

Vibration and Shock **Handbook**

Mechanical Engineering Series

Frank Kreith - Series Editor

Published Titles

Distributed Generation: The Power Paradigm for the New Millennium

Anne-Marie Borbely & Jan F. Kreider

Elastoplasticity Theory

Vlado A. Lubarda

Energy Audit of Building Systems: An Engineering Approach

Moncef Krarti

Engineering Experimentation

Euan Somerscales

Entropy Generation Minimization

Adrian Bejan

Finite Element Method Using MATLAB, 2nd Edition

Young W. Kwon & Hyochoong Bang

Fluid Power Circuits and Controls: Fundamentals and Applications

John S. Cundiff

Fundamentals of Environmental Discharge Modeling

Lorin R. Davis

Heat Transfer in Single and Multiphase Systems

Greg F. Naterer

Introductory Finite Element Method

Chandrakant S. Desai & Tribikram Kundu

Intelligent Transportation Systems: New Principles and Architectures

Sumit Ghosh & Tony Lee

Mathematical & Physical Modeling of Materials Processing Operations

Olusegun Johnson Ilegbusi, Manabu Iguchi & Walter E. Wahnsiedler

Mechanics of Composite Materials

Autar K. Kaw

Mechanics of Fatigue

Vladimir V. Bolotin

Mechanics of Solids and Shells: Theories and Approximation

Gerald Wempner & Demosthenes Talaslidis

Mechanism Design: Enumeration of Kinematic Structures According to Function

Lung-Wen Tsai

Nonlinear Analysis of Structures

M. Sathyamoorthy

Practical Inverse Analysis in Engineering

David M. Trujillo & Henry R. Busby

Pressure Vessels: Design and Practice

Somnath Chattopadhyay

Principles of Solid Mechanics

Rowland Richards, Jr.

Thermodynamics for Engineers

Kau-Fui Wong

Vibration and Shock Handbook

Clarence W. de Silva

Viscoelastic Solids

Roderic S. Lakes

Vibration and Shock **Handbook**

Edited by
Clarence W. de Silva



Taylor & Francis
Taylor & Francis Group

Boca Raton London New York Singapore

A CRC title, part of the Taylor & Francis imprint, a member of the
Taylor & Francis Group, the academic division of T&F Informa plc.

Published in 2005 by
CRC Press
Taylor & Francis Group
6000 Broken Sound Parkway NW, Suite 300
Boca Raton, FL 33487-2742

© 2005 by Taylor & Francis Group, LLC
CRC Press is an imprint of Taylor & Francis Group

No claim to original U.S. Government works
Printed in the United States of America on acid-free paper
10 9 8 7 6 5 4 3 2 1

International Standard Book Number-10: 0-8493-1580-8 (Hardcover)
International Standard Book Number-13: 978-0-8493-1580-0 (Hardcover)
Library of Congress Card Number 2004065847

This book contains information obtained from authentic and highly regarded sources. Reprinted material is quoted with permission, and sources are indicated. A wide variety of references are listed. Reasonable efforts have been made to publish reliable data and information, but the author and the publisher cannot assume responsibility for the validity of all materials or for the consequences of their use.

No part of this book may be reprinted, reproduced, transmitted, or utilized in any form by any electronic, mechanical, or other means, now known or hereafter invented, including photocopying, microfilming, and recording, or in any information storage or retrieval system, without written permission from the publishers.

For permission to photocopy or use material electronically from this work, please access www.copyright.com (<http://www.copyright.com/>) or contact the Copyright Clearance Center, Inc. (CCC) 222 Rosewood Drive, Danvers, MA 01923, 978-750-8400. CCC is a not-for-profit organization that provides licenses and registration for a variety of users. For organizations that have been granted a photocopy license by the CCC, a separate system of payment has been arranged.

Trademark Notice: Product or corporate names may be trademarks or registered trademarks, and are used only for identification and explanation without intent to infringe.

Library of Congress Cataloging-in-Publication Data

Vibration and shock handbook / editor-in-chief, Clarence W. de Silva.

p. cm.

Includes bibliographical references and index.

ISBN 0-8493-1580-8 (alk. paper)

1. Vibration--Handbooks, manuals, etc. 2. Shock (Mechanics)--Handbooks, manuals, etc. I. De Silva, Clarence W.

TA355.V5197 2005

620.3--dc22

2004065847



Taylor & Francis Group
is the Academic Division of T&F Informa plc.

Visit the Taylor & Francis Web site at
<http://www.taylorandfrancis.com>

and the CRC Press Web site at
<http://www.crcpress.com>

Preface

With individual chapters authored by distinguished leaders and experienced professionals in their respective topics, this handbook provides engineers, technicians, designers, researchers, educators, and students with a convenient, thorough, up-to-date, and authoritative reference source on techniques, tools, and data for modeling, analysis, design, monitoring, instrumentation, modification, and control of vibration, shock, noise, and acoustics. The handbook consists of 45 chapters, grouped into nine sections. In these sections, the following are considered: fundamentals and analytical techniques; computer techniques, tools, and signal analysis including finite element methods and wavelet analysis and the use of MATLAB[®] toolboxes; shock and vibration methodologies, particularly for civil and mechanical engineering systems; instrumentation and testing methods, including sensors, exciters, signal acquisition, conditioning, and recording, and LabVIEW[®] tools for virtual instrumentation; vibration suppression, damping, and control; monitoring and diagnosis; design for and control of seismic vibration, and related regulatory issues; system design, application, and control implementation; and acoustics and noise suppression. Important information and results are summarized as windows, tables, graphs, and lists throughout the chapters for easy reference and information tracking. References are given at the end of each chapter for further information and study. An extensive glossary, which defines useful technical terms in the fields of vibration, shock, and acoustics, is provided at the end of the handbook. Cross-referencing is used throughout to indicate other places in the handbook where further information on a particular topic is provided.

In the handbook, equal emphasis is given to theory and practical application. The chapters are grouped into fundamentals, basic theory, advanced theory, analytical techniques, numerical techniques, experimental techniques, design methodology, practical problems and solutions, applications, regulatory considerations, and useful data. Analytical formulations, numerical methods, design approaches, control techniques, and commercial software tools are presented and illustrated. Commercial equipment, computer hardware, and instrumentation are described, analyzed, and demonstrated for field application, practical implementation, and experimentation. Examples and case studies are given throughout the handbook to illustrate the use and application of the included information. The material is presented in a format that is convenient for easy reference and recollection.

Mechanical vibration is a manifestation of oscillatory behavior in mechanical systems, as a result of either the repetitive interchange of kinetic and potential energies among components in the system, or a forcing excitation that is oscillatory. Such oscillatory responses are not limited to purely mechanical systems, and are found in electrical and fluid systems as well. In purely thermal systems, however, free natural oscillations are not possible, and an oscillatory excitation is needed to obtain an oscillatory response. Shock is vibration caused by brief, abrupt, and typically high-intensity excitations. Sound, noise, and acoustics are manifestations of pressure waves, sources of which are often vibratory dynamic systems.

Low levels of vibration mean reduced noise and an improved work environment. Vibration modification and control can be crucial in maintaining high performance and production efficiency, and

prolonging the useful life in industrial machinery. Consequently, a considerable effort is devoted today to studying and controlling the vibration and shock generated by machinery components, machine tools, transit vehicles, impact processes, civil engineering structures, fluid flow systems, and aircraft. Noise and acoustic problems can originate from undesirable vibrations and fluid–structure interactions, as found, for example, in automobile engines. Engine noise, environmental noise, and noise from high-speed and high-temperature exhaust gases in a vehicle will not only cause passenger discomfort and public annoyance, they will also result in damaging effects to the vehicle itself. Noise-suppression methods and devices, and sound-absorption material and structures are crucial in such situations. Before designing or controlling a system for good vibratory or acoustic performance, it is important to understand, analyze, and represent the dynamic characteristics of the system. This may be accomplished through purely analytical means, computer analysis of analytical models, testing and analysis of test data, or by a combination of these approaches. It follows that modeling, analysis, testing, and design are all important aspects of study in vibration, shock, and acoustics.

In recent years, educators, researchers, and practitioners have devoted considerable effort toward studying and controlling vibration, shock, and noise in a range of applications in various branches of engineering, particularly in civil, mechanical, aeronautical and aerospace, and production and manufacturing engineering. Specific applications are found in machine tools, transit vehicles, impact processes, civil engineering structures, construction machinery, industrial processes, product qualification and quality control, fluid flow systems, ships, and aircraft. This handbook is a contribution toward these efforts. In view of the analytical methods, practical considerations, design issues, and experimental techniques that are presented throughout the handbook, and in view of the simplified and snap-shot style presentation of formulas, data, and advanced theory, the handbook serves as a useful reference tool and an extensive information source for engineers and technicians in industry and laboratories, researchers, instructors, and students in the areas of vibration, shock, noise, and acoustics.

Clarence W. de Silva

Editor-in-Chief
Vancouver

Acknowledgments

I wish to express my gratitude to the authors of the chapters for their valuable and highly professional contributions. The assistance of my research engineer, Jian Zhang, in some graphics and formatting of the handbook was quite valuable. I am very grateful to Cindy Renee Carelli, Acquisitions Editor-Engineering, CRC Press, for her enthusiasm, characteristic vigor, and support throughout the project. The editorial and production staff at CRC Press and its affiliates, particularly Jessica Vakili, and Carol Cooper have done an excellent job in getting this handbook in print. Finally, I wish to lovingly acknowledge the patience and understanding of my family.

Editor-in-Chief

Clarence W. de Silva, P. Eng., Fellow ASME and Fellow IEEE, is Professor of Mechanical Engineering at the University of British Columbia, Vancouver, Canada, and has occupied the NSERC Research Chair in Industrial Automation since 1988. He has earned Ph.D. degrees from Massachusetts Institute of Technology (1978) and Cambridge University, England (1998). De Silva has also occupied the Mobil Endowed Chair Professorship in the Department of Electrical and Computer Engineering at the National University of Singapore. He has served as a consultant to several companies, including IBM and Westinghouse in the U.S., and has led the development of six industrial machines. He is recipient of the Killam Research Prize, Outstanding Engineering Educator Award of the Institute of Electrical and Electronics Engineers (IEEE) Canada, Education Award of the Dynamic Systems and Control Division of the American Society of Mechanical Engineers (ASME), Lifetime Achievement Award of the World Automation Congress, IEEE Third Millennium Medal, Meritorious Achievement Award of the Association of Professional Engineers of BC, and the Outstanding Contribution Award of the Systems, Man, and Cybernetics Society of the IEEE. As well as editing or coediting 12 volumes, he has authored or coauthored 16 technical books, over 150 journal papers, and about 200 conference papers and book chapters. He has served on the editorial boards of 12 international journals, in particular as the Editor-in-Chief of the *International Journal of Control and Intelligent Systems*, Editor-in-Chief of the *International Journal of Knowledge-Based Intelligent Engineering Systems*, Senior Technical Editor of *Measurements and Control*, and Regional Editor, North America, of *Engineering Applications of Artificial Intelligence — the International Journal of Intelligent Real-Time Automation*. He is a Lilly Fellow, Senior Fulbright Fellow to Cambridge University, Fellow of the Advanced Systems Institute of British Columbia, and a Killam Fellow.

Contributors

S. Akishita

Ritsumeikan University
Kusatsu, Japan

Haym Benaroya

Rutgers University
Piscataway, NJ

Su Huan Chen

Jilin University
Changchun, P.R. China

M. Dabestani

Furlong Research Foundation
London, UK

Marie D. Dahleh

Harvard University
Cambridge, MA

Kourosh Danai

University of Massachusetts
Amherst, MA

Chris “Flip” DeFilippo

National Instruments
Austin, TX

Clarence W. de Silva

The University of British
Columbia
Vancouver, BC, Canada

Ibrahim Esat

Brunel University
Middlesex, UK

Ebrahim Esmailzadeh

University of Ontario
Oshawa, ON, Canada

Giuseppe Failla

Università degli Studi
Mediterranea di Reggio Calabria
Italy

Mohamed S. Gadala

The University of British Columbia
Vancouver, BC, Canada

Seon M. Han

Texas Tech University
Lubbock, TX

P.S. Heyns

University of Pretoria
Pretoria, South Africa

Cheng Huang

National Research Council of Canada
Vancouver, Canada

S. Huang

National University of Singapore
Singapore

Hirokazu Iemura

Kyoto University
Kyoto, Japan

Sarvesh Kumar Jain

Madhav Institute of Technology and
Science
Madhya Pradesh, India

Nader Jalili

Clemson University
Clemson, SC

Takayuki Koizumi

Doshisha University
Kyoto-Hu, Japan

Christian Lalanne

Engineering Consultant
Jalles, France

Robert G. Landers

University of Missouri at Rolla
Rolla, MO

T.H. Lee

National University of Singapore
Singapore

Y.P. Leow

Singapore Institute of Manufacturing
Technology
Singapore

S.Y. Lim

Singapore Institute of Manufacturing
Technology
Singapore

Jiahao Lin

Dalian University of Technology
Liaoning, P.R. China

W. Lin

Singapore Institute of Manufacturing
Technology
Singapore

L.Y. Lu

National Kaohsiung First University
of Science and Technology
Kaohsiung, Taiwan

Chris K. Mechefske

Queen's University
Kingston, ON, Canada

Priyan Mendis

University of Melbourne
Melbourne, Victoria, Australia

Y.L. Mo

University of Houston
Houston, TX

Kiyoshi Nagakura

Railway Technical Research Institute
Tokyo-To, Japan

Tuan Ngo

University of Melbourne
Melbourne, Victoria, Australia

Teruo Obata

Teikyo University
Totigi-Ken, Japan

Kiyoshi Okura

Mitsuboshi Belting Ltd.
Hyogo-Ken, Japan

Randall D. Peters

Mercer University
Macon, GA

Mulyo Harris Pradono

Kyoto University
Kyoto, Japan

Nikolaos P. Politis

Rice University
Houston, TX

H. Sam Samarasekera

Sulzer Pumps (Canada), Inc.
Burnaby, BC, Canada

C. Scheffer

University of Stellenbosch
Pretoria, South Africa

Michael Sedlak

National Instruments
Austin, TX

Zhong-Sheng Liu

National Research Council of
Canada
Vancouver, Canada

Datong Song

National Research Council of Canada
Vancouver, Canada

Pol D. Spanos

Rice University
Houston, TX

K.K. Tan

National University of Singapore
Singapore

K.Z. Tang

National University of Singapore
Singapore

Y.B. Yang

National Taiwan University
Taipei, Taiwan

J.D. Yau

Tamkang University
Taipei, Taiwan

Yahui Zhang

Dalian University of Technology
Liaoning, P.R. China

Contents

SECTION I Fundamentals and Analysis

1	Time-Domain Analysis	<i>Clarence W. de Silva</i>	1-1
1.1	Introduction		1-1
1.2	Undamped Oscillator		1-2
1.3	Heavy Springs		1-12
1.4	Oscillations in Fluid Systems		1-14
1.5	Damped Simple Oscillator		1-16
1.6	Forced Response		1-27
2	Frequency-Domain Analysis	<i>Clarence W. de Silva</i>	2-1
2.1	Introduction		2-1
2.2	Response to Harmonic Excitations		2-2
2.3	Transform Techniques		2-14
2.4	Mechanical Impedance Approach		2-25
2.5	Transmissibility Functions		2-31
2.6	Receptance Method		2-37
	Appendix 2A Transform Techniques		2-40
3	Modal Analysis	<i>Clarence W. de Silva</i>	3-1
3.1	Introduction		3-1
3.2	Degrees of Freedom and Independent Coordinates		3-2
3.3	System Representation		3-4
3.4	Modal Vibrations		3-10
3.5	Orthogonality of Natural Modes		3-14
3.6	Static Modes and Rigid-Body Modes		3-15
3.7	Other Modal Formulations		3-22
3.8	Forced Vibration		3-28
3.9	Damped Systems		3-32
3.10	State-Space Approach		3-36
	Appendix 3A Linear Algebra		3-41
4	Distributed-Parameter Systems	<i>Clarence W. de Silva</i>	4-1
4.1	Introduction		4-1
4.2	Transverse Vibration of Cables		4-2

4.3	Longitudinal Vibrations of Rods	4-13
4.4	Torsional Vibration of Shafts	4-19
4.5	Flexural Vibration of Beams	4-26
4.6	Damped Continuous Systems	4-50
4.7	Vibration of Membranes and Plates	4-52
5	Random Vibration <i>Haym Benaroya</i>	5-1
5.1	Random Vibration	5-1
5.2	Single Degree of Freedom: The Response to Random Loads	5-2
5.3	Response to Two Random Loads	5-7
5.4	Multi-Degree-of-Freedom Vibration	5-12
5.5	Multi-Degree-of-Freedom: The Response to Random Loads	5-17
5.6	Continuous System Random Vibration	5-29

SECTION II Computer Techniques

6	Numerical Techniques <i>Marie D. Dahleh</i>	6-1
6.1	Introduction	6-1
6.2	Single-Degree-of-Freedom System	6-2
6.3	Systems with Two or More Degrees of Freedom	6-8
6.4	Finite Difference Method for a Continuous System	6-11
6.5	Matrix Methods	6-14
6.6	Approximation Methods for the Fundamental Frequency	6-18
6.7	Finite Element Method	6-20
	Appendix 6A Introduction to MATLAB®	6-24
7	Vibration Modeling and Software Tools <i>Datong Song, Cheng Huang, and Zhong-Sheng Liu</i>	7-1
7.1	Introduction	7-1
7.2	Formulation	7-2
7.3	Vibration Analysis	7-9
7.4	Commercial Software Packages	7-13
7.5	The Basic Procedure of Vibration Analysis	7-16
7.6	An Engineering Case Study	7-19
7.7	Comments	7-21
8	Computer Analysis of Flexibly Supported Multibody Systems <i>Ibrahim Esat and M. Dabestani</i>	8-1
8.1	Introduction	8-1
8.2	Theory	8-2
8.3	A Numerical Example	8-7
8.4	An Industrial Vibration Design Problem	8-11
8.5	Programming Considerations	8-16
8.6	VIBRATIO	8-17
8.7	Analysis	8-24
8.8	Comments	8-31
	Appendix 8A VIBRATIO Output for Numerical Example in Section 8.3	8-32

9	Finite Element Applications in Dynamics	<i>Mohamed S. Gadala</i>	9-1
9.1	Problem and Element Classification		9-2
9.2	Types of Analysis		9-20
9.3	Modeling Aspects for Dynamic Analysis		9-23
9.4	Equations of Motion and Solution Methods		9-27
9.5	Various Dynamic Analyses		9-33
9.6	Checklist for Dynamic FE Analysis		9-41
10	Vibration Signal Analysis	<i>Clarence W. de Silva</i>	10-1
10.1	Introduction		10-1
10.2	Frequency Spectrum		10-2
10.3	Signal Types		10-7
10.4	Fourier Analysis		10-7
10.5	Analysis of Random Signals		10-18
10.6	Other Topics of Signal Analysis		10-26
10.7	Overlapped Processing		10-28
11	Wavelets — Concepts and Applications	<i>Pol D. Spanos, Giuseppe Failla, and Nikolaos P. Politis</i>	11-1
11.1	Introduction		11-1
11.2	Time–Frequency Analysis		11-2
11.3	Time-Dependent Spectra Estimation of Stochastic Processes		11-11
11.4	Random Field Simulation		11-14
11.5	System Identification		11-15
11.6	Damage Detection		11-17
11.7	Material Characterization		11-18
11.8	Concluding Remarks		11-19

SECTION III Shock and Vibration

12	Mechanical Shock	<i>Christian Lallanne</i>	12-1
12.1	Definitions		12-2
12.2	Description in the Time Domain		12-3
12.3	Shock Response Spectrum		12-4
12.4	Pyroshocks		12-17
12.5	Use of Shock Response Spectra		12-18
12.6	Standards		12-24
12.7	Damage Boundary Curve		12-26
12.8	Shock Machines		12-28
12.9	Generation of Shock Using Shakers		12-44
12.10	Control by a Shock Response Spectrum		12-52
12.11	Pyrotechnic Shock Simulation		12-58
13	Vibration and Shock Problems of Civil Engineering Structures	<i>Priyan Mendis and Tuan Ngo</i>	13-1
13.1	Introduction		13-2
13.2	Earthquake-Induced Vibration of Structures		13-3

13.3	Dynamic Effects of Wind Loading on Structures	13-22
13.4	Vibrations Due to Fluid–Structure Interaction	13-33
13.5	Blast Loading and Blast Effects on Structures	13-34
13.6	Impact Loading	13-47
13.7	Floor Vibration	13-51
14	Reinforced Concrete Structures <i>Y.L. Mo</i>	14-1
14.1	Introduction	14-1
14.2	Analytical Models	14-6
14.3	Beams under Harmonic Excitations	14-18
14.4	Design for Explosions/Shocks	14-21
 SECTION IV Instrumentation and Testing		
15	Vibration Instrumentation <i>Clarence W. de Silva</i>	15-1
15.1	Introduction	15-1
15.2	Vibration Exciters	15-3
15.3	Control System	15-15
15.4	Performance Specification	15-21
15.5	Motion Sensors and Transducers	15-27
15.6	Torque, Force, and Other Sensors	15-50
	Appendix 15A Virtual Instrumentation for Data Acquisition, Analysis, and Presentation	15-73
16	Signal Conditioning and Modification <i>Clarence W. de Silva</i>	16-1
16.1	Introduction	16-2
16.2	Amplifiers	16-2
16.3	Analog Filters	16-15
16.4	Modulators and Demodulators	16-29
16.5	Analog–Digital Conversion	16-37
16.6	Bridge Circuits	16-43
16.7	Linearizing Devices	16-49
16.8	Miscellaneous Signal Modification Circuitry	16-56
16.9	Signal Analyzers and Display Devices	16-62
17	Vibration Testing <i>Clarence W. de Silva</i>	17-1
17.1	Introduction	17-1
17.2	Representation of a Vibration Environment	17-3
17.3	Pretest Procedures	17-24
17.4	Testing Procedures	17-37
17.5	Some Practical Information	17-52
18	Experimental Model Analysis <i>Clarence W. de Silva</i>	18-1
18.1	Introduction	18-1
18.2	Frequency-Domain Formulation	18-2
18.3	Experimental Model Development	18-8
18.4	Curve Fitting of Transfer Functions	18-10

18.5	Laboratory Experiments	18-18
18.6	Commercial EMA Systems	18-24

SECTION V Vibration Suppression and Control

19	Vibration Damping <i>Clarence W. de Silva</i>	19-1
19.1	Introduction	19-1
19.2	Types of Damping	19-2
19.3	Representation of Damping in Vibration Analysis	19-9
19.4	Measurement of Damping	19-16
19.5	Interface Damping	19-26
20	Damping Theory <i>Randall D. Peters</i>	20-1
20.1	Preface	20-2
20.2	Introduction	20-4
20.3	Background	20-12
20.4	Hysteresis — More Details	20-19
20.5	Damping Models	20-20
20.6	Measurements of Damping	20-23
20.7	Hysteretic Damping	20-27
20.8	Failure of the Common Theory	20-29
20.9	Air Influence	20-30
20.10	Noise and Damping	20-31
20.11	Transform Methods	20-34
20.12	Hysteretic Damping	20-36
20.13	Internal Friction	20-41
20.14	Mathematical Tricks — Linear Damping Approximations	20-43
20.15	Internal Friction Physics	20-44
20.16	Zener Model	20-45
20.17	Toward a Universal Model of Damping	20-48
20.18	Nonlinearity	20-58
20.19	Concluding Remark	20-65
21	Experimental Techniques in Damping <i>Randall D. Peters</i>	21-1
21.1	Electronic Considerations	21-2
21.2	Data Processing	21-3
21.3	Sensor Choices	21-7
21.4	Damping Examples	21-8
21.5	Driven Oscillators with Damping	21-19
21.6	Oscillator with Multiple Nonlinearities	21-21
21.7	Multiple Modes of Vibration	21-24
21.8	Internal Friction as Source of Mechanical Noise	21-28
21.9	Viscous Damping — Need for Caution	21-29
21.10	Air Influence	21-31
22	Structure and Equipment Isolation <i>Y.B. Yang, L.Y. Lu, and J.D. Yau</i>	22-1
22.1	Introduction	22-2
22.2	Mechanisms of Base-Isolated Systems	22-4

22.3	Structure–Equipment Systems with Elastomeric Bearings	22-9
22.4	Sliding Isolation Systems	22-17
22.5	Sliding Isolation Systems with Resilient Mechanism	22-36
22.6	Issues Related to Seismic Isolation Design	22-50
23	Vibration Control <i>Nader Jalili and Ebrahim Esmailzadeh</i>	23-1
23.1	Introduction	23-1
23.2	Vibration-Control Systems Concept	23-4
23.3	Vibration-Control Systems Design and Implementation	23-12
23.4	Practical Considerations and Related Topics	23-38
24	Helicopter Rotor Tuning <i>Kouros Danai</i>	24-1
24.1	Introduction	24-1
24.2	Neural Network-Based Tuning	24-4
24.3	Probability-Based Tuning	24-5
24.4	Adaptive Tuning	24-8
24.5	Case Study	24-12
24.6	Conclusion	24-17
 SECTION VI Monitoring and Diagnosis		
25	Machine Condition Monitoring and Fault Diagnostics <i>Chris K. Mechefske</i>	25-1
25.1	Introduction	25-2
25.2	Machinery Failure	25-2
25.3	Basic Maintenance Strategies	25-4
25.4	Factors which Influence Maintenance Strategy	25-7
25.5	Machine Condition Monitoring	25-8
25.6	Transducer Selection	25-10
25.7	Transducer Location	25-14
25.8	Recording and Analysis Instrumentation	25-14
25.9	Display Formats and Analysis Tools	25-16
25.10	Fault Detection	25-21
25.11	Fault Diagnostics	25-25
26	Vibration-Based Tool Condition Monitoring Systems <i>C. Scheffer and P.S. Heyns</i>	26-1
26.1	Introduction	26-1
26.2	Mechanics of Turning	26-2
26.3	Vibration Signal Recording	26-7
26.4	Signal Processing for Sensor-Based Tool Condition Monitoring	26-11
26.5	Wear Model/Decision-Making for Sensor-Based Tool Condition Monitoring	26-15
26.6	Conclusion	26-20
27	Fault Diagnosis of Helicopter Gearboxes <i>Kouros Danai</i>	27-1
27.1	Introduction	27-1
27.2	Abnormality Scaling	27-5
27.3	The Structure-Based Connectionist Network	27-8
27.4	Sensor Location Selection	27-11

27.5	A Case Study	27-14
27.6	Conclusion	27-23

28 Vibration Suppression and Monitoring in Precision Motion Systems *K.K. Tan,*

<i>T.H. Lee, K.Z. Tang, S. Huang, S.Y. Lim, W. Lin, and Y.P. Leow</i>	28-1
28.1 Introduction	28-1
28.2 Mechanical Design to Minimize Vibration	28-2
28.3 Adaptive Notch Filter	28-10
28.4 Real-Time Vibration Analyzer	28-17
28.5 Practical Insights and Case Study	28-29
28.6 Conclusions	28-35

SECTION VII Seismic Vibration

29 Seismic Base Isolation and Vibration Control *Hirokazu Iemura, Sarvesh Kumar Jain,*

<i>and Mulyo Harris Pradono</i>	29-1
29.1 Introduction	29-1
29.2 Seismic Base Isolation	29-4
29.3 Seismic Vibration Control	29-33

30 Seismic Random Vibration of Long-Span Structures *Jiahao Lin and Yahui Zhang*

30.1 Introduction	30-2
30.2 Seismic Random Excitation Fields	30-11
30.3 Pseudoexcitation Method for Structural Random Vibration Analysis	30-16
30.4 Long-Span Structures Subjected to Stationary Random Ground Excitations	30-27
30.5 Long-Span Structures Subjected to Nonstationary Random Ground Excitations	30-34
30.6 Conclusions	30-39

31 Seismic Qualification of Equipment *Clarence W. de Silva*

31.1 Introduction	31-1
31.2 Distribution Qualification	31-1
31.3 Seismic Qualification	31-6

SECTION VIII Design and Applications

32 Vibration Design and Control *Clarence W. de Silva*

32.1 Introduction	32-2
32.2 Specification of Vibration Limits	32-3
32.3 Vibration Isolation	32-5
32.4 Balancing of Rotating Machinery	32-15
32.5 Balancing of Reciprocating Machines	32-26
32.6 Whirling of Shafts	32-33
32.7 Design through Modal Testing	32-39
32.8 Passive Control of Vibration	32-45

32.9	Active Control of Vibration	32-61
32.10	Control of Beam Vibrations	32-67
	Appendix 32A MATLAB Control Systems Toolbox	32-73
33	Structural Dynamic Modification and Sensitivity Analysis <i>Su Huan Chen</i>	33-1
33.1	Introduction	33-2
33.2	Structural Dynamic Modification of Finite Element Model	33-2
33.3	Perturbation Method of Vibration Modes	33-4
33.4	Design Sensitivity Analysis of Structural Vibration Modes	33-8
33.5	High-Accuracy Modal Superposition for Sensitivity Analysis of Modes	33-11
33.6	Sensitivity of Eigenvectors for Free-Free Structures	33-13
33.7	Matrix Perturbation Theory for Repeated Modes	33-14
33.8	Matrix Perturbation Method for Closely Spaced Eigenvalues	33-16
33.9	Matrix Perturbation Theory for Complex Modes	33-22
34	Vibration in Rotating Machinery <i>H. Sam Samarasekera</i>	34-1
34.1	Introduction	34-1
34.2	Vibration Basics	34-6
34.3	Rotordynamic Analysis	34-18
34.4	Vibration Measurement and Techniques	34-39
34.5	Vibration Control and Diagnostics	34-39
35	Regenerative Chatter in Machine Tools <i>Robert G. Landers</i>	35-1
35.1	Introduction	35-1
35.2	Chatter in Turning Operations	35-3
35.3	Chatter in Face-Milling Operations	35-9
35.4	Time-Domain Simulation	35-14
35.5	Chatter Detection	35-18
35.6	Chatter Suppression	35-20
35.7	Case Study	35-24
36	Fluid-Induced Vibration <i>Seon M. Han</i>	36-1
36.1	Description of the Ocean Environment	36-1
36.2	Fluid Forces	36-16
36.3	Examples	36-23

SECTION IX Acoustics

37	Sound Levels and Decibels <i>S. Akishita</i>	37-1
37.1	Introduction	37-1
37.2	Sound Wave Characteristics	37-1
37.3	Levels and Decibels	37-3
38	Hearing and Psychological Effects <i>S. Akishita</i>	38-1
38.1	Introduction	38-1
38.2	Structure and Function of the Ear	38-1
38.3	Frequency and Loudness Response	38-2

38.4	Hearing Loss	38-4
38.5	Psychological Effects of Noise	38-4
39	Noise Control Criteria and Regulations <i>S. Akishita</i>	39-1
39.1	Introduction	39-1
39.2	Basic Ideas behind Noise Policy	39-1
39.3	Legislation	39-2
39.4	Regulation	39-4
39.5	Measures of Noise Evaluation	39-5
40	Instrumentation <i>Kiyoshi Nagakura</i>	40-1
40.1	Sound Intensity Measurement	40-1
40.2	Mirror–Microphone System	40-4
40.3	Microphone Array	40-6
41	Source of Noise <i>S. Akishita</i>	41-1
41.1	Introduction	41-1
41.2	Radiation of Sound	41-1
42	Design of Absorption <i>Teruo Obata</i>	42-1
42.1	Introduction	42-1
42.2	Fundamentals of Sound Absorption	42-2
42.3	Sound-Absorbing Materials	42-3
42.4	Acoustic Characteristic Computation of Compound Wall	42-6
42.5	Attenuation of Lined Ducts	42-10
42.6	Attenuation of Dissipative Mufflers	42-12
42.7	General Considerations	42-15
42.8	Practical Example of Dissipative Muffler	42-17
43	Design of Reactive Mufflers <i>Teruo Obata</i>	43-1
43.1	Introduction	43-1
43.2	Fundamental Equations	43-2
43.3	Effects of Reactive Mufflers	43-3
43.4	Calculation Procedure	43-5
43.5	Application Range of Model	43-6
43.6	Practical Example	43-13
44	Design of Sound Insulation <i>Kiyoshi Okura</i>	44-1
44.1	Theory of Sound Insulation	44-1
44.2	Application of Sound Insulation	44-13
45	Statistical Energy Analysis <i>Takayuki Koizumi</i>	45-1
45.1	Introduction	45-1
45.2	Power Flow Equations	45-2
45.3	Estimation of Sea Parameters	45-4
45.4	Application in Structures	45-7
	Glossary	G-1

Fundamentals and Analysis

1

Time-Domain Analysis

1.1	Introduction.....	1-1
1.2	Undamped Oscillator	1-2
	Energy Storage Elements • The Method of Conservation of Energy • Free Response	
1.3	Heavy Springs	1-12
	Kinetic Energy Equivalence	
1.4	Oscillations in Fluid Systems.....	1-14
1.5	Damped Simple Oscillator.....	1-16
	Case 1: Underdamped Motion ($\zeta < 1$) • Logarithmic Decrement Method • Case 2: Overdamped Motion ($\zeta > 1$) • Case 3: Critically Damped Motion ($\zeta = 1$) • Justification for the Trial Solution • Stability and Speed of Response	
1.6	Forced Response	1-27
	Impulse-Response Function • Forced Response • Response to a Support Motion	

Clarence W. de Silva

The University of British Columbia

Summary

This chapter concerns the modeling and analysis of mechanical vibrating systems in the time domain. Useful procedures of time-domain analysis are developed. Techniques of analyzing both free response and forced response are given. Examples of the application of Newton's force-motion approach, energy conservation approach, and Lagrange's energy approach are given. Particular emphasis is placed on the analysis of an undamped oscillator and a damped oscillator. Associated terminology, which is useful in vibration analysis, is defined.

1.1 Introduction

Vibrations can be analyzed both in the time domain and in the frequency domain. Free vibrations and forced vibrations may have to be analyzed. This chapter provides the basics of the time-domain representation and analysis of mechanical vibrations.

Free and natural vibrations occur in systems because of the presence of two modes of energy storage. When the stored energy is repeatedly interchanged between these two forms, the resulting time response of the system is oscillatory. In a mechanical system, natural vibrations can occur because *kinetic energy* (which is manifested as velocities of mass [inertia] elements) may be converted into *potential energy* (which has two basic types: *elastic potential energy* due to the deformation in spring-like elements, and *gravitation potential energy* due to the elevation of mass elements under the Earth's gravitational pull) and back to kinetic energy, repetitively, during motion. An oscillatory excitation (forcing function) is able to make a dynamic system respond with an oscillatory motion (at the same frequency as the forcing excitation) even in the absence of two forms of energy storage. Such motions are forced responses rather than natural or free responses.

An analytical model of a mechanical system is a set of equations. These may be developed either by the Newtonian approach, where Newton's Second Law is explicitly applied to each inertia element, or by the Lagrangian or Hamiltonian approach which is based on the concepts of energy (kinetic and potential energies). A time-domain analytical model is a set of differential equations with respect to the independent variable time (t). A frequency-domain model is a set of input–output transfer functions with respect to the independent variable frequency (ω). The time response will describe how the system moves (responds) as a function of time. The frequency response will describe the way the system moves when excited by a harmonic (sinusoidal) forcing input, and is a function of the frequency of excitation.

1.2 Undamped Oscillator

Consider the mechanical system that is schematically shown in Figure 1.1. The inputs (or excitation) applied to the system are represented by the force $f(t)$. The outputs (or response) of the system are represented by the displacement y . The system boundary (real or imaginary) demarcates the region of interest in the analysis. What is outside the system boundary is the environment in which the system operates. An analytical model of the system may be given by one or more equations relating the outputs to the inputs. If the rates of changes of the response (outputs) are not negligible, the system is a *dynamic* system. In this case the analytical model, in the time domain, becomes one or more differential equations rather than algebraic equations. System parameters (e.g., mass, stiffness, damping constant) are represented in the model, and their values should be known in order to determine the response of the system to a particular excitation. State variables are a minimum set of variables, which completely represent the dynamic state of a system at any given time t . These variables are not unique (more than one choice of a valid set of state variables is possible). For a simple oscillator (a single-degree-of-freedom (DoF) mass–spring–damper system) an appropriate set of state variables would be the displacement y and the velocity \dot{y} . An alternative set would be \dot{y} and the spring force.

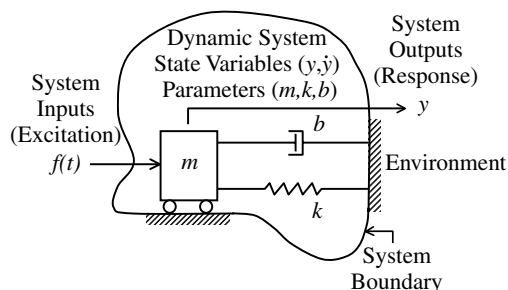


FIGURE 1.1 A mechanical dynamic system.

In the present section, we will first show that many types of oscillatory systems can be represented by the equation of an *undamped simple oscillator*. In particular, mechanical, electrical, and fluid systems will be considered. The *conservation of energy* is a straightforward approach for deriving the equations of motion for undamped oscillatory systems (which fall into the class of conservative systems). The equations of motion for mechanical systems may be derived using the *free-body diagram* approach, with the direct application of *Newton's Second Law*. An alternative and rather convenient approach is the use of *Lagrange's equations*. The natural (free) response of an undamped simple oscillator is a *simple harmonic motion*. This is a periodic, sinusoidal motion.

In the present section, we will first show that many types of oscillatory systems can be represented by the equation of an *undamped simple oscillator*. In particular, mechanical, electrical, and fluid systems will be considered. The *conservation of energy* is a straightforward approach for deriving the equations of motion for undamped oscillatory systems (which fall into the class of conservative systems). The equations of motion for mechanical systems may be derived using the *free-body diagram* approach, with the direct application of *Newton's Second Law*. An alternative and rather convenient approach is the use of *Lagrange's equations*. The natural (free) response of an undamped simple oscillator is a *simple harmonic motion*. This is a periodic, sinusoidal motion.

1.2.1 Energy Storage Elements

Mass (inertia) and spring are the two basic energy storage elements in mechanical systems. The concept of state variables may be introduced as well through these elements.

1.2.1.1 Inertia (m)

Consider an inertia element of lumped mass m , excited by force f , as shown in Figure 1.2.

The resulting velocity is v .

Newton's Second Law gives

$$m \frac{dv}{dt} = f \quad (1.1)$$

Kinetic energy stored in the mass element is equal to the work done by the force f on the mass. Hence,

$$\begin{aligned} \text{Energy } E &= \int f dx = \int f \frac{dx}{dt} dt = \int f v dt = \int \frac{m dv}{dt} v dt \\ &= m \int v dv \end{aligned}$$

or

$$\text{Kinetic energy KE} = \frac{1}{2} m v^2 \quad (1.2)$$

Note: v is an appropriate state variable for a mass element because it can completely represent the energy of the element.

Integrate Equation 1.1:

$$v(t) = v(0^-) + \frac{1}{m} \int_{0^-}^t f dt \quad (1.3)$$

Hence, with $t = 0^+$, we have

$$v(0^+) = v(0^-) + \frac{1}{m} \int_{0^-}^{0^+} f dt \quad (1.4)$$

Since the integral of a finite quantity over an almost zero time interval is zero, these results tell us that a finite force will not cause an instantaneous change in velocity in an inertia element. In particular, for a mass element subjected to finite force, since the integral on the right-hand side of Equation 1.4 is zero, we have

$$v(0^+) = v(0^-) \quad (1.5)$$

1.2.1.2 Spring (k)

Consider a massless spring element of lumped stiffness k , as shown in Figure 1.3. One end of the spring is fixed and the other end is free. A force f is applied at the free end, which results in a displacement (extension) x in the spring.

Hooke's Law gives

$$f = kx \quad \text{or} \quad \frac{df}{dt} = kv \quad (1.6)$$

Elastic potential energy stored in the spring is equal to the work done by the force on the spring. Hence,

$$\text{Energy } E = \int f dx = \int kx dx = \frac{1}{2} kx^2 = \int f \frac{dx}{dt} dt = \int f v dt = \int f \frac{1}{k} \frac{df}{dt} dt = \frac{1}{k} \int f df = \frac{1}{2k} f^2$$

or

$$\text{Elastic potential energy PE} = \frac{1}{2} kx^2 = \frac{1}{2} \frac{f^2}{k} \quad (1.7)$$

Note: f and x are both appropriate state variables for a spring, because both can completely represent the energy in the spring.

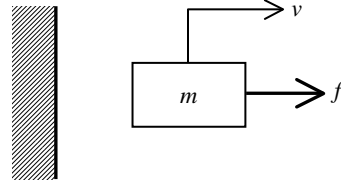


FIGURE 1.2 A mass element.

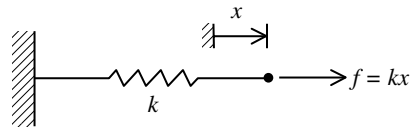


FIGURE 1.3 A spring element.

Integrate Equation 1.6:

$$f(t) = f(0^-) + \frac{1}{k} \int_{0^-}^t v \, dt \quad (1.8)$$

Set $t = 0^+$. We have

$$f(0^+) = f(0^-) + \frac{1}{k} \int_{0^-}^{0^+} v \, dt \quad (1.9)$$

From these results, it follows that at finite velocities there cannot be an instantaneous change in the force of a spring. In particular, from Equation 1.9 we see that when the velocities of a spring are finite:

$$f(0^+) = f(0^-) \quad (1.10)$$

Also, it follows that

$$x(0^+) = x(0^-) \quad (1.11)$$

1.2.1.3 Gravitation Potential Energy

The work done in raising an object against the gravitational pull is stored as gravitational potential energy of the object. Consider a lumped mass m , as shown in Figure 1.4, which is raised to a height y from some reference level.

The work done gives

$$\text{Energy } E = \int f \, dy = \int mg \, dy$$

Hence,

$$\text{Gravitational potential energy PE} = mgy \quad (1.12)$$

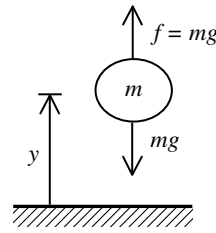


FIGURE 1.4 A mass element subjected to gravity.

1.2.2 The Method of Conservation of Energy

There is no energy dissipation in undamped systems which contain energy storage elements only. In other words, energy is conserved in these systems, which are known as *conservative systems*. For mechanical systems, conservation of energy gives

$$\text{KE} + \text{PE} = \text{const.} \quad (1.13)$$

These systems tend to be oscillatory in their natural motion, as noted before. Also, analogies exist with other types of systems (e.g., fluid and electrical systems). Consider the six systems sketched in Figure 1.5.

1.2.2.1 System 1 (Translatory)

Figure 1.5(a) shows a translatory mechanical system (an undamped oscillator) which has just one degree of freedom x . This may represent a simplified model of a rail car that is impacting against a snubber. The conservation of energy (Equation 1.13) gives

$$\frac{1}{2} m \dot{x}^2 + \frac{1}{2} k x^2 = \text{const.} \quad (1.14)$$

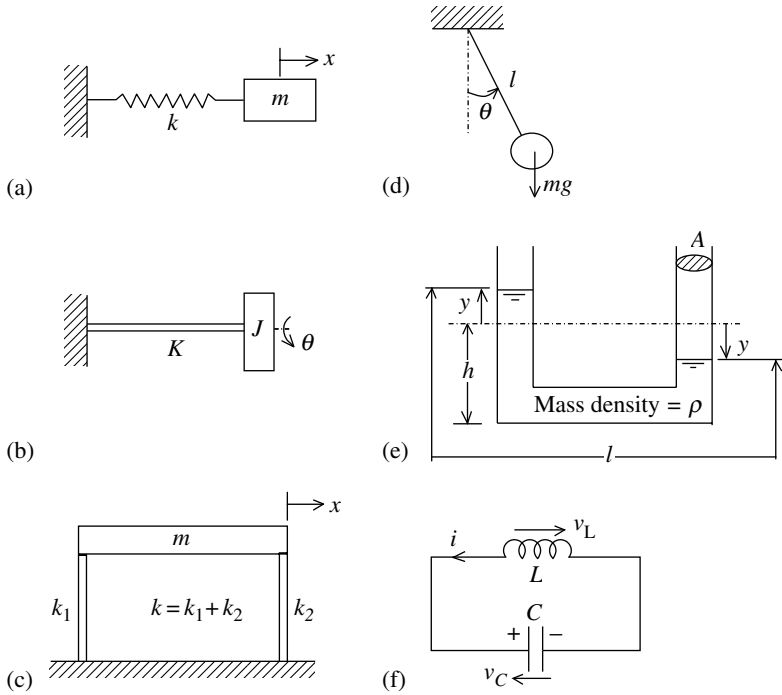


FIGURE 1.5 Six examples of single-degree-of-freedom oscillatory systems: (a) translatory; (b) rotatory; (c) flexural; (d) pendulous; (e) liquid slosh; (f) electrical.

Here, m is the mass and k is the spring stiffness. Differentiate Equation 1.14 with respect to time t . We obtain

$$m\dot{x}\ddot{x} + kx\dot{x} = 0$$

Since generally $\dot{x} \neq 0$ at all t , we can cancel it out. Hence, we obtain the equation of motion:

$$\ddot{x} + \frac{k}{m}x = 0 \quad (1.15)$$

1.2.2.2 System 2 (Rotatory)

Figure 1.5(b) shows a rotational system with the single DoF θ . It may represent a simplified model of a motor drive system. As before, the conservation energy gives

$$\frac{1}{2}J\dot{\theta}^2 + \frac{1}{2}K\theta^2 = \text{const.} \quad (1.16)$$

In this equation, J is the moment of inertia of the rotational element and K is the torsional stiffness of the shaft. Then, by differentiating Equation 1.16 with respect to t and canceling $\dot{\theta}$, we obtain the equation of motion:

$$\ddot{\theta} + \frac{K}{J}\theta = 0 \quad (1.17)$$

1.2.2.3 System 3 (Flexural)

Figure 1.5(c) is a lateral bending (flexural) system, which is a simplified model of a building structure. Again, a single DoF x is assumed. Conservation of energy gives

$$\frac{1}{2}m\dot{x}^2 + \frac{1}{2}kx^2 = \text{const.} \quad (1.18)$$

Here, m is the lumped mass at the free end of the support and k is the lateral bending stiffness of the support structure. Then, as before, the equation of motion becomes

$$\ddot{x} + \frac{k}{m}x = 0 \quad (1.19)$$

1.2.2.4 System 4 (Pendulous)

Figure 1.5(d) shows a simple pendulum. It may represent a swinging-type building demolisher or a ski lift, and has a single-DoF θ . We have

$$\text{KE} = \frac{1}{2}m(l\dot{\theta})^2$$

$$\text{Gravitational PE} = E_{\text{ref}} - mgl \cos \theta$$

Here, m is the pendulum mass, l is the pendulum length, and g is the acceleration due to gravity. Hence, conservation of energy gives

$$\frac{1}{2}ml^2\dot{\theta}^2 - mgl \cos \theta = \text{const.} \quad (1.20)$$

Differentiate with respect to t after canceling the common ml :

$$l\dot{\theta}\ddot{\theta} + g \sin \theta \dot{\theta} = 0$$

Since, $\dot{\theta} \neq 0$ at all t , we have the equation of motion:

$$\ddot{\theta} + \frac{g}{l} \sin \theta = 0 \quad (1.21)$$

This system is nonlinear, in view of the term $\sin \theta$.

For small θ , $\sin \theta$ is approximately equal to θ . Hence, the linearized equation of motion is

$$\ddot{\theta} + \frac{g}{l} \theta = 0 \quad (1.22)$$

1.2.2.5 System 5 (Liquid Slosh)

Consider a liquid column system shown in Figure 1.5(e). It may represent two liquid tanks linked by a pipeline. The system parameters are: area of cross section of each column = A ; mass density of liquid = ρ ; length of liquid mass = l .

We have

$$\text{KE} = \frac{1}{2}(\rho l A)\dot{y}^2$$

$$\text{Gravitational PE} = \rho A(h+y)\frac{g}{2}(h+y) + \rho A(h-y)\frac{g}{2}(h-y)$$

Hence, conservation of energy gives

$$\frac{1}{2}\rho l A\dot{y}^2 + \frac{1}{2}\rho A g(h+y)^2 + \frac{1}{2}\rho A g(h-y)^2 = \text{const.} \quad (1.23)$$

Differentiate:

$$l\dot{y}\ddot{y} + g(h+y)\dot{y} - g(h-y)\dot{y} = 0$$

But, we have

$$\dot{y} \neq 0 \quad \text{for all } t$$

Hence,

$$\ddot{y} + g(h+y) - g(h-y) = 0$$

or

$$\ddot{y} + \frac{2g}{l} y = 0 \quad (1.24)$$

1.2.2.6 System 6 (Electrical)

Figure 1.5(f) shows an electrical circuit with a single capacitor and a single inductor. Again, conservation of energy may be used to derive the equation of motion.

Voltage balance gives

$$v_L + v_C = 0 \quad (1.25)$$

where v_L and v_C are voltages across the inductor and the capacitor, respectively.

Constitutive equation for the inductor is

$$L \frac{di}{dt} = v_L \quad (1.26)$$

Constitutive equation for the capacitor is

$$C \frac{dv_C}{dt} = i \quad (1.27)$$

Hence, by differentiating Equation 1.26, substituting Equation 1.25, and using Equation 1.27, we obtain

$$L \frac{d^2 i}{dt^2} = \frac{dv_L}{dt} = -\frac{dv_C}{dt} = -\frac{i}{C}$$

or

$$LC \frac{d^2 i}{dt^2} + i = 0 \quad (1.28)$$

Now consider the energy conservation approach for this electrical circuit, which will give the same result. Note that power is given by the product vi .

1.2.2.7 Capacitor

$$\text{Electrostatic energy } E = \int vi \, dt = \int vC \frac{dv}{dt} dt = C \int v \, dv = \frac{Cv^2}{2} \quad (1.29)$$

Here, v denotes v_C . Also,

$$v = \frac{1}{C} \int i \, dt \quad (1.30)$$

Since the current i is finite for a practical circuit, we have $\int_0^+ i \, dt = 0$.

Hence, in general, the voltage across a capacitor cannot change instantaneously. In particular,

$$v(0^+) = v(0^-) \quad (1.31)$$

1.2.2.8 Inductor

$$\text{Electromagnetic energy } E = \int vi \, dt = \int L \frac{di}{dt} i \, dt = L \int i \, di = \frac{Li^2}{2}$$

Here, v denotes v_L . Also,

$$i = \frac{1}{L} \int v \, dt \quad (1.32)$$

Since v is finite in a practical circuit, we have $\int_0^+ v \, dt = 0$.

Hence, in general, the current through an inductor cannot change instantaneously. In particular,

$$i(0^+) = i(0^-) \quad (1.33)$$

Since the circuit in [Figure 1.5\(f\)](#) does not have a resistor, there is no energy dissipation. As a result, energy conservation gives

$$\frac{Cv^2}{2} + \frac{Li^2}{2} = \text{const.} \quad (1.34)$$

Differentiate Equation 1.34 with respect to t :

$$Cv \frac{dv}{dt} + Li \frac{di}{dt} = 0$$

Substitute the capacitor constitutive equation 1.27:

$$iv + Li \frac{di}{dt} = 0$$

Since $i \neq 0$ in general, we can cancel it. Now, by differentiating Equation 1.27, we have $di/dt = C(d^2v/dt^2)$. Substituting this in the above equation, we obtain

$$LC \frac{d^2v}{dt^2} + v = 0 \quad (1.35)$$

Similarly, we obtain

$$LC \frac{d^2i}{dt^2} + i = 0 \quad (1.36)$$

1.2.3 Free Response

The equation of free motion (i.e., without an excitation force) of the six linear systems considered above (Figure 1.5) is of the same general form:

$$\ddot{x} + \omega_n^2 x = 0 \quad (1.37)$$

This is the equation of an undamped, simple oscillator. The parameter ω_n is the *undamped natural frequency* of the system. For a mechanical system of mass m and stiffness k , we have

$$\omega_n = \sqrt{\frac{k}{m}} \quad (1.38)$$

To determine the time response x of this system, we use the trial solution:

$$x = A \sin(\omega_n t + \phi) \quad (1.39)$$

in which A and ϕ are unknown constants, to be determined by the initial conditions (for x and \dot{x}); say,

$$x(0) = x_0, \quad \dot{x}(0) = v_0 \quad (1.40)$$

Substitute the trial solution into Equation 1.37. We obtain

$$(-A\omega_n^2 + A\omega_n^2)\sin(\omega_n t + \phi) = 0$$

This equation is identically satisfied for all t . Hence, the general solution of Equation 1.37 is indeed Equation 1.39, which is periodic and sinusoidal.

This response is sketched in Figure 1.6. Note that this sinusoidal oscillatory motion has a *frequency* of oscillation of ω (radians/sec). Hence, a system that provides this type of natural motion is called a *simple oscillator*. In other words, the response exactly repeats itself in time periods of T or a cyclic frequency $f = 1/T$ (Hz). The frequency ω is in fact the *angular frequency* given by $\omega = 2\pi f$. Also, the response has an *amplitude* A , which is the peak value of the sinusoidal response. Now, suppose that we shift this response curve to the right through ϕ/ω . Consider the resulting curve to be the reference signal (with signal value = 0 at $t = 0$, and increasing). It should be clear that the response shown in Figure 1.6 leads the reference signal by a time period of ϕ/ω . This may be verified from the fact that the value of the reference signal at time t is the same as that of the signal in Figure 1.6 at time $t - \phi/\omega$. Hence, ϕ is termed the *phase angle* of the response, and it is a *phase lead*.

The left-hand-side portion of Figure 1.6 is the phasor representation of a sinusoidal response. In this representation, an arm of length A rotates in the counterclockwise direction at angular speed ω . This is the phasor. The arm starts at an angular position ϕ from the horizontal axis, at time $t = 0$. The projection of the arm onto the vertical (x) axis is the time response. In this manner, the phasor representation can conveniently indicate the amplitude, frequency, phase angle, and the actual time response (at any time t) of a sinusoidal motion. A repetitive (periodic) motion of the type 1.39 is called a *simple harmonic motion*, meaning it is a pure sinusoidal oscillation at a single frequency.

Next, we will show that the amplitude A and the phase angle ϕ both depend on the initial conditions. Substitute the initial conditions (Equation 1.40) into Equation 1.39 and its time derivative. We obtain

$$x_0 = A \sin \phi \quad (1.41)$$

$$v_0 = A\omega_n \cos \phi \quad (1.42)$$

Now divide Equation 1.41 by Equation 1.42, and also use the fact that $\sin^2 \phi + \cos^2 \phi = 1$. We obtain

$$\tan \phi = \omega_n \frac{x_0}{v_0}$$

$$\left(\frac{x_0}{A}\right)^2 + \left(\frac{v_0}{A\omega_n}\right)^2 = 1$$

Hence,

$$\text{Amplitude } A = \sqrt{x_0^2 + \frac{v_0^2}{\omega_n^2}} \quad (1.43)$$

$$\text{Phase } \phi = \tan^{-1} \frac{\omega_n x_0}{v_0} \quad (1.44)$$

Example 1.1

A simple model for a tracked gantry conveyor system in a factory is shown in Figure 1.7.

The carriage of mass (m) moves on a frictionless track. The pulley is supported on frictionless bearings, and its axis of rotation is fixed. Its moment of inertia about this axis is J . The motion of the carriage is restrained by a spring of stiffness k_1 , as shown. The belt segment that drives the carriage runs over the

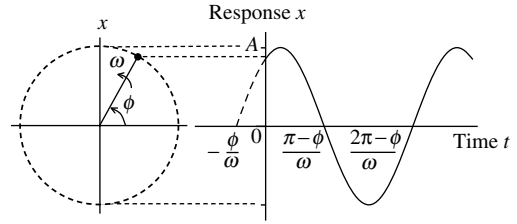


FIGURE 1.6 Free response of an undamped simple oscillator.

Eliminate the common velocity variable \dot{x} (which cannot be zero for all t). We obtain

$$\left(m + \frac{J}{r^2}\right)\ddot{x} + (k_1 + k_2)x = k_2x_{20} - k_1x_{10}$$

which is the same result as before.

Solution Using Lagrange's Equations

$$\text{Lagrangian } L = T - V = \frac{1}{2}m\dot{x}^2 + \frac{1}{2}J\dot{\theta}^2 - \frac{1}{2}k_1(x_{10} + x)^2 - \frac{1}{2}k_2(x_{20} - x)^2$$

Now, substituting for θ in terms of x (Equation v), we obtain

$$L = \frac{1}{2}\left(m + \frac{J}{r^2}\right)\dot{x}^2 - \frac{1}{2}k_1(x_{10} + x)^2 - \frac{1}{2}k_2(x_{20} - x)^2$$

Use Lagrange's equation (see Box 1.1):

$$\frac{d}{dt} \frac{\partial L}{\partial \dot{q}_i} - \frac{\partial L}{\partial q_i} = Q_i \quad \text{for } i = 1, 2, \dots, n$$

where the generalized coordinate $q_i = x$ and the corresponding generalized force $Q_i = 0$ because there are no nonconservative and external forces. We obtain

$$\begin{aligned} \frac{\partial L}{\partial \dot{x}} &= \left(m + \frac{J}{r^2}\right)\dot{x} \\ \frac{\partial L}{\partial x} &= -k_1(x_{10} + x) + k_2(x_{20} - x) \end{aligned}$$

From this, we obtain the equation of motion:

$$\left(m + \frac{J}{r^2}\right)\ddot{x} + (k_1 + k_2)x = k_2x_{20} - k_1x_{10}$$

which is identical to what we obtained before.

Natural Frequency

From the equivalent translational system, the natural frequency (undamped) of the system is obtained as

$$\omega_n = \sqrt{k_{eq}/m_{eq}} = \sqrt{(k_1 + k_2)/\left(m + \frac{J}{r^2}\right)} \quad (\text{vii})$$

Substitute for x and its derivatives into Equation vi using the compatibility condition (Equation v). We obtain the equivalent rotational system:

$$(r^2m + J)\ddot{\theta} + r^2(k_1 + k_2)\theta = rk_2x_{20} - rk_1x_{10}$$

The equivalent moment of inertia:

$$J_{eq} = r^2m + J$$

The equivalent torsional stiffness:

$$K_{eq} = r^2(k_1 + k_2)$$

Therefore, the corresponding natural frequency is

$$\omega_n = \sqrt{r^2(k_1 + k_2)/(r^2m + J)} = \sqrt{(k_1 + k_2)/\left(m + \frac{J}{r^2}\right)} \quad (\text{viii})$$

This result is identical to the previous result (vii). This is to be expected, as the system has not changed (only the response variable was changed).

Common methods of developing equations of motion for mechanical systems are summarized in Box 1.1.

Box 1.1

APPROACHES FOR DEVELOPING EQUATIONS OF MOTION

1. Conservative Systems (No Nonconservative Forces/No Energy Dissipation):

Kinetic energy = T

Potential energy = V

Conservation of energy: $T + V = \text{const.}$

Differentiate with respect to time t

2. Lagrange's Equations:

Lagrangian $L = T - V$

$$\frac{d}{dt} \frac{\partial L}{\partial \dot{q}_i} - \frac{\partial L}{\partial q_i} = Q_i \quad \text{for } i = 1, 2, \dots, n$$

n = number of DoFs

Q_i = generalized force corresponding to generalized coordinate q_i .

Find Q_i using:

$$\delta W = \sum Q_i \delta q_i$$

where δW = work done by nonconservative forces in a general incremental motion ($\delta q_1, \delta q_2, \dots, \delta q_n$).

3. Newtonian Approach:

$$\sum \text{Forces} = \frac{d}{dt} \sum \text{Linear Momentum}$$

$$\sum \text{Torques} = \frac{d}{dt} \sum \text{Angular Momentum}$$

(About centroid or a fixed point)

1.3 Heavy Springs

A heavy spring has its mass and flexibility properties continuously distributed throughout its body. In that sense it has an infinite number of DoF(s), and a single coordinate cannot represent its motion. However, for many practical purposes, a lumped-parameter approximation with just one lumped mass to represent the inertial characteristics of the spring may be sufficient. Such an approximation may be obtained by using the energy approach. Here, we represent the spring by a lumped-parameter "model" such that the original spring and the model have the same net kinetic energy and potential energy. This *energy equivalence* is used in deriving a lumped mass parameter for the model. Even though damping (energy dissipation) is neglected in the present analysis, it is not difficult to incorporate that as well in the model.

1.3.1 Kinetic Energy Equivalence

Consider the uniform, heavy spring shown in Figure 1.9, with one end fixed and the other end moving at velocity v .

Note that:

k = stiffness of spring

m_s = mass of spring

l = length of spring

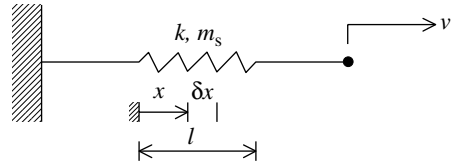


FIGURE 1.9 A uniform heavy spring.

Local speed of element δx of the spring is given by $(x/l)v$. Element mass = $(m_s/l)\delta x$. Hence,

$$\text{Element KE} = \frac{1}{2} \frac{m_s}{l} \delta x \left(\frac{x}{l} v \right)^2$$

In the limit, we have $\delta x \rightarrow dx$. Then,

$$\text{Total KE} = \int_0^l \frac{1}{2} \frac{m_s}{l} dx \left(\frac{x}{l} v \right)^2 = \frac{1}{2} \frac{m_s v^2}{l^3} \int_0^l x^2 dx = \frac{1}{2} \frac{m_s v^2}{3} \quad (1.45)$$

Hence, the equivalent lumped mass concentrated at the free end = $(1/3) \times$ spring mass.

Note: This derivation assumes that one end of the spring is fixed. Furthermore, the conditions are assumed to be *uniform* along the spring.

An example of utilizing this result is shown in Figure 1.10. Here, a system with a heavy spring and a lumped mass is approximated by a light spring (having the same stiffness) and a lumped mass.

Another example is shown in Figure 1.11. In this case, it is not immediately clear which of the approximations shown on the right-hand side is most appropriate.

Example 1.2

A uniform heavy spring of mass m_s and stiffness k is attached at one end to a mass m that is free to roll on a frictionless horizontal plane. The other end is anchored to a vertical post. A schematic diagram of this arrangement is shown in Figure 1.12.

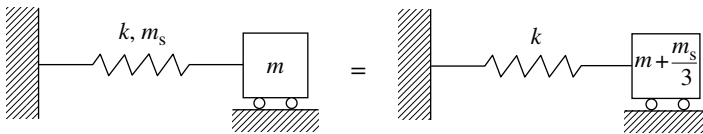


FIGURE 1.10 Lumped-parameter approximation for an oscillator with heavy spring.

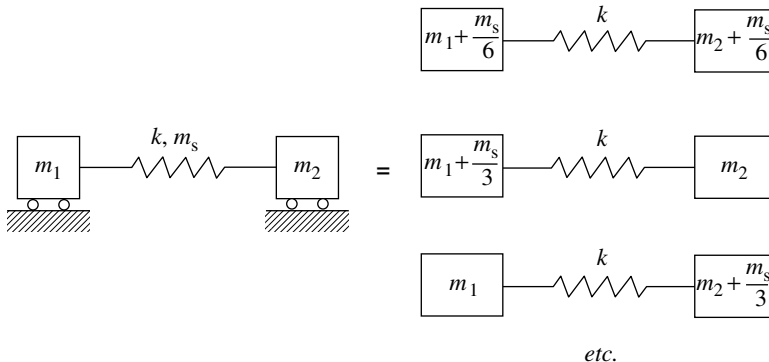


FIGURE 1.11 An example where lumped-parameter approximation for spring is ambiguous.

The unstretched length of the spring is l . Assume that, when the velocity of the connected mass is v , the velocity distribution along the spring is given by

$$v_s(x) = v \sin \frac{\pi x}{2l}$$

where x is the distance of a point along the spring, as measured from the fixed end. We will determine an equivalent lumped mass located at the moving end of the spring (i.e., at the moving mass m) to represent the inertia effects of the spring.

Consider an element of length δx at location x of the spring. Since the spring is uniform, we have element mass $= (m_s/l)\delta x$. Also, according to the given assumption, element velocity $= v \sin(\pi x/2l)$. Hence, kinetic energy of the spring is

$$\begin{aligned} \int_0^l \frac{1}{2} \left(v \sin \frac{\pi x}{2l} \right)^2 \frac{m_s}{l} dx &= \frac{1}{2} \frac{m_s}{l} v^2 \int_0^l \sin^2 \frac{\pi x}{2l} dx = \frac{1}{4} \frac{m_s}{l} v^2 \int_0^l \left[1 - \cos \frac{\pi x}{l} \right] dx \\ &= \frac{1}{4} \frac{m_s}{l} v^2 \left[x - \frac{l}{\pi} \sin \frac{\pi x}{l} \right]_0^l = \frac{1}{4} \frac{m_s}{l} v^2 l = \frac{1}{2} \frac{m_s}{2} v^2 \end{aligned}$$

It follows that the equivalent lumped mass to be located at the moving end of the spring is $m_s/2$. This result is valid only for the assumed velocity distribution, and corresponds to the first mode of motion only. In fact, a linear velocity distribution would be more realistic in this low frequency (quasi-static motion) region, which will give an equivalent lumped mass of $(1/3)m_s$, as we have seen before. Such approximations will not be valid for high frequencies (say, higher than $\sqrt{k/m_s}$).

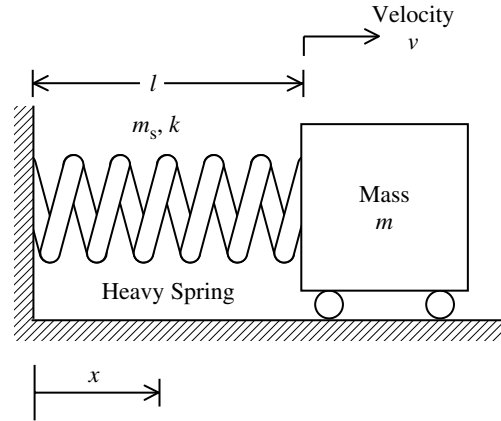


FIGURE 1.12 A heavy spring connected to a rolling stock.

1.4 Oscillations in Fluid Systems

Fluid systems can undergo oscillations (vibrations) quite analogous to mechanical and electrical systems. Again, the reason for their natural oscillation is the ability to store and repeatedly interchange two types of energy — kinetic energy and potential energy. The kinetic energy comes from the velocity of fluid particles during motion. The potential energy arises primarily from the following three main sources:

1. Gravitational potential energy
2. Compressibility of the fluid volume
3. Flexibility of the fluid container

A detailed analysis of these three effects is not undertaken here. However, we have seen from the example in Figure 1.5(e) how a liquid column can oscillate due to repeated interchange between kinetic energy and gravitational potential energy. Now, let us consider another example.

Example 1.3

Consider a cylindrical wooden peg of uniform cross section and height h , floating in a tank of water, as in Figure 1.13(a). It is pushed by hand until completely immersed in water, in an upright orientation. When released, the object will oscillate up and down while floating in the tank. Let ρ_b and ρ_l be the mass

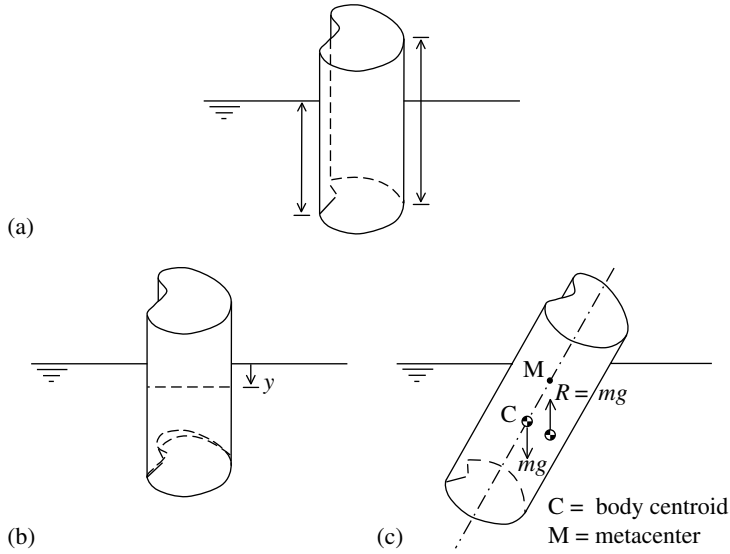


FIGURE 1.13 (a) A buoyancy experiment; (b) upright oscillations of the body; (c) restoring buoyancy couple due to a stable metacenter.

densities of the body (peg) and the liquid (water), respectively. The natural oscillations and the stability of this system may be studied as below.

Suppose that, under equilibrium in the upright position of the body, the submersed length is l . The mass of the body is

$$m = Ah\rho_b \quad (\text{i})$$

where A is the area of cross section (uniform).

By the Archimedes principle, the buoyancy force R is equal to the weight of the liquid displaced by the body. Hence,

$$R = Al\rho_1 g \quad (\text{ii})$$

For equilibrium, we have

$$R = mg \quad (\text{iii})$$

or

$$Al\rho_1 g = Ah\rho_b g$$

Hence,

$$l = \frac{\rho_b}{\rho_1} h \quad \text{for } \rho_b < \rho_1 \quad (\text{iv})$$

For a vertical displacement y from the equilibrium position, the equation of motion is (Figure 1.13(b))

$$m\ddot{y} = mg - A(l + y)\rho_1 g$$

Substitute Equation ii and Equation iii. We obtain

$$m\ddot{y} = -A\rho_1 g y$$

Substitute Equation i:

$$Ah\rho_b \ddot{y} + A\rho_1 g y = 0$$

or

$$\ddot{y} + \frac{\rho_l g}{\rho_b h} y = 0$$

The natural frequency of oscillations is

$$\omega_n = \sqrt{\frac{\rho_l g}{\rho_b h}}$$

Note that this result is independent of the area of the cross section of the body.

Assumptions made:

1. The tank is very large compared to the body. The change in liquid level is negligible as the body is depressed into the water.
2. Fluid resistance (viscous effects, drag, etc.) is negligible.
3. Dynamics of the liquid itself is negligible. Hence, “added inertia” due to liquid motion is neglected.

To study stability of the system, note that the buoyancy for R acts through the centroid of the volume of displaced water (Figure 1.13(c)). Its line of action passes through the central axis of the body at point M . The point is known as the *metacenter*. Let C be the centroid of the body.

If M is above C , then, when tilted, there will be a restoring couple that will tend to restore the body to its upright position. Otherwise the body will be in an unstable situation, and the buoyancy couple will tend to tilt it further towards a horizontal configuration.

1.5 Damped Simple Oscillator

Now we will consider free (natural) response of a simple oscillator in the presence of energy dissipation (damping).

Assume viscous damping, and consider the oscillator shown in Figure 1.14. The free-body diagram of the mass is shown separately.

We use the following notation:

- ω_n = undamped natural frequency
- ω_d = damped natural frequency
- ω_r = resonant frequency
- ω = frequency of excitation

The concept of resonant frequency will be addressed in Chapter 2.

Usually, the viscous damping constant of a single DoF is denoted by b (but, sometimes c is used instead of b , particularly for multi-DoF systems).

Apply Newton's Second Law. From the free-body diagram in Figure 1.14, we have the equation of motion $m\ddot{x} = -kx - b\dot{x}$

or

$$m\ddot{x} + b\dot{x} + kx = 0 \quad (1.46)$$

or

$$\ddot{x} + 2\zeta\omega_n\dot{x} + \omega_n^2 x = 0 \quad (1.47)$$

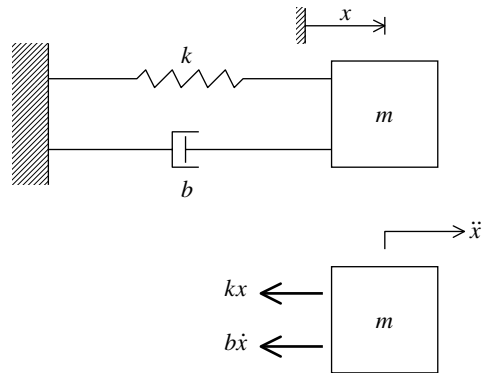


FIGURE 1.14 A damped simple oscillator and its free-body diagram.

This is a free (or unforced, or *homogeneous*) equation of motion. Its solution is the free (natural) response of the system and is also known as the *homogeneous solution*. Note that $\omega_n = \sqrt{k/m}$, which is the natural frequency when there is no damping, and

$$2\zeta\omega_n = \frac{b}{m} \quad (1.48)$$

Hence,

$$\zeta = \frac{1}{2} \sqrt{\frac{m}{k}} \frac{b}{m}$$

or

$$\zeta = \frac{1}{2} \frac{b}{\sqrt{km}} \quad (1.49)$$

Note that ζ is called the *damping ratio*. The formal definition of, and the rationale for, this terminology will be discussed later.

Assume an exponential solution:

$$x = C e^{\lambda t} \quad (1.50)$$

This is justified by the fact that linear systems have exponential or oscillatory (i.e., complex exponential) free responses. A more detailed justification will be provided later.

Substitute Equation 1.50 into Equation 1.47 to obtain

$$[\lambda^2 + 2\zeta\omega_n\lambda + \omega_n^2]C e^{\lambda t} = 0$$

Note that $C e^{\lambda t}$ is not zero in general. It follows that, when λ satisfies the equation

$$\lambda^2 + 2\zeta\omega_n\lambda + \omega_n^2 = 0 \quad (1.51)$$

then Equation 1.50 will represent a solution of Equation 1.47.

Equation 1.51 is called the *characteristic equation* of the system. This equation depends on the natural dynamics of the system, not on forcing excitation or initial conditions.

The solution of Equation 1.51 gives the two roots:

$$\lambda = -\zeta\omega_n \pm \sqrt{\zeta^2 - 1}\omega_n = \lambda_1 \text{ and } \lambda_2 \quad (1.52)$$

These are called *eigenvalues* or *poles* of the system.

When $\lambda_1 \neq \lambda_2$, the general solution is

$$x = C_1 e^{\lambda_1 t} + C_2 e^{\lambda_2 t} \quad (1.53)$$

The two unknown constants C_1 and C_2 are related to the integration constants and can be determined by two initial conditions which should be known.

If $\lambda_1 = \lambda_2 = \lambda$, we have the case of repeated roots. In this case, the general solution (Equation 1.53) does not hold because C_1 and C_2 would no longer be independent constants to be determined by two initial conditions. The repetition of the roots suggests that one term of the homogenous solution should have the multiplier t (a result of the double integration of zero). Then the general solution is

$$x = C_1 e^{\lambda t} + C_2 t e^{\lambda t} \quad (1.54)$$

We can identify three categories of damping level, as discussed below, and the nature of the response will depend on the particular category of damping.

1.5.1 Case 1: Underdamped Motion ($\zeta < 1$)

In this case it follows from Equation 1.52 that the roots of the characteristic equation are

$$\lambda = -\zeta\omega_n \pm j\sqrt{1 - \zeta^2}\omega_n = -\zeta\omega_n \pm j\omega_d = \lambda_1 \quad \text{and} \quad \lambda_2 \quad (1.55)$$

where the damped natural frequency is given by

$$\omega_d = \sqrt{1 - \zeta^2}\omega_n \quad (1.56)$$

Note that λ_1 and λ_2 are complex conjugates. The response (Equation 1.53) in this case may be expressed as

$$x = e^{-\zeta\omega_n t} [C_1 e^{j\omega_d t} + C_2 e^{-j\omega_d t}] \quad (1.57)$$

The term within the square brackets of Equation 1.57 has to be real, because it represents the time response of a real physical system. It follows that C_1 and C_2 have to be complex conjugates.

Note:

$$e^{j\omega_d t} = \cos \omega_d t + j \sin \omega_d t$$

$$e^{-j\omega_d t} = \cos \omega_d t - j \sin \omega_d t$$

So, an alternative form of the general solution would be

$$x = e^{-\zeta\omega_n t} [A_1 \cos \omega_d t + A_2 \sin \omega_d t] \quad (1.58)$$

Here, A_1 and A_2 are the two unknown constants. By equating the coefficients it can be shown that

$$A_1 = C_1 + C_2 \quad \text{and} \quad A_2 = j(C_1 - C_2) \quad (1.59)$$

Hence,

$$C_1 = \frac{1}{2}(A_1 - jA_2) \quad \text{and} \quad C_2 = \frac{1}{2}(A_1 + jA_2) \quad (1.60)$$

1.5.1.1 Initial Conditions

Let $x(0) = x_0$, $\dot{x}(0) = v_0$ as before. Then,

$$x_0 = A_1 \quad \text{and} \quad v_0 = -\zeta\omega_n A_1 + \omega_d A_2 \quad (1.61)$$

or

$$A_2 = \frac{v_0}{\omega_d} + \frac{\zeta\omega_n x_0}{\omega_d} \quad (1.62)$$

Yet, another form of the solution would be

$$x = A e^{-\zeta\omega_n t} \sin(\omega_d t + \phi) \quad (1.63)$$

Here, A and ϕ are the unknown constants with

$$A = \sqrt{A_1^2 + A_2^2} \quad \text{and} \quad \sin \phi = \frac{A_2}{\sqrt{A_1^2 + A_2^2}} \quad (1.64)$$

Also,

$$\cos \phi = \frac{A_1}{\sqrt{A_1^2 + A_2^2}} \quad \text{and} \quad \tan \phi = \frac{A_2}{A_1} \quad (1.65)$$

Note that the response $x \rightarrow 0$ as $t \rightarrow \infty$. This means the system is *asymptotically stable*.

1.5.2 Logarithmic Decrement Method

The damping ratio ζ may be experimentally determined from the free response by the logarithmic decrement method. To illustrate this approach, note from Equation 1.63 that the period of damped oscillations is

$$T = \frac{2\pi}{\omega_d} \quad (1.66)$$

Also, from Equation 1.63, we have

$$\frac{x(t)}{x(t+nT)} = \frac{A e^{-\zeta\omega_n t} \sin(\omega_d t + \phi)}{A e^{-\zeta\omega_n(t+nT)} \sin[\omega_d(t+nT) + \phi]}$$

But, $\sin[\omega_d(t+nT) + \phi] = \sin(\omega_d t + \phi + 2n\pi) = \sin(\omega_d t + \phi)$.

Hence,

$$\frac{x(t)}{x(t+nT)} = \frac{e^{-\zeta\omega_n t}}{e^{-\zeta\omega_n(t+nT)}} = e^{\zeta\omega_n nT} \quad (1.67)$$

Take the natural logarithm of Equation 1.67, the logarithmic decrement,

$$\zeta\omega_n nT = \ln \left[\frac{x(t)}{x(t+nT)} \right]$$

However,

$$\omega_n T = \omega_n \frac{2\pi}{\omega_d} = \frac{\omega_n 2\pi}{\sqrt{1-\zeta^2}\omega_n} = \frac{2\pi}{\sqrt{1-\zeta^2}}$$

Hence, with $x(t)/x(t+nT) = r$ we have the logarithmic decrement.

$$\frac{2\pi n\zeta}{\sqrt{1-\zeta^2}} = \ln r$$

Note that $(1/n)\ln r$ is the “per-cycle” logarithmic decrement and $(1/2\pi n)\ln r$ is the “per-radian” logarithmic decrement. The latter is

$$\frac{\zeta}{\sqrt{1-\zeta^2}} = \frac{1}{2\pi n} \ln r = \alpha \quad (1.68)$$

Then, we have

$$\zeta = \sqrt{\frac{\alpha^2}{1+\alpha^2}} \quad (1.69)$$

This is the basis of the logarithmic decrement method of measuring damping. Start by measuring a point $x(t)$ and another point $x(t+nT)$ at n cycles later. For high accuracy, pick the peak points of the response curve for the measurement of $x(t)$ and $x(t+nT)$. From Equation 1.68 it is clear that, for small damping, $\zeta = \alpha$ = per-radian logarithmic decrement.

1.5.3 Case 2: Overdamped Motion ($\zeta > 1$)

In this case, roots λ_1 and λ_2 of the characteristic equation (Equation 1.51) are real. Specifically, we have

$$\lambda_1 = -\zeta\omega_n + \sqrt{\zeta^2 - 1}\omega_n < 0 \quad (1.70)$$

$$\lambda_2 = -\zeta\omega_n - \sqrt{\zeta^2 - 1}\omega_n < 0 \quad (1.71)$$

and the response equation (Equation 1.53) is nonoscillatory. Also, it should be clear from Equation 1.70 and Equation 1.71 that both λ_1 and λ_2 are negative. Hence, $x \rightarrow 0$ as $t \rightarrow \infty$. This means the system is asymptotically stable.

From the initial conditions

$$x(0) = x_0, \quad \dot{x}(0) = v_0$$

we obtain

$$x_0 = C_1 + C_2 \quad (i)$$

and

$$v_0 = \lambda_1 C_1 + \lambda_2 C_2 \quad (ii)$$

Multiply the first initial condition (Equation i) by λ_1 :

$$\lambda_1 x_0 = \lambda_1 C_1 + \lambda_1 C_2 \quad (iii)$$

Subtract Equation iii from Equation ii:

$$v_0 - \lambda_1 x_0 = C_2(\lambda_2 - \lambda_1)$$

We obtain

$$C_2 = \frac{v_0 - \lambda_1 x_0}{\lambda_2 - \lambda_1} \quad (1.72)$$

Similarly, multiply the first initial condition (Equation i) by λ_2 and subtract from Equation ii. We obtain

$$v_0 - \lambda_2 x_0 = C_1(\lambda_1 - \lambda_2)$$

Hence,

$$C_1 = \frac{v_0 - \lambda_2 x_0}{\lambda_1 - \lambda_2} \quad (1.73)$$

1.5.4 Case 3: Critically Damped Motion ($\zeta = 1$)

Here, we have repeated roots, given by

$$\lambda_1 = \lambda_2 = -\omega_n \quad (1.74)$$

The response for this case is given by (see Equation 1.54)

$$x = C_1 e^{-\omega_n t} + C_2 t e^{-\omega_n t} \quad (1.75)$$

Since the term $e^{-\omega_n t}$ goes to zero faster than t goes to infinity, we have $t e^{-\omega_n t} \rightarrow 0$ as $t \rightarrow \infty$. Hence, the system is asymptotically stable.

Now use the initial conditions $x(0) = x_0$, $\dot{x}(0) = v_0$. We obtain

$$x_0 = C_1$$

$$v_0 = -\omega_n C_1 + C_2$$

Hence,

$$C_1 = x_0 \quad (1.76)$$

$$C_2 = v_0 + \omega_n x_0 \quad (1.77)$$

Note: When $\zeta = 1$ we have the critically damped response because below this value the response is oscillatory (underdamped) and above this value, the response is nonoscillatory (overdamped). It follows

that we may define the damping ratio as

$$\zeta = \text{damping ratio} = \frac{\text{damping constant}}{\text{damping constant for critically damped conditions}} \quad (1.78)$$

1.5.5 Justification for the Trial Solution

In the present analysis, the trial solution (Equation 1.50) has been used for the response of a linear system having constant parameter values. A justification for this is provided now.

1.5.5.1 First-Order System

Consider a first-order (homogeneous, no forcing input) linear system given by

$$\left(\frac{d}{dt} - \lambda \right) x = \dot{x} - \lambda x = 0 \quad (1.79)$$

This equation can be written as

$$\frac{dx}{x} = \lambda dt$$

Integrate:

$$\ln x = \lambda t + \ln C$$

Here, $\ln C$ is the constant of integration. Hence,

$$x = C e^{\lambda t} \quad (1.80)$$

This is then the general form of the free response of a first-order system. It incorporates one constant of integration, and hence will need one initial condition.

1.5.5.2 Second-Order System

We can write the equation of a general second-order (homogeneous, unforced) system in the operational form:

$$\left(\frac{d}{dt} - \lambda_1 \right) \left(\frac{d}{dt} - \lambda_2 \right) x = 0 \quad (1.81)$$

By reasoning as before, the general solution would be of the form $x = C_1 e^{\lambda_1 t} + C_2 e^{\lambda_2 t}$. Here, C_1 and C_2 are the constants of integration, which are determined using two initial conditions.

1.5.5.3 Repeated Roots

The case of repeated roots deserves a separate treatment. First, consider

$$\frac{d^2 x}{dt^2} = 0 \quad (1.82)$$

Integrate twice:

$$\frac{dx}{dt} = C; \quad x = Ct + D \quad (1.83)$$

Note the term with t in this case. Hence, a suitable trial solution for the system

$$\left(\frac{d}{dt} - \lambda \right) \left(\frac{d}{dt} - \lambda \right) x = 0 \quad (1.84)$$

would be $x = C_1 e^{\lambda t} + C_2 t e^{\lambda t}$.

The main results for the free (natural) response of a damped oscillator are given in Box 1.2.

Box 1.2

FREE (NATURAL) RESPONSE OF A DAMPED SINGLE OSCILLATOR

System Equation: $m\ddot{x} + b\dot{x} + kx = 0$ or $\ddot{x} + 2\zeta\omega_n\dot{x} + \omega_n^2x = 0$

Undamped natural frequency $\omega_n = \sqrt{k/m}$

Damping ratio $\zeta = b/2\sqrt{km}$

Characteristic Equation: $\lambda^2 + 2\zeta\omega_n\lambda + \omega_n^2 = 0$

Roots (Eigenvalues or Poles): λ_1 and $\lambda_2 = -\zeta\omega_n \pm \sqrt{\zeta^2 - 1}\omega_n$

Response:

$$x = C_1 e^{\lambda_1 t} + C_2 e^{\lambda_2 t} \text{ for unequal roots } (\lambda_1 \neq \lambda_2)$$

$$x = (C_1 + C_2 t)e^{\lambda t} \text{ for equal roots } (\lambda_1 = \lambda_2 = \lambda)$$

Initial Conditions: $x(0) = x_0$ and $\dot{x}(0) = v_0$

Case 1: Underdamped ($\zeta < 1$)

Poles are complex conjugates: $-\zeta\omega_n \pm j\omega_d$

Damped natural frequency $\omega_d = \sqrt{1 - \zeta^2}\omega_n$

$$x = e^{-\zeta\omega_n t} [C_1 e^{j\omega_d t} + C_2 e^{-j\omega_d t}] = e^{-\zeta\omega_n t} [A_1 \cos \omega_d t + A_2 \sin \omega_d t] = A e^{-\zeta\omega_n t} \sin(\omega_d t + \phi)$$

$$A_1 = C_1 + C_2 \quad \text{and} \quad A_2 = j(C_1 - C_2)$$

$$C_1 = \frac{1}{2}(A_1 - jA_2) \quad \text{and} \quad C_2 = \frac{1}{2}(A_1 + jA_2)$$

$$A = \sqrt{A_1^2 + A_2^2} \quad \text{and} \quad \tan \phi = \frac{A_2}{A_1}$$

Initial conditions give:

$$A_1 = x_0 \quad \text{and} \quad A_2 = \frac{v_0 + \zeta\omega_n x_0}{\omega_d}$$

Logarithmic Decrement per Radian:

$$\alpha = \frac{1}{2\pi n} \ln r = \frac{\zeta}{\sqrt{1 - \zeta^2}}$$

where $r = x(t)/[x(t + nT)]$ = decay ratio over n complete cycles.

For small ζ : $\zeta \cong \alpha$

Case 2: Overdamped ($\zeta > 1$)

Poles are real and negative: $\lambda_1, \lambda_2 = -\zeta\omega_n \pm \sqrt{\zeta^2 - 1}\omega_n$

$$x = C_1 e^{\lambda_1 t} + C_2 e^{\lambda_2 t}$$

$$C_1 = \frac{v_0 - \lambda_2 x_0}{\lambda_1 - \lambda_2} \quad \text{and} \quad C_2 = \frac{v_0 - \lambda_1 x_0}{\lambda_2 - \lambda_1}$$

Case 3: Critically Damped ($\zeta = 1$)

Two identical poles: $\lambda_1 = \lambda_2 = \lambda = -\omega_n$

$$x = (C_1 + C_2 t)e^{-\omega_n t} \quad \text{with} \quad C_1 = x_0 \quad \text{and} \quad C_2 = v_0 + \omega_n x_0$$

1.5.6 Stability and Speed of Response

The free response of a dynamic system, particularly a vibrating system, can provide valuable information concerning the natural characteristics of the system. The free (unforced) excitation may be obtained, for example, by giving an initial-condition excitation to the system and then allowing it to respond freely. Two important characteristics which can be determined in this manner are:

1. Stability
2. Speed of response

The stability of a system implies that the response will not grow without bounds when the excitation force itself is finite. This is known as bounded-input bounded-output (BIBO) stability. In particular, if the free response eventually decays to zero, in the absence of a forcing input, the system is said to be *asymptotically stable*. We have seen that a damped simple oscillator is asymptotically stable, but an undamped oscillator, while being stable in a general (BIBO) sense, is not asymptotically stable.

The speed of response of a system indicates how fast the system responds to an excitation force. It is also a measure of how fast the free response (1) rises or falls if the system is oscillatory; or (2) decays, if the system is nonoscillatory. Hence, the two characteristics, stability and speed of response, are not completely independent. In particular, for nonoscillatory (overdamped) systems these two properties are very closely related. It is clear then that stability and speed of response are important considerations in the analysis, design, and control of vibrating systems.

The level of stability of a linear dynamic system depends on the real parts of the eigenvalues (or poles), which are the roots of the characteristic equation. Specifically, if all the roots have real parts that are negative, then the system is stable. Also, the more negative the real part of a pole, the faster the decay of the free response component corresponding to that pole. The inverse of the negative real part is the time constant. The smaller the time constant, the faster the decay of the corresponding free response, and hence, the higher the level of stability associated with that pole. We can summarize these observations as follows:

Level of stability. Depends on decay rate of free response (and hence on time constants or real parts of poles)

Speed of response. Depends on natural frequency and damping for oscillatory systems and decay rate for nonoscillatory systems

Time constant. Determines stability and decay rate of free response (and speed of response in nonoscillatory systems)

Now let us consider the specific case of a damped simple oscillator given by Equation 1.47.

Case 1 ($\zeta < 1$)

The free response is given by $x = A e^{-\zeta\omega_n t} \sin(\omega_d t + \phi)$

$$\text{Time constant } \tau = \frac{1}{\zeta\omega_n} \quad (1.85)$$

The system is asymptotically stable. The larger $\zeta\omega_n$, the more stable the system. Also, the speed of response increases with both ω_d and $\zeta\omega_n$.

Case 2 ($\zeta > 1$)

The response is nonoscillatory, and is given by

$$x = A_1 e^{\lambda_1 t} \text{ (decays slower)} + A_2 e^{\lambda_2 t} \text{ (decays faster)}$$

where $\lambda_1 = -\zeta\omega_n + \sqrt{\zeta^2 - 1}\omega_n$ and $\lambda_2 = -\zeta\omega_n - \sqrt{\zeta^2 - 1}\omega_n$.

This system has two time constants:

$$\tau_1 = \frac{1}{|\lambda_1|} \quad \text{and} \quad \tau_2 = \frac{1}{|\lambda_2|} \quad (1.86)$$

Note that τ_1 is the dominant (slower) time constant. The system is also asymptotically stable. The larger the $|\lambda_1|$ the faster and more stable the system.

Consider an underdamped system and an overdamped system with damping ratios ζ_u and ζ_o , respectively. We can show that the underdamped system is more stable than the overdamped system if and only if

$$\zeta_o - \sqrt{\zeta_o^2 - 1} < \zeta_u \quad (1.87a)$$

or equivalently,

$$\zeta_o > \frac{\zeta_u^2 + 1}{2\zeta_u} \quad (1.87b)$$

where $\zeta_o > 1 > \zeta_u > 0$ by definition.

Proof

To be more stable, we should have the underdamped pole located farther away than the dominant overdamped pole from the imaginary axis of the pole plane; thus

$$\zeta_u \omega_n > \zeta_o \omega_n - \sqrt{\zeta_o^2 - 1} \omega_n$$

Hence,

$$\zeta_u > \zeta_o - \sqrt{\zeta_o^2 - 1}$$

Now, bring the square-root term to the left-hand side and square it:

$$\zeta_o^2 - 1 > (\zeta_o - \zeta_u)^2 = \zeta_o^2 - 2\zeta_o\zeta_u + \zeta_u^2$$

Hence,

$$2\zeta_o\zeta_u > \zeta_u^2 + 1$$

or

$$\zeta_o > \frac{\zeta_u^2 + 1}{2\zeta_u}$$

This completes the proof. \square

To explain this result further, consider an undamped ($\zeta = 0$) simple oscillator of natural frequency ω_n . Its poles are at $\pm j\omega_n$ (on the imaginary axis of the pole plane). Now let us add damping and increase ζ from 0 to 1. Then the complex conjugates poles $-\zeta\omega_n \pm j\omega_d$ will move away from the imaginary axis as ζ increases (because $\zeta\omega_n$ increases) and hence the level of stability will increase. When ζ reaches the value 1 (critical damping) we obtain two identical and real poles at $-\omega_n$. When ζ is increased beyond 1, the poles will be real and unequal, with one pole having a magnitude smaller than ω_n and the other having a magnitude larger than ω_n . The former (closer to the “origin” of zero) is the dominant pole, and will determine both stability and the speed of response of the overdamped system. It follows that, as ζ increases beyond 1, the two poles will branch out from the location $-\omega_n$, one moving towards the origin (becoming less stable) and the other moving away from the origin. It is now clear that as ζ is increased beyond the point of critical damping, the system becomes less stable. Specifically, for a given value of $\zeta_u < 1$, there is a value of $\zeta_o > 1$, governed by Equation 1.87, above which the overdamped system is less stable and slower than the underdamped system.

Example 1.4

Consider the simple oscillator shown in Figure 1.14, with parameters $m = 4$ kg, $k = 1.6 \times 10^3$ N/m, and the two cases of damping:

1. $b = 80$ N/m/sec
2. $b = 320$ N/m/sec

We will study the nature of the free response in each case.

The undamped natural frequency of the system is

$$\omega_n = \sqrt{\frac{k}{m}} = \sqrt{\frac{1.6 \times 10^3}{4}} \text{ rad/sec} = 20.0 \text{ rad/sec}$$

Case 1

$$2\zeta\omega_n = \frac{b}{m} \quad \text{or} \quad 2\zeta \times 20 = \frac{80}{4}$$

Then,

$$\zeta_u = 0.5$$

The system is underdamped in this case.

Case 2

$$2\zeta \times 20 = \frac{320}{4}$$

Then,

$$\zeta_o = 2.0$$

The system is overdamped in this case.

Case 3

The characteristic equation is

$$\lambda^2 + 2 \times 0.5 \times 20\lambda + 20^2 = 0$$

or

$$\lambda^2 + 20\lambda + 20^2 = 0$$

The roots (eigenvalues or poles) are

$$\lambda = -10 \pm j\sqrt{20^2 - 10^2} = -10 \pm j10\sqrt{3}$$

The free (no force) response is given by

$$x = A e^{-10t} \sin(10\sqrt{3}t + \phi)$$

The amplitude A and the phase angle ϕ can be determined using initial conditions.

$$\text{Time constant } \tau = \frac{1}{10} = 0.1 \text{ sec}$$

Case 4

The characteristic equation is

$$\lambda^2 + 2 \times 2 \times 20\lambda + 20^2 = 0$$

or

$$\lambda^2 + 80\lambda + 20^2 = 0$$

The roots are

$$\begin{aligned}\lambda &= -40 \pm \sqrt{40^2 - 20^2} = -40 \pm 20\sqrt{3} \\ &= -5.36, -74.64\end{aligned}$$

The free response is given by

$$x = C_1 e^{-5.36t} + C_2 e^{-74.64t}$$

The constants C_1 and C_2 can be determined using initial conditions. The second term on the right-hand side goes to zero much faster than the first term, as shown in Figure 1.15. Hence, the first term will dominate and will determine the dominant time constant, level of stability, and speed of response. Specifically, the response may be approximated as

$$x \cong C_1 e^{-5.36t}$$

Hence,

$$\text{Time constant } \tau = \frac{1}{5.36} = 0.19 \text{ sec}$$

This value is double that of Case 1. Consequently, it is clear that the underdamped system (Case 1) decays faster than the overdamped system (Case 2). In fact, according to Equation 1.87b, with $\zeta_u = 0.5$ we have

$$\zeta_u > \frac{0.5^2 + 1}{2 \times 0.5} = 1.25$$

Hence, an overdamped system of damping ratio greater than 1.25 will be less stable than the underdamped system of damping ratio 0.5.

Table 1.1 summarizes some natural characteristics of a damped simple oscillator under three different levels of damping. The nature of the natural response for these three cases is sketched in Figure 1.16. In general, the natural response of a system is governed by its eigenvalues (or poles), which are the roots of the characteristic equation. The poles may be marked on a complex plane (s-plane), with the horizontal axis representing the real part and the vertical axis representing the imaginary part. The nature of the free response depending on the pole location of the system is shown in Figure 1.17.

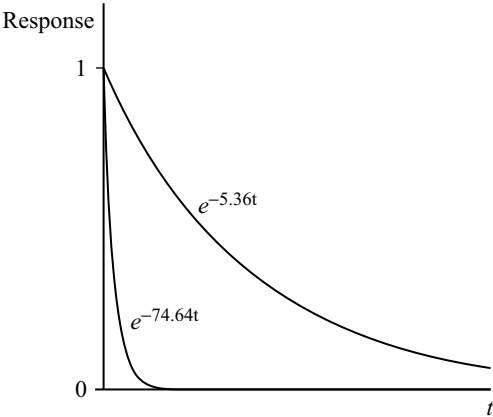


FIGURE 1.15 The free (homogeneous) response components of an overdamped system.

TABLE 1.1 Natural Characteristics of a Damped Oscillator

	Damping Ratio		
	$\zeta < 1$	$\zeta > 1$	$\zeta = 1$
Level of damping	Underdamped	Overdamped	Critically damped
Oscillatory response	Yes	No	No
Stability	Asymptotically stable (less stable than $\zeta = 1$ case but not necessarily less stable than the overdamped case)	Asymptotically stable (less stable than the critically damped case)	Asymptotically stable (most stable)
Speed of response	Better than overdamped	Lower than critical	Good
Time constant	$1/(\zeta\omega_n)$	$1/(\zeta\omega_n \pm \sqrt{\zeta^2 - 1}\omega_n)$	$1/\omega_n$

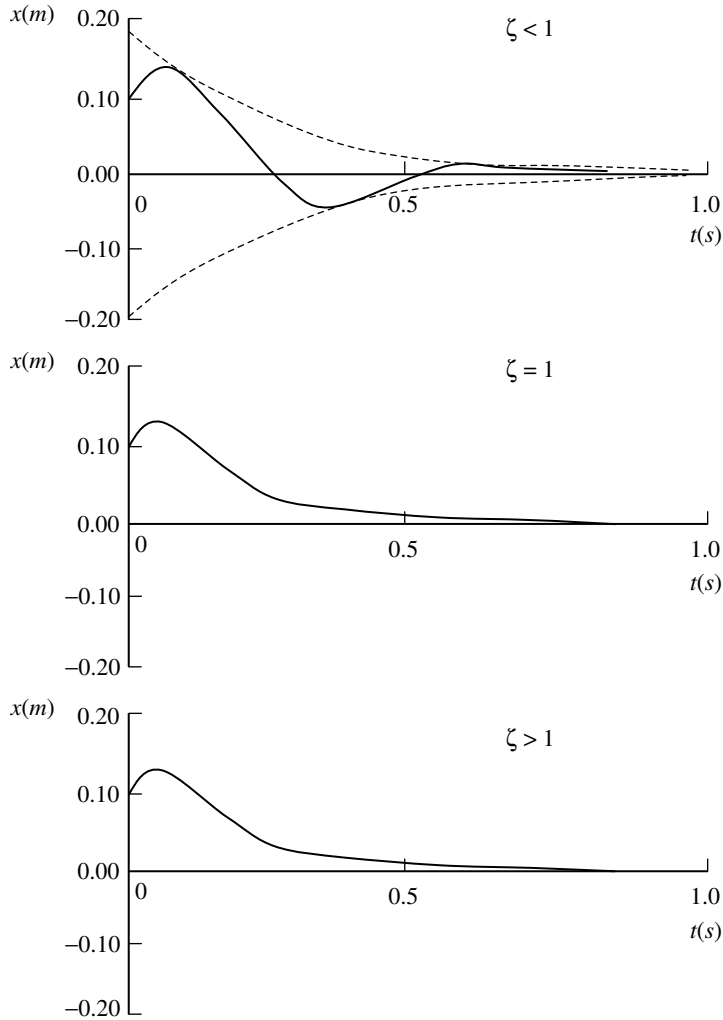


FIGURE 1.16 Free response of a damped oscillator: (a) underdamped; (b) critically damped; (c) overdamped.

1.6 Forced Response

The *free response* of a vibratory system is the response to some initial excitation and in the absence of any subsequent forcing input. This corresponds to the “natural” response of the system. Mathematically, it is the homogeneous solution, because it is obtained by solving the homogeneous equation of the system (i.e., without the input terms). The natural response, the free response, and the homogeneous solution are synonymous, in the absence of a forcing input to the system.

The *forced response* of a dynamic (vibratory) system is the response of the system to a forcing input. When there is a forcing excitation (i.e., an input) on a system, the equation of motion will be nonhomogeneous (i.e., the right-hand side will not be zero). Then, the total solution (total response T) will be given by the sum of the homogeneous solution (H) and the particular integral (P), subject to the system initial conditions. This may be determined by the mathematical solution of the equation of motion. The total response can be separated into the terms that depend on the initial conditions (X) and the terms that depend on the forcing excitation (F). This is in fact the physical interpretation of the total solution. Note that X is called the “free response,” “initial-condition response,” or the “zero-input

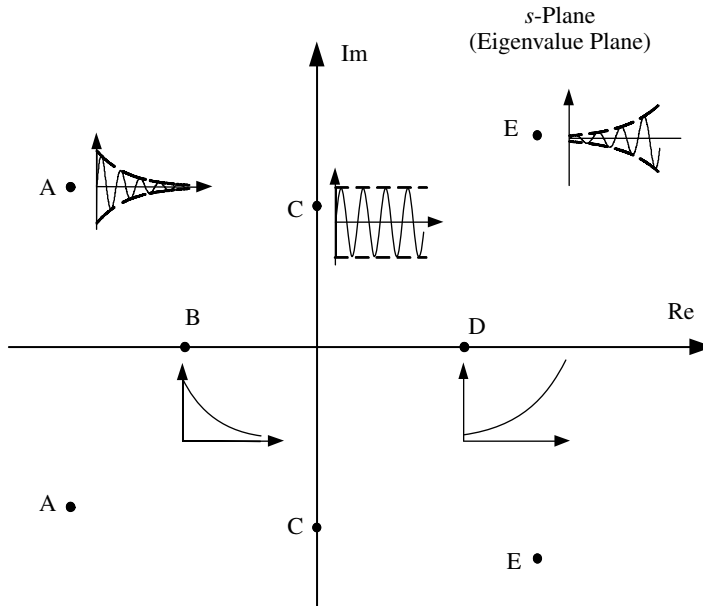


FIGURE 1.17 Dependence of free response (or stability) on the pole location. (A and B are stable; C is marginally stable; D and E are unstable.)

response.” The term F is called the “forced response” or the “zero-initial-condition response” or the “zero-state response.” In general H is not identical to X and P is not identical to F . But, when there is no forcing excitation (no input), by definition H and X will be identical. Furthermore, under steady-state conditions the homogeneous part or initial-condition response will die down (assuming that there is some damping, and the system is stable). Then, F will become equal to P . Note that, even when the initial conditions are zero, F and P may not be identical because F may contain a natural response component that is excited by the forcing input. This component will die out with time, however.

The total response will depend on the natural characteristics of the system (as for the free response) and also on the nature of the forcing excitation. Mathematically, then, the total response will be determined by both the homogeneous solution and the particular solution. The complete solution will require a knowledge of the input (forcing excitation) and the initial conditions.

The behavior of a dynamic system when subjected to a certain forcing excitation may be studied by analyzing a model of the system. This is commonly known as system-response analysis. System response may be studied either in the *time domain*, where the independent variable of the system response is time, or in the *frequency domain*, where the independent variable of the system response is frequency. Time-domain analysis and frequency-domain analysis are equivalent. Variables in the two domains are connected through the Fourier (integral) transform. The preference of one domain over the other depends on such factors as the nature of the excitation input, the type of the available analytical model, the time duration of interest, and the quantities that need to be determined. The frequency-domain analysis will be addressed in [Chapter 2](#).

1.6.1 Impulse-Response Function

Principle of superposition. Consider a linear dynamic (vibratory) system. The principle of superposition holds for a linear system. More specifically, if y_1 is the system response to excitation $u_1(t)$ and y_2 is the response to excitation $u_2(t)$, then $\alpha y_1 + \beta y_2$ is the system response to input $\alpha u_1(t) + \beta u_2(t)$ for any

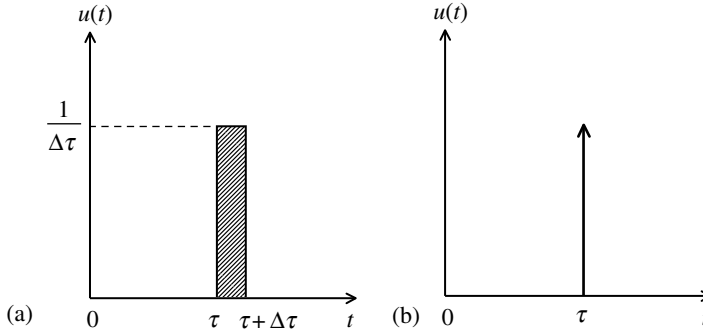


FIGURE 1.18 Illustrations of (a) unit pulse and (b) unit impulse.

constants α and β and any excitation functions $u_1(t)$ and $u_2(t)$. This is true for both time-variant-parameter linear systems and constant-parameter linear systems.

Unit impulse. A *unit pulse* of width $\Delta\tau$ starting at time $t = \tau$ is shown in Figure 1.18(a). Its area is unity. A *unit impulse* is the limiting case of a unit pulse when $\Delta\tau \rightarrow 0$. Unit impulse acting at time $t = \tau$ is denoted by $\delta(t - \tau)$ and is graphically represented as in Figure 1.18(b). In mathematical analysis, this is known as the *Dirac delta function*. It is mathematically defined by the two conditions:

$$\delta(t - \tau) = \begin{cases} 0 & \text{for } t \neq \tau \\ \infty & \text{for } t = \tau \end{cases} \quad (1.88)$$

and

$$\int_{-\infty}^{\infty} \delta(t - \tau) dt = 1 \quad (1.89)$$

The Dirac delta function has the following well-known and useful properties:

$$\int_{-\infty}^{\infty} f(t) \delta(t - \tau) dt = f(\tau) \quad (1.90)$$

and

$$\int_{-\infty}^{\infty} \frac{d^n f(t)}{dt^n} \delta(t - \tau) dt = \left. \frac{d^n f(t)}{dt^n} \right|_{t=\tau} \quad (1.91)$$

for any well-behaved time function $f(t)$.

Impulse-response function. The system response (output) to a unit-impulse excitation (input) acted at time $t = 0$ is known as the *impulse-response function* and is denoted by $h(t)$.

1.6.2 Forced Response

The system output to an arbitrary input may be expressed in terms of its impulse-response function. This is the essence of the impulse-response approach to determining the forced response of a dynamic system.

Without loss of generality, assume that the system input $u(t)$ starts at $t = 0$; that is,

$$u(t) = 0 \quad \text{for } t < 0 \quad (1.92)$$

For a *physically realizable system*, the response does not depend on the future values of the input. Consequently,

$$y(t) = 0 \quad \text{for } t < 0 \quad (1.93)$$

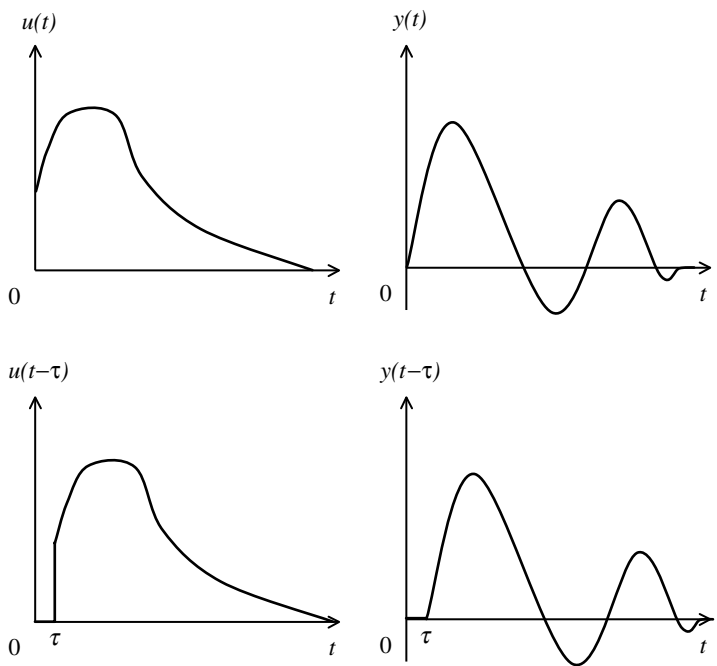


FIGURE 1.19 Response to a delayed input.

and

$$h(t) = 0 \quad \text{for } t < 0 \tag{1.94}$$

where $y(t)$ is the response of the system to any general excitation $u(t)$.

Furthermore, if the system is a *constant-parameter system*, then the response does not depend on the time origin used for the input. Mathematically, this is stated as follows: if the response to input $u(t)$ satisfying Equation 1.92 is $y(t)$, which satisfies Equation 1.93, then the response to input $u(t - \tau)$, which satisfies,

$$u(t - \tau) = 0 \quad \text{for } t < \tau \tag{1.95}$$

is $y(t - \tau)$, and it satisfies

$$y(t - \tau) = 0 \quad \text{for } t < \tau \tag{1.96}$$

This situation is illustrated in Figure 1.19. It follows that the delayed-impulse input $\delta(t - \tau)$, having time delay τ , produces the delayed response $h(t - \tau)$.

Convolution integral. A given input $u(t)$ can be divided approximately into a series of pulses of width $\Delta\tau$ and magnitude $u(\tau) \Delta\tau$. In Figure 1.20, as $\Delta\tau \rightarrow 0$, the pulse shown by the shaded area becomes an impulse acting at $t = \tau$, having the magnitude $u\tau d\tau$. The value of this impulse is given by $\delta(t - \tau)u(\tau)d\tau$. In a linear, constant-parameter system, it produces the response $h(t - \tau)u(\tau)d\tau$. By integrating over the entire time duration of the input $u(t)$, the overall response $y(t)$ is obtained as

$$y(t) = \int_0^\infty h(t - \tau)u(\tau)d\tau \tag{1.97}$$

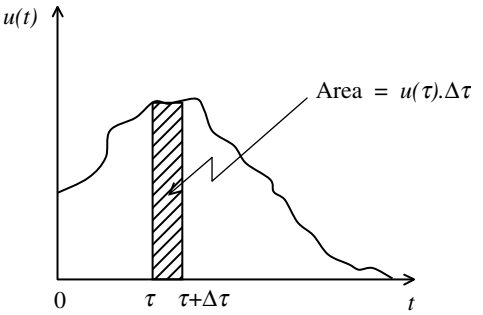


FIGURE 1.20 A general input treated as a continuous series of impulses.

Equation 1.97 is known as the *convolution integral*. This is in fact the forced response, under zero initial conditions.

In view of Equation 1.94, it follows that $h(t - \tau) = 0$ for $\tau > t$. Consequently, the upper limit of integration in Equation 1.97 could be made equal to t without affecting the result. Similarly, in view of Equation 1.92, the lower limit of integration in Equation 1.97 could be made $-\infty$. Furthermore, by introducing the change of variable $\tau \rightarrow t - \tau$, an alternative version of the convolution integral is obtained. Several valid versions of the convolution integral (or response equation) for a linear, constant-parameter system are given below:

$$y(t) = \int_0^{\infty} h(\tau)u(t - \tau)d\tau \quad (1.97a)$$

$$y(t) = \int_{-\infty}^{\infty} h(t - \tau)u(\tau)d\tau \quad (1.97b)$$

$$y(t) = \int_{-\infty}^{\infty} h(\tau)u(t - \tau)d\tau \quad (1.97c)$$

$$y(t) = \int_{-\infty}^t h(t - \tau)u(\tau)d\tau \quad (1.97d)$$

$$y(t) = \int_{-\infty}^t h(\tau)u(t - \tau)d\tau \quad (1.97e)$$

$$y(t) = \int_0^t h(t - \tau)u(\tau)d\tau \quad (1.97f)$$

$$y(t) = \int_0^t h(\tau)u(t - \tau)d\tau \quad (1.97g)$$

In fact, the lower limit of integration in the convolution integral could be any value satisfying $\tau \leq 0$, and the upper limit could be any value satisfying $\tau \geq t$. The use of a particular pair of integration limits depends on whether the functions $h(t)$ and $u(t)$ implicitly satisfy the conditions given by Equation 1.93 and Equation 1.94, or whether these conditions have to be imposed on them by means of the proper integration limits. It should be noted that the two versions given by Equation 1.97f and Equation 1.97g take these conditions into account explicitly and therefore are valid for all inputs and impulse-response functions.

It should be emphasized that the response given by the convolution integral assumes a zero initial state, and is known as the *zero-state response*, because the impulse response itself assumes a zero initial state. As we have stated, this is not necessarily equal to the “particular solution” in mathematical analysis. Also, as t increases ($t \rightarrow \infty$), this solution approaches the *steady-state response* denoted by y_{ss} , which is typically the particular solution. The impulse response of a system is the inverse Laplace transform of the transfer function. Hence, it can be determined using Laplace transform techniques. This aspect will be addressed in [Chapter 3](#). Some useful concepts of forced response are summarized in Box 1.3.

1.6.3 Response to a Support Motion

An important consideration in vibration analysis and in the testing of machinery and equipment is the response to a support motion. To illustrate the method of analysis, consider the linear, single-DoF system consisting of mass m , spring constant k , and damping constant b , subjected to support motion (displacement) $u(t)$. Vertical and horizontal configurations of this system are shown in [Figure 1.21](#).

Both configurations possess the same equation of motion, provided the support motion $u(t)$ and the mass response (displacement) y are measured from the fixed points that correspond to the initial, static-equilibrium position of the system. In the vertical configuration, the compressive force in the spring exactly balances the weight of the mass when it is in static equilibrium. In the horizontal configuration, the spring is unstretched when in static equilibrium. It may be easily verified that the equation of motion

Box 1.3

CONCEPTS OF FORCED RESPONSE

Total Response (T) = Homogeneous Solution (H) + Particular Integral (P)

= Free Response (X) + Forced Response (F)

= Initial-Condition Response (X) + Zero-Initial-Condition Response (F)

= Zero-Input Response (X) + Zero-State Response (F)

Note: In general, $H \neq X$ and $P \neq F$

With no input (no forcing excitation), by definition, $H \equiv X$

At steady state, F becomes equal to P .

Convolution Integral: Response $y = \int_0^t h(t - \tau)u(\tau)d\tau = \int_0^t h(\tau)u(t - \tau)d\tau$, where u = excitation (input) and h = impulse-response function (response to a unit-impulse input).

Damped Simple Oscillator: $\ddot{y} + 2\zeta\omega_n\dot{y} + \omega_n^2y = \omega_n^2u(t)$

$$\text{Poles (eigenvalues)} \lambda_1, \lambda_2 = \begin{cases} -\zeta\omega_n \pm \sqrt{\zeta^2 - 1}\omega_n & \text{for } \zeta \geq 1 \\ -\zeta\omega_n \pm j\omega_d & \text{for } \zeta < 1 \end{cases}$$

ω_n = undamped natural frequency, ω_d = damped natural frequency, ζ = damping ratio.

Note: $\omega_d = \sqrt{1 - \zeta^2}\omega_n$.

Impulse-Response Function (Zero Initial Conditions):

$$h(t) = \begin{cases} \frac{\omega_n}{\sqrt{1 - \zeta^2}} \exp(-\zeta\omega_n t) \sin \omega_d t & \text{for } \zeta < 1 \\ \frac{\omega_n}{2\sqrt{\zeta^2 - 1}} [\exp \lambda_1 t - \exp \lambda_2 t] & \text{for } \zeta > 1 \\ \omega_n^2 t \exp(-\omega_n t) & \text{for } \zeta = 1 \end{cases}$$

Unit Step Response (Zero Initial Conditions):

$$y_{\text{step}}(t) = \begin{cases} 1 - \frac{1}{\sqrt{1 - \zeta^2}} \exp(-\zeta\omega_n t) \sin(\omega_d t + \phi) & \text{for } \zeta < 1 \\ 1 - \frac{1}{2\sqrt{\zeta^2 - 1}\omega_n} [\lambda_1 \exp \lambda_2 t - \lambda_2 \exp \lambda_1 t] & \text{for } \zeta > 1 \\ 1 - (\omega_n t + 1) \exp(-\omega_n t) & \text{for } \zeta = 1 \end{cases}$$

with

$$\cos \phi = \zeta$$

Note:

$$\text{Impulse Response} = \frac{d}{dt} (\text{Step Response})$$

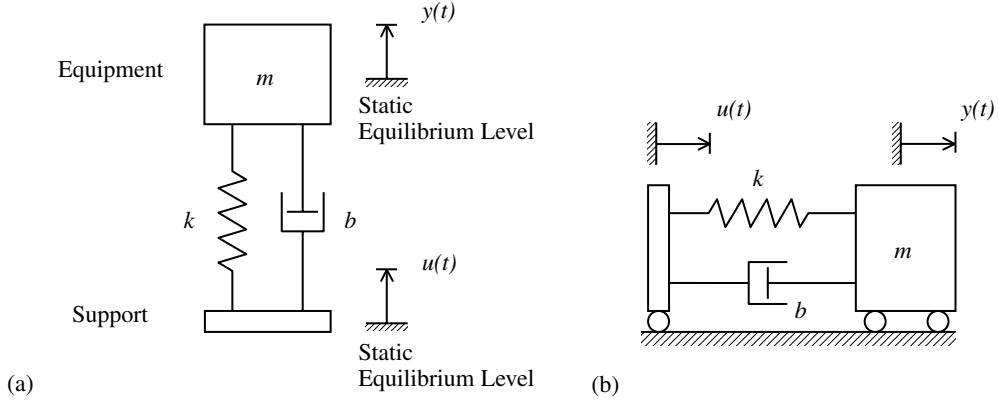


FIGURE 1.21 A system subjected to support motion: (a) vertical configuration; (b) horizontal configuration.

is given by

$$m\ddot{y} + b\dot{y} + ky = ku(t) + bu(t) \quad (1.98)$$

in which $(\dot{}) = d/dt$ and $(\ddot{}) = d^2/dt^2$. The two parameters ω_n and ζ are undamped natural frequency and damping ratio, respectively, given by $\omega_n = \sqrt{k/m}$ and $2\zeta\omega_n = b/m$, as usual. This results in the equivalent equation of motion:

$$\ddot{y} + 2\zeta\omega_n\dot{y} + \omega_n^2y = \omega_n^2u(t) + 2\zeta\omega_n\dot{u}(t) \quad (1.99)$$

There are several ways to determine the response y from Equation 1.99 once the excitation function $u(t)$ is specified. The procedure used below is to first solve the modified equation:

$$\ddot{y} + 2\zeta\omega_n\dot{y} + \omega_n^2y = \omega_n^2u(t) \quad (1.100)$$

This can be identified as the equation of motion of the single-DoF system shown in Figure 1.15. Once this response is known, the response of the system (Equation 1.99) is obtained by applying the principle of superposition.

1.6.3.1 Impulse Response

Many important characteristics of a system can be studied by analyzing the system response to an impulse or a step-input excitation. Such characteristics include system stability, speed of response, time constants, damping properties, and natural frequencies. In this way, a knowledge of the system response to an arbitrary excitation is gained. A unit impulse or a unit step are baseline inputs or test inputs. Responses to such inputs can also serve as the basis for system comparison. In particular, it is usually possible to determine the degree of nonlinearity in a system by exciting it at two input intensity levels, separately, and checking whether proportionality is retained at the output; or by applying a harmonic excitation and checking whether limit cycles are encountered by the response.

The response of the system (Equation 1.100) to a unit impulse $u(t) = \delta(t)$ may be conveniently determined by the Laplace transform approach. Here, we will use a time-domain approach, instead. First, integrate Equation 1.100 over the almost zero time interval from $t = 0^-$ to $t = 0^+$. We obtain

$$\dot{y}(0^+) = \dot{y}(0^-) - 2\zeta\omega_n[y(0^+) - y(0^-)] - \omega_n^2 \int_{0^-}^{0^+} y \, dt + \omega_n^2 \int_{0^-}^{0^+} u(t) \, dt \quad (1.101)$$

Suppose that the system starts from rest. Hence, $y(0^-) = 0$ and $\dot{y}(0^-) = 0$. Also, when an impulse is applied over an infinitesimal time period $[0^-, 0^+]$ the system will not be able to move through a finite distance during that period. Hence, $y(0^+) = 0$ as well, and furthermore, the integral of y on the right-hand side of Equation 1.101 will also be zero. Now, by the definition of a unit impulse, the integral of u

on the right-hand side of Equation 1.101 will be unity. Hence, we have $y(0^+) = \omega_n^2$. It follows that as soon as a unit impulse is applied to the system (Equation 1.100) the initial conditions will become

$$y(0^+) = 0 \quad \text{and} \quad \dot{y}(0^+) = \omega_n^2 \quad (1.102)$$

Also, beyond $t = 0^+$ the excitation $u(t) = 0$, according to the definition of an impulse. Then, the impulse response of the system (Equation 1.100) is obtained by its homogeneous solution (as carried out before, under free response), but with the initial conditions given in Equation 1.102. The three cases of damping ratio ($\zeta < 1$, $\zeta > 1$, and $\zeta = 1$) should be considered separately. We obtain the following results:

$$y_{\text{impulse}}(t) = h(t) = \frac{\omega_n}{\sqrt{1 - \zeta^2}} \exp(-\zeta \omega_n t) \sin \omega_d t \quad \text{for } \zeta < 1 \quad (1.103a)$$

$$y_{\text{impulse}}(t) = h(t) = \frac{\omega_n}{2\sqrt{\zeta^2 - 1}} [\exp \lambda_1 t - \exp \lambda_2 t] \quad \text{for } \zeta > 1 \quad (1.103b)$$

$$y_{\text{impulse}}(t) = h(t) = \omega_n^2 t \exp(-\omega_n t) \quad \text{for } \zeta = 1 \quad (1.103c)$$

An explanation concerning the dimensions of $h(t)$ is appropriate here. Note that $y(t)$ has the same dimensions as $u(t)$. Since $h(t)$ is the response to a unit impulse, $\delta(t)$, it follows that they have the same dimensions. The magnitude of $\delta(t)$ is represented by a unit area in the $u(t)$ versus t plane. Consequently, $\delta(t)$ has the dimensions of (1/time) or (frequency). Clearly then, $h(t)$ also has the dimensions of (1/time) or (frequency).

1.6.3.2 The Riddle of Zero Initial Conditions

For a second-order system, zero initial conditions correspond to $y(0) = 0$ and $\dot{y}(0) = 0$. It is clear from Equations 1.103 that $h(0) = 0$, but $\dot{h}(0) \neq 0$, which appears to violate the zero-initial-conditions assumption. This situation is characteristic in a system response to an impulse and its derivatives. This may be explained as follows. When an impulse is applied to a system at rest (zero initial state), the highest derivative of the system differential equation momentarily becomes infinity.

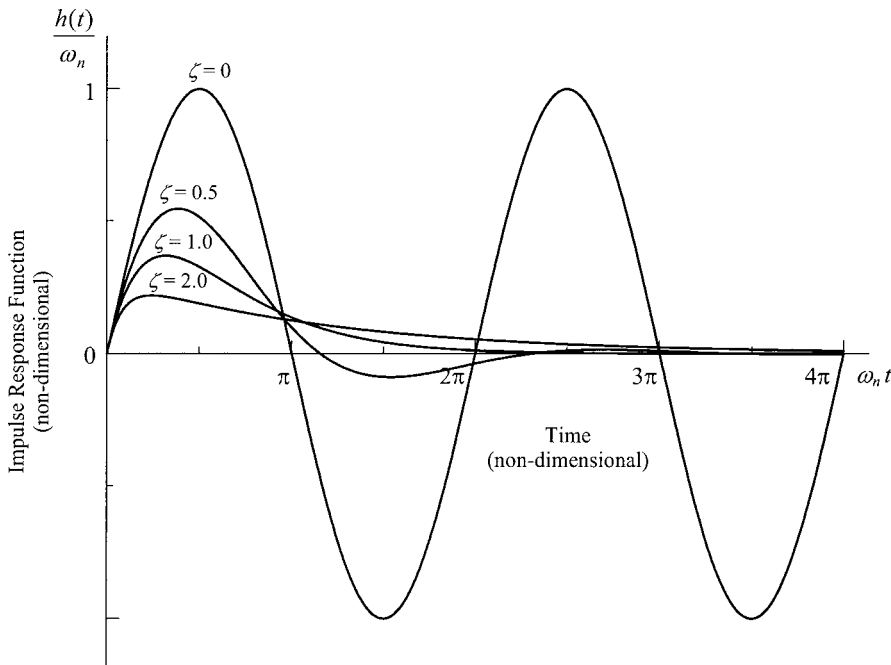


FIGURE 1.22 Impulse-response functions of a damped oscillator.

As a result, the next lower derivative becomes finite (nonzero) at $t = 0^+$. The remaining lower derivatives maintain their zero values at that instant. When an impulse is applied to the system given by Equation 1.100, for example, the acceleration $\ddot{y}(t)$ becomes infinity, and the velocity $\dot{y}(t)$ takes a nonzero (finite) value shortly after its application ($t = 0^+$). The displacement $y(t)$, however, would not have sufficient time to change at $t = 0^+$. The impulse input is therefore equivalent to a velocity initial condition, in this case. This initial condition is determined by using the integrated version (Equation 1.101) of the system (Equation 1.100), as has been done.

The impulse-response functions given by Equations 1.103 are plotted in Figure 1.22 for some representative values of the damping ratio. It should be noted that for $0 < \zeta < 1$ the angular frequency of damped vibrations is ω_d , the *damped natural frequency*, which is smaller than the *undamped natural frequency* ω_n .

1.6.3.3 Step Response

A unit-step excitation is defined by

$$u(t) = \begin{cases} 1 & \text{for } t > 0 \\ 0 & \text{for } t \leq 0 \end{cases} \quad (1.104)$$

Unit-impulse excitation $\delta(t)$ may be interpreted as the time derivative of $u(t)$,

$$\delta(t) = \frac{du(t)}{dt} \quad (1.105)$$

Note that Equation 1.105 re-establishes the fact that for a nondimensional $u(t)$, the dimension of $\delta(t)$ is $(\text{time})^{-1}$. Then, since a unit step is the integral of a unit impulse, the step response can be obtained directly as the integral of the impulse response; thus,

$$y_{\text{step}}(t) = \int_0^t h(\tau) d\tau \quad (1.106)$$

This result also follows from the convolution integral (Equation 1.97g) because, for a delayed unit step, we have

$$u(t - \tau) = \begin{cases} 1 & \text{for } \tau < t \\ 0 & \text{for } \tau \geq t \end{cases} \quad (1.107)$$

Thus, by integrating Equations 1.103 with zero initial conditions, the following results are obtained for step response:

$$y_{\text{step}}(t) = 1 - \frac{1}{\sqrt{1 - \zeta^2}} \exp(-\zeta \omega_n t) \sin(\omega_d t + \phi) \quad \text{for } \zeta < 1 \quad (1.108a)$$

$$y_{\text{step}} = 1 - \frac{1}{2\sqrt{1 - \zeta^2} \omega_n} [\lambda_1 \exp \lambda_2 t - \lambda_2 \exp \lambda_1 t] \quad \text{for } \zeta > 1 \quad (1.108b)$$

$$y_{\text{step}} = 1 - (\omega_n t + 1) \exp(-\omega_n t) \quad \text{for } \zeta = 1 \quad (1.108c)$$

with

$$\cos \phi = \zeta \quad (1.109)$$

The step responses given by Equations 1.108 are plotted in Figure 1.23 for several values of damping ratio.

Note that, since a step input does not cause the highest derivative of the system equation to approach infinity at $t = 0^+$, the initial conditions that are required to solve the system equation remain unchanged at $t = 0^+$, provided that there are no derivative terms on the input side of the system equation. If there are derivative terms in the input, then, for example, a step can become an impulse and the situation changes.

Now, the response of the system in Figure 1.21, when subjected to a unit step of support excitation (see Equation 1.99), is obtained by using the principle of superposition, as the sum of the unit-step

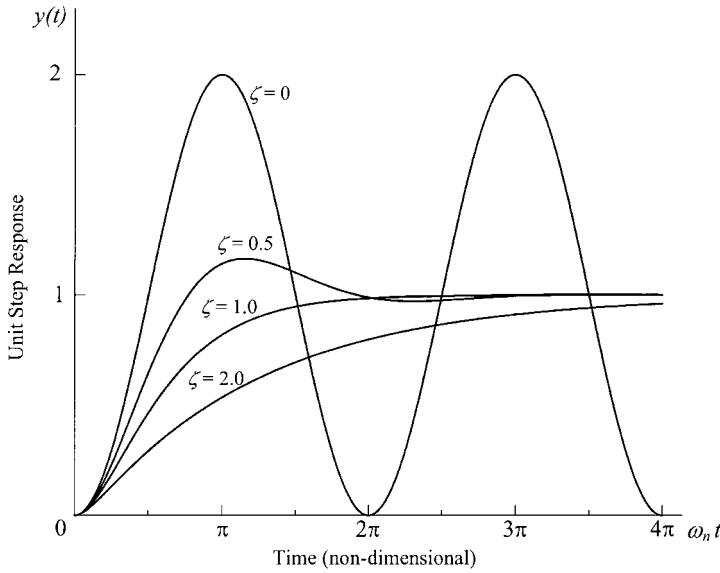


FIGURE 1.23 Unit-step response of a damped simple oscillator.

response and $(2\zeta/\omega_n)$ times the unit-impulse response of Equation 1.100. Thus, from Equation 1.103 and Equation 1.108, we obtain the step response of the system in Figure 1.21 as

$$y(t) = 1 - \frac{\exp(-\zeta\omega_n t)}{\sqrt{1-\zeta^2}} [\sin(\omega_d t + \phi) - 2\zeta \sin \omega_d t] \quad \text{for } \zeta < 1 \quad (1.110a)$$

$$y(t) = 1 + \frac{1}{2\sqrt{1-\zeta^2}\omega_n} [\lambda_2 \exp \lambda_2 t - \lambda_1 \exp \lambda_1 t] \quad \text{for } \zeta > 1 \quad (1.110b)$$

$$y(t) = 1 + (\omega_n t - 1)\exp(-\omega_n t) \quad \text{for } \zeta = 1 \quad (1.110c)$$

1.6.3.4 Liebnitz's Rule

The time derivative of an integral whose limits of integration are also functions of time may be obtained using Liebnitz's rule. It is expressed as

$$\frac{d}{dt} \int_{a(t)}^{b(t)} f(\tau, t) d\tau = f[b(t), t] \frac{db(t)}{dt} - f[a(t), t] \frac{da(t)}{dt} + \int_{a(t)}^{b(t)} \frac{\partial f}{\partial t}(\tau, t) d\tau \quad (1.111)$$

By repeated application of Liebnitz's rule to Equation 1.97g, we can determine the i th derivative of the response variable; thus,

$$\begin{aligned} \frac{d^i y(t)}{dt^i} = & \left[h(t) + \frac{dh(t)}{dt} + \cdots + \frac{d^{i-1}h(t)}{dt^{i-1}} \right] u(0) + \left[h(t) + \frac{dh(t)}{dt} + \cdots + \frac{d^{i-2}h(t)}{dt^{i-2}} \right] \frac{du(0)}{dt} \\ & + \cdots + h(t) \frac{d^{i-1}u(0)}{dt^{i-1}} + \int_0^t h(\tau) \frac{d^i u(t-\tau)}{dt^i} d\tau \end{aligned} \quad (1.112)$$

From this result, it follows that the zero-state response to input $[d^i u(t)]/dt^i$ is $[d^i y(t)]/dt^i$, provided that all lower-order derivatives of $u(t)$ vanish at $t = 0$. This result verifies the fact that, for instance, the first derivative of the unit-step response gives the impulse-response function.

It should be emphasized that the convolution integral (Equation 1.97) gives the forced response of a system, assuming that the initial conditions are zero. For nonzero initial conditions, the homogeneous

solution (e.g., Equation 1.54 or Equation 1.58) should be added to this zero-initial-condition response and then the unknown constants should be evaluated by using the initial conditions. Care should be exercised in the situation in which there is an initial velocity in the system and to this an impulsive excitation is applied. In this case, one approach would be to first determine the velocity at $t = 0^+$ by adding to the initial velocity at $t = 0^-$, the velocity change in the system due to the impulse. The initial displacement will not change, however, due to the impulse. Once the initial conditions at $t = 0^+$ are determined in this manner, the complete solution can be obtained as usual.

Bibliography

- Benaroya, H. 1998. *Mechanical Vibration*, Prentice Hall, Upper Saddle River, NJ.
- Crandall, S.H., Karnopp, D.C., Kurtz, E.F., and Prodmore-Brown, D.C. 1968. *Dynamics of Mechanical and Electromechanical Systems*, McGraw-Hill, New York.
- den Hartog, J.P. 1956. *Mechanical Vibrations*, McGraw-Hill, New York.
- de Silva, C.W. 2000. *VIBRATION—Fundamentals and Practice*, CRC Press, Boca Raton, FL.
- de Silva, C.W. 2004. *MECHATRONICS—An Integrated Approach*, CRC Press, Boca Raton, FL.
- Dimarogonas, A. 1996. *Vibration for Engineers*, 2nd ed., Prentice Hall, Upper Saddle River, NJ.
- Inman, D.J. 1996. *Engineering Vibration*, Prentice Hall, Englewood Cliffs, NJ.
- Irwin, J.D. and Graf, E.R. 1979. *Industrial Noise and Vibration Control*, Prentice Hall, Englewood Cliffs, NJ.
- Meirovitch, L. 1986. *Elements of Vibration Analysis*, 2nd ed., McGraw-Hill, New York.
- Rao, S.S. 1995. *Mechanical Vibrations*, 3rd ed., Addison-Wesley, Reading, MA.
- Shearer, J.L. and Kulakowski, B.T. 1990. *Dynamic Modeling and Control of Engineering Systems*, MacMillan, New York.
- Shearer, J.L., Murphy, A.T., and Richardson, H.H. 1971. *Introduction to System Dynamics*, Addison-Wesley, Reading, MA.
- Steidel, R.F. 1979. *An Introduction to Mechanical Vibrations*, 2nd ed., Wiley, New York.
- Thomson, W.T. and Dahleh, M.D. 1998. *Theory of Vibration with Applications*, 5th ed., Prentice Hall, Upper Saddle River, NJ.
- Volterra, E. and Zachmanoglou, E.C. 1965. *Dynamics of Vibrations*, Charles E. Merrill Books, Columbus, OH.

2

Frequency-Domain Analysis

2.1	Introduction	2-1
2.2	Response to Harmonic Excitations	2-2
	Response Characteristics • Measurement of Damping Ratio (Q-Factor Method)	
2.3	Transform Techniques	2-14
	Transfer Function • Frequency-Response Function (Frequency Transfer Function)	
2.4	Mechanical Impedance Approach	2-25
	Interconnection Laws	
2.5	Transmissibility Functions	2-31
	Force Transmissibility • Motion Transmissibility • General Case • Peak Values of Frequency-Response Functions	
2.6	Receptance Method	2-37
	Application of Receptance	
	Appendix 2A Transform Techniques	2-40

Clarence W. de Silva

The University of British Columbia

Summary

This chapter presents the frequency-domain analysis of mechanical vibrating systems. In the frequency domain, the independent variable is frequency. The response of a vibrating system to harmonic excitations under various levels of damping (overdamped, underdamped, and critically damped) is analyzed. Frequency transfer function techniques including impedance, mobility, force transmissibility, motion transmissibility, and receptance are studied. Transform techniques (Fourier and Laplace) are applicable in the frequency-domain analysis. The Q-factor method of measuring damping is derived. Component interconnection laws are established for frequency-domain analysis. The emphasis is on single-degree-of-freedom (single-DoF) systems.

2.1 Introduction

In many vibration problems, the primary excitation force typically has a repetitive periodic nature, and in some cases this periodic forcing function may be even purely sinusoidal. Examples are excitations due to mass eccentricity and misalignments in rotational components, tooth meshing in gears, and electromagnetic devices excited by AC or periodic electrical signals. In basic terms, the frequency-response of a dynamic system is the response to a pure sinusoidal excitation. As the amplitude and the frequency of the excitation are changed, the response also changes. In this manner, the response of the system over a range of excitation frequencies can be determined. This represents the frequency response. In this case, frequency (ω) is the independent variable and hence we are dealing with the *frequency domain*.

Frequency-domain considerations are applicable even when the signals are not periodic. In fact, a time signal can be transformed into its frequency spectrum through the Fourier transform. For a given time signal, an equivalent Fourier spectrum, which contains all the frequency (sinusoidal) components of the signal, can be determined either analytically or computationally. Hence, a time-domain representation and analysis has an equivalent frequency-domain representation and analysis, at least for linear dynamic systems. For this reason, and also because of the periodic nature of typical vibration signals, frequency-response analysis is extremely useful in the subject of mechanical vibrations. The response to a particular form of “excitation” is what is considered in the frequency-domain analysis. Hence, we are specifically dealing with the subject of “forced response” analysis, albeit in the frequency domain.

2.2 Response to Harmonic Excitations

Consider a simple oscillator with an excitation force $f(t)$, as shown in Figure 2.1.

The equation of motion is given by

$$m\ddot{x} + b\dot{x} + kx = f(t) \quad (2.1)$$

Suppose that $f(t)$ is sinusoidal (i.e., harmonic). Pick the time reference such that

$$f(t) = f_0 \cos \omega t \quad (2.2)$$

where

ω = excitation frequency

f_0 = forcing excitation amplitude

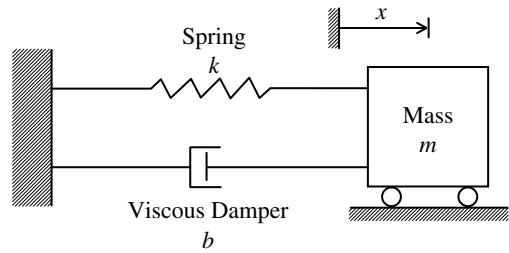


FIGURE 2.1 A forced simple oscillator.

For a system subjected to a forcing excitation, we have

$$\begin{aligned} \text{Total Response} &= \text{Homogeneous Response } x_h + \text{Particular Response } x_p \\ &\quad \begin{matrix} T \\ \text{(Natural Response)} \end{matrix} \quad \begin{matrix} H \\ \text{(Enforced Response)} \end{matrix} \\ &= \text{Free Response} \quad + \quad \text{Forced Response} \\ &\quad \begin{matrix} X \\ \text{(Depends only on initial conditions)} \\ \text{does not contain enforced response} \\ \text{and depends entirely on the} \\ \text{natural/homogeneous response} \end{matrix} \quad \begin{matrix} F \\ \text{(Depends only on } f_0) \\ \text{but contains a natural/homogeneous component} \end{matrix} \end{aligned}$$

Using these concepts, we analyze the forced problem, which may be written as

$$\ddot{x} + \frac{b}{m}\dot{x} + \frac{k}{m}x = \frac{f_0}{m} \cos \omega t = u(t) \quad (2.3)$$

or

$$\ddot{x} + 2\zeta\omega_n\dot{x} + \omega_n^2x = a \cos \omega t = u(t) \quad (2.4)$$

where $u(t)$ is the modified excitation. Also,

ω_n = undamped natural frequency

ζ = damping ratio

The total response is given by

$$x = x_h + x_p \quad (2.5)$$

with

$$x_h = C_1 e^{\lambda_1 t} + C_2 e^{\lambda_2 t} \quad (2.6)$$

The particular solution x_p , by definition, is one solution that satisfies Equation 2.4. It should be intuitively clear that this will be of the form

$$x_p = a_1 \cos \omega t + a_2 \sin \omega t \text{ \{except for the case: } \zeta = 0 \text{ and } \omega = \omega_n \text{\}} \quad (2.7)$$

where the constants a_1 and a_2 are determined by substituting Equation 2.7 into the system Equation 2.4 and equating the like coefficient. This is known as the method of undetermined coefficients.

We will consider several important cases.

2.2.1 Response Characteristics

Case 1: Undamped oscillator with excitation frequency \neq natural frequency

We have

$$\ddot{x} + \omega_n^2 x = a \cos \omega t \quad \text{with } \omega \neq \omega_n \quad (2.8)$$

Homogeneous solution:

$$x_h = A_1 \cos \omega_n t + A_2 \sin \omega_n t \quad (2.9)$$

Particular solution:

$$x_p = \frac{a}{(\omega_n^2 - \omega^2)} \cos \omega t \quad (2.10)$$

It can be easily verified that x_p given by Equation 2.10 satisfies the forced system Equation 2.4, with $\zeta = 0$. Hence, it is a particular solution.

Complete solution:

$$x = \underbrace{A_1 \cos \omega_n t + A_2 \sin \omega_n t}_H + \underbrace{\frac{a}{(\omega_n^2 - \omega^2)} \cos \omega t}_P \quad (2.11)$$

Satisfies the homogeneous equation Satisfies the equation with input

Now A_1 and A_2 are determined using the initial conditions:

$$x(0) = x_0 \text{ and } \dot{x}(0) = v_0 \quad (2.12)$$

Specifically, we obtain

$$x_0 = A_1 + \frac{a}{\omega_n^2 - \omega^2} \quad (2.13a)$$

$$v_0 = A_2 \omega_n \quad (2.13b)$$

Hence, the complete response is

$$x = \underbrace{\left[x_0 - \frac{a}{(\omega_n^2 - \omega^2)} \right] \cos \omega_n t + \frac{v_0}{\omega_n} \sin \omega_n t}_{\substack{H \\ \text{Homogeneous solution}}} + \underbrace{\frac{a}{\omega_n^2 - \omega^2} \cos \omega t}_{\substack{P \\ \text{Particular solution}}} \quad (2.14a)$$

$$= \underbrace{x_0 \cos \omega_n t + \frac{v_0}{\omega_n} \sin \omega_n t}_{\substack{X \\ \text{Free response} \\ \text{(depends only on initial conditions)} \\ \text{comes from } x_h \\ \text{*Sinusoidal at } \omega_n}} + \underbrace{\frac{a}{(\omega_n^2 - \omega^2)} \frac{[\cos \omega t - \cos \omega_n t]}{2 \sin \frac{(\omega_n + \omega)}{2} t \sin \frac{(\omega_n - \omega)}{2} t}}_{\substack{F \\ \text{Forced response (depends on input)} \\ \text{comes from both } x_h \text{ and } x_p \\ \text{*Will exhibit a beat phenomenon for } \omega_n - \omega; \text{ i.e.,} \\ \text{ } (\omega_n + \omega)/2 \text{ wave modulated by } (\omega_n - \omega)/2 \text{ wave}}} \quad (2.14b)$$

This is a stable response in the sense of bounded-input bounded-output (BIBO) stability, as it is bounded and does not increase steadily.

Note: If there is no forcing excitation, the homogeneous solution H and the free response X will be identical. With a forcing input, the natural response (the homogeneous solution) will be influenced by it in general, as is clear from Equation 2.14b.

Case 2: Undamped oscillator with $\omega = \omega_n$ (resonant condition)

In this case, the x_p that was used before is no longer valid. This is the degenerate case, because otherwise the particular solution cannot be distinguished from the homogeneous solution and the former will be completely absorbed into the latter. Instead, in view of the “double-integration” nature of the forced system equation when $\omega = \omega_n$, we use the particular solution (P):

$$x_p = \frac{at}{2\omega} \sin \omega t \quad (2.15)$$

This choice of particular solution is strictly justified by the fact that it satisfies the forced system equation.

Complete solution:

$$x = A_1 \cos \omega t + A_2 \sin \omega t + \frac{at}{2\omega} \sin \omega t \quad (2.16)$$

Initial conditions:

$$x(0) = x_0 \text{ and } \dot{x}(0) = v_0.$$

We obtain

$$x_0 = A_1 \quad (2.17a)$$

$$v_0 = \omega A_2 \quad (2.17b)$$

The total response is

$$x = \underbrace{x_0 \cos \omega t + \frac{v_0}{\omega} \sin \omega t}_{\substack{X \\ \text{Free response (depends on initial conditions)} \\ \text{*Sinusoidal at } \omega}} + \underbrace{\frac{at}{2\omega} \sin \omega t}_{\substack{F \\ \text{Forced response (depends on input)} \\ \text{*Amplitude increases linearly}}} \quad (2.18)$$

Since the forced response increases steadily, this is an *unstable* response in the BIBO sense. Furthermore, the homogeneous solution H and the free response X are identical, and the particular solution P is identical to the forced response F in this case.

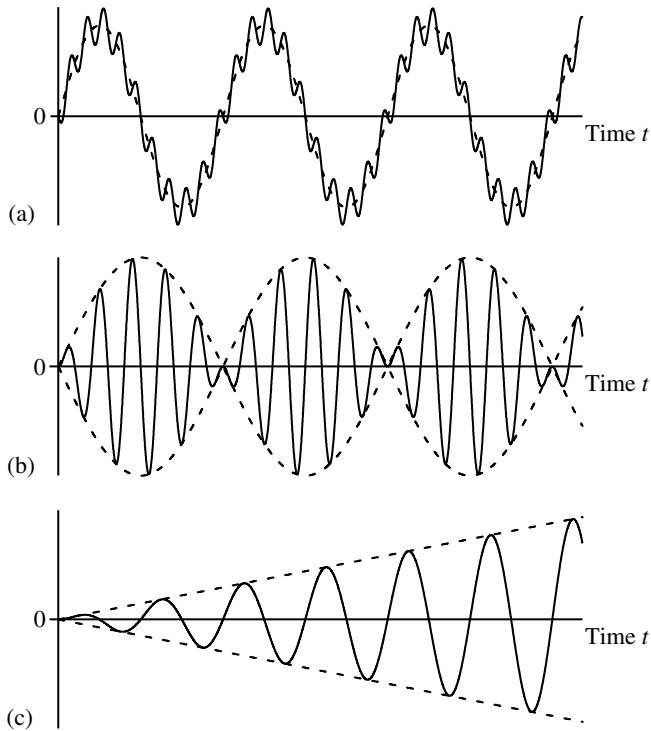


FIGURE 2.2 Forced response of a harmonically excited undamped simple oscillator: (a) for a large frequency difference; (b) for a small frequency difference (beat phenomenon); (c) response at resonance.

Note that the same system (undamped oscillator) gives a bounded response for some excitations, while producing an unstable (steady linear increase) response when the excitation frequency is equal to its natural frequency. Hence, the system is not quite unstable, but is not quite stable either. In fact, the undamped oscillator is said to be marginally stable. When the excitation frequency is equal to the natural frequency it is reasonable for the system to respond in a complementary and steadily increasing manner because this corresponds to the most “receptive” excitation. Specifically, in this case, the excitation complements the natural response of the system. In other words, the system is “in resonance” with the excitation, and the condition is called a resonance. We will address this aspect for the more general case of a damped oscillator, in the sequel.

Figure 2.2 shows typical forced responses of an undamped oscillator when there is a large difference between the excitation and the natural frequencies (Case 1); a small difference between the excitation and the natural frequencies when a beat phenomenon is clearly manifested (also Case 1); and for the resonant case (Case 2).

Case 3: Damped oscillator

The equation of forced motion is

$$\ddot{x} + 2\zeta\omega_n\dot{x} + \omega_n^2x = a \cos \omega t \quad (2.19)$$

Particular Solution (Method 1):

Since derivatives of both odd order and even order are present in this equation, the particular solution should have terms corresponding to odd and even derivatives of the

forcing function (i.e., $\sin \omega t$ and $\cos \omega t$). Hence, the appropriate particular solution will be of the form:

$$x_p = a_1 \cos \omega t + a_2 \sin \omega t \quad (2.20)$$

Substitute Equation 2.20 into Equation 2.19. We obtain

$$-\omega^2 a_1 \cos \omega t - \omega^2 a_2 \sin \omega t + 2\zeta\omega_n[-\omega a_1 \sin \omega t + \omega a_2 \cos \omega t] + \omega_n^2[a_1 \cos \omega t + a_2 \sin \omega t] = a \cos \omega t$$

Equate like coefficients:

$$-\omega^2 a_1 + 2\zeta\omega_n \omega a_2 + \omega_n^2 a_1 = a$$

$$-\omega^2 a_2 - 2\zeta\omega_n \omega a_1 + \omega_n^2 a_2 = 0$$

Hence, we have

$$(\omega_n^2 - \omega^2)a_1 + 2\zeta\omega_n \omega a_2 = a \quad (2.21a)$$

$$-2\zeta\omega_n \omega a_1 + (\omega_n^2 - \omega^2)a_2 = 0 \quad (2.21b)$$

This can be written in the matrix–vector form:

$$\begin{bmatrix} (\omega_n^2 - \omega^2) & 2\zeta\omega_n \omega \\ -2\zeta\omega_n \omega & (\omega_n^2 - \omega^2) \end{bmatrix} \begin{bmatrix} a_1 \\ a_2 \end{bmatrix} = \begin{bmatrix} a \\ 0 \end{bmatrix} \quad (2.21c)$$

The solution is

$$\begin{bmatrix} a_1 \\ a_2 \end{bmatrix} = \frac{1}{D} \begin{bmatrix} (\omega_n^2 - \omega^2) & -2\zeta\omega_n \omega \\ 2\zeta\omega_n \omega & (\omega_n^2 - \omega^2) \end{bmatrix} \begin{bmatrix} a \\ 0 \end{bmatrix} \quad (2.22)$$

with the determinant

$$D = (\omega_n^2 - \omega^2)^2 + (2\zeta\omega_n \omega)^2 \quad (2.23)$$

On simplification, we obtain

$$a_1 = \frac{(\omega_n^2 - \omega^2)}{D} a \quad (2.24a)$$

$$a_2 = \frac{2\zeta\omega_n \omega}{D} a \quad (2.24b)$$

This is the method of undetermined coefficients.

Particular Solution (Method 2): Complex Function Method

Consider

$$\ddot{x} + 2\zeta\omega_n \dot{x} + \omega_n^2 x = a e^{j\omega t} \quad (2.25)$$

where the excitation is complex. (Note: $e^{j\omega t} = \cos \omega t + j \sin \omega t$.)

The resulting complex particular solution is

$$x_p = X(j\omega) e^{j\omega t} \quad (2.26)$$

Note that we should take the real part of this solution as the true particular solution.

First substitute Equation 2.26 into Equation 2.25:

$$X[-\omega^2 + 2\zeta\omega_n j\omega + \omega_n^2] e^{j\omega t} = a e^{j\omega t}$$

Hence, since $e^{j\omega t} \neq 0$ in general,

$$X = \frac{a}{[-\omega^2 + 2\zeta\omega_n j\omega + \omega_n^2]} \quad (2.27)$$

The characteristic polynomial of the system is

$$\Delta(\lambda) = \lambda^2 + 2\zeta\omega_n\lambda + \omega_n^2 \quad (2.28a)$$

or, with the Laplace variable s ,

$$\Delta(s) = s^2 + 2\zeta\omega_n s + \omega_n^2 \quad (2.28b)$$

If we set $s = j\omega$, we have

$$\Delta(j\omega) = -\omega^2 + 2\zeta\omega_n j\omega + \omega_n^2 \quad (2.28c)$$

Note that Equation 2.28c is the denominator of Equation 2.27. Hence, Equation 2.27 can be written as

$$X = \frac{a}{\Delta(j\omega)} \quad (2.29)$$

It follows from Equation 2.26 that the complex particular solution is

$$x_p = \frac{a}{\Delta(j\omega)} e^{j\omega t} \quad (2.30)$$

Next let

$$\Delta(j\omega) = |\Delta| e^{j\phi} \quad (2.31)$$

Then, by substituting Equation 2.31 in Equation 2.30, we obtain

$$x_p = \frac{a}{|\Delta|} e^{j(\omega t - \phi)} \quad (2.32)$$

where it is clear from Equation 2.31 that

$$|\Delta| = \text{magnitude of } \Delta(j\omega)$$

$$\phi = \text{phase angle of } \Delta(j\omega)$$

The actual real particular solution is the real part of Equation 2.32 and is given by

$$x_p = \frac{a}{|\Delta|} \cos(\omega t - \phi) \quad (2.33)$$

It can easily be verified that this result is identical to what was obtained previously by Method 1, as given by Equation 2.20 together with Equations 2.23 and 2.24.

In passing, we will note here that the frequency-domain transfer function (i.e., response and excitation in the frequency domain) of the system Equation 2.19 is:

$$G(j\omega) = \frac{1}{\Delta} = \left[\frac{1}{s^2 + 2\zeta\omega_n s + \omega_n^2} \right]_{s=j\omega} \quad (2.34)$$

This frequency transfer function (also known as the frequency-response function) is obtained from the Laplace transfer function $G(s)$ by setting $s = j\omega$. We will discuss this aspect in more detail later.

The particular section (P) is equal to the steady-state solution, because the homogeneous solution dies out due to damping.

The particular solution (Equation 2.33) has the following characteristics:

1. The frequency is the same as the excitation frequency ω .
2. The amplitude is amplified by the magnitude $1/|\Delta| = |G(j\omega)|$.

3. The response is “lagged” by the phase angle ϕ of Δ (or “led” by the phase angle of $G(j\omega)$, denoted by $\angle G(j\omega)$).
4. Since the homogeneous solution of a stable system decays to zero, the particular solution is also the *steady-state* solution.

Resonance

The amplification ($|G(j\omega)| = 1/|\Delta|$) is maximum (i.e., resonance) when $|\Delta|$ is a minimum or $|\Delta|^2$ is a minimum. As noted earlier, this condition of peak amplification of a system when excited by a sinusoidal input is called resonance and the associated frequency of excitation is called resonant frequency. We can determine the resonance of the system (Equation 2.19) as follows:

Equation 2.28c is $\Delta = \omega_n^2 - \omega^2 + 2\zeta\omega_n\omega j$

Hence,

$$|\Delta|^2 = (\omega_n^2 - \omega^2)^2 + (2\zeta\omega_n\omega)^2 = D \quad (2.35)$$

The resonance corresponds to a minimum value of D , or

$$\frac{dD}{d\omega} = 2(\omega_n^2 - \omega^2)(-2\omega) + 2(2\zeta\omega_n)^2\omega = 0 \quad \text{For a minimum.} \quad (2.36)$$

Hence, with straightforward algebra, the required condition for resonance is

$$-\omega_n^2 + \omega^2 + 2\zeta^2\omega_n^2 = 0$$

or

$$\omega^2 = (1 - 2\zeta^2)\omega_n^2$$

or

$$\omega = \sqrt{1 - 2\zeta^2}\omega_n$$

This is the resonant frequency, and is denoted as

$$\omega_r = \sqrt{1 - 2\zeta^2}\omega_n \quad (2.37)$$

Note that $\omega_r \leq \omega_d \leq \omega_n$, where ω_d is the damped natural frequency given by $\omega_d = \sqrt{1 - \zeta^2}\omega_n$. These three frequencies (resonant frequency, damped natural frequency, and undamped natural frequency) are almost equal for small ζ (i.e., for light damping).

The magnitude and the phase angle plots of $G(j\omega)$ are shown in [Figure 2.3](#). These curves correspond to the amplification and the phase change of the particular response (the steady-state response) with respect to the excitation input. This pair, the magnitude and phase angle plots of a transfer function with respect to frequency, is termed a Bode plot. Usually, logarithmic scales are used for both magnitude (e.g., decibels) and frequency (e.g., decades). In summary, the steady-state response of a linear system to a sinusoidal excitation is completely determined by the frequency transfer function of the system. The total response is determined by adding H to P and substituting initial conditions, as usual.

For an undamped oscillator ($\zeta = 0$), we notice from Equation 2.34 that the magnitude of $G(j\omega)$ becomes infinity when the excitation frequency is equal to the natural frequency (ω_n) of the oscillator. This frequency (ω_n) is clearly the resonant frequency (as well as natural frequency) of the oscillator. This fact has been further supported by the nature of the corresponding time response (see Equation 2.18 and [Figure 2.2\(c\)](#)), which grows (linearly) with time.

2.2.2 Measurement of Damping Ratio (Q-Factor Method)

The frequency transfer function of a simple oscillator (Equation 2.19) may be used to determine the damping ratio. This frequency-domain method is also termed the *half-power* point method, for reasons that should become clear from the following development.

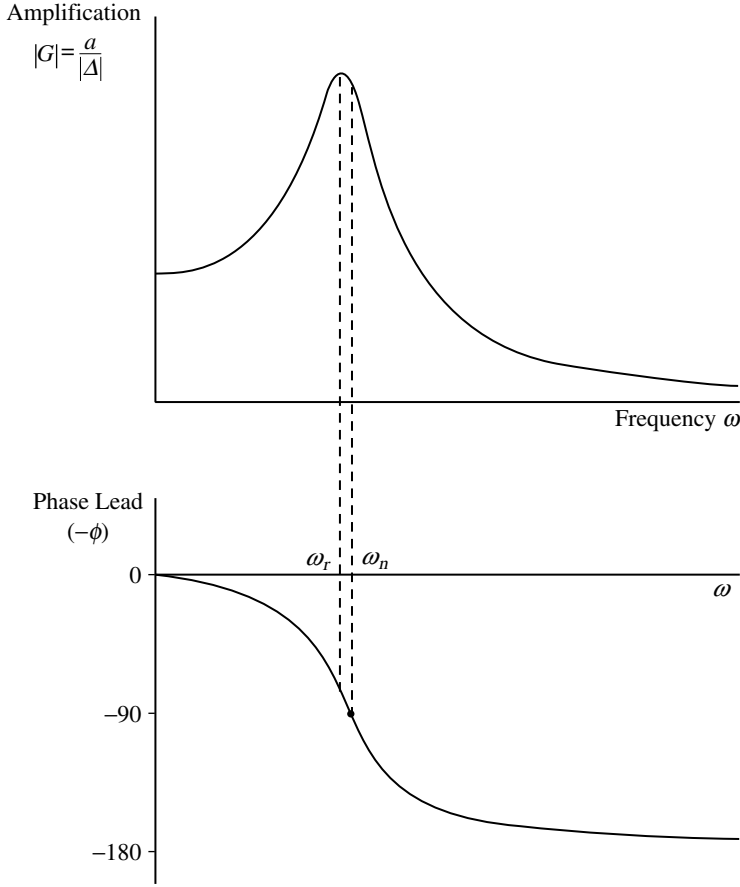


FIGURE 2.3 Magnitude and phase angle curves of a simple oscillator (A Bode plot).

First we assume that $\zeta < 1/\sqrt{2}$. Strictly speaking, we should assume that $\zeta < 1/2\sqrt{2}$.

Without loss of generality, consider the normalized (or, non-dimensionalized) transfer function

$$G(j\omega) = \left[\frac{\omega_n^2}{s^2 + 2\zeta\omega_n s + \omega_n^2} \right]_{s=j\omega} = \frac{\omega_n^2}{\omega_n^2 - \omega^2 + 2\zeta\omega_n j\omega} \quad (2.38)$$

As noted before, the transfer function $G(s)$, where s is the Laplace variable, can be converted into the corresponding frequency transfer function simply by setting $s = j\omega$. Its value at the undamped natural frequency is

$$G(j\omega)|_{\omega=\omega_n} = \frac{1}{2\zeta j} \quad (2.39a)$$

Hence, the magnitude of $G(j\omega)$ (amplification) at $\omega = \omega_n$ is

$$|G(j\omega)|_{\omega=\omega_n} = \frac{1}{2\zeta} \quad (2.39b)$$

For small ζ we have $\omega_r \cong \omega_n$. Hence, $1/2\zeta$ is approximately the peak magnitude at resonance (the resonant peak). The actual peak is slightly larger.

It is clear from Equation 2.39a that the phase angle of $G(j\omega)$ at $\omega = \omega_n$ is $-\pi/2$.

When power is half of the peak power value (e.g., because the displacement squared is proportional to potential energy), then the velocity squared is proportional to kinetic energy, and power is the rate of

change of energy. Therefore, when the amplification is $1/\sqrt{2}$ of the peak value we have half-power points, given by:

$$\frac{1}{\sqrt{2}} \frac{1}{2\zeta} = \left| \frac{\omega_n^2}{\omega_n^2 - \omega^2 + 2j\zeta\omega_n\omega} \right| = \left| \frac{1}{1 - \left(\frac{\omega}{\omega_n}\right)^2 + 2j\zeta\left(\frac{\omega}{\omega_n}\right)} \right| \quad (2.40)$$

Square Equation 2.40:

$$\frac{1}{2 \times 4\zeta^2} = \frac{1}{\left[1 - \left(\frac{\omega}{\omega_n}\right)^2\right]^2 + 4\zeta^2\left(\frac{\omega}{\omega_n}\right)^2}$$

Hence,

$$\left(\frac{\omega}{\omega_n}\right)^4 - 2\left(\frac{\omega}{\omega_n}\right)^2 + 1 + 4\zeta^2\left(\frac{\omega}{\omega_n}\right)^2 = 8\zeta^2$$

or

$$\left(\frac{\omega}{\omega_n}\right)^4 - 2(1 - 2\zeta^2)\left(\frac{\omega}{\omega_n}\right)^2 + \underbrace{(1 - 8\zeta^2)}_{>0} = 0 \quad (2.41)$$

Now assume that $\zeta^2 < 1/8$ or $\zeta < 1/2\sqrt{2}$. Otherwise, we will not obtain two positive roots for $(\omega/\omega_n)^2$. Solve for $(\omega/\omega_n)^2$, which will give two roots ω_1^2 and ω_2^2 for ω^2 . Next, assume $\omega_2^2 > \omega_1^2$. Compare $(\omega^2 - \omega_1^2)(\omega^2 - \omega_2^2) = 0$ with Equation 2.41.

Sum of roots:

$$\frac{\omega_2^2 + \omega_1^2}{\omega_n^2} = 2(1 - 2\zeta^2) \quad (2.42)$$

Product of roots:

$$\frac{\omega_2^2 \omega_1^2}{\omega_n^4} = (1 - 8\zeta^2) \quad (2.43)$$

Hence,

$$\begin{aligned} \left(\frac{\omega_2 - \omega_1}{\omega_n}\right)^2 &= \left(\frac{\omega_2^2 + \omega_1^2 - 2\omega_2\omega_1}{\omega_n^2}\right) = 2(1 - 2\zeta^2) - 2\sqrt{1 - 8\zeta^2} \\ &= 2 - 4\zeta^2 - 2\left[1 - \frac{1}{2} \times 8\zeta^2 + O(\zeta^4)\right] \\ &\cong 2 - 4\zeta^2 - 2 + 8\zeta^2 \quad \{\text{because } O(\zeta^4) \rightarrow 0 \text{ for small } \zeta\} \\ &\cong 4\zeta^2 \end{aligned}$$

or

$$\frac{\omega_2 - \omega_1}{\omega_n} \cong 2\zeta$$

Hence, the damping ratio

$$\zeta \cong \frac{(\omega_2 - \omega_1)}{2\omega_n} = \frac{\Delta\omega}{2\omega_n} \cong \frac{\omega_2 - \omega_1}{\omega_2 + \omega_1} \quad (2.44)$$

It follows that, once the magnitude of the frequency-response function $G(j\omega)$ is experimentally determined, the damping ratio can be estimated from Equation 2.44, as illustrated in [Figure 2.4](#).

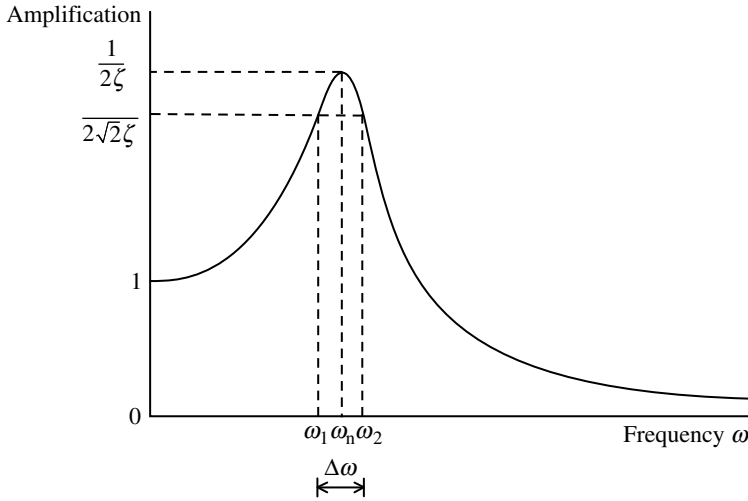


FIGURE 2.4 The Q-factor method of damping measurement.

The Q-factor, which measures the sharpness of resonant peak, is defined by

$$\text{Q-factor} = \frac{\omega_n}{\Delta\omega} = \frac{1}{2\zeta} \quad (2.45)$$

The term originated from the field of electrical tuning circuits where a sharp resonant peak is a desirable thing (*quality factor*). Some useful results on the frequency-response of a simple oscillator are summarized in Box 2.1.

Example 2.1

A dynamic model of a fluid coupling system is shown in Figure 2.5. The fluid coupler is represented by a rotatory viscous damper with damping constant b . It is connected to a rotatory load of moment of inertia J , restrained by a torsional spring of stiffness k , as shown. We now obtain the frequency transfer function of the system that relates the restraining torque τ of the spring to the angular displacement excitation $\alpha(t)$ that is applied at the free end of the fluid coupler. If $\alpha(t) = \alpha_0 \sin \omega t$, what is the magnitude (i.e., amplitude) of τ at steady state?

Solution

Newton's Second Law gives

$$J\ddot{\theta} = b(\dot{\alpha} - \dot{\theta}) - k\theta$$

Hence,

$$J\ddot{\theta} + b\dot{\theta} + k\theta = b\dot{\alpha} \quad (i)$$

Motion transfer function is

$$\frac{\theta}{\alpha} = \frac{bs}{Js^2 + bs + k} \quad (ii)$$

Note that the frequency transfer function is obtained simply by setting $s = j\omega$.

The restraining torque of the spring is $\tau = k\theta$. Hence,

$$\frac{\tau}{\alpha} = \frac{k\theta}{\alpha} = \frac{kbs}{Js^2 + bs + k} = G(s) \quad (iii)$$

Box 2.1

HARMONIC RESPONSE OF A SIMPLE OSCILLATOR

Undamped Oscillator:

$$\ddot{x} + \omega_n^2 x = a \cos \omega t; \quad x(0) = x_0, \quad \dot{x}(0) = v_0$$

$$x = \underbrace{x_0 \cos \omega_n t + \frac{v_0}{\omega_n} \sin \omega_n t}_X + \underbrace{\frac{a}{\omega_n^2 - \omega^2} [\cos \omega t - \cos \omega_n t]}_F \quad \text{for } \omega \neq \omega_n$$

$$x = \text{Same } X + \frac{at}{2\omega} \sin \omega t \quad \text{for } \omega = \omega_n \text{ (resonance)}$$

Damped Oscillator:

$$\ddot{x} + 2\zeta\omega_n\dot{x} + \omega_n^2 x = a \cos \omega t$$

$$x = H + \underbrace{\frac{a}{|\omega_n^2 - \omega^2 + 2j\zeta\omega_n\omega|}}_P \cos(\omega t - \phi)$$

where

$$\tan \phi = \frac{2\zeta\omega_n\omega}{\omega_n^2 - \omega^2}; \quad \phi = \text{phase lag.}$$

Particular solution P is also the steady-state response.

Homogeneous solution $H = A_1 e^{\lambda_1 t} + A_2 e^{\lambda_2 t}$
 where λ_1 and λ_2 are roots of $\lambda^2 + 2\zeta\omega_n\lambda + \omega_n^2 = 0$
 (characteristic equation)

A_1 and A_2 are determined from initial conditions: $x(0) = x_0, \dot{x}(0) = v_0$

Resonant Frequency: $\omega_r = \sqrt{1 - 2\zeta^2} \omega_n$

The magnitude of P will peak at resonance.

Damping Ratio:

$$\zeta = \frac{\Delta\omega}{2\omega_n} = \frac{\omega_2 - \omega_1}{\omega_2 + \omega_1} \quad \text{for low damping}$$

where, $\Delta\omega = \text{half-power bandwidth} = \omega_2 - \omega_1$

Note: Q-factor = $\frac{\omega_n}{\Delta\omega} = \frac{1}{2\zeta}$ for low damping.

Then, the corresponding frequency-response function (frequency transfer function) is

$$G(j\omega) = \frac{k b j \omega}{(k - J \omega^2) + b j \omega} \quad (\text{iv})$$

For a harmonic excitation of

$$\alpha = \alpha_0 e^{j\omega t} \quad (\text{v})$$

we have

$$\tau = |G(j\omega)|\alpha_0 e^{(j\omega t + \phi)} \quad (\text{vi})$$

at steady state.

Here, the phase lead of τ with respect to α is

$$\begin{aligned} \phi &= \angle G(j\omega) = \angle j\omega - \angle(k - J\omega^2 + bj\omega) \\ &= \frac{\pi}{2} - \tan^{-1} \frac{b\omega}{(k - J\omega^2)} \end{aligned} \quad (\text{vii})$$

The magnitude of the restraining torque, at steady state, is

$$\begin{aligned} \tau_0 &= \alpha_0 |G(j\omega)| = \alpha_0 \frac{kb\omega}{|k - J\omega^2 + bj\omega|} \\ &= \frac{\alpha_0 kb\omega}{\sqrt{(k - J\omega^2)^2 + b^2\omega^2}} \end{aligned}$$

Hence,

$$\tau_0 = \frac{J\alpha_0\omega_n^2\omega \times 2\zeta\omega_n}{\sqrt{(\omega_n^2 - \omega^2)^2 + (2\zeta\omega_n\omega)^2}} \quad (\text{viii})$$

or

$$\tau_0 = \frac{\alpha_0 k 2\zeta\omega_n\omega}{\sqrt{(\omega_n^2 - \omega^2)^2 + (2\zeta\omega_n\omega)^2}} \quad (\text{ix})$$

with $k/J = \omega_n^2$; $b/J = 2\zeta\omega_n$; and ω_n equal to the undamped natural frequency of the load.

Now, define the normalized frequency

$$r = \frac{\omega}{\omega_n} \quad (\text{x})$$

Then, from (ix) we have

$$\tau_0 = \frac{2k\alpha_0\zeta r}{\sqrt{(1 - r^2)^2 + (2\zeta r)^2}} \quad (\text{xi})$$

For $r = 1$:

$$\tau_0 = \frac{2k\alpha_0\zeta}{2\zeta} = k\alpha_0 \quad (\text{xii})$$

This means, at resonance, the applied twist is directly transmitted to the load spring.

For small r :

$$\tau_0 = \frac{2k\alpha_0\zeta r}{1} \quad (\text{xiii})$$

which is small, and becomes zero at $r = 0$. Hence, at low frequencies, the transmitted torque is small.

For larger r :

$$\tau_0 = \frac{2k\alpha_0\zeta r}{r^2} = \frac{2k\alpha_0\zeta}{r} \quad (\text{xiv})$$

which is small and goes to zero. Hence, at high frequencies as well, the transmitted torque is small.

The variation of τ_0 with the frequency ratio r is sketched in [Figure 2.6](#).

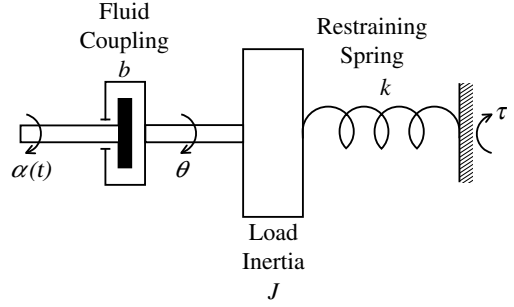


FIGURE 2.5 A fluid coupling system.

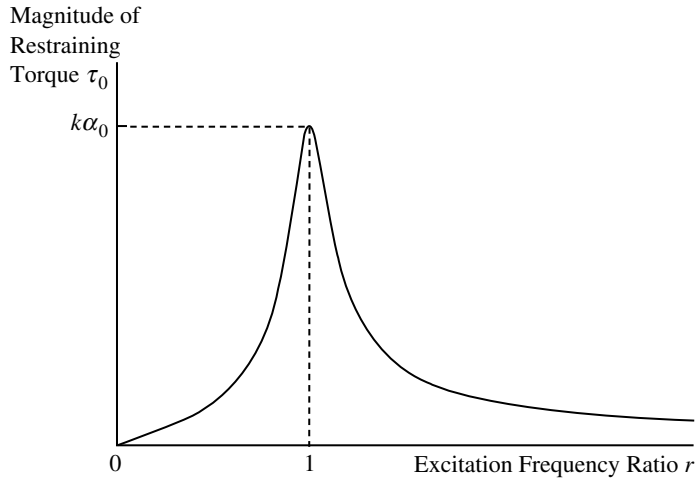


FIGURE 2.6 Variation of the steady-state transmitted torque with frequency.

2.3 Transform Techniques

Concepts of frequency-response analysis originate from the nature of the response of a dynamic system to a sinusoidal (i.e., harmonic) excitation. These concepts can be generalized because the time-domain analysis, where the independent variable is time (t), and the frequency-domain analysis, where the independent variable is frequency (ω), are linked through the Fourier transformation. Analytically, it is more general and versatile to use the Laplace transformation, where the independent variable is the Laplace variable (s) which is complex (i.e., non-real). This is true because analytical Laplace transforms may exist even for time functions that do not have “analytical” Fourier transforms. But with compatible definitions, the Fourier transform results can be obtained from the Laplace transform results simply by setting $s = j\omega$. In the present section, we will formally introduce the Laplace transformation and the Fourier transformation, and will illustrate how these techniques are useful in the response analysis of vibrating systems. The preference of one domain over another will depend on such factors as the nature of the excitation input, the type of the analytical model available, the time duration of interest, and the quantities that need to be determined.

2.3.1 Transfer Function

The Laplace transform of a piecewise-continuous function $f(t)$ is denoted here by $F(s)$ and is given by the Laplace transformation

$$F(s) = \int_0^{\infty} f(t) \exp(-st) dt \quad (2.46)$$

in which s is a complex independent variable known as the Laplace variable, expressed as

$$s = \sigma + j\omega \quad (2.47)$$

and $j = \sqrt{-1}$. Laplace transform operation is denoted as $\mathcal{L}f(t) = F(s)$. The inverse Laplace transform operation is denoted by $f(t) = \mathcal{L}^{-1}F(s)$ and is given by

$$f(t) = \frac{1}{2\pi j} \int_{\sigma-j\infty}^{\sigma+j\infty} F(s) \exp(st) ds \quad (2.48)$$

The integration is performed along a vertical line parallel to the imaginary (vertical) axis, located at σ from the origin in the complex Laplace plane (s -plane). For a given piecewise-continuous function

$f(t)$, the Laplace transform exists if the integral in Equation 2.46 converges. A sufficient condition for this is

$$\int_0^{\infty} |f(t)| \exp(-\sigma t) dt < \infty \quad (2.49)$$

Convergence is guaranteed by choosing a sufficiently large and positive σ . This property is an advantage of the Laplace transformation over the Fourier transformation. (For a more complete discussion of the Fourier transformation, see later in this chapter and in [Chapter 4](#).)

By the use of Laplace transformation, the convolution integral equation can be converted into an algebraic relationship. To illustrate this, consider the convolution integral which gives the response $y(t)$ of a dynamic system to an excitation input $u(t)$, with zero initial conditions. By definition (Equation 2.46), its Laplace transform is written as

$$Y(s) = \int_0^{\infty} \int_0^{\infty} h(\tau) u(t - \tau) d\tau \exp(-st) dt \quad (2.50)$$

Note that $h(t)$ is the impulse-response function of the system. Since the integration with respect to t is performed while keeping τ constant, we have $dt = d(t - \tau)$. Consequently,

$$Y(s) = \int_{-\tau}^{\infty} u(t - \tau) \exp[-s(t - \tau)] d(t - \tau) \int_0^{\infty} h(\tau) \exp(-s\tau) d\tau$$

The lower limit of the first integration can be made equal to zero, in view of the fact that $u(t) = 0$ for $t < 0$. Again using the definition of Laplace transformation, the foregoing relation can be expressed as

$$Y(s) = H(s)U(s) \quad (2.51)$$

in which

$$H(s) = \mathcal{L}h(t) = \int_0^{\infty} h(t) \exp(-st) dt \quad (2.52)$$

Note that, by definition, the transfer function of a system, denoted by $H(s)$, is given by Equation 2.51. More specifically, the system transfer function is given by the ratio of the Laplace-transformed output and the Laplace-transformed input, with zero initial conditions. In view of Equation 2.52, it is clear that the system transfer function can be expressed as the Laplace transform of the impulse-response function of the system. The transfer function of a linear and constant-parameter system is a unique function that completely represents the system. A physically realizable, linear, constant-parameter system possesses a unique transfer function, even if the Laplace transforms of a particular input and the corresponding output do not exist. This is clear from the fact that the transfer function is a system model and does not depend on the system input itself.

Note: The transfer function is also commonly denoted by $G(s)$. However, in the present context we use $H(s)$ in view of its relation to $h(t)$. Some useful Laplace transform relations are given in [Table 2.1](#). Also, note that the Fourier transform (set $s = j\omega$) is given by

Forward:

$$F(j\omega) = \int_0^{\infty} f(t) \exp(-j\omega t) dt$$

Inverse:

$$f(t) = \int_{-j\infty}^{j\infty} F(j\omega) \exp(j\omega t) d\omega$$

Consider the n th-order linear, constant-parameter dynamic system given by

$$a_n \frac{d^n y}{dt^n} + a_{n-1} \frac{d^{n-1} y}{dt^{n-1}} + \cdots + a_0 y = b_0 u + b_1 \frac{du(t)}{dt} + \cdots + b_m \frac{d^m u(t)}{dt^m} \quad (2.53)$$

TABLE 2.1 Important Laplace Transform Relations

$\mathcal{L}^{-1}F(s) = f(t)$	Conversion $\mathcal{L}f(t) = F(s)$
$\frac{1}{2\pi j} \int_{\sigma-j\infty}^{\sigma+j\infty} F(s) \exp(st) ds$	$\int_0^\infty f(t) \exp(-st) dt$
$k_1 f_1(t) + k_2 f_2(t)$	$k_1 F_1(s) + k_2 F_2(s)$
$\exp(-at)f(t)$	$F(s+a)$
$f(t-\tau)$	$\exp(-s\tau)F(s)$
$f^{(n)}(t) = \frac{d^n f(t)}{dt^n}$	$s^n F(s) - s^{n-1}f(0^+) - s^{n-2}f'(0^+) - \dots - f^{(n-1)}(0^+)$
$\int_{-\infty}^t f(t) dt$	$\frac{F(s)}{s} + \frac{\int_{-\infty}^0 f(t) dt}{s}$
Impulse function, $\delta(t)$	1
Step function, $\mathcal{U}(t)$	$\frac{1}{s}$
t^n	$\frac{n!}{s^{n+1}}$
$\exp(-at)$	$\frac{1}{s+a}$
$\sin \omega_n t$	$\frac{\omega_n}{s^2 + \omega_n^2}$
$\cos \omega_n t$	$\frac{s}{s^2 + \omega_n^2}$

for physically realizable systems, $m \leq n$. By applying a Laplace transformation and then integrating by parts, it may be verified that

$$\mathcal{L} \frac{d^k f(t)}{dt^k} = s^k \hat{F}(s) - s^{k-1} f(0) - s^{k-2} \frac{df(0)}{dt} - \dots + \frac{d^{k-1} f(0)}{dt^{k-1}} \tag{2.54}$$

By definition, the initial conditions are set to zero in obtaining the transfer function. This results in

$$H(s) = \frac{b_0 + b_1 s + \dots + b_m s^m}{a_0 + a_1 s + \dots + a_n s^n} \tag{2.55}$$

for $m \leq n$. Note that Equation 2.55 contains all the information that is contained in Equation 2.53. Consequently, the transfer function is an analytical model of a system. The transfer function may be employed to determine the total response of a system for a given input, even though it is defined in terms of the response under zero initial conditions. This is quite logical because the analytical model of a system is independent of the system's initial conditions.

The denominator polynomial of a transfer function is the system's *characteristic polynomial*. Its roots are the poles or the eigenvalues of the system. If all the eigenvalues have negative real parts, the system is stable. The response of a stable system is bounded (that is, remains finite) when the input is bounded (which is the BIBO stability). The zero-input response of an asymptotically stable system approaches zero with time.

2.3.2 Frequency-Response Function (Frequency Transfer Function)

The Fourier integral transform of the impulse-response function is given by

$$H(f) = \int_{-\infty}^\infty h(t) \exp(-j2\pi ft) dt \tag{2.56}$$

where f is the *cyclic frequency* (measured in cps or hertz). This is known as the frequency-response function (or frequency transfer function) of a system. The Fourier transform operation is denoted as $\mathcal{F}h(t) = H(f)$.

In view of the fact that $h(t) = 0$ for $t < 0$, the lower limit of integration in Equation 2.56 could be made zero. Then, from Equation 2.52, it is clear that $H(f)$ is obtained simply by setting $s = j2\pi f$ in $H(s)$. Hence, strictly speaking, we should use the notation $H(j2\pi f)$ and not $H(f)$. However, for notational simplicity, we denote $H(j2\pi f)$ by $H(f)$. Furthermore, since the angular frequency $\omega = 2\pi f$, we can express the frequency-response function by $H(j\omega)$, or simply by $H(\omega)$ for notational convenience. It should be noted that the frequency-response function, like the Laplace transfer function, is a complete representation of a linear, constant-parameter system. In view of the fact that both $u(t) = 0$ and $y(t) = 0$ for $t < 0$, we can write the Fourier transforms of the input and the output of a system directly by setting $s = j2\pi f = j\omega$ in the corresponding Laplace transforms. Specifically, we have, according to the notation used here

$$U(f) = U(j2\pi f) = U(j\omega)$$

and

$$Y(f) = Y(j2\pi f) = Y(j\omega).$$

Then, from Equation 2.51, we have

$$Y(f) = H(f)U(f) \quad (2.57)$$

Note: Sometimes, for notational convenience, the same lowercase letters are used to represent the Laplace and Fourier transforms as well as the original time-domain variables.

If the Fourier integral transform of a function exists, then its Laplace transform also exists. The converse is not generally true, however, because of the poor convergence of the Fourier integral in comparison to the Laplace integral. This arises from the fact that the factor $\exp(-\sigma t)$ is not present in the Fourier integral. For a physically realizable, linear, constant-parameter system, $H(f)$ exists even if $U(f)$ and $Y(f)$ do not exist for a particular input. The experimental determination of $H(f)$, however, requires system stability. For the n th-order system given by Equation 2.53, the frequency-response function is determined by setting $s = j2\pi f$ in Equation 2.55 as

$$H(f) = \frac{b_0 + b_1 j2\pi f + \cdots + b_m (j2\pi f)^m}{a_0 + a_1 j2\pi f + \cdots + a_n (j2\pi f)^n} \quad (2.58)$$

This, generally, is a complex function of f that has a magnitude denoted by $|H(f)|$ and a phase angle denoted by $\angle H(f)$.

A further interpretation of the frequency-response function can be given in view of the developments given in Section 2.2. Consider a harmonic input having cyclic frequency f , expressed by

$$u(t) = u_0 \cos 2\pi ft \quad (2.59a)$$

In analysis, it is convenient to use the complex input

$$u(t) = u_0 (\cos 2\pi ft + j \sin 2\pi ft) = u_0 \exp(j2\pi ft) \quad (2.59b)$$

and take only the real part of the final result. Note that Equation 2.59b does not implicitly satisfy the requirement of $u(t) = 0$ for $t < 0$. Therefore, an appropriate version of the convolution integral, where the limits of integration automatically account for this requirement, should be used. For instance, we can write

$$y(t) = \operatorname{Re} \left[\int_{-\infty}^t h(\tau) u_0 \exp[j2\pi f(t - \tau)] d\tau \right] \quad (2.60a)$$

or

$$y(t) = \operatorname{Re} \left[u_0 \exp(j2\pi ft) \int_{-\infty}^t h(\tau) \exp(-j2\pi f\tau) d\tau \right] \quad (2.60b)$$

in which $\operatorname{Re}[\cdot]$ denotes the real part. As $t \rightarrow \infty$, the integral term in Equation 2.60b becomes the frequency-response function $H(f)$, and the response $y(t)$ becomes the steady-state response y_{ss} . Accordingly,

$$y_{ss} = \operatorname{Re}[H(f)u_0 \exp(j2\pi ft)] \quad (2.61a)$$

or

$$y_{ss} = u_0 |H(f)| \cos(2\pi ft + \phi) \quad (2.61b)$$

for a harmonic excitation, in which the phase lead angle $\phi = \angle H(f)$. It follows from Equation 2.61b that, when a harmonic excitation is applied to a stable, linear, constant-parameter dynamic system having frequency-response function $H(f)$, its steady-state response will also be harmonic at the same frequency, but with an amplification factor of $|H(f)|$ in its amplitude and a phase lead of $\angle H(f)$. This result has been established previously, in Section 2.2. Consequently, the frequency-response function of a stable system can be experimentally determined using a sine-sweep test or a sine-dwell test. With these methods, a harmonic excitation is applied as the system input, and the amplification factor and the phase-lead angle in the corresponding response are determined at steady state. The frequency of excitation is varied continuously for a sine sweep and in steps for a sine dwell. The sweep rate should be slow enough, and the dwell times should be long enough, to guarantee steady-state conditions at the output. The pair of plots of $|H(f)|$ and $\angle H(f)$ against f completely represent the complex frequency-response function, and are Bode plots or Bode diagrams, as noted earlier. In Bode plots, logarithmic scales are normally used for both frequency f and magnitude $|H(f)|$.

Impulse Response

The impulse-response function of a system can be obtained by taking the inverse Laplace transform of the system transfer function. For example, consider the damped simple oscillator given by the normalized transfer function:

$$H(s) = \frac{\omega_n^2}{s^2 + 2\zeta\omega_n s + \omega_n^2} \quad (2.62)$$

The characteristic equation of this system is given by

$$s^2 + 2\zeta\omega_n s + \omega_n^2 = 0 \quad (2.63)$$

The eigenvalues (poles) are given by its roots. Three possible cases exist, as given below.

Case 1: ($\zeta < 1$)

This is the case of complex eigenvalues λ_1 and λ_2 . Since the coefficients of the characteristic equation are real, the complex roots should occur in conjugate pairs. Hence,

$$\lambda_1, \lambda_2 = -\zeta\omega_n \pm j\omega_d \quad (2.64)$$

in which

$$\omega_d = \sqrt{1 - \zeta^2} \omega_n \quad (2.65)$$

is the damped natural frequency.

Case 2: ($\zeta > 1$)

This case corresponds to real and unequal eigenvalues,

$$\lambda_1, \lambda_2 = -\zeta\omega_n \pm \sqrt{\zeta^2 - 1} \omega_n = -a, -b \quad (2.66)$$

with $a \neq b$, in which

$$ab = \omega_n^2 \quad (2.67)$$

and

$$a + b = 2\zeta\omega_n \quad (2.68)$$

Case 3: ($\zeta = 1$)

In this case, the eigenvalues are real and equal:

$$\lambda_1 = \lambda_2 = -\omega_n \quad (2.69)$$

In all three cases, the real parts of the eigenvalues are negative. Consequently, these second-order systems of a damped simple oscillator are always stable.

The impulse-response functions $h(t)$ corresponding to these three cases are determined by taking the inverse Laplace transform (Table 2.1) of Equation 2.62 for $\zeta < 1$, $\zeta > 1$, and $\zeta = 1$, respectively. The following results are obtained:

$$y_{\text{impulse}}(t) = h(t) = \frac{\omega_n}{\sqrt{1 - \zeta^2}} \exp(-\zeta\omega_n t) \sin \omega_d t \quad \text{for } \zeta < 1 \quad (2.70a)$$

$$y_{\text{impulse}}(t) = h(t) = \frac{ab}{(b - a)} [\exp(-at) - \exp(-bt)] \quad \text{for } \zeta > 1 \quad (2.70b)$$

$$y_{\text{impulse}}(t) = h(t) = \omega_n^2 t \exp(-\omega_n t) \quad \text{for } \zeta = 1 \quad (2.70c)$$

Step Response

Unit-step function is defined by

$$\mathcal{U}(t) = \begin{cases} 1 & \text{for } t > 0 \\ 0 & \text{for } t \leq 0 \end{cases} \quad (2.71)$$

Unit-impulse function $\delta(t)$ may be interpreted as the time derivative of $\mathcal{U}(t)$; thus,

$$\delta(t) = \frac{d\mathcal{U}(t)}{dt} \quad (2.72)$$

Note that Equation 2.72 re-establishes the fact that for non-dimensional $\mathcal{U}(t)$, the dimension of $\delta(t)$ is $(\text{time})^{-1}$. Since $\mathcal{L}\mathcal{U}(t) = 1/s$ (see Table 2.1), the unit-step response of the dynamic system (Equation 2.62) can be obtained by taking the inverse Laplace transform of

$$Y_{\text{step}}(s) = \frac{1}{s} \frac{\omega_n^2}{(s^2 + 2\zeta\omega_n s + \omega_n^2)} \quad (2.73)$$

which follows from Equation 2.73.

To facilitate using Table 2.1, partial fractions of Equation 2.73 are determined in the form

$$\frac{a_1}{s} + \frac{a_2 + a_3 s}{(s^2 + 2\zeta\omega_n s + \omega_n^2)}$$

in which the constants a_1 , a_2 , and a_3 are determined by comparing the numerator polynomial; thus,

$$\omega_n^2 = a_1(s^2 + 2\zeta\omega_n s + \omega_n^2) + s(a_2 + a_3 s)$$

Then $a_1 = 1$, $a_2 = -2\zeta\omega_n$, and $a_3 = 1$.

The following results are obtained:

$$y_{\text{step}}(t) = 1 - \frac{1}{\sqrt{1 - \zeta^2}} \exp(-\zeta\omega_n t) \sin(\omega_d t + \phi) \quad \text{for } \zeta < 1 \quad (2.74a)$$

$$y_{\text{step}} = 1 - \frac{1}{(b - a)} [b \exp(-at) - a \exp(-bt)] \quad \text{for } \zeta > 1 \quad (2.74b)$$

$$y_{\text{step}} = 1 - (\omega_n t + 1) \exp(-\omega_n t) \quad \text{for } \zeta = 1 \quad (2.74c)$$

In Equation 2.74c,

$$\cos \phi = \zeta \quad (2.75)$$

Transfer Function Matrix

Consider the state-space model of a linear dynamic system as given by

$$\dot{\mathbf{x}} = \mathbf{A}\mathbf{x} + \mathbf{B}\mathbf{u} \quad (2.76a)$$

$$\mathbf{y} = \mathbf{C}\mathbf{x} + \mathbf{D}\mathbf{u} \quad (2.76b)$$

where, \mathbf{x} = the n th order state vector, \mathbf{u} = the r th order input vector, \mathbf{y} = the m th order output vector, \mathbf{A} = the system matrix, \mathbf{B} = the input gain matrix, \mathbf{C} = the output (measurement) gain matrix, and \mathbf{D} = the feedforward gain matrix. We can express the input–output relation between u and y , in the Laplace domain, by a transfer function matrix of the order $m \times r$.

To obtain this relation, let us Laplace transform the Equations 2.76a and 2.76b and use zero initial conditions for \mathbf{x} ; thus,

$$s\mathbf{X}(s) = \mathbf{A}\mathbf{X}(s) + \mathbf{B}\mathbf{U}(s) \quad (2.77a)$$

$$\mathbf{Y}(s) = \mathbf{C}\mathbf{X}(s) + \mathbf{D}\mathbf{U}(s) \quad (2.77b)$$

From Equation 2.77a it follows that,

$$\mathbf{X}(s) = (s\mathbf{I} - \mathbf{A})^{-1}\mathbf{B} + \mathbf{U}(s) \quad (2.78)$$

in which \mathbf{I} is the n th order identity matrix. By substituting Equation 2.78 into Equation 2.77b, we obtain the transfer relation

$$\mathbf{Y}(s) = [\mathbf{C}(s\mathbf{I} - \mathbf{A})^{-1}\mathbf{B} + \mathbf{D}]\mathbf{U}(s) \quad (2.79a)$$

or

$$\mathbf{Y}(s) = \mathbf{G}(s)\mathbf{U}(s) \quad (2.79b)$$

The transfer-function matrix $\mathbf{G}(s)$ is an $m \times r$ matrix given by

$$\mathbf{G}(s) = \mathbf{C}(s\mathbf{I} - \mathbf{A})^{-1}\mathbf{B} + \mathbf{D} \quad (2.80)$$

In practical systems with dynamic delay, the excitation $u(t)$ is not fed forward into the response y . Consequently, $\mathbf{D} = 0$ for systems that we normally encounter. For such systems

$$\mathbf{G}(s) = \mathbf{C}(s\mathbf{I} - \mathbf{A})^{-1}\mathbf{B} \quad (2.81)$$

Several examples are given now to illustrate the approaches of obtaining transfer function models when the time domain differential equation models are given, and to indicate some uses of a transfer function model. Some useful results in the frequency domain are summarized in Box 2.2.

Example 2.2

Consider the simple oscillator equation given by

$$m\ddot{y} + b\dot{y} + ky = ku(t) \quad (i)$$

Note that $u(t)$ can be interpreted as a displacement input (e.g., support motion) or $ku(t)$ can be interpreted as the input force applied to the mass. Take the Laplace transform of the system equation (i) with zero initial conditions; thus,

$$(ms^2 + bs + k)Y(s) = kU(s) \quad (ii)$$

The corresponding transfer function is

$$G(s) = \frac{Y(s)}{U(s)} = \frac{k}{ms^2 + bs + k} \quad (iii)$$

Box 2.2

USEFUL FREQUENCY-DOMAIN RESULTS

Laplace Transform (\mathcal{L}):

$$F(s) = \int_0^{\infty} f(t) \exp(-st) dt$$

Fourier Transform (\mathcal{F}):

$$F(j\omega) = \int_{-\infty}^{\infty} f(t) \exp(-j\omega t) dt$$

Note: May use $F(\omega)$ to denote $F(j\omega)$

Note: Set $s = j\omega = j2\pi f$ to convert Laplace results into Fourier results.

ω = angular frequency (rad/sec)

f = cyclic frequency (cps or Hz)

Transfer function $H(s)$ = output/input in Laplace domain, with zero initial conditions.

Frequency transfer function (or frequency-response function) = $H(j\omega)$

Note: Notation $(G(s))$ is also used to denote a system transfer function

Note:

$$H(s) = \mathcal{L}h(t)$$

$h(t)$ = impulse-response function = response to a unit impulse input.

Frequency response:

$$Y(j\omega) = H(j\omega)U(j\omega)$$

where

$U(j\omega)$ = Fourier spectrum of input $u(t)$

$Y(j\omega)$ = Fourier spectrum of output $y(t)$

Note:

$|H(j\omega)|$ = response amplification for a harmonic excitation of frequency ω

$\angle H(j\omega)$ = response phase “lead” for a harmonic excitation

Multivariable Systems:

State-Space Model:

$$\dot{\mathbf{x}} = \mathbf{Ax} + \mathbf{Bu}$$

$$\mathbf{y} = \mathbf{Cx} + \mathbf{Du}$$

Transfer-Matrix Model:

$$\mathbf{Y}(s) = \mathbf{G}(s)\mathbf{U}(s)$$

where

$$\mathbf{G}(s) = \mathbf{C}(s\mathbf{I} - \mathbf{A})^{-1}\mathbf{B} + \mathbf{D}$$

or, in terms of the undamped natural frequency ω_n and the damping ratio ζ , where $\omega_n^2 = k/m$ and $2\zeta\omega_n = b/m$, the transfer function is given by

$$G(s) = \frac{\omega_n^2}{s^2 + 2\zeta\omega_n s + \omega_n^2} \quad (\text{iv})$$

This is the transfer function corresponding to the displacement output. It follows that the output velocity transfer function is

$$\frac{sY(s)}{U(s)} = sG(s) = \frac{s\omega_n^2}{s^2 + 2\zeta\omega_n s + \omega_n^2} \quad (\text{v})$$

and the output acceleration transfer function is

$$\frac{s^2 Y(s)}{U(s)} = s^2 G(s) = \frac{s^2 \omega_n^2}{s^2 + 2\zeta\omega_n s + \omega_n^2} \quad (\text{vi})$$

In the output acceleration transfer function, we have $m = n = 2$. This means that if the acceleration of the mass that is caused by an applied force is measured, the input (applied force) is instantly felt by the acceleration. This corresponds to a feedforward action of the input excitation or a lack of dynamic delay. For example, this is the primary mechanism through which road disturbances are felt inside a vehicle that has very hard suspension.

Example 2.3

Again let us consider the simple oscillator differential equation

$$\ddot{y} + 2\zeta\omega_n \dot{y} + \omega_n^2 y = \omega_n^2 u(t) \quad (\text{i})$$

By defining the state variables as

$$\mathbf{x} = [x_1, x_2]^T = [y, \dot{y}]^T \quad (\text{ii})$$

a state model for this system can be expressed as

$$\dot{\mathbf{x}} = \begin{bmatrix} 0 & 1 \\ -\omega_n^2 & -2\zeta\omega_n \end{bmatrix} \mathbf{x} + \begin{bmatrix} 0 \\ \omega_n^2 \end{bmatrix} u(t) \quad (\text{iii})$$

If we consider both displacement and velocity as outputs, we have

$$\mathbf{y} = \mathbf{x} \quad (\text{iv})$$

Note that the output gain matrix \mathbf{C} is the identity matrix in this case. From Equation 2.79b and Equation 2.81 it follows that:

$$\mathbf{Y}(s) = \begin{bmatrix} s & -1 \\ \omega_n^2 & s + 2\zeta\omega_n \end{bmatrix}^{-1} \begin{bmatrix} 0 \\ \omega_n^2 \end{bmatrix} U(s) \quad (\text{v})$$

$$\mathbf{Y}(s) = \frac{1}{[s^2 + 2\zeta\omega_n s + \omega_n^2]} \begin{bmatrix} s + 2\zeta\omega_n & 1 \\ -\omega_n^2 & s \end{bmatrix} \begin{bmatrix} 0 \\ \omega_n^2 \end{bmatrix} U(s)$$

$$\mathbf{Y}(s) = \frac{1}{[s^2 + 2\zeta\omega_n s + \omega_n^2]} \begin{bmatrix} \omega_n^2 \\ s\omega_n^2 \end{bmatrix} U(s) \quad (\text{vi})$$

The transfer function matrix is

$$\mathbf{G}(s) = \begin{bmatrix} \omega_n^2/\Delta(s) \\ s\omega_n^2/\Delta(s) \end{bmatrix} \quad (\text{vii})$$

in which $\Delta(s) = s^2 + 2\zeta\omega_n s + \omega_n^2$ is the characteristic polynomial of the system. The first element in the only column in $G(s)$ is the displacement-response transfer function and the second element is the velocity-response transfer function. These results agree with the expressions obtained in the previous example.

Now, let us consider the acceleration \ddot{y} as an output and denote it by y_3 . It is clear from the system equation (i) that

$$y_3 = \ddot{y} = -2\zeta\omega_n \dot{y} - \omega_n^2 y + \omega_n^2 u(t) \quad (\text{viii})$$

or, in terms of the state variables,

$$y_3 = -2\zeta\omega_n x_2 - \omega_n^2 x_1 + \omega_n^2 u(t) \quad (\text{ix})$$

Note that this output explicitly contains the input variable. The feedforward situation implies that the matrix \mathbf{D} is non-zero for the output y_3 . Now,

$$Y_3(s) = -2\zeta\omega_n X_2(s) - \omega_n^2 X_1(s) + \omega_n^2 U(s) = -2\zeta\omega_n \frac{s\omega_n^2}{\Delta(s)} U(s) - \omega_n^2 \frac{\omega_n^2}{\Delta(s)} U(s) + \omega_n^2 U(s)$$

which simplifies to

$$Y_3(s) = \frac{s^2 \omega_n^2}{\Delta(s)} U(s) \quad (\text{x})$$

This again confirms the result for the acceleration output transfer function that was obtained in the previous example.

Example 2.4

- Briefly explain an approach that you could use to measure the resonant frequency of a mechanical system. Do you expect this measured frequency to depend on whether displacement, velocity, or acceleration is used as the response variable? Justify your answer.
- A vibration test setup is schematically shown in Figure 2.7.

In this experiment, a mechanical load is excited by a linear motor and its acceleration response is measured by an accelerometer and charge amplifier combination. The force applied to the load by the linear motor is also measured, using a force sensor (strain-gauge type). The frequency-response function acceleration/force is determined from the sensor signals, using a spectrum analyzer.

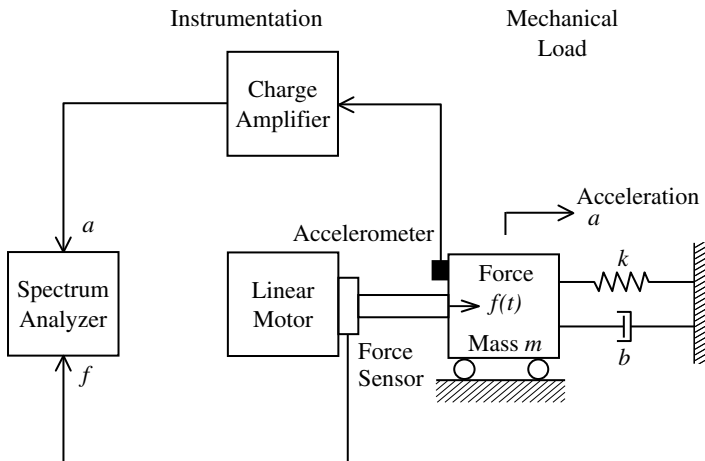


FIGURE 2.7 Measurement of the acceleration spectrum of a mechanical system.

Suppose that the mechanical load is approximated by a damped oscillator with mass m , stiffness k , and damping constant b , as shown in Figure 2.7. If the force applied to this load is $f(t)$ and the displacement in the same direction is y , show that the equation of motion of the system is given by

$$m\ddot{y} + b\dot{y} + ky = f(t)$$

Obtain an expression for the acceleration frequency-response function $G(j\omega)$ in the frequency domain, with excitation frequency ω as the independent variable. Note that the applied force f is the excitation input and the acceleration a of the mass is the response, in this case.

Express $G(j\omega)$ in terms of (normalized) frequency ratio $r = \omega/\omega_n$, where ω_n is the undamped natural frequency.

Giving all the necessary steps, determine an expression for r at which the acceleration frequency-response function will exhibit a resonant peak. What is the corresponding peak magnitude of $|G|$?

For what range of values of damping ratio ζ would such a resonant peak be possible?

Solution

- (a) For a single DoF system, apply a sinusoidal forcing excitation at the DoF and measure the displacement response at the same location. Vary the excitation frequency ω in small steps, and for each frequency at steady state determine the amplitude ratio of the (displacement response/forcing excitation). The peak amplitude ratio will correspond to the resonance. For a multi-DoF system, several tests may be needed, with excitations applied at different locations of freedom and the response measured at various locations as well (see Chapters 10 and 11). In the frequency domain we have,

$$|\text{Velocity response spectrum}| = \omega x |\text{Displacement response spectrum}|$$

$$|\text{Acceleration response spectrum}| = \omega x |\text{Velocity response spectrum}|$$

It follows that the shape of the frequency-response function will depend on whether the displacement, velocity, or acceleration is used as the response variable. Hence it is likely that the frequency at which the peak amplification occurs (i.e., resonance) will also depend on the type of response variable that is used.

- (b) A free-body diagram of the mass element is shown in Figure 2.8.

Newton's Second Law gives

$$m\ddot{y} = f(t) - b\dot{y} - ky \quad (\text{i})$$

Hence, the equation of motion is

$$m\ddot{y} + b\dot{y} + ky = f(t) \quad (\text{ii})$$

The displacement transfer function is

$$\frac{y}{f} = \frac{1}{(ms^2 + bs + k)} \quad (\text{iii})$$

Note that, for notational convenience, the same lowercase letters are used to represent the Laplace transforms as well as the original time-domain variables (y and f). The acceleration transfer function is obtained by multiplying Equation iii by s^2 . (From Table 2.1, the Laplace transform of d/dt is s , with zero initial conditions). Hence

$$\frac{a}{f} = \frac{s^2}{(ms^2 + bs + k)} = G(s) \quad (\text{iv})$$

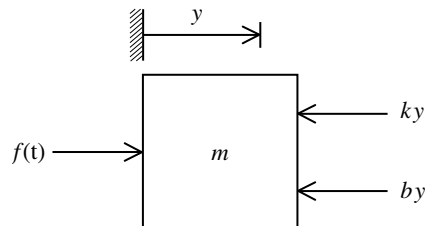


FIGURE 2.8 Free-body diagram.

In the frequency domain, the corresponding frequency-response function is obtained by substituting $j\omega$ for s . Hence,

$$G(j\omega) = \frac{-\omega^2}{(-m\omega^2 + bj\omega + k)} \quad (\text{v})$$

Divide throughout by m and use $b/m = 2\zeta\omega_n$ and $k/m = \omega_n^2$, where ω_n = undamped natural frequency and ζ = damping ratio.

Then,

$$G(j\omega) = \frac{-\omega^2/m}{(\omega_n^2 - \omega^2 + 2j\zeta\omega_n\omega)} = \frac{-r^2/m}{1 - r^2 + 2j\zeta rr} \quad (\text{vi})$$

where $r = \omega/\omega_n$. The magnitude of $G(j\omega)$ gives the amplification of the acceleration signal with respect to the forcing excitation:

$$|G(j\omega)| = \frac{r^2/m}{\sqrt{(1 - r^2)^2 + (2\zeta r)^2}} \quad (\text{vii})$$

Its peak value corresponds to the peak value of

$$p(r) = \frac{r^4}{(1 - r^2)^2 + (2\zeta r)^2} \quad (\text{viii})$$

and gives the resonance. This occurs when $dp/dr = 0$. Hence,

$$[(1 - r^2)^2 + (2\zeta r)^2]4r^3 - r^4[2(1 - r^2)(-2r) + 8\zeta^2 r] = 0$$

The solution is

$$r = 0 \quad \text{or} \quad [(1 - r^2)^2 + 4\zeta^2 r^2] + r^2[1 - r^2 - 2\zeta^2] = 0$$

The first result ($r = 0$) corresponds to static conditions and is ignored. Hence, the resonant peak occurs when

$$(1 - r^2)^2 + 4\zeta^2 r^2 + r^2 - r^4 - 2\zeta^2 r^2 = 0$$

which has the valid root

$$r = \frac{1}{\sqrt{1 - 2\zeta^2}} \quad (\text{ix})$$

Note that r has to be real and positive. It follows that, for a resonance to occur we need

$$0 < \zeta < \frac{1}{\sqrt{2}}$$

Substitute in (vii), the resonant value of r , to obtain

$$|G|_{\text{peak}} = \frac{\frac{1}{m(1 - 2\zeta^2)}}{\sqrt{\left(1 - \frac{1}{1 - 2\zeta^2}\right)^2 + \frac{4\zeta^2}{1 - 2\zeta^2}}}$$

or

$$|G|_{\text{peak}} = \frac{1}{2m\zeta\sqrt{1 - \zeta^2}} \quad (\text{x})$$

2.4 Mechanical Impedance Approach

Any type of force or motion variable may be used as input and output variables in defining a system transfer function. In vibration studies, three particular choices are widely used. The corresponding

frequency transfer functions are named impedance functions, mobility functions, and transmissibility functions. These are described in the present section and in the subsequent section, and their use is illustrated.

Through variables (force) and across variables (velocity), when expressed in the frequency domain (as Fourier spectra), are used in defining the two important frequency transfer functions: mechanical impedance and mobility. In the case of impedance functions, velocity is considered the input variable and the force is the output variable; whereas in the case of mobility functions, the converse applies. Specifically,

$$M = \frac{1}{Z} \quad (2.82)$$

It is clear that mobility (M) is the inverse of impedance (Z). Either transfer function may be used in a given problem. One can define several other versions of frequency transfer functions that might be useful in the modeling and analysis of mechanical systems. Some of the relatively common ones are listed in Table 2.2.

Note that in the frequency domain, since $\text{acceleration} = j\omega \times \text{velocity}$; and $\text{displacement} = \text{velocity}/(j\omega)$, the alternative types of transfer functions as defined in Table 2.2, are related to mechanical impedance and mobility through a factor of $j\omega$; specifically,

$$\begin{aligned} \text{dynamic inertia} &= \text{force/acceleration} = \text{impedance}/(j\omega) \\ \text{acceleration} &= \text{acceleration/force} = \text{mobility} \times (j\omega) \\ \text{dynamic stiffness} &= \text{force/displacement} = \text{impedance} \times j\omega \\ \text{receptance} &= \text{displacement} = \text{mobility}/(j\omega) \end{aligned}$$

In these definitions, the variable (force, acceleration, and displacement) should be interpreted as the corresponding Fourier spectra.

The time-domain constitutive relations for the mass, spring, and the damper elements are well known. The corresponding transfer relations are obtained by replacing the derivative operator d/dt by the Laplace operator s . The frequency transfer functions are obtained by substituting $j\omega$ or $j2\pi$ for s . These results are derived below.

Mass Element:

$$m \frac{dv}{dt} = f$$

In the frequency domain,

$$mj\omega v = f \quad \text{or} \quad \frac{f}{v} = mj\omega$$

Hence,

$$Z_m = mj\omega \quad (2.83a)$$

and

$$M_m = \frac{1}{mj\omega} \quad (2.83b)$$

TABLE 2.2 Definitions of Useful Mechanical Transfer Functions

Transfer Function	Definition (in the Frequency Domain)
Dynamic stiffness	Force/displacement
Receptance, dynamic flexibility, or compliance	Displacement/force
Impedance (Z)	Force/velocity
Mobility (M)	Velocity/force
Dynamic inertia	Force/acceleration
Accelerance	Acceleration/force
Force transmissibility (T_f)	Transmitted force/applied force
Motion transmissibility (T_m)	Transmitted velocity/applied velocity

TABLE 2.3 Impedance and Mobility Functions of Basic Mechanical Elements

Element	Frequency Transfer Function (Set $s = j\omega = j2\pi f$)		
	Impedance	Mobility	Receptance
Mass, m	$Z_m = ms$	$M_m = \frac{1}{ms}$	$R_m = \frac{1}{ms^2}$
Spring, k	$Z_k = \frac{k}{s}$	$M_k = \frac{s}{k}$	$R_k = \frac{1}{k}$
Damper, b	$Z_b = b$	$M_b = \frac{1}{b}$	$R_b = \frac{1}{bs}$

Spring Element:

$$f = kx \quad \text{or} \quad \frac{df}{dt} = kv$$

In the frequency domain,

$$j\omega f = kv \quad \text{or} \quad \frac{f}{v} = \frac{k}{j\omega}$$

Hence,

$$Z_k = \frac{k}{j\omega} \tag{2.84a}$$

and

$$M_k = \frac{j\omega}{k} \tag{2.84b}$$

Damper Element:

$$f = bv \quad \text{or} \quad \frac{f}{v} = b$$

Then,

$$Z_b = b \tag{2.85a}$$

or

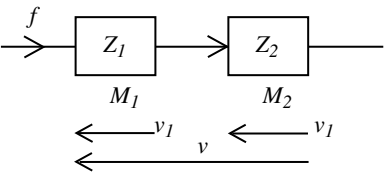
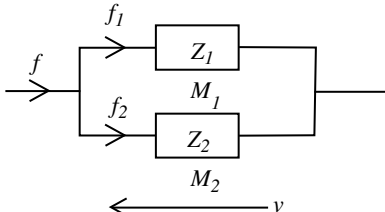
$$M_b = \frac{1}{b} \tag{2.85b}$$

These results are summarized in Table 2.3.

2.4.1 Interconnection Laws

Any general impedance element or a mobility element may be interpreted as a *two-port element* in which, under steady conditions, energy (or power) transfer into the device takes place at the *input port* and energy (or power) transfer out of the device takes place at the output port. Each port of a two-port element has a *through variable*, such as force or current, and an *across variable*, such as velocity or voltage, associated with it. Through variables are called *flux variables*, and across variable are called *potential variables*. Through variables are not always the same as *flow variables* (velocity and current). Similarly, across variables are not the same as *effort variables* (force and voltage). For example, force is an effort variable, but it is also a through variable. Similarly, velocity is a flow variable and is also an across variable. The concept of effort and flow variables is useful in giving unified definitions for electrical and mechanical impedance. However, in component interconnecting and circuit analysis, mechanical impedance is not analogous to electrical impedance. The definition of mechanical impedance is force/velocity in the frequency domain. This is a ratio of (through variable)/(across variable); whereas electrical impedance, defined as voltage/current in the frequency domain, is a ratio of

TABLE 2.4 Interconnection Laws for Impedance and Mobility

Series Connections	Parallel Connections
 <div>$v = v_1 + v_2$$\frac{v}{f} = \frac{v_1}{f} + \frac{v_2}{f}$$M = M_1 + M_2$$\frac{1}{Z} = \frac{1}{Z_1} + \frac{1}{Z_2}$</div>	 <div>$f = f_1 + f_2$$\frac{f}{v} = \frac{f_1}{v} + \frac{f_2}{v}$$Z = Z_1 + Z_2$$\frac{1}{M} = \frac{1}{M_1} + \frac{1}{M_2}$</div>

(across variable)/(through variable). Since both force and voltage are “effort” variables, and velocity and current are “flow” variables, it is then convenient to use the definition

$$\text{Impedance (electrical or mechanical)} = \frac{\text{Effort}}{\text{Flow}}$$

In other words, impedance measures how much effort is needed to drive a system at unity flow. Nevertheless, this definition does not particularly help us to analyze interconnected systems with mechanical impedance, because mechanical impedance cannot be manipulated using the rules for electrical impedance. For example, if two electric components are connected in series, the current (through variable) will be the same for both components, and the voltage (across variable) will be additive. Accordingly, the impedance of a series-connected electrical system is just the sum of the impedances of the individual components. Now consider two mechanical components connected in series. Here the force (through variable) will be the same for both components, and velocity (across variable) will be additive. Hence, it is mobility, not impedance, that is additive in the case of series-connected mechanical components. It can be concluded that, in circuit analysis, mobility behaves like electrical impedance and mechanical impedance behaves like electrical admittance. Hence, the “generalized series element” is electrical impedance or mechanical mobility, and the “generalized parallel element” is electrical admittance or mechanical impedance. The corresponding interconnection laws are summarized in Table 2.4.

Now, two examples are given to demonstrate the use of impedance and mobility methods in frequency-domain problems.

Example 2.5

Consider the simple oscillator shown in Figure 2.9(a). A schematic mechanical circuit is given in Figure 2.9(b). Note here that in this circuit, the broken line from the mass to the ground represents how the inertia force of the mass is felt by, or virtually transmitted to, the ground. This is the case because the net force that generates the acceleration in the mass (i.e., the inertia force) has to be transmitted to the ground at the reference point of the force source. This is the same reference with respect to which the velocity of the mass is expressed. If the input is the force $f(t)$, the source element is a force source. The corresponding response is the velocity v , and in this situation, the transfer function $V(f)/F(f)$ is a mobility function. On the other hand, if the input is the velocity $v(t)$, the source element is a velocity source. Then, f is the output, and the transfer function $F(f)/V(f)$ is an impedance function.

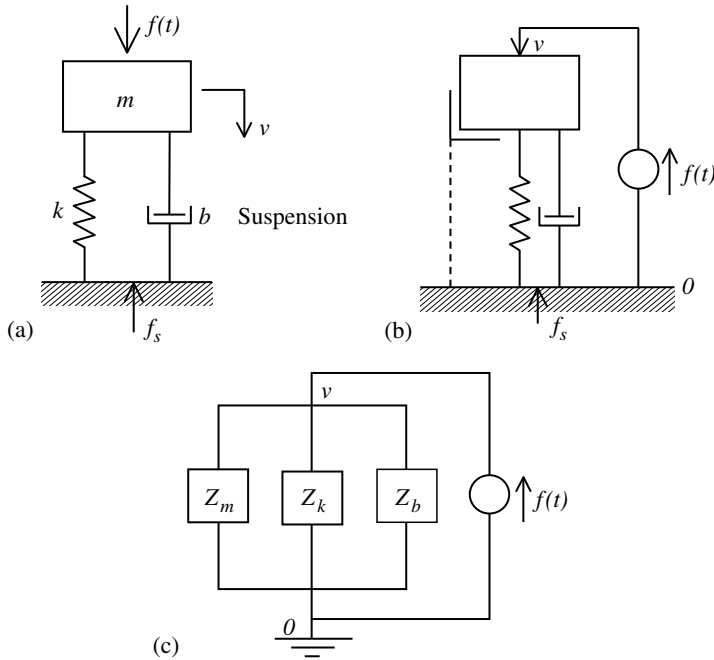


FIGURE 2.9 (a) A ground-based mechanical oscillator; (b) schematic mechanical circuit; (c) impedance circuit.

Suppose that a known forcing function is applied to this system (with zero initial conditions) using a force source, and the velocity is measured. Now, if we were to move the mass exactly at this predetermined velocity (using a velocity source), the force generated at the source will be identical to the originally applied force. In other words, mobility is the reciprocal (inverse) of impedance, as noted earlier. This reciprocity should be intuitively clear because we are dealing with the same system and same initial conditions. Owing to this property, we may use either the impedance representation or the mobility representation, depending on whether the elements are connected in parallel or in series, and irrespective of whether the input is a force or a velocity. Once the transfer function is determined in one form, its reciprocal gives the other form.

In the present example, the three elements are connected in parallel, as is clear from the mechanical circuit shown in Figure 2.9(c). Hence, the impedance representation is appropriate. The overall impedance function of the system is

$$Z(f) = \frac{F(f)}{V(f)} = Z_m + Z_k + Z_b = ms + \frac{k}{s} + b \Big|_{s=j2\pi f} = \frac{ms^2 + bs + k}{s} \Big|_{s=j2\pi f} \quad (2.86)$$

Then, the mobility function is

$$M(f) = \frac{V(f)}{F(f)} = \frac{s}{ms^2 + bs + k} \Big|_{s=j2\pi f} \quad (2.87)$$

Note that, if in fact the input is the force, the mobility function will govern the system behavior. In this case, the characteristic polynomial of the system is $s^2 + bs + k$, which corresponds to a simple oscillator, and accordingly the (dependent) velocity response of the system would be governed by this. If, on the other hand, the input is the velocity, the impedance function will govern the system behavior. The characteristic polynomial of the system, in this case, is s , which corresponds to a simple integrator. The (dependent) force response of the system would be governed by an integrator-type behavior. To explore

this behavior further, suppose that the velocity source has a constant value. The inertia force will be zero. The damping force will be constant. The spring force will increase linearly. Hence, the net force will have an integration (linearly increasing) effect. If the velocity source provides a linearly increasing velocity (constant acceleration), the inertia force will be constant, the damping force will increase linearly, and the spring force will increase quadratically.

Example 2.6

Consider the system shown in Figure 2.10(a). In this example, the motion of the mass, m , is not associated with an external force. The support motion, v , however, is associated with a force, f .

The schematic mechanical circuit representation shown in Figure 2.10(b), and the corresponding impedance circuit shown in Figure 2.10(c), indicate that the spring and the damper are connected in parallel and that the mass is connected in series with this pair. By impedance addition for parallel elements and mobility addition for series elements, it follows that the mobility function is

$$\frac{V(f)}{F(f)} = M_m + \frac{1}{(Z_k + Z_b)} = \frac{1}{ms} + \frac{1}{(k/s + b)} \Big|_{s=j2\pi f} = \frac{ms^2 + bs + k}{ms(bs + k)} \Big|_{s=j2\pi f} \quad (2.88)$$

It follows that, when the support force is the input (force source) and the support velocity is the output, the system characteristic polynomial is $ms(bs + k)$, which is known to be inherently unstable due to the presence of a free integrator, and has a non-oscillatory transient response.

The impedance function that corresponds to support velocity input (velocity source) is the reciprocal of the previous mobility function; thus,

$$\frac{F(f)}{V(f)} = \frac{ms(bs + k)}{ms^2 + bs + k} \Big|_{s=j2\pi f} \quad (2.89)$$

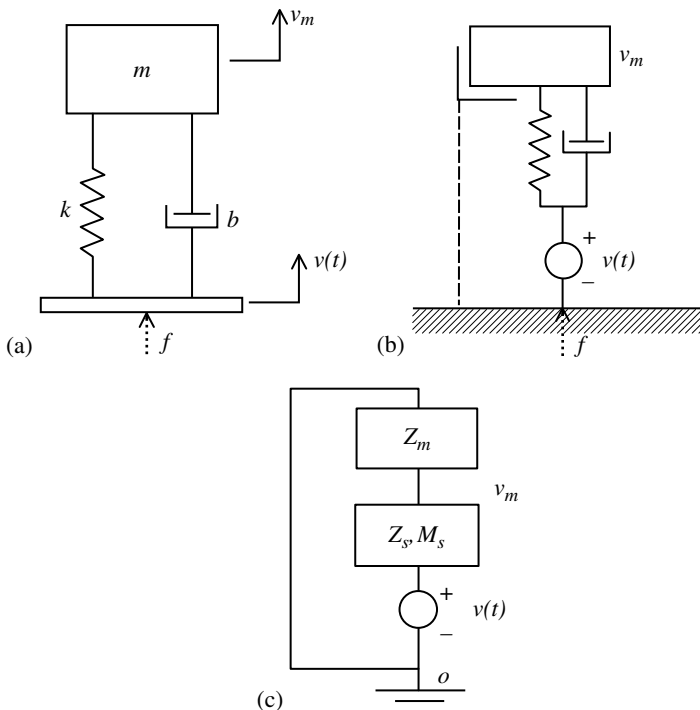


FIGURE 2.10 (a) An oscillator with support motion; (b) schematic mechanical circuit; (c) impedance circuit.

and

$$\frac{V_m(f)}{F(f)} = \frac{1}{ms} \Big|_{s=j2\pi f} \quad (2.90)$$

The resulting impedance function $F(f)/V_m(f)$ is not admissible and is physically non-realizable because V_m cannot be an input as there is no associated force. This is confirmed by the fact that the corresponding transfer function is a differentiator, which is not physically realizable. The mobility function $V_m(f)/F(f)$ corresponds to a simple integrator. Physically, when a force, f , is applied to the support, it is transmitted to the mass, unchanged, through the parallel spring–damper unit. Accordingly, when f is constant, a constant acceleration is produced at the mass causing its velocity to increase linearly (an integration behavior).

Maxwell's principle of reciprocity can be demonstrated by noting that the mobility function $V_m(f)/F(f)$, obtained in this example, will be identical to the mobility function when the locations of f and V_m are reversed (i.e., when a force, f , is applied to the mass m and the resulting motion, V_m , of the support, which is not restrained by a force, is measured), with the same initial conditions. The reciprocity property is valid for linear, constant-parameter systems in general and is particularly useful in vibration analysis and the testing of multi-DoF systems; for example, to determine a transfer function that is difficult to measure, by measuring its symmetrical counterpart in the transfer function matrix.

2.5 Transmissibility Functions

Transmissibility functions are transfer functions that are particularly useful in the analysis of vibration isolation in machinery and other mechanical systems. Two types of transmissibility function, force transmissibility and motion transmissibility, can be defined (see Table 2.2). Due to a reciprocity characteristic in linear systems, it can be shown that these two transfer functions are equal and, consequently, it is sufficient to consider only one of them. Let us, however, consider both types first and show their equivalence.

2.5.1 Force Transmissibility

Consider a mechanical system that is supported on a rigid foundation through a suspension system. If a forcing excitation is applied to the system, the force is not directly transmitted to the foundation. The suspension system acts as a vibration isolation device. Force transmissibility determines the fraction of the forcing excitation that is transmitted to the support structure (foundation) through the suspension, at different excitation frequencies, and is defined as

$$\text{Force Transmissibility, } T_f = \frac{\text{Force Transmitted to Support, } F_s}{\text{Applied Force, } F} \quad (2.91)$$

Note that this is defined in the frequency domain, and that accordingly F_s and F should be interpreted as the Fourier spectra of the corresponding forces.

A schematic representation of the force transmissibility mechanism is shown in Figure 2.11(a). The reason for the suspension force f_s being not equal to the applied force f is attributed to the inertia paths (broken line in the figure) that are present in a mechanical system.

2.5.2 Motion Transmissibility

Consider a mechanical system that is supported by suspension on a structure that may be subjected to undesirable motions (e.g., guideway deflections, vehicle motions, seismic disturbances). Motion transmissibility determines the fraction of the support motion that is transmitted to the system through

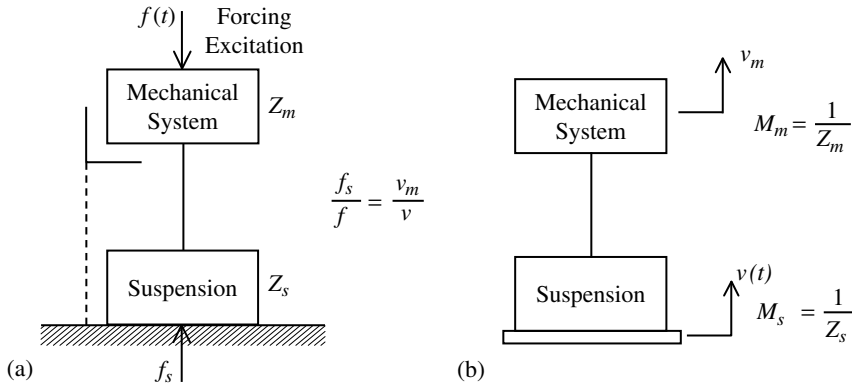


FIGURE 2.11 (a) An inertial system with ground-based suspension; (b) the counterpart (complementary) system with support motion.

its suspension at different frequencies. It is defined as

$$\text{Motion Transmissibility, } T_m = \frac{\text{System Motion, } V_m}{\text{Support Motion, } V} \quad (2.92)$$

The velocities V_m and V are expressed in the frequency domain, as Fourier spectra.

A schematic representation of the motion transmissibility mechanism is shown in Figure 2.11(b). Typically, the motion of the system is taken as the velocity of one of its critical masses. Different transmissibility functions are obtained when different mass points (or DoFs) of the system are considered.

Next, two examples are given to show a reciprocity property that makes the force transmissibility and the motion transmissibility functions identical in complementary (reciprocal) systems.

System Suspended on a Rigid Base (Force Transmissibility)

Consider the system suspended on a rigid base and excited by force $f(t)$, as shown earlier in Figure 2.9(a). Here the system is the inertia element m , and the suspension is the parallel spring and damper combination. We have noted that the three elements m , k , and b are all in parallel.

Here, $Z_m = m j \omega$; $Z_b = b$; and $Z_k = k / j \omega$, as given in Table 2.3. Now, because the elements are connected in parallel, we have (see Table 2.4)

$$\frac{f}{v} = Z_m + Z_b + Z_k \quad (2.93)$$

Hence,

$$\frac{v}{f} = \frac{1}{Z_m + Z_b + Z_d} \quad (2.94)$$

Also, suspension impedance is

$$\frac{f_s}{v} = Z_b + Z_k = Z_s \quad (2.95)$$

where f_s is the force transmitted to the support structure (foundation). Then,

$$\frac{f_s}{f} = \frac{Z_b + Z_k}{Z_m + Z_b + Z_k} = \frac{Z_s}{Z_m + Z_s} \quad (2.96)$$

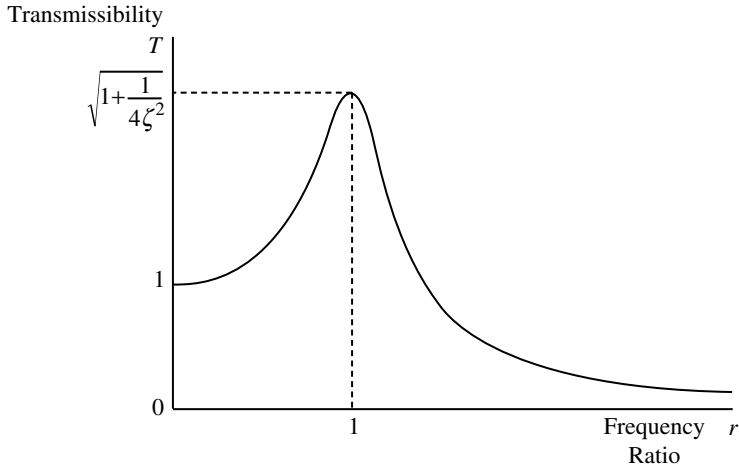


FIGURE 2.12 Transmissibility curve for a simple mechanical oscillator.

This result should be immediately clear since force is divided among parallel branches in proportion to their impedance values (because the velocity is common). Now,

$$\text{Force Transmissibility Magnitude, } |T_f| = \left| \frac{\text{Force Transmitted to Support}}{\text{Applied Force to System}} \right| = \left| \frac{Z_s}{Z_m + Z_s} \right| \quad (2.97)$$

Substitute parameters

$$\begin{aligned} |T_f| &= \left| \frac{f_s}{f} \right| = \left| \frac{b + \frac{k}{j\omega}}{mj\omega + b + \frac{k}{j\omega}} \right| = \left| \frac{bj\omega + k}{k - m\omega^2 + bj\omega} \right| = \sqrt{\frac{b^2\omega^2 + k^2}{(k - m\omega^2)^2 + b^2\omega^2}} \\ &= \sqrt{\frac{(2\zeta\omega_n\omega)^2 + \omega_n^4}{(\omega_n^2 - \omega^2)^2 + (2\zeta\omega_n\omega)^2}} \end{aligned}$$

On simplification, we obtain

$$|T_f| = \sqrt{\frac{1 + 4\zeta^2 r^2}{(1 - r^2)^2 + 4\zeta^2 r^2}} \quad (2.98)$$

where the normalized frequency is

$$\frac{\omega}{\omega_n} = r$$

At $r = 0$, we have $|T_f| = 1$.

At $r = 1$,

$$|T_f| = \sqrt{1 + \frac{1}{4\zeta^2}} \quad (2.99)$$

This transmissibility magnitude curve is shown in Figure 2.12.

System with Support Motion (Motion Transmissibility)

Consider again the system suspended on a moving platform as shown in Figure 2.10(a). For this system, we have $Z_m = mj\omega$ and $M_m = 1/mj\omega$ for the mass element. Since the damper and the spring are

connected in parallel, the corresponding impedances are additive. Hence, we have

$$Z_s = Z_b + Z_k = b + \frac{k}{j\omega} \quad \text{and} \quad M_s = \frac{1}{b + \frac{k}{j\omega}}$$

$$\text{Motion Transmissibility Magnitude, } T_m = \left| \frac{\text{Motion of system inertia}}{\text{Applied support motion}} \right| = \left| \frac{M_m}{M_m + M_s} \right| \quad (2.100)$$

This directly follows from the fact that the velocity is divided among series elements in proportion to their mobilities (because the force is common).

However,

$$\frac{M_m}{M_m + M_s} = \frac{1}{1 + \frac{M_s}{M_m}} = \frac{1}{1 + \frac{Z_m}{Z_s}} = \frac{Z_s}{Z_m + Z_s} \quad (2.101)$$

Hence,

$$|T_m| = \left| \frac{Z_s}{Z_m + Z_s} \right| \quad (2.102)$$

It follows that

$$T_f = T_m \quad (2.103)$$

This establishes the reciprocity property.

2.5.3 General Case

Consider an inertial system with a ground-based suspension, as shown in Figure 2.11(a), and its counterpart with a moving support, as shown in Figure 2.11(b).

The corresponding impedance circuits are shown in Figure 2.13.

For system (a), we have

$$\frac{f_s}{f} = \frac{Z_s}{Z_m + Z_s}$$

For system (b), we have

$$\frac{V_m}{v} = \frac{M_m}{M_m + M_s} = \frac{1}{1 + \frac{M_s}{M_m}} = \frac{1}{1 + \frac{Z_m}{Z_s}} = \frac{Z_s}{Z_s + Z_m}$$

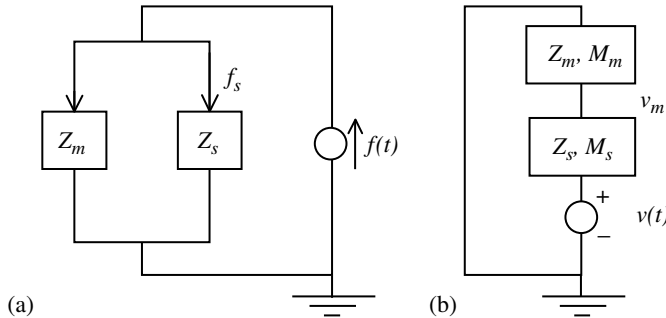


FIGURE 2.13 Impedance circuits: (a) inertial system with ground-based suspension; (b) system and suspension with support motion.

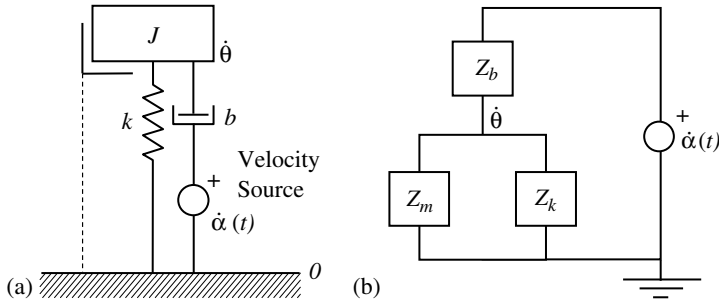


FIGURE 2.14 (a) Schematic mechanical circuit of the fluid coupling system; (b) impedance circuit.

It follows that

$$\frac{f_s}{f} = \frac{V_m}{v} \quad \text{and} \quad T_f = T_m \quad (2.104)$$

for this more general situation.

Example 2.7

Consider again the problem of a fluid coupling system shown in Figure 2.5 and studied in Example 2.1. A schematic mechanical circuit for the system is shown in Figure 2.14(a). The corresponding impedance circuit is shown in Figure 2.14(b). Let us use the impedance method to solve the same problem.

For this problem, we have: input angular velocity = $\dot{\alpha}(t)$; angular velocity of the load = $\dot{\theta}$; and load impedance $Z_l = Z_m + Z_k$. In view of the series connection of Z_b and Z_l , we have

$$\frac{\dot{\theta}}{\dot{\alpha}} = \frac{M_l}{M_l + M_b} = \frac{1/M_b}{1/M_b + 1/M_l} = \frac{Z_b}{Z_b + Z_m + Z_k} \quad (i)$$

For the torsional spring,

$$\frac{\tau}{\dot{\theta}} = Z_k \quad (ii)$$

Multiply Equation (i) and Equation (ii) together.

$$\frac{\tau}{\dot{\alpha}} = \frac{Z_k Z_b}{(Z_b + Z_m + Z_k)} \quad (iii)$$

Since the time derivative corresponds to multiplication by $j\omega$ in the frequency domain, we can write (iii) in the form

$$\frac{\tau}{\alpha} = j\omega \frac{Z_k Z_b}{(Z_b + Z_m + Z_k)} \quad (iv)$$

Substitute $Z_b = b$, $Z_m = j\omega J$, and $Z_k = k/j\omega$. We obtain $\tau/\alpha = kbj\omega/((k - J\omega^2) + bj\omega)$, which is identical to what we obtained in Example 2.1.

2.5.4 Peak Values of Frequency-Response Functions

The peak values of a frequency transfer function correspond to the resonances. The frequencies at these points are called resonant frequencies. Since a transfer function is the ratio of a response variable to an input variable, it is reasonable to obtain different peak frequencies for the same excitation input, if the response variable that is considered is different. Some results obtained for a damped oscillator model are summarized in Table 2.5.

TABLE 2.5 Some Practical Frequency-Response Functions and Their Peaks

System	Response/Excitation	Frequency-Response Function (Normalized)	Normalized Frequency (r_p)	Peak Magnitude (Normalized)
Simple oscillator	Displacement/force	$\frac{1}{(1 - r^2) + 2j\zeta r}$	$\sqrt{1 - 2\zeta^2}$	$\frac{1}{2\zeta\sqrt{1 - \zeta^2}}$
Simple oscillator with velocity response	Velocity/force	$\frac{j r}{(1 - r^2) + 2j\zeta r}$	1	$\frac{1}{2\zeta}$
Simple oscillator with acceleration response	Acceleration/force	$\frac{-r^2}{(1 - r^2) + 2j\zeta r}$	$\frac{1}{\sqrt{1 - 2\zeta^2}}$	$\frac{1}{2\zeta\sqrt{1 - \zeta^2}}$
Fluid coupling system	Torque/displacement	$\frac{2j\zeta r}{(1 - r^2) + 2j\zeta r}$	1	1
Force transmissibility	Force/force	$\frac{1 + 2j\zeta r}{(1 - r^2) + 2j\zeta r}$	$\frac{\sqrt{\sqrt{1 + 8\zeta^2} - 1}}{2\zeta}$	$\sqrt{1 + \frac{1}{4\zeta^2}}$ (for small ζ)
Motion transmissibility	Velocity/velocity	Same	Same	Same

2.6 Receptance Method

Receptance is another name for dynamic flexibility or compliance, and is given by the transfer function (output displacement)/(input force) in the frequency domain (see Table 2.2). Also, as has been mentioned previously, it is directly related to mobility through

$$\text{Receptance} = \frac{\text{Mobility}}{j\omega} \quad (2.105)$$

and this relationship should be clear due to the fact that velocity = $j\omega \times$ displacement, with zero initial conditions, in the frequency domain. Hence, the receptance functions for the basic elements mass (m), spring (k), and damper (b) can be derived from the mobility functions of these elements, as given in Table 2.3. As a result, the interconnection laws given for mobility (M) will be valid for receptance (R) as well. Specifically, for two receptance elements R_1 and R_2 connected in series, we have the combined receptance

$$\text{Series: } R = R_1 + R_2 \quad (2.106)$$

because the displacement is additive and the force is common. For two receptance elements connected in parallel, the combined receptance R is given by

$$\text{Parallel: } \frac{1}{R} = \frac{1}{R_1} + \frac{1}{R_2} \quad (2.107)$$

because the forces are additive and the displacement is common. The inverse of receptance is dynamic stiffness.

2.6.1 Application of Receptance

The receptance method is widely used in the frequency-domain analysis of multi-DoF systems. This is true particularly because the receptance of a multicomponent system can be expressed in a convenient form in terms of the receptances of its constituent components. In deriving such relations, we use the conditions of continuity (forces balance at points of interconnection, or nodes) and compatibility (relative displacements in a loop add to zero). In fact, Equation 2.106 and Equation 2.107 are special cases of receptance relations for multicomponent systems.

It should be clear from Table 2.3 that the receptance R_m of an inertia element ($-1/(\omega^2 m)$), and the receptance R_k of a spring element ($1/k$), are real quantities, unlike the corresponding mobility functions. The receptance R_b of a damper ($1/(bj\omega)$) is imaginary, however. It follows that receptance functions of undamped systems are real, and we will have to deal with real quantities only in the receptance analysis of undamped systems. This makes the analysis quite convenient. Also, since the displacement response of an undamped system becomes infinite when excited by a harmonic force at its natural frequency, we see that the receptance function of an undamped system goes to infinity (or its inverse becomes zero) at its natural frequencies. This property can be utilized in determining an undamped natural frequency (say, the fundamental natural frequency) of a system using the receptance method. In particular, the characteristic equations for a system with two interconnected components are

$$\text{Series: } \frac{1}{R_1 + R_2} = 0 \quad (2.108)$$

$$\text{Parallel: } R_1 + R_2 = 0 \quad (2.109)$$

and their solutions will give the undamped natural frequencies of the combined system. Now, we will consider two examples to illustrate the application of receptance techniques.

Undamped Simple Oscillator

Consider the simple oscillator shown in Figure 2.9, but assume that the damper is not present. As was noted earlier, the mass and the spring elements are connected in parallel. Hence, the characteristic

equation of the undamped system is

$$R_m + R_k = 0 \quad (2.110)$$

or

$$-\frac{1}{\omega^2 m} + \frac{1}{k} = 0 \quad (2.111)$$

or

$$-k + \omega^2 m = 0$$

whose positive solution is

$$\omega = \omega_n = \sqrt{\frac{k}{m}}$$

which gives the undamped natural frequency.

Dynamic Absorber

Dynamic absorbers are commonly used for vibration suppression in machinery over narrow frequency ranges. Specifically, a dynamic absorber can “absorb” the vibration energy from the main system (machine) at a specific frequency (the tuned frequency) and thereby completely balance the vibration excitation in the system.

Consider a machine of equivalent mass M and equivalent stiffness K that is mounted on a rigid foundation, as modeled in Figure 2.15(a). A dynamic absorber, which is a lightly damped oscillator, of mass m and stiffness k is mounted on the machine. The damping is neglected in the model. The machine receives a vibration excitation $f(t)$, and the objective of the absorber is to counteract this excitation. A schematic mechanical circuit of the system is shown in Figure 2.15(b). The overall system can be considered to consist of two subsystems: the subsystem a , representing the machine, has M and K connected in parallel with the excitation source; and the subsystem b , representing the vibrating absorber,

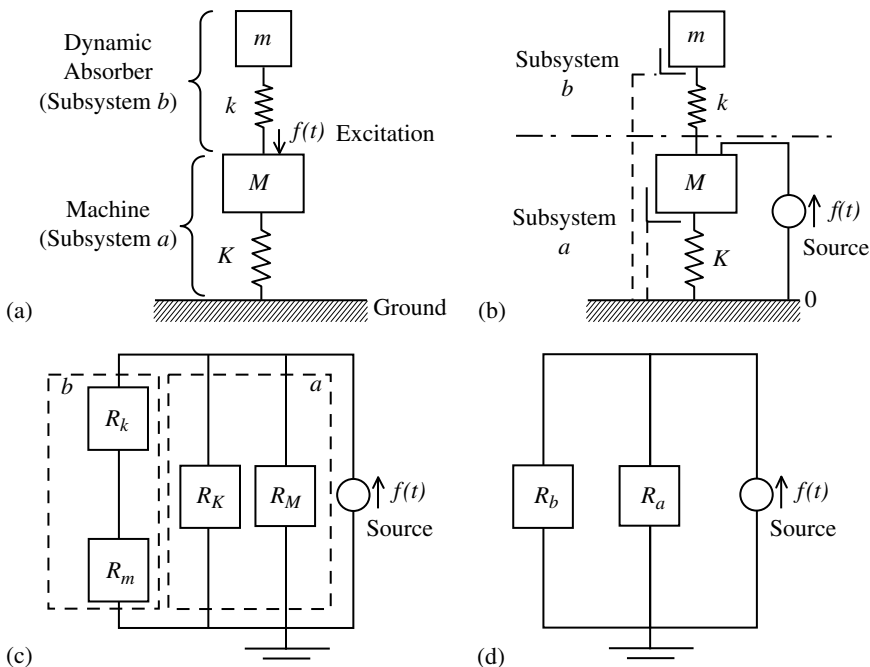


FIGURE 2.15 (a) A machine with a vibration absorber; (b) schematic mechanical circuit; (c) component receptance circuit; and (d) subsystem receptance circuit.

Box 2.3

CONCEPTS OF RECEPTION

$$\text{Receptance, } R \quad = \quad \frac{\text{Displacement}}{\text{Force}}$$

(Compliance, Dynamic Flexibility)

Receptance = Mobility/ $j\omega$

Series Connection: $R = R_1 + R_2$

Parallel Connection: $1/R = 1/R_1 + 1/R_2$

Note: R is real for undamped systems.

Natural Frequency: $R \rightarrow \infty$ (undamped case)

Characteristic Equation:

For system with series components: $1/\sum R_i = 0$

For system with parallel components: $\sum 1/R_i = 0$

has m and k connected in series, as is clear from Figure 2.15(b). The corresponding receptance circuit, indicating the two subsystems with receptances R_a and R_b , is shown in Figure 2.15(d).

Since M and K are connected in parallel, from Equation 2.107 we have

$$\frac{1}{R_a} = -\omega^2 M + K \quad (2.112)$$

Since m and k are connected in series, from Equation 2.106 we have

$$R_b = -\frac{1}{\omega^2 m} + \frac{1}{k} \quad (2.113)$$

Now, since the subsystems a and b are connected in parallel, from Equation 2.109, the characteristic equation of the overall system is given by

$$R_a + R_b = 0 \quad (2.114)$$

Substitute Equations 2.112 and 2.113 in Equation 2.114. We obtain

$$\frac{1}{-\omega^2 M + K} + \frac{1}{-\omega^2 m} + \frac{1}{k} = 0 \quad (2.115)$$

On simplification, after multiplying throughout by the common denominator, we obtain the characteristic equation

$$mM\omega^4 - (kM + Km + km)\omega^2 + kK = 0 \quad (2.116)$$

This will give two positive roots for ω , which are the two undamped natural frequencies of the system. Typically, the natural frequency of the vibration absorber has to be tuned to the frequency of excitation in order to achieve effective vibration suppression, as discussed in Chapter 12 (Enunciations 1–26).

Here, we have only considered *direct receptance* functions, where the considered excitation and response are both for the same node. For more complex, multicomponent, multi-DoF systems, we will need to consider *cross receptance* functions, where the response is considered at a node other than where the excitation force is applied. Such situations are beyond the scope of the present, introductory material. Some concepts of receptance are summarized in Box 2.3.

Bibliography

- Bendat, J.S. and Piersol, A.G. 1971. *Random Data: Analysis and Measurement Procedures*, Wiley, New York.
- den Hartog, J.P. 1956. *Mechanical Vibrations*, McGraw-Hill, New York.
- de Silva, C.W. 2004. *MECHATRONICS—An Integrated Approach*, CRC Press, Boca Raton, FL.
- de Silva, C.W. 2000. *VIBRATION—Fundamentals and Practice*, CRC Press, Boca Raton, FL.
- Inman, D.J. 1996. *Engineering Vibration*, Prentice Hall, Englewood Cliffs, NJ.
- Irwin, J.D. and Graf, E.R. 1979. *Industrial Noise and Vibration Control*, Prentice Hall, Englewood Cliffs, NJ.
- Randall, R.B. 1977. *Application of B&K Equipment to Frequency Analysis*, Bruel and Kjaer, Naerum, Denmark.
- Rao, S.S. 1995. *Mechanical Vibrations*, 3rd ed., Addison-Wesley, Reading, MA.
- Shearer, J.L., Murphy, A.T., and Richardson, H.H. 1971. *Introduction to System Dynamics*, Addison-Wesley, Reading, MA.
- Thomson, W.T. and Dahleh, M.D. 1998. *Theory of Vibration with Applications*, 5th ed., Prentice Hall, Upper Saddle River, NJ.

Appendix 2A

Transform Techniques

2A.1 Introduction

Many people use “transforms” without even knowing it. A transform is simply a number, variable, or function in a different form. For example, since $10^2 = 100$, one can use the exponent (2) to represent the number 100. Doing this for all numbers (i.e., using their exponent to the base 10) results in a “table of logarithms.” One can perform mathematical computations using only logarithms. The logarithm transforms all numbers into their exponential equivalents; a table of such transforms (i.e., a log table) enables a user to quickly transform any number into its exponent, do the computations using exponents (where a product becomes an addition and a division becomes a subtraction), and transform the result back into the original form (i.e., by an inverse logarithm). It is seen that the computations become simpler by using logarithms, but at the cost of the time and effort for transformation and inverse transformation.

Other common transforms include the Laplace transform, Fourier transform, and Z transform. In particular, the Laplace transform provides a simple, algebraic way to solve (i.e., integrate) a linear differential equation. Most functions that we use are of the form t^n , $\sin \omega t$, or e^t , or some combination of them. Thus, in the expression

$$y = f(t)$$

the function y is quite likely to be a power, a sine, or an exponential function. Also, often, we must work with derivatives and integrals of these functions and differential equations containing these functions. These tasks can be greatly simplified by the use of the Laplace transform.

Concepts of frequency-response analysis originate from the nature of the response of a dynamic system to a sinusoidal (i.e., harmonic) excitation. These concepts can be generalized because the time-domain analysis, where the independent variable is time (t), and the frequency-domain analysis, where the independent variable is frequency (ω), are linked through the Fourier transformation. Analytically, it is more general and versatile to use the Laplace transformation, where the independent variable is the Laplace variable (s), which is complex (nonreal). This is true because analytical Laplace transforms may exist even for time functions that do not have “analytical” Fourier transforms. However, with compatible definitions, the Fourier transform results can be obtained from the Laplace transform results simply by setting $s = j\omega$. In the present appendix, we will formally introduce the Laplace transformation and the

Fourier transformation, and will illustrate how these techniques are useful in the analysis of mechatronic systems. The preference of one domain over another will depend on such factors as the nature of the excitation input, the type of the analytical model available, the time duration of interest, and the quantities that need to be determined.

2A.2 Laplace Transform

The Laplace transformation relates the time domain to the *Laplace domain* (also called *s-domain* or complex frequency domain). The Laplace transform, $Y(s)$, of a piecewise-continuous function or signal, $y(t)$, is given, by definition, as

$$Y(s) = \int_0^{\infty} y(t) \exp(-st) dt \quad (2A.1)$$

and is denoted using the Laplace operator, \mathcal{L} , as

$$Y(s) = \mathcal{L}y(t) \quad (2A.1)^*$$

Here, s is a complex independent variable known as the Laplace variable, defined by

$$s = \sigma + j\omega \quad (2A.2)$$

where σ is a real-valued constant that will make the transform (Equation 2A.1) finite, ω is simply frequency, and $j = \sqrt{-1}$. The real value (σ) can be chosen sufficiently large so that the integral in Equation 2A.1 is finite even when the integral of the signal itself (i.e., $\int y(t) dt$) is not finite. This is the reason, for example, the Laplace transform functions better than the Fourier transform, which will be defined later, from the analytical point of view. The symbol s can be considered to be a constant, when integrating with respect to t , in Equation 2A.1.

The inverse relation (i.e., obtaining y from its Laplace transform) is

$$y(t) = \frac{1}{2\pi j} \int_{\sigma-j\omega}^{\sigma+j\omega} Y(s) \exp(st) ds \quad (2A.3)$$

and is denoted using the inverse Laplace operator, \mathcal{L}^{-1} , as

$$y(t) = \mathcal{L}^{-1}Y(s) \quad (2A.3)^*$$

The integration in Equation 2A.3 is performed along a vertical line parallel to the imaginary (vertical) axis, located at σ from the origin in the complex Laplace plane (the s -plane). For a given piecewise-continuous function, $y(t)$, the Laplace transform exists if the integral in Equation 2A.1 converges. A sufficient condition for this is

$$\int_0^{\infty} |y(t)| \exp(-\sigma t) dt < \infty \quad (2A.4)$$

Convergence is guaranteed by choosing a sufficiently large and positive σ . This property is an advantage of the Laplace transformation over the Fourier transformation.

2A.2.1 Laplace Transforms of Some Common Functions

Now we determine the Laplace transform of some useful functions using the definition (Equation 2A.1). Usually, however, we use Laplace transform tables to obtain these results.

Laplace Transform of a Constant

Suppose our function $y(t)$ is a constant, B . Then the Laplace transform is

$$\mathcal{L}(B) = Y(s) = \int_0^{\infty} B e^{-st} dt = B \left. \frac{e^{-st}}{-s} \right|_0^{\infty} = \frac{B}{s}$$

Laplace Transform of the Exponential

If $y(t)$ is e^{at} , its Laplace transform is

$$\mathcal{L}(e^{at}) = \int_0^{\infty} e^{-st} e^{at} dt = \int_0^{\infty} e^{(a-s)t} dt = \frac{1}{(a-s)} e^{(a-s)t} \Big|_0^{\infty} = \frac{1}{s-a}$$

Note: If $y(t)$ is e^{-at} , it is obvious that the Laplace transform is

$$\mathcal{L}(e^{-at}) = \int_0^{\infty} e^{-st} e^{-at} dt = \int_0^{\infty} e^{-(a+s)t} dt = \frac{-1}{(a+s)} e^{-(a+s)t} \Big|_0^{\infty} = \frac{1}{s+a}$$

This result can be obtained from the previous result simply by replacing a with $-a$.

Laplace Transform of Sine and Cosine

In the following, the letter $j = \sqrt{-1}$. If $y(t)$ is $\sin \omega t$, the Laplace transform is

$$\mathcal{L}(\sin \omega t) = \int_0^{\infty} e^{-st} (\sin \omega t) dt$$

Consider the identities:

$$e^{j\omega t} = \cos \omega t + j \sin \omega t$$

$$e^{-j\omega t} = \cos \omega t - j \sin \omega t$$

If we add and subtract these two equations, respectively, we obtain the expressions for the sine and the cosine in terms of $e^{j\omega t}$ and $e^{-j\omega t}$:

$$\cos \omega t = \frac{1}{2} (e^{j\omega t} + e^{-j\omega t})$$

$$\sin \omega t = \frac{1}{2j} (e^{j\omega t} - e^{-j\omega t})$$

$$\mathcal{L}(\cos \omega t) = \frac{1}{2} \mathcal{L}(e^{j\omega t}) + \frac{1}{2} \mathcal{L}(e^{-j\omega t})$$

$$\mathcal{L}(\sin \omega t) = \frac{1}{2} \mathcal{L}(e^{j\omega t}) - \frac{1}{2} \mathcal{L}(e^{-j\omega t})$$

We have just seen that

$$\mathcal{L}(e^{at}) = \frac{1}{s-a}, \quad \mathcal{L}(e^{-at}) = \frac{1}{s+a}$$

Hence,

$$\mathcal{L}(e^{j\omega t}) = \frac{1}{s-j\omega}, \quad \mathcal{L}(e^{-j\omega t}) = \frac{1}{s+j\omega}$$

Substituting these expressions, we obtain:

$$\mathcal{L}(\cos \omega t) = \frac{1}{2} \left[\frac{1}{s-j\omega} \right] + \frac{1}{2} \left[\frac{1}{s+j\omega} \right] = \frac{1}{2} \left[\frac{s+j\omega}{s^2-(j\omega)^2} + \frac{s-j\omega}{s^2-(j\omega)^2} \right] = \frac{s}{s^2+\omega^2}$$

$$\begin{aligned} \mathcal{L}(\sin \omega t) &= \frac{1}{2j} \mathcal{L}(e^{j\omega t} - e^{-j\omega t}) = \frac{1}{2j} \left[\frac{1}{s-j\omega} \right] - \frac{1}{2j} \left[\frac{1}{s+j\omega} \right] = \frac{1}{2j} \left[\frac{s+j\omega}{s^2-(j\omega)^2} + \frac{s-j\omega}{s^2-(j\omega)^2} \right] \\ &= \frac{1}{2j} \left[\frac{2j\omega}{s^2+\omega^2} \right] = \frac{\omega}{s^2+\omega^2} \end{aligned}$$

Transform of a Derivative

Let us transform a derivative of a function. Specifically, the derivative of a function y of t is denoted by $\dot{y} = dy/dt$. Its Laplace transform is given by

$$\mathcal{L}(\dot{y}) = \int_0^{\infty} e^{-st} \dot{y} dt = \int_0^{\infty} e^{-st} \frac{dy}{dt} dt \quad (2A.5)$$

Now, we integrate by parts, to eliminate the derivative within the integrand.

Integration by parts: From calculus we know that $d(uv) = u dv + v du$.

By integrating we obtain $uv = \int u dv + \int v du$

Hence,

$$\int u dv = uv - \int v du \quad (2A.6)$$

This is known as integration by parts.

In Equation 2A.5, let

$$u = e^{-st} \quad \text{and} \quad v = y$$

Then,

$$dv = dy = \frac{dy}{dt} dt = \dot{y} dt$$

$$du = \frac{du}{dt} dt = -s e^{-st} dt.$$

Substitute in Equation 2A.5 to integrate by parts:

$$\begin{aligned} \mathcal{L}(\dot{y}) &= \int_0^{\infty} e^{-st} dy = \int u dv = uv - \int v du = e^{-st} y(t) \Big|_0^{\infty} - \int_0^{\infty} -s e^{-st} y(t) dt = -y(0) + s\mathcal{L}[y(t)] \\ &= s\mathcal{L}(y) - y(0) \end{aligned}$$

where $y(0)$ = initial value of y . This says that the Laplace transform of a first derivative, \dot{y} , equals s times the Laplace transform of the function y minus the initial value of the function (the initial condition).

Note: We can determine the Laplace transforms of the second and higher derivatives by repeated application of the result for the first derivative. For example, the transform of the second derivative is given by

$$\mathcal{L}[\ddot{y}(t)] = \mathcal{L}\left[\frac{d\dot{y}(t)}{dt}\right] = s\mathcal{L}[\dot{y}(t)] - \dot{y}(0) = s\{s\mathcal{L}[y(t)] - y(0)\} - \dot{y}(0) \quad \text{or}$$

$$\mathcal{L}[\ddot{y}(t)] = s^2\mathcal{L}[y(t)] - sy(0) - \dot{y}(0)$$

2A.2.2 Table of Laplace Transforms

Table 2A.1 shows the Laplace transforms of some common functions. Specifically, the table lists functions as $y(t)$, and their Laplace transforms (on the right) as $Y(s)$ or $\mathcal{L}y(t)$. If one is given a function, one can obtain its Laplace transform from the table. Conversely, if one is given the transform, one can obtain the function from the table.

Some general properties and results of the Laplace transform are given in **Table 2A.2**.

In particular, note that with zero initial conditions, differentiation can be interpreted as multiplication by s . Also, integration can be interpreted as division by s .

TABLE 2A.1 Laplace Transform Pairs

$y(t) = \mathcal{L}^{-1}[Y(s)]$	$\mathcal{L}[y(t)] = Y(s)$
B	B/s
e^{-at}	$\frac{1}{s+a}$
e^{at}	$\frac{1}{s-a}$
$\sinh at$	$\frac{a}{s^2 - a^2}$
$\cosh at$	$\frac{s}{s^2 - a^2}$
$\sin \omega t$	$\frac{\omega}{s^2 + \omega^2}$
$\cos \omega t$	$\frac{s}{s^2 + \omega^2}$
$e^{-at} \sin \omega t$	$\frac{\omega}{(s+a)^2 + \omega^2}$
$e^{-at} \cos \omega t$	$\frac{s+a}{(s+a)^2 + \omega^2}$
Ramp t	$\frac{1}{s^2}$
$e^{-at}(1-at)$	$\frac{s}{(s+a)^2}$
$y(t)$	$Y(s)$
$\frac{dy}{dt} = \dot{y}$	$sY(s) - y(0)$
$\frac{d^2y}{dt^2} = \ddot{y}$	$s^2Y(s) - sy(0) - \dot{y}(0)$
$\frac{d^3y}{dt^3} = \dddot{y}$	$s^3Y(s) - s^2y(0) - s\dot{y}(0) - \ddot{y}(0)$
$\int_a^t y(t)dt$	$\frac{1}{s}Y(s) - \frac{1}{s} \int_0^a y(t)dt$
$af(t) + bg(t)$	$aF(s) + bG(s)$
Unit step $U(t) = \begin{cases} 1 & \text{for } t \geq 0 \\ 0 & \text{for otherwise} \end{cases}$	$\frac{1}{s}$
Delayed step $cU(t-b)$	$\frac{c}{s}e^{-bs}$
Pulse $c[U(t) - U(t-b)]$	$c\left(\frac{1 - e^{-bs}}{s}\right)$
Impulse function $\delta(t)$	1
Delayed impulse $\delta(t-b) = \dot{U}(t-b)$	e^{-bs}
Sine pulse	$\left(\frac{\omega}{s^2 + \omega^2}\right)(1 + e^{-(\pi s/\omega)})$

TABLE 2A.2 Important Laplace Transform Relations

$\mathcal{L}^{-1}F(s) = f(t)$	$\mathcal{L}f(t) = F(s)$
$\frac{1}{2\pi j} \int_{\sigma-j\infty}^{\sigma+j\infty} F(s)\exp(st)ds$	$\int_0^\infty f(t)\exp(-st)dt$
$k_1f_1(t) + k_2f_2(t)$	$k_1F_1(s) + k_2F_2(s)$
$\exp(-at)f(t)$	$F(s + a)$
$f(t - \tau)$	$\exp(-\tau s)F(s)$
$f^{(n)}(t) = \frac{d^n f(t)}{dt^n}$	$s^n F(s) - s^{n-1}f(0^+) - s^{n-2}f'(0^+) - \dots - f^{(n-1)}(0^+)$
$\int_{-\infty}^t f(t)dt$	$\frac{F(s)}{s} + \frac{\int_{-\infty}^0 f(t)dt}{s}$
t^n	$\frac{n!}{s^{n+1}}$
$t^n e^{-at}$	$\frac{n!}{(s + a)^{n+1}}$

2A.3 Response Analysis

The Laplace transform method can be used in the response analysis of dynamic systems, mechatronic and control systems in particular. We will give examples for the approach.

Example 2A.1

The capacitor–charge equation of the RC circuit shown in Figure 2A.1 is

$$e = iR + v \quad (\text{i})$$

For the capacitor,

$$i = C \frac{dv}{dt} \quad (\text{ii})$$

Substitute Equation (ii) in (i) to get the circuit equation

$$e = RC \frac{dv}{dt} + v \quad (\text{iii})$$

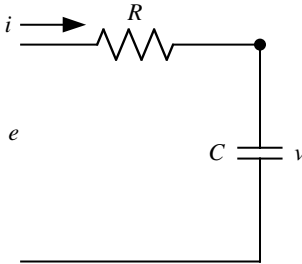


FIGURE 2A.1 An RC circuit with applied voltage, e , and voltage, v , across the capacitor.

Take the Laplace transform of each term in Equation (iii), with all initial conditions = 0

$$E(s) = RCsV(s) + V(s)$$

The transfer function expressed as the output/input ratio (in the transform form) is

$$\frac{V(s)}{E(s)} = \frac{V(s)}{sRCV(s) + V(s)} = \frac{1}{sRC + 1} = \frac{1}{\tau s + 1} \quad (\text{iv})$$

where $\tau = RC$.

The actual response can now be found from Table 2A.1 for a given input E . The first step is to get the transform into proper form (like Line 2)

$$\frac{1}{\tau s + 1} = \frac{1/\tau}{s + (1/\tau)} = \frac{a}{s + a} = a \left(\frac{1}{s + a} \right)$$

where $a = 1/\tau$. Suppose that input (excitation), e , is a unit impulse. Its Laplace transform (see Table 2A.1)

is $E = 1$. Then from Equation (iv)

$$V(s) = \frac{1}{\tau s + 1}$$

From Line 2 of Table 2A.1, the response is

$$v = a e^{-at} = \frac{1}{\tau} e^{-t/\tau} = \frac{1}{RC} e^{-t/RC}$$

A common transfer function for an overdamped second-order system (e.g., one with two RC circuit components of Figure 2A.1) would be

$$\frac{V(s)}{E(s)} = \frac{1}{(1 + \tau_1 s)(1 + \tau_2 s)}$$

This can be expressed as “partial fractions” in the form

$$\frac{A}{1 + \tau_1 s} + \frac{B}{1 + \tau_2 s}$$

and solved in the usual manner.

Example 2A.2

The transfer function of a thermal system is given by

$$G(s) = \frac{2}{(s + 1)(s + 3)}$$

If a unit-step input is applied to the system, with zero initial conditions, what is the resulting response?

Solution

Input: $U(s) = 1/s$ (for a unit step)

Since

$$\frac{Y(s)}{U(s)} = \frac{2}{(s + 1)(s + 3)}$$

the output (response) is

$$Y(s) = \frac{2}{s(s + 1)(s + 3)}$$

Its inverse Laplace transform gives the time response. For this, first convert the expression into partial fractions as

$$\frac{2}{s(s + 1)(s + 3)} = \frac{A}{s} + \frac{B}{(s + 1)} + \frac{C}{(s + 3)} \quad (i)$$

The unknown, A , is determined by multiplying Equation (i) throughout by s and then setting $s = 0$. We obtain

$$A = \frac{2}{(0 + 1)(0 + 3)} = \frac{2}{3}$$

Similarly, B is obtained by multiplying Equation (i) throughout by $(s + 1)$ and then setting $s = -1$. We obtain

$$B = \frac{2}{(-1)(-1 + 3)} = -1$$

Next, C is obtained by multiplying Equation (i) throughout by $(s + 3)$ and then setting $s = -3$. We obtain

$$C = \frac{2}{(-3)(-3 + 1)} = \frac{1}{3}$$

Hence,

$$Y(s) = \frac{2}{3s} - \frac{1}{(s + 1)} + \frac{1}{3(s + 3)}$$

Take the inverse transform using Line 2 of [Table 2A.1](#)

$$y(t) = \frac{2}{3} - e^{-t} + \frac{1}{3}e^{-3t}$$

Example 2A.3

The transfer function of a damped simple oscillator is known to be of the form

$$\frac{Y(s)}{U(s)} = \frac{\omega_n^2}{(s^2 + 2\zeta\omega_n s + \omega_n^2)}$$

where ω_n is the undamped natural frequency and ζ the damping ratio.

Suppose that a unit step input (i.e., $U(s) = 1/s$) is applied to the system. Using Laplace transform tables, determine the resulting response with zero initial conditions.

Solution

$$Y(s) = \frac{1}{s} \frac{\omega_n^2}{(s^2 + 2\zeta\omega_n s + \omega_n^2)}$$

The corresponding partial fractions are of the form:

$$Y(s) = \frac{A}{s} + \frac{Bs + C}{(s^2 + 2\zeta\omega_n s + \omega_n^2)} = \frac{\omega_n^2}{s(s^2 + 2\zeta\omega_n s + \omega_n^2)} \quad (\text{i})$$

We need to determine A , B , and C .

Multiply Equation (i) throughout by s and set $s = 0$. We obtain:

$$A = 1$$

Next, note that the roots of the characteristic equation,

$$s^2 + 2\zeta\omega_n s + \omega_n^2 = 0$$

are

$$s = -\zeta\omega_n \pm \sqrt{\zeta^2 - 1}\omega_n = -\zeta\omega_n \pm j\omega_d$$

These are the poles of the system and are complex conjugates. Two equations for B and C are obtained by multiplying Equation (i) by $s + \zeta\omega_n - \sqrt{\zeta^2 - 1}\omega_n$ and setting $s = -\zeta\omega_n + \sqrt{\zeta^2 - 1}\omega_n$, and by multiplying Equation (i) by $s + \zeta\omega_n + \sqrt{\zeta^2 - 1}\omega_n$ and setting $s = -\zeta\omega_n - \sqrt{\zeta^2 - 1}\omega_n$. We obtain $B = -1$ and $C = 0$. Consequently,

$$Y(s) = \frac{1}{s} - \frac{s}{(s^2 + 2\zeta\omega_n s + \omega_n^2)} = \frac{1}{s} - \frac{s + \zeta\omega_n}{[(s + \zeta\omega_n)^2 + \omega_d^2]} + \frac{\zeta}{\sqrt{1 - \zeta^2}} \frac{\omega_d}{[(s + \zeta\omega_n)^2 + \omega_d^2]}$$

where $\omega_d = \sqrt{1 - \zeta^2}\omega_n$ is the damped natural frequency.

Now, use Table 2A.1 to obtain the inverse Laplace transform:

$$\begin{aligned}
 y_{\text{step}}(t) &= 1 - e^{-\zeta\omega_n t} \cos \omega_d t - \frac{\zeta}{\sqrt{1-\zeta^2}} e^{-\zeta\omega_n t} \sin \omega_d t = 1 - \frac{e^{-\zeta\omega_n t}}{\sqrt{1-\zeta^2}} [\sin \phi \cos \omega_d t + \cos \phi \sin \omega_d t] \\
 &= 1 - \frac{e^{-\zeta\omega_n t}}{\sqrt{1-\zeta^2}} \sin(\omega_d t + \phi)
 \end{aligned}$$

where

$$\cos \phi = \zeta = \text{damping ratio}, \quad \sin \phi = \sqrt{1-\zeta^2}$$

Example 2A.4

The open-loop response of a plant to a unit impulse input, with zero initial conditions, was found to be $2 e^{-t} \sin t$. What is the transfer function of the plant?

Solution

By linearity, since a unit impulse is the derivative of a unit step, the response to a unit impulse is given by the derivative of the result given in the previous example; thus,

$$\begin{aligned}
 y_{\text{impulse}}(t) &= \frac{\zeta\omega_n}{\sqrt{1-\zeta^2}} e^{-\zeta\omega_n t} \sin(\omega_d t + \phi) - \frac{\omega_d}{\sqrt{1-\zeta^2}} e^{-\zeta\omega_n t} \cos(\omega_d t + \phi) \\
 &= \frac{\omega_n}{\sqrt{1-\zeta^2}} e^{-\zeta\omega_n t} [\cos \phi \sin(\omega_d t + \phi) - \sin \phi \cos(\omega_d t + \phi)]
 \end{aligned}$$

or

$$y_{\text{impulse}}(t) = \frac{\omega_n}{\sqrt{1-\zeta^2}} e^{-\zeta\omega_n t} \sin \omega_d t$$

Compare this with the given expression. We have

$$\frac{\omega_n}{\sqrt{1-\zeta^2}} = 2, \quad \zeta\omega_n = 1, \quad \omega_d = 1$$

However,

$$\omega_n^2 = (\zeta\omega_n)^2 + \omega_d^2 = 1 + 1 = 2$$

Hence,

$$\omega_n = \sqrt{2}$$

Hence,

$$\zeta = \frac{1}{\sqrt{2}}$$

The system transfer function is

$$\frac{\omega_n^2}{(s^2 + 2\zeta\omega_n s + \omega_n^2)} = \frac{2}{s^2 + 2s + 2}$$

Example 2A.5

Express the Laplace transformed expression

$$X(s) = \frac{s^3 + 5s^2 + 9s + 7}{(s+1)(s+2)}$$

as partial fractions. From the result, determine the inverse Laplace function, $x(t)$.

Solution

$$X(s) = s + 2 + \frac{2}{s+1} - \frac{1}{s+2}$$

From Table 2A.1, we get the inverse Laplace transform

$$x(t) = \frac{d}{dt}\delta(t) + 2\delta(t) + 2e^{-t} - e^{-2t}$$

where $\delta(t)$ is the unit impulse function.

2A.4 Transfer Function

By the use of Laplace transformation, a *convolution integral* equation can be converted into an algebraic relationship. To illustrate this, consider the convolution integral which gives the response, $y(t)$, of a dynamic system to an excitation input, $u(t)$, with zero initial conditions, as discussed in Chapter 2. By definition (Equation 2A.1), its Laplace transform is written as

$$Y(s) = \int_0^\infty \int_0^\infty h(\tau)u(t-\tau)d\tau \exp(-st)dt \quad (2A.7)$$

Note that $h(t)$ is the *impulse response function* of the system. Since integration with respect to t is performed while keeping τ constant, we have $dt = d(t-\tau)$. Consequently,

$$Y(s) = \int_{-\tau}^\infty u(t-\tau)\exp[-s(t-\tau)]d(t-\tau) \int_0^\infty h(\tau)\exp(-s\tau)d\tau$$

The lower limit of the first integration can be made equal to zero, in view of the fact that $u(t) = 0$ for $t < 0$. Again, by using the definition of Laplace transformation, the foregoing relation can be expressed as

$$Y(s) = H(s)U(s) \quad (2A.8)$$

in which

$$H(s) = Lh(t) = \int_0^\infty h(t)\exp(-st)dt \quad (2A.9)$$

Note that, by definition, the transfer function of a system, denoted by $H(s)$, is given by Equation 2A.8. More specifically, the system transfer function is given by the ratio of the Laplace-transformed output and the Laplace-transformed input with zero initial conditions. In view of Equation 2A.9, it is clear that the system transfer function can be expressed as the Laplace transform of the impulse-response function of the system. The transfer function of a linear and constant-parameter system is a unique function that completely represents the system. A physically realizable, linear, constant-parameter system possesses a unique transfer function, even if the Laplace transforms of a particular input and the corresponding output do not exist. This is clear from the fact that the transfer function is a system model and does not depend on the system input itself.

Note: The transfer function is also commonly denoted by $G(s)$. However, in the present context, we use $H(s)$ in view of its relation to $h(t)$.

Consider the n th-order linear, constant-parameter dynamic system given by

$$a_n \frac{d^n y}{dt^n} + a_{n-1} \frac{d^{n-1} y}{dt^{n-1}} + \cdots + a_0 y = b_0 u + b_1 \frac{du(t)}{dt} + \cdots + b_m \frac{d^m u(t)}{dt^m} \quad (2A.10)$$

for a physically realizable system, $m \leq n$. By applying Laplace transformation and then integrating by parts, it may be verified that

$$L \frac{d^k f(t)}{dt^k} = s^k \hat{F}(s) - s^{k-1} f(0) - s^{k-2} \frac{df(0)}{dt} - \cdots + \frac{d^{k-1} f(0)}{dt^{k-1}} \quad (2A.11)$$

By definition, the initial conditions are set to zero in obtaining the transfer function. This results in

$$H(s) = \frac{b_0 + b_1 s + \cdots + b_m s^m}{a_0 + a_1 s + \cdots + a_n s^n} \quad (2A.12)$$

for $m \leq n$. Note that Equation 2A.12 contains all the information that is contained in Equation 2A.10. Consequently, transfer function is an analytical model of a system. The transfer function may be employed to determine the total response of a system for a given input, even though it is defined in terms of the response under zero initial conditions. This is logical because the analytical model of a system is independent of the initial conditions of the system.

2A.5 Fourier Transform

The Fourier transform, $Y(f)$, of a signal, $y(t)$, relates the time domain to the frequency domain. Specifically,

$$Y(f) = \int_{-\infty}^{+\infty} y(t) \exp(-j2\pi ft) dt = \int_{-\infty}^{+\infty} y(t) e^{-j\omega t} dt \quad (2A.13)$$

Using the Fourier operator, F , terminology:

$$Y(f) = Fy(t) \quad (2A.14)$$

Note that if $y(t) = 0$ for $t < 0$, as in the conventional definition of system excitations and responses, the Fourier transform is obtained from the Laplace transform by simply changing the variable according to $s = j2\pi f$ or $j\omega$. The Fourier is a special case of the Laplace, where, in Equation 2A.2, $\sigma = 0$:

$$Y(f) = Y(s)|_{s=j2\pi f} \quad (2A.15)$$

or

$$Y(\omega) = Y(s)|_{s=j\omega} \quad (2A.16)$$

The (complex) function $Y(f)$ is also termed the (continuous) *Fourier spectrum* of the (real) signal, $y(t)$. The inverse transform is given by:

$$y(t) = \int_{-\infty}^{+\infty} Y(f) \exp(j2\pi ft) df \quad (2A.17)$$

or

$$y(t) = F^{-1}Y(f)$$

Note that according to the definition given by Equation 2A.13, the Fourier spectrum, $Y(f)$, is defined for the entire frequency range $f(-\infty, +\infty)$ which includes negative values. This is termed the *two-sided spectrum*. Since, in practical applications it is not possible to have “negative frequencies,” the *one-sided spectrum* is usually defined only for the frequency range $f(0, \infty)$.

In order that a two-sided spectrum has the same amount of *power* as a one-sided spectrum, it is necessary to make the one-sided spectrum double the two-sided spectrum for $f > 0$.

If the signal is not sufficiently transient (fast-decaying or damped), the infinite integral given by Equation 2A.13 might not exist, but the corresponding Laplace transform might still exist.

2A.5.1 Frequency-Response Function (Frequency Transfer Function)

The Fourier integral transform of the impulse-response function is given by

$$H(f) = \int_{-\infty}^{\infty} h(t) \exp(-j2\pi ft) dt \quad (2A.18)$$

where f is the *cyclic frequency* (measured in cycles/sec or hertz). This is known as the frequency-response function (or frequency transfer function) of a system. Fourier transform operation is denoted as $Fh(t) = H(f)$. In view of the fact that $h(t) = 0$ for $t < 0$, the lower limit of integration in Equation 2A.18 can be made zero. Then, from Equation 2A.9, it is clear that $H(f)$ is obtained simply by setting $s = j2\pi f$ in $H(s)$. Hence, strictly speaking, we should use the notation $H(j2\pi f)$ and not $H(f)$. However, for notational simplicity, we denote $H(j2\pi f)$ by $H(f)$. Furthermore, since the angular frequency $\omega = 2\pi f$, we can express the frequency-response function as $H(j\omega)$, or simply by $H(\omega)$ for notational convenience. It should be noted that the frequency-response function, like the Laplace transfer function, is a complete representation of a linear, constant-parameter system. In view of the fact that both $u(t) = 0$ and $y(t) = 0$ for $t < 0$, we can write the Fourier transforms of the input and the output of a system directly by setting $s = j2\pi f = j\omega$ in the corresponding Laplace transforms.

Then, from Equation 2A.8, we have

$$Y(f) = H(f)U(f) \quad (2A.19)$$

Note: Sometimes, for notational convenience, the same lowercase letters are used to represent the Laplace and Fourier transforms as well as the original time-domain variables.

If the Fourier integral transform of a function exists, then its Laplace transform also exists. The converse is not generally true, however, because of the poor convergence of the Fourier integral in comparison to the Laplace integral. This arises from the fact that the factor $\exp(-\sigma t)$ is not present in the Fourier integral. For a physically realizable, linear, constant-parameter system, $H(f)$ exists even if $U(f)$ and $Y(f)$ do not exist for a particular input. The experimental determination of $H(f)$, however, requires system stability. For the n th-order system given by Equation 2A.10, the frequency-response function is determined by setting $s = j2\pi f$ in Equation 2A.12 as

$$H(f) = \frac{b_0 + b_1 j2\pi f + \cdots + b_m (j2\pi f)^m}{a_0 + a_1 j2\pi f + \cdots + a_n (j2\pi f)^n} \quad (2A.20)$$

This, generally, is a complex function of f , which has a magnitude denoted by $|H(f)|$ and a phase angle denoted by $\angle H(f)$.

2A.6 The s -Plane

We have noted that the Laplace variable s is a complex variable, with a real part and an imaginary part. Hence, to represent it we will need two axes at right angles to each other—the real axis and the imaginary axis. These two axes form a plane, which is called the s -plane. Any general value of s (or any variation or trace of s) may be marked on the s -plane.

2A.6.1 An Interpretation of Laplace and Fourier Transforms

In the Laplace transformation of a function, $f(t)$, we multiply the function by e^{-st} and integrate with respect to t . This process may be interpreted as determining the “components” $F(s)$ of $f(t)$ in the “direction” e^{-st} , where s is a complex variable. All such components $F(s)$ should be equivalent to the original function, $f(t)$.

In the Fourier transformation of $f(t)$ we multiply it by $e^{-j\omega t}$ and integrate with respect to t . This is the same as setting $s = j\omega$. Hence, the Fourier transform of $f(t)$ is $F(j\omega)$. Furthermore, $F(j\omega)$ represents the components of $f(t)$ that are in the direction of $e^{-j\omega t}$. Since $e^{-j\omega t} = \cos \omega t - j \sin \omega t$, in the Fourier transformation we determine the sinusoidal components of frequency ω , of a time

function $f(t)$. Since s is complex, $F(s)$ is also complex and so is $F(j\omega)$. Hence, they all will have a real part and an imaginary part.

2A.6.2 Application in Circuit Analysis

The fact that $\sin \omega t$ and $\cos \omega t$ are 90° out of phase is further confirmed in view of

$$e^{j\omega t} = \cos \omega t + j \sin \omega t \quad (2A.21)$$

Consider the R – L – C circuit shown in Figure 2A.2. For the capacitor, the current, i , and the voltage, v , are related through

$$i = C \frac{dv}{dt} \quad (2A.22)$$

If the voltage $v = v_0 \sin \omega t$, the current $i = v_0 \omega C \cos \omega t$. Note that the magnitude of v/i is $1/\omega C$ (or $1/2\pi fC$ where $\omega = 2\pi f$; f is the cyclic frequency and ω is the angular frequency). But v and i are out of phase by 90° . In fact, in the case of a capacitor, i leads v by 90° . The equivalent circuit resistance of a capacitance is called *reactance*, and is given by

$$X_C = \frac{1}{2\pi fC} \quad (2A.23)$$

$$= \frac{1}{\omega C} \quad (2A.24)$$

Note that this parameter changes with the frequency.

We cannot add the reactance of the capacitor and the resistance of the resistor algebraically; we must add them vectorially because the voltages across a capacitor and resistor in series are not in phase, unlike in the case of a resistor. Also, the resistance in a resistor does not change with frequency. In a series circuit, as in Figure 2A.2, the current is identical in each element, but the voltages differ in both amplitude and phase; in a parallel circuit, the voltages are identical, but the currents differ in amplitude and phase.

Similarly, for an inductor,

$$v = L \frac{di}{dt} \quad (2A.25)$$

The corresponding reactance is

$$X_L = \omega L = 2\pi fL \quad (2A.26)$$

If the voltage (E) across R in Figure 2A.2(a) is in the direction shown in Figure 2A.2(b) (i.e., pointing to the right), then the voltage across the inductor, L , must point up (90° leading) and the voltage across the capacitor, C , must point down (90° lagging). Since the current (I) is identical in each component of a

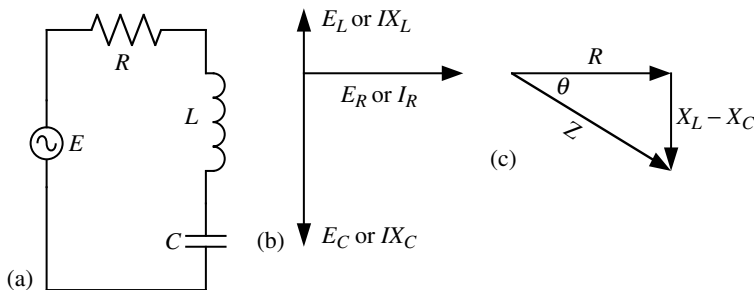


FIGURE 2A.2 (a) Series RLC circuit; (b) phases of voltage drops; (c) impedance triangle.

series circuit, we see the directions of IR , IX_L and IX_C as in [Figure 2A.2\(b\)](#), giving the impedance triangle shown in [Figure 2A.2\(c\)](#).

To express these reactances in the s -domain, we simply substitute s for $j\omega$:

$$\begin{aligned} -jX_C &= \frac{1}{sC} \\ jX_L &= sL \end{aligned}$$

The series impedance of the RLC circuit can be expressed as

$$Z = R + jX_L - jX_C = R + sL + \frac{1}{sC}$$

In this discussion, note the use of $\sqrt{-1}$ or j to indicate a 90° phase change.

3

Modal Analysis

3.1	Introduction	3-1
3.2	Degrees of Freedom and Independent Coordinates	3-2
	Nonholonomic Constraints	
3.3	System Representation	3-4
	Stiffness and Flexibility Matrices • Inertia Matrix • Direct Approach for Equations of Motion	
3.4	Modal Vibrations	3-10
3.5	Orthogonality of Natural Modes	3-14
	Modal Mass and Normalized Modal Vectors	
3.6	Static Modes and Rigid-Body Modes	3-15
	Static Modes • Linear Independence of Modal Vectors • Modal Stiffness and Normalized Modal Vectors • Rigid-Body Modes • Modal Matrix • Configuration Space and State Space	
3.7	Other Modal Formulations	3-22
	Nonsymmetric Modal Formulation • Transformed Symmetric Modal Formulation	
3.8	Forced Vibration	3-28
	First Mode (Rigid-Body Mode) • Second Mode (Oscillatory Mode)	
3.9	Damped Systems	3-32
	Proportional Damping	
3.10	State-Space Approach	3-36
	Modal Analysis • Mode Shapes of Nonoscillatory Systems • Mode Shapes of Oscillatory Systems	
	Appendix 3A Linear Algebra	3-41

Clarence W. de Silva

The University of British Columbia

Summary

This chapter presents the modal analysis of lumped-parameter mechanical vibrating systems. In the considered systems, inertia, flexibility, and damping characteristics are lumped at a finite number of discrete points in the system. Techniques for determining the natural frequencies and mode shapes of vibration are given. The orthogonality of mode shapes is established. The existence of natural modes in damped systems is investigated. Proportional damping is discussed. Both free vibration and forced vibration of multi-degree-of-freedom (multi-DoF) systems are analyzed.

3.1 Introduction

Complex vibrating systems usually consist of components that possess distributed energy-storage and energy-dissipative characteristics. In these systems, inertial, stiffness, and damping properties vary (piecewise) continuously with respect to the spatial location. Consequently, partial differential equations, with spatial coordinates (e.g., Cartesian coordinates x , y , z) and time t as independent variables are necessary to represent their vibration response.

A distributed (continuous) vibrating system may be approximated (modeled) by an appropriate set of lumped masses properly interconnected using discrete spring and damper elements. Such a model is termed *lumped-parameter model* or *discrete model*. An immediate advantage resulting from this lumped-parameter representation is that the system equations become ordinary differential equations. Often, linear springs and linear viscous damping elements are used in these models. The resulting linear ordinary differential equations can be solved by the modal analysis method. The method is based on the fact that these idealized systems (models) have preferred frequencies and geometric configurations (or *natural modes*) in which they tend to execute free vibration. An arbitrary response of the system can be interpreted as a linear combination of these *modal vibrations*, and as a result its analysis may be conveniently done using modal techniques.

Modal analysis is an important tool in vibration analysis, diagnosis, design, and control. In some systems, mechanical malfunction or failure can be attributed to the excitation of their preferred motion such as modal vibrations and resonances. By modal analysis, it is possible to establish the extent and location of severe vibrations in a system. For this reason, it is an important diagnostic tool. For the same reason, modal analysis is also a useful method for predicting impending malfunctions or other mechanical problems. Structural modification and substructuring are techniques of vibration analysis and design that are based on modal analysis. By sensitivity analysis methods using a modal model, it is possible to determine which degrees of freedom (DoFs) of a mechanical system are most sensitive to addition or removal of mass and stiffness elements. In this manner, a convenient and systematic method can be established for making structural modifications to eliminate an existing vibration problem, or to verify the effects of a particular modification. A large and complex system can be divided into several subsystems which can be independently analyzed. By modal analysis techniques, the dynamic characteristics of the overall system can be determined from the subsystem information. This approach has several advantages, including: (1) subsystems can be developed by different methods such as experimentation, finite element method, or other modeling techniques and assembled to obtain the overall model; (2) the analysis of a high order system can be reduced to several lower order analyses; and (3) the design of a complex system can be carried out by designing and developing its subsystems separately. These capabilities of structural modification and substructure analysis which are possessed by the modal analysis method make it a useful tool in the design development process of mechanical systems. Modal control, a technique that employs modal analysis, is quite effective in the vibration control of complex mechanical systems.

3.2 Degrees of Freedom and Independent Coordinates

The geometric configuration of a vibrating system can be completely determined by a set of independent coordinates. This number of independent coordinates, for most systems, is termed the number of DoFs of the system. For example, a particle freely moving on a plane requires two independent coordinates to completely locate it (e.g., x and y Cartesian coordinates or r and θ polar coordinates); its motion has two DoF. A rigid body that is free to take any orientation in (three-dimensional) space needs six independent coordinates to completely define its position. For instance, its centroid is positioned using three independent Cartesian coordinates (x, y, z). Any axis fixed in the body and passing through its centroid can be oriented by two independent angles (θ, ϕ). The orientation of the body about this body axis can be fixed by a third independent angle (ψ). Altogether, six independent coordinates have been utilized; the system has six DoF.

Strictly speaking, the number of DoF is equal to the number of independent, incremental, generalized coordinates that are needed to represent a general motion. In other words, it is the number of incremental independent motions that are possible. For holonomic systems (i.e., systems possessing holonomic constraints only), the number of independent incremental generalized coordinates is equal to the number of independent generalized coordinates; hence, either definition may be used for the number of DoF. If, on the other hand, the system has nonholonomic

constraints, the definition based on incremental coordinates should be used, because in these systems the number of independent incremental coordinates is in general less than the number of independent coordinates that are required to completely position the system.

3.2.1 Nonholonomic Constraints

Constraints of a system that cannot be represented by purely algebraic equations in its generalized coordinates and time are termed nonholonomic constraints. For a nonholonomic system, more coordinates than the number of DoF are required to completely define the position of the system. The number of excess coordinates is equal to the number of nonalgebraic relations that define the nonholonomic constraints in the system. Examples for nonholonomic systems are afforded by bodies rolling on surfaces and bodies whose velocities are constrained in some manner.

Example 3.1

A good example for a nonholonomic system is provided by a sphere rolling, without slipping, on a plane surface. In Figure 3.1, the point O denotes the center of the sphere at a given instant, and P is an arbitrary point within the sphere. The instantaneous point of contact with the plane surface is denoted by Q , so that the radius of the sphere is $OQ = a$. This system requires five independent generalized coordinates to position it. For example, the center O is fixed by the Cartesian coordinates x and y . Since the sphere is free to roll along any arbitrary path on the plane and return to the starting point, the line OP can assume any arbitrary orientation for any given position for the center O . This line can be oriented by two independent coordinates θ and ϕ , defined as in Figure 3.1. Furthermore, since the sphere is free to spin about the z -axis and is also free to roll on any trajectory (and return to its starting point), it follows that the sphere can take any orientation about the line OP (for a specific location of point O and line OP). This position can be oriented by the angle ψ . These five generalized coordinates x , y , θ , ϕ , and ψ are independent. The corresponding incremental coordinates δx , δy , $\delta \theta$, $\delta \phi$, and $\delta \psi$ are, however, not independent, as a result of the constraint of rolling without slipping. It can be shown that two independent differential equations can be written for this constraint, and that consequently there exist only three independent incremental coordinates; the system actually has only three DoF.

To establish the equations for the two nonholonomic constraints note that the incremental displacements δx and δy of the center O about the instantaneous point of contact Q can be written

$$\delta x = a \delta \beta, \quad \delta y = -a \delta \alpha$$

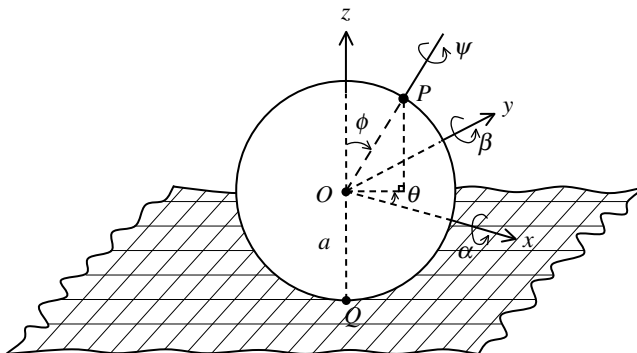


FIGURE 3.1 Rolling sphere on a plane (an example of a nonholonomic system).

in which the rotations of α and β are taken as positive about the positive directions of x and y , respectively (Figure 3.1). Next, we will express $\delta\alpha$ and $\delta\beta$ in terms of the generalized coordinates. Note that $\delta\theta$ is directed along the z direction and has no components along the x and y directions. On the other hand, $\delta\phi$ has the components $\delta\phi \cos \theta$ in the positive y direction and $\delta\phi \sin \theta$ in the negative x direction. Furthermore, the horizontal component of $\delta\psi$ is $\delta\psi \sin \phi$. This in turn has the components $(\delta\psi \sin \phi) \cos \theta$ and $(\delta\psi \sin \phi) \sin \theta$ in the positive x and y directions, respectively. It follows that

$$\delta\alpha = -\delta\phi \sin \theta + \delta\psi \sin \phi \cos \theta$$

$$\delta\beta = \delta\phi \cos \theta + \delta\psi \sin \phi \sin \theta$$

Consequently, the two nonholonomic constraint equations are

$$\delta x = a(\delta\phi \cos \theta + \delta\psi \sin \phi \sin \theta)$$

$$\delta y = a(\delta\phi \sin \theta - \delta\psi \sin \phi \cos \theta)$$

Note that these are differential equations that cannot be directly integrated to give algebraic equations. A particular choice for the three independent incremental coordinates associated with the three DoF in the present system of a rolling sphere would be $\delta\theta$, $\delta\phi$, and $\delta\psi$. The incremental variables $\delta\alpha$, $\delta\beta$, and $\delta\theta$ will form another choice. The incremental variables δx , δy , and $\delta\theta$ will also form a possible choice. Once three incremented displacements are chosen in this manner, the remaining two incremental generalized coordinates are not independent and can be expressed in terms of these three incremented variables using the constraint differential equations.

Example 3.2

A relatively simple example for a nonholonomic system is a single-dimensional rigid body (a straight line) moving on a plane such that its velocity is always along the body axis. The idealized motion of a ship in calm water is a practical situation representing such a system. This body needs three independent coordinates to completely define all possible configurations that it can take. For example, the centroid of the body can be fixed by two Cartesian coordinates x and y on the plane, and the orientation of the axis through the centroid may be fixed by a single angle θ . Note that, for a given location (x, y) of the centroid, any arbitrary orientation (θ) for the body axis is feasible, because, as in the previous example, any arbitrary trajectory can be followed by this body and return the centroid to the starting point, but with a different orientation of the axis of the body. Since the velocity is always directed along the body axis, a nonholonomic constraint exists and it is expressed as

$$\frac{dy}{dx} = \tan \theta$$

It follows that there are only two independent incremental variables; the system has only two DoF. Some useful definitions and properties that were discussed in this section are summarized in Box 3.1.

3.3 System Representation

Some damped systems do not possess real modes. If a system does not possess real modes, modal analysis could still be used, but the results would only be approximately valid. In modal analysis it is convenient to first neglect damping and develop the fundamental results, and then subsequently extend the results to damped systems, for example, by assuming a suitable damping model that possesses real modes. Since damping is an energy dissipation phenomenon, it is usually possible to determine a model that possesses real modes and also has an energy dissipation capacity equivalent to that of the actual system.

Box 3.1

SOME DEFINITIONS AND PROPERTIES OF MECHANICAL SYSTEMS

Holonomic constraints	Constraints that can be represented by purely algebraic relations
Nonholonomic constraints	Constraints that require differential relations for their representation
Holonomic system	A system that possesses holonomic constraints only
Nonholonomic system	A system that possesses one or more nonholonomic constraints
Number of DoFs	The number of independent incremental coordinates that are needed to represent general incremental motion of a system = number of independent incremental motions = $2 \times$ number of DoF (typically)
Order of a system	
For a holonomic system	
Number of independent incremental coordinates	= Number of independent coordinates = number of DoF
For a nonholonomic system	
Number of independent incremental coordinates	< Number of independent coordinates

Consider the three undamped system representations (models) shown in Figure 3.2. The motion of system (a) consists of the *translatory* displacements y_1 and y_2 of the lumped masses m_1 and m_2 . The masses are subjected to the external excitation forces (inputs) $f_1(t)$ and $f_2(t)$ and the restraining forces of the discrete, tensile-compressive stiffness (spring) elements k_1 , k_2 , and k_3 . Only two independent

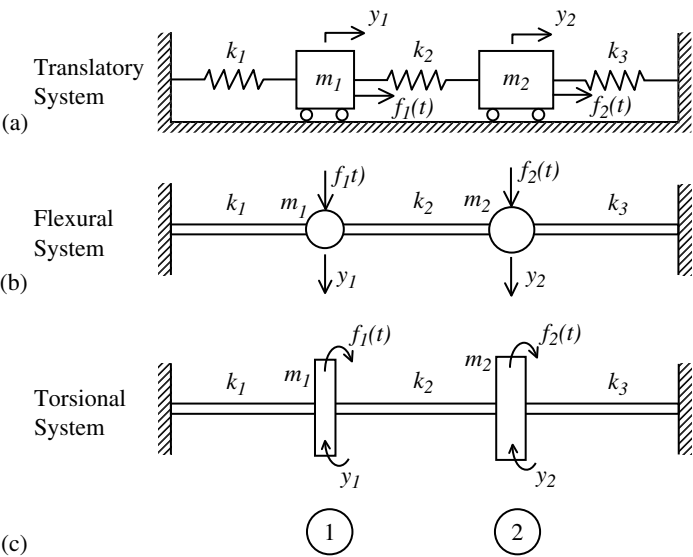


FIGURE 3.2 Three types of two-DoF systems.

incremental coordinates (δy_1 and δy_2) are required to completely define the incremental motion of the system subject to its inherent constraints. It follows that the system has two DoF.

In system (b), shown in Figure 3.2, the elastic stiffness to the *transverse* displacements y_1 and y_2 of the lumped masses is provided by three bending (*flexural*) springs that are considered massless. This flexural system is very much analogous to the translatory system (a) even though the physical construction and the motion itself are quite different. System (c) in Figure 3.2 is the analogous *torsional* system. In this case, the lumped elements m_1 and m_2 should be interpreted as polar moments of inertia about the shaft axis, and k_1 , k_2 , and k_3 as the torsional stiffness in the connecting shafts. Furthermore, the motion coordinates y_1 and y_2 are rotations and the external excitations $f_1(t)$ and $f_2(t)$ are torques applied at the inertia elements. Practical examples where these three types of vibration system models may be useful are: (a) a two-car train, (b) a bridge with two separate vehicle loads, and (c) an electric motor and pump combination.

The three systems shown in Figure 3.2 are analogous to each other in the sense that the dynamics of all three systems can be represented by similar equations of motion. For modal analysis, it is convenient to express the system equations as a set of coupled second-order differential equations in terms of the displacement variables (coordinates) of the inertia elements. Since in modal analysis we are concerned with linear systems, the system parameters can be given by a mass matrix and a stiffness matrix, or by a flexibility matrix. Lagrange's equations of motion directly yield these matrices; however, we will now present an intuitive method for identifying the stiffness and mass matrices.

The linear, lumped-parameter, undamped systems shown in Figure 3.2 satisfy the set of dynamic equations

$$\begin{bmatrix} m_{11} & m_{12} \\ m_{21} & m_{22} \end{bmatrix} \begin{bmatrix} \ddot{y}_1 \\ \ddot{y}_2 \end{bmatrix} + \begin{bmatrix} k_{11} & k_{12} \\ k_{21} & k_{22} \end{bmatrix} \begin{bmatrix} y_1 \\ y_2 \end{bmatrix} = \begin{bmatrix} f_1 \\ f_2 \end{bmatrix}$$

or

$$\mathbf{M}\ddot{\mathbf{y}} + \mathbf{K}\mathbf{y} = \mathbf{f} \quad (3.1)$$

Here, \mathbf{M} is the inertia matrix which is the generalized case of mass matrix, and \mathbf{K} is the stiffness matrix. There are many ways to derive Equation 3.1. Below, we will describe an approach, termed the *influence coefficient method*, which accomplishes the task by separately determining \mathbf{K} and \mathbf{M} .

3.3.1 Stiffness and Flexibility Matrices

In the systems shown in Figure 3.2 suppose the accelerations \ddot{y}_1 and \ddot{y}_2 are both zero at a particular instant, so that the inertia effects are absent. The stiffness matrix \mathbf{K} is given under these circumstances by the constitutive relation for the spring elements:

$$\begin{bmatrix} f_1 \\ f_2 \end{bmatrix} = \begin{bmatrix} k_{11} & k_{12} \\ k_{21} & k_{22} \end{bmatrix} \begin{bmatrix} y_1 \\ y_2 \end{bmatrix}$$

or

$$\mathbf{f} = \mathbf{K}\mathbf{y} \quad (3.2)$$

in which \mathbf{f} is the force vector $[f_1, f_2]^T$ and \mathbf{y} is the displacement vector $[y_1, y_2]^T$. Both are column vectors. The elements of the stiffness matrix, in this two-DoF case, are explicitly given by

$$\mathbf{K} = \begin{bmatrix} k_{11} & k_{12} \\ k_{21} & k_{22} \end{bmatrix}$$

Suppose that $y_1 = 1$ and $y_2 = 0$ (i.e., give a unit displacement to m_1 while holding m_2 at its original position). Then k_{11} and k_{21} are the forces needed at location 1 and location 2, respectively, to maintain this static configuration. For this condition it is clear that $f_1 = k_1 + k_2$ and $f_2 = -k_2$. Accordingly,

$$k_{11} = k_1 + k_2, \quad k_{21} = -k_2$$

Similarly, suppose that $y_1 = 0$ and $y_2 = 1$. Then k_{12} and k_{22} are the forces needed at location 1 and location 2, respectively, to maintain the corresponding static configuration. It follows that

$$k_{12} = -k_2, \quad k_{22} = k_2 + k_3$$

Consequently, the complete stiffness matrix can be expressed in terms of the stiffness elements in the system as

$$\mathbf{K} = \begin{bmatrix} k_1 + k_2 & -k_2 \\ -k_2 & k_2 + k_3 \end{bmatrix}$$

From the foregoing development, it should be clear that the stiffness parameter k_{ij} represents the force that is needed at the location i to obtain a unit displacement at location j . Hence, these parameters are termed *stiffness influence coefficients*.

Observe that the stiffness matrix is symmetric. Specifically,

$$k_{ij} = k_{ji} \quad \text{for } i \neq j$$

or

$$\mathbf{K}^T = \mathbf{K} \quad (3.3)$$

Note, however, that \mathbf{K} is not diagonal in general ($k_{ij} \neq 0$ for at least two values of $i \neq j$). This means that the system is statically coupled (or *flexibly coupled*).

Flexibility matrix \mathbf{L} is the inverse of the stiffness matrix

$$\mathbf{L} = \mathbf{K}^{-1} \quad (3.4)$$

To determine the flexibility matrix using the influence coefficient approach, we have to start with a constitutive relation of the form

$$\mathbf{y} = \mathbf{L}\mathbf{f} \quad (3.5)$$

Assuming that there are no inertia forces at a particular instant, we then proceed as before. For the systems in Figure 3.2, for example, we start with $f_1 = 1$ and $f_2 = 0$. In this manner, we can determine the elements l_{11} and l_{21} of the flexibility matrix

$$\mathbf{L} = \begin{bmatrix} l_{11} & l_{12} \\ l_{21} & l_{22} \end{bmatrix}$$

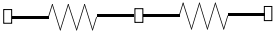
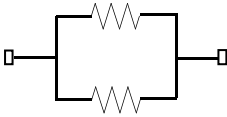
However, here, the result is not as straightforward as in the previous case. For example, to determine l_{11} , we will have to find the flexibility contributions from either side of m_1 . The flexibility of the stiffness element k_1 is $1/k_1$. The combined flexibility of k_2 and k_3 , which are connected in series, is $1/k_2 + 1/k_3$ because the displacements (*across variables*) are additive in series. The two flexibilities on either side of m_1 are applied in parallel at m_1 . Since the forces (*through variables*) are additive in parallel, the stiffness will also be additive. Consequently,

$$\frac{1}{l_{11}} = \frac{1}{(1/k_1)} + \frac{1}{(1/k_2 + 1/k_3)}$$

After some algebraic manipulation we get

$$l_{11} = \frac{k_2 + k_3}{k_1 k_2 + k_2 k_3 + k_3 k_1}$$

TABLE 3.1 Combination Rules for Stiffness and Flexibility Elements

Connection	Graphical Representation	Combined Stiffness	Combined Flexibility
Series		$\frac{1}{(1/k_1 + 1/k_2)}$	$l_1 + l_2$
Parallel		$k_1 + k_2$	$\frac{1}{(1/l_1 + 1/l_2)}$

Since there is no external force at m_2 in the assumed loading configuration, the deflections at m_2 and m_1 are proportioned according to the flexibility distribution along the path. Accordingly,

$$l_{21} = \left[\frac{1/k_3}{1/k_3 + 1/k_2} \right] l_{11}$$

or

$$l_{21} = \frac{k_2}{k_1 k_2 + k_2 k_3 + k_3 k_1}$$

Similarly, we can obtain

$$l_{12} = \frac{k_2}{k_1 k_2 + k_2 k_3 + k_3 k_1}$$

and

$$l_{22} = \frac{k_1 + k_2}{k_1 k_2 + k_2 k_3 + k_3 k_1}$$

Note that these results confirm the symmetry of flexibility matrices

$$l_{ij} = l_{ji} \quad \text{for } i \neq j$$

or

$$\mathbf{L}^T = \mathbf{L} \tag{3.6}$$

Also, we can verify the fact that \mathbf{L} is the inverse of \mathbf{K} . The series–parallel combination rules for stiffness and flexibility that are useful in the present approach are summarized in Table 3.1.

The flexibility parameters l_{ij} represent the displacement at the location i when a unit force is applied at location j . Hence, these parameters are termed *flexibility influence coefficients*.

3.3.2 Inertia Matrix

The mass matrix, which is used in the case of translatory motions, can be generalized as inertia matrix \mathbf{M} in order to include rotatory motions as well. To determine \mathbf{M} for the systems shown in Figure 3.2, suppose the deflections y_1 and y_2 are both zero at a particular instant so that the springs are in their static equilibrium configuration. Under these conditions, the equation of motion 3.1 becomes

$$\mathbf{f} = \mathbf{M}\ddot{\mathbf{y}} \tag{3.7}$$

For the present two-DoF case, the elements of \mathbf{M} are denoted by

$$\mathbf{M} = \begin{bmatrix} m_{11} & m_{12} \\ m_{21} & m_{22} \end{bmatrix}$$

To identify these elements, first set $\ddot{y}_1 = 1$ and $\ddot{y}_2 = 0$. Then, m_{11} and m_{21} are the forces needed at the locations 1 and 2, respectively, to sustain the given accelerations; specifically, $f_1 = m_1$ and $f_2 = 0$. It follows that

$$m_{11} = m_1, \quad m_{21} = 0$$

Similarly, by setting $\ddot{y}_1 = 0$ and $\ddot{y}_2 = 1$, we get

$$m_{12} = 0, \quad m_{22} = m_2$$

Then, the mass matrix is obtained as

$$\mathbf{M} = \begin{bmatrix} m_1 & 0 \\ 0 & m_2 \end{bmatrix}$$

It should be clear now that the inertia parameter m_{ij} represents the force that should be applied at the location i in order to produce a unit acceleration at location j . Consequently, these parameters are called *inertia influence coefficients*.

Note that the mass matrix is symmetric in general; specifically

$$m_{ij} = m_{ji} \quad \text{for } i \neq j$$

or

$$\mathbf{M}^T = \mathbf{M} \tag{3.8}$$

Furthermore, when the independent displacements of the lumped inertia elements are chosen as the motion coordinates, as is typical, the inertia matrix becomes diagonal. If not, it can be made diagonal by using straightforward algebraic substitutions so that each equation contains the second derivative of just one displacement variable. Hence, we may assume

$$m_{ij} = 0 \quad \text{for } i \neq j \tag{3.9}$$

Then the system is said to be inertially uncoupled. This approach to finding \mathbf{K} and \mathbf{M} is summarized in Box 3.2. It can be conveniently extended to damped systems for determining the damping matrix \mathbf{C} .

Box 3.2

INFLUENCE COEFFICIENT METHOD OF
DETERMINING SYSTEM MATRICES
(UNDAMPED CASE)

Stiffness Matrix (\mathbf{K})	Mass Matrix (\mathbf{M})
1. Set $\ddot{\mathbf{y}} = 0$ $\mathbf{f} = \mathbf{K}\mathbf{y}$	1. Set $\mathbf{y} = 0$ $\mathbf{f} = \mathbf{M}\ddot{\mathbf{y}}$
2. Set $y_j = 1$ and $y_i = 0$ for all $i \neq j$	2. Set $\ddot{y}_j = 1$ and $\ddot{y}_i = 0$ for all $i \neq j$
3. Determine \mathbf{f} from the system diagram, that is needed to main equilibrium = j th column of \mathbf{K}	3. Determine \mathbf{f} to maintain this condition = j th column of \mathbf{M}
Repeat for all j	Repeat for all j

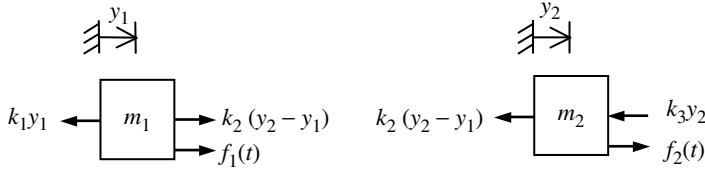


FIGURE 3.3 Free-body diagram of the two-DoF system.

3.3.3 Direct Approach for Equations of Motion

The influence coefficient approach that was described in the previous section is a rather indirect way of obtaining the equations of motion 3.1 for a multi-DoF system. The most straightforward approach, however, is to sketch a free-body diagram for the system, mark the forces or torques on each inertia element, and finally, apply Newton's Second Law. This approach is now illustrated for the system shown in Figure 3.2(a). The equations of motion for the systems in Figures 3.2(b) and (c) will follow analogously.

The free-body diagram of the system in Figure 3.2(a) is sketched in Figure 3.3. Note that all the forces on each inertia element are marked.

Application of Newton's Second Law to the two mass elements separately gives

$$m_1 \ddot{y}_1 = -k_1 y_1 + k_2 (y_2 - y_1) + f_1(t)$$

$$m_2 \ddot{y}_2 = -k_2 (y_2 - y_1) - k_3 y_2 + f_2(t)$$

The terms can be rearranged to obtain the following two coupled, second order, linear, ordinary differential equations:

$$m_1 \ddot{y}_1 + (k_1 + k_2) y_1 - k_2 y_2 = f_1(t)$$

$$m_2 \ddot{y}_2 - k_2 y_1 + (k_2 + k_3) y_2 = f_2(t)$$

which may be expressed in the vector-matrix form as

$$\begin{bmatrix} m_1 & 0 \\ 0 & m_2 \end{bmatrix} \begin{bmatrix} \ddot{y}_1 \\ \ddot{y}_2 \end{bmatrix} + \begin{bmatrix} k_1 + k_2 & -k_2 \\ -k_2 & k_2 + k_3 \end{bmatrix} \begin{bmatrix} y_1 \\ y_2 \end{bmatrix} = \begin{bmatrix} f_1(t) \\ f_2(t) \end{bmatrix}$$

Observe that this result is identical to what we obtained by the influence coefficient approach.

Another convenient approach that would provide essentially the same result is the energy method through the application of Lagrange's equations. Two common types of models used in vibration analysis and applications are summarized in Box 3.3.

3.4 Modal Vibrations

Among the infinite number of relative geometric configurations the lumped masses in a multi-DoF system could assume under free motion (i.e., with $\mathbf{f}(t) = 0$), when excited by an arbitrary initial state, there is a finite number of configurations that are naturally preferred by the system. Each of these configurations will have an associated frequency of motion. These motions are termed *modal motions*. By choosing the initial displacement $\mathbf{y}(0)$ proportional to a particular modal configuration, with zero initial velocity, $\dot{\mathbf{y}}(0) = 0$, that particular mode can be excited at the associated natural frequency of motion. The displacements of different DoF retain this initial proportion at all times. This constant proportion in displacement can be expressed as a vector $\boldsymbol{\psi}$ for that mode, and represents the mode shape. Note that each modal motion is a harmonic motion executed at a specific frequency ω known as the *natural frequency* (undamped). In view of these general properties of modal motions,

Linear	Nonlinear
Coupled second-order equations	
$\mathbf{M}\ddot{\mathbf{y}} + \mathbf{C}\dot{\mathbf{y}} + \mathbf{K}\mathbf{y} = \mathbf{f}(t)$	$\mathbf{M}\ddot{\mathbf{y}} = \mathbf{h}(\mathbf{y}, \dot{\mathbf{y}}, \mathbf{f}(t))$
Response vector:	
$\mathbf{y} = [y_1, y_2, \dots, y_p]^T$; p = number of DoF	
Excitation vector: $\mathbf{f}(t) = [f_1, f_2, \dots, f_p]^T$	
\mathbf{M} = mass matrix	
\mathbf{C} or \mathbf{B} = damping matrix	
\mathbf{K} = stiffness matrix	
Coupled first-order equations (state-space models)	
$\dot{\mathbf{x}} = \mathbf{A}\mathbf{x} + \mathbf{B}\mathbf{u}$	$\dot{\mathbf{x}} = \mathbf{a}(\mathbf{x}, \mathbf{u})$
$\mathbf{y} = \mathbf{C}\mathbf{x}$	$\mathbf{y} = \mathbf{y}(\mathbf{x})$
State vector $\mathbf{x} = [x_1, x_2, \dots, x_n]^T$; n = order of the system	
Input (excitation) vector $\mathbf{u} = [u_1, u_2, \dots, u_m]^T$	
Output (response) vector $\mathbf{y} = [y_1, y_2, \dots, y_p]^T$	
Notes:	
1. Definition of state: If $\mathbf{x}(t_0)$, and \mathbf{u} from t_0 to t_1 , are known, $\mathbf{x}(t_1)$ can be determined completely	
2. State vector \mathbf{x} contains a minimum number (n) of elements	
3. State model is not unique (different state models are possible for the same system)	
4. One approach to obtaining a state model is to use $\mathbf{x} = \begin{bmatrix} \mathbf{y} \\ \dot{\mathbf{y}} \end{bmatrix}$	

$$\mathbf{y} = \boldsymbol{\Psi} \cos \omega t \quad (3.10)$$
$$\mathbf{y} = \boldsymbol{\psi} e^{j\omega t} \quad (3.11)$$
$$\mathbf{M}\ddot{\mathbf{y}} + \mathbf{K}\mathbf{y} = \mathbf{0} \quad (3.12)$$
$$[\omega^2 \mathbf{M} - \mathbf{K}] \boldsymbol{\Psi} = 0 \quad (3.13)$$
$$\det[\omega^2 \mathbf{M} - \mathbf{K}] = 0 \quad (3.14)$$

© 2005 by Taylor & Francis Group, LLC

results a mode shape vector Ψ_i that determines up to one unknown parameter which can be used as a scaling parameter. Extra care should be exercised, however, when determining mode shapes for zero natural frequencies (i.e., rigid-body modes) and repeated natural frequencies (i.e., for systems with a dynamic symmetry). We shall return to these considerations in later sections.

Example 3.3

Consider a mechanical system modeled as in Figure 3.4. This is obtained from the systems in Figure 3.2 by setting $m_1 = m$, $m_2 = \alpha m$, $k_1 = k$, $k_2 = \beta k$, and $k_3 = 0$. The corresponding mass matrix and the stiffness matrix are

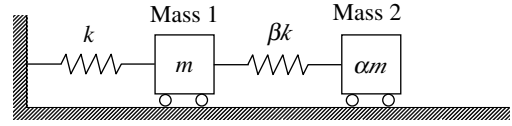


FIGURE 3.4 A modal vibration example.

$$\mathbf{M} = \begin{bmatrix} m & 0 \\ 0 & \alpha m \end{bmatrix}, \quad \mathbf{K} = \begin{bmatrix} (1 + \beta)k & -\beta k \\ -\beta k & \beta k \end{bmatrix}$$

The natural frequencies are given by the roots of the characteristic equation

$$\det \begin{bmatrix} \omega^2 m - (1 + \beta)k & \beta k \\ \beta k & \omega^2 \alpha m - \beta k \end{bmatrix} = 0$$

By expanding the determinant, this can be expressed as

$$[\omega^2 m - (1 + \beta)k][\omega^2 \alpha m - \beta k] - \beta^2 k^2 = 0$$

or

$$\omega^4 \alpha m^2 - \omega^2 km[\beta + \alpha(1 + \beta)] + \beta k^2 = 0$$

Let us define a frequency parameter $\omega_0 = \sqrt{k/m}$. This parameter is identified as the natural frequency of an undamped simple oscillator (single-DoF mass-spring system) with mass m and stiffness k . Consequently, the characteristic equation of the given 2 DoF system can be written as

$$\alpha \left(\frac{\omega}{\omega_0} \right)^4 - (\alpha + \beta + \alpha\beta) \left(\frac{\omega}{\omega_0} \right)^2 + \beta = 0$$

whose roots are

$$\left(\frac{\omega_1}{\omega_0} \right)^2, \left(\frac{\omega_2}{\omega_0} \right)^2 = \frac{1}{2\alpha} \{ \alpha + \beta + \alpha\beta \} \left\{ 1 \mp \sqrt{1 - \frac{4\alpha\beta}{(\alpha + \beta + \alpha\beta)^2}} \right\}$$

The mode shapes are obtained by solving for Ψ in

$$\begin{bmatrix} \omega^2 m - (1 + \beta)k & \beta k \\ \beta k & \omega^2 \alpha m - \beta k \end{bmatrix} \Psi = 0$$

or

$$\begin{bmatrix} \left(\frac{\omega}{\omega_0} \right)^2 - (1 + \beta) & \beta \\ \beta & \alpha \left(\frac{\omega}{\omega_0} \right)^2 - \beta \end{bmatrix} \Psi = 0$$

In a mode shape vector, only the ratio of the elements is needed. This is because, in determining a mode shape, we are concerned about the relative motions of the lumped masses, not the absolute motions.

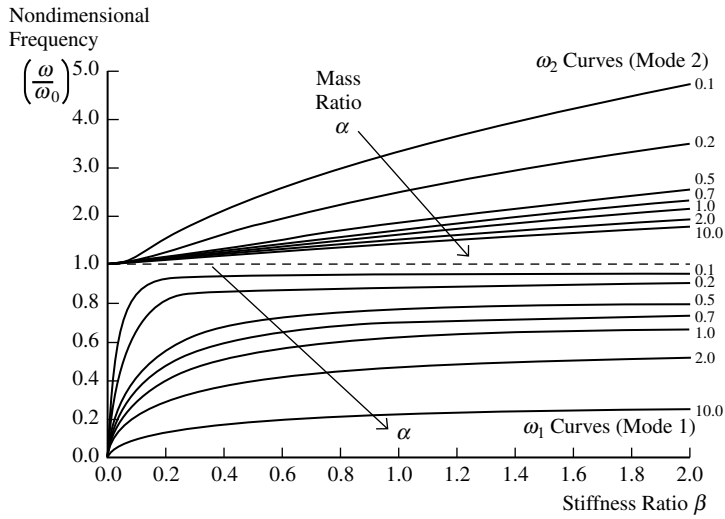


FIGURE 3.5 Dependence of natural frequencies (ω/ω_0) on mass ratio (α) and stiffness ratio (β) .

From the above equation, it is clear that this ratio is given by

$$\frac{\psi_2}{\psi_1} = \frac{(1 + \beta) - \left(\frac{\omega}{\omega_0}\right)^2}{\beta} = \frac{\beta}{\beta - \alpha\left(\frac{\omega}{\omega_0}\right)^2}$$

which is evaluated by substituting the appropriate value for (ω/ω_0) , depending on the mode, into any one of the right-hand-side expressions above.

The dependence of the natural frequencies on the parameters α and β is illustrated by the curves in Figure 3.5. Some representative values of the natural frequencies and mode shape ratios are listed in Table 3.2.

Note that, when $\beta = 0$, the spring connecting the two masses does not exist and the system reduces to two separate systems: a simple oscillator of natural frequency ω_0 and a single mass particle (of zero natural frequency). It is clear that in this case $\omega_1/\omega_0 = 0$ and $\omega_2/\omega_0 = 1$. This fact can be established from the expressions for natural frequencies of the original system by setting $\beta = 0$. The mode corresponding to $\omega_1/\omega_0 = 0$ is a rigid-body mode in which the free mass moves indefinitely (zero frequency) and the other mass (restrained mass) stands still. It follows that the mode shape ratio $(\psi_2/\psi_1)_1 \rightarrow \infty$. In the second mass, the free mass stands still and the restrained mass moves. Hence, $(\psi_2/\psi_1)_1 = 0$. These results are also obtained from the general expressions for the mode shape ratios of the original system.

TABLE 3.2 The Dependence of Natural Frequencies and Mode Shapes on Inertia and Stiffness

α	0.5				1.0				2.0			
β	ω_1/ω_0	ω_2/ω_0	$(\psi_2/\psi_1)_1$	$(\psi_2/\psi_1)_2$	ω_1/ω_0	ω_2/ω_0	$(\psi_2/\psi_1)_1$	$(\psi_2/\psi_1)_2$	ω_1/ω_0	ω_2/ω_0	$(\psi_2/\psi_1)_1$	$(\psi_2/\psi_1)_2$
0	0	1.0	∞	0	0	1.0	∞	0	0	1.0	∞	0
0.5	0.71	1.41	2.0	-1.0	0.54	1.31	2.41	-0.41	0.40	1.26	2.69	-0.19
1.0	0.77	1.85	1.41	-1.41	0.62	1.62	1.62	-0.62	0.47	1.51	1.78	-0.28
2.0	0.79	2.52	1.19	-1.69	0.66	2.14	1.28	-0.78	0.52	1.93	1.37	-0.37
5.0	0.81	3.92	1.07	-1.87	0.69	3.24	1.10	-0.91	0.55	2.86	1.14	-0.44
∞	0.82	∞	1.0	-2.0	0.71	∞	1.0	-1.0	0.57	∞	1.0	-0.5

When $\beta \rightarrow \infty$, the spring connecting the two masses becomes rigid and the two masses act as a single mass $(1 + \alpha)m$ restrained by a spring of stiffness k . This simple oscillator has a squared natural frequency of $\omega_0^2/(1 + \alpha)$. This is considered the smaller natural frequency of the corresponding system: $(\omega_1/\omega_0)^2 = 1/(1 + \alpha)$. The larger natural frequency ω_2 approaches ∞ in this case and it corresponds to the natural frequency of a massless spring. These limiting results can be derived from the general expressions for the natural frequencies of the original system by using the fact that for small $|x| \ll 1$, the expression $\sqrt{1 - x}$ is approximately equal to $1 - (1/2)x$. (Proof: Use the Taylor series expansion.) In the first mode, the two masses move as one unit and hence the mode shape ratio $(\psi_2/\psi_1)_1 = 1$. In the second mode, the two masses move in opposite directions restrained by an infinitely stiff spring. This is considered the static mode which results from the redundant situation of associating two DoF to a system that actually has only one lumped mass $(1 + \alpha)m$. In this case, the mode shape ratio is obtained from the general result as follows: For large β , we can neglect α in comparison. Hence,

$$\left(\frac{\omega_2}{\omega_0}\right)^2 = \frac{1}{2\alpha} \{\beta + \alpha\beta\} \{1 + 1\} = (1 + \alpha) \frac{\beta}{\alpha}$$

By substituting this result in the expression for the mode shape ratio, we obtain

$$\left(\frac{\psi_2}{\psi_1}\right)_2 = \frac{\beta}{\beta - \alpha\left(\frac{\omega_2}{\omega_0}\right)^2} = \frac{\beta}{\beta - \alpha(1 + \alpha)\frac{\beta}{\alpha}} = -\frac{1}{\alpha}$$

Finally, consider the case $\alpha = 0$ (with $\beta \neq 0$). In this case, only one mass m restrained by a spring of stiffness k is present. The spring of stiffness βk has an open end. The first mode corresponds to a simple oscillator of natural frequency ω_0 . Hence, $\omega_1/\omega_0 = 1$. The open end has the same displacement as the point mass. Consequently, $(\psi_2/\psi_1)_1 = 1$. These results can be derived from the general expressions for the original system. In the second mode the simple oscillator stands still and the open-ended spring oscillates (at an infinite frequency). Hence $\omega_2/\omega_0 = \infty$, and this again corresponds to a static mode situation which arises by assigning two DoF to a system that has only one DoF associated with its inertia elements. Since the lumped mass stands still, we have $(\psi_2/\psi_1)_2 = \infty$.

Note that, when $\alpha = 0$ and $\beta = 0$, the system reduces to a simple oscillator and the second mode is completely undefined. Hence, the corresponding results cannot be derived from the general results for the original system.

3.5 Orthogonality of Natural Modes

Let us write Equation 3.13 explicitly for the two distinct modes i and j . Distinct modes are defined as those having distinct natural frequencies (i.e., $\omega_i \neq \omega_j$).

$$\omega_i^2 \mathbf{M} \boldsymbol{\psi}_i - \mathbf{K} \boldsymbol{\psi}_i = 0 \quad (3.15)$$

$$\omega_j^2 \mathbf{M} \boldsymbol{\psi}_j - \mathbf{K} \boldsymbol{\psi}_j = 0 \quad (3.16)$$

Premultiply Equation 3.15 by $\boldsymbol{\psi}_j^T$ and Equation 3.16 by $\boldsymbol{\psi}_i^T$

$$\omega_i^2 \boldsymbol{\psi}_j^T \mathbf{M} \boldsymbol{\psi}_i - \boldsymbol{\psi}_j^T \mathbf{K} \boldsymbol{\psi}_i = 0 \quad (3.17)$$

$$\omega_j^2 \boldsymbol{\psi}_i^T \mathbf{M} \boldsymbol{\psi}_j - \boldsymbol{\psi}_i^T \mathbf{K} \boldsymbol{\psi}_j = 0 \quad (3.18)$$

Take the transpose of Equation 3.18, which is a scalar:

$$\omega_j^2 \boldsymbol{\psi}_j^T \mathbf{M}^T \boldsymbol{\psi}_i - \boldsymbol{\psi}_j^T \mathbf{K}^T \boldsymbol{\psi}_i = 0$$

This, in view of the symmetry of \mathbf{M} and \mathbf{K} as expressed in Equation 3.8 and Equation 3.3, becomes

$$\omega_j^2 \boldsymbol{\psi}_j^T \mathbf{M} \boldsymbol{\psi}_i - \boldsymbol{\psi}_j^T \mathbf{K} \boldsymbol{\psi}_i = 0$$

By subtracting this result from Equation 3.17, we get

$$(\omega_i^2 - \omega_j^2)\boldsymbol{\psi}_i^T \mathbf{M} \boldsymbol{\psi}_j = 0$$

Now, because $\omega_i \neq \omega_j$, it follows that

$$\boldsymbol{\psi}_i^T \mathbf{M} \boldsymbol{\psi}_j = \begin{cases} 0 & \text{for } i \neq j \\ M_i & \text{for } i = j \end{cases} \quad (3.19)$$

Equation 3.19 is a useful *orthogonality condition* for natural modes.

Even though the foregoing condition of **M**-orthogonality was proved for distinct (unequal) natural frequencies it is generally true, even if two or more modes have repeated (equal) natural frequencies. Indeed, if a particular natural frequency is repeated r times, there will be r arbitrary elements in the modal vector. As a result, we are able to determine r independent mode shapes that are orthogonal with respect to the **M** matrix. An example is given later in the problem of Figure 3.6. Note further that any such mode shape vector corresponding to a repeated natural frequency will also be **M**-orthogonal to the mode shape vector corresponding to any of the remaining distinct natural frequencies. Consequently, we conclude that the entire set of n mode shape vectors is **M**-orthogonal even in the presence of various combinations of repeated natural frequencies.

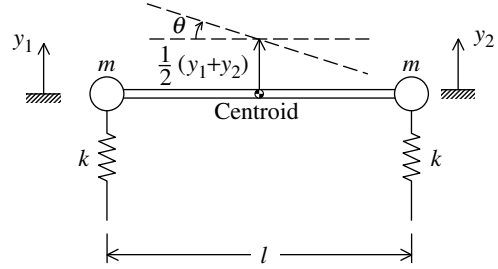


FIGURE 3.6 A simplified vehicle model for heave and pitch motions.

3.5.1 Modal Mass and Normalized Modal Vectors

Note that, in Equation 3.19, a parameter M_i has been defined to denote $\boldsymbol{\psi}_i^T \mathbf{M} \boldsymbol{\psi}_i$. This parameter is termed the *generalized mass* or *modal mass* for the i th mode. Since the modal vectors $\boldsymbol{\psi}_i$ are determined for up to one unknown parameter, it is possible to set the value of M_i arbitrarily. The process of specifying the unknown scaling parameter in the modal vector, according to some convenient rule, is called the *normalization* of modal vectors. The resulting modal vectors are termed *normal modes*. A particularly useful method of normalization is to set each modal mass to unity ($M_i = 1$). The corresponding normal modes are said to be *normalized with respect to the mass matrix*, or **M**-normal. Note that, if $\boldsymbol{\psi}_i$ is normal with respect to **M**, then it follows from Equation 3.18 that $-\boldsymbol{\psi}_i$ is also normal with respect to **M**. Specifically,

$$(-\boldsymbol{\psi}_i)^T \mathbf{M} (-\boldsymbol{\psi}_i) = \boldsymbol{\psi}_i^T \mathbf{M} \boldsymbol{\psi}_i = 1 \quad (3.20)$$

It follows that **M**-normal modal vectors are still arbitrary up to a multiplier of -1 . A convenient practice for eliminating this arbitrariness is to make the first element of each normalized modal vector positive.

3.6 Static Modes and Rigid-Body Modes

3.6.1 Static Modes

Modes corresponding to infinite natural frequencies are known as static modes. For these modes, the modal mass is zero; in the normalization process with respect to **M** static modes cannot be included. If we assign a DoF for a massless location, the resulting mass matrix **M** becomes singular ($\det \mathbf{M} = 0$) and a static mode arises. We have come across two similar situations in a previous example; in one case the stiffness of the spring connecting two masses is made infinite so that they act as a single mass in the limit, and in the other case one of the two masses is made equal to zero so that only one mass is left. We should take extra precautions to avoid such situations by using proper modeling practices; the presence of a static mode amounts to assigning a DoF to a system that it does not actually possess. In a static mode, the system behaves like a simple massless spring.

In the literature of experimental modal analysis, the static modes are represented by a *residual flexibility* term in the transfer functions. Note that, in this case, modes of natural frequencies that are

higher than the analysis bandwidth or the maximum frequency of interest are considered static modes. Such issues of experimental modal analysis will be discussed in [Chapter 18](#).

3.6.2 Linear Independence of Modal Vectors

In the absence of static modes (i.e., modal masses $M_i \neq 0$), the inertia matrix \mathbf{M} will be nonsingular. Then the orthogonality condition 3.19 implies that the modal vectors are *linearly independent*, and consequently, they will form a *basis* for the n -dimensional space of all possible displacement trajectories \mathbf{y} for the system. Any vector in this *configuration space* (or displacement space), therefore, can be expressed as a linear combination of the modal vectors.

Note that we have assumed in the earlier development that the natural frequencies are distinct (or unequal). Nevertheless, linearly independent modal vectors are possessed by modes of equal natural frequencies as well. An example is the situation where these modes are physically uncoupled. These modal vectors are not unique, however; there will be arbitrary elements in the modal vector equal in number to the repeated natural frequencies. Any linear combination of these modal vectors can also serve as a modal vector at the same natural frequency. To explain this point further, without loss of generality suppose that $\omega_1 = \omega_2$. Then, from Equation 3.15, we have

$$\omega_1^2 \mathbf{M} \boldsymbol{\psi}_1 - \mathbf{K} \boldsymbol{\psi}_1 = 0$$

$$\omega_1^2 \mathbf{M} \boldsymbol{\psi}_2 - \mathbf{K} \boldsymbol{\psi}_2 = 0$$

Multiply the first equation by α , the second equation by β , and add the resulting equations. We get

$$\omega_1^2 \mathbf{M}(\alpha \boldsymbol{\psi}_1 + \beta \boldsymbol{\psi}_2) - \mathbf{K}(\alpha \boldsymbol{\psi}_1 + \beta \boldsymbol{\psi}_2) = 0$$

This verifies that any linear combination $\alpha \boldsymbol{\psi}_1 + \beta \boldsymbol{\psi}_2$ of the two modal vectors $\boldsymbol{\psi}_1$ and $\boldsymbol{\psi}_2$ will also serve as a modal vector for the natural frequency ω_1 . The physical significance of this phenomenon should be clear in Example 3.4.

3.6.3 Modal Stiffness and Normalized Modal Vectors

It is possible to establish an alternative version of the orthogonality condition given as Equation 3.19 by substituting it into Equation 3.18. This gives

$$\boldsymbol{\psi}_i^T \mathbf{K} \boldsymbol{\psi}_j = \begin{cases} 0 & \text{for } i \neq j \\ K_i & \text{for } i = j \end{cases} \quad (3.21)$$

This condition is termed **K-orthogonality**.

Since the **M-orthogonality** condition (Equation 3.19) is true even for the case of repeated natural frequencies, it should be clear that the **K-orthogonality** condition (Equation 3.21) is also true, in general, even with repeated natural frequencies. The newly defined parameter K_i represents the value of $\boldsymbol{\psi}_i^T \mathbf{K} \boldsymbol{\psi}_i$ and is known as the *generalized stiffness* or *modal stiffness* corresponding to the i th mode.

Another useful way to *normalize* modal vectors is to choose their unknown parameters so that all modal stiffnesses are unity ($K_i = 1$ for all i). This process is known as normalization with respect to the stiffness matrix. The resulting normal modes are said to be **K-normal**. These normal modes are still arbitrary up to a multiplier of -1 . This can be eliminated by assigning positive values to the first element of all modal vectors.

Note that it is not possible to normalize a modal vector simultaneously with respect to both \mathbf{M} and \mathbf{K} , in general. To understand this further, we may observe that $\omega_i^2 = K_i/M_i$ and consequently we are unable to pick both K_i and M_i arbitrarily. In particular, for the **M-normal** case $K_i = \omega_i^2$ and for the **K-normal** case $M_i = 1/\omega_i^2$.

3.6.4 Rigid-Body Modes

Rigid-body modes are those for which the natural frequency is zero. Modal stiffness is zero for rigid-body modes, and as a result it is not possible to normalize these modes with respect to the stiffness matrix. Note that when rigid-body modes are present the stiffness matrix becomes *singular* ($\det \mathbf{K} = 0$). Physically, removal of a spring that connects two DoF results in a rigid-body mode. In Example 3.3 we came across a similar situation. In experimental modal analysis applications, low-stiffness connections or restraints, which might be present in a test object, could result in approximate rigid-body modes that would become prominent at low frequencies.

Some important results of modal analysis that we have discussed thus far are summarized in Table 3.3.

Example 3.4

Consider a light rod of length l having equal masses m attached to its ends. Each end is supported by a spring of stiffness k as shown in Figure 3.6. Note that this system may represent a simplified model of a vehicle in heave and pitch motions. Gravity effects can be eliminated by measuring the displacements y_1 and y_2 of the two masses about their respective static equilibrium positions. Assume small front-to-back rotations θ in the pitch motion and small up-and-down displacements $(1/2)(y_1 + y_2)$ of the centroid in its heave motion.

3.6.4.1 Equation of Heave Motion

From Newton's Second Law for rigid-body motion, we get

$$2m \frac{1}{2}(\ddot{y}_1 + \ddot{y}_2) = -ky_1 - ky_2$$

3.6.4.2 Equation of Pitch Motion

Note that, for small angles of rotation, $\theta = (y_1 - y_2)/l$. The moment of inertia of the system about the centroid is $2m(l/2)^2 = (1/2)ml^2$. Hence, by Newton's Second Law for rigid-body rotation, we have

$$\frac{1}{2}ml^2 \left(\frac{\ddot{y}_1 - \ddot{y}_2}{l} \right) = -\frac{l}{2}ky_1 + \frac{l}{2}ky_2$$

These two equations of motion can be written as

$$\ddot{y}_1 + \ddot{y}_2 + \omega_0^2(y_1 + y_2) = 0$$

$$\ddot{y}_1 - \ddot{y}_2 + \omega_0^2(y_1 - y_2) = 0$$

TABLE 3.3 Some Important Results of Modal Analysis

System	$\mathbf{M}\ddot{\mathbf{y}} + \mathbf{K}\mathbf{y} = \mathbf{f}(t)$
Symmetry	$\mathbf{M}^T = \mathbf{M}$ and $\mathbf{K}^T = \mathbf{K}$
Modal problem	$[\omega^2 \mathbf{M} - \mathbf{K}]\boldsymbol{\psi} = 0$
Characteristic equation (gives natural frequencies)	$\det[\omega^2 \mathbf{M} - \mathbf{K}] = 0$
\mathbf{M} -orthogonality	$\boldsymbol{\psi}_i^T \mathbf{M} \boldsymbol{\psi}_j = \begin{cases} 0 & \text{for } i \neq j \\ M_i & \text{for } i = j \end{cases}$
\mathbf{K} -orthogonality	$\boldsymbol{\psi}_i^T \mathbf{K} \boldsymbol{\psi}_j = \begin{cases} 0 & \text{for } i \neq j \\ K_i & \text{for } i = j \end{cases}$
Modal mass (generalized mass)	M_i
Modal stiffness (generalized stiffness)	K_i
Natural frequency	$\omega_i = \sqrt{K_i/M_i}$
\mathbf{M} -normal case	$M_i = 1, K_i = \omega_i^2$
\mathbf{K} -normal case	$K_i = 1, M_i = 1/\omega_i^2$
Presence of rigid-body modes	$\det \mathbf{K} = 0, K_i = 0$, and $\omega_i = 0$
Presence of static modes	$\det \mathbf{M} = 0, M_i = 0$, and $\omega_i \rightarrow \infty$

in which $\omega_0 = \sqrt{k/m}$. By straightforward algebraic manipulation, a pair of completely uncoupled equations of motion are obtained; thus

$$\ddot{y}_1 + \omega_0^2 y_1 = 0$$

$$\ddot{y}_2 + \omega_0^2 y_2 = 0$$

It follows that the resulting mass matrix and the stiffness matrix are both diagonal. In this case, there is an infinite number of choices for mode shapes, and any two linearly independent second-order vectors can serve as modal vectors for the system. Two particular choices are shown in Figure 3.7. Any of these mode shapes will correspond to the same natural frequency ω_0 .

In each of these two choices, the mode shapes have been chosen so that they are orthogonal with respect to both \mathbf{M} and \mathbf{K} . This fact is verified below. Note that, in the present example

$$\mathbf{M} = \begin{bmatrix} 1 & 0 \\ 0 & 1 \end{bmatrix} \quad \text{and} \quad \mathbf{K} = \begin{bmatrix} \omega_0^2 & 0 \\ 0 & \omega_0^2 \end{bmatrix}$$

For Case 1:

$$[1 \quad 1]\mathbf{M} \begin{bmatrix} 1 \\ -1 \end{bmatrix} = 0 \quad \text{and} \quad [1 \quad 1]\mathbf{K} \begin{bmatrix} 1 \\ -1 \end{bmatrix} = 0$$

For Case 2:

$$[1 \quad 0]\mathbf{M} \begin{bmatrix} 0 \\ 1 \end{bmatrix} = 0 \quad \text{and} \quad [1 \quad 0]\mathbf{K} \begin{bmatrix} 0 \\ 1 \end{bmatrix} = 0$$

In general, since both elements of each eigenvector can be picked arbitrarily, we can write

$$\boldsymbol{\psi}_1 = \begin{bmatrix} 1 \\ a \end{bmatrix} \quad \text{and} \quad \boldsymbol{\psi}_2 = \begin{bmatrix} 1 \\ b \end{bmatrix}$$

where a and b are arbitrary, limited only by the orthogonality requirement for $\boldsymbol{\psi}_1$ and $\boldsymbol{\psi}_2$. The \mathbf{M} -orthogonality requires

$$[1 \quad a] \begin{bmatrix} 1 & 0 \\ 0 & 1 \end{bmatrix} \begin{bmatrix} 1 \\ b \end{bmatrix} = 0$$

and \mathbf{K} -orthogonality requires

$$[1 \quad a] \begin{bmatrix} \omega_0^2 & 0 \\ 0 & \omega_0^2 \end{bmatrix} \begin{bmatrix} 1 \\ b \end{bmatrix} = 0$$

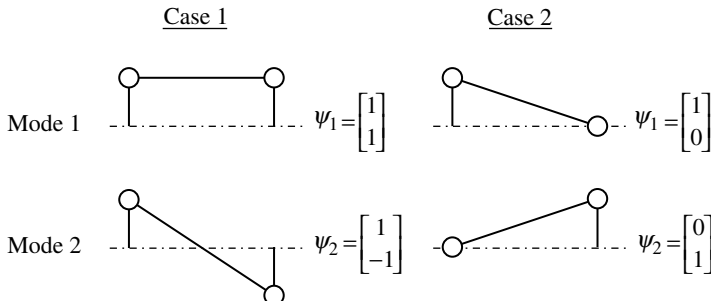


FIGURE 3.7 Two possibilities of mode shapes for the symmetric heave-pitch vehicle.

Both conditions give $1 + ab = 0$, which corresponds to $ab = -1$. Note that Case 1 corresponds to $a = 1$ and $b = -1$ and Case 2 corresponds to $a = 0$ and $b \rightarrow \infty$. More generally, we can pick as modal vectors

$$\psi_1 = \begin{bmatrix} 1 \\ a \end{bmatrix} \quad \text{and} \quad \psi_2 = \begin{bmatrix} 1 \\ -1/a \end{bmatrix}$$

such that the two mode shapes are both **M**-orthogonal and **K**-orthogonal. In fact, if this particular system is excited by an arbitrary initial displacement, it will undergo free vibrations at frequency ω_0 while maintaining the initial displacement ratio. Hence, if **M**-orthogonality and **K**-orthogonality are not required, any arbitrary second-order vector may serve as a modal vector to this system.

Example 3.5

An example for a system possessing a rigid-body mode is shown in Figure 3.8. This system, a crude model of a two-car train, can be derived from the system shown in Figure 3.4 by removing the end spring (inertia restraint) and setting $\alpha = 1$ and $\beta = 1$. The equation for unforced motion of this system is

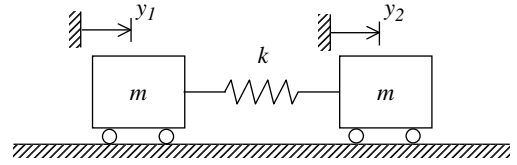


FIGURE 3.8 A simplified model of a two-car train.

$$\begin{bmatrix} m & 0 \\ 0 & m \end{bmatrix} \begin{bmatrix} \ddot{y}_1 \\ \ddot{y}_2 \end{bmatrix} + \begin{bmatrix} k & -k \\ -k & k \end{bmatrix} \begin{bmatrix} y_1 \\ y_2 \end{bmatrix} = \begin{bmatrix} 0 \\ 0 \end{bmatrix}$$

Note that $\det \mathbf{M} = m^2 \neq 0$ and hence the system does not possess static modes. This should also be obvious from the fact that each DoF (y_1 and y_2) has an associated, independent mass element. On the other hand, $\det \mathbf{K} = k^2 - k^2 = 0$ which signals the presence of rigid-body modes.

The characteristic equation of the system is

$$\det \begin{bmatrix} \omega^2 m - k & k \\ k & \omega^2 m - k \end{bmatrix} = 0$$

or

$$(\omega^2 m - k)^2 - k^2 = 0$$

The two natural frequencies are given by the roots: $\omega_1 = 0$ and $\omega_2 = \sqrt{2k/m}$. Note that the zero natural frequency corresponds to the rigid body mode. The mode shapes can reveal further interesting facts.

3.6.4.3 First Mode (Rigid-Body Mode)

In this case, we have $\omega = 0$. Consequently, from Equation 3.15, the mode shape is given by

$$\begin{bmatrix} -k & k \\ k & -k \end{bmatrix} \begin{bmatrix} \psi_1 \\ \psi_2 \end{bmatrix} = \begin{bmatrix} 0 \\ 0 \end{bmatrix}$$

which has the general solution $\psi_1 = \psi_2$, or

$$\begin{bmatrix} \psi_1 \\ \psi_2 \end{bmatrix} = \begin{bmatrix} a \\ a \end{bmatrix}$$

The parameter a can be chosen arbitrarily. The corresponding modal mass is

$$M_1 = [a \quad a] \begin{bmatrix} m & 0 \\ 0 & m \end{bmatrix} \begin{bmatrix} a \\ a \end{bmatrix} = 2ma^2$$

If the modal vector is normalized with respect to \mathbf{M} , we have $M_1 = 2ma^2 = 1$. Then, $a = \pm 1/\sqrt{2m}$ and the corresponding normal mode vector would be

$$\begin{bmatrix} \psi_1 \\ \psi_2 \end{bmatrix}_1 = \begin{bmatrix} \frac{1}{\sqrt{2m}} \\ \frac{1}{\sqrt{2m}} \end{bmatrix} \quad \text{or} \quad \begin{bmatrix} -\frac{1}{\sqrt{2m}} \\ -\frac{1}{\sqrt{2m}} \end{bmatrix}$$

which is arbitrary up to a multiplier of -1 . If the first element of the normal mode is restricted to be positive, the former vector (one with positive elements) should be used.

We have already noted that it is not possible to normalize a rigid-body mode with respect to \mathbf{K} . Specifically, the modal stiffness for the rigid-body mode is

$$K_1 = \begin{bmatrix} a & a \end{bmatrix} \begin{bmatrix} k & -k \\ -k & k \end{bmatrix} \begin{bmatrix} a \\ a \end{bmatrix} = 0$$

for any choice for a , as expected.

3.6.4.4 Second Mode

For this mode, $\omega_2 = \sqrt{2k/m}$. By substituting into Equation 3.15 we get

$$\begin{bmatrix} k & k \\ k & k \end{bmatrix} \begin{bmatrix} \psi_1 \\ \psi_2 \end{bmatrix}_2 = \begin{bmatrix} 0 \\ 0 \end{bmatrix}$$

the solution of which gives the corresponding modal vector (mode shape).

The general solution is $\psi_2 = -\psi_1$, or

$$\begin{bmatrix} \psi_1 \\ \psi_2 \end{bmatrix}_2 = \begin{bmatrix} a \\ -a \end{bmatrix}$$

in which a is arbitrary. The corresponding modal mass is given by

$$M_2 = \begin{bmatrix} a & -a \end{bmatrix} \begin{bmatrix} m & 0 \\ 0 & m \end{bmatrix} \begin{bmatrix} a \\ -a \end{bmatrix} = 2ma^2$$

and the modal stiffness is given

$$K_2 = \begin{bmatrix} a & -a \end{bmatrix} \begin{bmatrix} k & -k \\ -k & k \end{bmatrix} \begin{bmatrix} a \\ -a \end{bmatrix} = 4ka^2$$

Then, for \mathbf{M} -normality we must have $2ma^2 = 1$ or $a = \pm 1/\sqrt{2m}$.

It follows that the \mathbf{M} -normal mode vector would be

$$\begin{bmatrix} \psi_1 \\ \psi_2 \end{bmatrix}_1 = \begin{bmatrix} \frac{1}{\sqrt{2m}} \\ -\frac{1}{\sqrt{2m}} \end{bmatrix} \quad \text{or} \quad \begin{bmatrix} -\frac{1}{\sqrt{2m}} \\ \frac{1}{\sqrt{2m}} \end{bmatrix}$$

The corresponding value of the modal stiffness is $K_2 = 2k/m$, which is equal to ω_2^2 , as expected. Similarly, for \mathbf{K} -normality we must have $4Ka^2 = 1$, or $a = \pm 1/\sqrt{4K}$. Hence, the \mathbf{K} -normal modal vector would be

$$\begin{bmatrix} \psi_1 \\ \psi_2 \end{bmatrix}_2 = \begin{bmatrix} \frac{1}{\sqrt{4k}} \\ -\frac{1}{\sqrt{4k}} \end{bmatrix} \quad \text{or} \quad \begin{bmatrix} -\frac{1}{\sqrt{4k}} \\ \frac{1}{\sqrt{4k}} \end{bmatrix}$$

The corresponding value of the modal mass is $M_2 = m/(2k)$ which is equal to $1/\omega_2^2$, as expected.

The mode shapes of the system are shown in Figure 3.9. Note that in the rigid-body mode both masses move in the same direction through the same distance, with the connecting spring maintained in the unstretched configuration. In the second mode, the two masses move in opposite directions with equal amplitudes. This results in a *node point* halfway along the spring. A node is a point in the system that remains stationary under a modal motion. It follows that, in the second mode, the system behaves like an identical pair of simple oscillators, each possessing twice the stiffness of the original spring (see Figure 3.10). The corresponding natural frequency is $\sqrt{2k/m}$, which is equal to ω_2 .

Orthogonality of the two modes may be verified with respect to the mass matrix as

$$\begin{bmatrix} 1 & 1 \end{bmatrix} \begin{bmatrix} m & 0 \\ 0 & m \end{bmatrix} \begin{bmatrix} 1 \\ -1 \end{bmatrix} = 0$$

and, with respect to the stiffness matrix, as

$$\begin{bmatrix} 1 & 1 \end{bmatrix} \begin{bmatrix} k & -k \\ -k & k \end{bmatrix} \begin{bmatrix} 1 \\ -1 \end{bmatrix} = 0$$

Since \mathbf{K} is singular, due to the presence of the rigid-body mode, the first orthogonality condition (Equation 3.19), and not the second (Equation 3.21), is the useful result for this system. In particular, since \mathbf{M} is nonsingular, the orthogonality of the modal vectors with respect to the mass matrix implies that they are linearly independent vectors by themselves. This is further verified by the nonsingularity of the *modal matrix*; specifically

$$\det[\boldsymbol{\psi}_1, \boldsymbol{\psi}_2] = \det \begin{bmatrix} 1 & 1 \\ 1 & -1 \end{bmatrix} \neq 0$$

Since \mathbf{M} is a scalar multiple of the identity matrix, we note that the modal vectors are in fact orthogonal, as is clear from

$$\boldsymbol{\psi}_1^T \boldsymbol{\psi}_2 = \begin{bmatrix} 1 & 1 \end{bmatrix} \begin{bmatrix} 1 \\ -1 \end{bmatrix} = 0$$

3.6.5 Modal Matrix

An n -DoF system has n modal vectors $\boldsymbol{\psi}_1, \boldsymbol{\psi}_2, \dots, \boldsymbol{\psi}_n$, which are independent. The $n \times n$ square matrix $\boldsymbol{\Psi}$ whose columns are the modal vectors is known as the modal matrix

$$\boldsymbol{\Psi} = [\boldsymbol{\psi}_1, \boldsymbol{\psi}_2, \dots, \boldsymbol{\psi}_n] \quad (3.22)$$

Since the mass matrix \mathbf{M} can always be made nonsingular through proper modeling practices (in choosing the DoF), it can be concluded that the modal matrix is nonsingular

$$\det \boldsymbol{\Psi} \neq 0 \quad (3.23)$$

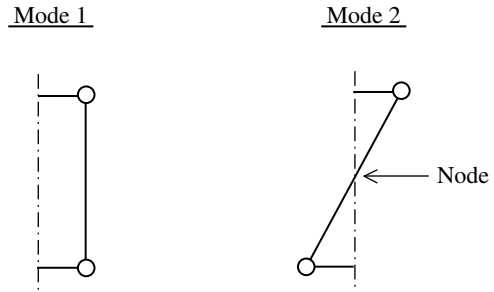


FIGURE 3.9 Mode shapes of the two-car train example.

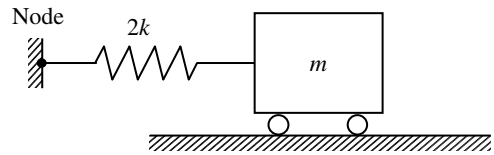


FIGURE 3.10 Equivalent system for mode 2 of the two-car train example.

and the inverse Ψ^{-1} exists. Before showing this fact, note that the orthogonality conditions (Equation 3.19 and Equation 3.21) can be written in terms of the modal matrix as

$$\Psi^T \mathbf{M} \Psi = \text{diag}[M_1, M_2, \dots, M_n] = \bar{\mathbf{M}} \quad (3.24)$$

$$\Psi^T \mathbf{K} \Psi = \text{diag}[K_1, K_2, \dots, K_n] = \bar{\mathbf{K}} \quad (3.25)$$

in which $\bar{\mathbf{M}}$ and $\bar{\mathbf{K}}$ are the *diagonal* matrices of modal masses and modal stiffnesses, respectively.

Next, we use the result from linear algebra, which states that the determinant of the product of two square matrices is equal to the product of the determinants. Also, a square matrix and its transpose have the same determinant. Then, by taking the determinant of both sides of Equation 3.24, it follows that

$$\det \Psi^T \mathbf{M} \Psi = (\det \Psi)^2 \det \mathbf{M} = \det \bar{\mathbf{M}} = M_1, M_2, \dots, M_n \quad (3.26)$$

Here, we have also used the fact that in Equation 3.24 the RHS matrix is diagonal. Now, $M_i \neq 0$ for all i since there are no static modes in a well-posed modal problem. It follows that

$$\det \Psi \neq 0 \quad (3.27)$$

which implies that Ψ is nonsingular.

3.6.6 Configuration Space and State Space

All solutions of the displacement response \mathbf{y} span a Euclidean space known as the *configuration space*. This is an n -Euclidean space (L^n). This is also the *displacement space*.

The trace of the displacement vector \mathbf{y} is not a complete representation of the dynamic response of a vibrating system because the same \mathbf{y} can correspond to more than one *dynamic state* of the system. Hence, \mathbf{y} is not a state vector. However,

$$\begin{bmatrix} \mathbf{y} \\ \dot{\mathbf{y}} \end{bmatrix}_{2n}$$

is a state vector, because it includes both displacement and velocity and completely represents the state of the system. This *state vector* spans the *state space* (L^{2n}) which is a $2n$ -Euclidean space.

3.6.6.1 State Vector

This is a vector \mathbf{x} consisting of a minimal set of response variables of a dynamic system such that, with knowledge of the initial state $\mathbf{x}(t_0)$ and the subsequent input $\mathbf{u}[t_0, t_1]$ to the system over a finite time interval $[t_0, t_1]$, the end state $\mathbf{x}(t_1)$ can be *uniquely* determined. Each point in a state space uniquely (and completely) determines the state of the dynamic system under these conditions.

Note: Configuration space can be thought of as a subspace of the state space, which is obtained by projecting the state space into the subspace formed by the axes of the \mathbf{y} vector.

For an n -DoF vibrating system (see Equation 3.1), the displacement response vector \mathbf{y} is of order n . If we know the initial condition $\mathbf{y}(0)$ and the forcing excitation $\mathbf{f}(t)$, it is not possible to completely determine $\mathbf{y}(t)$ in general. However, if we know $\mathbf{y}(0)$ and $\dot{\mathbf{y}}(0)$ as well as $\mathbf{f}(t)$, then it is possible to completely determine $\mathbf{y}(t)$ and $\dot{\mathbf{y}}(t)$. This says what we have noted before; \mathbf{y} alone does not constitute a state vector, but \mathbf{y} and $\dot{\mathbf{y}}$ together do. In this case, the order of the state space is $2n$, which is twice the number of DoF.

3.7 Other Modal Formulations

The modal problem (eigenvalue problem) studied in the previous sections consists of the solution of

$$\omega^2 \mathbf{M} \boldsymbol{\psi} = \mathbf{K} \boldsymbol{\psi} \quad (3.28)$$

which is identical to Equation 3.13. The natural frequencies (eigenvalues) are given by solving the characteristic equation 3.14. The corresponding mode shape vectors (eigenvectors) $\boldsymbol{\psi}_i$ are determined by

substituting each natural frequency ω_i into Equation 3.13 and solving for a nontrivial solution. This solution will have at least one arbitrary parameter. Hence, $\boldsymbol{\psi}$ represents the relative displacements at the various DoF of the vibrating system and not the absolute displacements. Now, two other formulations are given for the modal problem.

The first alternative formulation given below involves the solution of the eigenvalue problem of a nonsymmetric matrix ($\mathbf{M}^{-1}\mathbf{K}$). The other formulation given consists of first transforming the original problem into a new set of motion coordinates, then solving the eigenvalue problem of a symmetric matrix ($\mathbf{M}^{-1/2}\mathbf{K}\mathbf{M}^{-1/2}$), and then transforming the resulting modal vectors back to the original motion coordinates. Of course, all three of these formulations will give the same end result for the natural frequencies and mode shapes of the system, because the physical problem would remain the same regardless of what formulation and solution approach are employed. This fact will be illustrated using an example.

3.7.1 Nonsymmetric Modal Formulation

Consider the original modal formulation given by Equation 3.28 that we have studied. Since the inertia matrix \mathbf{M} is nonsingular, its inverse \mathbf{M}^{-1} exists. The premultiplication of Equation 3.28 by \mathbf{M}^{-1} gives

$$\omega^2 \boldsymbol{\psi} = \mathbf{M}^{-1} \mathbf{K} \boldsymbol{\psi} \quad (3.29)$$

This vector–matrix equation is of the form

$$\lambda \boldsymbol{\psi} = \mathbf{S} \boldsymbol{\psi} \quad (3.30)$$

where $\lambda = \omega^2$ and $\mathbf{S} = \mathbf{M}^{-1}\mathbf{K}$. Equation 3.30 represents the standard matrix eigenvalue problem for matrix \mathbf{S} . It follows that

Squared natural frequencies = eigenvalues of $\mathbf{M}^{-1}\mathbf{K}$

Mode shape vectors = eigenvectors of $\mathbf{M}^{-1}\mathbf{K}$

3.7.2 Transformed Symmetric Modal Formulation

Now consider the free (unforced) system equations

$$\mathbf{M} \ddot{\mathbf{y}} + \mathbf{K} \mathbf{y} = \mathbf{0} \quad (3.31)$$

whose modal problem needs to be solved. First, we define the square root of matrix \mathbf{M} , as denoted by $\mathbf{M}^{1/2}$, such that

$$\mathbf{M}^{1/2} \mathbf{M}^{1/2} = \mathbf{M} \quad (3.32)$$

Since \mathbf{M} is symmetric, $\mathbf{M}^{1/2}$ also has to be symmetric. Next, we define $\mathbf{M}^{-1/2}$ as the inverse of $\mathbf{M}^{1/2}$. Specifically,

$$\mathbf{M}^{-1/2} \mathbf{M}^{1/2} = \mathbf{M}^{1/2} \mathbf{M}^{-1/2} = \mathbf{I} \quad (3.33)$$

where \mathbf{I} is the identity matrix. Note that $\mathbf{M}^{-1/2}$ is also symmetric.

Once $\mathbf{M}^{-1/2}$ is defined in this manner, we transform the original problem 3.31 using the coordinate transformation

$$\mathbf{y} = \mathbf{M}^{-1/2} \mathbf{q} \quad (3.34)$$

Here, \mathbf{q} denotes the transformed displacement vector, which is related to the actual displacement vector \mathbf{y} through the matrix transformation using $\mathbf{M}^{-1/2}$.

By differentiating Equation 3.34 twice, we get

$$\ddot{\mathbf{y}} = \mathbf{M}^{-1/2} \ddot{\mathbf{q}} \quad (3.35)$$

Substitute Equation 3.34 and Equation 3.35 into Equation 3.31. This gives

$$\mathbf{M}\mathbf{M}^{-1/2} \ddot{\mathbf{q}} + \mathbf{K}\mathbf{M}^{-1/2} \mathbf{q} = 0$$

Premultiply this result by $\mathbf{M}^{-1/2}$ and use the fact that

$$\mathbf{M}^{-1/2} \mathbf{M} \mathbf{M}^{-1/2} = \mathbf{M}^{-1/2} \mathbf{M}^{1/2} \mathbf{M}^{1/2} \mathbf{M}^{-1/2} = \mathbf{I}$$

which follows from Equation 3.32 and Equation 3.33. We get

$$\ddot{\mathbf{q}} + \mathbf{M}^{-1/2} \mathbf{K} \mathbf{M}^{-1/2} \mathbf{q} = 0 \quad (3.36)$$

Equation 3.36 is the transformed problem, whose modal response may be given by

$$\mathbf{q} = e^{j\omega t} \phi \quad (3.37)$$

where ω represents a natural frequency and ϕ represents the corresponding modal vector, as usual. Then, in view of Equation 3.34, we have

$$\mathbf{y} = e^{j\omega t} \mathbf{M}^{-1/2} \phi = e^{j\omega t} \boldsymbol{\psi} \quad (3.38)$$

It follows that the natural frequencies of the original problem 3.31 are identical to the natural frequencies of the transformed problem 3.36, and the modal vectors $\boldsymbol{\psi}$ of the original problem are related to the modal vectors ϕ of the transformed problem through

$$\boldsymbol{\psi} = \mathbf{M}^{-1/2} \phi \quad (3.39)$$

Substitute the modal response 3.37 into Equation 3.36. We get

$$\lambda \phi = \mathbf{P} \phi \quad (3.40)$$

where $\lambda = \omega^2$ and $\mathbf{P} = \mathbf{M}^{-1/2} \mathbf{K} \mathbf{M}^{-1/2}$.

Equation 3.40, just like Equation 3.30, represents a standard matrix eigenvalue problem. But now matrix \mathbf{P} is symmetric. As a result, its eigenvectors ϕ will not only be real but also orthogonal.

The solution steps for the present, transformed, and symmetric modal problem are:

1. Determine $\mathbf{M}^{-1/2}$.
2. Solve for eigenvalues λ and eigenvectors ϕ of $\mathbf{M}^{-1/2} \mathbf{K} \mathbf{M}^{-1/2}$. Eigenvalues are squares of the natural frequencies of the original system.
3. Determine the modal vectors $\boldsymbol{\psi}$ of the original system by using $\boldsymbol{\psi} = \mathbf{M}^{-1/2} \phi$.

The three approaches of modal analysis which we have studied are summarized in Table 3.4.

TABLE 3.4 Three Approaches of Modal Analysis

Approach	Standard	Nonsymmetric Matrix Eigenvalue	Symmetric Matrix Eigenvalue
Modal formulation	$[\omega^2 \mathbf{M} - \mathbf{K}] \boldsymbol{\psi} = 0$	$\omega^2 \boldsymbol{\psi} = \mathbf{M}^{-1} \mathbf{K} \boldsymbol{\psi}$	$\omega^2 \phi = \mathbf{M}^{-1/2} \mathbf{K} \mathbf{M}^{-1/2} \phi$
Squared natural frequencies (ω_i^2)	Roots of $\det[\omega^2 \mathbf{M} - \mathbf{K}] = 0$	Eigenvalues of $\mathbf{M}^{-1} \mathbf{K}$	Eigenvalues of $\mathbf{M}^{-1/2} \mathbf{K} \mathbf{M}^{-1/2}$
Mode-shape vectors ($\boldsymbol{\psi}_i$)	Nontrivial solutions of $[\omega_i^2 \mathbf{M} - \mathbf{K}] \boldsymbol{\psi} = 0$	Eigenvectors of $\mathbf{M}^{-1} \mathbf{K}$	Determine eigenvectors ϕ_i of $\mathbf{M}^{-1/2} \mathbf{K} \mathbf{M}^{-1/2}$. Then $\boldsymbol{\psi}_i = \mathbf{M}^{-1/2} \phi_i$

Example 3.6

We will use the 2-DoF vibration problem given in [Figure 3.4](#) (Example 3.3) to demonstrate the fact that all three approaches summarized in [Table 3.4](#) will lead to the same results.

Consider the special case of $\alpha = 0.5$ and $\beta = 0.5$. Then we have

$$\mathbf{M} = \begin{bmatrix} m & 0 \\ 0 & \frac{m}{2} \end{bmatrix} \quad \text{and} \quad \mathbf{K} = \begin{bmatrix} \frac{3}{2}k & -\frac{k}{2} \\ -\frac{k}{2} & \frac{k}{2} \end{bmatrix}$$

Approach 1

Using the standard approach, we obtain the modal results given in [Table 3.3](#). Specifically, we get the natural frequencies (normalized with respect to $\omega_0 = \sqrt{k/m}$)

$$\frac{\omega_1}{\omega_0} = \frac{1}{\sqrt{2}} \quad \text{and} \quad \frac{\omega_2}{\omega_0} = \sqrt{2}$$

and the mode shapes

$$\left(\frac{\psi_2}{\psi_1} \right)_1 = 2 \quad \text{and} \quad \left(\frac{\psi_2}{\psi_1} \right)_2 = -1$$

Let us now obtain these results using the other two approaches of modal analysis.

Approach 2

$$\mathbf{M}^{-1} = \begin{bmatrix} \frac{1}{m} & 0 \\ 0 & \frac{2}{m} \end{bmatrix},$$

$$\mathbf{M}^{-1}\mathbf{K} = \begin{bmatrix} \frac{1}{m} & 0 \\ 0 & \frac{2}{m} \end{bmatrix} \begin{bmatrix} \frac{3}{2}k & -\frac{k}{2} \\ -\frac{k}{2} & \frac{k}{2} \end{bmatrix} = \begin{bmatrix} \frac{3}{2}\frac{k}{m} & -\frac{1}{2}\frac{k}{m} \\ -\frac{k}{m} & \frac{k}{m} \end{bmatrix} = \omega_0^2 \begin{bmatrix} \frac{3}{2} & -\frac{1}{2} \\ -1 & 1 \end{bmatrix}$$

Note that this is not a symmetric matrix. We solve the eigenvalue problem of

$$\begin{bmatrix} \frac{3}{2} & -\frac{1}{2} \\ -1 & 1 \end{bmatrix}$$

Eigenvalues λ are given by

$$\det \begin{bmatrix} \lambda - \frac{3}{2} & \frac{1}{2} \\ 1 & \lambda - 1 \end{bmatrix} = 0$$

or

$$\left(\lambda - \frac{3}{2} \right) (\lambda - 1) - \frac{1}{2} = 0$$

or

$$\lambda^2 - \frac{5}{2}\lambda + 1 = 0$$

the roots of which are

$$\lambda_1, \lambda_2 = \frac{1}{2}, 2$$

It follows that $\omega_1/\omega_0 = 1/\sqrt{2}$ and $\omega_2/\omega_0 = \sqrt{2}$ as before.

The eigenvector corresponding to λ_1 (mode 1) is given by

$$\begin{bmatrix} \frac{1}{2} & -\frac{3}{2} & \frac{1}{2} \\ 1 & \frac{1}{2} & -1 \end{bmatrix} \begin{bmatrix} \psi_1 \\ \psi_2 \end{bmatrix}_1 = \begin{bmatrix} 0 \\ 0 \end{bmatrix}$$

The solution is $(\psi_2/\psi_1)_1 = 2$ as before.

The eigenvector corresponding to λ_2 (mode 2) is given by

$$\begin{bmatrix} 2 & -\frac{3}{2} & \frac{1}{2} \\ 1 & 2 & -1 \end{bmatrix} \begin{bmatrix} \psi_1 \\ \psi_2 \end{bmatrix}_2 = \begin{bmatrix} 0 \\ 0 \end{bmatrix}$$

The solution is $(\psi_2/\psi_1)_2 = -1$ as before.

Approach 3

Since \mathbf{M} is diagonal, it is easy to obtain $\mathbf{M}^{1/2}$. We simply take the square root of the diagonal elements; thus,

$$\mathbf{M}^{1/2} = \begin{bmatrix} \sqrt{m} & 0 \\ 0 & \sqrt{\frac{m}{2}} \end{bmatrix}$$

Its inverse is given by inverting the diagonal elements; thus

$$\mathbf{M}^{-1/2} = \begin{bmatrix} \frac{1}{\sqrt{m}} & 0 \\ 0 & \sqrt{\frac{2}{m}} \end{bmatrix}$$

Now,

$$\begin{aligned} \mathbf{M}^{-1/2} \mathbf{K} \mathbf{M}^{-1/2} &= \begin{bmatrix} \frac{1}{\sqrt{m}} & 0 \\ 0 & \sqrt{\frac{2}{m}} \end{bmatrix} \begin{bmatrix} \frac{3}{2}k & -\frac{k}{2} \\ -\frac{k}{2} & \frac{k}{2} \end{bmatrix} \begin{bmatrix} \frac{1}{\sqrt{m}} & 0 \\ 0 & \sqrt{\frac{2}{m}} \end{bmatrix} = \begin{bmatrix} \frac{3}{2} \frac{k}{m} & -\frac{1}{\sqrt{2}} \frac{k}{m} \\ -\frac{1}{\sqrt{2}} \frac{k}{m} & \frac{k}{m} \end{bmatrix} \\ &= \omega_0^2 \begin{bmatrix} \frac{3}{2} & -\frac{1}{\sqrt{2}} \\ -\frac{1}{\sqrt{2}} & 1 \end{bmatrix} \end{aligned}$$

Note that, as expected, this is a symmetric matrix. We solve for eigenvalues and eigenvectors of

$$\begin{bmatrix} \frac{3}{2} & -\frac{1}{\sqrt{2}} \\ -\frac{1}{\sqrt{2}} & 1 \end{bmatrix}$$

Eigenvalues are given by

$$\det \begin{bmatrix} \lambda - \frac{3}{2} & \frac{1}{\sqrt{2}} \\ \frac{1}{\sqrt{2}} & \lambda - 1 \end{bmatrix} = 0$$

or

$$\left(\lambda - \frac{3}{2}\right)(\lambda - 1) - \frac{1}{2} = 0$$

or

$$\lambda^2 - \frac{5}{2}\lambda + 1 = 0$$

which is identical to the characteristic equation obtained in the first two approaches. It follows that the same two natural frequencies are obtained by this method. The eigenvector ϕ_1 for mode 1 is given by

$$\begin{bmatrix} \frac{1}{2} - \frac{3}{2} & \frac{1}{\sqrt{2}} \\ \frac{1}{\sqrt{2}} & \frac{1}{2} - 1 \end{bmatrix} \begin{bmatrix} \phi_1 \\ \phi_2 \end{bmatrix}_1 = \begin{bmatrix} 0 \\ 0 \end{bmatrix}$$

which gives $(\phi_2/\phi_1)_1 = [\sqrt{2}]$.

Accordingly, we may use

$$\begin{bmatrix} \phi_1 \\ \phi_2 \end{bmatrix}_1 = \begin{bmatrix} 1 \\ \sqrt{2} \end{bmatrix}$$

The eigenvector ϕ_2 for mode 2 is given by

$$\begin{bmatrix} 2 - \frac{3}{2} & \frac{1}{\sqrt{2}} \\ \frac{1}{\sqrt{2}} & 2 - 1 \end{bmatrix} \begin{bmatrix} \phi_1 \\ \phi_2 \end{bmatrix}_2 = \begin{bmatrix} 0 \\ 0 \end{bmatrix}$$

which gives $(\phi_2/\phi_1)_2 = -1/\sqrt{2}$.

Accordingly, we use

$$\begin{bmatrix} \phi_1 \\ \phi_2 \end{bmatrix}_2 = \begin{bmatrix} 1 \\ -\frac{1}{\sqrt{2}} \end{bmatrix}$$

Now, we transform these eigenvectors back to the original coordinate system using Equation 3.39. We get

$$\begin{bmatrix} \psi_1 \\ \psi_2 \end{bmatrix}_1 = \begin{bmatrix} \frac{1}{\sqrt{m}} & 0 \\ 0 & \sqrt{\frac{2}{m}} \end{bmatrix} \begin{bmatrix} 1 \\ \sqrt{2} \end{bmatrix} = \begin{bmatrix} \frac{1}{\sqrt{m}} \\ \frac{2}{\sqrt{m}} \end{bmatrix}$$

which gives $(\psi_2/\psi_1)_1 = 2$ as before.

Also,

$$\begin{bmatrix} \psi_1 \\ \psi_2 \end{bmatrix}_2 = \begin{bmatrix} \frac{1}{\sqrt{m}} & 0 \\ 0 & \sqrt{\frac{2}{m}} \end{bmatrix} \begin{bmatrix} 1 \\ -\frac{1}{\sqrt{2}} \end{bmatrix} = \begin{bmatrix} \frac{1}{\sqrt{m}} \\ -\frac{1}{\sqrt{m}} \end{bmatrix}$$

which gives $(\psi_2/\psi_1)_2 = -1$ as before.

3.8 Forced Vibration

The forced motion of a linear, n -DoF, undamped system is given by the nonhomogeneous equation of motion 3.1:

$$\mathbf{M}\ddot{\mathbf{y}} + \mathbf{K}\mathbf{y} = \mathbf{f}(t) \quad (3.41)$$

Even though the following discussion is based on this undamped model, the results can be easily extended to the damped case.

We have observed that the modal vectors form a basis for the *configuration space*. In other words, it is possible to express the response \mathbf{y} as a linear combination of the modal vectors $\boldsymbol{\psi}_i$:

$$\mathbf{y} = q_1\boldsymbol{\psi}_1 + q_2\boldsymbol{\psi}_2 + \cdots + q_n\boldsymbol{\psi}_n \quad (3.42)$$

The parameters q_i are a set of *generalized coordinates* and are functions of time t . Equation 3.42 is written in the vector–matrix form

$$\mathbf{y} = [\boldsymbol{\psi}_1, \boldsymbol{\psi}_2, \dots, \boldsymbol{\psi}_n] \begin{bmatrix} q_1 \\ q_2 \\ \vdots \\ q_n \end{bmatrix}$$

or

$$\mathbf{y} = \boldsymbol{\Psi}\mathbf{q} \quad (3.43)$$

and can be viewed as a coordinate transformation from the trajectory space to the *canonical space* of generalized coordinates (principal coordinates or natural coordinates). Note that the inverse transformation exists because the modal matrix $\boldsymbol{\Psi}$ is nonsingular. On substituting Equation 3.43 into Equation 3.41, we obtain

$$\mathbf{M}\boldsymbol{\Psi}\ddot{\mathbf{q}} + \mathbf{K}\boldsymbol{\Psi}\mathbf{q} = \mathbf{f}(t)$$

This result is premultiplied by $\boldsymbol{\Psi}^T$ and the orthogonality conditions (Equation 3.24 and Equation 3.25) are substituted to obtain the canonical form of the system equation:

$$\bar{\mathbf{M}}\ddot{\mathbf{q}} + \bar{\mathbf{K}}\mathbf{q} = \bar{\mathbf{f}}(t) \quad (3.44)$$

in which $\bar{\mathbf{M}}$ and $\bar{\mathbf{K}}$ are the diagonal matrices given by Equation 3.24 and Equation 3.25, and the transformed forcing vector is given by

$$\bar{\mathbf{f}}(t) = \boldsymbol{\Psi}^T \mathbf{f}(t) \quad (3.45)$$

Since $\bar{\mathbf{M}}$ and $\bar{\mathbf{K}}$ are diagonal matrices, Equation 3.44 corresponds to the set of n uncoupled *simple oscillator* equations:

$$M_i \ddot{q}_i + K_i q_i = \bar{f}_i(t) \quad \text{for } i = 1, 2, \dots, n \quad (3.46)$$

In other words, the coordinate transformation 3.43 using the modal matrix has uncoupled the equations of forced motion. It follows from Equation 3.46 that the natural frequencies of the system are given by

$$\omega_i^2 = K_i/M_i \quad \text{for } i = 1, 2, \dots, n \quad (3.47)$$

as we have noted before.

It is particularly convenient to employ \mathbf{M} -normal modal vectors. In this case, $\bar{\mathbf{M}}$ becomes the n th order identity matrix, and $\bar{\mathbf{K}}$ the diagonal matrix having ω_i^2 as its diagonal elements; thus

$$\bar{\mathbf{M}} = \mathbf{I} \quad (3.48)$$

$$\bar{\mathbf{K}} = \text{diag}[\omega_1^2, \omega_2^2, \dots, \omega_n^2] \quad (3.49)$$

The corresponding uncoupled equations 3.46 take the form

$$\ddot{q}_i + \omega_i^2 q_i = \bar{f}_i(t) \quad \text{for } i = 1, 2, \dots, n \quad (3.50)$$

in which the forcing terms $\bar{f}_i(t)$ are given by Equation 3.45, Ψ being \mathbf{M} -normal.

Typically, the initial conditions for the original system are provided as the initial position $\mathbf{y}(0)$ and the initial velocity $\dot{\mathbf{y}}(0)$. The corresponding initial conditions for the transformed equations of motion are obtained using Equation 3.43 as

$$\mathbf{q}(0) = \Psi^{-1} \mathbf{y}(0) \quad (3.51)$$

$$\dot{\mathbf{q}}(0) = \Psi^{-1} \dot{\mathbf{y}}(0) \quad (3.52)$$

The complete response of the original system can be conveniently obtained by first solving the simple oscillator equation 3.50 and then transforming the results back into the trajectory space using Equation 3.43.

The complete solution to this linear system can be viewed as the sum of the initial condition response in the absence of the forcing function and the forced response with zero initial conditions, as discussed in [Chapter 2](#). For the simple oscillator equation 3.50, the initial condition response q_{iI} is given by

$$q_{iI} = q_i(0) \cos \omega_i t + \frac{\dot{q}_i(0)}{\omega_i} \sin \omega_i t \quad (3.53)$$

The impulse response function (i.e., response to a unit impulse excitation) for the undamped oscillator equation is

$$h_i(t) = \frac{1}{\omega_i} \sin \omega_i t \quad \text{for } t \geq 0 \quad (3.54)$$

The forced response q_{iF} , with zero initial conditions, is obtained using the *convolution integral* method; specifically

$$q_{iF} = \int_0^t \bar{f}_i(\tau) h_i(t - \tau) d\tau \quad (3.55)$$

The complete solution in the canonical domain is

$$q_i = q_{iI} + q_{iF} = q_i(0) \cos \omega_i t + \frac{\dot{q}_i(0)}{\omega_i} \sin \omega_i t + \frac{1}{\omega_i} \int_0^t \bar{f}_i(\tau) \sin \omega_i(t - \tau) d\tau \quad i = 1, 2, \dots, n \quad (3.56)$$

Each of the n responses is a modal response that is the contribution from that mode to the actual response \mathbf{y} . This approach is summarized in Box 3.4. Next, we will illustrate this approach of solving for the forced vibration by means of an example.

Box 3.4

MODAL APPROACH TO FORCED RESPONSE

Forced system: $\mathbf{M}\ddot{\mathbf{y}} + \mathbf{K}\mathbf{y} = \mathbf{f}(t)$

Number of DoFs = n

Modal transformation: $\mathbf{y} = \mathbf{\Psi}\mathbf{q}$

where modal matrix $\mathbf{\Psi} = [\boldsymbol{\psi}_1, \boldsymbol{\psi}_2, \dots, \boldsymbol{\psi}_n]$ = matrix of mode shape vectors.

We obtain the diagonalized system

$$\bar{\mathbf{M}}\ddot{\mathbf{q}} + \bar{\mathbf{K}}\mathbf{q} = \bar{\mathbf{f}}(t)$$

or

$$M_i\ddot{q}_i + K_i q_i = f_i(t); \quad i = 1, 2, \dots, n$$

where

$$\bar{\mathbf{M}} = \mathbf{\Psi}^T \mathbf{M} \mathbf{\Psi} = \text{diag}[M_1, M_2, \dots, M_n]$$

$$\bar{\mathbf{K}} = \mathbf{\Psi}^T \mathbf{K} \mathbf{\Psi} = \text{diag}[K_1, K_2, \dots, K_n]$$

$$\bar{\mathbf{f}}(t) = \mathbf{\Psi}^T \mathbf{f}(t) = [\bar{f}_1, \bar{f}_2, \dots, \bar{f}_n]^T$$

Initial conditions:

$$\mathbf{q}(0) = \mathbf{\Psi}^{-1} \mathbf{y}(0)$$

$$\dot{\mathbf{q}}(0) = \mathbf{\Psi}^{-1} \dot{\mathbf{y}}(0)$$

Steps: Use \mathbf{M} -normal case: $M_i = 1$, $K_i = \omega_i^2$

Then,

$$\ddot{q}_i + \omega_i^2 q_i = \bar{f}_i(t); \quad i = 1, 2, \dots, n$$

1. Free, initial-condition response (zero-input response)

$$q_{iF} = q_i(0) \cos \omega_i t + \frac{\dot{q}_i(0)}{\omega_i} \sin \omega_i t$$

2. Forced, zero initial-condition response

$$q_{iF} = \frac{1}{\omega_i} \int_0^t \bar{f}_i(\tau) \sin \omega_i(t - \tau) d\tau$$

3. $q_i = q_{iF} + q_{iF}$

4. Transform back to \mathbf{y} using $\mathbf{y} = \mathbf{\Psi}\mathbf{q}$

Example 3.7

Let us consider again the system shown in Figure 3.8. A step-input force $f(t)$ given by

$$f(t) = \begin{cases} f_0 & \text{for } t \geq 0 \\ 0 & \text{for } t < 0 \end{cases}$$

is applied to the left-hand mass (DoF y_1). Assume that the system starts from rest ($\mathbf{y}(0) = 0$ and $\dot{\mathbf{y}}(0) = 0$).

As before, the \mathbf{M} -normal modal matrix of the system is

$$\mathbf{\Psi} = \begin{bmatrix} \frac{1}{\sqrt{2m}} & \frac{1}{\sqrt{2m}} \\ \frac{1}{\sqrt{2m}} & -\frac{1}{\sqrt{2m}} \end{bmatrix} = \frac{1}{\sqrt{2m}} \begin{bmatrix} 1 & 1 \\ 1 & -1 \end{bmatrix}$$

No forcing input is applied to the second DoF (y_2). Hence, the overall forcing input vector is

$$\mathbf{f}(t) = \begin{bmatrix} f_0 \\ 0 \end{bmatrix} \quad \text{for } t \geq 0$$

From Equation 3.45, the transformed forcing input vector is obtained as

$$\tilde{\mathbf{f}}(t) = \mathbf{\Psi}^T \mathbf{f}(t) = \frac{1}{\sqrt{2m}} \begin{bmatrix} 1 & 1 \\ 1 & -1 \end{bmatrix} \begin{bmatrix} f_0 \\ 0 \end{bmatrix} = \frac{f_0}{\sqrt{2m}} \begin{bmatrix} 1 \\ 1 \end{bmatrix} \quad \text{for } t \geq 0$$

From Equation 3.51 and Equation 3.52, the initial conditions for the modal (canonical) variables are obtained as $\dot{\mathbf{q}}(0) = 0$ and $\mathbf{q}(0) = 0$. The modal responses $q_1(t)$ and $q_2(t)$ are obtained using Equation 3.56.

3.8.1 First Mode (Rigid-Body Mode)

Note that

$$\lim_{\omega_i \rightarrow 0} \frac{\sin \omega_i(t - \tau)}{\omega_i} = t - \tau$$

It follows that

$$q_1(t) = \int_0^t \frac{f_0(t - \tau)}{\sqrt{2m}} d\tau = \frac{f_0 t^2}{2\sqrt{2m}}$$

3.8.2 Second Mode (Oscillatory Mode)

$$q_2(t) = \frac{1}{\omega_2} \int_0^t \frac{f_0}{\sqrt{2m}} \sin \omega_2(t - \tau) d\tau = \frac{f_0}{\omega_2^2 \sqrt{2m}} (1 - \cos \omega_2 t)$$

The overall response in the physical trajectory space is obtained by transforming the modal responses using Equation 3.43; thus

$$\mathbf{y} = \frac{1}{\sqrt{2m}} \begin{bmatrix} 1 & 1 \\ 1 & -1 \end{bmatrix} \begin{bmatrix} \frac{f_0 t^2}{2\sqrt{2m}} \\ \frac{f_0 (1 - \cos \omega_2 t)}{\omega_2^2 \sqrt{2m}} \end{bmatrix} = \frac{f_0}{2m} \begin{bmatrix} \frac{t^2}{2} + \frac{1}{\omega_2^2} (1 - \cos \omega_2 t) \\ \frac{t^2}{2} - \frac{1}{\omega_2^2} (1 - \cos \omega_2 t) \end{bmatrix}$$

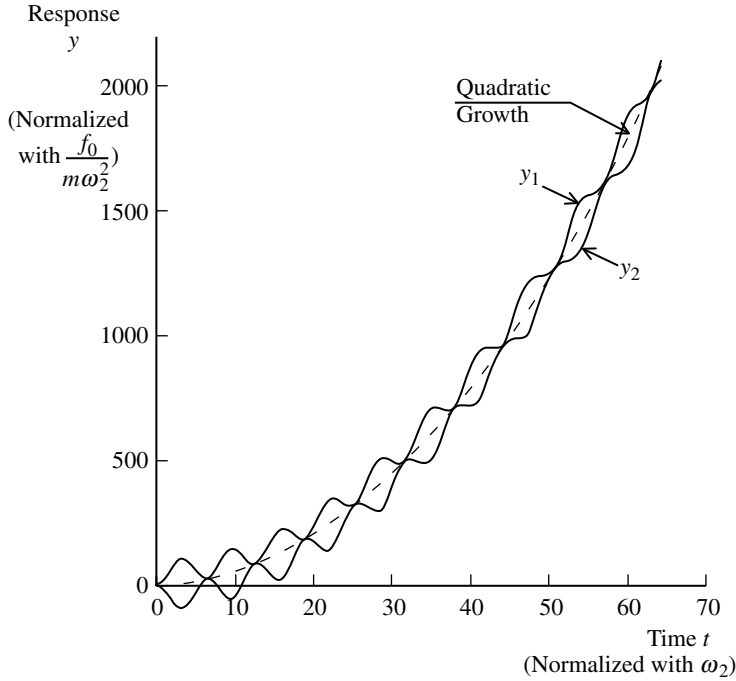


FIGURE 3.11 Forced response obtained through modal analysis.

with $\omega_2^2 = 2k/m$. The response of both masses grows (unstable) quadratically in an oscillatory manner, as shown in Figure 3.11.

3.9 Damped Systems

Let us examine the possibility of extending the modal analysis results to damped systems. Damping is an energy dissipation phenomenon. In lumped-parameter models of vibrating systems, damping force can be represented by a resisting force at each lumped mass. In view of Equation 3.1, then, the system equations for a damped system can be written as

$$\mathbf{M}\ddot{\mathbf{y}} + \mathbf{K}\mathbf{y} = \mathbf{f}(t) - \mathbf{d} \quad (3.57)$$

in which \mathbf{d} is the damping force vector. Modeling of damping is usually quite complicated. Often, a linear model, whose energy dissipation capacity is equivalent to that of the actual system, is employed. Such a model is termed as an *equivalent damping* model. The most popular model for damping is the *linear viscous model*, in which the damping force is proportional to the relative velocity. In lumped-parameter dynamic models, (linear) viscous damping elements may be assigned across pairs of DoF or across a DoF and a fixed reference. The damping force for such a model may be expressed as

$$\mathbf{d} = \mathbf{C}\dot{\mathbf{y}} \quad (3.58)$$

in which \mathbf{C} is the *damping matrix*. The resulting damped system equation is

$$\mathbf{M}\ddot{\mathbf{y}} + \mathbf{C}\dot{\mathbf{y}} + \mathbf{K}\mathbf{y} = \mathbf{f}(t) \quad (3.59)$$

To determine the elements of \mathbf{C} for a given system model by the influence coefficient approach, the same procedure outlined previously for obtaining the elements of \mathbf{K} may be used, except that the velocities \dot{y}_i should be used in place of the displacements y_i . The coefficients c_{ij} are termed as *damping influence coefficients*.

3.9.1 Proportional Damping

Because the modal vectors are orthogonal with respect to both \mathbf{M} and \mathbf{K} , the transformation 3.43 will decouple the undamped system equation 3.41. It should be clear, however, that the same transformation will not diagonalize the \mathbf{C} matrix in general. As we have observed in the previous section, decoupling or *modal decomposition*, is a convenient tool in response analysis. This is because each uncoupled modal equation is a simple oscillator equation with a well-known solution that can be transformed back (or, recombined) to obtain the total response. This simple procedure cannot be used for damped systems unless the modal vectors are orthogonal with respect to \mathbf{C} as well.

In modal vibration, all DoF move in the same displacement proportion, as given by the modal vector. This type of synchronous motion may not be possible in damped systems. Another way to state this is that most damped systems do not possess real modes. If we try to excite such a damped system at one of its natural frequencies, we will notice that the constant proportion, given by the modal vector (for the undamped system), is violated during motion. Furthermore, if the undamped system has a (fixed) node point in the particular mode, that point would not remain fixed but would move in a cyclic manner when set to vibrate at the natural frequency of the mode.

Note that viscous damping is just a model for energy dissipation. If we become rather restrictive in choosing the parameters of viscous damping, we will be able to develop an equivalent damping matrix, with respect to which, the modal vectors of the undamped system would be orthogonal. In other words, we require that the transformed damping matrix $\bar{\mathbf{C}}$ be a diagonal matrix; thus

$$\Psi^T \mathbf{C} \Psi = \text{diag}[C_1, C_2, \dots, C_n] = \bar{\mathbf{C}} \quad (3.60)$$

In this case, the corresponding viscous damping model is termed *proportional damping* or *Rayleigh damping* (after the person who first identified this simplification).

Modal decomposition of Equation 3.59, assuming proportional damping using the transformation 3.43, results in the canonical form (uncoupled modal equation)

$$\bar{\mathbf{M}}\ddot{\mathbf{q}} + \bar{\mathbf{C}}\dot{\mathbf{q}} + \bar{\mathbf{K}}\mathbf{q} = \bar{\mathbf{f}}(t) \quad (3.61)$$

or

$$M_i \ddot{q}_i + C_i \dot{q}_i + K_i q_i = \bar{f}_i(t) \quad \text{for } i = 1, 2, \dots, n$$

Equation 3.61 can be written in the standard form for a damped simple oscillator:

$$\ddot{q}_i + 2\zeta_i \omega_i \dot{q}_i + \omega_i^2 q_i = \bar{f}_i(t) \quad \text{for } i = 1, 2, \dots, n \quad (3.62)$$

in which, the modal matrix is assumed \mathbf{M} -normal (i.e., $M_i = 1$). It can be concluded that a proportionally damped system possesses real modal vectors that are identical to the modal vectors of its undamped counterpart. The damped natural frequency, however, is smaller than the undamped natural frequency and is given by

$$\omega_{di} = \sqrt{1 - \zeta_i^2} \omega_i \quad (3.63)$$

One way to guarantee proportional damping is to pick a damping matrix that satisfies

$$\mathbf{C} = c_m \mathbf{M} + c_k \mathbf{K} \quad (3.64)$$

From modal transformation (see Equation 3.61), it follows that Equation 3.64 corresponds to

$$\text{Modal damping constant } C_i = c_m M_i + c_k K_i$$

or

$$2\zeta_i \omega_i = c_m + c_k \omega_i^2$$

or

$$\text{Modal damping ratio } \zeta_i = \frac{1}{2} \left(\frac{c_m}{\omega_i} + c_k \omega_i \right) \quad (3.64a)$$

Equation 3.64, however, is not the only way to achieve real modes in a damped system (Equation 3.60). The first term on the right-hand side (RHS) of Equation 3.64 is termed the *inertial damping matrix*. The corresponding damping force on each lumped mass in the model will be proportional to the momentum. This term may represent the energy loss associated with a momentum and is termed *momentum damping*. Physically, this is incorporated by assigning a viscous damper between each DoF and its fixed reference, with the damping constant proportional to the mass concentrated at that location.

The second term in Equation 3.64 is termed the *stiffness damping matrix*. The corresponding damping force is proportional to the rate of change of the local deformation forces (stresses) in flexible structural members and joints. It may be interpreted as a simplified model for *structural damping*. Physically, this model is realized by assigning a viscous damper across every spring element in the model, with the damping constant proportional to the stiffness. It is known that rate of change of stresses or rate of change of strains will give rise to *viscoelastic damping*, which is associated with plasticity and viscoelasticity. This type of damping is known as *strain-rate damping*.

Usually, structural damping is most appropriately modeled as being present across (lumped) stiffness elements. Coulomb damping is modeled as acting between an inertia element and its fixed reference point. These intuitive observations also support the damping model given by Equation 3.64. Some terminology and properties of damped systems are summarized in Box 3.5.

Example 3.8

Let us examine the lumped-parameter damped model shown in Figure 3.12 to determine whether it has real modes.

Note that if we modify the model as in Figure 3.13, the damping matrix will become proportional to the stiffness matrix. This will be a case of proportional damping and the modified (damping) system will possess real modes with modal vectors that are identical to those for the corresponding undamped system. It should be verified that the equations of motion for this modified system (Figure 3.13) are

$$\begin{bmatrix} m & 0 \\ 0 & m \end{bmatrix} \ddot{\mathbf{y}} + \begin{bmatrix} 2c & -c \\ -c & 2c \end{bmatrix} \dot{\mathbf{y}} + \begin{bmatrix} 2k & -k \\ -k & 2k \end{bmatrix} \mathbf{y} = \begin{bmatrix} 0 \\ f(t) \end{bmatrix}$$

Notice the similarity between the stiffness matrix and the damping matrix.

Another damped system that possesses classical modes is shown in Figure 3.14. In this model, the damping matrix is proportional to the mass (inertia) matrix. It may be easily verified that the system equations are

$$\begin{bmatrix} m & 0 \\ 0 & m \end{bmatrix} \ddot{\mathbf{y}} + \begin{bmatrix} c & 0 \\ 0 & c \end{bmatrix} \dot{\mathbf{y}} + \begin{bmatrix} 2k & -k \\ -k & 2k \end{bmatrix} \mathbf{y} = \begin{bmatrix} 0 \\ f(t) \end{bmatrix}$$

Here, notice the similarity between the inertia matrix and the damping matrix.

Returning to the original system shown in Figure 3.12, the equations of motion can be written as

$$\begin{bmatrix} m & 0 \\ 0 & m \end{bmatrix} \ddot{\mathbf{y}} + \begin{bmatrix} c_1 + c_2 & -c_2 \\ -c_2 & c_2 \end{bmatrix} \dot{\mathbf{y}} + \begin{bmatrix} 2k & -k \\ -k & 2k \end{bmatrix} \mathbf{y} = \begin{bmatrix} 0 \\ f(t) \end{bmatrix}$$

From these equations, it is not obvious whether this system possesses real modes. The undamped natural frequencies are given by the roots of the characteristic equation

$$\det \begin{bmatrix} \omega^2 m - 2k & k \\ k & \omega^2 m - 2k \end{bmatrix} = 0$$

Box 3.5

TERMINOLOGY AND PROPERTIES OF DAMPED SYSTEMS

Characteristic equation:

$$\det[\mathbf{M}s^2 + \mathbf{C}s + \mathbf{K}] = 0$$

Roots s are the eigenvalues λ_i

$\text{Im}(\lambda_i) = \omega_{di} =$ damped natural frequencies

$|\lambda_i| = \omega_i =$ undamped natural frequencies

$-\text{Re}(\lambda_i)/\omega_i = \zeta_i =$ modal damping ratios

$\sqrt{1 - 2\zeta_i^2}\omega_i = \omega_{ri} =$ resonant frequencies

$$\sqrt{1 - \zeta_i^2}\omega_i = \omega_{di}$$

Existence of real modes:

- Condition for existence of modes that are identical to undamped modes

$$\mathbf{\Psi}^T \mathbf{C} \mathbf{\Psi} = \text{diagonal matrix}$$

where

$\mathbf{\Psi} =$ modal matrix of undamped modes

- Another (equivalent) condition

$$\mathbf{M}^{-1} \mathbf{C} \mathbf{M}^{-1} \mathbf{K} = \mathbf{M}^{-1} \mathbf{K} \mathbf{M}^{-1} \mathbf{C} \quad (\text{Prove})$$

i.e., $\mathbf{M}^{-1} \mathbf{C}$ and $\mathbf{M}^{-1} \mathbf{K}$ must commute

- Special case:

Proportional damping $\mathbf{C} = c_m \mathbf{M} + c_k \mathbf{K}$

\Rightarrow Modal damping constant $C_i = c_m M_i + c_k K_i$

Modal damping ratio $\zeta_i = \frac{1}{2} \left(\frac{c_m}{\omega_i} + c_k \omega_i \right)$

The natural frequencies are $\omega_1 = \sqrt{k/m}$ and $\omega_2 = \sqrt{3k/m}$. The corresponding mode shapes are given by the nontrivial solution of

$$\begin{bmatrix} \omega_i^2 m - 2k & k \\ k & \omega_i^2 m - 2k \end{bmatrix} \begin{bmatrix} \psi_1 \\ \psi_2 \end{bmatrix}_i = \begin{bmatrix} 0 \\ 0 \end{bmatrix} \quad \text{for } i = 1, 2$$

Also, let us normalize the modal vectors by choosing the first element of each vector to be unity. Then, by following the usual procedure of modal analysis, we will obtain the normalized modal vectors

$$\mathbf{\psi}_1 = \begin{bmatrix} 1 \\ 1 \end{bmatrix} \quad \text{and} \quad \mathbf{\psi}_2 = \begin{bmatrix} 1 \\ -1 \end{bmatrix}$$

The modal matrix is

$$\Psi = [\psi_1, \psi_2] = \begin{bmatrix} 1 & 1 \\ 1 & -1 \end{bmatrix}$$

Consequently, we obtain

$$\Psi^T \mathbf{M} \Psi = \bar{\mathbf{M}} = \begin{bmatrix} 2m & 0 \\ 0 & 2m \end{bmatrix}$$

$$\Psi^T \mathbf{K} \Psi = \bar{\mathbf{K}} = \begin{bmatrix} 2k & 0 \\ 0 & 6k \end{bmatrix}$$

$$\Psi^T \mathbf{C} \Psi = \bar{\mathbf{C}} = \begin{bmatrix} c_1 & c_1 \\ c_1 & c_1 + 4c_2 \end{bmatrix}$$

and

$$\Psi^T \mathbf{f}(t) = \bar{\mathbf{f}}(t) = \begin{bmatrix} f(t) \\ -f(t) \end{bmatrix}$$

Notice that the transformed damping matrix $\bar{\mathbf{C}}$ is not diagonal in general and, consequently, real modes will not exist. This is to be expected without the condition of proportional damping. Proportional damping is realized in this model if $c_1 = 0$. Then, $\bar{\mathbf{C}}$ will be diagonal and the transformed systems equations will be uncoupled. The uncoupled model equations are

$$2m\ddot{q}_1 + 2kq_1 = f(t)$$

$$2m\ddot{q}_2 + 4c_2\dot{q}_2 + 6kq_2 = -f(t)$$

The first mode is always undamped for this choice of damping model. This confirms that, in the case of proportional damping, it is not generally possible to pick an arbitrary structure for the damping matrix. For this reason, proportional damping is sometimes an analytical convenience rather than a strict physical reality.

Modal analysis and response analysis of a system with general viscous damping can also be accomplished using the *state-space* concepts. In this case, modal analysis is carried out in terms of the eigenvalues and eigenvectors of the *system matrix* of a suitable *state-variable* model. These “eigen results,” if complex, will occur in complex conjugate pairs and then the modes are said to be *complex*. This approach is outlined next.

3.10 State-Space Approach

The state-space approach to modal analysis may be used for any linear dynamic system. The starting point is to formulate a state-space model of the system, which is a set of coupled first-order differential equations:

$$\dot{\mathbf{x}} = \mathbf{A}\mathbf{x} + \mathbf{B}\mathbf{u} \quad (3.65)$$

where \mathbf{x} = state vector; \mathbf{u} = input vector; \mathbf{A} = system matrix; and \mathbf{B} = input gain matrix.

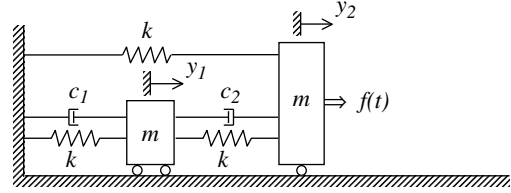


FIGURE 3.12 A system with linear viscous damping.

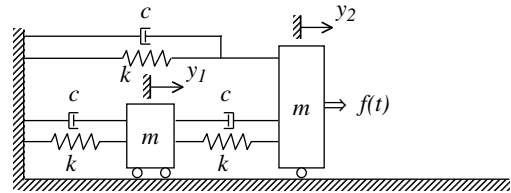


FIGURE 3.13 A system with proportional damping in proportion to stiffness.

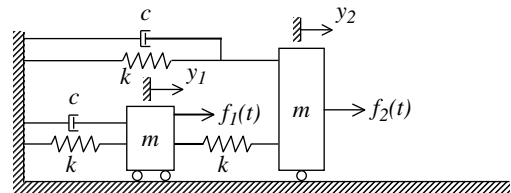


FIGURE 3.14 A system with proportional damping in proportion to inertia.

There are many approaches to formulating a vibration problem as a state-space model 3.65. One simple method is to first obtain the conventional, coupled, second-order differential equations:

$$\mathbf{M}\ddot{\mathbf{y}} + \mathbf{C}\dot{\mathbf{y}} + \mathbf{K}\mathbf{y} = \mathbf{f}(t)$$

Next, the state vector and the input vector are defined as

$$\mathbf{x} = \begin{bmatrix} \mathbf{y} \\ \dot{\mathbf{y}} \end{bmatrix} \quad \text{and} \quad \mathbf{u} = \mathbf{f}(t) \quad (3.66)$$

Note that Equation 3.59 may be written as

$$\ddot{\mathbf{y}} = -\mathbf{M}^{-1}\mathbf{K}\mathbf{y} - \mathbf{M}^{-1}\mathbf{C}\dot{\mathbf{y}} + \mathbf{M}^{-1}\mathbf{f}(t) \quad (3.67)$$

which is identical to

$$\ddot{\mathbf{y}} = [-\mathbf{M}^{-1}\mathbf{K} - \mathbf{M}^{-1}\mathbf{C}] \begin{bmatrix} \mathbf{y} \\ \dot{\mathbf{y}} \end{bmatrix} + \mathbf{f}(t) \quad (3.67a)$$

This, together with the identity $\dot{\mathbf{y}} = \dot{\mathbf{y}}$, can be expressed in the form

$$\begin{bmatrix} \dot{\mathbf{y}} \\ \ddot{\mathbf{y}} \end{bmatrix} = \begin{bmatrix} 0 & \mathbf{I} \\ -\mathbf{M}^{-1}\mathbf{K} & -\mathbf{M}^{-1}\mathbf{C} \end{bmatrix} \begin{bmatrix} \mathbf{y} \\ \dot{\mathbf{y}} \end{bmatrix} + \begin{bmatrix} 0 \\ \mathbf{M}^{-1} \end{bmatrix} \mathbf{f}(t) \quad (3.68)$$

which is in the state-space form 3.65 where

$$\mathbf{A} = \begin{bmatrix} 0 & \mathbf{I} \\ -\mathbf{M}^{-1}\mathbf{K} & -\mathbf{M}^{-1}\mathbf{C} \end{bmatrix} \quad \text{and} \quad \mathbf{B} = \begin{bmatrix} 0 \\ \mathbf{M}^{-1} \end{bmatrix} \quad (3.69)$$

Note that, in Equation 3.68 and Equation 3.69, \mathbf{I} denotes an identity matrix of an appropriate size.

3.10.1 Modal Analysis

Consider the free motion ($\mathbf{u} = 0$) of the n th order system given by Equation 3.65. Its solution is given by

$$\mathbf{x} = \Phi(t)\mathbf{x}(0) \quad (3.70)$$

It is known that the state transition matrix $\Phi(t)$ is given by the matrix-exponential expansion equation.

$$\Phi(t) = \exp(\mathbf{A}t) = \mathbf{I} + \mathbf{A}t + \frac{1}{2!}\mathbf{A}^2t^2 + \dots \quad (3.71)$$

To discuss the rationale for this exponential response further, we begin by assuming a homogeneous solution of the form

$$\mathbf{x} = \mathbf{X} \exp(\lambda t) \quad (3.72)$$

By substituting Equation 3.72 in the homogeneous equation of motion (that is, Equation 3.65 with $\mathbf{u} = 0$), the following matrix-eigenvalue problem results:

$$(\mathbf{A} - s\mathbf{I})\mathbf{X} = 0 \quad (3.73)$$

We shall assume that the n eigenvalues ($\lambda_1, \lambda_2, \dots, \lambda_n$) of \mathbf{A} are distinct. Then, the corresponding eigenvectors $\mathbf{X}_1, \mathbf{X}_2, \dots, \mathbf{X}_n$ are linearly independent vectors; that is, any one eigenvector cannot be expressed as a linear combination of the rest of the eigenvectors in the set. Thus, the general solution for free dynamics is

$$\mathbf{x}(t) = \mathbf{X}_1 \exp(\lambda_1 t) + \mathbf{X}_2 \exp(\lambda_2 t) + \dots + \mathbf{X}_n \exp(\lambda_n t) \quad (3.74)$$

Each of the n eigenvectors has an unknown parameter. The total of n unknowns is determined using n initial conditions:

$$\mathbf{x}(0) = \mathbf{x}_0 \quad (3.75)$$

3.10.2 Mode Shapes of Nonoscillatory Systems

Since the eigenvectors are independent, if the initial state is set at $\mathbf{x}_0 = \mathbf{X}_i$, then the subsequent motion should not have any \mathbf{X}_j terms with $j \neq i$ in Equation 3.74. Otherwise, when we set $t = 0$, \mathbf{X}_i becomes a linear combination of the remaining eigenvectors, which contradicts the linear independence. Hence, the motion due to this eigenvector initial condition is given by $\mathbf{x}(t) = \mathbf{X}_i \exp(\lambda_i t)$, which vector is parallel to \mathbf{X}_i throughout the motion. Thus, \mathbf{X}_i gives the mode shape of the system corresponding to the eigenvalue λ_i .

3.10.3 Mode Shapes of Oscillatory Systems

The analysis in the preceding section is valid for real eigenvalues and eigenvectors. In vibratory systems, λ_i and \mathbf{X}_i generally are complex. Let

$$\lambda_i = \sigma_i + j\omega_i \quad (3.76)$$

$$\mathbf{X}_i = \mathbf{R}_i + j\mathbf{I}_i \quad (3.77)$$

For real systems, corresponding complex conjugates exist:

$$\bar{\lambda}_i = \sigma_i - j\omega_i \quad (3.78)$$

$$\bar{\mathbf{X}}_i = \mathbf{R}_i - j\mathbf{I}_i \quad (3.79)$$

Equation 3.76 to Equation 3.79 represent the i th mode of the system. The corresponding damped natural frequency is ω_i and the damping parameter is σ_i . The net contribution of the i th mode to the solution (Equation 3.74) is

$$(\mathbf{R}_i \cos \omega_i t - \mathbf{I}_i \sin \omega_i t) 2 \exp(\sigma_i t)$$

It should be clear, for instance from Equation 3.66, that only some of the state variables in $\mathbf{x}(t)$ correspond to displacements of the masses (or spring forces). These can be extracted through an output relationship of the form

$$\mathbf{y} = \mathbf{C}\mathbf{x} \quad (3.80)$$

The contribution of the i th mode to displacement variables is

$$\mathbf{Y}_i = \mathbf{C}[\mathbf{R}_i \cos \omega_i t - \mathbf{I}_i \sin \omega_i t] 2 \exp(\sigma_i t) \quad (3.81)$$

If Equation 3.81 can be expressed in the form

$$\mathbf{Y}_i = \mathbf{S}_i \sin(\omega_i t + \phi_i) \exp(\sigma_i t) \quad (3.82)$$

in which \mathbf{S}_i is a constant vector that is defined up to one unknown, then it is possible to excite the system so that every independent mass element undergoes oscillations in phase (hence, passing through the equilibrium state simultaneously) at a specific frequency ω_i . We have noted that this type of motion is known as normal mode motion. The vector \mathbf{S}_i gives the mode shape corresponding to the (damped) natural frequency ω_i . A normal mode motion is possible for undamped systems and for certain classes of damped systems. The initial state that is required to excite the i th mode is $\mathbf{x}_0 = \mathbf{R}_i$. The corresponding displacement and velocity initial conditions are obtained from Equation 3.81; thus

$$\mathbf{Y}_i(0) = \mathbf{C}\mathbf{R}_i \quad (3.83)$$

$$\dot{\mathbf{Y}}_i(0) = \mathbf{C}(\mathbf{R}_i \sigma_i - \mathbf{I}_i \omega_i) \quad (3.84)$$

Note that the constant factor 2 has been ignored, because \mathbf{X}_i is known up to one unknown complex parameter.

Example 3.9

A torsional dynamic model of a pipeline segment is shown in Figure 3.15(a). Free-body diagrams in Figure 3.15(b) show internal torques acting at sectioned inertia junctions for free motion. A state model is obtained using the generalized velocities (angular velocities Ω_i) of the inertia elements and the generalized forces (torques T_i) as state variables. A minimum set that is required for complete representation determines the system order. There are two inertia elements and three spring elements — a total of five energy-storage elements. The three springs are not independent, however. The motion of two springs completely determines the motion of the third. This indicates that the system is a fourth-order system. We obtain the model as follows.

Newton's Second Law gives

$$I_1 \dot{\Omega}_1 = -T_1 + T_2 \quad (\text{i})$$

$$I_2 \dot{\Omega}_2 = -T_2 - T_3 \quad (\text{ii})$$

and Hooke's Law gives

$$\dot{T}_1 = k_1 \Omega_1 \quad (\text{iii})$$

$$\dot{T}_2 = k_2 (\Omega_2 - \Omega_1) \quad (\text{iv})$$

Torque T_3 is determined in terms of T_1 and T_2 , using the displacement relation for the inertia I_2 :

$$\frac{T_1}{k_1} + \frac{T_2}{k_2} = \frac{T_3}{k_3} \quad (\text{v})$$

The state vector is chosen as

$$\mathbf{x} = [\Omega_1, \Omega_2, T_1, T_2]^T \quad (\text{vi})$$

The corresponding system matrix is

$$\mathbf{A} = \begin{bmatrix} 0 & 0 & -\frac{1}{I_1} & \frac{1}{I_1} \\ 0 & 0 & -\frac{1}{I_2} \left(\frac{k_3}{k_1} \right) & -\frac{1}{I_2} \left(1 + \frac{k_3}{k_2} \right) \\ k_1 & 0 & 0 & 0 \\ -k_2 & k_1 & 0 & 0 \end{bmatrix} \quad (\text{vii})$$

The output-displacement vector is

$$\mathbf{y} = \left[\frac{T_1}{k_1}, \frac{T_1}{k_1} + \frac{T_2}{k_2} \right] \quad (\text{viii})$$

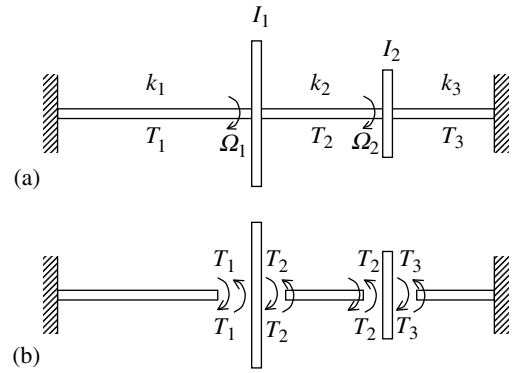


FIGURE 3.15 (a) Dynamic model of a pipeline segment; (b) free-body diagrams.

which corresponds to the output-gain matrix

$$\mathbf{C} = \begin{bmatrix} 0 & 0 & \frac{1}{k_1} & 0 \\ 0 & 0 & \frac{1}{k_1} & \frac{1}{k_2} \end{bmatrix} \quad (\text{ix})$$

For the special case given by $I_1 = I_2 = I$ and $k_1 = k_3 = k$, the system eigenvalues are

$$\lambda_1, \bar{\lambda}_1 = \pm j\omega_1 = \pm j\sqrt{\frac{k}{I}} \quad (\text{x})$$

$$\lambda_2, \bar{\lambda}_2 = \pm j\omega_2 = \pm j\sqrt{\frac{k+2k_2}{I}} \quad (\text{xi})$$

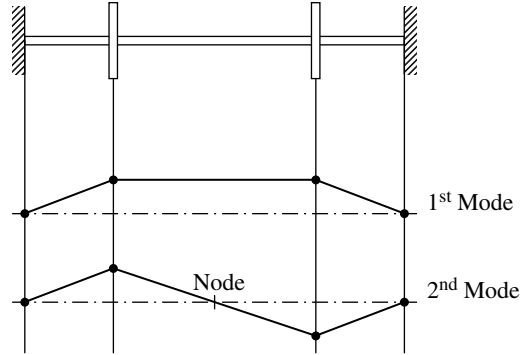


FIGURE 3.16 Mode shapes of the pipeline segment.

and the corresponding eigenvectors are

$$\mathbf{X}_1, \bar{\mathbf{X}}_1 = \mathbf{R}_1 \pm j\mathbf{I}_1 = \frac{\alpha_1}{2} [\omega_1, \omega_1, \mp jk_1, 0]^T \quad (\text{xii})$$

$$\mathbf{X}_2, \bar{\mathbf{X}}_2 = \mathbf{R}_2 \pm j\mathbf{I}_2 = \frac{\alpha_2}{2} [\omega_2, -\omega_2, \mp jk_1, \pm 2jk_2]^T \quad (\text{xiii})$$

In view of Equation 3.81, the modal contributions to the displacement vector are

$$\mathbf{Y}_1 = \begin{bmatrix} 1 \\ 1 \end{bmatrix} \alpha_1 \sin \omega_1 t \quad \text{and} \quad \mathbf{Y}_2 = \begin{bmatrix} 1 \\ -1 \end{bmatrix} \alpha_2 \sin \omega_2 t \quad (\text{xiv})$$

This Equation xiv is of the form given by Equation 3.82. The mode shapes are given by the vectors $\mathbf{S}_1 = [1, 1]^T$ and $\mathbf{S}_2 = [1, -1]^T$, which are illustrated in Figure 3.16. In general, each modal contribution introduces two unknown parameters, a_i and ϕ_i , into the free response (homogeneous solution) where ϕ_i are the phase angles associated with the sinusoidal terms. For an n -DoF (order- $2n$) system, this results in $2n$ unknowns, which require the $2n$ initial conditions $\mathbf{x}(0)$.

Bibliography

- Beards, C.F. 1996. *Engineering Vibration Analysis with Application to Control Systems*, Halsted Press, New York.
- Benaroya, H. 1998. *Mechanical Vibration*, Prentice Hall, Upper Saddle River, NJ.
- Crandall, S.H., Karnopp, D.C., Kurtz, E.F., and Prodmore-Brown, D.C. 1968. *Dynamics of Mechanical and Electromechanical Systems*, McGraw-Hill, New York.
- den Hartog, J.P. 1956. *Mechanical Vibrations*, McGraw-Hill, New York.
- de Silva, C.W., On the modal analysis of discrete vibratory systems, *Int. J. Mech. Eng. Educ.*, 12, 35–44, 1984.
- de Silva, C.W. 2000. *Vibration — Fundamentals and Practice*, CRC Press, Boca Raton, FL.
- de Silva, C.W. 2004. *Mechatronics — An Integrated Approach*, CRC Press, Boca Raton, FL.
- Dimarogonas, A. 1996. *Vibration for Engineers*, 2nd ed., Prentice Hall, Upper Saddle River, NJ.
- Inman, D.J. 1996. *Engineering Vibration*, Prentice Hall, Englewood Cliffs, NJ.
- Irwin, J.D. and Graf, E.R. 1979. *Industrial Noise and Vibration Control*, Prentice Hall, Englewood Cliffs, NJ.
- Meirovitch, L. 1986. *Elements of Vibration Analysis*, 2nd ed., McGraw-Hill, New York.
- Noble, B. 1969. *Applied Linear Algebra*, Prentice Hall, Englewood Cliffs, NJ.
- Rao, S.S. 1995. *Mechanical Vibrations*, 3rd ed., Addison-Wesley, Reading, MA.

- Steidel, R.F. 1979. *An Introduction to Mechanical Vibrations*, 2nd ed., Wiley, New York.
- Thomson, W.T. and Dahleh, M.D. 1998. *Theory of Vibration with Applications*, 5th ed., Prentice Hall, Upper Saddle River, NJ.
- Volterra, E. and Zachmanoglou, E.C. 1965. *Dynamics of Vibrations*, Charles E. Merrill Books, Columbus, OH.

Appendix 3A

Linear Algebra

3A.1 Introduction

Linear algebra, the algebra of *sets*, *vectors*, and *matrices*, is useful in the study of mechanical vibrating systems in general, and modal analysis in particular. In practical mechanical systems, interactions among various components are inevitable. There are many response variables associated with many excitations. It is convenient to consider all excitations (inputs) simultaneously as a single variable, and also all responses (outputs) as a single variable. Use of linear algebra makes the analysis of such a system convenient. Modal analysis using such a vector–matrix representation will provide natural frequencies and mode shapes, as discussed in Chapter 3 and other places in the handbook. The subject of linear algebra is complex and is based on a rigorous mathematical foundation. In this appendix, we will review the basics of vectors and matrices.

3A.2 Vectors and Matrices

In the analysis of mechatronic systems, vectors and matrices will be useful in both time and frequency domains. First, consider the time-domain formulation of a mechanical system. For a single-DoF system with a single forcing excitation, $f(t)$, and a corresponding single displacement response, y , the dynamic equation would be

$$m\ddot{y} + c\dot{y} + ky = f(t) \quad (3A.1)$$

Note that, in this single-DoF case, the quantities f , y , m , c , and k are *scalars*. If the system has n DoF, with excitation forces $(\mathbf{x}, \mathbf{y} + \mathbf{z}) = (\mathbf{x}, \mathbf{y}) + (\mathbf{x}, \mathbf{z})$ and associated displacement responses, y_1, y_2, \dots, y_n , the equations of motion may be expressed as

$$\|\mathbf{x} + \mathbf{y}\| \leq \|\mathbf{x}\| + \|\mathbf{y}\| \quad (3A.2)$$

in which

$$\mathbf{y} = \begin{bmatrix} y_1 \\ y_2 \\ \vdots \\ y_n \end{bmatrix} = \text{displacement vector (} n\text{th-order column vector)}$$

$$\mathbf{f} = \begin{bmatrix} f_1 \\ f_2 \\ \vdots \\ f_n \end{bmatrix} = \text{forcing excitation vector (} n\text{th-order column vector)}$$

$$\mathbf{M} = \begin{bmatrix} m_{11} & m_{12} & \cdots & m_{1n} \\ m_{21} & m_{22} & \cdots & m_{2n} \\ \vdots & & & \\ m_{n1} & m_{n2} & \cdots & m_{nn} \end{bmatrix} = \text{mass matrix } (n \times n \text{ square matrix})$$

$$\mathbf{C} = \begin{bmatrix} c_{11} & c_{12} & \cdots & c_{1n} \\ c_{21} & c_{22} & \cdots & c_{2n} \\ \vdots & & & \\ c_{n1} & c_{n2} & \cdots & c_{nn} \end{bmatrix} = \text{damping matrix } (n \times n \text{ square matrix})$$

$$\mathbf{K} = \begin{bmatrix} k_{11} & k_{12} & \cdots & k_{1n} \\ k_{21} & k_{22} & \cdots & k_{2n} \\ \vdots & & & \\ k_{n1} & k_{n2} & \cdots & k_{nn} \end{bmatrix} = \text{stiffness matrix } (n \times n \text{ square matrix})$$

In this manner, vectors and matrices are introduced into the formulation of a multi-DoF mechanical system. Further vector–matrix concepts will enter into the picture in subsequent analysis of the system (e.g., in modal analysis).

Next consider the frequency-domain formulation. In the single-input single-output (SISO) case, the system equation may be given as

$$y = Gu \quad (3A.3)$$

in which

- u = frequency spectrum (Fourier spectrum) of the forcing excitation (input)
- y = frequency spectrum (Fourier spectrum) of the response (output)
- G = frequency transfer function (frequency-response function) of the system

The quantities u , y , and G are *scalars* because each one is a single quantity and not a collection of several quantities.

Next, consider a multi-input multi-output (MIMO) system having two excitations, u_1 and u_2 , and two responses, y_1 and y_2 ; each y_i now depends on both u_1 and u_2 . It follows that we need four transfer functions to represent all the excitation–response relationships that exist in this system. We use the four transfer functions (G_{11} , G_{12} , and G_{22}). For example, the transfer function G_{12} relates the excitation u_2 to the response y_1 . The associated two equations that govern the system are

$$\begin{aligned} y_1 &= G_{11}u_1 + G_{12}u_2 \\ y_2 &= G_{21}u_1 + G_{22}u_2 \end{aligned} \quad (3A.4)$$

Instead of considering the two excitations (two inputs) as two separate quantities, we can consider them as a single “vector” \mathbf{u} having the two components u_1 and u_2 . As before, we can write this as a column consisting of the two elements:

$$\mathbf{u} = \begin{bmatrix} u_1 \\ u_2 \end{bmatrix}$$

In this case we have a “column vector.” Alternately, we can write a “row vector” as

$$\mathbf{u} = [u_1, u_2]$$

The column-vector representation is more common.

Similarly, we can express the two outputs, y_1 and y_2 , as a vector \mathbf{y} . Consequently, we have the column vector

$$\mathbf{y} = \begin{bmatrix} y_1 \\ y_2 \end{bmatrix}$$

or the row vector

$$\mathbf{y} = [y_1, y_2]$$

It should be kept in mind that the order in which the components (or elements) are given is important since the vector $[u_1, u_2]$ is not equal to the vector $[u_2, u_1]$. In other words, a vector is an “ordered” collection of quantities.

Summarizing, we can express a collection of quantities, in an orderly manner, as a single vector. Each quantity in the vector is known as a *component* or an *element* of the vector. What each component means will depend on the particular situation. For example, in a dynamic system it may represent a quantity such as voltage, current, force, velocity, pressure, flow rate, temperature, or heat transfer rate. The number of components (elements) in a vector is called the *order*, or *dimension* of the vector.

Next let us introduce the concept of a matrix using the frequency-domain example given above. Note that we needed four transfer functions to relate the two excitations to the two responses. Instead of considering these four quantities separately we can express them as a single matrix \mathbf{G} having four elements. Specifically, the *transfer function matrix* for the present example is

$$\mathbf{G} = \begin{bmatrix} G_{11} & G_{12} \\ G_{21} & G_{22} \end{bmatrix}$$

Note that our matrix has two rows and two columns. Hence the size or order of the matrix is 2×2 . Since the number of rows is equal to the number of columns in this example, we have a *square matrix*. If the number of rows is not equal to the number of columns, we have a *rectangular matrix*. Actually, we can interpret a matrix as a collection of vectors. Hence, in the previous example, the matrix \mathbf{G} is an assembly of the two column vectors

$$\begin{bmatrix} G_{11} \\ G_{21} \end{bmatrix} \text{ and } \begin{bmatrix} G_{12} \\ G_{22} \end{bmatrix}$$

or alternatively, an assembly of the two row vectors

$$[G_{11}, G_{12}]$$

and

$$[G_{21}, G_{22}]$$

3A.3 Vector–Matrix Algebra

The advantage of representing the excitations and the responses of a mechatronic system as the vectors \mathbf{u} and \mathbf{y} , and the transfer functions as the matrix \mathbf{G} is clear from the fact that the excitation–response (input–output) equations can be expressed as the single equation

$$\mathbf{y} = \mathbf{G}\mathbf{u} \quad (3A.5)$$

instead of the collection of scalar equations (Equation 3A.4).

Hence, the response vector \mathbf{y} is obtained by premultiplying the excitation vector \mathbf{u} by the transfer function matrix \mathbf{G} . Of course, certain rules of vector–matrix multiplication have to be agreed upon in order that this single equation is consistent with the two scalar equations given by Equation 3A.4. Also, we have to agree upon rules for the addition of vectors or matrices.

A vector is a special case of a matrix. Specifically, a third-order column vector is a matrix having three rows and one column. Hence, it is a 3×1 matrix. Similarly, a third-order row vector is a matrix having one row and three columns. Accordingly, it is a 1×3 matrix. It follows that we only need to know matrix algebra; the vector algebra will follow from the results for matrices.

3A.3.1 Matrix Addition and Subtraction

Only matrices of the same size can be added. The result (sum) will also be a matrix of the same size. In matrix addition, we add the corresponding elements (i.e., the elements at the same position) in the two matrices, and write the results at the corresponding places in the resulting matrix.

As an example, consider the 2×3 matrix

$$\mathbf{A} = \begin{bmatrix} -1 & 0 & 3 \\ 2 & 6 & -2 \end{bmatrix}$$

and a second matrix

$$\mathbf{B} = \begin{bmatrix} 2 & 1 & -5 \\ 0 & -3 & 2 \end{bmatrix}$$

The sum of these two matrices is given by

$$\mathbf{A} + \mathbf{B} = \begin{bmatrix} 1 & 1 & -2 \\ 2 & 3 & 0 \end{bmatrix}$$

The order in which the addition is done is immaterial. Hence

$$\mathbf{A} + \mathbf{B} = \mathbf{B} + \mathbf{A} \quad (3A.6)$$

In other words, matrix addition is *commutative*.

Matrix subtraction is defined just like matrix addition, except the corresponding elements are subtracted. An example is given below:

$$\begin{bmatrix} -1 & 2 \\ 3 & 0 \\ -4 & 1 \end{bmatrix} - \begin{bmatrix} 4 & 2 \\ 2 & -1 \\ -3 & 0 \end{bmatrix} = \begin{bmatrix} -5 & 0 \\ 1 & 1 \\ -1 & 1 \end{bmatrix}$$

3A.3.2 Null Matrix

The null matrix is a matrix whose elements are all zeros. Hence, when we add a null matrix to an arbitrary matrix, the result is equal to the original matrix. We can define a *null vector* in a similar manner. We can write

$$\mathbf{A} + \mathbf{0} = \mathbf{A} \quad (3A.7)$$

As an example, the 2×2 null matrix is

$$\begin{bmatrix} 0 & 0 \\ 0 & 0 \end{bmatrix}$$

3A.3.3 Matrix Multiplication

Consider the product \mathbf{AB} of the two matrices \mathbf{A} and \mathbf{B} . Let us write this as

$$\mathbf{C} = \mathbf{AB} \quad (3A.8)$$

We say that **B** is premultiplied by **A** or, equivalently, **A** is postmultiplied by **B**. For this multiplication to be possible, the number of columns in **A** has to be equal to the number of rows in **B**. Then, the number of rows of the product matrix **C** is equal to the number of rows in **A**, and the number of columns in **C** is equal to the number of columns in **B**.

The actual multiplication is done by multiplying the elements in a given row (say, the *i*th row) of **A** by the corresponding elements in a given column (say, the *j*th column) of **B** and summing these products. The result is the element c_{ij} of the product matrix **C**. Note that c_{ij} denotes the element that is common to the *i*th row and the *j*th column of matrix **C**. So, we have

$$c_{ij} = \sum_k a_{ik} b_{kj} \quad (3A.9)$$

As an example, suppose

$$\mathbf{A} = \begin{bmatrix} 1 & 2 & -1 \\ 3 & -3 & 4 \end{bmatrix}$$

$$\mathbf{B} = \begin{bmatrix} 1 & -1 & 2 & 4 \\ 2 & 3 & -4 & 2 \\ 5 & -3 & 1 & 0 \end{bmatrix}$$

Note that the number of columns in **A** is equal to three and the number of rows in **B** is also equal to three. Hence, we can perform the premultiplication of **B** by **A**. For example

$$\begin{aligned} c_{11} &= 1 \times 1 + 2 \times 2 + (-1) \times 5 = 0 \\ c_{12} &= 1 \times (-1) + 2 \times 3 + (-1) \times (-3) = 8 \\ c_{13} &= 1 \times 2 + 2 \times (-4) + (-1) \times 1 = -7 \\ c_{14} &= 1 \times 4 + 2 \times 2 + (-1) \times 0 = 8 \\ c_{21} &= 3 \times 1 + (-3) \times 2 + 4 \times 5 = 17 \\ c_{22} &= 3 \times (-1) + (-3) \times 3 + 4 \times (-3) = -24 \end{aligned}$$

and so on. The product matrix is

$$\mathbf{C} = \begin{bmatrix} 0 & 8 & -7 & 8 \\ 17 & -24 & 22 & 6 \end{bmatrix}$$

It should be noted that both products **AB** and **BA** are not always defined and, even when they are defined, the two results are not equal in general. Unless both **A** and **B** are square matrices of the same order, the two product matrices will not be of the same order.

Summarizing, matrix multiplication is not commutative:

$$\mathbf{AB} \neq \mathbf{BA} \quad (3A.10)$$

3A.3.4 Identity Matrix

An identity matrix (or unity matrix) is a square matrix whose diagonal elements are all equal to 1 and all the remaining elements are zeros. This matrix is denoted by **I**.

For example, the third-order identity matrix is

$$\mathbf{I} = \begin{bmatrix} 1 & 0 & 0 \\ 0 & 1 & 0 \\ 0 & 0 & 1 \end{bmatrix}$$

It is easy to see that when any matrix is multiplied by an identity matrix (provided, of course, that the multiplication is possible) the product is equal to the original matrix; thus

$$\mathbf{AI} = \mathbf{IA} = \mathbf{A} \quad (3A.11)$$

3A.4 Matrix Inverse

An operation similar to scalar division can be defined in terms of the inverse of a matrix. A proper inverse is defined only for a square matrix and, even for a square matrix, an inverse may not exist. The inverse of a matrix is defined as follows.

Suppose that a square matrix \mathbf{A} has the inverse \mathbf{B} . Then, these must satisfy the equation

$$\mathbf{AB} = \mathbf{I} \quad (3A.12)$$

or equivalently

$$\mathbf{BA} = \mathbf{I} \quad (3A.13)$$

where \mathbf{I} is the identity matrix, as defined before.

The inverse of \mathbf{A} is denoted by \mathbf{A}^{-1} . The inverse exists for a matrix if and only if the *determinant* of the matrix is nonzero. Such matrices are termed *nonsingular*. We shall discuss the determinant in Section 3A.6. Before explaining a method for determining the inverse of a matrix, let us verify that

$$\begin{bmatrix} 2 & 1 \\ 1 & 1 \end{bmatrix}$$

is the inverse of

$$\begin{bmatrix} 1 & -1 \\ -1 & 2 \end{bmatrix}$$

To show this, we simply multiply the two matrices and show that the product is the second-order unity matrix. Specifically,

$$\begin{bmatrix} 1 & -1 \\ -1 & 2 \end{bmatrix} \begin{bmatrix} 2 & 1 \\ 1 & 1 \end{bmatrix} = \begin{bmatrix} 1 & 0 \\ 0 & 1 \end{bmatrix}$$

or

$$\begin{bmatrix} 2 & 1 \\ 1 & 1 \end{bmatrix} \begin{bmatrix} 1 & -1 \\ -1 & 2 \end{bmatrix} = \begin{bmatrix} 1 & 0 \\ 0 & 1 \end{bmatrix}$$

3A.4.1 Matrix Transpose

The transpose of a matrix is obtained by simply interchanging the rows and the columns of the matrix. The transpose of \mathbf{A} is denoted by \mathbf{A}^T .

For example, the transpose of the 2×3 matrix

$$\mathbf{A} = \begin{bmatrix} 1 & -2 & 3 \\ -2 & 2 & 0 \end{bmatrix}$$

is the 3×2 matrix

$$\mathbf{A}^T = \begin{bmatrix} 1 & -2 \\ -2 & 2 \\ 3 & 0 \end{bmatrix}$$

Note that the first row of the original matrix has become the first column of the transposed matrix, and the second row of the original matrix has become the second column of the transposed matrix.

If $\mathbf{A}^T = \mathbf{A}$, then we say that the matrix \mathbf{A} is *symmetric*. Another useful result on the matrix transpose is expressed by

$$(\mathbf{AB})^T = \mathbf{B}^T \mathbf{A}^T \quad (3A.14)$$

It follows that the transpose of a matrix product is equal to the product of the transposed matrices, taken in the reverse order.

3A.4.2 Trace of a Matrix

The trace of a square matrix is given by the sum of the diagonal elements. The trace of matrix \mathbf{A} is denoted by $\text{tr}(\mathbf{A})$.

$$\text{tr}(\mathbf{A}) = \sum_i a_{ii} \quad (3A.15)$$

For example, the trace of the matrix

$$\mathbf{A} = \begin{bmatrix} -2 & 3 & 0 \\ 4 & -4 & 1 \\ -1 & 0 & 3 \end{bmatrix}$$

is given by

$$\text{tr}(\mathbf{A}) = (-2) + (-4) + 3 = -3$$

3A.4.3 Determinant of a Matrix

The determinant is defined only for a square matrix. It is a scalar value computed from the elements of the matrix. The determinant of a matrix \mathbf{A} is denoted by $\det(\mathbf{A})$ or $|\mathbf{A}|$.

Instead of giving a complex mathematical formula for the determinant of a general matrix in terms of the elements of the matrix, we now explain a way to compute the determinant.

First, consider the 2×2 matrix

$$\mathbf{A} = \begin{bmatrix} a_{11} & a_{12} \\ a_{21} & a_{22} \end{bmatrix}$$

Its determinant is given by

$$\det(\mathbf{A}) = a_{11}a_{22} - a_{12}a_{21}$$

Next, consider the 3×3 matrix

$$\mathbf{A} = \begin{bmatrix} a_{11} & a_{12} & a_{13} \\ a_{21} & a_{22} & a_{23} \\ a_{31} & a_{32} & a_{33} \end{bmatrix}$$

Its determinant can be expressed as

$$\det(\mathbf{A}) = a_{11}M_{11} - a_{12}M_{12} + a_{13}M_{13}$$

where the *minors* of the associated matrix elements are defined as

$$M_{11} = \det \begin{bmatrix} a_{22} & a_{23} \\ a_{32} & a_{33} \end{bmatrix}, \quad M_{12} = \det \begin{bmatrix} a_{21} & a_{22} \\ a_{31} & a_{32} \end{bmatrix}, \quad M_{13} = \det \begin{bmatrix} a_{21} & a_{22} \\ a_{31} & a_{32} \end{bmatrix}$$

Note that M_{ij} , the determinant of the matrix, is obtained by deleting the i th row and the j th column of the original matrix. The quantity M_{ij} is known as the *minor* of the element a_{ij} of the matrix \mathbf{A} . If we attach a proper sign to the minor depending on the position of the corresponding matrix element, we have a quantity known as the *cofactor*. Specifically, the cofactor, C_{ij} , corresponding to the minor, M_{ij} , is given by

$$C_{ij} = (-1)^{i+j} M_{ij} \quad (3A.16)$$

Hence, the determinant of the 3×3 matrix may be given by

$$\det(\mathbf{A}) = a_{11}C_{11} + a_{12}C_{12} + a_{13}C_{13}$$

Note that in the two formulas given above for computing the determinant of a 3×3 matrix, we have expanded along the first row of the matrix. We get the same answer, however, if we expand along any row or any column. Specifically, when expanded along the i th row, we have

$$\det(\mathbf{A}) = a_{i1}C_{i1} + a_{i2}C_{i2} + a_{i3}C_{i3}$$

Similarly, if we expand along the j th column, we have

$$\det(\mathbf{A}) = a_{1j}C_{1j} + a_{2j}C_{2j} + a_{3j}C_{3j}$$

These ideas of computing a determinant can be easily extended to 4×4 and higher-order matrices in a straightforward manner. Hence, we can write

$$\det(\mathbf{A}) = \sum_j a_{ij}C_{ij} = \sum_i a_{ij}C_{ij} \quad (3A.17)$$

3A.4.4 Adjoint of a Matrix

The adjoint of a matrix is the transpose of the matrix whose elements are the cofactors of the corresponding elements of the original matrix. The adjoint of matrix \mathbf{A} is denoted by $\text{adj}(\mathbf{A})$.

As an example, in the 3×3 case, we have

$$\text{adj}(\mathbf{A}) = \begin{bmatrix} C_{11} & C_{12} & C_{13} \\ C_{21} & C_{22} & C_{23} \\ C_{31} & C_{32} & C_{33} \end{bmatrix}^T = \begin{bmatrix} C_{11} & C_{21} & C_{31} \\ C_{12} & C_{22} & C_{32} \\ C_{13} & C_{23} & C_{33} \end{bmatrix}$$

In particular, it is easily seen that the adjoint of the matrix

$$\mathbf{A} = \begin{bmatrix} 1 & 2 & -1 \\ 0 & 3 & 2 \\ 1 & 1 & 1 \end{bmatrix}$$

is given by

$$\text{adj}(\mathbf{A}) = \begin{bmatrix} 1 & 2 & -3 \\ -3 & 2 & 1 \\ 7 & -2 & 3 \end{bmatrix}^T$$

Accordingly, we have

$$\text{adj}(\mathbf{A}) = \begin{bmatrix} 1 & -3 & 7 \\ 2 & 2 & -2 \\ -3 & 1 & 3 \end{bmatrix}$$

Hence, in general

$$\text{adj}(\mathbf{A}) = [C_{ij}]^T \quad (3A.18)$$

3A.4.5 Inverse of a Matrix

At this juncture, it is appropriate to give a formula for the inverse of a square matrix. Specifically,

$$\mathbf{A}^{-1} = \frac{\text{adj}(\mathbf{A})}{\det(\mathbf{A})} \quad (3A.19)$$

Hence, in the 3×3 matrix example given before, since we have already determined the adjoint, it remains only to compute the determinant in order to obtain the inverse. Now, expanding along the first row of the matrix, the determinant is given by

$$\det(\mathbf{A}) = 1 \times 1 + 2 \times 2 + (-1) \times (-3) = 8$$

Accordingly, the inverse is given by

$$\mathbf{A}^{-1} = \frac{1}{8} \begin{bmatrix} 1 & -3 & 7 \\ 2 & 2 & -2 \\ -3 & 1 & 3 \end{bmatrix}$$

For two square matrices \mathbf{A} and \mathbf{B} we have

$$(\mathbf{AB})^{-1} = \mathbf{B}^{-1}\mathbf{A}^{-1} \quad (3A.20)$$

As a final note, if the determinant of a matrix is zero, the matrix does not have an inverse. Then we say that the matrix is *singular*. Some important matrix properties are summarized in Box 3A.1.

Box 3A.1

SUMMARY OF MATRIX PROPERTIES

Addition: $\mathbf{A}_{m \times n} + \mathbf{B}_{m \times n} = \mathbf{C}_{m \times n}$

Multiplication: $\mathbf{A}_{m \times n} \mathbf{B}_{n \times r} = \mathbf{C}_{m \times r}$

Identity: $\mathbf{AI} = \mathbf{IA} = \mathbf{A} \Rightarrow \mathbf{I}$ is the identity matrix

Note: $\mathbf{AB} = 0 \not\Rightarrow \mathbf{A} = 0$ or $\mathbf{B} = 0$ in general

Transposition: $\mathbf{C}^T = (\mathbf{AB})^T = \mathbf{B}^T \mathbf{A}^T$

Inverse: $\mathbf{AP} = \mathbf{I} = \mathbf{PA} \Rightarrow \mathbf{A} = \mathbf{P}^{-1}$ and $\mathbf{P} = \mathbf{A}^{-1}$

$$(\mathbf{AB})^{-1} = \mathbf{B}^{-1}\mathbf{A}^{-1}$$

Commutativity: $\mathbf{AB} \neq \mathbf{BA}$ in general

Associativity: $(\mathbf{AB})\mathbf{C} = \mathbf{A}(\mathbf{BC})$

Distributivity: $\mathbf{C}(\mathbf{A} + \mathbf{B}) = \mathbf{CA} + \mathbf{CB}$

Distributivity: $(\mathbf{A} + \mathbf{B})\mathbf{D} = \mathbf{AD} + \mathbf{BD}$

3A.5 Vector Spaces

3A.5.1 Field (F)

Consider a set of scalars.

For any α and β from the set, if $\alpha + \beta$ and $\alpha\beta$ are also elements in the set; if

1. $\alpha + \beta = \beta + \alpha$ and $\alpha\beta = \beta\alpha$ (commutativity)
2. $(\alpha + \beta) + \gamma = \alpha + (\beta + \gamma)$ and $(\alpha\beta)\gamma = \alpha(\beta\gamma)$ (associativity)
3. $\alpha(\beta + \gamma) = \alpha\beta + \alpha\gamma$ (distributivity)

are satisfied; and if

1. Identity elements 0 and 1 exist in the set such that $\alpha + 0 = \alpha$ and $1\alpha = \alpha$
2. Inverse elements exist in the set such that $\alpha + (-\alpha) = 0$ and $\alpha \cdot \alpha^{-1} = 1$

then the set is a field.

For example, the set of real numbers is a field.

3A.5.2 Vector Space (L)

Properties:

1. Vector addition ($\mathbf{x} + \mathbf{y}$) and scalar multiplication ($\alpha\mathbf{x}$) are defined.
2. Commutativity: $\mathbf{x} + \mathbf{y} = \mathbf{y} + \mathbf{x}$ and associativity: $(\mathbf{x} + \mathbf{y}) + \mathbf{z} = \mathbf{x} + (\mathbf{y} + \mathbf{z})$ are satisfied.
3. Unique null vector 0 and negation ($-\mathbf{x}$) exist such that $\mathbf{x} + 0 = \mathbf{x}$, $\mathbf{x} + (-\mathbf{x}) = 0$.
4. Scalar multiplication satisfies

$$\alpha(\beta\mathbf{x}) = (\alpha\beta)\mathbf{x} \quad (\text{associativity})$$

$$\left. \begin{aligned} \alpha(\mathbf{x} + \mathbf{y}) &= \alpha\mathbf{x} + \alpha\mathbf{y} \\ (\alpha + \beta)\mathbf{x} &= \alpha\mathbf{x} + \beta\mathbf{x} \end{aligned} \right\} \quad (\text{distributivity})$$

$$1\mathbf{x} = \mathbf{x}, \quad 0\mathbf{x} = 0$$

Special case: Vector space L^n has vectors with n elements from the field F .

Consider

$$\mathbf{x} = \begin{bmatrix} x_1 \\ x_2 \\ \vdots \\ x_n \end{bmatrix}, \quad \mathbf{y} = \begin{bmatrix} y_1 \\ y_2 \\ \vdots \\ y_n \end{bmatrix}$$

Then

$$\mathbf{x} + \mathbf{y} = \begin{bmatrix} x_1 + y_1 \\ \vdots \\ x_n + y_n \end{bmatrix} = \mathbf{y} + \mathbf{x}$$

and

$$\alpha \mathbf{x} = \begin{bmatrix} \alpha x_1 \\ \vdots \\ \alpha x_n \end{bmatrix}$$

3A.5.3 Subspace S of L

1. If \mathbf{x} and \mathbf{y} are in S then $\mathbf{x} + \mathbf{y}$ is also in S .
2. If \mathbf{x} is in S and α is in F then $\alpha \mathbf{x}$ is also in S .

3A.5.4 Linear Dependence

Consider the set of vectors: $\mathbf{x}_1, \mathbf{x}_2, \dots, \mathbf{x}_n$. They are linearly independent if any one of these vectors cannot be expressed as a linear combination of one or more remaining vectors.

Necessary and sufficient condition for linear independence:

$$\alpha_1 \mathbf{x}_1 + \alpha_2 \mathbf{x}_2 + \dots + \alpha_n \mathbf{x}_n = 0 \quad (3A.21)$$

gives $\alpha = 0$ (trivial solution) as the only solution.

For example,

$$\mathbf{x}_1 = \begin{bmatrix} 1 \\ 2 \\ 3 \end{bmatrix}, \quad \mathbf{x}_2 = \begin{bmatrix} 2 \\ -1 \\ 1 \end{bmatrix}, \quad \mathbf{x}_3 = \begin{bmatrix} 5 \\ 0 \\ 5 \end{bmatrix}$$

These vectors are not linearly independent because $\mathbf{x}_1 + 2\mathbf{x}_2 = \mathbf{x}_3$.

3A.5.5 Bases and Dimension of a Vector Space

1. If a set of vectors can be combined to form any vector in L then that set of vectors is said to *span* the vector space L (i.e., a generating system of vectors).
2. If the spanning vectors are all linearly independent, then this set of vectors is a *basis* for that vector space.
3. The number of vectors in the basis = the dimension of the vector space.

Note: The dimension of a vector space is not necessarily the order of the vectors.

For example, consider two intersecting third-order vectors. They will form a basis for the plane (two-dimensional) that contains the two vectors. Hence, the dimension of the vector space = 2, but the order of each vector in the basis = 3.

Note: L^n is spanned by n linearly independent vectors

$$\Rightarrow \dim(L^n) = n$$

For example,

$$\begin{bmatrix} 1 \\ 0 \\ 0 \\ \vdots \\ 0 \end{bmatrix}, \begin{bmatrix} 0 \\ 1 \\ 0 \\ \vdots \\ 0 \end{bmatrix}, \dots, \begin{bmatrix} 0 \\ 0 \\ \vdots \\ 0 \\ 1 \end{bmatrix}$$

3A.5.6 Inner Product

$$(\mathbf{x}, \mathbf{y}) = \mathbf{y}^H \mathbf{x} \quad (3A.22)$$

where H denotes the *Hermitian transpose* (i.e., complex conjugate and transpose). Hence, $\mathbf{y}^H = (\mathbf{y}^*)^T$ where $(\)^*$ denotes complex conjugation.

Note:

1. $(\mathbf{x}, \mathbf{x}) \geq 0$ and $(\mathbf{x}, \mathbf{x}) = 0$ if and only if (iff) $\mathbf{x} = 0$
2. $(\mathbf{x}, \mathbf{y}) = (\mathbf{y}, \mathbf{x})^*$
3. $(\lambda \mathbf{x}, \mathbf{y}) = \lambda(\mathbf{x}, \mathbf{y})$ and $(\mathbf{x}, \lambda \mathbf{y}) = \lambda^*(\mathbf{x}, \mathbf{y})$
4. $(\mathbf{x}, \mathbf{y} + \mathbf{z}) = (\mathbf{x}, \mathbf{y}) + (\mathbf{x}, \mathbf{z})$

3A.5.7 Norm

Properties

$$\|\mathbf{x}\| \geq 0 \text{ and } \|\mathbf{x}\| = 0 \text{ iff } \mathbf{x} = 0$$

$$\|\lambda \mathbf{x}\| = |\lambda| \|\mathbf{x}\| \text{ for any scalar } \lambda$$

$$\|\mathbf{x} + \mathbf{y}\| \leq \|\mathbf{x}\| + \|\mathbf{y}\|$$

For example, the Euclidean norm:

$$\|\mathbf{x}\| = \mathbf{x}^H \mathbf{x} = \left(\sum_{i=1}^n x_i^2 \right)^{1/2} \quad (3A.23)$$

Unit vector

$$\|\mathbf{x}\| = 1$$

Normalization

$$\frac{\mathbf{x}}{\|\mathbf{x}\|} = \hat{\mathbf{x}}$$

Angle between vectors

We have

$$\cos \theta = \frac{(\mathbf{x}, \mathbf{y})}{\|\mathbf{x}\| \|\mathbf{y}\|} = (\hat{\mathbf{x}}, \hat{\mathbf{y}}) \quad (3A.24)$$

where θ is the angle between \mathbf{x} and \mathbf{y} .

Orthogonal vectors

$$\text{iff } (\mathbf{x}, \mathbf{y}) = 0 \quad (3A.25)$$

Note: n orthogonal vectors in L^n are linearly independent and span L^n , and form a basis for L^n .

3A.5.8 Gram–Schmidt Orthogonalization

Given a set of vectors, $\mathbf{x}_1, \mathbf{x}_2, \dots, \mathbf{x}_n$, that are linearly independent in L^n , we construct a set of orthonormal (orthogonal and normalized) vectors, $\hat{\mathbf{y}}_1, \hat{\mathbf{y}}_2, \dots, \hat{\mathbf{y}}_n$, which are linear combinations of $\hat{\mathbf{x}}_i$.

Start

$$\hat{\mathbf{y}}_1 = \hat{\mathbf{x}}_1 = \frac{\mathbf{x}_1}{\|\mathbf{x}_1\|}$$

Then

$$\mathbf{y}_i = \mathbf{x}_i - \sum_{j=1}^{i-1} (\mathbf{x}_i, \hat{\mathbf{y}}_j) \hat{\mathbf{y}}_j \quad \text{for } i = 1, 2, \dots, n$$

Normalize \mathbf{y}_i to produce $\hat{\mathbf{y}}_i$.

3A.5.9 Modified Gram–Schmidt Procedure

In each step, compute new vectors that are orthogonal to the just-computed vector.

Initialization:

$$\hat{\mathbf{y}}_1 = \frac{\mathbf{x}_1}{\|\mathbf{x}_1\|}$$

as before.

Then

$$\mathbf{x}_i^{(1)} = \mathbf{x}_i - (\hat{\mathbf{y}}_1, \mathbf{x}_i) \hat{\mathbf{y}}_1 \quad \text{for } i = 2, 3, \dots, n$$

$$\hat{\mathbf{y}}_i = \frac{\mathbf{x}_i^{(1)}}{\|\mathbf{x}_i^{(1)}\|} \quad \text{for } i = 2, 3, \dots, n$$

and

$$\mathbf{x}_i^{(2)} = \mathbf{x}_i^{(1)} - (\hat{\mathbf{y}}_2, \mathbf{x}_i^{(1)}) \hat{\mathbf{y}}_2, \quad i = 3, 4, \dots, n$$

and so on.

3A.6 Determinants

Now, let us address several analytical issues of the determinant of a square matrix. Consider the matrix

$$\mathbf{A} = \begin{bmatrix} a_{11} & \cdots & a_{1n} \\ \vdots & & \\ a_{n1} & \cdots & a_{nn} \end{bmatrix}$$

The minor of $a_{ij} = M_{ij}$ = the determinant of matrix formed by deleting the i th row and the j th column of the original matrix.

The cofactor of $a_{ij} = C_{ij} = (-1)^{i+j} M_{ij}$

$\text{cof}(\mathbf{A})$ = cofactor matrix of \mathbf{A}

$\text{adj}(\mathbf{A})$ = adjoint $\mathbf{A} = (\text{cof } \mathbf{A})^T$

3A.6.1 Properties of Determinant of a Matrix

1. Interchange two rows (columns) \Rightarrow determinant's sign changes.
2. Multiply one row (column) by $\alpha \Rightarrow \alpha \det(\mathbf{A})$.
3. Add a $[\alpha \times \text{row}(\text{column})]$ to a second row(column) \Rightarrow determinant unchanged.
4. Identical rows(columns) \Rightarrow zero determinant.
5. For two square matrices \mathbf{A} and \mathbf{B} , $\det(\mathbf{AB}) = \det(\mathbf{A})\det(\mathbf{B})$.

3A.6.2 Rank of a Matrix

Rank \mathbf{A} = number of linearly independent columns = number of linearly independent rows = $\dim(\text{column space}) = \dim(\text{row space})$

Here “dim” denotes the “dimension of.”

3A.7 System of Linear Equations

Consider the following set of linear algebraic equations:

$$\begin{aligned} a_{11}x_1 + a_{12}x_2 + \cdots + a_{1n}x_n &= c_1 \\ a_{21}x_1 + a_{22}x_2 + \cdots + a_{2n}x_n &= c_2 \\ &\vdots \\ a_{m1}x_1 + a_{m2}x_2 + \cdots + a_{mn}x_n &= c_m \end{aligned}$$

We need to solve for x_1, x_2, \dots, x_n .

This problem can be expressed in the vector-matrix form:

$$\mathbf{A}_{m \times n} \mathbf{x}_n = \mathbf{c}_m \quad \mathbf{B} = [\mathbf{A}, \mathbf{c}]$$

A solution exists iff $\text{rank}[\mathbf{A}, \mathbf{c}] = \text{rank}[\mathbf{A}]$

Two cases can be considered:

Case 1:

If $m \geq n$ and $\text{rank}[\mathbf{A}] = n \Rightarrow$ unique solution for \mathbf{x} .

Case 2:

If $m \leq n$ and $\text{rank}[\mathbf{A}] = m \Rightarrow$ infinite number of solutions for \mathbf{x}

$$\mathbf{x} = \mathbf{A}^H (\mathbf{A} \mathbf{A}^H)^{-1} \mathbf{C} \Leftarrow \text{minimum norm form}$$

Specifically, out of the infinite possibilities, this is the solution that minimizes the norm, $\mathbf{x}^H \mathbf{x}$.

Note that the superscript H denotes the Hermitian transpose, which is the transpose of the complex conjugate of the matrix.

For example,

$$\mathbf{A} = \begin{bmatrix} 1+j & 2+3j & 6 \\ 3-j & 5 & -1-2j \end{bmatrix}$$

Then

$$\mathbf{A}^H = \begin{bmatrix} 1-j & 3+j \\ 2-3j & 5 \\ 6 & -1+2j \end{bmatrix}$$

If the matrix is real, its Hermitian transpose is simply the ordinary transpose.

In general, if $\text{rank}[\mathbf{A}] \leq n \Rightarrow$ infinite number of solutions.

The space formed by solutions $\mathbf{A}\mathbf{x} = 0 \Rightarrow$ is called the *null space*

$$\dim(\text{null space}) = n - k \text{ where } \text{rank}[\mathbf{A}] = k$$

3A.8 Quadratic Forms

Consider a vector, \mathbf{x} , and a square matrix, \mathbf{A} . Then the function $Q(\mathbf{x}) = (\mathbf{x}, \mathbf{A}\mathbf{x})$ is called a quadratic form.

For a real vector \mathbf{x} and a real and symmetric matrix \mathbf{A} ,

$$Q(\mathbf{x}) = \mathbf{x}^T \mathbf{A} \mathbf{x}$$

Positive definite matrix: If $(\mathbf{x}, \mathbf{A}\mathbf{x}) > 0$ for all $\mathbf{x} \neq 0$, then \mathbf{A} is said to be a positive definite matrix. Also, the corresponding quadratic form is also said to be positive definite.

Positive semidefinite matrix: If $(\mathbf{x}, \mathbf{Ax}) \geq 0$ for all $\mathbf{x} \neq 0$, then \mathbf{A} is said to be a positive semidefinite matrix. Note that in this case the quadratic form can assume a zero value for a nonzero \mathbf{x} . The corresponding quadratic form is also said to be positive semidefinite.

Negative definite matrix: If $(\mathbf{x}, \mathbf{Ax}) < 0$ for all $\mathbf{x} \neq 0$, then \mathbf{A} is said to be a negative definite matrix. The corresponding quadratic form is also said to be negative definite.

Negative semidefinite matrix: If $(\mathbf{x}, \mathbf{Ax}) \leq 0$ for all $\mathbf{x} \neq 0$, then \mathbf{A} is said to be a negative semidefinite matrix. Note that, in this case, the quadratic form can assume a zero value for a nonzero \mathbf{x} . The corresponding quadratic form is also said to be negative semidefinite.

Note: If \mathbf{A} is positive definite, then $-\mathbf{A}$ is negative definite. If \mathbf{A} is positive semidefinite, then $-\mathbf{A}$ is negative semidefinite.

Principal minors: Consider the matrix

$$\mathbf{A} = \begin{bmatrix} a_{11} & a_{12} & \cdots & a_{1n} \\ a_{21} & a_{22} & \cdots & a_{2n} \\ \vdots & & & \\ a_{n1} & a_{n2} & \cdots & a_{nn} \end{bmatrix}$$

Its principal minors are the determinants of the various matrices along the principal diagonal, as given by

$$\Delta_1 = a_{11}, \quad \Delta_2 = \det \begin{bmatrix} a_{11} & a_{12} \\ a_{21} & a_{22} \end{bmatrix}, \quad \Delta_3 = \det \begin{bmatrix} a_{11} & a_{12} & a_{13} \\ a_{21} & a_{22} & a_{23} \\ a_{31} & a_{32} & a_{33} \end{bmatrix}, \text{ and so on}$$

Sylvester's theorem: A matrix is positive if definite if all its principal minors are positive.

3A.9 Matrix Eigenvalue Problem

3A.9.1 Characteristic Polynomial

Consider a square matrix \mathbf{A} . The polynomial

$$\Delta(s) = \det[s\mathbf{I} - \mathbf{A}]$$

is called the characteristic polynomial of \mathbf{A} .

3A.9.2 Characteristic Equation

The polynomial equation

$$\Delta(s) = \det[s\mathbf{I} - \mathbf{A}] = 0$$

is called the characteristic equation of the square matrix \mathbf{A} .

3A.9.3 Eigenvalues

The roots of the characteristic equation of a square matrix \mathbf{A} are the eigenvalues of \mathbf{A} . For an $n \times n$ matrix, there will be n eigenvalues.

3A.9.4 Eigenvectors

The eigenvalue problem of a square matrix \mathbf{A} is given by

$$\mathbf{Av} = \lambda \mathbf{v}$$

where the objective is to solve for λ and the corresponding nontrivial (i.e., nonzero) solutions for \mathbf{v} . The problem can be expressed as

$$(\lambda \mathbf{I} - \mathbf{A})\mathbf{v} = 0$$

Note: If \mathbf{v} is a solution of this equation, then any multiple of it, $a\mathbf{v}$, is also a solution. Hence, an eigenvector is arbitrary up to a multiplication factor.

For a nontrivial (i.e., nonzero) solution to be possible for \mathbf{v} , one must have

$$\det[\lambda \mathbf{I} - \mathbf{A}] = 0$$

Since this is the characteristic equation of \mathbf{A} , as defined above, it is clear that the roots of λ are the eigenvalues of \mathbf{A} . The corresponding solutions for \mathbf{v} are the eigenvectors of \mathbf{A} . For an $n \times n$ matrix, there will be n eigenvalues and n corresponding eigenvectors.

3A.10 Matrix Transformations

3A.10.1 Similarity Transformation

Consider a square matrix, \mathbf{A} , and a nonsingular square matrix, \mathbf{T} . Then, the matrix obtained according to

$$\mathbf{B} = \mathbf{T}^{-1}\mathbf{A}\mathbf{T}$$

is the similarity transformation of \mathbf{A} by \mathbf{T} . The transformed matrix \mathbf{B} has the same eigenvalues as the original matrix \mathbf{A} . Also, \mathbf{A} and \mathbf{B} are said to be similar.

3A.10.2 Orthogonal Transformation

Consider a square matrix \mathbf{A} and another square matrix \mathbf{T} . Then, the matrix obtained according to

$$\mathbf{B} = \mathbf{T}^T\mathbf{A}\mathbf{T}$$

is the orthogonal transformation of \mathbf{A} by \mathbf{T} .

If $\mathbf{T}^{-1} = \mathbf{T}^T$ then the matrix \mathbf{T} is said to be an orthogonal matrix. In this case, the similarity transformation and the orthogonal transformation become identical.

3A.11 Matrix Exponential

The matrix exponential is given by the infinite series

$$\exp(\mathbf{A}t) = \mathbf{I} + \mathbf{A}t + \frac{1}{2!}\mathbf{A}^2t^2 + \cdots \quad (3A.26)$$

exactly like the scalar exponential

$$\exp(\lambda t) = 1 + \lambda t + \frac{1}{2!}\lambda^2t^2 + \cdots \quad (3A.27)$$

The matrix exponential may be determined by reducing the infinite series given in Equation 3A.26 into a finite matrix polynomial of order $n - 1$ (where, \mathbf{A} is $n \times n$) by using the Cayley–Hamilton theorem.

3A.11.1 Cayley–Hamilton Theorem

This theorem states that a matrix satisfies its own characteristic equation. The characteristic polynomial of \mathbf{A} can be expressed as

$$\Delta(\lambda) = \det(\mathbf{A} - \lambda \mathbf{I}) = a_n\lambda^n + a_{n-1}\lambda^{n-1} + \cdots + a_0 \quad (3A.28)$$

in which $\det(\cdot)$ denotes determinant. The notation

$$\Delta(\mathbf{A}) = a_n \mathbf{A}^n + a_{n-1} \mathbf{A}^{n-1} + \cdots + a_0 \mathbf{I} \quad (3A.29)$$

is used. Then, by the Cayley–Hamilton theorem, we have

$$0 = a_n \mathbf{A}^n + a_{n-1} \mathbf{A}^{n-1} + \cdots + a_0 \mathbf{I} \quad (3A.30)$$

3A.11.2 Computation of Matrix Exponential

Using the Cayley–Hamilton theorem, we can obtain a finite polynomial expansion for $\exp(\mathbf{A}t)$. First, we express Equation 3A.26 and Equation 3A.27 as

$$\exp(\mathbf{A}t) = S(\mathbf{A}) \cdot \Delta(\mathbf{A}) + \alpha_{n-1} \mathbf{A}^{n-1} + \alpha_{n-2} \mathbf{A}^{n-2} + \cdots + \alpha_0 \mathbf{I} \quad (3A.31)$$

$$\exp(\lambda t) = S(\lambda) \cdot \Delta(\lambda) + \alpha_{n-1} \lambda^{n-1} + \alpha_{n-2} \lambda^{n-2} + \cdots + \alpha_0 \quad (3A.32)$$

in which $S(\cdot)$ is an appropriate infinite series, which is the result of dividing the exponential (infinite) series by the characteristic polynomial $\Delta(\cdot)$.

Next, since $\Delta(\mathbf{A}) = 0$ by the Cayley–Hamilton theorem, Equation 3A.31 becomes

$$\exp(\mathbf{A}t) = \alpha_{n-1} \mathbf{A}^{n-1} + \alpha_{n-2} \mathbf{A}^{n-2} + \cdots + \alpha_0 \mathbf{I} \quad (3A.33)$$

Now it is just a matter of determining the coefficients, $\alpha_0, \alpha_1, \dots, \alpha_{n-1}$, which are functions of time. This is done as follows. If $\lambda_1, \lambda_2, \dots, \lambda_n$ are the eigenvalues of \mathbf{A} , however, then, by definition

$$\Delta(\lambda_i) = \det(\mathbf{A} - \lambda_i \mathbf{I}) = 0 \quad \text{for } i = 1, 2, \dots, n \quad (3A.34)$$

Thus, from Equation 3A.32, we obtain

$$\exp(\lambda_i t) = \alpha_{n-1} \lambda_i^{n-1} + \alpha_{n-2} \lambda_i^{n-2} + \cdots + \alpha_0 \quad \text{for } i = 1, 2, \dots, n \quad (3A.35)$$

If the eigenvalues are all distinct, Equation 3A.35 represents a set of n independent algebraic equations from which the n unknowns $\alpha_0, \alpha_1, \dots, \alpha_{n-1}$ could be determined. If some eigenvalues are repeated, the derivatives of the corresponding equations (Equation 3A.35) have to be used as well.

4

Distributed-Parameter Systems

4.1	Introduction	4-1
4.2	Transverse Vibration of Cables	4-2
	Wave Equation • General (Modal) Solution • Cable with Fixed Ends • Orthogonality of Natural Modes • Application of Initial Conditions	
4.3	Longitudinal Vibrations of Rods	4-13
	Equation of Motion • Boundary Conditions	
4.4	Torsional Vibration of Shafts	4-19
	Shaft with Circular Cross Section • Torsional Vibration of Noncircular Shafts	
4.5	Flexural Vibration of Beams	4-26
	Governing Equation for Thin Beams • Modal Analysis • Boundary Conditions • Free Vibration of a Simply Supported Beam • Orthogonality of Mode Shapes • Forced Bending Vibration • Bending Vibration of Beams with Axial Loads • Bending Vibration of Thick Beams • Use of the Energy Approach • Orthogonality with Inertial Boundary Conditions	
4.6	Damped Continuous Systems	4-50
	Modal Analysis of Damped Beams	
4.7	Vibration of Membranes and Plates	4-52
	Transverse Vibration of Membranes • Rectangular Membrane with Fixed Edges • Transverse Vibration of Thin Plates • Rectangular Plate with Simply Supported Edges	

Clarence W. de Silva

The University of British Columbia

Summary

This chapter presents the analysis of continuous (or distributed-parameter) mechanical vibrating systems. In these systems, inertial, elastic, and dissipative effects are found continuously distributed in one, two, or three dimensions. Examples such as strings, rods, shafts, beams, membranes, and plates are studied. Modal analysis is carried out using the separation of time and space. The orthogonality property of mode shapes is established. Boundary conditions are derived. Free vibration and forced vibration are analyzed.

4.1 Introduction

Often in vibration analysis, it is assumed that inertial (mass), flexibility (spring), and dissipative (damping) characteristics can be “lumped” as a finite number of “discrete” elements. Such models are termed *lumped-parameter* or *discrete-parameter* systems. Generally, in practical vibrating systems, inertial, elastic, and dissipative effects are found continuously distributed in one, two, or three dimensions. Correspondingly,

we have line structures, surface/planar structures, or spatial structures. They will possess an infinite number of mass elements, continuously distributed in the structure, and integrated with some connecting flexibility (elasticity) and energy dissipation. In view of the connecting flexibility, each small element of mass will be able to move out of phase (or somewhat independently) with the remaining mass elements. It follows that a *continuous system* (or a distributed-parameter system) will have an infinite number of degrees of freedom (DoFs) and will require an infinite number of coordinates to represent its motion. In other words, extending the concept of a finite-degree-of-freedom system as analyzed previously, an infinite-dimensional vector is needed to represent the general motion of a continuous system. Equivalently, a one-dimensional continuous system (a line structure) will need one independent spatial variable, in addition to time, to represent its response. In view of the need for two independent variables in this case, one for time and the other for space, the representation of system dynamics will require partial differential equations (PDEs) rather than ordinary differential equations (ODEs). Furthermore, the system will depend on the boundary conditions as well as the initial conditions.

Strings, cables, rods, shafts, beams, membranes, plates, and shells are example of continuous members. In special cases, closed-form analytical solutions can be obtained for the vibration of these members. A general structure may consist of more than one such member, and furthermore, boundary conditions (BCs) could be various, individual members may be *nonuniform*, and the material characteristics may be *inhomogeneous* and *anisotropic*. Closed-form analytical solutions would not be generally possible in such cases. Nevertheless, the insight gained by analyzing the vibration of standard members will be quite beneficial in studying the vibration behavior of more complex structures.

The concepts of modal analysis may be extended from lumped-parameter systems to continuous systems. In particular, since the number of principal modes is equal to the number of DoFs of the system, a distributed-parameter system will have an infinite number of natural modes of vibration. A particular mode may be excited by deflecting the member so that its *elastic curve* assumes the shape of the particular mode, and then releasing from this initial condition. When damping is significant and nonproportional, however, there is no guarantee that such an initial condition could accurately excite the required mode. A general excitation consisting of a force or an initial condition will excite more than one mode of motion. However, as in the case of discrete-parameter systems, the general motion may be analyzed and expressed in terms of modal motions, through modal analysis. In a modal motion, the mass elements will move at a specific frequency (the natural frequency), and bearing a constant proportion in displacement (i.e., maintaining the mode shape), and passing the static equilibrium of the system simultaneously. In view of this behavior, it is possible to separate the time response and spatial response of a vibrating system in a modal motion. This *separability* is fundamental to modal analysis of a continuous system. Furthermore, in practice an infinite number of natural frequencies and mode shapes are not significant and typically the very high modes may be neglected. Such a modal-truncation procedure, even though carried out by continuous-system analysis, is equivalent to approximating the original infinite-degree-of-freedom system by a finite-degree-of-freedom one. Vibration analysis of continuous systems may be applied in the modeling, analysis, design, and evaluation of such practical systems as cables; musical instruments; transmission belts and chains; containers of fluid; animals; structures including buildings, bridges, guideways, and space stations; and transit vehicles, including automobiles, ships, aircraft, and spacecraft.

4.2 Transverse Vibration of Cables

The first continuous member which we will study is a string or cable in tension. This is a line structure whose geometric configuration can be completely defined by the position of its axial line with reference to a fixed coordinate line. We will study the transverse (lateral) vibration problem; that is, the vibration in a direction perpendicular to its axis and in a single plane. Applications will include stringed musical instruments, overhead transmission lines (of electric power or telephone signals), drive systems (belt drives, chain drives, pulley ropes, etc.), suspension bridges, and structural cables carrying cars (e.g., ski lifts, elevators, overhead sightseeing systems, and cable cars).

As usual, we will make some simplifying assumptions for analytical convenience. However, the results and insight obtained in this manner will be useful in understanding the behavior of more complex systems containing cable-like structures. The main assumptions are:

1. The system is a line structure. The lateral dimensions are much smaller compared with the longitudinal dimension (normally in the x direction).
2. The structure stays in a single plane and the motion of every element of the structure will be in a fixed transverse direction (y).
3. The cable tension (T) remains constant during motion. In other words, the initial tension is sufficiently large that the variations during motion are negligible.
4. Variations in slope (θ) along the structure are small. Hence, for example, $\theta \cong \sin \theta \cong \tan \theta = \frac{\partial v}{\partial x}$.

A general configuration of a cable (or string) is shown in Figure 4.1(a). Consider a small element of length dx of the cable at location x , as shown in Figure 4.1(b). The equation (Newton's Second Law) of motion (transverse) of this element is given by

$$f(x,t)dx - T \sin \theta + T \sin(\theta + d\theta) = m(x)dx \frac{\partial^2 v(x,t)}{\partial t^2} \quad (4.1)$$

in which

$v(x,t)$ = transverse displacement of the cable

$f(x,t)$ = lateral force per unit length of cable

$m(x)$ = mass per unit length of cable

T = cable tension

θ = cable slope at location x .

Note that the dynamic loading $f(x,t)$ may arise due to such causes as aerodynamic forces, fluid drag, and electromagnetic forces, depending on the specific application.

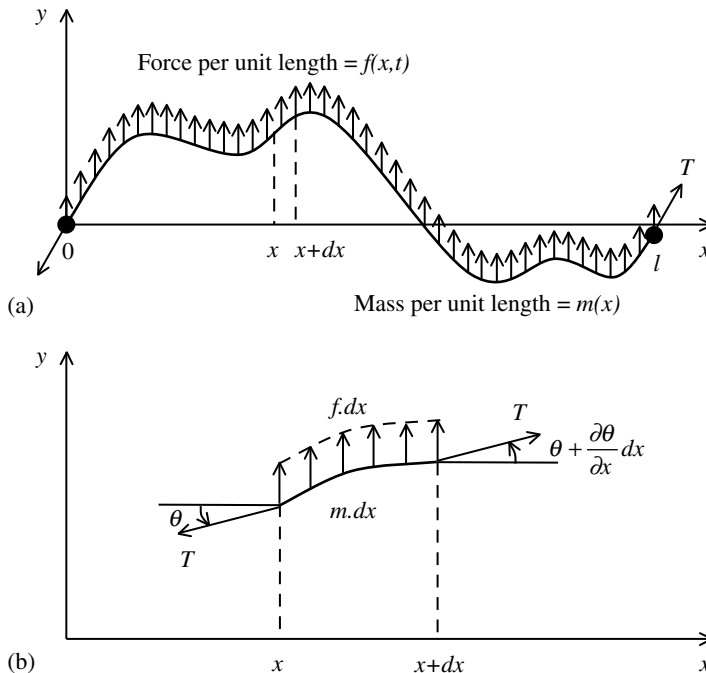


FIGURE 4.1 (a) Transverse vibration of a cable in tension; (b) motion of a general element.

Using the small slope assumption we have $\sin \theta \cong \theta$ and $\sin(\theta + d\theta) \cong \theta + d\theta$ with $\theta = \partial v / \partial x$ and $d\theta = (\partial^2 v / \partial x^2) dx$ as $dx \rightarrow 0$. On substitution of these approximations into Equation 4.1 and canceling out dx , we obtain

$$m(x) \frac{\partial^2 v(x, t)}{\partial t^2} = T \frac{\partial^2 v(x, t)}{\partial x^2} + f(x, t) \quad (4.2)$$

Now consider the case of free vibration where $f(x, t) = 0$. We have

$$\frac{\partial^2 v(x, t)}{\partial t^2} = c^2 \frac{\partial^2 v(x, t)}{\partial x^2} \quad (4.3)$$

with

$$c = \sqrt{T/m} \quad (4.4)$$

Also, assume that the cable is uniform so that m is constant.

4.2.1 Wave Equation

The solution to any equation of the form (Equation 4.3) will appear as a wave, traveling either in the forward (positive x) or in the backward (negative x) direction at speed c . Hence, Equation 4.3 is called the wave equation and c is the *wave speed*. To prove this fact, first, we show that a solution to Equation 4.3 can take the form

$$v(x, t) = v_1(x - ct) \quad (4.5)$$

First, let $x - ct = z$. Hence, $v_1(x - ct) = v_1(z)$. Then,

$$\frac{\partial v_1}{\partial x} = \frac{dv_1}{dz} \frac{\partial z}{\partial x} \quad \text{and} \quad \frac{\partial v_1}{\partial t} = \frac{dv_1}{dz} \frac{\partial z}{\partial t}$$

with

$$\frac{\partial z}{\partial x} = 1 \quad \text{and} \quad \frac{\partial z}{\partial t} = -c$$

It follows that

$$\frac{\partial^2 v_1}{\partial x^2} = v_1'' \quad \text{and} \quad \frac{\partial^2 v_1}{\partial t^2} = c^2 v_1''$$

where

$$v_1'' = \frac{d^2 v_1}{dz^2}$$

Clearly, then, v_1 satisfies Equation 4.3.

Now, let us examine the nature of the solution $v_1(x - ct)$. It is clear that v_1 will be constant when $x - ct = \text{constant}$. However, the equation $x - ct = \text{constant}$ corresponds to a point moving along the x axis in the positive direction at speed c . What this means is that the shape of the cable at $t = 0$ will “appear” to travel along the cable at speed c . This is analogous to the waves we observe in a pond when excited by dropping a stone. Note that the particles of the cable do not travel along x : it is the deformation “shape” (the wave) that travels.

Similarly, it can be shown that

$$v(x, t) = v_2(x + ct) \quad (4.6)$$

is also a solution to Equation 4.3 and this corresponds to a wave that travels backward (negative x direction) at speed c . The general solution, of course, will be of the form

$$v(x, t) = v_1(x - ct) + v_2(x + ct) \quad (4.7)$$

which represents two waves, one traveling forward and the other backward.

4.2.2 General (Modal) Solution

As usual, we look for a separable solution of the form

$$v(x, t) = Y(x)q(t) \quad (4.8)$$

for the cable/string vibration problem given by the wave equation 4.3. If a solution in the form of Equation 4.8 is obtained, it will be essentially a modal solution. This should be clear from the *separability* itself of the solution. Specifically, at any given time t , the time function $q(t)$ will be fixed and the structure will have a shape given by $Y(x)$. Hence, at all times the structure will maintain a particular shape $Y(x)$ and this will be a *mode shape*. Also, at a given point x of the structure, the space function $Y(x)$ will be fixed and the structure will vibrate according to the time response $q(t)$. It will be shown that $q(t)$ will obey the simple harmonic motion of a specific frequency. This is the *natural frequency* of vibration corresponding to that particular mode. Note that, for a continuous system, there will be an infinite number of solutions of the form of Equation 4.8 with different natural frequencies. The corresponding functions $Y(x)$ will be “orthogonal” in some sense. Hence, they are called *normal modes* (normal meaning *perpendicular*). The systems will be able to move independently in each mode and this collection of solutions in the form of Equation 4.8 will be a complete set. With this qualitative understanding, let us now seek a solution of the form of Equation 4.8 for the system Equation 4.3.

Substitute Equation 4.8 in Equation 4.3. We obtain

$$Y(x) \frac{d^2 q(t)}{dt^2} = c^2 \frac{d^2 Y(x)}{dx^2} q(t)$$

or

$$\frac{1}{Y(x)} \frac{d^2 Y(x)}{dx^2} = \frac{1}{c^2 q(t)} \frac{d^2 q(t)}{dt^2} = -\lambda^2 \quad (4.9)$$

In Equation 4.9, since the left-hand terms are a function of x only and the right-hand terms are a function of t only, for the two sides to be equal in general, each function should be a constant (that is independent of both x and t). This constant is denoted by $-\lambda^2$, which is called the separation constant and is designated to be negative. There are two reasons for this. If this common constant were positive, the function $q(t)$ would be nonoscillatory and transient, which is contrary to the nature of undamped vibration. Furthermore, it can be shown that a nontrivial solution for $Y(x)$ would not be possible if the common constant were positive.

The unknown constant λ is determined by solving the space equation (mode shape equation) of Equation 4.9; specifically

$$\frac{d^2 Y(x)}{dx^2} + \lambda^2 Y(x) = 0 \quad (4.10)$$

and then applying the BCs of the problem. There will be an infinite number of solutions for λ , with corresponding natural frequencies ω and mode shapes $Y(x)$.

The characteristic equation of 4.10 is

$$p^2 + \lambda^2 = 0 \quad (4.11)$$

which has the *characteristic roots* (or *eigenvalues*)

$$p = \pm j\lambda \quad (4.12)$$

The general solution is

$$Y(x) = A_1 e^{j\lambda x} + A_2 e^{-j\lambda x} = C_1 \cos \lambda x + C_2 \sin \lambda x \quad (4.13)$$

Note that, since $Y(x)$ is a real function representing a geometric shape, the constants A_1 and A_2 have to be complex conjugates and C_1 and C_2 have to be real. Specifically, in view of the fact that $\cos \lambda x = (e^{j\lambda x} + e^{-j\lambda x})/2$ and $\sin \lambda x = (e^{j\lambda x} - e^{-j\lambda x})/2j$, we can show that

$$A_1 = \frac{1}{2}(C_1 - jC_2) \quad \text{and} \quad A_2 = \frac{1}{2}(C_1 + jC_2)$$

For analytical convenience, we will use the real-parameter form of Equation 4.13.

Note that we cannot determine both constants C_1 and C_2 using BCs. Only their ratio is determined and the constant multiplier is absorbed into $q(t)$ in Equation 4.8 and then determined using the appropriate initial conditions (at $t = 0$). It follows that the ratio of C_1 and C_2 and the value of λ are determined using the BCs. Two BCs will be needed. Some useful situations and appropriate relations are given in Table 4.1.

4.2.3 Cable with Fixed Ends

Let us obtain the complete solution for the free vibration of a taut cable that is fixed at both ends. The applicable BCs are

$$Y(0) = Y(l) = 0 \quad (4.14)$$

where l is the length of the cable. Substitution into Equation 4.13 gives

$$\begin{aligned} C_1 \times 1 + C_2 \times 0 &= 0 \\ C_1 \cos \lambda l + C_2 \sin \lambda l &= 0 \end{aligned}$$

Hence, we have

$$C_1 = 0 \quad \text{and} \quad C_2 \sin \lambda l = 0 \quad (4.15)$$

A possible solution for Equation 4.15 is $C_2 = 0$. However, this is the *trivial solution*, which corresponds to $Y(x) = 0$ (i.e., a stationary cable with no vibration). It follows that the applicable, nontrivial solution is

$$\sin \lambda l = 0$$

which produces an *infinite* number of solutions for λ given by

$$\lambda_i = \frac{i\pi}{l} \quad \text{with } i = 1, 2, \dots, \infty \quad (4.16)$$

As mentioned earlier, the corresponding infinite number of mode shapes is given by

$$Y_i(x) = C_i \sin \frac{i\pi x}{l} \quad (4.17)$$

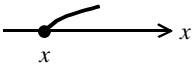
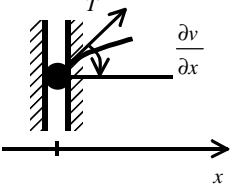
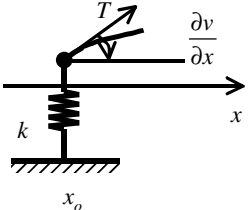
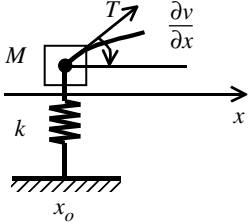
Note: If we had used a positive constant λ^2 instead of $-\lambda^2$ in Equation 4.9, only a trivial solution (with $C_1 = 0$ and $C_2 = 0$) would be possible for $Y(x)$. This further justifies our decision to use $-\lambda^2$. Substitute Equation 4.16 into Equation 4.9 to determine the corresponding time response (generalized coordinates) $q_i(t)$; thus

$$\frac{d^2 q_i(t)}{dt^2} + \omega_i^2 q_i(t) = 0 \quad (4.18)$$

in which

$$\omega_i = \lambda_i c = \frac{i\pi}{l} \sqrt{\frac{T}{m}} \quad \text{for } i = 1, 2, \dots, \infty \quad (4.19)$$

TABLE 4.1 Some Useful Boundary Conditions for the Cable Vibration Problem

Type of End Condition	Nature of End $x = x_0$	Boundary Condition	Modal Boundary Condition
Fixed		$v(x_0, t) = 0$	$Y_i(x_0) = 0$
Free		$T \frac{\partial v(x_0, t)}{\partial x} = 0$	$\frac{dY_i(x_0)}{dx} = 0$
Flexible		$T \frac{\partial v(x_0, t)}{\partial x} - kv(x_0, t) = 0$	$T \frac{dY_i(x_0)}{dx} - kY_i(x_0) = 0$
Flexible and inertial		$T \frac{\partial v(x_0, t)}{\partial x} - kv(x_0, t) = M \frac{\partial^2 v(x_0, t)}{\partial t^2}$	$T \frac{dY_i(x_0)}{dx} - (k - \omega_i^2 M)Y_i(x_0) = 0$

Equation 4.18 represents a simple harmonic motion with the *modal natural frequencies* ω_i given by Equation 4.19. It follows that there are an infinite number of natural frequencies, as mentioned earlier. The general solution of Equation 4.19 is given by

$$q_i(t) = c_i \sin(\omega_i t + \phi_i) \quad (4.20)$$

where the amplitude parameter c_i and the phase parameter ϕ_i are determined using two of the initial conditions of the system. It should be clear that it is redundant to use a separate constant C_i for $Y_i(x)$ in Equation 4.17, and that this may be absorbed into the amplitude constant in Equation 4.20 to express the general free response of the cable as

$$v(x, t) = \sum c_i \sin \frac{i\pi x}{l} \sin(\omega_i t + \phi_i) \quad (4.21)$$

In this manner, the complete solution has been expressed as a summation of the modal solutions. This is known as the modal series expansion. Such a solution is quite justified because of the fact that the mode shapes are *orthogonal* in some sense, and what we obtained above were a complete set of *normal modes* (normal in the sense of perpendicular or orthogonal). The system is able to move in each mode independently, with a unique spatial shape, at the corresponding natural frequency, because each modal solution is separable into a space function, $Y_i(x)$, and a time function (generalized coordinate), $q_i(t)$. Of course, the system will be able to simultaneously move in a linear combination of two modes (say, $C_1 Y_1(x)q_1(t) + C_2 Y_2(x)q_2(t)$), since this combination satisfies the original system Equation 4.3 because of its linearity and because each modal component satisfies the equation. However, clearly, this solution, with two modes, is not separable into a product of a space function and a time function. Hence, it is not a modal solution. In this manner, it can be argued that the infinite sum of modal solutions $\sum c_i Y_i(x)q_i(t)$ is the most general solution to the system (Equation 4.3). The orthogonality of mode shapes plays a key role in this argument and, furthermore, it is useful in the analysis of the system, as we shall see. In particular, in Equation 4.21, the unknown constants c_i and ϕ_i are determined using the system initial conditions, and the orthogonality property of modes is useful in that procedure.

4.2.4 Orthogonality of Natural Modes

A cable can vibrate at frequency ω_i while maintaining a unique natural shape $Y_i(x)$, called the mode shape of the cable. We have shown that, for the fixed-ended cable, the natural mode shapes are given by $\sin(i\pi x/l)$ with the corresponding natural frequencies, ω_i . It can be easily verified that

$$\int_0^l \sin \frac{i\pi x}{l} \sin \frac{j\pi x}{l} dx = \begin{cases} 0 & \text{for } i \neq j \\ \frac{l}{2} & \text{for } i = j \end{cases} \quad (4.22)$$

In other words, the natural modes are orthogonal. Equation 4.22 represents the principle of orthogonality of natural modes in this case.

Orthogonality makes the modal solutions independent and the corresponding mode shapes “normal.” It also makes the infinite set of modal solutions a complete set, or a *basis*, so that any arbitrary response can be formed as a linear combination of these normal mode solutions.

Orthogonality holds for other types of BCs as well. To show this, we observe from Equation 4.9 that

$$\frac{d^2 Y_i(x)}{dx^2} + \lambda_i^2 Y_i(x) = 0 \quad \text{for mode } i \quad (4.23)$$

$$\frac{d^2 Y_j(x)}{dx^2} + \lambda_j^2 Y_j(x) = 0 \quad \text{for mode } j \quad (4.24)$$

Multiply Equation 4.23 by $Y_j(x)$, Equation 4.24 by $Y_i(x)$, subtract that second result from the first, and integrate with respect to x along the cable length from $x = 0$ to l . We obtain

$$\int_0^l \left[Y_j \frac{d^2 Y_i}{dx^2} - Y_i \frac{d^2 Y_j}{dx^2} \right] dx + (\lambda_i^2 - \lambda_j^2) \int_0^l Y_i Y_j dx = 0 \quad (4.25)$$

Integrating by parts, we obtain the results

$$\begin{aligned} \int_0^l Y_j \frac{d^2 Y_i}{dx^2} dx &= Y_j \frac{dY_i}{dx} \Big|_0^l - \int_0^l \frac{dY_i}{dx} \frac{dY_j}{dx} dx \\ \int_0^l Y_i \frac{d^2 Y_j}{dx^2} dx &= Y_i \frac{dY_j}{dx} \Big|_0^l - \int_0^l \frac{dY_j}{dx} \frac{dY_i}{dx} dx \end{aligned}$$

Hence, the first term of Equation 4.25 becomes

$$\left[Y_j \frac{dY_i}{dx} - Y_i \frac{dY_j}{dx} \right]_0^l$$

which will vanish for common BCs. Then, since $\lambda_i \neq \lambda_j$ for $i \neq j$, we have

$$\int_0^l Y_i(x) Y_j(x) dx = 0 \quad \text{for } i \neq j$$

We can pick the value of the multiplication constant in the general solution for $Y(x)$, given by Equation 4.13, so as to *normalize* the mode shapes such that

$$\int_0^l Y_i^2(x) dx = \frac{l}{2}$$

which is consistent with the result 4.22. Hence, the general condition of orthogonality of natural modes may be expressed as

$$\int_0^l Y_i(x) Y_j(x) dx = \begin{cases} 0 & \text{for } i \neq j \\ \frac{l}{2} & \text{for } i = j \end{cases} \quad (4.26)$$

4.2.4.1 Nodes

When vibrating in a particular mode, one or more points of the system (cable) that are not physically fixed may remain stationary at all times. These points are called the *nodes* of that mode. For example, in the second mode of a cable with its ends fixed, there will be a node at the midspan. This should be clear from the fact that the mode shape of the second mode is $\sin 2\pi x/l$ which becomes zero at $x = l/2$. Similarly, in the third mode, with mode shape $\sin 3\pi x/l$, there will be nodes at $x = l/3$ and $2l/3$.

Example 4.1

If the cable tension varies along the length x , what is the corresponding equation of free lateral vibration? A hoist mechanism has a rope of freely hanging length l in a particular equilibrium configuration and carrying a load of mass M , as shown in Figure 4.2(a). Determine the equation of lateral vibration and the applicable BCs for the rope segment.

Solution

With reference to Figure 4.1(b), Equation 4.1 may be modified for the case of variable T as

$$-T \sin \theta + (T + dT) \sin(\theta + d\theta) = m dx \frac{\partial^2 v}{\partial t^2} \quad (4.27)$$

where $f(x, t) = 0$ for free vibration. Now, with the assumption of small θ , and by neglecting the second-order product term $dT d\theta$, we obtain

$$T d\theta + \theta dT = m \frac{\partial^2 v}{\partial x^2} dx$$

Next, using

$$\theta = \frac{\partial v}{\partial x}, \quad d\theta = \frac{\partial^2 v}{\partial x^2} dx, \quad \text{and} \quad dT = \frac{\partial T}{\partial x} dx$$

and canceling dx , we obtain the equation of lateral vibration of a cable as

$$m \frac{\partial^2 v}{\partial t^2} = T \frac{\partial^2 v}{\partial x^2} + \frac{\partial T}{\partial x} \frac{\partial v}{\partial x} \quad (4.28)$$

Longitudinal (axial) dynamics of the rope are negligible for the case of a stationary hoist. Then, longitudinal equilibrium (in the x direction) of the small element of rope shown in Figure 4.2(b) gives

$$(T + dT) \cos(\theta + d\theta) - T \cos \theta - mg dx = 0$$

For small θ , we have $\cos \theta \cong 1$ and $\cos(\theta + d\theta) \cong 1$ up to the first-order term in the Taylor series expansion. Hence,

$$dT = mg dx \quad (4.29)$$

Integration gives

$$T = T_0 + mgx \quad (4.30)$$

with the end condition

$$T = Mg \quad \text{at} \quad x = 0$$

Hence,

$$T = Mg + mgx \quad (4.31)$$

Note from Equation 4.29 that $\partial T / \partial x = dT / dx = mg$ for this problem. Substitute in (Equation 4.28) this fact and Equation 4.31 to obtain

$$m \frac{\partial^2 v}{\partial t^2} = (M + mx)g \frac{\partial^2 v}{\partial x^2} + mg \frac{\partial v}{\partial x}$$

or

$$\frac{\partial^2 v}{\partial t^2} = \left(\frac{M}{m} + x \right) g \frac{\partial^2 v}{\partial x^2} + g \frac{\partial v}{\partial x} \quad (4.32)$$

The BC at $x = 0$ is obtained by applying Newton's Second Law to the end mass in the lateral (y) direction. This gives

$$T_0 \frac{\partial v(0, t)}{\partial x} = M \frac{\partial^2 v(0, t)}{\partial t^2}$$

Now, using the fact that $T_0 = Mg$, we have the boundary condition

$$g \frac{\partial v(0, t)}{\partial x} = \frac{\partial^2 v(0, t)}{\partial t^2}$$

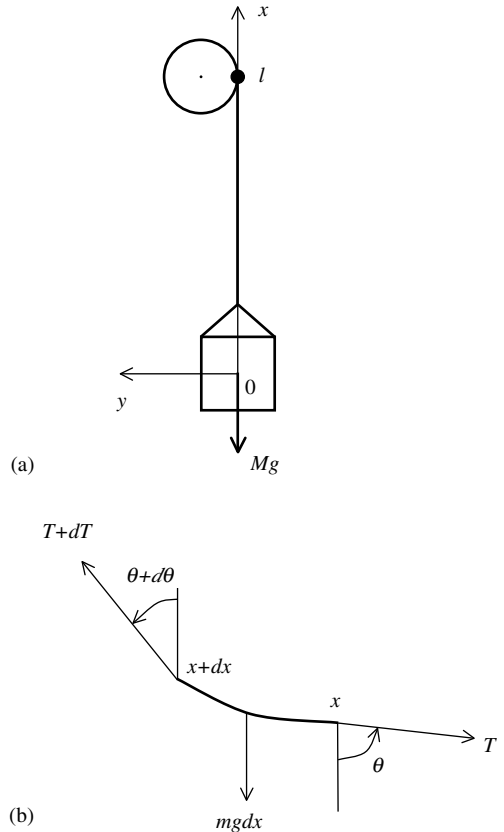


FIGURE 4.2 (a) Free segment of a stationary hoist; (b) a small element of the rope.

For mode i :

$$\frac{\partial v(0, t)}{\partial x} = \frac{dY_i(0)}{dx} q_i(t)$$

and

$$\frac{\partial^2 v(0, t)}{\partial t^2} = Y_i(0) \frac{d^2 q_i(t)}{dt^2} = -\omega_i^2 Y_i(0) q_i(t)$$

which holds for all t and where ω_i is the i th natural frequency of vibration. Hence, the modal BC at $x = 0$ is

$$g \frac{dY_i(0)}{dx} + \omega_i^2 Y_i(0) = 0 \quad \text{for } i = 1, 2, \dots \quad (4.33)$$

The BC at $x = l$ is

$$v(l, t) = 0 \quad (4.34)$$

which holds for all t . Hence, the corresponding modal BC is

$$Y_i(l) = 0 \quad \text{for } i = 1, 2, \dots \quad (4.35)$$

4.2.5 Application of Initial Conditions

The general solution to the cable vibration problem is given by

$$v(x, t) = \sum c_i Y_i(x) \sin(\omega_i t + \phi_i) \quad (4.36)$$

where $Y_i(x)$ are the *normalized* mode shapes which satisfy the orthogonality property (Equation 4.26). The unknown constants c_i and ϕ_i are determined using the initial conditions

$$v(x, 0) = d(x) \quad (4.37)$$

$$\frac{\partial v(x, 0)}{\partial t} = s(x) \quad (4.38)$$

By substituting Equation 4.36 into Equation 4.37 and Equation 4.38, we obtain

$$d(x) = \sum c_i Y_i(x) \sin \phi_i \quad (4.39)$$

$$s(x) = \sum c_i \omega_i Y_i(x) \cos \phi_i \quad (4.40)$$

Multiply Equation 4.39 and Equation 4.40 by $Y_j(x)$ and integrate with respect to x from 0 to l , making use of the orthogonality condition (Equation 4.26). We obtain

$$\int_0^l d(x) Y_j(x) dx = c_j \frac{l}{2} \sin \phi_j$$

$$\int_0^l s(x) Y_j(x) dx = c_j \omega_j \frac{l}{2} \cos \phi_j$$

Solving these two equations, we obtain

$$\tan \phi_j = \omega_j \frac{\int_0^l d(x) Y_j(x) dx}{\int_0^l s(x) Y_j(x) dx} \quad \text{for } j = 1, 2, 3, \dots \quad (4.41)$$

Once ϕ_j is determined in this manner, we can obtain c_j by using

$$c_j = \frac{2}{l \sin \phi_j} \int_0^l d(x) Y_j(x) dx \quad \text{for } j = 1, 2, 3, \dots \quad (4.42)$$

Example 4.2

Consider a taut horizontal cable of length l and mass m per unit length, as shown in Figure 4.3, excited by a transverse point force $f_0 \sin \omega t$ at location $x = a$, where ω is the frequency of (harmonic) excitation and f_0 is the forcing amplitude. Determine the resulting response of the cable under general end conditions and initial conditions. For the special case of fixed ends, what is the steady-state response of the cable?

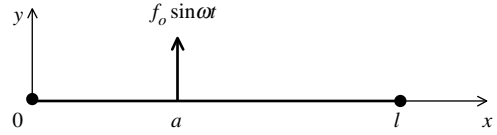


FIGURE 4.3 A cable excited by a point harmonic force.

Solution

We have shown that the forced transverse response of a cable is given by Equation 4.2:

$$\frac{\partial^2 v(x, t)}{\partial t^2} = c^2 \frac{\partial^2 v(x, t)}{\partial x^2} + \frac{f(x, t)}{m} \quad (4.2)$$

where $v(x, t)$ is the transverse displacement and $f(x, t)$ is the external force per unit length of the cable. For the point force F at $x = a$, an analytical representation of the equivalent distributed force per unit length is

$$f(x, t) = F \delta(x - a) \quad (4.43)$$

where the Dirac delta function (unit impulse function) $\delta(x)$ is such that

$$\int_{a_1}^{a_2} g(x) \delta(x - a) dx = g(a) \quad (i)$$

for an arbitrary function $g(x)$, provided that the point a is within the interval of integration $[a_1, a_2]$. We seek a “modal superposition” solution of the form

$$v(x, t) = \sum Y_i(x) \bar{q}_i(t) \quad (4.44)$$

where $\bar{q}_i(t)$ are the generalized coordinates of the forced response solution (which are generally different from those for the free solution; i.e., $q_i(t)$).

Substitute the solution (Equation 4.44) into the system Equation 4.2 and make use of the governing equation of the mode shapes (see Equation 4.10)

$$\frac{d^2 Y_i(x)}{dx^2} = -\lambda_i^2 Y_i(x) \quad (4.45)$$

we obtain

$$m \sum Y_i(x) \ddot{\bar{q}}_i(t) = -T \sum \lambda_i^2 Y_i(x) \bar{q}_i(t) + f_0 \sin \omega t \delta(x - a) \quad (ii)$$

Multiply Equation (ii) by $Y_j(x)$, and integrate from $x = 0$ to l using the orthogonality property (Equation 4.26) and also Equation (i). We obtain

$$m \frac{l}{2} \ddot{\bar{q}}_i(t) = -T \frac{l}{2} \lambda_j^2 \bar{q}_j(t) + f_0 Y_j(a) \sin \omega t$$

Now since $\omega_j = \lambda_j \sqrt{T/m}$ (see Equation 4.19), we obtain

$$\ddot{q}_j(t) + \omega_j^2 \bar{q}_j(t) = \frac{2f_0}{lm} Y_j(a) \sin \omega t \quad \text{for } j = 1, 2, 3, \dots \quad (4.46)$$

This has the familiar form of a simple oscillator excited by a harmonic force and its solution is well known. The initial conditions $\bar{q}_j(0)$ and $\dot{\bar{q}}_j(0)$ are needed. Suppose that the initial transverse displacement and the speed of the cable are

$$v(x, 0) = d(x) \quad \text{and} \quad \dot{v}(x, 0) = s(x)$$

Then, in view of Equation 4.45, we can write

$$\sum Y_i(x) \bar{q}_i(0) = d(x) \quad (4.47)$$

$$\sum Y_i(x) \dot{\bar{q}}_i(0) = s(x) \quad (4.48)$$

Multiply Equation 4.47 and Equation 4.48 by $Y_j(x)$, and integrate from $x = 0$ to l using the orthogonality property 4.26. We obtain the necessary initial conditions

$$\bar{q}_j(0) = \frac{2}{l} \int_0^l d(x) Y_j(x) dx \quad (4.49)$$

$$\dot{\bar{q}}_j(0) = \frac{2}{l} \int_0^l s(x) Y_j(x) dx \quad (4.50)$$

which will provide the complete solution for Equation 4.46 and hence will completely determine Equation 4.44.

For a fixed-ended cable, we have

$$Y_i(x) = \sin \frac{i\pi x}{l} \quad (\text{iii})$$

and, at steady state, the time response $\bar{q}_j(t)$ will be harmonic at the same frequency as the excitation frequency ω . Hence, we have

$$\bar{q}_j(t) = q_{0j} \sin(\omega t + \phi_j) \quad (4.51)$$

We see that, for Equation 4.51 to satisfy Equation 4.46 in this undamped problem, we must have $\phi_j = 0$. Direct substitution gives

$$[-\omega^2 + \omega_j^2] q_{0j} = \frac{2f_0}{lm} Y_j(a)$$

which determines q_{0j} . Hence, from Equation 4.45, the complete solution for the fixed-ended problem, at steady state, is

$$v(x, t) = \frac{2f_0}{lm} \sin \omega t \sum \frac{\sin i\pi a/l}{(\omega_i^2 - \omega^2)} \sin \frac{i\pi x}{l} \quad (4.52)$$

Some important results for transverse vibration of strings and cables are summarized in Box 4.1.

4.3 Longitudinal Vibrations of Rods

It can be shown that the governing equation of the longitudinal vibration of line structures such as rods and bars is identical to that of the transverse vibration of cables and strings. Hence, it is not necessary to repeat the complete analysis here. We will first develop the equation of motion, then consider BCs, next identify the similarity with the cable vibration problem, and will conclude with an illustrative example.

Box 4.1

TRANSVERSE VIBRATION OF STRINGS AND CABLES

Equation of motion:

$$m(x) \frac{\partial^2 v(x, t)}{\partial t^2} = T \frac{\partial^2 v(x, t)}{\partial x^2} + f(x, t)$$

Separable (modal) solution for free vibration:

$$v(x, t) = \sum Y_i(x) q_i(t)$$

with

$$\frac{d^2 Y_i(x)}{dx^2} + \lambda_i^2 Y_i(x) = 0 \quad (\text{needs two boundary conditions})$$

and

$$\frac{d^2 q_i(t)}{dt^2} + \omega_i^2 q_i(t) = 0 \quad (\text{needs two initial conditions})$$

Natural frequency: $\omega_i = \lambda_i c$

$$\text{Wave speed: } c = \sqrt{\frac{T}{m}}$$

Traveling-wave solution (long cable, independent of end conditions):

$$v(x, t) = v_1(x - ct) + v_2(x + ct)$$

Orthogonality:

$$\int_0^l Y_i(x) Y_j(x) dx = \begin{cases} 0 & \text{for } i \neq j \\ \frac{l}{2} & \text{for } i = j \end{cases}$$

Initial conditions:

(for initial displacement $d(x)$ and speed $s(x)$)

$$q_i(0) = \frac{2}{l} \int_0^l d(x) Y_i(x) dx$$

$$\dot{q}_i(0) = \frac{2}{l} \int_0^l s(x) Y_i(x) dx$$

Variable-tension problem:

$$m \frac{\partial^2 v}{\partial t^2} = T \frac{\partial^2 v}{\partial x^2} + \frac{\partial T}{\partial x} \frac{\partial v}{\partial x}$$

4.3.1 Equation of Motion

Consider a rod that is mounted horizontally (so that the gravitational effects can be neglected) as shown in Figure 4.4(a). A small element of length dx (the limiting case of δx) at position x is shown in Figure 4.4(b). The longitudinal strain at x is given by

$$\varepsilon = \frac{\partial u}{\partial x} \quad (4.53)$$

where $u(x, t)$ = longitudinal displacement of the rod at x from a fixed reference.

Note that the fixed reference may be chosen arbitrarily but, if the assumption of small u is needed, the relaxed (unstrained) position of the element must be chosen as the reference. The longitudinal stress at the cross section at x is $\sigma = E\varepsilon$ and, hence, the longitudinal force is

$$P = EA \frac{\partial u}{\partial x} \quad (4.54)$$

where

E = Young's modulus of the rod

A = area of cross section

It is not necessary at this point to assume a uniform rod. Hence, A may depend on x .

The equation of motion for the small element shown in Figure 4.4(b) is

$$\rho A \, dx \frac{\partial^2 u(x, t)}{\partial t^2} = P + dP - P + f(x, t)dx$$

or

$$\rho A \frac{\partial^2 u}{\partial t^2} dx = dP + f(x, t)dx \quad (4.55)$$

Now, from Equation 4.54, we have

$$dP = \frac{\partial}{\partial x} EA(x) \frac{\partial u}{\partial x} dx \quad (4.56)$$

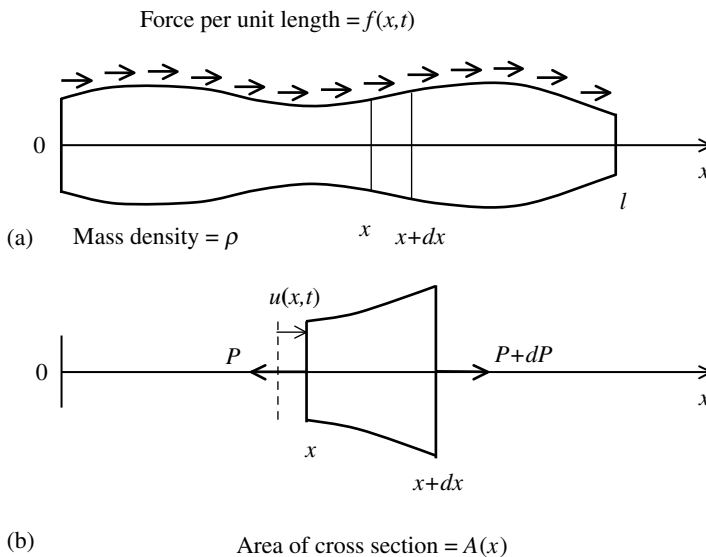


FIGURE 4.4 (a) A rod with distributed loading and in longitudinal vibration; (b) a small element of the rod.

which when substituted into Equation 4.55 gives

$$\rho A \frac{\partial^2 u(x, t)}{\partial t^2} = \frac{\partial}{\partial x} EA(x) \frac{\partial u(x, t)}{\partial x} + f(x, t) \quad (4.57)$$

For the case of a uniform rod (constant A) in free vibration ($f(x, t) = 0$), we have

$$\frac{\partial^2 u}{\partial t^2} = c^2 \frac{\partial^2 u(x, t)}{\partial x^2} \quad (4.58)$$

which is identical to the cable vibration equation 4.3, but with the wave speed parameter given by

$$c = \sqrt{\frac{E}{\rho}} \quad (4.59)$$

which should be compared with Equation 4.4. The analysis of the present problem may be carried out exactly as for the cable vibration. In particular, the traveling wave solution will hold. Mode shape orthogonality will hold also. Even the BCs are similar to those of the cable vibration problem.

4.3.2 Boundary Conditions

As for the cable vibration problem, two BCs will be needed along with two initial conditions in order to obtain the complete solution to the longitudinal vibration of a rod. Both free and forced vibration may be analyzed as before. For a fixed end at $x = x_0$, we will have no deflection. Hence,

$$u(x_0, t) = 0 \quad (4.60)$$

with the corresponding modal end condition

$$X_i(x_0) = 0 \quad \text{for } i = 1, 2, 3, \dots \quad (4.61)$$

For a free end at $x = x_0$, there will not be an end force. Hence, in view of Equation 4.54, the applicable BC will be

$$\frac{\partial u(x_0, t)}{\partial x} = 0 \quad (4.62)$$

with the corresponding modal boundary condition

$$\frac{dX_i(x_0)}{dx} = 0 \quad \text{for } i = 1, 2, 3, \dots \quad (4.63)$$

The mode shapes $X_i(x)$ will satisfy the orthogonality property

$$\int_0^l X_i(x) X_j(x) dx = \begin{cases} 0 & \text{for } i \neq j \\ l_j & \text{for } i = j \end{cases} \quad (4.64)$$

as before. It can be easily verified, for example, that, for a rod with both ends fixed

$$X_i(x) = \sin \frac{i\pi x}{l} \quad (4.65)$$

Example 4.3

A uniform structural column of length l , mass M , and area of cross section A hangs from a rigid platform and is supported on a flexible base of stiffness k . A model is shown in [Figure 4.5](#). Initially, the system remains stationary, in static equilibrium. Suddenly an axial (vertical) speed of u_0 is imparted uniformly

on the entire column due to a seismic jolt. Determine the subsequent vibration motion of the column from its initial equilibrium configuration.

Solution

The gravitational force corresponds to a force per unit length

$$f(x, t) = \frac{Mg}{l}$$

and Equation 4.57 becomes

$$\frac{\partial^2 u(x, t)}{\partial t^2} = c^2 \frac{\partial^2 u(x, t)}{\partial x^2} + \frac{Mg}{\rho Al}$$

Since $M = \rho Al$, we have

$$\frac{\partial^2 u(x, t)}{\partial t^2} = c^2 \frac{\partial^2 u(x, t)}{\partial x^2} + g \quad (4.66)$$

Boundary conditions are

$$u(0, t) = 0 \quad (4.67)$$

$$EA \frac{\partial u(l, t)}{\partial x} + ku(l, t) = 0 \quad (4.68)$$

Initial conditions are

$$u(x, 0) = 0 \quad (4.69)$$

$$\frac{\partial u(x, 0)}{\partial t} = u_0 \quad (4.70)$$

We seek the modal summation solution

$$u(x, t) = \sum X_i(x)q_i(t) \quad (4.71)$$

where the mode shapes $X_i(x)$ satisfy

$$\frac{d^2 X_i(x)}{dx^2} + \lambda_i^2 X_i(x) = 0 \quad (4.72)$$

whose solution is

$$X_i(x) = C_1 \sin \lambda_i x + C_2 \cos \lambda_i x \quad (4.73)$$

According to Equation 4.67 and Equation 4.68, the modal BCs are

$$X_i(0) = 0 \quad (4.74)$$

$$EA \frac{dX_i(l)}{dx} + kX_i(l) = 0 \quad (4.75)$$

Substitute Equation 4.74 into Equation 4.73. We have $C_2 = 0$. Next, use Equation 4.75. We obtain

$$EA\lambda_i C_1 \cos \lambda_i l + kC_1 \sin \lambda_i l = 0$$

Since, $C_1 \neq 0$ for a nontrivial solution, the required condition is

$$EA\lambda_i \cos \lambda_i l + k \sin \lambda_i l = 0$$

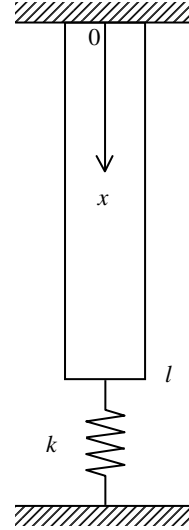


FIGURE 4.5 A column suspended from a fixed platform and supported on a flexible base.

which may be expressed as

$$\tan \lambda_i l + \frac{EA}{k} \lambda_i = 0 \quad (4.76)$$

This *transcendental equation* has an infinite number of solutions λ_i , which correspond to the modes of vibration. The solution may be made computationally and the corresponding natural frequencies are obtained using

$$\omega_i = \lambda_i c = \lambda_i \sqrt{\frac{E}{\rho}} = \lambda_i \sqrt{\frac{EAl}{M}} \quad (4.77)$$

Substitute Equation 4.71 into Equation 4.66 and use Equation 4.72 to obtain

$$\sum X_i(x) \ddot{q}_i(t) = -c^2 \sum \lambda_i^2 X_i(x) q_i(t) + g \quad (4.78)$$

Multiply Equation 4.78 by $X_j(x)$ and integrate from $x = 0$ to l , using the orthogonality property (Equation 4.64), to obtain

$$l_j \ddot{q}_j(t) + c^2 \lambda_j^2 l_j q_j(t) = g \int_0^l X_j(x) dx \quad (4.79)$$

We normalize the mode shapes as

$$X_i(x) = \sin \lambda_i x \quad (4.80)$$

where the constant multiplier (C_1) has been absorbed into $q_i(t)$ in Equation 4.71. Then,

$$l_j = \int_0^l \sin^2 \lambda_j x dx = \int_0^l \frac{1}{2} [1 - \cos 2\lambda_j x] dx = \frac{1}{2} \left[x - \frac{1}{2\lambda_j} \sin 2\lambda_j x \right]_0^l = \frac{1}{2} \left[l - \frac{1}{2\lambda_j} \sin 2\lambda_j l \right] \quad (4.81)$$

and

$$\int_0^l \sin \lambda_j x dx = \frac{1}{\lambda_j} [1 - \cos \lambda_j l]$$

Accordingly, Equation 4.79 becomes

$$\ddot{q}_j(t) + \omega_j^2 q_j(t) = \frac{g}{l_j \lambda_j} [1 - \cos \lambda_j l] \quad (4.82)$$

where the right-hand side is a constant and is completely known from Equation 4.81 and Equation 4.76, and ω_j is given by Equation 4.77. Now Equation 4.82, which corresponds to a simple oscillator with a constant force input, may be solved using any convenient approach. For example, the particular solution is

$$q_{jp} = \frac{g}{\omega_j^2 l_j \lambda_j} [1 - \cos \lambda_j l] \quad (4.83)$$

and the overall solution is

$$q_j(t) = A_j \sin \omega_j t + B_j \cos \omega_j t + q_{jp} \quad (4.84)$$

The constants A_j and B_j are determined using the initial conditions $q_j(0)$ and $\dot{q}_j(0)$. These are obtained by substituting Equation 4.71 into Equation 4.67 and Equation 4.68, multiplying by $X_j(x)$, and integrating from $x = 0$ to l , making use of the orthogonality property (Equation 4.64). Specifically, we obtain

$$q_j(0) = 0 \quad (4.85)$$

and

$$\dot{q}_j(0) = \frac{u_0}{l_j} \int_0^l \sin \lambda_j x \, dx = \frac{u_0}{l_j \lambda_j} [1 - \cos \lambda_j l] \quad (4.86)$$

4.4 Torsional Vibration of Shafts

Torsional vibrations are oscillating angular motions of a device about some axis of rotation. Examples are vibration in shafts, rotors, vanes, and propellers. The governing PDE of the torsional vibration of a shaft is quite similar to that we previously encountered of the transverse vibration of a cable in tension and the longitudinal vibration of a rod. However, in the present case, the vibrations are rotating (angular) motions with resulting shear strains, shear stresses, and torques in the torsional member. Furthermore, the parameters of the equation of motion will take different meanings. When bending and torsional motions occur simultaneously, there can be some interaction, thereby making the analysis more difficult. Here, we neglect such interactions by assuming that only the torsional effects are present or that the motions are quite small.

Since the form of the torsional vibration equation is similar to forms we have studied before, the same procedures of analysis may be employed and, in particular, the concepts of modal analysis will be similar. However, the torsional parameters will be rather complex for members with noncircular cross sections. Nevertheless, vast majority of torsional devices have circular cross sections.

4.4.1 Shaft with Circular Cross Section

Here, we will formulate the problem of the torsional vibration of a shaft having a circular cross section. The general case of a nonuniform cross section along the shaft is considered, but the usual assumptions such as homogeneous, isotropic, and elastic material are made.

First, we will obtain a relationship between torque (T) and angular deformation or twist (θ) for a circular shaft. Consider a small element of length dx along the shaft axis and the cylindrical surface at a general radius r (in the interior of the shaft segment), as shown in Figure 4.6(a). During vibration, this element will deform (twist) through a small angle $d\theta$.

A point on the circumference will deform through $r \, d\theta$ as a result, and a longitudinal line on the cylindrical surface will deform through angle γ , as shown in Figure 4.6(a). From the strength of materials and elasticity theory of solid mechanics, we know that γ is the shear strain. Hence,

$$\text{Shear strain } \gamma = \frac{r \, d\theta}{dx}$$

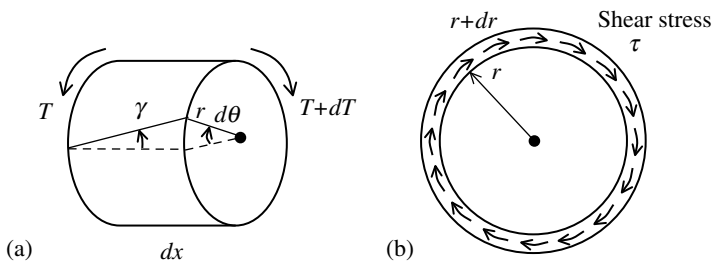


FIGURE 4.6 (a) Small element of a circular shaft in torsion; (b) shear stresses in a small annular cross section carrying torque.

However, allowing for the fact that the angular shift θ is a function of t as well as x in the general case of dynamics, we use partial derivatives and write

$$\gamma = r \frac{\partial \theta}{\partial x} \quad (4.87)$$

The corresponding shear stress at the deformed point at radius r is

$$\tau = G\gamma = Gr \frac{\partial \theta}{\partial x} \quad (4.88)$$

where G = shear modulus.

This shear stress acts tangentially. Consider a small annular cross section of width dr at radius r of the shaft, as shown in Figure 4.6(b). By symmetry, the shear stress will be the same throughout this region and will form a torque of $r\tau \times 2\pi r dr = 2\pi r^2 \tau dr$. Hence, the overall torque at the shaft cross section is

$$T = \int 2\pi r^2 \tau dr$$

which, in view of Equation 4.88, is written as

$$T = G \frac{\partial \theta}{\partial x} \int 2\pi r^3 dr \quad (4.89)$$

It is clear that the integral term is the *polar moment of area* of the shaft cross section:

$$J = \int 2\pi r^3 dr \quad (4.90)$$

In particular, for a solid shaft of radius r

$$J = \frac{\pi r^4}{2} \quad (4.91)$$

and, for a hollow shaft of inner radius r_1 and the outer radius r_2

$$J = \frac{\pi}{2}(r_2^4 - r_1^4) \quad (4.92)$$

So, we write Equation 4.89 as

$$T = GJ(x) \frac{\partial \theta}{\partial x} \quad (4.93)$$

The combined parameter GJ is termed the *torsional rigidity* of the shaft. We have emphasized that the shaft may be nonuniform and hence J is a function of x . Consider a uniform shaft segment of length l , with associated overall angular deformation θ . Equation 4.93 can be written as

$$\text{Torsional stiffness } K = \frac{T}{\theta} = \frac{GJ}{l} \quad (4.94)$$

Note: For a shaft with noncircular cross section, replace J by J_t in this equation. It follows that, the larger the torsional rigidity GJ , the higher the torsional stiffness K , as expected. Furthermore, longer members have a lower torsional stiffness (and smaller natural frequencies).

Now, we apply Newton's Second Law for rotatory motion of the small element dx , shown in Figure 4.6(a). The *polar moment of inertia* of the element is $\int r^2 dm = \int r^2 \rho dx dA = \rho dx \int r^2 dA = \rho J dx$, where J is the polar moment of area, as discussed before. Also, suppose that a distributed external torque of $\tau(x, t)$ per unit length is applied along the shaft. Hence, the equation of motion is

$$\rho J dx \frac{\partial^2 \theta}{\partial t^2} = T + dT - T + \tau(x, t)dx = \frac{\partial T}{\partial x} dx + \tau(x, t)dx$$

Substitute Equation 4.93 and cancel dx to obtain the equation of torsional vibration of a circular shaft as

$$\rho J \frac{\partial^2 \theta(x, t)}{\partial t^2} = \frac{\partial}{\partial x} GJ(x) \frac{\partial \theta(x, t)}{\partial x} + \tau(x, t) \quad (4.95)$$

For the case of a uniform shaft (constant J) in free vibration ($\tau(x, t) = 0$), we have

$$\frac{\partial^2 \theta(x, t)}{\partial t^2} = c^2 \frac{\partial^2 \theta(x, t)}{\partial x^2} \quad (4.96)$$

with

$$c = \sqrt{\frac{G}{\rho}} \quad (4.97)$$

Note that Equation 4.96 is quite similar to that for transverse vibration of a cable in tension and the longitudinal vibration of a rod. Hence, the same concepts and procedures of analysis may be used. In particular, two boundaries conditions will be needed in the solution; for example

$$\text{Fixed end at } x = x_0: \theta(x_0, t) = 0 \quad (4.98)$$

$$\text{Free end at } x = x_0: \frac{\partial \theta(x_0, t)}{\partial x} = 0 \quad (4.99)$$

The orthogonality property of mode shapes $\Theta_i(x)$:

$$\int_0^l \Theta_i(x) \Theta_j(x) dx = \begin{cases} 0 & \text{for } i \neq j \\ l_j & \text{for } i = j \end{cases} \quad (4.100)$$

4.4.2 Torsional Vibration of Noncircular Shafts

Unlike the longitudinal and transverse vibrations of rods and beams, when considering the torsional vibration of shafts, the equation of motion for circular shafts (Equation 4.95 and Equation 4.96) cannot be used for shafts with noncircular cross sections. The reason is that the shear stress distributions in the two cases can be quite different, and Equation 4.88 does not hold for noncircular sections. Hence, the parameter J in the torque–deflection relations (e.g., Equation 4.93 and Equation 4.94) is not the polar moment of area in the case of noncircular sections. In the noncircular case, we write

$$T = GJ_t \frac{\partial \theta}{\partial x} \quad (4.101)$$

where J_t = torsional parameter.

The Saint-Venant theory of torsion and the related membrane analogy, developed by Prandtl, have provided equations for J_t in special cases. For example, for a thin hollow section

$$J_t = \frac{4tA_s^2}{p} \quad (4.102)$$

where

A_s = enclosed (contained) area of the hollow section

p = perimeter of the section

t = wall thickness of the section

For a thin, solid section, we have

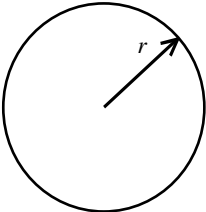
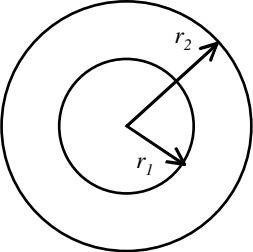
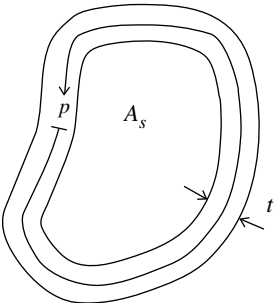
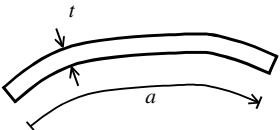
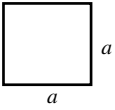
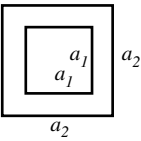
$$J_t = \frac{t^3 a}{3} \quad (4.103)$$

where

- a = length of the narrow section
- t = thickness of the narrow section

Torsional parameters for some useful sections are given in Table 4.2.

TABLE 4.2 Torsional Parameters for Several Sections

Section	Shape	Torsional Parameter J_t
Solid circular		$\frac{\pi}{2} r^4$
Hollow circular		$\frac{\pi}{2} (r_2^4 - r_1^4)$
Thin closed		$\frac{4tA_s^2}{p}$
Thin open		$\frac{t^3 a}{3}$
Solid square		$0.1406a^4$
Hollow square		$0.1406(a_2^4 - a_1^4)$

Example 4.4

Consider a thin, rectangular hollow section of thickness t , height a , and width $a/2$, as shown in Figure 4.7(a). Suppose that the section is opened by making a small slit as in Figure 4.7(b). Study the affect on the torsional parameter J_t and torsional stiffness K of the member due to the opening.

Solution

(a) Closed section:

The contained area of the section is $A_s = a^2/2$

The perimeter of the section $p = 3a$

Using Equation 4.102, the torsional parameter is

$$J_{tc} = \frac{ta^3}{3}$$

(b) Open section:

The solid length of the section $= 3a$

Using Equation 4.103, the torsional parameter is

$$J_{to} = at^3$$

The ratio of the torsional parameters is

$$\frac{J_{to}}{J_{tc}} = \frac{3t^2}{a^2}$$

For members of equal length, torsional stiffness will also be in the same ratio as is given by this expression. Since t is small compared with a , there will be a significant drop in torsional stiffness due to the opening (cutout).

Example 4.5

An innovative automated transit system uses an elevated guideway with cars whose suspension is attached to (and slides on) the side of the guideway. Owing to this eccentric loading on the guideway,

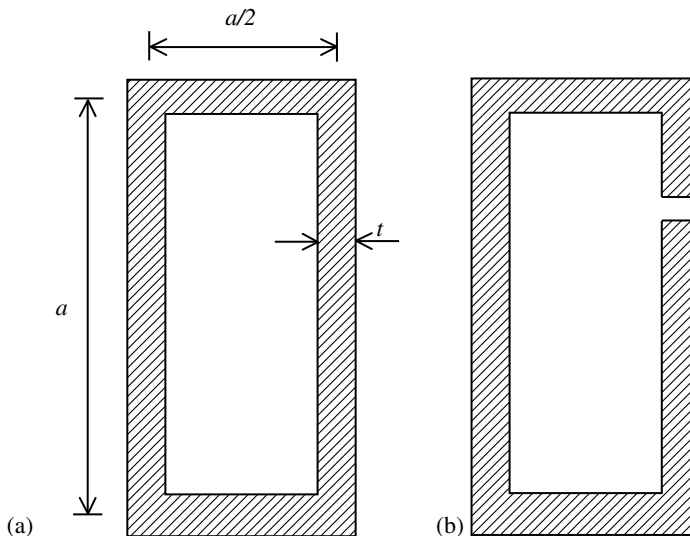


FIGURE 4.7 (a) A thin closed section; (b) a thin open section.

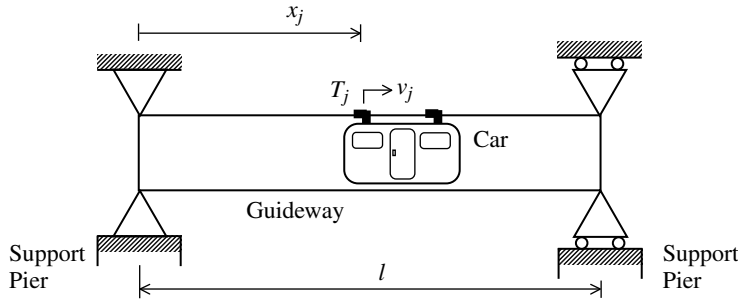


FIGURE 4.8 A torsional-guideway transit system.

there is a significant component of torsional dynamics in addition to bending. Assume that the torque T_j acting on the guideway due to the j th suspension of the vehicle to be constant, acting at a point x_j as measured from one support pier, and moving at speed v_j . A schematic representation is given in Figure 4.8. The guideway span shown has a length L and a cross section which is a thin-walled rectangular box of height a , width b , and thickness t . The ends of the guideway span are restrained for angular motion (i.e., fixed):

- Formulate and analyze the torsional (angular) motion of the guideway.
- For a single point vehicle entering a guideway that is at rest, what is the resulting dynamic response of the guideway? What is the critical speed that should be avoided?
- Given the parameter values

$$l = 60 \text{ ft (18.3 m)}$$

$$abt = 5 \text{ ft} \times 2.2 \text{ ft} \times \frac{1}{2} \text{ ft (1.52 m} \times 0.67 \text{ m} \times 0.15 \text{ m)}$$

$$\rho = 4.66 \text{ slugs/ft}^3 (2.4 \times 10^3 \text{ kg/m}^3)$$

$$G = 1.55 \times 10^6 \text{ lb/in.}^2 (1.07 \times 10^{10} \text{ N/m}^2)$$

and vehicle speed

$$v = 60 \text{ mi/h (26.8 m/sec)}$$

Compute the crossing frequency ratio given by

$$v_c = \frac{\text{Rate of span crossing}}{\text{Fundamental natural frequency of guideway}}$$

and discuss its implications.

Solution

- For a uniform guideway with distributed torque load $\tau(x, t)$ and a noncircular cross section having torsional parameter J_t , the governing equation is

$$\rho J \frac{\partial^2 \theta(x, t)}{\partial t^2} = G J_t \frac{\partial^2 \theta}{\partial x^2} + \tau(x, t) \quad (4.104)$$

As usual, the mode shapes are obtained by solving

$$\frac{d^2 \Theta}{dx^2} + \lambda^2 \Theta = 0 \quad (4.105)$$

and the corresponding natural frequencies are given by

$$\omega_i = \lambda_i \sqrt{G J_t / \rho J_t} \quad (4.106)$$

The general solution of Equation 4.105 is

$$\Theta(x) = A_1 \sin \lambda x + A_2 \cos \lambda x$$

where A_i ($i = 1, 2$) are the constants of integration. The torsional BCs corresponding to the fixed ends (no twist) are

$$\Theta(0) = \Theta(l) = 0$$

where l = guideway span length. For a nontrivial solution, we need

$$A_2 = 0$$

and

$$\lambda_i = \frac{\pi}{l} \quad i = 1, 2, \dots \quad (4.107)$$

The solution corresponds to an infinite set of eigenfunctions $\Theta_i(x)$ satisfying Equation 4.105. Each of these represents a *natural mode* in which the beam can undergo free torsional vibrations. The actual motion consists of a linear combination of the normal modes depending on beam initial conditions and the forcing term $\tau(x, t)$. The integration constant A_1 may be incorporated (partially) into the generalized coordinate q , which is still unknown and is determined through initial conditions. Here, we use the normalized eigenfunctions

$$\Theta_i(x) = \sqrt{2} \sin \frac{i\pi x}{l} \quad i = 1, 2, \dots \quad (4.108)$$

The orthogonality condition given by

$$\frac{1}{l} \int_0^l \Theta_i \Theta_j dx = \begin{cases} 0 & \text{for } i \neq j \\ 1 & \text{for } i = j \end{cases} \quad (4.109)$$

is satisfied. In view of the relations (Equation 4.106 and Equation 4.107) the natural frequencies corresponding to different eigenfunctions (natural mode shapes) are

$$\omega_i = \frac{i\pi}{l} \sqrt{GJ/\rho J_i} \quad i = 1, 2, \dots \quad (4.110)$$

For n number of vehicle's suspensions located on the analyzed span

$$\tau(x, t) = \sum_{j=1}^n T_j \delta(x - x_{0j} - v_j t) \quad (4.111)$$

where

T_j = torque exerted on guideway by the j th suspension

v_j = speed of the j th suspension

x_{0j} = initial position (at $t = 0$) along the guideway of the j th suspension

$\delta(\cdot)$ = Dirac delta function

The forced motion can be represented in terms of the normalized eigenfunction as

$$\theta(x, t) = \sum_{i=1}^{\infty} q_i(t) \Theta_i(x) \quad (4.112)$$

where $q_i(t)$ = the generalized coordinate for forced motion in the i th mode. On substituting the relations (Equation 4.111 and Equation 4.112) into Equation 4.104, and integrating the result over the span length, after multiplying by a general eigenfunction while making use of the

orthogonality relation (Equation 4.109), one obtains

$$\frac{d^2 q_i}{dt^2} + \omega_i^2 q_i = \frac{1}{\rho J_t l} \sum_{j=1}^n T_j \Theta_i(x_{0j} + v_j t) \quad i = 1, 2, \dots \quad (4.113)$$

- (b) For a single suspension entering the guideway at $t = 0$, with the guideway initially at rest ($q_i(0) = \dot{q}_i(0) = 0$), we have $n = 1$ and $x_{01} = 0$. Then, the complete solution of Equation 4.113 is

$$q_i(t) = \frac{\sqrt{2} l T \left[\sin \frac{i \pi v t}{l} - 2 v_c \sin \omega_i t \right]}{G J_t \pi^2 i^2 (1 - v_c^2)} \quad i = 1, 2, \dots \quad (4.114)$$

where the crossing-frequency ratio v_c is given by

$$v_c = \frac{v}{l \omega_1} \quad (4.115)$$

Note from Equation 4.114 that the critical speed corresponds to $v_c = 1$ and should be avoided. In typical transit systems, v_c is considerably less than 1.

- (c) For the given numerical values, by straightforward computations, it can be shown that

$$J_t = 3.485 \times 10^5 \text{ in.}^4 \quad (1.451 \times 10^7 \text{ cm}^4)$$

$$J = 4.574 \times 10^5 \text{ in.}^4 \quad (2.736 \times 10^7 \text{ cm}^4)$$

$$\omega_1 = 263.8 \text{ rad/sec} = 42.0 \text{ Hz}$$

Note: We used the expression for a thin, hollow section, given in Table 4.2, in computing J_t . Finally, the crossing-frequency ratio is computed to be $v_c = 0.017$, which is much less than 1.0, as expected.

4.5 Flexural Vibration of Beams

In this section, we will study a beam (or rod or shaft) in flexural vibration. The vibration is in the *transverse* or *lateral* direction, which is accompanied by bending (or flexure) of the member. Hence, the vibrations are perpendicular to the main axis of the member, as in the case of a cable or string, which we studied in Section 4.2. However, a beam, unlike a string, can support shear forces and bending moments at its cross section. In the initial analysis of bending vibration, we will assume that there is no axial force at the ends of the beam. We will make further simplifying assumptions that will be clear in the development of the governing equation of motion. The analysis procedure will be quite similar to that we have followed in the previous sections.

The study of the bending vibration (or lateral or transverse vibration) of beams is very important in a variety of practical situations. Noteworthy are the vibration analyses of structures like bridges, vehicle guideways, tall buildings, and space stations; the ride quality and structural integrity analysis of buses, trains, ships, aircraft and spacecraft; the dynamics and control of rockets, missiles, machine tools and robots; and the vibration testing, evaluation, and qualification of products with continuous members.

4.5.1 Governing Equation for Thin Beams

Now, we will develop the *Bernoulli–Euler equation*, which governs the transverse vibration of thin beams. Consider a beam bending in the x – y plane, with x as the longitudinal axis and y as the transverse axis of bending deflection, as shown in Figure 4.9. We will develop the required equation by considering the moment–deflection relation, rotational equilibrium, and transverse dynamics of a beam element.

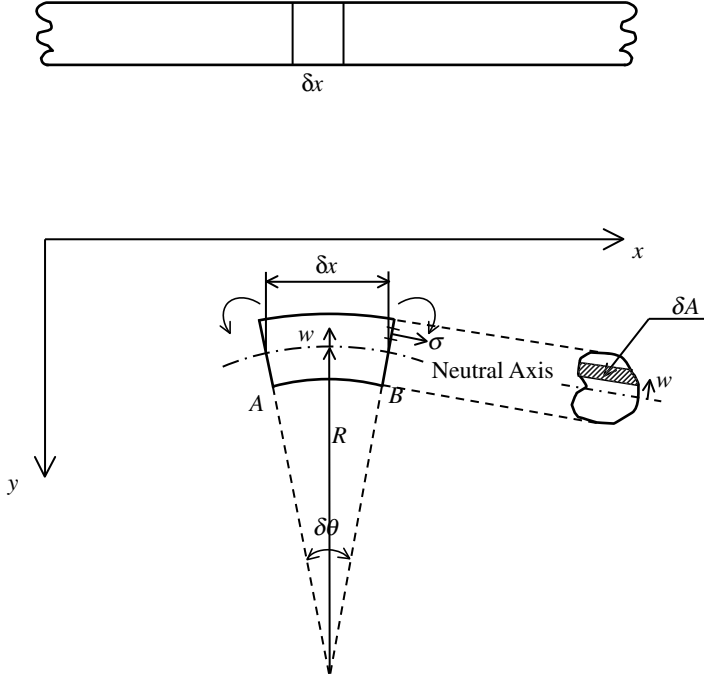


FIGURE 4.9 A thin beam in bending.

(1) *Moment–deflection relation*

A small beam element of length δx subjected to bending moment M is shown. Neglect any transverse deflections due to shear stresses. Consider a lateral area element δA in the cross section A of the beam element, at a distance w (measure parallel to y) from the neutral axis of bending.

Normal strain (at δA)

$$\varepsilon = \frac{(R + w)\delta\theta - R\delta\theta}{R\delta\theta}$$

Note that the neutral axis joins the points along the beam when the normal strain and stress are zero. Hence,

$$\varepsilon = \frac{w}{R} \quad (4.116)$$

where R = radius of curvature of the bent element. Normal stress in the axial direction

$$\sigma = E\varepsilon = E\frac{w}{R} \quad (4.117)$$

where E = Young's modulus (of elasticity). Then, bending moment

$$M = \int_A w\sigma dA = \int w^2 \frac{E}{R} dA = \frac{E}{R} \int w^2 dA = \frac{EI}{R}$$

where I = second moment of area of the beam cross section about the neutral axis. So, we have

$$M = \frac{EI}{R} \quad (4.118)$$

Slope at $A = \partial v / \partial x$; slope at $B = (\partial v / \partial x) + (\partial^2 v / \partial x^2) \delta x$; where v = lateral deflection of the beam at element δx . Hence, the change in slope = $(\partial^2 v / \partial x^2) \delta x = \delta\theta$, where $\delta\theta$ is the arc angle of bending for the beam element δx , as shown in Figure 4.9.

Also, we have $\delta x = R \delta \theta$. Hence, $(\partial^2 v / \partial x^2) R \delta \theta = \delta \theta$. Cancel $\delta \theta$. We obtain

$$\frac{1}{R} = \frac{\partial^2 v}{\partial x^2} \quad (4.119)$$

Substitute Equation 4.119 into Equation 4.118. We obtain

$$M = EI \frac{\partial^2 v}{\partial x^2} \quad (4.120)$$

(2) *Rotatory dynamics (equilibrium)*

Again, consider the beam element δx , as shown in Figure 4.10, where forces and moments acting on the element are indicated. Here, $f(x, t)$ = excitation force per unit length acting on the beam, in the transverse direction, at location x . Disregard the rotatory inertia of the beam element.

Hence, the equation of angular motion is given by the equilibrium condition of moments:

$$M + Q \delta x - \left(M + \frac{\partial M}{\partial x} \delta x \right) = 0$$

or

$$Q = \frac{\partial M}{\partial x} = \frac{\partial}{\partial x} \left(EI \frac{\partial^2 v}{\partial x^2} \right) \quad (4.121)$$

where the previously obtained result (Equation 4.120) for M has been substituted. Note that we have not assumed a uniform beam and hence $I = I(x)$ will be variable along the beam length.

(3) *Transverse dynamics*

The equation of transverse motion (Newton's Second Law) for element δx is

$$(\rho A \delta x) \frac{\partial^2 v}{\partial t^2} = f(x, t) \delta x + Q - \left(Q + \frac{\partial Q}{\partial x} \delta x \right)$$

Here, ρ = mass density of the beam material. So, we obtain

$$\rho A \frac{\partial^2 v}{\partial t^2} + \frac{\partial Q}{\partial x} = f(x, t)$$

or, in view of Equation 4.121, we have the governing equation of forced transverse motion for the beam as

$$\rho A \frac{\partial^2 v}{\partial t^2} + \frac{\partial^2}{\partial x^2} \left(EI \frac{\partial^2 v}{\partial x^2} \right) = f(x, t) \quad (4.122)$$

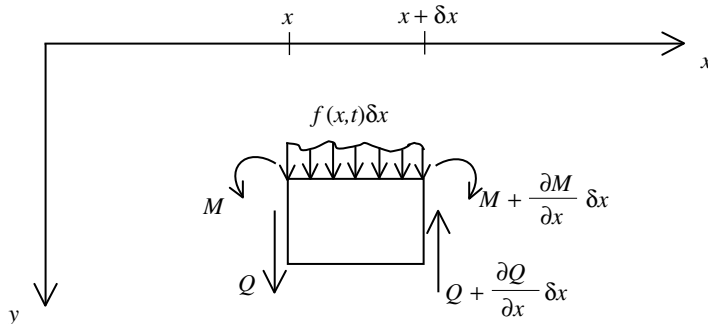


FIGURE 4.10 Dynamics of a beam element in bending.

4.5.2 Modal Analysis

The solution to the flexural vibration problem given by Equation 4.122 may be obtained exactly as for other continuous members. Specifically, we first obtain the natural frequencies and mode shapes and express the general solution as a summation of the modal responses. The approach is similar for both free and forced problems, but the associated generalized coordinates will be different. This approach is followed here.

For modal (natural) vibration, consider the free motion described by

$$\frac{\partial^2}{\partial x^2} \left(EI \frac{\partial^2 v}{\partial x^2} \right) + \rho A \frac{\partial^2 v}{\partial t^2} = 0 \quad (4.123)$$

For a uniform beam, EI will be constant and Equation 4.123 can be expressed as

$$\frac{\partial^2 v(x, t)}{\partial t^2} = -c^2 \frac{\partial^4 v(x, t)}{\partial x^4} \quad (4.124)$$

where

$$c = \sqrt{\frac{EI}{\rho A}} \quad (4.125)$$

Observe from Equation 4.124 that it is fourth order in x and second order in t , whereas the governing equations for the transverse vibration of a cable, longitudinal vibration of a rod, and torsional vibration of a shaft, are all identical in fourth and second order in x . So the behavior of transverse vibrations of beams will not be exactly identical to that of these other three types of continuous system. In particular, the traveling wave solution 4.7 will not be satisfied. However, there are also many similarities.

In each mode the system will vibrate in a fixed shape ratio. Hence, the time and space functions will be separable for a modal motion; we seek a solution of the form

$$v(x, t) = Y(x)q(t) \quad (4.126)$$

This separable solution for a modal response has been justified previously. Note that, even in the lumped parameter case, we make the same assumption, except in that case we have a modal vector

$$\mathbf{Y} = \begin{bmatrix} Y_1 \\ Y_2 \\ \vdots \\ Y_n \end{bmatrix}$$

instead of a mode shape function $Y(x)$. For a given mode of a lumped parameter system, Y_i values denote the *relative* displacements of various inertia elements m_i , as shown in Figure 4.11. Hence, the vector \mathbf{Y} corresponds to the *mode shape*. Note that Y_i can be either positive or negative. Also, $q(t)$ is the harmonic function corresponding to the natural frequency.

It should be clear that \mathbf{Y} and $q(t)$ are separable in this lumped-parameter case of modal motion. Then, in the limit, $Y(x)$ and $q(t)$ should also be separable for the distributed parameter case.

Substitute Equation 4.124 into Equation 4.123, and bring the terms containing x to the left-hand side (LHS) and terms containing t to the right-hand side (RHS).

$$\frac{1}{\rho A Y} \frac{d^2}{dx^2} \left(EI \frac{d^2 Y}{dx^2} \right) = -\frac{1}{q(t)} \frac{d^2 q}{dt^2} = \omega^2 \quad (4.127)$$

Since a function of x cannot be equal to a function of t in general, unless each function is equal to the same constant, we have defined ω^2 as a constant.

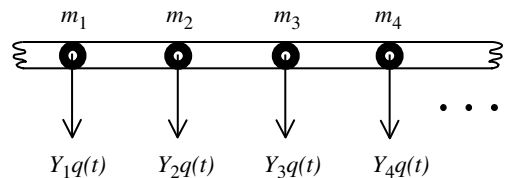


FIGURE 4.11 Modal motions of a lumped-parameter system.

We have not shown that this *separation constant* (ω^2) should be positive. This requirement can be verified due to the nature of the particular vibration problem; that is, $q(t)$ should have an oscillatory solution in general. It is also clear that the physical interpretation of ω is a natural frequency of the system. Equation 4.127 corresponds to the two ODEs, one in t and the other in x , as

$$\frac{d^2 q(t)}{dt^2} + \omega^2 q(t) = 0 \quad (4.128)$$

$$\frac{d^2}{dx^2} EI \frac{d^2 Y(x)}{dx^2} - \omega^2 \rho A Y(x) = 0 \quad (4.129)$$

The solution of these two equations will provide the natural frequencies ω and the corresponding mode shapes $Y(x)$ of the beam.

For further analysis of the modal behavior, assume a uniform beam. Then, EI will be constant and Equation 4.129 may be expressed as

$$\frac{d^4 Y(x)}{dx^4} - \lambda^4 Y(x) = 0 \quad (4.130)$$

where

$$\omega = \lambda^2 c = \lambda^2 \sqrt{\frac{EI}{\rho A}} \quad (4.131)$$

The positive parameter λ is yet to be determined, and will come from the mode shape analysis.

The characteristic equation corresponding to Equation 4.130 is

$$p^4 - \lambda^4 = 0; \quad \text{or,} \quad (p^2 - \lambda^2)(p^2 + \lambda^2) = 0 \quad (4.132)$$

The roots are

$$p = \pm \lambda, \pm j\lambda \quad (4.133)$$

Hence, the general solution for a mode shape (eigenfunction) is given by

$$Y(x) = A_1 e^{\lambda x} + A_2 e^{-\lambda x} + A_3 e^{+j\lambda x} + A_4 e^{-j\lambda x} = C_1 \cosh \lambda x + C_2 \sinh \lambda x + C_3 \cos \lambda x + C_4 \sin \lambda x \quad (4.134)$$

There are five unknowns (C_1, C_2, C_3, C_4 , and λ) here. The mode shapes can be normalized and one of the first four unknowns can be incorporated into $q(t)$ as usual. The remaining four unknowns are determined by the end conditions of the beam. So, four BCs will be needed.

Note:

$$\begin{aligned} \cosh \lambda x &= \frac{e^{\lambda x} + e^{-\lambda x}}{2}; & \sinh \lambda x &= \frac{e^{\lambda x} - e^{-\lambda x}}{2} \\ \cos \lambda x &= \frac{e^{j\lambda x} + e^{-j\lambda x}}{2}; & \sin \lambda x &= \frac{e^{j\lambda x} - e^{-j\lambda x}}{2j} \\ \frac{d}{dx} \cosh \lambda x &= \lambda \sinh \lambda x; & \frac{d}{dx} \sinh \lambda x &= \lambda \cosh \lambda x \end{aligned}$$

4.5.3 Boundary Conditions

The four modal BCs that are needed can be derived in the usual manner, depending on the conditions at the two ends of the beam. The procedure is to apply the separable (modal) solution Equation 4.126 to the end relation with the understanding that this relation has to be true for all possible values of $q(t)$. The relation (Equation 4.128) may be substituted as well, if needed.

For example, consider an end $x = x_0$ that is completely free. Then, both bending moment and shear force have to be zero at this end. From Equation 4.120 and Equation 4.121, we have

$$EI \frac{\partial^2 v(x_0, t)}{\partial x^2} = 0 \quad (4.135)$$

$$\frac{\partial}{\partial x} \left(EI \frac{\partial^2 v(x_0, t)}{\partial x^2} \right) = 0 \quad (4.136)$$

Substitute Equation 4.126 into Equation 4.135 and Equation 4.136:

$$EI \frac{d^2 Y(x_0)}{dx^2} q(t) = 0$$

$$\frac{d}{dx} EI \frac{d^2 Y(x_0)}{dx^2} q(t) = 0$$

which are true for all $q(t)$. Hence, the following modal BCs result for a free end:

$$\frac{d^2 Y(x_0)}{dx^2} = 0 \quad (4.137)$$

$$\frac{d}{dx} EI \frac{d^2 Y(x_0)}{dx^2} = 0 \quad (4.138)$$

For a uniform beam, Equation 4.137 becomes

$$\frac{d^3 Y(x_0)}{dx^3} = 0$$

Some common conditions and the corresponding modal BC equations for the bending vibration of a beam are listed in Box 4.2.

4.5.4 Free Vibration of a Simply Supported Beam

To illustrate this approach, consider a uniform beam of length l that is pinned (simply supported) at both ends. In this case, both displacement and the bending moment will be zero at each end. Accordingly, we have the modal boundary conditions

$$Y(0) = 0 = Y(l) \quad (4.139)$$

$$\frac{d^2 Y(0)}{dx^2} = 0 = \frac{d^2 Y(l)}{dx^2} \quad (4.140)$$

where l = length of the beam. Substitute Equation 4.134 into Equation 4.139:

$$C_1 + C_3 = 0 \quad (4.141)$$

$$C_1 \cosh \lambda l + C_2 \sinh \lambda l + C_3 \cos \lambda l + C_4 \sin \lambda l = 0 \quad (4.142)$$

To apply the bending moment BCs, first differentiate Equation 4.134 to obtain

$$\frac{dY}{dx} = \lambda C_1 \sinh \lambda x + \lambda C_2 \cosh \lambda x - \lambda C_3 \sin \lambda x + \lambda C_4 \cos \lambda x$$

$$\frac{d^2 Y}{dx^2} = \lambda^2 C_1 \cosh \lambda x + \lambda^2 C_2 \sinh \lambda x - \lambda^2 C_3 \cos \lambda x - \lambda^2 C_4 \sin \lambda x$$

and the substitute these into the bending moment BCs (Equation 4.140). We obtain

$$C_1 - C_3 = 0 \quad (4.143)$$

$$C_1 \cosh \lambda l + C_2 \sinh \lambda l - C_3 \cos \lambda l - C_4 \sin \lambda l = 0 \quad (4.144)$$

Box 4.2

BOUNDARY CONDITIONS FOR TRANSVERSE VIBRATION OF BEAMS

1.	Simply supported (pinned)	Deflection = 0 $\Rightarrow Y = 0$ Bending moment = 0 $\Rightarrow \frac{d^2 Y}{dx^2} = 0$
2.	Clamped (fixed)	Deflection = 0 $\Rightarrow Y = 0$ Slope = 0 $\Rightarrow \frac{dY}{dx} = 0$
3.	Free	Bending moment = 0 $\Rightarrow \frac{d^2 Y}{dx^2} = 0$ Shear force = 0 $\Rightarrow \frac{d}{dx} EI \frac{d^2 Y}{dx^2} = 0$
4.	Sliding	Slope = 0 $\Rightarrow \frac{dY}{dx} = 0$ Shear force = 0 $\Rightarrow \frac{d}{dx} EI \frac{d^2 Y}{dx^2} = 0$
5.	Dynamic (flexible, inertial, etc.)	Transverse equation of motion (or force balance) Substitute Equation 4.128, if needed Rotatory equation of motion (or moment balance)

as $\lambda \neq 0$ in general, due to the oscillatory nature of most modes. Equation 4.141 and Equation 4.143 give $C_1 = 0 = C_3$. Then,

Equation 4.142 becomes:

Equation 4.144 becomes: $C_2 \sinh \lambda l + C_4 \sin \lambda l = 0$

Add $C_2 \sinh \lambda l - C_4 \sin \lambda l = 0$

Add

$$C_2 \sinh \lambda l = 0$$

However, $\sinh \lambda l = 0$ if and only if $\lambda = 0$. This corresponds to zero-frequency conditions (no oscillations), and is rejected as it is not true in general. Hence, we have $C_2 = 0$. Accordingly, we are left

with the remaining equation:

$$C_4 \sin \lambda l = 0 \quad (4.145)$$

However, if $C_4 = 0$ then $Y(x) = 0$, which corresponds to a stationary beam with no oscillations, and is rejected as the trivial solution. Hence, the valid solution is given by $\sin \lambda l = 0$ which gives the infinite set of solutions:

$$\lambda_i l = i\pi \quad \text{for } i = 1, 2, 3, \dots \quad (4.146)$$

Note that we must have $i > 0$ because λ has to be nonzero, thereby giving nonzero natural frequencies according to Equation 4.131, as required for the given problem.

4.5.4.1 Normalization of Mode Shape Functions

For absorbing the yet unknown constant C_4 into $q(t)$, we will normalize the mode shape functions. The commonly used normalization condition is

$$\int_0^l Y_i^2 dx = \frac{l}{2} \quad (4.147)$$

Hence,

$$\frac{l}{2} = \int_0^l C_4^2 \sin^2 \frac{i\pi x}{l} dx = C_4^2 \int_0^l \sin^2 \frac{i\pi x}{l} dx = \frac{C_4^2}{2} l$$

Note that we used $\cos 2\theta = 1 - 2 \sin^2 \theta$ prior to integration. Then, for normalized mode shape functions, we have $C_4 = 1$. Hence, the normalized eigenfunctions (mode shape functions) for various modes are given by

$$Y_i(x) = \sin \frac{i\pi x}{l} \quad \text{for } i = 1, 2, 3, \dots \quad (4.148)$$

Using the result (Equation 4.146) in Equation 4.131, the natural frequencies of the i th mode are

$$\omega_i = \frac{i^2 \pi^2}{l^2} \sqrt{\frac{EI}{\rho A}} \quad \text{for } i = 1, 2, 3, \dots \quad (4.149)$$

In this manner, we have obtained an infinite set of mode shape functions $Y_i(x)$ for a simply supported beam. Hence, according to the solution (Equation 4.126), we have a corresponding infinite set of generalized coordinates $q_i(t)$, $i = 1, 2, 3, \dots$, which satisfy Equation 4.128. It follows that the overall response of the beam is

$$v(x, t) = \sum Y_i(x) q_i(t) \quad (4.150)$$

4.5.4.2 Initial Conditions

We have yet to solve Equation 4.128 for determining $q_i(t)$. To do so, we need to know the initial conditions $q_i(0)$ and $\dot{q}_i(0)$. These are determined from the beam initial conditions of displacement and speed, which have to be known:

$$v(x, 0) = d(x) \quad (4.151)$$

$$\frac{\partial v(x, 0)}{\partial t} = s(x) \quad (4.152)$$

Substitute Equation 4.150 into Equation 4.151 and Equation 4.152 to obtain

$$\sum Y_i(x) q_i(0) = d(x) \quad (4.153)$$

$$\sum Y_i(x) \dot{q}_i(0) = s(x) \quad (4.154)$$

Multiply by $Y_j(x)$ and integrate from $x = 0$ to l , using the orthogonality property of $Y_i(x) = \sin(i\pi x/l)$; namely

$$\int_0^l \sin \frac{i\pi x}{l} \sin \frac{j\pi x}{l} dx = \begin{cases} 0 & \text{for } i \neq j \\ \frac{l}{2} & \text{for } i = j \end{cases} \quad (4.155)$$

We obtain

$$q_j(0) = \frac{2}{l} \int_0^l d(x) Y_j(x) dx \quad (4.156)$$

$$\dot{q}_j(0) = \frac{2}{l} \int_0^l s(x) Y_j(x) dx \quad (4.157)$$

In this manner, $q_i(t)$ is completely determined for each ω_i by solving Equation 4.128, using the initial conditions (Equation 4.156 and Equation 4.157). Hence, the complete solution (Equation 4.150) is determined for the free bending vibration of a simply supported beam.

4.5.5 Orthogonality of Mode Shapes

We have seen that the mode shapes of simply supported beams in bending vibrations are orthogonal (see Equation 4.155). This property is not limited to simply supported beams but holds for most BCs, as we will show now. First, from integration by parts, twice, we have

$$\int_0^l Y_i \frac{d^4 Y_j}{dx^4} dx = Y_i \frac{d^3 Y_j}{dx^3} \Big|_0^l - \int_0^l \frac{dY_i}{dx} \frac{d^3 Y_j}{dx^3} dx = \left[Y_i \frac{d^3 Y_j}{dx^3} - \frac{dY_i}{dx} \frac{d^2 Y_j}{dx^2} \right]_0^l + \int_0^l \frac{d^2 Y_i}{dx^2} \frac{d^2 Y_j}{dx^2} dx \quad (4.158)$$

Now consider two separate modes, i and j , which have the modal equations

$$\text{Mode } i: \frac{d^4 Y_i}{dx^4} = \lambda_i^4 Y_i \quad (a)$$

$$\text{Mode } j: \frac{d^4 Y_j}{dx^4} = \lambda_j^4 Y_j \quad (b)$$

Multiply Equation (a) by Y_j , multiply Equation (b) by Y_i , integrate both with respect to x from 0 to l , make use of Equation 4.158 and subtract the second result from the first. We obtain

$$\begin{aligned} (\lambda_i^4 - \lambda_j^4) \int_0^l Y_i Y_j dx &= \int_0^l \left(Y_j \frac{d^4 Y_i}{dx^4} - Y_i \frac{d^4 Y_j}{dx^4} \right) dx \\ &= \left[Y_j \frac{d^3 Y_i}{dx^3} - \frac{dY_j}{dx} \frac{d^2 Y_i}{dx^2} \right]_0^l - \left[Y_i \frac{d^3 Y_j}{dx^3} - \frac{dY_i}{dx} \frac{d^2 Y_j}{dx^2} \right]_0^l \end{aligned} \quad (4.159)$$

Clearly, the two RHS terms are zero for typical BCs, such as pinned, fixed, free, and sliding. Now, since $\lambda_i \neq \lambda_j$ for $i \neq j$ (unequal modes), we have

$$\int_0^l Y_i Y_j dx = 0 \quad \text{for } i \neq j \quad l_j \quad \text{for } i = j \quad (4.160)$$

Note that normalized mode shape functions may be used here to obtain the constant $l_j = l/2$.

4.5.5.1 Case of Variable Cross Section

The orthogonality of mode shapes holds for nonuniform beams as well. Here, EI is not constant. We use integration by parts:

$$\int_0^l Y_j \frac{d^2}{dx^2} EI \frac{d^2 Y_i}{dx^2} dx = \left[Y_j \underbrace{\frac{d}{dx} EI \frac{d^2 Y_i}{dx^2}}_Q \right]_0^l - \left[\frac{dY_j}{dx} \underbrace{EI \frac{d^2 Y_i}{dx^2}}_M \right]_0^l + \int_0^l EI \frac{d^2 Y_j}{dx^2} \frac{d^2 Y_i}{dx^2} dx \quad (4.161)$$

Again, the first two terms on the RHS are zero for typical BCs. Then, as before, we use the modal equations (Equation 4.129) for two different modes, i and j :

$$\frac{d^2}{dx^2} EI \frac{d^2 Y_i}{dx^2} = \omega_i^2 \rho A Y_i$$

$$\frac{d^2}{dx^2} EI \frac{d^2 Y_j}{dx^2} = \omega_j^2 \rho A Y_j$$

Multiply the first equation by Y_j , the second equation by Y_i , subtract the second result from the first, integrate the result from $x = 0$ to l , and finally use Equation 4.161 to cancel the equal terms. We obtain

$$\begin{aligned} (\omega_i^2 - \omega_j^2) \int_0^l \rho A Y_i Y_j dx - \left[Y_j \frac{d}{dx} EI \frac{d^2 Y_i}{dx^2} - Y_i \frac{d}{dx} EI \frac{d^2 Y_j}{dx^2} \right]_0^l \\ + \left[\frac{dY_j}{dx} EI \frac{d^2 Y_i}{dx^2} - \frac{dY_i}{dx} EI \frac{d^2 Y_j}{dx^2} \right]_0^l = 0 \end{aligned} \quad (4.162)$$

Now, as before, for common BCs, the second and third boundary terms in Equation 4.162 will vanish. Hence, after canceling the term $\omega_i^2 - \omega_j^2$, which is $\neq 0$ $i \neq j$, we obtain the orthogonality condition for nonuniform beams as

$$\int_0^l \rho A Y_i Y_j dx = \begin{cases} 0 & \text{for } i \neq j \\ \alpha_j & \text{for } i = j \end{cases} \quad (4.163)$$

The general steps for the modal analysis of a distributed-parameter vibrating system are summarized in Box 4.3.

4.5.6 Forced Bending Vibration

The equation of motion is

$$\frac{\partial^2}{\partial x^2} EI \frac{\partial^2 v}{\partial x^2} + \rho A \frac{\partial^2 v}{\partial t^2} = f(x, t) \quad (4.164)$$

Assume a separable, forced response:

$$v(x, t) = \sum_i \bar{q}_i(t) Y_i(x) \quad (4.165)$$

where $\bar{q}_i(t)$ are the generalized coordinates in the forced case. Substitute Equation 4.165 into Equation 4.164 in the beam equation:

$$\sum_i \bar{q}_i(t) \frac{d^2}{dx^2} EI \frac{d^2 Y_i(x)}{dx^2} + \rho A \sum_i \ddot{\bar{q}}_i(t) Y_i(x) = f(x, t)$$

Box 4.3

MODAL ANALYSIS OF CONTINUOUS SYSTEMS

Equation of free (unforced) motion:

$$L(x, t)v(x, t) = 0 \quad (i)$$

where

$v(x, t)$ = system response

$L(x, t)$ = partial differential operator in space (x) and time (t)

Model solution:

Assume a separable solution

$$v(x, t) = Y(x)q(t) \quad (ii)$$

because a modal response is separable in time and space.

Note:

$Y(x)$ = mode shape

$q(t)$ = generalized coordinate for free response

Note: For two- and three-dimensional space systems, time and space will still be separable for a modal response. However, the space function itself may not be separable along each coordinate direction.

Steps:

1. Substitute Equation (ii) in Equation (i) and separate the space function (of x) and the time function (of t), each of which should be equal to the same constant.
2. Solve the resulting ODE for $Y(x)$ using system boundary conditions. We obtain an infinite set of mode shapes $Y_i(x)$, up to one unknown (removed by normalization), and natural frequencies ω_i .
3. Solve the ODE for $q(t)$ using system initial conditions to determine $q_i(t)$ for mode i . (The orthogonality of $Y_i(x)$ will be needed to establish the initial conditions for $q_i(t)$.)
4. Overall response

$$v(x, t) = \sum_i Y_i(x)q_i(t)$$

The first term on the LHS, on using the mode shape equation 4.129, becomes $\bar{q}_i(t)\rho A\omega_i^2 Y_i(x)$. Multiply the result by $Y_j(x)$ and integrate with respect to $x[0, l]$. We obtain

$$\omega_j^2 \bar{q}_j(t) \int_0^l \rho A Y_j^2(x) dx + \ddot{\bar{q}}_j(t) \int_0^l \rho A Y_j^2(x) dx = \underbrace{\int_0^l Y_j(x) f(x, t) dx}_{f_j(t)}$$

Each of the two integrals on the LHS evaluates α_j according to Equation 4.163. Hence,

$$\ddot{\bar{q}}_j(t) + \omega_j^2 \bar{q}_j(t) = \frac{1}{\alpha_j} f_j(t) \quad \text{for } j = 1, 2, 3, \dots \quad (4.166)$$

We can then solve this equation to determine the generalized coordinates $\bar{q}_j(t)$, using the knowledge of the forcing function $f_j(t)$ and the initial conditions $\bar{q}_j(0)$ and $(d\bar{q}_j/dt)(0)$. Specifically, if the initial displacement and speed of the beam are given by Equation 4.151 and Equation 4.152, respectively, by following the procedure that was adopted to obtain the results (Equation 4.156 and Equation 4.157), we determine

$$\bar{q}_j(0) = \frac{1}{\alpha_j} \int_0^l \rho A d(x) Y_j(x) dx \quad (4.167)$$

$$\frac{d\bar{q}_j(0)}{dt} = \frac{1}{\alpha_j} \int_0^l \rho A s(x) Y_j(x) dx \quad (4.168)$$

Finally, we obtain the overall response of the forced system as

$$v(x, t) = \sum_i \bar{q}_j(t) Y_j(x) \quad (4.169)$$

The main steps in the forced response analysis are summarized in Box 4.4.

Box 4.4

FORCED RESPONSE OF CONTINUOUS SYSTEMS

Equation of forced motion:

$$L(x, t)v(x, t) = L_1(x, t)f(x, t) \quad (i)$$

where

$v(x, t)$ = forced response of the system

$f(x, t)$ = distributed force per unit space

L and L_1 are partial differential operators in space and time

Steps:

1. Substitute the modal expansion

$$v(x, t) = \sum Y_i(x) \bar{q}_i(t) \quad (ii)$$

in Equation (i), where

$Y_i(x)$ = mode shapes

$\bar{q}_i(t)$ = generalized coordinates for forced motion

2. Multiply by $Y_j(x)$ and integrate with respect to space (x) using orthogonality

$$\int_0^l m(x) Y_i(x) Y_j(x) dx = 0 \quad \text{for } i \neq j \quad (iii)$$

Note: Additional boundary terms are present in Equation (iii) when there are lumped elements at the system boundary.

3. Determine the initial conditions for $\bar{q}_j(t)$. We require Equation (iii) for this.
4. Solve the ODE for $\bar{q}_j(t)$ using the initial conditions.
5. Substitute the results into Equation (ii).

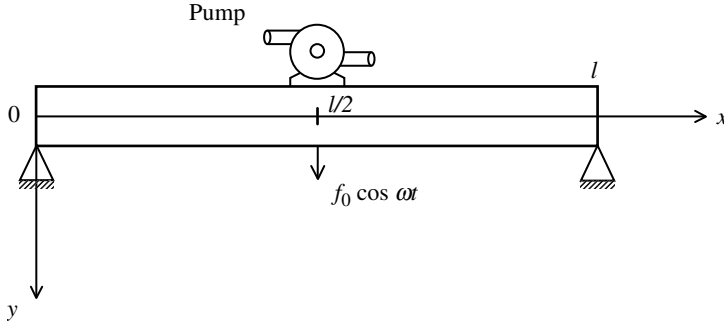


FIGURE 4.12 A pump mounted on a simply supported beam.

Example 4.6

A pump is mounted at the midspan of a simply supported thin beam of uniform cross section and length l . The pump rotation generates a transverse force $f_0 \cos \omega t$, as schematically shown in Figure 4.12. Initially, the system starts from rest, from the static equilibrium position of the beam, such that

$$v(x, t) = 0 \quad \text{and} \quad \frac{\partial v(x, t)}{\partial t} = 0 \quad \text{at } t = 0$$

It is necessary to obtain the transverse response $v(x, t)$ of the beam in the form of a modal summation during operation of the pump.

First, determine $q_j(t)$ in terms of f_0 , ω , ω_j and the beam parameters ρ , A , and l , assuming that the beam is completely undamped. Are all modes of the beam excited by the pump? If the beam is lightly damped, what would be its steady-state response?

In particular, what is the steady-state response of the beam at the pump location? Sketch its amplitude as a function of the excitation frequency ω .

Solution

Using the Dirac delta function $\delta(x)$, we can express the equation of forced motion of the beam as

$$EI \frac{\partial^4 v}{\partial x^4} + \rho A \frac{\partial^2 v}{\partial t^2} = f_0 \cos \omega t \delta\left(x - \frac{l}{2}\right) \quad (4.170)$$

Substitute $v(x, t) = \sum_i Y_i(x) q_i(t)$, where normalized mode shapes for the simply supported beam are $Y_i(x) = \sin i\pi x/l$, multiply by $Y_j(x)$, integrate over $x = [0, l]$ and use the orthogonality of mode shapes. We obtain

$$EI \left(\frac{i\pi}{l}\right)^4 \frac{l}{2} q_j(t) + \rho A \frac{l}{2} \ddot{q}_j = f_0 \cos \omega t \sin \frac{j\pi}{2}$$

Note:

$$\int_{a^-}^{a^+} p(x) \delta(x - a) dx = p(a)$$

Hence, from Equation 4.149, we obtain

$$\ddot{q}_j + \omega_j^2 q_j = \alpha_j \cos \omega t \quad (4.171)$$

where

$$\alpha_j = \frac{2f_0}{\rho A l} \sin j \frac{\pi}{2}$$

The given initial conditions are satisfied if and only if $q_j(0) = 0$ and $\dot{q}_j(0) = 0$ for all j .

Hence, the complete solution is

$$q_j(t) = \frac{\alpha_j}{(\omega_j^2 - \omega^2)} [\cos \omega t - \cos \omega_j t] \quad (4.172)$$

It follows that the total response is

$$v(x, t) = \frac{2f_0}{\rho A l} \sum \frac{\sin j\pi/2}{(\omega_j^2 - \omega^2)} \sin j \frac{\pi x}{l} [\cos \omega t - \cos \omega_j t] \quad (4.173)$$

Clearly, $\sin(j\pi/2) = 0$ for even values of j . We see that even modes of the beam are not excited by the pump. This is to be expected because, for even modes, the midspan is a node point and has no motion. If the beam is lightly damped, its natural response terms ($\cos \omega_j t$) will decay to zero with time. Hence, the steady-state response will be

$$v_{ss}(x, t) = \frac{2f_0}{\rho A l} \cos \omega t \sum \frac{\sin j\pi/2 \sin j\pi x/l}{(\omega_j^2 - \omega^2)} \quad (4.174)$$

At the pump location ($x = l/2$), the steady-state response is

$$v_{ss}(l/2, t) = \frac{2f_0}{\rho A l} \cos \omega t \sum \frac{\sin^2 j\pi/2}{(\omega_j^2 - \omega^2)} = \frac{2f_0}{\rho A l} \cos \omega t \left[\frac{1}{(\omega_1^2 - \omega^2)} + \frac{1}{(\omega_3^2 - \omega^2)} + \frac{1}{(\omega_5^2 - \omega^2)} + \cdots \right]$$

Note again that only the odd modes contribute to the response. Furthermore, for a simply supported beam

$$\omega_j = j^2 \omega_1 \quad \text{for } j = 1, 2, 3, \dots$$

where

$$\omega_1 = \left(\frac{\pi}{l} \right)^2 \sqrt{\frac{EI}{\rho A}}$$

Nondimensionalize the midspan response at steady state as

$$\bar{v} = \frac{\rho A l \omega_1^2}{2f_0} v_{ss}(l/2, t) = \left[\frac{1}{(1^4 - \bar{\omega}^2)} + \frac{1}{(3^4 - \bar{\omega}^2)} + \frac{1}{(5^4 - \bar{\omega}^2)} + \cdots \right] \cos \omega t$$

Its amplitude is

$$v_0(\bar{\omega}) = \left| \frac{1}{(1^4 - \bar{\omega}^2)} + \frac{1}{(3^4 - \bar{\omega}^2)} + \frac{1}{(5^4 - \bar{\omega}^2)} + \cdots \right|$$

The characteristic of the amplitude as a function of the nondimensional excitation frequency is sketched in [Figure 4.13](#).

Example 4.7

Perform a modal analysis to determine natural frequencies and mode shapes of transverse vibration of a thin cantilever (i.e., a beam with “fixed–free” or “clamped–free” end conditions). The coordinate system and the beam parameters are as shown in [Figure 4.14](#).

Solution

As usual, the mode shapes are given by

$$Y(x) = C_1 \cosh \lambda x + C_2 \sinh \lambda x + C_3 \cos \lambda x + C_4 \sin \lambda x \quad (4.134)$$

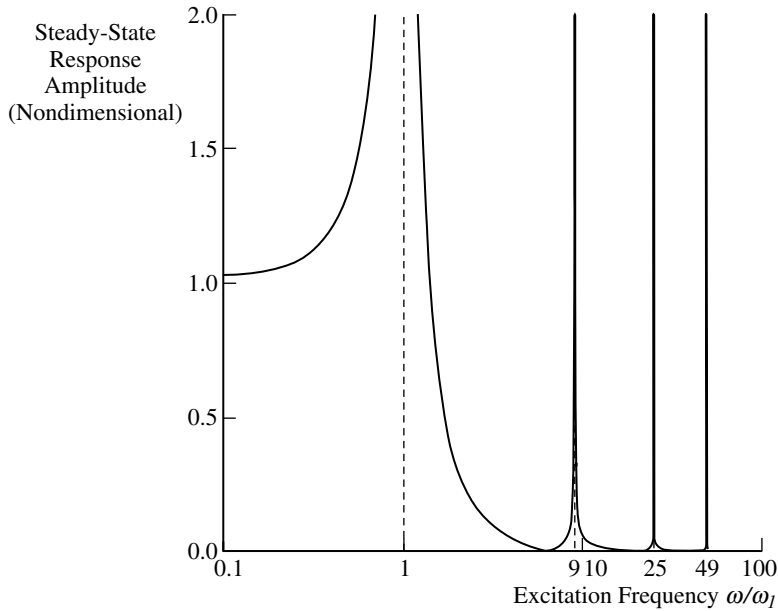


FIGURE 4.13 Amplitude of the steady response at the pump as a function of excitation frequency.

Its first three derivatives are

$$\frac{dY(x)}{dx} = C_1 \lambda \sinh \lambda x + C_2 \lambda \cosh \lambda x - C_3 \lambda \sin \lambda x + C_4 \lambda \cos \lambda x \quad (4.175)$$

$$\frac{d^2 Y(x)}{dx^2} = C_1 \lambda^2 \cosh \lambda x + C_2 \lambda^2 \sinh \lambda x - C_3 \lambda^2 \cos \lambda x - C_4 \lambda^2 \sin \lambda x \quad (4.176)$$

$$\frac{d^3 Y(x)}{dx^3} = C_1 \lambda^3 \sinh \lambda x + C_2 \lambda^3 \cosh \lambda x + C_3 \lambda^3 \sin \lambda x - C_4 \lambda^3 \cos \lambda x \quad (4.177)$$

The BCs of the beam are

$$\text{At } x = 0 : v(0, t) = 0 \quad \text{and} \quad \frac{\partial v(0, t)}{\partial x} = 0$$

$$\text{At } x = l : EI \frac{\partial^2 v(l, t)}{\partial x^2} = 0 \quad \text{and} \quad EI \frac{\partial^3 v(l, t)}{\partial x^3} = 0$$

The corresponding modal BCs are

$$Y(0) = 0; \quad \frac{dY(0)}{dx} = 0; \quad \frac{d^2 Y(l)}{dx^2} = 0; \quad \frac{d^3 Y(l)}{dx^3} = 0 \quad (4.178)$$

Substitute Equation 4.134, Equation 4.175 to Equation 4.177 into Equation 4.178. We obtain

$$C_1 + C_3 = 0 \quad (i)$$

$$C_2 + C_4 = 0 \quad (ii)$$

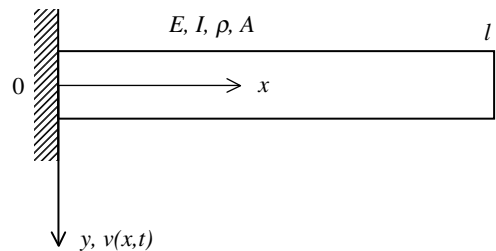


FIGURE 4.14 A cantilever in bending vibration.

$$C_1 \cosh \lambda l + C_2 \sinh \lambda l - C_3 \cos \lambda l - C_4 \sin \lambda l = 0 \quad (\text{iii})$$

$$C_1 \sinh \lambda l + C_2 \cosh \lambda l + C_3 \sin \lambda l - C_4 \cos \lambda l = 0 \quad (\text{iv})$$

Eliminate C_1 and C_2 in Equation (iii) and Equation (iv) by substituting Equation (i) and Equation (ii). We obtain

$$[\cosh \lambda l + \cos \lambda l]C_3 + [\sinh \lambda l + \sin \lambda l]C_4 = 0 \quad (\text{v})$$

$$[\sinh \lambda l - \sin \lambda l]C_3 + [\cosh \lambda l + \cos \lambda l]C_4 = 0 \quad (\text{vi})$$

or, in the vector-matrix form

$$\begin{bmatrix} \cosh \lambda l + \cos \lambda l & \sinh \lambda l + \sin \lambda l \\ \sinh \lambda l - \sin \lambda l & \cosh \lambda l + \cos \lambda l \end{bmatrix} \begin{bmatrix} C_3 \\ C_4 \end{bmatrix} = \begin{bmatrix} 0 \\ 0 \end{bmatrix} \quad (4.179)$$

The trivial solution of Equation 4.179 is $C_3 = 0 = C_4$. Then, from Equation (i) and Equation (ii), we also have $C_1 = 0 = C_2$. This solution corresponds to $Y(x) = 0$ and is not acceptable in general for a vibrating system. Hence, the matrix in Equation 4.179 must be noninvertible (i.e., singular). Hence, the determinant of the matrix must vanish (see Appendix 3A); thus

$$(\cosh \lambda l + \cos \lambda l)^2 - (\sinh \lambda l + \sin \lambda l)(\sinh \lambda l - \sin \lambda l) = 0$$

or

$$\cosh^2 \lambda l + 2 \cosh \lambda l \cos \lambda l + \cos^2 \lambda l - \sinh^2 \lambda l + \sin^2 \lambda l = 0$$

However, it is well known that

$$\cosh^2 \lambda l - \sinh^2 \lambda l = 1 \quad \text{and} \quad \cos^2 \lambda l + \sin^2 \lambda l = 1$$

Hence,

$$\cos \lambda l \cosh \lambda l = -1 \quad (4.180)$$

This equation has an infinite number of solutions λ_i for $i = 1, 2, 3, \dots$ giving an infinite number of natural frequencies:

$$\omega_i = \lambda_i^2 \sqrt{\frac{EI}{\rho A}} \quad (4.181)$$

The corresponding mode shapes are given by Equation 4.134 subject to Equation (i), Equation (ii), and Equation (v) or Equation (vi). This gives $Y_i(x) = C_3(\cos \lambda_i x - \cosh \lambda_i x) + C_4(\sin \lambda_i x - \sinh \lambda_i x)$ with

$$C_3 = -\frac{[\sinh \lambda_i l + \sin \lambda_i l]}{[\cosh \lambda_i l + \cos \lambda_i l]} C_4$$

It follows that

$$Y_i(x) = C_4[\sin \lambda_i x - \sinh \lambda_i x] + C_4 \left[\frac{\sinh \lambda_i l + \sin \lambda_i l}{\cosh \lambda_i l + \cos \lambda_i l} \right] [-\cos \lambda_i x + \cosh \lambda_i x]$$

The unknown multiplier C_4 simply scales the mode shape and is absorbed into the generalized coordinate $q_i(t)$ as usual. In fact, this is a process of normalization of mode shapes, where $C_4 = 1$ is used. So, we have the normalized mode shapes:

$$Y_i(x) = a \sin \lambda_i x + b \sinh \lambda_i x + \alpha_i [c \cos \lambda_i x + d \cosh \lambda_i x] \quad (4.182)$$

with

$$a = 1, \quad b = -1, \quad c = -1, \quad d = 1 \quad \text{and} \quad \alpha_i = \frac{\sinh \lambda_i l + \sin \lambda_i l}{\cosh \lambda_i l + \cos \lambda_i l} \quad (4.183)$$

The first three roots of Equation 4.180 are

$$\lambda_1 l = 1.875104; \quad \lambda_2 l = 4.694091; \quad \lambda_3 l = 7.854757$$

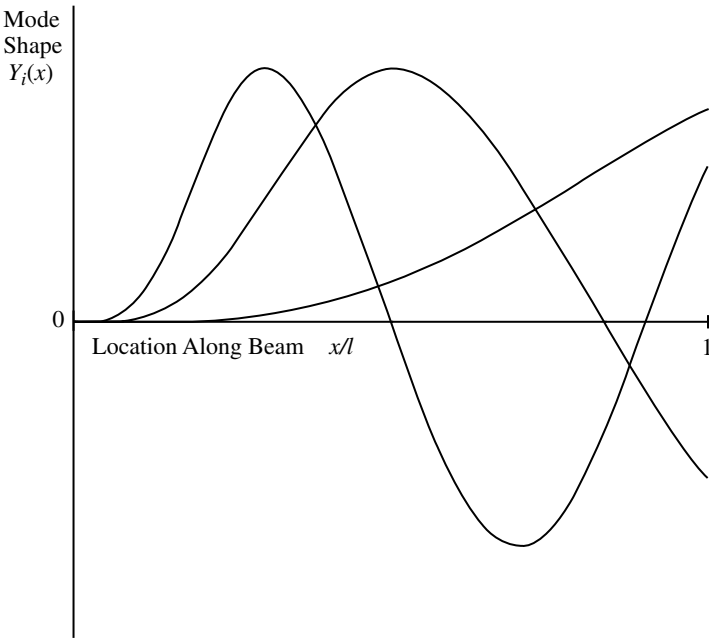


FIGURE 4.15 First three modes of a cantilever (fixed–free beam) in transverse vibration.

The corresponding three mode shapes are sketched in Figure 4.15. Note, in particular, that the node points are not physically fixed but remain stationary during a modal motion. This completes the solution.

The modal information corresponds to the infinite set of natural frequencies that are obtained by solving Equation 4.180 subject to Equation 4.181, and the mode shapes are given by Equation 4.182 subject to Equation 4.183. Modal information corresponding to other common BCs may also be put in this form. Table 4.3 summarizes such data. Table 4.4 provides numerical values corresponding to this modal information for the first three modes.

TABLE 4.3 Modal Information for Bending Vibration of Beams

End Conditions	Natural Frequencies $\omega_i = \lambda_i^2 \sqrt{EI/\rho A}$ where λ_i are roots of	Mode Shapes $Y_i(x) = a \sin \lambda_i x + b \sinh \lambda_i x + c \cos \lambda_i x + d \cosh \lambda_i x$				
		a	b	c	d	α_i
Pinned–pinned	$\sin \lambda_i l = 0$ $i = 1, 2, 3, \dots$	1	0	0	0	0
Fixed–fixed	$\cosh \lambda_i l \cos \lambda_i l = 1$ $i = 1, 2, 3, \dots$	1	–1	–1	1	$\frac{\sinh \lambda_i l - \sin \lambda_i l}{\cosh \lambda_i l - \cos \lambda_i l}$
Free–free	$\cosh \lambda_i l \cos \lambda_i l = 1$ $i = 0, 1, 2, \dots$	1	1	–1	–1	Same
Fixed–pinned	$\tanh \lambda_i l = \tan \lambda_i l$ $i = 1, 2, 3, \dots$	1	–1	–1	1	Same
Fixed–free	$\cosh \lambda_i l \cos \lambda_i l = -1$	1	–1	–1	1	$\frac{\sinh \lambda_i l + \sin \lambda_i l}{\cosh \lambda_i l + \cos \lambda_i l}$
Fixed–sliding	$\tanh \lambda_i l = -\tan \lambda_i l$	1	–1	–1	1	$\frac{\cosh \lambda_i l + \cos \lambda_i l}{\sin \lambda_i l - \sinh \lambda_i l}$
Pinned–free	$\tanh \lambda_i l = \tan \lambda_i l$	1	α_i	0	0	$\frac{\sin \lambda_i l}{\sinh \lambda_i l}$

TABLE 4.4 Roots of the Frequency Equation for Bending Vibration of Beams

End Conditions	First Three Roots $\lambda_i l$
Pinned–pinned	π 2π 3π
Fixed–fixed	4.730041 7.853205 10.995608
Free–free	0 4.730041 7.853205 10.995608
Fixed–pinned	3.926602 7.068583 10.210176
Fixed–free	1.875104 4.694091 7.854757
Fixed–sliding	2.365020 5.497804 8.639380
Pinned–free	0 3.926602 7.068583 10.210176

4.5.7 Bending Vibration of Beams with Axial Loads

In practice, beam-type members that undergo flexural (transverse) vibrations may carry axial forces. Examples are structural members such as columns, struts, and towers. Generally, a tension will increase the natural frequencies of bending and compression will decrease them. Hence, one way to avoid the excitation of a particular natural frequency (and mode) of bending vibration is to use a suitable tension or compression in the axial direction.

The equation of motion for the transverse motion of a thin beam subjected to an axial tension P may be easily derived by following the procedure that led to Equation 4.122. For simplicity, assume a thin beam subjected to a constant tensile force P . A small element δx of the beam is shown in Figure 4.16. The vertical component (in the positive y direction) of the axial force is

$$-P \sin \theta + P \sin(\theta + \delta\theta) \cong -P\theta + P(\theta + \delta\theta) = P \delta\theta$$

because the slope $\theta = \partial v / \partial x$ is small. Also, the change in slope is

$$\delta\theta = \frac{\partial^2 v}{\partial x^2} \delta x$$

It is clear that the previous equation of transverse dynamics of element δx has to be modified simply by adding the term $P(\partial^2 v / \partial x^2) \delta x$ to the $f(x, t) \delta x$ side of the equation. Then, the resulting equation of transverse vibration will be

$$\rho A \frac{\partial^2 v}{\partial t^2} + \frac{\partial^2}{\partial x^2} \left(EI \frac{\partial^2 v}{\partial x^2} \right) - P \frac{\partial^2 v}{\partial x^2} = f(x, t) \quad (4.184)$$

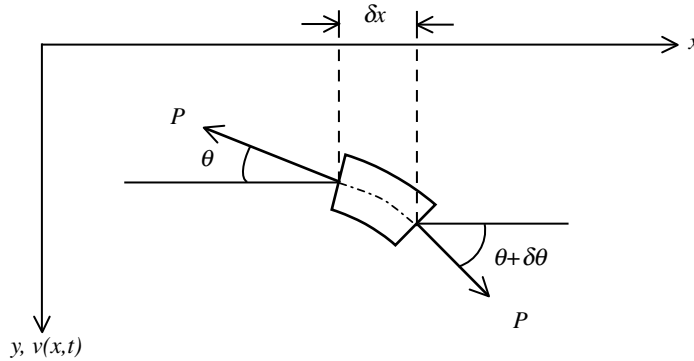


FIGURE 4.16 Beam element in transverse vibration and subjected to axial tension.

For modal analysis of a uniform beam, then, we use the equation of free motion

$$\rho A \frac{\partial^2 v}{\partial t^2} + EI \frac{\partial^4 v}{\partial x^4} - P \frac{\partial^2 v}{\partial x^2} = 0 \quad (4.185)$$

With a separable (modal) solution of the form

$$v(x, t) = Y(x)q(t) \quad (4.186)$$

we have

$$\frac{\ddot{q}(t)}{q(t)} = - \frac{EI (d^4 Y/dx^4) - P (d^2 Y/dx^2)}{\rho A Y} = -\omega^2 \quad (4.187)$$

which gives, as before, the time response equation of the generalized coordinates

$$\ddot{q}(t) + \omega^2 q(t) = 0 \quad (4.188)$$

and the mode shape equation

$$EI \frac{d^4 Y}{dx^4} - P \frac{d^2 Y}{dx^2} - \rho A \omega^2 Y = 0 \quad (4.189)$$

Note that the mode shape equation is still fourth order, but is different. The analysis, however, may be done as before by using four BCs at the two ends of the beam to determine the natural frequencies (an infinite set) and the corresponding normalized mode shapes.

4.5.8 Bending Vibration of Thick Beams

In our derivation of the governing equation for the lateral vibration of thin beams (known as the Bernoulli–Euler beam equation), we neglected the following effects in particular:

1. Deformation and associated lateral motion due to shear stresses
2. Moment of inertia of beam elements in rotatory motion

Note, however, that we did use the fact that shear forces (Q) are present in a beam cross section, even though the resulting deformations were not taken into account. Also, in writing the equation for rotational motion of a beam element δx , we simply summed the moments to zero, without including the inertia moment. These assumptions are valid for a beam whose cross-sectional dimensions are small compared with its length. However, for a thick beam, the effect of shear deformation and rotatory inertia must be included in deriving the governing equation. The resulting equation is known as the *Timoshenko beam equation*. Important steps in the derivation of the equation of motion for the forced transverse vibration of beams, including the effects of shear deformation and rotatory inertia, are given now.

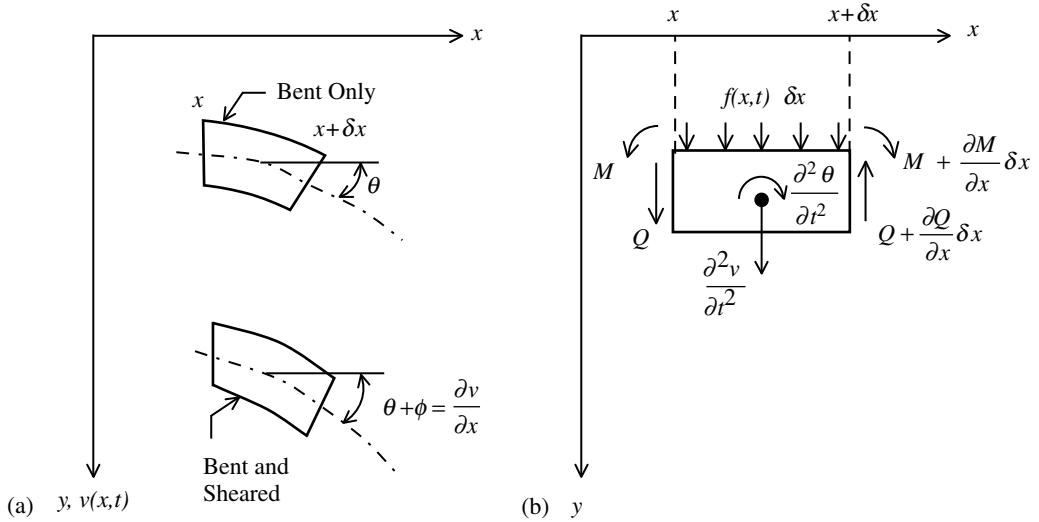


FIGURE 4.17 A Timoshenko beam element: (a) combined effect of bending and shear; (b) dynamic effects including rotatory inertia.

Consider a small element δx of a beam. Figure 4.17(a) illustrates the contribution of the bending of an element and the deformation due to transverse shear stresses towards the total slope of the beam neutral axis. Let

θ = angle of rotation of the beam element due to bending

ϕ = increase in slope of the element due to shear deformation in transverse shear (this is equal to shear strain)

Then, the total slope of the beam element is

$$\frac{\partial v}{\partial x} = \theta + \phi \quad (4.190)$$

Here, v and x take the usual meanings, as for a thin beam.

Figure 4.17(b) shows an element δx of the beam with the forces, moments, and the linear and angular accelerations marked. With the sign convention shown in Figure 4.17(b), the linear shear-stress–shear-strain relation can be stated as

$$Q = -kGA\phi \quad (4.191)$$

where the Timoshenko shear coefficient

$$k = \frac{\text{Average shear stress on beam cross section at } x}{\text{Shear stress at the neutral axis at } x}$$

and

$$G = \text{shear modulus}$$

The equation for translatory motion is

$$f(x, t)\delta x + Q - \left(Q + \frac{\partial Q}{\partial x}\delta x\right) = (\rho A \delta x) \frac{\partial^2 v}{\partial t^2}$$

Hence,

$$f(x, t) - \frac{\partial Q}{\partial x} = \rho A \frac{\partial^2 v}{\partial t^2} \quad (4.192)$$

The equation for the rotatory motion of the element, taking into account the rotatory inertia, is

$$M + \frac{\partial M}{\partial x} \delta x - M - Q \delta x = (I\rho \delta x) \frac{\partial^2 \theta}{\partial t^2}$$

which becomes

$$\frac{\partial M}{\partial x} - Q = I\rho \frac{\partial^2 \theta}{\partial t^2} \quad (4.193)$$

From the elementary theory of bending, as before

$$M = EI \frac{\partial \theta}{\partial x} \quad (4.194)$$

The relationship between the shear modulus and the modulus of elasticity is known to be

$$E = 2(1 + \nu)G \quad (4.195)$$

where ν = Poisson's ratio. This relation may be substituted if desired.

Manipulation of these equations yields

$$\begin{aligned} EI \frac{\partial^4 \nu}{\partial x^4} + \rho A \frac{\partial^2 \nu}{\partial t^2} - \rho I \left(1 + \frac{E}{kG} \right) \frac{\partial^4 \nu}{\partial x^2 \partial t^2} + \frac{\rho^2 I}{kG} \frac{\partial^4 \nu}{\partial t^4} \\ = f(x, t) - \frac{EI}{kGA} \frac{\partial^2 f(x, t)}{\partial x^2} + \frac{\rho I}{kGA} \frac{\partial^2 f(x, t)}{\partial t^2} \end{aligned} \quad (4.196)$$

This is the Timoshenko beam equation for forced transverse motion. Note that this equation is fourth order in time, whereas the thin beam equation is second order in time. The modal analysis may proceed as before, by using the free ($f = 0$) equation and a separable solution. However, the resulting differential equation for the generalized coordinates will be fourth order in time and, as a result, additional natural frequency bands will be created. The reason is the independent presence of shear and bending motions. The differential equation of mode shapes will be fourth order in x and the solution procedure will be as before, through the use of four BCs at the two ends of the beam.

4.5.9 Use of the Energy Approach

So far, we have used only the direct, Newtonian approach in deriving the governing equations for continuous members in vibration. Of course, the same results may be obtained by using the Lagrangian (energy) approach. The general approach here is to first express the Lagrangian L of the system as

$$L = T^* - V \quad (4.197)$$

where

T^* = total kinetic co-energy (equal to kinetic energy T for typical systems)

V = total potential energy

Then, for a virtual increment (variation) of the system through incrementing the system variable, the following condition will hold:

$$\int_{t_1}^{t_2} [\delta L + \delta W] dt = 0 \quad (4.198)$$

where δL is the increment in the Lagrangian and δW is the work done by the external forces on the system due to the increment. Finally, using the arbitrariness of the variation, the equation of motion, along with the BCs, can be obtained. This approach is illustrated now.

First, consider the free motion. We can easily extend the result to the case of forced motion. Kinetic energy is given by

$$T = \frac{1}{2} \int_0^l \rho A \, dx \left(\frac{\partial v}{\partial t} \right)^2 = \frac{1}{2} \int_0^l \rho A \left(\frac{\partial v}{\partial t} \right)^2 dx \quad (4.199)$$

Potential energy due to bending results from work needed to bend the beam (angle denoted by $\theta = \partial v / \partial x$ as usual) under bending moment M ; thus

$$V = \frac{1}{2} \int_{\text{End 1}}^{\text{End 2}} M \, d\phi = \frac{1}{2} \int_0^l EI \left(\frac{\partial^2 v}{\partial x^2} \right)^2 dx \quad (4.200)$$

Before proceeding further, note the following steps of variation and integration by parts with respect to t :

$$\delta \int_{t_1}^{t_2} \frac{1}{2} \left(\frac{\partial v}{\partial t} \right)^2 dt = \int_{t_1}^{t_2} \frac{\partial v}{\partial t} \delta \left(\frac{\partial v}{\partial t} \right) dt = \int_{t_1}^{t_2} \frac{\partial v}{\partial t} \frac{\partial \delta v}{\partial t} dt = \left[\frac{\partial v}{\partial t} \delta v \right]_{t_1}^{t_2} - \int_{t_1}^{t_2} \frac{\partial^2 v}{\partial t^2} \delta v \, dt \quad (4.201)$$

Note that we interchanged the operations δ and $\partial/\partial t$ prior to integrating by parts. Also, by convention, we assume that no variations are performed at the starting and ending times (t_1 and t_2) of integration. Hence,

$$\delta v(t_1) = 0 \quad \text{and} \quad \delta v(t_2) = 0 \quad (4.202)$$

Similarly, variation and integration by parts with respect to x are done as follows:

$$\begin{aligned} \delta \int_0^l \frac{1}{2} EI \left(\frac{\partial^2 v}{\partial x^2} \right)^2 dx &= \int_0^l EI \frac{\partial^2 v}{\partial x^2} \delta \left(\frac{\partial^2 v}{\partial x^2} \right) dx = \int_0^l EI \frac{\partial^2 v}{\partial x^2} \frac{\partial}{\partial x} \delta \left(\frac{\partial v}{\partial x} \right) dx \\ &= \left[EI \frac{\partial^2 v}{\partial x^2} \delta \left(\frac{\partial v}{\partial x} \right) \right]_0^l - \int_0^l \frac{\partial}{\partial x} EI \frac{\partial^2 v}{\partial x^2} \delta \left(\frac{\partial v}{\partial x} \right) dx = \left[EI \frac{\partial^2 v}{\partial x^2} \delta \left(\frac{\partial v}{\partial x} \right) \right]_0^l - \int_0^l \frac{\partial}{\partial x} EI \frac{\partial^2 v}{\partial x^2} \frac{\partial \delta v}{\partial x} dx \\ &= \left[EI \frac{\partial^2 v}{\partial x^2} \delta \left(\frac{\partial v}{\partial x} \right) \right]_0^l - \left[\frac{\partial}{\partial x} EI \frac{\partial^2 v}{\partial x^2} \delta v \right]_0^l + \int_0^l \frac{\partial^2}{\partial x^2} EI \frac{\partial^2 v}{\partial x^2} \delta v \, dx \end{aligned} \quad (4.201a)$$

Now, for the case of free vibration ($\delta W = 0$), substitute Equation 4.201 and Equation 4.201a in δT , and δV of Equation 4.199 and Equation 4.200, to obtain

$$\begin{aligned} \int_{t_1}^{t_2} \delta L \, dt = 0 &= - \int_{t_1}^{t_2} dt \int_0^l dx \left[\rho A \frac{\partial^2 v}{\partial t^2} + \frac{\partial^2}{\partial x^2} EI \frac{\partial^2 v}{\partial x^2} \right] \delta v + \int_0^l dx \rho A \left[\frac{\partial v}{\partial t} \delta v \right]_{t_1}^{t_2} \\ &\quad - \int_{t_1}^{t_2} dt \left[EI \frac{\partial^2 v}{\partial x^2} \delta \left(\frac{\partial v}{\partial x} \right) \right]_0^l + \int_{t_1}^{t_2} dt \left[\frac{\partial}{\partial x} EI \frac{\partial^2 v}{\partial x^2} \delta v \right]_0^l \end{aligned} \quad (4.203)$$

Since Equation 4.203 holds for all arbitrary variations $\delta v(t)$, its coefficient should vanish. Hence,

$$\rho A \frac{\partial^2 v}{\partial t^2} + \frac{\partial^2}{\partial x^2} EI \frac{\partial^2 v}{\partial x^2} = 0 \quad (4.204)$$

which is the same Bernoulli–Euler beam equation for free motion as we had derived before.

The second integral term on the RHS of Equation 4.203 has no consequence. We conventionally pick $\delta v(t_1) = 0$ and $\delta v(t_2) = 0$ at the time points t_1 and t_2 .

The third integral term on the RHS of Equation 4.203 gives some BCs. Specifically, if the slope BC $\partial v / \partial x$ is zero (i.e., fixed end), then the corresponding bending moment at the end is arbitrary, as expected. However, if the slope at the boundary is arbitrary, then the bending moment $EI(\partial^2 v / \partial x^2)$ at the end should be zero (i.e., pinned or free end).

The last integral term on the RHS of Equation 4.203 gives some other BCs. Specifically, if the displacement BC v is zero (i.e., pinned or fixed end) then the corresponding shear force at the

end is arbitrary. However, if the displacement at the boundary is arbitrary, then the shear force $(\partial/\partial x)EI(\partial^2 v/\partial x^2)$ at that end should be zero (i.e., free or sliding end).

Next, consider a forced beam with force per unit length given by $f(x, t)$. Then, the work done by $f(x, t)dx$ in a small element dx of the beam, when moved through a displacement of δv , is

$$f(x, t)dx \delta v \quad (4.205)$$

Then, by combining Equation 4.205 with Equation 4.203, for arbitrary variation δv , we obtain the forced vibration equation

$$\rho A \frac{\partial^2 v}{\partial t^2} + \frac{\partial^2}{\partial x^2} EI \frac{\partial^2 v}{\partial x^2} = f(x, t) \quad (4.206)$$

Note that external forces and moments applied at the ends of the beam can be incorporated into the BCs in the same manner.

4.5.10 Orthogonality with Inertial Boundary Conditions

It can be verified that the conventional orthogonality condition (Equation 4.163) holds for beams in transverse vibration, under common noninertial BCs. When an inertia element (rectilinear or rotatory) is present at an end of the beam, this condition is violated. A modified and more general orthogonality condition can be derived for application to beams with inertial boundary conditions.

To illustrate the procedure, consider a beam with a mass m attached at the end $x = l$, as shown in Figure 4.18(a). A free-body diagram giving the sign convention for shear force Q acting on m is shown in Figure 4.18(b).

The BCs at $x = l$ are:

1. Bending moment vanishes, because there is no rotatory inertia at the end that is free. Hence,

$$EI \frac{\partial^2 v(l, t)}{\partial x^2} = 0 \quad (4.207)$$

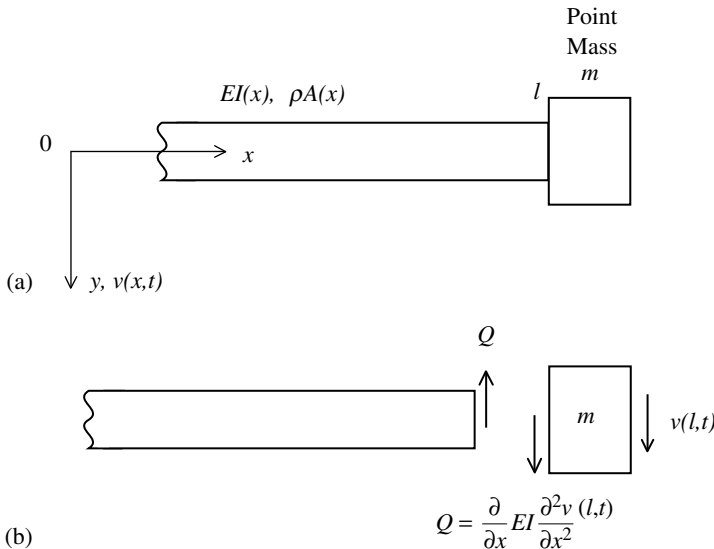


FIGURE 4.18 (a) A beam with an end mass in transverse vibration; (b) free-body diagram showing the shear force acting on the end mass.

2. Equation of rectilinear motion of the end mass

$$m \frac{\partial^2 v(l, t)}{\partial t^2} = \frac{\partial}{\partial x} EI \frac{\partial^2 v(l, t)}{\partial x^2} \quad (4.208)$$

In the usual manner, by substituting $v(x, t) = Y_i(x)q_i(t)$ for mode i , along with $\ddot{q}_i(t) = -\omega_i^2 q_i(t)$, into Equation 4.207 and Equation 4.208, with the understanding that the result should hold for any $q_i(t)$, we obtain the corresponding modal boundary conditions:

$$\frac{d^2 Y_i(l)}{dx^2} = 0 \quad (4.209)$$

$$\frac{d}{dx} EI \frac{d^2 Y_i(l)}{dx^2} + \omega_i^2 m Y_i(l) = 0 \quad (4.210)$$

for mode i .

Now, we return to Equation 4.162:

$$(\omega_i^2 - \omega_j^2) \int_0^l \rho A Y_i Y_j dx - \left[Y_j \frac{d}{dx} EI \frac{d^2 Y_i}{dx^2} - Y_i \frac{d}{dx} EI \frac{d^2 Y_j}{dx^2} \right]_0^l \left[\frac{dY_j}{dx} EI \frac{d^2 Y_i}{dx^2} - \frac{dY_i}{dx} EI \frac{d^2 Y_j}{dx^2} \right]_0^l = 0 \quad (4.162)$$

The second and the third terms of Equation 4.162 will vanish at $x = 0$ for noninertial BCs, as usual. At $x = l$, the third term will vanish in view of Equation 4.209. So, we are left with the second term at $x = l$. Substitute Equation 4.210:

$$\left(Y_j \frac{d}{dx} EI \frac{d^2 Y_i}{dx^2} - Y_i \frac{d}{dx} EI \frac{d^2 Y_j}{dx^2} \right)_l = -(\omega_i^2 - \omega_j^2) m Y_i(l) Y_j(l) \quad (4.211)$$

Substitute Equation 4.211 into Equation 4.162 and cancel $\omega_i^2 - \omega_j^2 \neq 0$ for $i \neq j$. We obtain

$$\int_0^l \rho A Y_i Y_j dx + m Y_i(l) Y_j(l) = \begin{cases} 0 & \text{for } i \neq j \\ \alpha_j & \text{for } i = j \end{cases} \quad (4.212)$$

This is the modified and more general orthogonality property. If the mass is at $x = 0$, the direction of Q that acts on m will reverse and, hence, the second term in Equation 4.212 will become $-m Y_i(0) Y_j(0)$.

4.5.10.1 Rotatory Inertia

If there is a free rotatory inertia at $x = l$, without an associated rectilinear inertia, then the shear force will vanish, giving

$$\frac{d}{dx} EI \frac{d^2 Y_i(l)}{dx^2} = 0 \quad (4.213)$$

The equation of rotational motion of J will give

$$EI \frac{d^2 Y_i(l)}{dx^2} - \omega_i^2 J \frac{dY_i(l)}{dx} = 0 \quad (4.214)$$

Here, the second term in Equation 4.162 will vanish in view of Equation 4.213. Then, by substituting Equation 4.214 into the third term of Equation 4.162, we obtain the modified orthogonality relation

$$\int_0^l \rho A Y_i Y_j dx + J \frac{dY_i(l)}{dx} \frac{dY_j(l)}{dx} = \begin{cases} 0 & \text{for } i \neq j \\ \alpha_j & \text{for } i = j \end{cases} \quad (4.215)$$

4.6 Damped Continuous Systems

All practical mechanical systems have some form of energy dissipation (damping). When the level of dissipation is small, damping is neglected, as we have done thus far in this chapter. Yet, some effects of damping (e.g., the fact that at steady state the natural [modal] vibration components decay to zero leaving only the steady forcing component) are tacitly assumed even in undamped analysis.

The natural behavior of a system is expected to change due to the presence of damping. In particular, the system's natural frequencies will decrease (and be called damped natural frequencies) as a result of damping. Furthermore, it is quite possible that a damped system would not possess "real" modes in which it could independently vibrate. Mathematically, in that case, the modes will become complex (as opposed to real) and, physically, all the points of the system will not move, maintaining a constant phase at a given damped natural frequency. In other words, a real solution that is separable in space (x) and time (t) may not be possible for the free vibration problem of a damped system. Also, node points of an undamped system may vary with time as a result of damping. With light damping, of course, such effects of damping will be negligible.

Since there are damped systems that do not possess real natural modes of vibration, care should be exercised when extending the results of modal analysis from an undamped system to a damped one. However, in some cases, the mode shapes will remain the same after including damping (even though the natural frequencies will change). This is analogous to the case of proportional damping, which was discussed in the section on lumped-parameter (multi-degree-of-freedom) vibrating systems. The modal analysis of a damped system will become significantly easier if we assume that the mode shapes will remain the same as those for the undamped system. Even when the actual type of damping in the system results in complex modes, for analytical convenience, an equivalent damping model that gives real modes is used in simplified analysis. This is analogous to the use of proportional damping in lumped-parameter systems.

4.6.1 Modal Analysis of Damped Beams

Consider the problem of free damped transverse vibration of a thin beam, given by

$$\frac{\partial^2}{\partial x^2} EI \frac{\partial^2 v}{\partial x^2} + L \left(\frac{\partial v}{\partial t} \right) + \rho A \frac{\partial^2 v}{\partial t^2} = 0 \quad (4.216)$$

where L is a spatial differential operator (in x). Consider the following two possible models of damping:

$$1. \quad L = \frac{\partial^2}{\partial x^2} E^* I \frac{\partial^2}{\partial x^2} \quad (4.217)$$

$$2. \quad L = c \quad (4.218)$$

Model 1 corresponds to the Kelvin–Voigt model of material (internal) damping given by the stress–strain relation

$$\sigma = E\varepsilon + E^* \frac{\partial \varepsilon}{\partial t} \quad (4.219)$$

where E^* is the damping parameter of the beam material. Hence, we obtain the damped beam equation simply by replacing E in the undamped beam equation by $E + E^* (\partial/\partial t)$. Also, E^* is independent of the frequency of vibration for the *viscoelastic damping* model, but will be frequency dependent for the *hysteretic damping* model. Modal analysis is done regardless of any frequency dependence of E^* and, in the final modal result for a particular modal frequency ω_i , the appropriate frequency function for $E^*(\omega)$ is used with $\omega = \omega_i$ if the damping is of the hysteretic type. It can be easily verified that the mode shapes of the damped system with model 4.217 are identical to those of the undamped system, regardless of whether the beam cross section is uniform or not.

In Model 2 (Equation 4.218), the operator is a constant c . This corresponds to external damping of the linear viscous type, distributed along the beam length. For example, imagine a beam resting on a

foundation of viscous damping material. For Model 2, it can be shown that the damped mode shapes are identical to the undamped ones, assuming that the beam cross section is uniform. If the beam is nonuniform, the damped and the undamped mode shapes are identical if we assume that the damping constant c varies along the beam in proportion to the area of cross section $A(x)$ of the beam. We shall show this in the example given below.

Example 4.8

Perform the modal analysis for transverse vibration of a thin nonuniform beam with linear viscous damping distributed along its length and satisfying the beam equation

$$\frac{\partial^2}{\partial x^2} EI(x) \frac{\partial^2 v}{\partial x^2} + \rho A(x) b \frac{\partial v}{\partial t} + \rho A(x) \frac{\partial^2 v}{\partial t^2} = 0 \quad (4.220)$$

Determine damped natural frequencies, modal damping ratios, and the response $v(x, t)$ as a modal series expansion, given $v(x, 0) = d(x)$ and $\dot{v}(x, 0) = s(x)$.

Solution

Substitute the separable solution

$$v(x, t) = Y(x)q(t) \quad (4.221)$$

into Equation 4.220. We obtain

$$\frac{d^2}{dx^2} EI \frac{d^2 Y(x)}{dx^2} q(t) + \rho A(x) b Y(x) \dot{q}(t) + \rho A(x) Y(x) \ddot{q}(t) = 0$$

Group the functions of x and t separately and equate to the same constant ω^2 , as usual:

$$\frac{\frac{d^2}{dx^2} EI \frac{d^2 Y(x)}{dx^2}}{\rho A(x) Y(x)} = - \frac{\ddot{q}(t) + b \dot{q}(t)}{q(t)} = \omega^2 \quad (4.222)$$

We have

$$\frac{d^2}{dx^2} EI \frac{d^2 Y(x)}{dx^2} - \omega^2 \rho A Y(x) = 0 \quad (4.223)$$

and

$$\ddot{q}(t) + b \dot{q}(t) + \omega^2 q(t) = 0 \quad (4.224)$$

Note that Equation 4.223 is identical to that for the undamped beam. Hence, with known BCs, we will obtain the same mode shapes $Y_i(x)$ and the same *undamped* natural frequencies ω_i in the usual manner. However, the equation of modal generalized coordinates $q(t)$ given by Equation 4.224 is different from that for the undamped case ($b = 0$). We write, for mode i

$$\ddot{q}_i(t) + 2\zeta_i \omega_i \dot{q}_i(t) + \omega_i^2 q_i(t) = 0 \quad (4.225)$$

where

$$\zeta_i = \frac{b}{2\omega_i} \quad (4.226a)$$

is the modal damping ratio for mode i . Damped natural frequencies are

$$\omega_{di} = \sqrt{1 - \zeta_i^2} \omega_i \quad (4.226b)$$

Equation 4.225 can be solved in the usual manner, with initial conditions $q_i(0)$ and $\dot{q}_i(0)$ determined *a priori*, using known $v(x, 0)$ and $\dot{v}(x, 0)$.

The modal series solution is

$$v(x, t) = \sum Y_i(x)q_i(t) \quad (4.227)$$

The initial conditions are

$$\sum Y_i(x)q_i(0) = d(x) \quad (4.228)$$

$$\sum Y_i(x)\dot{q}_i(0) = s(x) \quad (4.229)$$

Multiply Equation 4.228 and Equation 4.229 by $\rho A(x)Y_j(x)$ and integrate from $x = 0$ to l using the orthogonality condition

$$\int_0^l \rho A(x)Y_i(x)Y_j(x)dx = \begin{cases} 0 & \text{for } i \neq j \\ \alpha_j & \text{for } i = j \end{cases} \quad (4.230)$$

We obtain

$$q_j(0) = \frac{1}{\alpha_j} \int_0^l d(x)\rho A(x)dx \quad (4.231)$$

$$\dot{q}_j(0) = \frac{1}{\alpha_j} \int_0^l s(x)\rho A(x)dx \quad (4.232)$$

This completes the solution for the free damped beam. The forced damped case can be analyzed in the same manner as for the forced undamped case because the mode shapes are the same.

4.7 Vibration of Membranes and Plates

The cables, rods, shafts, and beams whose vibration we have studied thus far in this chapter are *one-dimensional members* or *line structures*. These continuous members need one spatial variable (x), in addition to the time variable (t), as an independent variable to represent their governing equation of motion. Membranes and plates are *two-dimensional members* or *planar structures*. They need two independent spatial variables (x and y) in addition to time (t), for representing their dynamics.

A membrane may be interpreted as a two-dimensional extension of a string or cable. In particular, it has to be in tension and cannot support any bending moment. A plate is a two-dimensional extension of a beam. It can support a bending moment. Their governing equations will, therefore, resemble two-dimensional versions of their respective one-dimensional counterparts. Modal analysis will also follow the familiar steps, after accounting for the extra dimension. In this section, we will give an introduction to the modal analysis of membranes and plates. For simplicity, only special cases of rectangular members with relatively simple BCs will be considered. Analysis of more complicated boundary geometries and conditions will follow analogous procedures, but requires a greater effort and produces more complicated results.

4.7.1 Transverse Vibration of Membranes

Consider a stretched membrane (in tension) that lies on the x - y plane, as shown in [Figure 4.19](#). Transverse vibration $v(x, y, t)$ in the z -direction is of interest. By following a procedure that is somewhat analogous to the derivation of the cable equation, we can obtain the governing equation as

$$\frac{\partial^2 v(x, y, t)}{\partial t^2} = c^2 \left[\frac{\partial^2}{\partial x^2} + \frac{\partial^2}{\partial y^2} \right] v(x, y, t) \quad (4.233)$$

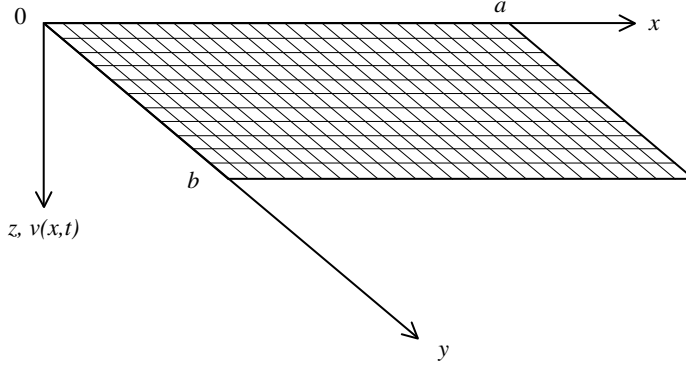


FIGURE 4.19 A membrane or a plate in Cartesian coordinates.

with

$$c = \sqrt{\frac{T'}{m'}} \quad (4.234)$$

where

T' = tension per unit length of membrane section (assumed constant)

m' = mass per unit surface area of membrane

For modal analysis, we seek a separable solution of the form

$$v(x, y, t) = Y(x)Z(y)q(t) \quad (4.235)$$

Substitute Equation 4.235 into Equation 4.233. We obtain

$$Y(x)Z(y)\ddot{q}(t) = c^2 \left[\frac{1}{Y(x)} \frac{d^2 Y(x)}{dx^2} + \frac{1}{Z(y)} \frac{d^2 Z(y)}{dy^2} \right] \quad (4.236)$$

Since Equation 4.236 is true for all possible values of t , x , and y that are independent, the three function groups should separately equal the constants; thus

$$\frac{1}{Y(x)} \frac{d^2 Y}{dx^2} = -\alpha^2 \quad \text{or} \quad \frac{d^2 Y(x)}{dx^2} + \alpha^2 Y(x) = 0 \quad (4.237)$$

$$\frac{1}{Z(y)} \frac{d^2 Z(y)}{dy^2} = -\beta^2 \quad \text{or} \quad \frac{d^2 Z(y)}{dy^2} + \beta^2 Z(y) = 0 \quad (4.238)$$

$$\frac{\ddot{q}(t)}{q(t)} = -\omega^2 \quad \text{or} \quad \ddot{q}(t) + \omega^2 q(t) = 0 \quad (4.239)$$

with

$$\omega^2 = c^2(\alpha^2 + \beta^2) \quad (4.240)$$

The argument for using positive constants α^2 , β^2 , and ω^2 is similar to that we gave for the one-dimensional case. Next, Equation 4.237 and Equation 4.238 have to be solved using two end conditions for each direction, as usual. This will provide an infinite number of solutions α_i and β_j , and the corresponding natural frequencies

$$\omega_{ij}^2 = c(\alpha_i^2 + \beta_j^2)^{1/2} \quad \text{for } i = 1, 2, 3, \dots \text{ and } j = 1, 2, 3, \dots \quad (4.241)$$

along with the mode shape components $Y_i(x)$ and $Z_j(y)$ for the two dimensions.

4.7.2 Rectangular Membrane with Fixed Edges

Consider a rectangular membrane of length a and width b as shown in Figure 4.19 and with the four edges fixed. The BCs are

$$v(0, y, t) = 0; \quad v(a, y, t) = 0; \quad v(x, 0, t) = 0; \quad v(x, b, t) = 0$$

Using these in solving Equation 4.237 and Equation 4.238, as usual, we obtain

$$Y_i(x) = \sin \alpha_i x \quad \text{with } \alpha_i = \frac{i\pi}{a} \quad (4.242)$$

$$Z_j(y) = \sin \beta_j y \quad \text{with } \beta_j = \frac{j\pi}{b} \quad (4.243)$$

$$\omega_{ij} = c[\alpha_i^2 + \beta_j^2]^{1/2} = \pi c \left[\frac{i^2}{a^2} + \frac{j^2}{b^2} \right]^{1/2} \quad \text{for } i = 1, 2, 3, \dots \text{ and } j = 1, 2, 3 \quad (4.244)$$

Note that the spatial mode shapes are given by

$$Y_i(x)Z_j(y) = \sin \frac{i\pi x}{a} \sin \frac{j\pi y}{b} \quad (4.245)$$

4.7.3 Transverse Vibration of Thin Plates

Consider a thin plate of thickness h in a Cartesian coordinate system as shown in Figure 4.19. The usual assumptions as for the derivation of the Bernoulli–Euler beam equation are used. In particular, h is assumed small compared with the surface dimensions (a and b for a rectangular plate). Then, shear deformation and rotatory inertia can be neglected, and also normal stresses in the transverse direction (z) can be neglected. Furthermore, any end forces in the planar directions (x and y) are neglected. The governing equation is

$$\frac{\partial^2 v(x, y, t)}{\partial t^2} + c^2 \left[\frac{\partial^2}{\partial x^2} + \frac{\partial^2}{\partial y^2} \right] v(x, y, t) = 0 \quad (4.246)$$

with

$$c^2 = \frac{E'I'}{\rho A'} = \frac{Eh^2}{12(1 - \nu^2)\rho} \quad (4.247)$$

where

$$E' = \frac{E}{(1 - \nu^2)} \quad (4.248)$$

$$I' = \frac{h^3}{12} = \text{second moment of area per unit length of section} \quad (4.249)$$

$A' = h$ = area per unit length of section

ρ = mass density of material

E = Young's modulus of elasticity of the plate material

ν = Poisson's ratio of the plate material

If we attempt modal analysis by assuming a completely separable solution of the form $v(x, y, t) = Y(x)Z(y)q(t)$ in Equation 4.246, a separable grouping of functions of x and y will not be achieved in general. However, the space and the time will be separable in modal motions. Hence, we seek a solution of the form

$$v(x, y, t) = Y(x, y)q(t) \quad (4.250)$$

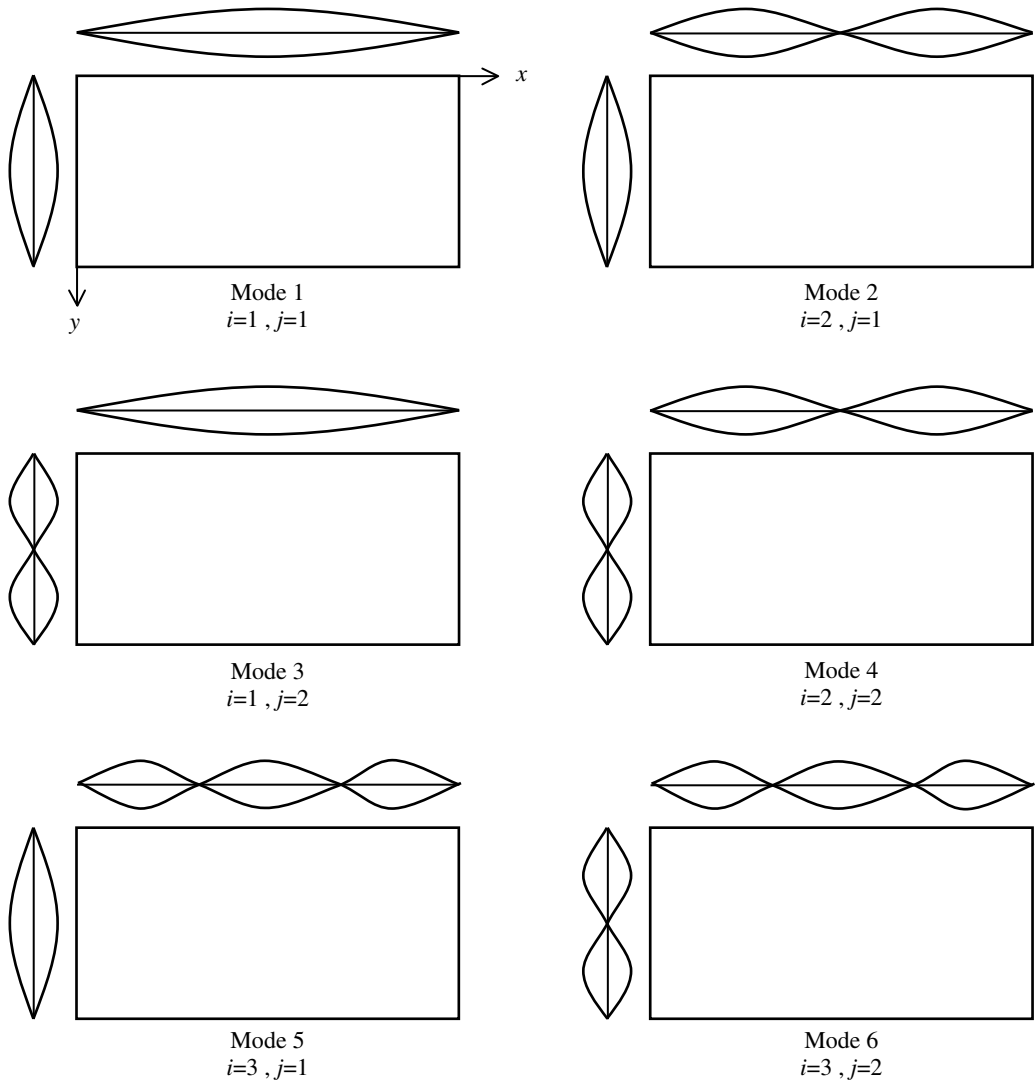


FIGURE 4.20 Mode shapes of transverse vibration of a simply supported rectangular plate.

We will obtain

$$\ddot{q}(t) + \omega^2 q(t) = 0 \quad (4.251)$$

and

$$\nabla^2 \nabla^2 Y(x, y) - \lambda^4 Y(x, y) = 0 \quad (4.252)$$

with the natural frequencies ω given by

$$\omega = \lambda^2 c \quad (4.253)$$

and ∇^2 is the Laplace operator given by

$$\nabla^2 = \frac{\partial^2}{\partial x^2} + \frac{\partial^2}{\partial y^2} \quad (4.254)$$

and, hence, $\nabla^2 \nabla^2$ is the biharmonic operation ∇^4 given by

$$\nabla^4 = \frac{\partial^4}{\partial x^4} + 2 \frac{\partial^4}{\partial x^2 \partial y^2} + \frac{\partial^4}{\partial y^4} \quad (4.255)$$

The solution of Equation 4.252 will require two sets of BCs for each edge of the plate (as for a beam), but will be mathematically involved. Instead of a direct solution, a logical trial solution that satisfies Equation 4.252 and the BCs is employed next for a simply supported rectangular plate. The solution tried is in fact the correct solution for the particular problem.

4.7.4 Rectangular Plate with Simply Supported Edges

As a special case, we now consider a thin rectangular plate of length a , width b , and thickness h , as shown in Figure 4.19, whose edges are simply supported. For each edge, the BCs are the displacement in zero and the bending moment about the edge zero. Specifically, we have

$$\begin{aligned} v(x, y, t) = 0 \text{ and } M_x = E'I' \left(\frac{\partial^2 v}{\partial x^2} + \nu \frac{\partial^2 v}{\partial y^2} \right) = 0 \text{ for } x = 0 \text{ and } a; 0 \leq y \leq b \\ v(x, y, t) = 0 \text{ and } M_y = E'I' \left(\frac{\partial^2 v}{\partial y^2} + \nu \frac{\partial^2 v}{\partial x^2} \right) = 0 \text{ for } y = 0 \text{ and } b; 0 \leq x \leq a \end{aligned} \quad (4.256)$$

where E' and I' are as given in Equation 4.248 and Equation 4.249. In this case, the mode shapes are found to be

$$Y_{ij}(x, y) = \sin \frac{i\pi x}{a} \sin \frac{j\pi y}{b} \quad \text{for } i = 1, 2, \dots \text{ and } j = 1, 2, \dots \quad (4.257)$$

which clearly satisfy the BCs (Equation 4.256) and the governing model equation 4.252, with an infinite set of solutions for λ given by

$$\lambda_{ij}^2 = \pi^2 \left(\frac{i^2}{a^2} + \frac{j^2}{b^2} \right) \quad (4.258)$$

Hence, from Equation 4.253, the natural frequencies are

$$\omega_{ij} = \pi^2 c \left(\frac{i^2}{a^2} + \frac{j^2}{b^2} \right) \quad (4.259)$$

where c is given by Equation 4.247. The overall response, then, is given by

$$v(x, y, t) = \sum_{i=1}^{\infty} \sum_{j=1}^{\infty} \left[A_{ij} \sin \omega_{ij} t + B_{ij} \cos \omega_{ij} t \right] \sin \frac{i\pi x}{a} \sin \frac{j\pi y}{b} \quad (4.260)$$

The unknown constants A_{ij} and B_{ij} are determined by the system initial conditions $v(x, y, 0)$ and $\dot{v}(x, y, 0)$. The first six mode shapes of transverse vibration of a rectangular plate are sketched in Figure 4.20.

Bibliography

- Benaroya, H. 1998. *Mechanical Vibration*, Prentice Hall, Upper Saddle River, NJ.
- Cao, Y., Modi, V.J., de Silva, C.W., and Misra, A.K., On the control of space platform-based variable geometry manipulator, *Adv. Astronaut. Sci.*, 103, Part 1, 305–326, 1999.
- Caron, M., Modi, V.J., Pradhan, S., de Silva, C.W., and Misra, A.K., Planar dynamics of flexible manipulators with slewing deployable links, *J. Guidance Control Dyn.*, 21, 4, 572–580, 1998.
- Chen, Y., Modi, V.J., de Silva, C.W., and Misra, A.K., On the performance of variable geometry manipulators: part I — three dimensional order N formulation, *Acta Astronaut.*, 49, 1, 1–12, 2001.

- Chen, Y., Modi, V.J., de Silva, C.W., and Misra, A.K., On the performance of variable geometry manipulators: part II — computer implementation and dynamical study, *Acta Astronaut.*, 49, 1, 13–30, 2001.
- Crandall, S.H., Karnopp, D.C., Kurtz, E.F., and Prodmor-Brown, D.C. 1968. *Dynamics of Mechanical and Electromechanical Systems*, McGraw-Hill, New York.
- den Hartog, J.P. 1956. *Mechanical Vibrations*, McGraw-Hill, New York.
- de Silva, C.W., A technique to model the simply supported Timoshenko beam in the design of mechanical vibrating systems, *Int. J. Mech. Sci.*, 17, 389–393, 1975.
- de Silva, C.W., Dynamic beam model with internal damping, rotatory inertia and shear deformation, *AIAA J.*, 14, 5, 676–680, 1976.
- de Silva, C.W. 2000. *VIBRATION—Fundamentals and Practice*, CRC Press, Boca Raton, FL.
- de Silva, C. W., Buyukozturk, O., and Wormley, D. N., Postcracking compliance of RC beams, *J. Struct. Div., Trans. ASCE*, 105, ST1, 35–51, 1979.
- de Silva, C.W., and Wormley, D. N., Material optimization in a torsional guideway transit system, *J. Adv. Transp.*, 13, 3, 41–60, 1979.
- de Silva, C.W., and Wormley, D.N., Torsional analysis of cutout beams, *J. Struct. Div., Trans. ASCE*, 106, ST9, 1933–1946, 1980.
- de Silva, C.W., Wormley, D.N. 1983. *Automated Transit Guideways: Analysis and Design*, D.C. Heath and Co., Lexington, KY.
- Dimarogonas, A. 1996. *Vibration for Engineers*, 2nd ed., Prentice Hall, Upper Saddle River, NJ.
- Inman, D.J. 1996. *Engineering Vibration*, Prentice Hall, Englewood Cliffs, NJ.
- Kim, S.W., Misra, A.K., Modi, V.J., Cyril, X., and De Silva, C.W., Modelling of contact dynamics of two flexible multi-body systems, *Acta Astronaut.*, 45, 11, 669–677, 1999.
- Meirovitch, L. 1986. *Elements of Vibration Analysis*, 2nd ed., McGraw-Hill, New York.
- Rao, S. S. 1995. *Mechanical Vibrations*, 3rd ed., Addison-Wesley, Reading, MA.
- Thomson, W.T., and Dahleh, M.D. 1998. *Theory of Vibration with Applications*, 5th ed., Prentice Hall, Upper Saddle River, NJ.
- Volterra E. and Zachmanoglou, E.C. 1965. *Dynamics of Vibrations*, Charles E. Merrill Books, Columbus, OH.
- Zhang, J., Modi, V.J., and De Silva, C.W., Parametric dynamical study of a novel manipulator, *Adv. Astronaut. Sci.*, 110, 115–136, 2001.

5

Random Vibration

5.1	Random Vibration	5-1
5.2	Single Degree of Freedom: The Response to Random Loads	5-2
	Formulation • Derivation of Equations • Response Correlations • Response Spectral Density	
5.3	Response to Two Random Loads	5-7
5.4	Multi-Degree-of-Freedom Vibration	5-12
	Deterministic Vibration • Solution by Frequency Response Function • Modal Analysis	
5.5	Multi-Degree-of-Freedom: The Response to Random Loads	5-17
	Response due to a Single Random Force • Response to Multiple Random Forces • Impulse-Response Approach • Modal Analysis Approach	
5.6	Continuous System Random Vibration	5-29
	Transverse Vibration of Beams • Random Transverse Vibration	

Haym Benaroya

Rutgers University

Summary

This chapter summarizes the key ideas of linear random vibration. This discipline focuses on determining the response statistics of an oscillator or structure to input forces that are definable only in terms of their statistics. Typical problems include the following: (1) given the power spectrum of the force, find the power spectrum of the response; (2) given the mean value and variance of the force, find the mean value and variance of the response. The methodology is built upon the linear theory of vibration for discrete single- and multi-degree-of-freedom (DoF) systems, and continuous systems. The approaches are essentially the direct method and the modal analysis method. The direct method may also be called a transfer matrix method (see Chapter 2). Modal analysis (see Chapters 3 and 4) has the same benefit in random vibration as is done in deterministic vibration studies: it can be computationally more efficient. A number of examples are given, as are a list of representative references.

5.1 Random Vibration

The discipline of random vibration of structures was borne of the need to understand how structures respond to dynamic loads that are too complex to model deterministically. Examples include aerodynamic loading on aircraft and earthquake loading of structures. Essentially, the question that must be answered is: *given the statistics (read: uncertainties) of the loading, what are the statistics (read: most likely values with bounds) of the response?* Generally, for engineering applications the statistics of greatest concern are the mean, or average value, and the variance, or scatter. These concepts are discussed in detail subsequently.

Suppose that we are aircraft designers currently working on the analysis and design of a wing for a new airplane. As engineers, we are very familiar with the mechanics of solids and can size the wing for static loads. Also, we have vibration experience and can evaluate the response of the wing to a harmonic

or impulsive forcing. However, this wing provides lift to an airplane flying through a turbulent atmosphere. Even though we are not fluid dynamicists, we know that turbulence is a very complicated physical process. In fact, the fluid (air) motion is so complicated that probabilistic models are required to model the behavior. *Here, a plausibly deterministic but very complicated dynamic process is taken to be random for the purposes of modeling.* Wing design requires force data resulting from the interaction between fluid and structure. Such data can be shown as the time history in Figure 5.1.

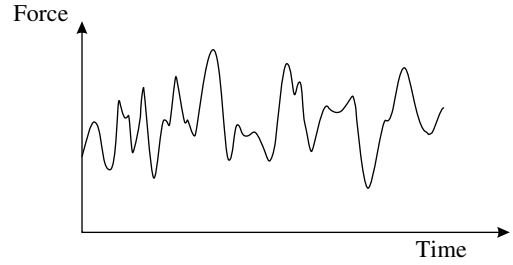


FIGURE 5.1 Turbulent force history.

The challenge is to make sense of such intricate fluctuations. The analyst and designer must run scale model tests. A wing section is set up in the wind tunnel and representative aerodynamic forces are generated. Data on wind forces and structural response are gathered and analyzed. With additional data analysis, it is possible to estimate the force magnitudes. Estimates of the mean values of these forces can be calculated, as well as of the range of possible forces. With these estimates, it is possible to study the behavior of the wing under a variety of realistic loading scenarios using the tools of probability and statistics to model this complex physical problem. This text introduces the use of probabilistic information in mechanical systems, primarily structural and dynamic systems. These tools are applicable to all the sciences and engineering, even though this text focuses on the mechanical sciences and engineering.

5.2 Single Degree of Freedom: The Response to Random Loads

Consider the second-order differential equation¹ governing the linear motion of an oscillator

$$\ddot{X}(t) + 2\zeta\omega_n\dot{X}(t) + \omega_n^2X(t) = F(t) \quad (5.1)$$

where the input force per unit mass is given by stationary random process $F(t)$ and the output displacement by random process $X(t)$. Note that it is customary to use upper case letters $X(t)$ to represent random processes, and lower case letters $x(t)$ to represent the realizations of a random process. The notation here is standard: $2\zeta\omega_n = c/m$ where c = viscous damping and m = mass; and $\omega_n^2 = k/m$ where k = stiffness.

We assume that the reader understands the concepts of *impulse response* and *convolution*. We would also like to present *a priori* the results which are derived in the subsequent section; the mean value of the response μ_X and the spectral density of the output $S_{XX}(\omega)$:

$$\mu_X = H(0)\mu_F$$

$$S_{XX}(\omega) = |H(\omega)|^2 S_{FF}(\omega)$$

$$|H(\omega)|^2 = \left[\frac{1/\omega_n^2}{\sqrt{(1 - \omega^2/\omega_n^2)^2 + (2\zeta\omega/\omega_n)^2}} \right]^2$$

These equations tell us that the mean value of the response μ_x is proportional to the mean value of the force μ_F , and that the response spectral density $S_{XX}(\omega)$ is proportional to the force spectral density $S_{FF}(\omega)$. For both results, the proportionality constants depend on the structural or system parameters.

¹In this instance, the system parameters ζ and ω_n are deterministic and, therefore, so is the governing equation of motion. If ζ and ω_n are either random variables or processes then the governing equation is random. The case of random parameters is much more complicated because the system itself is random rather than just the forcing. We would have to solve the problem for the "many randomly prescribed systems" rather than for just one system with randomly prescribed forces.

By previewing the end results, the reader will hopefully be able to better follow the mathematical manipulations which follow.

5.2.1 Formulation

Consider the linear system defined by Equation 5.1 and assume random process input $F(t)$ to be stationary, with mean μ_F and power spectrum $S_{FF}(\omega)$. The stationarity assumption for the forcing means that transient dynamic behavior cannot be directly considered here.² Thus, the initial loading transients of an earthquake, a wind gust, or an extreme ocean wave cannot be considered as stationary. Assuming that the character of the loading does not change, steady-state behavior can be assumed to be statistically stationary.

5.2.2 Derivation of Equations

Begin with the convolution equation for the deterministic response of a linear oscillator

$$X(t) = \int_{-\infty}^{\infty} g(\tau)F(t - \tau)d\tau \quad (5.2)$$

where $g(t)$ is the impulse response given by

$$g(t) = \frac{1}{\omega_d} e^{-\zeta\omega_n t} \sin \omega_d t$$

and stationary random load per unit mass $F(t)$ is applied at $t = -\infty$, that is, long before the present time. This ensures that the impulse response is stationary. Beginning with Equation 5.2, take the expected value of both sides and use the linear property of mathematical expectation to interchange it with the integral:

$$\begin{aligned} E\{X(t)\} &= \int_{-\infty}^{\infty} g(\tau)E\{F(t - \tau)\}d\tau = E\{F(t)\} \int_{-\infty}^{\infty} g(\tau)d\tau \\ &= \mu_F \int_{-\infty}^{\infty} g(\tau)d\tau = \mu_F H(0) \end{aligned}$$

where the fact that $F(t)$ is stationary was utilized in the second and third equations,³ and $H(\omega)$ is the frequency response function; $H(0) = H(\omega)|_{\omega=0}$. Therefore, we arrive at the first important result

$$\mu_X = H(0)\mu_F = \frac{1}{\omega_n^2} \mu_F,$$

which shows us that since μ_F is time independent, then so must be $E\{x(t)\}$.

In order to derive the output spectral density, we must work through the intermediate results involving the correlation function.

5.2.3 Response Correlations

For a stationary process, the autocorrelation function is given by

$$R_{XX}(\tau) = \int_{-\infty}^{\infty} x(t)x(t + \tau)f_X(x)dx$$

where $f_X(x)$ is the probability density function of the process. We cannot take the Fourier transform of this equation to find the response spectral density because we do not know the response density

²There are, however, clever ways by which stationary solutions can be utilized in nonstationary cases. One possibility is to multiply the stationary process by a deterministic time function such that the product is an *evolutionary*, or nonstationary, process. For example, use $A(t)F(t)$ as the forcing function where $A(t)$ is a deterministic transient function and $F(t)$ is stationary.

³The force is stationary and has a constant mean value.

function $f_X(x)$. There are two other equivalent ways to proceed: (i) utilize the ergodic definition of the autocorrelation,⁴ or (ii) use Equation 5.2, utilizing available information on $F(t)$, as follows.

First, derive the cross-correlation between $F(t)$ and $X(t)$. Multiply both sides of Equation 5.2 by $F(t - \alpha_1)$ and take the expected values of both sides:

$$E\{X(t)F(t - \alpha_1)\} = \int_{-\infty}^{\infty} g(\tau_1)E\{F(t - \tau_1)F(t - \alpha_1)\}d\tau_1$$

where $E\{F(t - \tau_1)F(t - \alpha_1)\} = R_{FF}(\tau_1 - \alpha_1)$ and $E\{X(t)F(t - \alpha_1)\} = R_{XF}(\alpha_1)$, the cross-correlation between loading $F(t)$ and response $X(t)$. Thus,

$$R_{XF}(\alpha_1) = \int_{-\infty}^{\infty} g(\tau_1)R_{FF}(\tau_1 - \alpha_1)d\tau_1 \quad (5.3)$$

and R_{FF} is known from experimental data. Next, multiply both sides of Equation 5.2 by $X(t + \alpha_2)$ and take expected values of both sides:

$$\begin{aligned} E\{X(t + \alpha_2)X(t)\} &= \int_{-\infty}^{\infty} g(\tau_2)E\{X(t + \alpha_2)F(t - \tau_2)\}d\tau_2 \\ R_{XX}(\alpha_2) &= \int_{-\infty}^{\infty} g(\tau_2)R_{XF}(\tau_2 + \alpha_2)d\tau_2 \end{aligned} \quad (5.4)$$

Substitute Equation 5.3 into Equation 5.4 to find

$$R_{XX}(\tau) = \int_{-\infty}^{\infty} \int_{-\infty}^{\infty} g(\alpha)g(\beta)R_{FF}(\tau + \beta - \alpha)d\alpha d\beta \quad (5.5)$$

which is a double convolution. To evaluate the variance, we use

$$\sigma_X^2 = E\{X(t)^2\} - E^2\{X(t)\} = R_{XX}(0) - [H(0)E\{F(t)\}]^2$$

While this information on the correlation is of interest, a more important result is the response spectral density that we derive in the next section.

5.2.4 Response Spectral Density

Begin with the Fourier transform relation between power spectrum and correlation function

$$S_{XX}(\omega) = \frac{1}{2\pi} \int_{-\infty}^{\infty} R_{XX}(\tau)e^{-i\omega\tau} d\tau,$$

and substitute Equation 5.5 for $R_{XX}(\tau)$, with $\lambda = \tau + \beta - \alpha$:

$$\begin{aligned} S_{XX}(\omega) &= \frac{1}{2\pi} \int_{-\infty}^{\infty} e^{-i\omega\tau} \left[\int_{-\infty}^{\infty} \int_{-\infty}^{\infty} g(\alpha)g(\beta)R_{FF}(\lambda)d\alpha d\beta \right] d\tau \\ &= \int_{-\infty}^{\infty} g(\alpha)e^{-i\omega\alpha} d\alpha \int_{-\infty}^{\infty} g(\beta)e^{+i\omega\beta} d\beta \times \frac{1}{2\pi} \int_{-\infty}^{\infty} R_{FF}(\lambda)e^{-i\omega\lambda} d\lambda \\ &= H(\omega)H^*(\omega)S_{FF}(\omega) \end{aligned}$$

by definition, where $*$ denotes complex conjugate and therefore

$$S_{XX}(\omega) = |H(\omega)|^2 S_{FF}(\omega) \quad (5.6)$$

This is the *fundamental* result for random vibration and linear systems theory that allows us to evaluate the output spectral density, given the input spectral density and the system frequency response.

⁴ $R_{xx}(\tau) = \lim_{T \rightarrow \infty} \frac{1}{2T} \int_{-T}^{+T} x(t)x(t + \tau)dt.$

It is emphasized here that the derivation of Equation 5.6 made use of the convolution equation that is valid for linear systems and structures. Any generalization for nonlinear behavior requires problem-specific approaches.

Example 5.1 Oscillator Response to White Noise

Consider a simple application of the above ideas to an oscillator. What is the response of a damped oscillator to a force with white noise density?

Solution

The governing equation of motion is

$$\ddot{X}(t) + 2\zeta\omega_n\dot{X}(t) + \omega_n^2X(t) = F(t)$$

where $F(t)$ is the external force per unit mass, the system transfer function is given by

$$H(\omega) = \frac{1}{\omega_n^2 + i2\zeta\omega_n\omega + (i\omega)^2}$$

and the squared magnitude of $H(\omega)$ is given by

$$|H(\omega)|^2 = \frac{1}{(\omega_n^2 - \omega^2)^2 + (2\zeta\omega_n\omega)^2}$$

Therefore, given any input spectral density $S_{FF}(\omega)$, the response spectral density is

$$S_{XX}(\omega) = |H(\omega)|^2 S_{FF}(\omega) = \frac{S_{FF}(\omega)}{(\omega_n^2 - \omega^2)^2 + (2\zeta\omega_n\omega)^2}$$

Suppose, for mathematical simplicity, that the forcing is white noise, $S_{FF}(\omega) = S_0$. Then,

$$S_{XX}(\omega) = \frac{S_0}{(\omega_n^2 - \omega^2)^2 + (2\zeta\omega_n\omega)^2} \quad (5.7)$$

and the mean-square response is given by

$$E\{X(t)^2\} = \int_{-\infty}^{\infty} S_{XX}(\omega) d\omega = \frac{\pi m^2 S_0}{kc} = \frac{\pi S_0}{2\omega_n^3 \zeta}$$

The mean-square response can also be written in terms of a one-sided spectrum

$$E\{X(t)^2\} = \frac{\pi m^2 S_0}{kc} = \frac{m^2 W_0}{4kc}$$

where the one-sided density W_0 is related to the two-sided density by $S_0 = \pi W_0/4$.

This integral is not standard, but can be found in texts on random vibration.⁵ Even though infinite mean-square energy is input to the system,⁶ it responds with finite mean-square energy. See Figure 5.2 for plots of the components of Equation 5.7. Only the positive frequency ranges are plotted as they are

⁵For example, the integral of this example problem is a specialized version of

$$\int_{-\infty}^{\infty} \left| \frac{B_0 + i\omega B_1}{A_0 + i\omega A_1 - \omega^2 A_2} \right|^2 d\omega = \frac{\pi(A_0 B_1^2 + A_2 B_0^2)}{A_0 A_1 A_2}$$

where

$$A_0 = \omega_n^2, \quad A_1 = 2\zeta\omega_n, \quad A_2 = 2, \quad B_0 = 1, \quad B_1 = 0.$$

⁶The energy input equals to the area under the spectral density, which for white noise is

$$\int_{-\infty}^{\infty} S_0 d\omega = \infty.$$

symmetric about the abscissae. White noise is useful and frequently used, even though it is nonphysical, because it leads to good approximate results.

Example 5.2 Response to Colored Noise

Suppose the same system as in the last example is subjected to more complex loading, where the spectral density of the forcing is not a constant, but a function of ω . How would the above analysis change?

Solution

The output spectral density becomes a more complex function of frequency, for example, if the loading density is similar to those found for wind loads. Then, the mean-square response must be evaluated numerically.

The applied problems are always solved numerically, although hopefully after some significant analytical exposition. There are numerical methods that are specifically geared to handling uncertainties. Of particular note is the group known as Monte Carlo methods. These methods utilize the massive computational power available today to account for uncertainties. This is accomplished by generating random numbers that are used to represent random parameters. For each of these generated random values, the program recalculates the problem. After running enough cycles to ensure the convergence of the statistics, these numerical realizations are averaged to find the mean value and variance of the relevant parameters.

We summarize the key results for the random vibration of a single-DoF linear oscillator in Table 5.1 to Table 5.3. Figure 5.3 shows some of the most important correlation and spectral density pairs.

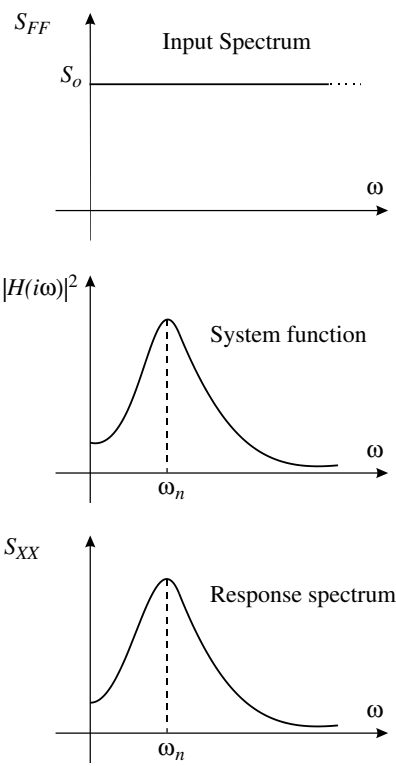


FIGURE 5.2 $S_{FF}(\omega)$, $|H(i\omega)|^2$, $S_{XX}(\omega)$.

TABLE 5.1 Mean-Value Response

$\mu_X = H(0)\mu_F$
$ H(\omega) ^2 = \left[\frac{1/\omega_n^2}{\sqrt{(1 - \omega^2/\omega_n^2)^2 + (2\zeta\omega/\omega_n)^2}} \right]^2$
μ_F is known from force data

TABLE 5.2 Output Correlation Function/Variance

$R_{XX}(\tau) = \int_{-\infty}^{\infty} \int_{-\infty}^{\infty} g(\alpha)g(\beta)R_{FF}(\tau + \beta - \alpha)d\alpha d\beta$
$\sigma_X^2 = R_{XX}(0) - [H(0)E\{F(t)\}]^2$
$R_{FF}(\tau + \beta - \alpha)$ is known from force data

TABLE 5.3 Output Spectral Density

$S_{XX}(\omega) = |H(\omega)|^2 S_{FF}(\omega)$

$|H(\omega)|^2$ from structural parameters

$S_{FF}(\omega)$ is the input force power spectrum

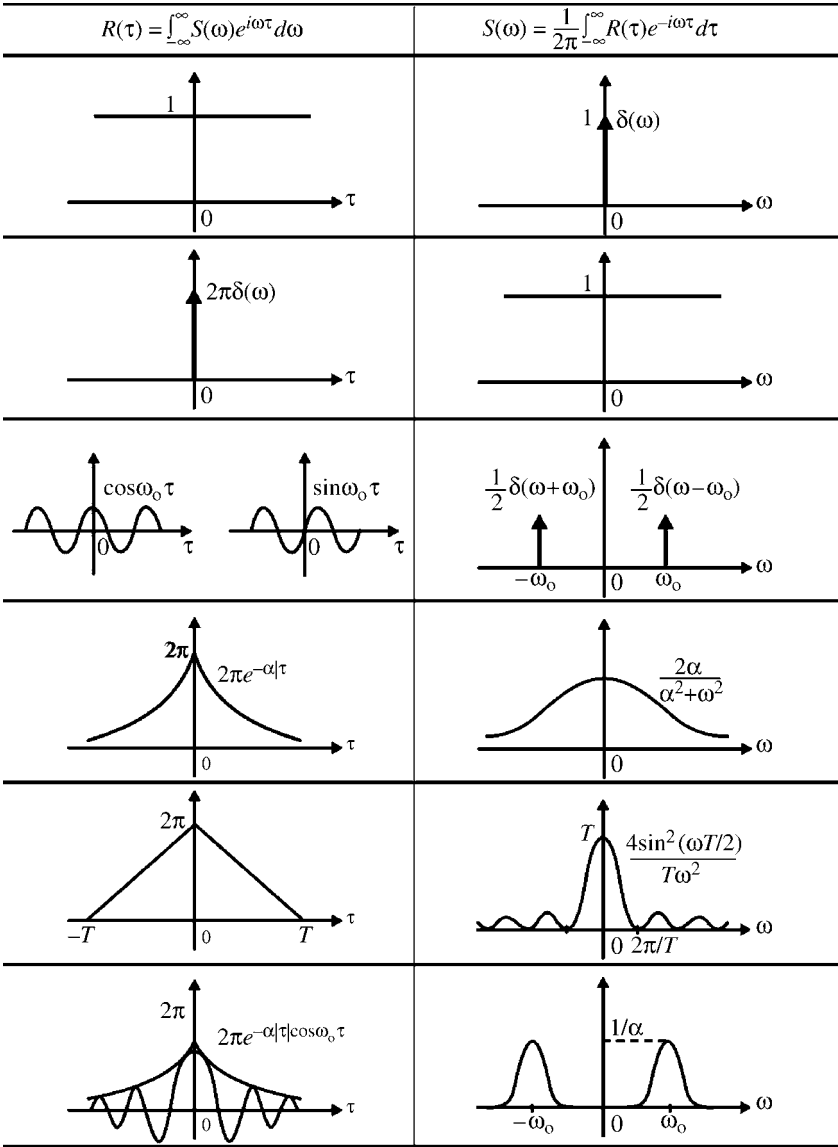


FIGURE 5.3 Correlation functions and corresponding power spectral densities.

5.3 Response to Two Random Loads

Previously, the system responses were due to a single randomly varying force. In general, the situation is more complicated, because more than one load may act on a system and the resulting response depends not only on the properties of each force, but also on the correlation between the two forces.

Consider the response of the system to two random loadings, $P(t)$ and $Q(t)$, acting simultaneously but at different points on the system, as shown in Figure 5.4. We are interested in calculating the response statistics of the displacement $X(t)$ at an arbitrary point on the system. Assume that $E\{P(t)\} = 0$ and $E\{Q(t)\} = 0$. Also, by utilizing available data, we are able to estimate $R_{PP}(\tau)$ and $R_{QQ}(\tau)$. Our interest is in evaluating $R_{XX}(\tau)$ and its Fourier transform $S_{XX}(\omega)$. Using linear superposition and the convolution integral, the response due to both forces is given by

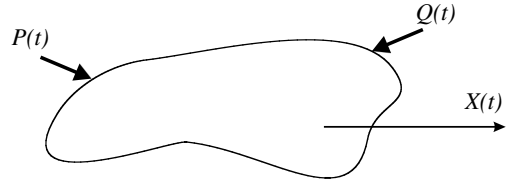


FIGURE 5.4 Response to two random loads.

$$X(t) = \int_{-\infty}^{\infty} [g_{XP}(\tau_1)P(t - \tau_1) + g_{XQ}(\tau_1)Q(t - \tau_1)]d\tau_1$$

Similarly, for $X(t + \tau)$:

$$X(t + \tau) = \int_{-\infty}^{\infty} [g_{XP}(\tau_2)P(t + \tau - \tau_2) + g_{XQ}(\tau_2)Q(t + \tau - \tau_2)]d\tau_2$$

where g_{XP} is the impulse response function at coordinate X due to force P and g_{XQ} is the impulse response function at X due to Q . Then,

$$R_{XX}(\tau) = E\{X(t)X(t + \tau)\} = E\left\{\int_{-\infty}^{\infty} [g_{XP}(\tau_1)P(t - \tau_1) + g_{XQ}(\tau_1)Q(t - \tau_1)]d\tau_1 \times \int_{-\infty}^{\infty} [g_{XP}(\tau_2)P(t + \tau - \tau_2) + g_{XQ}(\tau_2)Q(t + \tau - \tau_2)]d\tau_2\right\}$$

Now expand the product, and then move the expectation operator to the random processes, as follows:

$$\begin{aligned} R_{XX}(\tau) = & \int_{-\infty}^{\infty} g_{XP}(\tau_1) \left[\int_{-\infty}^{\infty} g_{XP}(\tau_2) E\{P(t - \tau_1)P(t + \tau - \tau_2)\} d\tau_2 \right] d\tau_1 \\ & + \int_{-\infty}^{\infty} g_{XP}(\tau_1) \left[\int_{-\infty}^{\infty} g_{XQ}(\tau_2) E\{P(t - \tau_1)Q(t + \tau - \tau_2)\} d\tau_2 \right] d\tau_1 \\ & + \int_{-\infty}^{\infty} g_{XQ}(\tau_1) \left[\int_{-\infty}^{\infty} g_{XP}(\tau_2) E\{Q(t - \tau_1)P(t + \tau - \tau_2)\} d\tau_2 \right] d\tau_1 \\ & + \int_{-\infty}^{\infty} g_{XQ}(\tau_1) \left[\int_{-\infty}^{\infty} g_{XQ}(\tau_2) E\{Q(t - \tau_1)Q(t + \tau - \tau_2)\} d\tau_2 \right] d\tau_1 \end{aligned}$$

In this expression

$$E\{P(t - \tau_1)P(t + \tau - \tau_2)\} = R_{PP}(\tau + \tau_1 - \tau_2)$$

$$E\{Q(t - \tau_1)Q(t + \tau - \tau_2)\} = R_{QQ}(\tau + \tau_1 - \tau_2)$$

The expectations in the second and third terms are cross-correlations of the form $R_{PQ}(\tau) = E\{P(t)Q(t + \tau)\}$. Therefore, the autocorrelation of the response becomes

$$\begin{aligned} R_{XX}(\tau) = & \int_{-\infty}^{\infty} g_{XP}(\tau_1) \left[\int_{-\infty}^{\infty} g_{XP}(\tau_2) R_{PP}(\tau + \tau_1 - \tau_2) d\tau_2 \right] d\tau_1 \\ & + \int_{-\infty}^{\infty} g_{XP}(\tau_1) \left[\int_{-\infty}^{\infty} g_{XQ}(\tau_2) R_{PQ}(\tau + \tau_1 - \tau_2) d\tau_2 \right] d\tau_1 \\ & + \int_{-\infty}^{\infty} g_{XQ}(\tau_1) \left[\int_{-\infty}^{\infty} g_{XP}(\tau_2) R_{QP}(\tau + \tau_1 - \tau_2) d\tau_2 \right] d\tau_1 \\ & + \int_{-\infty}^{\infty} g_{XQ}(\tau_1) \left[\int_{-\infty}^{\infty} g_{XQ}(\tau_2) R_{QQ}(\tau + \tau_1 - \tau_2) d\tau_2 \right] d\tau_1 \end{aligned}$$

The importance of this result is primarily in the observation that we cannot derive $R_{XX}(\tau)$ unless the cross-correlations $R_{PQ}(\tau)$ and $R_{QP}(\tau)$ are also known. Using the Fourier transform relation between $R_{XX}(\tau)$ and $S_{XX}(\omega)$, that is

$$S_{XX}(\omega) = \frac{1}{2\pi} \int_{-\infty}^{\infty} R_{XX}(\tau) e^{-i\omega\tau} d\tau$$

we obtain

$$\begin{aligned} S_{XX}(\omega) = & H_{XP}^*(\omega)H_{XP}(\omega)S_{PP}(\omega) + H_{XP}^*(\omega)H_{XQ}(\omega)S_{PQ}(\omega) \\ & + H_{XQ}^*(\omega)H_{XP}(\omega)S_{QP}(\omega) + H_{XQ}^*(\omega)H_{XQ}(\omega)S_{QQ}(\omega) \end{aligned} \quad (5.8)$$

where

$$H_{XP}^*(\omega)H_{XP}(\omega) = |H_{XP}(\omega)|^2$$

$$H_{XQ}^*(\omega)H_{XQ}(\omega) = |H_{XQ}(\omega)|^2$$

and

$$S_{PQ}(\omega) = \frac{1}{2\pi} \int_{-\infty}^{\infty} R_{PQ}(\tau) e^{-i\omega\tau} d\tau$$

As expected, the evaluation of the output spectral density requires knowledge about the cross-spectra $S_{PQ}(\omega)$ and $S_{QP}(\omega)$. If there are more than two forces, then we will have additional cross-spectra between each pair of forces.

Examining Equation 5.8 closely, we find that we can write $S_{XX}(\omega)$ as

$$S_{XX}(\omega) = \begin{bmatrix} H_{XP}^*(\omega) & H_{XQ}^*(\omega) \end{bmatrix} \begin{bmatrix} S_{PP}(\omega) & S_{PQ}(\omega) \\ S_{QP}(\omega) & S_{QQ}(\omega) \end{bmatrix} \begin{bmatrix} H_{XP}(\omega) \\ H_{XQ}(\omega) \end{bmatrix} \quad (5.9)$$

Example 5.3 Conjugates of Cross Spectra

It was briefly mentioned that $R_{PQ}(\tau) = R_{QP}(-\tau)$. How are $S_{PQ}(\omega)$ and $S_{QP}(\omega)$ related?

Solution

By the definition of spectral density

$$S_{PQ}(\omega) = \frac{1}{2\pi} \int_{-\infty}^{\infty} R_{PQ}(\tau) \exp(-i\omega\tau) d\tau$$

Replacing $R_{PQ}(\tau)$ with $R_{QP}(-\tau)$

$$S_{PQ}(\omega) = \frac{1}{2\pi} \int_{-\infty}^{\infty} R_{QP}(-\tau) \exp(-i\omega\tau) d\tau$$

Letting $-\tau = t$

$$S_{PQ}(\omega) = \frac{1}{2\pi} \int_{-\infty}^{\infty} R_{QP}(t) \exp(i\omega t) dt$$

Then,

$$S_{PQ}(\omega) = S_{QP}(-\omega) = S_{QP}^*(\omega)$$

Example 5.4 Response Spectrum due to Two Random Loads

Consider a mass–spring–damper system in [Figure 5.5](#) subject to two random forces $P(t)$ and $Q(t)$. Find the response spectrum $S_{XX}(\omega)$ assuming that

$$S_{PP}(\omega) = S_P, \quad S_{PQ}(\omega) = 0, \quad S_{QQ}(\omega) = S_Q$$

Solution

The equation of motion for this system is given by

$$m\ddot{X} + c\dot{X} + kX = P(t) + Q(t)$$

First, assume that $Q(t) = 0$ in order to first obtain $H_{XP}(\omega)$. Taking the Fourier transform, the equation of motion is given by

$$(-m\omega^2 + ci\omega + k)X(\omega) = P(\omega)$$

Then, the frequency response function $H_{XP}(\omega)$ is

$$H_{XP}(\omega) = \frac{1}{(-m\omega^2 + ci\omega + k)}$$

or

$$H_{XP}(\omega) = \frac{1}{m(-\omega^2 + 2\omega_n \zeta i\omega + \omega_n^2)}$$

Similarly, $H_{XQ}(\omega)$ is obtained by setting $P(t) = 0$ and is also given by

$$H_{XQ}(\omega) = \frac{1}{m(-\omega^2 + 2\omega_n \zeta i\omega + \omega_n^2)}$$

Then, the spectral density of the response is given by

$$S_{XX}(\omega) = \begin{bmatrix} (m(\omega_n^2 - \omega^2 - 2\omega_n \zeta i\omega))^{-1} & (m(\omega_n^2 - \omega^2 - 2\omega_n \zeta i\omega))^{-1} \end{bmatrix} \begin{bmatrix} S_{PP}(\omega) & S_{PQ}(\omega) \\ S_{QP}(\omega) & S_{QQ}(\omega) \end{bmatrix} \\ \times \begin{bmatrix} (m(\omega_n^2 - \omega^2 + 2\omega_n \zeta i\omega))^{-1} \\ (m(\omega_n^2 - \omega^2 + 2\omega_n \zeta i\omega))^{-1} \end{bmatrix} = \frac{S_{PP}(\omega) + S_{PQ}(\omega) + S_{QP}(\omega) + S_{QQ}(\omega)}{m^2[(\omega_n^2 - \omega^2)^2 + (2\omega_n \zeta)^2]}$$

In our case, the spectral density is reduced to

$$S_{XX}(\omega) = \frac{S_P + S_Q}{m^2[(\omega_n^2 - \omega^2)^2 + (2\omega_n \zeta)^2]}$$

Spectral densities are rather complicated expressions to evaluate in general. A number of special cases will help better understand the effects of the cross-terms:

1. $P(t)$ and $Q(t)$ arise from independent sources and are, therefore, uncorrelated.⁷ Then, $R_{PQ}(\tau) = 0$, $R_{QP}(\tau) = 0$ and $S_{PQ}(\omega) = 0$, $S_{QP}(\omega) = 0$.
2. $P(t)$ and $Q(t)$ are directly correlated; that is, $Q(t) = kP(t)$ where k is a constant.
3. $P(t)$ and $Q(t)$ are exponentially correlated, $E\{P(t)Q(t + \tau)\} = k_{PQ} \exp\{-\alpha\tau\}$ where k_{PQ} is a constant.
4. $P(t)$ and $Q(t)$ are correlated in a “simplified” exponential; that is, with a triangular correlation defined by $E\{P(t)Q(t + \tau)\} = \bar{k}_{PQ}(1 - \tau/\tau_1)$, $-\tau_1 \leq \tau \leq \tau_1$.

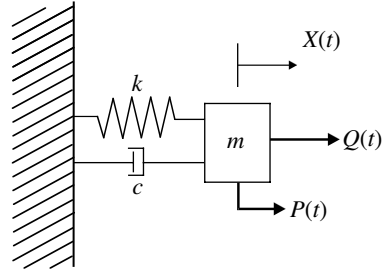


FIGURE 5.5 Single-DoF system subjected to two random loads.

⁷Independence implies that

$$E\{P(t_1)Q(t_2)\} = E\{P(t_1)\}E\{Q(t_2)\}$$

They are uncorrelated if

$$\text{Cov}(P(t_1)Q(t_2)) = E\{P(t_1)Q(t_2)\} - E\{P(t_1)\}E\{Q(t_2)\} = 0$$

Independent processes are always uncorrelated whereas uncorrelated processes may not be independent.

We consider in more detail the first two cases listed above. Where the loads are independent, because the cross-correlations are identically zero, the output spectral density is just the sum of the two respective spectral densities obtained with the forces acting separately:

$$\begin{aligned} S_{XX}(\omega) &= H_{XP}(\omega)H_{XP}^*(\omega)S_{PP}(\omega) + H_{XQ}(\omega)H_{XQ}^*(\omega)S_{QQ}(\omega) \\ &= |H_{XP}(\omega)|^2 S_{PP}(\omega) + |H_{XQ}(\omega)|^2 S_{QQ}(\omega) \end{aligned} \quad (5.10)$$

We note that the output spectral density for a linear system follows a strict interpretation of the principle of linear superposition only when the forces are *uncorrelated*.

For the case where $Q(t) = kP(t)$, we have

$$\begin{aligned} R_{PQ}(\tau) &= E\{P(t)kP(t + \tau)\} = kR_{PP}(\tau) \\ R_{QP}(\tau) &= E\{kP(t)P(t + \tau)\} = kR_{PP}(\tau) \\ R_{QQ}(\tau) &= E\{kP(t)kP(t + \tau)\} = k^2 R_{PP}(\tau) \end{aligned}$$

Then, we can obtain the respective spectral densities

$$\begin{aligned} S_{PQ}(\omega) &= S_{QP}(\omega) = kS_{PP}(\omega) \\ S_{QQ}(\omega) &= k^2 S_{PP}(\omega) \end{aligned}$$

leading to the spectral density of the response

$$\begin{aligned} S_{XX}(\omega) &= H_{XP}^*(\omega)H_{XP}(\omega)S_{PP}(\omega) + H_{XP}^*(\omega)H_{XQ}(\omega)kS_{PP}(\omega) + H_{XQ}^*(\omega)H_{XQ}(\omega)kS_{PP}(\omega) \\ &\quad + H_{XQ}^*(\omega)H_{XQ}(\omega)k^2 S_{PP}(\omega) = (H_{XP} + kH_{XQ})(H_{XP}^* + kH_{XQ}^*)S_{PP}(\omega) \\ &= |H_{XP}(\omega) + kH_{XQ}(\omega)|^2 S_{PP}(\omega) \end{aligned} \quad (5.11)$$

This last expression is related to the relative phase between the two functions $H_{XP}(\omega)$ and $H_{XQ}(\omega)$. The addition of two frequency response functions $H_{XP} + kH_{XQ}$ is shown graphically in Figure 5.6.

Suppose $S_{PP}(\omega) = S_{QQ}(\omega) = S(\omega)$. Then, from Equation 5.10, for independent loadings

$$S_{XX}(\omega) = [|H_{XP}|^2 + |H_{XQ}|^2]S(\omega) \quad (5.12)$$

If the forces are directly correlated with parameter $k = 1$, Equation 5.11 yields

$$S_{XX}(\omega) = |H_{XP} + H_{XQ}|^2 S(\omega) = [|H_{XP}|^2 + |H_{XQ}|^2 + 2|H_{XP}||H_{XQ}|\cos \phi]S(\omega) \quad (5.13)$$

where ϕ is the phase difference between H_{XP} and H_{XQ} as shown in Figure 5.6. The law of cosines is used for the second relation. Therefore, a comparison of Equation 5.12 with Equation 5.13 shows that the results of an uncorrelated loading will be identical to those that are correlated where $\cos \phi = 0$, that is, $\phi = \pm \pi/2$. This is when the two vectors in Figure 5.6 are perpendicular to each other. For other values of ϕ , the spectral density in the correlated case may have any value in the range defined by $[|H_{XP}|^2 \pm |H_{XQ}|^2]S(\omega)$ depending on the value of ϕ .

If, at some frequency, $H_{XP} = -H_{XQ}$, the spectral density at that frequency for the correlated case with $k = 1$ will be zero. For any case where $H_{XP} = H_{XQ}$, the spectral density with correlation will be twice that obtained without correlation.

Another specialized result is where $Q(t)$ follows $P(t)$ after a lag of τ_0 so that $Q(t) = P(t + \tau_0)$.

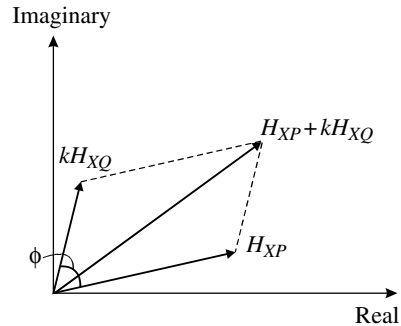


FIGURE 5.6 Addition of frequency-response functions.

Then,

$$R_{PQ}(\tau) = E\{P(t)P(t + \tau_0 + \tau)\} = R_{PP}(\tau_0 + \tau)$$

with the respective spectral density

$$\begin{aligned} S_{PQ}(\omega) &= \frac{1}{2\pi} \int_{-\infty}^{\infty} R_{PQ}(\tau) e^{-i\omega\tau} d\tau = \frac{1}{2\pi} \int_{-\infty}^{\infty} R_{PP}(\tau_0 + \tau) e^{-i\omega\tau} d\tau \\ &= \frac{1}{2\pi} e^{i\omega\tau_0} \int_{-\infty}^{\infty} R_{PP}(\tau_0 + \tau) e^{-i\omega(\tau_0 + \tau)} d(\tau_0 + \tau) = e^{i\omega\tau_0} S_{PP}(\omega) \end{aligned}$$

Since $S_{PQ}(\omega) = S_{QP}(\omega)$ are complex conjugates

$$S_{QP}(\omega) = e^{-i\omega\tau_0} S_{PP}(\omega)$$

Also, $S_{PP}(\omega) = S_{QQ}(\omega)$. Then,

$$S_{XX}(\omega) = [H_{XP}(\omega)H_{XP}^*(\omega) + e^{i\omega\tau_0}H_{XP}(\omega)H_{XQ}^*(\omega) + e^{-i\omega\tau_0}H_{XQ}(\omega)H_{XP}^*(\omega) + H_{XQ}(\omega)H_{XQ}^*(\omega)]S_{PP}(\omega)$$

5.4 Multi-Degree-of-Freedom Vibration

In this section, a review of deterministic vibration is provided. These results are used in the next section, where the forcing is taken to be a random process.

5.4.1 Deterministic Vibration

Consider a case where there is more than one DoF. The equations of motion can be written as

$$[m]\{\ddot{x}(t)\} + [c]\{\dot{x}(t)\} + [k]\{x(t)\} = \{F(t)\}$$

For an N -DoF system, the matrices $[m]$, $[c]$ and $[k]$ are of dimension $N \times N$, and the response $\{x(t)\}$ and force $\{F(t)\}$ vectors are of dimension $N \times 1$.

For purposes of demonstration and discussion, the necessary concepts will be introduced primarily by working through the solution of a two-DoF system. All these ideas transfer to larger systems, but with the two-DoF model we can demonstrate the key ideas without the complications of the major algebraic and numerical demands made by the larger systems.

For the system shown in Figure 5.7, we can derive the coupled equations of motion using either Newton's Second Law of motion applied to a free body diagram for each mass, as shown in Figure 5.8, or by Lagrange's equation. In either case, we find the governing equations to be

$$\begin{aligned} m_1\ddot{x}_1(t) + (c_1 + c_2)\dot{x}_1(t) + (k_1 + k_2)x_1(t) - c_2\dot{x}_2(t) - k_2x_2(t) &= F_1(t), \\ m_2\ddot{x}_2(t) + c_2\dot{x}_2(t) - c_2\dot{x}_1(t) - k_2x_1(t) + k_2x_2(t) &= F_2(t) \end{aligned}$$

or in matrix form

$$\begin{bmatrix} m_1 & 0 \\ 0 & m_2 \end{bmatrix} \begin{Bmatrix} \ddot{x}_1(t) \\ \ddot{x}_2(t) \end{Bmatrix} + \begin{bmatrix} c_1 + c_2 & -c_2 \\ -c_2 & c_2 \end{bmatrix} \begin{Bmatrix} \dot{x}_1(t) \\ \dot{x}_2(t) \end{Bmatrix} + \begin{bmatrix} k_1 + k_2 & -k_2 \\ -k_2 & k_2 \end{bmatrix} \begin{Bmatrix} x_1(t) \\ x_2(t) \end{Bmatrix} = \begin{Bmatrix} F_1(t) \\ F_2(t) \end{Bmatrix} \quad (5.14)$$

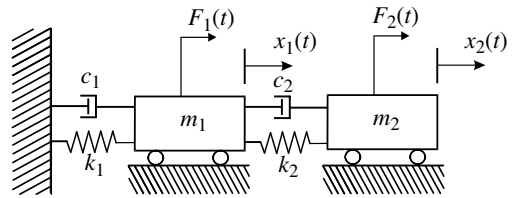


FIGURE 5.7 Two-DoF mass–spring–damper system.

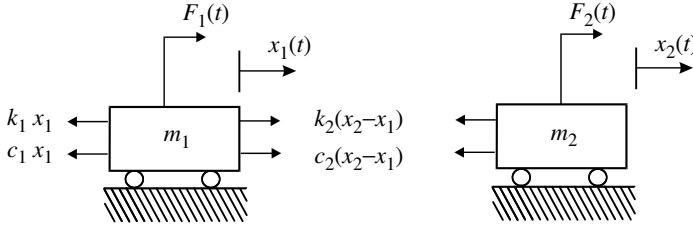


FIGURE 5.8 Free body diagram of a two-DoF system.

In this case, the mass, damping, and stiffness matrices are given by

$$[m] = \begin{bmatrix} m_1 & 0 \\ 0 & m_2 \end{bmatrix}, \quad [c] = \begin{bmatrix} c_1 + c_2 & -c_2 \\ -c_2 & c_2 \end{bmatrix}, \quad [k] = \begin{bmatrix} k_1 + k_2 & -k_2 \\ -k_2 & k_2 \end{bmatrix}$$

5.4.2 Solution by Frequency Response Function

Begin by taking the Fourier transform of the equations of motion, obtaining

$$(-\omega^2[m] + i\omega[c] + [k])\{X(\omega)\} = \{F(\omega)\}$$

where $\{X(\omega)\}$ and $\{F(\omega)\}$ are Fourier transforms of $\{x(t)\}$ and $\{F(t)\}$, respectively. The matrix $(-\omega^2[m] + i\omega[c] + [k])$ is denoted as $[Z(\omega)]$. Then,

$$\{X(\omega)\} = [Z(\omega)]^{-1}\{F(\omega)\}$$

The matrix $[Z(\omega)]^{-1}$ is identical to the frequency response matrix denoted as $[H(\omega)]$:

$$\{X(\omega)\} = [H(\omega)]\{F(\omega)\} \quad (5.15)$$

For the two-DoF system in Figure 5.7

$$[H(\omega)] = \frac{1}{\det[Z]} \begin{bmatrix} -m_2\omega^2 + i\omega c_2 + k_2 & i\omega c_2 + k_2 \\ i\omega c_2 + k_2 & -m_1\omega^2 + i\omega(c_1 + c_2) + (k_1 + k_2) \end{bmatrix}$$

$$\det[Z] = \omega^4 m_1 m_2 - i\omega^3 (m_1 c_2 + c_1 m_2 + c_2 m_2) + i\omega (c_1 k_2 + k_1 c_2)$$

$$- \omega^2 (m_1 k_2 + c_1 c_2 + k_1 m_2 + k_2 m_2) + k_1 k_2$$

Note that the frequency response function of a two-DoF system is given as a matrix with dimension of 2×2 . To clarify the meaning of each element, let us expand Equation 5.15:

$$X_1(\omega) = H_{11}(\omega)F_1(\omega) + H_{12}(\omega)F_2(\omega)$$

$$X_2(\omega) = H_{21}(\omega)F_1(\omega) + H_{22}(\omega)F_2(\omega)$$

Now, the meaning of each element is clear. Each element $H_{ij}(\omega)$ is the frequency response function for coordinate i due to a force at j . In general, $[H(\omega)]$ is a symmetric matrix since $[m]$, $[c]$ and $[k]$ are symmetric.

For a deterministic response, recall that the impulse response function is related to the frequency response function by

$$g_{ij}(t) = \frac{1}{2\pi} \int_{-\infty}^{\infty} H_{ij}(\omega) \exp(i\omega t) d\omega$$

which is written for each element in the matrix. For the two-DoF system

$$\begin{aligned} g_{11}(t) &= \frac{1}{2\pi} \int_{-\infty}^{\infty} \frac{-m_2 \omega^2 + i\omega c_2 + k_2}{\det[Z]} \exp(i\omega t) d\omega \\ g_{12}(t) &= \frac{1}{2\pi} \int_{-\infty}^{\infty} \frac{i\omega c_2 + k_2}{\det[Z]} \exp(i\omega t) d\omega \\ g_{21}(t) &= \frac{1}{2\pi} \int_{-\infty}^{\infty} \frac{i\omega c_2 + k_2}{\det[Z]} \exp(i\omega t) d\omega = g_{12}(t) \\ g_{22}(t) &= \frac{1}{2\pi} \int_{-\infty}^{\infty} \frac{-m_1 \omega^2 + i\omega(c_1 + c_2) + (k_1 + k_2)}{\det[Z]} \exp(i\omega t) d\omega \end{aligned}$$

Again, $[g(t)]$ is a symmetric matrix.

Using the convolution integral, the response $x_i(t)$ due to F_j is

$$x_i(t) = \int_{-\infty}^{\infty} g_{ij}(\tau) F_j(t - \tau) d\tau$$

The total response $x_i(t)$ of mass m_i is then equal to the sum of the individual responses to each of the forces. In our case, the responses are

$$\begin{aligned} x_1(t) &= \int_{-\infty}^{\infty} [g_{11}(\tau) F_1(t - \tau) + g_{12}(\tau) F_2(t - \tau)] d\tau \\ x_2(t) &= \int_{-\infty}^{\infty} [g_{21}(\tau) F_1(t - \tau) + g_{22}(\tau) F_2(t - \tau)] d\tau \end{aligned}$$

We can extend our analysis to a system with N DoF. The equations of motion are written in matrix form as

$$[m]\{\ddot{x}(t)\} + [c]\{\dot{x}(t)\} + [k]\{x(t)\} = \{F(t)\}$$

where $\{x(t)\}$ and $\{F(t)\}$ are response and force vectors and the frequency response matrix is given by

$$[H(\omega)] = (-\omega^2[m] + i\omega[c] + [k])^{-1}$$

The impulse response matrix $[g(t)]$ is given by

$$[g(t)] = \frac{1}{2\pi} \int_{-\infty}^{\infty} [H(\omega)] \exp(i\omega t) d\omega$$

and the response matrix is given by

$$\{x(t)\} = \int_{-\infty}^{\infty} [g(\tau)] \{F(t - \tau)\} d\tau$$

Note that the impulse response vector is not trivial to evaluate, much less the convolution integrals. More importantly, this method becomes much harder for each additional DoF. Therefore, this method is rarely used, and we often rely on *modal analysis*.

5.4.3 Modal Analysis

Let us first consider an undamped system in free vibration with equations of motion

$$[m]\{\ddot{x}(t)\} + [k]\{x(t)\} = 0$$

If we assume that $\{x(t)\}$ is harmonic with frequency ω ,

$$\{x(t)\} = A_0 \{u\} e^{i\omega t}$$

the equations of motion are reduced to the eigenvalue problem given by

$$(-\omega^2[m] + [k])\{u\} = \{0\} \quad (5.16)$$

The goal is to find the nonzero vector $\{u\}$. Therefore, equations must be linearly dependent,⁸ or there should be no inverse for $(-\omega^2[m] + [k])$. This can be satisfied if the determinant of $(-\omega^2[m] + [k])$ is zero:

$$|-\omega^2[m] + [k]| = 0$$

There are several values of ω^2 which can make the determinant equal zero, and these values of ω^2 are called *eigenvalues*. For each nonrepeating eigenvalue, there is a corresponding vector $\{u\}$ that satisfies Equation 5.16. This vector is called the *eigenvector*. Physically, the eigenvalues of this problem are the *natural frequencies* squared, and the eigenvectors are the *mode shapes*, since they represent the respective motion of each modal coordinate.

By solving this eigenvalue problem, we can obtain N sets of eigenvalues ω_i^2 with corresponding eigenvectors $\{u\}_i$ for an N -DoF system.⁹ It is customary that the eigenvalues are arranged in ascending order

$$\omega_1^2 < \omega_2^2 < \dots < \omega_N^2$$

The eigenvectors can be *normalized with respect to the mass matrix*,

$$\{u\}_i^T [m] \{u\}_i = 1, \quad i = 1, 2, \dots, N$$

where

$$\{u\}_i = \begin{Bmatrix} u_{1i} \\ \vdots \\ u_{Ni} \end{Bmatrix}$$

For the i th and j th set of eigenvalues and eigenvectors, we can write

$$-\omega_i^2 [m] \{u\}_i + [k] \{u\}_i = \{0\}$$

$$-\omega_j^2 [m] \{u\}_j + [k] \{u\}_j = \{0\}$$

Multiplying the first equation by $\{u\}_j^T$ and the second equation by $\{u\}_i^T$, we obtain

$$-\omega_i^2 \{u\}_j^T [m] \{u\}_i + \{u\}_j^T [k] \{u\}_i = \{0\} \quad (5.17)$$

$$-\omega_j^2 \{u\}_i^T [m] \{u\}_j + \{u\}_i^T [k] \{u\}_j = \{0\} \quad (5.18)$$

Take the transpose of Equation 5.18,

$$-\omega_j^2 \{u\}_j^T [m]^T \{u\}_i + \{u\}_j^T [k]^T \{u\}_i = \{0\}$$

Since $[m]$ and $[k]$ are symmetric, $[m] = [m]^T$ and $[k] = [k]^T$, and

$$-\omega_j^2 \{u\}_j^T [m] \{u\}_i + \{u\}_j^T [k] \{u\}_i = \{0\} \quad (5.19)$$

⁸An example of a linear dependent equation is

$$\begin{bmatrix} 1 & 2 \\ 2 & 4 \end{bmatrix} \begin{Bmatrix} u_1 \\ u_2 \end{Bmatrix} = \begin{Bmatrix} 0 \\ 0 \end{Bmatrix}$$

or

$$u_1 + 2u_2 = 0$$

$$2u_1 + 4u_2 = 0$$

In this case, u_1 and u_2 need not be zeros. Instead, the equations are satisfied as long as $u_1 = 2u_2$. Therefore, there is an infinite number of solutions.

⁹An eigenvalue problem will be demonstrated in the next example.

Subtracting Equation 5.19 from Equation 5.17, we obtain

$$(\omega_j^2 - \omega_i^2)\{u\}_j^T[m]\{u\}_i = 0$$

If the eigenvalues are unique ($\omega_j^2 \neq \omega_i^2$), then

$$\{u\}_j^T[m]\{u\}_i = 0, \quad i \neq j$$

From Equation 5.19, similarly

$$\{u\}_j^T[k]\{u\}_i = 0, \quad i \neq j$$

That is, the eigenvectors are *orthogonal (or normal) to each other with respect to the mass and the stiffness matrices*. If the eigenvectors are normalized with respect to the mass matrix, Equation 5.19 with $i = j$ can be written as

$$-\omega_i^2\{u\}_i^T[m]\{u\}_i + \{u\}_i^T[k]\{u\}_i = \{0\}$$

and therefore

$$\{u\}_i^T[k]\{u\}_i = \omega_i^2$$

In summary, we just found that the eigenvectors have the following properties:

$$\{u\}_i^T[m]\{u\}_j = \begin{cases} 1, & i = j \\ 0, & i \neq j \end{cases}$$

and

$$\{u\}_i^T[k]\{u\}_j = \begin{cases} \omega_i^2, & i = j \\ 0, & i \neq j \end{cases}$$

If we construct a matrix composed of eigenvectors

$$[P] = [\{u\}_1 \quad \cdots \quad \{u\}_N] \quad (5.20)$$

we can write

$$[p]^T[m][p] = [I]$$

$$[p]^T[k][p] = \begin{bmatrix} \omega_1^2 & 0 & 0 \\ 0 & \ddots & 0 \\ 0 & 0 & \omega_N^2 \end{bmatrix} = \text{diag}(\omega^2)$$

where $[I]$ is the identity matrix and $[P]$ is called the *modal matrix*.

Now, let us return to our original equations of motion given by

$$[m]\{\ddot{x}(t)\} + [c]\{\dot{x}(t)\} + [k]\{x(t)\} = \{F(t)\}$$

We restrict our problem to the proportional damping case, where $[c]$ is a linear combination of $[m]$ and $[k]$:

$$[c] = \alpha[m] + \beta[k]$$

with constant α and β .

Let us define a new set of coordinates $\{z(t)\}$, so that

$$\{x(t)\} = [P]\{z(t)\} \quad (5.21)$$

where $[p]$ is the modal matrix defined in Equation 5.20. The equations of motion then become

$$[m][P]\{\ddot{z}(t)\} + [c][P]\{\dot{z}(t)\} + [k][P]\{z(t)\} = \{F(t)\}$$

Multiplying by $[P]^T$,

$$[P]^T[m][P]\{\ddot{z}(t)\} + [P]^T[c][P]\{\dot{z}(t)\} + [P]^T[k][P]\{z(t)\} = [P]^T\{F(t)\}$$

which reduces to

$$\{\ddot{z}(t)\} + (\alpha[I] + \beta \times \text{diag}(\omega^2))\{\dot{z}(t)\} + \text{diag}(\omega^2)\{z(t)\} = [P]^T\{F(t)\}$$

or

$$\begin{aligned} \ddot{z}_1(t) + (\alpha + \beta\omega_1^2)\dot{z}_1(t) + \omega_1^2 z_1(t) &= \{u\}_1^T\{F(t)\} \\ &\vdots \\ \ddot{z}_N(t) + (\alpha + \beta\omega_N^2)\dot{z}_N(t) + \omega_N^2 z_N(t) &= \{u\}_N^T\{F(t)\} \end{aligned}$$

It is clear now why proportional damping is considered. The damping matrix $[c]$ becomes diagonalized so that the equations of motion are *decoupled*. The coordinates $z_i(t)$ are called the *modal coordinates*, and $\{u\}_i^T\{F(t)\}$ are called the *modal forces*. We often let

$$(\alpha + \beta\omega_i^2) = 2\omega_i\zeta_i$$

$$\{u\}_i^T\{F(t)\} = q_i(t)$$

to simplify the equations to

$$\begin{aligned} \ddot{z}_1(t) + 2\omega_1\zeta_1\dot{z}_1(t) + \omega_1^2 z_1(t) &= q_1(t) \\ &\vdots \\ \ddot{z}_N(t) + 2\omega_N\zeta_N\dot{z}_N(t) + \omega_N^2 z_N(t) &= q_N(t) \end{aligned} \tag{5.22}$$

The solution to these equations can be obtained using the impulse response function and the convolution integral for each coordinate

$$z_i(t) = \int_{-\infty}^{\infty} g_i(\tau)g_i(t - \tau)d\tau, \quad i = 1, 2, \dots, N$$

where

$$g_i(t) = \begin{cases} \frac{1}{\omega_{d_i}} e^{-\zeta_i\omega_i t} \sin \omega_{d_i} t, & t \geq 0 \\ 0, & t < 0 \end{cases}$$

and

$$\omega_{d_i} = \omega_i \sqrt{1 - \zeta_i^2}$$

Once we find all the $z_i(t)$, we recover the physical coordinates by using the transformation in Equation 5.21 or

$$\{x(t)\} = [P]\{z(t)\}$$

5.5 Multi-Degree-of-Freedom: The Response to Random Loads

From the analysis of the Single-DoF system, we know that knowledge of the frequency response function $H(\omega)$ is crucial in obtaining the response statistics to random loads. For a system with more than one DoF, there is more than one frequency response function $H(\omega)$. For an N -DoF system, the frequency response functions will be given as an $N \times N$ symmetric matrix $\mathbf{H}(\omega)$.

In the single-DoF system, the response statistics were given in terms of the mean response μ_X and the spectral density of the response $S_{XX}(\omega)$. We will find here that the response statistics of an N -DoF system are given in terms of the mean response for each DoF, $\mu_{X_1}, \dots, \mu_{X_N}$, and a matrix of spectral densities of the response $\mathbf{S}(\omega)$, which is also of dimension $N \times N$.

We present *a priori* the results which are derived in the subsequent section; the mean response vector μ_X and the matrix spectral density of the output $\mathbf{S}_{XX}(\omega)$:

$$\begin{aligned}\mu_X &= \mathbf{H}_{XX}(0)\mu_F \\ \mathbf{S}_{XX}(\omega) &= \mathbf{H}_{XX}^*(\omega)\mathbf{S}_{FF}(\omega)\mathbf{H}_{XX}^T(\omega)\end{aligned}$$

Here, we will first obtain the frequency response function of a typical two-DoF system. We will then consider a two-DoF system subjected to a single random load. Finally, we will expand our analysis to an N -DoF system subjected to N random loads.

5.5.1 Response due to a Single Random Force

When a body vibrates, points on the body move relative to each other. To describe this relative motion of two points on a body subjected to random loading, we must know both their cross-spectral densities and cross-correlations, and also the spectral densities and the autocorrelation function of the individual motions of each point. This requirement is true even though there is only one force acting on the system. This is similar to the problem of the single mass loaded by two random loads.

Consider a body excited by a single randomly varying force $P(t)$ with autocorrelation $R_{TT}(\tau)$ and spectral density $S_{PP}(\omega)$. Owing to this loading, two points on the body have displacements $X(t)$ and $Y(t)$ with means μ_X and μ_Y , autocorrelations $R_{XX}(\tau)$ and $R_{YY}(\tau)$, and spectral densities $S_{XX}(\omega)$ and $S_{YY}(\omega)$, respectively. Note again that upper case letters are used to signify random processes.

We know the following from our earlier studies

$$E\{X(t)\} = H_{XP}(0)\mu_P$$

$$E\{Y(t)\} = H_{YP}(0)\mu_P$$

and

$$S_{XX}(\omega) = |H_{XP}(\omega)|^2 S_{PP}(\omega) \quad (5.23)$$

$$S_{YY}(\omega) = |H_{YP}(\omega)|^2 S_{PP}(\omega) \quad (5.24)$$

where

$$H_{XP}(\omega) = \int_{-\infty}^{\infty} g_{XP}(\tau) e^{-i\omega\tau} d\tau$$

$$H_{YP}(\omega) = \int_{-\infty}^{\infty} g_{YP}(\tau) e^{-i\omega\tau} d\tau$$

and

$$X(t) = \int_{-\infty}^{\infty} g_{XP}(\tau) P(t - \tau) d\tau$$

$$Y(t) = \int_{-\infty}^{\infty} g_{YP}(\tau) P(t - \tau) d\tau$$

With these relations, we can now find the expressions for the cross-correlation $R_{XY}(\tau)$ and cross-spectral density $S_{XY}(\omega)$. Using the definition of a cross-correlation function, we obtain

$$\begin{aligned} R_{XY}(\tau) &= E\{X(t)Y(t+\tau)\} = E\left\{\int_{-\infty}^{\infty} g_{XP}(\tau_1)P(t-\tau_1)d\tau_1 \int_{-\infty}^{\infty} g_{YP}(\tau_2)P(t+\tau-\tau_2)d\tau_2\right\} \\ &= \int_{-\infty}^{\infty} g_{XP}(\tau_1) \left[\int_{-\infty}^{\infty} g_{YP}(\tau_2) E\{P(t-\tau_1)P(t+\tau-\tau_2)\} d\tau_2 \right] d\tau_1 \\ &= \int_{-\infty}^{\infty} g_{XP}(\tau_1) \left[\int_{-\infty}^{\infty} g_{YP}(\tau_2) R_{PP}(\tau+\tau_1-\tau_2) d\tau_2 \right] d\tau_1 \end{aligned}$$

Even though we have an explicit expression, it is generally not easy to interpret.

The cross-spectral density can be derived by using the Fourier transform relation between $R_{XY}(\tau)$ and $S_{XY}(\omega)$. Thus,

$$\begin{aligned} S_{XY}(\omega) &= \frac{1}{2\pi} \int_{-\infty}^{\infty} R_{XY}(\tau) e^{-i\omega\tau} d\tau = \frac{1}{2\pi} \int_{-\infty}^{\infty} \int_{-\infty}^{\infty} g_{XP}(\tau_1) \int_{-\infty}^{\infty} g_{YP}(\tau_2) R_{PP}(\tau+\tau_1-\tau_2) d\tau_2 d\tau_1 e^{-i\omega\tau} d\tau \\ &= \frac{1}{2\pi} \int_{-\infty}^{\infty} g_{XP}(\tau_1) e^{+i\omega\tau_1} \int_{-\infty}^{\infty} g_{YP}(\tau_2) e^{-i\omega\tau_2} \int_{-\infty}^{\infty} R_{PP}(\tau+\tau_1-\tau_2) e^{-i\omega(\tau+\tau_1-\tau_2)} d\tau d\tau_2 d\tau_1 \end{aligned} \quad (5.25)$$

In order to integrate this last expression, it is easier to proceed by transforming the variables in the innermost integral according to

$$\lambda \equiv \tau + \tau_1 - \tau_2 \quad \text{and} \quad d\lambda = d\tau$$

where τ_1 and τ_2 are dummy variables. Then, Equation 5.25 becomes

$$\begin{aligned} S_{XY}(\omega) &= \frac{1}{2\pi} \int_{-\infty}^{\infty} g_{XP}(\tau_1) e^{+i\omega\tau_1} d\tau_1 \int_{-\infty}^{\infty} g_{YP}(\tau_2) e^{-i\omega\tau_2} d\tau_2 \int_{-\infty}^{\infty} R_{PP}(\lambda) e^{-i\omega\lambda} d\lambda \\ &= H_{XP}^*(\omega) H_{YP}(\omega) S_{PP}(\omega) \end{aligned} \quad (5.26)$$

Where points X and Y coincide, this result reduces to the classical fundamental relation $S_{XX}(\omega) = |H_{XP}|^2 S_{PP}(\omega)$.

Equation 5.23, Equation 5.24 and Equation 5.26 can be written in matrix form

$$\begin{bmatrix} S_{XX}(\omega) & S_{XY}(\omega) \\ S_{YX}(\omega) & S_{YY}(\omega) \end{bmatrix} = \begin{bmatrix} H_{XP}^*(\omega) \\ H_{YP}^*(\omega) \end{bmatrix} S_{PP}(\omega) \begin{bmatrix} H_{XP}(\omega) & H_{YP}(\omega) \end{bmatrix} \quad (5.27)$$

or

$$\begin{bmatrix} S_{XX}(\omega) & S_{XY}(\omega) \\ S_{YX}(\omega) & S_{YY}(\omega) \end{bmatrix} = \begin{bmatrix} H_{XP}^*(\omega) S_{XX}(\omega) H_{XP}(\omega) & H_{XP}^*(\omega) S_{XY}(\omega) H_{YP}(\omega) \\ H_{YP}^*(\omega) S_{YX}(\omega) H_{XP}(\omega) & H_{YP}^*(\omega) S_{YY}(\omega) H_{YP}(\omega) \end{bmatrix}$$

Example 5.5 Response Spectra for a Two-Degree-of-Freedom System Subjected to a Single Random Force

Consider the mass–spring–damper system shown in Figure 5.9. Assume that the random force $F_1(t)$ is a white noise random process with $S_{F_1 F_1}(\omega) = S_0$ and $F_2(t) = 0$. (i) Find the frequency response functions $H_{11}(\omega)$ and $H_{21}(\omega)$, and (ii) find the spectral densities $S_{X_1 X_1}(\omega)$, $S_{X_1 X_2}(\omega)$ and $S_{X_2 X_2}(\omega)$.

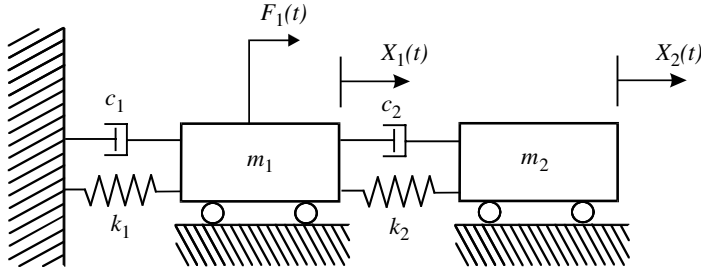


FIGURE 5.9 Two-DoF system excited by a single random force.

Solution

The equation of motion for this system has been obtained as Equation 5.14 with $F_2(t) = 0$. We found previously that the frequency response function for this system is given by

$$[H(\omega)] = \frac{1}{\det[Z]} \begin{bmatrix} -m_2\omega^2 + i\omega c_2 + k_2 & i\omega c_2 + k_2 \\ i\omega c_2 + k_2 & -m_1\omega^2 + i\omega(c_1 + c_2) + (k_1 + k_2) \end{bmatrix}$$

where

$$\det[Z] = \omega^4 m_1 m_2 - i\omega^3 (m_1 c_2 + c_1 m_2 + c_2 m_2) + i\omega (c_1 k_2 + k_1 c_2) - \omega^2 (m_1 k_2 + c_1 c_2 + k_1 m_2 + k_2 m_2) + k_1 k_2$$

Since $F_2 = 0$, the frequency response functions due to F_2 , $H_{12}(\omega)$ and $H_{22}(\omega)$, are zero. The frequency response functions due to F_1 are given by

$$H_{11}(\omega) = \frac{-m_2\omega^2 + i\omega c_2 + k_2}{\det[Z]}$$

$$H_{21}(\omega) = \frac{i\omega c_2 + k_2}{\det[Z]}$$

Using Equation 5.27, the response spectra are given by

$$S_{X_1 X_1}(\omega) = H_{11}^*(\omega) H_{11}(\omega) S_{F_1 F_1}(\omega) = S_0 \frac{(k_2 - m_2\omega^2)^2 + (\omega c_2)^2}{(\det[Z])^2}$$

$$S_{X_2 X_2}(\omega) = H_{22}^*(\omega) H_{22}(\omega) S_{F_1 F_1}(\omega) = S_0 \frac{k_2^2 + (\omega c_2)^2}{(\det[Z])^2}$$

$$S_{X_1 X_2}(\omega) = H_{11}^*(\omega) H_{21}(\omega) S_{F_1 F_1}(\omega) = S_0 \frac{(-m_2\omega^2 - i\omega c_2 + k_2)(i\omega c_2 + k_2)}{(\det[Z])^2}$$

$$S_{X_2 X_1}(\omega) = H_{21}^*(\omega) H_{11}(\omega) S_{F_1 F_1}(\omega) = S_0 \frac{(-m_2\omega^2 + i\omega c_2 + k_2)(-i\omega c_2 + k_2)}{(\det[Z])^2}$$

Note that $S_{X_2 X_1}(\omega) = S_{X_1 X_2}(-\omega) = S_{X_1 X_2}^*(\omega)$.

5.5.2 Response to Multiple Random Forces

Consider a multi-DoF system subjected to multiple random forces. The goal is to obtain the relation equivalent to Equation 5.27 for the general response for N DoF by first considering the response of a Single-DoF to N forces, and then generalizing to N DoF. This will be done in two ways. First, by extending the impulse-response method leading to the convolution integral, and then by utilizing the modal

analysis approach where the coupled physical equations of motion are decoupled in a new *modal* coordinate system.

5.5.3 Impulse-Response Approach

Let us start by expressing the response $X_k(t)$ using the impulse-response functions $g_{ki}(t)$. Recall that $g_{ki}(t)$ is the impulse response of mass m_k to force $F_i(t)$. By linear superposition, the total response $X_k(t)$ of mass m_k is equal to the sum of the individual responses to each of the N forces

$$X_k(t) = \sum_{i=1}^N X_{ki}(t) = \sum_{i=1}^N \int_{-\infty}^{\infty} g_{ki}(\tau) F_i(t - \tau) d\tau$$

Assuming that the forces are stationary with respective means μ_{F_i} and cross-correlations $R_{F_i F_j}(\tau)$, the mean and correlation of the response can be found as follows:

$$\begin{aligned} E\{X_k(t)\} &= \sum_{i=1}^N \int_{-\infty}^{\infty} g_{ki}(\tau) E\{F_i(t - \tau)\} d\tau \\ \mu_{X_k} &= \sum_{i=1}^N \mu_{F_i} \int_{-\infty}^{\infty} g_{ki}(\tau) d\tau = \sum_{i=1}^N \mu_{F_i} H_{ki}(0) \end{aligned}$$

In matrix form

$$\boldsymbol{\mu}_X = \mathbf{H}_{XX}(0) \boldsymbol{\mu}_F$$

This is a static response and, therefore, can be ignored here and added on at the end of the computations. We next evaluate the expressions for the response correlations and spectral densities, from which we can evaluate the mean-square response. By definition, the correlations are given by

$$\begin{aligned} R_{X_k X_j}(\tau) &= E\{X_k(t) X_j(t + \tau)\} = E\left\{ \sum_{m=1}^N X_{km}(t) \sum_{n=1}^N X_{jn}(t + \tau) \right\} \\ &= E\left\{ \sum_{m=1}^N \int_{-\infty}^{\infty} g_{km}(\zeta) F_m(t - \zeta) d\zeta \sum_{n=1}^N \int_{-\infty}^{\infty} g_{jn}(\xi) F_n(t + \tau - \xi) d\xi \right\} \\ &= \sum_{m=1}^N \sum_{n=1}^N \int_{-\infty}^{\infty} \int_{-\infty}^{\infty} g_{km}(\zeta) g_{jn}(\xi) E\{F_m(t - \zeta) F_n(t + \tau - \xi)\} d\zeta d\xi \\ &= \sum_{m=1}^N \sum_{n=1}^N \int_{-\infty}^{\infty} \int_{-\infty}^{\infty} g_{km}(\zeta) g_{jn}(\xi) R_{F_m F_n}(\tau - \xi + \zeta) d\zeta d\xi \end{aligned}$$

The response spectral density is by definition

$$S_{X_k X_j}(\omega) = \frac{1}{2\pi} \int_{-\infty}^{\infty} R_{X_k X_j}(\tau) \exp(-i\omega\tau) d\tau$$

Before substituting the correlation function into this equation, multiply it by $\exp(-i\omega[\zeta - \xi]) \times \exp(i\omega[\zeta - \xi])$. Also, define $\nu = \tau - \xi + \zeta$ with $d\nu = d\tau$. All of these manipulations allow us to put the spectral density in the following form:

$$\begin{aligned} S_{X_k X_j}(\omega) &= \sum_{m=1}^N \sum_{n=1}^N \int_{-\infty}^{\infty} g_{km}(\zeta) \exp(i\omega\zeta) d\zeta \int_{-\infty}^{\infty} g_{jn}(\xi) \exp(-i\omega\xi) d\xi \times \frac{1}{2\pi} \int_{-\infty}^{\infty} R_{F_m F_n}(\nu) \exp(-i\omega\nu) d\nu \\ &= \sum_{m=1}^N \sum_{n=1}^N H_{km}^*(\omega) H_{jn}(\omega) S_{F_m F_n}(\omega) \end{aligned}$$

where the star denotes complex conjugate. In matrix form

$$S_{X_k X_j}(\omega) = \mathbf{H}_k^*(\omega) \mathbf{S}_{FF}(\omega) \mathbf{H}_j^T(\omega) \quad (5.28)$$

In this notation, $\mathbf{H}_k^*(\omega)$ is a row vector of dimension $1 \times N$

$$\mathbf{H}_k^*(\omega) = [H_{k1}^*(\omega) \quad \cdots \quad H_{kN}^*(\omega)]$$

$\mathbf{H}_j^T(\omega)$ is a column vector of dimension $N \times 1$

$$\mathbf{H}_j^T(\omega) = \begin{bmatrix} H_{j1}(\omega) \\ \vdots \\ H_{jN}(\omega) \end{bmatrix}$$

and $\mathbf{S}_{FF}(\omega)$ is a matrix of dimension $N \times N$

$$\mathbf{S}_{FF}(\omega) = \begin{bmatrix} S_{F_1 F_1}(\omega) & \cdots & S_{F_1 F_N}(\omega) \\ \vdots & \ddots & \vdots \\ S_{F_N F_1}(\omega) & \cdots & S_{F_N F_N}(\omega) \end{bmatrix}$$

Equation 5.28 can now be generalized for any X_k and X_j

$$\mathbf{S}_{XX}(\omega) = \mathbf{H}^*(\omega) \mathbf{S}_{FF}(\omega) \mathbf{H}^T(\omega) \quad (5.29)$$

where

$$\mathbf{H}(\omega) = \begin{bmatrix} H_{11}(\omega) & \cdots & H_{1N}(\omega) \\ \vdots & \ddots & \vdots \\ H_{N1}(\omega) & \cdots & H_{NN}(\omega) \end{bmatrix}$$

and

$$\mathbf{S}_{XX}(\omega) = \begin{bmatrix} S_{X_1 X_1}(\omega) & \cdots & S_{X_1 X_N}(\omega) \\ \vdots & \ddots & \vdots \\ S_{X_N X_1}(\omega) & \cdots & S_{X_N X_N}(\omega) \end{bmatrix}$$

Let us recall Equation 5.6, Equation 5.9, and Equation 5.27. Equation 5.6 is the response spectral density of a single-DoF system to a single random force, Equation 5.9 is the response spectral density of a single-DoF system to two random forces, and Equation 5.27 is the response spectral densities of a two-DoF system due to a single force. Comparing them with Equation 5.29, we realize that they are all special cases of this equation.

For a zero mean, the mean-square response of the j th coordinate is given by the relation

$$\sigma_{X_j}^2 = \int_{-\infty}^{\infty} S_{X_j X_j}(\omega) d\omega \quad (5.30)$$

Example 5.6 Spacecraft Design Problem (based on Wirsching et al., p. 228)

A rocket mounting is to be designed. The rocket of mass $m_1 = 181$ kg is mounted on a supporting structure of mass $m_2 = 362$ kg using structural brackets that can be modeled as springs of constant $k = 1.40$ MN/m. There is also damping with coefficient $c = 3.50$ kNsec/m. When the engine fires, the thrust can be interpreted as being composed of a mean value thrust and a random fluctuating thrust.

The random variations are due to factors such as fluctuations in fuel mix and eccentricities in thrust direction. The mean thrust is given by $\mu_T = 16$ kN and the random component is given by T , which is a random function of time. T is characterized as white noise of intensity $1980 \text{ N}^2/\text{Hz}$ over the frequency range 0–50 Hz. The mean thrust can be viewed as a static load while the random thrust as the dynamic load.

The design must consider that components in the supporting structure will be damaged if the acceleration is too large. Also, the structural brackets will fail if the relative displacement between the rocket and the supporting structure is too large. Both these design issues are difficult because the input is random. Therefore, there is a trade-off between the cost of making a component stronger and making it more reliable. The probabilistic framework allows the analyst to quantitatively understand the trade-off.

Solution

The goal of the analysis is to determine the acceleration of the supporting mass \ddot{X}_2 and the relative displacement $Z = X_2 - X_1$.

First we solve the mean value problem. The mean value acceleration is

$$a = \frac{F}{m_1 + m_2} = \frac{16,000}{181 + 362} = 29.46 \text{ m/sec}^2 = \frac{29.46}{9.81} = 3.00g$$

The mean force in the bracket is found by applying the equation of motion to m_2

$$\mu_{F_b} = m_2 a_2 = 362 \times 29.46 = 10665 \text{ N} = 10.66 \text{ kN}$$

The mean bracket deflection is

$$\mu_Z = \frac{\mu_{F_b}}{k} = \frac{10.66 \times 10^3}{1.40 \times 10^6} = 7.61 \times 10^{-3} \text{ m} = 7.61 \text{ mm}$$

While the mean value is the single most important descriptor of randomness, the variance is important because it is a measure of the scatter of possible results. In order to calculate the variance, we need to derive the response spectral density and the frequency response function (see Equation 5.30). This we compute next. The equations of motion are given by

$$\begin{aligned} m_1 \ddot{X}_1 - k(X_2 - X_1) - c(\dot{X}_2 - \dot{X}_1) &= F(t) \\ m_2 \ddot{X}_2 + k(X_2 - X_1) + c(\dot{X}_2 - \dot{X}_1) &= 0 \end{aligned}$$

Given the problem statement, the variables of interest are (Z, X_2) . Transform variables using $Z = X_2 - X_1$. The equations of motion become

$$\begin{aligned} m_1 \ddot{X}_2 - m_1 \ddot{Z} - kZ - c\dot{Z} &= F(t) \\ m_2 \ddot{X}_2 + kZ + c\dot{Z} &= 0 \end{aligned}$$

To derive the frequency response function, assume harmonic excitation

$$\mathbf{F}(t) = \begin{bmatrix} F_0 \\ 0 \end{bmatrix} e^{i\omega t}$$

and harmonic response of the form

$$\begin{bmatrix} Z(t) \\ \ddot{X}_2 \end{bmatrix} = \begin{bmatrix} Z_0 \\ \ddot{X}_0 \end{bmatrix} e^{i\omega t}$$

Substitute these equations into the matrix equation of motion to find

$$\begin{aligned} m_1 \ddot{X}_0 + m_1 \omega^2 Z_0 - kZ_0 - i c \omega Z_0 &= F_0 \\ m_2 \ddot{X}_0 + kZ_0 + i c \omega Z_0 &= 0 \end{aligned}$$

The frequency response function is then found to be

$$\mathbf{H}(\omega) = \frac{1}{\Delta(\omega)} \begin{bmatrix} m_2 & -m_1 \\ -k - i c \omega & m_1 \omega^2 - k - i c \omega \end{bmatrix}$$

$$\Delta(\omega) = m_1 m_2 \omega^2 - k(m_1 + m_2) - i c \omega(m_1 + m_2)$$

There is only one applied force, and the spectral density function matrix is

$$\mathbf{S}_F(\omega) = \begin{bmatrix} S_0 & 0 \\ 0 & 0 \end{bmatrix}$$

Apply Equation 5.29 to find

$$\mathbf{S}_{XX}(\omega) = \begin{bmatrix} S_{ZZ} & S_{Z\ddot{X}} \\ S_{\ddot{X}Z} & S_{\ddot{X}\ddot{X}} \end{bmatrix} = \frac{S_0}{|\Delta(\omega)|^2} \begin{bmatrix} m_2^2 & -k m_2 + i c m_2 \omega \\ -k m_2 + i c m_2 \omega & k^2 + (c \omega)^2 \end{bmatrix}$$

To determine the root mean square of relative displacement $Z(t)$, note that the spectral density function of $Z(t)$ is the top term on the diagonal of $S_{XX}(\omega)$:

$$S_{ZZ}(\omega) = S_0 \frac{m_2^2}{|\Delta(\omega)|^2}$$

The mean-square value of $Z(t)$ is then

$$\sigma_Z^2 = \int_{-\infty}^{\infty} S_{ZZ}(\omega) d\omega = \frac{\pi S_0 m_2^2}{c k (m_1 + m_2)^2}$$

The above are for a two-sided spectrum. The given spectrum is one-sided, therefore, $S_0 = W_0/4\pi$. Then, with appropriate substitutions, we find $\sigma_Z \approx 0.212$ mm. In summary, the relative displacement has mean and root mean-square

$$\mu_Z = 7.61 \text{ mm}, \quad \sigma_Z = 0.212 \text{ mm}$$

The force in the spring has mean and root mean-square

$$\mu_{F_b} = k \mu_Z = 1.40 \times 10^6 \times 7.61 = 10.65 \text{ kN}$$

$$\sigma_{F_b} = k \sigma_Z = 1.40 \times 10^6 \times 0.212 = 0.297 \text{ kN}$$

Finally, the spectral density of the acceleration is the second diagonal term of $S_X(\omega)$:

$$S_{\ddot{X}\ddot{X}} = S_0 \frac{k^2 + (c \omega)^2}{|\Delta(\omega)|^2}$$

$$\sigma_{\ddot{X}}^2 = \int_{-\infty}^{\infty} S_{\ddot{X}\ddot{X}}(\omega) d\omega$$

and

$$\sigma_{\ddot{X}}^2 = \pi S_0 \left[\frac{k}{c(m_1 + m_2)^2} + \frac{c}{(m_1 + m_2)m_1 m_2} \right]$$

Upon making the appropriate substitutions, we find

$$\sigma_{\ddot{X}} = 0.852 \text{ m/sec}^2 = 0.087g$$

In summary, the mean and standard deviation of \ddot{X}_2 are

$$\mu_{\ddot{X}_2} = 3g, \quad \sigma_{\ddot{X}_2} = 0.087g$$

See Example 5.1 for a discussion on the above nonstandard integrals.

A designer would now use these mean and standard deviation numbers to decide how reliable to make the components. For example, if we assume that F_b and \ddot{X}_2 are normal density, we can specify a design based

on $\mu \pm 3\sigma$, which tells us the probability of exceeding this 6σ range is less than 0.1%. If this design is too expensive, then the designer will try a design based on $\mu \pm 3\sigma$, one that will have a higher probability of failure. In this way, a trade-off study is performed weighing cost against probability of failure. Figure 5.10 demonstrates a design based on 5% failure probability.

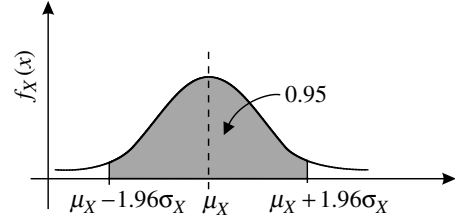


FIGURE 5.10 Normal density with 5% failure probability.

5.5.4 Modal Analysis Approach

The response of a multi-DoF discrete system loaded by random forces is generally a very complicated problem to formulate and solve. Here, to demonstrate one possible approach, we study the modal analysis of such a structure and work through some of the intricacies.

We will start the analysis at the point where the modal equations of motion have been formulated and the assumption of proportional damping has been made. From Equation 5.22, for a random vibration, the modal equations in indicial notation are

$$\ddot{Z}_i + 2\zeta_i\omega_i\dot{Z}_i + \omega_i^2 Z_i = Q_i(t), \quad i = 1, 2, \dots, N \quad (5.31)$$

where the parameters are familiar. We further assume that the modal forces $Q_i(t)$ are *ergodic* random excitations. The transformation between physical and modal spaces is

$$X_j(t) = \sum_{i=1}^N u_{ji} Z_i(t)$$

and the transformation between physical and modal forces is

$$Q_j(t) = \sum_{i=1}^N u_{ji} F_i(t) = \mathbf{u}_j^T \mathbf{F} \quad (5.32)$$

where \mathbf{u}_i is the modal vector for the i th DoF and

$$\mathbf{u}_i = \begin{bmatrix} u_{1i} \\ \vdots \\ u_{Ni} \end{bmatrix}$$

In matrix form, we can write

$$\mathbf{X} = \mathbf{PZ}$$

$$\mathbf{Q} = \mathbf{P}^T \mathbf{F}$$

where \mathbf{P} is the modal matrix given by

$$\mathbf{P} = [\mathbf{u}_1 \quad \cdots \quad \mathbf{u}_N]$$

For a two-DoF system, we can be specific

$$\begin{aligned} X_j(t) &= \sum_{i=1}^2 u_{ji} Z_i(t) = u_{j1} Z_1(t) + u_{j2} Z_2(t), \quad j = 1, 2 \\ Q_j(t) &= \sum_{i=1}^2 u_{ji} F_i(t) = u_{j1} F_1(t) + u_{j2} F_2(t), \quad j = 1, 2 \end{aligned} \quad (5.33)$$

for each DoF j of a two-DoF structure. Our goal in this analysis is to evaluate the statistics of the response, that is, to find autocorrelations and cross-correlations, $R_{X_k X_j}(\tau)$, and its Fourier transform, the power spectrum, $S_{X_k X_j}(\omega)$.

Begin with the definition of the autocorrelation and substitute Equation 5.33 for $X_j(t)$:

$$R_{X_k X_j}(\tau) = E\{X_j(t)X_j(t + \tau)\} = E\left\{\sum_{l=1}^n \sum_{m=1}^n u_{kl}u_{jm}Z_l(t)Z_m(t + \tau)\right\} \quad (5.34)$$

where $Z_i(t)$ is the solution to Equation 5.31:

$$Z_i(t) = \int_0^t Q_i(\tau)g_i(t - \tau)d\tau \quad (5.35)$$

$$g_i(\tau) = \frac{1}{\omega_{d_i}} \exp(-\zeta_i \omega_i \tau) \sin \omega_{d_i} \tau \quad (5.36)$$

$$\omega_{d_i} = \omega_i(1 - \zeta_i^2)^{1/2} \quad (5.37)$$

Note that, since the impulse response function $g(t)$ is zero for $t < 0$, the lower limit on the integral defining $Z(t)$ can be made $-\infty$ without changing the value of the integral.

Substituting Equation 5.35 to Equation 5.37 into Equation 5.34 and letting the expectation operate only on the stochastic terms, we have

$$R_{X_k X_j}(\tau) = \sum_{l=1}^n \sum_{m=1}^n \int_{-\infty}^{t+\tau} \int_{-\infty}^t u_{kl}u_{jm}E\{Q_l(\theta_1)Q_m(\theta_2)\}g_l(t - \theta_1)g_m(t + \tau - \theta_2)d\theta_1 d\theta_2 \quad (5.38)$$

where θ_1 and θ_2 are dummy time variables, and

$$R_{Q_l Q_m}(\theta_2 - \theta_1) = E\{Q_l(\theta_1)Q_m(\theta_2)\}$$

owing to the assumed ergodicity (and thus stationarity) of the forcing. If the system is lightly damped and has well-separated modal frequencies, as is the case in many engineering structures, the response due to $Q_l(t)$ is almost statistically independent of the response due to $Q_m(t)$. The cross-correlation terms that arise in Equation 5.38 are then almost zero, with the only nonzero terms arising for $m = l$:

$$R_{Q_l Q_l}(\theta_2 - \theta_1) = E\{Q_l(\theta_1)Q_l(\theta_2)\}$$

Now that we have the correlation function for the response in terms of the correlation function for the random forcing, we can proceed to evaluate the response spectral density, from which we can evaluate probabilities of occurrence. To do this, the following transformation of variables is first necessary:

$$\begin{aligned} u_1 &\equiv t - \theta_1, & u_2 &\equiv t + \tau - \theta_2, \\ du_1 &= -d\theta_1, & du_2 &= -d\theta_2 \end{aligned}$$

resulting in the response correlation

$$R_{X_k X_j}(\tau) = \sum_{l=1}^n \sum_{m=1}^n \int_{-\infty}^{\infty} \int_{-\infty}^{\infty} u_{kl}u_{jm}R_{Q_l Q_m}(u_1 - u_2 + \tau)g_l(u_1)g_m(u_2)du_1 du_2$$

The power spectral density for response $X(t)$ is equal to the Fourier transform of the correlation function

$$\begin{aligned} S_{X_k X_j}(\partial \varepsilon \omega) &= \frac{1}{2\pi} \int_{-\infty}^{\infty} R_{X_k X_j}(\tau) e^{-i\omega \tau} d\tau \\ &= \frac{1}{2\pi} \int_{-\infty}^{\infty} \left\{ \sum_{l=1}^n \sum_{m=1}^n \int_0^{\infty} \int_0^{\infty} u_{kl}u_{jm}R_{Q_l Q_m}(u_1 - u_2 + \tau)g_l(u_1)g_m(u_2)du_1 du_2 \right\} e^{-i\omega \tau} d\tau \end{aligned}$$

or, recalling and utilizing the assumption that the processes are ergodic, and, therefore, by averaging in time

$$S_{X_k X_j}(\omega) = \sum_{l=1}^n \sum_{m=1}^n u_{kl} u_{jm} \left\{ \lim_{T \rightarrow \infty} \frac{1}{2\pi} \int_{-T}^T g_l(u_1) du_1 \lim_{T \rightarrow \infty} \frac{1}{2\pi} \int_{-T}^T g_m(u_2) du_2 \right. \\ \left. \times \lim_{T \rightarrow \infty} \frac{1}{2\pi} \int_{-T}^T R_{Q_l Q_m}(u_1 - u_2 + \tau) e^{-i\omega\tau} d\tau \right\}$$

where the lower limits on the integrals were set to $-T$ since $g(t)$ is zero for $t < 0$, and thus the change in lower limit does not affect the values of the integrals. Using the change of variables

$$\gamma \equiv u_1 - u_2 + \tau, \quad d\gamma = d\tau$$

we obtain

$$S_{X_k X_j}(\omega) = \sum_{l=1}^n \sum_{m=1}^n u_{kl} u_{jm} \left\{ \lim_{T \rightarrow \infty} \frac{1}{2\pi} \int_{-T}^T g_l(u_1) \exp(i\omega u_1) du_1 \right. \\ \left. \times \lim_{T \rightarrow \infty} \frac{1}{2\pi} \int_{-T}^T g_m(u_2) \exp(-i\omega u_2) du_2 \lim_{T \rightarrow \infty} \frac{1}{2\pi} \int_{-T-u_2+u_1}^{T-u_2+u_1} R_{Q_l Q_m}(\gamma) e^{-i\omega\gamma} d\gamma \right\}$$

In the last integral, we make the physical argument that $R_{Q_l Q_m}(\gamma) \rightarrow 0$ as $|\gamma|$ increases and, therefore, the limits can be replaced by $-T$ and T , respectively.¹⁰ Then,

$$H_l(-\omega) = \lim_{T \rightarrow \infty} \frac{1}{2\pi} \int_{-T}^T g_l(u_1) \exp(i\omega u_1) du_1 \\ H_m(\omega) = \lim_{T \rightarrow \infty} \frac{1}{2\pi} \int_{-T}^T g_m(u_2) \exp(-i\omega u_2) du_2 \\ S_{Q_l Q_m}(\omega) = \lim_{T \rightarrow \infty} \frac{1}{2\pi} \int_{-T-u_2+u_1}^{T-u_2+u_1} R_{Q_l Q_m}(\gamma) e^{-i\omega\gamma} d\gamma$$

with the resulting response spectral density

$$S_{X_k X_j}(\omega) = \sum_{l=1}^n \sum_{m=1}^n u_{kl} u_{jm} H_l(-\omega) H_m(\omega) S_{Q_l Q_m}(\omega)$$

For a two-DoF system, we would have

$$S_{X_k X_j}(\omega) = \begin{bmatrix} u_{k1} & u_{k2} \end{bmatrix} \begin{bmatrix} H_1^*(\omega) & 0 \\ 0 & H_2^*(\omega) \end{bmatrix} \begin{bmatrix} S_{Q_1 Q_1}(\omega) & S_{Q_1 Q_2}(\omega) \\ S_{Q_2 Q_1}(\omega) & S_{Q_2 Q_2}(\omega) \end{bmatrix} \begin{bmatrix} H_1(\omega) & 0 \\ 0 & H_2(\omega) \end{bmatrix} \begin{bmatrix} u_{j1} \\ u_{j2} \end{bmatrix} \\ = u_{k1} u_{j1} H_1^*(\omega) H_1(\omega) S_{Q_1 Q_1}(\omega) + u_{k1} u_{j2} H_1^*(\omega) H_2(\omega) S_{Q_1 Q_2}(\omega) + u_{k2} u_{j1} H_2^*(\omega) H_1(\omega) S_{Q_2 Q_1}(\omega) \\ + u_{k2} u_{j2} H_2^*(\omega) H_2(\omega) S_{Q_2 Q_2}(\omega)$$

Suppose that we wish to find S_{XX} for a two-DoF system. Then

$$S_{XX} = \begin{bmatrix} u_{11} & u_{12} \\ u_{21} & u_{22} \end{bmatrix} \begin{bmatrix} H_1^*(\omega) & 0 \\ 0 & H_2^*(\omega) \end{bmatrix} \begin{bmatrix} S_{Q_1 Q_1}(\omega) & S_{Q_1 Q_2}(\omega) \\ S_{Q_2 Q_1}(\omega) & S_{Q_2 Q_2}(\omega) \end{bmatrix} \begin{bmatrix} H_1(\omega) & 0 \\ 0 & H_2(\omega) \end{bmatrix} \begin{bmatrix} u_{11} & u_{21} \\ u_{12} & u_{22} \end{bmatrix}$$

¹⁰Physically, we are stating that, as time difference (*trial mode*) increases, there will be an exponentially decaying correlation. This is borne out by experiments on physical systems.

In general, we can write

$$\mathbf{S}_{XX}(\omega) = \mathbf{P}\mathbf{H}^*(\omega)\mathbf{S}_{QQ}(\omega)\mathbf{H}(\omega)\mathbf{P}^T \quad (5.39)$$

where

$$\mathbf{H}(\omega) = \begin{bmatrix} H_1(\omega) & 0 & 0 \\ 0 & \ddots & 0 \\ 0 & 0 & H_N(\omega) \end{bmatrix}$$

$$H_i(\omega) = \frac{1}{-\omega^2 + i2\zeta_i\omega_i\omega + \omega_i^2}$$

The spectral densities of the modal forces $S_{Q_lQ_m}(\omega)$ can be obtained from $S_{FF}(\omega)$ using Equation 5.32. The autocorrelation $R_{Q_lQ_m}(\tau)$ is defined as

$$R_{Q_lQ_m}(\tau) = E\{Q_l(t)Q_m(t + \tau)\} = E\left\{\sum_{i=1}^N u_{il}F_i(t) \sum_{j=1}^N u_{jm}F_j(t + \tau)\right\} = \sum_{i=1}^N \sum_{j=1}^N u_{il}u_{jm}E\{F_i(t)F_j(t + \tau)\}$$

$$= \sum_{i=1}^N \sum_{j=1}^N u_{il}u_{jm}R_{F_iF_j}(\tau)$$

Taking the Fourier transform

$$S_{Q_lQ_m}(\omega) = \sum_{i=1}^N \sum_{j=1}^N u_{il}u_{jm}S_{F_iF_j}(\omega)$$

or

$$S_{Q_lQ_m}(\omega) = \mathbf{u}_l^T \mathbf{S}_{FF} \mathbf{u}_m$$

or

$$\mathbf{S}_{QQ}(\omega) = \mathbf{P}^T \mathbf{S}_{FF} \mathbf{P} \quad (5.40)$$

Substituting Equation 5.40 into Equation 5.39, we obtain

$$\mathbf{S}_{XX}(\omega) = \mathbf{P}\mathbf{H}^*(\omega)\mathbf{P}^T \mathbf{S}_{FF}(\omega)\mathbf{P}\mathbf{H}(\omega)\mathbf{P}^T$$

Comparing this result with Equation 5.29, we find that

$$\mathbf{H}_{XX}^*(\omega) = \mathbf{P}\mathbf{H}^*(\omega)\mathbf{P}^T$$

$$\mathbf{H}_{XX}(\omega) = \mathbf{P}\mathbf{H}(\omega)\mathbf{P}^T$$

which is a fully populated transfer function matrix of $X(t)$.

For lightly damped systems with well-spaced modal frequencies, the cross-terms in the double summation, those where $l \neq m$, contribute very little to the mean-square response given by $\int_{-\infty}^{\infty} S_{X_iX_j}(\omega)d\omega$. In this case, we can use the approximation

$$S_{X_iX_j}(\omega) \approx \sum_{l=1}^n u_{ji}^2 |\mathbf{H}_l(\omega)|^2 S_{Q_lQ_l}(\omega)$$

where

$$|H_l(\omega)|^2 = \left[\frac{1/\omega_l^2}{\sqrt{(1 - \omega^2/\omega_l^2)^2 + (2\zeta_l\omega/\omega_l)^2}} \right]^2$$

Suppose that we only account for the first three modes out of 1000 DoF. Then, the spectral density \mathbf{S}_{XX} based on three modes can be obtained by

$$\mathbf{S}_{XX}(\omega) = \mathbf{P}|_{1000 \times 3} \mathbf{H}^*(\omega)|_{3 \times 3} \mathbf{P}^T|_{3 \times 1000} \mathbf{S}_{FF}|_{1000 \times 1000} \mathbf{P}|_{1000 \times 3} \mathbf{H}(\omega)|_{3 \times 3} \mathbf{P}^T|_{3 \times 1000}$$

where

$$\mathbf{P}|_{1000 \times 3} = [\mathbf{u}_1 \quad \mathbf{u}_2 \quad \mathbf{u}_3]$$

$$\mathbf{H}(\omega)|_{3 \times 3} = \begin{bmatrix} H_1(\omega) & 0 & 0 \\ 0 & H_2(\omega) & 0 \\ 0 & 0 & H_3(\omega) \end{bmatrix}$$

Thus, we can easily see that the modal approach allows the analyst and designer to retain only those modes that are key to the problem at hand. If, as above, a thousand-DoF system can be adequately modeled as a three-DoF system because that is where all the energy is located, then a great deal of unnecessary computation is avoided.

5.6 Continuous System Random Vibration

Continuous models of vibrating systems are viewed as more realistic because the structural properties are distributed rather than being concentrated at discrete points. The price to pay for increased realism is increased complexity. The governing equations of motion go from being ordinary differential equations for the discrete models, to partial differential equations for the continuous ones, since displacement is a function of both time and position. For our elementary applications, deriving and solving the partial differential equations does not pose a great challenge. But, when we need to model nonuniform structures with varying cross sections and material properties, approximate techniques will be needed. Here our introduction to continuous systems will focus on strings and vibrating beams. These are found in most structures and machines, and understanding how they behave is of great use to modeling more complex systems. We will approach these studies using the direct and modal solutions.

5.6.1 Transverse Vibration of Beams

Begin with the equation of motion of a damped, forced, simply-supported beam with uniform properties

$$EI \frac{\partial^4 y}{\partial x^4} + c \frac{\partial y}{\partial t} + m \frac{\partial^2 y}{\partial t^2} = p(x, t) \quad (5.41)$$

where it is assumed the natural frequencies and the mode shapes have already been evaluated. To solve this problem, we will use the normal mode method, which depends on the modal orthogonality properties. First, expand the applied force $p(x, t)$ in terms of the modes,¹¹ then do the

¹¹The modes $Y_j(x)$ are the eigenfunctions of the problem

$$EI \frac{\partial^4 y}{\partial x^4} + m \frac{\partial^2 y}{\partial t^2} = 0$$

That is, they satisfy

$$EI \frac{d^4 Y_j}{dx^4} - \omega^2 m Y_j = 0, \quad j = 1, 2, \dots$$

and the boundary conditions at hand.

same with the structural displacement

$$p(x, t) = \sum_{j=1}^{\infty} p_j(t) Y_j(x)$$

Multiply both sides of this equation by $mY_k(x)$ and then integrate over the beam span

$$\int_0^L mp(x, t) Y_k(x) dx = \sum_{j=1}^{\infty} p_j(x, t) \int_0^L mY_j(x) Y_k(x) dx$$

On the right-hand side of this equation, we note that, by the orthogonality properties of the modes, the integral equals zero for $k \neq j$, and otherwise is normalized to 1 for $k = j$. Therefore, we are left with

$$\int_0^L mp(x, t) Y_j(x) dx = p_j(t) \quad (5.42)$$

Apply the same procedure to the response

$$y(x, t) = \sum_{j=1}^{\infty} y_j(t) Y_j(x) \quad (5.43)$$

and multiply and integrate as above to find

$$\int_0^L my(x, t) Y_j(x) dx = y_j(t)$$

$y(x, t)$ can be differentiated with respect to x and t so that all the terms in the equation of motion (Equation 5.41) can be put into the modal expansion form

$$\sum_{j=1}^{\infty} \left[EI y_j(t) \frac{d^4 Y_j}{dx^4} + c \frac{dy_j}{dt} Y_j + m \frac{d^2 y_j}{dt^2} Y_j \right] = \sum_{j=1}^{\infty} p_j(t) Y_j(x) \quad (5.44)$$

We know that the modes are defined by and satisfy the equation $EI d^4 Y_j/dx^4 = \omega_j^2 m Y_j$. Substituting this relation into Equation 5.44 leads to

$$\sum_{j=1}^{\infty} [\omega_j^2 m y_j(t) + c \dot{y}_j(t) + m \ddot{y}_j(t) - p_j(t)] Y_j(x) = 0$$

Since the eigenfunctions $Y_j(x)$ are not zero except for unrestrained motion, the expression in the square brackets must vanish for every j ,

$$\ddot{y}_j(t) + \frac{c}{m} \dot{y}_j(t) + \omega_j^2 y_j(t) = \frac{1}{m} p_j(t), \quad j = 1, 2, \dots \quad (5.45)$$

As for single-DoF systems, let $c/m = 2\zeta_j \omega_j$, that is,

$$\zeta_j = \frac{c}{2m\omega_j}$$

Equation 5.52 is the damped, forced, harmonic oscillator, with the well-known convolution solution,

$$\eta_j(t) = \frac{1}{m} \int_0^t p_j(\tau) g_j(t - \tau) d\tau \quad (5.46)$$

where $g_j(t)$ is the impulse response function for a damped oscillator. Once solved, $y_j(t)$ is substituted into the expansion equation

$$y(x, t) = \sum_{j=1}^{\infty} y_j(t) Y_j(x) = \frac{1}{m} \sum_{j=1}^{\infty} Y_j(x) \int_0^t p_j(\tau) g_j(t - \tau) d\tau$$

and substituting Equation 5.42 for $p_j(t)$ results in

$$y(x, t) = \sum_{j=1}^{\infty} Y_j(x) \int_0^t \left[\int_0^L p(\xi, t - \tau) Y_j(\xi) d\xi \right] g_j(t - \tau) d\tau \quad (5.47)$$

This is the complete steady-state time-domain solution.

5.6.2 Random Transverse Vibration

Assume that the loading $P(x, t)$ is random and represents an ensemble of functions of space and time. We need only the first two statistics of the load to proceed with the analysis of the response. Its mean value is denoted

$$E\{P(x, t)\} = \mu_p(x, t)$$

with autocorrelation

$$E\{P(x_1, t_1)P(x_2, t_2)\} = R_{pp}(x_1, x_2; t_1, t_2)$$

These statistics are available through data-gathering experiments performed on the loading to be experienced by the structure. Our goal in this analysis is to derive the statistics for the response, μ_Y and R_{YY} , which are functions of the statistics of the loading and the structural parameters.

For steady-state vibration problems, we may reasonably assume that the statistics of the loading are stationary. Begin with Equation 5.47 but now, for random loading $P(x, t)$

$$y(x, t) = \sum_{j=1}^{\infty} Y_j(x) \int_0^t \left[\int_0^L P(\xi, t - \tau) Y_j(\xi) d\xi \right] g_j(\tau) d\tau$$

where the shift τ has been placed within $p(x, t)$ and take the expectation of both sides

$$E\{Y(x, t)\} = \sum_{j=1}^{\infty} Y_j(x) \int_0^t \left[\int_0^L E\{P(\xi, t - \tau)\} Y_j(\xi) d\xi \right] g_j(\tau) d\tau$$

The impulse response function is $g(t)$, and for stationary loading, the expected value is a constant, $E\{P(\xi, t - \tau)\} = \mu_p(\xi)$. In order to simplify the following analysis, we assume that the loading has zero mean. This does not overly simplify the problem since a nonzero mean can be introduced later by simply shifting the response by the (constant) mean value. For zero mean loading, $\mu_p(x) = 0$, and the response is also zero mean, $E\{Y(x, t)\} = \mu_Y = 0$.

We need to relate the autocorrelation of the response to that for the loading. Begin with Equation 5.42:

$$\begin{aligned} R_{p_j p_k}(t_1, t_2) &= E\{P_j(t_1)P_k(t_2)\} = m^2 \int_0^L \int_0^L E\{P(x_1, t_1)P(x_2, t_2)\} Y_j(x_1)Y_k(x_2) dx_1 dx_2 \\ &= m^2 \int_0^L \int_0^L R_{pp}(x_1, x_2; t_1, t_2) Y_j(x_1)Y_k(x_2) dx_1 dx_2 \end{aligned} \quad (5.48)$$

where, for a stationary loading, $R_{pp}(x_1, x_2; t_1, t_2) = R_{pp}(x_1, x_2; \tau)$, where $\tau = t_2 - t_1$ and therefore, $R_{p_j p_k}(t_1, t_2) = R_{p_j p_k}(\tau)$. Using Equation 5.43, the response autocorrelation is

$$\begin{aligned} R_{YY}(x_1, x_2; t_1, t_2) &= E\{Y(x_1, t_1)Y(x_2, t_2)\} = \sum_{j=1}^{\infty} \sum_{k=1}^{\infty} E\{Y_j(t_1)Y_k(t_2)\} Y_j(x_1)Y_k(x_2) \\ &= \sum_{j=1}^{\infty} \sum_{k=1}^{\infty} R_{Y_j Y_k}(t_1, t_2) Y_j(x_1)Y_k(x_2) \end{aligned}$$

where, using Equation 5.46, with upper and lower limits extended to $\pm\infty$ without changing the final value of the integral due to the fact that the impulse response is zero outside the original limits

$$\begin{aligned} R_{Y_j Y_k}(t_1, t_2) &= \frac{1}{m^2} E \left\{ \int_{-\infty}^{\infty} P_j(t_1 - \theta) g_j(\theta) d\theta \int_{-\infty}^{\infty} P_k(t_2 - \kappa) g_k(\kappa) d\kappa \right\} \\ &= \frac{1}{m^2} \int_{-\infty}^{\infty} \int_{-\infty}^{\infty} E \{ P_j(t_1 - \theta) P_k(t_2 - \kappa) \} g_j(\theta) g_k(\kappa) d\theta d\kappa \\ &= \frac{1}{m^2} \int_{-\infty}^{\infty} \int_{-\infty}^{\infty} R_{P_j P_k}(t_1 - \theta, t_2 - \kappa) g_j(\theta) g_k(\kappa) d\theta d\kappa \end{aligned}$$

Since $P(x, t)$ is stationary, $R_{P_j P_k}(t_1 - \theta, t_2 - \kappa) = R_{P_j P_k}(t_2 - t_1 + \theta - \kappa)$ and $R_{Y_j Y_k}(t_1, t_2) = R_{Y_j Y_k}(t_2 - t_1)$. Therefore,

$$R_{Y_j Y_k}(t_1, t_2) = \frac{1}{m^2} \int_{-\infty}^{\infty} \int_{-\infty}^{\infty} R_{P_j P_k}(t_2 - t_1 + \theta - \kappa) g_j(\theta) g_k(\kappa) d\theta d\kappa \quad (5.49)$$

and

$$R_{YY}(x_1, x_2; t_2 - t_1) = \sum_{j=1}^{\infty} \sum_{k=1}^{\infty} R_{Y_j Y_k}(t_2 - t_1) Y_j(x_1) Y_k(x_2)$$

This last equation is a relation between the forcing and response autocorrelations. The spectral density of the response, $S_{YY}(\omega)$, is given by the Fourier transform of $R_{YY}(\tau)$

$$S_{YY}(\omega) = \sum_{j=1}^{\infty} \sum_{k=1}^{\infty} \left[\int_{-\infty}^{\infty} R_{Y_j Y_k}(\tau) e^{-i\omega\tau} d\tau \right] Y_j(x_1) Y_k(x_2) \quad (5.50)$$

where $\tau = t_2 - t_1$, and the term in the square brackets equals $S_{Y_j Y_k}(\omega)$, which now needs to be evaluated in terms that have already been derived.

By definition, we know the Fourier transform relation

$$S_{Y_j Y_k}(\omega) = \int_{-\infty}^{\infty} R_{Y_j Y_k}(\tau) e^{-i\omega\tau} d\tau$$

We can evaluate $R_{Y_j Y_k}$ by beginning with Equation 5.49

$$R_{Y_j Y_k}(\tau) = \frac{1}{m^2} \int_{-\infty}^{\infty} \int_{-\infty}^{\infty} R_{P_j P_k}(\tau + \theta - \kappa) g_j(\theta) g_k(\kappa) d\theta d\kappa$$

Take the Fourier transform of both sides, letting $\lambda = \tau + \theta - \kappa$, to find

$$S_{Y_j Y_k}(\omega) = \int_{-\infty}^{\infty} e^{-i\omega(\lambda - \theta + \kappa)} \frac{1}{m^2} \left[\int_{-\infty}^{\infty} \int_{-\infty}^{\infty} R_{P_j P_k}(\lambda) g_j(\theta) g_k(\kappa) d\theta d\kappa \right] d\lambda \quad (5.51)$$

where τ has been replaced by $\lambda - \theta + \kappa$ and $d\tau$ by $d\lambda$. Rewrite Equation 5.51 in a more useful form by separating the integrals according to dummy variables

$$S_{Y_j Y_k}(\omega) = \frac{1}{m^2} \int_{-\infty}^{\infty} g_j(\theta) e^{i\omega\theta} d\theta \int_{-\infty}^{\infty} g_k(\kappa) e^{-i\omega\kappa} d\kappa \int_{-\infty}^{\infty} R_{P_j P_k}(\lambda) e^{-i\omega\lambda} d\lambda \quad (5.52)$$

The Fourier transform of the impulse response function $g(t)$ is the frequency response function $H(\omega)$. Therefore, Equation 5.52 becomes

$$S_{Y_j Y_k}(\omega) = \frac{1}{m^2} H_j^*(\omega) H_k(\omega) S_{P_j P_k}(\omega) \quad (5.53)$$

where $H_j(\omega) = [\omega_j^2 - \omega^2 + 2\zeta_j\omega_j\omega]^{-1}$ and $S_{p_j p_k}(\omega)$, the spectral density of the modal force components, is derived assuming that the Fourier transform for $P_j(t)$ exists, as it does for most physical processes

$$P_j(t) = \frac{1}{2\pi} \int_{-\infty}^{\infty} P_j(\omega) e^{i\omega t} d\omega$$

Take the Fourier transform of Equation 5.48, to find

$$S_{p_j p_k}(\omega) = m^2 \int_0^L \int_0^L S_{pp}(\omega) Y_j(x_1) Y_k(x_2) dx_1 dx_2 \quad (5.54)$$

where $S_{pp}(\omega)$ is the spectral density of the loading, a quantity that is estimated from data. Substituting Equation 5.54 into Equation 5.53, we now have the expression for $S_{Y_j Y_k}(\omega)$, which can be substituted into Equation 5.50, resulting in

$$S_{YY}(x_1, x_2; \omega) = \frac{1}{m^2} \sum_{j=1}^{\infty} \sum_{k=1}^{\infty} H_j^*(\omega) H_k(\omega) S_{p_j p_k}(\omega) Y_j(x_1) Y_k(x_2)$$

One value of having such an equation is that the mean-square displacement can be evaluated

$$Y_{MS}(x) = R_{YY}(x, x; 0) = \int_{-\infty}^{\infty} S_{YY}(x, x; \omega) d\omega$$

Recall that if $\mu_Y(x) = 0$ then $Y_{MS}(x) = \sigma_Y^2(x)$, the variance.

The derivations are now complete, but what do they mean and what do they do for us? One of the functions of a probabilistic analysis is to help us bound our uncertainties so that we can understand how randomness in the forcing results in a scatter of possible structural responses. Furthermore, this scatter is not haphazard, but is defined by a standard deviation and possibly a density function. It is the variance that is used to bound the mean-value response.

Nomenclature

Symbol	Quantity	Symbol	Quantity
$E\{\cdot\}$	mathematical expectation	$\{u\}_i$	structural mode
$H(\omega)$	frequency response function	W_0	one-sided spectral density
$R_{XX}(\tau)$	autocorrelation function	$z(t)$	modal coordinates
$R_{XY}(\tau)$	cross-correlation function	μ	mean value (first moment)
$S_{XX}(\omega)$	power spectral density	σ^2	variance (second moment)
$S_{XY}(\omega)$	power cross-spectral density		

Acknowledgments

I am pleased to acknowledge my collaboration over the past few years with Dr. Seon Mi Han of Wood-Hole Oceanographic Institute. Seon has had input to this document and has prepared the figures. It is also a great pleasure to acknowledge the support provided by the Office of Naval Research and by our program manager Dr. Thomas Swean under Grant No. N00014-97-10017. Finally, I appreciate the invitation by Professor Clarence W. de Silva to prepare this chapter.

Bibliography

The discipline of random vibration includes thousands of references. Applications include wind and earthquake engineering, aerospace engineering, and ocean engineering to name the broad areas.

More recently, applications in materials engineering and biomechanical engineering have also broadened to include random effects. Therefore, we provide here a brief list of references.

- Augusti, G., Baratta, A., and Casciati, F. 1984. *Probabilistic Methods in Structural Engineering*, Chapman & Hall, London.
- Benaroya, H. 1998. *Mechanical Vibration: Analysis, Uncertainties, and Control*, Prentice Hall, Upper Saddle River, NJ.
- Bolotin, V.V. 1969. *Statistical Methods in Structural Mechanics*, Holden-Day, San Francisco, CA.
- Bolotin, V.V. 1984. *Random Vibrations of Elastic Systems*, Martinus Nijhoff, The Hague.
- Dimentberg, M.F. 1988. *Statistical Dynamics of Nonlinear and Time-Varying Systems*, Research Studies Press, England.
- Ibrahim, R.A. 1985. *Parametric Random Vibration*, Research Studies Press, England.
- Lin, Y.K. 1976. *Probabilistic Theory of Structural Dynamics*, Krieger, Malabar, FL.
- Madsen, H.O., Krenk, S., and Lind, N.C. 1986. *Methods of Structural Safety*, Prentice Hall, Englewood Cliffs, NJ.
- To, C.W.S. 2000. *Nonlinear Random Vibration: Analytical Techniques and Applications*, Swets & Zeitlinger, Lisse, The Netherlands.
- Vanmarcke, E. 1983. *Random Fields: Analysis and Synthesis*, MIT Press, Cambridge, MA.
- Wirsching, P.H., Paez, T.L., and Ortiz, K. 1995. *Random Vibrations: Theory and Practice*, Wiley-Interscience, New York.

II

Computer Techniques

6

Numerical Techniques

6.1	Introduction	6-1
6.2	Single-Degree-of-Freedom System	6-2
	Forced Single-Degree-of-Freedom System • Summary of Single-Degree-of-Freedom System	
6.3	Systems with Two or More Degrees of Freedom	6-8
	Example • Summary of Two-Degree-of-Freedom System	
6.4	Finite Difference Method for a Continuous System	6-11
	Bar • Beam • Summary of Finite Difference Methods for a Continuous System	
6.5	Matrix Methods	6-14
	Example: Three-Degree-of-Freedom System • Bisection Method • Directly Calculating the Eigenvalues and Eigenvectors from the Matrix Equation • Summary of Matrix Methods	
6.6	Approximation Methods for the Fundamental Frequency	6-18
	Rayleigh Method • Dunkerley's Formula • Summary of Approximations for the Fundamental Frequency	
6.7	Finite Element Method	6-20
	Bar Element • Beam • Summary of Finite Element Method	
	Appendix 6A Introduction to MATLAB®	6-24

Marie D. Dahleh
Harvard University

Summary

This chapter gives an overview of numerical techniques for vibration analysis. The centered difference approximation for the first, second, and fourth derivative are given. These form the basis for the finite difference approximation of both spring–mass systems and the continuous problem. The fourth-order Runge–Kutta method is presented. Both of these approaches are used to solve the single-degree-of-freedom (single-DoF) system. In order to demonstrate these techniques for the multiple-degree-of-freedom (multi-DoF) system a two-degree-of-freedom (two-DoF) system is explored. Finite element and finite difference methods are presented as solution techniques for the continuous problem (also see Chapter 9). The bar and beam are used for examples. The Rayleigh method and Dunkerley's formula are presented. These are methods for computing the fundamental frequency.

6.1 Introduction

This chapter presents numerical techniques for three classes of vibration problems; the single spring mass, the multiple spring mass, and the continuous model. The simplest oscillatory problem results when the problem can be modeled by the single spring–mass system. This system is modeled by a second-order constant coefficient differential equation, which can be solved analytically when either there is no forcing, or the forcing is harmonic. When the forcing is not harmonic, the finite difference method can be used to

solve this second-order equation or to solve the system of first-order equations, which is equivalent to the second-order equation. A larger computational problem arises when there are multiple springs and masses subjected to nonharmonic forcing. Again, the finite difference method can be used to compute the full solution. It is not always necessary to compute the full solution. Often, all that is needed is the fundamental frequency. This can be computed from the eigenvalues of a matrix problem. Both the numerical solution to the full problem and the matrix problem will be discussed. Finally, one may want to look at the vibration of a continuous element like a beam. Here, both the finite difference method and the finite element method will be discussed.

6.2 Single-Degree-of-Freedom System

The simple undamped spring–mass system oscillates with a frequency known as the natural frequency. The natural frequency is determined by the spring constant and the mass in the following way, $\omega = \sqrt{k/m}$. This relationship is derived by applying Newton's second law to the basic spring–mass system. The resulting equation is given by $m\ddot{x} = -kx$. The solution to this equation is harmonic with the frequency specified by the expression $\omega = \sqrt{k/m}$.

A more realistic vibration model of a simple oscillatory system includes a mass, a spring and a damper (see Figure 6.1). For simplicity, the mass is concentrated at the center of mass of the object, the spring is assumed to be of negligible mass, and, for the purposes of this discussion, the damping will be modeled by viscous damping. This is described by a force proportional to the velocity, denoted by \dot{x} . In the case of no external forcing, the system can be described by the following equation:

$$m\ddot{x} + c\dot{x} + kx = 0$$

where m , c , and k are constants and m is the mass, c is the damping coefficient, and k is the spring constant. This equation can be solved analytically by assuming a solution of the form

$$x = e^{st}$$

where s is a constant. Substitution into the differential equation yields the following quadratic equation:

$$(ms^2 + cs + k)e^{st} = 0$$

This equation is satisfied for all values of t when the following quadratic equation, known as the characteristic equation, is satisfied:

$$s^2 + \left(\frac{c}{m}\right)s + \frac{k}{m} = 0$$

The characteristic equation has two roots

$$s_1 = -\frac{c}{2m} + \sqrt{(c/2m)^2 - (k/m)}$$

and

$$s_2 = -\frac{c}{2m} - \sqrt{(c/2m)^2 - (k/m)}$$

The general solution is

$$x = A e^{s_1 t} + B e^{s_2 t}$$

The constants A and B are determined by the initial conditions $x(0)$ and $\dot{x}(0)$. The single spring–mass system exhibits three types of behavior, overdamped, underdamped and critically damped.

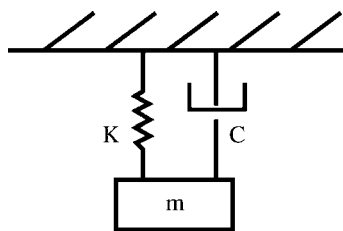


FIGURE 6.1 Single spring–mass system.

The overdamped state exists when k/m is larger than $(c/2m)^2$. No oscillations exist in this state. The underdamped case is oscillatory and results when $(c/2m)^2$ is larger than k/m . The limiting case between oscillatory and nonoscillatory motion occurs when $(c/2m)^2 = k/m$. When this condition is met, the system is said to be critically damped.

The next level of complexity results when the system is forced harmonically. The following equation serves as a model for this system:

$$m\ddot{x} + c\dot{x} + kx = F \sin \omega t$$

The solution of this equation is found by first computing the complementary function, which is the solution of the homogeneous equation discussed above, and then the particular solution. The details for computing a particular solution can be found in books on differential equations or mechanical vibrations (Thomson and Dahleh, 1998).

6.2.1 Forced Single-Degree-of-Freedom System

In general, when the oscillatory system is forced in a nonharmonic way, the resulting differential equation cannot be solved in closed form, and numerical methods must be employed to predict the behavior of the system. In this section, we consider two finite difference methods chosen for their simplicity. For a more detailed discussion of numerical methods for ordinary differential equations see Atkinson (1978) and Isaacson (1966).

The spring–mass system that is subjected to general forcing, $F(x, \dot{x}, t)$, can be modeled by the following differential equation:

$$m\ddot{x} + c\dot{x} + kx = f(x, \dot{x}, t)$$

$$x_0 = x(0)$$

$$\dot{x}_0 = \dot{x}(0)$$

where m , c , and k are constants and F is an arbitrary function. The two initial conditions, x_0 and \dot{x}_0 , are known.

In the first method, the second-order equation is integrated without change in form; in the second method, the second-order equation is rewritten as a system of two first-order equations and then the system of equations is integrated. Both methods approximate the first and second derivatives with the centered difference approximation for the derivatives. Finite difference methods are based on the Taylor expansion. The centered difference method for the first and second derivative results from a combination of the forward and backward Taylor expansion about the point x_i . To get the forward expansion, one writes the Taylor expansion for x_{i+1} . Similarly, the backward expression is obtained from the Taylor expansion about x_{i-1} . These are given by

$$x_{i+1} = x_i + h\dot{x}_i + \frac{h^2}{2}\ddot{x}_i + \frac{h^3}{6}\ddot{x}_i + \dots$$

$$x_{i-1} = x_i - h\dot{x}_i + \frac{h^2}{2}\ddot{x}_i - \frac{h^3}{6}\ddot{x}_i + \dots$$

where $h = \Delta t$. A second-order approximation is one which matches the Taylor expansion exactly up to and including terms of order h^2 ; that is, to determine a second-order expansion one neglects terms of order h^3 and higher. A second-order approximation for the first derivative is obtained by subtracting the backward difference from the forward difference. The resulting centered difference approximation is given by

$$\dot{x}_i = \frac{1}{2h}(x_{i+1} - x_{i-1}) - \frac{h^2}{6}\ddot{x}_i + \dots$$

Errors result when this expression is truncated after the first term. These errors depend on h^2 and the third derivative of x_i . If the error in the computed derivative is larger than order h^2 it may well arise from the neglected third derivative term.

The centered difference approximation for the second derivative is found by adding the forward and backward difference expansions and ignoring terms of order h^4 and higher. The resulting approximation is

$$\ddot{x}_i = \frac{1}{h^2}(x_{i-1} - 2x_i + x_{i+1}) + \frac{h^2}{12}x^{iv} + \dots$$

The truncation error that occurs for this expression depends on h^2 and the fourth derivative of x_i . Both the first and second derivative centered difference approximations are order h^2 . They can be used together to create a second-order approximation to a second-order ordinary differential equation such as that describing the spring–mass system.

6.2.1.1 Centered Difference Approximation

After substituting these two centered difference approximations into the differential equation and rearranging terms, one gets the following recurrence relation for the single spring–mass system:

$$x_{i+1} = h^2 f(x_i, t_i) - (fh^2 - 2m)x_i - (m - ch/2)x_{i-1}$$

with the initial conditions

$$x_0 = x(0)$$

$$\dot{x}_0 = \dot{x}(0)$$

The recurrence relation should be used to compute all values of x from the initial condition. By letting $i = 1$ in the recurrence relation, we get

$$x_2 = h^2 f(x_1, t_1) - (kh^2 - 2m)x_1 - (m - ch/2)x_0$$

In order to compute x_2 , both x_0 and x_1 are needed. The initial conditions provide x_0 . However, to start the calculation, we need an additional equation for x_1 . This equation is derived by substituting $i = 0$ into the Taylor expansion for x_{i+1} , using the initial conditions and ignoring terms of order h^2 and higher. Since the centered difference approximation is of order h^2 , it is consistent to compute x_1 with an error of order h^2 . For the point $i = 0$, the forward difference is given by

$$x_1 = x_0 + h\dot{x}_0$$

This equation allows one to find x_1 in terms of the two initial conditions, after which the recurrence relation can be used to find all subsequent discrete values of x .

6.2.1.2 Pseudocode for Centered Difference Approximation

The following is an example of the MATLAB[®] routine for the solution to the centered difference approximation of the general single-DoF spring–mass equations. The function f needs to be specified in a separate function file:

```
%initial conditions (index has to start at 1)
x(1) = x0
xd = x'0
%specify a time step
h = H
%specify the constants m, k, c.
m = M
k = K
c = C
%compute x(2) from the Taylor expansion
x(2) = x(1) + h * xd
%specify the total number of steps
TEND = tfinal
```

```

%compute the solution for all remaining times using the recurrence relation
t(1) = h
t(2) = 2 * h
for I = 3:TEND
Xi = h2 * f(xi-1, ti-1) - (k * h2 - 2 * m) * xi-1 - (m - c * h/2) * xi-2
T(i) = t(I - 1) + h
end

```

The method just presented has ignored terms of order h^2 and higher. This is known as the truncation error. The calculation will contain other errors such as round-off error due to the loss of significant figures. This loss is related to both the machine and the language used for the calculations. The round-off errors are also related to the time increment $h = \Delta t$ in a complicated way that is beyond the scope of this chapter. Better accuracy can be obtained by choosing a smaller Δt . However, the smaller the Δt , the larger the number of computations needed to reach the solution in a fixed time T . The increased number of computations affects both the total time of the calculation and the overall accuracy.

6.2.1.3 Runge–Kutta Methods

The centered difference approximation is not a self-starting method. In other words, the calculation that determines x_1 from the initial conditions does not come from the discretized equation, but rather from the Taylor expansion directly. An alternate way to solve this equation is to use what is known as a Runge–Kutta method. All of these methods approximate the differential equation with Taylor series expansions. The advantage of this class of methods is that they are self-starting. The disadvantage is that they only work on first-order equations (or systems of first-order equations). Before the Runge–Kutta method is discussed in detail, the second-order spring–mass equation has to be written as a system of two first-order equations. The equation for the single-DoF system, subjected to arbitrary forcing f is

$$m\ddot{x} + c\dot{x} + kx = f(x, \dot{x}, t)$$

It can be rewritten as the following system of first-order equations

$$\begin{aligned}\dot{x} &= u \\ \dot{u} &= \ddot{x} = \frac{1}{m}[f(x, u, t) - cu + kx]\end{aligned}$$

These equations are coupled and need to be solved together. Any Runge–Kutta method for the system of equations requires a Taylor series expansion of x and u about x_i and u_i . The Taylor expansion is given by

$$\begin{aligned}x_{i+1} &= x_i + \dot{x}_i h + \ddot{x}_i \frac{h^2}{2} + \cdots \\ u_{i+1} &= u_i + \dot{u}_i h + \ddot{u}_i \frac{h^2}{2} + \cdots\end{aligned}$$

As above, the time increment will be denoted by $h = \Delta t$. The first-order Runge–Kutta method (also known as Euler's method) is obtained by retaining terms of first-order and lower, i.e., the Euler approximation is given by

$$\begin{aligned}x_{i+1} &= x_i + \dot{x}_i h - o(h) \\ u_{i+1} &= u_i + \dot{u}_i h - o(h)\end{aligned}$$

The truncation error for Euler's method is order h . The error depends linearly on h .

Matching more terms in the Taylor expansion generates higher order Runge–Kutta methods. The most commonly used Runge–Kutta method is the fourth-order method that matches the Taylor expansion up to terms of order h^4 . This is a significant reduction in the error. For a derivation of this method see Cheney and Kincaid (1999).

TABLE 6.1 Fourth-Order Runge–Kutta Method for Spring–Mass Equation

t	x	$\dot{X} = u$	$\ddot{X} = G$
$T_1 = t_i$	$X_1 = x_i$	$U_1 = u_i$	$G_1 = G(T_1, X_1, U_1)$
$T_2 = t_i + h/2$	$X_2 = x_i + U_1 h/2$	$U_2 = u_i + G_1 h/2$	$G_2 = G(T_2, X_2, U_2)$
$T_3 = t_i + h/2$	$X_3 = x_i + U_2 h/2$	$U_3 = u_i + G_2 h/2$	$G_3 = G(T_3, X_3, U_3)$
$T_4 = t_i + h$	$X_4 = x_i + U_3 h$	$U_4 = u_i + G_3 h$	$G_4 = G(T_4, X_4, U_4)$

Source: Thomson and Dahleh 1998. *Theory of Vibration Applications*, 5th ed. With permission.

For the system of first-order equations given above, the fourth-order Runge–Kutta method requires four values of t , x , u , and, G where $G = 1/m[f(x, u, t) - cu + kx]$. It can be computed for each point i as follows in Table 6.1.

Combining these quantities in the following method gives the fourth-order Runge–Kutta method:

$$x_{i+1} = x_i + h/6(U_1 + 2U_2 + 2U_3 + U_4)$$
$$u_{i+1} = u_i + h/6(G_1 + 2G_2 + 2G_3 + G_4)$$

where it is recognized that the four values of U divided by six represent the average slope dx/dt and the four values of G divided by six result in an average of du/dt . A way to check the accuracy of a Runge–Kutta method is to Taylor expand G_1 , G_2 , G_3 , and G_4 and collect like terms. One will find that the above combination produces an expansion which is exact up to order h^4 .

6.2.1.4 Pseudocode for the Fourth-Order Runge–Kutta Method

For simplicity, the code is given for the single first-order equation

$\dot{x} = G(t, x)$ with the initial data $x(0) = x_0$.

The function G should be specified in a function file.

```
%initial conditions (index has to start at 1)
x(1) = x0;
%time step needs to be specified
h = H;
h2 = 2 * H;
%TEND is the total number of time steps
TEND = Tfinal;
T = h;
for I = 1:TEND
    G1 = H * G(t, x);
    G2 = H * G(t + h2, x = 0.5 * G1);
    G3 = H * G(t + h2, x = 0.5 * G2);
    G4 = h * G(t + h, x + G3);
    X = x + (G1 + 2 * G2 + 2 * G3 + G4)/6.0;
    t = (I + 1) * h;
end
```

6.2.1.5 Example

Solve numerically the differential equation

$$4\ddot{x} + 2000x = F(t)$$

with the initial conditions

$$x_0 = \dot{x}_0 = 0$$

The forcing is as shown in Figure 6.2.

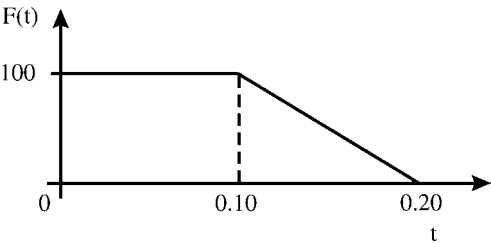


FIGURE 6.2 The forcing function for Example 6.2.1.5. (Source: Thomson and Dahleh 1998. *Theory of Vibration Applications*, 5th ed. With permission.)

6.2.1.5.1 Centered Difference

Using the centered difference approximation for the second derivative, one gets the following discrete equation

$$x_{i+1} = h^2/4F(t) - 500h^2x_i - x_{i-1} + 2x_i$$

This equation is valid for $i \geq 1$. From the initial conditions $x_0 = \dot{x}_0 = 0$, x_1 is computed by the following $x_1 = x_0 + \dot{x}_0 = 0 + 0$. A time step of $h = 0.02$ sec has been used in the calculation. The numerical solution as compared with the exact solution is given in Table 6.2. Table 6.3 contains the absolute errors for the two discrete solutions.

6.2.1.5.2 Runge–Kutta

In order to use the Runge–Kutta method, the second-order equation needs to be written as a system of first-order equations.

Let $u = \dot{x}$; then

$$\dot{u} = G(x, t) = .25 * F(t) - 500x$$

where $x(0) = 0$ and $u(0) = 0$.

This is now in a form which can be directly input into a fourth-order Runge–Kutta solver.

The Runge–Kutta method is more accurate then the centered difference approximation. This can be seen in Table 6.3, which gives the absolute value of the difference between the exact solution and the computed solutions. This is known as the absolute error. Moreover, the Runge–Kutta method is self-starting and can be used for a single variable or a system of variables as in the above example. The price that is paid is that the fourth-order Runge–Kutta method requires four function evaluations for the first derivative for each time step. This is offset by the fact that this method has higher accuracy and has a large stability region so one can take larger time steps.

TABLE 6.2 Solution to Example 6.2.1.5

Time t	Exact Solution	Central Difference	Runge–Kutta
0	0	0	0
0.02	0.00492	0.00500	0.00492
0.04	0.01870	0.01900	0.01869
0.06	0.03864	0.03920	0.03862
0.08	0.06082	0.06159	0.06076
0.10	0.08086	0.08167	0.08083
0.12	0.09451	0.09541	0.09447
0.14	0.09743	0.09807	0.09741
0.16	0.08710	0.08712	0.08709
0.18	0.06356	0.06274	0.06359
0.20	0.02949	0.02782	0.02956
0.22	−0.01005	−0.01267	−0.00955
0.24	−0.04761	−0.05063	−0.04750
0.26	−0.07581	−0.07846	−0.07571
0.28	−0.08910	−0.09059	−0.08903
0.30	−0.08486	−0.08461	−0.08485
0.32	−0.06393	−0.06171	−0.06400
0.34	−0.03043	−0.02646	−0.03056
0.36	0.00906	0.01407	0.00887
0.38	0.04677	0.05180	0.04656
0.40	0.07528	0.07916	0.07509
0.42	0.08898	0.09069	0.08886
0.44	0.08518	0.08409	0.08516
0.46	0.06436	0.06066	0.06423
0.48	0.03136	0.02511	0.03157

TABLE 6.3 Absolute Error for Centered Difference and for the Fourth-Order Runge–Kutta

Time t	Error for Central Difference	Error for Runge–Kutta All Times 1.0×10^{-3}
0	0	0
0.02	0.0001	0.0
0.04	0.0003	0.0100
0.06	0.0006	0.0180
0.08	0.0008	0.0600
0.10	0.0008	0.0300
0.12	0.0009	0.0400
0.14	0.0006	0.0200
0.16	0.0000	0.0100
0.18	0.0008	0.0300
0.20	0.0017	0.0700
0.22	0.0026	0.0500
0.24	0.0030	0.1100
0.26	0.0026	0.1000
0.28	0.0015	0.0700
0.30	0.0003	0.0100
0.32	0.0022	0.0700
0.34	0.0040	0.1300
0.36	0.0050	0.1900
0.38	0.0050	0.2100
0.40	0.0039	0.1900
0.42	0.0017	0.1200
0.44	0.0011	0.0200
0.46	0.0037	0.1300
0.48	0.0062	0.2100

Stability is a measure of how quickly errors in the computed solution grow or decay. There are very few numerical methods that are stable for all choices of time step. For most methods, there is a range of time steps which produce a stable method. The fourth-order Runge–Kutta method is stable for larger values of the time step than are the lower-order Runge–Kutta methods. A numerical method will not converge to a solution if the time step does not produce a stable method. Often, the stability criterion places a stricter limitation on the time step than accuracy does. For a more complete discussion of stability, see Strang (1986). In Table 6.3, the absolute error for both methods grows but it does not grow exponentially. Controlled error growth is the signature of a stable time step.

6.2.2 Summary of Single-Degree-of-Freedom System

- Unforced equation of motion $m\ddot{x} + c\dot{x} + kx = 0$.
- Forced equation of motion $m\ddot{x} + c\dot{x} + kx = f(x, \dot{x}, t)$.
- Centered difference approximation for the first derivative $\dot{x}_i = \frac{1}{2h}(x_{i+1} - x_{i-1})$.
- Centered difference approximation for the second derivative $\ddot{x}_i = \frac{1}{h^2}(x_{i-1} - 2x_i + x_{i+1})$.
- Fourth-order Runge–Kutta method.

6.3 Systems with Two or More Degrees of Freedom

A system that requires more than one coordinate to describe its motion is a multi-DoF system. These systems differ from single-DoF systems in that n DoF are described by n simultaneous differential equations and have n natural frequencies. When these systems are written in matrix notation, they look

just like the single-DoF system. The equations of motion of a viscously damped multi-DoF system can be written as follows:

$$[M]\ddot{\mathbf{x}} + [C]\dot{\mathbf{x}} + [K]\mathbf{x} = \mathbf{f}$$

where $[M]$, $[C]$, and $[K]$ are the mass, damping, and stiffness matrices, respectively; \mathbf{x} is the displacement vector; and \mathbf{f} is the force vector. Both the central difference method and Runge–Kutta can be applied to the matrix equation. The method follows exactly that given above where the scalar quantities are replaced by the matrix quantities.

6.3.1 Example

As an example, consider the two-DoF system shown in Figure 6.3.

In this example, $k_1 = k_2 = 36 \text{ kN/m}$, $m_1 = 100 \text{ kg}$, $m_2 = 25 \text{ kg}$, and $f = 4000 \text{ N}$ for $t > 0$ and 0 for $t \leq 0$. The initial conditions are all zero, i.e., $x_1 = \dot{x}_1 = x_2 = \dot{x}_2 = 0$. The equation of motion for this system is

$$100\ddot{x}_1 + 36,000x_1 - 36,000(x_2 - x_1) = 0$$

$$25\ddot{x}_2 + 36,000(x_2 - x_1) = f$$

This can be written in matrix notation as

$$\begin{bmatrix} 100 & 0 \\ 0 & 25 \end{bmatrix} \ddot{\mathbf{x}} + 36,000 \begin{bmatrix} 2 & -1 \\ -1 & 1 \end{bmatrix} \mathbf{x} = \mathbf{f}$$

where $\mathbf{x} = (x_1, x_2)^t$ and $\mathbf{f} = (0, f)^t$.

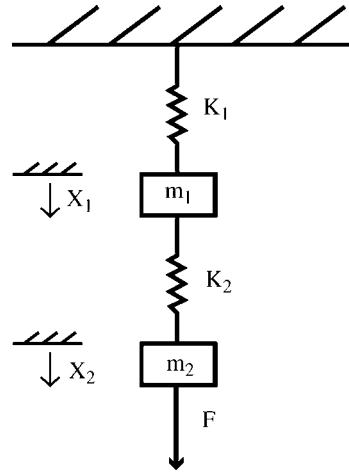


FIGURE 6.3 Two-DoF system. (Source: Thomson and Dahleh 1998. *Theory of Vibration Applications*, 5th ed. With permission.)

6.3.1.1 Centered Difference

Using the centered difference approximation for the second derivatives, one obtains the following two recurrence relations

$$x_1^{i+1} = (-720x_1^i + 360x_2^i)\Delta t^2 + 2x_1^i - x_1^{i-1}$$

$$x_2^{i+1} = (1440(x_1^i - x_2^i) + 160)\Delta t^2 + 2x_2^i - x_2^{i-1}$$

These two equations are only valid for $i \geq 3$. From the single-DoF system, we know that this method is not self-starting. In order to compute x_1^2 and x_2^2 , one needs to use an additional equation, which one obtains from the Taylor expansion. First one needs to compute the initial acceleration for the system. This is obtained from the differential equation and the initial data. For this problem, the initial acceleration is given by $\ddot{x}_1 = 0$ and $\ddot{x}_2 = 160$. Next, values for x_1^{-1} and x_2^{-1} are computed from the Taylor expansion

$$x_1^{-1} = x_1^0 - \Delta t \dot{x}_1 + \frac{\Delta t^2}{2} \ddot{x}_1 = 0$$

$$x_2^{-1} = 80\Delta t^2$$

Now, the recurrence relations can be used to compute the rest of the terms. An example of the MATLAB code for this calculation is the following.

6.3.1.2 Pseudocode for Example 6.3.1

The following is a MATLAB m file for Example 6.3.1.

```
clear
deltat = 0.01;
deltsq = deltat*deltat;
x2(1) = 0;
x1(1) = 0;
x2(2) = 160/2*deltsq;
x1(2) = (60*x2(2)*deltsq)/(1 + 120*deltsq);
x2ddot(2) = 1440*(x1(2) - x2(2)) + 160;
x1ddot(2) = -720*x1(2) + 360*x2(2);
for i = 3:51
    x2(i) = x2ddot(i - 1)*deltsq + 2*x2(i - 1) - x2(i - 2);
    x1(i) = x1ddot(i - 1)*deltsq + 2*x1(i - 1) - x1(i - 2);
    x2ddot(i) = 1440*(x1(i) - x2(i)) + 160;
    x1ddot(i) = -720*x1(i) + 360*x2(i);
end
```

Figure 6.4 gives the displacement of x_1 and x_2 over time for Example 6.3.1.

6.3.1.3 Runge–Kutta

Alternately, the system of second-order equations can be integrated using the fourth-order Runge–Kutta method. In order to use Runge–Kutta, the second-order system has to be written as a system of first-order equations. The following second-order system

$$\ddot{x}_1 = -720x_1 + 360x_2$$

$$\ddot{x}_2 = 1440(x_1 - x_2) + 160$$

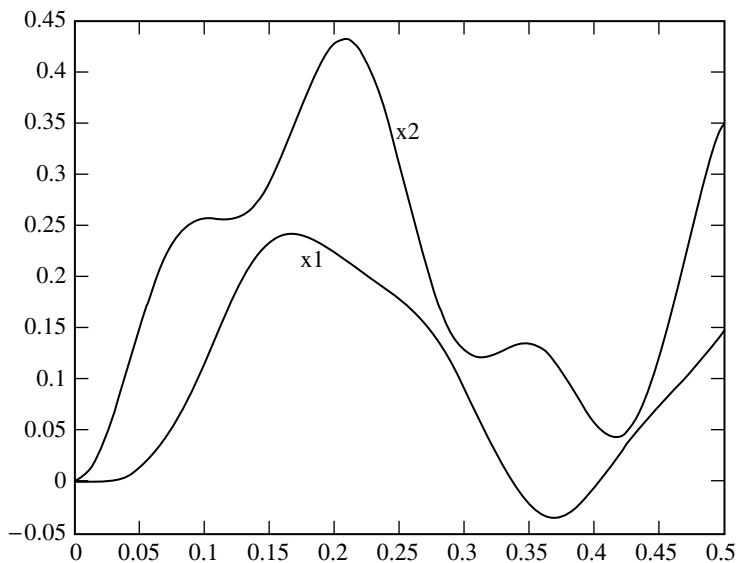


FIGURE 6.4 Displacement versus time. (Source: Thomson and Dahleh 1998. *Theory of Vibration Applications*, 5th ed. With permission.)

becomes the following first-order system

$$\begin{aligned}\dot{x}_1 &= x_3 \\ \dot{x}_2 &= x_4 \\ \dot{x}_3 &= -720x_1 + 360x_2 \\ \dot{x}_4 &= 1400(x_1 - x_2) + 160\end{aligned}$$

Two new variables have been introduced.

6.3.1.4 Integrating Ordinary Differential Equations Using MATLAB

There are several ODE solvers in MATLAB, especially in version six. The discussion here will be limited to the least complicated solvers. These are *ode23* and *ode45*, which are implementations of a second- and third-order, and a fourth- and fifth-order solver, respectively. Like all Runge–Kutta methods, these solvers work on first-order equations. If the equation is of higher order, it needs to be converted to a system of first-order equations. Then the equation should be written in vector form, i.e., $\mathbf{x}' = \mathbf{f}(\mathbf{x}, t)$. The user must write a MATLAB function routine which computes the values of $\mathbf{f} = (f_1, f_2, \dots, f_n)$ given the values of (\mathbf{x}, t) . Once this function file exists, it can be used as input in either *ode23* or *ode45*. The function call details are given in the on-line help facility in MATLAB. See the Appendix for an introduction to MATLAB.

6.3.2 Summary of Two-Degree-of-Freedom System

1. Equation of motion: $[\mathbf{M}]\ddot{\mathbf{x}} + [\mathbf{C}]\dot{\mathbf{x}} + [\mathbf{K}]\mathbf{x} = \mathbf{f}$.
2. Centered difference for systems of equations.
3. Runge–Kutta methods.
4. MATLAB commands for solution of ordinary differential equations — *ode23* and *ode45*.

6.4 Finite Difference Method for a Continuous System

6.4.1 Bar

A thin uniform rod is the first example of a continuous system that will be examined. The equation of motion for such a system is given by

$$\partial^2 u / \partial x^2 = 1/c^2 \partial^2 u / \partial t^2$$

where $c = \sqrt{E/\rho}$. E is the modulus of elasticity and ρ is the density of the rod. A complete derivation of this equation can be found in many books (see Thomson and Dahleh 1998). Separation of variables can be used to find a solution of the form $u(x, t) = U(x)G(t)$. This substitution gives the equation.

$$\frac{d^2 U}{dx^2} G(t) = \frac{1}{c^2} U(x) \frac{d^2 G(t)}{dt^2}$$

Upon rearrangement, this becomes

$$\frac{1}{U(x)} \frac{d^2 U}{dx^2} = \frac{1}{c^2 G(t)} \frac{d^2 G(t)}{dt^2}$$

The left-hand side of the equation is independent of t and the right-hand side is independent of x . Therefore, each side must equal a constant. Let this constant be denoted by α and $\alpha = -(\omega/c)^2$. There are now two differential equations, the displacement equation

$$d^2 U / dx^2 + \alpha^2 U = 0$$

U_{n+1} is the displacement of a point off the bar. We never compute U_{n+1} ; however, as one can see from a previous calculation, this value is used when the recurrence relationship is evaluated for $i = n$, $U_{n+1} - (2 - \lambda)U_n + U_{n-1} = 0$. Under the assumption that the stress is zero at the right-hand endpoint, the remaining constraint becomes

$$(2 - \lambda)U_n - 2U_{n-1} = 0$$

For a bar that has one fixed left-hand endpoint and a free right-hand end, the matrix problem is the following:

$$\begin{bmatrix} 2 - \lambda & -1 & 0 & 0 & \dots & 0 \\ -1 & 2 - \lambda & -1 & 0 & \dots & 0 \\ 0 & -1 & 2 - \lambda & -1 & \dots & 0 \\ & & & & & \\ 0 & & & -1 & 2 - \lambda & -1 \\ & & & & -2 & 2 - \lambda \end{bmatrix} \begin{bmatrix} U_2 \\ U_3 \\ U_4 \\ \\ U_{n-1} \\ U_n \end{bmatrix} = \begin{bmatrix} 0 \\ 0 \\ 0 \\ \\ 0 \\ 0 \end{bmatrix}$$

This matrix problem has a unique solution because there are $n - 1$ linearly independent equations and there are $n - 1$ unknowns.

6.4.1.1 Example

Consider a bar of unit length that is divided into four equal pieces. The left-hand end is fixed so that $U_1 = 0$, and the right-hand end is free. The eigenvalue problem for this system is the following:

$$\begin{bmatrix} 2 - \lambda & -1 & 0 & 0 \\ -1 & 2 - \lambda & -1 & 0 \\ 0 & -1 & 2 - \lambda & -1 \\ 0 & 0 & -2 & 2 - \lambda \end{bmatrix} \begin{bmatrix} U_2 \\ U_3 \\ U_4 \\ U_5 \end{bmatrix} = \begin{bmatrix} 0 \\ 0 \\ 0 \\ 0 \end{bmatrix}$$

The eigenvalues, λ , are $\lambda = [0.1522, 1.2346, 2.7654, 3.8478]$. The natural frequencies can be recovered from the eigenvalues since $\lambda = h^2 \omega / c$ and $c = \sqrt{E/\rho}$ is determined by the material properties of the bar.

6.4.2 Beam

A second example of finite difference approximation is given by looking at a centered difference approximation to compute the transverse vibration of a uniform beam. We will consider a special case of the Euler equation for the beam. The following fourth-order equation results when the flexural rigidity, (EI) , is constant:

$$d^4 W / dx^4 - \beta^4 W = 0$$

where β contains all of the material properties of the beam (i.e., $\beta^4 = \rho A \omega^2 / EI$).

The centered difference formula for the fourth derivative is given by

$$f^{iv} = 1/h^4 (f_{i+2} - 4f_{i+1} + 6f_i - 4f_{i-1} + f_{i-2})$$

In order to see that this expansion is in fact second-order, combine the Taylor expansions for f_{i+2} , f_{i+1} , f_i , f_{i-1} , and f_{i-2} , and notice that you obtain an approximation for the fourth derivative which exactly matches the combined Taylor approximations up to order h^2 . Using this approximation, the transverse beam equation at the interior mesh point becomes

$$W_{i+2} - 4W_{i+1} + (6 - \lambda)W_i - 4W_{i-1} + W_{i-2} = 0$$

where $\lambda = h^4 \beta^4$. This equation is valid for $i = 3, n - 2$. As before, the boundary conditions have to be used in order to have sufficient conditions to determine all n values for the deflection, W . There will be two additional constraints placed at each end. In this case, all of the types of boundary condition require fictitious points. In other words, they require that the beam be extended beyond the physical boundaries to include W_{-1} , W_0 , W_{n+1} , and W_{n+2} . Let us consider three types of boundary conditions: fixed end, free end, and simply-supported end. For simplicity, we will derive all of the conditions for the right-hand endpoint $x = L$.

Fixed end: When the end of the beam is fixed, both the deflection $W = 0$ and $dW/dx = 0$. As above, the centered difference approximation for the first derivative requires the introduction of a fictitious point. These conditions translate into

$$W_n = 0 \text{ and } dW/dx|_n = 1/h^2(W_{n+1} - W_{n-1}) = 0$$

These constraints reduce to the following:

$$W_{n+1} = W_{n-1}$$

Free end: The bending moment and the shear force are zero at the free end. These are given by a second and third derivative, respectively. Assuming the free end is located at N , the two fictitious points introduced are at $n + 1$ and $n + 2$. The discrete version of the two constraints is:

$$d^2W/dx^2|_n = 1/h^2(W_{n-1} - 2W_n + W_{n+1}) = 0$$

$$d^3W/dx^3|_n = 1/(2h^3)(W_{n+2} - 2W_{n+1} + 2W_{n-1} - W_{n-2}) = 0$$

Simply-supported end: The boundary conditions of this type require that the deflection and the moment are zero. When these are applied to the right-hand endpoint

$$W_n = 0 \\ d^2W/dx^2 = 1/h^2(W_{n+1} - 2W_n + W_{n-1}) = 0$$

Combining these two equations, one sees that the value of W at the fictitious point is equal to the value on the beam, i.e., $W_{n+1} = W_{n-1}$.

All three of these boundary condition types allow one to replace the fictitious values in the recurrence relations with values on the beam. The procedures followed are very similar to those outlined for the longitudinal vibration of a beam.

6.4.3 Summary of Finite Difference Methods for a Continuous System

1. Equation of motion for the bar: $\partial^2 u / \partial x^2 = 1/c^2 \partial^2 u / \partial t^2$.
2. Displacement equation for the bar: $d^2 U / dx^2 + \alpha^2 U = 0$.
3. Finite difference approximation: $U_{i+1} - (2 - \lambda)U_i + U_{i-1} = 0$.
4. Equation of motion for the beam: $d^4 W / dx^4 - \beta^4 W = 0$.
5. Centered difference approximation for the fourth derivative: $f^{iv} = 1/h^4(f_{i+2} - 4f_{i+1} + 6f_i - 4f_{i-1} + f_{i-2})$.
6. Finite difference approximation for the beam equation: $W_{i+2} - 4W_{i+1} + (6 - \lambda)W_i - 4W_{i-1} + W_{i-2} = 0$.

6.5 Matrix Methods

In the preceding section, the equations of motion are solved for the system. Often, one is not interested in the complete solution. Rather, one is interested in the natural frequencies and the normal modes. When the number of DoF is very high, only the lowest natural frequency needs to be computed. Several methods to find some, but not all, of the eigenvalues of the system will be presented.

6.5.1 Example: Three-Degree-of-Freedom System

A three-DoF system will be used as an example. The larger DoF systems work exactly in the same manner but produce larger calculations.

Let us consider the following spring-mass system in Figure 6.6.

The equation of motion for this system is

$$M \begin{bmatrix} 2 & 0 & 0 \\ 0 & 1 & 0 \\ 0 & 0 & 1 \end{bmatrix} \begin{bmatrix} \ddot{x}_1 \\ \ddot{x}_2 \\ \ddot{x}_3 \end{bmatrix} + K \begin{bmatrix} 3 & -1 & 0 \\ -1 & 2 & -1 \\ 0 & -1 & 1 \end{bmatrix} \begin{bmatrix} x_1 \\ x_2 \\ x_3 \end{bmatrix} = \begin{bmatrix} 0 \\ 0 \\ 0 \end{bmatrix}$$

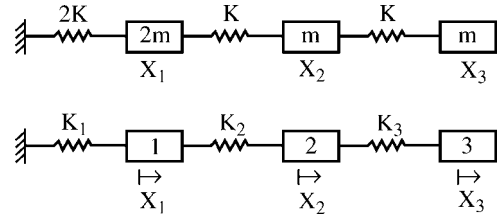


FIGURE 6.6 Three spring-mass system. (Source: Thomson and Dahleh 1998. *Theory of Vibration Applications*, 5th ed. With permission.)

Assuming a harmonic solution of the form $x = A \sin(\omega t)$ gives the following eigenvalue problem:

$$\left(-\lambda \begin{bmatrix} 2 & 0 & 0 \\ 0 & 1 & 0 \\ 0 & 0 & 1 \end{bmatrix} + k \begin{bmatrix} 3 & -1 & 0 \\ -1 & 2 & -1 \\ 0 & -1 & 1 \end{bmatrix} \right) \begin{bmatrix} x_1 \\ x_2 \\ x_3 \end{bmatrix} = \begin{bmatrix} 0 \\ 0 \\ 0 \end{bmatrix}$$

where $\lambda = \omega^2 m/k$. The eigenvalues are found by setting the characteristic equation of the determinant equal to zero. This gives the following polynomial:

$$\lambda^3 - 4.5\lambda^2 + 5\lambda - 1 = 0$$

It is a simple matter to graph this polynomial and see that there are three real roots to this equation.

6.5.2 Bisection Method

One method for calculating the roots of a nonlinear function is called the bisection method. This method finds the zeros of nonlinear functions by bracketing the zero in an interval $[a, b]$. The interval is chosen so that $f(a)$ and $f(b)$ are of opposite sign. If f is a continuous function and it is positive at one endpoint, say $f(a) > 0$, and it is negative at the other endpoint, $f(b) < 0$, then it has had to go through zero at some point in the interval. It is possible that it has gone through zero more than once in the interval. From Figure 6.7, one can see that one root is between $[0, 0.5]$; another is between $[1, 1.5]$; and a third root is in $[2.5, 3]$. In order to find all three roots, the bisection method has to be used three times; one for each interval. As an example, the MATLAB code for the first root is given below.

6.5.2.1 MATLAB Code for the Bisection Method

```
clear
%set an acceptable tolerance for the root
tol = 10e - 4
%endpoints of the interval
a = 0
b = 0.5
for i = 1:20
    c = 0.5*(a + b)
    if abs(f(c)) < tol, break, end
```

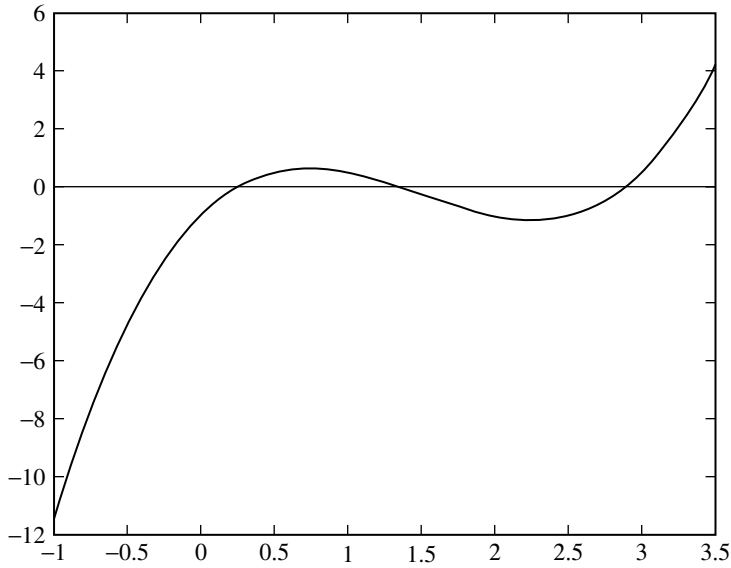


FIGURE 6.7 Graph of the cubic polynomial $\lambda^3 - 4.5\lambda^2 + 5\lambda - 1 = 0$. (Source: Thomson and Dahleh 1998. *Theory of Vibration Applications*, 5th ed. With permission.)

```

if f(a)*f(c) < 0
    b = c
else
    a = c
end
end
end

```

The root 0.2554 is found after ten iterations. As long as the initial interval is chosen so that the function has different signs at the endpoints, this method will always converge. There are nonlinear root finding methods, such as Newton's method, which when they converge do so more quickly. However, they may or may not converge.

6.5.2.2 MATLAB Function for Finding the Roots of a Polynomial

MATLAB has a built in root-finding method which requires the creation of a vector **c** that contains the coefficients of the polynomial in descending order. The MATLAB command *roots(c)*, produces the roots of the polynomial. For our example, **c** = [1, -4.5, 5, -1]. The roots of this equation are given by $\lambda = 2.8892, 1.3554, 0.2554$.

6.5.2.3 Mode Shapes

The mode shapes are determined by substituting each eigenvalue into the matrix problem and computing the corresponding eigenvector. As an example of how to compute the eigenvector for a given eigenvalue, we will compute the eigenvector associated with $\lambda = 2.8892$. The first step is to substitute this value of λ into the eigenvalue equation. This gives the following problem:

$$\begin{bmatrix} 2.489 & -1 & 0 \\ -1 & 1.745 & -1 \\ 0 & -1 & 0.744 \end{bmatrix} \begin{bmatrix} x_1 \\ x_2 \\ x_3 \end{bmatrix} = \begin{bmatrix} 0 \\ 0 \\ 0 \end{bmatrix}$$

The solution vector found by Gaussian elimination is given by

$$\mathbf{x} = (x_1, x_2, x_3)^t = (0.2992, 0.7446, 1.0)^t$$

6.5.3 Directly Calculating the Eigenvalues and Eigenvectors from the Matrix Equation

Ideally one would like to use a computer program such as MATLAB to compute both the eigenvalues and the eigenvectors directly from the matrix equation. In order to do this, the matrix equation needs to be rewritten slightly. In general, the matrix equation for the normal mode vibration is given by

$$[-\lambda \mathbf{M} + \mathbf{K}]x = 0$$

where \mathbf{M} and \mathbf{K} are the mass and stiffness matrices, respectively, both are square symmetric matrices, and λ is the eigenvalue related to the natural frequency by $\lambda = n\omega^2$. Premultiplying the preceding equation by \mathbf{M}^{-1} , we have another form of the equation:

$$[-\lambda \mathbf{I} + \mathbf{A}]x = 0$$

where $\mathbf{A} = \mathbf{M}^{-1}\mathbf{K}$ and \mathbf{A} is called the dynamic matrix. In general, \mathbf{A} is not symmetric. In order to use MATLAB to compute the eigenvectors and eigenvalues, the matrix must be symmetric. There is a standard transformation of coordinates that converts the matrix problem into a standard eigenvalue problem which can be solved by a computer. Assume that we have a transformation of coordinates which has the following form:

$$x = \mathbf{U}^{-1}y$$

When this transformation is substituted into the equation, we get

$$[-\lambda \mathbf{M}\mathbf{U}^{-1} + \mathbf{K}\mathbf{U}^{-1}]y = 0$$

Premultiplying the equation by \mathbf{U}^t gives

$$[-\lambda \mathbf{U}^t \mathbf{M} \mathbf{U}^{-1} + \mathbf{U}^t \mathbf{K} \mathbf{U}^{-1}]y = 0$$

From this equation, one can see that if either \mathbf{M} or \mathbf{K} equals $\mathbf{U}^t \mathbf{U}$, then the preceding equation is reduced to standard form, at which time it is possible to compute both the eigenvalues and eigenvectors directly. To see how this works, let us assume that $\mathbf{M} = \mathbf{U}^t \mathbf{U}$. The equation becomes

$$[-\lambda \mathbf{I} + \mathbf{U}^t \mathbf{K} \mathbf{U}^{-1}]y = 0$$

where $\lambda = \omega^2$. This equation is in standard form since $\mathbf{U}^t \mathbf{K} \mathbf{U}^{-1}$ is symmetric.

6.5.3.1 Example

To illustrate the use of the dynamic matrix and the standard computer form, we can use MATLAB to calculate the eigenvalues and eigenvectors for Example 6.5.1. The first step is to convert the problem into standard form. For this example, the dynamic matrix is given by

$$\mathbf{A} = \begin{bmatrix} 1.5 & -0.5 & 0 \\ -1.0 & 2.0 & -1.0 \\ 0 & -1.0 & 1.0 \end{bmatrix}$$

We can compute both the eigenvalues and the eigenvectors in MATLAB using the command $[U, D] = \text{eig}(A)$. The result of this command is two matrices, \mathbf{U} and \mathbf{D} . Matrix \mathbf{U} contains the eigenvectors as column vectors and \mathbf{D} is a diagonal matrix which has the eigenvalues on the diagonal. Continuing with our example, we get the following two matrices:

$$\mathbf{U} = \begin{bmatrix} 0.7569 & 0.3031 & 0.2333 \\ 0.2189 & -0.8422 & 0.5808 \\ -0.6158 & 0.4458 & 0.7799 \end{bmatrix}$$

and

$$\mathbf{D} = \begin{bmatrix} 1.3554 & 0 & 0 \\ 0 & 2.8892 & 0 \\ 0 & 0 & 0.2544 \end{bmatrix}$$

In order to use this transformation then, one has to be able to write \mathbf{M} or \mathbf{K} as $\mathbf{U}^t \mathbf{U}$. This is known as the Cholesky decomposition. In MATLAB, if one has a positive definite matrix \mathbf{M} , the matrix can be Cholesky-decomposed with the built in function *chol*. The command $U = chol(M)$ produces an upper triangular matrix \mathbf{U} such that $\mathbf{U}^t \mathbf{U} = \mathbf{M}$.

Cholesky decomposition is a special case of LU factorization where \mathbf{L} is a lower triangular matrix and \mathbf{U} is an upper triangular matrix. The computational procedure begins by writing the algebraic equations that result from the following calculation:

$$\begin{bmatrix} u_{11} & 0 & 0 \\ u_{12} & u_{22} & 0 \\ u_{13} & u_{23} & u_{33} \end{bmatrix} \begin{bmatrix} u_{11} & u_{12} & u_{13} \\ 0 & u_{22} & u_{23} \\ 0 & 0 & u_{33} \end{bmatrix} = \begin{bmatrix} m_{11} & m_{12} & m_{13} \\ m_{21} & m_{22} & m_{23} \\ m_{31} & m_{32} & m_{33} \end{bmatrix}$$

If the matrix \mathbf{M} is positive definite, then the above matrix multiplication results in six linearly independent equations.

6.5.4 Summary of Matrix Methods

1. Bisection method for the roots of a polynomial.
2. MATLAB command *roots* for finding the roots of a polynomial.
3. Cholesky decomposition.

6.6 Approximation Methods for the Fundamental Frequency

The smallest natural frequency, known as the fundamental frequency, of a multi-DoF system is often of greater interest than the high natural frequencies because its forced response in many cases is the largest. One approach to this problem is to extend the Rayleigh method to matrix problems. We will see that the Rayleigh frequency approaches the fundamental frequency from the high side.

6.6.1 Rayleigh Method

Let \mathbf{M} and \mathbf{K} be the mass and stiffness matrices, respectively, and \mathbf{x} is the assumed displacement vector for the amplitude of vibration. For harmonic motion, the maximum kinetic energy is

$$T_{\max} = 1/2 \omega \mathbf{x}^t \mathbf{M} \mathbf{x}$$

and the maximum potential energy is

$$U_{\max} = 1/2 \mathbf{x}^t \mathbf{K} \mathbf{x}$$

Since the maximum kinetic energy equals the maximum potential energy, these two quantities are equal. Equating these two and solving for ω^2 gives the Rayleigh quotient:

$$\omega^2 = \frac{\mathbf{x}^t \mathbf{K} \mathbf{x}}{\mathbf{x}^t \mathbf{M} \mathbf{x}}$$

It can be shown (Thomson and Dahleh, 1998) that this quotient approaches the lowest natural frequency from above and it is somewhat insensitive to the choice of amplitudes.

6.6.2 Dunkerley's Formula

Dunkerley's formula produces a lower bound for the fundamental frequency and can be used in conjunction with the Rayleigh method to get a good approximation for the fundamental frequency. Dunkerley's formula is based on the characteristic equation for the flexibility coefficients. The flexibility influence coefficient, a_{ij} , is defined as the displacement at i due to a unit force applied at j with all other forces equal to zero. This concept is most easily understood through an example.

6.6.2.1 Computation of the Flexibility Matrix

The procedure for computing the flexibility matrix and in particular, the computation of the flexibility matrix for the three spring–mass matrix systems shown in [Figure 6.6](#), are discussed.

Example

First, one applies a unit force to mass 1 with no other forces present, i.e., $f_1 = 1$, $f_2 = f_3 = 0$. The displacements are located in the first column of the flexibility matrix.

This gives

$$\begin{bmatrix} x_1 \\ x_2 \\ x_3 \end{bmatrix} = \begin{bmatrix} 1/k_1 & 0 & 0 \\ 1/k_1 & 0 & 0 \\ 1/k_1 & 0 & 0 \end{bmatrix} \begin{bmatrix} 1 \\ 0 \\ 0 \end{bmatrix}$$

In this case, springs k_2 and k_3 are not stretched and are displaced equally with mass 1. Now, a unit force is applied to mass 2 and there are no other forces. This allows us to write the second column of the matrix to get

$$\begin{bmatrix} x_1 \\ x_2 \\ x_3 \end{bmatrix} = \begin{bmatrix} 0 & 1/k_1 & 0 \\ 0 & 1/k_1 + 1/k_2 & 0 \\ 0 & 1/k_1 + 1/k_2 & 0 \end{bmatrix} \begin{bmatrix} 0 \\ 1 \\ 0 \end{bmatrix}$$

This time, the unit force is transmitted through k_1 and k_2 . The spring k_3 is not stretched. Finally, the force is applied to mass 3 and there are no other forces present. This gives the third column of the matrix:

$$\begin{bmatrix} x_1 \\ x_2 \\ x_3 \end{bmatrix} = \begin{bmatrix} 0 & 0 & 1/k_1 \\ 0 & 0 & 1/k_1 + 1/k_2 \\ 0 & 0 & 1/k_1 + 1/k_2 + 1/k_3 \end{bmatrix} \begin{bmatrix} 1 \\ 0 \\ 0 \end{bmatrix}$$

Since the flexibility matrix is the sum of the three previous matrices, it is given by

$$\begin{bmatrix} x_1 \\ x_2 \\ x_3 \end{bmatrix} = \begin{bmatrix} 1/k_1 & 1/k_1 & 1/k_1 \\ 1/k_1 & 1/k_1 + 1/k_2 & 1/k_1 + 1/k_2 \\ 1/k_1 & 1/k_1 + 1/k_2 & 1/k_1 + 1/k_2 + 1/k_3 \end{bmatrix} \begin{bmatrix} f_1 \\ f_2 \\ f_3 \end{bmatrix}$$

An interesting feature of the flexibility matrix is that it is symmetric about the diagonal. For simplicity of notation, let the ij element of the flexibility matrix be given by $a_{ij}m_j$. Dunkerley's formula is obtained from the characteristic equation of the flexibility matrix, which is obtained by computing the determinant of the following matrix:

$$\begin{vmatrix} a_{11}m_1 - 1/\omega^2 & a_{12} & a_{13} \\ a_{21} & a_{22}m_2 - 1/\omega^2 & a_{23} \\ a_{31} & a_{32} & a_{33}m_3 - 1/\omega^2 \end{vmatrix} = 0$$

A third-degree equation in $1/\omega^2$ is obtained by expanding the determinant. One obtains the following cubic equation:

$$(1/\omega^2)^3 - (a_{11}m_1 + a_{22}m_2 + a_{33}m_3)(1/\omega^2)^2 + \dots = 0$$

A cubic equation has three roots that are denoted by $(1/\omega_i^2)$ for $i = 1, 2, 3$. This allows the cubic equation to be factored:

$$(1/\omega^2 - 1/\omega_1^2)(1/\omega^2 - 1/\omega_2^2)(1/\omega^2 - 1/\omega_3^2) = 0$$

The highest two powers of this equation are given by

$$(1/\omega^2)^3 - (1/\omega_1^2 + 1/\omega_2^2 + 1/\omega_3^2)(1/\omega^2)^2 + \dots = 0$$

The coefficient of the second highest power is equal to the sum of the roots of the characteristic equation, which is also equal to the sum of the diagonal elements of the matrix \mathbf{A}^{-1} . This relationship is not just true for $n = 3$ but is more generally true for n greater than or equal to 3. For the general n -DoF system

$$1/\omega_1^2 + 1/\omega_2^2 + \dots + 1/\omega_n^2 = a_{11}m_1 + a_{22}m_2 + \dots + a_{nn}m_n$$

The fundamental frequency is the smallest natural frequency. Since $\omega_2, \omega_3, \dots$ are larger than ω_1 , the reciprocal of these frequencies is smaller than the reciprocal of the fundamental frequency. An estimate for the fundamental frequency is obtained by neglecting all of the higher modes in the left-hand side of the above equation. This estimate gives a value for ω_1 that is smaller than the true value of the fundamental frequency. Dunkerley's formula is a lower bound for the fundamental frequency and it is given by

$$1/\omega_1^2 < a_{11}m_1 + a_{22}m_2 + \dots + a_{nn}m_n$$

6.6.3 Summary of Approximations for the Fundamental Frequency

1. Rayleigh method

$$\omega^2 = \frac{\mathbf{x}^t \mathbf{K} \mathbf{x}}{\mathbf{x}^t \mathbf{M} \mathbf{x}}$$

2. Dunkerley's formula $1/\omega_1^2 < a_{11}m_1 + a_{22}m_2 + \dots + a_{nn}m_n$.

6.7 Finite Element Method

In the finite element method, complex structures are replaced by assemblages of simple structural elements known as finite elements. The elements are connected by joints or nodes. The force and moments at the ends of the elements are known from structural theory, the joints between the elements are matched for compatibility of displacement, and the force and moment at the joints are established by imposing the condition of equilibrium.

The accuracy obtainable from the finite element method depends on being able to duplicate the vibration mode shapes. Using only one finite element between structure joints or corners gives good results for the first lowest mode, because the static deflection curve is a good approximation to the lowest dynamic mode shape. For higher modes, several elements are necessary between structural joints. This leads to large matrices. The eigenvalues and eigenvectors need to be computed numerically.

This section introduces the basic idea of the finite element method as it applies to the simple vibration problem.

The basic idea behind the finite element method is to break up the structure into simple component structures. The structural elements for the bar and the beam are discussed here.

6.7.1 Bar Element

The force–displacement relationship for a uniform rod is

$$F = (EA/L)U$$

where E is the young's modulus, A is the cross sectional area, L is the length of the element and U is the displacement. Figure 6.8 shows this one-dimensional element. The two endpoints are the nodes.

For simplicity, assume the axial displacement at any point $s = x/L$ is linear:

$$U(x, t) = a(t) + b(t)x$$

and $U_1(t) = U(0, t)$, $U_2(t) = U(L, t)$. These two conditions uniquely determine the coefficients $a(t)$ and $b(t)$. They are given by the following:

$$a(t) = U_1(t)$$

and

$$b(t) = (U_2(t) - U_1(t))/L$$

Using the linear element, the displacement anywhere along the beam is given by

$$\begin{aligned} U(x, t) &= (1 - x/L)U_1(t) + x/LU_2(t) \\ &= \varphi_1 U_1(t) + \varphi_2 U_2(t) \end{aligned}$$

where

$$\varphi_1 = 1 - x/L \quad \text{and} \quad \varphi_2 = x/L$$

φ_1 and φ_2 are known as the mode shape, which can be seen in Figure 6.9.

These two mode shapes can be superimposed to create a linear function. An example of such a function is given in Figure 6.10.

The kinetic energy of the bar is given by

$$T = .5 \int_0^L \dot{u}^2 m dx = .5m \int_0^L ((1 - s)\dot{u}_1(t) + s\dot{u}_2(t))^2 ds = .5ml(1/3\dot{u}_1^2 + 1/3\dot{u}_1\dot{u}_2 + 1/3\dot{u}_2^2)$$

6.7.1.1 Mass Matrix

The generalized mass matrix is derived from the Lagrange equations using the following:

$$\frac{D}{Dt} \frac{\partial T}{\partial \dot{u}_1}$$

Given the kinetic energy for the bar, the Lagrange equations become

$$\begin{aligned} \frac{D}{Dt} \frac{\partial T}{\partial \dot{u}_1} &= mL(1/3\ddot{u}_1 + 1/6\ddot{u}_2) \\ \frac{D}{Dt} \frac{\partial T}{\partial \dot{u}_2} &= mL(1/3\ddot{u}_1 + 1/6\ddot{u}_2) \end{aligned}$$

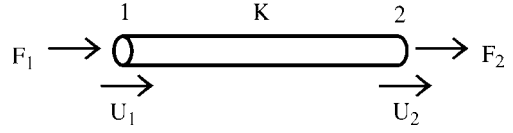


FIGURE 6.8 One dimensional element.

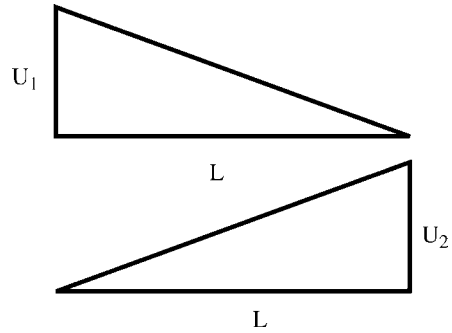


FIGURE 6.9 Linear mode shapes.

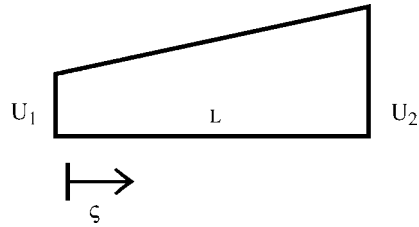


FIGURE 6.10 Superposition of the linear mode shapes.

The mass matrix for an axial element with a uniform mass distribution per unit length is given by

$$\frac{mL}{6} \begin{bmatrix} 2 & 1 \\ 1 & 2 \end{bmatrix}$$

6.7.1.2 Stiffness Matrix

The force–displacement relationship for a uniform bar is given by

$$\begin{bmatrix} F_1 \\ F_2 \end{bmatrix} = \frac{EA}{L} \begin{bmatrix} 1 & -1 \\ -1 & 1 \end{bmatrix} \begin{bmatrix} u_1 \\ u_2 \end{bmatrix}$$

6.7.1.3 Variable Properties

A simple approach to problems with variable properties is to use a large number of elements of short length. The variation of mass or stiffness over each element is small and can be neglected. In this model, the mass and stiffness for each element is constant and can be placed outside the integral. If a large number of elements are needed to capture the behavior, this will lead to a large matrix problem.

Example

A tapered rod is modeled as two uniform sections where $EA_1 = 2EA_2$ and $m_1 = 2m_2$, $k_2 = 2EA_2/L$. The displacement equation for this system is given by

$$\frac{-\omega^2 m_2}{6} \begin{bmatrix} 2(2+1) & 1 \\ 1 & 2 \end{bmatrix} + \frac{2EA_2}{L} \begin{bmatrix} 2+1 & -1 \\ -1 & 1 \end{bmatrix} \begin{bmatrix} u_1 \\ u_2 \end{bmatrix} = \begin{bmatrix} 0 \\ 0 \end{bmatrix}$$

This can be written as a standard eigenvalue problem where $\lambda = \omega^2 m_2 L / 12EA_2$.

The eigenvalue problem is the following

$$\begin{vmatrix} 3 - 6\lambda & -(1 + \lambda) \\ -(1 + \lambda) & (1 - 2\lambda) \end{vmatrix} = 0$$

The solution of the determinant requires computing the roots of a quadratic equation. The two roots are $\lambda = [0.6140, 1.1088]$. The two natural frequencies can be computed from λ . They are

$$\omega_1 = 1.4029 \sqrt{((EA_2)/(M_2 L))}$$

$$\omega_2 = 3.6477 \sqrt{((EA_2)/(M_2 L))}$$

The modes shapes are calculated by solving the eigenvalue problem. The two eigenvectors are

$$\mathbf{x}_1 = [0.5773, 1]^t$$

and

$$\mathbf{x}_2 = [-5258, 1]^t$$

6.7.2 Beam

When the ends of the element are rigidly connected to the adjoining structure, the elements act like a beam with the moments and lateral forces acting at the joints. Generally, the axial displacement $u_2 - u_1$ is small compared to the lateral displacement V of the beam.

The local coordinates of the beam element are lateral displacements, V , and rotation, θ , at the two ends. This results in four coordinates $V_1, \theta_1, V_2, \theta_2$. Four constraints uniquely determine a cubic polynomial. Therefore, the lateral displacement of a beam is assumed to be described by a cubic

polynomial

$$V(x) = p_1 + p_2 s + p_3 s^2 + p_4 s^4$$

where $s = x/L$ and p_i , the coefficients of the polynomials, are related to the lateral displacement and the rotation. The lateral displacement at the left-hand side determines V_1 :

$$V(0, t) = V_1(t) = p_1$$

The rotation at the left-hand end determines the second coefficient, θ_1 :

$$\frac{\partial V}{\partial x}(0, t) = \theta_1 = p_2$$

The remaining two coefficients are combinations of the variables and they are given by the following two constraints:

$$V(L, t) = V_2(t) \quad \text{and} \quad \frac{\partial V}{\partial x}(L, t) = \theta_2$$

Applying these two conditions, one obtains

$$p_3 = 1/L^2(-3v_1(t) - 2\theta_1(t)L + 3v_2(t) - \theta_2(t)L)$$

$$p_4 = 1/L^3(2v_1(t) + \theta_1(t)L - 2v_2(t) + \theta_2(t)L)$$

These coefficients can be represented by the following matrix equation:

$$\begin{bmatrix} p_1 \\ p_2 \\ p_3 \\ p_4 \end{bmatrix} = \begin{bmatrix} 1 & 0 & 0 & 0 \\ 0 & 1 & 0 & 0 \\ -3 & -2 & 3 & 1 \\ 2 & 1 & -2 & 1 \end{bmatrix} \begin{bmatrix} v_1 \\ L\theta_1 \\ v_2 \\ L\theta_2 \end{bmatrix}$$

The shape functions for the beam elements are determined by equating a single displacement to one, and all other displacement to zero. The first shape function is derived by letting $V_1 = 1$ and the remaining three variables zero; i.e., $V_2 = \theta_1 = \theta_2 = 0$. This gives

$$p_1 = 1 \quad p_2 = 0 \quad p_3 = -3 \quad p_4 = 2$$

The first shape function becomes

$$\varphi_1 = 1 - 3s^2 + 2s^3$$

A similar calculation for $\theta_1 = 1$ and $V_2 = V_1 = \theta_2 = 0$ yields

$$p_1 = 0 \quad p_2 = l \quad p_3 = -2l \quad p_4 = l$$

and the shape function becomes

$$\varphi_2 = ls - 2ls^2 + ls^3$$

The remaining two shape functions are determined similarly. The four shape functions for the beam are

$$\varphi_1 = 1 - 3s^2 + 2s^3$$

$$\varphi_2 = ls - 2ls^2 + ls^3$$

$$\varphi_3 = 3s^2 - 2s^3$$

$$\varphi_4 = -ls^2 + ls^3$$

6.7.2.1 Mass Matrix

Just as in the case of the bar, the generalized mass m_{ij} is given by

$$M_{ij} = \int_0^l \varphi_i \varphi_j m dx$$

Substitution of the above shape functions and integration yields the following mass matrix for the uniform beam element in terms of the end displacements:

$$\frac{mL}{420} \begin{bmatrix} 156 & 22L & 54 & -13L \\ 22L & 2L^2 & 13L & -3L^2 \\ 54 & 13L & 156 & -22L \\ -13L & -3L^2 & -22L & 4L^2 \end{bmatrix}$$

6.7.3 Summary of Finite Element Method

1. Linear finite element for a bar $\varphi_1 = 1 - x/L$ and $\varphi_2 = x/L$
2. Mass matrix for the bar

$$\frac{ML}{6} \begin{bmatrix} 2 & 1 \\ 1 & 2 \end{bmatrix}$$

3. Stiffness matrix for the bar

$$\begin{bmatrix} F_1 \\ F_2 \end{bmatrix} = \frac{EA}{L} \begin{bmatrix} 1 & -1 \\ -1 & 1 \end{bmatrix} \begin{bmatrix} u_1 \\ u_2 \end{bmatrix}$$

4. Cubic finite elements for the beam

$$\varphi_1 = 1 - 3\varsigma^2 + 2\varsigma^3$$

$$\varphi_2 = l\varsigma - 2l\varsigma^2 + l\varsigma^3$$

$$\varphi_3 = 3\varsigma^2 - 2\varsigma^3$$

$$\varphi_4 = -l\varsigma^2 + l\varsigma$$

Appendix 6A

Introduction to MATLAB®

MATLAB is a software package for numerical computation, visualization, and symbolic manipulation (also see Appendix 32A). It is an interactive environment with hundreds of built-in functions, which are in essence subroutines. These functions range from plotting commands, to those for finding the eigenvalues and eigenvectors of a matrix, to those for solving an ordinary differential equation, and much more. In addition to the built-in functions, MATLAB contains a programming language, which allows the user to write their own functions. The name MATLAB is an abbreviation of *matrix laboratory*. The original versions of MATLAB concentrated on numerical analysis of linear systems of equation. MATLAB is available from the Mathworks (www.mathworks.com).

The best way to learn MATLAB is by playing around with the different functions (Pratap, 2001). The first thing to note when you launch MATLAB is that it is a window-based environment. There are three windows: the command window, the graphics window, and the edit window. The command

window is the main window and it is the one in which you run all functions (built-in or user created). This is the window which appears when the program is launched, and it has the symbol \gg as a prompt. The graphics window is where all of the graphics are displayed, and the edit window is where users create and save all of their own programs, known as *m files*.

MATLAB provides routines for all of the basic areas of numerical analysis (numerical linear algebra, data analysis, Fourier transform, and interpolation), curve fitting, root-finding, numerical solution of ordinary differential equations, integration, and graphics. There are specialized tool boxes for signal processes and control systems to name two. With these hundreds of functions, it is imperative to have a good help facility. In the command window, the command *help functionname* provides online help. For example, type *help help* to get more information about help. There are three other commands for information: *lookfor*, *helpwin*, and *helpdesk*. *Lookfor* gives a list of functions with the keyword in their description. *Helpwin* gives a help window. *Helpdesk* is a web browser-based help.

Given the early history of MATLAB as a matrix laboratory, it should not be surprising that one of its strengths is its ability to manipulate vectors and matrices very well. A row vector is created by typing in the command window the following:

```
 $\gg x = [2, 3, 6, 4]$ 
```

This command will produce

```
 $x = \quad 2 \quad 3 \quad 6 \quad 4$ 
```

A common vector is created by entering the following

```
 $\gg x = [2; 1; 3; 4]$ 
```

This produces $x =$

```
2
1
3
4
```

The elements of a vector or matrix are separated by commas or by spaces, and the rows are separated by semicolons. Printing is suppressed by ending the line with a semicolon. The following command will produce a 2×2 matrix but it will not print it:

```
 $A = \begin{bmatrix} 2 & 4 \\ 1 & 5 \end{bmatrix}$ 
```

Providing that the operations make sense, it is easy to do operations on vectors and matrices in MATLAB. For example, if **A** and **B** are two matrices of the same size, the command $A + B$ adds the matrices.

There are several MATLAB commands given throughout the text of this chapter. Several books are available to get you started with MATLAB; for example, Hanselman and Littlefield (2001), Palm (2001), Pratap (2001), and Recktenwald (2000). The best way to learn more about these commands is to type help and the command name. This way, you get the most up-to-date information concerning the function.

References

- Atkinson, K. 1978. *An Introduction to Numerical Analysis*, 2nd ed., Wiley, New York.
- Cheney, E. and Kincaid, D. 1999. *Numerical Mathematics and Computing*, 4th ed., Brooks Cole, Monterey, CA.

- Hanselman, D. and Littlefield, B. 2001. *Mastering MATLAB 6: A Comprehensive Tutorial and Reference*, Prentice Hall, Upper Saddle River, NJ.
- Isaacson, E. and Keller, H. 1966. *Analysis of Numerical Methods*, Wiley, New York.
- Palm, W. 2001. *Introduction to MATLAB 6 for Engineers*, McGraw Hill, Boston.
- Pratap, R. 2001. *Getting Started with MATLAB 6: A Quick Introduction for Scientists and Engineers*, Oxford University Press, New York.
- Recktenwald, G. 2000. *Numerical Methods with MATLAB: Implementation and Application*, Prentice Hall, Upper Saddle River, NJ.
- Strang, G. 1986. *Introduction to Applied Mathematics*, Wellesley-Cambridge Press, Wellesley, MA.
- Thomson, W. and Dahleh, M. 1998. *Theory of Vibration with Applications*, 5th ed., Prentice Hall, Upper Saddle River, NJ.

Vibration Modeling and Software Tools

7.1	Introduction	7-1
7.2	Formulation	7-2
	Differential Formulation • Integral Formulation and Rayleigh–Ritz Discretization • Finite Element Method • Lumped Mass Matrix • Model Reduction	
7.3	Vibration Analysis	7-9
	Natural Vibration • Harmonic Response • Transient Response • Response Spectrum	
7.4	Commercial Software Packages	7-13
	ABAQUS • ADINA • ALGOR • ANSYS • COSMOSWorks • MSC.Nastran • ABAQUS/Explicit • DYNA3D • LS-DYNA	
7.5	The Basic Procedure of Vibration Analysis	7-16
	Planning • Preprocessing • Solution • Postprocessing • Engineering Judgment	
7.6	An Engineering Case Study	7-19
	Objectives • Modeling Strategy • Boundary Conditions • Material • Results	
7.7	Comments	7-21

Datong Song

National Research Council of Canada

Cheng Huang

National Research Council of Canada

Zhong-Sheng Liu

National Research Council of Canada

Summary

In this chapter, several aspects of vibration modeling are addressed. They include the formulation of the equations of motion both in differential form and integral form, the Rayleigh–Ritz method and the finite element methods, and model reduction. Natural vibration analysis and response analysis are discussed in detail. Several commercial finite element analysis (FEA) software tools are listed and their capabilities for vibration analysis are introduced. The basic procedure in using the commercial FEA software packages for vibration analysis is outlined (also see Chapter 6 and Chapter 9). The vibration analysis of a gearbox housing is presented to illustrate the procedure.

7.1 Introduction

Vibration phenomenon, common in mechanical devices and structures [2,9], is undesirable in many cases, such as machine tools. But this phenomenon is not always unwanted; for example, vibration is needed in the operation of vibration screens. Thus, reducing or utilizing vibration is among the challenging tasks that mechanical or structural engineers have to face. Vibration modeling has been used extensively for a better understanding of vibration phenomena. The vibration modeling here implies a process of converting an engineering vibration problem into a mathematical model, whereby the major vibration characteristics of the original problem can be accurately predicted. The mathematical model of vibration in its general sense consists of four components: a mass (inertia) term; a stiffness term; an

excitation force term; and a boundary condition term. These four terms are represented in differential equations of motion for discrete (or, lumped-parameter) systems, or boundary value problems for continuous systems. A damping term is included if damping effects are of concern. Depending on the nature of the vibration problem, the complexity of the mathematical model varies from simple spring–mass systems (see Chapter 1) to multi-degree-of-freedom (DoF) systems (see Chapter 3); from a continuous system (see Chapter 4) for a single structural member (beam, rod, plate, or shell) to a combined system for a built-up structure; from a linear system to a nonlinear system. The success of the mathematical model heavily depends on whether or not the four terms mentioned before can represent the actual vibration problem. In addition, the mathematical model must be sufficiently simplified in order to produce an acceptable computational cost. The construction of such a representative and simple mathematical model requires an in-depth understanding of vibration principles and techniques, extensive experience in vibration modeling, and ingenuity in using vibration software tools. Furthermore, it also requires sufficient knowledge of the vibration problem itself in terms of working conditions and specifications.

Except for few special cases that promise exact and explicit analytical solutions, vibration models have to be studied by means of approximate numerical methods such as the finite element method. The finite element method has been very successfully used for vibration modeling for the past two decades. Its success is attributed to the development of sophisticated software packages and the rapid growth of computer technology.

In this chapter, several aspects of the construction of mathematical models of linear vibration problems without damping will be addressed. The capabilities of the available software packages for vibration analysis are listed and the basic procedure for vibration analysis is summarized. As an illustration, an engineering example is given.

7.2 Formulation

7.2.1 Differential Formulation

In a majority of engineering vibration problems, the amplitude of vibrations is very small, so that the following assumptions hold: (1) a linear form of strain–displacement relationships, and (2) a linear form of stress–strain relationships (Hooke's Law). If the energy losses are negligible, it is straightforward to apply Newton's (second) law and Hooke's Law to derive the equations of motion, which appear as differential equations. Consider a single-DoF spring–mass system, as shown in Figure 7.1. The two laws are given by

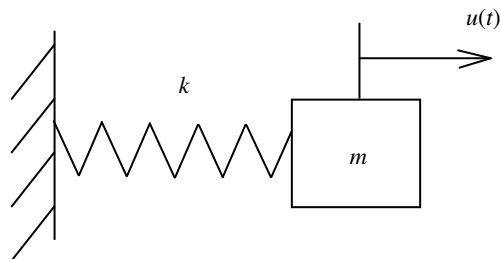


FIGURE 7.1 Single-DoF spring–mass system.

$$\begin{cases} m\ddot{u}(t) = -f, & \text{Newton's law} \\ f = ku(t), & \text{Hooke's Law} \end{cases} \quad (7.1)$$

The first equation describes the inertia force, and the second equation describes the elastic force. These two forces are essential for mechanical vibration to exist (see Chapter 1).

In a similar way, the differential equations are given directly when Newton's law plus Hooke's Law is applied to a multiple-DoF spring–mass system, shown in Figure 7.2

$$\begin{cases} \mathbf{M}\ddot{\mathbf{u}}(t) = -\mathbf{F}, & \text{Newton's law} \\ \mathbf{F} = \mathbf{K}\mathbf{u}(t), & \text{Hooke's Law} \end{cases} \quad (7.2)$$

where \mathbf{M} is the (diagonal) mass matrix, and \mathbf{K} is the stiffness matrix.

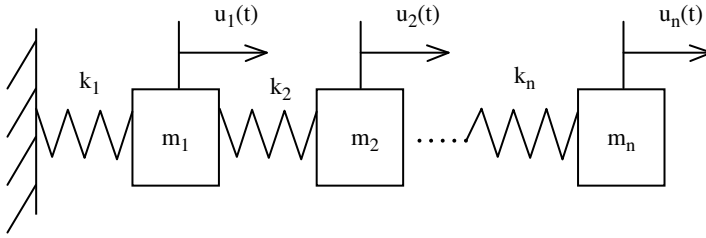


FIGURE 7.2 Multiple-DoF spring–mass system.

In the case of continua, the differential equations of motion can be derived by means of Newton's law and Hooke's Law in the same way as above. But in this case the boundary conditions have to be specified in order to make the problem statement complete (see Chapter 4). For example, as a direct consequence of Newton's law and Hooke's Law, the differential equation of bending vibration of a clamped–clamped Euler beam may be given as (Chapter 4)

$$\begin{cases} \rho \frac{\partial^2 u(x, t)}{\partial t^2} = -f, & \text{Newton's law} \\ f = EI \frac{\partial^4 u(x, t)}{\partial x^4}, & \text{Hooke's Law} \\ u(0, t) = u(l, t) = \frac{\partial u(0, t)}{\partial x} = \frac{\partial u(l, t)}{\partial x} = 0, & \text{Boundary conditions} \end{cases} \quad (7.3)$$

where ρ represents the mass per unit length, l the beam length, and EI the bending stiffness (flexural rigidity).

7.2.2 Integral Formulation and Rayleigh–Ritz Discretization

Besides the approach in which Newton's law and Hooke's Law are directly used to establish equations of motion, there are alternatives: Hamilton's principle, the minimum potential energy principle, and the virtual work principle; all of which appear in integral form. From a mathematical standpoint, the differential equations and the integral equations are equivalent in that one can be derived from another. However, they are very different in that the integral equations facilitate the application of the discretization schemes such as the finite element method, an element-wise application of Rayleigh–Ritz method. Therefore, Hamilton's principle, as one of the integral formulations, and its Rayleigh–Ritz discretization are briefly introduced here in order to provide a better understanding of the finite element method.

Denote T as the system kinetic energy, V the system potential energy, and δW the virtual work done by nonconservative forces. Hamilton's principle [11] states that the variation of the Lagrangian ($T - V$) Standard terminology plus the line integral of the virtual work done by the nonconservative forces during any time interval must be equal to zero. If the time interval is denoted by $[t_1, t_2]$, then Hamilton's principle can be expressed as

$$\delta \int_{t_1}^{t_2} (T - V) dt + \int_{t_1}^{t_2} \delta W dt = 0 \quad (7.4)$$

In the case of a continuum, we look for an approximate solution $u(x, y, z, t)$ in the form of

$$u(x, y, z, t) = \sum_{i=1}^n \varphi_i(x, y, z) q_i(t) \quad (7.5)$$

where $\varphi_i(x, y, z)$ is called a Rayleigh–Ritz shape function and $q_i(t)$ is called a generalized coordinate. In this way, the system kinetic energy and the system potential energy can be, respectively, expressed

as follows:

$$T = \frac{1}{2} \sum_{i=1}^n \sum_{j=1}^n m_{ij} \dot{q}_i \dot{q}_j \equiv \frac{1}{2} \dot{\mathbf{u}}^T(t) \mathbf{M} \dot{\mathbf{u}}(t) \quad (7.6)$$

and

$$V = \frac{1}{2} \sum_{i=1}^n \sum_{j=1}^n k_{ij} q_i q_j \equiv \frac{1}{2} \mathbf{u}^T(t) \mathbf{K} \mathbf{u}(t) \quad (7.7)$$

where $\mathbf{u}^T(t) \equiv [q_1, q_2, \dots, q_n]$, $\mathbf{M} \equiv [m_{ij}]$, $\mathbf{K} \equiv [k_{ij}]$.

The virtual work done by the generalized forces is

$$\delta W = \sum_{i=1}^n f_i(t) \delta q_i = \mathbf{F}^T \delta \mathbf{u}(t) \quad (7.8)$$

where $\mathbf{F}^T \equiv [f_1(t), f_2(t), \dots, f_n(t)]$ and $f_i(t)$ is the generalized force corresponding to the nonconservative force $f(x, y, z, t)$

$$f_i(t) = \int \varphi_i(x, y, z) f(x, y, z, t) dV \quad (7.9)$$

Substituting Equation 7.6, Equation 7.7 and Equation 7.8 into Hamilton's principle (Equation 7.4) and conducting a routine variation operation, one has

$$\int_{t_1}^{t_2} (\dot{\mathbf{u}}^T \mathbf{M} \delta \dot{\mathbf{u}} - \mathbf{u}^T \mathbf{K} \delta \mathbf{u} + \mathbf{F}^T \delta \mathbf{u}) dt = 0 \quad (7.10)$$

Applying the separation integration to the first term of the above equation and noting that the variations of the generalized coordinate $\delta \mathbf{u}$ at times t_1 and t_2 equal zero, Equation 7.10 is rewritten as

$$\int_{t_1}^{t_2} (-\mathbf{M} \ddot{\mathbf{u}}(t) - \mathbf{K} \mathbf{u}(t) + \mathbf{F}) \delta \mathbf{u} dt = 0 \quad (7.11)$$

Because $\delta \mathbf{u}$, the variation of the generalized coordinate vector, is arbitrary and independent, from the above equation one obtains

$$\mathbf{M} \ddot{\mathbf{u}}(t) + \mathbf{K} \mathbf{u} = \mathbf{F} \quad (7.12)$$

which is the vibration equation resulting from a Rayleigh–Ritz discretization.

7.2.3 Finite Element Method

In the finite element method (FEM) [7,10,12], a continuum is divided into a number of relatively small regions called elements that are interconnected at selected nodes. This procedure is called discretization. The deformation within each element is expressed by interpolating polynomials. The coefficients of these polynomials are defined in terms of the element nodal DoF that describe the displacements and slopes of selected nodes on the element. By using the connectivity between elements, the assumed displacement field can then be written in terms of the nodal DoF by means of the element shape function. Using the assumed displacement field, the kinetic energy and the strain energy of each element are expressed in the form of the element mass and stiffness matrices. The energy expressions for the entire continua can be obtained by adding the energy expressions of its elements. This leads to the assembled mass matrix and the assembled stiffness matrix, and finally to the finite element vibration equation.

The displacement in the interior of an element e is determined by a polynomial

$$u(x, y, z, t) = \mathbf{N} \mathbf{u}^e \quad (7.13)$$

where the matrix \mathbf{N} is called the shape function matrix of the element e , and \mathbf{u}^e the vector of the nodal DoF.

Based on the element displacement expression Equation 7.13, one can obtain the strain and the stress in the element e and finally the strain energy.

The strain and the stress in the element e are

$$\boldsymbol{\varepsilon} = \partial u(x, y, z, t) = \partial \mathbf{N} \mathbf{u}^e = \mathbf{B} \mathbf{u}^e \quad (7.14)$$

and

$$\boldsymbol{\sigma} = \mathbf{D} \boldsymbol{\varepsilon} = \mathbf{D} \mathbf{B} \mathbf{u}^e = \mathbf{S} \mathbf{u}^e \quad (7.15)$$

respectively, where ∂ is the differential operator matrix, $\mathbf{B} = \partial \mathbf{N}$ is the element strain matrix, \mathbf{D} is the elastic matrix, and $\mathbf{S} = \mathbf{D} \mathbf{B}$ is called the element stress matrix.

The strain energy in the element e is given by the element strain $\boldsymbol{\varepsilon}$ and stress $\boldsymbol{\sigma}$ as

$$V^e = \frac{1}{2} \int \boldsymbol{\varepsilon}^T \boldsymbol{\sigma} \, dV = \frac{1}{2} (\mathbf{u}^e)^T \mathbf{K}^e \mathbf{u}^e \quad (7.16)$$

where

$$\mathbf{K}^e = \int \mathbf{B}^T \mathbf{D} \mathbf{B} \, dV \quad (7.17)$$

is called the element stiffness matrix.

The velocity at a point (x, y, z) in the element e can be obtained from Equation 7.13 as

$$\dot{u}(x, y, z, t) = \mathbf{N} \dot{\mathbf{u}}^e \quad (7.18)$$

So the kinetic energy of the element e is

$$T^e = \frac{1}{2} \int \rho \dot{\mathbf{u}}^T \dot{\mathbf{u}} \, dV = \frac{1}{2} (\dot{\mathbf{u}}^e)^T \mathbf{M}^e \dot{\mathbf{u}}^e \quad (7.19)$$

where

$$\mathbf{M}^e = \int \rho \mathbf{N}^T \mathbf{N} \, dV \quad (7.20)$$

is called the element mass matrix.

The equivalent nodal force \mathbf{F}^e corresponding to the force \mathbf{f}^e applied onto the element e is determined by equaling the work done by \mathbf{F}^e to the work done by \mathbf{f}^e along any virtual displacement. This leads to the following:

$$(\delta \mathbf{u}^e)^T \mathbf{F}^e = \int \delta \mathbf{u}^T \mathbf{f}^e \, dV = (\delta \mathbf{u}^e)^T \left(\int \mathbf{N}^T \mathbf{f}^e \, dV \right) \quad (7.21)$$

Note that as the variation of the nodal displacement is arbitrary, one can obtain the expression of the equivalent nodal force \mathbf{F}^e from Equation 7.21 as

$$\mathbf{F}^e = \int \mathbf{N}^T \mathbf{f}^e \, dV \quad (7.22)$$

Now we have the kinetic energy, the strain energy, and the equivalent nodal force of the element e . But these quantities are expressed in the local coordinate system (X^e, Y^e, Z^e) of the element e , not in the global coordinate system (X, Y, Z) . In order to calculate the corresponding counterparts for the whole structure, it is necessary to transform the expressions of the kinetic energy, the strain energy, and the equivalent nodal force of the element e from the local coordinate system into the global one.

Let \mathbf{L} be the transformation matrix from the global coordinate system to the local coordinate system. Then the nodal displacement vector \mathbf{u}^e in the local coordinate system is related to the nodal displacement

vector $\bar{\mathbf{u}}^e$ in the global coordinate system by the following:

$$\mathbf{u}^e = \mathbf{L}\bar{\mathbf{u}}^e \quad (7.23)$$

Similarly, the equivalent nodal force vector \mathbf{F}^e in the local coordinate system is related to the equivalent nodal force vector $\bar{\mathbf{F}}^e$ in the global coordinate system by

$$\mathbf{F}^e = \mathbf{L}\bar{\mathbf{F}}^e \quad (7.24)$$

Substituting Equation 7.23 into Equation 7.16 and Equation 7.19, and noting that \mathbf{L} is a normal matrix ($\mathbf{L}^T = \mathbf{L}^{-1}$), the element stiffness and mass matrices in the global coordinate system can be, respectively, expressed as

$$\bar{\mathbf{K}}^e = \mathbf{L}^T \mathbf{K}^e \mathbf{L} \quad (7.25)$$

and

$$\bar{\mathbf{M}}^e = \mathbf{L}^T \mathbf{M}^e \mathbf{L} \quad (7.26)$$

The equivalent nodal force vector in the global coordinate system is solved from Equation 7.24

$$\bar{\mathbf{F}}^e = \mathbf{L}^T \mathbf{F}^e \quad (7.27)$$

In this way, we can obtain the total strain energy of the structure as

$$V = \sum_e \bar{V}^e = \frac{1}{2} \sum_e (\bar{\mathbf{u}}^e)^T \bar{\mathbf{K}}^e \bar{\mathbf{u}}^e = \frac{1}{2} \mathbf{u}^T \mathbf{K} \mathbf{u} \quad (7.28)$$

where the matrix

$$\mathbf{K} = \sum_e \bar{\mathbf{K}}^e \quad (7.29)$$

is called the global stiffness matrix of the structure. The vector \mathbf{u} is the global nodal displacement vector of the structure.

Similarly, the total kinetic energy of all of the elements can be written as

$$T = \sum_e \bar{T}^e = \frac{1}{2} \sum_e (\dot{\bar{\mathbf{u}}}^e)^T \bar{\mathbf{M}}^e \dot{\bar{\mathbf{u}}}^e = \frac{1}{2} \dot{\mathbf{u}}^T \mathbf{M} \dot{\mathbf{u}} \quad (7.30)$$

where the matrix

$$\mathbf{M} = \sum_e \bar{\mathbf{M}}^e \quad (7.31)$$

is called the global mass matrix. The vector $\dot{\mathbf{u}}$ is the global nodal velocity vector.

The total virtual work done by the external forces is

$$\delta W = \sum_e \delta \bar{W}^e = \sum_e (\delta \bar{\mathbf{u}}^e)^T \bar{\mathbf{F}}^e = (\delta \mathbf{u})^T \mathbf{F} \quad (7.32)$$

where the vector

$$\mathbf{F} = \sum_e \bar{\mathbf{F}}^e \quad (7.33)$$

is a global generalized force vector.

Substituting Equation 7.28, Equation 7.30, and Equation 7.32 into Hamilton's principle (Equation 7.4) and conducting the routine variation operation, one has

$$\mathbf{M}\ddot{\mathbf{u}} + \mathbf{K}\mathbf{u} = \mathbf{F} \quad (7.34)$$

which is the vibration equation resulting from the finite element discretization.

7.2.4 Lumped Mass Matrix

The element mass matrix given by Equation 7.20 is normally a full symmetric matrix, because the element shape functions are not orthogonal with each other. It is desirable to reduce this full matrix into a diagonal matrix. In practice, this is achieved by lumping the element mass at its nodes. For example, the consistent element mass matrix of a beam element is

$$\mathbf{M}^e = \frac{\rho A l}{420} \begin{bmatrix} 156 & 22l & 54 & -13l \\ 22l & 4l^2 & 13l & -3l^2 \\ 54 & 13l & 156 & -22l \\ -13l & -3l^2 & -22l & 4l^2 \end{bmatrix} \quad (7.35)$$

When the inertia effect associated with the rotational DoF is negligible, the element lumped mass matrix can be obtained by lumping one half of the total beam element mass at each of the two nodes along the translation DoF:

$$\mathbf{M}^e = \frac{\rho A l}{2} \begin{bmatrix} 1 & 0 & 0 & 0 \\ 0 & 0 & 0 & 0 \\ 0 & 0 & 1 & 0 \\ 0 & 0 & 0 & 0 \end{bmatrix} \quad (7.36)$$

When the inertia effect associated with the rotational DoF is not negligible, the mass moment of inertia of one half of the beam element about each node can be computed and included at the diagonal locations corresponding to the rotational DoF:

$$\mathbf{M}^e = \frac{\rho A l}{2} \begin{bmatrix} 1 & 0 & 0 & 0 \\ 0 & l^2/12 & 0 & 0 \\ 0 & 0 & 1 & 0 \\ 0 & 0 & 0 & l^2/12 \end{bmatrix} \quad (7.37)$$

7.2.5 Model Reduction

The finite element discretization of an engineering vibration problem usually generates a very large number of DoF. In particular, when automatic meshing schemes are not properly applied, or three-dimensional elements must be used, the number of elements created could become too great to be cost-effectively handled with limited computer capabilities. To solve this problem, modelers have to pay close attention to how the meshing is done in commercial software packages. Very often, simplification and idealization based on the nature of the problem of concern can tremendously reduce the number

of elements. For example, there could be two ways of generating the finite elements of a clamped-free steel beam with a metal block attached to its free end. One way is to mesh both the beam and the block using three-dimensional elements; the other way is to mesh the beam with one-dimensional beam elements and treat the block as a lumped mass, zero-dimensional element. It is obvious that the first approach will result in many more elements than the second approach. However, both approaches will give very similar results for the first several natural frequencies and the associated mode shapes. Another technique for reducing the number of elements comes from deleting the detailed features. The detailed features here imply those geometrical details, such as fillets, chamfers, small holes, and so on, which do not have significant contributions to the vibration behavior of the entire structure, but increase the number of elements. Generally these detailed features can be deleted without any visible effect on the results, if the global behavior of the vibration problem is of concern. Note that such detailed features may have to be kept if the localized behavior such as fatigue (stress) induced by vibration is to be evaluated.

When further model reduction is necessary, Guyan reduction [3] is considered. It was proposed two decades ago when computer capabilities were much more limited than today. In fact, Guyan reduction is still in use today and has been cast into many commercial software packages. In Guyan reduction, the model scale is reduced by removing those DoF (called slave DoF) that can be approximately expressed by the rest of the DoF (called master DoF) through a static relation. The DoF associated with zero mass or relatively small mass are likely candidates for slave DoF.

By rearranging the DoF \mathbf{u} so that those to be removed, denoted by \mathbf{u}^2 , appear last in the vector, and partitioning the mass and the stiffness matrices accordingly, one obtains

$$\begin{bmatrix} \mathbf{M}_{11} & \mathbf{M}_{12} \\ \mathbf{M}_{21} & \mathbf{M}_{22} \end{bmatrix} \begin{Bmatrix} \ddot{\mathbf{u}}^1 \\ \ddot{\mathbf{u}}^2 \end{Bmatrix} + \begin{bmatrix} \mathbf{K}_{11} & \mathbf{K}_{12} \\ \mathbf{K}_{21} & \mathbf{K}_{22} \end{bmatrix} \begin{Bmatrix} \mathbf{u}^1 \\ \mathbf{u}^2 \end{Bmatrix} = \begin{Bmatrix} \mathbf{F} \\ \mathbf{0} \end{Bmatrix} \quad (7.38)$$

If we assume $\mathbf{M}_{22} = \mathbf{0}$, and $\mathbf{M}_{21} = \mathbf{0}$, then the second equation in Equation 7.38 can be written as

$$\mathbf{u}^2 = -\mathbf{K}_{22}^{-1} \mathbf{K}_{21} \mathbf{u}^1 \quad (7.39)$$

Define the transformation

$$\mathbf{u} = \mathbf{Q} \mathbf{u}^1 \quad (7.40)$$

where the transformation matrix \mathbf{Q} is

$$\mathbf{Q} = \begin{bmatrix} \mathbf{I} \\ -\mathbf{K}_{22}^{-1} \mathbf{K}_{21} \end{bmatrix} \quad (7.41)$$

and \mathbf{I} is the unit (identity) matrix.

Substituting Equation 7.40 into Equation 7.38 and premultiplying the resulting equation by \mathbf{Q}^T , one obtains a new reduced-order model

$$\mathbf{Q}^T \mathbf{M} \mathbf{Q} \ddot{\mathbf{u}}^1 + \mathbf{Q}^T \mathbf{K} \mathbf{Q} \mathbf{u}^1 = \mathbf{F} \quad (7.42)$$

where

$$\mathbf{Q}^T \mathbf{M} \mathbf{Q} = \mathbf{M}_{11} - \mathbf{M}_{12} \mathbf{K}_{22}^{-1} \mathbf{K}_{21} + \mathbf{K}_{21}^T \mathbf{K}_{22}^{-1} \mathbf{M}_{22} \mathbf{K}_{22}^{-1} \mathbf{K}_{21} \quad (7.43)$$

and

$$\mathbf{Q}^T \mathbf{K} \mathbf{Q} = \mathbf{K}_{11} - \mathbf{K}_{12} \mathbf{K}_{22}^{-1} \mathbf{K}_{21} \quad (7.44)$$

Newton's law

$$\mathbf{M}\ddot{\mathbf{u}}(t) = -\mathbf{F}$$

Hooke's Law

$$\mathbf{F} = \mathbf{K}\mathbf{u}(t)$$

Hamilton's principle

$$\delta \int_{t_1}^{t_2} (T - V) dt + \int_{t_1}^{t_2} \delta W dt = 0$$

Finite element equation without damping

$$\mathbf{M}\ddot{\mathbf{u}} + \mathbf{K}\mathbf{u} = \mathbf{F}$$

$$\mathbf{M} = \sum_e \mathbf{L}^T \mathbf{M}^e \mathbf{L}, \quad \mathbf{K} = \sum_e \mathbf{L}^T \mathbf{K}^e \mathbf{L}, \quad \mathbf{F} = \sum_e \mathbf{L}^T \mathbf{F}^e$$

Guyan reduction scheme

$$\mathbf{Q}^T \mathbf{M} \mathbf{Q} \ddot{\mathbf{u}}^1 + \mathbf{Q}^T \mathbf{K} \mathbf{Q} \mathbf{u}^1 = \mathbf{F}$$

$$\mathbf{Q} = \begin{bmatrix} \mathbf{I} \\ -\mathbf{K}_{22}^{-1} \mathbf{K}_{21} \end{bmatrix}$$

7.3 Vibration Analysis

According to the vibration characteristics to be extracted, vibration analysis can be categorized into the following two types: natural vibration analysis, including modal analysis (see Chapter 1 and Chapter 3), and (forced) response analysis (see Chapter 2). Natural vibration analysis can extract natural vibration frequencies and the associated mode shapes, which is a matrix eigenvalue problem (see Chapter 3), and can result from a finite element discretization. The response analysis refers to the calculation of the response, which can be displacements, strain, or stress, when the system is subjected to time-varying excitation forces. The response analysis can be further divided into any one a combination of harmonic response analysis, transient response analysis, and response spectrum analysis, depending on the nature of excitation forces.

7.3.1 Natural Vibration

As noted in previous chapters, the natural vibration frequencies (or simply *natural frequencies*) and the associated mode shapes of a vibrating system are independent of excitation forces. In other words, they are intrinsic characteristics of the vibration problem. Therefore, they constitute an important part of vibration theory and vibration engineering. When vibration engineers specify design requirements in terms of vibration, they normally do so by restricting natural frequencies, and sometimes restricting mode shapes as well. For instance, in order to enhance the passenger comfort, vehicle designers have to ensure that the first few natural frequencies of the vehicle are not within a certain range; in order to avoid vibration resonance, the natural frequencies of a transmission shaft should be designed not to be identical or even close to the rotating speeds of the shaft; in order to effectively control vibration, vibration sensors and actuators have to be located at those places where the dominant mode shapes have large displacements.

From a mathematical standpoint, the natural vibration analysis of a multi-DoF system requires the solution of a matrix eigenvalue problem. According to the theory of second-order ordinary differential equations, the solution of Equation 7.34, when $\mathbf{F} = \mathbf{0}$, can be expressed as $\mathbf{u} = \mathbf{v} e^{i\omega t}$. By substituting $\mathbf{u} = \mathbf{v} e^{i\omega t}$ into Equation 7.34 and letting $\mathbf{F} = \mathbf{0}$, one can obtain

$$\omega^2 \mathbf{M} \mathbf{v} = \mathbf{K} \mathbf{v} \quad (7.45)$$

Equation 7.45 represents a generalized matrix eigenvalue problem. For an N -dimensional matrix pair (\mathbf{M}, \mathbf{K}) , there exist N pairs of solutions (ω_i, \mathbf{v}_i) , $\omega_i^2 \mathbf{M} \mathbf{v}_i = \mathbf{K} \mathbf{v}_i$ ($i = 1, 2, \dots, N$), where ω_i and \mathbf{v}_i are called the i th natural frequency and the associated i th mode shape, respectively.

The numerical methods for solving the matrix eigenvalue problem given by Equation 7.45 have been well developed with the symmetric and sparse features of (\mathbf{M}, \mathbf{K}) being fully considered. Those that have been used by commercial finite element software packages include the power method, the subspace iteration method, the LR method, the QR method, the Givens method, the Householder method, and the Lanczos method.

When conducting vibration modeling, modelers need to understand how idealization and simplification will affect the resulting natural frequencies and the associated mode shapes. Idealization and simplification cause a difference between the actual mass matrix \mathbf{M} and the resulting mass matrix \mathbf{M}_r ($\mathbf{M} = \mathbf{M}_r + \Delta \mathbf{M}$), and a difference between the actual stiffness matrix \mathbf{K} and the resulting stiffness matrix \mathbf{K}_r ($\mathbf{K} = \mathbf{K}_r + \Delta \mathbf{K}$). Rayleigh's quotient [9,11] can be used to determine the effect of $\Delta \mathbf{K}$ and $\Delta \mathbf{M}$ on a particular natural frequency. Rayleigh's quotient is defined as

$$R(\mathbf{x}) = \frac{\mathbf{x}^T \mathbf{K} \mathbf{x}}{\mathbf{x}^T \mathbf{M} \mathbf{x}} \quad (7.46)$$

Note that Rayleigh's quotient $R(\mathbf{x})$ becomes the square of the i th natural vibration frequency, $R(\mathbf{x}) = \omega_i^2$, when $\mathbf{x} = \mathbf{v}_i$. Thus, Rayleigh's quotient can be expressed as

$$\omega_i^2 + \Delta \omega_i^2 = \frac{(\mathbf{v}_i^T + \Delta \mathbf{v}_i^T)(\mathbf{K}_r + \Delta \mathbf{K})(\mathbf{v}_i + \Delta \mathbf{v}_i)}{(\mathbf{v}_i^T + \Delta \mathbf{v}_i^T)(\mathbf{M}_r + \Delta \mathbf{M})(\mathbf{v}_i + \Delta \mathbf{v}_i)} \quad (7.47)$$

where $\Delta \omega_i^2$ and $\Delta \mathbf{v}_i$ are the increase of the i th natural frequency and the variation of the i th mode shape, respectively, induced by $\Delta \mathbf{K}$ and $\Delta \mathbf{M}$. Because of the fact that $R(\mathbf{x})$ reaches the stationary value when \mathbf{x} is equal to the eigenvector \mathbf{v}_i , Equation 7.47 can be simplified as [1,4]

$$\Delta \omega_i^2 = \mathbf{v}_i^T (\Delta \mathbf{K} - \Delta \mathbf{M}) \mathbf{v}_i \quad (7.48)$$

Equation 7.48 indicates that an increase in stiffness leads to a rise in a natural frequency, but an increase in mass causes a decrease in a natural frequency, as is intuitively clear.

7.3.2 Harmonic Response

Harmonic response analysis determines the response of a vibration system (model) to harmonic excitation forces. A typical output is a plot showing response (usually displacement of a certain DoF) versus frequency. This plot indicates how the response at a certain DoF, as a function of excitation frequency, changes with excitation frequency. The harmonic response can also be used to calculate the response to a general periodic excitation force, if it can be satisfactorily approximated by a summation of its major harmonic components.

Consider a harmonic excitation force, $\mathbf{F}(t) = \mathbf{F}_0 e^{i\omega t}$. Substituting it into Equation 7.34, we have

$$\mathbf{M} \ddot{\mathbf{u}}(t) + \mathbf{K} \mathbf{u}(t) = e^{i\omega t} \mathbf{F}_0 \quad (7.49)$$

According to the theory of differential equations, its steady solution can be written as $\mathbf{u}(t) = e^{i\omega t} \mathbf{U}$. After substitution of $\mathbf{u}(t) = e^{i\omega t} \mathbf{U}$ into Equation 7.49, one obtains

$$(-\omega^2 \mathbf{M} + \mathbf{K}) \mathbf{U} = \mathbf{F}_0 \quad (7.50)$$

Harmonic response analysis will solve Equation 7.50 for \mathbf{U} against ω . There are many numerical methods available for solving Equation 7.50. The most efficient one is the modal superposition method.

In the modal superposition method, the response is expressed as a linear combination given by

$$\mathbf{u}(t) = \sum_{i=1}^j \mathbf{v}_i \hat{\mathbf{u}}_i(t) = \mathbf{\Phi} \hat{\mathbf{u}}(t) \quad (7.51)$$

where $\mathbf{\Phi} = [\mathbf{v}_1, \mathbf{v}_2, \dots, \mathbf{v}_j]$ is a modal matrix that contains the dominant mode shapes, and $\hat{\mathbf{u}}^T(t) = [\hat{\mathbf{u}}_1(t), \hat{\mathbf{u}}_2(t), \dots, \hat{\mathbf{u}}_j(t)]$ are called modal coordinates. Substituting Equation 7.51 into Equation 7.49 and premultiplying the result by $\mathbf{\Phi}^T$, we obtain

$$\ddot{\hat{\mathbf{u}}}(t) + \mathbf{\Lambda} \hat{\mathbf{u}}(t) = \mathbf{\Phi}^T e^{i\omega t} \mathbf{F}_0 \quad (7.52)$$

Note that the modal matrix $\mathbf{\Phi}$ has already been normalized against the mass matrix ($\mathbf{\Phi}^T \mathbf{M} \mathbf{\Phi} = \mathbf{I}$), and that $\mathbf{\Lambda} = \text{diag}(\omega_1, \omega_2, \dots, \omega_j)$.

Equation 7.52 represents a set of decoupled modal equations with a much smaller dimension than Equation 7.49. After solving Equation 7.52 for $\hat{\mathbf{u}}(t)$ and transforming $\hat{\mathbf{u}}(t)$ back to $\mathbf{u}(t)$ through Equation 7.51, we obtain $\mathbf{u}(t)$.

7.3.3 Transient Response

Transient response analysis (sometimes called time-history analysis) determines the dynamic response of a structure under the action of time-varying excitation. Excitation forces are explicitly defined in the time domain. The computed response usually includes the time-varying displacements, accelerations, strains, and stresses. Consider Equation 7.34 in its general form

$$\begin{cases} \mathbf{M} \ddot{\mathbf{u}}(t) + \mathbf{K} \mathbf{u}(t) = \mathbf{F}(t) \\ \mathbf{u}(0) = \mathbf{u}_0; \quad \dot{\mathbf{u}}(0) = \dot{\mathbf{u}}_0 \end{cases} \quad (7.53)$$

where $\mathbf{F}(t)$ is the excitation force, \mathbf{u}_0 is the initial displacement, and $\dot{\mathbf{u}}_0$ is the initial velocity. As in the harmonic response analysis, Equation 7.53 can be solved by the modal superposition method.

Substituting Equation 7.51 into Equation 7.53, premultiplying the result of the first equation by $\mathbf{\Phi}^T$, and premultiplying the result of the initial condition by $\mathbf{\Phi}^T \mathbf{M}$, we obtain

$$\begin{cases} \ddot{\hat{\mathbf{u}}}(t) + \mathbf{\Lambda} \hat{\mathbf{u}}(t) = \mathbf{\Phi}^T \mathbf{F}(t) \\ \hat{\mathbf{u}}(0) = \mathbf{\Phi}^T \mathbf{M} \mathbf{u}_0; \quad \dot{\hat{\mathbf{u}}}(0) = \mathbf{\Phi}^T \mathbf{M} \dot{\mathbf{u}}_0 \end{cases} \quad (7.54)$$

Equation 7.54 represents a set of decoupled modal equations, which can be solved by means of numerical integration techniques. After solving Equation 7.54 for $\hat{\mathbf{u}}(t)$ and transforming $\hat{\mathbf{u}}(t)$ back to $\mathbf{u}(t)$ through Equation 7.51, we can obtain $\mathbf{u}(t)$.

To implement the numerical integration techniques, the overall time period being studied has to be divided into a number of smaller time steps. If the time step is too large, portions of the response (such as spikes) could be missed or truncated. On the other hand, if the time step is too small, the analysis will take an excessively long time or even a prohibitive amount of time.

7.3.4 Response Spectrum

The excitation forces, resulting from earthquakes, winds, ocean waves, jet engine thrust, uneven roads, and so on, do not have repeated patterns, for a variety of reasons, and thus it is difficult to describe them using a deterministic time history. Such excitations are normally treated as random excitations. The assumption that such excitation forces are random is recognition of our lack of knowledge of the detailed

characteristics of the excitation forces. Some excitation forces, like those resulting from an uneven road, could be measured to any desired accuracy, and thus they would become deterministic rather than random. But it is not cost-effective and not convenient to do so. Therefore, engineers prefer to characterize these excitation forces by a statistical description that can be easily measured on any particular representative length of time history. Of the statistical descriptions, the autocorrelation function and the power spectral density function are the most important. Denote $f(t)$ as a stationary random excitation force, and $R_f(\tau)$ as its autocorrelation function and $S_f(\omega)$ as its power spectral density function. Their relations [6] are

$$R_f(\tau) = \lim_{T \rightarrow \infty} \frac{1}{T} \int_0^T f(t)f(t + \tau)dt \quad (7.55)$$

$$S_f(\omega) = \int_{-\infty}^{\infty} R_f(\tau)e^{-i\omega\tau} d\tau \quad (7.56)$$

The response spectrum analysis here calculates the power spectral density function of the response of a vibration model to a random excitation force, described by its power spectral density function (see Chapter 5). For the single DoF system given in Figure 7.1

$$m\ddot{u}(t) + ku(t) = f(t) \quad (7.57)$$

The power spectral density function of the response $u(t)$ is given by

$$S_u(\omega) = |H(\omega)|^2 S_f(\omega) \quad (7.58)$$

where

$$H(\omega) = (-m\omega^2 + k)^{-1} \quad (7.59)$$

is the frequency response function representing the natural vibration characteristic of the system.

In the case of the multiple-DoF system given by Equation 7.34, the random excitation force $\mathbf{F}(t)$ is a column vector. For the sake of simplicity, we assume all of the components in the vector $\mathbf{F}(t)$ are stationary and statistically independent. Accordingly, all of the components in the vector of the response $\mathbf{u}(t)$ are stationary. Under this assumption, the power spectral density function of the response $\mathbf{u}(t)$ is determined by

$$\mathbf{S}_u(\omega) = \mathbf{H}(\omega)\mathbf{S}_f(\omega)\mathbf{H}^T(\omega) \quad (7.60)$$

where $\mathbf{S}_f(\omega)$ is a diagonal matrix with its i th element as the power spectral density function of the i th element in $\mathbf{F}(t)$, and $\mathbf{H}(\omega)$ is the frequency response function matrix defined by

$$\mathbf{H}(\omega) = (-\mathbf{M}\omega^2 + \mathbf{K})^{-1} \quad (7.61)$$

From Equation 7.60 and Equation 7.61 one can see that the power spectral density function matrix of the response is correlated to the power spectral density function matrix of the excitation force by means of the frequency response matrix of the system $\mathbf{H}(\omega)$. In commercial finite element software packages, $\mathbf{H}(\omega)$ is often calculated by the truncated modal method in which $\mathbf{H}(\omega)$ is approximately expressed by the dominant natural frequencies and the associated mode shapes, neglecting the contributions of the other mode shapes to $\mathbf{H}(\omega)$, as given below.

$$\mathbf{H}(\omega) \approx \sum_i \frac{\mathbf{v}_i \mathbf{v}_i^T}{\omega_i^2 - \omega^2} \quad (7.62)$$

Natural vibration analysis (generalized eigenvalue problem)

$$\omega^2 \mathbf{M} \mathbf{v} = \mathbf{K} \mathbf{v}$$

Rayleigh's quotient

$$R(\mathbf{x}) = \frac{\mathbf{x}^T \mathbf{K} \mathbf{x}}{\mathbf{x}^T \mathbf{M} \mathbf{x}}$$

Harmonic response

$$(-\omega^2 \mathbf{M} + \mathbf{K}) \mathbf{U} = \mathbf{F}_0$$

$$\mathbf{u}(t) = \sum_{i=1}^j \mathbf{v}_i \hat{\mathbf{u}}_i(t) = \Phi \hat{\mathbf{u}}(t)$$

$$\ddot{\hat{\mathbf{u}}}(t) + \Lambda \hat{\mathbf{u}}(t) = \Phi^T e^{i\omega t} \mathbf{F}_0$$

Transient response

$$\begin{cases} \mathbf{M} \ddot{\mathbf{u}}(t) + \mathbf{K} \mathbf{u}(t) = \mathbf{F}(t) \\ \mathbf{u}(0) = \mathbf{u}_0; \quad \dot{\mathbf{u}}(0) = \dot{\mathbf{u}}_0 \end{cases}$$

$$\begin{cases} \ddot{\hat{\mathbf{u}}}(t) + \Lambda \hat{\mathbf{u}}(t) = \Phi^T \mathbf{F}(t) \\ \hat{\mathbf{u}}(0) = \Phi^T \mathbf{M} \mathbf{u}_0; \quad \hat{\dot{\mathbf{u}}}(0) = \Phi^T \mathbf{M} \dot{\mathbf{u}}_0 \end{cases}$$

Response spectrum analysis

$$\mathbf{S}_u(\omega) = \mathbf{H}(\omega) \mathbf{S}_f(\omega) \mathbf{H}^T(\omega)$$

$$\mathbf{H}(\omega) = (-\mathbf{M}\omega^2 + \mathbf{K})^{-1}$$

7.4 Commercial Software Packages

There are many commercial finite element analysis (FEA) software packages available for vibration analysis, and they have been so well developed that they have an extensive range of vibration analysis capabilities. Some software packages are intended for generic engineering structures, for example, ABAQUS, ADINA, ALGOR, ANSYS, COSMOSWorks, MSC/NASTRAN, DYNA3D, and LS-DYNA. The others are designed for the vibration analysis of specific vibration problems. For example, the software package Bridge and the software package LUSAS Bridge are for the vibration analysis of bridges.

Normally, FEA modeling software has the following three major components: a preprocessor, a solver, and a postprocessor. The preprocessor is responsible for building up geometries, meshing, specification of element types, material properties, and boundary conditions; the solver solves the matrix equations; the postprocessor provides visualization of results and outputs the results in different formats. Because of the fact that those CAD/CAE systems such as CATIA, Unigraphics, Pro/E, and Solidworks have powerful capabilities for building up geometries, vibration modelers often import geometries from such systems rather than building them up using the FEA modeling software packages themselves.

In this section, we will select the software packages ABAQUS, ADINA, ALGOR, ANSYS, COSMOSWorks, MSC/NASTRAN, ABAQUS/Explicit, DYNA3D, and LS-DYNA, and will briefly introduce their major capabilities for vibration analysis. In fact, the vibration analysis capability is only a small portion of their total capabilities. All of these packages can perform basic vibration analysis

including: (1) determination of natural mode shapes and frequencies, (2) transient response, (3) steady-state response resulting from harmonic loading, and (4) response spectrum analysis. In addition, each of them has its own strengths in some specific areas. These special capabilities are listed below.

7.4.1 ABAQUS

The ABAQUS software is for linear and nonlinear engineering analyses. Due to its wide range of functionality, ABAQUS usage spans many industries, including automotive, aerospace and defense, consumer electronics, manufacturing, medical, and rubber sealing.

Some special capabilities include

- Analysis of the coupled phenomena: thermo-mechanical, thermo-electrical, piezoelectric, pore fluid flow-mechanical, stress–mass diffusion, and shock and acoustic-structural
- Substructures and submodeling
- Material removal and addition
- Fracture mechanics design evaluation
- Parameterization and parametric studies
- User subroutines

7.4.2 ADINA

The ADINA system offers comprehensive finite element analyses of structures, fluids, and fluid flows with structural interactions. It is widely used in many fields, including the automotive, aerospace, manufacturing, nuclear, and biomedical industries, and in civil engineering and research.

Some special dynamic capabilities include

- Contact problems in statics and dynamics
- Substructuring in statics and dynamics
- Wave propagation and shock wave analysis

7.4.3 ALGOR

ALGOR's Professional Multiphysics includes capabilities for static structural analysis and Mechanical Event Simulation with linear and nonlinear material models, steady state and transient thermal analysis, electrostatic analysis, linear dynamics, and steady and unsteady fluid flow analysis. It is used in aerospace and space exploration; the automotive, transportation, consumer products, electronics, entertainment, manufacturing, chemical processing and medical industries; in the defense, power, and utility sectors; in civil engineering and scientific research; and in recreation and sports.

Some special features include

- Rigid-body motion
- Hertzian contact
- Submodeling
- Earthquake simulation
- Fluid–solid interaction
- The EAGLE programming language

7.4.4 ANSYS

ANSYS Software Suite offers capabilities for determining the structural, thermal, acoustic, electrostatic, magnetostatic, electromagnetic, and fluid-flow behavior of three-dimensional product designs, including

the effects of multiphysics. The software simulates complex thermal/mechanical, fluid/structural and electrostatic/structural interactions. It is widely used in the aerospace, automotive, biomedical engineering, chemical engineering, civil engineering, communications, consumer products, defense, electronic packaging, industrial and scientific equipment production, and micro-electromechanical systems (MEMS) industries.

Some special dynamic capabilities include

- Modal analysis of prestressed structures
- Dynamic Topological design optimization
- Substructuring and submodeling
- Coupled field analysis of thermal-structural, fluid-structural, electrostatic-structural, magneto-structural, acoustic-structural, thermal-electric, thermal-electromagnetic, fluid-thermal, piezo-electric fields, and an electromechanical circuit simulator
- A parametric design language

7.4.5 COSMOSWorks

COSMOSWorks offers a wide spectrum of specialized analysis tools to virtually test and analyze complicated parts and assemblies, and is seamlessly integrated with Solidworks. COSMOSWorks is used for linear stress, strain, displacement, thermal analysis, design, optimization, and nonlinear analysis. Combined with ASTAR (Post Dynamics), COSMOSWorks is capable of more advanced dynamic analysis. It is used in a wide range of industries, including aerospace and defense, automotive and transportation, civil engineering, consumer products, electrical and electronics, heavy equipment, marine, medical and power.

The special dynamic features of the ASTAR module are

- Support of uniform and multi-base motion systems; the multi-base motion capability allows engineers to model structures with nonuniform support excitations.
- Support of the gap-friction element, which lets engineers model drop-test and other dynamic contact problems.
- The provision for several damper options such as Rayleigh damping, modal damping, concentrated damping, and composite modal damping.

7.4.6 MSC.Nastran

In 1965, MSC participated in a NASA-sponsored project to develop a unified approach to computerized structural analysis. The program became known as NASTRAN (NASA Structural Analysis Program); one of the first efforts to consolidate structural mechanics into a single computer program. The suite of MSC.Software is used in the space, aircraft, and automotive industries; in rail vehicle development; in general machinery; and in medical and electromechanical devices. Its capabilities include stress, vibration, heat transfer, acoustics, aeroelasticity, and coupled system analysis.

MSC.NASTRAN's special dynamic capabilities include

- Damping
- Direct matrix input
- Dynamic equations of motion
- Residual vector methods
- Enforced motion
- Complex eigenvalue analysis
- Normal mode of preloaded structures
- Dynamic design optimization
- Test-analysis correlation

7.4.7 ABAQUS/Explicit

ABAQUS/Explicit uses explicit time integration for time stepping and addresses the following special types of analysis:

- Explicit dynamic response with or without adiabatic heating effects
- Fully coupled transient dynamic temperature–displacement procedure; explicit algorithms are used for both the mechanical and thermal response
- Annealing for multistep forming simulations
- Acoustic and coupled acoustic-structural analysis
- Automatic adaptive meshing, which allows robust solutions of highly nonlinear problems

7.4.8 DYNA3D

DYNA3D is an explicit finite element program for structural and continuum mechanics problems. Due to its explicit nature, DYNA3D uses small time steps to integrate the equations of motion and is especially efficient at solving transient dynamic problems.

The specific analysis capabilities of DYNA3D include

- Static analysis using dynamic relaxation
- Dynamic analysis with static initialization from a NIKE3D implicit analysis
- Various contact slideline options for different contact situations between two bodies

7.4.9 LS-DYNA

LS-DYNA is a general-purpose transient dynamic finite element program, and is suited for complex dynamics, vibration, and wave propagation problems. Its explicit algorithm can be used for high-speed impact, shock, and vibration problems. Falling impact, rubber elasticity, and impact on sports goods (rackets, bats, and helmets) are typical examples of problems that can be handled by LS-DYNA. It is widely used in earthquake engineering; crashworthiness and occupant safety analysis; metal forming; biomedical engineering; train crashworthiness testing; sports, airbag, and seat-belt deployment; and in military, manufacturing, metal cutting, and bird strike applications.

The special capabilities of LS-DYNA include

- FEM-rigid multi-body dynamics coupling
- Underwater shock analysis
- Failure analysis
- Crack propagation analysis
- Real-time acoustics
- Design optimization
- Implicit springback analysis
- Multi-physics coupling
- Adaptive re-meshing
- Smooth particle hydrodynamics
- The element-free meshless method

7.5 The Basic Procedure of Vibration Analysis

In this section, a typical procedure in using commercial software packages to conduct vibration analysis is outlined.

7.5.1 Planning

This is a very important part of the entire analysis process, as it helps to ensure the success of the modeling. The quality of the results is strongly dependent on how accurately the model represents the actual problem being investigated. In order to generate a representative finite element model, all influencing factors must be scrutinized to determine whether their effects are considerable or negligible in the final result. The aspects listed below should be given consideration in the planning stage.

- *Modeling objectives.* Why is the vibration analysis required? What is the major concern of designers? What are the working conditions? Does the FEA model have to be used for static stress analysis as well as vibration analysis? These considerations affect how the FEA model is to be built up.
- *Modeling considerations.* Which type of analysis is required: natural vibration analysis or response analysis? What types of elements should be used? Where are loads and constraints applied? Can the model reduction/simplification resulting from symmetrical geometries and loading conditions be applied? There are no universal guidelines for these, but the aspects below can help you to make decision:
 - If the stress varies linearly through the thickness of thin-walled regions, shell elements can be used. If it varies parabolically, then at least three solid, second-order elements are required through the thickness in order to resolve a representative state of stress.
 - If a frequency or buckling analysis is being conducted, a full three-dimensional analysis may be needed to identify non-symmetric mode shapes.
 - If the region of interest is local, then a submodel may be appropriate, as it will save considerable time achieving a solution.
 - Large gradients in stress levels will require a high mesh density to capture the behavior appropriately.
 - The effects of simplifications on boundary conditions should be well predicted, for example: some over-constrained boundary conditions may result in higher natural frequencies of the finite element model.

The degree of accuracy of a model is very much dependant on the level of planning that has been carried out. Careful planning is the key to a successful analysis.

7.5.2 Preprocessing

The preprocessor stage in a general FEA package involves the following:

- *Defining the element type as planned before the analysis.* This may be one-, two-, or three-dimensional.
- *Creating the geometry.* The geometry is drawn in one-, two-, or three-dimensional space according to what kind of elements are going to be used. The model may be created in the preprocessor, or it can be imported from other CAD or CAE systems *via* a neutral file format (IGES, STEP, ACIS, Parasolid, DXF, etc.). The same units should be applied in all models, otherwise the results will be difficult to interpret or, in extreme cases, the results will not show up mistakes made during the loading and restraining of the model.
- *Applying a mesh.* Mesh generation is the process of dividing the continuum into a number of discrete parts or finite elements. The finer the mesh, the more accurate the result, but the longer the processing time. Therefore, a compromise between accuracy and solution speed is usually made. The mesh may be created manually or generated automatically, or, as in most cases, in a combined manner.

Manual meshing is a long and tedious process for models with a fair degree of geometric complication, but with useful tools emerging in preprocessors, the task is becoming easier. Automatic mesh generators are very useful and popular. The mesh is created automatically by a mesh engine; the only requirement is to define the mesh density along the model's edges.

Automatic meshing has limitations as regards mesh quality and solution accuracy. Automatic brick element meshers are limited in function, but are steadily improving. Any mesh is usually applied to the model by simply selecting the mesh command on the preprocessor list of the user interface.

Usually a complex geometry needs to be decomposed into many smaller components in order to use the automatic meshing tool.

- *Assigning properties.* Material properties (Young's modulus; Poisson's ratio; the density; and if applicable, the coefficients of expansion, friction, thermal conductivity, damping effect, specific heat, etc.) will have to be defined. In addition element properties may need to be set. If two-dimensional elements are being used, the thickness property is required. One-dimensional beam elements require area, I_{xx} , I_{yy} , I_{zz} , J , and the direction of the beam axis in three-dimensional space. Shell elements, which are two-dimensional elements in three-dimensional space, require orientation and neutral surface offset parameters to be defined. Special elements such as mass, contact, spring, gap, coupling, damper, and so on require properties (specific to the element type) to be defined for their use.
- *Applying loads.* In the case of transient response analysis, some type of load is usually applied to the analysis model. The loading may be in the form of a point force, a pressure or a displacement, or a temperature or heat flux in a thermal analysis. The loads may be applied to a point, an edge, a surface, or even a complete body. The loads should be in the same unit system as the model geometry and material properties specified. In the case of modal analyses, a load does not have to be specified for the analysis to run.
- *Applying boundary conditions.* Structural boundary conditions are usually in the form of zero displacements; thermal boundary conditions are usually specified temperatures. A boundary condition may be specified to act in all directions (x, y, z), or in certain directions only. Boundary conditions can be placed on nodes, key points, lines, or areas. The boundary conditions applied on lines or areas can be of a symmetric or antisymmetric type, one allowing inplane rotations and out of plane translations, the other allowing in plane translations and out of plane rotations for a given line or area. The application of correct boundary conditions is critical to the accurate solution of the design problem.

7.5.3 Solution

The FEA solver can be logically divided into three main parts: the presolver, the mathematical-engine, and the postsolver. The presolver reads in the model created by the preprocessor and formulates the mathematical representation of the model. All the parameters defined during the preprocessing stage are used to do this, so if something has been omitted the presolver is very likely to stop the call to the mathematical-engine. If the model is correct, the solver proceeds to form the element stiffness matrix and the element mass matrix for the problem and calls the mathematical-engine, which calculates the result. The results are returned to the solver and the postsolver is used to calculate strains, stresses, velocities, response, and so on for each node within the component or continuum. All these results are sent to a result file that may be read by the postprocessor.

7.5.4 Postprocessing

Here the results of the analysis are read and interpreted. They can be presented in the form of a table, a contour plot, a deformed shape of the component, or the mode shapes and natural frequencies if frequency analysis is involved. Most postprocessors provide animation tools.

Contour plots are usually the most effective way of viewing results for structural type problems. Slices can be made through three-dimensional models to facilitate the viewing of internal stress and deformation patterns.

All postprocessors now include the calculation of stresses and strains in any of the x , y , or z directions; or indeed in a direction at an angle to the coordinate axes. The principal stresses and strains may also be plotted, or if required, the yield stresses and strains according to the main theories of failure (Von Mises, St Venant, Tresca, etc.).

7.5.5 Engineering Judgment

For many reasons, the vibration analysis results may not represent the actual vibration problem very well. Software packages will not reveal anything about this, and so it is the responsibility of modelers to make judgments.

Sound judgment comes from a thorough understanding of the actual vibration problem; indepth knowledge of vibration theory, FEA, and the software package used; and also rich experience in modeling. When you are not confident of your vibration analysis results you should check the following:

1. What units have been used, SI units or Imperial units? Are the units used consistent and compatible with the software package you are using?
2. What are the material's properties?
3. Is the boundary free or partially constrained, or flexibly connected to other parts?
4. How are the interconnections between different parts modeled (e.g., the interconnection between a two-dimensional plate and a three-dimensional block)?

Sometimes, a judgment is made by comparing your model's results and the results of different models that are similar in some sense to the one of concern, but which have been validated. A judgment can also be made by vibration measurements or testing under laboratory conditions or in real-life situations (see [Chapter 17](#) and [Chapter 18](#)). By properly exploiting the combined test and analysis data, modelers can effectively and reliably identify otherwise only approximately known structural properties (e.g., joint stiffness), material properties, and loading; validate and refine the FEA model (simplification validation, model updating, etc.) by using test results as reference data; identify unknown or badly known physical properties; and better assess uncertainties in the FEA model.

7.6 An Engineering Case Study

In this section, we illustrate the procedure for the vibration analysis of a gearbox housing, shown in [Figure 7.3](#). The vibration analysis was performed using ANSYS [5].

7.6.1 Objectives

The chief aim of the vibration analysis is to ensure that the gearbox housing is not subject to a dangerous resonant condition during the full range of operation. Specifically, the natural vibration frequencies of the gearbox housing have to be widely separated from the rotating speeds of the shafts. Hence, natural vibration analysis is required for this purpose. Furthermore, there are concerns about the strength of the gearbox, and so a static stress analysis is also required.

7.6.2 Modeling Strategy

The gearbox housing shown in [Figure 7.3](#) contains the following three subparts: the vertical cylinder, the front housing, and the rear housing, which are welded together. Because the FEA model has to be built up with the considerations of both vibration analysis and static stress analysis, some detailed

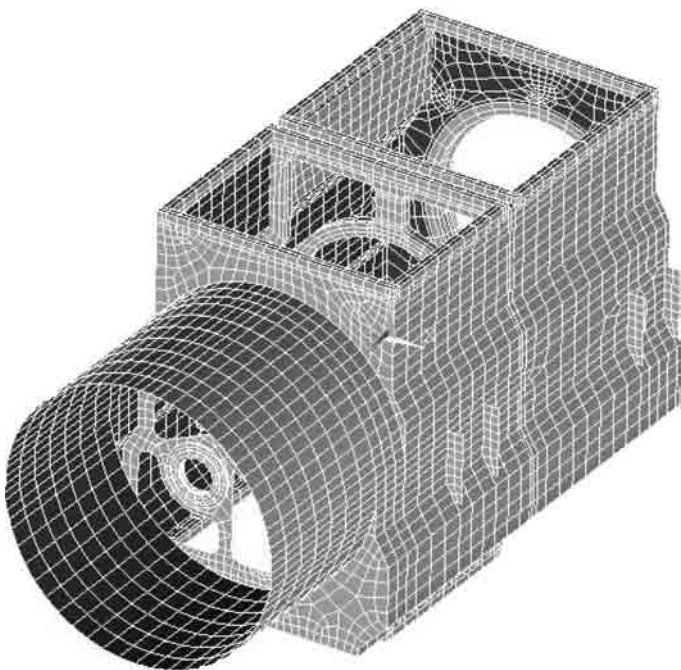


FIGURE 7.3 Finite element model of the gearbox housing. (Courtesy of Pacific Rim Engineered Products, Surrey, British Columbia.)

geometries such as fillets are not deleted but modeled with fine meshes. In addition, a sufficient level of attention is paid to the interconnections between different sections. To achieve a balance between the accuracy of the results and the size of finite element model, quadratic elements (midsize nodes) are used for both shell elements and solid elements. These usually yield better results at less expense than linear elements.

Three types of finite elements are used to model the different parts:

1. The front cylinder plate, side plates and bottom plate: shell elements with variable thickness; 8 nodes, 6 DoF per node.
2. The ribs and fringes: solid elements; 20 nodes, 3 DoF per node.
3. The gears, shafts, clutch, and bearings: lumped mass elements; 1 node, 6 DoF per node.

Because of the discrepancy in the DoF between the shell elements and the solid elements, the nodal rotating freedoms around the edges that connect shell elements and solid elements together are not constrained, and consequently each rotating freedom needs to be constrained by two nodal translation freedoms on solid elements near the edge, but not on the edge.

The total numbers of nodes, shell elements, and solid elements are given in Table 7.1, and the complete finite element model is shown in Figure 7.3.

TABLE 7.1 Total Size of the Finite Element Model of the Gearbox Housing

Nodes	36,523
Shell elements	4,060
Solid elements	3,760

TABLE 7.2 Material Properties

Density	7800 kg/m ³
Young's modulus	2.1×10^{11} Pa
Poisson coefficient	0.29

TABLE 7.3 The First 10 Natural Frequencies

No.	Frequency (Hz)
1	46.46
2	67.73
3	81.57
4	105.5
5	166.2
6	204.6
7	205.1
8	212.0
9	213.4
10	222.8

7.6.3 Boundary Conditions

The four mountings on each side are constrained completely and the front edge of the cylinder is also completely constrained.

7.6.4 Material

The mechanical properties of the material are given in Table 7.2.

7.6.5 Results

The first 10 natural frequencies and the associated mode shapes are calculated with a Lanczos algorithm. They are listed in Table 7.3.

The first and the fifth mode shapes are shown in [Figure 7.4](#) and [Figure 7.5](#), respectively.

7.7 Comments

Vibration modeling using the finite element method is extremely powerful. However, with comforting contour plots, one can be easily deceived into thinking that a superior result has been achieved. Nevertheless, the quality of the result directly depends upon how accurately the model represents the actual physical problem being investigated. This involves three things: sufficient understanding of the actual vibration problem, sufficient knowledge of vibration theory including FEA, and hands-on experience in running an FEA software package. In particular, modelers have to understand the limitations of the theories applied and the numerical methods used. For example, the FEA can predict global characteristics such as natural frequencies of vibration and mode shapes more accurately than localized features such as stresses. This is an intrinsic nature of finite element methods. Without knowing this, modelers might incorrectly use an unnecessarily fine mesh for mode shape analysis while applying coarse meshes to evaluate stress.

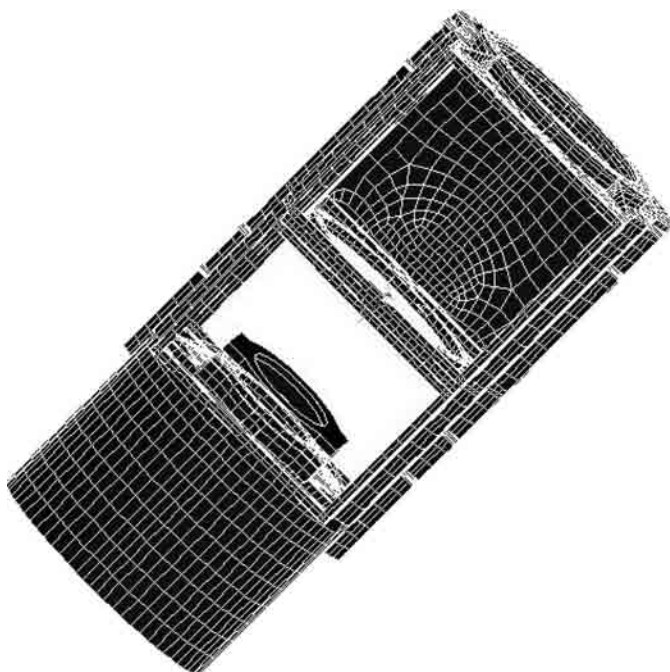


FIGURE 7.4 The first mode shape (46.5 Hz) of the gearbox housing. (Courtesy of Pacific Rim Engineered Products, Surrey, British Columbia.)

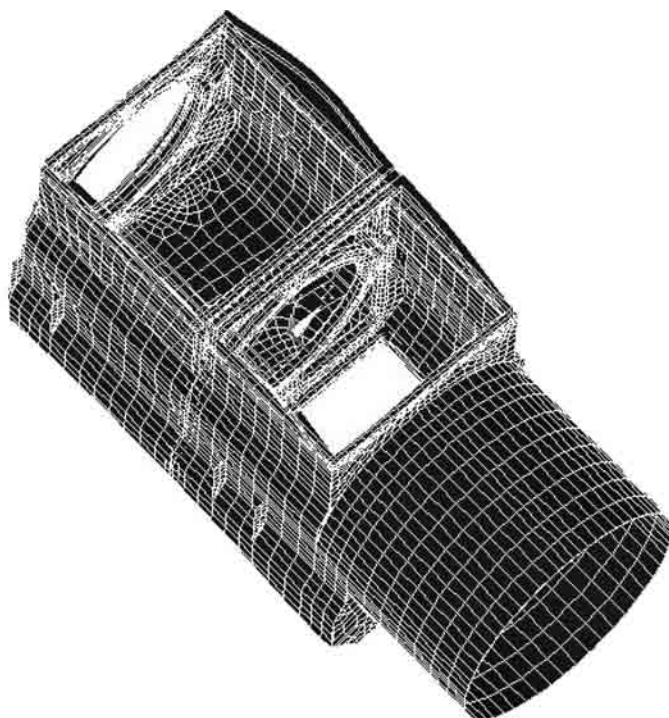


FIGURE 7.5 The fifth mode shape (166.2 Hz) of the gearbox housing. (Courtesy of Pacific Rim Engineered Products, Surrey, British Columbia.)

References

1. Chen, S. 1993. *Matrix Perturbation Theory in Structural Dynamics*, International Academic Publishers, Beijing.
2. den Hartog, J.P. 1984. *Mechanical Vibrations*, 4th ed., McGraw-Hill, New York.
3. Guyan, R.I., Reduction of stiffness and mass matrices, *AIAA Journal*, 3, 2, 380–381, 1965.
4. Hu, H.C. 1984. *Variational Principles of Theory of Elasticity with Applications*, Science Press, Beijing.
5. Moaveni, S. 1999. *Finite Element Analysis. Theory and Application with ANSYS*, Prentice Hall, Upper Saddle River, NJ.
6. Newland, D.E. 1993. *An Introduction to Random Vibration, Spectral and Wavelet Analysis*, Longman Scientific & Technical, New York.
7. Petyt, M. 1990. *Introduction to Finite Element Vibration Analysis*, Cambridge University Press, UK.
8. Rao, S.S. 1995. *Mechanical Vibrations*, 3rd ed., Addison-Wesley, Reading, MA.
9. Rayleigh, J.W.S. 1945. *Theory of Sound*, Vol. 1/2, Dover Publications, New York.
10. Turner, M.J., Clough, R.W., Martin, H.C., and Topp, L.J., Stiffness and deflection analysis of complex structures, *J. Aeronaut. Sci.*, 23, 805–823, 1956.
11. Washizu, K. 1982. *Variational Methods in Elasticity & Plasticity*, 3rd ed., Pergamon Press, UK.
12. Zienkiewicz, O.C. 1987. *The Finite Element Method*, 4th ed., McGraw-Hill, London.

Computer Analysis of Flexibly Supported Multibody Systems

8.1	Introduction	8-1
8.2	Theory	8-2
	Definitions and Assumptions • Equations of Motion for the Linear Model • Linear Momentum–Force Systems • Generalization of the Equations of Moment of Momentum • Assembly of Equations	
8.3	A Numerical Example	8-7
	A Uniform Rectangular Prism • VIBRATIO Output	
8.4	An Industrial Vibration Design Problem	8-11
	Static Deflection • Natural Frequencies • Transient Response Analysis • Frequency Analysis • A Flexibly Supported Engine — A Numerical Problem	
8.5	Programming Considerations	8-16
8.6	VIBRATIO	8-17
	Capabilities • Modeling on VIBRATIO	
8.7	Analysis	8-24
	Analysis Options • Eigenvalue Analysis • Linear Deflection Analysis • Frequency Analysis • Time-Domain Analysis	
8.8	Comments	8-31
	Appendix 8A VIBRATIO Output for Numerical Example in Section 8.3	8-32

Ibrahim Esat

Brunei University

M. Dabestani

Furlong Research Foundation

Summary

This chapter presents the Euler–Newton formulation of oscillatory behavior of a multibody system interconnected by discrete stiffness elements. Bodies are interconnected by springs, and/or dashpots (dampers). Connections are described in terms of end coordinates of springs relative to the coordinate system of the body to which it is attached. Stiffness characteristics are described along the three principal axes of springs. Orientation of springs and masses are described by using appropriate Euler angles. The model developed is linear, and gyroscopic influences are ignored. The chapter gives a detailed treatment of rigid bodies in three dimensional space using vector-matrix formulation. Complete formulation and assembly issues relating to programming aspects are presented. A software suite called VIBRATIO, based on the present formulation, is described. The capabilities of VIBRATIO are indicated and illustrative examples are given in both frequency and time domains. A student version of VIBRATIO is available at no cost to the users of this handbook at www.signal-research.com.

8.1 Introduction

There are many commercial software packages for analysis of kinematics and dynamics of multibody linkage systems. There are fewer software tools for analysis of vibration of multiple rigid-body systems

in 3-D space, even though some finite element analysis (FEA) packages offer rigid-body capability. Common FEA software packages treat rigid bodies using point masses or point inertias. Although this is not a serious restriction, when it comes to attaching discrete stiffness elements to a body away from its center of gravity (COG), the attachment is achieved by introducing “lever arms” with a very high Young’s modulus. One may argue that the error introduced in doing so is acceptable but how true this argument is depends on the problem, and there is no escape from the fact that this approach can create ill-conditioned stiffness matrices. The correct way, however, is to incorporate the created kinematic constraints into rigid-body geometries. This is the approach presented in this chapter. A typical rigid multibody system supported or interconnected by discrete spring elements, as considered here, is shown in Figure 8.1. The chapter presents a complete formulation of a multibody system flexibly supported by linear mountings. The formulations and methods proposed in this chapter are used in the VIBRATIO suite of vibration analysis software.

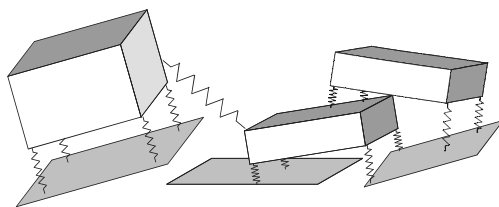


FIGURE 8.1 Schematic representation of a multibody system.

8.2 Theory

8.2.1 Definitions and Assumptions

- Springs have zero length.
- The stiffness parameters of the springs in their principal axes of deflection remain uncoupled.
- The amplitude of oscillation is small. No geometrical nonlinearity is involved. In other words, the orientation of both mountings and bodies remains unaffected by oscillations.
- The time-dependent effects of polymeric material are excluded.
- Gyroscopic effects are negligible.

These assumptions are acceptable for most engineering vibration problems with small amplitude vibration.

8.2.2 Equations of Motion for the Linear Model

To set up equations of motion for a dynamic system, the following steps are required:

- (i) Generation of the equations of internal reactions and external forces. The internal reactions due to damping and stiffness elements have to be expressed in a unified and structured fashion for formulation of the stiffness matrix. (The damping matrix structure is identical to the stiffness matrix structure, except that stiffness coefficients need to be replaced by damping coefficients.)
- (ii) Generation of the equations of linear momentum (force–acceleration equations).
- (iii) Generation of the equations of angular momentum (turning moment equations).

8.2.3 Linear Momentum–Force Systems

8.2.3.1 Stiffness and Damping Systems

The formulations applied in this chapter to obtain the stiffness matrix apply equally to the damping matrix by replacing stiffness parameters with their corresponding damping parameters.

Let us assume that spring stiffness parameters are described in a local three-dimensional (3-D) Cartesian coordinate frame, the axes of which coincide with the principal axes of the springs. The force

vector \mathbf{f} acting on the springs may be expressed as

$$\mathbf{f} = \mathbf{k}\mathbf{x} \quad (8.1)$$

where \mathbf{k} is the stiffness matrix (diagonal with principal stiffness values) and \mathbf{x} is the displacement vector (expressing the spring extension).

In general, it is convenient to describe the behavior of a system in the global coordinate frame, OXYZ. This is not a prerequisite for the formulation. It is equally possible to obtain equations of motion for each body in its own frame. In this chapter, all spring stiffness matrices will be expressed in a common global coordinate frame. The individual spring matrices will be transformed accordingly. Since the principal axes of the springs and the global coordinates are all orthogonal, an orthogonal transformation exists between the two frames. A vector, \mathbf{x} , in the local coordinates could be expressed as a vector, \mathbf{X} , in the global coordinate system. Using, \mathbf{T} , a transformation matrix

$$\mathbf{X} = \mathbf{T}\mathbf{x} \quad (8.2)$$

If we premultiply Equation 8.1 by \mathbf{T} , then we have $\mathbf{T}\mathbf{f} = \mathbf{T}\mathbf{k}\mathbf{x}$. But $\mathbf{T}\mathbf{f} = \mathbf{F}$.

Therefore, force vector, \mathbf{F} , in the global coordinate frame, may be written as

$$\mathbf{F} = \mathbf{T}\mathbf{k}\mathbf{x} \quad (8.3)$$

For consistency, \mathbf{x} needs to be replaced by \mathbf{X} . To replace \mathbf{x} by \mathbf{X} , Equation 8.2 may be used, giving $\mathbf{x} = \mathbf{T}^T\mathbf{X}$. This is true since $\mathbf{T}^{-1} = \mathbf{T}^T$ for orthogonal transformation matrices. Therefore,

$$\mathbf{F} = \mathbf{T}\mathbf{k}\mathbf{T}^T\mathbf{X} \quad (8.4)$$

Then introduce a new matrix \mathbf{K} , where

$$\mathbf{K} = \mathbf{T}\mathbf{k}\mathbf{T}^T$$

Now $\mathbf{T}\mathbf{k}\mathbf{T}^T$ is the stiffness matrix of the spring in the global coordinate system. The transformation matrix \mathbf{T} may be described in three Euler angles of rotation.

8.2.3.2 Generalization of the Equation of Linear Momentum

If the mass/inertia matrix in the Euler–Newton formulation is obtained relative to the axes passing through the center of mass, then the submatrix of the mass matrix corresponding to linear momentum is a diagonal matrix containing the mass elements; thus,

$$\mathbf{h}_i = \mathbf{m}_i\mathbf{v} \quad (8.5)$$

Here, \mathbf{h}_i is linear momentum, \mathbf{m}_i is a diagonal matrix, and \mathbf{v} is the velocity vector of the center of mass (casually known as COG) of the body.

The usual transformation to the global coordinate frame, $\mathbf{H}_i = \mathbf{T}\mathbf{m}_i\mathbf{T}^T\mathbf{v}$, leaves the mass matrix, \mathbf{m} , unchanged. Therefore, the force acting on a body, i (i.e., the rate of change of linear momentum), may be expressed simply as

$$\text{Force} = \dot{\mathbf{H}}_i = \frac{\partial \mathbf{H}_i}{\partial t} = \mathbf{m}\mathbf{a} \quad (8.6)$$

where \mathbf{a} is the acceleration vector of the COG.

8.2.4 Generalization of the Equations of Moment of Momentum

The equations of moment of momentum may be expressed as

$$\mathbf{h}_a = \mathbf{j}\boldsymbol{\omega} \quad (8.7)$$

where \mathbf{h}_a is the angular momentum vector, \mathbf{j} is the moments of inertia matrix and $\boldsymbol{\omega}$ is the angular velocity of the coordinate frame. (In this case, the frame is attached to the body.)

Here, \mathbf{j} may or may not be a diagonal matrix. However, it is always symmetric. Equation 8.7 is described in the local coordinate system of the rigid body and it has to be expressed in the global coordinate system for the final matrix assembly. As presented for the stiffness elements, transformation follows exactly the same steps as before. In this case, \mathbf{T} refers to the transformation matrix of mass relative to the global coordinate system. Transforming Equation 8.7 to the global coordinates, we get

$$\mathbf{H}_a = \mathbf{T}\mathbf{j}\mathbf{T}^T\Omega \quad (8.8)$$

Introduce a new matrix notation

$$\mathbf{J} = \mathbf{T}\mathbf{j}\mathbf{T}^T \quad (8.9)$$

The vector differentiation of \mathbf{H}_a gives the moment vector in the global coordinates

$$\mathbf{M} = \dot{\mathbf{H}}_a = \frac{\partial \mathbf{H}_a}{\partial t} + \boldsymbol{\omega} \times \mathbf{H}_a \quad (8.10)$$

where $\boldsymbol{\omega}$ is the angular velocity of the body (or the coordinate frame, as the body is fixed to the frame).

Note that $\boldsymbol{\omega} \times \mathbf{H}_a$ contains the product of angular velocity terms and this, for small and geometrically linear vibration problems, is small and may be ignored.

8.2.5 Assembly of Equations

To assemble the equations of motion, the internal forces acting on individual bodies due to their motion relative to each other are required. In Figure 8.2, two bodies (i and j) in motion are shown, connected by spring \mathbf{K}_p .

Motion of the origin of vector \mathbf{i} (which coincides with the COG of body i) is given by $\mathbf{x}_i = (x_i, y_i, z_i)$, and the angular rotation of the coordinates is given by $\boldsymbol{\alpha}_i = (\alpha_i, \beta_i, \gamma_i)$. Similarly, the motion of body j is described by $\mathbf{x}_j = (x_j, y_j, z_j)$ and $\boldsymbol{\alpha}_j = (\alpha_j, \beta_j, \gamma_j)$.

For small motions, displacements of the end points of the springs on each body, described in the *coordinate frame* of each body, are given by

$$\mathbf{d}_i = \mathbf{x}_i + \boldsymbol{\alpha}_i \times \mathbf{r}_{pi} \quad (8.11)$$

$$\mathbf{d}_j = \mathbf{x}_j + \boldsymbol{\alpha}_j \times \mathbf{r}_{pj} \quad (8.12)$$

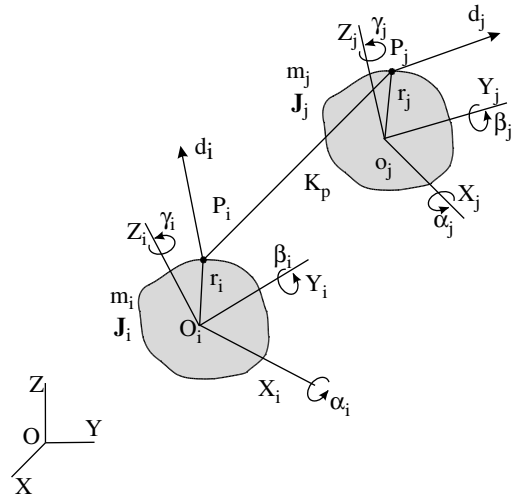


FIGURE 8.2 Two bodies connected by springs.

where \mathbf{r}_{pi} and \mathbf{r}_{pj} are the coordinates of the spring attachment relative to the bodies i and j in their respective coordinate frames, given as $\mathbf{r}_{pi} = (x_{pi}, y_{pi}, z_{pi})$ and $\mathbf{r}_{pj} = (x_{pj}, y_{pj}, z_{pj})$.

Cross-product terms in Equation 8.11 and Equation 8.12 can be converted into matrix form as

$$\boldsymbol{\alpha}_i \times \mathbf{r}_{pi} = \begin{bmatrix} 0 & z_{pi} & -y_{pi} \\ -z_{pi} & 0 & x_{pi} \\ y_{pi} & -x_{pi} & 0 \end{bmatrix} \begin{Bmatrix} \alpha_i \\ \beta_i \\ \gamma_i \end{Bmatrix} \quad (8.13)$$

and

$$\boldsymbol{\alpha}_j \times \mathbf{r}_{pj} = \begin{bmatrix} 0 & z_{pj} & -y_{pj} \\ -z_{pj} & 0 & x_{pj} \\ y_{pj} & -x_{pj} & 0 \end{bmatrix} \begin{Bmatrix} \alpha_j \\ \beta_j \\ \gamma_j \end{Bmatrix} \quad (8.14)$$

Let us choose the matrix notation \mathbf{R}_{pi} as

$$\mathbf{R}_{pi} = \begin{bmatrix} 0 & z_{pi} & -y_{pi} \\ -z_{pi} & 0 & x_{pi} \\ y_{pi} & -x_{pi} & 0 \end{bmatrix} \quad (8.15)$$

and \mathbf{R}_{pj} as

$$\mathbf{R}_{pj} = \begin{bmatrix} 0 & z_{pj} & -y_{pj} \\ -z_{pj} & 0 & x_{pj} \\ y_{pj} & -x_{pj} & 0 \end{bmatrix} \quad (8.16)$$

Therefore,

$$\mathbf{d}_i = \mathbf{x}_i + \boldsymbol{\alpha}_i \times \mathbf{r}_{pi}$$

which is

$$= \begin{Bmatrix} x_i \\ y_i \\ x_i \end{Bmatrix} + \begin{bmatrix} 0 & z_{pi} & -y_{pi} \\ -z_{pi} & 0 & x_{pi} \\ y_{pi} & -x_{pi} & 0 \end{bmatrix} \begin{Bmatrix} \alpha_i \\ \beta_i \\ \gamma_i \end{Bmatrix} \quad (8.17)$$

Using the new notation, we have

$$\mathbf{d}_i = \mathbf{x}_i + \mathbf{R}_{pi} \boldsymbol{\alpha}_i \quad (8.18)$$

Now \mathbf{d}_j is given by

$$\mathbf{d}_j = \mathbf{x}_j + \boldsymbol{\alpha}_j \times \mathbf{r}_{pj} \quad (8.19)$$

and can be written as

$$\mathbf{d}_j = \begin{Bmatrix} x_j \\ y_j \\ x_j \end{Bmatrix} + \begin{bmatrix} 0 & z_{pj} & -y_{pj} \\ -z_{pj} & 0 & x_{pj} \\ y_{pj} & -x_{pj} & 0 \end{bmatrix} \begin{Bmatrix} \alpha_j \\ \beta_j \\ \gamma_j \end{Bmatrix}$$

and therefore in matrix notation, we have

$$\mathbf{d}_j = \mathbf{x}_j + \mathbf{R}_{pj} \boldsymbol{\alpha}_j \quad (8.20)$$

To calculate the reactions acting on each body, the relative displacements between the connecting points (stretch) should be calculated.

The relative displacements are given by

$$\mathbf{d} = \mathbf{d}_j - \mathbf{d}_i \quad (8.21)$$

The reaction forces due to the relative displacements on each body are given by

$$\mathbf{F}_s = \mathbf{K}_p \mathbf{d} \quad (8.22)$$

For equal but opposite directions, we have

$$\mathbf{F}_s = -\mathbf{K}_p \mathbf{d} \quad (8.23)$$

Moments for spring forces acting at points \mathbf{r}_i and \mathbf{r}_j on bodies i and j , respectively, are given by

$$\mathbf{M}_i = \mathbf{r}_i \times \mathbf{F}\mathbf{s}_i \quad (8.24)$$

On body j , we have

$$\mathbf{M}_j = \mathbf{r}_j \times \mathbf{F}\mathbf{s}_j \quad (8.25)$$

The cross-products may be expressed in matrix form as

$$\mathbf{M}_i = \mathbf{r}_i \times \mathbf{F}\mathbf{s}_i = \begin{bmatrix} 0 & -z_{pi} & y_{pi} \\ z_{pi} & 0 & -x_{pi} \\ -y_{pi} & x_{pi} & 0 \end{bmatrix} \begin{Bmatrix} \mathbf{F}s_{xi} \\ \mathbf{F}s_{yi} \\ \mathbf{F}s_{zi} \end{Bmatrix} \quad (8.26)$$

$$\mathbf{M}_j = \mathbf{r}_j \times \mathbf{F}\mathbf{s}_j = \begin{bmatrix} 0 & -z_{pj} & y_{pj} \\ z_{pj} & 0 & -x_{pj} \\ -y_{pj} & x_{pj} & 0 \end{bmatrix} \begin{Bmatrix} \mathbf{F}s_{xj} \\ \mathbf{F}s_{yj} \\ \mathbf{F}s_{zj} \end{Bmatrix} \quad (8.27)$$

Note that the matrices in Equation 8.26 and Equation 8.27 are transposed forms of the matrices in Equation 8.15 and Equation 8.16

$$\mathbf{R}_{pi}^T = \begin{bmatrix} 0 & -z_{pi} & y_{pi} \\ z_{pi} & 0 & -x_{pi} \\ -y_{pi} & x_{pi} & 0 \end{bmatrix} \quad (8.28)$$

$$\mathbf{R}_{pj}^T = \begin{bmatrix} 0 & -z_{pj} & y_{pj} \\ z_{pj} & 0 & -x_{pj} \\ -y_{pj} & x_{pj} & 0 \end{bmatrix} \quad (8.29)$$

Now the equations of motion can be compiled for the translation of body i

$$\mathbf{m}_i \ddot{\mathbf{x}}_i + \mathbf{K}_p \mathbf{d}_i - \mathbf{K}_p \mathbf{d}_j = \mathbf{F}_i \quad (8.30)$$

In this case, \mathbf{F}_i is the vector of external forces acting on body i . Substituting \mathbf{d}_i and \mathbf{d}_j into Equation 8.30, from Equation 8.18 and Equation 8.20 we have

$$\mathbf{m}_i \ddot{\mathbf{x}}_i + \mathbf{K}_p(\mathbf{x}_i + \mathbf{R}_{pi}\boldsymbol{\alpha}_i) - \mathbf{K}_p(\mathbf{x}_j + \mathbf{R}_{pj}\boldsymbol{\alpha}_j) = \mathbf{F}_i \quad (8.31)$$

Expanding this, we get

$$\mathbf{m}_i \ddot{\mathbf{x}}_i + \mathbf{K}_p \mathbf{x}_i + \mathbf{K}_p \mathbf{R}_{pi} \boldsymbol{\alpha}_i - \mathbf{K}_p \mathbf{x}_j - \mathbf{K}_p \mathbf{R}_{pj} \boldsymbol{\alpha}_j = \mathbf{F}_i \quad (8.32)$$

Similarly, for body j , substituting the expressions for \mathbf{d}_i and \mathbf{d}_j , we get

$$\mathbf{m}_j \ddot{\mathbf{x}}_j + \mathbf{K}_p \mathbf{d}_i - \mathbf{K}_p \mathbf{d}_j = \mathbf{F}_j \quad (8.33)$$

Again, \mathbf{F}_j in this case is the vector of external forces acting on body j .

$$\mathbf{m}_j \ddot{\mathbf{x}}_j + \mathbf{K}_p(\mathbf{x}_i + \mathbf{R}_{pi}\boldsymbol{\alpha}_i) - \mathbf{K}_p(\mathbf{x}_j + \mathbf{R}_{pj}\boldsymbol{\alpha}_j) = \mathbf{F}_j \quad (8.34)$$

$$\mathbf{m}_j \ddot{\mathbf{x}}_j + \mathbf{K}_p \mathbf{x}_i + \mathbf{K}_p \mathbf{R}_{pi} \boldsymbol{\alpha}_i - \mathbf{K}_p \mathbf{x}_j - \mathbf{K}_p \mathbf{R}_{pj} \boldsymbol{\alpha}_j = \mathbf{F}_j \quad (8.35)$$

With Equation 8.32 and Equation 8.35, the force–acceleration equations are complete.

Moment Equations

The moment equation may be written for body i as shown in Equation 8.36, where \mathbf{M}_i is the external moment acting on body i .

$$\mathbf{J}_i \ddot{\boldsymbol{\alpha}}_i + \mathbf{r}_i \times (\mathbf{K}_p \mathbf{d}_i - \mathbf{K}_p \mathbf{d}_j) = \mathbf{M}_i \quad (8.36)$$

Substituting expressions for \mathbf{d}_i and \mathbf{d}_j and converting the cross-product to the matrix form, we get

$$\mathbf{J}_i \ddot{\alpha}_i + \mathbf{R}_{pi}^T (\mathbf{K}_p (\mathbf{x}_i + \mathbf{R}_{pi} \alpha_i) - \mathbf{K}_p (\mathbf{x}_j + \mathbf{R}_{pj} \alpha_j)) = \mathbf{M}_i \quad (8.37)$$

Expanding this, we get

$$\mathbf{J}_i \ddot{\alpha}_i + \mathbf{R}_{pi}^T \mathbf{K}_p \mathbf{x}_i + \mathbf{R}_{pi}^T \mathbf{K}_p \mathbf{R}_{pi} \alpha_i - \mathbf{R}_{pi}^T \mathbf{K}_p \mathbf{x}_j - \mathbf{R}_{pi}^T \mathbf{K}_p \mathbf{R}_{pj} \alpha_j = \mathbf{M}_i \quad (8.38)$$

The moment equation may be written for body j as given in Equation 8.39, where \mathbf{M}_j is the external moment acting on body j . Thus,

$$\mathbf{J}_j \ddot{\alpha}_j - \mathbf{r}_j \times (\mathbf{K}_p \mathbf{d}_i - \mathbf{K}_p \mathbf{d}_j) = \mathbf{M}_j \quad (8.39)$$

Substituting \mathbf{d}_i and \mathbf{d}_j and converting the cross-product to the matrix form, we get

$$\mathbf{J}_j \ddot{\alpha}_j - \mathbf{R}_{pj}^T (\mathbf{K}_p (\mathbf{x}_i + \mathbf{R}_{pi} \alpha_i) - \mathbf{K}_p (\mathbf{x}_j + \mathbf{R}_{pj} \alpha_j)) = \mathbf{M}_j \quad (8.40)$$

Expanding this, we get

$$\mathbf{J}_j \ddot{\alpha}_j - \mathbf{R}_{pj}^T \mathbf{K}_p \mathbf{x}_i - \mathbf{R}_{pj}^T \mathbf{K}_p \mathbf{R}_{pi} \alpha_i + \mathbf{R}_{pj}^T \mathbf{K}_p \mathbf{x}_j + \mathbf{R}_{pj}^T \mathbf{K}_p \mathbf{R}_{pj} \alpha_j = \mathbf{M}_j \quad (8.41)$$

If we then collect Equation 8.32 and Equation 8.38 for body i , then Equation 8.32 becomes

$$\mathbf{m}_i \ddot{\mathbf{x}}_i + \mathbf{K}_p \mathbf{x}_i + \mathbf{K}_p \mathbf{R}_{pi} \alpha_i - \mathbf{K}_p \mathbf{x}_j - \mathbf{K}_p \mathbf{R}_{pj} \alpha_j = \mathbf{F}_i \quad (8.42)$$

and Equation 8.38 becomes

$$\mathbf{J}_i \ddot{\alpha}_i + \mathbf{R}_{pi}^T \mathbf{K}_p \mathbf{x}_i + \mathbf{R}_{pi}^T \mathbf{K}_p \mathbf{R}_{pi} \alpha_i - \mathbf{R}_{pi}^T \mathbf{K}_p \mathbf{x}_j - \mathbf{R}_{pi}^T \mathbf{K}_p \mathbf{R}_{pj} \alpha_j = \mathbf{M}_i \quad (8.43)$$

Expressing Equation 8.42 and Equation 8.43 in matrix form, we have

$$\begin{bmatrix} \mathbf{m}_i & 0 \\ 0 & \mathbf{J}_i \end{bmatrix} \begin{Bmatrix} \ddot{\mathbf{x}}_i \\ \ddot{\alpha}_i \end{Bmatrix} + \begin{bmatrix} \mathbf{K}_p & \mathbf{K}_p \mathbf{R}_{pi} \\ \mathbf{R}_{pi}^T \mathbf{K}_p & \mathbf{R}_{pi}^T \mathbf{K}_p \mathbf{R}_{pi} \end{bmatrix} \begin{Bmatrix} \mathbf{x}_i \\ \alpha_i \end{Bmatrix} - \begin{bmatrix} \mathbf{K}_p & \mathbf{K}_p \mathbf{R}_{pj} \\ \mathbf{R}_{pi}^T \mathbf{K}_p & \mathbf{R}_{pi}^T \mathbf{K}_p \mathbf{R}_{pj} \end{bmatrix} \begin{Bmatrix} \mathbf{x}_j \\ \alpha_j \end{Bmatrix} = \begin{Bmatrix} \mathbf{F}_i \\ \mathbf{M}_i \end{Bmatrix} \quad (8.44)$$

Similarly, if we collect Equation 8.34 and Equation 8.41 for body j , then Equation 8.34 becomes

$$\mathbf{m}_j \ddot{\mathbf{x}}_j - \mathbf{K}_p \mathbf{x}_i - \mathbf{K}_p \mathbf{R}_{pi} \alpha_i + \mathbf{K}_p \mathbf{x}_j + \mathbf{K}_p \mathbf{R}_{pj} \alpha_j = \mathbf{F}_j \quad (8.45)$$

and Equation 8.41 becomes

$$\mathbf{J}_j \ddot{\alpha}_j - \mathbf{R}_{pj}^T \mathbf{K}_p \mathbf{x}_i - \mathbf{R}_{pj}^T \mathbf{K}_p \mathbf{R}_{pi} \alpha_i + \mathbf{R}_{pj}^T \mathbf{K}_p \mathbf{x}_j + \mathbf{R}_{pj}^T \mathbf{K}_p \mathbf{R}_{pj} \alpha_j = \mathbf{M}_j \quad (8.46)$$

Expressing Equation 8.45 and Equation 8.46 in the matrix form, we have

$$\begin{bmatrix} \mathbf{m}_j & 0 \\ 0 & \mathbf{J}_j \end{bmatrix} \begin{Bmatrix} \ddot{\mathbf{x}}_j \\ \ddot{\alpha}_j \end{Bmatrix} - \begin{bmatrix} \mathbf{K}_p & \mathbf{K}_p \mathbf{R}_{pi} \\ \mathbf{R}_{pj}^T \mathbf{K}_p & \mathbf{R}_{pj}^T \mathbf{K}_p \mathbf{R}_{pi} \end{bmatrix} \begin{Bmatrix} \mathbf{x}_i \\ \alpha_i \end{Bmatrix} + \begin{bmatrix} \mathbf{K}_p & \mathbf{K}_p \mathbf{R}_{pj} \\ \mathbf{R}_{pj}^T \mathbf{K}_p & \mathbf{R}_{pj}^T \mathbf{K}_p \mathbf{R}_{pj} \end{bmatrix} \begin{Bmatrix} \mathbf{x}_j \\ \alpha_j \end{Bmatrix} = \begin{Bmatrix} \mathbf{F}_j \\ \mathbf{M}_j \end{Bmatrix} \quad (8.47)$$

Overall, the equations of motion are now complete. Equation 8.44 and Equation 8.47 provide all that is needed to complete the final equations of motion. It is worth restating that the stiffness and damping matrices are identical in their structure. To obtain a damping matrix, all one needs to do is to replace the stiffness coefficients with the corresponding damping coefficients.

8.3 A Numerical Example

In order to illustrate the use of the equations given before, let us consider a rigid body flexibly supported by a number of springs. For this, the simplest starting point would be Equation 8.44

$$\begin{bmatrix} \mathbf{m}_i & 0 \\ 0 & \mathbf{J}_i \end{bmatrix} \begin{Bmatrix} \ddot{\mathbf{x}}_i \\ \ddot{\alpha}_i \end{Bmatrix} + \begin{bmatrix} \mathbf{K}_p & \mathbf{K}_p \mathbf{R}_{pi} \\ \mathbf{R}_{pi}^T \mathbf{K}_p & \mathbf{R}_{pi}^T \mathbf{K}_p \mathbf{R}_{pi} \end{bmatrix} \begin{Bmatrix} \mathbf{x}_i \\ \alpha_i \end{Bmatrix} - \begin{bmatrix} \mathbf{K}_p & \mathbf{K}_p \mathbf{R}_{pj} \\ \mathbf{R}_{pi}^T \mathbf{K}_p & \mathbf{R}_{pi}^T \mathbf{K}_p \mathbf{R}_{pj} \end{bmatrix} \begin{Bmatrix} \mathbf{x}_j \\ \alpha_j \end{Bmatrix} = \begin{Bmatrix} \mathbf{F}_i \\ \mathbf{M}_i \end{Bmatrix} \quad (8.48)$$

Since body j does not exist, all the terms relevant to body j will disappear. Furthermore, since we are dealing with a single mass, the suffix i is not needed either. However, for n number of springs, the stiffness matrices need to be summed-up. Summation has to be carried out for each stiffness p attached at a position on the body. We then have

$$\begin{bmatrix} \mathbf{m} & \mathbf{0} \\ \mathbf{0} & \mathbf{J} \end{bmatrix} \begin{Bmatrix} \ddot{\mathbf{x}} \\ \ddot{\boldsymbol{\alpha}} \end{Bmatrix} + \begin{bmatrix} \sum_{p=1}^n \mathbf{K}_p & \sum_{p=1}^n \mathbf{K}_p \mathbf{R}_p \\ \sum_{p=1}^n \mathbf{R}_p^T \mathbf{K}_p & \sum_{p=1}^n \mathbf{R}_p^T \mathbf{K}_p \mathbf{R}_p \end{bmatrix} \begin{Bmatrix} \mathbf{x} \\ \boldsymbol{\alpha} \end{Bmatrix} = \begin{Bmatrix} \mathbf{F} \\ \mathbf{M} \end{Bmatrix} \quad (8.49)$$

For a situation where the axes of the springs are parallel to the global coordinate system, no transformation of the stiffness matrix is needed. Hence, $\mathbf{k}_p = \mathbf{K}_p$. To obtain the submatrices of the stiffness matrix given in Equation 8.49, start with the stiffness matrix for spring p . Specifically,

$$\mathbf{K}_p = \begin{bmatrix} k_{px} & 0 & 0 \\ 0 & k_{py} & 0 \\ 0 & 0 & k_{pz} \end{bmatrix} \quad (8.50)$$

Now, $\mathbf{K}_p \mathbf{R}_p$ is given by

$$\mathbf{K}_p \mathbf{R}_p = \begin{bmatrix} k_{px} & 0 & 0 \\ 0 & k_{py} & 0 \\ 0 & 0 & k_{pz} \end{bmatrix} \begin{bmatrix} 0 & z_p & -y_p \\ -z_p & 0 & x_p \\ y_p & -x_p & 0 \end{bmatrix} \quad (8.51)$$

Expanding this, we get

$$\mathbf{K}_p \mathbf{R}_p = \begin{bmatrix} 0 & k_{px} z_p & -k_{px} y_p \\ -k_{py} z_p & 0 & k_{py} x_p \\ k_{pz} y_p & -k_{pz} x_p & 0 \end{bmatrix} \quad (8.52)$$

For $\mathbf{R}_p^T \mathbf{K}_p$, we have

$$\mathbf{R}_p^T \mathbf{K}_p = \begin{bmatrix} 0 & -z_p & y_p \\ z_p & 0 & -x_p \\ -y_p & x_p & 0 \end{bmatrix} \begin{bmatrix} k_{px} & 0 & 0 \\ 0 & k_{py} & 0 \\ 0 & 0 & k_{pz} \end{bmatrix} \quad (8.53)$$

Expanding this, we get

$$\mathbf{R}_p^T \mathbf{K}_p = \begin{bmatrix} 0 & -k_{py} z_p & k_{pz} y_p \\ k_{px} z_p & 0 & -k_{pz} x_p \\ -k_{px} y_p & k_{py} x_p & 0 \end{bmatrix} \quad (8.54)$$

Finally, $\mathbf{R}_p^T \mathbf{K}_p \mathbf{R}_p$ is given by

$$\mathbf{R}_p^T \mathbf{K}_p \mathbf{R}_p = \begin{bmatrix} 0 & -k_{py} z_p & k_{pz} y_p \\ k_{px} z_p & 0 & -k_{pz} x_p \\ -k_{px} y_p & k_{py} x_p & 0 \end{bmatrix} \begin{bmatrix} 0 & z_p & -y_p \\ -z_p & 0 & x_p \\ y_p & -x_p & 0 \end{bmatrix} \quad (8.55)$$

$$\mathbf{R}_p^T \mathbf{K}_p \mathbf{R}_p = \begin{bmatrix} k_{pz}y_p^2 + k_{py}z_p^2 & -k_{pz}x_p y_p & -k_y x_p z_p \\ -k_{pz}x_p y_p & k_{pz}x_p^2 + k_{px}z_p^2 & -k_{px}y_p z_p \\ -k_{py}x_p z_p & -k_{px}y_p z_p & k_{py}x_p^2 + k_{px}y_p^2 \end{bmatrix} \quad (8.56)$$

The overall stiffness matrix from Equation (8.48) for a single spring is given by

$$\begin{bmatrix} k_{px} & 0 & 0 & 0 & k_{px}z_p & -k_{px}y_p \\ 0 & k_{py} & 0 & -k_{py}z_p & 0 & k_{py}x_p \\ 0 & 0 & k_{pz} & k_{pz}y_p & -k_{pz}x_p & 0 \\ 0 & -k_{py}z_p & k_{pz}y_p & k_{pz}y_p^2 + k_{py}z_p^2 & -k_{pz}x_p y_p & -k_{py}x_p z_p \\ k_{px}z_p & 0 & -k_{pz}x_p & -k_{pz}x_p y_p & k_{pz}x_p^2 + k_{px}z_p^2 & -k_{px}y_p z_p \\ -k_{px}y_p & k_{py}x_p & 0 & -k_{py}x_p z_p & -k_{px}y_p z_p & k_{py}x_p^2 + k_{px}y_p^2 \end{bmatrix} \quad (8.57)$$

The mass matrix is diagonal and, for the inertia matrix, it is assumed that the principal axes of the body coincide with the global coordinate system. Specifically,

$$\mathbf{m} = \begin{bmatrix} m & 0 & 0 \\ 0 & m & 0 \\ 0 & 0 & m \end{bmatrix} \quad (8.58)$$

$$\mathbf{J} = \begin{bmatrix} I_{xx} & 0 & 0 \\ 0 & I_{yy} & 0 \\ 0 & 0 & I_{zz} \end{bmatrix} \quad (8.59)$$

Now, the overall equations of motion may be assembled for n springs.

$$\begin{bmatrix} m & 0 & 0 & 0 & 0 & 0 \\ 0 & m & 0 & 0 & 0 & 0 \\ 0 & 0 & m & 0 & 0 & 0 \\ 0 & 0 & 0 & I_{xx} & 0 & 0 \\ 0 & 0 & 0 & 0 & I_{yy} & 0 \\ 0 & 0 & 0 & 0 & 0 & I_{zz} \end{bmatrix} \begin{Bmatrix} \ddot{x} \\ \ddot{y} \\ \ddot{z} \\ \ddot{\alpha} \\ \ddot{\beta} \\ \ddot{\gamma} \end{Bmatrix} + \sum_{p=1}^n \begin{bmatrix} k_{px} & 0 & 0 & 0 & k_{px}z_p & -k_{px}y_p \\ 0 & k_{py} & 0 & -k_{py}z_p & 0 & k_{py}x_p \\ 0 & 0 & k_{pz} & k_{pz}y_p & -k_{pz}x_p & 0 \\ 0 & -k_{py}z_p & k_{pz}y_p & k_{pz}y_p^2 + k_{py}z_p^2 & -k_{pz}x_p y_p & -k_{py}x_p z_p \\ k_{px}z_p & 0 & -k_{pz}x_p & -k_{pz}x_p y_p & k_{pz}x_p^2 + k_{px}z_p^2 & -k_{px}y_p z_p \\ -k_{px}y_p & k_{py}x_p & 0 & -k_{py}x_p z_p & -k_{px}y_p z_p & k_{py}x_p^2 + k_{px}y_p^2 \end{bmatrix} \begin{Bmatrix} x \\ y \\ z \\ \alpha \\ \beta \\ \gamma \end{Bmatrix} = \begin{Bmatrix} F_x \\ F_y \\ F_z \\ M_x \\ M_y \\ M_z \end{Bmatrix} \quad (8.60)$$

8.3.1 A Uniform Rectangular Prism

A rectangular prism is supported by four springs as shown in Figure 8.3. Springs have stiffness values in all three directions (k_{px} , k_{py} , k_{pz} , where p is the spring number). The axes of each spring in which the stiffness values are measured are parallel to the principal axes of the springs, which in turn are parallel to the global coordinate system of the rectangular prism. Thus, no transformation is needed. The end of spring p is located at (x_p, y_p, z_p) , measured relative to the COG of the body. The mass of the prism is m and the principal moments of inertia are I_{xx} , I_{yy} , and I_{zz} . A simplified equation of motion of the system in 3-D space may be obtained from Equation 8.59. If one attempts to carry this out, one will realize that some terms will disappear because the z components of the positions are all zero and some will disappear because of the symmetry of points.

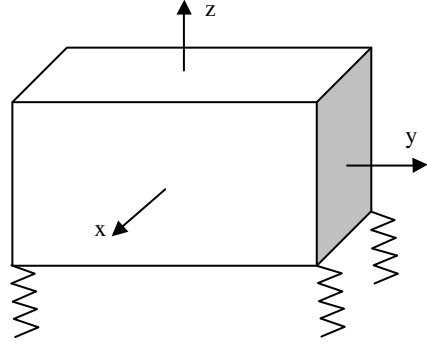


FIGURE 8.3 A rectangular prism supported on springs.

The body shown in Figure 8.3 corresponds to $m = 1000$ kg, moments of inertia $I_{xx} = 10$ kg m², $I_{yy} = 20$ kg m², and $I_{zz} = 30$ kg m², supported by four identical (thus, point suffix p is dropped) springs with stiffness values ($k_x = 10,000$ N/m, $k_y = 20,000$ N/m, $k_z = 30,000$ N/m). The positions of the springs are given as follows:

$$P1(1, 2, 0)$$

$$P2(1, -2, 0)$$

$$P3(-1, 2, 0)$$

$$P4(-1, -2, 0)$$

The coordinates imply that the COG is on the bottom plane of the prism. The system has six degrees of freedom and all six natural frequencies will be calculated.

Since stiffness parameters are on the Oxy plane, no coupling will occur between $(x$ and $\beta)$ and $(y$ and $\alpha)$. Similarly, the vertical motion is also uncoupled from the others due to symmetry. Thus,

$$\omega_x = \sqrt{\frac{\sum_{p=1}^4 k_{px}}{m}} = \sqrt{\frac{40,000}{1000}} = 6.32 \text{ rad/sec} = 1.0065 \text{ Hz}$$

$$\omega_y = \sqrt{\frac{\sum_{p=1}^4 k_{py}}{m}} = \sqrt{\frac{80,000}{1000}} = 8.94 \text{ rad/sec} = 1.4235 \text{ Hz}$$

$$\omega_z = \sqrt{\frac{\sum_{p=1}^4 k_{pz}}{m}} = \sqrt{\frac{120,000}{1000}} = 10.95 \text{ rad/sec} = 1.743 \text{ Hz}$$

$$\omega_\alpha = \sqrt{\frac{\sum_{p=1}^4 y_p^2 k_{pz}}{I_{xx}}} = \sqrt{\frac{4 \times 2^2 \times 30,000}{10}} = 219.09 \text{ rad/sec} = 34.87 \text{ Hz}$$

$$\omega_{\beta} = \sqrt{\frac{\sum_{p=1}^4 x_p^2 k_{pz}}{I_{yy}}} = \sqrt{\frac{4 \times 1^2 \times 30,000}{20}} = 77.45 \text{ rad/sec} = 12.32 \text{ Hz}$$
$$\omega_{\gamma} = \sqrt{\frac{\sum_{p=1}^4 (x_p^2 k_{py} + y_p^2 k_{px})}{I_{zz}}} = \sqrt{\frac{4(1^2 \times 20,000 + 2^2 \times 10,000)}{30}} = 89.44 \text{ rad/sec} = 14.23 \text{ Hz}$$

8.3.2 VIBRATIO Output

For the numerical problem given above, the output obtained from the software package VIBRATIO (see Appendix 8A for the full listing) is tabulated below.

Dominant Oscillation Direction	Frequencies
Frequency in X	1.01 Hz (60 CPM)
Frequency in Y	1.42 Hz (85 CPM)
Frequency in Z	1.74 Hz (105 CPM)
Frequency in alpha	34.87 Hz (2092 CPM)
Frequency in beta	12.33 Hz (740 CPM)
Frequency in gamma	14.24 Hz (854 CPM)

8.4 An Industrial Vibration Design Problem

In the analysis of vibration characteristics of an engine or an engine-generator set, flexibly supported rigid-body representations are commonly used. In the case study given here, an engine assembly system is considered. In designing an engine mounting system, engineers consider a number of issues. Particularly useful are: static deflection; natural frequencies and spread of these frequencies relative to the engine speed range; time response under shock or other transient loads; and frequency response of the system, especially when subjected to unbalanced engine-generated excitations.

8.4.1 Static Deflection

This problem involves the selection of mounting geometry and mount stiffness parameters. Here, the design engineer seeks to achieve a pure deflection with as little tilt as possible. In principle, there is nothing wrong with some mounts deflecting more than the others, but an excessive tilt normally indicates other problems such as a high degree of coupling between the modes of motion. However, achieving a pure vertical deflection, at least mathematically, is relatively easy and involves the selection of spring positions/stiffness values to satisfy the following conditions:

$$\sum_{p=1}^{n\text{-spring}} y_p k_{pz} = 0$$

and

$$\sum_{p=1}^{n\text{-spring}} x_p k_{pz} = 0.$$

Here, x_p and y_p are spring mount positions and k_{pz} is the spring stiffness in the z direction. In addition, the designer needs to ensure that the static deflection is well within the allowable deflection range, especially since it needs to account for any additional deflection due to vibration.

8.4.2 Natural Frequencies

Normally, design application demands that the natural frequencies are kept away from the running speed of an engine. Such a requirement is easy to satisfy for single-DoF systems. However, in real-life situations, the number of DoF(s) is six just for a single rigid body. Any change to the mounting configuration or stiffness parameters (or mass distribution) will affect all six natural frequencies. In order to be able to modify a natural frequency corresponding to a particular mode shape (e.g., resonance in the vertical direction), a vibration design engineer will attempt to decouple various modes of oscillation. Such a design requirement, however, is unrealistic for many engineering problems, even for a single rigid body, due to space considerations and is practically impossible for multiple rigid body systems. However, it is possible to achieve partial decoupling. For example, the condition given above for pure vertical deflection will also provide decoupling between the rocking motion about two-coordinate systems (about Ox and Oy) in the horizontal plane and vertical motion.

8.4.3 Transient Response Analysis

Static deflection analysis and modal analysis are normally essential (see Chapter 3). However, there are two more problem-specific analyses that a design engineer may need to perform depending on the problem. For example, in many engineering applications, the response of a flexibly supported system to a shock loading is very important. In this case, coupling among modes as well as stiffness of the system play an important role in determining the levels of shock transmission to the engine system. As a rule of thumb, the softer the spring the smaller the shock transferred to the flexibly mounted structure. Making mounting stiffness elements softer may not be a realistic option (see Chapter 32) as this can result in unacceptable static deflections and may even be in conflict with the requirements discussed above in relation to the positioning of a natural frequency relative to the operating speed of the engine and the static deflection.

8.4.4 Frequency Analysis

Frequency analysis is probably one of the most useful among the various types of analysis listed above. If the vibration problem is not transient, then it is a problem involving a steady-state vibration. The analysis of a steady-state vibration problem under sinusoidal excitation is normally referred to as frequency analysis (see Chapter 2). In mathematical terms, this is the particular solution of the differential equation of motion. Under a sinusoidal excitation, a vibrating system reaches a steady-state vibration and frequency analysis provides information of the amplitude of vibration as a function of excitation frequency. If there is more than one excitation force, then the resulting motion will be a combination of the results due to each excitation. Multiexcitation force analysis is sometimes referred to as harmonics analysis (see Chapter 2). Here, the designer needs to ensure that the highest amplitude of oscillation under harmonic excitation does not exceed the safe limits for the system and, in particular, for the mounts.

Although design considerations linked to static deflection, positioning of natural frequencies, decoupling of modes, and response to shock represent a large proportion of vibration design problems, there are other and more complex design specifications. For example, minimizing vibration at a point on a flexibly supported body may be considered a design objective. Such a requirement may then cause problems where the engineer intends to place a drive shaft coupling or an additional mounting at this position. Because the vibration (or deflection) is at its minimum at the assembly point, a coupling or additional mount will add a minimum constraint to the system.

Obviously, all the design objectives discussed above have to be satisfied within the physical constraints relating to the problem at hand. In general, these constraints are associated with space and the stiffness range of industrially available mountings.

8.4.5 A Flexibly Supported Engine — A Numerical Problem

The example considered here involves a study of an engine-mounting configuration. Mounting configurations are restricted by the geometry and little flexibility exists in modifying these positions. They are located by the engine manufacturer. To perform vibration analysis, the mass/moments of inertia values of the system, the coordinates of the mounting positions relative to the COG, and the forces acting on the system are needed. Although the mass is normally given or easy to obtain, moments of inertia and the COG are not always supplied by engine manufacturers. Even though it is possible to build a solid model of an engine in order to calculate moments of inertia, this is a rather tedious and costly task. The alternative is to define engine moments of inertia in an approximate manner. This can be done by assuming that the main assemblies of the engine are made of regular geometrical primitives representing approximate shapes without going into exact geometrical models. Such an approach works reasonably well, especially since the mass values of these primitives can be obtained in an exact manner. When calculating the moments of inertia and the overall mass of the assembly, its COG can also be calculated. Once these are obtained, the mount positions can be calculated relative to the COG. Having obtained the mass, the moments of inertia, the COG, and the mount position coordinates relative to the COG, the main step of analysis may be started. This involves selecting the mount stiffness parameters in such a way that the various conditions and objectives described above are met. The vibration design, like all engineering problems, involves reconciling many conflicting requirements.

Engine mass and moments of inertia (symmetry of mass distribution is assumed)
 $m = 250 \text{ kg}$ and moments of inertia $I_{xx} = 45 \text{ kg m}^2$, $I_{yy} = 80 \text{ kg m}^2$, and $I_{zz} = 110 \text{ kg m}^2$.

Mounts stiffness values:
($k_x = 150,000 \text{ N/m}$, $k_y = 150,000 \text{ N/m}$, $k_z = 300,000 \text{ N/m}$).

Mount positions (all in mm):

1	0.000	100.000	− 75.000
2	250.000	0.000	− 75.000
3	0.000	− 100.000	− 75.000
4	− 170.000	0.000	− 75.000

8.4.5.1 Satisfying Static Deflection

On running a static analysis under a vertical load of 2500 N (weight), the following results are obtained: (displacements are in mm and angles are in rad)

X	Y	Z	Alpha	Beta	Gamma	xc	yc	zc
0.1392	0.0000	2.1205	0.0000	0.0019	0.0000	1142.5000	0.0000	− 75.0000

In relation to the static deflection, there are two considerations: (i) overall deflection should not be more than what is allowed by the deflection range of the springs selected for the design, and (ii) the static position and orientation of the engine should not be outside what is allowed by spatial and other constraints; i.e., it should not tilt to one side excessively. In either case, stiffer springs will tend to solve

the problem. However, such a choice may not be the best for transients, shocks, and vibration transmission from the supporting frame. “Tilt” level calculated above is assumed to be small (0.0019 rad).

The results from the program also list the deflection at the mount positions (in mm) as: mass no. = 1

Mount no.	Position			Deflection		
	X	Y	Z	x	y	z
1	0.000	100.000	− 75.000	0.000	0.000	2.120
2	250.000	0.000	− 75.000	0.000	0.000	1.656
3	0.000	− 100.000	− 75.000	0.000	0.000	2.120
4	− 170.000	0.000	− 75.000	0.000	0.000	2.436

The maximum deflection is at the fourth mount position and is 2.436 mm. The mount selected should give a deflection range that would extend well beyond this to ensure that any additional deflection due to vibration could be accommodated.

The coordinates *xc*, *yc*, *zc* give the instantaneous center of rotation for this particular static deflection result. This point (as discussed above) may be used in some design applications as it remains stationary during the deflection.

8.4.5.2 Eigenvalue Analysis

The eigenvalue analysis (see Chapter 3 and Appendix 3A) will help ensure that the natural frequencies are not in the vicinity of the idling speed of the engine. It may also help to minimize the number of natural frequencies in the speed range of the engine.

Since the spring positions and their locations are already specified to satisfy the considerations for static deflection, it becomes difficult to modify them to satisfy the “natural frequency” requirements as well. However, all stiffness values could be increased together in the same proportion. This ensures that the “no tilt” condition is maintained. Of course, stiffening now reduces the static deflection and is likely to increase the vibration transmission to the frame.

The eigenvalue analysis results are listed below. Here, the natural frequencies spread from 1.98 to 12.09 Hz. The widest gap between these frequencies is between 3.17 and 8.69 Hz. It would be desirable to have the idling speed in the middle of this range. It is equally important that the cruising speed does not coincide with the two higher frequencies.

X	Y	Z	Alpha	Beta	Gamma
1.0000	0.0000	Frequency in X = 8.63 Hz (518 CPM)			
		− 0.0111	0.0000	− 0.2709	0.0000
0.0000	1.0000	Frequency in Y = 8.69 Hz (521 CPM)			
		0.0000	0.4403	0.0000	0.0484
− 0.0051	0.0000	Frequency in Z = 12.09 Hz (725 CPM)			
		− 1.0000	0.0000	0.0685	0.0000
0.0000	0.0797	Frequency in alpha = 1.98 Hz (119 CPM)			
		0.0000	− 1.0000	0.0000	− 0.0226
0.0869	0.0000	Frequency in beta = 3.17 Hz (190 CPM)			
		0.0215	0.0000	1.0000	0.0000
0.0000	− 0.0163	Frequency in gamma = 2.13 Hz (128 CPM)			
		0.0000	− 0.0625	0.0000	1.0000

In order to achieve decoupling between different motions, one practical technique is to minimize the distance between the COG and the “center of stiffness.” Center of stiffness is a crude term used in industry to ensure that the coupling between different motions of body is minimized. The definition of center of stiffness is similar to that of the COG. The *Ox* axis is located in such a

way that $\sum_p y_p k_{pz} = 0$ holds. Then this axis will pass through the center of stiffness. Similarly, $\sum_p x_p k_{pz} = 0$ will hold for the Oy axis passing through the center of stiffness. If the center of stiffness coincides with the COG and the axes defined by the first moment of stiffness coincide with the principal axis of mass, then full decoupling can be achieved. As far as the horizontal plane is concerned, this also ensures that the assembly is leveled. Note that the relationships are the same as the “no tilt” condition described above for static deflection. Normally, it may not be possible to achieve this in all three planes and the designer may choose to achieve this in one plane where the excitation forces are the greatest. However, it is common among designers to focus on the horizontal plane alone, purely due to deflection under gravity considerations.

8.4.5.3 Time Domain Analysis — Analysis of the System under a Shock Loading

Suppose that a 10 g, 10 msec, half sine shock is applied in the vertical, z , direction. The shock response in the z direction is shown in Figure 8.4. The shock response in the y direction is shown in Figure 8.5.

The results show that, in addition to static deflection, if the mounts were to withstand the applied shock, they should be able to deflect 9 mm in shear and more than 6 mm in the vertical directions.

8.4.5.4 Frequency Analysis

The frequency analysis specifications are given below.

The engine is subjected to an unbalanced force which is known to be proportional to the square of the engine running speed. In other words, this is given as $A\omega^2$. It is measured that when the engine speed is 300 rpm the unbalanced force is 250 N. A simple calculation shows that $A = 1.013$. The force menu option 20 in VIBRATIO provides the required excitation, which increases with the square of the running speed. The option 20 allows the A value to be linearly increased between the start and end frequencies during which the excitation is active. In our case, this is to be taken to be the same (frequency is independent of the A value). The vertical amplitude vs. frequency results are given in Figure 8.6. The amplitudes in other directions are much smaller and are not shown here. The analysis is not carried out beyond 15 Hz as we know already that the maximum resonance is at 12.09 Hz. According to the result, the selected mount should allow a 16 mm deflection on top of static deflection. Now, the designer should be in a position to make a decision on whether the selected

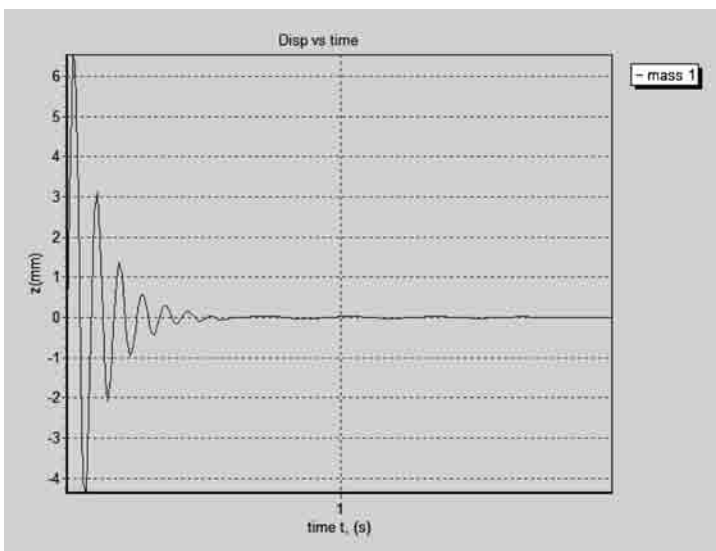


FIGURE 8.4 Shock response in the z direction.

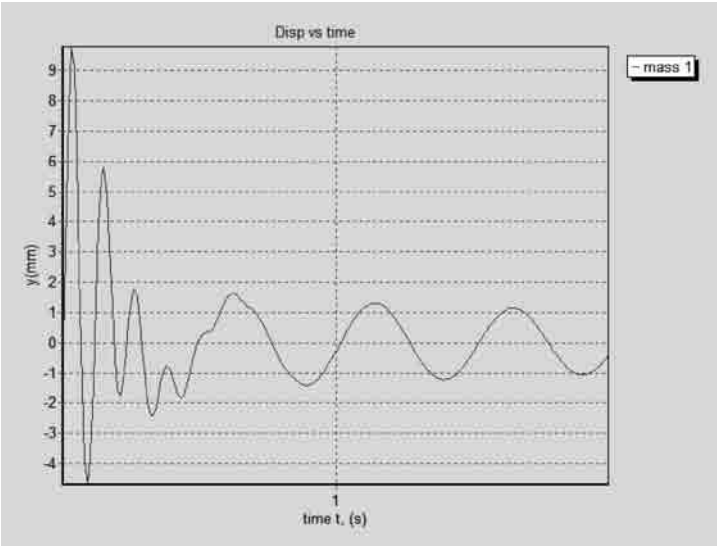


FIGURE 8.5 Shock response in the y direction.

spring type is acceptable or not. If the answer is no, then the whole analysis process has to be repeated to find an acceptable solution.

8.5 Programming Considerations

Equations developed in this chapter are formulated and structured in such a way that they can be used for developing general vibration analysis software. As the equations given above refer to bodies i and j , they can be placed in the global coordinates accordingly. Four submatrices (6×6) will be placed as follows:

$$\begin{bmatrix} \mathbf{K}_r & \mathbf{K}_r \mathbf{R}_{pi} \\ \mathbf{R}_{pi}^T \mathbf{K}_r & \mathbf{R}_{pi}^T \mathbf{K}_r \mathbf{R}_{pi} \end{bmatrix}$$
 will be placed, starting from position $6(i - 1) + 1, 6(i - 1) + 1$

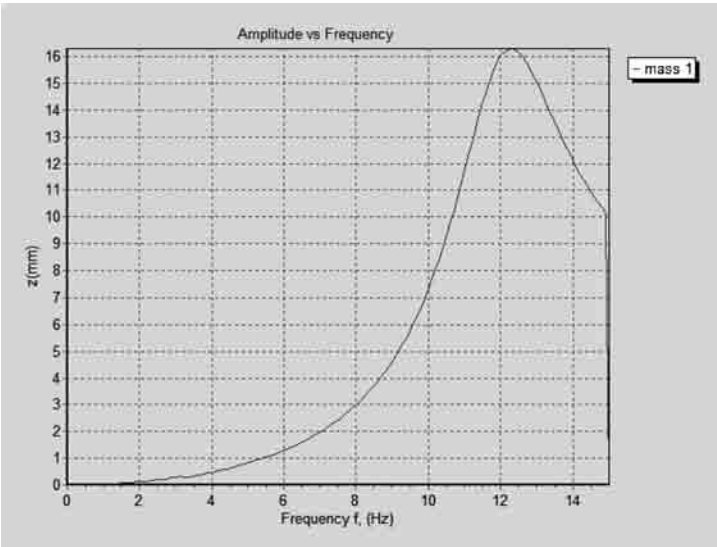


FIGURE 8.6 Frequency response in the z direction for unbalanced engine excitation.

$$\begin{aligned}
& - \begin{bmatrix} \mathbf{K}_r & \mathbf{K}_r \mathbf{R}_{pj} \\ \mathbf{R}_{pi}^T \mathbf{K}_r & \mathbf{R}_{pi}^T \mathbf{K}_r \mathbf{R}_{pj} \end{bmatrix} \text{ will be placed, starting from position } (6(i-1) + 1, 6(j-1) + 1) \\
& - \begin{bmatrix} \mathbf{K}_r & \mathbf{K}_r \mathbf{R}_{pi} \\ \mathbf{R}_{pj}^T \mathbf{K}_r & \mathbf{R}_{pj}^T \mathbf{K}_r \mathbf{R}_{pi} \end{bmatrix} \text{ will be placed, starting from position } (6(j-1) + 1, 6(i-1) + 1) \\
& \begin{bmatrix} \mathbf{K}_r & \mathbf{K}_r \mathbf{R}_{pj} \\ \mathbf{R}_{pj}^T \mathbf{K}_r & \mathbf{R}_{pj}^T \mathbf{K}_r \mathbf{R}_{pj} \end{bmatrix} \text{ will be placed, starting from position } (6(j-1) + 1, 6(j-1) + 1)
\end{aligned}$$

Entry to the global stiffness matrix must be additive (a new entry is added to the previously entered values to account for any contribution coming from other springs). In programming terms, the global stiffness matrix is constructed based on the spring count loop. Therefore, the data structure for a spring must be such that the end of the spring refers to the mass number. Hence, for a spring stiffness, submatrices could be located in the global matrix according to the mass numbers to which the ends of that spring are attached.

To start assembling the equations, the first step is to express the stiffness matrices in global coordinates. Here, it is assumed that the stiffness values are given in three orthogonal axes. These axes will be assumed to be the principal axes of the springs (in practice, this is not strictly correct and the assumption holds only for small deflections). The orientation of the principal axes relative to the global coordinates can be described in terms of Euler angles (or using direction cosines). Once the transformation matrix is obtained, then the stiffness can be expressed in the global coordinate system Equation 8.4. In developing one's own software, it is important to bear in mind the way the transformation matrix is constructed. Euler angles have to be applied one by one and the order in which they are processed is important. For example, to orient a given body, one may assume that, initially, its local coordinates are parallel to the principal coordinate frame. From here, the first Euler angle will rotate the body to a new orientation. Relative to this position, the next rotation will be applied, resulting in yet another orientation. Lastly, the third rotation will be applied relative to this orientation, giving the final position of the body under consideration. Assuming that these rotations are $\alpha \beta \gamma$ in the given order, the transformation matrix is built as

$$T = T(\alpha)T(\beta)T(\gamma)$$

In other words, any vector in the local coordinates will be transformed to the global coordinates in reverse order. To explain further, any vector in the local coordinates is first transformed by $T(\gamma)$, then the resulting vector is transformed by $T(\beta)$, and finally the resulting vector is transformed by $T(\alpha)$. The expression $\mathbf{X} = \mathbf{T}\mathbf{x}$ processes these matrices in that order.

Transformation will apply to spring stiffness matrices and inertia matrices. Therefore, the input to the vibration program has to account for Euler angles for each body and spring, and the order in which these rotations are performed.

Once the transformation is completed, all that remains is to perform the appropriate matrix algebra in order to construct the stiffness matrix for each spring and its location in the global stiffness matrix. The inertia matrix for each mass, after expressing it in the global coordinate frame by performing matrix transformation, will need to be placed in the appropriate location in the global inertia matrix.

8.6 VIBRATIO

8.6.1 Capabilities

VIBRATIO is a vibration analysis program designed to model flexibly supported multibody systems. An educational version is made available free of charge by the author of this chapter for the readers of

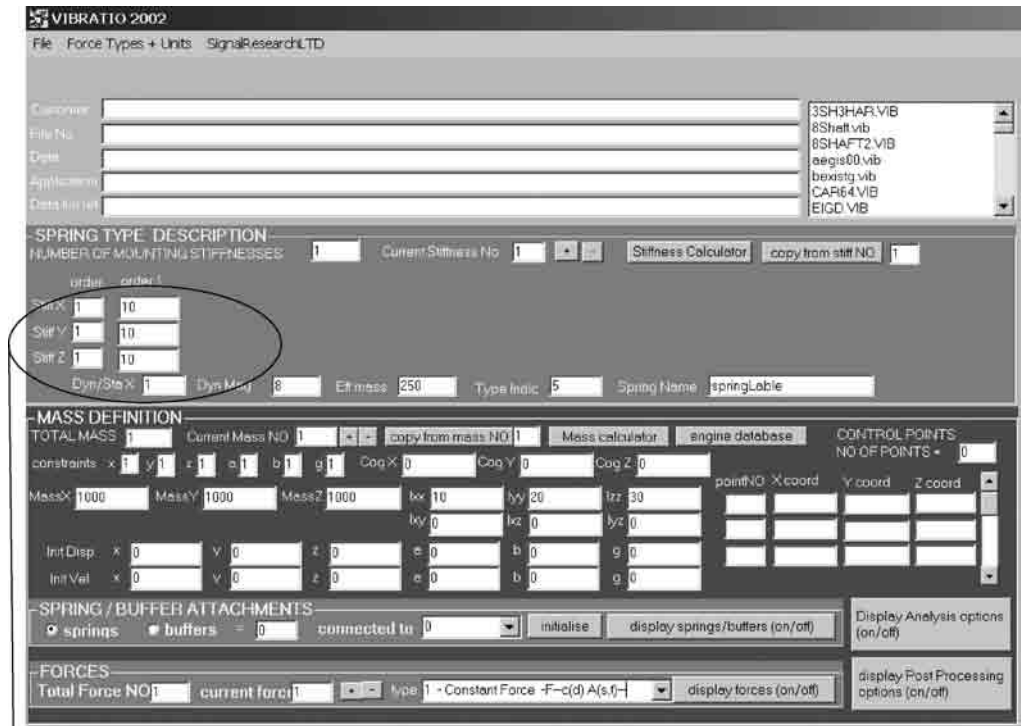
this handbook. The executable file could be downloaded from the website, www.signal-research.com. The educational version will allow analysis of a flexibly supported system not exceeding more than 10 masses (60 dof). For the purpose of supporting the theory presented in this handbook, four types of analysis are activated: static; eigenvalue (both damped and undamped); frequency domain; and time domain. Standard excitations for time and frequency domains will be based on the excitation functions available in the menu. Numerically defined excitations, and all the other modules, such as signal processing, finite-element shaft analysis, fatigue analysis, mass design, etc. are not available in this version.

8.6.2 Modeling on VIBRATIO

Click vibratio2002 from start/programs/vibratio2002 menu. The VIBRATIO screen shown in Figure 8.7 will be displayed. The top part of the frame gives inputs for application details. The date/time box can be double-clicked to produce current date and time. File options are listed in the file box. Only files with a VIB extension are filtered for the listing. You may also use the file menu to load VIBRATIO files. If you use any other extension to save your data, you will have to use the file menu to open it. VIB files are text files and can be read by any text editor. It is not advisable, however, to create these manually by using any editor other than VIBRATIO.

8.6.2.1 Entering Spring Data

The second section on this screen, titled “Spring Type Description,” is for entering spring stiffnesses. Here, the *types* of springs are defined, not the definition of individual springs.



Stiffnesses k_x , k_y and k_z .

FIGURE 8.7 VIBRATIO main window.

Order should always be set to 1. In general, it is assumed that the spring deflections can be described as polynomials, and “order” refers to order of the polynomial. Only linear capability is offered in the present version; thus, order must always be set to 1.

8.6.2.2 Entering Mass Data

When VIBRATIO runs, it automatically loads default mass data. To create a two-mass system, change “total mass” to 2. This is shown in Figure 8.8.

Normally, if these two masses are not the same then you will need to modify accordingly. Also, you may copy mass data from one previously defined mass to another by clicking the “copy from” button. CogX, CogY, CogZ are the centers of mass of the current mass relative to the COG of mass 1. It means that the program will not allow you to change the COG coordinates of mass 1. “Frame” shows that you have massX, massY, massZ values. For normal applications, mass does not have a directional property and values in each direction will be the same. There are applications where directional “effective mass” may be appropriate, such as modeling the ground mass for earthquake analysis.

Moment of inertia elements are calculated relative to the COG of current mass and about coordinates that are parallel to the coordinates of the global frame. The center of the global coordinate system coincides with the center of mass 1. If the principal coordinate system of the current body is not parallel to the global coordinate system, then cross-inertias I_{xy} , I_{xz} , I_{yz} need to be calculated. The full version of

VIBRATIO 2002
File Force Types + Units SignalResearchLTD

Customs: 3SH3HAR.VIB
File No: 8Shatt.vib
Date: 8SHAFT2.VIB
Application: segis00.vib
Data file ref: bevis0g.vib
CAP64.VIB
EIGD.VIB

SPRING TYPE DESCRIPTION
NUMBER OF MOUNTING STIFFNESSES: 1 Current Stiffness No: 1 Stiffness Calculator copy from stiff NO: 1
order: order1
Stiff X: 1 10
Stiff Y: 1 10
Stiff Z: 1 10
Dyn/Stiff X: 1 Dyn Mag: 8 Eff mass: 250 Type indic: 5 Spring Name: springLeble

MASS DEFINITION
TOTAL MASS: 2 Current Mass NO: 1 copy from mass NO: 1 Mass calculator engine database CONTROL POINTS
constraints: x 1 y 1 z 1 Cog X: 0 Cog Y: 0 Cog Z: 0 NO OF POINTS: 0
MassX: 1000 MassY: 1000 MassZ: 1000 Ixx: 10 Iyy: 20 Izz: 30 pointNO X coord Y coord Z coord
Ixy: 0 Ixz: 0 Iyz: 0
Init Disp: x 0 y 0 z 0 a 0 b 0 g 0
Init Vel: x 0 y 0 z 0 a 0 b 0 g 0

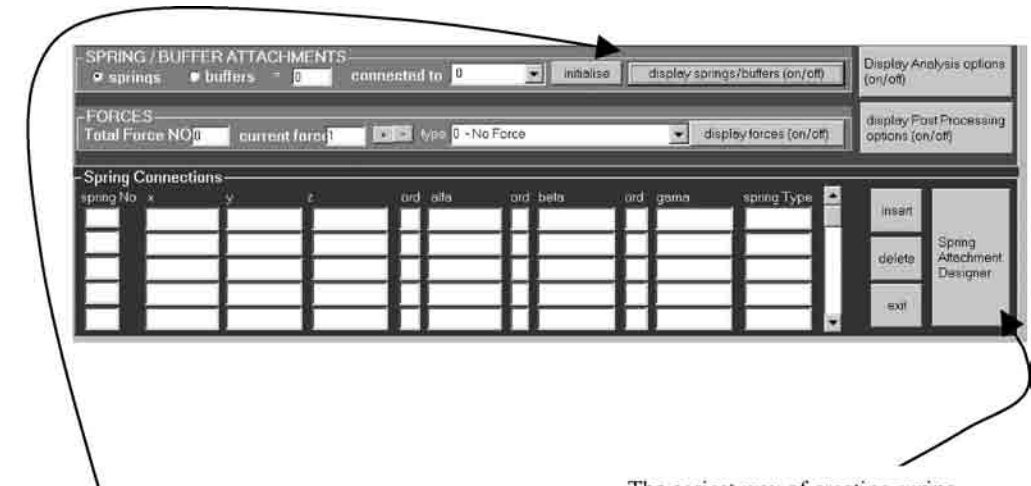
SPRING / BUFFER ATTACHMENTS
spring buffers = 0 connected to 0 initialise display springs/buffers (on/off) Display Analysis options (on/off)

FORCES
Total Force NO: 0 current force: 1 type: 0 - No Force display forces (on/off) display Post Processing options (on/off)

Replace total mass to be 2.

Click "+" button to view mass 2 properties.

FIGURE 8.8 Mass data entry.



Click “display springs/buffers (on/off)” button; Spring Connections table will appear.

The easiest way of creating spring attachments is to use “Spring Attachment Designer”. Click “Spring Attachment Designer”; the frame shown in Figure 8.10 will appear in the middle of the screen.

FIGURE 8.9 Entering spring data.

VIBRATIO offers a mass calculator that, among other things, can calculate the necessary transformation for given sets of Euler angles.

Control points: Here, you may enter the coordinates of points at which the linear deflection module will calculate the displacements. For time and frequency domain analyses this module is not used. Graphics programs come with options to create point tables for analyzing motions at those points.

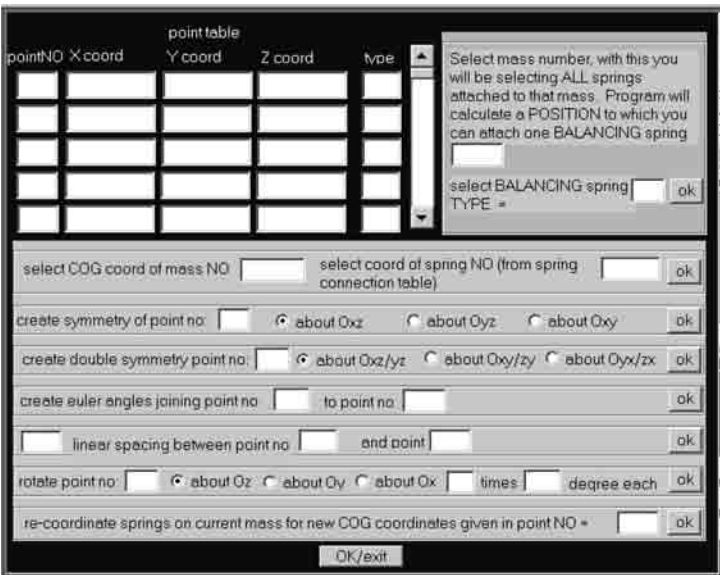


FIGURE 8.10 Spring attachment designer window.

Initial conditions: For each mass, initial conditions may be assigned (displacements and velocities) for time-domain analysis.

Now you have a two-mass system where both masses are identical.

8.6.2.3 Entering Spring Attachment Data

The process of entering spring data is illustrated in Figure 8.9 to Figure 8.11. The first step is to decide how these bodies are connected to the ground and to each other. Connection can be by a spring or a buffer. Buffers are not covered in this chapter. One needs to make sure that the spring option button is selected (spring option is selected as the default). Consider the option buttons. The “text box” refers to the total number of connections to be entered in this frame. Do not modify this one for now. What you enter in this box will depend on how you create these connections. The next very important action is to select “connected to” combo box. This refers to the mass number to which the current mass is connected. If the connection is to the ground, then “0” should be selected. Ground is called mass 0. Once you select a connection mass, “+” will appear in front of the mass number. This makes it easy to identify the masses to which a connection is made. If a “+” character had not been added, then the user would have to search all the mass numbers one by one to view the data. Even in a 10-mass system, this could involve checking 55 possible connections. Note that “connected to” lists mass numbers that are less than the current mass. For example, if the current mass number is 5, then the “connected to” list will have 4, 3, 2, 1, 0.

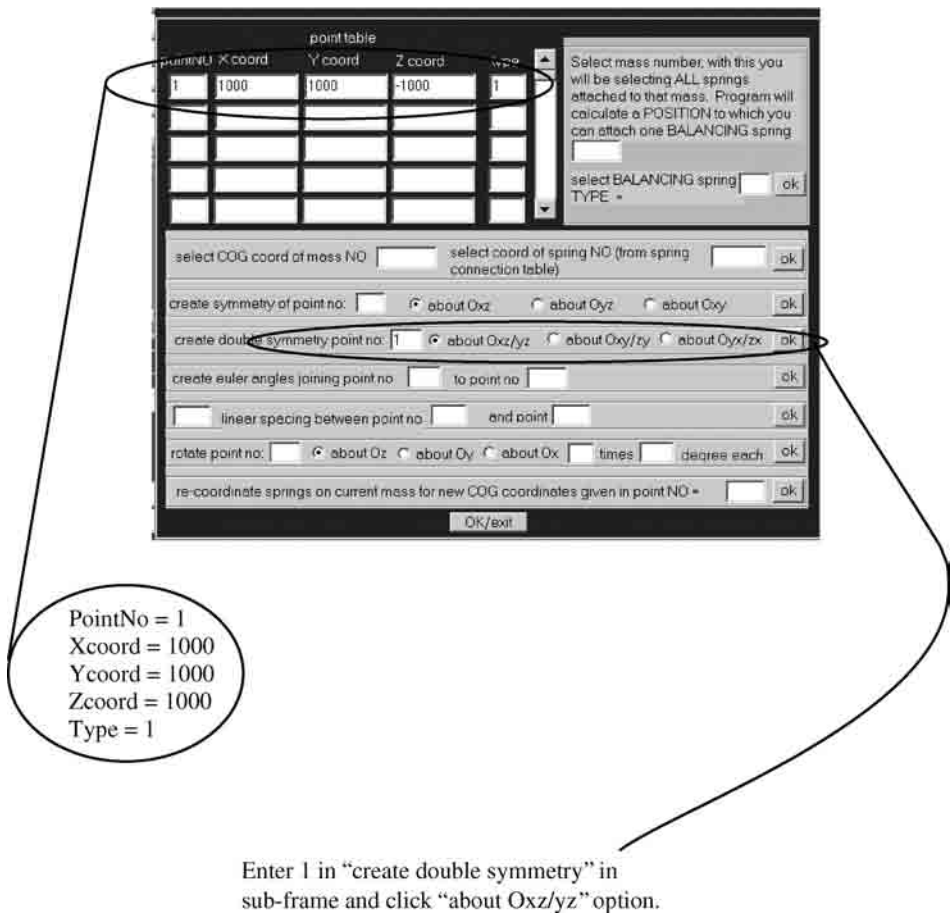
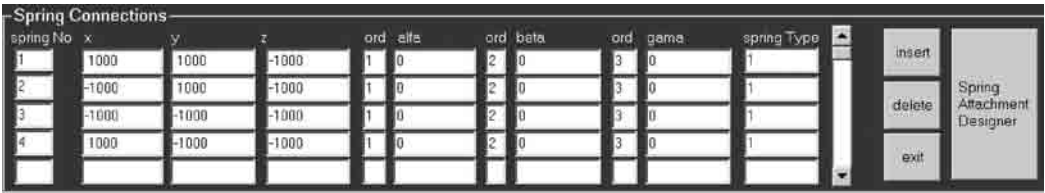


FIGURE 8.11 Spring data entry.



spring No	x	y	z	ord	alfa	ord	beta	ord	gamma	spring Type
1	1000	1000	-1000	1	0	2	0	3	0	1
2	-1000	1000	-1000	1	0	2	0	3	0	1
3	-1000	-1000	-1000	1	0	2	0	3	0	1
4	1000	-1000	-1000	1	0	2	0	3	0	1

Buttons: insert, delete, exit, Spring Attachment Designer

FIGURE 8.12 Four spring attachments generated by “spring attachment designer.”

To start entering connections, make sure that the current mass is 1, the “spring” rather than the “buffer” option is selected, and, in this case, “connected to” would be 0 (the only option). Also, make sure that you have pressed the “display springs/buffers” (on/off) button. Now you have three options:

- 1. Enter the total number of spring connections and start entering the data one by one, but make sure that you enter no more than the total connections you had specified. (This is rather tedious and most of the spring attachments will have identical angle values.)
- 2. Once you have selected the total number of springs, click the “initialize” button. This will fill all the cells with default numbers and you can simply modify these to create your own data.
- 3. An even easier approach is to follow the steps given below.

Enter values as shown in Figure 8.11. Point number is used as a reference in this frame only. Coordinates X, Y, Z are in mm and are relative to the body displayed currently and connecting to the “connected to” mass. If you want to attach springs to the next mass, you must display the mass in your main window (attachment is to the current mass). “Type” is the spring type. Spring type numbers were previously described.

Double symmetry means the point (point number 1, referring to the point above) will be duplicated by its symmetry about the *Oxz* plane. Then these two points will be doubled (four altogether) by taking their symmetry about *Oyz*. Click “ok” (for double symmetry) to complete the operation. The points shown in Figure 8.12 are now generated. Note that all the points have the same spring attachments (the same type). Remember that these four springs are between mass 1 and mass 0 (ground) and the coordinates are relative to mass 1.

To enter spring attachments between the second mass and the first mass, you need to click “+” to increase the Current Mass No. to 2. Having done that, you need to select the “connected to” combo box. When you click “2”, option 1 will appear: 0 and 1, see Figure 8.13. This figure shows how to choose mass number 1 to start creating a new set of spring attachment (between mass 2 and mass 1). As explained previously, mass 2 can connect to mass 1 and mass 0. If we are connecting mass 2 to



MASS DEFINITION

TOTAL MASS: 2 Current Mass NO: 2 copy from mass NO: 1

constraints: x: 1 y: 1 z: 1 a: 1 b: 1 g: 1 Cog X: 0 Cog Y: 0

Mass X: 1000 Mass Y: 1000 Mass Z: 1000 lx: 10 ly: 20
by: 0 lz: 0

Init Disp: x: 0 y: 0 z: 0 a: 0 b: 0
Init Vel: x: 0 y: 0 z: 0 a: 0 b: 0

SPRING / BUFFER ATTACHMENTS

☒ springs ☐ buffers = 0 connected to: 0 initial

FORCES

1

FIGURE 8.13 Selecting mass 2 and clicking the “connected to” combo box.

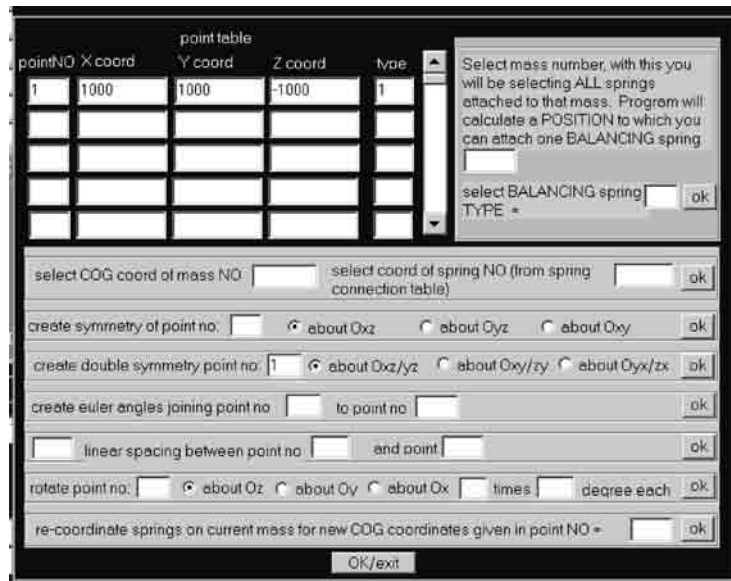


FIGURE 8.14 Use of “spring attachment designer” to create four attachments by double symmetry.

mass 1, then select 1. You may again click the “spring attachment designer” button to create attachment information.

The spring attachment frame will appear with exactly the last set of information (assuming that you have not cleared the text boxes before exiting the frame).

Figure 8.14 shows how to use “spring attachment designer” to create four attachments by double symmetry. Here, click the “ok” button on the “create double symmetry” subframe. Spring attachment information is now generated, between mass 2 and mass 1. Again, coordinates are relative to the current mass 2.

8.6.2.4 Entering Force Data

Make sure that your current mass is 1. When you run VIBRATIO, it assigns a single force of type 1 on mass 1. To see the force data, click “display forces” (on/off). You will see that the “Total Force No.” is 1, “current force” is 1, and “type” is also selected to be 1, as shown in Figure 8.15. In this case, “force” is a term that has a wider meaning. Specifically, “flags” on top of “force” magnitudes identify what is meant by “force.” Note that “flags” can take values between (and including) 0 and 4. Here, 0 means force does not exist; 1 means ordinary force, measured in N; 2 means prescribed displacement, measured in m; 3 means prescribed velocity, measured in m/sec; and 4 means prescribed acceleration, measured in m/sec².

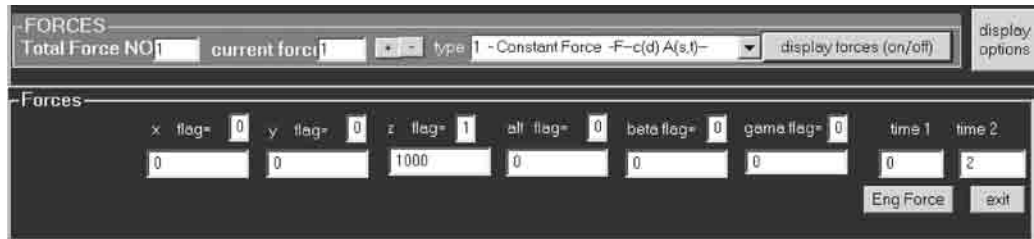


FIGURE 8.15 Default force vector.

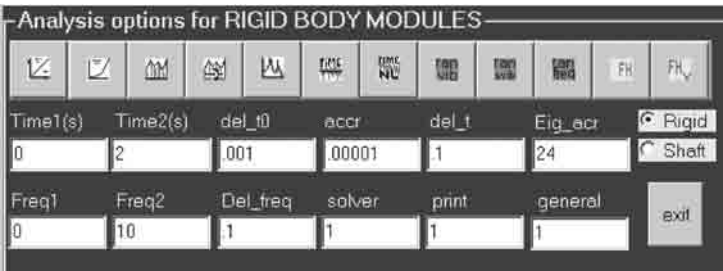


FIGURE 8.16 Analysis options and analysis control parameters.

Note that time 1 and time 2 describe the period in which this force is active. Also, x , y , z , and (α) alpha, (β) beta, (γ) gamma are “force” magnitudes.

Now we have created a two-mass system. Mass 1 is connected to the ground with four springs and mass 2 is connected to mass 1 with four springs. Springs attached to each mass are located at the four corners of the respective masses. There is a constant force acting on mass 1 for 2 sec (although this will be modified according to analysis). Now we are ready to perform analysis.

8.7 Analysis

8.7.1 Analysis Options

To see the analysis frame click the “display analysis options” button.

The analysis option frame as shown in Figure 8.16 will appear. Analysis options offered here are those relevant to the theory presented in this chapter and elsewhere in the handbook (see [Chapters 1 to 3](#)). The theory concerns rigid bodies connected to each other by flexible springs (and dampers). Since flexible shafting analysis is not available in the version provided to the reader, the “rigid” option has to be selected. The frame also contains a number of analysis parameters. Only some of the parameters are needed for a given analysis. For example, for deflection, eigenvalue, and eigenvalue (with damping), no parameters are needed. Once you select your analysis, parameters relevant to the analysis will remain visible and anything else will disappear.

Among analysis options, those shown in Figure 8.17 will be functional in your copy of the software. Starting from the left, the first button is for linear deflection, the third button is for eigenvalue analysis (ignores damping), the fourth button is for eigenvalue analysis (damping included), the fifth button is for frequency analysis, and the sixth and final button is for time-domain analysis. When you place your cursor on a button, the information box will identify its use.



FIGURE 8.17 Analysis options available for the provided version of software.

8.7.2 Eigenvalue Analysis

It is recommended that the first analysis you do is eigenvalue analysis. This will reveal whether you have any inconsistency/error in your data entry and if the created system is physically viable or not.

To perform eigenvalue analysis, click the third button as shown in [Figure 8.18](#). All the analysis parameter data boxes will disappear. The color of the selected button will change to red. This allows the user to enter any appropriate analysis parameter (in this case no parameter is needed).



FIGURE 8.18 Eigenvalue analysis button.



FIGURE 8.19 Postprocessing options.

When the button is clicked a second time, the analysis will be performed. To perform eigenvalue analysis for damped system, the procedure is the same but click the fourth button for this analysis.

To see results, you need to click the “display postprocessing options” (on/off) button. The postprocessing options will appear as shown in Figure 8.19. VIBRATIO has a basic text editor that may be used to display textual results. Click the “DISP TEXT” button to view eigenvalue results.

8.7.2.1 Eigenvalue/Vector Analysis Results

The editor window will open, and from the file menu you can then open “eigftext.txt.” You should obtain the results given below

X	Y	Z	Alpha	Beta	Gamma
Frequency in X = 1.26 Hz (76 CPM)					
Relative eigenvector values for mass = 1					
1.0000	0.0000	0.0000	0.0000	0.5025	0.0000
Relative eigenvector values for mass = 2					
− 0.6180	0.0000	0.0000	0.0000	− 0.3106	0.0000
Frequency in X = 0.48 Hz (29 CPM)					
Relative eigenvector values for mass = 1					
0.6180	0.0000	0.0000	0.0000	0.3106	0.0000
Relative eigenvector values for mass = 2					
1.0000	0.0000	0.0000	0.0000	0.5025	0.0000
Frequency in Y = 0.48 Hz (29 CPM)					
Relative eigenvector values for mass = 1					
0.0000	− 0.6180	0.0000	0.3098	0.0000	0.0000
Relative eigenvector values for mass = 2					
0.0000	− 1.0000	0.0000	0.5012	0.0000	0.0000
Frequency in Y = 1.26 Hz (76 CPM)					
Relative eigenvector values for mass = 1					
0.0000	− 1.0000	0.0000	0.5012	0.0000	0.0000
Relative eigenvector values for mass = 2					
0.0000	0.6180	0.0000	− 0.3098	0.0000	0.0000

(continued on next page)

(continued)

X	Y	Z	Alpha	Beta	Gamma
Frequency in Z = 1.78 Hz (107 CPM)					
Relative eigenvector values for mass = 1					
0.0000	0.0000	1.0000	0.0000	0.0000	0.0000
Relative eigenvector values for mass = 2					
0.0000	0.0000	-0.6180	0.0000	0.0000	0.0000
Frequency in Z = 0.68 Hz (41 CPM)					
Relative eigenvector values for mass = 1					
0.0000	0.0000	0.6180	0.0000	0.0000	0.0000
Relative eigenvector values for mass = 2					
0.0000	0.0000	1.0000	0.0000	0.0000	0.0000
Frequency in alpha = 25.26 Hz (1516 CPM)					
Relative eigenvector values for mass = 1					
0.0000	-0.0050	0.0000	-1.0000	0.0000	0.0000
Relative eigenvector values for mass = 2					
0.0000	0.0031	0.0000	0.6180	0.0000	0.0000
Frequency in alpha = 9.65 Hz (579 CPM)					
Relative eigenvector values for mass = 1					
0.0000	-0.0031	0.0000	-0.6180	0.0000	0.0000
Relative eigenvector values for mass = 2					
0.0000	-0.0050	0.0000	-1.0000	0.0000	0.0000
Frequency in beta = 17.89 Hz (1073 CPM)					
Relative eigenvector values for mass = 1					
0.0100	0.0000	0.0000	0.0000	-1.0000	0.0000
Relative eigenvector values for mass = 2					
-0.0062	0.0000	0.0000	0.0000	0.6180	0.0000
Frequency in beta = 6.83 Hz (410 CPM)					
Relative eigenvector values for mass = 1					
-0.0062	0.0000	0.0000	0.0000	0.6180	0.0000
Relative eigenvector values for mass = 2					
-0.0100	0.0000	0.0000	0.0000	1.0000	0.0000
Frequency in gamma = 14.57 Hz (874 CPM)					
Relative eigenvector values for mass = 1					
0.0000	0.0000	0.0000	0.0000	0.0000	-1.0000
Relative eigenvector values for mass = 2					
0.0000	0.0000	0.0000	0.0000	0.0000	0.6180
Frequency in gamma = 5.56 Hz (334 CPM)					
Relative eigenvector values for mass = 1					
0.0000	0.0000	0.0000	0.0000	0.0000	0.6180
Relative eigenvector values for mass = 2					
0.0000	0.0000	0.0000	0.0000	0.0000	1.0000

This is the result file created as a result of executing eigenvalue analysis (if you had performed eigenvalue analysis with damping you need to open the "eigdtext.txt" file). A successful eigenvalue analysis normally implies physically feasible data (of course, not always).

Now we are ready to perform other analysis options.

8.7.3 Linear Deflection Analysis

The linear deflection equations may be obtained from vibration equations by simply removing the acceleration and velocity terms. If the excitation (force) vector is made of constant values, then the

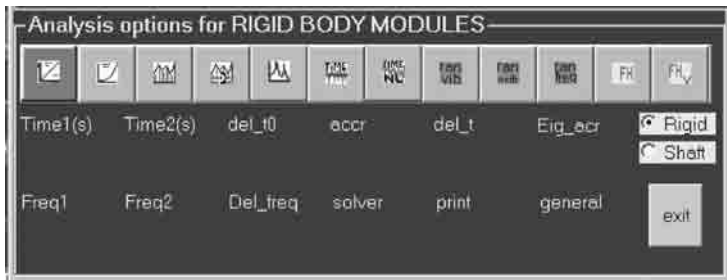


FIGURE 8.20 Linear deflection analysis; no control parameter is needed.

problem is a static deflection problem. By clicking the linear deflection button, you will see that no analysis parameters are needed. Next, click the red button. This will perform a static deflection analysis, as indicated in Figure 8.20.

Numerical results can be displayed using the “DISP TEXT” button from postprocessing options. The deflection results are saved in the “distext.txt” file. This file holds the results given in the next section. Note that, since force is acting on mass 1, mass 2 does not deflect relative to mass 1.

8.7.3.1 Linear Deflection Analysis Results

X	Y	Z	Alpha	Beta	Gamma
Deflections of mass no. = 1					
0.0000	0.0000	25.0000	0.0000	0.0000	0.0000
Center of rotation of mass no. = 1					
64,000.0000	64,000.0000	64,000.0000			
Deflections of mass no. = 2					
0.0000	0.0000	25.0000	0.0000	0.0000	0.0000
Center of rotation of mass no. = 2					
64,000.0000	64,000.0000	64,000.0000			

Deflection at control points (mm)

Mass no. = 1						
Position			Deflection			
Point no.	X	Y	Z	x	y	z
Mass no. = 2						
Position			Deflection			
Point no.	X	Y	Z	x	y	z

Deflections at coupling/mount positions

Mount no.	Position			Deflection		
	X	Y	Z	x	y	z
Mass no. = 1						
1	1000.000	1000.000	− 1000.000	0.000	0.000	25.000
2	− 1000.000	1000.000	− 1000.000	0.000	0.000	25.000
3	− 1000.000	− 1000.000	− 1000.000	0.000	0.000	25.000
4	1000.000	− 1000.000	− 1000.000	0.000	0.000	25.000

(continued on next page)

(continued)

Mount no.	Position			Deflection		
	X	Y	Z	x	y	z
Mass no. = 2						
5	1000.000	1000.000	− 1000.000	0.000	0.000	25.000
6	− 1000.000	1000.000	− 1000.000	0.000	0.000	25.000
7	− 1000.000	− 1000.000	− 1000.000	0.000	0.000	25.000
8	1000.000	− 1000.000	− 1000.000	0.000	0.000	25.000

Global and Local Deflections of Couplings/Mounts

Coordinates mount no.	Global Deflection			Local Deflection		
	x _p	y _p	z _p	X	Y	Z
Mass no. = 1						
1	0.00	0.00	25.00	0.00	0.00	25.00
2	0.00	0.00	25.00	0.00	0.00	25.00
3	0.00	0.00	25.00	0.00	0.00	25.00
4	0.00	0.00	25.00	0.00	0.00	25.00
Mass no = 2						
5	0.00	0.00	0.00	0.00	0.00	0.00
6	0.00	0.00	0.00	0.00	0.00	0.00
7	0.00	0.00	0.00	0.00	0.00	0.00
8	0.00	0.00	0.00	0.00	0.00	0.00

8.7.4 Frequency Analysis

In order to perform a frequency analysis, the force selection must be relevant to the frequency analysis. Force options between 16 and 21 are for frequency analysis. Option 16 (A Sin Wt) is chosen to demonstrate the frequency analysis, as shown in Figure 8.21.

Here, default excitation is in the z direction. Flag = 1 means this is an ordinary sinusoidal force with 1000 N excitation amplitude. It exists in the frequency range from 0 to 2 Hz (freq 1 and freq 2) acting in

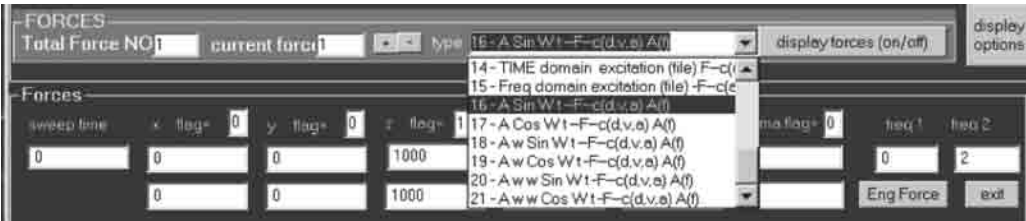


FIGURE 8.21 Frequency analysis options 16 to 21.

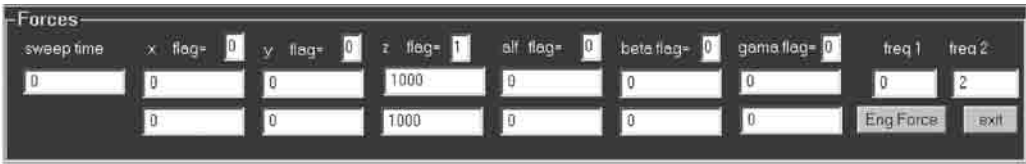


FIGURE 8.22 Constant force amplitude between 0 and 2 Hz.

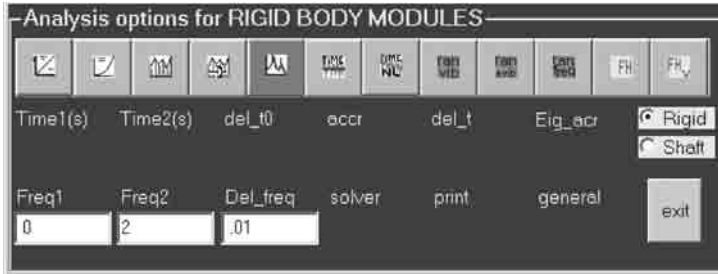


FIGURE 8.23 Frequency analysis parameters.

the z direction, as shown in Figure 8.22. You may have more than one force, with different amplitudes and different frequency ranges. Sweep time, in seconds (any number other than zero), refers to the time taken to sweep from freq 1 to freq 2 (see Chapter 17). If the sweep time is infinitely slow, then a zero entry signifies this (exactly the opposite meaning!). There are two amplitudes for each direction, the top entry refers to the amplitude at freq 1 and the bottom one refers to the amplitude at freq 2. Amplitudes between these frequencies vary linearly.

To execute a frequency analysis, select analysis options and click the button shown in Figure 8.23. Frequency analysis parameters: start frequency, end frequency, and frequency steps are shown in this figure.

Specifically, the options Freq 1 and Freq 2 will appear here. These relate to the frequency range to be analyzed. Del_freq is the frequency step. Your choice of frequency range should not be arbitrary. Either the problem dictates the range or you may be interested in amplitudes of the system at resonant frequencies. In the latter case, you may look at the eigenvalue results to identify which resonant frequencies will be exhibited in the selected range. For the example considered, the excitation force is in the z direction. Therefore, one needs to find out the resonant frequencies in the z direction (or coupled modes which include the z direction). If the eigenvalue results are studied, one can see that the resonant frequencies in the z direction are given as: 0.68 and 1.78 Hz. Therefore, analysis beyond 2 Hz in the z direction will not reveal any other resonances. Clicking the red button a second time will execute the analysis. To see the results you need to click the “display postprocessing” button, and from the postprocessing frame click the “plot freq” button. The frequency-plotting window will appear. The frequency motion in six directions will be plotted for mass 1. “+” can be used to move to the next mass. You may also display motion curves of all bodies together by choosing the “plot all” option. You will end up with the results shown in Figure 8.24.

8.7.5 Time-Domain Analysis

Forces 1 to 14 are for the time domain, although 13 and 14 are not available in this version of VIBRATIO. When option 1 is selected in the force “type” option, the default force would be 1000 N in the z direction, remaining active between 0 and 2 sec. Modify Time 2 to 0.01 sec (10 msec). You can use option 1 for a rectangular shock but there are also other shock options. Figure 8.25 shows a constant force, magnitude 10,000 N acting in the z direction between 0 and 0.1 sec.

To perform a time domain analysis, the button shown in Figure 8.26 needs to be clicked. Relevant analysis parameters will appear as shown in this figure. Time 1 and Time 2 give the range of the time domain analysis. If Time 1 is chosen not to start from 0, even though the resulting data will not be collected until Time 1 reaches, still the solution will be executed starting from start time = 0. In other words, if Time 1 is not zero then this will be the time when data recording starts. Analysis itself, irrespective of Time 1, always starts from 0 sec. del_t0 is the initial step length for integration

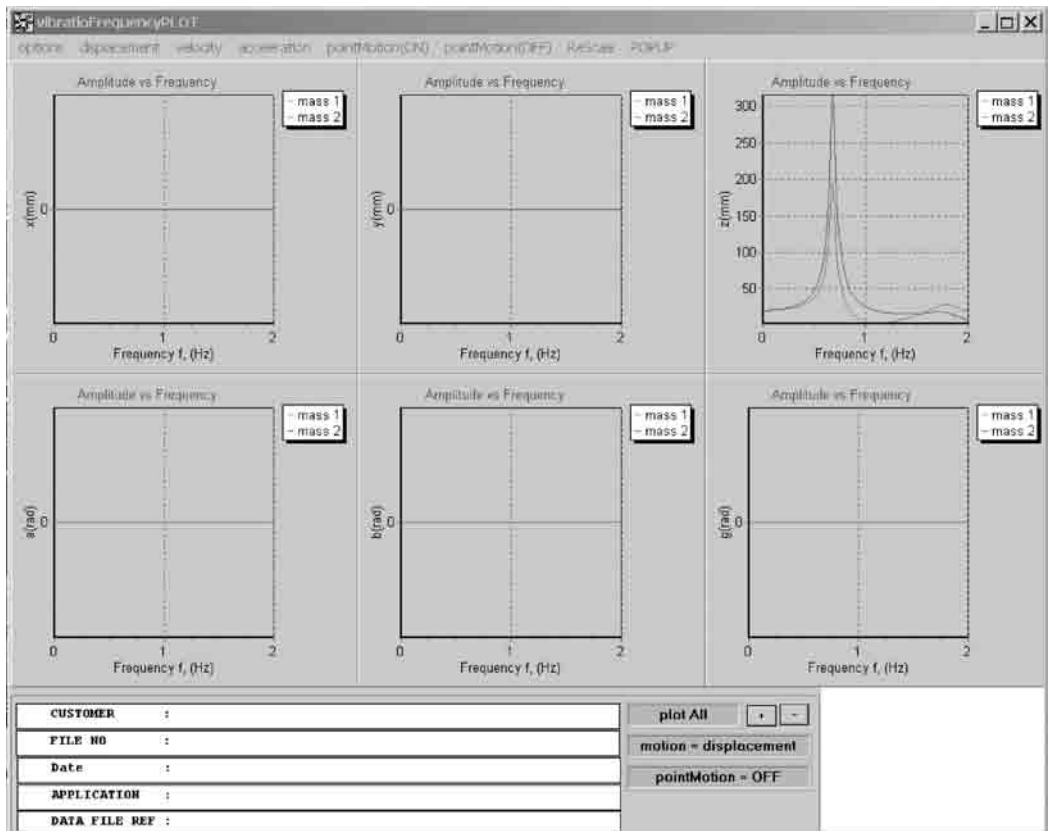


FIGURE 8.24 Frequency analysis results.

(The time-domain analysis uses variable step length Runge–Kutta and the time integration step where an algorithm automatically modifies the integration step to achieve the required accuracy). Accr is the accuracy of integration and del_t is the time step at which data is sampled. To execute, click the button again.

8.7.5.1 Time-Domain Results

Time domain results will be displayed by clicking the plot-time button on the postprocessing frame. The results shown in Figure 8.27 will be obtained, again from the “options” menu, when “plot all” is selected.

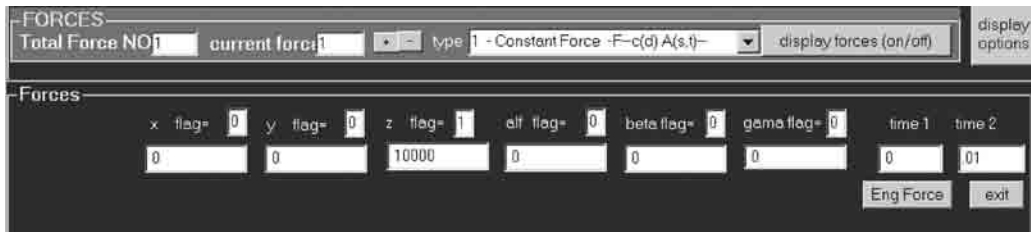


FIGURE 8.25 Constant force representation.

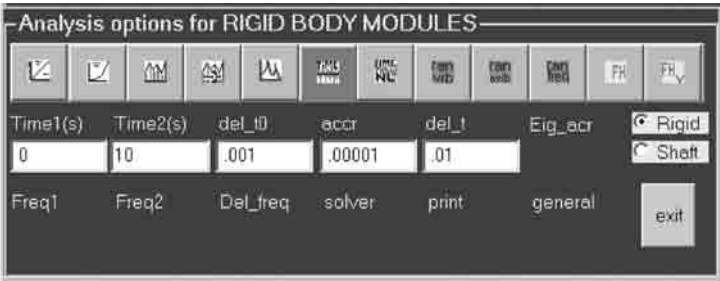


FIGURE 8.26 Time-domain analysis button and analysis control parameters.

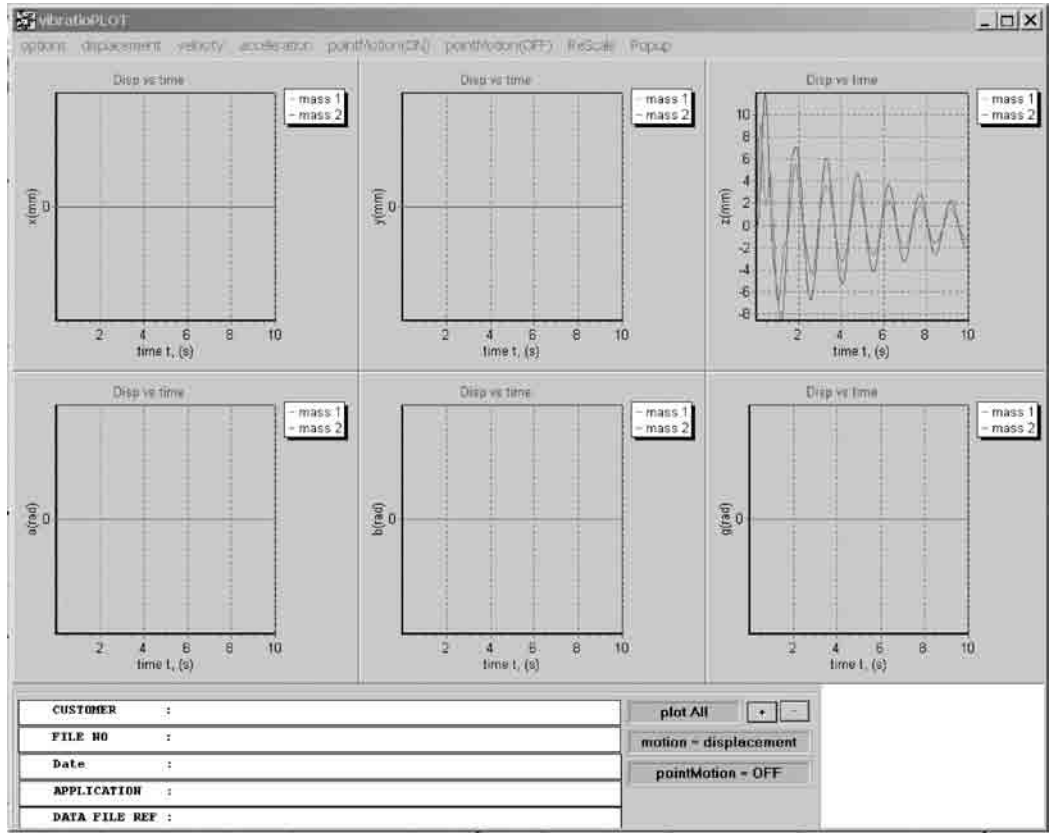


FIGURE 8.27 Time-domain results window.

8.8 Comments

This chapter presented a method of analyzing general multiple rigid-body systems interconnected by linear springs and linear dampers. The mathematical modeling was presented for small vibrations where nonlinear geometry effects and gyroscopic couplings were negligible and the deflection characteristics of the mountings were linear. There is a shortage of published material on general mathematical modeling of flexibly supported rigid multibody systems for vibration analysis. Detailed mathematics of time domain, frequency domain and eigenvalue/eigenvector analyses can be found in

standard vibration textbooks. Some are listed in the references section, but this list is not exhaustive. This chapter also gives a precise and clear formulation suitable for computational implementation. The formulation presented in this chapter forms the core of the vibration analysis suite “VIBRATIO”, a version of which is made available to the users of this handbook, at www.signal-research.com, as indicated in the text.

Bibliography

Bishop, R.F.D. and Johnson, D.C. 1960. *The Mechanics of Vibration*, Cambridge University Press, New York.

Caughey, T.K., Classical normal modes in damped linear dynamic systems, *J. Appl. Mech.*, 27, 269–271, 1960.

den Hartog, J.P. 1956. *Mechanical Vibration*, 4th ed., McGraw-Hill, New York.

de Silva, C.W. 2000. *VIBRATION: Fundamentals and Practice*, CRC Press, Boca Raton, FL.

Jacobsen, L.S. and Ayre, R.S. 1958. *Engineering Vibrations*, McGraw-Hill, New York.

Meirovitch, L. 1986. *Elements of Vibration Analysis*, 2nd ed., McGraw-Hill, New York.

Meirovitch, L. 1967. *Analytical Methods in Vibrations*, Macmillan, New York.

Ralston, A. 1965. *A First Course in Numerical Analysis*, McGraw-Hill, New York.

Thomson, W.T. 1988. *Theory of Vibrations with Applications*, 3rd ed., Prentice Hall, Englewood Cliffs, NJ.

Timoshenko, S., Young, D.H., and Weaver, W. Jr. 1974. *Vibration Problems in Engineering*, 4th ed., Wiley, New York.

VIBRATIO, information and download for the readers of this chapter, www.signal-research.com.

Wilkinson, J.H. 1965. *The Algebraic Eigenvalue Problem*, Clarendon Press, Oxford.

Appendix 8A

VIBRATIO Output for Numerical Example in Section 8.3

X	Y	Z	Alpha	Beta	Gamma
Frequency in X = 1.01 Hz (60 CPM)					
Relative eigenvector values for mass = 1					
1.0000	0.0000	0.0000	0.0000	0.0000	0.0000
Frequency in Y = 1.42 Hz (85 CPM)					
Relative eigenvector values for mass = 1					
0.0000	1.0000	0.0000	0.0000	0.0000	0.0000
Frequency in Z = 1.74 Hz (105 CPM)					
Relative eigenvector values for mass = 1					
0.0000	0.0000	1.0000	0.0000	0.0000	0.0000
Frequency in alpha = 34.87 Hz (2092 CPM)					
Relative eigenvector values for mass = 1					
0.0000	0.0000	0.0000	1.0000	0.0000	0.0000
Frequency in beta = 12.33 Hz (740 CPM)					
Relative eigenvector values for mass = 1					
0.0000	0.0000	0.0000	0.0000	1.0000	0.0000
Frequency in gamma = 14.24 Hz (854 CPM)					
Relative eigenvector values for mass = 1					
0.0000	0.0000	0.0000	0.0000	0.0000	1.0000

Finite Element Applications in Dynamics

9.1	Problem and Element Classification	9-2
	Geometric Modeling • Discrete Element Types in FE Programs • Truss and Beam Problems • Two-Dimensional Problems • Shell and Plate Problems • Three-Dimensional Solid Problems • Synopsis of Problem Classification and Element Choice	
9.2	Types of Analysis	9-20
9.3	Modeling Aspects for Dynamic Analysis	9-23
	Model Size and Choice of Master Degrees of Freedom • Lumped and Consistent Mass Modeling • Use of Symmetry	
9.4	Equations of Motion and Solution Methods	9-27
	Equation of Motion • Direct Integration Method • Modal Superposition Method • Damping Formulation	
9.5	Various Dynamic Analyses	9-33
	Modal Analysis • Transient Dynamic Analysis • Harmonic Response Analysis • Response Spectrum Analysis	
9.6	Checklist for Dynamic FE Analysis	9-41

Mohamed S. Gadala

The University of British Columbia

Summary

This chapter discusses the use of the finite element (FE) method in problems of vibrations and structural dynamics. The first three sections outline the main steps in modeling a physical problem for a specific dynamic analysis. Section 9.1 concentrates on the finite element aspect of the modeling process. The basis for geometric modeling is outlined and an overview of commonly used types of elements in typical commercial programs is presented. A summary of element capabilities is given at the end of the section (Table 9.1). Section 9.2 discusses the basis for classifying and choosing a particular type of dynamic analysis, including modal, harmonic or frequency response, transient and shock, and random analysis. Section 9.3 discusses some special aspects in modeling that are pertinent to dynamic system analysis; namely, choice of master and slave degrees of freedom (DoF), lumped vs. consistent mass modeling, and use of symmetry in dynamic analysis.

The second part of the chapter discusses solution methods and damping considerations, and outlines basic steps for performing various dynamic analyses. Section 9.4 briefly presents the theory and equations for various dynamic analyses. The analysis types included in the discussion are direct integration and modal superposition. In the direct integration analysis, both implicit and explicit schemes are discussed and an example of each is presented. Most of the theory and equations are presented in a summarized form without rigorous mathematical proofs. Section 9.5 describes details of various dynamic analyses and provides a brief discussion of the choice of the solution method for each analysis. Emphasis is placed on the basic steps required to perform a particular analysis type. Modal analysis, transient analysis (direct integration and mode superposition approaches),

frequency response harmonic analysis, and random response analysis are presented. The various methods of combination of modal responses are also discussed. Finally, Section 9.6 provides some general guidelines for a typical dynamic analysis using the FE method.

9.1 Problem and Element Classification

The first step in any finite element (FE) analysis is to build a model of the physical structure to be analyzed. This is an important step and normally requires extensive time and interaction with the analyst. The adequacy of the model, assumptions involved, and types of elements used for a specific structure and analysis type establish the accuracy level of the FE analysis. Much research effort is being devoted to automating this process by providing options for automatic mesh generation, automatic mesh refinement, error estimation, and error bounds. Such research has resulted in a significant reduction in the time needed for this step but the role of the analyst is still dominant and vital in obtaining a good mesh and model for the problem.

The modeling process can be divided into steps as follows:

- Build a geometric database for the structure. This includes description of the characteristic geometric features of the structure, such as boundaries, holes, intersections, curvatures, etc., in the finite element program database. The level of geometric detail has an important effect on the accuracy and the size of the model.
- Build a FE model for the geometric model. This may include important aspects such as:
 - Establishing the type of analysis to be performed,
 - Choosing the appropriate element or elements for building the model,
 - Considering aspects of symmetry in the structure, and
 - Establishing critical areas for increasing mesh density.
- Apply constraints and loading boundary conditions.
- Establish the material model(s) to be used in the analysis.
- Perform various options of model checks.
- Solve sample load cases and compare the results with hand calculations or experimental results in order to check the behavior and response of the model.
- Fine tune the model based on the results obtained from sample load cases.

Most of the time, the above steps are rather linked together, and an overall knowledge of the problem is required to perform a specific step. An important decision that should be made at the beginning of the analysis is to identify the category of the problem. This will have an impact on the first three steps mentioned above. In the first part of the present section, we provide a brief discussion on the geometric modeling aspects of the problem. The rest of the section then provides general guidelines on classifying the problem into one of the main categories available in typical commercial finite element programs; namely, truss, beam, two-dimensional, shell, or three-dimensional problems. We also provide simple examples for each type of problem. The concepts of element choice and problem classification are summarized in a table at the end of the section.

9.1.1 Geometric Modeling

Geometric modeling simply means transforming a physical problem into a geometric database in a FE program. The process is very similar to creating an engineering drawing or a model in a CAD program. Most FE programs have built-in preprocessors that are dedicated to generating the geometry database. Generally, FE preprocessors have similar capabilities to those available in CAD programs. In many cases an existing geometric database may be available for the structure in a CAD program and may be imported into the FE program database. However, there can be translation problems between the two databases, especially in three-dimensional and shell structures. In most cases, it is faster to regenerate the geometric database for the problem directly using the FE program.

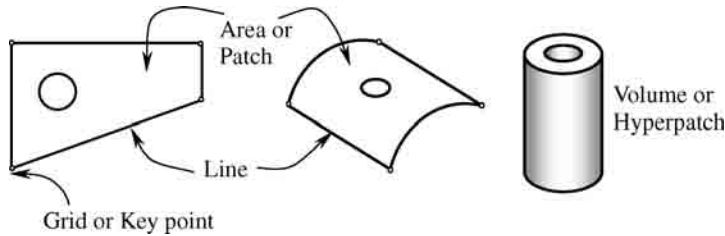


FIGURE 9.1 Geometric modeling entities.

Finite element programs use specific building blocks or entities to build the geometry of a structure (Kamel, 1991; *NISA User's Manual*, 1992; *ANSYS User's Manual*, 2003). The theory on which geometry generation is based is quite simple and basically relies on parametric cubic modeling of curves and surfaces in space. Figure 9.1 shows the basic entities used by most programs for building a geometric model. We define these basic geometric entities and briefly discuss their use in practical modeling of structures.

9.1.1.1 Key Point

A key point is a coordinate location in space. In two-dimensional space, a key point is uniquely defined by two coordinates (e.g., x, y ; r, θ). In three-dimensional space, a key point is uniquely defined by three coordinates (e.g., x, y, z ; r, θ, z). Key points are normally the starting building blocks in the geometry. Connection between key points will generate lines, surfaces, or volumes. On the other hand, most programs will be capable of extracting key points from the end points or corners of lines, surfaces, and volumes. Key points should not be confused with nodes, and should be considered only as spatial locations in space. One may place a node at the same location as a key point or leave the location without node generation.

9.1.1.2 Line or Line Segment

A line or line segment is a portion of a cubic spline curve bounded on both ends by a key point. A line may be straight or curved. The curvature of a line is limited only by its parametric cubic equation in the program. If a physical curve in the structure is presented by up to and including a third-order parametric cubic equation, it may be modeled exactly by a single line. In many practical situations, however, this is not the case. As an example, the parametric equation of a circle is not cubic and the recommended way to model a circle accurately is to break it into at least four lines. Breaking a space curve into many lines will always increase the accuracy of the geometric modeling but entails increasing the complexity of the model. The analyst should be careful in situations where the order of the line to be modeled is not known. A common case is the generation of the line of intersection between two surfaces. In such situations, it is important to break the intersection line into a few separate lines.

Most programs provide extensive methods for line generation. These may include generation by joining two grid points, cubic spline fitting of four grid points, best fitting a curve between several grid points, extracting the edges of a surface or a volume, intersection of surfaces, and mirroring and copying other lines.

9.1.1.3 Area or Patch

An area or a patch is a portion of a bi-cubic surface completely bounded by three line segments (for triangular areas) or four line segments (for quadrilateral areas). The same limitations discussed above for using line segments may be extended here by realizing that the area is modeled by parametric cubic equations in two directions representing the two edges of the area.

Most programs provide extensive methods for generating areas or patches. These include generation by sweeping the space between two lines, filling in the area between four edge lines, rotating a line about an axis, extracting the boundary surfaces of a volume, and intersection between volumes.

9.1.1.4 Volume or Hyperpatch

A volume or a hyperpatch is a portion of tri-cubic solid completely bounded by four areas (for tetrahedron volumes) or six areas (for brick volumes). The equations used to model the edge lines of a volume are still parametric cubic equations and the same restrictions discussed for lines can be extended to a volume in the three directions of the volume.

As for line and area generation, most programs provide a wide variety of methods for generating volumes. These may include generation by sweeping the volume between two surfaces, filling the volume between bounding surfaces, rotating an area about an axis, and copying and mirror imaging the existing volume.

An important addition in the generation of volumes is the ability of many programs to use solid primitives as building blocks (Kamel, 1991; *ANSYS User's Manual*, 2003). These solid primitives may include tetrahedrons, cubes, cylinders, conical volumes, spheres, torus elements, and other standard volumes. These may be used as building blocks that may be combined, subtracted, or intersected with each other. Many programs provide simple Boolean operations to use for such processes.

REMARKS

- In most modeling cases, it is faster to regenerate the geometric database of the problem directly using the FE program, especially in complicated and three-dimensional models.
- The basic building blocks in geometric modeling are key points, lines, areas, and volumes.
- Many programs provide the ability to create solid primitives as building blocks. These solid primitives may include tetrahedrons, cubes, cylinders, conical volumes, spheres, toruses, and other standard volumes.
- Boolean operations are normally used to combine, subtract, or intersect various geometric entities.

9.1.2 Discrete Element Types in FE Programs

Most commercial FE programs have extensive element libraries that may be used in static and dynamic analyses. For dynamic analysis, it may be convenient to classify elements into discrete and continuum types. Discrete types include concentrated (lumped) mass and inertia, spring, and damper elements, whereas continuum (distributed) types include all other one-dimensional (1-D), two-dimensional (2-D), and three-dimensional (3-D) deformable elements. In this section, we briefly discuss the discrete type of elements whereas the continuum type will be discussed in detail in subsequent sections.

9.1.2.1 Concentrated Mass/Inertia Element

A concentrated mass/inertia element represents a structural mass and moment of inertia concentrated at one point and has six DoF: three translational and three rotational. The mass and rotary (moment of) inertia may be assigned different values in the three coordinate directions (see Figure 9.2), even though, typically, the mass is the same in all three directions (see Chapter 8). The element is rigid with no geometrical properties and it only contributes to the global mass matrix of the structure. In building up a model, the element may be attached to a structural node of other deformable or elastic elements or be positioned in space and attached to structure nodes through rigid elements or elastic spring and/or damper elements. Most FE programs provide rotary inertia quantities for various components of the geometric model as part of the standard preprocessing data. These can be used to model parts of the structure as lumped mass and inertia that may be connected to the structure through elastic elements.

An example of the use of a concentrated mass and inertia element is the modeling of a heavy, rigid machine mounted on an elastic support. The mass and inertia effects of the machine may be represented by a concentrated or lumped mass/inertia element at the center of the machine. Care must be taken in connecting this element to the deformable elements of the structure or the support. In general, a rigid link may be used to connect the mass/inertia element to the nearest node of a deformable element rather than placing the mass/inertia element directly on that node (Cook et al., 1989). This will generally account for proper interaction between translational and rotational DoF of the mass and the structure.

It should be noted that some computational algorithms might have problems with zero diagonal values of the mass matrix. This happens if the inertia terms of the mass/inertia element are assigned as zero. This can be avoided by always assigning an arbitrary and small value to the rotary inertia terms.

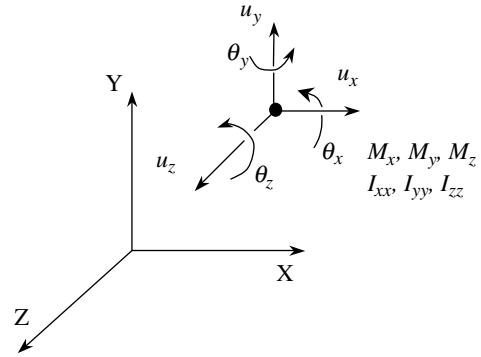


FIGURE 9.2 Three-dimensional mass/inertia element.

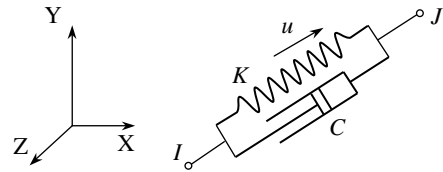


FIGURE 9.3 One-dimensional spring/damper element.

9.1.2.2 Spring and Damper Elements

Most programs provide 1-D spring and damper elements that can be used to model hydraulic cylinders, discrete dampers, and shock absorbers. The element normally has one spring constant and one damping coefficient (along the element axis defined by the nodes *I* and *J* as shown in Figure 9.3). It is easy to model 3-D stiffness and damping characteristics by replicating the element in the required directions. A mass may be attached to one or two nodes of the element. The force transmitted through the element nodes is the sum of the spring and the damping forces along the element axis.

REMARKS

- A concentrated mass/inertia element may be used to model lumped mass/inertia at specific points in the structure. Likewise, spring or damper elements may be used to model stiffness and damping characteristics between two points in the structure.
- A concentrated mass/inertia element represents a structural mass and inertia at a point and has six DoF: three translational and three rotational. Different mass and inertia values may be assigned in different directions.
- Three-dimensional stiffness and damping characteristics between two nodes may be modeled by replicating 1-D spring or damper elements in the required directions.

9.1.3 Truss and Beam Problems

Three-dimensional truss and beam elements are shown in Figure 9.4. The main difference between the two elements is the fact that beams may support bending moments and have rotations as extra DoF at

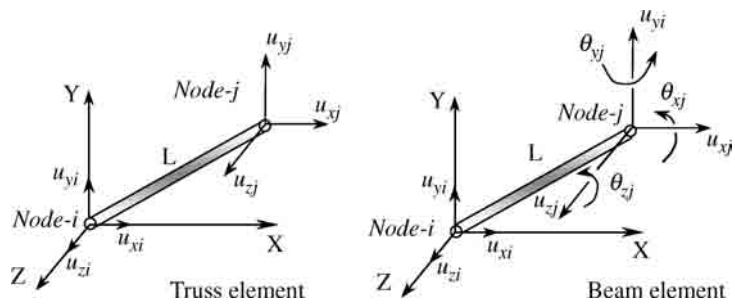


FIGURE 9.4 Three-dimensional truss and beam elements. (Nodal rotations for the beam element are only shown for node-j.)

each node. This means that a beam element may have loads along the beam axis and not necessary only at the end points.

The following conditions should be satisfied for a structure to be classified as a truss or a beam:

- *Geometry:*
 - Thin, slender, straight bars or rods with pin joints at both ends. Depending on the application, the element may be considered as a truss, a link, a cable, a spring, etc.

If the joints are fixed or the bar is curved, the problem will be classified as a beam type. Fixed joints may be created by completely fixing the beam ends to a wall or support, or to another member. This is normally realized if the joint is built-in, welded, or fully bolted to the support or to other members.
 - Geometry may be 1-D, 2-D, or 3-D.
- *Loading:*
 - For truss problems, loading may only be by tension or compression of the members. This may be achieved by having only concentrated loading at the joints (no bending moment) and no loadings along the member.

For beam problems, loading may be in any direction and may be applied along the member axis. This will generally create a bending moment and the member should have rotations as DoF.
 - Thermal loading may also be applied to the member.
 - Body or inertia forces will generally create a bending moment and violate the truss condition and so may be applied only to beam problems. Such loads may be applied, however, to truss elements under the simplification of assuming the inertia effects to be applied only at the nodes or the joints and ignoring the bending moment that will be created on the member.

Degrees of freedom: For 3-D truss elements, the DoF per node are the displacement in the three coordinate directions: u_x , u_y , and u_z . Two-dimensional truss members only have u_x and u_y as DoF. Three-dimensional beam elements have all six DoF: three translational, u_x , u_y , and u_z , as well as three rotational, θ_x , θ_y , and θ_z . Two-dimensional beam elements have u_x , u_y , and θ_z as DoF.

Element shapes: Various element shapes commonly available in commercial finite element programs are shown in Figure 9.5. The cross section of the element may be a solid or hollow prismatic section, e.g., a rectangular, circular, trapezoidal, or thin-walled section or a channel, thin-walled tubular, I-section, etc.

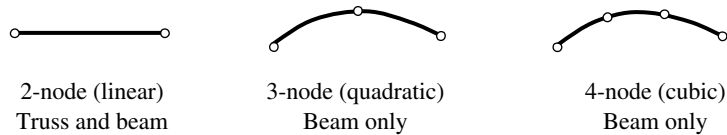


FIGURE 9.5 Various element shapes for truss and beam elements.

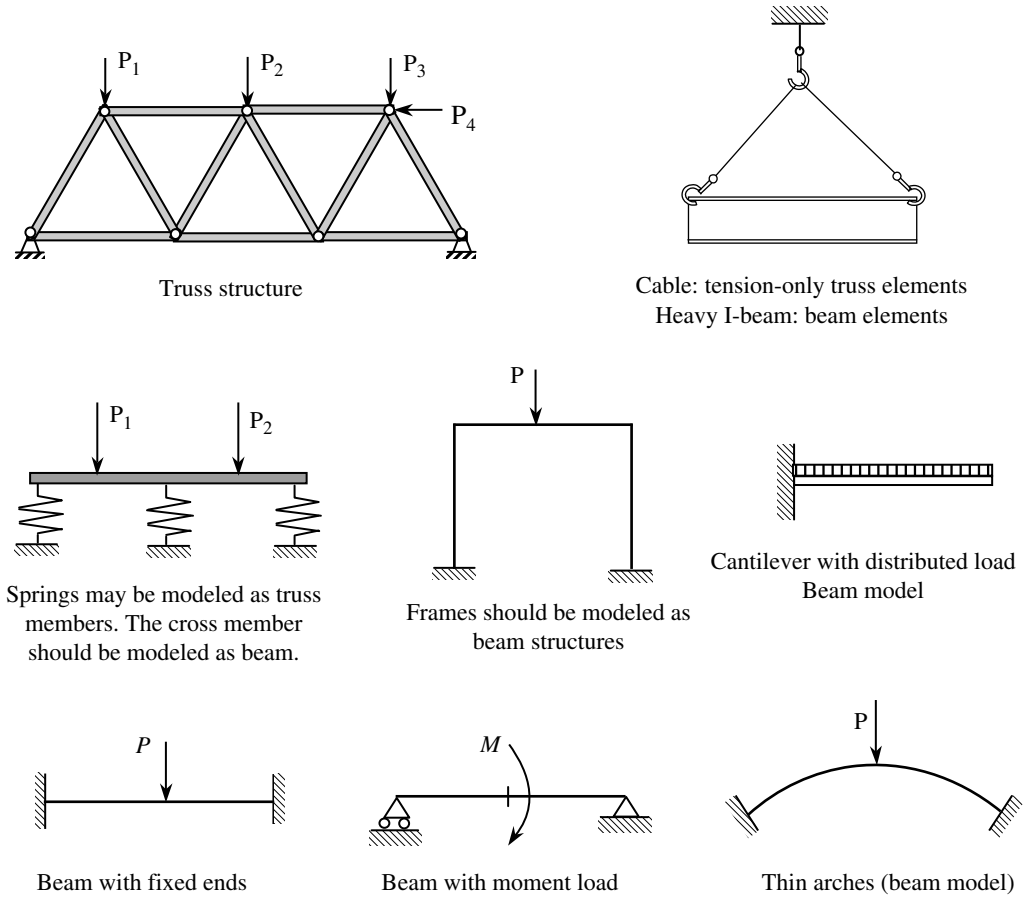


FIGURE 9.6 Typical applications for truss and beam elements.

The analyst will generally be required to identify the orientation of the beam cross section by specifying local axes or identifying key points for the program to locate the local axes. Most programs are capable of modeling variable cross section beam elements to avoid excessive subdivision of the beam into smaller elements.

Example applications: Figure 9.6 shows sample applications for the use of truss and beam elements.

REMARKS

- Truss elements have translational DoF whereas beam elements have both translational and rotational DoF at the nodes. Three-dimensional truss elements have 3 DoF/node (u_x , u_y , and u_z), whereas 3-D beam elements have 6 DoF/node (u_x , u_y , u_z , θ_x , θ_y , and θ_z).
- Truss structures may only carry loads at the end of each truss whereas beam structures may also carry loads along the beam length.
- Curved members should be modeled with beam elements.
- Problems with body and inertia forces should generally be modeled as beam elements. If lumping of the body forces is assumed and the effect of the bending moment created by body forces is neglected, the effect may be modeled with truss elements.

9.1.4 Two-Dimensional Problems

9.1.4.1 Two-Dimensional Plane Stress Problems

Figure 9.7 shows a typical structure, which may be considered as a 2-D plane stress problem.

The following geometry and load conditions should be satisfied for a structure to be categorized as a 2-D plane stress structure (Boresi and Chong, 2000).

Conditions:

- *Geometry:*
 - A flat, thin surface in one plane (e.g., xy -plane), simply connected or multiply connected with a small thickness in the third direction (e.g., z -direction).
 - The boundary of the structure in the xy -plane may be straight or curved.
- *Loading:*
 - Loading is restricted to the plane of the structure (e.g., xy -plane).
 - Thermal loading may also be applied to the plane (i.e., $T = T(x, y)$).
 - Body or inertia forces may be due to linear or angular acceleration in the plane of the structure.

Degrees of freedom: For 2-D elements, the DoF per node are the displacements in the two coordinate directions, u_x and u_y .

Typical element shapes (see Figure 9.8): Elements may be triangular or quadrilateral. Most programs provide the option of having 3, 6, or 9 nodes for triangular elements and 4, 8, or 12 nodes for quadrilateral elements. Increasing the number of nodes will increase the element accuracy at the expense of having more DoF and requiring more CPU time to solve the problem. This is normally called a “p-conversion” approach in finite elements. The same goal may be achieved by increasing the number of elements while fixing the number of nodes per element, which is usually called “h-conversion” (Zeng et al., 1992; Babuska and Guo, 1996). The choice of method to obtain greater accuracy is rather arbitrary and mostly depends on the availability of the option in the program. Only a limited number of programs provide extensive “p-conversion” options.

Example applications: Figure 9.9 shows some typical examples that may be modeled using a plane stress assumption. It should be noted such models cannot capture any out-of-plane modes of vibration. If such vibration modes are of concern, the model should be capable of capturing lateral displacement DoF and out-of-plane rotations. This may be realized by using shell or 3-D solid elements as will be discussed in the following sections.

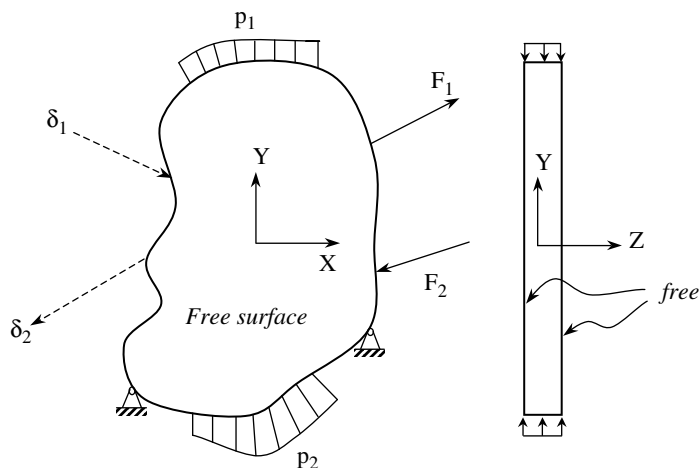


FIGURE 9.7 A general 2-D plane stress structure.

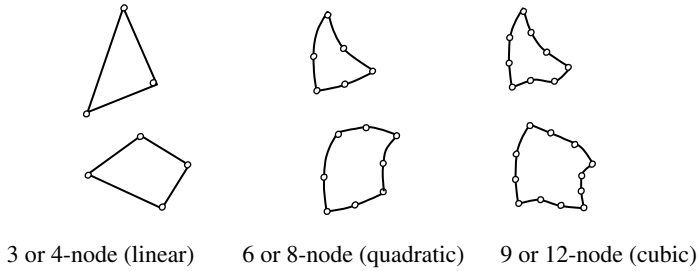


FIGURE 9.8 Typical plane stress elements.

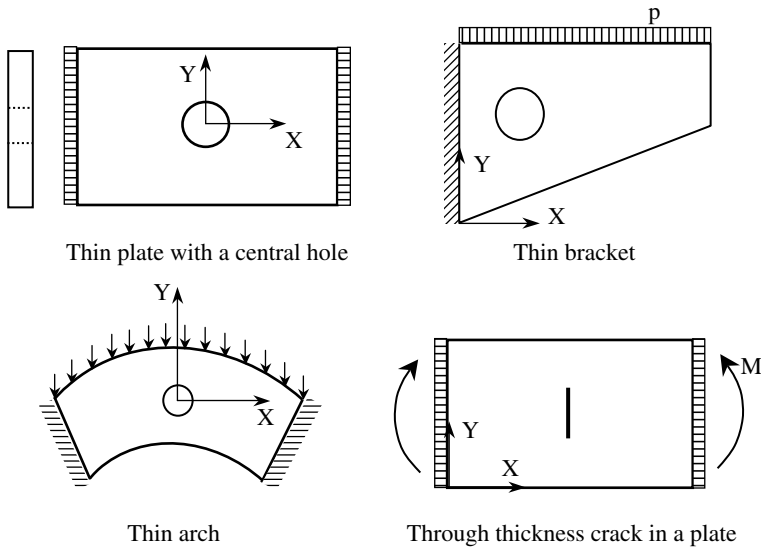


FIGURE 9.9 Typical plane stress examples.

9.1.4.2 Two-Dimensional Plane Strain Problems

Figure 9.10 shows a typical structure that may be considered as a 2-D plane strain.

The following geometry and load conditions should be satisfied for a structure to be categorized as a plane strain structure (Borelli and Chong, 2000).

Conditions:

- **Geometry:**
 - A flat surface in a plane (e.g., xy -plane), simply or multiply connected with large thickness in the third or z -direction (with much larger dimensions than in the xy -plane).
 - The boundary of the structure in the xy -plane may be straight or curved.
- **Loading:**
 - Loading is restricted to the plane of the structure (e.g., xy -plane) with possible uniform loading or constraint in the z -direction. The loading in the z -direction will remain only as a function of the x and y coordinates; i.e., $P_z = P_z(x, y)$.
 - Thermal loading may also be applied to the plane (i.e., $T = T(x, y)$).
 - Body or inertia forces may be applied to the plane.

Degrees of freedom: For 2-D plane strain elements, the DoF per node are the displacement in the two coordinate directions u_x and u_y . The plane strain assumption means that the strain in z -direction will be zero and that the stress will be nonzero, $\epsilon_z = 0$ and $\sigma_z \neq 0$.

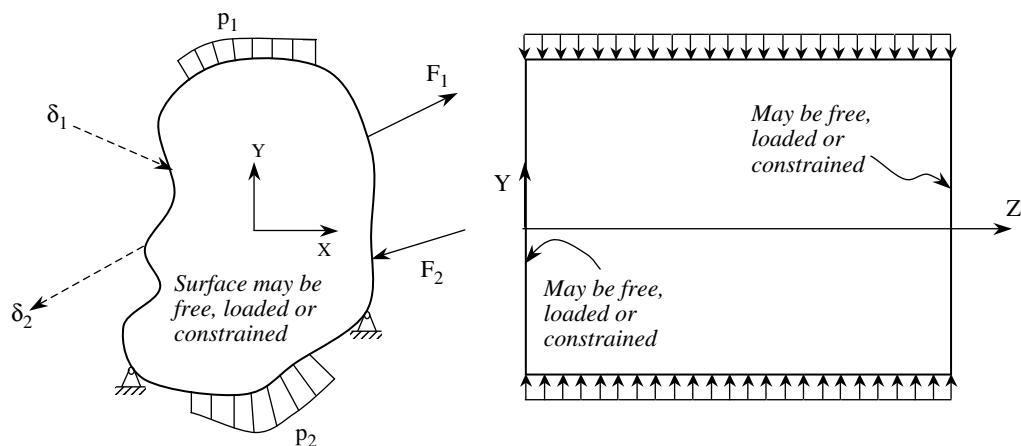


FIGURE 9.10 A general 2-D plane stress structure.

Typical element shapes: The same element shapes as in the case of plane stress are available in most commercial FE programs (see Figure 9.8). The comment above on p-conversion and h-conversion also applies here.

Example applications: Figure 9.11 shows some typical examples that may be modeled using a plane strain assumption. Once again, it should be noted that such a model cannot capture any out-of-plane modes of vibration. If such vibration modes are of concern, the model should be capable of capturing lateral displacement DoF and out-of-plane rotations. This may be realized by using shell or 3-D solid elements as will be discussed in the following sections.

9.1.4.3 Two-Dimensional Axisymmetric Problems

Axisymmetric problems are characterized by having an axis of symmetry or axis of revolution for geometry and loading. Referring to Figure 9.12, any arbitrary plane that passes by the axis of symmetry will be a plane of symmetry. Symmetry means that the two halves of the structure on each side of the plane of symmetry are mirror images of each other. Symmetry must be satisfied for all aspects affecting the response of the structure including geometry, load, constraint, and material properties.

The following conditions summarize the requirements for categorizing a problem as axisymmetric (Boresi and Chong, 2000).

Conditions:

- *Geometry:*
 - A solid of revolution formed by rotating a flat area (e.g., in the rz -plane) around an axis of symmetry (e.g., the z -axis).
 - The boundary of the flat area in the rz -plane may be straight or curved and the area may be simply or multiply connected.
- *Loading:*
 - Loading is restricted to the rz -plane with no variation of loading in the θ -direction. No loading in the θ -direction.
 - Thermal loading may be applied in the rz -plane (i.e., $T = T(r, z)$).
 - Body or inertia forces may be applied in the rz -plane.

Degrees of freedom: For 2-D-axisymmetric elements, the DoF per node are the displacements in the two coordinate directions u_r and u_z . Some programs use x and y coordinates to replace the r and z axes, respectively.

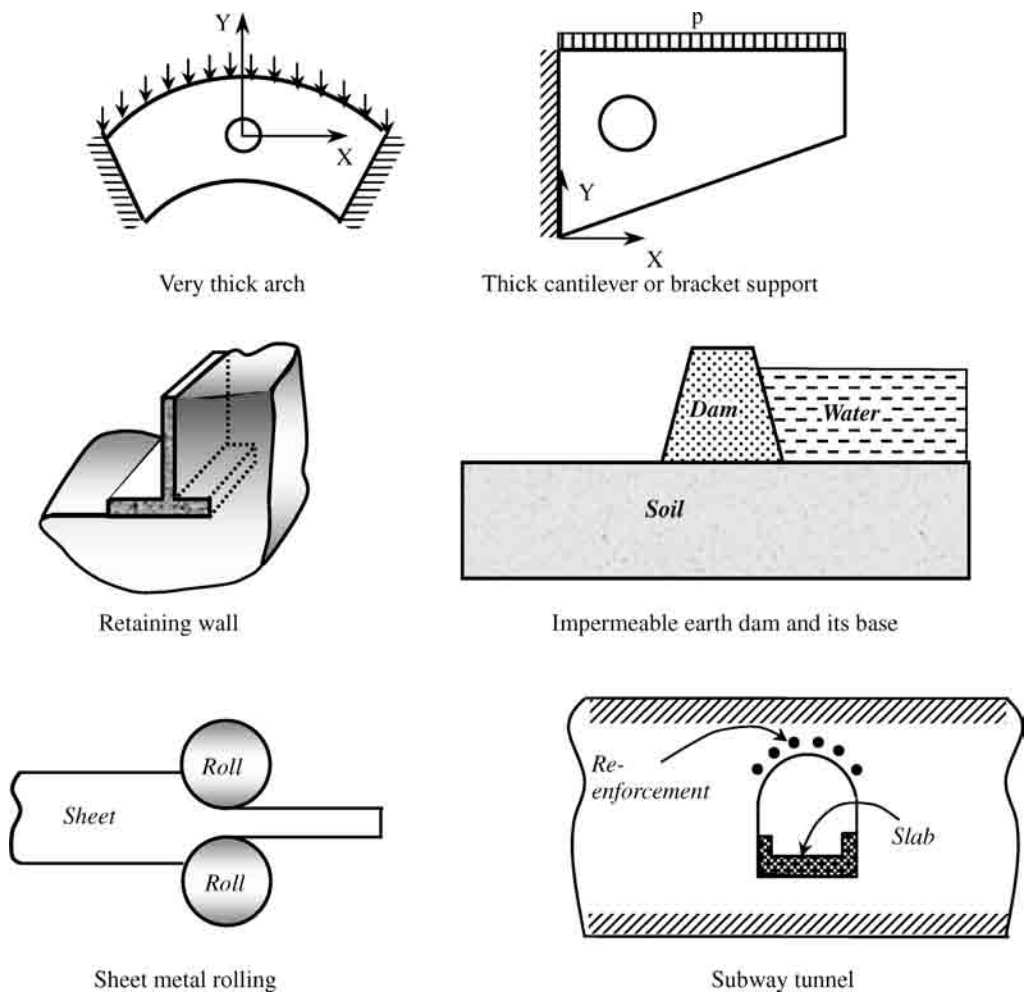


FIGURE 9.11 Typical plane strain examples.

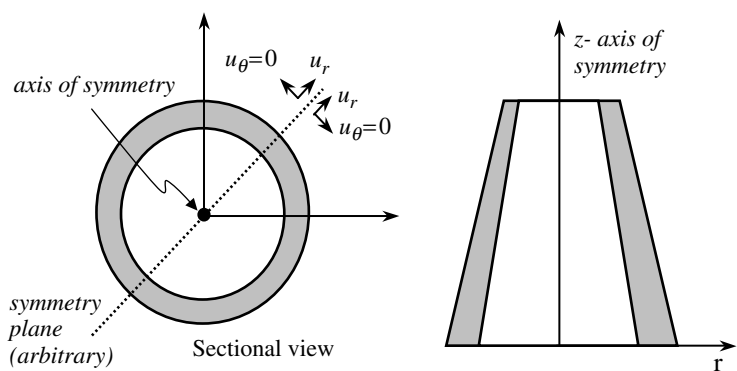


FIGURE 9.12 Axial symmetry conditions.

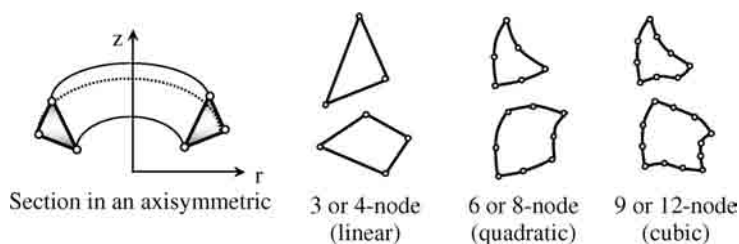


FIGURE 9.13 Typical axisymmetric elements.

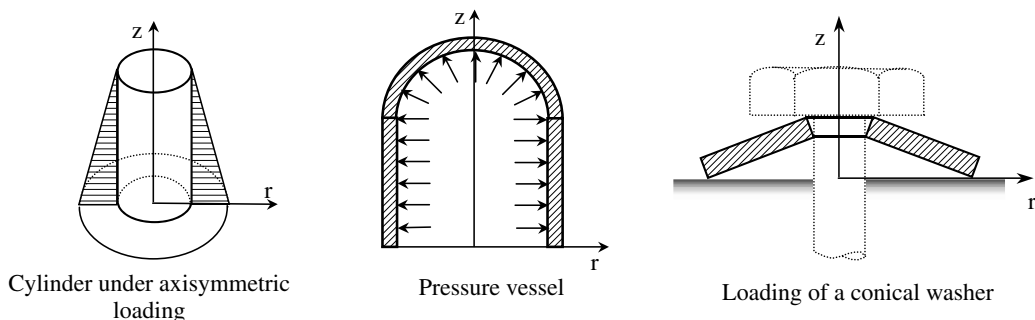


FIGURE 9.14 Typical axisymmetric examples.

Typical element shapes: Figure 9.13 shows typical axisymmetric element shapes that are commonly available in commercial FE programs. The elements are shaped as a torus with various cross sections as shown in the figure.

Application examples: Figure 9.14 shows typical axisymmetric examples.

9.1.5 Shell and Plate Problems

Shell and plate problems are quite similar to plane stress problems (see Figure 9.15). We first recall the conditions for a plane stress problem: (1) that the geometry has to be flat in one plane with a small thickness, and (2) that the load has to be in the same plane. If either of these two conditions is violated, the problem becomes a shell problem. For example, if the load is a moment about any direction other than the z -direction then it has an out-of-plane component, or if the geometry is not flat then the problem ceases to be a plane stress problem and should be modeled as a shell problem. Normally, shell structures would still maintain a small thickness in the direction normal to the surface of the shell. This maintains the condition that the stress normal to the shell surface will be zero, although there may still be a pressure applied to the surface of the shell.

The following summarizes the conditions for a shell structure.

- *Geometry:*
 - Thin surfaces or plates that have a thickness in the direction normal to the surface. The midsurface or midplane of the structure may be flat or curved.
 - The boundary or edges of the structure may be straight or curved.
- *Loading:*
 - Both in-plane and out-of-plane loadings are permitted.
 - Thermal loading may also be applied in all x -, y -, and z -directions.
 - Body or inertia forces may be due to linear or angular acceleration in all three directions.

Degrees of freedom: Three-dimensional shell elements have six DoF: three translational, u_x , u_y , and u_z , and three global rotational, θ_x , θ_y , and θ_z .

REMARKS

- Structures with a flat planar surface of a small thickness and with loading only in the plane (e.g., xy) of the structure (no out-of-plane loading or constraints) are categorized as plane stress structures. Such structures will have three nonzero stress components: σ_{xx} , σ_{yy} , and t_{xy} .
- Structures with a flat planar surface (e.g., xy) but a very large dimension in the third direction and with loading only in the plane of the structure (with possible uniform loading or constraints in the third direction) are categorized as plane strain structures. Such structures will have four nonzero stress components: σ_{xx} , σ_{yy} , σ_{zz} , and t_{xy} .
- Axisymmetric problems are characterized by having an axis of symmetry or axis of revolution (e.g., z -axis) for geometry and loading. Such structures will have four nonzero stress components: σ_{rr} , $\sigma_{\theta\theta}$, σ_{zz} , and t_{rz} .
- Two-dimensional problems may be modeled by elements having two translational DoF per node. The elements may be triangular with 3, 6, or 9 nodes or quadrilateral with 4, 8, or 12 nodes. Axisymmetric elements are shaped as a torus with triangular or quadrilateral cross-sections.
- Increasing the number of elements while fixing the nodes per element is called “h-conversion,” whereas increasing the number of nodes per element while fixing the number of elements is called “p-conversion.”
- Two-dimensional models cannot capture out-of-plane vibration modes. If such vibration modes are of concern, the model should be capable of capturing lateral displacement DoF and out-of-plane rotations.

Element shapes: Figure 9.16 shows some typical shell elements available in most commercial FE programs. To properly model a curved shell with linear elements that are flat requires using a large number of elements to capture the curvature. Quadratic and cubic elements, on the other hand, may have curvature in two directions and a much reduced number of elements will be needed to model a curved shell. Most programs are capable of modeling variable thickness shell and plate elements.

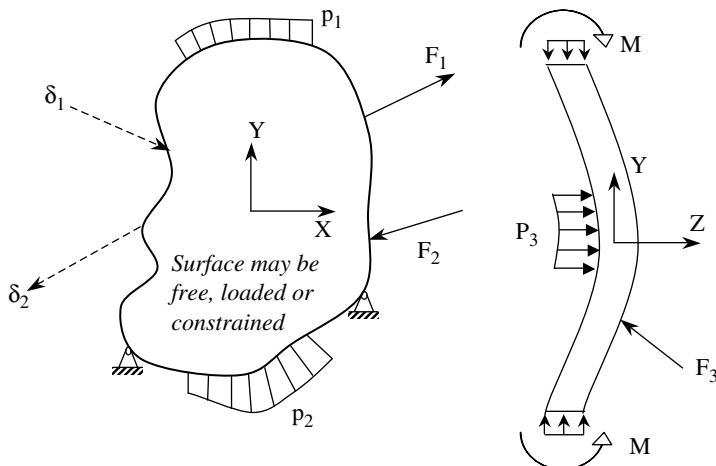


FIGURE 9.15 Shell and plate structures.

Some programs offer shell elements that only have membrane capabilities and others that have both membrane and bending capabilities.

In shell and plate analyses, it is important to note that linear elements, i.e., three-node triangles and four-node quadrilaterals, may behave in an unrealistically stiff manner in shear deformation when the element thickness to size ratio is very small. This phenomenon is normally called “shear locking” (Bathe and Dvorkin, 1985; Bathe, 1996; Luo, 1998; Cesar de Sa et al., 2002). The problem occurs when in-plane displacements are coupled with section rotations in the governing equation of

the element and when low-order interpolations (linear elements) are adopted. The same phenomenon is also evident in beam elements. Similarly, when in-plane displacements are coupled with section rotations in the governing equations and low-order interpolations are used, “membrane locking” will be evident.

Most programs provide various remedies for shear- and membrane-locking problems. These include selective/reduced integration, enhanced assumed strain method, mixed field method, etc. Depending on the availability of a particular method in the program, the user should initiate the remedy. The problem may also be alleviated by switching to higher order elements, such as quadratic or cubic elements.

Example applications: Figure 9.17 shows typical examples of applications for shell problems.

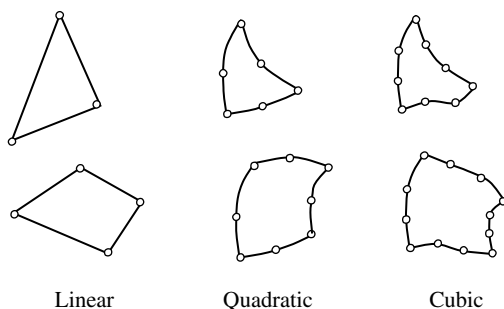


FIGURE 9.16 Typical shell elements.

REMARKS

- Shell structures are general 3-D surfaces of small thickness. Loading can be in plane and out of plane. All stress components except those normal to the surface will be nonzero.
- The shell element may be triangular with 3, 6, or 9 nodes or quadrilateral with 4, 8, or 12 nodes.
- Commercial programs offer shell elements with variable thickness and with membrane and/or bending capabilities.
- Linear elements may experience “shear locking”: nonphysical, high stiffness in shear. Various remedies are available in most programs.

9.1.6 Three-Dimensional Solid Problems

By default, if the problem is not one of those discussed in Section 9.1.3 to Section 9.1.5 then it will be classified as a 3-D problem. Three-dimensional problems are easily identified by their 3-D geometry and loading, as shown in Figure 9.18. Any of the categories of problems discussed above may be solved by using 3-D elements. The critical drawback is the substantial increase in analyst time for modeling and in CPU time in processing the solution (the time needed may be one order of magnitude larger than for a corresponding 2-D problem).

The following summarizes the conditions for a 3-D problem.

- *Geometry:*
 - A 3-D object with no apparent thickness or uniformity in any direction.
 - The boundary of the object may be straight or curved.

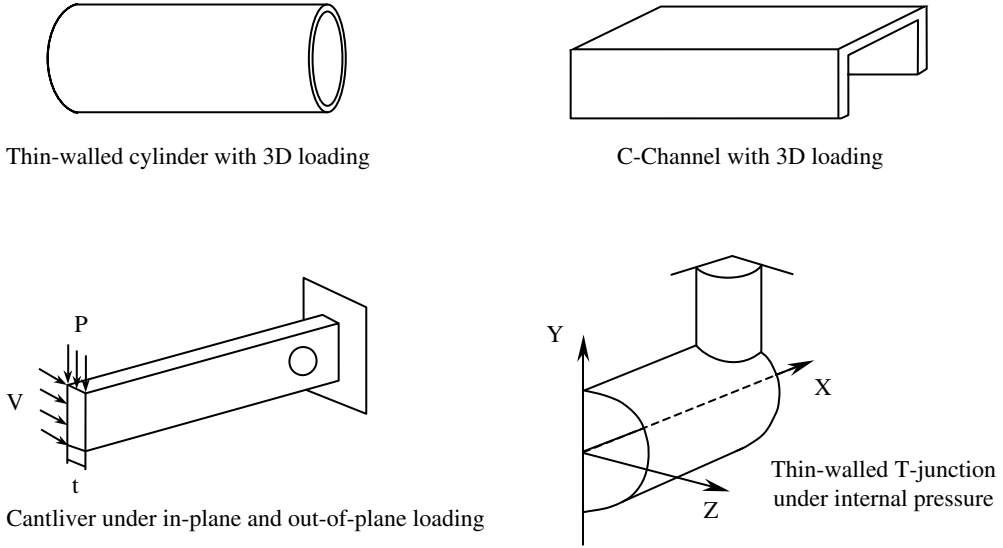


FIGURE 9.17 Typical shell and plate examples.

• *Loading:*

- Three-dimensional loading. An important note should be added here: 3-D elements normally have three displacement DoF and no rotational DoF. This means that moments cannot be directly applied to such elements and the moment effect should be simulated via concentrated forces or couples.
- Other loading, including thermal loading and body or inertia forces, may be applied in any direction.

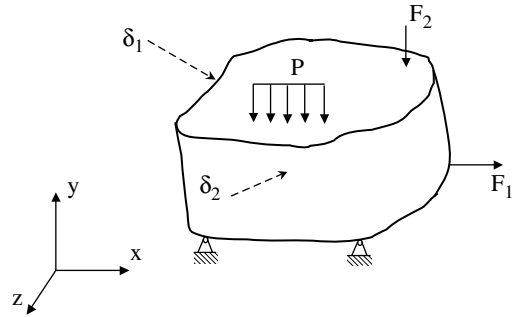


FIGURE 9.18 Three-dimensional problems.

Degrees of freedom: Three-dimensional solid elements have three translational DoF: u_x , u_y , and u_z . As mentioned above, concentrated moments should be modeled by an equivalent system of concentrated forces or couples.

Element shapes: Figure 9.19 shows some typical 3-D element shapes available in most commercial FE programs.

Example applications: Figure 9.20 shows some typical examples of 3-D structures requiring 3-D solid modeling and elements. It should be noted that if out-of-plane vibration modes of a 2-D structure are of concern, then a 3-D solid or shell model should be used even if the loading is in one plane.

Remarks

- Structures that are not classified as truss, beam, 2-D, or shell may be modeled with 3-D solid elements.
- Three-dimensional elements have three translational DoF per node (u_x , u_y , and u_z) and may have 4–32 nodes per element.

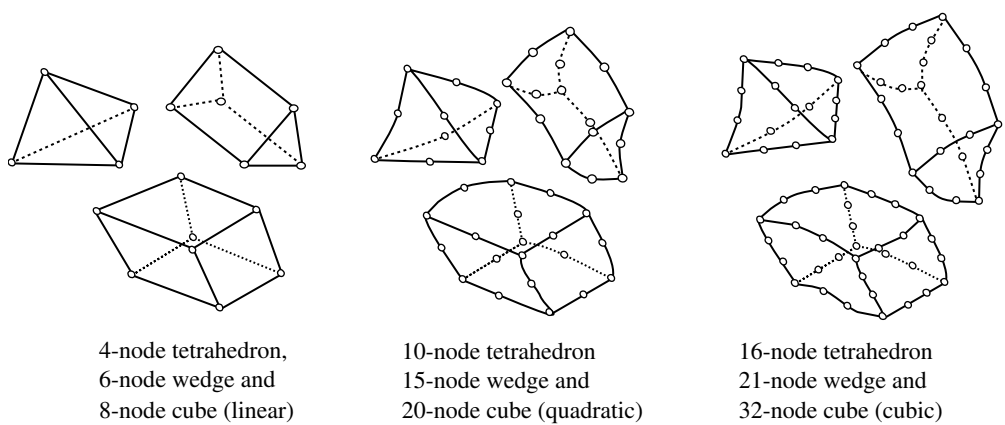


FIGURE 9.19 Typical 3-D solid element shapes.

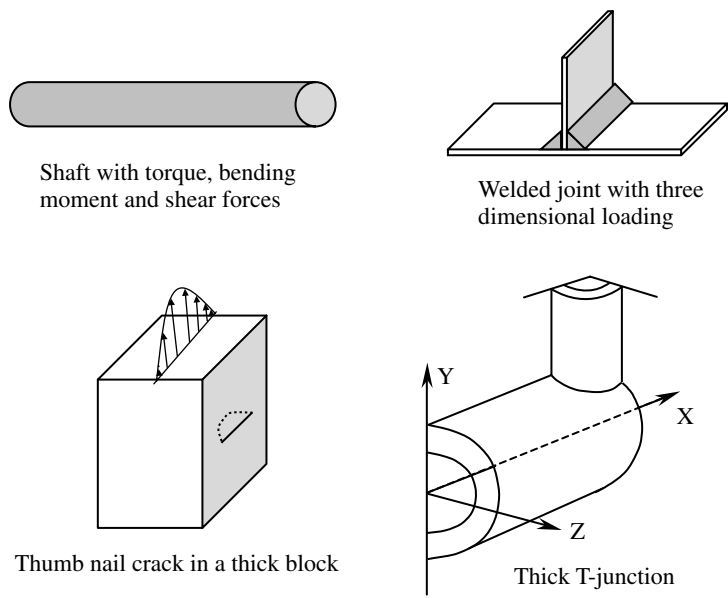


FIGURE 9.20 Typical 3-D examples.

9.1.7 Synopsis of Problem Classification and Element Choice

Table 9.1 summarizes the concepts discussed above (Section 9.1.2 to Section 9.1.6) for element choice and problem classification. The table also shows displacement and stress variations within each element as well as standard element output quantities. The displacement variation within the element represents the basic element assumption in FE analysis and is called the “shape function” or the “approximation function” assumption. The strain variation within the element follows by differentiating the displacement variation according to the strain–displacement relations. The number of nodes per element is linked to the shape function assumption. For example, in 2-D elements three-node triangles have linear shape functions and in 3-D elements eight-node bricks have linear shape functions. Elements with linear shape function are sometimes called low-order or linear elements. Such elements may be used quite efficiently in both linear and nonlinear analyses.

TABLE 9.1 Summary of Problem Classification and Corresponding Element Characteristics

Characteristics	Element			
	Truss	Beam	Two-Dimensional Plane Elements	
Dimension	1-, 2-, or 3-D	2- or 3-D	2-D	2-D
Applications	Trusses — only axial stiffness (acts as a spring between two nodes)	Frames with axial and bending stiffness	2-D plane stress or plane strain problems	2-D plane stress or plane strain problems
Degree of freedom	UX, UY, UZ	UX, UY, UZ, ROTX, ROTY, ROTZ	UX, UY	UX, UY
Geometry	Linear	Linear (principal axes found from third node)	Linear	Quadratic
Displacement	Linear	Axial: linear Bending: cubic	Linear	Quadratic
Stress/strain	Constant	Axial: constant Bending: linear	Constant (triangular) Linear/constant (Quad)	Linear (triangular) Quadratic/linear (Quad)
Loading	Only at end nodes (also possible mass) No distributed load	Line load Self-weight Centrifugal force	Edge pressure Self-weight Thermal Centrifugal force	Edge pressure Self-weight Thermal Centrifugal force
Stress output	Constant thermal Axial force or stress	Thermal Axial force Bending moment Shear in two perpendicular axes or alternatively outer fiber stresses	2-D stresses: σ_{xx} , σ_{yy} , τ_{xy} , σ_{zz} (plane strain) Stress intensities and principal stresses	2-D stresses: σ_{xx} , σ_{yy} , τ_{xy} , σ_{zz} (plane strain) Stress intensities and principal stresses

(continued on next page)

TABLE 9.1 (continued)

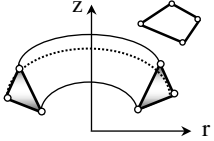
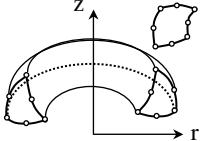
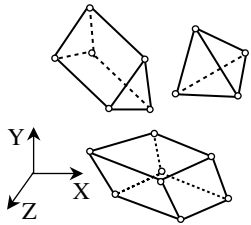
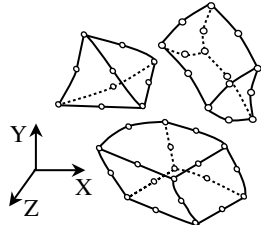
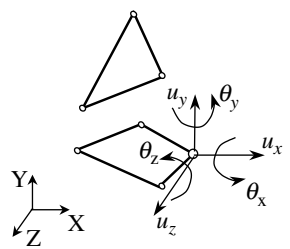
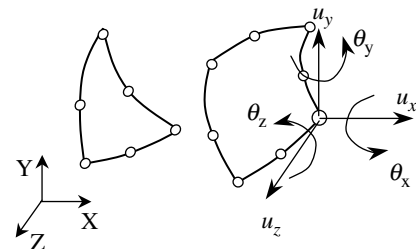
Characteristics	Element			
	Axisymmetric Solid		Three-Dimensional Solids	
				
Dimension	2-D	2-D	3-D	3-D
Applications	Axisymmetric structures with possible nonaxisymmetric loads	Axisymmetric structures with possible nonaxisymmetric loads	3-D solids with general loading	3-D solids with general loading
Degree of freedom	UR, UZ	UR, UZ	UX, UY, UZ	UX, UY, UZ
Geometry	Linear	Quadratic	Linear	Quadratic
Displacement	Linear	Quadratic	Linear	Quadratic
Stress/strain	Constant (triangular) Linear-constant (quad)	Linear (triangular) Quadratic/linear (quad)	Constant (tetrahedron) Linear/constant (hexahedron)	Linear (tetrahedron) Quadratic/linear (hexahedron)
Distributed loads	Pressure Self-weight Thermal Centrifugal force	Pressure Self-weight Thermal Centrifugal force	Pressure Self-weight Thermal Centrifugal force	Pressure Self-weight Thermal Centrifugal force
Stress output	Axisymmetric stresses: $\sigma_{rr}, \sigma_{zz}, \sigma_{\theta\theta}, \tau_{rz}$ Stress intensities and principal stresses	Axisymmetric stresses: $\sigma_{rr}, \sigma_{zz}, \sigma_{\theta\theta}, \tau_{rz}$ Stress intensities and principal stresses	3-D stresses: $\sigma_{xx}, \sigma_{yy}, \sigma_{zz}, \tau_{xy}, \tau_{yz}, \tau_{zx}$ Stress intensities and principal stresses	3-D stresses: $\sigma_{xx}, \sigma_{yy}, \sigma_{zz}, \tau_{xy}, \tau_{yz}, \tau_{zx}$ Stress intensities and principal stresses

TABLE 9.1 (continued)

Characteristics	Element	
	Three-Dimensional Shell Structures	
		
Dimension	3-D	3-D
Applications	3-D shell structures with general loading	3-D shell structures with general loading
Degree of freedom	UX, UY, UZ, ROTX, ROTY, ROTZ	UX, UY, UZ, ROTX, ROTY, ROTZ
Geometry	Linear	Quadratic
Displacement	In shell local coordinates: linear on midsurface and linear through the thickness	In shell local coordinates: quadratic on midsurface and linear through the thickness
Stress/strain	On the midsurface and in shell local coordinates: Triangle: constant Quad: linear/constant (linear through thickness)	On the midsurface and in shell local coordinates: Triangle: linear Quad: quadratic/linear (linear through thickness)
Distributed loads	Surface and edge pressure Self-weight Thermal Centrifugal force	Surface and edge pressure Self-weight Thermal Centrifugal force
Stress output	3-D stresses σ_{xx} , σ_{yy} , σ_{zz} , τ_{xy} , τ_{yz} , τ_{zx} (global) Local stresses Stress intensities and principal stresses	3-D stresses σ_{xx} , σ_{yy} , σ_{zz} , τ_{xy} , τ_{yz} , τ_{zx} (global) Local stresses Stress intensities and principal stresses

9.2 Types of Analysis

If the applied loading on the structure is to change with time, the designer should make a decision on whether or not a dynamic analysis is required. To be able to make this decision, information about the loading and the natural frequencies of the structure are required. From the loading point of view, we classify a general loading on a structure into one of four categories: steady, cyclic, transient, and random.

Figure 9.21 shows a schematic presentation of the four loading categories. Figure 9.21b shows two types of cyclic loading, one is a simple harmonic loading with amplitude of oscillation F_o , period $T = 2\pi$, and frequency $f = 1/T$. The second is a periodic loading with a period T . Using Fourier analysis, any periodic function with a period, T , may be decomposed into a series of harmonic sines and cosines with frequencies $f_1 = 1/T, 2f_1, 3f_1, \dots, nf_1$. Figure 9.21c shows a transient load with a duration T .

Some forcing functions do not lend themselves to simple frequency or time specifications. Figure 9.21d shows a typical time history of a forcing function of such a category that may be considered as random excitation. Transient and cyclic forcing functions are normally specified as force vs. time or frequency, respectively. On the other hand, random forcing functions are commonly specified as the magnitude of the input acceleration squared vs. frequency. This input data is normally called a power spectral density (PSD) input curve. Time history input may be used in the analysis of random excitation and the random input may be treated as transient. This would normally require extensive computer resources and CPU time due to the very large number of time steps that would be required to capture the peak response. Random excitation may occur from random sources such as road undulation on vehicles, noise, earthquakes, and seismic events on buildings, and wind and turbulent loading on airplanes. For practical purposes, PSD curves have been compiled for various random events and are normally available in most FE commercial programs.

In addition to the load specification, the second factor affecting the decision on the type of analysis is the natural frequency of the structure. Structures with mass and stiffness characteristics are capable of free vibrations after removing the initial excitation on the structure. Depending on the initial conditions of excitation, the structure may vibrate in one natural frequency or in a combination of more than one

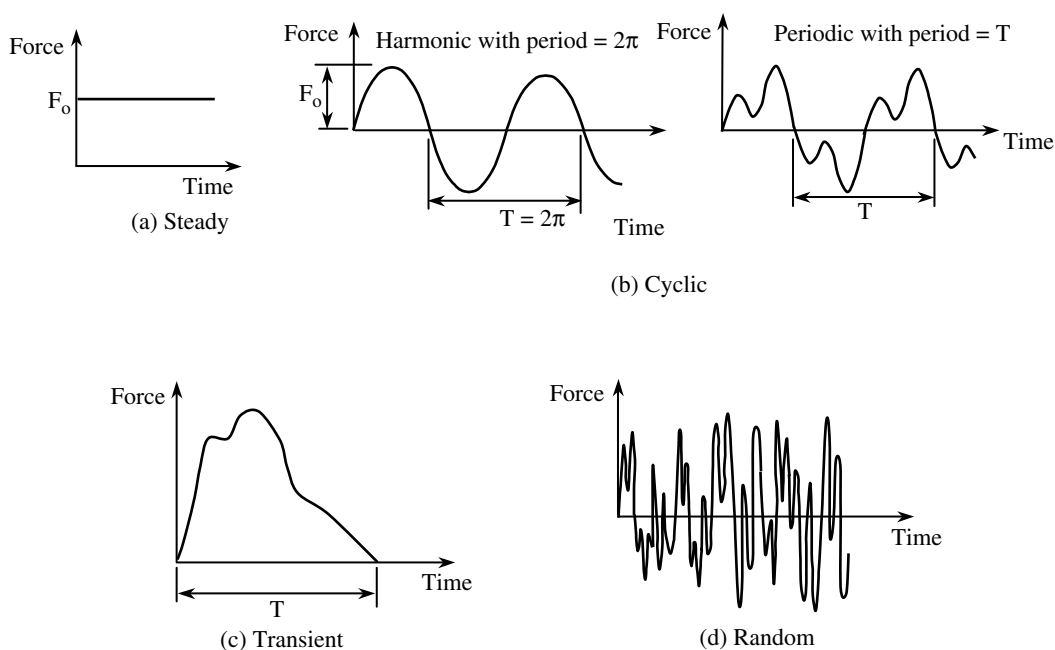


FIGURE 9.21 Various loading types.

natural frequency. In the latter case, the vibration will result in a complex periodic motion that may be decomposed into a series of harmonic motions vibrating at the first natural frequency (fundamental one) and its multiples. As indicated, these frequencies are called the natural or resonant frequencies of the system and they depend on the mass and elastic or stiffness characteristics of the system. In other words, the natural frequencies of a system are those frequencies that the system tends to vibrate under conditions of free vibration. Theoretically, a continuous system or structure has infinite DoF and infinite natural frequencies. From a practical modeling point of view, the structure will have a number of natural frequencies equal to the number of DoF used to model the structure. The mode shapes give the relative displacements of each point in the structure when it vibrates in one of the natural frequencies. Each natural frequency has a corresponding mode shape. The first mode shape corresponding to the first natural frequency of a structure represents the most flexible way in which the structure may deform or vibrate and corresponds to the least strain energy level in all modes. It is important to note that, a symmetric structure will have symmetric and antisymmetric mode shapes. This may be realized by considering the mode shapes of a simple beam as shown in Figure 9.22 where all odd number modes are symmetric and all even number modes are antisymmetric.

The information provided by the natural frequencies and mode shapes of a structure is vital in understanding the behavior of the structure under general excitation. If a structure is excited in one of its natural frequencies, then theoretical analysis of the structure response as an undamped system shows that the amplitude of the resulting vibration response reaches infinity. In practice, all structures possess a certain amount of damping that will limit the amplitude of vibration.

Determining the type of analysis required for a structure depends on the nature of the applied load and the magnitude of the first natural frequency or the fundamental frequency of the structure. The two main categories of analysis types are static and dynamic analyses. A steady load, i.e., a load that does not change with time (Figure 9.21a), would require simple static analysis. If the load varies with time, it does not necessarily mean that dynamic analysis needs to be performed. For example, if the loading is harmonic with a frequency less than approximately one third of the first natural frequency of the structure then static analysis will provide an accurate solution and we only need to solve the static problem for the peak load values. (For this frequency range, static analysis may provide a maximum difference of 12.5% in the response for undamped structures and for a forcing frequency less than one fourth of the natural frequency, the difference is only 6.7%.) In this case, the load is normally called “quasi-static.” We may apply the same rule to periodic loading after decomposing it into its harmonic components. In transient loading, we should consider the time of application of the load or the “rise time.” If the longest natural period corresponding to the first natural frequency of the structure is more than about twice the rise time, the loading should be classified as shock or impact loading and transient dynamic analysis would be required. If the longest natural period of a system is less than about one third of the rise time, it would be sufficient to perform static analysis and consider the loading to be quasi-static. If the longest natural period falls between the quasi-static and shock conditions then a transient dynamic analysis would be required and the load would be classified as transient loading. If the loading cannot be categorized as frequency dependent or time dependent, as for example the one shown schematically in Figure 9.21d, then it should be considered random.

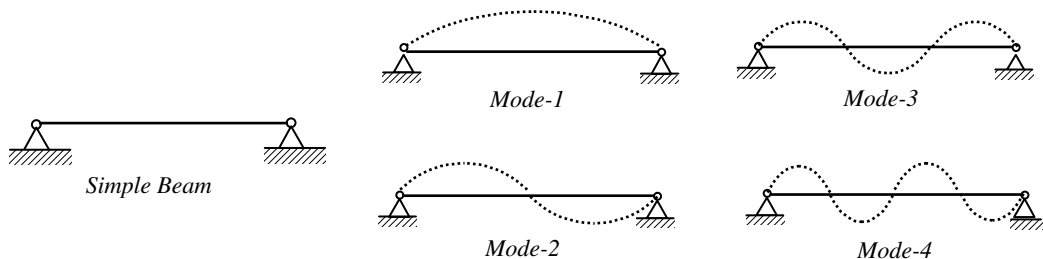


FIGURE 9.22 First four mode shapes of a simple beam.

From the above discussion, the following categories of dynamic analysis may be classified (Mirovitch, 1980):

Modal and natural frequency analysis: This is normally performed before any other type of dynamic analysis and will produce the natural frequencies and mode shapes of the structure. This information is vital for understanding the dynamic behavior of the structure and provides data for decoupling the dynamic equations in other analyses. One objective of this analysis is to make sure that the structure is not operating at a frequency close to one of its natural frequencies. A comfortable range for an operating frequency is three times higher than the nearest natural frequency from the lower side and three times smaller than the nearest natural frequency from the higher side. If the operating frequency is higher than the first natural frequency, then large vibration amplitudes or “shudder” will be evident upon passing the natural frequency and certain startup procedures may have to be devised.

Frequency response analysis: This type of analysis is performed if the loading on the structure is harmonic or periodic. In periodic loading, the loading function is first decomposed into its sine and cosine components using Fourier analysis. In this analysis, the response will be harmonic with the same loading frequency and with a possible phase shift. The output of such analysis would be displacements, velocities, and accelerations that may be used to calculate forces and stresses in the structure. The displacement output of this analysis defines the deformed shape of the structure, which, in general, is different from the structural mode shapes and may be used to calculate stresses and strains in the structure. Assuming linear conditions, the response to multiple frequency inputs may be simply summed up using the superposition technique.

Transient response analysis: This type of analysis is performed if the loading on the structure is classified as transient or shock. There are two general approaches to solving the equation of motion in transient analysis. One is the “direct integration approach” and the other is the “modal superposition approach.” In the direct integration approach, the system equations of motion are integrated directly in the time domain. The required number of time steps depends on the period and the assumptions specified for displacement, velocities, and accelerations within the time step. This number may be quite large and the solution to large size problems may become a computationally difficult task.

In the second method, the modal superposition approach, the equations of motion are first transformed to modal generalized displacements. In order to perform this transformation, the mode shapes of the structure should first be determined through a modal analysis. The transformation yields a set of decoupled second-order differential equations for the system that are easier to solve. The basic assumption in this approach is that the superposition of the structural response due to the first few lower mode shapes adequately represents the dynamic response of the structure under general transient loading. In practice, this means that only a fraction of the mode shapes of the structure are needed to accurately represent the dynamic behavior. This approach will be generally less accurate than the direct integration approach but will provide substantial savings in computation time for large size problems.

The output of transient analysis is time histories of displacements, velocities, and accelerations of the system that may be used to calculate forces and stresses.

Random response analysis: If the loading on the structure cannot be classified as frequency or time dependent, it is considered random. Problems with random loading may be solved using a “time history approach” or a “power spectral density (PSD) approach.” The time history approach treats the random input as a transient one and performs a step-by-step integration over the excitation period. This is normally very costly and requires intensive use of computational resources. If the structure has multiple random inputs in more than one direction, then the transient time history approach is more accurate and may be the preferred approach to solve the problem. Structures with random inputs in more than one direction may be analyzed by a modal superposition approach with special procedures to combine the modal responses (see Section 9.5.4 for details). In the PSD approach, the input will be acceleration as a function of frequency. This is normally specified as a discrete or continuous spectrum by providing values of the (G^2/f) vs. f , where G is the input acceleration and f is the frequency. This approach is most appropriate for a single input in one direction.

As mentioned above, most programs will have standard time history inputs or PSD inputs to simulate commonly used random excitations such as vibrations due to road irregularities, earthquakes and seismic inputs, vibration due to wind loads for aerospace parts, and wind loads for wind tunnel tests.

REMARKS

- Structural loading may be classified into four categories: steady (constant with time), cyclic (harmonic with period $T = 2\pi$ and frequency $f = 1/T$ or general periodic that may be decomposed into harmonics by Fourier analysis), transient with a duration T , and random.
- Random forcing functions are commonly specified as the magnitude of the input acceleration squared vs. frequency (PSD). Typical PSD curves have been compiled for various random events and are normally available in commercial FE programs.
- The natural frequencies of a system are those frequencies that the system tends to vibrate under conditions of free vibration. The mode shapes give the relative displacements of each point in the structure when it vibrates in one of the natural frequencies. Symmetric structures will generally have symmetric and antisymmetric mode shapes.
- If the loading is harmonic with a frequency of less than approximately one third of the first natural frequency of the structure, static analysis for the peak load levels suffices. In transient loading, if the longest natural period of a system is less than about one third of the rise time, loading is quasi-static and static analysis suffices.
- In transient loading, if the longest natural period corresponding to the first natural frequency of the structure is more than about twice the rise time of the load, it is necessary to classify the loading as shock or impact loading and transient dynamic analysis would be required.
- If the longest natural period falls between the quasi-static and shock conditions, a transient dynamic analysis would be required.

9.3 Modeling Aspects for Dynamic Analysis

Section 9.1 and Section 9.2 provide guidelines for problem and analysis classification. Once a decision has been made about the type of problem and the method of analysis to be used, the designer still has to finalize many details to create a working model for the structure. This section provides a brief discussion of the main aspects required to do this. This includes choice of model size and master DoF, lumped and consistent mass modeling, and use of symmetry. Another important aspect of modeling, damping, will be dealt with in Section 9.4.

9.3.1 Model Size and Choice of Master Degrees of Freedom

Using the same model for both static and dynamic analysis will make the FE solution to the dynamic problem more complicated and therefore much more memory and CPU resources will be required. Also, the results may not be necessarily more useful or accurate. Therefore, FE models for dynamic analysis should, in general, be kept simple.

Depending on the type of dynamic analysis, it may be possible to construct a much simpler model for the dynamic problem, possibly using spring, beam, and mass elements. If we consider modal analysis, for example, the objective is to find the mode shapes of the structure and the corresponding natural frequencies. In practice, we seldom need more than the very few lower natural frequencies and mode

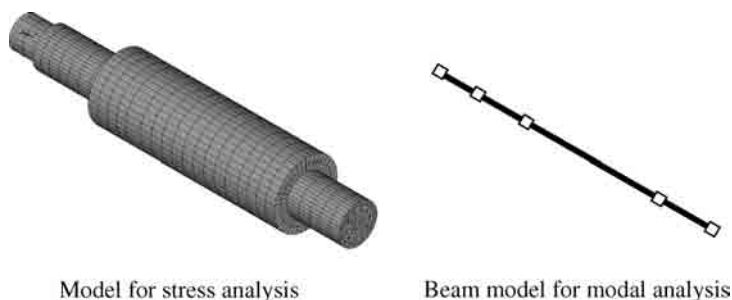


FIGURE 9.23 Static and dynamic models for a shaft.

shapes for a structure. Using a static model that may have thousands of DoF in a modal analysis is very time consuming and does not serve the purpose of the mode shape analysis. It may be better and more efficient to construct a mass spring/beam model for the modal analysis. Figure 9.23 shows a static analysis model for a shaft and a corresponding much simpler mode shape analysis model. In the mass/beam model for modal analysis, the beam properties may change to accommodate specific variations in the shaft geometry. It is also possible to extract accurate values for the spring and beam stiffnesses in 3-D using a detailed static model.

Most programs provide means for condensing or reducing the DoF in a dynamic analysis. A common condensation method used is the “Guyan reduction” (see e.g., Freed and Flanigan, 1991; Bouhaddi and Fillod, 1992; Deiters and Smith, 2000). In these condensation methods, the analyst specifies certain DoF to be masters and to be retained by the program, while all other DoF would be considered slaves and would be eliminated or condensed. The dynamic analysis is then carried out using the master DoF. Information pertaining to slave DoF is still available and may be extracted in subsequent runs that may involve stress or other detailed analyses or postprocessing. Reduction has the same effect as modal superposition in terms of reducing the problem size and the required CPU time.

Fundamental differences between the two methods may be realized due to the nature of reducing the system of equations. In the modal superposition technique, reduction is accomplished by assuming that the superposition of the structural response due to the first few lower mode shapes adequately represents the response of the structure. In other reduction methods, such as the Guyan reduction technique, we assume that the response of the system is accomplished from the response of certain predetermined master DoF. In the modal superposition technique, a modal analysis must be performed first and the final equations of motion are decoupled, whereas in the other reduction methods no modal analysis is necessary and the final equations of motion are generally full and coupled. Reduction of the total DoF to a set of master DoF has the effect of imposing displacement constraints on the system that increase the stiffness and subsequently overestimate the natural frequencies. The least affected modes are the lower ones. Therefore, reduction and modal superposition techniques should not be used, in general, for shock and impact loading (the modal superposition technique entirely ignores the response from higher modes).

The choice of master DoF may be performed automatically by the program. There is no assurance, however, that this will always produce the best choice of masters. The analyst may like to use the program for a first choice of master DoF and then augment the choice manually to improve the accuracy. Simple rules may be used to identify the master DoF (see *ANSYS User's Manual*, 2003). The general rule is to choose DoF with large mass and small stiffness or large mass to stiffness ratios as masters. Master DoF should be chosen in the direction of the expected response of the structure, e.g., in a beam or shell model, lateral DoF would be more appropriate than axial or membrane DoF, assuming that the load produces lateral deflections. Rotational DoF are seldom used as masters. It is also important to spread out and not cluster the master DoF so that they will be capable of producing the structural response. Finally, DoF with concentrated mass, a specified input force, or displacement should be retained as masters.

The question of how many master DoF are adequate is not an easy one to answer. The rule of thumb is to have having at least double the number of master DoF compared with the number of modes of interest. The other guideline is to use 10 to 50% of the total DoF as masters. In practice, the only sure way to test the adequacy of the number of master DoF is to run the analysis with two different choices and compare the results to make sure that the modes of interest are not substantially different.

REMARKS

- In general, dynamic analysis models should be simpler and much smaller in terms of the number of DoF (than static analysis ones). In modal analysis, it is better and more efficient to construct a mass spring/beam model for the structure.
- “Guyan reduction” may be used to reduce the model size by selecting master DoF for the analysis and condensing out slave DoF.
- Master DoF may initially be chosen by the program. The analyst should, however, ensure that the choice includes nodes with a large mass to stiffness ratio and with DoF in the direction of the expected response of the structure. Also, it is important to spread out and not cluster the master DoF.
- As a rule of thumb, the number of master DoF should be at least double the number of modes of interest or about 10 to 50% of the total DoF.

9.3.2 Lumped and Consistent Mass Modeling

The mass characteristic of the structure may be modeled as a lumped or consistent mass matrix. Lumped mass simply means dividing the total mass of the element by the number of nodes. This produces a diagonal mass matrix and may significantly reduce the numerical effort required to solve the dynamic equations. Considering rotational inertia terms in lumped mass assumptions is arbitrary and is normally ignored. If the lumped mass matrix has zero diagonal terms, the matrix will be positive semidefinite and the natural periods corresponding to the zero diagonal terms will be zero. This will have serious implications on the choice of the time step in explicit direct integration solution methods and will be discussed in Section 9.4. A lumped mass assumption implies a discontinuous acceleration field in the element and it usually gives good accuracy for lower modes and frequencies (Chan et al., 1993; Jensen, 1996). A consistent mass matrix is derived by introducing inertia forces in the virtual work formulation of a dynamic FE problem. This would normally lead to a full mass matrix making contributions to both translational and rotational DoF as well as coupling terms. Consistent mass representation usually provides better accuracy for higher modes and frequencies (Kim, 1993).

It may be concluded that, if no reduced integration is used to compute element stiffness, the element is compatible, and a consistent mass matrix is used, then the calculated natural frequencies will be an upper bound of the model frequencies (Cook et al., 1989). In some applications such as plates, shells, and 3-D solid elements, it has been found that the convergence rate of the natural frequency calculations for the lumped mass discretization is the same as that for a consistent mass formulation (Chan et al., 1993; Jensen, 1996).

Some FE programs provide a modified lumped mass modeling in which the diagonal translational terms are proportional to the diagonal terms of the corresponding consistent mass matrix. This yields more accurate results, in general, than the traditional lumped mass assumption. Several studies have been published on the merits of combining consistent and lumped mass formulations into some kind of modified lumped mass matrix (Chan et al., 1993; Kim, 1993; Jensen, 1996). The modified lumped mass matrix is generally a linear combination of the lumped and the consistent mass matrices. For an improved accuracy, the consistent mass should be weighted more than the lumped mass.

In building a lumped mass model for the structure, the analyst should realize that one of the objectives is to capture the few lower natural frequencies and mode shapes of the structure. To achieve this, the model should minimize the strain energy and maximize the kinetic energy of the structure. Minimizing the strain energy of the structure may be realized by accurately modeling the soft links in the load path. Structural supports are particularly difficult in this regard. Changing the support model from completely rigid to slightly flexible may shift the first natural frequency by as much as 40% (although it will not have much impact on the mode shape). Maximizing the kinetic energy is simply realized by accurate modeling of the system mass, especially in areas where the mass is large and the stiffness is small.

Care should be exercised when modeling masses attached to the system, e.g., a large “nonstructural” mass on top of a building (e.g., a mass of a machine, reservoir, etc.) or the mass of an engine in a car model. If the stiffness characteristic of the nonstructural mass is not important, it may be simply modeled as a rigid lumped mass with an offset mass center from the nearest node. Most programs have a rigid link capability to connect this mass to the structure. This kind of model is transformed internally to a nondiagonal mass matrix and may only be used with a consistent mass formulation for the structural mass. If the structural mass is modeled as lumped, the nonstructural mass will simply be added to the nearest node, which may not be an accurate representation of the physical model.

REMARKS

- A lumped mass matrix is a diagonal mass matrix that may be obtained by simply dividing the total mass by the number of DoF or alternatively by certain combinations of lumped and consistent mass terms. A consistent mass matrix is derived from FE virtual work equations and is normally a full mass matrix having translational, rotational, and coupling terms.
- Lumped mass may significantly reduce the numerical effort required to solve the dynamic equations without impacting the accuracy.
- Zero diagonal terms in the mass matrix should be avoided as much as possible.
- A lumped mass assumption usually gives good accuracy for lower modes and frequencies, whereas consistent mass representation usually gives better accuracy for higher modes and frequencies.

9.3.3 Use of Symmetry

Use of symmetry to reduce the analysis cost and computer time is rather tricky in modal analysis. As shown in Table 9.2, symmetric structures have both symmetric and nonsymmetrical mode shapes. If we only use a symmetric model with symmetric boundary conditions, all nonsymmetrical modes will be undetected. This will change the interpretation of the results and will have an impact on subsequent analyses using the modal data. If the objective is to perform only a modal analysis, it may be advisable to have a less detailed full model rather than a detailed half or quarter model. Also, if the

TABLE 9.2 Symmetric and Antisymmetric Boundary Conditions

Plane of symmetry	Symmetric Boundary Conditions						Antisymmetric Boundary Conditions					
	u_x	u_y	u_z	θ_x	θ_y	θ_z	u_x	u_y	u_z	θ_x	θ_y	θ_z
XY	—	—	0	0	0	—	0	0	—	—	—	0
XZ	—	0	—	0	—	0	0	—	0	—	0	—
YZ	0	—	—	—	0	0	—	0	0	0	—	—

objective is to perform frequency response or transient analysis using the modal data, it may be advisable to rely on a full model. Experienced analysts may use symmetric models and run the modal analysis with symmetric and antisymmetric boundary conditions to capture the response of all modes. Table 9.2 summarizes symmetric and antisymmetric boundary conditions for translational and rotational DoF.

9.4 Equations of Motion and Solution Methods

In this section, an overview of the equation of motion and the various solution methods available are provided. In most cases, detailed derivation of the equations is not given. The intention is to highlight various solution schemes and the practical aspects of choosing a particular one for a given system or a given dynamic analysis. A consideration of damping and its idealization are also discussed in this section.

9.4.1 Equation of Motion

The equations of motion describing the dynamic behavior of a structural system may be obtained from the extended Hamilton's principle for elastodynamics:

$$\delta \int_{t_0}^{t_f} (U - T) dt - \int_{t_0}^{t_f} \delta W dt = 0 \quad (9.1)$$

where

δ : first variation

t_0, t_f : two arbitrary time points at which the first variation vanishes

U : strain energy of the system

T : kinetic energy of the system

δW : virtual work of the external forces acting on the system during virtual displacements

The external forces may be conservative or nonconservative. Nonconcentrative forces, e.g., damping and follower forces, are deformation dependent, i.e., their magnitudes and/or directions depend on the deformations. Introducing the finite element discretization assumption and substituting expressions for the virtual work and the kinetic and strain energy terms into the above equation, we obtain the Lagrange equation which finally leads to the equations of motion of the system that may be written in the following form:

$$\mathbf{M}\ddot{\mathbf{u}} + \mathbf{C}\dot{\mathbf{u}} + \mathbf{K}\mathbf{u} = \mathbf{p}(t) \quad (9.2)$$

where \mathbf{M} , \mathbf{C} , and \mathbf{K} are, respectively, the global mass, global damping, and global stiffness matrices (made up by proper assembly of the element matrices); $\mathbf{p}(t)$ is the time-dependent applied force vector; and $\ddot{\mathbf{u}}$, $\dot{\mathbf{u}}$, and \mathbf{u} are the nodal acceleration, nodal velocity, and nodal displacement vectors, respectively.

The global mass and damping matrices are assembled from the element matrices that are given by (Cook et al., 1989; Bathe, 1996):

$$\mathbf{M}^{(e)} = \int_V \rho^{(e)} \mathbf{N}^T \mathbf{N} dV \quad (9.3)$$

$$\mathbf{C}^{(e)} = \int_V c_s^{(e)} \mathbf{N}^T \mathbf{N} dV \quad (9.4)$$

where $\rho^{(e)}$ and $c_s^{(e)}$ are the mass density and the viscous damping coefficient for an element e , and \mathbf{N} is the matrix of the element shape functions.

As indicated above, there are two general approaches to solving Equation 9.1. One is the direct integration approach and the other is the modal superposition approach. With the direct integration approach, the equations of motion are integrated directly in the time domain. In the second approach, the modal superposition method, the equations of motion are first transformed to modal generalized displacements through the use of the mode shapes of the structure. The transformation yields a set of

decoupled second-order differential equations for the system that are easier to solve. In the remaining part of this section, we describe the two solution approaches in more detail.

REMARKS

- Equation 9.2 is the general equation of motion for a dynamic system. Two solution methods are available: the direct integration approach and the modal superposition approach.

9.4.2 Direct Integration Method

With this method, the coupled equations of motion are integrated directly without special transformation. Direct integration schemes seek to satisfy the equilibrium equations of motion at discrete time points, $0, \Delta t, 2\Delta t, \dots, t, t + \Delta t, \dots$ etc. This requires assumptions for the variation of $\ddot{\mathbf{u}}$, $\dot{\mathbf{u}}$, and \mathbf{u} within the time step. These assumptions will determine the accuracy and convergence characteristics of a particular time integration scheme. They also govern the variation of these quantities with time and are different from the shape function assumptions for the element, which govern the displacement variation within the element, i.e., with spatial coordinates. Direct integration schemes may be categorized as “explicit” and “implicit” schemes. In explicit schemes, the equilibrium equations at time t are used to solve the unknowns at time $t + \Delta t$. These schemes are usually fast and efficient and require no factorization of the effective stiffness matrix provided that the mass and damping matrices can be formulated as diagonal matrices. The main drawback of these schemes is the requirement that the time step for the analysis has to be smaller than a critical value. On the other hand, in implicit schemes, the equilibrium equations at time $t + \Delta t$ are used to solve unknowns at time $t + \Delta t$. These schemes require factorization of the effective stiffness matrix of the structure at each time step but do not require the condition of a critical time step. In implicit schemes, the number of operations at each time step is proportional to the matrix order times half of the band width, $m = \alpha nb$, where m is the number of operations, n is the number of equations, α is a constant ≥ 2 , and b is half the band width.

Many integration schemes are available in commercial FE programs. These include Euler forward, Euler backward, central difference, Houbolt, Wilson- θ , and Newmark schemes (Belytschko and Hughes, 1983; Zeng et al., 1992). In the following, one example of an explicit scheme and one example of an implicit scheme are discussed.

9.4.2.1 The Central Difference Method

This is an explicit scheme in which the velocity and acceleration assumptions are given by

$$\left. \begin{aligned} {}^t\dot{\mathbf{u}} &= \frac{1}{2\Delta t} \left({}^{t+\Delta t}\mathbf{u} - {}^{t-\Delta t}\mathbf{u} \right) \\ {}^t\ddot{\mathbf{u}} &= \frac{1}{(\Delta t)^2} \left({}^{t+\Delta t}\mathbf{u} - 2 {}^t\mathbf{u} + {}^{t-\Delta t}\mathbf{u} \right) \end{aligned} \right\} \quad (9.5)$$

Using Equation 9.5 in the equilibrium equation at time (t) to obtain a solution at time $(t + \Delta t)$ gives

$$\left[\frac{1}{(\Delta t)^2} \mathbf{M} + \frac{1}{2(\Delta t)} \mathbf{C} \right] {}^{t+\Delta t}\mathbf{u} = {}^t\mathbf{p} - \left[\mathbf{K} - \frac{2}{(\Delta t)^2} \mathbf{M} \right] {}^t\mathbf{u} - \left[\frac{1}{(\Delta t)^2} \mathbf{M} - \frac{1}{2(\Delta t)} \mathbf{C} \right] {}^{t-\Delta t}\mathbf{u} \quad (9.6)$$

If the mass and damping matrices are diagonal, Equation 9.6 requires no assembly and no factorization of the effective stiffness matrix of the structure is required. The scheme is, however, conditionally stable and requires a time step smaller than a critical value given by

$$\Delta t_{cr} \leq T_n / \pi \quad (9.7)$$

where T_n is the smallest period in the FE assembly with n DoF. This is an important condition and should be examined carefully. If the mass matrix has a zero diagonal value, the corresponding period will be zero and Equation 9.7 cannot be satisfied. Introducing very small diagonal values may not provide a practical solution since the time step will be very small and the number of steps will be excessive. The scheme is generally applied when a lumped mass assumption with no zero diagonal terms and velocity-dependent damping are assumed. The initial conditions required for this scheme are the displacements, velocities, and accelerations at time $t = 0$.

9.4.2.2 The Newmark Method

This is a commonly used implicit scheme with the following assumptions:

$${}^{t+\Delta t}\dot{\mathbf{u}} = {}^t\dot{\mathbf{u}} + \left[(1 - \alpha) {}^t\ddot{\mathbf{u}} + \alpha {}^{t+\Delta t}\ddot{\mathbf{u}} \right] \Delta t \quad (9.8)$$

$${}^{t+\Delta t}\mathbf{u} = {}^t\mathbf{u} + {}^t\dot{\mathbf{u}} \Delta t + \left[\left(\frac{1}{2} - \beta \right) {}^t\ddot{\mathbf{u}} + \beta {}^{t+\Delta t}\ddot{\mathbf{u}} \right] (\Delta t)^2 \quad (9.9)$$

where α and β are user input parameters. Equation 9.8 and Equation 9.9 are solved for ${}^{t+\Delta t}\dot{\mathbf{u}}$ and ${}^{t+\Delta t}\ddot{\mathbf{u}}$, then substituted into the equilibrium equations at time $(t + \Delta t)$ to obtain:

$$\left[\mathbf{K} + \frac{\alpha}{\beta \Delta t} \mathbf{C} + \frac{1}{\beta (\Delta t)^2} \mathbf{M} \right] {}^{t+\Delta t}\mathbf{u} = {}^{t+\Delta t}\bar{\mathbf{p}} \quad (9.10)$$

where the right-hand side is a function of the parameters α , β , Δt , \mathbf{K} , \mathbf{M} , \mathbf{C} , ${}^t\mathbf{u}$, ${}^t\dot{\mathbf{u}}$, and ${}^t\ddot{\mathbf{u}}$. Equation 9.10 indicates that the scheme requires assembly and factorization of the effective stiffness matrix of the structure. The choice of parameters α and β will determine the stability of the scheme and may reduce the scheme to be equivalent to other known ones as follows:

- For $2\beta \geq \alpha \geq 1/2$, the scheme is unconditionally stable. This does not guarantee accuracy and only ensures that the results will not grow out of bounds (Belytschko and Hughes, 1983).
- A slightly more stringent criterion for unconditional stability that provides artificial damping in higher modes is given by using (Belytschko and Hughes, 1983):

$$\alpha \geq \frac{1}{2} \quad \text{and} \quad \beta \geq \frac{1}{4} \left(\alpha + \frac{1}{2} \right)^2$$

- A commonly used option gives $\alpha = 1/2$ and $\beta = 1/4$ which corresponds to a trapezoidal rule with constant average acceleration.
- Another option that corresponds to a linear acceleration assumption is given by $\alpha = 1/6$ and $\beta = 1/2$. This method is very good for small Dt but tends to be unstable for large Dt .

Table 9.3 summarizes the above choices for α and β .

TABLE 9.3 Typical Choices of α and β Parameters for the Newmark Scheme

α Value	β Value	Comments
$2\beta \geq \alpha \geq 1/2$	$2\beta \geq \alpha \geq 1/2$	No guarantee of accuracy
$\alpha \geq \frac{1}{2}$	$\beta \geq \frac{1}{4} \left(\alpha + \frac{1}{2} \right)^2$	Improved accuracy Provides artificial damping in higher modes
$\alpha \geq \frac{1}{2}$	$\beta \geq \frac{1}{4} \left(\alpha + \frac{1}{2} \right)^2$	Improved accuracy Corresponds to a trapezoidal rule with constant average acceleration
$\alpha \geq \frac{1}{2}$	$\beta \geq \frac{1}{4}$	Improved accuracy Provides artificial damping in higher modes Good for small Dt
$\alpha = 1/6$	$\beta = 1/2$	Improved accuracy Corresponds to a linear acceleration Very good for small Dt but tends to be unstable for large Dt

REMARKS

- In the direct integration approach, the equations of motion are integrated directly without special transformation. Such schemes may be categorized as explicit and implicit schemes.
- Explicit schemes are usually fast, efficient, and require no factorization of the effective stiffness matrix provided that the mass and damping are diagonal (refer to Equation 9.6 for an example). However, explicit schemes require the time step to be smaller than a critical value (Equation 9.7) that normally leads to very large number of steps.
- Implicit schemes require factorization of the effective stiffness matrix of the structure at each time step (refer to Equation 9.10 for an example) but do not require the condition of a critical time step.
- Although implicit schemes are unconditionally stable, accuracy is not always guaranteed without careful consideration of the step size (refer to Table 9.3).

9.4.3 Modal Superposition Method

In this method, the nodal displacement response is expressed in terms of the normal modes that may be found in an eigenvalue analysis. The coupled equations of motion, Equation 9.2, are first transformed into a set of independent or decoupled differential equations cast in modal generalized coordinates (Mirovitch, 1980). The dynamic response of the original system is then obtained by superimposing the responses of the uncoupled modal equations. The generalized coordinates (modal coordinates) are introduced by the following coordinate transformation

$$\mathbf{u} = \Phi \mathbf{q} \text{ and } u_i = \sum_{j=1}^m \varphi_{ij} q_j \quad (9.11)$$

where Φ is an $n \times m$ matrix called the eigenvector or mode shape matrix, m is the number of eigenvectors ($m \leq n$), n is the number of DoF of the system, and \mathbf{q} is a vector of size $m \times 1$ representing the number of mode-amplitude generalized or normal coordinates. The transformation given by Equation 9.11 represents a change of basis from nodal displacements (\mathbf{u}) to modal generalized coordinates (\mathbf{q}). In order for the equations to be decoupled in the modal generalized coordinate system, the triple product $\Phi^T \mathbf{C} \Phi$ has to be a diagonal matrix and the following orthogonality property is assumed for damping:

$$\Phi^T \mathbf{C} \Phi = \text{diag}(2\xi_i \omega_i) \quad (9.12)$$

where ξ_i is the damping ratio for mode i and $\text{diag}(2\xi_i \omega_i)$ indicates a diagonal matrix with the i th diagonal component of $2\xi_i \omega_i$. This form has been assumed by generalization of damping for a single DoF system. It is practically more convenient to define the damping by the damping ratios of each mode than it is to evaluate the damping matrix explicitly. Introducing Equation 9.11 and Equation 9.12 into the equation of motion, the following decoupled equations of motion are obtained:

$$\ddot{\mathbf{q}} + \text{diag}(2\xi_i \omega_i) \dot{\mathbf{q}} + \text{diag}(\omega_i^2) \mathbf{q} = \Phi^T \mathbf{p}(t) \quad (9.13)$$

If the components of the applied force vector have the same time function, so that $\mathbf{p}(t)$ can be expressed as

$$\mathbf{p}(t) = \bar{\mathbf{p}} g(t) \quad (9.14)$$

where $\bar{\mathbf{p}}$ is a constant vector and $g(t)$ is a function giving the time change of the load vector, then the modal load can be written as

$$f_r(t) = (\varphi_r^T \bar{\mathbf{p}}) g(t) = \Gamma_r g(t) \quad (9.15)$$

where φ_r^T is a row modal vector corresponding to mode r . The quantity Γ_r is referred to as the modal participation factor (*NISA User's Manual*, 1992). A particular use of this quantity is in ground motion types of excitation.

Once the generalized coordinates, \mathbf{q} , are evaluated, the physical response of the original system in terms of nodal displacements, velocities, accelerations, and stresses are recovered from Equation 9.11. For the stress recovery, it is noted that (*NISA User's Manual*, 1992; Kim et al., 1994):

$$\boldsymbol{\sigma}(t) = \mathbf{D}\mathbf{B}\ddot{\mathbf{u}}^{(e)}(t) = \mathbf{D}\mathbf{B}\boldsymbol{\Phi}^{(e)}\mathbf{q} = [\mathbf{D}\mathbf{B}\boldsymbol{\Phi}^{(e)}]\mathbf{q} = \mathbf{A}\mathbf{q} \quad \text{or} \quad \sigma_i(t) = \sum_{r=1}^m \Lambda_{ir}q_r \quad (9.16)$$

where $\sigma_i(t)$ represents a stress component in an element (i.e., σ_{xx} , σ_{yy} , σ_{xy} , etc.), Λ_{ir} lists the stress components corresponding to the r th mode at a typical point. That is, Λ_{ir} , $r = 1, 2, \dots, m$ are modal stresses which should be interpreted as stress shapes rather than absolute values of stress and the matrix \mathbf{D} is the material stress–strain matrix.

The above derivation of the mode superposition method shows the decoupling advantage of the normal coordinates, whereby the change of basis from nodal displacements to normal modes yields a set of uncoupled modal equations, with each equation cast in the form of a single DoF oscillator. As indicated above, another major advantage of the normal mode method is that a good approximation to the response may be obtained using a drastically reduced number of coordinates ($m \ll n$). For most types of loading, with the exclusion of shock and impact loading, the contributions of the lowest few modes are generally more pronounced than the higher modes. Furthermore, practical finite element idealization approximates the lower modes better and tends to be less reliable for higher modes of vibration.

REMARKS

- In the modal superposition approach, the equations of motion are first transformed into a set of decoupled equations cast in modal generalized coordinates. The response of the system is then obtained by superimposing the solutions of the decoupled modal equations (Equation 9.13 and Equation 9.16).
- The modal superposition approach may only be achieved for linear systems with proportional or directly assumed modal damping (refer to Section 9.4.4).
- In the modal superposition approach, a good approximation to the response may be obtained using a drastically reduced number of modes. For most types of loading, with the exclusion of shock and impact loading, the contributions of the lowest few modes are generally more pronounced than the higher modes.
- Practical FE idealization approximates the lower modes better and tends to be less reliable for higher modes of vibration.

9.4.4 Damping Formulation

Damping is a source of energy dissipation in the structure and it leads to decay of the free vibration amplitude with time. Damping sources in a structure include internal friction in the material, Coulomb friction in sliding and pin joints, and other viscous friction forces due to fluid friction (Beards, 1982; Fretzen, 1986). The overall damping of a system is normally quite difficult to obtain and, in general, must be determined experimentally (Kareem and Gurley, 1996). In free vibrations and modal analysis, the damping may be neglected or an overall small value for the system may be assumed. This is a reasonable assumption since in practice damping is small enough and can usually be assumed to be viscous. In forced vibrations, however, and when the forcing frequency is close to one of the system's natural frequencies, the response of the system is dominated by the specified damping values.

Commonly, damping is described in viscous or structural form. Both descriptions are used for their mathematical convenience but may not truly represent the actual damping behavior and mechanism. For viscous damping, the damping force is proportional to and opposes the velocity. With structural damping, the damping force is proportional in magnitude to the internal elastic force (i.e., to the displacement) and is in the opposite direction to the velocity. In practical FE analysis, most programs provide the following damping representation that may be used for dynamic analysis:

1. Discrete viscous damper elements (dashpots). As discussed in Section 9.1.2, these elements are damping counterparts of the spring elements and are discrete idealization of viscous damping in the structure. The damping matrix resulting from these elements, in general, cannot be decoupled as in Equation 9.12. Hence, these elements may be used only with direct integration solution methods.

2. Proportional viscous damping (Rayleigh damping). In this type, the following arbitrary form for the damping matrix is assumed:

$$\mathbf{C} = c_1 \mathbf{K} + c_2 \mathbf{M} \quad (9.17)$$

where c_1 and c_2 are constants to be determined and supplied by the user. A commonly used method in determining the constants c_1 and c_2 is to define two damping ratios ξ_1 and ξ_2 corresponding to two unequal natural frequencies ω_1 and ω_2 , respectively. Since \mathbf{C} is proportional to \mathbf{K} and/or \mathbf{M} , it satisfies the orthogonality property and we have

$$c_1 \omega_i^2 + c_2 = 2 \xi_i \omega_i \quad (9.18)$$

which leads to

$$\xi_i = \frac{c_1 \omega_i}{2} + \frac{c_2}{2 \omega_i} \quad (9.19)$$

Equation 9.19 is then used to calculate the coefficient c_1 and c_2 from the knowledge of the specified damping ratios ξ_1 and ξ_2 and their corresponding natural frequencies ω_1 and ω_2 . For the case when \mathbf{C} is only proportional to \mathbf{K} ($c_2 = 0$), the damping ratio is proportional to the natural frequency, and thus the higher modes will be damped more than the lower modes. Similarly, if \mathbf{C} is only proportional to \mathbf{M} ($c_1 = 0$), the damping ratio is inversely proportional to the natural frequency and the higher modes will have less damping than the lower modes. The relationship of Equation 9.19 is diagrammatically illustrated in Figure 9.24.

The above method for calculating the coefficients c_1 and c_2 should not restrict the use of proportional damping to only modal analysis. Proportional damping may be used in harmonic, modal, and transient analyses, as well as substructure and reduced types of analyses.

For direct transient dynamic analysis, different sets of constants c_1 and c_2 may be assigned to different parts of the model. This may result in a nonorthogonal global damping matrix. The damping orthogonality condition, however, is not required in direct transient dynamic analysis since the governing equations are directly integrated.

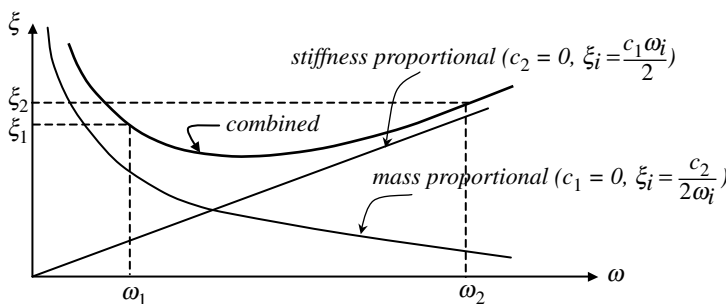


FIGURE 9.24 Proportional damping.

TABLE 9.4 Typical Damping Ratios for Various Systems and Materials

System/Material	Damping Ratio
Various metals in elastic range	< 0.01
Small diameter piping systems	0.01–0.02
Large building during earthquake	0.01–0.05
Large diameter piping systems	0.02–0.03
Welded joints and rigid metal structures	0.02–0.04
Prestressed concrete structures	0.02–0.05
Metal structures with joints	0.03–0.07
Transmission lines (aluminum or steel)	0.04
Reinforced concrete structures	0.04–0.07
Rubber	0.05
Bolted joints	0.07
Shock absorbers	0.30

3. Modal viscous damping, in which the damping ratios are directly specified for the participating modes. This type of damping can be used in modal dynamic analyses and usually provides good results for systems with small damping. In this type, the damping matrix is assumed to be diagonal with values of $2\xi_i\omega_i$, where i is the i th diagonal and ξ_i is the damping ratio for mode i with frequency ω_i .

Typical values of overall damping ratios for various systems are given in Table 9.4 (Adams and Askenazi, 1999).

REMARKS

- Damping is a source of energy dissipation in the structure and is generally difficult to quantify. Damping sources in a structure include internal, Coulomb, and viscous friction.
- The most common forms of damping provided by FE programs are discrete, proportional, and modal viscous damping.
- Discrete damping is modeled by special spring and damping elements in FE applications. The damping matrix resulting from these elements cannot, in general, be decoupled as in Equation 9.12. Hence, these elements may be used only with direct integration solution methods.
- Proportional viscous or Rayleigh damping (Equation 9.17) leads to a decoupled damping matrix and may be used in both direct integration as well as modal superposition approaches.
- A commonly used method to determine the coefficient of proportionality is through defining two modal damping ratios (Equation 9.19).
- In modal viscous damping, the damping ratios are directly specified for the participating modes and the damping matrix is assumed to be diagonal.

9.5 Various Dynamic Analyses

9.5.1 Modal Analysis

This is normally the first, and in certain cases the only, type of analysis required for a structure. It is used to obtain the dynamic characteristics of a system in terms of its natural frequencies or eigenvalues

and associated undamped free vibration natural modes or eigenvectors. These eigenmodes may then be used to decouple the general equations of motion in other types of dynamic analyses. Modal analysis is the first step required before performing mode superposition harmonic or transient analysis as well as spectrum analysis. The natural frequencies of the system may be obtained by solving the eigenvalue problem:

$$(\mathbf{K} - \omega^2 \mathbf{M})\bar{\varphi} = 0 \quad (9.20)$$

For a nontrivial solution, the coefficient matrix $(\mathbf{K} - \omega^2 \mathbf{M})$ is singular and its determinant is equal to zero, which yields the values of the natural frequencies. For each eigenvalue, ω_n , a corresponding mode shape, $\bar{\varphi}_i$, can be obtained from Equation 9.20. If the mass matrix has some zero diagonal values, the number of eigenpairs will be less than the total number of DoF by the number of zero entries on the diagonal of the mass matrix. For properly constrained structures, \mathbf{K} is positive definite and all natural frequencies are positive. If the structure is unconstrained or partially constrained, however, \mathbf{K} is positive semidefinite and the eigenvalues will contain zero frequencies representing the rigid-body modes. The calculated mode shapes from Equation 9.20 are normalized and they satisfy the orthogonality properties: $\varphi_i^T \mathbf{M} \varphi_j = 0$ and $\varphi_i^T \mathbf{K} \varphi_j = 0$ for $i \neq j$ and $\varphi_i^T \mathbf{M} \varphi_i = 1.0$ and $\varphi_i^T \mathbf{K} \varphi_i = \omega_i^2$, where $\varphi_i = \bar{\varphi}_i / \sqrt{m_i}$ and $m_i = \bar{\varphi}_i^T \mathbf{M} \bar{\varphi}_i$.

Several eigenvalue extraction methods are available. Among the most commonly used are the block Lanczos, Subspace Iteration, Power Dynamics, and Reduced Householder methods (Mirovitch, 1980; Belytschko and Hughes, 1983; Bathe, 1996). The Lanczos method is recommended for large models with many modes to be extracted (about 50 or more). It is also better suited for models containing different types of elements such as solid, shell, and beam elements with the possibility that some elements are distorted. The method is fast and efficient but requires more memory than the Subspace Iteration method. In contrast, the Subspace Iteration method is well suited for extracting lower numbers of modes (less than 50) in models with well-shaped elements and it requires less memory than the Lanczos method. The Power Dynamics method is used for very large models, with more than 100,000 DoF, and is especially useful for obtaining a solution for the first several modes of the model. The Reduced Householder method is recommended for finding all the modes in small to medium models of less than 10,000 DoF (ANSYS Users Manual, 2003).

The information obtained from an eigenvalue or modal analysis is vital in the analysis of dynamic systems. The designer's goal is to ensure that the loading frequency is not close to any natural frequency of the system and that the mode shapes do not produce excessive deformation in weak sections of the structure. With respect to the mode shapes, it is desirable to avoid mode shapes that are similar to deformation patterns obtained from the static loading on the structure. As stated previously, the comfortable range for an operating frequency is three times higher than the nearest natural frequency from the lower side and three times smaller than the nearest natural frequency from the higher side. The natural frequencies may be altered by changing the mass distribution or adjusting the geometry of the system. If the loading frequency is higher than one or more of the first natural frequencies then large vibrations or "shudder" may occur during startup and in certain cases special startup procedures may have to be devised. If the loading frequency is close to one of the natural frequencies, a large factor of safety should be used. For example, an operating frequency 20% away from a natural frequency may call for doubling the nominal loads applied on a shaft. In some very special applications, it may be desirable actually to operate the system at one of its natural frequencies and utilize the amplification in the response, e.g., ultrasonic welding equipment and certain nanoscale measuring instruments.

Modal analysis requires no special boundary conditions and the structure may be completely free or partially constrained. Special attention should be given to the application of constraints, since overconstraining a system will result in overprediction of the first modes, which are generally nonconservative in a modal analysis.

REMARKS

- Modal dynamic analysis is used to obtain the dynamic characteristics of a system in terms of its natural frequencies (eigenvalues) and natural modes (eigenvectors). It is normally the first (and may be the only) dynamic analysis to be performed and its results are required to decouple the equations of motion for other analyses.
- Common eigenvalue extraction methods include: Lanczos (recommended for large models with many modes to be extracted; about 50 or more); Subspace Iteration (recommended for extracting lower number of modes, less than 50); Power Dynamics (recommended for very large models of more than 100,000 DoF); and Householder (recommended to find all modes in small to medium sized models of less than 10,000 DoF).
- Modal analysis requires no special boundary conditions and the structure may be completely free.

9.5.2 Transient Dynamic Analysis

9.5.2.1 Direct Integration Method

As indicated above, with the direct integration method, the general equation of motion is integrated directly without transformation. The input loads are specified as a function of time and the response is calculated in the time domain. Transient analysis could be viewed as solving an equivalent static analysis problem for each time step in the domain. The response quantities may include the time history of displacements, velocities, and accelerations at each point in the structure. Most programs will also provide a stress history output that is calculated in a postprocessing phase. The output results are straightforward and easy to interpret. As in static analysis, structures undergoing transient analysis should be fully constrained and all rigid-body motion should be eliminated. Initial conditions of displacement and velocity are also required to perform the analysis.

As discussed in Section 9.4.2, direct integration may be performed through explicit or implicit schemes. It should be noted that while implicit schemes do not require a critical time step, the size of the time step will affect the accuracy of the solution. Most programs are capable of automatic time stepping, which should be seriously considered. If automatic time stepping is not available in the program, the rule of thumb is to use a time step that is at least one tenth of the load period. Smaller time steps may be required to capture peak response and sharp changes in the input load.

The equations of motion (Equation 9.2) may first be reduced in size before the start of the integration process by choosing certain master DoF as discussed above. The reduced equations are then solved by one of the direct integration schemes and the results may then be expanded to the full set of DoF.

The following steps may be used as general guidelines in performing direct integration transient dynamic analysis:

- *Build the FE model:* This will include identifying the problem type and the type(s) of elements to be used in the model. The mesh should be fine enough to capture the highest mode required for the analysis. If stresses are required, the intensity of the mesh should be adequate for stress calculations.
- *Apply the loads and boundary conditions:* All rigid-body modes should be constrained and the model should be fully constrained. Time-dependent loads are normally specified in a table format.
- *Specify initial conditions:* Initial conditions of displacement and velocity are required for transient analysis. Most programs assume zero initial conditions for acceleration. If initial accelerations are not zero, the analyst may apply appropriate acceleration loads over a small time interval. It should be noted that initial conditions are required for all unconstrained DoF.

- *Set solution control parameters, start solution and review results:* This includes mass and damping formulation, damping parameters, time integration, and time stepping parameters as well as parameters to control output and postprocessing options.

9.5.2.2 Mode Superposition Method

In this method, the uncoupled modal equation 9.13, repeated here for convenience,

$$\ddot{\mathbf{q}} + \text{diag}(2\xi_r\omega_r)\dot{\mathbf{q}} + \text{diag}(\omega_r^2)\mathbf{q} = \{f_r(t)\} = \Phi^T \mathbf{p}(t) \quad (9.21)$$

consist of m independent second-order differential equations with constant coefficients, where m is the number of the participating modes used in the mode superposition process.

At time $t = 0$, each modal equation is subject to the initial conditions $q_r(0) = \varphi_r^T \mathbf{Mu}_0$ and $\dot{q}_r(0) = \varphi_r^T \mathbf{M}\dot{\mathbf{u}}_0$. For the underdamped case ($\xi_r < 1$), the solution to a typical modal equation (excluding rigid-body modes) is

$$q_r(t) = e^{-\xi_r\omega_r t} [\alpha_r \sin \bar{\omega}_r t + \beta_r \cos \bar{\omega}_r t] + \int_0^t f_r(\tau) h_r(t - \tau) d\tau \quad (9.22)$$

where $h_r(t - \tau)$ is the unit-impulse response function, defined by

$$h_r(t - \tau) = \frac{1}{\bar{\omega}_r} e^{-\xi_r\omega_r(t-\tau)} \sin \bar{\omega}_r(t - \tau) \quad (9.23)$$

The first term in Equation 9.23 represents the free vibration response (homogenous solution) and the second term represents the particular solution (Duhamel integral). α_r and β_r are constants evaluated from the initial conditions and $\bar{\omega}_r$ is the damped natural frequency given by

$$\bar{\omega}_r = \omega_r \sqrt{1 - \xi_r^2} \quad (9.24)$$

The integral in Equation 9.22 may be evaluated in closed form if the applied loading $\mathbf{p}(t)$, and consequently $f_r(t)$, is a step input, ramp input, piecewise linear function of time, or harmonic input; otherwise, numerical integration is utilized to obtain the response.

The general steps of a typical modal transient analysis include building the model, extracting the required modes for the analysis, obtaining the modal transient analysis and, finally, expanding the modal superposition solution. It should be noted that most programs do not allow change of displacement constraints after the mode extraction step is performed; i.e., all displacement constraints should be specified before performing the modal analysis to extract the required modes. Some programs may require the full loading conditions to be specified in the modal extraction step. Initial conditions should be specified before performing the modal transient solution. This may include initial displacement and velocities.

REMARKS

- In transient analysis, the input loads are specified as a function of time and the response (displacement, velocity, acceleration, and stress) is calculated in the time domain. The structure should be fully constrained and initial conditions are required.
- Direct integration transient analysis may be performed with explicit (conditionally stable) or implicit (unconditionally stable) schemes.
- Prior to performing integration, the size of the equations may be reduced by choosing master DoF and condensing out slave DoF.
- Transient analysis with mode superposition requires an initial modal analysis run followed by the superposition of modal responses (Equation 9.22) obtained from the solution of the decoupled equations. The integral in Equation 9.22 may be evaluated in closed form for step, ramp, piecewise linear, and harmonic inputs; otherwise, numerical integration is utilized.

9.5.3 Harmonic Response Analysis

9.5.3.1 Direct Integration Method

Harmonic response analysis involves computing the steady-state response of a structure to a set of harmonic concentrated loads, pressure loads, and harmonic ground motion. The harmonic loads may be defined in terms of different amplitude and phase spectra. In general, the load vector may be represented in the form:

$$p_i(t) = p_i(\Omega)\sin[\Omega t + \Psi_i(\Omega)] \quad (9.25)$$

where $p_i(t)$ is a component of the forcing function having a magnitude, $p_i(\Omega)$, phase shift, $\psi_i(\Omega)$, and forcing frequency, Ω .

Substituting Equation 9.25 into Equation 9.2, we obtain:

$$\mathbf{M}\ddot{\mathbf{u}} + \mathbf{C}\dot{\mathbf{u}} + \mathbf{K}\mathbf{u} = \mathbf{p}(t) = \bar{\mathbf{p}}(\Omega)\sin[\Omega t + \bar{\Psi}(\Omega)] \quad (9.26)$$

Using direct integration schemes to solve Equation 9.26 is theoretically viable but not recommended practically for a few reasons. A large number of time steps would be normally required to obtain a meaningful response to a harmonic excitation and the equations have to be resolved for each forcing frequency. Also, if the damping is zero and a particular forcing frequency coincides with one of the natural frequencies, the matrix becomes singular and the solution process fails. If the forcing frequency is close to one of the natural frequencies, the matrix becomes ill conditioned and poses solution problems even if the damping is not zero. For these reasons, it is recommended to perform harmonic response analyses using the mode superposition method.

9.5.3.2 Mode Superposition Method

In the mode superposition method, Equation 9.26 is transformed into generalized modal coordinates and decoupled. For the r th mode, the equation takes the form:

$$\ddot{q}_r + 2\xi_r\omega_r\dot{q}_r + \omega_r^2 q_r = \bar{f}_r e^{i\Omega t} \quad (9.27)$$

where \bar{f}_r is the amplitude of modal load given by $\bar{f}_r = \boldsymbol{\varphi}_r^T \bar{\mathbf{p}}$. The steady-state modal response is given by

$$q_r(t) = \bar{q}_r e^{i\Omega t} \quad (9.28)$$

which when substituted into Equation 9.27 gives

$$\bar{q}_r(\Omega) = H_r(\Omega)\bar{f}_r(\Omega) \quad (9.29)$$

and

$$H_r(\Omega) = \frac{1}{\omega_r^2 \left[\left(1 - \frac{\Omega^2}{\omega_r^2} \right) + i \left(2\xi_r \frac{\Omega}{\omega_r} \right) \right]} \quad (9.30)$$

Equation 9.29 in the frequency domain is equivalent to Equation 9.22 in the time domain and $H_r(\Omega)$ is the Fourier transform of the unit-impulse response function $h_r(t)$.

The physical response is recovered from the generalized modal response through the transformation $\bar{\mathbf{u}} = \boldsymbol{\Phi}\bar{\mathbf{q}}$. The velocity and acceleration components are obtained from the corresponding displacement component through multiplication by Ω and Ω^2 , respectively. Finally, the stress components are obtained by the use of modal stresses (Equation 9.16). Most programs provide the option that the user can obtain the responses in either an amplitude–phase format or real–imaginary format and the actual value of all responses can also be obtained for a given value of Ωt .

The input to harmonic analysis constitutes the forcing frequency and the magnitude of the load vector at various points of load applications. For each loading case, all forces should have the same frequency. A change in the forcing frequency gives rise to a new load case. In harmonic analysis, as is the case in transient and static analyses, the structure should be fully constrained and all rigid-body motions should be eliminated. If the structure has rigid-body modes in one of the DoF, the analyst may use soft springs to ground the structure or utilize symmetry to provide constraints.

The general steps of a typical modal harmonic analysis are quite similar to those for the modal transient analysis, i.e., they include building the model, extracting the required modes for the analysis, obtaining the modal harmonic analysis and, finally, expanding the modal superposition solution. It should also be noted that most programs do not allow changes in displacement constraints after the mode extraction step, i.e., all displacement constraints should be specified before performing the modal analysis to extract the required modes. Some programs may require the full loading conditions to be specified in the modal extraction step.

REMARKS

- Harmonic response analysis involves computing the steady-state response of a structure to a set of harmonic loads and ground motion (Equation 9.26).
- Using direct integration schemes in harmonic analysis is theoretically viable but not recommended or used practically.
- Harmonic analysis with mode superposition requires an initial modal analysis run followed by the superposition of modal responses (Equation 9.28) obtained from the solution of the decoupled equations.
- The input to harmonic analysis constitutes the frequency and the magnitude of the load vector at all points of load applications. For each load case, all forces should have the same frequency. The structure should be fully constrained.

9.5.4 Response Spectrum Analysis

This analysis is an efficient alternative to transient dynamic analysis for estimating the maximum response under support excitations without regard to the time at which the maximum occurs. If the input loading is classified as a shock or impulse, this analysis is termed “shock spectrum analysis.” In theory, one may use a direct integration scheme to find the response as a function of time and then use the maximum value of the response. This may be prohibitive because of the very large number of time steps that will be required to capture the peak response. As a more efficient alternative, a modal analysis should be performed first and then a sufficient number of modes should be retained for the response spectrum analysis. Then the solution of the individual decoupled modal equation (Equation 9.13) for a viscous underdamped system under ground motion $w(t)$ is

$$q_r(t) = \frac{1}{\bar{\omega}_r} \int_0^t \ddot{w}(\tau) e^{-\xi_r \omega_r(t-\tau)} \sin[\bar{\omega}_r(t-\tau)] d\tau \quad (9.31)$$

The response function in Equation 9.31 is scanned over time to find the maximum scalar value $(q_r)_{\max}$. Then the physical value of the response of the i th DoF due to $(q_r)_{\max}$ may be given by

$$\bar{u}_{ir} = \Phi_{ir}(q_r)_{\max} \quad (9.32)$$

in which Φ_{ir} is the component of the modal vector, r , in direction i . Equation 9.32 is different from Equation 9.11 in which all the components of the modal vector, Φ_i , and the generalized response, q_i , are used and, therefore, actual and accurate physical displacements are obtained.

It can be readily seen that the quantities $(q_r)_{\max}$, and hence \bar{u}_{ir} , are only functions of the natural frequency and damping (in addition to the ground excitation). A shock (or response) spectrum curve for a certain value of damping may be defined as the maximum responses of all such single DoF systems with a given damping and plotted as a function of natural frequency. Similarly, the maximum acceleration and maximum velocity may also be determined and are termed as spectral acceleration and spectral velocity, respectively.

The mass matrix in response spectrum analysis may be lumped or modified lumped based on the consistent mass matrix. Response spectrum analysis using consistent mass generally lowers the resulting internal forces and moments in the structure and therefore produces less stresses and may be considered generally nonconservative (Gregory, 1990).

Unlike transient dynamic analysis, the contributions of the physical responses for each of the modes cannot be directly summed to obtain the total response. This is because the maxima for each mode occur at different times and the information on the time of maxima is not available in the shock spectra. Reasonable, but arbitrary, estimates of the maxima may be obtained by using one of the following commonly used modal combination methods (Wilson et al., 1981; *NISA User's Manual*, 1992; Roussel, 1994; Joshi and Gupta, 1998):

1. *The sum of absolute magnitudes (ABS or PEAK)*: The absolute sum of the modal responses is given by

$$R_{\text{tot}} = \sum_{r=1}^m |R_r| \quad (9.33)$$

in which R_r is the physical response (displacement, velocity, or acceleration) due to mode r and m is the number of modes considered. This method is conservative and is used if the natural frequencies are closely spaced (within 10% of each other) and/or when damping is large. It is also shown that the method may lead to unrealistically high calculated responses, e.g., in the coupled analysis of light secondary systems attached to heavy primary structures or in the decoupled analysis of systems when the centers of mass and stiffness do not coincide (Mertens, 1994).

2. *The square root of the sum of the squares (SRSS or RMS)*: The square root of the sum of the squares of the modal response is given by

$$R_{\text{tot}} = \sqrt{\sum_{r=1}^m R_r^2} \quad (9.34)$$

This method is applicable if the modes are statistically independent, which is the case when the natural frequencies are far apart and/or when damping is small. The SRSS method is commonly used in a wide range of applications. Some studies indicate, however, that the method may underestimate the response of structures with high-frequency modes, e.g., long-span bridges exposed to high wind velocities (Joshi and Gupta, 1998).

3. *The complete quadratic combination (CQC)*: The complete quadratic combination is given by the following formula (Wilson et al., 1981; Der Kiureghian and Nakamura, 1993):

$$R_{\text{tot}} = \sqrt{\sum_{r=1}^m \sum_{s=1}^m R_r \cdot R_s P_{rs}} \quad (9.35)$$

in which

$$P_{rs} = \frac{8\sqrt{\xi_r \xi_s}(\xi_r + \gamma \xi_s)\gamma^{3/2}}{(1 - \gamma^2) + 4\xi_r \xi_s(1 + \gamma^2) + 4\gamma^2(\xi_r^2 + \xi_s^2)} \quad (9.36)$$

where ξ_r and ξ_s are modal damping ratios and $\gamma = \omega_s/\omega_r$. This method encompasses the SRSS and ABS procedures for $\xi_r = \xi_s$. If $\gamma = 0$, the CQC method reduces to the former, and if $\gamma = 1$, it reduces to the latter. Certain modifications of the CQC method exist, aimed at improving response estimates for structures with high frequency modes (Der Kiureghian and Nakamura, 1993).

TABLE 9.5 Common Methods of Combining Modal Responses

Combinational Method	Comments
Sum of absolute magnitudes (ABS or PEAK)	Generally gives conservative results Used if the natural frequencies are closely spaced (within 10% of each other) and/or when damping is large
Square root of the sum of the squares (SRSS or RMS)	Use when natural frequencies are far apart and/or when damping is small May underestimate the response of structures with high frequency modes
Complete quadratic combination (CQC)	Combination of the SRSS and the ABS methods Certain modifications exist to correct the response of structures with high frequency modes
Combination of ABS and SRSS	Another form of combination of the SRSS and the ABS methods employed by simply adding the response of the two methods

4. *Combination of ABS and SRSS*: The absolute maxima of the modal responses is added to the square root of the sum of the squares of the remaining modal responses as follows (*NISA User’s Manual*, 1992):

$$R_{\max} = |R_j| + \sqrt{\sum_{r=1, r \neq j}^m R_r^2}$$

(9.37)

where

$$R_j = \max_r |R_r|$$

(9.38)

The above superposition rules are employed to get the response maxima due to ground excitation in one direction. Similarly, the maximum responses due to ground motions in other directions are computed separately. These maxima are then superimposed by using the SRSS or ABS procedures to get the total response.

A final note is given here on the use of spectrum analysis in earthquake-resistant design. Most building codes require the designer to consider the response of the structure due to simultaneous action of three translational components of ground motion: two in the horizontal plane and one in the vertical direction. Standard design practice is to calculate the peak responses of these inputs independently and then combine these peak responses according to rules similar to those discussed above (Menun and Der Kiureghian, 1998; Lopez et al., 2001).

Table 9.5 summarizes the above modal combination methods, their use and merits.

REMARKS

- Response spectrum and shock analysis are efficient alternatives to transient dynamic analysis for estimating the maximum response under support excitations without regard to the time at which the maximum occurs.
- In response spectrum analysis, the solution of the individual decoupled modal equation (Equation 9.13) for ground motion, $w(t)$, is obtained (Equation 9.31) and the maximum value of the response is recorded (with no reference to the time it occurs).
- Reasonable, but arbitrary, estimates of the maxima for the overall structure may be obtained by using various methods of combining the modal maximums (Table 9.5).

9.6 Checklist for Dynamic FE Analysis

1. Study the physical system and decide on the type of problem, i.e., beam, 2-D, shell, or 3-D, and the type of elements to be used. Typical questions to be addressed are:
 - Can the geometry be idealized as 2-D or shell or do we have to use 3-D analysis? (Section 9.1.2 to Section 9.1.6).
 - Can the loading and constraints be idealized as 2-D?
 - Are we concerned about responses that are not compatible with the loading type?
 - Are we interested in displacements, stresses, or natural frequencies?
 - Can we have a simple spring/mass model?
 - What type of element might be used in the analysis, i.e., linear, quadratic, or cubic (Section 9.1.7)? Generally, linear and quadratic elements are used for the majority of analyses. The choice between linear and quadratic elements is rather arbitrary and may depend on certain advanced analysis aspects. For linear analysis, there is little difference between the response of the two elements if the overall model has the same or similar total DoF.
2. Study all types of loading to identify the required analysis type. Important questions to be addressed are:
 - Is the load steady, cyclic, transient, or random (Section 9.2)?
 - What is the frequency content of the load? A simple Fourier analysis may be required to define the main harmonics of a transient load input.
 - What are the first few natural frequencies of the structure? This question will be answered in detail by performing a modal analysis. It is important, however, to have an approximate idea of the range of frequencies of the structure and to compare this to the loading frequency in order to identify the proper type of analysis (Section 9.2). In order to answer this question adequately, a very simplified mass/spring model and quick hand calculations may be considered.
 - What kind of data is required from the analysis? Data required may be in terms of displacements, velocities, accelerations, stresses, strains, etc. Also, identify if peak values or time histories are required. This decision may have an impact on what analysis type is required.
 - What is the type of analysis required (Section 9.2)?
3. Identify other data required to perform the analysis. This may include:
 - Material properties.
 - Damping consideration, modeling, and values (Section 9.4.4).
 - Identifying all load cases and all constraints of the system. Special attention must be paid to the modeling of constraints and nonstructural masses (Section 9.3).
 - If modal superposition is going to be used, how many modes are required for the analysis?
4. Start the actual modeling process, testing and verification of the model. Important issues to be considered may include:
 - A decision should be made of whether or not a simple or coarse model is required. In general, dynamic analysis of large models is quite costly. Dynamic analysis results (such as natural frequencies, mode shapes, and to some extent displacements, velocities, and accelerations) may be accurately obtained from a coarse model or even a mass/spring model. The main concern would be in obtaining stress and strain responses. In many cases, it may be advisable to have two different models — one for dynamic analysis and the other for stress analysis. The output from the dynamic model may be used as input to the stress model. In any case, if the model is large, it is advisable to have a coarser model for testing and basic understanding of the behavior of the structure (Section 9.3).
 - Choose a program to perform the analysis. The key issue in choosing a program would be the availability of the required analysis type. Other issues that may be considered include ease of model generation, ease of postprocessing, and cost effectiveness. It is always advisable to have the same program for all phases of the analysis, i.e., modeling, solution, and postprocessing.

- Build the model geometry (Section 9.1.1). In 2-D problems, the model geometry may be imported from a CAD program. In 3-D and shell problems, however, this process entails many problems and it may be faster for the analyst to build the model directly in a FE database.
 - Build the finite element model and apply load cases and constraints (Section 9.2).
 - Test the model. Most FE programs provide extensive testing capabilities that may be invoked to test the quality of the mesh and the continuity of the model. It is important to note that additional testing is required. The response of the system to simple load cases should be considered. Testing should involve load cases that may be easily verified. This may include computing structure response due to unit impulse, step input, or sudden release of an initial displacement. Also, simple static analysis runs can be very useful in this regard and may provide initial conditions for the final dynamic run.
5. Analyze the model for the actual load cases. The following important issues should be considered:
 - Identify solution parameters. This includes mass and damping formulation, damping parameters (Section 9.4.4), time integration, and time stepping parameters, as well as parameters to control output and postprocessing options. If modal analysis is considered, identify the modal extraction method (Section 9.5).
 - Check and apply restart capabilities in the program. Large size dynamic analyses should, in general, be done in steps and the restart option should be invoked.
 - If modal analysis is performed, a careful check of mode shapes will provide important information about the validity of the model and the appropriateness of solution steps to follow.
 - Identify solution control parameters that invoke the storage of specific data required for postprocessing.
 6. Postprocess the results. This is the final stage of the analysis and may involve:
 - Graphical and contour plots of various response quantities. This may be done in the form of time history plots, envelopes of maximum responses, or contour plots of stress maxima. The amount of output data associated with large dynamic analysis runs is vast and such graphical display of results is essential.
 - Most programs have extensive capabilities in results animation, search facilities, preparing output summaries, and some can also assist in report writing. Such capabilities may become important in processing the results of large problems.

References

- Adams, V. and Askenazi, A. 1999. *Building Better Products with Finite Element Analysis*, On Word Press, Santa Fe.
- ANSYS *User's Manual*, Revision 7.0, Swanson Analysis Systems Inc., Houston, 2003.
- Babuska, I. and Guo, B.Q., Approximation properties of the h - p version of the finite element method, *Comput. Methods Appl. Mech. Eng.*, 133, 319–346, 1996.
- Bathe, K.J. 1996. *Finite Element Procedures in Engineering Analysis*, Prentice Hall, New York.
- Bathe, K.J. and Dvorkin, E.N., A four-node plate bending element based on Mindlin–Reissner plate theory and a mixed interpolation, *Int. J. Numer. Methods Eng.*, 21, 367–383, 1985.
- Beards, C.F., Damping in structural joints, *Sound Vib. Dig.*, 14, 9–11, 1982.
- Belytschko, B. and Hughes, T.J.R., Eds. 1983. *Computational Methods for Transient Analysis*, North Holland, Amsterdam.
- Boresi, A.P. and Chong, K.P. 2000. *Elasticity in Engineering Mechanics*, 2nd ed., Wiley, New York.
- Bouhaddi, N. and Fillod, R., Method for selecting master DoF in dynamic substructuring using the Guyan condensation method, *Comput. Struct.*, 45, 941–946, 1992.
- Cesar de Sa, J.M.A., Natal, J.R.M., Fontes, R.A., and Almeida, P.M., Development of shear locking-free shell elements using an enhanced assumed strain formulation, *Int. J. Numer. Methods Eng.*, 53, 1721–1750, 2002.

- Chan, H.C., Cai, C.W., and Cheung, Y.K., Convergence studies of dynamic analysis by using the finite element method with lumped mass matrix, *J. Sound Vib.*, 165, 193–207, 1993.
- Cook, R.D., Malkus, D.S., and Plesha, M.E. 1989. *Concepts and Applications of Finite Element Analysis*, 3rd ed., Wiley, New York.
- Deiters, T.A. and Smith, K.S., Faster, easier finite element model reduction, *Exp. Tech.*, 24, 35–40, 2000.
- Der Kiureghian, A. and Nakamura, Y., CQC modal combination rule for high-frequency modes, *Earthquake Eng. Struct. Dyn.*, 22, 943–956, 1993.
- Freed, A.M. and Flanigan, C., Comparison of test-analysis model reduction methods, *Sound Vib.*, 25, 30–35, 1991.
- Fretzen, C.P., Identification of mass, damping, and stiffness matrices of mechanical systems, *ASME J. Vib. Acoust. Stress Reliab. Des.*, 108, 9–16, 1986.
- Gregory, F.M., Response spectra analysis. Consistent mass versus lumped mass, *ASME-Pressure Vessels Piping Div. (Publ.) PVP Seismic Eng.*, 197, 85–89, 1990.
- Jensen, M.S., High convergence order finite elements with lumped mass matrix, *Int. J. Numer. Methods Eng.*, 39, 1879–1888, 1996.
- Joshi, R.G. and Gupta, I.D., On the relative performance of spectrum superposition methods considering modal interaction effects, *Soil Dyn. Earthquake Eng.*, 17, 357–369, 1998.
- Kamel, H.A., Integration of solid modeling and finite element generation, *Comput. Methods Appl. Mech. Eng.*, 89, 485–496, 1991.
- Kareem, A. and Gurley, K., Damping in structures: its evaluation and treatment of uncertainty, *J. Wind Eng. Ind. Aerodyn.*, 59, 131–157, 1996.
- Kim, K., Review of mass matrices for eigenproblems, *Comput. Struct.*, 46, 1041–1048, 1993.
- Kim, H.M., Bartkiewicz, T.J., and Van Horn, D.A., Data recovery and model reduction methods for large structures, *Finite Elem. Anal. Des.*, 16, 85–98, 1994.
- Lopez, O.A., Chopra, A.K., and Hernandez, J.J., Evaluation of combination rules for maximum response calculation in multicomponent seismic analysis, *Earthquake Eng. Struct. Dyn.*, 30, 1379–1398, 2001.
- Luo, Y., Explanation and elimination of shear locking and membrane locking with field consistence approach, *Comput. Methods Appl. Mech. Eng.*, 162, 249–269, 1998.
- Menun, C. and Der Kiureghian, A., Replacement for the 30%, 40%, and SRSS rules for multicomponent seismic analysis, *Earthquake Spectra*, 14, 153–164, 1998.
- Mertens, P.G., New algebraic white-noise modal combination rule — GAC(A), *Nucl. Eng. Des.*, 147, 299–309, 1994.
- Mirovitch, L. 1980. *Computational Methods in Structural Dynamics*, Sijthoff and Noordhoff, Alphen a/d Rijn.
- NISA User's Manual, Engineering Mechanics Research Corp., Michigan, USA, 1992.
- Roussel, G., Algebraic modal combination method in seismic response spectrum analysis, *ASME-Pressure Vessels Piping Div. (Publ.) PVP Seismic Eng.*, 275-1, 211–216, 1994.
- Wilson, E.L., Der Kiureghian, A., and Bayo, E.P., A replacement for the SRSS method in seismic analysis, *Earthquake Eng. Struct. Dyn.*, 9, 187–194, 1981.
- Zeng, L.F., Wiberg, N.-E., and Bernspang, L., Adaptive finite element procedure for 2D dynamic transient analysis using direct integration, *Int. J. Numer. Methods Eng.*, 34, 997–1014, 1992.

10

Vibration Signal Analysis

10.1	Introduction	10-1
10.2	Frequency Spectrum	10-2
	Frequency • Amplitude Spectrum • Phase Angle • Phasor Representation of Harmonic Signals • RMS Amplitude Spectrum • One-Sided and Two-Sided Spectra • Complex Spectrum	
10.3	Signal Types	10-7
10.4	Fourier Analysis	10-7
	Fourier Integral Transform • Fourier Series Expansion • Discrete Fourier Transform • Aliasing Distortion • Another Illustration of Aliasing	
10.5	Analysis of Random Signals	10-18
	Ergodic Random Signals • Correlation and Spectral Density • Frequency Response Using Digital Fourier Transform • Leakage (Truncation Error) • Coherence • Parseval's Theorem • Window Functions • Spectral Approach to Process Monitoring • Cepstrum	
10.6	Other Topics of Signal Analysis	10-26
	Bandwidth • Transmission Level of a Band-Pass Filter • Effective Noise Bandwidth • Half-Power (or 3 dB) Bandwidth • Fourier Analysis Bandwidth • Resolution in Digital Fourier Results	
10.7	Overlapped Processing	10-28
	Order Analysis	

Clarence W. de Silva

The University of British Columbia

Summary

This chapter considers the nature and analysis of vibration signals. Both time-domain techniques and frequency-domain techniques are investigated, which are related through Fourier transform. Topics covered include signal types, signal sampling, aliasing error, truncation error, window functions, spectral analysis, bandwidth issues, and order analysis. Several applications of signal analysis in mechanical vibration are discussed.

10.1 Introduction

Numerous examples can be drawn from engineering applications for vibrating (dynamic) systems. A steam generator of a nuclear power plant that undergoes flow-induced vibration; a high-rise building subjected to seismic motions at its foundation; an incinerator tower subjected to aerodynamic disturbances; an airplane excited by atmospheric turbulence; a gate valve under manual operation; and a heating, ventilating, and air conditioning (HVAC) control panel stressed due to vibrations in its support structure are such examples.

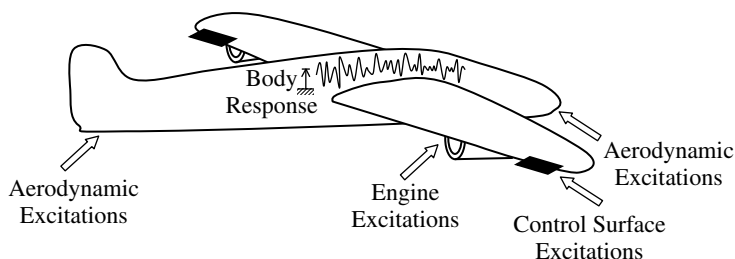


FIGURE 10.1 In-flight excitations and responses of an aircraft.

Consider an aircraft in flight, as schematically shown in Figure 10.1. There are many excitations on this dynamic system. For example, jet engine forces and control surface movements are intentional excitations, whereas aerodynamic disturbances are unintentional (and unwanted) excitations. The primary response of the aircraft to these excitations will be the motions in various degrees of freedom (DoF), including rigid-body and flexible (vibratory) mode motions.

Even though the inputs and outputs (excitations and responses) are functions of *time*, they can also be represented as functions of *frequency*, through *Fourier transformation*. The resulting *Fourier spectrum* of a signal can be interpreted as the set of frequency components which the original signal contains. This *frequency-domain* representation of a signal can highlight many salient characteristics of the signal and also those of the corresponding system. For this reason, frequency-domain methods, particularly Fourier analysis, are used in a wide variety of applications such as data acquisition and interpretation, experimental modeling and modal analysis, diagnostic techniques, signal/image processing and pattern recognition, acoustics and speech research, signal detection, telecommunications, and dynamic testing for design development, quality control, and qualification of products. Many such applications involve the study of mechanical vibrations.

10.2 Frequency Spectrum

Excitations (inputs) to a dynamic system progress with time, thereby producing responses (outputs) which themselves vary with time. These are signals that can be recorded or measured. A measured signal is a *time history*. Note that in this case the independent variable is *time* and the signal is represented in the *time domain*. A limited amount of information can be extracted by examining a time history. As an example, consider the time-history record shown in Figure 10.2. It can be characterized by parameters such as the following:

a_p = peak amplitude

T_p = period in the neighborhood of the peak = $2 \times$ interval between successive zero crossings near the peak

T_e = duration of the record

T_s = duration of strong response (i.e., the time interval beyond which no peaks occur that are larger than $a_p/2$)

N_z = number of zero crossings within T_s ($N_z = 14$ in Figure 10.2)

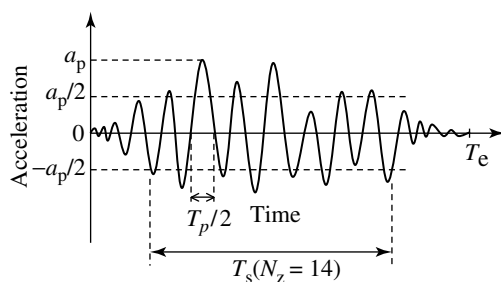


FIGURE 10.2 A time-history record.

It is obviously cumbersome to keep track of so many parameters and, furthermore, not all of them are equally significant in a given application. Note, however, that all the parameters listed above are directly

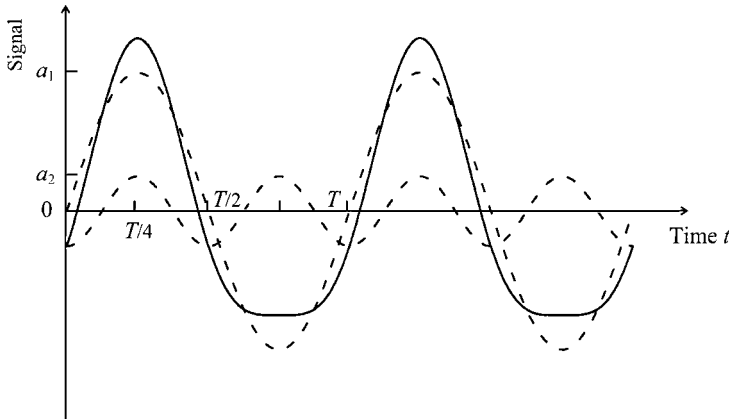


FIGURE 10.3 Time-domain representation of a periodic signal.

or indirectly related to either the *amplitude* or the frequency of zero crossings within a given time interval. This signifies the importance of a frequency variable in representing a time signal. This is probably the fundamental motivation for using frequency-domain representations. In this context, however, more rigorous definitions are needed for the parameters: amplitude and frequency. A third parameter, known as *phase angle*, is also needed for unique representation of a signal in the frequency domain.

10.2.1 Frequency

Let us further examine the basis of frequency-domain analysis. Consider the *periodic* signal of period T that is formed by combining two *harmonic* (or sinusoidal) components of periods T and $T/2$ and amplitudes a_1 and a_2 as shown in Figure 10.3. The *cyclic frequency* (cycles/sec, or hertz, or Hz) of the two components are $f_1 = 1/T$ and $f_2 = 2/T$. Note that in order to obtain the *angular frequency* (radians/sec), the cyclic frequency has to be multiplied by 2π .

10.2.2 Amplitude Spectrum

An alternative graphical representation of the periodic signal shown in Figure 10.3 is given in Figure 10.4. In this representation, the amplitude of each harmonic component of the signal is plotted against the corresponding frequency. This is known as the *amplitude spectrum* of the signal, and it forms the basis of the frequency-domain representation. Note that this representation is often more compact, and can be far more useful than the time-domain representation. Note further that in the frequency-domain representation, the independent variable is frequency.

10.2.3 Phase Angle

In its present form, Figure 10.4 does not contain all the information of Figure 10.3. For instance, if the high-frequency component in Figure 10.3 is shifted through half its period ($T/4$), the resulting signal is shown in Figure 10.5. This signal is quite different from that in Figure 10.3 but since the amplitudes and the frequencies of the two harmonic components are identical for both signals, they possess the same amplitude spectrum. So, what is lacking in Figure 10.3 in order to make

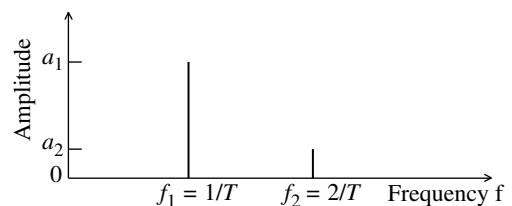


FIGURE 10.4 The amplitude spectrum of a periodic signal.

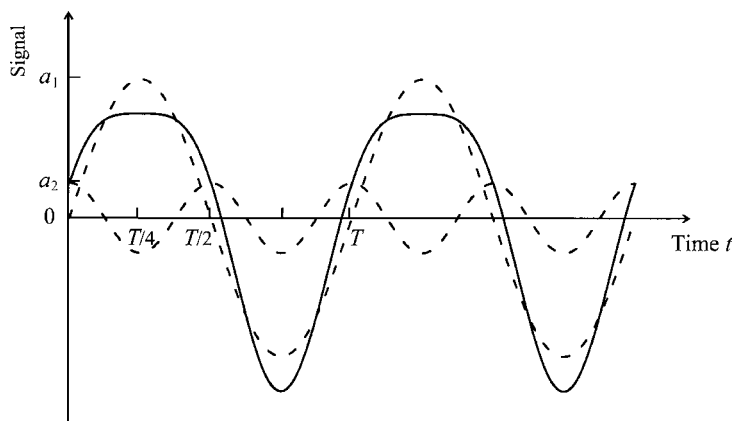


FIGURE 10.5 A periodic signal with an identical amplitude spectrum as for Figure 10.2.

it a unique representation of a signal, is the information concerning the exact location of the harmonic components with respect to the time reference or origin ($t = 0$). This is known as the phase information. For example, the distance of the first positive peak of each harmonic component from the time origin can be expressed as an angle (in radians) by multiplying it by $2\pi/T$. This is termed the *phase angle* of the particular component. In both signals (shown in Figure 10.3 and Figure 10.5) the phase angle of the first harmonic component is the same and equals $\pi/2$ according to the present convention. The phase angle of the second harmonic component is $\pi/2$ in Figure 10.3 and zero in Figure 10.5.

10.2.4 Phasor Representation of Harmonic Signals

A convenient geometric representation of a harmonic signal of the form

$$y(t) = a \cos(\omega t + \phi) \quad (10.1)$$

is possible by means of a phasor. This representation is illustrated in Figure 10.6. Specifically, consider a rotating arm of radius a , rotating in the counter-clockwise (ccw) direction at an angular speed of ω rad/sec. Suppose that the arm starts (i.e., at $t = 0$) at an angular position ϕ with respect to the y -axis (vertical axis) in the ccw sense. Then, it is clear from Figure 10.6(a) that the projection of the rotating arm on the y -axis gives the time signal $y(t)$. This is the phasor representation, where we have

Signal amplitude = length of the phasor

Signal frequency = angular speed of the phasor

Signal phase angle = initial position of the phasor with respect to the y -axis

It should be clear that a phase angle makes practical sense only when two or more signals are compared. This is so because for a given harmonic signal we can pick any point as the time reference ($t = 0$). However, when two harmonic signals are compared, as in Figure 10.6(b), we may consider one of those signals that starts (at $t = 0$) at its position peak as the reference signal. This will correspond to a phasor whose initial configuration coincides with the positive y -axis. As is clear from Figure 10.6(b), for this reference signal we have, $\phi = 0$. Then the phase angle ϕ of any other harmonic signal would correspond to the angular position of its phasor with respect to the reference phasor. Note that, in this example, the time shift between the two signals is ϕ/ω , which is also a direct representation of the phase. It should be clear, then, that the phase difference between two signals is also a representation of the *time lead* or *time lag* (delay) of one signal with respect to the other. Specifically, the phase that is ahead of the reference phasor is considered to “lead” the reference signal. In other words, the signal $a \cos(\omega t + \phi)$ has a phase lead of ϕ or a time lead of ϕ/ω with respect to the signal of $a \cos \omega t$.

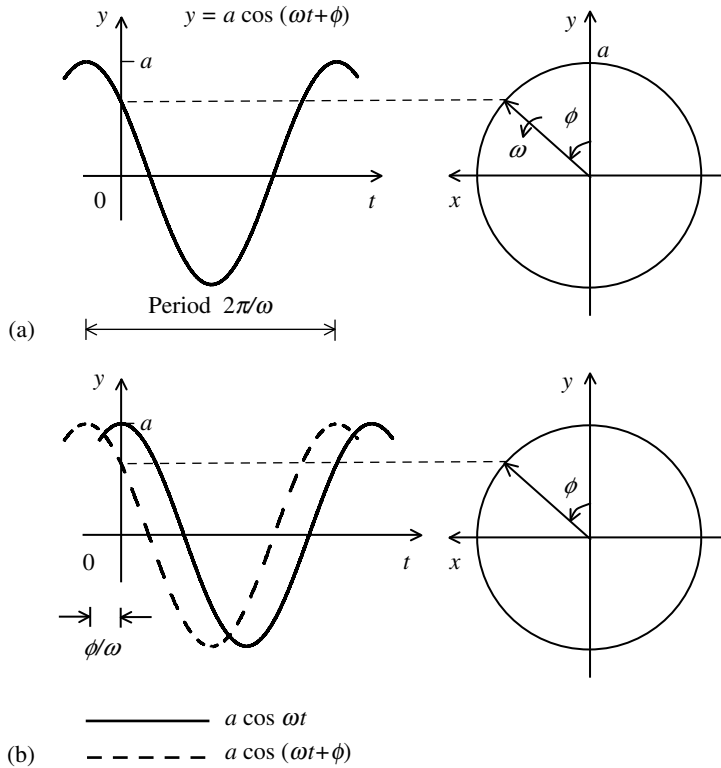


FIGURE 10.6 Phasor representation of a harmonic signal. (a) A phasor and the corresponding signal; (b) representation of a phase angle (phase lead) ϕ .

Another important observation may be made with regard to the phasor representation of a harmonic signal. A phasor may be expressed as the complex quantity

$$y(t) = a e^{j(\omega t + \phi)} = a \cos(\omega t + \phi) + ja \sin(\omega t + \phi) \quad (10.2)$$

whose real part is $a \cos(\omega t + \phi)$, which is in fact the signal of interest. It is clear from Figure 10.6 that, if we take the y -axis to be real and the x -axis to be imaginary, the complex representation 10.2 is indeed a complete representation of a phasor. By using the complex representation 10.2 for a harmonic signal, significant benefits of mathematical convenience could be derived in vibration analysis. It suffices to remember that practical vibrations are “real” signals, and regardless of the type of mathematical analysis that is used, only the real part of a complex signal of the form 10.2 will make physical sense.

10.2.5 RMS Amplitude Spectrum

If a harmonic signal $y(t)$ is averaged over one period T , the negative portion cancels out the positive portion, giving zero. Consider a harmonic signal of angular frequency ω (or cyclic frequency f), phase angle ϕ , and amplitude a , as given by

$$y(t) = a \cos(\omega t + \phi) = a \cos(2\pi f t + \phi) \quad (10.3)$$

Its average (mean) value is

$$y_{\text{mean}} = \frac{1}{T} \int_0^T y(t) dt = 0 \quad (10.4)$$

which can be verified by direct integration, while noting that

$$T = 1/f = 2\pi/\omega \quad (10.5)$$

For this reason, mean value is not a measure of the “strength” of a signal in general. Now let us define the *root mean square* (RMS) value of a signal. This is the square root of the mean value of the square of the signal. By direct integration, it can be shown that for a sinusoidal (or harmonic) signal; the RMS value is given by

$$y_{\text{RMS}} = \left[\frac{1}{T} \int_0^T y^2(t) dt \right]^{1/2} = \frac{a}{\sqrt{2}} \quad (10.6)$$

It follows that the *RMS amplitude spectrum* is obtained by dividing the amplitude spectrum by $\sqrt{2}$. For example, for the periodic signal formed by combining two harmonic components as in Figure 10.3, the RMS amplitude spectrum is shown in Figure 10.7. This again is a frequency-domain representation of a signal, and the independent variable is frequency.

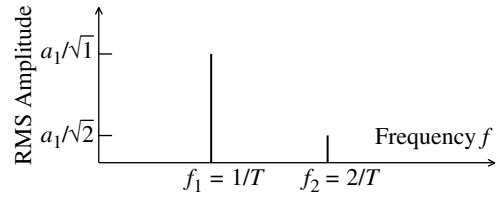


FIGURE 10.7 The RMS amplitude spectrum of a periodic signal.

10.2.6 One-Sided and Two-Sided Spectra

Mean squared amplitude spectrum of a signal (sometimes called *power spectrum* because the square of a variable such as voltage and velocity is a measure of quantities such as *power* and *energy*, even though it is not strictly the spectrum of power in the conventional sense) is obtained by plotting the mean squared amplitude of the signal against frequency. Note that these are *one-sided spectra* because only the positive *frequency band* is considered. This is a realistic representation because one cannot talk about negative frequencies for a real system. But, from a mathematical point of view, we may consider negative frequencies as well. In a spectral representation it is at times convenient to consider the entire frequency band (consisting of both negative and positive values of frequency). It then becomes a *two-sided spectrum*. In this case the spectral component at each frequency value should be equally divided between the positive and the negative frequency values (hence, the spectrum is *symmetric*), such that the overall mean squared amplitude (or power or energy) remains the same.

We have seen that for a harmonic signal component of amplitude a and frequency f (e.g., $a \cos(2\pi f + \phi)$) the RMS amplitude is $a^2/2$ at frequency f , whereas the two-side spectrum has a magnitude of $a^2/4$ at both the frequency values $-f$ and $+f$.

Note that, even though it is possible to interpret the meaning of a negative time (which represents the past, previous to the starting point), it is not possible to give a realistic meaning to a negative frequency. This concept is introduced primarily for analytical convenience.

10.2.7 Complex Spectrum

We have shown that for unique representation of a signal in the frequency domain, both amplitude and phase information should be provided for each frequency component. Alternatively, the spectrum can be expressed as a *complex* function of frequency, having a *real part* and an *imaginary part*. For instance, for a harmonic component given by $a \cos(2\pi f_i + \phi)$ the two-sided complex spectrum can be expressed as

$$Y(f_i) = \frac{a_i}{2} (\cos \phi_i + j \sin \phi_i) = \frac{a_i}{2} e^{j\phi_i}$$

and,

$$Y(-f_i) = \frac{a_i}{2} (\cos \phi_i - j \sin \phi_i) = \frac{a_i}{2} e^{-j\phi_i} \quad (10.7)$$

in which j is the *imaginary unity* as given by $j = \sqrt{-1}$. Note that the spectral component at the negative frequency is the *complex conjugate* of that at the positive frequency. This concept of complex spectrum is

the basis of (complex) *Fourier series expansion* (FSE), which we shall consider in detail in a later section. It should be clear that the complex conjugate of a spectrum is obtained by changing either j to $-j$ or ω to $-\omega$ (or f to $-f$).

10.3 Signal Types

Signals can be classified into different types depending on their characteristics. Note that the signal itself is a time function, but its frequency-domain representation can bring up some of its salient features. Signals particularly important to us here are the excitations and responses of vibrating systems. These can be divided into two broad classes: *deterministic signals* and *random signals* depending on whether we are dealing with deterministic vibrations or random vibrations. Consider a damped cantilever beam that is subjected to a sinusoidal base excitation of frequency ω and amplitude u_0 in the lateral direction (Figure 10.8). In the steady state, the tip of the beam will also oscillate at the same frequency, but with a different amplitude y_0 and, furthermore, there will be a phase shift by an angle ϕ . For a given frequency and known beam properties, the quantities y_0 and ϕ can be completely determined. Under these conditions the tip response of the cantilever is a deterministic signal in the sense that when the experiment is repeated, the same response is obtained. Furthermore, the response can be expressed as a mathematical relationship in terms of parameters whose values are determined with 100% certainty, and probabilities are not associated with these parameters (such parameters are termed *deterministic parameters*). Random signals are nondeterministic (or *stochastic*) signals. Their mathematical representation requires probability considerations. Furthermore, if the process were to be repeated there would always be some uncertainty as to whether an identical response signal could be obtained again.

Deterministic signals can be classified as *periodic*, *quasi-periodic*, and *transient*. Periodic signals repeat exactly at equal time periods. The frequency (Fourier) spectrum of a periodic signal constitutes a series of equally spaced impulses. Furthermore, a periodic signal will have a Fourier series representation. This implies that a periodic signal can be expressed as the sum of sinusoidal components whose frequency ratios are rational numbers (not necessarily integers). Quasi-periodic (or almost periodic) signals also have discrete Fourier spectra, but the spectral lines are not equally spaced. Typically, a quasi-periodic signal can be generated by combining two or more sinusoidal components, provided that at least two of the components have as their frequency ratio an irrational number. Transient signals have continuous Fourier spectra. These types of signals cannot be expressed as a sum of sinusoidal components (or a Fourier series). All signals that are not periodic or quasi-periodic can be classified as transient. Most often, highly damped (overdamped) signals with exponentially decaying characteristics are termed transient, even though various other forms of signals such as exponentially increasing (unstable) responses, sinusoidal decays (underdamped responses), and sinesweeps (sinewaves with variable frequency) also fall into this category. Table 10.1 gives examples for these three types of deterministic signals. The corresponding amplitude spectra are sketched in Figure 10.9. A general classification of signals, with some examples is given in Box 10.1.

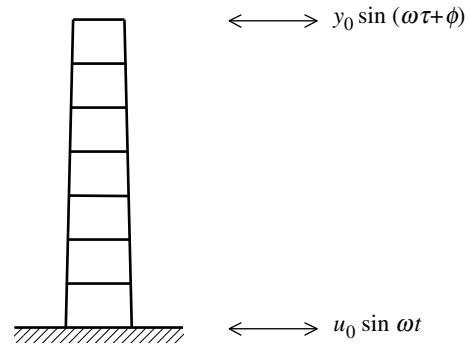


FIGURE 10.8 Response to base excitations of a tall structure (cantilever).

10.4 Fourier Analysis

Fourier analysis is the key to frequency analysis of vibration signals. The frequency-domain representation of a time signal is obtained through the Fourier transform. One immediate advantage

TABLE 10.1 Deterministic Signals

Primary Classification	Nature of the Fourier Spectrum	Example
Periodic	Discrete and equally spaced	$y_0 \sin \omega t + y_1 \sin \frac{5}{3} \omega t + \phi$
Quasi-periodic	Discrete and irregularly spaced	$y_0 \sin \omega t + y_1 \sin(\sqrt{2} \omega t + \phi)$
Transient	Continuous	$y_0 \exp(-\lambda t) \sin(\omega t + \phi)$

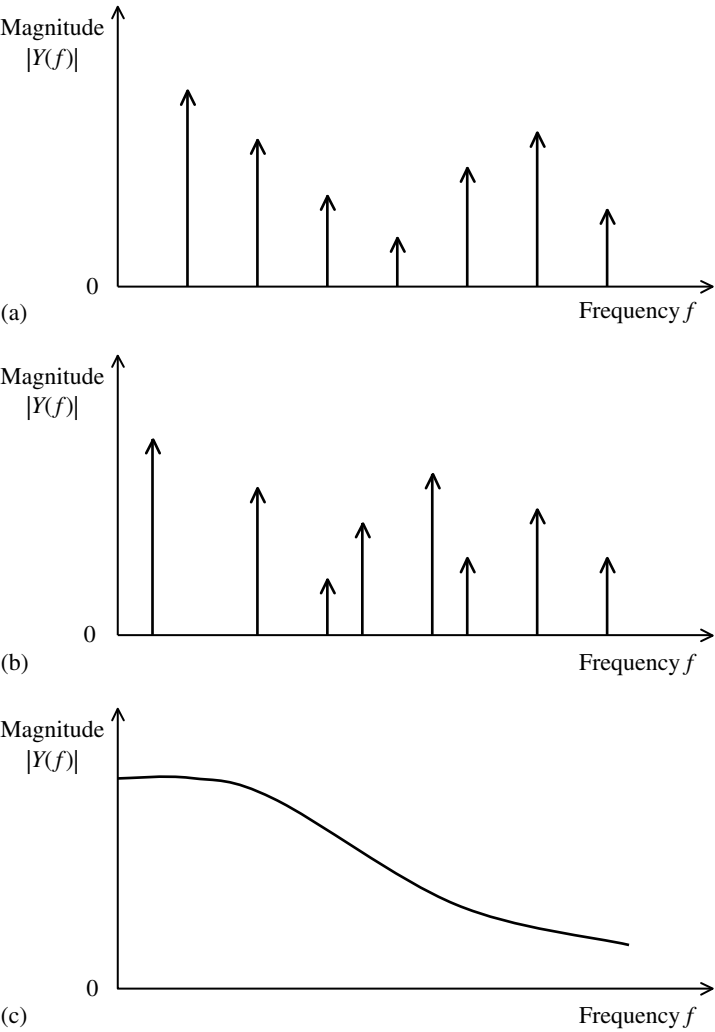
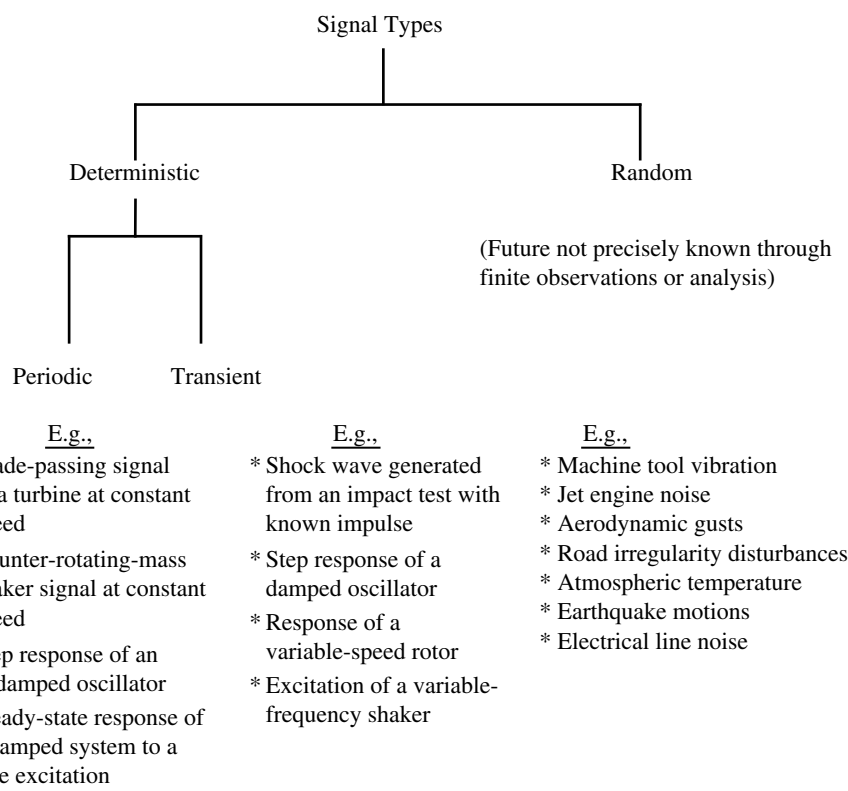


FIGURE 10.9 Magnitude spectra for three types of deterministic signals. (a) Periodic; (b) quasi-periodic; (c) transient.

of the Fourier transform is that, through its use, differential operations (differentiation and integration) in the time domain are converted into simpler algebraic operations (multiplication and division). Transform techniques are quite useful in mathematical applications. For example, a simple, yet versatile transformation from products into sums is accomplished through the use of the *logarithm*. Three versions of Fourier transform are important to us. The Fourier integral transform (FIT) can be applied to any general signal, whereas the FSE is applicable only to periodic signals, and the discrete Fourier

Box 10.1

SIGNAL CLASSIFICATION



transform (DFT) is used for discrete signals. As we shall see, all three versions of transform are interrelated. In particular, we have to use the DFT in digital computation of both FIT and FSE.

10.4.1 Fourier Integral Transform

The *Fourier spectrum* $X(f)$ of a time signal $x(t)$ is given by the *forward transform* relation

$$X(f) = \int_{-\infty}^{\infty} x(t) \exp(-j2\pi ft) dt \tag{10.8}$$

with $j = \sqrt{-1}$ and f the cyclic frequency variable. When Equation 10.8 is multiplied by $\exp(j2\pi f\tau)$ and integrated with respect to f using the *orthogonality property* (which can be considered as a definition of the *Dirac delta function* δ)

$$\int_{-\infty}^{\infty} \exp[j2\pi f(t - \tau)] df = \delta(t - \tau) \tag{10.9}$$

we get the *inverse transform* relation

$$x(t) = \int_{-\infty}^{\infty} X(f) \exp(2j\pi ft) df \quad (10.10)$$

The forward transform is denoted by the operator \mathfrak{F} and the inverse transform by \mathfrak{F}^{-1} . Hence, the Fourier transform pair is given by

$$X(f) = \mathfrak{F}x(t) \text{ and } x(t) = \mathfrak{F}^{-1}X(f) \quad (10.11)$$

Note that for *real* systems, $x(t)$ is a real function but $X(f)$ is a *complex* function in general. Hence, the Fourier spectrum of a signal can be represented by the *magnitude* $|X(f)|$ and the *phase angle* $\angle X(f)$ of the (complex) Fourier spectrum $X(f)$. Alternatively, the *real part* $\text{Re } X(f)$ and the *imaginary part* $\text{Im } X(f)$ together can be used to represent the Fourier spectrum.

According to the present definition, the Fourier spectrum is defined for negative frequency values as well as positive frequencies (i.e., a *two-sided spectrum*). The *complex conjugate* of a complex value is obtained by simply reversing the sign of the imaginary part; in other words, replacing j with $-j$. By noting that replacing j with $-j$ in the forward transform relation is identical to replacing f with $-f$, it should be clear that the Fourier spectrum (of real signals) for negative frequencies is given by the complex conjugate $X^*(f)$ of the Fourier spectrum for positive frequencies. As a result, only the positive-frequency spectrum needs to be specified and the negative-frequency spectrum can be conveniently derived from it, through complex conjugation.

The *Laplace transform* is similar to the FIT. Laplace transform is defined by the forward and inverse relations

$$X(s) = \int_0^{\infty} x(t) \exp(-st) dt \quad (10.12)$$

and

$$x(t) = \frac{1}{2\pi j} \int_{\sigma-j\infty}^{\sigma+j\infty} X(s) \exp(st) ds \quad (10.13)$$

Since the signal itself is zero for $t < 0$, it is seen that for all practical purposes, Fourier transform results can be deduced from the Laplace transform analysis, simply by substituting $s = j2\pi f = j\omega$ and $\sigma = 0$.

10.4.2 Fourier Series Expansion

For a periodic signal $x(t)$ of period T , the FSE is given by

$$x(t) = \Delta F \sum_{n=-\infty}^{\infty} A_n \exp(j2\pi nt/T) \quad (10.14)$$

with $\Delta F = 1/T$. Strictly speaking (see FIT relations) this is the inverse transform relation. The scaling factor ΔF is not essential but is introduced so that the Fourier coefficients A_n will have the same units as the Fourier spectrum. The Fourier coefficients are obtained by multiplying the inverse transform relation by $\exp(-j2\pi mt/T)$ and integrating with respect to t from 0 to T using the orthogonality condition

$$\frac{1}{T} \int_0^T \exp[j2\pi(n-m)t/T] dt = \delta_{mn} \quad (10.15)$$

Note that the *Kronecker delta* δ_{mn} is defined as

$$\delta_{mn} = \begin{cases} 1 & \text{for } m = n \\ 0 & \text{for } m \neq n \end{cases} \quad (10.16)$$

for integer values of m and n . The forward transform that results is given by

$$A_n = \int_0^T x(t) \exp(-j2\pi nt/T) dt \quad (10.17)$$

Note that A_n are complex quantities in general.

It can be shown that for periodic signals, FSE is a special case of FIT, as expected. Consider a Fourier spectrum consisting of a sum of equidistant impulses separated by the frequency interval $\Delta F = 1/T$:

$$X(f) = \Delta F \sum_{n=-\infty}^{\infty} A_n \delta(f - n \cdot \Delta F) \quad (10.18)$$

This is shown in Figure 10.10 (only the magnitudes $|A_n|$ can be plotted in this figure because A_n is complex in general). If we substitute this spectrum into the inverse FIT relation given earlier, we get the inverse FSE relation 10.14. Furthermore, this shows that the Fourier spectrum of a periodic signal is a series of equidistant impulses.

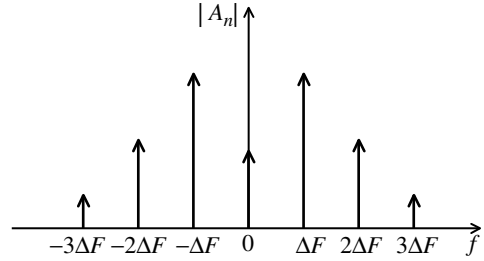


FIGURE 10.10 Fourier spectrum of a periodic signal and its relation to Fourier series.

10.4.3 Discrete Fourier Transform

The DFT relates an N -element *sequence of sampled (discrete) data signal*

$$\{x_m\} = [x_0, x_1, \dots, x_{N-1}] \quad (10.19)$$

to an N -element sequence of spectral results

$$\{X_n\} = [X_0, X_1, \dots, X_{N-1}] \quad (10.20)$$

through the forward transform relation

$$X_n = \Delta T \sum_{m=0}^{N-1} x_m \exp(-j2\pi mn/N) \quad (10.21)$$

with $n = 0, 1, \dots, N-1$. The values X_n are called the *spectral lines*. It can be shown that these quantities approximate the values of the Fourier spectrum (continuous) at the corresponding discrete frequencies. Let us identify ΔT as the *sampling period* (i.e., the time step between two adjacent points of sampled data).

The inverse transform relation is obtained by multiplying the forward transform relation by $\exp(j2\pi mr/N)$ and summing over $n = 0$ to $N-1$, using the orthogonality property

$$\frac{1}{N} \sum_{n=0}^{N-1} \exp[j2\pi n(r-m)/N] = \delta_{rm} \quad (10.22)$$

Note that this orthogonality relation can be considered as a definition of *Kronecker delta*. The inverse transform is

$$x_m = \Delta F \sum_{n=0}^{N-1} X_n \exp(j2\pi mn/N) \quad (10.23)$$

The data record length is given by

$$T = N \cdot \Delta T = 1/\Delta F \quad (10.24)$$

The DFT is a transform in its own right, independent of the FIT. It is possible, however, to interpret this transformation as the *trapezoidal integration* approximation of FIT. We have deliberately chosen appropriate scaling factors ΔT and ΔF in order to maintain this equivalence, and it is very useful in computing the Fourier spectrum of a general signal or the Fourier coefficients of a periodic signal using a digital computer. Proper interpretation of the digital results is crucial, however, in using DFT to compute (an approximate) Fourier spectrum of a (continuous) signal. In particular, two types of error: aliasing

TABLE 10.2 Unified Definitions for Three Fourier Transform Types

Relation Name	Fourier Integral Transform	Discrete Fourier Transform (DFT)	Fourier Series Expansion (FSE)
Forward transform	$X(f) = \int_{-\infty}^{\infty} x(t) \exp(-j2\pi ft) dt$	$X_n = \Delta T \sum_{m=0}^{N-1} x_m \exp(-j2\pi mn/N),$ $n = 0, 1, \dots, N - 1$	$A_n = \int_0^T x(t) \exp(-j2\pi nt/T) dt$ $n = 0, 1, \dots$
Inverse transform	$x(t) = \int_{-\infty}^{\infty} X(f) \exp(j2\pi ft) df$	$x_m = \Delta F \sum_{n=0}^{N-1} X_n \exp(j2\pi mn/N),$ $m = 0, 1, \dots, N - 1$	$x(t) = \Delta F \sum_{n=-\infty}^{\infty} A_n \times \exp(j2\pi nt/T)$
Orthogonality	$\int_{-\infty}^{\infty} \exp[j2\pi f(\tau - t)] df = \delta(\tau - t)$	$\frac{1}{N} \sum_{n=0}^{N-1} \exp[j2\pi n(r - m)/N] = \delta_{rm}$	$\frac{1}{T} \int_0^T \exp[j2\pi(r - n)t/T] dt = \delta_{rn}$
Notes	$T = N\Delta T$	$\Delta F = 1/T$	$X(f) = \Delta F \sum_{n=-\infty}^{\infty} A_n \delta(f - n/T)$

TABLE 10.3 Important Properties of the Fourier Transform

Function of Time	Fourier Spectrum
$x(t)$	$X(f)$
$k_1 x_1(t) + k_2 x_2(t)$	$k_1 X_1(f) + k_2 X_2(f)$
$x(t) \exp(-j2\pi ta)$	$X(f + a)$
$x(t + \tau)$	$X(f) \exp(j2\pi f\tau)$
$\frac{d^n x(t)}{dt^n}$	$(j2\pi f)^n X(f)$
$\int_{-\infty}^t x(t) dt$	$\frac{X(f)}{j2\pi f}$

and leakage (or truncation error) should be considered. This subject will be addressed later. The three transform relations, corresponding inverse transforms, and the orthogonality relations are summarized in Table 10.2.

The link between the time-domain signals and models and the corresponding frequency-domain equivalents is the FIT. Table 10.3 provides some important properties of the FIT and the corresponding time-domain relations that are useful in the analysis of signals and system models. These properties may be easily derived from the basic FIT relations (Equation 10.8 through Equation 10.10). It should be noted that, inherent in the definition of the DFT given in Table 10.2 is the N -point periodicity of the two sequences; that is, $X_n = X_{n+iN}$ and $x_m = x_{m+iN}$, for $i = \pm 1, \pm 2, \dots$

The definitions given in Table 10.2 may differ from the versions available in the literature by a multiplicative constant. However, it is observed that according to the present definitions, the DFT may be interpreted as the trapezoidal integration of the FIT. The close similarity between the definitions of the FSE and the DFT is also noteworthy. Furthermore, according to the last row in Table 10.2, the FSE can be expressed as a special FIT consisting of an equidistant set of impulses of magnitude A_n/T located at $f = n/T$.

10.4.4 Aliasing Distortion

Recalling that the primary task of digital Fourier analysis is to obtain a discrete approximation to the FIT of a piecewise continuous function, it is advantageous to interpret the DFT as a discrete (digital computer) version of the FIT rather than an independent discrete transform. Accordingly, the results from a DFT must be consistent with the exact results obtained if the FIT were used. The definitions given in Table 10.2 are consistent in this respect because the DFT is given as the trapezoidal integration of the FIT. However, it should be clear that if $X(f)$ is the FIT of $x(t)$, then the sequence of sampled values $\{X(n \cdot \Delta F)\}$ is not exactly the DFT of the sampled data sequence $\{x(m \cdot \Delta T)\}$. Only an approximate relationship exists.

A further advantage of the definitions given in Table 10.2 is apparent when dealing with the FSE. As we have noted, the FIT of a periodic function is a set of impulses. We can avoid dealing with impulses by

relating the complex Fourier coefficients to the DFT sequence of sampled data from the periodic function via the present definitions.

Aliasing distortion is an important consideration when dealing with sampled data from a continuous signal. This error may enter into computation in both the time domain and the frequency domain, depending on the domain in which the results are presented. We will address this issue next.

10.4.4.1 Sampling Theorem

The basic relationships between the FIT, the DFT, and the FSE are summarized in Table 10.4. By means of straightforward mathematical procedures, the relationship between the FIT and the DFT can be established. Even though $\{X(n \cdot \Delta F)\}$ is not the DFT of $\{x(m \cdot \Delta T)\}$, the results in Table 10.4 show that $\{\tilde{X}(n \cdot \Delta F)\}$ is the DFT of $\{\tilde{x}(m \cdot \Delta T)\}$ where the periodic functions $\tilde{X}(f)$ and $\tilde{x}(t)$ are as defined as in Table 10.4. This situation is illustrated in Figure 10.11. It should be recalled that $X(f)$ is a complex function in general, and as such it cannot be displayed as a single curve in a two-dimensional coordinate system. Both the magnitude and the phase angle variations with respect to frequency f are needed. For brevity, only the magnitude $|X(f)|$ is shown in Figure 10.11(a). Nevertheless, the argument presented applies to the phase angle $\angle X(f)$ as well.

It is obvious that in the time interval $[0, T]$, $x(t) = \tilde{x}(t)$ and $x_m = \tilde{x}_m$. However, $\tilde{X}(n \cdot \Delta F)$ is only approximately equal to $X(n \cdot \Delta F)$ in the frequency interval $[0, F]$. This is known as the aliasing distortion in the frequency domain. As ΔT decreases (i.e., as F increases) $\tilde{X}(f)$ will become closer to $X(f)$ in the frequency interval $[0, F/2]$, as is clear from Figure 10.11(c). Furthermore, due to the F -periodicity of $\tilde{X}(f)$, its value in the frequency range $[F/2, F]$ will approximate $X(f)$ in the frequency range $[-F/2, 0]$.

It is clear from the preceding discussion that if a time signal $x(t)$ is sampled at equal steps of ΔT , no information regarding its frequency spectrum $X(f)$ is obtained for frequencies higher than $f_c = 1/(2\Delta T)$. This fact is known as *Shannon's sampling theorem*, and the limiting (cut-off) frequency is called the *Nyquist frequency*. In vibration signal analysis, a sufficiently small sample step ΔT should be chosen in order to reduce aliasing distortion in the frequency domain, depending on the highest frequency of interest in the analyzed signal. This however, increases the signal processing time and the computer storage requirements, which is undesirable, particularly in real-time analysis. It can also result in stability problems in numerical computations. The Nyquist sampling criterion requires that the sampling rate ($1/\Delta T$) for a signal should be at least twice the highest frequency of interest. Instead of making the sampling rate very high, a moderate value that satisfies the Nyquist sampling criterion is used in practice, together with an *antialiasing filter* to remove the distorted frequency components. It should be noted that the DFT results in the frequency interval $[f_c, 2f_c]$ are redundant because they merely approximate the frequency spectrum in the negative frequency interval $[-f_c, 0]$ which is known for real signals. This fact is known as the Hermitian property.

The last column of Table 10.4 presents the relationship between the FSE and the DFT. It is noted that the sequence $\{\tilde{A}_n\}$ rather than the sequence of complex Fourier series coefficients $\{A_n\}$ represents the DFT

TABLE 10.4 Unified Fourier Transform Relationships

Description	Relationship	
	DFT and FIT	DFT and FSE
Given	$x(t) \xrightarrow{\text{FIT}} X(f)$	$x(t) \xrightarrow{\text{FSE}} \{A_n\}$
Form	$\tilde{x}(t) = \sum_{k=-\infty}^{\infty} x(t + kT)$ $\tilde{X}(f) = \sum_{k=-\infty}^{\infty} X(f + kF)$	$\tilde{A}_n = \sum_{k=-\infty}^{\infty} A_{n+kN}$
Then	$\{\tilde{x}_m\} \xrightarrow{\text{DFT}} \{\tilde{X}_n\}$	$\{\tilde{x}_m\} \xrightarrow{\text{DFT}} \{\tilde{A}_n\}$
Where	$\tilde{x}_m = \tilde{x}(m \cdot \Delta T)$, $\tilde{X}_n = \tilde{X}(n \cdot \Delta F)$ $F = 1/\Delta T$, $T = 1/\Delta F$	$x_m = x(m \cdot \Delta T)$ $N = T/\Delta T$

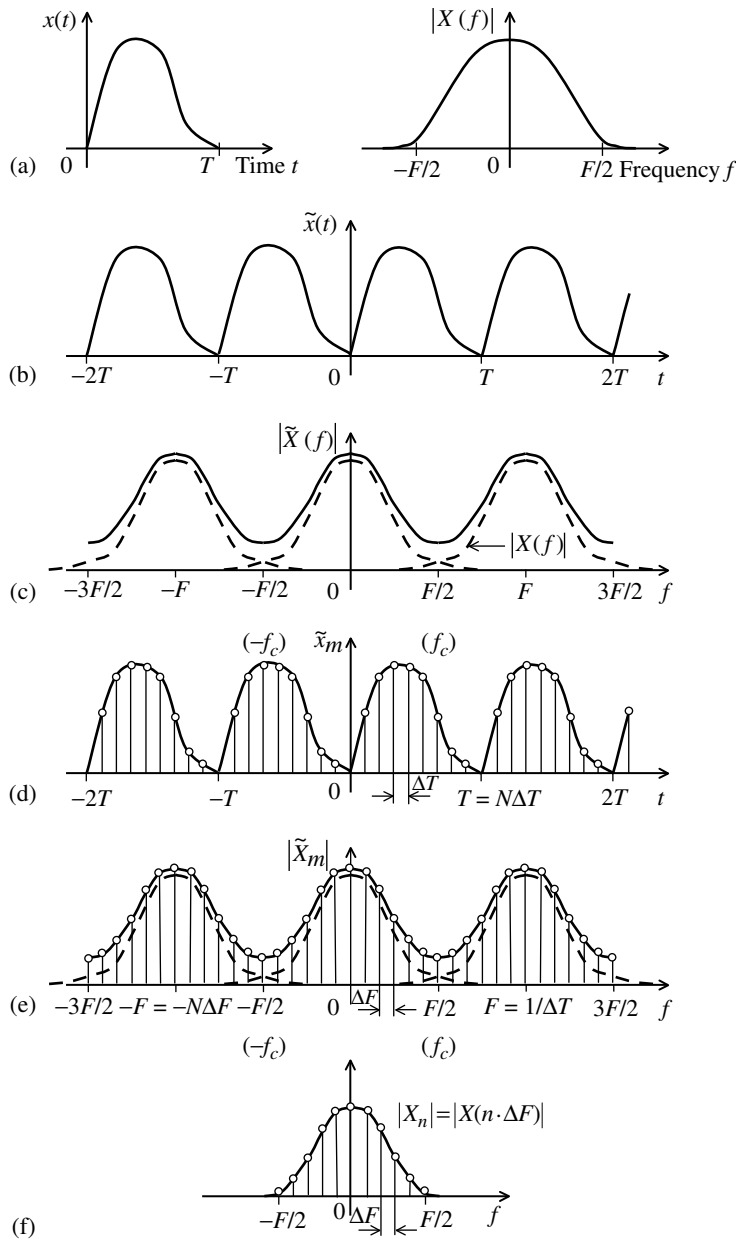


FIGURE 10.11 Relationship between FIT and DFT, with an illustration of aliasing error. (a) Fourier integral transformation (FIT) of a signal; (b) periodicity arranged time signal; (c) periodicity of the frequency spectrum; (d) sampled time signal; (e) sampled frequency spectrum (with aliasing error); (f) sampled original spectrum (no aliasing error).

of the sampled data sequence $\{x(m \cdot \Delta T)\}$. In practice, however, $A_n \rightarrow 0$ as $n \rightarrow \infty$. Consequently, \tilde{A}_n is a good approximator to A_n in the range $[-N/2 \leq n \leq N/2]$ for sufficiently large N . This basic result is useful in determining the Fourier coefficients of a periodic signal using discrete data that are sampled at time steps of $\Delta T = 1/F$, in which F is the fundamental frequency of the periodic signal. Again the aliasing error $(\tilde{A}_n - A_n)$ may be reduced by increasing the sampling rate (i.e., by decreasing ΔT or increasing N).

10.4.4.2 Aliasing Distortion in the Time Domain

In vibration applications it is sometimes required to reconstruct the signal from its Fourier spectrum. Inverse DFT is used for this purpose and is particularly applicable in digital equalizers in vibration testing. Due to sampling in the frequency domain, the signal becomes distorted. The aliasing error ($\tilde{x}_m - x(m\Delta T)$) is reduced by decreasing the sample period ΔF . It should be noted that no information regarding the signal for times greater than $T = 1/\Delta F$ is obtained from the analysis.

By comparing Figure 10.11(a) with (c), or (e) with (f), it should be clear that the aliasing error in \tilde{X} in comparison with the original spectrum X is caused by “folding” of the high-frequency segment of X beyond the Nyquist frequency into the low-frequency segment of X . This is illustrated in Figure 10.12.

10.4.4.3 Antialiasing Filter

It should be clear from Figure 10.12 that, if the original signal is low-pass filtered at a cut-off frequency equal to the Nyquist frequency, then the aliasing distortion would not occur due to sampling. A filter of this type is called an antialiasing filter. In practice, it is not possible to achieve perfect filtering. Hence, some aliasing could remain even after using an antialiasing filter. Such residual errors may be reduced by using a filter cut-off frequency that is slightly less than the Nyquist frequency. The resulting spectrum would then only be valid up to this filter cut-off frequency (and not up to the theoretical limit of Nyquist frequency).

Example 10.1

Consider 1024 data points from a signal, sampled at 1 msec intervals.

$$\text{Sample rate } f_s = 1/0.001 \text{ samples/sec} = 1000 \text{ Hz} = 1 \text{ kHz}$$

$$\text{Nyquist frequency} = 1000/2 \text{ Hz} = 500 \text{ Hz}$$

Due to aliasing, approximately 20% of the spectrum (i.e., spectrum beyond 400 Hz) will be distorted. Here we may use an antialiasing filter.

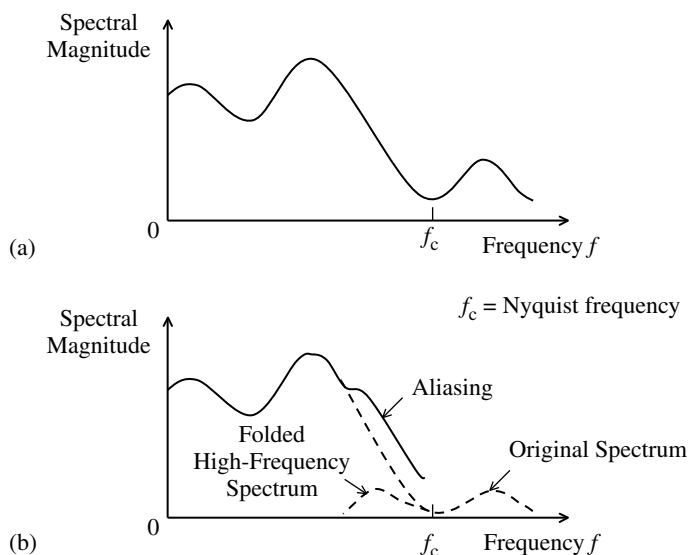


FIGURE 10.12 Aliasing distortion of frequency spectrum. (a) Original spectrum; (b) distorted spectrum due to aliasing.

Box 10.2

SIGNAL SAMPLING CONSIDERATIONS

The maximum useful frequency in digital Fourier results is half the sampling rate.

Nyquist frequency or cut-off frequency or computational bandwidth:

$$f_c = \frac{1}{2} \times \text{sampling rate}$$

Aliasing distortion:

High-frequency spectrum beyond Nyquist frequency folds on to the useful spectrum, thereby distorting it.

Summary:

1. Pick a sufficiently small sample step ΔT in the time domain, to reduce the aliasing distortion in the frequency domain.
2. The highest frequency for which the Fourier transform (frequency-spectrum) information would be valid, is the Nyquist frequency $f_c = 1/(2\Delta T)$.
3. DFT results that are computed for the frequency range $[f_c, 2f_c]$ merely approximate the frequency spectrum in the negative frequency range $[-f_c, 0]$.

Suppose that a digital Fourier transform computation provides 1024 frequency points of data up to 1000 Hz. Half of this number is beyond the Nyquist frequency and will not give any new information about the signal.

$$\text{Spectral line separation} = 1000/1024 \text{ Hz} = 1 \text{ Hz (approximately)}$$

Keep only the first 400 spectral lines as the useful spectrum.

Note: Almost 500 spectral lines may be retained if an accurate antialiasing filter is used.

Some useful information on signal sampling is summarized in Box 10.2.

10.4.5 Another Illustration of Aliasing

A simple illustration of aliasing is given in [Figure 10.13](#). Here, two sinusoidal signals of frequency, $f_1 = 0.2 \text{ Hz}$ and $f_2 = 0.8 \text{ Hz}$, are shown ([Figure 10.13\(a\)](#)). Suppose that the two signals are sampled at the rate of $f_s = 1 \text{ sample/sec}$. The corresponding Nyquist frequency is $f_c = 0.5 \text{ Hz}$. It is seen that, at this sampling rate, the data samples from the two signals are identical. In other words, the high-frequency signal cannot be distinguished from the low-frequency signal. Hence, a high-frequency signal component of frequency 0.8 Hz will appear as a low-frequency signal component of frequency 0.2 Hz. This is aliasing, as is clear from the signal spectrum shown in [Figure 10.13](#). Specifically, the spectral segment of the signal beyond the Nyquist frequency (f_c) cannot be recovered.

It is apparent from [Figure 10.11\(e\)](#) that the aliasing error becomes increasingly prominent for frequencies of the spectrum closer to the Nyquist frequency. With reference to the expression for $\tilde{X}(f)$ in [Table 10.4](#), it should be clear that when the true Fourier spectrum $X(f)$ has a steep roll-off prior to $F/2$ ($= f_c$), the influence of the $X(f - nF)$ segments for $n \geq 2$ and $n \leq -1$ is negligible in the discrete spectrum in the frequency range $[0, F/2]$. Hence the aliasing distortion in the frequency band $[0, F/2]$ comes primarily from $X(f - F)$, which is the true spectrum shifted to the right through F . Therefore,

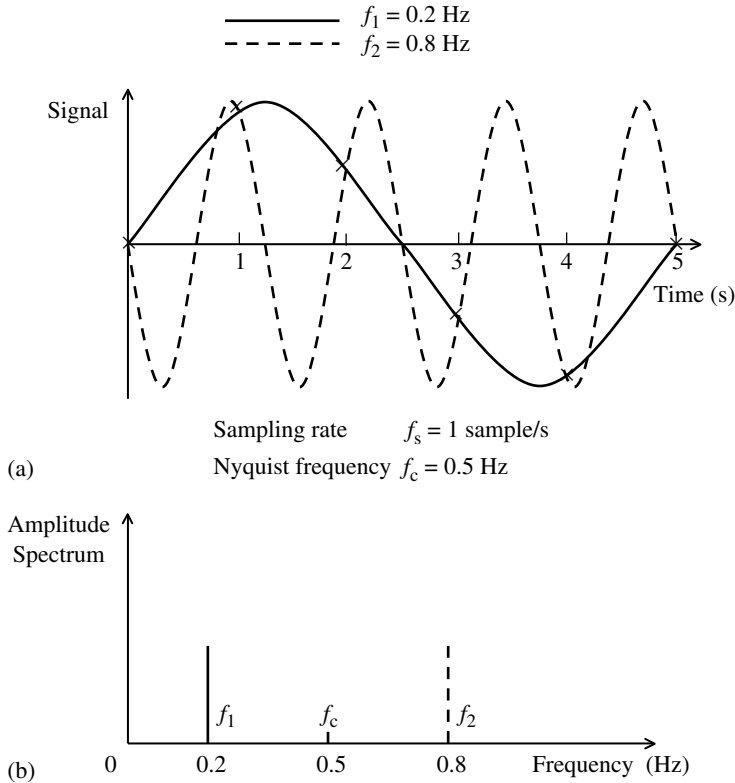


FIGURE 10.13 A simple illustration of aliasing. (a) Two harmonic signals with identical sampled data; (b) Frequency spectra of the two harmonic signals.

a reasonably accurate expression for the aliasing error is

$$e_n = X(-(F - n \cdot \Delta F)) = X(n \cdot \Delta F - F) = X_{-(N-n)} = X_{n-N} \quad n = 0, 1, 2, \dots, N/2 \quad (10.25)$$

Note from Equation 10.8 that the spectral value obtained when f in the complex exponential is replaced by $-f$ is the same as the spectral value obtained when j is replaced by $-j$. Since the signal $x(t)$ is real, it follows that the Fourier spectrum for the negative frequencies is simply the complex conjugate of the Fourier spectrum for the positive frequencies; thus

$$X(-f) = X^*(f) \quad (10.26)$$

or, in the discrete case

$$X_{n-N} = X_{N-n}^* \quad (10.27)$$

It follows from Equation 10.25 that the aliasing distortion is given by

$$e_n = X_{N-n}^* \quad \text{for } n = 0, 1, 2, \dots, N/2 \quad (10.28)$$

This result confirms that aliasing can be interpreted as folding of the complex conjugate of the true spectrum beyond the Nyquist frequency $f_c (= F/2)$ over to the original spectrum. In other words, due to aliasing, frequency components higher than the Nyquist frequency appear as lower frequency components (due to folding). These aliasing components enter into the digital Fourier results in the useful frequency range $[0, f_c]$.

Aliasing reduces the valid frequency range in digital Fourier results. Typically, the useful frequency limit is $f_c/1.28$ so that the last 20% of the spectral points near the Nyquist frequency should be neglected.

It should be clear that if a low-pass filter with its cut-off frequency set at f_c is used on the time signal prior to sampling and digital Fourier analysis, the aliasing distortion can be virtually eliminated. Analog hardware filters may be used for this purpose. They are the *antialiasing filters*. Note that sometimes $f_c/1.28 (\cong 0.8f_c)$ is used as the filter cut-off frequency. In this case, the computed spectrum is accurate up to $0.8f_c$ and not up to f_c .

The buffer memory of a typical commercial Fourier analyzer can store $N = 2^{10} = 1024$ samples of data from the time signal. This is the size of the data block analyzed in each digital Fourier transform calculation. This will result in $N/2 = 512$ spectral points (spectral lines) in the frequency range $[0, f_c]$. Out of this only the first 400 spectral lines (approximately 80%) are considered free of aliasing distortion.

Example 10.2

Suppose that the frequency range of interest in a particular vibration signal is 0–200 Hz. We are interested in determining the sampling rate (digitization speed) and the cut-off frequency for the antialiasing (low-pass) filter.

The Nyquist frequency f_c is given by $f_c/1.28 = 200$

Hence, $f_c = 256$ Hz

The sampling rate (or digitization speed) for the time signal that is needed to achieve this range of analysis is $F = 2f_c = 512$ Hz. With this sampling frequency, the cut-off frequency for the antialiasing filter could be set at a value between 200 and 256 Hz.

10.5 Analysis of Random Signals

Random (stochastic) signals are generated by some random mechanism. Each time the mechanism is operated a new time history (sample function) is generated. The chance of any two sample functions becoming identical is governed by some probabilistic law. If all sample functions are identical (with unity probability), then the corresponding signal is a deterministic signal. A random process is denoted by $\tilde{X}(t)$, while any sample function of it is denoted by $x(t)$. No numerical computations can be performed on $\tilde{X}(t)$ because it is not known for certain. Its Fourier transform, for instance, can be written down as an analytical expression, but cannot be numerically computed. However, once the signal is generated, numerical computations can be performed on that sample function $x(t)$ because it is a completely known function of time.

10.5.1 Ergodic Random Signals

At any given time t_1 , $\tilde{X}(t_1)$ is a random variable which has a certain probability distribution. Consider a well-behaved function $f\{\tilde{X}(t)\}$ of this random variable (which is also a random variable). Its expected value (statistical mean) is $E[f\{\tilde{X}(t)\}]$. This is also known as the ensemble average because it is equivalent to the average value at t of a collection (ensemble) of a large number of sample functions $x(t)$.

Consider the function $f\{x(t)\}$ of one sample function $x(t)$. Its temporal (time) mean is expressed by

$$\lim_{T \rightarrow \infty} \frac{1}{2T} \int_{-T}^T f\{x(t)\} dt$$

Now, if

$$E[f\{\tilde{X}(t_1)\}] = \lim_{T \rightarrow \infty} \frac{1}{2T} \int_{-T}^T f\{x(t)\} dt \quad (10.29)$$

then the random signal is said to be ergodic. It should be noted that the right-hand side of Equation 10.29 does not depend on time. Consequently, the left-hand side should also be independent of the time point t_1 .

For analytical convenience, random vibration signals are usually assumed to be ergodic (the ergodic hypothesis). Using this hypothesis, the properties of a random signal could be determined by performing computations on a sufficiently long record (sample function) of the signal. Since the ergodic hypothesis is not exactly satisfied for vibration signals, and since it is impossible to analyze infinitely long data records, the accuracy of the numerical results depends on various factors such as the record length, sampling rate, frequency range of interest, and the statistical nature of the random signal (e.g., closeness to a deterministic signal, frequency content, periodicity, damping characteristics). Accuracy can be improved in general, by averaging the results for more than one data record.

10.5.2 Correlation and Spectral Density

If for a random signal $\tilde{X}(t)$, the joint statistical properties of $\tilde{X}(t_1)$ and $\tilde{X}(t_2)$ depend on the time difference $(t_2 - t_1)$ and not on t_1 itself, then the signal is said to be stationary. Consequently, the statistical properties of a stationary $\tilde{X}(t)$ will be independent of t . It is noted from Equation 10.29 that ergodic random signals are necessarily stationary. However, in general the converse is not true.

The cross-correlation function of two random signals $\tilde{X}(t)$ and $\tilde{Y}(t)$ is given by $E[\tilde{X}(t)\tilde{Y}(t + \tau)]$. If the signals are stationary, this expected value is a function of τ (not t) and is denoted by $\phi_{xy}(\tau)$. In view of the ergodic hypothesis, the cross-correlation function may be expressed as

$$\phi_{xy}(\tau) = \lim_{T \rightarrow \infty} \left[\frac{1}{T} \int_0^T x(t)y(t + \tau)dt \right] \quad (10.30)$$

The FIT of $\phi_{xy}(\tau)$ is the cross-spectral density function which is denoted by $\Phi_{xy}(f)$. When the two signals are identical, we have the autocorrelation function $\phi_{xx}(\tau)$ in the time domain and the power spectral density (PSD) $\Phi_{xx}(f)$ in the frequency domain. The continuous and the discrete versions of the correlation theorem are given in the first row of Table 10.5. It follows that the cross-spectral density may be estimated using the DFT (FFT) of the two signals, as $[X_n]^* Y_n / T$ in which T is the record length and $[X_n]^*$ is the complex conjugate of $[X_n]$.

Parseval's theorem (second row of Table 10.5) follows directly from the correlation theorem. Consequently, the mean square value of a random signal may be obtained from the area under the PSD curve. This suggests a hardware-based method of estimating the PSD as illustrated by the functional diagram in Figure 10.14(a). Alternatively, a software-based digital Fourier analysis could be used (Figure 10.14(b)). A single sample function would not give the required accuracy, and averaging is usually needed. In real-time digital analysis, the running average as well as the current estimate is usually computed. In the running average, it is desirable to give a higher weighting to the more recent estimates. The fluctuations in the PSD estimate about the local average could be reduced by selecting a large filter

TABLE 10.5 Some Useful Fourier Transform Results

Description	Continuous	Discrete
Correlation theorem	If $z(\tau) = \int_{-\infty}^{\infty} x(t)y(t + \tau)dt$ Then $Z(f) = [X(f)]^* Y(f)$	$z_m = \Delta T \sum_{r=0}^{N-1} x_r y_{r+m}$ $Z_n = [X_n]^* Y_n$
Parseval's theorem	If $y(t) \xrightarrow{\text{FIT}} Y(f)$ Then $\int_{-\infty}^{\infty} y^2(t)dt = \int_{-\infty}^{\infty} Y(f) ^2 df$	$\{y_m\} \xrightarrow{\text{DFT}} \{Y_n\}$ $\Delta T \sum_{m=0}^{N-1} y_m^2 = \Delta F \sum_{n=0}^{N-1} Y_n ^2$
Convolution theorem	If $y(t) = \int_{-\infty}^{\infty} h(\tau)u(t - \tau)d\tau = \int_{-\infty}^{\infty} h(t - \tau)u(\tau)d\tau$ Then $Y(f) = H(f)U(f)$	$y_m = \Delta T \sum_{r=0}^{N-1} h_r u_{m-r} = \Delta T \sum_{r=0}^{N-1} h_{m-r} u_r$ $Y_n = H_n U_n$

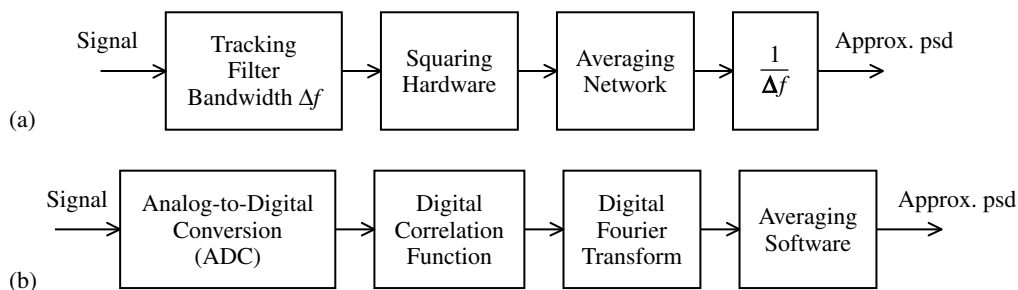


FIGURE 10.14 Power spectral density computation. (a) Narrow-band filtering method; (b) correlation and Fourier transformation method.

bandwidth Δf and a large record length T . A measure of these fluctuations is given by

$$\varepsilon = \frac{1}{\sqrt{\Delta f T}} \quad (10.31)$$

It should be noted that a large Δf results in reduction of the precision of the estimates while improving the appearance. To offset this, T has to be increased further.

10.5.3 Frequency Response Using Digital Fourier Transform

Vibration test programs usually require a resonance search type pretesting. In order to minimize the damage potential, it is carried out at a much lower intensity than the main test. The objective of such exploratory tests is to determine the significant frequency-response functions of the test specimen. These provide the natural frequencies, damping ratios, and mode shapes of the test specimen. Such frequency-response data are useful in planning and conducting the main test. For example, more attention is required when testing in the vicinity of the resonance points (slower sweep rates, larger dwell periods, etc.). Also, the frequency-response data are useful in determining the most desirable test input directions and intensities. The degree of nonlinearity and time variance of the test object can be determined by conducting more than one frequency-response test at different input intensities. If the deviation of the frequency-response function is sufficiently small, then linear, time-invariant analysis is considered to be satisfactory. Often, frequency-response tests are conducted at full test intensity. In such cases, it is considered as a part of the main test rather than a prescreening test. Other uses of the frequency-response function include the following: it can be employed as a system model (experimental model) for further analysis of the test specimen (experimental modal analysis). Most desirable frequency range and sweep rates for vibration testing can be estimated by examining frequency-response functions.

The time response $h(t)$ to a unit impulse is known as the impulse-response function. For each pair of input and output locations (A,B) of the test specimen, a corresponding single response function would be obtained (assuming linearity and time-invariance). Entire collection of these responses would determine the response of the test specimen to an arbitrary input signal. The response $y(t)$ at B to an arbitrary input $u(t)$ applied at A, is given by

$$y(t) = \int_{-\infty}^{\infty} h(\tau)u(t - \tau)d\tau = \int_{-\infty}^{\infty} h(t - \tau)u(\tau)d\tau \quad (10.32)$$

The right-hand side of Equation 10.32 is the convolution integral of $h(t)$ and $u(t)$ and is denoted by $h(t) * u(t)$. By substituting the inverse FIT relations (Table 10.2) in Equation 10.32, the frequency-response function (frequency-transfer function) $H(f)$ is obtained as the ratio of the (complex) FITs of the output and the input. It exists for physically realizable (casual) systems even when the individual FITs of the input and output signals do not converge. The continuous convolution theorem and the discrete

counterpart are given in the last row of Table 10.5. The discrete convolution can be interpreted as the trapezoidal integration of Equation 10.32. Frequency-response function is a valid representation (model) for linear, time-invariant systems. It is related to the system transfer function $G(s)$ (ratio of the Laplace transforms of output and input with zero initial conditions) through

$$H(f) = \frac{Y(f)}{U(f)} = G(2\pi f) \quad (10.33)$$

But for notational convenience, the frequency-response function corresponding to $G(s)$ may be denoted by either $G(f)$ or $G(\omega)$, where ω is the angular frequency and f is the cyclic frequency.

Using Fourier transform theory, three methods of determining $H(f)$ can be established. First, using any transient excitation signal to a system at rest and the corresponding output, $H(f)$ is determined from their FITs (Table 10.5). Second, if the input is sinusoidal, the signal amplification of the steady-state output is the magnitude $|H(f)|$ at the input frequency, and the phase lead of the steady-state output is the corresponding phase angle $\angle H(f)$. Third, using a random input signal and the corresponding input and output spectral density functions, $H(f)$ is determined as the ratio

$$H(f) = \Phi_{yy}(f)/\Phi_{uu}(f) \quad (10.34)$$

10.5.4 Leakage (Truncation Error)

In digital processing of vibration signals (e.g., accelerometer signals), sampled data are truncated to eliminate less significant parts. This is of course essential in real-time processing because, in that case, only sufficiently short segments of continuously acquisitioned data are processed at a time. The computer memory (and buffer) limitations, the speed and cost of processing, the frequency range of importance, the sampling rate, and the nature of the signal (level of randomness, periodicity, decay rate, etc.) should be taken into consideration in selecting the truncation point of data.

The effect of direct truncation of a signal $x(t)$ on its Fourier spectrum is shown in Figure 10.15. In the time domain, truncation is accomplished by multiplying $x(t)$ by the box-car function $b(t)$. This is equivalent to a convolution ($X(f) * B(f)$) in the frequency domain. This procedure introduces ripples (side lobes) into the true spectrum. The resulting error ($X(f) - X(f) * B(f)$) is known as leakage or truncation error. Similar leakage effects arise in the time domain, as a result of truncation of the frequency spectrum. The truncation error may be reduced by suppressing the side lobes, which requires modification of the truncation function (window) from the box-car shape $b(t)$ to a more desirable shape. Commonly used windows are the Hanning, Hamming, Parzen, and Gaussian windows.

10.5.5 Coherence

Random vibration signals $\tilde{X}(t)$ and $\tilde{Y}(t)$ are said to be statistically independent if their joint probability distribution is given by the product of the individual distributions. A special case of this is the uncorrelated signals which satisfy

$$E[\tilde{X}(t_1)\tilde{Y}(t_2)] = E[\tilde{X}(t_1)]E[\tilde{Y}(t_2)] \quad (10.35)$$

In the stationary case, the means $\mu_x = E[\tilde{X}(t)]$ and $\mu_y = E[\tilde{Y}(t)]$ are time independent. The autocovariance functions are given by

$$\psi_{xx}(\tau) = E[\{\tilde{X}(t) - \mu_x\}\{\tilde{X}(t + \tau) - \mu_x\}] = \phi_{xx}(\tau) - \mu_x^2 \quad (10.36)$$

$$\psi_{yy}(\tau) = E[\{\tilde{Y}(t) - \mu_y\}\{\tilde{Y}(t + \tau) - \mu_y\}] = \phi_{yy}(\tau) - \mu_y^2 \quad (10.37)$$

and the cross-covariance function is given by

$$\psi_{xy}(\tau) = E[\{\tilde{X}(t) - \mu_x\}\{\tilde{Y}(t + \tau) - \mu_y\}] = \phi_{xy}(\tau) - \mu_x\mu_y \quad (10.38)$$

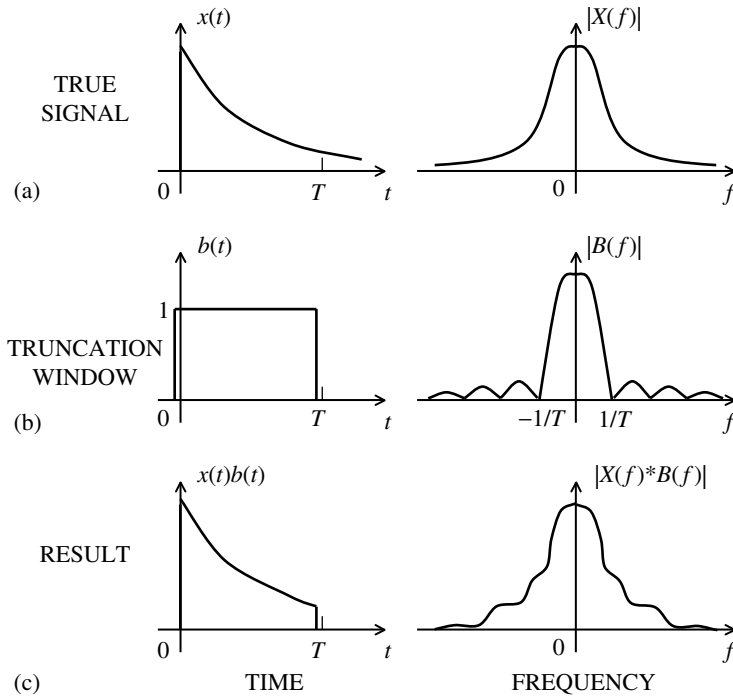


FIGURE 10.15 Illustration of truncation error. (a) Signal and its frequency spectrum; (b) a rectangular (box-car) window and its frequency spectrum; (c) truncated signal and its frequency spectrum.

For uncorrelated signals $\phi_{xy}(\tau) = \mu_x \mu_y$ and $\psi_{xy}(\tau) = 0$. The correlation function coefficient is defined by

$$\rho_{xy}(\tau) = \frac{\psi_{xy}(\tau)}{\sqrt{\psi_{xx}(0)\psi_{yy}(0)}} \quad (10.39)$$

which satisfies $-1 \leq \rho_{xy}(\tau) \leq 1$.

For uncorrelated signals we have $\rho_{xy}(\tau) = 0$. This function measures the degree of correlation of the two signals. In the frequency domain, the correlation is determined by its (ordinary) coherence function

$$\gamma_{xy}^2(f) = \frac{|\Phi_{xy}(f)|^2}{\Phi_{xx}(f)\Phi_{yy}(f)} \quad (10.40)$$

which satisfies the condition $0 \leq \gamma_{xy}^2(f) \leq 1$. In this definition, the signals are assumed to have zero means. Alternatively, the FIT of the covariance functions may be used. If the signals are uncorrelated (or better, independent) the coherence function vanishes. On the other hand, if $\tilde{Y}(t)$ is the response of a linear, time-invariant system to an input $\tilde{X}(t)$, then

$$\Phi_{xy}(f) = \Phi_{xx}(f)H(f) \quad (10.41)$$

$$\Phi_{yy}(f) = \Phi_{xx}(f)|H(f)|^2 \quad (10.42)$$

Consequently, the coherence function becomes unity for this ideal case. In practice, however, the coherence function of an excitation and the corresponding response is usually less than unity. This is due to deviations such as measurement noise, system nonlinearities, and time-variant effects. Consequently, the coherence function is commonly used as a measure of the accuracy of frequency-response estimates.

10.5.6 Parseval's Theorem

For a pair of rapidly decaying (aperiodic) deterministic signals $x(t)$ and $y(t)$, the cross-correlation function is given by

$$\phi_{xy}(\tau) = \int_{-\infty}^{\infty} x(t)y(t + \tau)dt \quad (10.43)$$

This is equivalent to Equation 10.30, for a pair of ergodic, random (stochastic) signals $x(t)$ and $y(t)$. By using the definition of the inverse FIT (see Table 10.2) in Equation 10.43, and by following straightforward mathematical manipulation, it may be shown that

$$\Phi_{xy}(f) = [X(f)]^* Y(f) \quad (10.44)$$

in which the cross-spectral density $\Phi_{xy}(f)$ is the FIT of $\phi_{xy}(\tau)$, as given by

$$\Phi_{xy}(f) = \int_{-\infty}^{\infty} \phi_{xy}(\tau) \exp(-j2\pi f\tau) d\tau \quad (10.45)$$

and $[\]^*$ denotes the complex conjugation operation. This result, which is known as the correlation theorem (see Table 10.5) has applications in the evaluation of the correlation functions and PSD functions of finite-record-length data.

The inverse FIT relation corresponding to Equation 10.45 is

$$\phi_{xy}(\tau) = \int_{-\infty}^{\infty} \Phi_{xy}(f) \exp(j2\pi f\tau) df \quad (10.46)$$

From Equation 10.44, we have

$$\phi_{xy}(\tau) = \int_{-\infty}^{\infty} [X(f)]^* Y(f) \exp(j2\pi f\tau) df \quad (10.47)$$

If we set $\tau = 0$ and $x = y$ in Equation 10.47, we get

$$\phi_{xy}(0) = \int_{-\infty}^{\infty} |Y(f)|^2 df \quad (10.48)$$

Similarly, from Equation 10.43, we get

$$\phi_{xy}(0) = \int_{-\infty}^{\infty} y^2(t) dt \quad (10.49)$$

By comparing Equation 10.48 and Equation 10.49, we obtain Parseval's theorem and thus

$$\int_{-\infty}^{\infty} y^2(t) dt = \int_{-\infty}^{\infty} |Y(f)|^2 df \quad (10.50)$$

By using the discrete correlation theorem in an analogous manner, we can establish the discrete version of Equation 10.50:

$$\Delta T \sum_{m=0}^{N-1} y_m^2 = \Delta F \sum_{n=0}^{N-1} |Y_n|^2 \quad (10.51)$$

These results are listed in the second row of Table 10.5.

10.5.7 Window Functions

Consider the unit box-car function $w(t)$, defined as

$$w(t) = \begin{cases} 1 & \text{for } -0 \leq t < T \\ 0 & \text{otherwise} \end{cases} \quad (10.52)$$

TABLE 10.6 Some Common Window Functions

Function Name	Time-Domain Representation $[w(t)]$	Frequency-Domain Representation $[W(f)]$
Box-car	$\begin{cases} 1 & \text{for } 0 \leq t < T \\ 0 & \text{otherwise} \end{cases}$	$\frac{1}{j2\pi f} [1 - \cos 2\pi fT + j \sin 2\pi fT]$
Hanning	$\begin{cases} \frac{1}{2} + \frac{1}{2} \cos \frac{\pi t}{T} & \text{for } t < T \\ 0 & \text{otherwise} \end{cases}$	$\frac{T \sin 2\pi fT}{2\pi fT[1 - (2fT)^2]}$
Parzen	$\begin{cases} 1 - 6\left[\frac{t}{T}\right]^2 + 6\left[\frac{ t }{T}\right]^3 & \text{for } t < \frac{T}{2} \\ 2\left[1 - \frac{ t }{T}\right]^3 & \text{for } \frac{T}{2} < t \leq T \\ 0 & \text{otherwise} \end{cases}$	$\frac{3}{4} T \left[\frac{\sin \pi fT/2}{\frac{1}{2} \pi fT} \right]^4$
Bartlett	$\begin{cases} 1 - \frac{ t }{T} & \text{for } t \leq T \\ 0 & \text{otherwise} \end{cases}$	$T \left[\frac{\sin \pi fT}{\pi fT} \right]^4$

This is shown in Figure 10.15(b). The FIT of $w(t)$ is

$$W(f) = \frac{1}{j2\pi f} [1 - \cos 2\pi fT + j \sin 2\pi fT]$$

(10.53)

Clearly, this (rectangular) window function produces side lobes (leakage) in the frequency domain.

In spectral analysis of vibration signals, it is often required to segment the time history into several parts, and then perform spectral analysis on the individual results to observe the time development of the spectrum. If segmenting is done by simple truncation (multiplication by the box-car window), the process would introduce rapidly fluctuating side lobes into spectral results. Window functions, or smoothing functions other than the box-car function, are widely used to suppress the side lobes (leakage error). Some common smoothing functions are defined in Table 10.6.

A graphical comparison of these four window types is given in Figure 10.16. Hanning windows are very popular in practical applications. A related window is the Hamming window, which is simply a Hanning window with rectangular cut-offs at the two ends. A Hamming window will have characteristics similar to those of a Hanning window, except that the side lobe fall-off rate at higher frequencies is less in the Hamming window.

From Figure 10.16(b), we observe that the frequency-domain weight of each window varies with the frequency range of interest. Obviously, the box-car window is the worst. In practical applications, the performance of any window could be improved by simply increasing the window length T . In addition, a window in the shape of a Gaussian function may be used when a rapid roll-off without side lobes is desired.

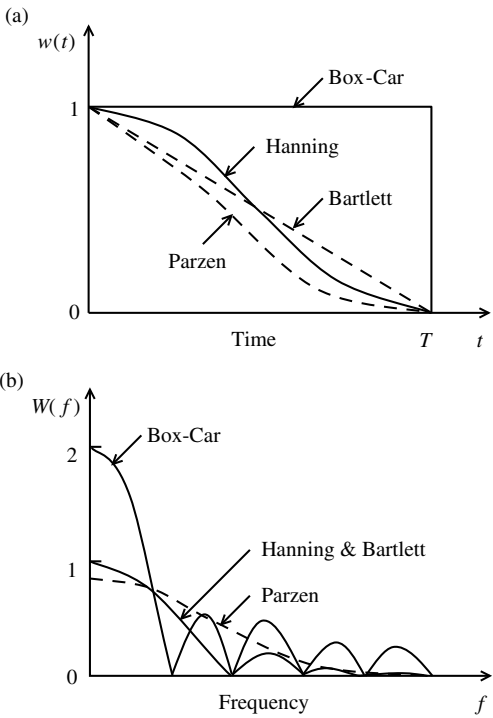


FIGURE 10.16 Some common window functions. (a) Time-domain function; (b) frequency spectrum.

TABLE 10.7 Signal Types and Appropriate Windows

Signal Type	Window
Periodic with period = T	Rectangular
Rapid transients within $[0, T]$	Gaussian
Periodic with period $\neq T$	Flat-top cosine
Quasi-periodic	Hamming
Slow transients beyond $[0, T]$	Hanning
Nonstationary random	Gaussian
Beat-like signals with period $\approx T$	Bartlett (triangular)
Narrow-band random	Rectangular
Stationary random	Hamming
Important low-level components mixed with widely spaced high-level spectral components	Parzen
Broad-band random (white noise, pink noise, etc.)	Gaussian

Characteristics of the signal that is being analyzed and also the nature of the system that generates the signal should be considered in choosing an appropriate truncation window. In particular, the Hanning window is recommended for signals generated by heavily damped systems and the Hamming window is recommended for use with lightly damped systems. Table 10.7 lists some useful signal types and appropriate window functions.

10.5.8 Spectral Approach to Process Monitoring

In mechanical systems, component degradation may be caused by vibrating excitations, which can result in malfunction or failure. In this sense, continuous monitoring during testing of mechanical deterioration in various critical components of a vibratory system is of prime importance. This usually cannot be done by simple visual observation, unless malfunction is detected by operability monitoring of the system. However, since mechanical degradation is always associated with a change in vibration level, by continuously monitoring the development of Fourier spectra in time (during system operation) at various critical locations of the system, it is possible to conveniently detect any mechanical deterioration and impending failure. In this respect, real-time Fourier analysis is very useful in process monitoring and failure detection and prediction. Special-purpose real-time analyzers with the capability of spectrum comparison (often done by an external command) are available for this purpose.

Various mechanical deteriorations manifest themselves at specific frequency values. A change in spectrum level at a particular frequency (and its multiples) would indicate a specific type of mechanical degradation or component failure. An example is given in Figure 10.17, which compares the Fourier spectrum at a monitoring location of a vibratory system at the start of test with the Fourier spectrum after some mechanical degradation has taken place. To facilitate spectrum comparison within a narrow-frequency band, it is customary to plot such Fourier spectra on a linear frequency axis. It is seen that the overall spectrum levels have increased as a result of mechanical degradation. Also, a significant change has occurred near 30 Hz. This information is useful in diagnosing the cause of degradation or malfunction. Figure 10.17 might indicate, for example, impending failure of a component having resonant frequency close to 30 Hz.

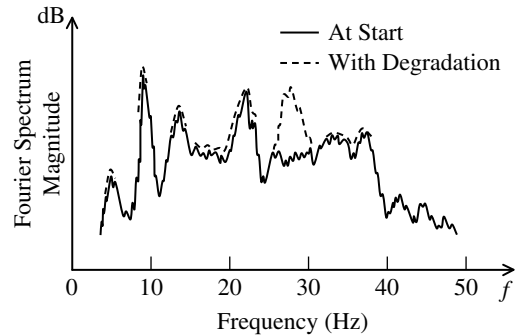


FIGURE 10.17 Effect of mechanical degradation on a monitored Fourier spectrum.

10.5.9 Cepstrum

A function known as the *cepstrum* is sometimes used to facilitate the analysis of Fourier spectrum in detecting mechanical degradation. The cepstrum (complex) $C(\tau)$ of a Fourier spectrum $Y(f)$ is defined by

$$C(\tau) = \mathcal{F}^{-1} \log Y(f) \quad (10.54)$$

The independent variable τ is known as quefrency, and it has the units of time.

An immediate advantage of cepstrum arises from the fact that the logarithm of the Fourier spectrum is taken. From Equation 10.33 it is clear that, for a system having frequency-transfer function $H(f)$, and excited by a signal having Fourier spectrum $U(f)$, the response Fourier spectrum $Y(f)$ could be expressed in the logarithmic form:

$$\log Y(f) = \log H(f) + \log U(f) \quad (10.55)$$

Since the right-hand side terms are added rather than multiplied, any variation in $H(f)$ at a particular frequency will be less affected by a possible low-spectrum level in the excitation $U(f)$ at that frequency, when considering $\log Y(f)$ rather than $Y(f)$. Consequently, any degradation will be more conspicuous in the cepstrum than in the Fourier spectrum. Another advantage of cepstrum is that it is better capable of detecting variation in phenomena that manifest themselves as periodic components in the Fourier spectrum (for example, harmonics and sidebands). Such phenomena, which appear as repeated peaks in the Fourier spectrum, occur as a single peak in the cepstrum, and so any variations can be detected more easily.

10.6 Other Topics of Signal Analysis

In this section, we will briefly address some other important topics of signal analysis. We will start by discussing bandwidth in different contexts then we will present several practically useful analysis procedures and results on vibration signals.

10.6.1 Bandwidth

Bandwidth has different meanings depending on the particular context and application. For example, when studying the response of a dynamic system, the bandwidth relates to the fundamental resonant frequency, and correspondingly to the speed of response for a given excitation. In band-pass filters, the bandwidth refers to the frequency band within which the frequency components of the signal are allowed through the filter, the frequency components outside the band being rejected by it. With respect to measuring instruments, bandwidth refers to the range frequencies within which the instrument measures a signal accurately. Note that these various interpretations of bandwidth are somewhat related. For example, if a signal passes through a band-pass filter, then we know that its frequency content is within the bandwidth of the filter; but we cannot determine the actual frequency content of the signal through

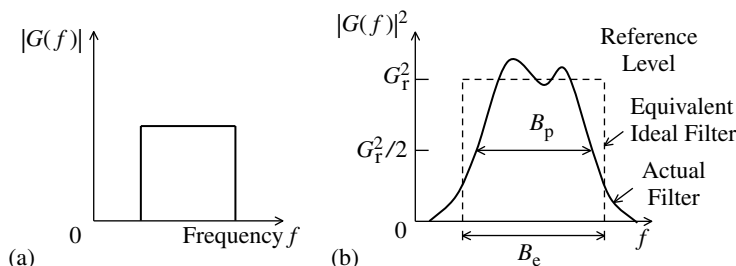


FIGURE 10.18 Characteristics of (a) an ideal band-pass filter; (b) a practical band-pass filter.

such an observation. In this context, the bandwidth appears to represent a frequency uncertainty in the observation (i.e., the larger the bandwidth of the filter, the less certain the actual frequency content of a signal that is allowed through the filter).

10.6.2 Transmission Level of a Band-Pass Filter

Practical filters can be interpreted as dynamic systems. In fact all physical, dynamic systems (e.g., mechanical structures) are analog filters. It follows that the filter characteristic can be represented by the frequency-transfer function $G(f)$ of the filter. A magnitude squared plot of such a filter transfer function is shown in Figure 10.18. In a logarithmic plot the magnitude-squared curve is obtained by simply doubling the corresponding magnitude (Bode plot) curve. Note that the actual filter transfer function (Figure 10.18(b)) is not flat like the ideal filter shown in Figure 10.18(a). The reference level G_r is the average value of the transfer function magnitude in the neighborhood of its peak.

10.6.3 Effective Noise Bandwidth

Effective noise bandwidth of a filter is equal to the bandwidth of an ideal filter that has the same reference level and that transmits the same amount of power from a white noise source. Note that white noise has a constant (flat) PSD. Hence, for a noise source of unity PSD, the power transmitted by the practical filter is given by

$$\int_0^{\infty} |G(f)|^2 df$$

which, by definition, is equal to the power $G_r^2 B_e$ transmitted by the equivalent ideal filter. Hence, the effective noise bandwidth B_e is given by

$$B_e = \int_0^{\infty} |G(f)|^2 df / G_r^2 \quad (10.56)$$

10.6.4 Half-Power (or 3 dB) Bandwidth

Half of the power from a unity-PSD noise source, as transmitted by an ideal filter, is $G_r^2 B_r / 2$. Hence, $G_r / \sqrt{2}$ is referred to as the *half-power level*. This is also known as a 3 dB level because $20 \log_{10} \times \sqrt{2} = 10 \log_{10} 2 = 3$ dB. (Note: 3 dB refers to a power ratio of 2 or an amplitude ratio of $\sqrt{2}$. Furthermore, 20 dB corresponds to an amplitude ratio of 10 or a power ratio of 100). The 3 dB (or half-power) bandwidth corresponds to the width of the filter transfer function at the half-power level. This is denoted by B_p in Figure 10.18(b). Note that B_e and B_p are different in general. However, in an ideal case where the magnitude-squared filter characteristic has linear rise and fall-off segments, these two bandwidths are equal (see Figure 10.19).

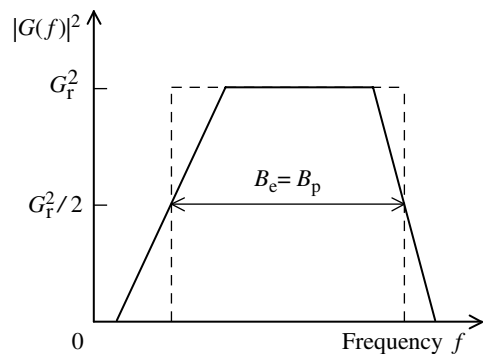


FIGURE 10.19 An idealized filter with linear segments.

10.6.5 Fourier Analysis Bandwidth

In Fourier analysis, bandwidth is interpreted, again, as the *frequency uncertainty* in the spectral results. In analytical FIT results, which assume that the entire signal is available for analysis, the spectrum is

continuously defined over the entire frequency range $[-\infty, \infty]$ and the frequency increment df is infinitesimally small ($df \rightarrow 0$). There is no frequency uncertainty in this case, and the analysis bandwidth is infinitesimally narrow.

In digital Fourier transform, the discrete spectral lines are generated at frequency intervals of ΔF . This finite frequency increment ΔF , which is the frequency uncertainty, is therefore the analysis bandwidth B for this analysis. Note that $\Delta F = 1/T$, where T is the record length (or window length for a rectangular window). It follows also that the minimum frequency that has a meaningful accuracy is the bandwidth. This interpretation for analysis bandwidth is confirmed by noting the fact that harmonic components of frequency less than ΔF (or period greater than T) cannot be studied by observing a signal record of length less than T . Analysis bandwidth carries information regarding distinguishable minimum frequency separation in computed results. In this sense bandwidth is directly related to the frequency resolution of analyzed results. The accuracy of analysis increases by increasing the record length T (or decreasing the analysis bandwidth B).

When a time window other than the rectangular window is used to truncate a measured vibration signal, then reshaping of data occurs according to the shape of the window. This reshaping reduces leakage due to suppression of side lobes of the Fourier spectrum of the window. At the same time, however, an error is introduced due to the information lost through data reshaping. This error is proportional to the bandwidth of the window itself. The effective noise bandwidth of a rectangular window is only slightly less than $1/T$, because the main lobe of its Fourier spectrum is nearly rectangular. Hence, for all practical purposes, the effective noise bandwidth can be taken as the analysis bandwidth. Note that data truncation (multiplication in the time domain) is equivalent to convolution of the Fourier spectrum (in the frequency domain). The main lobe of the spectrum uniformly affects all spectral lines in the discrete spectrum of the data signal. It follows that a window main lobe having a broader bandwidth (effective noise bandwidth) introduces a larger error into the spectral results. Hence, in digital Fourier analysis, bandwidth is taken as the effective noise bandwidth of the time window that is employed.

10.6.6 Resolution in Digital Fourier Results

Resolution is the frequency separation between spectral lines in digital Fourier-analysis results. For a data record of length T , the resolution is $\Delta F = 1/T$ irrespective of the type of window used. There is a noteworthy distinction between analysis bandwidth and resolution. Suppose that we have a data record of length T . If we double the length by augmenting it with trailing zeros, digital Fourier analysis of the resulting record of length $2T$ will yield a spectral line separation of $1/(2T)$. Thus, the resolution is halved. But, unless the true signal value is also zero in the second time interval $t[T, 2T]$, no new information is presented in the augmented record of duration $[0, 2T]$ in comparison to the original record of duration $[0, T]$. So, the analysis bandwidth (a measure of accuracy) will remain unchanged. If, on the other hand, the signal itself was sampled over $[0, 2T]$ and the resulting $2N$ data points were used in digital Fourier analysis, the bandwidth as well as the resolution would be halved.

Some relations that are useful in the digital computation of spectral results for signals are summarized in Box 10.3.

10.7 Overlapped Processing

Digital Fourier analysis is performed on blocks of sampled data (e.g., $2^{10} = 1024$ samples at a time). In overlapped processing, each data block is made to include part of the previous data block that was analyzed. After completing a computation, the overlapped data at the end of the computed block is moved to the beginning of the block, and the leading vacancy is filled with new data so that the end data in one block is identical to the beginning data in the next block, in the overlapped region. In other words, the overlapped portions of each data block (the two end portions) are processed twice. It follows that if there is 50% (or more) overlapping then the entire data block is processed twice. Three main reasons can

Box 10.3

USEFUL RELATIONS FOR DIGITAL SPECTRAL COMPUTATIONS

$$\mathcal{F} y(t) \xrightarrow[\text{(FFT)}]{\text{DFT}} Y(f)$$

Fourier spectrum

$$\frac{1}{T} Y^*(f) Y(f)$$

= Power spectral density (PSD)

Power spectrum

= $B \times$ Power spectral density

$$= \frac{B}{T} Y^*(f) Y(f)$$

Energy spectrum

= $T \times$ Power spectrum

$$= B Y^*(f) Y(f)$$

Energy spectral density

= $\frac{1}{B} \times$ Energy spectrum

$$= Y^*(f) Y(f)$$

RMS spectra

(always shown for
+ve frequencies only)

$$= \left[\frac{2}{B} \int_f^{f+B} |Y(f')|^2 df' \right]^{1/2}$$

* one sided
* like $|Y(f)|$ but smoother
* no phase information
* increase $B \rightarrow$ high
bandwidth

Note:

T = Record length

B = Bandwidth of digital analysis (minimum frequency for which meaningful results are obtained) \rightarrow includes window effect

Periodic or stationary signals
(infinite energy)

Use power spectra

Transient signals (finite energy)

Energy spectra can be used

One-sided spectrum = $2 \times$ (+ve frequency part of two-sided spectrum)

Coherent output power = coherence $\gamma_{yy}^2 \times$ output power \leftarrow could be power spectrum (spectrum or spectral density) or PSD of the output

be given for using overlapped processing in digital Fourier analysis:

1. It is an effective means of averaging spectral results.
2. It reduces the waiting time for assembling the data buffer.
3. It reduces the error caused by the end shaping effect of time windows (when a window other than the rectangle window is used).

From reasons 1 and 2, it is clear that, due to overlapping, the statistical error of computations is reduced for the same speed of computation, and the computing power is more efficiently used. To explain reason 3, let us examine [Figure 10.20](#). This example shows a 50% overlap in data. It is seen that the window function can be assumed to be relatively flat, at least over 50% of the window length (record length). Then the entire data block will correspond to the flat part of the window in three successive analyses. Consequently, the shaping error (or the error due to increased analysis bandwidth) that is caused by a nonrectangular time window is virtually eliminated by overlapped processing. The flatness of a time window is determined by its effective noise bandwidth B_e . The effective record length T_e is defined as

$$T_e = \frac{1}{B_e} \quad (10.57)$$

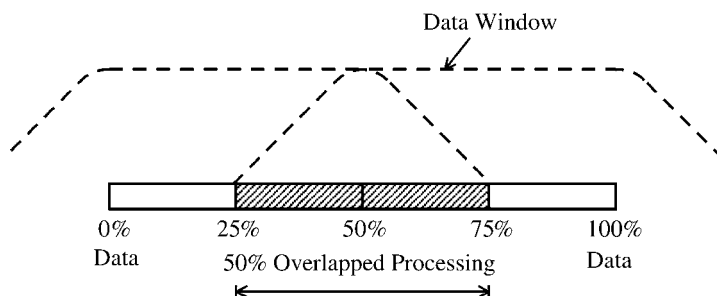


FIGURE 10.20 Overlapped processing of windowed signals.

which provides a measure for the flat segment of the window. The percentage effective record length is given by T_e as a percentage of the actual record length T . The degree of overlapping is chosen using the relation

$$\% \text{overlap} = 100 \left(1 - \frac{T_e}{T} \right) \quad (10.58)$$

Example 10.3

For a Hamming window, $B_e = 1.4/T$. Hence, a typical value for the percentage overlap is

$$100 \left(1 - \frac{1}{1.4} \right) = 29\%$$

We might want to use a conservative overlap and even go up to 50% in this case because the window is not quite flat.

10.7.1 Order Analysis

Speed related vibrations in rotation machinery may be analyzed through order analysis. Machinery vibrations under start-up (accelerating) and shut-down (decelerating) conditions are analyzed in this manner. Orders represent the rotating-speed-related frequency components in a response signal. The ratio of the response frequency to the rotating speed is termed “order.”

Order analysis is done essentially through digital Fourier analysis of a rotating-speed-related response signal. Practically, this may be accomplished in many ways. The format in which the spectral results are presented will depend on the procedure used in order analysis. Some of the typical formats of data presentation are given below.

10.7.1.1 Speed-Spectral Map

As the rotating speed of a machine is changing in a given range, the Fourier spectrum of the response signal is determined for equal increments of speed. The results are presented as a speed spectral map which is a three-dimensional cascade diagram (or *waterfall display*). The two base axes of the plot are spectral frequency and rotating speed. The third axis gives the spectral magnitude (see Figure 10.21). These types of plots are useful in identifying order-related components during start-up or coast-down conditions. Note that for each speed the frequency band of digital Fourier analysis is kept the same (i.e., fixed sampling rate). Each distinct crest trace denotes an order-related resonance. The fact that these traces are almost straight lines indicates the significance of order (the ratio, frequency/rotating speed) in exciting these resonances.

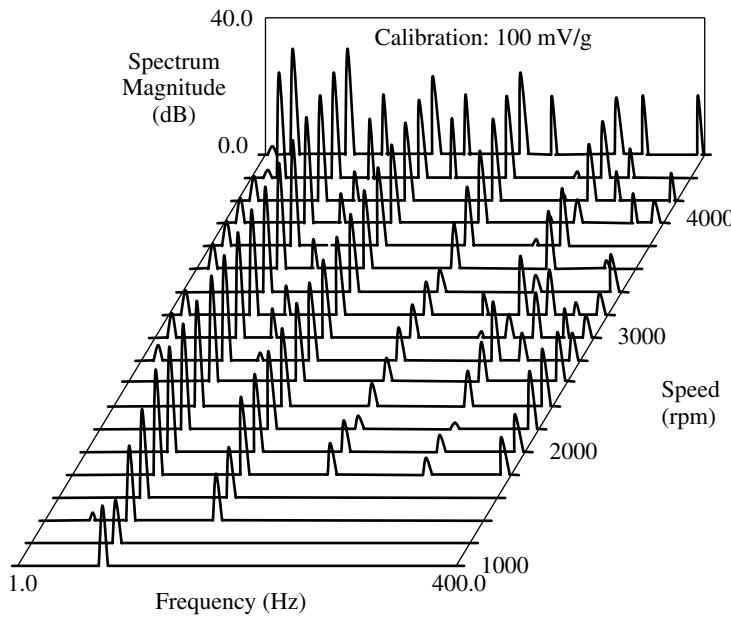


FIGURE 10.21 A speed-spectral map obtained from order analysis.

10.7.1.2 Time-Spectral Map

Under variable speed conditions (not necessarily accelerating or decelerating) the response signal is Fourier analyzed at equal increments of time. The results are plotted in a *cascade diagram*, with frequency and time as the base axes. The third axis again represents the magnitude of the Fourier spectrum (see Figure 10.22). In this case, the crest traces are not necessarily straight, and can change their orientation arbitrarily. This variation in crest orientation is determined by the degree of speed variation.

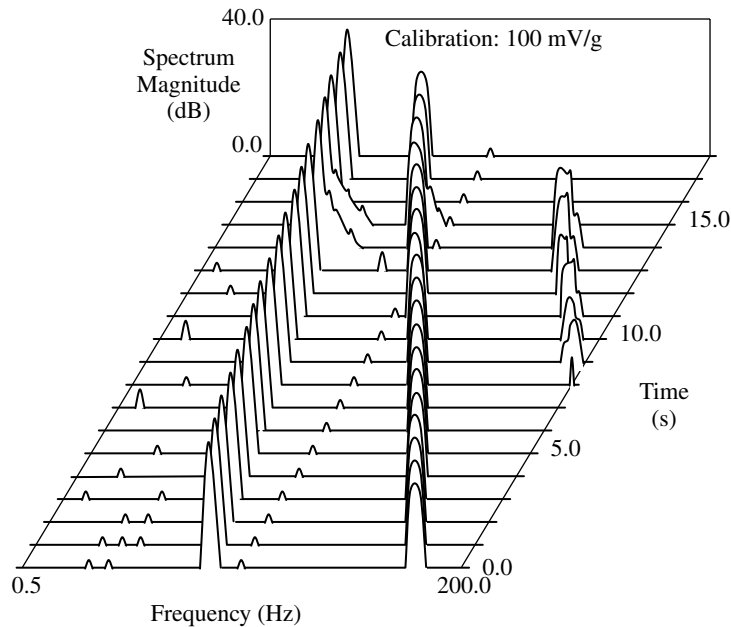


FIGURE 10.22 A time-spectral map obtained from order analysis.

10.7.1.3 Order Tracking

In order tracking, a “tracking frequency multiplier” monitors the rotating speed of the machine (as for a speed-spectral map). But, in the present case, the sampling rate of the response signal (for Fourier analysis) is changed in proportion to the rotating speed. Note that, in this manner, the maximum useful frequency (approximately $400/512 \times \text{Nyquist Frequency}$) is increased as the rotating speed increases, so that the aliasing effects are reduced. If the same sampling rate is used for high speeds (as in the Speed-Spectral Map discussed above), aliasing error can be significant at high rotating speeds.

In presenting order tracking spectral results, the frequency axis is typically calibrated in orders. Both speed-spectral maps and time-spectral maps may be presented in this manner. Other types of data presentation may be used as well in order analysis. For example, instead of the Fourier spectrum of the response signal, power spectrum or composite power spectrum (in which the total signal power is computed in specified frequency bands and presented as a function of the rotating speed) may be used in the schemes described in this section.

Order analysis provides information on most severe operating speeds with respect to vibration (and dynamic stress). For example, suppose that, for a given speed of operation, two major resonances occur, one at 10 Hz and the other at 80 Hz. Then, the structure of the system (rotating machine and its support fixtures) should be modified to change and preferably damp out these resonances. Furthermore, the most desirable operating speed can be chosen in terms of the lowest resonant peaks by observing a speed-spectral map.

Bibliography

- Bendat, J.S. and Piersol, A.G. 1971. *Random Data: Analysis and Measurement Procedures*, Wiley-Interscience, New York.
- Brigham, E.O. 1974. *The Fast Fourier Transform*, Prentice Hall, Englewood Cliffs, NJ.
- Broch, J.T. 1980. *Mechanical Vibration and Shock Measurements*, Bruel and Kjaer, Naerum.
- de Silva, C.W. 1983. *Dynamic Testing and Seismic Qualification Practice*, D.C. Heath and Co., Lexington, MA.
- de Silva, C.W., Optimal estimation of the response of internally damped beams to random loads in the presence of measurement noise, *J. Sound Vib.*, 47, 4, 485–493, 1976.
- de Silva, C.W., The digital processing of acceleration measurements for modal analysis, *Shock Vib. Dig.*, 18, 10, 3–10, 1986.
- de Silva, C.W. 2000. *Vibration — Fundamentals and Practice*, CRC Press, Boca Raton, FL.
- de Silva, C.W. 2004. *Mechatronics — An Integrated Approach*, CRC Press, Boca Raton, FL.
- Ewins, D.J. 1984. *Modal Testing: Theory and Practice*, Research Studies Press Ltd, Letchworth.
- MATLAB Control Systems Toolbox, The Math Works, Inc., Natick, MA, 2004.
- Meirovitch, L. 1980. *Computational Methods in Structural Dynamics*, Sijthoff & Noordhoff, Rockville, MD.
- Randall, R.B. 1977. *Application of B&K Equipment to Frequency Analysis*, Bruel and Kjaer, Naerum.

Wavelets — Concepts and Applications

Pol D. Spanos

Rice University

Giuseppe Failla

Università degli Studi

Mediterranea di Reggio Calabria

Nikolaos P. Politis

Rice University

11.1	Introduction	11-1
11.2	Time–Frequency Analysis	11-2
	Gabor Transform • Wavelet Transform • Wavelet Families	
11.3	Time-Dependent Spectra Estimation of Stochastic Processes	11-11
11.4	Random Field Simulation	11-14
11.5	System Identification	11-15
11.6	Damage Detection	11-17
11.7	Material Characterization	11-18
11.8	Concluding Remarks	11-19

Summary

Section 11.1 provides a brief introduction to wavelet concepts in vibration-related applications. Aspects of time–frequency analysis are discussed in Section 11.2. Specifically, the Gabor and wavelet transforms are outlined. Further, several wavelet families commonly used in vibration-related applications are presented. Estimation of time-dependent spectra of stochastic processes is considered in Section 11.3. Section 11.4 to Section 11.7 discuss applications of wavelet analysis in vibration-related applications. In particular, applications in random field simulation, system identification, damage detection, and material characterization are examined. Section 11.8 provides an overview and concluding remarks on the applicability and usefulness of the wavelet analysis in vibration theory. To enhance the usefulness of this chapter, a list of readily available references in the form of books and archival articles is provided.

11.1 Introduction

Wavelets-based representations offer an important option for capturing localized effects in many signals. This is achieved by employing representations *via* double integrals (continuous transforms), or *via* double series (discrete transforms). Seminal to these representations are the processes of *scaling* and *shifting* of a generating (*mother*) function. Over a period of several decades, wavelet analysis has been set on a rigorous mathematical framework and has been applied to quite diverse fields. Wavelet families associated with specific mother functions have proven quite appropriate for a variety of problems. In this context, fast decomposition and reconstruction algorithms ensure computational efficiency, and rival classical spectral analysis algorithms such as the fast Fourier transform (FFT). The field of vibration analysis has benefited from this remarkable mathematical development in conjunction with vibration monitoring, system identification, damage detection, and several other tasks. There is a voluminous body

of literature focusing on wavelet analysis. However, this chapter has the restricted objective of, on one hand, discussing concepts closely related to vibration analysis, and on the other hand, citing sources that can be readily available to a potential reader. In view of this latter objective, almost exclusively books and archival articles are included in the list of references. First, theoretical concepts are briefly presented; for more mathematical details, the reader may consult references [1–23]. Next, the theoretical concepts are supplemented by vibration-analysis-related sections on time-varying spectra estimation, random field synthesis, structural identification, damage detection, and material characterization. It is noted that most of the mathematical developments pertain to the interval $[0,1]$ relating to dimensionless independent variables derived by normalization with respect to the spatial or temporal “lengths” of the entire signals.

11.2 Time–Frequency Analysis

A convenient way to introduce the wavelet transform is through the concept of time–frequency representation of signals. In the classical Fourier theory, a signal can be represented either in the time or in the frequency domain, and the Fourier coefficients define the average spectral content over the entire duration of the signal. The Fourier representation is appropriate for signals that are stationary, in terms of parameters which are deemed important for the problem in hand, but becomes inadequate for nonstationary signals, in which important parameters may evolve rapidly in time.

The need for a time–frequency representation is obvious in a broad range of physical problems, such as acoustics, image processing, earthquake and wind engineering, and a plethora of others. Among the time–frequency representations available to date, the wavelet transform has unique features in terms of efficacy and versatility. In mathematical terms, it involves the concept of *scale* as a counterpart to the concept of frequency in the Fourier theory. Thus, it is also referred to as time-scale representation. Its formulation stems from a generalization of a previous time–frequency representation, known as the Gabor transform. For completeness, and to underscore the significant advantages achieved by the development of the wavelet transform, the Gabor transform is briefly discussed in Section 11.2.1. Section 11.2.2 is entirely devoted to the wavelet transform, and the most commonly used wavelet families are described in Section 11.2.3.

11.2.1 Gabor Transform

The first steps in time–frequency analysis trace back to the work of Gabor [24], who applied in signal analysis fundamental concepts developed in quantum mechanics by Wigner a decade earlier [25]. Given a function $f(t)$ belonging to the space of finite-energy one-dimensional functions, denoted by $L^2(\mathbb{R})$, Gabor introduced the transform

$$G_f(\omega, t_0) = \int_{-\infty}^{\infty} f(t) \overline{g(t - t_0)} e^{-i\omega(t - t_0)} dt \quad (11.1)$$

where $g(t)$ is a window and the bar ($\bar{}$) denotes complex conjugation. This transform, generally referred to as the *continuous Gabor transform* (CGT) or the short-time Fourier transform of $f(t)$, is a complete representation of $f(t)$. That is, the original function $f(t)$ can be reconstructed as

$$f(t) = \frac{1}{2\pi \|g\|^2} \int_{-\infty}^{\infty} \int_{-\infty}^{\infty} G_f(\omega, t_0) g(t - t_0) e^{i\omega(t - t_0)} d\omega dt_0 \quad (11.2)$$

where $\|g\|^2 = \int_{-\infty}^{\infty} |g(t)|^2 dt$. The Gabor transform (Equation 11.1) may be seen as the projection of $f(t)$ onto the family $\{g_{(\omega, t_0)}(t); \omega, t_0 \in \mathbb{R}\}$ of *shifted* and *modulated* copies (atoms) of $g(t)$ expressed in the form

$$g_{(\omega, t_0)}(t) = e^{i\omega(t - t_0)} g(t - t_0) \quad (11.3)$$

These time–frequency atoms, also referred to as Gabor functions, are shown in [Figure 11.1](#) for three different values of ω . Clearly, if $g(t)$ is an appropriate window function, then Equation 11.1 may be regarded as the standard Fourier transform of the function $f(t)$, localized at the time t_0 . In this context, t_0 is the

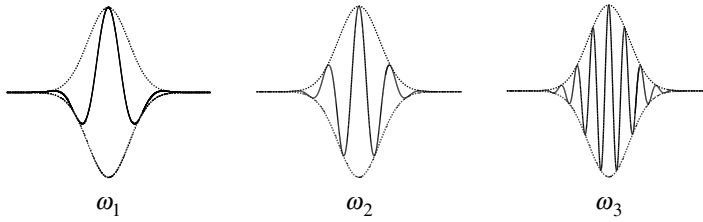


FIGURE 11.1 Plots of Gabor function $g(\omega, t_0)$ versus the independent variable x for three values of the frequency ω ; the effective support is the same for the three values of the frequency.

time parameter which gives the center of the window, and ω is the frequency parameter which is used to compute the Fourier transform of the windowed signal.

As intuition suggests, the accuracy of the CGT representation (Equation 11.2) of $f(t)$ depends on the window function $g(t)$, which must exhibit good localization properties both in the time and the frequency domains. As discussed in Ref. [6], a measure of the localization properties may be obtained by the average and the standard deviation of the density $|g(t)|^2$ in the time domain. That is,

$$\langle t \rangle = \int_{-\infty}^{\infty} t |g(t)|^2 dt \quad (11.4a)$$

$$\sigma_t^2 = \int_{-\infty}^{\infty} (t - \langle t \rangle)^2 |g(t)|^2 dt \quad (11.4b)$$

The counterparts of Equation 11.4a and Equation 11.4b in the frequency domain are

$$\langle \omega \rangle = \int_{-\infty}^{\infty} \omega |\hat{G}(\omega)|^2 d\omega \quad (11.5a)$$

$$\sigma_\omega^2 = \int_{-\infty}^{\infty} (\omega - \langle \omega \rangle)^2 |\hat{G}(\omega)|^2 d\omega \quad (11.5b)$$

where $\hat{G}(\omega)$ denotes the Fourier transform of $g(t)$ given by the equation

$$\hat{G}(\omega) = \frac{1}{\sqrt{2\pi}} \int_{-\infty}^{\infty} g(t) e^{-i\omega t} dt \quad (11.6)$$

The well-known *Heisenberg uncertainty principle* is in actuality a mathematically proven property and states that the values σ_t and σ_ω cannot be independently small [6]. Specifically, for an arbitrary window normalized so that $\|g\|^2 = 1$, it can be shown that

$$\sigma_t \sigma_\omega \geq \frac{1}{2} \quad (11.7)$$

Thus, high resolution in the time domain (small value of σ_t) may be generally achieved only at the expense of a poor resolution (bigger than a minimum value σ_ω) in the frequency domain and *vice versa*. Note that the optimal time–frequency resolution, that is $\sigma_t \sigma_\omega = 1/2$, may be attained when the Gaussian window

$$g(t) = \frac{1}{\sqrt{4\pi\sigma_t^2}} \exp\left(-\frac{t^2}{4\sigma_t^2}\right) \quad (11.8)$$

is selected.

Clearly, as a time–frequency representation, the Gabor transform exhibits considerable limitations. The time support, governed by the window function $g(t)$, is equal for all of the Gabor functions (Equation 11.3) for all frequencies (see Figure 11.1). In order to achieve good localization of high-frequency components, narrow windows are required; as a result of that, low-frequency components are poorly represented. Thus, a more flexible representation with nonconstant windowing is quite desirable,

to enhance the time resolution for short-lived high-frequency phenomena and frequency resolution for long-lasting low-frequency phenomena.

11.2.2 Wavelet Transform

The preceding shortcomings of the Gabor transform have been overcome with significant effectiveness and efficiency by wavelets-based signal representation. Its two formulations, continuous and discrete, are described in the ensuing sections. Because of the numerous applications of wavelets beyond time–frequency analysis, the t -time domain will be replaced by a generic x -space domain. For succinctness, the formulation will be developed for scalar functions only, but generalization for multidimensional spaces is well established in the literature [1–22].

11.2.2.1 Continuous Wavelet Transform

The concept of wavelet transform was introduced first by Goupillaud et al. for seismic records analysis [26,27]. In analogy to the Gabor transform, the idea consists of decomposing a function $f(x)$ into a two-parameter family of elementary functions, each derived from a basic or *mother wavelet*, $\psi(x)$. The first parameter, a , corresponds to a dilation or compression of the mother wavelet that is generally referred to as *scale*. The second parameter, b , determines a *shift* of the mother wavelet along the x -domain. In mathematical terms

$$W_f(a, b) = \frac{1}{\sqrt{a}} \int_{-\infty}^{\infty} f(x) \overline{\psi\left(\frac{x-b}{a}\right)} dx \quad (11.9)$$

where $a \in \mathbb{R}^+$, $b \in \mathbb{R}$. In the literature, Equation 11.9 is generally referred to as *continuous wavelet transform* (CWT). Note that the factor $a^{-1/2}$ is a normalization factor, included to insure that the mother wavelet and any dilated wavelet $a^{-1/2}\psi(x/a)$ have the same total energy [26]. Clearly, alternative normalizations may also be chosen [1].

An example of wavelet functions is shown in Figure 11.2 for different values of the scale parameter a . As a result of scaling, all the wavelet functions exhibit the same number of cycles within the x -support of the mother wavelet. Obviously, the spatial and frequency localization properties of the wavelet transform depend on the value of the parameter a . As a approaches zero, the dilated wavelet $a^{-1/2}\psi(x/a)$ is highly concentrated at the point $x = 0$; the wavelet transform, $W_f(a, b)$, then gives increasingly sharper spatial resolution displaying the small-scale/higher-frequency features of the function $f(x)$, at various locations b . However, as a approaches $+\infty$, the wavelet transform $W_f(a, b)$ gives increasingly coarser spatial resolution, displaying the large-scale/low-frequency features of the function $f(x)$.

For the function $f(x)$ to be reconstructable from the set of coefficients (Equation 11.9), in the form

$$f(x) = \frac{1}{\pi c_\psi} \int_0^\infty \int_{-\infty}^\infty W_f(a, b) \psi_{a,b}(x) \frac{da}{a^2} db \quad (11.10)$$

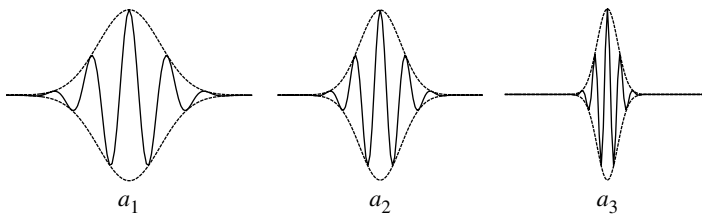


FIGURE 11.2 Plots versus time of wavelet functions corresponding to three different values of a scale a of the same mother function; the effective time support increases with the magnitude of the scale.

where $\psi_{a,b}(x) = a^{-1/2}\psi[(x-b)/a]$, the wavelet function $\psi(\cdot)$ must satisfy the admissibility condition

$$c_\psi = \int_{-\infty}^{\infty} \frac{|\hat{\Psi}(\omega)|^2}{|\omega|} d\omega < \infty \quad (11.11)$$

where $\hat{\Psi}(\omega)$ denotes the Fourier transform of $\psi(x)$. As pointed out in Ref. [26], the condition 11.11 includes a set of subconditions, such as:

1. The analyzing wavelet $\psi(\cdot)$ is absolutely integrable and square integrable. That is,

$$\int_{-\infty}^{\infty} |\psi(x)| dx < \infty \quad (11.12a)$$

$$\int_{-\infty}^{\infty} |\psi(x)|^2 dx < \infty \quad (11.12b)$$

2. The Fourier transform $\hat{\Psi}(\omega)$ must be sufficiently small at the vicinity of the origin $\omega = 0$, or in mathematical terms

$$\int_{-\infty}^{\infty} \frac{|\hat{\Psi}(\omega)|}{|\omega|} d\omega < \infty \quad (11.13)$$

Subcondition 2, then, implies that $\hat{\Psi}(0) = 0$; that is, $\int_{-\infty}^{\infty} \psi(x) dx = 0$. Therefore, for an analyzing wavelet to be admissible, its real and imaginary parts must both be symmetric with respect to the x -axis.

From the reconstruction formula (Equation 11.10), it can be shown that

$$\|f\|^2 = \frac{1}{\pi c_\psi} \int_0^\infty \int_{-\infty}^\infty |W_f(a, b)|^2 \frac{da}{a^2} db \quad (11.14)$$

Based on Equation 11.14, the square modulus of the wavelet transform (Equation 11.9) is often taken as an energy density in a spatial-scale domain. Extensive use of this concept has been made for spectra estimation purposes, as discussed in Section 11.3.

Note that the reconstruction wavelet in Equation 11.10 can be different from the analyzing wavelet used in Equation 11.9. That is, under some admissibility conditions on $\chi(x)$ [1], the original function $f(x)$ may be reconstructed as

$$f(x) = \frac{1}{c_{\psi\chi}} \int_0^\infty \int_{-\infty}^\infty W_f(a, b) \chi_{a,b}(x) \frac{da}{a^2} db \quad (11.15)$$

where $\chi_{a,b}(x) = a^{-1/2}\chi[(x-b)/a]$ and $c_{\psi\chi}$ is a constant parameter depending on the Fourier transforms of both $\psi(x)$ and $\chi(x)$. This property, referred to as redundancy in mathematical terms, may be advantageous in some applications for reducing the error due to noise in signal reconstruction [28,29], but highly undesirable for signal coding or compression purposes [1]. Further, under certain conditions [1], the following simplified reconstruction formula holds

$$f(x) = \frac{1}{k_\psi} \int_0^\infty W_f(a, x) \frac{da}{a^{3/2}} \quad (11.16)$$

where k_ψ is a constant parameter given by the equation

$$k_\psi = \sqrt{2\pi} \int_0^\infty \frac{\hat{\Psi}(\omega)}{\omega} d\omega \quad (11.17)$$

Use of this formula has been made, in a discrete version, in the approximation theory of functional spaces [1] and also in structural identification applications, as discussed in Section 11.5.

11.2.2.2 Discrete Wavelet Transform

For numerical applications, where fast decomposition or reconstruction algorithms are generally required, a discrete version of the CWT is to prefer. In this sense, a natural way to define a *discrete wavelet transform* (DWT) is

$$W_f(j, k) = \frac{1}{\sqrt{a_0^j}} \int_{-\infty}^{\infty} f(x) \overline{\psi(a_0^{-j}x - kb_0)} dx, \quad j, k \in \mathbb{Z} \quad (11.18)$$

Equation 11.18 is derived from a straightforward discretization of the CWT (Equation 11.9) by considering the discrete lattice $a = a_0^j$, $a_0 > 1$, $b = kb_0a_0^j$, $b_0 \neq 0$. In developing Equation 11.18, however, the main mathematical concern is to ensure that *sampling* the CWT on a discrete set of points does not lead to a loss of information about the wavelet-transformed function $f(x)$. Specifically, the original function $f(x)$ must be fully recoverable from a discrete set of wavelet coefficients. That is,

$$f(x) = \sum_{j,k \in \mathbb{Z}} W_f(j, k) \psi_{j,k}(x) \quad (11.19)$$

where $\psi_{j,k}(x) = a_0^{-j/2} \psi(a_0^{-j}x - kb_0)$. Another crucial aspect in Equation 11.18 involves selecting the wavelet functions $\psi_{j,k}(x)$ such that Equation 11.19 may be regarded as the expansion of $f(x)$ in a *basis*, thus eliminating the redundancy of the CWT.

This issues are addressed by using the theory of Hilbert space *frames*, introduced in 1952 by Duffin and Schaeffer in context with non-harmonic Fourier series [30]. In general, if $h_\lambda(x) \in L^2(\mathbb{R})$ and Λ is a countable set, a family of functions $\{h_\lambda(x); \lambda \in \Lambda\}$ constitutes a *frame*, if for any $f(x) \in L^2(\mathbb{R})$

$$A\|f\|^2 \leq \sum_{\lambda \in \Lambda} |\langle f, h_\lambda \rangle|^2 \leq B\|f\|^2 \quad (11.20)$$

where $\langle f, h_\lambda \rangle = \int_{-\infty}^{\infty} f(x) \overline{h_\lambda(x)} dx$ and $A > 0$, $B < \infty$, the so-called *frame bounds*, are independent of $f(x)$ [1]. The concept of frame may be interpreted as an extension of the concept of basis, in the sense that the reconstruction of the original function is possible *via* stable numerical expressions in terms of the set $\{h_\lambda(x); \lambda \in \Lambda\}$. For instance, if the frame is *tight*, that is $A = B$, the simple formula

$$f(x) = \sum_{\lambda \in \Lambda} \langle f, h_\lambda \rangle h_\lambda(x) \quad (11.21)$$

holds [29].

In contrast to a basis, however, the vectors of a frame may be linearly dependent and, for this, a certain degree of redundancy is still retained in the reconstruction formula (Equation 11.21) [29,31].

The concept of frame has played a crucial role in the formulation of the DWT. The first wavelet frames were constructed by Daubechies et al. [32]. Later, Battle [33] constructed orthonormal bases with an exponential decay. The ensemble of these results has demonstrated the advantages of the wavelet transform over the Gabor transform. In fact, it has been shown that discrete versions of Gabor transform are not capable of generating orthonormal bases [32] due to the so-called Balian–Low phenomenon [1].

Mallat [34] has shown that the orthonormal wavelet bases proposed by Battle can all be derived by a *multiresolution analysis*. The latter involves representing an arbitrary $f(x) \in L^2(\mathbb{R})$ as a limit of successive approximations, at different resolutions. That is, if $\{V_j\}_{j \in \mathbb{Z}}$ is a sequence of subspaces of $L^2(\mathbb{R})$, and f_j is the orthogonal projection of $f(x)$ on V_j , in a multiresolution analysis the following conditions hold

$$\lim_{j \rightarrow -\infty} f_j = f \quad (11.22a)$$

$$\lim_{j \rightarrow \infty} f_j = 0 \quad (11.22b)$$

Each approximation f_j , then, represents a smoothed version of $f(x)$ and, in the limit, more and more localized smoothing functions lead to the function $f(x)$. From a mathematical point of view [29,31], a

multiresolution analysis requires that

1. The subspaces V_j 's are closed and embedded, that is

$$\cdots \subset V_2 \subset V_1 \subset V_0 \subset V_{-1} \subset V_{-2} \subset \cdots \quad (11.23)$$

where $V_{-m} \rightarrow L^2(\mathbb{R})$ for $m \rightarrow \infty$ and $f \in V_m \Leftrightarrow f(2 \cdot) \in V_{m-1}$.

2. A scaling function $\phi(x) \in L^2(\mathbb{R})$ exists, such that, for each j , the family of functions

$$\phi_{j,k}(x) = 2^{-j/2} \phi(2^{-j}x - k), \quad k \in \mathbb{Z} \quad (11.24)$$

spans the subspace V_j and constitutes a Riesz basis for V_j , that is, there exists $0 < C' \leq C'' < \infty$ such that

$$C' \sum_k |c_k|^2 \leq \int_{-\infty}^{\infty} \left| \sum_k c_k \phi_{j,k}(x) \right|^2 dx \leq C'' \sum_k |c_k|^2 \quad (11.25)$$

for all sequences of numbers $(c_k)_{k \in \mathbb{Z}}$. Equation 11.25 is a more stringent condition of Equation 11.20 and includes the latter as a special case.

The concept of multiresolution analysis offers a straightforward and mathematically coherent approach to discrete wavelet analysis. Given a scaling function $\phi(x)$ as in 2, in fact, families of orthonormal wavelet bases

$$\psi_{j,k}(x) = 2^{-j/2} \psi(2^{-j}x - k), \quad j, k \in \mathbb{Z} \quad (11.26)$$

can be developed by appropriate algorithms. For this, Mallat has used the frequency response of a high-pass filter [35], while Daubechies has devised a systematic approach to build orthonormal wavelet bases with compact support in the x -domain [36]. Specifically, for each even integer $2M$, the Daubechies scaling function $\phi(x)$ can be computed as

$$\phi(x) = \sqrt{2} \sum_{k=0}^{2M-1} h_{k+1} \phi(2x - k) \quad (11.27)$$

where h_k 's are $2M$ coefficients obtained by imposing M orthogonality conditions and M accuracy conditions to enhance the rate of convergence of the approximation to the original function $f(x)$. In turn, the mother wavelet is related to the scaling function $\phi(x)$ by the equation

$$\psi(x) = \sqrt{2} \sum_{k=0}^{2M-1} g_{k+1} \phi(2x - k) \quad (11.28)$$

where g_k 's are the same as h_k 's but reversed in order and with alternate signs. Numerical values of both series h_k 's and g_k 's are readily available in the literature [16].

Also based on multiresolution analysis concepts, a wavelet decomposition algorithm for image analysis has been developed [34,35]. If associated to Daubechies wavelets, the algorithm becomes quite efficient from a computational point of view, since no numerical integration is involved to compute wavelet and scale coefficients. It relies on the projection of $f(x)$ onto a sufficiently fine scale j of the set 11.24. That is,

$$f(x) \approx f_j(x) = \sum_k c_k^j \phi_{j,k}(x) \quad (11.29)$$

where, for orthogonal wavelets,

$$c_k^j = \int_{-\infty}^{\infty} f(x) \phi_{j,k}(x) dx \quad (11.30)$$

Based on Equation 11.22a and Equation 11.22b, the projection $f_j(x)$ can be rewritten in terms of the projection $f_{j+1}(x)$ onto the coarser scale $(j+1)$ and the incremental *detail* $\delta_{j+1}(x)$, that is the pieces of

information contained in the subspace V_j and lost when “moving” to the subspace V_{j+1} . Therefore,

$$f_j(x) = f_{j+1}(x) + \delta_{j+1}(x) = f_{j+1}(x) + \delta_{j+1}(x) + \cdots + \delta_{j+1}(x) \approx \delta_{j+1}(x) + \cdots + \delta_{j+1}(x) \quad (11.31)$$

As a fundamental result of multiresolution analysis, the details $\delta_j(x)$ can be decomposed in terms of the set of wavelet functions at the same scale. That is,

$$\delta_j(x) = \sum_k d_k^j \psi_{j,k}(x) \quad (11.32)$$

where d_k^j 's are the wavelet coefficients of $f(x)$. Based on Equation 11.28, both wavelet and scale coefficients can be computed recursively by the closed-form expressions

$$c_k^j = \sum_{l=0}^{2M-1} h_{l+1} c_{2k+l-1}^{j-1} \quad (11.33a)$$

$$d_k^j = \sum_{l=0}^{2M-1} g_{l+1} c_{2k+l-1}^{j-1} \quad (11.33b)$$

Similarly, the reconstruction algorithm can be implemented by the formula

$$c_k^{j-1} = \sum_l h_{k-2l+2} c_l^j + g_{k-2l+2} d_l^j \quad (11.34)$$

The reconstruction algorithm described by Equation 11.34 lends itself to interpretation as a scale linear system [37,38]. Based on this concept, applications have also been developed for random field simulation [39].

11.2.3 Wavelet Families

A great number of wavelet families with various properties are available. Selecting an optimal family for a specific problem is not, in general, an easy task and there are properties that prove more important to certain fields of application. For instance, symmetry may be of great help for preventing dephasing in image processing, while regularity is critical for building smooth reconstructed signals or accurate nonlinear regression estimates. Compactly supported wavelets, either in the time or in the frequency domain, may be preferable for enhanced time or frequency resolution. The number of vanishing moments, M , that is the highest integer m for which the equation

$$\int_{-\infty}^{\infty} x^m \psi(x) dx = 0, \quad m = 0, 1, \dots, M-1 \quad (11.35)$$

holds is important in signal processing for compression, or in damage detection for enhancement of singularities in the vibration modes. Also, in some cases, wavelets may be required to be *progressive*. In mathematical terms, this means that their Fourier transform is defined only for positive frequencies. That is,

$$\hat{\Psi}(\omega) = 0, \quad \text{for } \omega < 0 \quad (11.36)$$

The progressive wavelet transform of a real-valued signal $f(t)$ and the associated *analytic signal*

$$z_f(t) = f(t) + iH[f(t)] \quad (11.37)$$

are related by the equation

$$W_f(a, b) = \frac{1}{2} W_{z_f}(a, b) \quad (11.38)$$

where $H[\cdot]$ denotes the Hilbert transform operator [40]. Equation 11.38 is quite useful for structural identification. Note also that significant reduction of computational costs is generally achieved if orthogonal wavelets in the frequency or in the x -domain are used.

A brief description of the most-used families is given below. A distinction is made between real and complex wavelets, and the most relevant properties for application purposes are discussed. A more exhaustive review may be found in Ref. [15].

11.2.3.1 Real Wavelets

1. *Daubechies orthonormal wavelets* — A family of bases, each corresponding to a particular value of the parameter M in Equation 11.27 and Equation 11.28 [36]. Closed-form expressions for $\phi(x)$ in Equation 11.27 are available only for $M = 1$, to which the well-known Haar basis corresponds. In this case, the scaling function and the mother wavelet are

$$\phi(x) = \begin{cases} 1, & 0 \leq x < 1, \\ 0, & \text{elsewhere,} \end{cases} \quad \psi(x) = \begin{cases} 1, & 0 \leq x < \frac{1}{2}, \\ -1, & \frac{1}{2} \leq x < 1, \\ 0, & \text{elsewhere.} \end{cases} \quad (11.39)$$

Various algorithms, however, are available in the literature for determining $\phi(x)$ and $\psi(x)$ numerically for $M > 1$.

Daubechies wavelets support both CWT and DWT, although the latter is most generally performed due to the fast decomposition and reconstruction algorithm mentioned in Section 11.2.2.2. Both $\phi(x)$ and $\psi(x)$ are compactly supported in the x -domain, and the support is equal to the segment $[0; 2M - 1]$. Also, M is equal to the number of vanishing moments of the wavelet function. Note that most Daubechies wavelets are not symmetric; regularity and harmonic-like shape increases with M .

2. *Meyer wavelets* — Families of wavelets [10], each defined for a particular choice of an auxiliary function $v(\omega)$ which appears in the following expression for the Fourier transform of the mother wavelet:

$$\hat{\Psi}(\omega) = \begin{cases} \frac{1}{\sqrt{2\pi}} e^{i\omega/2} \sin\left[\frac{\pi}{2} v\left(\frac{3}{2\pi}|\omega| - 1\right)\right], & \frac{2}{3}\pi \leq |\omega| \leq \frac{4}{3}\pi, \\ \frac{1}{\sqrt{2\pi}} e^{i\omega/2} \cos\left[\frac{\pi}{2} v\left(\frac{3}{4\pi}|\omega| - 1\right)\right], & \frac{4}{3}\pi \leq |\omega| \leq \frac{8}{3}\pi, \\ 0, & |\omega| \notin \left[\frac{2}{3}\pi, \frac{8}{3}\pi\right], \end{cases} \quad (11.40)$$

for $v(\omega)$ to be an admissible auxiliary function it is required that

$$v(\omega) = \begin{cases} 0, & \omega \leq 0, \\ 1, & \omega \geq 1, \end{cases} \quad (11.41a)$$

$$v(\omega) + v(1 - \omega) = 1, \quad 0 \leq \omega \leq 1 \quad (11.41b)$$

The most common form of $v(\omega)$ in the literature is

$$v(\omega) = \omega^4(35 - 84\omega + 70\omega^2 - 20\omega^3), \quad 0 \leq \omega \leq 1 \quad (11.42)$$

The mother wavelet, for which only numerical expressions are available, is then constructed by inverse Fourier-transforming Equation 11.40.

Meyer wavelets are suitable for both CWT and DWT. Unlike Daubechies wavelets, they are compact in the frequency domain but not in the x -domain. Because of their fast decay, however, an effective x -support $[-8, 8]$ is generally assumed. Appealing features of Meyer wavelets are orthogonality, infinite regularity, and symmetry.

3. *Mexican Hat wavelets* — A family of wavelets in the x -domain [15] related to a mother function that is proportional to the second derivative of the Gaussian probability density function.

That is,

$$\psi(x) = \frac{2}{\sqrt{3}} \pi^{-1/4} (1 - x^2) e^{-x^2/2} \quad (11.43)$$

The Mexican Hat wavelets allow CWT only. Unlike Daubechies or Meyer wavelets, Mexican Hat wavelets are not compact both in the frequency and in the x -domain, although an effective support $[-5, 5]$ may be considered for practical calculations. They are infinitely regular and symmetric.

4. *Biorthogonal wavelets* — Families of wavelets derived by generalizing the ordinary concept of wavelet bases, and creating a pair of *dual wavelets*, say $(\psi(x), \tilde{\psi}(x))$, satisfying the following properties [41,42]:

$$\int_{-\infty}^{\infty} \psi_{j,k}(x) \tilde{\psi}_{j',k'}(x) dx = \delta_{jj'} \delta_{kk'} \quad (11.44)$$

where the symbol δ_{mn} denotes the Kronecker delta. One wavelet, say $\psi(x)$, may be used for reconstruction and the dual one, $\tilde{\psi}(x)$, for decomposition. Therefore, Equation 11.18 and Equation 11.19 can be rewritten as

$$W_f(j, k) = 2^{-j/2} \int_{-\infty}^{\infty} f(x) \psi_{j,k}(2^{-j}x - k) dx, \quad j, k \in \mathbb{Z} \quad (11.45)$$

$$f(x) = \sum_{j,k \in \mathbb{Z}} W_f(j, k) \tilde{\psi}_{j,k}(x) \quad (11.46)$$

Biorthogonal wavelets support both CWT and DWT. The properties of a biorthogonal basis are specified in terms of a pair of integers (N_d, N_r) . These integers, in analogy with the Daubechies wavelets, govern the regularity and the number of vanishing moments N_d of the decomposition wavelet $\psi(x)$, and the regularity and the number of vanishing moments N_r of the reconstruction wavelet $\tilde{\psi}(x)$. Obviously, this feature allows a greater number of choices for signal decomposition and reconstruction. Both wavelet functions $\psi(x)$ and $\tilde{\psi}(x)$ are symmetric.

11.2.3.2 Complex Wavelets

5. *Harmonic wavelets* — A Family of bases defined in the frequency domain by the formula [16,43,44]:

$$\hat{\Psi}_{m,n}(\omega) = \begin{cases} \frac{1}{2\pi(n-m)}, & m\pi \leq \omega \leq n\pi, \\ 0, & \text{elsewhere,} \end{cases} \quad (11.47)$$

where m and n are positive numbers but not necessarily integers. The pair of values m, n is referred to as *level* m, n and represents, for harmonic wavelets, the scale index j . A harmonic wavelet basis thus corresponds to a complete set of adjacent levels m, n , spanning all the positive frequency axis. By inverse-Fourier transforming Equation 11.47, the corresponding wavelet functions at a generic step k on the x -domain take the complex form:

$$\psi_{m,n,k}(x) = \frac{\exp\left[in2\pi\left(x - \frac{k}{n-m}\right)\right] - \exp\left[im2\pi\left(x - \frac{k}{n-m}\right)\right]}{i2\pi(n-m)\left(x - \frac{k}{n-m}\right)} \quad (11.48)$$

A common choice for the pairs m, n is $m, n = 0, 1, 2, 4, \dots; 2^j, 2^{j+1}, \dots$. In this case, all the wavelets have octave bands, except for the first one.

Harmonic wavelets have been devised in context with a DWT, for which extremely fast decomposition and reconstruction algorithms exist. They exhibit a compact support in the frequency domain (see Equation 11.47), while in the x -domain their rate of decay away from

the wavelet's center is relatively low and proportional to x^{-1} . Further, they satisfy relevant orthogonality properties [16].

From Equation 11.48, it is seen that the real part of the wavelet is even, while the imaginary part is odd. For signal processing, this ensures that harmonic components in a signal can be detected regardless of the phase. Note that this feature cannot be achieved by real wavelets such as the Meyer wavelets, which are all self-similar, being derived from a unique mother wavelet by scaling and shifting. Also, note that orthonormal basis of real wavelets can be generated by considering either the real or the imaginary parts only of Equation 11.48. For instance, the well-known Shannon wavelets correspond to the imaginary parts of Equation 11.48, for $m, n = 1, 2; 2, 4; 4, 8; \dots$. Harmonic wavelets are used in many mechanics applications such as acoustics, vibration monitoring, and damage detection [45–49].

6. *Complex Gaussian wavelets* — Families of wavelets, each corresponding to a p th order derivative of a complex Gaussian function. That is,

$$\psi_p(x) = C_p \frac{d^p}{dx^p} (e^{-ix} e^{-x^2/2}), \quad p = 1, 2, \dots \quad (11.49)$$

where C_p is a normalization constant such that $\|\psi(x)\|^2 = 1$. Complex Gaussian wavelets support the CWT only. They have no finite support in the x -domain, although the interval $[-5, 5]$ is generally taken as effective support. Despite their lack of orthogonality, they are quite popular in image-processing applications due to their regularity [1].

7. *Complex Morlet wavelets* — Families of [50], each obtained as the derivative of the classical Morlet wavelet $\psi_0(x) = e^{-x^2/2} e^{i\omega_0 x}$. That is,

$$\psi_p(x) = \frac{d^p}{dx^p} (e^{-x^2/2} e^{i\omega_0 x}), \quad p = 1, 2, \dots \quad (11.50)$$

Except for $\psi_0(x)$, which does not satisfy the admissibility condition (Equation 11.11) in a strict sense, all the other members of the family are proper wavelets. For practical purposes, however, $\psi_0(x)$ is generally considered admissible for $\omega_0 \geq 5$. Complex Morlet wavelets support the CWT only and are not orthogonal. However, they are all progressive, that is, they satisfy the condition posed by Equation 11.36. Further, for the Morlet wavelet $\psi_0(x)$, there exists a relation between the scale parameter a and the frequency ω at which its Fourier transform focuses. That is,

$$a = \frac{\omega_0}{\omega} \quad (11.51)$$

Complex Morlet wavelets are then applied for structural identification purposes, as shown in Section 11.5.

11.3 Time-Dependent Spectra Estimation of Stochastic Processes

Wavelets-based approaches are significant tools for joint time–frequency analysis of problems related to vibrations of mechanical and structural systems. This applies both to the characterization of the system excitation, the system identification, and the system response determination. Several examples exist in nature of stochastic phenomena with a time-dependent frequency content. The frequency content of earthquake records, for instance, evolves in time due to the dispersion of the propagating seismic waves [51,52]. Further, sudden changes in the wave frequency at a given location of the sea surface are often induced by fast-moving meteorological fronts [53]. Also, a rapid change in the frequency content is generally associated with waves at the breaking stage. Similarly, turbulent gusts of time-varying frequency content are often embedded in wind fields.

Appropriate description of such phenomena is obviously crucial for design and reliability assessments. In an early attempt, concepts of traditional Fourier spectral theory were generalized to provide spectral estimates, such as the Wigner–Ville method [25,54] or the CGT of Equation 11.1. However, it soon

became clear that the extension of the traditional concept of a spectrum is not unique, and proposed time-varying spectra could have contradictory properties [6,55].

Wavelet analysis is readily applicable for estimating time-varying spectral properties, and a significant effort has been devoted to formulating “wavelet energy principles” that work as alternatives to classical Fourier methods. Measures of a time-varying frequency content were first obtained by “sectioning,” at different time instants, the wavelet coefficients mean square map [49,56–58]. Developing consistent spectral estimates from such sections, however, is not straightforward. From a theoretical point of view, it either requires an appropriate wavelet-based definition of time-varying spectra, or it must relate to well-established notions of time-varying spectra. From a numerical point of view, it involves certain difficulties in converting the scale axis to a frequency axis, especially when the wavelet functions are not orthogonal in the frequency domain; that is, when the frequency content of wavelet functions at adjacent scales do overlap.

Early investigations on wavelet-based spectral estimates may be found in references such as [44,59–64], where wavelet analysis was applied in the context of earthquake engineering problems. In a particular approach, a modified Littlewood Paley (MLP) wavelet basis can be introduced, whose mother wavelet is defined in the frequency domain by the equation

$$\hat{\psi}(\omega) = \begin{cases} \frac{1}{\sqrt{2(\sigma-1)\pi}}, & \pi \leq |\omega| \leq \sigma\pi, \\ 0, & \text{elsewhere} \end{cases} \quad (11.52)$$

In Equation 11.52, the symbol σ denotes a scalar factor, to be adjusted depending on the desired frequency resolution. The MLP wavelets are orthogonal in the frequency domain, that is, wavelets at adjacent scales span nonoverlapping intervals. The MLP wavelets have been used in conjunction with a discretized version of the CWT proposed by Alkemade [65] for a finite-energy process $f(t)$

$$f(t) = \sum_{i,j} \frac{K\Delta b}{a_j} W_f(a_j, b_i) \psi_{a_j, b_i}(t) \quad (11.53)$$

where $a_j = \sigma^j$, Δb is a time step, and K is a constant parameter depending on σ .

In many instances, Equation 11.53 can be construed as representing realizations of a *stochastic process*, and in this case, the following estimate of its instantaneous mean-square value of $f(t)$ has been constructed

$$E[f^2(t)]|_{t=b_i} = K \sum_j \frac{E[W_f(a_j, b_i)]^2}{a_j} \quad (11.54)$$

where $E[\cdot]$ is the mathematical expectation operator over the ensemble of realizations. From Equation 11.54, and based on the orthogonality properties of the MLP wavelets, the following quantity

$$S_f(\omega)|_{t=b_i} = \sum_j K \frac{E[W_f(a_j, b_i)]^2}{a_j} |\hat{\psi}_{a_j, b_i}(\omega)|^2 \quad (11.55)$$

where the symbol $\hat{\psi}_{a_j, b_i}(\omega)$ denotes the Fourier transform of the wavelet function $\psi_{a_j, b_i}(t)$, can be taken as a measure of the time-varying power spectral density (PSD) of the process $f(t)$. Based on Equation 11.55, closed-form expressions can be derived between the input and the output PSDs [63]. In this context, linear-response statistics, such as the instantaneous rate of crossings of the zero level or the instantaneous rate of occurrence of the peaks, have been estimated with considerable accuracy. Analysis of nonlinear systems has also been attempted by an equivalent statistical linearization procedure [61,66].

Wavelet analysis for spectral estimation has also been pursued by Kareem et al., who have used the squared wavelet coefficients of a DWT to estimate the PSD of stationary processes [56]. To improve the frequency resolution of the DWT, where only adjacent octave bands can be accounted for, a CWT can be implemented based on a complex Morlet wavelet basis. The latter is preferable due to the one-to-one

correspondence between the scale a and the center frequency (Equation 11.51), which allows minimizing the overlap between spectral estimates at adjacent scales. Further, the product of wavelet coefficients can be used as a measure of the cross-correlation between two nonstationary signals $x(t)$ and $y(t)$ [56]. This concept can be refined by the introduction of a wavelet *coherence* measure [57,58] expressed by the equation

$$(c^W(a, b))^2 = \frac{|S_{xy}^W(a, b)|^2}{S_{xx}^W(a, b)S_{yy}^W(a, b)} \quad (11.56)$$

In this equation, the local spectrum $S_{ij}^W(a, b)$ is defined as

$$S_{ij}^W(a, b) = \int_T \overline{W_i}(a, b) W_j(a, b) d\tau \quad (11.57)$$

where the time integration window T depends on the desired time resolution. The local spectrum (Equation 11.57), owing to the time average over T , allows smoothing of potential measurement noise effects. Measures of higher-order correlation can also be introduced [56,58], such as the wavelet *bicoherence*

$$(b_{xxy}^W(a_1, a_2, b))^2 = \frac{|B_{xxy}^W(a_1, a_2, b)|^2}{\int_T |W_x(a_1, \tau) W_x(a_2, \tau)|^2 d\tau \int_T |W_y(\tilde{a}, \tau)|^2 d\tau} \quad (11.58)$$

where $1/\tilde{a} = 1/a_1 + 1/a_2$, and

$$B_{xxy}^W(a_1, a_2, b) = \int_T W_x(a_1, \tau) W_x(a_2, \tau) W_y(\tilde{a}, \tau) d\tau \quad (11.59)$$

Related remedies can be adopted to suppress spurious correlations induced by statistical noise, based on a reference noise map created from artificially simulated signals [58].

Signal energy representation concepts have been examined in Ref. [67] by using quasi-orthogonal Daubechies wavelets in the frequency domain to simulate earthquake ground motion accelerations. Further, Massel has used wavelet analysis to capture time-varying frequency composition of sea-surface records due to fast-moving atmospheric fronts in deep water, wave growth, and breaking or disintegration of mechanically generated wave trains [68]. In this regard, absolute value wavelet maps and a spectral measure called global wavelet energy spectrum, defined by the equation

$$E_3(a) = \int_0^\infty E_1(a, b) db \quad (11.60)$$

are used. The symbol $E_1(\tau, b)$ denotes a time-scale energy density

$$E_1(a, b) = \frac{|W_f(a, b)|^2}{a} \quad (11.61)$$

The scale in Equation 11.61 is readily translated into frequency by selecting the Morlet wavelet basis.

Spanos and Failla [69] have applied wavelet analysis to estimate the evolutionary power spectral density (EPSD) of nonstationary oscillatory processes defined as [70]

$$f(t) = \int_{-\infty}^\infty A(\omega, t) e^{i\omega t} dZ(\omega) \quad (11.62)$$

The symbol $A(\omega, t)$ denotes a slowly varying time- and frequency-dependent modulating function, and $Z(\omega)$ is a complex random process with orthogonal increments such that $E[|dZ(\omega)|^2] = S_{f_0f_0}(\omega) d\omega$, where $S_{f_0f_0}(\omega)$ is the two-sided PSD of the zero-mean stationary process

$$f_0(t) = \int_{-\infty}^\infty e^{i\omega t} dZ(\omega) \quad (11.63)$$

The two-sided EPSD of $f(t)$ is then taken as

$$S_{ff}(\omega, t) = |A(\omega, t)|^2 S_{f_0 f_0}(\omega) \quad (11.64)$$

Due to its localization properties, the wavelet transform of $f(t)$ (Equation 11.62) may be approximated as an oscillatory stochastic process. That is,

$$W_f(a, b) \approx \int_{-\infty}^{\infty} A(\omega, b) e^{i\omega b} dZ'(\omega) \quad (11.65)$$

where $dZ'(\omega) = \sqrt{2\pi a} \bar{\Psi}(\omega a) dZ(\omega)$. Based on Equation 11.65, the following integral relation is found between the mean-squared wavelet coefficients at each scale a and the EPSD of $f(t)$. That is,

$$E[W_f(a, b)^2] = 4\pi a \int_0^{\infty} |\hat{\Psi}(\omega a)|^2 S_{ff}(\omega, b) d\omega \quad (11.66)$$

A sufficient number of Equations 11.66, one for each scale a , can be solved by a standard solution algorithm, applicable for both orthogonal and nonorthogonal bases in the frequency domain. This procedure has proved quite accurate using both the Littlewood–Paley and the real Morlet wavelet bases.

11.4 Random Field Simulation

The use of wavelets for random field synthesis can be examined within the more general framework of scale-type methods. The latter have been developed to improve the computational performances of Monte Carlo simulations. Classical methods such as the spectral approach [71] or the autoregressive moving average (ARMA) [72] are not readily applicable for this purpose, especially when using nonuniform meshes or when enhancement of local resolution is desirable. To address these shortcomings, Fournier et al. [73] have proposed a “random midpoint method” to synthesize fractional Brownian motion; that is, a scale-type method where values of the random field for points within a coarser scale are generated first, and then the generated samples are used to determine values for a finer scale. This approach has been extended by Lewis [74] into a “generalized stochastic subdivision method,” suitable for a broad class of stationary processes, and by Fenton and Vanmarcke [75] into a “local average subdivision method,” which includes a random field smoothing procedure producing averages of the field for an increasingly finer scale.

An interpretation of scale-type approaches in the context of random field synthesis has been given by Zeldin and Spanos [39] using compactly supported Daubechies wavelets. Specifically, a synthesis algorithm has been developed that includes the previous methods proposed by Lewis [74] and Fenton and Vanmarcke [75] as a particular case. To synthesize a sample of a given process, the closed-form expressions

$$r_{k,l}^{j,i} = E[d_k^j d_l^i] = \int_{-\infty}^{\infty} \int_{-\infty}^{\infty} R_f(x_1, x_2) \psi_{j,k}(x_1) \psi_{i,l}(x_2) dx_1 dx_2 \quad (11.67)$$

$$b_{k,l}^{j,i} = E[c_k^j c_l^i] = \int_{-\infty}^{\infty} \int_{-\infty}^{\infty} R_f(x_1, x_2) \phi_{j,k}(x_1) \psi_{i,l}(x_2) dx_1 dx_2 \quad (11.68)$$

$$a_{k,l}^{j,i} = E[c_k^j c_l^i] = \int_{-\infty}^{\infty} \int_{-\infty}^{\infty} R_f(x_1, x_2) \phi_{j,k}(x_1) \phi_{i,l}(x_2) dx_1 dx_2 \quad (11.69)$$

given in Refs. [21,39] are considered to relate the autocorrelation function $R_f(x_1, x_2)$ of the process to the coefficients of its wavelet transform, which in this case are random variables. The synthesis algorithm is based on the wavelet reconstruction algorithm developed by Mallat [34,35], which proceeds from coarse to fine scales to determine the wavelet coefficients. Some relevant properties of wavelet ensure the computational efficiency of the algorithm. Specifically, using the quasi-differential properties of wavelets showed by Belkin [76], the coefficients d_k^j 's are derived directly from c_k^j 's by the approximate

linear combination

$$d_k^j = \sum_l \alpha_{k,l}^j c_l^j + \beta_k^j u_k \quad (11.70)$$

where u_k 's are uncorrelated, zero mean, unit variance random variables, statistically independent of c_k^j 's. For a wide class of stochastic processes, wavelet coefficients prove weakly correlated as the difference $k - l$ increases and, for this, the summation in Equation 11.70 is generally restricted to adjacent elements only. The algorithm is completed by an error-assessment procedure which allows refining of the triggering scale j in order to fit the sought target statistical properties of the synthesized field.

Further studies on the role of wavelet analysis in stochastic mechanics applications may be found in Ref. [21], which has showed how wavelet bases can be used in approximate Karhunen–Loève expansions. Any stationary process can then be represented as

$$f(t) = \sum_{j,k} d_k^j \psi_{j,k}(t) \quad (11.71)$$

where d_k^j 's are uncorrelated random variables and $\psi_{j,k}(t)$ are a nonorthogonal wavelet-like basis.

11.5 System Identification

Wavelet analysis lends itself to system-identification applications. For instance, frequency localization properties allow detection and decoupling of individual vibration modes of multi-degree-of-freedom (multi-DoF) linear systems. The wavelet representation of the system response can be truncated to an appropriate scale parameter in order to filter measurement noise. Also, the wavelet transform coefficients can be related directly to the system parameters, as long as specific bases are used.

Early investigations trace back to the work by Robertson et al. [77], who have used the DWT for the estimation of the impulse-response function of multi-DoF systems. Compared with alternative time-domain techniques, the DWT-based extraction procedure offers significant advantages. It is robust since singularities in the procedure-related matrices can generally be avoided by selecting orthonormal wavelet functions. Further, the reconstructed impulse-response function captures the low-frequency components, referred to as static modes and mode shape errors, which ordinarily are difficult to estimate.

An important application of wavelet analysis to structural identification is due to Staszewski [78], who has used complex Morlet wavelets for modal damping estimation. Specifically, Staszewski has interpreted in terms of the wavelet transform some concepts already used in well-established methods, where the Hilbert transform has been applied to a free-vibration linear response [79]. In the case of light damping, the free response in each mode $x_j(t)$ may be approximated in the complex plane by an analytical signal, given by Equation 11.37. The modulus of the Morlet wavelet transform of $x_j(t)$ can be expressed as

$$|W_{x_j}(a, b)| \approx A_j e^{-\zeta_j \omega_j b} |\bar{\Psi}(\pm i a_j \omega_j \sqrt{1 - \zeta_j^2})| \quad (11.72)$$

where A_j is the residue magnitude, and ω_j and ζ_j are the mode natural frequency and damping ratio, respectively. In Equation 11.72, the symbol a_j denotes the specific scale value, related to the mode natural frequency ω_j by the closed-form relation 11.51, typical of Morlet wavelets. Assuming that the natural frequency ω_j has been previously computed, the damping ratio ζ_j can then be estimated as the slope of a straight line, representing the cross section wavelet modulus (Equation 11.72) plotted in a semilogarithmic scale. That is,

$$\ln|(W_{x_j}(a, b))| \approx -\zeta_j \omega_j b + \ln(A_j |\bar{\Psi}(\pm i a_j \omega_j \sqrt{1 - \zeta_j^2})|) \quad (11.73)$$

Staszewski has also proposed an alternative damping estimation method based on the *ridge* and *skeletons* of the wavelet transform. A ridge is a curve of local maxima in the mean-square wavelet map, and the

corresponding skeleton is given by the values of the wavelet transform restricted to the ridge. As a result of the localization properties of the wavelet transform, the ridges and skeletons of the wavelet transform can be detected separately for each mode. Specifically, the real part of the skeleton of the wavelet transform gives the impulse-response function for each single mode from which a straightforward estimate of the damping ratio is obtained from a logarithmic equation analogous to Equation 11.73. A generalization of the method for nonlinear systems can also be formulated [80].

Ruzzene et al. [81] have also presented a damping estimation algorithm based on the same concepts and leading to analogous results. Certain issues have been addressed in detail concerning the frequency resolution of the adopted wavelet basis, crucial for detecting coupled modes, and appropriate algorithms for ridges extraction [50]. Lardies and Gouttebroze [82] have estimated modal parameters *via* ambient records without input measurements. To this end, the random decrement method (see Ref. [83] and the references therein) has been used to convert ambient vibration response into a free vibration response. Also, a modified Morlet wavelet basis has been developed with enhanced properties for modal parameters estimation. The method devised by Staszewski and by Ruzzene et al. has also been implemented by Slavic et al. [84] by replacing the Morlet wavelets by Gabor wavelets, whose time and frequency resolution may be adjusted by an appropriate parameter. Explicit conditions have been given on the frequency *bandwidths* of the Gabor wavelet transform, in order to estimate the instantaneous frequencies of two adjacent modes.

Damping coefficients have been estimated using a logarithmic decrement formula, where the ratio of the wavelet transform at two subsequent extremes of the pseudo-period $T_j = 2\pi/\omega_j$ of the response in each mode is involved for a selected wavelet transform scale [85,86]. For the procedure to estimate the damping coefficient associated with the fundamental mode, it is sufficient to adapt the analyzing scale so that the higher frequency modes are filtered. For an arbitrary mode j , low-pass filtering is used to cancel the fundamental and the first $j - 1$ modes. Ghanem and Romeo [87] have formulated a wavelet-Galerkin method for time-varying systems, where both damping and stiffness parameters are computed by solving a matrix equation. The latter is built by a standard Galerkin method by projecting the solution of the differential equation of motion onto a subspace described by the wavelet scaling functions of a compactly supported Daubechies wavelet basis. The method is accurate for both free and forced vibration responses. A formulation for nonlinear systems has also been proposed [88]. Another application is due to Yu and Xiao [89], who have used wavelet transform to identify the parameters of a Preisach model of hysteresis (see Refs. [69,90] and the references therein). The output function of the Preisach model is expanded in terms of the scaling functions of a given wavelet basis. Then, the coefficients of such an expansion are determined by fitting a number of experimental data points with a minimum energy method. From the output function, the so-called Preisach function can be determined in a closed form.

A comprehensive application of wavelet-analysis concepts to system-identification problems has been given by Le and Argoul [91]. They have developed closed-form expressions to compute the damping ratio, the natural frequency and the shape of each mode, based on ridges and skeletons of the wavelet transformed free vibration response. As an alternative, Yin et al. [92] have proposed to apply the wavelet transform to the frequency response function (FRF) of the system. Specifically, given the FRF of an N -DoF system in the form

$$H(\omega) = \sum_{r=1}^N \left[\frac{A_r}{i\omega - \lambda_r} + \frac{\bar{A}_r}{i\omega - \bar{\lambda}_r} \right] \quad (11.74)$$

where λ_r is the r th complex pole and A_r the r th residue, a complex fractional function

$$\psi_y(x) = \frac{1}{(1 + ix)^{y+1}} = e^{-(y+1)\log(1+ix)}, \quad y \in \mathbb{R}^+ \quad (11.75)$$

is selected as a wavelet basis. Based on Equation 11.75, a closed-form expression can be established for the CWT of Equation 11.74 multiplied by $(\sqrt{a})^{-\gamma}$. Specifically,

$$\begin{aligned} H_\gamma(a, b) &= a^{-(\gamma+1)/2} \int_{-\infty}^{\infty} H(\omega) \bar{\psi}_\gamma \left(\frac{\omega - b}{a} \right) d\omega \\ &= 2\pi a^{(\gamma+1)/2} \sum_{r=1}^N \left(\frac{A_r}{(a + ib - \lambda_r)^{\gamma+1}} + \frac{\bar{A}_r}{(a + ib - \bar{\lambda}_r)^{\gamma+1}} \right) \end{aligned} \quad (11.76)$$

Natural frequencies and damping ratios can be estimated by locating the maxima of Equation 11.76 in the (a, b) plane.

11.6 Damage Detection

Properties of the wavelet transform are also quite appealing for damage-detection purposes. Early investigations in this field [93,94] used wavelet analysis to detect local faults in machineries. Specifically, visual inspection of the modulus and phase of the wavelet transform was used to localize the fault [93]. Further, it was shown that transient vibrations due to developing damage are disclosed by the local maxima of the mean-square wavelet map [94]. These investigations gave a qualitative approach to damage detection as no estimate of the damage amplitude was provided. Additional studies have confirmed the correlation between local maxima of the wavelet transform and damage in beams and plates [95–97], and a first attempt to estimate the damage amplitude was made by Okafor and Dutta [98]. Specifically, Daubechies wavelets were used to wavelet transform the mode shapes of a damaged cantilever beam, and a regression analysis by a least-square method was conducted to correlate the peaks of the wavelet coefficients with the corresponding damage amplitude.

A consistent mathematical framework for wavelet analysis of damaged beams is due to Hong et al. [99]. The focal concept is that defects in structures, even if small, may affect significantly the vibration mode shapes, depending on the location and the kind of damage. Such variations may not be apparent in the measured data but become detectable as singularities if wavelet analysis is used due to its high resolution properties. Specifically, Hong et al. have shown that the singularity of the vibration modes can be described in terms of Lipschitz regularity, a concept also encountered in the theory of differential equations, widely used in image processing where object contours correspond to irregularities in the intensity [100,101]. In mathematical terms, a function $f(x)$ is Lipschitz $\alpha \geq 0$ at $x = x_0$ if there exists $K > 0$, and a polynomial of order m (m is the largest integer satisfying $m \leq \alpha$), $p_m(x)$, such that and a polynomial of order m , $p_m(x)$, such that

$$f(x) = p_m(x) + \varepsilon(x) \quad (11.77)$$

$$|\varepsilon(x)| \leq K|x - x_0|^\alpha \quad (11.78)$$

The wavelet transform of Lipschitz α functions enjoys some properties. Mallat and Hwang [100] have shown that for a wavelet basis with a number of vanishing moments $\alpha \leq n$, a local Lipschitz singularity at x_0 corresponds to maxima lines of the wavelet transform modulus. That is, local maxima with asymptotic decay across scales. Near the cone of influence $x = x_0$, such moduli satisfy the equation

$$|W_f(a, x)| \leq Aa^{\alpha+1/2}, \quad A > 0 \quad (11.79)$$

from which the Lipschitz exponent is computed as

$$\log_2 |W_f(a, x)| \leq \log_2 A + \left(\alpha + \frac{1}{2} \right) \log_2 a \quad (11.80)$$

By plotting the wavelet coefficients on a logarithmic scale, A and α may be computed by setting the equality sign in Equation 11.80 and minimizing the error in the least-square sense. Hong et al. have

applied Equation 11.79 to the first mode shape of a damaged cantilever beam *via* a Mexican Hat wavelet transform. The first mode shape is preferable since it is the most accurately determined by modal testing; it features the lowest curvature; and sets off the singularity better. A correlation between damage size and the magnitude of the Lipschitz exponent has been found from a number of beams with different damage parameters.

Some of the ideas presented by Hong et al. may also be found in the work by Douka et al., who have pursued crack identification in beams and plates using Daubechies wavelets [102,103]. The first mode vibration response has been considered and the singularity induced by local defects has been characterized in terms of Equation 11.79. The Lipschitz exponent has been used to describe the kind of singularity, and the parameter A has been taken as the factor relating the depth of the crack to the amplitude of the wavelet transform. Specifically, a second-order polynomial law has been found for the intensity factor as a function of the crack depth. The work by Douka et al. has pointed out the importance of the number of vanishing moments M of the chosen wavelet basis. It is intuitive that the capability of setting off singularities in a regular function increases with M . However, wavelet functions with high M exhibit a long support and lack space resolution. A compromise, then, must be achieved, depending on the application in hand. Further insight into some mathematical details of both the methods developed by Hong et al. and Douka et al. may be found in Haase and Widjajakusuma [50]. Specifically, a fast algorithm to determine the maxima lines of the wavelet transform has been devised. Also, the performance of various wavelet bases, such as the Gaussian family of wavelets, has been assessed versus Daubechies wavelets used by Douka et al.

Another approach for damage-detection problems has been proposed by Yam et al. [104]. Clearly, detection of small and incipient damage cannot be pursued by computing modal parameters that change only if the amount of damage is significant. Thus, a method has been devised based on the energy variation of the vibration response due to the occurrence of damage. The method is implemented in two steps. The first involves the construction of damage feature proxy vectors using the energy at various scales of the wavelet transformed vibration response. Then, classification and identification of the structural damage status is pursued by using artificial neural networks (ANNs), which offer significant advantages compared with genetic algorithms (GAs) developed by Moslem and Nafaspour for damage-identification purposes [105]. Genetic-algorithm-based damage detection, in fact, requires repeatedly searching among numerous damage parameters to find the optimal solution of the objective function.

Yet another approach for applications of wavelet analysis to damage detection has been discussed by Paget et al. [106], who have developed a procedure to detect impact damage in composite plates. It is based on Lamb waves generated and received by embedded piezoceramic transducers. The Lamb waves can be quite effective since they can propagate over long distances in the composite material and can interfere with damage. To characterize the damage, the Lamb waves are wavelet transformed using an original wavelet basis, devised from the recurrent waveforms of the Lamb waves. The changes in the Lamb waves interacting due to the occurrence of damage are captured by the amplitude change of the wavelet coefficients. From this effect, an estimate of the impact energy and the damage level is obtained based on experimental results.

11.7 Material Characterization

Material properties description is another application for wavelet analysis. Intuition suggests that multiscale analysis is a natural way of describing microstructure or material heterogeneity. Various, in fact, are the examples of multiscale microstructures, such as porosity distributions in ceramics, defects, dislocations, grain boundaries, and pores. It is important, however, to understand how information at different scales is related, and whether large or small scales affect macroscopic material properties such as deformation, toughness, and electrical conductance. Further interest towards a multiscale description of material properties is motivated by the need of alternatives to the standard finite element method (FEM).

The latter, although capable in principle, cannot simulate the actual behavior of materials such as aluminum alloys, where pores may attain a size up to $500\text{ }\mu\text{m}$ and inclusions may attain a size of 3 to $6\text{ }\mu\text{m}$ in diameter. Further, in FEM-based methods, the constitutive response of the material at increasing scales is not the result of microstructural analysis at smaller scales, but it is rather assumed on the basis of macroscopic experiments.

Willam et al. [107] have performed *multiresolution* homogenization based on a recursive Schur reduction method in conjunction with the Haar wavelet transform. The method allows coarse-grained parameters, such as Young's modulus of elasticity, to be extracted from fine-grained properties at the meso- and micro-scales. Also, progressive elastic degradation can be modeled, which initiates at a quite fine scale and evolves into a macroscopic zero stiffness at the continuum level.

Frantziskonis [108] has focused on stationary and isotropic porous media. The geometry of porous media is generally described in terms of a fundamental function, defined as unity for spatial locations in the matrix, and as zero for locations in the pores or flaws. At a solid-flaw interface, the porous medium is represented mathematically through a local jump in the fundamental function. It has been found that such a jump can be captured by a wavelet transform, as long as the finest scale is small enough relative to the size of the pores. From this fact, a relationship between the energy of the wavelet transform of the porous medium, and the variance and the correlation distance of the solid phase can be derived. In the presence of heterogeneous materials, with multiscale porosity, the role of porosity at each scale has been identified through the variation of the energy of the wavelet transform as a function of scale. Peaks of the energy reveal the dominant scale in determining macroscopic properties of the materials, such as mechanical failure. Specifically, a biorthogonal spline with four vanishing moments has been employed as a wavelet basis. The results obtained have been subsequently extended in a second study, addressing the crack formation in an aluminum alloy with distributed pores and inclusions [109]. The problem, implemented for a one-dimensional solid, is tackled by wavelet transforming the flexibility function, assumed to vary along the longitudinal axis of the one-dimensional solid. The relationship between the energy of the wavelet transform and the variance of the flexibility is used to detect the dominant scale in the crack-formation process.

Note that an application of a two-dimensional wavelet transform has been described in Ciliberto et al. [110] for porosity classification on carbon fiber-reinforced plastics.

11.8 Concluding Remarks

Concepts of wavelets-based continuous and discrete representations have been reviewed. Further, an overview of vibration-related applications for evolutionary spectrum estimation, random field simulation, system identification, damage detection, and material characterization has been included. The list of references is not exhaustive. However, these references can serve as readily available resources for canvassing the multitude of concepts and applications of this remarkable tool for capturing and representing localization features of many physical phenomena. Wavelets-based algorithms and commercial codes are an indispensable family of tools of vibration analysis and offer, in many cases, a potent improvement over the classical Fourier-transform-based approaches.

Acknowledgments

The support of this work through a grant from the U.S. Department of Energy is gratefully acknowledged.

Nomenclature

Symbol	Quantity	Symbol	Quantity
$E[\cdot]$	the operator of mathematical expectation	ω	frequency
$R(\cdot, \cdot)$	correlation function	ζ	damping ratio
$H[\cdot]$	Hilbert transform operator	a	scale
$\langle \cdot, \cdot \rangle$	inner product	b	shift
\subset	inclusion	$\psi(x)$	mother wavelet
$\{; ; \}$	set of all elements with a specified property	$\phi(x)$	scale function
$ \cdot $	absolute value	x	spatial variable
$\ \cdot\ $	norm	W	wavelet transform
\mathbb{Z}	the set of integer numbers	i	$\sqrt{-1}$
\mathbb{C}	the set of complex numbers	δ_{mn}	Kronecker delta defined as
$\overline{(\cdot)}$	complex conjugate		$\delta_{mn} = \begin{cases} 0 & \text{for } m \neq n \\ 1 & \text{for } m = n \end{cases}$

References

1. Carmona, R., Hwang, W.-L., and Torr sani, B. 1998. *Practical Time–Frequency Analysis: Gabor and Wavelet Transforms with an Implementation in S.*, Academic Press, San Diego.
2. Chan, Y.T. 1995. *Wavelet Basics*, Kluwer, Boston.
3. Chui, C.K. 1992. *An Introduction to Wavelets*, Academic Press, New York.
4. Chui, C.K. 1992. *Wavelets: A Tutorial in Theory and Applications*, Academic Press, New York.
5. Chui, C.K., Montefusco, L., and Puccio, L. 1994. *Wavelets: Theory, Algorithms, and Applications*, Academic Press, New York.
6. Cohen, L. 1995. *Time–Frequency Analysis*, Prentice Hall, Englewood Cliffs, NJ.
7. Daubechies, I. 1992. *Ten Lectures on Wavelets*, Society for Industrial and Applied Mathematics, Philadelphia.
8. Hern ndez, E. and Weiss, G.L. 1996. *A First Course on Wavelets*, CRC Press, Boca Raton, FL.
9. Hubbard, B.B. 1996. *The World According to Wavelets: The Story of a Mathematical Technique in the Making*, A.K. Peters, Wellesley, MA.
10. Jaffard, S., Meyer, Y., and Ryan, R.D. 2001. *Wavelets: Tools for Science & Technology*, Society for Industrial and Applied Mathematics, Philadelphia.
11. Kahane, J.-P. and Lemari -Rieusset, P.-G. 1995. *Fourier Series and Wavelets*, Gordon & Breach, Luxembourg.
12. Kaiser, G. 1994. *A Friendly Guide to Wavelets*, Birkh user, Boston.
13. Mallat, S.G. 1998. *A Wavelet Tour of Signal Processing*, Academic Press, San Diego.
14. Meyer, Y. 1990. *Ondelettes*, Hermann, Paris.
15. Misiti, M. 1997. *Wavelet Toolbox for Use with Matlab*, Math Works, Natick, MA.
16. Newland, D.E. 1993. *An Introduction to Random Vibrations, Spectral and Wavelet Analysis*, 3rd ed., Longman Scientific & Technical, New York, Harlow, UK.
17. Qian, S. and Chen, D. 1996. *Joint Time–Frequency Analysis: Methods and Applications*, Prentice Hall, Upper Saddle River, NJ.
18. Qian, S. 2001. *Introduction to Time–Frequency and Wavelet Transforms*, Prentice Hall, Upper Saddle River, NJ.
19. Strang, G. and Nguyen, T. 1996. *Wavelets and Filter Banks*, Cambridge Press, Wellesley, MA.
20. Vetterli, M. and Kovacevic, J. 1995. *Wavelets and Subband Coding*, Prentice Hall, Englewood Cliffs, NJ.

21. Walter, G.G. 1994. *Wavelets and Other Orthogonal Systems with Applications*, CRC Press, Boca Raton, FL.
22. Young, R.K. 1993. *Wavelet Theory and Its Applications*, Kluwer, Boston.
23. Spanos, P.D. and Zeldin, B.A., A state-of-the-art report on computational stochastic mechanics: wavelets concepts, *Probab. Eng. Mech.*, 12, 244, 1997.
24. Gabor, D., Theory of communication, *J. Inst. Electr. Eng.*, 93, 429, 1946.
25. Wigner, E.P., On the quantum correction for thermodynamic equilibrium, *Phys. Rev.*, 40, 749, 1932.
26. Goupillaud, P., Grossmann, A., and Morlet, J., Cycle-octave and related transforms in seismic signal analysis, *Geoexploration*, 23, 85, 1984.
27. Grossmann, A. and Morlet, A., Decomposition of hardy functions into square integrable wavelets of constant shape, *SIAM J. Math. Anal.*, 15, 723, 1984.
28. Holschneider, M. and Tchamitchian, P., Pointwise analysis of Riemann's 'nondifferentiable' function, *Invent. Math.*, 105, 157, 1991.
29. Cohen, A. and Kovacevic, J., Wavelets: the mathematical background, *Proc. IEEE*, 84, 514, 1996.
30. Duffin, R.J. and Schaeffer, A.C., A class of nonharmonic Fourier series, *Trans. Am. Math. Soc.*, 72, 341, 1952.
31. Daubechies, I., The wavelet transform, time–frequency localization and signal analysis, *IEEE Trans. Inf. Theory*, 36, 961, 1990.
32. Daubechies, I., Grossmann, A., and Meyer, Y., Painless nonorthogonal expansions, *J. Math. Phys.*, 27, 1271, 1986.
33. Battle, G., A block spin construction of ondelettes. I. Lemarie functions, *Commun. Math. Phys.*, 110, 601, 1987.
34. Mallat, S.G., Multifrequency channel decompositions of images and wavelet models, *IEEE Trans. Acoust. Speech Signal Process.*, 37, 2091, 1989.
35. Mallat, S.G., A theory for multiresolution signal decomposition: the wavelet representation, *IEEE Trans. Pattern Anal. Machine Intell.*, 11, 674, 1989.
36. Daubechies, I., Orthogonal bases of compactly supported wavelets, *Commun. Pure Appl. Math.*, 41, 909, 1988.
37. Basseville, M., Benveniste, A., Chou, K.C., Golden, S.A., Nikoukhah, R., and Willsky, A.S., Modeling and estimation of multiresolution stochastic processes, *IEEE Trans. Inf. Theory*, 38, 766, 1992.
38. Basseville, M., Benveniste, A., and Willsky, A.S., Multiscale autoregressive processes. Part I: Schur–Levinson parametrizations, *IEEE Trans. Signal Process.*, 40, 1915, 1992.
39. Zeldin, B.A. and Spanos, P.D., Random field representation and synthesis using wavelet bases, *ASME J. Appl. Mech.*, 63, 946, 1996.
40. Carmona, R.A., Hwang, W.L., and Torresani, B., Characterization of signals by the ridges of their wavelet transforms, *IEEE Trans. Signal Process.*, 45, 2586, 1997.
41. Kim, H.O., Kim, R.Y., and Lim, J.K., Characterizations of biorthogonal wavelets which are associated with biorthogonal multiresolution analyses, *Appl. Comput. Harmonic Anal.*, 11, 263, 2001.
42. Spanos, P.D. and Rao, V.R.S., Random field representation in a biorthogonal wavelet basis, *J. Eng. Mech.*, 127, 194, 2001.
43. Newland, D.E., Wavelet analysis of vibration, Part I: Theory, *J. Vib. Acoust.*, 116, 409, 1994.
44. Spanos, P.D., Tratskas, P.N., and Tezcan, J., Stochastic processes evolutionary spectrum estimation via the wavelet spectrum, *J. Comput. Methods Appl. Mech. Eng.*, 194, 12–16, 1367–1383, 2005.
45. Newland, D.E., Wavelet analysis of vibration, Part II: Wavelet maps, *J. Vib. Acoust.*, 116, 417, 1994.
46. Newland, D.E., Some properties of discrete wavelet maps, *Probab. Eng. Mech.*, 9, 59, 1994.
47. Newland, D.E. and Butler, G.D. 1998. Application of time–frequency analysis to strong motion data with damage, *Proceedings of the 69th Shock and Vibration Symposium*, Minneapolis, St Paul, MN.

48. Newland, D.E., Ridge and phase identification in the frequency analysis of transient signals by harmonic wavelets, *J. Vib. Acoust.*, 121, 149, 1999.
49. Newland, D.E. and Butler, G.D. 1999. Time-varying cross-spectra by harmonic wavelets for soil motion damage, *Proceedings of the ASME DETC: 17th ASME Biennial Conference on Mechanical Vibration and Noise*, Las Vegas, NV, p. 1335.
50. Haase, M. and Widjajakusuma, J., Damage identification based on ridges and maxima lines of the wavelet transform, *Int. J. Eng. Sci.*, 41, 1423, 2003.
51. Trifunac, M.D., Response envelope spectrum and interpretation of strong earthquake ground motion, *Bull. Seismol. Soc. Am.*, 61, 343, 1971.
52. Spanos, P.D., Donley, M., and Roesset, J. 1987. Evolutionary power spectrum estimation of earthquake accelerograms, September 19, 1985, Mexico. In *Stochastic Approaches in Earthquake Engineering: U.S.–Japan Joint Seminar, Boca Raton, Florida, USA, May 6–7*, Y.K. Lin and R. Minai, Eds., p. 322. Springer, Berlin.
53. Massel, S.R. 1996. *Ocean Surface Waves: Their Physics and Prediction*, World Scientific, River Edge, NJ.
54. Ville, J., Theorie et applications de la notion de signal analytique, *Cables Transm.*, 2, 61, 1948.
55. Loynes, R.M., On the concept of the spectrum for nonstationary processes, *J. R. Stat. Soc. Ser. B Methodol.*, 30, 1, 1968.
56. Gurley, K. and Kareem, A., Applications of wavelet transforms in earthquake, wind, and ocean engineering, *Eng. Struct.*, 21, 149, 1999.
57. Gurley, K., Kijewski, T., and Kareem, A., First- and higher-order correlation detection using wavelet transforms, *J. Eng. Mech.*, 129, 188, 2003.
58. Kareem, A. and Kijewski, T., Time–frequency analysis of wind effects on structures, *J. Wind Eng. Ind. Aerodyn.*, 90, 1435, 2002.
59. Basu, B. and Gupta, V.K., Non-stationary seismic response of multi-DoF systems by wavelet transform, *Earthquake Eng. Struct. Dyn.*, 26, 1243, 1997.
60. Basu, B. and Gupta, V.K., Seismic response of single-DoF systems by wavelet modeling of nonstationary processes, *J. Eng. Mech.*, 124, 1142, 1998.
61. Basu, B. and Gupta, V.K., Stochastic seismic response of single-DoF systems through wavelets, *Eng. Struct.*, 22, 1714, 2000.
62. Basu, B. and Gupta, V.K., Wavelet-based non-stationary response analysis of a friction base-isolated structure, *Earthquake Eng. Struct. Dyn.*, 29, 1659, 2000.
63. Tratskas, P. and Spanos, P.D., Linear multi-DoF system stochastic response by using the harmonic wavelet transform, *J. Appl. Mech.*, 70, 724, 2003.
64. Spanos, P.D. and Failla, G., Evolutionary spectra estimation using wavelets, *J. Eng. Mech.*, 130, 2004.
65. Alkemade, J.A.H. 1993. The finite wavelet transform with an application to seismic processing. In *Wavelets: An Elementary Treatment of Theory and Applications*, T.H. Koornwinder, Ed., p. 183. World Scientific, Hackensack, NJ.
66. Basu, B. and Gupta, V.K., On equivalent linearization using the wavelet transform, *J. Vib. Acoust.*, 121, 429, 1999.
67. Iyama, J. and Kuwamura, H., Application of wavelets to analysis and simulation of earthquake motions, *Earthquake Eng. Struct. Dyn.*, 28, 255, 1999.
68. Massel, S.R., Wavelet analysis for processing of ocean surface wave records, *Ocean Eng.*, 28, 957, 2001.
69. Spanos, P. D., Cacciola, P., and Redhorse, J., Random vibration of SMA systems via Preisach formalism, *Nonlinear Dyn.*, 36, 405, 2004.
70. Priestley, M.B. 1981. *Spectral Analysis and Time Series*, Academic Press, New York.
71. Shinozuka, M. and Deodatis, G., Stochastic process models for earthquake ground motion, *Probab. Eng. Mech.*, 3, 114, 1988.
72. Spanos, P.D. and Mignolet, M.P., Simulation of homogeneous two-dimensional random fields: Part II — MA and ARMA models, *J. Appl. Mech.*, 114, 270, 1992.

73. Fournier, A., Fussell, D., and Carpenter, L., Computer rendering of stochastic models, *Commun. ACM*, 25, 371, 1982.
74. Lewis, J.P., Generalized stochastic subdivision, *ACM Trans. Graph.*, 6, 167, 1987.
75. Fenton, G.A. and Vanmarcke, E.H., Simulation of random fields via local average subdivision, *J. Eng. Mech.*, 116, 1733, 1990.
76. Belkin, G., On the representation of operators in bases of compactly supported wavelets, *J. Numer. Anal.*, 6, 1716, 1993.
77. Robertson, A.N., Park, K.C., and Alvin, K.F., Extraction of impulse response data via wavelet transform for structural system identification, *Proc. Des. Eng. Tech. Conf. DE-84.1 ASME-95*, 1323, 1995.
78. Staszewski, W.J., Identification of damping in multi-DoF systems using time-scale decomposition, *J. Sound Vib.*, 203, 283, 1997.
79. Jones, D.I.G. 1988. Application of damping treatments. In *Shock and Vibration Handbook*, 3rd ed., C.M. Harris, Ed. McGraw-Hill, New York.
80. Staszewski, W.J., Identification of non-linear systems using multi-scale ridges and skeletons of the wavelet transform, *Shock Vib. Dig.*, 214, 639, 1998.
81. Ruzzene, M., Fasana, A., Garibaldi, L., and Piombo, B., Natural frequencies and dampings identification using wavelet transform: application to real data, *Mech. Syst. Signal Process.*, 11, 207, 1997.
82. Lardies, J. and Gouttebroze, S., Identification of modal parameters using the wavelet transform, *Int. J. Mech. Sci.*, 44, 2263, 2002.
83. Spanos, P.D. and Zeldin, B.A., Generalized random decrement method for analysis of vibration data, *J. Vib. Acoust., Trans. ASME*, 120, 806, 1998.
84. Slavic, J., Simonovski, I., and Boltezar, M., Damping identification using a continuous wavelet transform: application to real data, *J. Sound Vib.*, 262, 291, 2003.
85. Lamarque, C.H., Pernot, S., and Cuer, A., Damping identification in multi-DoF systems via a wavelet-logarithmic decrement. Part 1: Theory, *J. Sound Vib.*, 235, 361, 2000.
86. Hans, S., Ibraim, E., Pernot, S., Boutin, C., and Lamarque, C.H., Damping identification in multi-DoF system via a wavelet-logarithmic decrement. Part 2: Study of a civil engineering building, *J. Sound Vib.*, 235, 375, 2000.
87. Ghanem, R. and Romeo, F., A wavelet-based approach for the identification of linear time-varying dynamical systems, *J. Sound Vib.*, 234, 555, 2000.
88. Ghanem, R. and Romeo, F., Wavelet-based approach for model and parameter identification of non-linear systems, *Int. J. Non-Linear Mech.*, 36, 835, 2001.
89. Yu, Y., Xiao, Z., Lin, E.-B., and Naganathan, N., Analytic and experimental studies of a wavelet identification of Preisach model of hysteresis, *J. Magn. Magn. Mater.*, 208, 255, 2000.
90. Mayergoyz, I.D. 2003. *Mathematical Models of Hysteresis and Their Applications*, 1st ed., Academic Press, Boston.
91. Le, T.-P. and Argoul, P., Continuous wavelet transform for modal identification using free decay response, *J. Sound Vib.*, 277, 73, 2004.
92. Yin, H.P., Duhamel, D., and Argoul, P., Natural frequencies and damping estimation using wavelet transform of a frequency response function, *J. Sound Vib.*, 271, 999, 2004.
93. Staszewski, W.J. and Tomlinson, G.R., Application of the wavelet transform to fault detection in a spur gear, *Mech. Syst. Signal Process.*, 8, 289, 1994.
94. Wang, W.J. and McFadden, P.D., Application of orthogonal wavelets to early gear damage detection, *Mech. Syst. Signal Process.*, 9, 497, 1995.
95. Liew, K.M. and Wang, Q., Application of wavelet theory for crack identification in structures, *J. Eng. Mech.*, 124, 152, 1998.
96. Deng, X. and Wang, Q., Crack detection using spatial measurements and wavelet analysis, *Int. J. Fracture*, 91, L23, 1998.

97. Wang, Q. and Deng, X., Damage detection with spatial wavelets, *Int. J. Solids Struct.*, 36, 3443, 1999.
98. Okafor, A.C., Chandrashekhara, K., and Jiang, Y.P., Location of impact in composite plates using waveform-based acoustic emission and Gaussian cross-correlation techniques, *Proc. SPIE — Int. Soc. Opt. Eng.*, 2718, 291, 1996.
99. Hong, J.-C., Kim, Y.Y., Lee, H.C., and Lee, Y.W., Damage detection using the Lipschitz exponent estimated by the wavelet transform: applications to vibration modes of a beam, *Int. J. Solids Struct.*, 39, 1803, 2002.
100. Mallat, S. and Hwang, W.L., Singularity detection and processing with wavelets, *IEEE Trans. Inf. Theory*, 38, 617, 1992.
101. Grossmann, A. 1986. Wavelet transform and edge detection. In *Stochastic Processes in Physics and Engineering*, M. Hazewinkel, Ed. Reidel, Dodrecht.
102. Douka, E., Loutridis, S., and Trochidis, A., Crack identification in beams using wavelet analysis, *Int. J. Solids Struct.*, 40, 3557, 2003.
103. Douka, E., Loutridis, S., and Trochidis, A., Crack identification in plates using wavelet analysis, *J. Sound Vib.*, 270, 279, 2004.
104. Yam, L.H., Yan, Y.J., and Jiang, J.S., Vibration-based damage detection for composite structures using wavelet transform and neural network identification, *Compos. Struct.*, 60, 403, 2003.
105. Moslem, K. and Nafaspour, R., Structural damage detection by genetic algorithms, *AIAA J.*, 40, 1395, 2002.
106. Paget, C.A., Grondel, S., Levin, K., and Delebarre, C., Damage assessment in composites by Lamb waves and wavelet coefficients, *Smart Mater. Struct.*, 12, 393, 2003.
107. Willam, K., Rhee, I., and Beylkin, G., Multiresolution analysis of elastic degradation in heterogeneous materials, *Meccanica*, 36, 131, 2001.
108. Frantziskonis, G., Wavelet-based analysis of multiscale phenomena: application to material porosity and identification of dominant scales, *Probab. Eng. Mech.*, 17, 349, 2002.
109. Frantziskonis, G., Multiscale characterization of materials with distributed pores and inclusions and application to crack formation in an aluminum alloy, *Probab. Eng. Mech.*, 17, 359, 2002.
110. Ciliberto, A., Cavaccini, G., Salvetti, O., and Chimenti, M., Porosity detection in composite aeronautical structures, *Infrared Phys. Technol.*, 43, 139, 2002.

III

Shock and Vibration

12

Mechanical Shock

12.1	Definitions	12-2
	Shock • Simple (or Perfect) Shock • Half-Sine Shock • Versed-Sine (or Haversine) Shock • Terminal Peak Sawtooth Shock or Final Peak Sawtooth Shock • Rectangular Shock	
12.2	Description in the Time Domain	12-3
12.3	Shock Response Spectrum	12-4
	Need • Shock Response Spectrum Definition • Response of a Linear One-Degree-of-Freedom System • Definitions • Standardized Shock Response Spectrum • Choice of Damping • Shock Response Spectra Domains • Algorithms for Calculation of the Shock Response Spectra • Choice of the Digitization Frequency of the Signal • Use of Shock Response Spectra for the Study of Systems with Several Degrees of Freedom	
12.4	Pyroshocks	12-17
12.5	Use of Shock Response Spectra	12-18
	Severity Comparison of Several Shocks • Test Specification Development from Real Environment Data	
12.6	Standards	12-24
	Types of Standards • Installation Conditions of Test Item • Uncertainty Factor • Bump Test	
12.7	Damage Boundary Curve	12-26
	Definition • Analysis of Test Result	
12.8	Shock Machines	12-28
	Main Types • Impact Shock Machines • Shock Simulators (Programmers) • Limitations • Pneumatic Machines • High Impact Shock Machines • Specific Test Facilities	
12.9	Generation of Shock Using Shakers	12-44
	Principle Behind the Generation of a Simple Shape Signal versus Time • Main Advantages • Pre- and Postshocks • Limitations of Electrodynamic Shakers • The Use of Electrohydraulic Shakers	
12.10	Control by a Shock Response Spectrum	12-52
	Principle • Principal Shapes of Elementary Signals • Comparison of WAVSIN, SHOC Waveforms, and Decaying Sinusoid • Criticism of Control by a Shock Response Spectrum	
12.11	Pyrotechnic Shock Simulation	12-58
	Simulation Using Pyrotechnic Facilities • Simulation Using Metal-to-Metal Impact • Simulation Using Electrodynamic Shakers • Simulation Using Conventional Shock Machines	

Christian Lalanne
Engineering Consultant

Summary

Transported or on-board equipment is very frequently subjected to mechanical shocks in the course of its useful lifetime (in material handling, transportation, etc.). This kind of environment, although of extremely short duration (from a fraction of a millisecond to a few dozen milliseconds), is often severe and cannot be neglected. What is presented in this chapter is summarized here. After a brief recapitulation of the shock shapes most widely used in tests, the shock response spectrum (SRS) is presented with its numerous definitions and calculation methods. The main properties of the spectrum are described, showing that important characteristics of the original signal can be drawn from it, such as its amplitude or the velocity change associated with the movement during a shock.

The SRS is the ideal tool for comparing the severity of several shocks and for drafting specifications. Recent standards require writing test specifications from real environment measurements associated with the life profile of the material (test tailoring). The process that makes it possible to transform a set of recorded shocks into a specification of the same severity is detailed.

Packages must protect the equipment contained within them from various forms of disturbance related to handling and possible free fall drop and impact onto a floor. A method to characterize the shock fragility of the packaged product, using the "damage boundary curve" (DBC), and to choose the characteristics of the cushioning material constituting the package is described.

The principle of shock machines that are currently most widely used in laboratories is described. To reduce costs by restricting the number of changes in test facilities, specifications expressed in the form of a simple shock (half-sine, rectangle, sawtooth with a final peak) can occasionally be tested using an electrodynamic exciter. The problems encountered, which stress the limitations of such means, are set out together with the consequences of modifications, that have to be made to the shock profile on the quality of the simulation.

Determining a simple shape shock of the same severity as a set of shocks on the basis of their response spectrum is often a delicate operation. Thanks to progress in computerization and control facilities, this difficulty can sometimes be overcome by expressing the specification in the form of a response spectrum and by controlling the exciter directly from that spectrum. In practical terms, as the exciter can only be driven with a signal that is a function of time, the software of the control rack determines a time signal with the same spectrum as the specification displayed. The principles of composition of the equivalent shock are described with the shapes of the basic signals commonly used, while their properties and the problems that can be encountered, both in the generation of the signal and with respect to the quality of the simulation obtained, are emphasized.

Pyrotechnic devices or equipment (cords, valves, etc.) are frequently used in satellite launchers due to the very high degree of accuracy that they provide in operating sequences. Shocks induced in structures by explosive charges are extremely severe, with very specific characteristics. It is shown that they cannot be correctly simulated in the laboratory by conventional means and that their simulation requires specific tools.

12.1 Definitions

12.1.1 Shock

Shock occurs when a force, a position, a velocity, or an acceleration is abruptly modified and creates a transient state in the system considered. The modification is normally regarded as *abrupt* if it occurs in a time period that is short compared with the natural period concerned (AFNOR, 1993). Shock is defined as a vibratory excitation having a duration between the natural period of the excited mechanical system and two times that period (Figure 12.1).

12.1.2 Simple (or Perfect) Shock

A shock whose signal can be represented exactly in simple mathematical terms is called a simple (or perfect) shock. Standards generally specify one of the three following: half-sine (approached by a versed sine waveform), terminal peak sawtooth, and rectangular shock (approached by a trapezoidal waveform).

12.1.3 Half-Sine Shock

This is a simple shock for which the acceleration–time curve has the form of a half-period (part positive or negative) of a sinusoid.

12.1.4 Versed-Sine (or Haversine) Shock

This is a simple shock for which the acceleration–time curve has the form of one period of the curve representative of the function $[1 - \cos(\)]$, with this period starting from the zero value of this function. It is thus a signal ranging between two minima of a sine wave.

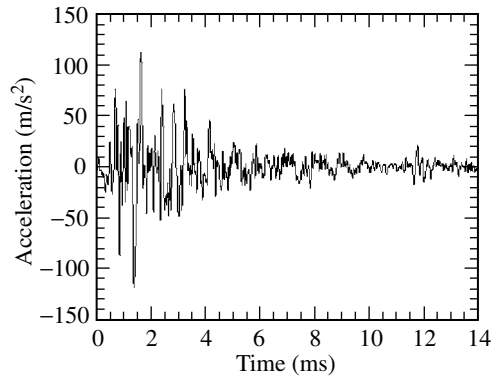


FIGURE 12.1 Example of a shock. (Source: Lalanne, *Chocs Mécaniques*, Hermes Science Publications. With permission.)

12.1.5 Terminal Peak Sawtooth Shock or Final Peak Sawtooth Shock

This is a simple shock for which the acceleration–time curve has the shape of a triangle, where acceleration increases linearly up to a maximum value and then instantly decreases to zero.

12.1.6 Rectangular Shock

This is a simple shock for which the acceleration–time curve increases instantaneously up to a given value, remains constant throughout the signal, and decreases instantaneously to zero. In practice, what is carried out are trapezoidal shocks.

12.1.6.1 Trapezoidal Shock

This is a simple shock for which the acceleration–time curve grows linearly up to a given value, remains constant during a certain time period, after which it decreases linearly to zero.

12.2 Description in the Time Domain



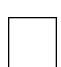

Three parameters are necessary to describe a shock in the time domain: its amplitude, its duration, τ , and its form.

The physical parameter expressed in terms of time is generally an acceleration, $\ddot{x}(t)$, but can be also a velocity, $\dot{v}(t)$, a displacement, $x(t)$, or a force, $F(t)$.

In the first case, which we will consider in particular in this chapter, the *velocity change* corresponding to the shock movement is equal to (Table 12.1)

$$\Delta V = \int_0^{\tau} \ddot{x}(t) dt \quad (12.1)$$

TABLE 12.1 Main Simple Shock Waveforms (Amplitude, \bar{x}_m , Duration, τ , Velocity Change, ΔV)

Waveform		Function	ΔV
Half-sine		$\bar{x}(t) = \bar{x}_m \sin\left(\frac{\pi}{\tau}t\right)$	$\frac{2}{\pi} \bar{x}_m \tau$
Versed-sine		$\bar{x}(t) = \frac{\bar{x}_m}{2} \left(1 - \cos \frac{2\pi}{\tau}t\right)$	$\frac{1}{2} \bar{x}_m \tau$
Rectangle		$\bar{x}(t) = \bar{x}_m$	$\bar{x}_m \tau$
Terminal peak sawtooth		$\bar{x}(t) = \bar{x}_m \frac{t}{\tau}$	$\frac{1}{2} \bar{x}_m \tau$

12.3 Shock Response Spectrum

12.3.1 Need

Very often, the problem is to evaluate the relative severity of several shocks (shocks measured in the real environment, measured shocks with respect to standards, establishment of a specification, etc.).

A shock is an excitation of short duration, which induces transitory dynamic stress in structures. These stresses are a function of the following:

- The characteristics of the shock (amplitude, duration, and shape).
- The dynamic properties of the structure (resonant frequencies, Q factors; [see Chapter 19](#)).

The severity of a shock can thus be estimated only according to the characteristics of the system that undergoes it. The evaluation of this severity requires in addition the knowledge of the mechanism leading to a degradation of the structure. The two most common mechanisms are as follows:

- The exceeding of a value threshold of the stress in a mechanical part can lead to either a permanent deformation (acceptable or not) or a fracture, or at any rate, a functional failure.
- If the shock is repeated many times (e.g., the shock recorded on the landing gear of an aircraft, the operation of an electromechanical contactor), the fatigue damage accumulated in the structural elements can lead in the long term to fracture (Lalanne, 2002c).

The comparison would be difficult to carry out if one used a fine model of the structure, and in any case this is not always available, particularly at the stage of the development of the specification of dimensioning. One searches for a method of general nature, which leads to results that can be extrapolated to any structure.

12.3.2 Shock Response Spectrum Definition

In a thesis on the study of earthquakes' effects on buildings, Biot (1932) proposed a method consisting of applying the shock under consideration to a "standard" mechanical system, which thus does not claim to be a model of the real structure. It is composed of a support and of N linear one-degree-of-freedom (one-DoF) resonators, comprising each one are a mass, m_i a spring of stiffness, k_i and a damping device, c_i , chosen such that the fraction of critical damping (damping ratio) $\xi = c_i / (2\sqrt{k_i m_i})$ is the same for all N resonators. A model for the shock response spectrum (SRS) is shown in [Figure 12.2](#) ([also see Chapter 17](#)).

When the support is subjected to the shock, each mass, m_i , has a specific movement response according to its natural frequency, $f_{0i} = (1/2\pi)\sqrt{k_i/m_i}$ and to the chosen damping ratio, ξ , while a

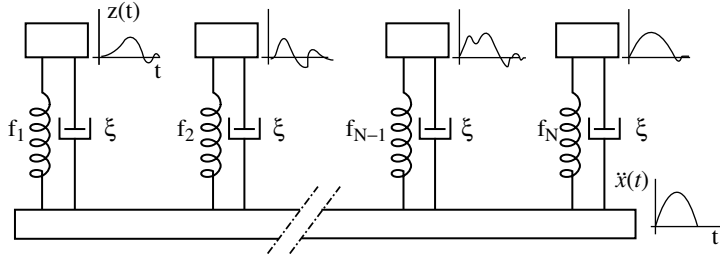


FIGURE 12.2 Model of the SRS. (Source: Lalanne, *Chocs Mecaniques*, Hermes Science Publications. With permission.)

stress, σ_i , is induced in the elastic element. The analysis consists of seeking the largest stress, σ_{m_i} , observed at each frequency in each spring.

For applications deviating from the assumptions of definition of the SRS (linearity, only one DoF), it is desirable to observe a certain prudence if one wishes to estimate quantitatively the response of a system starting from the spectrum (Bort, 1989). The response spectra are more often used to compare the severity of several shocks.

It is known that the tension static diagram of many materials comprises a more-or-less linear arc on which the stress is proportional to the deformation. In dynamics, this proportionality can be allowed within certain limits for the peaks of the deformation.

If a mass–spring–damper system is supposed to be linear, it is then appropriate to compare two shocks by the maximum response stress, σ_m , that they induce or by the maximum relative displacement, z_m , that they generate. This occurs since it is supposed

$$\sigma_m = Kz_m \quad (12.2)$$

z_m is a function only of the dynamic properties of the system, whereas σ_m is also a function, via K , of the properties of the materials which constitute it.

The curve giving the largest relative displacement, z_{sup} multiplied by ω_0^2 ($\omega_0 = 2\pi f_0$) according to the natural frequency, f_0 , for a given damping ratio ξ , is the SRS.

12.3.3 Response of a Linear One-Degree-of-Freedom System

12.3.3.1 Shock Defined by a Force

Consider a mass–spring–damping system subjected to a force, $F(t)$, applied to the mass (Figure 12.3). The differential equation of the movement is written as

$$m \frac{d^2 z}{dt^2} + c \frac{dz}{dt} + kz = F(t) \quad (12.3)$$

where $z(t)$ is the relative displacement of the mass, m , relative to its support in response to the shock, $F(t)$. This equation can be expressed in the form (Lalanne, 2002b):

$$\frac{d^2 z}{dt^2} + 2\xi\omega_0 \frac{dz}{dt} + \omega_0^2 z = \frac{F(t)}{m} \quad (12.4)$$

where $\xi = c/2\sqrt{km}$ (damping ratio) and $\omega_0 = \sqrt{k/m}$ (natural frequency).

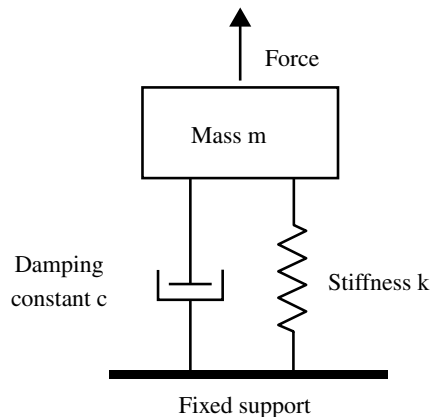


FIGURE 12.3 Linear one-Dof system subjected to a force. (Source: Lalanne, *Chocs Mecaniques*, Hermes Science Publications. With permission.)

12.3.3.2 Shock Defined by an Acceleration

Let us set $\ddot{x}(t)$ as an acceleration applied to the base of a linear one-DoF mechanical system, with $\ddot{y}(t)$ the absolute acceleration response of the mass, m , and $z(t)$ the relative displacement of the mass, m , with respect to the base (Figure 12.4).

The equation of the movement is written as above:

$$m \frac{d^2 y}{dt^2} = -k(y - x) - c \left(\frac{dy}{dt} - \frac{dx}{dt} \right) \quad (12.5)$$

that is

$$\frac{d^2 y}{dt^2} + 2\xi\omega_0 \frac{dy}{dt} + \omega_0^2 y = \omega_0^2 x(t) + 2\xi\omega_0 \frac{dx}{dt} \quad (12.6)$$

or while setting $z(t) = y(t) - x(t)$

$$\frac{d^2 z}{dt^2} + 2\xi\omega_0 \frac{dz}{dt} + \omega_0^2 z = -\frac{d^2 x}{dt^2} \quad (12.7)$$

The differential equation (Equation 12.7) can be integrated by parts or by using the Laplace transformation. If the excitation is an acceleration of the support, the response relative displacement is given, for zero initial conditions, by an integral called *Duhamel's integral*:

$$z(t) = \frac{-1}{\omega_0 \sqrt{1 - \xi^2}} \int_0^t \ddot{x}(\alpha) e^{-\xi\omega_0(t-\alpha)} \sin \omega_0 \sqrt{1 - \xi^2} (t - \alpha) d\alpha \quad (12.8)$$

where α is an integration variable homogeneous with time.

The absolute acceleration of the mass is given by

$$\begin{aligned} \ddot{y}(t) = & \frac{\omega_0}{\sqrt{1 - \xi^2}} \int_0^t \ddot{x}(\alpha) e^{-\xi\omega_0(t-\alpha)} [(1 - 2\xi^2) \sin \omega_0 \sqrt{1 - \xi^2} (t - \alpha) \\ & + 2\xi \sqrt{1 - \xi^2} \cos \omega_0 \sqrt{1 - \xi^2} (t - \alpha)] d\alpha \end{aligned} \quad (12.9)$$

12.3.4 Definitions

12.3.4.1 Response Spectrum

This is a curve representative of the variations of the largest response of a linear one-DoF system subjected to a mechanical excitation, plotted against its natural frequency, $f_0 = \omega_0/2\pi$, for a given value of its damping ratio (see Chapter 17).

12.3.4.2 Absolute Acceleration Shock Response Spectrum

In the most usual cases where the excitation is defined by an absolute acceleration of the support or by a force applied directly to the mass, the response of the system can be characterized by the absolute acceleration of the mass (which can be measured using an accelerometer fixed to this mass). The response spectrum is then called the *absolute acceleration SRS*.

12.3.4.3 Relative Displacement Shock Spectrum

In similar cases, we often calculate the relative displacement of the mass with respect to the displacement of the base of the system. This displacement is proportional to the stress created in the

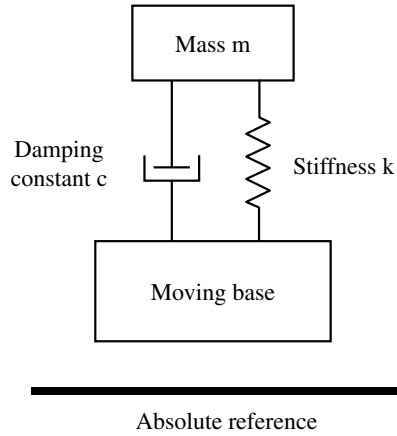


FIGURE 12.4 Linear one-DoF system subjected to acceleration. (Source: Lalanne, *Chocs Mecaniques*, Hermes Science Publications. With permission.)

spring (since the system is regarded as linear). In practice, one generally expresses in ordinates the quantity $\omega_0^2 z_{\text{sup}}$, which is called the *equivalent static acceleration* (Biot, 1941). This product has the dimensions of acceleration, but does not represent the absolute acceleration of the mass, except when damping is zero. However, when damping is close to the current values observed in mechanics, and in particular when $\xi = 0.05$, as a first approximation one can assimilate $\omega_0^2 z_{\text{sup}}$ to the absolute acceleration \ddot{y}_{sup} of the mass, m (Lalanne, 1975, 2002b).

The quantity $\omega_0^2 z_{\text{sup}}$ is termed *pseudo-acceleration*. In the same way, one terms the product $\omega_0 z_{\text{sup}}$ *pseudo-velocity*. The spectrum giving $\omega_0^2 z_{\text{sup}}$ vs. the natural frequency is named the *relative displacement shock spectrum*.

In each of these two important categories, the response spectrum can be defined in various ways according to how the largest response at a given frequency is characterized.

12.3.4.4 Primary Positive Shock Response Spectrum or Initial Positive Shock Response Spectrum

This is the highest positive response observed during the shock.

12.3.4.5 Primary (or Initial) Negative Shock Response Spectrum

This is the highest negative response observed during the shock.

12.3.4.6 Secondary (or Residual) Shock Response Spectrum

This is the largest response observed after the end of the shock. Here also, the spectrum can be positive or negative.

Example

An example giving standardized primary and residual relative displacement SRS curves for a half-sine pulse is shown in Figure 12.5.

12.3.4.7 Positive (or Maximum Positive) Shock Response Spectrum

This is the largest positive response due to the shock, without reference to the duration of the shock. It thus corresponds to the envelope of the positive primary and residual spectra.

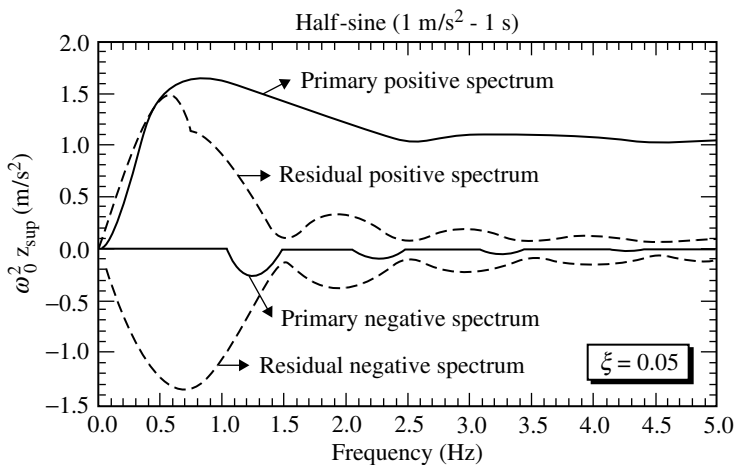


FIGURE 12.5 Standardized primary and residual relative displacement SRS of a half-sine pulse. (Source: Lalanne, *Chocs Mecaniques*, Hermes Science Publications. With permission.)

12.3.4.8 Negative (or Maximum Negative) Shock Response Spectrum

This is the largest negative response due to the shock, without reference to the duration of the shock. As before, it corresponds to the envelope of the negative primary and residual spectra.

12.3.4.9 Maximax Shock Response Spectrum

This is the envelope of the absolute values of the positive and negative spectra.

12.3.4.10 Choice of Shock Response Spectrum

Which spectrum must be used? Absolute acceleration SRS can be useful when absolute acceleration is the parameter easiest to compare with a characteristic value (as in a study of the effects of a shock on a man, a comparison with the specification of an electronics component, etc.).

In practice, it is very often the stress (and thus the relative displacement) which seems the most interesting parameter. The spectrum is primarily used to study the behavior of a structure, to compare the severity of several shocks (the stress created is a good indicator), to write test specifications (as it is also a comparison between the real environment and the test environment), or to dimension a suspension (relative displacement and stress are then useful).

The damage is assumed to be proportional to the largest value of the response, i.e., to the amplitude of the spectrum at the frequency considered, and it is of little importance for the system whether this maximum, z_m , takes place during or after the shock. The most interesting spectra are thus the positive and negative spectra that are most frequently used in practice, with the maximax spectrum.

The distinction between positive and negative spectra must be made each time the system, if dissymmetrical, behaves differently, for example under different tension and compression. It is, however, useful to know these various definitions so as to be able to correctly interpret the curves published.

The *Shock Response Spectrum* is a curve representative of the variations of the largest response of a linear one-DoF system subjected to a mechanical excitation, plotted against its natural frequency, for a given value of its damping ratio.

The response can be defined by the pseudo-acceleration, $\omega_0^2 z_{sup}$ (*relative displacement shock spectrum*) or by the absolute acceleration of the mass (*absolute acceleration SRS*). For the usual values of Q , the spectra are very close.

The most interesting spectra are the positive and negative spectra, which are most frequently used in practice, with the maximax spectrum.

The relation between the various types of SRS that have been discussed here is shown in Figure 12.6.

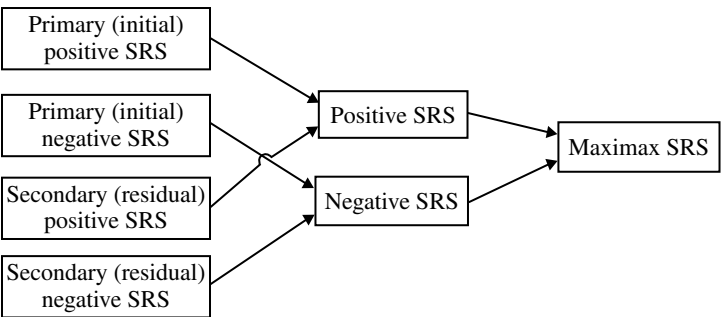


FIGURE 12.6 Relation between the different types of SRS.

12.3.5 Standardized Shock Response Spectrum

12.3.5.1 Definition

For a given shock, the spectra plotted for various values of the duration and the amplitude are similar in shape. It is thus useful, for simple shocks, to have a standardized or reduced spectrum plotted in dimensionless coordinates, while plotting on the abscissa the product $f_0 \tau$ (instead of f_0) or $\omega_0 \tau$ and on the ordinate the spectrum/shock pulse amplitude ratio, $\omega_0^2 z_m / \ddot{x}_m$, which, in practice, amounts to tracing the spectrum of a shock of duration equal to 1 sec and amplitude 1 m/sec². This is shown in Figure 12.7.

These standardized spectra can be used for two purposes:

- Plotting of the spectrum of a shock of the same form, but of arbitrary amplitude and duration.
- Investigating the characteristics of a simple shock of which the spectrum envelope is a given spectrum (resulting from measurements from the real environment).

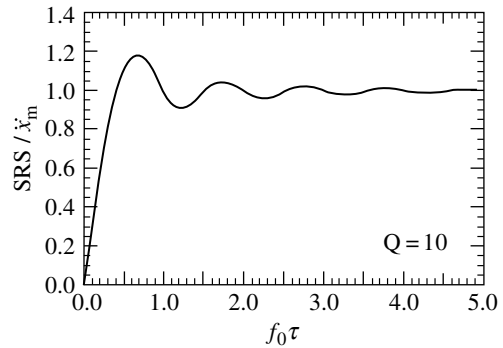


FIGURE 12.7 Standardized positive SRS of a terminal peak sawtooth pulse. (Source: Lalanne, *Chocs Mecaniques*, Hermes Science Publications. With permission.)

12.3.5.2 Standardized Shock Response Spectra of Simple Shocks

Figure 12.8 to Figure 12.15 give the reduced SRSs for various pulse forms, with unit amplitude and unit duration, for several values of damping. To obtain the spectrum of a particular shock of arbitrary amplitude, \ddot{x}_m , and duration, τ (different from 1) from these spectra, it is enough to regraduate the scales as follows:

- For the amplitude, multiply the reduced values by \ddot{x}_m .
- For the abscissae (x -axis values), replace each value $\phi (= f_0 \tau)$ by $f_0 = \phi / \tau$.

We will see later on how these spectra can be used for the calculation of test specifications.

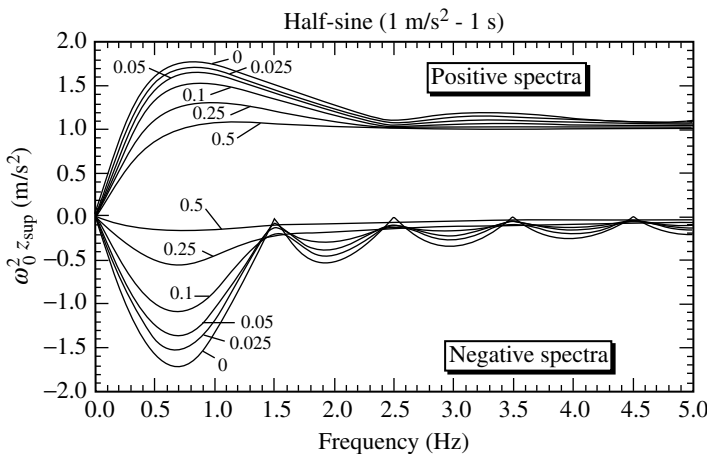


FIGURE 12.8 Standardized positive and negative relative displacement SRS of a half-sine pulse. (Source: Lalanne, *Chocs Mecaniques*, Hermes Science Publications. With permission.)

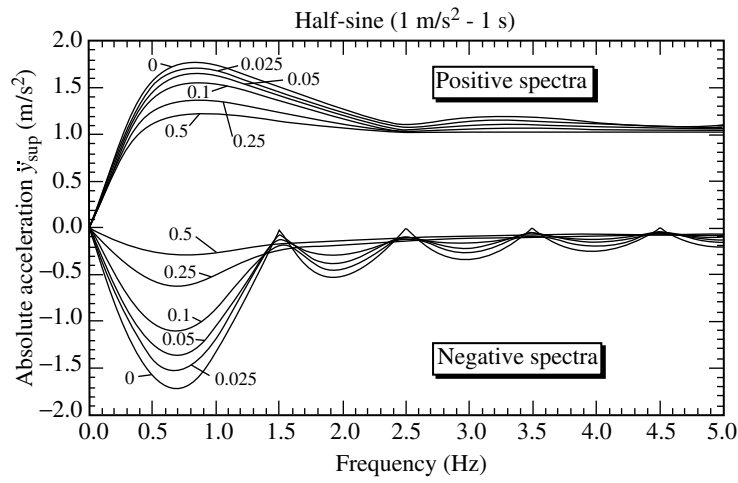


FIGURE 12.9 Standardized positive and negative absolute acceleration SRS of a half-sine pulse. (Source: Lalanne, *Chocs Mecaniques*, Hermes Science Publications. With permission.)

12.3.5.2.1 Half-Sine Pulse

Figure 12.8 and Figure 12.9 show the standardized SRS curves in this case.

12.3.5.2.2 Versed Sine Pulse

Figure 12.10 shows the standardized SRS curves in this case.

12.3.5.2.3 Terminal Peak Sawtooth Pulse

Figure 12.11 and Figure 12.12 show the standardized SRS curves for terminal peak sawtooth (TPS) pulse.

12.3.5.2.4 Rectangular Pulse

Figure 12.13 gives the standardized SRS curves for a rectangular pulse shock.

12.3.5.2.5 Trapezoidal Pulse

Figure 12.14 presents the standardized SRS curve for a trapezoidal pulse. A comparison of various SRS curves is given in Figure 12.15.

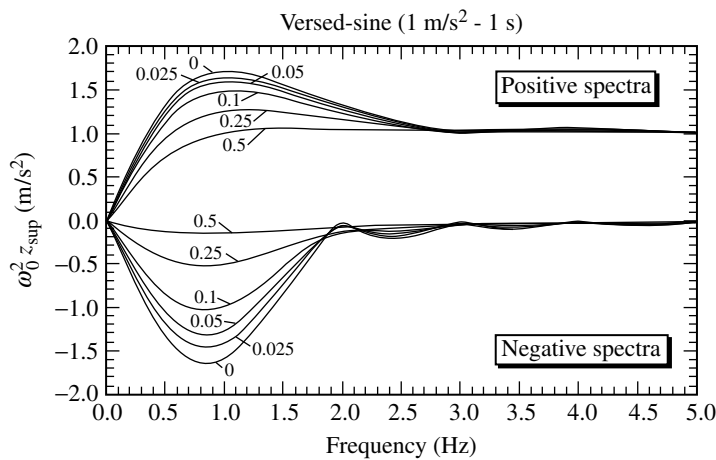


FIGURE 12.10 Standardized positive and negative relative displacement SRS of a versed sine pulse. (Source: Lalanne, *Chocs Mecaniques*, Hermes Science Publications. With permission.)

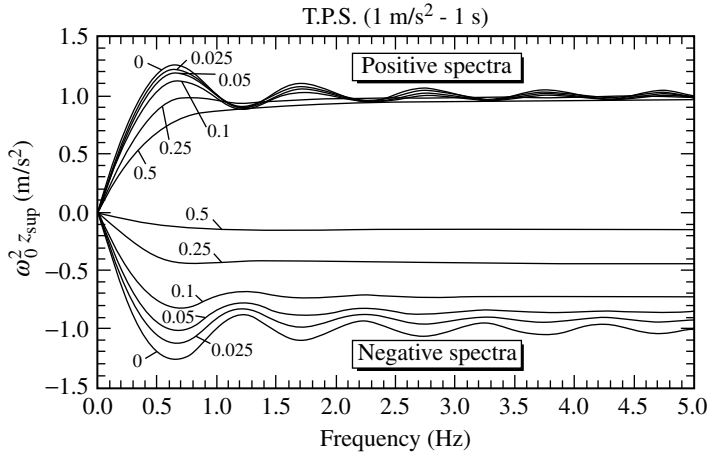


FIGURE 12.11 Standardized positive and negative relative displacement SRS of a TPS pulse. (Source: Lalanne, *Chocs Mecaniques*, Hermes Science Publications. With permission.)

12.3.6 Choice of Damping

The choice of damping should be carried out according to the structure subjected to the shock. When this is not known, or studies are being carried out with a view to comparison with other already calculated spectra, the outcome is that one plots the shock response spectra with a damping ratio equal to 0.05 (i.e., $Q = 10$; see Chapter 19). It is an approximately average value for the majority of structures. Unless otherwise specified, as noted on the curve, it is the value chosen conventionally. With the spectra varying relatively little with damping, this choice is often not very important. To limit possible errors, the selected value should, however, be systematically noted on the diagram.

12.3.7 Shock Response Spectra Domains

Three domains can be schematically distinguished for shock spectra.

1. An *impulse domain* at low frequencies, in which the amplitude of the spectrum (and thus of the response) is lower than the amplitude of the shock: The system reduces the effects of the shock. It is thus

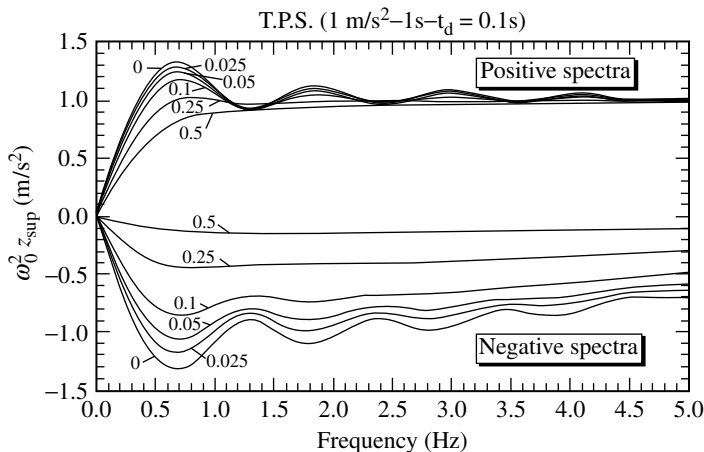


FIGURE 12.12 Standardized positive and negative relative displacement SRS of a TPS pulse with nonzero decay time. (Source: Lalanne, *Chocs Mecaniques*, Hermes Science Publications. With permission.)

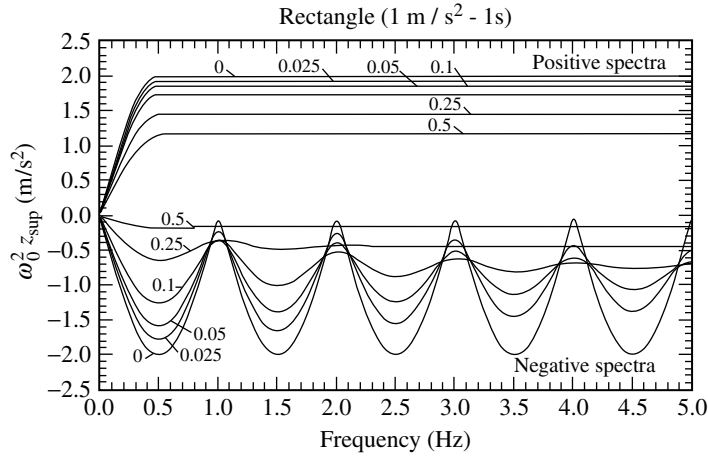


FIGURE 12.13 Standardized positive and negative relative displacement SRS of a rectangular pulse. (Source: Lalanne, *Chocs Mecaniques*, Hermes Science Publications. With permission.)

in this impulse region that it would be advisable to choose the natural frequency of an isolation system to the shock, from which we can deduce the stiffness envisaged of the insulating material:

$$k = m\omega_0^2 = 4\pi^2 f_0^2 m \quad (12.10)$$

with m being the mass of the material to be protected.

The shock here is of very short duration with respect to the natural period of the system. In this impulse region ($0 \leq f_0 \tau \leq 0.2$):

- The form of the shock has little influence on the amplitude of the spectrum. Only (for a given damping value) the velocity change ΔV associated with the shock, equal to the algebraic surface under the curve $\ddot{x}(t)$ is important.
- The slope p at the origin of the spectrum plotted for zero damping in linear scales is proportional to the velocity change ΔV corresponding to the shock pulse (Lalanne, 2002b):

$$p = \frac{d(\omega_0^2 z_{sup})}{df_0} = 2\pi\Delta V \quad (12.11)$$

This relation is approximate if damping is small.

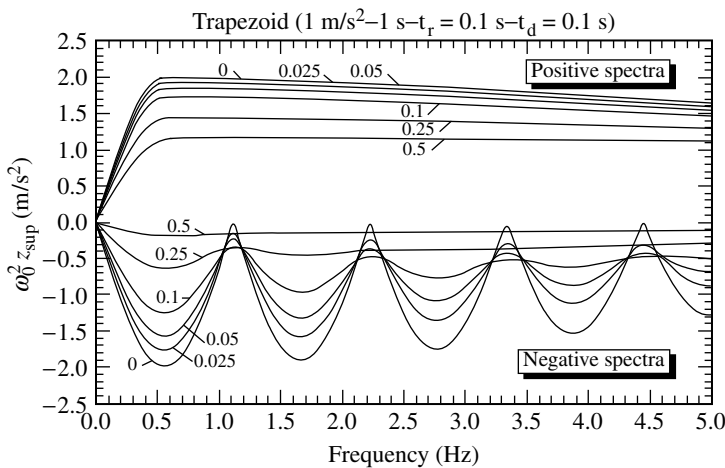


FIGURE 12.14 Standardized positive and negative relative displacement SRS of a trapezoidal pulse. (Source: Lalanne, *Chocs Mecaniques*, Hermes Science Publications. With permission.)

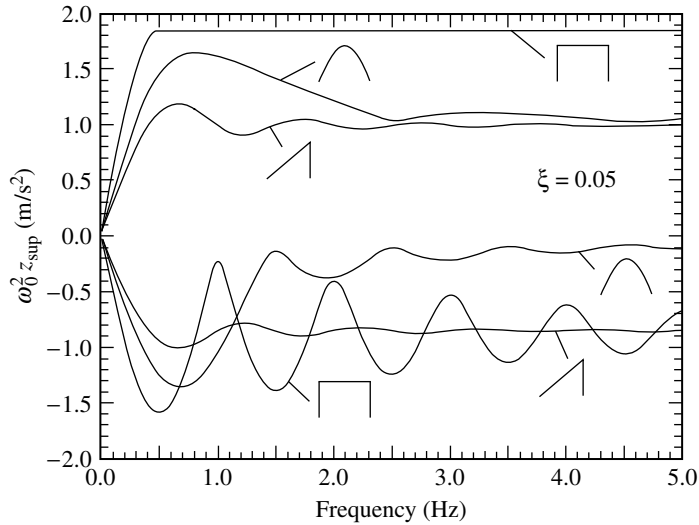


FIGURE 12.15 Comparison between the SRS of the three main simple shock waveforms.

- The positive and negative spectra are in general the residual spectra (it is sometimes necessary that the frequency of spectrum is very small, and there can be exceptions for certain long shocks in particular). They are nearly symmetrical so long as damping is small.

2. A *static domain* in the range of the high frequencies, where the positive spectrum tends towards the amplitude of the shock whatever the damping: All occurs here as if the excitation were a static acceleration (or a very slowly varying acceleration), as the natural period of the system is small compared with the duration of the shock. This does not apply to rectangular shocks or to the shocks with zero rise time. Real shocks having necessarily a rise time different from zero, this restriction remains theoretical.

3. An *intermediate domain* in which there is dynamic amplification of the effects of the shock, the natural period of the system being close to the duration of the shock: This amplification, which is more or less significant depending on the shape of the shock and the damping of the system, does not exceed 1.77 for shocks of traditional simple shape (half-sine, versed sine, TPS). Much larger values are reached in the case of oscillatory shocks, made up, for example, by a few periods of a sinusoid.

Various domains of an SRS are illustrated in Figure 12.16.

Example

Consider a half-sine shock pulse, amplitude $\ddot{x}_m = 50 \text{ m/sec}^2$, duration $\tau = 11 \text{ msec}$, positive SRS (relative displacement) for a damping ratio $\xi = 0.05$.

The slope p of the SRS (Figure 12.16) at the origin is equal to $p = 30.6/15 = 2.04 \text{ m/sec}$, yielding

$$\Delta V \approx \frac{p}{2\pi} = \frac{2.04}{2\pi} \approx 0.325 \text{ m/sec}$$

a value to be compared with the surface under the half-sine shock pulse (Table 12.1):

$$\Delta V = \frac{2}{\pi} \ddot{x}_m \tau = \frac{2}{\pi} \times 50 \times 11 \times 10^{-3} \approx 0.35 \text{ m/sec}$$

12.3.8 Algorithms for Calculation of the Shock Response Spectra

Various algorithms have been developed to solve the second-order differential equation (Equation 12.7; O'Hara, 1962; Gaberson, 1980; Smallwood, 1981; Cox, 1983; Hughes and Belytschko, 1983; Irvine, 1986;

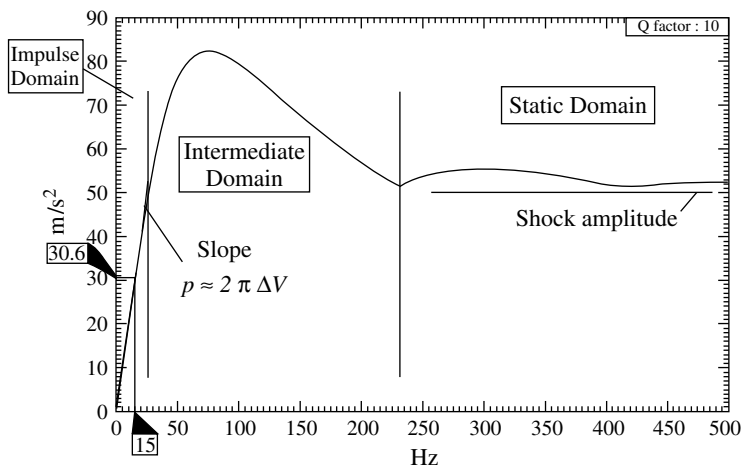


FIGURE 12.16 Shock response spectra domains.

Dokainish and Subbaraj, 1989; Colvin and Morris, 1990; Hale and Adhami, 1991; Mercer and Lincoln, 1991; Seipel, 1991; Merritt, 1993; Grivelet, 1996). Very reliable results are obtained in particular with those of Cox (1983) and Smallwood (1986, 2002).

12.3.9 Choice of the Digitization Frequency of the Signal

The SRS is obtained by considering the largest peak of the response of a one-DoF system. This response is in general calculated by the algorithms with the same temporal step as that of the shock signal.

First of all, the digitization (sampling) frequency must be sufficient to correctly represent the signal itself and in particular not to truncate its peaks. Two cases are shown in Figure 12.17 and Figure 12.18.

When the natural frequency of the one-DoF system is lower than the smallest shock frequency, the detection of peaks of the response can be carried out accurately even if the signal digitization (sampling) frequency is insufficient for correctly describing the shock (Figure 12.17). The error on the SRS is then only related to the poor digitization (sampling) of shock and results in an inaccuracy on the velocity change associated with the shock, i.e., on the SRS slope at low frequency.

Even if the sampling frequency allows a good representation of the shock, it can be insufficient for the response when the natural frequency of the system is higher than the maximum frequency of

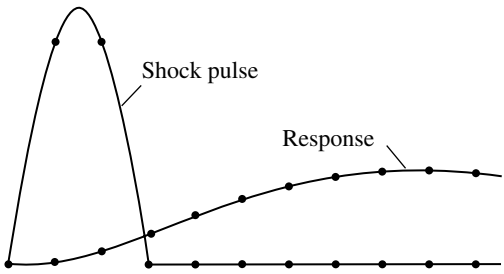


FIGURE 12.17 Sampling frequency sufficient for the response and too low for the shock pulse (error on the slope of SRS at low frequency).

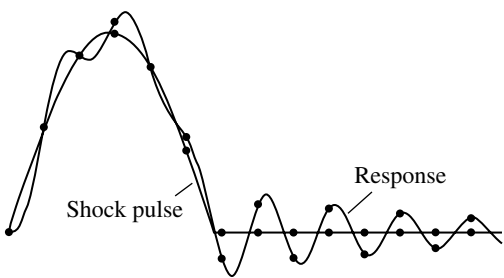


FIGURE 12.18 Sampling frequency sufficient for the shock pulse and too low for the response (error on the SRS at high frequency).

the signal (Figure 12.18). The error is here related to the detection of the largest peak of the response, which occurs throughout shock (primary spectrum).

Figure 12.19 shows the error made in the more stringent case when the points surrounding the peak are symmetrical with respect to the peak.

If we set

$$S_F = \frac{\text{Sample frequency}}{\text{SRS maximum frequency}}$$

it can be shown that, in this case, the error made according to the sampling factor, S_F , is equal to (Sinn and Bosin, 1981; Wise, 1983)

$$e_s = 100 \left[1 - \cos \left(\frac{\pi}{S_F} \right) \right] \tag{12.12}$$

The sampling frequency must be higher than 16 times the maximum frequency of the spectrum so that the error made at high frequency is lower than 2% (23 times the maximum frequency for an error lower than 1%). The rule of thumb often used to specify a sampling factor equal to ten can lead to an error of about 5%. Percentage error as a function of the sampling factor is plotted in Figure 12.20. Also see Table 12.2.

Algorithms use generally the same sampling frequency for the shock input and the response of the one-DoF system. This choice led to define the sampling frequency according to the highest SRS frequency. In order to decrease the computing time, it could be interesting to determine a sampling frequency varying with each natural frequency (Smallwood, 2002).

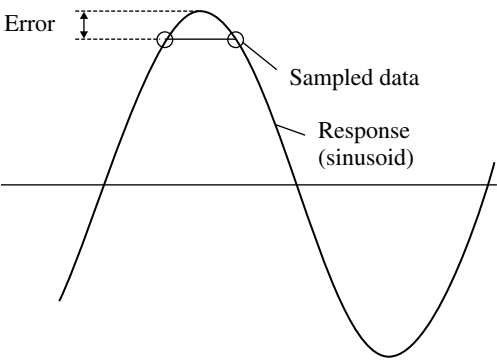


FIGURE 12.19 Error made in measuring the amplitude of the peak. (Source: Lalanne, *Chocs Mecaniques*, Hermes Science Publications. With permission.)

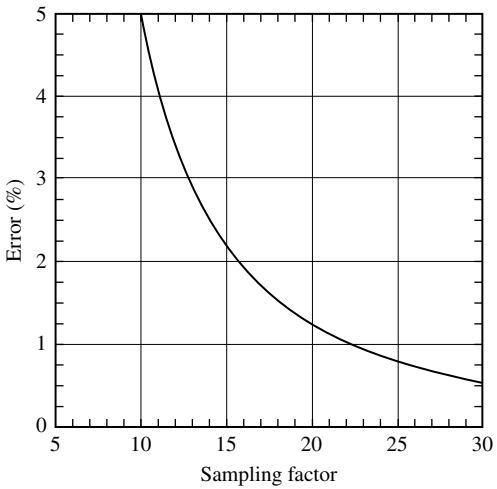


FIGURE 12.20 Error made in measuring the amplitude of the peak plotted against sampling factor. (Source: Lalanne, *Chocs Mecaniques*, Hermes Science Publications. With permission.)

Note: The sampling frequency must be higher than 16 times the maximum frequency of the spectrum so that the error made at high frequency is lower than 2%.

TABLE 12.2 Some Sampling Factors with Corresponding Error on the SRS

SRS Maximum Frequency Multiplied by	Error (%)
23	1
16	2
10	5

12.3.10 Use of Shock Response Spectra for the Study of Systems with Several Degrees of Freedom

By definition, the response spectrum gives the largest value of the response of a linear single-DoF system subjected to a shock. If the real structure is comparable to such a system, the SRS can be used to evaluate this response directly. This approximation is often possible, with the displacement response being mainly due to the first mode. In general, however, the structure comprises several modes, which are simultaneously excited by the shock. The response of the structure consists of the algebraic sum of the responses of each excited mode.

The maximum response of each one of these modes can be read on the SRS, but the following apply.

- One does not have any information concerning the moment of occurrence of these maxima. The phase relationships between the various modes are not preserved and the exact way in which the modes are combined cannot be known simply.
- The SRS is plotted for a given constant damping over all the frequency range, whereas this damping varies from one mode to another in the structure.

It thus appears difficult to use an SRS to evaluate the response of a system presenting more than one mode. However, it happens that this is the only possible means. The problem is to know how to combine these “elementary” responses so as to obtain the total response and to determine, if need be, any suitable participation factors dependent on the distribution of the masses of the structure, of the shapes of the modes, etc.

When there are several modes, several proposals have been made to limit the value of the total response of the mass j of the one of the DoF starting from the values read on the SRS, as follows.

- Add the values with the maxima of the responses of each mode, without regard to the phase (Benioff, 1934).
- Sum the absolute values of the maximum modal responses (Biot, 1932). As it is not probable that the values of the maximum responses take place all at the same moment with the same sign, the real maximum response is lower than the sum of the absolute values. This method gives an upper limit of the response and thus has a practical advantage: the errors are always on the side of safety. However, it sometimes leads to excessive safety factors (Shell, 1966).
- Perform an algebraic sum of the maximum responses of the individual modes. A study showed that, in the majority of the practical problems, the distribution of the modal frequencies and the shape of the excitation are such that the possible error remains probably lower than 10% (Rubin, 1958; Fung and Barton, 1958).
- Add to the response of the first mode a fixed percentage of the responses of the other modes, or increase in the response of the first mode by a constant percentage (Clough, 1955).
- Combine the responses of the modes by taking the square root of the sum of the squares to obtain an estimate of the most probable value (Merchant and Hudson, 1962). This criterion gives values of the total response lower than the sum of the absolute values and provides a more realistic evaluation of the average conditions (Ostrem and Rumerman, 1965; Ridler and Blader, 1969).
- Average the sum of the absolute values and the square root of the sum of the squares (Jennings, 1958). One can also choose to define positive and negative limiting values starting from a system of weighted averages. For example, the relative displacement response of the mass j is estimated by

$$\max_{t \geq 0} |z_j(t)| = \frac{\sqrt{\sum_{i=1}^n (z_m^2)_i} + p \sum_{i=1}^n |z_m|_i}{p + 1} \quad (12.13)$$

where the terms $|z_m|_i$ are the absolute values of the maximum responses of each mode and p is a weighting factor (Merchant and Hudson, 1962).

12.4 Pyroshocks

The aerospace industry uses many pyrotechnic devices such as explosive bolts, squib valves, jet cord, and pin pushers. During their operation, these devices generate shocks which are characterized by very strong acceleration levels at very high frequencies that can be sometimes dangerous for the structures, but especially for the electric and electronic components involved. An example of a pyroshock is given in Figure 12.21.

Pyroshock intensity is often classified according to the distance from the point of detonation of the device. Agreement on classifying intensity according to this criterion is not unanimous. Two fields are generally considered (Table 12.3):

- The near-field, close to the source (material within about 15 cm of point of detonation of the device, or about 7.5 cm for less intense pyrotechnic devices), in which the effects of the shocks are primarily related to the propagation of a stress wave in the material.
- The far-field (material beyond about 15 cm for intense pyrotechnic devices, or beyond 7.5 cm for less intense devices) in which the shock is then propagated whilst attenuating in the structure and from which the effects of this wave combine with a damped oscillatory response of the structure at its frequencies of resonance (or the structural response only).

Three fields are sometimes suggested: the near-field, the mid-field (same definition as the far-field above, between 15 and 60 cm, or 7.5 and 15 cm for the less intense shocks), and the far-field, where only the structural response effect persists.

An investigation by Moening (1986) showed that the causes of observed failures on the American launchers between 1960 and 1986 (63 due to pyroshocks) are mainly the difficulty in evaluating these shocks *a priori*, especially the lack of consideration of these excitations during design and the absence of rigorous test specifications.

Such shocks have the following general characteristics.

- The levels of acceleration are very important; the shock amplitude is not simply related to the quantity of explosive used (Hughes, 1983). The quantity of metal cut by a jet cord is, for example, a more significant factor than the mass of the explosive.

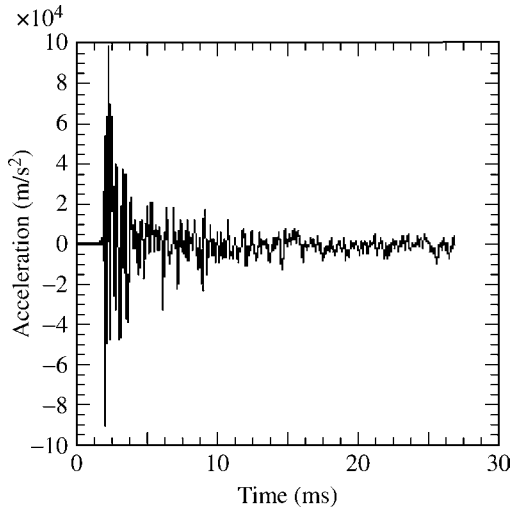


FIGURE 12.21 Example of a pyroshock. (Source: Lalanne, *Chocs Mecaniques*, Hermes Science Publications. With permission.)

TABLE 12.3 Characteristics of Each Pyroshock Intensity Domain

Field	Distance from the Source (cm)	Intense Pyrotechnic Devices (cm)	Shock Amplitude Frequency Content
Near field (stress wave propagation effect)	< 7.5	< 15	> 5000g, up to 300,000g above 100,000 Hz
Far-field (stress wave propagation effect + structural response effect)	> 7.5	> 15	1000 to 5000g above 10,000 Hz

Source: Lalanne, *Chocs Mecaniques*, Hermes Science Publications. With permission.

- The signals assume an oscillatory shape.
- The shocks have very close components according to three axes; their positive and negative response spectra are curves that are roughly symmetrical with respect to the axis of the frequencies. They begin at zero frequency with a very small slope at the origin, grow with the frequency until a maximum located at some kHz, even a few tens of kHz, is reached, and then tend according to the rule towards the amplitude of the temporal signal. Due to their contents at high frequencies, such shocks can damage electric or electronic components.
- The *a priori* estimate of the shock levels is neither easy nor precise.

These characteristics make pyroshocks difficult to measure, requiring sensors that are able to accept amplitudes of 100,000g, frequencies being able to exceed 100 kHz, with important transverse components. They are also difficult to simulate.

The dispersions observed in the response spectra of shocks measured under comparable conditions are often important, 3 dB with more than 8 dB compared with the average value, according to the authors (Smith, 1984, 1986). The reasons for this dispersion are in general related to inadequate instrumentation and the conditions of measurement (Smith, 1986):

- The fixing of the sensors on the structure using insulated studs or wedge which act like mechanical filters.
- Zero shift, due to the fact that high accelerations make the crystal of the accelerometer work in a temporarily nonlinear field (this shift can affect the calculation of the SRS).
- Saturation of the amplifiers.
- Resonance of the sensors.

With correct instrumentation, the results of measurements carried out under the same conditions are actually very close. The spectrum does not vary with the tolerances of manufacture and the assembly tolerances.

12.5 Use of Shock Response Spectra

12.5.1 Severity Comparison of Several Shocks

A shock, A, is regarded as more severe than a shock, B, if it induces in each resonator a larger stress. One then carries out an extrapolation, which is certainly open to criticism, by supposing that, if shock A is more severe than shock B when it is applied to all the standard resonators, it is also more severe with respect to an arbitrary real structure (which cannot be linear nor have a single DoF).

12.5.2 Test Specification Development from Real Environment Data

12.5.2.1 Synthesis of Spectra

Let us consider the most complex case where the real environment, described by curves of acceleration against time, is supposed to be composed of p different events (handling shock, inter-stage cutting shock on a satellite launcher, etc.), with each one of these events itself characterized by r_i successive measurements.

These r_i measurements allow a statistical description of each event. The following procedure holds for each one (Lalanne, 2002b; see Figure 12.22).

- Calculate the SRS of each signal recorded with the damping ratio of the principal mode of the structure if this value is known, if not, use the conventional value 0.05. In the same way, the

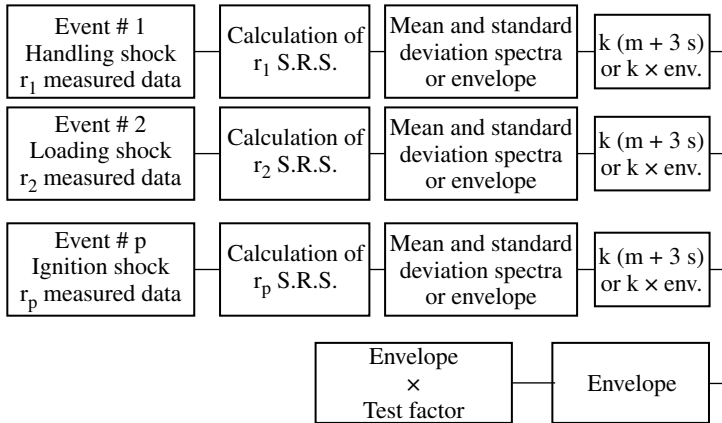


FIGURE 12.22 Process of developing a specification from real shocks measurements.

frequency band of analysis will have to envelop the principal resonant frequencies of the structure (known or foreseeable frequencies).

- If the number of measurements is sufficient, calculate the mean spectrum, m (mean of the points at each frequency) as well as the standard deviation spectrum (s), then the mean spectrum + α standard deviations, according to the frequency; if it is insufficient, make the envelope of the spectra.

The value of α can be either arbitrary (for example 2.5 or 3) or the result of a statistical calculation. It is often considered that the SRS amplitudes obey to a log-normal distribution. If y_i is the logarithm of the SRS amplitude, $y_j = \log_{10} \text{SRS}_j$, the real environment envelope (for a given probability P_0 of not exceeding at the confidence level π_0) can be defined by

$$\text{SRS}_{\text{Env}} = 10^{m_y + \alpha s_y} \quad (12.14)$$

where m_y and s_y are, respectively, the mean and the standard deviation of the y_j values:

$$m_y = \frac{1}{r_i} \sum_{j=1}^{r_i} y_j \quad (12.15)$$

$$s_y = \sqrt{\frac{\sum_{j=1}^{r_i} (y_j - m_y)^2}{r_i - 1}} \quad (12.16)$$

The number of standard deviations, α , is given in Table 12.4 for different values of r_i , P_0 , and π_0 . SRS_{Env} can also be defined as the upper one-sided normal tolerance interval for which 100 $P_0\%$ of the values will lie below the limit with 100 $\pi_0\%$ confidence.

- Apply the mean spectrum or the mean spectrum + α standard deviations a statistical uncertainty coefficient (Lalanne, 2002d), calculated for a probability of tolerated maximum failure (taking into account the uncertainties related to the dispersion of the real environment and of the mechanical strength), or contractual (if one uses the envelope).

TABLE 12.4 Number of Standard Deviations Corresponding to a Given Probability of not Exceeding, P_0 , at the Confidence Level, π_0

$r_i \backslash P_0$	$\pi_0 = 0.75$				$\pi_0 = 0.90$				$\pi_0 = 0.95$			
	0.75	0.90	0.95	0.99	0.75	0.90	0.95	0.99	0.75	0.90	0.95	0.99
3	1.464	2.501	3.152	4.396	2.602	4.258	5.310	7.340	3.804	6.158	7.655	10.552
4	1.256	2.134	2.680	3.726	1.972	3.187	3.957	5.437	2.619	4.416	5.145	7.042
5	1.152	1.961	2.463	3.421	1.698	2.742	3.400	4.666	2.149	3.407	4.202	5.741
6	1.087	1.860	2.336	3.243	1.540	2.494	3.091	4.242	1.895	3.006	3.707	5.062
7	1.043	1.791	2.250	3.126	1.435	2.333	2.894	3.972	1.732	2.755	3.399	4.641
8	1.010	1.740	2.190	3.042	1.360	2.219	2.755	3.783	1.617	2.582	3.188	4.353
9	0.984	1.702	2.141	2.977	1.302	2.133	2.649	3.641	1.532	2.454	3.031	4.143
10	0.964	1.671	2.103	2.927	1.257	2.065	2.568	3.532	1.465	2.355	2.911	3.981
15	0.899	1.577	1.991	2.776	1.119	1.866	2.329	3.212	1.268	2.068	2.566	3.520
20	0.865	1.528	1.933	2.697	1.046	1.765	2.208	3.052	1.167	1.926	2.396	3.295
30	0.825	1.475	1.869	2.613	0.966	1.657	2.080	2.884	1.059	1.778	2.220	3.064
40	0.803	1.445	1.834	2.568	0.923	1.598	2.010	2.793	0.999	1.697	2.126	2.941
50	0.788	1.426	1.811	2.538	0.894	1.560	1.965	2.735	0.961	1.646	2.065	2.863

Source: Lalanne, *Chocs Mecaniques*, Hermes Science Publications. With permission.

Each event thus being synthesized in only one spectrum, one proceeds to an envelope of all the spectra obtained to deduce from it an SRS covering the totality of the shocks of the life profile. After multiplication by a test factor, which takes account of the number of tests performed to demonstrate the resistance of the equipment (Lalanne, 2002d), this spectrum will be used as reference “real environment” for the determination of the specification.

The reference spectrum can consist of the positive and negative spectra or the envelope of their absolute value (maximax spectrum). In this last case, the specification will have to be applied according to the two corresponding half-axes of the test item.

12.5.2.2 Nature of the Specification

There is an infinity of shocks having a given response spectrum. This property is related to the very great loss of information in computing the SRS, since one retains only the largest value of the response according to the time to constitute the SRS at each natural frequency.

According to the characteristics of the spectrum and available means, the specification can be expressed in the forms given below.

- It can be a simple shape signal according to the time realizable on the usual shock machines (half-sine, TPS, rectangular pulse).

One can thus try to find a shock of simple form, in which the spectrum is closed to the reference spectrum, characterized by its form, its amplitude, and its duration. It is in general desirable that the positive and negative spectra of the specification, respectively, cover the positive and negative spectra of the field environment. If this condition cannot be obtained by application of only one shock (owing to the particular shape of the spectra, and the limitations of the facilities), the specification will be made up of two shocks, one on each half-axis. The envelope must be approaching the reference SRS as well as possible, if possible on all the spectrum in the frequency band retained for the analysis, if not in a frequency band surrounding the resonant frequencies of the test item (if they are known).

- It can be a SRS. In this case, the specification is directly the reference SRS.

12.5.2.3 Choice of Shape

The choice of the shape of a shock is carried out by a comparison of the shapes of the positive and negative spectra of the real environment with those of the spectra of the usual shocks of simple shape (half-sine, TPS, rectangle; [Figure 12.23](#)).

12.5.2.4 Amplitude

The amplitude of a shock is obtained by plotting the horizontal straight line that closely envelops the positive reference SRS at high frequency (Figure 12.24). This line cuts the y -axis at a point which gives the amplitude sought (here, one uses the property of the spectrum at high frequencies, which tends in this zone towards the amplitude of the signal in the time domain).

12.5.2.5 Duration

The shock duration is given by the coincidence of a particular point of the reference spectrum (Figure 12.24) and the reduced spectrum of the simple shock selected above.

One in general considers the abscissa, f_{01} , of the first point which reaches the value of the asymptote at the high frequencies (amplitude of shock) as shown in Figure 12.25. Table 12.5 joins together some values of this abscissa for the most usual simple shocks according to the Q factor (Lalanne, 2002b). Another possibility is to use the coordinates of the first (higher) peak of the SRS, as given in Table 12.6.

Notes:

1. If the calculated duration must be rounded (in milliseconds), the higher value should always be considered, so that the spectrum of the specified shock remains always higher or equal to the reference spectrum.

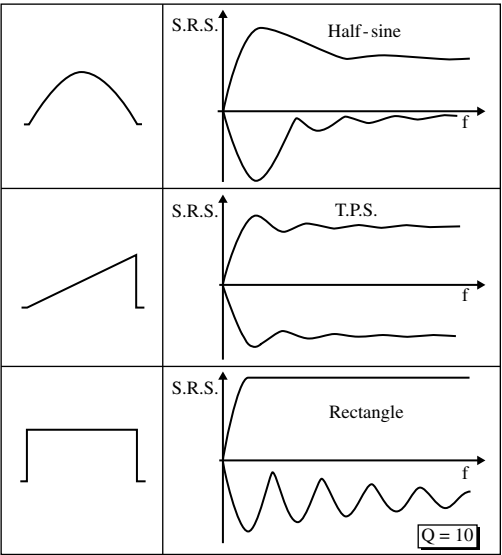


FIGURE 12.23 Shapes of the SRS of the realizable shocks on the usual machines. (Source: Lalanne, *Chocs Mecaniques*, Hermes Science Publications. With permission.)

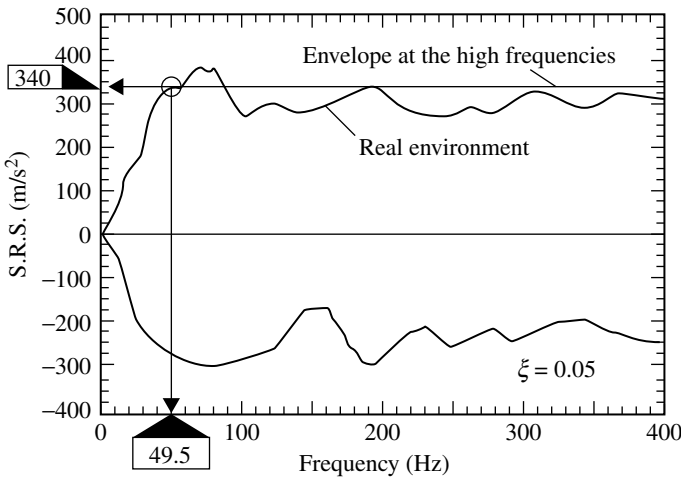


FIGURE 12.24 Determination of the amplitude and duration of the specification. (Source: Lalanne, *Chocs Mecaniques*, Hermes Science Publications. With permission.)

- 2. It is in general difficult to carry out shocks of duration lower than 2 msec on standard shock machines (except for very light equipment).

One will validate the specification by checking that the positive and negative spectra of the shock thus determined will envelop the respective reference spectra and one will verify, if the resonant frequencies of the test item are known, that one does not overtest exaggeratedly at these frequencies.

Example

As an example, let us consider the positive and negative spectra characterizing the real environment plotted in Figure 12.24, which is a result of a true synthesis. It is noted that the negative spectrum preserves a significant level throughout the entire frequency domain (the beginning of the spectrum being excluded).

The most suitable simple shock shape is the TPS. The shock amplitude, whatever its waveform, is equal to 340 m/sec². The abscissa, f_{01} , of the first point that reaches the value of the asymptote is equal to 0.415. From this value, $f_0 = 49.5$ Hz, the duration is given by $\tau = 0.415/49.5 = 0.0084$ sec.

The duration of the shock will thus be (rounding up) $\tau = 9$ msec, which slightly moves the spectrum towards the left and makes it possible to better cover the low frequencies. Figure 12.26 shows the spectra of the environment and those of the TPS pulse thus determined.

The main steps of deriving a shock test specification from the SRS of a real environment are outlined in Table 12.7.

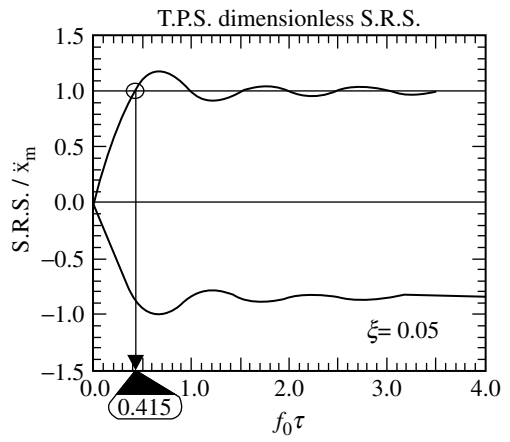


FIGURE 12.25 Determination of the shock duration. (Source: Lalanne, *Chocs Mecaniques*, Hermes Science Publications. With permission.)

TABLE 12.5 Values of the Dimensionless Frequency Corresponding to the First Passage of the SRS by the Amplitude Unit

Q	ξ	f_{01}		
		Half-sine	TPS	Rectangle
3	0.1667	0.358	0.564	0.219
4	0.1250	0.333	0.499	0.205
5	0.1000	0.319	0.468	0.197
6	0.0833	0.310	0.449	0.192
7	0.0714	0.304	0.437	0.188
8	0.0625	0.293	0.427	0.185
9	0.0556	0.295	0.421	0.183
10*	0.0500	0.293	0.415	0.181
15	0.0333	0.284	0.400	0.176
20	0.0250	0.280	0.392	0.174
30	0.0167	0.276	0.385	0.172
40	0.0125	0.274	0.382	0.170
50	0.0100	0.272	0.379	0.170
∞	0.0000	0.267	0.371	0.167

(*) Conventional value

TABLE 12.6 Values of the Dimensionless Frequency and Amplitude Corresponding to the First Peak of the SRS

Q	ξ	Half-sine		TPS		Rectangle	
		f_0 peak	SRS Peak	f_0 peak	SRS Peak	f_0 peak	SRS Peak
3	0.1667	0.875	1.4249	0.723	1.0462	0.508	1.5880
4	0.1250	0.86	1.4958	0.700	1.0894	0.504	1.6731
5	0.1000	0.845	1.5425	0.688	1.1182	0.503	1.7292
6	0.0833	0.840	1.5757	0.681	1.1387	0.502	1.7690
7	0.0714	0.830	1.600	0.676	1.1541	0.502	1.7985
8	0.0625	0.83	1.6194	0.672	1.1660	0.501	1.8214
9	0.0556	0.830	1.6346	0.669	1.1755	0.501	1.8396
10*	0.0500	0.826	1.6470	0.667	1.1832	0.501	1.8545
15	0.0333	0.820	1.6854	0.661	1.2073	0.501	1.9005
20	0.0250	0.820	1.7054	0.658	1.2199	0.501	1.9244
30	0.0167	0.815	1.7258	0.656	1.2328	0.501	1.9490
40	0.0125	0.810	1.7363	0.654	1.2393	0.501	1.9615
50	0.0100	0.813	1.7426	0.653	1.2433	0.501	1.9691
∞	0.0000	0.810	1.7685	0.650	1.2596	0.500	2.000

(*) Conventional value

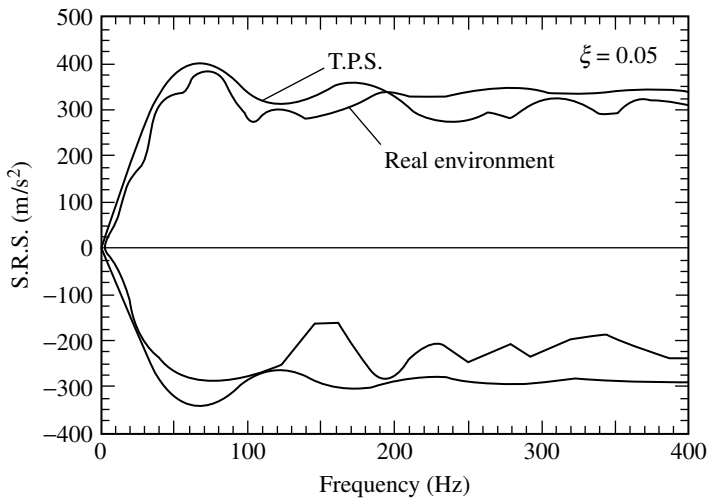


FIGURE 12.26 SRS of the specification and of the real environment. (Source: Lalanne, *Chocs Mecaniques*, Hermes Science Publications. With permission.)

12.5.2.6 Difficulties

The response spectra of shocks measured in the real environment often have a complicated shape which is impossible to envelop by the spectrum of a shock of simple shape realizable with the usual test facilities of the drop table type. This problem arises in particular when the spectrum presents an important peak (Smallwood and Witte, 1972). The spectrum of a shock of simple shape will be (see Figure 12.27): either an envelope of the peak, which will lead to significant overtesting compared with the other frequencies, or envelope of the spectrum except the peak, consequently leading to undertesting at the frequencies close to the peak, if one knows that the material does not have any resonance in the frequency band around the peak. The simulation of shocks of pyrotechnic origin leads to this kind of situation.

TABLE 12.7 Deriving a Shock Test Specification from the SRS of the Real Environment

Specification	Determined by
Shock waveform	Comparing the shape of the SRS of the real environment (reference) to that of the SRS of the simple shape shocks (half-sine, TPS or rectangular waveform)
Shock amplitude	The SRS amplitude at high frequency
Shock duration	Writing that the abscissa of the first point which reaches the value of the asymptote at high frequencies (amplitude of shock) is the same for the reduced SRS of the chosen simple shock and the reference SRS

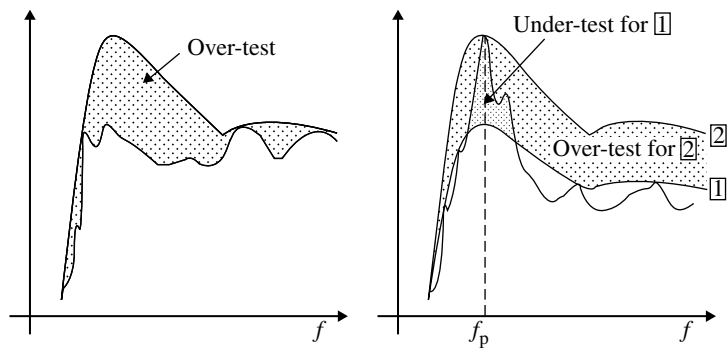


FIGURE 12.27 Examples of SRS that are difficult to envelop with the SRS of a simple shock. (Source: Lalanne, *Chocs Mecaniques*, Hermes Science Publications. With permission.)

Shock pulses of simple shape (half-sine, TPS) have, in logarithmic scales, a slope of 6 dB/octave (i.e., 45°) at low frequencies incompatible with those larger ones, of spectra of pyrotechnic shocks (>9 dB/octave). When the levels of acceleration do not exceed the possibilities of the shakers, simulation with control using spectra is of interest (Section 12.10).

Note: In general, it is not advisable to choose a simple shock shape as a specification when the real shock is oscillatory in nature. In addition to overtesting at low frequencies (the oscillatory shock is with very small velocity change), the amplitude of the simple shock thus calculated is more sensitive to the value of the *Q* factor in the intermediate frequency range.

12.6 Standards

12.6.1 Types of Standards

There are two types of standards: (1) those which specify *arbitrary shock pulses* (IEC, ISO, MIL STD 810 C, ...), and (2) those which require *test tailoring* (GAM EG 13, 1986; DEF STAN, 1999; MIL STD 810 F, 2000; NATO, 2000).

For the first case, the most frequently specified shock shapes are the half-sine, the TPS, and the rectangular (or trapezoidal) waveforms. In these standards, a table proposes several values of levels and durations, with preferred combinations (for example, 30g, 18 msec or 50g, 11 msec).

To take account of the limitations of test facilities and unavoidable signal distortions, the shock carried out is regarded as acceptable if the time acceleration signal lies between two tolerance limits. Two shocks included within these limits can, however, have very different effects (which can be evaluated with the SRS; Lalanne, 2002b).

Some examples of standards are given in Figure 12.28 and Figure 12.29.

In the second case, the test specification is preferably written from real measurements corresponding to the life profile of the material. The data to be used can be any of the following, in the preferential order:

- Functional real environment time history measurements of the material.
- Data measured under similar conditions and estimated to be representative.
- Data issued from prediction or calculation.
- *Default* values (fallback levels), obviously more arbitrary in character, to be used if measured data not available (classical pulse shock or SRS).

Derivation of the test specification and subsequent test should be carried out, in the preferential order as follows:

- For measured data of the same event, if the measured pulse shapes are very similar, use direct reproduction of the measured data under shaker waveform control (if possible). If the measured shock shapes are very different, use the following method.
- For measured data of different shock events use a synthesis of measurements using SRS (see Section 12.5.2). Test on shaker with SRS control if possible. If not possible, test on shock machine with a classical pulse having the same SRS.
- If there is no measured data of the real shock, but measured data under similar conditions, use the method as above.
- If there are no measured data, fallback levels and provisional values are to be replaced by results of measurement as soon as possible.

The transformation shock spectrum-signal has an infinite number of solutions, and very different signals can have identical response spectra. Standards often require specifying in addition to the spectrum other complementary data such as the duration of the signal time, the velocity change during the shock or the number of cycles (less easy), in order to deal with the spectrum and the couple amplitude/duration of the signal at the same time (see Section 12.10.4).

It is not correct to decompose a SRS into two separate domains in order to be able to meet a shock requirement (a low frequency component and a high frequency component). If the specimen has no significant low natural frequency, it is permissible to allow the low frequency domain of the SRS to fall out of tolerance in order to satisfy the high frequency part of the requirement.

The tolerance on the SRS amplitude should be, for example (MIL STD 810 F), -1.5 dB, $+3$ dB over the specified frequency range; a tolerance of $+3$ dB, $+6$ dB being permissible over a limited frequency range.

It is generally required to determine the positive and negative spectra (absolute acceleration or relative displacement) at $Q = 10$, at at least $1/12$ -octave frequency intervals.

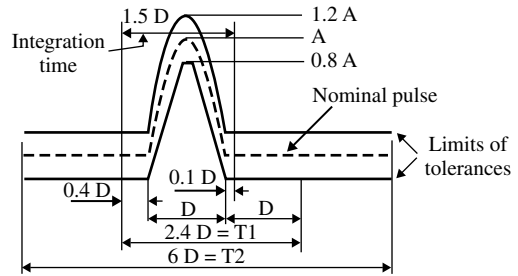


FIGURE 12.28 Half-sine pulse (NATO Stanag 4370, AECTP 403). T_1 : minimum time during which the pulse shall be monitored for shocks produced using a conventional shock-testing machine; T_2 : minimum time during which the pulse shall be monitored for shocks produced using a vibration generator.

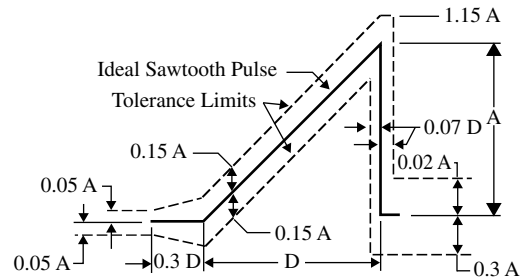


FIGURE 12.29 TPS pulse (MIL STD 810 F). D : duration of nominal pulse; A : peak acceleration of nominal pulse.

In the absence of accurate information on the number of shocks which the material will undergo in its service life, a minimum is often required of three shocks in both directions along each of the three orthogonal axes, a total of 18 shocks.

12.6.2 Installation Conditions of Test Item

- The test item should be mechanically fastened to the shock machine, directly by its normal means of attachment or by means of a fixture.
- The mounting configuration should enable the test item to be subjected to shocks along the various axes and directions as specified.
- External connections necessary for measuring purposes should add minimum restraint and mass.
- The fixture should not modify the dynamic behavior of the test item.
- Material intended for use with isolators should be tested with its isolators.
- The direction of gravity or any loading factors (mechanisms, shock isolators, etc.) must be taken into account by compensation or by suitable simulation.

12.6.3 Uncertainty Factor

An uncertainty factor may be added to the resulting envelope if confidence in the data is low or in order to take account of the dispersion of levels in the real environment when the data set is small. This factor can be arbitrary, of the order of 3 to 6 dB, for example, or determined from a reliability computation, taking account of the statistical distributions of the real environment and of the material strength (Lalanne, 2002d).

It is important that all uncertainties be clearly defined and that uncertainties are not superimposed upon estimates that already account for uncertainties.

Note: The purpose of the test is to demonstrate that the equipment has at least the specified strength at the time of its design. However, for obvious reasons of cost, this demonstration is generally conducted only on one specimen. To take into account the variability of the strength of the material, it is possible to increase the test severity by applying a “test factor.” This second factor depends on the number of tests to be conducted and on the coefficient of variation of the material strength (Lalanne, 2002d).

12.6.4 Bump Test

A *bump test* is a test in which a simple shock is repeated many times (DEF STAN, 1999; IEC, 1987b; AFNOR, 1993). Standardized severities are proposed. For example, half-sine, 10 g, 16 ms, 3000 bumps (shock) per axis, 3 bumps a second.

The purpose of this test is not to simulate any specific service condition. It is simply considered that it could be useful as a general ruggedness test to provide some confidence in the suitability of equipment for transportation in wheeled vehicles. It is intended to produce in the specimen effects similar of those resulting from repetitive shocks likely those encountered during transportation.

In this test, the equipment is always fastened (with its isolators if it is normally used with isolators) to the bump machine during conditioning.

12.7 Damage Boundary Curve

12.7.1 Definition

Products are placed in a package to be protected from possible free-fall drops and impacts onto a floor or a shipping platform during transport or handling. This packaging is often made up of a cushioning material (for example, honeycomb or foam) which absorbs the impact energy (related to the impact velocity) either by inelastic deformation, and which generates a shock at the entry of the material, whose

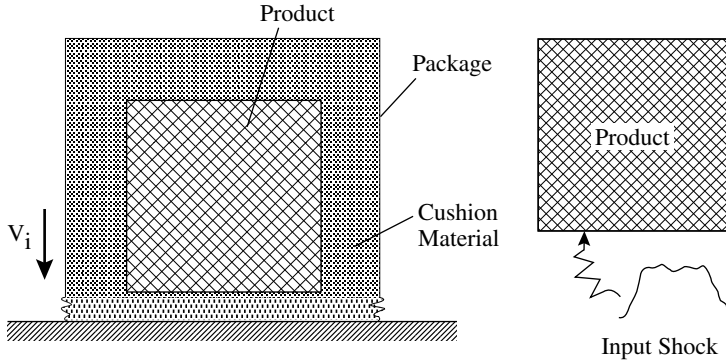


FIGURE 12.30 Shock transmitted to product during the crushing of package.

shape is often comparable to a rectangular or a trapezoid pulse (Figure 12.30). Alternatively, it can be made of an elastic material, which produces at the material entry a shock with a near half-sine waveform.

After determination of the shock environment, a statistical analysis allows one to specify the design drop height, with a given percentage of loss tolerated.

To choose the characteristics of the cushioning material constituting the package, it is first of all necessary to determine the shock fragility of the product that would be subjected to a shock with one of these two forms.

It can be considered that the severity of a shock is related to its amplitude and to its associated velocity change (we saw that these two parameters intervene in the SRS). We thus determine the largest acceleration and the largest velocity change that the unpackaged product subjected to these shocks can support.

At the time of two series of tests carried out on a shock machine, we note, for a given acceleration, the *critical velocity change* or, for a given velocity change, the *critical maximum shock acceleration* that leads to a damage on the material (deformation, fracture, faulty operation after the shock, etc.).

Results are expressed on a diagram of the acceleration–velocity change by a curve defined as the *damage boundary curve* (DBC; ASTM D3332), as shown in Figure 12.31.

Variable velocity change tests begin with a short-duration shock, then the duration is increased (by preserving constant acceleration) until the appearance of damage (functional or physical). The critical velocity change is equal to the velocity change just lower than that producing damage (ASTM, 1994).

The variable acceleration tests are performed on a new material, starting with a small acceleration level and with a rather large velocity change (at least 1.5 times the critical velocity change previously determined).

The tests should be carried out in the more penalizing impact configuration (unit orientation).

12.7.2 Analysis of Test Results

Damage can occur if the acceleration and the velocity change are together higher than the critical acceleration and the critical velocity change.

From the critical velocity change, the critical drop height can be calculated. If V_i is the impact velocity, V_R is the rebound velocity, and α is the

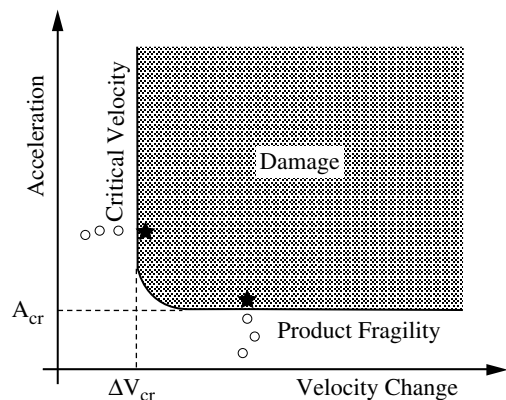


FIGURE 12.31 Damage boundary curve (rectangular shock pulse).

rate of rebound ($V_R = -\alpha V_i$), the velocity change ΔV is equal to

$$\begin{aligned}\Delta V &= V_R - V_i = -(V_i + \alpha V_i) \\ &= -(1 + \alpha)V_i\end{aligned}\quad (12.17)$$

and the free-fall drop height H_{cr} to

$$H_{cr} = \frac{V_i^2}{2g} = \frac{\Delta V^2}{2g(1 + \alpha)^2} \quad (12.18)$$

If this critical height is lower than the design height defined from the real use conditions of the product, it is necessary to use a package with a medium cushioning and then to define its characteristics (crush stress, thickness) so that maximum acceleration at the time of impact is lower than the critical acceleration. If not, no protection is necessary.

Tests are in general carried out with a rectangular shock waveform, for two reasons.

- As the rectangular shock is most severe (see SRSs), the result is conservative, as seen in Figure 12.32.
- The DBC is made up only of two lines, which makes it possible to determine the curve from only two set of tests (saving time) by destroying only two specimens. A much more significant number of sets of tests would be necessary to determine the curve from a half-sine shock waveform.

Note: If, for cost reasons, the same product is used to determine the critical velocity change or the critical acceleration, it undergoes several shocks before failure. The test result is usable only if the product fails in a brittle mode. If the material is ductile, each shock damages the product by an effect of fatigue, which should be taken into account (Burgess, 1996, 2000).

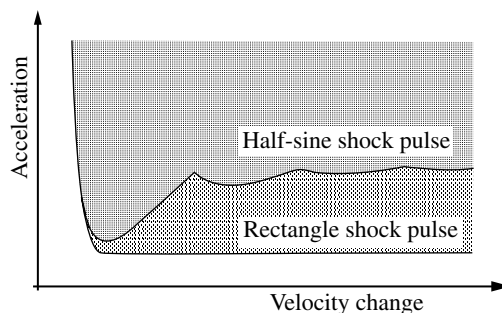


FIGURE 12.32 DBC comparison of half-sine and rectangular shock pulses.

12.8 Shock Machines

12.8.1 Main Types

A shock machine, whatever its standard, is primarily a device allowing modification over a short time period of the velocity of the material to be tested (also, see Chapter 15). Two principal categories are usually distinguished (Lalanne, 2002b):

- The first category is that of *impulse* machines, which increase the velocity of the test item during the shock. The initial velocity is in general zero. The air gun, which creates the shock during the setting of the velocity in the tube, is an example.
- The second category is that of *impact* machines, which decrease the velocity of the test item throughout the shock and/or which change its direction.

The test facilities now used are classified as follows:

- In free fall machines, the impact is made on a shock simulator (in American literature these devices are termed “shock programmers”) adapted to the shape of the specified shock (elastomer discs, conical or cylindrical lead pellets, pneumatic shock simulators, etc.). To increase the impact velocity, which is limited by the drop height, that is, by the height of the guide columns, the fall can be accelerated by the use of bungee cords.
- In pneumatic machines, the velocity is derived from a pneumatic actuator.
- In electrodynamic exciters, the shock is specified either by the shape of a temporal signal, its amplitude and its duration, or by a SRS.

- Exotic machines are designed to carry out shocks that are nonrealizable by the preceding methods, generally because their amplitude and duration characteristics are not compatible with the performances from these means. The desired shapes, not being normal, are not possible with the shock simulators delivered by the manufacturers.

We will try to show in the following sections how mechanical shocks could be simulated on materials in the laboratory. The facilities described are the most current, but the list is far from being exhaustive. Many other processes were or are still used to satisfy particular needs (Nelson and Prasthofer, 1974; Powers, 1974, 1976; Conway et al., 1976).

12.8.2 Impact Shock Machines

Most machines with free or accelerated drop testing belong to the category of impact shock machines. The machine itself allows the setting of velocity of the test item.

The shock is carried out by impact, with the help of the shock simulator (programmer), which formats the acceleration of braking according to the desired shape. The impact can be without rebound when the velocity is zero at the end of the shock, or with rebound when the velocity changes sign during the movement. Laboratory machines of this type consist of two vertical guide rods on which the table carrying the test item slides (Figure 12.33).

The impact velocity is obtained by gravity, after the dropping of the table from a certain height or using bungee cords allowing one to obtain a larger impact velocity.

Let us consider a free fall shock machine for which the friction of the shock table on the guidance system can be neglected. The necessary drop height, H , to obtain the desired impact velocity, v_i , is given by

$$H = \frac{v_i^2}{2g} \quad (12.19)$$

where g is the acceleration of gravity (9.81 m/sec^2).

These machines are limited by the possible drop height, that is, by the height of the columns and the height of the test item when the machine is provided with a gantry. It is difficult to increase the height of the machine due to overcrowding and problems with guiding the table.

However, the impact velocity can be increased using a force complementary to gravity by means of bungee cords tended before the test and exerting a force generally directed downwards. The acceleration produced by the cords is in general much higher than gravity, which then becomes negligible. This idea was used to design horizontal (Lonborg, 1963) and vertical machines (Marshall et al., 1965; La Verne Root and Bohs, 1969), this last configuration being less cumbersome.

During impact, the velocity of the table changes quickly and forces of great amplitude appear between the table and machine bases. To generate a shock of a given shape, it is necessary to control the amplitude of the force throughout the stroke during its velocity change. This is carried out using a shock simulator (programmer).

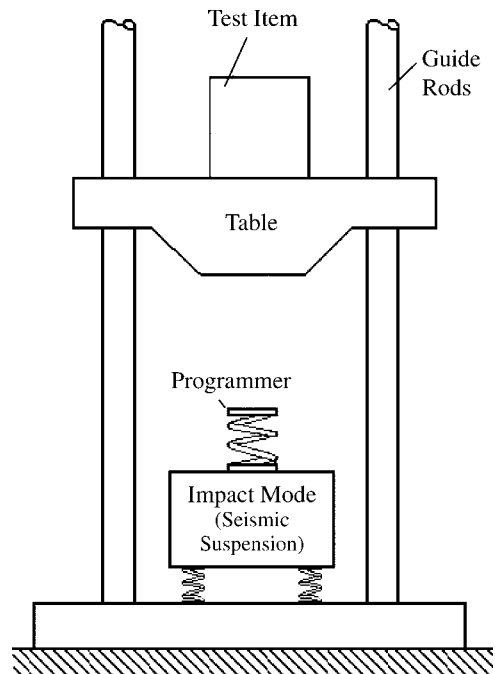


FIGURE 12.33 Elements of a shock-test machine. (Source: Lalanne, *Chocs Mecaniques*, Hermes Science Publications. With permission.)

12.8.2.1 Universal Shock-Test Machines

12.8.2.1.1 Impact Mode

As an example, the MRL[®] Company (Monterey Research Laboratory) has marketed a machine allowing the carrying out of shocks according to two modes: impulse and impact (Bresk and Beal, 1966). In the two test configurations, the test item is installed on the upper face of the table. The table is guided by two rods that are fixed at a vertical frame.

To carry out a test according to the impact mode (the general case), one raises the table by the height required by means of a hoist attached to the top of the frame, using the intermediary assembly for raising and dropping (see Figure 12.34). By opening the blocking system in a high position, the table falls under the effect of gravity or owing to the relaxation of elastic cords if the fall is accelerated. After rebound, as seen on the shock simulator (programmer), the table is again blocked to avoid a second impact.

12.8.2.1.2 Impulse Mode

The impulse mode shocks (see Figure 12.35) are obtained while placing the table on the piston of the shock simulator (used for the realization of initial peak sawtooth shock pulses). The piston of this hydropneumatic shock simulator (programmer) propels the table upward according to an appropriate force profile to produce the specified acceleration signal. The table is stopped in its stroke to prevent its falling down for a second time on the shock simulator (programmer).

12.8.3 Shock Simulators (Programmiers)

We will describe only the most frequently used shock simulators to carry out half-sine, TPS and trapezoid shock pulses.

12.8.3.1 Half-Sine Pulse

These shocks are obtained using an elastic material interposed between the table and the solid mass reaction.

12.8.3.1.1 Shock Duration

The shock duration is calculated by supposing that the table and the shock simulator (programmer), for this length of time, constitute a linear mass–spring system with only one DoF. From the differential equation of the movement (valid only during the elastomeric material compression and its relaxation, so long as there is contact between the table and the shock simulator, i.e., during a half-period)

$$m \frac{d^2x}{dt^2} + kx = 0 \quad (12.20)$$

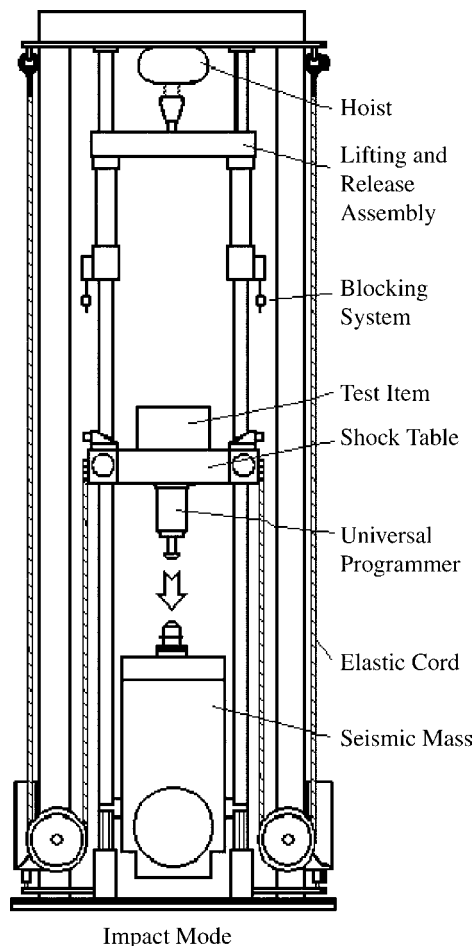


FIGURE 12.34 MRL universal shock-test machine (impact mode). (Source: Lalanne, *Chocs Mécaniques*, Hermes Science Publications. With permission.)

the shock duration τ can be deduced:

$$\tau = \pi \sqrt{\frac{m}{k}} \quad (12.21)$$

where m is the mass of the moving assembly (table + fixture + test item) and k is the stiffness constant of the shock simulator (programmer).

This expression shows that, theoretically, the duration can be regarded as a function alone of the mass, m , and of the stiffness of the target. It is, in particular, independent of the impact velocity. The mass, m , and the duration, τ , being known, we deduce from it the stiffness constant, k , of the target:

$$k = m \frac{\pi^2}{\tau^2} \quad (12.22)$$

12.8.3.1.2 Impact Velocity

Let us set v_i as the impact velocity of the table and v_R as the velocity of rebound. The elastomeric shock simulators often have a coefficient of restitution, α ($v_R = -\alpha v_i$), of about 50%. In a first approximation, we will consider that the rebound is perfect ($\alpha = 1$). The impact velocity is then equal to $\Delta V/2$, where ΔV is the velocity change given by Table 12.1:

$$\Delta V = \frac{2}{\pi} \ddot{x}_m \tau$$

12.8.3.1.3 Maximum Deformation of the Shock Simulator (Programmer)

If x_m is the maximum deformation of the shock simulator (programmer) during the shock, it becomes, by equalizing the kinetic loss of energy and the deformation energy during the compression of the shock simulator (programmer)

$$\frac{1}{2} m v_i^2 = \frac{1}{2} k x_m^2 \quad (12.23)$$

yielding

$$x_m = v_i \sqrt{\frac{m}{k}} \quad (12.24)$$

12.8.3.1.4 Shock Amplitude

From Equation 12.20, one has, in absolute terms, $m \ddot{x}_m = k x_m$, yielding $\ddot{x}_m = x_m (k/m)$ and, according to Equation 12.24

$$\ddot{x}_m = v_i \sqrt{\frac{k}{m}} \quad (12.25)$$

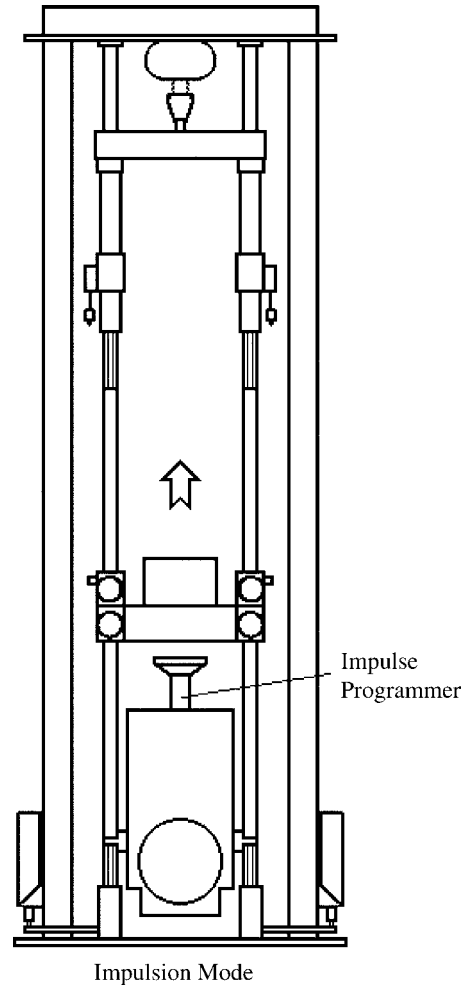


FIGURE 12.35 MRL universal shock-test machine (impulse mode). (Source: Lalanne, *Chocs Mecaniques*, Hermes Science Publications. With permission.)

where the impact velocity, v_i is equal to

$$v_i = \sqrt{2gH} \quad (12.26)$$

where g is the acceleration of gravity ($1g = 9.81 \text{ m/sec}^2$) and H is the drop height.

This relation, established theoretically for perfect rebound, remains usable in practice as long as the rebound velocity remains higher than approximately 50% of the impact velocity. Having determined k from m and τ , it is enough to act on the impact velocity, that is, on the drop height, to obtain the required shock amplitude.

12.8.3.1.5 Characteristics of the Target

For a cylindrical shock simulator (programmer), we have

$$k = \frac{ES}{L} \quad (12.27)$$

where S and L are, respectively, the cross section and the height of the shock simulator (programmer) and where E is Young's modulus of material in compression.

Depending on the materials available, that is the possible values of E , one chooses the values of L and S that lead to a realizable shock simulator (by avoiding too large a height-to-diameter ratio to eliminate the risks from buckling). When the table has a large surface, it is possible to place four shock simulators to distribute the effort. The cross section of each shock simulator (programmer) is then calculated starting from the value of S determined above and divided by four.

If the surface of impact is planar, a wave created at the time of the impact is propagated in the cylinder and makes several up and down excursions (Figure 12.36). From it, at the beginning of the signal the appearance of a high frequency oscillation that distorts the desired half-sine pulse results.

To avoid this phenomenon, the front face of the shock simulator (programmer) is designed to be slightly conical (Figure 12.37) in order to insert the load material gradually (open module). The shock thus created is between a half-sine and a versed-sine pulse. In addition, a good empirical rule is to limit the maximum dynamic deformation of the shock simulator (programmer) from 10 to 15% of its initial thickness to avoid distortion of the half-sine due to damping of the material. If this limit is exceeded, the shape obtained risks nonlinear tendencies.

Example

Consider the realization of a half-sine shock 340 m/sec^2 , 9 msec. It is supposed that the mass of the moving assembly (table + fixture + test item) is equal to 470 kg (test item + fixture mass: 150 kg). From Equation 12.22

$$k = m \frac{\pi^2}{\tau^2} = 470 \frac{\pi^2}{(0.009)^2} \approx 5.727 \times 10^7 \text{ N/m}$$

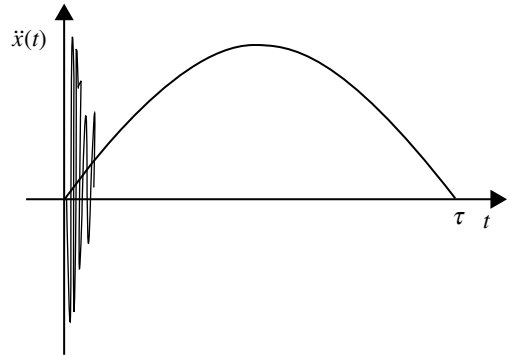


FIGURE 12.36 High frequencies at impact. (Source: Lalanne, *Chocs Mecaniques*, Hermes Science Publications. With permission.)

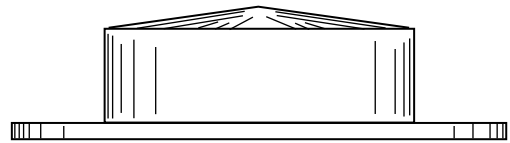


FIGURE 12.37 Impact module with conical impact face (open module). (Source: Lalanne, *Chocs Mecaniques*, Hermes Science Publications. With permission.)

The impact velocity is calculated from Equation 12.25:

$$v_i = \ddot{x}_m \sqrt{\frac{m}{k}} = \ddot{x}_m \frac{\tau}{\pi} = 340 \frac{0.009}{\pi} \approx 0.974 \text{ m/sec}$$

which leads to the drop height, $H = (v_i^2/2g) \approx 48 \times 10^{-3} \text{ m}$. During the impact, the elastomeric target will be deformed to a height equal to Equation 12.24:

$$x_m = v_i \sqrt{\frac{m}{k}} = \ddot{x}_m \left(\frac{\tau}{\pi} \right)^2 = 300 \left(\frac{0.009}{\pi} \right)^2 \approx 2.79 \times 10^{-3} \text{ m}$$

The velocity change during the shock is equal to $\Delta V = (2/\pi)\ddot{x}_m\tau = (2/\pi)340 \times 0.009 \approx 1.91 \text{ m/sec}$. It is checked that $\Delta V = 2v_i$.

With L being the height of the target, its diameter D is calculated from $k = ES/L$:

$$D^2 = \frac{4}{\pi} \frac{k}{E} L$$

If the target is an elastomer of Young's modulus, $E = 5 \times 10^7 \text{ N/m}^2$ yielding, if $L = 0.015 \text{ m}$, $D \approx 0.148 \text{ m}$. It remains to check that the stress in the material does not exceed the acceptable value.

The manufacturers provide cylindrical modules made up of an elastomer sandwiched between two metal plates. The shock simulator (programmer) is composed of stacked modules of various stiffnesses (Figure 12.38). A relatively low number of different modules allows the covering of a broad range of shock durations by combinations of these elements (Brooks, 1966; Brooks and Mathews, 1966; Gray, 1966; Bresk, 1967).

The modules are in general distributed between the bottom of the table and the top of the solid mass of reaction to regularly distribute the load at the time of the shock in the lower part of the table. One thus avoids exciting its bending mode at lower frequency and amplifying the vibrations due to resonance of the table.

The shock simulators for very short duration shock are made up of a high strength and high Young's modulus thermoplastic material. The selected plastic is highly resilient and very hard. It is used within its yield stress and can thus be useful almost indefinitely. Reproducibility is very good.

The shock simulator (programmer) is composed of a cylinder of this material attached to a planar circular plate screwed to the lower part of the table of the shock machine.

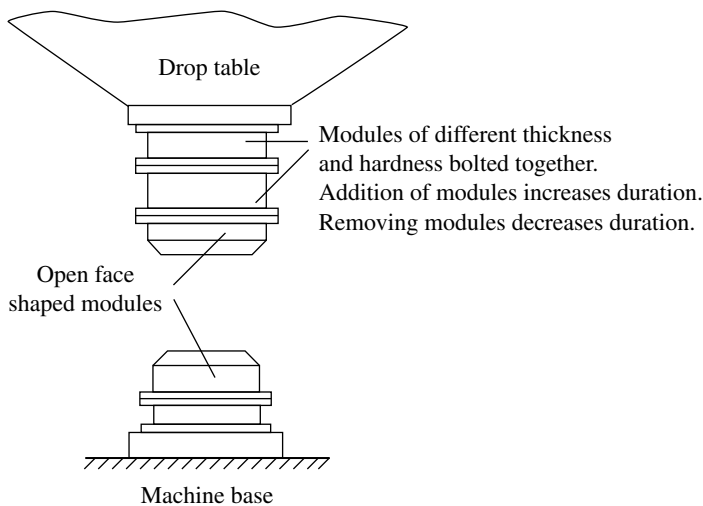


FIGURE 12.38 Distribution of the modules (half-sine shock pulse). (Source: Lalanne, *Chocs Mecaniques*, Hermes Science Publications. With permission.)

12.8.3.2 Terminal Peak Sawtooth Shock Pulse

To generate a TPS shock pulse, any target made up of an inelastic material (crushable material) with a curve dynamic deflection-load which follows a cubic law is thus appropriate (McWhirter, 1961). This curve is approximated by using shock simulators of conical shape.

The material generally used is lead or honeycomb. The cones can be calculated as follows:

- Crushed length:

$$x_m = \frac{\ddot{x}_m \tau^2}{3} \quad (12.28)$$

yielding the height of the cone, $h > 1.2 x_m$ (to allow material to become deformed to the necessary height).

- Force maximum:

$$F_m = S_m \sigma_{cr} = m \ddot{x}_m \quad (12.29)$$

where S_m is the cross section of the cone at height x_m and σ_{cr} is the crush stress of material constituting the target yielding:

$$S_m = \frac{m \ddot{x}_m}{\sigma_{cr}} \quad (12.30)$$

When all the kinetic energy of the table is dissipated by the crushing of the lead, acceleration decreases to zero. The shock machine must have a very rigid solid mass of reaction, so that the time of decay to zero is not too long and satisfies the specification. The speed of this decay to zero is a function of the mass of reaction and of the mass of the table: if the solid mass of reaction has a nonnegligible elasticity, the time, already nonzero because of the imperfections inherent in the shock simulator (programmer), can become too long and unacceptable.

For lead, the order of magnitude of σ_{cr} is 760 kg/cm^2 ($7.6 \times 10^7 \text{ N/m}^2 = 76 \text{ MPa}$). The range of possible durations lies between approximately 2 and 20 msec.

For each machine and each shock, it is necessary to carry out preliminary tests to check that the shock simulator (programmer) is well calculated. The shock simulators are destroyed with each test. It is thus a relatively expensive method. One prefers to use, if possible, a *Universal Programmer* (Section 12.8.3.4).

Example

TPS shock pulse, 340 m/sec^2 , 9 msec (example of Section 12.5.2.5)

Unit table mass: 320 kg

Fixture + test item mass: 150 kg

Conical lead shock simulator ($\sigma_{cr} = 760 \text{ kg/cm}^2 = 7.6 \times 10^7 \text{ N/m}^2$)

The impact velocity is calculated from Table 12.1:

$$\Delta V = v_i = \frac{\ddot{x}_m \tau}{2} = \frac{340 \times 0.009}{2} \approx 1.53 \text{ m/sec}$$

which leads to the theoretical drop height $H = (v_i^2/2g) \approx 0.119 \text{ m}$. During the impact, the target will be deformed to a height equal to Equation 12.28:

$$x_m = \frac{\ddot{x}_m \tau^2}{3} = \frac{340 \times 0.009^2}{3} \approx 9.18 \times 10^{-3} \text{ m}$$

yielding the height of the target $h \geq 1.2 x_m \approx 1.2 \times 9.18 \times 10^{-3} \approx 0.011 \text{ m}$.

The cross section of the cone at height x_m is equal to Equation 12.30

$$S_m = \frac{m\ddot{x}_m}{\sigma_{cr}} = \frac{470 \times 340}{7.6 \times 10^7} \approx 2.1 \times 10^{-3} \text{ m}^2$$

corresponding to a diameter (at height x_m) $D \approx 0.052 \text{ m}$.

12.8.3.3 Rectangular Pulse – Trapezoidal Pulse

This test is carried out by impact. A cylindrical shock simulator (programmer) consists of a material which is crushed with constant force (lead, honeycomb) or using the Universal Shock simulator (programmer). In the first case, the characteristics of the shock simulator (programmer) can be calculated as follows:

- The cross section is given according to the shock amplitude to be realized using the relation

$$F_m = m\ddot{x}_m = S\sigma_{cr} \quad (12.31)$$

yielding

$$S = \frac{m\ddot{x}_m}{\sigma_{cr}} \quad (12.32)$$

- Starting from the dynamics of the impact without rebound, the length of crushing is equal to

$$x_m = \frac{\ddot{x}_m \tau^2}{2} \quad (12.33)$$

and that of the shock simulator (programmer) must be at least equal to $1.4x_m$ in order to allow a correct crushing of the matter with constant force.

The shock amplitude is controlled by the cross section of the shock simulator (programmer), the crush stress of material, and the mass of the total carriage mass. The duration is affected only by the impact velocity.

This method produces relatively disturbed signals, because of the impact between two plane surfaces. They are adapted only for shocks of short duration, because of the limits of deformation. A long duration requires a plastic deformation over a big length, but it is difficult to maintain the constant force of resistance on such a stroke. The honeycombs lend themselves better to the realization of a long duration shock (Gray, 1966).

Example

Rectangular shock pulse, 340 m/sec², 9 msec

Unit table mass: 320 kg

Fixture + test item mass: 150 kg

Cylindrical lead shock simulator ($\sigma_{cr} = 760 \text{ kg/cm}^2 = 7.6 \times 10^7 \text{ N/m}^2$)

The impact velocity is calculated from Table 12.1:

$$\Delta V = v_i = \ddot{x}_m \tau = 340 \times 0.009 = 3.06 \text{ m/sec}$$

which leads to the theoretical drop height $H = (v_i^2/2g) \approx 0.477 \text{ m}$. During the impact, the target will be deformed to a height equal to Equation 12.33:

$$x_m = \frac{\ddot{x}_m \tau^2}{2} = \frac{340 \times 0.009^2}{2} \approx 13.8 \times 10^{-3} \text{ m}$$

yielding the height of the target $h \geq 1.4x_m \approx 1.4 \times 13.8 \times 10^{-3} \approx 0.019 \text{ m}$.

TABLE 12.8 Characteristics of the Target for the Half-Sine, Sawtooth, and Rectangular Pulses

	Half-Sine	TPS	Rectangle
Maximum deformation of the shock simulator (programmer)	$x_m = \frac{\ddot{x}_m \tau^2}{\pi^2}$	$x_m = \frac{\ddot{x}_m \tau^2}{3}$	$x_m = \frac{\ddot{x}_m \tau^2}{2}$
Shock simulator (programmer) cross section at height x_m	$\frac{S}{h} = \frac{\pi^2 m}{E \tau^2}$	$S_m = \frac{m \ddot{x}_m}{\sigma_{cr}}$	$S = \frac{m \ddot{x}_m}{\sigma_{cr}}$
Shock simulator (programmer) height		$h \geq 1.2 \frac{\ddot{x}_m \tau^2}{3}$	$h \geq 1.4 \frac{\ddot{x}_m \tau^2}{2}$
Impact velocity	$v_i = \frac{\ddot{x}_m \tau}{\pi}$	$v_i = \frac{\ddot{x}_m \tau}{2}$	$v_i = \ddot{x}_m \tau$
Free fall height	$H = \frac{v_i^2}{2g}$		

The cross section of the cylinder is equal to Equation 12.32

$$S_m = \frac{m \ddot{x}_m}{\sigma_{cr}} = \frac{470 \times 340}{7.6 \times 10^7} \approx 2.1 \times 10^{-3} \text{ m}^2$$

corresponding to a diameter $D \approx 0.052 \text{ m}$.

Table 12.8 recapitulates the main relations allowing the predimensioning of targets for generating half-sine, sawtooth and rectangular shock pulses.

12.8.3.4 Universal Shock Simulator (Programmer)

MTS^{®1} has manufactured a shock simulator (programmer), known as *Universal*, still used in many laboratories, to produce half-sine, TPS, and trapezoidal shock pulses after various adjustments.

This shock simulator (programmer) consists of a cylinder fixed under the table of the machine, filled with a gas under pressure, and, in the lower part of a piston, a rod and a head (Figure 12.39).

12.8.3.4.1 Generating a Half-Sine Shock Pulse

The chamber is put under sufficient pressure so that, during the shock, the piston cannot move (Figure 12.39). The shock pulse is thus formatted only by the compression of the stacking of elastomeric cylinders (modular shock simulators), placed under the piston head. One is thus brought back to the case of Section 12.8.3.1.

12.8.3.4.2 Generating a Terminal Peak Sawtooth Shock Pulse

The gas pressure (nitrogen) in the cylinder is selected so that, after compression of elastomer during duration, τ , the piston, assembled in the cylinder as indicated in Figure 12.40, is suddenly released for a force corresponding to the required maximum acceleration, \ddot{x}_m .

The pressure that was exerted before separation over the whole area of the piston applies only after separation to one area equal to that of the rod, producing a negligible resistant force.

Acceleration thus passes very quickly from \ddot{x}_m to zero, as shown in Figure 12.41. The rise phase is not perfectly linear, but corresponds rather to an arc of versed-sine (since if the pressure were sufficiently strong, one would obtain a versed-sine by compression of the elastomer alone).

¹Registered trademark of MTS Systems Corporation.

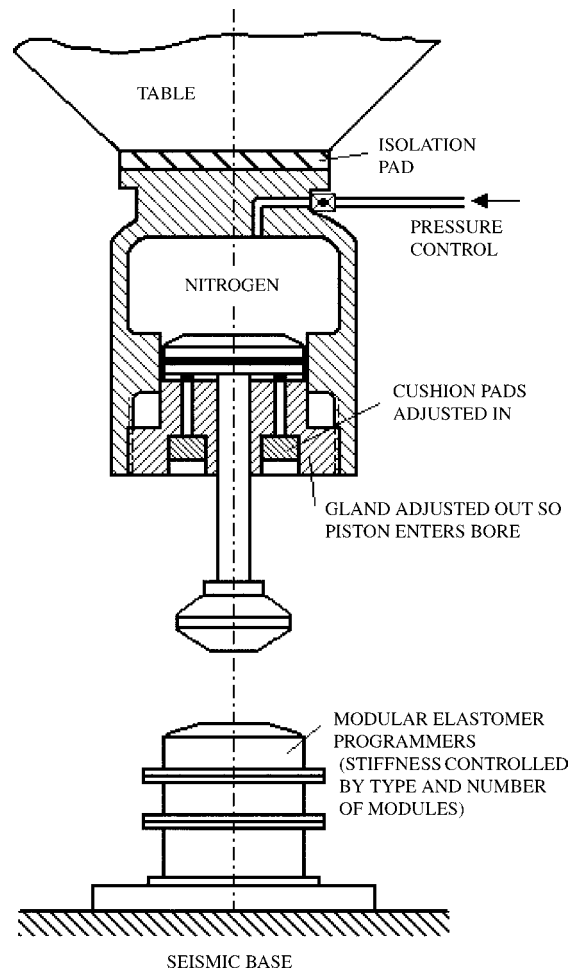


FIGURE 12.39 MTS® *Universal* shock simulator (half-sine and rectangle pulse configuration). (Source: Lalanne, *Chocs Mecaniques*, Hermes Science Publications. With permission.)

12.8.3.4.3 Trapezoidal Shock Pulse

The assembly here is the same as that of the half-sine pulse (Figure 12.39). At the time of the impact, there is:

- Compression of the elastomer until the force exerted on the piston balances the compressive force produced by nitrogen (this phase gives the first part [rise] of the trapezoid).
- Up and down displacement of the piston in the part of the cylinder of smaller diameter, approximately with constant force, since volume varies little (this phase corresponds to the horizontal part of the trapezoid).
- Relaxation of elastomer: decay to zero acceleration.

The rise and decay parts are not perfectly linear for the same reason as in the case of the TPS pulse.

12.8.4 Limitations

12.8.4.1 Limitations of the Shock Machines

The limitations are often represented graphically by straight lines plotted in logarithmic scales, delimiting the domain of realizable shocks (amplitude, duration). The shock machine is

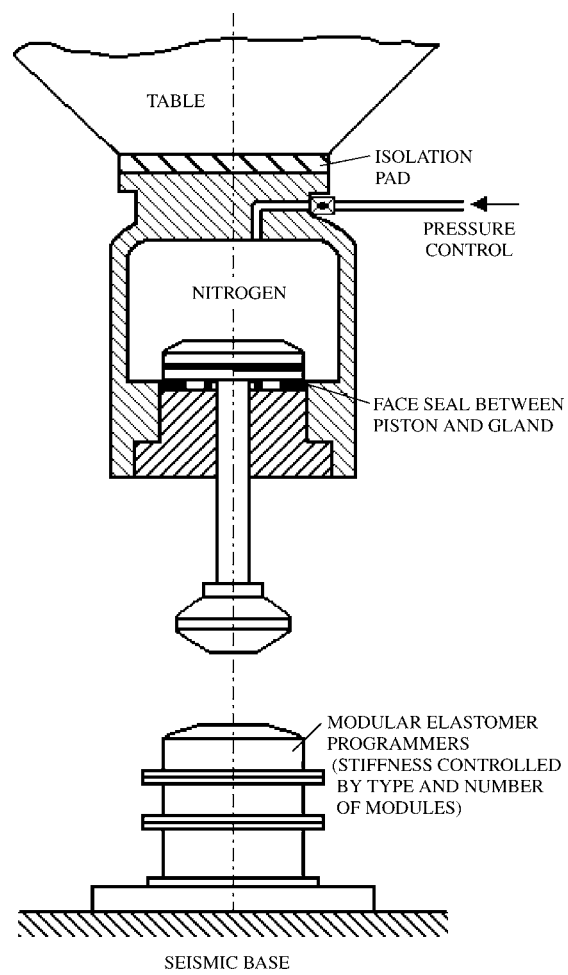


FIGURE 12.40 MTS® Universal shock simulator (TPS pulse configuration). (Source: Lalanne, *Chocs Mecaniques*, Hermes Science Publications. With permission.)

limited by (IMPAC 6060F Operating Manual; Figure 12.42):

- The allowable maximum force on the table. To carry out a shock of amplitude \ddot{x}_m , the force generated on the table, given by

$$F = [m_{\text{table}} + m_{\text{programmer}} + m_{\text{fixture}} + m_{\text{test item}}]\ddot{x}_m \tag{12.34}$$

must be lower than or equal to the acceptable maximum force, F_{max} . Knowing the total carriage mass, the relation (Equation 12.34) allows calculation of the possible maximum acceleration under the test conditions

$$(\ddot{x}_m)_{\text{max}} = F_{\text{max}}/[m_{\text{table}} + m_{\text{programmer}} + m_{\text{fixture}} + m_{\text{test item}}] \tag{12.35}$$

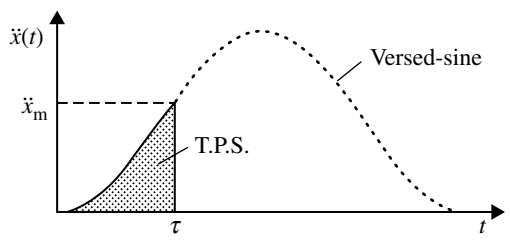


FIGURE 12.41 Realization of a TPS shock pulse. (Source: Lalanne, *Chocs Mecaniques*, Hermes Science Publications. With permission.)

This limitation is represented on the abacus by a horizontal line constant, \ddot{x}_m .

- This emphasizes maximum free fall height, H , or the maximum impact velocity, that is the velocity change, ΔV of the shock pulse. If v_R is the rebound velocity, equal to a percentage α of the impact velocity, we have

$$\begin{aligned}\Delta V &= v_R - v_i = -(1 + \alpha)v_i \\ &= -(1 + \alpha)\sqrt{2gH} \\ &= \int_0^\tau \ddot{x}(t)dt\end{aligned}\tag{12.36}$$

yielding

$$H = \frac{\Delta V^2}{2g(1 + \alpha)^2}\tag{12.37}$$

where α is a function of the shape of the shock and of the type of shock simulator (programmer) used. In practice, there are losses of energy by friction during the fall and especially in the shock simulator (programmer) during the realization of the shock. Taking account of these losses is difficult to calculate analytically and so one can set:

$$H = \beta \frac{\Delta V^2}{2g}\tag{12.38}$$

where β takes into account at the same time losses of energy and rebound. As an example, the manufacturer of machine IMPAC 60 × 60 (MRL) gives Table 12.9, according to the type of shock simulators (*IMPAC 6060F Operating Manual*).

The limitation related to the drop height can be represented by parallel straight lines on a diagram giving the velocity change, ΔV , as a function of the drop height in logarithmic scales. The velocity change being, for all simple shocks, proportional to the product $\ddot{x}_m \tau$, we have

$$\Delta V = \lambda \ddot{x}_m \tau = \sqrt{2gH/\beta}\tag{12.39}$$

Some typical values for the amplitude × duration product are given in Table 12.10.

On logarithmic scales (\ddot{x}_m, τ), the limitation relating to the velocity change is represented by parallel, inclined straight lines (Figure 12.42).

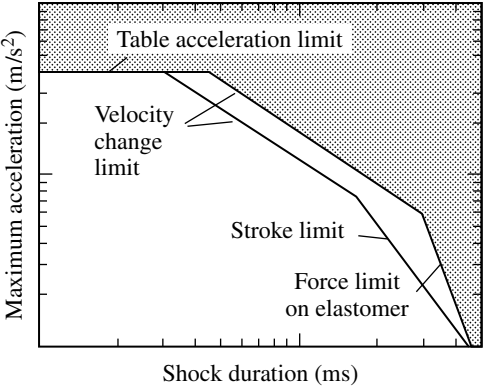


FIGURE 12.42 Abacus of the limitations of a shock machine. (Source: Lalanne, *Chocs Mecaniques*, Hermes Science Publications. With permission.)

TABLE 12.9 Loss Coefficient β

Shock Simulator (Programmer)	Value of β
Elastomer (half-sine pulse)	0.556
Lead (rectangle pulse)	0.2338
Lead (TPS pulse)	1.544

Source: Lalanne, *Chocs Mecaniques*, Hermes Science Publications. With permission.

TABLE 12.10 Amplitude × Duration Limitation

Waveform	Shock Simulator (Programmer)	$(\ddot{x}_m \tau)_{\max}$ (m/sec)
Half-sine	Elastomer	17.7
TPS	Lead cone	10.8
	<i>Universal</i> shock simulator (programmer)	7.0
Rectangle	<i>Universal</i> shock simulator (programmer)	9.2

Source: Lalanne, *Chocs Mecaniques*, Hermes Science Publications. With permission.

12.8.4.2 Limitations of Shock Simulators

Elastomeric materials are used to generate shocks of:

- Half-sine shape (or versed-sine with a conical frontal module to avoid the presence of high frequencies).
- TPS and rectangular shapes, in association with a *Universal* shock simulator.

Elastomer shock simulators are limited by the allowable maximum force, a function of Young’s modulus, and their dimensions (Figure 12.42). This limitation is in fact related to the need to maintain the stress lower than the yield stress of the material, so that the target can be regarded as a pure stiffness. The maximum stress, σ_{\max} , developed in the target at the time of the shock can be expressed according to Young’s modulus, E , to the maximum deformation, x_m , and to the thickness, h , of the target according to

$$\sigma_{\max} = E \frac{x_m}{h} \tag{12.40}$$

with, for an impact with perfect rebound, $x_m = \ddot{x}_m \tau^2 / \pi^2$. It is necessary that, if R_e is the elastic ultimate stress

$$\frac{E \ddot{x}_m \tau^2}{h \pi^2} < R_e \tag{12.41}$$

that is

$$h > \frac{E \ddot{x}_m \tau^2}{R_e \pi^2} \tag{12.42}$$

Taking into account the mass of the carriage assembly, this limitation can be transformed into maximum acceleration ($F_m = m \ddot{x}_m$). With four shock simulators used simultaneously, the maximum acceleration is naturally multiplied by four. This limitation is represented on the abacus of Figure 12.42 by the straight lines of greater slope.

The *Universal* shock simulator is limited (*MRL 2680 Operating Manual*):

- By the acceptable maximum force.
- By the stroke of the piston: for each waveform, the displacement during the shock is always proportional to the product $\ddot{x}_m \tau^2$.

This limitation is provided by the manufacturer.

In short, the domain of the realizable shock pulses is limited on this diagram by straight lines representative of the conditions given in Table 12.11.

TABLE 12.11 Summary of Limitations on the Domain of Realizable Shock Pulses

$\ddot{x}_m = \text{constant}$	Acceptable force on the table or on the <i>Universal</i> shock simulator
$\ddot{x}_m \tau = \text{constant}$	Drop height (ΔV)
$\ddot{x}_m \tau^2 = \text{constant}$	Piston stroke of the <i>Universal</i> shock simulator
$\ddot{x}_m \tau^4 = \text{constant}$	Acceptable force for elastomers

Source: Lalanne, *Chocs Mecaniques*, Hermes Science Publications. With permission.

12.8.5 Pneumatic Machines

Pneumatic machines in general consist of a cylinder separated into two parts by a plate bored to let pass the rod of a piston located lower down (Figure 12.43). The rod crosses the higher cylinder, comes out of the cylinder, and supports a table receiving the test item.

The surface of the piston subjected to the pressure is different according to whether it is on the higher face or the lower face, as long as it is supported in the higher position on the Teflon^{®2} seat (Thorne, 1964).

Initially, the moving piston, rod, and table rose by filling the lower cylinder (reference pressure). The higher chamber is then inflated to a pressure of approximately five times the reference pressure. When the force exerted on the higher face of the piston exceeds the force induced by the pressure of reference, the piston releases. The useful surface area of the higher face increases quickly and the piston is subjected in a very short time to a significant force exerted towards the bottom. It involves the table, which compresses the shock simulators (elastomers, lead cones, etc.) placed on the top of the body of the jack.

This machine is assembled on four rubber bladders filled with air to uncouple it from the floor of the building. The body of the machine is used as a solid mass of reaction. The interest behind this lies in its performance and its compactness. An industrial pneumatic shock machine is shown in Figure 12.44.

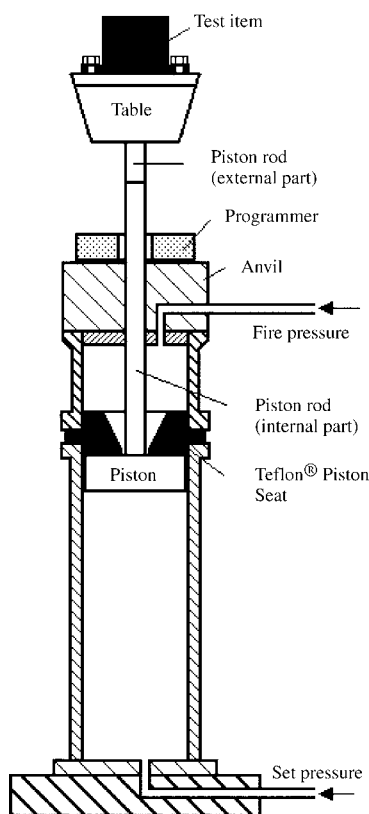


FIGURE 12.43 The principle of pneumatic machines. (Source: Lalanne, *Chocs Mecaniques*, Hermes Science Publications. With permission.)

12.8.6 High Impact Shock Machines

The first machine was developed in 1939 to simulate the effects of underwater explosions (mines) on the equipment onboard military ships. Such explosions, which generally occur at large distances from the ships, create shocks that are propagated in all the structures.

The procedure consisted of specifying the machine to be used, the method of assembly, the adjustment of the machine and so on, and not of a SRS or a simple shape shock.

Two models of machines of this type were built to test lightweight and medium weight equipment.

12.8.6.1 Lightweight High Impact Shock Machine

The lightweight high impact shock machine, the first built, consists of a welded frame of standard steel sections and two hammers, one sliding vertically, the other describing an arc of a circle in a vertical plane, according to a pendular motion (Figure 12.45).

²Registered trademark of E.I. du Pont de Nemours & Company, Inc., Wilmington, DE.

A target plate carrying the test item can be placed to receive one or the other of the hammers. The combination of the two movements and the two positions of the target makes it possible to deliver shocks according to three perpendicular directions without disassembling the test item. Each hammer weighs approximately 200 kg and can fall a maximum height of 1.50 m (Conrad, 1952). The target is a plate of steel of 86 cm × 122 cm × 1.6 cm, reinforced and stiffened on its back face by I-beams.

In each of the three impact positions of the hammer, the target plate is assembled on springs in order to absorb the energy of the hammer with a limited displacement (38 mm to the maximum). Rebound of the hammer is prevented.

Several intermediate standardized plates simulate various conditions of assembly of the equipment on board. These plates are inserted between the target and the equipment tested to provide certain insulation at the time of impact and to restore a shock considered comparable with the real shock.

The mass of the equipment tested on this machine should not exceed 100 kg. For fixed test conditions (direction of impact, equipment mass, intermediate plate), the shape of the shock obtained is not very sensitive to the drop height. The duration of the produced shocks is about 1 msec and the amplitudes range between 5000 and 10,000 m/sec².

12.8.6.2 Medium Weight High Impact Shock Machine

This machine was designed to test equipment whose mass, including the fixture, is less than 2500 kg (Figure 12.46). It consists of a hammer weighing 1360 kg that swings through an arc of a circle at an angle greater than 180° and comes to strike an anvil at its lower face. Under the impact, this anvil, fixed under the table carrying the test item, moves vertically upwards. The movement of this unit is limited to approximately 8 cm at the top and 4 cm at the bottom (Vigness, 1947, 1961a; Conrad, 1951; Lazarus, 1967) by stops that halt it and reverse its movement. The equipment being tested is fixed on the table via a group of steel channel beams (and not directly to the rigid anvil structure), so that the natural frequency of the test item on this support metal structure is about 60 Hz.



FIGURE 12.44 Benchmark® SM 105 pneumatic shock machine. SM 105 and Benchmark are registered trademarks owned by Benchmark Electronics, Hunstville, Inc. (courtesy Benchmark Electronics).

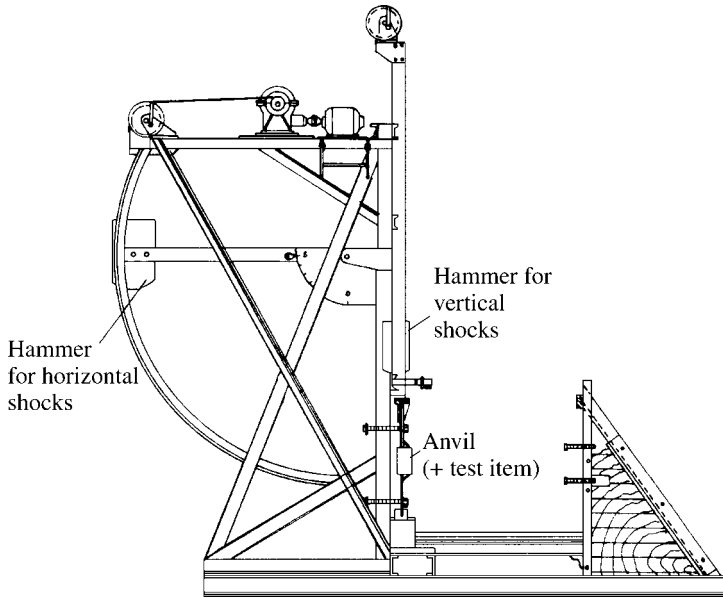


FIGURE 12.45 High impact shock machine for lightweight equipment. (Source: Lalanne, *Chocs Mecaniques*, Hermes Science Publications. With permission.)

The shocks obtained are similar to those produced with the machine for light equipment (Lazarus, 1967).

The shocks carried out on all these facilities are not very reproducible and are sensitive to the ageing of the machine and the assembly (the results can differ after dismantling and reassembling the equipment on the machine under identical conditions, in particular at high frequencies; Vigness, 1961b).

These machines can also be used to generate simple shape shocks such as half-sine or TPS pulses (Vigness, 1963), while inserting either an elastic or a plastic material between the hammer and the anvil carrying the test item. One thus obtains durations of about 10 msec at 20 msec for the half-sine pulse and 10 msec for the TPS pulse.

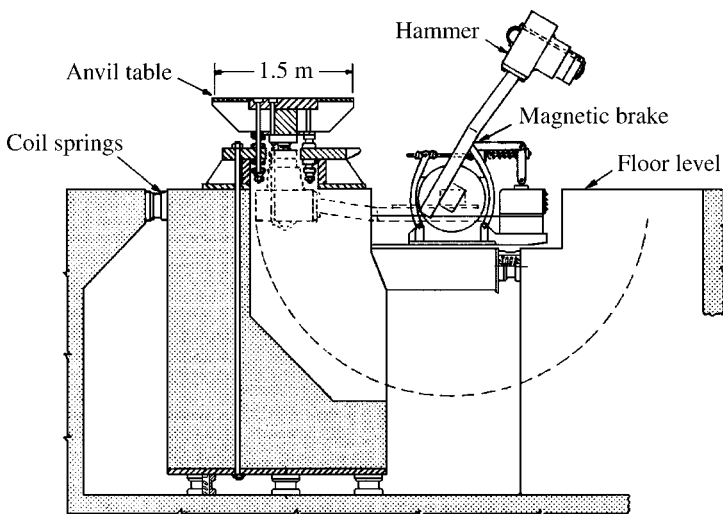


FIGURE 12.46 High impact machine for medium weight equipment. (Source: Lalanne, *Chocs Mecaniques*, Hermes Science Publications. With permission.)

12.8.7 Specific Test Facilities

When the impact velocity of standard machines is insufficient, one can use other means to obtain the desired velocity. For example:

- One can use drop testers, equipped with two vertical (or inclined) guide cables (McWhirter, 1963; Lalanne, 1975). The drop height can reach a few tens of meters. It is wise to make sure that the guidance is correct and, in particular, and that friction is negligible. It is also desirable to measure the impact velocity (using photoelectric cells or any other device).
- One can also use gas guns, which initially use the expansion of a gas (often air) under pressure in a tank to propel a projectile carrying the test item towards a target equipped with a shock simulator fixed at the extremity of a gun on a solid reaction mass (McWhirter, 1961; McWhirter, 1963; Yarnold, 1965; Lazarus, 1967; Lalanne, 1975). One finds the impact mode to be as above. It is necessary that the shock created at the time of the velocity setting in the gun is of low amplitude with regard to the specified shock carried out at the time of the impact. Another operating mode consists of using the phase of the velocity setting to program the specified shock, the projectile then being braked at the end of the gun by a pneumatic device, with a small acceleration with respect to the principal shock. A major disadvantage of guns is related to the difficulty of handling cables instrumentation, which must be wound or unreel in the gun, in order to follow the movement of the projectile.
- Alternatively, one can use inclined-plane impact testers (Vigness, 1961a; Lazarus, 1967). These were especially conceived to simulate shocks undergone during too severe handling operations or in trains. They are made up primarily of a carriage on which the test item is fixed, traveling on an inclined rail and coming to run up against a wooden barrier (Figure 12.47).

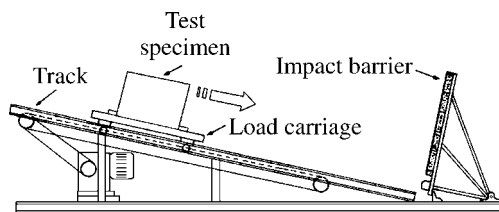


FIGURE 12.47 Inclined plane impact tester (CONBUR tester). (Source: Lalanne, *Chocs Mecaniques*, Hermes Science Publications. With permission.)

The shape of the shock can be modified by using elastomeric “bumpers” or springs. Tests of this type are often named “CONBUR tests.”

12.9 Generation of Shock Using Shakers

In about the mid-1950s, with the development of electrodynamic exciters for the realization of vibration tests, the need for a realization of shocks on this facility was quickly felt. This simulation on a shaker, when possible, indeed presents a certain number of advantages (Coty and Sannier, 1966).

12.9.1 Principle Behind the Generation of a Simple Shape Signal versus Time

The objective is to carry out on the shaker a shock of simple shape (half-sine, triangle, rectangle, etc.) of given amplitude and duration similar to that made on the classical shock machines. This technique was mainly developed during the years 1955 to 1965 (Wells and Mauer, 1961).

The transfer function between the electric signal of the control applied to the coil and acceleration to the input of the test item is not constant. It is thus necessary to calculate the signal of control according to this transfer function and the signal to be realized.

The process is as follows (Favour et al., 1969; Magne, 1971):

- Measurement of the transfer function of the installation (including the fixture and the test item) using a calibration signal; the measurement of the transfer function of the installation can be made using a calibration signal of the shock type, random vibration or sometimes by fast swept sine (Favour, 1974; Lalanne, 2002a).
- Calculation of the Fourier transform of the signal specified at the input of the test item.
- By division of this transform by the transfer function, calculation of the Fourier transform of the signal of control.
- Calculation of the control signal vs. time by inverse transformation.

In all cases, the procedure consists of measurement and calculation of the signal of control to $-n$ dB (-12 , -9 , -6 , and/or -3). The specified level is applied only after several adjustments on a lower level. These adjustments are necessary because of the sensitivity of the transfer function to the amplitude of the signal (nonlinearities). The development can be carried out using a dummy item representative of the mass of the specimen. However, particularly if the mass of the test specimen is significant (with respect to that of the moving element), it is definitely preferable to use the real test item or a model with dynamic behavior very near to it.

If random vibration is used as the calibration signal, its root-mean-square (rms) value is calculated in order to be lower than the amplitude of the shock (but not too distant in order to avoid the effects of any nonlinearities). This type of signal can result in application to the test item of many substantial peaks of acceleration compared with the shock itself.

12.9.2 Main Advantages

The realization of the shocks on shakers has very interesting advantages:

- Possibility of obtaining very diverse shocks shapes.
- Use of the same means for the tests with vibrations and shocks, without disassembly (saving time) and with the same fixtures (Wells and Mauer, 1961; Hay and Oliva, 1963).
- Possibility of a better simulation of the real environment, in particular by direct reproduction of a signal of measured acceleration (or of a given shock spectrum).
- Better reproducibility than on the traditional shock machines.
- Very easy realization of the test on two directions of an axis.
- No need to use a shock machine.

In practice, however, one is rather quickly limited by the possibilities of the exciters, which therefore do not make it possible to generalize their use for shock simulation.

12.9.3 Pre- and Postshocks

12.9.3.1 Requirements

The velocity change, $\Delta V = \int_0^\tau \ddot{x}(t)dt$ (τ = shock duration), associated with shocks of simple shape (half-sine, rectangle, TPS, etc.) is different from zero. At the end of the shock, the velocity of the table of the shaker must, however, be zero. It is thus necessary to devise a method to satisfy this need.

12.9.3.2 Solutions

One way of bringing back the variation of velocity associated with the shock to zero can be the addition of a negative acceleration to the principal signal so that the area under the pulse has the same value on the

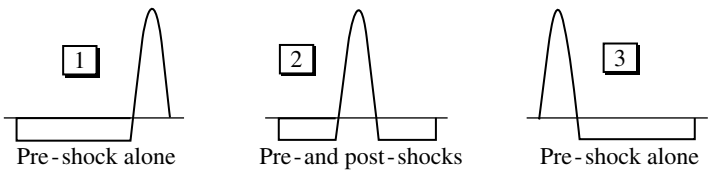


FIGURE 12.48 Possibilities for pre- and postshock positioning. (Source: Lalanne, *Chocs Mecaniques*, Hermes Science Publications. With permission.)

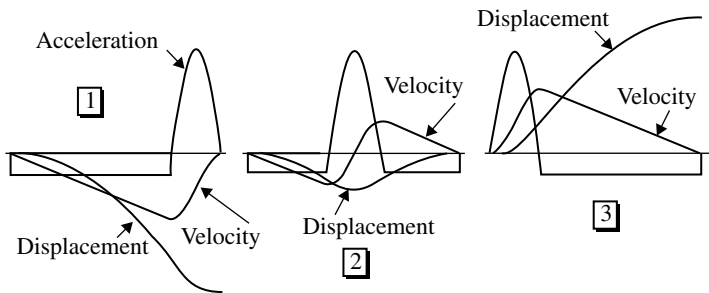


FIGURE 12.49 Kinematics of the movement with preshock alone [1], symmetrical pre and postshocks [2] and postshock alone [3]. (Source: Lalanne, *Chocs Mecaniques*, Hermes Science Publications. With permission.)

side of positive accelerations and on the side of negative accelerations (Lalanne, 2002b). Various solutions are possible *a priori* (Figure 12.48):

- A preshock alone.
- A postshock alone.
- Pre- and postshocks, possibly of equal durations.

Preshock alone [1], which requires a less powerful power amplifier, thus seems preferable to postshock alone [3]. The use of symmetrical pre- and postshocks is however better, because of a certain number of additional advantages (Magne and Leguay, 1972; Figure 12.49).

- The final displacement is minimal. If the specified shock is symmetrical (with respect to the vertical line $\pi/2$), this residual displacement is zero (Young, 1964).
- For the same duration, τ , of the specified shock and for the same value of maximum velocity, the possible maximum level of acceleration is twice as big.
- The maximum force is provided at the moment when acceleration is maximum, that is, when the velocity is zero (one will be able to thus have the maximum current). The solution with symmetrical pre- and postshocks requires minimal electric power.

Another parameter is the shape of these pre- and postshocks, the most used shapes being the triangle, the half-sine, and the rectangle (Figure 12.50).

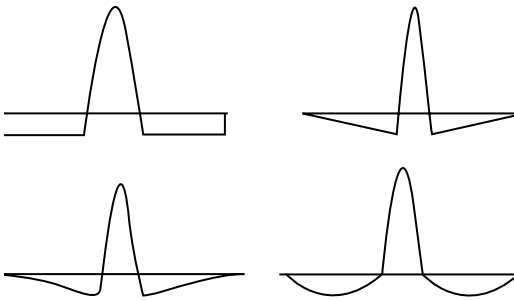


FIGURE 12.50 Shapes of pre- and postshock pulses. (Source: Lalanne, *Chocs Mecaniques*, Hermes Science Publications. With permission.)

Owing to discontinuities at the ends of the pulse, the rectangular compensation is seldom satisfactory (Smallwood, 1985). One often prefers a versed-sine applied to the entire signal (Hanning window), which has the advantages of being zero and smoothed at the ends (first zero derivative) and presenting symmetrical pre- and postshocks.

In all the cases, the amplitude of pre- and postshocks must remain small with respect to that of the principal shock (preferably lower than approximately 10%), in order not to deform too much the temporal signal and consequently, the shock spectrum. For a given shape of pre- and postshock, this choice thus imposes the duration.

12.9.3.2.1 Optimized Pre- and Postpulses

Another method was developed (Fandrich, 1981) in order to take into account the tolerances on the shape of the signal allowed by the standards (R.T. Fandrich refers to standard MIL-STD 810 C) and to best use the possibilities of the shaker.

The solution suggested consists of defining the following:

1. One must define a preshock made up of the first two terms of the development in a Fourier series of a rectangular pulse (with coefficients modified after a parametric analysis). The table being in equilibrium in a median position before the test, the objective of this preshock is twofold:
 - To give to a velocity, just before the principal shock, having a value close to one of the two limits of the shaker so that, during the shock, the velocity can use the entire range of variation permitted by the machine.
 - To place, in the same way, the table as close as possible to one of the thrusts so that the moving element can move during the shock in the entire space between the two thrusts (limitation in displacement equal, according to the machines, to 2.54 or 5.08 cm).
2. One must also define a postshock composed of one period of a signal of the shape, $Kt^\gamma \sin(2\pi f_1 t)$, where the constants K , γ , and f_1 are evaluated in order to cancel the acceleration, the velocity, and the displacement at the end of the movement of the table.

The frequency and the exponent are selected in order to respect the ratio of the velocity to the displacement at the end of the principal shock. The amplitude of the postshock is adjusted to obtain the desired velocity change.

Figure 12.51 shows the total signal obtained in the case of a principal shock half-sine 30g, 11 msec. This methodology has been improved to provide a more general solution (Lax, 2001).

Note: The realization of shocks on free or accelerated fall machines imposes *de facto* preshocks and/or postshocks, the existence of which the user is not always aware, but that can modify the shock severity at

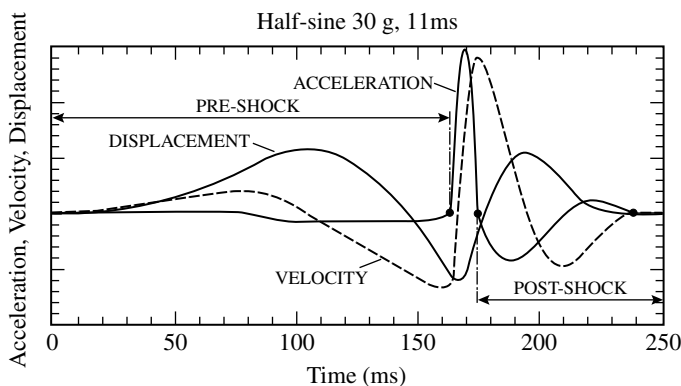


FIGURE 12.51 Overall movement in a half-sine shock. (Source: Lalanne, *Chocs Mecaniques*, Hermes Science Publications. With permission.)

low frequencies. The movement of shock starts with dropping the table from the necessary height to produce the specified shock and finishes with stopping the table after rebound on the shock simulator (Lalanne, 2002b). The preshock takes place during the fall of the table, the postshock during its rebound (Figure 12.52). These pre- and postshocks modify the SRS low frequency and can lead to an unexpected behavior of material when its natural frequency is low.

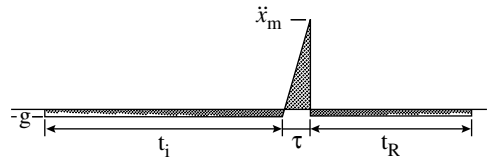


FIGURE 12.52 Shock performed. (Source: Lalanne, *Chocs Mecaniques*, Hermes Science Publications. With permission.)

12.9.3.3 Incidence on the Shock Response Spectra

Figure 12.53 shows the response, $\omega_0^2 z(t)$, of a one-DoF system ($f_0 = 4$ Hz, $\xi = 0.05$) to a TPS shock (the example of Section 12.5.2.5):

- For $z_0 = \dot{z}_0 = 0$ (conditions of the response spectrum).
- In the case of a shock with impact (free fall).
- In the case of a shock on shaker (half-sine symmetrical pre and postshocks with amplitude equal to 34 m/sec^2).

We observed in this example the differences between the theoretical response at 4 Hz and the responses actually obtained on the shaker and shock machine. According to the test facility used, the shock applied can underest or overtest the material. For the estimate of shock severity, one must take account of the whole of the signal of acceleration.

In Figure 12.54, for $\xi = 0.05$, is the SRS of:

- The nominal shock, calculated under the usual conditions of the spectra ($z_0 = \dot{z}_0 = 0$).
- The realizable shock on shaker, with its pre- and postshocks.
- The realizable shock by impact, taking of account of the fall and rebound phases.

One notes in this example that for:

- $f_0 \leq 6$ Hz, the spectrum of the shock by impact is lower than the nominal spectrum, but higher than the spectrum of the shock on the shaker.
- $6 \text{ Hz} < f_0 < 30$ Hz, the spectrum of the shock on the shaker is much overestimated.
- $f_0 < 30$ Hz, all the spectra are superimposed.

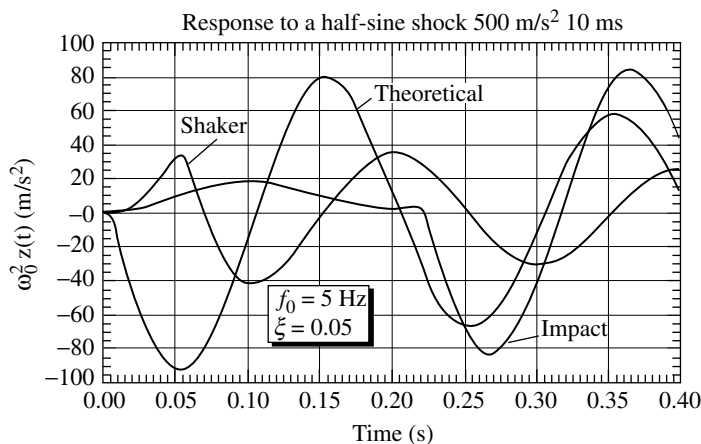


FIGURE 12.53 Influence of the realization mode of a TPS shock on the response of a one-DoF system. (Source: Lalanne, *Chocs Mecaniques*, Hermes Science Publications. With permission.)

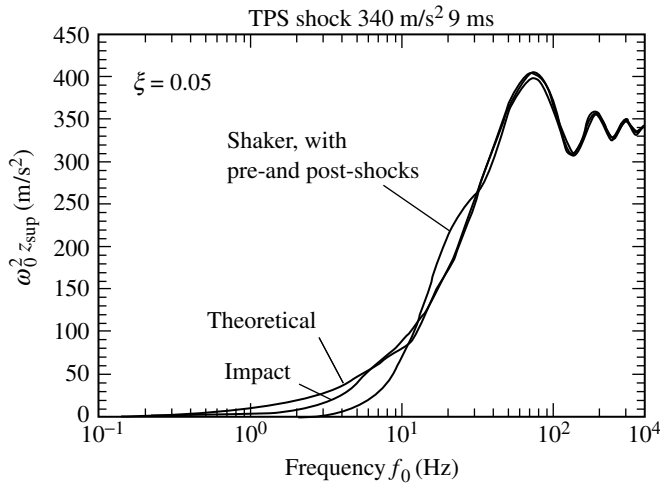


FIGURE 12.54 Influence of the realization mode of a TPS shock on the SRS. (Source: Lalanne, *Chocs Mecaniques*, Hermes Science Publications. With permission.)

This result appears logical when we remember that the slope of the shock spectrum at the origin is, for zero damping, proportional to the velocity change associated with the shock. The compensation signal, added to bring the velocity change back to zero, thus makes the slope of the spectrum at the origin zero. In addition, the response spectrum of the compensated signal can be larger than the spectrum of the theoretical signal close to the frequency corresponding to the inverse of the duration of the compensation signal. It is thus advisable to make sure that the variations observed are not in a range that includes the resonant frequencies of the test item.

It is necessary to add pre- and/or postshock to the specified shock in order to bring back the velocity of the shaker table to zero at the end of the shock pulse. The use of pre- and postshocks is best. Their amplitude must remain small with respect to that of the principal shock (lower than approximately 10%).

The realization of shocks on free or accelerated fall machines also imposes pre- and postshocks.

These pre- and postshocks lead to differences at low frequency between the spectrum of the specified shock and the spectrum of the shock actually carried out on the test facility.

12.9.4 Limitations of Electrodynamic Shakers

12.9.4.1 Mechanical Limitations

Performances of electrodynamic shakers (see Chapter 15) are limited in the following fields (Miller, 1964; Magne and Leguay, 1972).

- They are limited in terms of the maximum stroke of the coil-table unit (according to the machines being used, 25.4 to 75 mm peak-to-peak). At the time of the realization of a usual simple shock on shaker, the displacement starts from the equilibrium position (rest) of the coil, passes through a maximum, then returns to the initial position. In fact only half of the available stroke is used. For better use of the capacities of the machine, it is possible to shift the rest position from the central value towards one of the extreme values (Figure 12.55; Miller, 1964; McClanahan and Fagan, 1966; Smallwood and Witte, 1972).

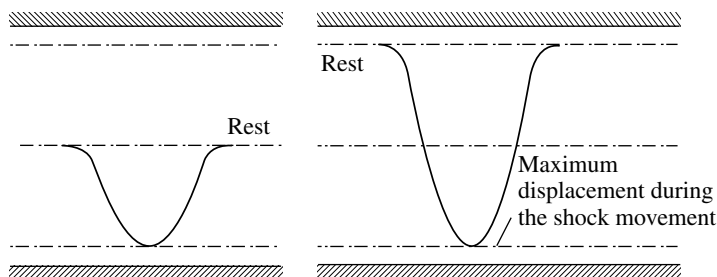


FIGURE 12.55 Displacement of the coil of the shaker. (Source: Lalanne, *Chocs Mecaniques*, Hermes Science Publications. With permission.)

- The maximum velocity is also limited (Young, 1964): 1.5 to 3 m/sec in sine mode (in shock, one can admit a larger velocity with nontransistorized amplifiers (electronic tubes), because these amplifiers can generally accept a very short overvoltage). During the movement of the moving element in the air-gap of the magnetic coils, there is an electromotive force (emf) produced which is opposed to the voltage supply. The velocity must thus have a value such that this emf is lower than the acceptable maximum output voltage of the amplifier. The velocity must in addition be zero at the end of the shock movement (Smallwood and Witte, 1972; Galef, 1973).
- There is a limit to maximum acceleration, related to the maximum force. McClanahan and Fagan (1965) consider that the realizable maxima shock levels are approximately 20% below the vibratory limit levels in velocity and in displacement. The majority of authors agree that the limits in force are, for the shocks, larger than those indicated by the manufacturer (in sine mode). The determination of the maximum force and the maximum velocity is based, in vibration, on considerations of the fatigue of the shaker mechanical assembly. Since the number of shocks that the shaker will carry out is very much lower than the number of cycles of vibrations that it will undergo during its life, the parameter maximum force can be, for the shock applications, increased considerably.

Another reasoning consists of considering the acceptable maximum force, given by the manufacturer in random vibration mode, expressed by its rms value. Knowing that one can observe random peaks being able to reach 4.5 times this value (limitation of control system), one can admit the same limitation in shock mode. One finds other values in the literature, such as:

- ≤ 4 times the maximum force in sine mode, with the *proviso* of not exceeding 300g on the armature assembly (Hug, 1972).
- > 8 times the maximum force in sine mode in certain cases (very short shocks; 0.4 msec, for example; Gallagher and Adkins, 1966). Dinicola (1964) and Keegan (1973) give a factor of about ten for the shocks of duration lower than 5 msec.

The limits of velocity, displacement, and force are not affected by the mass of the specimen.

12.9.4.1.1 Abacuses

For a given shock and for given pre- and postshocks shapes, the velocity and the displacement can be calculated as a function of time by integration of the expressions of the acceleration, as well as the maximum values of these parameters, in order to compare them with the characteristics of the facilities.

From these data, abacuses can be established allowing quick evaluation of the possibility of realization of a specified shock on a given test facility (characterized by its limits of velocity and

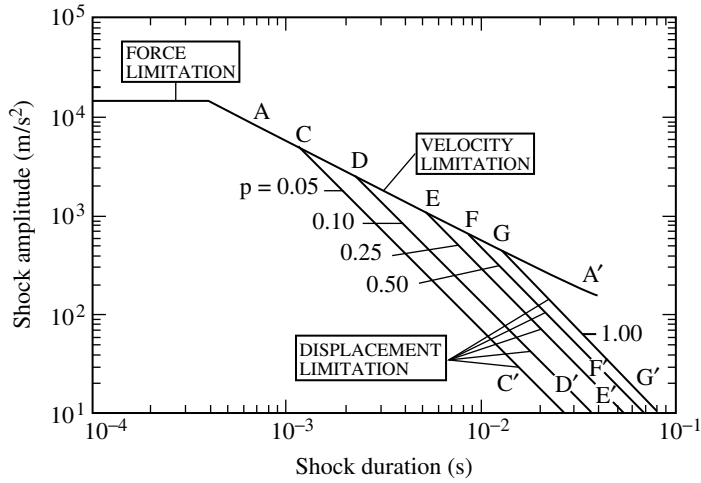


FIGURE 12.56 Abacus of the realization domain of a shock. (Source: Lalanne, *Chocs Mecaniques*, Hermes Science Publications. With permission.)

of displacement). These abacuses are made up of straight-line segments on logarithmic scales (Figure 12.56).

- AA' corresponding to the limitation of velocity: the condition $v_m \leq v_L$ (v_L = acceptable maximum velocity on the facility considered) results in a relationship of the form $\ddot{x}_m \tau \leq \text{constant}$ (independent of p , the ratio of the absolute values of the pre- and postshocks amplitude and of the principal shock amplitude).
- CC, DD, and so on, the greater slope corresponding to the limitation in displacement for various values of p ($p = 0.05, 0.10, 0.25, 0.50$, and 1.00).

A particular shock will be thus realizable on the shaker only if the point of coordinates τ, \ddot{x}_m (duration and amplitude of the shock considered) is located under these lines, this useful domain increasing when p increases.

Example

TPS shock pulse, 340 m/sec^2 , 9 msec
 (example of Section 12.5.2.5)
 Unit table mass: 192 kg
 Shaker: 135 kN (maximum velocity:
 1.78 m/sec , maximum stroke: $\pm 12.7 \text{ mm}$; see
 Figure 12.57)
 Test item + fixture mass: 150 kg
 Maximum acceleration without load:
 $(135,000/192) \approx 703 \text{ m/sec}^2$
 Maximum acceleration with test item and
 fixture: $(135,000/(192 + 150)) \approx 395 \text{ m/sec}^2$

The TPS shock pulse (340 m/sec^2 , 9 msec) is realizable on this shaker with $p = 0.05$.

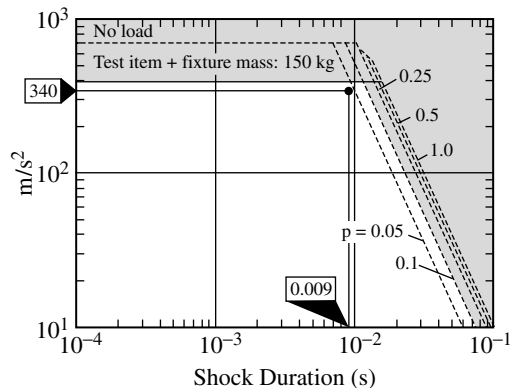


FIGURE 12.57 Shaker 135 kN , $\pm 12.7 \text{ mm}$ — TPS pulse with half-sine symmetrical pre- and postshocks.

The limitation can also be due to:

- The resonance of the moving element (a few thousands Hertz; although it is kept to the maximum by design, the resonance of this element can be excited in the presence of signals with very short rise time).
- The strength of the material (very great accelerations can involve a separation of the coil of the moving component).

Mechanical limitations of electrodynamic shakers for shocks:

- Maximum stroke of the coil-table unit: 25.4 to 75 mm peak-to-peak.
- Maximum acceleration, related to the maximum force: according to the author, ≤ 4 times the maximum force in sine mode, with the *proviso* of not exceeding 300g on the armature assembly, more than eight times the maximum force in sine mode in certain cases (very short shocks; 0.4 msec, for example).
- Maximum velocity: 1.5 to 3 m/sec in sine mode.

12.9.4.2 Electronic Limitations

1. Limitation of the output voltage of the amplifier (Smallwood, 1974), which limits coil velocity.
2. Limitation of the acceptable maximum current in the amplifier, related to the acceptable maximum force (i.e., with acceleration).
3. Limitation of the bandwidth of the amplifier.
4. Limitation in power, which relates to the shock duration (and the maximum displacement) for a given mass.

Current transistor amplifiers make it possible to increase the low frequency bandwidth but do not handle even short over tensions well, and thus are limited in mode shock (Miller, 1964).

12.9.5 The Use of Electrohydraulic Shakers

Shocks are realizable on the electrohydraulic exciters, but with additional stresses.

- Contrary to the case of the electrodynamic shakers, one cannot obtain via these means shocks of amplitude larger than realizable accelerations in the steady mode.
- The hydraulic vibration machines are in addition strongly nonlinear (Favour, 1974).

However, their long stroke, required for long duration shocks, is an advantage.

12.10 Control by a Shock Response Spectrum

12.10.1 Principle

The exciters are actually always controlled by a signal that is a function of time. An acceleration–time signal gives only one SRS. However, there is an infinity of acceleration–time signals with a given spectrum. The general principle thus consists in searching out one of the signals, $\ddot{x}(t)$, having the specified spectrum.

Historically, the simulation of shocks with spectrum control was first carried out using analog and then digital methods (Smallwood and Witte, 1973; Smallwood, 1974).

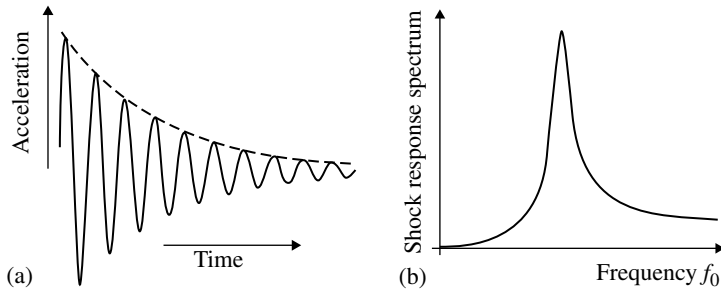


FIGURE 12.58 Elementary shock (a) and its SRS (b). (Source: Lalanne, *Chocs Mecaniques*, Hermes Science Publications. With permission.)

From the data of selected points on the shock spectrum to be simulated, the calculator of the control system uses an acceleration signal with a very tight spectrum. For that, the calculation software proceeds as follows (Lalanne, 2002b):

- At each frequency, f_0 , of the reference shock spectrum, the software generates an elementary acceleration signal, for example, a decaying sinusoid. Such a signal has the property of having a SRS presenting a peak of the frequency of the sinusoid whose amplitude is a function of the damping of the sinusoid (Figure 12.58). With an identical shock spectrum, this property makes it possible to realize shocks on the shaker that would be unrealizable with a control carried out by a temporal signal of simple shape. For high frequencies, the spectrum of the sinusoid tends roughly towards the amplitude of the signal.
- All the elementary signals are added by possibly introducing a given delay (and variable) between each one of them in order to control to a certain extent the total duration of the shock, which is primarily due to the lower frequency components (Figure 12.59).
- The total signal being thus made up, the software proceeds to processes correcting the amplitudes of each elementary signal so that the spectrum of the total signal converges towards the reference spectrum after some iterations.

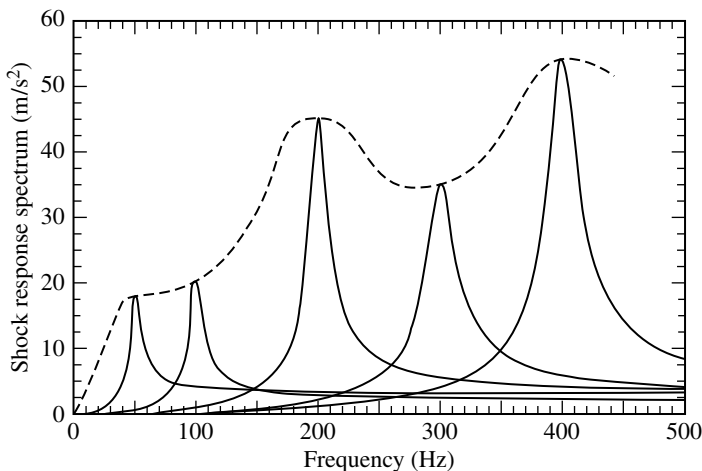


FIGURE 12.59 SRS of the components of the required shock. (Source: Lalanne, *Chocs Mecaniques*, Hermes Science Publications. With permission.)

The operator must provide to the software with, at each frequency of the reference spectrum:

- The frequency of the spectrum
- Its amplitude
- A delay
- The damping of sinusoids or other parameters characterizing the number of oscillations of the signal

When a satisfactory spectrum time signal has been obtained, it remains to be checked that the maximum velocity and displacement during the shock are within the authorized limits of the test facility (by integration of the acceleration signal). Lastly, after measurement of the transfer function of the facility, one calculates the electric excitation which will make it possible to reproduce on the table the acceleration pulse with the desired spectrum, as in the case of control from a signal according to the time (Powers, 1974).

12.10.2 Principal Shapes of Elementary Signals

12.10.2.1 Decaying Sinusoid

The shocks measured in the field environment are very often responses of structures to an excitation applied upstream, and are thus composed of the superposition of several modal responses of a damped sine type (Smallwood and Witte, 1973; Crimi, 1978; Boissin et al., 1981; Smallwood, 1985). Electrodynamical shakers are completely adapted to the reproduction of this type of signal. According to this, one should be able to reconstitute a given SRS from such signals of the form:

$$\left. \begin{aligned} a(t) &= A e^{-\eta\Omega t} \sin \Omega t & t \geq 0 \\ a(t) &= 0 & t < 0 \end{aligned} \right\} \quad (12.43)$$

where $\Omega = 2\pi f$, f = frequency of the sinusoid, and η = damping factor.

Velocity and displacement are not zero at the end of the shock with this type of signal. These nonzero values are very awkward for a test on a shaker. Compensation can be carried out in several ways:

1. By truncating the total signal until it is realizable on the shaker. This correction can, however, lead to an important degradation of the corresponding spectrum (Smallwood and Witte, 1972).
2. By adding to the total signal (sum of all the elementary signals) a highly damped decaying sinusoid at low frequency, shifted in time, defined to compensate for the velocity and the displacement (Smallwood and Nord, 1974; Smallwood 1975, 1985).
3. By adding to each component two exponential compensation functions, with a phase in the sinusoid (Nelson and Prasthofer, 1974; Smallwood, 1975).

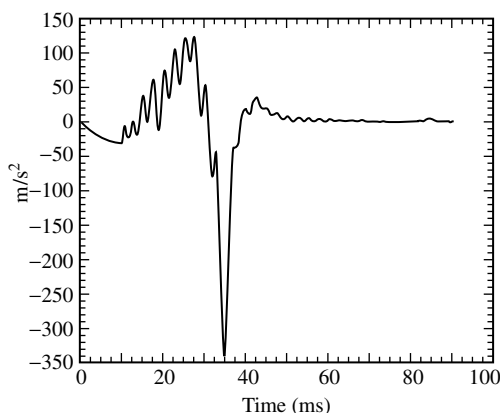


FIGURE 12.60 Shock pulse generated from decaying sinusoids, compensated by a decaying sinusoid. (Source: Lalanne, *Chocs Mécaniques*, Hermes Science Publications. With permission.)

Example

The reference SRS is that of Figure 12.24 (Section 12.5.2.5). Examples of acceleration signals generated from decaying sinusoids and having approximately the same SRS are shown in Figure 12.60 and Figure 12.61 in the cases of a compensation by a decaying sinusoid and by two exponential functions.

12.10.2.2 ZERD Function

The use of a decaying sinusoid with its compensation waveform modifies the response spectrum at the low frequencies and, in certain cases, can harm the quality of simulation. Fisher and Posehn (1977) proposed using a waveform, which they named “ZERD” (Zero Residual Displacement), defined by the expression:

$$a(t) = A e^{-\eta\Omega t} \left[\frac{1}{\Omega} \sin \Omega t - t \cos(\Omega t + \phi) \right] \quad (12.44)$$

where $\phi = \arctan(2\eta/1 - \eta^2)$. This function resembles a damped sinusoid and has the advantage of leading to zero velocity and displacement at the end of the shock (Figure 12.62).

Example

The reference SRS is that of Figure 12.24 (Section 12.5.2.5). Figure 12.63 shows an example of acceleration signal generated from ZERD functions having approximately the same SRS.

12.10.2.3 WAVSIN Waveform

Yang (1970, 1972) and Smallwood (1974, 1975, 1985) proposed (initially for the simulation of the earthquakes) a signal of the form:

$$\left. \begin{aligned} a(t) &= a_m \sin 2\pi b t \sin 2\pi f t & 0 \leq t \leq \tau \\ a(t) &= 0 & \text{elsewhere} \end{aligned} \right\} \quad (12.45)$$

where

$$f = Nb \quad (12.46)$$

$$\tau = \frac{1}{2b} \quad (12.47)$$

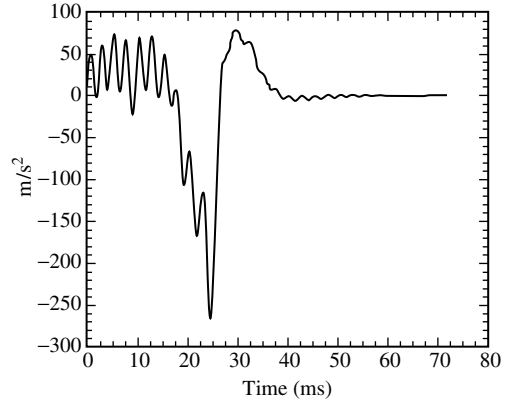


FIGURE 12.61 Acceleration signal generated from decaying sinusoids, compensated by two exponential functions. (Source: Lalanne, *Chocs Mecaniques*, Hermes Science Publications. With permission.)

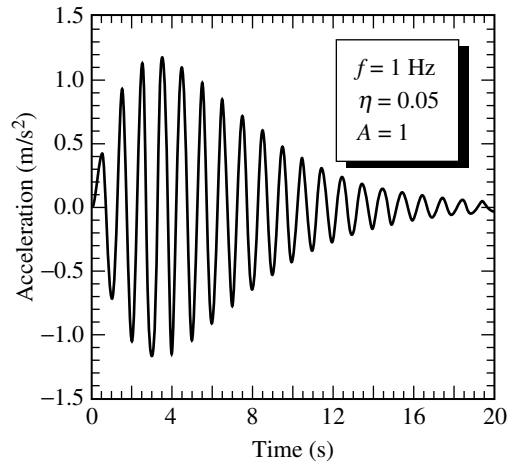


FIGURE 12.62 ZERD waveform of D.K. Fisher and M.R. Posehn (example).

where N is an integer (which must be odd and higher than on 1). The first term of $a(t)$ is a window of half-sine form of half-period τ . The second describes N half-cycles of a sinusoid of greater frequency (f), modulated by the preceding window (Figure 12.64).

This function leads also to zero velocity and displacement at the end of the shock.

Example

Figure 12.65 shows an example of acceleration signal generated from WAVSIN functions having approximately the same SRS as the reference SRS of Figure 12.24 (Section 12.5.2.5).

12.10.3 Comparison of WAVSIN, SHOC Waveforms, and Decaying Sinusoid

The cases treated by Smallwood (1974) seem to show that these three methods give similar results. It is noted, however, in practice, that, according to the shape of the reference spectrum, one or other of these waveforms allows a better convergence. The ZERD waveform very often gives good results.

12.10.4 Criticism of Control by a Shock Response Spectrum

Whatever the method adopted, simulation on a test facility of shocks measured in the real world requires the calculation of their SRSs and the search for an equivalent shock.

If the specification must be presented in the form of a time-dependent shock pulse, the test requester must define the characteristics of shape, duration, and amplitude of the signal, with the already quoted difficulties.

If the specification is given in the form of an SRS, the operator inputs in the control system the given spectrum, but the shaker is always controlled by a signal according to the time calculated and according to procedures described in the preceding sections. It is known that the transformation shock spectrum signal has an infinite number of solutions, and that very different signals can have identical SRSs. This phenomenon is related to the loss of most of the information initially contained in the signal, $\ddot{x}(t)$, during the calculation of the spectrum (Metzgar, 1967).

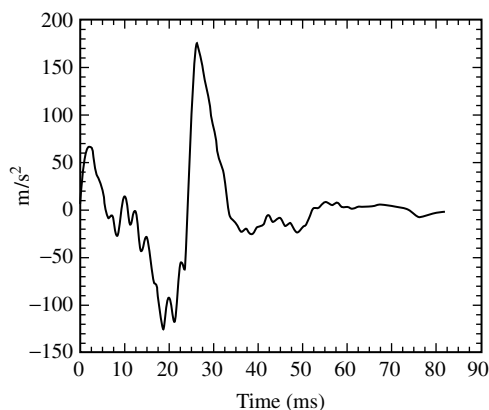


FIGURE 12.63 Acceleration signal generated from ZERD functions.

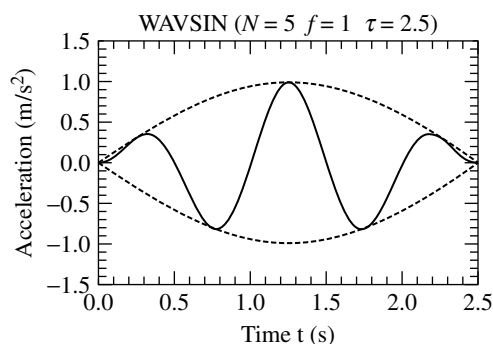


FIGURE 12.64 Example of WAVSIN waveform. (Source: Lalanne, *Chocs Mecaniques*, Hermes Science Publications. With permission.)

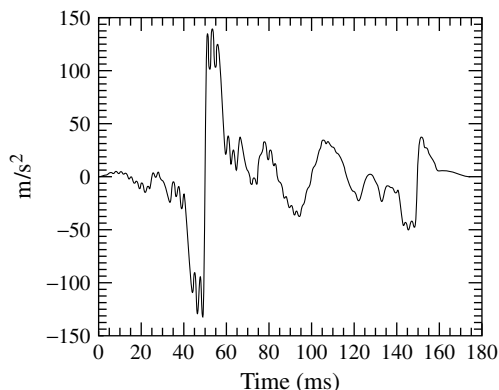


FIGURE 12.65 Acceleration signal generated from WAVSIN functions.

The oscillatory shock pulses have a spectrum that presents an important peak to the frequency of the signal. This peak can, according to choice of parameters, exceed by a factor of five the amplitude of the same spectrum at the high frequencies; that is, five times the amplitude of the signal itself. Being given a point of the specified spectrum of amplitude, S , it is thus enough to have a signal vs. time of amplitude $S/5$ to reproduce the point. For a simple shaped shock, this factor does not exceed two in the most extreme case. All these remarks show that the determination of a signal of the same spectrum can lead to very diverse solutions, the validity of which one can question.

If any particular precaution is not taken, the signals created by these methods have, in a general way, one duration much larger and an amplitude much smaller than the shocks that were used to calculate the reference SRS (a factor of about ten in both cases). Figure 12.66 and Figure 12.67 give an example.

In the face of such differences between the excitations, one can legitimately wonder whether the SRS is a sufficient condition to guarantee a representative test. It is necessary to remember that this equivalence is based on the behavior of a linear system that one chooses the Q factor *a priori*. One must be aware of the following.

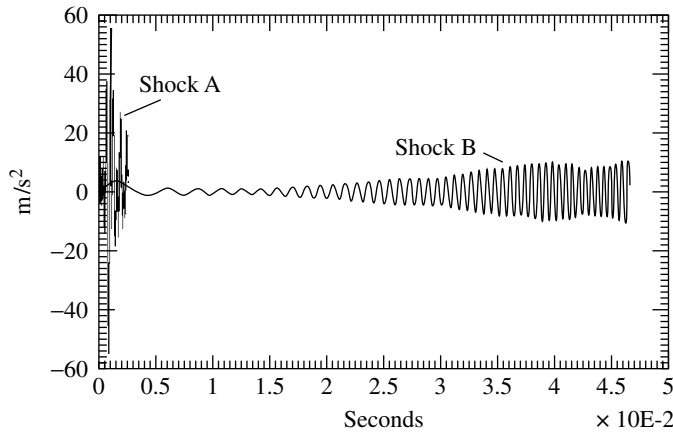


FIGURE 12.66 Example of shocks having spectra near the SRS.

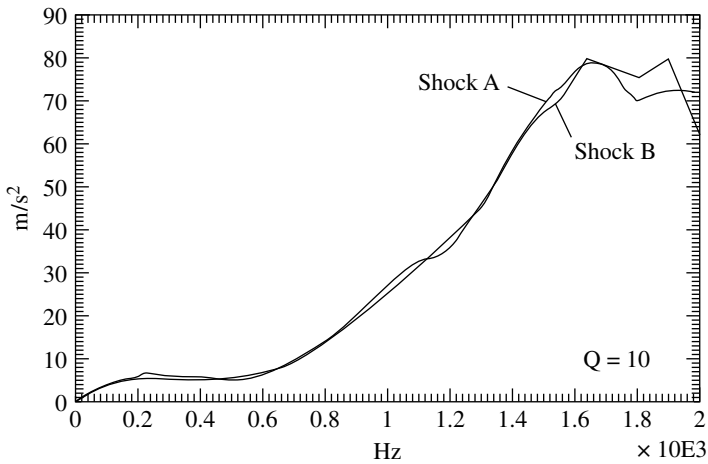


FIGURE 12.67 SRS of the shocks shown in Figure 12.66.

- The behavior of the structure is in practice far from linear and that the equivalence of the spectrum does not lead to stresses of the same amplitude. Another effect of these nonlinearities appears sometimes by the inaptitude of the system to correct the drive waveform to take account of the transfer function of the installation.
- Even if the amplitudes of the peaks of acceleration and the maximum stresses of the resonant parts of the tested structure are identical, the damage by the fatigue generated by accumulation of the stress cycles is rather different when the number of shocks to be applied is significant.
- The tests carried out by various laboratories do not have the same severity.

These questions did not receive a really satisfactory response. By prudence rather than by rigorous reasoning, many agree, however, on the need for placing parapets, while trying to supplement the specification defined by a spectrum with complementary data (ΔV , duration of the shock, require SRS at two different values of damping, etc.; Favour, 1974; Smallwood, 1974, 1975, 1985).

There is an infinity of acceleration–time signals with a given spectrum. Several elementary waveforms can be used to build a signal of acceleration having a given SRS. They give similar results.

Without particular precaution, the signals thus obtained generally have one duration much larger and an amplitude much smaller than the shocks which were used to calculate the reference SRS. A complementary parameter (shock duration, velocity change, etc.) is often specified with the SRS to limit this effect.

12.11 Pyrotechnic Shock Simulation

Many works have been published on the characterization, measurement, and simulation of shocks of pyrotechnic origin, generated by bolt cutters, explosive valves, separation nuts, and so on (Zimmerman, 1993). The test facilities suggested are many, ranging from traditional machines to very exotic means.

The tendency today is to consider that the best simulation of shocks measured in near-field can be obtained only by subjecting the material to the shock produced by the real device.

For shocks in the far-field, simulation can be carried out either using the real pyrotechnic source and a particular mechanical assembly, using specific equipment using explosives, or by impacting metal to metal if the structural response is more important. When the real shock is practically made up only of the response of the structures, a simulation on a shaker is possible (when performances by this means are allowed).

12.11.1 Simulation Using Pyrotechnic Facilities

The simplest solution consists of making functional, real pyrotechnic devices on real structures. The simulation is perfect but (Conway et al., 1976; Luhrs, 1976):

- It can be expensive and destructive.
- One cannot apply an uncertainty factor (Lalanne, 2002d) to cover the variability of this shock without being likely to create unrealistic local damage (a larger load, which requires an often expensive modification of the devices and can be much more destructive). To avoid this problem, an expensive solution consists of carrying out several tests in a statistical matter.

One often prefers to carry out a simulation on a reusable assembly, the excitation still being pyrotechnic in nature. Several devices have been designed, some examples of which are as follows:

- A test facility made up of a cylindrical structure (Ikola, 1964), which comprises a “consumable” sleeve cut out for the test by an explosive cord. Preliminary tests are carried out to calibrate the facility while acting on the linear charge of the explosive cord and/or the distance between the equipment to be tested (fixed on the structure as in the real case if possible) and the explosive cord.
- A greater number of small explosive charges near the equipment to be tested on the structure in “flowers pots.” The number of pots to be used on each axis depends on the amplitude of the shock, the size of the equipment, and the local geometry of the structure. The shape of the shock can be modified within certain limits by use of damping devices, placing the pot closer to or further from the equipment, or by putting suitable padding in the pot (Aerospace Systems pyrotechnic shock data, 1970).
- A test facility made up of a basic rectangular steel plate (Figure 12.68) suspended horizontally. This plate receives on its lower part, directly or by the intermediary of an “expendable” item, an explosive load (chalk line, explosive in plate or bread).

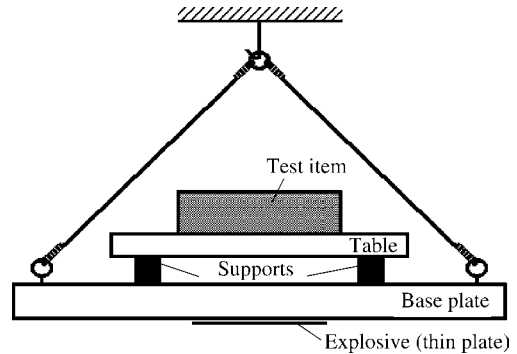


FIGURE 12.68 Plate with resonant system subjected to detonation. (Source: Lalanne, *Chocs Mecaniques*, Hermes Science Publications. With permission.)

A second plate supporting the test item rests on the base plate via four elastic supports (Thomas, 1973). The reproducibility of the shocks is better if the explosive charge is not in direct contact with the base plate.

12.11.2 Simulation Using Metal-to-Metal Impact

The shock obtained by a metal-to-metal impact has similar characteristics to those of a pyrotechnical shock in an intermediate field: great amplitude; short duration; high frequency content; SRS comparable with a low frequency slope of 12 dB per octave, etc. The simulation is in general satisfactory up to approximately 10 kHz.

The shock can be created by the impact of a hammer on the structure itself, a Hopkinson bar or a resonant plate (Bai and Thatcher, 1979; Luhrs, 1981; Davie, 1985; Dokainish and Subbaraj, 1989; Davie and Batemen, 1992).

With all these devices, the amplitude of the shock is controlled while acting on the velocity of impact. The frequency components are adjusted by modifying the resonant geometry of system (changing the length of the bar between two points of fixing, adding or removing runners, etc.) or by the addition of a deformable material between the hammer and the anvil.

12.11.3 Simulation Using Electrodynamic Shakers

The limitation relating to the stroke of the electrodynamic shaker is not very constraining for the pyrotechnical shocks since they are at high frequencies. The possibilities are limited especially by the acceptable maximum force and then concern the maximum acceleration of the shock

(Conway et al., 1976; Luhrs, 1976; Powers, 1976; Caruso, 1977). If one agrees to cover only part of the SRS where material has resonant frequencies, then when one makes a possible simulation on the shaker, which gives a better approach to matching the real spectrum.

Exciters have the advantage of allowing the realization of any signal shape such as shocks of simple shapes (Dinicola, 1964; Gallagher and Adkins, 1966), but also of reproducing a specified SRS (direct control from an SRS; see Section 12.10.1).

It is possible, in certain cases, to reproduce the real SRS up to 1000 Hz. If one is sufficiently far away from the source of the shock, the transient has a lower level of acceleration and the only limitation is the bandwidth of the shaker, which is about 2000 Hz. Certain facilities of this type were modified to make it possible to simulate the effects of pyrotechnical shocks up to 4000 Hz. One can thus manage to simulate shocks whose spectrum can reach 7000g (Moening, 1986).

12.11.4 Simulation Using Conventional Shock Machines

We saw that, generally, the method of development of a specification of a shock consists of replacing the transient of the real environment, whose shape is in general complex, with a simple shape shock, such as half-sine, triangle, trapezoid, and so on, starting from the SRS equivalence criterion, with the application of a given or calculated uncertainty factor (Lalanne, 2002d) to the shock amplitude (Luhrs, 1976).

With the examination of the shapes of the response spectra of standard simple shocks, it seems that the signal best adapted is the TPS pulse, whose spectra are also appreciably symmetrical. SRSs of the pyrotechnical shocks with, in general, averages close to zero have a very weak slope at low frequencies. The research of the characteristics of such a triangular pulse (amplitude, duration) having an SRS envelope of that of a pyrotechnical shock led often to a duration of about 1 msec and to an amplitude being able to reach several tens of thousands of msec⁻². Except in the case of very

TABLE 12.12 Advantages and Drawbacks of Various Test Facilities for the Pyroshock Simulation

Shock Facility	Field	Advantages	Drawbacks
Real pyrotechnic devices on real structures	Near	Very good simulation	Expensive, generally destructive, no uncertainty factor/test factor
Reusable assembly with pyrotechnic excitation	Near	Good simulation	Necessity of preliminary tests, no uncertainty factor/test factor, use of explosive (specific conditions to ensure safety), expensive
Metal to metal impact	Near	Good simulation, no explosive charge	Necessity of preliminary tests, limitations in acceleration and frequency (approximately 10 kHz)
Electrodynamic shaker	Far	Easy implementation, control using any time history signal or SRS, possibility of using an uncertainty factor or a test factor	Necessity of one test by axis, maximum frequency up to about 1 to 2 kHz
Conventional shock-test machine	Far	Easy implementation, possibility of using an uncertainty factor or a test factor	Use of a shock pulse with velocity change instead of an oscillatory shock pulse (over test at low frequency), necessity of one test by axis, shock duration higher than 2 msec (0.1 msec using a specific device for very light test item), limitation in amplitude, useable for very small test items only

small test items, it is in general not possible to carry out such shocks on the usual drop tables due to certain limitations:

- Limitation in amplitude (acceptable maximum force on the table).
- Duration limit: the pneumatic shock simulators do not allow it to go below 3 to 4 msec; even with the lead shock simulators, it is difficult to obtain a duration of less than 2 msec and a larger shock duration leads to a significant overttest at low frequency.
- The SRSs of the pyrotechnical shocks are much more sensitive to the choice of damping than simple shocks carried out on shock machines.

A comparison of some pyroshock-test facilities is given in [Table 12.12](#).

References

- Aerospace Systems pyrotechnic shock data (Ground test and flight), Final Report, Contract NAS 5, 15208, June 1966, March 1970.
- ASTM D3332, *Standard Test Method for Mechanical-Shock Fragility of Products, Using Shock Machines*. American Society for Testing and Materials, Philadelphia, PA.
- Bai, M. and Thatcher, W., High G pyrotechnic shock simulation using metal-to-metal impact, *Shock Vib. Bull.*, 49, Part 1, 97–100, 1979.
- Benioff, H., The physical evaluation of seismic destructiveness, *Bull. Seismol. Soc. Am.*, 398–403, 1934.
- Biot, M.A. 1932. Transient oscillations in elastic systems, Thesis No. 259, Aeronautics Department, California Institute of Technology, Pasadena.
- Biot, M.A., A mechanical analyzer for the prediction of earthquake stresses, *Bull. Seismol. Soc. Am.*, 31, 2, 151–171, 1941.
- Boissin, B., Girard, A., and Imbert, J.F. 1981. Methodology of uniaxial transient vibration test for satellites, In *Recent Advances in Space Structure Design-Verification Techniques*, ESA SP 1036, pp. 35–53.
- Bort, R.L., Use and misuse of shock spectra, *Shock Vib. Bull.*, 60, Part 3, 79–86, 1989.
- Bresk, F., Shock programmers, *IES Proc.*, 141–149, 1967.
- Bresk, F. and Beal, J., Universal impulse impact shock simulation system with initial peak sawtooth capability, *IES Proc.*, 405–416, 1966.
- Brooks, R.O., Shock springs and pulse shaping on impact shock machines, *Shock Vib. Bull.*, 35, Part 6, 23–40, 1966.
- Brooks, R.O. and Mathews, F.H., Mechanical shock testing techniques and equipment, *IES Tutorial Lect. Ser.*, 69, 1966.
- Burgess, G., Effects of fatigue on fragility testing and the damage boundary curve, *J. Test. Eval.*, 24, 6, 419–426, 1996.
- Burgess, G., Extension and evaluation of fatigue model for product shock fragility used in package design, *J. Test. Eval.*, 28, 2, 116–120, 2000.
- Caruso, H., Testing the Viking lander, *J. Environ. Sci.*, March/April, 11–17, 1977.
- Clough, R.W., On the importance of higher modes of vibration in the earthquake response of a tall building, *Bull. Seismol. Soc. Am.*, 45, 4, 289–301, 1955.
- Colvin, V.G. and Morris, T.R., Algorithms for the rapid computation of response of an oscillator with bounded truncation error estimates, *Int. J. Mech. Sci.*, 32, 3, 181–189, 1990.
- Conrad, R. W., Characteristics of the navy medium weight high-impact shock machine, NRL Report 3852, September 14, 1951.
- Conrad, R.W., Characteristics of the light weight high-impact shock machine, NRL Report 3922, January 23, 1952.
- Conway, J.J., Pugh, D.A., and Sereno, T.J., Pyrotechnic shock simulation, *IES Proc.*, 12–16, 1976.
- Coty, A. and Sannier, B. 1966. Essais de chocs sur excitateur de vibrations, Note Technique No. 170/66/EM, LRBA, France, December 1966.

- Cox, F.W., Efficient algorithms for calculating shock spectra on general purpose computers, *Shock Vib. Bull.*, 53, Part 1, 143–161, 1983.
- Crimi, P., Analysis of structural shock transmission, *J. Spacecraft*, 15, 2, 79–84, 1978.
- Davie, N.T., Pyrotechnic shock simulation using the controlled response of a resonating bar fixture, *IES Proc.*, 344–351, 1985.
- Davie, N.T. and Bateman, V.I. 1992. Pyroshock simulation for satellite components using a tunable resonant fixture — Phase 1, SAND 92-2135, October 1992.
- DEF STAN 00 35, *Environmental Handbook for Defence Materials, Environmental Test Methods*, Part 3, Ministry of Defence, Issue 3, May 7, 1999.
- Dinicola, D.J., A method of producing high-intensity shock with an electro-dynamic exciter, *IES Proc.*, 253–256, 1964.
- Dokainish, M.A. and Subbaraj, K., A survey of direct time-integration methods in computational structural dynamics: I. Explicit methods; II. Implicit methods, *Comput. Struct.*, 32, 6, 1371–1389, 1989, see also 1387–1401.
- Fandrich, R.T., Optimizing pre and postpulses for shaker shock testing, *Shock Vib. Bull.*, 51, Part 2, 1–13, 1981.
- Favour, J.D., Transient waveform control — a review of current techniques, *J. Environ. Sci.*, November/December, 9–19, 1974.
- Favour, J.D., Lebrun, J.M., and Young, J.P., Transient waveform control of electromagnetic test equipment, *Shock Vib. Bull.*, 40, Part 2, 157–171, 1969.
- Fisher, D.K. and Posehn, M.R., Digital control system for a multiple-actuator shaker, *Shock Vib. Bull.*, 47, Part 3, 79–96, 1977.
- Fung, Y.C. and Barton, M.V., Some shock spectra characteristics and uses, *J. Appl. Mech.*, 25, 365–372, 1958.
- Gaberson, H.A., Shock spectrum calculation from acceleration time histories, *Civil Engineering Laboratory* TN 1590, September 1980.
- Galef, A.E., Approximate response spectra of decaying sinusoids, *Shock Vib. Bull.*, 43, Part 1, 61–65, 1973.
- Gallagher, G.A. and Adkins, A.W., Shock testing a spacecraft to shock response spectrum by means of an electrodynamic exciter, *Shock Vib. Bull.*, 35, Part 6, 41–45, 1966.
- GAM EG 13, 1ère Partie, Recueil des Fascicules d'Essais, Ministère de la Défense, Délégation Générale pour l'Armement, France, Juin 1986.
- Gray, R.P., Shock test programming — some recent developments, *Test Eng.*, May, 28–41, 1966.
- Grivelet, P., SRS calculation using prony and wavelet transforms, *Shock Vib. Bull.*, 1, 67, 123–132, 1996.
- Hale, M.T. and Adhami, R., Time–frequency analysis of shock data with application to shock response spectrum waveform synthesis, *Proc. IEEE*, 213–217, 1991, Southeastcon, 91 CH 2998-3, April 1991.
- Hay, W.A. and Oliva, R.M., An improved method of shock testing on shakers, *IES Proc.*, 241–246, 1963.
- Hug, G., *Méthodes d'essais de chocs au moyen de vibreurs électrodynamiques*. IMEX, France, 1972.
- Hughes, M.E., Pyrotechnic shock test and test simulation, *Shock Vib. Bull.*, 53, Part 1, 83–88, 1983.
- Hughes, T.J.R. and Belytschko, T., A precis of developments in computational methods for transient analysis, *J. Appl. Mech.*, 50, 1033–1041, 1983.
- IEC 60068-2-27, Environmental testing, Part 2: Tests, Test Ea and guidance: Shock, June 1987a.
- IEC 60068-2-29, Ed. 2.0, Basic Environmental Testing Procedures, Part 2: Tests, Test Eb and guidance: Bump, 1987b.
- Ikola, A.L., Simulation of the pyrotechnic shock environment, *Shock Vib. Bull.*, 34, Part 3, 267–274, 1964.
- IMPAC 6060F — *Shock Test Machine — Operating Manual*, MRL 335 Monterey Research Laboratory, Inc.
- Irvine, M. 1986. *Structural Dynamics for the Practising Engineer*. Unwin Hyman, London, pp. 114–153.
- Jennings, R.L. 1958. The response of multi-storied structures to strong ground motion, MSc Thesis, University of Illinois, Urbana.

- Keegan, W.B. 1973. Capabilities of electrodynamic shakers when used for mechanical shock testing, NASA Report N74-19083, July 1973.
- Lalanne, C. 1975. La simulation des environnements de chocs mécaniques, Rapport CEA-R-4682 (1) et (2), Commissariat à l'Energie Atomique, France, 1975.
- Lalanne, C. 2002a. *Mechanical Vibration and Shock, Sinusoidal Vibration*, Vol. I. Taylor & Francis, New York.
- Lalanne, C. 2002b. *Mechanical Vibration and Shock, Mechanical Shock*, Vol. II. Taylor & Francis, New York.
- Lalanne, C. 2002c. *Mechanical Vibration and Shock, Fatigue Damage*, Vol. IV. Taylor & Francis, New York.
- Lalanne, C. 2002d. *Mechanical Vibration and Shock, Specification Development*, Vol. V. Taylor & Francis, New York.
- La Verne Root and Bohs, C., Slingshot shock testing, *Shock Vib. Bull.*, 39, Part 5, 73–81, 1969.
- Lax, R., A new method for designing MIL-STD shock tests, *Test Eng. Manage.*, 63, 3, 10–13, 2001.
- Lazarus, M., Shock testing, *Mach. Des.*, October 12, 200–214, 1967.
- Lonborg, J.O., A slingshot shock tester, *IES Proc.*, 457–460, 1963.
- Luhrs, H., Equipment sensitivity to pyrotechnic shock, *IES Proc.*, 3–4, 1976.
- Luhrs, H.N., Pyrotechnic shock testing — past and future, *J. Environ. Sci.*, Vol. XXIV, 6, 17–20, 1981.
- Magne, M. 1971. Essais de chocs sur excitateur électrodynamique — méthode numérique, Note CEA-DAM Z — SDA/EX — DO 0016, Commissariat à l'Energie Atomique, France, December 1971.
- Magne, M., and Leguay, P. 1972. Réalisation d'essais aux chocs par excitateurs électrodynamique, Rapport CEA-R-4282, Commissariat à l'Energie Atomique, France, 1972.
- Marshall, S., La Verne Root, and Sackett, L., 10 000 g Slingshot shock tests on a modified sand-drop machine, *Shock Vib. Bull.*, 35, Part 6, 1965.
- McClanahan, J.M. and Fagan, J., Shock capabilities of electro-dynamic shakers, *IES Proc.*, 251–256, 1965.
- McClanahan, J.M. and Fagan, J., Extension of shaker shock capabilities, *Shock Vib. Bull.*, 35, Part 6, 111–118, 1966.
- McWhirter, M., Shock machines and shock test specifications, *IES Proc.*, 497–515, 1963.
- McWhirter, M., *Methods of Simulating Shock and Acceleration and Testing Techniques*. Sandia Corporation SCDC 2939, 1961.
- Mercer, C.A. and Lincoln, A.P., Improved evaluation of shock response spectra, *Shock Vib. Bull.*, 62, Part 2, 350–359, 1991.
- Merchant, H.C. and Hudson, D.E., Mode superposition in multi-DoF systems using earthquake response spectrum data, *Bull. Seismol. Soc. Am.*, 52, 2, 405–416, 1962.
- Merritt, R.G., A note on variation in computation of shock response spectra, *IES Proc.*, 2, 330–335, 1993.
- Metzgar, K.J., A test oriented appraisal of shock spectrum synthesis and analysis, *IES Proc.*, 69–73, 1967.
- Miller, W.R., Shaping shock acceleration waveforms for optimum electrodynamic shaker performance, *Shock Vib. Bull.*, 34, Part 3, 345–354, 1964.
- MIL STD 810 F, Test Method Standard for Environmental Engineering Considerations and Laboratory Tests, Department of Defence, January 1, 2000.
- Moening, C., Views of the world of pyrotechnic shock, *Shock Vib. Bull.*, 56, Part 3, 3–28, 1986.
- NATO Standardization Agreement, STANAG 4370, Environmental Testing, Allied Environmental Conditions and Test Publications (AECTP) 400, Mechanical Environmental Tests, Method 403, Classical waveform shock, Edition 2, June 2000.
- Nelson, D.B. and Prasthofer, P.H., A case for damped oscillatory excitation as a natural pyrotechnic shock simulation, *Shock Vib. Bull.*, 44, Part 3, 57–71, 1974.
- O'Hara, G.J. 1962. A numerical procedure for shock and Fourier analysis, NRL Report 5772, June 5, 1962.
- Operating manual for the MRL 2680 Universal programmer, MRL 519, Monterey Research Laboratory, Inc.
- Ostrem, F.E. and Rumerman, M.L. 1965. Final report. *Shock and Vibration Transportation Environmental criteria*, NASA Report CR 77220.
- Powers, D.R., Development of a pyrotechnic shock test facility, *Shock Vib. Bull.*, 44, Part 3, 73–82, 1974.

- Powers, D.R., Simulation of pyrotechnic shock in a test laboratory, *IES Proc.*, 5–9, 1976.
- Ridler, K.D. and Blader, F.B., Errors in the use of shock spectra, *Environ. Eng.*, July, 7–16, 1969.
- Rubin, S., Response of complex structures from reed-gage data, *J. Appl. Mech.*, 35, 1958.
- Seipel, W.F., The SRC shock response spectra computer program, *Shock Vib. Bull.*, 62, Part 1, 300–309, 1991.
- Selected ASTM Standards on Packaging*, 4th Ed., ASTM, Philadelphia, 1994.
- Shell, E.H., Errors inherent in the specification of shock motions by their shock spectra, *IES Proc.*, 439–448, 1966.
- Sinn, L.A. and Bosin, K.H., Sampling rate detection requirements for digital shock response spectra calculations, *IES Proc.*, 174–180, 1981.
- Smallwood, D.O., Methods used to match shock spectra using oscillatory transients, *IES Proc.*, 28 April–1 May, 409–420, 1974.
- Smallwood, D.O. 1975. Time history synthesis for shock testing on shakers, Sand 75-5368.
- Smallwood, D.O., An improved recursive formula for calculating shock response spectra, *Shock Vib. Bull.*, 51, Part 2, 211–217, 1981.
- Smallwood, D.O. 1985. Shock testing by using digital control, Sand 85-03552 J.
- Smallwood, D.O., Shock response spectrum at low frequency, *Shock Vib. Bull.*, 56, Part 1, 279–288, 1986.
- Smallwood, D.O., Calculation of the shock response spectrum (SRS) with a change in sample rate, *ESTECH 2002 Proc.*, April 28–May 1, 2002.
- Smallwood, D.O. and Nord, A.R., Matching shock spectra with sums of decaying sinusoids compensated for shaker velocity and displacement limitations, *Shock Vib. Bull.*, 44, Part 3, 43–56, 1974.
- Smallwood, D.O. and Witte, A.F., The use of shaker optimized periodic transients in watching field shock spectra, *Shock Vib. Bull.*, 43, Part 1, 139–150, 1973, or Sandia Report, SC-DR-710911, May 1972.
- Smith, J. L. 1984. Shock response spectra variational analysis for pyrotechnic qualification testing of flight hardware, NASA Technical Paper 2315, N84-23676, May 1984.
- Smith, J.L. 1986. Effects of variables upon pyrotechnically induced shock response spectra, NASA Technical Paper 2603.
- Thomas, C.L., Pyrotechnic shock simulation using the response plate approach, *Shock Vib. Bull.*, 43, Part 1, 119–126, 1973.
- Thorne, L.F., The design and the advantages of an air-accelerated impact mechanical shock machine, *Shock Vib. Bull.*, 33, Part 3, 81–84, 1964.
- Vibrations et Chocs Mécaniques — Vocabulaire, Norme AFNOR NF E 90-001 (NF ISO 2041), June 1993.
- Vigness, I., Some characteristics of navy high impact type shock machines, *SESA Proc.*, 5, 1, 101–110, 1947.
- Vigness, I. 1961a. Shock testing machines. *Shock and Vibration Handbook*, Vol. 2, C.M. Harris and C.E. Crede, eds., McGraw-Hill, New York, chap. 26.
- Vigness, I. 1961b. *Navy High Impact Shock Machines for High Weight and Medium Weight Equipment*. U.S. Naval Research Laboratory, Washington, DC, NRL Report 5618, AD 260-008, June 1961b.
- Vigness, I. and Clements, E.W. 1963. *Sawtooth and Half-sine Shock Impulses from the Navy Shock Machine for Medium Weight Equipment*. U.S. Naval Research Laboratory, NRL Report 5943, June 3, 1963.
- Wells, R.H. and Mauer, R.C., Shock testing with the electrodynamic shaker, *Shock Vib. Bull.*, 29, Part 4, 96–105, 1961.
- Wise, J.H., The effects of digitizing rate and phase distortion errors on the shock response spectrum, *IES Proc.*, 36–43, 1983.
- Yang, R.C. 1970. Safeguard BMD system-development of a waveform synthesis technique, Document No. SAF-64, The Ralph M. Parsons Company, August 28, 1970.
- Yang, R.C. and Saffell, H.R., Development of a waveform synthesis technique. A supplement to response spectrum as a definition of shock environment, *Shock Vib. Bull.*, 42, Part 2, 45–53, 1972.
- Yarnold, J.A.L., High velocity shock machines, *Environ. Eng.*, 17, 11–16, 1965, November.
- Young, F.W., Shock testing with vibration systems, *Shock Vib. Bull.*, 34, Part 3, 355–364, 1964.
- Zimmerman, R.M., Pyroshock — bibliography, *IES Proc.*, 471–479, 1993.

13

Vibration and Shock Problems of Civil Engineering Structures

13.1	Introduction	13-2
13.2	Earthquake-Induced Vibration of Structures	13-3
	Seismicity and Ground Motions • Influence of Local Site Conditions • Response of Structures to Ground Motions • Dynamic Analysis • Earthquake Response Spectra • Design Philosophy and the Code Approach • Analysis Options for Earthquake Effects • Soil–Structure Interaction • Active and Passive Control Systems • Worked Examples	
13.3	Dynamic Effects of Wind Loading on Structures	13-22
	Introduction • Wind Speed • Design Structures for Wind Loading • Along and Across-Wind Loading • Wind Tunnel Tests • Comfort Criteria: Human Response to Building Motion • Dampers • Comparison with Earthquake Loading	
13.4	Vibrations Due to Fluid–Structure Interaction	13-33
	Added Mass and Inertial Coupling • Wave-Induced Vibration of Structure	
13.5	Blast Loading and Blast Effects on Structures	13-34
	Explosions and Blast Phenomenon • Explosive Air-Blast Loading • Gas Explosion Loading and Effect of Internal Explosions • Structural Response to Blast Loading • Material Behaviors at High Strain Rate • Failure Modes of Blast-Loaded Structures • Blast Wave–Structure Interaction • Effect of Ground Shocks • Technical Design Manuals for Blast-Resistant Design • Computer Programs for Blast and Shock Effects	
13.6	Impact loading	13-47
	Structural Impact between Two Bodies — Hard Impact and Soft Impact • Example — Aircraft Impact	
13.7	Floor Vibration	13-51
	Introduction • Types of Vibration • Natural Frequency of Vibration • Vibration Caused by Walking • Design for Rhythmic Excitation • Example — Vibration Analysis of a Reinforced Concrete Floor	

Priyan Mendis
University of Melbourne

Tuan Ngo
University of Melbourne

Summary

This chapter provides a concise guide to vibration theory, sources of dynamic loading and effects on structures, options for dynamic analyses, and methods of vibration control. Section 13.1 gives an introduction to

different types of dynamic loads. Section 13.2 covers the basic theory underlying earthquake engineering and seismic design. In this section, seismic codes and standards are reviewed including American, British, and European practices. Active and passive control systems for seismic mitigation are also discussed. This section contains analytical and design examples on seismic analysis and building response to earthquakes. Section 13.3 introduces the nature of wind loading, dynamic effects, and the basic principles of wind design. This section includes formulae, charts, graphs, and tables on both static and dynamic approaches for designing structures to resist wind loads. Types of dampers to reduce vibration in tall buildings under wind loads are also introduced. Section 13.4 gives a brief overview of vibration due to fluid–structure interaction. Section 13.5 extensively covers the effects of explosion on structures. An explanation of the nature of explosions and the mechanism of blast waves in free air is given. This section also introduces different methods to estimate blast loads and structural response. Section 13.6 deals with the impact loading. An analytical example of aircraft impact on a building is given. Section 13.7 looks in detail at the problems of floor vibration. Charts and tables are given for designing floor slabs to avoid excessive vibrations. A comprehensive list of references is provided.

13.1 Introduction

The different types of dynamic loading considered in this chapter include: earthquakes, wind, floor vibrations, blast effects, and impact- and wave-induced vibration. The effects of these loadings on different engineering structures are also discussed. It is standard practice to use equivalent static horizontal forces when designing buildings for earthquake and wind resistance. This is the simplest way of obtaining the dimensions of structural members. Dynamic calculations may follow to check, and perhaps modify, the design. However, vibrations caused by extreme loads such as blast and impact must be assessed by methods of dynamical analysis or by experiment.

Some examples of dynamic loading are shown in Figure 13.1. The first (a) is a record of fluctuating wind velocity. Corresponding fluctuating pressures will be applied to the structure. The random nature of the loading is evident, and it is clear that statistical methods are required for establishing an appropriate design loading. The next figure (b) shows a typical earthquake *accelerogram*. As shown, the maximum ground acceleration of the El-Centro earthquake was about 0.33g. The third figure (c) shows the characteristic shape of the air pressure impulse caused by a

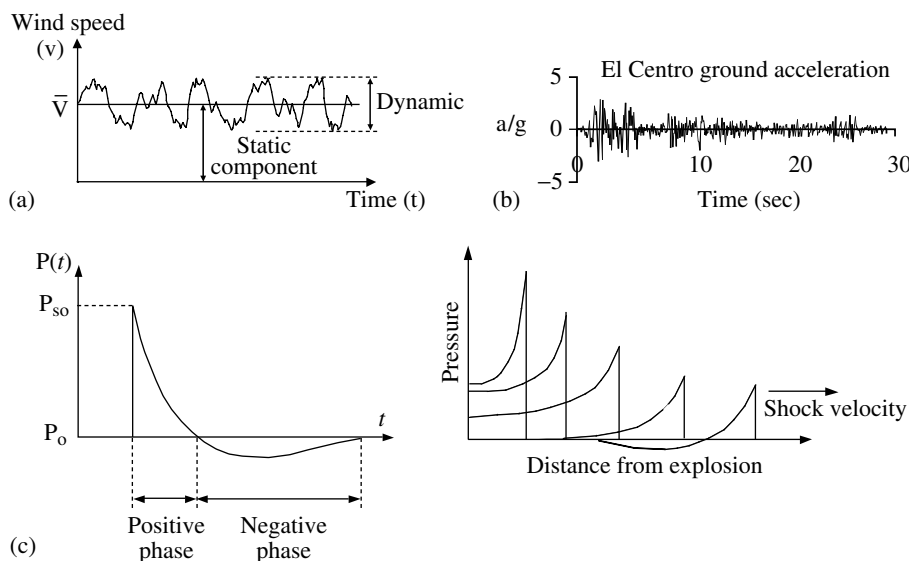


FIGURE 13.1 Examples of dynamic loading. (a) Fluctuating wind velocity; (b) earthquake accelerogram; (c) pressure time history for bomb blasts.

bomb blast. The shapes of air-blast curves are usually quite similar, having an initial peak followed by an almost linear decay and often followed by some suction. The duration of the impulsive loads and their amplitudes depend on many factors, for example, distance from blast and charge weight.

Vibration of structures is undesirable for a number of reasons, as follows:

1. Overstressing and collapse of structures
2. Cracking and other damage requiring repair
3. Damage to safety-related equipment
4. Impaired performance of equipment or delicate apparatus
5. Adverse human response

With modern forms of construction, it is feasible to design structures to resist the forces arising from dynamic loadings such as major earthquakes. The essential requirement is to prevent total collapse and consequent loss of life. For economic reasons, however, it is the accepted practice to absorb the earthquake energy by ductile deformation, therefore accepting that repair might be required.

Some forms of loading are quite well defined and may be quantified by observation or experiment. Many forms of loading are not at all well defined and require judgment on the part of the engineer. London's Millennium Bridge, which is a 350-m pedestrian bridge, opened in June 2000. However, local authorities shut it down after two days due to vibration problems. Engineers found that the "synchronous lateral excitation" caused the problem and fitted 91 dampers to reduce the excessive movement. In January 2001, a 2000-strong crowd marched across the bridge to check the performance of the structure before it was reopened to the public.

Data on certain types of dynamic loading, such as earthquakes and wind, are readily available in many design codes. Other types of loading are less well covered, though much data may be available in published research papers. One of the aims of this chapter is to discuss the nature of the most important types of dynamic loading and to direct the reader to relevant literature for further information.

13.2 Earthquake-Induced Vibration of Structures

13.2.1 Seismicity and Ground Motions

The most common cause of earthquakes is thought to be the violent slipping of rock masses along major geological fault lines in the Earth's crust, or lithosphere. These fault lines divide the global crust into about 12 tectonic plates, which are rigid, relatively cool slabs about 100 km thick. Tectonic plates float on the molten mantle of the Earth and move relative to one another at the rate of 10 to 100 mm/year.

The basic mechanism causing earthquakes in the plate boundary regions appears to be that the continuing deformation of the crustal structure eventually leads to stresses/strains which exceed the material strength. A rupture will then initiate at some critical point along the fault line and will propagate rapidly through the highly stressed material at the plate boundary. In some cases, the plate margins are moving away from one another. In those cases, molten rock appears from deep in the Earth to fill the gap, often manifesting itself as volcanoes. If the plates are pushing together, one plate tends to dive under the other and, depending on the density of the material, it may resurface in the form of volcanoes. In both these scenarios, there may be volcanoes and earthquakes at the plate boundaries, both being caused by the same mechanism of movement in the Earth's crust. Another possibility is that the plate boundaries will slide sideways past each other, essentially retaining the local surface area of the plate. It is believed that approximately three quarters of the world's earthquakes are accounted for by this rubbing–sticking–slipping mechanism, with ruptures occurring on faults on boundaries between tectonic plates.

Earthquake occurrence maps tend to outline the plate boundaries. Such earthquakes are referred to as interplate earthquakes.

Earthquakes do occur at locations away from the plate boundaries. Such events are known as intraplate earthquakes and they are much less frequent than interplate earthquakes. They are also much less predictable than events at the plate margins and they have been observed to be far more severe. For example, the Eastern United States, which is located well away from the tectonic plate boundaries of California, has recorded the largest earthquakes in the history of European settlement in the country. These major intraplate earthquakes occurred in the middle of last century in South Carolina on the East Coast and Missouri in the interior. However, because of the low population density at the time, the damage caused was minimal. It is significant to note, however, that these intraplate earthquakes, although very infrequent, were considerably larger than the moderately sized interplate earthquakes that frequently occur along the plate boundaries in California. (It is thought that, because tectonic plates are not homogeneous or isotropic, areas of local high stress are developed as the plate attempts to move as a rigid body. Accordingly, rupture within the plate, and the consequent release of energy, are believed to give rise to these intraplate events.)

The point in the Earth's crustal system where an earthquake is initiated (the point of rupture) is called the hypocenter or focus of the earthquake. The point on the Earth's surface directly above the focus is called the epicenter and the depth of the focus is the focal depth. Earthquake-occurrence maps usually indicate the location of various epicenters of past earthquakes and these epicenters are located by seismological analysis of the effect of earthquake waves on strategically located receiving instruments called seismometers.

When an earthquake occurs, several types of seismic wave are radiated from the rupture. The most important of these are the body waves (primary (P) and secondary (S) waves). P waves are essentially sound waves traveling through the Earth, causing particles to move in the direction of wave propagation with alternate expansions and compressions. They tend to travel through the Earth with velocities of up to 8000 m/sec (up to 30 times faster than sound waves through air). S waves are shear waves with particle motion transverse to the direction of propagation. S waves tend to travel at about 60% of the velocity of P waves, so they always arrive at seismometers after the P waves. The time lag between arrivals often provides seismologists with useful information about the distance of the epicenter from the recorder.

The total strain energy released during an earthquake is known as the magnitude of the earthquake and it is measured on the Richter scale. It is defined quite simply as the amplitude of the recorded vibrations on a particular kind of seismometer located at a particular distance from the epicenter. The magnitude of an earthquake by itself, which reflects the size of an earthquake at its source, is not sufficient to indicate whether structural damage can be expected at a particular site. The distance of the structure from the source has an equally important effect on the response of a structure, as do the local ground conditions. The local intensity of a particular earthquake is measured on the subjective Modified Mercalli scale (Table 13.1) which ranges from 1 (barely felt) to 12 (total destruction). The Modified Mercalli scale is essentially a means by which damage may be assessed after an earthquake. In a given location, where there has been some experience of the damaging effects of earthquakes, albeit only subjective and qualitative, regions of varying seismic risk may be identified. The Modified Mercalli scale is sometimes used to assist in the delineation of these regions. A particular earthquake will be associated with a range of local intensities, which generally diminish with distance from the source, although anomalies due to local soil and geological conditions are quite common.

Modern seismometers (or seismographs) are sophisticated instruments utilizing, in part, electromagnetic principles. These instruments can provide digitized or graphical records of earthquake-induced accelerations in both the horizontal and vertical directions at a particular site. Accelerometers provide records of earthquake accelerations and the records may be appropriately integrated to provide velocity records and displacement records. Peak accelerations, velocities, and displacements are all in turn significant for structures of differing stiffness (Figure 13.2).

TABLE 13.1 Modified Mercalli Intensity Scale

- I. Not felt except by a very few under especially favorable circumstances
- II. Felt only by a few persons at rest, especially on upper floors of buildings. Delicately suspended objects may swing
- III. Felt quite noticeably indoors, especially on upper floors of buildings, but many people do not recognize it as an earthquake. Standing motor cars may rock slightly. Vibration like passing truck. Duration estimated
- IV. During the day felt indoors by many, outdoors by few. At night some awakened. Dishes, windows, and doors disturbed; walls make creaking sound. Sensation like heavy truck striking building. Standing motorcars rock noticeably
- V. Felt by nearly everyone; many awakened. Some dishes, windows, etc., broken; a few instances of cracked plaster; unstable objects overturned. Disturbance of trees, poles, and other tall objects sometimes noticed. Pendulum clocks may stop
- VI. Felt by all; many frightened and run outdoors. Some heavy furniture moved; a few instances of fallen plaster or damaged chimneys. Damage slight
- VII. Everybody runs outdoors. Damage negligible in buildings of good design and construction, slight to moderate in well-built ordinary structures; considerable in poorly built or badly designed structures. Some chimneys broken. Noticed by persons driving motor cars
- VIII. Damage slight in specially designed structures; considerable in ordinary substantial buildings, with partial collapse; great in poorly built structures. Panel walls thrown out of frame structures. Fall of chimneys, factory stacks, columns, monuments, walls. Heavy furniture overturned. Sand and mud ejected in small amounts. Changes in well water. Persons driving motorcars disturbed
- IX. Damage considerable in specially designed structures; well-designed frame structures thrown out of plumb; great in substantial buildings, with partial collapse. Buildings shifted off foundations. Ground cracked conspicuously. Underground pipes broken
- X. Some well-built wooden structures destroyed; most masonry and frame structures destroyed with foundations; ground badly cracked. Rails bent. Landslides considerable from riverbanks and steep slopes. Shifted sand and mud. Water splashed over banks
- XI. Few, if any (masonry), structures remain standing. Bridges destroyed. Broad fissures in ground. Underground pipelines completely out of service. Earth slumps and land slips in soft ground. Rails bent greatly
- XII. Damage total. Waves seen on ground surfaces. Lines of sight and level distorted. Objects thrown upward into the air

Source: Data from Wood, H.O. and Neumann, Fr., *Bull. Seis. Soc. Am.*, 21, 277–283, 1931.

13.2.2 Influence of Local Site Conditions

Local geological and soil conditions may have a significant influence on the amplitude and frequency content of ground motions. These conditions affect the earthquake motions experienced (and hence the structural response) in one, or more, of the following ways:

- Interaction between the bedrock earthquake motion and the soil column will modify the actual ground accelerations input to the structure. This manifests itself by an increase in the amplitude of the ground motion over and above that at the bedrock, and a filtering of the motion so that the range of frequencies present becomes narrow with the high-frequency components being eliminated. This condition particularly arises in areas where soft sediments and alluvial soil overly bedrock. The degree of amplification is dependent on the strength of shaking at the bedrock. Because of nonlinear effects in the soil, the amplification ratio is less in strong shaking than under base motions of lower amplitude.
- The soil properties in the proximity of the structure contribute significantly to the effective stiffness of the structural foundation. This may be a significant parameter in determining the overall structural response, especially for structures that would be characterized as stiff under other environmental loadings.
- The strength (and response) of the local soil under earthquake shaking may be critical to the overall stability of the structure.

It is also important that information on relevant geological features, such as faulting, be assessed. Geological information on suspected active faults near the site can assist in providing a basis for

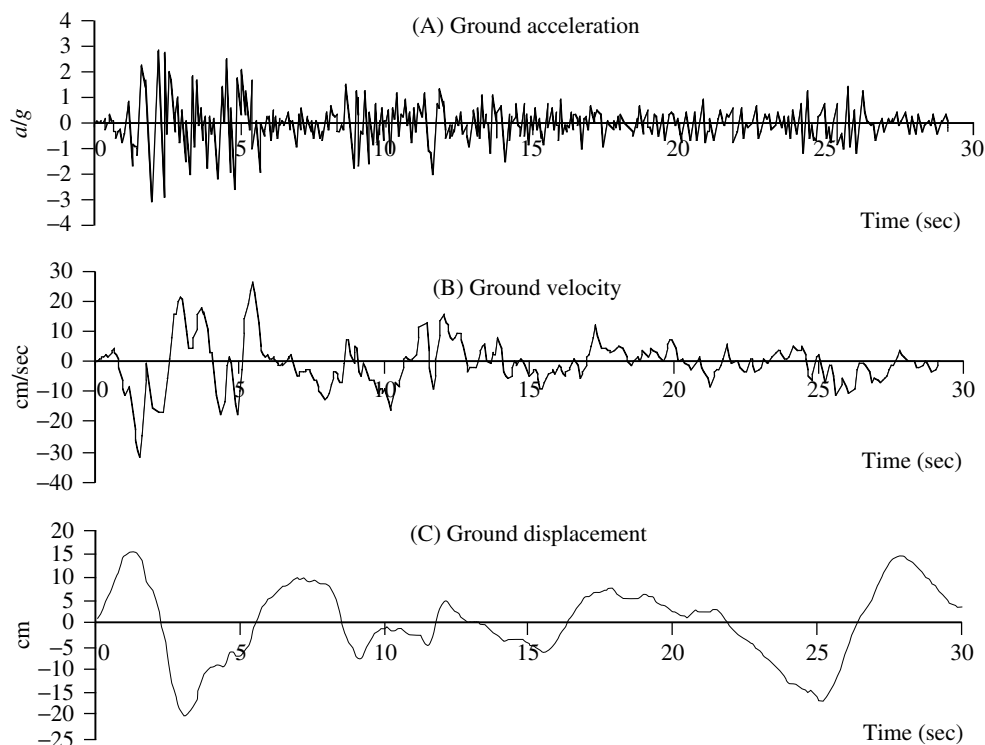


FIGURE 13.2 El-Centro earthquake, north-south component. (A) Record of the ground acceleration; (B) ground velocity, obtained by integration of (A); (C) ground displacement, obtained by integration of (B).

evaluating the intensity of a likely earthquake. It is usual to use this information, together with the regional seismicity data, to determine the likely level of seismic activity.

13.2.3 Response of Structures to Ground Motions

The effect of ground motion on the various categories of structures is dictated almost entirely by the distribution of mass and stiffness in the structure. It is important to appreciate that, in an earthquake, loads are not applied to the structure. Rather, earthquake loading arises because of accelerations generated by the foundation level(s) of the structure intercepting and being influenced by transient ground motions. Specifically, the product of the structural mass and the total acceleration produces the inertia loading experienced by the structure. This is an expression of Newton's Second Law. It is important to appreciate that the total acceleration is the absolute acceleration of the structure, namely, the sum of the ground acceleration and that of the structure relative to the ground.

If the structure is stiff there is little, if any, additional acceleration relative to the ground motion and, therefore, the earthquake loading experienced is essentially proportional to the building mass, that is, $F_{eq} \propto M$.

For structures that are flexible, for example, those in the high-rise or long-span category, the absolute acceleration is low. This occurs because the ground acceleration and the acceleration of the building relative to the ground tend to oppose one another. In this case, the earthquake loading is approximately proportional to the square root of the mass, that is $F_{eq} \propto M^{0.5}$.

For structures in the cantilever category, which are essentially vertical, it is the horizontal accelerations that are significant; whereas for structures that are largely horizontal in extent, the effect of the vertical accelerations is dominant. Moreover, if the plan distributions of mass and stiffness are dissimilar in vertical structures, significant twisting motions may arise.

The peak ground acceleration is of importance in the response of stiff structures and peak ground displacements are of importance in the response of flexible structures, with peak ground velocity being of importance for structures of intermediate stiffness. Stiff structures tend to move in unison with the ground while flexible structures, such as high-rise buildings, experience the ground moving beneath them, their upper floors tending to remain motionless.

13.2.4 Dynamic Analysis

13.2.4.1 Equations of Motion for Linear Single-Degree-of-Freedom Systems

Consider the linear single-degree-of-freedom (single-DoF) system shown in Figure 13.3 subjected to a time varying ground displacement, $z(t)$. Let the relative displacement of the system to the ground be, $y(t)$; y is then the extension of the spring and dashpot. From the equation of motion, it follows that

$$m(\ddot{y} + \ddot{z}) = -ky - c\dot{y} \quad (13.1)$$

Rearranging Equation 13.1, and replacing m , k , and c by the system's radial frequency ω and damping ratio ξ , gives

$$\ddot{y} + 2\xi\omega\dot{y} + \omega^2y = -\ddot{z} \quad (13.2)$$

Given a description of the input motion, $z(t)$, (for example, from an accelerograph recording), the solution of Equation 13.2 provides a complete time history of the response of a structure with a given natural period and damping ratio, and can also be used to derive maximum responses for constructing a response spectrum (Figure 13.6). Owing to the random nature of earthquake ground motion, numerical solution techniques are needed for Equation 13.2, as described by Clough and Penzien (1993).

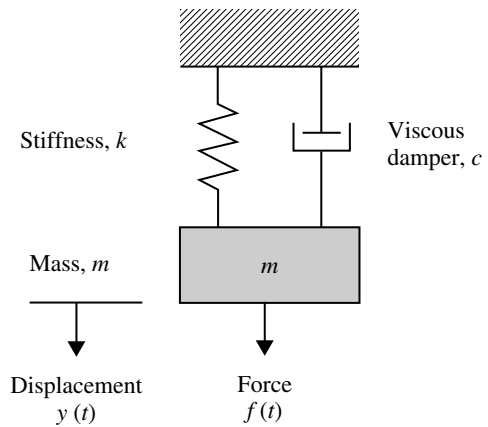


FIGURE 13.3 Single-DoF system.

13.2.4.2 Equations of Motion for Linear Multiple-Degree-of-Freedom Systems

The dynamic response of many linear multiple-degree-of-freedom (multi-DoF) systems can be split into decoupled natural modes of vibration (Figure 13.4), each mode effectively representing a single-DoF system. A modified form of Equation 13.2 then applies to each mode, which for mode i becomes

$$\ddot{Y}_i + 2\xi_i\omega_i\dot{Y}_i + \omega_i^2Y_i = \frac{L_i}{M_i}\ddot{z} \quad (13.3)$$

Here, Y_i is the generalized modal response in the i th mode. (L_i/M_i) is a participation factor, which depends on the mode shape and mass distribution, and describes the participation of the mode in overall response to a particular direction of ground motion. For a two-dimensional (2D) structure with n lumped masses, responding in one horizontal direction

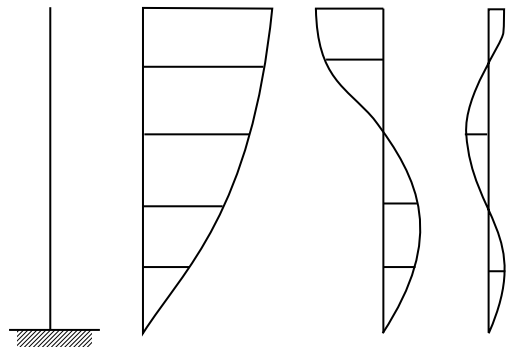


FIGURE 13.4 Typical modes for multistory buildings.

$$\frac{L_i}{M_i} = \frac{\sum_{j=1}^n \phi_{ij}m_j}{\sum_{j=1}^n \phi_{ij}^2m_j} \quad (13.4)$$

In Equation 13.4, ϕ_{ij} , describes the modal displacement of the j th mass in the i th mode. The higher modes often have very low values of (L_i/M_i) , and their contribution can then be omitted. In this way, the computational effort is greatly reduced. In cases where only the first mode in each direction is significant (often the case for low- to medium-rise building structures), equivalent static analysis may be sufficient, as described later.

13.2.5 Earthquake Response Spectra

13.2.5.1 Elastic Response Spectra

For design purposes, it is generally sufficient to know only the maximum value of the response due to an earthquake. A plot of the maximum value of a response quantity as a function of the natural vibration frequency of the structure, or as a function of a quantity which is related to the frequency such as natural period, constitutes the *response spectrum* for that quantity (see Chapter 17 and Chapter 31).

The peak relative displacement is usually called S_d and the peak strain energy of the oscillator is

$$SE = \frac{1}{2}KS_d^2$$

$$SE = \frac{1}{2}M\frac{K}{M}S_d^2$$

or

$$SE = \frac{1}{2}MS_v^2$$

Hence, the pseudo-relative velocity and acceleration spectra are defined as

$$S_v = \omega S_d \quad (13.5)$$

$$S_a = \omega^2 S_d \quad (13.6)$$

Figure 13.5 shows that a record of peak relative displacement response of an single-DoF oscillator can be plotted for a given earthquake, given damping, and a range of periods, typical of structures.

The structure's natural period (T or $1/n$) is conventionally taken as the abscissa, and curves are drawn for various levels of damping (Figure 13.6). It should be noted that the response spectrum gives no information about the duration of response (and hence the number of damaging cycles) that the structure experiences, which can have a very significant influence on the damage sustained.

13.2.5.2 Smoothed Design Spectra

Owing to the highly random nature of earthquake ground motions, the response spectrum for a real earthquake record contains many sharp peaks and troughs, especially for low levels of damping. The peaks and troughs are determined by a number of uncertain factors, such as the precise location of the earthquake source, which are unlikely to be known precisely in advance. Therefore, spectra for design purposes are usually smoothed envelopes of spectra for a range of different earthquakes; indeed, one of the advantages of response spectrum analysis over time history analysis is that it can represent the envelope response to a number of different possible earthquake sources from a single analysis, and is not dependent on the precise characteristic of one particular ground motion record. Codes of practice such as UBC (2000) and Eurocode 8 (ENV 1998, 1994-8) provide smoothed spectra for design purposes.

13.2.5.3 Ductility-Modified Response Spectrum Analysis

In a ductile structure, or subassemblage, the resistance, R , may be sustained at displacements that are several times those at first yield, Δ_y , as represented in Figure 13.7.

For yielding single-DoF systems, ductility-modified acceleration response spectra can be drawn, representing the maximum acceleration response of a system as a function of its initial (elastic) period, T , damping ratio, ξ , and displacement ductility ratio, μ (μ is the ratio of maximum displacement,

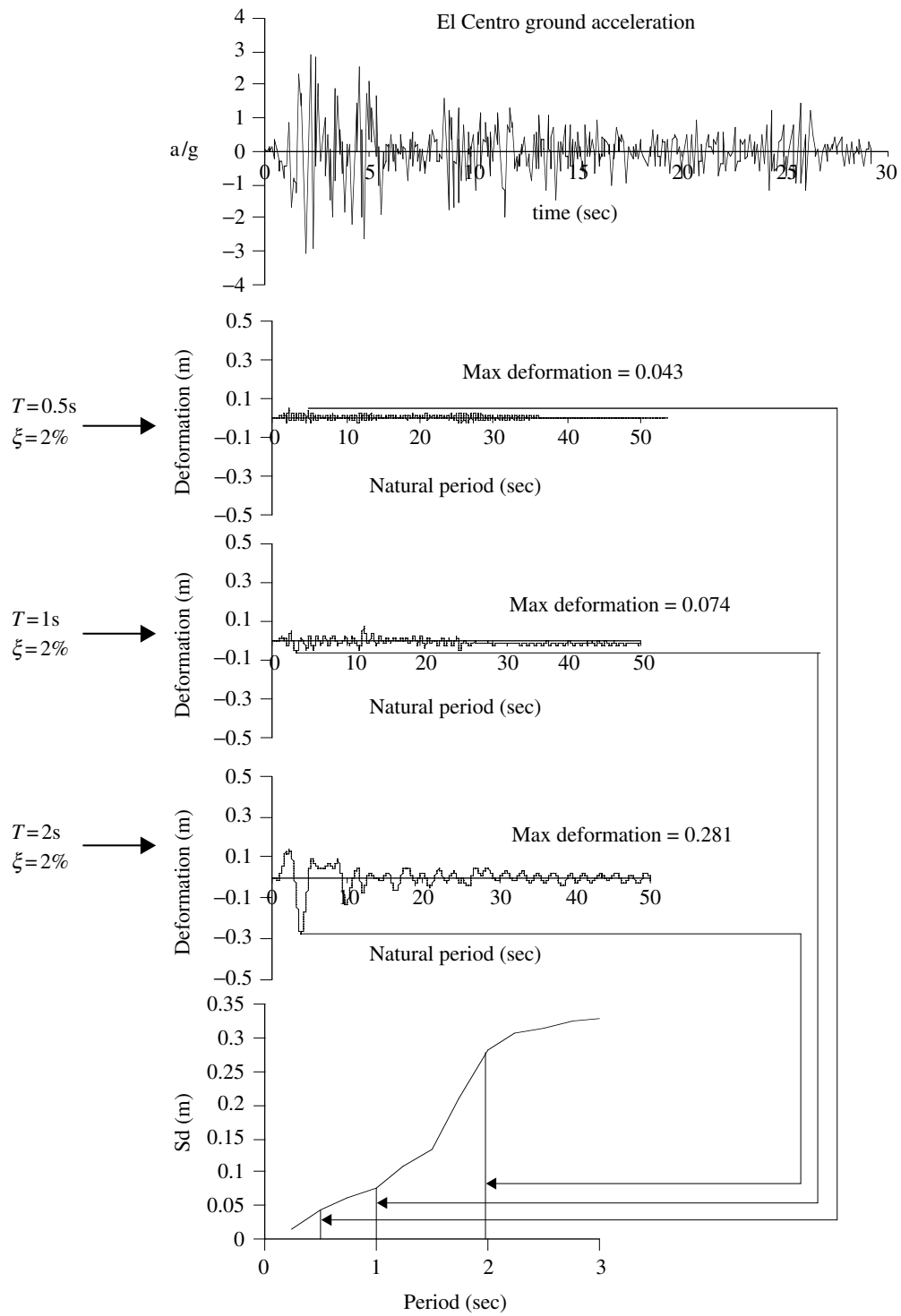


FIGURE 13.5 Compilation of (relative) displacement response spectra.

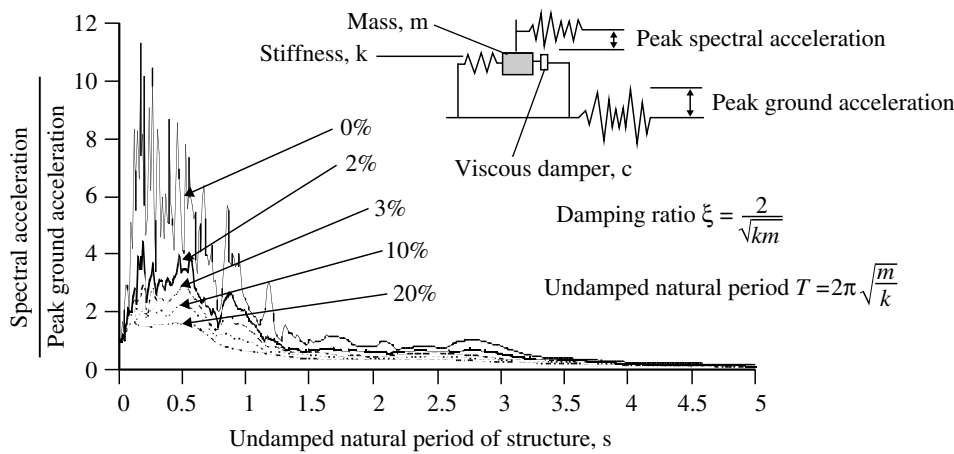


FIGURE 13.6 Acceleration response spectrum for El-Centro 1940 earthquake.

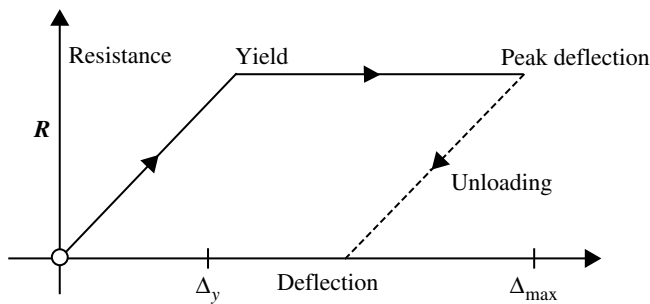


FIGURE 13.7 A simple bilinear elasto-plastic curve of response, representative of ductile performance.

Δ_{max} , to yield displacement, Δ_y). The reduction in acceleration response of the yielding system compared with the elastic one is period dependent; for structural periods greater than the predominant earthquake periods, the reduction is approximately $1/\mu$, for very stiff systems there is no reduction, while at intermediate periods a reduction factor between $1/\mu$ and 1 applies.

To derive peak accelerations and internal forces, the system can be treated as linear elastic and the ductility-modified spectrum used exactly like a normal elastic spectrum. However, deflections derived from this treatment must be multiplied by μ to allow for the plastic deformation.

It is now standard practice to analyze multi-DoF systems in the same way. That is, a yielding multi-DoF system is treated as elastic, and an appropriate ductility-modified spectrum is substituted for an elastic one. Acceleration and force responses are derived directly and deflections are multiplied by μ . However, this procedure is not (contrary to the case for single-DoF systems) rigorously correct. Although it gives satisfactory answers for regular structures, it can be seriously in error for structures (such as those with weak stories) where the plasticity demand is not evenly distributed. Nevertheless, most codes of practice allow the use of ductility-modified spectra for design, and give appropriate values for the reduction factors (called q , or behavior factors in Eurocode 8 and R factors in UBC) to apply to elastic response spectra.

13.2.6 Design Philosophy and the Code Approach

In areas of the world recognized as being prone to major earthquakes, the engineer is faced with the dilemma of being required to design for an event, the magnitude of which has only a small chance of

occurring during the life of the facility. If the designer adopts conservative performance criteria for the facility, the client (often society) is faced with costs which may be out of proportion to the risks involved. On the other hand, to ignore the possibility of a major earthquake could be construed as negligent in these circumstances.

To overcome this problem, a *dual design philosophy* has been developed, by which procedure:

1. A moderate earthquake, such as may reasonably be expected at the site, is used as a basis for the seismic design. The facility should be proportioned to resist such an earthquake without significant damage. This “damageability” limit state should ensure safety, limited nonstructural damage, and the continued performance of facilities and services, particularly in those with important postearthquake functions. The list includes hospitals, police, fire and civil defense facilities, water supply, telecommunications, electricity generation and distribution systems, and so on. Almost as important is the maintenance of road and rail communications, particularly for food distribution (including warehouses and their contents). Similarly, the protection of industrial complexes, in their own right, as well as the protection of individual items of equipment in other buildings and facilities, is a necessary consequence of adoption of this limit state.
2. The most severe, credible earthquake that may be expected to occur at the site is used to test safety. In this ultimate limit state, significant structural and nonstructural damage is expected but neither collapse nor loss of life should occur.

The main strategy for preventing collapse has traditionally been provision of ductility. This is the opposite quality to brittleness, and may be defined as the ability to sustain repeated excursions beyond the elastic limit without fracture. Owing to the cyclic, imposed displacement nature of earthquake loading, a ductile structure can absorb very large amounts of energy without collapse; the designer must think in terms of designing for maximum imposed displacements, rather than imposed loads.

Achieving ductility is partly a matter of choosing the right structural system, and partly a matter of detailing. In the former category comes the important concept of “capacity design,” as described by Paulay (1993). This involves ensuring a hierarchy of strengths within a structure to ensure that yielding occurs in ductile modes (such as flexure) rather than brittle modes (such as buckling or, for reinforced concrete, shear). There are other aspects of structural form which are important, particularly regularity in elevation (to avoid “soft” or weak stories) and regularity in plan (to minimize torsional response). These aspects are described in many textbooks and are quantified in some codes of practice (Park and Paulay, 1975).

Detailing of the structure is also important to ensure ductility. For concrete structures, this primarily involves reinforcement detailing and in steel structures connection detailing. The latter aspect has been particularly recognized following the failure of H-welded connections in the Northridge earthquake of 1994 (Burdekin, 1996). The primary reliance is on empirical solutions to these problems, as described in codes of practice, such as Eurocode 8 (ENV 1998, 1994-8) Part 1.3 and UBC/IBC (2000). Textbooks discussing these issues for concrete include Paulay and Priestley (1992), Booth (1994), Penelis and Kappos (1996), FEMA 273/274, FEMA 356/357 “NEHRP guidelines for seismic rehabilitation of buildings,” FEMA 368/369 “NEHRP recommended provisions for seismic regulations for new buildings and other structures,” and FEMA 306/307/308 “Evaluation and repair of earthquake damaged concrete and masonry buildings.” Textbooks covering failures of steel structures in recent earthquakes include Burdekin (1996) and FEMA 350-354 (2000).

Another important aspect of detailing is to allow for the maximum inelastic deflections caused by the design earthquake. Nonseismic-resisting elements of a structure such as cladding and infill walls must be able to accommodate these deflections safely, as must (crucially) the gravity load-bearing structure, which still suffers the seismic displacements even when not contributing to seismic resistance. In addition, adequate separation between adjacent structures must be provided. Codes of practice (e.g., Eurocode 8 and UBC) give guidance on suitable limits.

13.2.6.1 Performance-Based Design

In recent years, seismic design codes throughout the world have been shifting toward the adoption of performance-based design philosophy. The goal of a performance-based design procedure is to produce structures that have predictable seismic performance under multiple levels of earthquake intensity. In order to do so, it is important that the behavior of the structures is targeted in advance, both in the elastic as well as the inelastic ranges of deformation. The four important parameters in seismic design, strength, stiffness, ductility, and deformation, become the primary elements of a performance-based design procedure and have to be designed rationally. The next generation of codes is expected to be based on performance-based principles such as Asian Model Concrete Code (ACMC, 2001).

13.2.7 Analysis Options for Earthquake Effects

Analysis is only one part of the design process; conceptual design, detailing, and proper construction are the other vital components for ensuring good seismic performance. This section provides a brief theoretical review of the basis for seismic analysis, describing the main analytical techniques currently used by designers. More details are given by Clough and Penzien (1993), a standard general text for dynamic analysis, and Chopra (2001), which deals specifically with concerns for earthquake engineers.

Essentially, an earthquake engineer is faced with four possible methods of analysis/design for earthquake loading on a structure. In all methods, the dual damage criteria discussed above may be applied. The four analysis/design options available are:

- Dynamic time history analysis
- Response spectrum analysis
- Equivalent static approach (or force-based approach)
- Displacement-based approach

Equivalent static methods are usually adequate for conventional, regular building structures under about 75 m in height. A response spectrum analysis is required for taller buildings, because higher mode effects may become important, and also for buildings with plan or elevational eccentricities because torsional effects or nonstandard mode shapes may be significant. Codes of practice such as Eurocode 8 and UBC (2000) specify the degree of eccentricity at which such analysis is required. Unusual or very important structures may require nonlinear time history analysis, and this may also be required where the inaccuracies implicit in the use of ductility-modified response spectrum analysis become unacceptable. Displacement-based approach is a new method for seismic design, which is gaining popularity. The above four analysis options are discussed next.

13.2.7.1 Dynamic Time History Analysis

The most rigorous form of dynamic analysis involves stepping a nonlinear model of the structure through a complete time history of earthquake ground motions. The advantage of the method is that it can give direct information on nonlinear response, the duration of response (and hence the number of loading cycles), and the relative phasing of response between various parts. The method involves subjecting an appropriate finite element computer model of the building, or structural system, to a given, previously recorded, earthquake record and examining its response in real time. Response peaks are generally of most interest. The analysis must be performed for a number of different earthquake time histories to reduce dependence on the random characteristics of a particular record.

There are certain special circumstances where this procedure is useful but, for general seismic design, it is of little value as the actual earthquake that the structure may have to resist cannot be guaranteed to have sufficiently similar characteristics to the design earthquake. In particular, the intensity, duration, and frequency content of the earthquake may be unsuitable especially if, as often happens, the record comes from another country or continent. Moreover, the method is expensive and time-consuming, so that only for special structures can its use be justified. If, in addition, inelastic response calculations are involved, another level of complexity (and uncertainty) is introduced. Response then becomes

dependent, often heavily so, on the nonlinear models chosen and this is in addition to that inherent in choosing to use one particular record.

13.2.7.2 Response Spectrum Analysis

13.2.7.2.1 Response Spectrum Analysis of Single-Degree-of-Freedom Systems

With a knowledge of the natural period and damping of an single-DoF system, its peak (i.e., spectral) acceleration, S_a , can be determined directly from an appropriate response spectrum (see Chapter 17). In undamped systems, this peak response occurs when the equivalent spring is at its maximum extension point, so that the maximum force in the spring is given by

$$F = mS_a \quad (13.7)$$

From Equation 13.7, the peak (i.e., spectral) displacement, S_x , of the spring is given by

$$S_x = \frac{F}{k} = mS_a \frac{T^2}{4\pi^2 m} = \frac{S_a T^2}{4\pi^2} \quad (13.8)$$

For structures with relatively small viscous damping, the same relationships are still approximately true, because the maximum acceleration occurs when the velocity is low and hence the damping force (which is velocity proportional) is also low. Therefore, Equation 13.7 and hence also Equation 13.8 are still very good approximations for lightly damped systems.

Thus the two most important parameters of structural response — maximum force and displacement — can be determined for a linear single-DoF system directly from the acceleration response spectrum, provided only that the mass, natural period, and damping are known.

It is important to realize that the spectral acceleration, S_a , is an absolute value (the true acceleration of the structure in space) whereas the spectral displacement, S_x , is a relative value, measured in relation to the ground, which itself is moving in the earthquake. This at first sight may seem confusing, until it is remembered that the absolute acceleration of the mass is determined by the force on it (Equation 13.7), which itself is determined by the relative compression of the spring with respect to the ground (Equation 13.8).

13.2.7.2.2 Response Spectrum Analysis of Multi-Degree-of-Freedom Systems

By considering the response of each mode separately, a response spectrum analysis is also possible for an multi-DoF system, if generalized modal quantities are used (compare Equation 13.2 and Equation 13.3). For example, for a 2D structure with n lumped masses, responding in one horizontal direction, Equation 13.4 is modified to give the maximum base shear in the i th mode as

$$F_i = \frac{\left(\sum_{j=1}^n \phi_{ij} m_j \right)^2}{\sum_{j=1}^n \phi_{ij}^2 m_j} S_a = m_{\text{eff},i} S_a \quad (13.9)$$

where S_a is the spectral acceleration corresponding to the damping and frequency of mode i .

Higher modes with low effective masses, $m_{\text{eff},i}$, may contribute little to response and can usually be neglected. Since the sum of effective masses, $m_{\text{eff},i}$, of all modes equals the total mass, a good test of whether the first r modes are sufficient to capture response adequately is

$$\sum_{i=1}^r m_{\text{eff},i} \geq 0.9 \sum_{i=1}^n m_i = 0.9 \text{ (total mass)} \quad (13.10)$$

A response spectrum analysis gives the maximum response of the structure for each mode of vibration considered. Although it is rigorously correct to add the response in each mode at any time to obtain the total response, the maximum responses in each mode, calculated from response spectrum analysis, do

not occur simultaneously, and hence simple addition produces an overestimate of response. A common and usually adequate approximation is the square root of the sum of the squares (SRSS) rule, where the maximum total response is estimated as the SRSS combination of the individual modal responses. However, this may not be conservative enough for closely spaced or high-frequency modes, and other methods, such as the complete quadratic combination (CQC) method, are available (Gupta, 1990).

There are many commercially available computer programs which can perform response spectrum analysis, and it is now regarded as a standard rather than a specialist technique.

13.2.7.3 Equivalent Static Analysis (Force-Based Approach)

This is the type of analysis presented in most contemporary codes of practice, and it is conditional for its accuracy upon response being dominated by one mode of vibration in each direction. In the case of buildings, a quantity usually referred to as the “total base shear” is calculated from the product of the weight of the building and a coefficient. This coefficient takes into account the location and importance of the structure, its ductility or energy absorption capacity, its dynamic characteristics, and the local soil conditions and their effect on structural responses. Once the total base shear has been calculated, it is distributed up the structure as a series of horizontal loads at each floor level and the structure is analyzed with these equivalent horizontal loads applied.

The maximum lateral base shear is first calculated. Equation 13.11 gives the relevant formulae in UBC (2000). Other current codes follow similar formats

$$V = \frac{C_v IW}{RT} \text{ but } V \leq \frac{2.5C_a I}{R} W \text{ and } \geq 0.11C_a IW \quad (13.11)$$

In addition, $V \geq (0.8ZN_v I/R)W$ (high seismicity, Zone 4 only), where:

V = ultimate seismic base shear (force units, e.g., kN)

C_v, C_a = seismic coefficients, depending on the zone factor Z as given in UBC

I = importance factor = 1 to 1.25 in UBC

R = reduction coefficient depending on the ductility of structure = 2.8 to 8.5 in UBC

T = first mode period of the building (sec)

W = building weight (force units, e.g., kN)

Z = zone factor expressed as the peak ground acceleration on rock (in gravity units) for a 475-year return period = 0.075 to 0.4 in UBC

N_v = factor allowing for proximity to active faults = 1.0 to 2.0 in UBC

(V/W) represents the shape of a standard design response spectrum with a peak amplification on ground acceleration for 5% damping of 2.5, and a minimum value at long period to allow for the uncertainty in long-period motions and for proximity to active faults.

The base shear calculated by these methods is then applied to the structure as a set of horizontal forces, with a vertical distribution based on the first mode shape of regular vertical cantilever structures. Horizontal distribution follows the mass distribution, with some additional allowance for torsional effects.

13.2.7.4 Displacement-Based Approach

In the development of performance-based earthquake engineering, which stresses the inelastic behavior of structural system under severe earthquake ground motions (high seismic region), displacement rather than force has been recognized as the most suitable and direct performance or damage indicator. Deformation-controlled design can be achieved either by using the traditional force/strength-based design procedure together with a check on the displacement/drift limit, or by employing a direct displacement-based procedure. The idea of displacement-based design was introduced by Gulkan and Sozen (1974). They developed the concept of substitute structure to estimate the nonlinear structural response through an equivalent elastic model, assuming a linear behavior and a viscous

damping equivalent to the nonlinear response. This idea has been adopted recently by Priestley and Kowalsky (2000) for a direct displacement design of single-DoF and multi-DoF reinforced concrete structures. Another direct displacement-based design approach was proposed by Fajfar (2000) based on the capacity spectrum method (Chopra and Goel, 1999).

In all the above references, seismic demand is specified as either a displacement response spectrum (D-T format) or an acceleration displacement response spectrum (ADRS format). For a general-purpose spectrum, nonlinear elastic behavior of a structural system can be accounted for by either an equivalent elastic response spectrum or an inelastic response spectrum. The former is associated with effective viscous damping ξ_{eff} and the latter is directly constructed based on the relation between reduction factors and ductility. Although the elastic acceleration design spectrum is available from codes, it is not appropriate to be a basis for the determination of the elastic displacement design spectrum because the displacement increases with period even at longer periods.

13.2.8 Soil–Structure Interaction

Structural analyses usually assume that ground motions are applied *via* a rigid base, thus neglecting the effect of ground compliance on response. Although this rigid base assumption may lead to an underestimate of deflections, it is usually conservative as far as forces are concerned, because ground compliance reduces stiffness and usually moves structural periods farther from resonance with the ground motion. However, this conservatism may not always apply, and Eurocode 8 Part 5 lists the following cases where soil–structure interaction (SSI) should be investigated:

1. Structures where P-Delta (second order) effects need to be considered
2. Structures with massive or deep-seated foundations, such as bridge piers, offshore caissons, and silos
3. Slender, tall structures such as towers and chimneys
4. Structures supported on very soft soils with an average shear wave velocity less than 100 m/sec

Allowance for SSI effects is usually a specialist task. The simplest method is to present the soil flexibility by discrete springs connected to the foundation. These require a knowledge of the shear stiffness of the soil. Further information is given by Pappin (1991) and Wolf (1985, 1994).

13.2.9 Active and Passive Control Systems

Alternative strategies of designing for earthquake resistance involve modification of the dynamic characteristics of structure to improve seismic response. The systems can be classified as either passive or active. The basic role of these systems is to absorb a portion of the input energy, thereby reducing energy dissipation demand on primary structural members and minimizing possible structural damage.

The most common type of passive system involves lengthening the structure's fundamental period of vibration by mounting the superstructure on bearings with a low horizontal stiffness; this is known as base or seismic isolation. Where this increases, the fundamental period above the predominant periods of earthquake excitation, the acceleration (but not necessarily displacement) response is significantly reduced. Usually, additional damping is provided in the seismic isolation bearing to control deflections.

The principle of seismic isolation is illustrated by Figure 13.8. The reduction in response, often of the order of 50, has proved highly effective in recent earthquakes in reducing damage to both building structure and building contents. UBC (2000) provides codified guidance for seismic isolation of buildings while AASHTO (1991) and Eurocode 8 (ENV 1998, 1994-8) Part 2 treat bridge structures. Seismic isolation has been incorporated in many hundreds of recent structures, particularly in bridges, and also in buildings such as hospitals with contents that must remain functional after an earthquake. It has also been used to improve the seismic resistance of existing structures. Another form of passive

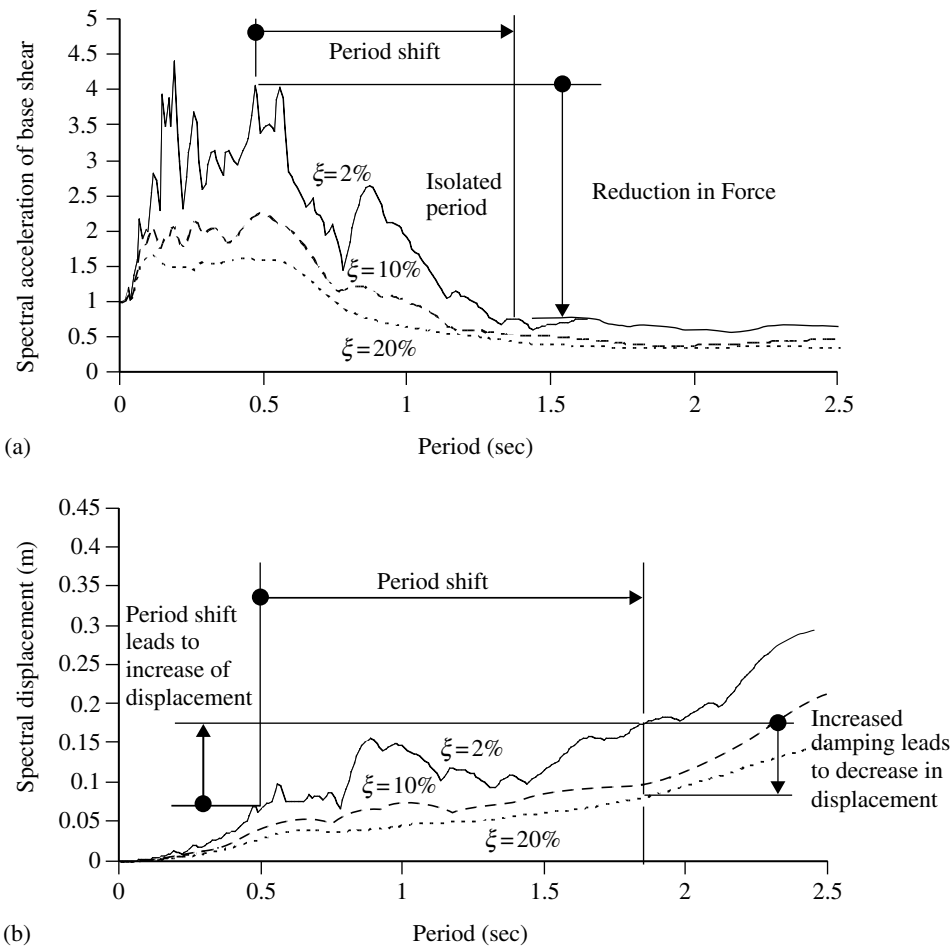


FIGURE 13.8 Effect of seismic isolation on forces and displacements for an earthquake with predominant period around 0.5 sec. (a) Effect of period shift on design forces; (b) Effect of period shift and damping on relative displacement between ground and structure.

system is the provision of additional structural damping in the form of discrete viscous, frictional, or hysteretic dampers.

Active systems modify the dynamic characteristics of a structure in real time during an earthquake, by computer-controlled devices such as active mass dampers. Presently, very few buildings are actually constructed in this way, but there has been a recent large international research effort (Casciati, 1996; Kabori, 1996; Soong, 1996). Owing to their adaptability, active systems are less dependent for their effectiveness on the precise nature of the input motion (a concern for passive systems, particularly where they are very close to the earthquake source) but they must have a very high degree of reliability to ensure they function during the crucial few seconds of an earthquake.

13.2.10 Worked Examples

Example 13.1 Seismic Analysis of a 30-Story Frame

A 30-story building has the effective stiffness, $K_e = 2.5 \times 10^3$ kN/m, together with a mass per unit height of $m = 30$ tons/m.

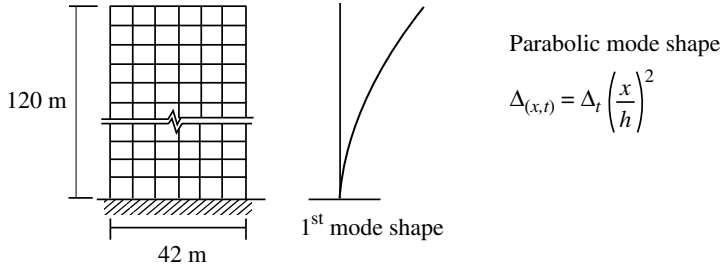


FIGURE 13.9 First mode shape of the 30-story frame.

The mass of the building is uniform over its height of 120 m. An appropriate first mode shape for the structure is the parabola, as shown in Figure 13.9.

For this frame, using the response spectrum for 2% damping (Figure 13.10), find:

1. The peak tip deflection
2. The peak base shear
3. The overturning moment
4. The peak interstory drift at the top of the frame
5. The peak acceleration at the top of the frame

The effective mass, M_e or M_i , (see Equation 13.4)

$$M_e = \phi^2 m = \int_0^H m(x) \left(\frac{x}{H} \right)^4 dx = \frac{m(x)}{5} \frac{x^5}{H^4} \Big|_0^H = \frac{mH}{5} = \frac{30 \times 120}{5} = 720 \text{ tons}$$

This is the effective mass tributary to one frame.

The effective earthquake mass, M_{eq} or L_i (see Equation 13.4)

$$M_{eq} = \phi m = \int_0^H m(x) \left(\frac{x}{H} \right)^2 dx = \frac{m(x)}{3} \frac{x^3}{H^2} \Big|_0^H = \frac{mH}{3} = \frac{30 \times 120}{3} = 1200 \text{ tons}$$

The natural period is 3.37 sec, a long-period structure, given:

$$K_{eq} = 2.5 \times 10^3 \text{ kN/m}$$

$$T = 2\pi(720/2500)^{0.5}$$

The participation factor is

$$PF = \frac{M_{eq}}{M_e} = \frac{1200}{720} = 1.667$$

(i) *Peak tip deflection*

From Figure 13.9

$$S_d = 0.32 \text{ m} = 320 \text{ mm} = PF \times S_d$$

$$\Delta_{tip} = 1.667 \times 320 = 533.44 \text{ mm}$$

(ii) *Peak base shear* = $PF \times F_{max}$

$$V_0 = PF(\Delta_{tip} K_e) = 1.667(0.53344 \times 2500) = 2.22 \text{ MN}$$

(iii) *Peak overturning moment*

$$M_{ot} = V_0 \bar{x}$$

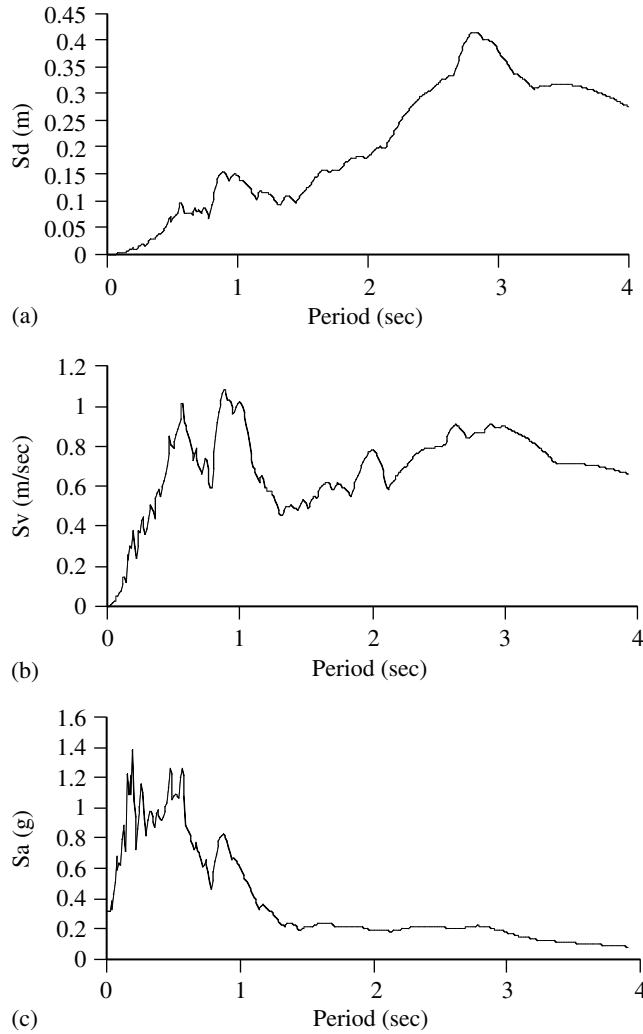
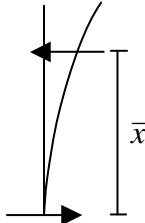


FIGURE 13.10 (a) Deformation (or displacement); (b) pseudo-velocity, and (c) pseudo-acceleration response spectra. El-Centro ground motion. Damping ratio $\xi = 2\%$.

$$\bar{x} = \frac{\int_0^H xm(x) \left(\frac{x}{H} \right)^2 dx}{\int_0^H m(x) \left(\frac{x}{H} \right)^2 dx} = \frac{\int_0^H m(x) \frac{x^3}{H^2} dx}{\int_0^H m(x) \frac{x^2}{H^2} dx}$$


$$\bar{x} = \frac{3H}{4} = \frac{3 \times 120}{4} = 90 \text{ m}$$

$$M_{ot} = 2223.11 \times 90 = 2.0008 \times 10^5 \text{ kN m}$$

$$\text{Equivalent static loading} = m(t)\omega^2 \times \text{PF} \times S_d \left(\frac{x}{H} \right)^2$$

TABLE 13.2 Calculation Details for Structure's Response to an Earthquake

Height (m)	Height (ft)	T (sec)	C_t	C_v	C_a	N_v	N_a	R	I	Z
208.00	682.41	4.01	0.03	0.96	0.36	1.00	1.00	3.50	1.00	0.40
Level	Story Height (m)	Height (m)	Story Weight (kN)	$W_i H_i$	Force (kN)	Shear (kN)	Moment (kN m)			
Top	0	212	0	0	19,778	19,778	0			
52	4.0	208.0	9,300.0	1,934,400	1,319	21,097	79,113			
51	4.0	204.0	9,300.0	1,897,200	1,294	22,391	163,503			
50	4.0	200.0	9,300.0	1,860,000	1,268	23,659	253,067			
49	4.0	196.0	9,300.0	1,822,800	1,243	24,902	347,705			
48	4.0	192.0	16,900.0	3,244,800	2,213	27,115	447,315			
47	4.0	188.0	16,900.0	3,177,200	2,167	29,282	555,776			
46	4.0	184.0	16,900.0	3,109,600	2,120	31,402	672,903			
45	4.0	180.0	16,900.0	3,042,000	2,074	33,477	798,511			
44	4.0	176.0	16,900.0	2,974,400	2,028	35,505	932,418			
43	4.0	172.0	16,900.0	2,906,800	1,982	37,487	1,074,437			
42	4.0	168.0	16,900.0	2,839,200	1,936	39,423	1,224,386			
41	4.0	164.0	16,900.0	2,771,600	1,890	41,313	1,382,079			
40	4.0	160.0	16,900.0	2,704,000	1,844	43,157	1,547,331			
39	4.0	156.0	16,900.0	2,636,400	1,798	44,955	1,719,960			
38	4.0	152.0	16,900.0	2,568,800	1,752	46,707	1,899,779			
37	4.0	148.0	16,900.0	2,501,200	1,706	48,412	2,086,606			
36	4.0	144.0	16,900.0	2,433,600	1,660	50,072	2,280,254			
35	4.0	140.0	16,900.0	2,366,000	1,613	51,685	2,480,541			
34	4.0	136.0	16,900.0	2,298,400	1,567	53,252	2,687,282			
33	4.0	132.0	16,900.0	2,230,800	1,521	54,774	2,900,292			
32	4.0	128.0	16,900.0	2,163,200	1,475	56,249	3,119,386			
31	4.0	124.0	16,900.0	2,095,600	1,429	57,678	3,344,381			
30	4.0	120.0	16,900.0	2,028,000	1,383	59,061	3,575,092			
29	4.0	116.0	16,900.0	1,960,400	1,337	60,398	3,811,335			

28	4.0	112.0	16,900.0	1,892,800	1,291	61,688	4,052,926
27	4.0	108.0	16,900.0	1,825,200	1,245	62,933	4,299,679
26	4.0	104.0	16,900.0	1,757,600	1,199	64,131	4,551,410
25	4.0	100.0	16,900.0	1,690,000	1,152	65,284	4,807,936
24	4.0	96.0	16,900.0	1,622,400	1,106	66,390	5,069,072
23	4.0	92.0	16,900.0	1,554,800	1,060	67,450	5,334,633
22	4.0	88.0	16,900.0	1,487,200	1,014	68,465	5,604,435
21	4.0	84.0	16,900.0	1,419,600	968	69,433	5,878,293
20	4.0	80.0	16,900.0	1,352,000	922	70,355	6,156,024
19	4.0	76.0	16,900.0	1,284,400	876	71,230	6,437,442
18	4.0	72.0	16,900.0	1,216,800	830	72,060	6,722,364
17	4.0	68.0	16,900.0	1,149,200	784	72,844	7,010,605
16	4.0	64.0	16,900.0	1,081,600	738	73,581	7,301,981
15	4.0	60.0	16,900.0	1,014,000	691	74,273	7,596,306
14	4.0	56.0	16,900.0	946,400	645	74,918	7,893,398
13	4.0	52.0	16,900.0	878,800	599	75,518	8,193,071
12	4.0	48.0	16,900.0	811,200	553	76,071	8,495,141
11	4.0	44.0	16,900.0	743,600	507	76,578	8,799,424
10	4.0	40.0	16,900.0	676,000	461	77,039	9,105,735
9	4.0	36.0	16,900.0	608,400	415	77,454	9,413,890
8	4.0	32.0	16,900.0	540,800	369	77,822	9,723,705
7	4.0	28.0	16,900.0	473,200	323	78,145	10,034,994
6	4.0	24.0	16,900.0	405,600	277	78,422	10,347,575
5	4.0	20.0	16,900.0	338,000	230	78,652	10,661,261
4	4.0	16.0	16,900.0	270,400	184	78,837	10,975,870
3	4.0	12.0	16,900.0	202,800	138	78,975	11,291,216
2	4.0	8.0	16,900.0	135,200	92	79,067	11,607,116
1	4.0	4.0	16,900.0	67,600	46	79,113	11,923,384
GF	4.0	0.0	16,900.0	0	0	79,113	11,923,384
Sum			865,300.0 kN	87,012,000 kN m	79,113 kN	Seismic base shear	Seismic overturning moment

Distribution of lateral forces

UBC (2000) specifies the load at the top to be

$$F_t = 0.07TV = 19.778 \text{ MN}$$

Extracting calculation for level 48,

$$W_i H_i = 16.9 \times 192 = 3.245 \times 10^3 \text{ MN}$$

$$F_x = \frac{(V - F_t)(W_{48} H_{48})}{\sum_i^{52} W_i H_i} = \frac{(79.113 - 19.778)(3.245 \times 10^3)}{87.012 \times 10^3} = 2.21 \text{ MN}$$

$$\text{Shear force} = \text{Shear}_{49} + F_{48} = 24.9 + 2.21 = 27.1 \text{ MN}$$

$$\text{Moment} = \text{Moment}_{49} + (\text{Shear}_{49} \times \text{story height}) = 347.7 + (24.9 \times 4) = 447.3 \text{ MN m}$$

13.3 Dynamic Effects of Wind Loading on Structures

13.3.1 Introduction

The turbulent nature of the wind is characterized by sudden gusts superimposed upon a mean wind velocity. The wind vector at a point may be regarded as the sum of the mean wind vector (static component) and a dynamic component

$$V(z, t) = \bar{V}(z) + v(z, t) \quad (13.12)$$

Wind is a phenomenon of great complexity because of the many flow situations arising from the interaction of wind with structures. Wind is composed of a multitude of eddies of varying sizes and rotational characteristics carried along in a general stream of air moving relative to the Earth's surface. These eddies give wind its gusty or turbulent character. The gustiness of strong winds in the lower levels of the atmosphere largely arises from interaction with surface features. The average wind speed over a time period of the order of 10 min or more tends to increase with height, while the gustiness tends to decrease with height.

A further consequence of turbulence is that dynamic loading on a structure depends on the size of the eddies. Large eddies, whose dimensions are comparable with the structure, give rise to well-correlated pressures as they envelop the structure. On the other hand, small eddies result in pressures at various parts of the structure being practically uncorrelated. Eddies generated around a typical structure are shown in Figure 13.12.

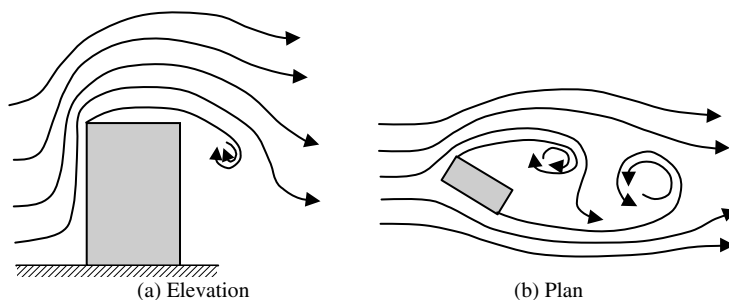


FIGURE 13.12 Generation of eddies. (a) Elevation; (b) plan.

Some structures, particularly those that are tall or slender, respond dynamically to the wind. The best-known structural collapse due to wind was the Tacoma Narrows Bridge which occurred in 1940 at a wind speed of only about 19 m/sec. It failed after it had developed a joint torsional and flexural mode of oscillation.

There are several different phenomena giving rise to dynamic response of structures in wind. These include buffeting, vortex shedding, galloping, and flutter. Slender structures are likely to be sensitive to dynamic response in line with the wind direction as a consequence of turbulence buffeting. Transverse or crosswind response is more likely to arise from vortex shedding or galloping, but may be excited by turbulence buffeting also. Flutter is a coupled motion, often a combination of bending and torsion, and can result in instability.

An important problem associated with the wind-induced motion of buildings is concerned with the human response to vibration. At this point, it will suffice to note that humans are surprisingly sensitive to vibration, to the extent that motions may feel uncomfortable even if they correspond to relatively unimportant stresses. The next few sections give a brief introduction to the dynamic response of structures in wind. More details can be found in wind engineering texts (e.g., Sachs, 1978; Holmes, 2001).

13.3.2 Wind Speed

At great heights above the surface of the Earth, where frictional effects are negligible, air movements are driven by pressure gradients in the atmosphere, which in turn are the thermodynamic consequence of variable solar heating of the Earth. This upper level wind speed is known as the gradient wind velocity.

Different terrains can be categorized according to the roughness length. Table 13.3 shows the different categories specified in the Australian/New Zealand wind code, AS/NZS 1170.2 (2002). Closer to the surface, the wind speed is affected by frictional drag of the air over the terrain. There is a boundary layer within which the wind speed varies from almost zero, at the surface, to the gradient wind speed at a height known as the gradient height. The thickness of this boundary layer, which may vary from 500 to 3000 m, depends on the type of terrain, as depicted in Figure 13.13. As can be seen, the gradient height within a large city center is much higher than it is over the sea where the surface roughness is less.

In practice, it has been found useful to start with a reference wind speed based on statistical analysis of wind speed records obtained at meteorological stations throughout the country. The definition of the reference wind speed varies from one country to another. For example, in Australia/New Zealand, it is the 3-sec gust wind speed at a height of 10 m above the ground assuming terrain category 2. Maps of reference wind speeds applying to various countries are usually available.

An engineering wind model for Australia has been developed by Melbourne (1992) from the Deaves and Harris (1978) model. This model is based on extensive full-scale data and on the classic logarithmic law in which the mean velocity profile in strong winds applicable in noncyclonic regions (neutral stability conditions) is given by Equation 13.13

$$\bar{V}_z \approx \frac{u^*}{0.4} \left[\log_e \left(\frac{z}{z_0} \right) + 5.75 \left(\frac{z}{z_g} \right) - 1.88 \left(\frac{z}{z_g} \right)^2 - \left(\frac{z}{z_g} \right)^3 + 0.25 \left(\frac{z}{z_g} \right)^4 \right] \quad (13.13)$$

The numerical values are based on a mean gradient wind speed of 50 m/sec.

TABLE 13.3 Terrain Category and Roughness Length (z_0)

Terrain Category	Roughness Length (z_0)
Exposed open terrain with few or no obstructions and water surfaces at serviceability wind speeds	0.002
Water surfaces, open terrain, grassland with few, well-scattered obstructions having heights generally from 1.5 to 10 m	0.02
Terrain with numerous closely spaced obstructions 3 to 5 m high such as areas of suburban housing	0.2
Terrain with numerous large, high (10.0 to 30.0 m high) and closely spaced obstructions such as large city centers and well-developed industrial complexes	2

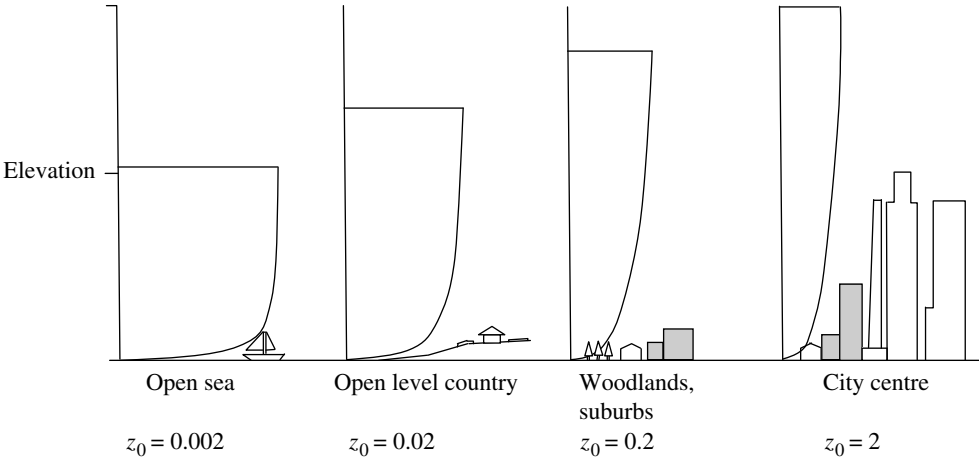


FIGURE 13.13 Mean wind profiles for different terrains.

For values of $z < 30.0$ m the z/z_g values become insignificant and the above equation simplifies to

$$\bar{V}_z \approx \frac{u^*}{0.4} \log_e \left(\frac{z}{z_0} \right) \tag{13.14}$$

where:

\bar{V}_z = the design hourly mean wind speed at height z , in m/sec

u^* = the friction velocity

$$u^* = \sqrt{\frac{\text{surface friction shear stress}}{\text{atmospheric density}}}$$

z = the distance or height above ground, in m

z_g = the gradient height in meters (the value ranges from 2700 to 4500 m), see Table 13.4 (derived by the authors)

$$z_g = \frac{u^*}{6 \times 10^{-4}}$$

As given in Table 13.3, there is an interaction between roughness length and terrain category, so it is necessary to define a terrain category to find the design hourly wind speeds and gust wind speeds. The link between hourly mean and gust wind speeds is as follows:

$$V = \bar{V} \left[1 + 3.7 \left(\frac{\sigma_v}{\bar{V}_z} \right) \right] \tag{13.15}$$

where

$$\sigma_v = 2.63 \eta u^* \left[0.538 + 0.09 \log_e \left(\frac{z}{z_0} \right) \right]^{\eta^{16}} \tag{13.16}$$

TABLE 13.4 Roughness Length, Friction Velocity, and Gradient Height

Terrain Category	z_0 (m)	u^*	z_g (m)
1	0.002	1.662	2769
2	0.02	1.910	3184
3	0.2	2.243	3738
4	2	2.708	4514

$$\eta = 1.0 - \left(\frac{z}{z_g} \right) \quad (13.17)$$

For design, the basic wind speed is classified into three different speeds as follows:

$V_s = V_{20 \text{ yr}}$ = serviceability limit state design speed having an estimated probability of exceedance of 5% in any one year, for the serviceability limit states

$V_p = V_{50 \text{ yr}}$ = permissible, or working, stress design wind speed and can be obtained directly from V_u using the relation $V_p = V_u/(1.5)^{0.5}$

$V_u = V_{1000 \text{ yr}}$ = ultimate limit state design wind speed having an estimated probability of exceedance of 5% in a lifetime of 50 years, for the ultimate limit states

Using rigorous analysis incorporating probability distribution of wind speed and direction, basic design wind speeds for different directions and different return periods can be derived. For example, AS/NZS 1170.2 provides a wind direction multiplier, which varies from 0.80 for wind from the east to 1.0 for wind from the west, and having wind speeds up to a 2000-year return period.

13.3.3 Design Structures for Wind Loading

The characteristics of wind pressures are a function of the characteristics of the approaching wind, the geometry of the structure, and the geometry and proximity of the upwind structures. The pressures are not steady, but highly fluctuating, partly as a result of the gustiness of the wind, but also because of local vortex shedding at the edges of the structures themselves. The fluctuating pressures result in fatigue damage to structures, and in dynamic excitation, if the structure happens to be dynamically wind sensitive. The pressures are also not uniformly distributed over the surface of the structure, but vary with position.

The complexities of wind loading should be kept in mind when designing a structure. Because of the many uncertainties involved, the maximum wind loads experienced by a structure during its lifetime may vary widely from those assumed in the design. Thus, the failure or nonfailure of a structure in a windstorm cannot necessarily be taken as an indication of the nonconservativeness, or conservativeness, of the wind-loading standard. The standards do not apply to buildings or structures that are of unusual shape or location. Wind loading governs the design of some types of structures, such as tall buildings and slender towers. Experimental wind tunnel data may be used in place of the coefficients given in the code for these structures.

13.3.3.1 Types of Wind Design

Typically, for wind-sensitive structures, three basic wind effects need to be considered:

- *Environmental wind studies* — to study the wind effects on the surrounding environment caused by erecting the structure (e.g., a tall building). This study is particularly important to assess the impact of wind on pedestrians and motor vehicles and so on, which utilize the public domain within the vicinity of the proposed structure.
- *Wind loads for facade* — to assess design wind pressures throughout the surface area of the structure to design the cladding system. Owing to the significant cost of typical facade systems in proportion to the overall cost of very tall buildings, engineers cannot afford the luxury of conservatism in assessing design wind loads. With due consideration to the complex building shapes and dynamic characteristics of the wind and building structure, even the most advanced wind codes generally cannot accurately assess design loads. Wind tunnel tests to assess design loads for cladding are now a normal industry practice, with the aim of minimizing initial capital costs, and more significantly, to avoid the expensive maintenance costs associated with malfunctions due to leakage and/or structural failure.

- *Wind loads for structure* — to determine the design wind load so as to design the lateral load-resisting structural system of a structure and therefore satisfy the various design criteria.

13.3.3.2 Design Criteria

In terms of designing a structure for lateral wind loads, the following design criteria need to be satisfied:

- *Stability* against overturning, uplift, and/or sliding of the structure as a whole.
- The *strength* of the structural components of the building, and stresses that must be withstood without failure during the life of the structure.
- *Serviceability*, for example for buildings, where interstory and overall deflections are within acceptable limits. The control of deflection and drift is imperative for tall buildings in order to limit damage and cracking to nonstructural members such as the facade, internal partitions, and ceilings.

As adopted by most international codes, to satisfy stability and strength limit state requirements, ultimate limit state wind speed is used. In many codes, such a speed has a 5% probability of being exceeded in a 1-year period.

An additional criterion that requires careful consideration in wind-sensitive structures such as tall buildings is the control of accelerations when subjected to wind loads under serviceability conditions. Acceptability criteria for vibrations in buildings are frequently expressed in terms of acceleration limits for a 1- or 5-year return period wind speed, and are based on human tolerance to vibration discomfort in the upper levels of buildings. Wind response is relatively sensitive to both mass and stiffness, and response accelerations can be reduced by increasing either or both of these parameters. However, this is in conflict with earthquake design optimization where loads are minimized in buildings by reducing both the mass and stiffness. Increasing the damping results in a reduction in both the wind and earthquake responses.

The detailed procedure described in wind codes is subdivided into static analysis and dynamic analysis methods. The static approach is based on a quasi-steady assumption. It assumes that the building is a fixed rigid body in the wind. The static method is not appropriate for tall or slender structures or structures susceptible to vibration in the wind. In practice, static analysis is normally appropriate for structures up to 50 m in height. The subsequently described dynamic method is for exceptionally tall, slender, or vibration-prone buildings. The codes not only provide some detailed design guidance with respect to dynamic response, but also state specifically that a dynamic analysis must be undertaken to determine overall forces on any structure with both a height (or length) to breadth ratio greater than five, and a first mode frequency less than one.

Wind-loading codes may give the impression that wind forces are relatively constant with time. In reality, wind forces vary significantly over short time intervals, with large amplitude fluctuations at high-frequency intervals. The magnitude and frequency of the fluctuations is dependent on many factors associated with the turbulence of the wind and local gusting effects caused by the structure and surrounding environment.

To simplify this complex wind characteristic, most international codes have adopted a simplified approach by utilizing a quasi-steady assumption. This approach simply uses a single value equivalent, static wind pressure, to represent the maximum peak pressure the structure would experience.

13.3.3.3 Static Analysis

This method assumes the quasi-steady approximation. It approximates the peak pressures on the building surfaces by the product of gust dynamic wind pressure and the mean pressure coefficients. The mean pressure coefficients are measured in a wind-tunnel or full-scale tests and are given by $p_{\text{bar}}/q_{z(\text{bar})}$. The implied assumption is that the pressures on the building surface (external and internal) faithfully follow the variations in upwind velocity. Thus, it is assumed that a peak value of wind speed is accompanied by a peak value of pressure or load on the structure. The quasi-steady model has been found to be fairly good for small structures.

In static analysis, gust wind speed, V_z , is used to calculate the forces, pressures, and moments on the structure.

The main advantages and disadvantages of the quasi-steady/peak gust format can be summarized as follows:

- Advantages:
 - Simplicity.
 - Continuity with previous practice.
 - Pressure coefficients should need little adjustment for different upwind terrain types.
 - Existing meteorological data on wind gusts are used directly.
- Disadvantages:
 - The approach is not suitable for very large structures, or for those with significant dynamic response.
 - The response characteristics of the gust anemometers and the natural variability of the peak gusts tend to be incorporated into the wind load estimates.
 - The quasi-steady assumption does not work well for cases where the mean pressure coefficient is near zero.

However, the advantages outweigh the disadvantages — certainly for smaller, stiff structures for which the code is mainly intended.

The philosophy used in specifying the peak loads in AS/NZS 1170.2 has been to approximate the real values of the extremes. In many cases, this has required the adjustment of the quasi-steady pressures with factors such as area reduction factors and local pressure factors.

The dynamic wind pressure at height z is given by

$$\bar{q}_z = 0.6 \bar{V}_z^2 \times 10^{-3} \quad (13.18)$$

where

\bar{V}_z = the design gust wind speed at height z , in meters per second = $VM_{(z,cat)}M_zM_tM_i$

V = the basic wind speed

The multiplying factors (M) take into account the type of terrain (M_t), height above ground level (M_z), topography, and the importance of the structure (M_i). The above derivation essentially forms the basis of most international codes.

The mean base overturning moment M_{bar} is determined by summing the moments resulting from the net effect of the mean pressure and leeward sides of the structure given by

$$\bar{F}_z = \sum c_{p,e} \bar{q}_z A_z$$

or for structures with discrete elements:

$$\bar{F}_d = \sum c_d \bar{q}_z A_z \quad (13.19)$$

where

\bar{F}_z = the hourly mean net horizontal force acting on a structure at height z

$C_{p,e}$ = the pressure coefficients for both windward and leeward surfaces

A_z = the area of a structure or a part of a structure, at height z , in square meters

\bar{F}_d = the hourly mean drag force acting on discrete elements

C_d = the drag force coefficient for an element of the structure

13.3.4 Along and Across-Wind Loading

Not only is the wind approaching a building a complex phenomenon, but the flow pattern generated around a building is complicated by the distortion of the mean flow, the flow

separation, the vortex formation, and the wake development. Large wind pressure fluctuations due to these effects occur on the surface of a building. As a result, large aerodynamic loads are imposed on the structural system and intense localized fluctuating forces act on the facade of such structures. Under the collective influence of these fluctuating forces, a building vibrates in rectilinear and torsional modes, as illustrated in Figure 13.14. The amplitude of such oscillations is dependant on the nature of aerodynamic forces and the dynamic characteristics of the building.

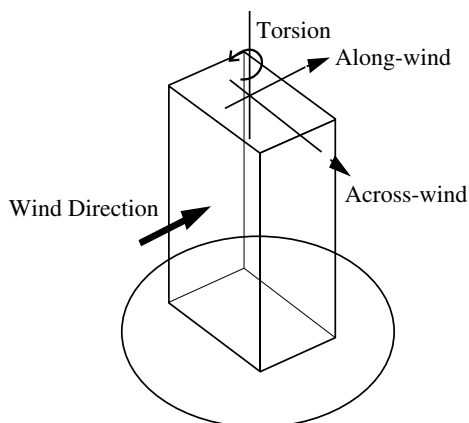


FIGURE 13.14 Wind response directions.

13.3.4.1 Along-Wind Loading

The along-wind loading or response of a building due to the gusting wind can be assumed to consist of a mean component due to the action of the mean wind speed (e.g., the mean hourly wind speed), and a fluctuating component due to wind speed variations from the mean. The fluctuating wind is a random mixture of gusts or eddies of various sizes, with the larger eddies occurring less often (i.e., with a lower average frequency) than smaller eddies. The natural frequency of vibration of most structures is sufficiently higher than the component of the fluctuating load effect imposed by the larger eddies. That is, the average frequency with which large gusts occur is usually much less than any of the structure's natural frequencies of vibration and so they do not force the structure to respond dynamically. The loading due to those larger gusts (which are sometimes referred to as "background turbulence") can therefore be treated in similar way to that due to the mean wind speed. The smaller eddies, however, because they occur more often, may induce the structure to vibrate at or near one of the structure's natural frequencies of vibration. This in turn induces a magnified dynamic load effect in the structure which can be significant.

The separation of wind loading into mean and fluctuating components is the basis of the so-called "gust factor" approach, which is the basis of many design codes. The mean load component is evaluated from the mean wind speed using pressure and load coefficients. The fluctuating loads are determined separately by a method which makes an allowance for the intensity of turbulence at the site, size reduction effects, and dynamic amplification (Davenport, 1967; Vickery, 1971).

The dynamic response of buildings in the along-wind direction can be predicted with reasonable accuracy by the gust factor approach, provided the wind flow is not significantly affected by the presence of neighboring tall buildings or surrounding terrain.

13.3.4.2 Across-Wind Loading

There are many examples of slender structures that are susceptible to dynamic motion perpendicular to the direction of the wind. Tall chimneys, street lighting standards, towers, and cables frequently exhibit this form of oscillation, which can be very significant, especially if the structural damping is small. Crosswind excitation of modern tall buildings and structures can be divided into three mechanisms (AS/NZS 1170.2, 2002). These and higher time derivatives are described as follows:

1. The most common source of crosswind excitation is that associated with "vortex shedding." Tall buildings are bluff (as opposed to streamlined) bodies that cause the flow to separate from the surface of the structure, rather than follow the body contour (Figure 13.15). For a

particular structure, the shed vortices have a dominant periodicity that is defined by the Strouhal number. Hence, the structure is subjected to a periodic pressure loading, which results in an alternating crosswind force. If the natural frequency of the structure coincides with the shedding frequency of the vortices, large amplitude displacement response may occur, and this

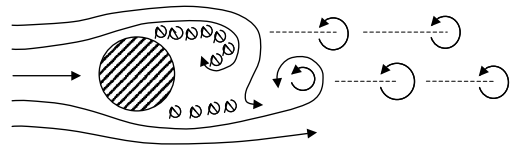


FIGURE 13.15 Vortex formation in the wake of a bluff object.

is often referred to as critical velocity effect. The asymmetric pressure distribution created by the vortices around the cross section results in an alternating transverse force as they are shed. If the structure is flexible, oscillation will occur transverse to the wind, and the conditions for resonance would exist if the vortex shedding frequency coincided with the natural frequency of the structure. This situation could give rise to very large oscillations and possibly failure.

In practice, vertical structures are exposed to a turbulent wind in which both the wind speed and the turbulence level vary with height, so that excitation due to vortex shedding is effectively broadband. Therefore, the term “wake excitation” is used to include all forms of excitation associated with the wake and not just those associated with the critical wind velocity.

2. The “incident turbulence” mechanism refers to the situation where the turbulence properties of the natural wind give rise to changing wind speeds and directions that directly induce varying lift and drag forces and pitching moments on the structure over a wide band of frequencies. The ability of incident turbulence to produce significant contributions to crosswind response depends very much on the ability to generate a crosswind (lift) force on the structure as a function of longitudinal wind speed and angle of attack. In general, this means that sections with a high lift curve slope or pitching moment curve slope, such as a streamlined bridge deck section or a flat deck roof, are possible candidates for this effect.
3. Higher derivatives of crosswind displacement: there are three commonly recognized displacement-dependent excitations (i.e., “galloping,” “flutter,” and “lock-in”), all of which are also dependent on the effects of turbulence (turbulence affects the wake development, and hence, the aerodynamic derivatives). Many formulae are available to calculate these effects (Holmes, 2001). Recently, computational fluid dynamics techniques have also been used (Tamura, 1999) to evaluate these effects.

13.3.5 Wind Tunnel Tests

There are many situations in which analytical methods cannot be used to estimate certain types of wind loads and the associated structural response. For example, when the aerodynamic shape of the building is rather uncommon, or the building is very flexible so that its motion affects the aerodynamic forces acting on the building. In such situations, more accurate estimates of wind effects on buildings are obtained through aeroelastic model tests in a boundary-layer wind tunnel.

Wind tunnel tests currently being conducted on buildings and other structures can be divided into two types. The first is concerned with the determination of wind-loading effects to enable the design of a wind-resistant structure. The second is concerned with the flow fields induced around the structure, such as its effects on pedestrian comfort and safety at ground level or air intake concentration levels of exhaust pollutants.

Wind tunnel studies involve blowing wind on the subject building model and its surrounding at various angles relative to the building orientation, representing the wind directions. This is typically achieved by placing the complete model on a rotating platform within the wind tunnel. Once testing is



FIGURE 13.16 Wind tunnel test.

complete for a select direction, the platform is simply rotated by a chosen increment to represent a new wind direction. A typical wind tunnel model is illustrated in Figure 13.16.

The design wind speed is based on meteorological data for the given city or area, which are analyzed to produce the required probability distribution of gust wind speeds. By appropriate integration processes and the application of necessary scaling factors, directional wind speeds for the wind tunnel can be determined.

Although wind tunnel testing attempts to duplicate a complex problem, the actual models are quite simple and are based on the premise that the fundamental mode of displacement for a structure such as a tall building can be approximated by a straight line. In general terms, it is not necessary to achieve a correct mass density distribution along the building height as long as the mass moment of inertia about the pivot point is the same as the prototype density distribution. The pivot point is typically chosen to obtain a mode shape which provides the best agreement with the calculated fundamental mode shapes of the prototype. Springs are located near the pivot points to achieve the correct frequencies of vibrations in the two fundamental sway modes corresponding to the orthogonal building axis. An electromagnet or oil dashpot provides the model with a damping corresponding to that of the full scale tower. In addition to the stiffness and damping compatibility, it is essential that structural length scale, timescale, and the inertial force are the same between the model and the full structure.

Buildings of similar size located in close proximity to the proposed building can cause large increases in across-wind responses. Fortunately, in wind tunnel studies, surroundings comprising existing and/or future buildings can easily be incorporated with relatively minor costs.

13.3.6 Comfort Criteria: Human Response to Building Motion

There are no generally accepted international standards for comfort criteria. A considerable amount of research has been carried out into the important physiological and psychological parameters that affect human perceptions of motion and vibration in the low-frequency range of 0 to 1 Hz encountered in tall buildings. These parameters include the occupant's expectations and experience, activity, body posture, and orientation; visual and acoustic cues; and the amplitude, frequency, and acceleration of both the translational and rotational motion to which the occupant is subjected. Table 13.5 gives some guidance on the general human perception levels.

TABLE 13.5 Human Perception Levels

Level	Acceleration (m/sec ²)	Effect
1	<0.05	Humans cannot perceive motion
2	0.05 to 0.1	Sensitive people can perceive motion; hanging objects may move slightly
3	0.1 to 0.25	The majority of people will perceive motion; the level of motion may affect desk work; long-term exposure may produce motion sickness
4	0.25 to 0.4	Desk work becomes difficult or almost impossible; ambulation still possible
5	0.4 to 0.5	People strongly perceive motion; it is difficult to walk naturally; standing people may lose their balance
6	0.5 to 0.6	Most people cannot tolerate the motion and are unable to walk naturally
7	0.6 to 0.7	People cannot walk or tolerate the motion
8	>0.85	Objects begin to fall and people may be injured

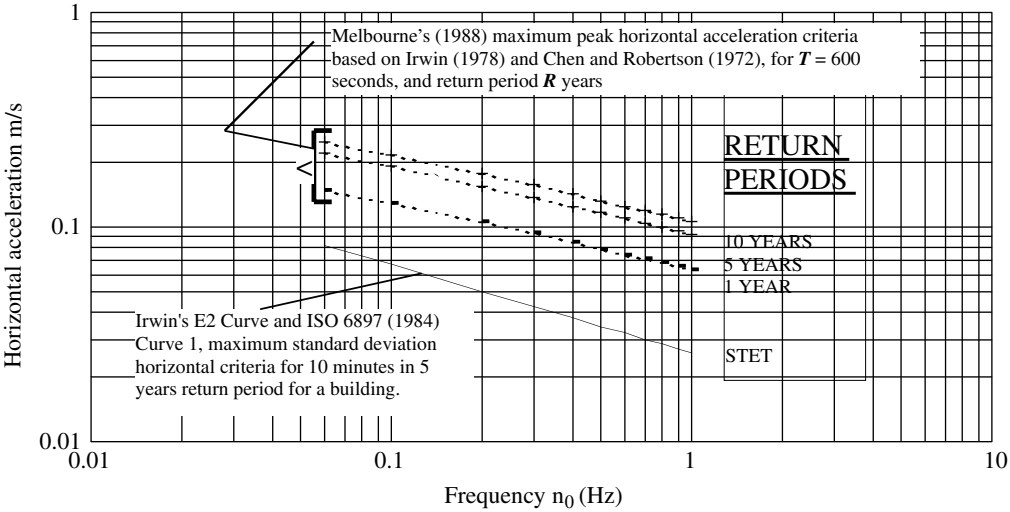


FIGURE 13.17 Horizontal acceleration criteria for occupancy comfort in buildings.

Acceleration limits are a function of the frequency of the vibration felt. Upper limits have been recommended for corresponding frequencies of vibration with the relationship suggested by Irwin (1978). Peak acceleration limits as suggested by Melbourne (1988) and Chen (1987) have been plotted along with the Irwin E2 curve in Figure 13.17. To obtain the peak acceleration, the root-mean-square (rms) value can be multiplied by a peak factor. The peak factor is generally between 3 and 4.

13.3.7 Dampers

The damping in a mechanical or structural system is a measure of the rate at which the energy of motion of the system is dissipated. All real systems have some damping. An example is friction in a bearing. Another example is the viscous damping created by the oil within an automotive shock absorber. In many systems, damping is not helpful and it has to be overcome by the system input. In the case of wind-sensitive structures such as tall buildings, however, it is beneficial, as damping reduces motion, making the building feel more stable to its occupants.

Controlling vibrations by increasing the effective damping can be a cost-effective solution. Occasionally, it is the only practical and economical solution.

The types of damping systems that can be implemented include:

- Tuned mass damper (TMD; an example is given in Figure 13.18)
- Distributed viscous dampers
- Tuned liquid column dampers (TLCD), also known as liquid column vibration absorbers (LCVA)
- Tuned sloshing water dampers (TSWD)
- Impact-type dampers
- Visco-elastic dampers
- Semiactive dampers
- Active dampers

While general design philosophy tends to favor passive damping systems due to their lower capital and maintenance costs, active or semiactive dampers may be the ideal solution for certain vibration problems. More details about passive and active systems to control vibrations are given by Soong and Constantinou (1994).

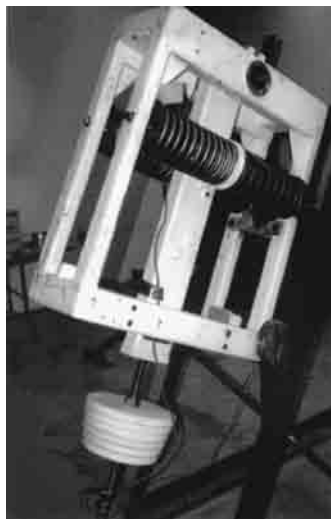


FIGURE 13.18 One of the TMDs designed for the skybridge legs of the Petronas Towers by RWDI Inc. (12 TMDs were installed, three in each of the four legs).

13.3.8 Comparison with Earthquake Loading

Extremes of wind loading, which may be as much as three or four times the loading associated with the mean result, are possible, and a significant contribution to this extreme is often supplied by the resonant component in the turbulence of the wind. Resonance refers to a condition in which the periodicity of forcing is identical to that of the structure, with a consequential amplification of response that is limited only by the level of damping of the structure. A typical wind contains a wide range of frequency components in its turbulence, so it is always possible that the peak response has a resonant component.

Earthquake ground motions are characterized by a series of rather random spikes, with the range of frequencies present (i.e., the range of intervals between zero crossings on the ground acceleration record) being somewhat narrower than for normal wind turbulence. Structures that are stiff will move essentially in unison with the ground motion. For more flexible structures, response is analogous to that from a series of impulses, with the dominant frequency in the response being that of the structure itself. This frequency, the natural frequency of the structure, is dependent on the mass and stiffness of the system.

Wind loading depends on exposed area; earthquake loading depends on the (hidden) mass of the structure. Structures attract wind loadings which increase steadily with the major dimension (height or span, say). The earthquake loading experienced by such structures increases much less rapidly, with the result that, for high-rise structures, wind loading is almost always the dominant lateral loading. This assumes elastic responses for both regimes of loading.

Wind loading depends on topography and, in urban areas, on the proximity of other buildings. Earthquake loading, on the other hand, depends to a marked degree on the foundation materials. It is universally observed that buildings founded on soft soils perform much worse than those founded on rock.

The most important differences between wind and earthquake loading are summarized in Table 13.6.

TABLE 13.6 Main Differences between Wind and Earthquake Loading

Characteristic	Wind	Earthquake
Source of loading	External force due to wind pressures	Applied base motion from ground vibration
Type and duration of loading	Wind storm of several hours duration. Loads fluctuate, but are predominantly in one direction	Transient cyclic loads of at most a few minutes total duration. Loads change repeatedly in direction
Predictability	Good statistical basis is generally available	Poor
Sensitivity of loading to return period	Moderate; +15% typical for $\times 10$ on return period	High; maximum credible earthquake often greatly in excess of "design" values
Influence of local soil conditions	Little effect on dynamic sensitivity	Soil conditions can be very important
Spectral peak input range	Gust: <0.1 Hz	Usually 1 to 5 Hz
Main factors affecting building response	External shape of building or structure. Generally only global dynamic properties are important. Dynamic considerations affect only a small fraction of building structures	Response is governed by global dynamic properties (fundamental period, damping, and mass) but plan and vertical regularity of structure also important. All structures are affected dynamically
Normal design basis	Elastic response is required	Inelastic response is usually permitted, but ductility must be provided
Design of nonstructural elements	Applied loading is concentrated on external cladding	Entire building contents are shaken and must be appropriately designed

Source: Data from Maguire, J.R. and Wyatt, T.A., 1999. *Dynamics — An Introduction for Civil and Structural Engineers*, Thomas Telford, London.

13.4 Vibrations Due to Fluid–Structure Interaction

The principles of vibration due to fluids such as water are very similar to those of wind action presented in the previous section. The fluid flow can significantly affect the vibrational characteristics of a structure. The presence of a quiescent fluid decreases the natural frequencies and increases the damping of the structure. Similar to wind, a turbulent fluid flow exerts random pressures on a structure, and these random pressures induce a random response leading to large structural deformations or failure. More details on fluid–structure interaction can be found in text books (e.g., Tiejens and Prandtl, 1957; Milne-Thompson, 1968).

13.4.1 Added Mass and Inertial Coupling

A real fluid is viscous and compressible. In contrast, a perfect fluid is nonviscous and incompressible. Fluid damping is absent in perfect fluids, and therefore, for a structure oscillating in a quiescent perfect fluid, the fluid-force component is associated with the fluid inertia called the added mass. This is of practical importance when the fluid density is comparable to the density of the structure, because then the added mass becomes a significant fraction of the total mass in dynamic motion. Added mass and fluid damping associated with single and multiple cylindrical structures are discussed in detail by Chen (1987). For example, the added mass for a circular cylinder of radius a and height h is equal to $\pi a^2 h$. Added masses for different cross-sectional shapes are presented by Milne-Thompson (1968).

13.4.2 Wave-Induced Vibration of Structure

This effect is similar to wind; however, the density is very much larger than wind, thus making the structural damping less effective. Therefore, it is essential to ensure that resonance does not occur.

The fluid forces which act in line with the direction of wave propagation (Figure 13.19) can be found using a generalized form of Morrison's equation comprising both drag (proportional to area times velocity squared) and inertia forces (proportional to immersed volume times acceleration). More details can be found in Muga and Wilson (1970).

Flexible structures will resonate with the wave if the structural natural period equals the wave period or a harmonic of the wave period. Since the wave frequencies of importance are ordinarily less than 0.2 Hz, such a resonance occurs only for exceptionally flexible structures such as offshore platforms. The amplitude of structural response at resonance is a balance between the wave force and the structural stiffness times the damping.

The above discussion considers only the in-line forces. These in-line forces produce an in-line response. However, substantial transverse vibrations also occur for ocean flows around circular cylinders. These vibrations are associated with periodic vortex shedding, which was discussed under wind-induced vibration.

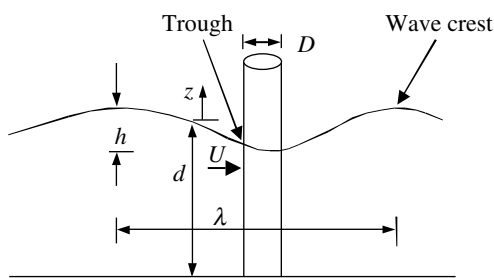


FIGURE 13.19 A circular cylindrical structure exposed to ocean waves.

13.5 Blast Loading and Blast Effects on Structures

The use of vehicle bombs to attack city centers has been a feature of campaigns by terrorist organizations around the world. A bomb explosion within or very near a building can have catastrophic effects, destroying or severely damaging portions of the building's external and internal structural frames, collapsing walls, blowing out large expanses of windows, and shutting down critical life-safety systems, such as fire detection and suppression, ventilation, light, water, sewage, and power systems. Loss of life and injuries to occupants can result from many causes, including direct blast effects, structural collapse, debris impact, fire, and smoke. The indirect effects can combine to inhibit or prevent timely evacuation, thereby contributing to additional casualties. In addition, major catastrophes resulting from gas-chemical explosions or nuclear leakage result in large dynamic loads, greater than the original design loads, of many structures. Owing to the threat of such extreme loading conditions, efforts have been made during the past three decades to develop methods of structural analysis and design to resist blast loads. The analysis and design of structures subjected to blast loads requires a detailed understanding of blast phenomena and the dynamic response of various structural elements.

13.5.1 Explosions and Blast Phenomenon

An explosion is defined as a large-scale, rapid, and sudden release of energy. Explosions can be categorized on the basis of their nature as physical, nuclear, or chemical events. In physical explosions, energy may be released from the catastrophic failure of a cylinder of compressed gas, volcanic eruptions, or even the mixing of two liquids at different temperatures. In a nuclear explosion, energy is released from the formation of different atomic nuclei by the redistribution of the protons and neutrons within the interacting nuclei; whereas the rapid oxidation of fuel elements (carbon and hydrogen atoms) is the main source of energy in the case of chemical explosions.

Explosive materials can be classified according to their physical state as solids, liquids, or gases. Solid explosives are mainly high explosives, for which blast effects are best known. They can also be classified on the basis of their sensitivity to ignition as secondary or primary explosive. The latter is one that can be easily detonated by simple ignition from a spark, flame, or impact. Materials such as mercury fulminate and lead azide are primary explosives. Secondary explosives detonate creating blast (shock) waves, which

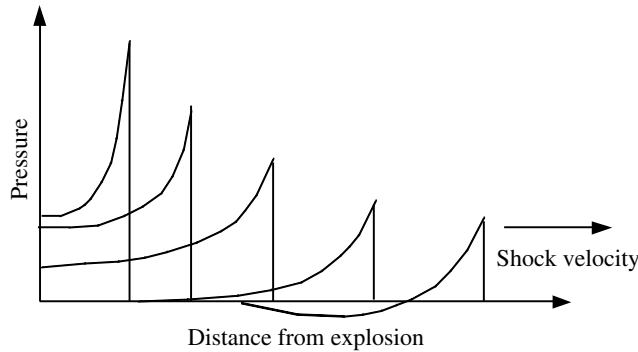


FIGURE 13.20 Blast wave propagation.

result in damage to the surroundings. Examples include trinitrotoluene (TNT) and ammonium nitrate and fuel oil (ANFO).

The detonation of a condensed high explosive generates hot gases under pressure of up to 300 kbar and a temperature of about 3000 to 4000°C. The hot gas expands, forcing out the volume it occupies. As a consequence, a layer of compressed air (blast wave) forms in front of this gas volume, containing most of the energy released by the explosion. The blast wave instantaneously increases to a value of pressure above the ambient atmospheric pressure. This is referred to as the side-on overpressure, and decays as the shock wave expands outward from the explosion source. After a short time, the pressure behind the front may drop below the ambient pressure (see Figure 13.20 and Figure 13.21). During such a negative phase, a partial vacuum is created and air is sucked in. This is also accompanied by high suction winds that carry the debris for long distances away from the explosion source.

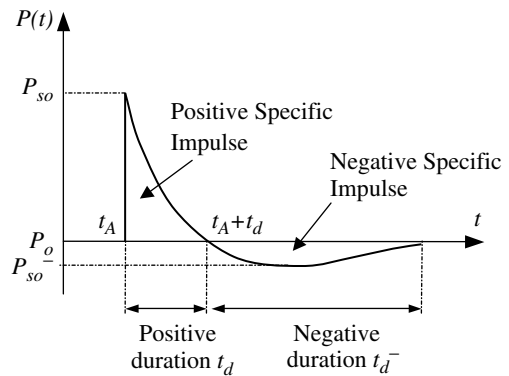


FIGURE 13.21 Blast wave pressure — time history.

13.5.2 Explosive Air-Blast Loading

The threat for a conventional bomb is defined by two equally important elements, the bomb size, or charge weight, W , and the standoff distance, R , between the blast source and the target (Figure 13.22). For example, the blast that occurred at the basement of the World Trade Center in 1993 had the charge weight of 816.5 kg TNT. The Oklahoma City bomb in 1995 had a charge weight of 1814 kg at a stand off of 4.5 m (Longinow and Mniszewski, 1996). As terrorist attacks may range from a small letter bomb to a gigantic truck bomb, as experienced in Oklahoma City, the mechanics of a conventional explosion and their effects on the target must be addressed.

The observed characteristics of air-blast waves are found to be affected by the physical properties of the explosion source. Figure 13.21 shows a typical blast pressure profile. At an arrival time of t_A after the explosion, pressure at that position suddenly increases to a peak value of overpressure, P_{so} , over the ambient pressure, P_0 . The pressure then decays to the ambient pressure at time t_d until it reaches a partial vacuum of peak underpressure P_{so}^- , and eventually returns to the ambient pressure at time $t_d + t_d^-$. The quantity P_{so} is usually referred to as the peak side-on overpressure, incident peak overpressure, or merely the peak overpressure (TM 5-1300, 1990).

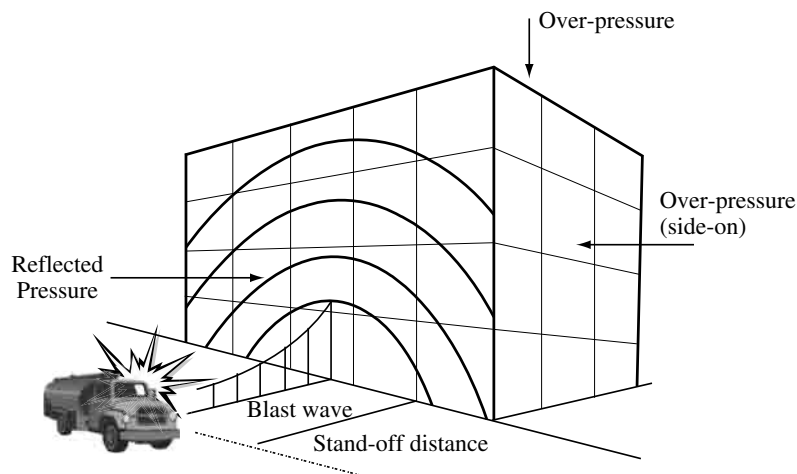


FIGURE 13.22 Blast loads on a building.

The incident peak overpressure, P_{so} , is amplified by a reflection factor as the shock wave encounters an object or structure in its path. Except for the specific focusing of high-intensity shock waves at near 45° incidence, these reflection factors are typically greatest for normal incidence (a surface adjacent and perpendicular to the source) and diminish with the angle of obliquity or angular position relative to the source. Reflection factors depend on the intensity of the shock wave. For large explosions at normal incidence these reflection factors may enhance the incident pressures by as much as an order of magnitude.

Throughout the pressure–time profile, two main phases can be observed; the portion above ambient pressure is called positive phase of duration t_d , while that below ambient is called negative phase of duration, t_d^- . The negative phase is of a longer duration and a lower intensity than the positive duration. The duration of the positive-phase blast wave increases with range, resulting in a lower amplitude, longer duration shock pulse the further a target structure is situated from the burst. Charges situated extremely close to a target structure impose a highly impulsive, high-intensity pressure load over a localized region of the structure; charges situated further away produce a lower-intensity, longer-duration uniform pressure distribution over the entire structure. Eventually, the entire structure is engulfed in the shock wave, with reflection and diffraction effects creating focusing and shadow zones in a complex pattern around the structure. During the negative phase, the weakened structure may be subjected to impact by debris that may cause additional damage.

If the exterior building walls are capable of resisting the blast load, the shock front penetrates through window and door openings, subjecting the floors, ceilings, walls, contents, and people within to sudden pressures and fragments from shattered windows, doors, and other fixtures. Building components not capable of resisting the blast wave will fracture and be further fragmented and moved by the dynamic pressure that immediately follows the shock front. Building contents and people will be displaced and tumbled in the direction of blast wave propagation. In this manner the blast will propagate through the building.

13.5.2.1 Blast Wave Scaling Laws

All blast parameters are primarily dependent on the amount of energy released by a detonation in the form of a blast wave and the distance from the explosion. A universal normalized description of the blast effects can be given by scaling distance relative to $(E/P_0)^{1/3}$, and pressure relative to P_0 , where E is the energy release (kJ) and P_0 the ambient pressure (typically 100 kN/m^2). For convenience, however, it is general practice to express the basic explosive input or charge weight W as an equivalent mass of TNT. Results are then given as a function of the dimensional distance parameter (scaled distance)

$Z = R/W^{1/3}$, where R is the actual effective distance from the explosion. W is generally expressed in kilograms. Scaling laws provide parametric correlations between a particular explosion and a standard charge of the same substance.

13.5.2.2 Prediction of Blast Pressure

Blast wave parameters for conventional high-explosive materials have been the focus of a number of studies during the 1950s and 1960s. Estimations of peak overpressure due to a spherical blast based on the scaled distance $Z = R/W^{1/3}$ were introduced by Brode (1955) as

$$P_{so} = \frac{6.7}{Z^3} + 1 \text{ bar } (P_{so} > 10 \text{ bar})$$

$$P_{so} = \frac{0.975}{Z} + \frac{1.455}{Z^2} + \frac{5.85}{Z^3} - 0.019 \text{ bar } (0.1 \text{ bar} < P_{so} < 10 \text{ bar})$$
(13.20)

Newmark and Hansen (1961) introduced a relationship to calculate the maximum blast overpressure, P_{so} , in bars, for a high-explosive charge detonated at the ground surface as

$$P_{so} = 6784 \frac{W}{R^3} + 93 \left(\frac{W}{R^3} \right)^{\frac{1}{2}}$$
(13.21)

Another expression of the peak overpressure in kPa was introduced by Mills (1987), in which W is expressed as the equivalent charge weight in kg of TNT, and Z is the scaled distance

$$P_{so} = \frac{1772}{Z^3} - \frac{114}{Z^2} + \frac{108}{Z}$$
(13.22)

As the blast wave propagates through the atmosphere, the air behind the shock front is moving outward at a lower velocity. The velocity of the air particles, and hence the wind pressure, depends on the peak overpressure of the blast wave. This later velocity of the air is associated with the dynamic pressure, $q(t)$. The maximum value, q_s , say, is given by

$$q_s = 5P_{so}^2/2(P_{so} + 7P_0)$$
(13.23)

If the blast wave encounters an obstacle perpendicular to the direction of propagation, reflection increases the overpressure to a maximum reflected pressure P_r as

$$P_r = 2P_{so} \left\{ \frac{7P_0 + 4P_{so}}{7P_0 + P_{so}} \right\}$$
(13.24)

A full discussion and extensive charts for predicting blast pressures and blast durations are given by TM 5-1300 (1990) and Mays and Smith (1995). Some representative numerical values of peak-reflected overpressure are given in Table 13.7.

TABLE 13.7 Peak-Reflected Overpressures P_r (in MPa) with Different W – R Combinations

R (m)	W			
	100 kg TNT	500 kg TNT	1000 kg TNT	2000 kg TNT
1	165.8	354.5	464.5	602.9
2.5	34.2	89.4	130.8	188.4
5	6.65	24.8	39.5	60.19
10	0.85	4.25	8.15	14.7
15	0.27	1.25	2.53	5.01
20	0.14	0.54	1.06	2.13
25	0.09	0.29	0.55	1.08
30	0.06	0.19	0.33	0.63

For design purposes, reflected overpressure can be idealized by an equivalent triangular pulse of maximum peak pressure P_r and time duration t_d , which yields the reflected impulse i_r :

$$i_r = \frac{1}{2} P_r t_d \quad (13.25)$$

The reflection effect dissipates as the perturbation propagates to the edges of the obstacle at a velocity related to the speed of sound (U_s) in the compressed and heated air behind the wave front. Denoting the maximum distance from an edge as S (for example, the lesser of the height or half the width of a conventional building), the additional pressure due to reflection is considered to reduce from $P_r - P_{so}$ to 0 in time $3S/U_s$. Conservatively, U_s can be taken as the normal speed of sound, about 340 m/sec, and the additional impulse to the structure evaluated on the assumption of a linear decay.

After the blast wave has passed the rear corner of a prismatic obstacle, the pressure similarly propagates on to the rear face; linear build-up over duration $5S/U_s$ has been suggested. For skeletal structures, the effective duration of the net overpressure load is thus small, and the drag loading based on the dynamic pressure is then likely to be dominant. Conventional wind-loading pressure coefficients may be used, with the conservative assumption of instantaneous build-up when the wave passes the plane of the relevant face of the building, the loads on the front and rear faces being numerically cumulative for the overall load effect on the structure. Various formulations have been put forward for the rate of decay of the dynamic pressure loading; a parabolic decay (i.e., corresponding to a linear decay of equivalent wind velocity) over a time equal to the total duration of positive overpressure is a practical approximation.

13.5.3 Gas Explosion Loading and Effect of Internal Explosions

In the circumstances of a progressive build-up of fuel in a low-turbulence environment, typical of domestic gas explosions, flame propagation on ignition is slow and the resulting pressure pulse is correspondingly extended. The specific energy of combustion of a hydrocarbon fuel is very high (46,000 kJ/kg for propane, compared with 4520 kJ/kg for TNT) but widely differing effects are possible according to the conditions at ignition.

Internal explosions often produce complex pressure loading profiles as a consequence of having two loading phases. The first results from the blast overpressure reflection and, due to the confinement provided by the structure, re-reflection will occur. Depending on the degree of confinement of the structure, the confined effects of the resulting pressures may cause different degrees of damage to the structure. On the basis of the confinement effect, target structures can be described as either vented or unvented. The latter must be stronger to resist a specific explosion yield than a vented structure where some of the explosion energy would be dissipated by the breaking of window glass or fragile partitions.

Generally, venting following the failure of windows (typically at 7 kN/m²) greatly reduces the peak values of internal pressures. A study of this problem at the Building Research Establishment (Ellis and Crowhurst, 1991) showed that an explosion fuelled by a 200 ml aerosol canister in a typical domestic room produced a peak pressure of 9 kN/m² with a pulse duration over 0.1 sec. This is long by comparison with the natural frequency of wall panels in conventional building construction, and a quasi-static design pressure is commonly advocated. Much higher pressures with a shorter timescale are generated in turbulent conditions. Suitable conditions arise in buildings in multiroom explosions on the passage of the blast through doorways, but can also be created by obstacles closer to the release of the gas. These may be presumed to occur on a release of gas due to a failure of industrial pressure vessels or pipelines.

13.5.4 Structural Response to Blast Loading

Complexity in analyzing the dynamic response of blast-loaded structures involves the effect of high strain-rates, nonlinear inelastic material behavior, uncertainties of blast-load calculations, and time-dependent deformations. Therefore, to simplify the analysis, a number of assumptions related to the response of structures and loads have been proposed and widely accepted. To establish the principles of

this analysis, the structure is idealized as an single-DoF system and the link between the positive duration of the blast load and the natural period of vibration of the structure is established. This leads to blast-load idealization and simplifies the classification of the blast-loading regimes.

13.5.4.1 Elastic Single-Degree-of-Freedom Systems

The simplest discretization of transient problems is by means of the single-DoF approach. The actual structure can be replaced by an equivalent system of one concentrated mass and one weightless spring, representing the resistance of the structure against deformation. Such an idealized system is illustrated in Figure 13.23. The structural mass, M , is under the effect of an external force, $F(t)$, and the structural resistance, R , is expressed in terms of the vertical displacement, y , and the spring constant, K .

The blast load can also be idealized as a triangular pulse having a peak force F_m and positive-phase duration t_d (see Figure 13.23). The forcing function is given as

$$F(t) = F_m \left(1 - \frac{t}{t_d}\right) \quad (13.26)$$

The blast impulse is approximated as the area under the force–time curve, and is given by

$$I = \frac{1}{2} F_m t_d \quad (13.27)$$

The equation of motion of the undamped elastic single-DoF system for a time ranging from 0 to the positive-phase duration, t_d , is given by Biggs (1964) as

$$M\ddot{y} + Ky = F_m \left(1 - \frac{t}{t_d}\right) \quad (13.28)$$

The general solution can be expressed as

$$\begin{aligned} \text{Displacement } y(t) &= \frac{F_m}{K} (1 - \cos \omega t) + \frac{F_m}{K t_d} \left(\frac{\sin \omega t}{\omega} - t \right) \\ \text{Velocity } \dot{y}(t) &= \frac{dy}{dt} = \frac{F_m}{K} \left[\omega \sin \omega t + \frac{1}{t_d} (\cos \omega t - 1) \right] \end{aligned} \quad (13.29)$$

in which ω is the natural circular frequency of vibration of the structure and T is the natural period of vibration of the structure given as

$$\omega = \frac{2\pi}{T} = \sqrt{\frac{K}{M}} \quad (13.30)$$

The maximum response is defined by the maximum dynamic deflection y_m , which occurs at time t_m . The maximum dynamic deflection y_m can be evaluated by setting dy/dt in Equation 13.29 equal to zero, that is, when the structural velocity is zero. The dynamic load factor (DLF) is defined as the ratio of the maximum dynamic deflection y_m to the static deflection y_{st} which would have resulted from the static

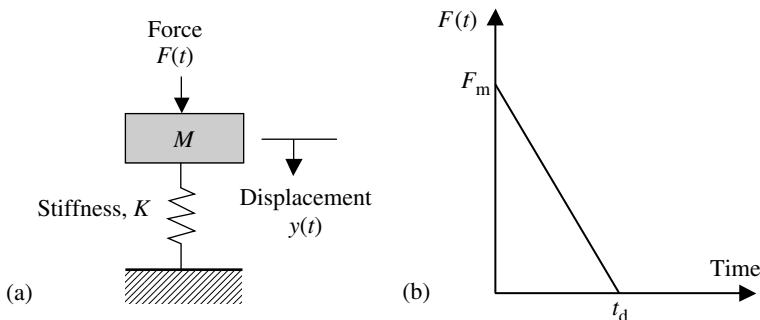


FIGURE 13.23 (a) Single-DoF system and (b) blast loading.

application of the peak load F_m , as follows:

$$DLF = \frac{y_{\max}}{y_{st}} = \frac{y_{\max}}{F_m/K} = \psi(\omega t_d) = \Psi\left(\frac{t_d}{T}\right) \quad (13.31)$$

The structural response to blast loading is significantly influenced by the ratio t_d/T or ωt_d ($t_d/T = \omega t_d/2\pi$). Three loading regimes are categorized as follows:

1. $\omega t_d < 0.4$: impulsive loading regime
2. $\omega t_d < 0.4$: quasi-static loading regime
3. $0.4 < \omega t_d < 40$: dynamic loading regime

13.5.4.2 Elasto-Plastic Single-Degree-of-Freedom Systems

Structural elements are expected to undergo large inelastic deformation under a blast load or high-velocity impact. The exact analysis of dynamic response is then only possible by a step-by-step numerical solution requiring non-linear dynamic finite-element software. However, the degree of uncertainty in both the determination of the loading, and the interpretation of acceptability of the resulting deformation, is such that the solution of a postulated equivalent ideal elasto-plastic single-DoF system (Biggs, 1964) is commonly used. Interpretation is based on the required ductility factor $\mu = y_m/y_e$ (Figure 13.24).

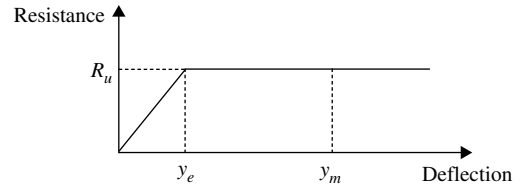


FIGURE 13.24 Simplified resistance function of an elasto-plastic single-DoF system.

For example, a uniform simply supported beam has first mode shape $\phi(x) = \sin \pi x/L$ and the equivalent mass is $M = (1/2)mL$, where L is the span of the beam and m is mass per unit length. The equivalent force corresponding to a uniformly distributed load of intensity p is $F = (2/\pi)pL$. The response of the ideal bilinear elasto-plastic system can be evaluated in closed form for the triangular load pulse comprising rapid rise and linear decay, with maximum value F_m and duration t_d . The result for the maximum displacement is generally presented in chart form (TM 5-1300) as a family of curves for

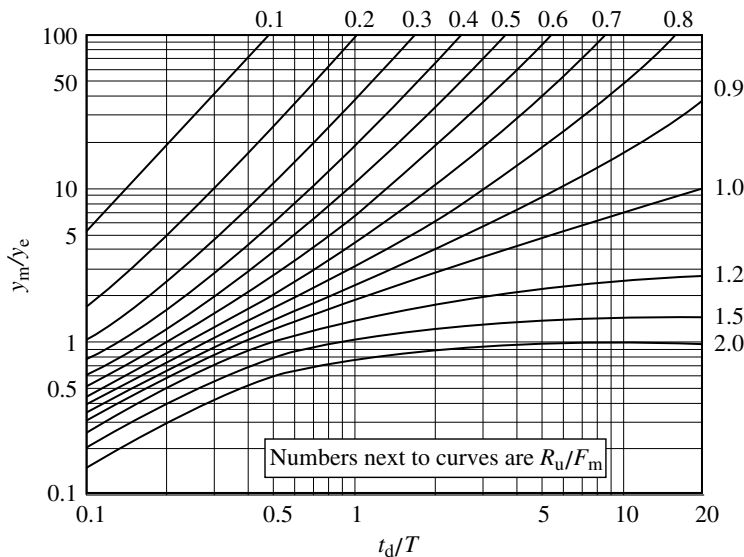


FIGURE 13.25 Maximum response of an elasto-plastic single-DoF system to a triangular load (TM 5-1300).

selected values of R_u/F_m showing the required ductility μ as a function of t_d/T , in which R_u is the structural resistance of the beam and T is the natural period (Figure 13.25).

13.5.5 Material Behaviors at High Strain Rate

Blast loads typically produce very high strain-rates in the range of 100 to 10,000 sec^{-1} . This high straining (loading) rate would alter the dynamic mechanical properties of target structures and, accordingly, the expected damage mechanisms for various structural elements. For reinforced concrete structures subjected to blast effects, the strength of concrete and steel reinforcing bars can increase significantly due to the strain-rate effect. Figure 13.26 shows approximate ranges of the expected strain rates for different loading conditions. It can be seen that the ordinary static strain rate is located in the range of 10^{-6} to 10^{-5} sec^{-1} , while blast pressures normally yield loads associated with strain rates in the range of 100 to 10,000 sec^{-1} .

13.5.5.1 Dynamic Properties of Concrete under High Strain Rates

The mechanical properties of concrete under dynamic loading conditions can be quite different from that under static loads. While the dynamic stiffness does not change very much compared with the static stiffness, the stresses that are sustained for a certain period under dynamic conditions may gain values that are remarkably higher than the static compressive strength (Figure 13.27). Strength magnification factors as high as four in compression and up to six in tension for strain rates in the range of 100 to 1000 sec^{-1} have been reported (Grote et al., 2001).

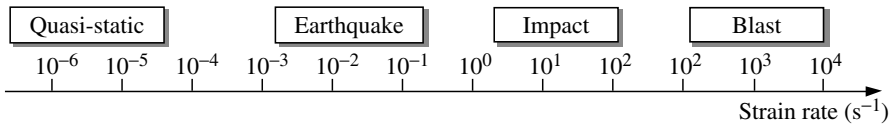


FIGURE 13.26 Strain rates associated with different types of loading.

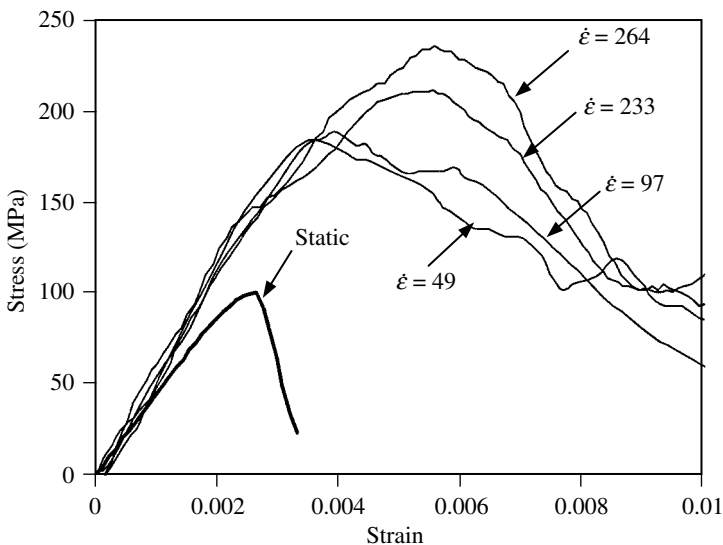


FIGURE 13.27 Stress–strain curves of concrete at different strain rates. (Source: Data from Ngo, T. et al., *Proc. 18th Australasian Conf. on Mechanics of Structures and Materials*, Perth, Australia. With permission.)

For the increase in peak compressive stress (f'_c), a dynamic increase factor (DIF) is introduced in the Comité Euro-International du Béton (CEB-FIP; 1990) model (Figure 13.28) for strain-rate enhancement of concrete as follows:

$$\text{DIF} = \left(\frac{\dot{\epsilon}}{\dot{\epsilon}_s} \right)^{1.026\alpha} \quad \text{for } \dot{\epsilon} \leq 30 \text{ sec}^{-1} \quad (13.32)$$

$$\text{DIF} = \gamma \left(\frac{\dot{\epsilon}}{\dot{\epsilon}_s} \right)^{1/3} \quad \text{for } \dot{\epsilon} > 30 \text{ sec}^{-1} \quad (13.33)$$

where

$\dot{\epsilon}$ = strain rate

$\dot{\epsilon}_s = 30 \times 10^{-6} \text{ sec}^{-1}$ (quasi-static strain rate)

$\log \gamma = 6.156\alpha - 2$

$\alpha = 1/(5 + 9f'_c/f_{co})$

$f_{co} = 10 \text{ MPa} = 1450 \text{ psi}$

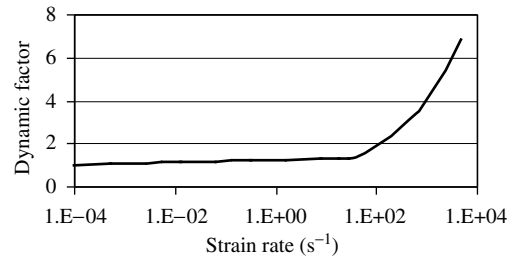


FIGURE 13.28 Dynamic increase factor for peak stress of concrete (CEB-FIP model).

13.5.5.2 Dynamic Properties of Reinforcing Steel under High Strain Rates

Owing to the isotropic properties of metallic materials, their elastic and inelastic response to dynamic loading can easily be monitored and assessed. Norris et al. (1959) tested steel with two different static yield strengths (330 and 278 MPa) under tension at strain rates ranging from 10^{-5} to 0.1 sec^{-1} . Strength increases of 9–21% and 10–23% were observed for the two steel types, respectively. Dowling and Harding (1967) conducted tensile experiments using the tensile version of the Split Hopkinson's Pressure Bar (SHPB) on mild steel using strain rates varying between 10^{-3} and 2000 sec^{-1} . It was concluded from this test series that materials of body-centered cubic (BCC) structure (such as mild steel) showed the greatest strain rate sensitivity, the lower yield tensile strength of mild steel was almost doubled, the ultimate tensile stress was increased by about 50%, the upper yield tensile strength considerably increased, and the ultimate tensile strain decreased by different percentages, depending on the strain rate.

Malvar (1998) also studied the strength enhancement of steel reinforcing bars under the effect of high strain rates. This was described in terms of the DIF, which can be evaluated for different steel grades and for yield stresses, f_y , ranging from 290 to 710 MPa as

$$\text{DIF} = \left(\frac{\dot{\epsilon}}{10^{-4}} \right)^{\alpha} \quad (13.34)$$

where for calculating yield stress $\alpha = \alpha_{fy}$,

$$\alpha_{fy} = 0.074 - 0.04 (f_y/414) \quad (13.35)$$

and for ultimate stress calculation $\alpha = \alpha_{fu}$

$$\alpha_{fu} = 0.019 - 0.009 (f_y/414) \quad (13.36)$$

13.5.6 Failure Modes of Blast-Loaded Structures

Blast-loading effects on structural members may produce both local and global responses associated with different failure modes. The type of structural response depends mainly on the loading rate, the orientation of the target with respect to the direction of the blast wave propagation, and boundary conditions. The general failure modes associated with blast loading can be flexure, direct shear, or punching shear. Local responses are characterized by localized breaching and spalling, and generally

result from the close-in effects of explosions, while global responses are typically manifested as flexural failure.

13.5.6.1 Global Structural Behavior

The global response of structural elements is generally a consequence of transverse (out of plane) loads with long exposure time (quasi-static loading), and is usually associated with global membrane (bending) and shear responses. Therefore, the global response of above-ground reinforced concrete structures subjected to blast loading is referred to as membrane/bending failure.

The second global failure mode to be considered is shear failure. It has been found that under the effect of both static and dynamic loads, four types of shear failure can be identified: diagonal tension, diagonal compression, punching shear, and direct (dynamic) shear (Woodson, 1993). The first two types are common in reinforced concrete elements under static loads, while punching shear is associated with local shear failure; for example, the familiar case is column punching through flat slabs. These shear response mechanisms have relatively minor structural effect in case of blast loading and can be neglected. The fourth type of shear failure is direct (dynamic) shear. This failure mode is primarily associated with transient short duration dynamic loads that result from blast effects, and it depends mainly on the intensity of the pressure waves. The associated shear force is many times higher than the shear force associated with flexural failure modes. The high shear stresses may lead to a direct global shear failure and it may occur very early (within a few milliseconds of shock wave arrival to the facing structure's surface) even prior to any significant bending deformations.

13.5.6.2 Localized Structural Behavior

The close-in effect of an explosion may cause localized shear or flexural failure in the closest structural elements. This depends mainly on the distance between the explosion center and the target, and the relative strength/ductility of the structural elements. The localized shear failure takes the form of localized punching and spalling, which produces low and high-speed fragments. The punching effect is frequently referred to as breaching, which is well known in high-velocity impact applications and in the case of explosions close to the surface of structural members. Breaching failures are typically accompanied by spalling and scabbing of concrete covers, as well as fragments and debris (Figure 13.29).



FIGURE 13.29 Breaching failure due to a close-in explosion of 6000 kg TNT equivalent (photograph by Tuan Ngo).

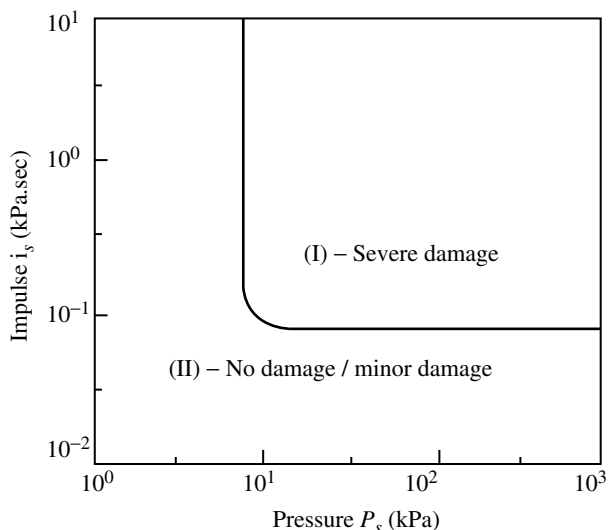


FIGURE 13.30 Typical pressure-impulse (P - I) diagram.

13.5.6.3 Pressure-Impulse (P - I) Diagrams

The P - I diagram is an easy way to mathematically relate a specific damage level to a combination of blast pressures and the corresponding impulses for a particular structural element. An example P - I diagram is given in Figure 13.30. This figure shows the levels of damage of a structural member, in which region (I) corresponds to severe structural damage and region (II) refers to no or minor damage. There are other P - I diagrams that are concerned with human responses to blasts, in which three categories of blast-induced injury are identified as primary, secondary, and tertiary injury (Baker et al., 1983).

13.5.7 Blast Wave-Structure Interaction

The structural behavior of an object or structure exposed to such a wave may be analyzed by dealing with two main issues. Firstly, blast-loading effects, that is, forces that result from the action of the blast pressure; secondly, the structural response, or the expected damage criteria associated with such loading effects. It is important to consider the interaction of the blast waves with target structures. This might be quite complicated in the case of complex structural configurations. However, it is possible to consider some equivalent simplified geometry. Accordingly, in analyzing the dynamic response to blast loading, two types of target structures can be considered: diffraction-type and drag-type structures. As these names imply, the former would be affected mainly by diffraction (engulfing) loading and the latter by drag loading. It should be emphasized that actual buildings will respond to both types of loading and the distinction is made primarily to simplify the analysis. The structural response will depend upon the size, shape, and weight of the target, how firmly it is attached to the ground, and also on the existence of openings in each face of the structure.

13.5.8 Effect of Ground Shocks

Above ground or shallow-buried structures can be subjected to ground shock resulting from the detonation of explosive charges that are on, or close to, the ground surface. The energy imparted to the

ground by the explosion is the main source of ground shock. A part of this energy is directly transmitted through the ground as direct-induced ground shock, while part is transmitted through the air as air-induced ground shock. Air-induced ground shock results when the air-blast wave compresses the ground surface and sends a stress pulse into the ground underlayers. Generally, motion due to air-induced ground shock is maximum at the ground surface and attenuates with depth (TM 5-1300, 1990). The direct-induced shock results from the direct transmission of explosive energy through the ground. For a point of interest on the ground surface, the net experienced ground shock results from a combination of both the air-induced and direct-induced shocks.

13.5.8.1 Loads from Air-Induced Ground Shock

To overcome complications of predicting actual ground motion, one-dimensional wave propagation theory has been employed to quantify the maximum displacement, velocity, and acceleration in terms of the already known blast wave parameters (TM 5-1300). The maximum vertical velocity at the ground surface, V_v , is expressed in terms of the peak incident overpressure, P_{so} , as

$$V_v = \frac{P_{so}}{\rho C_p} \quad (13.37)$$

where ρ and C_p are, respectively, the mass density and the wave seismic velocity in the soil.

By integrating the vertical velocity in Equation 13.37 with time, the maximum vertical displacement at the ground surface, D_v , can be obtained as

$$D_v = \frac{i_s}{1000\rho C_p} \quad (13.38)$$

Accounting for the depth of soil layers, an empirical formula is given by TM 5-1300 to estimate the vertical displacement in meters so that

$$D_v = 0.09W^{1/6}(H/50)^{0.6}(P_{so})^{2/3} \quad (13.39)$$

where W is the explosion yield in 10^9 kg and H is the depth of the soil layer in meters.

13.5.8.2 Loads from Direct Ground Shock

As a result of the direct transmission of the explosion energy, the ground surface experiences vertical and horizontal motions. Some empirical equations were derived (TM 5-1300) to predict the direct-induced ground motions in three different ground media; dry soil, saturated soil, and rock media. The peak vertical displacement in m/sec at the ground surface for rock, $D_{V_{rock}}$ and dry soil, $D_{V_{soil}}$ are given as

$$D_{V_{rock}} = \frac{0.25R^{1/3}W^{1/3}}{Z^{1/3}} \quad (13.40)$$

$$D_{V_{soil}} = \frac{0.17R^{1/3}W^{1/3}}{Z^{2.3}} \quad (13.41)$$

The maximum vertical acceleration, A_v , in m/sec^2 for all ground media is given by

$$A_v = \frac{1000}{W^{1/8}Z^2} \quad (13.42)$$

13.5.9 Technical Design Manuals for Blast-Resistant Design

This section summarizes applicable military design manuals and computational approaches to predicting blast loads and the responses of structural systems. Although the majority of these design guidelines were focused on military applications, this knowledge is relevant for civil design practice.

Structures to Resist the Effects of Accidental Explosions, TM 5-1300 (U.S. Departments of the Army, Navy, and Air Force, 1990): This manual appears to be the most widely used publication by both military and civilian organizations for designing structures to prevent the propagation of explosion, and to provide protection for personnel and valuable equipment. It includes step-by-step analysis and design procedures, including information on such items as (1) blast, fragment, and shock-loading; (2) principles of dynamic analysis; (3) reinforced and structural steel design; and (4) a number of special design considerations, including information on tolerances and fragility, as well as shock isolation. Guidance is provided for the selection and design of security windows, doors, utility openings, and other components that must resist blast and forced-entry effects.

A Manual for the Prediction of Blast and Fragment Loadings on Structures, DOE/TIC-11268 (U.S. Department of Energy, 1992): This manual provides guidance to the designers of facilities subject to accidental explosions and aids in the assessment of the explosion-resistant capabilities of existing buildings.

Protective Construction Design Manual, ESL-TR-87-57 (Air Force Engineering and Services Center, 1989): This manual provides procedures for the analysis and design of protective structures exposed to the effects of conventional (nonnuclear) weapons, and is intended for use by engineers with a basic knowledge of weapons effects, structural dynamics, and hardened protective structures.

Fundamentals of Protective Design for Conventional Weapons, TM 5-855-1 (U.S. Department of the Army, 1986): This manual provides procedures for the design and analysis of protective structures subjected to the effects of conventional weapons. It is intended for use by engineers involved in designing hardened facilities.

The Design and Analysis of Hardened Structures to Conventional Weapons Effects (DAHS CWE, 1998): This new joint services manual, written by a team of more than 200 experts in conventional weapons and protective structures engineering, supersedes U.S. Department of the Army TM 5-855-1, *Fundamentals of Protective Design for Conventional Weapons* (1986), and Air Force Engineering and Services Centre ESL-TR-87-57, *Protective Construction Design Manual* (1989).

Structural Design for Physical Security — State of the Practice Report (Conrath et al., 1995): This report is intended to be a comprehensive guide for civilian designers and planners who wish to incorporate physical security considerations into their designs or building retrofit efforts.

13.5.10 Computer Programs for Blast and Shock Effects

Computational methods in the area of blast effects mitigation are generally divided into those used for the prediction of blast loads on the structure and those for the calculation of structural responses to the loads. Computational programs for blast prediction and structural response use both first-principle and semiempirical methods. Programs using the first-principle method can be categorized into uncouple and couple analyses. The uncouple analysis calculates blast loads as if the structure (and its components) were rigid, and then applies these loads to a responding model of the structure. The shortcoming of this procedure is that, when the blast field is obtained with a rigid model of the structure, the loads on the structure are often overpredicted, particularly if significant motion or the failure of the structure occurs during the loading period.

For a coupled analysis, the blast simulation module is linked with the structural response module. In this type of analysis, the computational fluid mechanics (CFD) model for blast-load prediction is solved simultaneously with the computational solid mechanics (CSM) model for structural response. By accounting for the motion of the structure while the blast calculation proceeds, the pressures that arise due to the motion and failure of the structure can be predicted more accurately. Examples of this type of computer software are AUTODYN, DYNA3D, LS-DYNA, and ABAQUS. [Table 13.8](#) provides a listing of computer programs that are currently being used to model blast effects on structures.

Prediction of the blast-induced pressure field on a structure and its response involves highly nonlinear behavior. Computational methods for blast-response prediction must therefore be validated by comparing calculations to experiments. Considerable skill is required to evaluate the output of the

TABLE 13.8 Examples of Computer Programs Used to Simulate Blast Effects and Structural Response

Name	Purpose and Type of Analysis	Author/Vendor
BLASTX	Blast prediction, CFD ^a	SAIC
CTH	Blast prediction, CFD	Sandia National Laboratories
FEFLO	Blast prediction, CFD	SAIC
FOIL	Blast prediction, CFD	Applied Research Associates, Waterways Experiment Station
SHARC	Blast prediction, CFD	Applied Research Associates, Inc.
DYNA3D	Structural response, CFD (coupled analysis)	Lawrence Livermore National Laboratory (LLNL)
ALE3D	Coupled analysis	Lawrence Livermore National Laboratory (LLNL)
LS-DYNA	Structural response, CFD (coupled analysis)	Livermore Software Technology Corporation (LSTC)
Air3D	Blast prediction, CFD	Royal Military Science College, Cranfield University
CONWEP	Blast prediction (empirical)	U.S. Army Waterways Experiment Station
AUTODYN	Structural response, CFD (coupled analysis)	Century Dynamics
ABAQUS	Structural response, CFD (coupled analysis)	ABAQUS Inc.

^a CFD, computational fluid mechanics.

computer software, both as to its correctness and its appropriateness to the situation modeled; without such judgment, it is possible through a combination of modeling errors and poor interpretation to obtain erroneous or meaningless results. Therefore, successful computational modeling of specific blast scenarios by engineers unfamiliar with these programs is difficult, if not impossible.

13.6 Impact Loading

Impact effects on structures arise over a very broad range of circumstances, from high-velocity missiles or aircraft impact to high-mass ship or vehicle collisions. The requirement may be for the structure to withstand the impact without serious damage, or major inelastic deformation may be permitted.

13.6.1 Structural Impact between Two Bodies — Hard Impact and Soft Impact

Impact loads differ from blast loads in duration, and they are applied to a localized area. Blast loads propagate as a wave front, while an impact load is caused by the force resulting from the collision between a moving object and a structure. Impact loading can be classified as either hard or soft, depending upon the relative characteristics of the impactor and the target structure. Impulsive loading can be considered to be a special case of soft impact. Soft impact occurs when the impactor deforms substantially with respect to a hard structure, and a portion of the impactor's kinetic energy is absorbed by the impactor's plastic deformation. For hard impact, the striking object is rigid and the kinetic energy is transmitted to the target and absorbed by deformation and damage in the structure.

Impact problems essentially involve all three fundamental conservation laws: conservation of mass, conservation of momentum, and conservation of energy. These three laws are outlined in the following equations (Zukas, 1990), respectively

$$\int_v \rho \, dV = \text{const} \quad (13.43)$$

$$F = m \, dv/dt \quad (13.44)$$

$$\sum E_i + \sum \frac{1}{2} \rho v_i^2 = \sum E_f + \sum \frac{1}{2} \rho v_f^2 + W \quad (13.45)$$

where

ρ = material density

V = volume

F = force

m = mass

v = velocity

E = stored internal energy

W = work

i, f = initial and final states

Upon impact, stresses and strains are induced in the target material. The layers of particles in the target are compressed upon contact, creating compressive stress. When the compression stress between two layers is equal to the applied pressure, compression supports the entire pressure. Through this process, stress waves are developed similar to the shock waves generated by blast loading. The stress waves propagate throughout the material at a speed inherent to that material and reflect multiple times as interfaces are reached.

Various types of stress waves are developed, depending on the energy imparted into the target. The impact velocity determines the strain rate, mode of response, and the type of impact damage (Zukas et al., 1982). If the impact is below a certain level, only elastic stress waves are generated. Higher velocity impacts create inelastic stress waves. Historically, impact has been considered a localized phenomenon that may cause plastic deformation and/or failure of the target and/or the impactor. During an impact event, some or all of the kinetic energy of the impactor is transferred to the target. This process is a function of the wave propagation in the target, the impactor's deformation of the target upon contact, and the contact velocity. Because the impact has been considered to be localized, the local behavior deformation and penetration has been the prime consideration.

Impact causes elastic and plastic stress waves, and propagation through the structural thickness can cause failure by spalling. Such effects usually occur within microseconds of the impact, and may be referred to as the early time response. The overall dynamic response of the structure usually occurs on a timescale several orders of magnitude longer, and can thus reasonably be decoupled from the early time response and subjected to an initial check against spalling.

Impact imparts impulsive loadings to a structure, producing responses within the structure. Three different types of solutions to the impact problem are available: theoretical (analytical), semiempirical, and numerical. Theoretical methods provide closed-form solutions for the governing partial differential

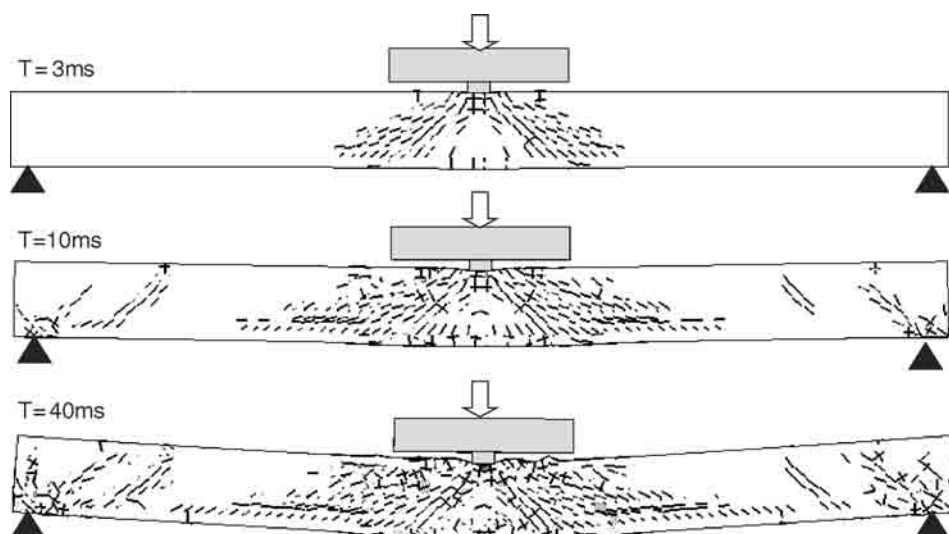


FIGURE 13.31 Transient deformation of a reinforced concrete beam under impact at midspan. (Source: Data from Ngo, T. et al., *Proc. of 18th Australasian Conference on the Mechanics of Structures and Materials*, Perth, Australia. 2004a. With permission.)

equations. Semiempirical methods rely on extensive test data to produce a curve-fit solution for a class of similar impact problems. Numerical solutions replace the continuous system with discrete domains and treat the problem as it progresses over time (Figure 13.31).

13.6.2 Example — Aircraft Impact

Design loads resulting from aircraft impacts are governed by the absorption of kinetic energy from the aircraft by the building at its maximum deflection. These loads are limited by the yield, buckling, and crushing of the aircraft. Total impact load $F(t)$ at the interface of the collapsing aircraft and the building is given by

$$F(t) = F_c + \mu[m(t)]V(t) \quad (13.46)$$

in which $m(t)$ is the mass of the aircraft reaching the building per unit time; μ is a coefficient for change in momentum (which can be taken conservatively as one); F_c is the crushing load, a constant which can be determined from the design acceleration for failure of the aircraft; and $V(t)$ is the velocity of the aircraft.

Figure 13.32 compares the impact loads produced by a Boeing 707-320 and a Boeing 767, which hit the World Trade Center. It should be noted that World Trade Center was designed to resist the equivalent impact of a Boeing 707.

Figure 13.33 compares the impact loads produced by different aircraft. The peak loads and the duration of loading for different aircraft are given in Table 13.9. These loads were calculated by the method suggested by Kar in 1979 (Mendis and Ngo, 2002).

Kinsella and Jowett (1981) suggested a more accurate method in which the crash event is treated as a combination of the separate time-dependent impacts of the aircraft's frame and engines. The frame is classed as a soft missile which will suffer considerable deformation, and a finite difference method of calculation is employed to describe its perfectly plastic impact. The engines, which are considered separately, are assumed to constitute a much harder missile which will undergo little deformation. The results obtained by this method for a Phantom F4 aircraft are shown in Figure 13.34. This method gave a maximum load of 233 MN compared with the 145 MN obtained from Kar's method.

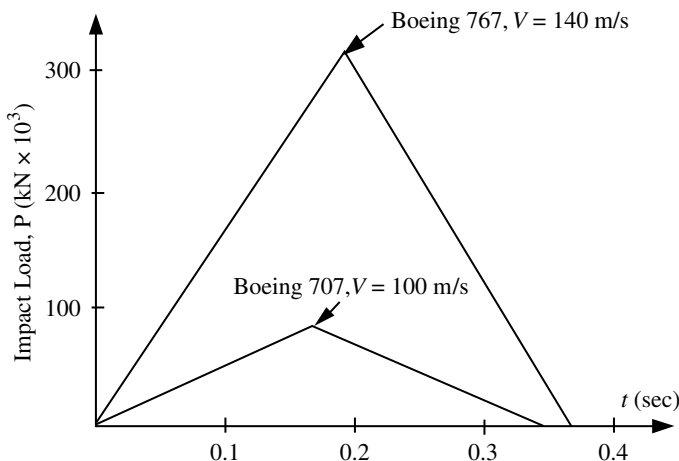


FIGURE 13.32 Impact load–time history for aircraft impact.

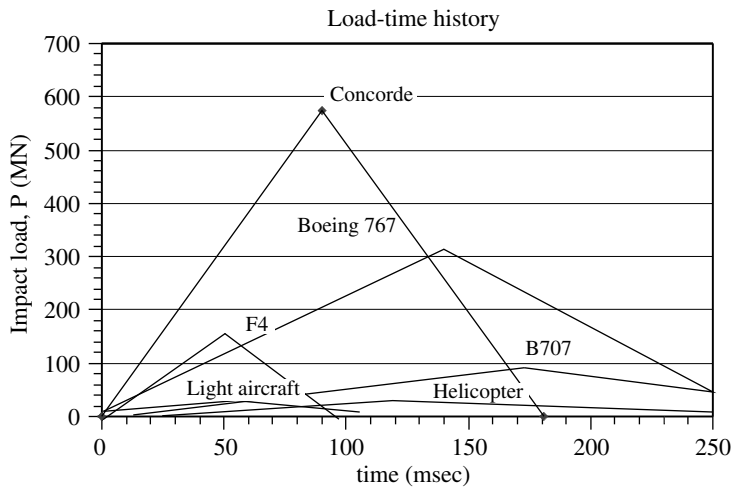


FIGURE 13.33 Comparison of impact loads for different aircraft.

TABLE 13.9 Examples of Aircraft and Peak Impact Loads

Aircraft	Mass (kg)	Length (m)	Velocity V_0 (m/sec)	Peak Load (MN)	Duration (msec)
Aust. SUPAPUP light aircraft	340	5.7	51.3	4.6	111
Westland Sea King helicopter	9,500	17	63.9	19.6	266
Boeing 707-320	91,000	40	103.6	92	386
Phantom F4 aircraft	22,000	19.2	210	145	91
Boeing 767-300 ER	187,000	54.9	140	320	362
Supersonic Concorde	138,000	62.2	344	568	181

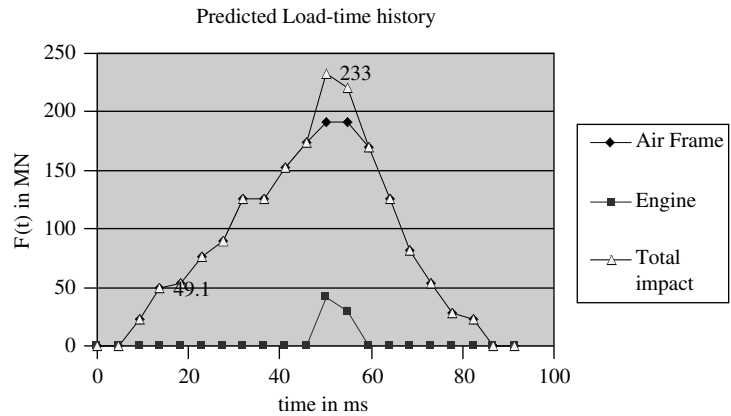


FIGURE 13.34 Impact loads of Phantom F4 aircraft. (Source: Data from Kinsella, K. and Jowett, J. 1981. *The Dynamic Load Arising from a Crashing Military Combat Aircraft*, Safety and Reliability Directorate, Wigshaw, U.K. With permission.)

13.7 Floor Vibration

13.7.1 Introduction

Annoying floor vibrations may be caused by occupant activities. Walking, dancing, jumping, aerobics, and audience participation at music concerts and sporting events are some prime examples of occupant activities that create floor vibrations. The operation of mechanical equipment is another cause for concern. Heating, ventilation, and air-conditioning systems, if not properly isolated, can cause serious vibration problems. The current trend towards longer spans and lighter floor systems has resulted in a significant increase in the number of floor vibration complaints by building owners and occupants.

Most of the sources contributing to reported human discomfort rest on the floor system itself. However, human activities or machinery off a floor can cause significant floor vibrations. On more than one occasion, aerobics on one floor of a high-rise building has been reported to cause vibration discomfort on another level in the building. The vibrations caused by automobiles on parking levels below have been reported to disrupt sensitive laboratory work on upper floors. Other equipment and activities off the floor that can contribute to a floor vibration problem are ground or air traffic, drilling, the impact of falling objects, and other construction-related events.

When the natural frequency of a floor system is close to a forcing frequency and the deflection of the system is significant, motion will be perceptible, and perhaps even annoying. Perception is related to the activity of the occupants: a person at rest or engaged in quiet work will tolerate less vibration than a person performing an active function, such as dancing or aerobics. If a floor system dissipates the imparted energy in a very short period of time, the motion is likely to be perceived as less annoying. Thus, the damping characteristics of the system affect acceptability.

In design guidelines for floor vibration analysis, limits are stated as a minimum natural frequency of a structural system. These limits depend on the permissible peak accelerations (as a fraction of gravitational acceleration) on the mass affected by an activity, the environment in which the vibration occurs, the effectiveness of interaction between connected structural components, and the degree of damping, among other factors.

Recently, excessive floor vibrations have become a common problem due to a decrease in the natural frequency at which buildings vibrate due, in turn, to increased floor spans and a decrease in the amount of damping and mass used in standard construction practice, because of the availability of stronger and lighter materials. Some methods have been developed in the recent past to check the floor vibrations of structures. These methods are summarized in this section. More details can be found in the texts given in the list of references.

13.7.2 Types of Vibration

13.7.2.1 Walking

A walking person's foot touching the floor causes a vibration of the floor system. This vibration may be annoying to other persons sitting or lying in the same area, such as an office, a church, or a residence. Although more than one person may be walking in the same area at the same time, their footsteps are normally not synchronized. Therefore, the analysis is based on the effect of the impact of the individual walking.

13.7.2.2 Rhythmic Activities

In some cases, more than a few people may engage in a coordinated activity that is at least partially synchronized. Spectators at sporting events, rock concerts, and other entertainment events often move in unison in response to music, a cheer, or other stimuli. In these cases, the vibration is caused by many people moving together, usually at a more or less constant tempo.

The people disturbed by the vibration may be those participating in the rhythmic activity, or those in nearby part of the structure engaged in a more quiet activity. The people engaged in the rhythmic activity

have higher level of tolerance for the induced vibrations, while those nearby will have a lower level of tolerance.

13.7.2.3 Mechanical Equipment

Mechanical equipment may produce a constant impulse at a fixed frequency, causing the structure to vibrate.

13.7.2.4 Analysis Methods

Because the nature of the input varies for these three types of loads, each of the three requires a somewhat different solution. However, all cases require knowledge of an important response parameter of the floor system, its natural frequency of vibration, and all three analysis methods are based on finding a required minimum frequency.

13.7.3 Natural Frequency of Vibration

The natural frequency of a floor system is important for two reasons. It determines how the floor system will respond to forces causing vibrations. It is also important in determining how human occupants will perceive the vibrations. It has been found that certain frequencies set up resonance with internal organs of the human body, making these frequencies more annoying to people.

Figure 13.35 shows the human sensitivity over a range of frequencies during various activities. The human body is most sensitive to frequencies in the range of 4 to 8 Hz. This range of natural frequencies is commonly found in typical floor systems. Recommended acceleration limits for vibrations due to rhythmic activities are given in Table 13.10.

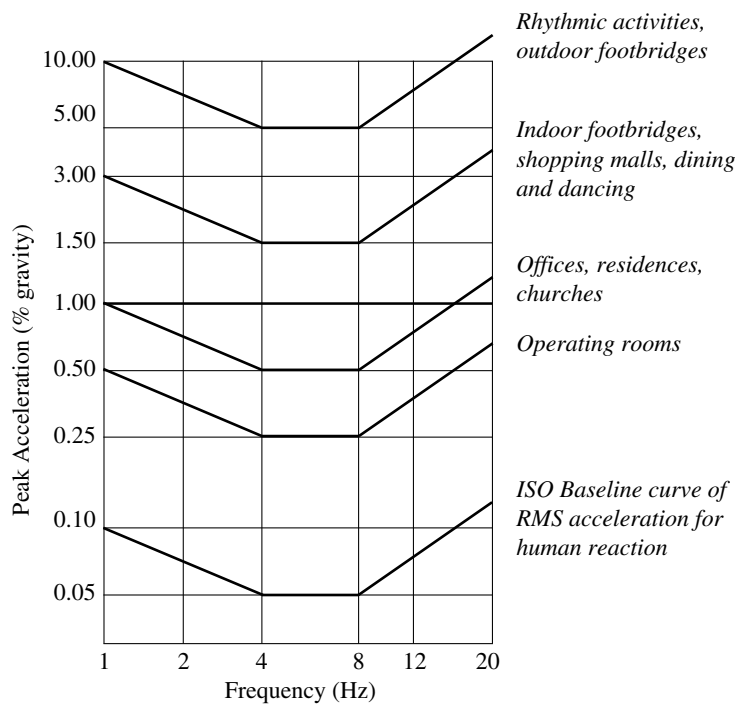


FIGURE 13.35 Recommended permissible peak vibration acceleration levels acceptable for human comfort while in different environments. (Source: Data from Mast, R.F., Vibration of precast prestressed concrete floors, PCI J., Nov–Dec, 2001. With permission.)

TABLE 13.10 Recommended Acceleration Limits for Vibrations Due to Rhythmic Activities

Occupancies Affected by the Vibration	Acceleration Limit (%g)
Office and residential	0.4–0.7
Dining and weightlifting	1.5–2.5
Rhythmic activity only	4–7

Source: Data from Alen, D.E., Building vibration from human activities, *Concr. Int.*, 66–73, 1990.

13.7.3.1 Computing the Natural Frequency

The natural frequency of a vibrating beam is determined by the ratio of its stiffness to its mass (or weight). The deflection of simple-span beam is also dependent on its weight and stiffness. A simple relationship exists between the self-weight deflection and the natural frequency of a uniformly loaded simple-span beam on rigid supports:

$$f_n = 0.18\sqrt{g/\Delta_j} \tag{13.47}$$

where

f_n = natural frequency in the fundamental mode of vibration

g = acceleration due to gravity

Δ_j = instantaneous simple-span deflection of floor panel due to dead load plus actual live load

13.7.3.2 Computing Deflection

The equation for the deflection Δ_j for a uniformly loaded simple-span beam is

$$\Delta_j = \frac{5wl^4}{384EI} \tag{13.48}$$

where

l = span length of member

I = gross moment of inertia, for prestressed concrete members

Many vibration problems are more critical when the mass (or weight) is low.

For continuous spans of equal length, the natural frequency is the same as for simple spans. This may be understood by examining Figure 13.36. For static loads, all spans deflect downward simultaneously, and continuity significantly reduces the deflection. But for vibration, one span deflects downward while the adjacent spans deflect upward. An inflection point exists at the supports, and the deflection and natural frequency are the same as for a simple span.

For unequal continuous spans, and for partially continuous spans with supports, the natural frequency may be increased by a small amount.

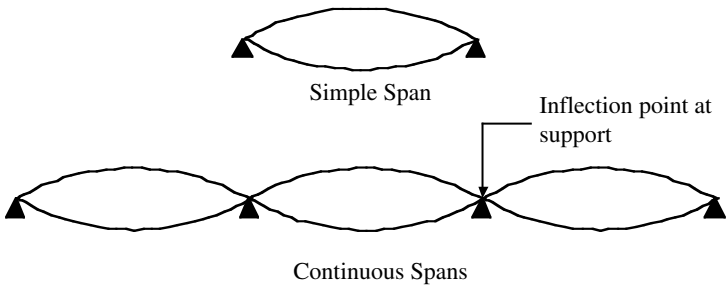


FIGURE 13.36 Natural frequency of simple and continuous spans.

13.7.3.3 Damping

Damping determines how quickly a vibration will decay and die out. This is important because human perception and tolerance of vibration or motion is dependent on how long it lasts. Damping of a floor system is highly dependent on the nonstructural items (partitions, ceilings, furniture, and other items) present. The modal damping ratio of a bare structure undergoing low-amplitude vibrations can be very low, on the order of 1%. Nonstructural elements may increase this damping ratio up to 5% (see Table 13.11). It must be appreciated that the results of a vibration analysis are highly influenced by the choice of the assumed damping, which can vary widely.

13.7.3.4 Resonance

Resonance occurs when the frequency of a forcing input nearly matches the natural frequency of a system. In order to avoid excessive amplification of vibration, the natural frequency must be higher than the frequency of the input forces by an amount related to the damping of the floor system.

13.7.4 Vibration Caused by Walking

Vibrations caused by walking can often be objectionable in lighter constructions of wood or steel. Because of the greater mass and stiffness of concrete floor systems, vibrations caused by walking are seldom a problem in these systems. However, when designing concrete floor systems of long span, the serviceability requirement on vibrations may become critical.

13.7.4.1 Minimum Natural Frequency

People are most sensitive to vibrations when engaged in sedentary activities while seated or lying. Much more vibration is tolerated by people who are standing, walking, or active in other ways. Thus, different criteria are given for offices, residences, and churches than for shopping malls and footbridges.

An empirical formula, based on the resonant effects of walking, has been developed to determine the minimum natural frequency of a floor system needed to prevent disturbing vibrations caused by walking:

$$f_n \geq 2.861 \ln \left(\frac{K}{\beta W} \right) \tag{13.49}$$

where

K = a constant, given in Table 13.11

β = modal damping ratio

W = weight of area of floor panel affected by a point load

13.7.5 Design for Rhythmic Excitation

Rhythmic excitation may occur when a group of people exercise or respond to a musical beat. Because a group is acting in unison at a constant frequency, the input forces are much more powerful than those produced by random walking. Resonance can occur when the input frequency is at or near the

TABLE 13.11 Values of K and β

Occupancies Affected by the Vibration	K (kN)	β
Offices, residences, churches	58	0.02 ^a ; 0.03 ^b ; 0.05 ^c
Shopping malls	20	0.02
Outdoor footbridges	8	0.01

^a For floors with few nonstructural components and furnishings, open work areas, and churches.

^b For floors with nonstructural components and furnishings, and cubicles.

^c For floors with full-height partitions.

Source: Data from Alen, D.E. and Murray, T.M., Design criterion for vibrations due to walking, *Am. Inst. Steel Const. Eng. J.*, Fourth Quarter, 117–129, 1993

fundamental frequency of vibration, and so the fundamental frequency of the floor must be sufficiently higher than the input frequency as to prevent resonance.

13.7.5.1 Harmonics

A harmonic of frequency is any higher frequency that is equal to the fundamental frequency multiplied by an integer. For instance, if the frequency of an input excitation is 2.5 Hz, the harmonics are $2.5 \times 2 = 5$ Hz, $2.5 \times 3 = 7.5$ Hz, and so on. If the fundamental frequency of a floor system is equal to a harmonic of the exciting frequency, resonance may occur.

This process is less efficient than one which is in resonance striking at each cycle of vibration. Nevertheless, the 2.5 Hz forcing frequency can cause resonance in the 5 Hz fundamental frequency due to the input force striking every second cycle in the fundamental frequency.

Higher harmonics should not be confused with higher modes of vibration. The second mode of vibration of a simple span has a frequency four times the fundamental frequency. This high a frequency is almost never excited. Harmonics refers to the forcing frequency, compared with the fundamental mode of vibration.

13.7.5.2 Minimum Natural Frequency

The following design criterion for minimum natural frequency for a floor subjected to rhythmic excitation is based on the dynamic response of the floor system to dynamic loading. The objective is to avoid the possibility of being close to a resonant condition:

$$f_n \geq f \sqrt{1 + \frac{k}{a_0/g} \frac{\alpha_i w_p}{w_t}} \quad (13.50)$$

where

f = forcing frequency = $(i) (f_{\text{step}})$

f_{step} = step frequency

i = number of harmonic = 1, 2, 3

k = a dimensionless constant (1.3 for dancing, 1.7 for a lively concert or sport events, 2.0 for aerobics)

α_i = dynamic coefficient

a_0/g = ratio of peak acceleration limited to the acceleration due to gravity

W_p = effective distributed weight per unit area of participants

W_t = effective total distributed weight per unit area of participants (weight of participants plus weight of floor system).

The natural frequency of the floor system, f_n , can be found as discussed previously.

13.7.6 Example — Vibration Analysis of a Reinforced Concrete Floor

A concrete floor of a tall building is analyzed in this example. The plan view and structural configuration of the building are shown in Figure 13.37. Perimeter columns are spaced at 12 m centers and are connected by spandrel beams to support the facade. The example floor will be used for aerobic exercises and needs to be checked for vibration. Aerobic exercises are usually undertaken in the range of 2 to 2.75 Hz, with a maximum value in the order of 3.0 Hz. Ideally aerobic

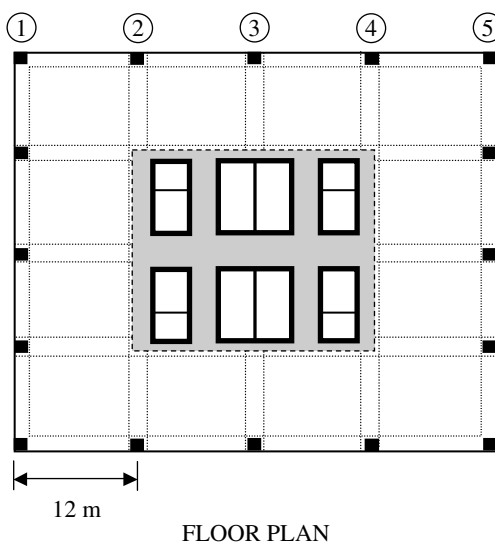


FIGURE 13.37 Structural configuration.

exercise floors should be designed so that the floor's natural frequency exceeds the third harmonic by a factor of 1.2, resulting in $f_n > 1.2 \times 3 \times 2.75 = 9.9$ Hz. This is not always achievable in practice, especially for long span floors that have the natural frequency in the range from 4 to 8 Hz. Hence, a floor with natural frequency greater than 7.5 Hz is considered a minimum standard, although in some cases floor vibrations may be quite noticeable.

The modal analysis of the floor system was carried out with the assumed damping factor β of 2% (see Table 13.11). It was found that the floor natural frequency is 6.75 Hz, which may result in some problems in floor vibration. To reduce the vibration problem the following approaches can be used:

- Reduce mass (normally not very effective)
- Increase damping (e.g., using dampers)
- Reduce vibration transmission (stiffening joists at columns may reduce transmission)

Bibliography

- AASHTO *Guide Specifications for Seismic Isolation Design*. American Association of State Highway and Transportation Officials (AASHTO), Washington, 1991.
- Alen, D.E., Building vibration from human activities, *Concr. Int.*, 66–73, 1990.
- Alen, D.E. and Murray, T.M., Design criterion for vibrations due to walking, *Am. Inst. Steel Const. Eng. J.*, Fourth Quarter, 117–129, 1993.
- Asian Model Concrete Code (ACMC)*, International Committee on Concrete Model Code for Asia (ICCMC), 2001.
- AS/NZS 1170.2, *Structural Design Actions — Wind*, Standards Australia/New Zealand, 2002.
- Baker, W.E., Cox, P.A., Westine, P.S., Kulesz, J.J., and Strehlow, R.A. 1983. *Explosion Hazards and Evaluation*, Elsevier, New York.
- Biggs, J.M. 1964. *Introduction to Structural Dynamics*, McGraw-Hill, New York.
- Booth, E., Ed. 1994. *Concrete Structures in Earthquake Regions*, Longmans, Harlow, Essex.
- Brode, H.L., Numerical solution of spherical blast waves, *J. Appl. Phys.*, 26, 766–775, 1955.
- Burdekin, M., Ed. 1996. *Seismic Design of Steel Structures after Northridge and Kobe*, SECED/Institution of Structural Engineers, Rotterdam.
- Casciati, F. 1996. Active control of structures in European seismic areas. In *Proceedings of the Eleventh World Conference on Earthquake Engineering*, Pergamon Press, Oxford.
- Chen, P.W. and Robertson, L.E., Human perception thresholds of horizontal motion, *J. Struct. Div.*, 92, 8, 1681–1695, 1972.
- Chen, S.S. 1987. *Flow-Induced Vibration of Circular Cylindrical Structures*, Hemisphere, Washington.
- Chopra, A.K. 1981. *Dynamics of Structures, A Primer*, Earthquake Engineering Research Institute, Oakland, CA.
- Chopra, A.K. 2001. *Dynamics of Structures: Theory and Applications to Earthquake Engineering*, Prentice Hall, Upper Saddle River, NJ.
- Chopra, A.K. and Goel, R.K., Capacity–demand–diagram methods based on inelastic design spectrum, *Earthquake Spectra*, 15, 4, 637–656, 1999.
- Clough, R.W. and Penzien, J. 1993. *Dynamics of Structures*, McGraw-Hill, New York.
- Collins, J.A. 1993. *Failure of Materials in Mechanical Design*, 2nd ed., Wiley Interscience, New York.
- Comité Euro-International du Béton 1990. *CEB-FIP Model Code 1990*, Redwood Books, Trowbridge, Wiltshire.
- Conrath, E.J., Krauthammer, T., Marchand, K.A. and Mlakar, P.F. 1995. *Structural Design for Physical Security — State of the Practice Report*, American Society of Civil Engineers, ASCE, New York.
- DAHS CWE 1998. *Technical Manual — Design and Analysis of Hardened Structures to Conventional Weapons Effects*, U.S. Army Corps of Engineers (CEMP-ET), Washington.
- Davenport, A.G., Gust loading factors, *J. Struct. Div.*, 93, 11–34, 1967.
- Deaves, D.M. and Harris, R.I. 1978. *A Mathematical Model of the Structure of Strong Winds*, Report 76, Construction Industry Research and Information Association, London, U.K.

- DOE/TIC-11268. 1992. *A Manual for the Prediction of Blast and Fragment Loadings on Structures*, U.S. Department of Energy, Washington.
- Dowling, A.R. and Harding, J. 1967. Tensile properties of mild steel under high strain rates. In *Proceedings of the First HERF Conference*, University of Denver, Denver.
- Ellis, B.R. and Crowhurst, D. 1991. The response of several LPS maisonettes to small gas explosions. *IStructE/BRE Seminar: Structural Design for Hazardous Loads: The Role of Physical Tests*.
- ENV. 1998. *Design Provisions for Earthquake Resistance of Structures*, CEN (European Committee for Standardisation), Brussels (various dates), ENV 1994-8.
- ESL-TR-87-57. 1989. *Protective Construction Design Manual*, U.S. Air Force Engineering and Services Center.
- Fajfar, P., A nonlinear analysis method for performance-based seismic design, *Earthquake Spectra*, 16, 3, 573–592, 2000.
- FEMA 306/307/308 - NEHRP. 1998. *Evaluation and Repair of Earthquake Damaged Concrete and Masonry Buildings*, USA.
- FEMA 273/274 - NEHRP. 2000. *Guidelines for Seismic Rehabilitation of Buildings*, 1997 Edition, FEMA 356/357, USA.
- FEMA 350-354. 2000.
- FEMA 368/369 - NEHRP. 2000 *Recommended Provisions for Seismic Regulations for New Buildings and Other Structures*, USA.
- Grote, D., Park, S., and Zhou, M., Dynamic behaviour of concrete at high strain rates and pressures, *J. Impact Eng.*, 25, 869–886, 2001.
- Gulkan, P. and Sozen, M.A., Inelastic responses of reinforced concrete structures to earthquake motions, *J. Am. Concrete Inst.*, 71, 12, 604–610, 1974.
- Gupta, A.K. 1990. *Response Spectrum Method in Seismic Analysis and Design of Structures*, Blackwell, Oxford.
- Holmes, J. 2001. *Wind Loading of Structures*, Spon Press, London.
- Irwin, A.W., Human response to dynamic motion of structures, *Struct. Engineer*, 56A, 1978.
- Izzudin, B.A. and Smith, D.L. 1996. Response of offshore structures to explosion loading. In *Proceedings of the Sixth Offshore and Polar Engineering Conference*, pp. 323–330, Los Angeles, CA.
- Kabori, T. 1996. Active and hybrid structural control research in Japan. In *Proceedings of the Eleventh World Conference on Earthquake Engineering*, Pergamon Press, Oxford.
- Kar, K., Impactive effects of tornado missiles and aircraft, *J. Struct. Div.*, 105 (11), 2243–2260, 1979.
- Kinsella, K. and Jowett, J. 1981. *The Dynamic Load Arising from a Crashing Military Combat Aircraft*, Safety and Reliability Directorate, Wigshaw, U.K.
- Krauthammer, T. 1994. Buildings subjected to short duration dynamic effects. In *Proceedings of First Cradington Conference*, November, Building Research Establishment, Bedford, England.
- Longinow, A. and Mniszewski, K.R. 1996. Protecting buildings against vehicle bomb attacks. In *Practice Periodical on Structural Design and Construction*, pp. 51–54, ASCE, New York.
- Maguire, J.R. and Wyatt, T.A. 1999. *Dynamics — An Introduction for Civil and Structural Engineers*, Thomas Telford, London.
- Malvar, L.J., Review of static and dynamic properties of steel reinforcing bars, *ACI Mater. J.*, 95(5), 609–616, 1998.
- Mast, R.F., Vibration of precast prestressed concrete floors, *PCI J.*, Nov–Dec, 2001.
- Mays, C.G. and Smith, P.D. 1995. *Blast Effects on Buildings*, TTL, London.
- Melbourne, W. 1988, Definition of wind pressure on tall buildings, In *Proceedings of the Third International Conference on Tall Buildings*, Chicago, USA.
- Melbourne, W. 1992. Towards an engineering wind model. In *Course Notes on Wind Engineering*, Monash University, Melbourne.
- Mendis, P.A. and Ngo, T. 2002. Assessment of tall buildings under blast loading and aircraft impact. In *Toward a Better Built Environment, Innovation, Sustainability and Information Technology*, International Association of Bridge and Structural Engineering, Australia.

- Mills, C. A. 1987. The design of concrete structure to resist explosions and weapon effects. In *Proceedings of the First International Conference on Concrete for Hazard Protections*, pp. 61–73.
- Milne-Thompson, L.M. 1968. *Theoretical Hydrodynamics*, McMillan, New York.
- Muga, B. and Wilson, J. 1970. *Dynamic Analysis of Ocean Structures*, Plenum Press, New York.
- Newmark, N.M. and Hansen, R.J. 1961. Design of blast resistant structures. In *Shock and Vibration Handbook*, Vol. 3, Harris, C.M. and Crede, C.E., Eds., McGraw-Hill, New York.
- Ngo, T., Mendis, P., Hongwei, M., and Mak, S. 2004a. High strain rate behaviour of concrete cylinders subjected to uniaxial compressive impact loading. In *Proceedings of 18th Australasian Conference on the Mechanics of Structures and Materials*, Perth, Australia.
- Ngo, T., Mendis, P., and Itoh, A. 2004b. Modelling reinforced concrete structures subjected to impulsive loading using the Modified Continuum Lattice Model. In *Proceedings of 18th Australasian Conference on the Mechanics of Structures and Materials*, Perth, Australia.
- Norris, G.H., Hansen, R.J., Holly, M.J., Biggs, J.M., Namyet, S., and Minami, J.K. 1959. *Structural Design for Dynamic Loads*, McGraw-Hill, New York.
- Pappin, J.W. 1991. Design of foundation and soil structures for seismic loading. In *Cyclic Loading of Soils*, M.P. O'Reilly and S.F. Brown, eds., pp. 306–366, Blackie, London.
- Park, R. and Paulay, T. 1975. *Reinforced Concrete Structures*, Wiley, New York.
- Paulay, T. and Priestley, M.J.N. 1992. *Seismic Design of Reinforced Concrete and Masonry Buildings*, Wiley, New York.
- Paulay, T. 1993. Simplicity and confidence in seismic design. In *Fourth Mallet-Milne Lecture*, Wiley, Chichester.
- Penelis, G. and Kappos, A. 1996. *Earthquake Resistant Concrete Structures*, E. & F.N. Spon, London.
- Priestley, M.J.N. and Kowalsky, M.J., Direct displacement-based seismic design of concrete buildings, *Bull. N.Z. Soc. Earthquake Eng.*, 33 (4), 421–444, 2000.
- Sachs, P. 1978. *Wind Forces in Engineering*, Pergamon Press, Oxford.
- Soong, T.T. 1996. Active research control in the US. In *Proceedings of the 11th World Conference on Earthquake Engineering*, Pergamon Press, Oxford.
- Soong, T. and Constantinou, M., Eds. 1994. *International Centre for Mechanical Sciences*, Springer, Wien.
- Tamura, T., Reliability on CFD estimation for wind–structure interaction problems, *J. Wind Eng. Ind. Aerodyn.*, 81, May–Jul, 117–143, 1999.
- Tiejens, O.G. and Prandtl, L. 1957. *Applied Hydro & Aeromechanics*, Dover Publications, New York.
- TM 5-1300. 1990. *The Design of Structures to Resist the Effects of Accidental Explosions*, Technical Manual. U.S. Department of the Army, Navy, and Air Force, Washington DC.
- TM 5-855-1. 1986. *Fundamentals of Protective Design for Conventional Weapons*, U.S. Department of the Army, Washington.
- Uniform Building Code*, Vol. 2. Structural Engineering Design Provisions, International Conference Building Officials, Whittier, 2000.
- Vickery, B.J., On the reliability of gust loading factors, *Civil Eng. Trans.*, 13, 1–9, 1971.
- Wolf, J.P. 1985. *Dynamic Soil–Structure Interaction*, Prentice Hall, Englewood Cliffs, NJ.
- Wolf, J.P. 1994. *Foundation Vibration Analysis Using Simple Physical Models*, Prentice Hall, Englewood Cliffs, NJ.
- Wood, H.O. and Neumann, Fr., Modified Mercalli intensity scale of 1931, *Bull. Seis. Soc. Am.*, 21, 277–283, 1931.
- Woodson, S.C. 1993. *Response of slabs: in plane forces and shear effects*. In *Structural Concrete Slabs under Impulsive Loads*, T. Krauthammer, Ed., pp. 51–68. Research Library, U.S. Army Engineer Waterways Experiment Station, Vicksburg, MS.
- Yamada, M., Goto, T. 1975. The criteria to motions in tall buildings. In *Proceedings of Pan Pacific Tall Buildings Conference*, pp. 233–244, Hawaii.
- Zukas, J.A. 1990. *High Velocity Impact Dynamics*, Wiley, New York.
- Zukas, J.A., Nicholas, S.T. and Swift, H.F. 1982. *Impact Dynamics*. Wiley, New York.

14

Reinforced Concrete Structures

14.1	Introduction	14-1
	Basic Concepts • Natural Frequencies • Viscous Damping • Damped Harmonic Excitation	
14.2	Analytical Models	14-6
	Model-Based Simulation • Flexural Behavior • Shear Behavior • Time-History Analysis	
14.3	Beams under Harmonic Excitations	14-18
	Mechanical Properties • Design for Machine Vibration	
14.4	Design for Explosions/Shocks	14-21
	Column • Shear Walls	

Y.L. Mo
University of Houston

Summary

This chapter concerns vibration and shock in reinforced concrete structures, addressing how to design reinforced concrete structures that will be subjected to vibration or shock, for example, due to a missile attack. The chapter is intended to apply vibration theory to concrete structures. Section 14.1 describes the fundamental properties of vibration theory. Section 14.2 proposes analytical models for reinforced concrete structures that are subjected to flexure, shear, and dynamic loading. Section 14.3 discusses reinforced concrete beams under harmonic excitations, including mechanical properties and designs for machine vibration. Section 14.4 indicates the step-by-step procedure for designing reinforced concrete columns or walls that will be subjected to seismic loads or shocks, respectively.

14.1 Introduction

14.1.1 Basic Concepts

Reinforced concrete structures are capable of free and forced vibration when disturbed from their equilibrium configuration (see Chapter 1 and Chapter 2). Free vibration takes place when a structure vibrates under the action inherent to the structure itself without being impressed by external forces. The structure under *free vibration* vibrates at its *natural frequency*, which is one of the dynamic properties of the structure. Forced vibration takes place under the excitation of an external force and at the frequency of the exciting force, which is independent of the natural frequency of the structure. When the frequency of the exciting force coincides with the natural frequency of a structure, resonance occurs and dangerously large amplitudes may result. Therefore, the calculation of natural frequency and the examination of resonance are of practical importance. Also, in reality, the influence of viscous dampening on a vibrating structure should be taken into account. In this section, the fundamental dynamic properties are introduced.

14.1.2 Natural Frequencies

An undamped single-degree-of-freedom (single-DoF) system (Figure 14.1) is used to explain natural frequency. Figure 14.1(c) shows the free-body diagram with inclusion of the inertial force $m\ddot{y}$. This force is equal to the mass, m , multiplied by the acceleration, \ddot{y} , and should always be directed negatively with respect to the corresponding coordinate; note that k is the spring constant of the system. The summation of forces in the y -direction directly gives the following equation of motion:

$$m\ddot{y} + ky = 0 \quad (14.1)$$

To solve Equation 14.1, we assume

$$y = A \cos wt \quad (14.2)$$

or

$$y = B \sin wt \quad (14.3)$$

where A and B are constants depending on the initiation of the motion and w is a quantity denoting a physical characteristic of the system. The substitution of Equation 14.2 or Equation 14.3 into Equation 14.1 gives

$$(-mw^2 + k)A \cos wt = 0 \quad (14.4)$$

If this equation is to be satisfied at any time, the factor in parentheses must be equal to zero:

$$-mw^2 + k = 0 \quad (14.5)$$

The positive root of Equation 14.5

$$w = \sqrt{\frac{k}{m}} \text{ rad/sec} \quad (14.6)$$

is known as the circular or angular natural frequency of the system (Paz, 1997; Clough and Penzien, 1993).

Note: The Greek symbol ω is commonly used rather than w to denote this natural frequency in the literature, which is expressed in rad/sec and is called “angular” natural frequency.

The “cyclic” natural frequency f is usually expressed in hertz (Hz) or cycles per second (cps). The quantity w differs from the natural frequency f only by the constant factor, 2π . The period, T , is usually expressed in seconds per cycle (i.e., the value reciprocal to the natural frequency, f). Therefore, it gives

$$f = \frac{1}{T} = \frac{w}{2\pi} \quad (14.7)$$

Example 14.1

Determine the natural frequency of the system shown in Figure 14.2, consisting of a weight of $W = 230 \text{ kN}$ attached to a horizontal reinforced concrete cantilever beam through the coil spring k_2 .

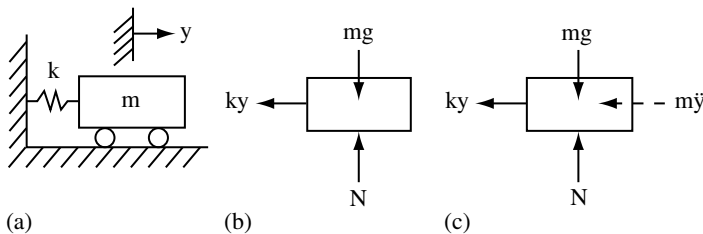


FIGURE 14.1 Free-body diagrams: (a) showing single-DoF; (b) showing only external forces; (c) showing external and inertial forces.

The cantilever beam has a cross section of 305 mm (h) \times 152 mm (b), modulus of elasticity $E = 30 \text{ kN/mm}^2$, and a length $L = 3 \text{ m}$. The coil spring has stiffness $k_2 = 200 \text{ N/mm}$.

Solution

The deflection, Δ , at the free end of a cantilever beam that is acted upon by a static force, P , at the free end is given by

$$\Delta = \frac{PL^3}{3EI}$$

The corresponding spring constant, k_1 , is then

$$k_1 = \frac{P}{\Delta} = \frac{3EI}{L^3}$$

where $I = (1/12)bh^3$ (for rectangular section) when the contribution of reinforcing bars is neglected. The cantilever and the coil spring of this system are connected as springs in series. Consequently, the equivalent spring constant is

$$\frac{1}{k_e} = \frac{1}{k_1} + \frac{1}{k_2}$$

Substituting corresponding numerical values, we obtain

$$I = \frac{1}{12} \times 152(305)^3 = 3.59 \times 10^8 \text{ mm}^4$$

$$k_1 = \frac{3 \times 30,000 \times 3.59 \times 10^8}{(3000)^3} = 1197 \text{ N/mm}$$

and

$$\frac{1}{k_e} = \frac{1}{1197} + \frac{1}{200}$$

$$k_e = 171 \text{ N/mm}$$

The natural frequency for this system is then given by Equation 14.6 as

$$\omega = \sqrt{k_e/m} \quad (m = W/g \text{ and } g = 9.8 \text{ m/sec}^2)$$

$$\omega = \sqrt{171 \times 9.8/230}$$

$$\omega = 2.7 \text{ rad/sec}$$

or, using Equation 14.7

$$f = 0.43 \text{ Hz}$$

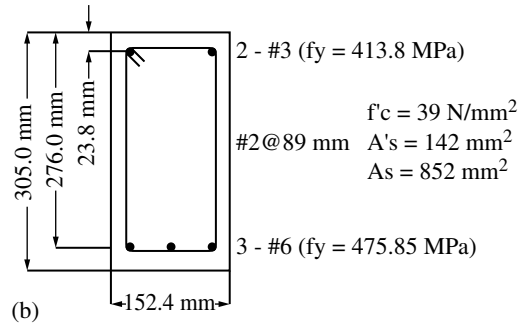
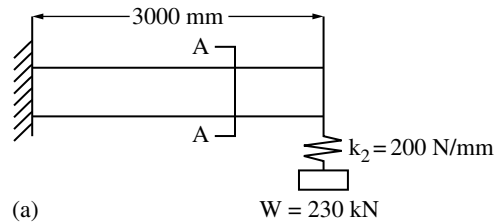


FIGURE 14.2 System for Example 14.1.

14.1.3 Viscous Damping

Let us assume that we have modeled a structural system as a simple oscillator with viscous damping, as shown in Figure 14.3. In this figure, m and k are the mass and spring constant of the oscillator, respectively, and c is the viscous *damping coefficient* (or *damping constant*). The summation of forces in

the y -direction gives the differential equation of motion.

$$m\ddot{y} + c\dot{y} + ky = 0 \tag{14.8}$$

To solve Equation 14.8, we try $y = C e^{pt}$. Substituting this function into Equation 14.8 results in the equation

$$mCp^2 e^{pt} + cCp e^{pt} + kC e^{pt} = 0 \tag{14.9}$$

After cancellation of the common factors, Equation 14.9 reduces to an equation called the characteristic equation for the system, given by

$$mp^2 + cp + k = 0 \tag{14.10}$$

The roots of this quadratic equation are

$$p_1, p_2 = -\frac{c}{2m} \pm \sqrt{\left(\frac{c}{2m}\right)^2 - \frac{k}{m}} \tag{14.11}$$

For a system oscillating with critical damping, the expression under the radical in Equation 14.11 is equal to zero, that is

$$\left(\frac{c_{cr}}{2m}\right)^2 - \frac{k}{m} = 0 \tag{14.12}$$

$$c_{cr} = 2\sqrt{km} \tag{14.13}$$

where c_{cr} designates the *critical damping* value (Clough and Penzien, 1993; Paz, 1997).

In general, the damping of the system is expressed as

$$c = \xi c_{cr} \tag{14.14}$$

where ξ is the *damping ratio* of the system.

Note: Often the symbol ζ is used instead of ξ to denote the damping ratio.

The dampening value depends on structural materials. According to Dowrick (1987), the values for concrete structures are listed in Table 14.1. It can be seen from this table that for reinforced and prestressed concrete the values are 5 and 2%, respectively.

Example 14.2

A reinforced concrete beam consists of a weight of 5.0 kN and a stiffness of $k = 4.0$ kN/cm. Find

- 1. the undamped natural frequency
- 2. the damping coefficient

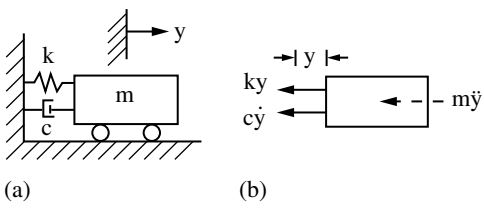


FIGURE 14.3 (a) Viscous damped oscillator; (b) free-body diagram.

TABLE 14.1 Typical Damping Ratios for Concrete Structures

Type of Construction	Damping ξ , % of Critical
Concrete frame, with all walls of flexible construction	5
Concrete frame, with stiff cladding and all internal walls flexible	7
Concrete frame, with concrete or masonry shear walls	10
Concrete and/or masonry shear wall buildings	10
Prestressed concrete	2

Notes: (1) The term *frame* indicates beam and column bending structures as distinct from shear structures. (2) The term *concrete* includes both reinforced and prestressed concrete in buildings. For isolated prestressed concrete members such as in bridge decks, damping values less than 5% may be appropriate, e.g., a value of 1 to 2% may apply if the structure remains substantially uncracked.

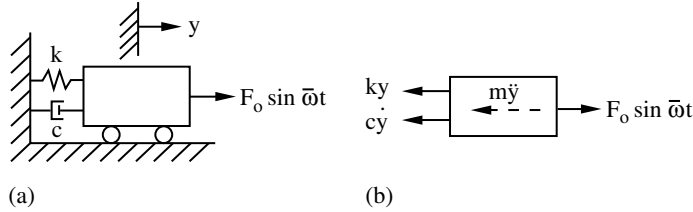


FIGURE 14.4 (a) Damped oscillator harmonically excited; (b) free-body diagram.

Solution

1. $w = \sqrt{k/m} = \sqrt{(4.0 \text{ kN/cm} \times 980 \text{ cm/sec}^2)/5.0 \text{ kN}} = 28.0 \text{ rad/sec.}$
2. $c = \xi c_{cr} = 0.05 \times 2 \times \sqrt{(5.0 \times 4.0)/980} = 14 \text{ N sec/cm.}$

14.1.4 Damped Harmonic Excitation

Now consider the case of one-DoF system in Figure 14.4, vibration due to an external load of a sine function under the influence of viscous damping. The differential equation of motion is obtained by equating to zero the sum of the forces in the free-body diagram of Figure 14.4(b). Hence,

$$m\ddot{y} + c\dot{y} + ky = F_0 \sin \bar{\omega}t \quad (14.15)$$

The total response is then obtained by summing the complementary solution and the particular solution

$$y(t) = e^{-\xi \bar{\omega} t} (A \cos w_D t + B \sin w_D t) + \frac{y_{st} \sin(\bar{\omega} t - \theta)}{\sqrt{(1 - r^2)^2 + (2r\xi)^2}} \quad (14.16)$$

where r is the frequency ratio that is equal to forced vibration frequency, $\bar{\omega}$, divided by natural frequency, w .

Note: A further discussion of this topic is found in Chapter 2.

By examining the transient component of the response, it may be seen that the presence of the exponential factor, $e^{-\xi \bar{\omega} t}$, will cause this component to vanish, leaving only the steady-state motion, Y , which is given by the second term of Equation 14.16.

The ratio of the steady-state amplitude of Y to the static deflection y_{st} , defined above, is known as the *dynamic magnification factor*, D .

$$D = \frac{Y}{y_{st}} = \frac{1}{\sqrt{(1 - r^2)^2 + (2r\xi)^2}} \quad (14.17)$$

D varies with the frequency ratio, r , and the damping ratio, ξ . Equation 14.17 is plotted in Figure 14.5 (Paz, 1997; Clough and Penzien, 1993). It can be seen from this figure that $0.8 \leq r \leq 1.2$ is in the resonance zone. Therefore, for design, $r > 1.2$ or $r < 0.8$ is required to avoid resonance.

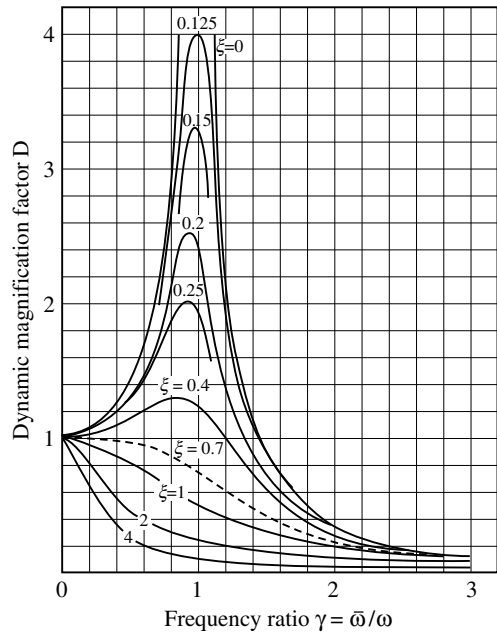


FIGURE 14.5 Dynamic magnification factor as a function of the frequency ratio for various amounts of damping.

14.2 Analytical Models

14.2.1 Model-Based Simulation

When a structure is analyzed for its vibrational characteristics, it first must be presented by a simple model that reflects its mechanical properties adequately. In many analyses, mass is assumed to be concentrated at the nodes of the models. By using this assumption, a single-story structure can be simplified as a single-DoF system subjected to a time-varying force, $F(t)$. In general, dynamic models of reinforced concrete structures depend on the structural systems. Figure 14.6 indicates the structural systems and the corresponding dynamic models (Mo, 1994).

14.2.2 Flexural Behavior

Using the trilinear theory (Mo, 1992), the primary curve (the load–deflection curve) of a reinforced/ prestressed concrete beam can be determined. The trilinear theory is described as follows. To find the load–deflection curve of a beam, first the moment–curvature relationship of each section needs to be determined. The trilinear moment–curvature relationship is shown in Figure 14.7. The first branch of the trilinear curve represents the behavior of the reinforced concrete section until flexural cracking (M_c, ψ_c). The second branch describes the behavior from the cracking until the yielding of the longitudinal steel (M_y, ψ_y). The third branch gives the postyield behavior until flexural failure (M_u, ψ_u). For a given cross section, the shape of the moment–curvature curve can be determined by using the following equations. Basically, the parabola–rectangle stress–strain curve of concrete specified in the CEB code (1978) and the elastic–plastic stress–strain curve of steel are used in the computation.

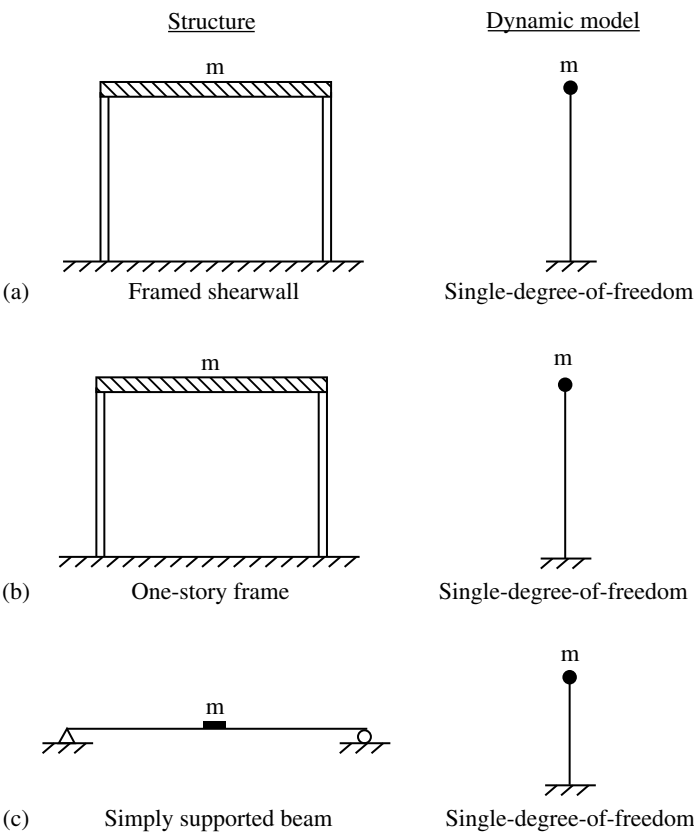


FIGURE 14.6 Structures and corresponding dynamic models.

Moment–curvature curve:

1. Cracking state

$$M_c = \frac{bh^2}{6}f_r = \frac{bh^2}{6}(7.5\sqrt{f'_c}) \quad (14.18)$$

where

$$\psi_c = \frac{M_c}{EI} \quad (14.19)$$

and

M_c = cracking moment

f'_c = concrete compressive strength in psi

f_r = concrete rupture strength in psi

ψ_c = cracking curvature

b = beam width

h = beam depth

E = concrete Young's modulus

I = moment of inertia

2. Yielding state (Figure 14.8)

$$\epsilon_c = \epsilon_y \frac{x_y}{d - x_y} \quad (14.20)$$

$$\epsilon_{sc} = \epsilon_y \frac{x_y - d'}{d - x_y} \quad (14.21)$$

$$M_y = k_1 f'_c b x_y (d - 0.375 x_y) + \frac{x_y - d'}{x_y} \epsilon_c (E_s - E_c) A'_s (d - d') \quad (14.22)$$

and

$$\psi_y = \frac{\epsilon_c}{x_y} \quad (14.23)$$

where

$$k_1 = \frac{\epsilon_c}{\epsilon_0} \left(1 - \frac{1}{3} \frac{\epsilon_c}{\epsilon_0} \right) \quad (14.24)$$

M_y = yielding moment

y_y = yielding curvature

ϵ_{sc} = compression steel strain

ϵ_c = concrete strain when tension steel yields

ϵ_y = steel yielding strain

d = effective depth

d' = distance between surface of concrete compression block and center of compression steel

x_y = distance between surface of concrete compression block and neutral axis when tension steel yields

A'_s = area of compression steel

E_s = steel Young's modulus

E_c = concrete Young's modulus

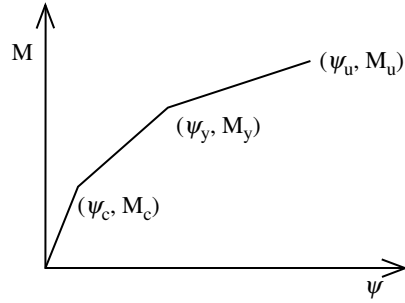


FIGURE 14.7 Trilinear moment–curvature curve.

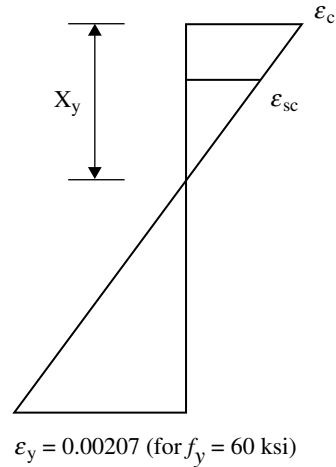


FIGURE 14.8 Strain diagram at yielding state.

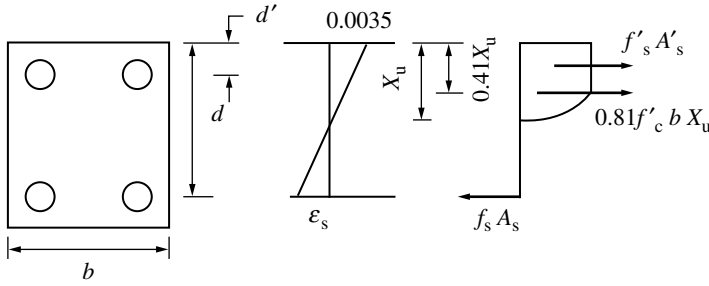


FIGURE 14.9 Stress and strain diagrams at ultimate state.

3. Ultimate state (Figure 14.9)

If

$$x_u \geq d'$$

then

$$M_u = 0.81f'_c b x_u (d - 0.41x_u) + \frac{x_u - d'}{x_u} \times 0.0035(E_s - E_c)A'_s(d - d') \quad (14.25a)$$

If

$$x_u < d'$$

then

$$M_u = f_s A_s (d - 0.41x_u) + \frac{d' - x_u}{x_u} \times 0.0035 E_s A'_s (d' - 0.41x_u) \quad (14.25b)$$

$$\psi_u = \frac{0.0035}{x_u} \quad (14.26)$$

where

M_u = ultimate moment

ψ_u = curvature corresponding to ultimate moment

x_u = distance between surface of concrete compression block and neutral axis at ultimate state

f_s = steel stress at ultimate state

A_s = area of tension steel

Load–deflection curve:

Once the trilinear moment–curvature is found, we can convert it into the load–deflection curve (Figure 14.10).

$$M = \frac{P}{2} \frac{L}{2}, \quad \therefore P = \frac{4M}{L} \quad (14.27)$$

where

M = moment

P = load

L = beam length

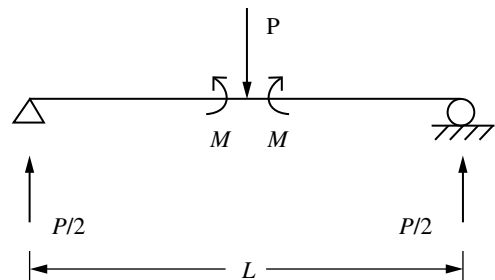


FIGURE 14.10 Simple beam with a concentrated load.

Curvature diagram:

1. Cracking state (Figure 14.11)

$$\theta_c = \frac{1}{2} \frac{L}{2} \frac{M_c}{EI} = \frac{M_c L}{4EI} \quad (14.28)$$

$$\begin{aligned} \delta_c &= \theta_A \frac{L}{2} - \frac{1}{3} \frac{L}{2} \theta_A = \frac{2}{3} \frac{L}{2} \theta_A \\ &= \frac{M_c L^2}{12EI} \end{aligned} \quad (14.29)$$

where

θ_c = rotation at point A at cracking state

δ_c = midspan deflection at cracking state

2. Yielding state (Figure 14.12)

$$\begin{aligned} \theta_y &= (\text{area of triangle}) + (\text{area of trapezoid}) \\ &= \frac{1}{2} L_1 \psi_c + \frac{1}{2} (\psi_c + \psi_y) L_2 \end{aligned} \quad (14.30)$$

$$\begin{aligned} \delta_y &= (\text{first moment of triangle}) + (\text{first moment of trapezoid}) \\ &= \frac{2}{3} L_1 \frac{1}{2} L_1 \psi_c + L_3 \frac{1}{2} (\psi_c + \psi_y) L_2 = \frac{1}{3} \psi_c L_1^2 + \frac{1}{2} (\psi_c + \psi_y) L_2 L_3 \end{aligned} \quad (14.31)$$

where

$$L_3 = L_1 + \frac{\psi_c L_2 \frac{L_2}{2} + (\psi_y - \psi_c) \frac{L}{2} \frac{2L_2}{3}}{\psi_c L_2 + \frac{1}{2} L_2 (\psi_y - \psi_c)} \quad (14.32)$$

θ_y = rotation at point A at yielding state

δ_y = midspan deflection at yielding state

3. Ultimate state (Figure 14.13)

$$\begin{aligned} \theta_u &= (\text{area of triangle}) + (\text{area of first trapezoid}) + (\text{area of second trapezoid}) \\ &= \frac{1}{2} L_1 \psi_c + \frac{1}{2} (\psi_c + \psi_y) L_2 + \frac{1}{2} (\psi_y + \psi_u) L_4 \end{aligned} \quad (14.33)$$

δ_u = (first moment of triangle) + (first moment of first trapezoid)
+ (first moment of second trapezoid)

$$\begin{aligned} &= \frac{2}{3} L_1 \frac{1}{2} L_1 \psi_c + L_3 \frac{1}{2} (\psi_c + \psi_y) L_2 + L_5 \frac{1}{2} (\psi_y + \psi_u) L_4 \\ &= \frac{1}{3} \psi_c L_1^2 + \frac{1}{2} (\psi_c + \psi_y) L_2 L_3 \\ &\quad + \frac{1}{2} (\psi_y + \psi_u) L_4 L_5 \end{aligned} \quad (14.34)$$

where

$$L_3 = L_1 + \frac{\psi_c L_2 \frac{L_2}{2} + (\psi_y - \psi_c) \frac{L_2}{2} \frac{2}{3} L_2}{\psi_c L_2 + \frac{1}{2} L_2 (\psi_y - \psi_c)} \quad (14.35)$$

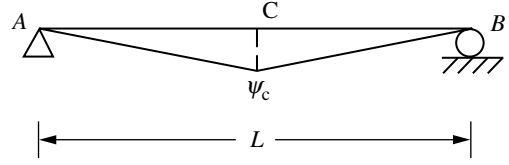


FIGURE 14.11 Curvature diagram at cracking state.

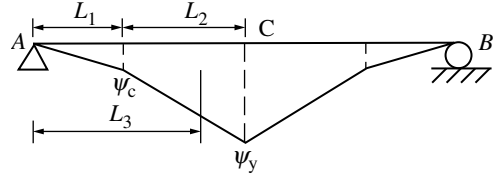


FIGURE 14.12 Curvature diagram at yielding state.

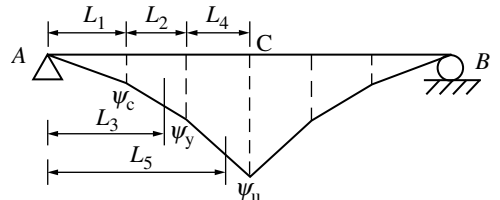


FIGURE 14.13 Curvature diagram at ultimate state.

$$L_5 = L_1 + L_2 + \frac{\psi_y L_4 \frac{L_4}{2} + (\psi_u - \psi_y) \frac{L_4}{2} \frac{2}{3} L_4}{\psi_y L_4 + \frac{1}{2} L_4 (\psi_u - \psi_y)} \quad (14.36)$$

θ_u = rotation at a point A at ultimate state

δ_u = midspan deflection at ultimate state

In this section, the maximum concrete strain at ultimate state (ϵ_{cu}) is assumed to be 0.0035 according to the CEB code (1978). If the ACI code (2002) is employed, the value is 0.003. However, in seismic structures there will be more stirrups. In these situations, reinforced concrete beams are confined. Therefore, the maximum concrete strain at ultimate state for *confined concrete* can be used as follows (Dowrick, 1987):

$$\epsilon_{cu} = 0.003 + 0.02 \left(\frac{b}{l_c} \right) + \left(\frac{\rho_v f_{yv}}{138} \right)^2 \quad (14.37)$$

where

b = beam width

l_c = distance from the critical section to the point of contraflexure

ρ_v = ratio of volume of confining steel (including the compression steel) to volume of concrete confined

f_{yv} = yielding stress of confining steel

14.2.3 Shear Behavior

Structural walls in a frame building should be so proportioned that they possess the necessary stiffness needed to reduce the relative inter-story distortions caused by explosion-induced motions. Such walls are termed structural (or shear) walls because their behavior is governed by shear if the ratio of height to length is less than unity. Their additional function is to reduce the possibility of damage to nonstructural elements that most buildings contain.

Buildings stiffened by structural walls are considerably more effective than rigid frame buildings with regard to damage control, overall safety, and integrity of the structure. This performance is due to the fact that structural walls are considerably stiffer than regular frame elements and thus can respond to or absorb the greater lateral forces induced by the earthquake motions, while controlling inter-story drift.

The past three decades saw a rapid development of knowledge regarding shear in reinforced concrete. Various rational models that are based on the smeared-crack concept can satisfy Navier's three principles of mechanics of materials (i.e., they satisfy stress equilibrium, strain compatibility, and constitutive laws of materials). These rational or mechanics-based models on the "smeared-crack level" (in contrast to the "discrete-crack level" or "local level") include: the compression field theory (CFT) (Vecchio and Collins, 1981); the rotating-angle softened truss model (RA-STM) (Belarbi and Hsu, 1994, 1995; Pang and Hsu 1995); the fixed-angle softened truss model (FA-STM) (Pang and Hsu, 1996; Hsu and Zhang, 1997; Zhang and Hsu, 1998); the softened membrane model (SMM) (Hsu and Zhu, 1999; Zhu, 2000); and the cyclic SMM (Mansour, 2001).

Vecchio and Collins (1981) proposed the earliest rational theory, CFT, to predict the nonlinear behavior of cracked reinforced concrete membrane elements. However, the CFT is unable to take into account the tension stiffening of the concrete in the prediction of deformations because the tensile stress of concrete was assumed to be zero.

The RA-STM, a rational theory developed at the University of Houston (UH) in 1994–1995, has two advantages over the CFT. (1) The tensile stress of concrete is taken into account so that the deformations can be correctly predicted. (2) The average stress–strain curve of steel bars embedded in concrete is derived on the “smeared crack level” so that it can be correctly used in the equilibrium and compatibility equations, which are based on continuous materials.

By 1996, the UH group reported that the FA-STM was capable of predicting the “concrete contribution” (V_c) by assuming the cracks to be oriented at the fixed angle.

Other significant advancements include the improvements on the softened truss models (rotating-angle and fixed-angle). As they were, these models could predict the ascending response curves of shear panels, but not the post-peak descending curves. By incorporating two new Hsu/Zhu ratios into the FA-STM, a new SMM was established (Hsu and Zhu, 1999; Zhu, 2000), which can satisfactorily predict entire response curves, including both the ascending and the descending branches.

More recently, Mansour et al. (2001a) tested 15 reinforced concrete panels under reversed cyclic stresses. Tests results showed that the orientation of the steel grids in a panel has an important effect on the shear stiffness, the shape of the hysteretic loops, the shear ductility, and the energy dissipation capacity of the panel. The cyclic SMM proposed by Mansour et al. (2001a) is able to predict rationally the pinching effect in the hysteretic loops, the shear ductility, and the energy dissipation capacity of the panels. In this chapter, only RA-STM will be introduced, as described below.

14.2.3.1 Principle of Transformation

The stresses in a membrane element are best analyzed by the principle of stress transformation (Hsu, 1993). Figure 14.14(a) shows a concrete element in the stationary l – t coordinate system, defined by the directions of the longitudinal and transverse steel. To find the three stress components in various directions, a rotating d – r coordinate system is introduced in Figure 14.14(b). The d – r axes have been rotated counterclockwise by an angle of α with respect to the stationary l – t axes. The three stress components in this rotating coordinate system are σ_d , σ_r , and τ_{dr} (or τ_{rd}). The relationship between the rotating stress components, σ_d , σ_r , and τ_{dr} , and the stationary stress components, σ_l , σ_t , and τ_{lt} , is the stress transformation. This relationship is a function of the angle α .

The relationship between the rotating d – r axes and the stationary l – t axes is shown by the transformation geometry in Figure 14.14(c). A positive unit length on the l axis will have projections of $\cos \alpha$ and $-\sin \alpha$ on the d and r axes, respectively. A positive unit length on the t axis should give

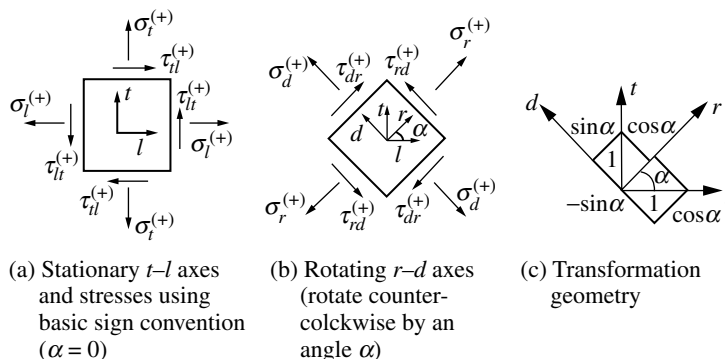


FIGURE 14.14 Transformation of stresses.

projections of $\sin \alpha$ and $\cos \alpha$. Hence, the rotation matrix $[R]$ is

$$[R] = \begin{bmatrix} \cos \alpha & \sin \alpha \\ -\sin \alpha & \cos \alpha \end{bmatrix} \quad (14.38)$$

The relationship between the stresses in the l - t coordinate $[\sigma_{lt}]$ and the stresses in the d - r coordinate $[\sigma_{dr}]$ is

$$[\sigma_{lt}] = [R]^T [\sigma_{dr}] [R] \quad (14.39)$$

where

$$[\sigma_{lt}] = \begin{bmatrix} \sigma_l & \tau_{lt} \\ \tau_{tl} & \sigma_t \end{bmatrix} \quad (14.40)$$

$$[\sigma_{dr}] = \begin{bmatrix} \sigma_d & \tau_{dr} \\ \tau_{rd} & \sigma_r \end{bmatrix} \quad (14.41)$$

If the d - r axes are defined as the principal axes, τ_{dr} must vanish. Introducing the reinforced concrete sign convention, performing the matrix multiplications and noticing that $\tau_{lt} = \tau_{tl}$ and $\tau_{dr} = \tau_{rd}$ gives the following equations when only the concrete struts are considered.

$$\sigma_{lc} = \sigma_d \cos^2 \alpha + \sigma_r \sin^2 \alpha \quad (14.42)$$

$$\sigma_{tc} = \sigma_d \sin^2 \alpha + \sigma_r \cos^2 \alpha \quad (14.43)$$

$$\tau_{ltc} = (-\sigma_d + \sigma_r) \sin \alpha \cos \alpha \quad (14.44)$$

14.2.3.2 Equilibrium Equations

When one studies a concrete element reinforced orthogonally with longitudinal and transverse steel bars, as shown in Figure 14.15(a), the three stress components σ_l , σ_t , and τ_{lt} are the applied stresses on the reinforced concrete element viewed as a whole. The stresses on the concrete strut itself are denoted as σ_{lc} , σ_{tc} , and τ_{ltc} , as shown in Figure 14.15(b). The longitudinal and transverse steel provide the smeared stresses of $\rho_l f_l$ and $\rho_t f_t$, as shown in Figure 14.15(c).

It is significant to recognize the difference between the two sets of stresses: σ_l , σ_t , and τ_{lt} for the reinforced concrete element and σ_{lc} , σ_{tc} , and τ_{ltc} for concrete struts. Both sets of stresses (σ_l , σ_t , τ_{lt} and σ_{lc} , σ_{tc} , τ_{ltc}) satisfy the transformation equations. In summing the concrete stresses and the steel stresses in the l and t directions, a fundamental assumption is made according to Hsu (1993). It is assumed that the

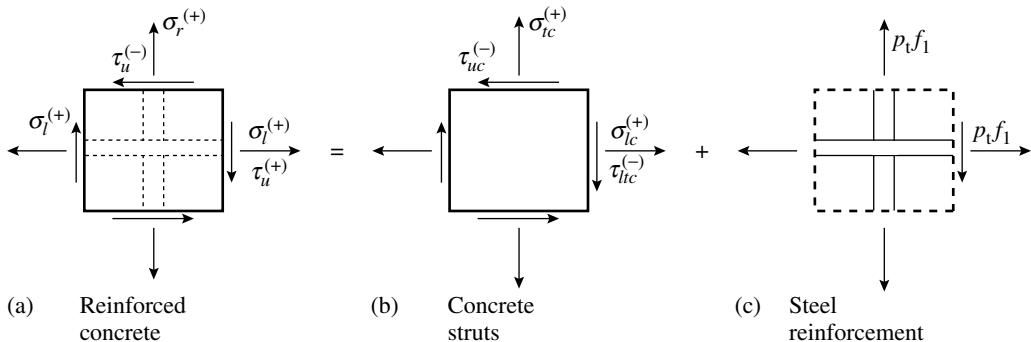


FIGURE 14.15 Stress condition in reinforced concrete.

steel reinforcement can take only axial stresses. Any possible dowel action is neglected. Hence, the superposition principle for concrete and steel becomes valid and gives the general equilibrium equations for reinforced concrete:

$$\sigma_l = \sigma_d \cos^2 \alpha + \sigma_r \sin^2 \alpha + \rho_l f_l \quad (14.45)$$

$$\sigma_t = \sigma_d \sin^2 \alpha + \sigma_r \cos^2 \alpha + \rho_t f_t \quad (14.46)$$

$$\tau_{lt} = (-\sigma_d + \sigma_r) \sin \alpha \cos \alpha \quad (14.47)$$

14.2.3.3 Compatibility Equations

The same principle of transformation for stresses can be applied to strains. Therefore, the following compatibility equations can be derived:

$$\varepsilon_l = \varepsilon_d \cos^2 \alpha + \varepsilon_r \sin^2 \alpha \quad (14.48)$$

$$\varepsilon_t = \varepsilon_d \sin^2 \alpha + \varepsilon_r \cos^2 \alpha \quad (14.49)$$

$$\frac{\gamma_{lt}}{2} = (\varepsilon_d + \varepsilon_r) \sin \alpha \cos \alpha \quad (14.50)$$

14.2.3.4 Constitutive Laws

Softened compression stress–strain relationship of concrete. The truss model has been applied to treat the shear and torsion of reinforced concrete since the turn of the 20th century. However, the prediction based on the truss model consistently overestimated the shear and torsional strengths of tested specimens. This nagging mystery has plagued researchers for over half a century. The source of this difficulty was first understood by Peter (1964). He realized that a reinforced concrete panel element subjected to tension is actually subjected to biaxial compression–tension stresses. Viewing the action as a two-dimensional problem, he discovered that the compressive strength in one direction was reduced by cracking due to tension in the perpendicular direction. After applying the softening effect of concrete struts to the nine test panels, Peter concluded that a reduction of 15% of the effective compressive strength should be taken into account in biaxial compression–tension stresses. Apparently, the mistake in applying the truss model theory before 1964 was the use of the compressive stress–strain relationship of concrete that was obtained from the uniaxial test of standard cylinders without considering the two-dimensional softening effect.

Peter's tests could not delineate the variables that govern the softening parameter because of technical difficulties in the biaxial testing of large panels. The quantification of the softening phenomenon, therefore, did not occur for almost two decades, when a unique “shear rig” test facility was built in 1981 by Vecchio and Collins (1981). Based on their tests of 17 panels, each 89 cm² and 7 cm thick, they proposed a softening parameter that was a function of the ratio of the tensile principal strains to the compression principal strain, $\varepsilon_r/\varepsilon_d$.

The discovery and the quantification of this softening phenomenon have allowed a major breakthrough in understanding the shear problem in reinforced concrete. During the past 20 years, a number of diverse analytical models have been proposed according to the test results (Peter, 1964; Robinson and Demorieux, 1968; Vecchio and Collins, 1981; Schlaich et al. 1982; Schlaich and Schafer, 1983; Vecchio and Collins, 1986; Eibl and Neuroth, 1988; Miyahara et al. 1988; Kollegger and Mehlhorn, 1990; Mikame et al. 1991; Ueda et al. 1991; Hsu, 1993; Vecchio and Collins, 1993; Vecchio et al. 1994; Belarbi and Hsu, 1995). The effect of these softening models on low-rise framed shear walls is studied by Mo and Rothert (1997). In this section, the softening model proposed by Belarbi and Hsu (1994, 1995) is briefly introduced.

The original softening model derived from test data proposed the use of a *softening parameter* ζ , where ζ is a function of the ratio of principal tensile strain to principal compressive strain (ϵ_r/ϵ_d). The proposed model by Belarbi and Hsu (1995) involves modification of the Hognestad parabola (Figure 14.16), which is used as the base curve describing the uniaxial compressive response of concrete.

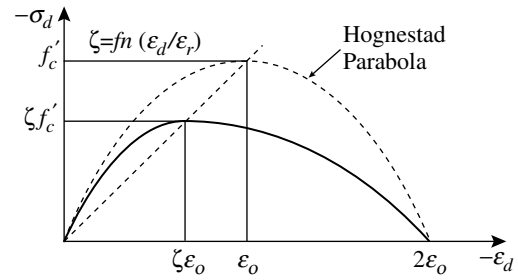


FIGURE 14.16 Compression softening models with Hognestad curve.

$$\sigma_d = \begin{cases} \zeta f'_c \left[2 \left(\frac{\epsilon_d}{\zeta \epsilon_o} \right) - \left(\frac{\epsilon_d}{\zeta \epsilon_o} \right)^2 \right], & \epsilon_d / \zeta \epsilon_o \leq 1 \\ \zeta f'_c \left[1 - \left(\frac{\epsilon_d / \zeta \epsilon_o - 1}{2 / \zeta - 1} \right)^2 \right], & \epsilon_d / \zeta \epsilon_o > 1 \end{cases} \quad (14.51a)$$

$$\zeta = \frac{0.9}{\sqrt{1 + 600 \epsilon_r}} \quad (14.51b)$$

Tensile stress–strain relationship of concrete. From the tests involving panels subjected to shear, it was clear that the tensile stress of concrete, σ_r , is not zero as assumed in the simple truss model. Based on the tests of 35 full-size panels (Hsu, 1993), a set of formulas were recommended as follows:

$$\text{If } \epsilon_r \leq \epsilon_{cr}, \quad \sigma_r = E_c \epsilon_r \quad (14.52)$$

$$\text{If } \epsilon_r > \epsilon_{cr}, \quad \sigma_r = f_{cr} \left(\frac{\epsilon_r}{\epsilon_{cr}} \right)^{0.4} \quad (14.53)$$

where

$E_c = 47,000 \sqrt{f'_c}$, and both f'_c and $\sqrt{f'_c}$ are in pounds per square inch

ϵ_{cr} = strain at cracking of concrete = 0.00008

$f_{cr} = 3.75 \sqrt{f'_c}$

Stress–strain relationship of steel. The stress–strain curve of a steel bar in concrete relates the average stress to the average strain of a long bar crossing several cracks, whereas the stress–strain curve of a bare bar relates the stress to the strain at a local point (Okamura and Maekawa, 1991). In other words, a steel bar in concrete is stiffened by the tensile stress of the concrete. If the tensile strength of concrete is neglected, as it is in the most of truss models, the following equations are used:

$$\text{If } \epsilon_t \leq \epsilon_{ly}, \quad f_l = E_s \epsilon_l \quad (14.54)$$

$$\text{If } \epsilon_l > \epsilon_{ly}, \quad f_l = f_{ly} \quad (14.55)$$

where

E_s = modulus of elasticity of steel bars

f_{ly} = yield stress of longitudinal steel bars

ϵ_{ly} = yield strain of longitudinal steel bars

It was recommended by Belarbi and Hsu (1995) that both the tensile strength of concrete, presented in the previous section, and the average stress–strain curve of steel stiffened by concrete, be taken into account. In this model, the following equations are used for describing the stress–strain relationship of steel:

$$\text{If } \epsilon_l E_s \leq f'_{ly}, \quad f_l = E_s \epsilon_l \quad (14.56)$$

$$\text{If } \varepsilon_l E_s \leq f'_{ly}, \quad f_l = \left[1 - \frac{2 - \alpha/45^\circ}{1000\rho_l} \right] [(0.91 - 2B)f_{ly} + (0.02 + 0.25B)E_s \varepsilon_l] \quad (14.57)$$

where

$$B = (1/\rho_l)(f_{cr}/f_{ly})^{1.5} \quad (14.58)$$

$$f'_{ly} = [1 - (2 - \alpha/45^\circ)/1000\rho_l](0.93 - 2B)f_{ly} \quad (14.59)$$

14.2.3.5 Solution Procedures

Figure 14.17 shows a framed shear wall. This kind of shear wall will be analyzed in this section. As discussed by Hsu and Mo (1985), in the design of low-rise structural walls, the boundary elements are reinforced to resist the applied bending moment, while the webs are designed to resist the applied shear force. The size and shape of the boundary elements do not have a significant influence on the shear behavior, as long as they are sufficient to carry the required bending moment. The effect of the boundary elements on structural walls has been studied by Mo and Kuo (1998). Owing to the restriction of the boundary elements, the strain of transverse steel in low-rise framed shear walls can be neglected, as verified by the PCA tests; i.e., $\varepsilon_t = 0$. Therefore, adding Equation 14.48 and Equation 14.49 gives

$$\varepsilon_r = \varepsilon_l - \varepsilon_d \quad (14.60)$$

Inserting $\varepsilon_r \sin^2 \alpha = \varepsilon_r - \varepsilon_r \cos^2 \alpha$ into Equation 14.20 gives

$$\cos^2 \alpha = \frac{\varepsilon_r - \varepsilon_l}{\varepsilon_r - \varepsilon_d} \quad (14.61)$$

Substituting Equation (14.60) and Equation (14.61) into Equation 14.45 results in

$$f_l = \frac{1}{\rho_l} \left[\sigma_l - \sigma_d \frac{(-\varepsilon_d)}{(\varepsilon_l - 2\varepsilon_d)} - \sigma_r \frac{(\varepsilon_l - \varepsilon_d)}{(\varepsilon_l - 2\varepsilon_d)} \right] \quad (14.62)$$

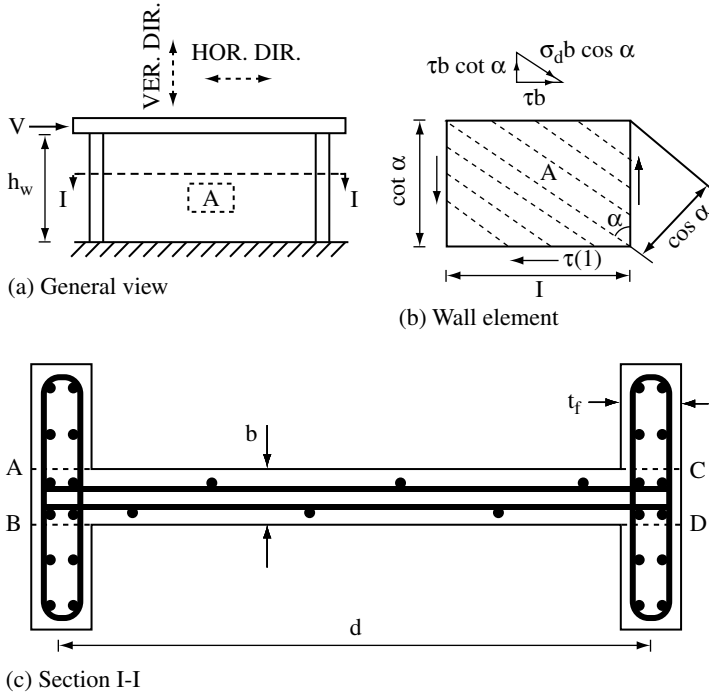


FIGURE 14.17 A framed shear wall.

Neglecting the tensile strength of concrete, i.e., $\sigma_r = 0$, gives

$$f_l = \frac{1}{\rho_l} \left[\sigma_l - \sigma_d \frac{(-\varepsilon_d)}{(\varepsilon_l - 2\varepsilon_d)} \right] \quad (14.63)$$

For low-rise framed shear walls, the average shear stress τ on the horizontal cross section is defined as

$$\tau = \frac{V}{bd} \quad (14.64)$$

where d is the effective depth, which is defined as the distance between the centroids of the longitudinal bars in the two flanges, b is the width of the web, and V is the horizontal shear force. The deflection at the top of the shear wall, δ , is determined by

$$\delta = \gamma h \quad (14.65)$$

where h = height of the shear wall.

Based on the softened truss model theory presented above, the algorithm is shown in Figure 14.18 (Mo and Jost, 1993; Mo and Shiau, 1993) and is explained below.

1. Select a given ε_d .
2. Assume a value of ε_l .
3. Calculate ε_r from Equation 14.60.
4. Calculate ζ using Equation 14.51b.
5. Calculate σ_d from Equation 14.51a.
6. Calculate σ_r from Equation 14.52 or Equation 14.53.
7. Calculate f_l from Equation 14.62 or Equation 14.63.
8. Check f_l using Equation 14.54 and Equation 14.55 or from Equation 14.56 to Equation 14.59.
- 9a. If the calculated value for f_l determined in Step 8 is not sufficiently close to the value shown in step 7, repeat steps 2 to 7.
- 9b. If the calculated value for f_l determined in Step 8 is sufficiently close to the value shown in Step 7, proceed to calculate τ (or V) and γ (or δ) from Equation 14.47 (or Equation 14.64) and Equation 14.49 (or Equation 14.65), respectively. This will provide one set of solutions.

Select other values of ε_d and repeat Steps 1 to 9 for each ε_d . This will provide a number of sets of quantities. From these sets of quantities, one can plot the shear stress vs. distortion curve (or shear force vs. deflection curve), the longitudinal steel strain vs. deflection curve, and the longitudinal steel strain vs. concrete strain curve. In general, the maximum ε_d value can be chosen as 0.003 with an increment of 0.00005.

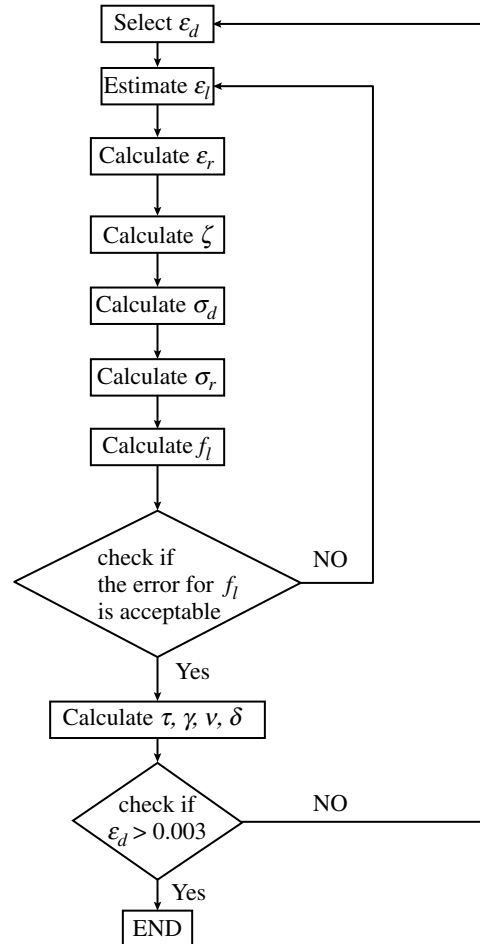


FIGURE 14.18 Algorithm for framed shear wall analysis.

14.2.4 Time-History Analysis

To accurately determine the dynamic behavior of concrete structures, the *time-history analysis* (Clough and Penzien, 1993; Paz, 1997) is preferred. This section will show an example for single-DoF systems, such as simple beams, torsional box tubes, spandrel beams, continuous beams, one-story frames and one-story framed shear walls. All of these structures will be discussed later.

In time-history analysis, a framed shear wall can be modeled as a nonlinear single-DoF system (Figure 14.19). The dynamic incremental equilibrium is shown in Figure 14.19(c).

The equation of the equilibrium is

$$m\Delta\ddot{y}_i + c_i\Delta\dot{y}_i + k_i\Delta y_i = \Delta F_i \quad (14.66)$$

where m is the mass at the top.

c_i and k_i are calculated for values of velocity and displacement corresponding to time t and assumed to remain constant during the increment of time Δt . Incremental acceleration, incremental velocity, and incremental displacement are $\Delta\ddot{y}_i$, $\Delta\dot{y}_i$, and Δy_i , respectively.

To perform the step-by-step integration of Equation 14.66, the linear acceleration method is employed. In this method, it is assumed that the acceleration may be expressed by a linear function of time during the time interval Δt . Let t_i and $t_{i+1} = t_i + \Delta t$ be, respectively, the designation for the time at the beginning and at the end of the time interval Δt . When the acceleration is assumed to be a linear function of time for the interval of time t_i to $t_{i+1} = t_i + \Delta t$, as shown in Figure 14.20, the acceleration may be expressed as

$$\ddot{y}(t) = \ddot{y}_i + \frac{\Delta\ddot{y}_i}{\Delta t}(t - t_i) \quad (14.67)$$

Integrating Equation 14.67 twice with respect to time between the limits t_i and $t = t_i + \Delta t$ and using the incremental displacement Δy as the basic variable gives

$$\Delta\ddot{y}_i = \frac{6}{\Delta t^2}\Delta y_i - \frac{6}{\Delta t}\dot{y}_i - 3\ddot{y}_i \quad (14.68)$$

and

$$\Delta\dot{y}_i = \frac{3}{\Delta t}\Delta y_i - 3\dot{y}_i - \frac{\Delta t}{2}\ddot{y}_i \quad (14.69)$$

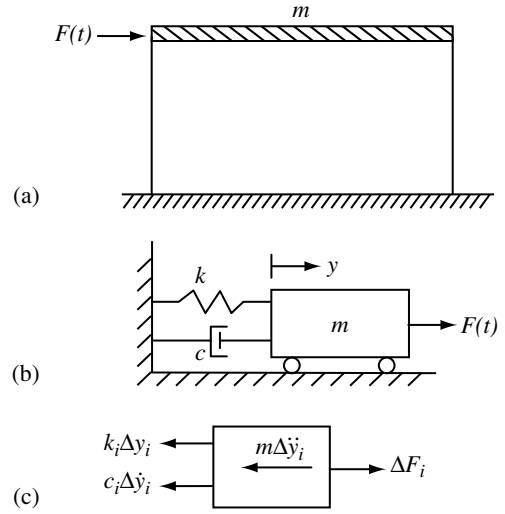


FIGURE 14.19 (a) Framed shear wall with a mass m at the top; (b) model for a nonlinear single-DoF system, and (c) free body diagram showing the incremental inertial force, the incremental damping force, the incremental spring force and the incremental external force.

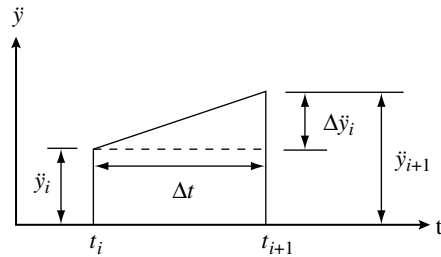


FIGURE 14.20 Linear variation of acceleration during time interval.

The substitution of Equation 14.68 and Equation 14.69 into Equation 14.66 leads to the following form of the equation of motion:

$$m\left(\frac{6}{\Delta t^2}\Delta y_i - \frac{6}{\Delta t}\dot{y}_i - 3\ddot{y}_i\right) + c_i\left(\frac{3}{\Delta t}\Delta y_i - 3\dot{y}_i - \frac{\Delta t}{2}\ddot{y}_i\right) + k_i\Delta y_i = \Delta F_i \quad (14.70)$$

Transferring all the terms containing the unknown incremental displacement, Δy_i , to the left-hand side gives

$$\bar{k}_i\Delta y_i = \Delta \bar{F}_i \quad (14.71)$$

where

$$\bar{k}_i = k_i + \frac{6m}{\Delta t^2} + \frac{3c_i}{\Delta t} \quad (14.72)$$

and

$$\Delta \bar{F}_i = \Delta F_i + m\left(\frac{6}{\Delta t}\dot{y}_i + 3\ddot{y}_i\right) + c_i\left(3\dot{y}_i + \frac{\Delta t}{2}\ddot{y}_i\right) \quad (14.73)$$

It should be noted that Equation 14.71 is equivalent to the static incremental-equilibrium equation and may be solved for the incremental displacement by simply dividing the equivalent incremental load, $\Delta \bar{F}_i$, by the equivalent spring constant \bar{k}_i .

The displacement y_{i+1} and the velocity \dot{y}_{i+1} at time $t_{i+1} = t_i + \Delta t$ are

$$y_{i+1} = y_i + \Delta y_i \quad (14.74)$$

and

$$\dot{y}_{i+1} = \dot{y}_i + \Delta \dot{y}_i \quad (14.75)$$

The acceleration \ddot{y}_{i+1} at the end of the time step is obtained directly from the differential equation of motion to avoid the errors that generally might tend to accumulate from step to step. It follows

$$\ddot{y}_{i+1} = \frac{1}{m}[F(t_{i+1}) - c_{i+1}\dot{y}_{i+1} - k_{i+1}y_{i+1}] \quad (14.76)$$

where the coefficients c_{i+1} and k_{i+1} are now evaluated at time t_{i+1} .

After the displacement, velocity, and acceleration have been determined at time $t_{i+1} = t_i + \Delta t$, the procedure just outlined is repeated to calculate these quantities at the following time step, $t_{i+2} = t_{i+1} + \Delta t$.

In general, sufficiently accurate results can be obtained if the time interval is taken to be no longer than one tenth of the natural period of the structure (Clough and Penzien, 1993; Paz, 1997).

14.3 Beams under Harmonic Excitations

14.3.1 Mechanical Properties

A 6-m-long beam is simply supported. The cross section and material properties are shown in Figure 14.2(b).

$$f'_c = 39 \text{ N/mm}^2$$

$$A'_s = 142 \text{ mm}^2$$

$$d = 305 - 12.7 - 6.35 - \frac{1}{2}(19.05) = 276 \text{ mm}$$

$$A_s = 852 \text{ mm}^2$$

Find the moment (M)–curvature (f) relationship of the cross section at the midspan and the force (P)–displacement (d) relationship of the beam.

Solution

1. Moment–curvature relationship

$$E = 1500\sqrt{f'_c} \text{ (N/mm}^2\text{)} = 29614.9 \text{ N/mm}^2$$

Using the derived equations in Section 14.2.2 gives

$$M_u = 86,122,000 \text{ N mm,}$$

$$\psi_u = 5.63 \times 10^{-5} \text{ rad/mm}$$

$$M_y = 82,491,700 \text{ N mm,}$$

$$\psi_y = 1.22 \times 10^{-5} \text{ rad/mm}$$

$$M_c = 9,263,000 \text{ N mm} \quad \psi_c = 8.66 \times 10^{-7} \text{ rad/mm}$$

They are plotted in Figure 14.21, and the corresponding loads are determined below.

2. Force–displacement relationship

$$P_U = \frac{4 \times 86,122,000}{6000} = 57,415 \text{ N}$$

$$P_Y = \frac{4 \times 82,491,700}{6000} = 54,994 \text{ N}$$

$$P_C = \frac{4 \times 9,263,000}{6000} = 6175 \text{ N}$$

The corresponding deflections can be determined as follows:

1. Cracking state (Figure 14.22)

$$\delta_c = \frac{M_c L^2}{12EI}$$

$$= \frac{9,263,000 \times (6000)^2}{12 \times (29,614.9) \times \frac{1}{12} \times (152.4) \times (305)^3}$$

$$= 2.6 \text{ mm}$$

2. Yielding state (Figure 14.23)

$$L_1 = 3000 \times \frac{9,263,000}{82,491,700} = 336.9 \text{ mm}$$

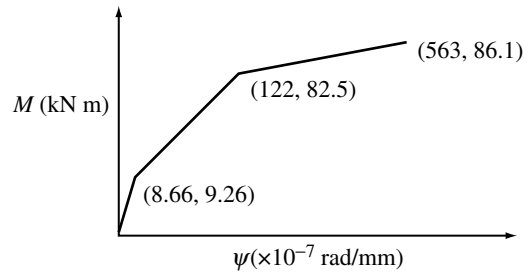


FIGURE 14.21 Moment–curvature curve for the example beam.

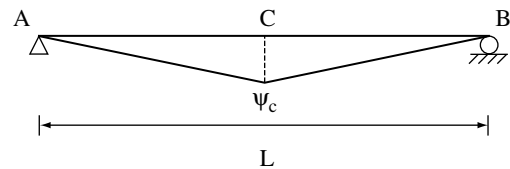


FIGURE 14.22 Curvature diagram at cracking state.

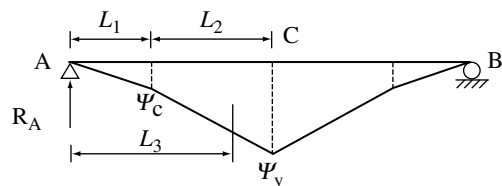


FIGURE 14.23 Curvature diagram at yielding state.

$$L_2 = 3000 - 336.9 = 2663.1 \text{ mm}$$

$$L_3 = 336.9 + \frac{8.66 \times 10^{-7} \times 2663.1 \times \frac{2663.1}{2} + (1.22 \times 10^{-5} - 8.66 \times 10^{-7}) \times \frac{2663.1}{2} \times \frac{2}{3} \times 2663.1}{8.66 \times 10^{-7} \times 2663.1 + \frac{1}{2} \times 2663.1 \times (1.22 \times 10^{-5} - 8.66 \times 10^{-5})}$$

$$= 2053 \text{ mm}$$

$$\delta_y = \frac{1}{3} \times 8.66 \times 10^{-7} \times (342.2)^2 + \frac{1}{2} \times (8.66 \times 10^{-7} + 1.22 \times 10^{-5}) \times (2663.1) \times 2053 = 35.75 \text{ mm}$$

3. Ultimate state (Figure 14.24)

$$L_1 = 3000 \times \frac{9,263,000}{86,122,000} = 322.7 \text{ mm}$$

$$L_2 = 3000 \times \frac{82,491,600}{86,122,000} - 322.7$$

$$= 2550.8 \text{ mm}$$

$$L_4 = 3000 - 322.7 - 2550.8 = 126.5 \text{ mm}$$

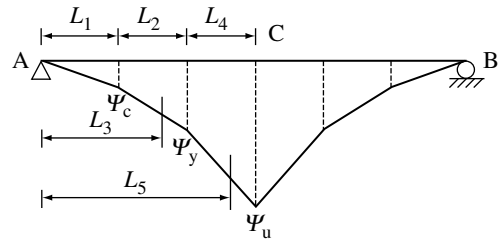


FIGURE 14.24 Curvature diagram at yielding state.

$$L_3 = 322.7 + \frac{8.66 \times 10^{-7} \times 2550.8 \times \frac{2550.8}{2} + (1.22 \times 10^{-5} - 8.66 \times 10^{-7}) \times \frac{2550.8}{2} \times \frac{2}{3} \times 2550.8}{8.66 \times 10^{-7} \times 2550.8 + \frac{1}{2} \times 2550.8 \times (1.22 \times 10^{-5} - 8.66 \times 10^{-7})}$$

$$= 1967.3 \text{ mm}$$

$$L_5 = 322.7 + 2550.8 + \frac{1.22 \times 10^{-5} \times 126.5 \times \frac{126.5}{2} + (5.63 \times 10^{-5} - 1.22 \times 10^{-5}) \times \frac{126.5}{2} \times \frac{2}{3} \times 126.5}{1.22 \times 10^{-5} \times 126.5 + \frac{1}{2} \times 126.5 \times (5.63 \times 10^{-5} - 1.22 \times 10^{-5})}$$

$$= 2950.4 \text{ mm}$$

$$\delta_u = \frac{1}{3} \times 8.66 \times 10^{-7} \times (322.7)^2$$

$$+ \frac{1}{2} \times (8.66 \times 10^{-7} + 1.22 \times 10^{-5})$$

$$\times 2550.8 \times 1967.3$$

$$+ \frac{1}{2} \times (5.63 \times 10^{-5} + 1.22 \times 10^{-5})$$

$$\times 126.5 \times 2950.4 = 45.6 \text{ mm}$$

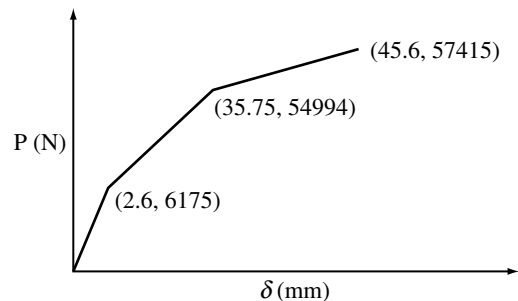


FIGURE 14.25 Load-deflection curve.

The load-deflection curve is shown in Figure 14.25.

14.3.2 Design for Machine Vibration

The same beam as described in Section 14.3.1 is supporting a machine with a rotating frequency of 9 Hz at the midspan of the beam. The mass of the rotating machine and the beam is 1 N sec²/mm. Check if resonance will occur.

Solution

Find the stiffness, k , the natural frequency, f , and the frequency ratio, r , for each of the three states, namely the elastic, cracking, and yield states.

1. Elastic state

$$k = \frac{617.5}{2.6} = 2375 \text{ N/mm}$$

$$f = \frac{1}{2\pi} \sqrt{\frac{2375}{1}} = 7.76 \text{ Hz}$$

$$r = \frac{7.76}{9} = 0.862$$

Since $0.8 < r < 1.2$, it is in the resonance zone. The beam needs to be redesigned to avoid resonance.

2. Cracking state

$$k = \frac{5499.4 - 617.5}{35.75 - 2.6} = 1472.7 \text{ N/mm}$$

$$f = \frac{1}{2\pi} \sqrt{\frac{1472.7}{1}} = 6.11 \text{ Hz}$$

$$r = \frac{6.11}{9} = 0.68 < 0.8$$

OK

3. Yield state

$$k = \frac{5741.5 - 5499.4}{45.6 - 35.75} = 245.8 \text{ N/mm}$$

$$f = \frac{1}{2\pi} \sqrt{\frac{245.8}{1}} = 2.50 \text{ Hz}$$

$$r = \frac{2.50}{9} = 0.28 < 0.8$$

OK

14.4 Design for Explosions/Shocks

14.4.1 Column

A 3-m-tall viaduct column supporting a mass of 50 N sec²/cm is subjected to a shock acceleration that is the same as the 1940 El Centro seismogram.

14.4.1.1 Load–Displacement Relationship

Using the same procedures presented in Section 14.3, the moment–curvature relationship of the cross section and the force–displacement relationship of the column can be determined. It is assumed that the force–displacement relationship of the column was found to be the same as that shown in [Figure 14.25](#).

14.4.1.2 Dynamic Response

To perform the dynamic response analysis, the computer program in Mo (1994) can be used. The required input data may be determined as follows:

$$\text{Stiffness 1} = \frac{0.6175}{2.6} = 0.2375 \text{ T/mm}$$

$$\text{Stiffness 2} = \frac{5.4994 - 0.6175}{35.75 - 2.6} = 0.1473 \text{ T/mm}$$

$$\text{Stiffness 3} = \frac{5.7415 - 5.4994}{45.6 - 35.75} = 0.246 \text{ T/mm}$$

$$\delta_c = 2.6 \text{ mm}$$

$$\delta_y = 35.75 \text{ mm}$$

$$\delta_u = 45.6 \text{ mm}$$

Result:

Maximum deflection = 38.33 mm

14.4.2 Shear Walls

14.4.2.1 Design Approach

14.4.2.1.1 Design Considerations

To insure ductile failure, the two design limitations for overreinforcement and minimum reinforcement can be derived in terms of the inclination angle, α , of the diagonal concrete struts.

1. *Overreinforcement.* Mo (1987) shows the inclination angle of the diagonal compression struts in the “lower balanced reinforcement,” α_{lb} , to be

$$\alpha_{lb} = \cos^{-1} \left\{ \frac{1}{2} \left[\left(\frac{\epsilon_{ly}}{2\epsilon_0} \right) \left(\sqrt{1 + \frac{8\epsilon_0^2}{\epsilon_{ly}^2}} - 1 \right) \right] \right\} \quad (14.77)$$

α_{lb} is a function of only one variable — the yield strain of longitudinal steel ϵ_{ly} . In underreinforced design, the chosen angle α should be greater than α_{lb} .

2. *Minimum reinforcement.* Mo (1987) also shows the inclination angle for minimum reinforcement, α_m , to be

$$\alpha_m = \cos^{-1} \left[\left(0.0025 \frac{f_{ly}}{f'_c} \right)^{1/3} \right] \quad (14.78)$$

α_m is a function of two variables — the yield strain in longitudinal steel, ϵ_{ly} , and the concrete strength, f'_c . Equation 14.77 and Equation 14.78 give the lower and upper limits, respectively, for the range of α , which insures ductile failure.

After the range of the inclination angle, α , is found, a preliminary angle, α , can be selected within this range. The wall size, bd , can then be determined by substituting $\tau = V/bd$ and $\sigma_d = f'_c \cos \alpha$ into $\tau = \sigma_d \sin \alpha \cos \alpha$ (Hsu and Mo, 1985; Mo, 1988).

$$bd = \frac{V}{f'_c \sin \alpha \cos^2 \alpha} \quad (14.79)$$

The effective length, d , in Equation 14.79 is usually given in design and the web width, b , needs to be chosen by the designer. After the wall size, bd , is determined, the actual inclination angle, α , can be refined by solving α in Equation 14.79.

The longitudinal steel can be determined from $A_l f_l = \tau b d \cot \alpha$ (Hsu and Mo, 1985; Mo, 1988), noting that $\tau b d$ becomes V_n at maximum shear

$$A_l f_l = V_n \cot \alpha \quad (14.80)$$

The transverse (horizontal) steel can be determined by the specified minimum value (Hsu, 1993):

$$\rho_t = 0.0045 \quad (14.81)$$

14.4.2.1.2 Design Procedure

For a given dynamic loading history (or seismogram) and given material properties (f'_c, f_{ly}, ξ), the procedure to design the size of the wall, the vertical steel, and the horizontal steel is as follows:

1. Assume a shear force (V_n).
2. Determine the range of α using Equation 14.77 and Equation 14.78.
3. Select an α value and find b and d using Equation 14.79. After b and d are selected, the actual angle of inclination can be refined.
4. Determine the longitudinal steel using Equation 14.80 and the horizontal steel using Equation 14.81.
5. Determine the load–deflection relationship using the algorithm mentioned in Figure 14.18.
6. Calculate the stiffness at the ultimate state.
7. Determine the natural period at the ultimate state.
8. Select the time interval $\Delta t \leq 0.1$ times the natural period at the ultimate state.
9. Calculate the initial stiffness using the load–deflection relationship.
10. Calculate the damping coefficient using Equation 14.14.
11. Calculate the effective stiffness using Equation 14.72.
12. Calculate the incremental effective force using Equation 14.73.
13. Solve for the incremental displacement using Equation 14.71.
14. Calculate the incremental velocity using Equation 14.69.
15. Calculate displacement and velocity at the end of time interval using Equation 14.74 and Equation 14.75.
16. Calculate shear force using the load–deflection relationship.
17. Calculate acceleration at the end of time interval by Equation 14.76. Steps 9 to 17 will provide one set of solutions.
18. Repeat Steps 9 to 17 for each time interval. This will provide a number of sets of solutions.
19. Determine the calculated maximum shear force in the entire loading history.
 - a. If the value of the calculated maximum shear force is not greater than the shear force assumed, the design is finished.
 - b. If the value of the calculated maximum shear forces is greater than the shear force assumed, reassume a new value for shear force V_n and repeat Steps 2 to 19 until Step 19a is satisfied.

The algorithm presented in this section has been extended to box tubes subjected to dynamic shear and torsion and to hybrid reinforced concrete frame–steel wall systems.

14.4.2.2 Missile Impact

A shear wall 10 ft (3.05 m) high by 15 ft (4.57 m) wide (Figure 14.26(a)) is designed to withstand a missile impact having the force–time relationship shown in Figure 14.26(b) and acting at the top of the wall (Mo, 1988). For simplicity, the force–time relationship of the missile impact is used instead of the earthquake seismogram. It is assumed that the mass at the top of the wall and one third of the mass of the wall m are 0.5 kip sec²/in. (0.088 kN sec²/mm). The material properties are given as follows: $f_{ly} = 60$ ksi (414 MPa), $f'_c = 4000$ psi (27.6 MPa), $E_s = 29 \times 10^6$ psi (2.0×10^5 MPa), $\varepsilon_0 = 0.002$, and $\xi = 0.07$. The wall thickness, b , and the reinforcement of the wall, ρ_l and ρ_t , are to be determined.

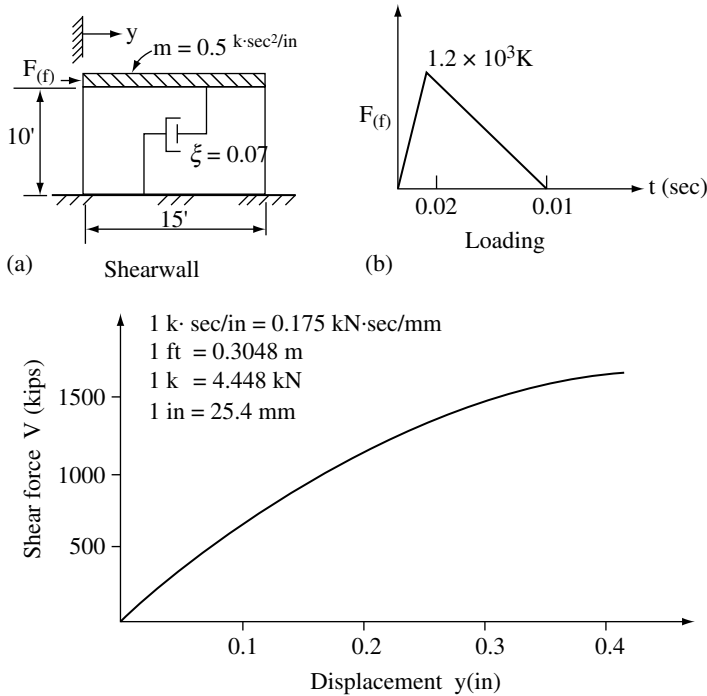


FIGURE 14.26 Shear wall subjected to missile impact.

The design of the boundary columns, which should be able to withstand the bending moment, will not be considered in this example.

Solution

1. Assume $V_n = 1600$ kips (7117 kN)
2. Determine the range of α

$$\alpha > \cos^{-1} \left\{ \frac{1}{2} \left[\left(\frac{0.00207}{2(0.002)} \right) \left(\sqrt{1 + \frac{8(0.002)^2}{(0.00207)^2}} - 1 \right) \right] \right\} \quad (14.77)$$

$$\alpha = 60.4^\circ$$

$$\alpha \leq \cos^{-1} \left[\left(\frac{(0.0025)(60,000)}{4000} \right)^{1/3} \right] \quad (14.78)$$

$$\alpha = 70.4^\circ$$

$$\therefore 60.4^\circ < \alpha \leq 70.4^\circ$$

3. Select $\alpha = 60.4^\circ$ and $d = 180$ in. (4572 mm)

$$b \geq \frac{1,600,000}{(180)(4000) \sin 60.4 \cos^2 60.4} \quad (14.79)$$

$$b \geq 10.48 \text{ in. (266 mm)}$$

Let us select $b = 12$ in. (305 mm). Calculate $\alpha = 62.9^\circ$ from Equation 14.79.

$$\alpha = 62.9^\circ < 70.4^\circ$$

OK

4. Determine ρ_l and ρ_t

$$\rho_l = \frac{1,600,000 \cot 62.9}{(12)(180)(60,000)} = 0.0063 \quad (14.80)$$

$$\rho_t = 0.0045 \quad (14.81)$$

5. Determine the load–deflection relationship using the algorithm mentioned in Figure 14.18. The load–deflection relationship is determined as shown in Figure 14.26(c).
6. Calculate the stiffness at the ultimate state

$$k_u = \frac{1609.9}{0.415} = 3879.3 \text{ kip/in. (679 kN/mm)}$$

7. Determine the natural period at the ultimate state

$$T_u = 2\pi \sqrt{\frac{0.5}{3879.3}} = 0.071 \text{ sec} \quad (14.82)$$

8. Select Δt

$$\Delta t = (0.1)(0.071) = 0.0071 \text{ sec}$$

Let us select $\Delta t = 0.005 \text{ sec}$

$$\Delta t = 0.005 < 0.0071 \text{ sec}$$

OK

9. Calculate the initial stiffness k

$$k = \frac{572.2}{0.0778} = 7354.8 \text{ kip/in. (1288 kN/mm)}$$

10. Calculate the damping coefficient C

$$C = (0.07)(2)[(0.5)(7354.8)]^{1/2} = 8.49 \text{ kip sec/in. (1.49 kN sec/mm)} \quad (14.83)$$

11. Calculate the effective stiffness \bar{k}

$$\bar{k} = 7354.8 + \frac{6(0.5)}{(0.005)^2} + \frac{3(8.49)}{0.005} = 132,448.8 \text{ kip/in. (23194 kN/mm)}$$

12. Calculate the incremental effective force

$$\Delta F = 300 \text{ kips (1334 kN)}$$

$$\Delta \bar{F} = 300 + (0.5) \left[\frac{6(0)}{0.005} + 3(0) \right] + (8.49) \left[3(0) + \frac{0.005(0)}{2} \right] = 300 \text{ kips (1334 kN)}$$

13. Determine the incremental displacement Δy

$$\Delta y = \frac{300}{132,448.8} = 0.002265 \text{ in. (0.058 mm)} \quad (14.84)$$

14. Determine the incremental velocity
- $\Delta\dot{y}$

$$\Delta\dot{y} = \frac{3}{0.005}(0.002265) - 3(0) - \frac{0.005}{2}(0) = 1.359 \text{ in./sec (34.52 mm/sec)} \quad (14.85)$$

15. Calculate the displacement and velocity at the end of the time interval

$$y_{i+1} = 0 + 0.002265 = 0.002265 \text{ in. (0.058 mm)} \quad (14.86)$$

$$\dot{y}_{i+1} = 0 + 1.359 = 1.359 \text{ in./sec (34.52 mm/sec)} \quad (14.87)$$

16. Determine the shear force
- V
- . From Figure 14.26(c),
- $V = 16.7$
- kips (74.3 kN) when
- $y = 0.002265$
- in. (0.058 mm).

17. Calculate the acceleration at the end of the time interval

$$\ddot{y}_{i+1} = \frac{1}{0.5}[300 - (8.49)(1.359) - 16.7] = 543.5 \text{ in./sec}^2 (13,805 \text{ mm/sec}^2)$$

Steps 9 to 17 provide one set of solutions.

18. Repeating Steps 9 to 17 for each time interval gives a number of sets of solutions, as illustrated in Table 14.2.

TABLE 14.2 Nonlinear Response — Linear Acceleration Step-by-Step Method for Design Example

t (sec)	F (kip)	\dot{y} (in.)	\ddot{y} (in./sec)	V (kip)	\ddot{y} (in./sec)	k_p (kip/in.)	\bar{k} (kip/in.)	ΔF (kip)	$\Delta \bar{F}$ (kip)	Δy (in.)	$\Delta \dot{y}$ (in./sec)
0	0	0	0	0	0	7355	132,449	300	300	0.0023	1.36
0.005	300	0.0023	1.36	17	544	7355	132,449	300	1977	0.0149	3.50
0.010	600	0.0172	4.86	126	865	7355	132,449	300	4658	0.0352	4.37
0.015	900	0.0524	9.23	385	947	7355	132,449	300	7514	0.0567	3.96
0.020	1200	0.1091	13.19	700	776	5549	129,971	-75	9309	0.0716	1.45
0.025	1125	0.1807	14.64	1015	4	4399	128,341	-75	9004	0.0702	-1.81
0.030	1050	0.2509	12.83	1300	-669	4060	127,846	-75	6852	0.0536	-4.66
0.035	975	0.3045	8.17	1455	-1063	2892	126,084	-75	3349	0.0266	-5.89
0.040	900	0.3311	2.28	1530	-1347	2820	125,976	-75	-709	-0.0056	-6.83
0.045	825	0.3255	-4.55	989	-280	4621	128,659	-75	-3322	-0.0258	-1.13
0.050	750	0.2997	-5.68	870	-164	4621	128,659	-75	-3846	-0.0299	-0.49
0.055	675	0.2698	-6.17	732	-31	4621	128,659	-75	-3948	-0.0307	0.17
0.060	600	0.2391	-6.00	590	101	4621	128,659	-75	-3645	-0.0283	0.78
0.065	525	0.2108	-5.22	459	202	4621	128,659	-75	-3009	-0.0234	1.13
0.070	450	0.1874	-4.10	351	253	4621	128,659	-75	-2232	-0.0173	1.28
0.075	375	0.1701	-2.82	271	246	4621	128,659	-75	-1449	-0.0113	1.05
0.080	300	0.1588	-1.77	219	186	4621	128,659	-75	-888	-0.0069	0.69
0.085	225	0.1519	-1.07	187	90	4621	128,659	-75	-603	-0.0047	0.17
0.090	150	0.1472	-0.90	165	-19	4621	128,659	-75	-661	-0.0051	-0.34
0.095	75	0.1421	-1.24	142	-116	4621	128,659	-75	-1019	-0.0079	-0.74
0.100	0	0.1342	-1.97	105	-183	4621	128,659	0	-1502	-0.0117	-0.64
0.105	0	0.1225	-2.62	51	-67	4621	128,659	0	-1723	-0.0134	-0.03
0.110	0	0.1091	-2.64	0	36	4621	120,000	0	-1532	-0.0128	0.16
0.115	0	0.0963	-2.49	0	0	0	120,000	0	-1491	-0.0124	0
0.120	0	0.839	-2.49	0	0	0	120,000	0	-1491	-0.0124	0
0.125	0	0.0715	-2.49	0	0	0	120,000	0	-1491	-0.0124	0
0.130	0	0.0591	-2.49	0	0	0	120,000	0	-1491	-0.0124	0

1 kip = 4.448 kN; 1 in. = 25.4 mm; 1 in./sec = 25.4 mm/sec; 1 in./sec² = 25.4 mm/sec²; 1 kip/in. = 0.175 kN/mm.

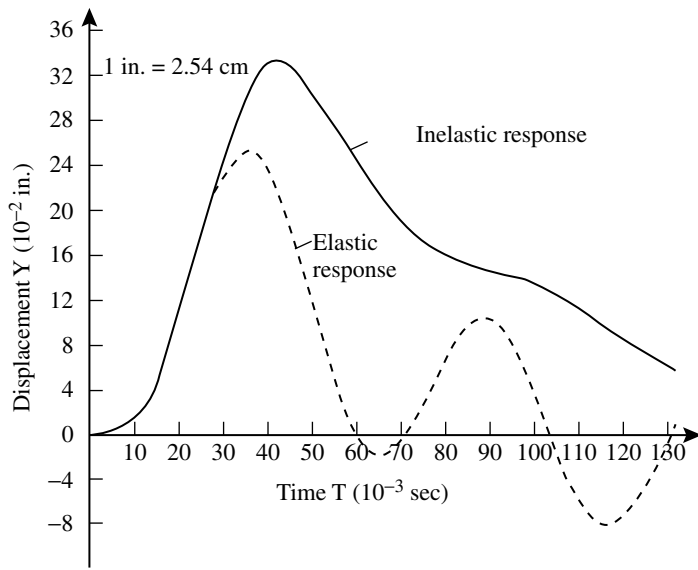


FIGURE 14.27 Comparison of inelastic with elastic response.

19. Determine the calculated maximum shear force. From Table 14.2, $V_{\max} = 1530$ kips (6805 kN) < assumed $V_n = 1600$ kips (7117 kN).
OK

The dynamic *inelastic response* calculated in Table 14.2 is plotted in Figure 14.27. Also plotted for comparison is the linear elastic response obtained by a similar step-by-step analysis. The effect of the inelastic response on the displacement shows up clearly in this comparison.

14.4.2.3 Explosion Interaction

The basic algorithm of Section 14.2.4 is modified to allow the analysis of a framed shear wall which interacts with a steel structure as shown in Figure 14.28.

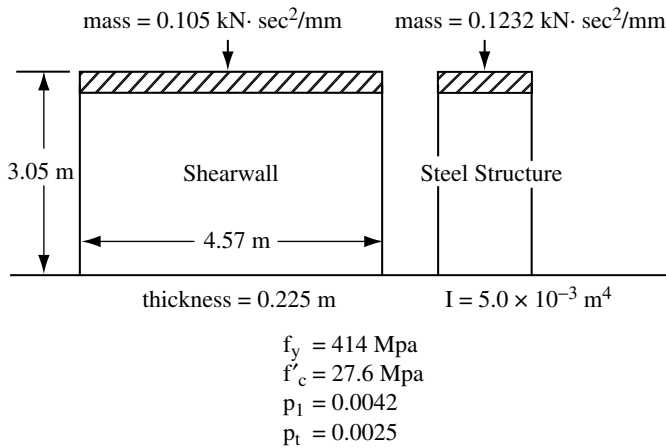


FIGURE 14.28 A framed shear wall that interacts with a steel structure.

When a collision between the two structures is assumed to be elastic, the new velocities \dot{y}_{i1}^* and \dot{y}_{i2}^* can be computed by assuming the conservation of momentum and energy:

$$m_1 \dot{y}_{i1} + m_2 \dot{y}_{i2} = m_1 \dot{y}_{i1}^* + m_2 \dot{y}_{i2}^* \quad (14.88)$$

and

$$\frac{1}{2} m_1 \dot{y}_{i1}^2 + \frac{1}{2} m_2 \dot{y}_{i2}^2 = \frac{1}{2} m_1 \dot{y}_{i1}^{*2} + \frac{1}{2} m_2 \dot{y}_{i2}^{*2} \quad (14.89)$$

These equations give the post-impact velocity as a function of the preimpact velocity:

$$\dot{y}_{i1}^* = \dot{y}_{i1} - \frac{2R}{1+R} (\dot{y}_{i1} - \dot{y}_{i2}) \quad (14.90)$$

and

$$\dot{y}_{i2}^* = \dot{y}_{i2} - \frac{2}{1+R} (\dot{y}_{i2} - \dot{y}_{i1}) \quad (14.91)$$

where R is the mass ratio m_2/m_1 and \dot{y}_{i1}^* and \dot{y}_{i2}^* are the relative postimpact velocities for systems 1 and 2 at time t_i .

The algorithm in Section 14.2.4 may be modified to accommodate explosion interaction by allowing for two structures instead of one and inserting the following step. If the two structures collide, (a) determine the postimpact velocities using Equation 14.90 and Equation 14.91, and (b) recalculate the acceleration using the postimpact velocities.

When the explosion interaction occurs, the response is shown in Figure 14.29(c) and Figure 14.29(d) with the assumption that the initial gap between the two structures is zero. For Figure 14.29(a) and Figure 14.29(b), the gap is so large that the two structures cannot collide. A comparison of Figure 14.29(b) and Figure 14.29(d) shows that the maximum force is significantly greater when the explosion interaction occurs than it is when no explosion interaction occurs.

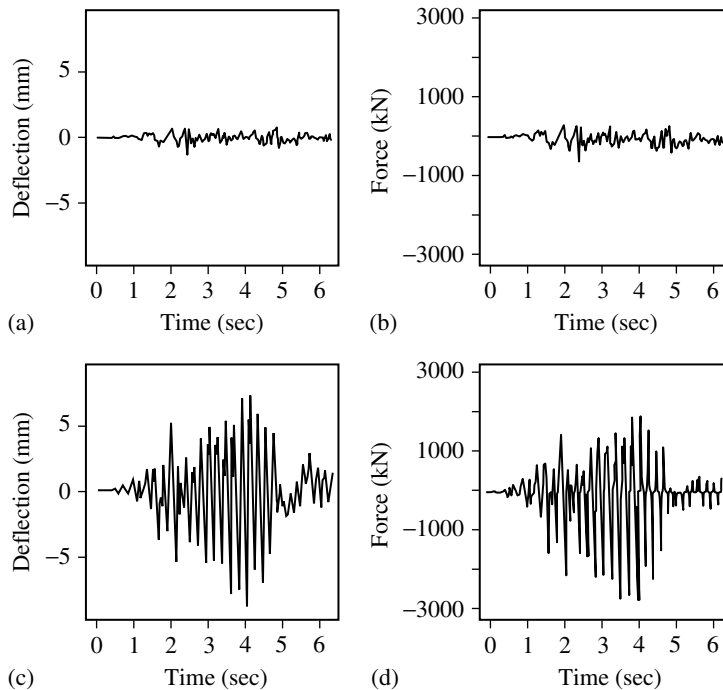


FIGURE 14.29 In (a) and (b) no explosion interaction occurs, but in (c) and (d) explosion interaction does occur.

References

- ACI Committee 318, 2002. *Building Code Requirements for Reinforced Concrete (ACI 318-02)*, American Concrete Institute, Detroit, 443pp.
- Belarbi, A. and Hsu, T.T.C., Constitutive laws of concrete in tension and reinforcing bars stiffened by concrete, *Struct. J. Am. Concr. Inst.*, 91, 4, 465–474, 1994.
- Belarbi, A. and Hsu, T.T.C., Constitutive laws of softened concrete in biaxial tension–compression, *Struct. J. Am. Concr. Inst.*, 92, 5, 562–573, 1995.
- CEB–FIP 1978. *Model Code for Concrete Structures*, 3rd ed., Comité Euro-International du Béton/Fédération Internationale de la Précontrainte, Paris, 348pp.
- Clough, R.W. and Penzien, J. 1993. *Dynamics of Structures*, 2nd ed., McGraw-Hill, New York, 738pp.
- Dowrick, D.J. 1987. *Earthquake Resistant Design*, 2nd ed., Wiley, New York, 529pp.
- Eibl, J. and Neuroth, U. 1988. *Untersuchungen zur Druckfestigkeit von bewehrtem Beton bei gleichzeitig wirkendem Querkzug*, Institut für Massivbau und Baustofftechnologie, Universität Karlsruhe.
- Hsu, T.T.C. 1993. *Unified Theory of Reinforced Concrete*, CRC Press, Boca Raton, FL, 313p.
- Hsu, T.T.C. and Mo, Y.L., Softening of concrete in low-rise shear walls, *J. Am. Concr. Inst.*, 82, 6, 883–889, 1985.
- Hsu, T.T.C. and Zhang, L.X., Nonlinear analysis of membrane elements by fixed-angle softened-truss model, *Struct. J. Am. Concr. Inst.*, 94, 5, 483–492, 1997.
- Hsu, T.T.C. and Zhu, R.H. 1999. Post-yield behavior of reinforced concrete membrane elements — The Hsu/Zhu ratios. In *Proceedings Volume, US–Japan Joint Seminar on Post-Peak Behavior of Reinforced Concrete Structures Subjected to Seismic Loads — Recent Advances and Challenges on Analysis and Design*. Tokyo/Lake Yamanaka, Japan, October 25–29, 1, pp. 43–60.
- Kollegger, J. and Mehlhorn, G. 1990. Experimentell Untersuchungen zur Bestimmung der Druckfestigkeit des gerissenen Stahlbetons bei einer Querkzugbeanspruchung, Report 413, Deutscher Ausschuss für Stahlbeton, Berlin, Germany.
- Mansour, M.Y. 2001. Behavior of reinforced concrete membrane elements under cyclic shear: experiments to theory, Ph.D. Thesis, Department of Civil and Environmental Engineering, University of Houston, Houston, TX.
- Mansour, M.Y., Hsu, T.T.C., and Lee, J.Y., Cyclic stress–strain curve of concrete and steel bars in membrane elements, *J. Struct. Eng., ASCE*, 127, 12, 2001a.
- Mikame, A., Uchida, K., and Noguchi, H. 1991. A study of compressive deterioration of cracked concrete. In *Proceedings of the International Workshop on Finite Element Analysis of Reinforced Concrete*, Columbia University, New York.
- Miyahara, T., Kawakami, T., and Maekawa, K., Nonlinear behavior of cracked reinforced concrete plate element under uniaxial compression, *Concrete library international, Jpn Soc. Civil Engrs*, 11, 306–319, 1988.
- Mo, Y.L., Discussion of “shear design and analysis of low-rise structural walls, by S. T. Mau and T. T. C. Hsu”, *ACI Struct. J.*, 84, 1, 91–92, 1987.
- Mo, Y.L., Analysis and design of low-rise structural walls under dynamically applied shear forces, *ACI Struct. J.*, 85, 2, 180–189, 1988.
- Mo, Y.L., Investigation of reinforced concrete frame behavior — theory and tests, *Mag. Concr. Res.*, 44, 160, 163–173, 1992.
- Mo, Y.L. 1994. *Dynamic Behavior of Concrete Structures*, Elsevier, Amsterdam, 37–38.
- Mo, Y.L. and Jost, S.D., Tool for dynamic analysis of reinforced concrete framed shearwalls, *Comput. Struct.*, 46, 4, 659–667, 1993.
- Mo, Y.L. and Kuo, J.Y., Experimental studies on low-rise structural walls, *Mater. Struct.*, RILEM, 31, August–November, 465–472, 1998.
- Mo, Y.L. and Rothert, H., Effect of softening models on behavior of reinforced concrete framed shearwalls, *ACI Struct. J.*, 94, 6, 730–744, 1997.

- Mo, Y.L. and Shiau, W.C., Ductility of low-rise structural walls, *Mag. Concr. Res.*, 45, 163, 131–138, 1993.
- Okamura, H. and Maekawa, K. 1991. *Nonlinear Analysis and Constitutive Models of Reinforced Concrete*, University of Tokyo, Tokyo, Japan, ISBN 7655-1506-0.
- Pang, X.B. and Hsu, T.T.C., Behavior of reinforced concrete membrane elements in shear, *Struct. J. Am. Concr. Inst.*, 92, 6, 665–679, 1995.
- Pang, X.B. and Hsu, T.T.C., Fixed-angle softened-truss model for reinforced concrete, *Struct. J. Am. Concr. Inst.*, 93, 2, 197–207, 1996.
- Paz, M. 1997. *Structural Dynamics*, 4th ed., Van Reinhold, New York, 626pp.
- Peter, J., 1964. Zur Bewehrung von Scheiben und Schalen fur Hauptspannungen schiefwinklig zur Bewehrungsrichtung, Dissertation, Lehrstuhl fur Massivbau, Technische Hochschule Stuttgart, Germany.
- Robinson, J.R. and Demorieux, J.M., Essais de Traction–Compression sur Modeles d'ame de Poutre en Beton Arme, Institutde Recherches Appliquees du Beton Arme (IRABA), Part I, June; Part II May, 1968, 1972.
- Schlaich, J. and Schafer, K. 1983. Zur Druck-Querzug-Festigkeit des Stahlbetons, Beton- und Stahlbetonbau, March, pp. 73–78.
- Schlaich, J., Schafer, K., and Schelling, G. 1982. *Druck and Querzug in bewehrten Betonelementen*. Bericht, Institut fur Massivbau, Unversitat Stuttgart, November.
- Ueda, M., Noguchi, H., Shirai, N., and Morita, S. 1991. Introduction to activity of new RC. In *Proceedings of the International Workshop on Finite Element Analysis of Reinforced Concrete*, Columbia University, New York
- Vecchio, F.J. and Collins, M.P. 1981. *Stress–strain characteristic of reinforced concrete in pure shear*, IABSE Colloquium, Advanced Mechanics of Reinforced Concrete, Delft, Final Report. International Association of Bridge and Structural Engineering, Zurich.
- Vecchio, F.J. and Collins, M.P., The modified compression field theory for reinforced concrete elements subjected to shear, *ACI J.*, 83, 2, 219–231, 1986.
- Vecchio, F. and Collins, M.P., Compression response of cracked reinforced concrete, *J. Struct. Eng.*, ASCE, 119, 12, 3590–3610, 1993.
- Vecchio, F.J., Collins, M.P., and Aspiotis, J., High-strength concrete elements subjected to shear, *ACI Struct. J.*, 91, 4, 423–433, 1994.
- Zhang, L.X. and Hsu, T.T.C., Behavior and analysis of 100 MPa concrete membrane elements, *J. Struct. Eng.*, ASCE, 124, 1, 24–34, 1998.
- Zhu, R.H., 2000. Softened membrane model for reinforced concrete elements considering poisson effect, Ph.D. Dissertation, Department of Civil and Environmental Engineering, University of Houston, Houston, TX.

Further Reading

- Specific topics related to reinforced concrete structures subjected to vibration and shock can be found from the following references.
- De Silva, C.W. 2000. *Vibration — Fundamentals and Practice*, CRC Press, Boca Raton, FL.
- Dowrick, D.J. 1987. *Earthquake Resistant Design*, 2nd ed., Wiley, New York.
- FEMA, 2000. *Prestandard and Commentary for the Seismic Rehabilitation of Buildings*, FEMA 356. Federal Emergency Management Agency, Washington, DC, November.
- FEMA, 2000. *Global topics Report on the Prestandard and Commentary for the Seismic Rehabilitation of Buildings*, FEMA 357. Federal Emergency Management Agency, Washington, DC, November.
- Hsu, T.T.C. 1993. *Unified Theory of Reinforced Concrete*, CRC Press, Boca Raton.

- JSCE, Earthquake resistant design codes in Japan, Earthquake engineering committee, *Jpn Soc. Civil Engrs*, 2000, Tokyo.
- Mo, Y.L. 1994. *Dynamic Behavior of Concrete Structures*, Elsevier, Amsterdam.
- Okamura, H., Maekawa, K. 1991. *Nonlinear Analysis and Constitutive Models of Reinforced Concrete*, University of Tokyo, Tokyo, ISBN 7655-1506-0.
- Paulay, T., Priestley, M.J.N. 1992. *Seismic Design of Reinforced Concrete and Masonry Buildings*, Wiley, New York.

IV

Instrumentation and Testing

15

Vibration Instrumentation

15.1	Introduction	15-1
15.2	Vibration Exciters	15-3
	Shaker Selection • Dynamics of Electromagnetic Shakers	
15.3	Control System	15-15
	Components of a Shaker Controller • Signal-Generating Equipment	
15.4	Performance Specification	15-21
	Parameters for Performance Specification • Linearity • Instrument Ratings • Accuracy and Precision	
15.5	Motion Sensors and Transducers	15-27
	Potentiometer • Variable-Inductance Transducers • Mutual-Induction Proximity Sensor • Selfinduction Transducers • Permanent-Magnet Transducers • Alternating Current Permanent-Magnet Tachometer • Alternating Current Induction Tachometer • Eddy Current Transducers • Variable-Capacitance Transducers • Piezoelectric Transducers	
15.6	Torque, Force, and Other Sensors	15-50
	Strain Gage Sensors • Miscellaneous Sensors	
	Appendix 15A Virtual Instrumentation for Data Acquisition, Analysis, and Presentation	15-73

Clarence W. de Silva

The University of British Columbia

Summary

Devices useful in instrumenting a mechanical vibrating system are presented in this chapter. Shakers, which generate vibration excitations, are discussed and compared. A variety of sensors, including motion sensors, proximity sensors, force/torque sensors, and other miscellaneous sensors, are considered. Performance specification in the time domain and the frequency domain is addressed. Rating parameters of instruments are given.

15.1 Introduction

Measurement and associated experimental techniques play a significant role in the practice of vibration. Academic exposure to vibration instrumentation usually arises in laboratories, in the context of learning, training, and research. In vibration practice, perhaps the most important task of instrumentation is the measurement or sensing of vibration. Vibration sensing is useful in the following applications:

1. Design and development of a product
2. Testing (screening) of a finished product for quality assurance
3. Qualification of a good-quality product to determine its suitability for a specific application

4. Mechanical aging of a product prior to carrying out a test program
5. Exploratory testing of a product to determine its dynamic characteristics such as resonances, mode shapes, and even a complete dynamic model
6. Vibration monitoring for performance evaluation
7. Control and suppression of vibration

Figure 15.1 indicates a procedure typical of experimental vibration, highlighting the essential instrumentation. Vibrations are generated in a device, the test object, in response to some excitation. In some experimental procedures, primarily in vibration testing (see Figure 15.1), the excitation signal has to be generated in a signal generator in accordance with some requirement (specification), and applied to the object through an exciter after amplification and conditioning. In some other situations, primarily in performance monitoring and vibration control, the excitations are generated as an integral part of the operating environment of the vibrating object and may originate either within the object (e.g., engine excitations in an automobile) or in the environment with which the object interacts during operation (e.g., road disturbances on an automobile). Sensors are needed to measure vibrations in the test object. In particular, a control sensor is used to check whether the specified excitation is applied to the object, and one or more response sensors may be used to measure the resulting vibrations at key locations of the object.

The sensor signals have to be properly conditioned, for example by filtering and amplification, and modified, for example through modulation, demodulation, and analog-to-digital conversion, prior to recording, analyzing, and display. The purpose of the controller is to guarantee that the excitation is correctly applied to the test object. If the signal from the control sensor deviates from the required excitation, the controller modifies the signal to the exciter so as to reduce this deviation. Furthermore, the controller will stabilize or limit (compress) the vibrations in the object. It follows that instruments in experimental vibration may be generally classified into the following categories:

1. Signal-generating devices
2. Vibration exciters
3. Sensors and transducers
4. Signal conditioning/modifying devices
5. Signal analysis devices
6. Control devices
7. Vibration recording and display devices

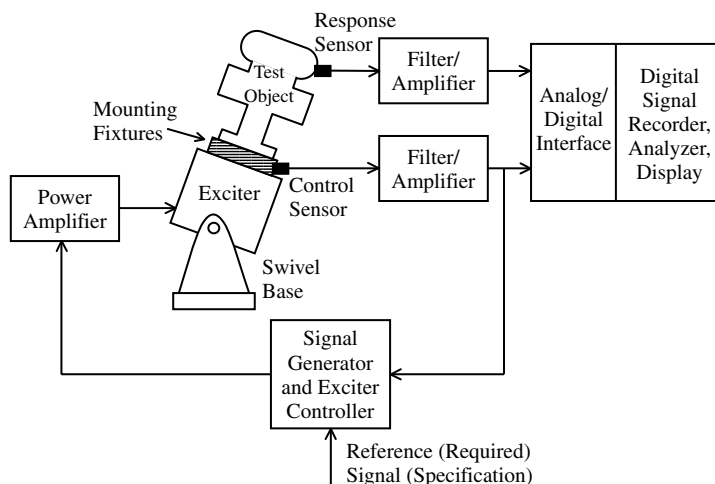


FIGURE 15.1 Typical instrumentation in experimental vibration.

Note that one instrument may perform the tasks of more than one category listed here. Also, more than one instrument may be needed to carry out tasks in a single category. In the following sections we will provide some examples of the types of vibration instrumentation, giving characteristics, operating principles, and important practical considerations. Also, we will describe several experiments which can be found in a typical vibration laboratory.

An experimental vibration system generally consists of four main subsystems:

1. Test object
2. Excitation system
3. Control system
4. Signal acquisition and modification system

These are schematically shown in Figure 15.2. Note that various components shown in Figure 15.1 may be incorporated into one of these subsystems. In particular, component matching hardware and object mounting fixtures may be considered interfacing devices that are introduced through the interaction between the main subsystems, as shown in Figure 15.2. Some important issues of vibration testing and instrumentation are summarized in Box 15.1.

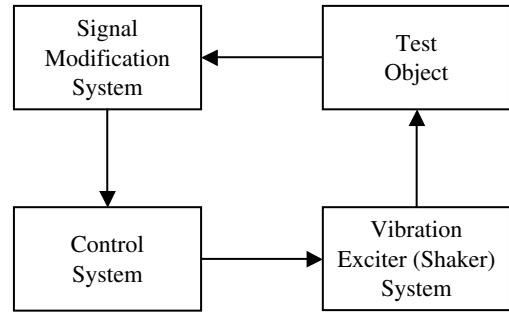


FIGURE 15.2 Interactions between major subsystems of an experimental vibration system.

15.2 Vibration Exciters

Vibration experimentation may require an external exciter to generate the necessary vibration. This is the case in controlled experiments such as product testing where a specified level of vibration is applied to the test object and the resulting response is monitored. A variety of vibration exciters are available, with different capabilities and principles of operation.

Three basic types of vibration exciters (shakers) are widely used: hydraulic shakers, inertial shakers, and electromagnetic shakers. The operation-capability ranges of typical exciters in these three categories are summarized in Table 15.1. Stroke, or maximum displacement, is the largest displacement the exciter is capable of imparting onto a test object whose weight is assumed to be within its design load limit. Maximum velocity and acceleration are similarly defined. Maximum force is the largest force that could be applied by the shaker to a test object of acceptable weight (one within the design load). The values given in Table 15.1 should be interpreted with caution. Maximum displacement is achieved only at very low frequencies. The achievement of maximum velocity corresponds to intermediate frequencies in the operating frequency range of the shaker. Maximum acceleration and force ratings are usually achieved at high frequencies. It is not feasible, for example, to operate a vibration exciter at its maximum displacement and its maximum acceleration simultaneously.

Consider a loaded exciter that is executing harmonic motion. Its displacement is given by

$$x = s \sin \omega t \quad (15.1)$$

in which s is the displacement amplitude (or stroke). Corresponding velocity and acceleration are

$$\dot{x} = s\omega \cos \omega t \quad (15.2)$$

$$\ddot{x} = -s\omega^2 \sin \omega t \quad (15.3)$$

Box 15.1

VIBRATION INSTRUMENTATION

Vibration Testing Applications for Products:

- Design and Development
- Production Screening and Quality Assessment
- Utilization and Qualification for Special Applications

Testing Instrumentation:

- Exciter (excites the test object)
- Controller (controls the exciter for accurate excitation)
- Sensors and Transducers (measure excitations and responses and provide excitation error signals to controller)
- Signal Conditioning (converts signals to appropriate form)
- Recording and Display (perform processing, storage, and documentation)

Exciters:

- Shakers
 1. Electrodynamic (high bandwidth, moderate power, complex and multifrequency excitations)
 2. Hydraulic (moderate to high bandwidth, high power, complex and multifrequency excitations)
 3. Inertial (low bandwidth, low power, single-frequency harmonic excitations)
- Transient/Initial Condition
 1. Hammers (impulsive, bump tests)
 2. Cable Release (step excitations)
 3. Drop (impulsive)

Signal Conditioning:

- Filters Amplifiers
- Amplifiers
- Modulators/Demodulators
- ADC/DAC

Sensors:

- Motion (displacement, velocity, acceleration)
- Force (strain, torque)

If the velocity amplitude is denoted by v and the acceleration amplitude by a , it follows from Equation 15.2 and Equation 15.3 that

$$v = \omega s \quad (15.4)$$

and

$$a = \omega v \quad (15.5)$$

TABLE 15.1 Typical Operation-Capability Ranges for Various Shaker Types

Shaker Type	Typical Operational Capabilities					
	Frequency	Maximum Displacement (Stroke)	Maximum Velocity	Maximum Acceleration	Maximum Force	Excitation Waveform
Hydraulic (electrohydraulic)	Low (0.1–500 Hz)	High (20 in; 50 cm)	Intermediate (50 in/sec; 125 cm/sec)	Intermediate (20 g)	High (100,000 lbf; 450,000 N)	Average flexibility (simple to complex and random)
Inertial (counter-rotating mass)	Intermediate (2–50 Hz)	Low (1 in; 2.5 cm)	Intermediate (50 in/sec; 125 cm/sec)	Intermediate (20 g)	Intermediate (1,000 lbf; 4,500 N)	Sinusoidal only
Electromagnetic (electrodynamic)	High (2–10,000 Hz)	Low (1 in; 2.5 cm)	Intermediate (50 in/sec; 125 cm/sec)	High (100 g)	Low to intermediate (450 lbf; 2,000 N)	High flexibility and accuracy (simple to complex and random)

An idealized performance curve of a shaker has a constant displacement–amplitude region, a constant velocity–amplitude region, and a constant acceleration–amplitude region for low, intermediate, and high frequencies, respectively, in the operating frequency range. Such an ideal performance curve is shown in Figure 15.3(a) on a frequency–velocity plane. Logarithmic axes are used. In practice, typical shaker performance curves would be fairly smooth yet nonlinear, curves, similar to those shown in Figure 15.3(b). As the mass increases, the performance curve compresses. Note that the acceleration limit of a shaker depends on the mass of the test object (load). Full load corresponds to the heaviest object that could be tested. The “no load” condition corresponds to a shaker without a test object. To standardize the performance curves, they are usually defined at the rated load of the shaker. A performance curve in the frequency–velocity plane may be converted to a curve in the frequency–acceleration plane simply by increasing the slope of the curve by a unit magnitude (i.e., 20 db/decade).

Several general observations can be made from Equation 15.4 and Equation 15.5. In the constant-peak displacement region of the performance curve, the peak velocity increases proportionally with the excitation frequency, and the peak acceleration increases with the square of the excitation frequency. In the constant-peak velocity region, the peak displacement varies inversely with the excitation frequency, and the peak acceleration increases proportionately. In the constant-peak acceleration region, the peak displacement varies inversely with the square of the excitation frequency, and the peak velocity varies inversely with the excitation frequency. This further explains why rated stroke, maximum velocity, and maximum acceleration values are not simultaneously realized.

15.2.1 Shaker Selection

Vibration testing is accomplished by applying a specified excitation to the test package, using a shaker apparatus, and monitoring the response of the test object. Test excitation may be represented by its response spectrum. The test requires that the response spectrum of the actual excitation, known as the test response spectrum (TRS), envelops the response spectrum specified for the particular test, known as the required response spectrum (RRS).

A major step in the planning of any vibration testing program is the selection of a proper shaker (exciter) system for a given test package. The three specifications that are of primary importance in selecting a shaker are the force rating, the power rating, and the stroke (maximum displacement) rating. Force and power ratings are particularly useful in moderate to high frequency excitations and the stroke rating is the determining factor for low frequency excitations. In this section, a procedure is given to determine conservative estimates for these parameters in a specified test for a given test package. Frequency domain considerations are used here.

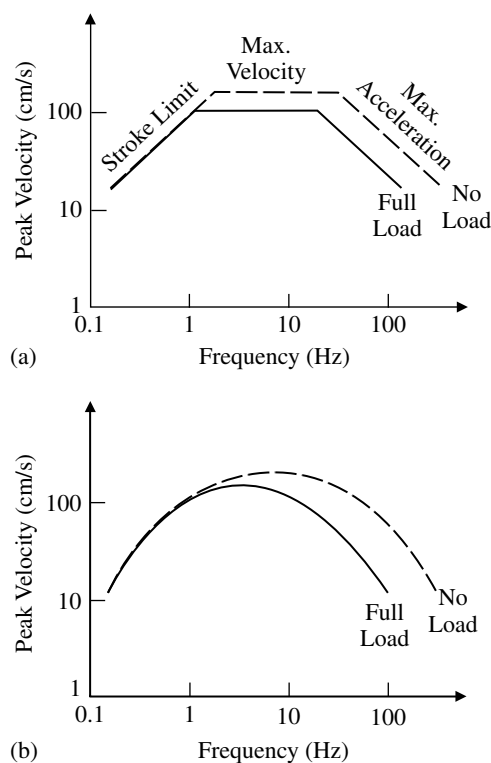


FIGURE 15.3 Performance curve of a vibration exciter in the frequency–velocity plane (log): (a) ideal; (b) typical.

15.2.1.1 Force Rating

In the frequency domain, the (complex) force at the exciter (shaker) head is given by

$$F = mH(\omega)a_s(\omega) \quad (15.6)$$

in which ω is the excitation frequency variable, m is the total mass of the test package including mounting fixture and attachments, $a_s(\omega)$ is the Fourier spectrum of the support-location (exciter head) acceleration, and $H(\omega)$ is frequency response function that takes into account the flexibility and damping effects (dynamics) of the test package apart from its inertia. In the simplified case where the test package can be represented by a simple oscillator of natural frequency ω_n and damping ratio by ζ_t , this function becomes

$$H(\omega) = \{1 + 2j\zeta_t\omega/\omega_n\} / \{1 - (\omega/\omega_n)^2 + 2j\zeta_t\omega/\omega_n\} \quad (15.7)$$

in which $j = \sqrt{-1}$. This approximation is adequate for most practical purposes. The static weight of the test object is not included in Equation 15.6. Most heavy-duty shakers, which are typically hydraulic, have static load support systems such as pneumatic cushion arrangements that can exactly balance the dead load. The exciter provides only the dynamic force. In cases where shaker directly supports the gravity load, in the vertical test configuration Equation 15.6 should be modified by adding a term to represent this weight.

A common practice in vibration test applications is to specify the excitation signal by its response spectrum. This is simply the peak response of a simple oscillator expressed as a function of its natural frequency when its support location is excited by the specified signal. Clearly, the damping of the simple oscillator is an added parameter in a response spectrum specification. Typical damping ratios (ζ_r) used in response spectra specifications are less than 0.1 (or 10%). It follows that an approximate relationship between the Fourier spectrum of the support acceleration and its response spectrum is

$$a_s = 2j\zeta_r a_r(\omega) \quad (15.8)$$

The magnitude $|a_r(\omega)|$ is the response spectrum.

Equation 15.8 substituted into Equation 15.6 gives

$$F = mH(\omega)2j\zeta_r a_r(\omega) \quad (15.9)$$

In view of Equation 15.7, for test packages having low damping the peak value of $H(\omega)$ is approximately $1/(2j\zeta_t)$; this should be used in computing the force rating if the test package has a resonance within the frequency range of testing. On the other hand, if the test package is assumed to be rigid, then $H(\omega) \cong 1$. A conservative estimate for the force rating is

$$F_{\max} = m(\zeta_r/\zeta_t)|a_r(\omega)|_{\max} \quad (15.10)$$

It should be noted that $|a_r(\omega)|_{\max}$ is the peak value of the specified (required) response spectrum (RRS) for acceleration.

15.2.1.2 Power Rating

The exciter head does not develop its maximum force when driven at maximum velocity. Output power is determined by using

$$p = \text{Re}[Fv_s(\omega)] \quad (15.11)$$

in which $v_s(\omega)$ is the Fourier spectrum of the exciter velocity, and $\text{Re} [\]$ denotes the real part of a complex function. Note that $a_s = j\omega v_s$. Substituting Equation 15.6 and Equation 15.8 into Equation 15.11 gives

$$p = (4m\zeta_r^2/\omega)\text{Re}[jH(\omega)a_r^2(\omega)] \quad (15.12)$$

It follows that a conservative estimate for the power rating is

$$p_{\max} = 2m(\zeta_r^2/\zeta_t)[|a_r(\omega)|^2/\omega]_{\max} \quad (15.13)$$

Representative segments of typical acceleration RRS curves have slope n , as given by

$$a = k_1 \omega^n \quad (15.14)$$

It should be clear from Equation 15.13 that the maximum output power is given by

$$p_{\max} = k_2 \omega^{2n-1} \quad (15.15)$$

This is an increasing function for $n > 1/2$ and a decreasing function for $n < 1/2$. It follows that the power rating corresponds to the highest point of contact between the acceleration RRS curve and a line of slope equal to $1/2$. A similar relationship may be derived if velocity RRS curves (having slopes $n - 1$) are used.

15.2.1.3 Stroke Rating

From Equation 15.8, it should be clear that the Fourier spectrum, x_s , of the exciter displacement time history can be expressed as

$$x_s = 2\zeta_r a_r(\omega)/j\omega^2 \quad (15.16)$$

An estimate for stroke rating is

$$x_{\max} = 2\zeta_r [a_r(\omega)/\omega^2]_{\max} \quad (15.17)$$

This is of the form

$$x_{\max} = k\omega^{n-2} \quad (15.18)$$

It follows that the stroke rating corresponds to the highest point of contact between the acceleration RRS curve and a line of slope equal to two.

Example 15.1

A test package of overall mass 100 kg is to be subjected to dynamic excitation represented by the acceleration RRS (at 5% damping) as shown in Figure 15.4. The estimated damping of the test package is 7%. The test package is known to have a resonance within the frequency range of the specified test. Determine the exciter specifications for the test.

Solution

From the development presented in the previous section, it is clear that the point F (or P) in Figure 15.4 corresponds to the force and output power ratings, and the point S corresponds to the stroke rating. The co-ordinates of these critical points are $F, P = (4.2 \text{ Hz}, 4.0 \text{ g})$, and $S = (0.8 \text{ Hz}, 0.75 \text{ g})$. Equation 15.10 gives the force rating as

$$F_{\max} = 100 \times (0.05/0.07) \times 4.0 \times 9.81 \text{ N} = 2803 \text{ N}$$

Equation 15.13 gives the power rating as

$$p_{\max} = 2 \times 100 \times (0.05^2/0.07) \times [(4.0 \times 9.81)^2/4.2 \times 2\pi] \text{ watts} = 417 \text{ W}$$

Equation 15.17 gives the stroke rating as

$$x_{\max} = 2 \times 0.05 \times [(0.75 \times 9.8)/(0.8 \times 2\pi)^2] \text{ m} = 3 \text{ cm}$$

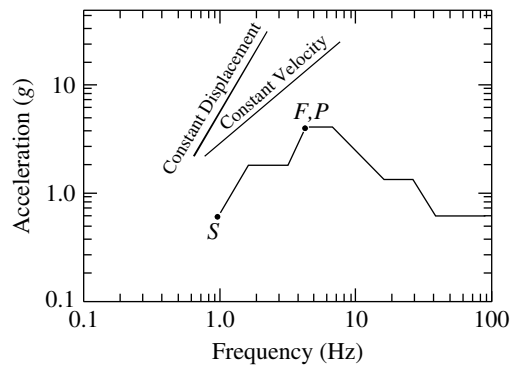


FIGURE 15.4 Test excitation specified by an acceleration RRS (5% damping).

15.2.1.4 Hydraulic Shakers

A typical hydraulic shaker consists of a piston-cylinder arrangement (also called a ram), a servo-valve, a fluid pump, and a driving electric motor. Hydraulic fluid (oil) is pressurized (typical operating pressure: 4000 psi) and pumped into the cylinder through a servo-valve by means of a pump that is driven by an electric motor (typical power, 150 hp). The flow (typical rate: 100 gal/min) that enters the cylinder is controlled (modulated) by the servo-valve, which, in effect, controls the resulting piston (ram) motion. A typical servo-valve consists of a two-stage spool valve, which provides a pressure difference and a controlled (modulated) flow to the piston, which sets it in motion.

The servo-valve itself is moved by means of a linear torque motor, which is driven by the excitation-input signal (electrical). A primary function of the servo-valve is to provide a stabilizing feedback to the ram. In this respect, the servo-valve complements the main control system of the test setup. The ram is coupled to the shaker table by means of a link with some flexibility. The cylinder frame is mounted on the support foundation with swivel joints. This allows for some angular and lateral misalignment, which might be caused primarily by test-object dynamics as the table moves.

Two-degree-of-freedom (Two-DoF) testing requires two independent sets of actuators, and three-DoF testing requires three independent actuator sets. Each independent actuator set can consist of several actuators operated in parallel, using the same pump and the same excitation-input signal to the torque motors.

If the test table is directly supported on the vertical actuators, they must withstand the total dead weight (i.e., the weight of the test table, the test object, the mounting fixtures, and the instrumentation). This requirement is usually prevented by providing a pressurized air cushion in the gap between the test table and the foundation walls. Air should be pressurized so as to balance the total dead weight exactly (typical required gage pressure: 3 psi).

Figure 15.5(a) shows the basic components of a typical hydraulic shaker. The corresponding operational block diagram is shown in Figure 15.5(b). It is desirable to locate the actuators in a pit in the test laboratory so that the test tabletop is flushed with the test laboratory floor under no-load conditions. This minimizes the effort required to place the test object on the test table. Otherwise, the test object has to be lifted onto the test table with a forklift. Also, installation of an aircushion to support the system dead weight is difficult under these circumstances of elevated mounting.

Hydraulic actuators are most suitable for heavy load testing and are widely used in industrial and civil engineering applications. They can be operated at very low frequencies (almost direct current [DC]), as well as at intermediate frequencies (see Table 15.1). Large displacements (stroke) are possible at low frequencies.

Hydraulic shakers have the advantage of providing high flexibility of operation during the test; their capabilities include variable-force and constant-force testing and wide-band random-input testing. The velocity and acceleration capabilities of hydraulic shakers are moderate. Although any general excitation-input motion (for example, sine wave, sine beat, wide-band random) can be used in hydraulic shakers, faithful reproduction of these signals is virtually impossible at high frequencies because of distortion and higher-order harmonics introduced by the high noise levels that are common in hydraulic systems. This is only a minor drawback in heavy-duty, intermediate-frequency applications. Dynamic interactions are reduced through feedback control.

15.2.1.5 Inertial Shakers

In inertial shakers, or “mechanical exciters,” the force that causes the shaker-table motion is generated by inertia forces (accelerating masses). Counter-rotating-mass inertial shakers are typical in this category. To understand their principle of operation, consider two equal masses rotating in opposite directions at the same angular speed ω and in the same circle of radius r (see Figure 15.6). This produces a resultant force equal to $2m\omega^2r \cos \omega t$ in a fixed direction (the direction of symmetry of the two rotating arms). Consequently, a sinusoidal force with a frequency of ω and an amplitude proportional to ω^2 is generated. This reaction force is applied to the shaker table.

Figure 15.7 shows a sketch of a typical counter-rotating-mass inertial shaker. It consists of two identical rods rotating at the same speed in opposite directions. Each rod has a series of slots in which to

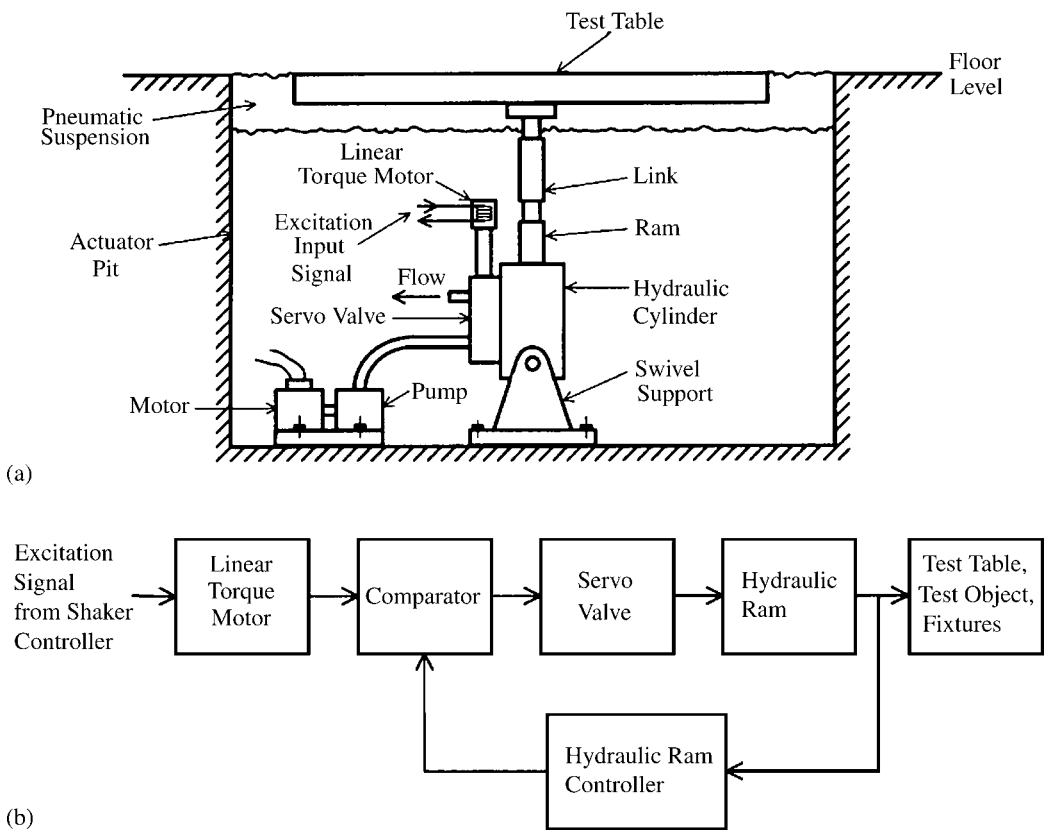


FIGURE 15.5 A typical hydraulic shaker arrangement: (a) schematic diagram; (b) operational block diagram.

place weights. In this manner, the magnitude of the eccentric mass can be varied to achieve various force capabilities. The rods are driven by a variable-speed electric motor through a gear mechanism that usually provides several speed ratios. A speed ratio is selected depending on the required test-frequency range. The whole system is symmetrically supported on a carriage that is directly connected to the test table. The test object is mounted on the test table. The preferred mounting configuration is horizontal so that the excitation force is applied to the test object in a horizontal direction. In this configuration, there are no variable gravity moments (weight \times distance to center of gravity) acting on the drive mechanism. Figure 15.7 shows the vertical configuration. In dynamic testing of large structures, the carriage can be mounted directly on the structure at a location where the excitation force should be applied. By incorporating two pairs of counter-rotating masses, it is possible to generate test moments as well as test forces.

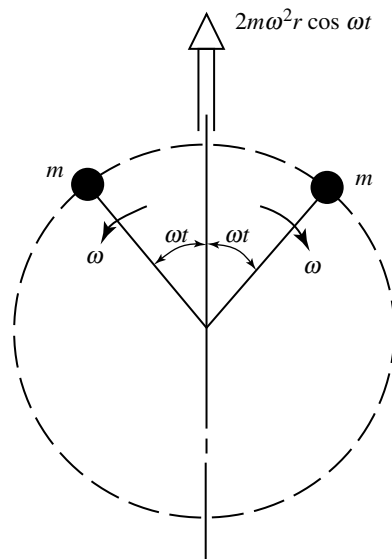


FIGURE 15.6 Principle of operation of a counter-rotating-mass inertial shaker.

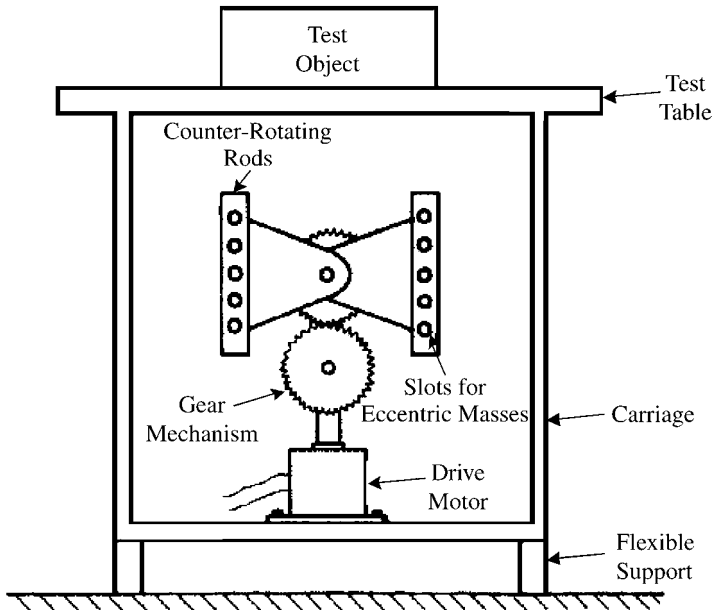


FIGURE 15.7 Sketch of a counter-rotating-mass inertial shaker.

Reaction-type shakers driven by inertia are widely used for the prototype testing of civil engineering structures. Their first application dates back to 1935. Inertial shakers are capable of producing intermediate excitation forces. The force generated is limited by the strength of the carriage frame. The frequency range of operation and the maximum velocity and acceleration capabilities are also intermediate for inertial shakers whereas the maximum displacement capability is typically low. A major limitation of inertial shakers is that their excitation force is exclusively sinusoidal and that the force amplitude is directly proportional to the square of the excitation frequency. As a result, complex and random excitation testing, constant-force testing (for example, transmissibility tests and constant-force sine-sweep tests), and flexibility to vary the force amplitude or the displacement amplitude during a test are not generally feasible with this type of shakers. Excitation frequency and amplitude can be varied during testing, however, by incorporating a variable-speed drive for the motor. The sinusoidal excitation generated by inertial shakers is virtually undistorted, which gives them an advantage over the other types of shakers when used in sine-dwell and sine-sweep tests. Small portable shakers with low-force capability are available for use in on-site testing.

15.2.1.6 Electromagnetic Shakers

In electromagnetic shakers or “electrodynamic exciters,” the motion is generated using the principle of operation of an electric motor. Specifically, the excitation force is produced when a variable excitation signal (electrical) is passed through a moving coil placed in a magnetic field.

The components of a commercial electromagnetic shaker are shown in Figure 15.8. A steady magnetic field is generated by a stationary electromagnet that consists of field coils wound on a ferromagnetic base that is rigidly attached to a protective shell structure. The shaker head has a coil wound around it. When the excitation electrical signal is passed through this drive coil, the shaker head, which is supported on flexure mounts, will be set in motion. The shaker head consists of the test table on which the test object is mounted. Shakers with interchangeable heads are available. The choice of appropriate shaker head is based on the geometry and mounting features of the test object. The shaker head can be turned to different angles by means of a swivel joint. In this manner, different directions of excitation (in biaxial and triaxial testing) can be obtained.

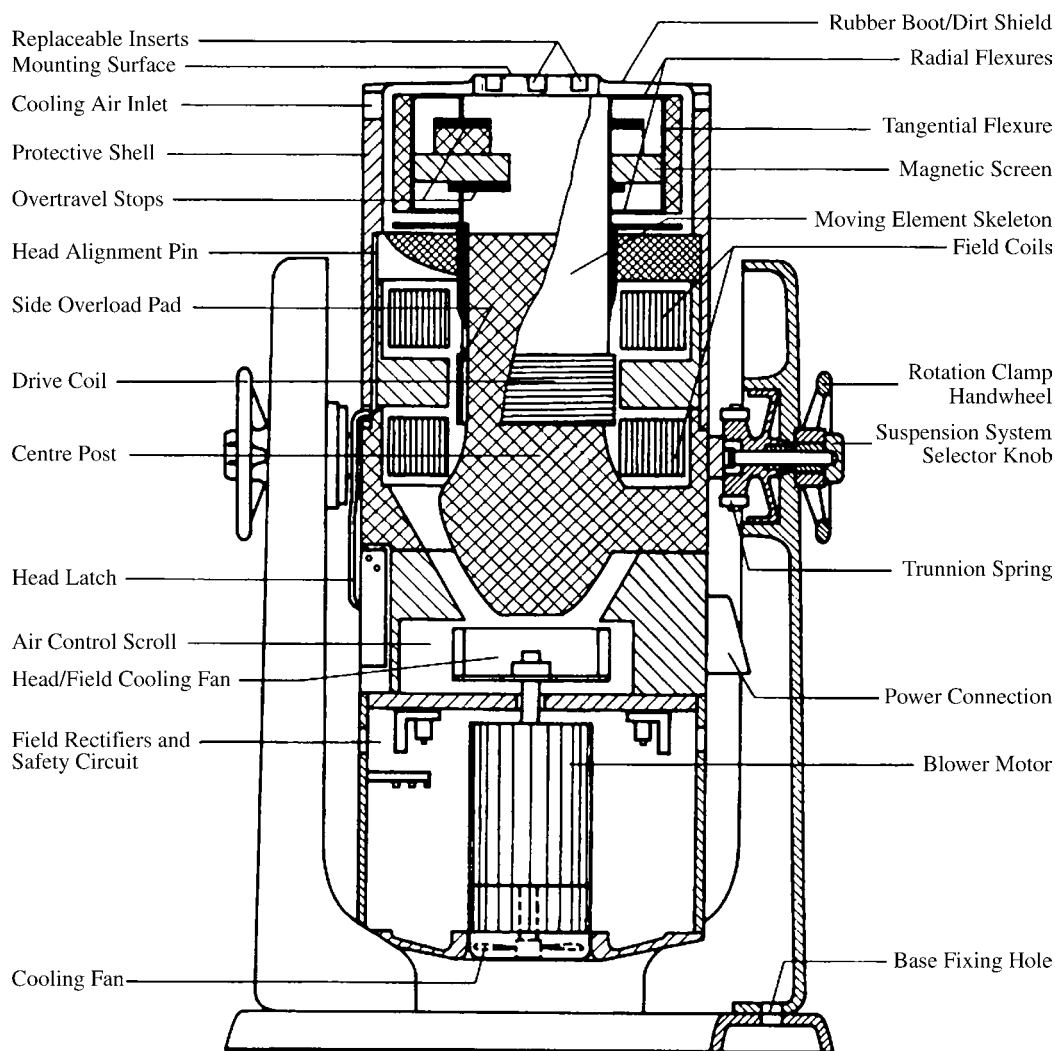


FIGURE 15.8 Schematic sectional view of a typical electromagnetic shaker, manufactured by Bruel and Kjaer, Denmark.

15.2.2 Dynamics of Electromagnetic Shakers

Consider a single axis electromagnetic shaker (Figure 15.8) with a test object having a single natural frequency of importance within the test frequency range. The dynamic interactions between the shaker and the test object give rise to two significant natural frequencies (and correspondingly, two significant resonances). These appear as peaks in the frequency response curve of the test setup. Furthermore, the natural frequency (resonance) of the test package alone causes a “trough” or depression (antiresonance) in the frequency response curve of the overall test setup. To explain this characteristic, consider the dynamic model shown in Figure 15.9. The following mechanical parameters are defined for Figure 15.9(a): m , k , and b are the mass, stiffness, and equivalent viscous damping constant, respectively, of the test package, and m_e , k_e , and b_e are the corresponding parameters of the exciter (shaker). Also, in the equivalent electrical circuit of the shaker head, as shown in Figure 15.9(b), the following electrical parameters are defined: R_e and L_e are the resistance and (leakage) inductance and k_b is the back electromotive force (back emf) of the linear motor. Assuming that the gravitational forces are supported

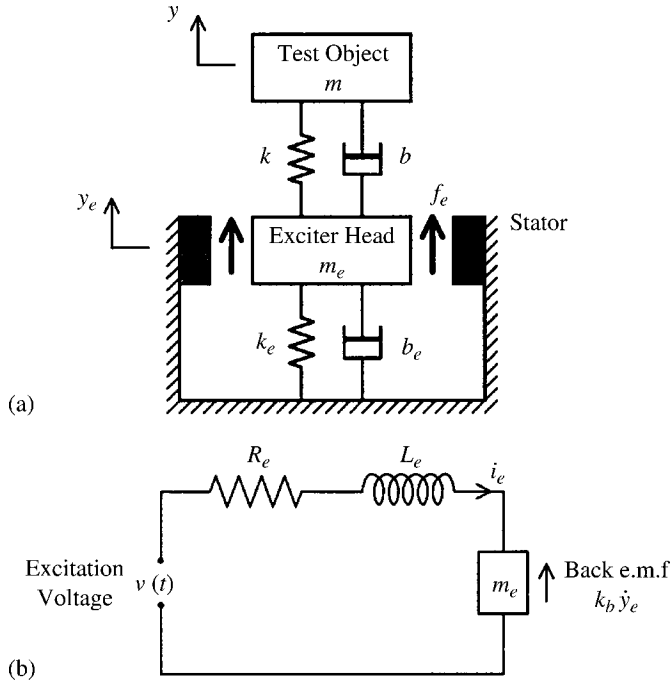


FIGURE 15.9 Dynamic models of an electromagnetic shaker and a flexible test package: (a) mechanical model; (b) electrical model.

by the static deflections of the flexible elements, and that the displacements are measured from the static equilibrium position, we have the following system equations:

$$\text{Test object: } m\ddot{y} = -k(y - y_e) - b(\dot{y} - \dot{y}_e) \quad (15.19)$$

$$\text{Shaker head: } m_e\ddot{y}_e = f_e + k(y - y_e) + b(\dot{y} - \dot{y}_e) - k_e y - b_e \dot{y}_e \quad (15.20)$$

$$\text{Electrical: } L_e \frac{di_e}{dt} + R_e i_e + k_b \dot{y}_e = v(t) \quad (15.21)$$

The electromagnetic force f_e generated in the shaker head is a result of the interaction of the magnetic field generated by the current i_e with coil of the moving shaker head and the constant magnetic field (stator) in which the head coil is located. Here, we have

$$f_e = k_b i_e \quad (15.22)$$

Note that $v(t)$ is the voltage signal that is applied by the amplifier to the shaker coil, y_e is the displacement of the shaker head, and y is the displacement response of the test package.

It is assumed that k_b has consistent electrical and mechanical units (V/m/sec and N/A). Usually, the electrical time constant of the shaker is quite small compared with the primarily mechanical time constants of the shaker and the test package. In such cases, the $L_e di_e/dt$ term in Equation 15.21 may be neglected. Consequently, the equations from Equation 15.19 through Equation 15.22 may be expressed in the Laplace (frequency) domain, with the Laplace variable s taking the place of the derivative d/dt , as

$$(ms^2 + bs + k)y = (bs + k)y_e \quad (15.23)$$

$$[m_e s^2 + (b + b_e)s + (k + k_e)]y_e = (bs + k)y + \frac{k_b}{R_e}v - \frac{k_b^2 s}{R_e}y_e \quad (15.24)$$

It follows that the transfer function of the shaker head motion with respect to the excitation voltage is given by

$$\frac{y_e}{v} = \frac{k_b}{R_e} \frac{\Delta(s)}{\Delta_d(s)} \quad (15.25)$$

where $\Delta(s)$ is the characteristic function of the primary dynamics of the test object

$$\Delta(s) = ms^2 + bs + k \quad (15.26)$$

and $\Delta_d(s)$ is the characteristic function of the primary dynamic interactions between the shaker and the test object

$$\Delta_c(s) = mm_e s^4 + [m(b_e + b + b_o) + m_e b]s^3 + [m(k_e + k) + m_e k + b(b_e + b_o)]s^2 + [bk_e + (b_e + b_o)k]s + kk_e \quad (15.27)$$

where

$$b_o = \frac{k_b^2}{R_e} \quad (15.28)$$

It is clear that under low damping conditions $\Delta_d(s)$ will produce two resonances as it is fourth order in s , and similarly $\Delta(s)$ will produce one antiresonance (trough) corresponding to the resonance of the test object. Note that in the frequency domain, $s = j\omega$, and hence the frequency response function given by Equation 15.25, is in fact

$$\frac{y_e}{v} = \frac{k_b}{R_e} \frac{\Delta(j\omega)}{\Delta_d(j\omega)} \quad (15.29)$$

The magnitude of this frequency response function for a typical test system is sketched in Figure 15.10. Note that this curve is for the “open-loop” case where there is no feedback from the shaker controller. In practice, the shaker controller will be able to compensate for the resonances and anti-resonances to some degree, depending on its effectiveness.

The main advantages of electromagnetic shakers are their high frequency range of operation, their high degree of operating flexibility, and the high level of accuracy of the generated shaker motion. Faithful reproduction of complex excitations is possible because of the advanced electronics and control systems used in this type of shakers. Electromagnetic shakers are not suitable for heavy-duty applications (large test objects), however. High test-input accelerations are possible at high frequencies when electromagnetic shakers are used, but their displacement and velocity capabilities are limited to low or intermediate values (see Table 15.1).

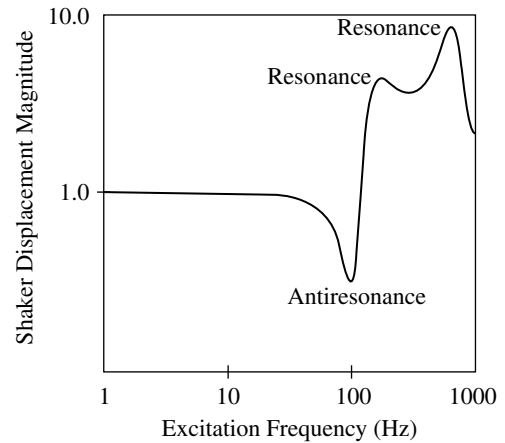


FIGURE 15.10 Frequency response curve of a typical electromagnetic shaker with a test object.

15.2.2.1 Transient Exciters

Other varieties of exciters are commonly used in transient-type vibration testing. In these tests, either an impulsive force or an initial excitation is applied to the test object and the resulting response is monitored. The excitations and the responses are “transient” in this case. Hammer test, drop tests, and pluck tests fall into this category. For example, a hammer test may be conducted by hitting the object with an instrumented hammer and then measuring the response of the object. The hammer has a force sensor at its tip, as sketched in Figure 15.11. A piezoelectric or strain-gage type force sensor may be used. More sophisticated hammers have impedance heads in place of force sensors. An impedance head measures force and acceleration simultaneously. The results of a hammer test will depend on many factors; for example, the dynamics of the hammer body, how firmly the hammer is held during the impact, how quickly the impact is applied, and whether there are multiple impacts.

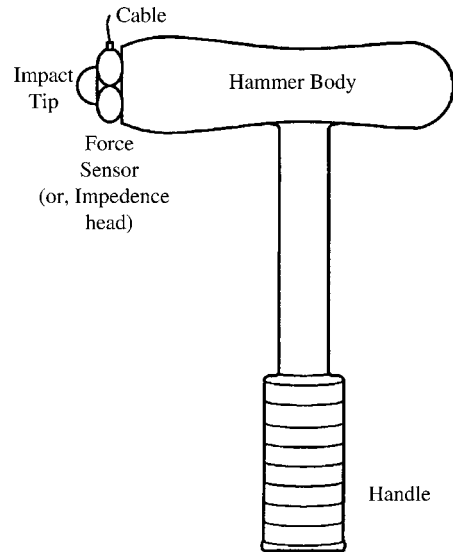


FIGURE 15.11 An instrumented hammer used in bump tests or hammer tests.

15.3 Control System

The two primary functions of the shaker control system in vibration testing are (1) to guarantee that the specified excitation is applied to the test object and (2) to ensure that the dynamic stability (motion constraints) of the test setup is preserved. An operational block diagram illustrating these control functions is given in Figure 15.12. The reference input to the control system represents the desired excitation force that should be applied to the test object. In the absence of any control, however, the force reaching the test object will be distorted, primarily because of: (1) dynamic interactions and nonlinearities of the shaker, the test table, the mounting fixtures, the auxiliary instruments, and the test object itself; (2) noise and errors in the signal generator, amplifiers, filters, and other equipment; and (3) external loads and disturbances acting on the test object and other components (for example, external restraints, aerodynamic forces, friction). To compensate for these distorting factors, response measurements (displacements, velocities, acceleration, and so on) are made at various locations in the test setup and are used to control the system dynamics. In particular, the responses of the shaker, the test table, and the test object are measured. These responses are used to compare the actual excitation felt by

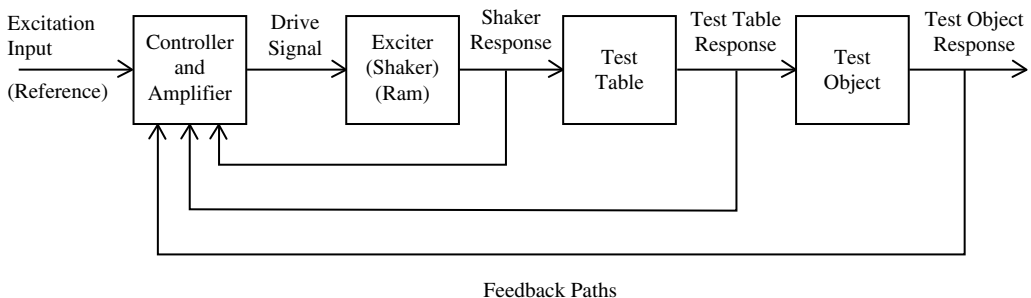


FIGURE 15.12 Operational block diagram illustrating a general shaker control system.

the test object at the shaker interface, with the desired (specified) input. The drive signal to the shaker is modified, depending on the error that is present.

Two types of control are commonly employed in shaker apparatus: simple manual control and complex automatic control. Manual control normally consists of simple, open-loop, trial-and-error methods of manual adjustments (or calibration) of the control equipment to obtain a desired dynamic response. The actual response is usually monitored (on an oscilloscope or frequency analyzer screen, for example) during manual-control operations. The pretest adjustments in manual control can be very time-consuming; as a result, the test object might be subjected to overtesting, which could produce cumulative damage, is undesirable, and could defeat the test purpose. Furthermore, the calibration procedure for the experimental setup must be repeated for each new test object.

The disadvantages of manual control suggest that automatic control is desirable in complex test schemes in which high accuracy of testing is desired. The first step of automatic control involves automatic measurement of the system response, using control sensors and transducers. The measurement is then fed back into the control system, which instantaneously determines the best drive signal to actuate the shaker in order to get the desired excitation. This may be done by either analog or digital methods.

Primitive control systems require an accurate mathematical description of the test object. This dependency of the control system on the knowledge of test-object dynamics is clearly undesirable. Performance of a good control system should not be considerably affected by the dynamic interactions and nonlinearities of the test object or by the nature of the excitation. Proper selection of feedback signals and control-system components can reduce such effects and will make the system robust.

In the response-spectrum method of vibration testing, it is customary to use displacement control at low frequencies, velocity control at intermediate frequency, and acceleration control at high frequencies. This necessitates feedback of displacement, velocity, and acceleration responses. Generally, however, the most important feedback is the velocity feedback. In sine-sweep tests, the shaker velocity must change steadily over the frequency band of interest. In particular, the velocity control must be precise near the resonances of the test object. Velocity (speed) feedback has a stabilizing effect on the dynamics, which is desirable. This effect is particularly useful in ensuring stability in motion when testing is done near resonances of lightly damped test objects. On the contrary, displacement (position) feedback can have a destabilizing effect on some systems, particularly when high feedback gains are used.

The controller usually consists of various instruments, equipment, and computation hardware and software. Often, the functions of the data-acquisition and processing system overlap with those of the controller to some extent. As an example, consider the digital-controller of vibration testing apparatus. First, the responses are measured through sensors (and transducers), filtered, and amplified (conditioned). These data channels may be passed through a multiplexer, whose purpose is to select one data channel at a time for processing. Most modern data acquisition hardware does not need a separate multiplexer to handle multiple signals. The analog data are converted into digital data using analog-to-digital converters (ADCs). The resulting sampled data are stored on a disk or as a block data in the computer memory. The reference input signal (typically, a signal recorded on an FM tape) is also sampled (if it is not already in the digital form), using an ADC, and fed into the computer. Digital processing is done on the reference signal and the response data, with the objective of computing the command signal to drive the shaker. The digital command signal is converted into an analog signal, using a digital-to-analog converter (DAC), and amplified (conditioned) before it is used to drive the exciter.

The nature of the control components depends to a large extent on the nature and objectives of the particular test to be conducted. Some of the basic components in a shaker controller are described in the following subsections.

15.3.1 Components of a Shaker Controller

15.3.1.1 Compressor

A compressor circuit is incorporated in automatic excitation control devices to control the excitation-input level automatically. The level of control depends on the feedback signal from a control sensor and

the specified (reference) excitation signal. Usually, the compressor circuit is included in the excitation-signal generator (for example, in a sine generator). The control by this means may be done on the basis of a single-frequency component (e.g., the fundamental frequency).

15.3.1.2 Equalizer (Spectrum Shaper)

Random-signal equalizers are used to shape the spectrum of a random signal in a desired manner. In essence, an equalizer consists of a bank of narrow-band filters (for example, 80 filters) in parallel over the operating frequency range. By passing the signal through each filter, the spectral density (or the mean square value) of the signal in that narrow frequency band (for example, each one-third-octave band) is determined. This is compared with the desired spectral level, and automatic adjustment is made in that filter in case there is an error. In some systems, response-spectrum analysis is made in place of power spectral density analysis. In that case, the equalizer consists of a bank of simple oscillators, whose resonant frequencies are distributed over the operating frequency range of the equalizer. The feedback signal is passed through each oscillator, and the peak value of its output is determined. This value is compared with the desired response spectrum value at that frequency. If there is an error, automatic gain adjustment is made in the appropriate excitation signal components.

Random-noise equalizers are used in conjunction with random signal generators. They receive feedback signals from the control sensors. In some digital control systems, there are algorithms (software) that are used to iteratively converge the spectrum of the excitation signal felt by the test object into the desired spectrum.

15.3.1.3 Tracking Filter

Many vibration tests are based on single-frequency excitations. In such cases, the control functions should be performed on the basis of the amplitudes of the fundamental-frequency component of the signal. A tracking filter is simply a frequency-tuned band-pass filter. It automatically tunes the center frequency of its very narrow-band-pass filter to the frequency of a carrier signal. Then, when a noisy signal is passed through the tuned filter, the output of the filter will be the required fundamental frequency component in the signal. Tracking filters also are useful in obtaining amplitude–frequency plots using an $X-Y$ plotter. In such cases, the frequency value comes from the signal generator (sweep oscillator), which produces the carrier signal to the tracking filter. The tracking filter then determines the corresponding amplitude of a signal that is fed into it. Most tracking filters have dual channels so that two signals can be handled (tracked) simultaneously.

15.3.1.4 Excitation Controller (Amplitude Servo-Monitor)

An excitation controller is typically an integral part of the signal generator. It can be set so that automatic sweep between two frequency limits can be performed at a selected sweep rate (linear or logarithmic). More advanced excitation controllers have the capability of an automatic switch-over between constant-displacement, constant-velocity and constant-acceleration excitation-input control at specified frequencies over the sweep frequency interval. Consequently, integrator circuits should be present within the excitation controller unit to determine velocities and displacements from acceleration signals. Sometimes, integration is performed by a separate unit called a *vibration meter*. This unit also offers the operator the capability of selecting the desired level of each signal (acceleration, velocity, or displacement). There is an automatic cut-off level for large displacement values that could result from noise in acceleration signals. A compressor is also a subcomponent of the excitation controller. The complete unit is sometimes known as an amplitude servo-monitor.

15.3.2 Signal-Generating Equipment

Shakers are force-generating devices that are operated using drive (excitation) signals generated from a source. The excitation-signal source is known as the signal generator. Three major types of signal generators are used in vibration testing applications: (1) oscillators, (2) random-signal generators, and (3) storage devices. In some units, oscillators and random-signal generators are combined. We shall

discuss these two generators separately, however, because of their difference in function. It also should be noted that almost any digital signal (deterministic or random) can be generated by a digital computer using a suitable computer program; the signal eventually can be passed through a DAC to obtain the corresponding analog signal. These 'digital' signal generators along with analog sources such as magnetic tape players (FM) are classified into the category of storage devices.

The dynamic range of equipment is the ratio of the maximum and minimum output levels (expressed in decibels) at which it is capable of operating without significant error. This is an important specification for many types of equipment, particularly for signal-generating devices. The output level of the signal generator should be set to a value within its dynamic range.

15.3.2.1 Oscillators

Oscillators are essentially single-frequency generators. Typically, sine signals are generated, but other waveforms (such as rectangular and triangular pulses) are also available in most oscillators. Normally, an oscillator has two modes of operation: (1) sweeping up and down between two frequency limits and (2) dwelling at a specified frequency. In the sweep operation, the sweep rate should be specified. This can be done either on a linear scale (Hz/min) or on a logarithmic scale (octaves/min). In the dwell operation, the frequency points (or intervals) should be specified. In either case, a desired signal level can be chosen using the gain-control knob. An oscillator that is operated exclusively in the sweep mode is called a sweep oscillator.

The early generation of oscillators employed variable inductor-capacitor types of electronic circuits to generate signals oscillating at a desired frequency. The oscillator is tuned to the required frequency by varying the capacitance or inductance parameters. A DC voltage is applied to energize the capacitor and to obtain the desired oscillating voltage signal, which subsequently is amplified and conditioned. Modern oscillators use operational amplifier circuits along with resistor, capacitor, and semiconductor (SC) elements. Also common are crystal (quartz) parallel-resonance oscillators, used to generate voltage signals accurately at a fixed frequency. The circuit is activated using a DC-voltage source. Other frequencies of interest are obtained by passing this high-frequency signal through a frequency converter. The signal is then conditioned (amplified and filtered). Required shaping (for example, rectangular pulse) is obtained using a shape circuit. Finally, the required signal level is obtained by passing the resulting signal through a variable-gain amplifier. A block diagram of an oscillator, illustrating various stages in the generation of a periodic signal, is given in Figure 15.13.

A typical oscillator offers a choice of several (typically six) linear and logarithmic frequency ranges and a sizable level of control capability (for example, 80 dB). Upper and lower frequency limits in a sweep can be preset on the front panel to any of the available frequency ranges. Sweep-rate settings are continuously

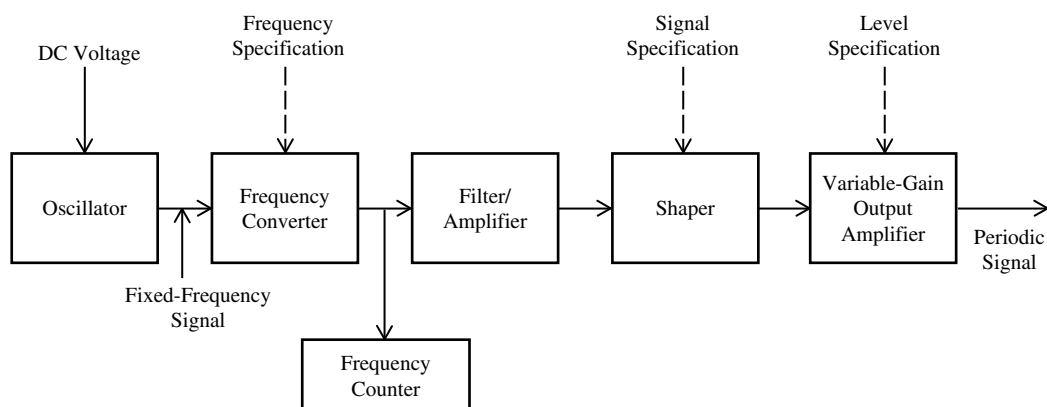


FIGURE 15.13 Block diagram of an oscillator-type signal generator.

variable (typically, 0 to 10 octaves/min in the logarithmic range, and 0 to 60 kHz/min in the linear range), but one value must be selected for a given test or part of a test. Most oscillators have a repetitive-sweep capability, which allows the execution of more than one sweep continuously, for example, for mechanical aging and in product-qualification single-frequency tests. Some oscillators also have the capability of varying the signal level (amplitude) during each test cycle (sweep or dwell). This is known as level programming. Also, automatic switching between acceleration, velocity, and displacement excitations at specified frequency points in each test cycle can be implemented with some oscillators. A frequency counter, which is capable of recording the fundamental frequency of the output signal, is usually an integral component of the oscillator.

15.3.2.2 Random Signal Generators

In modern random-signal generators, SC devices (e.g., zener diodes) are used to generate a random signal that has a required (e.g., Gaussian) distribution. This is accomplished by applying a suitable DC voltage to a SC circuit. The resulting signal is then amplified and passed through a bank of conditioning filters, which effectively acts as a spectrum shaper. In this manner, the bandwidth of the signal can be adjusted in a desired manner. Extremely wideband signals (white noise), for example, can be generated for random-excitation vibration testing in this manner. The block diagram in Figure 15.14 shows the essential steps in a random-signal generation process. A typical random-signal generator has several (typically eight) bandwidth selections over a wide frequency range (for example, 1 Hz to 100 kHz). A level-control capability (typically 80 dB) is also available.

15.3.2.3 Tape Players

Vibration testing for product qualification may be performed using a tape player as the signal source. A tape player is essentially a signal reproducer. The test-input signal that has a certain specified response spectrum is obtained by playing a magnetic tape and mixing the contents in the several tracks of the tape in a desirable ratio. Typically, each track contains a sine-beat signal, with a particular beat frequency, amplitude, and number of cycles per beat, or a random-signal component with a desired spectral characteristic).

In frequency modulation (FM) tapes, the signal amplitude is proportional to the frequency of a carrier signal. The carrier signal is recorded on the tape. When played back, the actual signal is reproduced, based on detecting the frequency content of the carrier signal in different time points. The FM method is usually favorable, particularly for low-frequency testing (below 100 Hz).

Performance of a tape player is determined by several factors, including tape type and quality, signal reproduction and recording circuitry, characteristics of the magnetic heads, and the tape-transport mechanism. Some important specifications for tape players are (1) the number of tracks per tape (for example, 14 or 28); (2) the available tape speeds (for example, 3.75, 7.5, 15, or 30 in./sec); (3) reproduction filter-amplifier capabilities (for example, 0.5% third-harmonic distortion in a 1 kHz signal recorded at 15 in./sec tape speed, peak-to-peak output voltage of 5 V at 100 Ω load, signal-to-noise ratio of 45 dB, output impedance of 50 Ω); and (4) the available control options and their capabilities (for example, stop, play, reverse, fast-forward, record, speed selection, channel selection). Tape player specifications for vibration testing are governed by an appropriate regulatory agency, according to a

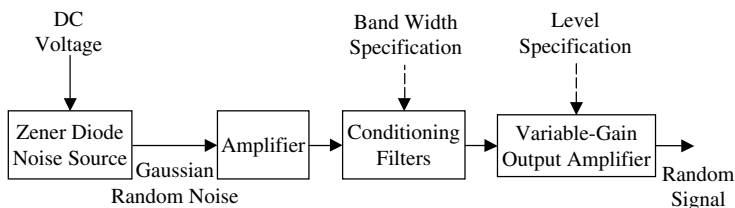


FIGURE 15.14 Block diagram of a random signal generator.

specified standard (e.g., the Communication and Telemetry Standard of the Intermediate Range Instrumentation Group (IRIG Standard 106-66)).

A common practice in vibration testing is to generate the test-input signal by repetitively playing a closed tape loop. In this manner, the input signal becomes periodic but has the desired frequency content. Frequency modulation players can be fitted with special loop adaptors for playing tape loops. In spectral (Fourier) analysis of such signals, the analyzing-filter bandwidth should be several times more than the repetition frequency (tape speed/loop length). Extraneous noise is caused by discontinuities at the tape joint. This can be suppressed by using suitable filters or gating circuits.

A technique that can be employed to generate low-frequency signals with high accuracy is to record the signal first at a very low tape speed and then play it back at a high tape speed (for example, r times higher). This has the effect of multiplying all frequency components in the signal by the speed ratio (r). Consequently, the filter circuits in the tape player will allow some low-frequency components in the signal that would normally be cut off and will cut off some high-frequency components that would normally be allowed. Hence, this process is a way of emphasizing the low-frequency components in a signal.

15.3.2.4 Data Processing

A controller generally has some data processing functions, as well. A data-acquisition and processing system usually consists of response sensors (and transducers), signal conditioners, an input–output (I/O) board including a multiplexer, ADCs, etc., and a digital computer, with associated I/O devices. The functions of a digital data-acquisition and processing system may be quite general, as listed below:

1. Measuring, conditioning, sampling, and storing the response signals and operational data of test object (using input commands, as necessary)
2. Digital processing of the measured data according to the test objectives (and using input commands, as necessary)
3. Generating drive signals for the control system
4. Generating and recording test results (responses) in a required format

The capacity and the capabilities of a data-acquisition and processing systems are determined by such factors as:

1. The number of response data channels that can be handled simultaneously
2. The data-sampling rate (samples per second) for each data channel
3. Computer memory size
4. Computer processing speed
5. External storage capability (hard disks, floppy disks, and so forth)
6. The nature of the input and output devices
7. Software features

Commercial data-acquisition and processing systems with a wide range of processing capabilities are available for use in vibration testing. Some of the standard processing capabilities are the following:

1. Response-spectrum analysis
2. FFT analysis (spectral densities, correlations, coherence, Fourier spectra, and so on)
3. Frequency-response function, transmissibility, and mechanical-impedance analysis
4. Natural-frequency and mode-shape analysis
5. System-parameter identification (for example, damping parameters)

Most processing is done in real time, which means that the signals are analyzed as they are being measured. The advantage of this is that outputs and command signals are available simultaneously as the monitoring is done, so that any changes can be detected as they occur (for example, degradation in the

test object or deviations in the excitation signal from the desired form) and automatic feedback control can be effected. For real-time processing to be feasible, the data-acquisition rate (sampling rate) and the processing speed of the computer should be sufficiently fast. In real-time frequency analysis, the entire frequency range is analyzed at a given instant, as opposed to analyzing narrow bands separately. Results are presented as Fourier spectra, power spectral densities, cross-spectral densities, coherence functions, correlation functions, and response-spectra curves. Averaging of frequency plots can be done over small frequency bands (for example, one-third-octave analysis), or the running average of each instantaneous plot can be determined.

15.4 Performance Specification

Proper selection and integration of sensors and transducers are crucial in “instrumenting” a vibrating system. The response variable that is being measured (for example, acceleration) is termed the *measurand*. A measuring device passes through two stages in making a measurement. First, the measurand is sensed. Then, the measured signal is transduced (converted) into a form that is particularly suitable for signal conditioning, processing, or recording. Often, the output from the *transducer* stage is an electrical signal. It is common practice to identify the combined sensor–transducer unit as either a sensor or a transducer.

The measuring device itself might contain some of the signal-conditioning circuitry and recording (or display) devices or meters. These are components of an overall measuring system. For our purposes, we shall consider these components separately.

In most applications, the following four variables are particularly useful in determining the response and structural integrity of a vibrating system (in each case the usual measuring devices are indicated in parentheses):

1. Displacement (potentiometer or LVDT)
2. Velocity (tachometer)
3. Acceleration (accelerometer)
4. Stress and strain (strain gage)

It is somewhat common practice to measure acceleration first and then determine velocity and displacement by direct integration. Any noise and DC components in the measurement, however, could give rise to erroneous results in such cases. Consequently, it is good practice to measure displacement, velocity, and acceleration by using separate sensors, particularly when the measurements are employed in feedback control of the vibratory system. It is not recommended to differentiate a displacement (or velocity) signal to obtain velocity (or acceleration), because this process would amplify any noise present in the measured signal. Consider, for example, a sinusoidal signal given by $A \sin \omega t$. Since $d/dt(A \sin \omega t) = A\omega \cos \omega t$, it follows that any high-frequency noise would be amplified by a factor proportional to its frequency. Also, any discontinuities in noise components would produce large deviations in the results. Using the same argument, it may be concluded that the acceleration measurements are desirable for high-frequency signals and the displacement measurements are desirable for low-frequency signals. It follows that the selection of a particular measurement transducer should depend on the frequency content of the useful portion of the measured signal.

Transducers are divided into two broad categories: active transducers and passive transducers. Passive transducers do not require an external electric source for activation. Some examples are electromagnetic, piezoelectric, and photovoltaic transducers. Active transducers, however, do not possess self-contained energy sources and thus need external activation. A good example is a resistive transducer, such as a potentiometer.

In selecting a particular transducer (measuring device) for a specific vibration application, special attention should be given to its ratings, which usually are provided by the manufacturer, and the required performance specifications as provided by the customer (or developed by the system designer).

15.4.1 Parameters for Performance Specification

A *perfect measuring device* can be defined as one that possesses the following characteristics:

1. Output instantly reaches the measured value (fast response).
2. Transducer output is sufficiently large (high gain, low output impedance, high sensitivity).
3. Output remains at the measured value (without drifting or being affected by environmental effects and other undesirable disturbances and noise) unless the measurand itself changes (stability and robustness).
4. The output signal level of the transducer varies in proportion to the signal level of the measurand (static linearity).
5. Connection of a measuring device does not distort the measurand itself (loading effects are absent and impedances are matched).
6. Power consumption is small (high input impedance).

All these properties are based on dynamic characteristics and therefore can be explained in terms of dynamic behavior of the measuring device. In particular, items 1 to 4 can be specified in terms of the device (response), either in the *time domain* or in the *frequency domain*. Items 2, 5, and 6 can be specified using the *impedance* characteristics of a device. First, we shall discuss response characteristics that are important in performance specification of a sensor/transducer unit.

15.4.1.1 Time-Domain Specifications

Several parameters that are useful for the time-domain performance specification of a device are as follows:

1. *Rise time* (T_r): This is the time taken to pass the steady-state value of the response for the first time. In overdamped systems, the response is nonoscillatory; consequently, there is no overshoot. So that the definition is valid for all systems, rise time is often defined as the time taken to pass 90% of the steady-state value for the first time. Rise time is often measured from 10% of the steady-state value in order to leave out irregularities occurring at start-up and time lags that might be present in a system. Rise time represents the speed of response of a device: a small rise time indicates a fast response.
2. *Delay time* (T_d): This is usually defined as the time taken to reach 50% of the steady-state value for the first time. This parameter is also a measure of the speed of response.
3. *Peak time* (T_p): This is the time at the first peak. This parameter also represents the speed of response of the device.
4. *Settling time* (T_s): This is the time taken for the device response to settle down within a certain percentage (e.g., $\pm 2\%$) of the steady-state value. This parameter is related to the degree of damping present in the device as well as the degree of stability.
5. *Percentage overshoot* (PO): This is defined as

$$PO = 100(M_p - 1)\% \quad (15.30)$$

using the normalized-to-unity step response curve, where M_p is the peak value. Percentage overshoot is a measure of damping or relative stability in the device.

6. *Steady-state error*: This is the deviation of the actual steady-state value from the desired value. Steady-state error may be expressed as a percentage with respect to the (desired) steady-state value. In a measuring device, steady-state error manifests itself as an offset. This is a systematic (deterministic) error that normally can be corrected by recalibration. In servo-controlled devices, steady-state error can be reduced by increasing the loop gain or by introducing a lag compensation. Steady-state error can be completely eliminated using the integral control (*reset*) action.

For the best performance of a measuring device, we wish to have the values of all the foregoing parameters as small as possible. In actual practice, however, it might be difficult to meet all specifications, particularly under conflicting requirements. For instance, T_r can be decreased by increasing the dominant natural frequency ω_n of the device. This, however, increases the PO and sometimes the T_s . On the other hand, the PO and T_s can be decreased by increasing device damping, but this has the undesirable effect of increasing T_r .

15.4.1.2 Frequency-Domain Specifications

Since any time signal can be decomposed into sinusoidal components through Fourier transformation, it is clear that the response of a system to an arbitrary input excitation also can be determined using transfer-function (frequency response-function) information for that system. For this reason, one could argue that it is redundant to use both time-domain specifications and frequency-domain specifications, as they carry the same information. Often, however, both specifications are used simultaneously, because this can provide a better understanding of the system performance. Frequency-domain parameters are more suitable in representing some characteristics of a system under some types of excitation.

Consider a device with the frequency-response function (transfer function) $G(j\omega)$. Some useful parameters for performance specification of the device in the frequency domain are:

1. Useful frequency range (operating interval): This is given by the flat region of the frequency response magnitude, $|G(j\omega)|$, of the device.
2. Bandwidth (speed of response): This may be represented by the primary natural frequency (or resonant frequency) of the device.
3. Static gain (steady-state performance): Since static conditions correspond to zero frequencies; this is given by $G(0)$.
4. Resonant frequency (speed and critical frequency region) ω_r : This corresponds to the lowest frequency at which $|G(j\omega)|$ peaks.
5. Magnitude at resonance (stability): This is given by $|G(j\omega_r)|$.
6. Input impedance (loading, efficiency, interconnectability): This represents the dynamic resistance as felt at the input terminals of the device. This parameter will be discussed in more detail under component interconnection and matching.
7. Output impedance (loading, efficiency, interconnectability): This represents the dynamic resistance as felt at the output terminals of the device.
8. Gain margin (stability): This is the amount by which the device gain could be increased before the system becomes unstable.
9. Phase margin (stability): This is the amount by which the device phase lead could be decreased (i.e., phase lag increased) before the system becomes unstable.

15.4.2 Linearity

A device is considered linear if it can be modeled by linear differential equations, with time t as the independent variable. Nonlinear devices are often analyzed using linear techniques by considering small excursions about an operating point. This linearization is accomplished by introducing incremental variables for the excitations (inputs) and responses (outputs). If one increment can cover the entire operating range of a device with sufficient accuracy, it is an indication that the device is linear. If the input/output relations are nonlinear algebraic equations, that represents a *static nonlinearity*. Such a situation can be handled simply by using nonlinear calibration curves, which linearize the device without introducing nonlinearity errors. If, on the other hand, the input/output relations are nonlinear differential equations, analysis usually becomes quite complex. This situation represents a *dynamic nonlinearity*.

Transfer-function representation is a “linear” model of an instrument. Hence, it implicitly assumes linearity. According to industrial terminology, a linear measuring instrument provides a measured value that varies linearly with the value of the measurand. This is consistent with the definition of static linearity.

All physical devices are *nonlinear* to some degree. This stems from any deviation from the ideal behavior, due to causes such as saturation, deviation from Hooke's Law in elastic elements, Coulomb friction, creep at joints, aerodynamic damping, backlash in gears and other loose components, and component wearout. Nonlinearities in devices are often manifested as some peculiar characteristics. In particular, the following properties are important in detecting nonlinear behavior in dynamic systems:

1. *Saturation*: The response does not increase when the excitation is increased beyond some level. This may result from such causes as magnetic saturation, which is common in transformer devices such as differential transformers, plasticity in mechanical components, or nonlinear deformation in springs.
2. *Hysteresis*: In this case, the input/output curve changes depending on the direction of motion, resulting in a hysteresis loop. This is common in: loose components such as gears, which have backlash; in components with nonlinear damping, such as Coulomb friction; and in magnetic devices with ferromagnetic media and various dissipative mechanisms (e.g., eddy current dissipation).
3. *The jump phenomenon*: Some nonlinear devices exhibit an instability known as the jump phenomenon (or *fold catastrophe*). Here, the frequency response (transfer) function curve suddenly jumps in magnitude at a particular frequency, while the excitation frequency is increased or decreased. A device with this nonlinearity will exhibit a characteristic "tilt" of its resonant peak either to the left (softening nonlinearity) or to the right (hardening nonlinearity). Furthermore, the transfer function itself may change with the level of input excitation in the case of nonlinear devices.
4. *Limit cycles*: A limit cycle is a closed trajectory in the state space that corresponds to sustained oscillations without decay or growth. The amplitude of these oscillations is independent of the location at which the response began. In the case of a stable limit cycle, the response will return to the limit cycle irrespective of the location near the limit cycle from which the response was initiated. In the case of an unstable limit cycle, the response will steadily move away from the location with the slightest disturbance.
5. *Frequency creation*: At steady state, nonlinear devices can create frequencies that are not present in the excitation signals. These frequencies might be harmonics (integer multiples of the excitation frequency), subharmonics (integer fractions of the excitation frequency), or nonharmonics (usually rational fractions of the excitation frequency).

Several methods are available to reduce or eliminate nonlinear behavior in vibrating systems. They include calibration (in the static case), use of linearizing elements, such as resistors and amplifiers to neutralize the nonlinear effects, and the use of nonlinear feedback. It is also good practice to take the following precautions:

1. Avoid operating the device over a wide range of signal levels.
2. Avoid operation over a wide frequency band.
3. Use devices that do not generate large mechanical motions.
4. Minimize Coulomb friction.
5. Avoid loose joints and gear coupling (i.e., use *direct-drive* mechanisms).

15.4.3 Instrument Ratings

Instrument manufacturers do not usually provide complete dynamic information for their products. In most cases, it is unrealistic to expect complete dynamic models (in the time or the frequency domain) and associated parameter values for complex instruments. Performance characteristics provided by manufacturers and vendors are primarily static parameters. Known as instrument ratings, these are available as parameter values, tables, charts, calibration curves, and empirical equations. Dynamic characteristics such as transfer functions (e.g., transmissibility curves expressed with respect to excitation

frequency) might also be provided for more sophisticated instruments, but the available dynamic information is never complete. Furthermore, the definitions of rating parameters used by manufacturers and vendors of instruments are in some cases not the same as analytical definitions used in textbooks. This is particularly true in relation to the term *linearity*. Nevertheless, instrument ratings provided by manufacturers and vendors are very useful in the selection, installation, operation, and maintenance of instruments. Some of these performance parameters are indicated below.

15.4.3.1 Rating Parameters

Typical rating parameters supplied by instrument manufacturers are:

1. Sensitivity
2. Dynamic range
3. Resolution
4. Linearity
5. Zero drift and full-scale drift
6. Useful frequency range
7. Bandwidth
8. Input and output impedances

The conventional definitions given by instrument manufacturers and vendors are summarized below.

Sensitivity of a transducer is measured by the magnitude (peak, root-mean-square [RMS] value, etc.) of the output signals corresponding to a unit input of the measurand. This may be expressed as the ratio of (incremental output)/(incremental input) or, analytically, as the corresponding partial derivative. In the case of vectorial or tensorial signals (e.g., displacement, velocity, acceleration, strain, force), the direction of sensitivity should be specified.

Cross-sensitivity is the sensitivity along directions that are orthogonal to the direction of primary sensitivity; it is expressed as a percentage of the direct sensitivity. High sensitivity and low cross-sensitivity are desirable for measuring instruments. Sensitivity to parameter changes, disturbances, and noise has to be small in any device, however; this is an indication of its *robustness*. Often, sensitivity and robustness are conflicting requirements.

Dynamic range of an instrument is determined by the allowed lower and upper limits of its input or output (response) so as to maintain a required level of measurement accuracy. This range is usually expressed as a ratio, in *decibels*. In many situations, the lower limit of the dynamic range is equal to the resolution of the device. Hence, the dynamic range is usually expressed as the ratio (range of operation)/(resolution), in decibels.

Resolution is the smallest change in a signal that can be detected and accurately indicated by a transducer, a display unit, or other instrument. It is usually expressed as a percentage of the maximum range of the instrument or as the inverse of the dynamic range ratio, as defined above. It follows that dynamic range and resolution are very closely related.

Linearity is determined by the calibration curve of an instrument. The curve of output amplitude (a peak or rms value) vs. input amplitude under static conditions within the dynamic range of an instrument is known as the *static calibration curve*. Its closeness to a straight line measures the degree of linearity. Manufacturers provide this information either as the maximum deviation of the calibration curve from the least squares straight-line fit of the calibration curve or from some other reference straight line. If the least squares fit is used as the reference straight line, the maximum deviation is called *independent linearity* (or more correctly, the independent nonlinearity, because the larger the deviation, the greater the nonlinearity). Nonlinearity may be expressed as a percentage of either the actual reading at an operating point or the full-scale reading.

Zero drift is defined as the drift from the null reading of the instrument when the measurand is maintained steady for a long period. Note that in this case, the measurand is kept at zero or any other level that corresponds to null reading of the instrument. Similarly, *full-scale drift* is defined with respect to the full-scale reading (the measurand is maintained at the full-scale value). Usual causes of drift include

instrument instability (e.g., instability in amplifiers), ambient changes (e.g., changes in temperature, pressure, humidity, and vibration level), changes in power supply (e.g., changes in reference DC voltage or alternating current [AC] line voltage), and parameter changes in an instrument (due to aging, wearout, nonlinearities, etc.). Drift due to parameter changes that are caused by instrument nonlinearities is known as *parametric drift*, *sensitivity drift*, or *scale-factor drift*. For example, a change in spring stiffness or electrical resistance due to changes in ambient temperature results in a parametric drift. Note that the parametric drift depends on the measurand level. Zero drift, however, is assumed to be the same at any measurand level if the other conditions are kept constant. For example, a change in reading caused by thermal expansion of the readout mechanism due to changes in the ambient temperature is considered a zero drift. In electronic devices, drift can be reduced by using AC circuitry rather than direct current (DC) circuitry. For example, AC-coupled amplifiers have fewer drift problems than DC amplifiers. Intermittent checking for the instrument response level for zero input is a popular way to calibrate for zero drift. In digital devices, this can be done automatically and intermittently, between sample points, when the input signal can be bypassed without affecting the system operation.

Useful frequency range corresponds to the interval of both flat gain and zero phase in the frequency response characteristics of an instrument. The maximum frequency in this band is typically less than half (say, one fifth of) the dominant resonant frequency of the instrument. This is a measure of instrument bandwidth.

Bandwidth of an instrument determines the maximum speed or frequency at which the instrument is capable of operating. High bandwidth implies faster speed of response. Bandwidth is determined by the dominant natural frequency, ω_n , or the dominant resonant frequency, ω_r , of the transducer. (Note: For low damping, ω_r is approximately equal to ω_n .) It is inversely proportional to the rise time and the dominant time constant. Half-power bandwidth is also a useful parameter. Instrument bandwidth must be several times greater than the maximum frequency of interest in the measured signal. The bandwidth of a measuring device is important, particularly when measuring transient signals. Note that the bandwidth is directly related to the useful frequency range.

15.4.4 Accuracy and Precision

The instrument ratings mentioned above affect the overall *accuracy* of an instrument. Accuracy can be assigned either to a particular reading or to an instrument. Note that instrument accuracy depends not only on the physical hardware of the instrument but also on the operating conditions (e.g., design conditions that are the normal, steady operating conditions or extreme transient conditions, such as emergency start-up and shutdown). *Measurement accuracy* determines the closeness of the measured value to the true value. *Instrument accuracy* is related to the worst accuracy obtainable within the dynamic range of the instrument in a specific operating environment. *Measurement error* is defined as

$$\text{Error} = (\text{measured value}) - (\text{true value}) \quad (15.31)$$

Correction, which is the negative of error, is defined as

$$\text{Correction} = (\text{true value}) - (\text{measured value}) \quad (15.32)$$

Each of these can also be expressed as a percentage of the true value. The accuracy of an instrument may be determined by measuring a parameter whose true value is known, and is near the extremes of the dynamic range of the instrument, under certain operating conditions. For this purpose, standard parameters or signals that can be generated at very high levels of accuracy would be needed. The National Institute for Standards and Testing (NIST) is usually responsible for the generation of these standards. Nevertheless, accuracy and error values cannot be determined to 100% exactness in typical applications, because the true value is not known. In a given situation, we can only make estimates for accuracy, by using ratings provided by the instrument manufacturer or by analyzing data from previous measurements and models.

Causes of error include instrument instability, external noise (disturbances), poor calibration, inaccurate information (e.g., poor analytical models, inaccurate control), parameter changes (e.g., due to environmental changes, aging, and wearout), unknown nonlinearities, and improper use of the instrument.

Errors can be classified as *deterministic* (or *systematic*) and *random* (or *stochastic*). Deterministic errors are those caused by well-defined factors, including nonlinearities and offsets in readings. These usually can be removed by applying proper calibration and analytical practices. Error ratings and calibration charts are used to remove systematic errors from instrument readings. Random errors are caused by uncertain factors entering into the instrument response. These include device noise, line noise, and the effects of unknown random variations in the operating environment. A statistical analysis using sufficiently large amounts of data is necessary to estimate random errors. The results are usually expressed as a mean error, which is the systematic part of random error, and a standard deviation or confidence interval for instrument response.

Precision is not synonymous with accuracy. Reproducibility (or repeatability) of an instrument reading determines the precision of an instrument. Two or more identical instruments that have the same high offset error might be able to generate responses at high precision, even though these readings are clearly inaccurate. For example, consider a timing device (clock) that very accurately indicates time increments (say, up to the nearest microsecond). If the reference time (starting time) is set incorrectly, the time readings will be in error, even though the clock has a very high precision.

Instrument error may be represented by a random variable that has a mean value μ_e and a standard deviation σ_e . If the standard deviation is zero, the variable is considered deterministic. In that case, the error is said to be deterministic or repeatable. Otherwise, the error is said to be random. The precision of an instrument is determined by the standard deviation of error in the instrument response. Readings of an instrument may have a large mean value of error (e.g., large offset), but if the standard deviation is small, the instrument has a high precision. Hence, a quantitative definition for precision is

$$\text{Precision} = (\text{measurement range})/\sigma_e \quad (15.33)$$

Lack of precision originates from random causes and poor construction practices. It cannot be compensated for by recalibration, just as the precision of a clock cannot be improved by resetting the time. On the other hand, accuracy can be improved by recalibration. Repeatable (deterministic) accuracy is inversely proportional to the magnitude of the mean error μ_e .

In selecting instruments for a particular application, in addition to matching instrument ratings with specifications, several additional features should be considered. These include geometric limitations (size, shape, etc.); environmental conditions (e.g., chemical reactions including corrosion, extreme temperatures, light, dirt accumulation, electromagnetic fields, radioactive environments, shock and vibration); power requirements; operational simplicity; availability; the past record and reputation of the manufacturer and of the particular instrument; and cost-related economic aspects (initial cost, maintenance cost, cost of supplementary components such as signal-conditioning and processing devices, design life and associated frequency of replacement, and cost of disposal and replacement). Often, these considerations become the ultimate deciding factors in the selection process.

15.5 Motion Sensors and Transducers

Motion sensing is considered the most important measurement in vibration applications. Other variables, such as force, torque, stress, strain, and material properties, are also important, either directly or indirectly, in the study of vibration. This section will describe some useful measuring devices of motion in the field of mechanical vibration.

15.5.1 Potentiometer

The potentiometer, or *pot*, is a displacement transducer. This active transducer consists of a uniform coil of wire or a film of high-resistive material, such as carbon, platinum, or conductive plastic, whose resistance is proportional to its length. A fixed voltage, v_{ref} is applied across the coil (or film) using an external, constant DC voltage supply. The transducer output signal, v_o , is the DC voltage between the movable contact (wiper arm) sliding on the coil and one terminal of the coil, as shown schematically in Figure 15.15(a). Slider displacement x is proportional to the output voltage

$$v_o = kx \quad (15.34)$$

This relationship assumes that the output terminals are open-circuit, which means that infinite-impedance load (or resistance in the present DC case) is present at the output terminal, so that the output current is zero. In actual practice, however, the load (the circuitry into which the pot signal is fed, e.g., conditioning or processing circuitry) has a finite impedance. Consequently, the output current (the current through the load) is nonzero, as shown in Figure 15.15(b). The output voltage thus drops to \tilde{v}_o , even if the reference voltage, v_{ref} , is assumed to remain constant under load variations (i.e., the voltage source has zero output impedance). This consequence is known as the *loading effect* of the transducer. Under these conditions, the linear relationship given by Equation 15.34 is no longer valid. This causes an error in the displacement reading. Loading can affect the transducer reading in two ways: by changing the reference voltage (i.e., loading the voltage source) or by loading the transducer. To reduce these effects, a voltage source that is not seriously affected by load variations (e.g., a regulated or stabilized power supply that has low output impedance) and data acquisition circuitry (including signal-conditioning circuitry) that has high input impedance should be used.

The resistance of a potentiometer should be chosen with care. On the one hand, an element with high resistance is preferred because this results in reduced power dissipation for a given voltage, which has the added benefit of reduced thermal effects. On the other hand, increased resistance increases the output impedance of the potentiometer and results in loading nonlinearity error unless the load resistance is also increased proportionately. Low-resistance pots have resistances less than 10 Ω . High-resistance pots can have resistances on the order of 100 k Ω . Conductive plastics can provide high resistances, typically about 100 Ω /mm, and are increasingly used in potentiometers. Reduced friction (low mechanical loading), reduced wear, reduced weight, and increased resolution are advantages of using conductive plastics in potentiometers.

15.5.1.1 Potentiometer Resolution

The force required to move the slider arm comes from the motion source, and the resulting energy is dissipated through friction. This energy conversion, unlike pure mechanical-to-electrical conversions,

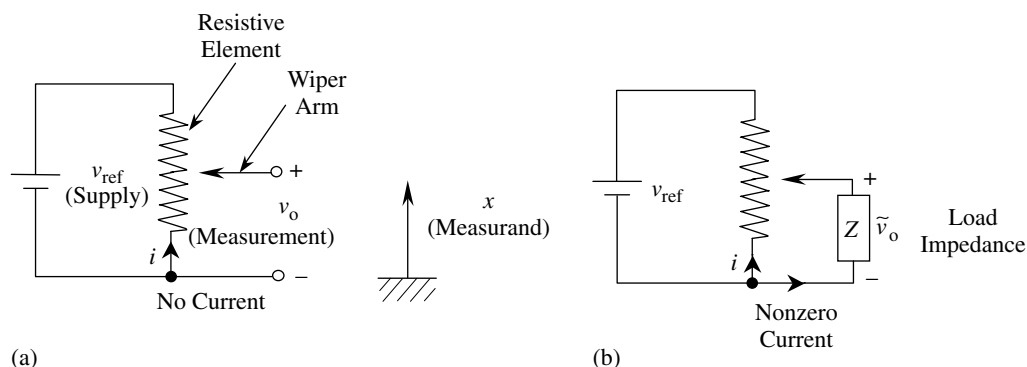


FIGURE 15.15 (a) Schematic diagram of a potentiometer; (b) potentiometer loading.

involves relatively high forces, and the energy is wasted rather than converted into the output signal of the transducer. Furthermore, the electrical energy from the reference source is also dissipated through the resistor coil (or film), resulting in an undesirable temperature rise. These are two obvious disadvantages of this *resistively coupled transducer*. Another disadvantage is the finite *resolution* in coil-type pots.

Coils, instead of straight wire, are used to increase the resistance per unit travel of the slider arm in the coil-type pot. However, the slider contact jumps from one turn to the next in this case. Accordingly, the resolution of a coil-type potentiometer is determined by the number of turns in the coil. For a coil that has N turns, the resolution, r , expressed as a percentage of the output range, is given by

$$r = \frac{100}{N} \% \quad (15.35)$$

Resolutions better (smaller) than 0.1% (i.e., 1000 turns) are available with coil potentiometers. Infinitesimal (incorrectly termed infinite) resolutions are now possible with high-quality resistive film potentiometers that use conductive plastics, for example. In this case, the resolution is limited by other factors, such as mechanical limitations and signal-to-noise ratio. Nevertheless, resolutions on the order of 0.01 mm are possible with good rectilinear potentiometers.

Some limitations and disadvantages of potentiometers as displacement measuring devices are as follows:

1. The force needed to move the slider (against friction and arm inertia) is provided by the vibration source. This mechanical loading distorts the measured signal itself.
2. High-frequency (or highly transient) measurements are not feasible because of such factors as slider bounce, friction and inertia resistance, and induced voltages in the wiper arm and primary coil.
3. Variations in the supply voltage cause error.
4. Electrical loading error can be significant when the load resistance is low.
5. Resolution is limited by the number of turns in the coil and by the coil uniformity. This will limit small-displacement measurements such as fine vibrations.
6. Wearout and heating up (with associated oxidation) in the coil (film) and slider contact cause accelerated degradation.

There are several advantages associated with potentiometer devices, however, including the following:

1. They are relatively less costly.
2. Potentiometers provide high-voltage (low-impedance) output signals, requiring no amplification in most applications. Transducer impedance can be varied simply by changing the coil resistance and supply voltage.

15.5.1.2 Optical Potentiometer

The optical potentiometer, shown schematically in Figure 15.16(a), is a displacement sensor. A layer of photoresistive material is sandwiched between a layer of regular resistive material and a layer of conductive material. The layer of resistive material has a total resistance of R_c , and it is uniform (i.e., it has a constant resistance per unit length). The photoresistive layer is practically an electrical insulator when no light is projected on it. The displacement of the moving object whose displacement is being measured causes a moving light beam to be projected on a rectangular area of the photoresistive layer. This light-projected area attains a resistance of R_p , which links the resistive layer, which is above the photoresistive layer, and the conductive layer, which is below it. The supply voltage to the potentiometer is v_{ref} and the length of the resistive layer is L . The light spot is projected at a distance x from one end of the resistive element, as shown in Figure 15.16(a).

An equivalent circuit for the optical potentiometer is shown in Figure 15.16(b). Here, it is assumed that a load of resistance R_L is present at the output of the potentiometer, the voltage across which is v_o . Current through the load is v_o/R_L . Hence, the voltage drop across $(1 - \alpha)R_c + R_L$, which is also the voltage across R_p , is given by $[(1 - \alpha)R_c + R_L]v_o/R_L$. Note that $\alpha = x/L$ is the fractional position of

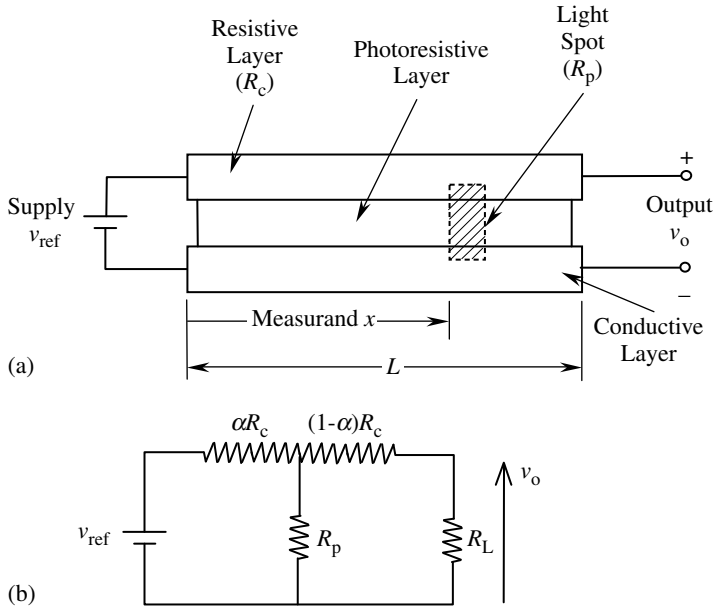


FIGURE 15.16 (a) An optical potentiometer; (b) equivalent circuit ($\alpha = x/L$).

the light spot. The current balance at the junction of the three resistors in Figure 15.16(b) is

$$\frac{v_{ref} - [(1 - \alpha)R_c + R_L]v_o/R_L}{\alpha R_c} = \frac{v_o}{R_L} + \frac{[(1 - \alpha)R_c + R_L]v_o/R_L}{R_p}$$

which can be written as

$$\frac{v_o}{v_{ref}} \left\{ \frac{R_c}{R_L} + 1 + \frac{x}{L} \frac{R_c}{R_p} \left[\left(1 - \frac{x}{L} \right) \frac{R_c}{R_L} + 1 \right] \right\} = 1 \quad (15.36)$$

When the load resistance R_L is quite large in comparison to the element resistance R_c , we have $R_c/R_L \approx 0$. Hence, Equation 15.36 becomes

$$\frac{v_o}{v_{ref}} = \frac{1}{\left[\frac{x}{L} \frac{R_c}{R_p} + 1 \right]} \quad (15.37)$$

This relationship is still nonlinear in v_o/v_{ref} vs. x/L . The nonlinearity decreases, however, with decreasing R_c/R_p .

15.5.2 Variable-Inductance Transducers

Motion transducers that employ the principle of electromagnetic induction are termed variable-inductance transducers. When the flux linkage (defined as magnetic flux density times the number of turns in the conductor) through an electrical conductor changes, a voltage is induced in the conductor. This, in turn, generates a magnetic field that opposes the primary field. Hence, a mechanical force is necessary to sustain the change of flux linkage. If the change in flux linkage is brought about by a relative motion, the mechanical energy is directly converted (induced) into electrical energy. This is the basis of electromagnetic induction, and it is the principle of operation of electrical generators and variable-inductance transducers. Note that, in these devices, the change of flux linkage is caused by a mechanical motion, and mechanical-to-electrical energy transfer takes place under near-ideal conditions.

The induced voltage or change in inductance may be used as a measure of the motion. Variable-inductance transducers are generally electromechanical devices coupled by a magnetic field.

There are many different types of variable-inductance transducers. Three primary types are:

1. Mutual-induction transducers
2. Selfinduction transducers
3. Permanent-magnet transducers

Variable-inductance transducers that use a nonmagnetized ferromagnetic medium to alter the reluctance (magnetic resistance) of the flux path are known as *variable-reluctance transducers*. Some of the mutual-induction transducers and most of the selfinduction transducers are of this type. Permanent-magnet transducers do not fall into category of variable-reluctance transducers.

15.5.2.1 Mutual-Induction Transducers

The basic arrangement of a mutual-induction transducer is constituted of two coils, the *primary windings* and the *secondary windings*. One of the coils, the primary windings, carries an AC excitation that induces a steady AC voltage in the other coil, the secondary windings. The level (amplitude, RMS value, etc.) of the induced voltage depends on the flux linkage between the coils. In mutual-induction transducers, a change in the flux linkage is effected by one of the two common techniques. One technique is to move an object made of ferromagnetic material within the flux path. This changes the reluctance of the flux path, with an associated change of the flux linkage in the secondary coil. This is the operating principle of the linear-variable differential transformer (LVDT), the rotatory-variable differential transformer (RVDT), and the mutual-induction proximity probe. All of these are variable-reluctance transducers. The other common way to change the flux linkage is to move one coil with respect to the other. This is the operating principle of the resolver, the synchro-transformer, and some types of AC tachometer. These are not variable-reluctance transducers, however.

The motion can be measured by using the secondary signal in several ways. For example, the AC signal in the secondary windings may be demodulated by rejecting the *carrier frequency* (primary-winding excitation frequency) and directly measuring the resulting signal, which represents the motion. This method is particularly suitable for measuring transient motions. Alternatively, the amplitude or the rms value of the secondary (induced) voltage may be measured. Another method is to measure the change of inductance in the secondary circuit directly by using a device such as an inductance bridge circuit.

15.5.2.2 Linear-Variable Differential Transformer

The LVDT is a displacement (vibration) measuring device, which can overcome most of the shortcomings of the potentiometer. It is considered a passive transducer because the measured displacement provides energy for “changing” the induced voltage, even though an external power supply is used to energize the primary coil, which in turn induces a steady carrier voltage in the secondary coil. The LVDT is a variable-reluctance transducer of the mutual induction type. In its simplest form, the LVDT consists of an insulating, nonmagnetic cylinder that has a primary coil in the midsegment and a secondary coil symmetrically wound in the two end segments, as depicted schematically in [Figure 15.17\(a\)](#). The primary coil is energized by an AC supply of voltage v_{ref} . This will generate, by mutual induction, an AC of the same frequency in the secondary winding. A core made of ferromagnetic material is inserted coaxially into the cylindrical form without actually touching it, as shown. As the core moves, the reluctance of the flux path changes.

Hence, the degree of flux linkage depends on the axial position of the core. The two secondary coils are connected in series opposition so that the potentials induced in these two coil segments oppose each other, therefore, the net induced voltage is zero when the core is centered between the two secondary winding segments. This is known as the *null position*. When the core is displaced from this position, a nonzero induced voltage will be generated. At steady state, the amplitude v_o of this induced voltage is proportional, in the linear (operating) region, to the core displacement x . Consequently, v_o may be used as a measure of the displacement. Note that, because of its opposed secondary windings, the LVDT

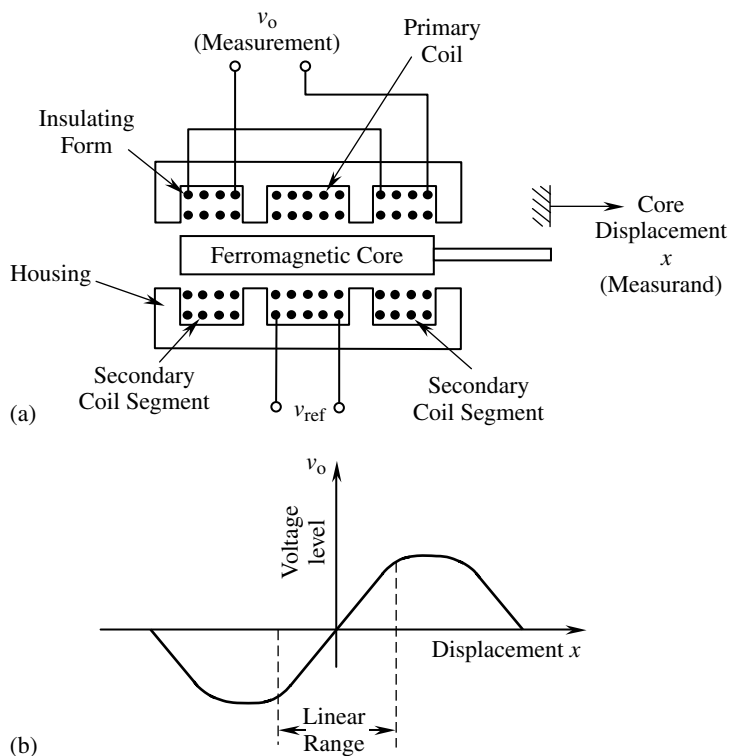


FIGURE 15.17 (a) Schematic diagram of an LVDT; (b) a typical operating curve.

provides the direction as well as the magnitude of displacement. If the output signal is not demodulated, the direction is determined by the phase angle between the primary (reference) voltage and the secondary (output) voltage, including the carrier signal.

For an LVDT to measure transient motions accurately, the frequency of the reference voltage (the carrier frequency) has to be about ten times larger than the largest significant frequency component in the measured motion. For quasi-dynamic displacements and slow transients on the order of a few hertz, a standard AC supply (at 60 Hz line frequency) is adequate. The performance, particularly the sensitivity and accuracy, is known to improve with the excitation frequency, however. Since the amplitude of the output signal is proportional to the amplitude of the primary signal, the reference voltage should be regulated to obtain accurate results. In particular, the power source should have a low output impedance.

The output signal from a differential transformer is normally not in phase with the reference voltage. Inductance in the primary windings and the leakage inductance in the secondary windings are mainly responsible for this phase shift. Since demodulation involves extraction of the modulating signal by rejecting the carrier frequency component from the secondary signal, it is important to understand the size of this phase shift. An error known as *null voltage* is present in some differential transformers. This manifests itself as a nonzero reading at the null position (i.e., at zero displacement). This is usually 90° out of phase from the main output signal and, hence, is known as *quadrature error*. Nonuniformities in the windings (unequal impedances in the two segments of the secondary windings) are a major reason for this error. The null voltage may also result from harmonic noise components in the primary signal and nonlinearities in the device. Null voltage is usually negligible (typically about 0.1% of the full scale). This error can be eliminated from the measurements by employing appropriate signal-conditioning and calibration practices.

15.5.2.3 Signal Conditioning

Signal conditioning associated with differential transformers includes filtering and amplification. Filtering is needed to improve the signal-to-noise ratio of the output signal. Amplification is necessary to increase the signal strength for data acquisition and processing. Since the reference frequency (carrier frequency) is embedded in the output signal, it is also necessary to interpret the output signal properly, particularly for transient motions. Two methods are commonly used to interpret the amplitude-modulated output signal from a differential transformer: (1) rectification; (2) demodulation.

In the first method, *rectification*, the AC output from the differential transformer is rectified to obtain a DC signal. This signal is amplified and then low-pass filtered to eliminate any high-frequency noise components. The amplitude of the resulting signal provides the transducer reading. In this method, phase shift in the LVDT output must be checked separately to determine the direction of motion. In the second method, *demodulation*, the carrier frequency component is rejected from the output signal by comparing it with a phase-shifted and amplitude-adjusted version of the primary (reference) signal. Note that phase shifting is necessary because the output signal is not in phase with the reference signal. The modulating signal which is extracted in this manner is subsequently amplified and filtered. As a result of advances in miniature integrated circuit (LSI and VLSI) technology, differential transformers with built-in microelectronics for signal conditioning are commonly available today. DC differential transformers have built-in oscillator circuits to generate the carrier signal powered by a DC supply. The supply voltage is usually on the order of 25 V, and the output voltage is about 5 V. Let us illustrate the demodulation approach to signal conditioning for an LVDT, using an example.

Example 15.2

Figure 15.18 shows a schematic diagram of a simplified signal conditioning system for an LVDT. The system variables and parameters are as indicated in Figure 15.18. In particular:

- $u(t)$ = displacement of the LVDT core (to be measured)
- ω_c = frequency of the carrier voltage
- v_o = output signal of the system (measurement)

The resistances R_1 , R_2 , and R , and the capacitance C are as marked. In addition, you may introduce a transformer parameter r for the LVDT, as required.

1. Explain the functions of the various components of the system shown in Figure 15.18.
2. Write equations for the amplifier and filter circuits and, using them, give expressions for the voltage signals v_1 , v_2 , v_3 , and v_o marked in Figure 15.18. Note that the excitation in the primary coil is $v_p \sin \omega_c t$.

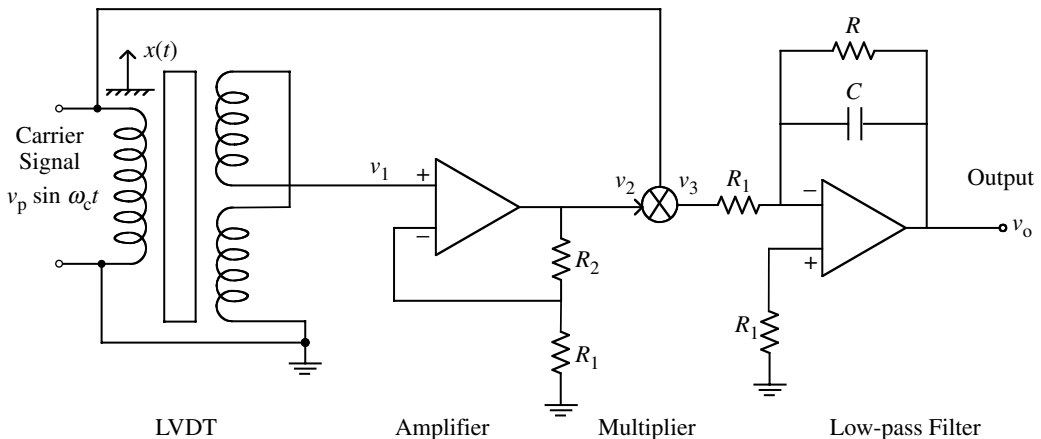


FIGURE 15.18 Signal-conditioning system for an LVDT.

3. Suppose that the carrier frequency is $\omega_c = 500$ rad/s and the filter resistance is $R = 100$ k Ω . If no more than 5% of the carrier component passes through the filter, estimate the required value of the filter capacitance, C . Also, what is the useful frequency range (measurement bandwidth) of the system in rad/sec, with these parameter values?

Solution

1. The LVDT has a primary coil that is excited by an AC voltage of $v_p \sin \omega_c t$. The ferromagnetic core is attached to the moving object whose displacement $x(t)$ is to be measured. The two secondary coils are connected in *series opposition* so that the LVDT output is zero at the null position, and that the direction of motion can be detected as well. The amplifier is a noninverting type. It amplifies the output of the LVDT which is an AC (carrier) signal of frequency ω_c , which is modulated by the core displacement $x(t)$.

The multiplier circuit determines the product of the primary (carrier) signal and the secondary (LVDT output) signal. This is an important step in demodulating the LVDT output.

The product signal from the multiplier has a high-frequency ($2\omega_c$) carrier component, added to the modulating component ($x(t)$). The low-pass filter removes this unnecessary high-frequency component to obtain the demodulated signal which is proportional to the core displacement $x(t)$.

2. Noninverting Amplifier: Note that the potentials at the positive and negative terminals of the operational amplifier (opamp) are nearly equal. Also, currents through these leads are nearly zero. (These are the two common assumptions used for an opamp.) Then, the current balance at node A gives

$$\frac{v_2 - v_1}{R_2} = \frac{v_1}{R_1}$$

or

$$v_2 = \frac{R_1 + R_2}{R_1} v_1$$

Then,

$$v_2 = k v_1 \quad (i)$$

with

$$k = \frac{R_1 + R_2}{R_1} = \text{amplifier gain}$$

Loss-Pass Filter: Since the $+$ lead of the opamp has approximately a zero potential (ground), the voltage at point B is also approximately zero. The current balance for node B gives

$$\frac{v_3}{R_1} + \frac{v_o}{R} + C\dot{v}_o = 0$$

Hence,

$$\tau \frac{dv_o}{dt} + v_o = -\frac{R}{R_1} v_3 \quad (ii)$$

where $\tau = RC$ = filter time constant. The transfer function of the filter is

$$\frac{v_o}{v_3} = -\frac{k_o}{(1 + \tau s)} \quad (iii)$$

with the filter gain $k_o = R/R_1$. In the frequency domain

$$\frac{v_o}{v_3} = -\frac{k_o}{(1 + \tau j\omega)} \quad (15.38)$$

Finally, neglecting the phase shift in the LVDT, we have

$$v_1 = v_p r u(t) \sin \omega_c t$$

$$v_2 = v_p r k u(t) \sin \omega_c t$$

or

$$v_3 = v_p^2 r k u(t) \sin^2 \omega_c t$$

$$v_3 = \frac{v_p^2 r k}{2} u(t) [1 - \cos 2 \omega_c t] \quad (\text{iv})$$

Owing to the low-pass filter, with an appropriate cut-off frequency, the carrier signal will be filtered out. Then,

$$v_o = \frac{v_p^2 r k_o}{2} u(t) \quad (15.39)$$

3. Filter magnitude = $k_o / \sqrt{1 + \tau^2 \omega^2}$. For no more than 5% of the carrier ($2\omega_c$) component to pass through, we must have

$$\frac{k_o}{\sqrt{1 + \tau^2 (2\omega_c)^2}} \leq \frac{5}{100} k_o \quad (\text{v})$$

or, $400 \leq 1 + 4\tau^2 \omega_c^2$; or, $\tau^2 \omega_c^2 \geq 399/4$; or $\tau \omega_c \geq 10$ (approximately). Pick $\tau \omega_c = 10$. With $R = 100 \text{ k}\Omega$ and $\omega_c = 500 \text{ rad/s}$, we have, $C \times 100 \times 10^3 \times 500 = 10$. Hence, $C = 0.2 \text{ }\mu\text{F}$.

According to the carrier frequency (500 rad/sec), we should be able to measure displacements $u(t)$ up to about 50 rad/sec. However, the flat region of the filter extends to approximately $\omega \tau = 0.1$, which, with the present value of $\tau = 0.02 \text{ sec}$, gives a bandwidth of only 5 rad/sec.

Advantages of the LVDT include the following:

1. It is essentially a noncontacting device with no frictional resistance. Its near-ideal electro-mechanical energy conversion and lightweight core will result in very small resistive forces. Hysteresis (both magnetic hysteresis and mechanical backlash) is negligible.
2. It has low output impedance, typically on the order of $100 \text{ }\Omega$ (signal amplification is usually not needed).
3. Directional measurements (positive/negative) are obtained.
4. It is available in small sizes (e.g., 1 cm long with maximum travel of 2 mm).
5. It has a simple and robust construction (inexpensive and durable).
6. Fine resolutions are possible (theoretically, infinitesimal resolution; practically, much finer resolution than that of a coil potentiometer).

The RVDT operates using the same principle as the LVDT, except that in an RVDT, a rotating ferromagnetic core is used. The RVDT is used for measuring angular displacements. The rotating core is shaped such that a reasonably wide linear operating region is obtained. Advantages of the RVDT are essentially the same as those cited for the LVDT. The linear range is typically $\pm 40^\circ$ with a nonlinearity error less than 1%.

In variable-inductance devices, the induced voltage is generated through the rate of change of the magnetic flux linkage. Therefore, displacement readings are distorted by velocity, and similarly, velocity readings are affected by acceleration. For the same displacement value, the transducer reading will depend on the velocity at that displacement. This error is known to increase with the ratio: (cyclic velocity of the core)/(carrier frequency). Hence, these *rate errors* can be reduced by increasing the carrier frequency. The reason for this is as follows.

At high frequencies, the induced voltage due to the transformer effect (frequencies of the primary signal) is greater than the induced voltage due to the rate (velocity) effect of the moving member. Hence, the error will be small. To estimate a lower limit for the carrier frequency in order to reduce rate effects,

we may proceed as follows:

1. For LVDT: max speed of operation/stroke of LVDT = ω_o
The excitation frequency of the primary coil should be chosen as at least $5\omega_o$.
2. For RVDT: for ω_o use the maximum angular frequency of operation (of the rotor).

15.5.3 Mutual-Induction Proximity Sensor

This displacement transducer operates on the mutual-induction principle. A simplified schematic diagram of such a device is shown in Figure 15.19(a). The insulated “E core” carries the primary windings in its middle limb. The two end limbs carry secondary windings that are connected in series. Unlike the LVDT and the RVDT, the two voltages induced in the secondary winding segments are additive in this case. The region of the moving surface (target object) that faces the coils has to be made of ferromagnetic material so that as it moves, the magnetic reluctance and the flux linkage will change. This, in turn, changes the induced voltage in the secondary windings, and this change is a measure of the displacement. Note that, unlike the LVDT, which has an “axial” displacement configuration, the proximity probe has a “transverse” displacement configuration. Hence, it is particularly suitable for measuring transverse displacements or proximities of moving objects (e.g., transverse vibrations of a beam or whirling of a rotating shaft). We can see from the operating curve shown in Figure 15.19(b) that the displacement-voltage relation of a proximity probe is nonlinear. Hence, these proximity sensors should be used only for measuring small displacements, such as linear vibrations (e.g., a linear range of 5.0 mm or 0.2 in.), unless accurate nonlinear calibration curves are available. Since the proximity sensor is a noncontacting device, mechanical loading is small and the product life is long. Because a ferromagnetic object is used to alter the reluctance of the flux path, the mutual-induction proximity sensor is a variable-reluctance device. The operating frequency limit is about one tenth the excitation frequency of the primary coil (carrier frequency). As for an LVDT, demodulation of the induced voltage (secondary) would be required to obtain direct (DC) output readings.

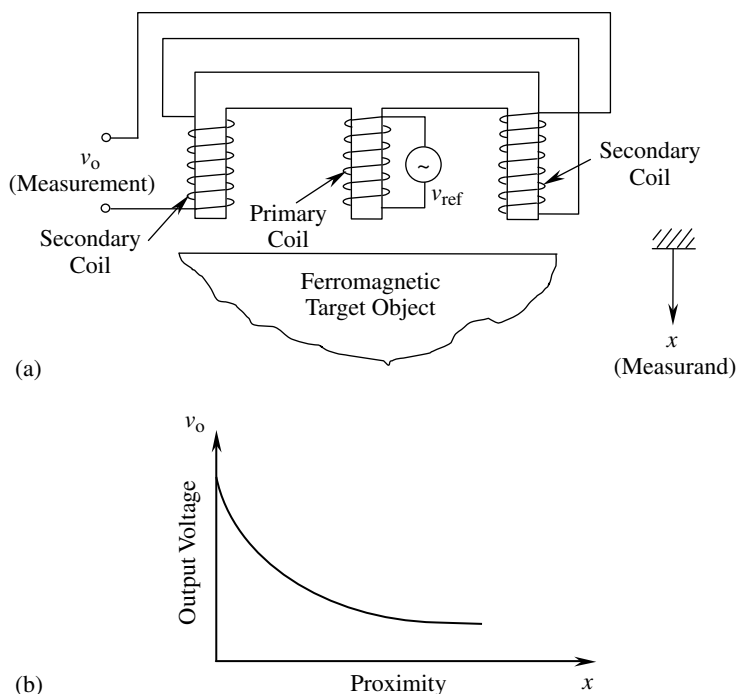


FIGURE 15.19 (a) Schematic diagram of the mutual-induction proximity sensor; (b) operating curve.

15.5.4 Selfinduction Transducers

These transducers are based on the principle of selfinduction. Unlike mutual-induction transducers, only a single coil is employed. This coil is activated by an AC supply voltage, v_{ref} . The current produces a magnetic flux, which is linked with the coil. The level of flux linkage (or selfinductance) can be varied by moving a ferromagnetic object within the magnetic field.

This changes the reluctance of the flux path and the inductance in the coil. This change is a measure of the displacement of the ferromagnetic object. The change in inductance is measured using an inductance measuring circuit (e.g., an inductance bridge). Note that selfinduction transducers are usually variable-reluctance devices.

A typical selfinduction transducer is a self-induction proximity sensor. A schematic diagram of this device is shown in Figure 15.20. This device can be used as a displacement or vibration sensor for transverse displacements. For instance, the distance between the sensor tip and ferromagnetic surface of a moving object, such as a beam or shaft, can be measured. Applications are essentially the same as those for mutual-induction proximity sensors. High-speed displacement (vibration) measurements can result in velocity error (rate error) when variable-inductance displacement sensors, including selfinduction transducers, are used. This effect may be reduced by increasing the carrier frequency, as in other AC-powered variable-inductance sensors.

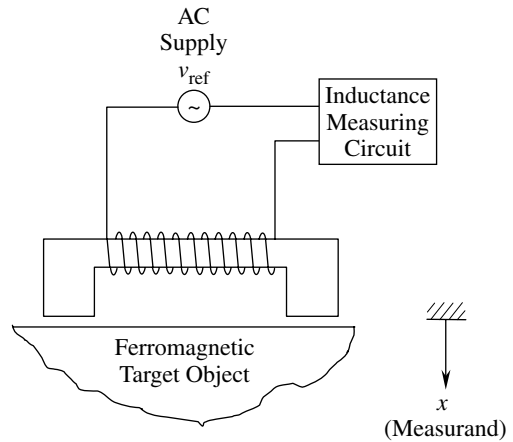


FIGURE 15.20 Schematic diagram of a selfinduction proximity sensor.

15.5.5 Permanent-Magnet Transducers

In discussing this third type of variable-inductance transducer, we will first consider the permanent-magnet DC velocity sensors (DC tachometers). A distinctive feature of permanent-magnet transducers is that they have a permanent magnet to generate a uniform and steady magnetic field. A relative motion between the magnetic field and an electrical conductor induces a voltage that is proportional to the speed at which the conductor crosses the magnetic field. In some designs, a unidirectional magnetic field generated by a DC supply (i.e., an electromagnet) is used in place of a permanent magnet. Nevertheless, this is generally termed a permanent-magnet transducer.

The principle of electromagnetic induction between a permanent magnet and a conducting coil is used in speed measurement by permanent-magnet transducers. Depending on the configuration, either rectilinear speeds or angular speeds can be measured. Schematic diagrams of the two configurations are shown in Figure 15.21. Note that these are passive transducers, because the energy for the output signal v_o is derived from the motion (measured signal) itself. The entire device is usually enclosed in a steel casing to isolate it from ambient magnetic fields.

In the rectilinear velocity transducer, as shown in Figure 15.21(a), the conductor coil is wrapped on a core and placed centrally between two magnetic poles, which produce a cross-magnetic field. The core is attached to the moving object whose velocity must be measured. The velocity v is proportional to the induced voltage, v_o . An alternative design, consisting of a moving-magnet and fixed-coil arrangement, may be used as well, thus eliminating the need for any sliding contacts (slip rings and brushes) for the output leads, and thereby reducing mechanical loading error, wearout, and related problems. The tachogenerator (or tachometer) is a very common permanent-magnet device. The principle of operation of a DC tachogenerator is shown in Figure 15.21(a). The rotor is directly connected to the rotating object. The output signal that is induced in the rotating coil is picked up as DC voltage, v_o , using a suitable

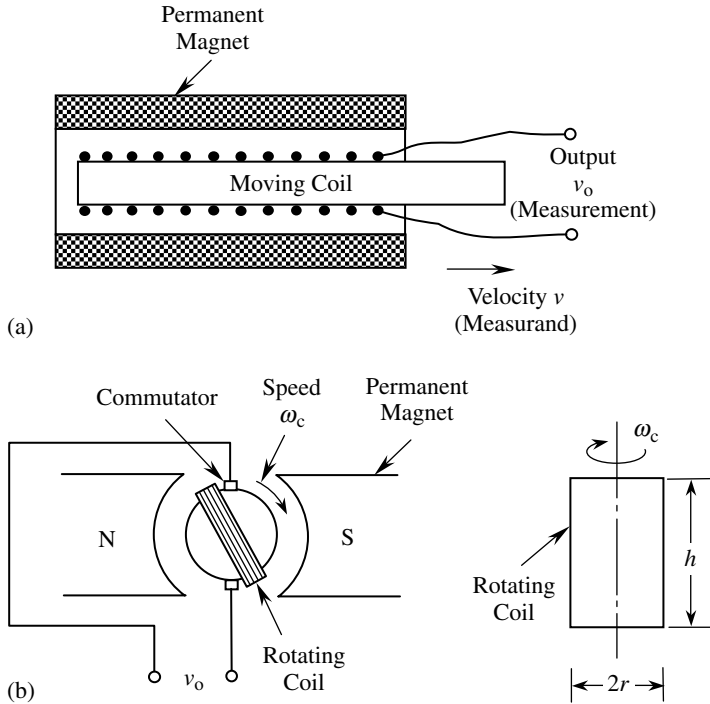


FIGURE 15.21 Permanent-magnet transducers: (a) rectilinear velocity transducer; (b) DC tachometer-generator.

commutator device, which typically consists of a pair of low-resistance carbon brushes, that is stationary but makes contact with the rotating coil through split slip rings so as to maintain the positive direction of induced voltage throughout each revolution. The induced voltage is given by

$$v_o = (2nhr\beta)\omega_c \quad (15.40)$$

for a coil of height h and width $2r$ that has n turns, moving at an angular speed ω_c in a uniform magnetic field of flux density β . This proportionality between v_o and ω_c is used to measure the angular speed ω_c .

When tachometers are used to measure transient velocities, some error will result from the rate (acceleration) effect. This error generally increases with the maximum significant frequency that must be retained in the transient velocity signal. Output distortion can also result because of reactive (inductive and capacitive) loading of the tachometer. Both types of error can be reduced by increasing the load impedance.

For an illustration, consider the equivalent circuit of a tachometer with an impedance load, as shown in Figure 15.22. The induced voltage $k\omega_c$ is represented by a voltage source. Note that the constant k depends on the coil geometry, the number of turns, and the magnetic flux density (see Equation 15.40). Coil resistance is denoted by R , and leakage inductance is denoted by L_ℓ . The load impedance is Z_L . From straightforward circuit analysis in the frequency domain, the output voltage at the load is given by

$$v_o = \left[\frac{Z_L}{R + j\omega L_\ell + Z_L} \right] k\omega_c \quad (15.41)$$

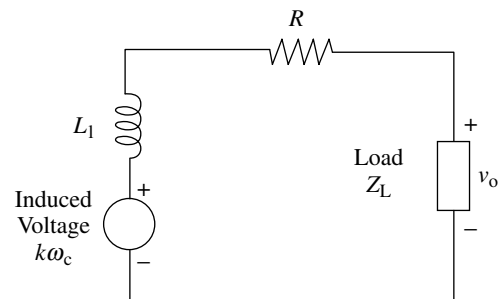


FIGURE 15.22 Equivalent circuit for a tachometer with an impedance load.

It can be seen that because of the leakage inductance, the output signal attenuates more at higher frequencies ω of the velocity transient. In addition, loading error is present. If Z_L is much larger than the coil impedance, however, the ideal proportionality, as given by

$$v_o = k\omega_c \quad (15.42)$$

is achieved.

Some tachometers operate in a different manner. For example, *digital tachometers* generate voltage pulses at a frequency proportional to the angular speed. These are considered to be digital transducers.

15.5.6 Alternating Current Permanent-Magnet Tachometer

This device has a permanent magnet rotor and two separate sets of stator windings as schematically shown in Figure 15.23(a). One set of windings is energized using an AC reference voltage. Induced voltage in the other set of windings is the tachometer output. When the rotor is stationary or moving in a quasi-static manner, the output voltage is a constant-amplitude signal much like the reference voltage. As the rotor moves at a finite speed, an additional induced voltage that is proportional to the rotor speed is generated in the secondary windings. This is due to the rate of change of flux linkage from the magnet in the secondary coil. The net output is an amplitude-modulated signal whose amplitude is proportional to the rotor speed. For transient velocities, it will be necessary to demodulate this signal in order to extract the transient velocity signal (i.e., the modulating signal) from the modulated output. The direction of velocity is determined from the phase angle of the modulated signal with respect to the carrier signal. Note that in an LVDT, the amplitude of the AC magnetic flux is altered by the position of the ferromagnetic core. But in an AC permanent-magnet tachometer, the DC magnetic flux generated by the magnetic rotor is linked with the stator windings, and the associated induced voltage is caused by the speed of rotation of the rotor.

For low-frequency applications (5 Hz or less), a standard AC supply (60 Hz) may be used to power an AC tachometer. For moderate-frequency applications, a 400 Hz supply is widely used. Typical sensitivity of an AC permanent-magnet tachometer is on the order of 50 to 100 mV/rad/sec.

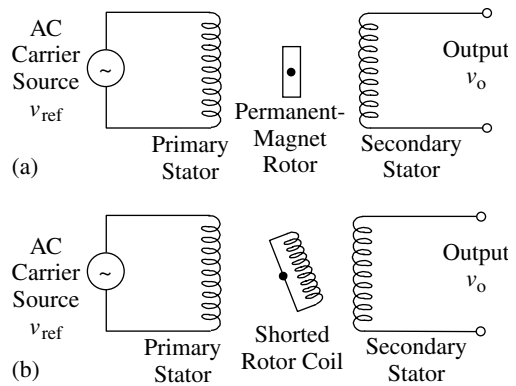


FIGURE 15.23 (a) AC permanent-magnet tachometer; (b) AC induction tachometer.

15.5.7 Alternating Current Induction Tachometer

These tachometers are similar in construction to the two-phase induction motors. The stator arrangement is identical to that of the AC permanent-magnet tachometer. The rotor, however, has windings that are shorted and not energized by an external source, as shown in Figure 15.23(b). One set of stator windings is energized with an AC supply. This induces a voltage in the rotor windings, and it has two components. One component is due to the direct transformer action of the supply AC. The other component is induced by the speed of rotation of the rotor and its magnitude is proportional to the speed of rotation. The nonenergized stator windings provide the output of the tachometer. Voltage induced in the output stator windings is due to both the primary stator windings and the rotor windings. As a result, the tachometer output has a carrier AC component and a modulating component that is proportional to the speed of rotation. Demodulation would be needed to extract the output component that is proportional to the angular speed of the rotor.

The main advantage of AC tachometers over their DC counterparts is the absence of slip-ring and brush devices. In particular, the signal from a DC tachometer usually has a voltage ripple, known as *commutator ripple*, which is generated as the split segments of the slip ring pass over the brushes. The frequency of the commutator ripple depends on the speed of operation; consequently, filtering out its effects using a notch filter is difficult (a tunable notch filter is necessary). Also, there are problems with frictional loading and contact bounce in DC tachometers, and these problems are absent in AC tachometers. It is known, however, that the output of an AC tachometer is somewhat nonlinear at high speeds due to the saturation effect. Furthermore, for measuring transient speeds, a sufficiently high carrier frequency and signal demodulation would be necessary. Another disadvantage of AC tachometers is that their output signal level depends on the supply voltage; hence, a stabilized voltage source that has a very small output impedance is necessary for accurate measurements.

15.5.8 Eddy Current Transducers

If a conducting (i.e., low-resistivity) medium is subjected to a fluctuating magnetic field, eddy currents are generated in the medium. The strength of eddy currents increases with the strength of the magnetic field and the frequency of the magnetic flux. This principle is used in eddy current proximity sensors. Eddy current sensors may be used as either dimensional gaging devices or high-frequency vibration sensors.

A schematic diagram of an eddy current proximity sensor is shown in [Figure 15.24\(a\)](#). Unlike variable-inductance proximity sensors, the target object of the eddy current sensor does not have to be made of a ferromagnetic material. A conducting target object is needed; however, a thin film conducting material, such as household aluminum foil glued onto a nonconducting target object, is adequate. The probe head has two identical coils, which form two arms of an impedance bridge. The coil closer to the probe face is the *active coil*. The other coil is the *compensating coil*. It compensates for ambient changes, particularly thermal effects. The other two arms of the bridge consist of purely resistive elements (see [Figure 15.24\(b\)](#)). The bridge is excited by a radio-frequency voltage supply. The frequency can range from 1 to 100 MHz. This signal is generated from a radio-frequency converter (an oscillator) that is typically powered by a 20 V DC supply. In the absence of the target object, the output of the impedance bridge is zero, which corresponds to the balanced condition. When the target object is moved close to the sensor, eddy currents are generated in the conducting medium because of the radio-frequency magnetic flux from the active coil. The magnetic field of the eddy currents opposes the primary field that generates these currents. Hence, the inductance of the active coil increases, creating an imbalance in the bridge. The resulting output from the bridge is an amplitude-modulated signal containing the radio-frequency carrier. This signal is demodulated by removing the carrier. The resulting signal (the modulating signal) measures the transient displacement (vibration) of the target object. Low-pass filtering is used to remove the high-frequency leftover noise in the output signal once the carrier is removed. For large displacements, the output is not linearly related to the displacement. Furthermore, the sensitivity of the eddy current probe depends nonlinearly on the nature of the conducting medium, particularly its resistivity. For example, for low resistivities, sensitivity increases with resistivity; for high resistivities, sensitivity decreases with resistivity. A calibrating unit is usually available with commercial eddy current sensors to accommodate various target objects and nonlinearities. The gage factor is usually expressed in volts/millimeter. Note that eddy current probes can also be used to measure resistivity and surface hardness (which affects resistivity) in metals.

The facial area of the conducting medium on the target object has to be slightly larger than the frontal area of the eddy current probe head. If the target object has a curved surface, its radius of curvature has to be at least four times the diameter of the probe. These are not serious restrictions, because the typical diameter of the probe head is about 2 mm. Eddy current sensors are medium-impedance devices; 1000 Ω output impedance is typical. Sensitivity is on the order of 5 V/mm. Since the carrier frequency is very high, eddy current devices are suitable for highly transient vibration measurements — for example,

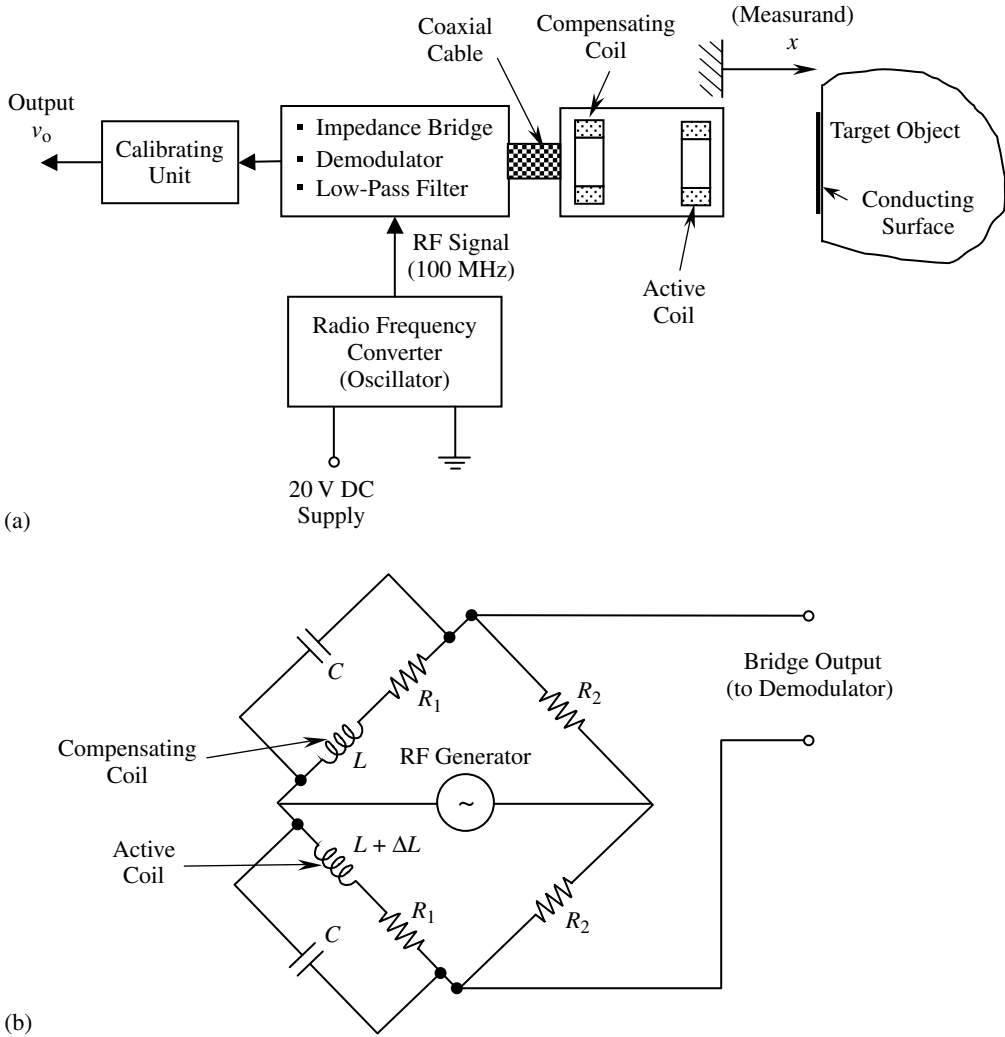


FIGURE 15.24 Eddy current proximity sensor: (a) schematic diagram; (b) impedance bridge.

bandwidths up to 100 kHz. Another advantage of an eddy current sensor is that it is a noncontacting device; there is no mechanical loading on the moving (target) object.

15.5.9 Variable-Capacitance Transducers

Capacitive or *reactive* transducers are commonly used to measure small transverse displacement such as vibrations, large rotations, and fluid level oscillations. They may also be employed to measure angular velocities. In addition to analog capacitive sensors, digital (pulse-generating) capacitive tachometers are also available.

Capacitance C of a two-plate capacitor is given by

$$C = \frac{kA}{x} \quad (15.43)$$

where A is the common (overlapping) area of the two plates, x is the gap width between the two plates, and k is the *dielectric constant* which depends on dielectric properties of the medium between the two plates. A change in any one of these three parameters may be used in the sensing process.

Schematic diagrams for measuring devices that use this feature are shown in Figure 15.25. In Figure 15.25(a), angular displacement of one of the plates causes a change in A . In Figure 15.25(b), a transverse displacement of one of the plates changes x . Finally, in Figure 15.25(c), a change in k is produced as the fluid level between the capacitor plates changes. Liquid oscillations may be sensed in this manner. In all three cases, the associated change in capacitance is measured directly or indirectly, and is used to estimate the measurand. A popular method is to use a capacitance bridge circuit to measure the change in capacitance, in a manner similar to that by which an inductance bridge is used to measure changes in inductance. Other methods include measuring a change in such quantities as charge (using a charge amplifier), voltage (using a high input-impedance device in parallel), and current (using a very low impedance device in series), as these changes will be results of the change in capacitance in a suitable circuit. An alternative method is to make the capacitor a part of an inductance–capacitance ($L - C$) oscillator circuit; the natural frequency of the oscillator ($1/\sqrt{LC}$) measures the capacitance. (Incidentally, this method may also be used to measure inductance.)

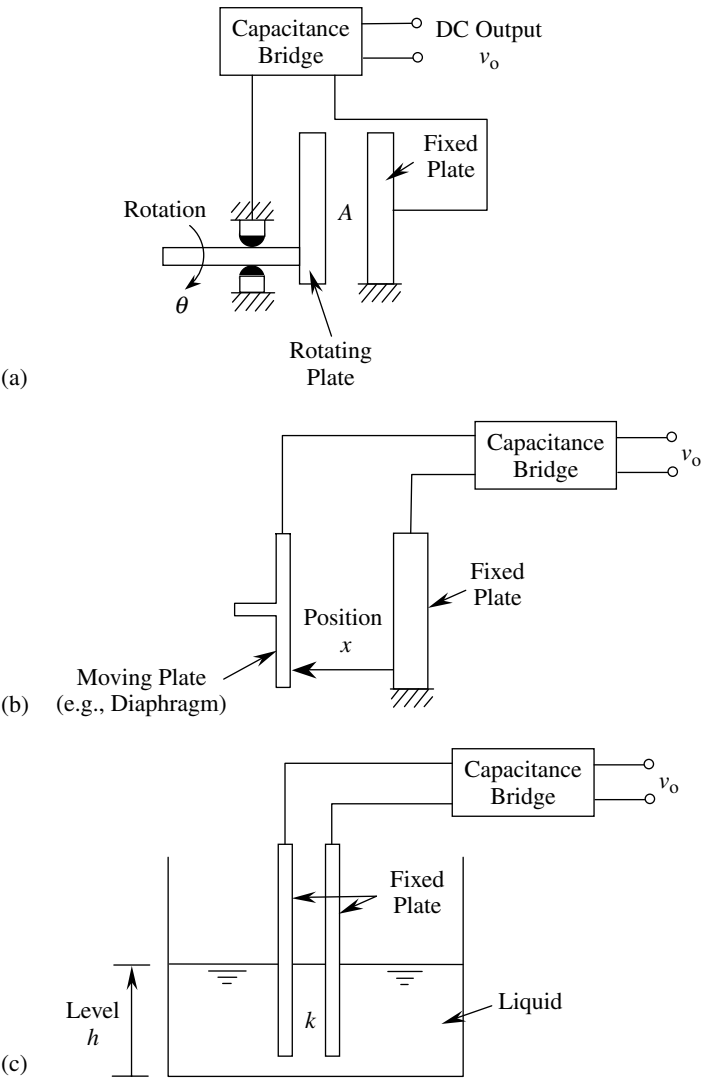


FIGURE 15.25 Schematic diagrams of capacitive sensors: (a) capacitive rotation sensor; (b) capacitive displacement sensor; (c) capacitive liquid oscillation sensor.

15.5.9.1 Capacitive Displacement Sensors

Consider the arrangement shown in Figure 15.25(a). Since the common area A is proportional to the angle of rotation θ , Equation 15.43 may be written as

$$C = K\theta \quad (15.44)$$

where K is a sensor constant. This is a linear relationship between C and θ . The capacitance may be measured by any convenient method. The sensor is linearly calibrated to give the angle of rotation.

For the arrangement shown in Figure 15.25(b), the sensor relationship is

$$C = \frac{K}{x} \quad (15.45)$$

The constant K has a different meaning here. Note that Equation 15.45 is a nonlinear relationship. A simple way to linearize this transverse displacement sensor is to use an inverting amplifier, as shown in Figure 15.26. Note that C_{ref} is a fixed, reference capacitance. Since the gain of the operational amplifier is very high, the voltage at the negative lead (point A) is zero for most practical purposes (because the positive lead is grounded). Furthermore, since the input impedance of the opamp is also very high, the current through the input leads is negligible. These are the two common assumptions used in opamp analysis. Accordingly, the charge balance equation for node point A is

$$v_{\text{ref}}C_{\text{ref}} + v_oC = 0$$

Now, in view of Equation 15.45, we obtain the following linear relationship for the output voltage, v_o , in terms of the displacement, x :

$$v_o = -\frac{v_{\text{ref}}C_{\text{ref}}}{K}x \quad (15.46)$$

Hence, measurement of v_o gives the displacement through linear calibration. The sensitivity of the device can be increased by increasing v_{ref} and C_{ref} . The reference voltage could be DC as well as AC. With an AC reference voltage, the output voltage is a modulated signal that has to be demodulated to measure transient displacements.

15.5.9.2 Capacitive Angular Velocity Sensor

The schematic diagram for an angular velocity sensor that uses a rotating-plate capacitor is shown in Figure 15.27. Since the current sensor has negligible resistance, the voltage across the capacitor is almost equal to the supply voltage v_{ref} , which is constant. It follows that the current in the circuit is given by

$$i = \frac{d}{dt}(Cv_{\text{ref}}) = v_{\text{ref}} \frac{dC}{dt}$$

which, in view of Equation 15.44, may be expressed as

$$\frac{d\theta}{dt} = \frac{i}{Kv_{\text{ref}}} \quad (15.47)$$

This is a linear relationship for the angular velocity in terms of the measured current i . Care must be exercised to guarantee that the current-measuring device does not interfere with the basic circuit.

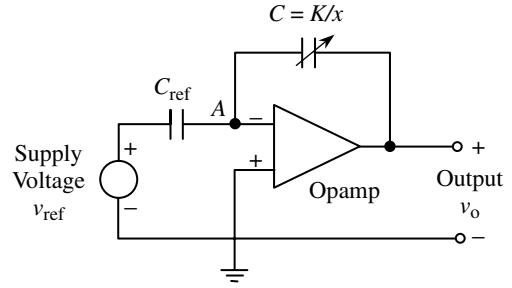


FIGURE 15.26 Inverting amplifier circuit used to linearize the capacitive transverse displacement sensor.

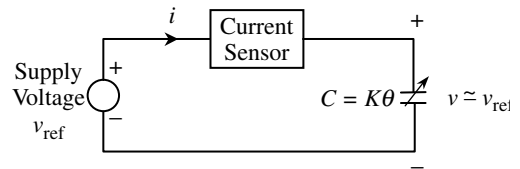


FIGURE 15.27 Rotating-plate capacitive angular velocity sensor.

An advantage of capacitance transducers is that, because they are noncontacting devices, mechanical loading effects are negligible. There is some loading due to inertial and frictional resistance in the moving plate. This can be eliminated by using the moving object itself to function as the moving plate. Variations in the dielectric properties due to humidity, temperature, pressure, and impurities introduce errors. A capacitance bridge circuit can compensate for these effects. Extraneous capacitances, such as cable capacitance, can produce erroneous readings in capacitive sensors. This problem can be reduced by using a charge amplifier to condition the sensor signal. Another drawback of capacitance displacement sensors is low sensitivity. For a transverse displacement transducer, the sensitivity is typically less than one picofarad (pF) per millimeter ($1 \text{ pF} = 10^{-12} \text{ F}$). This problem is not serious, because high supply voltages and amplifier circuitry can be used to increase the sensor sensitivity.

15.5.9.3 Capacitance Bridge Circuit

Sensors that are based on the change in capacitance (reactance) will require some means of measuring that change. Furthermore, changes in capacitance that are not caused by a change in the measurand, for example, changes in humidity, temperature, and so on, will cause errors and should be compensated for. Both these goals are accomplished using a capacitance bridge circuit. An example is shown in Figure 15.28.

In this circuit:

Z_2 = reactance (i.e., capacitive impedance) of the capacitive sensor (of capacitance C_2)

$$= \frac{1}{j\omega C_2}$$

Z_1 = reactance of the compensating capacitor C_1

$$= \frac{1}{j\omega C_1}$$

Z_4, Z_3 = bridge completing impedances (typically reactances)

v_{ref} = excitation AC voltage

$$= v_a \sin \omega t$$

v_o = bridge output

$$= v_b \sin(\omega t - \phi)$$

ϕ = phase lag of the output with respect to the excitation.

Using the two assumptions for the opamp (potentials at the negative and positive leads are equal and the current through these leads is zero), we can write the current balance equations

$$\frac{v_{\text{ref}} - v}{Z_1} + \frac{v_o - v}{Z_2} = 0 \quad (\text{i})$$

$$\frac{v_{\text{ref}} - v}{Z_3} + \frac{0 - v}{Z_4} = 0 \quad (\text{ii})$$

where v is the common voltage at the opamp leads. Next, eliminate v in Equation i and Equation ii to obtain

$$v_o = \frac{(Z_4/Z_3 - Z_2/Z_1)}{1 + Z_4/Z_3} v_{\text{ref}} \quad (15.48)$$

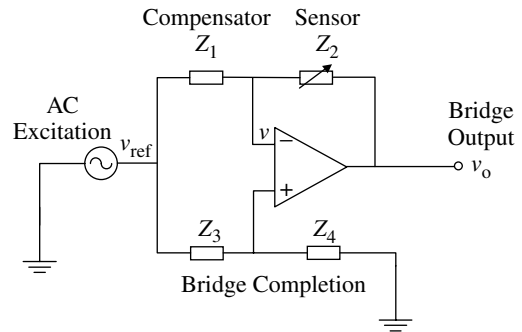


FIGURE 15.28 A bridge circuit for capacitive sensors.

It is noted that, when

$$\frac{Z_2}{Z_1} = \frac{Z_4}{Z_3} \quad (15.49)$$

the bridge output $v_o = 0$, and the bridge is said to be balanced. Since all capacitors in the bridge are similarly affected by ambient changes, a balanced bridge will maintain that condition even under ambient changes, unless the sensor reactance Z_2 is changed due to the measurand itself. It follows that the ambient effects are compensated for (at least up to the first order) by a bridge circuit. From Equation 15.48 it is clear that the bridge output due to a sensor change of δZ , starting from a balanced state, is given by

$$\delta v_o = -\frac{v_{\text{ref}}}{Z_1(1 + Z_4/Z_3)} \delta Z \quad (15.50)$$

The amplitude and phase angle of δv_o with respect to v_{ref} will determine δZ , assuming that Z_1 and Z_4/Z_3 are known.

15.5.10 Piezoelectric Transducers

Some substances, such as barium titanate and single-crystal quartz, can generate an electrical charge and an associated potential difference when they are subjected to mechanical stress or strain. This piezoelectric effect is used in piezoelectric transducers. Direct application of the piezoelectric effect is found in pressure and strain measuring devices, and many indirect applications also exist. They include piezoelectric accelerometers and velocity sensors, and piezoelectric torque sensors and force sensors. It is also interesting to note that piezoelectric materials deform when subjected to a potential difference (or charge). Some delicate test equipments (e.g., that used for vibration testing) use piezoelectric actuating elements (reverse piezoelectric action) to create fine motions. Also, piezoelectric valves (e.g., flapper valves), which are directly actuated using voltage signals, are used in pneumatic and hydraulic control applications and in ink-jet printers. Miniature stepper motors based on the reverse piezoelectric action are available.

Consider a piezoelectric crystal in the form of a disc with two electrodes plated on the two opposite faces. It is essentially a charge source. Furthermore, since the crystal is a dielectric medium, this device has a capacitor, which may be modeled by a capacitance, C , as in Equation 15.43. Accordingly, a piezoelectric sensor may be represented as a charge source with a capacitive impedance in series (Figure 15.29), in an equivalent circuit. The impedance from the capacitor is given by

$$Z = \frac{1}{j\omega C} \quad (15.51)$$

As is clear from Equation 15.51, the output impedance of piezoelectric sensors is very high, particularly at low frequencies. For example, a quartz crystal may present an impedance of several megohms at 100 Hz, increasing hyperbolically with decreasing frequencies. This is one reason why piezoelectric sensors have a limitation on the useful lower frequency. The other reason is charge leakage.

15.5.10.1 Sensitivity

The sensitivity of a piezoelectric crystal may be represented either by its charge sensitivity or by its voltage sensitivity. Charge sensitivity is defined as

$$S_q = \frac{\partial q}{\partial F} \quad (15.52)$$

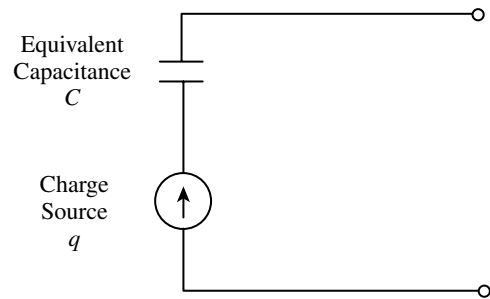


FIGURE 15.29 Equivalent circuit representation of a piezoelectric sensor.

where q denotes the generated charge and F denotes the applied force. For a crystal with surface area A , Equation 15.52 may be expressed as

$$S_q = \frac{1}{A} \frac{\partial q}{\partial p} \tag{15.53}$$

where p is the stress (normal or shear) or pressure applied to the crystal surface. Voltage sensitivity S_v is given by the change in voltage due to a unit increment in pressure (or stress) per unit thickness of the crystal. Thus, in the limit, we have

$$S_v = \frac{1}{d} \frac{\partial v}{\partial p} \tag{15.54}$$

where d denotes the crystal thickness. Now, since

$$\delta q = C \delta v \tag{15.55}$$

by using Equation 15.43 for a capacitor element, the following relationship between charge sensitivity and voltage sensitivity is obtained:

$$S_q = k S_v \tag{15.56}$$

Note that k is the dielectric constant of the crystal capacitor, as defined by Equation 15.43.

Example 15.3

A barium titanate crystal has a charge sensitivity of 150.0 picocoulombs per newton (pC/N). (*Note:* 1 pC = 1×10^{-12} coulombs; coulombs = farads \times volts.) The dielectric constant for the crystal is 1.25×10^{-8} farads per meter (F/m). What is the voltage sensitivity of the crystal?

Solution

The voltage sensitivity of the crystal is given by

$$S_v = \frac{150.0 \text{ pC/N}}{1.25 \times 10^{-8} \text{ F/m}} = \frac{150.0 \times 10^{-12} \text{ C/N}}{1.25 \times 10^{-8} \text{ F/m}}$$

or

$$S_v = 12.0 \times 10^{-3} \text{ V}\cdot\text{m/N} = 12.0 \text{ mV}\cdot\text{m/N}$$

The sensitivity of a piezoelectric element depends on the direction of loading. This is because the sensitivity depends on the crystal axis. Sensitivities of several piezoelectric materials along their most sensitive crystal axis are listed in Table 15.2.

15.5.10.2 Piezoelectric Accelerometer

Next we will discuss a piezoelectric motion transducer or vibration sensor, the piezoelectric accelerometer, in more detail. A piezoelectric velocity transducer is simply a piezoelectric accelerometer with a built-in integrating amplifier in the form of a miniature integrated circuit.

Accelerometers are acceleration-measuring devices. It is known from Newton's Second Law that a force (f) is necessary to accelerate a mass (or inertia element), and its magnitude is given by the

TABLE 15.2 Sensitivities of Several Piezoelectric Materials

Material	Charge Sensitivity S_q (pC/N)	Voltage Sensitivity S_v (mV m/N)
Lead zirconate titanate (PZT)	110	10
Barium titanate	140	6
Quartz	2.5	50
Rochelle salt	275	90

product of mass (M) and acceleration (a). This product (Ma) is commonly termed *inertia force*. The rationale for this terminology is that if a force of magnitude Ma were applied to the accelerating mass in the direction opposing the acceleration, then the system could be analyzed using static equilibrium considerations. This is known as *d'Alembert's principle*. The force that causes acceleration is itself a measure of the acceleration (mass is kept constant). Accordingly, mass can serve as a front-end element to convert acceleration into a force. This is the principle of operation of common accelerometers. There are many different types of accelerometers, ranging from strain gage devices to those that use electromagnetic induction. For example, force that causes acceleration can be converted into a proportional displacement using a spring element, and this displacement may be measured using a convenient displacement sensor. Examples of instruments of which operate this way are differential-transformer accelerometers, potentiometer accelerometers, and variable-capacitance accelerometers. Alternatively, the strain at a suitable location of a member that was deflected due to inertia force may be determined using a strain gage. This method is used in strain gage accelerometers. Vibrating-wire accelerometers use the accelerating force to create tension in a wire. The force is measured by detecting the natural frequency of vibration of the wire (which is proportional to the square root of tension). In servo force-balance (or null-balance) accelerometers, the inertia element is restrained from accelerating by detecting its motion and feeding back a force (or torque) to exactly cancel out the accelerating force (torque). This feedback force is determined, for instance, by knowing the motor current, and it is a measure of the acceleration.

The advantages of piezoelectric accelerometers (also known as *crystal accelerometers*) over other types of accelerometers are their light weight and high-frequency response (up to about 1 MHz). However, piezoelectric transducers are inherently high-output-impedance devices that generate small voltages (on the order of 1 mV). For this reason, special impedance-transforming amplifiers (e.g., charge amplifiers) have to be employed to condition the output signal and to reduce loading error.

A schematic diagram for a compression-type piezoelectric accelerometer is shown in Figure 15.30. The crystal and the inertia mass are restrained by a spring of very high stiffness. Consequently, the fundamental natural frequency or resonant frequency of the device becomes high (typically 20 kHz). This gives a reasonably wide, useful range (typically up to 5 kHz). The lower limit of the useful range (typically 1 Hz) is set by factors such as the limitations of the signal-conditioning systems, the mounting methods, the charge leakage in the piezoelectric element, the time constant of the charge-generating dynamics, and the signal-to-noise ratio. A typical frequency response curve for a piezoelectric accelerometer is shown in Figure 15.31.

In compression-type crystal accelerometers, the inertia force is sensed as a compressive normal stress in the piezoelectric element. There are also piezoelectric accelerometers that sense the inertia force as a shear strain or tensile strain. For an accelerometer, acceleration is the signal that is being measured (the measurand). Hence, accelerometer sensitivity is commonly expressed in terms of electrical charge per unit acceleration or

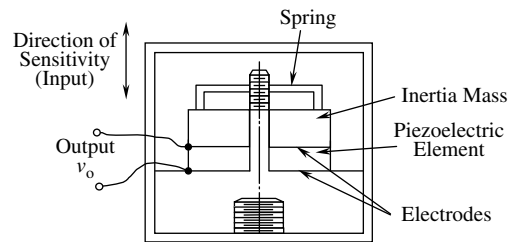


FIGURE 15.30 A compression-type piezoelectric accelerometer.

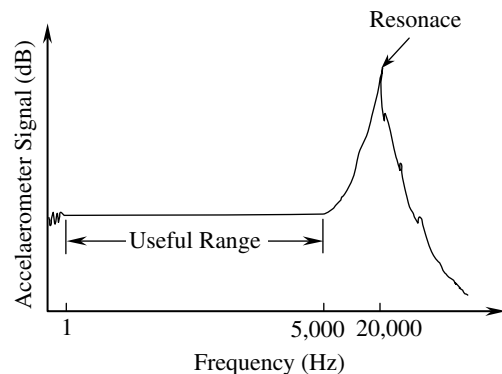


FIGURE 15.31 A typical frequency-response curve for a piezoelectric accelerometer.

voltage per unit acceleration (compare this with Equation 15.53 and Equation 15.54). Acceleration is measured in units of acceleration due to gravity (g), and charge is measured in picocoulombs (pC), which are units of 10^{-12} coulombs (C). Typical accelerometer sensitivities are 10 pC/g and 5 mV/g. Sensitivity depends on the piezoelectric properties and on the mass of the inertia element. If a large mass is used, the reaction inertia force on the crystal will be large for a given acceleration, thus generating a relatively large output signal. A large accelerometer mass results in several disadvantages, however. In particular:

1. The accelerometer mass distorts the measured motion variable (mechanical loading effect).
2. A heavier accelerometer has a lower resonant frequency and, hence, a lower useful frequency range (Figure 15.31).

For a given accelerometer size, improved sensitivity can be obtained by using the shear-strain configuration. In this configuration, several shear layers can be used (e.g., in a *delta arrangement*) within the accelerometer housing, thereby increasing the effective shear area and, hence, the sensitivity in proportion to the shear area. Another factor that should be considered in selecting an accelerometer is its *cross-sensitivity* or transverse sensitivity. Cross-sensitivity primarily results from manufacturing irregularities in the piezoelectric element, such as material unevenness and incorrect orientation of the sensing element. Cross-sensitivity should be less than the maximum error (a percentage) that is allowed for the device (typically 1%).

The technique employed to mount the accelerometer to an object can significantly affect the useful frequency range of the accelerometer. Some common mounting techniques are:

1. Screw-in base
2. Glue, cement, or wax
3. Magnetic base
4. Spring-base mount
5. Hand-held probe

Drilling holes in the object can be avoided by using the second to fifth methods, but the useful range can decrease significantly when spring-base mounts or hand-held probes are used (giving a typical upper limit of 500 Hz). The first two methods usually maintain the full useful range, whereas the magnetic attachment method reduces the upper frequency limit to some extent (typically 1.5 kHz).

Piezoelectric signals cannot be read using low-impedance devices. The two primary reasons for this are:

1. High output impedance in the sensor results in small output signal levels and large loading errors.
2. The charge can quickly leak out through the load.

15.5.10.3 Charge Amplifier

The charge amplifier, which has a very high input impedance and a very low output impedance, is the commonly used signal-conditioning device for piezoelectric sensors. Clearly, the impedance at the charge amplifier output is much smaller than the output impedance of the piezoelectric sensor. These impedance characteristics of a charge amplifier virtually eliminate loading error. Also, by using a charge amplifier circuit with a large time constant, charge leakage speed can be decreased. For example, consider a piezoelectric sensor and charge amplifier combination, as represented by the circuit in Figure 15.32. Let us examine how the charge leakage rate is slowed down by using this arrangement. Sensor capacitance, feedback capacitance of the charge amplifier, and feedback resistance of the charge amplifier are denoted by C , C_f , and R_f , respectively. The capacitance of the cable that connects the sensor to the charge amplifier is denoted by C_c .

For an opamp of gain, K , the voltage at its negative input is $-v_o/K$, where v_o is the voltage at the amplifier output. Note that the positive input of the opamp is grounded (zero potential). Current balance

at point A gives

$$\dot{q} + C_c \frac{\dot{v}_o}{K} + C_f \left(\dot{v}_o + \frac{\dot{v}_o}{K} \right) + \frac{v_o + v_o/K}{R_f} = 0 \quad (15.57)$$

Since gain, K , is very large (typically 10^5 to 10^9) compared to unity, this differential equation may be approximated to

$$R_f C_f \frac{dv_o}{dt} + v_o = -R_f \frac{dq}{dt} \quad (15.58)$$

Alternatively, instead of using Equation 15.57 it is possible to directly obtain Equation 15.58 from the two common assumptions (equal inverting and noninverting lead potentials and zero lead currents) for an opamp. In accordance with these assumptions the potential at the negative (inverting) lead is zero, as the positive lead is grounded. Also, as a result, the voltage across C_c is zero. Hence, the current balance at point A gives

$$\dot{q} + \frac{v_o}{R_f} + C_f \dot{v}_o = 0$$

This is identical to Equation 15.58. The corresponding transfer function is

$$\frac{v_o(s)}{q(s)} = -\frac{R_f s}{[R_f C_f s + 1]} \quad (15.59)$$

where s is the Laplace variable. Now, in the frequency domain ($s = j\omega$), we have

$$\frac{v_o(j\omega)}{q(j\omega)} = -\frac{R_f j\omega}{[R_f C_f j\omega + 1]} \quad (15.60)$$

Note that the output is zero at zero frequency ($\omega = 0$). Hence, a piezoelectric sensor cannot be used for measuring constant (DC) signals. At very high frequencies, on the other hand, the transfer function approaches the constant value $-1/C_f$ which is the calibration constant for the device.

From Equation 15.58 or Equation 15.59, which represent a first-order system, it is clear that the time constant τ_c of the sensor-amplifier unit is

$$\tau_c = R_f C_f \quad (15.61)$$

Suppose that the charge amplifier is properly calibrated (by the factor $-1/C_f$) so that the frequency transfer function (Equation 15.60) can be written as

$$G(j\omega) = \frac{j\tau_c \omega}{[j\tau_c \omega + 1]} \quad (15.62)$$

Magnitude M of this transfer function is given by

$$M = \frac{\tau_c \omega}{\sqrt{\tau_c^2 \omega^2 + 1}} \quad (15.63)$$

As $\omega \rightarrow \infty$, note that $M \rightarrow 1$. Hence, at infinite frequency, there is no error. Measurement accuracy depends on the closeness of M to 1. Suppose that we want the accuracy to be better than a specified value M_0 . Accordingly, we must have

$$\frac{\tau_c \omega}{\sqrt{\tau_c^2 \omega^2 + 1}} > M_0 \quad (15.64)$$

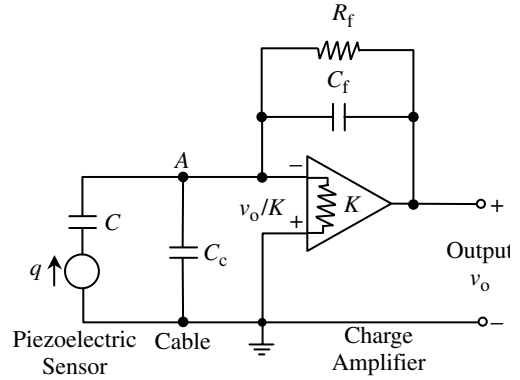


FIGURE 15.32 A piezoelectric sensor and charge amplifier combination.

or

$$\tau_c \omega > \frac{M_0}{\sqrt{1 - M_0^2}} \quad (15.65)$$

If the required lower frequency limit is ω_{\min} , the time constant requirement is

$$\tau_c > \frac{M_0}{\omega_{\min} \sqrt{1 - M_0^2}} \quad (15.66)$$

or

$$R_f C_f > \frac{M_0}{\omega_{\min} \sqrt{1 - M_0^2}} \quad (15.67)$$

It follows that a specified lower limit on the frequency of operation, for a specified level of accuracy, may be achieved by increasing the charge-amplifier time constant (i.e., by increasing R_f , C_f , or both). For instance, an accuracy better than 99% is obtained if

$$\frac{\tau_c \omega}{\sqrt{\tau_c^2 \omega^2 + 1}} > 0.99; \quad \text{or} \quad \tau_c \omega > 7.0$$

The minimum frequency of a transient signal that can tolerate this level of accuracy is $\omega_{\min} = 7.0/\tau_c$. Now ω_{\min} can be set by adjusting the time constant.

15.6 Torque, Force, and Other Sensors

The forced vibrations in a mechanical system depend on the forces and torques (excitations) applied to the system. Also, the performance of the system may be specified in terms of forces and torques that are generated, as for machine-tool operations such as grinding, cutting, forging, extrusion, and rolling. Performance monitoring and evaluation, failure detection and diagnosis, and vibration testing may depend considerably on the accurate measurement of associated forces and torques. In mechanical applications such as parts assembly, slight errors in motion can generate large forces and torques. These observations highlight the importance of measuring forces and torques. The strain gage is a sensor that is commonly used in this context. There are numerous other types of sensors and transducers that are useful in the context of mechanical vibration. In this section, we will outline several of these sensors.

15.6.1 Strain Gage Sensors

Many types of force and torque sensors, as well as motion sensors such as accelerometers, are based on strain gage measurements. Hence, strain gages are very useful in vibration instrumentation. Although strain gages measure strain, the measurements can be directly related to stress and force. Note, however, that strain gages may be used in a somewhat indirect manner, using auxiliary front-end elements, to measure other types of variables, including displacement and acceleration.

15.6.1.1 Equations for Strain Gage Measurements

The change of electrical resistance in material when it is mechanically deformed is the property used in resistance-type strain gages. The resistance R of a conductor that has length ℓ and area of cross section A , is given by

$$R = \rho \frac{\ell}{A} \quad (15.68)$$

where ρ denotes the resistivity of the material. Taking the logarithm of Equation 15.68, we attain $\log R = \log \rho + \log(\ell/A)$. Now, taking the differential, we obtain

$$\frac{dR}{R} = \frac{d\rho}{\rho} + \frac{d(\ell/A)}{\ell/A} \quad (15.69)$$

The first term on the right-hand side of Equation 15.69 depends on the change in resistivity, and the second term represents deformation. It follows that the change in resistance comes from the change in shape as well as from the change in the resistivity of the material. For linear deformations, the two terms on the right-hand side of Equation 15.69 are linear functions of strain, ϵ ; the proportionality constant of the second term, in particular, depends on Poisson's ratio of the material. Hence, the following relationship can be written for a strain gage element:

$$\frac{\delta R}{R} = S_s \epsilon \quad (15.70)$$

The constant S_s is known as the *sensitivity* or *gage factor* of the strain gage element. The numerical value of this constant ranges from 2 to 6 for most *metallic strain gage* elements and from 40 to 200 for *SC strain gages*. These two types of strain gage will be discussed later. The change in resistance of a strain gage element, which determines the associated strain (Equation 15.70), is measured using a suitable electrical circuit.

Resistance strain gages are based on resistance change due to strain, or the *piezoresistive* property of materials. Early strain gages were fine metal filaments. Modern strain gages are manufactured primarily as metallic foil (for example, using the copper–nickel alloy known as constantan) or SC elements (e.g., silicon with trace impurity boron). They are manufactured by first forming a thin film (foil) of metal or a single crystal of SC material and then cutting it into a suitable grid pattern, either mechanically or by using photoetching (chemical) techniques. This process is much more economical and is more precise than making strain gages with metal filaments. The strain gage element is formed on a backing film of electrically insulated material (e.g., plastic). This element is cemented onto the member whose strain is to be measured. Alternatively, a thin film of insulating ceramic substrate is melted onto the measurement surface, on which the strain gage is mounted directly. The direction of sensitivity is the major direction of elongation of the strain gage element (Figure 15.33(a)). To measure strains in more than one direction, multiple strain gages (e.g., various rosette configurations) are available as single units. These units have more than one direction of sensitivity. Principal strains in a given plane (the surface of the object on which the strain gage is mounted) can be determined by using these multiple strain gage units. Typical foil-type strain gages produce a relatively large output signal. A large accelerometer mass results in several disadvantages, however. In particular:

1. The accelerometer mass distorts the measured motion variable (mechanical loading effect).
2. A heavier accelerometer has a lower resonant frequency and, hence, a lower useful frequency range (Figure 15.31).

A direct way to obtain strain gage measurement is to apply a constant DC voltage across a series-connected strain gage element and a suitable resistor, and to measure the output voltage v_o across the strain gage under open-circuit conditions using a voltmeter with high input impedance. It is known as a *potentiometer circuit* or *ballast circuit* (see Figure 15.34(a)). This arrangement has several weaknesses. Any ambient temperature variation will directly introduce some error because of associated change in the strain gage resistance and the resistance of the connecting circuitry. Also, measurement accuracy will be affected by possible variations in the supply voltage v_{ref} . Furthermore, the electrical loading error will be significant unless the load impedance is very high. Perhaps, the most serious disadvantage of this circuit is that the change in signal due to strain is usually a very small percentage of the total signal level in the circuit output.

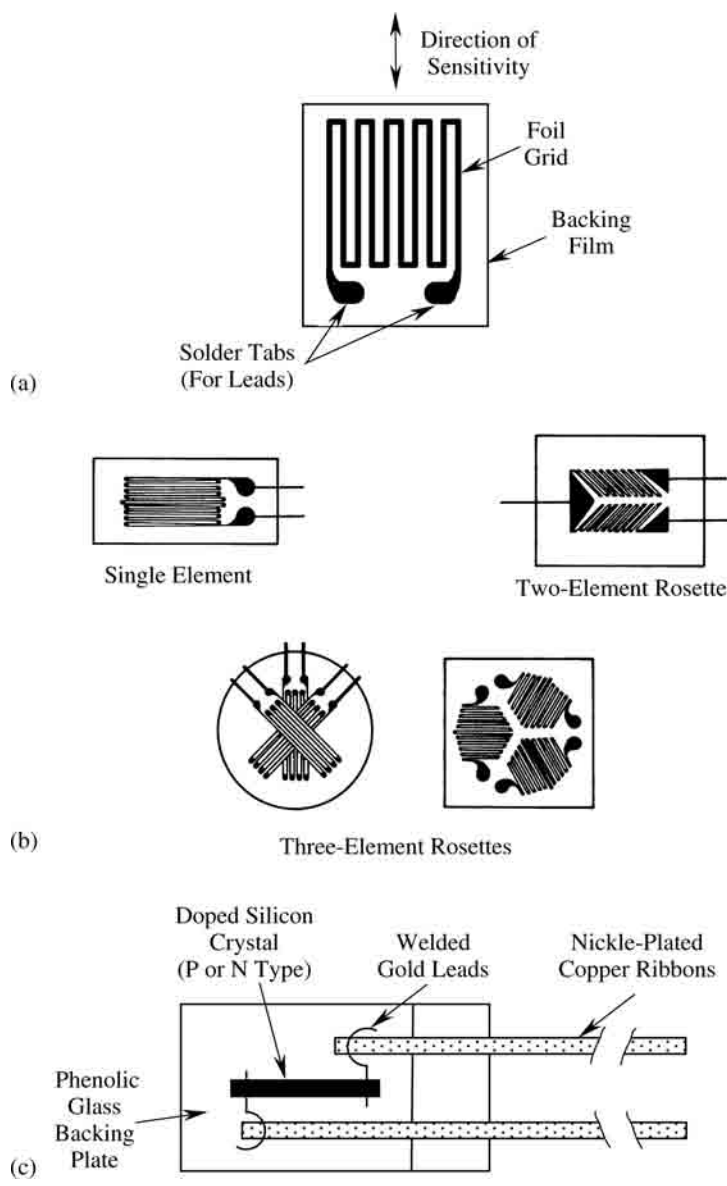


FIGURE 15.33 (a) Strain gage nomenclature; (b) typical foil-type strain gages; (c) a SC strain gage.

A more favorable circuit for use in strain gage measurements is the *Wheatstone bridge*, shown in Figure 15.34(b). One or more of the four resistors R_1 , R_2 , R_3 , and R_4 in the circuit may represent strain gages. To obtain the output relationship for the Wheatstone bridge circuit, assume that the load impedance R_L is very high. Hence, the load current, i , is negligibly small. Then, the potentials at nodes A and B are

$$v_A = \frac{R_1}{(R_1 + R_2)} v_{\text{ref}} \quad \text{and} \quad v_B = \frac{R_3}{(R_3 + R_4)} v_{\text{ref}}$$

and the output voltage $v_o = v_A - v_B$ is given by

$$v_o = \left[\frac{R_1}{(R_1 + R_2)} - \frac{R_3}{(R_3 + R_4)} \right] v_{\text{ref}} \tag{15.71}$$

By using straightforward algebra, we obtain

$$v_o = \frac{(R_1 R_4 - R_2 R_3)}{(R_1 + R_2)(R_3 + R_4)} v_{\text{ref}} \quad (15.72)$$

When this output voltage is zero, the bridge is said to be “balanced.” It follows from Equation 15.72 that, for a balanced bridge

$$\frac{R_1}{R_2} = \frac{R_3}{R_4} \quad (15.73)$$

Note that Equation 15.73 is valid for any value of R_L , not just for large R_L , because when the bridge is balanced, current i will be zero, even for small R_L .

15.6.1.2 Bridge Sensitivity

Strain gage measurements are calibrated with respect to a balanced bridge. When the strain gages in the bridge deform, the balance is upset. If one of the arms of the bridge has a variable resistor, it can be changed to restore the balance. The amount of this change corresponds to the amount by which the resistance of the strain gages changed, thereby measuring the applied strain. This is known as the *null-balance method* of strain measurement. This method is inherently slow because of the time required to balance the bridge each time a reading is taken. Hence, the null-balance method is generally not suitable for dynamic (time-varying) measurements. This approach to strain measurement can be sped up by using servo balancing, whereby the output error signal is fed back into an actuator that automatically adjusts the variable resistance so as to restore the balance.

A more common method, which is particularly suitable for making dynamic readings from a strain gage bridge, is to measure the output voltage resulting from the imbalance caused by the deformation of active strain gages in the bridge. To determine the *calibration constant* of a strain gage bridge, the sensitivity of the bridge output to changes in the four resistors in the bridge should be known. For small changes in resistance, this may be determined using the differential relation (or, equivalently, the first-order approximation for the Taylor series expansion):

$$\delta v_o = \sum_{i=1}^4 \frac{\partial v_o}{\partial R_i} \delta R_i \quad (15.74)$$

The partial derivatives are obtained directly from Equation 15.71. Specifically,

$$\frac{\partial v_o}{\partial R_1} = \frac{R_2}{(R_1 + R_2)^2} v_{\text{ref}} \quad (15.75)$$

$$\frac{\partial v_o}{\partial R_2} = \frac{R_1}{(R_1 + R_2)^2} v_{\text{ref}} \quad (15.76)$$

$$\frac{\partial v_o}{\partial R_3} = \frac{R_4}{(R_1 + R_4)^2} v_{\text{ref}} \quad (15.77)$$

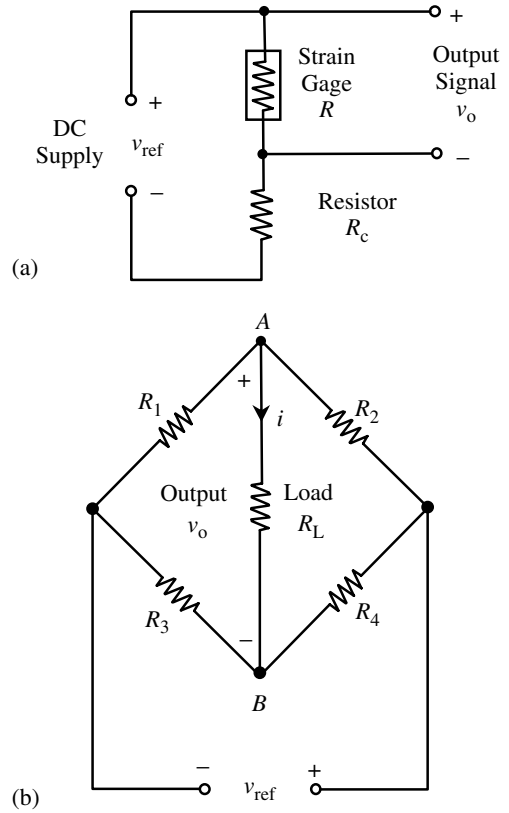


FIGURE 15.34 (a) A potentiometer circuit (ballast circuit) for strain gage measurements; (b) a Wheatstone bridge circuit for strain gage measurements.

$$\frac{\partial v_o}{\partial R_4} = \frac{R_3}{(R_3 + R_4)^2} v_{\text{ref}} \quad (15.78)$$

The required relationship is obtained by substituting the equations from Equation 15.75 to Equation 15.78 into Equation 15.74; thus

$$\frac{\delta v_o}{v_{\text{ref}}} = \frac{(R_2 \delta R_1 - R_1 \delta R_2)}{(R_1 + R_2)^2} - \frac{(R_4 \delta R_3 - R_3 \delta R_4)}{(R_3 + R_4)^2} \quad (15.79)$$

This result is subject to Equation 15.73, because changes are measured from the balanced condition. Note that, from Equation 15.79, if all four resistors are identical (in value and material), resistance changes due to ambient effects cancel out among the first-order terms ($\delta R_1, \delta R_2, \delta R_3, \delta R_4$), producing no net effect on the output voltage from the bridge. Closer examination of Equation 15.79 will reveal that only the adjacent pairs of resistors (e.g., R_1 with R_2 and R_3 with R_4) have to be identical in order to achieve this environmental compensation. Even this requirement can be relaxed. Compensation is achieved if R_1 and R_2 have the same temperature coefficient and if R_3 and R_4 have the same temperature coefficient.

15.6.1.3 The Bridge Constant

Numerous activating combinations of strain gages are possible in a bridge circuit. For example, there might be tension in R_1 and compression in R_2 , as in the case of two strain gages mounted symmetrically at 45° about the axis of a shaft in torsion. In this manner, the overall sensitivity of a strain gage bridge can be increased. It is clear from Equation 15.79 that, if all four resistors in the bridge are active, the best sensitivity is obtained if all four differential terms have the same sign, for example, when R_1 and R_4 are in tension and R_2 and R_3 are in compression. If more than one strain gage is active, the bridge output may be expressed as

$$\frac{\delta v_o}{v_{\text{ref}}} = k \frac{\delta R}{4R} \quad (15.80)$$

where

$$k = \frac{\text{bridge output in the general case}}{\text{bridge output if only one strain gage is active}}$$

This constant is known as the *bridge constant*. The larger the bridge constant is, the better the sensitivity of the bridge.

Example 15.4

A strain gage load cell (force sensor) consists of four identical strain gages, which form a Wheatstone bridge and are mounted on a rod that has a square cross section. One opposite pair of strain gages is mounted axially and the other pair is mounted in the transverse direction, as shown in Figure 15.35(a). To maximize the bridge sensitivity, the strain gages are connected to the bridge as shown in Figure 15.35(b). Determine the bridge constant k in terms of *Poisson's ratio* ν of the rod material.

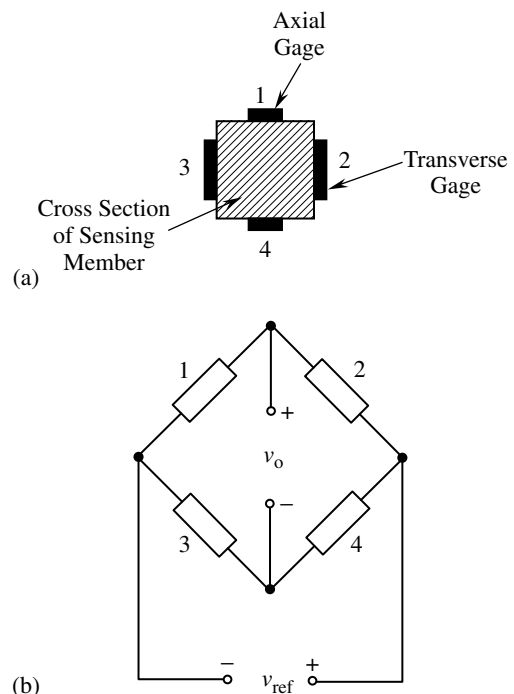


FIGURE 15.35 A strain-gage force sensor: (a) mounting configuration; (b) bridge circuit.

Solution

Suppose that $\delta R_1 = \delta R$. Then, for the given configuration, we have

$$\delta R_2 = -\nu \delta R$$

$$\delta R_3 = -\nu \delta R$$

$$\delta R_4 = \delta R$$

Note that, from the definition of Poisson's ratio, transverse strain $= (-\nu) \times$ longitudinal strain. Now, it follows from Equation 15.79 that

$$\frac{\delta v_o}{v_{\text{ref}}} = 2(1 + \nu) \frac{\delta R}{4R} \quad (15.81)$$

according to which the bridge constant is given by

$$k = 2(1 + \nu)$$

15.6.1.4 The Calibration Constant

The calibration constant, C , of a strain gage bridge relates the strain that is measured to the output of the bridge. Specifically,

$$\frac{\delta v_o}{v_{\text{ref}}} = C\varepsilon \quad (15.82)$$

Now, in view of Equation 15.70 and Equation 15.80, the calibration constant may be expressed as

$$C = \frac{k}{4} S_s \quad (15.83)$$

where k is the *bridge constant* and S_s is the *sensitivity* or *gage factor* of the strain gage. Ideally, the calibration constant should remain constant over the measurement range of the bridge (i.e., independent of strain ε and time t) and should be stable with respect to ambient conditions. In particular, there should not be any creep, non-linearities such as hysteresis, or thermal effects.

Example 15.5

A schematic diagram of a strain gage accelerometer is shown in Figure 15.36(a). A point mass of weight W is used as the acceleration sensing element, and a light cantilever with a rectangular cross section, which is mounted inside the accelerometer casing, converts the inertia force of the mass into a strain. The maximum bending strain at the root of the cantilever is measured using four identical active SC strain gages. Two of the strain gages (A and B) are mounted axially on the top surface of the cantilever, and the remaining two (C and D) are mounted on the bottom surface, as shown in Figure 15.36(b). In order to maximize the sensitivity of the accelerometer, indicate the

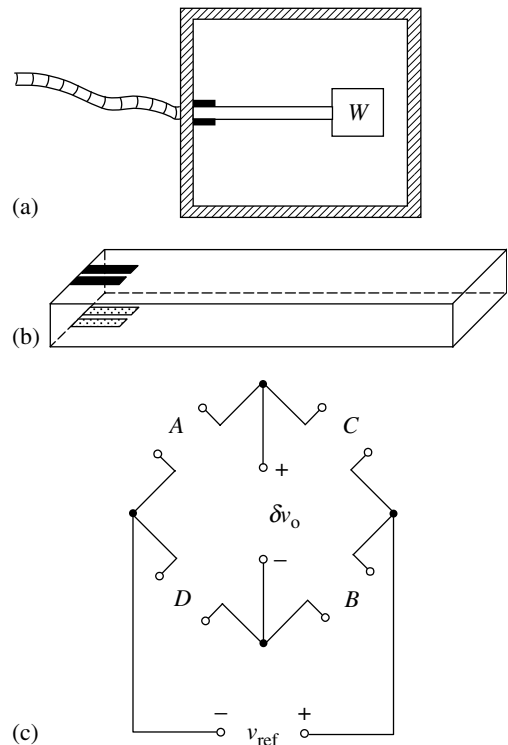


FIGURE 15.36 A strain gage accelerometer: (a) schematic diagram; (b) strain gage mounting configuration; (c) bridge connections.

manner in which the four strain gages (A, B, C, and D) should be connected to a Wheatstone bridge circuit. What is the bridge constant of the resulting circuit?

Obtain an expression relating the applied acceleration a (in units of g , which denotes acceleration due to gravity) to the bridge output δv_o (measured using a bridge balanced at zero acceleration) in terms of the following parameters:

W = weight of the seismic mass at the free end of the cantilever element

E = Young's modulus of the cantilever

ℓ = length of the cantilever

b = cross-sectional width of the cantilever

h = cross-sectional height of the cantilever

S_s = sensitivity (gage factor) of each strain gage

v_{ref} = supply voltage to the bridge

If $W = 0.02$ lb, $E = 10 \times 10^6$ lbf/in.², $\ell = 1$ in., $b = 0.1$ in., $h = 0.05$ in., $S_s = 200$, and $v_{\text{ref}} = 20$ V, determine the sensitivity of the accelerometer in mV/ g .

If the yield strength of the cantilever element is 10×10^3 lbf/in.², what is the maximum acceleration that could be measured using the accelerometer?

Is the cross-sensitivity (i.e., the sensitivity in the two directions orthogonal to the direction of sensitivity shown in Figure 15.36(a)) small given your arrangement of the strain gage bridge? Explain.

Note: For a cantilever subjected to force F at the free end, the maximum stress at the root is given by

$$\sigma = \frac{6F\ell}{bh^2} \quad (15.84)$$

with the present notation.

Solution

The bridge sensitivity is maximized by connecting the strain gages A, B, C, and D to the bridge as shown in Figure 15.36(c). This follows from Equation 15.79, noting that the contributions from all four strain gages are positive when δR_1 and δR_4 are positive and δR_2 and δR_3 are negative. The bridge constant for the resulting arrangement is $k = 4$. Hence, from Equation 15.80, we have

$$\frac{\delta v_o}{v_{\text{ref}}} = \frac{\delta R}{R}$$

or, from Equation 15.82 and Equation 15.83

$$\frac{\delta v_o}{v_{\text{ref}}} = S_s \varepsilon$$

Also,

$$\varepsilon = \frac{\sigma}{E} = \frac{6F\ell}{Eb h^2}$$

where F denotes the inertia force

$$F = \frac{W}{g} \ddot{x} = Wa$$

Note that \ddot{x} is the acceleration in the direction of sensitivity and $\ddot{x}/g = a$ is the acceleration in units of g . Thus,

$$\varepsilon = \frac{6W\ell}{Eb h^2} a \quad (15.85)$$

or

$$\delta v_o = \frac{6W\ell}{Ebh^2} S_s v_{\text{ref}} a \quad (15.86)$$

Now, with the given values

$$\begin{aligned} \frac{\delta v_o}{a} &= \frac{6 \times 0.02 \times 1 \times 200 \times 20}{10 \times 10^6 \times 0.1 \times (0.05)^2} \text{ V/g} = 0.192 \text{ V/g} = 192 \text{ mV/g} \\ \frac{\varepsilon}{a} &= \frac{1}{S_s v_{\text{ref}}} \frac{\delta v_o}{a} = \frac{0.192}{200 \times 20} \text{ strain/g} \\ \text{yield strain} &= \frac{\text{yield strength}}{E} = \frac{10 \times 10^3}{10 \times 10^6} = 1 \times 10^{-3} \text{ strain} \end{aligned}$$

Hence,

$$\text{number of gs to yielding} = \frac{1 \times 10^{-3}}{48 \times 10^{-6}} g = 20.8g$$

Cross-sensitivity comes from accelerations in the two directions (y and z) orthogonal to the direction of sensitivity (x). In the lateral (y) direction, the inertia force causes lateral bending. This will produce equal tensile (or compressive) strains in B and D , and equal compressive (or tensile) strains in A and C . According to the bridge circuit, we see that these contributions cancel each other. In the axial (z) direction, the inertia force causes equal tensile (or compressive) stresses in all four strain gages. These also will cancel out, as is clear from the following relationship for the bridge:

$$\frac{\delta v_o}{v_{\text{ref}}} = \frac{(R_C \delta R_A - R_A \delta R_C)}{(R_A + R_C)^2} - \frac{(R_B \delta R_D - R_D \delta R_B)}{(R_D + R_B)^2} \quad (15.87)$$

with

$$R_A = R_B = R_C = R_D = R$$

which gives

$$\frac{\delta v_o}{v_{\text{ref}}} = \frac{(\delta R_A - \delta R_C - \delta R_D + \delta R_B)}{4R} \quad (15.88)$$

It follows that this arrangement is good with respect to cross-sensitivity problems.

15.6.1.5 Data Acquisition

As noted earlier, the two common methods of measuring strains using a Wheatstone bridge circuit are (1) the null-balance method and (2) the imbalance output method. One possible scheme for using the first method is shown in [Figure 15.37\(a\)](#). In this particular arrangement, two bridge circuits are used. The *active bridge* contains the active strain gages, dummy gages, and bridge-completion resistors. The *reference bridge* has four resistors, one of which is micro-adjustable, either manually or automatically. The output from the each of the two bridges is fed into a difference amplifier, which provides an amplified difference of the two signals. This error signal is indicated on a null detector, such as a galvanometer. Initially, both bridges are balanced. When the measurement system is in use, the active gages are subjected to the strain that is being measured. This upsets the balance, giving a net output that is indicated on the null detector. In manual operation of the null-balance mechanism, the resistance knob in the reference bridge is adjusted carefully until the galvanometer indicates a null reading. The knob can be calibrated to indicate the measured strain directly. In servo operation, which is much faster than the manual method, the error signal is fed into an actuator that automatically adjusts the variable resistor in the reference bridge until the null balance is achieved. Actuator movement measures the strain.

For measuring dynamic strains in vibrating systems, either the servo null-balance method or the imbalance output method should be employed. A schematic diagram for the imbalance output method is

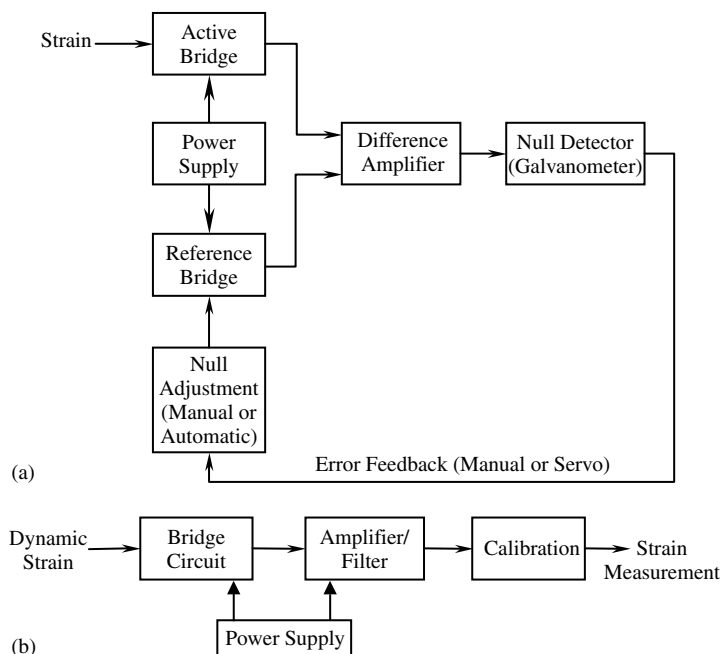


FIGURE 15.37 Strain gage bridge measurement: (a) null-balance method; (b) imbalance output method.

shown in Figure 15.37(b). In this method, the output from the active bridge is directly measured as a voltage signal and calibrated to provide the measured strain. An AC bridge may be used, where the bridge is powered by an AC voltage. The supply frequency should be about ten times the maximum frequency of interest in the dynamic strain signal (bandwidth). A supply frequency on the order of 1 kHz is typical. This signal is generated by an oscillator and is fed into the bridge. The transient component of the output from the bridge is very small (typically less than 1 mV and sometimes a few microvolts). This signal must be amplified, demodulated (especially if the signals are transient), and filtered to provide the strain reading. The calibration constant of the bridge should be known in order to convert the output voltage to strain.

Strain gage bridges powered by DC voltages are very common. They have the advantages of portability and simplicity with regard to necessary circuitry. The advantages of AC bridges include improved stability (reduced drift), improved accuracy, and reduced power consumption.

15.6.1.6 Accuracy Considerations

Foil gages are available with resistances as low as 50 Ω and as high as several kilohms. The power consumption of the bridge decreases with increased resistance. This has the added advantage of decreased heat generation. Bridges with a high range of measurement (e.g., a maximum strain of 0.01 m/m) are available. The accuracy depends on the linearity of the bridge, environmental (particularly temperature) effects, and mounting techniques. For example, a calibration error occurs in the case of zero shift, due to the strains produced when the cement that is used to mount the strain gage dries. Creep will introduce errors during static and low-frequency measurements. Flexibility and hysteresis of the bonding cement will bring about errors during high-frequency strain measurements. Resolutions on the order of 1 $\mu\text{m/m}$ (i.e., one *microstrain*) are common. The cross-sensitivity should be small (say, less than 1% of the direct sensitivity). Manufacturers usually provide the values of the cross-sensitivity factors for their strain gages. This factor, when multiplied by the cross strain present in a given application, gives the error in the strain reading due to cross-sensitivity.

Often, measurements of strains in moving members are needed, for example, in real-time monitoring and failure detection in machine tools. If the motion is small or the device has a limited stroke, strain gages mounted on the moving member can be connected to the signal-conditioning circuitry and the power source using coiled flexible cables. For large motions, particularly in rotating shafts, some form of commutating arrangement must be used. Slip rings and brushes are commonly used for this purpose. When AC bridges are used, a mutual-induction device (rotary transformer) can be used, with one coil located on the moving member and the other coil stationary. To accommodate and compensate for errors caused by commutation (e.g., losses and glitches in the output signal), it is desirable to place all four arms of the bridge, rather than just the active arms, on the moving member.

15.6.1.7 Semiconductor Strain Gages

In some low-strain applications (e.g., dynamic torque measurement), the sensitivity of foil gages is not adequate to produce an acceptable strain gage signal. SC strain gages are particularly useful in such situations. The strain element of a SC strain gage is made of a single crystal of *piezoresistive* material such as silicon, doped with a trace impurity such as boron. A typical construction is shown in Figure 15.38. The sensitivity (gage factor) of a SC strain gage is about two orders of magnitude higher than that of a metallic foil gage (typically, 40 to 200). The resistivity is also higher, providing reduced power consumption and heat generation. Another advantage of SC strain gages is that they deform elastically until fracture. In particular, mechanical hysteresis is negligible. Furthermore, they are smaller and lighter, providing less cross-sensitivity, reduced distribution error (i.e., improved spatial resolution), and negligible error due to mechanical loading. The maximum strain that is measurable using a SC strain gage is typically 0.003 m/m (i.e., 3000 $\mu\epsilon$). Strain gage resistance can be several hundred ohms (typically, 120 Ω or 350 Ω).

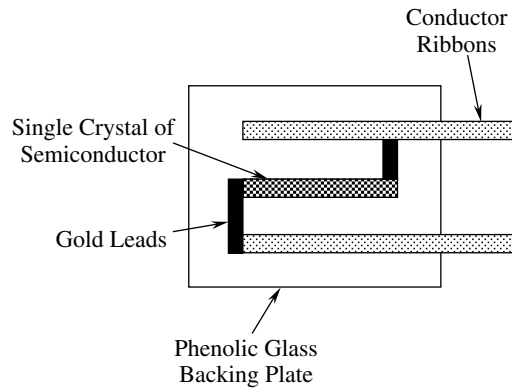


FIGURE 15.38 Details of a semiconductor strain gage.

There are several disadvantages associated with SC strain gages, however, which can be interpreted as advantages of foil gages. Undesirable characteristics of SC gages include the following:

1. The strain–resistance relationship is more nonlinear.
2. They are brittle and difficult to mount on curved surfaces.
3. The maximum strain that can be measured is an order of magnitude smaller (typically, less than 0.01 m/m).
4. They are more costly.
5. They have a much higher temperature sensitivity.

The first disadvantage is illustrated in Figure 15.39. There are two types of SC strain gages: the P-type and the N-type. In P-type strain gages, the direction of sensitivity is along the (1, 1, 1) crystal axis, and the element produces a “positive” (P) change in resistance in response to a positive strain. In N-type strain gages, the direction of sensitivity is along the (1, 0, 0) crystal axis, and the element responds with a “negative” (N) change in resistance to a positive strain. In both types, the response is nonlinear and can be approximated by the quadratic relationship

$$\frac{\delta R}{R} = S_1 \epsilon + S_2 \epsilon^2 \quad (15.89)$$

The parameter S_1 represents the *linear sensitivity*, which is positive for P-type gages and negative for N-type gages. Its magnitude is usually somewhat larger for P-type gages, thereby providing

better sensitivity. The parameter S_2 represents the degree of nonlinearity, which is usually positive for both types of gage. Its magnitude, however, is typically a little smaller for P-type gages. It follows that P-type gages are less nonlinear and have higher strain sensitivities. The nonlinear relationship given by Equation 15.89 or the nonlinear characteristic curve (Figure 15.39) should be used when measuring moderate to large strains with SC strain gages. Otherwise, the nonlinearity error will be excessive.

15.6.1.8 Force and Torque Sensors

Torque and force sensing is useful in vibration applications, including the following:

1. In vibration control of machinery where a small motion error can cause large damaging forces or performance degradation.
2. In high-speed vibration control when motion feedback alone is not fast enough (here, force feedback and feedforward force control can be used to improve the accuracy and bandwidth).
3. In vibration testing, monitoring, and diagnostic applications, where torque and force sensing can detect, predict, and identify abnormal operation, malfunction, component failure, or excessive wear (e.g., in monitoring machine tools such as milling machines and drills).
4. In experimental modal analysis where both excitation forces and response motioning may be needed to experimentally determine the system model.

In most applications, torque (or force) is sensed by detecting either an effect or the cause of torque (or force). There are also methods for measuring torque (or force) directly. Common methods of torque sensing include the following:

1. Measuring the strain in a sensing member between the drive element and the driven load, using a strain gage bridge.
2. Measuring the displacement in a sensing member (as in the first method), either directly, using a displacement sensor, or indirectly, by measuring a variable, such as magnetic inductance or capacitance, that varies with displacement.
3. Measuring the reaction in the support structure or housing (by measuring a force) and the associated lever arm length.
4. In electric motors, measuring the field or armature current that produces motor torque; in hydraulic or pneumatic actuators, measuring the actuator pressure.
5. Measuring the torque directly, for example, using piezoelectric sensors.
6. Employing the servo method to balance the unknown torque with a feedback torque generated by an active device (say, a servomotor) whose torque characteristics are known precisely.
7. Measuring the angular acceleration in a known inertia element when the unknown torque is applied.

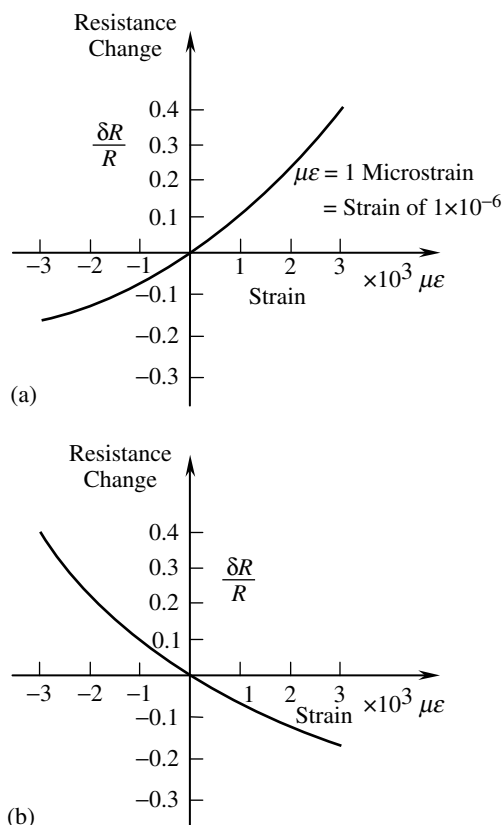


FIGURE 15.39 Nonlinear behavior of a semiconductor (silicon/boron) strain gage: (a) a P-type gage; (b) an N-type gage.

Note that force sensing may be accomplished by essentially the same techniques. Some types of force sensor (e.g., the strain gage force sensor) have been introduced before. Now, we will limit our discussion primarily to torque sensing. The extension of torque-sensing techniques to the task of force sensing is somewhat straightforward.

15.6.1.9 Strain Gage Torque Sensors

The most straightforward method of torque sensing is to connect a torsion member between the drive unit and the load-in series, and to measure the torque in the torsion member. If a circular shaft (solid or hollow) is used as the torsion member, the torque–strain relationship is relatively simple. A complete development of the relationship is found in standard textbooks on elasticity, solid mechanics, or strength of materials. With reference to Figure 15.40, it can be shown that the torque, T , may be expressed in terms of the direct strain, ϵ , on the shaft surface along a principal stress direction (i.e., at 45° to the shaft axis) as

$$T = \frac{2GJ}{r} \epsilon \quad (15.90)$$

where G = shear modulus of the shaft material, J = polar moment of area of the shaft, and r = shaft radius (outer). This is the basis of torque sensing using strain measurements.

Using the general bridge Equation 15.82 along with Equation 15.83 in Equation 15.90, we can obtain torque, T , from bridge output, δv_o :

$$T = \frac{8GJ}{kS_s r} \frac{\delta v_o}{v_{ref}} \quad (15.91)$$

where S_s is the gage factor (or sensitivity) of the strain gages. The bridge constant, k , depends on the number of active strain gages used. Strain gages are assumed to be mounted along a principal direction.

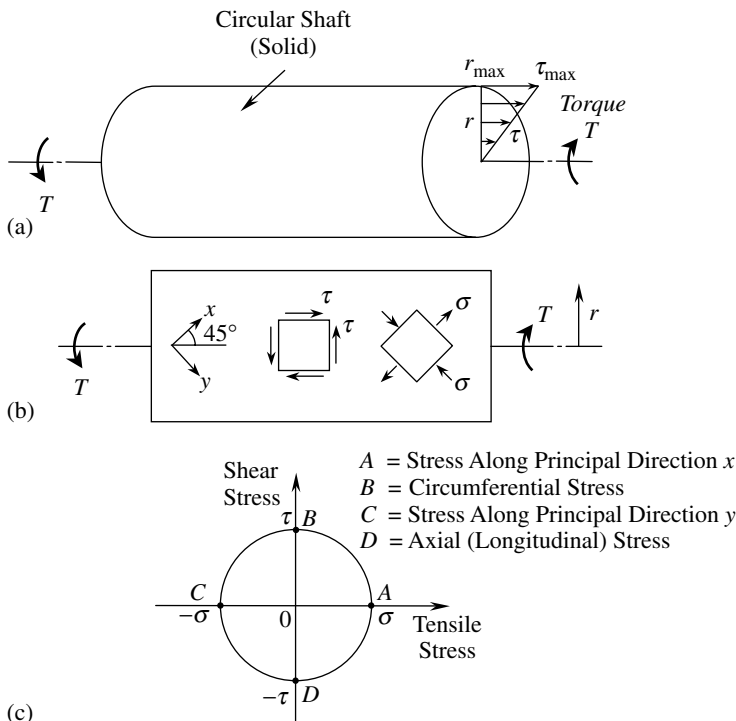


FIGURE 15.40 (a) Linear distribution of shear stress in a circular shaft under pure torsion; (b) pure shear state of stress and principal directions x and y ; (c) Mohr's circle.

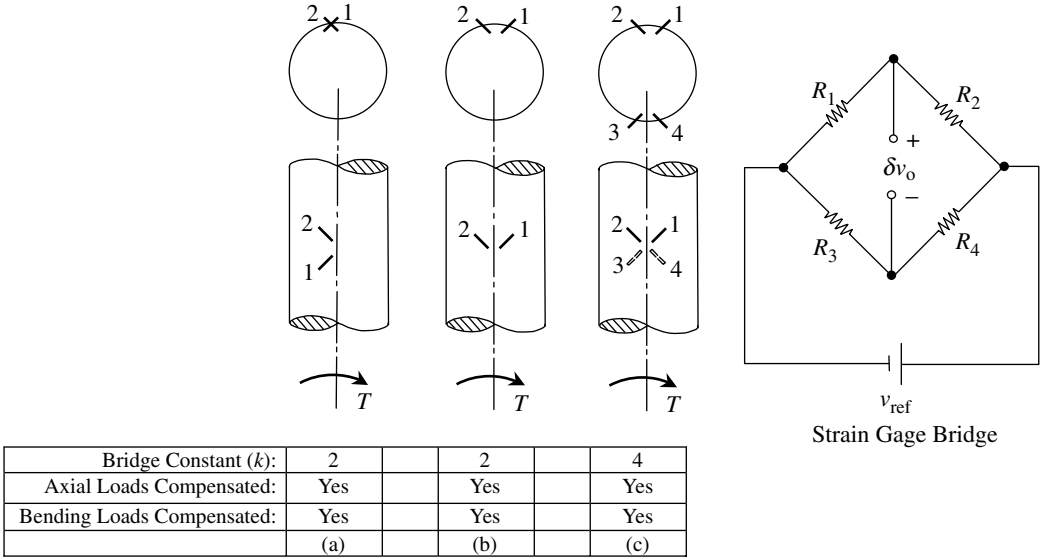


FIGURE 15.41 Strain gage configurations for a circular shaft torque sensor.

Three possible configurations are shown in Figure 15.41. In configurations (a) and (b), only two strain gages are used, and the bridge constant, k , is equal to 2. Note that both axial loads and bending are compensated with the given configurations because resistance in both gages will be changed by the same amount (the same sign and same magnitude) that cancels out, up to first order, for the bridge circuit connection shown in Figure 15.41. Configuration (c) has two pairs of gages, mounted on the two opposite surfaces of the shaft. The bridge constant is doubled in this configuration, and here again, the sensor clearly selfcompensates for axial and bending loads up to first order [$O(\delta R)$].

For a circular-shaft torque sensor that uses SC strain gages, design criteria for obtaining a suitable value for the polar moment of area (J) are listed in Table 15.3. Note that ϕ is a safety factor.

Although the manner in which strain gages are configured on a torque sensor can be exploited to compensate for cross-sensitivity effects arising from factors such as tensile and bending loads, it is advisable to use a torque-sensing element that inherently possesses low sensitivity to these factors that cause error in a torque measurement. A tubular torsion element is convenient for analytical purposes because of the simplicity of the associated expressions for design parameters. Unfortunately, such an

TABLE 15.3 Design Criteria for a Strain Gage Torque-Sensing Element

Criterion	Specification	Governing Formula for the Polar Moment of Area (J)
Strain capacity of strain gage element	ϵ_{\max}	$\geq \frac{\phi r}{2G} \frac{T_{\max}}{\epsilon_{\max}}$
Strain gage nonlinearity	$N_p = \frac{\text{Max strain error}}{\text{Strain range}} \times 100\%$	$\geq \frac{25\phi r S_2}{G S_1} \frac{T_{\max}}{N_p}$
Sensor sensitivity (output voltage)	$v_o = K_a \delta v_o$ where K_a = transducer gain	$\leq \frac{K_a k S_s r v_{\text{ref}}}{8G} \frac{T_{\max}}{v_o}$
Sensor stiffness (system bandwidth and gain)	$K = \frac{\text{Torque}}{\text{Twist angle}}$	$\geq \frac{L}{G} K$

element is not very rigid to bending and tensile loading. Alternative shapes and structural arrangements have to be considered if inherent rigidity (insensitivity) to cross-loads is needed. Furthermore, a tubular element has the same strain at all locations on the element surface. This does not provide a choice with respect to mounting locations of strain gages in order to maximize the torque sensor sensitivity. Another disadvantage of the basic tubular element is that the surface is curved; therefore, much care is needed in mounting fragile SC gages, which could be easily damaged by even slight bending. Hence, a sensor element that has flat surfaces to mount the strain gages would be desirable. A torque-sensing element that has the aforementioned desirable characteristics (i.e., inherent insensitivity to cross-loading, nonuniform strain distribution on the surface, and the availability of flat surfaces to mount strain gages) is shown in Figure 15.42. Note that two sensing elements are connected radially between the drive unit and the driven member. The sensing elements undergo bending while transmitting a torque between the driver and the driven member. Bending strains are measured at locations of high sensitivity and are taken to be proportional to the transmitted torque. Analytical determination of the calibration constant is not easy for such complex sensing elements, but experimental determination is straightforward. Note that the strain gage torque sensor measures the direction as well as the magnitude of the torque transmitted through it.

15.6.1.10 Deflection Torque Sensors

Instead of measuring strain in the sensor element, the actual deflection (twisting or bending) can be measured and used to determine torque, through a suitable calibration constant. For a circular-shaft (solid or hollow) torsion element, the governing relationship is given by

$$T = \frac{GJ}{L} \theta \quad (15.92)$$

The calibration constant GJ/L must be small in order to achieve high sensitivity. This means that the element stiffness should be low. This will limit the bandwidth (which measures speed of response) and gain (which determines steady-state error) of the overall system. The twist angle, θ , is very small (e.g., a fraction of a degree) in systems with high bandwidth. This requires very accurate measurement of θ in order to determine the torque T . A type of displacement sensor that could be used is described as follows. Two ferromagnetic gear wheels are splined at two axial locations of the torsion element. Two stationary proximity probes of the magnetic induction type (selfinduction or mutual induction) are placed radially, facing the gear teeth, at the two locations. As the shaft rotates, the gear teeth change the flux linkage of the proximity sensor coils. The resulting output signals of the two probes are pulse sequences, shaped somewhat like sine waves. The phase shift of one signal with respect to the other determines the relative angular deflection of one gear wheel with respect to the other, assuming that the two probes are synchronized under no-torque conditions. Both the magnitude and the direction of the transmitted torque are determined using this method. A 360° phase shift corresponds to a relative deflection by an integer multiple of the gear pitch. It follows that deflections less than half the pitch can be measured

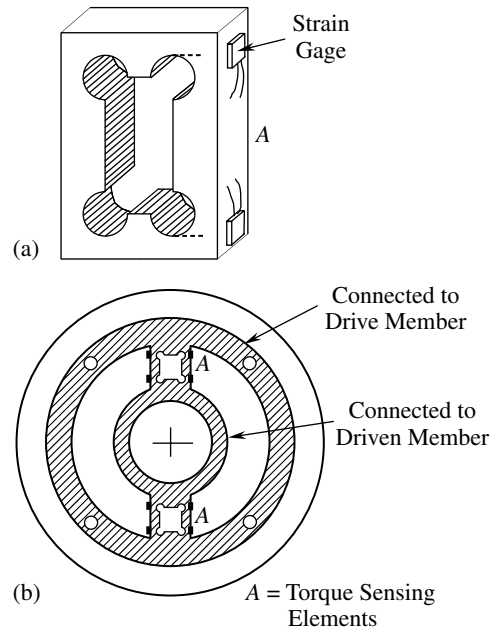


FIGURE 15.42 Use of a bending element in torque sensing: (a) sensing element; (b) element configuration.

without ambiguity. Assuming that the output signals of the two probes are sine waves (narrow-band filtering can be used to achieve this), the phase shift will be proportional to the angle of twist, θ .

15.6.1.11 Variable-Reluctance Torque Sensor

A torque sensor that is based on the sensor element deformation and that does not require a contacting commutator is a variable-reluctance device that operates like a differential transformer (RVDT or LVDT). The torque-sensing element is a ferromagnetic tube that has two sets of slits, typically oriented along the two principal stress directions of the tube (45°) under torsion. When a torque is applied to the torsion element, one set of gaps closes and the other set opens as a result of the principal stresses normal to the slit axes. Primary and secondary coils are placed around the slitted tube, and they remain stationary. One segment of the secondary coil is placed around one set of slits, and the second segment is placed around the other, perpendicular, set. The primary coil is excited by an AC supply, and the induced voltage, v_o , in the secondary coil is measured. As the tube deforms, it changes the magnetic reluctance in the flux linkage path, thus changing the induced voltage. The two segments of the secondary coil should be connected so that the induced voltages are absolutely additive (algebraically subtractive), because one voltage increases and the other decreases, to obtain the best sensitivity. The output signal should be demodulated, by removing the carrier frequency component, to measure transient torques effectively. Note that the direction of torque is given by the sign of the demodulated signal.

15.6.1.12 Reaction Torque Sensors

The foregoing methods of torque sensing use a sensing element that is connected between the drive member and the driven member. A major drawback of such an arrangement is that the sensing element modifies the original system in an undesirable manner, particularly by decreasing the system stiffness and adding inertia. Not only will the overall bandwidth of the system decrease, but the original torque will also be changed (mechanical loading) because of the inclusion of an auxiliary sensing element. Furthermore, under dynamic conditions, the sensing element will be in motion, thereby making the torque measurement more difficult. The reaction method of torque sensing eliminates these problems to a large degree. This method can be used to measure torque in a rotating machine. The supporting structure (or housing) of the rotating machine (e.g., a motor, pump, compressor, turbine, or generator) is cradled by releasing its fixtures, and the effort necessary to keep the structure from moving is measured. A schematic representation of the method is shown in [Figure 15.43\(a\)](#). Ideally, a lever arm is mounted on the cradled housing, and the force required to fix the housing is measured using a force sensor (load cell). The reaction torque on the housing is given by

$$T_R = F_R \cdot L \quad (15.93)$$

where

F_R = reaction force measured using load cell

L = lever arm length

Alternatively, strain gages or other types of force sensors could be mounted directly at the fixture locations (e.g., at the mounting bolts) of the housing to measure the reaction forces without cradling the housing. Then, the reaction torque is determined with a knowledge of the distance of the fixture locations from the shaft axis.

The reaction-torque method of torque sensing is widely used in dynamometers (reaction dynamometers) that determine the transmitted power in rotating machinery through torque and shaft speed measurements. A drawback of reaction-type torque sensors can be explained using [Figure 15.43\(b\)](#). A motor with rotor inertia, J , which rotates at angular acceleration, $\ddot{\theta}$, is shown. By Newton's Third Law (action equals reaction), the electromagnetic torque generated at the rotor of the motor, T_m , and the frictional torques, T_{f1} and T_{f2} , will be reacted back onto the stator and housing. By applying

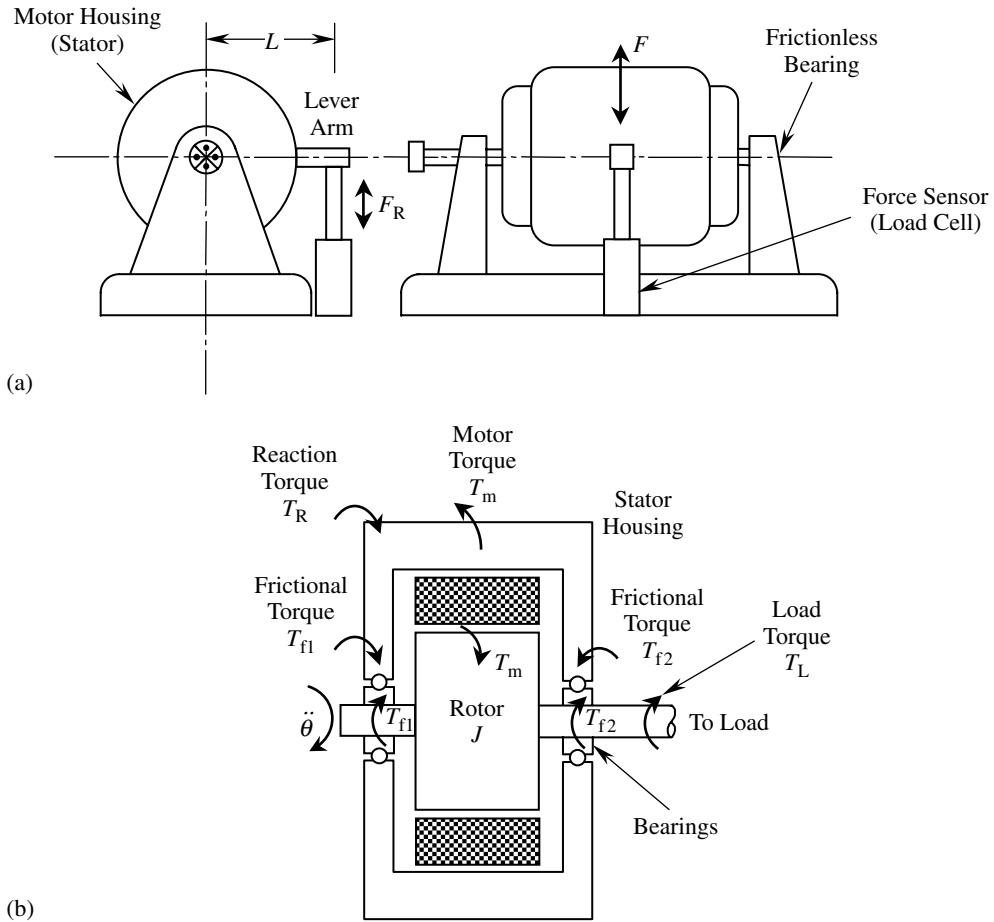


FIGURE 15.43 (a) Schematic representation of a reaction torque sensor setup (reaction dynamometer); (b) various torque components.

Newton's Second Law to the motor rotor and the housing combination, we obtain

$$T_L = T_R - J\ddot{\theta} \quad (15.94)$$

Note that T_L is the variable which must be measured. Under accelerating or decelerating conditions, the reaction torque, T_R , is not equal to the actual torque, T_L , that is transmitted. One method of compensating for this error is to measure the shaft acceleration, compute the inertia torque, and adjust the measured reaction torque using this inertia torque. Note that the frictional torque in the bearings does not enter the final Equation 15.94. This is an advantage of this method.

15.6.2 Miscellaneous Sensors

Motion and force/torque sensors of the types described thus far are widely used in vibration instrumentation. Several other types of sensors are also useful. A few of them are indicated now.

15.6.2.1 Stroboscope

Consider an object that executes periodic motions such as vibrations or rotations in a fairly dark environment. Suppose that a light is flashed at the object at the same frequency as the moving object. Since the object completes a full cycle of motion during the time period between two adjacent flashes,

the object will appear to be stationary. This is the principle of operation of a stroboscope. The main components of a stroboscope are a high-intensity strobe lamp and circuitry to vary the frequency of the electrical pulse signal that energizes the lamp. The flashing frequency may be varied either manually using a knob or according to the frequency of an external periodic signal (trigger signal) that is applied to the stroboscope.

It is clear that by synchronizing the stroboscope with a moving (vibrating, rotating) object so that the object appears stationary, and then noting the flashing (strobe) frequency, the frequency of vibration or speed of rotation of the object can be measured. In this sense, the stroboscope is a noncontacting vibration frequency sensor or a tachometer (rotating speed sensor). Note that the object appears stationary for any integer multiple of the synchronous flashing frequency. Hence, once the strobe is synchronized with the moving object, it is good practice to check whether the strobe also synchronizes at an integer fraction of that flashing frequency. (Typically, trying $1/2$, $1/3$, $1/5$, and $1/7$ the original synchronous frequency is adequate.) The lowest synchronous frequency thus obtained is the correct speed (frequency) of the object. Since the frequency of visual persistence of a human is about 15 Hz, the stationary appearance will not be possible using a stroboscope below this frequency. Hence, the low-frequency limit for a stroboscope is about 15 Hz.

In addition to serving as a sensor for vibration frequency and rotating speed, the stroboscope has many other applications. For example, by maintaining the strobe (flashing) frequency close (but not equal) to the object frequency, the object will appear to move very slowly. In this manner, visual inspection of objects that execute periodic motions at high speed is possible. Also, stroboscopes are widely used in dynamic balancing of rotating machinery. In this case, it is important to measure the phase angle of the resultant imbalance force with respect to a coordinate axis (direction) that is fixed to the rotor. Suppose that a radial line is marked on the rotor. If we synchronize a stroboscope with the rotor such that the marked line appears not only stationary but also oriented in a fixed direction (e.g., horizontal or vertical), we in effect make the strobe signal in phase with the rotation of the rotor. Then by comparing the imbalance force signal of the rotor (obtained, for example, by an accelerometer or a force sensor at the bearings of the rotor) with the synchronized strobe signal (with a fixed reference), by means of an oscilloscope or a phase meter, it is possible to determine the orientation of the imbalance force with respect to a fixed body reference of the rotating machine.

15.6.2.2 Fiber Optic Sensors and Lasers

The characteristic component in a fiber optic sensor is a bundle of glass fibers (typically a few hundred) that can carry light. Each optical fiber may have a diameter on the order of 0.01 mm. There are two basic types of fiber optic sensors. In one type, the “indirect” or the *extrinsic* type, the optical fiber acts only as the medium in which the sensed light is transmitted. In this type, the sensing element itself does not consist of optical fibers. In the second type, the “direct” or the *intrinsic* type, the optical fiber bundle itself acts as the sensing element. When the conditions of the sensed medium change, the light-propagation properties of the optical fibers change, providing a measurement of the change in the conditions. Examples of the first (extrinsic) type of sensor include fiber optic position sensors and tactile (distributed touch) sensors. The second (intrinsic) type of sensor is found, for example, in fiber optic gyroscopes, fiber optic hydrophones, and some types of micro-displacement or force sensors.

A schematic representation of a fiber optic position sensor (or proximity sensor or displacement sensor) is shown in [Figure 15.44\(a\)](#). The optical fiber bundle is divided into two groups: transmitting fibers and receiving fibers. Light from the light source is transmitted along the first bundle of fibers to the target object whose position is being measured. Light reflected onto the receiving fibers by the surface of the target object is carried to a photodetector. The intensity of the light received by the photodetector will depend on the position, x , of the target object. In particular, if $x = 0$, the transmitting bundle will be completely blocked off and the light intensity at the receiver will be zero. As x is increased, the received light intensity will increase, because more light will be

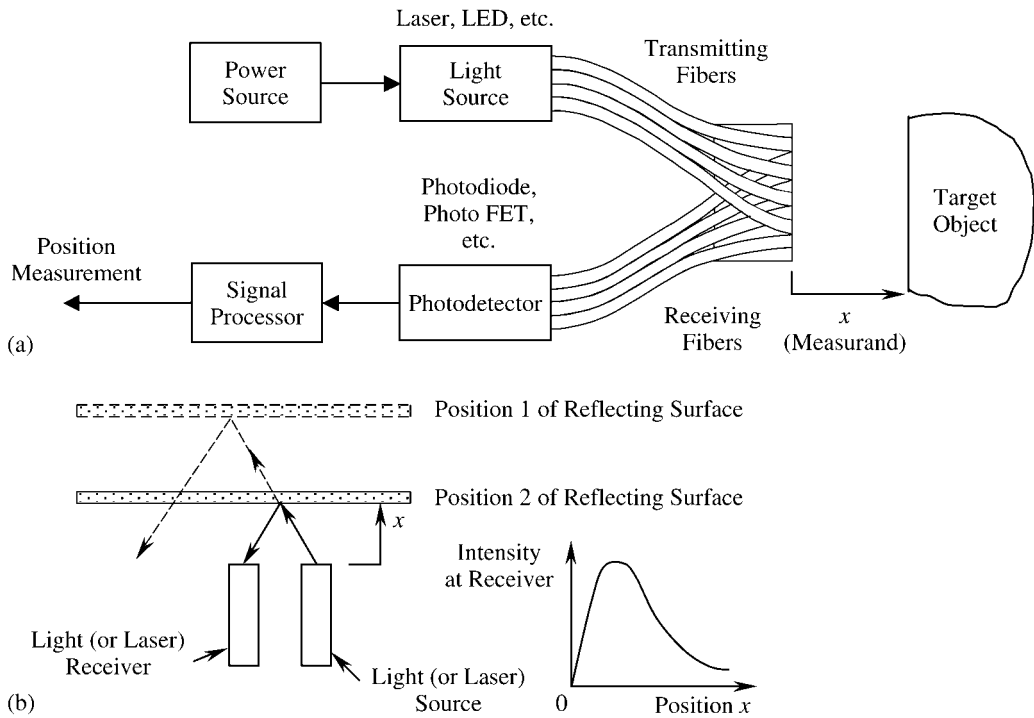


FIGURE 15.44 (a) A fiber-optic proximity sensor; (b) nonlinear characteristic curve.

reflected onto the receiving bundle tip. This will reach a peak at some value of x . When x is increased beyond that value, more light will be reflected outside the receiving bundle; hence, the intensity of the received light will decrease. Hence, in general, the proximity–intensity curve for an optical proximity sensor will be nonlinear and will have the shape shown in Figure 15.44(b). Using this (calibration) curve, we can determine the position (x) once the intensity of the light received at the photosensor is known. The light source could be a *laser* (or light amplification by stimulated emission of radiation; structured light), infrared light-source, or some other type, such as a light-emitting diode (LED). The light sensor (photodetector) could be some light-sensitive discrete SC element such as a photodiode or a photo field effect transistor (photo FET). Very fine resolutions, better than 1×10^{-6} cm, can be obtained using a fiber optic position sensor. An *optical encoder* is a digital (or pulse-generating) motion transducer. Here, a light beam is intercepted by a moving disk that has a pattern of transparent windows. The light that passes through, as detected by a photosensor, provides the transducer output. These sensors may also be considered in the extrinsic category.

The advantages of fiber optics include insensitivity to electrical and magnetic noise (due to optical coupling), safe operation in explosive, high-temperature, hazardous environments and high sensitivity. Furthermore, mechanical loading and wear problems do not exist because fiber optic position sensors are noncontacting devices with stationary sensor heads. The disadvantages include direct sensitivity to variations in the intensity of the light source and dependence on ambient conditions (ambient light, dirt, moisture, smoke, etc.).

As an example of an *intrinsic* application of fiber optics in sensing, consider a straight optical fiber element that is supported at each end. In this configuration almost 100% of the light at the source end will transmit through the optical fiber and will reach the detector (receiver) end. Then, suppose that a slight load is applied to the optical fiber segment at its mid span. The fiber will deflect slightly due to the

load, and as a result the amount of light received at the detector can significantly drop. For example, a deflection of just $50\text{ }\mu\text{m}$ can result in a drop in intensity at the detector by a factor of 25. Such an arrangement may be used in deflection, force, and tactile sensing. Another intrinsic application is the fiber optic gyroscope, as described below.

15.6.2.3 Fiber-Optic Gyroscope

This is an angular speed sensor that uses fiber optics. Contrary to the implication of its name, however, it is not a gyroscope in the conventional sense. Two loops of optical fibers wrapped around a cylinder are used in this sensor. One loop carries a monochromatic light (or laser) beam in the clockwise direction, and the other loop carries a beam from the same light (or laser) source in the counterclockwise direction. Since the laser beam traveling in the direction of rotation of the cylinder has a higher frequency than that of the other beam, the difference in frequencies of the two laser beams received at a common location will measure the angular speed of the cylinder. This may be accomplished through interferometry, as the light and dark patterns of the detected light will measure the frequency difference. Note that the length of the optical fiber in each loop can exceed 100 m. Angular displacements can be measured with the same sensor simply by counting the number of cycles and clocking the fractions of cycles. Acceleration can be determined by digitally determining the rate of change of speed.

15.6.2.4 Laser Doppler Interferometer

The laser produces electromagnetic radiation in the ultraviolet, visible, or infrared bands of the spectrum. A laser can provide a single-frequency (*monochromatic*) light source. Furthermore, the electromagnetic radiation in a laser is *coherent* in the sense that all waves generated have constant phase angles. The laser uses oscillations of atoms or molecules of various elements. The helium–neon (HeNe) laser and the SC laser are commonly used in industrial applications.

As noted earlier, the laser is useful in fiber optics, but it can also be used directly in sensing and gaging applications. The laser Doppler interferometer is one such sensor. It is useful in the accurate measurement of small displacements, for example, in strain measurements. To explain the operation of this device, we should explain two phenomena: the Doppler effect and light wave interference. Consider a wave source (e.g., a light source or sound source) that is moving with respect to a receiver (observer). If the source moves toward the receiver, the frequency of the received wave appears to have increased; if the source moves away from the receiver, the frequency of the received wave appears to have decreased. The change in frequency is proportional to the velocity of the source relative to the receiver. This phenomenon is known as the *Doppler effect*. Now consider a monochromatic (single-frequency) light wave of frequency, f (say, 5×10^{14} Hz), emitted by a laser source. If this ray is reflected by a target object and received by a light detector, the frequency of the received wave is

$$f_2 = f + \Delta f \quad (15.95)$$

The frequency increase Δf will be proportional to the velocity, v , of the target object, which is assumed to be positive when moving toward the light source. Hence,

$$\Delta f = cv \quad (15.96)$$

Now by comparing the frequency, f_2 , of the reflected wave, with the frequency

$$f_1 = f \quad (15.97)$$

of the original wave, we can determine Δf and, hence, the velocity, v , of the target object.

The change in frequency Δf due to the Doppler effect can be determined by observing the fringe pattern due to light wave interference. To understand this, consider the two waves

$$v_1 = a \sin 2\pi f_1 t \quad (15.98)$$

and

$$v_2 = a \sin 2\pi f_2 t \quad (15.99)$$

If we add these two waves, the resulting wave is

$$v = v_1 + v_2 = a(\sin 2\pi f_1 t + \sin 2\pi f_2 t)$$

which can be expressed as

$$v = 2a \sin \pi(f_2 + f_1)t \cos \pi(f_2 - f_1)t \quad (15.100)$$

It follows that the combined signal will beat at the beat frequency $\Delta f/2$. When f_2 is very close to f_1 (i.e., when Δf is small compared with f), these beats will appear as dark and light lines (fringes) in the resulting light wave. This is known as *wave interference*. Note that Δf can be determined by two methods:

1. By measuring the spacing of the fringes
2. By counting the beats in a given time interval or by timing successive beats using a high-frequency clock signal

The velocity of the target object is determined in this manner. Displacement can be obtained simply by digital integration or by accumulating the count. A schematic diagram for the laser Doppler interferometer is shown in Figure 15.45. Industrial interferometers usually employ a HeNe laser that has waves of two frequencies close together. In that case, the arrangement shown in Figure 15.45 has to be modified to take into account the two frequency components.

Note that there are laser interferometers that directly measure *displacement* rather than speed. They are based on measuring *phase difference* between the direct and the returning laser, not the Doppler effect (frequency difference). In this case, integration is not needed to obtain displacement from a measured velocity.

15.6.2.5 Ultrasonic Sensors

Audible sound waves have frequencies in the range of 20 Hz to 20 kHz. Ultrasound waves are pressure waves, just like sound waves, but their frequencies are higher than the audible frequencies. Ultrasonic sensors are used in many applications, including displacement and vibration sensing, medical imaging, ranging for cameras with autofocusing capability, level sensing, machine monitoring, and speed sensing. For example, in medical applications, ultrasound probes of frequencies 40 kHz, 75 kHz, 7.5 MHz and 10 MHz are commonly used. Ultrasound can be generated according to several principles. For example, high-frequency (gigahertz) oscillations in piezoelectric crystals subjected to electrical potentials are used to generate very high-frequency ultrasound. Another method is to use the magnetostrictive property of ferromagnetic material. Ferromagnetic materials deform when subjected to magnetic fields. Respondent oscillations generated by this principle can produce ultrasonic waves. Another method of generating ultrasound is to apply a high-frequency voltage to a metal-film capacitor. A microphone can serve as an ultrasound detector (receiver).

Analogous to the case of fiber-optic sensing, there are two common ways of employing ultrasound in a sensor. In one approach, the *intrinsic* method, the ultrasound signal undergoes change as it passes through an object, due to acoustic impedance and the absorption characteristics of the object. The resulting signal (image) may be interpreted to determine properties of the object, such as texture, firmness, and deformation. This approach is utilized, for example, in machine monitoring and object

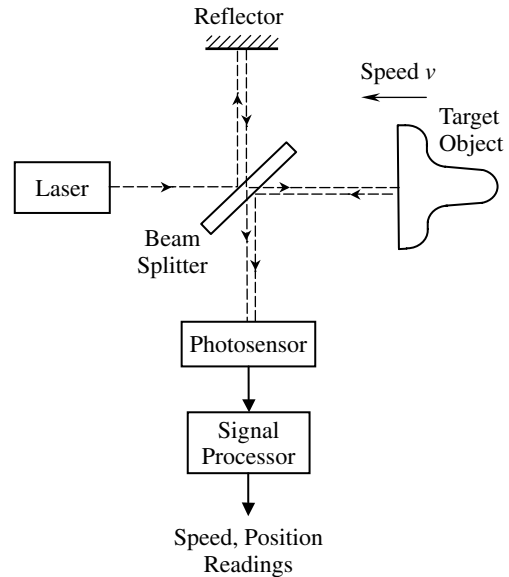


FIGURE 15.45 A laser Doppler interferometer for measuring velocity and displacement.

firmness sensing. In the other approach, the *extrinsic* method, the time for an ultrasound burst to travel from its source to some object and then back to a receiver is measured. This approach is used in distance, position, and vibration measurement and in dimensional gauging.

In distance (vibration, proximity, displacement) measurement using ultrasound, a burst of ultrasound is projected at the target object, and the time taken for the echo to be received is clocked. A signal processor computes the position of the target object, possibly compensating for environmental conditions. This configuration is shown in Figure 15.46. Alternatively, the velocity of the target object can be measured, using the Doppler effect, by measuring (clocking) the change in frequency between the transmitted wave and the received wave. The “beat” phenomenon may be employed here. Position measurements with fine resolution (e.g., a fraction of a millimeter) can be achieved using the ultrasonic method. Since the speed of ultrasonic wave propagation depends on the temperature of the medium (typically air), errors will enter into the ultrasonic readings unless the sensor is adjusted to compensate for temperature variations.

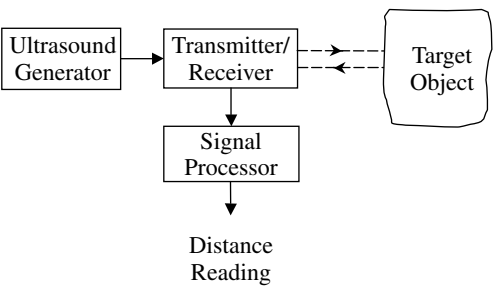


FIGURE 15.46 An ultrasonic position sensor.

15.6.2.6 Gyroscopic Sensors

Consider a rigid body spinning about an axis at angular speed, ω . If the moment of inertia of the body about that axis is J , the angular momentum H about the same axis is given by

$$H = J\omega \tag{15.101}$$

Newton’s Second Law (torque = rate of change of angular momentum) tells us that to rotate (precess) the spinning axis slightly, a torque has to be applied, because precession causes a change in the spinning angular momentum vector (the magnitude remains constant but the direction changes), as shown in Figure 15.47(a). This is the principle of operation of a gyroscope. Gyroscopic sensors are commonly used in control systems for stabilizing vehicle systems.

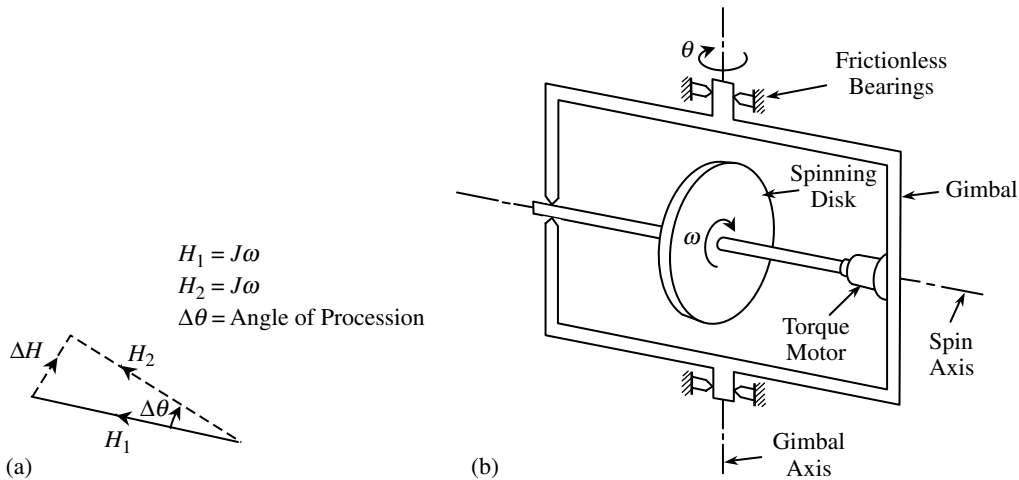


FIGURE 15.47 (a) Illustration of the gyroscopic torque needed to change the direction of an angular momentum vector; (b) a simple single-axis gyroscope for sensing angular displacements.

TABLE 15.4 Rating Parameters of Several Sensors and Transducers

Transducer	Measurand	Measurand Frequency Max/Min	Output Impedance	Typical Resolution	Accuracy	Sensitivity
Potentiometer	Displacement	10 Hz/DC	Low	0.1 mm	0.1%	200 mV/mm
LVDT	Displacement	2500 Hz/DC	Moderate	0.001 mm or less	0.3%	50 mV/mm
Resolver	Angular displacement	500 Hz/DC (limited by excitation frequency)	Low	2 min	0.2%	10 mV/deg
Tachometer	Velocity	700 Hz/DC	Moderate (50 Ω)	0.2 mm/sec	0.5%	5 mV/mm/sec; 75 mV/rad/sec
Eddy current proximity sensor	Displacement	100 kHz/DC	Moderate	0.001 mm 0.05% full scale	0.5%	5 V/mm
Piezoelectric accelerometer	Acceleration (and velocity, etc.)	25 kHz/1 Hz	High	1 mm/sec ²	1%	0.5 mV/m/sec ²
Semiconductor strain gage	Strain (displacement, acceleration, etc.)	1 kHz/DC (limited by fatigue)	200	1 to 10 μ sec (1 μ sec = 10^{-6} unity strain)	1%	1 V/ ϵ , 2000 μ sec max
Loadcell	Force (10–1000 N)	500 Hz/DC	Moderate	0.01 N	0.05%	1 mV/N
Laser	Displacement/shape	1 kHz/DC	100 Ω	1.0 μ m	0.5%	1 V/mm
Optical encoder	Motion	100 kHz/DC	500 Ω	10 bit	\pm 1/2 bit	10 ⁴ /rev

Consider the gyroscope shown in [Figure 15.47\(b\)](#). The disk is spun about frictionless bearings using a torque motor. Since the gimbal (the framework on which the disk is supported) is free to turn about the frictionless bearings on the vertical axis, it will remain fixed with respect to an inertial frame, even if the bearing housing (the main structure in which the gyroscope is located) rotates. Hence, the relative angle between the gimbal and the bearing housing (angle θ in the figure) can be measured, and this gives the angle of rotation of the main structure. In this manner, angular displacements in systems such as aircraft, space vehicles, ships, and land vehicles can be measured and stabilized with respect to an inertial frame. Note that bearing friction introduces an error that must be compensated for, perhaps by recalibration before a reading is taken.

The *rate gyro*, which has the same arrangement as shown in [Figure 15.47\(b\)](#), except with a slight modification, can be used to measure angular speeds. In this case, the gimbal is not free but is restrained by a torsional spring. A viscous damper is provided to suppress any oscillations. By analyzing this gyro as a mechanical tachometer, we will note that the relative angle of rotation, θ , gives the angular speed of the structure about the gimbal axis.

Several areas can be identified where new developments and innovations are being made in sensor technology:

1. Microminiature sensors: IC-based, with built-in signal processing.
2. Intelligent sensors: built-in reasoning or information preprocessing to provide high-level knowledge.
3. Integrated and distributed sensors: sensors are integral with the components and agents of the overall multiagent system that communicate with each other.
4. Hierarchical sensory architectures: low level sensory information is preprocessed to match higher level requirements.

These four areas of activity are also representative of future trends in sensor technology development. To summarize, rating parameters of a selected set of sensors/transducers are listed in [Table 15.4](#).

References

- Broch, J.T. 1980. *Mechanical Vibration and Shock Measurements*, Bruel and Kjaer, Naerum, Denmark.
- Buzdugan, G., Mihaiescu, E., and Rades, M. 1986. *Vibration Measurement*, Martinus Nijhoff Publishers, Dordrecht, The Netherlands.
- de Silva, C.W., Selection of Shaker specifications in seismic qualification tests, *J. Sound Vib.*, 91, 2, 21–26, 1983.
- de Silva, C.W., Shaker test-fixture design, *Meas. Control*, 17, 6, 152–155, 1983.
- de Silva, C.W., Sensory information acquisition for monitoring and control of intelligent mechatronic systems, *Int. J. Inf. Acquisition*, 1, 1, 89–99, 2004.
- de Silva, C.W. 1989. *Control Sensors and Actuators*, Prentice Hall, Englewood Cliffs, NJ.
- de Silva, C.W. 2004. *MECHATRONICS—An Integrated Approach*, CRC Press, Boca Raton, FL.
- de Silva, C.W., Price, T.E., and Kanade, T., A torque sensor for direct-drive manipulators, *J. Eng. Ind., Trans. ASME*, 109, 2, 122–127, 1987.
- de Silva, C.W. 2000. *VIBRATION—Fundamentals and Practice*, CRC Press, Boca Raton, FL.
- Ewins, D.J. 1984. *Modal Testing: Theory and Practice*, Research Studies Press Ltd., Letchworth, England.
- McConnell, K.G. 1995. *Vibration Testing*, Wiley, New York.
- Randall, R.B. 1977. *Application of B&K Equipment to Frequency Analysis*, Bruel and Kjaer, Naerum, Denmark.

Appendix 15A

Virtual Instrumentation for Data Acquisition, Analysis, and Presentation

Michael Sedlak, and Chris “Flip” DeFilippo

National Instruments

Source: Lab VIEW Sound and Vibration User Manual, April 2004 Edition. With permission.

Summary

The proper acquisition, analysis, and presentation of shock and vibration data demand careful configuration and execution of the measurement system. This Appendix provides a review of the fundamental considerations, which have to be made when acquiring, analyzing, and presenting shock as vibration data. Additionally, the Appendix indicates some tips and techniques for programming such tests using modern software packages. Specifically, this Appendix refers to the graphical programming environment LabVIEW and the Sound and Vibration Toolkit, and supplements the material presented in Chapter 10 and in Chapter 15 to Chapter 18.

List of Abbreviations

Symbol	Quantity	Symbol	Quantity
ADC	Analog-to-Digital Converter (A/D)	IEPE	Integrated Electronic Piezoelectric Excitation
AI	Analog Input	IMD	Intermodulation Distortion
ANSI	American National Standards Institute	JTFA	Joint Time Frequency Analysis
AO	Analog Output	NI	National Instruments
DAC	Digital-to-Analog Converter (D/A)	PXI	PCI eXtensions For Instrumentation
DAQ	Data Acquisition	RMS	Root Mean Square
DFT	Discrete Fourier Transform	RPM	Revolutions per Minute
DOF	Degree of Freedom	SDOF	Single Degree of Freedom
DSA	Dynamic Signal Acquisition	SRS	Shock Response Spectrum
DUT	Device Under Test	STFT	Short Time Fourier Transform
DZT	Discrete Zak Transform	SVL	Sound and Vibration Library
EU	Engineering Unit	SVT	Sound and Vibration Toolkit
FFT	Fast Fourier Transform	THD	Total Harmonic Distortion
FRF	Frequency Response Function	VI	LabVIEW Virtual Instrument
IEC	International Electrotechnical Commission		

15A.1 Dynamic Signals

This Appendix introduces how to properly obtain data to analyze with the LabVIEW Sound and Vibration Toolkit, as well as issues that can affect the quality of the data. One can simulate data with the generation Virtual Instruments (VIs) located on the Generation palette as well as with other VIs. The Appendix particularly supplements the material presented in [Chapter 10](#) and in Chapter 15 to [Chapter 18](#), on vibration instrumentation, testing, data acquisition, and analysis.

15A.1.1 Acquiring and Simulating Dynamic Signals

This section discusses obtaining data and some key issues when acquiring or simulating dynamic signals to ensure valid measurement results. The three techniques that allow one to obtain data

are as follows:

- Acquisition of data with a data acquisition (DAQ) device or system
- Reading of data from a file
- Simulation of data with a generation VI (LabVIEW Virtual Instrument) or other source

It is important that you keep certain considerations in mind when you obtain your data. Measurement and analysis software such as the LabVIEW Sound and Vibration Toolkit does not compensate for inaccurate data. Therefore, the test equipment and test procedure should be calibrated to ensure accurate results. Generally, the test equipment should have specifications at least ten times better than those of the device under test (DUT). Use a verifiable and repeatable test procedure to get accurate results.

Whether one is obtaining the data from a DAQ system, reading the data from a file, or simulating the data, aliasing and time continuity are common issues, which should be considered in the measurement analysis.

15A.1.1.1 Aliasing

When a dynamic signal is discretely sampled, aliasing is the phenomenon in which frequency components greater than the Nyquist frequency are erroneously shifted to lower frequencies (see [Chapter 10](#)). The Nyquist frequency is calculated with the following formula:

$$f_{\text{Nyquist}} = \text{sample rate}/2$$

When acquiring data with an NI Dynamic Signal Acquisition (DSA) device, aliasing protection is automatic in any acquisition. The sharp antialiasing filters on DSA devices track the sample rate and filter out (attenuate) all frequencies above the Nyquist frequency.

When performing frequency measurements with an NI E Series DAQ device, you must take steps to eliminate aliasing. These antialiasing steps can include the following actions:

- Increasing the sample rate
- Applying an external low-pass filter
- Using an inherently band-limited DUT

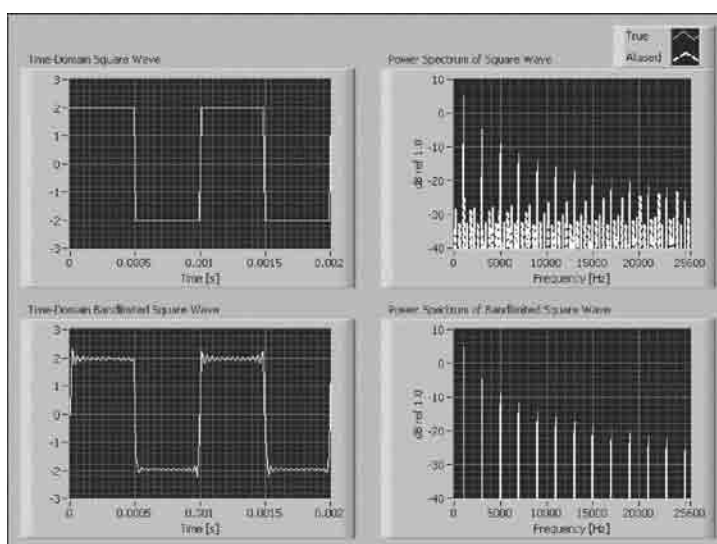


FIGURE 15A.1 Simulated data aliasing.

Simulated data also can exhibit aliasing. The signals often are generated according to a time-domain expression and, therefore, have high-frequency components that are aliased in the discretely sampled data. [Figure 15A.1](#) shows an example of this aliasing for a simulated square wave.

The only way to protect data from aliasing is to apply appropriate aliasing protection before the data are generated or acquired. Aliasing occurs when the data are generated or sampled, and it is not possible to remove aliased components from the data without detailed knowledge of the original signal. In general, it is not possible to distinguish between true frequency components and aliased frequency components. Therefore, accurate frequency measurements require adequate alias protection.

15A.1.1.2 Time Continuity

When you acquire data in a continuous acquisition, you can use the t_0 parameter in the waveform data-type to ensure there are no gaps between successive blocks of waveforms returned by sequential calls to the DAQmx Read VI or AI Read VI. When signals are generated with one of the waveform generation VIs, in the Generation palette or the Waveform Generation palette, the t_0 of the current waveform is one sample period later than the timestamp of the last sample in the previous waveform. Continuity is enforced in this way until the generation is reset.

The waveform data type is integral for testing time continuity in the Sound and Vibration Toolkit. If you read data from a file or simulate a signal using one of the VIs in the Signal Generation palette, wire a t_0 that meets the continuous timestamp condition to the waveform data type connected to the measurement analysis VIs. This action prevents unexpected resets of the measurement analysis due to detected discontinuities in the input signal.

15A.2 Measurement Configuration Considerations

This section describes how the analog input (AI), analog output (AO), timing, and triggering configuration affect your measurements.

15A.2.1 Input Signal Considerations

One must consider the following configuration before acquiring dynamic signals and performing shock and vibration measurements.

15A.2.1.1 Input Pseudodifferential and Differential Configuration

DSA devices such as the National Instruments PXI-4461 supports two terminal configurations for AI, differential and pseudodifferential. The term pseudodifferential refers to the fact that there is a 50 Ω resistance between the outer BNC shell and chassis ground. One can configure the NI PXI-4461 input channels on a per-channel basis. Therefore, you can have one channel configured for differential mode and the other channel configured for pseudodifferential mode. Configure the channels based on how the signal source or DUT is referenced. Refer to [Table 15A.1](#) to determine how to configure the channel based on the source reference.

If the signal source is floating, use the pseudodifferential channel configuration. A floating signal source does not connect to the building ground system. Instead, the signal source has an isolated ground-reference point. Some examples of floating signal sources are outputs of transformers without grounded center taps, battery-powered devices, nongrounded accelerometers, and most instrumentation

TABLE 15A.1 Input Channel Configuration

Source Reference	Channel Configuration
Floating, ground referenced	Pseudodifferential
Ground referenced	Differential

microphones. An instrument or device that has an isolated output is considered to be a floating signal source. It is important to provide a ground reference for a floating signal. If no ground-reference point is provided — for example, in selecting differential mode with a floating microphone — the microphone outputs can drift outside the NI PXI-4461 common-mode range.

If the signal source is ground-referenced, use either the differential or pseudodifferential channel configurations. A ground-referenced signal source connects in some way to the building system ground. Therefore, it is already connected to a ground-reference point with respect to the NI PXI-4461, assuming the PXI or CompactPCI chassis and controller are plugged into the same power system. Nonisolated outputs of instruments and devices that plug into the building power system fall into this category.

Provide only one ground-reference point for each channel by properly selecting differential or pseudodifferential configuration. If you provide two ground-reference points — for example, if you select pseudodifferential mode with a grounded accelerometer — the difference in ground potential results in currents in the ground system that can cause measurement errors. The 50 W resistor on the signal ground is usually sufficient to reduce this current to negligible levels, but results can vary depending on the system setup.

The NI PXI-4461 is automatically configured for differential mode when powered on or when power is removed from the device. This configuration protects the 50 W resistor on the signal ground.

15A.2.1.2 Gain

DSA devices such as the NI PXI-4461 often offer variable gain settings for each AI channel. Each gain setting corresponds to a particular AI range, and each range is centered on 0 V. The gain settings are specified in decibels (dB), where the 0 dB reference is the default input range of ± 10 V.

Positive gain values amplify the signal before the analog-to-digital converter (ADC) digitizes it. This signal amplification reduces the range of the measurement. However, amplifying the signal before digitization allows better resolution by strengthening weak signal components before they reach the ADC. Conversely, negative gains attenuate the signal before they reach the ADC. This attenuation increases the effective measurement range though it sacrifices some resolution for weak signal components.

In general, select the voltage range that provides the greatest dynamic range and the least distortion. For example, consider an accelerometer with a 100 mV/g sensitivity rating with an absolute maximum output voltage of 5 V_{pk}. In this case, the ± 10 V_{pk} is appropriate, corresponding to 0 dB gain. However, the ± 3.16 V_{pk} setting maximizes the dynamic range if one knows the stimulus is limited, for example, to 20 g or 2 V_{pk}.

15A.2.1.3 Input Coupling

One can configure each AI channel for either alternating current (AC) or direct current (DC) coupling. If you select DC coupling, any DC offset present in the source signal is passed to the ADC. The DC-coupling configuration is usually best if the signal source has only small amounts of offset voltage or if the DC content of the acquired signal is important.

If the source has a significant amount of unwanted offset, select AC coupling to take full advantage of the input dynamic range.

15A.2.1.4 Integrated Electronic Piezoelectric Excitation

If you attach an Integrated Electronic Piezoelectric Excitation (IEPE) accelerometer or microphone to an AI channel that requires excitation from your DSA device, you must enable the IEPE excitation circuitry for that channel to generate the required current.

One can independently configure IEPE signal conditioning on a per-channel basis. It is common to set the excitation from 0 to 20 mA with 20 mA resolution.

A DC voltage offset is generated equal to the product of the excitation current and sensor impedance when IEPE signal conditioning is enabled. To remove the unwanted offset, enable AC coupling. Using DC coupling with IEPE excitation enabled is appropriate only if the offset does not exceed the voltage range of the channel.

15A.2.1.5 Nyquist Frequency and Bandwidth

Further discussion of DSA measurement configuration requires a brief introduction of two concepts:

- Nyquist frequency
- Nyquist bandwidth

Any sampling system, such as an ADC, is limited in the bandwidth of the signals it can represent. Specifically, a sampling rate of f_s can only represent signals with a maximum frequency of $f_s/2$. This maximum frequency is known as the Nyquist frequency. The bandwidth from 0 Hz to the Nyquist frequency is the Nyquist bandwidth.

15A.2.1.6 Analog-to-Digital Conversion

ADC is discussed in [Chapter 16](#). DSA devices commonly use a conversion method known as delta–sigma modulation. If the data rate is 51.2 kS/sec, each ADC actually samples its input signal at 6.5536 MS/sec, 128 times the data rate, and produces one-bit samples that are applied to the digital filter. This filter then expands the data to 24 bits, rejects signal components greater than the Nyquist frequency of 25.6 kHz, and digitally resamples the data at 51.2 kS/sec.

The one-bit, 6.5536 MS/sec data stream from the ADC contains all of the information necessary to produce 24-bit samples at 51.2 kS/sec. The delta–sigma ADC achieves this conversion from high speed to high resolution by adding a large amount of random noise to the signal so that the resulting quantization noise, although large, is restricted to frequencies above the Nyquist frequency, 25.6 kHz in this case. This noise is not correlated with the input signal and is almost completely rejected by the digital filter.

The resulting output of the filter is a band-limited signal with a large dynamic range. One of the advantages of a delta–sigma ADC is that it uses a one-bit digital-to-analog converter (DAC) as an internal reference. As a result, the delta–sigma ADC is free from the kind of differential nonlinearity (DNL) and associated noise that is inherent in most high-resolution ADCs.

15A.2.1.7 Antialias Filters

A digitizer may sample signals containing frequency components above the Nyquist limit. The process by which the digitizer modulates out-of-band components, returning them to the Nyquist bandwidth, is known as aliasing. The greatest danger of aliasing is that there is no straightforward way to know whether it has happened by looking at the ADC output. If an input signal contains several frequency components or harmonics, some of these components may be represented correctly while others are aliased.

Low-pass filtering to eliminate components above the Nyquist frequency, either before or during the digitization process, can guarantee that the digitized data set is free of aliased components. The NI PXI-4461 employs both digital and analog low-pass filters to achieve this protection.

In addition to the ADC built-in digital filtering, DSA devices may also feature a fixed-frequency analog filter. The analog filter removes high-frequency components in the analog signal path before they reach the ADC. This filtering addresses the possibility of high-frequency aliasing from the narrow-bands that are not covered by the digital filter.

15A.2.1.8 Input Filter Delay

The input filter delay is the time required for digital data to propagate through the ADC digital filter. For example, a signal experiences a delay equal to 6.3 msec at 10 kS/sec. This delay is an important factor for stimulus–response measurements, control applications, or any application where loop time is critical. In this case, it is often advantageous to maximize the sample rate and minimize the time required for 63 sample clock cycles to elapse.

The input filter delay also makes an external digital trigger appear to occur 63 sample clocks later than expected. Alternatively, the acquired buffer appears to begin 63 samples earlier than expected. This delay occurs because external digital triggering is a predigitization event.

15A.2.1.9 **Overload Detection**

It is desirable to ensure that the DSA device includes overload detection in both the analog domain (predigitization) and digital domain (postdigitization). An analog overrange can occur independently from a digital overrange, and *vice versa*. For example, an IEPE accelerometer might have a resonant frequency that, when stimulated, can produce an overrange in the analog signal. However, because the delta-sigma technology of the ADC uses very sharp antialiasing filters, the overrange is not passed into the digitized signal. Conversely, a sharp transient on the analog side might not overrange, but the step response of the delta-sigma antialiasing filters might result in clipping in the digital data.

Modern DSA devices allow you to programmatically poll the digital and analog overload detection circuitry on a per-channel basis to monitor for an overload condition. If an overload is detected, consider any data acquired at that time corrupt.

15A.2.2 **Output Signal Considerations**

This section describes the theory of operation of the output components of DSA devices such as the NI PXI-4461.

15A.2.2.1 **Output Pseudodifferential and Differential Configuration**

The output channel terminal configuration options are very similar to those for the input channels. The NI PXI-4461 output channels are configurable on a per-channel basis. As with the input channels, you should configure the output channel based on how the DUT is referenced. Refer to Table 15A.2 to determine how to configure the output channel based on the DUT reference.

If the DUT inputs are floating, use the pseudodifferential channel configuration. The term pseudodifferential refers to the fact that there is a 50 W resistance between the outer BNC shell and chassis ground. A floating DUT does not connect in any way to the building ground system. Instead, the DUT has an isolated ground-reference point. Transformer inputs without center ground taps, battery-powered devices, or any instruments that have an isolated input are all examples of floating DUTs. One should provide a ground-reference for a floating DUT input. If no ground-reference point is provided — for example, in selecting differential mode with a floating shaker table input amplifier — the outputs can float outside the common-mode range of the amplifier input.

If the DUT input is ground referenced, use the differential channel configuration. A single-ended DUT connects in some way to the building system ground. Therefore, it is already connected to a ground-reference point with respect to the NI PXI-4461, assuming the PXI or CompactPCI chassis and controller are plugged into the same power system. Nonisolated inputs of instruments that plug into the building power system fall into this category.

You should provide only one ground-reference point for each channel by properly selecting the differential or pseudodifferential configuration. If you provide two ground-reference points — for example, by selecting the pseudodifferential output mode for a single-ended amplifier as the DUT — the difference in ground potential results in currents in the ground system that can cause errors in the output signal. The 50 W resistor on the signal ground is usually sufficient to reduce this current to negligible levels, but results can vary depending on the system setup.

The NI PXI-4461 is automatically configured for the differential mode when powered on or when power is removed from the device. Using the differential mode by default protects the 50 W resistor on the signal ground.

TABLE 15A.2 Output Channel Configuration

DUT Reference	Output Channel Configuration
Floating	Pseudodifferential
Ground referenced	Differential

TABLE 15A.3 NI PXI-4461 Gain Ranges

Gain (Referenced to $\pm 10 V_{pk}$) (dB)	Voltage Range (V_{pk})
0	± 10
-20	± 1
-40	± 0.1

15A.2.2.2 Attenuation

Modern DSA devices offer variable gain settings for AO. Most gain settings correspond to a particular AO range, always centered at 0 V. These gain settings can be specified in dB, where the 0 dB reference corresponds to the default output range.

Table 15A.3 summarizes the three output gain options available on the NI PXI-4461.

In general, select the gain that provides the greatest dynamic range and the least distortion. The $\pm 1 V_{pk}$ setting maximizes the dynamic range if you know the stimulus is limited to, for example, $0.5 V_{pk}$. You can minimize system distortion by providing sufficient headroom between the stimulus setting ($0.5 V_{pk}$) and the range setting ($\pm 1 V_{pk}$). In some cases in which distortion performance is critical, you can reduce the overall dynamic range to improve the distortion characteristics by selecting the $\pm 10 V_{pk}$ setting.

15A.2.2.3 Digital-to-Analog Conversion

Digital-to-analog conversion (DAC) is discussed in [Chapter 16](#). The delta-sigma DACs on the NI PXI-4461 function in a way analogous to delta-sigma ADCs. The digital data first passes through a digital interpolation filter, then the resampling filter of the DAC, and finally goes to the delta-sigma modulator.

In the ADC, the delta-sigma modulator is an analog circuit that converts high-resolution analog signals to high-rate, 1-bit digital data, whereas in the DAC the delta-sigma modulator is a digital circuit that converts high-resolution digital data to high-rate, 1-bit digital data. As in the ADC, the modulator frequency shapes the quantization noise so that almost all of its energy is above the Nyquist frequency.

The digital 1-bit data is then sent directly to a 1-bit DAC. This DAC can have only one of two analog values, and therefore is inherently perfectly linear.

15A.2.2.4 Anti-imaging and Interpolation Filters

A sampled signal repeats itself throughout the frequency spectrum. These repetitions begin above one half the sample rate, f_s , and, theoretically, continue up through the spectrum to infinity. Images remain in the sample data because the data actually represent only the frequency components below one half f_s (the baseband).

15A.2.2.5 Output Filter Delay

Output filter delay, or the time required for digital data to propagate through the DAC and interpolation digital filters, varies depending on the sample rate. This delay is an important factor for stimulus-response measurements, control applications, and every application where loop time is critical.

15A.3 Scaling and Calibration

This Appendix discusses using the SVL Scale Voltage to EU VI located on the Scaling palette to scale a signal to engineering units (EU) and using the Calibration VIs located on the Calibration palette.

15A.3.1 Scaling to Engineering Units

This section discusses scaling data to the appropriate EU so one can perform measurement analysis.

Typically, scaling a signal to the appropriate EU occurs before any analysis is performed. Use the SVL Scale Voltage to EU VI to scale the signal to the appropriate EU. All measurement VIs in the Sound and

Vibration Toolkit expect input signals and return results with the appropriate units, such as time-domain signals in the correct EU, frequency spectra in decibels with the proper reference, phase information in degrees or radians, and so on. To handle units properly, the high-level VIs need the signal to be scaled to the appropriate EU.

If you use any method outside of the Sound and Vibration Toolkit to apply scaling to a waveform, do not use the SVL Scale Voltage to EU VI. NI provides several tools and methods to apply scaling to a waveform. These include, but are not limited to, NI-DAQmx tasks or global channels created with Measurement and Automation Explorer (MAX), the DAQ Assistant, or the DAQmx Create Virtual Channel VI.

15A.3.2 Performing System Calibration

One typically performs system calibration with a dedicated calibrator, such as a pistonphone for microphones or a handheld shaker for accelerometers. If you are calibrating a microphone, consider using the SVL Calibrate Microphone VI. If you are calibrating an accelerometer, consider using the SVL Calibrate Accelerometer VI. These VIs are very similar to the general-purpose SVL Calibrate Sensor VI, but they offer the advantage of having default values commonly found for pistonphones or hand-held shakers. All of the Calibration VIs use the characteristics of the calibrator, such as reference calibration value and frequency, to perform the calibration.

15A.3.2.1 Propagation Delay Calibration

The Sound and Vibration Toolkit provides VIs for calibrating the propagation delay of the measurement system. National Instruments DSA devices like the NI PXI-4461 and NI PCI-4451 can acquire and generate signals on the same device. The input and output channels have analog and digital circuitry, such as antialiasing and anti-imaging filters, that introduce a certain delay to the signal. The propagation delay is the number of samples ranging from the time a sample is first written to the output channel, to the time when that sample is digitized on the input channel, assuming there is no delay from the output channel to the input channel. This delay varies by DSA device.

There are two ways to determine the propagation delay of the DSA device. You can refer to the documentation for the DSA device to find the propagation delay specifications, also referred to as group delay. You also can measure the propagation delay in samples with the SVL Measure Propagation Delay VIs. The SVL Measure Propagation Delay VIs allow you to measure the delay introduced in the input and output circuitry for a specific device at the desired sample rate. Connect the DSA device output channel directly to the input channel, as displayed in Figure 15A.2, to measure the device propagation delay.

Note: Do not put a DUT in the signal path when measuring the propagation delay for a DAQ device.

For an E or S Series DAQ device from NI, you should expect to measure a one-sample propagation delay due to the time required for the signal to traverse the signal path between the DAC on the analog output channel and the ADC on the analog input channel. Figure 15A.3 shows the time domain data for the propagation delay measurement of an NI PCI-6052E.

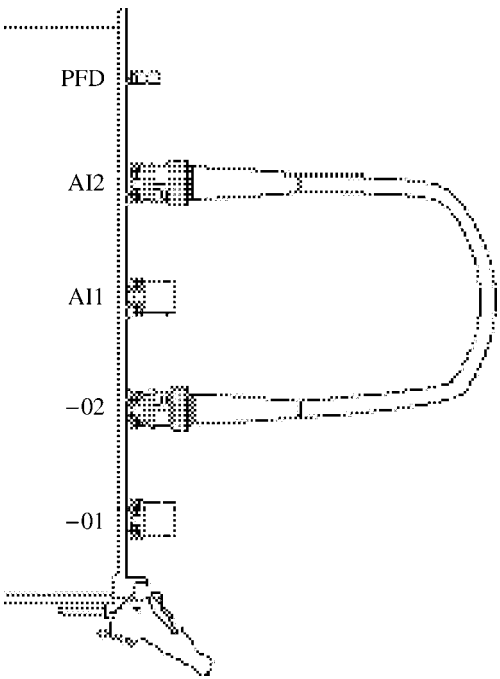


FIGURE 15A.2 15A.2 Measuring the device propagation delay.

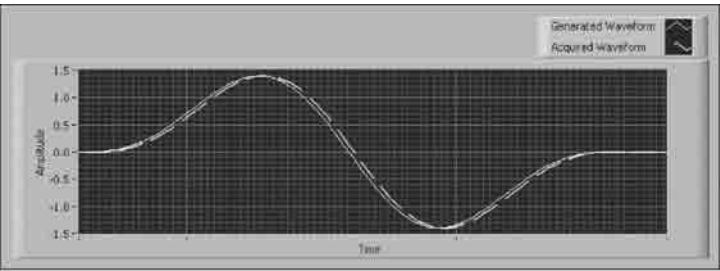


FIGURE 15A.3 Propagation delay measurement of an NI PCI-6052E.

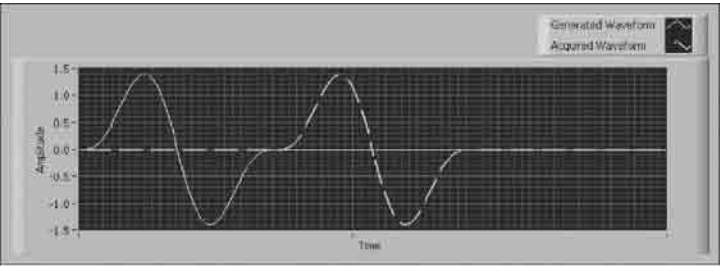


FIGURE 15A.4 NI PXI-4461 propagation delay with a 204.8 kHz sample rate.

For DSA devices, or any other device which has onboard filtering on either the input, output, or both channels, you should expect to measure a propagation delay consistent with the sum of the delays specified for the onboard filters on the input and output channels. Figure 15A.4 shows the delay of a smooth pulse generated and acquired by an NI PXI-4461 with a 204.8 kHz sample rate.

Not all DSA devices have a constant propagation delay across the entire range of supported sample rates. For example, the NI PXI-4461 propagation delay is dependent on the output update rate. Figure 15A.5 shows the total propagation delay vs. sample rate relationship for the NI PXI-4461 from output to input as a function of the sample rate.

As illustrated by Figure 15A.3, Figure 15A.4, and Figure 15A.5, the propagation delay can vary significantly with different sample rates and devices. To ensure measurement accuracy in your I/O applications, determine and account for the propagation delay of the DAQ device at the same sample rate used in your application.

It is important to remove the effects of the delay due to the data acquisition system for two reasons. First, there is always a delay between the generated output signal and the acquired input on the device even when the output and input channels are hardware synchronized. Second, the anti-imaging and antialiasing filters of the device introduce additional delays. You must account for this delay to perform accurate dynamic measurements. Use the *device propagation delay [samples]* input on the examples found in the LabVIEW program directory under “\examples\Sound” and “Vibration\Audio Measurements\” to remove the delay due to the DAQ device.

The anti-imaging and antialiasing filters have a low-pass filter effect on the data. This effect results in a transient response at sharp transitions in the data. These transitions are common at the start and stop of a

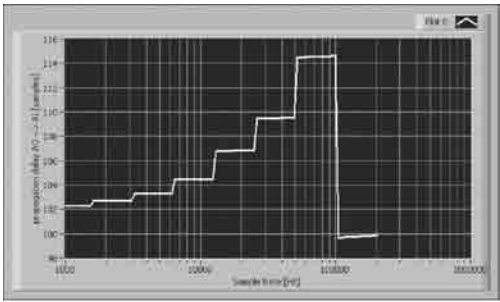


FIGURE 15A.5 NI PXI-4461 propagation delay vs. sample rate.

generation, at a change in frequency (swept sine), and when the amplitude changes (amplitude sweep). The swept-sine analysis and audio measurements examples in the Sound and Vibration Toolkit account for this transient behavior in the device response to achieve the highest degree of accuracy.

The propagation delay of the DUT is also an important specification in some applications. For example, the propagation delay for the DUT is a required input when performing audio measurements and when measuring the frequency response using swept sine. If the DUT and the propagation medium can successfully pass the pulse signal used by the SVL Measure Propagation Delay VIs without excessive attenuation, then this measurement also applies when measuring the propagation delay of the DUT and the propagation medium. Figure 15A.6 shows the wiring diagram for this configuration.

The DUT propagation delay is the delay of the entire system minus the device delay. Remember to measure the device delay without the DUT connected.

The propagation delay for an analog DUT is a constant time delay rather than a delay of samples. Use the following equation to convert the measured delay in samples to the equivalent delay in seconds:

$$\text{delay}[\text{sec}] = \text{delay}[\text{samples}] / \text{sample rate}[\text{Hz}]$$

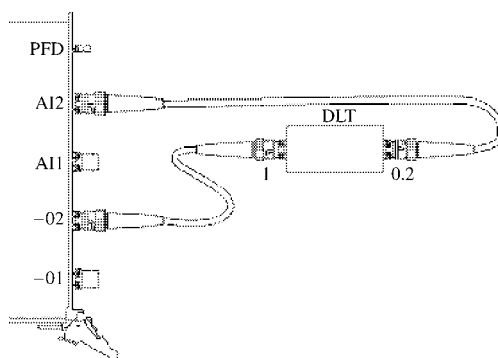


FIGURE 15A.6 Measuring the DUT propagation delay.

15A.4 Limit Testing Analysis

This Appendix discusses using the polymorphic SVT Limit Testing VI located on the Limit Testing palette.

You can use Limit Testing to perform analysis on any type of measured result produced by the Sound and Vibration Toolkit, including the following measurements:

- Waveform
- Spectrum
- Peak
- Octave
- Swept sine
- Scalar

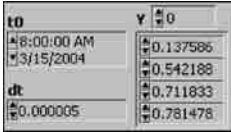

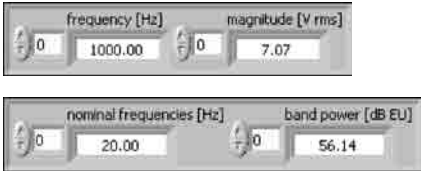

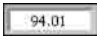
15A.4.1 Limit Testing Overview

You can use the SVT Limit Testing VI to analyze almost any measured result produced by the Sound and Vibration Toolkit. Refer to [Table 15A.4](#) for examples of data-types supported by the SVT Limit Testing VI and VIs that generate supported data-types.

15A.4.2 Using the SVT Limit Testing VI

Limit testing allows one to specify an envelope around the data to define a pass range. You can enter a scalar to the upper limit, lower limit, or both to specify a constant ceiling and floor for the data to perform tests such as range detection. You can enter an upper limit mask, lower limit mask, or both to the SVT Limit Testing VI to define a pass range that varies in shape and level based on acceptable results at any given point in the measurement. You also can create a discontinuous mask which allows you to perform limit testing on only a part of the results while ignoring the rest.

TABLE 15A.4 Compatible Data Types for SVT Limit Testing VI

Data-type		Output VIs
Waveform measurement		AI read, DAQmx read, waveform generation, weighting, integration, vibration level, sound level
Frequency spectrum measurement		Baseband FFT, baseband subset FFT, zoom FFT, extended measurements
XY data		ANSI and IEC octave, swept sine
Peak measurement		Distortion, single-tone, extended measurements
Scalar measurement		Calibration, vibration level, sound level, ANSI and IEC octave, distortion, single-tone, extended measurements

You must enter at least one limit, or the SVT Limit Testing VI returns an error. You can visually display the input signal, failures, upper limit, and lower limit by creating an indicator from the *output values* terminal.

The upper limit and lower limit inputs to the SVT Limit Testing VI must be compatible with the input signal. Table 15A.5 lists the criteria that must be met for each input signal type that is compatible with the SVT Limit Testing VI.

In Table 15A.5, the following abbreviations apply:

- dt is the time spacing, in seconds, between elements.
- df is the frequency spacing, in hertz, between elements.
- N is the number of elements in the array.
- $f(i)$ is the i th frequency element.
- S is the signal.
- U is the upper mask limit.
- L is the lower mask limit.

Limit testing covers a broad range of data testing from range detection to discontinuous mask testing of a swept-sine frequency response spectrum. [Figure 15A.7](#), [Figure 15A.9](#), [Figure 15A.11](#), and

TABLE 15A.5 Criteria for Upper and Lower Limits

Input Signal Type	Criteria on Input Limit Masks
Waveform data type ($t0$, dt , [signal])	$dt > 0$, $dt_S = dt_U = dt_L$, $N_S = N_U = N_L$
Frequency spectrum ($f0$, df , [spectrum])	$f0_S = f0_U = f0_L$, $df_S = df_U = df_L$, $N_S = N_U = N_L$
Octave spectrum, swept-sine spectrum, XY data ([X], [Y])	$[X]_S = [X]_U = [X]_L$, $N_S = N_U = N_L$
Identified peaks, harmonic components, multitone phases ([frequency, amplitude])	$f(i)_S = f(i)_U = f(i)_L$, $N_S = N_U = N_L$

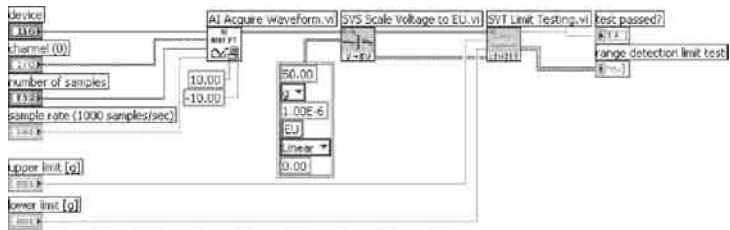


FIGURE 15A.7 Range detection performed in engineering units.

Figure 15A.13 illustrate some, but not all, of the different ways one can use the SVT Limit Testing VI in your application.

Figure 15A.7 illustrates a range-detection test. Scaled waveform data and upper and lower limits are input to the SVT Limit Testing VI. The VI checks that the data fall within the envelope specified by the upper and lower limits. Figure 15A.8 shows the output results for the range detection test.

Figure 15A.9 shows a pass/fail test on the measured THD. This test only checks the upper limit of the measurement, therefore, only the upper limit is wired to the VI. The upper limit should have the same units as the input measurement. In this case, both the THD and the upper limit are expressed as percentages. Figure 15A.10 shows the THD test output results.

Figure 15A.11 shows a continuous mask test on a power spectrum. Formula nodes define both the upper and lower limits in this VI, making this a more complex test than the one in Figure 15A.9. Figure 15A.12 shows the output graph for the power spectrum continuous mask test.

Figure 15A.13 shows a discontinuous mask test on a swept-sine frequency response. A discontinuous mask test can track and test the results at different magnitudes and ranges, as well as stop testing at defined intervals. For example, one might use the envelope defined by the upper and lower limit masks in this example for a DUT such as a notch filter. Figure 15A.14 shows the output graph for the discontinuous mask test.

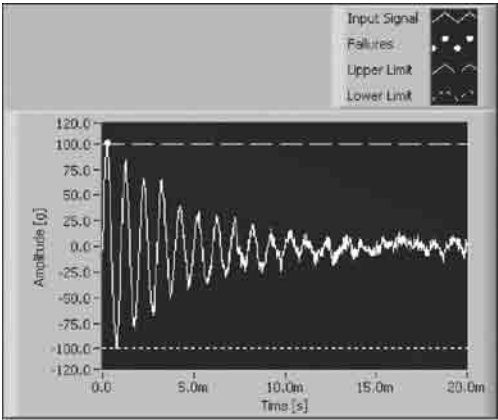


FIGURE 15A.8 Range detection test on a time-domain signal.

15A.5 Integration

This Appendix discusses the integration process, including basic theory and implementation in the time and frequency domains.

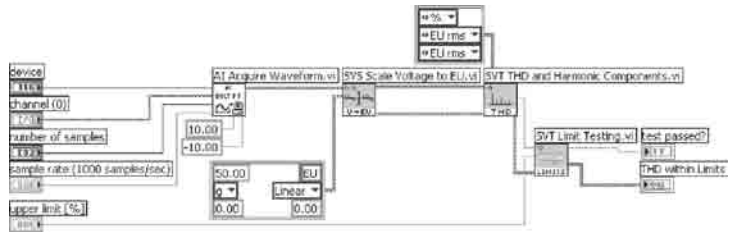


FIGURE 15A.9 Test scalar measurement.

The Sound and Vibration Toolkit contains the following integration VIs:

- SVT Integration VI located on the Integration palette for time-domain integration
- SVT Integration (frequency) VI located on the Frequency Analysis >> Extended Measurements palette for frequency-domain integration

15A.5.1 Introduction to Integration

The conversion between acceleration, velocity, and displacement is based on one of the fundamental laws in Newtonian physics, represented by the following equations:

$$\dot{x} = \frac{d}{dt}(x)$$

$$\ddot{x} = \frac{d}{dt}(\dot{x}) = \frac{d^2}{dt^2}(x)$$

Velocity is the first derivative of displacement with respect to time. *Acceleration* is the first derivative of velocity and the second derivative of displacement with respect to time. Therefore, given acceleration, perform a single integration with respect to time to compute the velocity or perform a double integration with respect to time to compute the displacement.

When representing the acceleration of a point by a simple sinusoid, the velocity and the displacement of the point are well known and represented by the following equations:

$$a = A \sin(\omega t) \tag{15A.1}$$

$$v = -\frac{A}{\omega} \cos(\omega t) = \frac{A}{\omega} \sin\left(\omega t - \frac{\pi}{2}\right) \tag{15A.2}$$

$$d = -\frac{A}{\omega^2} \sin(\omega t) = \frac{A}{\omega^2} \sin(\omega t - \pi)$$

Note: The initial condition is arbitrarily set to zero in Equation 15A.1 and Equation 15A.2. The amplitude of the velocity is inversely proportional to the frequency of vibration. The amplitude of the displacement is inversely proportional to the square of the frequency of vibration. Furthermore, the phase of the velocity lags the acceleration by 90°. The phase of the displacement lags the acceleration by 180°. Figure 15A.15 illustrates the relationship between acceleration, velocity, and displacement.

The integration of a sinusoid is known in closed form. Integration of an arbitrary waveform typically requires a numerical approach. You can use several numerical integration schemes to evaluate an integral in the time domain.

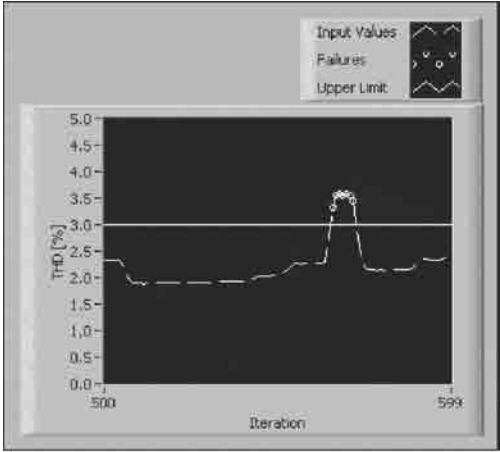


FIGURE 15A.10 Limit testing on THD measurements.

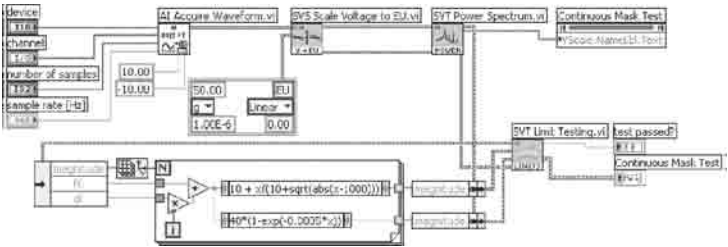


FIGURE 15A.11 Continuous mask test on power spectrum.

In the frequency domain, you can define any arbitrary band-limited waveform as a sum of sinusoids. Because the amplitude and phase relationships are known for sinusoids, you can carry out the integration in the frequency domain.

15A.5.2 Implementing Integration

If you need to perform measurements on velocity or displacement data when you have only acquired acceleration or velocity data, respectively, integrate the measured signal to yield the desired data. You can perform integration either in the time domain as a form of signal conditioning or in the frequency domain as a stage of analysis. When performed in the frequency domain, integration is one of the extended measurements for frequency analysis.

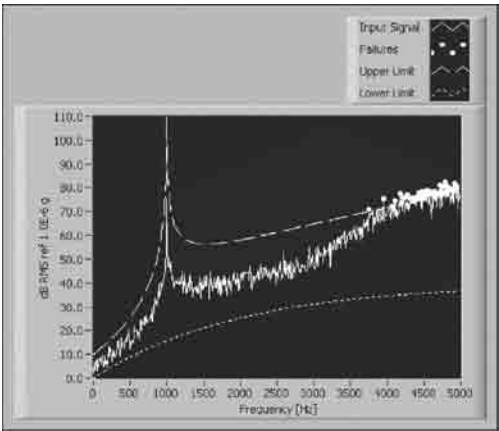


FIGURE 15A.12 Continuous mask test on a power spectrum.

15A.5.2.1 Challenges when Integrating Vibration Data

Converting acceleration data to velocity or displacement data presents a pair of unique challenges. First, measured signals typically contain some unwanted DC components. The second challenge is the fact that many transducers, especially vibration transducers, have lower-frequency limits. A transducer cannot accurately measure frequency components below the lower-frequency limit of the transducer.

15A.5.2.1.1 DC Component

Even though a DC component in the measured signal might be valid, the presence of a DC component indicates that the DUT has a net acceleration along the axis of the transducer. For a typical vibration measurement, the DUT is mounted or suspended in the test setup. The net acceleration of the DUT is zero. Therefore, any DC component in the measured acceleration is an artifact and should be ignored.

15A.5.2.1.2 Transducers

Most acceleration and velocity transducers are not designed to accurately measure frequency components close to DC (see Chapter 15). Closeness to DC is relative and depends on the specific transducer. A typical accelerometer can accurately measure components down to about 10 Hz. A typical velocity probe can accurately measure components down to 2 to 3 Hz. Inaccurately measured low-frequency vibrations can dominate the response when the signal is integrated because integration attenuates low-frequency components less than high-frequency components.

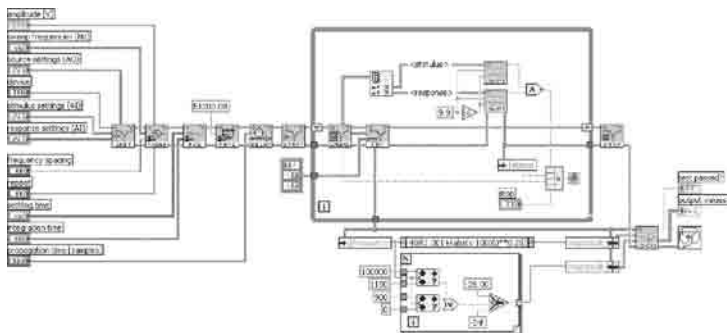


FIGURE 15A.13 Discontinuous mask test on swept-sine frequency response.

15A.5.2.1.3 Implementing Integration Using the Sound and Vibration Toolkit

Both the SVT Integration VI and the SVT Integration (frequency) VI address the challenges of converting acceleration data to velocity or displacement data.

15A.5.3 Time-Domain Integration

This section presents examples of and discussion about time-domain integration.

15A.5.3.1 Single-Shot Acquisition and Integration

The following example shows how one can use integration to convert acceleration data into displacement data in a single-shot acquisition and integration. In this example, the acquired waveform is sampled at 51.2 kHz and is double integrated. Figure 15A.16 shows the block diagram for the VI.

Because the integration is implemented with filters, there is a transient response associated with integration while the filters settle. You should take care to avoid the transient region when making further measurements. Figure 15A.17 shows the results of a single-shot acquisition and integration of a 38 Hz sine wave. You can see the transient response in the first 200 msec of the integrated signal.

15A.5.3.2 Continuous Acquisition and Integration

The more common case for time-domain integration occurs with continuous acquisition. Figure 15A.18 shows the block diagram for a VI designed for continuous acquisition and integration.

In this example, the high-pass cut-off frequency used for the integration is 10 Hz. Additionally, the integration is explicitly reset in the first iteration of the VI and performed continuously thereafter. In this example, this additional wiring is optional because the SVT Integration VI automatically resets the first time it is called and runs continuously thereafter.

If you use the block diagram in Figure 15A.18 in a larger application that requires starting and stopping the data acquisition process more than once, NI suggests setting the *reset filter* control to “TRUE” for the first iteration of the while loop. Setting the reset filter control to TRUE causes the filter to reset every time the data acquisition process starts. Set the reset filter control to “FALSE” for subsequent iterations of the while loop.

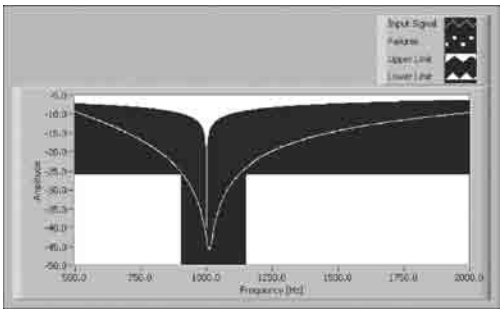


FIGURE 15A.14 Discontinuous mask test on a swept-sine frequency response.

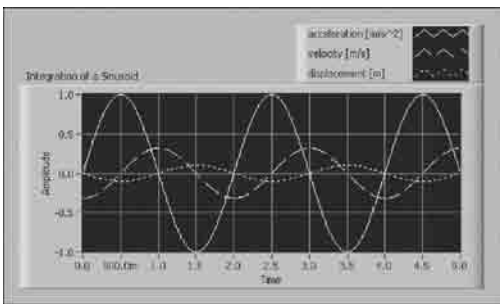


FIGURE 15A.15 Integration of a 0.5 Hz sine wave.

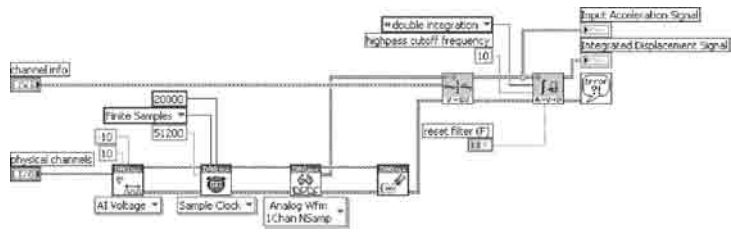


FIGURE 15A.16 Block diagram for single-shot acquisition and integration.

Figure 15A.19 shows the results of the continuous acquisition and integration of the same 38 Hz sinusoid used in the single-shot acquisition and integration example.

As in single-shot acquisition and integration, continuous acquisition and integration has an initial transient response. Take care to avoid making additional measurements until the response of the filters settles. Once the filters settle, you can use the integrated signals for additional analysis.

Figure 15A.20 shows the frequency response for time-domain single integration. Figure 15A.21 shows the frequency response for time-domain double integration.

In Figure 15A.20, one can see the characteristic 20 dB per decade roll-off of the magnitude response of the single integration. In Figure 15A.21, one can see the characteristic 40 dB per decade roll-off of the magnitude response of the double integration.

Upper and lower frequency limits exist for which you can obtain a specified degree of accuracy in the magnitude response. For example, sampling at a rate of 51.2 kHz, the magnitude response of the integrator is accurate to within 1 dB from 1.17 to 9.2 kHz for single integration and from 1.14 to 6.6 kHz for double integration. The accuracy ranges change with the sampling frequency and the high-pass cut-off frequency. The attenuation of the single integration filter at 9.2 kHz is -95 dB. The attenuation of the double integration filter at 6.6 kHz is -185 dB. Accuracy at high frequencies usually is not an issue.

15A.5.4 Frequency-Domain Integration

You can use the following strategies to obtain the spectrum of an integrated signal:

- Perform the integration in the time domain before computing the spectrum.
- Compute the spectrum before performing the integration in the frequency domain.

The following example demonstrates the implementation of the strategies used to obtain the spectrum of an integrated signal. Figure 15A.22 shows the block diagram for the example VI.

The *high-pass cutoff frequency* parameter of the SVT Integration VI is wired with a constant of 10 Hz. The SVT Integration (frequency) VI does not have a high-pass cutoff frequency parameter. Instead, the SVT Integration (frequency) VI sets the DC component of the integrated signal to zero if the spectrum scale is linear or to negative infinity (-Inf) if the spectrum scale is in decibels.

Figure 15A.23 shows the results of integrating in the time and frequency domains.

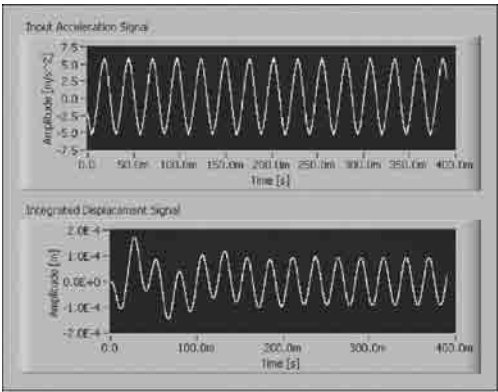


FIGURE 15A.17 Transient response in single-shot acquisition and integration.

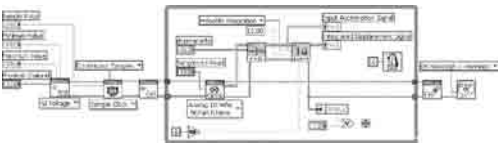


FIGURE 15A.18 Continuous acquisition and integration.

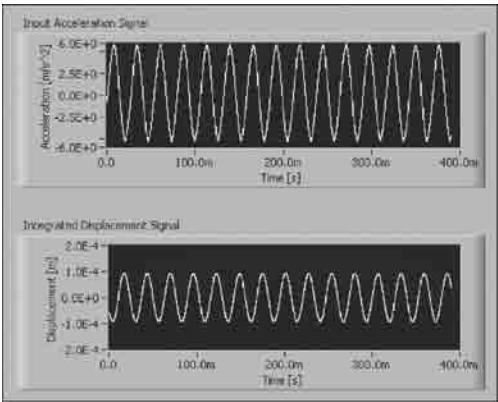


FIGURE 15A.19 Settled response of continuous acquisition and integration.

The power spectrum is computed after the time-domain integration filters settle. The frequency-domain integration scales the spectrum at each frequency line. No settling time is necessary for the frequency-domain integration because integration filters are not involved in the frequency-domain integration.

Perform frequency-domain integration in the following situations to maximize performance:

- When the integrated signal is not needed in the time domain
- When spectral measurements are made

15A.6 Vibration-Level Measurements

This Appendix briefly discusses the analysis concepts associated with performing vibration-level measurements and how one can use the Vibration Level VIs located on the Vibration Level palette to perform vibration-level measurements.

15A.6.1 Measuring the Root Mean Square Level

A basic requirement of vibration measurements is measuring the level of the signal returned by an accelerometer. The level of the accelerometer signal generally is expressed in root-mean-square (RMS) acceleration (g_{rms}).

15A.6.1.1 Single-Shot Buffered Acquisition

The block diagram in Figure 15A.24 illustrates a VI designed to perform a single-shot acquisition and compute the RMS levels.

The sampling frequency is 10 kS/sec. A buffer containing 1 sec of data is returned by the read VI.

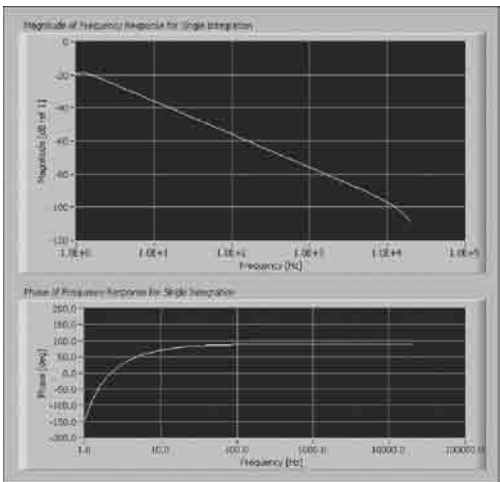


FIGURE 15A.20 Frequency response for single integration.

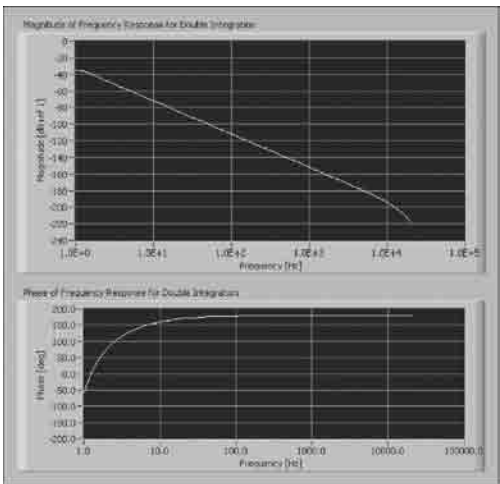


FIGURE 15A.21 Frequency response for double integration.

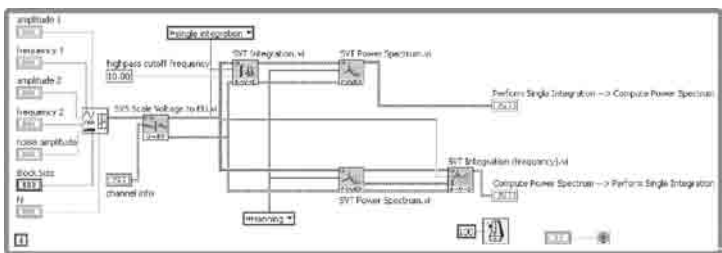


FIGURE 15A.22 Integration in the time domain and in the frequency domain.

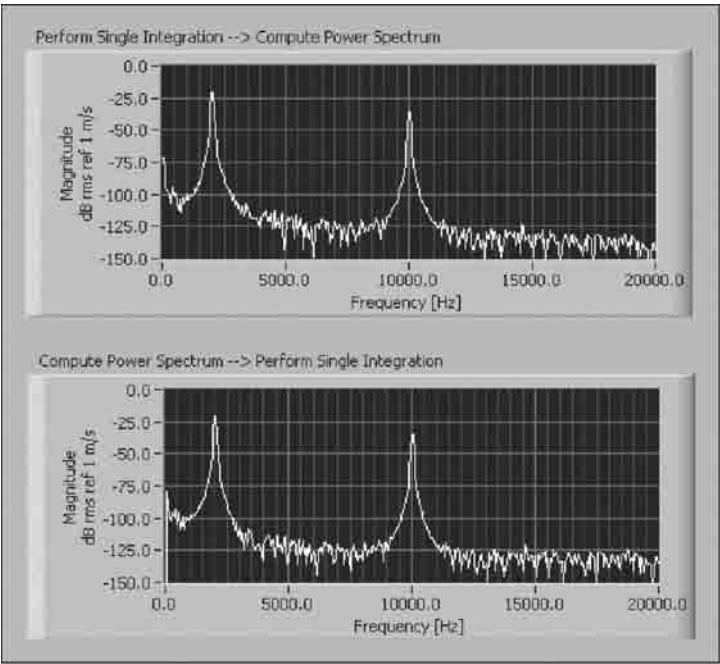


FIGURE 15A.23 Power spectra of the integrated signal.

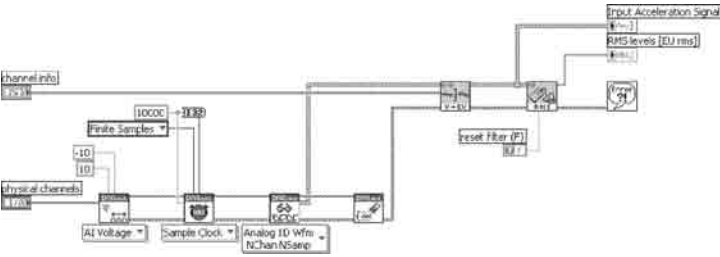


FIGURE 15A.24 Single-shot buffered acquisition and RMS level VI.

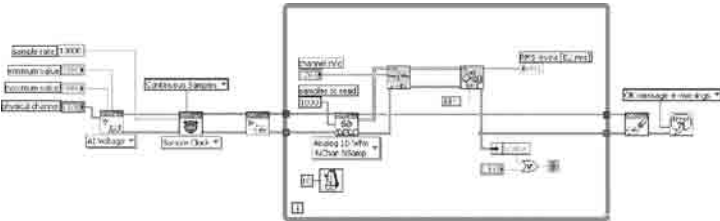


FIGURE 15A.25 Continuous data acquisition and RMS level VI.

15A.6.1.2 Continuous Signal Acquisition

One can use the block diagram in Figure 15A.24 with a while loop to continuously acquire signals from an accelerometer and display the vibration level in a chart. The block diagram in Figure 15A.25 illustrates how to measure the RMS value once every 100 msec and display the results in a strip chart. In this example, the RMS value is computed based on the last 100 msec of acquired data.

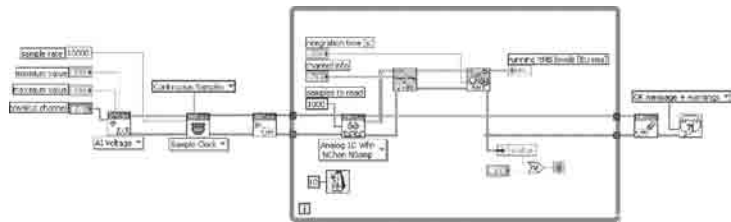


FIGURE 15A.26 Running RMS VI.

Note: Set the *restart averaging* control on the SVT RMS Level VI to TRUE. Otherwise, the SVT RMS Level VI accumulates intermediate results to compute the RMS vibration level over the entire data acquisition instead of just over the last block of data.

15A.6.2 Performing a Running RMS Level Measurement

The SVT Running RMS Level VI returns the RMS value computed over the last N seconds, which is the integration time. The block diagram in Figure 15A.26 illustrates an application using the SVT Running RMS Level VI. The sampling frequency is 10 kS/sec. The read VI reads 1000 samples at a time.

15A.6.3 Computing the Peak Level

Use the SVT Peak Level VI to compute the peak level of a signal. In peak-hold averaging, the largest measured level value of all previous values is computed and returned until a new value exceeds the current maximum. The new value becomes the new maximum value and is the value returned until a new value exceeds it.

15A.6.4 Computing the Crest Factor

The crest factor is the ratio of the peak value over the RMS value of a given signal and indicates the shape of the waveform. The crest factor is defined by the following equation:

$$F_c = \frac{V_{pk}}{V_{rms}}$$

where

F_c is the crest factor.

V_{pk} is the peak value of the signal.

V_{rms} is the RMS value of the signal.

The block diagram in Figure 15A.27 illustrates an application using the SVT Crest Factor VI. Along with the crest factors, the SVT Crest Factor VI also returns the peak and RMS levels.

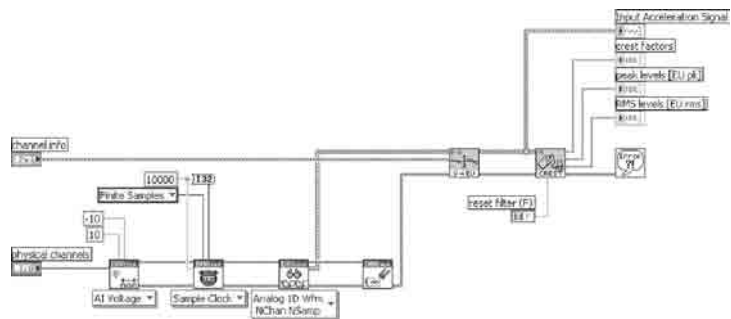


FIGURE 15A.27 Crest factor VI.

15A.7 Frequency Analysis

This Appendix discusses methods used by the Frequency Analysis VIs located on the Frequency Analysis palette for windowing, averaging, and performing frequency-domain measurements.

The Frequency Analysis VIs offer various frequency measurements based on the discrete Fourier transform (DFT).

For simplicity, the remainder of this document uses the term FFT to denote both the FFT and the DFT.

15A.7.1 FFT Fundamentals

The FFT resolves the time waveform into its sinusoidal components. The FFT takes a block of time-domain data and returns the frequency spectrum of that data. The FFT is a digital implementation of the Fourier transform. Thus, the FFT does not yield a continuous spectrum. Instead, the FFT returns a discrete spectrum where the frequency content of the waveform is resolved into a finite number of frequency lines, or bins.

15A.7.1.1 Number of Samples

The computed spectrum is completely determined by the sampled time waveform input to the FFT. If an arbitrary signal is sampled at a rate equal to f_s over an acquisition time, T , N samples are acquired. Compute T with the following equation:

$$T = \frac{N}{f_s}$$

where

T is the acquisition time.

N is the number of samples acquired.

f_s is the sampling frequency.

Compute N with the following equation:

$$N = Tf_s$$

where

N is the number of samples acquired.

T is the acquisition time.

f_s is the sampling frequency.

15A.7.1.2 Frequency Resolution

Because of the properties of the FFT, the spectrum computed from the sampled signal has a frequency resolution, d_f . Calculate the frequency resolution with the following equation:

$$d_f = \frac{1}{T} = \frac{f_s}{N}$$

where

d_f is the frequency resolution.

T is the acquisition time.

f_s is the sampling frequency.

N is the number of samples.

Note: The frequency resolution is determined solely by the acquisition time. The frequency resolution improves as the acquisition time increases.

15A.7.1.3 Maximum Resolvable Frequency

The sampling rate of the time waveform determines the maximum resolvable frequency. According to the Shannon Sampling Theorem, the maximum resolvable frequency must be half the sampling frequency. To calculate the maximum resolvable frequency, use the following equation:

$$f_{\max} = f_{\text{Nyquist}} = \frac{f_s}{2}$$

where

f_{\max} is the maximum resolvable frequency

f_{Nyquist} is the Nyquist frequency

f_s is the sampling frequency

15A.7.1.4 Minimum Resolvable Frequency

The minimum resolvable frequency is 0 (DC). The term *baseband analysis* is often used to describe analysis from 0 to f_{Nyquist} .

15A.7.1.5 Number of Spectral Lines

The number of lines in the spectrum is half the number of samples, N , in the waveform. Directly specify the number of lines in the spectrum for the Zoom FFT VIs, in the Sound and Vibration Toolkit. Specify the number of data samples to control the number of spectral lines for the Baseband FFT and the Baseband Subset VIs.

15A.7.1.6 Relationship between Time-Domain and Frequency-Domain Specifications and Parameters

Table 15A.6 summarizes the relationship of time-domain specifications to frequency-domain parameters.

Use the information in Table 15A.7 if you prefer to specify the spectrum parameters and determine the required data-acquisition parameters from these specifications.

TABLE 15A.6 Time-Domain Specifications to Frequency-Domain Parameters

Time Domain	Frequency Domain			
	f_{Nyquist}	f_{\max}	Number of Lines	df
f_s	$\frac{f_s}{2}$	$f_s \cdot E_b$	$E_b \cdot N$	$\frac{1}{T} = \frac{f_s}{N}$
N				
T				

f_s is the sampling frequency, E_b is the effective bandwidth, N is the number of samples acquired, and T is the acquisition time.

TABLE 15A.7 Frequency-Domain Specifications to Time-Domain Parameters

Frequency Domain	Time Domain		
	f_s	N	T
f_{\max}	$\frac{f_{\max}}{E_b}$	Number of lines	$\frac{1}{df} = \frac{\text{Number of lines}}{f_{\max}}$
Number of lines in the spectrum			
df			

f_{\max} is the maximum resolvable frequency, E_b is the effective bandwidth, and df is the frequency resolution.

In Table 15A.6 and Table 15A.7, E_b is the ratio of the alias-free bandwidth to the sampling frequency. In traditional instruments, E_b is typically 1/256. However, the alias-free bandwidth depends on the hardware used to acquire the dynamic signal. E_b can have a maximum value of 0.5. This maximum value corresponds to a perfect antialiasing filter. For example, if 1024 samples are input to the FFT algorithm, the computed spectrum has 512 nonDC spectral lines. The computed spectrum has a total of 513 lines including the DC component. Acquire these same 1024 samples on an instrument with a standard 1/256 effective bandwidth, then use the equation in Table 15A.6 to find the expected number of alias-free lines in the computed spectrum. Complete the necessary calculations with the following equations:

$$\begin{aligned} \text{Number of lines} &= E_b N \\ \text{Number of lines} &= \frac{1}{2.56} \times 1024 = 400 \text{ lines} \end{aligned}$$

E_b is entirely a hardware property. However, mathematically, you can use the FFT to compute the frequency spectrum up to the Nyquist frequency. Remember to account for the presence or absence of an antialiasing filter when performing the frequency analysis. The Frequency Analysis VIs compute every spectral line, alias-free or not. Use the frequency range to limit the analysis to the alias-free region of the spectrum with FFT subset and zoom FFT measurements. Use the SVT Get Spectrum Subset VI to limit the analysis to the alias-free region of the spectrum with baseband FFT measurements.

Note: Table 15A.6 shows that the sampling frequency and the block size acquired during each cycle of a continuous acquisition completely determine the frequency-domain parameters in baseband FFT analysis. However, many stand-alone instruments are operated by specifying the frequency range of interest and the number of lines in the FFT. Table 15A.7 shows how a stand-alone instrument uses the frequency range of interest and the number of lines in the FFT to determine an appropriate sampling frequency and block size.

15A.7.2 Increasing Frequency Resolution

Increasing the frequency resolution helps one to distinguish two individual tones that are close together. For example, if you analyze a signal that contains two tones at 1000 and 1100 Hz, use a sampling frequency of 10,000 Hz. Acquire data for 10 msec and the frequency resolution is 100 Hz. Figure 15A.28 shows the results of this analysis. In this particular case, you cannot distinguish one tone from the other.

Increase the acquisition time to 1 sec to achieve a frequency resolution of 1 Hz. Figure 15A.29 shows the results obtained with a 1 sec acquisition time. You can distinguish the individual tones with the increased acquisition time.

The following strategies achieve a finer frequency resolution:

- Decrease the sampling frequency, f_s . Decreasing f_s usually is not practical because decreasing f_s reduces the frequency range.
- Increase the number of samples, N . Increasing N yields an increased number of lines over the original frequency range.

Implement the decreased f_s strategy with zoom FFT analysis. Use baseband FFT and FFT-subset analyses to implement the increased N strategy. Baseband FFT analysis and FFT-subset analysis both achieve the same frequency resolution. However, FFT subset analysis only computes a narrow subset of the spectrum.

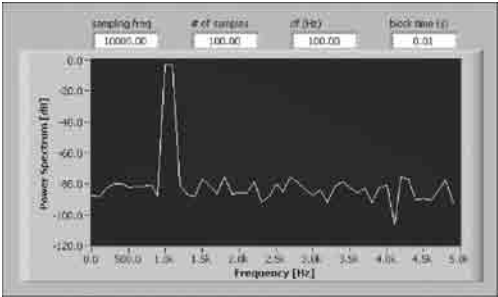


FIGURE 15A.28 Power spectrum obtained with an acquisition time of 10 msec.

Refer to Section 15A.7.2.1 and Section 15A.7.2.5 for examples that demonstrate the importance of frequency resolution in frequency analysis. The examples illustrate how to achieve a finer frequency resolution with the frequency analysis tools in the Sound and Vibration Toolkit.

15A.7.2.1 Zoom FFT Analysis

In some applications, it is necessary to obtain the spectral information with a very fine frequency resolution over a limited portion of the baseband span. In other words, you must zoom in on a spectral region to observe the details of that spectral region. Use the zoom FFT to obtain spectral information over a limited portion of the baseband span and with greater resolution. Just as in baseband analysis, the acquisition time determines the frequency resolution of the computed spectrum. The number of samples used in the transform determines the number of lines computed in the spectrum.

Zoom FFT analysis achieves a finer frequency resolution than the baseband FFT. The Zoom FFT VI acquires multiple blocks of data and downsamples to simulate a lower sampling frequency. The block size is decoupled from the achievable frequency resolution because the Zoom FFT VI accumulates the decimated data until you acquire the required number of points. Because the transform operates on a decimated set of data, you only need to compute a relatively small spectrum. The data are accumulated, so do not think of the acquisition time as the time required to acquire one block of samples. Instead, the acquisition time is the time required to accumulate the required set of decimated samples.

The Zoom FFT VIs complete the following steps to process the sampled data:

1. Modulate the acquired data to center the analysis band at 0 frequency.
2. Filter the modulated data in the time domain to isolate the analysis band and prevent aliasing when the data are resampled at a lower sampling frequency.
3. Decimate the filtered data to reduce the effective sampling frequency.
4. Accumulate the decimated data until sufficient samples are available to compute the spectrum.
5. Use the Discrete Zak Transform (DZT) to efficiently compute the desired spectral lines.
6. Demodulate, or shift, the computed spectrum.

15A.7.2.2 Frequency Resolution of the Zoom FFT VIs

Use the Zoom FFT VIs to compute the spectrum of a signal over a narrow frequency range with an arbitrarily fine frequency resolution. To get an approximation of the frequency resolution seen with the Zoom FFT VIs, use the following formula:

$$\text{frequency resolution} \approx \frac{\text{stop frequency} - \text{start frequency}}{\text{number of lines}}$$

Note: The exact frequency resolution is returned as d_f in the spectrum computed by the Zoom FFT VIs.

15A.7.2.3 Zoom Measurement

The following example demonstrates a zoom measurement of the power spectrum.

Acquire a sine wave at 1390 Hz with a National Instruments DSA device and the VI displayed in Figure 15A.30.

Acquire the signal at 51.2 kHz. The VI reads the data in blocks of 2048 samples. Compute the frequency resolution of this measurement using baseband analysis with the following equation:

$$\frac{51,200 \text{ Hz}}{2048} = 25 \text{ Hz}$$

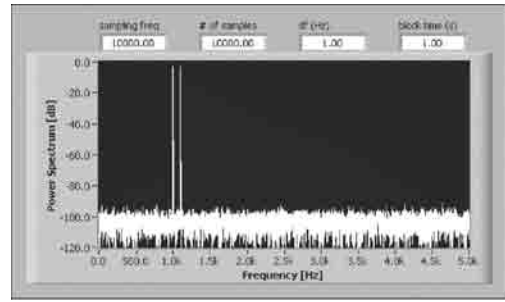


FIGURE 15A.29 Power spectrum obtained with an acquisition time of 1 sec.

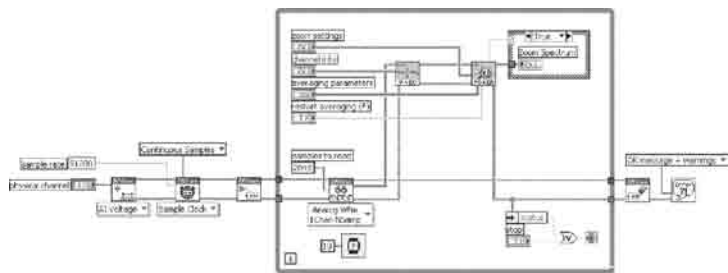


FIGURE 15A.30 Performing a zoom power spectrum measurement.

Use the SVT Zoom Power Spectrum VI located on the Zoom FFT palette to analyze a narrowband with a much finer frequency resolution. Figure 15A.31 shows the result of limiting the measurement to the frequency band between 1 and 2 kHz and computing 400 lines. Derive the frequency resolution of the computed spectrum with the following equation:

$$\frac{2000 - 1000 \text{ Hz}}{400 \text{ lines}} = 2.5 \text{ Hz}$$

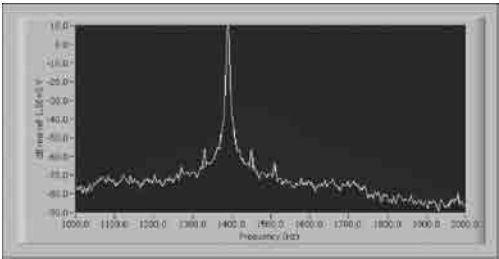


FIGURE 15A.31 Zoom power spectrum measurement results.

15A.7.2.4 Zoom Settings

Figure 15A.32 shows the *zoom settings* control used to acquire the zoom measurement results displayed in Figure 15A.31. Use this control to specify the frequency range, window, number of lines, and percent overlap used in the zoom analysis.

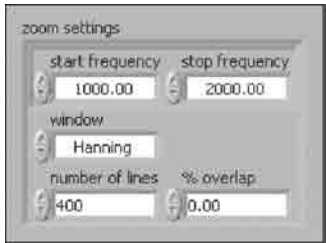


FIGURE 15A.32 Zoom settings control.

15A.7.2.5 Subset Analysis

The Baseband Subset VIs located on the Baseband Subset palette allow one to compute a subset of the baseband FFT measurement. Subset analysis uses the DZT to compute a subset of the baseband FFT. The frequency resolution for spectral measurements computed with the Baseband Subset VIs equals the frequency resolution for measurements made with the Baseband FFT VIs. The acquisition time determines the frequency resolution. The only way to achieve a finer frequency resolution is to increase the length of the time record. In the case of baseband or subset analysis, a longer time record implies a larger block size.

The Baseband Subset VIs algorithm computes only the desired spectral lines. The only programming difference between the Baseband Subset VIs and the Baseband FFT VIs is the additional parameter *frequency range*. The frequency range parameter specifies which spectral lines the Baseband Subset VI computes. The computed spectral lines are always inclusive of the start frequency and the stop frequency.

Note: Setting the start frequency to 0 Hz and the stop frequency to f_{max} yields the same spectrum as the corresponding Baseband FFT VI. If you set the stop frequency to -1 , the baseband subset VIs return the Nyquist frequency as the highest frequency in the computed spectrum.

The following consideration can help you decide when to use the Baseband Subset VIs instead of the Baseband FFT VIs:

- The required block size yields an acceptable frequency resolution.
- The analysis of a narrow subset of the baseband span requires better processing performance than the Baseband FFT VI can provide.

15A.8 Transient Analysis

This Appendix discusses performing transient analysis with the Transient Analysis VIs located on the Transient Analysis palette.

15A.8.1 Transient Analysis with the Sound and Vibration Toolkit

Transient analysis is the analysis of nonstationary signals. The Transient Analysis VIs offer two different techniques for extracting information about transient signals. Use the short-time Fourier transform (STFT) for signals in which the frequency content changes relatively slowly with time. Use the shock-response spectrum (SRS) for shock signals.

You can use the STFT VIs to extract frequency information as a function of time directly from the signal of interest. Additionally, in the case of a rotating machine where a tachometer signal is simultaneously acquired with the signal of interest, the STFT VIs can extract frequency information as a function of the rotational speed.

The results generated by the STFT are typically displayed on a waterfall display or on a colormap. The STFT VIs return the information needed to properly scale the axes of the displays. You can pass the information directly to a Waterfall Display VI. Use property nodes for the colormap display.

You can use the SVT SRS VI to evaluate the severity of a shock signal. The results generated by the SRS are typically displayed on an X–Y graph.

Note: Other LabVIEW toolkits are available that provide additional transient analysis capabilities. The Order Analysis Toolkit is designed for rotating machinery analysis and monitoring. The Signal Processing Toolkit has tools, such as wavelets and joint time-frequency analysis (JTFA), for the analysis of fast transients.

15A.8.2 Performing an STFT vs. Time

The STFT available in the Sound and Vibration Toolkit can compute multiple Fourier transforms on the time-domain signal with or without overlapping.

For example, analyze a waveform containing 10 sec of data acquired at 51.2 kS/sec. The signal is a chirp signal with the following attributes:

- Start frequency = 10 Hz
- End frequency = 10,000 Hz

Figure 15A.33 shows the signal corresponding to the first 200 msec of the waveform.

Figure 15A.34 shows the result of applying a baseband FFT on the entire waveform.

Note: No window is applied on the signal.

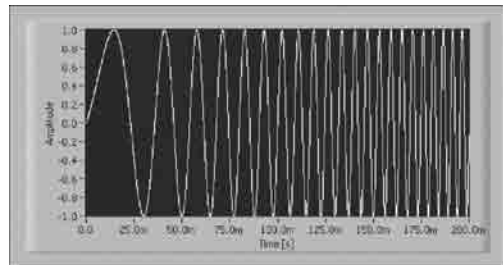


FIGURE 15A.33 Chirp signal.

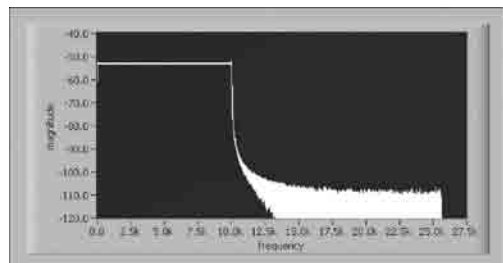


FIGURE 15A.34 Baseband FFT on a chirp signal.

The spectrum is flat from 10 Hz to 10 kHz. Only noise is measured at frequencies above 10 kHz. Unfortunately, this measurement does not provide any information about how the frequency content of the signal changes with time. However, the STFT can reveal useful information about the time dependence of the frequency content.

Instead of computing a single FFT on the whole data set, you can divide the data set into smaller blocks and compute FFTs on these smaller data blocks. For example, divide the signal into 100 msec blocks and perform an FFT on each of the blocks with the SVT STFT vs. Time VI.

Subdivide the time-domain signal by configuring the *time segment* control displayed in Figure 15A.35.

Leave *from [s]* and *to [s]* each equal to -1.00 to ensure that the entire signal is used in the STFT computation. In this particular example, the -1.00 setting in both *from [s]* and *to [s]* is equivalent to setting *from [s]* to 0 and *to [s]* to 10.

Create a 100 msec time increment by setting *time increment* to 100.00 and *time increment units (%)* to msec. The 100 msec time increment causes the SVT STFT vs. Time VI to compute one FFT every 100 msec. Setting time increment is independent from selecting the FFT block size.

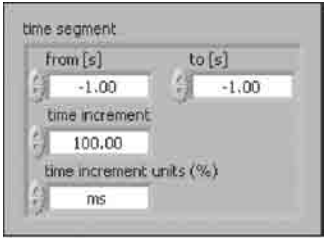


FIGURE 15A.35 Time segment control.

15A.8.2.1 Selecting the FFT Block Size

In addition to the time segment, one can adjust the FFT block size. For example, analyze a chirp signal having the following attributes:

- Start frequency = 10 Hz
- End frequency = 10,000 Hz

The measurement is performed using the following settings:

- Acquisition time = 10 sec
- Sampling frequency = 51.2 kS/sec
- FFT block size = 1024 samples or 512 lines (400 alias-free lines)
- Time increment = 100 msec.

Based on the sampling frequency of 51,200 Hz, a 1024 sample FFT requires a 20 msec block of data, leading to a frequency resolution of 50 Hz.

Because the time increment is 100 msec and a 1024 sample FFT only requires a 20 msec block, only one block out of five is used for computation. Figure 15A.36 shows the result obtained with a 1024 sample FFT.

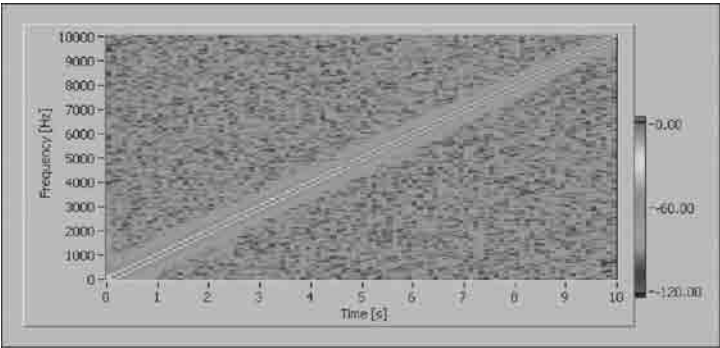


FIGURE 15A.36 STFT using a 1024 sample block size.

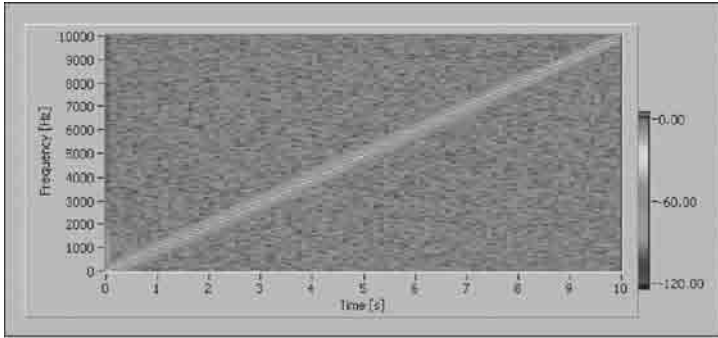


FIGURE 15A.37 STFT using a 4096 sample block size.

If you select an FFT Block size of 4096 samples, or 1600 alias-free lines, the resolution improves, as illustrated in Figure 15A.37. However, the increased resolution comes with the expense of extra processing.

15A.8.2.2 Overlapping

Overlapping is a method that uses a percentage of the previous data block to compute the FFT of the current data block. When combined with windowing, overlapping maximizes the use of the entire data set. If no overlapping is used, the part of the signal close to the window edges becomes greatly attenuated. The attenuation of the signal near the window edges could result in the loss of information in the region near the window edges.

Note: Set the desired overlapping rate by specifying % in the time increment units (%) in the time increment control. Refer to [Figure 15A.35](#) for the location of this control. No overlapping, or 0%, corresponds to a time increment of 100%. An overlapping of 75% corresponds to a time increment of 25%. An overlapping of 50% corresponds to a time increment of 50%, and so forth. The advantage of using the time increment control is that one can specify values greater than 100%. For example, a time increment of 200% corresponds to computing an FFT on every other block of data.

Figure 15A.38 and [Figure 15A.39](#) illustrate the overlapping process. Figure 15A.38 shows a 50% overlap.

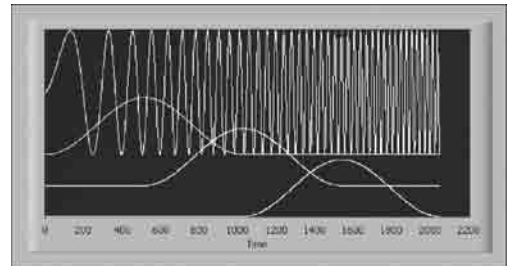


FIGURE 15A.38 50% overlap.

Figure 15A.39 shows the resulting subdivisions when one uses a 50% overlap and a Hamming window.

15A.8.2.3 Using the SVT STFT vs. Time VI

The following example illustrates how to use the SVT STFT vs. Time VI. [Figure 15A.40](#) shows the block diagram.

The example in Figure 15A.40 acquires 10 sec of data at a sample rate of 51.2 kHz. After scaling, the signal is sent to the SVT STFT vs. Time VI. The result is displayed on the intensity graph in [Figure 15A.41](#).

Note: Use the X scale and Y scale offset and multiplier properties to properly scale the axes of the intensity graph. In this example, the X scale range is 0 to 10 sec. The Y scale range is 0 to 25,600 Hz. The Nyquist frequency is 25,600 Hz. You can adjust the Z scale so that only the relevant part of the signal is displayed. In other words, you can hide noise in the displayed signal by increasing the minimum limit of the Z-axis. Refer to the *LabVIEW Help* for information about the offset and multiplier properties for graph controls.

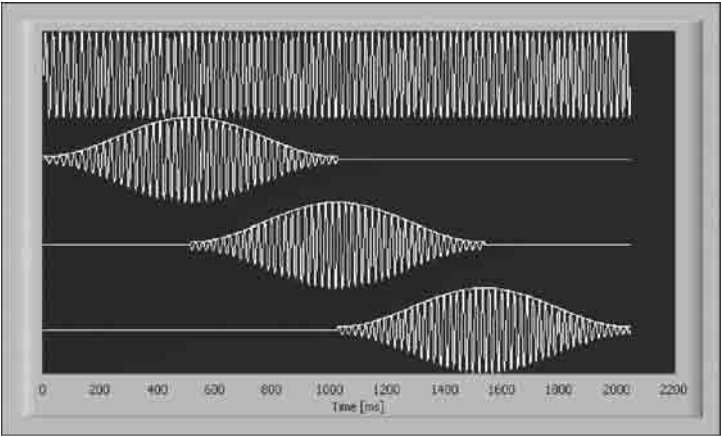


FIGURE 15A.39 Subdivisions of the time-domain waveform.

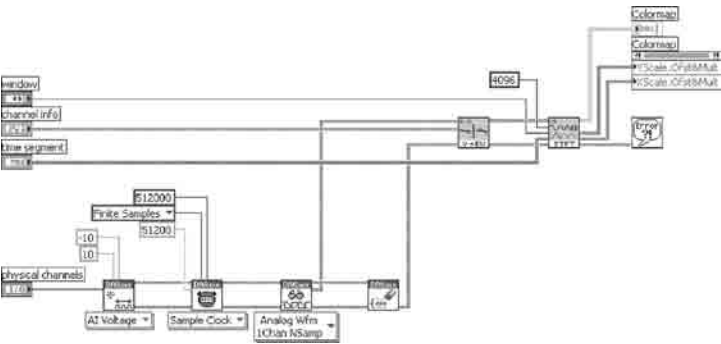


FIGURE 15A.40 Use of the SVT STFT vs. Time VI.

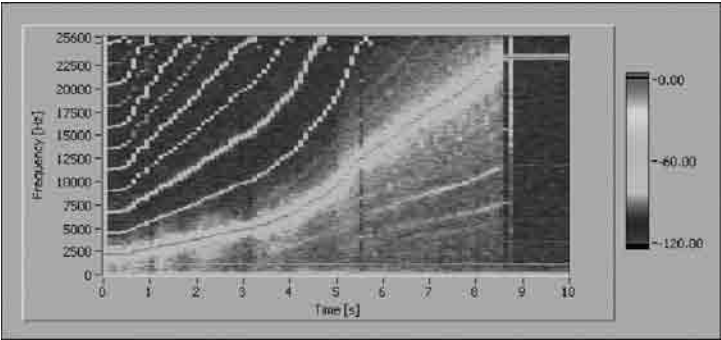


FIGURE 15A.41 STFT vs. time graph.

15A.8.3 Performing an STFT vs. Rotational Speed

Analyzing the frequency content as a function of the rotational speed is helpful when dealing with measurements on rotating machinery. Use the SVT STFT vs. RPM (analog) VI to analyze the frequency content as a function of the rotational speed.

15A.8.3.1 Converting the Pulse Train to Rotational Speed

Use the SVT Convert to RPM (analog) VI to convert a pulse train acquired by a tachometer or encoder to the rotational speed expressed in rotations per minute (RPM).

Note: For simplicity, the remainder of this Appendix uses the term tachometer to denote both a tachometer and an encoder.

In this example, an accelerometer is mounted at the test location for an engine run-up. A tachometer is used to measure the speed of the shaft and returns one pulse per revolution as a transistor–transistor logic (TTL) signal. Use the *tach info* control to specify the characteristics of the pulses generated by the tachometer. Figure 15A.42 shows the settings for the tachometer info control.

Figure 15A.43 shows a simulated tachometer signal.

You can use the SVT Convert to RPM (analog) VI to measure the rotational speed in RPM as a function of time. Figure 15A.44 shows the result obtained with the SVT Convert to RPM (analog) VI and a simulated tachometer signal.

15A.8.3.2 STFT vs. RPM

You also can display the STFT of an input signal as a function of the rotational speed based on the tachometer signal. Two input signals are needed, the signal of interest and the signal from the tachometer. Again, an engine run-up serves as a good example of computing an STFT as a function of the rotational speed.

During an engine run-up, the sound pressure close to the engine is measured with a microphone. Figure 15A.45 shows the signal acquired by the microphone.

The signal from the tachometer is also acquired. The measured tachometer signal is converted to RPM with the SVT Convert to RPM (analog) VI. Figure 15A.46 shows the rotational speed as a function of time, as computed by the SVT Convert to RPM (analog) VI.

Using the SVT STFT vs. RPM (analog) VI allows you to measure the frequency content of the signal as a function of the rotational speed of the engine. Figure 15A.47 displays the results obtained with the SVT STFT vs. RPM (analog) VI on an intensity graph.

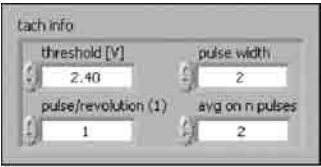


FIGURE 15A.42 Tachometer info control.

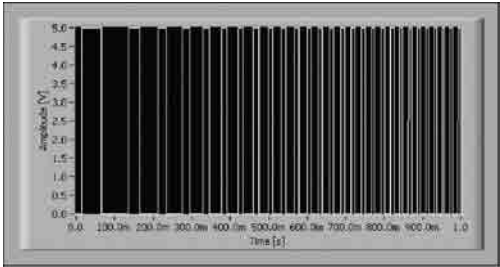


FIGURE 15A.43 Tachometer signal.

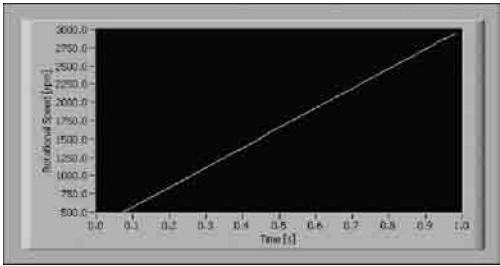


FIGURE 15A.44 Result from SVT convert to RPM (analog) VI.

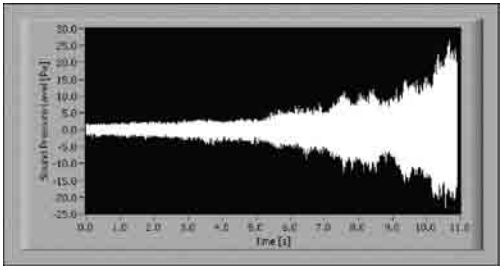


FIGURE 15A.45 Microphone signal obtained during engine run-up.

15A.8.4 Measuring a Shock Response Spectrum

Obtain the SRS by applying the acquired shock pulse to a series of single degree of freedom (SDOF) systems. Plot the system maximum response as resonance frequency of the system.

An SDOF mechanical system consists of the following components:

- Mass, whose value is represented with the variable m
- Spring, whose stiffness is represented with the variable k
- Damper, whose damping coefficient is represented with the variable c

The resonance frequency f_N , and the critical damping factor, z , characterize an SDOF system, where

$$f_N = \frac{1}{2\pi} \sqrt{\frac{k}{m}}$$
$$\zeta = \frac{c}{2\sqrt{km}}$$

For light damping, where z is less than or equal to 0.05, the peak value of the frequency response occurs in the immediate vicinity of f_N and is given by the following equation, where Q is the resonant gain:

$$Q = \frac{1}{2\zeta}$$

Figure 15A.48 illustrates the response of an single-DoF system to a half-sine pulse with a 10g acceleration amplitude and 10 msec duration. The top graph shows the time-domain acceleration. The middle graph is the single-DoF system response with a 50 Hz resonance frequency. The bottom graph is the single-DoF system response with a 150 Hz resonance frequency. In both cases, z is 0.05.

Use the signals shown in Figure 15A.48 to construct the SRS. For example, the *maximax*, the absolute maximum response of the calculated shock response over the entire signal duration, uses the absolute maximum system response as a function of the system natural frequency. Figure 15A.49 illustrates the maximax SRS for the same half-sine pulse.

Note: Each computed SRS is specific to the pulse used to perform the measurement.

You can use other types of shock spectra depending on the application. These spectra include the initial shock response from the system response over the pulse duration or from the residual shock

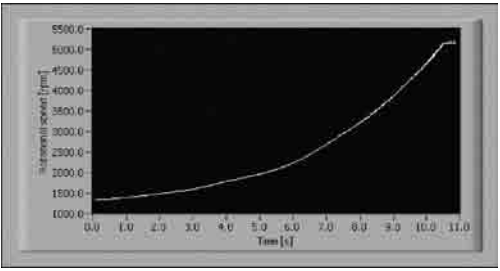


FIGURE 15A.46 Rotational speed as a function of time during engine run-up.

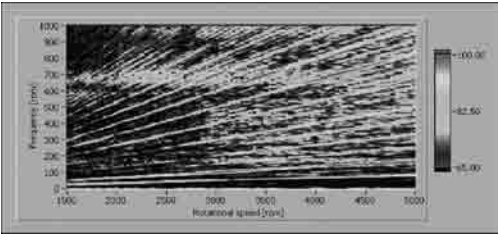


FIGURE 15A.47 Intensity graph of sound pressure level for an engine run-up.

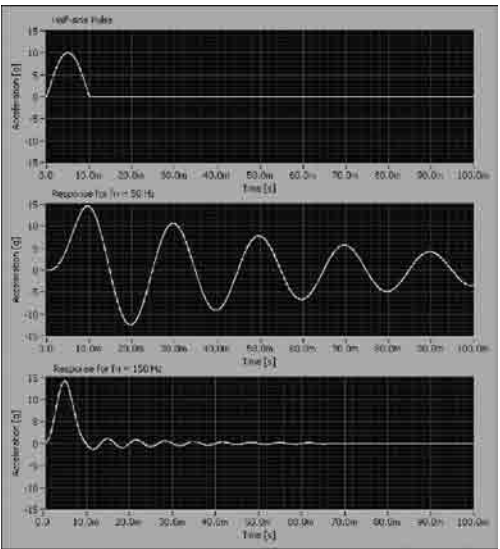


FIGURE 15A.48 Single-DoF system response to a half-sine shock.

spectrum from the system response after the pulse. You can use the positive maximum, the negative maximum, or the absolute maximum response signal value.

The Sound and Vibration Toolkit uses the Smallwood algorithm to compute the SRS. The SVT Shock Response Spectrum VI also offers the ability to preprocess the time-domain signal to improve SRS results. You can remove any DC component or apply a low-pass filter with a selectable cut-off frequency.

The SVT Shock Response Spectrum VI can compute the SRS from the absolute acceleration response or from the relative displacement response. Use the *model* control on the SVT Shock Response Spectrum VI to select the appropriate response.

Figure 15A.50 shows how to use the SVT Shock Response Spectrum VI. The example in Figure 15A.50 acquires 1000 samples of data from an accelerometer during a shock. The shock signal triggers the acquisition. The program stores 100 samples before the trigger to properly capture the entire shock signal.

Figure 15A.51 displays the acquired time-domain signal and the computed SRS.

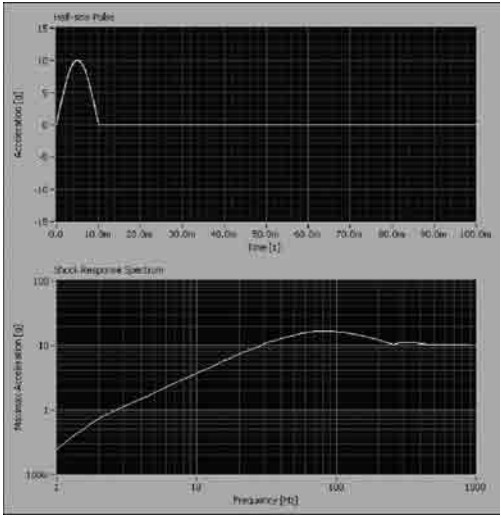


FIGURE 15A.49 Half-sine pulse SRS (Maximax).

15A.9 Waterfall Display

This Appendix discusses using the Waterfall Display VIs located on the Waterfall Display palette.

15A.9.1 Using the Display VIs

Waterfall display is a visualization technique that permits the visual representation of various analyses of nonstationary signals, such as machine run-up, coast down, transients, and others.

Use the Waterfall Display VIs to display FFT spectra from frequency analysis or transient analysis and octave spectra from octave analysis in waterfall graphs. Refer to *Front Panel Displays* in the *LabVIEW Help* for more information about displaying octave results.

Specific Waterfall Display VIs display the results of frequency analysis and octave analysis in a waterfall graph. The waterfall display opens in an external window called the *Waterfall* window.

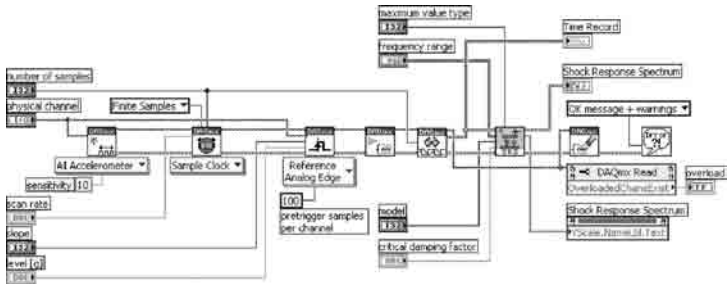


FIGURE 15A.50 Using the SVT shock response spectrum VI.

Complete the following basic steps to display results on a waterfall graph:

- 1. Initialize the display.
- 2. Send data to the display.
- 3. Close the waterfall display.

Figure 15A.52 shows the Waterfall window.

15A.9.1.1 Initializing the Display

Use the SVL Initialize Waterfall Display VI to create a reference to a waterfall display. If you are displaying octave spectra, use the SVT Initialize Waterfall Display for Octave VI. Both of the initializing VIs also enable one to define graph properties, including the window title, the bounds of the external window, and the colors used in the waterfall display.

15A.9.1.2 Sending Data to the Display

The Waterfall window does not open until it receives data sent to it. Use the SVL Send Data to Waterfall VI to send data to a waterfall display. Use the SVT Send Data to Waterfall for Octave VI to send octave data to a waterfall display.

The SVL Send Data to Waterfall VI is polymorphic and accepts an array of spectra, such as that returned by a power spectrum, a two-dimensional (2D) array, or a STFT.

15A.9.1.3 Waterfall Display for Frequency Analysis

The following example shows how to accumulate 20 spectra and display them in a waterfall graph. Figure 15A.53 shows the block diagram for the VI.

Twenty data blocks of 1024 samples are acquired. The power spectrum is computed on each block. The autoindexing capability of the For Loop is used to build an array of 20 spectra. The array of spectra is sent to the waterfall display. Refer to the *LabVIEW Help* for information about autoindexing.

15A.9.1.4 Waterfall Display for Transient Analysis

This example illustrates how to use the waterfall display in conjunction with the Transient Analysis VIs. Figure 15A.54 shows the block diagram for the example VI.

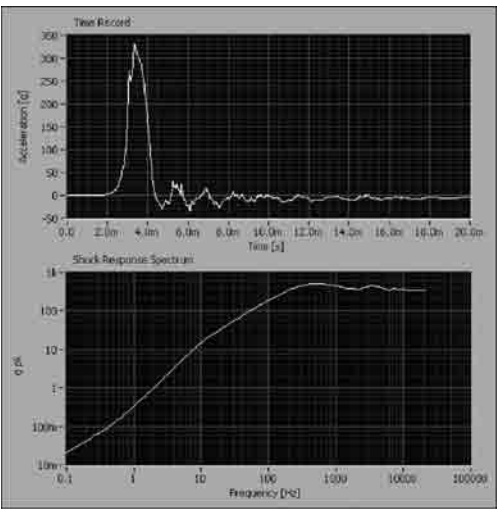


FIGURE 15A.51 Acquired SRS (Maximax).

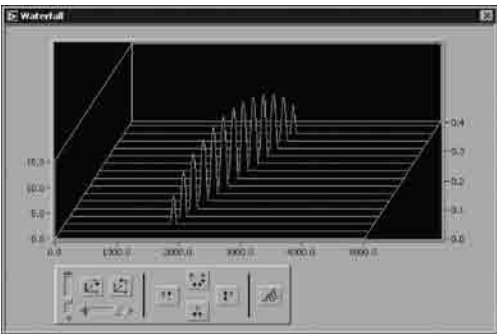


FIGURE 15A.52 Waterfall display for frequency analysis.

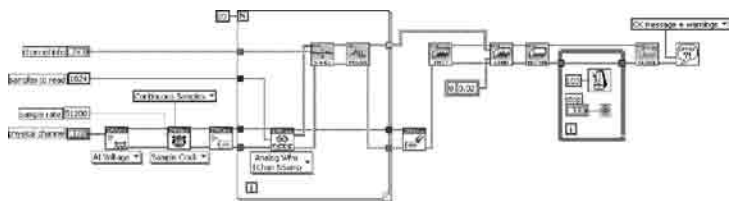


FIGURE 15A.53 Waterfall display for frequency analysis VI block diagram.

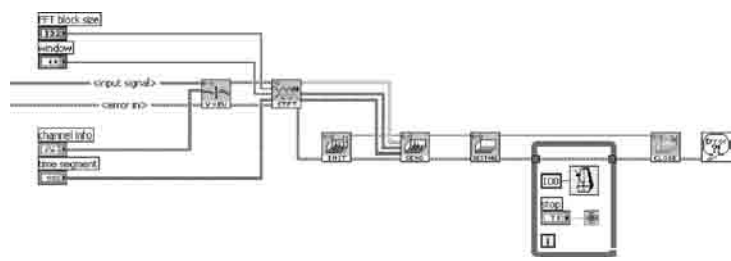


FIGURE 15A.54 STFT VI block diagram.

The data are scaled and sent to the SVT STFT vs. Time VI. The SVT STFT vs. Time VI returns a 2D array. You can use the results in the 2D array in an intensity graph or connect the 2D array directly to the SVL Send Data to Waterfall VI. Figure 15A.54 shows the 2D array connected directly to the Waterfall VI. The while loop keeps the waterfall display open until the *Stop* control is set to TRUE.

Note: Connect f_0 and Δf and y_0 and Δy on the SVL Send Data to Waterfall VI to ensure the graph shows the proper scales.

Figure 15A.55 shows the result obtained with the STFT VI illustrated in Figure 15A.54.

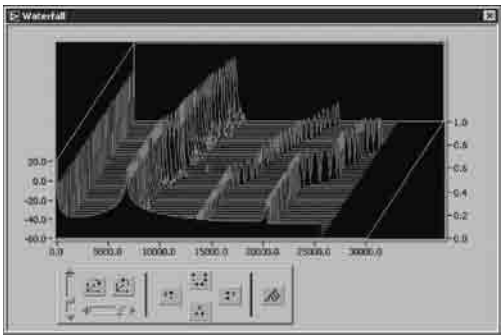


FIGURE 15A.55 STFT waterfall display.

15A.9.1.5 Waterfall Display for Octave Spectra

To display octave spectra in a waterfall display, use the SVT Initialize Waterfall Display for Octave and SVT Send Data to Waterfall for Octave VIs. Figure 15A.56 shows the block diagram for a VI displaying octave spectra in a waterfall display.

Figure 15A.57 shows the waterfall display created by the VI in Figure 15A.56.

15A.10 Swept-Sine Measurements

This Appendix discusses using the swept-sine VIs located on the Swept Sine palette (see Chapter 17). The swept-sine measurements include dynamic measurements for stimulus level, response level, frequency response (gain and phase), THD, and individual harmonic distortion.

15A.10.1 Swept-Sine Overview

Swept sine is a technique for characterizing the frequency response of the DUT. Two techniques are commonly used in swept-sine measurements. The first technique slowly sweeps through a range of

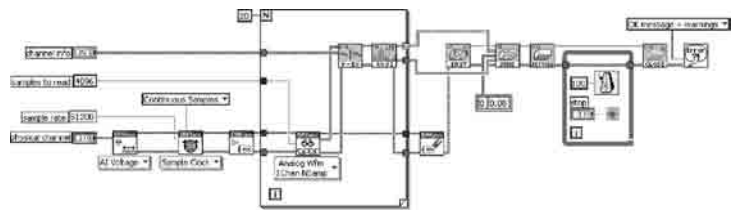


FIGURE 15A.56 Block diagram for VI displaying octave spectra.

frequencies in a manner similar to a chirp. Figure 15A.58 shows an example of the excitation signal for this form of swept-sine measurement.

The second technique steps through a range of frequencies. Figure 15A.59 shows an example of the excitation signal for this form of swept-sine measurement. The swept sine implemented in the Sound and Vibration Toolkit generates an excitation signal that steps through a range of test frequencies, similar to the signal in Figure 15A.59. Both techniques can yield similar results. However, they require very different measurement analysis processes.

Swept-sine frequency-response measurements compare a response signal to the stimulus tone in order to compute the FRF of the DUT. The magnitude of the FRF is equivalent to gain and represents the ratio of the output level to the input level for each test frequency. The phase of the FRF is equivalent to the phase lag introduced by the DUT for each test frequency.

Swept-sine measurements require a signal source. The stimulus signal is always a single tone that excites the DUT at the test frequency. Since the stimulus is a single tone, swept-sine analysis can measure the harmonic distortion while simultaneously measuring the linear response.

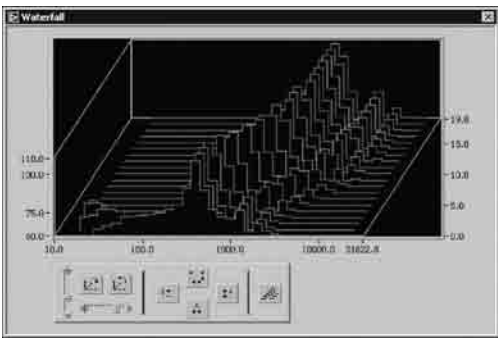


FIGURE 15A.57 Waterfall display for octave spectra analysis.

15A.10.2 Choosing Swept-Sine vs. FFT Measurements

The frequency response of the DUT is a useful tool. The Sound and Vibration Toolkit provides two distinct techniques to measure the frequency response. The swept-sine technique performs single-tone

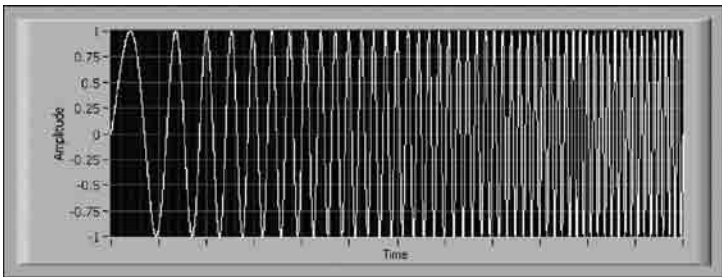


FIGURE 15A.58 Sweeping swept sine example.

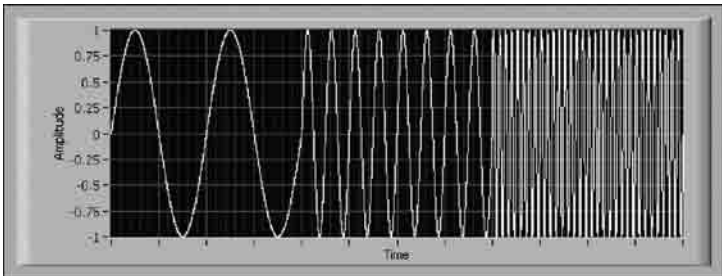


FIGURE 15A.59 Stepping swept sine example.

TABLE 15A.8 Swept Sine and FFT Differences

Swept-Sine Frequency Response	FFT-Based Frequency Response
Single-tone excitation	Broadband excitation
Can measure harmonics	Cannot measure harmonics
Arbitrary test frequencies	Linearly spaced frequency resolution
Longer test time for many test frequencies	
Better dynamic range possibility	

measurements at each test frequency. The FFT-based technique measures the response over the entire acquisition bandwidth. Table 15A.8 lists the basic differences between swept-sine and FFT-based techniques for measuring frequency response.

Swept-sine measurements offer superior dynamic range over FFT-based measurements because you can optimize the signal level and input ranges at each test frequency. FFT-based techniques must specify a signal level and input ranges appropriate for the maximum broadband response.

Figure 15A.60 shows the simulated frequency response function for a four-DoF system. The peak at 17.6 Hz has a magnitude roughly 1000 times larger than the peak at 5.8 Hz. To use an FFT-based technique, use broadband excitation to excite the entire frequency range of interest, to measure the frequency response. This situation forces one to set the input range so that the overall response does not overload the DUT or the acquisition device. Therefore, when you measure the response at 5.8 Hz, you lose 60 dB of measurement dynamic range. The swept-sine technique allows you to tailor the excitation amplitude to the specific test frequency, preserving the full measurement dynamic range.

FFT-based measurements are limited to a linearly spaced frequency resolution determined by the sample rate and the block size. Refer to [Appendix 15A.7](#) for more information on FFT-based measurements. When the response changes rapidly, this frequency resolution may not yield enough information about the dynamic response. Also, a linear resolution may yield an excessive amount of information in frequency regions where the dynamic response is relatively constant. Swept-sine analysis has the ability to test arbitrary frequency resolutions that are linear, logarithmic, or adapted to the dynamic response of the DUT. When the frequency resolution is adapted to the DUT dynamic response, you can test more frequencies in regions where the dynamic response is of interest to your application and fewer where it is not.

The main benefit of swept-sine analysis is the ability to measure harmonic distortion simultaneously with linear response. FFT-based analysis offers a speed advantage for broadband measurements with many test frequencies.

15A.10.3 Taking a Swept-Sine Measurement

Use the SVT Initialize Swept Sine VI to create a new swept-sine task for the designated device, source channel settings, and acquisition channel settings. Swept sine in the Sound and Vibration Toolkit only supports measurements on a single device with output and input capabilities.

Use configure swept sine VIs in the configure swept sine palette to configure the scaling, test frequencies, averaging, delays, and other measurement settings. These configuration VIs allow control over basic and advanced measurement parameters. The order in which you place the configuration VIs is important, as it allows you to customize a swept-sine measurement. For example, you can easily generate

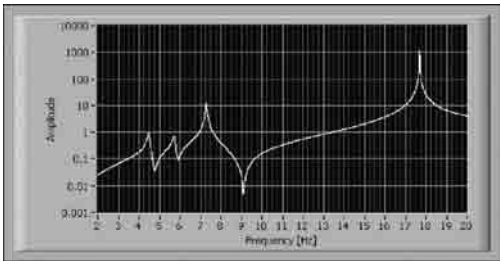


FIGURE 15A.60 Swept-sine and FFT measurements.

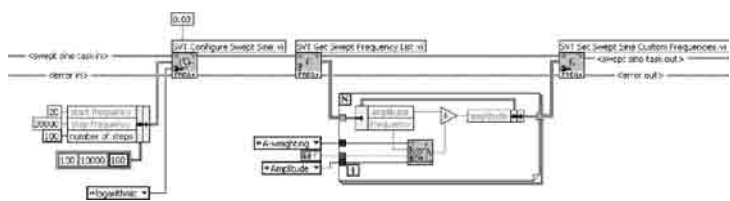


FIGURE 15A.61 Customizing a swept-sine measurement.

100 logarithmically spaced test frequencies in the audio range, then apply inverse A-weighted scaling to the excitation level by adding code similar to that in Figure 15A.61 into your swept-sine application.

You can use the swept-sine configuration VIs to customize your swept-sine application. For example, to speed up a swept-sine measurement, reduce the settling or integration time specified by the SVT Set Swept Sine Averaging VI. You also can configure the device IEPE with the SVT Set Swept Sine Coupling and IEPE Excitation (DAQmx) VI. You also can reduce the *block duration* input to SVT Set Swept Sine Block Duration VI.

Note: The minimum block duration is limited by the capabilities of the computer processing the measurement. A very small block duration can result in a loss of continuous processing, causing the swept-sine measurement to stop and return an error.

Use the SVT Start Swept Sine VI to begin the generation and acquisition. The VI fills the device output buffer with zeros before writing the first test frequency excitation.

The SVT Swept Sine Engine VI continually acquires data and processes it to remove samples acquired during delays, transitions, and settling periods. The SVT Swept Sine Engine VI performs measurement analysis on samples acquired during integration periods. The SVT Swept Sine Engine VI updates the excitation to excite the DUT at the next test frequency after it integrates sufficient data at the current test frequency.

Note: The transition to the next excitation tone, both frequency and amplitude, always occurs at a zero crossing to minimize transients introduced to the DUT.

Use the Read Swept Sine Measurements VIs in the Read Swept Sine Measurements palette to read the raw measurements, scale the measurements, and perform additional conversions to display and report the data in the desired format.

Use the SVT Close Swept Sine VI to stop the generation and acquisition, and clear the swept-sine task.

15A.10.4 Swept-Sine Measurement Example

This example of a swept-sine application measures the frequency response and harmonic distortion of a notch filter. In this example, a NI PXI-4461 generates the excitation signal and acquires the stimulus and response signals.

Figure 15A.62 illustrates the connection scheme used in this example to measure the dynamic response of the DUT using a swept-sine measurement. The acquired stimulus signal on the analog input channel 0, the AI0, is the generated excitation signal from the analog output channel 0, AO0.

The NI PXI-4461 converts the desired stimulus signal from digital data to an analog signal and outputs that signal on AO0. The excitation signal is

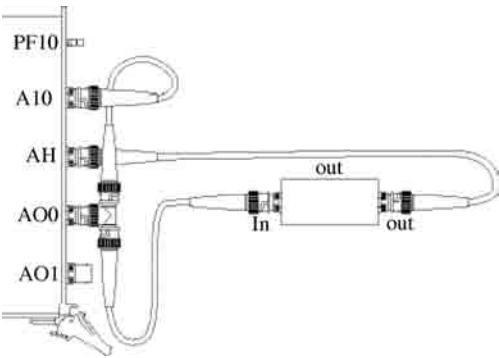


FIGURE 15A.62 Swept-sine measurement connection diagram.

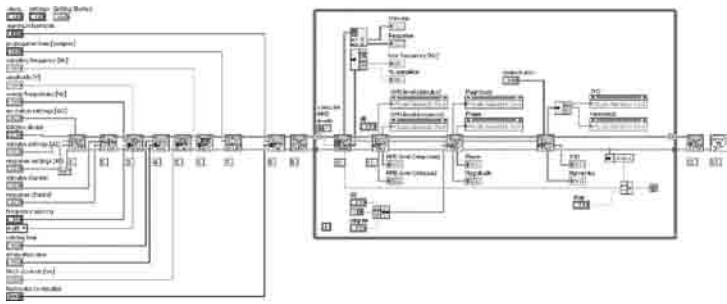


FIGURE 15A.63 Block diagram of SVXMPL_swept sine FRF DAQmx VI.

TABLE 15A.9 Swept Sine Measurement Steps

Step Number	Description	Optional or Required
1	Initialize a swept-sine measurement by specifying the hardware device and channel settings	Required
2	Specify the scaling that will be applied to the acquired stimulus and response data.	Optional
3	Configure the source by specifying the test frequencies, amplitude, and whether or not the sweep automatically restarts after completion	Required
4	Set the settling and integration parameters to allow sufficient time for the DUT to settle before the measurement is performed at the new test frequency and that there is sufficient integration time to achieve the desired level of accuracy	Required
5	Set the block duration input terminal for the measurement to be small enough to give a reasonable test time and large enough so that it does not put the test computer at risk of being unable to continuously generate and read the signals. The smaller the block size, the faster the swept sine can transition from one test frequency to the next	Optional
6	Explicitly set the sample rate for the measurement. The rate is automatically selected if this VI is not used. The same rate is used for input and output channels	Optional
7	Specify the <i>propagation time</i> terminal input specific to the DAQ device being used for the measurement. You can measure the device propagation time using the SVL Measure Propagation Delay VI. Refer to Appendix 3, <i>Scaling and Calibration</i> , for more information	Optional
8	Configure the harmonic distortion measurement by specifying the maximum harmonic to use in the computation of the THD. Only those harmonics specified in the <i>harmonics to visualize</i> array return individual harmonic components	Required if performing distortion measurements
9	Start the swept sine to perform the hardware configuration and start the output and input tasks. Channel synchronization is performed internally in this VI	Required
10	Generate the excitation and acquire the stimulus and response data at each test frequency	Required
11	Convert the raw data to the specified format in order to display and report measurement results	Required
12	Stop the swept-sine measurement and clear the output and input tasks to release the device	Required

connected to both the stimulus input channel AI0 and the input terminal of the DUT. The response signal is connected from the output terminal of the DUT to the response input channel AI1.

The DUT for this example is a notch filter centered at 1 kHz.

Figure 15A.63 shows the block diagram of the example SVXMPL_swept sine FRF DAQmx VI, which ships with the Sound and Vibration Toolkit.

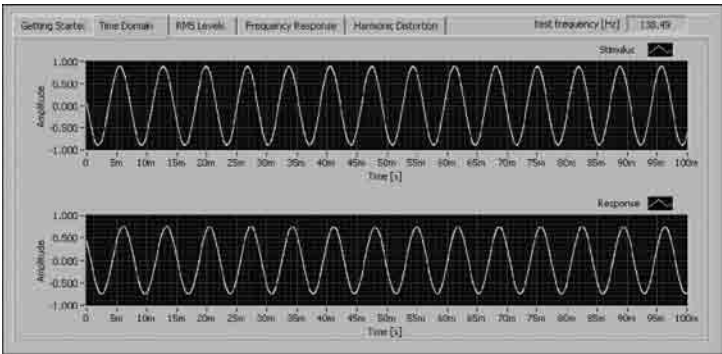


FIGURE 15A.64 Time-domain results.

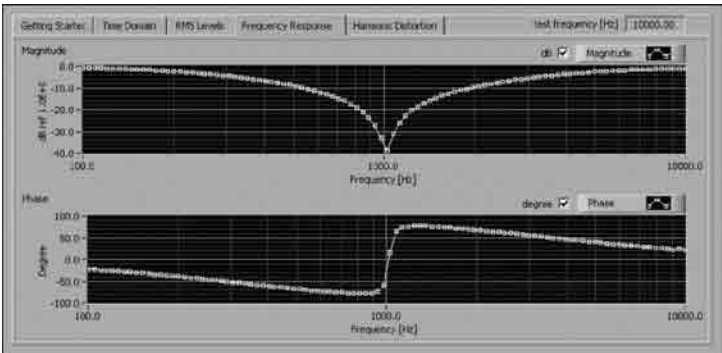


FIGURE 15A.65 Magnitude and phase response of a 1 kHz notch filter.

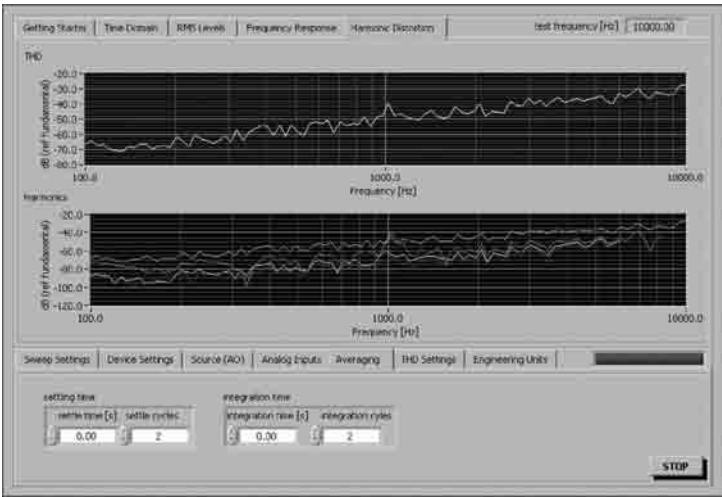


FIGURE 15A.66 THD vs. frequency.

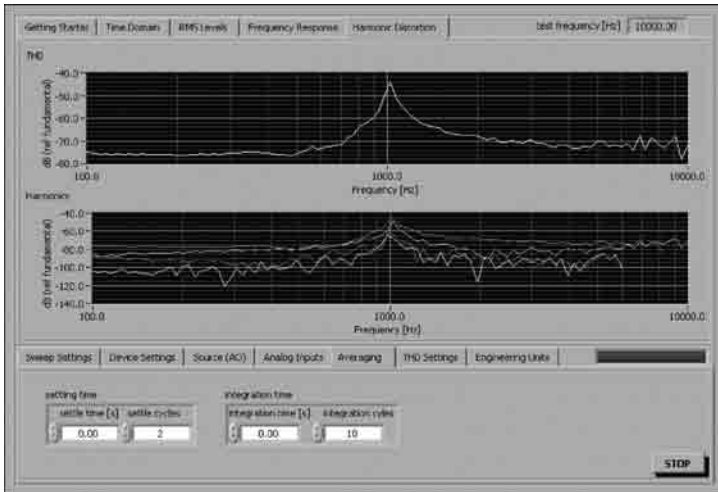


FIGURE 15A.67 THD vs. frequency results.

Table 15A.9 documents the actions performed by the VIs in Figure 15A.63. Some steps are required and must be done for the VI to function correctly. The optional steps allow you to customize your measurement.

The while loop in Figure 15A.63 controls the synchronized generation and acquisition. Display controls and measurement indicators are updated inside the while loop. This loop allows for the monitoring of intermediate results.

Many of the steps in Table 15A.9 are configuration steps. Through the Sound and Vibration Toolkit swept-sine configuration VIs, you can specify numerous configuration parameters to achieve fine control of the swept-sine measurement parameters. For many applications two or three configuration VIs are sufficient.

It is important to allow for the propagation delay of the DAQ or DSA device. This delay is specific to the device used to perform the measurement. To determine the device propagation delay, refer to the device documentation or measure the delay with the SVL Measure Propagation Delay VI.

Figures 15A.64 to 15A.67 display measurement results obtained with the SVXMPL_swept sine FRF DAQmx VI example program. Figure 15A.64 shows the time-domain stimulus and response signals for the 138.49 Hz test frequency. From the time-domain data, you can see that the notch filter has attenuated the signal and introduced a phase shift.

Figure 15A.65 shows the magnitude and phase responses of the notch filter at all the test frequencies in the magnitude and phase spectra in the Bode plot.

In addition to measuring the frequency response, this example simultaneously measures the harmonic distortion at each test frequency. Figure 15A.66 shows the graph of THD vs. frequency.

You expect to see a peak in the THD at the notch frequency. The peak occurs because the fundamental frequency is attenuated at the notch frequency. However, the graph indicates that this measurement has failed to accurately identify the power in the harmonic distortion components. For the example in Figure 15A.66, the number of *integration cycles* is two. More integration cycles must be specified to perform accurate harmonic distortion measurements. If you change the number of integration cycles to ten and rerun the example, you obtain the THD vs. frequency results displayed in Figure 15A.67.

Now, with a sufficient number of integration cycles specified, you can see the characteristic peak in the THD at the center frequency of the notch filter.

Bibliography

- Crocker and Malcolm, J. 1998. *Handbook of Acoustics*, Wiley, New York.
- Design Response of Weighting Networks for Acoustical Measurements*, ANSI S1.42-2001, American National Standards Institute, Washington, 1986.
- Electroacoustics — Sound Level Meters*, International Standard IEC 61672, 1st ed., 2002–2005, International Electrotechnical Commission, Geneva, Switzerland, 2002.
- Hassall, J.R. and Zaveri, K. 1988. *Acoustic Noise Measurements*, Bruel & Kjaer, Nærum, Denmark.
- Measurement of Audio-Frequency Noise Voltage Level in Sound Broadcasting*, ITU-R Recommendation 468-4, 1986.
- Octave-Band and Fractional Octave-Band Filters*, International Standard IEC 1260, 1st ed., 1995-07. International Electrotechnical Commission, Geneva, Switzerland, 1995.
- Preferred Frequencies for Measurements*, International Standard IEC 266, 1st ed., 1975-07-15, International Electrotechnical Commission, Geneva, Switzerland, 1975.
- Psophometer for Use on Telephone-Type Circuits*, ITU-T Recommendation O.41, Revised, 1993–1996. Telecommunication Standardization Sector of the International Telecommunication Union, 1995.
- Randall, R.B. 1987. *Frequency Analysis*, Brÿel & Kjaer, Nærum, Denmark.
- Smallwood, D., An improved recursive formula for calculating shock response spectra, *Shock Vib. Bull.*, 51, Pt 2, 211–217, 1981, May 1981.
- Specification for Octave-Band and Fractional Octave-Band Analog and Digital Filters*, ANSI S1.11-1986, Acoustical Society of America, New York, 1986b.
- Specification for Sound Level Meters*, ANSI S1.4-1983, American National Standards Institute, Washington, 1983.

16

Signal Conditioning and Modification

16.1	Introduction	16-2
16.2	Amplifiers	16-2
	Operational Amplifier • Use of Feedback in Opamp • Voltage, Current, and Power Amplifiers • Instrumentation Amplifiers • Amplifier Performance Ratings • Component Interconnection	
16.3	Analog Filters	16-15
	Passive Filters and Active Filters • Low-Pass Filters • High-Pass Filters • Band-Pass Filters • Band-Reject Filters	
16.4	Modulators and Demodulators	16-29
	Amplitude Modulation • Application of Amplitude Modulation • Demodulation	
16.5	Analog–Digital Conversion	16-37
	Digital-to-Analog Conversion • Analog-to-Digital Conversion • Analog-to-Digital Converter Performance Characteristics • Sample-and-Hold Circuitry • Digital Filters	
16.6	Bridge Circuits	16-43
	Wheatstone Bridge • Constant-Current Bridge • Bridge Amplifiers • Impedance Bridges	
16.7	Linearizing Devices	16-49
	Linearization by Software • Linearization by Hardware Logic • Analog Linearizing Circuitry • Offsetting Circuitry • Proportional-Output Circuitry	
16.8	Miscellaneous Signal Modification Circuitry	16-56
	Phase Shifters • Voltage-to-Frequency Converter • Frequency-to-Voltage Converter • Voltage-to-Current Converters • Peak-Hold Circuits	
16.9	Signal Analyzers and Display Devices	16-62
	Signal Analyzers • Oscilloscopes	

Clarence W. de Silva

The University of British Columbia

Summary

This chapter concerns the conditioning of signals in a vibrating system and the conversion of signals in one form to another as needed. Amplification, filtering, modulation, demodulation, analog/digital conversion, voltage/frequency conversion, voltage/current conversion, linearization, bridge circuits, and signal analysis and display devices are presented. Hardware, software, and techniques are considered. Issues of impedance and loading associated with the interconnection of components are addressed.

16.1 Introduction

Signal modification is an important function in many applications of vibration. The tasks of signal modification may include: *signal conditioning* (e.g., amplification, and analog and digital filtering); *signal conversion* (e.g., analog-to-digital conversion, digital-to-analog conversion, voltage-to-frequency conversion, and frequency-to-voltage conversion); *modulation* (e.g., amplitude modulation, frequency modulation, phase modulation, pulse-width modulation, pulse-frequency modulation, and pulse-code modulation); and *demodulation* (the reverse process of modulation). In addition, many other types of useful signal modification operations can be identified. For example, *sample and hold circuits* are used in digital data acquisition systems. Devices such as *analog and digital multiplexers* and *comparators* are needed in many applications of data acquisition and processing. Phase shifting, curve shaping, offsetting, and linearization can also be classified as signal modification. This chapter describes signal conditioning and modification operations that are useful in vibration applications. Signal modification plays a crucial role in component interfacing. When two devices are interfaced, it is essential to ensure that a signal leaving one device and entering the other will do so at proper signal levels (voltage, current, power), in the proper form (analog, digital), and without distortion (loading and impedance considerations). A signal should be properly modified for transmission by amplification, modulation, digitizing, and so on, so that the signal/noise ratio of the transmitted signal is sufficiently large at the receiver. The significance of signal modification is clear from these observations.

16.2 Amplifiers

The level of an electrical signal can be represented by variables such as voltage, current, and power. Analogous across variables, through variables, and power variables can be defined for other types of signals (e.g., mechanical) as well. Signal levels at various interface locations of components in a vibratory system have to be properly adjusted for proper performance of these components and of the overall system. For example, input to an actuator should possess adequate power to drive the actuator. A signal should maintain its signal level above some threshold during transmission so that errors due to signal weakening will not be excessive. Signals applied to digital devices must remain within the specified, logic levels. Many types of sensors produce weak signals that have to be upgraded before they can be fed into a monitoring system, data processor, controller, or data logger.

Signal amplification concerns the proper adjustment of a signal level for performing a specific task. Amplifiers are used to accomplish signal amplification. An amplifier is an active device that needs an external power source to operate. Even though active circuits, amplifiers in particular, can be developed in the monolithic form using an original integrated-circuit (IC) layout so as to accomplish a particular amplification task, it is convenient to study their performance using the *operational amplifier* (opamp) as the basic element. Of course, operational amplifiers are widely used not only for modeling and analyzing other types of amplifier but also as basic elements in building other kinds of amplifier. For these reasons, our discussion on amplifiers will revolve around the operational amplifier.

16.2.1 Operational Amplifier

The origin of the operational amplifier dates to the 1940s when the vacuum tube operational amplifier was introduced. The operational amplifier, or *opamp*, got its name due to the fact that originally it was used almost exclusively to perform mathematical operations; for example, it was used in analog computers. Subsequently, in the 1950s, the transistorized opamp was developed. It used discrete elements such as *bipolar junction transistors* and *resistors*. The opamp was still too large in size, consumed too much power, and was too expensive for widespread use in general applications. This situation changed in the late 1960s when IC opamp was developed in the monolithic form as a single IC chip. Today, the IC opamp, which consists of a large number of circuit elements on a *substrate*, typically of a single *silicon crystal* (the monolithic form), is a valuable component in almost any signal modification device.

An opamp could be manufactured in the discrete-element form using perhaps ten bipolar junction transistors and as many discrete resistors; alternatively (and preferably), it may be manufactured in the modern monolithic form as an IC chip that may be equivalent to over 100 discrete elements. In any form, the device has an *input impedance*, Z_i , an *output impedance*, Z_o , and a gain, K . Hence, a schematic model for an opamp can be given as in Figure 16.1(a). The conventional symbol of an opamp is shown in Figure 16.1(b). Typically, there are about six terminals (lead connections) to an opamp. For example, there may be two input leads (a *positive lead* with voltage v_{ip} and a *negative lead* with voltage v_{in}), an output lead (voltage v_o), two bipolar power supply leads ($+v_s$ and $-v_s$), and a ground lead.

Note from Figure 16.1(a) that, under open-loop (no feedback) conditions

$$v_o = K v_i \quad (16.1)$$

in which the input voltage, v_i , is the differential input voltage defined as the algebraic difference between the voltages at the positive and negative lead; thus

$$v_i = v_{ip} - v_{in} \quad (16.2)$$

The *open loop voltage gain* K is very high (10^5 to 10^9) for a typical opamp. Furthermore, the input impedance, Z_i , could be as high as $1 \text{ M}\Omega$ and the output impedance is low, of the order of 10Ω . Since v_o is typically 1 to 10 V, from Equation 16.1 it follows that $v_i \cong 0$ since K is very large. Hence, from Equation 16.2, we have $v_{ip} \cong v_{in}$. In other words, the voltages at the two input leads are nearly equal. Now, if we apply a large voltage differential v_i (say, 1 V) at the input then, according to Equation 16.1, the output voltage should be extremely high. This never happens in practice, however, since the device saturates quickly beyond moderate output voltages (of the order of 15 V).

From Equation 16.1 and Equation 16.2, it is clear that if the negative input lead is grounded (i.e., $v_{in} = 0$), then

$$v_o = K v_{ip} \quad (16.3)$$

and, if the positive input lead is grounded (i.e., $v_{ip} = 0$)

$$v_o = -K v_{in} \quad (16.4)$$

Accordingly, v_{ip} is termed *noninverting input* and v_{in} is termed *inverting input*.

Example 16.1

Consider an opamp having an open-loop gain of 1×10^5 . If the saturation voltage is 15 V, determine the output voltage in the following cases:

1. $5 \mu\text{V}$ at the positive lead and $2 \mu\text{V}$ at the negative lead.
2. $-5 \mu\text{V}$ at the positive lead and $2 \mu\text{V}$ at the negative lead.
3. $5 \mu\text{V}$ at the positive lead and $-2 \mu\text{V}$ at the negative lead.
4. $-5 \mu\text{V}$ at the positive lead and $-2 \mu\text{V}$ at the negative lead.
5. 1 V at the positive lead and negative lead grounded.
6. 1 V at the negative lead and positive lead grounded.

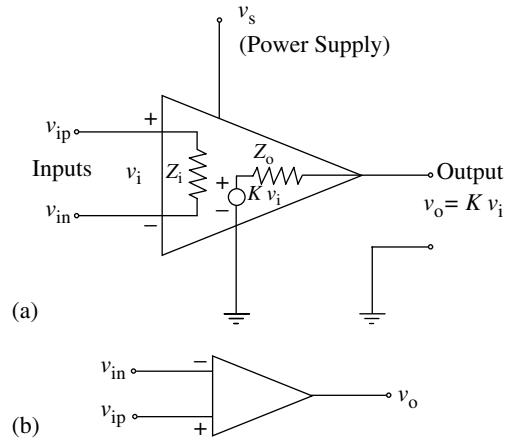


FIGURE 16.1 Operational amplifier: (a) a schematic model; (b) conventional symbol.

TABLE 16.1 Solution to Example 16.1

v_{ip}	v_{in}	v_i	v_o
$5\ \mu\text{V}$	$2\ \mu\text{V}$	$3\ \mu\text{V}$	$0.3\ \text{V}$
$-5\ \mu\text{V}$	$2\ \mu\text{V}$	$-7\ \mu\text{V}$	$-0.7\ \text{V}$
$5\ \mu\text{V}$	$-2\ \mu\text{V}$	$7\ \mu\text{V}$	$0.7\ \text{V}$
$-5\ \mu\text{V}$	$-2\ \mu\text{V}$	$-3\ \mu\text{V}$	$-0.3\ \text{V}$
$1\ \text{V}$	0	$1\ \text{V}$	$15\ \text{V}$
0	$1\ \text{V}$	$-1\ \text{V}$	$-15\ \text{V}$

Solution

This problem can be solved using Equation 16.1 and Equation 16.2. The results are given in Table 16.1. Note that, in the last two cases, the output will saturate and Equation 16.1 will no longer hold.

Field effect transistors (FET), for example, metal oxide semiconductor field effect transistors (MOSFET), could be used in the IC form of an opamp. The MOSFET type has advantages over many other types; for example, such opamps have higher input impedance and more stable output (almost equal to the power supply voltage) at saturation. This makes the MOSFET opamps preferable over bipolar junction transistor opamps in many applications.

In analyzing operational amplifier circuits under unsaturated conditions, we use the following two characteristics of an opamp:

1. Voltages of the two input leads should be (almost) equal.
2. Currents through each of the two input leads should be (almost) zero.

As explained earlier, the first property is credited to high open-loop gain and the second property to high input impedance in an operational amplifier. We shall repeatedly use these two properties to obtain input–output equations for amplifier systems.

16.2.2 Use of Feedback in Opamp

The operation amplifier is a very versatile device, primarily due to its very high input impedance, low output impedance, and very high gain. However, it cannot be used without modification as an amplifier because it is not very stable, as shown in Figure 16.1. Two factors that contribute to this problem are:

1. Frequency response
2. Drift

Stated in another way, opamp gain, K , does not remain constant; it can vary with the frequency of the input signal (i.e., frequency-response function is not flat in the operating range); also, it can vary with time (i.e., *drift*). The frequency-response problem arises due to circuit dynamics of an operational amplifier. This problem is usually not severe unless the device is operated at very high frequencies. The drift problem arises due to the sensitivity of gain, K , to environmental factors such as temperature, light, humidity, and vibration, and as a result of variation of K due to aging. Drift in an opamp can be significant and steps should be taken to remove that problem.

It is virtually impossible to avoid drift in gain and frequency-response error in an operational amplifier. However, an ingenious way has been found to remove the effect of these two problems at the amplifier output. Since gain K is very large, by using feedback we can virtually eliminate its effect at the amplifier output. This *closed loop* form of an opamp is preferred in almost every application. In particular, the *voltage follower* and *charge amplifier* are devices that use the properties of high Z_i , low Z_o , and high K of an opamp, along with feedback through a precision resistor, to eliminate errors due to nonconstant K . In summary, the operational amplifier is not very useful in its *open-loop* form, particularly because gain, K , is not steady. However, since K is very large, the problem can be removed by using feedback. It is this *closed-loop* form that is commonly used in the practical applications of an opamp.

In addition to the nonsteady nature of gain, there are other sources of error that contribute to the less than ideal performance of an operational amplifier circuit. Noteworthy are:

1. *offset current* present at input leads due to bias currents that are needed to operate the solid-state circuitry
2. *offset voltage* that might be present at the output even when the input leads are open
3. unequal gains corresponding to the two input leads (i.e., the *inverting gain* not equal to the *noninverting gain*)

Such problems can produce nonlinear behavior in opamp circuits, and they can be reduced by proper circuit design and through the use of compensating circuit elements.

16.2.3 Voltage, Current, and Power Amplifiers

Any type of amplifier can be constructed from scratch in the monolithic form as an IC chip, or in the discrete form as a circuit containing several discrete elements such as discrete bipolar junction transistors or discrete FETs, discrete diodes, and discrete resistors. However, almost all types of amplifiers can also be built using operational amplifier as the basic element. Since we are already familiar with opamps and since opamps are extensively used in general amplifier circuitry, we prefer to use the latter approach, which uses discrete opamps for the modeling of general amplifiers.

If an electronic amplifier performs a voltage amplification function, it is termed a *voltage amplifier*. These amplifiers are so common that, the term “amplifier” is often used to denote a voltage amplifier. A voltage amplifier can be modeled as

$$v_o = K_v v_i \quad (16.5)$$

in which

v_o = output voltage
 v_i = input voltage
 K_v = voltage gain

Voltage amplifiers are used to achieve voltage compatibility (or level shifting) in circuits.

Current amplifiers are used to achieve current compatibility in electronic circuits. A *current amplifier* may be modeled by

$$i_o = K_i i_i \quad (16.6)$$

in which

i_o = output current
 i_i = input current
 K_i = current gain

Note that voltage follower has $K_v = 1$ and, hence, it may be considered to be a current amplifier. Also, it provides impedance compatibility and acts as a buffer between a low-current (high-impedance) output device (the device that provides the signal) and a high-current (low-impedance) input device (the device that receives the signal) that are interconnected. Hence, the name *buffer amplifier* or *impedance transformer* is sometimes used for a current amplifier with unity voltage gain.

If the objective of signal amplification is to upgrade the associated power level, then a *power amplifier* should be used for that purpose. A simple model for a power amplifier is

$$p_o = K_p P_i \quad (16.7)$$

in which

p_o = output power
 P_i = input power
 K_p = power gain

It is easy to see from Equation 16.5 to Equation 16.7 that

$$K_p = K_v K_i \tag{16.8}$$

Note that all three types of amplification could be achieved simultaneously from the same amplifier. Furthermore, a current amplifier with unity voltage gain (for example, a voltage follower) is a power amplifier as well. Usually, voltage amplifiers and current amplifiers are used in the first stages of a signal path (e.g., sensing, data acquisition, and signal generation) where signal levels and power levels are relatively low. Power amplifiers are typically used in the final stages (e.g., actuation, recording, and display) where high signal levels and power levels are usually required.

Figure 16.2(a) shows an opamp-based voltage amplifier. Note the feedback resistor, R_f , that serves the purposes of stabilizing the opamp and providing an accurate voltage gain. The negative lead is grounded through an accurately known resistor, R . To determine the voltage gain, recall that the voltages at the two input leads of an opamp should be virtually equal. The input voltage, v_i , is applied to the positive lead of

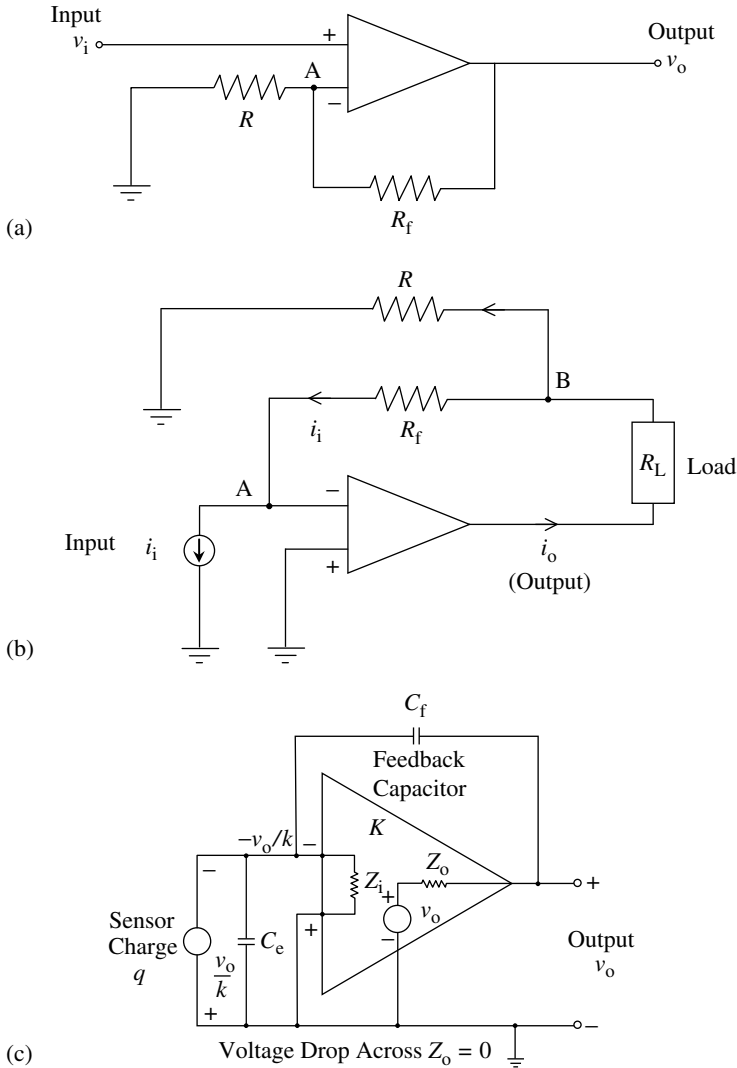


FIGURE 16.2 (a) A voltage amplifier; (b) a current amplifier; (c) a charge amplifier.

the opamp. Then the voltage at point A should also be equal to v_i . Next, recall that the current through the input lead of an opamp is virtually zero. Hence, by writing the current balance equation for the node point A, we have

$$\frac{v_o - v_i}{R_f} = \frac{v_i}{R}$$

This gives the amplifier equation

$$v_o = \left(1 + \frac{R_f}{R}\right)v_i \quad (16.9a)$$

Hence, the voltage gain is given by

$$K_v = 1 + \frac{R_f}{R} \quad (16.9b)$$

Note the K_v depends on R and R_f and not on the opamp gain. Hence, the voltage gain can be accurately determined by selecting the two resistors, R and R_f , precisely. Also note that the output voltage has the same sign as the input voltage. Hence, this is a *noninverting amplifier*. If the voltages are of the opposite sign, we will have an *inverting amplifier*.

A current amplifier is shown in Figure 16.2(b). The input current, i_i , is applied to the negative lead of the opamp as shown and the positive lead is grounded. There is a feedback resistor R_f connected to the negative lead through the load R_L . The resistor R_f provides a path for the input current since the opamp takes in virtually zero current. There is a second resistor R through which the output is grounded. This resistor is needed for current amplification. To analyze the amplifier, note that the voltage at point A (i.e., at the negative lead) should be zero because the positive lead of the opamp is grounded (zero voltage). Furthermore, the entire input current, i_i , passes through resistor, R_f , as shown. Hence, the voltage at point B is $R_f i_i$. Consequently, current through resistor R is $R_f i_i / R$, which is positive in the direction shown. It follows that the output current, i_o , is given by

$$i_o = i_i + \frac{R_f}{R} i_i$$

or

$$i_o = \left(1 + \frac{R_f}{R}\right)i_i \quad (16.10a)$$

The current gain of the amplifier is

$$K_i = 1 + \frac{R_f}{R} \quad (16.10b)$$

This gain can be accurately set using the high-precision resistors, R and R_f .

16.2.3.1 Charge Amplifiers

The principle of capacitance feedback is utilized in charge amplifiers. These amplifiers are commonly used for conditioning the output signals from piezoelectric transducers. A schematic diagram for the charge amplifier is shown in Figure 16.2(c). The feedback capacitance is denoted by C_f and the connecting cable capacitance by C_c . The charge amplifier views the sensor as a charge source (q), even though there is an associated voltage. Using the fact that charge = voltage \times capacitance, a charge balance equation can be written:

$$q + \frac{v_o}{K} C_c + \left(v_o + \frac{v_o}{K}\right) C_f = 0 \quad (16.11)$$

From this, we obtain

$$v_o = -\frac{K}{(K+1)C_f + C_c} q \quad (16.12a)$$

If the feedback capacitance is large in comparison with the cable capacitance, the latter can be neglected. This is desirable in practice. In any event, for large values of gain, K , we have the approximate relationship

$$v_o = -\frac{q}{C_f} \quad (16.12b)$$

Note that the output voltage is proportional to the charge generated at the sensor and depends only on the feedback parameter, C_f . This parameter can be appropriately chosen in order to obtain the required output impedance characteristics. Actual charge amplifiers also have a feedback resistor, R_f , in parallel with the feedback capacitor, C_f . Then, the relationship corresponding to Equation 16.12a becomes a first-order ordinary differential equation, which in turn determines the time constant of the charge amplifier. This time constant should be high. If it is low, the charge generated by the piezoelectric sensor will leak out quickly, giving erroneous results at low frequencies.

16.2.4 Instrumentation Amplifiers

An instrumentation amplifier is typically a special-purpose voltage amplifier dedicated to a particular instrumentation application. Examples include amplifiers used for producing the output from a bridge circuit (bridge amplifier) and amplifiers used with various sensors and transducers. An important characteristic of an instrumentation amplifier is the adjustable gain capability. The gain value can be adjusted manually in most instrumentation amplifiers. In more sophisticated instrumentation amplifiers, gain is *programmable* and can be set by means of digital logic. Instrumentation amplifiers are normally used with low-voltage signals.

16.2.4.1 Differential Amplifier

Usually, an instrumentation amplifier is also a *differential amplifier* (sometimes termed difference amplifier). Note that in a differential amplifier both input leads are used for signal input, whereas in a single-ended amplifier one of the leads is grounded and only one lead is used for signal input. Ground-loop noise can be a serious problem in single-ended amplifiers. Ground-loop noise can be effectively eliminated by using a differential amplifier, because noise loops are formed with both inputs of the amplifier using a differential amplifier allows that these noise signals are subtracted at the amplifier output. Since the noise level is almost the same for both inputs, it is canceled out. Note that any other noise (e.g., 60 Hz line noise) that might enter both inputs with the same intensity will also be canceled out in the output of a differential amplifier.

A basic differential amplifier that uses a single opamp is shown in Figure 16.3(a). The input–output equation for this amplifier can be obtained in the usual manner. For instance, since current through the opamp is negligible, current balance at point B gives

$$\frac{v_{i2} - v_B}{R} = \frac{v_B}{R_f} \quad (i)$$

in which v_B is the voltage at B. Similarly, current balance at point A gives

$$\frac{v_o - v_A}{R_f} = \frac{v_A - v_{i1}}{R} \quad (ii)$$

Now, we use the property

$$v_A = v_B \quad (iii)$$

for an operational amplifier to eliminate v_A and v_B from Equation i and Equation ii. This gives

$$\frac{v_{i2}}{(1 + R/R_f)} = \frac{(v_o R/R_f + v_{i1})}{(1 + R/R_f)}$$

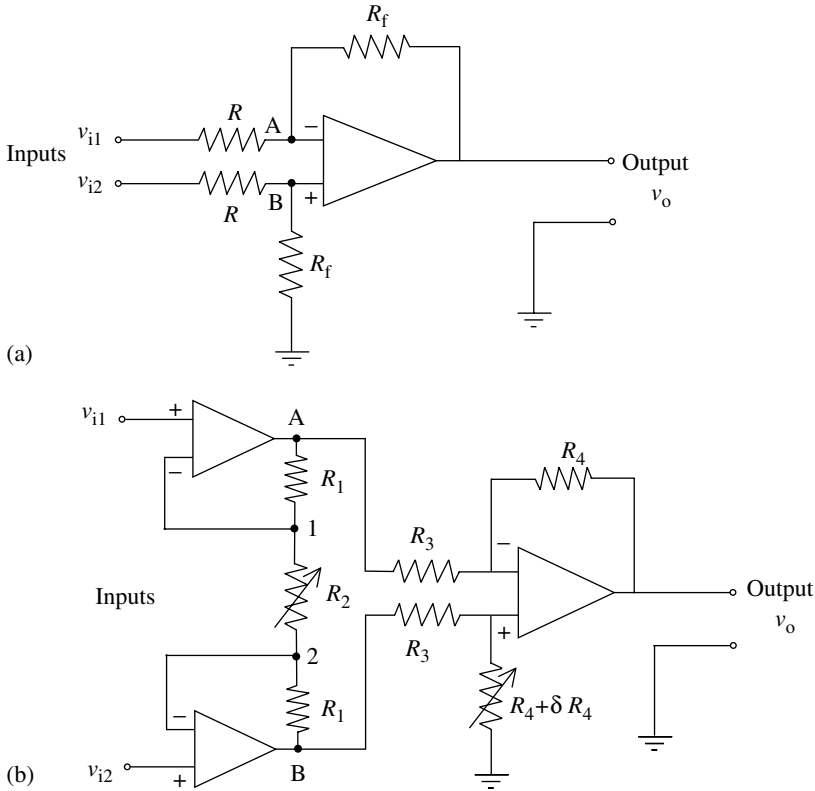


FIGURE 16.3 (a) A basic differential amplifier; (b) a basic instrumentation amplifier.

or

$$v_o = \frac{R_f}{R} (v_{i2} - v_{i1}) \quad (16.13)$$

Two things are clear from Equation 16.13. First, the amplifier output is proportional to the difference between, and not the absolute value of, the two inputs v_{i1} and v_{i2} . Second, voltage gain of the amplifier is R_f/R . This is known as the *differential gain*. Note that the differential gain can be accurately set by using high-precision resistors R and R_f .

The basic differential amplifier, shown in Figure 16.3(a) and discussed above, is an important component of an instrumentation amplifier. In addition, an instrumentation amplifier should possess the adjustable gain capability. Furthermore, it is desirable to have a very high input impedance and very low output impedance at each input lead. An instrumentation amplifier that possesses these basic requirements is shown in Figure 16.3(b). The amplifier gain can be adjusted using the precisely variable resistor, R_2 . Impedance requirements are provided by two voltage-follower-type amplifiers, one for each input, as shown. The variable resistance, δR_4 , is necessary to compensate for errors due to unequal *common-mode gain*. Let us first consider this aspect and then obtain an equation for the instrumentation amplifier.

16.2.4.2 Common Mode

The voltage that is “common” to both input leads of a differential amplifier is known as the *common-mode voltage*. This is equal to the smaller of the two input voltages. If the two inputs are equal, then the common-mode voltage is obviously equal to each one of the two inputs. When $v_{i1} = v_{i2}$, ideally, the output voltage v_o should be zero. In other words, ideally, *common-mode signals* are rejected by a

differential amplifier. However, since the operational amplifiers are not ideal and since they usually do not have exactly identical gains with respect to the two input leads, the output voltage v_o will not be zero when the two inputs are identical. This *common-mode error* can be compensated for by providing a variable resistor with fine resolution at one of the two input leads of the differential amplifier. As shown in Figure 16.3(b), to compensate for the common-mode error (i.e., to achieve a satisfactory level of common-mode rejection), first the two inputs are made equal and then δR_4 is varied carefully until the output voltage level is sufficiently small (minimum). Usually, the δR_4 that is required to achieve this compensation is small compared with the nominal feedback resistance R_4 .

Since ideally $\delta R_4 = 0$, we shall neglect δR_4 in the derivation of the instrumentation amplifier equation. Now, note from the basic characteristics of an opamp with no saturation (voltages at the two input leads have to be almost identical) that, in Figure 16.3(b), the voltage at point 2 should be v_{i2} and the voltage at point 1 should be v_{i1} . Furthermore, current through each input lead of an opamp is negligible. Hence, current through the circuit path $B \rightarrow 2 \rightarrow 1 \rightarrow A$ has to be the same. This gives the current continuity equations

$$\frac{v_B - v_{i2}}{R_1} = \frac{v_{i2} - v_{i1}}{R_2} = \frac{v_{i1} - v_A}{R_1}$$

in which V_A and V_B are the voltages at points A and B, respectively. Hence, we obtain the two equations

$$v_B = v_{i2} + \frac{R_1}{R_2}(v_{i2} - v_{i1})$$

$$v_A = v_{i1} - \frac{R_1}{R_2}(v_{i2} - v_{i1})$$

Now, by subtracting the second equation from the first, we have the equation for the first stage of the amplifier; thus

$$v_B - v_A = \left(1 + \frac{2R_1}{R_2}\right)(v_{i2} - v_{i1}) \quad (i)$$

From the previous result (see Equation 16.13) for a differential amplifier, we have (with $\delta R_4 = 0$)

$$v_o = \frac{R_4}{R_3}(v_B - v_A) \quad (ii)$$

Note that only the resistor R_2 is varied to adjust the gain (differential gain) of the amplifier. In Figure 16.3(b), the two input opamps (the voltage-follower opamps) do not have to be exactly identical as long as the resistors R_1 and R_2 are chosen so that they are accurate. This is so because the opamp parameters such as open-loop gain and input impedance do not enter the amplifier equations provided that their values are sufficiently high, as noted earlier.

16.2.5 Amplifier Performance Ratings

Main factors that affect the performance of an amplifier are:

1. Stability
2. Speed of response (bandwidth, slew rate)
3. Unmodeled signals

We have already discussed the significance of some of these factors.

The level of stability of an amplifier, in the conventional sense, is governed by the dynamics of the amplifier circuitry and may be represented by a *time constant*. However, a more important consideration for an amplifier is the “parameter variation” due to aging, temperature, and other environmental factors. Parameter variation is also classified as a stability issue in the context of devices such as amplifiers, because it pertains to the steadiness of the response when the input is maintained steady. Of particular importance is *temperature drift*. This may be specified as drift in the output signal per unit change in temperature (e.g., $\mu V/^\circ C$).

The speed of response of an amplifier dictates the ability of the amplifier to faithfully respond to transient inputs. Conventional time-domain parameters such as *rise time* may be used to represent this. Alternatively, in the frequency domain, speed of response may be represented by a *bandwidth* parameter. For example, the frequency range over which the frequency-response function is considered constant (flat) may be taken as a measure of bandwidth. Since there is some nonlinearity in any amplifier, bandwidth can depend on the signal level itself. Specifically, *small-signal bandwidth* refers to the bandwidth that is determined using small input signal amplitudes.

Another measure of the speed of response is the slew rate. Slew rate is defined as the largest possible rate of change in the amplifier output for a particular frequency of operation. Since, for a given input amplitude, the output amplitude depends on the amplifier gain, slew rate is usually defined for unity gain.

Ideally, for a linear device, the frequency-response function (transfer function) does not depend on the output amplitude (i.e., the product of the DC gain and the input amplitude). However, for a device that has a limited slew rate, the bandwidth, or the maximum operating frequency at which output distortions may be neglected, will depend on the output amplitude. The larger the output amplitude, the smaller the bandwidth for a given slew rate limit.

We have noted that stability problems and frequency-response errors are prevalent in the open-loop form of an operational amplifier. These problems can be eliminated using feedback because the effect of the open-loop transfer function on the closed loop transfer function is negligible if the open-loop gain is very large, which is the case for an operational amplifier.

Unmodeled signals can be a major source of amplifier error. Unmodeled signals include:

1. Bias currents
2. Offset signals
3. Common-mode output voltage
4. Internal noise

In analyzing operational amplifiers, we assume that the current through the input leads is zero. This is not strictly true because bias currents for the transistors within the amplifier circuit have to flow through these leads. As a result, the output signal of the amplifier will deviate slightly from the ideal value.

Another assumption that we make in analyzing opamps is that the voltage is equal at the two input leads. However, in practice, offset currents and voltages are present at the input leads, due to minute discrepancies inherent to the internal circuits within an opamp.

16.2.5.1 Common-Mode Rejection Ratio

Common-mode error in a differential amplifier was discussed earlier. We noted that ideally the common-mode input voltage (the voltage common to both input leads) should have no effect on the output voltage of a differential amplifier. However, since a practical amplifier has imbalances in the internal circuitry (for example, gain with respect to one input lead is not equal to the gain with respect to the other input lead and, furthermore, bias signals are needed for operation of the internal circuitry), there will be an error voltage at the output that depends on the common-mode input. The common-mode rejection ratio (CMRR) of a differential amplifier is defined as

$$\text{CMRR} = \frac{K v_{\text{cm}}}{v_{\text{ocm}}} \quad (16.14)$$

in which

- K = gain of the differential amplifier (i.e., differential gain)
- v_{cm} = common-mode voltage (i.e., voltage common to both input leads)
- v_{ocm} = common-mode output voltage (i.e., output voltage due to common-mode input voltage)

Note that, ideally, $v_{\text{ocm}} = 0$ and CMRR should be infinity. It follows that the larger the CMRR, the better the differential amplifier performance.

The three types of unmodeled signals mentioned above can be considered as noise. In addition, there are other types of noise signals that degrade the performance of an amplifier. For example, ground-loop

noise can enter the output signal. Furthermore, stray capacitances and other types of unmodeled circuit effects can generate internal noise. Usually in amplifier analysis, unmodeled signals (including noise) can be represented by a noise voltage source at one of the input leads. Effects of unmodeled signals can be reduced by using suitably connected compensating circuitry, including variable resistors that can be adjusted to eliminate the effect of unmodeled signals at the amplifier output (e.g., see δR_4 in [Figure 16.3\(b\)](#)). Some useful information about operational amplifiers is summarized in Box 16.1.

Box 16.1

OPERATIONAL AMPLIFIERS

Ideal Opamp Properties:

- Infinite open-loop differential gain
- Infinite input impedance
- Zero output impedance
- Infinite bandwidth
- Zero output for zero differential input

Ideal Analysis Assumptions:

- Voltages at the two input leads are equal.
- Current through either input lead is zero.

Definitions:

- Open-loop gain = $\left| \frac{\text{Output voltage}}{\text{Voltage difference at input leads}} \right|$ with no feedback
- Input impedance = $\frac{\text{Voltage between an input lead and ground}}{\text{Current through that lead}}$ with other input lead grounded and the output in open circuit
- Output impedance = $\frac{\text{Voltage between output lead and ground in open circuit}}{\text{Current through that lead}}$ with normal input conditions
- Bandwidth = frequency range in which the frequency response is flat (gain is constant)
- Input bias current = average (DC) current through one input lead
- Input offset current = difference in the two input bias currents
- Differential input voltage = voltage at one input lead with the other grounded when the output voltage is zero
- Common-mode gain = $\frac{\text{Output voltage when input leads are at the same voltage}}{\text{Common input voltage}}$
- Common-mode rejection ratio (CMRR) = $\frac{\text{Open loop differential gain}}{\text{Common-mode gain}}$
- Slew rate = speed at which steady output is reached for a step input

16.2.6 Component Interconnection

When two or more components are interconnected, the behavior of the individual components in the overall system can deviate significantly from their behavior of each component when they operate independently. The matching of components in a multicomponent system should be done carefully in order to improve system performance and accuracy, particularly with respect to their impedance characteristics. This is particularly true in vibration instrumentation.

16.2.6.1 Impedance Characteristics

When components such as measuring instruments, digital processing boards, process (plant) hardware, and signal-conditioning equipment are interconnected, it is necessary to *match* impedances properly at each interface in order to realize the devices' rated performance level. One adverse effect of improper impedance matching is the *loading effect*. For example, in a measuring system, the measuring instrument can distort the signal that is being measured. The resulting error can far exceed other types of measurement error. Loading errors will result from connecting a measuring device with low input impedance to a signal source.

Impedance can be interpreted either in the traditional electrical sense or in the mechanical sense, depending on the signal that is being measured. For example, a heavy accelerometer can introduce an additional dynamic load that will modify the actual acceleration at the monitoring location. Similarly, a voltmeter can modify the currents (and voltages) in a circuit. In mechanical and electrical systems, loading errors can appear as phase distortions as well. Digital hardware also can produce loading errors. For example, an ADC board can load the amplifier output from a strain-gage bridge circuit, thereby significantly affecting digitized data.

Another adverse effect of improper impedance consideration is inadequate output signal levels, which can make signal processing and transmission very difficult. Many types of transducers (e.g., piezoelectric accelerometers, impedance heads, and microphones) have high output impedances in the order of a thousand megohms. These devices generate low output signals, and they require conditioning to step up the signal level. *Impedance-matching amplifiers*, which have high input impedances (megohms) and low output impedances (a few ohms), are used for this purpose (e.g., charge amplifiers are used in conjunction with piezoelectric sensors). A device with a high input impedance has the further advantage that it usually consumes less power (v^2/R is low) for a given input voltage. The fact that a low input impedance device extracts a high level of power from the preceding output device may transpire to be the reason for a loading error.

16.2.6.2 Cascade Connection of Devices

Consider a standard two-port electrical device. The *output impedance*, Z_o , of such a device is defined as the ratio of the open-circuit (i.e., no-load) voltage at the output port to the short-circuit current at the output port.

Open-circuit voltage at the output is the output voltage present when there is no current flowing at the output port. This is the case if the output port is not connected to a load (impedance). As soon as a load is connected at the output of the device, a current will flow through it and the output voltage will drop to a value less than that of the open-circuit voltage. To measure open-circuit voltage, the rated input voltage is applied at the input port and maintained constant, and the output voltage is measured using a voltmeter that has a very high (input) impedance. To measure short-circuit current, a very low-impedance ammeter is connected at the output port.

The *input impedance*, Z_i , is defined as the ratio of the rated input voltage to the corresponding current through the input terminals while the output terminals are maintained as an open circuit.

Note that these definitions are associated with electrical devices. A generalization is possible that includes both electrical and mechanical devices; one must interpret voltage and velocity as *across variables*, and current and force as *through variables*. Then, mechanical *mobility* can be used in place of electrical impedance in the associated analysis.

Example 16.2

Input impedance, Z_i , and output impedance, Z_o , can be represented schematically as in Figure 16.4(a). Note that v_o is the open-circuit output voltage. When a load is connected at the output port, the voltage across the load will be different from v_o . This is caused by the presence of a current through Z_o . In the frequency domain, v_i and v_o are represented by their respective *Fourier spectra*. The corresponding transfer relation can be expressed in terms of the complex frequency-response (transfer) function $G(j\omega)$ under open-circuit (no-load) conditions:

$$v_o = Gv_i \quad (16.15)$$

Now, consider two devices connected in cascade, as shown in Figure 16.4(b). It can be easily verified that the following relations apply:

$$v_{o1} = G_1 v_i \quad (i)$$

$$v_{i2} = \frac{Z_{i2}}{Z_{o1} + Z_{i2}} v_{o1} \quad (ii)$$

$$v_o = G_2 v_{i2} \quad (iii)$$

These relations can be combined to give the overall input/output relation

$$v_o = \frac{Z_{i2}}{Z_{o1} + Z_{i2}} G_2 G_1 v_i \quad (16.16a)$$

We see from Equation 16.16a that the overall frequency-transfer function differs from the ideally expected product ($G_2 G_1$) by the factor

$$\frac{Z_{i2}}{Z_{o1} + Z_{i2}} = \frac{1}{Z_{o1}/Z_{i2} + 1} \quad (16.16b)$$

Note that cascading has “distorted” the frequency-response characteristics of the two devices. If $Z_{o1}/Z_{i2} \ll 1$, this deviation becomes insignificant. From this observation, it can be concluded that, when frequency-response characteristics (i.e., dynamic characteristics) are important in a cascaded device, cascading should be done such that the output impedance of the first device is much smaller than the input impedance of the second device.

16.2.6.3 AC-Coupled Amplifiers

The DC component of a signal can be blocked off by connecting that signal through a capacitor. (Note that the impedance of a capacitor is $1/(j\omega C)$ and, hence, at zero frequency there will be an infinite impedance.) If the input lead of a device has a series capacitor, we say that the input is AC coupled and, if the output lead has a series capacitor, then the output is AC coupled. Typically, an AC-coupled amplifier has a series capacitor both at the input lead and the output lead. Hence, its frequency-response function will have a high-pass characteristic; in particular, the DC components will be filtered out. Errors due to bias currents and offset signals are negligible for an AC-coupled amplifier. Furthermore, in an AC-coupled amplifier, stability problems are not very serious.

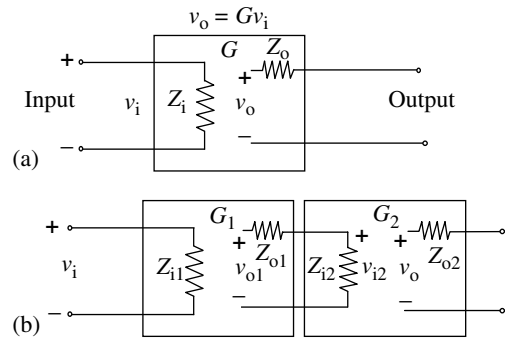


FIGURE 16.4 (a) Schematic representation of input impedance and output impedance; (b) the influence of cascade connection of devices on the overall impedance characteristics.

16.3 Analog Filters

Unwanted signals can seriously degrade the performance of a vibration monitoring and analysis system. External disturbances, error components in excitations, and noise generated internally within system components and instrumentation are such spurious signals. A filter is a device that allows only the desirable part of a signal to pass through, rejecting the unwanted part.

In typical applications of acquisition and processing of a vibration signal, the filtering task requires allowing certain frequency components through and filtering out certain other frequency components in the signal. In this context, we can identify four broad categories of filters:

1. Low-pass filters
2. High-pass filters
3. Band-pass filters
4. Band-reject (or notch) filters

The ideal frequency-response characteristic of each of these four types of filter is shown in Figure 16.5. Note that only the magnitude of the frequency-response function is shown.

It is understood, however, that the phase distortion of the input signal also should be small, within the *pass band* (the allowed frequency range). Practical filters are less than ideal. Their frequency-response functions do not exhibit sharp cutoffs as in Figure 16.5 and, furthermore, some phase distortion will be unavoidable.

A special type of band-pass filter that is widely used in acquisition and monitoring of vibration signals (e.g., in vibration testing) is the *tracking filter*. This is simply a band-pass filter with a narrow pass band that is frequency tunable. The center frequency (the mid-value) of the pass band is variable, usually by coupling it to the frequency of a carrier signal. In this manner, signals whose frequency varies with some basic variable in the system (e.g., rotor speed, frequency of a harmonic excitation signal, frequency of a sweep oscillator) can be accurately tracked in the presence of noise. The inputs to a tracking filter are the signal that is being tracked and the variable *tracking frequency* (*carrier input*). A typical tracking filter that can simultaneously track two signals is schematically shown in Figure 16.6.

Filtering can be achieved using *digital filters* as well as *analog filters*. Before digital signal processing became efficient and economical, analog filters were exclusively used for signal filtering and they are still widely used. In an analog filter, the signal is passed through an analog circuit.

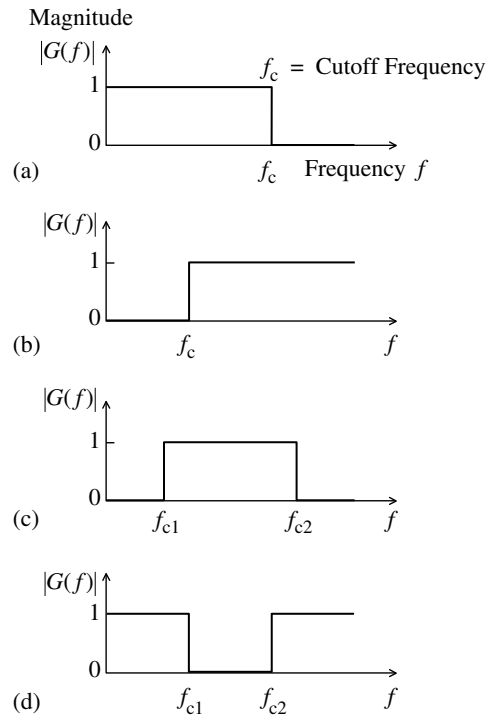


FIGURE 16.5 Ideal filter characteristics: (a) low-pass filter; (b) high-pass filter; (c) band-pass filter; (d) band-reject (notch) filter.

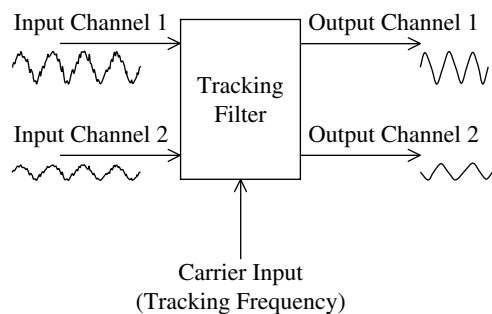


FIGURE 16.6 Schematic representation of a two-channel tracking filter.

The dynamics of the circuit will be such that the desired signal components will be passed through and the unwanted signal components will be rejected. Earlier versions of analog filters employed discrete circuit elements such as discrete transistors, capacitors, resistors, and even discrete inductors. Since inductors have several shortcomings, including susceptibility to electromagnetic noise, unknown resistance effects, and large size. These days, they are rarely used in filter circuits. Furthermore, owing to well-known advantages of IC devices, analog filters in the form of monolithic IC chips are today extensively used in modem applications and are preferred over discrete-element filters. Digital filters that employ digital signal processing to achieve filtering are also widely used nowadays.

16.3.1 Passive Filters and Active Filters

Passive analog filters employ analog circuits containing only passive elements, such as resistors and capacitors (and sometimes inductors). An external power supply is not needed in a passive filter. Active analog filters employ active elements and components, such as transistors and operational amplifiers in addition to passive elements. Since external power is needed for the operation of the active elements and components, an active filter is characterized by the need of an external power supply. Active filters are widely available in a monolithic IC form and are usually preferred over passive filters.

Advantages of active filters include the following:

1. Loading effects are negligible because active filters can provide a very high input impedance and very low output impedance.
2. They can be used with low-level signals because signal amplification and filtering can be provided by the same active circuit.
3. They are widely available in a low cost and compact IC form.
4. They can be easily integrated with digital devices.
5. They are less susceptible to noise from electromagnetic interference than passive filters.

Commonly mentioned disadvantages of active filters are the following:

1. They need an external power supply.
2. They are susceptible to "saturation"-type nonlinearity at high signal levels.
3. They can introduce many types of internal noise and unmodeled signal errors (offset, bias signals, etc.).

Note that advantages and disadvantages of passive filters can be directly inferred from the disadvantages and advantages of active filters as given above.

16.3.1.1 Number of Poles

Analog filters are dynamic systems and they can be represented by transfer functions, assuming linear dynamics. The number of poles of a filter is the number of poles in the associated transfer function. This is also equal to the order of the characteristic polynomial of the filter transfer function (i.e., *order of the filter*). Note that poles (or eigenvalues) are the roots of the characteristic equation.

In our discussion, we will show simplified versions of filters, typically consisting of a single filter stage. The performance of such a basic filter can be improved at the expense of circuit complexity (and an increased pole count). Only simple discrete-element circuits are shown for passive filters. Simple operational-amplifier circuits are given for active filters. Even here, much more complex devices are commercially available, but our purpose is to illustrate underlying principles rather than to provide descriptions and data sheets for commercial filters.

16.3.2 Low-Pass Filters

The purpose of a low-pass filter is to allow through all signal components below a certain (cutoff) frequency and block all signal components above that cutoff. Analog low-pass filters are widely used as *antialiasing filters* in digital signal processing. An error known as *aliasing* will enter the digitally processed results of a signal if the original signal has frequency components above half the *sampling frequency*. (Half the sampling frequency is called the *Nyquist frequency*.) Hence, aliasing distortion can be eliminated if, prior to sampling and digital processing, the signal is filtered using a low-pass filter with its cutoff set at Nyquist frequency. This is one of numerous applications of analog low-pass filters. Another typical application would be to eliminate high-frequency noise in a measured vibration response.

A single-pole, passive low-pass filter circuit is shown in Figure 16.7(a). An active filter corresponding to the same low-pass filter is shown in Figure 16.7(b). It can be shown that the two circuits have identical transfer functions. Hence, it might seem that the opamp in Figure 16.7(b) is redundant. This is not true, however. If two passive filter stages, each similar to Figure 16.7(a), are connected together, the overall transfer function is not equal to the product of the transfer functions of the individual stages. The reason for this apparent ambiguity is the circuit loading that arises due to the fact that the input impedance of the second stage is not sufficiently larger than the output impedance of the first stage. However, if two active filter stages, similar to those in Figure 16.7(b), are connected together, such loading errors will be negligible because the opamp with feedback (i.e., a voltage follower) introduces a very high input impedance and very low output impedance, while maintaining the voltage gain at unity.

To obtain the filter equation for the scenario depicted in Figure 16.7(a), note that, since the output is open circuit (zero load current), the current through capacitor C is equal to the current through resistor R . Hence,

$$C \frac{dv_o}{dt} = \frac{v_i - v_o}{R}$$

or

$$\tau \frac{dv_o}{dt} + v_o = v_i \quad (16.17)$$

where the filter time constant is

$$\tau = RC \quad (16.18)$$

From Equation 16.17, it follows that the filter transfer function is

$$\frac{v_o}{v_i} = G(s) = \frac{1}{(\tau s + 1)} \quad (16.19)$$

From this transfer function, it is clear that an analog low-pass filter is essentially a *lag circuit* (i.e., it provides a phase lag).

It can be shown that the active filter stage in Figure 16.7(b) has the same input/output equation. First, since current through an opamp lead is almost zero, we have from the previous analysis of the passive circuit stage

$$\frac{v_A}{v_i} = \frac{1}{(\tau s + 1)} \quad (i)$$

in which v_A is the voltage at the node point A. Now, since the opamp with feedback resistor is in fact a voltage follower, we have

$$\frac{v_o}{v_A} = 1 \quad (ii)$$

Next, by combining Equation i and Equation ii, we obtain Equation 16.19, as required. As mentioned earlier, a main advantage of the active filter version is that the resulting loading error is negligible.

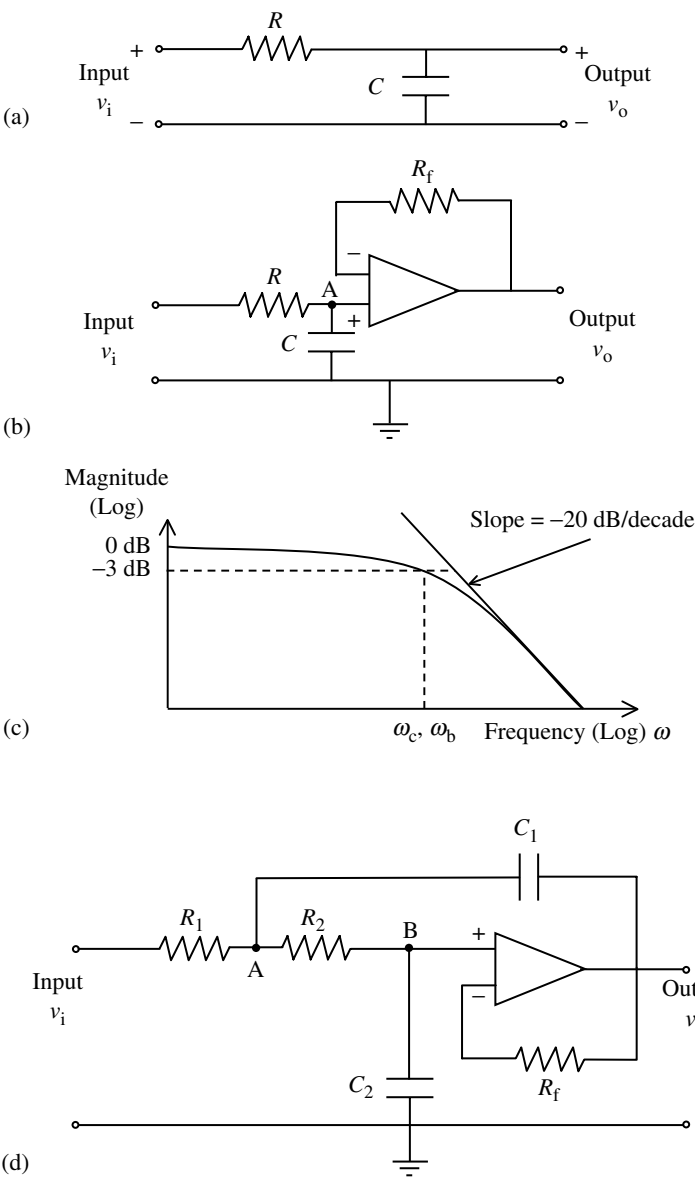


FIGURE 16.7 A single-pole low-pass filter: (a) a passive filter stage; (b) an active filter stage; (c) the frequency-response characteristic; (d) a two-pole, low-pass Butterworth filter.

The frequency-response function corresponding to Equation 16.19 is obtained by setting $s = j\omega$; thus

$$G(j\omega) = \frac{1}{(\tau j\omega + 1)} \tag{16.20}$$

This gives the response of the filter when a sinusoidal signal of frequency, ω , is applied. The magnitude $|G(j\omega)|$ of the frequency-transfer function gives the signal amplification and phase angle $\angle G(j\omega)$ gives the phase lead of the output signal with respect to the input. The magnitude curve (*Bode magnitude curve*) is shown in Figure 16.7(c). Note from Equation 16.20 that, for small frequencies (i.e., $\omega \ll 1/\tau$), the magnitude is approximately unity. Hence, $1/\tau$ can be considered the

cutoff frequency ω_c :

$$\omega_c = \frac{1}{\tau} \quad (16.21)$$

Example 16.3

Show that the cutoff frequency given by Equation 16.21 is also the *half-power bandwidth* for the low-pass filter. Show that, for frequencies much larger than this, the filter transfer function on the Bode magnitude plane (i.e., log magnitude vs. log frequency) can be approximated by a straight line with slope -20 dB/decade. This slope is known as the *roll-off rate*.

Solution

The frequency corresponding to half power (or $1/2$ magnitude) is given by

$$\frac{1}{|\tau j\omega + 1|} = \frac{1}{\sqrt{2}}$$

or

$$\frac{1}{\tau^2 \omega^2 + 1} = \frac{1}{2}$$

or

$$\tau^2 \omega^2 + 1 = 2$$

or

$$\tau^2 \omega^2 = 1$$

Hence, the half-power bandwidth is

$$\omega_b = \frac{1}{\tau} \quad (16.22)$$

This is identical to the cutoff frequency given by Equation 16.11.

Now, for $\omega \gg 1/\tau$ (i.e., $\tau\omega \gg 1$) Equation 16.20 can be approximated by

$$G(j\omega) = \frac{1}{\tau j\omega}$$

This has the magnitude

$$|G(j\omega)| = \frac{1}{\tau\omega}$$

In the log scale

$$\log_{10}|G(j\omega)| = -\log_{10} \omega - \log_{10} \tau$$

It follows that the \log_{10} (magnitude) vs. \log_{10} (frequency) curve is a straight line with slope -1 . In other words, when frequency increases by a factor of ten (i.e., a decade), the \log_{10} magnitude decreases by unity (i.e., by 20 dB). Hence, the roll-off rate is -20 dB/decade. These observations are shown in [Figure 16.7\(c\)](#). Note that an amplitude change by a factor of $\sqrt{2}$ (or power by a factor of 2) corresponds to 3 dB. Hence, when the DC (zero-frequency) magnitude is unity (0 dB), the half power magnitude is -3 dB.

Cutoff frequency and the roll-off rate are the two main design specifications for a low-pass filter. Ideally, we would like a low-pass filter magnitude curve to be flat until the required pass-band limit (cutoff frequency) and then roll off very rapidly. The low-pass filter shown in Figure 16.7 only

approximately meets these requirements. In particular, the roll-off rate is not as large as is desirable. We would like a roll-off rate of at least -40 dB/decade and, preferably, -60 dB/decade in practical filters.

This can be realized by using a higher order filter (i.e., a filter having many poles). The low-pass Butterworth filter is a widely used filter of this type.

16.3.2.1 Low-Pass Butterworth Filter

A low-pass Butterworth filter having two poles can provide a roll-off rate of -40 dB/decade, and one having three poles can provide a roll-off rate of -60 dB/decade. Furthermore, the steeper the slope of the roll-off, the flatter is the filter magnitude curve within the pass band.

A two-pole, low-pass Butterworth filter is shown in Figure 16.7(d). We could construct a two-pole filter simply by connecting two single-pole stages of the type shown in Figure 16.7(b). Then, we would require two opamps, whereas the circuit shown in Figure 16.7(d) achieves the same objective by using only one opamp (i.e., at a lower cost).

Example 16.4

Show that the opamp circuit in Figure 16.7(d) is a low-pass filter having two poles. What is the transfer function of the filter? Estimate the cutoff frequency under suitable conditions. Show that the roll-off rate is -40 dB/decade.

Solution

To obtain the filter equation, we write the current balance equations. Specifically, the sum of the currents through R_1 and C_1 passes through R_2 . The same current passes through C_2 because current through the opamp lead must be zero. Hence,

$$\frac{v_i - v_A}{R_1} + C_1 \frac{d}{dt}(v_o - v_A) = \frac{v_A - v_B}{R_2} = C_2 \frac{dv_B}{dt} \quad (i)$$

Also, since the opamp with a feedback resistor R_f is a voltage follower (with unity gain), we have

$$v_B = v_o \quad (ii)$$

From Equation i and Equation ii, we obtain

$$\frac{v_i - v_A}{R_1} + C_1 \frac{dv_o}{dt} - C_1 \frac{dv_A}{dt} = C_2 \frac{dv_o}{dt} \quad (iii)$$

$$\frac{v_A - v_o}{R_2} = C_2 \frac{dv_o}{dt} \quad (iv)$$

Now, defining the constants

$$\tau_1 = R_1 C_1 \quad (16.23)$$

$$\tau_2 = R_2 C_2 \quad (16.24)$$

$$\tau_3 = R_1 C_2 \quad (16.25)$$

and introducing the Laplace variable, s , we can eliminate v_A by substituting Equation iv into Equation iii; thus

$$\frac{v_o}{v_i} = \frac{1}{[\tau_1 \tau_2 s^2 + (\tau_2 + \tau_3)s + 1]} = \frac{\omega_n^2}{[s^2 + 2\zeta\omega_n^2 + \omega_n^2]} \quad (16.26)$$

This second-order transfer function becomes oscillatory if $(\tau_2 + \tau_3)^2 < 4\tau_1 \tau_2$. Ideally, we would like to have a zero resonant frequency, which corresponds to a damping ratio value $\zeta = 1/\sqrt{2}$. Since the undamped natural frequency is

$$\omega_n = \frac{1}{\sqrt{\tau_1 \tau_2}} \quad (16.27)$$

the damping ratio is

$$\zeta = \frac{\tau_2 + \tau_3}{\sqrt{4\tau_1\tau_2}} \quad (16.28)$$

and the resonant frequency is

$$\omega_r = \sqrt{1 - 2\zeta^2} \omega_n \quad (16.29)$$

we have, under ideal conditions (i.e., for $\omega_r = 0$),

$$(\tau_2 + \tau_3)^2 = 2\tau_1\tau_2 \quad (16.30)$$

The frequency-response function of the filter is (see Equation 16.26)

$$G(j\omega) = \frac{\omega_n^2}{[\omega_n^2 - \omega^2 + 2j\zeta\omega_n\omega]} \quad (16.31)$$

Now, for $\omega \ll \omega_n$, the filter frequency response is flat with a unity gain. For $\omega \gg \omega_n$, the filter frequency response can be approximated by

$$G(j\omega) = -\frac{\omega_n^2}{\omega^2}$$

In a log (magnitude) vs. log (frequency) scale, this function is a straight line with slope equals to -2 . Hence, when the frequency increases by a factor of ten (i.e., one decade), the \log_{10} (magnitude) drops by 2 units (i.e., 40 dB). In other words, the roll-off rate is -40 dB/decade. Also, ω_n can be taken as the filter cutoff frequency. Hence,

$$\omega_c = \frac{1}{\sqrt{\tau_1\tau_2}} \quad (16.32)$$

It can be easily verified that, when $\zeta = 1/\sqrt{2}$, the frequency is identical to the half-power bandwidth (i.e., the frequency at which the transfer function magnitude becomes $1/\sqrt{2}$).

Note that, if two single-pole stages (of the type shown in Figure 16.7(b)) are cascaded, the resulting two-pole filter has an overdamped (nonoscillatory) transfer function, and it is not possible to achieve $\zeta = 1/\sqrt{2}$, as in the present case. Also, note that a three-pole, low-pass Butterworth filter can be obtained by cascading the two-pole unit shown in Figure 16.7(d) with a single-pole unit as shown in Figure 16.7(b). Higher order low-pass Butterworth filters can be obtained in a similar manner by cascading an appropriate selection of basic units.

16.3.3 High-Pass Filters

Ideally, a high-pass filter allows through it all signal components above a certain (cutoff) frequency and blocks off all signal components below that frequency. A single-pole, high-pass filter is shown in Figure 16.8. As for the low-pass filter that was discussed earlier, the passive filter stage (Figure 16.8(a)) and the active filter stage (Figure 16.8(b)) have identical transfer functions. The active filter is desirable, however, because of its many advantages, including negligible loading error due to the high input impedance and low output impedance of the opamp voltage follower that is present in this circuit.

The filter equation is obtained by considering current balance in Figure 16.8(a), noting that the output is in open circuit (zero load current). Accordingly,

$$C \frac{d}{dt} (v_1 - v_o) = \frac{v_o}{R}$$

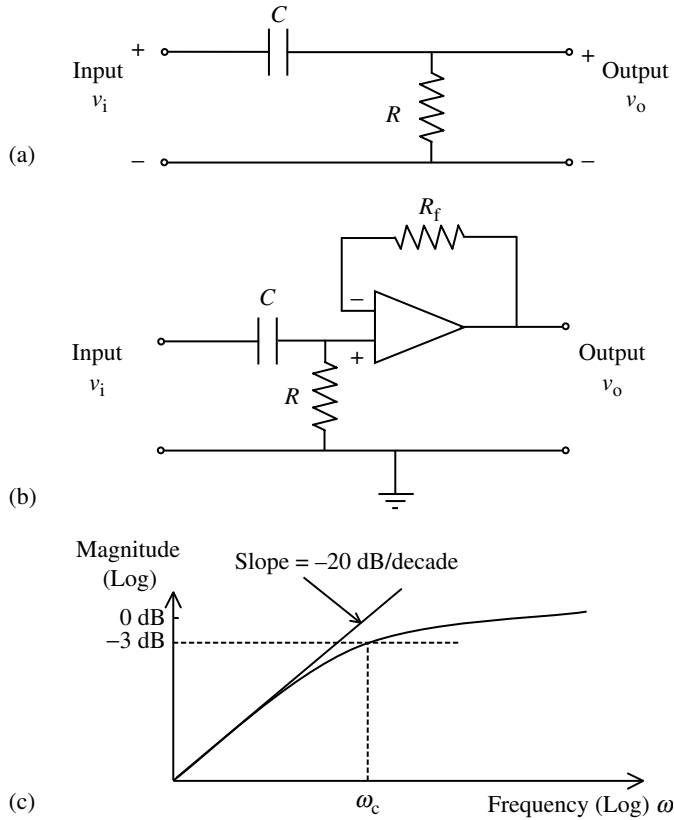


FIGURE 16.8 A single-pole high-pass filter: (a) a passive filter stage; (b) an active filter stage; (c) frequency-response characteristic.

or

$$\tau \frac{dv_o}{dt} + v_o = \tau \frac{dv_i}{dt} \quad (16.33)$$

in which the filter time constant is

$$\tau = RC \quad (16.34)$$

Introducing the Laplace variable, s , the filter transfer function is obtained as

$$\frac{v_o}{v_i} = G(s) = \frac{\tau s}{(\tau s + 1)} \quad (16.35)$$

Note that this corresponds to a *lead circuit* (i.e., an overall phase lead is provided by this transfer function). The frequency-response function is

$$G(j\omega) = \frac{\tau j\omega}{(\tau j\omega + 1)} \quad (16.36)$$

Since its magnitude is zero for $\omega \ll 1/\tau$ and is unity for $\omega \gg 1/\tau$, we have the cutoff frequency

$$\omega_c = \frac{1}{\tau} \quad (16.37)$$

Signals above this cutoff frequency are allowed undistorted by an ideal high-pass filter, and signals below the cutoff are completely blocked off. The actual behavior of the basic high-pass filter discussed

above is not perfect, as observed from the frequency-response characteristic shown in Figure 16.8(c). It can be easily verified that the half-power bandwidth of the basic high-pass filter is equal to the cutoff frequency given by Equation 16.37, as in the case of the basic low-pass filter. The roll-up slope of the single-pole high-pass filter is 20 dB/decade. Steeper slopes are desirable. Multiple-pole, high-pass Butterworth filters can be constructed to give steeper roll-up slopes and reasonably flat pass-band magnitude characteristics.

16.3.4 Band-Pass Filters

An ideal band-pass filter passes all signal components within a finite frequency band and blocks off all signal components outside that band. The lower frequency limit of the pass band is called the *lower cutoff frequency* (ω_{c1}), and the upper frequency limit of the band is called the *upper cutoff frequency* (ω_{c2}).

The most straightforward way to form a band-pass filter is to cascade a high-pass filter of cutoff frequency ω_{c1} with a low-pass filter of cutoff frequency ω_{c2} . Such an arrangement is shown in Figure 16.9. The passive circuit shown in Figure 16.9(a) is obtained by connecting the circuits shown in Figure 16.7(a) and Figure 16.8(a). The passive circuit shown in Figure 16.9(b) is obtained by connecting a voltage follower opamp circuit to the original passive circuit. Passive and active filters have the same transfer function, assuming that loading problems are not present in the passive filter. Since loading errors can be serious in practice, however, the active version is preferred.

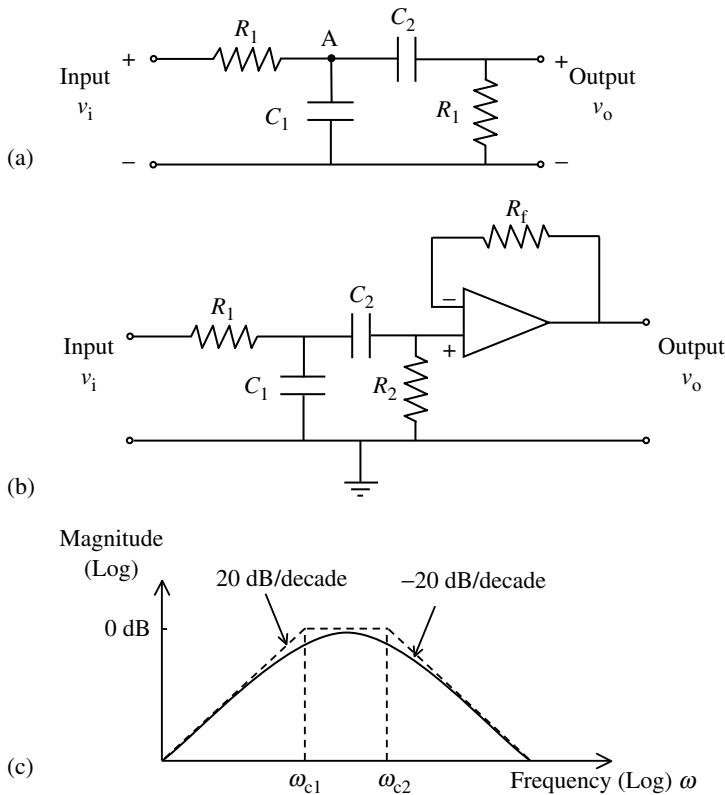


FIGURE 16.9 Band-pass filter: (a) a basic passive filter stage; (b) a basic active filter stage; (c) frequency-response characteristic.

To obtain the filter equation, first consider the high-pass portion of the circuit shown in Figure 16.9(a). Since the output is open circuit (zero current), we have from Equation 16.35:

$$\frac{v_o}{v_A} = \frac{\tau_2 s}{(\tau_2 s + 1)} \quad (i)$$

in which

$$\tau_2 = R_2 C_2 \quad (16.38)$$

Next, writing the current balance at node A of the circuit, we have

$$\frac{v_i - v_A}{R_1} = C_1 \frac{dv_A}{dt} + C_2 \frac{d}{dt}(v_A - v_o) \quad (ii)$$

Introducing the Laplace variable, s , we obtain

$$v_i = (\tau_1 s + \tau_3 s + 1)v_A - \tau_3 s v_o \quad (iii)$$

in which

$$\tau_1 = R_1 C_1 \quad (16.39)$$

and

$$\tau_3 = R_1 C_2 \quad (16.40)$$

Now, on eliminating v_A by substituting Equation i in Equation iii, we obtain the band-pass filter transfer function

$$\frac{v_o}{v_i} = G(s) = \frac{\tau_2 s}{[\tau_1 \tau_2 s^2 + (\tau_1 + \tau_2 + \tau_3)s + 1]} \quad (16.41)$$

We can show that the roots of the characteristic equation

$$\tau_1 \tau_2 s^2 + (\tau_1 + \tau_2 + \tau_3)s + 1 = 0 \quad (16.42)$$

are real and negative. The two roots are denoted by $-\omega_{c1}$ and $-\omega_{c2}$ and they provide the two cutoff frequencies shown in Figure 16.9(c). It can be verified that, for this basic band-pass filter, the roll-up slope is +20 dB/decade and the roll-down slope is -20 dB/decade. These slopes are not sufficient in many applications. Furthermore, the flatness of the frequency response within the pass band of the basic filter is not adequate either. More complex (higher order) band-pass filters with sharper cutoffs and flatter pass bands are commercially available.

16.3.4.1 Resonance-Type Band-Pass Filters

There are many applications where a filter with a very narrow pass band is required. The tracking filter mentioned in the beginning of the section on analog filters is one such application. A filter circuit with a sharp resonance can serve as a narrow-band filter. Note that the cascaded RC circuit shown in Figure 16.9 does not provide an oscillatory response (the filter poles are all real) and, hence, it does not form a resonance-type filter. A slight modification to this circuit using an additional resistor, R_1 , as shown in Figure 16.10(a), will produce the desired effect.

To obtain the filter equation, note that, for the voltage follower unit

$$v_A = v_o \quad (i)$$

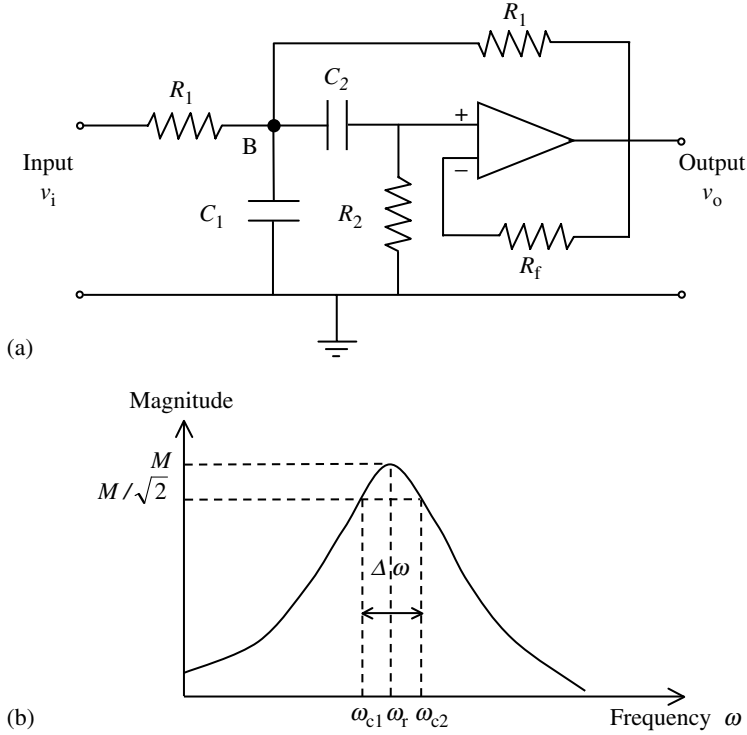


FIGURE 16.10 A resonance-type narrow-band-pass filter: (a) an active filter stage; (b) frequency-response characteristic.

Next, since current through an opamp lead is zero, for the high-pass circuit unit (see Equation 16.35), we have

$$\frac{v_A}{v_B} = \frac{\tau_2 s}{(\tau_2 s + 1)} \quad (\text{ii})$$

in which

$$\tau_2 = R_2 C_2$$

Finally, current balance at node B gives

$$\frac{v_i - v_B}{R_1} = C_1 \frac{dv_B}{dt} + C_2 \frac{d}{dt}(v_B - v_A) + \frac{v_B - v_o}{R_1}$$

or, by using the Laplace variable, we obtain

$$v_i = (\tau_1 s + \tau_3 s + 2)v_B - \tau_3 s v_A - v_o \quad (\text{iii})$$

Now, by eliminating v_A and v_B in the equations from Equation i to Equation iii, we obtain the filter transfer function

$$\frac{v_o}{v_i} = G(s) = \frac{\tau_2 s}{[\tau_1 \tau_2 s^2 + (\tau_1 + \tau_2 + \tau_3)s + 2]} \quad (16.43)$$

It can be shown that, unlike Equation 16.41, the present characteristic equation

$$\tau_1 \tau_2 s^2 + (\tau_1 + \tau_2 + \tau_3)s + 2 = 0 \quad (16.44)$$

can possess complex roots.

Example 16.5

Verify that the band-pass filter shown in Figure 16.10(a) can have a frequency response with a resonant peak as shown in Figure 16.10(b). Verify that the half-power bandwidth $\Delta\omega$ of the filter is given by $2\zeta\omega_r$ at low damping values. (Note: ζ = damping ratio and ω_r = resonant frequency.)

Solution

We may verify that the transfer function given by Equation 16.43 can have a resonant peak by showing that the characteristic equation (Equation 16.44) can have complex roots. For example, if we use parameter values $C_1 = 2$, $C_2 = 1$, $R_1 = 1$, and $R_2 = 2$, we have $\tau_1 = 2$, $\tau_2 = 2$, and $\tau_3 = 1$. The corresponding characteristic equation is

$$4s^2 + 5s + 2 = 0$$

It has the roots

$$-\frac{5}{8} \pm j\frac{\sqrt{7}}{8}$$

is obviously complex.

To obtain an expression for the half-power bandwidth of the filter, note that the filter transfer function may be written as

$$G(s) = \frac{ks}{(s^2 + 2\zeta\omega_n s + \omega_n^2)} \quad (16.45)$$

in which

ω_n = undamped natural frequency

ζ = damping ratio

k = a gain parameter

The frequency-response function is given by

$$G(j\omega) = \frac{kj\omega}{[\omega_n^2 - \omega^2 + 2j\zeta\omega_n\omega]} \quad (16.46)$$

For low damping, resonant frequency $\omega_r \cong \omega_n$. The corresponding peak magnitude M is obtained by substituting $\omega = \omega_n$ in Equation 16.46 and taking the transfer function magnitude; thus

$$M = \frac{k}{2\zeta\omega_n} \quad (16.47)$$

At half-power frequencies, we have

$$|G(j\omega)| = \frac{M}{\sqrt{2}}$$

or

$$\frac{k\omega}{\sqrt{(\omega_n^2 - \omega^2)^2 + 4\zeta^2\omega_n^2\omega^2}} = \frac{k}{2\sqrt{2}\zeta\omega_n}$$

This gives

$$(\omega_n^2 - \omega^2)^2 = 4\zeta^2 \omega_n^2 \omega^2 \quad (16.48)$$

the positive roots of which provide the pass band frequencies ω_{c1} and ω_{c2} . Note that the roots are given by

$$\omega_n^2 - \omega^2 = \pm 2\zeta \omega_n \omega$$

Hence, the two roots, ω_{c1} and ω_{c2} , satisfy the following two equations:

$$\omega_{c1}^2 + 2\zeta \omega_n \omega_{c1} - \omega_n^2 = 0$$

$$\omega_{c2}^2 - 2\zeta \omega_n \omega_{c2} - \omega_n^2 = 0$$

Accordingly, by solving these two quadratic equations and selecting the appropriate sign, we obtain

$$\omega_{c1} = -\zeta \omega_n + \sqrt{\omega_n^2 + \zeta^2 \omega_n^2} \quad (16.49)$$

$$\omega_{c2} = \zeta \omega_n + \sqrt{\omega_n^2 + \zeta^2 \omega_n^2} \quad (16.50)$$

The half-power bandwidth is

$$\Delta\omega = \omega_{c2} - \omega_{c1} = 2\zeta \omega_n \quad (16.51)$$

Now, since $\omega_n \cong \omega_r$, for low ζ we have

$$\Delta\omega = 2\zeta \omega_r \quad (16.52)$$

A notable shortcoming of a resonance-type filter is that the frequency response within the bandwidth (pass band) is not flat. Hence, quite nonuniform signal attenuation takes place inside the pass band.

16.3.5 Band-Reject Filters

Band-reject filters, or *notch filters*, are commonly used to filter out a narrow band of noise components from a signal. For example, 60 Hz line noise in signals can be eliminated by using a notch filter with a notch frequency of 60 Hz.

An active circuit that could serve as a notch filter is shown in [Figure 16.11\(a\)](#). This is known as the Twin T circuit because its geometric configuration resembles two T-shaped circuits connected together. To obtain the filter equation, note that the voltage at point P is v_o because of unity gain of the voltage follower. Now, we write the current balance at nodes A and B; thus

$$\begin{aligned} \frac{v_i - v_B}{R} &= 2C \frac{dv_B}{dt} + \frac{v_B - v_o}{R} \\ C \frac{d}{dt}(v_i - v_A) &= \frac{v_A}{R/2} + C \frac{d}{dt}(v_A - v_o) \end{aligned}$$

Next, since the current through the positive lead of the opamp (voltage follower) is zero, we have the current through point P as

$$\frac{v_B - v_o}{R} = C \frac{d}{dt}(v_o - v_A)$$

These three equations are written in the Laplace form as

$$v_i = 2(\tau s + 1)v_B - v_o \quad (i)$$

$$\tau s v_i = 2(\tau s + 1)v_A - \tau s v_o \quad (ii)$$

$$v_B = (\tau s + 1)v_o - \tau s v_A \quad (iii)$$

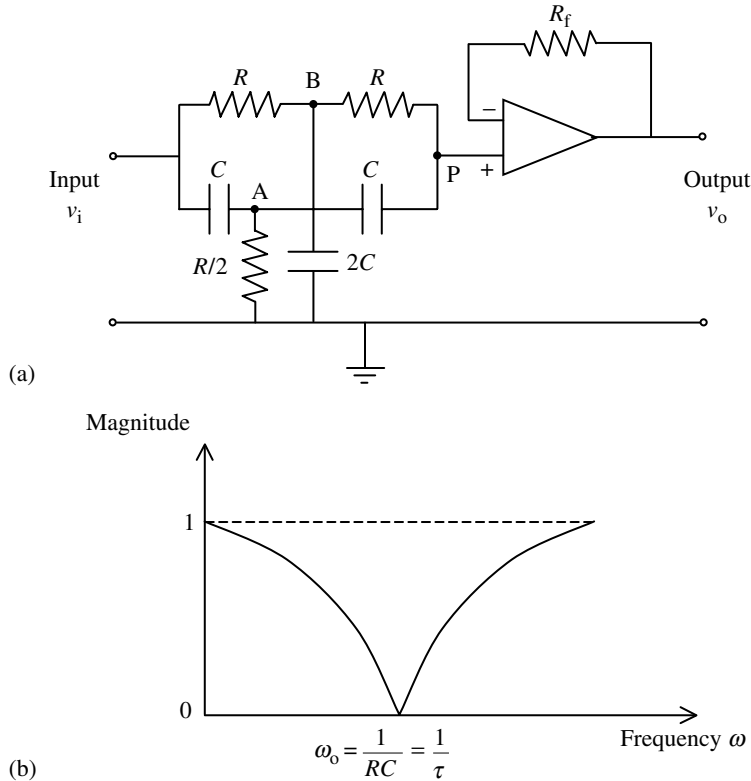


FIGURE 16.11 A notch filter: (a) an active Twin T filter circuit; (b) frequency-response characteristic.

in which

$$\tau = RC \quad (16.53)$$

Finally, eliminating v_A and v_B in Equation i to Equation iii, we obtain

$$\frac{v_o}{v_i} = G(s) = \frac{(\tau^2 s^2 + 1)}{(\tau^2 s^2 + 4\tau s + 1)} \quad (16.54)$$

The frequency-response function of the filter is

$$G(j\omega) = \frac{(1 - \tau^2 \omega^2)}{(1 - \tau^2 \omega^2 + 4j\tau\omega)} \quad (16.55)$$

with $s = j\omega$. Note that the magnitude of this function becomes zero at frequency

$$\omega_o = \frac{1}{\tau} \quad (16.56)$$

This is known as the notch frequency. The magnitude of the frequency-response function of the notch filter is sketched in Figure 16.11(b). It is noticed that any signal component at frequency ω_o will be completely eliminated by the notch filter. Sharp roll-down and roll-up are needed to allow the other (desirable) signal components through without too much attenuation.

Whereas the previous three types of filters achieve their frequency-response characteristics through the poles of the filter transfer function, a notch filter achieves its frequency-response characteristic through its zeros (roots of the numerator polynomial equation). Some useful information about filters is summarized in Box 16.2.

Box 16.2

FILTERS

Active Filters (Need External Power)**Advantages:**

- Smaller loading errors (have high input impedance and low output impedance, and hence do not affect the input circuit conditions and output signals)
- Lower cost
- Better accuracy

Passive Filters (No External Power, Use Passive Elements)**Advantages:**

- Useable at very high frequencies (e.g., radio frequency)
- No need for a power supply

Filter Types

- Low pass: Allows frequency components up to cutoff and rejects the higher frequency components
- High pass: Rejects frequency components up to cutoff and allows the higher frequency components
- Band pass: Allows frequency components within an interval and rejects the rest
- Notch (or band reject): Rejects frequency components within an interval (usually narrow) and allows the rest

Definitions

- Filter order: Number of poles in the filter circuit or transfer function
- Antialiasing filter: Low-pass filter with cutoff at less than half the sampling rate (i.e., Nyquist frequency), for digital processing
- Butterworth filter: A high-order filter with a very flat pass band
- Chebyshev filter: An optimal filter with uniform ripples in the pass band
- Sallen-Key filter: An active filter whose output is in phase with input

16.4 Modulators and Demodulators

Sometimes signals are deliberately modified to maintain the accuracy during signal transmission, conditioning, and processing. In signal *modulation*, the data signal, known as the *modulating signal*, is used to vary a property (such as amplitude or frequency) of a *carrier signal*. We say that the carrier signal is modulated by the data signal. After transmitting or conditioning the modulated signal, the data signal is usually recovered by removing the carrier signal. This is known as *demodulation* or *discrimination*.

Many modulation techniques exist, and several other types of signal modification (e.g., digitizing) could be classified as signal modulation even though they might not be commonly termed as such. Four types of modulation are illustrated in [Figure 16.12](#). In *amplitude modulation* (AM), the amplitude of a periodic carrier signal is varied according to the amplitude of the data signal (modulating signal), frequency of the carrier signal (*carrier frequency*) being kept constant. Suppose that the transient signal

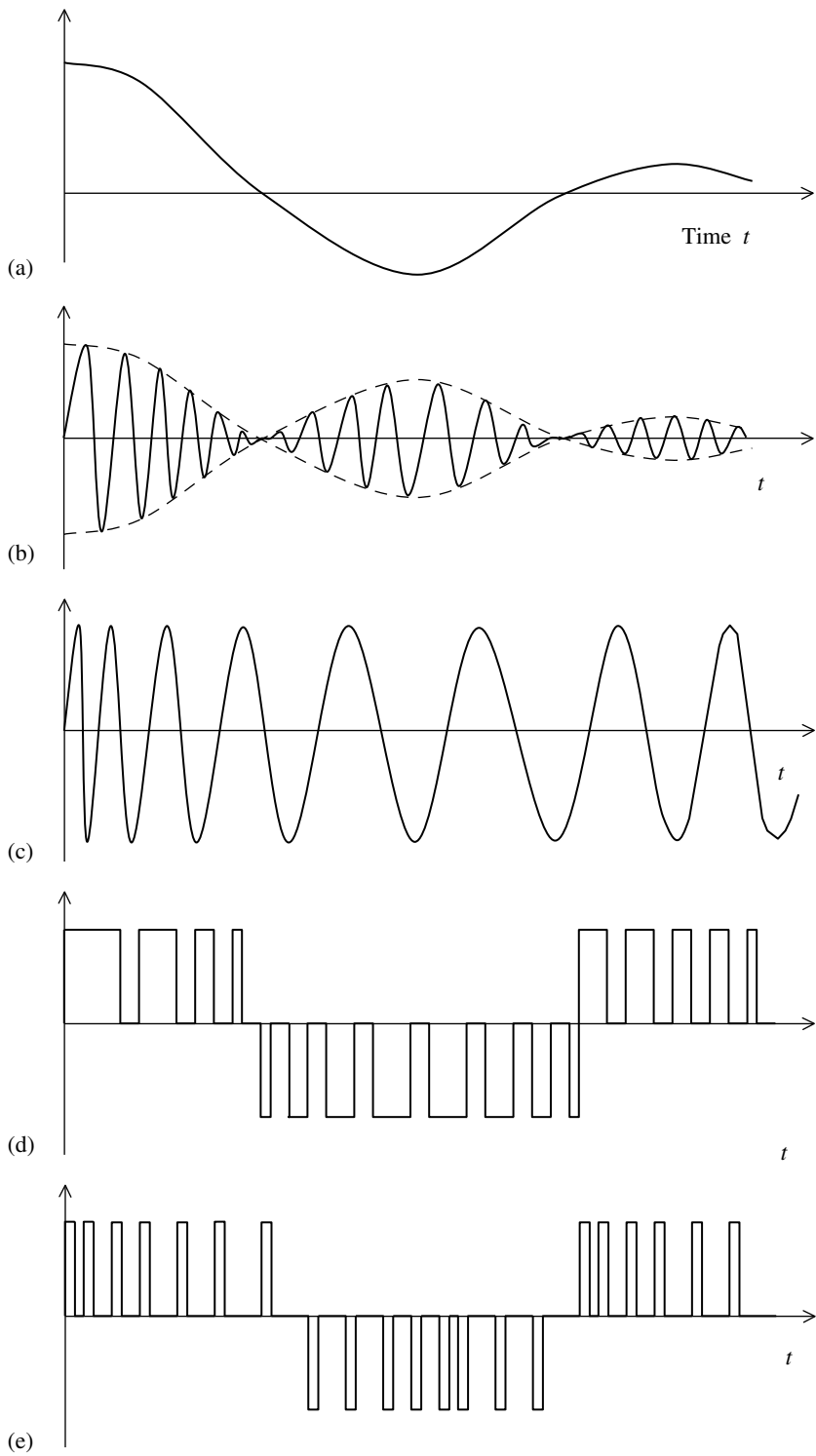


FIGURE 16.12 (a) Modulating signal (data signal); (b) amplitude-modulated (AM) signal; (c) frequency-modulated (FM) signal; (d) pulse-width-modulated (PWM) signal; (e) pulse-frequency-modulated (PFM) signal.

shown in Figure 16.12(a) is used as the modulating signal. A high-frequency sinusoidal signal is used as the carrier signal. The resulting amplitude-modulated signal is shown in Figure 16.12(b). Amplitude modulation is used in telecommunications, radio and TV signal transmission, instrumentation, and signal conditioning. The underlying principle is useful in other applications such as fault detection and diagnosis in rotating machinery.

In *frequency modulation* (FM), the frequency of the carrier signal is varied in proportion to the amplitude of the data signal (modulating signal), while the amplitude of the carrier signal is kept constant. If the data signal shown in Figure 16.12(a) is used to frequency modulate a sinusoidal carrier signal, then the result will appear as shown in Figure 16.12(c). Since information is carried as frequency rather than amplitude, any noise that might alter the signal amplitude will have virtually no effect on the transmitted data. Hence, FM is less susceptible to noise than AM. Furthermore, since the carrier amplitude is kept constant in FM, signal weakening and noise effects that are unavoidable in long-distance data communication will have less effect than in the case of AM, particularly if the data signal level is low in the beginning. However, more sophisticated techniques and hardware are needed for signal recovery (demodulation) in FM transmission, because FM demodulation involves frequency discrimination rather than amplitude detection. Frequency modulation is also widely used in radio transmission and in data recording and replay.

In *pulse-width modulation* (PWM), the carrier signal is a pulse sequence. The pulse width is changed in proportion to the amplitude of the data signal, while keeping the pulse spacing constant. This is illustrated in Figure 16.12(d). Pulse-width modulated signals are extensively used in controlling electric motors and other mechanical devices such as valves (hydraulic, pneumatic) and machine tools. Note that, in a given short time interval, the average value of the pulse-width modulated signal is an estimate of the average value of the data signal in that period. Hence, PWM signals can be used directly in controlling a process without one having to demodulate it. Advantages of PWM include better energy efficiency (less dissipation) and better performance with nonlinear devices. For example, a device may stick at low speeds due to Coulomb friction. This can be avoided by using a PWM signal that provides the signal amplitude that is necessary to overcome friction while maintaining the required average control signal, which might be very small.

In *pulse-frequency modulation* (PFM) as well, the carrier signal is a pulse sequence. In this method, the frequency of the pulses is changed in proportion to the data signal level, while the pulse width is kept constant. PFM has the advantage of ordinary frequency modulation. Additional advantages result due to the fact that electronic circuits (digital circuits, in particular) can handle pulses very efficiently. Furthermore, pulse detection is not susceptible to noise because it involves distinguishing between the presence and absence of a pulse rather than accurate determination of the pulse amplitude (or width). PFM may be used in place of PWM in most applications with better results.

Another type of modulation is *phase modulation* (PM). In this method, the phase angle of the carrier signal is varied in proportion to the amplitude of the data signal.

Conversion of discrete (sampled) data into the digital (binary) form is also considered to be modulation. In fact, this is termed *pulse-code modulation* (PCM). In this case, each discrete data sample is represented by a binary number containing a fixed number of binary digits (bits). Since each digit in the binary number can take only two values, 0 or 1, it can be represented by the absence or presence of a voltage pulse. Hence, each data sample can be transmitted using a set of pulses. This is known as *encoding*. At the receiver, the pulses have to be interpreted (or decoded) in order to determine the data value. As with any other pulse technique, PCM is quite immune to noise because decoding involves detection of the presence or absence of a pulse rather than determination of the exact magnitude of the pulse signal level. Also, since pulse amplitude is constant, long-distance signal transmission (of this digital data) can be accomplished without the danger of signal weakening and associated distortion. Of course, there will be some error introduced by the digitization process itself, which is governed by the finite word size (or dynamic range) of the binary data element. This is known as quantization error and is unavoidable in signal digitization.

In any type of signal modulation, it is essential to preserve the algebraic sign of the modulating signal (data). Different types of modulators handle this in different ways. For example, in PCM an extra *sign bit* is added to represent the sign of the transmitted data sample. In AM and FM, a *phase-sensitive demodulator* is used to extract the original (modulating) signal with the correct algebraic sign. Note that, in these two modulation techniques, a sign change in the modulating signal can be represented by a 180° phase change in the modulated signal. This is not noticeable in Figure 16.12(b) and (c). In PWM and PFM, a sign change in the modulating signal can be represented by changing the sign of the pulses, as shown in Figure 16.12(d) and (e). In PM, a positive range of phase angles (say 0 to π) can be assigned for the positive values of the data signal and a negative range of phase angles (say $-\pi$ to 0) can be assigned for the negative values of the signal.

16.4.1 Amplitude Modulation

Amplitude modulation can naturally enter into many physical phenomena. More important, perhaps, is the deliberate (artificial) use of AM to facilitate data transmission and signal conditioning. Let us first examine the related mathematics.

Amplitude modulation is achieved by multiplying the data signal (modulating signal), $x(t)$, by a high frequency (periodic) carrier signal, $x_c(t)$. Hence, amplitude-modulated signal, $x_a(t)$, is given by

$$x_a(t) = x(t)x_c(t) \quad (16.57)$$

Note that the carrier could be any periodic signal such as one which is harmonic (sinusoidal), square wave, or triangular. The main requirement is that the fundamental frequency of the carrier signal (*carrier frequency*), f_c , be significantly larger (say, by a factor of five or ten) than the highest frequency of interest (*bandwidth*) of the data signal. Analysis can be simplified by assuming a sinusoidal carrier frequency; thus

$$x_c(t) = a_c \cos 2\pi f_c t \quad (16.58)$$

16.4.1.1 Modulation Theorem

Modulation theorem is also known as the *frequency-shifting theorem*, and it relates the fact that if a signal is multiplied by a sinusoidal signal, the Fourier spectrum of the product signal is simply the Fourier spectrum of the original signal shifted through the frequency of the sinusoidal signal. In other words, the Fourier spectrum, $X_a(f)$, of the amplitude-modulated signal, $x_a(t)$, can be obtained from the Fourier spectrum, $X(f)$, of the data signal, $x(t)$, simply by shifting through the carrier frequency, f_c .

To mathematically explain the modulation theorem, we use the definition of the Fourier integral transform to obtain

$$X_a(f) = a_c \int_{-\infty}^{\infty} x(t) \cos 2\pi f_c t \exp(-j2\pi ft) dt$$

However, since

$$\cos 2\pi f_c t = \frac{1}{2} [\exp(j2\pi f_c t) + \exp(-j2\pi f_c t)]$$

we have

$$\begin{aligned} X_a(f) &= \frac{1}{2} a_c \int_{-\infty}^{\infty} x(t) \exp[-j2\pi(f - f_c)t] dt + \frac{1}{2} a_c \int_{-\infty}^{\infty} x(t) \exp[-j2\pi(f + f_c)t] dt \\ X_a(f) &= \frac{1}{2} a_c [X(f - f_c) + X(f + f_c)] \end{aligned} \quad (16.59)$$

Equation 16.59 is the mathematical statement of the modulation theorem. It is illustrated by an example in Figure 16.13. Consider a transient signal, $x(t)$, with a (continuous) Fourier spectrum, $X(f)$, whose magnitude, $|X(f)|$, is as shown in Figure 16.13(a). If this signal is used to modulate the AM of a high-frequency sinusoidal signal, the resulting modulated signal, $x_a(t)$, and the magnitude of its

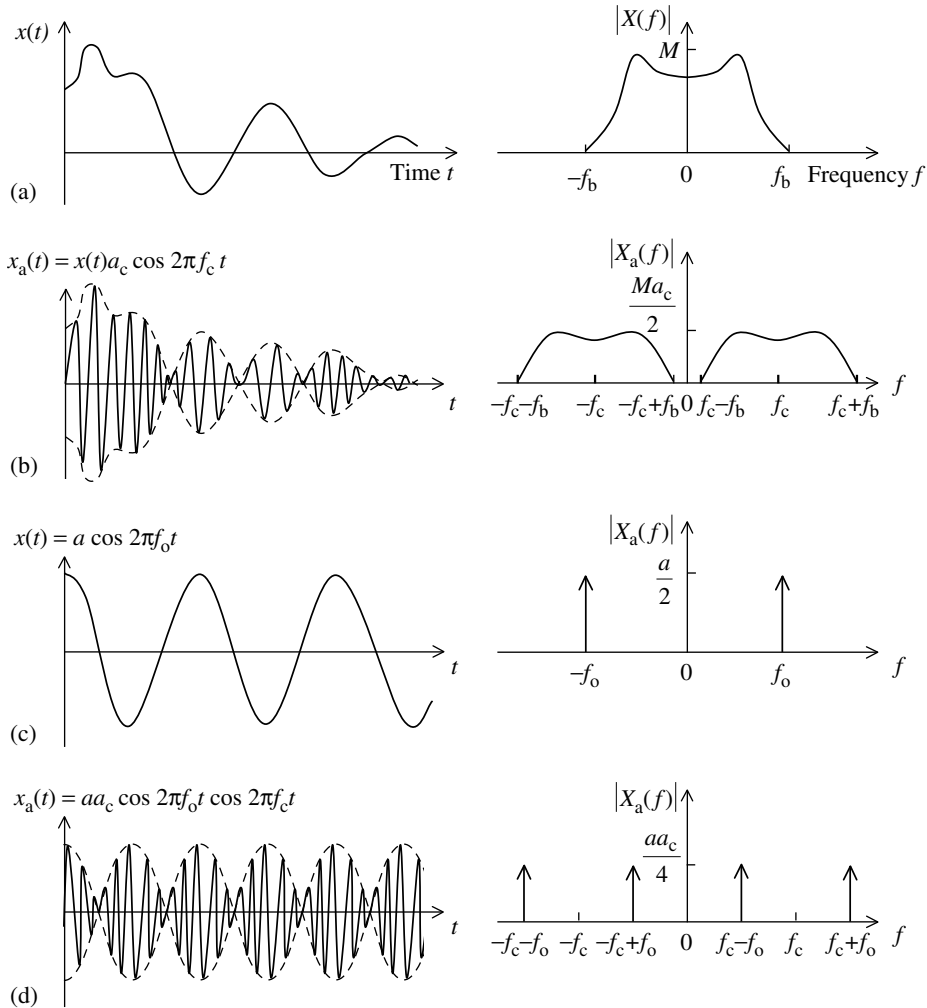


FIGURE 16.13 Illustration of the modulation theorem: (a) a transient data signal and its Fourier spectrum magnitude; (b) amplitude-modulated signal and its Fourier spectrum magnitude; (c) a sinusoidal data signal; (d) amplitude modulation by a sinusoidal signal.

Fourier spectrum are as shown in Figure 16.13(b). It should be kept in mind that the magnitude has been multiplied by $a_c/2$. Note that the data signal is assumed to be *band limited*, with bandwidth f_b . Of course, the theorem is not limited to band-limited signals but, for practical reasons, we need to have some upper limit on the useful frequency of the data signal. Also for practical reasons (not for the theorem itself), the carrier frequency, f_c , should be several times larger than f_b so that there is a reasonably wide frequency band from 0 to $(f_c - f_b)$, within which the magnitude of the modulated signal is virtually zero. The significance of this should be clear when we discuss applications of amplitude modulation.

Figure 16.13 shows only the magnitude of the frequency spectra. It should be remembered, however, that every Fourier spectrum has a phase angle spectrum as well. This is not shown for conciseness, but clearly the phase-angle spectrum is also similarly affected (frequency shifted) by AM.

16.4.1.2 Side Frequencies and Side Bands

The modulation theorem, as described above, assumed transient data signals with associated continuous Fourier spectra. The same ideas are applicable to periodic signals (with discrete spectra) as well. The case

of periodic signals is merely a special case of what was discussed above. This case can be analyzed by using Fourier integral transform itself, from the beginning. If this method is chosen, however, we will have to cope with impulsive spectral lines. Alternatively, Fourier series expansion could be employed to avoid the introduction of impulsive discrete spectra into the analysis. However, as shown in Figure 16.13(c) and (d), no analysis is actually needed for the periodic signal case because a final answer can be deduced from the transient signal results. Specifically, each frequency component, f_o , that has amplitude $a/2$ in the Fourier series expansion of the data signal will be shifted by $\pm f_c$ to the two new frequency locations $f_c + f_o$ and $-f_c + f_o$ with an associated amplitude $aa_c/4$. The negative frequency component $-f_o$ should also be considered in the same way, as illustrated in Figure 16.13(d). Note that the modulated signal does not have a spectral component at carrier frequency, f_c , but rather on each side of it, at $f_c \pm f_o$. Hence, these spectral components are termed side frequencies. When a band of *side frequencies* is present, we have a *side band*. Side frequencies are very useful in fault detection and diagnosis of rotating machinery.

16.4.2 Application of Amplitude Modulation

The main hardware component of an amplitude modulator is an *analog multiplier*. They are commercially available in the monolithic IC form, or one can be assembled using IC opamps and other discrete circuit elements. A schematic representation of an amplitude modulator is shown in Figure 16.14. In practice, to achieve satisfactory modulation, other components such as signal preamplifiers and filters are needed.

There are many applications of AM. In some applications, modulation is performed intentionally. In others, modulation occurs naturally as a consequence of the physical process, and the resulting signal is used to meet a practical objective. Typical applications of AM include the following:

1. Conditioning of general signals (including DC, transient, and low-frequency) by exploiting the advantages of AC signal conditioning hardware
2. Improvement of the immunity of low-frequency signals to low-frequency noise
3. Transmission of general signals (DC, low-frequency, etc.) by exploiting the advantages of AC signals
4. Transmission of low-level signals under noisy conditions
5. Transmission of several signals simultaneously through the same medium (e.g., same telephone line, same transmission antenna, etc.)
6. Fault detection and diagnosis of rotating machinery

The role of AM in many of these applications should be obvious if one understands the frequency-shifting property of AM. Several other types of application are also feasible due to the fact that the power of the carrier signal can be increased somewhat arbitrarily, irrespective of the power level of the data (modulating) signal. Let us discuss, one by one, the six categories of application mentioned above.

AC signal conditioning devices such as AC amplifiers are known to be more “stable” than their DC counterparts. In particular, *drift* problems are not as severe and nonlinearity effects are lower in AC signal conditioning devices. Hence, instead of conditioning a DC signal using DC hardware, we can first use the

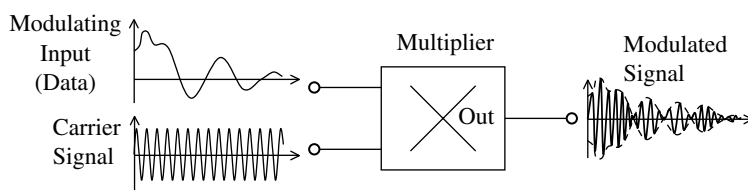


FIGURE 16.14 Representation of an amplitude modulator.

signal to modulate a high-frequency carrier signal. Then, the resulting high-frequency modulated signal may be conditioned more effectively using AC hardware.

The frequency-shifting property of AM can be exploited in making low-frequency signals immune to low-frequency noise. Note from Figure 16.13 that, by AM, low-frequency spectrum of the modulating signal can be shifted into a very high-frequency region by choosing a sufficiently large carrier frequency, f_c . Then, any low-frequency noise (within the band 0 to $f_c - f_b$) will not distort the spectrum of the modulated signal. Hence, this noise can be removed by a high-pass filter (with cutoff at $f_c - f_b$) without affecting the data. Finally, the original data signal can be recovered by demodulation. Note that the frequency of a noise component can be within the bandwidth, f_b , of the data signal and, hence, if AM is not employed, noise can directly distort the data signal.

Transmission of AC signals is more efficient than that of DC signals. Advantages of AC transmission include lower problems with energy dissipation. Hence, a modulated signal can be transmitted over long distances more effectively than could the original data signal alone. Furthermore, transmission of low-frequency (large wave-length) signals requires large antennas. Hence, when AM is employed (with an associated reduction in signal wave length), the size of broadcast antenna can be effectively reduced.

Transmission of weak signals over long distances is not desirable because signal weakening and corruption by noise could produce disastrous results. By increasing the power of the carrier signal to a sufficiently high level, the strength of the modulated signal can be elevated to an adequate level for long-distance transmission.

It is impossible to transmit two or more signals in the same frequency range simultaneously using a single telephone line. This problem can be resolved by using carrier signals with significantly different carrier frequencies to modulate the amplitude of the data signals. By choosing carrier frequencies that are sufficiently farther apart, the spectra of the modulated signals can be made nonoverlapping, thereby making simultaneous transmission possible. Similarly, with AM, simultaneous broadcasting by several radio (AM) broadcast stations in the same broadcast area has become possible.

16.4.2.1 Fault Detection and Diagnosis

A use of the AM principle that is particularly important in the practice of mechanical vibration is in the fault detection and diagnosis of rotating machinery. In this method, modulation is not deliberately introduced, but rather results from the dynamics of the machine. Flaws and faults in a rotating machine are known to produce periodic forcing signals at frequencies higher than, and typically at an integer multiple of, the rotating speed of the machine. For example, backlash in a gear pair will generate forces at the tooth-meshing frequency (equal to the number of teeth \times gear rotating speed). Flaws in roller bearings can generate forcing signals at frequencies proportional to the rotating speed times the number of rollers in the bearing race. Similarly, blade passing in turbines and compressors and eccentricity and unbalance in rotors can produce forcing components at frequencies that are integer multiples of the rotating speed. The resulting vibration response will be an amplitude-modulated signal, where the rotating response of the machine modulates the high-frequency forcing response. This can be confirmed experimentally by Fourier analysis (fast Fourier transform or FFT) of the resulting vibration signals. For a gear box, for example, it will be noticed that, instead of obtaining a spectral peak at the gear tooth-meshing frequency, two side bands are produced around that frequency. Faults can be detected by monitoring the evolution of these side bands. Furthermore, since side bands are the result of modulation of a specific forcing phenomenon (e.g., gear-tooth meshing, bearing-roller hammer, turbine-blade passing, imbalance, eccentricity, misalignment, etc.), one can trace the source of a particular fault (i.e., diagnose the fault) by studying the Fourier spectrum of the measured vibrations.

Amplitude modulation is an integral part of many types of sensors. In these sensors, a high-frequency carrier signal (typically the AC excitation in a primary winding) is modulated by the motion. Actual motion can be detected by demodulation of the output. Examples of sensors that generate modulated outputs are differential transformers (LVDT, RVDT), magnetic-induction proximity sensors, eddy-current proximity sensors, AC tachometers, and strain-gage devices that use AC bridge circuits.

Signal conditioning and transmission is facilitated by AM in these cases. However, the signal has to be demodulated at the end for most practical purposes such as analysis and recording.

16.4.3 Demodulation

Demodulation, or discrimination or detection, is the process of extracting the original data signal from a modulated signal. In general, demodulation must be phase sensitive in the sense that the algebraic sign of the data signal should be preserved and determined by the demodulation process. In *full-wave demodulation*, an output is generated continuously. In *half-wave demodulation*, no output is generated for every alternate half-period of the carrier signal.

A simple and straightforward method of demodulation is by the detection of the envelope of the modulated signal. For this method to be feasible, the carrier signal must be quite powerful (i.e., the signal level has to be high) and the carrier frequency also should be very high. An alternative method of demodulation that generally provides more reliable results involves the further step of modulation performed on the already-modulated signal, followed by low-pass filtering. This method will be explained by referring to Figure 16.13.

Consider the amplitude-modulated signal, $x_a(t)$, shown in Figure 16.13(b). If this signal is multiplied by the sinusoidal carrier signal, $2/a_c \cos 2\pi f_c t$, we obtain

$$\tilde{x}(t) = \frac{2}{a_c} x_a(t) \cos 2\pi f_c t \quad (16.60)$$

Now, by applying the modulation theorem (Equation 16.59) to Equation 16.60, we obtain the Fourier spectrum of $\tilde{x}(t)$ as

$$\tilde{X}(f) = \frac{1}{2} \frac{2}{a_c} \left[\frac{1}{2} a_c \{X(f - 2f_c) + X(f)\} + \frac{1}{2} a_c \{X(f) + X(f + 2f_c)\} \right]$$

or

$$\tilde{X}(f) = X(f) + \frac{1}{2} X(f - 2f_c) + \frac{1}{2} X(f + 2f_c) \quad (16.61)$$

The magnitude of this spectrum is shown in Figure 16.15(a). Note that we have recovered the spectrum, $X(f)$, of the original data signal, except for the two side bands that are present at locations far removed (centered at $\pm 2f_c$) from the bandwidth of the original signal. Hence, we can easily use a low-pass filter on this signal, $\tilde{x}(t)$, using a filter with cutoff at f_b to recover the original data signal. A schematic representation of this method of amplitude demodulation is shown in Figure 16.15(b).

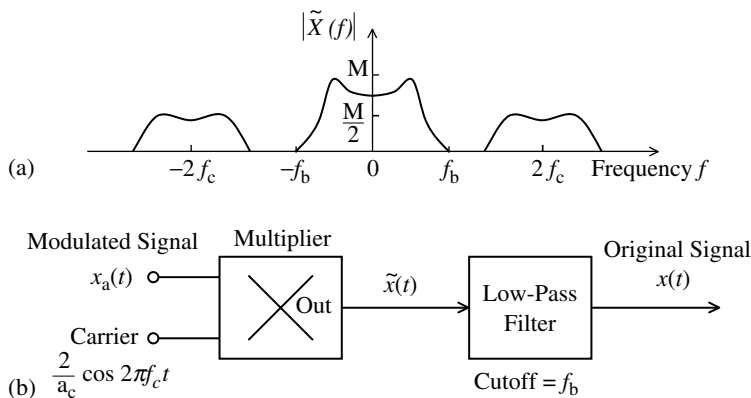


FIGURE 16.15 Amplitude demodulation: (a) spectrum of the signal after the second modulation; (b) demodulation schematic diagram (modulation + filtering).

16.5 Analog–Digital Conversion

Data-acquisition systems in machine condition monitoring, fault detection and diagnosis, and vibration testing employ digital computers for various tasks including signal processing, data analysis and reduction, parameter identification, and decision making. Typically, the measured response (output) of a dynamic system is available in the analog form as a continuous signal (function of continuous time). Furthermore, typically, the excitation signals (inputs) for a dynamic system have to be provided in the analog form.

Inputs to a digital device, say from a digital computer, and outputs from a digital device are necessarily present in the digital form. Hence, when a digital device is interfaced with an analog device, the interface hardware and associated driver software must perform several important functions. Two of the most important interface functions are *digital-to-analog conversion* (DAC) and *analog-to-digital conversion* (ADC). A digital output from a digital device has to be converted into the analog form for it to be fed into an analog device such as actuator or analog recording or display unit. Also, an analog signal has to be converted into the digital form according to an appropriate code before it is read by a digital processor or computer. Digital-to-analog converters are simpler and lower in cost than analog-to-digital converters. Furthermore, some types of analog-to-digital converters employ a digital-to-analog converter to perform their function. For these reasons, we will first discuss DAC.

16.5.1 Digital-to-Analog Conversion

The function of a DAC is to convert a sequence of digital words stored in a data register (called a DAC register), typically in straight binary form, into an analog signal. The data in the DAC register may come from a data bus of a computer. Each binary digit (bit) of information in the register may be present as a state of a *bistable* (two-stage) logic device, which can generate a voltage pulse or a voltage level to represent that bit. For example, the *off* state of a bistable logic element, the absence of a voltage pulse, a low level of a voltage signal, or no change in a voltage level can represent binary 0. Then, the *on* state of a bistable device, the *presence* of a voltage pulse, a *high level* of a voltage signal, or a *change* in a voltage level will represent binary 1. The combination of these bits, which form the digital word in the DAC register, will correspond to some numerical value for the output signal. The purpose of DAC is to generate an output voltage (signal level) that has this numerical value and maintain the value until the next digital word is converted. Since a voltage output cannot be arbitrarily large or small, for practical reasons, some form of scaling will have to be employed in the DAC process. This scale will depend on the reference voltage, v_{ref} , used in the particular DAC circuit.

A typical DAC unit is an active circuit in the IC form, which may consist of a data register (digital circuits), solid-state switching circuits, resistors, and operational amplifiers powered by an external power supply that can provide a reference voltage. The reference voltage will determine the maximum value of the output (*full-scale voltage*). An IC chip that represents the DAC is usually one of many components mounted on a *printed circuit* (PC) board. This PC board may be identified by several names including input/output (I/O) board, I/O card, interface board, and data acquisition and control board. Typically, the same board will provide both DAC and ADC capabilities for many output and input channels.

There are many types and forms of DAC circuits. The form will depend mainly on the manufacturer, the requirements of the user, or of the particular application. Most DACs are variations of two basic types: the *weighted* (or *summer* or *adder*) type and the *ladder* type. The latter type of DAC is more desirable, though the former can be somewhat simpler and less expensive.

16.5.1.1 DAC Error Sources

For a given digital word, the analog output voltage from a DAC is not exactly equal to what is given by the analytical formulas. The difference between the actual output and the ideal output is the error. The DAC error can be normalized with respect to the full-scale value.

There are many causes of DAC error. Typical error sources include parametric uncertainties and variations, circuit time constants, switching errors, and variations and noise in the reference voltage. Several types of error sources and representations are discussed below.

1. **Code ambiguity:** In many digital codes (for example, in the straight binary code), incrementing a number by a least significant bit (LSB) will involve more than one bit-switching. If the speed of switching from 0 to 1 is different from that for 1 to 0, and if switching pulses are not applied to the switching circuit simultaneously, the bit-switchings will not take place simultaneously. For example, in a 4-bit DAC, incrementing from decimal 2 to decimal 4 will involve changing the digital word from 0011 to 0100. This requires two bit-switchings from 1 to 0 and one bit-switching from 0 to 1. If 1 to 0 switching is faster than the 0 to 1 switching, then an intermediate value given by 0000 (decimal 0) will be generated, with a corresponding analog output. Hence, there will be a momentary code ambiguity and associated error in the DAC signal. This problem can be reduced (and eliminated in single bit increments) if a *gray code* is used to represent the digital data. Improved switching circuitry will also help reduce this error.
2. **Settling time:** The circuit hardware in a DAC unit will have some dynamics, with associated time constants and perhaps oscillations (underdamped response). Hence, the output voltage cannot instantaneously settle to its ideal value upon switching. The time required for the analog output to settle within a certain band (say $\pm 2\%$ of the final value or $\pm 1/2$ resolution), following the application of the digital data, is termed settling time. Naturally, settling time should be smaller for better (faster and more accurate) performance. As a guideline, the settling time should be approximately half the data arrival time. Note that the data arrival time is the time interval between the arrival of two successive data values, and is given by the inverse of the data arrival rate.
3. **Glitches:** Switching of a circuit will involve sudden changes in magnetic flux due to current changes. This will induce voltages that produce unwanted signal components. In a DAC circuit, these induced voltages due to rapid switching can cause signal spikes that will appear in the output. The error due to these noise signals is not significant at low conversion rates.
4. **Parametric errors:** Resistor elements in a DAC might not be precise, particularly when resistors within a wide range of magnitudes are employed, as in the case in a weighted-resistor DAC. These errors appear in the analog output. Furthermore, aging and environmental changes (primarily, change in temperature) will change the values of circuit parameters, resistance in particular. This also will result in DAC error. These types of error, which are due to the imprecision of circuit parameters and variations of parameter values, are termed parametric errors. Effects of such errors can be reduced by several ways, including the use of compensation hardware (and perhaps software) and directly, by using precise and robust circuit components and employing good manufacturing practices.
5. **Reference voltage variations:** Since the analog output of a DAC is proportional to the reference voltage, v_{ref} , any variations in the voltage supply will directly appear as an error. This problem can be overcome by using stabilized voltage sources with sufficiently low output impedance.
6. **Monotonicity:** Clearly, the output of a DAC should change by its resolution ($\delta y = v_{\text{ref}}/2^n$) for each step of one LSB increment in the digital value. This ideal behavior might not exist in some real DACs due to errors such as those mentioned above. At least the analog output should not decrease as the value of the digital input increases. This is known as the monotonicity requirement that should be met by a practical DAC.
7. **Nonlinearity:** Suppose that the digital input to a DAC is varied from [0 0...0] to [1 1...1] in steps of one LSB. Ideally the analog output should increase in constant jumps of $\delta y = v_{\text{ref}}/2^n$, giving a staircase-shaped analog output. If we draw the best linear fit for this ideally monotonic staircase response, it will have a slope equal to the resolution/step. This slope is known as the ideal scale factor. Nonlinearity of a DAC is measured by the largest deviation of the DAC output from this best linear fit. Note that, in the ideal case, the nonlinearity is limited to half the resolution $(1/2)\delta y$.

One cause of nonlinearity is clearly the faulty bit-transitions. Another cause is circuit nonlinearity in the conventional sense. Specifically, owing to nonlinearities in circuit elements such as opamps and resistors, the analog output will not be proportional to the value of the digital word dictated by the bit-switchings (faulty or not). This latter type of nonlinearity can be accounted for by using calibration.

16.5.2 Analog-to-Digital Conversion

Analog signals, which are continuously defined with respect to time, have to be sampled at discrete time points and the sample values have to be represented in the digital form (according to a suitable code) to be read into a digital system such as a microcomputer. An ADC is used to accomplish this. For example, since response measurements of dynamic systems are usually available as analog signals, these signals have to be converted into the digital form before passing on to a signal analysis computer. Hence, the computer interface for the measurement channels should contain one or more ADCs.

DACs and ADCs are usually situated on the same digital interface board. However, the ADC process is more complex and time consuming than the DAC process. Furthermore, many types of ADCs use DACs to accomplish the analog-to-digital conversion. Hence, ADCs are usually more costly than and their conversion rate is usually slower than that of DACs. Several types of ADCs are commercially available. The principle of operation varies depending on the type.

16.5.3 Analog-to-Digital Converter Performance Characteristics

For ADCs that use a DAC internally, the same error sources that were discussed previously for DACs apply. Code ambiguity at the output register is not a problem because the converted digital quantity is transferred instantaneously to the output register. Code ambiguity in the DAC register can still cause error in ADCs that use a DAC. Conversion time is a major factor as it is much larger for an ADC. In addition to resolution and dynamic range, quantization error will be applicable to an ADC. These considerations that govern the performance of an ADC are discussed below.

16.5.3.1 Resolution and Quantization Error

The number of bits, n , in an ADC register determines the resolution and dynamic range of the ADC. For an n -bit ADC, the output register size is n bits. Hence, the smallest possible increment of the digital output is one LSB. The change in the analog input that results in a change of one LSB at the output is the resolution of the ADC. The range of digital outputs is from 0 to $2^n - 1$ for the unipolar (unsigned) case. This represents the dynamic range. Hence, as for a DAC, the dynamic range of an n -bit ADC is given by the ratio

$$DR = 2^n - 1 \quad (16.62)$$

or, in decibels

$$DR = 20 \log_{10}(2^n - 1) \text{ dB} \quad (16.63)$$

The *full-scale value* of an ADC is the value of the analog input that corresponds to the maximum digital output.

Suppose that an analog signal within the dynamic range of the ADC is converted. Since the analog input (sample value) has infinitesimal resolution and the digital representation has a finite resolution (one LSB), an error is introduced in the ADC process. This is known as the *quantization error*. A digital number increments in constant steps of 1 LSB. If an analog value falls at an intermediate point within a single-LSB step, then there is a quantization error. Rounding of the digital output can be accomplished as follows. The magnitude of the error when quantized up is compared with that when quantized down, say, using two hold elements and a differential amplifier. Then, we retain the digital value corresponding to the lower error magnitude. If the analog value is below the 1/2 LSB mark, then the corresponding digital value is represented by the value in the beginning of the step. If the analog value is above the 1/2

LSB mark, then the corresponding digital value is the value at the end of the step. It follows that, with this type of rounding, the quantization error does not exceed $1/2$ LSB.

16.5.3.2 Monotonicity, Nonlinearity, and Offset Error

Considerations of monotonicity and nonlinearity are important for an ADC as well as for a DAC. The input is an analog signal and the output is digital in the case of ADC. Disregarding quantization error, the digital output of an ADC will increase in constant steps in the shape of an ideal staircase when the analog input is increased from zero in steps of the device resolution (δy). This is the ideally *monotonic* case. The best straight-line fit to this curve has a slope equal to $1/\delta y$ (LSB/V). This is the ideal gain or ideal scale factor. However, there will still be an *offset error* of $1/2$ LSB because the best linear fit will not pass through the origin. Adjustments can be made for this offset error.

Incorrect bit-transitions can take place in an ADC due to various errors that might be present and due to circuit malfunctions. The best linear fit under such faulty conditions will have a slope different from the ideal gain. The difference is the gain error. Nonlinearity is the maximum deviation of the output from the best linear fit. It is clear that, with perfect bit transitions, in the ideal case, a nonlinearity of $1/2$ LSB will be present. Nonlinearities larger than this result from incorrect bit-transitions. As in the case of DAC, another source of nonlinearity in an ADC is the existence of circuit nonlinearities that would deform the analog input signal before being converted into the digital form.

16.5.3.3 Analog-to-Digital Converter Conversion Rate

It is clear that ADC is much more time consuming than DAC. The conversion time is a very important factor because the rate at which conversion can take place governs many aspects of data acquisition, particularly in real-time applications. For example, the data sampling rate has to synchronize with the ADC conversion rate. This, in turn, will determine the Nyquist frequency (half the sampling rate) which is the maximum value of useful frequency present in the sampled signal. Furthermore, the sampling rate will dictate storage and memory requirements. Another important consideration related to the ADC conversion rate is the fact that a signal sample must be maintained at that value during the entire process of conversion into the digital form. This requires a hold circuit and this circuit should be able to perform accurately at the largest possible conversion time for the particular ADC unit.

The total time taken to convert an analog signal will depend on other factors besides the time taken for conversion from sampled data to digital data. For example, in multiple-channel data acquisition, the time taken to select the channel has to be counted. Furthermore, time needed to sample the data and time needed to transfer the converted digital data into the output register have to be included. The *conversion rate* for an ADC is the inverse of the overall time needed for a conversion cycle. Typically, however, conversion rate depends primarily on the bit conversion time in the case of one comparison-type ADC and on the integration time in the case of an integration-type ADC. A typical time period for a comparison step or counting step in an ADC is $\Delta t = 5 \mu\text{sec}$. Hence, for an eight-bit successive-approximation ADC the conversion time is $40 \mu\text{sec}$. The corresponding sampling rate is in the order of (less than) $1/40 \times 10^{-6} = 25 \times 10^3$ samples/sec (or 25 kHz). The maximum conversion rate for an eight-bit counter ADC is about $5 \times (2^8 - 1) = 1275 \mu\text{sec}$. The corresponding sampling rate would be of the order of 780 samples/sec. Note that this is considerably slow. The maximum conversion time for a dual-slope ADC can be still larger (slower).

16.5.4 Sample-and-Hold Circuitry

In typical applications of data acquisition that use ADC, the analog input to ADC can be very transient. Furthermore, ADC is not instantaneous (conversion time is much larger than the DAC time). Specifically, the incoming analog signal might be changing at a rate higher than the ADC conversion rate. Then, the input signal value will vary during the conversion period and there will be an ambiguity as to the input value corresponding to a digital output value. Hence, it is necessary to sample the analog input signal and maintain the input to the ADC at this value until the ADC is completed. In other words,

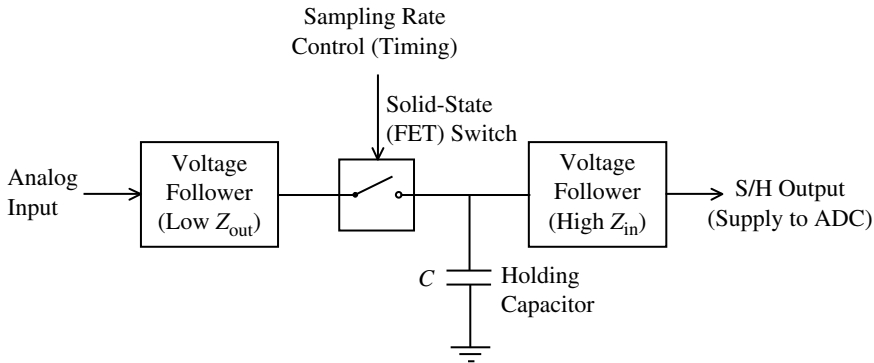


FIGURE 16.16 A sample and hold circuit.

since we are typically converting analog signals that can vary at a high speed, it is often necessary to *sample and hold* (S/H) the input signal for each ADC cycle. Each data sample must be generated and captured by the S/H circuit on the issue of the “start conversion” (SC) control signal, and the captured voltage level has to be maintained constant until the “conversion complete” (CC) control signal is issued by the ADC unit.

The main element in an S/H circuit is the holding capacitor. A schematic diagram of a S/H circuit is shown in Figure 16.16. The analog input signal is supplied through a voltage follower to a solid-state switch. The switch typically uses a field-effect transistor (FET), such as the metal-oxide semiconductor field effect transistor (MOSFET).

The switch is closed in response to a “sample pulse” and is opened in response to a “hold pulse.” Both control pulses are generated by the control logic unit of the ADC. During the time interval between these two pulses, the holding capacitor is charged to the voltage of the sampled input. This capacitor voltage is then supplied to the ADC through a second voltage follower.

The functions of the two voltage followers are now explained. When the FET switch is closed in response to a sample command (pulse), the capacitor must be charged as quickly as possible. The associated time constant (charging time constant) τ_c is given by

$$\tau_c = R_s C \quad (16.64)$$

in which

R_s = source resistance

C = capacitance of the holding capacitor

Since τ_c must be very small for fast charging and, since C is fixed by the holding requirements (typically C is of the order of 100 pF where $1 \text{ pF} = 1 \times 10^{-12} \text{ F}$), we need a very small source resistance. The requirement is met by the input voltage follower (which is known to have a very low output impedance), thereby providing a very small R_s . Furthermore, since a voltage follower has a unity gain, the voltage at the output of this input voltage follower is equal to the voltage of the analog input signal, as required.

Next, once the FET switch is opened in response to a hold command (pulse), the capacitor should not discharge. This requirement is met due to the presence of the output voltage follower. Since the input impedance of a voltage follower is very high, the current through its leads is almost zero. Because of this, the holding capacitor has a virtually zero discharge rate under hold conditions. Furthermore, we like the output of this second voltage follower to be equal to the voltage of the capacitor. This condition is also satisfied due to the fact that a voltage follower has a unity gain. Hence, the sampling will be almost instantaneous and the output of the S/H circuit will be maintained (almost) constant during the holding period due to the presence of the two voltage followers. Note that the practical S/H circuits are *zero-order-hold* devices by definition.

16.5.5 Digital Filters

A filter is a device that eliminates undesirable frequency components in a signal and passes only the desirable frequency components through. In *analog filtering*, the filter is a physical, dynamic system, typically an electric circuit. The signal to be filtered is applied (input) to this dynamic system. The output of the dynamic system is the filtered signal. It follows that any physical dynamic system can be interpreted as an analog filter.

An analog filter can be represented by a differential equation with respect to time. It takes an analog input signal, $u(t)$, that is defined continuously in time, t , and generates an analog output, $y(t)$. A digital filter is a device that accepts a sequence of discrete input values (say, sampled from an analog signal at sampling period Δt).

$$\{u_k\} = \{u_0, u_1, u_2, \dots\} \quad (16.65)$$

and generates a sequence of discrete output values:

$$\{y_k\} = \{y_0, y_1, y_2, \dots\} \quad (16.66)$$

Hence, a digital filter is a discrete-time system and it can be represented by a *difference equation*.

An n th order linear difference equation can be written in the form

$$a_0 y_k + a_1 y_{k-1} + \dots + a_n y_{k-n} = b_0 u_k + b_1 u_{k-1} + \dots + b_m u_{k-m} \quad (16.67)$$

This is a *recursive algorithm* in the sense that it generates one value of the output sequence using previous values of the output sequence and all values of the input sequence up to the present time point. Digital filters represented in this manner are termed *recursive digital filters*. There are filters that employ digital processing, in which a block (a collection of samples) of the input sequence is converted in a one-shot computation into a block of the output sequence. Such filters are not recursive filters. Nonrecursive filters usually employ *digital Fourier analysis*, the FFT algorithm in particular. We restrict our discussion below to recursive digital filters. Our intention in the present section is to give a brief (and nonexhaustive) introduction to the subject of digital filtering.

16.5.5.1 Software Implementation and Hardware Implementation

In digital filters, signal filtering is accomplished through digital processing of the input signal. The sequence of input data (usually obtained by sampling and digitizing the corresponding analog signal) is processed according to the recursive algorithm of the particular digital filter. This generates the output sequence. This digital output can be converted into an analog signal using a DAC if so desired.

A recursive digital filter is an implementation of a recursive algorithm that governs the particular filtering (e.g., low-pass, high-pass, band-pass, and band-reject). The filter algorithm can be implemented either by *software* or by *hardware*. In software implementation, the filter algorithm is programmed into a digital computer. The *processor* (e.g., the microprocessor) of the computer can process an input data sequence according to the run-time filter program stored in the memory (in machine code) to generate the filtered output sequence.

Digital processing of data is accomplished by means of logic circuitry that can perform basic arithmetic operations such as addition. In the software approach, the processor of a digital computer makes use of these basic logic circuits to perform digital processing according to the instructions of a software program stored in the computer memory. Alternatively, a hardware digital processor can be put together to perform a somewhat complex, yet fixed, processing operation. In this approach, the program of computation is said to be in hardware. The hardware processor is then available as an IC chip whose processing operation is fixed and cannot be modified. The logic circuitry in the IC chip is designed to accomplish the required processing function. Digital filters implemented by this hardware approach are termed *hardware digital filters*.

The software implementation of digital filters has the advantage of flexibility; the filter algorithm can be easily modified by changing the software program that is stored in the computer. If, on the other hand, a large number of filters of a particular (fixed) structure are needed commercially, then it is economical to

design the filter as an IC chip and replicate the chip in mass production. In this manner, very low-cost digital filters can be produced. A hardware filter can operate at a much faster speed than a software filter because, in the former case, processing takes place automatically through logic circuitry in the filter chip without having to access the processor, a software program, and various data items stored in the memory. The main disadvantage of a hardware filter is that its algorithm and parameter values cannot be modified, and the filter is dedicated to a fixed function.

16.6 Bridge Circuits

A full bridge is a circuit having four arms which are connected in a lattice form. Four nodes are formed in this manner. Two opposite nodes are used for the excitation (voltage or current supply) of the bridge and the remaining two opposite nodes provide the bridge output.

A bridge circuit is used to make some form of measurement. Typical measurements include change in resistance, change in inductance, change in capacitance, oscillating frequency, or some variable (stimulus) that causes these. There are two basic methods of making the measurement:

1. Bridge balance method
2. Imbalance output method

A bridge is said to be balanced when the output voltage is zero. In the bridge-balance method, we start with a balanced bridge. Then, when one is preparing to make a measurement, the balance of the bridge will be upset due to the associated variation, resulting in a nonzero output voltage. The bridge can be balanced again by varying one of the arms of the bridge (assuming, of course, that some means is provided for the fine adjustments that may be required). The change that is required to restore the balance provides the measurement. In this method, the bridge can be balanced precisely using a servo device.

In the imbalance output method, we usually start with a balanced bridge. However, the bridge is not balanced again after undergoing the change due to the variable that is being measured. Instead, the output voltage of the bridge due to the resulting imbalance is measured and used as an indication of the measurement.

There are many types of bridge circuits. If the supply to the bridge is DC, then we have a *DC bridge*. Similarly, an *AC bridge* has an AC excitation. A *resistance bridge* has only resistance elements in its four arms. An *impedance bridge* has impedance elements consisting of resistors, capacitors, and inductors in one or more of its arms. If the bridge excitation is a constant-voltage supply, we have a *constant-voltage bridge*. If the bridge supply is a constant current source, we have a *constant-current bridge*.

16.6.1 Wheatstone Bridge

The Wheatstone bridge is a resistance bridge with a constant DC voltage supply (i.e., a constant-voltage resistance bridge). A Wheatstone bridge is used in strain-gage measurements, and also in force, torque, and tactile sensors that employ strain-gage techniques. Since a Wheatstone bridge is used primarily in the measurement of small changes in resistance, it could be used in other types of sensing applications as well (for example, in resistance temperature detectors or RTDs).

Consider the Wheatstone bridge circuit shown in [Figure 16.17\(a\)](#). The bridge output, v_o , may be expressed as

$$v_o = \frac{(R_1 R_4 - R_2 R_3)}{(R_1 + R_2)(R_3 + R_4)} v_{\text{ref}} \quad (16.68)$$

Note that the bridge-balance requirement is

$$\frac{R_1}{R_2} = \frac{R_3}{R_4} \quad (16.69)$$

Suppose that $R_1 = R_2 = R_3 = R_4 = R$ in the beginning. The bridge is balanced according to Equation 16.69 and then R_1 is increased by δR . For example, R_1 may represent the only active strain gage and the remaining three elements in the bridge are identical, dummy elements. Then, in view of Equation 16.68, the change in output due to the change δR is given by

$$\delta v_o = \frac{[(R + \delta R)R - R^2]}{(R + \delta R + R)(R + R)} v_{\text{ref}} - 0$$

or

$$\frac{\delta v_o}{v_{\text{ref}}} = \frac{\delta R/R}{(4 + 2\delta R/R)} \quad (16.70)$$

Note that the output is nonlinear in $\delta R/R$. If, however, $\delta R/R$ is assumed to be small in comparison to 2, we have the linearized relationship.

$$\frac{\delta v_o}{v_{\text{ref}}} = \frac{\delta R}{4R} \quad (16.71)$$

The error due to linearization, which is a measure of nonlinearity, may be given as the percentage

$$N_p = 100 \left(1 - \frac{\text{Linearized output}}{\text{Actual output}} \right) \% \quad (16.72)$$

Hence, from Equation 16.70 and Equation 16.71, we have

$$N_p = 50 \frac{\delta R}{R} \% \quad (16.73)$$

16.6.2 Constant-Current Bridge

When large resistance variations δR are required for a measurement, the Wheatstone bridge may not be satisfactory due to its nonlinearity, as indicated by Equation 16.70. The constant-current bridge has less nonlinearity and is preferred in such applications. However, it requires a current-regulated power supply, which is typically more costly than a voltage-regulated power supply.

As shown in Figure 16.17(b), the constant-current bridge uses a constant-current excitation, i_{ref} , instead of a constant-voltage supply. Note that the output equation for the constant-current bridge can be determined from Equation 16.68 simply by knowing the voltage at the current source. Suppose that this is the voltage, v_{ref} , with the polarity as shown in Figure 16.17(a). Now, since the load current is assumed small (high-impedance load), the current through R_2 is equal to the current through R_1 and is

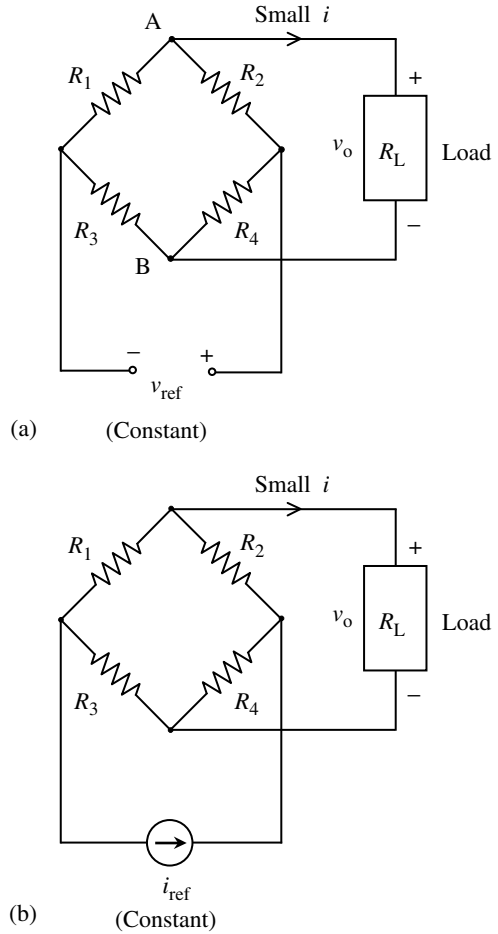


FIGURE 16.17 (a) Wheatstone bridge (the constant-voltage resistance bridge); (b) the constant-current bridge.

given by

$$\frac{v_{\text{ref}}}{(R_1 + R_2)}$$

Similarly, current through R_4 and R_3 is given by

$$\frac{v_{\text{ref}}}{(R_3 + R_4)}$$

Accordingly,

$$i_{\text{ref}} = \frac{v_{\text{ref}}}{(R_1 + R_2)} + \frac{v_{\text{ref}}}{(R_3 + R_4)}$$

or

$$v_{\text{ref}} = \frac{(R_1 + R_2)(R_3 + R_4)}{(R_1 + R_2 + R_3 + R_4)} i_{\text{ref}} \quad (16.74)$$

Substituting Equation 16.74 in Equation 16.68, we have the output equation for the constant-current bridge; thus,

$$v_o = \frac{(R_1 R_4 - R_2 R_3)}{(R_1 + R_2 + R_3 + R_4)} i_{\text{ref}} \quad (16.75)$$

Note that the bridge-balance requirement is again given by Equation 16.69.

To estimate the nonlinearity of a constant-current bridge, suppose that $R_1 = R_2 = R_3 = R_4 = R$ in the beginning and R_1 is changed by δR while the other resistors remain inactive. Again, R_1 will represent the active element (the sensing element) and may correspond to an active strain gage. The change in output, δv_o , is given by

$$\delta v_o = \frac{[(R + \delta R)R - R^2]}{(R + \delta R + R + R + R)} i_{\text{ref}} - 0$$

or

$$\frac{\delta v_o}{R i_{\text{ref}}} = \frac{\delta R/R}{(4 + \delta R/R)} \quad (16.76)$$

By comparing the denominator on the RHS of this equation with Equation 16.70, we observe that the constant-current bridge is more linear. Specifically, using the definition given by Equation 16.72, the *percentage nonlinearity* may be expressed as

$$N_p = 25 \frac{\delta R}{R} \% \quad (16.77)$$

It is noted that the nonlinearity is halved by using a constant-current excitation instead of a constant-voltage excitation.

16.6.3 Bridge Amplifiers

The output from a resistance bridge is usually very small in comparison to the reference, and it has to be amplified in order to increase the voltage level to a useful value (for example, in system monitoring or data logging). A *bridge amplifier* is used for this purpose. This is typically an *instrumentation amplifier* or a *differential amplifier*. The bridge amplifier is modeled as a simple gain, K_a , that multiplies the bridge output.

16.6.3.1 Half-Bridge Circuits

A half bridge may be used in some applications that require a bridge circuit. A half bridge has only two arms and the output is tapped from the mid-point of the two arms. The ends of the two arms are excited

by a positive voltage and a negative voltage. Initially, the two arms have equal resistances so that, nominally, the bridge output is zero. One of the arms has the active element. Its change in resistance results in a nonzero output voltage. It is noted that the half-bridge circuit is somewhat similar to a potentiometer circuit.

A half-bridge amplifier consisting of a resistance half-bridge and an output amplifier is shown in Figure 16.18. The two bridge arms have resistances R_1 and R_2 , and the amplifier uses a feedback resistance R_f . To obtain the output equation, we use the two basic facts for an unsaturated opamp; the voltages at the two leads are equal (due to high gain) and current in both leads is zero (due to high input impedance). Hence, voltage at node A is zero and the current balance equation at node A is

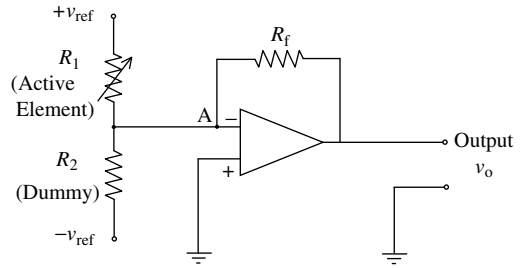


FIGURE 16.18 A half bridge with an output amplifier.

$$\frac{v_{\text{ref}}}{R_1} + \frac{(-v_{\text{ref}})}{R_2} + \frac{v_o}{R_f} = 0$$

This gives

$$v_o = R_f \left(\frac{1}{R_2} - \frac{1}{R_1} \right) v_{\text{ref}} \quad (16.78)$$

Now, suppose that initially $R_1 = R_2 = R$ and the active element R_1 changes by δR . The corresponding change in output is

$$\delta v_o = R_f \left(\frac{1}{R} - \frac{1}{R + \delta R} \right) v_{\text{ref}} - 0$$

or

$$\frac{\delta v_o}{v_{\text{ref}}} = \frac{R_f}{R} \frac{\delta R/R}{(1 + \delta R/R)} \quad (16.79)$$

Note that R_f/R is the amplifier gain. Now, in view of Equation 16.72, the percentage nonlinearity of the half-bridge circuit is

$$N_p = 100 \frac{\delta R}{R} \% \quad (16.80)$$

It follows that the nonlinearity of a half-bridge circuit is worse than that of the Wheatstone bridge.

16.6.4 Impedance Bridges

An impedance bridge contains general impedance elements, Z_1 , Z_2 , Z_3 , and Z_4 , in its four arms, as shown in Figure 16.19(a). The bridge is excited by an AC supply, v_{ref} . Note that v_{ref} represents a carrier signal and the output, v_o , has to be demodulated if a transient signal representative of the variation in one of the bridge elements is needed. Impedance bridges can be used, for example, to measure capacitances in *capacitive sensors* and changes of inductance in variable-inductance sensors and *eddy-current sensors*. Also, impedance bridges can be used as oscillator circuits. An oscillator circuit can serve as a constant-frequency source of a signal generator (in vibration testing) or it can be used to determine an unknown circuit parameter by measuring the oscillating frequency.

Analyzing using frequency-domain concepts, it is seen that the frequency spectrum of the impedance-bridge output is given by

$$v_o(\omega) = \frac{(Z_1 Z_4 - Z_2 Z_3)}{(Z_1 + Z_2)(Z_3 + Z_4)} v_{\text{ref}}(\omega) \quad (16.81)$$

This reduces to Equation 16.68 in the DC case of a Wheatstone bridge. The balanced condition is given by

$$\frac{Z_1}{Z_2} = \frac{Z_3}{Z_4} \quad (16.82)$$

This is used to measure an unknown circuit parameter in the bridge. Let us consider two examples.

16.6.4.1 Owen Bridge

The Owen bridge shown in Figure 16.19(b) may be used to measure the inductance L_4 or capacitance C_3 , by the bridge-balance method. To derive the necessary equation, note that the voltage–current relation for an inductor is

$$v = L \frac{di}{dt} \quad (16.83)$$

and for a capacitor it is

$$i = C \frac{dv}{dt} \quad (16.84)$$

It follows that the voltage/current transfer function (in the Laplace domain) for an inductor is

$$\frac{v(s)}{i(s)} = Ls \quad (16.85)$$

and that for a capacitor is

$$\frac{v(s)}{i(s)} = \frac{1}{Cs} \quad (16.86)$$

Accordingly, the impedance of an inductor element at frequency ω is

$$Z_L = j\omega L \quad (16.87)$$

and the impedance of a capacitor element at frequency ω is

$$Z_C = \frac{1}{j\omega C} \quad (16.88)$$

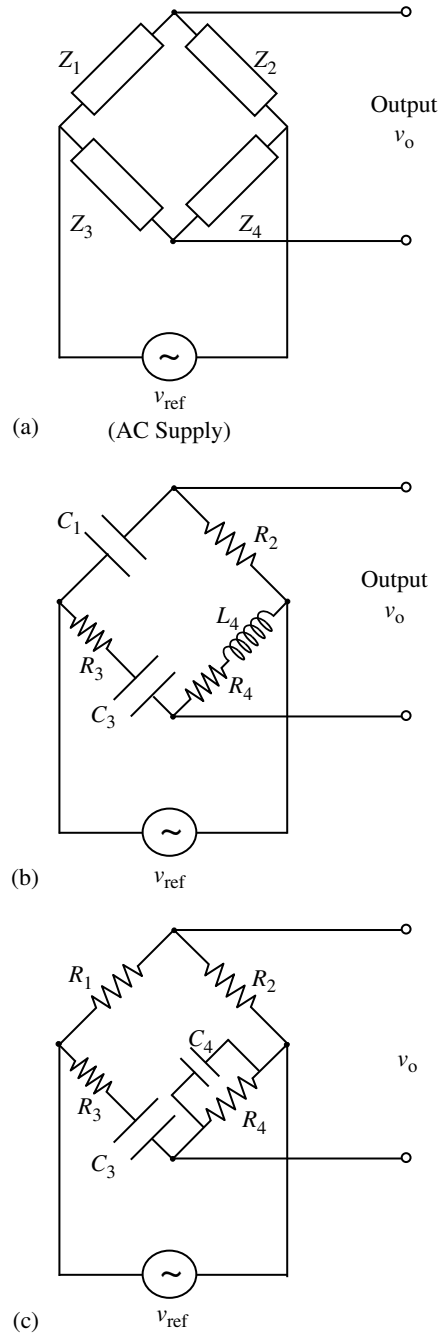


FIGURE 16.19 (a) General impedance bridge; (b) Owen bridge; (c) Wien-bridge oscillator.

Applying these results to the Owen bridge, we have

$$Z_1 = \frac{1}{j\omega C_1}$$

$$Z_2 = R_2$$

$$Z_3 = R_3 + \frac{1}{j\omega C_3}$$

$$Z_4 = R_4 + j\omega L_4$$

in which ω is the excitation frequency. Now, from Equation 16.82, we have

$$\frac{1}{j\omega C_1}(R_4 + j\omega L_4) = R_2 \left(R_3 + \frac{1}{j\omega C_3} \right)$$

By equating the real parts and the imaginary parts of this equation, we obtain the two equations

$$\frac{L_4}{C_1} = R_2 R_3$$

and

$$\frac{R_4}{C_1} = \frac{R_2}{C_3}$$

Hence, we have

$$L_4 = C_1 R_2 R_3 \quad (16.89)$$

and

$$C_3 = C_1 \frac{R_2}{R_4} \quad (16.90)$$

It follows that L_4 and C_3 can be determined with the knowledge of C_1 , R_2 , R_3 , and R_4 under balanced conditions. For example, with fixed C_1 and R_2 , an adjustable R_3 could be used to measure the variable L_4 , and an adjustable R_4 could be used to measure the variable C_3 .

16.6.4.2 Wien-Bridge Oscillator

Now consider the Wien-bridge oscillator shown in [Figure 16.19\(c\)](#). For this circuit, we have

$$Z_1 = R_1$$

$$Z_2 = R_2$$

$$Z_3 = R_3 + \frac{1}{j\omega C_3}$$

$$\frac{1}{Z_4} = \frac{1}{R_4} + j\omega C_4$$

Hence, from Equation 16.82, the bridge-balance requirement is

$$\frac{R_1}{R_2} = \left(R_3 + \frac{1}{j\omega C_3} \right) \left(\frac{1}{R_4} + j\omega C_4 \right)$$

Equating the real parts, we obtain

$$\frac{R_1}{R_2} = \frac{R_3}{R_4} + \frac{C_4}{C_3} \quad (16.91)$$

and, by equating the imaginary parts, we obtain

$$0 = \omega C_4 R_3 - \frac{1}{\omega C_3 R_4}$$

Hence,

$$\omega = \frac{1}{\sqrt{C_3 C_4 R_3 R_4}} \quad (16.92)$$

Equation 16.92 tells us that the circuit is an oscillator whose natural frequency is given by this equation under balanced conditions. If the frequency of the supply is equal to the natural frequency of the circuit, large-amplitude oscillations will take place. The circuit can be used to measure an unknown resistance (e.g., in strain-gage devices) by first measuring the frequency of the bridge signals at resonance (natural frequency). Alternatively, an oscillator that is excited at its natural frequency can be used as an accurate source of periodic signals (a signal generator).

16.7 Linearizing Devices

Nonlinearity is present in any physical device, to varying levels. If the level of nonlinearity in a system (component, device, or equipment) can be neglected without exceeding the error tolerance, then the system can be assumed to be linear.

In general, a linear system is one that can be expressed as one or more *linear differential equations*. Note that the *principle of superposition* holds for linear systems. Specifically, if the system response to an input, u_1 , is y_1 and the response to another input, u_2 , is y_2 , then the response to $a_1 u_1 + a_2 u_2$ is $a_1 y_1 + a_2 y_2$.

Nonlinearities in a system can appear in two forms:

1. Dynamic manifestation of nonlinearities
2. Static manifestation of nonlinearities

The useful operating region of many systems can exceed the frequency range where the frequency-response function is flat. The operating response of such a system is said to be dynamic. Examples include a typical dynamic system (e.g., automobile, aircraft, chemical process plant, robot), actuator (e.g., hydraulic motor), and controller (e.g., PID control circuitry). Nonlinearities of such systems can manifest themselves in a dynamic form such as the *jump phenomenon* (also known as the *fold catastrophe*), *limit cycles*, and *frequency creation*. Design changes, extensive adjustments, or reduction of the operating signal levels and bandwidths are generally necessary to reduce or eliminate these dynamic manifestations of nonlinearity. In many instances, such changes are not practical and we have to somehow manage with the presence of these nonlinearities under dynamic conditions. Design changes might involve replacing conventional gear drives with devices such as harmonic drives in order to reduce backlash, replacing nonlinear actuators with linear actuators, and using components that have negligible Coulomb friction and that make small motion excursions.

A wide majority of sensors, transducers, and signal-modification devices are expected to operate in the flat region of the frequency-response function. The input/output relation of these types of devices, in the operating range, is expressed (modeled) as a *static curve* rather than a differential equation. Nonlinearities in these devices will manifest themselves in the static operating curve in many forms. These manifestations include *saturation*, *hysteresis*, and *offset*.

In the first category of systems (plants, actuators, and compensators), if a nonlinearity is exhibited in the dynamic form, proper modeling and control practices should be employed in order to avoid unsatisfactory degradation of the system performance. In the second category of systems (sensors, transducers and signal modification devices), if nonlinearities are exhibited in the “static” operating curve, again the overall performance of the system will be degraded. Hence, it is important to “linearize” the output of such devices. Note that, in dynamic manifestations, it is not realistic to linearize the output because the response is in the dynamic form. The solution in that case is either to minimize nonlinearities

through design modifications and adjustments so that a linear approximation would be valid, or to take the nonlinearities into account in system modeling and control. In the present section, we are not concerned with this aspect. Instead, we are interested in the linearization of devices in the second category, whose operating characteristics can be expressed by static input–output curves.

Linearization of a static device can be attempted by making design changes and adjustments, as in the case of dynamic devices. However, since the response is static, and since we normally deal with an available (fixed) device whose internal hardware cannot be modified, we should consider ways of linearizing the input–output characteristic by modifying the output itself.

Static linearization of a device can be made in three ways:

1. Linearization using digital software
2. Linearization using digital (logic) hardware
3. Linearization using analog circuitry

In the software approach to linearization, the output of the device is read into a processor with software-programmable memory and the output is modified according to the program instructions. In the hardware approach, the device output is read by a device having fixed logic circuitry that processes (modifies) the data. In the analog approach, a linearizing circuit is directly connected at the output of the device so that the output of the linearizing circuit is proportional to the input of the device. We shall discuss these three approaches in the rest of this section, heavily emphasizing the analog-circuit approach.

Hysteresis-type static nonlinearity characteristics have the property that the input–output curve is not one to one. In other words, one input value may correspond to more than one (static) output value, and one output value may correspond to more than one input value. Let us disregard these types of nonlinearities. Our main concern is the linearization of a device having a single-valued static response curve that is not a straight line. An example of a typical nonlinear input–output characteristic is shown in Figure 16.20(a). Strictly speaking, a straight-line characteristic with a simple *offset*, as shown in Figure 16.20(b), is also a nonlinearity. In particular, note that superposition does not hold for an input–output characteristic of this type, given by

$$y = ku + c \quad (16.93)$$

It is very easy, however, to linearize such a device because the simple addition of a DC component will convert the characteristic into the linear form given by

$$y = ku \quad (16.94)$$

This method of linearization is known as offsetting. Linearization is more difficult in the general case where the characteristic curve could be much more complex.

16.7.1 Linearization by Software

If the nonlinear relationship between the input and the output of a nonlinear device is known, the input can be “computed” for a known value of the output. In the software approach of linearization, system

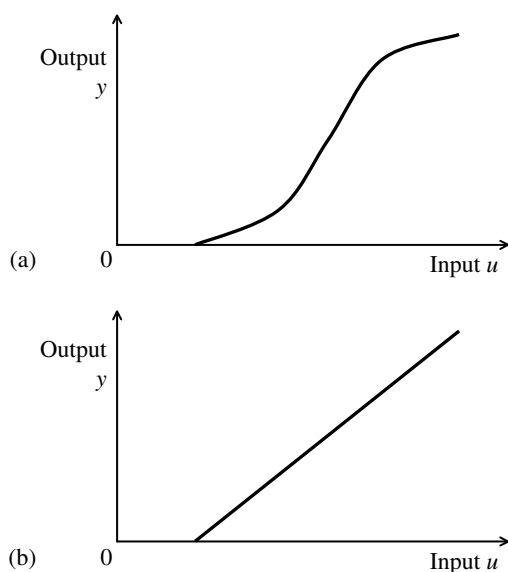


FIGURE 16.20 (a) A general static nonlinear characteristic; (b) an offset nonlinearity.

composed of a processor and memory that can be programmed using software (i.e., a digital computer) is used to compute the input using output data. Two approaches can be used. They are

1. Equation inversion
2. Table lookup

In the first method, the nonlinear characteristic of the device is known in the analytic (equation) form:

$$y = f(u) \quad (16.95)$$

in which

u = device input

y = device output

Assuming that this is a one-to-one relationship, a unique inverse given by the equation

$$u = f^{-1}(y) \quad (16.96)$$

can be determined. This equation is programmed into the read-and-write memory (RAM) of the computer as a *computation algorithm*. When the output values, y , are supplied to the computer, the processor will compute the corresponding input values, u , using the instructions (executable program) stored in the RAM.

In the table lookup method, a sufficiently large number of pairs of values (y, u) are stored in the memory of the computer in the form of a table of ordered pairs. These values should cover the entire operating range of the device. When a value for y is entered into the computer, the processor scans the stored data to check whether that value is present. If so, the corresponding value of u is read and this is the linearized output. If the value of y is not present in the data table, then the processor will *interpolate* the data in the vicinity of the value and will compute the corresponding output. In the *linear interpolation* method, the area of the data table where the y value falls is fitted with a straight line and the corresponding u value is computed using this straight line. Higher order interpolations use nonlinear interpolation curves such as quadratic and cubic polynomial equations (splines).

Note that the equation inversion method is usually more accurate than the table lookup method and it does not need excessive memory for data storage. However, it is relatively slow because data are transferred and processed within the computer using program instructions that are stored in the memory and that typically have to be accessed in a sequential manner. The table lookup method is fast. Since the accuracy depends on the number of stored data values, this is a memory-intensive method. For better accuracy, more data should be stored. However, since the entire data table has to be scanned to check for a given data value, this increase in accuracy is derived at the expense of speed as well as memory requirements.

16.7.2 Linearization by Hardware Logic

The software approach to linearization is flexible in the sense that the linearization algorithm can be modified (e.g., improved, changed) simply by modifying the program stored in the RAM. Furthermore, highly complex nonlinearities can be handled by the software method. As mentioned before, the method is relatively slow, however.

In the hardware logic method of linearization, the linearization algorithm is permanently implemented in the IC form using appropriate *digital logic circuitry* for data processing, and memory elements (e.g., *flip-flops*). Note that the algorithm and numerical values of parameters (except input values) cannot be modified without redesigning the IC chip, because a hardware device typically does not have *programmable memory*. Furthermore, it will be difficult to implement very complex linearization algorithms by this method and, unless the chips are mass produced for an extensive commercial market, the initial cost of chip development will make the production of linearizing chips economically infeasible. In bulk production, however, the per-unit cost will be very small. Furthermore, since the access of stored

program instructions and extensive data manipulation are not involved, the hardware method of linearization can be substantially faster than the software method.

A digital linearizing unit that has a processor and a read-only memory (ROM), whose program cannot be modified, also lacks the flexibility of a programmable software device. Hence, such a ROM-based device also falls into the category of hardware logic devices.

16.7.3 Analog Linearizing Circuitry

Three types of analog linearizing circuitry can be identified:

1. Offsetting circuitry
2. Circuitry that provides a proportional output
3. Curve shapers

We will describe each of these categories now.

An offset is a nonlinearity that can be easily removed using an analog device. This is accomplished by simply adding a DC offset of equal value to the response, but in the opposite direction. Deliberate addition of an offset in this manner is known as *offsetting*. The associated removal of original offset is known as *offset compensation*. There are many applications of offsetting. Unwanted offsets such as those present in ADC and DAC results can be removed by analog offsetting. Constant (DC) error components such as steady-state errors in dynamic systems due to load changes, gain changes, and other disturbances can be eliminated by offsetting. Common-mode error signals in amplifiers and other analog devices can also be removed by offsetting. In measurement circuitry such as potentiometer (ballast) circuits, where the actual measurement signal is a change, δv_o , in a steady output signal, v_o , the measurement can be completely wiped out due to noise. To reduce this problem, first the output should be offset by $-v_o$ so that the net output is δv_o and not $v_o + \delta v_o$. This output is subsequently conditioned by filtering and amplification. Another application of offsetting is the additive change of scale of a measurement, for example from a relative scale (e.g., velocity) to an absolute scale. In summary, some of the applications of offsetting are:

1. Removal of unwanted offsets and DC components in signals (e.g., in ADC, DAC, signal integration).
2. Removal of steady-state error components in dynamic system responses (e.g., due to load changes and gain changes in Type 0 systems. Note: Type 0 systems are open-loop systems having no free integrators).
3. Rejection of common-mode levels (e.g., in amplifiers and filters).
4. Error reduction when a measurement is an increment of a large steady output level (e.g., in ballast circuits for strain-gage and RTD sensors).
5. Scale changes in an additive manner (e.g., conversion from relative to absolute units or from absolute to relative units).

We can remove unwanted offsets in the simple manner as discussed above. Let us now consider more complex nonlinear responses that are nonlinear in the sense that the input–output curve is not a straight line. Analog circuitry can be used to linearize this type of response as well. The linearizing circuit used will generally depend on the particular device and the nature of its nonlinearity. Hence, often linearizing circuits of this type have to be discussed with respect to a particular application. For example, such linearization circuits are useful in *transverse-displacement capacitive sensor*. Several useful circuits are described below.

Consider the type of linearization that is known as *curve shaping*. A *curve shaper* is a linear device whose gain (output/input) can be adjusted so that response curves with different slopes can be obtained. Suppose that a nonlinear device having an irregular (nonlinear) input–output characteristic is to be linearized. First, we apply the operating input simultaneously to the device and the curve shaper, and the gain of the curve shaper is adjusted such that it closely matches that of the device in a small range

of operation. Now, the output of the curve shaper can be utilized for any task that requires the device output. The advantage here is that linear assumptions are valid with the curve shaper, which is not the case for the actual device. When the operating range changes, the curve shaper must be returned to the new range. Comparison (calibration) of the curve shaper and the nonlinear device can be done off line and, once a set of gain values corresponding to a set of operating ranges is determined in this manner for the curve shaper, it is possible to completely replace the nonlinear device with the curve shaper. Then the gain of the curve shaper can be adjusted depending on the actual operating range during system operation. This is known as *gain scheduling*. Note that we can replace a nonlinear device with a linear device (curve shaper) within a multicomponent system in this manner without greatly sacrificing the accuracy of the overall system.

16.7.4 Offsetting Circuitry

Common-mode outputs and offsets in amplifiers and other analog devices can be minimized by including a *compensating resistor* that can provide fine adjustments at one of the input leads. Furthermore, the larger is the feedback signal level in a feedback system, the smaller is the steady-state error. Hence, steady-state offsets can be reduced by reducing the *feedback resistance* (thereby increasing the feedback signal). Furthermore, since a ballast (potentiometer) circuit provides an output of $v_o + \delta v_o$ and a bridge circuit provides an output of δv_o , the use of a *bridge circuit* can be interpreted as an offset compensation method.

The most straightforward way of offsetting is by using a *differential amplifier* (or a *summing amplifier*) to subtract (or add) a DC voltage to the output of the nonlinear device. The DC level has to be variable so that various levels of offset can be provided using the same circuit. This is accomplished by using an adjustable resistance at the DC input lead of the amplifier.

An operational-amplifier circuit for offsetting is shown in Figure 16.21. Since the input, v_i , is connected to the negative lead of the opamp, we have an *inverting amplifier*, and the input signal will appear in the output, v_o , with its sign reversed. This is also a *summing amplifier* because two signals can be added together by this circuit. If the input, v_i , is connected to the positive lead of the opamp, we will have a *noninverting amplifier*.

The DC voltage, v_{ref} , provides the offsetting voltage. The resistor, R_c (compensating resistor), is variable so that different values of offset can be compensated using the same circuit. To obtain the circuit equation, we write the current balance equation for node A, using the usual assumption that the current through an input lead is zero for an opamp because of very high input impedance; thus

$$\frac{v_{\text{ref}} - v_A}{R_c} = \frac{v_A}{R_o}$$

or

$$v_A = \frac{R_o}{(R_o + R_c)} v_{\text{ref}} \quad (\text{i})$$

Similarly, the current balance at node B gives

$$\frac{v_i - v_B}{R} + \frac{v_o - v_B}{R} = 0$$

or

$$v_o = -v_i + 2v_B \quad (\text{ii})$$

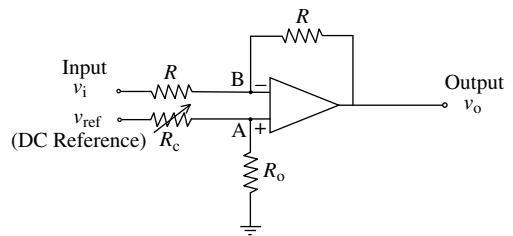


FIGURE 16.21 An inverting amplifier circuit for offset compensation.

Since $v_A = v_B$ for the opamp (because of very high open-loop gain), we can substitute Equation i into Equation ii. Then,

$$v_o = -v_i + \frac{2R_o}{(R_o + R_c)} v_{\text{ref}} \quad (16.97)$$

Note the sign of v_i is reversed at the output (because this is an inverting amplifier). This is not a problem because polarity can be reversed at input or output in connecting this circuit to other circuitry, thereby recovering the original sign. The important result here is the presence of a constant offset term on the RHS of Equation 16.97. This term can be adjusted by picking the proper value for R_c so as to compensate for a given offset in v_i .

16.7.5 Proportional-Output Circuitry

An operational-amplifier circuit may be employed to linearize the output of a capacitive transverse-displacement sensor. In constant-voltage and constant-current resistance bridges and in a constant-voltage half bridge, the relation between the bridge output, δv_o , and the measurand (the change in resistance in the active element) is nonlinear. The nonlinearity is least for the constant-current bridge and it is highest for the half bridge. Since δR is small compared with R , however, the nonlinear relations can be linearized without introducing large errors. However, the linear relations are inexact and are not suitable if δR cannot be neglected in comparison to R . Under these circumstances, the use of a linearizing circuit would be appropriate.

One way to obtain a proportional output from a Wheatstone bridge is to feed back a suitable factor of the bridge output into the bridge supply, v_{ref} . Another way is to use the opamp circuit shown in Figure 16.22. This should be compared with the Wheatstone bridge shown in Figure 16.17(a). Note that R represents the only active element (e.g., an active strain gage).

First, let us show that the output equation for the circuit in Figure 16.22 is similar to Equation 16.68. Using the fact that the current through an input lead of an unsaturated opamp can be neglected, we have the following current balance equations for nodes A and B:

$$\begin{aligned} \frac{v_{\text{ref}} - v_A}{R_4} &= \frac{v_A}{R_2} \\ \frac{v_{\text{ref}} - v_B}{R_3} + \frac{v_o - v_B}{R_1} &= 0 \end{aligned}$$

Hence,

$$v_A = \frac{R_2}{(R_2 + R_4)} v_{\text{ref}}$$

and

$$v_B = \frac{R_1 v_{\text{ref}} + R_3 v_o}{(R_1 + R_3)}$$

Now, using the fact $v_A = v_B$ for an opamp, we obtain

$$\frac{R_1 v_{\text{ref}} + R_3 v_o}{(R_1 + R_3)} = \frac{R_2}{(R_2 + R_4)} v_{\text{ref}}$$

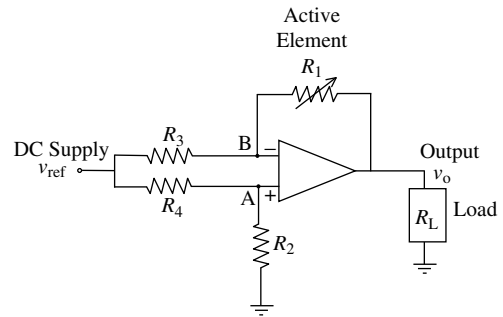


FIGURE 16.22 A proportional-output circuit for an active resistance element (strain gage).

Accordingly, we have the circuit output equation

$$v_o = \frac{(R_2 R_3 - R_1 R_4)}{R_3(R_2 + R_4)} v_{\text{ref}} \quad (16.98)$$

Note that this relation is quite similar to the Wheatstone bridge equation (Equation 16.68). The balance condition (i.e., $v_o = 0$) is again given by Equation 16.69.

Suppose that $R_1 = R_2 = R_3 = R_4 = R$ in the beginning (the circuit is balanced), so $v_o = 0$. Then suppose that the active resistance R_1 is changed by δR (say, owing to a change in strain in the strain gage R_1). Then, using Equation 16.98, we can write an expression for the change in circuit output as

$$\delta v_o = \frac{[R^2 - R(R + \delta R)]}{R(R + R)} v_{\text{ref}} - 0$$

or

$$\frac{\delta v_o}{v_{\text{ref}}} = -\frac{1}{2} \frac{\delta R}{R} \quad (16.99)$$

By comparing this result with Equation 16.71, we observe that the circuit output, δv_o , is proportional to the measurand, δR . Furthermore, note that the sensitivity of the circuit in Figure 16.22 (1/2) is double that of a Wheatstone bridge that has one active element (1/4), which is a further advantage of the proportional-output circuit. The sign reversal is not a drawback because it can be accounted for by reversing the load polarity.

16.7.5.1 Curve-Shaping Circuitry

A curve shaper can be interpreted as an amplifier whose gain is adjustable. A typical arrangement for a curve-shaping circuit is shown in Figure 16.23. The feedback resistance, R_f , is adjustable by some means. For example, a switching circuit with a bank of resistors (say, connected in parallel through solid-state switches as in the case of weighted-resistor DAC) can be used to switch the feedback resistance to the required value. Automatic switching can be realized by using Zener diodes that will start conducting at certain voltage levels. In both cases (external switching by switching pulses or automatic switching using Zener diodes), amplifier gain is variable in discrete steps. Alternatively, a potentiometer can be used as R_f so that the gain can be continuously adjusted (manually or automatically).

The output equation for the curve-shaping circuit shown in Figure 16.23 is obtained by writing the current balance at node A, noting that $v_A = 0$; thus

$$\frac{v_i}{R} + \frac{v_o}{R_f} = 0$$

or

$$v_o = -\frac{R_f}{R} v_i \quad (16.100)$$

It follows that the gain (R_f/R) of the amplifier can be adjusted by changing R_f .

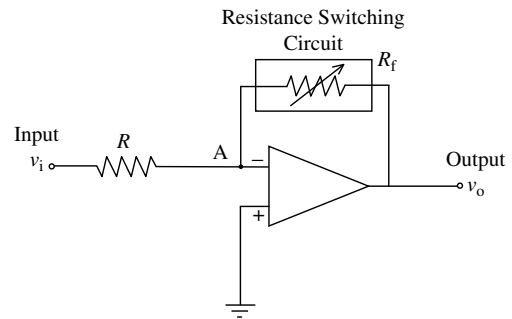


FIGURE 16.23 A curve-shaping circuit.

16.8 Miscellaneous Signal Modification Circuitry

In addition to the signal modification devices discussed so far in this chapter, there are many other types of circuitry that are used for signal modification and related tasks. Examples are phase shifters, voltage-to-frequency converters, frequency-to-voltage converters, voltage-to-current converts, and peak-hold circuits. The objective of the present section is to discuss briefly several of such miscellaneous circuits and components that are useful in the instrumentation of dynamic systems.

16.8.1 Phase Shifters

A sinusoidal signal given by

$$v = v_a \sin(\omega t + \phi) \quad (16.101)$$

has the following three representative parameters:

- v_a = amplitude
- ω = frequency
- ϕ = phase angle

Note that the phase angle represents the *time reference* (starting point) of the signal. The phase angle is an important consideration only when two or more signal components are compared. The Fourier spectrum of a signal is presented as its amplitude (magnitude) and the phase angle with respect to the frequency.

Phase-shifting circuits have many applications. When a signal passes through a system, its phase angle changes due to dynamic characteristics of the system. Consequently, the phase change provides very useful information about the dynamic characteristics of the system. Specifically, for a linear constant-coefficient system, this phase shift is equal to the phase angle of the *frequency-response function* (*frequency-transfer function*) of the system at that particular frequency. This phase-shifting behavior is, of course, not limited to electrical systems and is equally exhibited by other types of systems including mechanical vibrating systems. The phase shift between two signals can be determined by converting the signals into the electrical form (using suitable transducers) and shifting the phase angle of one signal through known amounts, using a phase-shifting circuit, until the two signals are in phase.

Another application of phase shifters is in signal demodulation. For example, one method of amplitude demodulation involves processing the modulated signal together with the carrier signal. This, however, requires the modulated signal and the carrier signal to be in phase. Usually, however, since the modulated signal has already transmitted through electrical circuitry having impedance characteristics, its phase angle has changed. Then, it is necessary to shift the phase angle of the carrier until the two signals are in phase, so that demodulation can be performed accurately. Hence, phase shifters are used in demodulating, for example, when demodulating LVDT displacement-sensor outputs.

A phase-shifter circuit, ideally, should not change the signal amplitude while changing the phase angle by a required amount. Practical phase shifters can introduce some degree of amplitude distortion (with respect to frequency) as well. A simple phase-shifter circuit can be constructed using resistance (R) and capacitance (C) elements. A resistance or a capacitor of such an RC circuit is made fine-adjustable so as to obtain a variable phase shifter.

An opamp-based phase shifter circuit is shown in Figure 16.24. We can show that this circuit provides a phase shift without distorting the signal amplitude. The circuit equation is obtained by writing the current balance equations at nodes A and B, noting, as usual, that the current through the opamp leads

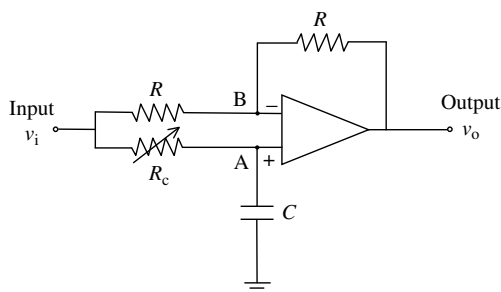


FIGURE 16.24 A phase-shifter circuit.

can be neglected due to high input impedance; thus

$$\frac{v_i - v_A}{R_C} = C \frac{dv_A}{dt}$$

$$\frac{v_i - v_B}{R} + \frac{v_o - v_B}{R} = 0$$

On simplifying and introducing the Laplace variable, we obtain

$$v_i = (\tau s + 1)v_A \quad (i)$$

and

$$v_B = \frac{1}{2}(v_i + v_o) \quad (ii)$$

in which, the circuit *time constant*, τ , is given by

$$\tau = R_C C$$

Since $v_A = v_B$ as a result of very high gain in the opamp, by substituting Equation ii into Equation i, we obtain

$$v_i = \frac{1}{2}(\tau s + 1)(v_i + v_o)$$

It follows that the transfer function $G(s)$ of the circuit is given by

$$\frac{v_o}{v_i} = G(s) = \frac{(1 - \tau s)}{(1 + \tau s)} \quad (16.102)$$

It is seen that the magnitude of the frequency-response function $G(j\omega)$ is

$$|G(j\omega)| = \frac{\sqrt{1 + \tau^2 \omega^2}}{\sqrt{1 + \tau^2 \omega^2}}$$

or

$$|G(j\omega)| = 1 \quad (16.103)$$

and the phase angle of $G(j\omega)$ is

$$\angle G(j\omega) = -\tan^{-1} \tau \omega - \tan^{-1} \tau \omega$$

or

$$\angle G(j\omega) = -2 \tan^{-1} \tau \omega = -2 \tan^{-1} R_C C \omega \quad (16.104)$$

As needed, the transfer function magnitude is unity, indicating that the circuit does not distort the signal amplitude over the entire bandwidth. Equation 16.104 gives the *phase lead* of the output, v_o , with respect to the input, v_i . Note that this angle is negative, indicating that actually a *phase lag* is introduced. The phase shift can be adjusted by varying the resistance, R_C .

16.8.2 Voltage-to-Frequency Converter

A voltage-to-frequency converter (VFC) generates a periodic output signal whose frequency is proportional to the level of an input voltage. Since such an *oscillator* generates a periodic output according to the voltage excitation, it is also called a *voltage-controlled oscillator* (VCO).

A common type of VFC uses a capacitor. The time needed for the capacitor to be charged to a fixed voltage level will depend on the charging voltage (it is inversely proportional). Suppose that this voltage is governed by the input voltage. Then, if the capacitor is made to periodically charge and discharge, we have an output whose frequency (inverse of the charge–discharge period) is proportional to the charging voltage. The output amplitude will be given by the fixed voltage level to which the capacitor is charged in

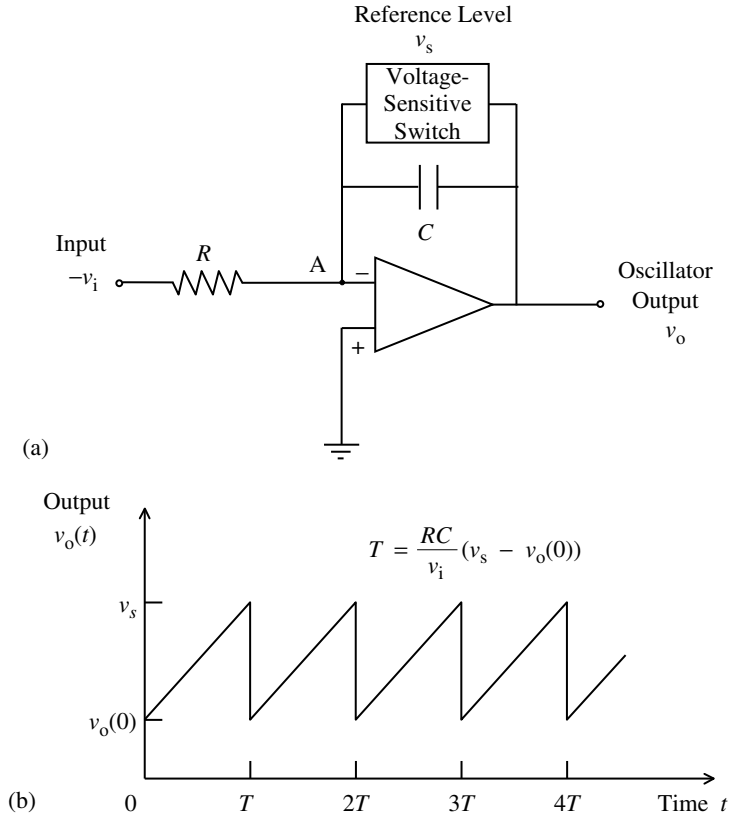


FIGURE 16.25 A voltage-to-frequency converter (voltage-controlled oscillator): (a) circuit; (b) output signal.

each cycle. Consequently, we have a signal with a fixed amplitude and a frequency that depends on the charging voltage (input).

A VFC (or VCO) circuit is shown in Figure 16.25(a). The voltage-sensitive switch closes when the voltage across it exceeds a reference level, v_s , and it opens again when the voltage across it falls below a lower limit, $v_o(0)$. The *programmable unijunction transistor* (PUT) is such a switching device.

Note that the polarity of the input voltage, v_i , is reversed. Suppose that the switch is open. Then, current balance at node A of the opamp circuit gives

$$\frac{v_i}{R} = C \frac{dv_o}{dt}$$

As usual, $v_A = \text{voltage at positive lead} = 0$ because the opamp has a very high gain, and current through the opamp leads $= 0$ because the opamp has a very high input impedance. The capacitor charging equation can be integrated for a given value of v_i . This gives

$$v_o(t) = \frac{1}{RC} v_i t + v_o(0)$$

The switch is closed when the voltage across the capacitor $v_o(t)$ equals the reference level v_s . Then, the capacitor will be immediately discharged through the closed switch. Hence, the capacitor charging time, T , is given by

$$v_s = \frac{1}{RC} v_i T + v_o(0)$$

Accordingly,

$$T = \frac{RC}{v_i}(v_s - v_o(0)) \quad (16.105)$$

The switch opens again when the voltage across the capacitor drops to $v_o(0)$, and the capacitor again begins to charge from $v_o(0)$ up to v_s . This charging and instantaneous discharge cycle repeats periodically. The corresponding output signal is as shown in Figure 16.25(b). This is a periodic (*sawtooth*) wave with period T . The frequency of oscillation of the output ($1/T$) is given by

$$f = \frac{v_i}{RC(v_s - v_o(0))} \quad (16.106)$$

It is seen that the oscillator frequency is proportional to the input voltage v_i . The oscillator amplitude is v_s , which is fixed.

VCOs have many applications. One application is in *analog-to-digital conversion*. In the VCO type analog-to-digital converters, the analog signal is converted into an oscillating signal using a VCO. Then, the oscillator frequency is measured using a *digital counter*. This count, which is available in the digital form, is representative of the input analog signal level. Another application is in digital voltmeters. Here, the same method as for ADC is used. Specifically, the voltage is converted into an oscillator signal and its frequency is measured using a digital counter. The count can be scaled and displayed to provide the voltage measurement. A direct application of the VCO is apparent from the fact it is actually a *frequency modulator*, providing a signal whose frequency is proportional to the input (modulating) signal. Hence, the VCO is useful in applications that require frequency modulation. Also, a VCO can be used as a signal (wave) generator for variable-frequency applications; for example, it can be used for excitation inputs for shakers in vibration testing, excitations for frequency-controlled DC motors, and pulse signals for translator circuits of stepping motors.

16.8.3 Frequency-to-Voltage Converter

A frequency-to-voltage converter (FVC) generates an output voltage whose level is proportional to the frequency of its input signal. One way to obtain a FVC is to use a digital counter to count the signal frequency and then use a DAC to obtain a voltage proportional to the frequency. A schematic representation of this type of FVC is shown in Figure 16.26(a).

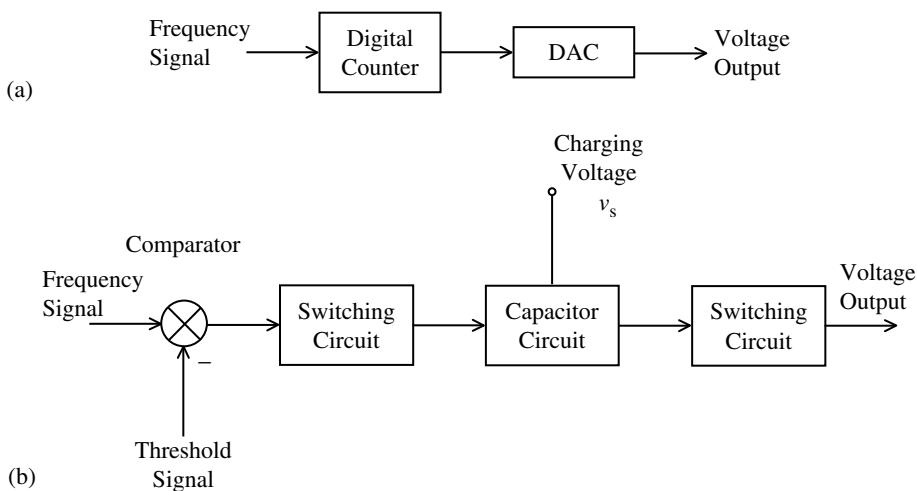


FIGURE 16.26 Frequency-to-voltage converters: (a) digital counter method; (b) capacitor charging method.

An alternative FVC circuit is schematically shown in Figure 16.26(b). In this method, the frequency signal is supplied to a comparator along with a threshold voltage level. The sign of the comparator output will depend on whether the input signal level is larger or smaller than the threshold level. The first sign change (negative to positive) in the comparator output is used to trigger a switching circuit that will respond by connecting a capacitor to a fixed charging voltage. This will charge the capacitor. The next sign change (positive to negative) of the comparator output will cause the switching circuit to short the capacitor, thereby instantaneously discharging it. This charging–discharging process will be repeated in response to the oscillator input. Note that the voltage level to which the capacitor is charged each time will depend on the switching period (charging voltage is fixed), which is in turn governed by the frequency of the input signal. Hence, the output voltage of the capacitor circuit will be representative of the frequency of the input signal. Since the output is not steady due to the ramp-like charging curve and instantaneous discharge, a smoothing circuit is provided at the output to remove the noisy ripples.

Applications of FVC include demodulation of frequency-modulated signals, frequency measurement in mechanical vibration applications, and conversion of pulse outputs in some types of sensors and transducers into analog voltage signals.

16.8.4 Voltage-to-Current Converters

Measurement and feedback signals are usually transmitted as current levels in the range of 4 to 20 mA rather than as voltage levels. This is particularly useful when the measurement site is not close to the monitoring room. Since the measurement itself is usually available as a voltage, it has to be converted into current by using a voltage-to-current converter (VCC). For example, pressure transmitters and temperature transmitters in operability testing systems provide current outputs that are proportional to the measured values of pressure and temperature.

There are many advantages to transmitting current rather than voltage. In particular, the voltage level will drop due to resistance in the transmitting path, but the current through a conductor will remain unchanged unless the conductor is branched. Hence, current signals are less likely to acquire errors due to signal weakening. Another advantage of using current instead of voltage as the measurement signal is that the same signal can be used to operate several devices in series (for example, a display, a plotter, and a signal processor simultaneously), without causing errors through signal weakening due to the power lost at each device, because the same current is applied to all devices. A VCC should provide a current proportional to an input voltage without being affected by the load resistance to which the current is supplied.

An operational-amplifier-based voltage-to-current convert circuit is shown in Figure 16.27. Using the fact that the currents through the input leads of an unsaturated opamp can be neglected (due to very high input impedance), we write the current summation equations for the two nodes, A and B, thus:

$$\frac{v_A}{R} = \frac{v_P - v_A}{R}$$

and

$$\frac{v_i - v_B}{R} + \frac{v_P - v_B}{R} = i_o$$

Accordingly, we have

$$2v_A = v_P \quad (i)$$

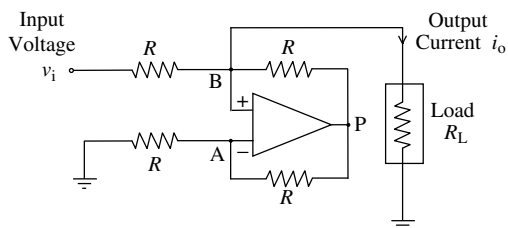


FIGURE 16.27 A voltage-to-current converter.

and

$$v_i - 2v_B + v_P = Ri_o \quad (\text{ii})$$

Now, using the fact that $v_A = v_B$ for the opamp (due to very high gain), we substitute Equation i into Equation ii. This gives

$$i_o = \frac{v_i}{R} \quad (16.107)$$

in which

i_o = output current

v_i = input voltage

It follows that the output current is proportional to the input voltage, irrespective of the value of the load resistance, R_L , as required for a VCC.

16.8.5 Peak-Hold Circuits

Unlike a S/H circuit that holds every sampled value of the signal, a peak-hold circuit holds only the largest value reached by the signal during the monitored period. Peak holding is useful in a variety of applications. In signal processing for shock and vibration studies, what are known as *response spectra* (e.g., a *shock response spectrum*) are determined by using a *response spectrum analyzer* that exploits a peak holding scheme. Suppose that a signal is applied to a simple oscillator (a single-degree-of-freedom second-order system with no zeros) and the peak value of the response (output) is determined. A plot of the peak output as a function of the natural frequency of the oscillator, for a specified damping ratio, is known as the response spectrum of the signal for that damping ratio. Peak detection is also useful in machine monitoring and alarm systems. In short, when just one representative value of a signal is needed in a particular application, the peak value is a leading contender.

Peak detection of a signal can be conveniently done using digital processing. For example, the signal may be sampled and the previous sample value replaced by the present sample value if and only if the latter is larger than the former. By sampling and then holding one value in this manner, the peak value of the signal is retained. Note that, usually, the time instant at which the peak occurs is not retained.

Peak detection can be done using analog circuitry as well. This is, in fact, the basis of analog spectrum analyzers. A peak-holding circuit is shown in Figure 16.28. The circuit consists of two voltage followers. The first voltage follower has a diode at its output that is forward biased by the positive output of the voltage follower and reverse-biased by a low-leakage capacitor, as shown. The second voltage follower presents the peak voltage that is held by the capacitor to the circuit output at a low output impedance, without loading the previous circuit stage (capacitor and first voltage follower). To understand the operation of the circuit, suppose that the input voltage, v_i , is larger than the voltage to which capacitor is charged (v). Since the voltage at the positive lead of the opamp is v_i and the voltage at the negative lead is v , the first opamp will be saturated. Since the differential input to the opamp is positive under these conditions, the opamp output will be positive. The output will charge the capacitor until the capacitor voltage, v , equals the input voltage, v_i . This voltage (call it v_o) is in turn supplied to the second voltage follower which presents the same value to its output (gain = 1 for a voltage follower), but at a very low impedance level. Note that the opamp output remains at the saturated value only for a very short time (the time taken by the capacitor to charge). Now, suppose that v_i is smaller than v . Then, the differential input of the opamp will be negative, and the opamp output will be saturated at the negative saturation level. This will reverse bias the diode. Hence, the output of the first opamp will be in open circuit, and as a result the voltage supplied to the output voltage follower

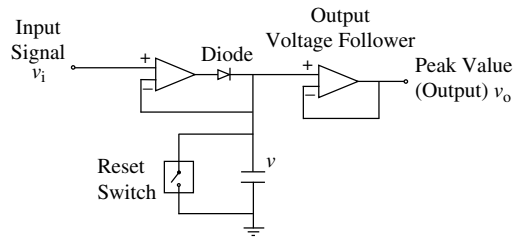


FIGURE 16.28 A peak-holding circuit.

would still be the capacitor voltage and not the output of the first opamp. It follows that the voltage level of the capacitor (and hence the output of the second voltage follower) would always be the peak value of the input signal. The circuit can be reset by discharging the capacitor through a solid-state switch that is activated by an external pulse.

16.9 Signal Analyzers and Display Devices

Vibration signal analysis may employ both analog and digital procedures. Since signal analysis results in extracting various useful bits of information from the signal, it is appropriate to consider the topic within the present context of signal modification as well. Here, we will introduce digital signal analyzers.

Signal display devices also make use of at least some signal processing. This may involve filtering and change of the signal level and format. More sophisticated signal display devices, particularly digital oscilloscopes, can carry out more complex signal analysis functions such as those normally available with digital signal analyzers. Oscilloscopes as well are introduced in the present section, though they may be treated under vibration instrumentation.

Signal-recording equipment commonly employed in vibration practice includes digital storage devices such as hard drives, floppy disks, and CD-ROMs, analog devices like tape recorders, strip-chart recorders and X - Y plotters, and digital printers. Tape recorders are used to record vibration data (transducer outputs) that are subsequently reproduced for processing or examination. Often, tape-recorded waveforms are also used to generate (by replay) signals that drive vibration test exciters (shakers). Tape recorders use tapes made of a plastic material that has a thin coating of a specially treated ferromagnetic substance. During the recording process, magnetic flux proportional to the recorded signal is produced by the recording head (essentially an electromagnet), which magnetizes the tape surface in proportion to the signal variation. Reproduction is the reverse process, whereby an electrical signal is generated at the reproduction head by electromagnetic induction in accordance with the magnetic flux of the magnetized (recorded) tape. Several signal-conditioning circuitries are involved in the recording and reproducing stages. Recording by FM is very common in vibration testing.

Strip-chart recorders are usually employed to plot time histories (that is, quantities that vary with time), although they also may be used to plot such data as frequency-response functions and response spectra. In these recorders, a paper roll unwinds at a constant linear speed, and the writing head moves across the paper (perpendicular to the paper motion) proportionally to the signal level. There are many kinds of strip-chart recorders, which are grouped according to the type of writing head that is employed. Graphic-level recorders, which use ordinary paper, employ such heads as ink pens or brushes, fiber pens, and sapphire styli. Visicoders are simple oscilloscopes that are capable of producing permanent records; they employ light-sensitive paper for this. Several channels of input data can be incorporated with a visicoder. Obviously, graphic-level recorders are generally limited by the number of writing heads possible (typically, one or two), but visicoders can have many more input channels (typically, 24). Performance specifications of these devices include paper speed, frequency range of operation, dynamic range, and power requirements.

In vibration experimentation, X - Y plotters are generally employed to plot frequency data (for example, PSD, frequency-response functions, response spectra, transmissibility curves), although they also can be used to plot time-history data. Many types of X - Y plotter are available, most of them using ink pens and ordinary paper. There are also hard-copy units that use heat-sensitive paper in conjunction with a heating element as the writing head. The writing head in an X - Y plotter is moved in the X and Y directions on the paper by two input signals that form the coordinates for the plot. In this manner, a trace is made on stationary plotting paper. Performance specifications of X - Y plotters are governed by such factors as paper size; writing speed (in./sec, cm/sec); dead band (expressed as a percentage of the full scale), which measures the resolution of the plotter head; linearity (expressed as a percentage of the full scale), which measures the accuracy of the plot; minimum trace separation (in., cm) for multiple plots on the same axes; dynamic range; input impedance; and maximum input (mV/in., mV/cm).

Today, the most widespread signal recording device is in fact the digital computer (memory, storage) and printer combination. This and the other (analog) devices used in signal recording and display make use of some signal modification to accomplish their functions. However, we will not discuss these devices in the present section.

16.9.1 Signal Analyzers

Modern signal analyzers employ digital techniques of signal analysis to extract useful information that is carried by the signal. Digital Fourier analysis using FFT is perhaps the single common procedure that is used in the vast majority of signal analyzers. As we have noted before, Fourier analysis will produce the frequency spectrum of a time signal. It should be clear, therefore, why the terms digital signal analyzer, FFT analyzer, frequency analyzer, spectrum analyzer, and digital Fourier analyzer are to some extent synonymous as used in the commercial instrumentation literature.

A signal analyzer typically has two (dual) or more (multiple) input signal channels. To generate results such as frequency response (transfer) functions, cross spectra, coherence functions, and cross-correlation functions, we need at least two data signals and hence a dual-channel analyzer.

In hardware analyzers, digital circuitry rather than software is used to carry out the mathematical operations. Clearly, these are very fast but less flexible (in terms of programmability and functional capability) for this reason. Digital signal analyzers, regardless of whether they use the hardware or the software approach, employ some basic operations. These operations, carried out in sequence, are:

1. Antialias filtering (analog)
2. Analog-to-digital conversion (i.e., single sampling)
3. Truncation of a block of data and multiplication by a window function
4. FFT analysis of the block of data

We have noted the following facts. If the sampling period of the ADC is ΔT (i.e., the sampling frequency is $1/\Delta T$) then the Nyquist frequency $f_c = 1/2\Delta T$. This Nyquist frequency is the upper limit of the useful frequency content of the sampled signal. The cutoff frequency of the antialiasing filter should be set at f_c or less. If there are N data samples in the block of data that is used in the FFT analysis, the corresponding record length is $T = N \cdot \Delta T$. Then, the spectral lines in the FFT results are separated at a frequency spacing of $\Delta F = 1/T$. In view of the Nyquist frequency limit, there will be only $N/2$ useful spectral lines of FFT result.

Strictly speaking, a real-time signal analyzer should analyze a signal instantaneously and continuously as the signal is received by the analyzer. This is usually the case with an analog signal analyzer. However, in digital signal analyzers, which are usually based on digital Fourier analysis, a block of data (i.e., N samples of record length T) is analyzed together to produce $N/2$ useful spectral lines (at frequency spacing $1/T$). This is, then, not a truly real-time analysis. For practical purposes, if the speed of analysis is sufficiently fast, the analyzer may be considered real time, which is usually the case with hardware analyzers and also modern, high-speed software analyzers.

The bandwidth B of a digital signal analyzer is a measure of its speed of signal processing. Specifically, for an analyzer that uses N data samples in each block of signal analysis, the associated processing time may be given by

$$T_c = \frac{N}{B} \quad (16.108)$$

Note that the larger the B , the smaller the T_c . The analyzer is considered real-time if the analysis time (T_c) of the data record is less than the generation time ($T = N \cdot \Delta T$) of the data record. Hence, we need

$$T_c < T$$

or

$$\frac{N}{B} < T$$

or

$$\frac{N}{B} < N \cdot \Delta T$$

or

$$\frac{1}{\Delta T} < B \quad (16.109)$$

In other words, a real-time analyzer has a bandwidth greater than its sampling rate.

A multichannel digital signal analyzer can analyze one or more signals simultaneously and generate (and display) results such as Fourier spectra, power spectral densities, cross spectral densities, frequency-response functions, coherence functions, autocorrelations, and cross correlations. They are able to perform high-resolution analysis on a small segment of the frequency spectrum of a signal. This is termed *zoom analysis*. Essentially, in this case, the spectral line spacing, ΔF , is decreased while keeping the number of lines (N), and hence the number of time data samples, the same. That means the record length ($T = 1/\Delta F$) has to be increased in proportion, for zoom analysis.

16.9.2 Oscilloscopes

An oscilloscope is used to observe one or two signals separately or simultaneously. Amplitude, frequency, and phase information of the signals can be obtained using an oscilloscope. In this sense, the oscilloscope is a signal modification as well as a measurement (monitoring) and display device. Both analog and digital oscilloscopes are available. A typical application of an oscilloscope is to observe (monitor) experimental data such as vibration signals of machinery as obtained from transducers. They are also useful in observing and examining vibration test results, such as frequency-response plots, PSD curves, and response spectra. Typically, only temporary records are available on an analog oscilloscope screen. The main component of an analog oscilloscope is the cathode-ray tube (CRT), which consists of an electron gun (cathode) that deflects an electron ray according to the input-signal level. The oscilloscope screen has a coating of electron-sensitive material, so that the electron ray that impinges on the screen leaves a temporary trace on it. The electron ray sweeps across the screen horizontally, so that waveform traces can be recorded and observed. Usually, two input channels are available. Each input may be observed separately, or the variations in one input may be observed against those of the other. In this manner, signal phasing can be examined. Several sensitivity settings for the input-signal-amplitude scale (in the vertical direction) and sweep-speed selections are available on the panel.

16.9.2.1 Triggering

The voltage level of the input signal deflects the electron gun proportionally in the vertical (y -axis) direction on the CRT screen. This alone will not show the time evolution of the signal. The true time variation of the signal is achieved by means of a sawtooth signal that is generated internally in the oscilloscope and used to move the electron gun in the horizontal (x -axis) direction. As the name implies, the sawtooth signal increases linearly in amplitude until a threshold value then suddenly drops to zero, and then repeats this cycle again. In this manner, the observed signal is repetitively swept across the screen and a trace of it can be observed as a result of the temporary retention of the illumination of the electron gun on the fluorescent screen. The sawtooth signal may be controlled (triggered) in several ways. For example, the *external trigger* mode uses an external signal from another channel (not the observed channel) to generate and synchronize the sawtooth signal. In the *line trigger* mode, the sawtooth signal is synchronized with the AC line supply (60 or 50 Hz). In the *internal trigger* mode, the observed signal (which is used to deflect the electron beam in the y direction) itself is used to generate (synchronize) the

sawtooth signal. Since the frequency and the phase of the observed signal and the trigger signal are perfectly synchronized in the last case, the trace on the oscilloscope screen will appear stationary. Careful observation of a signal can be made in this manner.

16.9.2.2 Lissajous Patterns

Suppose that two signals, x and y , are provided to the two channels of an oscilloscope. If they are used to deflect the electron beam in the horizontal and the vertical directions, respectively, a pattern known as Lissajous pattern will be observed on the oscilloscope screen. Useful information about the amplitude and phasing of the two signals may be observed by means of these patterns. Consider sine waves x and y . Several special cases of Lissajous patterns are given below.

1. *Same frequency, same phase:* Here,

$$x = x_o \sin(\omega t + \phi)$$

$$y = y_o \sin(\omega t + \phi)$$

Then we have

$$\frac{x}{x_o} = \frac{y}{y_o}$$

which gives a straight-line trace with a positive slope, as shown in Figure 16.29(a).

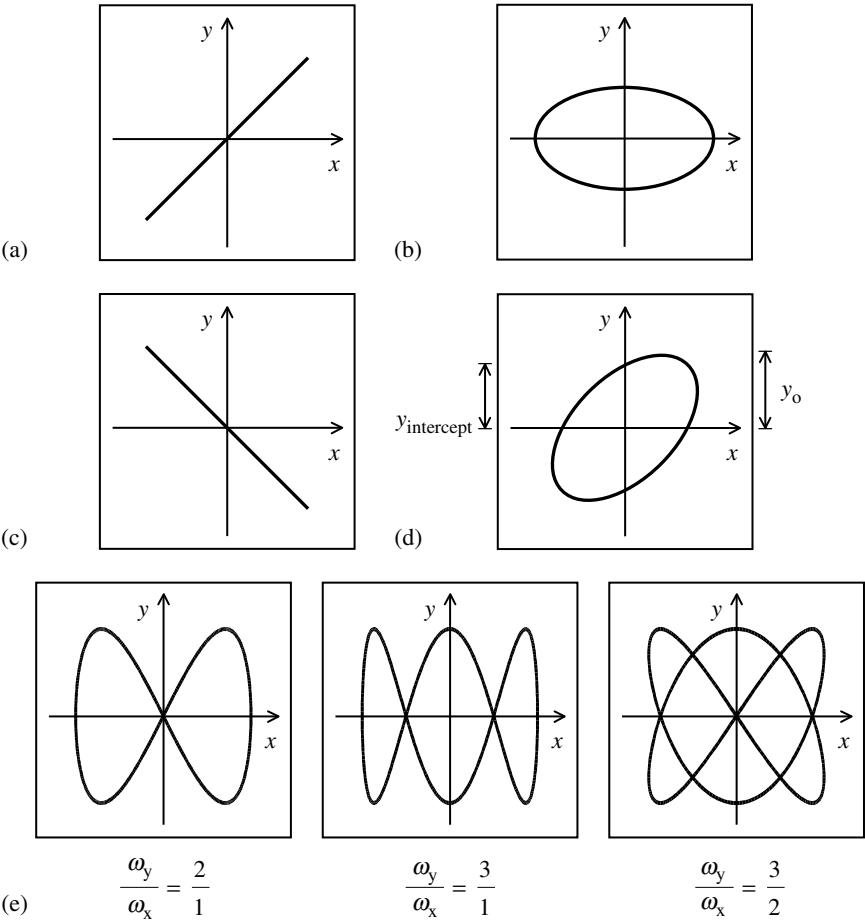


FIGURE 16.29 Some Lissajous patterns: (a) equal frequency and in-phase; (b) equal frequency and 90° out-of-phase; (c) equal frequency and 180° out-of-phase; (d) equal frequency and θ out-of-phase; (e) integral frequency ratio.

2. *Same frequency, 90° out-of-phase:* Here,

$$x = x_o \sin(\omega t + \phi)$$

$$y = y_o \sin(\omega t + \phi + \pi/2) = y_o \cos(\omega t + \phi)$$

Then we have

$$\left(\frac{x}{x_o}\right)^2 + \left(\frac{y}{y_o}\right)^2 = 1$$

which gives an ellipse, as shown in Figure 16.29(b).

3. *Same frequency, 180° out-of-phase:* Here,

$$x = x_o \sin(\omega t + \phi)$$

$$y = y_o \sin(\omega t + \phi + \pi) = -y_o \sin(\omega t + \phi)$$

Hence,

$$\frac{x}{x_o} + \frac{y}{y_o} = 0$$

which corresponds to a straight line with a negative slope, as shown in Figure 16.29(c).

4. *Same frequency, θ out-of-phase:*

$$x = x_o \sin(\omega t + \phi)$$

$$y = y_o \sin(\omega t + \phi + \theta)$$

When $\omega t + \phi = 0$, $y = y_{\text{intercept}} = y_o \sin \theta$.

Hence,

$$\sin \theta = \frac{y_{\text{intercept}}}{y_o}$$

In this case, we obtain a tilted ellipse as shown in Figure 16.29(d). The phase difference θ is obtained from the Lissajous pattern.

5. *Integral frequency ratio:*

$$\frac{\omega_y}{\omega_x} = \frac{\text{Number of } y\text{-peaks}}{\text{Number of } x\text{-peaks}}$$

Three examples are shown in Figure 16.29(e).

$$\frac{\omega_y}{\omega_x} = \frac{2}{1}, \quad \frac{\omega_y}{\omega_x} = \frac{3}{1}, \quad \frac{\omega_y}{\omega_x} = \frac{3}{2}$$

Note: The above observations are true for narrowband signals as well. Broadband random signals produce scattered (irregular) Lissajous patterns.

16.9.2.3 Digital Oscilloscopes

The basic uses of a digital oscilloscope are quite similar to those of a traditional analog oscilloscope. The main differences stem from the manner in which information is represented and processed “internally” within the oscilloscope. Specifically, a digital oscilloscope first samples a signal that arrives at one of its input channels and stores the resulting digital data within a memory segment. This is essentially a typical ADC operation. This digital data may be processed to extract and display the necessary information. The sampled data and the processed information may be stored on a floppy disk, if needed, for further processing using a digital computer. Also, some digital oscilloscopes have the

communication capability so that the information may be displayed on a video monitor or printed to provide a hard copy.

A typical digital oscilloscope has four channels so that four different signals may be acquired (sampled) into the oscilloscope and displayed. Also, it has various triggering options so that the acquisition of a signal may be initiated and synchronized by means of either an internal or an external trigger. Apart from the typical capabilities that are possible with an analog oscilloscope, a digital oscilloscope can automatically provide other useful features such as the following:

1. Automatic scaling of the acquired signal
2. Computation of signal features such as frequency, period, amplitude, mean, root-mean-square (rms) value, and rise time
3. Zooming into regions of interest of a signal record
4. Averaging of multiple signal records
5. Enveloping of multiple signal records
6. FFT capability, with various window options and antialiasing

These various functions are menu selectable. Typically, first a channel of the incoming data (signal) is selected and then an appropriate operation on the data is chosen from the menu (through menu buttons).

Bibliography

- Bendat, J.S. and Piersol, A.G. 1971. *Random Data: Analysis and Measurement Procedures*, Wiley-Interscience, New York.
- Brigham, E.O. 1974. *The Fast Fourier Transform*, Prentice Hall, Englewood Cliffs, NJ.
- Broch, J.T. 1980. *Mechanical Vibration and Shock Measurements*, Bruel and Kjaer, Naerum.
- de Silva, C.W. 1983. *Dynamic Testing and Seismic Qualification Practice*, D.C. Heath and Co., Lexington, KY.
- de Silva, C.W., and Palusamy, S.S., Experimental modal analysis — a modeling and design tool, *Mech. Eng.*, ASME, 106, 6, 56–65, 1984.
- de Silva, C.W., The digital processing of acceleration measurements for modal analysis, *Shock Vib. Dig.*, 18, 10, 3–10, 1986.
- de Silva, C.W. 1989. *Control Sensors and Actuators*, Prentice Hall, Englewood Cliffs, NJ.
- de Silva, C.W. 2000. *Vibration — Fundamentals and Practice*, CRC Press, Boca Raton, FL.
- de Silva, C.W. 2004. *Mechatronics — An Integrated Approach*, CRC Press, Boca Raton, FL.
- de Silva, C.W., Henning, S.J., and Brown, J.D., Random testing with digital control — application in the distribution qualification of microcomputers, *Shock Vib. Dig.*, 18, 3–13, 1986.
- Ewins, D.J. 1984. *Modal Testing: Theory and Practice*, Research Studies Press Ltd., Letchworth, UK.
- Meirovitch, L. 1980. *Computational Methods in Structural Dynamics*, Sijthoff & Noordhoff, Rockville, MD.
- Randall, R.B. 1977. *Application of B&K Equipment to Frequency Analysis*, Bruel and Kjaer, Naerum, Denmark.

17

Vibration Testing

17.1	Introduction	17-1
17.2	Representation of a Vibration Environment	17-3
	Test Signals • Deterministic Signal Representation • Stochastic Signal Representation • Frequency-Domain Representations • Response Spectrum • Comparison of Various Representations	
17.3	Pretest Procedures	17-24
	Purpose of Testing • Service Functions • Information Acquisition • Test-Program Planning • Pretest Inspection	
17.4	Testing Procedures	17-37
	Resonance Search • Methods of Determining Frequency- Response Functions • Resonance-Search Test Methods • Mechanical Aging • Test-Response Spectrum Generation • Instrument Calibration • Test-Object Mounting • Test-Input Considerations	
17.5	Some Practical Information	17-52
	Random Vibration Test Example • Vibration Shakers and Control Systems	

Clarence W. de Silva

The University of British Columbia

Summary

Vibration testing involves application of a vibration excitation to a test object and monitoring the resulting response. The first step in vibration testing is the generation of a test excitation according to some specification or objective. The applied excitation and the corresponding responses are measured at designated locations of the test object. Analysis of the test data will generate useful information about the tested object, which may be applicable in design development, manufacture, and utilization of the object. This chapter presents the basics of the planning of vibration tests, test signal representation and generation, vibration testing, and test data acquisition.

17.1 Introduction

Vibration testing is usually performed by applying a vibratory excitation to a test object and monitoring the structural integrity of the object and its performance of its intended function. The technique may be useful in several stages: (1) *design development*, (2) *production*, and (3) *utilization* of a product. In the initial design stage, the design weaknesses and possible improvements can be determined through the vibration testing of a preliminary design prototype or a partial product. In the production stage, the quality of the workmanship of the final product can be evaluated using both destructive and nondestructive vibrating testing. A third application termed *product qualification*, is intended for determining the adequacy of a product of good quality for a specific application (e.g., the seismic qualification of a nuclear power plant) or a range of applications.

The technology of vibration testing has evolved rapidly since World War II and the technique has been successfully applied to a wide spectrum of products ranging from small printed circuit boards and microprocessor chips to large missiles and structural systems. Until recently, however, much of the signal processing that was required in vibration testing was performed through analog methods. In these methods, the measured signal is usually converted into an electric signal, which in turn is passed through a series of electrical or electronic circuits to achieve the required processing. Alternatively, motion or pressure signals can be used in conjunction with mechanical or hydraulic (e.g., fluidic) circuits to perform analog processing. Today's complex test programs require the capability for the fast and accurate processing of a large number of measurements. The performance of analog signal analyzers is limited by hardware costs, size, data handling capacity and computational accuracy. Digital processing for the synthesis and analysis of vibration test signals and for the interpretation and evaluation of test results, began to replace the classical analog methods in late 1960s. Today, special-purpose digital analyzers with real-time digital Fourier analysis capability are commonly used in vibration testing applications. The advantages of incorporating digital processing into vibration testing include: flexibility and convenience with respect to the type of the signal that can be analyzed and the complexity of the nature of processing that can be handled; increased speed of processing, accuracy and reliability; reduction in operational costs; practically unlimited repeatability of processing; and reduction in the overall size and weight of the analyzer.

Vibration testing is usually accomplished using a shaker apparatus, as shown by the schematic diagram in Figure 17.1. The test object is secured to the shaker table in a manner representative of its installation during actual use (service). In-service operating conditions are simulated while the shaker table is actuated by applying a suitable input signal. The shakers of different types, with electromagnetic, electromechanical, or hydraulic actuators, are available. The shaker device may depend on the test requirement, availability, and cost. More than one signal may be required to simulate three-dimensional characteristics of the vibration environment. The test input signal is either stored on an analog magnetic tape or generated in real-time by a signal generator. The capability of the test object or a similar unit to withstand a "predefined" vibration environment is evaluated by monitoring the dynamic response (accelerations, velocities, displacements, strains, etc.) and functional operability variables (e.g., temperatures, pressures, flow rates, voltages, currents). Analysis of the response signals will aid in detecting existing defects or impending failures in various components of the test equipment. The control sensor output is useful in several ways, particularly in feedback control of the shaker, frequency-band equalization in real-time of the excitation signal, and the synthesizing of future test signals.

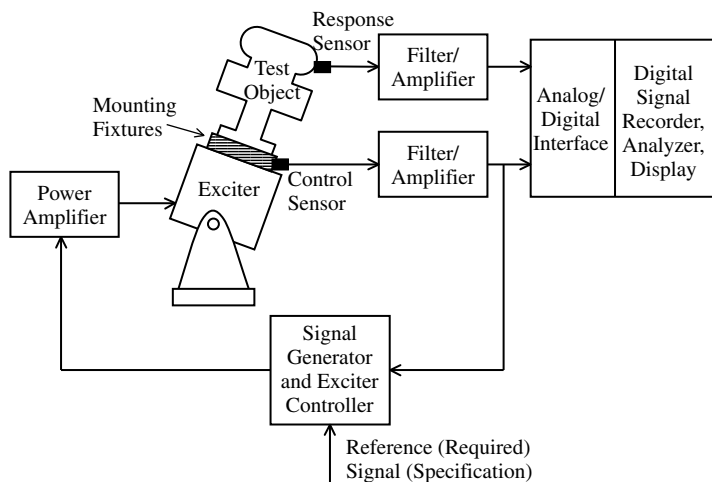


FIGURE 17.1 A typical vibration-testing arrangement.

The excitation signal is applied to the shaker through a shaker controller, which usually has a built-in power amplifier. The shaker controller compares the “control sensor” signal from the shaker–test object interface with the reference excitation signal from the signal generator. The associated error is used to control the shaker motion so as to push this error to zero. This is termed “equalization.” Hence, a shaker controller serves as an equalizer as well.

The signals that are monitored from the test object include test response signals and operability signals. The former category of signals provides the dynamic response of the test object, and may include velocities, accelerations, and strains. The latter category of signals are used to check whether the test object performs in-service functions (i.e., it operates properly) during the test excitation, and may include flow rates, temperatures, pressures, currents, voltages, and displacements. The signals may be recorded in a computer or a digital oscilloscope for subsequent analysis. When using an oscilloscope or a spectrum analyzer, some analysis can be done on line and the results are displayed immediately.

The most uncertain part of a vibration test program is the simulation of the test input. For example, the operating environment of a product such as an automobile is not deterministic and will depend on many random factors. Consequently, it is not possible to generate a single test signal that can completely represent all various operating conditions. As another example, in seismic qualification of equipment, the primary difficulty stems from the fact that the probability of accurately predicting the recurrence of an earthquake at a given site during the design life of the equipment is very small and that of predicting the nature of the ground motions if an earthquake were to occur is even smaller. In this case, the best that one can do is to make a conservative estimate for the nature of the ground motions due to the strongest earthquake that is reasonably expected. The test input should have (1) *amplitude*, (2) *phasing*, (3) *frequency content*, and (4) *damping* characteristics comparable to the expected vibration environment if satisfactory representation is to be achieved. A frequency-domain representation of the test inputs and responses can, in general, provide better insight regarding their characteristics than can a time domain representation, namely, a time history. Fortunately, frequency-domain information can be derived from time domain data by using Fourier transform techniques.

In vibration testing, Fourier analysis is used in three principal ways: first, to determine the frequency response of the test object in prescreening tests; second, to represent the vibration environment by its Fourier spectrum or its power spectral density (PSD) so that a test input signal can be generated to represent it; and third, to monitor the Fourier spectrum of the response at key locations in the test object and at control locations of the test table and use the information diagnostically or in controlling the exciter.

The two primary steps of a vibration testing scheme are:

Step 1: Specify the test requirements;

Step 2: Generate a vibration test signal that conservatively satisfies the specifications of Step 1.

17.2 Representation of a Vibration Environment

A complete knowledge of the vibration environment in which a device will be operating is not available to the test engineer or the test program planner. The primary reason for this is that the operating environment is a random process. When performing a vibration test, however, either a deterministic or a random excitation can be employed to meet the test requirements. This is known as the test environment.

Based on the vibration-testing specifications or product qualification requirements, the test environment should be developed to have the required characteristics of (1) intensity (amplitude), (2) frequency content (effect on the test-object resonances and the like), (3) decay rate (damping), and (4) phasing (dynamic interactions). Usually, these parameters are chosen to represent conservatively the worst possible vibration environment that is reasonably expected during the design life of the test object. So long as this requirement is satisfied, it is not necessary for the test environment to be identical to the operating vibration environment.

In vibration testing, the excitation input (test environment) can be represented in several ways. The common representations are (1) by time signal, (2) by response spectrum, (3) by Fourier spectrum, and (4) by PSD function. Once the required environment is specified by one of these forms, the test should be conducted either by directly employing them to drive the exciter or by using a more conservative excitation when the required environment cannot be exactly reproduced.

17.2.1 Test Signals

Vibration testing may employ both random and deterministic signals as test excitations. Regardless of its nature, the test input should conservatively meet the specified requirements for that test.

17.2.1.1 Stochastic vs. Deterministic Signals

Consider a seismic time-history record. Such a ground-motion record is not stochastic. It is true that earthquakes are random phenomena and the mechanism by which the time history was produced is a random process. Once a time history is recorded, however, it is known completely as a curve of response value versus time (a deterministic function of time). Therefore, it is a deterministic set of information. However, it is also a “sample function” of the original stochastic process, the earthquake, by which it was generated. Hence, valuable information about the original stochastic process itself can be determined by analyzing this sample function on the basis of the *ergodic hypothesis* (see Section 17.2.3). Some may think that an irregular time-history record corresponds to a random signal. It should be remembered that some random processes produce very smooth signals. As an example, consider the sine wave given by $a \sin(\omega t + \phi)$. Let us assume that the amplitude a and the frequency ω are deterministic quantities and the phase angle ϕ is a random variable. This is a random process. Every time this particular random process is activated, a sine wave is generated that has the same amplitude and frequency but, generally, a different phase angle. Nevertheless, the sine wave will always appear as smooth as a deterministic sine wave.

In a vibration-testing program, if we use a recorded time history to derive the exciter, it is a deterministic signal, even if it was originally produced by a random phenomenon such as an earthquake. Also, if we use a mathematical expression for the signal in terms of completely known (deterministic) parameters, it is again a deterministic signal. If the signal is generated by some random mechanism (whether computer simulation or physical) in real time, however, and if that signal is used as the excitation in the vibration test simultaneously as it is being generated, then we have a truly random excitation. Also, if we use a mathematical expression (with respect to time) for the excitation signal for which some of the parameters are not known numerically and the values are assigned to them during the test in a random manner, we again have a truly random test signal.

17.2.2 Deterministic Signal Representation

In vibration testing, time signals that are completely predefined can be used as test excitations. They should be capable, however, of subjecting the test object to the specified levels of intensity, frequency, decay rate, and phasing (in the case of simultaneous multiple test excitations).

Deterministic excitation signals (time histories) used in vibration testing are divided into two broad categories: single-frequency signals and multifrequency signals.

17.2.2.1 Single-Frequency Signals

Single-frequency signals have only one predominant frequency component at a given time. For the entire duration, however, the frequency range covered is representative of the frequency content of the vibration environment. For seismic-qualification purposes, for example, this range should be at least 1 to 33 Hz. Some typical single-frequency signals that are used as excitation inputs in vibration testing of equipment are shown in [Figure 17.2](#). The signals shown in the figure can be expressed by simple mathematical expressions. This is not a requirement, however. It is acceptable to store a very complex signal in a storage device and subsequently use it in the procedure. In picking a particular time history, we should give

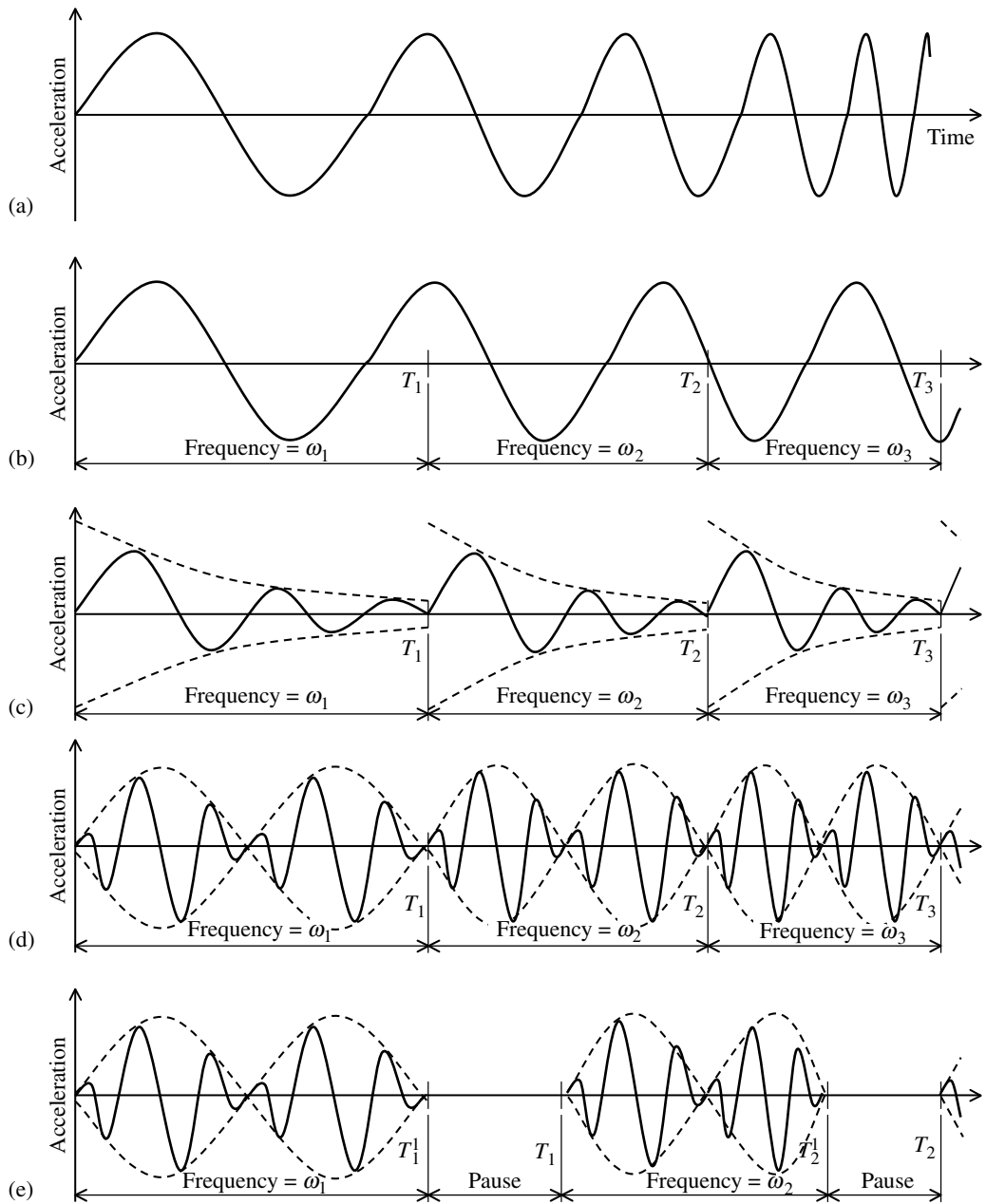


FIGURE 17.2 Typical single-frequency test signals: (a) sine sweep; (b) sine dwell; (c) sine decay; (d) sine beat; (e) sine beat with pause.

proper consideration to its ease of reproduction and the accuracy with which it satisfies the test specifications. Now, let us describe mathematically the acceleration signals shown in Figure 17.2.

17.2.2.2 Sine Sweep

We obtain a sine sweep by continuously varying the frequency of a sine wave. Mathematically,

$$u(t) = a \sin[\omega(t)t + \phi] \tag{17.1}$$

The amplitude, a , and the phase angle, ϕ , are usually constants and the frequency, $\omega(t)$, is a function of time. Both linear and exponential variations of frequency over the duration of the test are in common usage, but exponential variations are more common. For the linear variation (see Figure 17.3), we have

$$\omega(t) = \omega_{\min} + (\omega_{\max} - \omega_{\min}) \frac{t}{T_d} \quad (17.2)$$

in which

ω_{\min} = lowest frequency in the sweep

ω_{\max} = highest frequency in the sweep

T_d = duration of the sweep

For the exponential variation (see Figure 17.3), we have

$$\log \left[\frac{\omega(t)}{\omega_{\min}} \right] = \frac{t}{T_d} \log \left[\frac{\omega_{\max}}{\omega_{\min}} \right] \quad (17.3)$$

or

$$\omega(t) = \omega_{\min} \left[\frac{\omega_{\max}}{\omega_{\min}} \right]^{t/T_d} \quad (17.4)$$

This variation is sometimes incorrectly called logarithmic variation. This confusion arises because of its definition using Equation 17.3 instead of Equation 17.4. It is actually an inverse logarithmic (i.e., exponential) variation. Note that the logarithm in Equation 17.3 can be taken to any arbitrary base. If base ten is used, the frequency increments are measured in *decades* (multiples of ten); if base two is used, the frequency increments are measured in *octaves* (multiples of two). Thus, the number of decades in the frequency range from ω_1 to ω_2 is given by $\log_{10}(\omega_2/\omega_1)$; for example, with $\omega_1 = 1$ rad/sec and $\omega_2 = 100$ rad/sec, we have $\log_{10}(\omega_2/\omega_1) = 2$, which corresponds to two decades. Similarly, the number of octaves in the range ω_1 to ω_2 is given by $\log_2(\omega_2/\omega_1)$. Then, with $\omega_1 = 2$ rad/sec and $\omega_2 = 32$ rad/sec we have $\log_2(\omega_2/\omega_1) = 4$, a range of four octaves. Note that these quantities are ratios and have no physical units. The foregoing definitions can be extended for smaller units; for instance, one-third octave represents increments of $2^{1/3}$. Thus, if we start with 1 rad/sec and increment the frequency successively by one-third octave, we obtain 1, $2^{1/3}$, $2^{2/3}$, 2, $2^{4/3}$, $2^{5/3}$, 2^2 , and so on. It is clear, for example, that there are four one-third octaves in the frequency range from $2^{2/3}$ to 2^2 . Note that ω is known as the angular frequency (or radian frequency) and is usually measured in units of radians per second (rad/sec).

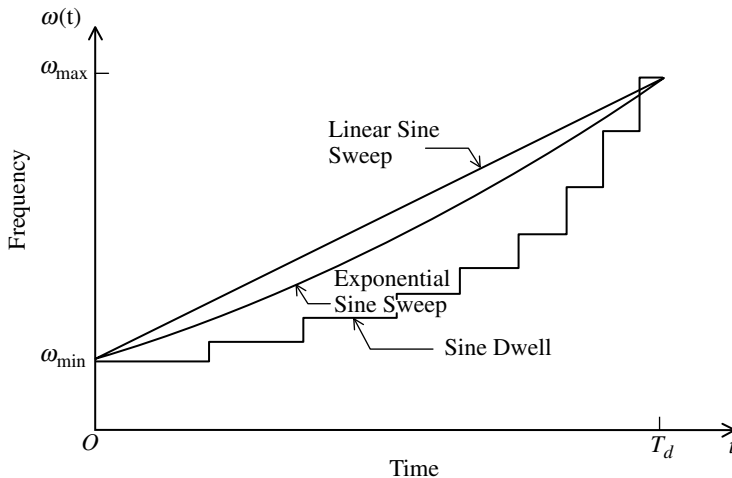


FIGURE 17.3 Frequency variation in some single-frequency vibration-test signals.

The more commonly used frequency is the cyclic frequency which is denoted by f . This is measured in hertz (Hz), which is identical to cycles per second (cps). It is clear that

$$f = \frac{\omega}{2\pi} \quad (17.5)$$

This is true because there are 2π radians in one cycle.

So that all important vibration frequencies of the test object (or its model) are properly excited, the sine sweep rate should be as slow as is feasible. Typically, rates of one octave per minute or slower are employed.

17.2.2.3 Sine Dwell

Sine-dwell signal is the discrete version of a sine sweep. The frequency is not varied continuously but is incremented by discrete amounts at discrete time points. This is shown graphically in [Figure 17.3](#). Mathematically, for the r th time interval, the dwell signal is

$$u(t) = a \sin(\omega_r t + \phi_r), \quad T_{r-1} \leq t \leq T_r \quad (17.6)$$

in which ω_r , a , and ϕ are kept constant during the time interval (T_{r-1}, T_r) . The frequency can be increased by a constant increment or the frequency increments can be made bigger with time (exponential-type increment). The latter procedure is more common. Also, the dwelling-time interval is usually made smaller as the frequency is increased. This is logical because, as the frequency increases, the number of cycles that occur during a given time also increases. Consequently, steady-state conditions may be achieved in a shorter time.

Sine-dwell signals can be specified using either a graphical form (see [Figure 17.3](#)) or a tabular form, giving the dwell frequencies and corresponding dwelling-time intervals. The amplitude is usually kept constant for the entire duration $(0, T_d)$, but the phase angle, ϕ , may have to be changed with each frequency increment in order to maintain the continuity of the signal.

17.2.2.4 Decaying Sine

Actual transient vibration environments (e.g., seismic ground motions) decay with time as the vibration energy is dissipated by some means. This decay characteristic is not present, however, in sine-sweep and sine-dwell signals. Sine-decay representation is a sine dwell with decay (see [Figure 17.2](#)). For an exponential decay, the counterpart of Equation 17.6 can be written as

$$u(t) = a \exp(-\lambda_r t) \sin(\omega_r t + \phi_r), \quad T_{r-1} \leq t \leq T_r \quad (17.7)$$

The damping parameter (the inverse of the time constant), λ , is typically increased with each frequency increment in order to represent the increased decay rates of a dynamic environment (or increased modal damping) at higher frequencies.

17.2.2.5 Sine Beat

When two sine waves having the same amplitude but different frequencies are mixed together (added or subtracted), a sine beat is obtained. This signal is considered to be a sine wave having the average frequency of the two original waves, which is amplitude-modulated by a sine wave of frequency equal to half the difference of the frequencies of the two original waves. The amplitude modulation produces a transient effect which is similar to that caused by the damping term in the sine-decay equation (Equation 17.7). The sharpness of the peaks becomes more prominent when the frequency difference of the two frequencies is made smaller.

Consider two cosine wave having frequencies $(\omega_r + \Delta\omega_r)$ and $(\omega_r - \Delta\omega_r)$ and the same amplitude $a/2$. If the first signal is subtracted from the second (that is, it is added with a 180° phase shift from the first wave), we obtain

$$u(t) = \frac{a}{2} [\cos(\omega_r - \Delta\omega_r)t - \cos(\omega_r + \Delta\omega_r)t] \quad (17.8)$$

By straightforward use of trigonometric identities, we obtain

$$u(t) = a(\sin \omega_r t)(\sin \Delta \omega_r t), \quad T_{r-1} \leq t \leq T_r \tag{17.9}$$

This is a sine wave of amplitude, a , and frequency, ω , modulated by a sine wave of frequency $\Delta\omega_r$. Sine-beat signals are commonly used as test excitation inputs in vibration testing. Usually, the ratio $\omega_r/\Delta\omega_r$ is kept constant. A typical value used is 20, in which case we obtain 10 cycles per beat. Here, cycles refer to the cycles at the higher frequency, ω_r , and a beat occurs at each half cycle of the smaller frequency, $\Delta\omega_r$. Thus, a beat is identified by a peak of amplitude a in the modulated wave and the beat frequency is $2\Delta\omega_r$.

As in the case of a sine dwell, the frequency, ω_r , of a sine-beat excitation signal is incremented at discrete time points, T_r , so as to cover the entire frequency interval of interest ($\omega_{\min}, \omega_{\max}$). It is a common practice to increase the size of the frequency increment and decrease the time duration at a particular frequency, for each frequency increment, just as is done for the sine dwell. The reasoning for this is identical to that given for sine dwell. The number of beats for each duration is usually kept constant (typically at a value over seven). A sine-beat signal is shown in [Figure 17.2\(d\)](#).

17.2.2.6 Sine Beat with Pauses

If we include pauses between sine-beat durations, we obtain a sine-beat signal with pauses. Mathematically, we have

$$u(t) = \begin{cases} a(\sin \omega_r t)(\sin \Delta \omega_r t), & \text{for } T_{r-1} \leq t \leq T_r', \\ 0, & \text{for } T_r' \leq t \leq T_r \end{cases} \tag{17.10}$$

This situation is shown in [Figure 17.2\(e\)](#). When a sine-beat signal with pauses is specified as a test excitation, we must give the frequencies, the corresponding time intervals, and the corresponding pause times. Typically, the pause time is also reduced with each frequency increment.

The single-frequency signal relations described in this section are summarized in [Table 17.1](#).

17.2.2.7 Multifrequency Signals

In contrast to single-frequency signals, multifrequency signals usually appear irregular and can have more than one predominant frequency component at a given time. Three common examples of multifrequency signals are aerodynamic disturbances, actual earthquake records, and simulated road disturbance signals used in automotive dynamic tests.

TABLE 17.1 Typical Single-Frequency Signals Used in Vibration Testing

Single Frequency Acceleration Signal	Mathematical Expression
Sine sweep	$u(t) = a \sin[\omega(t)t + \phi]$ $\omega(t) = \omega_{\min} + (\omega_{\max} - \omega_{\min})t/T_d \text{ (linear)}$ $\omega(t) = \omega_{\min} \left(\frac{\omega_{\max}}{\omega_{\min}} \right)^{t/T_d} \text{ (exponential)}$
Sine dwell	$u(t) = a \sin(\omega_r t + \phi_r) \quad T_{r-1} \leq t \leq T_r, \quad r = 1, 2, \dots, n$
Decaying sine	$u(t) = a \exp(-\lambda_r t) \sin(\omega_r t + \phi_r) \quad T_{r-1} \leq t \leq T_r, \quad r = 1, 2, \dots, n$
Sine beat	$u(t) = a(\sin \omega_r t)(\sin \Delta \omega_r t) \quad T_{r-1} \leq t \leq T_r, \quad r = 1, 2, \dots, n,$ $\omega_r/\Delta\omega_r = \text{constant}$
Sine beat with pauses	$u(t) = \begin{cases} a(\sin \omega_r t)(\sin \Delta \omega_r t), & \text{for } T_{r-1} \leq t \leq T_r' \\ = 0, & \text{for } T_r' \leq t \leq T_r \end{cases}$

17.2.2.8 Actual Excitation Records

Typically, actual excitation records such as overhead guideway vibrations are sample functions of random processes. By analyzing these deterministic records, however, characteristics of the original stochastic processes can be established, provided that the records are sufficiently long. This is possible because of the *ergodic hypothesis*. Results thus obtained are not quite accurate, because the actual excitation signals are usually nonstationary random processes and hence are not quite ergodic. Nevertheless, the information obtained by a Fourier analysis is useful in estimating the amplitude, phase, and frequency-content characteristics of the original excitation. In this manner, we can choose a past excitation record that can conservatively represent the design-basis excitation for the object that needs to be tested.

Excitation time histories can be modified to make them acceptably close to a design-basis excitation by using spectral-raising and spectral-suppressing methods. In spectral-raising procedures, a sine wave of required frequency is added to the original time history to improve its capability of excitation at that frequency. The sine wave should be properly phased such that the time of maximum vibratory motion in the original time history is unchanged by the modification. Spectral suppressing is achieved, essentially, by using a narrowband reject filter for the frequency band that needs to be removed. Physically, this is realized by passing the time history signal through a linearly damped oscillator that is tuned to the frequency to be rejected and connected in series with a second damper. The damping of this damper is chosen to obtain the required attenuation at the rejected frequency.

17.2.2.9 Simulated Excitation Signals

Random-signal-generating algorithms can be easily incorporated into digital computers. Also, physical experiments can be developed that have a random mechanism as an integral part. A time history from any such random simulation, once generated, is a sample function. If the random phenomenon is accurately programmed or physically developed so as to conservatively represent a design-basis excitation, a signal from such a simulation may be employed in vibration testing. Such test signals are usually available either as analog records on magnetic tapes or as digital records on a computer disk. Spectral-raising and spectral-suppressing techniques, mentioned earlier, also may be considered as methods of simulating vibration test excitations.

Before we conclude this section, it is worthwhile to point out that all test excitation signals considered in this section are oscillatory. Though the single-frequency signals considered may possess little resemblance to actual excitations on a device during operation, they can be chosen to possess the required decay, magnitude, phase, and frequency-content characteristics. During vibration testing, these signals, if used as excitations, will impose reversible stresses and strains on the test object, whose magnitudes, decay rates, and frequencies are representative of those that would be experienced during actual operation during the design life of the test object.

17.2.3 Stochastic Signal Representation

To generate a truly stochastic signal, a random phenomenon must be incorporated into the signal-generating process. The signal has to be generated in real time, and its numerical value at a given time is unknown until that time instant is reached. A stochastic signal cannot be completely specified in advance, but its statistical properties may be prespecified. There are many ways of obtaining random processes, including physical experimentation (for example, by tossing a coin at equal time steps and assigning a value to the magnitude over a given time step depending on the outcome of the toss), observation of processes in nature (such as outdoor temperature), and digital-computer simulation. The last procedure is the one commonly used in signal generation associated with vibration testing.

17.2.3.1 Ergodic Random Signals

A random process is a signal that is generated by some random (stochastic) mechanism. Generally, each time the mechanism is operated, a different signal (sample function) is generated. The likelihood of any two sample functions becoming identical is governed by some probabilistic law. The random process is

denoted by $X(t)$, and any sample function by $x(t)$. It should be remembered that no numerical computations can be made on $X(t)$ because it is not known for certain. Its Fourier transform, for instance, can be written as an analytical expression but cannot be computed. Once a sample function, $x(t)$, is generated, however, any numerical computation can be performed on it because it is a completely known function of time. This important difference may be somewhat confusing.

At any given time, t_1 , $X(t_1)$ is a random variable that has a certain probability distribution. Consider a well-behaved function, $f\{X(t_1)\}$, of this random variable (which is also a random variable). Its expected value (statistical mean) is denoted $E[f\{X(t_1)\}]$. This is also known as the ensemble average because it is equivalent to the average value at t_1 of a collection (ensemble) of a large number of sample functions of $X(t)$.

Now, consider the function $f\{x(t)\}$ of one sample function $x(t)$ of the random process. Its temporal (time) mean is expressed by

$$\lim_{T \rightarrow \infty} \frac{1}{2T} \int_{-T}^T f\{x(t)\} dt$$

Now, if

$$E[f\{X(t_1)\}] = \lim_{T \rightarrow \infty} \frac{1}{2T} \int_{-T}^T f\{x(t)\} dt \quad (17.11)$$

then the random signal is said to be ergodic. Note that the right-hand side of Equation 17.11 does not depend on time. Hence, the left-hand side also should be independent of the time point t_1 .

As a result of this relation (known as the *ergodic hypothesis*), we can obtain the properties of a random process merely by performing computations using one of its sample functions. The ergodic hypothesis links the stochastic domain of expectations and uncertainties and the deterministic domain of real records and actual numerical computations. Digital Fourier computations, such as correlation functions and spectral densities, would not be possible for random signals if not for this hypothesis.

17.2.3.2 Stationary Random Signals

If the statistical properties of a random signal, $X(t)$, are independent of the time point considered, it is stationary. In particular, $X(t_1)$ will have a probability density that is independent of t_1 , and the joint probability of $X(t_1)$ and $X(t_2)$ will depend only on the time difference, $t_2 - t_1$. Consequently, the mean value $E[X(t)]$ of a stationary random signal is independent of t , and the autocorrelation function defined by

$$E[X(t)X(t + \tau)] = \phi_{xx}(\tau) \quad (17.12)$$

which depends on τ and not on t . Note that ergodic signals are always stationary, but the converse is not always true.

Consider Parseval's theorem:

$$\int_{-\infty}^{\infty} x^2(t) dt = \int_{-\infty}^{\infty} |X(f)|^2 df \quad (17.13)$$

This can be interpreted as an energy integral, and its value is usually infinite for random signals. An appropriate measure for random signals is its power. This is given by its root-mean-square (RMS) value $E[X(t)^2]$. PSD $\Phi(f)$ is the Fourier transform of the autocorrelation function $\phi(\tau)$ and, similarly, the latter is the inverse Fourier transform of the former. Hence,

$$\phi_{xx}(\tau) = \int_{-\infty}^{\infty} \Phi_{xx}(f) \exp(j2\pi f \tau) df \quad (17.14)$$

Now, from Equation 17.12 and Equation 17.14, we obtain

$$\text{RMS value} = E[X(t)^2] = \phi_{xx}(0) = \int_{-\infty}^{\infty} \Phi_{xx}(f) df \quad (17.15)$$

It follows that the RMS value of a stationary random signal is equal to the area under its PSD curve.

17.2.3.3 Independent and Uncorrelated Signals

Two random signals $X(t)$ and $Y(t)$ are independent if their joint distribution is given by the product of the individual distributions. A special case is that of uncorrelated signals, which satisfy

$$E[X(t_1)Y(t_2)] = E[X(t_1)]E[Y(t_2)] \quad (17.16)$$

Consider the stationary case, with mean values

$$\mu_x = E[X(t)] \quad (17.17)$$

$$\mu_y = E[Y(t)] \quad (17.18)$$

The *autocovariance functions* are given by

$$\varphi_{xx}(\tau) = E[\{X(t) - \mu_x\}\{X(t + \tau) - \mu_x\}] = \phi_{xx}(\tau) - \mu_x^2 \quad (17.19)$$

$$\varphi_{yy}(\tau) = E[\{Y(t) - \mu_y\}\{Y(t + \tau) - \mu_y\}] = \phi_{yy}(\tau) - \mu_y^2 \quad (17.20)$$

and the *cross-covariance function* is given by

$$\varphi_{xy}(\tau) = E[\{X(t) - \mu_x\}\{Y(t + \tau) - \mu_y\}] = \phi_{xy}(\tau) - \mu_x\mu_y \quad (17.21)$$

For uncorrelated signals (Equation 17.16)

$$\phi_{xy}(\tau) = \mu_x\mu_y \quad (17.22)$$

and from Equation 17.21 it follows that

$$\varphi_{xy}(\tau) = 0 \quad (17.23)$$

The correlation-function coefficient is defined by

$$\rho_{xy}(\tau) = \frac{\varphi_{xy}(\tau)}{\sqrt{\varphi_{xx}(0)\varphi_{yy}(0)}} \quad (17.24)$$

which satisfies

$$-1 \leq \rho_{xy}(\tau) \leq 1 \quad (17.25)$$

For uncorrelated signals, $\rho_{xy}(\tau) = 0$. This function measures the degree of correlation of the two signals.

The correlation of two random signals, $X(t)$ and $Y(t)$, is measured in the frequency domain by its *ordinary coherence function*

$$\gamma_{xy}^2(f) = \frac{|\Phi_{xy}(f)|^2}{\Phi_{xx}(f)\Phi_{yy}(f)} \quad (17.26)$$

which satisfies the condition

$$0 \leq \gamma_{xy}^2(f) \leq 1 \quad (17.27)$$

17.2.3.4 Transmission of Random Excitations

When the excitation input to a system is a random signal, the corresponding system response will also be random. Consider the system shown by the block diagram in [Figure 17.4\(a\)](#). The response of the system

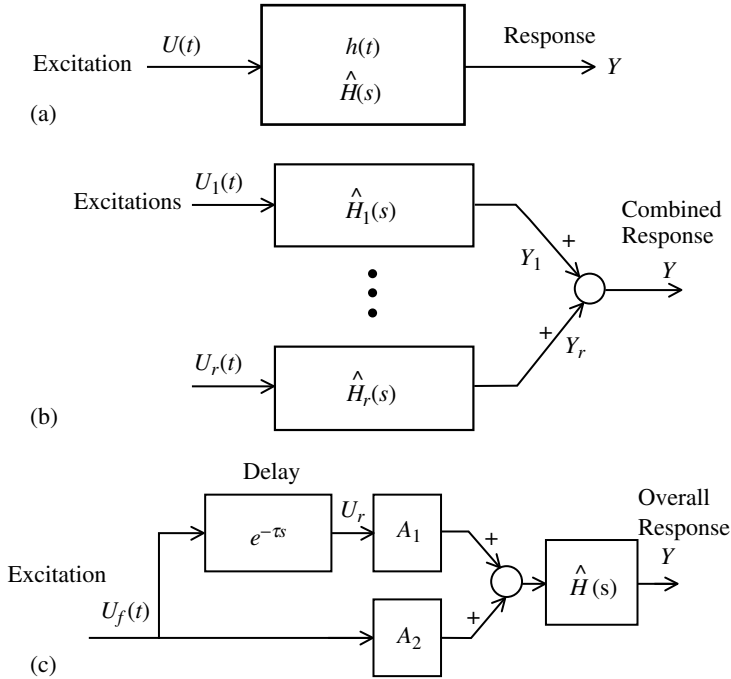


FIGURE 17.4 Combined response of a system to various random excitations: (a) system excited by a single input; (b) response to several random excitations; (c) response to a delayed excitation.

is given by the convolution integral

$$Y(t) = \int_{-\infty}^{\infty} h(t_1)U(t - t_1)dt_1 \quad (17.28)$$

in which the response PSD is given by the Fourier transform

$$\Phi_{yy}(f) = \Im\{E[Y(t)Y(t + \tau)]\} \quad (17.29)$$

Now, by using Equation 17.28 in Equation 17.29, in conjunction with the definition of Fourier transform, we can write

$$\Phi_{yy}(f) = \int_{-\infty}^{\infty} d\tau \exp(-j2\pi f\tau) E\left[\int_{-\infty}^{\infty} dt_1 h(t_1)U(t - t_1) \int_{-\infty}^{\infty} dt_2 h(t_2)U(t + \tau - t_2)\right]$$

which can be expressed as

$$\Phi_{yy}(f) = \int_{-\infty}^{\infty} dt_1 h(t_1) \int_{-\infty}^{\infty} dt_2 h(t_2) \int_{-\infty}^{\infty} d\tau \exp(-j2\pi f\tau) \phi_{uu}(\tau + t_1 - t_2)$$

Now, by letting $\tau' = \tau + t_1 - t_2$, we can write

$$\Phi_{yy}(f) = \left[\int_{-\infty}^{\infty} h(t_1)\exp(j2\pi ft_1)dt_1\right] \left[\int_{-\infty}^{\infty} h(t_2)\exp(-j2\pi ft_2)dt_2\right] \left[\int_{-\infty}^{\infty} \phi_{uu}(\tau')\exp(-j2\pi f\tau')d\tau'\right]$$

Note that $U(t)$ is assumed to be *stationary*.

Next, since the frequency-response function is given by the Fourier transform of the impulse response function, we obtain

$$\Phi_{yy}(f) = H^*(f)H(f)\Phi_{uu}(f) \quad (17.30)$$

in which $H^*(f)$ is the complex conjugate of $H(f)$. Alternatively, if $|H(f)|$ denotes the magnitude of the complex quantity, we can write

$$\Phi_{yy}(f) = |H(f)|^2 \Phi_{uu}(f) \quad (17.31)$$

By using Equation 17.30 or Equation 17.31, we can determine the PSD of the system response from the PSD of the excitation if the system-frequency-response function is known.

In a similar manner, it can be shown that the cross-spectral density function may be expressed as

$$\Phi_{uy}(f) = H(f) \Phi_{uu}(f) \quad (17.32)$$

Now, consider r stationary, independent, random excitations, U_1, U_2, \dots, U_r , (which are assumed to have zero-mean values, without loss of generality) applied to r subsystems, having transfer functions $\hat{H}_1(s), \hat{H}_2(s), \dots, \hat{H}_r(s)$, as shown in Figure 17.4(b). The total response, Y , consists of the sum of individual responses, Y_1, Y_2, \dots, Y_r . It can be shown that Y_1, Y_2, \dots, Y_r are also stationary, independent, zero-mean, random processes. By definition, we have

$$\phi_{yy}(\tau) = E[\{Y_1(t) + \dots + Y_r(t)\}\{Y_1(t + \tau) + \dots + Y_r(t + \tau)\}] \quad (17.33)$$

Now, for independent, zero-mean Y_i , Equation 17.33 becomes

$$\phi_{yy}(\tau) = E[Y_1(t)Y_1(t + \tau)] + \dots + E[Y_r(t)Y_r(t + \tau)] \quad (17.34)$$

Since Y_i are stationary, we have

$$\phi_{yy}(\tau) = \phi_{y_1y_1}(\tau) + \dots + \phi_{y_ry_r}(\tau) \quad (17.35)$$

On Fourier transformation, we obtain

$$\Phi_{yy}(f) = \Phi_{y_1y_1}(f) + \dots + \Phi_{y_ry_r}(f) \quad (17.36)$$

In view of Equation 17.31, it can be written

$$\Phi_{yy}(f) = \sum_{i=1}^r |H_i(f)|^2 \Phi_{u_iu_i}(f) \quad (17.37)$$

from which the response PSD can be determined if the input PSDs are known.

If all inputs, $U_i(t)$, have identical probability distributions (for example, when they are generated by the same mechanism), the corresponding PSDs will be identical. Note that this does not imply that the inputs are equal. They could be dependent, independent, correlated, or uncorrelated. In this case, Equation 17.37 becomes

$$\Phi_{yy}(f) = \left[\sum_{i=1}^r |H_i(f)|^2 \right] \Phi_{uu}(f) \quad (17.38)$$

in which $\Phi_{uu}(f)$ is the common input PSD.

Finally, consider the linear combination of two excitations, $U_f(t)$ and $U_r(t)$, with the latter excitation delayed in time by τ but otherwise identical to the former. This situation is shown in Figure 17.4(c). From Laplace transform tables, it is seen that the Laplace transforms of the two signals are related by

$$U_r(s) = \exp(-\tau s) U_f(s) \quad (17.39)$$

From Equation 17.39, it follows that (see Figure 17.4(c)):

$$Y(s) = (A_1 \exp(-\tau s) + A_2) H(s) U_f(s) \quad (17.40)$$

Consequently, we have

$$\Phi_{yy}(f) = |(A_1 \exp(-j2\pi f\tau) + A_2) H(f)|^2 \Phi_{uu}(f) \quad (17.41)$$

From this result, the net response can be determined when the phasing between the two excitations is known. This has applications, for example, in determining the response of a vehicle to road disturbances at the front and rear wheels.

17.2.4 Frequency-Domain Representations

In this section, we shall discuss the Fourier spectrum method and the PSD method of representing a test excitation. These are frequency-domain representations.

17.2.4.1 Fourier Spectrum Method

Since the time domain and the frequency domain are related through Fourier transformation, a time signal can be represented by its Fourier spectrum. In vibration testing, a required Fourier spectrum may be given as the test specification. Then, the actual input signal that is used to excite the test object should have a Fourier spectrum that envelops the required Fourier spectrum. The generation of a signal to satisfy this requirement might be difficult. Usually, digital Fourier analysis of the control sensor signal is necessary to compare the actual (test) Fourier spectrum with the required Fourier spectrum. If the two spectra do not match in a certain frequency band, the error (i.e., the difference in the two spectra) is fed back to correct the situation. This process is known as *frequency-band equalization*. Also, the sample step of the time signal in the digital Fourier analysis should be adequately small to cover the frequency range of interest in that particular vibration testing application. Advantages of using digital Fourier analysis in vibration testing include flexibility and convenience with respect to the type of the signal that can be analyzed, availability of complex processing capabilities, increased speed of processing, accuracy and reliability, reduction in the test cost, practically unlimited repeatability of processing, and reduction in the overall size and weight of the analyzer.

17.2.4.2 Power Spectral Density Method

The operational vibration environment of equipment is usually random. Consequently, a stochastic representation of the test excitation appears to be suitable for a majority of vibration-testing situations. One way of representing a stationary random signal is by its PSD. As noted before, the numerical computation of the PSD is not possible, however, unless the ergodicity is assumed for the signal. Using the ergodic hypothesis, we can compute the PSD of a random signal simply by using one sample function (one record) of the signal.

Three methods of determining the PSD of a random signal are shown in Figure 17.5. From Parseval’s theorem (Equation 17.13), we notice that the mean square value of a random signal may be obtained from the area under the PSD curve. This suggests the method shown in Figure 17.5(a) for estimating the PSD of a signal. The mean square value of a sample of the signal in the frequency band, Δf , having a certain center frequency is obtained by first extracting the signal components in the band and then squaring them. This is done for several samples and averaged to obtain a high accuracy. It is then divided by Δf . By repeating this for a range of center frequencies, an estimate for the PSD is obtained.

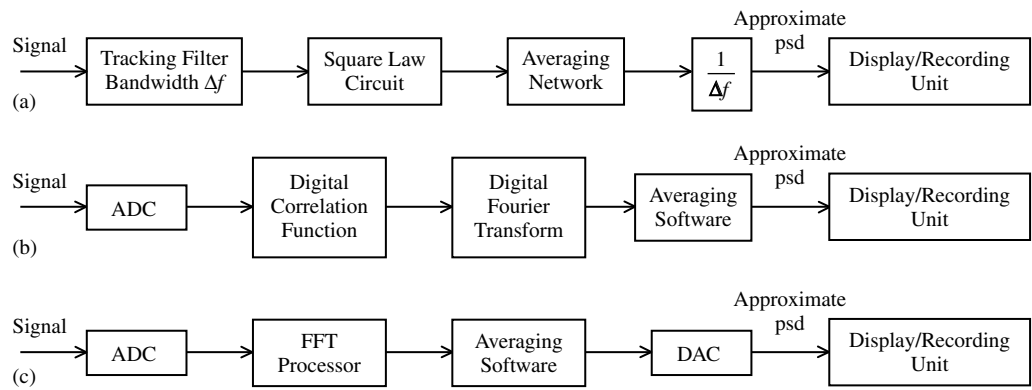


FIGURE 17.5 Some methods of PSD determination: (a) the filtering, squaring, and averaging method; (b) using an autocorrelation function; (c) using direct FFT.

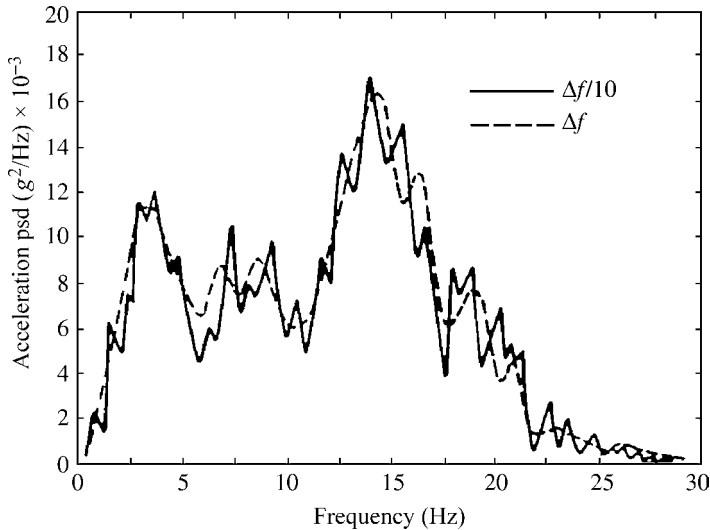


FIGURE 17.6 Effect of filter bandwidth on PSD results.

In the second scheme, shown in Figure 17.5(b), correlation function is first computed digitally. Its Fourier transform (by fast Fourier transform, or FFT) gives an estimate of the PSD.

In the third scheme, shown in Figure 17.5(c), the PSD is computed directly using FFT. Here, the Fourier spectrum of the sample record is computed and the PSD is estimated directly, without first computing the autocorrelation function.

In these numerical techniques of computing PSD, a single sample function will not give the required accuracy, and averaging results for a number of sample records is usually needed. In real-time digital analysis, the running average and the current estimate are normally computed. In the running average, it is desirable to give a higher weighting to the more recent estimates. The fluctuations about the local average in the PSD estimate could be reduced by selecting a larger filter bandwidth, Δf (see Figure 17.6), and a large record length T . A measure of this fluctuation is given by

$$\varepsilon = \frac{1}{\sqrt{\Delta f T}} \quad (17.42)$$

It should be noted that increasing Δf results in reduction of the precision of the estimates while improving the appearance. To offset this, T must be increased further, or averaging must be done for several sample records.

Generating a test-input signal with a PSD that satisfactorily compares with the required PSD can be a tedious task if one attempts to do it manually by mixing various signal components. A convenient method is to use an automatic multiband equalizer. By this means, the mean amplitude of the signal in each small frequency band of interest can be made to approach the spectrum of the specified vibration environment (see Figure 17.7). Unfortunately, this type of random-signal vibration testing can be more costly than testing with deterministic signals.

17.2.5 Response Spectrum

Response spectra are commonly used to represent signals associated with vibration testing. A given signal has a certain fixed response spectrum, but many different signals can have the same response spectrum. For this reason, as will be clear shortly, the original signal cannot be reconstructed from its response spectrum (unlike in the case of a Fourier spectrum). This is a disadvantage. However, the physical significance of a response spectrum makes it a good representation for a test signal.

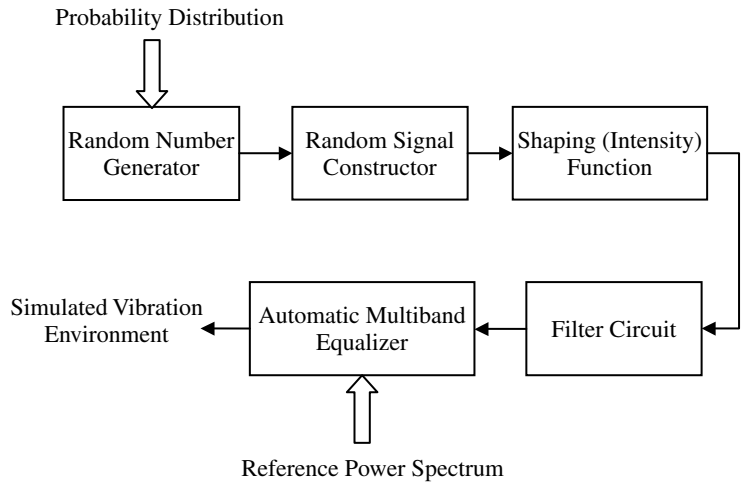


FIGURE 17.7 Generation of a specified random vibration environment.

If a given signal is applied to a single-degree-of-freedom (single-DoF) oscillator (of a specific natural frequency), and the response of the oscillator (mass) is recorded, we can determine the maximum (peak) value of that response. Suppose that we repeat the process for a number of different oscillators (having different natural frequencies) and then plot the peak response values thus obtained against the corresponding oscillator natural frequencies. This procedure is shown schematically in Figure 17.8. For an infinite number of oscillators (or for the same oscillator with continuously variable natural frequency), we get a continuous curve, which is called the response spectrum of the given signal. It is obvious, however, that the original signal cannot be completely determined from the knowledge of its response spectrum alone. As shown in Figure 17.8, for instance, another signal, when passed through a given oscillator, might produce the same peak response.

Note that we have assumed the oscillators to be undamped; the response spectrum obtained using undamped oscillators corresponds to $\zeta = 0$. If all the oscillators are damped, however, and have the same damping ratio, ζ , the resulting response spectrum will correspond to that particular ζ . It is, therefore, clear that ζ is also a parameter in the response-spectrum representation. We should specify the damping value as well when we represent a signal by its response spectrum.

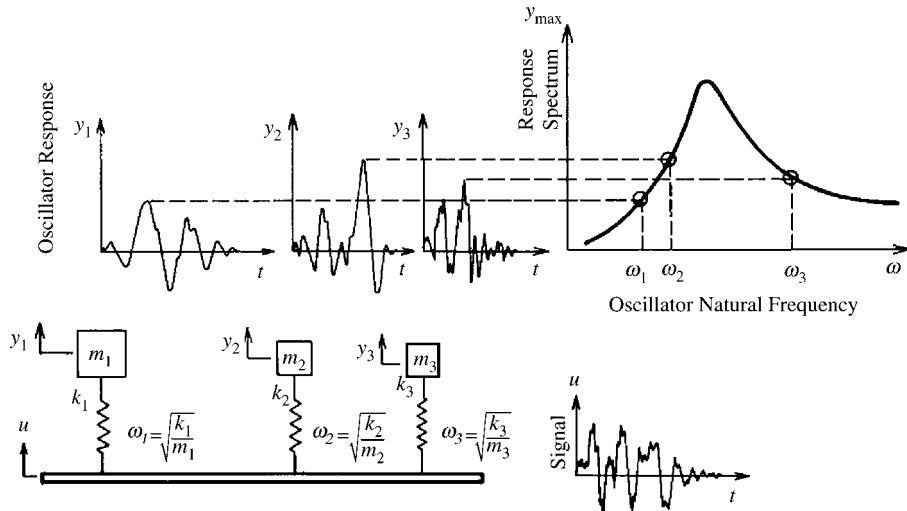


FIGURE 17.8 Definition of the response spectrum of a signal.

17.2.5.1 Displacement, Velocity, and Acceleration Spectra

It is clear that a motion signal can be represented by the corresponding displacement, velocity, or acceleration. First, consider a displacement signal, $u(t)$. The corresponding velocity signal is $\dot{u}(t)$ and the acceleration is $\ddot{u}(t)$.

Now consider an undamped simple oscillator, which is subjected to a support displacement $u(t)$, as shown in Figure 17.9. As usual, assuming that the displacements are measured with respect to a static equilibrium configuration, the gravity effect can be ignored. Then, the equation of motion is given by

$$m\ddot{y}_d = k(u - y_d) \quad (17.43)$$

or

$$\ddot{y}_d + \omega_n^2 y_d = \omega_n^2 u(t) \quad (17.44)$$

where the (undamped) natural frequency is given by

$$\omega_n = \sqrt{\frac{k}{m}} \quad (17.45)$$

Suppose that the support (displacement) excitation, $u(t)$, is a unit impulse $\delta(t)$. Then, the corresponding (displacement) response y is called the impulse-response function, and is denoted by $h(t)$. It is known that $h(t)$ is the inverse Laplace transform (with zero initial condition) of the transfer function of the system (Equation 17.44), as given by

$$H(s) = \frac{\omega_n^2}{(s^2 + \omega_n^2)} \quad (17.46)$$

The impulse-response function (to an impulsive support excitation) for an undamped, single-DoF oscillator having natural frequency ω_n is given by

$$h(t) = \omega_n \sin \omega_n t \quad (17.47)$$

The displacement response $y_d(t)$ of this oscillator, when excited by the displacement signal $u(t)$, is given by the convolution integral

$$y_d(t) = \omega_n \int_0^\infty u(\tau) \sin \omega_n(t - \tau) d\tau \quad (17.48)$$

The “velocity” response of the same oscillator, when excited by the velocity signal, $\dot{u}(t)$, is given by

$$y_v(t) = \omega_n \int_0^\infty \dot{u}(\tau) \sin \omega_n(t - \tau) d\tau \quad (17.49)$$

and the “acceleration” response when excited by the acceleration signal, $\ddot{u}(t)$, is

$$y_a(t) = \omega_n \int_0^\infty \ddot{u}(\tau) \sin \omega_n(t - \tau) d\tau \quad (17.50)$$

These results immediately follow from Equation 17.44. Specifically, differentiate Equation 17.44 once to obtain

$$\ddot{y}_v + \omega_n^2 y_v = \omega_n^2 \dot{u}(t) \quad (17.51)$$

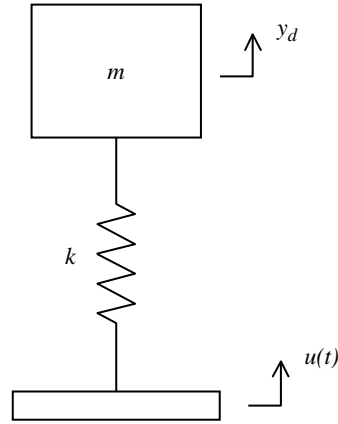


FIGURE 17.9 Undamped simple oscillator subjected to a support excitation.

and differentiate again, to obtain

$$\ddot{y}_a + \omega_n^2 y_a = \omega_n^2 \ddot{u}(t) \quad (17.52)$$

in which

$$y_v = \frac{dy_d}{dt} \quad (17.53)$$

$$y_a = \frac{d^2 y_d}{dt^2} = \frac{dy_v}{dt} \quad (17.54)$$

If the peak value of $y_d(t)$ is plotted against ω_n , we get the *displacement-spectrum* curve of the displacement signal, $u(t)$. If the peak value of $y_v(t)$ is plotted against ω_n , we get the *velocity-spectrum* curve of the displacement signal, $u(t)$. If the peak value of $y_a(t)$ is plotted against ω_n , we get the *acceleration-spectrum* curve of the displacement signal, $u(t)$. Now consider Equation 17.49. Integration by parts gives

$$y_v(t) = [\omega_n u(\tau) \sin \omega_n(t - \tau)]_0^\infty + \omega_n^2 \int_0^\infty u(\tau) \cos \omega_n(t - \tau) d\tau \quad (17.55)$$

The initial and final conditions for $u(t)$ are assumed to be zero. It follows that the first term in Equation 17.55 vanishes. The second term is $\omega_n [y_d(t + \pi/2\omega_n - \tau)]$, which is clear by noting that $\sin \omega_n(t + \pi/2\omega_n - \tau)$ is equal to $\cos \omega_n(t - \tau)$; thus

$$y_v(t) = -\omega_n y_d \left(t + \frac{\pi}{2\omega_n} \right) \quad (17.56)$$

If we integrate Equation 17.50 by parts twice, and apply the end conditions as before, we obtain

$$y_a(t) = -\omega_n^2 y_d(t) \quad (17.57)$$

By taking the peak values of response time histories, we see from Equation 17.56 and Equation 17.57 that

$$v(\omega_n) = \omega_n d(\omega_n) \quad (17.58)$$

$$a(\omega_n) = \omega_n^2 d(\omega_n) \quad (17.59)$$

in which $d(\omega_n)$, $v(\omega_n)$, and $a(\omega_n)$ represent the displacement spectrum, the velocity spectrum, and the acceleration spectrum, respectively, of the displacement time history, $u(t)$. It follows from Equation 17.58 and Equation 17.59 that

$$a(\omega_n) = \omega_n v(\omega_n) \quad (17.60)$$

17.2.5.2 Response-Spectra Plotting Paper

Response spectra are usually plotted on a frequency-velocity coordinate plane or on a frequency-acceleration coordinate plane. Values are normally plotted in logarithmic scale, as shown in [Figure 17.10](#). First, consider the axes shown in Figure 17.10(a). Obviously, constant velocity lines are horizontal for this coordinate system. From Equation 17.58, the constant-displacement line corresponds to

$$v(\omega_n) = c \omega_n$$

By taking logarithms of both sides, we obtain

$$\log v(\omega_n) = \log \omega_n + \log c$$

It follows that the constant-displacement lines have a slope of +1 on the logarithmic frequency-velocity plane. Similarly, from Equation 17.60, the constant-acceleration lines correspond to

$$\omega_n v(\omega_n) = c$$

Hence,

$$\log v(\omega_n) = -\log \omega_n + \log c$$

It follows that the constant-acceleration lines have a slope of negative one on the logarithmic frequency–velocity plane. Similarly, it can be shown from Equation 17.59 and Equation 17.60 that, on the logarithmic frequency–acceleration plane (Figure 17.10(b)), the constant-displacement lines have a slope of +2, and the constant-velocity lines have a slope of +1.

On the frequency–velocity plane, a point corresponds to a specific frequency and a specific velocity. The corresponding displacement at the point is obtained (Equation 17.58) by dividing the velocity value by the frequency value at that point. The corresponding acceleration at that point is obtained (Equation 17.60) by multiplying the particular velocity value by the frequency value. Any units may be used for displacement, velocity, and acceleration quantities. A typical logarithmic frequency–velocity plotting sheet is shown in Figure 17.11. Note that the sheet is already graduated on constant displacement, velocity, and acceleration lines. Also, a period axis (period = 1/cyclic frequency) is given for convenience in plotting. A plot of this type is called a *nomograph*.

17.2.5.3 Zero-Period Acceleration

Frequently, response spectra are specified in terms of accelerations rather than velocities. This is particularly true in vibration testing associated with product qualification, because typical operational disturbance records are usually available as acceleration time histories. No information is lost because the logarithmic frequency–acceleration plotting paper can be graduated for velocities and displacements as well. It is, therefore, clear that an acceleration quantity (peak) on a response spectrum has a corresponding velocity quantity (peak), and a displacement quantity (peak). In vibration testing, however, the motion variable that is in common usage is the acceleration. Zero-period acceleration (ZPA) is an important parameter that characterizes a response spectrum. It should be remembered, however, that zero-period velocity or zero-period displacement can be similarly defined.

ZPA is defined as the acceleration value (peak) at zero period (or infinite frequency) on a response spectrum. Specifically,

$$\text{ZPA} = \lim_{\omega_n \rightarrow \infty} a(\omega_n) \quad (17.61)$$

Consider the damped simple oscillator equation (for support motion excitation):

$$\ddot{y} + 2\zeta\omega_n\dot{y} + \omega_n^2 y = \omega_n^2 u(t) \quad (17.62)$$

By differentiating Equation 17.62 throughout, either once or twice, it is seen, as in Equation 17.51 and Equation 17.52, that if u and y initially refer to displacements, then the same equation is valid when both of them refer to either velocities or accelerations. Let us consider the case in which u and y refer to input and response acceleration variables, respectively. Consider a sinusoidal

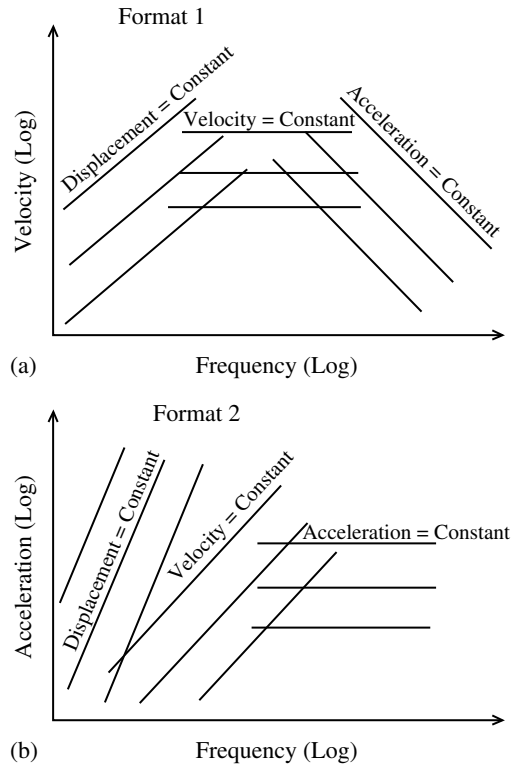


FIGURE 17.10 Response-spectra plotting formats: (a) frequency–velocity plane; (b) frequency–acceleration plane.

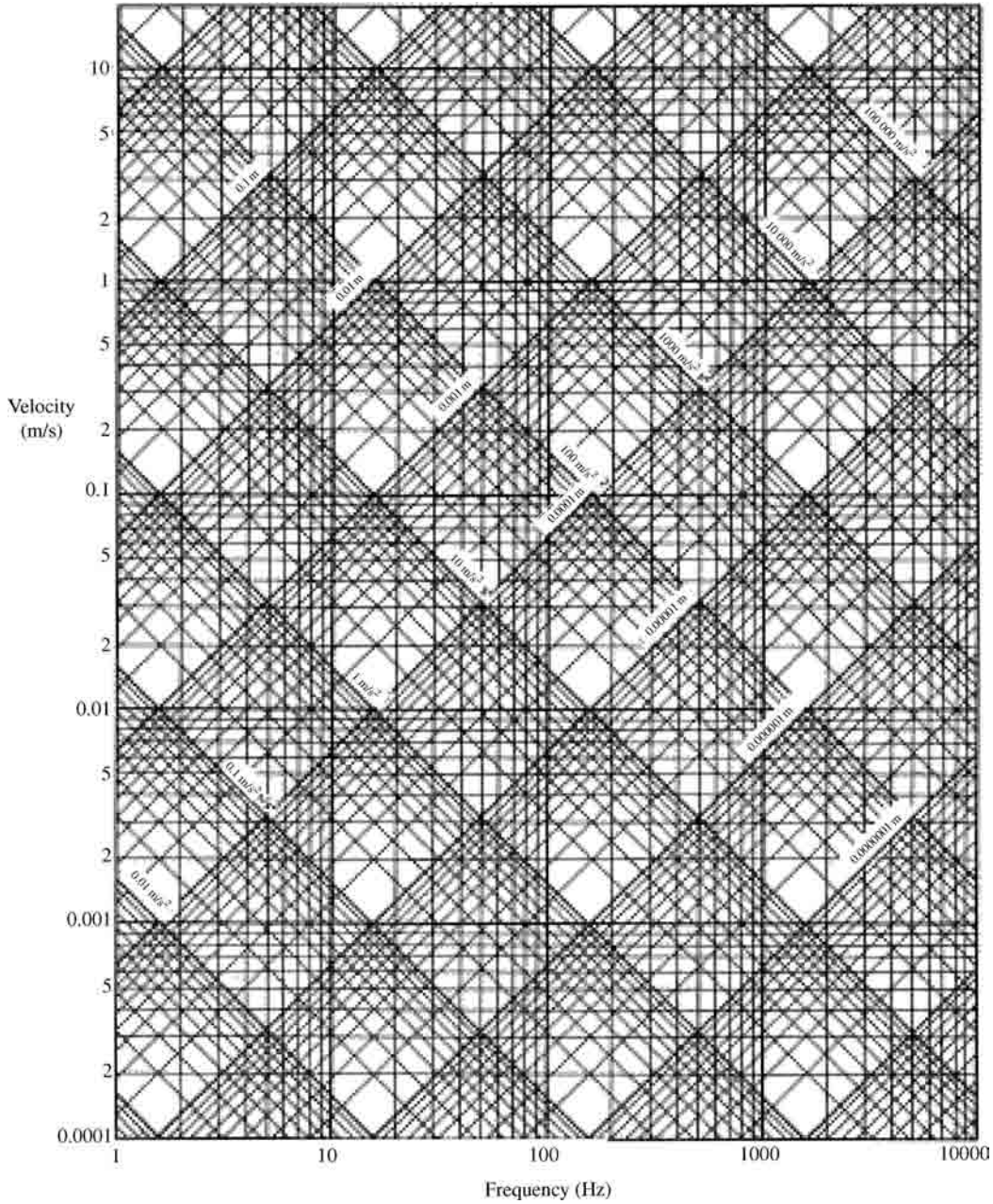


FIGURE 17.11 Response-spectra plotting sheet or nomograph (frequency–velocity plane).

signal, $u(t)$, given by

$$u(t) = A \sin \omega t \tag{17.63}$$

The resulting response, $y(t)$, neglecting the transient components (that is, the steady-state value), is given by

$$y(t) = A \frac{\omega_n^2}{\sqrt{(\omega_n^2 - \omega^2)^2 + 4\zeta^2 \omega_n^2 \omega^2}} \sin(\omega t + \phi) \tag{17.64}$$

Hence, the acceleration-response spectrum, given by $a(\omega_n) = [y(t)]_{\max}$, for a sinusoidal signal of frequency, ω , and amplitude, A , is

$$a(\omega_n) = A \frac{\omega_n^2}{\sqrt{(\omega_n^2 - \omega^2)^2 + 4\zeta^2 \omega_n^2 \omega^2}} \quad (17.65)$$

A plot of this response is shown in Figure 17.12. Note that $a(0) = 0$. Also,

$$\text{ZPA} = \lim_{\omega_n \rightarrow \infty} a(\omega_n) = A \quad (17.66)$$

It is worth observing that at the point $\omega_n = \omega$ (i.e., when the excitation frequency, ω , is equal to the natural frequencies, ω_n , of the simple oscillator), we have $a(\omega_n) = A/(2\zeta)$, which corresponds to an amplification by a factor of $1/(2\zeta)$ over the ZPA value.

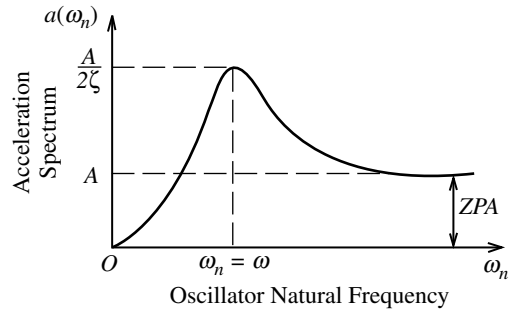


FIGURE 17.12 Response spectrum and ZPA of a sine signal.

17.2.5.4 Uses of Response Spectra

In vibration testing, response-spectra curves are employed to specify the dynamic environment to which the test object is required to be subjected. This specified response spectrum is known as the *required response spectrum* (RRS). In order to satisfy conservatively the test specification, the response spectrum of the actual test input excitation, known as the test response spectrum (TRS), should envelop the RRS. Note that, when response spectra are used to represent excitation input signals in vibration testing, the damping value of the hypothetical oscillators used in computing the response spectrum has no bearing on the actual damping that is present in the test object. In this application, the response spectrum is merely a representation of the shaker-input signal and, therefore, does not depend on system damping.

Another use of response spectra is in estimating the peak value of the response of a multi-DoF or distributed-parameter system when it is excited by a signal whose response spectrum is known. To understand this concept, we recall the fact that, for a multi-DoF or truncated (approximated) distributed-parameter system having distinct natural frequencies, the total response can be expressed as a linear combination of the individual modal responses. Specifically, the response $y(t)$ can be written

$$y(t) = \sum_{i=1}^r \alpha_i a(\omega_i) \exp \left[\frac{-\zeta_i \omega_i t}{\sqrt{1 - \zeta_i^2}} \right] \sin(\omega_i t + \phi_i) \quad (17.67)$$

in which the spectrum, $a(\omega_i)$, is comprised of the amplitude contributions from each mode (simple oscillator equation), with “damped” natural frequency, ω_i . Hence, $a(\omega_i)$ corresponds to the value of the response spectrum at frequency ω_i . The linear combination parameters, α_i , depend on the modal-participation factors and can be determined from system parameters. Since the peak values of all terms in the summation on the right-hand side of Equation 17.67 do not occur at the same time, we observe that

$$[y(t)]_{\text{peak}} < \sum_{i=1}^r \alpha_i a(\omega_i) \quad (17.68)$$

It follows that the right-hand side of the inequality (Equation 17.68) is a conservative upper-bound estimate (i.e., the absolute sum) for the peak response of the multi-DoF system. Some prefer to make the estimate less conservative by taking the square root of sum of the squares (SRSS):

$$[y(t)]_{\text{SRSS}} = \left[\sum_{i=1}^r \alpha_i^2 a^2(\omega_i) \right]^{1/2} \quad (17.69)$$

The latter method, however, has the risk of giving an estimate that is less than the true value. Note that, in this application, the damping value associated with the response spectrum is directly related to modal damping of the system. Hence, the response spectrum, $a(\omega_i)$, should correspond to the same damping ratio as that of the mode considered within the summation of the inequality (Equation 17.68). If all modal damping ratios, ζ_i , are identical or nearly so, the same response spectrum could be used to compute all terms in the inequality 17.68. Otherwise, different response-spectra curves should be used to determine each quantity, $a(\omega_i)$, depending on the applicable modal damping ratio, ζ_i .

17.2.6 Comparison of Various Representations

In this section, we shall state some major advantages and disadvantages of the four representations of the vibration environment that we have discussed.

Time-signal representation has several advantages. It can be employed to represent either deterministic or random vibration environment. It is an exact representation of a single excitation event. Also, when performing multiexcitation (multiple shaker) vibration testing, phasing between the various inputs can be conveniently incorporated simply by delaying each excitation with respect to the others. There are also disadvantages to time-signal representation. Since each time history represents just one sample function (a single event) of a random environment, it may not be truly representative of the actual vibration excitation. This can be overcome by using longer signals, which, however, will increase the duration of the test, which is limited by test specifications. If the random vibration is truly ergodic (or at least stationary), this problem will not be as serious. Furthermore, the problem does not arise when testing with deterministic signals. An extensive knowledge of the true vibration environment to which the test object is subjected is necessary, however, in order to conclude that it is stationary or that it could be represented by a deterministic signal. In this sense, time-signal representation is difficult to implement.

The response-spectrum method of representing a vibration environment has several advantages. It is relatively easy to implement. Since the peak response of a simple oscillator is used in its definition, it is representative of the peak response or structural stress of simple dynamic systems; hence, there is a direct relation to the behavior of the physical object. An upper bound for the peak response of a multi-DoF system can be conveniently obtained by the method outlined in Section 17.2.5.4. Also, by considering the envelope of a set of response spectra at the same damping value, it is possible to use a single response spectrum to conservatively represent more than one excitation event. The method also has disadvantages. It employs deterministic signals in its definition. Sample functions (single events) of random vibrations can be used, however. It is not possible to determine the original vibration signal from the knowledge of its response spectrum, because it uses the peak value of response of a simple oscillator (more than one signal can have the same response spectrum). Thus, a response spectrum cannot be considered a complete representation of a vibration environment. Also, characteristics such as the transient nature and the duration of the excitation event cannot be deduced from the response spectrum. For the same reason, it is not possible to incorporate information on excitation-signal phasing into the response-spectrum representation. This is a disadvantage in multiple excitation testing.

Fourier spectrum representation also has advantages. Since the actual dynamic environment signal can be obtained by inverse transformation, it has the same advantages as for the time-signal representation. In particular, since a Fourier spectrum is generally complex, phasing information of the test excitation can be incorporated into Fourier spectra, in multiple excitation testing. Furthermore, by considering an envelope Fourier spectrum (like an envelope response spectrum), it can be employed to represent conservatively more than one vibration environment. Also, it gives frequency-domain information (such as information about resonances), which is very useful in vibration testing situations. The disadvantages of Fourier spectrum representation include the following. It is a deterministic representation but, as in the response-spectrum method, a sample function (a single event) of a random vibration can be represented by its Fourier spectrum. Transient effects and event duration are hidden in this representation. Also, it is

somewhat difficult to implement, because complex procedures of multiband equalization might be necessary in the signal synthesis associated with this representation.

PSD representation has the following advantages. It takes the random nature of a vibration environment into account. As in response-spectrum and Fourier-spectrum representations, by taking an envelope PSD, it can be used to represent conservatively more than one environment. It can display important frequency-domain characteristics, such as resonances. Its disadvantages include the following. It is an exact representation only for truly stationary or ergodic random environments. In nonstationary situations, as in seismic ground motions, significant error could result. Also, it is not possible to obtain the original sample function (dynamic event) from its PSD. Hence, the transient characteristics and duration of the event are not known from its PSD. Since mean square values, not peak values, are considered, PSD representation is not structural-stress-related. Furthermore, since PSD functions are real (not complex), we cannot incorporate phasing information into them. This is a disadvantage in multiple excitation testing situations, but this problem can be overcome by considering either the cross spectrum (which is complex) or the cross correlation in each pair of test excitations.

Random vibration testing is compared with sine testing (single-frequency, deterministic excitations) in Box 17.1. A comparison of various representations of test excitations is given in Box 17.2.

Box 17.1

RANDOM TESTING VS. SINE TESTING

Advantages of Random Testing:

1. More realistic representation of the true environment
2. Many frequencies are applied simultaneously
3. All resonances, natural frequencies, and mode shapes are excited simultaneously

Disadvantages of Random Testing:

1. Needs more power for testing
2. Control is more difficult
3. More costly

Advantages of Sine Testing:

Appropriate for:

1. Fatigue testing of products that operate primarily at a known speed (frequency) under in-service conditions
2. Detecting sensitivity of a device to a particular excitation frequency
3. Detecting resonances, natural frequencies, modal damping, and mode shapes
4. Calibration of vibration sensors and control systems

Disadvantages of Sine Testing:

1. Usually not a good representation of the true dynamic environment
2. Because vibration energy is concentrated at one frequency, it can cause failures that would not occur in service (particularly single-resonance failures)
3. Since only one mode is excited at a time, it can hide multiple-resonance failures that might occur in service

Box 17.2

COMPARISON OF TEST EXCITATION REPRESENTATIONS

Property	Time Signal	Response Spectrum	Fourier Spectrum	Power Spectral Density
True representation of a deterministic environment?	Yes	Yes	Yes	No
True representation of a random environment?	One sample function	One sample function	One sample function	Yes
Frequency–time reversible?	Yes	No	Yes	No
Signal phasing possible for multiaxis testing?	Yes	No	Yes	No
Good representation of peak amplitude/stress events?	Yes	Yes	No	No
Explicit accounting for modal responses	No	Yes	Yes	Yes

In practice, the generation of an excitation signal for vibration testing may not follow any one of the analytical procedures and may incorporate a combination of them. For example, a combination of sine-beat signals of different frequencies with random phasing is one practical approach to the generation of a multifrequency, pseudo-random excitation signal. This approach is summarized in Box 17.3.

17.3 Pretest Procedures

The selection of a test procedure for the vibration testing of an object should be based on technical information regarding the test object and its intended use. Vendors usually prefer to use more established, conventional testing methods and are generally reluctant to incorporate modifications and

Box 17.3

TEST SIGNAL GENERATION

- Steps:
1. Generate a set of sine beats at discrete frequencies of interest for the vibration test, having specified amplitudes.
 2. Phase shift (time shift) the signal components from Step 1 according to a random number generator.
 3. Sum the signal components from Step 2.

improvements. This is primarily due to economic reasons, convenience, testing-time limitation, availability of the equipment and facilities (test-lab limitations), and similar factors. Regulatory agencies, however, usually modify their guidelines from time to time, and some of these requirements are mandatory.

Before conducting a vibration test on a test object, it is necessary to follow several pretest procedures. Such procedures are necessary in order to conduct a meaningful test. Some important pretest procedures include the following:

1. Understanding the purpose of the test
2. Studying the service functions of the test object
3. Acquiring information on the test object
4. Planning the test program
5. Conducting pretest inspection of the test object
6. Resonance-searching to gather dynamic information about the test object
7. Mechanically aging the test object

In the following sections, we shall discuss each of the first five items of these procedures to emphasize how they can contribute to a meaningful test. The last two items will be considered separately, in Section 17.4 on Testing Procedures.

17.3.1 Purpose of Testing

As noted before, vibration testing is useful in various stages of (1) design and development, (2) production and quality assurance, and (3) qualification and utilization of a product. Depending on the outcome of a vibration test, design modifications or corrective actions can be recommended for a preliminary design or a partial product. To determine the most desirable location (in terms of minimal noise and vibration), for the compressor in a refrigerator unit, for example, a resonance-search test could be employed. As another example, vibration testing can be employed to determine vibration-isolation material requirements in structures for providing adequate damping. Such tests fall into the first category of system development tests. They are beneficial for the designer and the manufacturer in improving the quality of performance of the product. Government regulatory agencies do not usually stipulate the requirements for this category of tests, but they sometimes stipulate minimal requirements for safety and performance levels of the final product, which can indirectly affect the development-test requirements. Custom-made items are exceptions for which the customers could stipulate the design-test requirements.

For special-purpose products, it is sometimes also necessary to conduct a vibration test on the final product before its installation for service operation. For mass-produced items, it is customary to select representative samples from each batch of the product for these tests. The purpose of such test is to detect any inferiorities in the workmanship or in the materials used. These tests fall into the second category, quality-assurance tests. These usually consist of a standard series of routine tests that are well established for a given product.

Distribution qualification and seismic qualification of devices and components are good examples of the use of the third category, qualification tests. A high-quality product such as a valve actuator, for instance, which is thoroughly tested in the design-development stage and at the final production stage, will need further dynamic tests or analysis if it is to be installed in a nuclear power plant. The purpose in this testing is to determine whether the product (valve actuator) will be crucial for system-safety-related functions. Government regulatory agencies usually stipulate basic requirements for qualification tests. These tests are necessarily application-oriented. The vendor or the customer might employ more elaborate test programs than those stipulated by the regulatory agency, but at least the minimum requirements set by the agency should be met before commissioning the plant.

The purpose of any vibration test should be clearly understood before incorporating it into a test program. A particular test might be meaningless under some circumstances. If it is known, for instance, that no resonances below 35 Hz exist in a particular piece of equipment that requires seismic

qualification, then it is not necessary to conduct a resonance search because the predominant frequency content of seismic excitations occurs below 35 Hz. If, however, the test serves a dual purpose, such as mechanical aging in addition to resonance detection, then it may still be conducted even if there are no resonances in the predominant frequency range of excitation.

If testing is performed on one test item selected from a batch of products to assure the quality of the entire batch or to qualify the entire batch, it is necessary to establish that all items in the batch are of identical design. Otherwise, testing of all items in the batch might be necessary unless some form-design similarity can be identified. "Qualification by similarity" is done in this manner.

The nature of the vibration testing that is employed will be usually governed by the test purpose. Single-frequency tests, using deterministic test excitations, for example, are well suited for design-development and quality-assurance applications. The main reason for this choice is that the test-input excitations can be completely defined; consequently, a complete analysis can be performed with relative ease, based on existing theories and dynamic models. Random or multifrequency tests are more realistic in a qualification test, however, because under typical service conditions, the dynamic environments to which an object is subjected are random and have multiple frequencies by nature (for example, seismic disturbances, ground-transit road disturbances, aerodynamic disturbances). Since random-excitation tests are relatively more expensive and complex in terms of signal generation and data processing, single-frequency tests might also be employed in qualification tests. Under some circumstances, single-frequency testing could add excessive conservatism to the test excitation. It is known, for instance, that single-frequency tests are justified in the qualification of line-mounted equipment (i.e., equipment mounted on pipe lines, cables, and similar "line" structures), which can encounter in-service disturbances that are amplified because of resonances in the mounting structure.

17.3.2 Service Functions

For product qualification by testing, it is required that the test object remain functional and maintain its structural integrity when subjected to a certain prespecified dynamic environment. In seismic qualification of equipment, for instance, the dynamic environment is an excitation that adequately represents the amplitude, phasing, frequency content, and transient characteristics (decay rate and signal duration) of the motions at the equipment-support locations, caused by the most severe seismic disturbance that has a reasonable probability of occurring during the design life of the equipment. Monitoring the proper performance of in-service functions (functional-operability monitoring) of a test object during vibration testing can be crucial in the qualification decision.

The intended service functions of the test object should be clearly defined prior to testing. For active equipment, functional operability is necessary during vibration testing. For passive equipment, however, only structural integrity need be maintained during testing.

17.3.2.1 Active Equipment

Equipment that should perform a mechanical motion (for example, valve closure, relay contact) or that produces a measurable signal (for example, an electrical signal, pressure, temperature, flow) during the course of performing its intended functions is termed active equipment. Some examples of active equipment are valve actuators, relays, motors, pumps, transducers, control switches, and data recorders.

17.3.2.2 Passive Equipment

Passive equipment typically performs containment functions and consequently should maintain a certain minimum structural strength or pressure boundary. Such equipment usually does not perform mechanical motions or produce measurable response signals, but it may have to maintain displacement tolerances. Some examples of passive equipment are piping, tanks, cables, supporting structures, and heat exchangers.

17.3.2.3 Functional Testing

When defining the intended functions of an object for test purposes, the following information should be gathered for each active component of the object that will be tested:

1. The maximum number of times a given function should be performed during the design life of the equipment
2. The best achievable precision (or monitoring tolerance) for each functional-operability parameter and the time duration for which a given precision is required
3. Mechanisms and states of malfunction or failure
4. Limits of the functional-operability parameters (electrical signals, pressures, temperatures, flow rates, mechanical displacements and tolerances, relay chatter, and so forth) that correspond to a state of malfunction or failure

It should be noted that, under a state of malfunction, the object will not perform the intended function properly. Under a failure state, however, the object will not perform its intended function at all.

For objects consisting of an assembly of several crucial components, it should be determined how a malfunction or failure of one component could result in the malfunction or failure of the entire unit. In such cases, any hardware redundancy (that is, when component failure does not necessarily cause unit failure) and possible interactive and chain effects (such as failure in one component overloading another, which could result in subsequent failure of the second component, and so on) should be identified. In considering functional precision, it should be noted that high precision usually means increased complexity of the test procedure. This is further complicated if a particular level of precision is required at a prescribed instant.

It is a common practice for the test object supplier (the customer) to define the functional test, including acceptance criteria and tolerances for each function, for the benefit of the test engineer. This information eventually is used in determining acceptance criteria for the tests of active equipment. Complexity of the required tests also depends on the precision requirements for the intended functions of the test object.

Examples of functional failure are sensor and transducer (measuring instrumentation) failure, actuator (motors, valves, and so forth) failure, chatter in relays, gyroscopic and electronic-circuit drift, and discontinuity of electrical signals because of short-circuiting. It should be noted that functional failures caused by mechanical excitation are often linked with the structural integrity of the test object. Such functional failures are primarily caused in two situations: (1) when displacement amplitude exceeds a certain critical value once or several times, or (2) when vibrations of moderate amplitudes occur for an extended period of time. Functional failures in the first category include, for example, short-circuiting, contact errors, instabilities and nonlinearities (in relays, amplifier outputs, etc.). Such failures are usually reversible, so that, when the excitation intensity drops, the system will function normally. Under the second category, slow degradation of components will occur because of aging, wear, and fatigue, which can cause drift, offset, etc., and subsequent malfunction or failure. This kind of failure is usually irreversible. We must emphasize that the first category of functional failure can be better simulated using high-intensity single-frequency testing and shock testing, and the second category by multifrequency or broadband random testing and low-intensity single-frequency testing.

For passive devices, a damage criterion should be specified. This could be expressed in terms of parameters such as cumulative fatigue, deflection tolerances, wear limits, pressure drops, and leakage rates. Often, damage or failure in passive devices can be determined by visual inspection and other nondestructive means.

17.3.3 Information Acquisition

In addition to information concerning service functions, as discussed in the previous section, and dynamic characteristics determined from a resonance search, as will be discussed later in this chapter, there are other characteristics of the test object that need to be studied in the development of a vibration

testing program. In particular, there are characteristics that cannot be described in exact quantitative terms. In determining the value of a piece of equipment, for instance, the monetary value (or cost) might be relatively easy to estimate, whereas it can be very difficult to assign a dollar value to its significance under service conditions. One reason for this is that a particular piece of equipment alone may not determine the proper operation of a complex system. Interaction of a particular unit with other subsystems in a complex operation would determine the importance attached to it and, hence, its value. In this sense, the true value of a test object is a relatively complex consideration. The service function of the test object is also an important consideration in determining its value. The value of a test object is important in planning a test program, because the cost of a test program and the effort expended therein are governed mainly by this factor.

Many features of a test object that are significant in planning a test program can be deduced from manufacturer's data for the particular object. The following information is representative:

1. Drawings (schematic or to scale when appropriate) of principal components and the whole assembly, with the manufacturer's name, identification numbers, and dimensions clearly indicated
2. Materials used, design strengths, fatigue life, and so on, of various components, and factors determining the structural integrity of the unit
3. Component weight and total weight of the unit
4. Design ratings, capacities, and tolerances for in-service operation of each crucial component
5. Description of the intended functions of each component and of the entire unit, clearly indicating the parameters that determine functional operability of the unit
6. Interface details (inter-component as well as for the entire assembly), including in-service mounting configurations and mounting details
7. Details of the probable operating site or operating environment (particularly with respect to the excitation events if product qualification is intended)
8. Details of any previous testing or analysis performed on that unit or a similar one

Scale drawings and component-weight information describe the size and geometry of the test object. This information is useful in determining the following:

1. The locations of sensors (accelerometers, strain gages, stroboscopes, and the like) for monitoring dynamic response of the test object during tests;
2. The necessary ratings for vibration test (shaker) apparatus (power, force, stroke, bandwidth, and so on);
3. The degree of dynamic interaction between the test object and the test apparatus;
4. The level of coupling between various DoFs and modal interactions in the test object;
5. The assembly level of the test object (for example, whether it can be treated as a single component, as a subsystem consisting of several components, or as an independent, stand-alone system)

In general, as the size and the assembly level increase, the tests become increasingly complex and difficult to perform. To test heavy, complex test objects, we require a large test apparatus with high power ratings and the capability of multiple excitation locations. In this case, the number of operability parameters that are monitored and the number of observation (sensor) locations also will increase.

17.3.3.1 Interface Details

The dynamics of a piece of equipment depend on the way the equipment is attached to its support structure. In addition to the mounting details, the dynamic response of equipments is affected by other interfacing linkages, such as wires, cables, conduits, pipes, and auxiliary instrumentation. In the vibration testing of equipment, such interface characteristics should be simulated appropriately. Dynamics of the test fixture and the details of the test object–fixture interface are very important considerations that affect the overall dynamics of the test object. If the interface characteristics are not properly represented during testing, a nonuniform test could result, in which case some parts of the test object are be overtested and

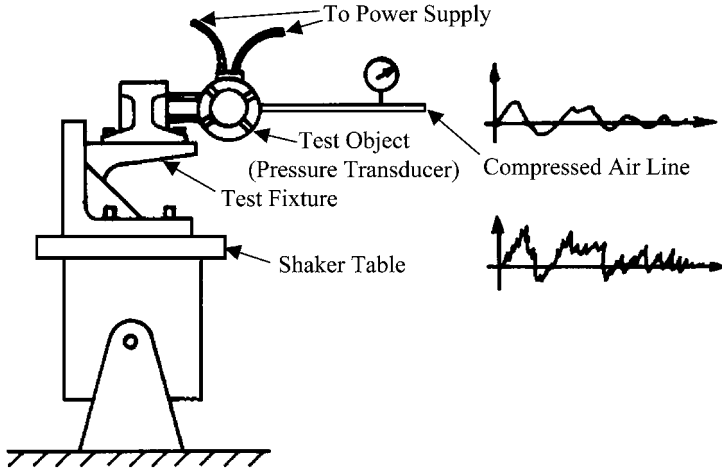


FIGURE 17.13 Influence of test fixture on the test excitation signal.

other parts undertested. This situation can bring about failures that are not representative of the failures that could take place in actual service. In effect, the testing could become meaningless if interface details are not simulated properly.

The test fixture is a structure attached to the shaker table and used to mount the test object (see Figure 17.13). Test-fixture dynamics can significantly modify the shaker-table motion before reaching the test object. Such modifications include filtering of the shaker motion and the introduction of auxiliary (cross-axis) motions. In the test set-up shown in Figure 17.13, for example, the direct motion will be modified to some extent by fixture dynamics. In addition, some transverse and rotational motion components will be transmitted to the test object by the test fixture because of its overhang.

To minimize interface-dynamic effects in vibration testing situations, an attempt should be made to (1) make the test fixture as light and as rigid as is feasible; (2) simulate in-service mounting conditions at the test object–fixture interface; and (3) simulate other interface linkages, such as cables, conduits, and instrumentation, to represent in-service conditions. Very often, the design of a proper test fixture can be a costly and time-consuming process. A trade-off is possible by locating the control sensors (accelerometers) at the mounting locations of the test object, and then using the error between the actual and the desired excitations through feedback to control the mounting-location excitations during testing.

17.3.3.2 Effect of Neglecting Interface Dynamics

We shall consider a simplified model to study some important effects of neglecting interface dynamics. In the model shown in Figure 17.14, the equipment and the mounting interface are modeled separately as single-DoF systems. Capital letters are used to denote the equipment parameters (mass, M ; stiffness, K ; and damping coefficient, C). When mounting-interface dynamics are included, the model appears as in Figure 17.14(a). When the mounting-interface dynamics are neglected, we obtain the single-DoF model shown in Figure 17.14(b). Note that, in the latter case, the shaker motion, $u(t)$, is directly applied to the equipment mounts whereas, in the former case, it is applied through the interface. If the equipment response in the two cases is denoted by y and \tilde{y} , respectively, one can see, by considering the system-frequency transfer functions, $Y(\omega)/U(\omega)$ and $\tilde{Y}(\omega)/U(\omega)$, that

$$\frac{\tilde{Y}(\omega)}{Y(\omega)} = \frac{Ms^2}{(Ms^2 + Cs + K)} \frac{(Cs + K)}{(cs + k)} + \frac{(ms^2 + cs + k)}{(cs + k)} \quad (17.70)$$

with $s = j\omega$. The following nondimensional parameters are defined:

$$\text{Mass ratio } \alpha = \frac{m}{M} \quad (17.71)$$

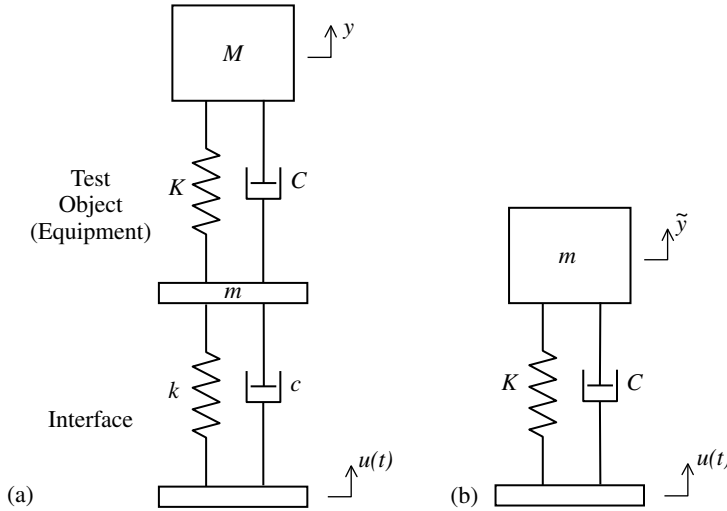


FIGURE 17.14 A simplified model to study the effect of interface dynamics: (a) with interface dynamics; (b) without interface dynamics.

$$\text{Natural frequency ratio } \beta = \frac{\omega_n}{\Omega_n} \quad (17.72)$$

$$\text{Normalized excitation frequency } \bar{\omega} = \frac{\omega}{\Omega_n} \quad (17.73)$$

in which the natural frequency (undamped) of the equipment is

$$\Omega_n = \sqrt{\frac{K}{M}} \quad (17.74)$$

and the mounting-interface natural frequency is

$$\omega_n = \sqrt{\frac{k}{m}} \quad (17.75)$$

Then, Equation 17.70 can be written

$$\frac{\tilde{Y}(\omega)}{Y(\omega)} = \frac{(\beta^2 + 2j\zeta\beta\bar{\omega} - \bar{\omega}^2)}{(\beta^2 + 2j\zeta\beta\bar{\omega})} - \frac{\bar{\omega}(1 + 2jZ\bar{\omega})}{\alpha(\beta^2 + 2j\zeta\beta\bar{\omega})(1 + 2jZ\bar{\omega} - \bar{\omega}^2)} \quad (17.76)$$

in which ζ and Z denote the damping ratios of the interface and the equipment, respectively.

The ratio $\tilde{Y}(\omega)/Y(\omega)$ is representative of the equipment-response amplification when interface-dynamic effects are neglected for a harmonic excitation. Figure 17.15 shows eight curves, corresponding to Equation 17.76, for the parameter combinations given in Table 17.2. Interpretation of the results becomes easier when peak values of the response ratios are compared for various parameter combinations. Sample results are given Table 17.2.

17.3.3.3 Effects of Damping

By comparing the cases from Case 1 to Case 4 in Table 17.2 with the cases from Case 5 to Case 8, respectively (comparing Case 1 with Case 5 and so forth), we see that increasing the interface damping has reduced the peak response (a favorable effect), irrespective of the values of the interface mass and natural frequency (α and β values).

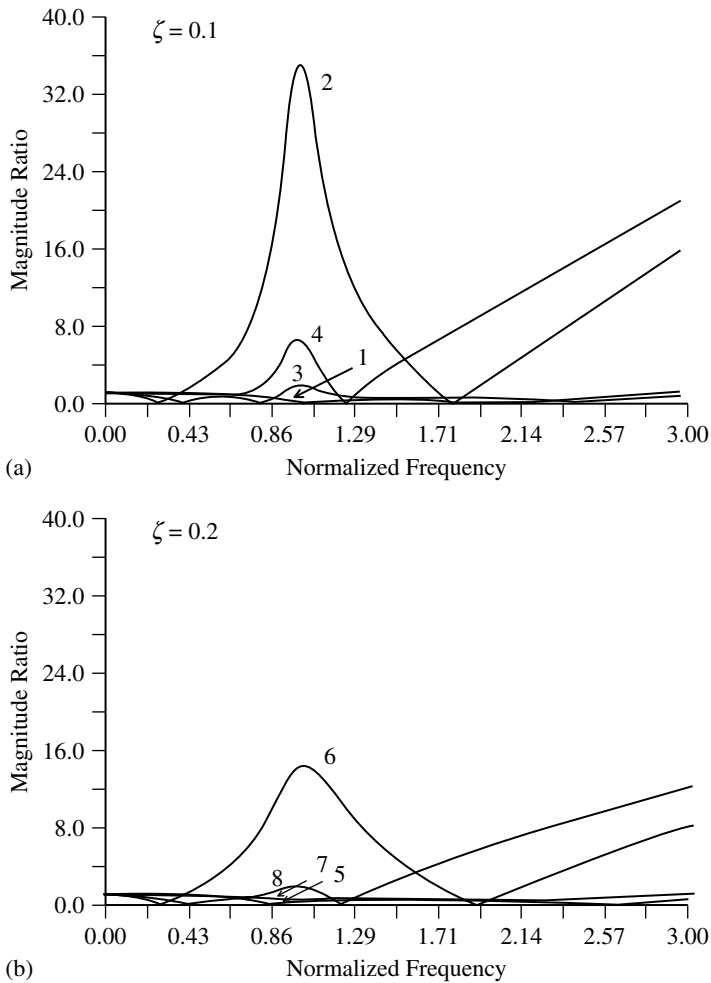


FIGURE 17.15 Response amplification when interface dynamic interactions are neglected.

17.3.3.4 Effects of Inertia

By comparing the cases from Case 1 to Case 4 in Table 17.2 with the cases from Case 5 to Case 8, respectively, we see that the interface inertia has a favorable effect in decreasing dynamic interaction, irrespective of the interface damping and natural frequency.

TABLE 17.2 Response Amplification Caused by Neglecting Interface Dynamics

Case (Curve No.)	Parameter Combination				Peak Value of Response Ratio
	ζ	α	β	Z	
1	0.1	2.0	2.0	0.1	1.11
2	0.1	0.5	0.5	0.1	38.80
3	0.1	0.5	2.0	0.1	2.77
4	0.1	2.0	0.5	0.1	17.80
5	0.2	2.0	2.0	0.2	0.89
6	0.2	0.5	0.5	0.2	18.40
7	0.2	0.5	2.0	0.2	1.71
8	0.2	2.0	0.5	0.2	5.98

17.3.3.5 Effect of Natural Frequency

By comparing the cases from Case 1 to Case 4 in [Table 17.2](#) with the cases from Case 5 to Case 8, respectively, we see that increasing the interface natural frequency has a favorable effect in decreasing dynamic interactions, irrespective of the interface damping and inertia.

17.3.3.6 Effect of Excitation Frequency

All the response plots ([see Figure 17.15](#)) diverge to ∞ as $\bar{\omega}$ increases. This indicates that, at very high excitation-input frequencies, dynamic-testing results can become meaningless because of the interactions with interface dynamics.

It can be concluded that, to reduce dynamic interactions caused by a mechanical interface, we should (1) increase interface damping as much as is feasible, (2) increase interface mass as much as is feasible, (3) increase interface natural frequency as much as is feasible, and (4) avoid testing at relatively high frequencies of excitation. It should be noted that, in the foregoing analysis and discussion, the mechanical interface was considered to include test fixtures and the shaker table as well.

17.3.3.7 Other Effects of Interface

The type of vibration test used sometimes depends on the mechanical interface characteristics. An example is the testing of line-mounted equipment. Single-frequency testing is preferred for such equipment so as to add a certain degree of conservatism because, as a result of interface resonances, line-mounted equipment could be subjected to higher levels of narrowband excitation through the support structure.

In vibration testing of multicomponent equipment cabinets, it is customary to test the empty cabinet first, with the components replaced by dummy weights, and then to test the individual components separately, using different test excitations depending on the component locations and their mounting characteristics. Mechanical interface details of individual components are important in such situations. As a result, interface information is an important constituent of the pretest information that is collected for a test object.

Most of the interface data, particularly information related to size and geometry (for example, mass, dimensions, configurations, and locations), can be gathered simply by observing the test object and using scale drawings supplied by the manufacturer. Knowledge of the size and number of anchor bolts used or the weld thickness, for example, can be obtained in this manner. When analysis is also used to augment testing, however, it is often necessary to know the loads transmitted (forces, moments, and so on), relative displacements, and stiffness values at the mechanical interface under in-service conditions. These must be determined by tests, by analysis (static or dynamic) of a suitable model, or from manufacturer's data.

17.3.4 Test-Program Planning

The test program to which a test object is subjected depends on several factors including the following:

1. The objectives and specific requirements of the test
2. In-service conditions, including equipment-mounting features, the vibration environment, and specifications of the test environment
3. The nature of the test object, including complexity, assembly level, and functional-operability parameters to be monitored
4. Test-laboratory capabilities, available testing apparatus, past experience, conventions, and established practices of testing

Some of these factors are based on solid technical reasons, whereas others depend on economics, convenience, and personal likes and dislikes.

Initially, it is not necessary to develop a detailed test procedure; this is required only at the stage of actual testing. In the initial stage it is only necessary to select the appropriate test method, based on factors such as those listed in the beginning of this section. Before conducting the tests, however, a test procedure should be prepared in sufficient detail. In essence, this is a pretest requirement.

Objectives and specific requirements of a test depend on such considerations as whether the test is conducted at the design stage, the quality-control stage or the utilization stage. The objective of a particular test could be to verify the outcome of a previously conducted test. In that case, it is necessary to assess the adequacy of one or a series of tests conducted at an earlier time (for instance, when the specifications and government regulations were less stringent). Often, this could be done by analysis alone. Some testing might be necessary at times, but it usually is not necessary to repeat the entire test program. If the previous tests were conducted for the frequency range 1 to 25 Hz, for example, and the present specifications require a wider range of 1 to 35 Hz, it might be adequate merely to demonstrate (by analysis or testing) that there are no significant resonances in the test object in the 25 to 35 Hz range.

If it is necessary to qualify the test object for several different dynamic environments, a generic test that represents (conservatively, but without the risk of overtesting) all these environments could be used. For this purpose, special test-excitation inputs must be generated, taking into account the variability of the excitation characteristics under the given set of environments. Alternatively, several tests might be conducted if the dynamic environments for which the test object is to be qualified are significantly different. Operating-basis earthquake (OBE) tests and safe-shutdown earthquake (SSE) tests in seismic qualification of nuclear power plant equipment, for example, represent two significantly different test conditions. Consequently, they cannot be represented by a single test. When qualifying an equipment for several geographic regions or locations, however, we might be able to combine all OBE tests into a single test and all SSE tests into another single test.

Another important consideration in planning a test program is the required accuracy for the test, including the accuracy for the excitation inputs, response and operability measurements, and analysis. This is related to the value of the test object and the objectives of the test.

When it is required to evaluate or qualify a group of equipment by testing a sample, it is first necessary to establish that the selected sample unit is truly representative of the entire group. When the items in the batch are not identical in all respects, some conservatism could be added to the tests to minimize the possibility of an incorrect qualification decision. It might be necessary to test more than one sample unit in such situations.

When planning a test procedure, we should clearly identify the standards, government regulations, and specifications that are applicable to a particular test. The pertinent sections of the applicable documents should be noted, and proper justification should be given if the tests deviate from regulatory-agency requirements.

The excitation input that is employed in a vibration test depends on the in-service vibration environment of the test object. The number of tests needed will also depend on this to some extent. Test orientation depends mainly on the mounting features and the mechanical interface details of the test object under in-service conditions. Mounting features might govern the nature of the test excitations used for a particular test.

Two distinct mounting types can be identified for most equipment: (1) *line-mounted equipment* and (2) *floor-mounted equipment*. Line-mounted equipment is equipment that is mounted upright or hanging from pipelines, cables, or similar line structures that are not rigid. Generally, devices such as valves, nozzles, valve actuators, and transducers are to be considered line-mounted equipment. Any equipment that is not line-mounted is considered floor-mounted. The supporting structure is considered to be relatively rigid in this case. Examples of such mounting structures are floors, walls, and rigid frames. Typical examples of floor-mounted equipment include motors, compressors, and cabinets of relays and switchgear.

Wide-band floor disturbances are filtered by line structures. Consequently, the environmental disturbances to which line-mounted equipment is subjected are generally narrowband disturbances. Accordingly, vibration testing of line-mounted equipment is best performed using narrowband random test excitations or single-frequency deterministic test excitations. Higher test intensities can be necessary for line-mounted equipment, because any low-frequency resonances that are present

in the mounting structure (which is relatively flexible in this case) can amplify the excitations before reaching the equipment.

Floor-mounted equipment often requires relatively wide-band random test excitations. As an example, consider a pressure transducer mounted on (1) a rigid wall, (2) a rigid I-section frame, (3) a pressurized gasline, or (4) a cabinet. In cases (1) and (2), wide-band random excitations with response spectra approximately equal to the floor-response spectra can be employed for vibration testing of the pressure transducer. For cases (3) and (4), however, flexibility of the support structure should be taken into consideration in developing the RRS specifications for vibration testing. In case (3), a single-frequency deterministic test, such as a sine-beat test or a sine-dwell test, can be employed, giving sufficient attention to testing at the equipment-resonant frequencies. In case (4), single-frequency tests can also be employed if the cabinet is considerably flexible and not rigidly attached to a rigid structure (a floor or a wall). Alternatively, a wide-band test on the cabinet itself, with the pressure transducer mounted on it, could be used.

Size, complexity, assembly level, and related features of a test object can significantly complicate and extend the test procedure. In such cases, testing the entire assembly might not be practical and testing of individual components or subassemblies might not be adequate because, in the in-service dynamic environment, the motion of a particular component could be significantly affected by the dynamics of other components in the assembly, the mounting structure, and other interface subsystems.

Functional-operability parameters to be monitored during testing should be predetermined. They depend on the purpose of the test, the nature of the test object, and the availability and characteristics of the sensors that are required to monitor these parameters. Malfunction or failure criteria should be related in some way to the monitored operability parameters; that is, each operability parameter should be associated with one or several components in the test object that are crucial to its operation.

The decision of whether to perform an active test (for example, whether a valve should be cycled during the test) and determination of the actuation time requirements (for example, the number of times the valve is cycled and at what instants during the test) should be made at this stage. The loading conditions for the test (that is, in-service loading simulation) also should be defined.

An important nontechnical factor that determines the nature of a vibration test is the availability of hardware (test apparatus) in the test laboratory. This is especially true when nonconventional vibration tests are required. Some specifications require three-DoF test inputs, for example, but most test laboratories have only one-DoF or two-DoF test machines. When two-DoF or one-DoF tests are used in place of three-DoF tests, it is first required to determine what additional orientations of the test object should be tested in order to add the required conservatism. Additionally, it should be verified by analysis or testing that the modified series of tests does not cause significant undertesting or overtesting of certain parts of the test object. Otherwise, some other form of justification should be provided for replacing the test.

Test plans prepared in the pretest stage should include an adequate description of the following important items:

1. Test purpose
2. Test-object details
3. Test environment, specifications, and standards
4. Functional-operability parameters and failure or malfunction criteria
5. Pretest inspection
6. Aging requirements
7. Test outline
8. Instrumentation requirements
9. Data-processing requirements
10. Methods of evaluation of the test results

17.3.4.1 Testing of Cabinet-Mounted Equipment

In the vibration testing of cabinet-mounted or panel-mounted equipment, the following is a standard procedure.

- Step 1:* Test the cabinet or panel with the equipment replaced by a dummy weight.
- Step 2:* Obtain the cabinet response at equipment-mounting locations and, based on these observations, develop the required vibration environment for testing (the RRS) of the equipment.
- Step 3:* Test the equipment separately, using the excitations developed in Step 2.

This procedure may not be satisfactory if there is a considerable degree of dynamic interaction between the equipment and the mounting cabinet. This could be illustrated by using a simplified model to represent cabinet-mounted equipment. The cabinet and the equipment are represented separately by single-DoF systems, as shown in Figure 17.16. Cabinet parameters are represented by upper-case letters and equipment parameters by lower-case letters. The cabinet responds when the equipment is replaced by a dummy weight of equal mass, which is denoted by $\tilde{y}(t)$. The test excitation applied to the cabinet base is denoted by $u(t)$. It can be shown that the frequency-response ratio in the two cases is given by

$$\frac{\tilde{Y}(\omega)}{Y(\omega)} = \frac{[ms^2(cs + k)]/(ms^2 + cs + k) + Ms^2 + Cs + K}{(M + m)s^2 + Cs + K} \quad (17.77)$$

with $s = j\omega$. Using the nondimensional parameters defined by the equations from Equation 17.71 to Equation 17.75, we obtain

$$\frac{\tilde{Y}(\omega)}{Y(\omega)} = \frac{(j\bar{\omega})^2 \alpha (2\zeta\beta j\bar{\omega} + \beta^2) + (j\bar{\omega})^2 + 2Zj\bar{\omega} + 1}{(1 + \alpha)(j\bar{\omega})^2 + 2Zj\bar{\omega} + 1} \quad (17.78)$$

in which ζ denotes the equipment damping ratio and Z denotes the cabinet damping ratio.

The ratio $\tilde{Y}(\omega)/Y(\omega)$ represents the amplification in the cabinet response when the equipment is replaced by a dummy weight for a harmonic excitation. Figure 17.17 shows eight curves obtained for the ζ , α , β , and Z combinations, as given in Table 17.2. Notice that the best response is obtained in Curve 6. It can be concluded that a dummy test procedure for cabinet-mounted equipment is satisfactory when

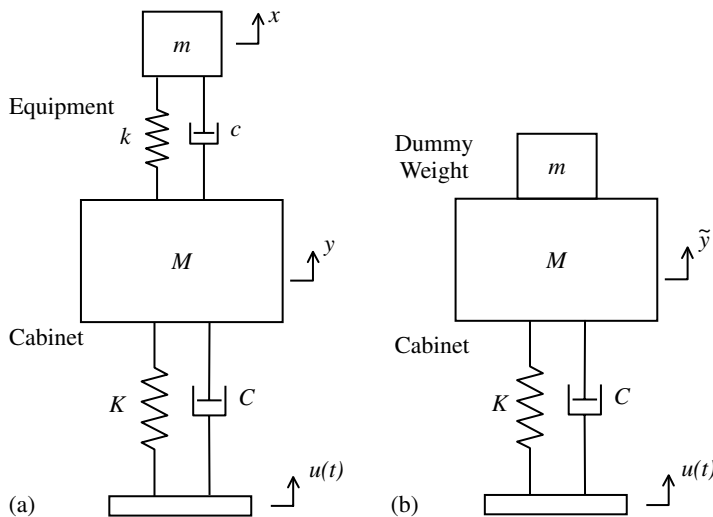


FIGURE 17.16 A simplified model for (a) an equipment cabinet test system; (b) a dummy-weight cabinet test system.

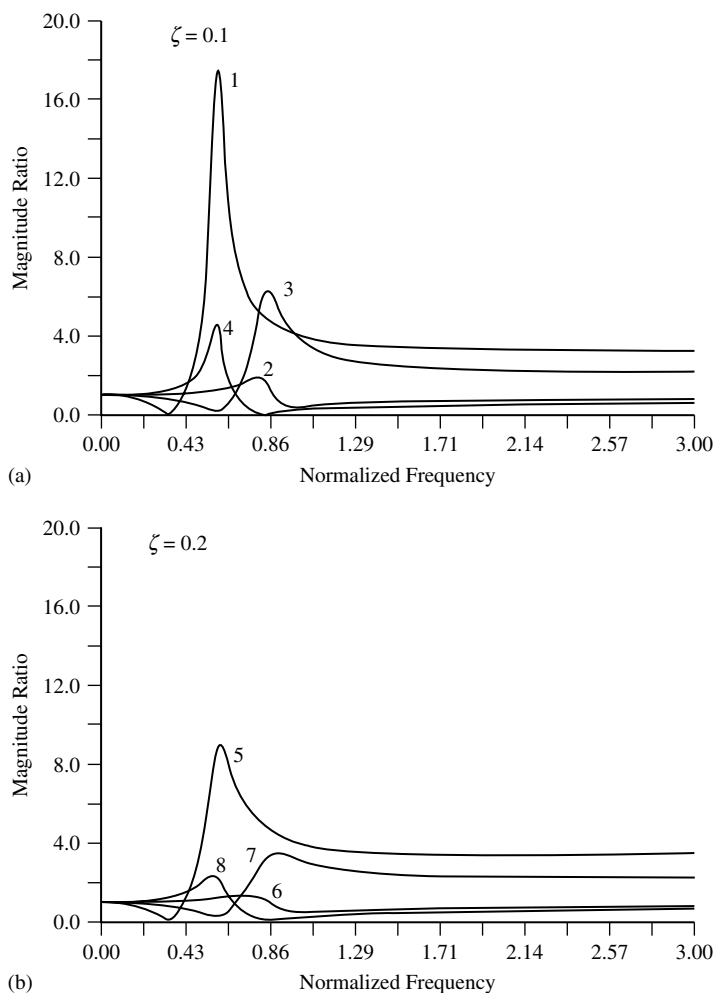


FIGURE 17.17 Cabinet response amplification in dummy-weight tests.

the equipment inertia and natural frequency are small in comparison to the values for the cabinet. Also, increasing the damping level has a favorable effect on test results.

17.3.5 Pretest Inspection

Pretest inspection of a test object is important at least for two major reasons. First, if the equipment supplied for testing is different from the piece of equipment or the group of equipment that is required to be qualified, then these differences must be carefully observed and recorded in sufficient detail. In particular, deviations in the model number, mounting features and other details of the mechanical interface, geometry, size, and significant dynamic features should be recorded. Second, before testing, the test object should be inspected for any damage, deficiencies, or malfunctions. Structural integrity usually can be determined by visual inspection alone. To determine malfunctions by operability monitoring, however, the test object must be actuated and the operating environment should be simulated.

If the equipment supplied for testing is not identical to that required to be tested, adequate justification must be provided for the differences to guarantee that the objectives of the test can be achieved by testing the equipment that is supplied. Otherwise, the test should be abandoned pending the arrival of the correct test object.

If any structural failure or operation malfunction is noted during pretest inspection, no corrective action should be taken by the test laboratory personnel unless those actions are notified to and fully authorized by the supplier of the test object. Otherwise, the test should be abandoned and the customer should be promptly notified of the anomalies.

It is important that the functional-operability pretest inspection is performed in the same functional environment as that is experienced under normal in-service conditions. When monitoring functional-operability parameters, it is necessary to guarantee that the monitoring instrumentation meets the required accuracy. Instrumentation data should be provided to the customer for review. This assures that the observed malfunction is real and not merely apparent, caused by a malfunction in the monitoring instrumentation and channels. The monitoring-equipment accuracy should be higher than that required for the operability parameter itself.

Justification is needed if some components in the test object are not actuated and monitored during pretest inspection. Also, the warm-up period and the total time of actuation should be justified. In particular, if the proper operation of the equipment is governed by the continuity of a parameter (such as an electrical signal), the time duration of monitoring should be noted. If, however, the proper function is governed by a change of state (such as the opening or closing of a valve, a switch, or a relay), the number of cycles of actuation is important.

17.4 Testing Procedures

Vibration testing may involve pretesting prior to the main tests. The objectives of pretesting may be (1) exploratory, in order to obtain dynamic information such as natural frequencies, mode shapes and damping about the test object; (2) preconditioning, in order to age or pass the “infant-mortality” stage so that the main test will be realistic and correspond to normal operating conditions. In the present section, we will describe both pretesting and main testing in an integrated manner.

17.4.1 Resonance Search

Vibration test programs usually require a resonance-search pretest. This is typically carried out at a lower excitation intensity than that used for the main test in order to minimize the damage potential (overtesting). The primary objective of a resonance-search test is to determine resonant frequencies of the test object. More elaborate tests are employed, however, to determine mode shapes and modal damping ratios in addition to resonant frequencies. Such frequency-response data on the test object are useful in planning and conducting the main test.

Frequency-response data usually are available as a set of complex frequency-response functions. There are tests that determine the frequency-response functions of a test object, and simpler tests are available to determine resonant frequencies alone. Some of the uses of frequency-response data are given below.

1. A knowledge of the resonant frequencies of the test object is important in conducting the main test. More attention should be given, for example, when performing a main test in the vicinity of resonant frequencies. In the resonance neighborhoods, lower sweep rates should be used if sine sweep is used in the main test, and larger dwell periods should be used if a sine dwell is part of the main test. Frequency-response data give the most desirable frequency range for conducting main tests.
2. From frequency-response data, it is possible to determine the most desirable test excitation directions and the corresponding input intensities.
3. The degree of nonlinearity and the time variance in the system parameters of the test object can be estimated by conducting more than one frequency-response test at different excitation levels. If the deviation in the frequency-response functions thus obtained is

sufficiently small, then a linear, time-invariant dynamic model is considered satisfactory in the analysis of the test object.

4. If no resonances are observed in the test object over the frequency range of interest, as determined by the operating environment for a given application, then a static analysis will be adequate to qualify the test object.
5. A set of frequency-response functions can be considered a dynamic model for the test specimen. This model can be employed in further studies of the test specimen by analytical means.

17.4.2 Methods of Determining Frequency-Response Functions

Three methods of determining frequency-response functions are outlined here.

17.4.2.1 Fourier Transform Method

If $y(t)$ is the response at location B of the test object, when a transient input, $u(t)$, is applied at location A , then the frequency-response function, $H(f)$, between locations A and B is given by the ratio of the Fourier integral transforms of the output, $y(t)$, and the input, $u(t)$:

$$H(f) = \frac{Y(f)}{U(f)} \quad (17.79)$$

In particular, if $u(t)$ is a unit impulse, then $U(f) = 1$ and, hence, $H(f) = Y(f)$.

17.4.2.2 Spectral Density Method

If the input excitation is a random signal, the frequency-response function between the input point and the output point can be determined as the ratio of the cross-spectral density, $\Phi_{uy}(f)$, of the input, $u(t)$, and the output, $y(t)$, and the PSD, $\Phi_{uu}(f)$, of the input:

$$H(f) = \frac{\Phi_{uy}(f)}{\Phi_{uu}(f)} \quad (17.80)$$

17.4.2.3 Harmonic Excitation Method

If the input signal is sinusoidal (harmonic) with frequency, f , the output also will be sinusoidal with frequency, f , at steady state but with a change in the phase angle. Then, the frequency-response function is obtained as a magnitude function and a phase-angle function. The magnitude, $|H(f)|$, is equal to the steady-state amplification of the output signal, and the phase angle, $\angle H(f)$, is equal to the steady-state phase lead of the output signal. This pair of curves, the magnitude plot and the phase angle plot, is called a *Bode plot* or Bode diagram.

17.4.3 Resonance-Search Test Methods

There are three basic types of resonance-search test methods. They are categorized according to the nature of the excitation used in the test; specifically, (1) impulsive excitation, (2) initial displacement, or (3) forced vibration. The first two categories are free-vibration tests; that is, response measurements are made on free decay of the test object following a momentary (initial) excitation. Typical tests belonging to each of these categories are described in the following sections.

17.4.3.1 Hammer (Bump) Test and Drop Test

In a resonance search using the impulsive-excitation method, an impulsive force (a large magnitude of force acting over a very short duration) is applied at a suitable location of the test object, and the resulting transient response of the object is observed, preferably at several locations. This is

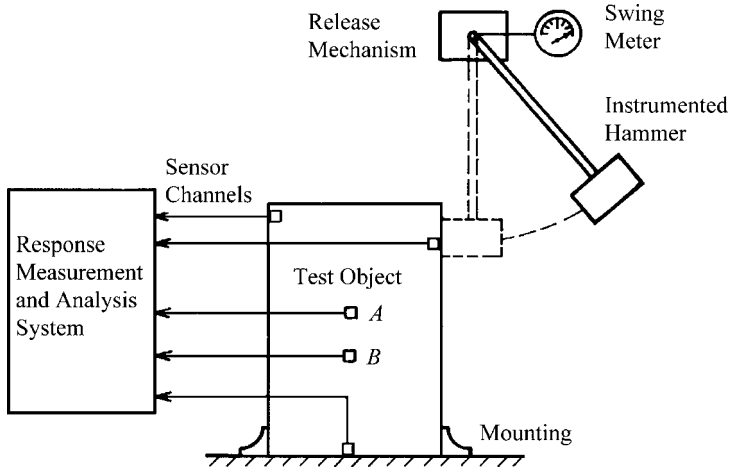


FIGURE 17.18 Schematic diagram of a hammer test arrangement.

equivalent to applying an initial velocity to the test object and letting it vibrate freely. By Fourier analysis of the response data, it is possible to obtain the resonant frequencies, corresponding mode shapes, and modal damping.

Hammer tests and drop tests belong to the impulsive-excitation category. A schematic diagram of the hammer-test arrangement is shown in Figure 17.18. A schematic diagram of the drop-test arrangement is shown in Figure 17.19. The angle of swing of the hammer or the drop height of the object determines the intensity of the applied impulse. Alternatively, the impulse can be generated using explosive cartridges (for relatively large structures) located suitably in the test object, or by firing small projectiles at the test object. The response is monitored at several locations of the test object. The response at the point of application of the impulse is always monitored. Response analysis can be done in real time, or the response can be recorded for subsequent analysis. A major concern in these tests is making sure that all significant resonances in the required frequency range are excited under the given excitation. Several tests for different configurations of the test object might be necessary to achieve this.

Proper selection of the response-monitoring locations is also important in obtaining meaningful test results. By changing the impulsive-force intensity and repeating the test, any significant nonlinear (or time-variant-parameter) behavior of the test object can be determined. A common practice is to monitor the impulsive-force signal during impact. In this way, poor impacts (for example, low-intensity impacts

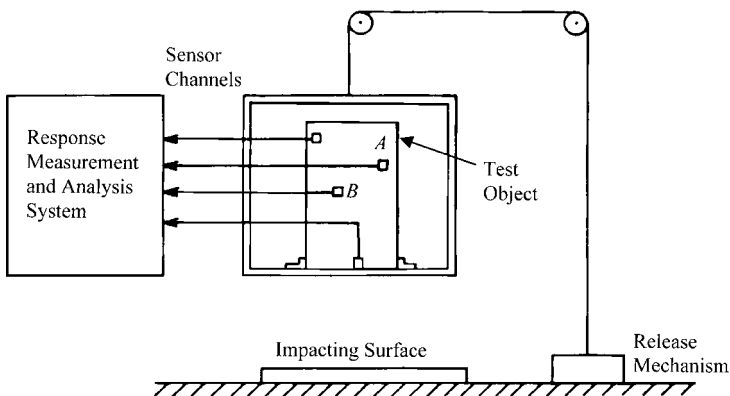


FIGURE 17.19 Schematic diagram of a drop test arrangement.

or multiple impacts caused by the bouncing back of a hammer) can be detected and the corresponding test results can be rejected.

17.4.3.2 Pluck Test

A resonance search on a test object can be performed by applying a displacement initial condition (rather than a velocity initial condition, as in impulsive tests) to a suitably mounted test object and measuring its subsequent response at various locations as it executes free vibrations. By properly selecting the locations and the magnitudes of the initial displacements, it is sometimes possible to excite various modes of vibration, provided that these modes are reasonably uncoupled.

The pluck test is the most common test that uses the initial-displacement method. A schematic diagram of the test set-up is shown in Figure 17.20. The test object is initially deflected by pulling it with a cable. When the cable is suddenly released, the test object will undergo free vibrations about its static-equilibrium position. The response is observed for several locations of the test object and analyzed to obtain the required parameters.

In Figure 17.18 to Figure 17.20, the frequency-response function between two locations (*A* and *B*, for example) is obtained by analyzing the corresponding two signals, using either the Fourier transform method (Equation 17.79) or the spectral-density method (Equation 17.80). These frequency-domain techniques will automatically provide the natural-frequency and modal-damping information. Alternatively, modal damping can be determined using time-domain methods, for example, by evaluating the logarithmic decrement of the response after passing it through a filter having a center frequency adjusted to the predetermined natural frequency of the test object for that mode. The accuracy of the estimated modal-damping value can be improved significantly by such filtering methods.

Often, the most difficult task in a natural-frequency search is the excitation of a single a mode. If two natural frequencies are close together, modal interactions of the two invariably will be present in the response measurements. Because of the closeness of the frequencies, the response curve will display a beat phenomenon, as shown in Figure 17.21, which makes it difficult to determine damping by the logarithmic-decrement method. It is difficult to distinguish between decay caused by damping and rapid drop-off caused by beating. In this case, one of the frequency components must be filtered out, using a very narrowband-pass filter, before computing damping.

The required testing time for the impulsive-excitation and initial-displacement test methods is relatively small in comparison with forced-vibration test durations. For this reason, these former (free-vibration) tests are often preferred in preliminary (exploratory) testing before the main tests. The directions and locations of impact or initial displacements should be properly chosen, however, so that as many significant modes as possible will be excited in the desired frequency range. If the

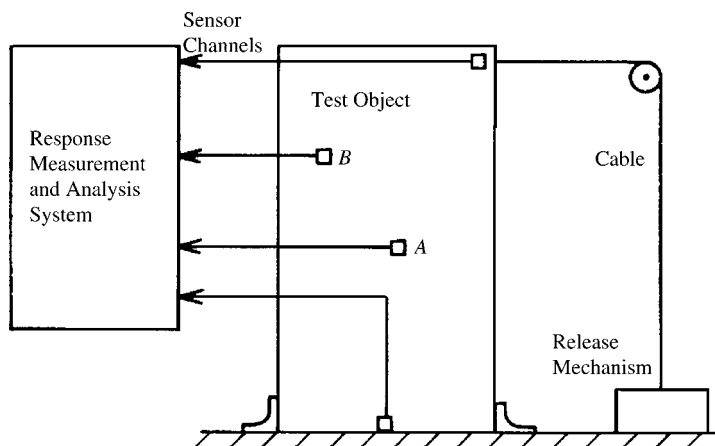


FIGURE 17.20 Diagram of a pluck test arrangement.

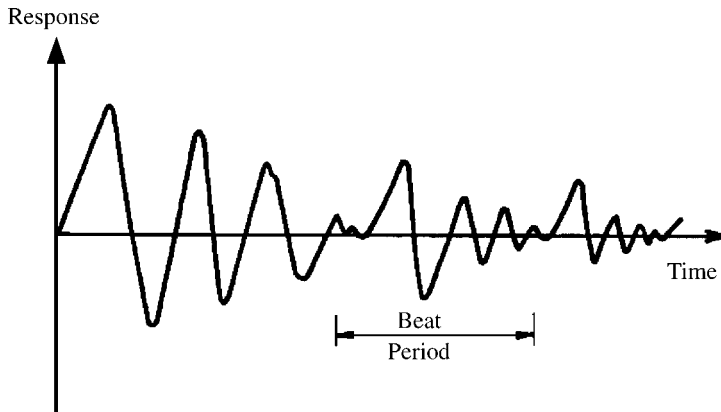


FIGURE 17.21 Beat phenomenon resulting from interaction of closely spaced modes.

impact is applied at a node point, (of a particular mode, for instance) it will be virtually impossible to detect that mode from the response data. Sometimes, a large number of monitoring locations are necessary to accurately determine mode shapes of the test object. This depends primarily on the size and dynamic complexity of the test object and the particular mode number. This, in turn, necessitates the use of more sensors (accelerometers and the like) and recorder channels. If a sufficient number of monitoring channels is not available, the test will have to be repeated, each time using a different set of monitoring locations. Under such circumstances, it is advisable to keep one channel (monitoring location) unchanged and to use it as the reference channel. In this manner, any deviations in the test-excitation input can be detected for different tests and properly adjusted or taken into account in subsequent analysis (for example, by normalizing the response data).

17.4.3.3 Shaker Tests

A convenient method of resonance search is by using a continuous excitation. A forced excitation, which typically is a sinusoidal signal or a random signal, is applied to the test object by means of a shaker, and the response is continuously monitored. The test set-up is shown schematically in Figure 17.22. For sinusoidal excitations, signal amplification and phase shift over a range of excitations will determine the frequency-response function. For random excitations, Equation 17.80 may be used to determine the frequency-response function.

One or several portable exciters (shakers) or a large shaker table similar to that used in the main vibration test can be employed to excite the test object. The number and the orientations of the shakers and the mounting configurations and monitoring locations of the test object should be chosen depending on the size and complexity of the test object, the required accuracy of the resonance-search results, and the modes of vibration that need to be excited. The shaker-test method has the advantage of being able to control the nature of the test-excitation input (for example, frequency content, intensity, and sweep rate), although it might be more complex and costly. The results from shaker tests are more accurate and more complete.

Test objects usually display a change in resonant frequencies when the shaker amplitude is increased. This is caused by inherent nonlinearities in complex structural systems. Usually, the

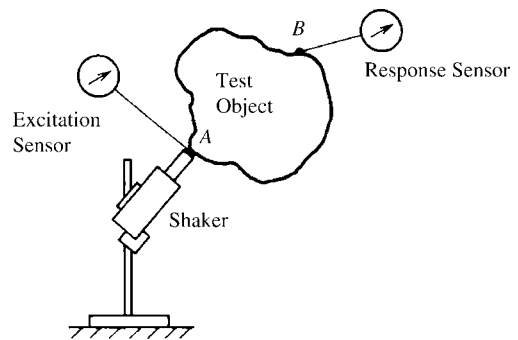


FIGURE 17.22 Schematic diagram of a shaker test for resonance search.

change appears as a spring-softening effect, which results in lower resonant frequencies at higher shaker amplitudes. If this nonlinear effect is significant, the resonant frequencies for the main test level cannot be accurately determined using a resonance search at low intensity. Some form of extrapolation of the test results, or analysis using an appropriate dynamic model, might be necessary in this case to determine the resonant-frequency information that might be required to perform the main test.

17.4.4 Mechanical Aging

Before performing a qualification test, it is usually necessary to age the test object to put it into a condition that represents its state following its operation for a predetermined period under in-service conditions. In this manner, it is possible to reduce the probability of burn-in failure (infant mortality) during testing. Some tests, such as design-development tests and quality-assurance tests, might not require prior aging.

The nature and degree of aging that is required depends on such factors as the intended function of the test object, the operating environment, and the purpose of the dynamic test. In qualification tests, it may be necessary to demonstrate that the test object still has adequate capability to withstand an extreme dynamic environment toward the end of its design life (that is, the period in which it can be safely operated without requiring corrective action). In such situations, it is necessary to age the test object to an extreme deterioration state, representing the end of the design life of the test object.

Test objects are aged by subjecting them to various environmental conditions (for example, high temperatures, radiation, humidity, and vibrations). Usually, it is not practical to age the equipment at the same rate as it would age under a normal service environment. Consequently, accelerated aging procedures are used to reduce the test duration and cost. Furthermore, the operating environment may not be fully known at the testing stage. This makes the simulation of the true operating environment virtually impossible. Usually, accelerated aging is done sequentially, by subjecting the test equipment to the various environmental conditions one at a time. Under in-service conditions, however, these effects occur simultaneously, with the possibility of interactions between different effects. Therefore, when sequential aging is employed, some conservatism should be added. The type of aging used should be consistent with the environmental conditions and operating procedures of the specific application of the test object. Often these conditions are not known in advance, in which case, standardized aging procedures should be used.

Our main concern in this section is mechanical aging, although other environmental conditions can significantly affect the dynamic characteristics of a test object. The two primary mechanisms of mechanical aging are material fatigue and mechanical wearout. The former mechanism plays a primary role if in-service operation consists of cyclic loading over relatively long periods of time. Wearout, however, is a long-term effect caused by any type of relative motion between components of the test object. It is very difficult to analyze component wearout, even if only the mechanical aspects are considered (that is the effects of corrosion, radiation, and the like are neglected). Some mechanical wearout processes resemble fatigue aging; however, they depend simultaneously on the number of cycles of load applications and the intensity of the applied load. Consequently, only the cumulative damage phenomenon, which is related to material fatigue, is usually treated in the literature.

Although mechanical aging is often considered a pretest procedure (for example, the resonance-search test), it actually is part of the main test. In a dynamic qualification program, if the test object malfunctions during mechanical aging, this amounts to failure in the qualification test. Furthermore, exploratory tests, such as resonance-search tests, are sometimes conducted at higher intensities than what is required to introduce mechanical aging into the test object.

17.4.4.1 Equivalence for Mechanical Aging

It is usually not practical to age a test object under its normal operating environment, primarily because of time limitations and the difficulty in simulating the actual operating environment. Therefore, it may

be necessary to subject the test object to an accelerated aging process in a dynamic environment of higher intensity than that present under normal operating conditions.

Two aging processes are said to be equivalent if the final aged condition attained by the two processes is identical. This is virtually impossible to realize in practice, particularly when the object and the environment are complex and the interactions of many dynamic causes have to be considered. In this case, a single most severe aging effect is used as the standard for comparison to establish the equivalence. The equivalence should be analyzed in terms of both the intensity and the nature of the dynamic excitations used for aging.

17.4.4.2 Excitation-Intensity Equivalence

A simplified relationship between the dynamic-excitation intensity, U , and the duration of aging, T , that is required to attain a certain level of aging, keeping the other environmental factors constant, may be given as

$$T = \frac{c}{U^r} \quad (17.81)$$

in which c is a proportionality constant and r is an exponent. These parameters depend on such factors as the nature and sequence of loading and characteristics of the test object. It follows from Equation 17.81 that, by increasing the excitation intensity by a factor n , the aging duration can be reduced by a factor of n^r . In practice, however, the intensity–time relationship is much more complex, and caution should be exercised when using Equation 17.81. This is particularly true if the aging is caused by multiple dynamic factors of varying characteristics that are acting simultaneously. Furthermore, there is usually an acceptable upper limit to n . It is unacceptable, for example, to use a value that will produce local yielding or any such irreversible damage to the equipment that is not present under normal operating conditions.

It is not necessary to monitor functional operability during mechanical aging. Furthermore, it can happen that, during accelerated aging, the equipment malfunctions but, when the excitation is removed, it operates properly. This type of reversible malfunction is acceptable in accelerated aging.

The time to attain a given level of aging is usually related to the stress level at a critical location of the test object. Since this critical stress can be related, in turn, to the excitation intensity, the relationship given by Equation 17.81 is justified.

17.4.4.3 Dynamic-Excitation Equivalence

The equivalence of two dynamic excitations that have different time histories can be represented using methods employed to represent dynamic excitations (for example, response spectrum, Fourier spectrum, and PSD). If the maximum (peak) excitation is the factor that primarily determines aging in a given system under a particular dynamic environment, then response-spectrum representation is well suited for establishing the equivalence of two excitations. If, however, the frequency characteristics of the excitation are the major determining factor for mechanical aging, then Fourier spectrum representation is favored for establishing the equivalence of two deterministic excitations, and PSD representation is suited for random excitations. When two excitation environments are represented by their respective PSD functions, $\Phi_1(\omega)$ and $\Phi_2(\omega)$, if the significant frequency range for the two excitations is (ω_1, ω_2) , then the degree of aging under the two excitations may be compared using the ratio

$$\frac{A_1}{A_2} = \frac{\int_{\omega_1}^{\omega_2} \Phi_1(\omega) d\omega}{\int_{\omega_1}^{\omega_2} \Phi_2(\omega) d\omega} \quad (17.82)$$

in which A denotes a measure of aging. If the two excitations have different frequency ranges of interest, a range consisting of both ranges might be selected for the integrations in Equation 17.82.

17.4.4.4 Cumulative Damage Theory

Miner's linear cumulative damage theory may be used to estimate the combined level of aging resulting from a set of excitation conditions. Consider m excitations acting separately on a system. Suppose that each of these excitations produces a unit level of aging in N_1, N_2, \dots, N_m loading cycles, respectively, when acting separately. If, in a given dynamic environment, n_1, n_2, \dots, n_m loading cycles, respectively, from the m excitations actually have been applied to the system (possibly all excitations were acting simultaneously), the level of aging attained can be given by

$$A = \sum_{i=1}^m \frac{n_i}{N_i} \quad (17.83)$$

The unit level of aging is achieved, theoretically, when $A = 1$. Equation 17.83 corresponds to Miner's linear cumulative damage theory.

Because of various interactive effects produced by different loading conditions, when some or all of the m excitations act simultaneously, it is usually not necessary to have $A = 1$ under the combined excitation to attain the unit level of aging. Furthermore, it is extremely difficult to estimate $N_i, i = 1, \dots, m$. For such reasons, the practical value of A in Equation 17.83 for using in attaining a unit level of aging could vary widely (typically, from 0.3 to 3.0).

17.4.5 Test-Response Spectrum Generation

A vibration test may be specified by a RRS. In this case, the response spectrum of the actual excitation signal, that is, the TRS, should envelop the RRS during testing. It is customary for the purchaser (the owner of the test object) to provide the test laboratory with a multichannel FM tape or some form of signal storage device containing the components of the excitation input signal that should be used in the test. Alternatively, the purchaser may request that the test laboratory generate the required signal components under the purchaser's supervision. If sine beats are combined to generate the test excitations, each FM tape should be supplemented by tabulated data giving the channel number, the beat frequencies (Hz) in that channel, and the amplitude (g) of each sine-beat component. The RRS curve that is enveloped by the particular input should also be specified.

The excitation signal that is applied to the shaker-table actuator is generated by combining the contents of each channel in an appropriate ratio so that the response spectrum of the excitation that is actually felt at the mounting locations of the test object (the TRS) satisfactorily matches the RRS supplied to the test laboratory. Matching is performed by passing the contents of each channel through a variable-gain amplifier and mixing the resulting components according to variable proportions. These operations are performed by a waveform mixer. The adjustment of the amplifier gains is done by trial and error. The phase of the individual signal components should be maintained during the mixing process.

Each channel may contain a single-frequency component (such as sine beat) or a multifrequency signal of fixed duration (for example, 20 sec). If the RRS is complex, each channel may have to carry a multifrequency signal to achieve close matching of the TRS with the RRS. Also, a large number of channels might be necessary. The test excitation signal is generated continuously by repetitively playing the FM tape loop of fixed duration.

In product qualification, response spectra are usually specified in units of acceleration due to gravity (g). Consequently, the contents in each channel of the test-input FM tape represent acceleration motions. For this reason, the signal from the waveform mixer must be integrated twice before it is used to drive the shaker table. The actuator of the exciter is driven by this displacement signal, and its control may be done by feedback from a displacement sensor. However, if the control sensor is an accelerometer, as is typical, double integration of that signal will be needed as well. In typical test facilities, a double integration unit is built into the shaker system. It is then possible to use any type of signal (displacement, velocity, acceleration) as the excitation input and to decide

simultaneously on the number of integrations that are necessary. If the input signal is a velocity time history, for example, one integration should be chosen and so on.

The tape speed should be specified (for example, 7.5, 15 in./s) when the signals recorded on tapes are provided to generate input signals for vibration testing. This is important to ensure that the frequency content of the signal is not distorted. The speeding up of the tape has the effect of scaling up of each frequency component in the signal. It has also the effect, however, of filtering out very high-frequency components in the signal. If the excitation signals are available as digital records, then a DAC is needed to convert them into analog signals.

17.4.6 Instrument Calibration

The test procedure normally stipulates accuracy requirements and tolerances for various critical instruments that are used in testing. It is desirable that these instruments have current calibration records that are agreeable to an accepted standard. Instrument manufacturers usually provide these calibration records. Accelerometers, for example, may have calibration records for several temperatures (for example, -65 , 75 , 350°F) and for a range of frequencies (such as 1 to 1000 Hz). Calibration records for accelerometers are given in both voltage sensitivity (mV/g) and charge sensitivity (pC/g), along with percentage-deviation values. These tolerances and peak deviations for various test instruments should be provided for the purchaser's review before they are used in the test apparatus.

From the tolerance data for each sensor or transducer, it is possible to estimate peak error percentages in various monitoring channels in the test set-up, particularly in the channels used for functional-operability monitoring. The accuracy associated with each channel should be adequate to measure expected deviations in the monitored operability parameter.

It is good practice to calibrate sensor or transducer units, such as accelerometers and associated auxiliary devices, daily or after each test. These calibration data should be recorded under different scales when a particular instrument has multiple scales, and for different instrument settings.

17.4.7 Test-Object Mounting

When a test object is being mounted on a shaker table, care should be taken to simulate all critical interface features under normal installed conditions for the intended operation. This should be done as accurately as is feasible. Critical interface requirements are those that could significantly affect the dynamics of the test object. If the mounting conditions in the test set-up significantly deviate from those under installed conditions for normal operation, adequate justification should be provided to show that the test is conservative (that is, the motions produced under the test mounting conditions are more severe than in in-service conditions). In particular, local mounting that would not be present under normal installation conditions should be avoided in the test set-up.

In simulating in-service interface features, the following details should be considered as a minimum:

1. Test orientation of the test object should be its in-service orientation, particularly with respect to the direction of gravity (vertical), available DoF, and mounting locations.
2. Mounting details at the interface of the test object and the mounting fixture should represent in-service conditions with respect to the number, size, and strength of welds, bolts, nuts, and other hold-down hardware.
3. Additional interface linkages, including wires cables, conduits, pipes, instrumentation (dials, meters, gauges, sensors, transducers, and so on), and the supporting brackets of these elements, should be simulated at least in terms of mass and stiffness, and preferably in terms of size as well.
4. Any dynamic effects of adjacent equipment cabinets and supporting structures under in-service conditions should be simulated or taken into account in analysis.
5. Operating loads, such as those resulting from fluid flow, pressure forces, and thermal effects, should be simulated if they appear to significantly affect test object dynamics. In particular, the nozzle loads (fluid) should be simulated in magnitude, direction, and location.

The required mechanical interface details of the test object are obtained by the test laboratory at the information-acquisition stage. Any critical interface details that are simulated during testing should be included in the test report.

At least three control accelerometers should be attached to the shaker table near the mounting location of the test object. One control accelerometer measures the excitation-acceleration component applied to the test object in the vertical direction. The other two measure the excitation-acceleration components in two horizontal directions at right angles. The two horizontal (control) directions are chosen to be along the two major freedom-of-motion directions (or dynamic principal axes) of the test object. Engineering judgment may be used in deciding these principal directions of high response in the test object. Often, geometric principal axes are used. The control accelerometer signals are passed through a response-spectrum analyzer (or a suitably programmed digital computer) to compute the TRS in the vertical and two horizontal directions that are perpendicular.

Vibration tests generally require monitoring of the dynamic response at several critical locations of the test object. In addition, the tests may call for the determining of mode shapes and natural frequencies of the test object. For this purpose, a sufficient number of accelerometers should be attached to various key locations in the test object. The test procedure (document) should contain a sketch of the test object, indicating the accelerometer locations. Also, the type of accelerometers employed, their magnitudes and directions of sensitivity, and the tolerances should be included in the final test report.

17.4.8 Test-Input Considerations

In vibration testing, a significant effort goes into the development of test excitation inputs. Not only the nature but also the number and the directions of the excitations can have a significant effect on the outcomes of a test. This is so because the excitation characteristics determine the nature of a test.

17.4.8.1 Test Nomenclature

We have noted that a common practice in vibration testing is to apply synthesized vibration excitation to a test object that is appropriately mounted on a shaker table. Customarily, only translatory excitations as generated by linear actuators, are employed. Nevertheless the resulting motion of the test object usually consists of rotational components as well. A typical vibration environment may consist of three-dimensional motions, however. The specification of a three-dimensional test environment is a complex task, even after omitting the rotational motions at the mounting locations of the test object. Furthermore, practical vibration environments are random and they can be represented with sufficient accuracy only in a probabilistic sense.

Very often the type of testing that is used is governed mainly by the capabilities of the test laboratory to which the contract is granted. Test laboratories conduct tests using their previous experience and engineering judgment. Making extensive improvements to existing tests can be very costly and time-consuming, and this is not warranted from the point of view of the customer or the vendor. Regulatory agencies usually allow simpler tests if sufficient justification can be provided indicating that a particular test is conservative with respect to regulatory requirements.

The complexity of a shaker-table apparatus is governed primarily by the number of actuators that are employed and the number of independent directions of simultaneous excitation that it is capable of producing. Terminology for various tests is based on the number of independent directions of excitation used in the test. It would be advantageous to standardize this terminology to be able to compare different test procedures. Unfortunately, the terminology used to denote different types of tests usually depends on the particular test laboratory and the specific application. Attempts to standardize various test methods have become tedious, partly because of the lack of a universal nomenclature for dynamic testing. A justifiable grouping of test configurations is presented in this section. [Figure 17.23](#) illustrates the various test types.

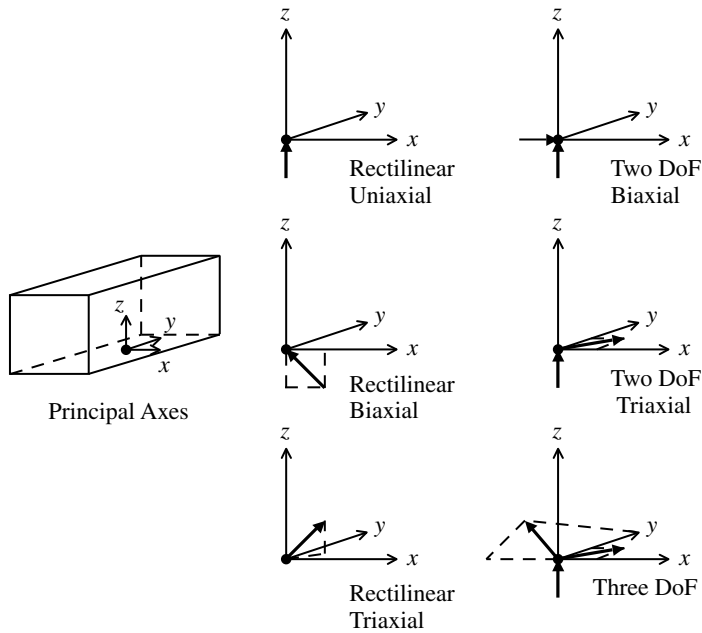


FIGURE 17.23 Vibration-test configurations.

In test nomenclature, the DoF refers to the number of directions of independent motions that can be generated simultaneously by means of independent actuators in the shaker table. According to this concept, three basic types of tests can be identified:

1. Single-DoF (or rectilinear) testing is that in which the shaker table employs only one exciter (actuator), producing test-table motions along the axis of that actuator. The actuator may not necessarily be in the vertical direction.
2. Two-DoF testing is that in which two independent actuators, oriented at right angles to each other, are employed. The most common configuration consists of a vertical actuator and a horizontal actuator. Theoretically, the motion of each actuator can be specified independently.
3. Three-DoF testing is that in which three actuators, oriented at mutually right angles, are employed. A desirable configuration consists of a vertical actuator and two horizontal actuators. At least theoretically, the motion of each actuator can be specified independently.

It is common practice to specify the directions of excitation with respect to the geometric principal axes of the test object. This practice is somewhat questionable, primarily because it does not take into account the flexibility and inertia distributions of the object. Flexibility and inertia elements in the test object have a significant influence on the level of dynamic coupling present in a given pair of directions. In this respect, it is more appropriate to consider *dynamic principal axes* rather than geometric principal axes of the test object. One useful definition is in terms of eigenvectors of an appropriate three-dimensional, frequency-response function matrix that takes into account the response at every critical location in the test object. The only difficulty in this method is that prior frequency-response testing or analysis is needed to determine the test input direction. For practical purposes, the vertical axis (the direction of gravity) is taken as one principal axis.

The single-DoF (rectilinear) test configuration has three subdivisions, based on the orientation of the vibration exciter (actuator) with respect to the principal axes of the test object. It is assumed that one principal axis of the test object is the vertical axis and that the three principal axes are

mutually perpendicular. The three subdivisions are as follows:

1. Rectilinear uniaxial testing, in which the single actuator is oriented along one of the principal axes of the test object
2. Rectilinear biaxial testing, in which the single actuator is oriented on the principal plane containing the vertical and one of the two horizontal principal axes (the actuator is inclined to both principal axes in the principal plane)
3. Rectilinear triaxial testing, in which the single actuator is inclined to all three orthogonal principal axes of the test object

The two-DoF test configuration has two subdivisions, based on the orientation of the two actuators with respect to the principal axes of the test object, as follows:

1. Two-DoF biaxial testing, in which one actuator is directed along the vertical principal axis and the other along one of the two horizontal principal axes of the test object
2. Two-DoF triaxial testing, in which one actuator is positioned along the vertical principal axis and the other actuator is horizontal but inclined to both horizontal principal axes of the test object

17.4.8.2 Testing with Uncorrelated Excitations

Simultaneous excitations in three orthogonal directions often produce responses (accelerations, stresses, etc.) that are very different from that which is obtained by vectorially summing the responses to separate excitations acting one at a time. This is primarily because of the nonlinear, time-variant nature of test specimens and test apparatus, their dynamic coupling, and the randomness of excitation signals. If these effects are significant, it is theoretically impossible to replace a three-DoF test, for example, with a sequence of three single-DoF tests. In practice, however, some conservatism can be incorporated into two-DoF and single-DoF tests to account for these effects. These tests with added conservatism may be employed when three-DoF testing is not feasible. It should be clear by now that rectilinear triaxial testing is generally not equivalent to three-degree-freedom testing, because the former merely applies an identical excitation in all three orthogonal directions, with scaling factors (direction cosines). One obvious drawback of rectilinear triaxial testing is that the input excitation in a direction at right angles to the actuator is theoretically zero, and the excitation is at its maximum along the actuator. In three-DoF testing using uncorrelated random excitations, however, no single direction has a zero excitation at all times, and also the probability is zero that the maximum excitation occurs in a fixed direction at all times.

Three-DoF testing is mentioned infrequently in the literature on vibration testing. A major reason for the lack of three-DoF testing might be the practical difficulty in building test tables that can generate truly uncorrelated input motions in three orthogonal directions. The actuator interactions caused by dynamic coupling through the test table and mechanical constraints at the table supports are primarily responsible for this. Another difficulty arises because it is virtually impossible to synthesize perfectly uncorrelated random signals to drive the actuators. Two-DoF testing is more common. In this case, the test must be repeated for a different orientation of the test object (for example, with a 90° rotation about the vertical axis), unless some form of dynamic-axial symmetry is present in the test object.

Test programs frequently specify uncorrelated excitations in two-DoF testing for the two actuators. This requirement lacks solid justification, because two uncorrelated excitations applied at right angles do not necessarily produce uncorrelated components in a different pair of orthogonal directions, unless the mean square values of the two excitations are equal. To demonstrate this, consider the two uncorrelated excitations, u and v , shown [Figure 17.24](#). The components u' and v' , in a different pair of orthogonal directions obtained by rotating the original coordinates through an angle θ in the counterclockwise direction, are given by

$$u' = u \cos \theta + v \sin \theta \quad (17.84)$$

$$v' = -u \sin \theta + v \cos \theta \quad (17.85)$$

Without loss of generality, we can assume that u and v have zero means. Then, u' and v' also will have zero means. Furthermore, since u and v are uncorrelated, we have

$$E(uv) = E(u)E(v) = 0 \quad (17.86)$$

From Equation 17.84 and Equation 17.85, we obtain

$$E(u'v') = E[(u \cos \theta + v \sin \theta) \times (-u \sin \theta + v \cos \theta)]$$

This, when expanded and substituted with Equation 17.86, becomes

$$E(u'v') = \sin \theta \cos \theta [E(v^2) - E(u^2)] \quad (17.87)$$

Since θ is any general angle, the excitation components u' and v' become uncorrelated if and only if

$$E(v^2) = E(u^2) \quad (17.88)$$

This is the required result. Nevertheless, a considerable effort, in the form of digital Fourier analysis, is expended by vibration-testing laboratories to determine the degree of correlation in test signals employed in two-DoF testing.

17.4.8.3 Symmetrical Rectilinear Testing

Single-DoF (rectilinear) testing that is performed with the test excitation applied along the line of symmetry with respect to an orthogonal system of three principal axes of the test object mainframe is termed symmetrical rectilinear testing. In product qualification literature, this test is often referred to as the 45° test. The direction cosines of the input orientation are $(1/\sqrt{3}, 1/\sqrt{3}, 1/\sqrt{3})$ for this test configuration. The single-actuator input intensity is amplified by a factor of $\sqrt{3}$ in order to obtain the required excitation intensity in the three principal directions. Note that symmetrical rectilinear testing falls into the category of rectilinear triaxial testing, as defined earlier. This is one of the widely used testing configurations in seismic qualification, for example.

17.4.8.4 Geometry vs. Dynamics

In vibration testing the emphasis is on the dynamic behavior rather than the geometry of the equipment. For a simple three-dimensional body that has homogeneous and isotropic characteristics, it is not difficult to correlate its geometry to its dynamics. A symmetrical rectilinear test makes sense for such systems. The equipment we come across is often much more complex, however. Furthermore, our interest is not merely in determining the dynamics of the mainframe of the equipment. We are more interested in the dynamic reliability of various critical components located within the mainframe. Unless we have some previous knowledge of the dynamic characteristics in various directions of the system components, it is not possible to draw a direct correlation between the geometry and the dynamics of the tested equipment.

17.4.8.5 Some Limitations

In a typical symmetrical rectilinear test, we deal with “black-box” equipment whose dynamics are completely unknown. The excitation is applied along the line of symmetry of the principal axes of the mainframe. A single test of this type does not guarantee excitation of all critical components located inside the equipment. Figure 17.25 illustrates this further. Consider the plane perpendicular to the direction of excitation. The dynamic effect caused by the excitation is minimal along any line on

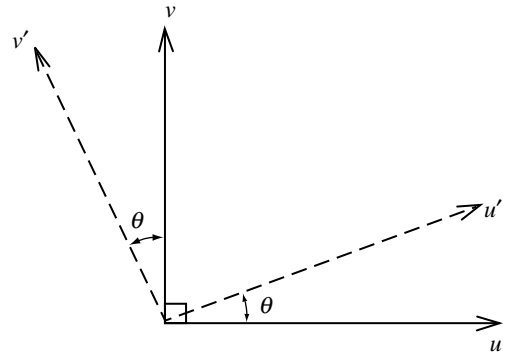


FIGURE 17.24 Effect of coordinate transformation on correlation.

this plane. (Any dynamic effect on this plane is caused by dynamic coupling among different body axes.) Accordingly, if there is a component (or several components) inside the equipment whose direction of sensitivity lies on this perpendicular plane, the single excitation might not excite that component. Since we deal with a black box, we do not know the equipment dynamics beforehand. Hence, there is no way of identifying the existence of such unexcited components. When the equipment is put into service, a vibration of sufficient intensity may easily overstress this component along its direction of sensitivity and may bring about component failure. It is apparent that at least three tests, performed in three orthogonal directions, are necessary to guarantee excitation of all components, regardless of their direction of sensitivity.

A second example is given in Figure 17.26. Consider a dual-arm component with one arm sensitive in the $O-O$ direction and the second arm sensitive in the $P-P$ direction. If component failure occurs when the two arms are in contact, a single excitation in either the $O-O$ direction or the $P-P$ direction will not bring about component failure. If the component is located inside a black box, such that either the $O-O$ direction or the $P-P$ direction is very close to the line of symmetry of the principal axes of the mainframe, a single symmetrical rectilinear test will not result in system malfunction. This may be true, because we do not have a knowledge of component dynamics in such cases. Again, under service conditions, a vibration of sufficient intensity can produce an excitation along the $A-A$ direction, subsequently causing system malfunction.

A further consideration in using rectilinear testing is dynamic coupling between the directions of excitation. In the presence of dynamic coupling, the sum of individual responses of the test object resulting from four symmetrical rectilinear tests is not equal to the response obtained when the excitations are applied simultaneously in the four directions. Some conservatism should be introduced when employing rectilinear testing for objects having a high level of dynamic coupling between the test directions. If the test-object dynamics are restrained to only one direction under normal operating conditions, however, then rectilinear testing can be used without applying any conservatism.

17.4.8.6 Testing Black Boxes

When the equipment dynamics are unknown, a single rectilinear test does not guarantee proper testing of the equipment. To ensure excitation of every component within the test object that has directional intensities, three tests should be carried out along three independent directions. The first test may be carried out with a single horizontal excitation, for example. The second test could then be performed with the equipment rotated through 90° about its vertical axis, and using the same horizontal excitation. The last test would be performed with a vertical excitation.

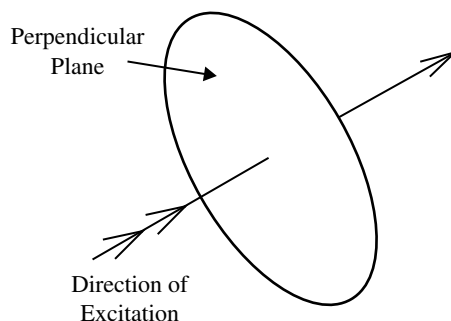


FIGURE 17.25 Illustration of the limitation of a single rectilinear test.

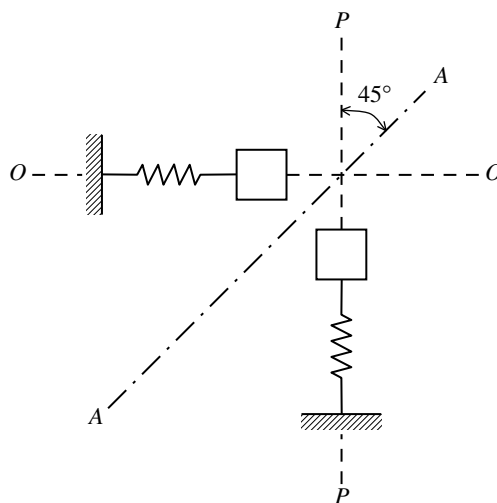


FIGURE 17.26 Illustrative example of the limitation of several rectilinear tests.

Alternatively, if symmetrical rectilinear tests are preferred, four such tests should be performed for four equipment orientations (for example, an original test, a 90° rotation, a 180° rotation, and a 270° rotation about the vertical axis). These tests also ensure excitation of all components that have directional intensities. This procedure might not be very efficient, however. The shortcoming of this series of four tests is that some of the components will be overtested. It is clear from Figure 17.27, for example, that the vertical direction is excited by all four tests. The method has the advantage, however, of simplicity of performance.

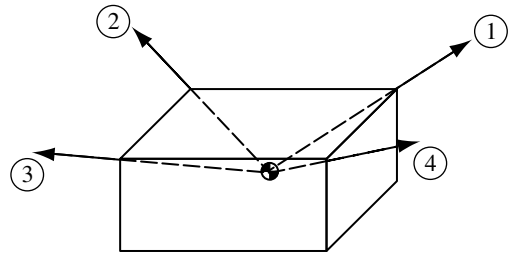


FIGURE 17.27 Directions of excitation in a sequence of four rectilinear tests.

17.4.8.7 Phasing of Excitations

The main purpose of rotating the test orientation in rectilinear testing is to ensure that all components within the equipment are excited. Phasing of different excitations also plays an important role, however, when several excitations are used simultaneously. To explore this concept further, it should be noted that a random input applied in the $A-B$ direction or in the $B-A$ direction has the same frequency and amplitude (spectral) characteristics. This is clear because the PSD of $u = \text{PSD}$ of $(-u)$, and the autocorrelation of $u = \text{autocorrelation}$ of $(-u)$. Hence, it is seen that, if the test is performed along the $A-B$ direction, it is of no use to repeat the test in the $B-A$ direction. It should be understood, however, that the situation is different when several excitations are applied simultaneously.

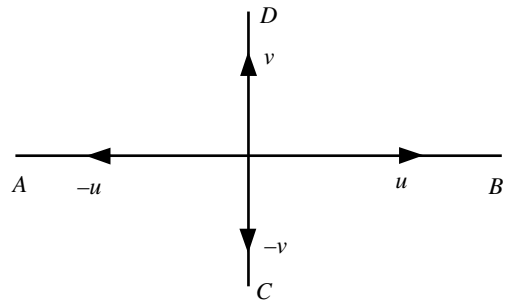


FIGURE 17.28 Significance of excitation phasing in two-DoF testing.

The simultaneous action of u and v is not the same as the simultaneous action of $-u$ and v (see Figure 17.28). The simultaneous action of u and v is the same, however, as the simultaneous action of $-u$ and $-v$. Obviously, this type of situation does not arise when there are no simultaneous excitations, as in rectilinear testing.

17.4.8.8 Testing a Gray or White Box

When some information regarding the true dynamics of the test object is available, it is possible to reduce the number of necessary tests. In particular, if the equipment dynamics are completely known, then a single test would be adequate. The best direction for excitation of the system in Figure 17.26, for example, is $A-A$. (Note that $A-A$ may be lined up in any arbitrary direction inside the equipment housing. In such a situation, knowledge of the equipment dynamics is crucial.) This also indicates that it is very important to accumulate and use any past experience and data on the dynamic behavior of similar equipment. Any test that does not use some previously known information regarding the equipment is a blind test, and it cannot be optimal in any respect. As more information is available, better tests can be conducted.

17.4.8.9 Overtesting in Multitest Sequences

It is well known that increasing the test duration increases aging of the test object because of prolonged stressing and load cycling of various components. This is the case when a test is repeated one or more times at the same intensity as that prescribed for a single test. The symmetrical rectilinear test requires four separate tests at the same excitation intensity as that prescribed for a single test. As a result, the

equipment becomes subjected to overtesting, at least in certain directions. The degree of overtesting is small if the tests are performed in only three orthogonal directions. In any event, a certain amount of dynamic coupling is present in the test-object's structure and, to minimize overtesting in these sequential tests, a smaller intensity than that prescribed for a single test should be employed. The value of the intensity-reduction factor clearly depends on the characteristics of the test object, the degree of reliability expected, and the intensity value itself. More research is necessary to develop expressions for intensity-reduction factors for various test objects.

17.5 Some Practical Information

Some useful practical information on vibration testing of products is given here.

TABLE 17.3 Random Vibration Tests for a Product Development Application

Vibration Test	Root-Mean-Square Value of Excitation (g)	Peak Value of the Excitation PSD (g^2/Hz)	Minimum Times the Random Vibration is Applied	Minimum Duration of Vibration (min)	Vibration Axes
A	2.7	0.01	1	60	Major horizontal axis
B	6.0	0.05	2	30	Major horizontal axis
C	3.2	0.01	1	15	All three
D	5.8	0.02	1	15	All three
E	4.9	0.01	1	15	All three
F	6.3	0.04	2	5	All three

TABLE 17.4 Capabilities of Five Commercial Control Systems for Vibration-Test Shakers

System	A	B	C	D	E
Random test	Yes	Yes	Yes	Yes	Yes
Sine test	Yes	Yes	Optional	No	Yes
Transient and shock tests	Yes	Yes	Optional	No	Yes
Hydraulic shaker	OK	OK	OK	OK	OK
Preprogrammed test set-ups	Max. 63	Max. 25	Max. 99	10 per disk	Not given
Amplitude scheduling	32 Levels and duration	Min. start: -25 dB; min. step: 0.25 dB; can pick step durations	10 Levels over 60 dB	0.5 dB steps; can pick no. of steps and rate	No
On-line reference modification	Yes	No	Yes	No	No
Use of measured spectra as reference	Yes	Yes (measurement-pass feature)	Yes	No	No
Transmissibility	Yes	Measurement option	Yes	No	Yes
Coherence	Yes	Measurement option	No	No	Yes
Correlation	Yes	No	No	No	Yes
Shock response spectrum	Yes	Yes	Optional	No	Yes
Sine on random	Yes	Sine bursts	Optional	No	No
Random on random	Yes	No	Optional	No	No

TABLE 17.5 Important Hardware Characteristics of Five Systems for Shaker Control

System	A	B	C	D	E
Reference spectrum break points	40	32	50	10	45
Spectrum resolution (number of spectral lines)	Can pick 100, 200, 400, 600, 800 lines	Can pick 64, 128, 256, 512 lines (optional 1024 lines)	Can pick 100, 200, 400, 800 lines	200 Lines 10 Hz spacing	Pick any number: 10 to 1000 lines (optional 2048 lines)
Nature or random drive signal	Not given	Gaussian, periodic pseudo-random	Gaussian	Gaussian	Pseudo-random
Measured signal averaging	RMS, peak-hold	Arithmetic peak-hold	True power	Peak pick	No
Operator interface	Keyboard, menu-driven RS 232	Keyboard, push button, dialog, set-up	Keyboard, push button, dialog, menu-driven	Keyboard 10 soft keys, dialog	Keyboard
Output devices	CRT screen, hard copy, video print, digital plot	Standard or graphics terminal, X-Y record printer, digital plot	Graphics terminal, video hard copier, digital plotter, X-Y recorder	Like IBM PC, Mono-chrome-9" Epson printer	Graphics terminal printer, hard copy, X-Y plotter
Memory	128K	64K	128K	64K	32K std, 64K option
Mass storage	Floppy drive 0.5 MB; hard drive 10 MB	One floppy drive, 256K	Hard + floppy 8, 20, 30B	Two floppy drives 360K each	Two floppy drives 256K each
Number of measurements (control input) channels	2 standard; 16 optional	2 standard; 4 optional, multiplexer optional	1 standard; 16, 31 optional	1 standard; 4 optional	Not given
Number of controller output channels	One	One	One	One	One

TABLE 17.6 Specifications of Five Shaker Control Systems

System	A	B	C	D	E
Accelerometer signal (controller input)	± 125 mV to ± 8 V full scale	10 mV RMS ^a to ± 8 V max. typically > 500 mV RMS	Max. 10 V peak, 3.5 V, RMS	1 to 1000 mV/g user picked	Not given
Controller output signal	2.4 V RMS (random) 20 V peak to peak (sine and random)	20 V $P-P$ max. 50 mA max.	20 V $P-P$ max.	10 V peak 3 V RMS	Not given
Input frequency ranges	Random: DC to 200, 500 Hz, 1, 2, 3, 4, 8 kHz;. Sine: 1–8 Hz; shock: 10–125 Hz, 312 Hz,..., 5kHz	Seven ranges max. freq.: 500 Hz–5 kHz, min. freq = 1 line	100, 500 Hz, 1, 2, 4, 5, 10 kHz	10–2000 Hz	10–5000 Hz
Control loop time	2.1 sec (2 kHz, 200 lines)	0.3 sec, 64 lines; 0.9 sec, 256 lines, 3 sec, 1024 lines (2kHz)	4 sec, 100 lines, 8 sec, 200 lines (2 kHz)	2 sec	2.5 sec for 256 lines at 2 kHz
Equalization time for 10 dB range	Within ± 3 dB in two loops	2 or 3 loops	Within ± 1 dB in one loop	Within ± 1 dB in 6 sec	Not given
Resolution	12 bit	12 bit			12 bit
Dynamic range	65 dB	65 dB	72 dB	60 dB	—
Control accuracy	± 1 dB at $Q = 30$, ± 2 dB at $Q = 50$ (100 Hz Resonance at 1 octave/min	± 1 dB (at 90% confidence)	± 1 dB over 72 dB	± 1 dB	± 1 dB (at 95% confidence)
Sine sweep rate	OK	0.1–100 oct/min (log) 1 Hz–100 kHz/min (linear)	0.1–100 oct/min max.; 0.1 Hz–6 kHz/min	N/A	0.001–10 oct/min; 1–6000 Hz/min

^a RMS, root-mean-square.

17.5.1 Random Vibration Test Example

Table 17.3 lists several random vibration tests in the frequency range of 0 to 500 Hz in an application related to product development.

17.5.2 Vibration Shakers and Control Systems

Table 17.4 lists capabilities of five commercial control systems that may be used for shaker control in random vibration testing of products.

Table 17.5 summarizes important hardware characteristics of the five control systems.

Table 17.6 gives some important specifications of the five control systems.

Bibliography

- Broch, J.T. 1980. *Mechanical Vibration and Shock Measurements*, Bruel and Kjaer, Naerum, Denmark.
- Buzdugan, G., Mihaiescu, E., and Rades, M. 1986. *Vibration Measurement*, Martinus Nijhoff Publishers, Dordrecht, The Netherlands.
- de Silva, C.W. and Palusamy, S.S., Experimental modal analysis—a modeling and design tool, *Mech. Eng., ASME*, 106, 56–65, 1984.
- de Silva, C.W. 1983. *Dynamic Testing and Seismic Qualification Practice*, D.C. Heath and Co., Lexington, MA.
- de Silva, C.W., A dynamic test procedure for improving seismic qualification guidelines, *J. Dyn. Syst. Meas. Control, Trans. ASME*, 106, 143–148, 1984.
- de Silva, C.W., Hardware and software selection for experimental modal analysis, *Shock Vib. Digest* 16, 3–10, 1984.
- de Silva, C.W., Matrix eigenvalue problem of multiple-shaker testing, *J. Eng. Mech. Div., Trans. ASCE*, 108, EM2, 457–461, 1982.
- de Silva, C.W., Optimal input design for the dynamic testing of mechanical systems, *J. Dyn. Syst. Meas. Control, Trans. ASME*, 109, 111–119, 1987.
- de Silva, C.W., Seismic qualification of electrical equipment using a uniaxial test, *Earthquake Eng. Struct. Dyn.*, 8, 337–348, 1980.
- de Silva, C.W., The digital processing of acceleration measurements for modal analysis, *Shock Vib. Digest*, 18, 3–10, 1986.
- de Silva, C.W., Sensory information acquisition for monitoring and control of intelligent mechatronic systems, *Int. J. Inf. Acquisit.*, 1, 1, 89–99, 2004.
- de Silva, C.W., Henning, S.J., and Brown, J.D., Random testing with digital control—application in the distribution qualification of microcomputers, *Shock Vib. Digest*, 18, 3–13, 1986.
- de Silva, C.W., Loceff, F., and Vashi, K.M., Consideration of an optimal procedure for testing the operability of equipment under seismic disturbances, *Shock Vib. Bull.*, 50, 149–158, 1980.
- de Silva, C.W. 2004. *MECHATRONICS—An Integrated Approach*, CRC Press, Boca Raton, FL.
- de Silva, C.W., Singh, M., and Zaldonis, J., Improvement of response spectrum specifications in dynamic testing, *J Eng. Industry, Trans. ASME*, 112, 4, 384–387, 1990.
- de Silva, C.W. 2000. *VIBRATION—Fundamentals and Practice*, CRC Press, Boca Raton, FL.
- Ewins, D.J. 1984. *Modal Testing: Theory and Practice*, Research Studies Press Ltd, Letchworth, U.K.
- McConnell, K.G. 1995. *Vibration Testing*, Wiley, New York.
- Meirovitch, L. 1980. *Computational Methods in Structural Dynamics*, Sijthoff & Noordhoff, Rockville, MD.
- Randall, R.B. 1977. *Application of B&K Equipment to Frequency Analysis*, Bruel and Kjaer, Naerum, Denmark.

18

Experimental Modal Analysis

18.1	Introduction	18-1
18.2	Frequency-Domain Formulation	18-2
	Transfer-Function Matrix • Principle of Reciprocity	
18.3	Experimental Model Development	18-8
	Extraction of the Time-Domain Model	
18.4	Curve Fitting of Transfer Functions	18-10
	Problem Identification • Single- and Multi-Degree-of-Freedom Techniques • Single-Degree-of-Freedom Parameter Extraction in the Frequency Domain • Multi-Degree of Freedom Curve Fitting • A Comment on Static Modes and Rigid-Body Modes • Residue Extraction	
18.5	Laboratory Experiments	18-18
	Lumped-Parameter System • Distributed-Parameter System	
18.6	Commercial EMA Systems	18-24
	System Configuration	

Clarence W. de Silva
The University of British Columbia

Summary

In experimental modal analysis (EMA), first the modal information (natural frequencies, modal damping ratios, and mode shapes) of a test object is determined through experimentation, and this information is then used to determine a model for the test object. Once an “experimental model” is obtained in this manner, it may be used in a variety of practical uses including system analysis, fault detection and diagnosis, design, and control. This chapter presents some standard techniques and procedures associated with EMA.

18.1 Introduction

Experimental modal analysis (EMA) is basically a procedure of “experimental modeling.” The primary purpose here is to develop a dynamic model for a mechanical system, using experimental data. In this sense, EMA is similar to “model identification” in control system practice, and may utilize somewhat related techniques of “parameter estimation.” It is the nature of the developed model, which may distinguish EMA from other conventional procedures of model identification. Specifically, EMA produces a *modal model* as the primary result, which consists of:

1. Natural frequencies
2. Modal damping ratios
3. Mode shape vectors

Once a modal model is known, standard results of modal analysis may be used to extract an *inertia (mass) matrix*, a *damping matrix*, and a *stiffness matrix*, which constitute a complete dynamic model for the experimental system, in the time domain. Since EMA produces a modal model (and in some cases a complete time-domain dynamic model) for a mechanical system from test data of the system, its uses can be

extensive. In particular, EMA is useful in mechanical systems, primarily with regard to vibration, in:

1. Design
2. Diagnosis
3. Control

In the area of design, the following three approaches that utilize EMA should be mentioned:

1. Component modification
2. Modal response specification
3. Substructuring

In component modification, we modify (i.e., add, remove, or vary) inertia (mass), stiffness, and damping parameters in a mechanical system and determine the resulting effect on the modal response (natural frequencies, damping ratios, and mode shapes) of the system. In modal response specification, we establish the best changes, from the design point of view, in system parameters (inertia, stiffness, and damping values and their degrees of freedom (DoF), in order to give a “specified” (prescribed) change in the modal response. In substructuring, two or more subsystem models are combined using dynamic interfacing components, and the overall model is determined. Some of the subsystem models used in this manner can be of analytical origin (e.g., finite element models).

Diagnosis of problems (faults, performance degradation, component deterioration, impending failure, etc.) of a mechanical system requires *condition monitoring* of the system, and analysis and evaluation of the monitored information. Often, analysis involves extraction of modal parameters using monitored data. Diagnosis may involve the establishment of changes (both gradual and sudden), patterns, and trends in these system parameters.

Control of a mechanical system may be based on modal analysis. Standard and well-developed techniques of modal control are widely used in mechanical system practice. In particular, vibration control, both active and passive, can use modal control. In this approach, the system is first expressed as a modal model, then control excitations, parameter adaptations, and so on are established that result in a specified (derived) behavior in various modes of the system. Of course, techniques of EMA are commonly used here, both in obtaining a modal model from test data and in establishing modal excitations and parameter changes that are needed to realize a prescribed behavior in the system.

The standard steps of EMA are as follows:

1. Obtain a suitable (admissible) set of test data, consisting of forcing excitations and motion responses for various pairs of DoF of the test object.
2. Compute the frequency transfer functions (the frequency response functions) of the pairs of test data, using Fourier analysis. Digital Fourier analysis using Fast Fourier Transform (FFT) is the standard way of accomplishing this. Either software-based (computer) equipment or hardware-based instrumentation may be used.
3. Curve fit analytical transfer functions to the computed transfer functions. Determine natural frequencies, damping ratios, and residues for various modes in each transfer function.
4. Compute mode shape vectors.
5. Compute inertia (mass) matrix \mathbf{M} , stiffness matrix \mathbf{K} , and damping matrix \mathbf{C} .

Some variations of these steps is possible in practice, and Step 5 is omitted in some situations. In the present chapter, we will study some standard techniques and procedures associated with the process of EMA.

18.2 Frequency-Domain Formulation

Frequency-domain analysis of vibrating systems is very useful in a wide variety of applications. The analytical convenience of frequency-domain methods results from the fact that differential equations in the time domain become algebraic equations in the frequency domain. Once the

necessary analysis is performed in the frequency domain, it is often possible to interpret the results without having to transform them back to the time domain through inverse Fourier transformation. In the context of the present chapter, frequency-domain representation is particularly important because it is the frequency transfer functions that are used for extracting the necessary modal parameters.

For the convenience of notation, we shall develop the frequency-domain results using the Laplace variable, s . As usual, the straightforward substitution of $s = j\omega$ or $s = j2\pi f$ gives the corresponding frequency-domain results.

18.2.1 Transfer-Function Matrix

Let us consider a linear mechanical system that is represented by

$$\mathbf{M}\ddot{\mathbf{y}} + \mathbf{C}\dot{\mathbf{y}} + \mathbf{K}\mathbf{y} = \mathbf{f}(t) \quad (18.1)$$

where

$\mathbf{f}(t)$ = forcing excitation vector (n th order column)
 \mathbf{y} = displacement response vector (n th order column)
 \mathbf{M} = mass (inertia) matrix ($n \times n$)
 \mathbf{C} = damping (linear viscous) matrix ($n \times n$)
 \mathbf{K} = stiffness matrix ($n \times n$)

If the assumption of *proportional damping* is made, the coordinate transformation

$$\mathbf{y} = \mathbf{\Psi}\mathbf{q} \quad (18.2)$$

decouples Equations 18.1 into the canonical form of modal equations

$$\bar{\mathbf{M}}\ddot{\mathbf{q}} + \bar{\mathbf{C}}\dot{\mathbf{q}} + \mathbf{K}\mathbf{q} = \mathbf{\Psi}^T\mathbf{f}(t) \quad (18.3)$$

where

$\mathbf{\Psi}$ = modal matrix ($n \times n$) of n independent modal vector vectors $[\boldsymbol{\psi}_1, \boldsymbol{\psi}_2, \dots, \boldsymbol{\psi}_n]$
 $\bar{\mathbf{M}}$ = diagonal matrix of modal masses M_i
 $\bar{\mathbf{C}}$ = diagonal matrix of modal damping constants C_i
 $\bar{\mathbf{K}}$ = diagonal matrix of modal stiffnesses K_i

Specifically, we have

$$\bar{\mathbf{M}} = \mathbf{\Psi}^T\mathbf{M}\mathbf{\Psi} \quad (18.4)$$

$$\bar{\mathbf{C}} = \mathbf{\Psi}^T\mathbf{C}\mathbf{\Psi} \quad (18.5)$$

$$\bar{\mathbf{K}} = \mathbf{\Psi}^T\mathbf{K}\mathbf{\Psi} \quad (18.6)$$

If the modal vectors are assumed to be \mathbf{M} -normal, then we have

$$M_i = 1$$

$$K_i = \omega_i^2$$

and furthermore, we can express C_i in the convenient form

$$C_i = 2\zeta_i\omega_i$$

where

ω_i = undamped natural frequency
 ζ_i = modal damping ratio

By Laplace transformation of the response canonical equations of modal motion (Equation 18.3), assuming zero initial conditions, we obtain

$$\begin{bmatrix} s^2 + 2\zeta\omega_1s + \omega_1^2 & & & 0 \\ & s^2 + 2\zeta\omega_2s + \omega_2^2 & & \\ & & \ddots & \\ 0 & & & s^2 + 2\zeta\omega_ns + \omega_n^2 \end{bmatrix} \mathbf{Q}(s) = \mathbf{\Psi}^T \mathbf{F}(s) \quad (18.7)$$

Laplace transforms of the modal response (or generalized coordinate) vector, $\mathbf{q}(t)$, and the forcing excitation vector, $\mathbf{f}(t)$, are denoted by the column vectors, $\mathbf{Q}(s)$ and $\mathbf{F}(s)$, respectively. The square matrix on the left-hand side of Equation 18.7 is a diagonal matrix. Its inverse is obtained by inverting the diagonal elements. Consequently, the following modal transfer relation results:

$$\mathbf{Q}(s) = \begin{bmatrix} G_1 & & & 0 \\ & G_2 & & \\ & & \ddots & \\ 0 & & & G_n \end{bmatrix} \mathbf{\Psi}^T \mathbf{F}(s) \quad (18.8)$$

in which the diagonal elements are the damped simple-oscillator transfer functions

$$G_i(s) = \frac{1}{[s^2 + 2\zeta_i\omega_i s + \omega_i^2]} \quad \text{for } i = 1, 2, \dots, n \quad (18.9)$$

Note that ω_i , the i th undamped natural frequency (in the time domain), is only approximately equal to the frequency of the i th *resonance* of the transfer function (in the frequency domain), as given by

$$\omega_{ri} = \sqrt{1 - 2\zeta_i^2} \omega_i \quad (18.10)$$

As we have discussed before, and as is clear from Equation 18.10, the approximation improves for decreasing modal damping. Consequently, in most applications of EMA, the resonant frequency is taken to be equal (approximately) to the natural frequency for a given mode.

From the time-domain coordinate transformation (Equation 18.2), the Laplace domain coordinate transformation relation is obtained as

$$\mathbf{Y}(s) = \mathbf{\Psi} \mathbf{Q}(s) \quad (18.11)$$

Substitute Equation 18.8 into Equation 18.11; thus

$$\mathbf{Y}(s) = \mathbf{\Psi} \begin{bmatrix} G_1 & & & 0 \\ & G_2 & & \\ & & \ddots & \\ 0 & & & G_n \end{bmatrix} \mathbf{\Psi}^T \mathbf{F}(s) \quad (18.12)$$

Equation 18.12 is the excitation–response (input–output) transfer relation. It is clear that the $n \times n$ *transfer function matrix*, \mathbf{G} , for the n -DoF system is given by

$$\mathbf{G}(s) = \mathbf{\Psi} \begin{bmatrix} G_1 & & & 0 \\ & G_2 & & \\ & & \ddots & \\ 0 & & & G_n \end{bmatrix} \mathbf{\Psi}^T \quad (18.13)$$

Notice in particular that $\mathbf{G}(s)$ is a symmetric matrix; specifically

$$\mathbf{G}^T(s) = \mathbf{G}(s) \quad (18.14)$$

which should be clear from the matrix transposition property, $(\mathbf{ABC})^T = \mathbf{C}^T \mathbf{B}^T \mathbf{A}^T$.

An alternative version of Equation 18.13 that is extensively used in EMA can be obtained by using the partitioned form (or assembled form) of the modal matrix in Equation 18.13. Specifically, we have

$$\mathbf{G}(s) = [\boldsymbol{\psi}_1, \boldsymbol{\psi}_2, \dots, \boldsymbol{\psi}_n] \begin{bmatrix} G_1 & & & \mathbf{0} \\ & G_2 & & \\ & & \ddots & \\ \mathbf{0} & & & G_n \end{bmatrix} \begin{bmatrix} \boldsymbol{\psi}_1^T \\ \boldsymbol{\psi}_2^T \\ \vdots \\ \boldsymbol{\psi}_n^T \end{bmatrix} \quad (18.15)$$

On multiplying out the last two matrices on the right-hand side of Equation 18.15 term by term, the following intermediate result is obtained:

$$\mathbf{G}(s) = [\boldsymbol{\psi}_1, \boldsymbol{\psi}_2, \dots, \boldsymbol{\psi}_n] \begin{bmatrix} G_1 \boldsymbol{\psi}_1^T \\ G_2 \boldsymbol{\psi}_2^T \\ \vdots \\ G_n \boldsymbol{\psi}_n^T \end{bmatrix}$$

Note that G_i are scalars while $\boldsymbol{\psi}_i$ are column vectors. The two matrices in this product can be multiplied out now to obtain the matrix sum

$$\mathbf{G}(s) = G_1 \boldsymbol{\psi}_1 \boldsymbol{\psi}_1^T + G_2 \boldsymbol{\psi}_2 \boldsymbol{\psi}_2^T + \dots + G_n \boldsymbol{\psi}_n \boldsymbol{\psi}_n^T = \sum_{r=1}^n G_r \boldsymbol{\psi}_r \boldsymbol{\psi}_r^T \quad (18.16)$$

in which $\boldsymbol{\psi}_r$ is the r th modal vector that is normalized with respect to the mass matrix. Notice that each term $\boldsymbol{\psi}_r \boldsymbol{\psi}_r^T$ in the summation (Equation 18.16) is an $n \times n$ matrix with the element corresponding to its i th row and k th column being $(\psi_i \psi_k)_r$. The ik th element of the transfer matrix $\mathbf{G}(s)$ is the transfer function $G_{ik}(s)$, which determines the transfer characteristics between the response location, i , and the excitation location, k . From Equation 18.16, this is given by

$$G_{ik}(s) = \sum_{r=1}^n G_r (\psi_i \psi_k)_r = \sum_{r=1}^n \frac{(\psi_i \psi_k)_r}{[s^2 + 2\zeta_r \omega_r s + \omega_r^2]} \quad (18.17)$$

with $s = j\omega = j2\pi f$ in the frequency domain. Note that $(\psi_i)_r$ is the i th element of the r th modal vector, and is a scalar quantity. Similarly, $(\psi_i \psi_k)_r$ is the product of the i th element and the k th element of the r th modal vector, and is also a scalar quantity. This is the numerator of each modal transfer function within the right-hand side summation of Equation 18.17, and is the *residue* of the pole (eigenvalue) of that mode.

Equation 18.17 is useful in EMA. Essentially, we start by determining the residues $(\psi_i \psi_k)_r$ of the poles in an admissible set of measured transfer functions. We can determine the modal vectors in this manner. In addition, by analyzing the measured transfer functions, the *modal damping ratios*, ζ_i , and the *natural frequencies*, ω_i , can be estimated. From these results, an estimate for the time-domain model (i.e., the matrices \mathbf{M} , \mathbf{K} , and \mathbf{C}) can be determined.

18.2.2 Principle of Reciprocity

By the symmetry of transfer matrix, as given by Equation 18.14, it follows that

$$G_{ik}(s) = G_{ki}(s) \quad (18.18)$$

This fact is further supported by Equation 18.17. This symmetry can be interpreted as *Maxwell's principle of reciprocity*. To understand this further, consider the complete set of transfer relations given by Equation 18.12 and Equation 18.13:

$$\begin{aligned} Y_1(s) &= G_{11}(s)F_1(s) + G_{12}(s)F_2(s) + \cdots + G_{1n}(s)F_n(s) \\ Y_2(s) &= G_{21}(s)F_1(s) + G_{22}(s)F_2(s) + \cdots + G_{2n}(s)F_n(s) \\ &\vdots \\ Y_n(s) &= G_{n1}(s)F_1(s) + G_{n2}(s)F_2(s) + \cdots + G_{nn}(s)F_n(s) \end{aligned} \quad (18.19)$$

Note that the diagonal elements, $G_{11}, G_{22}, \dots, G_{nn}$, are *driving-point transfer functions* (or autotransfer functions) and the rest are *cross-transfer functions*. Suppose that a single excitation, $F_k(s)$, is applied at the k th DoF with all the other excitations set to zero. The resulting response at the i th DoF is given by

$$Y_i(s) = G_{ik}(s)F_k(s) \quad (18.20)$$

Similarly, when a single excitation, $F_i(s)$, is applied at the i th DoF, the resulting response at the k th DoF is given by

$$Y_k(s) = G_{ki}(s)F_i(s) \quad (18.21)$$

In view of the symmetry that is indicated by Equation 18.18, it follows from Equation 18.20 and Equation 18.21 that if the two separate excitations, $F_k(s)$ and $F_i(s)$, are identical then the corresponding responses, $Y_i(s)$ and $Y_k(s)$, are also identical. In other words, the response at the i th DoF due to a single force at the k th DoF is equal to the response at the k th DoF when the same single force is applied at the i th DoF. This is the frequency-domain version of the principle of reciprocity.

Example 18.1

Consider the two-DoF system shown in Figure 18.1. Assume that the excitation forces, $f_1(t)$ and $f_2(t)$, act at the y_1 and y_2 DoFs, respectively. The equations of motion are given by

$$\begin{bmatrix} m & 0 \\ 0 & m \end{bmatrix} \ddot{\mathbf{y}} + \begin{bmatrix} c & 0 \\ 0 & c \end{bmatrix} \dot{\mathbf{y}} + \begin{bmatrix} 2k & -k \\ -k & 2k \end{bmatrix} \mathbf{y} = \mathbf{f}(t) \quad (i)$$

This system has proportional damping (specifically, it is clear that \mathbf{C} is proportional to \mathbf{M}) and hence possesses the same real modal vectors as does the undamped system. Let us first obtain the transfer matrix in the direct manner. By taking the Laplace transform (with zero initial conditions) of the equations of motion (i), we have

$$\begin{bmatrix} ms^2 + cs + 2k & -k \\ -k & ms^2 + cs + 2k \end{bmatrix} \mathbf{Y}(s) = \mathbf{F}(s) \quad (ii)$$

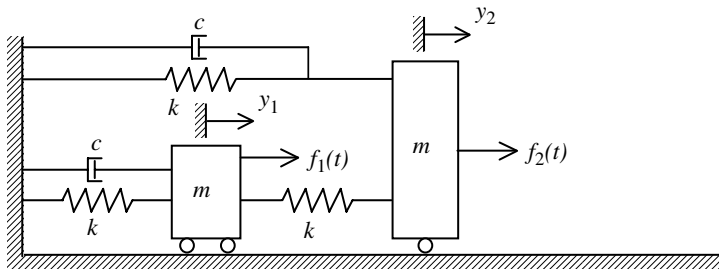


FIGURE 18.1 A vibrating system with proportional damping.

Hence, in the relation $\mathbf{Y}(s) = \mathbf{G}(s)\mathbf{F}(s)$, the transfer matrix \mathbf{G} is given by

$$\begin{aligned}\mathbf{G}(s) &= \begin{bmatrix} ms^2 + cs + 2k & -k \\ -k & ms^2 + cs + 2k \end{bmatrix}^{-1} \\ &= \frac{1}{[(ms^2 + cs + 2k)^2 - k^2]} \begin{bmatrix} ms^2 + cs + 2k & k \\ k & ms^2 + cs + 2k \end{bmatrix}\end{aligned}\quad (\text{iii})$$

The characteristic polynomial $\Delta(s)$ of the system is

$$\Delta(s) = (ms^2 + cs + 2k)^2 - k^2 = (ms^2 + cs + k)(ms^2 + cs + 3k) \quad (\text{iv})$$

and is common to the denominator of all four transfer functions in the matrix. Specifically,

$$G_{11}(s) = G_{22}(s) = \frac{ms^2 + cs + 2k}{\Delta(s)} \quad (\text{v})$$

$$G_{12}(s) = G_{21}(s) = \frac{k}{\Delta(s)} \quad (\text{vi})$$

This result implies that the characteristic equation characterizes the entire system (particularly, the natural frequencies and damping ratios) and, no matter what transfer function is measured (or analyzed), the same natural frequencies and modal damping are obtained.

We can put these transfer functions into the partial fraction form. For example,

$$\frac{ms^2 + cs + 2k}{(ms^2 + cs + k)(ms^2 + cs + 3k)} = \frac{A_1s + A_2}{(ms^2 + cs + k)} + \frac{A_3s + A_4}{(ms^2 + cs + 3k)} \quad (\text{vii})$$

By comparing the numerator coefficients, we find that $A_1 = A_3 = 0$ (this is the case when the modes are *real*; with complex modes, $A_1 \neq 0$ and $A_3 \neq 0$ in general) and $A_2 = A_4 = 1/2$. These results are summarized below:

$$G_{11}(s) = G_{22}(s) = \frac{1/(2m)}{[s^2 + 2\zeta_1\omega_1s + \omega_1^2]} + \frac{1/(2m)}{[s^2 + 2\zeta_2\omega_2s + \omega_2^2]} \quad (\text{viii})$$

$$G_{12}(s) = G_{21}(s) = \frac{1/(2m)}{[s^2 + 2\zeta_1\omega_1s + \omega_1^2]} - \frac{1/(2m)}{[s^2 + 2\zeta_2\omega_2s + \omega_2^2]} \quad (\text{ix})$$

with

$$\omega_1 = \sqrt{k/m}, \quad \omega_2 = \sqrt{3k/m}, \quad \zeta_1 = c/\sqrt{4mk}, \quad \text{and} \quad \zeta_2 = c/\sqrt{12mk}$$

By comparing the *residues* (numerators) of these expressions with the relation expressed in Equation 18.17, we can determine the \mathbf{M} -normal modal vectors. Specifically, by examining G_{11} :

$$(\psi_1^2)_1 = \frac{1}{2m}, \quad (\psi_1^2)_2 = \frac{1}{2m}$$

and by examining at G_{12} :

$$(\psi_1\psi_2)_1 = \frac{1}{2m}, \quad (\psi_1\psi_2)_2 = -\frac{1}{2m}$$

We need consider only two admissible transfer functions (e.g., G_{11} and G_{12} , or G_{11} and G_{21} , or G_{12} and G_{22} , or G_{21} and G_{22}) in order to completely determine the modal vectors. Specifically, we obtain

$$\begin{bmatrix} \psi_1 \\ \psi_2 \end{bmatrix}_1 = \begin{bmatrix} 1/\sqrt{2m} \\ 1/\sqrt{2m} \end{bmatrix} \quad \text{and} \quad \begin{bmatrix} \psi_1 \\ \psi_2 \end{bmatrix}_2 = \begin{bmatrix} 1/\sqrt{2m} \\ -1/\sqrt{2m} \end{bmatrix}$$

Note that the modal masses are unity for these modal vectors. Also, there is an arbitrariness in the sign. As usual, we have overcome this problem by making the first element of each modal vector positive.

18.3 Experimental Model Development

We have noted that the process of extracting modal data (natural frequencies, modal damping, and mode shapes) from measured excitation–response data is termed experimental modal analysis. Modal testing and the analysis of test data are the two main steps of EMA. Information obtained through EMA is useful in many applications, including the validation of analytical models for dynamic systems, fault diagnosis in machinery and equipment, *in situ* testing for requalification to revised regulatory specifications, and design development of mechanical systems.

In the present development, it is assumed that the test data are available in the frequency domain as a set of transfer functions. In particular, suppose that an *admissible* set of transfer functions is available. The actual process of constructing or computing these frequency transfer functions from measured excitation–response (input–output) test data (in the time domain) is known as *model identification* in the frequency domain. This step should precede the actual modal analysis in practice. Numerical analysis (or curve fitting) is the basic tool used for this purpose, and it will be discussed in a later section.

The basic result used in EMA is Equation 18.17 with $s = j\omega$ or $s = j2\pi f$ for the frequency-transfer functions. For convenience, however, the following notation is used:

$$G_{ik}(\omega) = \sum_{r=1}^n \frac{(\psi_i \psi_k)_r}{[\omega_r^2 - \omega^2 + 2j\zeta_r \omega_r \omega]} \quad (18.22)$$

$$G_{ik}(f) = \sum_{r=1}^n \frac{(\psi_i \psi_k)_r}{4\pi^2[f_1^2 - f^2 + 2j\zeta_r f_r f]} \quad (18.23)$$

where ω and f are used in place of $j\omega$ and $j2\pi f$ in the function notation $G(\cdot)$. As already observed in Example 18.1, it is not necessary to measure all n^2 transfer functions in the $n \times n$ transfer function matrix, \mathbf{G} , in order to determine the complete modal information. Owing to the symmetry of \mathbf{G} it follows that at most only $1/2n(n+1)$ transfer functions are needed. In fact, it can be “shown by construction” (i.e., in the process of developing the method itself) that only n transfer functions are needed. These n transfer functions cannot be chosen arbitrarily, however, even though there is a wide choice for the admissible set of n transfer functions. A convenient choice is to measure any one *row* or any one *column* of the transfer function matrix. It should be clear from the following development that any set of transfer functions that spans all n DoF of the system would be an admissible set provided that only one autotransfer function is included in the minimal set. Hence, for example, all the transfer functions on the main diagonals or on the main cross diagonal of \mathbf{G} , do not form an admissible set.

Suppose that the k th column (G_{ik} , $i = 1, 2, \dots, n$) of the transfer function matrix is measured by applying a single forcing excitation at the k th DoF and measuring the corresponding responses at all n DoF in the system. The main steps in extracting the modal information from this data are given below:

1. Curve fit the (measured) n transfer functions to expressions of the form given by Equation 18.22. In this manner determine the natural frequencies ω_r , the damping ratios ζ_r , and the residues $(\psi_i \psi_k)_r$, for the set of modes $r = 1, 2$, and so on.
2. The residues of a diagonal transfer function (i.e., point transfer functions or autotransfer function), G_{kk} , are $(\psi_k^2)_1, (\psi_k^2)_2, \dots, (\psi_k^2)_n$. From these, determine the k th row of the modal matrix; $(\psi_k)_1, (\psi_k)_2, \dots, (\psi_k)_n$. Note that \mathbf{M} -normality is assumed. However, the modal vectors are arbitrary up to a multiplier of -1 . Hence, we may choose this row to have all positive elements.
3. The residues of a nondiagonal transfer function, that is, a cross-transfer function, $G_{k+i,k}$ are $(\psi_{k+i} \psi_k)_1, (\psi_{k+i} \psi_k)_2, \dots, (\psi_{k+i} \psi_k)_n$. By substituting the values obtained in Step 2 into these values, determine the $k+i$ th row of the modal matrix; $(\psi_{k+i})_1, (\psi_{k+i})_2, \dots, (\psi_{k+i})_n$. The complete modal matrix Ψ is obtained by repeating this step for $i = 1, 2, \dots, n-k$ and $i = -1, -2, \dots, -k+1$. Note that the associated modal vectors are \mathbf{M} -normal.

The procedure just outlined for determining the modal matrix verifies, by construction, that only n transfer functions are needed to extract the complete modal information. It further reveals that it is not

essential to perform the transfer function measurements in a row fashion or column fashion. A diagonal element (i.e., a *point transfer function*, or an *autotransfer function*) should always be measured. The remaining $n - 1$ transfer functions must be off diagonal but otherwise can be chosen arbitrarily, provided that all n DoF are spanned either as an excitation point or as a measurement location (or both). This guarantees that no symmetric transfer function elements are included. This defines a minimal set of transfer function measurements. An *admissible set* of more than n transfer functions can be measured in practice so that redundant measurements are available in addition to the minimal set that is required. Such redundant data are useful for checking the accuracy of the modal estimates. Examples for an admissible (nonminimal) set, a minimal set, and an inadmissible set of transfer functions matrix elements are shown schematically in Figure 18.2. Note that the inadmissible set in this example contains 11 transfer function measurements but the sixth DoF is not covered by this set. On the other hand, a minimal set requires only six transfer functions.

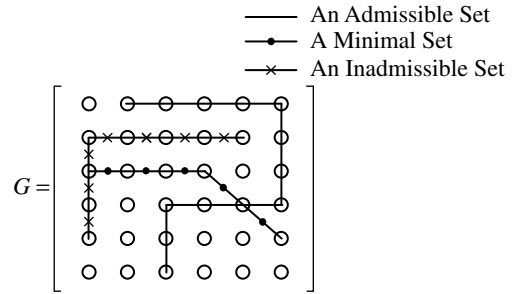


FIGURE 18.2 A nonminimal admissible set, a minimal set, and inadmissible set of possible transfer function measurements.

18.3.1 Extraction of the Time-Domain Model

Once the complete modal information is extracted by modal analysis, it is possible, at least in theory, to determine a time-domain model (\mathbf{M} , \mathbf{K} , and \mathbf{C} matrices) for the system. To obtain the necessary equations, first premultiply by $(\Psi^T)^{-1}$ and postmultiply by Ψ Equation 18.4, Equation 18.5, and Equation 18.6 to obtain

$$\mathbf{M} = (\Psi^T)^{-1} \bar{\mathbf{M}} \Psi^{-1} \quad (18.24)$$

where $\bar{\mathbf{M}} = \mathbf{I}$ = identity matrix

$$\mathbf{K} = (\Psi^T)^{-1} \bar{\mathbf{K}} \Psi^{-1} \quad (18.25)$$

$$\mathbf{C} = (\Psi^T)^{-1} \bar{\mathbf{C}} \Psi^{-1} \quad (18.26)$$

Since the modal matrix Ψ is nonsingular because \mathbf{M} is assumed nonsingular in the dynamic models that we use (i.e., each DoF has an associated mass, or the system does not possess static modes), the inverse transformations given by the equations from Equation 18.24 to Equation 18.26 are feasible. It appears, however, that two matrix inversions are needed for each result. Since \mathbf{M} , \mathbf{K} , and \mathbf{C} matrices are diagonal, their inverse is given by inverting the diagonal elements. This fact can be used to obtain each result through just one matrix inversion.

Equation 18.24, Equation 18.25, and Equation 18.26 are written as

$$\mathbf{M} = (\Psi \bar{\mathbf{M}}^{-1} \Psi^T)^{-1} \quad (18.27)$$

$$\mathbf{K} = (\Psi \bar{\mathbf{K}}^{-1} \Psi^T)^{-1} \quad (18.28)$$

$$\mathbf{C} = (\Psi \bar{\mathbf{C}}^{-1} \Psi^T)^{-1} \quad (18.29)$$

Note that for the present \mathbf{M} -normal case

$$\bar{\mathbf{M}}^{-1} = \mathbf{I} \quad (18.30)$$

$$\bar{\mathbf{K}}^{-1} = \text{diag}[1/\omega_1^2, 1/\omega_2^2, \dots, 1/\omega_n^2] \quad (18.31)$$

$$\bar{\mathbf{C}}^{-1} = \text{diag}[1/(2\zeta_1 \omega_1), 1/(2\zeta_2 \omega_2), \dots, 1/(2\zeta_n \omega_n)] \quad (18.32)$$

By substituting the equations from Equation 18.30 to Equation 18.32 into the equations from Equation 18.27 to Equation 18.29, we obtain the relations that can be used in computing the time-domain model:

$$\mathbf{M} = (\mathbf{\Psi}\mathbf{\Psi}^T)^{-1} \quad (18.33)$$

$$\mathbf{K} = \left(\mathbf{\Psi} \begin{bmatrix} 1/\omega_1^2 & & & \mathbf{0} \\ & 1/\omega_2^2 & & \\ & & \ddots & \\ \mathbf{0} & & & 1/\omega_n^2 \end{bmatrix} \mathbf{\Psi}^T \right)^{-1} \quad (18.34)$$

$$\mathbf{C} = \left(\mathbf{\Psi} \begin{bmatrix} 1/(2\zeta_1\omega_1) & & & \mathbf{0} \\ & 1/(2\zeta_2\omega_2) & & \\ & & \ddots & \\ \mathbf{0} & & & 1/(2\zeta_n\omega_n) \end{bmatrix} \mathbf{\Psi}^T \right)^{-1} \quad (18.35)$$

Alternatively, only one matrix inversion (that of $\mathbf{\Psi}$) is needed if we use the fact that

$$(\mathbf{\Psi}^T)^{-1} = (\mathbf{\Psi}^{-1})^T$$

Then,

$$\mathbf{M} = (\mathbf{\Psi}^{-1})^T \tilde{\mathbf{M}} \mathbf{\Psi}^{-1} \quad (18.36)$$

$$\mathbf{K} = (\mathbf{\Psi}^{-1})^T \tilde{\mathbf{K}} \mathbf{\Psi}^{-1} \quad (18.37)$$

$$\mathbf{C} = (\mathbf{\Psi}^{-1})^T \tilde{\mathbf{C}} \mathbf{\Psi}^{-1} \quad (18.38)$$

The main steps of EMA are summarized in Box 18.1. In practice, frequency-response data are less accurate at higher resonances. Some of the main sources of error are as follows:

- (1) Aliasing distortion in the frequency domain, due to finite sampling rate of data, will distort high-frequency results during digital computation.
- (2) Inadequate spectral-line resolution (or frequency resolution) and frequency coverage (bandwidth) can introduce errors at high-frequency resonances. The frequency resolution is fixed both by the signal record length (T) and the type of time window used in digital Fourier analysis, but the resonant peaks are sharper for higher frequencies. Frequency coverage depends on the data sampling rate.
- (3) Low signal-to-noise ratio (SNR) at high frequencies, in part due to noise and poor dynamic range of equipment and in part due to low signal levels, will result in data measurement errors. Signal levels are usually low at high frequencies because inertia in a mechanical system acts as a low-pass filter $1/(m\omega^2)$.
- (4) Computations involving high order matrices (multiplication, inversion, etc.) will lead to numerical errors in complex systems with many DoF.

It is customary, therefore, to extract modal information only for the first several modes. In that case, it is not possible to recover the mass, stiffness, and damping matrices. Even if these matrices are computed, their accuracy is questionable due to their sensitivity to the factors listed above.

18.4 Curve Fitting of Transfer Functions

Parameter estimation in vibrating systems can be interpreted as a technique of *experimental modeling*. This process requires experimental data in a suitable form, preferably excitation–response data, and is often represented as a set of transfer functions in the frequency domain. Parameter estimation using

Box 18.1

MAIN STEPS OF EXPERIMENTAL MODAL ANALYSIS

1. Measure an admissible set of excitation (u) and response (y) signals. (Cover all DoF; one response measurement should be for the excitation location.)
2. Group the signals, assign windows, and filter the signals.
3. Compute transfer functions using FFT and the spectral density method:

$$G_{uy} = \Phi_{uy} / \Phi_{uu}$$

4. Compute ordinary coherence functions

$$\gamma_{uy}^2 = \frac{|\Phi_{uy}|^2}{\Phi_{uu} \Phi_{yy}}$$

and choose the accurate transfer functions on this basis (γ_{uy} close to 1 \Rightarrow accept; γ_{uy} close to 0 \Rightarrow reject).

5. Curve fit n admissible transfer functions to expressions:

$$G_{ik} = \sum_{r=1}^n \frac{(\psi_i \psi_k)_r}{[\omega_r^2 - \omega^2 + 2j\zeta_r \omega_r \omega]}$$

Hence, extract:

Residues $(\psi_i \psi_k)_r \Rightarrow$ mode shapes vectors ψ_r which are \mathbf{M} -normal;

Natural frequencies (undamped), ω_r ;

Modal damping ratios (viscous), ζ_r .

6. Form the modal matrix $\Psi = [\psi_1, \psi_2, \dots, \psi_n]$;
Compute Ψ^{-1} .

7. Modal mass matrix $\bar{\mathbf{M}} = \mathbf{I}$;

Modal stiffness matrix $\bar{\mathbf{K}} = \text{diag}[\omega_1^2, \omega_2^2, \dots, \omega_n^2]$;

Modal damping matrix $\bar{\mathbf{C}} = \text{diag}[2\zeta_1 \omega_1, 2\zeta_2 \omega_2, \dots, 2\zeta_n \omega_n]$;

8. Compute the system model:

Mass matrix $\mathbf{M} = (\Psi^{-1})\Psi^{-1}$;

Stiffness matrix $\mathbf{K} = (\Psi^{-1})^T \bar{\mathbf{K}} \Psi^{-1}$;

Damping matrix $\mathbf{C} = (\Psi^{-1})\bar{\mathbf{C}}\Psi^{-1}$.

measured response data is termed *model identification* or, simply, identification in the literature on systems and control. We shall present a parameter estimation procedure that involves frequency transfer functions, which is particularly useful in EMA.

18.4.1 Problem Identification

Transfer functions that are computed from measured time histories using digital Fourier analysis (e.g., FFT) cannot be directly used in the modal analysis computations. The data must be available as analytical transfer functions. Therefore, it is important to represent the computed transfer functions with suitable analytical expressions. This is done, in practice, either by curve fitting

a suitable transfer function model into the computed data or by simplified methods such as “peak picking.” Accordingly, this conversion of data is an experimental modeling technique.

Identification of transfer function models from measured data is an essential step in EMA. Apart from that, it has other important advantages. In particular, analytical transfer function plots clearly identify system resonances and generate numerical values for the corresponding parameters (resonant frequencies, damping, phase angles, and magnitudes) in a convenient manner. This form represents a significant improvement over the crude transfer function plots, which are normally far less presentable and rather difficult to interpret.

18.4.2 Single- and Multi-Degree-of-Freedom Techniques

Several single-DoF techniques exist for extracting analytical parameters from experimental transfer functions. In particular, the methods of curve fitting (circle fitting) and peak picking are considered here. In a single-DoF method, only one resonance is considered at a time.

Single-DoF curve fitting, or more correctly, *single-resonance curve fitting* is the term used to denote any curve fitting procedure that fits a quadratic (second-order) transfer function into each resonance in the measured transfer function, one at a time. In the case of closely spaced modes (or closely spaced resonances), the associated error can be very large. The accuracy is improved if expressions of a higher order than quadratic are used for this purpose, but unacceptable errors can still exist. In peak picking, each resonance of experimental transfer function data is examined individually; the resonant frequency and the damping constant corresponding to that resonance are determined by comparing with an analytical single-DoF transfer function.

In multi-DoF curve fitting, or more appropriately, *multiresonance curve fitting*, all resonances (or modes) of importance are considered simultaneously and fitted into an analytical transfer function of suitable order. This method is generally more accurate but computationally more demanding than the single-resonance method. In choosing between the single-resonance and multiresonance methods, the required accuracy should be weighted against the cost and speed of computation.

18.4.3 Single-Degree-of-Freedom Parameter Extraction in the Frequency Domain

The theory of curve fitting by a circle (i.e., circle fitting) for each resonance of an experimentally determined transfer function is presented first. Next, the peak picking method will be described.

18.4.3.1 Circle-Fit Method

It can be shown that the *mobility* transfer function (velocity/force) of a single-DoF system with linear *viscous damping*, when plotted on the *Nyquist plane* of real axis and imaginary axis for the frequency transfer function, is a circle. Similarly, it can be shown that the *receptance* or *dynamic flexibility* or compliance transfer function (displacement/force) of a single-DoF system with *hysteretic damping*, when plotted on the Nyquist plane, is also a circle. Note that, for hysteretic damping, the damping constant (in the time domain) is not actually a constant but is inversely proportional to the frequency of motion. However, in this case, in the frequency domain, the damping term will be independent of frequency. The fact that such circle representations are possible for transfer functions of a single-DoF system may be used in fitting a circle to a transfer function that is computed from experimental data. This will lead to determining the analytical parameters for the transfer function. This approach is illustrated now through analytical development.

Case of Viscous Damping

Consider a single-DoF system with linear, viscous damping, as given by

$$m\ddot{y} + c\dot{y} + ky = f(t) \quad (18.39)$$

where m , k , and c are the mass, stiffness, and damping constants of the system elements, respectively, $f(t)$ is the excitation force, and y is the displacement response. Equation 18.39 may be expressed in the standard form:

$$\ddot{y} + 2\zeta\omega_n\dot{y} + \omega_n^2 y = \frac{1}{m}f(t) \quad (18.40)$$

Receptance

$$\frac{Y(s)}{F(s)} = \frac{1}{m[s^2 + 2\zeta\omega_n s + \omega_n^2]} \quad \text{with } s = j\omega \quad (18.41)$$

Mobility

$$\frac{V(s)}{F(s)} = \frac{sY(s)}{F(s)} = \frac{s}{m[s^2 + 2\zeta\omega_n s + \omega_n^2]} \quad \text{with } s = j\omega \quad (18.42)$$

Consider the mobility (velocity/force) transfer function given by

$$G(s) = \frac{s}{s^2 + 2\zeta\omega_n s + \omega_n^2} \quad (18.43)$$

where the constant parameter, m , in Equation 18.42 has been omitted, without loss of generality. In the frequency domain ($s = j\omega$), we have

$$G(j\omega) = \frac{j\omega}{\omega_n^2 - \omega^2 + 2j\zeta\omega_n\omega} \quad (18.44)$$

Multiply the numerator and the denominator of $G(j\omega)$ in Equation 18.44 by the complex conjugate of the denominator (i.e., $\omega_n^2 - \omega^2 - 2j\zeta\omega_n\omega$). Then, the denominator is converted to the square of its original magnitude, as given by

$$\Delta = (\omega_n^2 - \omega^2)^2 + (2\zeta\omega_n\omega)^2 \quad (18.45)$$

and the frequency transfer function (Equation 18.44) is converted into the form

$$G(j\omega) = \frac{j\omega}{\Delta} [\omega_n^2 - \omega^2 - 2j\zeta\omega_n\omega] \quad (18.46)$$

$$G(j\omega) = \text{Re} + j \text{Im} \quad \text{where} \quad \text{Re} = \frac{2\zeta\omega_n\omega^2}{\Delta} \quad \text{and} \quad \text{Im} = \frac{\omega}{\Delta}(\omega_n^2 - \omega^2) \quad (18.47)$$

Now, we can write

$$\text{Re} - \frac{1}{4\zeta\omega_n} = \frac{8\zeta^2\omega_n^2\omega^2 - 4\zeta^2\omega_n^2\omega^2 - (\omega_n^2 - \omega^2)^2}{4\zeta\omega_n\Delta} = \frac{4\zeta^2\omega_n^2\omega^2 - (\omega_n^2 - \omega^2)^2}{4\zeta\omega_n\Delta}$$

Hence, in view of Equation 18.47 we have

$$\begin{aligned} \left[\text{Re} - \frac{1}{4\zeta\omega_n} \right]^2 + \text{Im}^2 &= \left[\frac{4\zeta^2\omega_n^2\omega^2 - (\omega_n^2 - \omega^2)^2}{4\zeta\omega_n\Delta} \right]^2 + \frac{\omega^2(\omega_n^2 - \omega^2)^2}{\Delta^2} \\ &= \frac{16\zeta^4\omega_n^4\omega^4 - 8\zeta^2\omega_n^2\omega^2(\omega_n^2 - \omega^2)^2 + (\omega_n^2 - \omega^2)^4 + 16\zeta^2\omega_n^2\omega^2(\omega_n^2 - \omega^2)^2}{16\zeta^2\omega_n^2\Delta^2} \\ &= \frac{[4\zeta^2\omega_n^2\omega^2 + (\omega_n^2 - \omega^2)^2]^2}{16\zeta^2\omega_n^2\Delta^2} = \frac{\Delta^2}{16\zeta^2\omega_n^2\Delta^2} = \frac{1}{16\zeta^2\omega_n^2} = R^2 \end{aligned}$$

It follows that the transfer function, $G(j\omega)$, represents a circle in the real–imaginary plane, with the following properties:

$$\text{Circle radius } R = \frac{1}{4\zeta\omega_n} \quad (18.48)$$

$$\text{Circle center} = \left(\frac{1}{4\zeta\omega_n}, 0 \right) \quad (18.49)$$

Now, we may reintroduce the constant parameter, m , back into the transfer function, as in Equation 18.42. Then, we have

$$\begin{aligned} \text{Circle radius } R &= \frac{1}{4\zeta\omega_n m}, \\ \text{Center} &= \left(\frac{1}{4\zeta\omega_n m}, 0 \right) \end{aligned} \quad (18.50)$$

A sketch of this circle is shown in Figure 18.3(a). As mentioned before, the plane formed by the real and imaginary parts of $G(j\omega)$ as the Cartesian x and y axes, respectively, is the *Nyquist plane*. The plot of $G(j\omega)$ on this plane is the *Nyquist diagram*. It follows that the *Nyquist diagram* of the mobility function (Equation 18.42 or Equation 18.44) is a circle.

Case of Hysteretic Damping

Consider a single-DoF system with *hysteretic damping*. The equation motion is given by

$$\begin{aligned} m\ddot{y} + \frac{h}{\omega}\dot{y} + ky &= f(t) \\ \text{with } f(t) &= f_0 \sin \omega t \end{aligned} \quad (18.51)$$

Note the frequency dependent damping constant, with the hysteretic damping parameter, h , in the time domain. The receptance function, $G(j\omega)$, is given by

$$G(j\omega) = \frac{1}{(k - m\omega^2) + jh}$$

Note that the damping term, jh , is independent of frequency in the frequency domain for this case. As for the case of viscous damping, we can easily show that the Nyquist plot of this transfer function is a circle with

$$\text{Radius} = \frac{1}{2h} \quad \text{and} \quad \text{Center} = \left(0, -\frac{1}{2h} \right) \quad (18.52)$$

A sketch of the resulting circle is shown in Figure 18.3(b).

In general, for a multi-DoF viscous-damped system we have the “mobility” function

$$G_{ik}(j\omega) = j\omega \sum_{r=1}^n \frac{(\psi_i \psi_k)_r}{[\omega_r^2 - \omega^2 + 2j\zeta_r \omega_r \omega]} \quad (18.53)$$

If the resonances are not closely spaced we can assume that, near each resonance (r)

$$\begin{aligned} G_{ik} &= \text{constant offset (complex)} + \text{single DoF mobility function} \\ &= \text{constant offset} + \left[\frac{j\omega(\psi_i \psi_k)_r}{\omega_r^2 - \omega^2 + 2j\zeta_r \omega_r \omega} \right] \end{aligned} \quad (18.54)$$

We can curve fit each resonance r to a circle this way and thereby extract the $(\psi_i \psi_k)_r$ value (the residue) from the radius of the circle fit.

Note: This method cannot be used if the resonances are closely spaced and consequently if significant modal interactions are present.

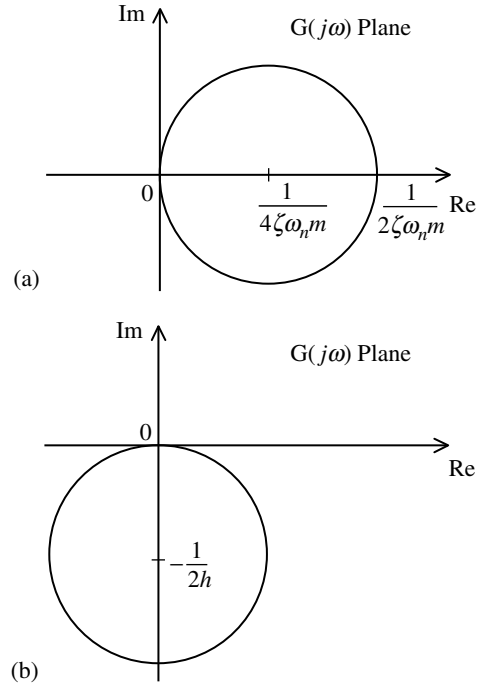


FIGURE 18.3 (a) Circle fit of a mobility function with viscous damping; (b) circle fit of a receptance function with hysteretic damping.

18.4.3.2 Peak-Picking Method

The peak-picking method is also a single-DoF method in view of the fact that each resonance of an experimentally determined transfer function is considered separately. The approach is to compare the resonance region with an analytical transfer function of a damped single-DoF system. One of three types of transfer functions, receptance, mobility, and accelerance as listed in Table 18.1, can be used for this purpose. Note that, when the level of damping is small, it can be assumed (approximately) that the resonance is at the undamped natural frequency $\omega_n = \sqrt{k/m}$. Substituting this value for ω in each of the frequency transfer functions, we can determine the transfer function value at resonance, denoted by $G_{\text{peak}}(j\omega)$. It is noted from Table 18.1 that this function value in general depends on the damping constant and the natural frequency. Since ω_n is known directly from the peak location of the transfer function, it is possible to compute c (or the damping ratio, ζ) by first determining the corresponding peak magnitude.

Specifically, from Table 18.1, it is clear that we should pick the imaginary part of the frequency transfer function for receptance or accelerance data and the real part of the transfer function for mobility data. Then, we pick the peak value of the chosen part of the transfer function and the frequency at the peak.

Table 18.2 gives normalized expressions for the three frequency transfer functions, receptance = displacement/force; mobility = velocity/force; accelerance = acceleration/force, in the frequency domain, in the case of a single-DoF mechanical system with (1) viscous damping and (2) hysteretic damping. It may be verified that their Nyquist diagrams are circles (either exactly or approximately), thereby enabling one to use the circle-fit method.

Note that $r = \omega/\omega_n$, where ω is the excitation frequency and ω_n is the undamped natural frequency; ζ is the damping ratio in the case of viscous damping; and $d = h/k$ where h is the hysteretic damping parameter and k is the system stiffness.

Peak picking is good in cases where modes are well separated and lightly damped. It does not work when the system is highly damped (or overdamped) or when the damping is zero (infinite peak). It is a quick approach that is appropriate for initial evaluations and trouble shooting.

TABLE 18.1 Some Frequency Transfer Functions Used in Peak Picking

Single-DoF system	$m\ddot{y} + c\dot{y} + ky = f(t)$
Receptance (dynamic flexibility, compliance) $G^r(j\omega) = \frac{\text{Displacement } y}{\text{Force } f}$	$\frac{1}{ms^2 + cs + k}$ with $s = j\omega$
Mobility $G^m(j\omega) = \frac{\text{Velocity } v}{\text{Force } f}$	$\frac{s}{ms^2 + cs + k}$ with $s = j\omega$
Accelerance $G^a(j\omega) = \frac{\text{Acceleration } a}{\text{Force } f}$	$\frac{s^2}{ms^2 + cs + k}$ with $s = j\omega$
Resonant peaks $G_{\text{peak}}(j\omega)$ (occur approximately at $\omega = \omega_n$ for light damping)	$G_{\text{peak}}^r = -\frac{j}{c\omega_n}$ $G_{\text{peak}}^m = \frac{1}{c}$ $G_{\text{peak}}^a = \frac{j\omega_n}{c}$

TABLE 18.2 Normalized Frequency Response Functions for Single-DoF Curve Fitting

Frequency Response Function	With Viscous Damping	With Hysteretic Damping
Receptance	$\frac{1}{1 - r^2 + 2j\zeta r}$	$\frac{1}{1 - r^2 + jd}$
Mobility	$\frac{j r}{1 - r^2 + 2j\zeta r}$	$\frac{j r}{1 - r^2 + jd}$
Accelerance	$\frac{-r^2}{1 - r^2 + 2j\zeta r}$	$\frac{-r^2}{1 - r^2 + jd}$

18.4.4 Multi-Degree of Freedom Curve Fitting

We shall now discuss a general multiresonance curve fitting method. The corresponding single-resonance method should also be clear from this general procedure. Note that many different versions of problem formulation and algorithm development are possible for least squares curve fitting, but the results should be essentially the same. The method presented here is a frequency-domain method as we are dealing with experimentally determined frequency transfer functions. In a comparable time-domain method, a suitable analytical expression of the complex exponential form is fitted into the experimental impulse response function obtained by the inverse Fourier transformation of measured transfer function. That method acquires additional error due to truncation (*leakage*) and finite sampling rate (*aliasing*) during the inverse FFT.

18.4.4.1 Formulation of the Method

The objective of the present multiresonance (multi-DoF) curve fitting procedure is to fit the computed (measured) transfer function data into an analytical expression of the form

$$G(s) = \frac{[b_0 + b_1s + \cdots + b_ms^m]}{[a_0 + a_1s + \cdots + a_{p-1}s^{p-1} + s^p]} \quad \text{for } m \leq p \quad (18.55)$$

The data for curve fitting are the N complex transfer function values $[G_1, G_2, \dots, G_N]$ computed at discrete frequencies $[\omega_1, \omega_2, \dots, \omega_N]$. Typically, if 1024 samples of time history were used in the FFT computations to determine the transfer function, we would have 512 valid spectral lines of transfer function data. However, near the high-frequency end, these data values become excessively distorted due to the aliasing error; only a part of the 512 spectral lines will be usable, typically the first 400 lines. In that case, we have $N = 400$. This value can be doubled by doubling the FFT block size (to 2048 words in the buffer), thereby doubling the record length or the sampling rate. It is acceptable to leave out part of the computed transfer function, not for poor accuracy but because that part falls outside the frequency band of interest in that particular modal analysis problem. A less wasteful practice is to pick the sampling rate of the measured time-history data to reflect the highest frequency of interest in the modal analysis.

The (complex) error in the estimated value at each frequency point (spectral line), ω_i , is given by

$$\tilde{e}_i = G(\omega_i) - G_i = \frac{[b_0 + b_1s_i + \cdots + b_ms_i^m]}{[a_0 + a_1s_i + \cdots + a_{p-1}s_i^{p-1} + s_i^p]} - G_i \quad (18.56)$$

with $s = j\omega$.

The characteristic equation of the dynamic model is given by

$$\Delta(s) = a_0 + a_1s + \cdots + a_{p-1}s^{p-1} + s^p = 0 \quad (18.57)$$

Its roots are the eigenvalues of the system. For damped systems, they occur in complex conjugates with negative real parts (*note*: $p = 2 \times \text{number of DoFs}$, in typical cases). For systems with *rigid-body modes*, zero eigenvalues will also be present. However, since there is some damping in the system and since the lowest frequency that is tested and analyzed is normally greater than zero even for systems with rigid-body modes, we have

$$\Delta(j\omega) \neq 0 \quad (18.58)$$

in the frequency range of interest. Hence, the estimation error given by Equation 18.56 can be expressed as

$$e_i = [b_0 + b_1s_i + \cdots + b_ms_i^m] - G_i[a_0 + a_1s_i + \cdots + a_{p-1}s_i^{p-1} + s_i^p] \quad (18.59)$$

with $s = j\omega$.

The quadratic error function is given by the sum of the squares of magnitude error for all discrete frequency points used in modal analysis; thus

$$J = \sum_{i=1}^N |e_i|^2 = \sum_{i=1}^N e_i^* e_i \quad (18.60)$$

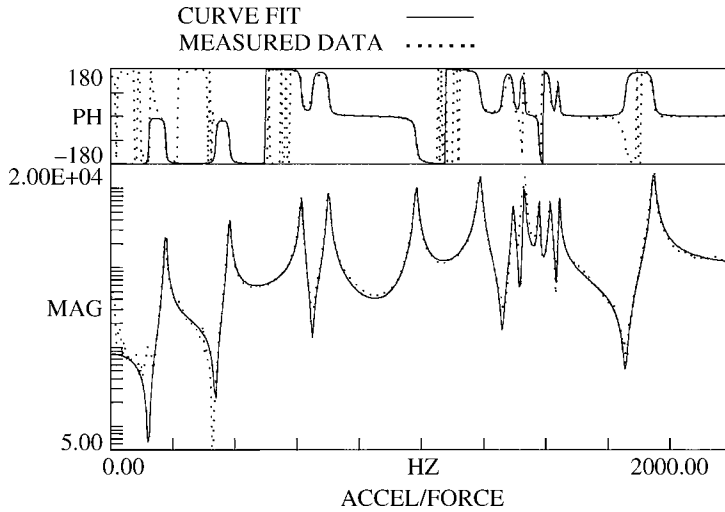


FIGURE 18.4 An example of multi-DoF curve fitting on experimental data.

Note that $[\]^*$ denotes the complex conjugate. Complex conjugation is achieved by simply replacing $(j\omega)$ with $(-j\omega)$ in Equation 18.59. It follows that Equation 18.60 can be written as

$$J = \sum_{i=1}^N \left\langle \left[b_0 + b_1(-j\omega_i) + \cdots + b_m(-j\omega_i)^m - G_i^* \{ a_0 + a_1(-j\omega_i) + \cdots + a_{p-1}(-j\omega_i)^{p-1} + (-j\omega_i)^p \} \right] \left[b_0 + b_1(j\omega_i) + \cdots + b_m(j\omega_i)^m - G_i \{ a_0 + a_1(j\omega_i) + \cdots + a_{p-1}(j\omega_i)^{p-1} + (j\omega_i)^p \} \right] \right\rangle \quad (18.61)$$

The basis of the least squares curve fitting method of parameter estimation is to pick the transfer function parameters b_i ; $i = 0, 1, \dots, m$ and a_i ; $i = 0, \dots, p - 1$, such that the quadratic error function, J , is a minimum. Analytically, this requires

$$\frac{\partial J}{\partial b_k} = 0 \quad k = 0, 1, \dots, m \quad (18.62)$$

$$\frac{\partial J}{\partial a_k} = 0 \quad k = 0, 1, \dots, p - 1 \quad (18.63)$$

Note that Equation 18.62 and Equation 18.63 correspond to $m + p + 1$ linear equations in the $m + p + 1$ unknowns b_i , $i = 0, 1, \dots, m$ and a_i , $i = 0, 1, \dots, p - 1$. A well-defined solution exists to this set of *nonhomogeneous equations* provided that the equations are *linearly independent*, which is guaranteed if the determinant of the coefficients of the unknown parameters does not vanish. It is a good practice to check for linear independence of the set of $m + p + 1$ equations using this determinant condition prior to performing further computations to solve the equations. The solution approach itself is primarily computational in nature and is not presented here. Figure 18.4 shows a result of multi-DoF curve fitting on an experimental frequency transfer function, as collected from a civil engineering structure. Note the close match of the magnitude but not the phase angle. This analysis resulted in the resonant frequency and damping ratio values that are given in Table 18.3.

18.4.5 A Comment on Static Modes and Rigid-Body Modes

Some test systems may possess static modes, and rigid-body modes under rare circumstances. Static modes arise in analytical models if we fail to assign an inertia (mass) element for each DoF. Rigid-body modes arise in analytical models if proper restraints are not provided for the inertia elements. In practice,

TABLE 18.3 Extracted Parameters in an Example of Experimental Modal Analysis

Mode No.	Resonant Frequency (Hz)	Damping Ratio (viscous)
1	1.773×10^2	1.170×10^{-2}
2	3.829×10^2	8.149×10^{-3}
3	6.145×10^2	6.033×10^{-3}
4	7.018×10^2	5.931×10^{-3}
5	9.839×10^2	4.580×10^{-3}
6	1.190×10^3	3.676×10^{-3}

however, static modes arise if a coordinate is assigned to a DoF that actually does not exist, or if some parts of the physical system are relatively light with stiff restraints (i.e., very high natural frequencies), and rigid-body modes arise in the presence of relatively heavy components restrained by very flexible elements (i.e., very low natural frequencies). Note that the assumed transfer function (Equation 18.55) allows for both these extremes. Specifically, if static modes are present it is necessary that the transfer function can be expressed as a sum of a constant term (static mode) and an ordinary transfer function (without a static mode). Hence, it will approach a nonzero constant value as the frequency, ω , increases. This requires $m = p$. If rigid-body modes are present, the characteristic polynomial $\Delta(s)$ of the model should have a factor s^2 . This corresponds to $a_0 = a_1 = 0$.

18.4.6 Residue Extraction

The estimated transfer functions as given by Equation 18.55 is in the form of the ratio of two polynomials; *the rational fraction form*. This has to be converted into the partial fraction form given by Equation 18.17 in order to extract the residues $(\psi_i \psi_k)_r$ that are needed for determining the mode shapes. For this, the natural frequencies, ω_r , and the modal damping ratios, ζ_r , should be computed first. These are given by the roots of the characteristic Equation 18.57 as

$$\lambda_r, \lambda_r^* = \zeta_r \omega_r \pm j \sqrt{1 - \zeta_r^2} \omega_r; \quad r = 1, 2, \dots, n \tag{18.64}$$

Once these eigenvalues are known, by solving Equation 18.57 using the estimated values for a_0, a_1, \dots, a_{p-1} , it is a straightforward task to compute the quadratic factors

$$\Delta_r(s) = s^2 + 2\zeta_r \omega_r s + \omega_r^2 \quad r = 1, 2, \dots, n \tag{18.65}$$

Note that, from Equation 18.17

$$(\psi_i \psi_k)_r = [G_{ik}(s) \Delta_r(s)]_{s=\lambda_r} \tag{18.66}$$

assuming distinct eigenvalues. This is true because, when the partial fraction form is multiplied by $\Delta_r(s)$, it will cancel out with the denominator of the partial fraction corresponding to the r th mode, leaving its residue. Then, when s is set equal to Δ_r , all the remaining partial fraction terms will vanish due to the fact that $\Delta_r(\lambda_r) = 0$, provided that the eigenvalues are distinct. Since $G_{ik}(s)$ are known from the estimated transfer functions, the residues can be computed using Equation 18.66. Finally, the mode shapes are determined using the procedure outlined earlier. Some curve fitting approaches are summarized in Box 18.2.

18.5 Laboratory Experiments

Testing and analysis are important in the practice of mechanical vibration and are integral in EMA. In this section, we will describe two experiments in the category of modal testing. One experiment deals with a lumped-parameter system and the other with a distributed-parameter (or continuous) system.

Box 18.2

CURVE FITTING OF TRANSFER FUNCTION DATA

Single-resonance curve fitting:

- (a) Viscous damping:
 - 1. Compute mobility (velocity/force) function near resonance.
 - 2. Scale the data.
 - 3. Curve fit to circle in the Nyquist plane (Argand diagram).
- (b) Hysteretic damping:
 - 1. Compute receptance (displacement/force) function near resonance.
 - 2. Scale the data.
 - 3. Curve fit to circle in the Nyquist plane (Argand diagram).

Multiresonance curve fitting:

- 1. Compute transfer function over the entire frequency range.
- 2. Scale the data.
- 3. Curve fit to a general polynomial ratio with static and rigid-body modes.

Both experiments have direct practical implications and have been used in an established undergraduate course in mechanical vibrations.

18.5.1 Lumped-Parameter System

A schematic representation of a prototype unit that is used in laboratory for modal testing is shown in [Figure 18.5](#). A view of the experimental system is shown in [Figure 18.6](#). The system is a crude representation of an engine unit that is supported on flexible mounts and subjected to unbalance forces and moments.

The test object is assumed to consist of lumped elements of inertia, stiffness, and damping. The rectangular metal box, which represents the engine housing, is mounted on four springs and damping elements at the four corners. Inside the box are two pairs of identical and meshed gears, which are driven by a single DC motor. Each gear has two slots at diametrically opposite locations in order to place the eccentric masses. Various types of unbalance excitations can be generated by placing the four eccentric masses at different combinations of locations on the gear wheels.

The drive motor is operated by a DC power supply with a speed control knob. The motor speed (and hence the gear speed) is measured using an optical encoder that is mounted on the drive shaft. It generates pulses as the encoder disk rotates with the shaft, in proportion to the angle of rotation. The pulse frequency of the encoder determines the shaft speed. A pair of accelerometers with magnetic bases is mounted on the top of the engine box. The locations that are used for this purpose are indicated in [Figure 18.5](#).

[Figure 18.6](#) shows, from left to right, the following components of the experimental system:

- 1. Digital spectrum analyzer
- 2. A combined instrument panel consisting of a vibration meter, a tunable band-pass filter, and a unit consisting of a conditioning amplifier and a phase meter

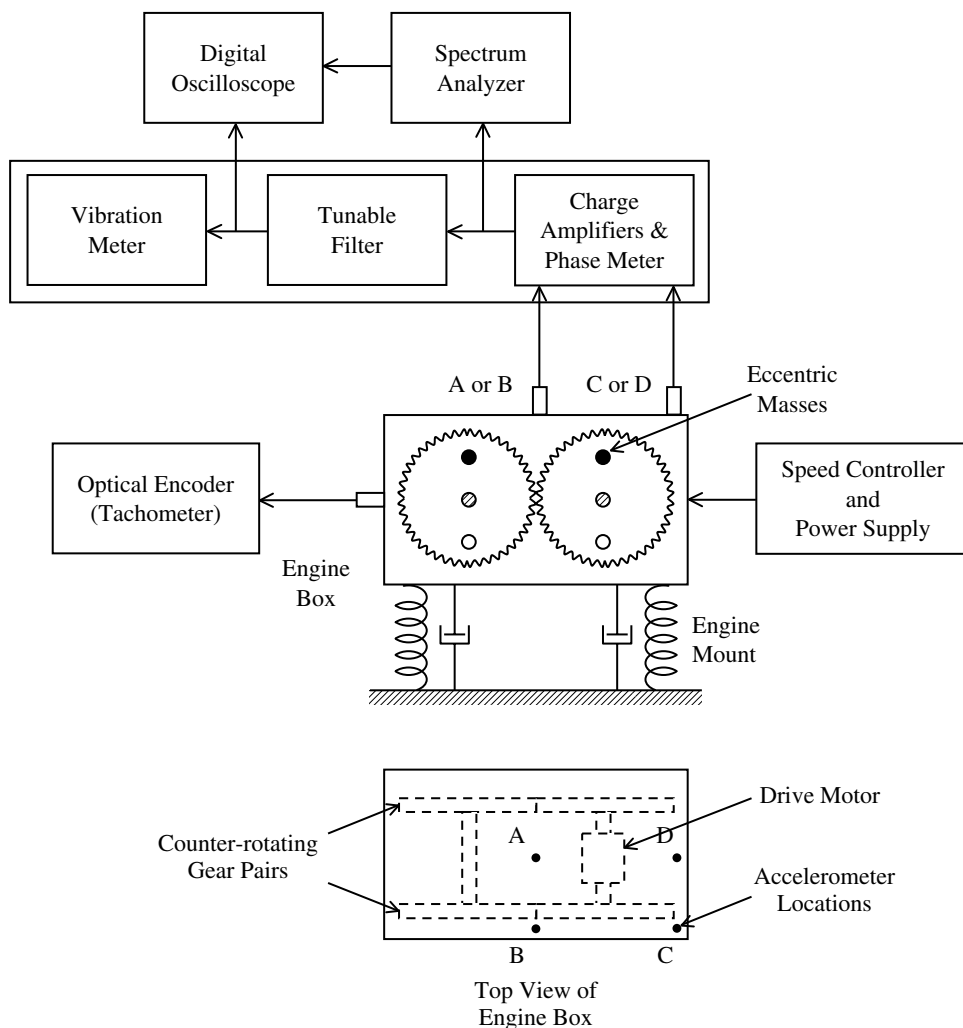


FIGURE 18.5 Schematic diagram of an experimental setup for modal testing in laboratory.

3. Power supply for the instrument panel, placed on top of the panel
4. Engine unit with two accelerometers mounted on top surface of the housing
5. Digital oscilloscope placed on a shelf top immediately above the engine unit
6. DC power supply and speed controller combination for the drive motor

The phase meter measures the phase difference between two input signals. The tunable filter is a band-pass filter and it can be tuned by a fine-adjustment dial so that a signal in a very narrow band (i.e., harmonic signal) can be filtered and measured. The vibration meter measures the magnitude (peak or rms value) of a signal. The choice of a displacement value (i.e., double integration), a velocity value (a single integration), or an acceleration value (no integration) is available, and can be selected using a knob.

By placing the eccentric masses at various locations on the gear wheels, different modes can be excited. For example, the placement of all four eccentric masses at the vertical radius location above the rotating axis will generate a net harmonic force in the vertical direction, as the motor is driven. This will excite the heave (up and down) mode of the engine box. If the two masses on a meshed pair are placed at the vertical radius location below the rotating axis while the masses on the other meshed

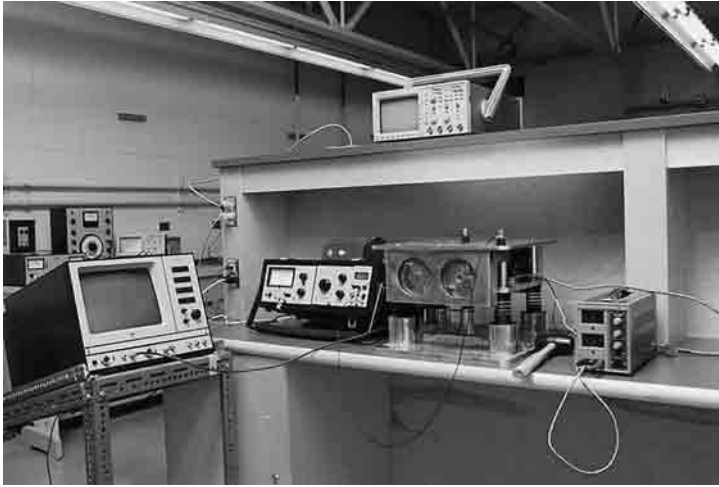


FIGURE 18.6 A view of an experimental setup for modal testing at the University of British Columbia.

pair are placed vertically above the rotating axis, then it will result a net moment (pitch) about a central horizontal axis of the engine box. This will excite the pitch mode, and so on. For a given arrangement of eccentric masses, two tests can be carried out, one in the frequency domain and the other in the time domain.

18.5.1.1 Frequency-Domain Test

Choose the “displacement” setting of the vibration meter. Start the motor and maintain the speed at a low value, say 4 Hz. Tune the filter, using its dial, until the vibration meter reading becomes the largest. The tuned frequency will be, in the ideal case, equal to the motor speed. Record the motor speed (i.e., the excitation frequency) and the magnitude of the displacement response. Increase the motor speed in 1-Hz steps and repeat the measurements, until reaching a reasonably high frequency, covering at least one resonance, say 25 Hz. Reduce the speed in steps of 1 Hz and repeat the measurements. Take some more measurements in the neighborhood of each resonance using smaller frequency steps. Plot the data as a frequency spectrum after compensating for the fact that the amplitude of the excitation force increases with the square of the drive speed (hence, divide the vibration magnitudes by square of the frequency). This experiment can be used, for example, to measure mode shapes, resonant frequencies, and damping ratios (by the half-power bandwidth method).

18.5.1.2 Time-Domain Tests

A test can be conducted to determine the damping ratio corresponding to a particular mode by the logarithmic decrement method. Here, first pick the eccentric mass arrangement so as to excite the desired mode. Next increase the motor speed and then fine-tune the operation at the desired resonance. Maintain the speed steady at this condition and observe the accelerometer signal using the oscilloscope, while making sure that at least ten complete cycles can be viewed on the screen. Suddenly, turn off the motor and record the decay of the acceleration signal using the oscilloscope. Another test that can be carried out is an impact (hammer) test. Here, use the spectrum analyzer to record and analyze a vibration response of the engine box through an accelerometer. Gently tap the engine box in different critical directions (e.g., at points A, B, C, and D in the vertical direction, in [Figure 18.5](#), or in the horizontal direction on the side of the engine box in the neighborhood of these points) and acquire the vibration signal using the spectrum analyzer. Process the signal using the spectrum analyzer, obtain the resonant frequencies, and compare them with those obtained from sine testing.

18.5.2 Distributed-Parameter System

All real vibrating systems have continuous components. Often, however, we make distributed-parameter assumptions depending on the properties and the operating frequency range of the vibrating system. When a lumped-parameter approximation is not adequate, a distributed-parameter analysis will be needed. Modal testing and comparison with analytic results can validate an analytical model.

The response of a distributed-parameter system will depend on the boundary conditions (the supporting conditions) as well as the initial conditions. For forced excitations, the response will depend on the nature of the excitation as well. Natural frequencies and mode shapes are system characteristics and depend on the boundary conditions, but not on the initial conditions and forcing excitations.

Consider the experimental setup schematically represented in Figure 18.7. A view of the setup is shown in Figure 18.8. The device that is tested is a ski. For analytical purposes, it may be approximated as a thin beam. The objective of the test is to determine the natural frequencies and mode shapes of the ski. Since the significant frequency range of the excitation forces on a ski, during use, is below 15 Hz, it is advisable to determine the modal information in the frequency range of about double the operating range (i.e., 0 to 30 Hz). In particular, in the design of a ski, natural frequencies below 15 Hz should be avoided, while keeping the unit as light and strong as possible. These are conflicting design requirements. It follows that modal testing can play an important role in the design development of a ski.

Consider the experimental setup that is sketched in Figure 18.7. The ski is firmly supported at its middle on the electrodynamic shaker. Two accelerometers are mounted on either side of the support and are movable along the ski. The accelerometer signals are acquired and conditioned using charge amplifiers. The two signals are observed in the x - y mode of the digital oscilloscope so that both the amplitudes and the phase difference can be measured. The sine-random signal generator is set to the sine mode so that a harmonic excitation is generated at the shaker head. The shape of the motion can be observed in slow motion by illuminating the ski with the hand-held stroboscope, with the strobe frequency set to within about ± 1 Hz of the excitation frequency.

In the experimental system shown in Figure 18.8, we observe, from left to right, the following components:

1. Electrodynamic shaker with the ski mounted on its exciter head (two accelerometers are mounted on the ski)
2. Hand-held stroboscope, placed beside the shaker

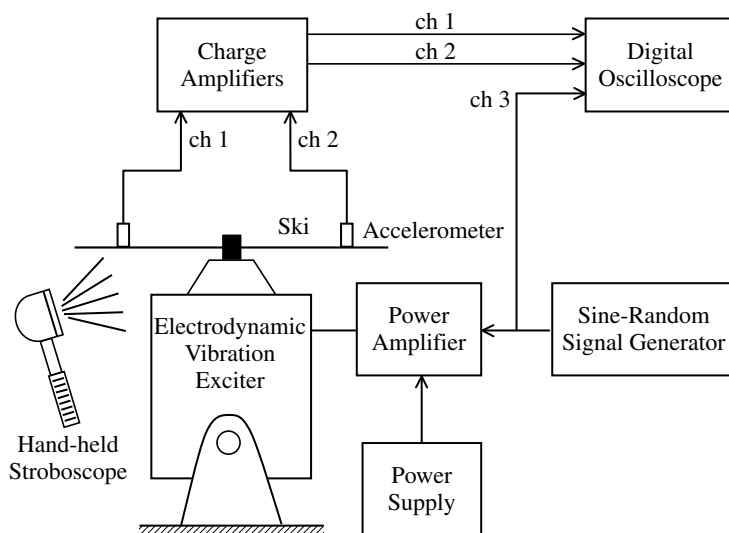


FIGURE 18.7 Schematic diagram of a laboratory setup for modal testing of a ski.

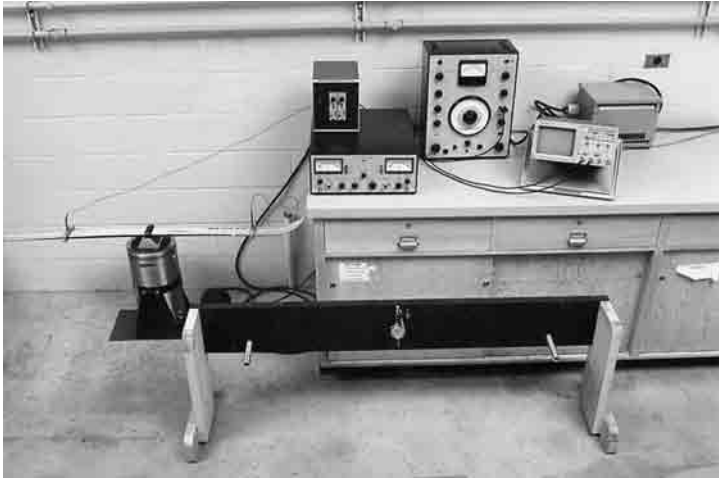


FIGURE 18.8 A view of the experimental system for modal testing of a ski at the University of British Columbia.

3. Power amplifier for driving the shaker, placed on top of the side table
4. Two charge amplifiers placed on top of the power amplifier and connected to the accelerometers
5. Sine-random signal generator, placed on the table top, next to the amplifier
6. Power supply for the shaker
7. Static load–deflection measurement device for determining the modulus of rigidity (EI) of the ski

Prior to modal testing, the modulus of rigidity of the ski is determined by supporting it on the two smooth end pegs of the loading structure, and loading at the midspan using incremental steps of 500-gm weights up to 4.0 kg, placed on a scale pan that is suspended at the midspan of the ski. The midspan deflection of the ski is measured using a spring-loaded dial gage that is mounted on the loading structure. If the midspan stiffness (force/deflection) as measured in this manner is k , it is known that the modulus of rigidity is

$$EI = \frac{k l^3}{48} \quad (18.67)$$

where l is the length of the ski. Note that this formula is for a simply supported ski, which is the case in view of the smooth supporting pegs. Also, weigh the ski and then compute m = mass per unit length. With this information, the natural frequencies and mode shapes can be computed for various end conditions. In particular, compute this modal information for the following supporting conditions:

1. Free–free
2. Clamped at the center

Next, perform modal testing using the experimental setup and compare the results with those computed using the analytical formulation.

The natural frequencies (actually, the resonant frequencies, which are almost equal to the natural frequencies in the present case of light damping) can be determined by increasing the frequency of excitation in small steps using the sine generator and noting the frequency values at which the amplitudes of the accelerometer signals reach local maxima, as observed on the oscilloscope screen. A mode shape is measured as follows. First, detect the corresponding natural frequency as above. While maintaining the shaker excitation at this frequency, place the accelerometer near the shaker head, and then move the other accelerometer from one end of the ski to the other in small steps of displacement and observe the amplitude ratio and the phase difference of the two accelerometer signals using the oscilloscope. Note that in-phase signals mean the motions of the two points are in the same direction,

and the out-of-phase signals mean the motions are in the opposite directions. The mode shapes can be verified by observing the modal vibrations in slow motion using the stroboscope, as indicated before. Node points are the vibration-free points. They can be detected from the mode shapes. In particular, a tiny piece of paper will remain stationary at a node while making large jumps on either side of the node. Also, the phase angle of the vibration signal, as measured by an accelerometer, will jump by 180° if the accelerometer is carefully moved across the node point.

18.6 Commercial EMA Systems

Commercially available EMA systems typically consist of an FFT analyzer, a modal analysis processor, a graphics terminal, and a storage device. Digital plotters, channel selectors, hard copy units, and other accessories can be interfaced, and the operation of the overall system can be coordinated through a host computer to enhance its capability. The selection of hardware for a particular application should address specific objectives as well as hardware capabilities. Software selection is equally important. Proper selection of an EMA system is difficult unless the underlying theory is understood. In particular, the determination of transfer functions via FFT analysis; extraction of natural frequencies, modal damping ratios, and mode shapes from transfer function data; and the construction of mass, stiffness, and damping matrices from modal data should be considered. We have already presented the underlying theory. In the present section, we will describe the features of a typical EMA system.

18.6.1 System Configuration

The extraction of modal parameters from dynamic test data is essentially a two-step procedure consisting of:

1. FFT analysis
2. Modal analysis

In the first step, appropriate frequency transfer functions are computed and stored. These raw transfer functions form the input data for the subsequent modal analysis, yielding modal parameters (natural frequencies, damping ratios, and mode shapes) and a linear differential equation model for the dynamic system (test object).

18.6.1.1 FFT Analysis Options

The basic hardware configuration of a commercial modal analysis system is shown in [Figure 18.9](#). Notice that the FFT analyzer forms the front end of the system. The excitation signal and the response measurements can be transmitted on line to the FFT analyzer (through charge amplifiers for piezoelectric sensors); many signals can be transmitted simultaneously in the multiple-channel case. Alternatively, all measurements may first be recorded on a multiple-track FM tape and subsequently fed into the analyzer through a multiplexer. In the first case, it is necessary to take the FFT analyzer to the test site; an FM tape recorder is needed at the test site in the second case.

Through advances in microelectronics and LSI technology, the FFT analyzer has rapidly evolved into a powerful yet compact instrument that is often smaller in size than the conventional tape recorder used in vibration data acquisition; either device can be used in the field with equal convenience. On-site FFT analysis, however, allows one to identify and reject unacceptable measurements (e.g., low signal levels and high noise components) during data acquisition, so that alternative data that might be needed for a complete modal identification can be collected without having to repeat the test at another time. The main advantage of the FM tape method is that data are available in analog form, free of quantization error (digital word-size dependent), aliasing distortion (data sampling-rate dependent), and signal truncation error (data block-size dependent). Sophisticated analog filtering is often necessary, however,

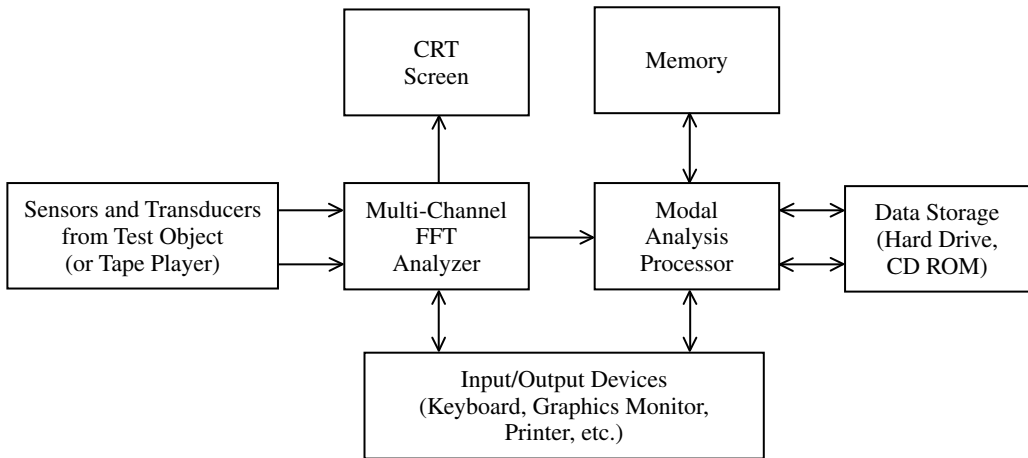


FIGURE 18.9 The configuration of a commercial experimental modal analysis system.

to remove extraneous noise entering from the recording process (e.g., line noise and tape noise), as well as from the measurement process (e.g., sensor and amplifier noise).

The analog-to-digital converter (ADC) is normally an integral part of the analyzer. The raw transfer functions, once computed, are stored on a floppy disk or hard disk as the “transfer function file.” This constitutes the input data file for modal extraction. Some analyzers, instead, compute power spectral densities with respect to the excitation signal and store these in the data file. From these data, it is possible instantly to compute coherence functions, transfer functions, and other spectral information using keyboard commands. Another procedure has been to compute Fourier spectra of all signals and store them as raw data, from which other spectral functions can be conveniently computed. Most analyzers have small CRT screens to display spectral results. Low-coherent transfer functions are detected by analytical or visual monitoring and are automatically discarded.

In principle, the same processor can be used for both FFT analysis and modal analysis. Some commercial modal analysis systems use a plug-in programmable FFT card in a common processor cage. Historically, however, the digital FFT analyzer was developed as a stand-alone hardware unit to be used as a powerful measuring instrument in a wide variety of applications, rather than just as a data processor. Uses include measurement of resonant frequencies and damping in vibration isolation applications, measurement of phase lag between two signals, estimation of signal noise levels, identification of the sources of noise in measured signals, and measurement of correlation in a pair of signals. Because of this versatility, most modal analysis systems do come with a standard FFT analyzer unit as the front end and a separate computer for modal analysis.

18.6.1.2 Modal Analysis Components

In addition to the transfer function file, the modal analysis processor needs geometric information about the test object, typically coordinates of the mass points and directions of the DoF. This information is stored in a “geometry file.” The results of modal analysis are usually stored in two separate files: the “parameter file” containing natural frequencies, modal damping ratios, mass matrix, stiffness matrix, and damping matrix; and the “mode shape file,” containing mode shape vectors that are used for graphics display and printout. Individual modes can be displayed on the CRT screen of the graphics monitor either as a static traces or in animated (dynamic) form. The graphics monitor and printer are standard components of the system. The entire system may be interfaced with other peripheral I/O devices using an IEEE-488 interface bus or the somewhat slower serial RS-232 interface. For example, the overall operation can be coordinated, and further processing done, using a host computer. A desktop (personal) computer may substitute for the modal analysis processor, graphics monitor, and storage devices in the standard system, resulting in a reasonable reduction of the overall cost. An alternative configuration that

TABLE 18.4 Comparative Data for Four Modal Analysis Systems

Description	System A	System B	System C	System D
Number of weighting window options available	3	10	5	4
Analyzer data channels	2	2	2	2
Maximum DoFs per analysis	750 @ 20 modes	450	725 @ 5 modes	750
Maximum number of modes analyzed	50 @ 250 DoF	20	10 (typical)	64
Multi-DoFs curve fitting	Yes	Yes	No	Yes
FFT Resolution (usable spectral lines/512)	400	400	400	400
Zoom analysis capability in FFT	Yes	Yes	Yes	Optional
Statistical error-band analysis	No	No	No	No
Static mode-shape extremes	Yes	Yes	Yes	Yes
Animated graphics capability	Yes	Yes	Yes	Yes
Color graphics capability	No	Yes	No	No
Hidden-line display	No	No	No	No
Color printing	No	No	Yes	No
Structural mass and stiffness matrices	No	No	No	Yes
Approximate cost	\$30,000	\$20,000	\$25,000	\$50,000

is particularly useful in data transfer and communication from remote test sites uses a voice-grade telephone line and a modem coupler to link the FFT analyzer to the main processor.

The first step in selecting a modal analysis system for a particular application is to understand the specific needs of that application. For industrial applications of modal testing, the following requirements are typically adequate:

1. Acceptance of a wide range of measured signals having a variety of transient and frequency band characteristics
2. Capability to handle up to 300 DoF of measured data in a single analysis
3. FFT with frequency resolution of at least 400 spectral lines per 512
4. Zoom analysis capability
5. Capability to perform statistical error-band analysis
6. Static display and plot of mode-shape extremes
7. Animated (dynamic) display of mode shapes
8. Color graphics
9. Hidden-line display
10. Color printing with high line resolution
11. Capability to generate an accurate time-domain model (mass, stiffness, and damping matrices)

The capabilities of four representative modal analysis systems are summarized in Table 18.4.

Bibliography

- Bendat, J.S. and Piersol, A.G. 1971. *Random Data: Analysis and Measurement Procedures*, Wiley-Interscience, New York.
- Brigham, E.O. 1974. *The Fast Fourier Transform*, Prentice Hall, Englewood Cliffs, NJ.
- de Silva, C.W., Seismic qualification of electrical equipment using a uniaxial test, *Earthquake Eng. Struct. Dyn.*, 8, 337–348, 1980.
- de Silva, C.W., Matrix eigenvalue problem of multiple-shaker testing, *J. Eng. Mech. Div., Trans. ASCE*, 108, 457–461, 1982.
- de Silva, C.W. 1983a. *Testing and Seismic Qualification Practice*, D.C. Heath and Co., Lexington, MA.
- de Silva, C.W., Selection of shaker specifications in seismic qualification tests, *J. Sound Vib.*, 91, 21–26, 1983b.
- de Silva, C.W., A Dynamic test procedure for improving seismic qualification guidelines, *J. Dyn. Syst. Meas. Control, Trans. ASME*, 106, 143–148, 1984a.

- de Silva, C.W., Hardware and software selection for experimental modal analysis, *Shock Vib. Dig.*, 16, 3–10, 1984b.
- de Silva, C.W., On the modal analysis of discrete vibratory systems, *Int. J. Mech. Eng. Educ.*, 12, 35–44, 1984c.
- de Silva, C.W., The digital processing of acceleration measurements for modal analysis, *Shock Vib. Dig.*, 18, 3–10, 1986.
- de Silva, C.W., Optimal input design for the dynamic testing of mechanical systems, *J. Dyn. Syst. Meas. Control, Trans. ASME*, 109, 111–119, 1987.
- de Silva, C.W. 2000. *VIBRATION — Fundamentals and Practice*, CRC Press, Boca Raton, FL.
- de Silva, C.W. 2004. *MECHATRONICS — An Integrated Approach*, CRC Press, Boca Raton, FL.
- de Silva, C.W., Henning, S.J., and Brown, J.D., Random testing with digital control — application in the distribution qualification of microcomputers, *Shock Vib. Dig.*, 18, 3–13, 1986.
- de Silva, C.W., Loceff, F., and Vashi, K.M., Consideration of an optimal procedure for testing the operability of equipment under seismic disturbances, *Shock Vib. Bull.*, 50, 149–158, 1980.
- de Silva, C.W. and Palusamy, S.S. Experimental modal analysis — a modeling and design tool, *Mech. Eng., ASME*, 106, 56–65, 1984.
- de Silva, C.W., Singh, M., and Zaldonis, J., Improvement of response spectrum specifications in dynamic testing, *J. Eng. Ind., Trans. ASME*, 112, 384–387, 1990.

V

Vibration Suppression and Control

19

Vibration Damping

19.1	Introduction	19-1
19.2	Types of Damping	19-2
	Material (Internal) Damping • Structural Damping • Fluid Damping	
19.3	Representation of Damping in Vibration Analysis	19-9
	Equivalent Viscous Damping • Complex Stiffness • Loss Factor	
19.4	Measurement of Damping	19-16
	Logarithmic Decrement Method • Step-Response Method • Hysteresis Loop Method • Magnification Factor Method • Bandwidth Method • General Remarks	
19.5	Interface Damping	19-26
	Friction in Rotational Interfaces • Instability	

Clarence W. de Silva
The University of British Columbia

Summary

Damping in vibrating systems occurs through the dissipation of mechanical energy. This chapter presents modeling, analysis, and measurement of mechanical damping. The types of damping covered include material internal damping (including viscoelastic damping and hysteretic damping), structural damping, fluid damping, interface damping, viscous damping, Coulomb friction, and Stribeck damping. Representations of various types of damping using equivalent viscous damping models are analyzed. Damping in rotating devices is also studied.

19.1 Introduction

Damping is the phenomenon by which mechanical energy is dissipated (usually by conversion into internal thermal energy) in dynamic systems. Knowledge of the level of damping in a dynamic system is important in the utilization, analysis, and testing of the system. For example, a device with natural frequencies within the seismic range (that is, less than 33 Hz) and which has relatively low damping, could produce damaging motions under resonance conditions when subjected to a seismic disturbance. This effect could be further magnified by low-frequency support structures and panels with low damping. This example shows that knowledge of damping in constituent devices, components, and support structures is important in the design and operation of complex mechanical systems. The nature and the level of component damping should be known in order to develop a dynamic model of the system and its peripherals. Knowledge of damping in a system is also important in imposing dynamic environmental limitations on the system (that is, the maximum dynamic excitation the system can withstand) under in-service conditions. Furthermore, knowledge of a system's damping can be useful in order to make design modifications in a system that has failed the acceptance test.

However, the significance of knowledge of damping levels in a test object for the development of test excitation (input) is often overemphasized. Specifically, if the response spectrum method is used to represent the required excitation in a vibration test, then there is no need for the damping value used in the development of the required response spectrum specification to be equal to the actual damping in the

test object. The only requirement is that the damping used in the specified response spectrum be equal to that used in the test response spectrum. The degree of dynamic interaction between the test object and the shaker table, however, will depend on the actual level of damping in these systems. Furthermore, when testing near the resonant frequency of a test object, it is desirable to know about the damping in the test object.

In characterizing damping in a dynamic system it is important, first, to understand the major mechanisms associated with mechanical energy dissipation in the system. Then a suitable damping model should be chosen to represent the associated energy dissipation. Finally, damping values (model parameters) should be determined, for example, by testing the system or a representative physical model, by monitoring system response under transient conditions during normal operation or by employing already available data.

19.2 Types of Damping

There is some form of mechanical energy dissipation in any dynamic system. In the modeling of systems, damping can be neglected if the mechanical energy that is dissipated during the time duration of interest is small in comparison to the initial total mechanical energy of excitation in the system. Even for highly damped systems, it is useful to perform an analysis with the damping terms neglected, in order to study several crucial dynamic characteristics, e.g., modal characteristics (undamped natural frequencies and mode shapes).

Several types of damping are inherently present in a mechanical system. If the level of damping that is available in this manner is not adequate for proper functioning of the system then external damping devices may be added either during the original design or during subsequent design modifications of the system. Three primary mechanisms of damping are important in the study of mechanical systems. They are:

1. Internal damping (of material)
2. Structural damping (at joints and interfaces)
3. Fluid damping (through fluid–structure interactions)

Internal (material) damping results from mechanical energy dissipation within the material due to various microscopic and macroscopic processes. Structural damping is caused by mechanical energy dissipation resulting from relative motions between components in a mechanical structure that has common points of contact, joints or supports. Fluid damping arises from the mechanical energy dissipation resulting from drag forces and associated dynamic interactions when a mechanical system or its components move in a fluid.

Two general types of external dampers may be added to a mechanical system in order to improve its energy dissipation characteristics. They are:

1. Passive dampers
2. Active dampers

Passive dampers are devices that dissipate energy through some kind of motion, without needing an external power source or actuators. Active dampers have actuators that need external sources of power. They operate by actively controlling the motion of the system that needs damping. Dampers may be considered as vibration controllers. In the present chapter, the emphasis will be on damping that is inherently present in a mechanical system.

19.2.1 Material (Internal) Damping

Internal damping of materials originates from the energy dissipation associated with microstructure defects, such as grain boundaries and impurities; thermoelastic effects caused by local temperature gradients resulting from nonuniform stresses, as in vibrating beams; eddy current effects in ferromagnetic

materials; dislocation motion in metals; and chain motion in polymers. Several models have been employed to represent energy dissipation caused by internal damping. This variety of models is primarily a result of the vast range of engineering materials; no single model can satisfactorily represent the internal damping characteristics of all materials. Nevertheless, two general types of internal damping can be identified: viscoelastic damping and hysteretic damping. The latter term is actually a misnomer, because all types of internal damping are associated with hysteresis loop effects. The stress (σ) and strain (ϵ) relations at a point in a vibrating continuum possess a hysteresis loop, such as the one shown in Figure 19.1. The area of the hysteresis loop gives the energy dissipation per unit volume of the material, per stress cycle. This is termed the per-unit-volume damping capacity, and is denoted by d . It is clear that d is given by the cyclic integral

$$d = \oint \sigma d\epsilon \quad (19.1)$$

In fact, for any damped device, there is a corresponding hysteresis loop in the displacement–force plane as well. In this case, the cyclic integral of force with respect to the displacement, which is the area of the hysteresis loop, is equal to the work done against the damping force. It follows that this integral (loop area) is the energy dissipated per cycle of motion. This is the *damping capacity* which, when divided by the material volume, gives the per-unit-volume damping capacity as before.

It should be clear that, unlike a pure elastic force (e.g., a spring force), a damping force cannot be a function of displacement (q) alone. The reason is straightforward. Consider a force $f(q)$ which depends on q alone. Then, for a particular displacement point, q , of the component the force will be the same regardless of the direction of motion (i.e., the sign of \dot{q}). It follows that, in a loading and unloading cycle, the same path will be followed in both directions of motion. Hence, a hysteresis loop will not be formed. In other words, the net work done in a complete cycle of motion will be zero. Next consider a force $f(q, \dot{q})$ which depends on both q and \dot{q} . Then, at a given displacement point, q , the force will depend on \dot{q} as well. Hence, force in one direction of motion will be different from that in the opposite direction. As a result, a hysteresis loop will be formed, which corresponds to work done against the damping force (i.e., energy dissipation). We can conclude then that the damping force has to depend on a relative velocity, \dot{q} , in some manner. In particular, Coulomb friction, which does not depend on the magnitude of \dot{q} , does depend on the sign (direction) of \dot{q} .

19.2.1.1 Viscoelastic Damping

For a linear viscoelastic material, the stress–strain relationship is given by a linear differential equation with respect to time, having constant coefficients. A commonly employed relationship is

$$\sigma = E\epsilon + E^* \frac{d\epsilon}{dt} \quad (19.2)$$

which is known as the Kelvin–Voigt model. In Equation 19.2, E is Young's modulus and E^* is a viscoelastic parameter that is assumed to be time independent. The elastic term $E\epsilon$ does not contribute to damping, and, as noted before, mathematically, its cyclic integral vanishes. Consequently, for the Kelvin–Voigt model, damping capacity per unit volume is

$$d_v = E^* \oint \frac{d\epsilon}{dt} d\epsilon \pi \quad (19.3)$$

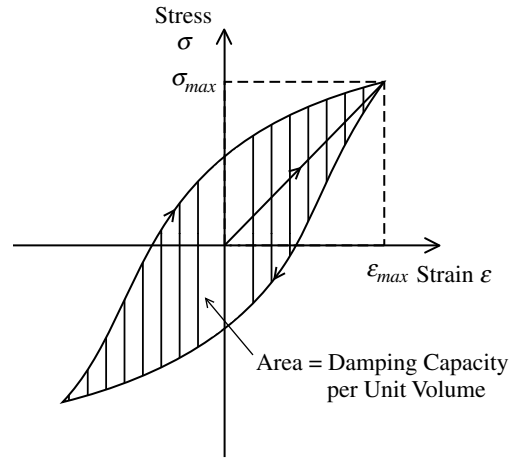


FIGURE 19.1 A typical hysteresis loop for mechanical damping.

For a material that is subjected to a harmonic (sinusoidal) excitation, at steady state, we have

$$\varepsilon = \varepsilon_{\max} \cos \omega t \quad (19.4)$$

When Equation 19.4 is substituted in Equation 19.3, we obtain

$$d_v = \pi \omega E^* \varepsilon_{\max}^2 \quad (19.5)$$

Now, $\varepsilon = \varepsilon_{\max}$ when $t = 0$ in Equation 19.4, or when $d\varepsilon/dt = 0$. The corresponding stress, according to Equation 19.2, is $\sigma_{\max} = E\varepsilon_{\max}$. It follows that

$$d_v = \frac{\pi \omega E^* \sigma_{\max}^2}{E^2} \quad (19.6)$$

These expressions for d_v depend on the frequency of excitation, ω .

Apart from the Kelvin–Voigt model, two other models of viscoelastic damping are also commonly used. They are, the Maxwell model given by

$$\sigma + c_s \frac{d\sigma}{dt} = E^* \frac{d\varepsilon}{dt} \quad (19.7)$$

and the standard linear solid model given by

$$\sigma + c_s \frac{d\sigma}{dt} = E\varepsilon + E^* \frac{d\varepsilon}{dt} \quad (19.8)$$

It is clear that the standard linear solid model represents a combination of the Kelvin–Voigt model and the Maxwell model, and is the most accurate of the three. But, for most practical purposes, the Kelvin–Voigt model is adequate.

19.2.1.2 Hysteretic Damping

It was noted above that the stress, and hence the internal damping force, of a viscoelastic damping material depends on the frequency of variation of the strain (and consequently the frequency of motion). For some types of material, it has been observed that the damping force does not significantly depend on the frequency of oscillation of strain (or frequency of harmonic motion). This type of internal damping is known as hysteretic damping.

Damping capacity per unit volume (d_h) for hysteretic damping is also independent of the frequency of motion and can be represented by

$$d_h = J \sigma_{\max}^n \quad (19.9)$$

A simple model that satisfies Equation 19.9, for the case of $n = 2$, is given by

$$\sigma = E\varepsilon + \frac{\tilde{E}}{\omega} \frac{d\varepsilon}{dt} \quad (19.10)$$

which is equivalent to using a viscoelastic parameter, E^* , that depends on the frequency of motion in Equation 19.2 according to $E^* = \tilde{E}/\omega$.

Consider the case of harmonic motion at frequency ω , with the material strain given by

$$\varepsilon = \varepsilon_0 \cos \omega t \quad (19.11)$$

Then, Equation 19.10 becomes

$$\sigma = E\varepsilon_0 \cos \omega t - \tilde{E}\varepsilon_0 \sin \omega t = E\varepsilon \cos \omega t + \tilde{E}\varepsilon_0 \cos\left(\omega t + \frac{\pi}{2}\right) \quad (19.12)$$

Note that the material stress has two components, as given by the right-hand side of Equation 19.12. The first component corresponds to the linear elastic behavior of a material and is in phase with the strain. The second component of stress, which corresponds to hysteretic damping, is 90° out of phase. (This stress component leads the strain by 90° .) A convenient mathematical representation is possible, by using the usual complex form of the response according to

$$\varepsilon = \varepsilon_0 e^{j\omega t} \quad (19.13)$$

Then, Equation 19.10 becomes

$$\sigma = (E + j\tilde{E})\varepsilon \quad (19.14)$$

It follows that this form of simplified hysteretic damping may be represented by using a complex modulus of elasticity, consisting of a real part which corresponds to the usual linear elastic (energy storage) modulus (or Young's modulus) and an imaginary part which corresponds to the hysteretic loss (energy dissipation) modulus.

By combining Equation 19.2 and Equation 19.10, a simple model for combined viscoelastic and hysteretic damping may be given by

$$\sigma = E\varepsilon + \left(E^* + \frac{\tilde{E}}{\omega}\right) \frac{d\varepsilon}{dt} \quad (19.15)$$

The equation of motion for a system whose damping is represented by Equation 19.15 can be deduced from the pure elastic equation of motion by simply substituting E by the operator

$$E + \left(E^* + \frac{\tilde{E}}{\omega}\right) \frac{\partial}{\partial t}$$

in the time domain.

Example 19.1

Determine the equation of flexural motion of a nonuniform slender beam whose material has both viscoelastic and hysteretic damping.

Solution

The Bernoulli–Euler equation of bending motion on an undamped beam subjected to a dynamic load of $f(x, t)$ per unit length, is given by

$$\frac{\partial^2}{\partial x^2} EI \frac{\partial^2 q}{\partial x^2} + \rho A \frac{\partial^2 q}{\partial t^2} = f(x, t) \quad (19.16)$$

Here, q is the transverse motion at a distance, x , along the beam. Then, for a beam with material damping (both viscoelastic and hysteretic) we can write

$$\frac{\partial^2}{\partial x^2} EI \frac{\partial^2 q}{\partial x^2} + \frac{\partial^2}{\partial x^2} \left(E^* + \frac{\tilde{E}}{\omega}\right) I \frac{\partial^3 q}{\partial t \partial x^2} + \rho A \frac{\partial^2 q}{\partial t^2} = f(x, t) \quad (19.17)$$

in which ω is the frequency of the external excitation $f(x, t)$ in the case of steady forced vibrations. In the case of free vibration, however, ω represents the frequency of free vibration decay. Consequently, when analyzing the modal decay of free vibrations, ω in Equation 19.17 should be replaced by the appropriate frequency (ω_i) of modal vibration in each modal equation. Hence, the resulting damped vibratory system possesses the same normal mode shapes as the undamped system. The analysis of the damped case is very similar to that for the undamped system.

19.2.2 Structural Damping

Structural damping is a result of mechanical energy dissipation caused by friction due to the relative motion between components and by impacting or intermittent contact at the joints in a mechanical system or structure. Energy dissipation behavior depends on the details of the particular mechanical system. Consequently, it is extremely difficult to develop a generalized analytical model that would satisfactorily describe structural damping. Energy dissipation caused by rubbing is usually represented by a Coulomb friction model. Energy dissipation caused by impacting, however, should be determined from the coefficient of restitution of the two members that are in contact.

The most common method of estimating structural damping is by measurement. The measured values, however, represent the overall damping in the mechanical system. The structural damping component is obtained by subtracting the values corresponding to other types of damping, such as material damping, present in the system (estimated by environment-controlled experiments, previous data, and so forth) from the overall damping value.

Usually, internal damping is negligible compared to structural damping. A large proportion of mechanical energy dissipation in tall buildings, bridges, vehicle guideways, and many other civil engineering structures and in machinery, such as robots and vehicles, takes place through the structural damping mechanism. A major form of structural damping is the slip damping that results from energy dissipation by interface shear at a structural joint. The degree of slip damping that is directly caused by Coulomb (dry) friction depends on such factors as joint forces (for example, bolt tensions), surface properties and the nature of the materials of the mating surfaces. This is associated with wear, corrosion, and general deterioration of the structural joint. In this sense, slip damping is time-dependent. It is a common practice to place damping layers at joints to reduce undesirable deterioration of the joints. Sliding causes shear distortions in the damping layers, causing energy dissipation by material damping and also through Coulomb friction. In this way, a high level of equivalent structural damping can be maintained without causing excessive joint deterioration. These damping layers should have a high stiffness (as well as a high specific-damping capacity) in order to take the structural loads at the joint.

For structural damping at a joint, the damping force varies as slip occurs at the joint. This is primarily caused by local deformations at the joint, which occur with slipping. A typical hysteresis loop for this case is shown in Figure 19.2(a). The arrows on the hysteresis loop indicate the direction of relative velocity. For idealized Coulomb friction, the frictional force (F) remains constant in each direction of relative motion. An idealized hysteresis loop for structural Coulomb damping is shown in Figure 19.2(b). The corresponding constitutive relation is

$$f = c \operatorname{sgn}(\dot{q}) \quad (19.18)$$

in which f is the damping force, q is the relative displacement at the joint and c is a friction parameter. A simplified model for structural damping caused by local deformation may be given by

$$f = c|q|\operatorname{sgn}(\dot{q}) \quad (19.19)$$

The corresponding hysteresis loop is shown in Figure 19.2(c). Note that the *signum function* is defined by

$$\operatorname{sgn}(v) = \begin{cases} 1 & \text{for } v \geq 0 \\ -1 & \text{for } v < 0 \end{cases} \quad (19.20)$$

19.2.3 Fluid Damping

Consider a mechanical component moving in a fluid medium. The direction of relative motion is shown parallel to the y -axis in Figure 19.3. Local displacement of the element relative to the surrounding fluid is denoted by $q(x, y, t)$.

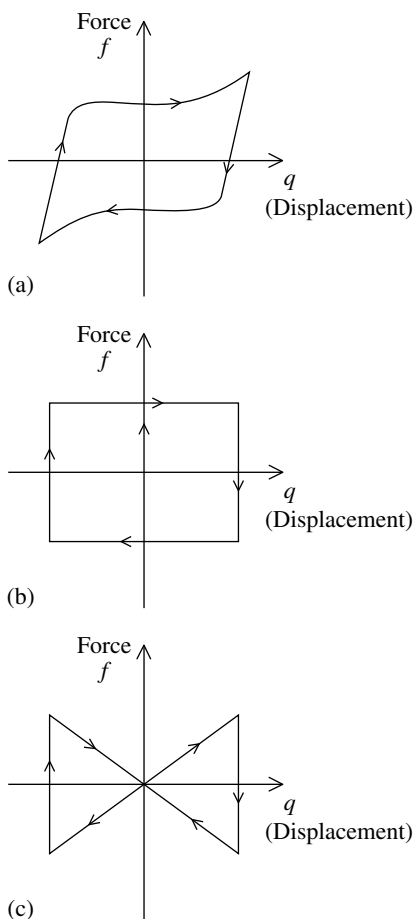


FIGURE 19.2 Some representative hysteresis loops: (a) typical structural damping; (b) Coulomb friction model; and (c) simplified structural damping model.

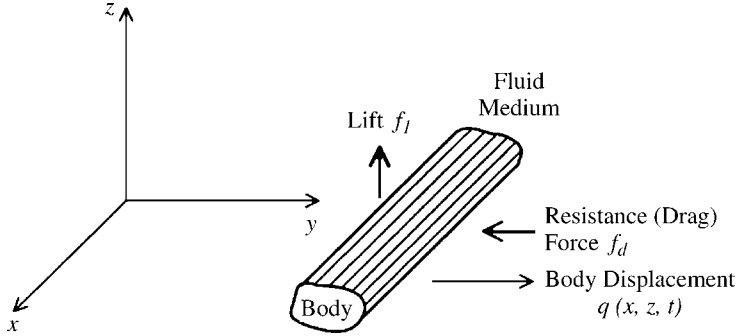


FIGURE 19.3 A body moving in a fluid medium.

The resulting drag force per unit area of projection on the x - z plane is denoted by f_d . This resistance is the cause of mechanical energy dissipation in fluid damping. It is usually expressed as

$$f_d = \frac{1}{2} c_d \rho \dot{q}^2 \text{sgn}(\dot{q}) \quad (19.21)$$

in which $\dot{q} = \partial q(x, z, t) / \partial t$ is the relative velocity. The drag coefficient, c_d , is a function of the Reynold's number and the geometry of the structural cross section. A net damping effect is

generated by viscous drag produced by the boundary layer effects at the fluid–structure interface, and by pressure drag produced by the turbulent effects resulting from flow separation at the wake. The two effects are illustrated in Figure 19.4. Fluid density is ρ . For fluid damping, the damping capacity per unit volume associated with the configuration shown in Figure 19.3 is given by

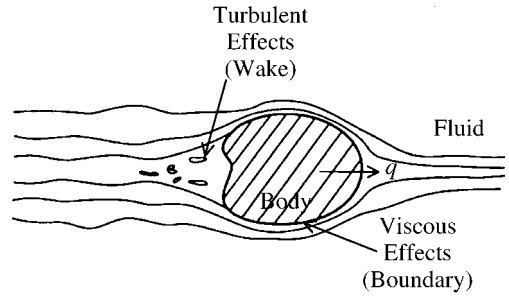


FIGURE 19.4 Mechanics of fluid damping.

$$d_f = \frac{\oint \int_0^{L_x} \int_0^{L_z} f_d \, dz \, dx \, dq(x, z, t)}{L_x L_z q_0} \quad (19.22)$$

in which, L_x and L_z are cross-sectional dimensions of the element in the x and y -directions, respectively, and q_0 is a normalizing amplitude parameter for relative displacement.

Example 19.2

Consider a beam of length L and uniform rectangular cross section that is undergoing transverse vibration in a stationary fluid. Determine an expression for the damping capacity per unit volume for this fluid–structure interaction.

Solution

Suppose that the beam axis is along the x -direction and the transverse motion is in the z -direction. There is no variation in the y -direction, and hence, the length parameters in this direction cancel out.

$$d_f = \frac{\oint \int_0^L f_d \, dx \, dq(x, t)}{L q_0}$$

or

$$d_f = \frac{\int_0^T \int_0^L f_d \dot{q}(x, t) \, dx \, dt}{L q_0} \quad (19.23)$$

in which T is the period of the oscillations. Assuming constant c_d , we substitute Equation 19.21 into Equation 19.23:

$$d_f = \frac{1}{2} \frac{c_d \rho}{L q_0} \int_0^L \int_0^T |\dot{q}|^3 dt dx \tag{19.24}$$

For steady-excited harmonic vibration at frequency ω and shape function $Q(x)$ (or for free-modal vibration at natural frequency ω and mode shape $Q(x)$) we have

$$q(x, t) = q_{\max} Q(x) \sin \omega t \tag{19.25}$$

In this case, with the change of variable $\theta = \omega t$, Equation 19.24 becomes

$$d_f = 2 c_d \rho \frac{q_{\max}^3}{L q_0} \int_0^L |Q(x)|^3 dx \omega^2 \int_0^{\pi/2} \cos^3 \theta d\theta$$

or

$$d_f = \frac{4}{3} c_d \rho q_{\max}^3 \omega^2 \frac{\int_0^L |Q(x)|^3 dx}{L q_0}$$

Note. The integration interval of $t = 0$ to T becomes $\theta = 0$ to 2π or four times that from $\theta = 0$ to $\pi/2$. If the normalizing parameter is defined as

$$q_0 = \frac{1}{L} q_{\max} \int_0^L |Q(x)|^3 dx$$

then, we get

$$d_f = \frac{4}{3} c_d \rho q_{\max}^2 \omega^2 \tag{19.26}$$

A useful classification of damping is given in Box 19.1.

Box 19.1

DAMPING CLASSIFICATION

Type of Damping	Origin	Typical Constitutive Relation
Internal damping	Material properties	Viscoelastic $\sigma = E\varepsilon + E^* \frac{d\varepsilon}{dt}$
		Hysteretic $\sigma = E\varepsilon + \frac{\tilde{E}}{\omega} \frac{d\varepsilon}{dt}$
Structural damping	Structural joints and interfaces	Structural deformation $f = c q \operatorname{sgn}(\dot{q})$
		Coulomb $f = c \operatorname{sgn}(\dot{q})$
		General interface $f = \begin{cases} f_s & \text{for } v = 0 \\ f_{sb}(v) \operatorname{sgn}(v) & \text{for } v \neq 0 \end{cases}$
Fluid damping	Fluid–structure interactions	$f_d = \frac{1}{2} c_d \rho \dot{q}^2 \operatorname{sgn}(\dot{q})$

19.3 Representation of Damping in Vibration Analysis

It is not practical to incorporate detailed microscopic representations of damping in the dynamic analysis of systems. Instead, simplified models of damping that are representative of various types of energy dissipation are typically used. Consider a general n -degree-of-freedom mechanical system. Its motion can be represented by the vector \mathbf{x} of n generalized coordinates, x_i , representing the independent motions of the inertia elements. For small displacements, linear spring elements can be assumed. The corresponding equations of motion may be expressed in the vector matrix form

$$\mathbf{M}\ddot{\mathbf{x}} + \mathbf{d} + \mathbf{K}\mathbf{x} = \mathbf{f}(t) \tag{19.27}$$

in which \mathbf{M} is the mass (inertia) matrix and \mathbf{K} is the stiffness matrix. The forcing-function vector is $\mathbf{f}(t)$. The damping force vector $\mathbf{d}(\mathbf{x}, \dot{\mathbf{x}})$ is generally a nonlinear function of \mathbf{x} and $\dot{\mathbf{x}}$. The type of damping used in the system model may be represented by the nature of \mathbf{d} that is employed in the system equations. The various damping models that may be used, as discussed in the previous section, are listed in Table 19.1. Only the linear viscous damping term given in Table 19.1 is amenable to simplified mathematical analysis. In simplified dynamic models, other types of damping terms are usually replaced by an equivalent viscous damping term. Equivalent viscous damping is chosen so that its energy dissipation per cycle of oscillation is equal to that for the original damping. The resulting equations of motion are expressed by

$$\mathbf{M}\ddot{\mathbf{x}} + \mathbf{C}\dot{\mathbf{x}} + \mathbf{K}\mathbf{x} = \mathbf{f}(t) \tag{19.28}$$

In modal analysis of vibratory systems, the most commonly used model is proportional damping, where the damping matrix satisfies

$$\mathbf{C} = c_m\mathbf{M} + c_k\mathbf{K} \tag{19.29}$$

The first term on the right-hand side of Equation 19.29 is known as the inertial damping matrix. The corresponding damping force on each concentrated mass is proportional to its momentum. It represents the energy loss associated with a change in momentum (for example, during an impact). The second term is known as the stiffness damping matrix. The corresponding damping force is proportional to the rate of change of the local deformation forces at joints near the concentrated mass elements. Consequently, it represents a simplified form of linear structural damping. If damping is of the proportional type, it follows that the damped motion can be uncoupled into individual modes. This means that, if the damping model is of the proportional type, the damped system (as well as the undamped system) will possess real modes.

TABLE 19.1 Some Common Damping Models Used in Dynamic System Equations

Damping Type	Simplified Model d_i
Viscous	$\sum_j c_{ij}\dot{x}_j$
Hysteretic	$\sum_j \frac{1}{\omega} c_{ij}\dot{x}_j$
Structural	$\sum_j c_{ij} x_j \operatorname{sgn}(\dot{x}_j)$
Structural Coulomb	$\sum_j c_{ij} \operatorname{sgn}(\dot{x}_j)$
Fluid	$\sum_j c_{ij} \dot{x}_j \dot{x}_j$

19.3.1 Equivalent Viscous Damping

Consider a linear, single-DoF system with viscous damping, subjected to an external excitation. The equation of motion, for a unit mass, is given by

$$\ddot{x} + 2\zeta\omega_n\dot{x} + \omega_n^2x = \omega_n^2u(t) \quad (19.30)$$

If the excitation force is harmonic, with frequency ω , we have

$$u(t) = u_0 \cos \omega t \quad (19.31)$$

Then, the response of the system at steady state is given by

$$x = x_0 \cos(\omega t + \phi) \quad (19.32)$$

in which the response amplitude is

$$x_0 = u_0 \frac{\omega_n^2}{[(\omega_n^2 - \omega^2) + 4\zeta^2\omega_n^2\omega^2]^{1/2}} \quad (19.33)$$

and the response phase lead is

$$\phi = -\tan^{-1} \frac{2\zeta\omega_n\omega}{(\omega_n^2 - \omega^2)} \quad (19.34)$$

The energy dissipation (i.e., damping capacity), ΔU , per unit mass in one cycle is given by the net work done by the damping force, f_d ; thus,

$$\Delta U = \oint f_d dx = \int_{-\phi/\omega}^{(2\pi-\phi)/\omega} f_d \dot{x} dt \quad (19.35)$$

Since the viscous damping force, normalized with respect to mass (see Equation 19.30), is given by

$$f_d = 2\zeta\omega_n\dot{x} \quad (19.36)$$

the damping capacity, ΔU_v , for viscous damping, can be obtained as

$$\Delta U_v = 2\zeta\omega_n \int_0^{2\pi/\omega} \dot{x}^2 dt \quad (19.37)$$

Finally, using Equation 19.32 in Equation 19.37 we get

$$\Delta U_v = 2\pi x_0^2 \omega_n \omega \zeta \quad (19.38)$$

For any general type of damping (see Table 19.1), the equation of motion becomes

$$\ddot{x} + \mathbf{d}(x, \dot{x}) + \omega_n^2x = \omega_n^2u(t) \quad (19.39)$$

The energy dissipation in one cycle (Equation 19.35) is given by

$$\Delta U = \int_{-\phi/\omega}^{(2\pi-\phi)/\omega} d(x, \dot{x}) \dot{x} dt \quad (19.40)$$

Various damping force expressions, $d(x, \dot{x})$, normalized with respect to mass, are given in Table 19.2. For fluid damping, for example, the damping capacity is

$$\Delta U_f = \int_{-\phi/\omega}^{(2\pi-\phi)/\omega} c|\dot{x}|\dot{x}^2 dt \quad (19.41)$$

By substituting Equation 19.32 in Equation 19.41 for steady, harmonic motion we obtain

$$\Delta U_f = \frac{8}{3} c x_0^3 \omega^2 \quad (19.42)$$

TABLE 19.2 Equivalent Damping Ratio Expressions for Some Common Types of Damping

Damping Type	Damping Force, $d(x, \dot{x})$, per Unit Mass	Equivalent Damping Ratio, ζ_{eq}
Viscous	$2\zeta\omega_n\dot{x}$	ζ
Hysteretic	$\frac{c}{\omega}\dot{x}$	$\frac{c}{2\omega_n\omega}$
Structural	$c x \operatorname{sgn}(\dot{x})$	$\frac{c}{\pi\omega_n\omega}$
Structural Coulomb	$c\operatorname{sgn}(\dot{x})$	$\frac{2c}{\pi x_0\omega_n\omega}$
Fluid	$c \dot{x} \dot{x}$	$\frac{4}{3\pi}\left(\frac{\omega}{\omega_n}\right)x_0c$

By comparing Equation 19.42 with Equation 19.38, the equivalent damping ratio for fluid damping is obtained as

$$\zeta_f = \frac{4}{3\pi}\left(\frac{\omega}{\omega_n}\right)x_0c \quad (19.43)$$

in which x_0 is the amplitude of steady-state vibrations, as given by Equation 19.33. For the other types of damping listed in Table 19.1, expressions for the equivalent damping ratio can be obtained in a similar manner. The corresponding equivalent damping ratio expressions are given in Table 19.2. It should be noted that, for nonviscous damping types, ζ is generally a function of the frequency of oscillation, ω , and the amplitude of excitation, u_0 . It should be noted that the expressions given in Table 19.2 are derived assuming harmonic excitation. Engineering judgment should be exercised when employing these expressions for nonharmonic excitations.

For multi-DoF systems that incorporate proportional damping, the equations of motion can be transformed into a set of one-DoF equations (modal equations) of the type given in Equation 19.30. In this case, the damping ratio and natural frequency correspond to the respective modal values and, in particular, $\omega = \omega_n$.

19.3.2 Complex Stiffness

Consider a linear spring of stiffness k connected in parallel with a linear viscous damper of damping constant c , as shown in Figure 19.5(a). Suppose that a force, f , is applied to the system, moving it through distance x from the relaxed position of the spring. Then we have

$$f = kx + c\dot{x} \quad (19.44)$$

Suppose that the motion is harmonic, as given by

$$x = x_0 \cos \omega t \quad (19.45)$$

It is clear that the spring force, kx , is in phase with the displacement, but the damping force, $c\dot{x}$, has a 90° phase lead with respect to the displacement. This is because the velocity, $\dot{x} = -x_0\omega \sin \omega t = x_0\omega \cos(\omega t + \pi/2)$, has a 90° phase lead with respect to x . Specifically, we have

$$f = kx_0 \cos \omega t + cx_0\omega \cos\left(\omega t + \frac{\pi}{2}\right) \quad (19.46)$$

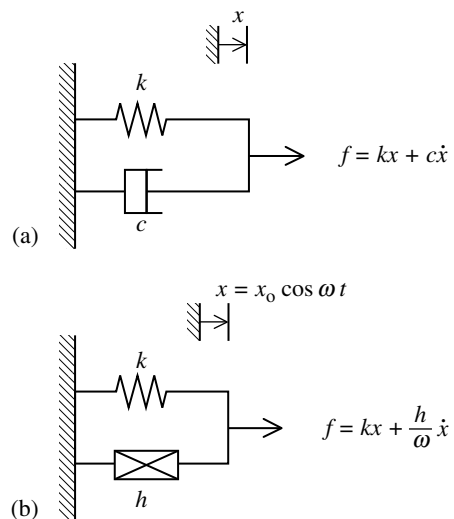


FIGURE 19.5 Spring element in parallel with (a) a viscous damper and (b) a hysteretic damper.

This same fact may be represented by using complex numbers, where the in-phase component is considered as the real part and the 90° phase lead component is considered as the imaginary part with each component oscillating at the same frequency ω . Then, we can write Equation 19.46 in the equivalent form

$$f = kx + j\omega cx \quad (19.47)$$

This is exactly what we get by starting with the complex representation of the displacement

$$x = x_0 e^{j\omega t} \quad (19.48)$$

and substituting it in Equation 19.44. We note that Equation 19.47 may be written as

$$f = k^* x \quad (19.49)$$

where k^* is a “complex” stiffness, given by

$$k^* = k + j\omega c \quad (19.50)$$

Clearly, the system itself and its two components (spring and damper) are real. Their individual forces are also real. The complex stiffness is simply a mathematical representation of the two force components (spring force and damping force), which are 90° out of phase, when subjected to harmonic motion. It follows that the linear damper may be “mathematically” represented by an “imaginary” stiffness. In the case of viscous damping this imaginary stiffness (and hence, the damping force magnitude) increases linearly with the frequency, ω , of the harmonic motion. The concept of complex stiffness when dealing with discrete dampers is analogous to the use of complex elastic modulus in material damping, as discussed earlier in this chapter.

We have noted that, for hysteretic damping, the damping force (or damping stress) is independent of the frequency in harmonic motion. It follows that a hysteretic damper may be represented by an equivalent damping constant of

$$c = \frac{h}{\omega} \quad (19.51)$$

which is valid for a harmonic motion (e.g., modal motion or forced motion) of frequency ω . This situation is shown in [Figure 19.5\(b\)](#). It can be seen that the corresponding complex stiffness is

$$k^* = k + jh \quad (19.52)$$

Example 19.3

A flexible system consists of a mass, m , attached to the hysteretic damper and spring combination shown in Figure 19.5(b). What is the frequency response function of the system relating an excitation force, f , applied to the mass and the resulting displacement response, x ? Obtain the resonant frequency of the system. Compare the results with the case for viscous damping.

Solution

For a harmonic motion of frequency ω , the equation of motion of the system is

$$m\ddot{x} + \frac{h}{\omega}\dot{x} + kx = f \quad (19.53)$$

With a forcing excitation of $f = f_0 e^{j\omega t}$ and the resulting steady-state response, $x = x_0 e^{j\omega t}$, where x_0 has a phase difference (i.e., it is a complex function) with respect to f_0 . Then, in the frequency domain, substituting the harmonic response $x = x_0 e^{j\omega t}$ into Equation 19.53 we get

$$\left[-\omega^2 m + \frac{h}{\omega} j\omega + k \right] x = f$$

resulting in the frequency transfer function

$$\frac{x}{f} = \frac{1}{[k - \omega^2 m + jh]} \quad (19.54)$$

Note that, as usual, this result is obtained simply by substituting $j\omega$ for d/dt . The magnitude of transfer function is at a maximum at resonance. This corresponds to a minimum value of

$$p(\omega) = (k - \omega^2 m)^2 + h^2$$

If we set $dp/d\omega = 0$, we get,

$$2(k - \omega^2 m)(-2\omega) = 0$$

Hence, the resonant frequency corresponds to the root of

$$k - \omega^2 m = 0$$

This gives the resonant frequency

$$\omega_r = \sqrt{\frac{k}{m}} \quad (19.55)$$

Note that, in the case of hysteretic damping, the resonant frequency is equal to the undamped natural frequency, ω_n , and, unlike in the case of viscous damping, does not depend on the level of damping itself. For convenience consider the system response as the spring force

$$f_s = kx \quad (19.56)$$

Then, a normalized transfer function is obtained, as given by

$$\frac{f_s}{f} = G(j\omega) = \frac{1}{\left[1 - \omega^2 \frac{m}{k} + j \frac{h}{k}\right]} \quad (19.57)$$

or,

$$\frac{f_s}{f} = \frac{1}{[1 - r^2 + j\alpha]} \quad (19.58)$$

where

$$r = \frac{\omega}{\omega_n} \quad \text{and} \quad \alpha = \frac{h}{k} \quad (19.59)$$

which are the normalized frequency and the normalized hysteretic damping, respectively. The magnitude of the transfer function is

$$\left| \frac{f_s}{f} \right| = \frac{1}{\sqrt{(1 - r^2)^2 + \alpha^2}} \quad (19.60)$$

and the phase angle (phase lead) is

$$\angle f_s/f = -\tan^{-1} \frac{\alpha}{(1 - r^2)} \quad (19.61)$$

These results are sketched in [Figure 19.6](#).

19.3.3 Loss Factor

We define the *damping capacity* of a device (damper) as the energy dissipated in a complete cycle of motion; specifically

$$\Delta U = \oint f_d dx \quad (19.62)$$

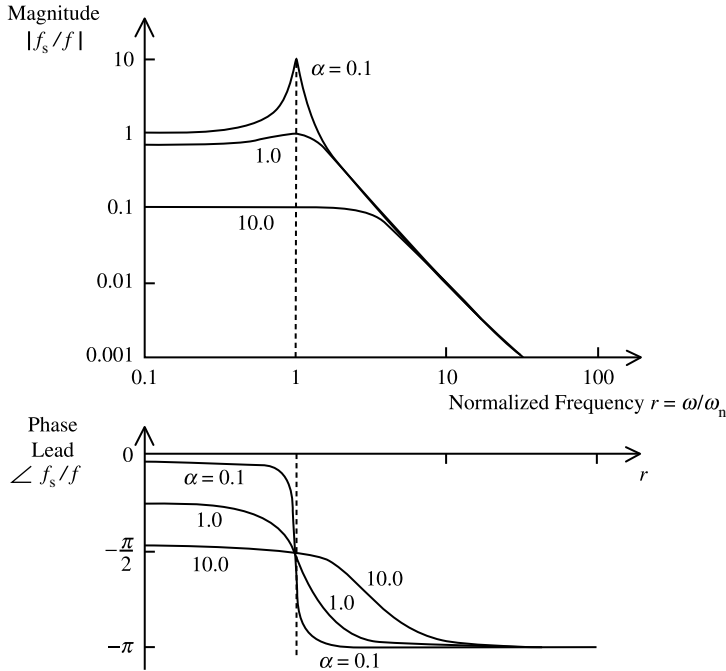


FIGURE 19.6 Frequency transfer function of a simple oscillator with hysteretic damping.

This is given by the area of the hysteresis loop in the displacement force plane. If the initial (total) energy of the system is denoted by U_{\max} , then the *specific damping capacity*, D , is given by the ratio

$$D = \frac{\Delta U}{U_{\max}} \quad (19.63)$$

The *loss factor*, η , is the specific damping capacity per radian of the damping cycle. Hence,

$$\eta = \frac{\Delta U}{2\pi U_{\max}} \quad (19.64)$$

Note that U_{\max} is approximately equal to the maximum kinetic energy and also to the maximum potential energy of the device when the damping is low.

Equation 19.38 gives the damping capacity per unit mass of a device with viscous damping as

$$\Delta U = 2\pi x_0^2 \omega_n \omega \zeta \quad (19.65)$$

Here, x_0 is the amplitude and ω is the frequency of harmonic motion of the device, ω_n is the undamped natural frequency and ζ is the damping ratio. The maximum potential energy per unit mass of the system is

$$U_{\max} = \frac{1}{2} \frac{k}{m} x_0^2 = \frac{1}{2} \omega_n^2 x_0^2 \quad (19.66)$$

Hence, from Equation 19.64, the loss factor for a viscous damped simple oscillator is given by

$$\eta = \frac{2\pi x_0^2 \omega_n \omega \zeta}{2\pi \times \frac{1}{2} \omega_n^2 x_0^2} = \frac{2\omega \zeta}{\omega_n} \quad (19.67)$$

For free decay of the system, we have $\omega = \omega_d \cong \omega_n$, where the latter approximation holds for low damping. For forced oscillation, the worst response conditions occur when $\omega = \omega_d \cong \omega_n$, which is what one must consider with regard to energy dissipation. In either case, the loss factor is approximately

given by

$$\eta = 2\zeta$$

(19.68)

For other types of damping, Equation 19.68 will still hold when the equivalent damping ratio, ζ_{eq} , (see Table 19.2) is used in place of ζ .

The loss factors of some common materials are given in Table 19.3. Definitions of useful damping parameters, as defined here, are summarized in Table 19.4. Expressions of loss factors for some useful damping models are given in Table 19.5.

TABLE 19.3 Loss Factors of Some Useful Materials

Material	Loss Factor $\eta \cong 2\zeta$
Aluminum	2×10^{-5} to 2×10^{-3}
Concrete	0.02 to 0.06
Glass	0.001 to 0.002
Rubber	0.1 to 1.0
Steel	0.002 to 0.01
Wood	0.005 to 0.01

TABLE 19.4 Definitions of Damping Parameters

Parameter	Definition	Mathematical Formula
Damping capacity (ΔU)	Energy dissipated per cycle of motion (area of displacement–force hysteresis loop)	$\oint f_d \, dx$
Damping capacity per volume (d)	Energy dissipated per cycle per unit material volume (area of strain–stress hysteresis loop)	$\oint \sigma \, d\varepsilon$
Specific damping capacity (D)	Ratio of energy dissipated per cycle (ΔU) to the initial maximum energy (U_{\max}) <i>Note:</i> for low damping, U_{\max} = maximum potential energy = maximum kinetic energy	$\frac{\Delta U}{U_{\max}}$
Loss factor (η)	Specific damping capacity per unit angle of cycle. <i>Note:</i> for low damping, $\eta = 2 \times$ damping ratio	$\frac{\Delta U}{2\pi U_{\max}}$

TABLE 19.5 Loss Factors for Several Material Damping Models

Material Damping Model	Stress–Strain Constitute Relation	Loss Factor (η)
Viscoelastic Kelvin–Voigt	$\sigma = E\varepsilon + E^* \frac{d\varepsilon}{dt}$	$\frac{\omega E^*}{E}$
Hysteretic Kelvin–Voigt	$\sigma = E\varepsilon + \frac{\tilde{E}}{\omega} \frac{d\varepsilon}{dt}$	$\frac{\tilde{E}}{E}$
Viscoelastic standard linear solid	$\sigma + c_s \frac{d\sigma}{dt} = E\varepsilon + E^* \frac{d\varepsilon}{dt}$	$\frac{\omega E^*}{E} \frac{(1 - c_s E/E^*)}{(1 + \omega^2 c_s^2)}$
Hysteretic standard linear solid	$\sigma + c_s \frac{d\sigma}{dt} = E\varepsilon + \frac{\tilde{E}}{\omega} \frac{d\varepsilon}{dt}$	$\frac{\tilde{E}}{E} \frac{(1 - \omega c_s E/\tilde{E})}{(1 + \omega^2 c_s^2)}$

19.4 Measurement of Damping

Damping may be represented by various parameters (such as specific damping capacity, loss factor, Q-factor, and damping ratio) and models (such as viscous, hysteretic, structural, and fluid). Before attempting to measure damping in a system, we need to decide on a representation (model) that will adequately characterize the nature of mechanical energy dissipation in the system. Next, we should decide on the parameter or parameters of the model that need to be measured.

It is extremely difficult to develop a realistic yet tractable model for damping in a complex piece of equipment operating under various conditions of mechanical interaction. Even if a satisfactory damping model is developed, experimental determination of its parameters could be tedious. A major difficulty arises because it usually is not possible to isolate various types of damping (for example, material, structural, and fluid) from an overall measurement. Furthermore, damping measurements must be conducted under actual operating conditions for them to be realistic.

If one type of damping (say, fluid damping) is eliminated during the actual measurement then it would not represent the true operating conditions. This would also eliminate possible interacting effects of the eliminated damping type with the other types. In particular, overall damping in a system is not generally equal to the sum of the individual damping values when they are acting independently. Another limitation of computing equivalent damping values using experimental data arises because it is assumed for analytical simplicity that the dynamic system behavior is linear. If the system is highly nonlinear, a significant error could be introduced into the damping estimate. Nevertheless, it is customary to assume linear viscous behavior when estimating damping parameters using experimental data.

There are two general ways by which damping measurements can be made: using a time–response record and using a frequency–response function of the system to estimate damping.

19.4.1 Logarithmic Decrement Method

This is perhaps the most popular time–response method that is used to measure damping. When a single-DoF oscillatory system with viscous damping (see Equation 19.30) is excited by an impulse input (or an initial condition excitation), its response takes the form of a time decay (see Figure 19.7), given by

$$y(t) = y_0 \exp(-\zeta \omega_n t) \sin \omega_d t \quad (19.69)$$

in which the damped natural frequency is given by

$$\omega_d = \sqrt{1 - \zeta^2} \omega_n \quad (19.70)$$

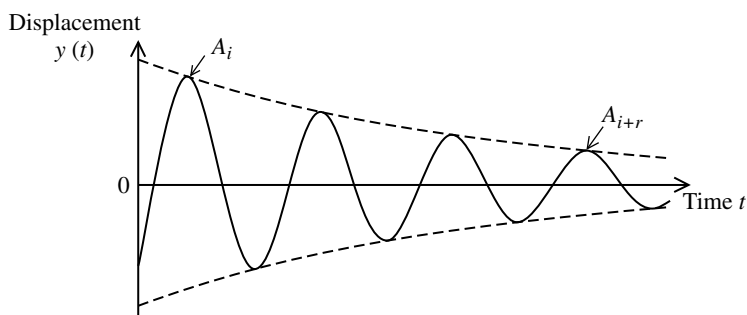


FIGURE 19.7 Impulse response of a simple oscillator.

If the response at $t = t_i$ is denoted by y_i , and the response at $t = t_i + 2\pi r/\omega_d$ is denoted by y_{i+r} , then, from Equation 19.69, we have

$$\frac{y_{i+r}}{y_i} = \exp\left(-\zeta \frac{\omega_n}{\omega_d} 2\pi r\right), \quad i = 1, 2, \dots, n$$

In particular, suppose that y_i corresponds to a peak point in the time decay function, having magnitude A_i , and that y_{i+r} corresponds to the peak point r cycles later in the time history, and its magnitude is denoted by A_{i+r} (see Figure 19.7). Even though the above equation holds for any pair of points that are r periods apart in the time history, the peak points seem to be the appropriate choice for measurement in the present procedure, as these values would be more prominent than any arbitrary points in a response–time history. Then,

$$\frac{A_{i+r}}{A_i} = \exp\left(-\zeta \frac{\omega_n}{\omega_d} 2\pi r\right) = \exp\left[-\frac{\zeta}{\sqrt{1-\zeta^2}} 2\pi r\right]$$

where Equation 19.70 has been used. Then, the logarithmic decrement δ is given by (per unit cycle)

$$\delta = \frac{1}{r} \ln\left(\frac{A_i}{A_{i+r}}\right) = \frac{2\pi\zeta}{\sqrt{1-\zeta^2}} \quad (19.71)$$

or the damping ratio may be expressed as

$$\zeta = \frac{1}{\sqrt{1 + (2\pi/\delta)^2}} \quad (19.72)$$

For low damping (typically, $\zeta < 0.1$), $\omega_d \cong \omega_n$ and Equation 19.71 become

$$\frac{A_{i+r}}{A_i} \cong \exp(-\zeta 2\pi r) \quad (19.73)$$

or

$$\zeta = \frac{1}{2\pi r} \ln\left(\frac{A_i}{A_{i+r}}\right) = \frac{\delta}{2\pi} \quad \text{for } \zeta < 0.1 \quad (19.74)$$

This is in fact the “per-radian” logarithmic decrement.

The damping ratio can be estimated from a free-decay record, using Equation 19.74. Specifically, the ratio of the extreme amplitudes in prominent r cycles of decay is determined and substituted into Equation 19.74 to get the equivalent damping ratio.

Alternatively, if n cycles of damped oscillation are needed for the amplitude to decay by a factor of two, for example, then, from Equation 19.74, we get

$$\zeta = \frac{1}{2\pi n} \ln(2) = \frac{0.11}{n} \quad \text{for } \zeta < 0.1 \quad (19.75)$$

For slow decays (low damping), we have

$$\ln\left(\frac{A_i}{A_{i+1}}\right) \cong \frac{2(A_i - A_{i+1})}{(A_i + A_{i+1})} \quad (19.76)$$

Then, from Equation 19.74, we get

$$\zeta = \frac{A_i - A_{i+1}}{\pi(A_i + A_{i+1})} \quad \text{for } \zeta < 0.1 \quad (19.77)$$

Any one of Equation 19.72, Equation 19.74, Equation 19.75, and Equation 19.77 could be employed in computing ζ from test data. It should be noted that the results assume single-DoF system behavior. For multi-DoF systems, the modal damping ratio for each mode can be determined using this method if the initial excitation is such that the decay takes place primarily in one mode of vibration.

In other words, substantial modal separation and the presence of “real” modes (not “complex” modes with nonproportional damping) are assumed.

19.4.2 Step–Response Method

This is also a time–response method. If a unit-step excitation is applied to the single-DoF oscillatory system given by Equation 19.30, its time–response is given by

$$y(t) = 1 - \frac{1}{\sqrt{1 - \zeta^2}} \exp(-\zeta \omega_n t) \sin(\omega_d t + \phi) \quad (19.78)$$

in which $\phi = \cos \zeta$. A typical step–response curve is shown in Figure 19.8. The time at the first peak (peak time), T_p , is given by

$$T_p = \frac{\pi}{\omega_d} = \frac{\pi}{\sqrt{1 - \zeta^2} \omega_n} \quad (19.79)$$

The response at peak time (peak value), M_p , is given by

$$M_p = 1 + \exp(-\zeta \omega_n T_p) = 1 + \exp\left(\frac{-\pi \zeta}{\sqrt{1 - \zeta^2}}\right) \quad (19.80)$$

The percentage overshoot, PO, is given by

$$PO = (M_p - 1) \times 100\% = 100 \exp\left(\frac{-\pi \zeta}{\sqrt{1 - \zeta^2}}\right) \quad (19.81)$$

It follows that, if any one parameter of T_p , M_p or PO is known from a step–response record, the corresponding damping ratio, ζ , can be computed by using the appropriate relationship from the following:

$$\zeta = \sqrt{1 - \left(\frac{\pi}{T_p \omega_n}\right)^2} \quad (19.82)$$

$$\zeta = \frac{1}{\sqrt{1 + \frac{1}{\left[\frac{\ln(M_p - 1)}{\pi}\right]^2}}} \quad (19.83)$$

$$\zeta = \frac{1}{\sqrt{1 + \frac{1}{\left[\frac{\ln(PO/100)}{\pi}\right]^2}}} \quad (19.84)$$

It should be noted that when determining M_p the response curve should be normalized to unit steady-state value. Furthermore, the results are valid only for single-DoF systems and modal excitations in multi-DoF systems.

19.4.3 Hysteresis Loop Method

For a damped system, the force versus displacement cycle produces a hysteresis loop. Depending on the inertial and elastic characteristics and other conservative loading conditions (e.g., gravity) in the system,

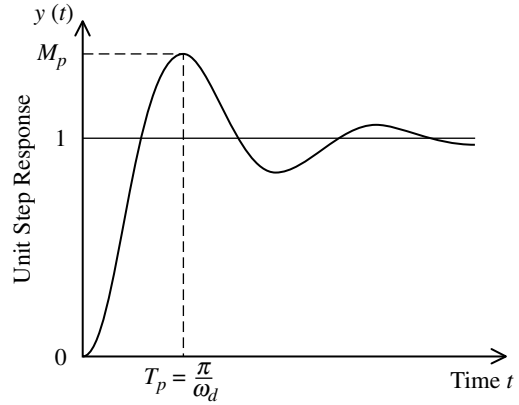


FIGURE 19.8 A typical step–response of a simple oscillator.

the shape of the hysteresis loop will change. But the work done by conservative forces (e.g., inertial, elastic, and gravitational) in a complete cycle of motion will be zero. Consequently, the net work done will be equal to the energy dissipated due to damping only. Accordingly, the area of the displacement–force hysteresis loop will give the damping capacity, ΔU (see Equation 19.62). The maximum energy in the system can also be determined from the displacement–force curve. Then, the loss factor, η , can be computed using Equation 19.64, and the damping ratio from Equation 19.68. This method of damping measurement may also be considered basically as a time domain method.

Note that Equation 19.65 is the work done against (i.e., energy dissipation in) a single loading–unloading cycle per unit mass. It should be recalled that $2\zeta\omega_n = c/m$, where c = viscous damping constant and m = mass. Accordingly, from Equation 19.65, the energy dissipation per unit mass and per hysteresis loop is $\Delta U = \pi x_0^2 \omega c/m$. Hence, without normalizing with respect to mass, the energy dissipation per hysteresis loop of viscous damping is

$$\Delta U_v = \pi x_0^2 \omega c \quad (19.85)$$

Equation 19.85 can be derived by performing the cyclic integration indicated in Equation 19.62 with the damping force $f_d = c\dot{x}$, harmonic motion $x = x_0 e^{j\omega t}$ and the integration interval $t = 0$ to $2\pi/\omega$.

Similarly, in view of Equation 19.51, the energy dissipation per hysteresis loop of hysteretic damping is

$$\Delta U_h = \pi x_0^2 h \quad (19.86)$$

Now, since the initial maximum energy may be represented by the initial maximum potential energy, we have

$$U_{\max} = \frac{1}{2} k x_0^2 \quad (19.87)$$

Note that the stiffness, k , may be measured as the average slope of the displacement–force hysteresis loop. Hence, in view of Equation 19.64, the loss factor for hysteretic damping is given by

$$\eta = \frac{h}{k} \quad (19.88)$$

Then, from Equation 19.68, the equivalent damping ratio for hysteretic damping is

$$\zeta = \frac{h}{2k} \quad (19.89)$$

Example 19.4

A damping material was tested by applying a loading cycle of -900 to 900 N and back to -900 N to a thin bar made of the material and measuring the corresponding deflection. The smoothed load vs. deflection curve obtained in this experiment is shown in [Figure 19.9](#). Assuming that the damping is predominantly of the hysteretic type, estimate

1. The hysteretic damping constant
2. The equivalent damping ratio

Solution

Approximating the top and the bottom segments of the hysteresis loop by triangles, we estimate the area of the loop as

$$\Delta U_h = 2 \times \frac{1}{2} \times 2.5 \times 900 \text{ N mm}$$

Alternatively, we may obtain this result by counting the squares within the hysteresis loop. The deflection amplitude is

$$x_0 = 8.5 \text{ mm}$$

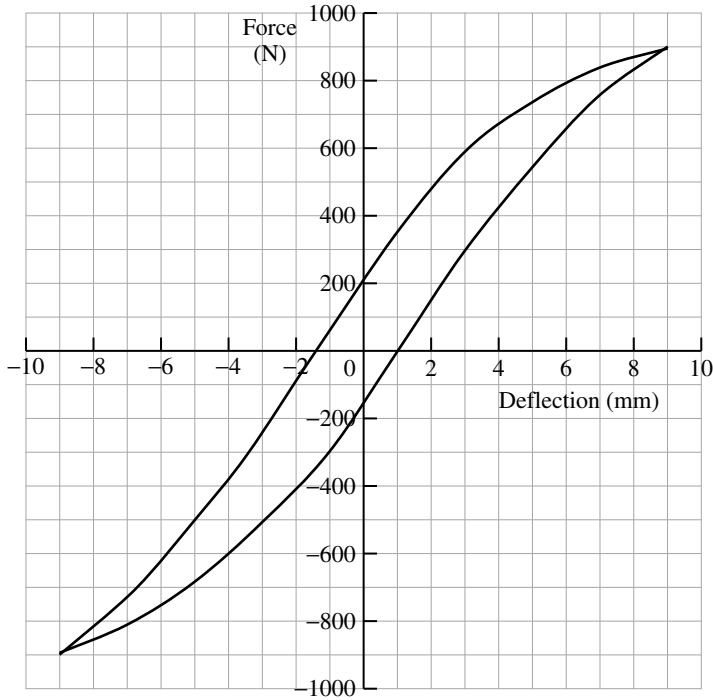


FIGURE 19.9 An experimental hysteresis loop of a damping material.

Hence, from Equation 19.86 we have

$$h = \frac{2 \times \frac{1}{2} \times 2.5 \times 900}{\pi \times 8.5^2} \text{ N/mm} = 9.9 \text{ N/mm}$$

The stiffness of the damping element is estimated as the average slope of the hysteresis loop; thus

$$k = \frac{600}{4.5} \text{ N/mm} = 133.3 \text{ N/mm}$$

Hence, from Equation 19.89, the equivalent damping ratio is

$$\zeta = \frac{9.9}{2 \times 133.3} \approx 0.04$$

19.4.4 Magnification Factor Method

This is a frequency–response method. Consider a single-DoF oscillatory system with viscous damping. The magnitude of its frequency–response function is

$$|H(\omega)| = \frac{\omega_n^2}{\left[(\omega_n^2 - \omega^2)^2 + 4\zeta^2 \omega_n^2 \omega^2 \right]^{1/2}} \quad (19.90)$$

A plot of this expression with respect to ω , the frequency of excitation, is given in Figure 19.10. The peak value of magnitude occurs when the denominator of the expression is at its minimum. This corresponds to

$$\frac{d}{d\omega} \left[(\omega_n^2 - \omega^2)^2 + 4\zeta^2 \omega_n^2 \omega^2 \right] = 0 \quad (19.91)$$

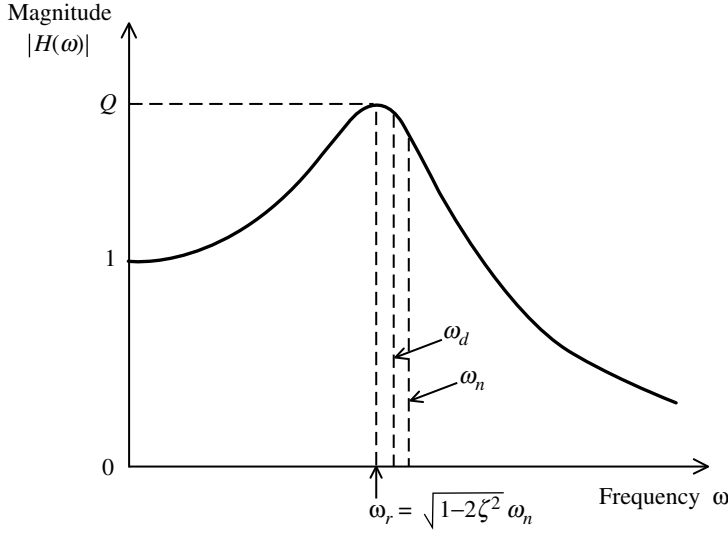


FIGURE 19.10 The magnification factor method of damping measurement applied to a single-DoF system.

The resulting solution for ω is termed the resonant frequency, ω_r

$$\omega_r = \sqrt{1 - 2\zeta^2} \omega_n \quad (19.92)$$

It is noted that $\omega_r < \omega_d$ (see Equation 19.70), but for low damping ($\zeta < 0.1$), the values of ω_n , ω_d , and ω_r are nearly equal. The amplification factor, Q , which is the magnitude of the frequency–response function at resonant frequency, is obtained by substituting Equation 19.92 in Equation 19.90:

$$Q = \frac{1}{2\zeta\sqrt{1 - \zeta^2}} \quad (19.93)$$

For low damping ($\zeta < 0.1$), we have

$$Q = \frac{1}{2\zeta} \quad (19.94)$$

In fact, Equation 19.94 corresponds to the magnitude of the frequency–response function at $\omega = \omega_n$.

It follows that, if the magnitude curve of the frequency–response function (or a Bode plot) is available, then the system damping ratio, ζ , can be estimated using Equation 19.94. When using this method, the frequency–response curve must be normalized so that its magnitude at zero frequency (termed *static gain*) is unity.

For a multi-DoF system modal damping values may be estimated from the magnitude of the Bode plot of its frequency–response function, provided that the modal frequencies are not too closely spaced and the system is lightly damped. Consider the logarithmic (to the base ten) magnitude plot shown in Figure 19.11. The magnitude is expressed in decibels (dB), which is calculated by multiplying the $\log_{10}(\text{magnitude})$ by a factor of 20. At the i th resonant frequency, ω_i , the amplification factor, q_i (in dB), is obtained by drawing an asymptote to the preceding segment of the curve and measuring the peak value from the asymptote. Then,

$$Q_i = (10)^{q_i/20} \quad (19.95)$$

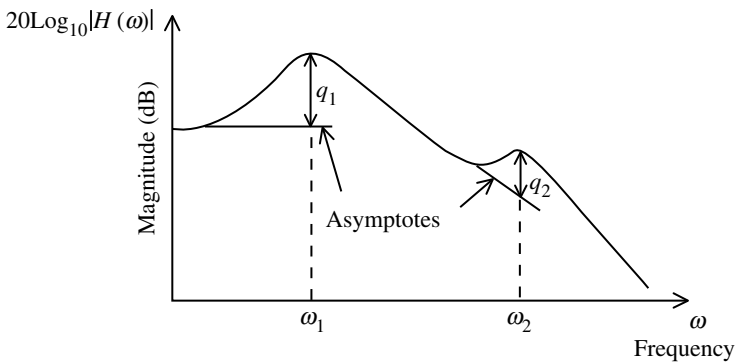


FIGURE 19.11 Magnification factor method applied to a multi-DoF system.

and the modal damping ratio

$$\zeta = \frac{1}{2Q_i}, \quad i = 1, 2, \dots, n \tag{19.96}$$

If the significant resonances are closely spaced, curve-fitting to a suitable function may be necessary in order to determine the corresponding modal damping values. The Nyquist plot may also be used in computing damping using frequency domain data.

19.4.5 Bandwidth Method

The bandwidth method of damping measurement is also based on frequency–response. Consider the frequency–response function magnitude given by Equation 19.90 for a single-DoF, oscillatory system with viscous damping. The peak magnitude is given by Equation 19.94 for low damping. Bandwidth (half-power) is defined as the width of the frequency–response magnitude curve when the magnitude is $(1/\sqrt{2})$ times the peak value. This is denoted by $\Delta\omega$ (see Figure 19.12). An expression

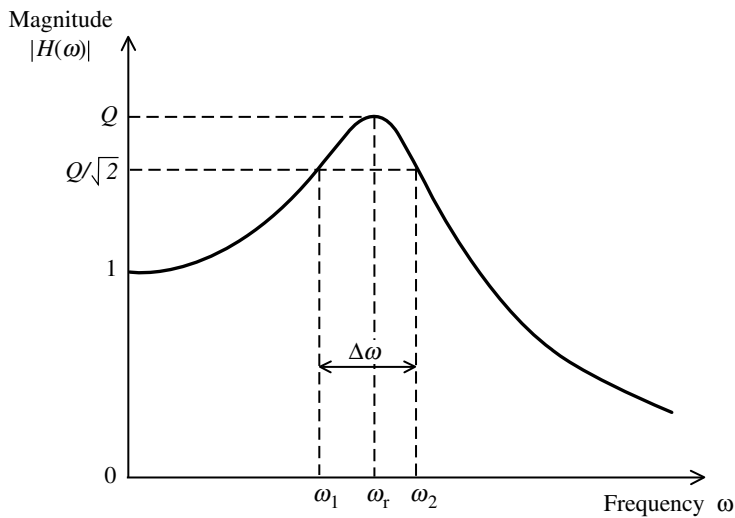


FIGURE 19.12 Bandwidth method of damping measurement in a single-DoF system.

for $\Delta\omega = \omega_2 - \omega_1$ is obtained below using Equation 19.90. By definition, ω_1 and ω_2 are the roots of the equation

$$\frac{\omega_n^2}{\left[(\omega_n^2 - \omega^2)^2 + 4\zeta^2 \omega_n^2 \omega^2\right]^{1/2}} = \frac{1}{\sqrt{2} \times 2\zeta} \quad (19.97)$$

for ω . Equation 19.97 can be expressed in the form

$$\omega^4 - 2(1 - 2\zeta^2)\omega_n^2 \omega^2 + (1 - 8\zeta^2)\omega_n^4 = 0 \quad (19.98)$$

This is a quadratic equation in ω^2 , having roots ω_1^2 and ω_2^2 , which satisfy

$$(\omega^2 - \omega_1^2)(\omega^2 - \omega_2^2) = \omega^4 - (\omega_1^2 + \omega_2^2)\omega^2 + \omega_1^2 \omega_2^2 = 0$$

Consequently,

$$\omega_1^2 + \omega_2^2 = 2(1 - 2\zeta^2)\omega_n^2 \quad (19.99)$$

and

$$\omega_1^2 \omega_2^2 = (1 - 8\zeta^2)\omega_n^4 \quad (19.100)$$

It follows that

$$(\omega_2 - \omega_1)^2 = \omega_1^2 + \omega_2^2 - 2\omega_1 \omega_2 = 2(1 - 2\zeta^2)\omega_n^2 - 2\sqrt{1 - 8\zeta^2}\omega_n^2$$

For small ζ (in comparison to 1), we have

$$\sqrt{1 - 8\zeta^2} \cong 1 - 4\zeta^2$$

Hence,

$$(\omega_2 - \omega_1)^2 \cong 4\zeta^2 \omega_n^2$$

or, for low damping

$$\Delta\omega = 2\zeta\omega_n = 2\zeta\omega_r \quad (19.101)$$

From Equation 19.101 it follows that the damping ratio can be estimated from the bandwidth using the relation

$$\zeta = \frac{1}{2} \frac{\Delta\omega}{\omega_r} \quad (19.102)$$

For a multi-DoF system with widely spaced resonances, the foregoing method can be extended to estimate modal damping. Consider the frequency–response magnitude plot (in dB) shown in [Figure 19.13](#).

Since a factor of $\sqrt{2}$ corresponds to 3 dB, the bandwidth corresponding to a resonance is given by the width of the magnitude plot at 3 dB below that resonant peak. For the i th mode, the damping ratio is given by

$$\zeta_i = \frac{1}{2} \frac{\Delta\omega_i}{\omega_i} \quad (19.103)$$

The bandwidth method of damping measurement indicates that the bandwidth at a resonance is a measure of the energy dissipation in the system in the neighborhood of that resonance. The simplified

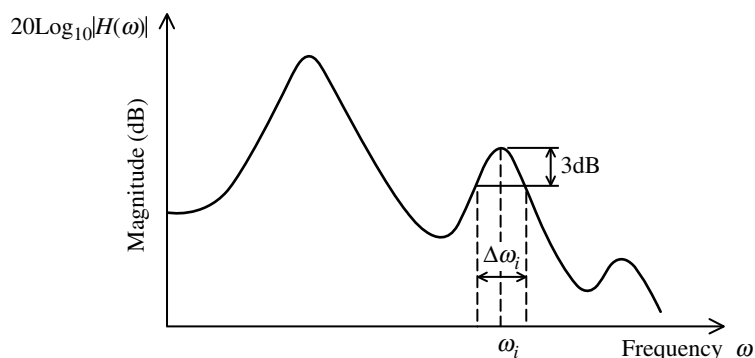


FIGURE 19.13 Bandwidth method of damping measurement in a multi-DoF system.

relationship given by Equation 19.103 is valid for low damping, however, and is based on linear system analysis. Several methods of damping measurement are summarized in Box 19.2.

19.4.6 General Remarks

There are limitations to the use of damping values that are experimentally determined. For example, consider time–response methods for determining the modal damping of a device for higher modes. The customary procedure is to first excite the system at the desired resonant frequency, using a harmonic exciter, and then to release the excitation mechanism. In the resulting transient vibration, however, there invariably will be modal interactions, except in the case of proportional damping. In this type of test, it is tacitly assumed that the device can be excited in the particular mode. In essence, proportional damping is assumed in modal damping measurements. This introduces a certain amount of error into the measured damping values.

Expressions used in computing damping parameters from test measurements are usually based on linear system theory. However, all practical devices exhibit some nonlinear behavior. If the degree of nonlinearity is high, the measured damping values will not be representative of the actual behavior of the system. Furthermore, testing to determine damping is usually performed at low amplitudes of vibration. The corresponding responses could be an order of magnitude lower than, for instance, the amplitudes exhibited under extreme operating conditions. Damping in practical devices increases with the amplitude of motion, except for relatively low amplitudes (see Figure 19.14 illustrating nonlinear behavior). Consequently, the damping values determined from experiments should be extrapolated when they are used to study the behavior of the system under various operating conditions. Alternatively, damping could be associated with a stress level in the device. Different components in a device are subjected to varying levels of stress, however, and it might be difficult to obtain a representative stress value for the entire device. One of the methods recommended for estimating damping in structures under seismic disturbances, for example, is by analyzing earthquake response records for structures that are similar to the one being considered. Some typical damping ratios that are applicable under operating basis earthquake (OBE) and safe-shutdown earthquake (SSE) conditions for a range of items are given in Table 19.6.

When damping values are estimated using frequency–response magnitude curves, accuracy becomes poor at very low damping ratios ($< 1\%$). The main reason for this is the difficulty in obtaining a sufficient number of points in the magnitude curve near a poorly damped resonance when the frequency–response function is determined experimentally. As a result, the magnitude curve is poorly defined in the neighborhood of a weakly damped resonance. For low damping ($< 2\%$), time–response methods are particularly useful. At high damping values, the rate of decay can be so fast that the measurements contain large errors. Modal interference in closely spaced modes can also affect measured damping results.

Box 19.2

DAMPING MEASUREMENT METHODS

Method	Measurements	Formulas
Logarithmic decrement method	A_i = first significant amplitude; A_{i+r} = amplitude after r cycles	Logarithmic decrement $\delta = \frac{1}{r} \ln \frac{A_i}{A_{i+r}} \text{ (per cycle)}$ $\frac{\delta}{2\pi} = \frac{\zeta}{\sqrt{1-\zeta^2}} \text{ (per radian)}$ <p>or,</p> $\zeta = \frac{1}{\sqrt{1+(2\pi/\delta)^2}}$ <p>For low damping</p> $\zeta = \frac{\delta}{2\pi}$ $\zeta = \frac{A_i - A_{i+1}}{\pi(A_i + A_{i+1})}$
Step response method	M_p = first peak value normalized r.t. steady-state value; PO = percentage overshoot (over steady-state value)	$M_p = 1 + \exp\left[\frac{-\pi\zeta}{\sqrt{1-\zeta^2}}\right]$ $\text{PO} = 100 \exp\left[\frac{-\pi\zeta}{\sqrt{1-\zeta^2}}\right]$
Hysteresis loop method	ΔU = area of displacement–force hysteresis loop; x_0 = maximum displacement of the hysteresis loop; k = average slope of the hysteresis loop	Hysteretic damping constant $h = \frac{\Delta U}{\pi x_0^2}$ <p>Loss factor</p> $\eta = \frac{h}{k}$ <p>Equivalent damping ratio</p> $\zeta = \frac{h}{2k}$
Magnification factor method	Q = amplification at resonance, w.r.t. zero-frequency value	$Q = \frac{1}{2\zeta\sqrt{1-\zeta^2}}$ <p>For low damping</p> $\zeta = \frac{1}{2Q}$
Bandwidth method	$\Delta\omega$ = bandwidth at $1/\sqrt{2}$ of resonant peak (i.e., half-power bandwidth); ω_r = resonant frequency	$\zeta = \frac{\Delta\omega}{2\omega_r}$

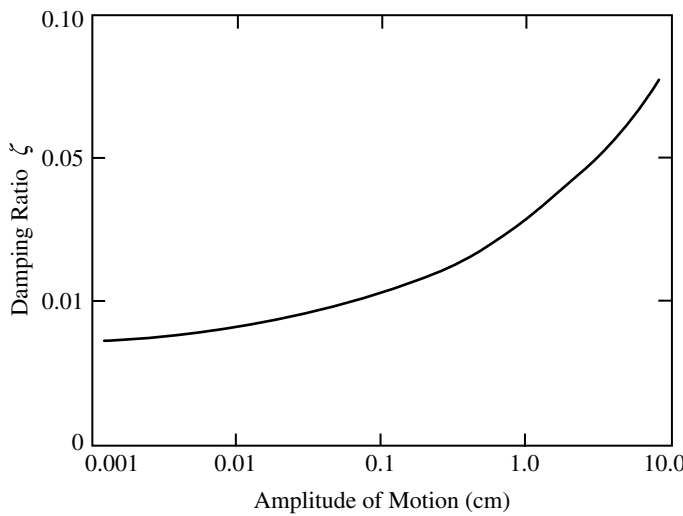


FIGURE 19.14 Effect of vibration amplitude on damping in structures.

TABLE 19.6 Typical Damping Values Suggested by ASME for Seismic Applications

System	Damping Ratio ($\zeta\%$)	
	OBE	SSE
Equipment and large diameter piping systems (> 12 in. diameter)	2	3
Small diameter piping systems (\leq 12 in. diameter)	1	2
Welded steel structures	2	4
Bolted steel structures	4	7
Prestressed concrete structures	2	5
Reinforced concrete structures	4	7

19.5 Interface Damping

In many practical applications damping is generated at the interface of two sliding surfaces. This is the case, for example, in bearings, gears, screws, and guideways. Even though this type of damping is commonly treated under structural damping, due to its significance we will consider it again here in more detail, as a category of its own.

Interface damping was formally considered by DaVinci in the early 1500s and again by Coulomb in the 1700s. The simplified model used by them is the well-known Coulomb friction model as given by

$$f = \mu R \operatorname{sgn}(v) \tag{19.104}$$

where

- f = the frictional force that opposes the motion
- R = the normal reaction force between the sliding surfaces
- v = the relative velocity between the sliding surfaces
- μ = the coefficient of friction

Note that the signum function “sgn” is used to emphasize that f is in the opposite direction of v . This simple model is not expected to provide accurate results in all cases of interface damping. It is known that, apart from the loading conditions, interface damping depends on a variety of factors such as material properties, surface characteristics, nature of lubrication, geometry of the moving parts, and the magnitude of the relative velocity.

A somewhat more complete model for interface damping, incorporating the following characteristics, is shown in Figure 19.15:

1. Static and dynamic friction, with stiction and stick–slip behavior.
2. Conventional Coulomb friction (Region 1).
3. A drop in dynamic friction, with a negative slope, before increasing again. This is known as the “Stribeck effect” (Region 2).
4. Conventional viscous damping (Region 3).

These characteristics cover the behavior of interface damping that is commonly observed in practice. In particular, suppose that a force is exerted to generate a relative motion between two surfaces. For small values of the force, there will not be a relative motion, in view of friction. The minimum force, f_s , that is needed for the motion to start is the static frictional force. The force that is needed to maintain the motion will drop instantaneously to f_d , as the motion begins. It is as though initially the two surfaces were “stuck” and f_s is the necessary breakaway force. Hence, this characteristic is known as stiction. The minimum force f_d that is needed to maintain the relative motion between the two surfaces is called dynamic friction. In fact, under dynamic conditions, it is possible for “stick–slip” to occur where repeated sticking and breaking away cycles of intermittent motion take place. Clearly, such “chattering” motion corresponds to instability (for example, in machine tools). It is an undesirable effect and should be avoided.

After the relative motion begins, conventional Coulomb type damping behavior may dominate for small relative velocities, as represented in Region 1. For lubricated surfaces, at low relative velocities, there will be some solid-to-solid contact that generates a Coulomb-type damping force. As the relative speed increases, the degree of this solid-to-solid contact will decrease and the damping force will drop, as in Region 2 of Figure 19.15. This characteristic is known as the Stribeck effect. Since the slope of the friction curve is negative in Regions 1 and 2, this corresponds to the unstable region. As the relative velocity is further increased, in fully lubricated surfaces, viscous-type damping will dominate, as shown in Region 3 of Figure 19.15. This is the stable region. It follows that a combined model of interface damping may be expressed as

$$f = \begin{cases} f_s & \text{for } v = 0 \\ f_{sb}(v)\text{sgn}(v) + bv & \text{for } v \neq 0 \end{cases} \quad (19.105)$$

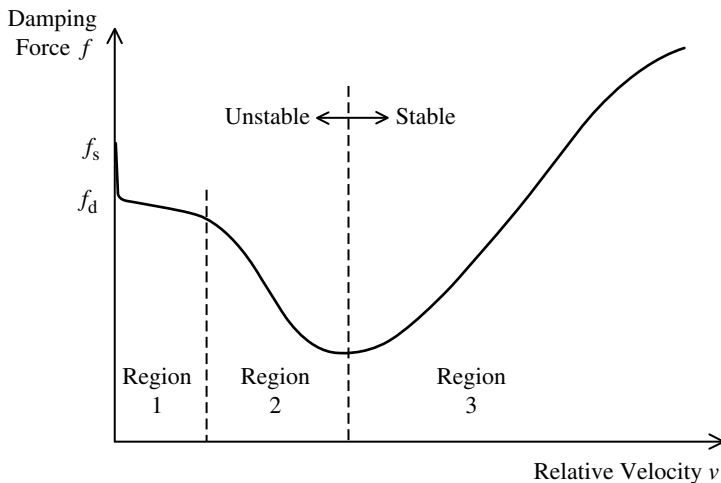


FIGURE 19.15 Main characteristics of interface damping.

Note that $f_{sb}(v)$ is a nonlinear function of velocity that will represent both dynamic friction (for $v > 0$) and the Stribeck effect. Models that have been used to represent this effect include the following

$$f_{sb} = \frac{f_d}{1 + (v/v_c)^2} \quad (19.106)$$

$$f_{sb} = f_d e^{-(v/v_c)^2} \quad (19.107)$$

and

$$f_{sb} = (f_d + \alpha|v|^{1/2})\text{sgn}(v) \quad (19.108)$$

Note that f_d represents dynamic Coulomb friction and v_c and α are modal parameters.

Example 19.5

An object of mass m rests on a horizontal surface and is attached to a spring of stiffness k , as shown in Figure 19.16. The mass is pulled so that the extension of the spring is x_0 , and is moved from rest from that position. Determine the subsequent sliding motion of the object. The coefficient of friction between the object at the horizontal surface is μ .

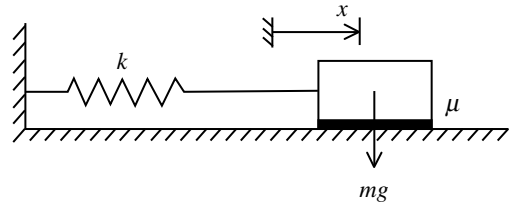


FIGURE 19.16 An object sliding against Coulomb friction.

Solution

Note that, when the object moves to the left, the frictional force, μmg acts to the right, and *vice versa*. Now, consider the first cycle of motion, starting from rest with $x = x_0$ moving to the left, coming to rest with the spring compressed and then moving to the right.

First Half Cycle (Moving to Left)

The equation of motion is

$$m\ddot{x} = -kx + \mu mg \quad (i)$$

or

$$\ddot{x} + \omega_n^2 x = \mu g \quad (ii)$$

where $\omega_n = \sqrt{k/m}$ is the undamped material frequency. Equation ii has a homogeneous solution of

$$x_h = A_1 \sin(\omega_n t) + A_2 \cos(\omega_n t) \quad (iii)$$

and a particular solution of

$$x_p = \frac{\mu g}{\omega_n^2} \quad (iv)$$

Hence, the total solution is

$$x = A_1 \sin(\omega_n t) + A_2 \cos(\omega_n t) + \frac{\mu g}{\omega_n^2} \quad (v)$$

Using the initial conditions $x = x_0$ and $\dot{x} = 0$ at $t = 0$, we get $A_1 = 0$ and $A_2 = x_0 - (\mu g/\omega_n^2)$. Hence, Equation v becomes

$$x = \left(x_0 - \frac{\mu g}{\omega_n^2}\right) \cos(\omega_n t) + \frac{\mu g}{\omega_n^2} \quad (vi)$$

At the end of this half cycle we have $\dot{x} = 0$ or $\sin \omega_n t = 0$. Hence the corresponding time is $t = \pi/\omega_n$. Substituting this in Equation vi, the corresponding position of the object

is (note: $\cos \pi = -1$)

$$x_{l1} = -\left(x_0 - \frac{2\mu g}{\omega_n^2}\right) \quad (\text{vii})$$

Second Half Cycle (Moving to Right)

The equation of motion is

$$m\ddot{x} = -kx - \mu mg \quad (\text{viii})$$

or

$$\ddot{x} + \omega_n^2 x = -\mu g \quad (\text{ix})$$

The corresponding response is given by

$$x = B_1 \sin(\omega_n t) + B_2 \cos(\omega_n t) - \frac{\mu g}{\omega_n^2} \quad (\text{x})$$

Using the initial conditions $x = -(x_0 - (2\mu g/\omega_n^2))$ and $\dot{x} = 0$ at $t = \pi/\omega_n$, we get $B_1 = 0$ and $B_2 = x_0 - (3\mu g/\omega_n^2)$. Hence, Equation x becomes

$$x = \left(x_0 - \frac{3\mu g}{\omega_n^2}\right) \cos(\omega_n t) - \frac{\mu g}{\omega_n^2} \quad (\text{xi})$$

The object will come to rest ($\dot{x} = 0$) next at $t = 2\pi/\omega_n$, hence the position of the object at the end of the present half cycle would be

$$x_1 = x_0 - \frac{4\mu g}{\omega_n^2} \quad (\text{xii})$$

The response for the next cycle is determined by substituting x_1 as given by Equation xii with Equation vi for the left motion and with Equation xi for the right motion. Then, we can express the general response as

$$\text{left motion in cycle } i: x = [x_0 - (4i - 3)\Delta] \cos \omega_n t + \Delta \quad (\text{xiii})$$

$$\text{right motion in cycle } i: x = [x_0 - (4i - 1)\Delta] \cos \omega_n t - \Delta \quad (\text{xiv})$$

where

$$\Delta = \frac{\mu g}{\omega_n^2} \quad (\text{xv})$$

Note that the amplitude of the harmonic part of the response should be positive for that half cycle of motion to be possible. Hence, we must have

$$x_0 > (4i - 3)\Delta \text{ for left motion in cycle } i$$

$$x_0 > (4i - 1)\Delta \text{ for right motion in cycle } i$$

Also note from Equation xiii and Equation xiv that the equilibrium position for the left motion is $+\Delta$ and for the right motion is $-\Delta$. A typical response curve is sketched in [Figure 19.17](#).

19.5.1 Friction in Rotational Interfaces

Friction in gear transmissions, rotary bearings, and other rotary joints has a somewhat similar behavior. Of course, the friction characteristics will depend on the nature of the devices and also the loading conditions, but, experiments have shown that the frictional behavior of these devices may be represented by the interface damping model given here. Typically, experimental results are presented as

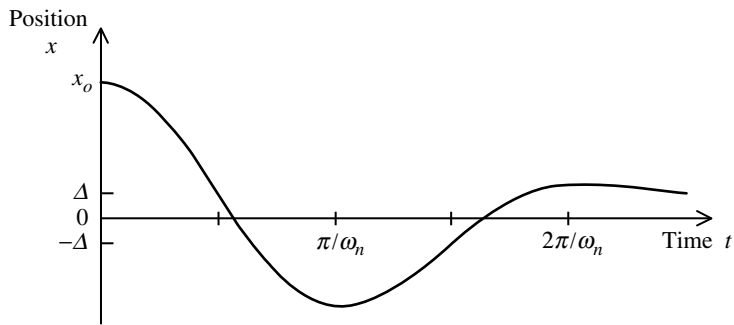


FIGURE 19.17 A typical cyclic response under Coulomb friction.

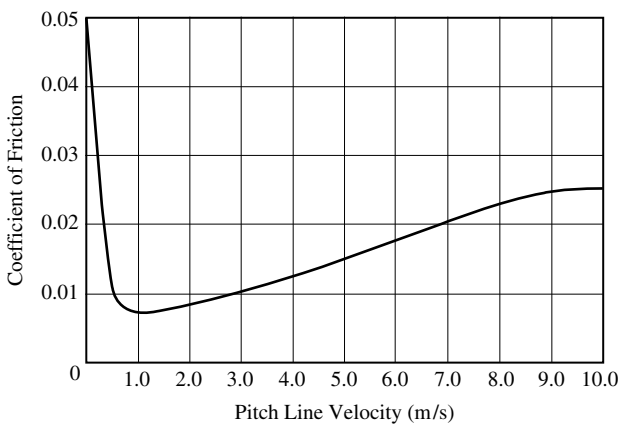


FIGURE 19.18 Frictional characteristics of a pair of spur gears.

curves of coefficient of friction (frictional force/normal force) vs. relative velocity of the two sliding surfaces. In the case of rotary bearings, the rotational speed of the shaft is used as the relative velocity, while for gears; the pitch line velocity is used. Experimental results for a pair of spur gears are shown in Figure 19.18.

What is interesting to notice from the result is the fact that, for this type of rotational device, the damping behavior may be approximated by two straight line segments in the velocity–friction plane; the first segment having a sharp negative slope and the second segment having a moderate positive slope that represents the equivalent viscous damping constant, as shown in Figure 19.19.

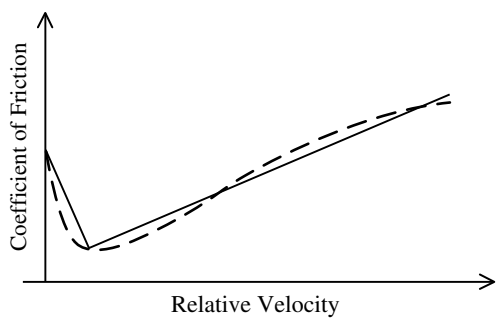


FIGURE 19.19 A friction model for rotatory devices.

19.5.2 Instability

Unstable behavior or self-excited vibrations, such as stick–slip and chatter, that are exhibited by interacting devices such as metal removing tools (e.g., lathes, drills, and milling machines) may be easily

explained using the interface damping model. In particular, it is noted that the model has a region of negative slope (or negative damping constant), which corresponds to low relative velocities, and a region of positive slope, which corresponds to high relative velocities. Consider the single-DoF model:

$$m\ddot{x} + b\dot{x} + kx = 0 \quad (19.109)$$

without an external excitation force. Initially the velocity is $\dot{x} = 0$. But, in this region, the damping constant, b , will be negative and hence the system will be unstable. Hence, a slight disturbance will result in a steadily increasing response. Subsequently, \dot{x} will increase above the critical velocity where b will be positive and the system will be stable. As a result, the response will steadily decrease. This growing and decaying cycle will be repeated at a frequency that primarily depends on the inertia and stiffness parameters (m and k) of the system. Chatter is caused in this manner in interfaced devices.

Bibliography

- Blevins, R.D. 1977. *Flow-Induced Vibration*, Van Nostrand Reinhold, New York.
- den Hartog, J.P. 1956. *Mechanical Vibrations*, McGraw-Hill, New York.
- de Silva, C.W., Dynamic beam model with internal damping, rotatory inertia and shear deformation, *AIAA J.*, 14, 5, 676–680, 1976.
- de Silva, C.W., Optimal estimation of the response of internally damped beams to random loads in the presence of measurement noise, *J. Sound Vib.*, 47, 4, 485–493, 1976.
- de Silva, C.W., An algorithm for the optimal design of passive vibration controllers for flexible systems, *J. Sound Vib.*, 74, 4, 495–502, 1982.
- de Silva, C.W. 2000. *VIBRATION — Fundamentals and Practice*, CRC Press, Boca Raton, FL.
- de Silva, C.W. 2004. *MECHATRONICS — An Integrated Approach*, CRC Press, Boca Raton, FL.
- Ewins, D.J. 1984. *Modal Testing: Theory and Practice*. Research Studies Press Ltd, Letchworth, England.
- Inman, D.J. 1996. *Engineering Vibration*, Prentice Hall, Englewood Cliffs, NJ.
- Irwin, J.D. and Graf, E.R. 1979. *Industrial Noise and Vibration Control*, Prentice Hall, Englewood Cliffs, NJ.
- Van de Vegte, J. and de Silva, C.W., Design of passive vibration controls for internally damped beams by modal control techniques, *J. Sound Vib.*, 45, 3, 417–425, 1976.

20

Damping Theory

20.1	Preface	20-2
20.2	Introduction	20-4
	General Considerations of Damping • Specific Considerations • The Pendulum as an Instrument for the Study of Material Damping • “Plenty of Room at the Bottom”	
20.3	Background	20-12
	Terminology • General Technical Features • Active vs. Passive Damping • Magnetorheological Damping • Portevin–LeChatelier Effect • Noise • Viscoelasticity • Memory Effects • Early History of Viscoelasticity • Creep • Stretched Exponentials • Fractional Calculus • Modified Coulomb Damping Model • Relaxation	
20.4	Hysteresis — More Details	20-19
20.5	Damping Models	20-20
	Viscous Damped Harmonic Oscillator • Definition of Q • Damping “Redshift” • Driven System • Damping Capacity • Coulomb Damping • Thermoelastic Damping	
20.6	Measurements of Damping	20-23
	Sensor Considerations • Common-Mode Rejection • Example of Viscous Damping • Another Way to Measure Damping	
20.7	Hysteretic Damping	20-27
	Equivalent Viscous (Linear) Model • Examples from Experiment of Hysteretic Damping	
20.8	Failure of the Common Theory	20-29
20.9	Air Influence	20-30
20.10	Noise and Damping	20-31
	General Considerations • Example of Mechanical $1/f$ Noise • Phase Noise	
20.11	Transform Methods	20-34
	General Considerations • Bit Reversal • Wavelet Transform • Heisenberg’s Famous Principle	
20.12	Hysteretic Damping	20-36
	Physical Basis • Ruchhardt’s Experiment • Physical Pendulum	
20.13	Internal Friction	20-41
	Measurement and Specification of Internal Friction • Nonoscillatory Sample • Isochronism of Internal Friction Damping	
20.14	Mathematical Tricks — Linear Damping Approximations	20-43
	Viscous Damping • Hysteretic Damping	

Randall D. Peters
Mercer University

20.15 Internal Friction Physics	20-44
Basic Concepts • Dislocations and Defects	
20.16 Zener Model	20-45
Assumptions • Frequency Dependence of Modulus and Loss • Successes — Models of Viscoelasticity • Failure of Viscoelasticity	
20.17 Toward a Universal Model of Damping	20-48
Damping Capacity Quadratic in Frequency • Pendula and Universal Damping • Modified Coulomb Model — Background • Modified Coulomb Damping Model — Equations of Motion • Model Output • Experimental Examples • Damping and Harmonic Content	
20.18 Nonlinearity	20-58
General Considerations • Harmonic Content • Nonlinearity/Complexity and Future Technologies • Microdynamics, Mesomechanics, and Mesodynamics • Example of the Importance of Mesoanelastic Complexity	
20.19 Concluding Remark	20-65

Summary

This introductory chapter synthesizes the many, though largely disjointed attributes of friction as they relate to damping. Among other means, events selected from the history of physics are used to show that damping models have suffered from the inability of physicists to describe friction from first principles. To support fundamental arguments on which the chapter is based, evidence is provided for a claim that important nonlinear properties have been mostly missing from classical damping models. The chapter illustrates how the mechanisms of internal friction responsible for hysteretic damping in solids can lead to serious errors of interpretation. Such is the case even though hysteretic damping often masquerades as a linear phenomenon. One attempt to correct common model deficiencies is the author's work toward a "universal damping model," that is described in Section 20.17. Section 20.17 is developed in a "canonical" damping form. It shows the value of a direct, as opposed to an indirect, involvement of energy in model development. To keep a better perspective on how the treatment of damping is likely to evolve in the future, the last section of the chapter addresses some of the remarkable complexities of damping that are only beginning to be discovered. The manner in which technology has played a role in some of these discoveries is addressed in [Chapter 21](#).

20.1 Preface

The sheer volume of published material on the subject is a testament to the difficulty of selecting topics for inclusion in a chapter on damping. Viscoelasticity alone is the basis for several voluminous engineering handbooks. The present chapter is purposely different from similarly titled chapters of other reference books. There is little repetition of well-known and proven classical methods, for which the reader is referred to excellent other sources, such as de Silva (2000) and [Chapter 19](#) of the present handbook. They provide solution techniques for many of the routine problems of engineering. The goal of the present chapter is to provide assistance with problems that are not routine, problems that are being encountered more frequently as technology advances. It is thought that this goal is best served by revisiting fundamental issues of the physics responsible for damping.

Once a multibody system has come to steady state, its damping treatment can be far less formidable than its description during approach to steady state. When dealing with limit cycles involving aeroelasticity and joints in helicopters, nonlinearity has a profound influence on the transient behavior. Attempts to model it have been largely unsuccessful, forcing the empirical selection of elastomers to reduce the vibration. (In the old days hydraulic dampers were used; Hodges 2003). At a much lower level

of sophistication, our understanding is quite limited on some common phenomena, such as the negative damping character of sound generated by a violin or a clarinet. Historically, when technology “hit the wall” because of too much theoretical handwaving, it became apparent that fundamental assumptions needed to be examined. In physics, a complete alteration of conventional wisdom was sometimes necessary, one of the best examples being the events that gave birth to quantum mechanics. Hopefully, from the multitude of seemingly disparate (but assumed by the author to be connected) observations which follow, the purpose for the architecture of this chapter can be partially realized. The enormous complexity of damping in general makes it unrealistic to hope for complete success.

Physics played a prominent role in developing the classical foundations of damping, starting in the 19th century. Subsequently, engineers uncovered many features of the subject that physicists never even thought about. In recent years, however, physics has been circumstantially forced to reconsider damping fundamentals. With the advent of personal computing, and an increased awareness of the importance of nonlinearity, new discoveries point to serious limitations of the classical foundation. The field of mechanics was severely limited until it began tackling problems of nonlinearity (not of damping type), and became concerned with previously ignored features giving unique system properties. Just as these unique properties could only be solved by techniques more sophisticated than the equations of linear type, there is mounting evidence that nonlinear damping may be the key to understanding some bewildering engineering cases.

It is important to try to identify the major mechanisms responsible for energy dissipation. This is easier said than done, since a host of different friction processes are usually at work. Moreover, the description of friction from first principles remains a daunting task. Thus we are forced to work with phenomenological models. There are also conflicts of nomenclature, with a given word meaning two different things from one profession to another. Thus, much of this chapter will attempt to define carefully terms while focusing on the physics, the treatment of which follows naturally along the lines of historical developments.

Engineers tend to be interested in higher frequencies and higher amplitudes of vibration than are scientists. A perfect damping model would be unconcerned with such differences of application; however, such a model is far from being realized. Because small-amplitude, long-period (low and slow) oscillations provide a valuable means for studying many processes of damping in general, much of this chapter focuses in that direction.

From the multitude of choices available to writers on the subject of damping, this author has selected a single (hopefully) unifying theme — nonlinear damping, especially as found in low and slow oscillations. Because it is a field still in its infancy, many of the ideas that follow are more speculative than one would prefer; however, they deserve discussion because of their perceived importance. To this author’s knowledge, damping has not been previously treated in the manner of this chapter. Concerning the earliest relevant paper (Peters, 2001a, 2001b), the following was indicated by oft-cited Prof. A.V. Granato: “I don’t know of anyone thinking about internal friction along the lines you have mentioned.”

There are two important elements to the unifying theme of nonlinear dissipation: (i) the influence of nonlinear damping on multibody systems in their approach to steady state, and (ii) the close connection between damping and mechanical noise. When vibration decay is not exponential because of nonlinearity, there are significant ramifications and they are only beginning to be appreciated.

The novel features of this chapter are possible because of dramatic improvements in both sensing and data collection/analysis in the last decade. Demonstrating that a decay is not purely exponential requires both (i) a good linear sensor and (ii) the means to study readily long-time records when the damping is small (high Q). The first prerequisite has been met through the use of this author’s patented fully differential capacitive sensor. The second has been realized with the availability of good, inexpensive analog-to-digital (A/D) converters having user-friendly, yet powerful Windows-based software. In addition to the “preview” software that comes with Dataq’s A/D converter, a proven means for identifying nonexponential decay has been the analysis of records imported to Microsoft Excel. Details of these novel methods will be provided in the various sections that follow.

There are many examples in the engineering literature of nonlinear damping; even Coulomb damping is nonlinear because the friction force involves the algebraic sign of the velocity rather than the velocity itself, as in linear viscous damping. What has been realized for the first time in the course of writing this chapter is the following. As will be shown in the subsequent material, a decay process is not usually a pure exponential. Whatever the reason for a pure exponential, whether fundamentally linear (viscous) or nonlinear (hysteretic present model), the quality factor Q for such a pure exponential decay is constant. When there is a second mechanism, such as amplitude-dependent damping (even if it is the only mechanism), the Q now becomes time dependent. This is significant to mode coupling for the following reason. When a pair of modes couple because of elastic nonlinearity (a process that is impossible assuming linear dynamics), the strength of the coupling is proportional to the product of the individual amplitudes of the pair.

Consequently, variability in Q can influence the evolution to steady state. It is a factor in determining which modes ultimately survive and/or dominate. Moreover, the distribution of the modes which remain depends on initial conditions, including the intensity of excitation.

Long ago, musicians learned to deal with nonlinearity, due in part to properties of the ear that are responsible for aural harmonics. A pair of purely harmonic signals can beat in the ear to produce a “sound” that does not exist when sensed with a linear detector. For example, consider a strong and undistorted 500 Hz signal sounded simultaneously with a pure 1003-Hz sound. The ear will hear a 3-Hz beat due to the superposition of the ear’s aural second harmonic of the first with the fundamental of the second. However, there’s more to this story. Conductors call for *fortissimo* and *pianissimo* sounds, not only because of the ear’s nonlinearity, but also because of nonlinearities inherent to musical instruments. For example, it is easy with a good microphone and LabView ([see Appendix 15A](#)) to demonstrate that the timbre of stringed instruments is intensity dependent. Not only is the mix of harmonics, as displayed in a fast Fourier transform (FFT) power spectrum, different according to volume, but their distribution also changes with time.

Noise is not typically treated in an engineering discussion of damping; however, mechanical noise is an important part of the technical material included in this chapter. Believing that there is a great deal of connectivity among vibration, damping, and noise, evidence will be provided in support of a premise — that the most important and least understood form of internal mechanical damping (material = hysteretic = “universal”) is closely allied with the most important and least understood form of noise ($1/f$ = flicker = pink). If this premise is true, then the foundations of damping physics need reconstruction on several counts. Evidence in support of the premise will be provided through tidbits of experimental discoveries from a host of independent investigations. It is hoped that the unusual and lengthy introduction that follows will be beneficial in this regard. Historical elements serve to synthesize the many parts and are offered without apology. Following the introduction, some practical and novel equations of damping will eventually be provided. Even if readers find little identification with the philosophies that birthed them, it is hoped they will at least carefully examine the equations that are presented here in Section 20.17 for the first time.

20.2 Introduction

20.2.1 General Considerations of Damping

The etymology of the word “damping” is difficult to determine. It is obviously allied with the word damper, commonly defined as a “device that decreases the amplitude of electronic, mechanical, aerodynamic or acoustical oscillations,” used for centuries, for example, to describe the sound attenuator pedal on the piano. Perhaps the German word *dampfen* (to choke) has had an influence in the evolution of the word. One can only wonder if water, as a moistening agent, played any role. Certainly, liquid water is important to some cases of energy dissipation in oscillators. Moreover, friction determined by the viscosity of a fluid (gas or liquid) is an important type of damping. A curious piece of history, in the

celebrated work of Stokes, is why his expression “index of friction” did not take precedence over our modern word, viscosity. Peculiar terminology is also encountered to describe damping, such as the engineering device known as a dashpot, which is a mechanical damper. The vibrating part is attached to a piston that moves in a liquid-filled chamber.

We will see that the number of adjectives used to describe various types of damping is extensive. This multiplicity of terms to describe the loss of oscillatory energy to heat is no doubt an indicator of the complexity of damping phenomena in general. We will attempt (i) to identify similarities and differences among various types of damping, while (ii) explaining some of the physics responsible for the characteristics observed. Conceptual ideas and techniques of both theory and experiment will be provided, targeting the lowest level of sophistication for which semimeaningful results can be obtained. The reader should be aware that a “grand-unified” theory of damping does not exist, nor is it likely that one will ever be created.

Damping causes a portion of the energy of an oscillator, otherwise periodically exchanged between potential and kinetic forms, to be irreversibly converted to heat, sometimes by way of acoustical noise. Whether by suitable choice of materials during design of passive equipment, or by using feedback in active control of a sophisticated system, control of damping is important since mechanical vibrations can be detrimental or even catastrophic. An oft-quoted example of catastrophe is the Tacoma Narrows bridge, which collapsed in high winds on November 7, 1940. Like the vibration of a clarinet reed, this disaster is probably best described by the term negative damping, which can drive parametric oscillations.

The optimal amount of damping for a given system might fall anywhere in a wide range from great to extremely small, depending on system needs. The engineering world frequently wants oscillations to be as close to critically damped as possible. Physics experiments, such as those searching for the elusive gravitational wave (centered at the Laser Interferometer Gravitational Observatories, or Laser Interferometer Gravitational Wave Observatories [LIGO], in the United States; GEO600 in Germany [involving the British]; VIRGO in Italy [with the French], and TAMA in Japan), want damping in some of their components to be as small as possible. Frequency standards the world over require very small damping to insure high precision for timekeeping.

For the specific components of a system, a successful design frequently requires identification of the specific mechanisms primarily responsible for the dissipation of energy. Even after identifying the dominant sources, the theoretical difficulty of their treatment can also range from great to small, depending on the type of damping. For dashpot fluid damping, adequate models have existed for decades. For material damping, on the other hand, theories of internal friction are numerous and largely lacking in self-consistency.

The fundamental mechanisms responsible for damping are in most cases nonlinear; however, the oscillator's motion can itself be approximated in many cases by a linear second-order differential equation. If the potential energy is quadratic in the displacement, then the undamped linear equation of motion is that of the simple harmonic oscillator, because its solution is a combination of the sine and cosine (harmonic) functions. This undamped equation comprises the sum of two terms, one being a displacement and the other term an acceleration. The constant parameter multiplying each term of the pair depends on the nature of the system. For example, in the case of a mass–spring oscillator, the acceleration is multiplied by the mass, and the displacement by the spring constant. Thus, the equation corresponds to Newton's Second Law applied to a Hooke's Law (idealized) spring. In an electronic L–C oscillator, the “displacement” corresponds to the charge on the capacitor (divided by C) and the “acceleration” corresponds to the second time derivative of the capacitor's charge (multiplied by inductance L).

The usual means to describe damping, which is always present with oscillation, is to add a velocity term to the aforementioned displacement and acceleration. Although the damping could derive from several causes, there is usually a single dominant process. For example, the damping of current in a series-connected resistor, inductor, capacitor (RLC) circuit may depend mostly on Joule heating in the resistor R , in spite of the fact that there must also be energy loss in the form of radiation. Thus, the equation of motion includes a first-time derivative of the capacitor's charge (current) multiplied by R , in accord with Ohm's law.

Whether radiation is important for damping of the RLC circuit depends on the amount of coupling to the environment. If the circuit communicates with a final amplifier connected to an antenna, then radiation may become more important than Joule losses. The frequency of oscillation is a key parameter in this case, and also for damping problems in general. Unfortunately for some common systems, theoretical efforts to account properly for the effects of frequency have proven largely unsuccessful — except for models of phenomenological type developed by empiricism.

20.2.2 Specific Considerations

The mass–spring oscillator is the textbook example of harmonic motion, for which one of the most sophisticated mechanical oscillators ever built is the LaCoste version of vertical seismometer. Significant portions of the experimental data presented in this chapter were generated with an instrument designed around the LaCoste zero-length spring (LaCoste, 1934). The instrument used for this data collection was part of the World Wide Standardized Seismograph Network (WWSSN) during the 1960s. The spring of this seismometer is responsible for hysteretic damping of the instrument, rather than viscous damping as commonly assumed. Contrary to popular belief, air damping is not important for this seismograph at its nominal operating period, which is typically greater than 15 sec. Since every long-period pendulum apparently exhibits similar behavior, we thus find strong synergetic evidence in support of an old (mostly unheeded) claim that hysteretic damping (friction force independent of frequency) is universal (Kimball and Lovell, 1927). Their claim in 1927 to have discovered a universal form of internal friction (damping) is strengthened since the same behavior is seen in three distinctly different systems: (i) a mass–spring oscillator (as demonstrated by Gunar Streckeisen, details given later); (ii) a pendulum whose restoration depends on the Earth’s gravitational field (demonstrated by several independent groups); and (iii) a rotating rod strained by a transverse deflection (1927 experiments of Kimball and Lovell).

The assumption of universality for hysteretic damping is a key point of this chapter. It will be shown that the damping of even a vibrating gas column (Ruchhardt’s experiment to measure the ratio of heat capacities) is likely also hysteretic. The models that are described represent a departure from common theories of damping. Interestingly, the author’s model has similarities to ordinary sliding friction, as given to us by Charles Augustin Coulomb. It effectively modifies the Coulomb coefficient of kinetic friction to yield an effective energy-dependent internal friction coefficient. The energy dependence is necessary to obtain exponential decay, as opposed to the linear decay of Coulomb damping. Just as with conventional Coulomb damping, its form is nonlinear, involving the algebraic sign of the velocity. We will see that the damping capacity predicted by the model permits an equivalent viscous form. Yet the underlying physics is related to creep of secondary type as opposed to the primary creep of viscoelasticity.

It is this author’s opinion that much of the existing theory of damping is not the best means for modeling dissipation. The difficulties arise from approximating oscillator decay with linear mathematics. Although most individuals recognize the oft-stated caveat that viscous damping is an approximation to the actual physics of dissipation, they do not recognize some of the many serious limitations of the approximation. The situation is similar to the place in which we found ourselves at the beginning of the era labeled “deterministic chaos.” The “butterfly effect” (Lorenz, 1972) has radically altered the thinking of many, but only in relationship to large-amplitude motions of a pendulum, where the instrument is no longer isochronous because of nonlinearity. As an archetype of chaos, the pendulum must be rigid and capable of “winding” (displacement greater than π) before chaos is possible. Nonlinearity is a prerequisite for the chaos, but it is not sufficient, since there are many examples of highly nonlinear but nonchaotic motions. For example, amplitude jumps of nonlinear oscillators, during a frequency sweep of an external drive, have been known for many years. They were observed before chaos was recognized, in systems like the Duffing and Van der Pol oscillators. Yet chaos, with its sensitive dependence on initial conditions (responsible for the butterfly effect), was not contemplated at the time. As with most significant advances, Lorenz’s discovery was by accident, as he modeled convection in the atmosphere. The author’s confrontation with complexity that derives from mesoscale structures in metals was likewise unexpected. “Strange phenomena” (as Richard Feynman would probably have labeled them)

were encountered while using his patented fully differential capacitive sensor to study various mechanical systems, mainly oscillators.

As with chaos, the pendulum may ultimately serve as an archetype of complexity. When operated at low energy, especially through a combination of long period and small amplitude, the free decay of the physical pendulum departs radically from the predictions based on linear equations of motion. Such complexity can be easily demonstrated when the pendulum is fabricated from soft alloy metals. For example, Figure 20.1 illustrates the decay of a rod pendulum constructed with ordinary (heavy-gauge lead–tin) solder of the type used for joining electrical conductors (Peters, 2002a, 2002b, 2002c).

The “jerkiness” (discontinuities) in the record of Figure 20.1 is in no way related to amplitude jumps of the type previously mentioned; rather, these are jumps of the Portevin–Le Chatelier (PLC) type (Portevin and Le Chatelier, 1923). They are a fundamental, yet “dirty” phenomenon that physics has chosen for decades to try and ignore (even though materials science and engineering took early note of the PLC effect). The most obvious and profound thing that can be said about Figure 20.1 is the following: the presence of PLC jerkiness means that the concept of a potential energy function is not really valid, since the requirement for its definition is that a closed integral of the force with respect to displacement must vanish.

No matter the form of hysteresis, which is the cause for damping, it disallows the curl of the force to be zero, so that potential energy is never formally meaningful for a macroscopic oscillator (since there is always damping). In those cases where the damping is essentially continuous (not true for the example of Figure 20.1), the assumption of a potential energy function retains some computational meaning. For oscillators influenced by the PLC effect, this is no longer true. The resulting properties are important to a variety of technology issues, such as sensor performance, since noise is no longer the simple thermal form predicted by the fluctuation–dissipation theorem (used to characterize white, i.e., Johnson, noise).

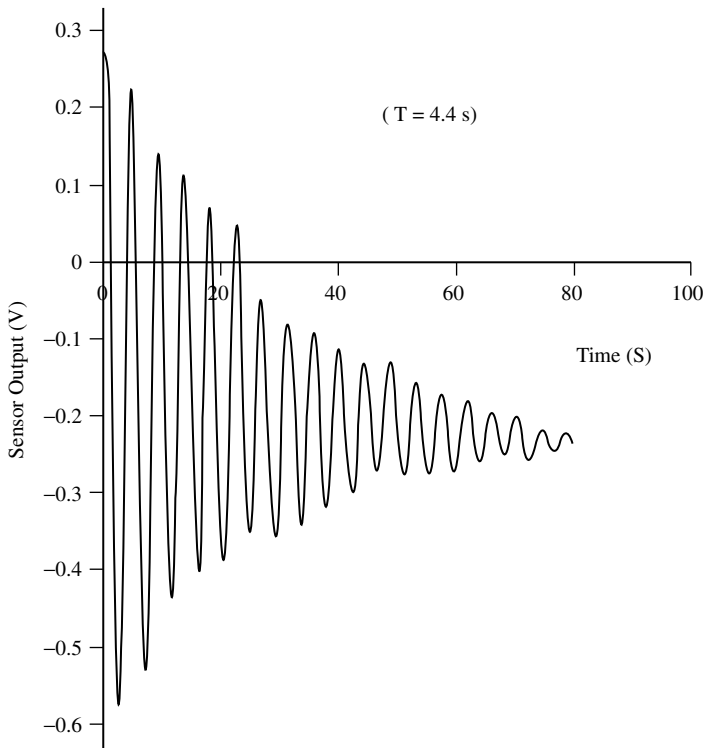


FIGURE 20.1 Free-decay of a rod pendulum fabricated from solder.

Practical means for dealing with systems influenced by “stiction” have been known by engineers for decades. Because of metastabilities in the assumed potential function, the system is prone to latching (stuck in a localized potential well). One means for mastering the metastabilities (unstuck the part designed to move) is to “dither” the system. The process has become more sophisticated in the last decade, which saw a major growth of interest in stochastic resonance. In the definition by Bulsara and Gammaitoni (1996):

A stochastic resonance is a phenomenon in which a nonlinear system is subjected to a periodic modulated signal so weak as to be normally undetectable, but it becomes detectable due to resonance between the weak deterministic signal and stochastic noise.

The phenomenon is related to dithering (Gammaitoni, 1995). It is a case where the signal-to-noise ratio (SNR) can be increased by the counterintuitive act of raising the level of noise. Such a gain in SNR is not possible with a harmonic potential.

In recent studies of granular materials, “tapping” has become a popular means to study behavior that violates the fundamental theorem of calculus. Years ago, this author used tapping as a means to accelerate creep in wires under tension. Evidently, hammering the table on which the extensometer rested caused vibrational excitations of the wire that stimulated length changes of discontinuous PLC type. Because of the broad spectral character of an impulse, various eigenmodes of the wire (see [Chapter 4](#)) could be thus readily excited. After “hammering-down” under load, a silver wire could by this same means be stimulated, after partial load removal, to exhibit length contractions. Since the total number of atoms is fixed, the process must involve exchange of atoms between the surface of the sample and its volume.

Extensometer studies of wires at elevated temperature have also displayed strange behavior. A polycrystalline silver wire of diameter 0.1 mm and approximate length 30 cm was found to exhibit large fluctuations when heated in air to within 100 K of its melting point, using a vertical furnace (Peters, 1993a, 1993b). The large fluctuation in length at these temperatures (reminiscent of critical phenomena and visible to the naked eye) may be associated with oxide states of the metal, since the experiments were not performed in vacuum. When cycled in temperature, fluctuations in the length of a gold wire were found to exhibit dramatic hysteresis. With influence from Prof. Tom Erber of Illinois Tech University, it was postulated in (Peters, 1993a) that there may be some mesoscale quantization of fundamental type responsible for the thermal hysteresis (hysteron).

Mechanical hysteresis resulting from mesoanelastic defect structures is evidently ubiquitous. Piezotranslators, which are used as actuators in atomic force microscopes and other nanotechnology applications, are afflicted with high levels of hysteresis when operating open loop. This behavior is consistent with the anomalously large damping that was observed with a pendulum (reported elsewhere in this document) in which there was a steel/PZT interface for the knife-edge.

Even the common strain gauge exhibits complex hysteresis behavior. The normally large hysteresis that is observed in preliminary cycling of a gauge is typically reduced by significant amounts after repeated cycling, a type of work hardening (if strained well below failure limits). It should be noted that the hysteresis of all the discussions in this chapter is not to be confused with backlash (as in a gear train).

All of these experiments are in keeping with the premise that *mesoanelastic complexity* determines the nature of hysteretic damping. It is seen that there are a plethora of examples where strain (and thus damping) of a sample is not simple, is not smooth, but more like the complex behavior of granular materials. In the case of polycrystalline metals, the same grains that are made visible by methods of acid etching decoration are evidently responsible for mesoscale (nonsmooth) internal friction damping. To assume that damping is quantal at the atomic scale, rather than the mesoscale, is without experimental justification. Nevertheless, this is a popular assumption with which estimates of the noise floor of an instrument such as a seismometer is estimated, to calculate SNR.

20.2.3 The Pendulum as an Instrument for the Study of Material Damping

Because of its early contributions to physics, which in those days was called natural philosophy, one might be tempted to believe that the pendulum is only important to (i) the history of science or (ii) teaching of fundamental principles. A single observation should be sufficient to resist this temptation — (as already noted) the pendulum has in the last 30 years become the primary archetype for the new science of chaos. Additionally, many of the data sets of this document, which show significant and previously unpublished results, were generated with a pendulum.

To a student of elementary physics, the choice of a pendulum may seem unsophisticated. Yet, to the author, who has spent 15 intense years trying to understand harmonic oscillators, the pendulum is the most versatile instrument with which to understand damping. It has been central to the development of science in general. It was studied by Galileo, Huygens, Newton, Hooke, and all the best-known scientists of the Renaissance period. It served to establish collision laws, conservation laws, the nature of Earth's gravitational field and, most of all, it was the basis for Newton's two-body central force theory. This theory was foundational to the development of classical mechanics, which is central to all of physics and engineering. Historian Richard Westfall has remarked: "Without the pendulum, there would be no Principia" (Westfall, 1990).

In 1850, Sir George Gabriel Stokes published a foundational paper (Stokes, 1850). His treatment of pendulum damping permitted the understanding, decades later, of a number of important phenomena in physics and engineering. For example, his studies were foundational to the Navier–Stokes equations of fluid mechanics. Moreover, viscous flow known as Stokes' Law was the basis for Millikan's famous oil drop experiment that determined the charge of the electron.

Stokes noted in his paper that, "... pendulum observations may justly be ranked among those most distinguished by modern exactness." He also noted

The present paper contains one or two applications of the theory of internal friction to problems which are of some interest, but which do not relate to pendulums. ... the resistance thus determined proves to be proportional, for a given fluid and a given velocity, not to the surface, but to the radius of the sphere. ... Since the index of friction of air is known from pendulum experiments, we may easily calculate the terminal velocity of a globule [water] of given size. ... The pendulum thus, in addition to its other uses, affords us some interesting information relating to the department of meteorology.

The last statement of this quotation speaks to some of the errors in the "common theory" of his day. In similar manner, some of the common-to-physics damping models of today are erroneously applied. Those who hold the viscous damping linear model in unwarranted regard, fail to recognize the limitations under which it is valid. There are frequent misapplications for reason of experimental deficiencies. We can all profit by taking seriously the following well-known words of Kelvin:

When you can measure what you are speaking about, and express it in numbers, you know something about it. But when you cannot measure it, when you cannot express it in numbers, your knowledge is of a meager and unsatisfactory kind. It may be the beginning of knowledge but you have scarcely in your thoughts advanced to the state of science. William Thomson, Lord Kelvin (1824 to 1907)

Simple (viscous) flow of the Stokes' Law type is possible only according to the restrictive conditions that Stokes spelled out in his paper. We now specify those conditions for viscous flow according to the nondimensional parameter given us late in the 19th century by Osborne Reynolds. Specifically, Stokes' Law is valid only for $Re = \rho v L / \eta < 60$ (approximately, for spheres); where ρ is the density of the retarding fluid, v is the speed of the object relative to the fluid, L is a characteristic dimension of the object, and η is the viscosity of the fluid. The requirement is not generally met for oscillators, and recent experiments have shown that contributions to the damping from air drag proportional to the square of

the velocity cannot generally be ignored (Nelson and Olssen, 1986). This is just one example of how two or more damping types must sometimes be folded into an adequate model of dissipation. A novel method for combining all the common forms of damping in one mathematical expression is provided in this document. Additionally, it is shown how to calculate analytically the history of the amplitude of free-decay for such cases.

Considering the importance of Stokes' work, it is surprising that some of his requests for further experiments were apparently never seriously considered. On page 75 of his paper, one reads the following: "Moreover, experiments on the decrement of the arc of vibration are almost wholly wanting." Having noted this, Stokes appealed to experimentalists to generate such data. In the 19th century, collecting the data he requested would have been labor-intensive and therefore the experiments were probably never attempted. Sensors and data processing of the modern age now make them straightforward, but the pendulum has by now been viewed by too many as a relic rather than the important instrument described by Stokes. Much of the author's efforts have been directed at showing that the pendulum is still an important research instrument. For example, one physical pendulum of simple design was the basis for the generalized model of damping (modified Coulomb) that is here presented. Another has been used to illustrate surprisingly rich complexities of the motion that results from the ubiquitous defects of its structure (Peters 2002a, 2002b, 2002c). Thus studying the complex motions of "low and slow" physical pendula could yield significant new insight into the defect properties of materials — a field where relatively little first-principles progress has been made.

20.2.4 "Plenty of Room at the Bottom"

Richard Feynman gave a now-famous talk in 1959 titled, "There's plenty of room at the bottom" (presented at the American Physical Society's annual meeting at CalTech). Drawing on observations from biology, he spoke of a solid-state physics world involving "... strange phenomena that occur in complex situations." In the 44 years since Feynman's prophetic comments, there have been spectacular achievements in very large-scale integrated (VLSI) electronics, microelectromechanical systems (MEMS), and even nanotechnology. Progress in the mechanical (including sensor) realm has been much slower than in electronics; consequently, our present processing power far exceeds our acquisition (and actuator) capabilities.

One of the major obstacles to miniaturization involves dramatic change to physical properties that can occur as the size of a system shrinks below the mesoscale toward the atomic. For example, VLSI electronics is already beginning to be impacted by quantum properties of the atom, as component size continues to decrease in accord with Moore's law (Moore, 1965). Among other things, Feynman predicted that lubrication would no longer be "classical" at such a scale. On a related note, a paper by Nobel Laureate Edward M. Purcell (Purcell, 1977) draws a striking contrast between our macroscopic world and that of micro-organisms. At low Reynolds number, inertia becomes unimportant, and mechanics is dominated by viscous effects. The adoption of a new paradigm will be necessary for engineers to deal with these differences.

In the article "Plenty of room indeed" (Roukes, 2001), it is noted that there is an anticipated "dark side" of efforts to build truly useful micro- and nano-sized devices. Gaseous atoms and molecules constantly adsorb and desorb from device surfaces. This process is known to exchange momentum with the surface, even permitting scientific study of the gas–solid interface (Peters, 1990). The smaller the device, the less stable it will be because of adsorption/desorption. As Roukes has noted, this instability may pose a real disadvantage in various futuristic electromechanical signal-processing applications (Cleland and Roukes, 2002).

There is direct evidence, provided in the present chapter, that we need to be more concerned with noise: (i) the evacuated pendulum where it is speculated that outgassing influenced its free-decay, and (ii) the seismometer free-decay that showed both amplitude and phase noise and evidence for nonlinear damping. Concerning (i), when the vacuum chamber pressure is reduced, the preexisting steady state (normal rate balance between adsorption and desorption) becomes disturbed, so that there is a complex

emission of gases from the surface of the pendulum. The emission is not likely to be spatially uniform, but more like the jets seen on Halley's comet when photographed by the Giotto spacecraft in 1986. In case (ii), the noise is seen to derive from mesoanelastic complexity of the structure of the pendulum itself rather than involving gases.

Miniaturized devices have the potential to serve as on-chip clocks, and the importance of phase noise to clocks is well documented. There is another, more subtle issue that points out the importance of phase noise. One of the best means for improving SNR is the technique of phase-sensitive detection, first employed by Robert Dicke at Princeton to improve solar experiments. The performance of miniaturized electromechanical sensors using "lock-in" amplifier methods may be influenced significantly by mechanical phase noise.

Phase noise of miniaturized devices is still mostly speculative. In addition to the mechanism just mentioned (adsorption/desorption), there is the matter that constitutes the theme of this chapter, defect organization. It is not possible to grow materials without dislocations and/or other disturbances to crystalline order, such as vacancies, interstitials, or substitutional impurities. Thus, "when mother nature fills the vacuum she abhors, she rarely does so with perfection."

Long before defects organize to the point of incipient failure (at much larger strains), they still influence vibration. They may even be a primary source of $1/f$ noise. Electronic noise of $1/f$ type is known to involve defects by means of trapping states, and these states derive from crystalline defects sometimes involving the surface. The interaction of the surface and the volume of a solid are important. For example, consider pure copper single crystals of the type used by the author in his doctoral work. A practical joke suggested by Vic Pare (that we never conducted because of the cost of these samples) would be to have a 98-lb weakling bend one by hand, then ask an NFL linebacker to straighten it back out! The striking irreversibility is the result of work hardening as dislocations develop at the surface and propagate into the bulk where they entangle.

In the case of polycrystalline materials, the memory features of hysteresis may be important according to the method of their fabrication. Wires are typically produced by pulling through successively smaller dies. This "swaging" may be conducive to the exchange of monolayer groups of atoms between the volume and the surface during fluctuation length changes. The fluctuation–dissipation theorem does not hold or, if it does, only in terms of larger entities than the atom. Thus, there are many yet-to-be-quantified elements of noise in the vibration of miniaturized devices. Feynman was right when he spoke of strange phenomena of the solid state.

Technology of the future is expected to be confronted increasingly with damping problems that must address issues of scaling — to deal with some factors discussed in this chapter, which, to the author's knowledge, have not been previously published. Until small (MEMS) oscillators become more common to the engineering world, we must study the mechanisms responsible for their damping by other than traditional means. One approach is similar to experimental techniques for the verification of the kinetic theory of gases. As noted by Present in his textbook (Present, 1958), there are two ways that Brownian motion can be studied: either (i) with small objects and an unsophisticated detector, or (ii) with larger objects and a very sensitive detector. It is the latter that provided some of our present knowledge of damping at the mesoscale. The fully differential capacitive transducer, whose patent label is "symmetric differential capacitive" (SDC), is a robust new technology that is sensitive, linear, and user-friendly (Peters, 1993a, 1993b). As with other sensitive detectors that have been used to predict the properties of small objects by studying larger ones, small-energy studies of various macroscopic pendula are demonstrating some of the "strange phenomena" of complex type predicted by Feynman.

From the author's perspective, we of the physics community have been guilty of two significant errors: (i) oversimplification of many problems by assuming a linear equation of motion based on viscous damping, and (ii) losing sight of fundamental issues by working with inappropriate, overly complicated damping models. The goal of this chapter is to assist progress toward a healthier balance between these extremes. It is hoped that readers will be thus better equipped to identify, and then dismantle, some of the impediments to the development of future technologies.

20.3 Background

20.3.1 Terminology

The large number of mechanisms capable of energy dissipation has resulted in a host of adjectives to describe damping phenomena in mechanical systems. They include (nonexhaustive list): viscous, eddy current, Coulomb, sliding, friction, structural, fluid, thermoelastic, internal friction, viscoelastic, material, solid, phonon–phonon, phonon–electron, and hysteretic. For present purposes, damping types will be grouped according to one of the following three categories: (i) fluid (including viscous), (ii) Coulomb, and (iii) hysteretic. Although hysteretic damping has come to be associated in engineering circles with a particular form of material damping in solids, it should be noted that all forms of damping involve hysteresis (for which the Greek meaning of the word is “to come late”). In a plot of periodic stress vs. strain, which is a straight line for displacements of a nondissipative, idealized substance, hysteresis causes the line to open into a loop. The size of the loop — more specifically the area inside this hysteresis loop — is a measure of the amount of nonrecoverable work done per cycle because of the damping. An actual force of friction is not readily recognizable in those cases that are labeled “internal friction.” The word friction is used in a generic sense, meaning any process responsible for conversion of the oscillator’s coherent motion into incoherent thermal activity.

With each of viscous, eddy current, and Coulomb damping, a force external to the oscillator is responsible for the dissipation of energy. The external force is associated respectively with (i) laminar fluid flow, (ii) induced currents, and (iii) surface friction. The surface friction case is not necessarily the trivial textbook presentation involving a coefficient of kinetic friction and a normal force. The cases just mentioned, along with thermoelastic damping; which is of internal rather than external origin, are much easier to treat theoretically than other cases. Viscous damping and eddy current damping (over the full range of the motion) are adequately described by a velocity term, which yields a linear equation of motion. Coulomb damping, however, is not proportional to velocity, but rather depends only on the algebraic sign of the velocity. The equation of motion is consequently nonlinear. Additionally, and unlike most other forms, Coulomb damping is not exponential. The turning points lie along a straight line when the motion is plotted vs. time. Similarly, if eddy current damping exists only over a small part of the motion, the decay is linear rather than exponential (Singh et al., 2002).

20.3.2 General Technical Features

Historically, viscous damping has been the model of choice because the resulting equation of motion is mathematically attractive and, for the RLC circuit, the form is appropriate. For mechanical oscillators, it is not generally appropriate, since viscous damping amounts to some part of the system moving in an external Newtonian fluid that removes energy because of a friction force that is proportional to velocity.

The defects responsible for material damping, such as dislocations, are also responsible for creep, so that high strength and high damping tend to be incompatible attributes. Magnesium alloys tend to be better than many other metals in this regard. Hardness of a material is neither a prerequisite for toughness nor for small damping, as recognized by those familiar with the mechanical properties of cast iron.

On a different scale, defects determine “how things break”; concerning which Marder and Fineberg have stated the following:

the strength of solids calculated from an excessively idealized starting point comes out completely wrong; it is not determined by performance under ideal conditions, but instead by the survival of the most vulnerable spot under the most adverse of conditions. (Marder and Fineberg, 1996)

Three famous scientists are primarily responsible for the highly popular viscous damping model of the simple harmonic oscillator; they are Lord Kelvin (Thomson and Tait, 1873), G.G. Stokes and

H.A. Lorentz. Stokes is best known for his equations of fluid dynamics that also include the name Navier. Stokes' Law, which describes the terminal velocity of a raindrop, was developed through his treatment of the damping of a pendulum. Not only does his law provide a basis for the simplest approximation for damping of a macroscopic oscillator, it was used by Robert Millikan to determine the charge of the electron. It should be noted that harmonic oscillation in a fluid (even at low Reynolds number) is much more complicated than steady-flow viscous friction. This topic is treated in [Chapter 21, Section 21.9](#).

The first individual to use the term "simple harmonic oscillator" was probably Lord Kelvin. Such an oscillator is a key tool of experimental physics and also the foundation for much of theoretical physics. It is the basis for communication via electromagnetic waves and even esoteric theories of superfluids and superconductors.

Much of the underpinnings of theory involving harmonic oscillation derive from the work of Hendrik Anton Lorentz (1853–1928). Lorentz is well known for a variety of classical physics contributions, such as (i) the transformation of special relativity associated with Einstein and (ii) the force law for the acceleration of charged particles, both of which bear his name. Before the existence of electrons was proved, Lorentz proposed that light waves were due to oscillations of an electric charge in the atom. For his development of a mathematical theory of the electron, he received the Nobel Prize in 1902. The importance of his contributions is further realized by noting that it is common practice to describe the lineshape of atomic spectra by the term Lorentzian. The Lorentzian is equivalent to the resonance response of the driven viscous-damped simple harmonic oscillator.

It is easy to show how resistance in an electric network is responsible for damping; however, it is a challenge to understand anelastic processes of mechanical damping in terms of viscosity. From comments of his Ph.D. dissertation, it has been said that even Lorentz was never apparently satisfied with the velocity damping term in his equation — not knowing just how to relate it to the underlying physics. It is also clear from Stokes' paper that he recognized the need for caution in the use of his law of viscous friction. It appears that both Lorentz and Stokes were very careful compared with the carelessness with which the viscous model has been employed by many individuals in recent years.

The failure of solids influenced by "hysteretic" damping to be adequately described by the methods of viscoelasticity is not widely appreciated. It is unfortunate that too few people have expanded their view of damping to include other important types, such as derive from the anelasticity of solids. It is important in this work to recognize some subtle differences, for example, inelastic (not elastic) is not to be equated with anelastic (other than elastic).

20.3.3 Active vs. Passive Damping

With improvements in cost/performance of electronics, active damping is increasingly popular. Using force-feedback with integration/differentiation circuitry (opamps), a mechanical oscillator can sometimes be tailored for a specific purpose. A sophisticated example of this technology is the broad-band seismometer that began to replace earlier version (passive) instruments roughly 35 years ago. The Sprengnether–LaCoste spring instrument that was used for some of the experiments reported in this document has been superseded by force-feedback units such as the Streckeisen STS-1 and STS-2.

In lieu of feedback, another way actively to influence the damping of a mechanical oscillator is to connect the sensor to an amplifier having a negative input resistance. The seismometers marketed by Lennartz Electronics in Germany use this in a patented technique to improve the performance of ordinary, off-the-shelf electrodynamic geophones.

Active damping depends on the nature of the transfer function of the composite system (electronics plus mechanical). The characteristics of the transfer function are determined by the location of its poles and zeros in the complex plane. Seismometers operate nominally near 0.707 of critical damping. This is done for two reasons: (i) the instrument is easier to adjust and (ii) the interpretation of earthquake records is simpler. Of course, to increase damping is to decrease sensitivity because of the fluctuation–dissipation theorem.

The force-feedback technique is not practical for some situations, regardless of cost. Additionally, it must be recognized that the method is not the answer to all problems, since electronics cannot compensate for a poor mechanical design. The description of commercial products is in some cases highly exaggerated, giving the impression that almost any sensor can perform flawlessly in this manner. Some accelerometers have employed dithering to offset the effects of “stiction” in bearings. The dithering was necessary because the potential energy function is not truly harmonic, being afflicted with the consequences of nonlinear damping. Even with sensing schemes that do not use a bearing, the effects of nonlinearity persist. In “Seismic Sensors and their Calibration” (Bormann and Bergmann, 2002), Erhard Wielandt, in talking about transient disturbances in the spring of a seismometer, says the following:

Most new seismometers produce spontaneous transient disturbances, quasi-miniature earthquakes caused by stress in the mechanical components.

In other words, internal friction from defects at the mesoscale cause behavior that is in some ways similar to ordinary sliding friction, where the static coefficient is greater than the kinetic coefficient. The postulate of Bantel and Newman is consistent with this idea (Bantel and Newman, 2000) when they refer to their observations as being consistent with a “stick–slip” model of internal friction.

It is seen then that one must use a detector that responds faithfully to the signal around which the servo-network functions. The linearity and sensitivity of that sensor are of paramount importance, since the basis for force-feedback design is linear system theory. For some less-challenging cases, the design approach is straightforward, since software packages like MATLAB (see Chapter 6 and Appendix 32A) have built in functions to describe behavior.

20.3.4 Magnetorheological Damping

A recent approach to damping control, that is quite different from the servo-networks mentioned above, is one that uses an magnetorheological (MR) fluid. It takes advantage of the large variation in viscosity of certain compound fluids according to the size of an applied magnetic field. J. David Carlson (Carlson, 2002) describes how an MR sponge damper is activated during the spin cycle of a washing machine to keep it from “walking out of the room.” The peak in the Lorentzian (resonance response) of the machine is shown in his article to be substantially lowered by supplying current to the electromagnet of the damper.

20.3.5 Portevin–LeChatelier Effect

Physics, engineering, geoscience, and mathematics have all contributed greatly to a better understanding of damping phenomena; however, there has been little cross-discipline exchange of ideas and lessons learned. Some of the impediments to strong interdisciplinary programs derive from (i) the complexity of damping problems in general and (ii) the tendency for physics and mathematics research to be, on the one hand, less pragmatic and, on the other hand, highly specialized — focused on specific energy dissipation mechanisms. A good example of (i) involves the PLC effect, discovered in 1923. Why physics mostly ignored this early example of “dirty science” by two of their own number is not easily understood, although the birthing of quantum mechanics around this time may have been a factor. Had history turned in a different direction, perhaps we would already be able to explain from first principles the most important, but still barely understood, form of noise known as $1/f$, or flicker, or pink noise. Even though R.B. Johnson (well known for his discovery of white electronics noise in a resistor) was one of the first to see this form of noise, it still is not explained from first principles — although recent discoveries suggest an intimate connection with fractal geometry involving self-similarity. Such geometry is associated with the mesoscale of materials where the grain, rather than the atom, is the basic element of statistical mechanics.

For alloys, the PLC effect appears to be, in some ways, what the Barkhausen effect is to magnetic systems. In the case of ferrous materials, the noise which derives from the mesoscale has long been recognized; however, similar noise of mechanical type has not been seriously studied. This oversight is even more puzzling when one considers the admonition by G. Venkataraman, as recorded in the

proceedings of a Fermi conference, for scientists to get involved in what he felt should become an important new field (Venkataraman, 1982).

20.3.6 Noise

Noise is purposely discussed in this chapter (also see the chapters in Section IX of this handbook) because it has been a, largely, missing component of efforts to understand the physics of damping. A feel for the importance of noise to damping research is to be gleaned from a comment by Kip Thorne in his foreword to the English translation of a book by V.B. Braginsky et al. (1985). Mainly because of instrumental needs of the Laser Interferometer Gravitational Wave Observatories (LIGO), Thorne writes,

The central problem of such experiments is to construct an oscillator that is as perfectly simple harmonic as possible, and the largest obstacle to such construction is the oscillator's dissipation. If dissipation were perfectly smooth, it would not be much of an obstacle, but the fluctuation–dissipation theorem of statistical mechanics guarantees that any dissipation is accompanied by fluctuating forces. The stronger the dissipation, the larger the fluctuating forces, and the more seriously they mask the signals that the experimenter seeks to detect.

This comment by Thorne suggests a frequently important impediment to dialogue between engineering and physics — concern for different issues. LIGO is trying to minimize damping, whereas many engineering problems are concerned with just the opposite — making the damping as large as possible without compromising strength. More detailed discussions of noise are provided later.

20.3.7 Viscoelasticity

Within the world of polymers, damping is frequently described by the expression “viscoelasticity.” This word, around which handbooks have been written (e.g., Lakes, 1998), is a combination of the two words, viscous and elastic. We like to think of ideal fluids as being viscous in the manner described by Newton. Likewise, ideal solids that obey Hooke's Law (stress proportional to strain) are described as elastic. Unfortunately, nature contains neither ideal solids nor ideal fluids. Real springs do not obey Hooke's Law, but rather are influenced by “anelasticity” (other than elastic) which gives rise to hysteresis in the stress–strain relationship. Real fluids usually have some (if not near total) degree of non-Newtonian character. Thus an envisioned “mixing” of fluid-like and solid-like character has dominated the thinking of those who, through the decades, attempted to develop theoretical models of damping.

It should be noted that the springs and dashpots used in models of viscoelasticity do not actually exist. They serve as a phenomenological means for (hopefully) understanding the elementary processes which their arrangement is designed to mimic. Consider, for example, high polymers, in which the interwoven structure of the long-chain molecules is one of extensive mechanical interference. (One popular visualization is that of an entanglement of a huge number of long, writhing snakes.) An increase of temperature is met with overall length reduction (negative temperature coefficient of expansion for the so-called entropy spring), which stands in stark contrast with metals. Such behavior is clearly important to damping since, as noted by Gross years ago, “...thermal movement interferes with the orientation and disorientation of the molecules and ultimately causes delay in the expansion and contraction of the specimen” (Gross, 1952).

20.3.8 Memory Effects

In this same article, Gross is one of the first to mention “memory” properties of creep. He describes a by-then old demonstration in which a “firmly suspended metal or plastic wire is twisted first in one direction for a long time and then in the other direction for a short time. Immediately after release,

the deflection will be in the direction of the last twisting, but it decreases rapidly. Presently, a reversal occurs, and the wire begins to turn in the other direction, corresponding to the first twisting — the memory of the recent short-term handling has been obliterated by that of the more remote but longer lasting and therefore more impressive one!” Perhaps this old demonstration (sometimes today called the anelastic after-effect) is not so startling to those familiar with more modern shape-memory-alloys, which are expected by many to play increasingly important roles in the applied science of damping.

20.3.9 Early History of Viscoelasticity

Those who provided seminal influence in the development of the theories of viscoelasticity during the 19th century were some of the most famous names in physics, like Maxwell and Kelvin. Maxwell is best known for the electromagnetic equations associated with his name. He is far less known for two other significant contributions: (i) kinetic theory of gases and (ii) viscoelasticity — both of which are important to theories of oscillator damping. Maxwell’s interest in the problem of viscoelasticity is first documented in a paper during his teen years, titled “The Equilibrium of Elastic Solids.” Through his development with Boltzmann of the kinetic theory of gases, Maxwell showed a counterintuitive property of the viscosity of a gas. The viscosity does not decrease significantly as the pressure is reduced, until the mean free path between collisions of the molecules begins to approach dimensions of the chamber holding the gas. Important even to modern innovations such as MEMS oscillators, his surprising prediction was quickly verified by experiment. Maxwell’s model of viscoelasticity combines a purely elastic spring with a purely viscous dashpot (fluid damper in which the friction force is proportional to the velocity).

Kelvin, probably the first to include a viscous damping term in the equation of motion of the simple harmonic oscillator, developed a similar model of viscoelasticity. Each of the two models is usually represented in literature (without original references) as containing a single spring and a single dashpot. They differ in that one connects the pair in series (Maxwell), while the other connects them in parallel (Kelvin–Voigt).

Both the Maxwell model and the Kelvin–Voigt model have been found by engineers to be less useful than the standard linear model (SLM) of anelasticity, largely advanced in the 20th century by Clarence Zener (Zener, 1948). In the three-component Zener model, a spring is connected in series with a parallel combination of spring and dashpot. Curiously, Zener is widely associated with electronics because of the common diode named after him, but fewer people know of his work in anelasticity. No doubt, his understanding of anelasticity helped him to better understand the complex processes at work in his diode.

20.3.10 Creep

The prevailing models of anelasticity appear frequently in the literature, but mostly in relationship to primary creep. Some of the papers exceptional to this rule are those by Berdichevsky (Berdichevsky et al., 1997). Recent work of a more heuristic type has shown that the equations of viscoelasticity are also able to accommodate secondary creep, in which the decay of strain rate with time has disappeared (Peters, 2001a, 2001b).

The importance of creep (and relaxation) physics to damping warrants some discussion. When a sample is subjected to a constant stress, the strain evolves through three phases of creep: (i) primary, (ii) secondary, and (iii) tertiary. An example of the first two of these phases is shown in [Figure 20.2](#).

In the primary stage, the sample is deformed by anelastic processes involving defects of the crystalline structure. Influence of the disordering mechanisms is progressively reduced as the sample undergoes work hardening (such as pinning of dislocations). Work hardening would result in a purely exponential creep, in the absence of thermal effects which strive to undo the hardening (via diffusion processes). (At zero Kelvin, the creep would eventually cease, if described by a single time constant.) In the secondary stage, a balance between work hardening and thermal softening is attained, in which the strain vs. time has converted from exponential to linear. This balance cannot continue forever, if the stress is larger than

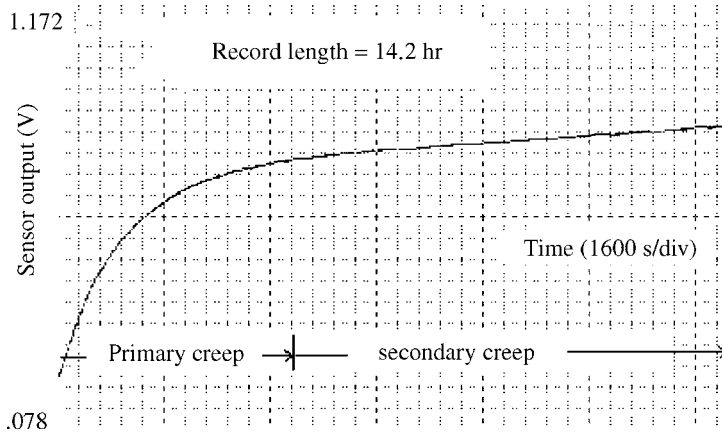


FIGURE 20.2 Example of creep in the spring of a vertical seismometer.

a threshold associated with failure (the elastic limit), and thus a final complex fracture of the sample finally occurs as the sample passes through the tertiary stage. Although one might want to divorce the issues of tertiary creep from considerations of damping, there is clearly a link between damping and failure, involving defects. We will return to this point later.

In Figure 20.2, creep resulted from the instrument having been severely disturbed (relocated accidentally by plumbers working in the building). As with any long-period mechanical oscillator, it is necessary for this instrument to stabilize after a major rebalancing. Primary creep is seen to have endured for about 5 h and what is labeled secondary creep in the figure does not continue indefinitely with the implied constant rate. Thus, the instrument will typically stabilize after one or several days, when the period of oscillation is of the order of 20 sec.

The total amount of creep in Figure 20.2 deserves mention. In the indicated 14.2 h, the mass of the seismometer moved a vertical distance of only 0.25 mm, which can be ascertained from the ordinate axis using the sensor calibration constant of 2000 V/m.

20.3.11 Stretched Exponentials

Systems typically demonstrate a more complex behavior than can be simply described by the SLM of viscoelasticity. In 1847, Kohlrausch (1847) discovered that the decay of the residual charge on a glass Leyden jar followed a *stretched exponential* law. The functional form that he discovered is often associated with a broad distribution of relaxation times, and has been found to describe a remarkably wide range of physical processes. To describe damping that is of the stretched exponential type, Kelvin chains or Maxwell elements in parallel have been used. Although an improved fit to the data can be realized by this means, the technique results in a high number of material parameters which have to be identified.

20.3.12 Fractional Calculus

A promising alternative to multiexponential decay models is to replace classical rheological dashpots by “fractional” elements. It is claimed that with only a few parameters, material behavior of many viscoelastic media can be described over large ranges of time and/or frequency (Hilfer, 2000). It may also be possible with fractional derivatives to treat the discontinuities that are sometimes present in decay (Asa, 1996). The disadvantages of fractional calculus are (i) the increasing computational/storage requirements and (ii) the esoteric mathematics, which is alien to the training of most.

20.3.13 Modified Coulomb Damping Model

Published here formally for the first time, with details described later, the heuristic “modified Coulomb” model is an alternative to all of the aforementioned damping models. It is thought to be closely related to secondary creep (Peters, 2001a, 2001b) and (like fractional calculus) accomplishes good fits with a small number of parameters. Developed from energy considerations, its equations are expressed in canonical form involving the quality factor Q .

20.3.14 Relaxation

Formally, relaxation is defined by the behavior of a sample subjected to a constant strain. Because of the mechanisms just discussed in relationship to creep, the stress relaxes exponentially toward zero (in the simplest approximation). In practice, the definition just given can be misleading since the word relaxation is used to describe a host of processes in which some quantity decays exponentially in time — for example, the relaxation of strain at constant stress in the Kelvin–Voigt model of viscoelasticity.

Some of the viscoelastic models using dashpots and springs have been quite successful in the limited regime of their applicability. For example, the Zener (Debye) model, which will be discussed again later, has been used for years to describe a particular form of damping in solids, which derives from relaxations associated with dislocations. Seminal experimental work of this type was conducted by Berry and Nowick in the 1950s (Berry and Norwich, 1958). A well-known theoretical model to describe dislocation damping was developed by Granato and Lucke (Granato and Lucke, 1956). The Granato model is that of a vibrating string (bowed Frank–Read source), where the end points of the “string” are points on the dislocation line that have been pinned. Recent theory shows that the Granato model is not always adequate; that “dislocation interactions may alter substantially the dislocation component of the spectrum observed during internal friction experiments.” (Greaney et al., 2002) (excellent introductory material on this subject is to be found online at <http://mid-ohio.mse.berkeley.edu/alex/rachel/rachel/rachel.html>).

Bordoni (1954) performed experiments that led to his observation of relaxation-type internal friction processes where the acoustic attenuation is seen to peak at certain temperatures. The so-called Bordoni peaks occur at low temperatures or at ultrasonic frequencies. These losses, which are maximum when dislocation relaxations can take place in step with the driving frequency, were first observed in the FCC metals: lead, copper, aluminum, and silver.

Dislocation damping as just described is characterized by a temperature-dependent relaxation that exhibits Arrhenius behavior. By plotting the internal friction vs. reciprocal temperature, one may estimate the activation energy of the process responsible for the damping. The following quotation from the introduction of the Berry paper assists in defining some of the many expressions used historically to describe damping:

Internal friction is often loosely described as the ability of a solid to damp out vibrations. More strictly, it is a measure of the vibrational energy dissipated by the operation of specific mechanisms within the solid. Internal friction arises even at the smallest stress levels if Hooke’s Law does not properly describe the static stress–strain curve of the material. The nonelastic behavior which Zener has called anelasticity arises when the strain in the material is dependent on variables other than stress.

In a recent private communication, Prof. Granato has indicated the following:

Dislocations do follow the Zener (or Debye) form fairly well for the damping, but not for the elastic modulus. This is because the response to a stress is given as a Fourier series. The higher order terms in the series have little effect on the damping, but a strong effect on the modulus at high frequencies. This makes the modulus fall off more slowly than with the reciprocal frequency.

20.4 Hysteresis — More Details

Hysteresis and creep are common to many systems, such as electromechanical actuators, especially when used at high drive levels. Their transfer function is influenced by “rate-independent memory effects.” The state of the actuator depends not only on the present value of the input signal but also on the nature of their past amplitudes, especially the extremum values, but not on rates of the past (Visintin, 1996). This statement is in support of the author’s secondary creep model of hysteretic damping, where the amplitude of the previous turning point determines the magnitude of the internal friction force for the half-cycle that follows. One of the most dramatic examples of a memory effect is the demonstration mentioned above, by Gross in the 1950s, concerning a twisted wire.

Damping complexities derive from the defect structures that are found in real materials and which give rise to hysteresis, which in the Greek language means to “come late.” Although, almost everybody seems to appreciate magnetic hysteresis at some level, too few individuals (at least in physics) have been trained in the mechanisms of mechanical hysteresis responsible for damping. Dislocations, for example, are usually an add-on chapter to a solid-state physics text — even though they are known to be indispensable with regard to actual, as opposed to idealized, properties of materials.

In the case of ferrous materials, the magnetization of a specimen lags behind the field generated by an electric current, to which the specimen responds. In the case of real springs that do not obey Hooke’s Law $F = -kx$, the displacement x lags behind the spring’s restoring force F . It is convenient to express the resulting hysteresis in terms of “intrinsic” variables instead of x and F . Thus, the strain ϵ (fractional change in the spring’s length if it were a wire in tension) lags the stress σ (force per unit area). Usually in engineering practice, the stress is reckoned with respect to the external force (negative of the spring F), so that the equivalent to Hooke’s Law is $\sigma = E\epsilon$, where E is an elastic modulus descriptive of the material from which the spring is fabricated. In the case of a straight wire, E would be Young’s modulus but, for coil springs, E is determined primarily by the shear modulus. Some of the ways in which hysteresis can be represented for a freely decaying oscillator are shown in Figure 20.3. The generalized coordinate q would be spring elongation for the force case shown, or it would be strain when the ordinate quantity is stress. The graph of velocity vs. displacement is referred to as a phase-space plot. It is commonly used in describing chaotic systems and, if “strobed” at the frequency of the oscillator, becomes the Poincaré section. Notice that the circulation is of opposite sign when using external force as opposed to spring force, in addition to the curves occupying different quadrants. It is important to recognize this difference, particularly when discussing negative damping where the oscillation amplitude builds in time, as illustrated in the right hand part of the figure.

Although not very common in mechanical oscillators, it is possible to realize negative damping. One example is that of an optically driven pendulum, because of the LiF crystals that were placed in its support structure (containing a high density of color centers produced by radiation) (Coy and Molnar, 1997). An interesting feature of this pendulum was its unwillingness to entrain to the driving laser.

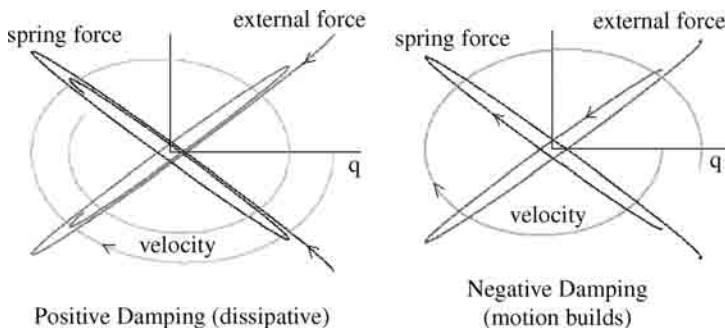


FIGURE 20.3 Three different ways to represent hysteresis damping for an oscillator in free-decay. Cases of both positive and negative damping are illustrated.

There are also examples of negative damping from aerodynamics, such as flutter. Since buildings and bridges can experience negative damping in catastrophic manner (Tacoma Narrows bridge as an example), it is not a subject to be ignored.

Another example of hysteresis that is very much like negative damping (though not usually labeled as such) is to be found in a heat engine (Peters, 2001a, 2001b). The motion is not simple harmonic; rather, the speed with which the hysteresis curve is traversed (in pressure vs. volume) increases as the size of the hysteresis loop increases. A larger loop (greater work done by the gas) results in higher revolutions per minute (r/min) of the engine as opposed to a larger amplitude of the motion at constant period. The gas pressure provides a force similar to the Hooke's Law force of the spring in a mass/spring oscillator.

It is usually assumed that hysteresis loops are "smooth," which is not necessarily true. For example, in the case of magnetic hysteresis, the "jerky" parts known as the Barkhausen effect (Barkhausen, 1919) are well known. The equivalent jerky behavior in metallic alloys is known as the Portevin–LeChatelier effect (Portevin and LeChatelier, 1923). Although we have historically avoided these cases that appear to be intractable in a mathematics sense (not obeying the fundamental theorem of calculus), their presence is undeniable testimony of the complex nature of hysteresis.

20.5 Damping Models

20.5.1 Viscous Damped Harmonic Oscillator

As first seen by students in a textbook, the equation of motion for a damped, driven harmonic oscillator is likely as follows:

$$m\ddot{x} + c\dot{x} + kx = F(t) \quad (20.1)$$

where m is mass, k is spring constant, c is a "constant" of viscous damping, and $F(t)$ is the external force driving the oscillator. It is convenient to work with a coefficient of performance, or quality factor Q , and rewrite Equation 20.1 in canonical form as

$$\ddot{x} + \frac{\omega_0}{Q}\dot{x} + \omega_0^2 x = \omega_0^2 \frac{F(t)}{k}, \text{ with } \omega_0^2 = \frac{k}{m} \quad (20.2)$$

For $F(t) = 0$ and an assumed solution, $x = A \exp(p\theta)$ with $\theta = \omega_0 t$, the differential equation becomes algebraic (quadratic) in $x(\theta)$, with the roots given by

$$p = -\frac{1}{2Q} \pm \sqrt{\frac{1}{4Q^2} - 1} \quad (20.3)$$

Depending on the value of Q , the motion is either overdamped (nonoscillatory), critically damped, or underdamped. Here, we restrict our attention to the last case corresponding to $Q > 1/2$, in which the square root term of Equation 20.3 is imaginary. Moreover, we are mostly concerned with systems in which $Q \gg 1$.

20.5.2 Definition of Q

The quality factor Q is in general defined as 2π times the ratio of the energy of the oscillator to the energy lost to friction per cycle. For viscous damping (and hysteretic damping, later discussed), the Q is independent of the amplitude of oscillation. For other types of damping, we will see that the Q is not constant. In the case of the viscous damped oscillator, $Q = \omega_0/2\beta$ where β appears in the solution as an amplitude decay "constant." The parameter β is not really constant, as discussed in [Chapter 21, Section 21.9](#).

$$x = A e^{-\beta t} e^{\pm j\omega_0 t \sqrt{1-1/4Q^2}} \quad (20.4)$$

Since x is real, we use the real part of Equation 20.4 and employ Euler's identity to obtain

$$x(t) = A e^{-\beta t} \cos(\omega_1 t - \phi), \text{ with } \omega_1 = \sqrt{\omega_0^2 - \beta^2} \quad (20.5)$$

where ϕ is a constant determined by the initial conditions.

20.5.3 Damping “Redshift”

It is seen that the frequency of oscillation depends on the damping constant, β ; however, the fractional change $\Delta\omega/\omega_0$ is almost always negligibly small. For example, the reduction in frequency is only 1.4% for $Q = 3$, which is close to critical damping of $Q = 0.5$. At these small values of Q , the lifetime of a freely decaying oscillator is so short that the frequency is ill-defined because of the Heisenberg uncertainty principle. At larger Q s, where the frequency is well-defined, the shift is negligible; i.e., at $Q = 100$, the fractional shift is only 1.3×10^{-5} . In the case of internal friction (hysteretic) damping, there is no redshift anyway because the oscillator is isochronous.

20.5.4 Driven System

When $F(t)$ is not zero, but rather corresponds to harmonic drive at angular frequency ω and amplitude A , the response involves the sum of Equation 20.5 (transient) and a particular solution (steady state).

$$x_p(t) = A_p \cos(\omega t - \delta), \text{ with } \delta = \tan^{-1} \left(\frac{2\omega\beta}{\omega_0^2 - \omega^2} \right). \quad (20.6)$$

The system resonates (amplitude a maximum) at $\omega \rightarrow \omega_R = \sqrt{\omega_0^2 - 2\beta^2}$, and the variation of the amplitude with ω at steady state at any drive frequency ω is given by

$$A_p = \frac{A\omega^2}{\sqrt{(\omega_0^2 - \omega^2)^2 + 4\omega^2\beta^2}} \quad (20.7)$$

The resonance response curve described by Equation 20.7 is called the Lorentzian. More frequently in physics, the term is used to describe pressure-broadened line widths (Milonni and Eberly, 1988). As noted previously, Lorentz was never apparently content with the damping term, $2\beta \, dx/dt$. In his Ph.D. dissertation concerned with the damping of electron oscillators through electromagnetic radiation, he was not able to satisfactorily describe the damping from first principles. Although we might be tempted to say that this failure derived from his classical (prequantum mechanics) description of the problem, such a viewpoint is an oversimplification.

20.5.5 Damping Capacity

20.5.5.1 Viscous Damping

The loss per cycle, called the damping capacity, is computed for the viscous damping case as follows (per unit mass):

$$d_v = 2\beta \oint \dot{x} \, dx = 2\beta\omega A^2 \int_0^{2\pi} \sin^2 \theta \, d\theta = 2\pi\beta\omega A^2 \quad (20.8)$$

where A is the amplitude of the oscillation. Because the total energy per unit mass is $\omega^2 A^2/2$, we see that $Q = \omega/(2\beta)$.

20.5.5.2 Hysteretic Damping, Linear Approximation

The equation of motion in this case is given by $m\ddot{x} + h/\omega\dot{x} + kx = 0$ where h is a constant. The energy loss in one cycle is given by

$$-\Delta E = md_h = \frac{h}{\omega} \int_0^T \dot{x}^2 dt = \frac{h}{\omega} \omega A^2 \int_0^{2\pi} \cos^2 \theta d\theta = \pi h A^2 \rightarrow d_h = \frac{\pi}{m} h A^2 \quad (20.9)$$

so that $Q = m\omega^2/h$.

20.5.5.3 Hysteretic Damping, Modified Coulomb Model

The nonlinear equation of motion introduced in this chapter to describe hysteretic damping is as follows:

$$\ddot{x} + c\sqrt{\frac{2E}{k}} \text{sgn}(\dot{x}) + \omega^2 x = 0 = \ddot{x} + \frac{\pi\omega}{4Q_h} \sqrt{\omega^2 x^2 + \dot{x}^2} \text{sgn}(\dot{x}) + \omega^2 x = \ddot{x} + cA_{\text{prev}} \text{sgn}(\dot{x}) + \omega^2 x \quad (20.10)$$

where, in the last expression, the subscript “prev” implies amplitude at the last (previous) turning point of the motion. This particular form for the damping term (Peters, 2002a, 2002b, 2002c), thought to result from secondary as opposed to primary creep (Peters, 2001a, 2001b), is not as computationally useful as the middle expression involving the Q . The damping capacity is given by

$$-\Delta E = md_h = 4cmA \int_0^{\pi/2} A \cos \theta d\theta \rightarrow d_h = 4cA^2 \quad (20.11)$$

yielding $Q = \pi\omega^2/(4c)$, so that the constant in the nonlinear model is related to the linear approximation constant through

$$c = \pi h/(4m)$$

20.5.6 Coulomb Damping

One of the simplest friction models is that in which a Hooke’s Law spring is connected on one end to a mass that slides on a level table. The other end of the spring is connected to a stationary wall. The friction force of the mass against the table is of the type first described quantitatively by Charles Augustin Coulomb (1736–1806), although Leonardo da Vinci is probably the first to consider it scientifically. The equation of motion and its solution, for the free-decay of an oscillator damped by Coulomb friction, is given by

$$\begin{aligned} m\ddot{x} + f \text{sgn}(\dot{x}) + kx &= 0 \\ \text{Solution} & \\ x(t) &= [x_0 - (2n + 1)\Delta_x] \cos \omega t + (-1)^n \Delta_x \end{aligned} \quad (20.12)$$

The equation is nonlinear because of the sign of the velocity term, but it is easily integrated numerically; additionally, it is one of the few nonlinear equations for which an analytic solution is known and is given above (for more details, the reader is referred to Peters and Pritchett, 1997). The integer, n , specifies the number of half-cycle turning points from $t = 0$, and Δ_x is the decrement (linear, not logarithmic, having units of m) per half-cycle. There are occasions to use Equation 20.12; for example, problems in civil engineering where relative motion of members (slipping) occurs at a structural joint. The work against friction in one cycle can be obtained from energy considerations and is given by

$$f(4x_0 - 8\Delta_x) = \frac{1}{2} kx_0^2 - \frac{1}{2} k(x_0 - 4\Delta_x)^2 \quad (20.13)$$

which, for small decrement, yields

$$\Delta_x = \frac{f}{k} = \frac{f}{m\omega^2} \quad (20.14)$$

Damping characteristics for the models presently treated are summarized in Box 20.1.

Box 20.1

DAMPING CHARACTERISTICS

Type	Equation of Motion	Damping Capacity	Q
Viscous	$\ddot{x} + 2\beta\dot{x} + \omega_0^2x = 0$	$2\pi\beta\omega A^2m$	$\frac{\omega}{2\beta}$
Hysteretic (linear approximation)	$\ddot{x} + \frac{h}{m\omega}\dot{x} + \omega^2x = 0$	πhA^2	$\frac{m\omega^2}{h}$
Hysteretic (modified Coulomb)	$\ddot{x} + c_hA \operatorname{sgn}(\dot{x}) + \omega^2x = 0$	$4c_hA^2m$	$\frac{\pi\omega^2}{4c_h}$
Coulomb	$\ddot{x} + \frac{f}{m}\operatorname{sgn}(\dot{x}) + \omega^2x = 0$	$4fA$	$\frac{\pi m\omega^2A}{4f}$
Amplitude dependent	$\ddot{x} + c_fA^2 \operatorname{sgn}(\dot{x}) + \omega^2x = 0$	$4c_fA^3m$	$\frac{\pi\omega^2}{4c_fA}$

20.5.7 Thermoelastic Damping

A microphone with Labview was used to analyze vibratory data of an aluminum rod. A rod of 1 m length can be excited to ear-piercing intensities by holding it at its center between thumb and finger of one hand, and stroking along the length with the other hand that is coated with violin-bow rosin. The decay of this “singing rod”, which is a common part of physics demonstration equipment, was found to be in agreement with the following theoretical expression for thermoeleastic damping (Landau and Lifshitz, 1965):

$$\frac{1}{Q_{\text{Th.d}}} = \frac{\kappa T \alpha^2 \rho \omega}{9C^2}$$

(20.15)

where ω is the vibrational angular frequency, T is the temperature, ρ is the density of the bar, C is the heat capacity per unit volume, α is its thermal expansion coefficient, and κ is the thermal conductivity. The expression assumes adiabatic vibrations and there is no thermoelastic dissipation in pure shear oscillations (e.g., torsional oscillations of a bar) because the volume does not change and hence there is no local oscillation of the temperature. Notice, in particular, that the Q is inversely proportional to frequency, unlike viscous damping that is proportional to the frequency, or hysteretic damping that is proportional to the square of the frequency. Thermoelastic damping is important for high-frequency compressional oscillations in materials with significant thermal coefficients, and especially for metals because of their large thermal conductivity.

The demonstration of comparable behavior in polymers (entropy spring, but opposite sign compared with metals) is quite easy. Stretch a rubber band between the hands and immediately touch it to the forehead. The increase in temperature is easily sensed. Conversely, releasing the tension in the band cools it enough to be sensed by placing the band to a part of the face that is sensitive to temperature change. Equation 20.15 does not apply to polymers.

20.6 Measurements of Damping

20.6.1 Sensor Considerations

The challenge to any measurement is to accomplish the task without significantly altering the system under study (see Chapter 15). For measurements on mechanical oscillators of the type described in

this document, two types of sensor are generally superior to every other kind: (i) optical and (ii) capacitive. Optical sensors are probably the least perturbative but they do not readily yield themselves to large dynamic range with good linearity (and small quantization errors for digital type). Inductive sensors, such as the linear variable differential transformer (LVDT), are known from seismology to be inherently more noisy (up to 100 times) because of ferromagnetic granularity. Additionally, transformers are not amenable to miniaturization, and the components are inherently less stable. It is therefore a mystery why the widespread use of the fully differential inductive sensor (LVDT) continues when we have available the superior fully differential capacitive sensor, which is electrically equivalent (apart from its reactance type) and capable of miniaturization to the MEMS level. The challenge with really small capacitive sensors is the increase in output reactance of the device as they approach femtoFarad levels of individual capacitors.

All measurements reported in this document were taken with the fully differential unit whose patent name is “symmetric differential capacitive” (see Peters, 1993a, 1993b). It is especially useful for studying mechanical oscillators of macroscopic size and, morphed to various forms, it recently has found application in MEMS. It is capable of great sensitivity when configured in the form of an array, as shown in Figure 20.4.

Various lines in Figure 20.4 correspond to narrow insulator strips, such as the single vertical line in the set that connects to the amplifier. In the cross-connected static set, the plates labeled “1” are electrically distinct from the others labeled “2”. The total-plate arrangement constitutes a symmetric AC bridge, and the central position of the moving set ($x = 0$ as shown in the figure) corresponds to bridge balance with $V_0 = 0$. Displacement away from balance gives a voltage output that is linear between $-w/4$ and $w/4$, as illustrated in the graph at the bottom of Figure 20.4.

The oscillator frequency is typically tens of kHz, and the amplifier is of instrumentation type (Horowitz and Hill, 1989). Unlike a bridge null detector, the linear response through $x = 0$ is realized

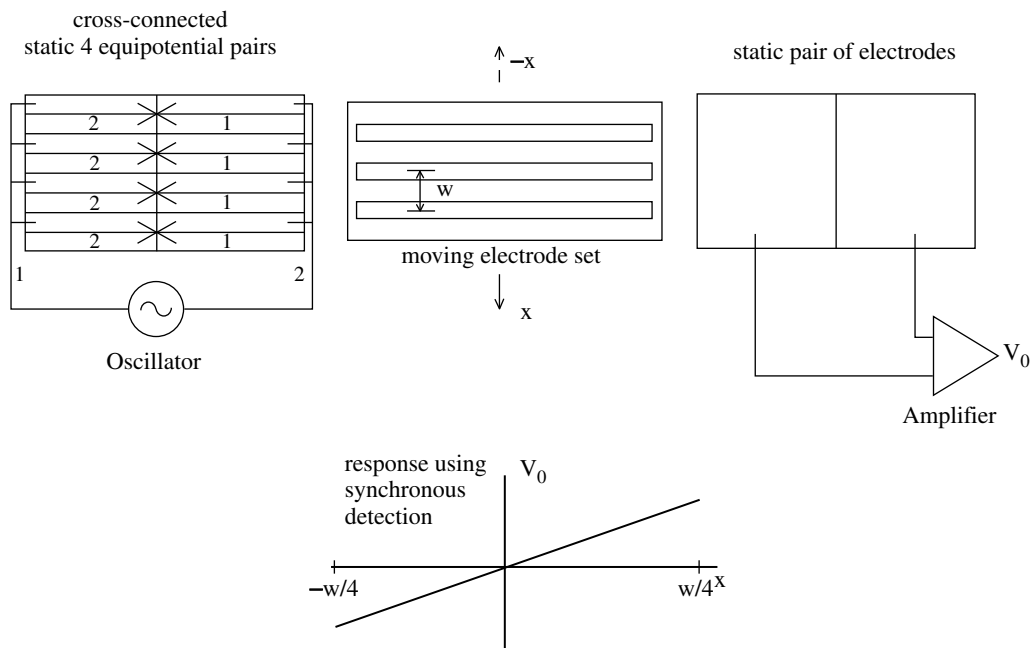


FIGURE 20.4 Illustration of a fully differential capacitive transducer array. For clarity, the three electrode-sets are shown separated from their operating positions (parallel with a small separation gap, with the moving electrodes in the middle).

when synchronous detection is employed. This can be accomplished with a lock-in amplifier, but the most recent Cavendish balance to employ the sensor uses diodes (Tel-Atomic Inc., online at <http://www.telatomic.com/sdct1.html>).

A tutorial (“detailed explanation”) of the SDC sensor using diodes can also be found at this website.

In Figure 20.4, four individual SDC units have been shown connected in parallel. The total number, N , of individual units in an array depends on the characteristic width, w , for which the total range of detectable motion is $w/2$. If the requirement on range is small, then N can in principle be made very large, which is desirable for the following reason. The sensitivity of this position sensor is inversely proportional to w if output capacitance of the device is not a factor. As w is reduced, however, the degrading influence of increased output reactance (capacitive) is more significant than the improved sensitivity that would result if the sensor could be connected to an amplifier with infinite input impedance. Since the instrumentation amplifier’s input capacitance is not negligible, shrinking w is beneficial only if the output reactance can by some means be kept low. This is accomplished with the array of individual units. In principle, the output capacitance could be held reasonably constant as N approaches 100, by using photolithographic techniques and small spacing between the parallel electrodes. The concept has been deemed feasible because of existing technologies as well as the following: although not in the form of an array, Auburn University has fabricated a mesoscale accelerometer around the SDC sensor. The prototype was built on printed wire board (PWB) under U.S. Army contract (Dean, 2002).

No doubt the popular silicon-based MEMS accelerometers marketed by Analog Devices utilize the impedance advantages of an array, employing a large number of “fingers” in a force-feedback arrangement. Although employed mostly otherwise, the first case of a fully differential capacitive transducer using force-feedback was one based on simultaneous action of actuator and sensor functions in a single unit of nonlinear type (Peters et al., 1991).

20.6.2 Common-Mode Rejection

In attempts to measure damping, one can be confronted with difficulties of mode mixing. For example, the historical Cavendish experiment, using optical detection, has been traditionally difficult unless the instrument is placed in a very quiet location to avoid pendulous swinging of the boom. The high-frequency pendulous motion (of the order of 1 Hz) as a “noise” becomes superposed on the low-frequency torsional signal. The computerized Cavendish balance sold by Tel-Atomic overcomes this problem by means of a mechanical common-mode rejection feature. An SDC sensor placed near one boom end is connected in electrical phase opposition to a second SDC sensor placed near the other end of the boom. The boom itself serves as the moving electrode for both sensors. Neither sensor has a first-order response to boom motion parallel to its long axis. Pendulous motion perpendicular to the boom orientation is largely canceled.

20.6.3 Example of Viscous Damping

The aforementioned Sprengnether–LaCoste spring seismometer is well-suited to the demonstration of viscous damping, when damping is imposed in the following manner: the instrument was built with a Faraday Law (velocity) detector; i.e., a coil that moves with the mass of the instrument, in the field of a stationary magnet. As originally employed, the coil was connected to the amplifier of a recorder. In the present configuration, however, the velocity detector is not employed, since its sensitivity is severely limited at low frequencies. Instead, an SDC array of the type shown in Figure 20.4 is used to measure the position of the mass (a pair of lead weights, total mass 11 kg). If the instrument is operated with the coil open-circuit, there is no induced current. By connecting a resistor across the coil (through very fine copper wires that go to terminals on the case), mass motion induces a current. The induced current opposes the motion through Lenz’s Law, resulting in damping. The damping depends on the size of the

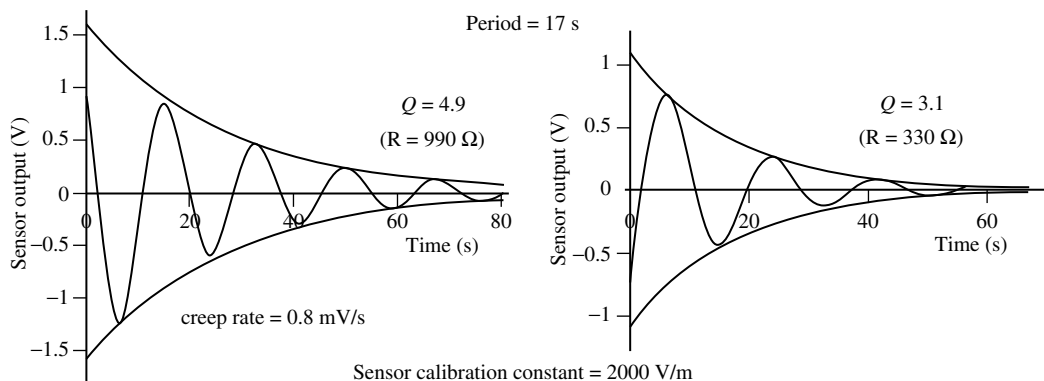


FIGURE 20.5 Examples of induced current damping of a vertical seismometer using two different resistors.

current and is thus an inverse function of the resistor's magnitude through Ohm's Law. The phenomenon is illustrated in Figure 20.5.

As compared with the "undamped" instrument, whose Q is approximately 80 at a period of 17 sec, it is seen that the addition of a 990-ohm resistor lowered the Q by more than an order of magnitude to 4.9. A 330-ohm resistor reduced it even further to 3.1. The amount of damping is also governed by the resistance of the coil winding, which is 480 ohm.

The envelopes that have been fitted to the decay curves were the basis for estimating the Q . The decay data were imported to Excel by first outputting the Dataq DI-154RS A/D generated record as a *.dat (CSV) file. The fits were produced by trial and error using the drag and autofill functions. Notice that the 990-ohm resistor (first) case is not as pure an exponential decay as the other case because of creep. The rate of creep is greater at large initial amplitudes of the motion.

20.6.4 Another Way to Measure Damping

Curve fitting (full nonlinear, in general) is the best way to estimate damping parameters, especially if the decay is not exponential. For more routine cases, simpler methods can be used. Among the host of ways that have been defined to specify the damping of an oscillator, one of the most common uses the logarithmic decrement. The solution to Equation 20.1 with zero right-hand side is given by

$$x(t) = x_0 e^{-\beta t} \cos(\omega t + \phi). \quad (20.16)$$

The full-cycle turning points, $x_N = x_0 e^{-\beta NT}$, with $N = 0, 1, 2, \dots$ can be used to compute the logarithmic decrement through

$$\beta T = \frac{1}{N} \ln \frac{x_0}{x_N} \quad (20.17)$$

Unfortunately, an estimate based on Equation 20.17 can be difficult due to the presence of either or both of two problems: (i) mean position offset in the decay record or (ii) asymmetry of the decay, where the turning points on one side of equilibrium decay at a different rate than those on the other side. Case (ii) occurs more often than one might expect; it is frequently a consequence of material complexity and not the result of nonlinearity in the electronics of the detector. It is important, however, to be sure that the detector is either linear or that corrections for the nonlinearity be utilized before estimating the damping.

A method to provide partial compensation uses half-cycle turning points $n = 2N$, and works with a minimum of three such points.

$$\beta T = -2 \ln[1 - (x_{n-1} - x_{n+1})/(x_{n-1} - x_n)] \quad (20.18)$$

Advantage is taken of random error reduction by using Equation 20.18 on a set of turning points (optimal number sometimes being about a dozen). The calculations are straightforward in a spreadsheet such as Excel by means of the autofill function.

20.7 Hysteretic Damping

20.7.1 Equivalent Viscous (Linear) Model

The few mechanical oscillators governed by Equation 20.1 tend to be those in which there is an external control, such as eddy current damping. For oscillators in which the damping derives from internal friction of its members, the following linear approximate form of the hysteretic damping model has been used:

$$m\ddot{x} + \frac{h}{\omega}\dot{x} + kx = F \quad (20.19)$$

It should be noted that hysteresis is the cause for all damping; however, engineers have come to use the term “hysteretic damping” for systems described by Equation 20.19. This equation differs in two important ways from Equation 20.1. For the viscous damped oscillator, Q is proportional to the frequency, but for the hysteretic damped oscillator, Q is proportional to the square of the frequency. Also, viscous damping changes the frequency of the oscillator, since $\omega_1 < \omega_0$ and, for resonance, the frequency is even lower. However, the hysteretic oscillator is isochronous, requiring only a single frequency $\omega = \sqrt{k/m} \rightarrow \omega_r$ to describe all features of the motion. For example, it is easy to show that the oscillator resonates at this frequency. Off resonance, the response is not the standard Lorentzian. To show this, assume steady state and use the phasor method given to us by Steinmetz, 1893 (complex exponential form for the variables); i.e., $F = F_0 e^{j\omega t}$ and $x = x_0 e^{j\omega t}$ to get the frequency transfer function

$$\frac{kx}{F} = \frac{1}{1 - \omega^2 \frac{m}{k} + j \frac{h}{k}} = \frac{1}{1 - r^2 + j\alpha} = Z, \text{ with } r = \frac{\omega}{\omega_r} \text{ and } \alpha = \frac{h}{k} = \frac{1}{Q} \quad (20.20)$$

for which the real and imaginary parts are given by

$$\text{Re } Z = \frac{1 - r^2}{(1 - r^2)^2 + \alpha^2}, \quad \text{Im } Z = \frac{-\alpha}{(1 - r^2)^2 + \alpha^2} \quad (20.21)$$

which is expressible in polar form as

$$Z = |Z| e^{j\delta}, \text{ where } |Z| = \frac{1}{\sqrt{(1 - r^2)^2 + \alpha^2}} \text{ and } \delta = -\tan^{-1} \frac{\alpha}{1 - r^2} \quad (20.22)$$

It is interesting to compare the steady-state response of the driven, hysteretic damped oscillator with that of the driven, viscous damped oscillator; i.e., Equation 20.22 compared with normalized Equation 20.7. A Bode plot comparison (log–log, for the amplitude case) is provided in [Figure 20.6](#). At small values of the damping parameter α (large Q), there is insignificant difference between the two cases. At large values, however, the difference is significant.

20.7.2 Examples from Experiment of Hysteretic Damping

The vertical seismometer that was used for several of the present studies is known to decay according to hysteretic damping. In Section 20.16.4 titled “Failure of Viscoelasticity”, details are provided of the work by Gunar Streckeisen (1974) that showed this to be true. Decay curves of the instrument are

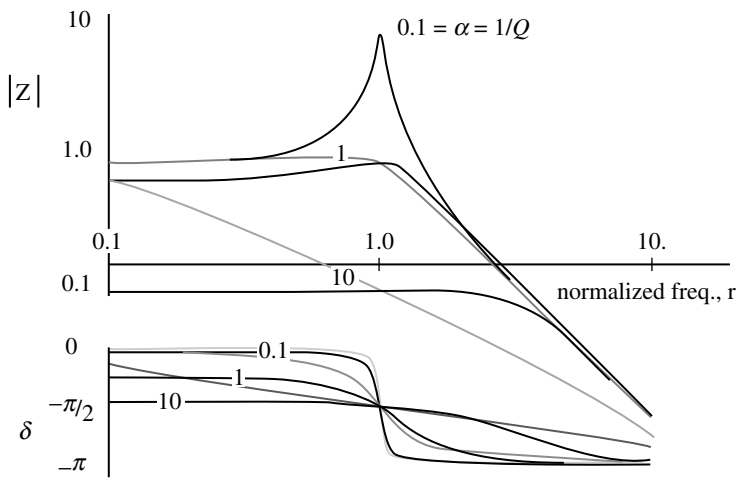


FIGURE 20.6 Bode plot comparison of steady-state driven system with (i) hysteretic damping (dark curves) and (ii) viscous damping (light curves).

frequently a near-perfect exponential, once corrected for secular drift of the record. Sometimes, this drift is the result of creep in the spring of the instrument, but it may also be the result of other factors, such as (i) temperature change, or (ii) barometric pressure variation, or even (iii) tidal influence. The temperature sensitivity is due to the difference of thermal coefficients of the materials from which the instrument is constructed, and the pressure variation is a buoyancy effect. Tidal influence is the smallest of the three, which causes minute accelerations of the crust of the Earth with a period of about 12 h.

In the discussions which follow, two different decay records are provided. In both cases, the initial amplitude of oscillation is quite large, being a significant fraction of 1 mm, and the period for the two cases is different — the first case being 17 sec and the second one 21 sec. The first case time record, shown in Figure 20.7, contains 9800 points. Once a 12 $\mu\text{V/s}$ (upward) drift was removed, the decay (left curve) is seen to be “nearly textbook” exponential.

The adjective “nearly” is appropriate because there is a 12% difference in the decay constants defining the upper and lower turning points (0.0022 top, 0.0025 bottom), which were determined by trial and error “eyeball” exponential fits using Excel. In this author’s experience, such is the norm for virtually all mechanical oscillations; perfectly symmetric exponential decays have rarely been seen in the hundreds of cases studied.

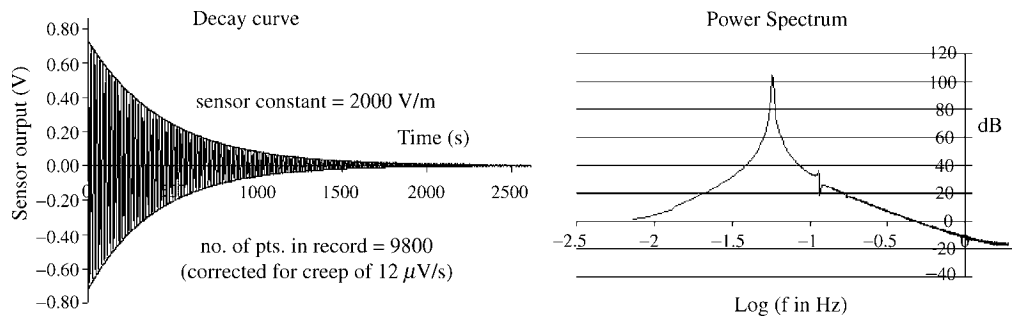


FIGURE 20.7 Free-decay of a vertical seismometer due to hysteretic damping. The period of oscillation is 17 sec.

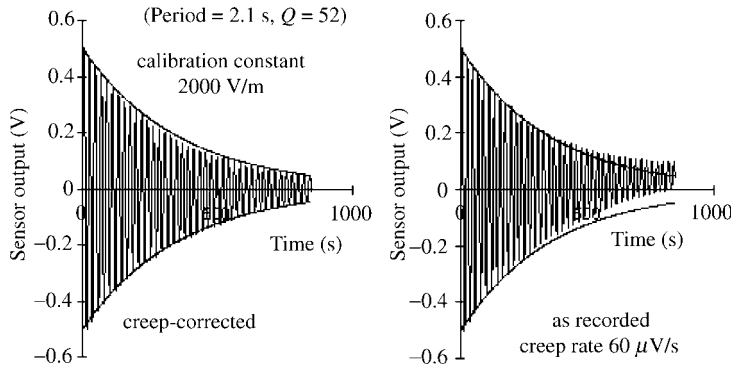


FIGURE 20.8 Free-decay of a seismometer due to hysteretic damping.

Because there are roughly 150 oscillations in the time record of Figure 20.7, it is not possible to resolve individual turning points of the motion, but the oscillations are very nearly that of a pure damped sinusoid, as noted from the right-side graph of the figure. This spectrum was generated with a 4096-point FFT, comprising the first 1090 sec of the time record. The second harmonic is the only distortion observed, and it is about 65 dB below the fundamental. For the case presented in Figure 20.7, $Q = 80$.

Another example of free-decay hysteretic damping is provided in Figure 20.8. As usual, the record was afflicted by drift, possibly from creep in the spring, in this case a constant rate of $60 \mu\text{V/s}$, as observed in the graph on the right. All of these graphs were produced with Excel, as noted earlier in the discussion of induced current damping. As with the decay curve of Figure 20.7, the creep-corrected graph on the left was generated by adding a secular term to the raw data. Once corrected, the decay is a near-perfect exponential of hysteretic type. We will see other examples (from pendulum studies) in which two damping mechanisms are simultaneously active in a decay.

The Q values corresponding to Figure 20.7 and Figure 20.8 are consistent with hysteretic damping; i.e., 80 for the 17-sec oscillation and 52 for the 21-sec oscillation. As noted elsewhere in this document, $Q\alpha\omega^2$ for hysteretic damping as opposed to an exponent of 1 for viscous damping. Of course, one must collect data over a very much larger range of frequencies to verify this, as was done by Streckeisen (1974).

20.8 Failure of the Common Theory

Many mechanical oscillator studies in decades past, mainly by engineers, have shown that the so-called decay constant β is proportional to ω^{-1} instead of being constant (e.g., Bert, 1973). The damping for these cases came to be called “material”, “structural”, or “hysteretic.” A common way to obtain the correct frequency dependence was to divide the velocity by frequency and call the result an “equivalent viscous” form of damping. The adjective “equivalent” draws attention to the fact that internal friction in a solid cannot really result from fluid effects. Moreover, elsewhere in this document, there is plenty of support for the position that the linear equations of viscous damping type cannot produce truly meaningful (predictive) models when doing modal analysis on multibody systems.

An important early work by Kimball and Lovell (1927) is evidently the first experiment to show that internal friction (“force”) of many solids is virtually independent of frequency. In other words, their elegant technique, in which a rotating rod is deflected by a transverse force, was the first to demonstrate the “universality” of hysteretic damping. Although both researchers were physicists at General Electric in the time of Steinmetz, few physicists of the 21st century know of this important work. As with the important contributions of Portevin and LeChatelier, their study of systems influenced by “dirty physics” was evidently ignored in favor of the “clean” new quantum mechanics of that era.

It is interesting that a bell made of lead does not tinkle at room temperature, but it can be made to do so at 77 K, by immersion in liquid nitrogen. This demonstration, which is often employed in physics “circuses,” shows clearly that the internal friction of lead at audio frequencies can be reduced substantially by lowering the temperature. An important lesson to be learned from these observations is that damping, in general, is a complex function of temperature, frequency, conductivity, ... (who knows where to terminate this list). Not only is a multitude of state variables necessary for a complete description of dissipation, but the previous history of stress–strain cycling may also be critical. Such is the nature of defect structures responsible for damping.

20.9 Air Influence

Even when operating an oscillator in high vacuum, there is a significant remanent damping that derives from internal friction. This fact is illustrated in Figure 20.9, which provides data for two different “simple” pendula. They are simple in the sense that the bob mass is concentrated near the bottom of the pendulum structure. In the figure, decay time (reciprocal of the decay constant, β) has been plotted against the natural log of the pressure in mtorr. Pressure reduction was done with a high-quality roughing pump, and the pressure was measured with (i) a mechanical gauge in the range $8 \text{ torr} < P < 760 \text{ torr}$ and (ii) a thermocouple vacuum gauge for $0 < P < 100 \text{ mtorr}$. In the range from 100 mtorr to 8 torr, the pressure could not be accurately measured with either of these gauges. Similarly, pressures below 1 mtorr could not be presently measured, but in similar other experiments with this pump, and using an ion gauge, it was easy to pump below 0.01 mtorr.

The period of each pendulum was very close to 1 sec, and the starting amplitude of the motion for every case was about 25 mrad. The heavier pendulum used a pair of pointed steel supports resting on single-crystalline silicon wafers to provide the axis of rotation. At the bottom of the pendulum was attached a solid lead ball whose mass was approximately 1 kg. The lighter pendulum was supported by a steel knife-edge resting on hard ceramic flats, and a large (10.3 cm dia.) lightweight (143 g) hollow metal sphere was attached at the bottom to provide as much air drag as possible. The motion was measured with an SDC sensor feeding the computer through a Dataq DI-154RS A/D converter.

Although air damping is evident in Figure 20.9, it is not as influential as one might expect, at least for the heavy pendulum. Moreover, at atmospheric pressure, it was easy to demonstrate the importance of nonlinear drag. As also noted in Nelson and Olssen (1986), this form of fluid friction caused a significant amplitude-dependent damping.

The remanent damping, once air influence is eliminated (pressure below 1 mtorr), is substantial relative to atmospheric damping, for both pendula. Removing the air increased the Q from 7500 to

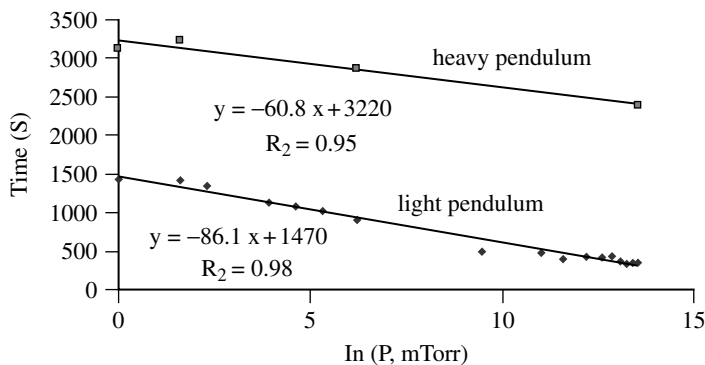


FIGURE 20.9 Pendulum damping as a function of pressure in a vacuum chamber.

10,100 for the heavy pendulum and, for the light pendulum, the increase was from 1000 to 4600. We thus see that even a pendulum designed to be heavily influenced by air drag also has significant damping that depends on the material from which the pendulum is fabricated or on the material upon which it rests.

The difference in internal friction damping between the heavy and light instruments was not expected to be so great. Although this might be due to the difference in axis-type (points for the heavy instrument and knife-edge for the light), no systematic effort was made to determine the primary source of the damping difference. In addition to different axis designs, the means for holding the instruments together were different. The light pendulum used a large-diameter solid brass wire between the axis and the lower mass, and the heavy pendulum used an aluminum tube.

Both of the pendula used to generate [Figure 20.9](#) were relatively high-frequency instruments (period of 1 sec). The pivot was located, in each case, near the top end of the instrument. As such, they stand in stark contrast with the instruments that motivated this paper, where long-period pendula were used. A simple instrument to demonstrate some of the complexities of long-period instruments is a rod-pendulum of adjustable period (refer to [Figure 20.1](#) above). The closer the axis to the center, the longer the period and the greater the influence of internal friction. It is easy to show that the sensitivity of a pendulum to external forces is proportional to the square of the period. Similarly, the ability to detect influence of internal configurational change is quadratic in the period.

20.10 Noise and Damping

20.10.1 General Considerations

Damping is inseparable from noise issues having nothing to do with undesirable sounds that might be produced by oscillation. In the simplest cases, the noise associated with damping can be described by the fluctuation–dissipation theorem. The viscous damped, thermally driven oscillator is a classic example of thermodynamic equilibrium, for which this theorem is applicable. The classic electronics analogous case is the Johnson noise of a resistor, described by the Nyquist (white) noise formula.

The largest obstacle to constructing a perfectly simple harmonic oscillator is the oscillator's dissipation. If damping were perfectly smooth, this would not be so great a challenge. However, the fluctuation–dissipation theorem of statistical mechanics guarantees that damping is accompanied by fluctuating forces. The larger the damping, the larger the fluctuating forces, i.e., the larger the noise. It is a standard problem in statistical mechanics to show that the magnitude of relative fluctuation is inversely proportional to the square root of the number of particles involved. In the case of internal friction noise, defects associated with mesoscale structures cause the effective number of particles responsible for the noise to be much smaller than the total number of atoms in a sample. Unfortunately, the fluctuation–dissipation theorem probably does not apply. It has been long known that it does not apply to the Barkhausen effect (Barkhausen, 1919). It has been recently demonstrated that it does not apply to structural glass (Grigera and Israeloff, 1999). The close relationship postulated by the author between the PLC effect and the Barkhausen effect implies that the fluctuation–dissipation theorem should also not generally apply to internal friction damping.

Internal friction noise is not white but rather more like $1/f$ (or flicker = pink) noise, a ubiquitous form that has not yet been explained from first principles. A frequently cited paper on self-organized criticality states the following:

We shall see that the dynamics of a critical state has a specific temporal fingerprint, namely “flicker noise,” in which the power spectrum $S(f)$ scales as $1/f$ at low frequencies. Flicker noise is characterized by correlations extended over a wide range of timescales, a clear indication of some sort of cooperative effect. Flicker noise has been observed, for example, in the light from quasars, the intensity of sunspots, the current through resistors, the sand flow in an hourglass, the flow of rivers such as the Nile, and even stock exchange price indices. Despite the ubiquity of flicker noise, its origin is not well understood. Indeed, one may say

that because of its ubiquity, no proposed mechanism to date can lay claim as the single general underlying root of $1/f$ noise. We shall argue that flicker noise is in fact not noise but reflects the intrinsic dynamics of self-organized critical systems. Another signature of criticality is spatial self-similarity. It has been pointed out that nature is full of self-similar “fractal” structures, though the physical reason for this is not understood. (Bak, 1988)

It should be noted that controversy exists concerning this self-organized criticality paper, summarized in the following excerpt from Bak’s book on $1/f$ noise called *How Nature Works: The Science of Self-Organized Criticality* (page 95):

In an earlier work (CFJ), performed while an undergraduate student in Aarhus, Denmark, (Kim Christensen) showed that our analysis of $1/f$ noise in the original sandpile article was not fully correct. Fortunately, we have since been able to recover from that fiasco in a joint project by showing that for a large class of models, $1/f$ noise does indeed emerge in the SOC state.

In the last few years, mathematicians have been drawn to “... an analogy, in which three areas of mathematics and physics, usually regarded as separate, are intimately connected. The analogy is tentative and tantalizing, but nevertheless fruitful. The three areas are eigenvalue asymptotics in wave physics, dynamical chaos, and prime number theory” (Berry and Keating, 1999). Some mathematicians speculate that a dynamical system (perhaps some form of a mesoanelastic pendulum, in the thinking of this author) could become a “machine” to generate prime numbers.

20.10.2 Example of Mechanical $1/f$ Noise

Shown in Figure 20.10 is an example of mechanical flicker noise made worse by creep that originates in the spring (LaCoste type) of a Sprengnether vertical seismometer. The data are from two separate time records, the first run preceding the second run by about a half-hour. Just before collecting the data of the first run, a clamping pin was removed from the seismometer. Used to constrain the mass from moving, this pin had been left in place overnight to determine the amount of electronics noise, including drift. The measured electronics noise (white = $1/f^0$) was more than an order of magnitude smaller than the smallest (high frequency) noise components of mechanical (seismometer) type. The peak-to-peak amplitude of the oscillation in both cases was 0.5 mm (calibration constant for the sensor being 2000 V/m). The peak-to-peak amplitude for SNR = 1 for this system is of the order of $1\ \mu\text{m}$.

Although the spring force was not unloaded with the pin in place overnight, nevertheless, its removal caused a significant change to defect structures in the spring, as noted by the residuals between the data and their harmonic fits (magnified by a factor of ten).

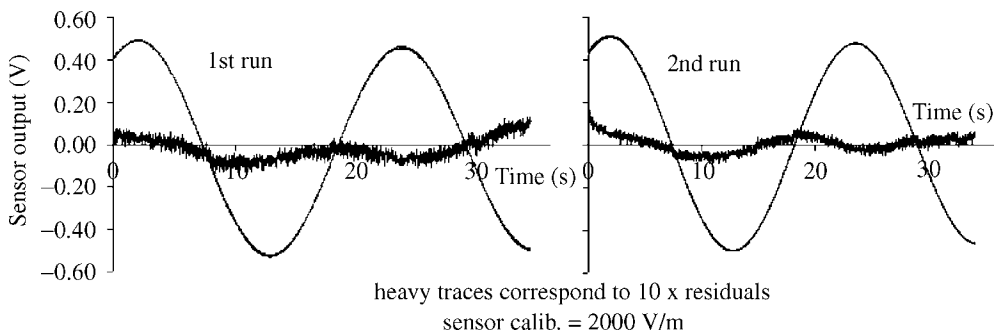


FIGURE 20.10 Evidence in support of $1/f$ mechanical noise in a seismometer.

The flicker character of the noise was demonstrated by computing power spectra of the residuals (not shown). The log–log plot, generated with the FFT (Cooley–Tukey FFT), showed $1/f$ frequency dependence for the second run. The larger noise of the first run was concentrated in the upper frequencies. The relaxation toward $1/f$ character suggests that flicker noise is a remanent of “work hardening.” To demonstrate that the flicker noise was not due to the electronics, sensor output was recorded with the mass of the instrument locked. The electronics noise proved to be more than an order of magnitude smaller and “white” in character, probably mainly the result of A/D quantization (see Chapter 16).

Because the spring was not in equilibrium at the time the pin was removed (perhaps because of temperature change while the system was clamped), a great deal of initial molecular rearrangement occurred, involving atoms at grain boundaries. It is seen that the amount of fluctuations has noticeably decreased during the half-hour separating the two runs. Although the creep-noise would be undoubtedly much greater if the spring were relaxed altogether, it is not easy in such a case to quickly rebalance the seismometer to oscillate with a period in excess of 20 sec. These observations are in keeping with known properties of sensitive seismometers, as noted by Erhardt Wieland in “Instrumental self noise — transient disturbances” (ed. Borman and Bergmann, 2002):

Most new seismometers produce spontaneous transient disturbances, quasi miniature earthquakes caused by stresses in the mechanical components. Although they do not necessarily originate in the spring, their waveform at the output seems to indicate a sudden and permanent (step-like) change in the spring force. Long-period seismic records are sometimes severely degraded by such disturbances. The transients often die out within some months or years; if not, and especially when their frequency increases, corrosion must be suspected. Manufacturers try to mitigate the problem with a low-stress design and by aging the components or the finished seismometer (by extended storage, vibrations, or alternate heating and cooling cycles). It is sometimes possible to relieve internal stresses by hitting the pier around the seismometer with a hammer, a procedure that is recommended in each new installation. (Wielandt, 2001)

Material damping noise appears to have features that are similar to Barkhausen noise — a magnetic phenomenon involving a system far-from-equilibrium. Such noise is associated with the granular nature of ferromagnetic domains and has consequence in the design of electronic instruments using iron alloys. For example, it is known (though not widely) that the popular LVDT is inherently less sensitive than a capacitive sensor of equivalent electrical type, because of its ferrous component (the rod-component that moves). As noted by Wielandt (2001), the capacitive sensor “...can be a hundred times better than that of the inductive type.” Fully differential capacitive sensors, being electrically equivalent to the LVDT have still greater advantages borne of the higher symmetry. Additionally, by configuring the capacitive device as an array, it is possible for the sensitivity to also be greater.

Barkhausen noise and hysteretic damping noise may be much more similar than has been realized — involving granularity at the mesoscale, intermediate between micro- and macrophenomena. For such systems, first principle methods are very difficult to employ due to complexities that originate from a host of nonlinear interactions. For example, in the case of internal friction of solids, damping derives from stress–strain hysteresis determined by defect structures in the solid. Involving roughly 10^{12} atoms per “grain” in metal specimens, flicker noise evidently derives from self-similar structures of fractal geometry with a higher degree of spatial correlation than is true of white noise. The ubiquitousness of $1/f$ noise is consistent with the labeling of hysteretic damping as “universal,” as first suggested by Kimball and Lovell (1927).

20.10.3 Phase Noise

The previous example was concerned with amplitude noise. It is also possible to see phase noise of mechanical type, as illustrated in Figure 20.11.

For the sensor calibration constant of 2000 V/m, it is seen that the initial amplitude of oscillation is 1.3 mrad, which is much too large to observe the discontinuities of mechanical Barkhausen type.

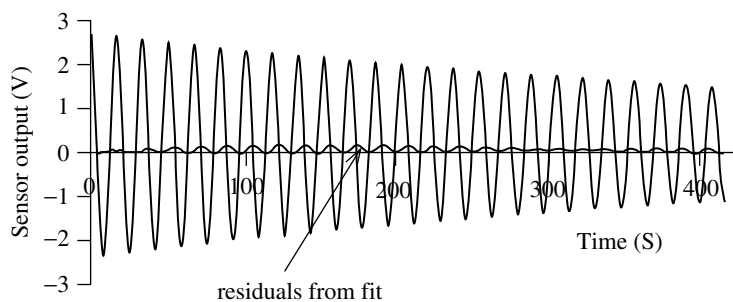


FIGURE 20.11 Illustration of phase noise in the free-decay of a vertical seismometer.

The phase noise is made obvious by comparing the decay to a “reference,” i.e., by looking at the residuals from an Excel-generated fit to the data. By adjusting in a computer-generated damped sinusoid, (i) the initial values of amplitude and phase, (ii) the decay parameter, and (iii) the frequency, one can visually by trial and error come close to an optimum fit to the data. Having done so with Figure 20.11, the striking feature of the residuals (difference between data and fit) is the structure that looks something like “beats” but is not. The phase noise responsible for this behavior is thought to be consistent with $1/f$ mechanical noise. To visualize the noise, it is convenient to think in terms of a small randomizing (noise) vector whose tail is positioned at the head of the phasor used to generate the record. The component of the noise vector that is in the direction of the phasor generates amplitude noise as in Figure 20.10, whereas the perpendicular component is responsible for the phase noise of Figure 20.11.

Vibration phase noise imposes a serious limit on the performance of precision quartz crystal oscillators, since they are sensitive to acceleration. The phase noise in these oscillators can be observed by beating against a reference oscillator of known character; i.e., the reference serves the same purpose as the computer “fit” of Figure 20.11. To reduce the phase noise, crystals are isolated with low natural frequency vibration isolators (as described in the marketing literature of Wenzel Assoc., Austin, X).

20.11 Transform Methods

20.11.1 General Considerations

For linear systems, the Laplace and Fourier transforms (Laplace being more general) have been pre-eminent tools with which to study equations of motion (see Appendix 2A and Chapter 10). The author’s transform experience (like most physicists) is mainly with Fourier transforms (FT). The discrete FT can be understood in terms of phasors (Peters, 1992). For linear differential equations, transforms are the means to convert differential forms to an equivalent algebraic form. Unfortunately, they cannot be directly employed on nonlinear equations due to the failure of superposition. Nevertheless, the linear approximations continue to be very valuable, so a chapter on damping deserves to mention some of their properties.

Ideas concerning the FFT were evidently originally treated by Gauss in the early 1800s, but the digital signal processing (DSP) “explosion” of the 1960s was largely due to the work of Cooley and Tukey (1965). For an interesting historical account about an “accident” in the publication of their paper, the reader is referred to Cipra (1993), who says the following about the FFT:

The Fourier transform stands at the center of signal processing, which encompasses everything from satellite communications to medical imaging, from acoustics to spectroscopy. Fourier analysis, in the guise of x-ray crystallography, was essential to Watson and Crick’s discovery of the double helix, and it continues to be important for the study of protein and viral structures. The Fourier transform is a fundamental tool, both theoretically and

computationally, in the solution of partial differential equations. As such, it is at the heart of mathematical physics, from Fourier’s analytic theory of heat to the most modern treatments of quantum mechanics. Any kind of wave phenomenon — be it seismic, tidal, or electromagnetic — is a candidate for Fourier analysis. Many statistical processes, such as the removal of “noise” from data and computing correlations, are also based on working with Fourier transforms.

Concerning the last statement about noise, this author has used autocorrelation as a powerful means for identifying short-lived, low-frequency periodic signals in time records that do not readily show up in power spectra (FFTs). For example, they are the means for studying free-earth oscillations — eigenmodes excited by rapid relaxations of the Earth under tidal stressing (12 h periodic) (Peters, 2000). The FFT is used to generate the autocorrelation by means of the Wiener–Khintchine theorem (Press et al., 1986).

The great advantage of the FFT compared with the DFT has to do with degeneracy. The DFT proceeds to calculate the components of every “vector” in the reciprocal space (frequency reciprocal to time, units of “second”, or wave number (spatial frequency) reciprocal to displacement, units of “meter”) with disregard for the fact that many components have the same value, apart from a change of sign.

20.11.2 Bit Reversal

The key to the power of the FFT (central processor unit [CPU] time proportional to $n \log n$) compared with the discrete Fourier transform (DFT) (CPU time proportional to n^2) is the bit reversal scheme of the Cooley–Tukey algorithm. It is illustrated very simply by the following. Instead of a practically sized number of samples in the record to be transformed (minimum of $n = 1024$, typically), consider (for pedagogy) $n = 8$, distributed on the unit circle as shown in Figure 20.12.

Observe that the roots of unity in the complex plane, which have been numbered 0 to 7, divide the “pie” into eight equal pieces. (The algorithm requires that n be expressible as a power of 2). The usual decimal counting scheme for the eight “vectors” is as indicated, traversing the phasor diagram (circle on left) sequentially. In the Cooley–Tukey algorithm, a choice is made to reverse the bits of the binary representation of the vector. Usually, the least significant bit is on the right and the most significant bit on the left, so that decimal counting is as shown on the right in the table, from 0 to 7. With bit reversal, “lsb” becomes the leftmost binary digit and the “msb” is the rightmost digit. Thus, for example, binary 110 (usually 6) becomes 3.

Using bit reversal, the phasor diagram is not traversed in the usual phasor (circulatory) sense, but rather in a “flip-flop” back and forth across the circle. By this means, there is no needless repetition in the calculation of “vector” components (real and imaginary values of a given term in the transform). For example, 5 is the simple negative of 1. It is much faster to reverse the sign on 1 to get 5 than to

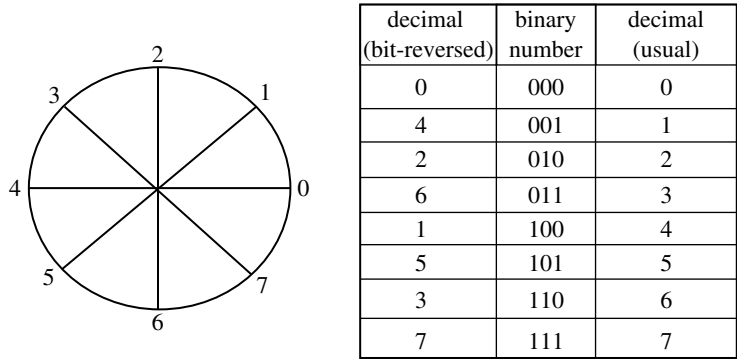


FIGURE 20.12 Graphical illustration of why the Cooley–Tukey FFT algorithm is significantly faster than the original DFT.

needlessly calculate values for sine and cosine terms a second time. The saving in time is substantial as n gets large, since there are then a great number of circulations of the phasor circle. For a 1K record, the FFT computes the transform 102.4 times faster than does the DFT. Additional details are provided in Peters (2003a, 2003b, 2003c).

20.11.3 Wavelet Transform

Recent work suggests that the wavelet transform (WT) may in the future replace the FT in some applications (see Chapter 11). It uses the Haar function, which is orthogonal on $[0,1]$, as opposed to the orthogonality of the harmonic functions (sine and cosine) corresponding to $[0,2\pi]$ (Strang, 1993). It is claimed that the WT is better able to address features of the Heisenberg uncertainty principle than the FFT.

20.11.4 Heisenberg's Famous Principle

The heart and soul of quantum mechanics is the Heisenberg uncertainty principle. As noted elsewhere in this chapter, it has things to say about damping models. According to well-known physicist Hans Bethe (1992), the principle has received "bad press":

Many people believe that the uncertainty principle has made everything uncertain. It is quite the opposite. Without the uncertainty principle there could not exist any atoms, there could not be any certainty in the behavior of matter. So it is in fact a certainty principle.

Curiously, a failure figured in Heisenberg's discovery of the principle. During his thesis defense, in front of great theoretical physicist Arnold Sommerfeld (his director) and the famous experimentalist Wilhelm Wien, he proved unable to derive the magnifying power of a simple microscope. The scandal culminated with Professor Wien asking him to explain how a battery works, and he could not answer that question either. Knowing his extraordinary theoretical giftings, Sommerfeld gave him the highest possible grade to compensate for Wien's choice of an F. Thus, Heisenberg was awarded his doctorate.

Later, in an ironic turn of events, Heisenberg chose a microscope to illustrate features of the matrix quantum mechanics that he originated, and which corrected problems with the Bohr wave mechanics theory. His greatest source of embarrassment served to make Heisenberg famous!

20.12 Hysteretic Damping

20.12.1 Physical Basis

The model of simple harmonic oscillation with viscous damping assumes dissipation from an externally acting force. It is not suited to a conceptual understanding of hysteretic damping. To accommodate internal friction requires more than a single mass connected to the elastic component responsible for restoration. Two systems are pedagogically useful in this regard, one being a long-period physical pendulum (mechanical), and the other being the oscillator used by Ruchhardt to measure the ratio of heat capacities of a gas (mainly thermodynamic). Because of widespread confusion concerning the difference between viscous and hysteretic damping, both cases are presented here. The treatments are provided as evidence for the premise that hysteretic damping is the more important case for applied physics and engineering.

It is common knowledge that the damping of a mechanical oscillator results from the conversion of mechanical energy into thermal energy. One might expect, then, that a direct consideration of thermodynamics could yield conceptual understanding of the underlying physics. Although an ideal gas is rarely considered in this context, there is a classic experiment which speaks to its relevance. It is the ingenious technique used first in 1929 by Ruchhardt to measure γ , the ratio of heat capacity at constant pressure to that at constant volume (Zemansky, 1957).

20.12.2 Ruchhardt's Experiment

Consider a piston of mass m moving in a cylinder of cross-sectional area A , alternately compressing and expanding a volume of ideal gas V_0 about the residual pressure P_0 . Assume that there is no sliding friction between the piston and the cylinder. A small displacement x of the mass results in volume change $\Delta V = V - V_0 = Ax$. There is a restoring force $F = A\Delta P$, where the pressure difference ΔP relates to ΔV through an assumed adiabatic process; i.e., the period of the motion is assumed too short for appreciable heat transfer into and out of the gas. Using $PV^\gamma = \text{constant}$, one obtains

$$\gamma P_0 V_0^{\gamma-1} \Delta V + V_0^\gamma \Delta P = 0 \quad (20.23)$$

from which one obtains

$$m\ddot{x} + \frac{\gamma P_0 A^2}{V_0} x = 0 \quad (20.24)$$

This is the equation of motion of a simple harmonic oscillator. There is no damping because of the assumed adiabatic process. By measuring the period $T = 2\pi/\omega = 2\pi\sqrt{V_0 m / \gamma P_0 A^2}$, one can estimate γ .

Historically, it appears that such measurements slightly underestimate γ , which can be understood as follows.

The ideal gas equation of state $PV = NkT$ yields, through differentiation

$$\begin{aligned} P_0 x A + V_0 \frac{F}{A} &= Nk\Delta T \\ m\ddot{x} + \frac{P_0 A^2}{V_0} x &= \frac{NkA}{V_0} \Delta T(t) = F_d(t) \end{aligned} \quad (20.25)$$

Notice the difference between Equation 20.24 and Equation 20.25. In Equation 20.25, damping is possible (a type of “negative drive” term) from temperature variations associated with heat transfer during traversal of the cycle. If it were possible for the oscillation to be isothermal ($\Delta T = 0$ at very low frequency, essentially quasistatic), then the frequency would be lower than that of the adiabatic case, since $\gamma > 1$ is missing from Equation 20.25. In the isothermal case, there would also be no damping, since the heat into the gas during compression would be balanced by that which leaves during expansion. The only way to get damping is for the paths of compression and expansion in a plot of pressure vs. volume to separate, i.e., for there to be hysteresis. Reality must correspond to something between the two extremes of adiabatic and isothermal, with experiment obviously favoring adiabatic. The process must depart somewhat from adiabatic, however, since there is damping, which Equation 20.25 shows to derive from temperature variations yielding hysteresis. It is interesting to look at the temperature variations relative to a “driving force,” $F'_d(t)$. In the Ruchhardt experiment, there must be small variations $\Delta T'(t)$ that lag behind $x(t)$. (These are not the reversible temperature variations of the adiabat, onto which the $\Delta T'(t)$ are superposed.) By comparing with Equation 20.25, the right-hand zero of Equation 20.24 may be replaced with a damping force that can be written in terms of the velocity as

$$F'_d(t) \propto \Delta T'(t) \rightarrow -\frac{c}{\omega} \dot{x} \quad (20.26)$$

where $c = \text{constant}$. Notice that the multiplier on the velocity is not simply a constant, but rather a constant divided by the angular frequency. The use of velocity is mathematically convenient, but the magnitude of the velocity (speed) is not expected to be a first order influence on the temperature changes of hysteresis type. The derivative of x with respect to time not only shifts the phase by 90° , which accommodates the lag with which heat is transferred, but it also introduces a frequency multiplier through the chain rule. Thus, to make damping proportional to the velocity would cause increased dissipative heat flow and thus increased damping as the frequency is increased. Since this does not happen, and lest we introduce a nonphysical term into the equation, it is necessary to divide by the frequency. Replacing the right-hand-side zero of Equation 20.24 with Equation 20.26, we obtain the

modified equation of motion, with damping

$$m\ddot{x} + \frac{c}{\omega}\dot{x} + \frac{\gamma P_0 A^2}{V_0}x = 0 \quad (20.27)$$

Additional justification for the form of the damping term in Equation 20.27 can be realized by looking at cases where there is negative damping, i.e., $c < 0$. Such is true when the gas is caused to cycle as an engine. An illustrative case study was that of a low temperature Stirling engine (Peters, 2002a, 2002b, 2002c), in which reasonable agreement between theory and experiment was realized through the use of an equation based on the same arguments used to derive Equation 20.27.

It is seen that a straightforward modeling of Ruchhardt's experiment to include damping yields an equation of motion that is in the form of hysteretic damping. It appears that, for many systems in which the dissipation is dominated by internal friction, hysteretic damping is a near universal form.

20.12.3 Physical Pendulum

In the paper by Speake et al. (1999), one finds the following statement:

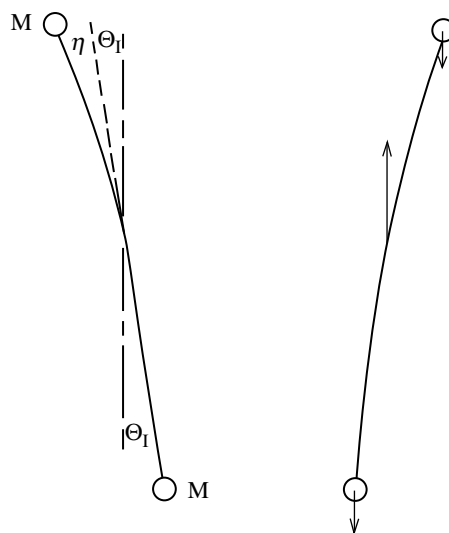
the logarithmic decrement (Q^{-1}) varied as the inverse of the square of the frequency. We interpreted this as evidence that, in Cu–Be over this frequency range, the imaginary component of Young's modulus was independent of frequency, contrary to that which was predicted by the Maxwell model.

To fit their theory with experiment, they used a “modified” Maxwell model with a distribution of time constants that ranged from 30 sec to more than 4000 sec. Motivation for their continued modeling efforts derived partly from the observation by Kuroda (1995) that anelasticity was cause for some of the huge errors that have been present in estimates of the Newtonian gravitational constant, G , by the time-of-swing method.

Although it gives agreement with their particular experiment, the model of Speake et al. (1999) does not have the blessing of Occam's razor. Moreover, their claim that damping derived primarily from their flex pivot of Cu–Be may not be true. Other studies suggest that the material defining the axis of a long-period pendulum is for many cases no more important (and sometimes much less important) to the damping than the material from which the pendulum proper is constructed. A model which also agrees with experiment of the type they conducted, but which is simpler, is now presented.

Illustrated in Figure 20.13 is an idealized long-period mechanical oscillator which could be labeled a “physical pendulum.” The top and bottom masses are the same, M , assumed to be much greater than the mass of the connecting structure, which is represented by the curved line.

A primary mechanism for internal friction damping can be understood by looking at the external forces acting on the pendulum, which are pictured in the “negative displacement” (b) case. The upward “normal” force that acts through the pivot (usually a knife-edge) is opposed by the pair of bob-weights situated left and right, respectively, of the axis of rotation. As the pendulum swings alternately between positive and negative displacements, the structure undergoes periodic flexure. It should be pointed out that internal friction could still be operative throughout the structure even without net bending; i.e., there



(a) positive displacement (b) negative displacement

FIGURE 20.13 Idealized physical pendulum used to develop the modified Coulomb damping model.

could be complementary pieces of the structure undergoing compression and tension. Even if the oscillator were in the weightlessness of space, a drive torque would result in dynamic reactionary forces that give rise to damping by this means.

Assume that the masses are separated a distance $2L$ and the axis of rotation is ΔL above the geometric center. Applying Newton's Second Law, with the lower mass causing a restoring torque and the upper mass a "destoring" torque, yields

$$\ddot{\theta}_1 + \frac{g}{2L} \left(1 + \frac{\Delta L}{L}\right) \theta_1 - \frac{g}{2L} \left(1 - \frac{\Delta L}{L}\right) \theta_2 = 0, \quad \theta_2 = \theta_1 + \eta \quad (20.28)$$

(Note: Equation 20.28 can be rewritten to accommodate larger displacements, where elastic nonlinearity gives rise to unusual behavior. The amplitude trend of the period is opposite to that of the gravitational nonlinearity, thus providing for improved isochronism. For details refer to Peters, 2003a, 2003b, 2003c).

The difference in displacement of the masses involves an elastic term proportional to θ_1 and a dissipative term that depends on its time rate of change, i.e.

$$\eta = c \left(\theta_1 \cos \delta - \frac{\dot{\theta}_1}{\omega} \sin \delta \right), \quad \omega = \sqrt{g \frac{\Delta L}{L^2}} \quad (20.29)$$

where c is a dimensionless constant. This result can be obtained by the complex exponential Steinmetz (phasor) method. The equation is consistent with the common assumption that stress and strain are related through a complex constant. The angle δ is the phase angle with which η strain) lags behind θ_1 (stress). To describe the motion of the lower mass, we can ignore the elastic part of η , since it does not contribute to the damping (or if the rod does not bend, assuming there still is damping as noted previously). We thus remove the subscript, and after some algebra obtain the result

$$\ddot{\theta} + \frac{\alpha}{\omega} \dot{\theta} + \omega^2 \theta = 0, \quad \alpha = \frac{gc}{2L} \sin \delta, \quad \text{for } \Delta L \ll L \quad (20.30)$$

which can also, in terms of $Q = 2\pi E/(-\Delta E)$, be expressed as

$$\ddot{\theta} + \frac{\omega}{Q} \dot{\theta} + \omega^2 \theta = 0, \quad Q = \frac{2L}{gc\delta} \omega^2, \quad \delta \ll 1 \quad (20.31)$$

If, as a material property, δ is independent of frequency, then Q is quadratic in the frequency; i.e., the damping of the pendulum due to internal friction is inversely proportional to the square of the frequency — even though the internal friction (determined by δ) is itself frequency-independent. It is important to note that the frequency dependence of internal friction is not to be equated with the frequency dependence of the Q of the oscillator, even though internal friction is frequently stated as simply $1/Q$. This will be discussed in greater detail in Section 20.13.2.

20.12.3.1 Test of Q Dependencies

The dependence of Q on frequency and length in Equation 20.31 was tested experimentally with a physical pendulum. Two Pb spheres, each of mass approximately 1 kg, were each drilled through a diameter to allow the insertion of the shaft of an aluminum alloy arrow (length approx. 70 cm) of the type commonly used with compound hunting bows. A second hole was drilled perpendicular to the first and tapped for a set screw. The shaft was sawed into two pieces, which were rigidly rejoined around a carbon-steel knife-edge using force fit and epoxy to machined protuberances above and below the knife-edges. The knife-edges extend perpendicularly outward on opposite sides of the arrow at its center.

20.12.3.2 Simple Method to Measure Damping

Although an SDC sensor could have been employed instead, the experiments to be described were performed with a measurement technique that warrants description because of its novel simplicity — yet it is reasonably accurate. To measure both period and damping, a small "flag" was super-glued to the top of the upper shaft. This flag was a small, thin, U-shaped piece of plastic in which the upper legs of the U were about 1 mm wide, with a spacing between centers of about 0.5 cm. An infra-red photogate of the

type used in general education laboratories was mounted so the flag would trip the photogate during pendulum oscillation. Two different timing measurements were then performed, using a Pasco Smart Timer. In every run, the pendulum was displaced initially about 10° by hand and then released. There was no need for precision initialization.

In the pendulum mode of the timer, the period was directly measured. For this case, the photogate was positioned, relative to the U-shaped flag (for which one vertical arm is slightly longer than the other), so as to be interrupted only once by the pendulum per pass. In the time-interval mode, the flag was positioned so that both arms interrupted the photogate beam. The reciprocal of this time of interruption proved to be a reasonable measure of the instantaneous speed of the pendulum at the position of the photogate, which was that of maximum kinetic energy. The time intervals were recorded manually for traversals separated by one period, through five cycles of oscillation. These numbers were then typed into Excel and their reciprocals graphed. A trendline (using the option to print the slope) was applied to the near linearly declining graph. The decrement of this line (fractional decrease per cycle) proved to be a good approximation to the logarithmic decrement of the motion, which could have been estimated with exceptional precision by means of the other techniques mentioned in this chapter.

In the first set of experiments, the sphere on the lower shaft was maintained at a constant distance from the knife-edge, while the mass on the upper shaft was positioned at increasingly greater distances from the knife-edge to lengthen the period. Over the full range of periods considered, the distance between the two masses changed by a small amount around its nominal value of 67 cm. The results of this first study are shown in the left graph of Figure 20.14, where the log-decrement has been plotted vs. the square of the period. The Q of the pendulum (π/Δ) may be calculated for any value of the period using the indicated slope of 0.0004. For example, the Q at a period of 10 sec was 76, this being near the shortest period considered. Near the other extreme of $T = 35$ sec, $Q = 6$. At the shortest possible periods, damping due to air drag would begin to become important.

The reasonable fit of the linear regression vs. period squared is consistent with the prediction by Equation 20.31 that Q should be quadratic in the frequency.

The Equation 20.31 also indicates that the log-decrement should be proportional to the reciprocal of the distance, L , between the masses. To test this prediction, the period of the pendulum was measured as a function of mass separation, also using the smart timer. In generating the data for the right graph of Figure 20.14, the period was maintained constant at 20 sec. For every datum, the top sphere was always only slightly closer to the knife-edge than the lower sphere. At 0.049, the intercept of the trendline differs enough from zero, relative to the size of the error bars, to imply a systematic error. Possible sources of the error include: (i) the masses are of finite size, rather than being points as assumed by the model, and (ii) a nonnegligible mass from parts other than the spheres. Nevertheless, the data show a clear size dependence of the Q .

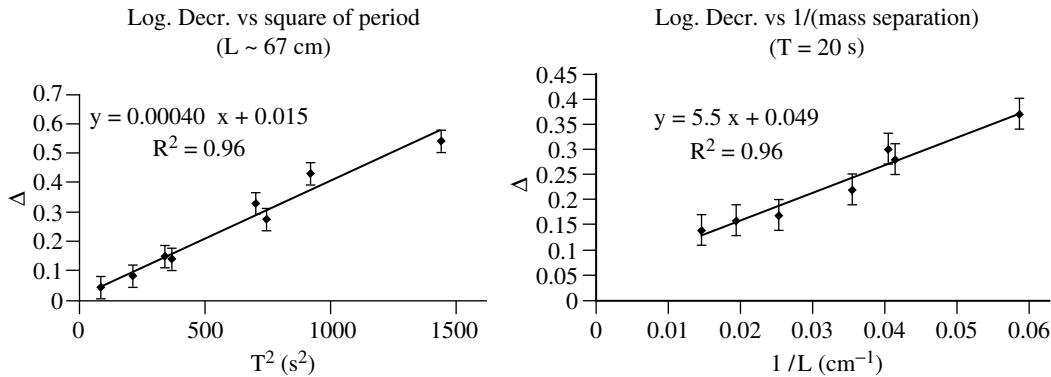


FIGURE 20.14 Results of experiments to test the dependencies of Q on (i) frequency and (ii) length of pendulum.

The experiments just described do not permit one readily to isolate the source of the damping, which, for the cases in [Figure 20.14](#), had the knife-edge resting on silicon wafers (integrated circuit stock material). It is not known to what extent the dissipation was dominated by strain in the knife-edge–silicon interface or by flexure of the aluminum arrow. Although the model that generated equation 20.31 assumed only the latter, there is nevertheless theoretical and experimental basis for model acceptance, regardless of the details of the damping.

20.12.3.3 Highly Dissipative, yet Hard Materials

The same pendulum was used to demonstrate some counterintuitive features of internal friction damping by replacing the Si wafers with various materials. When very soft material, such as lead, was the support for the knife-edges, there was a significant increase of the damping, as expected. It was also found, however, that cast iron increased the log-decrement (10-sec period) by more than 40%. The same was also true of ceramic PZT wafers of the type used to ignite gas grills by striking the wafer impulsively. Both the cast iron and the lead–zirconate–titanate samples are very hard, so the internal friction must derive from large defect densities in which atomic disorder is a sensitive function of stress. Some other hard interfaces, such as steel on glass, or steel on sapphire, did not show a difference from steel on Si, which suggests that the dominant source of damping for the pendulum in all these cases was flexure of the aluminum shaft.

The observation involving cast iron is consistent with its known excellent damping properties at higher frequencies — important, for example, to engine blocks. Some magnesium alloys have also been developed that have excellent damping characteristics without seriously sacrificing strength.

20.13 Internal Friction

20.13.1 Measurement and Specification of Internal Friction

Mechanical spectroscopy is a popular means for measuring internal friction of materials (Fantozzi, 1982). Typically, a torsion pendulum is used to stress harmonically a sample and the lag of the response (strain), relative to the stress, provides the loss tangent and thus the internal friction. In such experiments, it is widespread practice to report internal friction as Q^{-1} . There can be confusion because of this practice, depending on the nature of the measurement technique, i.e., whether one actually measures Q as opposed to measuring something proportional to the stress–strain lag angle. If Q is obtained from an oscillatory free decay, using the logarithmic decrement defined as follows, then there is no problem.

$$\Delta = \ln \frac{x_n}{x_{n+1}} = \beta T = \frac{\pi}{Q} \quad (20.32)$$

Here, x_n and x_{n+1} are adjacent turning point amplitudes separated by one period of the motion, T . In practice, it is very difficult to adjust a mechanical system to oscillate over a wide frequency range. The widest range known to the author, for a mass–spring system, involved the work of Gunar Streckeisen (1974), in which a vertical seismometer using the LaCoste spring was adjusted to have periods in the range between 7 and 140 sec. Because of the difficulties in attaining a wide range of eigenmodes, internal friction is typically determined with a specimen that does not oscillate. We now consider that case.

20.13.2 Nonoscillatory Sample

In the typical torsional pendulum used to measure internal friction, the sample is of very small mass. Such a pendulum was built, for example, around the original version of the fully differential capacitive sensor, to study magnetoelastic wires (Atalay and Squire, 1992). As with many delicate instruments, the Atalay and Squire instrument was of the type labeled “inverted.” A silk fiber at the top of the specimen was used to provide minimal tension in the sample. They used one linear rotary differential capacitance

transducer (LRDCT) (Peters, 1989) in the drive mode to provide a known stress to the delicate magnetoelastic sample and a second LRDCT to measure the strain magnitude and the angle by which it lags behind the stress because of an elasticity. As such, they were measuring the lag angle and not Q , as will now be shown.

Without an inertial term, the sample response x to a periodic external force F is governed by

$$F = Kx = (k + j\zeta)x = F_0 e^{j\omega t} \quad (20.33)$$

so that the transfer function is given by

$$\frac{x}{F} = k^{-1} - j \frac{\zeta}{k^2} \quad (20.34)$$

from which it is seen that the measurement does not yield Q^{-1} but rather the lag angle ζ/k , where k is constant. Perhaps the measured angle, which is an indicator of the internal friction, has been called Q^{-1} because $k = m\omega_0^2$ for an oscillator of frequency ω_0 , and $Q = m\omega_0^2/\zeta$ for the freely decaying oscillator. Bear in mind, however, that this expression for k does not apply to the nonoscillatory measurement just described. There is a frequency square difference between such a measurement and what would be measured if an adjustable oscillator were being considered.

An example of the importance of this issue is found in the article by Lakes and Quakenbush (1996), in which one reads from the abstract the following statement:

The damping, $\tan \delta$, followed a ν^{-n} dependence, with $n \approx 0.2$, over many decades of frequency ν . This dependence corresponds to a stretched exponential relaxation function, and is attributed to a dislocation-point defect mechanism. It is not consistent with a self-organized criticality dislocation model which predicts $\tan \delta \propto A^{-2}$. Dislocation damping in metals is relevant to development of high damping metals, the behavior of solders and of support wires in Cavendish balances.

The present arguments suggest that the experiment by Lakes and Quackenbush is (1996) not in strong disagreement with the SOC model; that the magnitude of the exponent difference between theory and experiment is really 0.2 and not 1.8 as they have indicated.

20.13.3 Isochronism of Internal Friction Damping

It is well known that, in the viscous damping free-decay case, the frequency of oscillation is lowered by damping according to

$$\omega_1 = \sqrt{\omega_0^2 - \beta^2} = \omega_0 \sqrt{1 - (2Q_v)^{-2}} \quad (20.35)$$

and the resonance frequency of the driven oscillator is lowered even further (Marion and Thornton, 1998). It is not well known how difficult it is to measure this damping “red-shift,” which brings in features of the Heisenberg uncertainty principle. Additionally, it is not well known that extensive damping experiments suggest that the frequency may not, for some systems, depend on the damping at all; i.e., the oscillator is isochronous. Isochronism cannot be realized with a linear homogeneous differential equation, but it can be realized with a nonlinear form that is obtained by modifying the damping term as follows:

$$\frac{\omega}{Q} \dot{x} \rightarrow \frac{\pi}{4} \frac{\omega}{Q} \sqrt{\omega^2 [x(t)]^2 + [\dot{x}(t)]^2} \text{sgn}(\dot{x}) \quad (20.36)$$

where $\text{sgn}(dx/dt)$ is the algebraic sign of the velocity — it causes the equation of motion to be nonlinear even if the square root term were not present. For small damping, the square root term can be shown to be equal to the time-dependent amplitude of the motion multiplied by the angular frequency.

Other damping types are possible and are indicated in Peters (2002a, 2002b, 2002c) (...universal...) where evidence is also provided for harmonic distortion in the waveform because of the nonlinearity. It is shown in Peters and Pritchett (1997) that the oscillation is isochronous.

For large values of Q , the lag angle (radian measure) is given by $\delta = 1/Q$. Researchers usually measure δ and specify the magnitude of the internal friction as Q^{-1} . As noted previously, Q is proportional to frequency for the viscous damped oscillator. Thus, for viscous damping, the internal friction is inversely proportional to the frequency.

For hysteretic damping we obtain the result

$$\tan \delta = \alpha = \frac{h}{k} \quad (20.37)$$

where the variables are defined in Equation 20.19. For small damping in which $\tan \delta = \delta = Q^{-1}$, we find that the internal friction for hysteretic damping is inversely proportional to the square of the frequency, since h is constant and $k = m\omega^2$.

20.14 Mathematical Tricks — Linear Damping Approximations

20.14.1 Viscous Damping

In the Hooke's Law expression, $F = -kx$, it is common practice to approximate hysteresis of oscillatory motion by letting k become a complex coefficient. This is also standard practice in a variety of fields, such as the description of lossy electromagnetic media. No doubt the practice has been further popularized by the standard approach of solving electrical engineering ac circuit problems by means of phasors, the technique developed by Steinmetz (1893).

We recognize in the expression $x(t) = x_0 e^{j\omega t} = x_0 \cos \omega t + jx_0 \sin \omega t$ that harmonic variation is contained in the real part (or alternatively the imaginary part) of the complex exponential form. Using Newton's Second Law, and representing the spring constant by $k e^{j\delta}$ with $\delta \ll 1$ (small damping), we obtain the damped harmonic oscillator equation

$$m\ddot{x} + kx + (jk\delta)x = 0 \quad (20.38)$$

where the approximations $\cos \delta \rightarrow 1$ and $\sin \delta \rightarrow \delta$ have been employed.

However, since $\dot{x} = j\omega x$, and $\frac{k}{m} = \omega^2$, Equation 20.38 can be rewritten as

$$\ddot{x} + \omega\delta\dot{x} + \omega^2 x = 0 \quad (20.39)$$

We thus see that the damping constant $\omega\delta = \omega/Q = 2\beta$ permits us to express the logarithmic decrement Δ in terms of the angle δ with which x lags F ; i.e., $\Delta = \beta T = \pi\delta$. (Note that we are making no distinction here between the periods with and without damping, since the difference is small and hard to measure.) If β were independent of frequency, then δ would be inversely proportional to the frequency, which is rarely realized in practice.

20.14.2 Hysteretic Damping

Equation 20.39 does not properly represent some of the most important engineering systems. For those labeled "hysteretic," we must use a different form for the complex spring constant. We assume that $F = -(k_{\text{complex}})x = (k + jh)x$ where h is a real constant. Since $dx/dt = j\omega x$, this yields the equation of motion

$$\ddot{x} + \frac{h}{m\omega}\dot{x} + \omega^2 x = 0 \quad (20.40)$$

Since h is assumed to be a true constant (independent of frequency), the lag angle between displacement and force is given by

$$\delta = \frac{h}{k} = \frac{1}{Q} = \frac{h}{m\omega^2} \quad (20.41)$$

which is seen to be inversely proportional to the square of the frequency. (Note that δ here is the same as α in Figure 20.6.) It should be noted that the complex form for the spring constant is not simply obtained using the common theory of viscoelasticity. Such theory requires a multitude of relaxation times (stretched exponentials) (Speake et al., 1999).

20.15 Internal Friction Physics

20.15.1 Basic Concepts

All damping derives from varying degrees of complexity because of the myriad interactions that are present, either internal of nonconservative type or external involving the environment. This is true even for systems that come closest to being governed by the textbook equations. For example, the author has attempted to produce ideal harmonic oscillators using viscous liquids for damping. Even they are complicated and do not strictly obey Stokes' Law of drag force proportional to the velocity. The nonlinear Navier–Stokes equation may be capable of describing them, but not in a simple form except to a first approximation that is not really very good relative to the precision that is possible with modern sensors.

Perhaps the closest to being an ideal viscous damped oscillator is that in which the damping force derives from eddy currents through Faraday's Law. A magnet is attached to the oscillator and, as it moves in proximity to a conductor, the time rate of change of magnetic flux gives rise to a retarding force that is proportional to velocity. Because there really is a force involved, and because of Lenz's Law, the damping term makes sense physically. This case might be completely ideal except for one factor — the magnet is part of a mechanical system that must possess structural integrity if it is to oscillate. Because of loads present in the structure (reactionary normal forces to the various weights), there will always be some creep. The creep is ultimately unavoidable, since there is apparently no stress threshold below which plastic deformation ceases to exist. It is important to realize that forces associated with inertial mass (Newton's Second Law) are just as important as the weights. Systems designed around an elastic member (such as a spring, in contrast to a simple pendulum) will experience damping in the weightlessness and the airlessness of space.

20.15.2 Dislocations and Defects

The extent to which mechanical defects, such as dislocations, have been ignored by large segments of the scientific community is surprising. The surprise is even greater when one considers the importance of defects in another field — that of electronics. Our present information age (world of computing) came into existence only after widespread recognition of the importance of the defects called impurities. The n-type and p-type semiconductor materials necessary to our modern age result from the substitution of silicon atoms with others of pentavalent and trivalent type in surprisingly small concentrations.

The strength of solids is very much less than as predicted by theories of an ideal (perfect) crystal. Dislocations are the primary culprits. Their influence on materials used in engineering has prompted the statement: "when mother nature fills the vacuum she abhors, she rarely does so with perfection." Unfortunately, few students exposed to fundamental science receive training in defect physics. Moreover, it is difficult to provide a self-consistent fundamental description of their properties, so very few scientists have more than a superficial knowledge of their importance.

"Viscoelasticity" is a misleading term. To combine the words viscous and elastic suggests that the state variables vary smoothly in time, i.e., as a fluid in the viscous part. Unfortunately, this is not true of hysteresis associated with either "domains" or with "grains." In the case of magnetic domains, it is quite easy to demonstrate nonsmooth (jerky) behavior that is called Barkhausen noise. Although the phenomenon was demonstrated by Barkhausen in 1919, only recent studies have begun to understand some of its complexities better (Urbach et al., 1995a,b).

A similar phenomenon, that must relate in some manner to the Barkhausen effect, is the PLC effect. Under applied stress, alloys frequently display discontinuous strain increase (jumps). The author has

even demonstrated strain recovery of a similar type, catalyzed by “tapping.” The polycrystalline metals that demonstrate these effects are obviously influenced by “granularity.” They differ from the “granular materials” that have become a hot topic of recent research. Even pure polycrystalline metals exhibit these features. The German word to describe the deformation of tin under large stresses is *zinnigeschrei* (=tin cries). Anyone who has ever bent large-diameter tungsten wire has experienced this phenomenon, since the nonsmooth strain can be both felt and heard.

There is still another type of material, thought to have great engineering potential in the future, that shows “granular” behavior — that of shape memory alloys (SMA). If an SMA specimen is cycled in temperature around the martensitic phase, it generates acoustic emissions (Amengual et al., 1987). For a figure taken from their work and other good pages about hysteresis, refer to the webpages of Prof. Sethna at <http://www.lassp.cornell.edu/sethna/hysteresis/ReturnPointMemory.html>. These emissions are probably related to the PLC effect and are characterized by surprising reproducibilities in spite of their complex behavior.

Thus, there is abundant experimental evidence against the overly simplistic view that hysteretic damping can be meaningfully described by simple, linear differential equations. The nonlinear terms necessary for a good mathematical treatment go beyond “chaos” to the world of “complexity.” Chaos of deterministic type, though bewildering to many, is in many cases tractable (using equations that can be integrated numerically). Damping problems are much more complex than deterministic chaos. The challenges to our understanding derive in part from the long time that it has taken before there were any serious investigations of the mesoscale, the place where defect structures abide. If, as with Zener, we use the word anelasticity to describe systems that are “other than” elastic, then the term *mesoanelastic complexity* is an appropriate label for this poorly understood physics that is important and yet mostly unknown to many fields of both science and engineering.

20.16 Zener Model

20.16.1 Assumptions

The SLM of viscoelasticity provides a sound basis for some damping phenomena, yet it fails badly as an approximation for hysteretic damping. Its prominence in both the worlds of physics and engineering warrants the following detailed discussion so that the failure case may be properly documented.

Following the example of Zener, the following linear differential equation relates the stress, σ , the strain, ε , and their first time derivatives:

$$\sigma(t) + \tau_\varepsilon \dot{\sigma} = E_1(\varepsilon + \tau_\sigma \dot{\varepsilon}) \quad (20.42)$$

The τ s are relaxation times (subscript ε meaning at constant strain and subscript σ at constant stress), and E_1 is the relaxed elastic modulus (ratio of stress to strain in a very slow process). Nominally, $\tau_\sigma > \tau_\varepsilon$, consistent with strain lagging stress. For periodic variations

$$\sigma(t) = \sigma_0 e^{j\omega t}, \quad \varepsilon(t) = \varepsilon_0 e^{j\omega t} \quad (20.43)$$

which, when substituted into Equation 20.42, yields

$$(1 + j\omega\tau_\varepsilon)\sigma_0 = E_1(1 + j\omega\tau_\sigma)\varepsilon_0 \quad (20.44)$$

The complex modulus of elasticity is defined by

$$E_C = \frac{1 + j\omega\tau_\sigma}{1 + j\omega\tau_\varepsilon} E_1 \quad (20.45)$$

and is seen to relate stress and strain according to

$$\sigma(t) = E_C \varepsilon(t) \quad (20.46)$$

From Equation 20.45, the real and imaginary parts of the modulus are found to be

$$\text{Real } (E_C) = \frac{1 + \omega^2 \tau_e \tau_\sigma}{1 + \omega^2 \tau_e^2} E_1 \quad (20.47)$$

$$\text{Imag } (E_C) = \frac{\omega(\tau_\sigma - \tau_e)}{1 + \omega^2 \tau_e^2} E_1 \quad (20.48)$$

The independent variable, or “frequency,” for all cases is the convenient dimensionless parameter, $\omega\tau = \omega\sqrt{\tau_e \tau_\sigma}$.

It is convenient to use polar form, so that

$$E_C = |E_C| e^{j\delta} \quad (20.49)$$

where $|E_C|$ is obtained by computing the square root of the sum of the squares of the real and imaginary parts. In this form, it is apparent that δ is a lag angle which determines the damping loss for the system. Moreover, from Equation 20.47 and Equation 20.48, it is seen to obey

$$\tan \delta = \frac{\omega(\tau_\sigma - \tau_e)}{1 + \omega^2 \tau_\sigma \tau_e} \quad (20.50)$$

20.16.2 Frequency Dependence of Modulus and Loss

The essential features of the Zener model are illustrated in Figure 20.15, where the “unrelaxed” high-frequency modulus obeys the relation $(E_1 E_2)/(E_1 + E_2) = E_1(\tau_\sigma/\tau_e)$.

In viscous damping models, the damping is quantified by the product βT , which is equal to the logarithmic decrement. The logarithmic decrement is directly proportional to the period when the damping “constant” β is truly constant. The graph in Figure 20.16 compares the logarithmic decrement computed by the standard model against a case where $\beta = \text{constant}$. Also shown in the figure is a set of hysteresis curves for $\omega\tau = 10, 1$, and 0.1 , respectively. Notice that the damping is large only for $\omega\tau$ near 1, in accord with the bottom plot of Figure 20.15. For that case, points (a) to (f) and back to (a) are shown, labels to illustrate work done by the stress in traversing the hysteresis loop. The algebraic sign of the work changes around the loop and the net work done in one cycle is just the area enclosed by the loop.

For damping based on the Zener (standard linear) model to agree with the simple viscous approximation, it is necessary that $\omega\tau \gg 1$; i.e., the period of the oscillator must be significantly shorter than the smaller of the relaxation times, as illustrated in the bottom graph of Figure 20.16.

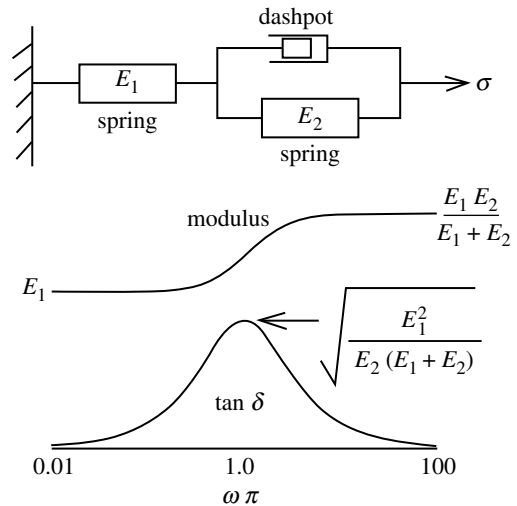


FIGURE 20.15 Zener Model of anelasticity. Bottom curves are “frequency” variation of modulus and loss respectively.

20.16.3 Successes — Models of Viscoelasticity

Viscoelasticity, as an approximation for damping, is evidently quite adequate for some materials. The assumption of fluid character as a basis for hysteresis is expected to be closest to correct when

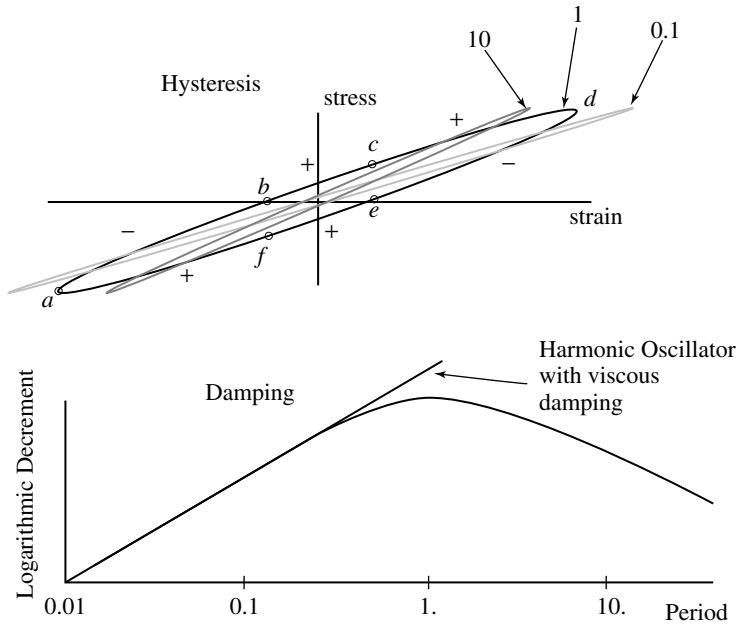


FIGURE 20.16 Characteristics of the Zener model.

applied to those cases in which variations in strain are almost continuous. The materials of rheological type for which this appears to be most true are solids built from long chain polymers, i.e., various plastics. Such materials can yield surprising results, however. Shown in Figure 20.17 are results from a study that used a nylon monofilament sample (8-lb fishing line). The pair of torsional free-decay records corresponds to two different temperatures — 290 K (room temperature) and 390 K (above the glass transition temperature of the nylon). Although a significant increase in the period was observed as the temperature was increased above the glass transition temperature (changing from 18.2 to 27.8 sec), the logarithmic decrement was found to be almost unchanged. This was not in keeping with the expectation that softening of the material at the higher temperature would result in significantly greater damping. The effect is just the opposite of what was mentioned concerning cast iron, which, though very hard, does not have small damping. Here, a softening does not result in significantly increased damping.

Although there was some creep observed for both the decays of Figure 20.17, the creep was more pronounced in the higher temperature case. This is illustrated by the lower curve of the bottom graph, which is a computer fit in which the secular term necessary for best fit was removed to illustrate the creep. In both decay cases, the log decrement was calculated by importing the A/D data (Dataq DI-154RS) to Excel and then using trial and error adjustment of parameters to achieve the best fit.

Although the damping of glasses is normally treated using the theory of viscoelasticity, Granato (2002) has recently modeled these materials via defects. In his paper, Granato states the following: “As dislocations carry the deformation in crystals, interstitials are the basic microscopic elements carrying the deformation in glasses near and above the glass temperature.”

20.16.4 Failure of Viscoelasticity

Unfortunately for the elegant theory of the Zener model that has been presented, there are many mechanical systems for which the Q is not proportional to frequency, but rather proportional to the square of the frequency. The logarithmic decrement ($\Delta = \pi/Q$) has been measured for a host of

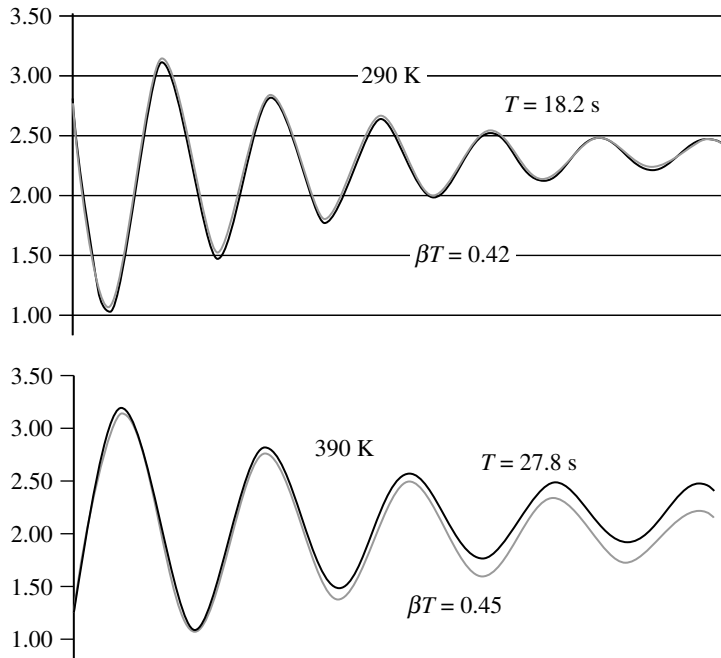


FIGURE 20.17 Torsional free-decay records of monofilament nylon at temperatures first below and then above the glass transition temperature. Although the modulus decreased dramatically at the higher temperature, the damping did not.

long-period mechanical oscillators, configured as some form of a pendulum. In all cases, these systems were described approximately by $\Delta = \beta T \alpha T^2$ rather than by $\beta T \alpha T$. Similar behavior has been noted in mechanical oscillators other than the pendulum — for example, in the geophysics research of Gunar Streckeisen and Erhard Wielandt, who are well known for the development of the widely employed STS-1 seismometer. During his pursuit of the Ph.D., Streckeisen (1974) measured the numerical damping (fraction of critical damping) of a vertical Sprengnether long-period seismometer 5100-V. After removing the magnet of the velocity transducer (to eliminate eddy currents and reduce viscous air damping, he found that the numerical damping was proportional to the square of the period between periods of 7 and 140 sec. He took about 30 measurements over this interval of periods, and showed that the damping increased from about 0.0008 to about 0.3 — a factor of roughly 400, not 20 as one would expect for viscous damping. To quote Wielandt (private communication), “the data are very clear.”

20.17 Toward a Universal Model of Damping

20.17.1 Damping Capacity Quadratic in Frequency

The quadratic dependence on frequency of Q (log decrement proportional to period squared) is equivalent to friction force being frequency-independent. In support for the claim of universality, it was noted in the Introduction (Section 20.2.2) that three very different systems showed this characteristic: (i) the vertical seismometer just discussed, (ii) various pendula, and (iii) the rotating rod direct measurement of internal friction first done by Kimball and Lovell (1927), who measured the transverse deflection of the end of a rod when it was rotated about a horizontal axis.

20.17.2 Pendula and Universal Damping

An example of one of the author's experiments that illustrate universal (hysteretic) damping is provided in [Figure 20.14](#). Other works that illustrate hysteretic damping include those by Peter Saulson of Syracuse University, who has been frequently cited in the literature (see Saulson et al., 1994).

The pioneering work of Braginsky (important to LIGO) has already been mentioned in the context of small force measurements and noise. He and his Moscow group members argue that the internal friction in fused silica may be roughly independent of frequency from 0.1 Hz to 10 kHz (Braginsky et al., 1993).

An oft-cited paper speaking to the issues of hysteretic damping is an article by Quinn et al. (1992) concerned with material problems in the construction of long-period pendula. (The type of pendulum on which they based their studies was first described in the scientific literature 2 years earlier (Peters, 1990).) In a follow-on paper, Speake et al. (1999) state the following: "The analogues of anelasticity and its resultant $1/f$ noise are seen in a wide range of other processes (for example, dielectric and magnetic ones) described in terms of frequency-dependent susceptibilities."

The jerkiness (discontinuous change) that is the hallmark of the Barkhausen effect may have been first seen mechanically in the experiments that generated the metastable states paper. From a consideration of the chapter by James Brophy (Brophy, 1965), it was postulated in this 1990 paper that the jerky behavior of a mesodynamic pendulum is a type of mechanical Barkhausen effect.

20.17.3 Modified Coulomb Model — Background

The results that follow grew naturally out of the application of fully differential capacitive sensors to the study of mechanical oscillators. Efforts to model internal friction influence on long-period pendula uncovered something surprising to most — that the foundation for physics laid by Charles Augustin Coulomb may be much broader than had been realized. Most individuals in the physics community do not associate Coulomb's name with contributions other than to the laws of electrostatics. Engineers, however, have long used his name in the context of sliding friction, since, in fact, Coulomb gave us the empirical description which involves static and kinetic coefficients. Because of his interest in the civil engineering of soils (Heyman, 1997), Coulomb also provided something else — a basis for understanding granular flows and even some types of fracture. Concerning the latter, the Mohr criterion, applied to the Coulomb failure envelope, defines a "coefficient of internal friction," which is used to predict brittle failure (Gere and Timoshenko, 1996).

Coulomb friction is empirically simple, at least as a first approximation, since it depends only on the normal force between surfaces and the algebraic sign of the velocity when there is relative motion. Like so many problems of multibody type, a complete theory of sliding friction is far from being realized. Simplistic textbook efforts to explain energy loss, by picturing "hills and valleys" of the surface of two solids in contact, are useless. An example of such naivete can be realized by trying to understand the phenomenon of optical contacting. Two orthogonally oriented fused silica cylindrical fibers, allowed to touch, can experience atomic bonding forces that are surprisingly strong, being much greater than the weak attraction of the van der Waals type. Cleanliness of the surfaces is paramount for success in such a demonstration, which speaks to another issue — a connection between internal friction and surface physics.

The conversion of mechanical energy to thermal energy must involve nonlinear (avalanche or cascade) processes. A heuristic description of defect structural interactions that generate heat and eventual failure is the phonon triangle of Tom Erber (Illinois Tech University) shown in Figure 20.18. The author has

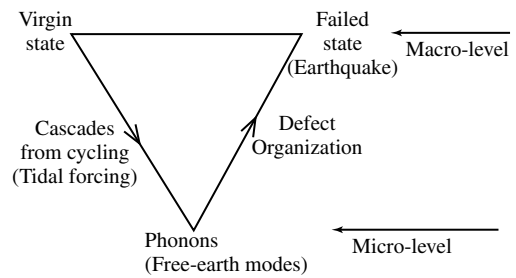


FIGURE 20.18 Heuristic description of how materials fail — processes connected with damping.

extended Erber's triangle to include the larger-scale Earth in an attempt to explain earthquakes. Everybody recognizes that the bending of a wire does not take it from the virgin initial state to the failed state along the macroscopic upper leg.

There must first be a downward path to the microlevel, through cascading. These cascades can cause Barkhausen noise in the case of ferromagnetic samples, and acoustic emission in nonmagnetic metallic alloys (PLC effect). Failure requires the upward path of defect organization, the mechanisms of which are not yet understood. One of the first theories with possible implications to the organization leg is that of self-organized criticality. In the magnetic case, Erber has used a fluxgate magnetometer to improve failure predictions, since magnetic hysteresis is proving to be a sensitive indicator of mesoscale structure changes during cycling toward failure. Inferred from these studies is some yet-to-be discovered connectivity between noise, damping, and failure.

Surface friction is expected somehow to be connected with internal friction, the biggest difference being that the surface has many more defect states with which to redistribute energy. The larger density of states of the surface (reduced order) is probably an important factor in the difference between surface friction and the modified internal friction model which follows.

20.17.4 Modified Coulomb Damping Model — Equations of Motion

In the following damping model for internal friction, Coulomb's law of sliding friction is modified by assuming that the coefficient of friction is not constant, but rather involves the energy of oscillation E in a power law; i.e.

$$m\ddot{x} + cm \left[\frac{2E}{k} \right]^\lambda \text{sgn}(\dot{x}) + kx = 0, \quad E = \frac{1}{2}m\dot{x}^2 + \frac{1}{2}kx^2 \quad (20.51)$$

where c = constant that is different for each λ . For Coulomb (sliding) friction $\lambda = 0$. For amplitude-independent damping of hysteretic type, $\lambda = \frac{1}{2}$. For amplitude-dependent (such as large Reynolds number fluid) damping, $\lambda = 1$. In all cases, if $c \ll 1$ (small damping), the damping capacity is quadratic in the frequency, so that the internal friction $Q^{-1} \sim \omega^{-2}$. Equation 20.51 is easily implemented, in spite of its nonlinearity, which we will see later to be a cause for harmonics in the decay.

It is convenient to rewrite Equation 20.51 in canonical form so as to involve the Q of the oscillator. For the case of hysteretic damping ($\lambda = \frac{1}{2}$), the equation becomes

$$\ddot{x} + \frac{\pi\omega}{4Q_h} \sqrt{\omega^2 x^2 + \dot{x}^2} \text{sgn}(\dot{x}) + \omega^2 x = 0 \quad (20.52)$$

Similarly, for amplitude-dependent damping ($\lambda = 1$)

$$\ddot{x} + \frac{\pi}{4y_0 Q_{f0}} (\omega^2 x^2 + \dot{x}^2) \text{sgn}(\dot{x}) + \omega^2 x = 0 \quad (20.53)$$

where y_0 is the initial value of the amplitude of x (largest maximum of x), and Q_f is found not to be constant, as in the case of hysteretic damping. Rather, in this case, the Q increases as the amplitude decreases. On the other hand, the Q of an oscillator influenced only by Coulomb ($\lambda = 0$, sliding) friction decreases with the amplitude, and the equation of motion in canonical form is given by

$$\ddot{x} + \frac{\pi\omega^2 y_0}{4Q_{c0}} \text{sgn}(\dot{x}) + \omega^2 x = 0 \quad (20.54)$$

In Equation 20.53 and Equation 20.54, the subscript 0 is used to identify the initial value of the time varying Q . Equation 20.54 is equivalent to equation 20.12 with $Q_{c0}/y_0 = \pi/(4\Delta_x)$.

As will be illustrated with some examples, it is possible for an oscillator to be influenced simultaneously by all three types of friction. One may treat such a system with the following equation of motion

$$\ddot{x} + \left[\frac{\pi\omega^2 y_0}{4Q_{c0}} + \frac{\pi\omega}{4Q_h} \sqrt{\omega^2 x^2 + \dot{x}^2} + \frac{\pi}{4y_0 Q_{f0}} (\omega^2 x^2 + \dot{x}^2) \right] \text{sgn}(\dot{x}) + \omega^2 x = 0 \quad (20.55)$$

At any instant during the decay, the total (time-dependent Q) is given by

$$\frac{1}{Q(t)} = \frac{1}{Q_c} + \frac{1}{Q_h} + \frac{1}{Q_f} \quad (20.56)$$

in which it is seen that the smallest Q in the set (largest damping term) is dominant in a manner reminiscent of capacitors connected in series.

It is instructive to look at the analytical solution for the time dependence of the amplitude (turning points, $y(t) = |x_{\max}|$), when all the Q s $\gg 1$. Such a solution is obtained from energy considerations by noting first that the time rate of change of the energy is zero in the absence of friction, i.e.

$$\dot{E} = \frac{d}{dt} \left(\frac{1}{2} m \dot{x}^2 + \frac{1}{2} k x^2 \right) = \dot{x}(m\ddot{x} + kx) = 0, \quad \text{no friction} \quad (20.57)$$

With friction, dE/dt is determined by the rate of doing work against the friction force; i.e., dE/dt is proportional to $\omega y f$, where f is the friction force. In the case of Coulomb friction, f is constant (determined by y_0), so dE/dt is proportional to $E^{1/2}$. For hysteretic damping, f is proportional to y , so dE/dt is proportional to E . For fluid damping, f is proportional to y^2 , so dE/dt is proportional to $E^{3/2}$. Thus, the general case is described by

$$\dot{E} = -(c_1 + c_2 \sqrt{E} + c_3 E) \sqrt{E} \quad (20.58)$$

Because the energy is proportional to y^2 , we can write down the equation for the time varying amplitude as

$$\dot{y} = -c - by - ay^2 \quad (20.59)$$

where a , b , and c are constants. The solution to this first-order equation can be found in integral tables, and the result depends on the size of c relative to the product ab . For present purposes, we will restrict ourselves to the case where Coulomb damping is not dominant, in which the solution involves an exponential. (For large c , one may develop the corresponding general case in terms of the tangent or its inverse.) The present result is as follows, using $r = (b^2 - 4ac)^{1/2}$, where $4ac < b^2$

$$\begin{aligned} \text{with } \alpha &= 2ay_0 + b - r, & \beta &= 2ay_0 + b + r, & p &= \frac{\alpha}{\beta} e^{-rt} \\ y &= \frac{b(p-1) + r(p+1)}{2a(1-p)} \end{aligned} \quad (20.60)$$

In the case where $c = 0$, Equation 20.60 can be simplified to the following form, which is useful for curve fitting:

$$\frac{1}{y} = \left(\frac{a}{b} + \frac{1}{y_0} \right) e^{bt} - \frac{a}{b} \quad (20.61)$$

For the case where $a = 0$, the better form for curve fitting is

$$y = \left(y_0 + \frac{c}{b} \right) e^{-bt} - \frac{c}{b} \quad (\text{until } y = 0) \quad (20.62)$$

Curve-fits based on the modified Coulomb damping model are summarized in Box 20.2.

Box 20.2

CURVE-FIT TO THE TURNING POINTS

If no damping

$$\dot{E} = \frac{d}{dt} \left(\frac{1}{2} m \dot{x}^2 + \frac{1}{2} k x^2 \right) = \dot{x}(m \ddot{x} + kx) = 0, \quad \text{no friction}$$

with damping (E prop. to y^2 , \dot{E} prop. to $\omega y \cdot$ friction force)

$$\dot{E} = -(c_1 + c_2 \sqrt{E} + c_3 E) \sqrt{E}$$

equivalent to (c for Coulomb, b for hysteretic, a for fluid)

$$\dot{y} = -c - by - ay^2$$

general solution

$$\text{with } \alpha = 2ay_0 + b - r, \quad \beta = 2ay_0 + b + r, \quad p = \frac{\alpha}{\beta} e^{-rt}$$

$$y = \frac{b(p-1) + r(p+1)}{2a(1-p)}$$

special case, $c = 0$

$$\frac{1}{y} = \left(\frac{a}{b} + \frac{1}{y_0} \right) e^{bt} - \frac{a}{b}$$

special case, $a = 0$

$$y = \left(y_0 + \frac{c}{b} \right) e^{-bt} - \frac{c}{b} \quad (\text{until } y = 0)$$

20.17.5 Model Output

Shown in [Figure 20.19](#) is a case in which the decay is influenced by all three types of friction. Notice how the Q rises initially, peaks at a value less than what would be true for hysteretic damping alone (constant Q case), and then later declines. The initial rise is due to the amplitude-dependent damping term (size determined by coefficient a), and the later decline is due to the Coulomb damping term (determined by coefficient b).

The code in [Table 20.1](#) that was used to generate Figure 20.19 has been reproduced here for two reasons: (i) to show the ease with which the modified Coulomb model may be numerically applied in general to a damping problem, and (ii) to illustrate an integration algorithm that has proven to be intuitive, simple, and powerful — the Cromer–Euler technique, which Alan Cromer first described as the “last point approximation (LPA)” (Cromer, 1981) in contrast to the unstable “first point approximation” given to us by Euler. Over the last 20 years, the author has employed the LPA in a host of applications that span from the generation of satellite ephemerides in the U.S. antisatellite program to both simple and several-body nonlinear problems of deterministic chaos type.

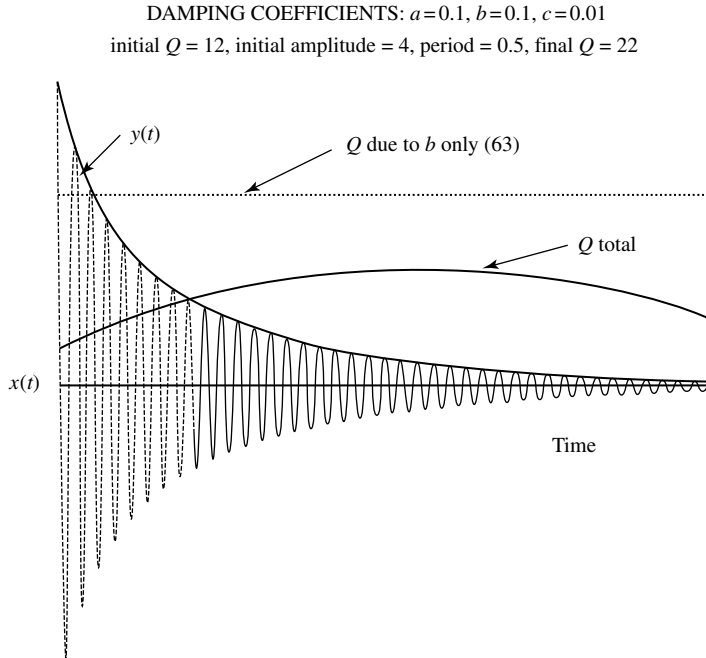


FIGURE 20.19 Model generated results based on Equation 20.55 and Equation 20.60.

20.17.6 Experimental Examples

The code of Table 20.1 is useful in determining the nature of a given experimental case. Too frequently in the past, it has been naively assumed that the entire decay record was exponential. Particularly when longer records are collected, it is found that most damping is nonlinear. In the two experimental examples that follow to backup this claim, one is a near-perfect (nonlinear) particular case of amplitude-dependent (fluid) damping, and the other is a mixture of amplitude-dependent and hysteretic damping, but devoid of any Coulombic influence. Coulomb friction frequently tends to be either “all or nothing,” depending on whether there is an unwanted mechanical contact that involves slippage. A notable exception is found in the case where a pendulum is influenced by eddy current damping in a narrow region of its total motion (Singh et al., 2002).

The pendulum that was used to generate the data displayed in Figure 20.14 was also used as follows. A large flat piece of plastic was attached to the bottom of the pendulum, so that its movement (normal vector to the surface in the direction of motion) would disturb a great amount of air in turbulent manner. As expected, there was a dominant initial (large level) amplitude-dependent damping, as shown in Figure 20.20.

The speed (maximum) was measured with a photogate as previously discussed. The expressions shown in the figure are consistent with Equation 20.59 and Equation 20.61. The data, which were collected by hand and typed into Excel, produced the “jagged” curve, and the computerized fit according to Equation 20.61 is the smooth curve of the pair. It is noteworthy that the quadratic drag of the air (determined by $a = 0.036$) is 40% greater than the viscous drag at the start of the decay. By cycle 37, the quadratic part has become much less significant than the constant Q viscous part, having become roughly 60% smaller.

The fluid damping “soup-can” pendulum data of Figure 20.21 was generated with a can of Bush’s black-eye peas. The container with enclosed unbroken contents, being a right circular cylinder of length 11 cm \times diameter 7.4 cm, was suspended horizontally by a pair of knife edges under opposing end-lips

TABLE 20.1 QuickBasic Code to Calculate Amplitude History $y(t)$ and Integrate Equation of Motion to Obtain $x(t)$; Accommodates Three Common Forms of Friction

```

CLS
REM: setup display
SCREEN 12: VIEW (0, 0) - (600, 470): WINDOW (-.2, - 5) - (1, 5)
REM: assign constants and initialize variables
pi = 3.1416: dt = 0.002: t = 0
x0 = 4: x = x0: y0 = x0: xd = 0
Period = .5: omega = 2*pi/period: b = .1: a = .1: c = .01
REM: print damping coefficients
PRINT "DAMPING COEFFICIENTS: a = "; a; ", b = "; b; ", c = "; c
r = SQR(b^2 - 4*a*c): alpha = 2*a*x0 + b - r
Beta = 2*a*x0 + b + r
REM: Use a, b and c — set Q's to dampen (quadratic, linear, and constant resp.)
qf = omega/2/a/y0: qh = omega/2/b: qc = y0*omega/2/c
REM: start integration loop
LOOP0:
t = t + dt
REM: analytically compute amplitude (y = magnitude of x) at each time point
p = alpha*EXP(-r*t)/beta
y = (b*(p - 1) + r*(p + 1))/2/a/(1 - p)
REM: integr. the eq. of motion to get x(t), using 3 fric. force/mass terms
REM: The coeff's ff, fh & fc correspond to: quadratic in speed (fluid),
REM: linear in speed (hysteretic), and independ. of speed (Coulomb) resp.
ff = (pi/4)*(1/y0)*(1/qf)*(omega^2*x^2 + xdot^2)
fh = (pi/4)*(omega/qh)*SQR(omega^2*x^2 + xdot^2)
fc = (pi/4)*omega^2*y0/qc
REM: check algebraic sign – USE SIGN BUT NOT MAGNITUDE OF VELOCITY
IF xdot > 0 THEN GOTO SKIP
ff = -ff: fh = -fh: fc = -fc
SKIP: xdoubledot = -ff - fh - fc - omega^2*x
xdot = xdot + xdoubledot*dt: x = x + xdot*dt
REM: calculate the energy and then the amplitude to evaluate Q
REM: could instead use analytical result q = (pi/4)*omega^2*x/abs(ff + fh + fc)
Energy = .5*xdot^2 + .5*omega^2*x^2
Amplitude = SQR(2*energy)/omega
REM: calculate loss per period due to friction
loss = ABS(ff + fh + fc)*4*amplitude
q = 2*pi*energy/loss
IF t < 1.2*dt THEN PRINT "initial Q = "; 10*INT(q)/10;
IF t < 20 THEN GOTO SKIP2
PRINT ", initial Amplitude = "; x0; ", Period = "; period;
PRINT ", final Q = "; 10*INT(q)/10
REM: DO GRAPH
SKIP2: PSET(.04*t, .5*q/omega): PSET (.04*t, .5*qh/omega), 4
PSET (.04*t, 4*x/y0): PSET (.04*t, 0): PSET (.04*t, 48*y/y0)
IF t > 20 OR y < 0 THEN GOTO pause
GOTO LOOP0
Pause: GOTO pause
RETURN: END: STOP

```

(Peters, 2002a, 2002b, 2002c). The motion of the can was measured with an SDC sensor connected to a Dataq A/D converter. Whereas experiments of similar type, with homogeneous fluid contents, have produced viscous decay records, the present case involved only friction of so-called “fluid” type; i.e., quadratic in the “velocity.” To generate the figure, the A/D record was exported to the Microsoft software package, Excel. Fits to the data were then obtained by adjusting, through trial and error, the a , b , and c

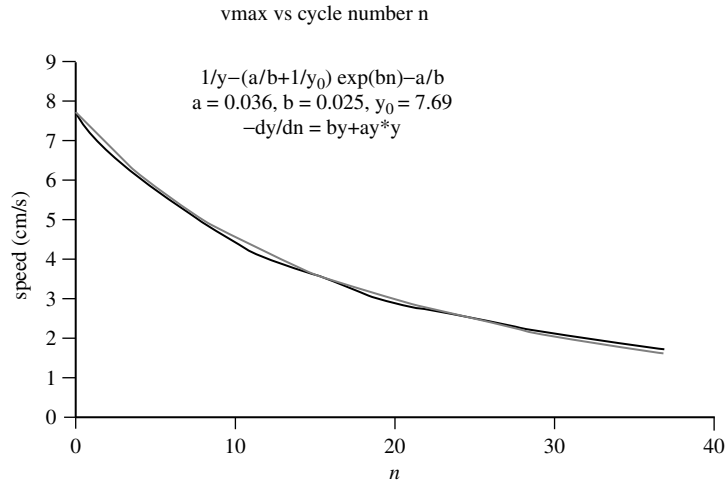


FIGURE 20.20 Decay of an air-damped pendulum as a function of cycle number n .

coefficients of a “fit” to the amplitude. For this case, the fit was easily accomplished because both b and c proved to be essentially zero.

The second case, involving an evacuated pendulum, was not a single pure type of damping, but can be seen in Figure 20.22 to have both hysteretic and amplitude-dependent contributions. Although fluid damping is amplitude-dependent in the same manner, with the damping term being proportional to the square of the amplitude, the word “fluid” is not used to describe this case since the system involved exclusively solid materials.

Not all decay records of this pendulum in vacuum yielded a mix of friction types as displayed in the figure. The effect was observed to be transient, and it is speculated that outgassing of components may have been a factor.

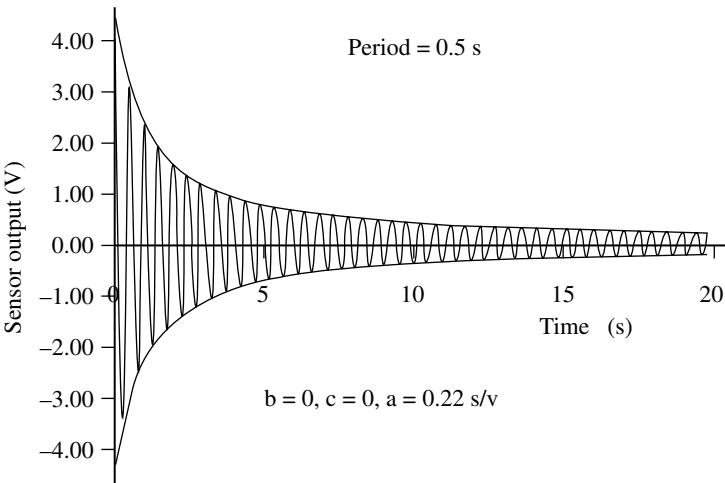


FIGURE 20.21 Example of fluid damping of a “soup-can” pendulum. The granular contents (black-eye peas and water) result in a friction force that is quadratic in the velocity.

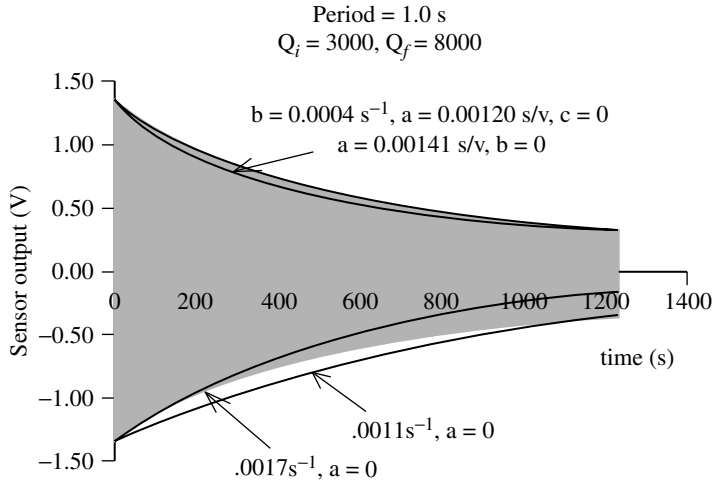


FIGURE 20.22 Example of a mix of two damping types, hysteretic and amplitude-dependent.

20.17.6.1 Numerical Integration

Instead of integrating the second-order equation of motion twice — first the acceleration, followed by the resulting velocity — more accurate results are obtained by integrating the equivalent pair of first-order equations (also see Chapter 6).

For example, the equation of the simple harmonic oscillator with viscous damping is expressible as

$$\dot{p} = -q - kp \quad \dot{q} = p \quad (20.63)$$

where the position variable has been represented by the generalized coordinate q (x elsewhere), and for the momentum $p = m dq/dt$, and here the mass, m , has been set to unity. Likewise, the spring constant has been set to unity. It is generally useful to distill a given problem to its most basic form when attempting to understand the physics. Constants that provide no useful information for trend analysis purposes are conveniently “normalized.” Such is common practice, for example, in modeling chaotic systems.

The second-order set can always be reduced mathematically to a first-order pair; however, the pair results naturally from the use of the Hamiltonian as opposed to the Newtonian formulation of mechanics.

20.17.7 Damping and Harmonic Content

Equation 20.52 to Equation 20.54 are the nonlinear, modified Coulomb damping model forms that correspond, respectively, to (i) hysteretic, (ii) amplitude-dependent, and (iii) Coulomb damping. The damping term for each of the three cases can be expressed as follows:

$$\frac{f}{m} = \frac{\pi}{4} \frac{\omega}{Q} [v] \quad (20.64)$$

where f is the friction force, and $[v]$ is the square wave whose fundamental in a Fourier series expansion is equal to the velocity of the oscillator times $4/\pi$; i.e., for a square wave $\pm h$, the amplitude of the fundamental is $\pm(4/\pi)h$. We see that all the damping types that have been considered in this chapter, when expressed in canonical form, correspond to a fundamental friction force $f = m\omega v/Q$. The simplicity of this result is probably why viscous damping has been viewed by so many physicists as “inviolable.” One must be careful, however, because (as noted in the previous section) only for the case of hysteretic damping is Q constant. For amplitude-dependent damping $Q_f = Q_{f0}(y_0/y)$ and for Coulomb damping

$Q_c = Q_{c0}(y/y_0)$. The time-dependent Q of nonexponential cases will have significant influence on mode development in many-body systems because of elastic nonlinearity (necessary for mode coupling).

There is another important subtlety of Equation 20.64. When only the fundamental of $[v]$ is retained, equivalent to viscous damping, Q is proportional to frequency. When all odd harmonics are included (full square wave), Q becomes proportional to frequency squared. This means that *harmonics in the friction force are responsible for the primary difference between hysteretic damping and viscous damping*. Something being presently considered is how, in an algorithmic sense, to modify Equation 20.52 to Equation 20.54 to provide for “dispersion,” i.e., means for providing Q dependence other than frequency squared. We posit the following: that hysteretic (exponential) damping is the idealized universal form of damping due to secondary creep. When there is an activation process of Zener (Debye) type, such as dislocation relaxation, then additional terms must be added to the hysteretic “background.” It may be that this can be accommodated by a suitable removal of harmonics from the square wave of the hysteretic case, and it may happen that Q is constant for systems that vary continuously. It is conjectured that the PLC effect, responsible for discontinuous changes, plays a role in those cases where Q is not constant. Equations of motion based on the modified Coulomb damping model are summarized in Box 20.3.

Box 20.3

EQUATIONS OF MOTION BASED ON NONLINEAR DAMPING

Equation of motion in terms of energy

$$m\ddot{x} + c m \left[\frac{2E}{k} \right]^2 \text{sgn}(\dot{x}) + kx = 0, \quad E = \frac{1}{2} m \dot{x}^2 + \frac{1}{2} kx^2$$

Hysteretic-only damping (exponential)

$$\ddot{x} + \frac{\pi\omega}{4Q_k} \sqrt{\omega^2 x^2 + \dot{x}^2} \text{sgn}(\dot{x}) + \omega^2 x = 0$$

Velocity-square (fluid) damping

$$\ddot{x} + \frac{\pi}{4y_0 Q_{f0}} (\omega^2 x^2 + \dot{x}^2) \text{sgn}(\dot{x}) + \omega^2 x = 0$$

Coulomb damping

$$\ddot{x} + \frac{\pi\omega^2 y_0}{4Q_{c0}} \text{sgn}(\dot{x}) + \omega^2 x = 0$$

All three damping types simultaneously active

$$\ddot{x} + \left[\frac{\pi\omega^2 y_0}{4Q_{c0}} + \frac{\pi\omega}{4Q_k} \sqrt{\omega^2 x^2 + \dot{x}^2} + \frac{\pi}{4y_0 Q_{f0}} (\omega^2 x^2 + \dot{x}^2) \right] \text{sgn}(\dot{x}) + \omega^2 x = 0$$

Quality factor

$$\frac{1}{Q(t)} = \frac{1}{Q_c} + \frac{1}{Q_k} + \frac{1}{Q_f}$$

20.18 Nonlinearity

20.18.1 General Considerations

Electrical nonlinearity is the type with which most engineers are familiar. It is the very basis for common nondigital forms of communication, such as that of frequency modulation type. A popular form of radio amateur communication is one in which the carrier and one of the two normal sidebands of a signal are suppressed before going to the antenna. At the receiver, the carrier is “regenerated” before going to the demodulator. The demodulator required for ultimate transduction by speaker is also a nonlinear device.

Nonlinearity of mechanical type is encountered throughout nature. The human ear, for example, is not linear, but rather characterized by both quadratic and cubic nonlinearities. If an intense, pure low frequency (inaudible) sound of frequency f is present with a higher frequency audible one of frequency F , then one typically hears (in addition to F) tones at $F \pm f$ due to the quadratic nonlinearity and $F \pm 2f$ due to the cubic nonlinearity.

Very high frequency acoustics (ultrasound) is employed for studies of elasticity. The quasi-linear features of ultrasonic propagation have been the basis for measuring second-order elastic constants (determined by velocity of propagation) and internal friction (by attenuation of the beam, i.e., damping). A commonly employed ultrasonic technique that has been used to study both linear and nonlinear phenomena is the pulse-echo method. By using a thin specimen and extending the pulse width, the overlapped signal can add constructively or destructively and, in the former case, resonance is approached as the width gets very large (Peters, 1973). The pulse-echo method was the basis for this author's Ph.D. dissertation (“Temperature dependence of the nonlinearity parameters of copper single crystals,” The University of Tennessee, 1968). The distinguished career of his professor, M.A. Breazeale, has focused on ultrasonic harmonic generation as a means to determine the shape of the interatomic potential of solids (Breazeale and Leroy, 1991). A longitudinal wave distorts because of the anharmonic potential (acoustic equivalence of optical frequency doubling with lasers in a KdP crystal). In like manner, phonon–phonon interactions are possible only because of nonzero elastic constants of order higher than second (second-order constants determining the harmonic potential). Because phonon–phonon interactions are part of damping, there must be consequences, at least for some cases, from nonlinear damping terms.

The unifying theme for this chapter is that damping is fundamentally nonlinear, in spite of the fact that linear approximations have prevailed in modeling and, for many purposes these linear models appear to be acceptable (Richardson and Potter, 1975). In their paper, Richardson and Potter state that “... an equivalent viscous damping component can always be derived, which will account for all of the energy loss from the system. Thus, in measuring the modal vibration parameters for the linear motion of a system, we don't care what the detailed damping mechanism really is.”

Although their statement may be true for steady state, it is not expected to be true for the transient processes that lead to steady conditions of oscillation. As demonstrated elsewhere in this chapter, mixtures of different damping types are common among oscillators, and only with viscous or hysteretic damping is the Q independent of amplitude. Other cases may result, for example, from the decay being a combination of hysteretic damping and amplitude-dependent damping. An example used to illustrate this combination was an outgassing pendulum oscillating in vacuum. Similarly, a long, “simple” pendulum, oscillating in air, is found to require a pair of terms — viscous damping and “fluid” damping (Nelson and Olssen, 1986). In the Nelson and Olsson experiment, the drag was found, because of the size of the Reynolds number, to involve both first- and second-power velocity terms. Their case can, incidentally, be treated by the modified Coulomb, generalized damping model of this document.

The presence of either amplitude-dependent damping or Coulomb damping is expected to play a role in determining what modes of a multibody system are actually excited by external forcing. Concerning the latter, Coulomb friction is the basis for exciting chaotic vibrations in mechanical systems (Moon, 1987). Without the nonlinear friction, the excitation would be impossible. In similar manner (although chaotic motion may be present but not in an obvious way), friction from rosin on a violin bow is used to

play the violin. Still another example of similar physics is the “singing rod” that was mentioned elsewhere as exhibiting thermoelastic damping.

Whatever combinations of normal modes are initially excited in a linear system are the only ones that can exist thereafter. Such is not the case, however, for many systems and, since nonlinearity is required for mode coupling, there must be nonlinearity in the equations of motion. There is no question about the existence and importance of elastic nonlinearity. Indeed, thermal expansion would be impossible in the absence of higher order elastic constants. The importance of nonlinear damping remains yet to be quantified, since models to include it have been few in number. For those who have found it advantageous to include the oldest and simplest type of nonlinearity in a damping model — Coulomb damping (sliding friction) — the improvements realized by their choice are unlikely to cause them to revisit the problem and try to solve it in terms of a viscous equivalent linear approximation.

There are many examples of damping of a single type other than viscous. In their efforts to improve the knowledge of the Newtonian gravitational constant $G = 6.67 \times 10^{-11} \text{ Nm}^2/\text{kg}^2$ (approx.), Bantel and Newman (2000) discovered a pure form of amplitude-dependent damping of internal friction type. They did their experiments at liquid helium temperature (4.2 K) and noted the following: “A striking feature noted in our data is the linearity of the amplitude dependence of Q^{-1} for the three metal fiber materials,” and also “Linearity implies that Q may depend on frequency but not on amplitude, while in fact Fig.1 displays a significant amplitude dependence (and hence nonlinearity) of internal friction in all fibers tested.” They also considered the temperature dependence of damping and note that there are two independent contributions in Cu–Be. One is linear and temperature-independent and the other amplitude-dependent and independent of temperature. Finally, it is worth noting their statement, “...our results are strongly suggestive of some kind of ‘stick–slip’ mechanism ...,” which lends strong support to the modified Coulomb internal friction damping model of the present document.

Repetition is felt to be warranted — such systems cannot always be reasonably described by an equivalent viscous form! For a case of amplitude-dependent Q , the equivalent form has no meaning unless the amplitude is fixed, i.e., it oscillates at steady state. Unfortunately, the evolution of the system to steady state is expected to depend on the damping form(s). Surely a model (not yet realized) that predicts what modes survive is worth much more than one which only characterizes the modes after they have reached steady state. The author and Prof. Dewey Hodges of Georgia Tech’s Aerospace School are planning projects to try to develop such predictive capability. The present state of the art applied to structures suggests that a truly predictive model cannot ignore damping nonlinearity.

As demonstrated by Bantel and Newman (2000), the mixture of damping types that can co-exist in a system may change with temperature. Early experiments by Berry and Nowick (1958) also showed, as have many investigators subsequently, that damping generally depends on aging. It is naive to believe that aging would not also change the mix of damping types, when there is more than one type. Thus, an adequate damping model must be able to easily accommodate several damping types that are simultaneously active. A variety of engineering techniques have evolved to treat such problems. The most “successful” ones suffer from the fact that an excessive number of parameters or coupled equations must be adjusted by trial and error to yield decent agreement with experiment. This is reminiscent of the state of high-energy (nuclear) physics before the standard model. The hallmark of physics success has always been *simplification*. As noted by Albert Einstein: “All physics is either impossible or trivial. It is impossible until you understand it. Then it becomes trivial.” It is hard to imagine, however, that certain damping physics could ever become trivial. Nevertheless, the simplifying nature of better conceptual understanding is a goal to strive for.

One of the remarkable things about the majority of damping models has been the absence of a direct consideration of energy in describing the dissipation process. After all, the most important quantity transformed by the damping is energy, so its inclusion is natural.

20.18.2 Harmonic Content

When the damping is nonlinear, the waveform of the oscillator in free-decay contains harmonics. The harmonic content is most obvious in the residuals (difference) after fitting a damped sinusoid to the record, as shown in [Figure 20.23](#).

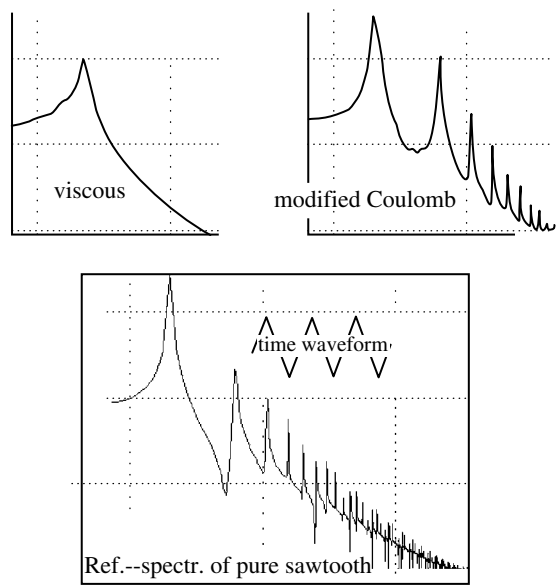


FIGURE 20.23 Harmonic differences between the residuals of the modified Coulomb damping model and the classic viscous damping model. For reference purposes, a pure sawtooth is included in the figure.

Residuals are still present for the viscous case because the equation of motion was integrated numerically and compared against the classic exponentially decaying sinusoid (solution to the equation) that was used for fitting in all cases. There is always some degree of mismatch with the fit because of rounding errors in the computer. In Figure 20.23, the fundamental is smaller for the viscous case because the fit is inherently more perfect by about an order of magnitude in most of the “eye-ball” fits that were performed by Excel after importation of the data.

A test for harmonic content was performed on the seismometer (17-sec period) data displayed in Figure 20.11 illustrating phase noise. The power spectrum of the residuals for that case is shown in Figure 20.24.

The third harmonic is especially noticeable in this case. That the other harmonics are not so “cleanly” displayed may result from the significant phase noise of the record.

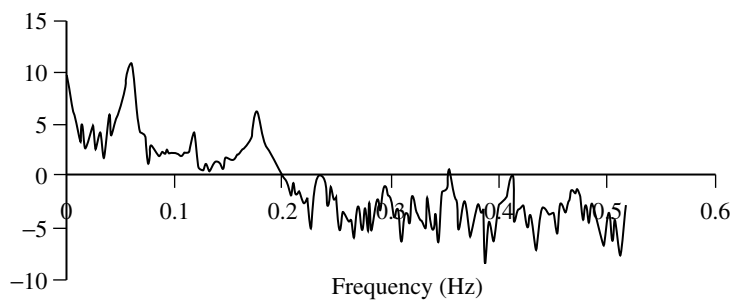


FIGURE 20.24 Power spectrum of residuals, Sprengnether vertical seismometer free-decay, showing harmonic content.

By looking at the FFT of residuals, rather than the experimental record itself, one finds evidence for a combination of both mechanical and electronic noise. At lower frequencies, the noise (largely mechanical) is approximately $1/f$, while at higher frequencies the noise (largely electronic) begins to be more nearly “white” (frequency-independent) because of discretization errors of the resolution-limited 12-bit A to D converter.

In general, more spectral information can be gleaned from a consideration of the residuals than from the experimental data alone, particularly as one looks for harmonic distortion of mechanical type. Spectral “fingerprints” may prove ultimately useful in determining to what extent damping models of engineering type need to be implemented in full nonlinear form as opposed to an “equivalent viscous” form that is more convenient mathematically.

The importance of the harmonics observed in Figure 20.24 in determining system evolution is not completely known. It was noted earlier that they are expected to influence the evolution of a multibody system to steady state. Presently, it appears that they may serve to validate damping models. From one model type to another, there can be significant differences in the spectral character of the residuals, as shown in Figure 20.25. As compared with Figure 20.23, the fit with the modified Coulomb (hysteretic case) model has been tweaked to reduce the fundamental somewhat, but the odd harmonics remain significant. Observe that the spectrum of the residuals is almost the same for this model and the simplified structural model (see de Silva, 2000, p. 354). This is true even though the temporal variation of the friction force is dramatically different for the two, as seen from the lower time traces that were used to obtain the residuals (which are too small to be seen in the graphs).

From this author’s perspective, the simplified structural model is unrealistic, since the friction force, given by $f = c|x|\operatorname{sgn}(\dot{x})$, vanishes for zero displacement (the absolute value of the displacement being used to get the hysteretic form of frequency dependence). This is seen in Figure 20.26, which compares hysteresis curves for several models. The modified Coulomb case shown is slightly different from Equation 20.52 that was used to generate Figure 20.25; Figure 20.26 was generated with the A_{prev} shown in Equation 20.10.

More studies of this type are obviously called for. The spectrum of residuals is a powerful means for the study of damping physics, and it needs to be more widely employed.

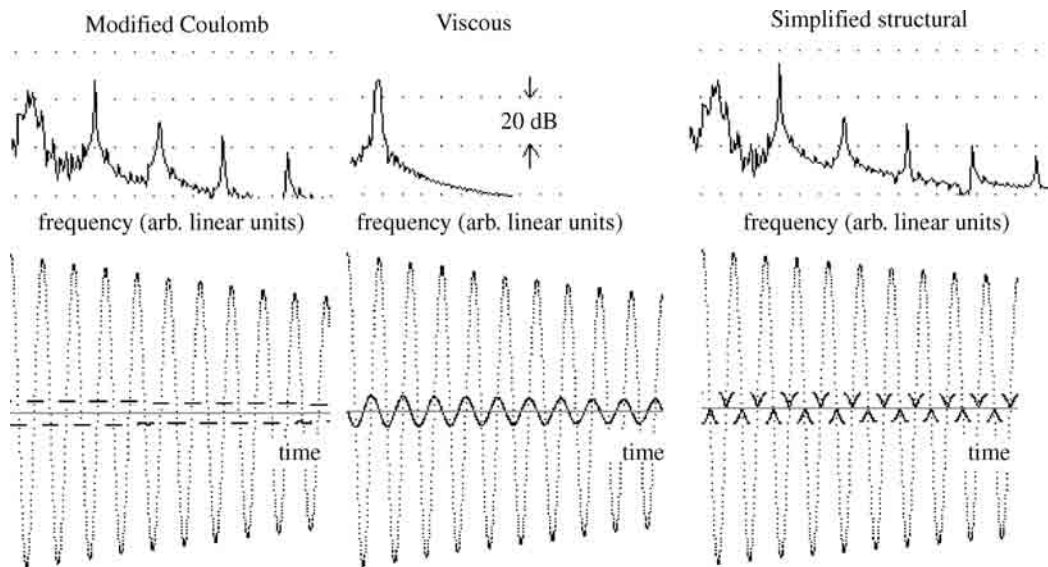


FIGURE 20.25 Illustration of the spectral difference of the residuals for three different damping models. The corresponding temporal records used to generate the spectra are also shown underneath each case.

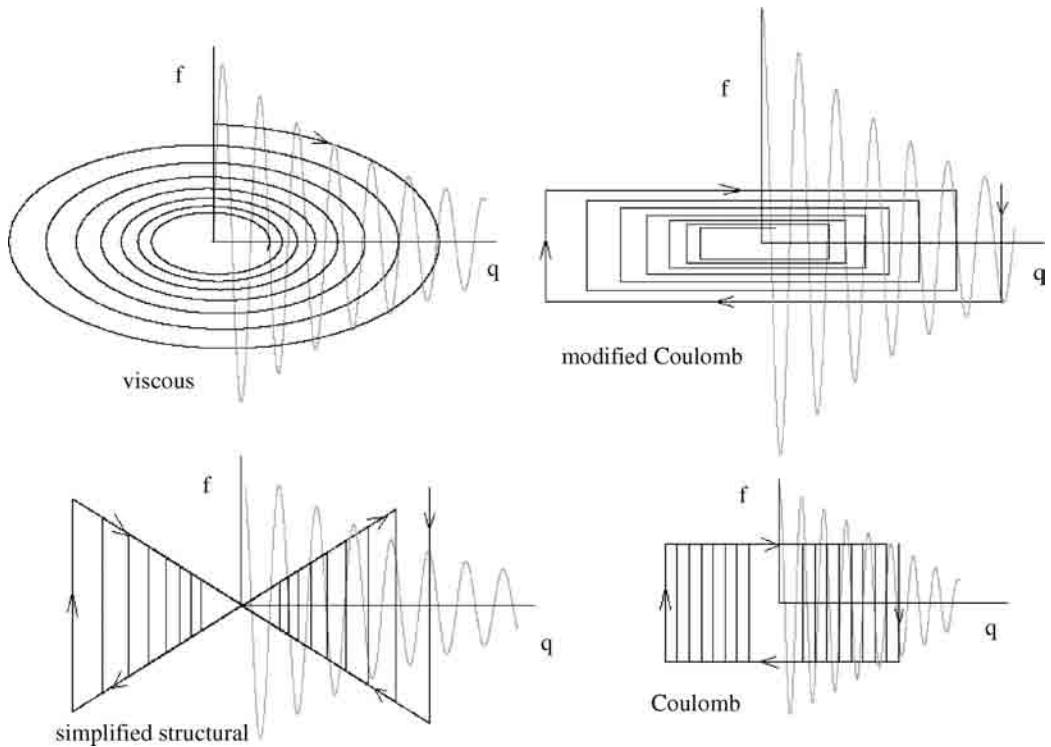


FIGURE 20.26 Comparison of hysteresis curves for some damping models.

20.18.3 Nonlinearity/Complexity and Future Technologies

Nonlinear damping models must improve if we are to overcome various technological barriers. One barrier is in the area of civil engineering. One of the pioneers of finite element modeling (FEM) is Prof. Emeritus Edward L. Wilson, of the University of California Berkeley. In Technical Note 19 (pertaining to “structural analysis programs”) — a document published by his company Computers and Structures Inc — Dr. Wilson says the following:

Linear viscous damping is a property of the computer model and is not a property of a real structure.

Expanding upon the statement, he notes:

the use of linear modal damping, as a percentage of critical damping, has been used to approximate the nonlinear behavior of structures. The energy dissipation in real structures is far more complicated and tends to be proportional to displacements rather than proportional to the velocity. The use of approximate “equivalent viscous damping” has little theoretical or experimental justification...the standard “state of the art” assumption of modal damping needs to be re-examined and an alternative approach must be developed [in reference to Rayleigh damping].

One of the hi-tech areas where modeling improvements are also sorely needed is that involving miniaturized mechanical systems. For example, MEMS devices have already encountered some of the “strange phenomena” of solid-state physics mentioned by Richard Feynman in his famous 1959 talk. To master or compensate for these phenomena, better understanding of the physics will be necessary.

20.18.4 Microdynamics, Mesomechanics, and Mesodynamics

At least three different broad fields of research have focused on problems associated with the structural defects that cause hysteresis. These are as follows.

20.18.4.1 Microdynamics

In the microdynamics world, the emphasis appears to have been primarily on “contact” friction. The 6th Microdynamics Workshop held at the Jet Propulsion Laboratory in 1999 produced the following statements (quoting Marie Levine’s Program Overview): (1) “We have demonstrated that microdynamics exist. The next step is to qualify and quantify microdynamics through rigorous testing and analysis techniques.” (2) Microdynamics is “defined as sub-micron nonlinear dynamics of materials, mechanisms (latches, joints, etc.) and other interface discontinuities.”

In this workshop, it was noted that frequency-based computational methods *cannot* be used to model quasi-static, transient, and nonstationary disturbances. One of the flight operations they have recommended to minimize adverse effects of microdynamics is dithering.

20.18.4.2 Mesomechanics

Ostermeyer and Popov (1999) have the following to say about mesomechanics: “Real physical objects inherently possess discrete internal structures. Great efforts are needed to formulate continuum models of really granular bodies. The history of the last two centuries in a multitude of ways has been marked by highly successful attempts at formulating and analyzing the continuum models of the discrete world. In spite of great advances of continuum mechanics, a number of physical processes are amenable to simulation within the framework of continuum approaches only to a very limited extent. Among these are primarily all the processes whereby the medium continuity is impaired; i.e., those of nucleation and accumulation of damages and cracks and failure of materials and constructions.”

Their paper speaks to one of the difficulties concerning granular materials that was mentioned earlier in this chapter — that the potential energy cannot be defined in the common manner. They introduce a temperature-dependent nonequilibrium interaction potential that is not constant in time due to the relaxation processes occurring in the system.

20.18.4.3 Mesodynamics

The author of this chapter is singlehandedly responsible for the use of the term “mesodynamics” in the context of mechanical oscillators. His research has been conducted independently of those doing mesomechanics; he came only recently to know of the latter. Whereas mesomechanics seems to have been largely concerned with failure, mesodynamics has been concerned with low-level hysteresis. It is probably closely related to the aforementioned microdynamics, except that the latter seems to have focused on surfaces (sliding friction), whereas mesodynamics is concerned with internal friction.

A group of individuals using “mesodynamics” to describe some of their computational physics is part of the Materials Science Division of Argonne National Laboratory. Their description of computational theory includes: (i) atomic-level simulation (using molecular dynamics); (ii) mesoscale simulation, i.e., “mesodynamics” (using FEM); and (iii) macroscale (continuum) simulation (FEM). Like the author of this chapter, they recognize that the mesoscale is not a continuum (meaning, for example, that the foundation of viscoelasticity is, for many cases, on shaky ground). They employ “dynamical simulation methods in which the microstructural elements (grain boundaries and grain junctions) are considered as the fundamental entities whose dynamical behavior determines microstructural evolution in space and time.”

At the Theoretical Division of Los Alamos National Laboratory, Brad Lee Holian has been modeling mesodynamics via nonequilibrium molecular-dynamics (NEMD). In his paper, “Mesodynamics from Atomistics: A New Route to Hall-Petch,” he notes that (i) the mesoscopic nonlinear elastic behavior must agree with the atomistic in compression; and (ii) the mesoscale cold curve in tension represents surface, rather than bulk cohesion, thereby decreasing inversely with grain size (Holian, 2003).

The complexity of mesodynamics, which this author has labeled “mesoanelastic complexity,” is responsible for much of the aforementioned “strange phenomena.” To those familiar with the Barkhausen effect and the PLC effect, they are less strange. It is thought that Richard Feynman, if he were still alive, would identify with mesodynamics because of material in his three-volume series (Feynman, 1970). For example, we have already noted his discussion of the Barkhausen effect, and he included in its entirety a reprint of the Bragg–Nye paper on bubbles which show two-dimensional defect structures such as dislocations, “grains,” and “recrystallization” boundaries after stirring (Bragg et al., 1947).

Another famous individual, whose work related in an unexpected way to the material of this chapter, was Enrico Fermi. In one of the first dynamics calculations carried out on a computer, he and colleagues treated a chain of harmonic oscillators coupled together by a nonlinear term (Fermi, 1940). The continuum limit of their model is the remarkable nonlinear partial differential equation known as the Korteweg–deVries equation, whose solution is a soliton, used to advantage in optical fibers. Damping of solitons, whether of the KdV type or the Sine Gordon (kink/antikink) type, is not to be described by linear mathematics. Incidentally, the Sine Gordon soliton is used in modeling dislocations (Nabarro, 1987). The earliest theory to describe dislocation damping using kink/anti-kink pairs was that of Seeger (1956).

20.18.5 Example of the Importance of Mesoanelastic Complexity

As noted earlier in this chapter, once hysteretic damping was finally recognized to be important to the Cavendish experiment, better agreement with theory and experiment was possible. Curiously, Henry Cavendish may have been the first person to encounter a “strange” phenomenon (which he did not discuss) (Cavendish, 1798). In his first mass swing to perturb the balance, which used a “fiber” made of copper (silvered), there was an anomalously small period of oscillation that was only 55 sec. The period reported for subsequent trials was about 421 sec.

Whereas the Michell–Cavendish apparatus was a torsion balance, the instrument of Figure 20.27 is a physical pendulum. The perturbing masses, M , were hung from a bicycle wheel whose axle was suspended from the ceiling. The long-period pendulum was placed under a bell jar so that the instrument would not be driven by air currents. By rotating the wheel at constant angular

velocity, the driving force on the pendulum was harmonic. (In the figure, the position of each M one-half period later are shown by the dashed circles.) Knowing the amount of damping, as determined from large amplitude free-decay, it was easy to estimate the number of orbits of the bell jar, at the resonance frequency of the pendulum, required to excite motion to a level above noise in the sensor. Surprisingly, if it were initially at rest, no amount of drive by this means was able to get the pendulum oscillating! The reason involves metastabilities of the defect structures. The potential well is not harmonic (parabolic), but is rather modulated by “fine structure.” When located in a deep metastability, the small gravitational force of the drive (in nanoNewtons) is not able to “unlatch” the system. If the pendulum had been dithered (a practice used in engineering) this problem could have been, at least partly, avoided. As it was, the pendulum rested on an isolation table of the type used in optics experiments.

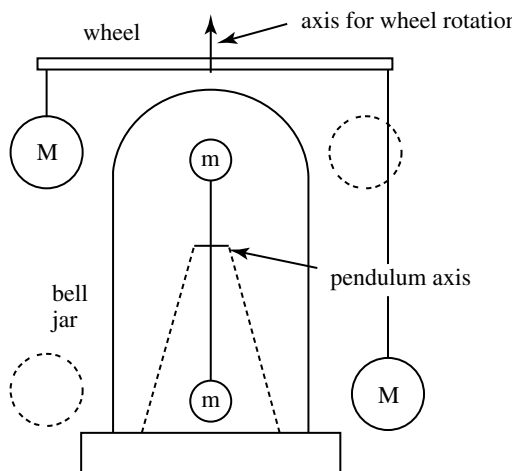


FIGURE 20.27 Physical pendulum used in the late 1980s to try and measure the Newtonian gravitational constant.

More recently, a Hungarian research team has used a similar apparatus and postulated that the anomalies of their experiment derive from gravity being other than prescribed by Newton (Sarkadi and Badonyi, 2001). Although they claim that there is a “strong dependence of gravitational attraction on the mass ratio of interacting bodies,” this author believes that additional experiments must be performed before such a claim has merit. It may be that the anomalous behavior of their pendulum is instead the result of mesoanelastic complexity, i.e., phenomena related to nonlinear damping.

The author’s most recent research on damping complexity is based on the premise that the most important scale for the treatment of internal friction is the mesoscale, and not the atomic scale (Peters 2004). Experiments to support this position center around a study of the SMA NiTiInol.

20.19 Concluding Remark

Much of the material of this part of the chapter on damping is clearly not appropriate to direct engineering application. It was deemed important to present some of the extensive background information responsible for birthing the practical equations of Section 20.17. In [Chapter 21](#), the reader will find practical aids to the measurement of damping.

Bibliography

- Amengual, A., Manosa, L.L., Marco, F., Picornell, C., Segui, C., and Torra, V., Systematic study of the martensitic transformation in a Cu–Zn–Al alloy, reversibility versus irreversibility via acoustic emission, *Thermochim. Acta*, 116, 195–308, 1987.
- Asa, F., Modal synthesis when modeling damping by use of fractional derivatives, *AIAA J.*, 34(5), 1051–1058, 1996.
- Atalay, S. and Squire, P., Torsional pendulum system for measuring the shear modulus and internal friction of magnetoelastic amorphous wires, *Meas. Sci. Technol.*, 3, 735–739, 1992.
- Bak, P., Tang, and Wiesenfeld, Self-organized criticality, *Phys. Rev. A*, 38, 364–374, 1988.
- Bantel, M.K. and Newman, R.D., High precision measurement of torsion fiber internal friction at cryogenic temperatures, *J. Alloys Compd.*, 310, 233–242, 2000.
- Barkhausen, H., *Phys. Z.*, 20, 401, 1919.
- Berdichevsky, V., Hazzledine, P., and Shoykhet, B., Micromechanics of diffusional creep, *Int. J. Eng. Sci.*, 35, 10/11, 1003–1032, 1997.
- Berry, M.V. and Keating, J.P., The Riemann zeros and eigenvalue asymptotics, *Siam Rev.*, 41, 2, 236–266, 1999.
- Berry, B. and Nowick, A., Internal friction study of aluminum alloys containing 4 weight percent copper, *National Advisory Committee for Aeronautics, Technical Note 4225*, online at <http://naca.larc.nasa.gov/reports/1958/naca-tn-4225>, 1958.
- Bert, C.W., Material damping: an introductory review of mathematical models, measures and experimental techniques, *J. Sound Vib.*, 29, 129–153, 1973.
- Bethe, H., Lecture at Cornell University online info. at <http://www.nd.edu/~bjanko/Copenhagen/Cop3.pdf>, 1992.
- Bordoni, P., Elastic and anelastic behavior of some metals at very low temperatures, *J. Acoust. Soc. Am.*, 26, 495, 1954.
- Bormann P. and Bergmann E., eds. 2002. *New Manual of Observatory Practice*, Institute of Geophysics, University of Stuttgart, online at <http://www.seismo.com/msop/nmsop/nmsop.html>.
- Bragg, Sir Lawrence, F.R.S., and Nye, J.F., A dynamical model of a crystal structure, *Proc. R. Soc. Lond., Ser. A, Math. Phys. Sci.*, 190, 1023, 474–481, 1947.
- Braginsky, V.B., Mitrofanov, V.P., and Panov, V.I. 1985. *Systems with Small Dissipation*, The University of Chicago Press, Chicago.

- Braginsky, V.B., Mitrofanov, V.P., and Okhrimenko, O.A., Isolation of test masses for gravitational wave antennae, *Phys. Lett. A*, 175, 82–84, 1993.
- Breazeale, M.A. and Leroy, O. 1991. *Physical Acoustics: Fundamentals and Applications*, Kluwer Academic/Plenum Publishers, New York.
- Brophy, J. 1965. Fluctuations in magnetic and dielectric solids. In *Fluctuation Phenomena in Solids*, R.E. Burgess, Ed., Academic Press, New York.
- Bulsara, A.R. and Gammaitoni, L., Tuning in to noise, *Phys. Today*, 49, 39–45, 1996.
- Carlson, J.D., Controlling vibration with MR fluid damping, *Sensor Technol. Design*, 19, 2, 2002, online at <http://www.sensorsmag.com/articles/0202/30/main.shtml>.
- Cavendish, H., Experiments to determine the density of the Earth, *Philos. Trans. R. Soc. Lond.*, 469–526, 1798.
- Cipra, B., The FFT: making technology fly, *SIAM News*, 26, 3, 1993, online at <http://www.siam.org/siamnews/mtc/mtc593.htm>.
- Cleland, A. and Roukes, M., Noise processes in nanomechanical resonators, *J. Appl. Phys.*, 92, 5, 2758–2770, 2002.
- Cooley, J. and Tukey, J., An algorithm for the machine calculation of complex Fourier Series, *Math. Comput.*, 19, 90, 297–301, 1965.
- Coy, D. and Molnar, M., Optically driven pendulum, *Proc. NCUR XI*, 1621–1626, 1997.
- Cromer, A., Stable solutions using the Euler approximation, *Am. J. Phys.*, 49, 5, 455–459, 1981.
- Dean, R., Low-cost, high precision MEMS accelerometer fabricated in laminate online at <http://www.eng.auburn.edu/ee/leap/MEMSFabricateTable.htm>, 2002.
- de Silva, C.W. 2000. *Vibration, Fundamentals and Practice*, CRC Press, Boca Raton, FL.
- Fantozzi, G., Esnouf Benoit, W., and Richie, I., *Prog. Mater. Sci.*, 27, 311, 1982.
- Fermi E., Pasta J., and Ulam S., Studies in nonlinear problems I, Los Alamos report (reproduced in R. Feynman, 1970: *Lectures on Physics*, Addison Wesley, Boston, 1940).
- Fraden, J. 1996. *Handbook of Modern Sensors, Physics, Designs, & Applications*, 2nd ed., AIP Press (Springer), Secaucus, NJ.
- Gammaitoni, L., Stochastic resonance and the dithering effect in threshold physical systems, *Phys. Rev. E*, 52, 469, 1995.
- Gere, J., Timoshenko, S. 1996. *Mechanics of Materials*, Chapman & Hall, London.
- Granato, A. 2002. High damping and the mechanical response of amorphous materials, Submitted to the Proceedings of the International Symposium on High Damping Materials in Tokyo, August 22, 2002 for publication in the Journal of Alloys and Compounds, private communication preprint.
- Granato, A. and Lucke, K., Theory of mechanical damping due to dislocations, *J. Appl. Phys.*, 27, 583, 1956.
- Greaney, P., Friedman, L., and Chrzan, D., Continuum simulation of dislocation dynamics: predictions for internal friction response, *Comput. Mater. Sci.*, 25, 387–403, 2002.
- Grigera, T. and Israeloff, N., Observation of fluctuation–dissipation theorem violations in a structural glass, *Phys. Rev. Lett.*, 83, 24, 5038–5041, 1999.
- Gross, B., The flow of solids, *Phys. Today*, 5, 8, 6–10, 1952.
- Heyman, J. 1997. *Coulomb's Memoir on Statics: An Essay in the History of Civil Engineering*. Imperial College Press, London, ISBN: 1860940560.
- Hilfer, P., ed. 2000. *Applications of Fractional Calculus in Physics*, World Scientific, London.
- Hodges, D. 2003. Private communication (Georgia Tech School of Aerospace).
- Holian, B. 2003. Mesodynamics from atomistics: a new route to Hall–Petch, private communication preprint.
- Horowitz, H. and Hill, W. 1989. *Art of Electronics*, 2nd ed., Cambridge University Press.
- Kimball, A. and Lovell, D., Internal friction in solids, *Phys. Rev.*, 30, 948–959, 1927.
- Kohlrusch, R., *Ann. Phys.*, 12, 392, 1847, online information at <http://www.ill.fr/AR-99/page/74magnetism.htm>.

- Kuroda, K., Does the time of swing method give a correct value of the Newtonian gravitational constant?, *Phys. Rev. Lett.*, 75, 2796–2798, 1995.
- LaCoste, L., A new type long period vertical seismograph, *Physics*, 5, 178–180, 1934.
- Lakes, R. 1998. *Viscoelastic Solids*, CRC Press, Boca Raton, FL.
- Lakes, R. and Quackenbush, J., Viscoelastic behavior in indium tin alloys over a wide range of frequency and time, *Philos. Mag Lett.*, 74, 227–232, 1996.
- Landau, L. and Lifshitz, E. 1965. *Theory of Elasticity*, Nauka, Moscow.
- Lorenz, E. 1972. Predictability: Does the flap of a butterfly's wings in Brazil set off a tornado in Texas, presented to AAAS, Washington, DC.
- Marder, M. and Fineberg, J., How things break, *Phys. Today*, 49, 24–29, 1996.
- Marion, J. and Thornton, S. 1988. *Classical Mechanics of Particles and Systems*, 3rd ed., HBJ, Academic Press, New York, p. 114.
- Milonni, P. and Eberly, J. 1988. *Lasers*. Wiley Interscience, Hoboken, NJ, p. 93.
- Moon, F. 1987. *Chaotic Vibrations, An Introduction for Applied Scientists and Engineers*, Wiley Interscience, Hoboken, NJ.
- Moore, G., Moore's law is described online at <http://www.intel.com/research/silicon/mooreslaw.htm>, 1965.
- Nabarro, F. 1987. *Theory of Crystal Dislocations*, Dover, New York.
- Nelson, R. and Olssen, M., The pendulum—rich physics from a simple system, *Am. J. Phys.*, 54, 112–121, 1986.
- Ostermeyer, G. and Popov, V., Many-particle non-equilibrium interaction potentials in the mesoparticle method, *Phys. Mesomech.*, 2, 31–36, 1999.
- Peters, R., Resonance generation of ultrasonic second harmonic in elastic solids, *J. Acoust. Soc. Am.*, 53, 6, 1673, 1973.
- Peters, R., Linear rotary differential capacitance transducer, *Rev. Sci. Instrum.*, 60, 2789, 1989.
- Peters, R., Metastable states of a low-frequency mesodynamic pendulum, *Appl. Phys. Lett.*, 57, 1825, 1990.
- Peters, R., Fourier transform construction by vector graphics, *Am. J. Phys.*, 60, 439, 1992.
- Peters, R., Fluctuations in the length of wires, *Phys. Lett. A*, 174, 3, 216, 1993a.
- Peters, R., Full-bridge capacitive extensometer, *Rev. Sci. Instrum.*, 64, 8, 2250–2255, 1993b. This paper describes an SDC sensor with cylindrical geometry. Other geometries, including the more common planar one, are described online at <http://physics.mercer.edu/petepag/sens.htm>.
- Peters, R. 2000. Autocorrelation Analysis of Data from a Novel Tiltmeter, abstract, *Amer. Geo. Union annual mtg.*, San Francisco.
- Peters, R. 2001a. The Stirling engine refrigerator — rich pedagogy from applied physics, online at <http://xxx.lanl.gov/html/physics/0112061>.
- Peters, R. 2001b. Creep and Mechanical Oscillator Damping, <http://arXiv.org/html/physics/0109067/>.
- Peters, R. 2002a. The pendulum in the 21st century—relic or trendsetter, *Proc. The Int'l Pendulum Project*, University of New South Wales, Australia, Proceedings, October, 2002.
- Peters, R. 2002b. The soup-can pendulum, *Proc. The Int'l Pendulum Project*, University of New South Wales, Australia, Proceedings, October, 2002.
- Peters, R. 2002c. Toward a universal model of damping—modified Coulomb friction online at <http://arxiv.org/html/physics/0208025>.
- Peters, R. 2003a. Graphical explanation of the speed of the Fast Fourier Transform, online at <http://arxiv.org/html/math.HO/0302212>.
- Peters, R. 2003b. Nonlinear damping of the 'linear' Pendulum, online at <http://arxiv.org/pdf/physics/0306081>.
- Peters, R. 2003c. Flex-Pendulum—basis for an improved timepiece, online at <http://arxiv.org/pdf/physics/0306088>.
- Peters, 2004. Friction at the Mesoscale. In *Contemporary Physics*, P. Knight, Ed., Vol. 45, no. 6, 475–490, Imperial College, London 2004.

- Peters, R. and Kwon, M., Desorption studies using Langmuir recoil force measurements, *J. Appl. Phys.*, 68, 1616, 1990.
- Peters, R. and Pritchett, T., The not-so-simple harmonic oscillator, *Am. J. Phys.*, 65, 1067–1073, 1997.
- Peters, R., Breazeale, M., and Pare, V., Temperature dependence of the nonlinearity parameters of Copper, *Phys. Rev.*, B1, 3245, 1970.
- Peters, R., Cardenas-Garcia, J., and Parten, M., Capacitive servo-device for microrobotic applications, *J. Micromech. Microeng.*, 1, 103, 1991.
- Portevin, A. and Le Chatelier, M., Tensile tests of alloys undergoing transformation, *C. R. Acad. Sci.*, 176, 507, 1923.
- Present, R. 1958. *The Kinetic Theory of Gases*. McGraw-Hill, New York.
- Press, W., Flannery, B., Teukolsky, S., and Vetterling, W. 1986. *Numerical Recipes—the Art of Scientific Computing*. Cambridge University Press.
- Purcell, E., Life at low Reynolds number, *Am. J. Phys.*, 45, 3–11, 1977.
- Richardson, M., and Potter, R. 1975. Viscous vs structural damping in modal analysis, *46th Shock and Vibration Symposium*.
- Roukes, M., Plenty of room indeed, *Scientific American*, 285, 48–57, 2001.
- Sarkadi, D. and Badonyi, L., A gravity experiment between commensurable masses, *J. Theor.*, 3–6, 2001.
- Saulson, P., Stebbins, R., Dumont, F., and Mock, S., The inverted pendulum as a probe of anelasticity, *Rev. Sci. Instrum.*, 65, 182–191, 1994.
- Seeger, A., On the theory of the low-temperature internal friction peak observed in metals, *Philos. Mag.*, 1, 1956.
- Singh, A., Mohapatra, Y., and Kumar, S., Electromagnetic induction and damping, quantitative experiments using a PC interface, *Am. J. Phys.*, 70, 424–427, 2002.
- Speake, C., Quinn, T., Davis, R., and Richman, S., Experiment and theory in anelasticity, *Meas. Sci. Technol.*, 10, 430–434, 1999. See also Quinn, Speake and Brown, 1992: Materials problems in the construction of long-period pendulums, *Philos. Mag. A* 65, 261–276, 1999.
- Steinmetz, C.P., *Complex Number Technique, paper given at the International Electrical Congress*, Chicago, 1893.
- Stokes, G., On the effect of the internal friction of fluids on the motion of pendulums, *Trans. Cambridge Philos. Soc.*, IX, 8, 1850, read December 9, 1850.
- Strang, G., Wavelet transforms versus Fourier Transforms, *Bull. Am. Math. Soc.*, 28, 288–305, 1993.
- Streckeisen, G. 1974. *Untersuchungen zur Messgenauigkeit langperiodischer Seismometer*, Diplomarbeit, Institut für Geophysik der ETH Zürich (communicated privately by E. Wielandt).
- Tabor, M. 1989. The FUP Experiment. In *Chaos and Integrability in Nonlinear Dynamics: Introduction*. Wiley, New York.
- Thomson, W., Tait, G. 1873. *Elements of Natural Philosophy, Part I*. The Clarendon Press, Oxford, (Thomson was later known as Lord Kelvin).
- Urbach, J., Madison, R., and Markert, J., Reproducibility of magnetic avalanches in an Fe–Ni–Co alloy, *Phys. Rev. Lett.*, 75, 4694, 1995a.
- Urbach, J., Madison, R., and Markert, J., Interface depinning, self-organized criticality, and the Barkhausen effect, *Phys. Rev. Lett.*, 75, 276, 1995b.
- Venkataraman, G. 1982. Fluctuations and mechanical relaxation. In *Mechanical and Thermal Behavior of Metallic Materials*, Caglioti, G. and Milone, A., eds., pp. 278–414. North-Holland, Amsterdam.
- Visintin, A. 1996. *Differential Models of Hysteresis*. Springer, Berlin.
- Westfall, R. 1990. Making a world of precision: Newton and the construction of a quantitative physics. In *Some Truer Method. Reflections on the Heritage of Newton*, F. Durham and R.D. Purrington, eds., pp. 59–87. Columbia University Press, New York.
- Wielandt, E. 2001. *Seismometry*, section Electronic Displacement Sensing, online at http://www.geophys.uni-stuttgart.de/seismometry/hbk_html/node1.html.
- Zemansky, M.W. 1957. *Heat and Thermodynamics*, 4th ed., McGraw-Hill, New York, p. 127.
- Zener, C. 1948. *Elasticity and Anelasticity of Metals*, Chicago Press, Chicago.

21

Experimental Techniques in Damping

21.1	Electronic Considerations	21-2
	Sensor Linearity • Frequency Issues • Data Acquisition	
21.2	Data Processing.....	21-3
	Language Type • Integration Technique • Fourier Transform	
21.3	Sensor Choices	21-7
	Direct Measurement • Indirect Measurement	
21.4	Damping Examples.....	21-8
	Case 1: Vibrating Bar — Linear with Significant Noise •	
	Case 2: Vibrating Reed — Example of Nonlinear Damping •	
	Case 3: Seismometer • Case 4: Rod Pendulum with Photogate	
	Sensor • Case 5: Rod Pendulum Influenced by Material under	
	the Knife-Edge • Hard Materials with Low Q • Anisotropic	
	Internal Friction	
21.5	Driven Oscillators with Damping	21-19
	MUL Apparatus • Driven Harmonic Oscillator	
21.6	Oscillator with Multiple Nonlinearities	21-21
21.7	Multiple Modes of Vibration.....	21-24
	The System • Some Experimental Results • Short Time	
	Fourier Transform • Nonlinear Effects — Mode Mixing	
21.8	Internal Friction as Source of Mechanical Noise.....	21-28
21.9	Viscous Damping — Need for Caution	21-29
21.10	Air Influence	21-31
	Brass and Solder Rod Pendula	

Randall D. Peters
Mercer University

Summary

This chapter is a continuation of [Chapter 20](#) and is concerned with practical experimental techniques for measuring damping. It begins with a discussion of the requirements placed on electronics. After demonstrating the importance of sensor linearity using a computer simulation, the issues of data acquisition and processing are addressed. The power of the Fast Fourier Transform is illustrated, not just for spectral analysis, but also (in “short time” form) for measuring the damping of each component when a system oscillates with multiple modes. Various sensor types are discussed in relation to their advantages and disadvantages for specific applications through the treatment of seven different systems studied in free decay. These seven cases differ with respect to factors such as (i) eigenfrequency, (ii) material type, and (iii) method of estimating the logarithmic decrement, and thus the Q of the decay. In the case of some solids, damping is shown to result largely from defects in the structures. A powerful test for nonlinear damping is demonstrated: simply looking at a graph of Q to see whether it changes with time. Two examples of driven oscillators are given. The first being very nearly linear, and the second being highly nonlinear, due to an anharmonic restoring force involving magnets plus several simultaneously acting damping mechanisms. The nonlinear system is used to illustrate difficulties in interpretation that can arise in driven systems due to

phenomena such as frequency and/or amplitude jumps involving hysteresis. Then an illustration is given of how elastic-type nonlinearities may couple with damping-type nonlinearities in order to determine which modes of a complex system survive during the transient approach to steady state. Mechanical noise, another important feature of nonlinear damping, is also examined. The magnitude of the $1/f$ character in an evacuated pendulum is shown to decrease with time, as the oscillator is allowed to stabilize against creep. The final sections address the common misconception that viscous air friction is the most important form of mechanical oscillator damping. Cases are chosen to demonstrate that (i) internal friction is nearly always also important, if not the most important, and moreover, that (ii) fluid damping is rarely simple — involving the density as well as the viscosity of the fluid. It is shown that damping has a complicated frequency dependence, as opposed to the simple (overly idealized) form predicted by common theory.

21.1 Electronic Considerations

21.1.1 Sensor Linearity

The importance of sensor linearity is often overlooked (see Chapter 15). It is naively assumed that one can simply employ a lookup table to provide calibration corrections. This assumption can result in serious misinterpretations of spectral data, especially in a multimode system. A classic example of artifacts (nonreal signals) that result from a nonlinear sensor is to be found in the ear. The phenomenon, known as aural harmonics, is well known to musicians and figures in the use of “fortissimo” and “pianissimo” in orchestral music. In this chapter we describe how the artifacts mentioned in Chapter 20 are generated. Figure 21.1 illustrates differences according to the nature of the nonlinearity.

The only “real” signals in Figure 21.1 are at frequencies f_1 and f_2 . The number and type of other “unreal” (artifact) signals depends on the type of nonlinearity. The sensor response for the left graph (quadratic) is of the form $V = ax + bx^2$, whereas for the right graph $V = ax + bx^2 + cx^3$. The influence of terms other than $V = ax$ (ideal, linear output voltage) was generated by (i) simulating the pair of harmonic signals, (ii) inputting these signals to each simulated sensor, respectively, and (iii) performing a Fast Fourier Transform (FFT) on the output.

Although it is possible to understand mathematically the various artifacts using trigonometric identities, the phenomenon is much easier to demonstrate with a computer. For Figure 21.1, all

Simulated harmonic distortion from Sensor Nonlinearity

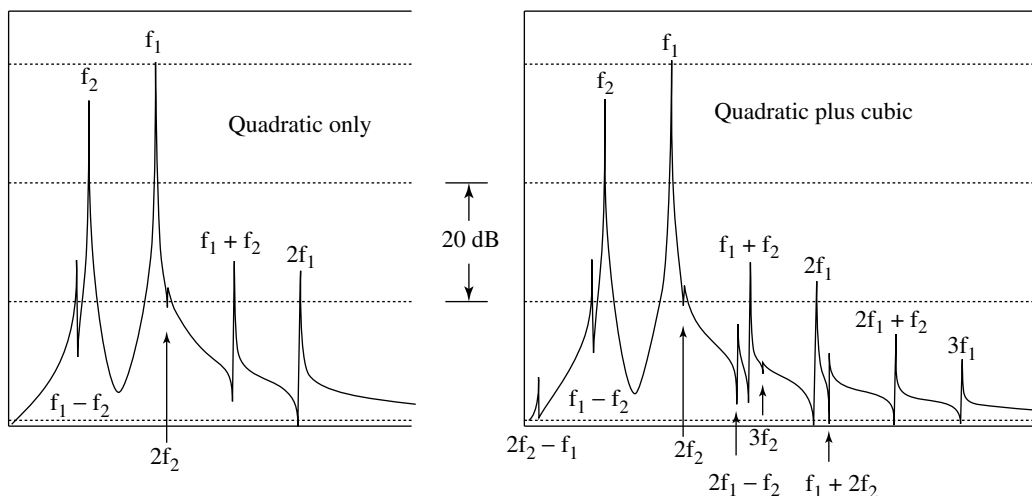


FIGURE 21.1 Spectral illustration of sum and difference artifact frequencies according to nonlinear sensor type.

numerical operations were performed with code written by the author using QuickBasic. It was used to (i) simulate the harmonic signal that was written to a data file, after which it was (ii) read by the FFT algorithm based on the details supplied in *Numerical Recipes* (Press et al., 1986).

21.1.2 Frequency Issues

The choice of a sensor depends largely on the frequencies to be measured. For higher frequencies an excellent instrument for data collection is a digital (storage) oscilloscope, where a microphone can often be directly connected to the instrument. At lower frequencies, a serial-port analog-to-digital converter (ADC) is generally adequate and user-friendly. Examples of each will be provided. The majority of examples considered in this chapter involve low frequencies, where the eigenmode is typically described not in terms of frequency but rather the period (reciprocal of frequency).

21.1.3 Data Acquisition

In the absence of sophisticated data collection and analysis tools, the true character of damping is not readily discovered. Proper characterization is important, since a crude estimate of the damping, based on a single parameter (such as the viscous linear model), may be inappropriate if the oscillator is driven at places (either frequency or amplitude) other than where the parameter was measured. Some of the examples from the experiment that follows were selected to demonstrate the importance of nonlinearity. The probability that an oscillator, selected at random, might have a Q that varies in time is proving to be more significant than anticipated. Were it not for dramatic improvements in numerical-type technology, this improved understanding of damping would not have been possible.

As with computer technology in general over the last decade, ADCs have become much more powerful. The Dataq model 700, for example, is superior (at lower frequencies) to many of the “plug-in” boards of the previous generation that were several times more expensive. The Dataq ADC operates through the USB port (Windows 98 and later), has 16-bit resolution and the software support is excellent. Especially useful for the present purposes are its ability to (i) easily perform data compression with which to view long records, (ii) quickly compute an FFT according to different, useful options, and (iii) easily output files to a spreadsheet.

21.2 Data Processing

21.2.1 Language Type

The author’s experience with software began with early computers and even included the loading of the Fortran compiler of a PDP-11 using punch-tape. He has programmed computers (or hardware-specific processors) with (i) machine code, (ii) assembly language, (iii) Fortran, and (iv) Basic, and he has acquired a rudimentary knowledge of Pascal and C++. The drudgery of machine coding was a factor in his quest to better understand the Fourier transform (Peters, 1992, 2003a, 2003b, 2003c, 2003d). His philosophy with regard to numerical methods is similar to his view of hardware: choose the simplest package (lowest level of sophistication) consistent with the desired results for the problem at hand. The reader may be surprised to learn that QuickBasic (which some have modernized to Visual Basic for Windows) is his favorite language. Nearly all simulation results presented in this chapter were generated with the DOS version of QuickBasic.

21.2.2 Integration Technique

Too few have discovered the powerful integration scheme in which Cromer (1981) modified the unstable Euler algorithm. The difference between the two methods involves the sequencing (order) of updates to the state vectors in the discrete approximation of the integrals. The method was called the “last point

approximation” (LPA) by Cromer, whereas the Euler technique would be called the “first point approximation” according to this nomenclature. The LPA was discovered by a high school student working for Cromer. She was attempting to simulate planetary motion with the Euler method and accidentally coded the LPA. The author first used the LPA to do intercept analyses for the U.S. antisatellite program — computing, among other things, orbital ephemerides. More recently he has used it in place of Runge Kutta techniques to do all kinds of mechanical system simulations, including nonlinear types with several DoF. A physics theorist at Texas Technical University, Professor Thomas Gibson, now regularly uses the LPA as part of the graduate-level course which he teaches in numerical methods.

21.2.3 Fourier Transform

With the Cooley–Tukey improvement to make it fast, the Fourier transform has become a tool of major software importance. Just as the integrated circuit dramatically changed hardware development, the FFT has had a profound influence on the evolution of scientific code.

Whereas many recognize the value of the FFT for viewing “raw” spectral data, few have discovered other powerful tools based in the FFT. For example, autocorrelation is unrivaled in its ability to uncover low-frequency signals of fairly short duration that are corrupted by noise. The number of cycles is not great enough (Heisenberg effect) for a well-defined line to be observed in the FFT by itself. Through the Wiener–Khinchin theorem, the autocorrelation overcomes this limitation. It is computed by multiplying the transform by its conjugate and then taking the inverse transform. The author has used this technique to study free oscillations of the earth (Peters, 2004).

21.2.3.1 Short Time Fourier Transform

A powerful software tool is one in which the Fourier transform is not computed over the entire length of a record. Instead, the record is subdivided (usually with some degree of overlap between adjacent subsections), and the FFT is computed for each subsection. Because the data are generally of the temporal (rather than spatial) type, the technique is called the short time Fourier transform (STFT). For equivalent processing, where the independent variable has units of meters rather than seconds (as in optics applications), the technique could just as well be called the short space Fourier transform.

The STFT is especially useful when waveforms are not pure harmonic, as from a single-degree-of-freedom (single-DoF) oscillator. For systems with multiple modes, whether they derive from eigenmodes as recognized by most, or from mechanical noise as recognized by a few (generated as part of the internal friction of load bearing members); the STFT is a powerful means for isolating and thus determining the temporal history of individual spectral components.

The most common form of the STFT is the canned programs that are a part of software packages such as LabVIEW. With the Dataq software it is easy to accomplish the same thing manually, since one can readily step in time from place to place of a stored record, computing the FFT at any position. The intensity at a given position is obtained by clicking on the displayed spectral line of interest, which provides the value either in dB (Dataq version) or in volts. The amplitude history in dB of the line is thus obtained (equally spaced-in-time values) with a simple click of the mouse. In this way, the free decay of a single component of the system can be readily extracted from the total system response. For the present purposes, the individual intensities were copied by hand to paper and later typed into a spreadsheet for plotting. The process is not laborious, since the number of necessary points is typically less than two dozen.

An example of a manually generated STFT is provided in [Figure 21.2](#). Unlike the methodology described above (operating on experimental data residing in a Dataq folder), the record of Figure 21.2 was generated by computer and written to an output file. The data correspond to three superposed, exponentially damped sinusoids.

From the upper graph (time record), it is not clear how the individual components are changing with time. The triplet of components becomes obvious in the frequency domain (lower left), and when the

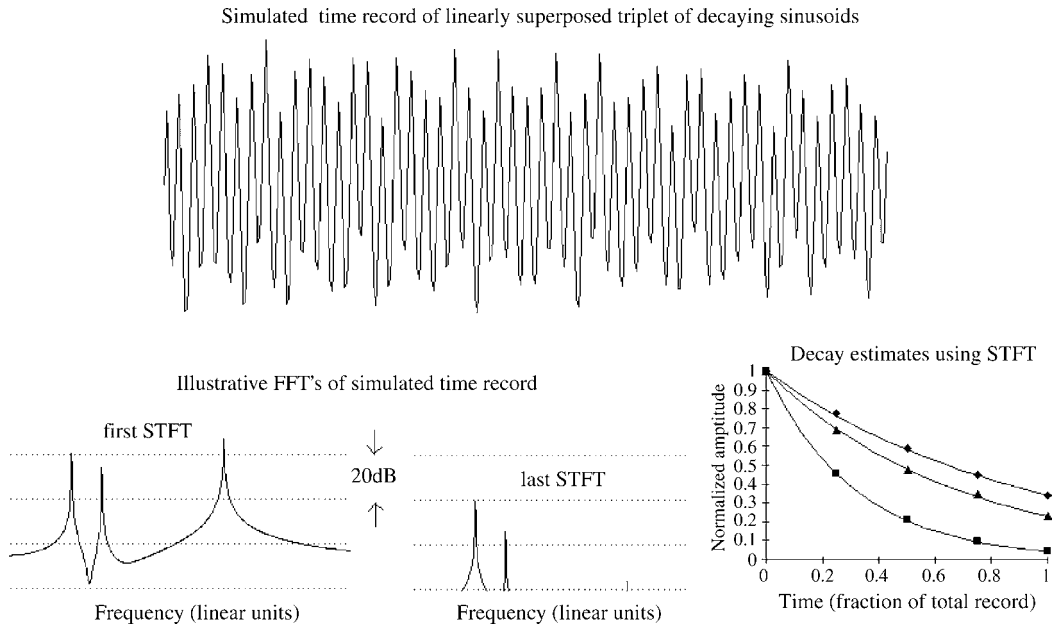


FIGURE 21.2 Example of separating the time decay of superposed components using the STFT.

intensities of each line are plotted *versus* time (lower right) the exponential character of each becomes visible. To test the viability of this method, the individual damping parameters were evaluated from a given STFT graph and found to be in excellent agreement with the values supplied to the simulation.

21.2.3.2 Example Use of the STFT

The majority of the examples given in this chapter avoid low-energy oscillations as space does not allow mesoanelastic regimes to be treated at length. The following case was chosen to illustrate (i) the importance of the Portevin–LeChatelier (PLC) effect on damping (Portevin and Le Chatelier, 1923), and (ii) the power of the STFT in eliminating the influence of clutter. The STFT benefit was expected, since the difference between a noisy record and a multimode case like the previous example is in the number of modes. The PLC effect is significant for high-energy internal friction dissipation even though the jumps for which the effect is known are not obvious at these energies. Evidently, this is a consequence of the large number of events, for which the average effect is a fairly smooth decay.

The scales for the two graphs of Figure 21.3 are different by nearly three orders of magnitude, with the level of the sensor output for each case being indicated (mid-range values). Two features are evident from a direct visual inspection: (i) the change from a smooth to a jerky decay in going from high to low levels, and (ii) a 4% increase in the frequency of oscillation at the lower energy. The latter is recognizable from the vertical lines that have been added (every fifth peak). One of the more interesting (and surprising to most) features of the lower graph is that phase of the oscillation is not significantly altered as the result of mean position jumps.

The following information is provided for those skeptical of the comments concerning the lower trace of Figure 21.3. From the study of hundreds of low-level decays in different mechanical oscillators, the author has become confident that the jumps shown are not sensor (or other electronic) artifacts. Prejudice against this conclusion has been considerable over the last 14 years, in spite of the fact that a similar phenomenon was noted (and accepted) in magnetic materials many years ago, i.e., the Barkhausen effect (Barkhausen, 1919). Unfortunately, the related phenomenon in mechanical systems (PLC effect) is hardly known among physicists.

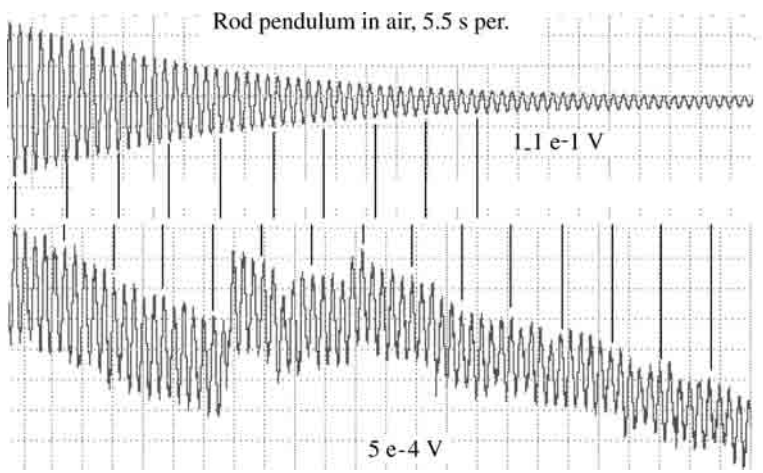


FIGURE 21.3 Illustration of the character changes in decay in going from high to low energies of a pendulum.

The value of the STFT for the study of data such as that of Figure 21.3 is illustrated in Figure 21.4. Whereas Figure 21.3 showed only the first and the last portions of a long record, here the STFT was applied to the entire record using 27 different FFTs.

As seen in the upper left curve, there is a sharp decrease in the damping in STFT No. 5. Thus, the intensity was replotted in each of the intervals from 0 to 5 and 5 to 27. Both intervals show a near perfect linear trendline fit, indicating exponential decay. Thus the Q was found to quickly change from 78 to 340 at an energy level in the region of 10^{-10} J. Although air damping was a factor in the early part of the record, it is not thought to be capable of causing the rapid change in Q that was observed. A similar sharp

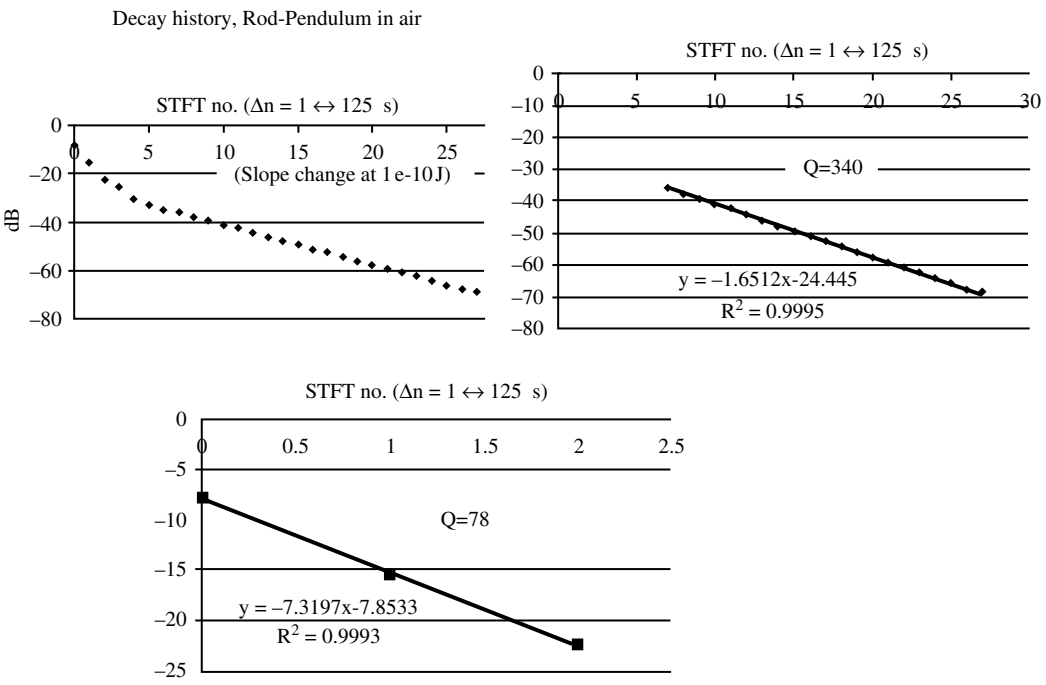


FIGURE 21.4 Example of the use of STFT analysis applied to a dataset, the first and last portions of which are shown in Figure 21.3.

change in the damping of this same pendulum was seen at roughly 10^{-11} J with the pendulum swinging in a high vacuum. The slope change was equally rapid for the vacuum case, but the change in Q was from 120 to 210. It is not known why the damping at low-level energy in a vacuum would have a lower Q than in air. Perhaps the difference derives from a different placement of the knife-edges on the silicon flats. Some of the damping of this pendulum is the result of the knife-edges being fabricated from brass rather than a harder metal such as carbon steel.

21.3 Sensor Choices

Box 21.1 shows some representative sensors for damping measurements. The list is far from exhaustive; for a detailed description of each (plus discussion of other types), the reader is referred to Fraden (1996). Of the transducer types indicated, position sensors are generally the most versatile; but the present chapter also provides examples of the use of (i) velocity, (ii) microphone, and (iii) photogate measurements.

In addition to the need for linearity (discussed in Section 21.1 above), the ideal sensor will be noninvasive. In reality, it is not possible to perform a measurement that does not at some level perturb the system under study. The least perturbative types of direct measurement are optical and electrical — capacitive, followed by inductive.

Some of the advantages and disadvantages of the devices indicated in Box 21.1 are provided below.

Box 21.1

SOME SENSOR TYPES

Representative Sensors for Damping Measurements					
Position	Velocity	Pressure	Time Interval	Acceleration	Force/Strain
Capacitive	Faraday law (electromagnetic)	Microphone	Photogate	Accelerometer	Strain gauge
LVDT		Pressure gauge			
Optical		Capacitive			
Encoder		Optoelectronic			
Shadow		Piezoresistive			
Potentiometric					

21.3.1 Direct Measurement

21.3.1.1 Position Sensors

The inductive linear variable differential transformer (LVDT) is a sensor that is commonly used in engineering applications. Thus, it has been a natural choice for many position-sensing purposes; but it is both more invasive and noisier than capacitive sensors. Wielandt (2001) notes the following concerning the advantage of capacitive over inductive sensors: “Their sensitivity is ... typically a hundred times better than that of the inductive type.”

Optical encoders are also readily available and have been used extensively. Because of their digital nature, based in a finite number of elements, their low-level resolution is poor compared to capacitive devices.

Optical sensing by shadow means is easy to employ — for example, using a solar cell of the type discussed later. The method is afflicted, however, by (i) an offset voltage, and (ii) the degrading influence of background light.

Potentiometers are very easy to use, but compared to other position sensors they are extremely invasive because of Coulomb friction in the slider and also the bearings that support it.

21.3.1.2 Velocity Sensor

The most important velocity sensor is that which functions on the basis of Faraday's law. Using a magnet and a coil, an electromagnetic force is generated in the wire of the coil when it experiences a changing magnetic flux. Prevalent in seismometers before the advent of broadband (feedback) instruments, its primary shortcoming is poor sensitivity at low frequencies.

21.3.1.3 Time Interval

Photogates have become the primary means for kinematic studies in introductory physics laboratories. Combined with compact, user-friendly timers, it is possible to measure both period and velocity. As illustrated later, they can be easily used to measure damping in slowly oscillating systems, but only in a limited amplitude range.

21.3.2 Indirect Measurement

In the cases of (i) pressure, (ii) acceleration, and (iii) force/stress sensing, the measurement is an indirect one. Consider, for example, the Ruchhardt experiment to measure the ratio of heat capacities of a gas (discussed in Chapter 20). The oscillation of the piston could be measured in several different ways. For instance, direct position sensing could be accomplished by attaching a small electrode to the piston and allowing it to move between stationary capacitor plates. Alternatively, a “flag” on the piston could be used to interrupt the light beam of a photogate. Depending on constraints, however, the easiest method might be an indirect measurement in which a pressure sensor monitors the gas through a catheter communicating with the cylinder of the apparatus.

Accelerometers can sometimes be connected directly to an oscillator, but only if the mass of the instrument is very small compared to the system being studied. As with the measurement of velocity, their sensitivity at low frequency is very poor (the second derivative of position yielding a response that is proportional to frequency-squared).

Strain gauges are easy to employ but also lack sensitivity (compared to position measurement), since they communicate with a very small portion of the oscillating sample (if noninvasive).

21.4 Damping Examples

21.4.1 Case 1: Vibrating Bar — Linear with Significant Noise

The simplest means to measure the Q of an oscillator whose frequency is in the range of the human ear is to use a microphone connected to a digital oscilloscope. In this case, the microphone was an inexpensive dynamic type and the oscilloscope was a Tektronix TDS 3054. A better choice, had it been available, would be an electret microphone. The ring-down of a xylophone bar, following a strong (sharp) hammer strike, is shown in Figure 21.5.

The voltage *versus* time of the microphone output was saved to memory in the oscilloscope, from which the digital record was output to a floppy disk, using the CSV format. Data from the disk were read into columns A and B of an Excel spreadsheet using “Open file.” An envelope fit was then performed on the turning points by placement of trial and error data into column C, using “autofill.” A separate graph was generated for each value of the constant b in the expression “ $= 0.04 * \exp(-b * A1)$ ” typed into Cell C1. (The lower turning points were obtained by typing “ $= -b1$ ” into Cell D1 and using autofill.

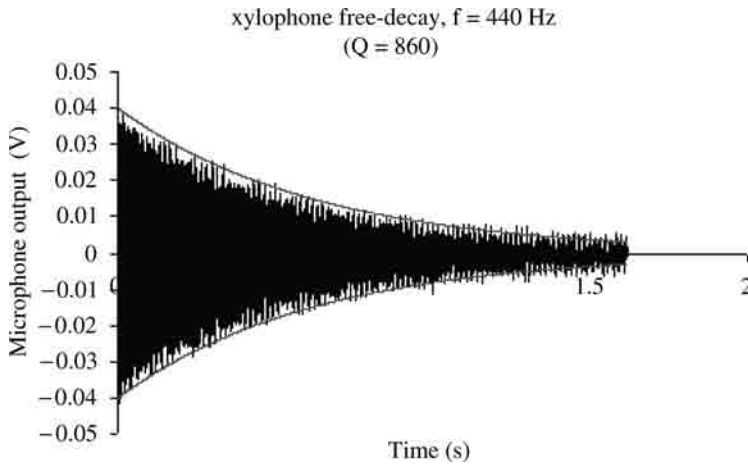


FIGURE 21.5 Free-decay record of a vibrating bar.

(Additional details concerning the use of Excel in this manner will be provided in the discussion of seismometer damping that follows.)

Although optimizing algorithms could be generated to perform such a fit (with a probable slight increase in accuracy), this visual technique is preferred here as it is more understandable, user-friendly, and its performance is proven. The total time required in Excel to generate Figure 21.5 using a 2K record (2048 points) is typically only a few minutes with a modern Pentium computer.*

Once a satisfactory fit was obtained ($b = 1.6$ in Figure 21.5), the Q was estimated using

$$Q = \frac{\pi}{\Delta} = \frac{\pi f}{b} \quad (21.1)$$

There is a fair amount of electronic noise in Figure 21.5 because the microphone was connected directly to the oscilloscope. The smallest bandwidth of the oscilloscope, at 20 MHz, causes a large amount of Johnson (white) noise. Narrowing the bandpass by means of a preamplifier would improve the quality of the data dramatically. Such is typically true of signal to noise ratio (SNR) improvement by tailoring the electronics to the need.

21.4.2 Case 2: Vibrating Reed — Example of Nonlinear Damping

To illustrate another sensing technique, the system shown in Figure 21.6 was used.

A 90° twist was given to a hacksaw blade after heating with a torch and quenching. One end was clamped to the vertical post shown and a piece of cardboard was taped to the other end. An incandescent lamp is placed above the cardboard, which vibrates horizontally, and a solar panel below the cardboard is used as a sensor. The solar panel in this case is a commercial unit that comes with a cigarette lighter plug for charging automobile batteries. The output from the panel goes to the Tektronix digital scope also in the picture.

Unlike other sensing schemes described in this chapter, the solar panel output is not bipolar but instead has a constant voltage offset corresponding to the equilibrium position of the reed.

The frequency of oscillation is too low to operate the oscilloscope with a.c. coupling. Thus, it is important to make the d.c. offset as small as possible. This was accomplished by shielding nonactive parts

*A disclaimer is in order at this point. Present comments by the author should not be interpreted as an endorsement of Microsoft products in general. Although QuickBasic and Excel have both proven unusually beneficial to the work described in this chapter, they are the only software packages marketed by the company to have received a strong endorsement from the author.

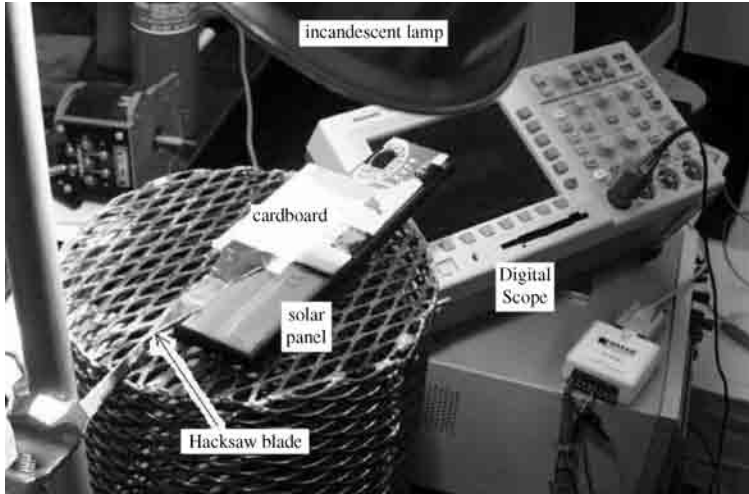


FIGURE 21.6 Setup for measurement of vibrating reed free-decay.

of the solar cell from the lamp. Although the d.c. offset could be removed with a voltage bucking battery, this was found to introduce unacceptable noise spikes. With the offset, the gain of the electronics was limited by the amount of vertical position shift allowed by the scope. The results of this study are illustrated in Figure 21.7.

The nonzero value of b (0.018) in Figure 21.7 indicates the presence of amplitude-dependent damping (refer to Equation 20.61, Chapter 20). The nonlinear damping in this case probably derives from the air, rather than internal friction of the hacksaw blade. Its presence causes the Q of the system to increase with time.

The Q of the system is calculated from the expression

$$Q = \frac{\pi}{(b + ay)\tau} \quad (21.2)$$

where τ is the period of oscillation. At the start of the record ($y = 0.12$) the Q is 390 and it approaches 2700 as the amplitude approaches zero.

21.4.3 Case 3: Seismometer

Since the ability of a seismometer to detect tremors is proportional to the square of the period of the instrument, they require a good low-frequency sensor. The most common sensor for the latest generation commercial instruments is a half-bridge (differential) capacitive type. Because of the greater sensitivity and linearity of the full-bridge symmetric differential capacitive (SDC) sensor mentioned in Chapter 20, it is well suited to these applications, being easy to employ. (The full-bridge character is described in a TEL-Atomic tutorial (Peters, 2002).) A significant advantage of the SDC symmetry (equivalent electrically to the inductive LVDT) is its relative insensitivity to construction imperfections, such as roughness of surface and nonparallelism of electrodes. Thus, construction can be done crudely without serious degradation of performance. For example, electrodes of the first prototype of the SDC sensor were fabricated from sheet

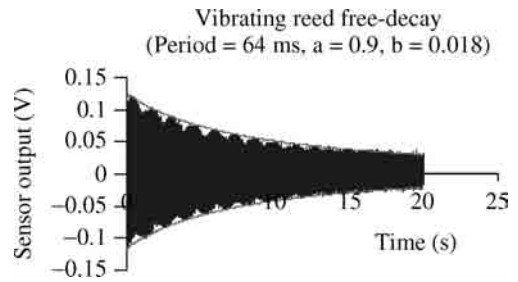


FIGURE 21.7 Vibrating reed decay with amplitude-dependent damping.

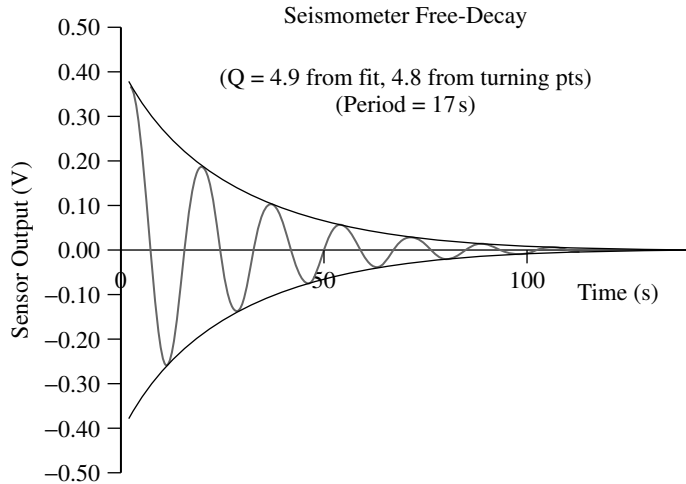


FIGURE 21.8 Free-decay record of the Sprengnether vertical seismometer, period 17 sec.

copper that was cut with shears and subsequently flattened by hammer on a hard plane surface. This stands in stark contrast to the optically polished surfaces necessary for the use of some sensors.

The Sprengnether vertical seismometer discussed at several points in [Chapter 20](#) was studied in a configuration for which $Q = 4.9$, as determined by an external $990\ \Omega$ resistor to provide induced-current damping. The resistor was connected across the coil that is part of the original equipment and which moves (with the mass of the instrument) in the field of a stationary magnet, i.e., a Faraday's law (velocity) detector. Excitation to initiate the free-decay study was accomplished by applying an alternating (square wave) current to the coil, reversing the direction of the current at each turning point of the motion of the mass. The fundamental (Fourier series) of a square-drive generated this way is shifted 90° from the mass motion, corresponding therefore to resonance. After cessation of the drive, data as shown in Figure 21.8 were collected with a Dataq DI-700 ADC (16-bit).

The graph in Figure 21.8 was generated with Excel after the Dataq record was saved to floppy disc as an *.dat (CSV) file. It was imported to Excel using "open file" with "comma delimiter." Once in Excel, these data were shifted one place to the right (from the default A column to the B column) to accommodate computer generation of a time-data column. The column of time values was generated according to the sample rate, the value of which is by default saved to the data file. To generate the time column, a 0 was placed in the first row, n corresponding to the start of data. Dropping down one row in the A column, " $= A_n + 1/(\text{sample rate})$ " was typed, to increment the time. Then the lower right hand corner "small solid square" of the box containing this time was grabbed and held with the left button of the mouse to autofill all the way to the last time point of the data. The computer-generated exponentials, which correspond to the turning points, were obtained by generating two additional columns. These were obtained by placing the cursor at a row corresponding to the time A_n (in column C) and then typing " $= A_0 * \exp(-(\omega/2Q) * A_n)$." The value of A_0 is obvious from the data and a first estimate for Q can be quickly obtained from about a dozen turning points (read with the Dataq software before the data are ever saved).

The technique is illustrated in [Table 21.1](#). For example, in the case of Figure 21.8, $Q = 4.8$ from the 13 turning points. Thus the argument of the exponential was set to 0.0385. Using autofill, the columnar (upper) exponential was then quickly produced. Then a second (adjacent) column D was generated in similar manner, by taking the negative of the last point and then autofilling to the top row. (When one autofills downward, the rate with which Excel traverses the rows increases exponentially after the last row of data has been passed; thus, it is much easier to fill upwards rather than downwards.)

Once the pair of exponentials being fitted to the data have been graphed, along with the data, it is simple to adjust the curves by varying the argument (in this case, small changes around 0.0385) until a

TABLE 21.1 Estimation of Q from the Turning Points

Use of Excel to estimate logarithmic decrement from turning points of the motion

Free-decay of Cavendish balance

	A	
1	-0.252	
2	0.247	
3	-0.185	
4	-0.194	
5	-0.133	
6	-0.155	
7	-0.095	
8	0.122	
9	-0.062	
10	0.107	
11	-0.037	
12	0.088	
13	0.024	
$-2*\ln(1-(A1-A13)/(A1-A2+A3-A4+A5-A6+A7-A8+A9-A10+A11-A12))$	0.292266	0.272743
$-2*\ln(1-(A2-A12)/(A2-A3+A4-A5+A6-A7+A8-A9+A10-A11))$	0.25322	
$(A15+A16)/2 = \text{mean}$		
(final estimate from computerized fit = 0.271)		

	A	B	C
Turning Pt (V)			
3	0.3643		
4	-0.2607		
5	0.1913		
6	-0.1343		
7	0.1029		
8	-0.0687		
9	0.0549		
10	-0.0371		
11	0.0298		
12	-0.0194		
13	0.0149		
14	-0.0109		
15	0.0071	0.6554	0.651
		0.6532	

Free-decay of Seismometer

1st set
 $B15 = -2*\ln(1-(A3-A15)/(A3-A4+A5-A6+A7-A8+A9-A10+A11-A12+A13-A14))$

2nd set
 $C15 = -2*\ln(1-(A4-A14)/(A4-A5+A6-A7+A8-A9+A10-A11+A12-A13))$

average yields $Q = 4.8 (\pi/0.653)$
(final estimate from computerized fit = 4.9)

good fit is obtained (using autofill each time). The fit is rapid and accurate when there are not too many parameters to vary, since the eye is well suited to this operation. Upon obtaining the best-fit by this means, the preliminary value of $Q = 4.8$ was altered to the final value of $Q = 4.9$.

Note that in Table 21.1 a new Excel worksheet was employed (column A no longer the time as in the discussion above). The voltages corresponding to the turning points (maximum and minimum) were each read by placing the cursor at an extremum and manually recording the value displayed in turn by the Dataq software. These values were then typed into Excel, as opposed to the “file open” method for importing large datasets, i.e., as used to generate Figure 21.7.

21.4.4 Case 4: Rod Pendulum with Photogate Sensor

One of the simplest ways to measure damping at larger levels is to use a photogate of the type common to general education physics laboratories. The infrared beam of the photogate is tripped by a “flag” attached

to the oscillator. The rod pendulum pictured in Figure 21.9 was studied by this means. Figure 21.10 shows a closeup of the flag which is attached to the top of the pendulum and which passes through the photogate during oscillation.

As seen in the figures, various parts of the pendulum are clamped to a vertical steel rod. Both upper and lower masses are made of lead, each with a pair of holes drilled in it — one to pass the brass rod of the pendulum through and the other (after tapping) to hold a thumbscrew for securing the mass at different vertical positions on the rod.

This mechanical oscillator is a compound pendulum; the period can be made long as the knife-edge (also clamped to the rod) approaches the center of mass. At long periods, the instrument is not very responsive to external accelerations of the supporting frame; but it is sensitive to internal structural changes. Low-frequency instability is encountered as the upper parts of the instrument experience creep, particularly in the materials just above the knife-edge. The upper pendulum has similarities to an inverted pendulum, except that it is rigidly connected to the lower pendulum, and causes the oscillator to eventually exhibit double-well (Duffing) characteristics. This happens at larger amplitudes as the period is increased toward really long times. The tendency toward mesoanelastic complexity depends on the dimensions of the rod. As expected because of the well-known engineering properties of rods and tubes, a large diameter, thin-wall tube will behave differently from a solid rod made from the same amount of material (same total mass). This will be true if the tube does not experience localized (sharp) deformation prone to creasing.

Damping measurements with a photogate require that the time required for the flag to pass through the beam be fairly small — thus larger amplitudes of motion are required than with other sensors. Of course really large motion would result in a period increase, consistent with long-understood pendulum dynamics. For amplitudes within the acceptable range (which in practice is not overly restrictive), the velocity of the pendulum as it passes through the equilibrium position is inversely proportional to the time

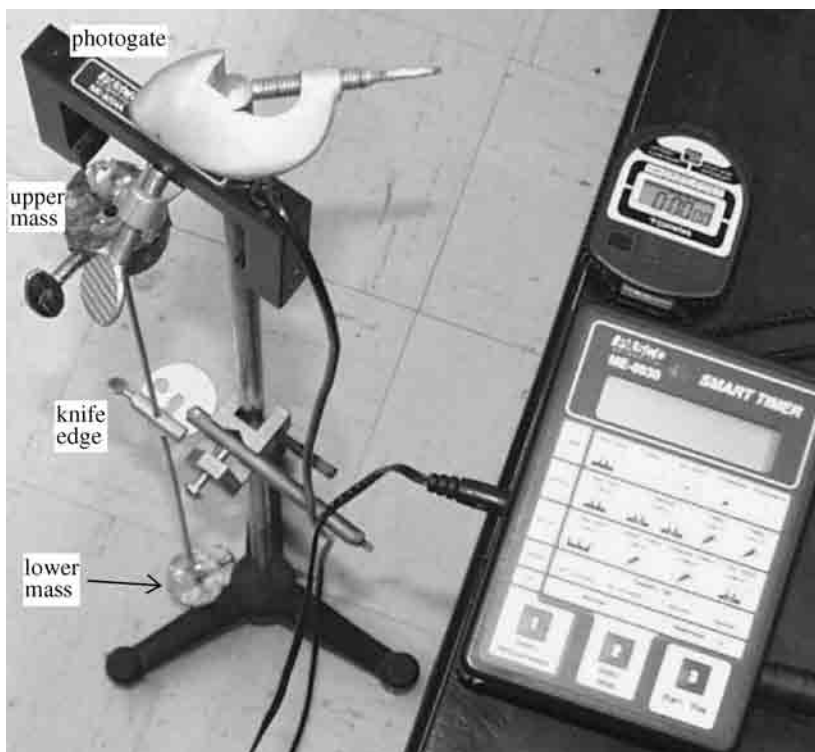


FIGURE 21.9 Rod pendulum in which damping measurements are made with a photogate.

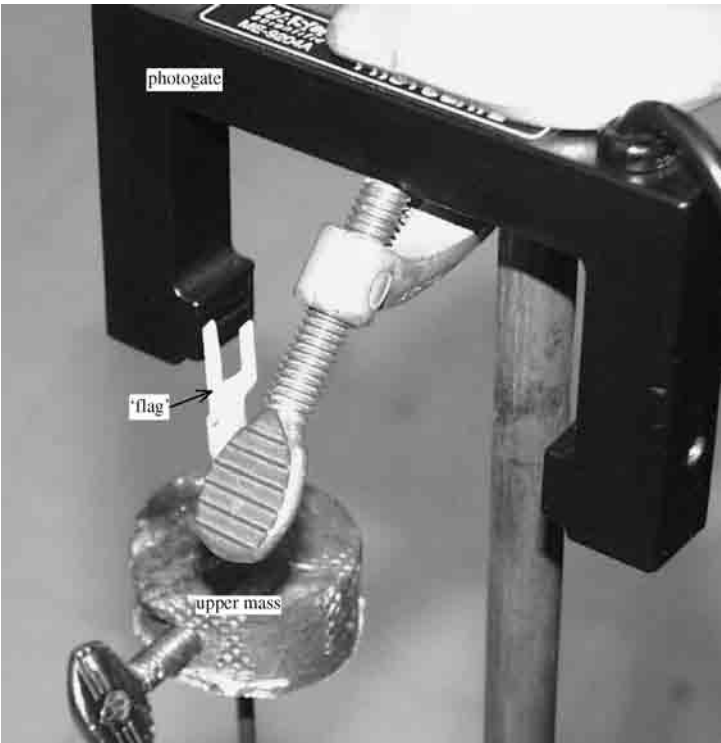


FIGURE 21.10 Top of the pendulum showing the upper mass and “flag” for tripping the photogate.

interval between interrupts of the photogate beam by the two vertical arms of the flag. If the period does not change with amplitude, then there is also an inverse relationship between the gate time and the amplitude. A plot of the inverse of these times *versus* cycle number is, for the constraints indicated, a reasonable approximation of the turning points of the free-decay.

In this case the single gate time interval measurements were made by a Pasco Smart Timer. It is a user-friendly instrument that also permits the period of the pendulum to be accurately measured by the flag (by using two different lengths of the flag arms). For experiments of this type, it may prove more convenient to measure the period with a stopwatch (infrequently as compared to the velocity). The sequentially increasing time intervals are read manually from the Smart Timer and recorded by hand, once per cycle. Of course, to do so requires that the period be long enough to permit these operations. The recorded values are conveniently analyzed by typing to a spreadsheet, which is then used to graph damping curves such as shown in Figure 21.11.

A pure exponential fit is not appropriate to the decay of Figure 21.11, in which the upper mass had been removed and a business card taped to the bottom of the pendulum to cause turbulent air damping (period near 1 sec). The fit shown, however, involving both linear and quadratic dampings, is seen to be quite reasonable. As in the case of the vibrating reed discussed earlier, this system is adequately described by the nonlinear damping equation 20.61 given in Chapter 20. For the data of Figure 21.11, $Q = 25$ initially and increases to 70 at the end of the record.

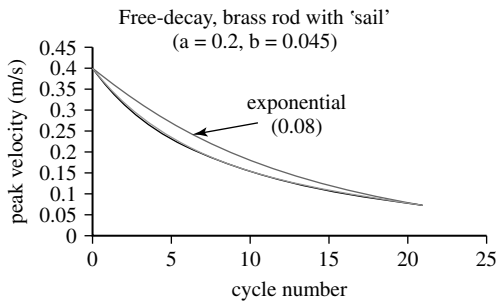


FIGURE 21.11 Free-decay of a pendulum as determined by photogate measurements.

Without the business card, and with the upper mass in place, the decay of this pendulum was found with the photogate measurement technique to be exponential, as expected for viscous damping with periods of about 5 sec. At periods in excess of about 10 sec, however, internal friction of the rod becomes more important than air damping. Although the decay is then still exponential at larger levels, the frequency dependence is not the same as required by linear air damping.

21.4.5 Case 5: Rod Pendulum Influenced by Material under the Knife-Edge

The data in Figure 21.11 were collected with the knife-edges resting on hard ceramic alumina flats. When supported by other materials, the damping of a rod pendulum can be influenced by anelastic flexure other than that of the rod. Hardness of the material does not guarantee low damping, as will be seen in the following examples. The data that follows were collected with a different pendulum, depicted in Figure 21.12.

The sensor in this case was an SDC unit, connected to the computer through the Dataq DI-700 A/D converter. The upper and lower masses are each approximately 1 kg and their separation distance on the aluminum hunting arrow from which the pendulum was fabricated was about 70 cm.

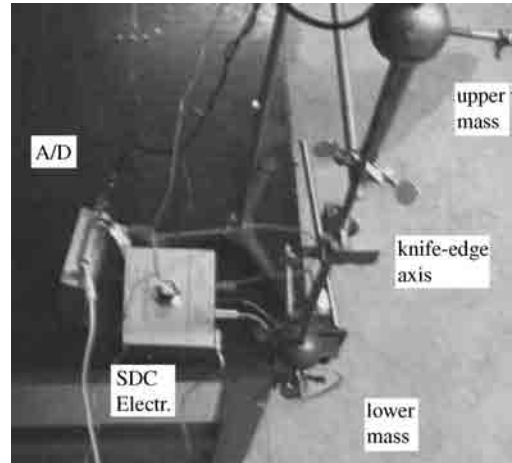


FIGURE 21.12 Long period rod pendulum used to study the influence of different materials under the knife-edge.

21.4.5.1 Lithium Fluoride Samples

The samples used to collect the data in Figure 21.13 were identical pairs, except that one pair had been irradiated with a huge dose of gamma rays. The resulting changes to the structure of the crystal are responsible not only for color centers as noted in the photograph in Figure 21.14, but also a dramatic change in the internal friction. It is clear from Figure 21.13 that internal friction in the LiF is the dominant source of damping of the rod pendulum that was used (Peters, 2003a, 2003b, 2003c, 2003d).

Lithium fluoride is used in thermoluminescent film badges (radiation monitors). When exposed to energetic radiation, atoms are “knocked” from their crystal lattice sites into metastable states corresponding to interstitial positions of the lattice. Upon ramping the temperature of the sample in an oven fitted with a photomultiplier tube, jumps from the metastable state are accompanied by the release of photons. The amount of light so generated is a measure of the dose that was received by the crystal. Because light flashes are observed with rather small changes in the temperature, it is reasonable to expect that mechanical strains might also cause a significant change to the defect state of such crystals. This postulate is confirmed by the data in Figure 21.13, which show a dramatic difference in the decay character of the pure (clear) crystals (bottom figure) and those which were extensively damaged by gammas (top figure).

In both of the decays in Figure 21.13 there is significant nonlinear damping, as evidenced in the early portions of each of the two records. The top case is nearly pure Coulombic, and the bottom case is partially amplitude dependent. This is revealed from estimates of the Q , shown in Figure 21.15.

The Q values in Figure 21.15 were computed from successive triplet-values of the turning points of the motion, read directly from the decay pattern displayed on the monitor by the Dataq software. The equation used is

$$Q = \frac{\pi}{-2 \ln[1 - (\theta_n - \theta_{n+2})/(\theta_n - \theta_{n+1})]}, \quad n = 0, 1, 2, \dots \quad (21.3)$$

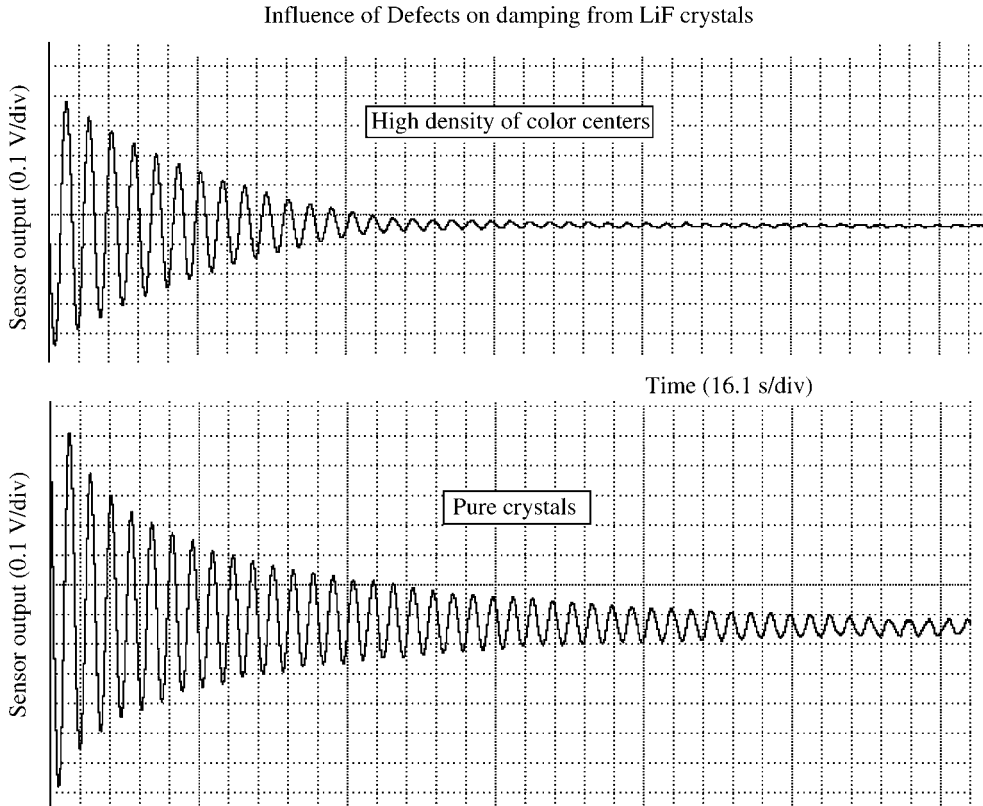


FIGURE 21.13 Illustration of damping difference according to specimen type under the knife-edge.

21.4.6 Hard Materials with Low Q

It is commonly (and mistakenly) thought that hard materials must necessarily also have low damping. The following two examples show that this is not necessarily so. Even though cast iron is very hard, it is also quite dissipative, which makes it an ideal material for engine blocks. Figure 21.16 shows a decay curve for the steel knife-edges of the pendulum resting on cast iron samples.

At the start of the record the damping with cast iron is nearly twice as great as that of steel-on-sapphire or steel-on-silicon, where the Q was found to be of the order of 80. This large damping measurement is consistent with the known excellent properties of cast iron for use in engine blocks, although the frequencies for such applications are much higher.

Figure 21.17 is another very hard material which has large damping — the ceramic piezoelectric wafer formed from lead, zirconium, and titanium (PZT), which by means of a mechanical impulse is commonly used to generate an electric spark to ignite a gas grill. The secular decline of Q based on the short temporal record indicates Coulomb damping. It is consistent with the nearly straight-line turning points for the early part of the long-term record, also shown. The long-term record

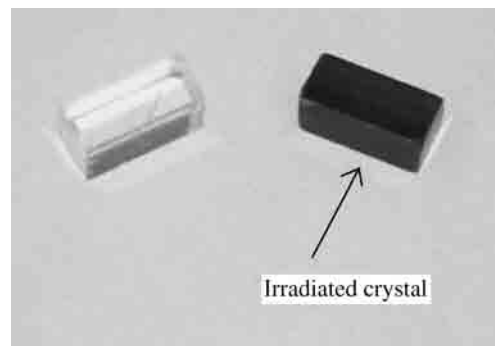


FIGURE 21.14 Photograph of LiF single crystals used to obtain the data in Figure 21.13.

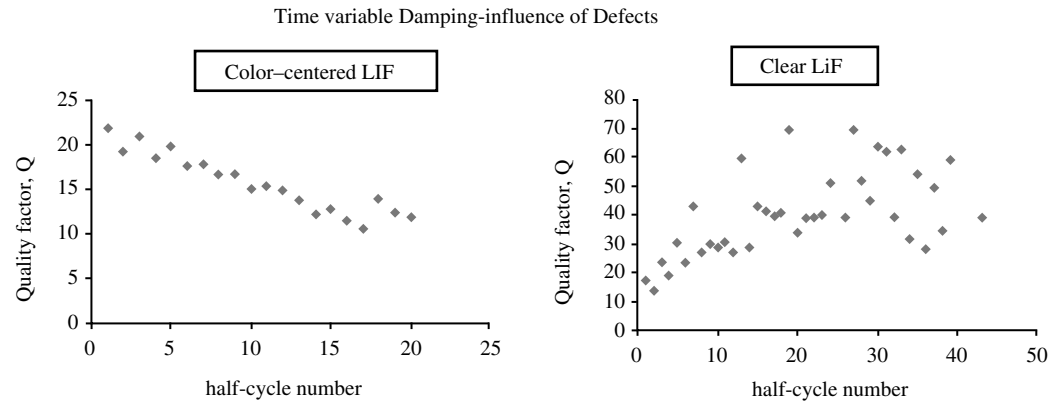


FIGURE 21.15 Temporal dependence of the Q, LiF crystal experiments.

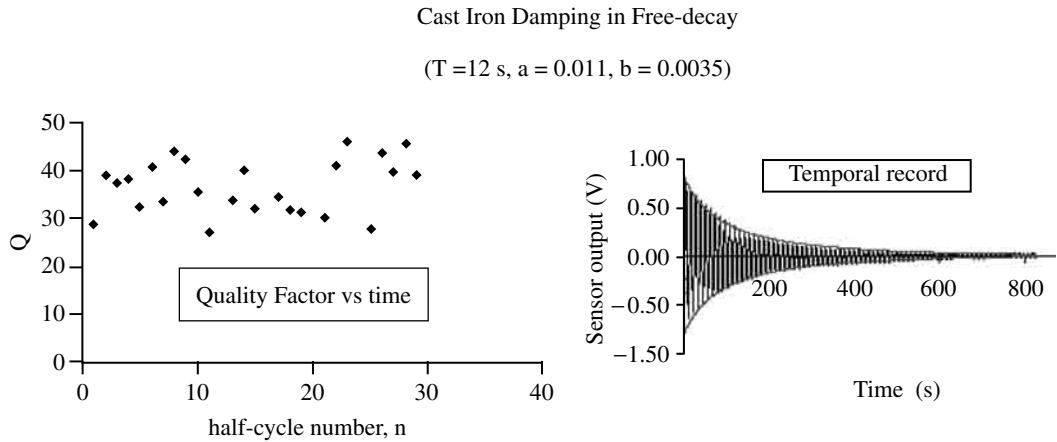


FIGURE 21.16 Data collected using cast iron samples.

is labeled as anomalous because it does not appear to be consistent with several simultaneously acting dissipation mechanisms. Instead, the strong Coulomb damping seen early on seems to disappear later, once the amplitude has dropped below a particular level. This suggests activation processes of a quantal type. It would be interesting to study the PZT wafers in a different pendulum configuration, and not operating “open-circuit” as in the present case, but rather with different resistors connected between the top and bottom of the wafers.

21.4.7 Anisotropic Internal Friction

With Polaroid material (H sheet) placed under the knife-edges it was found that the damping depends on the direction of the long-chain polymeric molecules. The direction of the molecules in a sample is readily determined by looking through the Polaroid at reflected light from a polished floor. When the reflection occurs close to the Brewster angle, only the horizontal component of the electric field is significant in the reflected light for unpolarized incident light. The direction of the molecules is thus determined by rotating the sample until the minimum of level of light is found. When this occurs the molecular chains are situated horizontally.

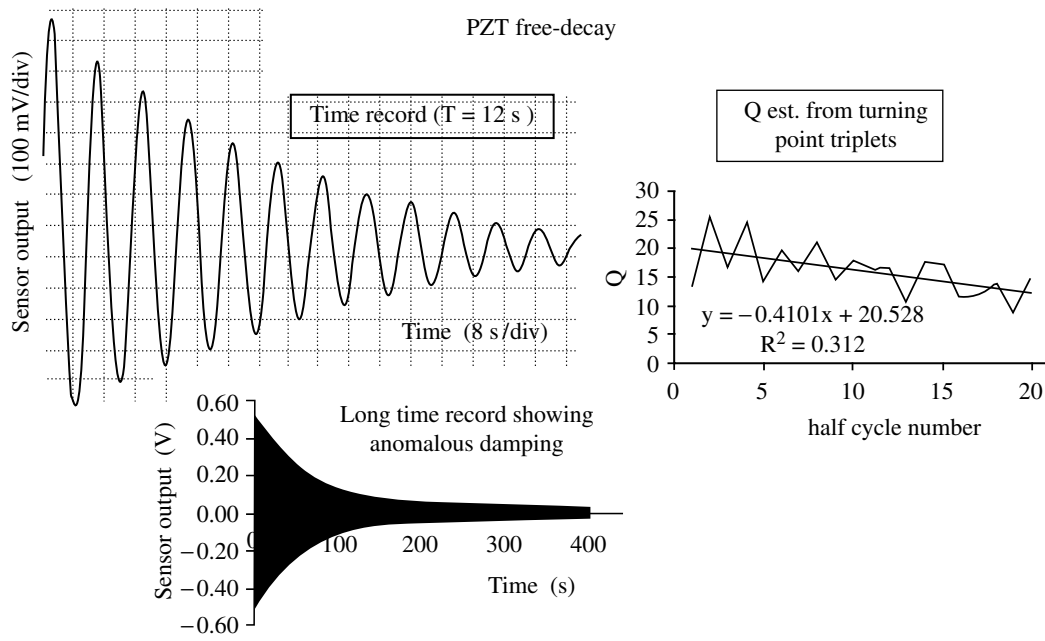


FIGURE 21.17 Data from an experiment involving PZT ceramic wafers.

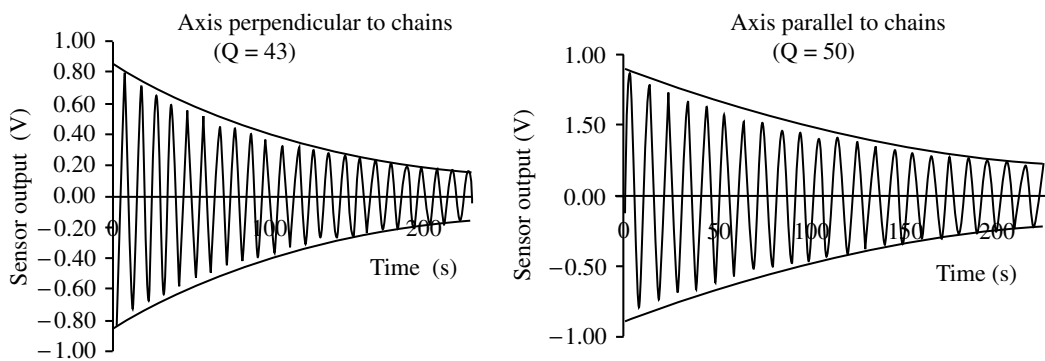


FIGURE 21.18 Free-decay curves showing anisotropy of the internal friction in polaroid material.

It was reasoned that the molecular properties of Polaroid might result in mechanical as well as optical anisotropies. This postulate proved to be true, as shown in Figure 21.18.

When oscillating on silicon at a period of 10 sec, previous studies have found that the instrument decays consistently with a Q of 80 (uncertainty 3%). In the present study, half a dozen free-decay records were obtained for (i) edges parallel to the chains and (ii) edges perpendicular to the chains. The average Q of oscillation was estimated at 50 for the parallel case and 43 for the perpendicular case. Reproducibility proved slightly better for the parallel case (4%) as compared to the perpendicular case (5%). Additional details are documented elsewhere (Peters, 2003a, 2003b, 2003c, 2003d).

21.4.7.1 Summary, Free-Decay Q Estimation

All of the techniques so far described are methods based on free-decay, which is especially important for nonlinear systems. With linear systems it is also possible to use steady-state methods, as noted in Box 21.2 (last column; de Silva, 2000). Box 21.2 summarizes the techniques used in the present chapter to estimate the logarithmic decrement, βT , from which $Q = \pi/(\beta T)$.

Damping (Q Estimation) Techniques ($Q = \pi/\beta T$, T = Period)					
Logarithmic Decrement (Full-Cycle, N)	Turning Points (Half-Cycle, n)	Nonlinear Fit to Envelope	Time τ to $1/e$ ($0.3679x_0$)	Short Time Fourier Transform	Bandwidth, Magnification Factor, Hysteresis Loop, Step-Response
$\beta T = \frac{1}{N} \ln \frac{x_0}{x_N}$	$\beta T = -2 \ln \left[\frac{1 - (x_{n-1} - x_{n+1})}{(x_{n-1} - x_{n+1})} \right]$	$-\dot{y} = ay^2 + by + c$	$\beta T = T/\tau$	$-\beta T = \frac{T \ln 10}{20}$ [slope(dB/s)]	de Silva (2000), p. 379

The best method is to use a full nonlinear fit; the worst is to measure the time to 1/e. The expression in Box 21.2 for the logarithmic decrement, using the STFT, is equivalent to

$$Q = 27.29 \frac{f}{\left| \frac{\text{dB}}{\text{s}} \right|}$$

(21.4)

where f is the frequency in Hz and the STFT slope is specified in dB per s.

21.5 Driven Oscillators with Damping

This chapter has been mainly concerned with oscillators in free-decay. It is also possible to make quantitative predictions from measurements at steady state. Confidence in predictions, however, depends on the nature of the damping. Such data are of limited value for most nonlinear systems, unless supplemented with free-decay data.

21.5.1 MUL Apparatus

Some of the techniques applicable to driven systems are illustrated by the multipurpose undergraduate laboratory (MUL) apparatus shown in Figure 21.19, that has been used by students in the physics department at Mercer University.

For the purpose of measuring the Lorenz force (basis for defining the current unit, the ampere) a constant current is supplied through the posts to the pivoted-on-points brass wire on which a weight, W , is shown hanging on one of the horizontal arms of the wire. Current enters the wire through one post *via* the banana plug inserted into a drilled hole. It thereafter travels through the lower (invisible) shorter

straight segment of the wire located between the poles of the drive magnet; and it finally exits through the banana plug on the opposite post. When carrying a current, the force on the wire from the part inside the magnet causes vertical deflection, the direction up or down being determined by the direction of the current. This results in a rotation about the pivot points (indented tops of the posts). The position is measured by the capacitive sensor, S (one of several variants of the SDC patent).

The sensitivity of this current balance depends on the location of the center of mass of the oscillatory wire, which is determined in part by the position of the rare earth magnet, M, which hangs from a steel nut on the threaded part of the heavier brass rod having a 90° bend. The upper end of this threaded rod is held by a plexiglass member that also holds the ends of the oscillatory wire.

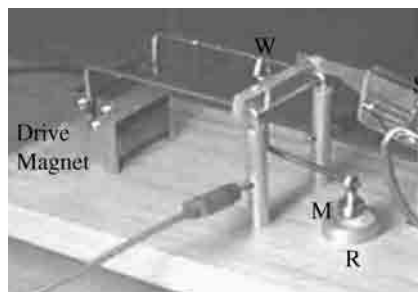


FIGURE 21.19 Apparatus for studying resonance and the Lorenz force law.

21.5.2 Driven Harmonic Oscillator

The MUL becomes a driven harmonic oscillator when the excitation current is a.c. rather than the d.c. used for the Lorenz force study. The damping is determined primarily by eddy currents in the aluminum ring, R, that lies on the wooden base underneath and in close proximity to magnet M.

The apparatus is useful for studying both free-decay and driven oscillation. Engineering students Brandon R. Bowden and James D. Sipe have programmed LabVIEW to generate both free-decay curves and resonances.

An example Lorentzian (resonance response) is given in Figure 21.20. (Additional information is found in a laboratory writeup (Peters, 1998).)

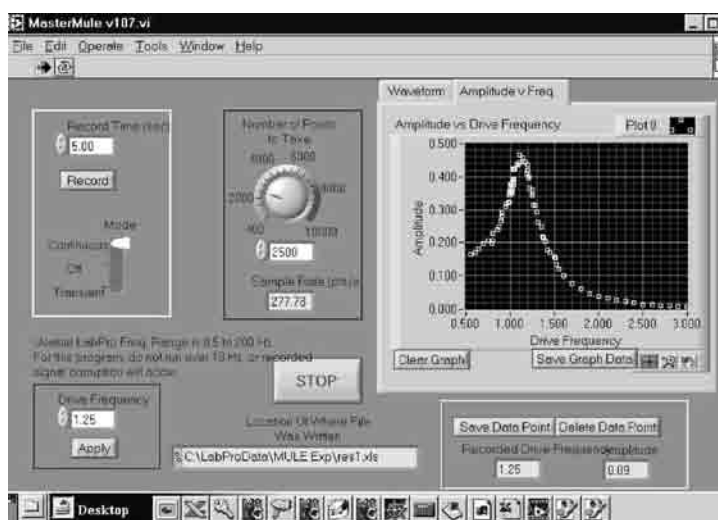


FIGURE 21.20 Screens from the LabVIEW program used with the MUL to study both transient and resonance phenomena.

21.6 Oscillator with Multiple Nonlinearities

An oscillator can have significant nonlinearities of both the elastic and damping types. An example is the mechanical system pictured in Figure 21.21.

The instrument is a modified extensometer that was sold by TEL-Atomic and which was designed around the SDC sensor to measure Young's modulus and thermal expansion coefficients. The wire sample normally used with the instrument (along with a hollow power resistor that fits in the black clamp) has been removed, and two rare earth magnets have been employed. One magnet is superglued to the bottom of the pan where the weights are normally placed, as shown in Figure 21.22; and the other magnet is attached to the bottom of the inductor that is sitting on the top of the oscillator (cased instrument, Pasco) used for drive. The pair of magnets are positioned in close proximity so as to repel each other, thus supporting the mass of the moveable arm of the extensometer.

The study of nonlinear systems requires a linear sensor; i.e., any nonlinear contributions from the detector must be negligible. Figure 21.23 shows the calibration results for the instrument and its linear response for the range of amplitudes used in the study.

The potential energy of this oscillator was assumed to have the following form

$$U(x) = \frac{b}{x^n} + cx \quad (21.5)$$

and the parameters were estimated by measuring x as small masses were placed on the pan. A linear regression fit to a log-log plot (using the sensor calibration constant of 550 V/m) yielded $b = 1.02 \times 10^{-5}$, $n = 1.526$, and $c = 0.304$ (system international units). Anharmonicity of the

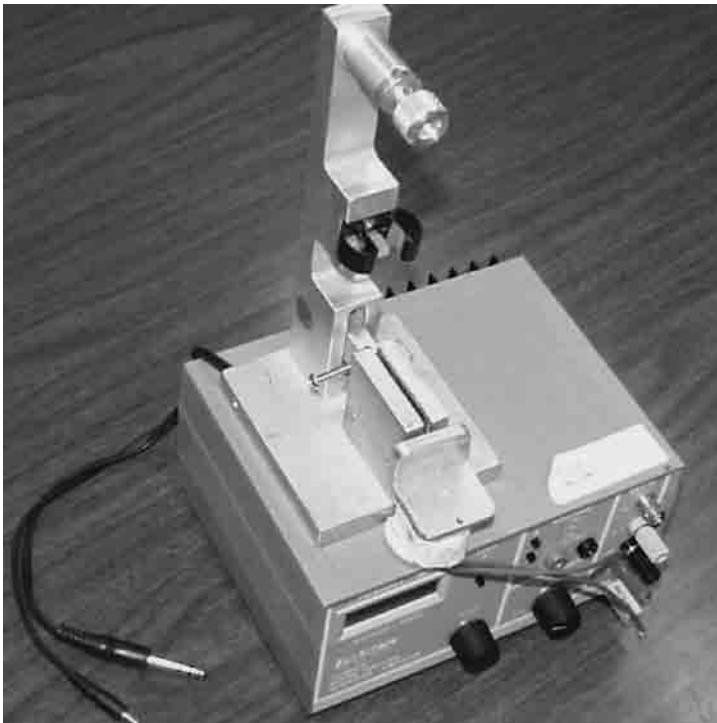


FIGURE 21.21 Mechanical oscillator with multiple nonlinearities.

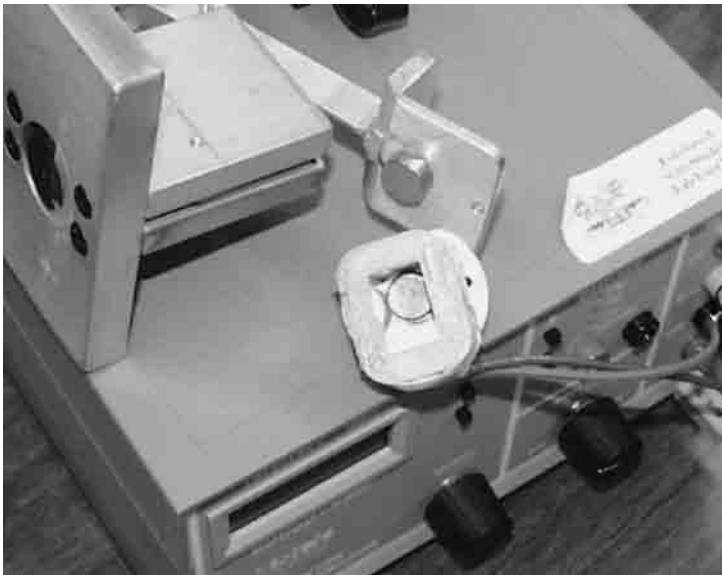


FIGURE 21.22 Closeup picture of the oscillator in [Figure 21.21](#) (nonoperational configuration), showing placement of the rare earth magnets.

potential is readily apparent in the plot shown in [Figure 21.24](#), with the force of restoration being greater in compression (x decreasing) than it is in extension. This feature is reminiscent of interatomic potentials, with anharmonicity being responsible for thermal expansion.

Because of the elastic nonlinearity, the mean position depends on the amplitude of the oscillation, as is evident in the free-decay curve in [Figure 21.25](#).

The damping of this oscillator was also found to be nonlinear, as seen in [Figure 21.26](#).

The oscillator exhibits hysteresis when driven at larger amplitudes, as shown in [Figure 21.27](#), where it can be seen that the location of an amplitude jump depends on which way the oscillator is adjusted, either up or down in frequency. Such jumps (well known with oscillators with nonlinear elasticity) stand in stark contrast with the behavior of a linear oscillator, as can be seen by comparing [Figure 21.27](#) with the screen picture in [Figure 21.20](#).

A surprise from this study involves the frequency of oscillation. In general, the oscillator did not entrain to the drive. Moreover, the preferred frequencies were not necessarily the same as the free-decay frequency of 6.01 Hz. Some of the frequencies (measured with power spectra) are indicated in

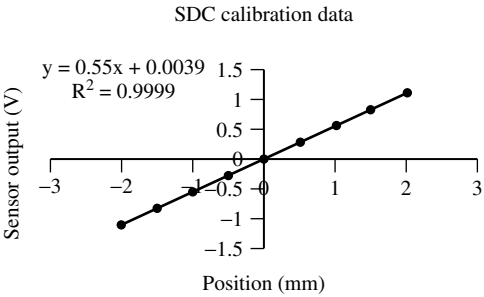


FIGURE 21.23 Calibration data for the sensor used with the oscillator having multiple nonlinearities.

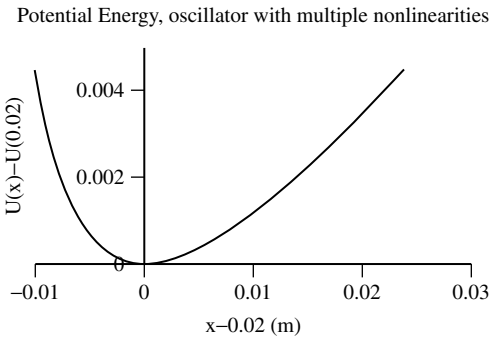


FIGURE 21.24 Plot of the potential energy function of the oscillator.

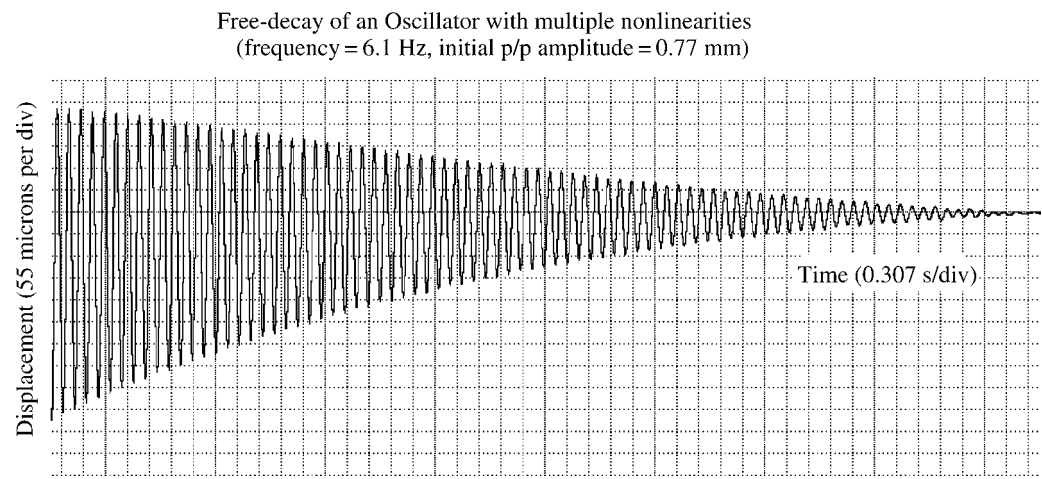


FIGURE 21.25 Free-decay curve showing the mean position shift as a function of oscillator amplitude. (Decreasing sensor voltage corresponds to increasing x .) The frequency of oscillation is 6.01 Hz.

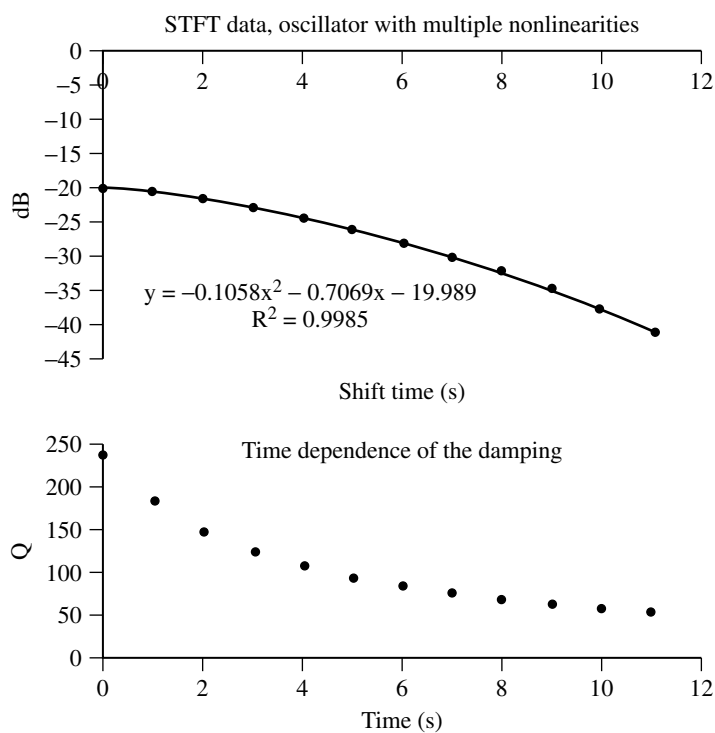


FIGURE 21.26 Free-decay character as determined using the short time Fourier transform.

Figure 21.27. The 3% frequency jumps observed in Figure 21.27 (in going from 5.46 Hz to 6.20 Hz) are not real but rather artifacts of the finite resolution of the 1024 point transforms that were employed.

Figure 21.27 demonstrates why nonlinear damping measurements should be done in free-decay. Figure 21.25 demonstrates how exponential fits make no sense for some oscillators. Fortunately, the STFT can be used to determine the amplitude dependence of the Q .

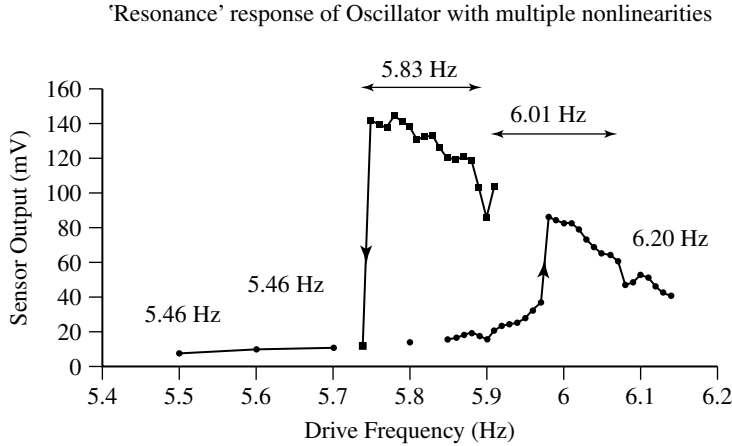


FIGURE 21.27 Resonance response (steady state) of the driven oscillator.

21.7 Multiple Modes of Vibration

21.7.1 The System

In engineering, multimode oscillations are common. Many, if not most, cases have mode mixing features even though they may in some cases be too small to be readily observed. The importance of nonlinearity to these problems is not widely appreciated, so a case to illustrate salient features is provided here. Free-decay records were obtained with an oscillator in the form of a vertically oriented (hanging) tungsten wire, of length 24 cm and diameter 0.31 mm. It was clamped at the top end, and at the bottom a rectangular plate was attached that was 11.3 cm long, 1.3 cm wide, and 0.8 mm thick. The plate was cut from double-sided copper circuit board. The board was positioned between the stationary plates of a capacitive sensor, as shown in Figure 21.28.

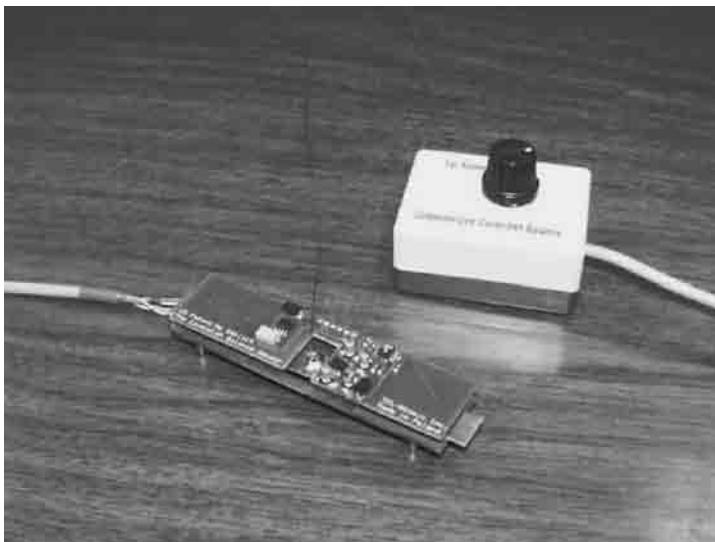


FIGURE 21.28 Photograph of the detector used to monitor the multimode oscillator.

For the picture, the apparatus was disassembled and the plate allowed to rest on the top of the bottom electrode set. Operationally, the plate was positioned midway between the upper and lower static electrode sets (separation distance of 4 mm); and there was no mechanical contact during oscillation. As can be seen, the top of the circuit board containing the upper electrode set contains more than a dozen electronic components; these are of the surface mount technology type. The detector is of the SDC type and this particular embodiment is manufactured in Poland for TEL-Atomic Inc., Jackson, MI, for use in the Computerized Cavendish Balance.

As can be seen in the picture, the wire was rather kinked instead of straight, which is expected to be a significant source of nonlinearity. For this reason, not to mention that it is very difficult to make larger diameter tungsten wires reasonably straight, no serious attempt was undertaken to remove the kinks.

21.7.2 Some Experimental Results

An example decay record generated with this apparatus is illustrated in Figure 21.29.

21.7.3 Short Time Fourier Transform

When multiple modes are present in a decay, as in Figure 21.29, it is not possible to readily estimate Q for all of the various modes using time data. The decays can be estimated using the FFT, in a technique called the short time Fourier transform, which is built-in to various software packages related to acquisition systems, such as LabVIEW (see Appendix 15A). With the versatile software supplied with the Dataq A/D converter, it is straightforward to employ an equivalent manual technique. Using the number of points to define the FFT a value (always a power of 2 total) that is substantially smaller than the number of points in the record, a manual scan is performed in which one simply increments from start to finish, calculating a separate FFT at each position in time along the way. As an illustration of this powerful tool, Figure 21.30 shows spectra corresponding to the start and the finish of the data in Figure 21.29.

All the modes decay in time, and the rate of decay is especially large for those modes that correspond to sum and difference frequencies of the primary modes at 1.19 and 2.19 Hz. Table 21.2 gives the spectral intensities in dB for the two times considered. Where the rows are blank for the end of record case, the values were insignificantly small.

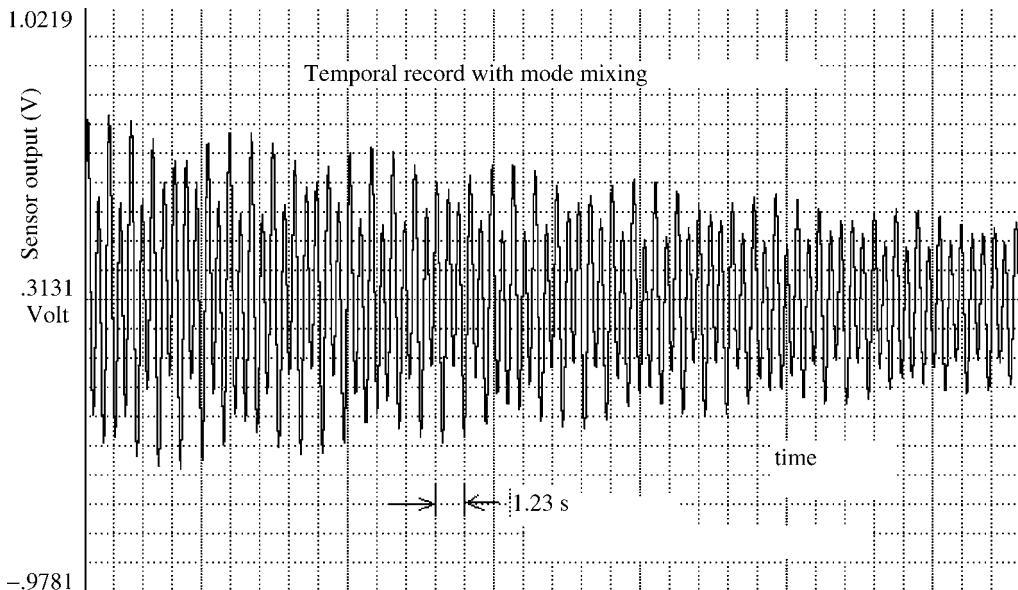


FIGURE 21.29 Example free-decay of a multimode wire oscillator.

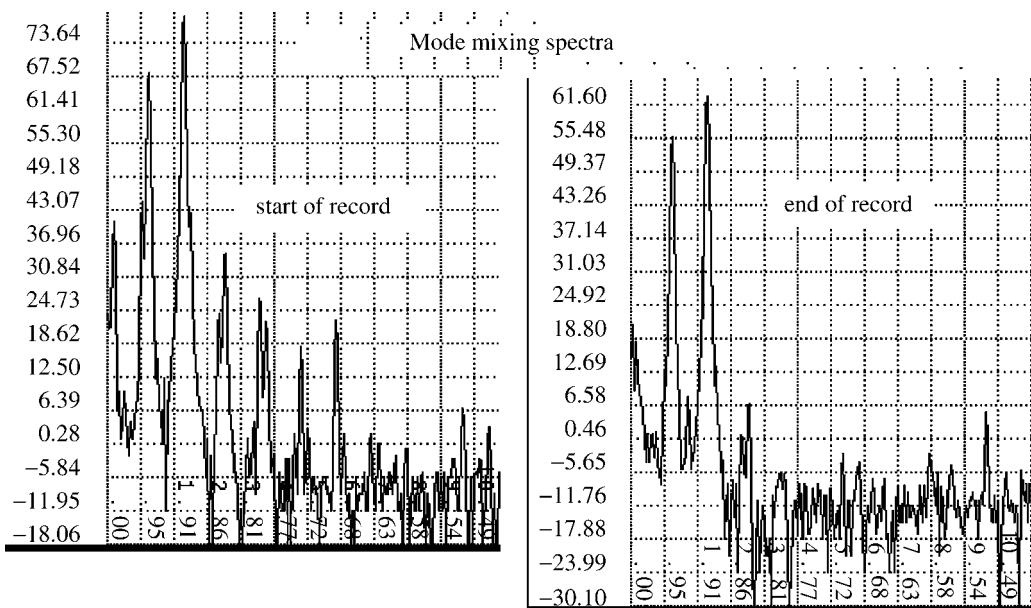


FIGURE 21.30 Beginning and end spectra corresponding to the temporal data from Figure 21.29. Ordinate values are spectral intensity in dB, abscissa values are frequency in Hz (linear scale).

The decibel values in the table are referenced to the bit-size (16 corresponding to 65536) of the ADC. In terms of the sensor output voltage, V , it is defined by Dataq as:

$$\text{dB} = 20 \log_{10}(32,768 \times V/\text{FS}) \tag{21.6}$$

where FS is the full-scale voltage as determined by the gain setting.

Elsewhere in this chapter, the decibel is calculated with a different reference. For example, for an FFT spectral line having real and imaginary components R and I , respectively (voltage based), the intensity in dB is calculated using

$$\text{dB} = 20 \log_{10} \left[\sqrt{R^2 + I^2} / \left(\frac{n}{2} \right) \right] \tag{21.7}$$

where n is the number of points in the FFT. This is convenient for determining noise levels. For example, from later graphs showing electronics noise, the floor of the SDC sensor is found to be of the order of -120 dB, corresponding to a microvolt. The position resolution defined by this noise level is about 500 nm, i.e., the wavelength of visible light.

TABLE 21.2 Spectral Intensities for Some of the Lines Shown in Figure 21.30

Frequency (Hz)	Start of Record (dB)	End of Record (dB)
2.19	78.3	63.0
1.19	68.1	55.6
1.00	44.6	
0.19	40.8	
3.38	35.0	6.7
4.34	26.7	
4.53	22.4	
6.53	22.9	
5.53	17.8	

Of the two primary modes of this kinked-wire case study, the higher frequency (2.19 Hz) is the twisting mode and the lower frequency (1.19 Hz) is the swinging mode. The swinging mode is a little higher frequency than that which would result if the wire were completely flexible, yielding a near simple pendulum (1.02 Hz for 24 cm length). The swinging mode is two dimensional (pendulum equivalent called conical), but the sensor only responds (first order) to motion perpendicular to the long axis of the electrodes. It should also be noted that this motion is attenuated, relative to the twisting response, because of the mechanical common-mode rejection feature discussed in [Chapter 20](#).

The manual STFT was used on the data that generated [Figure 21.29](#) to estimate the decay history of three different modes — both of the primary ones (twist and swing) and also the mode whose frequency is the difference between the frequencies of the primaries, i.e., 1 Hz. [Figure 21.31](#) shows the results, where a Hanning window was used, and the total number of points in the record permitted five equally time-spaced FFTs, when working with a 1024 point transform.

Although the decay of the twisting mode is seen to be reasonably exponential, there was large beating between the modes (readily observed in [Figure 21.29](#)). Beating alone would not yield a mix signal whose frequency is 1.0 Hz. However, beating in a linear system can cause amplitude variations in the weaker swinging mode.

21.7.4 Nonlinear Effects — Mode Mixing

At least two signals in the spectra are the result of nonlinearity, i.e., the lines corresponding to the sum and difference of the frequencies of the primary pair — at 3.38 and 1.00 Hz, respectively. If the system of oscillator and detector were completely linear, then no such sum and difference cases would be possible. It is also to be noted that these mixtures are not the result of sensor nonlinearity, which as noted previously one must be careful to avoid.

The amplitude of a mix signal was expected to approximately obey the following relation:

$$A_m \propto A_1 A_2 \quad (21.8)$$

To test this premise, the STFT was used to estimate the amplitudes of each of the three components indicated in Equation 21.8. The amplitudes were all normalized, relative to the starting value for each case, and the results used to generate the graphs in [Figure 21.32](#).

The amplitude of oscillation for a given mode, at the time of the transform, is found by using the peak value in dB of the intensity of the spectral line for that mode, according to

$$A \propto 10^{\text{dB}/20} \quad (21.9)$$

where the factor of 20 is used since the spectral intensities were calculated in terms of voltages. Although calibration constants (in V/m and V/rad) could be used to express the amplitude in meters or in radians, corresponding to the mode, nothing is gained by doing so for the present purposes.

The mixing index for these cases is defined by the expression

$$\text{index} = \frac{A_m}{\sqrt{A_1 A_2}} \quad (21.10)$$

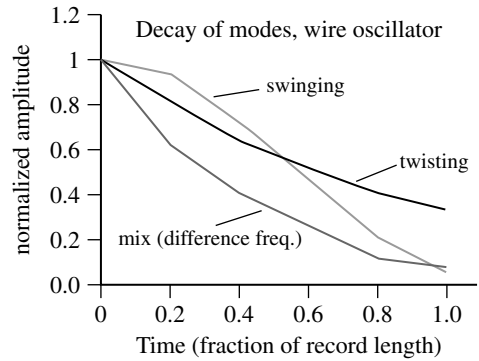


FIGURE 21.31 Decay of modes of the wire oscillator, determined by the manual STFT.

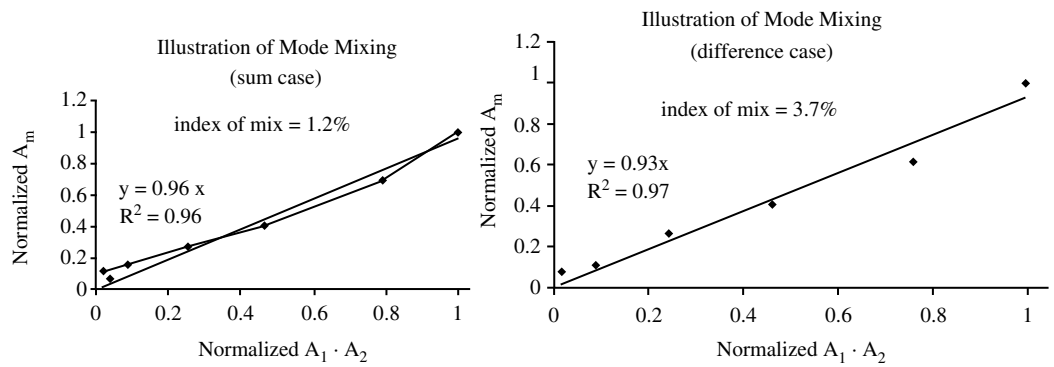


FIGURE 21.32 Evidence in support of nonlinear mixing according to Equation 21.8.

which is similar to expressions encountered in optics. It can be seen that the sum and difference frequencies are approximated reasonably well by theoretical expectation.

21.8 Internal Friction as Source of Mechanical Noise

Chapter 20 claims that internal friction is responsible not only for damping but also for significant mechanical noise of $1/f$ type. Figure 21.33 is provided in support of that claim.

The pendulum in these experiments (lead spheres near the ends of an aluminum tube with a pair of steel-points for the axis) was operated in a high vacuum to eliminate the influence of air. The electronics

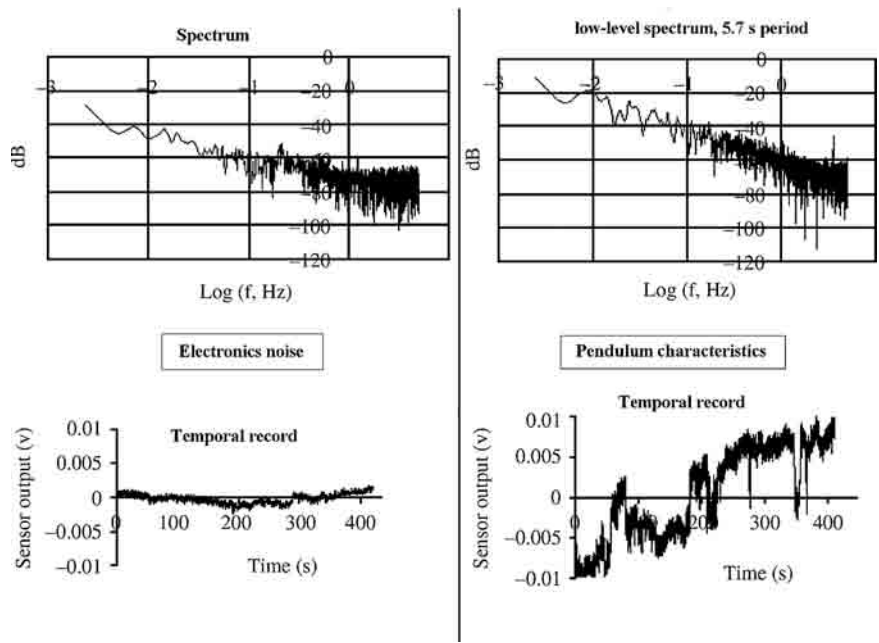


FIGURE 21.33 Power spectrum and associated temporal record showing mechanical $1/f$ noise (right pair). For reference, electronics noise is also provided (left pair).

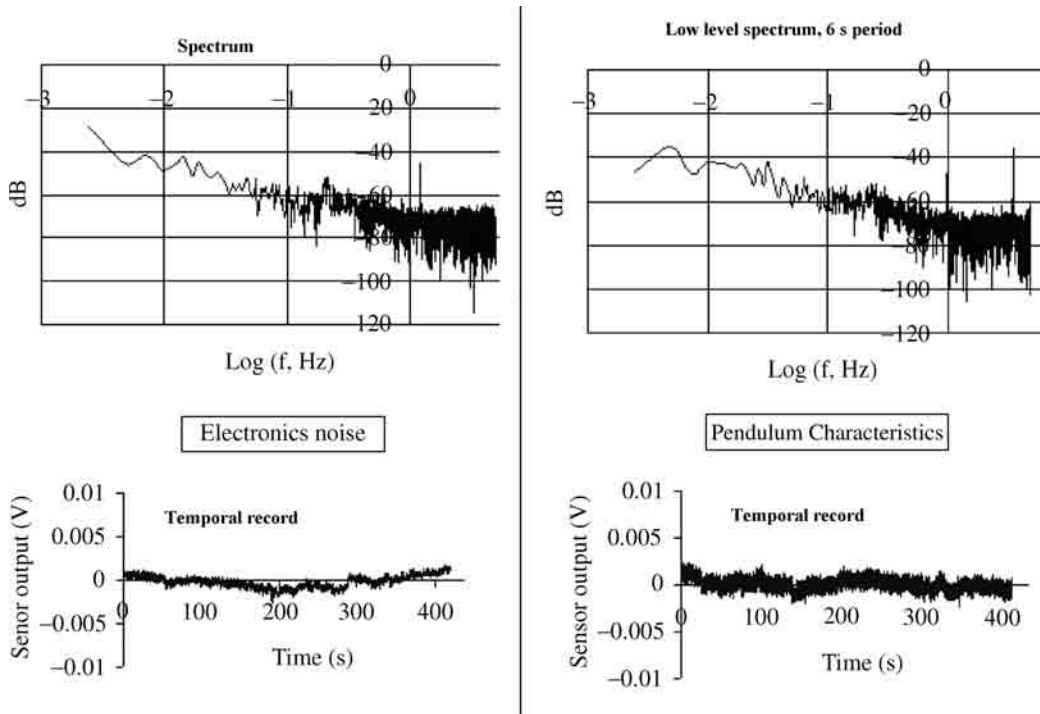


FIGURE 21.34 Same as Figure 21.33, but after the pendulum had stabilized.

noise was obtained by removing the top mass and measuring the motion after oscillation reached a minimum (frequency approximately 1 Hz); some pendulous mode remains because of pump noise transmitted through the vacuum hose. Similarly, the pump vibrations excite a vibratory mode in the long-period pendulum (sharp spectral line at 3.5 Hz, right spectrum). In this vibratory mode the lead masses move in the same direction relative to the stationary axis (similar to the bending mode of the carbon dioxide molecule). It is interesting to note that there is no coherent oscillation to be seen above noise corresponding to the period of 5.7 sec. The mechanical noise is seen to include bistability, which is not uncommon for this type of system before hardening, following a significant force disturbance. The data in Figure 21.33 were collected after replacing the upper mass, which had been removed to measure the electronics noise, and after pumping to the operating pressure (below $5 \mu\text{m Hg}$).

The mechanical noise is seen to be $1/f$ for $f < 1.5$ Hz, which is where electronics begins to contribute noticeably. Everywhere below 1 Hz, the electronics noise is an order of magnitude smaller than the mechanical noise.

After the pendulum had stabilized overnight and been allowed to oscillate through a number of free-decays (initialization by tilting the chamber), the data shown in Figure 21.34 was collected.

It can be seen that the mechanical noise has mostly settled out, leaving the remnant electronics noise.

21.9 Viscous Damping — Need for Caution

Recent experiments have shown important subtleties of viscous damping (Peters, 2003a, 2003b, 2003c, 2003d). It is true that the dissipation at a specified frequency can be adequately modeled by simply multiplying the velocity term in the differential equation by a coefficient. It is not proper, however, to call

this coefficient a constant, since the damping coefficient is frequency dependent and also involves the density as well as the viscosity of the fluid in which oscillation takes place.

Some engineers have known about the history term, which is most simply treated in the case of a sphere executing simple harmonic motion. The friction force acting on the sphere in this case can be reasonably approximated by

$$f_{\text{harmonic}} = 6\pi\eta a \left(1 + C_H \frac{a}{\delta}\right) v, \quad \delta = \sqrt{\frac{2\eta}{\omega\rho}}, \quad (C_H \rightarrow 1 \text{ as } \nu \rightarrow 0) \quad (21.11)$$

where ω is the angular frequency of oscillation, a is the radius of the sphere; and for the fluid, η and ρ are its viscosity and density, respectively. Only in the limit of zero frequency does the damping reduce to the form that one expects on the basis of Stokes' law of viscous friction (steady flow).

Using Equation 21.11 in the equation of motion for a pendulum yields for the Q

$$Q_v = \frac{I\omega}{6\pi\eta a \left(1 + \frac{a}{\delta}\right) L^2}, \quad \delta = \sqrt{\frac{2\eta}{\omega\rho}} \quad (21.12)$$

where I is the moment of inertia, and L is the distance from the axis to the center of the sphere. Typically, the ratio a/δ is significantly greater than unity so that the damping is governed by the surface area of the sphere rather than by its radius. These complexities of viscous damping are summarized in Box 21.3.

Reasonable experimental validation of the estimate for Q was provided, as demonstrated in Figure 21.35.

The instrument in this case was a compound pendulum in which a mass was located above the axis of rotation, as well as the usual situation of mass below the axis. The water damping was provided through a small sphere at the bottom of the pendulum, immersed in water held by a rectangular container.

If the history term in Equation 21.12 is ignored there can be huge errors. For example, in the case of water damping, the damping can be underestimated by 1000 to 3000%, as shown in Figure 21.36.

At low frequencies, it is also important to correct for the influence of hysteretic damping of the pendulum. Figure 21.37 shows the large errors that occur when one fails to do so.

For some cases, buoyancy and added mass of the fluid are also quite significant to the frequency of oscillation, as shown in Figure 21.38.

Box 21.3

COMPLEXITIES OF VISCOUS DAMPING

Friction force is not a function only of viscosity η ; it also depends on density ρ and angular frequency ω

$$f_{\text{harmonic}} = 6\pi\eta a \left(1 + C_H \frac{a}{\delta}\right) v, \quad \delta = \sqrt{\frac{2\eta}{\omega\rho}}, \quad (C_H \rightarrow 1 \text{ as } \nu \rightarrow 0)$$

resulting in a complicated frequency dependence for the Q of viscous damping

$$Q_v = \frac{I\omega}{6\pi\eta a \left(1 + \frac{a}{\delta}\right) L^2}, \quad \delta = \sqrt{\frac{2\eta}{\omega\rho}}$$

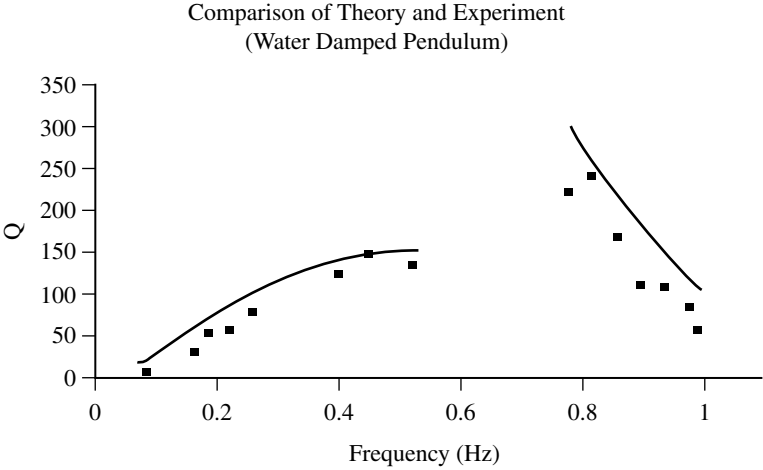


FIGURE 21.35 Comparison of theory and experiment for a pendulum damped by water.

21.10 Air Influence

As seen from Figure 21.37, low-frequency motions are likely to be influenced more by internal friction than by any fluids that interact with the oscillator. The most important fluid is of course air, and a true delineation between external and internal effects requires that the oscillator be studied in a high vacuum. It is not enough to just remove most of the air, since the viscosity of gases is surprisingly constant until the mean free path between collisions becomes a significant fraction of chamber dimensions.

Theoretically, it is possible to roughly estimate air influence, although only in the simplest of geometries, such as a sphere. In such cases, Equation 21.11 could be used (with accounts for the history term, using appropriate values for the viscosity and density). It is also possible in some cases to estimate air influence experimentally, as in the example that follows.

21.10.1 Brass and Solder Rod Pendula

Because of its malleability, the internal friction of solder (lead–tin alloy) is large, compared to that of much harder brass. A pendulum of each material was studied, both having a length of about 50 cm and a

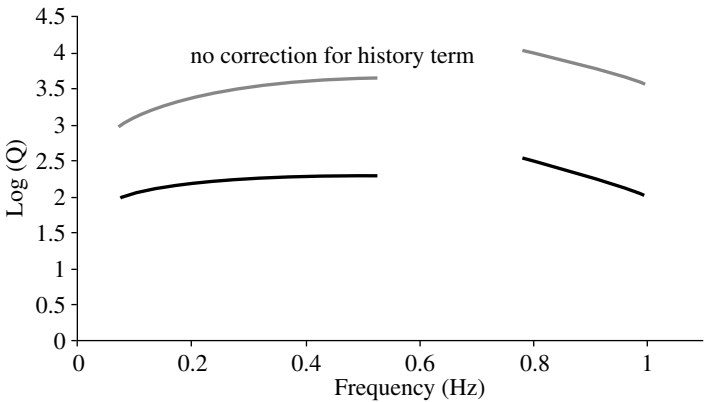


FIGURE 21.36 Illustration of how huge errors can occur in damping estimates if one ignores the history term.

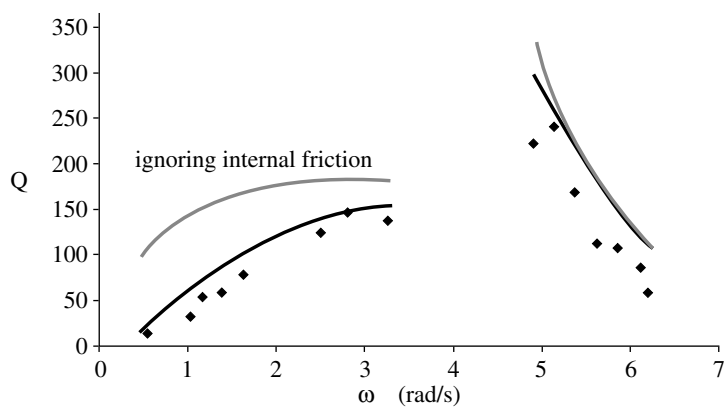


FIGURE 21.37 Illustration of significant low-frequency errors that result from a failure to recognize the hysteretic damping component of the pendulum.

diameter of about 3 mm. The technique used was the photogate method described in Section 21.4.4 (Case 4 above). Unlike the previous study, no lead masses were clamped on the rod — but it used the same adjustable knife-edge.

Figure 21.39 clearly shows that the internal friction for the solder pendulum is much greater than that of the brass pendulum.

A nonlinear fit was generated for each decay curve, from which the history of the quality factor was graphed as a function of velocity amplitude, as shown in Figure 21.40.

Consider the pair of brass curves in Figure 21.40. The large difference in Q at 10 cm/sec (387 compared to 266) is in stark contrast with their near equality at 50 cm/sec. This is primarily a consequence of air drag that is quadratic in the velocity at the larger amplitude. It is more important to brass than to solder because of the small internal friction of the brass.

From the large difference in internal friction of the two materials, a first order correction for air influence on the solder pendulum is to simply subtract $1/Q$ of the brass from $1/Q$ (raw data) of the solder, to yield the reciprocal Q (corrected) due to internal friction of the solder. This has been done in Figure 21.41.

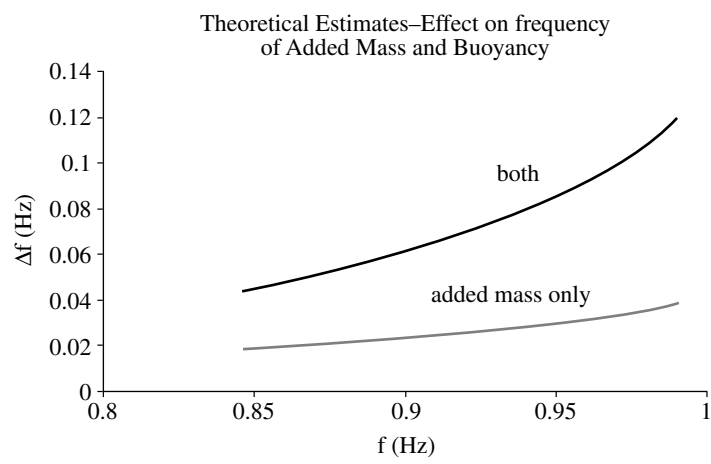


FIGURE 21.38 Example of how fluid properties influence the frequency as well as damping of an oscillator.

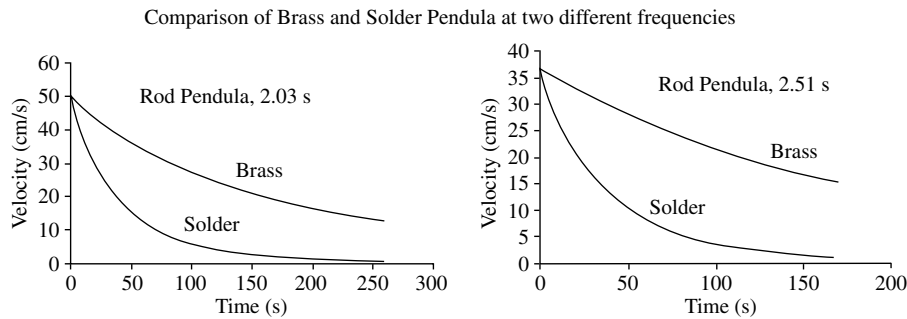


FIGURE 21.39 Free-decay curves for brass and solder pendula at two different frequencies, showing the larger internal friction of solder. The velocity is that of the peak value (amplitude) at the top of the pendulum, approx. 22 cm above the axis.

From [Figure 21.41](#) it can be seen that the internal friction damping is not simply hysteretic (constant Q); rather it is a function of amplitude. It can also be seen, from the close proximity of the solid and dashed curves, that the air influence on the solder pendulum is much less than that of the internal friction. By contrast, air influence is of comparable magnitude to the internal friction in the case of the brass pendulum (or even larger, at large amplitude).

A minimum of two frequencies was considered for the study, since the frequency variation of the damping is different for external and internal frictions. (Note: although the period is a function of amplitude, the amount of nonisochronism is small compared to the damping changes and is ignored here.) The periods were matched for the two pendula at each of 2.03 and 2.51 sec. For hysteretic-only (internal friction) damping, the Q at the shorter period should in theory be 1.53 times that of the longer period, for both brass and solder. If the damping were viscous only, the factor should be 1.24. In the case of solder at 10 cm/sec (corrected), the ratio is $1.66 = 131/71$, and for brass it is $1.46 = 387/266$. Although the ratio for solder is greater than the expected 1.53, the difference is within experimental

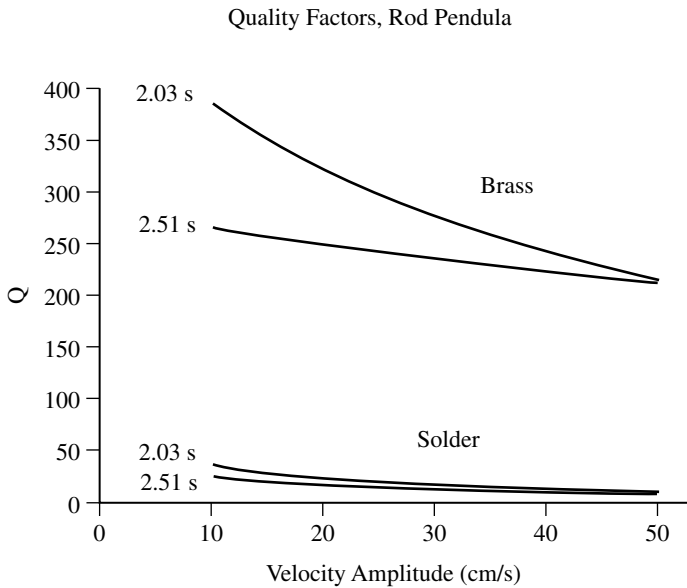


FIGURE 21.40 Illustration of amplitude-dependent damping in a rod pendulum made of (i) brass and (ii) solder. The two different matched periods of oscillation are indicated in seconds.

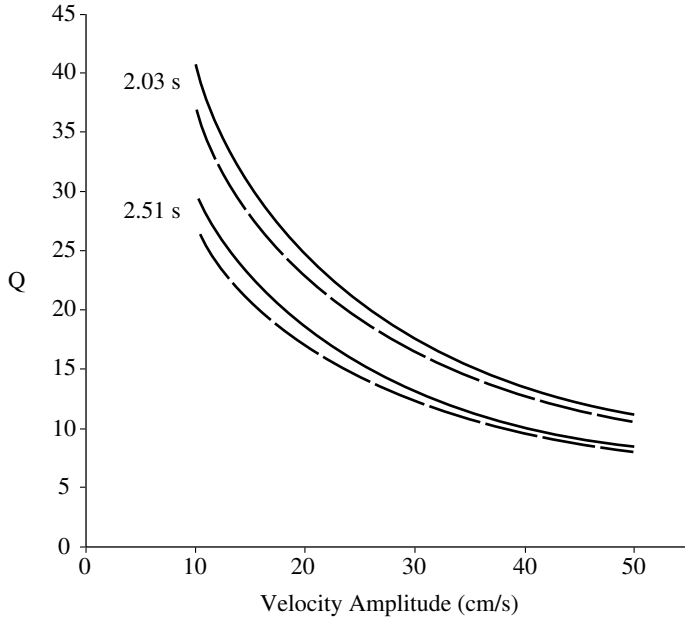


FIGURE 21.41 Amplitude dependence of the estimated quality factor due only to internal friction in the solder pendulum. Dashed lines show the Q before correction for air damping.

uncertainty for individual Q values, which from other, more detailed experiments were in the neighborhood of 5 to 10%.

The ratio for brass (1.46) is between 1.24 and 1.53, as expected, because of the comparable influence of air and internal friction.

References

- Barkhausen, H., *Z. Phys.*, 20, 401, 1919.
- Cromer, A., Stable solutions using the Euler approximation, *Am. J. Phys.*, 49(5), 455–459, 1981.
- de Silva, C.W. 2000. *Vibration, Fundamentals and Practice*. CRC Press, Boca Raton, FL.
- Fraden, J. 1996. *Handbook of Modern Sensors, Physics, Designs, & Applications*, 2nd ed., AIP Press (Springer), Secaucus, NJ.
- Peters, R., Fourier transform construction by vector graphics, *Am. J. Phys.*, 60, 439, 1992.
- Peters, R., Mercer physics laboratory experiment, described online at <http://physics.mercer.edu/labs/sho.htm>, 1998.
- Peters, R., Tutorial description of the symmetric differential capacitive (SDC) sensor, online at <http://www.telatonic.com/sdct2.html>, 2002.
- Peters, R., Graphical explanation of the speed of the Fast Fourier Transform, online at <http://arxiv.org/html/math.HO/0302212>, 2003a.
- Peters, R., Nonlinear damping of the “linear” pendulum, online at <http://arxiv.org/pdf/physics/03006081>, 2003b.
- Peters, R., Oscillator damping with more than one mechanism of internal friction dissipation, online at <http://arxiv.org/html/physics/0302003/>, 2003c.
- Peters, R., Anisotropic internal friction damping, online at <http://arxiv.org/html/physics/0302055>, 2003d.
- Peters, R., Folded pendulum measurements of the Earth’s free oscillations, online at <http://physics.mercer.edu/petepag/eigen.html>, 2004.

- Portevin, A. and Le Chatelier, M., Tensile tests of alloys undergoing transformation, *C. R. Acad. Sci.*, 176, 507, 1923.
- Press, W., Flannery, B., Teukolsky, S., and Vetterling, W. 1986. *Numerical Recipes — The Art of Scientific Computing*, Cambridge University Press, Cambridge.
- Wielandt, E., *Seismometry*, section: Electronic Displacement Sensing, online at http://www.geophys.uni-stuttgart.de/seismometry/hbk_html/node1.html, 2001.

22

Structure and Equipment Isolation

22.1	Introduction	22-2
22.2	Mechanisms of Base-Isolated Systems	22-4
	Elastomeric Isolation System • Sliding Isolation System • Sliding Isolation System with Resilient Mechanism • Electricite de France System • Concluding Remarks	
22.3	Structure–Equipment Systems with Elastomeric Bearings	22-9
	Formulation of Base Isolation Systems with Elastic Bearing • Free Vibration Analysis • Dynamics of Structure–Equipment Isolation Systems to Harmonic Excitations • Illustrative Example • Concluding Remarks	
22.4	Sliding Isolation Systems	22-17
	Mathematical Modeling and Formulation • Methods for Numerical Analysis • Simulation Results for Sliding Isolated Systems • Concluding Remarks	
22.5	Sliding Isolation Systems with Resilient Mechanism	22-36
	Mathematical Modeling and Formulation • Methods for Numerical Analysis • Simulation Results for Sliding Isolation with Resilient Mechanism • Concluding Remarks	
22.6	Issues Related to Seismic Isolation Design	22-50
	Design Methods • Static Analysis • Dynamic Analysis • Concluding Remarks	

Y.B. Yang

National Taiwan University

L.Y. Lu

National Kaohsiung First University
of Science and Technology

J.D. Yau

Tamkang University

Summary

In this chapter, a brief review will be given of the concept of isolation for suppressing the vibrations in structures and equipment subjected either to harmonic or seismic ground excitations. The mechanism of various isolation devices, including the elastomeric bearing, sliding bearing, resilient-friction base isolator, and Electricite de France system, will first be described in Section 22.2, together with their mathematical models. In Section 22.3, a closed form solution will be derived for the dynamic response of a structure–equipment system isolated by bearings of the elastomeric type, subjected to harmonic motions. Such a solution enables us to interpret the various behaviors of the structure and equipment under excitation. The elastomeric bearings can help increase the fundamental period of the structure, thereby, reducing the accelerations transmitted to the superstructure. In Section 22.4 and Section 22.5, the seismic behavior of a structure–equipment system isolated by a sliding support, with and without resilient force, will be studied using a state-space incremental-integration approach. With the introduction of a frictional sliding interface, the motion of the structure–equipment system will be uncoupled from the ground excitation, and the influence of the latter will be mitigated. The residual base displacement caused by the sliding isolator can be reduced

through inclusion of a resilient mechanism in the isolator. Nevertheless, the resilient mechanism can make the system more sensitive to the low-frequency components of excitation. In Section 22.6, issues related to design of base isolators will be discussed, along with the concepts underlying some design codes and guidelines. The notation used is listed at the end of the chapter.

22.1 Introduction

Conventionally, structural designers are concerned about the safety of buildings, bridges, and other civil engineering structures that are subjected to earthquakes. The recent history of earthquakes reveals that strong earthquakes, such as the 1994 Northridge earthquake (U.S.A.), 1995 Kobe earthquake (Japan), and 1999 Chi-Chi earthquake (Taiwan), can cause some badly designed structures or buildings to fail or collapse, and also cause some well-designed structures to malfunction due to the damage or failure of the equipment housed in the structure or building. Both the failures of structures and equipment, also known as *structural* and *nonstructural* failures, respectively, can cause serious harm to the residents or personnel working in a building. For the case where the equipment is part of a key service system, such as in hospitals, power stations, telecommunication centers, high-precision factories, and the like, the lives and economic losses resulting from the malfunctioning of the equipment can be tremendous. Thus, the maintenance of the safety of structures and attached equipment during a strong earthquake is a subject of high interest in earthquake engineering (also see Chapter 29 to Chapter 31). In this regard, *base isolation* has been proved to be an effective means for protecting the structures and attached equipment, which is made possible through reduction of the seismic forces transmitted from the ground to the superstructure (Yang et al., 2002).

For light secondary systems mounted on heavier primary systems, it was concluded that the response of the light secondary system, that is, the equipment, is affected by four major dynamic characteristics in earthquakes (Igusa and Der Kiureghian, 1985a, 1985b, 1985c; Yang and Huang, 1993). The first issue is *tuning*, which means that the natural frequency of the equipment is coincident with that of the structure. Such an effect may amplify the response of the equipment due to the fact that the light secondary system behaves as if it were a vibration absorber of the heavier primary system. The second issue is *interaction*, which is related to the feedback effect between the motions of the primary and secondary systems. Ignoring the feedback effect of interaction may result in an overestimation of the true response of the combined system. The third issue is *non-classical damping*, which may occur when the damping properties of the two systems are drastically different, such that the natural frequencies and mode shapes of the combined system can only be expressed in terms of complex numbers. Under such a circumstance, the conventional response spectrum analysis, based on modal superposition, becomes inapplicable. The last issue is *spatial coupling*, which relates to the effect of multiple support motions when the secondary system of interest is mounted at multiple locations. By considering the inelastic effect, Igusa (1990) proposed an equivalent linearization technique for investigating the response characteristics of an inelastic primary–secondary system with two degrees of freedom (DoF) under random vibrations. His results indicated that the existence of small nonlinearity is helpful for reducing the coupling system responses. With the concept of equivalent linearization, Huang et al. (1994) explored the response and reliability of a linear secondary system mounted on a yielding primary structure under white-noise excitations. It was concluded that the response of the secondary system could be reduced by increasing the equipment damping or by locating equipment at higher levels of the primary structure.

Owing to the fact that the mass and stiffness of a secondary system are much smaller than those of the primary structure, the interaction effect of the combined system, as well as the ill-conditioning in system matrices, may take place when one performs the dynamic analysis. To deal with this problem, some researchers chose to evaluate the response of the secondary systems from the floor motions. To avoid solving large eigenvalue problems and to account for the interaction between the building and equipment components, Villaverde (1986) applied the response spectrum technique to the analysis of a combined building–equipment system, by which the maximum response of light equipment mounted on the building under the earthquake is expressed in terms of the natural frequencies and mode shapes of

the building and equipment. To take into account the equipment–structure interactions, Suarez and Singh (1989) proposed an analytical scheme for computing the dynamic characteristics of the combined system, using the modal properties to compute the floor spectra. Lai and Soong (1990) presented a statistical energy analysis technique for evaluating the response of coupling primary–secondary structural systems, based on the concept of power-balance equation, that is, the power input to the primary system is equal to the dissipated energy of the primary system plus the transferred energy to the secondary system. Using a mean-square condensation procedure, Chen and Soong (1994) considered the effect of interaction by calculating the multi-DoF response of a primary–secondary system under random excitations. Later on, Chen and Soong (1996) derived an exact solution for the mean-square response of a structure–equipment system under dynamic loads, indicating that there exists an optimal damping ratio for reducing the vibration of equipment attached to the primary structure. Gupta and coworkers investigated the response of a secondary system with multiple supports on a primary structure subjected to earthquakes, taking into account the interaction effect between the equipment and structure (Dey and Gupta, 1998, 1999; Chaudhuri and Gupta, 2002). Their results indicated that when the soil–structure interaction (SSI) is taken into account, the response of the equipment–structure system will be affected by the SSI, unless a very stiff soil condition is considered.

On the other hand, a number of research works have been conducted by implementing isolation systems at the base of the equipment–structure system, aiming to reduce the earthquake forces transmitted from the ground. Based on a theoretical and experimental investigation, Kelly and Tsai (1985) showed that seismic protection can be achieved effectively for lightweight equipment mounted on an isolated structure installed with elastic bearings at the base. A hybrid isolation system with base-isolated floors was proposed by Inaudi and Kelly (1993), for the protection of highly sensitive devices mounted on a structure subjected to support motions. Considering the effects of torsion and translation, Yang and Huang (1998) studied the seismic response of light equipment items mounted on torsional buildings supported by elastic bearings. Their results indicated that the response of an equipment–structure system can be effectively reduced through installation of base isolators, and that there exists an optimal location for mounting the equipment. Juhn et al. (1992) presented a series of experimental results for the secondary systems mounted on a sliding base-isolated structure. They concluded that the acceleration response of the secondary system may be amplified when the input motions are composed of low-frequency vibrations. In this case, the sliding bearings are not considered to be an effective isolation device, which implies that the base-isolated structure is not suitable for a construction site with soft soil.

Concerning the use of sliding bearings (supports) as base isolators, Lu and Yang (1997) investigated the response of an equipment item attached to a sliding primary structure under earthquake excitations. Their results showed that the response of the equipment can be effectively reduced through the installation of a sliding support at the structural base, in comparison with that of a structure with fixed base. To overcome the discontinuous nature of the sliding and nonsliding phases of a structural system with sliding base, a fictitious spring model was proposed by Yang and coworkers for simulating the mechanism of sliding and nonsliding (Yang et al., 1990, 2000; Yang and Chen, 1999). Such a model will be described in a later section of this chapter. Agrawal (2000) adopted the same fictitious spring model in studying the response of an equipment item mounted on a torsionally coupled structure with sliding support. His results indicated that sliding supports could effectively reduce the equipment response, compared to that of a fixed-base structure. However, in the tuning region, where the natural frequency of the equipment coincides with the fundamental frequency of the structure, the equipment response may be adversely amplified due to the increase in eccentricity of the torsionally coupled structure.

The problem of building isolation has recently received more attention than ever from researchers and engineers, due to the construction of high-precision factories worldwide. More and more stringent requirements have been employed in this regard for removing the ambient or man-made vibrations (Rivin, 1995; Steinberg, 2000). To allow sensitive electronic equipment to operate in a harsh environment, Veprik and Babitsky (2000) proposed an optimization procedure for the design of vibration isolators aimed at minimizing the response of the internal components of electronic equipment. As for the protection of high-tech equipment from micro- or ambient

vibrations, Yang and Agrawal (2000) showed that passive hybrid floor isolation systems are more effective in mitigating the equipment response than passive or hybrid base isolation systems. Xu and coworkers studied the response of a batch of high-tech equipment mounted on a hybrid platform, which in turn is mounted on a building floor (Xu et al., 2003; Yang et al., 2003). Both their theoretical and experimental studies showed that the hybrid platform, which is composed of leaf springs, oil dampers, and an electron-magnetic actuator with velocity feedback control, is more effective in mitigating the velocity response of the high-tech equipment than the passive platform.

The objective of this chapter is to give an overview on the seismic behavior of various base isolators. The organization of this chapter can be summarized as follows. In Section 22.2, the mechanisms of various seismic isolators that are currently in use are introduced and explained. In Section 22.3, a structure–equipment system isolated by bearings of the elastomeric type is modeled by a three-DoF system composed of a spring and dashpot unit, for which a closed-form solution is obtained for the dynamic response of the isolated system subjected to harmonic earthquakes; remarks on the dynamic response of the system components are also made. In Section 22.4 and Section 22.5, the seismic behaviors of a structure–equipment system isolated by a sliding support, with and without resilient capability, will be investigated. Also presented are numerical methods based on the incremental-integration procedure for the analysis of structural systems with sliding-type isolators. Further information on seismic behavior and isolation of structures and equipment is found in [Chapter 29](#) to [Chapter 31](#).

22.2 Mechanisms of Base-Isolated Systems

Figure 22.1 shows a simplified model for a structural system subjected to a support motion.

For this single-DoF system, the equation of motion can be written as

$$m\ddot{x} + c\dot{x} + kx = -m\ddot{x}_g \quad (22.1)$$

where m denotes the mass, c the damping, k the stiffness, x the displacement of the system, and \ddot{x}_g the ground acceleration. By assuming the system to be linearly elastic, the response $x(t)$ can be obtained using Duhamel's integral (also see [Chapter 2](#) and [Chapter 14](#)), as

$$x(t) = \frac{1}{\Omega_d} \int_0^t \ddot{x}_g(\tau) e^{-\zeta\Omega_d(t-\tau)} \sin \Omega_d(t-\tau) d\tau \quad (22.2)$$

where the natural angular frequency, Ω , damped natural frequency, Ω_d , and damping ratio, ζ , of the system are defined as follows:

$$\Omega = \sqrt{\frac{k}{m}} \quad (22.3a)$$

$$\Omega_d = \Omega \sqrt{1 - \zeta^2} \quad (22.3b)$$

$$\zeta = \frac{c}{2m\Omega} \quad (22.3c)$$

Correspondingly, the natural period, T , and damped period, T_d , of the structure are

$$T = \frac{2\pi}{\Omega} = 2\pi \sqrt{\frac{m}{k}} \quad (22.4a)$$

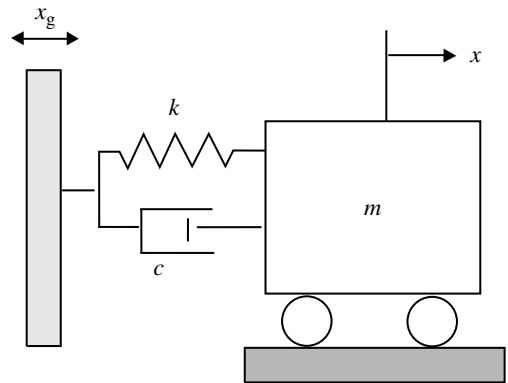


FIGURE 22.1 Model of a single-DoF system.

$$T_d = \frac{2\pi}{\Omega_d} = \frac{T}{\sqrt{1 - \zeta^2}} \quad (22.4b)$$

For a given support acceleration, \ddot{x}_g , the displacement, x , and acceleration, \ddot{x} , of the single-DoF system can be related to the natural period, T , and damping ratio, ζ , of the system. Thus, for a specific earthquake, by first selecting a damping ratio, ζ , and using Equation 22.2, one can compute the peak displacement x , for a structure with a period of vibration, T , with given values of m , c , and k . Repeating the above procedure for a wide range of periods, T , while keeping the damping ratio, ζ , constant, one can obtain response curves similar to those shown in Figure 22.2. By varying the damping ratio, ζ , one can construct the *displacement response spectra* and *pseudo-acceleration response spectra* for all single-DoF structures under a given earthquake, as schematically shown in Figures 22.2 and 22.3, respectively.

A general impression that is gained from Figure 22.2 and Figure 22.3 is that a structure with a shorter natural period has less displacement response when subjected to an earthquake, but it also has a larger acceleration response. Specifically, let us consider a structure of a constant damping ratio, ζ , with its period increased from T_1 to T_2 . As can be observed from the figures, the displacement of the structure increases from D_1 to D_2 , while the acceleration decreases from A_1 to A_2 . Such a feature is known as the *period shift* effect. On the other hand, by increasing damping ratio of the structure, the displacement of the structure decreases significantly, as can be seen from Figure 22.2. The same is also true with the acceleration response, as can be seen from Figure 22.3. Moreover, a larger damping ratio also makes the structure less sensitive to the variation in ground vibration characteristics, as indicated by the smoother response curves for structures having higher damping ratios, in both figures. From the aforementioned two response spectra, one observes that the philosophy of base isolation is to lengthen the vibration period of the structure to be protected, using base isolators of some kind, by which the earthquake force transmitted to the structure can be greatly reduced. In the meantime, some additional damping must be introduced on the base isolators in order to control the relative displacements across the base isolators with tolerable limits.

To fulfill the function of lengthening the period of vibration of the structure to be protected, the base isolators that are inserted between the structure and its foundation must be flexible in the horizontal direction, but stiff enough in the vertical direction so as to carry the heavy loads transmitted from the superstructure. With such devices, the natural period of vibration of the structure will be significantly lengthened and shifted away from the dominant frequency range of the expected earthquakes. The following is a summary of the fundamental features of four types of isolators frequently used in engineering practice.

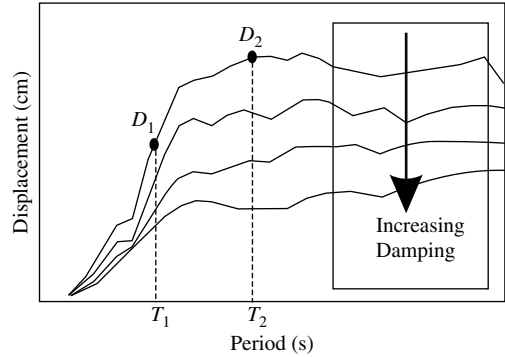


FIGURE 22.2 Schematic of displacement response spectra.

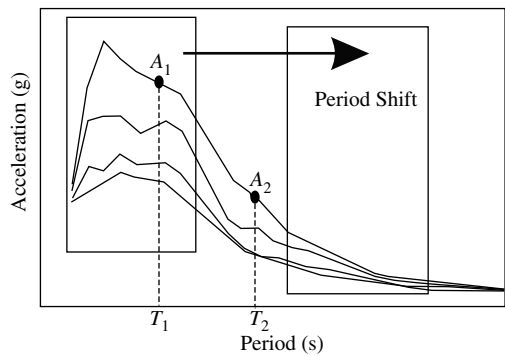


FIGURE 22.3 Schematic of pseudo-acceleration response spectra.

22.2.1 Elastomeric Isolation System

Elastomeric bearing is the type of base isolator most commonly known to researchers and engineers working on base isolation. It is usually composed of alternating layers of steel and hard rubber and, for this reason, it is also known as the *laminated rubber bearing*. This type of bearing is stiff enough to sustain the vertical loads, yet flexible under the lateral forces. The ability to deform horizontally enables the bearing to reduce significantly the structural base shear transmitted from the ground. While the major function of elastomeric bearings is to reduce the transmission of shear forces to the superstructure by lengthening the vibration period of the entire system, they must also provide sufficient rigidity under vertical loads. Let us consider a structure installed with elastomeric bearings, which is subjected to a support acceleration, \ddot{x}_g , as in Figure 22.4. By representing the isolated structure as a single-DoF system, based on the assumption that the superstructure is rigid in comparison with the stiffness of the elastic bearings, the equation of motion for the entire system can be written as

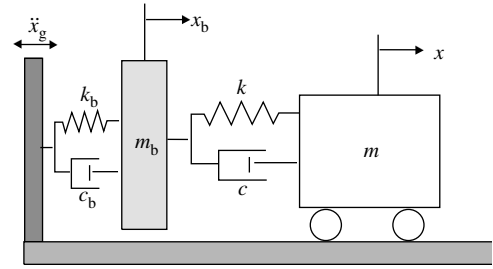


FIGURE 22.4 Model for base-isolation systems with elastic bearing.

$$\begin{bmatrix} m & 0 \\ 0 & m_b \end{bmatrix} \begin{Bmatrix} \ddot{x} \\ \ddot{x}_b \end{Bmatrix} + \begin{bmatrix} c & -c \\ -c & c + c_b \end{bmatrix} \begin{Bmatrix} \dot{x} \\ \dot{x}_b \end{Bmatrix} + \begin{bmatrix} k & -k \\ -k & k + k_b \end{bmatrix} \begin{Bmatrix} x \\ x_b \end{Bmatrix} = - \begin{Bmatrix} m\ddot{x}_g \\ m_b\ddot{x}_g \end{Bmatrix} \quad (22.5)$$

where m , c , and k denote the mass, damping, and stiffness of the superstructure, respectively, m_b , c_b , and k_b denote the mass, damping, and stiffness of the base raft, respectively, and x and x_b denote the displacements of the superstructure and the base, respectively.

In reality, the reduction in the seismic forces transmitted to a superstructure through the installation of laminated rubber bearings is achieved at the expense of large relative displacements across the bearings. If substantial damping can be introduced into the bearings or the isolation system, then the problem of large displacements can be alleviated. It is for this reason that the laminated rubber bearing with a central lead plug inserted has been devised (Yang et al., 2002). To simulate the dynamic properties of the lead-rubber bearing (LRB) system, an equivalent linearized system has been proposed, for which the equation of motion is

$$\begin{bmatrix} m & 0 \\ 0 & m_b \end{bmatrix} \begin{Bmatrix} \ddot{x} \\ \ddot{x}_b \end{Bmatrix} + \begin{bmatrix} c & -c \\ -c & c + c_{eq} \end{bmatrix} \begin{Bmatrix} \dot{x} \\ \dot{x}_b \end{Bmatrix} + \begin{bmatrix} k & -k \\ -k & k + k_{eq} \end{bmatrix} \begin{Bmatrix} x \\ x_b \end{Bmatrix} = - \begin{Bmatrix} m\ddot{x}_g \\ m_b\ddot{x}_g \end{Bmatrix} \quad (22.6)$$

where c_{eq} and k_{eq} respectively represent the equivalent linearized damping and stiffness coefficients of the LRB system. The dynamic behavior of a structure-equipment system isolated by elastomeric bearings with linearized damping and stiffness coefficients, when subjected to harmonic and earthquake excitations, will be investigated analytically and numerically, respectively, in Section 22.3.

22.2.2 Sliding Isolation System

Another means for increasing the horizontal flexibility of a base-isolated structure is to insert a *sliding* or *friction surface* between the foundation and the base of the structure. The shear force transmitted to the superstructure through the sliding interface is limited by the static frictional force, which equals the product of the coefficient of friction and the weight of the superstructure. The coefficient of friction is usually kept as low as is practical. However, it must be high enough to provide a frictional force that can sustain strong winds and minor earthquakes without sliding. Since the sliding system has no dominant

natural period, it is generally frequency-independent when the structure is subjected to earthquakes with a wideband frequency content. As mentioned previously, when a sliding structure is subjected to a ground motion, transitions may occur repeatedly between the sliding and nonsliding phases. To take into account such a phase transition, Yang et al. (1990) proposed the use of a fictitious spring between the structural base raft and the underlying ground to simulate the static–dynamic frictional force of the sliding device. With reference to Figure 22.5, the equation of motion for the structure with sliding base can be written as follows:

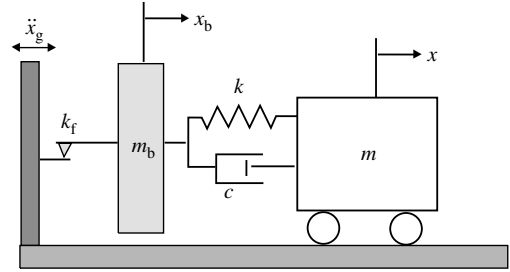


FIGURE 22.5 Model for base-isolation systems with sliding support.

$$\begin{bmatrix} m & 0 \\ 0 & m_b \end{bmatrix} \begin{Bmatrix} \ddot{x} \\ \ddot{x}_b \end{Bmatrix} + \begin{bmatrix} c & -c \\ -c & c \end{bmatrix} \begin{Bmatrix} \dot{x} \\ \dot{x}_b \end{Bmatrix} + \begin{bmatrix} k & -k \\ -k & k \end{bmatrix} \begin{Bmatrix} x \\ x_b \end{Bmatrix} + \begin{Bmatrix} 0 \\ f_r \end{Bmatrix} = - \begin{Bmatrix} m\ddot{x}_g \\ m_b\ddot{x}_g \end{Bmatrix} \quad (22.7)$$

where k_f is the stiffness of the fictitious spring and the frictional force, f_r , can be represented as

$$f_r = \begin{cases} k_f(x_b - x_{b0}) & \text{for non-sliding phase,} \\ \pm \mu(m + m_b)g & \text{for sliding phase} \end{cases} \quad (22.8)$$

with x_{b0} indicating the initial elongation of the fictitious spring in the current nonsliding phase, μ the coefficient of friction, and g the acceleration of gravity. The fictitious spring concept will be incorporated in the analysis of sliding structures in Section 22.4 of this chapter, when considering both harmonic and seismic excitations.

22.2.3 Sliding Isolation System with Resilient Mechanism

One particular problem with a sliding structure is the occurrence of residual displacements after earthquakes. To remedy such a drawback, the sliding surface is often made concave, so as to provide a recentering mechanism for the isolated structures. This is the idea behind the *friction pendulum system* (FPS), shown in Figure 22.6, which utilizes a spherical concave surface to produce a recentering force for the superstructure under excitations. To guarantee that a sliding structure can return to its original position, other mechanisms, such as high-tension springs and elastomeric bearings, can be used as an auxiliary system for providing the restoring forces. Previously, the sliding isolation systems have been successfully applied in the protection of important structures, such as nuclear power plants, emergency fire water tanks, large chemical storage tanks, and so on, from the damaging actions of severe earthquakes.

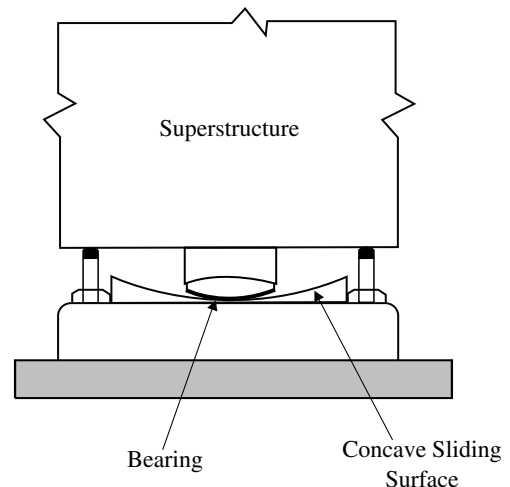


FIGURE 22.6 Friction pendulum system.

To improve the performance of sliding isolators under strong earthquakes, Mostaghel (1984) and Mostaghel and Khodaverdian (1987) proposed the *resilient-friction base isolator* (RFBI) for

controlling the transmission of shear force to the superstructures, while keeping the residual displacements within an allowable level. The RFBI device is basically made of a central rubber core and Teflon-coated steel plates, and offers a friction resistance for keeping the system in the nonsliding mode under wind excitations and small earthquakes, and a restoring force by the rubber ingredient for limiting the maximum sliding displacements. The equation of motion for a structure installed with RFBI, as shown in Figure 22.7, can be written as

$$\begin{bmatrix} m & 0 \\ 0 & m_b \end{bmatrix} \begin{Bmatrix} \ddot{x} \\ \ddot{x}_b \end{Bmatrix} + \begin{bmatrix} c & -c \\ -c & c + c_b \end{bmatrix} \begin{Bmatrix} \dot{x} \\ \dot{x}_b \end{Bmatrix} + \begin{bmatrix} k & -k \\ -k & k + k_b \end{bmatrix} \begin{Bmatrix} x \\ x_b \end{Bmatrix} + \begin{Bmatrix} 0 \\ f_r \end{Bmatrix} = - \begin{Bmatrix} m\ddot{x}_g \\ m_b\ddot{x}_g \end{Bmatrix} \quad (22.9)$$

The interfacial frictional force, f_r , existing in the RFBI and appearing in Equation 22.9 serves as the outlet for energy dissipation. The behavior of a structure–equipment system supported by sliding isolators with resilient mechanism subjected to both harmonic and earthquake excitations will be investigated in Section 22.5.

22.2.4 Electricite de France System

To limit effectively the acceleration of base-isolated structures and internal secondary systems, such as those of nuclear power plants, when subjected to strong earthquakes, the *Electricite de France* (EDF) system was proposed by Gueraud et al. (1985). The design concept of an EDF system is to arrange the elastomeric bearing and sliding device at the base of a structure in series. For low-level ground motions, the EDF system will behave as an elastomeric bearing and return to the original position after support motions, while for strong earthquakes, the EDF system will behave as a sliding device. The EDF system may have a residual displacement after some major earthquakes. Because of the sliding mechanism of the EDF system, the maximum horizontal acceleration of the superstructure is kept within a certain range (Gueraud et al., 1985; Park et al., 2002), while the shear force transmitted to the superstructure through the frictional interface is smaller than the static frictional force. For the mathematical model shown for the EDF system in Figure 22.8, the equations of motion for the nonsliding and sliding phases can be written as

(a) nonsliding phase:

$$\begin{Bmatrix} m\ddot{x} \\ m_b\ddot{x}_b \\ 0 \end{Bmatrix} + \begin{bmatrix} c & -c & 0 \\ -c & c & 0 \\ 0 & 0 & c_{EDF} \end{bmatrix} \begin{Bmatrix} \dot{x} \\ \dot{x}_b \\ \dot{x}_{EDF} \end{Bmatrix} + \begin{bmatrix} k & -k & 0 \\ -k & k + k_f & -k_f \\ 0 & -k_f & k_f + k_{EDF} \end{bmatrix} \begin{Bmatrix} x \\ x_b \\ x_{EDF} \end{Bmatrix} = \begin{Bmatrix} -m\ddot{x}_g \\ -m_b\ddot{x}_g \\ 0 \end{Bmatrix} \quad (22.10a)$$

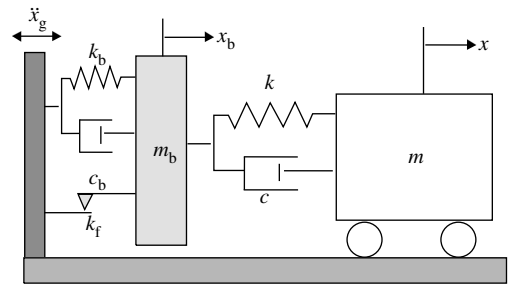


FIGURE 22.7 Model for base-isolation systems with RFBI device.

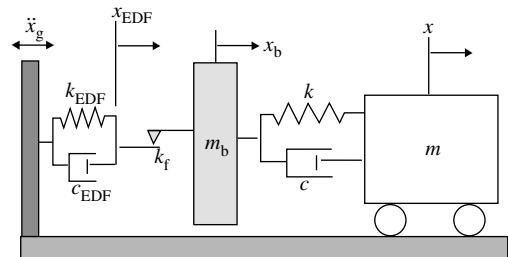


FIGURE 22.8 Model for base-isolation systems with EDF device.

(b) sliding phase:

$$\begin{aligned} & \begin{Bmatrix} m\ddot{x} \\ m_b\ddot{x}_b \\ 0 \end{Bmatrix} + \begin{bmatrix} c & -c & 0 \\ -c & c & 0 \\ 0 & 0 & c_{\text{EDF}} \end{bmatrix} \begin{Bmatrix} \dot{x} \\ \dot{x}_b \\ \dot{x}_{\text{EDF}} \end{Bmatrix} + \begin{bmatrix} k & -k & 0 \\ -k & k & 0 \\ 0 & 0 & k_{\text{EDF}} \end{bmatrix} \begin{Bmatrix} x \\ x_b \\ x_{\text{EDF}} \end{Bmatrix} \\ &= \begin{Bmatrix} -m\ddot{x}_g \\ -m_b\ddot{x}_g \mp \mu(m + m_b)g \\ \pm \mu(m + m_b)g \end{Bmatrix} \end{aligned} \quad (22.10b)$$

where c_{EDF} and k_{EDF} , respectively, denote the damping and stiffness of the EDF system, and x_{EDF} denotes the displacement of the system.

22.2.5 Concluding Remarks

To mitigate the transmission of earthquake forces to a structure, and the potentially earthquake-induced damage to the equipment attached to the structure, base isolation is an effective structural design philosophy. With the installation of base isolators, the natural period of vibration of the structure will be significantly lengthened and shifted away from the dominant frequency range of the expected earthquakes. In accordance, the earthquake force transmitted to the structure can be significantly reduced. In this section, the mechanisms of four types of base isolator frequently used in engineering practice are introduced. Since the base isolators, such as the elastomeric bearings or sliding isolations, have relatively flexible stiffness in the horizontal direction, the occurrence of residual displacements after earthquakes may cause certain problems on the structure to be protected. To remedy such a drawback and to further guarantee that a base-isolated structure can return to its original position, the RFBI is implemented for controlling the transmission of shear force to the superstructure, while keeping the residual displacement within an allowable level. On the other hand, to limit the acceleration level of internal secondary systems housed in a base-isolated structure under strong earthquakes, such as those of the nuclear power plants, the EDF system can be used as an alternative device for base isolation, even though some residual displacements may be induced after the earthquakes.

22.3 Structure–Equipment Systems with Elastomeric Bearings

Owing to the stringent requirements for normal functioning of high-tech facilities, such as printed circuit boards, semiconductor factories, and sensitive medical devices, the need to suppress excessive vibrations in sensitive structure–equipment systems has become an issue of great concern to structural designers. Besides, these high-tech facilities may suffer significant damages during a major earthquake. Using elastomeric isolation systems to reduce the earthquake forces transmitted from the ground is one of the most popular ways adopted by structural designers. In this section, the performance of elastomeric bearings in protecting structure–equipment systems against horizontal ground motions will be investigated.

22.3.1 Formulation of Base Isolation Systems with Elastic Bearing

By modeling the structure, internal equipment and the base of an isolated structure–equipment system as a lumped mass system, one can construct the mathematical model for the structure–equipment isolation system supported by an elastic bearing in [Figure 22.9](#). The following is the

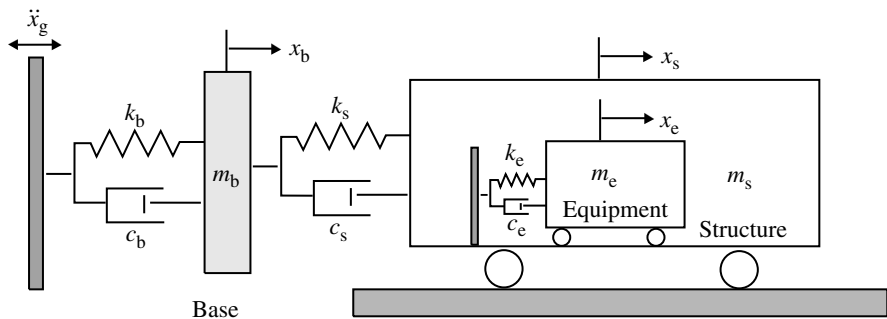


FIGURE 22.9 Model of a structure–equipment isolation system with elastic bearing.

equation of motion for the base-isolated structure–equipment system when it is subjected to a ground acceleration, \ddot{x}_g :

$$\begin{aligned} & \begin{Bmatrix} m_e \ddot{x}_e \\ m_s \ddot{x}_s \\ m_b \ddot{x}_b \end{Bmatrix} + \begin{bmatrix} c_e & -c_e & 0 \\ -c_e & c_s + c_e & -c_s \\ 0 & -c_s & c_s + c_b \end{bmatrix} \begin{Bmatrix} \dot{x}_e \\ \dot{x}_s \\ \dot{x}_b \end{Bmatrix} + \begin{bmatrix} k_e & -k_e & 0 \\ -k_e & k_s + k_e & -k_s \\ 0 & -k_s & k_s + k_b \end{bmatrix} \begin{Bmatrix} x_e \\ x_s \\ x_b \end{Bmatrix} \\ &= - \begin{Bmatrix} m_e \\ m_s \\ m_b \end{Bmatrix} \ddot{x}_g \end{aligned} \tag{22.11}$$

where m represents the mass, c the damping coefficient, and k the stiffness of the system. Also, the subscripts ‘e’, ‘s’, and ‘b’ are associated with the DoF of the equipment, structure, and base, respectively. The notations employed in Figure 22.9 have been defined in Table 22.1. It should be mentioned that the elastic bearing stiffness, k_b , appearing in Equation 22.11, is a parameter relating to the boundary conditions of the system considered here. A small value of k_b relative to the structural stiffness, k_s , means that the system is isolated by a set of soft bearings. In contrast, a large value of k_b means that the structure is rigidly supported.

TABLE 22.1 Definition of Symbols

Symbol	Definition
c_e, c_s	Damping coefficients of equipment and superstructure
k_e, k_s	Stiffness of equipment and superstructure
k_b	Stiffness of elastic bearing or resilient stiffness of isolation system
m_e, m_s, m_b	Masses of equipment, superstructure and base mat
$x_e(t), x_s(t), x_b(t)$	Relative-to-the-ground displacements of equipment, superstructure and base mat
$\ddot{x}_g(t)$	Ground acceleration
μ	Frictional coefficient of sliding isolation system
ω_b	Frequency of isolation system
ω_e, ω_s	Frequencies of equipment and superstructure
ω_g	Frequency of ground excitation
ζ_e, ζ_s	Damping ratios of equipment and structure

22.3.2 Free Vibration Analysis

By neglecting the damping and forcing terms in Equation 22.11, the equation of motion for free vibration can be written as

$$\begin{Bmatrix} m_e \ddot{x}_e \\ m_s \ddot{x}_s \\ m_b \ddot{x}_b \end{Bmatrix} + \begin{bmatrix} k_e & -k_e & 0 \\ -k_e & k_s + k_e & -k_s \\ 0 & -k_s & k_s + k_b \end{bmatrix} \begin{Bmatrix} x_e \\ x_s \\ x_b \end{Bmatrix} = \begin{Bmatrix} 0 \\ 0 \\ 0 \end{Bmatrix} \quad (22.12)$$

By solving the preceding equation, one can obtain the natural frequencies and vibration modes of the structure–equipment system with elastic bearings. As for the present problem, the horizontal stiffness of the elastic bearing is designed to be quite low compared with that of the superstructure. It follows that the superstructure in its entirety behaves essentially as a *rigid body* for the fundamental vibration mode shape of the combined system, which implies that the displacement responses for the equipment, structure, and base under free vibration can be approximately taken as the same, that is, $x_e = x_s = x_b = x$. By introducing such a condition into Equation 22.12, the equation of motion for the equivalent single-DoF base-isolated system can be written as

$$(m_e + m_s + m_b)\ddot{x} + k_b x = 0 \quad (22.13)$$

Equation 22.13 indicates that the fundamental frequency, ω_1 , of the base-isolated system can be approximated by $\omega_1 \approx \sqrt{k_b/(m_e + m_s + m_b)}$. Further, if the condition of fixed base is considered, that is, by letting the responses of the base be equal to zero, $x_b = \ddot{x}_b = 0$, the structure–equipment isolation system will be reduced to the case of a fixed-base system, such that the equation of motion becomes

$$\begin{Bmatrix} m_e \ddot{x}_e \\ m_s \ddot{x}_s \end{Bmatrix} + \begin{bmatrix} k_e & -k_e \\ -k_e & k_s + k_e \end{bmatrix} \begin{Bmatrix} x_e \\ x_s \end{Bmatrix} = \begin{Bmatrix} 0 \\ 0 \end{Bmatrix} \quad (22.14)$$

as is well known.

22.3.3 Dynamics of Structure–Equipment Isolation Systems to Harmonic Excitations

The advantage of a closed-form solution is that it allows us to examine the key parameters involved in the problem considered. This is what will be sought herein. For the case of a harmonic ground excitation, x_g , with amplitude, X_g , that is, with $x_g = X_g e^{i\omega t}$, one may derive from Equation 22.11 the following:

$$\begin{Bmatrix} m_e \ddot{x}_e \\ m_s \ddot{x}_s \\ m_b \ddot{x}_b \end{Bmatrix} + \begin{bmatrix} k_e & -k_e & 0 \\ -k_e & k_s + k_e & -k_s \\ 0 & -k_s & k_s + k_b \end{bmatrix} \begin{Bmatrix} x_e \\ x_s \\ x_b \end{Bmatrix} = \begin{Bmatrix} m_e \\ m_s \\ m_b \end{Bmatrix} X_g \omega^2 e^{i\omega t} \quad (22.15)$$

Correspondingly, the steady-state responses of the system can be expressed as

$$\begin{Bmatrix} x_e \\ x_s \\ x_b \end{Bmatrix} = \begin{Bmatrix} X_e \\ X_s \\ X_b \end{Bmatrix} e^{i\omega t} \quad (22.16)$$

where (X_e , X_s , and X_b) represent the amplitudes of the equipment, structure, and base, respectively.

Substituting Equation 22.16 into Equation 22.15 yields

$$\begin{bmatrix} k_e - m_e \omega^2 & -k_e & 0 \\ -k_e & k_s + k_e - m_s \omega^2 & -k_s \\ 0 & -k_s & k_s + k_b - m_b \omega^2 \end{bmatrix} \begin{Bmatrix} X_e \\ X_s \\ X_b \end{Bmatrix} = \begin{Bmatrix} m_e \\ m_s \\ m_b \end{Bmatrix} X_g \omega^2 \quad (22.17)$$

from which the amplitudes (X_e , X_s , and X_b) for the system can be solved as follows:

$$X_e = \frac{X_s + X_g f_e^2}{1 - f_e^2} \quad (22.18a)$$

$$X_b = \frac{X_s + \varepsilon_b f_s^2 X_g}{1 + k_b/k_s - \varepsilon_b f_s^2} \quad (22.18b)$$

$$X_s = \frac{\left[m_s + \frac{m_e}{1 - f_e^2} + \frac{m_b}{1 + k_b/k_s - \varepsilon_b f_s^2} \right] X_g \omega^2}{\frac{k_b - m_b \omega^2}{1 + k_b/k_s - \varepsilon_b f_s^2} - \left(m_s + \frac{m_e}{1 - f_e^2} \right) \omega^2} \quad (22.18c)$$

where the amplitudes of the equipment and base, that is, X_e and X_b , have been expressed in terms of the amplitude of the base, X_s . The parameters in Equation 22.18 are defined as

$$f_e = \omega/\omega_e \quad (22.19a)$$

$$f_s = \omega/\omega_s \quad (22.19b)$$

$$\varepsilon_b = m_b/m_s \quad (22.19c)$$

$$\omega_e = \sqrt{k_e/m_e} \quad (22.19d)$$

$$\omega_s = \sqrt{k_s/m_s} \quad (22.19e)$$

Finally, the state-steady absolute acceleration responses of the structure, equipment, and base can be expressed in terms of the ground acceleration \ddot{x}_g as

$$a_s = \ddot{x}_s + \ddot{x}_g = -(X_s + X_g) \omega^2 e^{i\omega t} = \frac{k_b \ddot{x}_g}{D(\omega)} \quad (22.20a)$$

$$a_e = \ddot{x}_e + \ddot{x}_g = -\frac{(X_s + X_g) \omega^2 e^{i\omega t}}{1 - f_e^2} = \frac{k_b \ddot{x}_g}{(1 - f_e^2) D(\omega)} \quad (22.20b)$$

$$a_b = \ddot{x}_b + \ddot{x}_g = \frac{[-X_s + X_g + (k_b/k_s) X_g] \omega^2 e^{i\omega t}}{1 + k_b/k_s - \varepsilon_b f_s^2} = \frac{(D^{-1}(\omega) + k_s^{-1}) k_b \ddot{x}_g}{1 + k_b/k_s - \varepsilon_b f_s^2} \quad (22.20c)$$

$$D(\omega) = (k_b - m_b \omega^2) - (1 + k_b/k_s - \varepsilon_b f_s^2) \left(m_s + \frac{m_e}{1 - f_e^2} \right) \omega^2 \quad (22.20d)$$

As can be seen, the acceleration response of each component in the structure–equipment system depends mainly on the stiffness of the elastic bearing, k_b . In particular, the use of a smaller bearing stiffness, k_b , can result in significant reduction of the shear forces transmitted to the superstructure, as indicated by Equation 22.20a. This explains why an elastic bearing can be effectively used as an isolator for reducing the base shear of the structure–equipment system. In contrast, if the bearing stiffness, k_b , is made to be infinitely large, that is, by letting $k_b \rightarrow \infty$, the acceleration responses in Equation 22.20, reduce to

$$a_s = \frac{(1 - f_e^2) \ddot{x}_g}{(1 - f_e^2)(1 - f_s^2) - \varepsilon_e f_s^2} \quad (22.21a)$$

$$a_e = \frac{\ddot{x}_g}{(1 - f_e^2)(1 - f_s^2) - \varepsilon_e f_s^2} \quad (22.21b)$$

$$a_b = \ddot{x}_g \quad (22.21c)$$

with the use of L'Hospital's Rule, where $\varepsilon_e = m_e/m_s$. As can be seen from Equation 22.21c, the acceleration of the structural base is equal to the ground acceleration. Clearly, the present problem has been reduced to a two-DoF system with a rigid base, for which the solutions have been given in Equation 22.21a and Equation 22.21b.

Some important high-tech facilities, such as semiconductor factories and medical devices, are very sensitive to vibrations, especially to those caused by resonance. To consider the effect of resonance, we shall let the ground excitation frequency, ω , coincide with the equipment frequency, ω_e , that is, by letting $f_e = 1$ or $\omega_e = \omega$. For this case, the acceleration responses of the system in Equation 22.20 reduce to

$$a_s = 0 \quad (22.22a)$$

$$a_e = \frac{-k_b \ddot{x}_g}{k_e[1 + (k_b - m_b \omega_e^2)/k_s]} \quad (22.22b)$$

$$a_b = \frac{k_b \ddot{x}_g}{k_s + k_b - m_b \omega_e^2} \quad (22.22c)$$

Because of the coincidence of the ground excitation frequency with the equipment frequency, the equipment behaves like a vibration absorber of the structure. For this reason, the response of the equipment is greatly amplified, as implied by Equation 22.22b, while the response of structure is completely suppressed, as indicated by Equation 22.22a. Moreover, if the frequency of the equipment is equal to the fundamental frequency of the structure–equipment isolation system, that is, $\omega_e (\approx \omega_1) = \sqrt{k_b/(m_e + m_s + m_b)}$, then the responses of the system in Equation 22.22 can further be expressed as follows:

$$a_s = 0 \quad (22.23a)$$

$$a_e = \frac{-k_b \ddot{x}_g}{k_e[1 + (m_s + m_e)\omega_e^2/k_s]} \quad (22.23b)$$

$$a_b = \frac{k_b \ddot{x}_g}{k_s + (m_s + m_e)\omega_e^2} \quad (22.23c)$$

Since the equipment mass is generally much smaller than the structural mass, the preceding equation can be further reduced to

$$a_s = 0 \quad (22.24a)$$

$$a_e = \frac{-k_b \ddot{x}_g}{k_e(1 + \omega_e^2/\omega_s^2)} \quad (22.24b)$$

$$a_b = \frac{k_b \ddot{x}_g}{k_s(1 + \omega_e^2/\omega_s^2)} \quad (22.24c)$$

As indicated by Equation 22.24b, the acceleration response of the equipment depends on the stiffness ratio, k_b/k_e , of the base to the equipment.

For the resonance condition of $\omega_e = \omega$, mentioned previously, let us consider the case when the structural frequency is equal to the equipment frequency, that is, $\omega_e = \omega_s$. For this case, the responses of the system in Equation 22.22 reduce to

$$a_s \approx 0 \quad (22.25a)$$

$$a_e \approx \frac{-k_b \ddot{x}_g}{\varepsilon_e[k_s(1 - \varepsilon_b) + k_b]} \quad (22.25b)$$

$$a_b = \frac{k_b \ddot{x}_g}{k_s(1 - \varepsilon_b) + k_b} \quad (22.25c)$$

which indicates that the acceleration response of the equipment may be greatly amplified, as implied by the relatively small mass ratio $\varepsilon_e (= m_e/m_s)$ and large stiffness ratio, k_b/k_s , in Equation 22.25b. Such a phenomenon has been referred to as the *tuning of equipment*.

On the other hand, when the excitation frequency, ω , coincides with the fundamental frequency, ω_1 , of the isolated system, that is, $\omega (\approx \omega_1) = \sqrt{k_b/(m_e + m_s + m_b)}$, resonant response may be induced on the structure–equipment isolation system. Considering that the first priority in design of high-tech

equipment is to reduce the vibrations of the equipment, rather than the structure, by comparing the denominators in Equation 22.20a and Equation 22.20b, one may assume that the condition $|1 - f_e^2| \geq 1$ or $f_e = \omega/\omega_e \geq \sqrt{2}$ remains satisfied for a good design, which is equivalent to

$$\frac{\omega_e}{\omega_s} \leq \sqrt{\frac{k_b/k_s}{2[1 + (m_b + m_e)/m_s]}} \tag{22.26}$$

Since the fundamental frequency, ω_s , of a base-isolated structure is generally low in practice, the horizontal stiffness of the equipment attached to the structure must be designed to be soft enough such that Equation 22.26 can be satisfied. Certainly, this is one of the guidelines to be obeyed in the design of equipment for the sake of vibration reduction.

22.3.4 Illustrative Example

The forgoing formulations have been made by neglecting the damping of the structural system and by assuming the ground motion to be of the harmonic type. In practice, there is always some damping with the structural system, while the ground motion may be random in nature. To deal with such problems, the only recourse is to use numerical methods that are readily available. In this section, the Newmark β method, proposed by Newmark (1959), with $\gamma = 1/2$ and $\beta = 1/4$, will be adopted for solving the second-order differential equation presented in Equation 22.11, which has the advantage of being numerically stable.

The example considered is the structure–equipment system isolated by elastomeric bearings, shown in Figure 22.9, with the data given in Table 22.2. As can be seen, the equipment has a frequency equal to five times the structural frequency, that is, $\omega_e = 5\omega_s$ ($= 8.34$ Hz). The 1940 El Centro earthquake (NS component) with a peak ground acceleration (PGA) of 341.55 gal is adopted as the ground excitation, as given in Figure 22.10. By an eigenvalue analysis, the natural frequencies solved for the base-isolated system are 2.46, 21.41, and 52.74 rad/sec. Because of the installation of elastic bearings on the structure–equipment system, the fundamental frequency of the system decreases significantly and is approximately equal to $\omega_1 \approx \sqrt{k_b(m_e + m_s + m_b)} = 2.51$ rad/sec, according to Section 22.3.2. From this example, one observes that the use of a single-DoF system to model a base-isolated system can give a generally good result for the first frequency of vibration.

As can be seen from Figure 22.11, for the structural acceleration of the system, the main-shock response of the fixed-base structure has been effectively eliminated due to installation of the elastic bearings. However, as indicated by Figure 22.12, because of the installation of soft bearings, the base displacement response of the isolated system is much larger and decays much slowly, even after the main shocks.

In Figure 22.13 the acceleration response of the equipment for the isolated and fixed-base cases are compared. As can be seen, the main-shock response of the fixed-base structure has been effectively suppressed through the installation of the elastic bearings. Furthermore, the equipment response appears to be almost identical to the structure response shown in Figure 22.11, due to the fact that the equipment

TABLE 22.2 System Parameters Used in Simulation (Section 22.3.4)

Equipment		Superstructure		Isolation System	
Parameter	Value	Parameter	Value	Parameter	Value
Mass m_e	3 t ($= m_s/100$)	Mass m_s	300 t	Mass m_b	100 t ($= m_s/3$)
Horizontal stiffness k_e	8258 kN/m	Horizontal stiffness k_s	33,030 kN/m	Horizontal stiffness k_b	2546 kN/m
Damping	15.74 kN m/s	Damping	314.79 kN m/s	Damping	50.46 kN m/s
Frequency $\omega_e = \sqrt{k_e/m_e}$	52.47 rad/sec	Frequency $\omega_s = \sqrt{k_s/m_s}$	10.46 rad/sec	Frequency $\omega_b = \sqrt{k_b/m_b}$	5.05 rad/sec

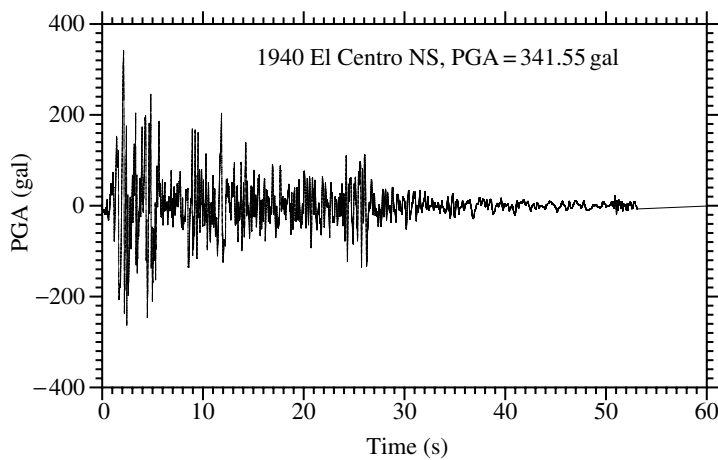


FIGURE 22.10 Waveform of 1940 El Centro earthquake (NS component).

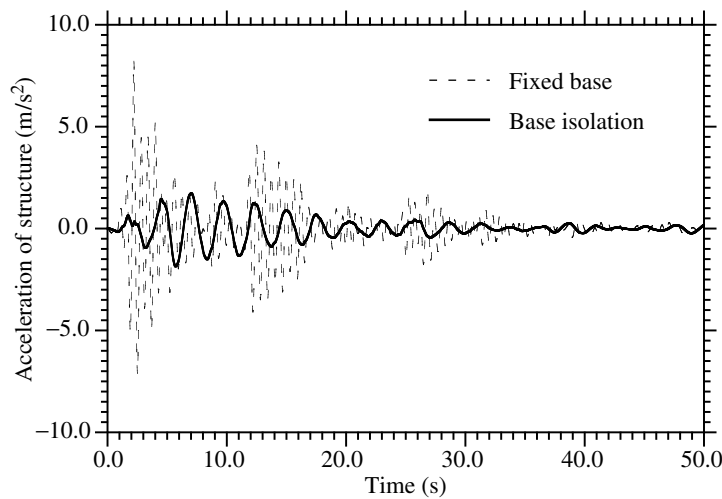


FIGURE 22.11 Comparison of structural accelerations.

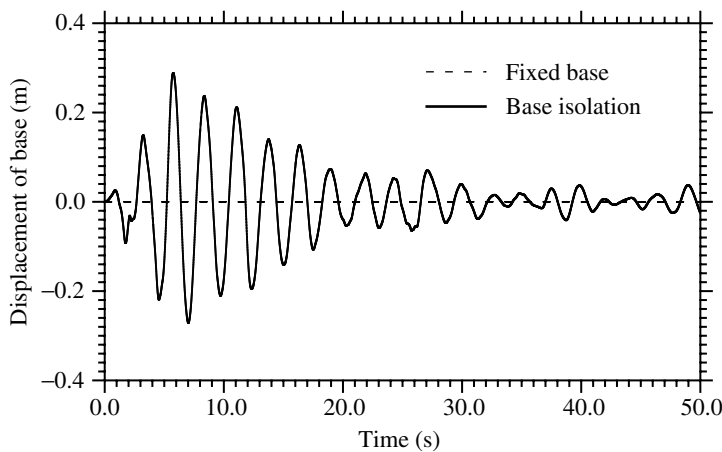


FIGURE 22.12 Comparison of base displacements.

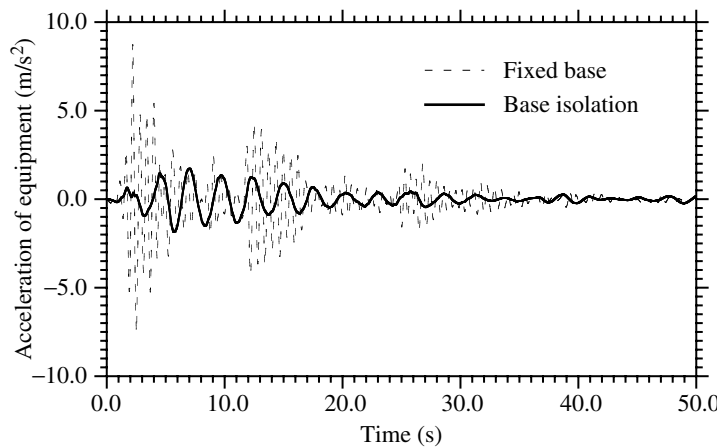


FIGURE 22.13 Comparison of equipment accelerations.

is rigidly attached to the structure, as implied by the relatively higher frequency of the equipment. As for the present example, the effectiveness of the elastic bearings in reducing the equipment response is ascertained.

For high-tech equipment, engineers may be concerned about the effect on equipment tuning induced by external excitations, such as earthquakes and traffic-induced vibrations. To investigate this effect on the structure–equipment isolation system considered, the maximum equipment acceleration was plotted as a function of the frequency ratio, ω_e/ω_s , in Figure 22.14. As can be seen, the response of the equipment is greatly amplified when it has a frequency close to the fundamental frequency of the structure–equipment isolation system, that is, when $\omega_e = 2.51$ rad/sec or $\omega_e/\omega_s = 0.24$. To avoid such a situation, it is suggested that isolators be mounted at both the structure base and equipment base. From Figure 22.14, one observes that the use of a small horizontal stiffness for the equipment will generally lead to greater equipment response due to tuning effect. However, as the stiffness of the equipment is further reduced, the equipment will reach another isolation state, in which the equipment response will be substantially suppressed, as indicated by the region with relatively small values of ω_e/ω_s . The margin for such a frequency ratio of ω_e/ω_s can be obtained by substituting the parameters in Table 22.2 into

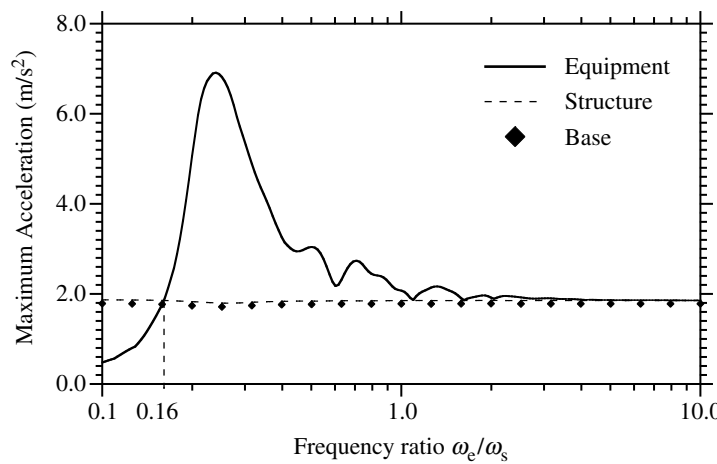


FIGURE 22.14 Maximum accelerations of structure–equipment isolation systems.

Equation 22.26, which yields a critical ratio of $\omega_c/\omega_s = 0.168$, very close to the value of 0.16 marked in Figure 22.14.

22.3.5 Concluding Remarks

This section investigates the dynamic response of a mathematical model of a structure–equipment system isolated by elastomeric bearings and subjected to ground excitations. Based on the closed-form solution of a structure–equipment isolation system subjected to harmonic support motions, one observes that the coincidence of the ground excitation frequency with the equipment frequency will make the equipment behave like a vibration absorber of the structure, of which the acceleration response will be greatly amplified. For the case that the first priority in design is to reduce the vibration of the equipment rather than that of the structure, Equation 22.26 provides a guideline for the design of equipment, which has been verified in the numerical example.

22.4 Sliding Isolation Systems

Sliding isolation can be an effective means for the seismic protection of structural systems. By implementing sliding isolators under the base mat of a structure, the transmission of ground excitation to the structure can be greatly reduced. Currently, applications of sliding isolation systems can be found elsewhere (Naeim and Kelly, 1999). A *sliding isolator* usually consists of a slider with frictional surfaces. For this reason, it is also referred to as a *friction isolator*. When subjected to an earthquake, the slider will slide along the frictional contact surfaces whenever the horizontal seismic force exceeds the maximum frictional force of the support, which, by Coulomb's theory, is equal to the normal contact force multiplied by the static (or dynamic) coefficient of friction of the sliding surfaces. Because of this, the seismic force transmitted to the superstructure is generally less than the maximum frictional force of the isolator. Obviously, the maximum frictional force is an important parameter for the design of a sliding isolation system, because it decides when the system starts to slide and how large the shear force is to be transmitted to the superstructure.

The motion of a sliding structure consists of two different states, namely, the sliding state and the stick (or nonsliding) state. At any instant of motion, the structure can only belong to one of the two states. Although in each state the sliding structure can be modeled as a linear system, the governing equations of motion for the two states are different. As a result, the overall behavior of the sliding structure is nonlinear. Such nonlinearity has resulted in the occurrence of subharmonic resonance in the frequency response of a sliding structure (Mostaghel et al., 1983; Westermo and Udawadia, 1983), making the dynamic response much more complicated. In some applications, a sliding isolation system has been designed with an automatic recentering mechanism (or resilient mechanism), so that the structure can slide back to its original position after the earthquake (Mokha et al., 1991). This type of sliding systems has been called the *resilient sliding isolation system*, which will be investigated in Section 22.5. The implementation of a recentering mechanism offers some advantages, but will inevitably introduce some disadvantages, as will be discussed in Section 22.5.

The purpose of this section is to investigate the seismic behavior of a sliding isolated structure and also the behavior of an equipment item mounted on the structure. No consideration will be made for the recentering mechanism. The nonlinear dynamic equation for a structure with an underneath friction element is first formulated. Next, two numerical approaches will be presented for solving the nonlinear equation, the *shear balance method* and *fictitious spring method*. Finally, using some assumed data, the harmonic response and seismic behavior of a sliding structure, together with the equipment mounted on it, will be presented. In this section, the frictional coefficient of the sliding system is assumed to be of the Coulomb type, that is, a time-invariant constant. For simplification, no distinction will be made between the static and dynamic frictional coefficients, or between the dynamic and maximum static frictional force.

22.4.1 Mathematical Modeling and Formulation

22.4.1.1 Equation of Motion

A sliding isolated structure with an attached equipment item, as schematically shown in Figure 22.15, can be represented as a mass–spring–dashpot system of three DoF, as shown in Figure 22.16, for which the notations employed have been defined in Table 22.1. When the structural system is excited by an earthquake, the equation of motion can be written as

$$\mathbf{M}\ddot{\mathbf{x}}(t) + \mathbf{C}\dot{\mathbf{x}}(t) + \mathbf{K}\mathbf{x}(t) = -\mathbf{M}\mathbf{L}_1\ddot{x}_g(t) + \mathbf{L}_2f(t) \quad (22.27)$$

where the vector \mathbf{x} denotes the dynamic responses of the whole structural system

$$\mathbf{x}(t) = \begin{Bmatrix} x_e(t) \\ x_s(t) \\ x_b(t) \end{Bmatrix} \quad (22.28)$$

The mass, damping, and stiffness matrices in Equation 22.27 are defined as

$$\mathbf{M} = \begin{bmatrix} m_e & 0 & 0 \\ 0 & m_s & 0 \\ 0 & 0 & m_b \end{bmatrix},$$

$$\mathbf{C} = \begin{bmatrix} c_e & -c_e & 0 \\ -c_e & c_e + c_s & -c_s \\ 0 & -c_s & c_s \end{bmatrix}, \quad (22.29)$$

$$\mathbf{K} = \begin{bmatrix} k_e & -k_e & 0 \\ -k_e & k_e + k_s & -k_s \\ 0 & -k_s & k_s \end{bmatrix}$$

and the force distribution vectors as

$$\mathbf{L}_1 = \begin{Bmatrix} 1 \\ 1 \\ 1 \end{Bmatrix}, \quad \mathbf{L}_2 = \begin{Bmatrix} 0 \\ 0 \\ 1 \end{Bmatrix} \quad (22.30)$$

Note that in Equation 22.27, the isolator frictional force, $f(t)$, which is not a constant, is moved to the right-hand side of the equation. This nonlinear force requires a special treatment in an analysis procedure, as will be explained later on.

For a systematic treatment, the above equation of motion can be further written in a state space form as shown below (Meirovitch, 1990):

$$\dot{\mathbf{z}}(t) = \mathbf{A}\mathbf{z}(t) + \mathbf{E}\ddot{x}_g(t) + \mathbf{B}f(t) \quad (22.31)$$

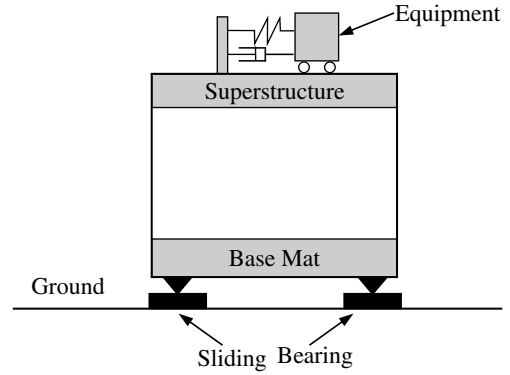


FIGURE 22.15 Schematic for an isolated structure–equipment system with sliding bearing.

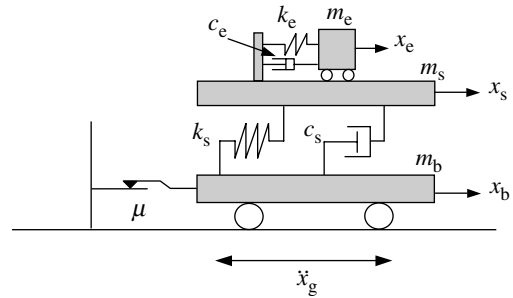


FIGURE 22.16 Model for an isolated structure–equipment system with sliding support.

where the state vector $\mathbf{z}(t)$ and the system matrix \mathbf{A} are defined as

$$\mathbf{z}(t) = \begin{bmatrix} \dot{\mathbf{x}}(t) \\ \mathbf{x}(t) \end{bmatrix}, \quad \mathbf{A} = \begin{bmatrix} -\mathbf{M}^{-1}\mathbf{C} & -\mathbf{M}^{-1}\mathbf{K} \\ \mathbf{I} & \mathbf{0} \end{bmatrix} \quad (22.32)$$

and the excitation and friction distribution vectors as

$$\mathbf{E} = \begin{bmatrix} -\mathbf{L}_1 \\ \mathbf{0} \end{bmatrix}, \quad \mathbf{B} = \begin{bmatrix} \mathbf{M}^{-1}\mathbf{L}_2 \\ \mathbf{0} \end{bmatrix} \quad (22.33)$$

22.4.1.2 Conditions for Stick and Sliding States

As mentioned above, the motion of a sliding structure at any instant has two possible states, namely, the stick (or nonsliding) and sliding states. The following are the conditions that must be satisfied by the sliding structure:

- (1) In stick state

$$|f(t)| < f_{\max} = \mu W \quad (22.34a)$$

$$\dot{x}_b(t) = 0 \quad (22.34b)$$

where μ is the coefficient of friction and W is the total weight of the structure. According to the preceding equations, the frictional force in the stick state is an unknown with a magnitude less than the maximum frictional force, f_{\max} , which equals the product of μ and W , while the sliding velocity of the structure is simply zero. Whenever the frictional force satisfies Equation 22.34a, the sliding system remains in the stick state, otherwise it changes into the sliding state.

- (2) In sliding state

$$f(t) = -\text{sgn}(\dot{x}_b(t))f_{\max} = -\text{sgn}(\dot{x}_b(t))\mu W \quad (22.35a)$$

$$\dot{x}_b(t) \neq 0 \quad (22.35b)$$

where the function $\text{sgn}(x)$ denotes the sign of the variable x . According to Equation 22.35a and Equation 22.35b, the frictional force in the sliding state has a magnitude equal to the maximum frictional force, but directed in a sense opposite to that of the sliding velocity. On the other hand, the sliding velocity of the isolator remains as an unknown.

22.4.2 Methods for Numerical Analysis

Two numerical methods commonly used for the analysis of sliding isolated structural systems, the shear balance method and fictitious spring method, will be introduced in this section. By employing the discrete-time state-space formula, both methods can be cast in an incremental form that is suitable for the analysis of sliding systems with multiple DoF.

22.4.2.1 Shear Balance Method

Consider the state-space equation, Equation 22.31, and assume that both the ground acceleration and frictional force vary linearly within each time interval, as shown in Figure 22.17. Equation 22.31 may be written in the following incremental form (Meirovitch, 1990)

$$\mathbf{z}[k+1] = \mathbf{A}_d\mathbf{z}[k] + \mathbf{E}_0\ddot{x}_g[k] + \mathbf{E}_1\ddot{x}_g[k+1] + \mathbf{B}_0f[k] + \mathbf{B}_1f[k+1] \quad (22.36)$$

where the symbol $x[k]$ denotes that the variable x is evaluated at the k th time step. The other coefficient

matrices in equation 22.36 are defined as

$$\mathbf{A}_d = e^{\mathbf{A}\Delta t} = \sum_{i=0}^{\infty} \frac{(\Delta t)^i}{i!} \mathbf{A}^i \quad (22.37)$$

$$\mathbf{B}_0 = \left[(\mathbf{A})^{-1} \mathbf{A}_d + \frac{1}{\Delta t} (\mathbf{A})^{-2} (\mathbf{I} - \mathbf{A}_d) \right] \mathbf{B} \quad (22.38a)$$

$$\mathbf{B}_1 = \left[-(\mathbf{A})^{-1} + \frac{1}{\Delta t} (\mathbf{A})^{-2} (\mathbf{A}_d - \mathbf{I}) \right] \mathbf{B} \quad (22.38b)$$

where Δt denotes the size of the time step considered for analysis. The matrices \mathbf{E}_0 and \mathbf{E}_1 can be computed in a way similar to \mathbf{B}_0 and \mathbf{B}_1 , except that the matrix \mathbf{B} in Equation 22.38a and Equation 22.38b should be replaced by the matrix \mathbf{E} . In some applications, the system matrix \mathbf{A} may not be invertible, that is, \mathbf{A}^{-1} does not always exist. If this is the case, one may compute \mathbf{B}_0 and \mathbf{B}_1 (and similarly \mathbf{E}_0 and \mathbf{E}_1) by the following formulas:

$$\mathbf{B}_0 = \mathbf{A}_d^* \mathbf{B}, \quad \mathbf{B}_1 = (\hat{\mathbf{A}}_d - \mathbf{A}_d^*) \mathbf{B} \quad (22.39)$$

where

$$\mathbf{A}_d^* = \sum_{i=0}^{\infty} \frac{(\Delta t)^{i+1}}{i!(i+2)} \mathbf{A}^i, \quad \hat{\mathbf{A}}_d = \sum_{i=0}^{\infty} \frac{(\Delta t)^{i+1}}{(i+1)!} \mathbf{A}^i \quad (22.40)$$

Note that, on the right-hand side of Equation 22.36, the only unknown at the k th time step is the frictional force $f[k+1]$; therefore, $f[k+1]$ must be determined before the next time step response $\mathbf{z}[k+1]$ is computed. Wang et al. (1998) proposed the shear balance method for computing the frictional force $f[k+1]$. By this method, the sliding structure is first assumed to be in the stick state at the $(k+1)$ th step, for which the condition given in Equation 22.34b must be satisfied

$$\dot{\mathbf{x}}_b[k+1] = \mathbf{D}\mathbf{z}[k+1] = 0 \quad (22.41)$$

where \mathbf{D} is a relation matrix, equal to $\mathbf{D} = [0 \ 0 \ 1 \ 0 \ 0 \ 0]$ for the model shown in Figure 22.16. Substituting $\mathbf{z}[k+1]$ in Equation 22.36 into Equation 22.41, one may solve for the *estimated frictional force* at the $(k+1)$ th time step as

$$\bar{f}[k+1] = -(\mathbf{D}\mathbf{B}_1)^{-1} \mathbf{D}(\mathbf{A}_d \mathbf{z}[k] + \mathbf{B}_0 f[k] + \mathbf{E}_0 \ddot{\mathbf{x}}_g[k] + \mathbf{E}_1 \ddot{\mathbf{x}}_g[k+1]) \quad (22.42)$$

where $\bar{f}[k+1]$ with an overbar signifies that the frictional force is an estimate obtained by assuming the sliding structure to be at the stick state. Such a value may not be the actual one if the system is not in the stick state. The physical meaning for $\bar{f}[k+1]$ is that it represents the *balanced shear force* required at the $(k+1)$ th time step for the structure to remain in the stick state. Therefore, the sign of $\bar{f}[k+1]$ indicates the direction of the resistant force provided by the isolation system. In spite of the fact that $\bar{f}[k+1]$ may not be the actual frictional force, it plays an important role for determining the actual state (stick or sliding) and the actual frictional force of the sliding isolated structure, as will be described below based on Equation 22.34a and Equation 22.35a.

- (1) The system is in the “stick state” if $|\bar{f}[k+1]| < f_{\max}$ and the frictional force is

$$f[k+1] = \bar{f}[k+1] \quad (22.43)$$

- (2) The system is in the “sliding state” if $|\bar{f}[k+1]| \geq f_{\max}$ and the frictional force is

$$f[k+1] = \text{sgn}(\bar{f}[k+1])f_{\max} \quad (22.44)$$

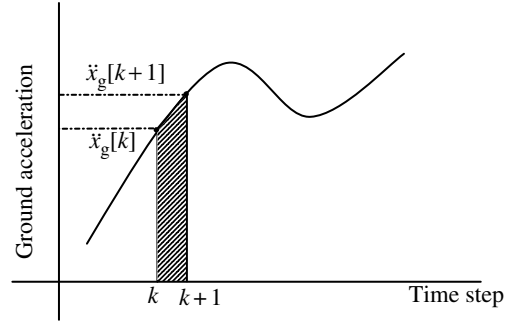


FIGURE 22.17 Force integration scheme with linear interpolation.

As can be seen, the term $-\text{sgn}(\dot{x}_b[k+1])$ in Equation 22.35a is replaced by $\text{sgn}(\tilde{f}[k+1])$ in Equation 22.44. Such a replacement is justified since the sign of $\tilde{f}[k+1]$ indicates the direction of the resistant force at the $(k+1)$ th time step. Once the correct frictional force, $f[k+1]$, is determined by using either Equation 22.43 or Equation 22.44, it can be substituted into Equation 22.36 to obtain the response $\mathbf{z}[k+1]$ for the next time step. The computational flow-chart for the shear balance method has been given in Figure 22.18.

22.4.2.2 Fictitious Spring Method

The fictitious spring method was first proposed by Yang et al. (1990) for the analysis of a sliding structure. Later, Lu and Yang (1997) reformulated the method into a state-space form for the analysis of equipment

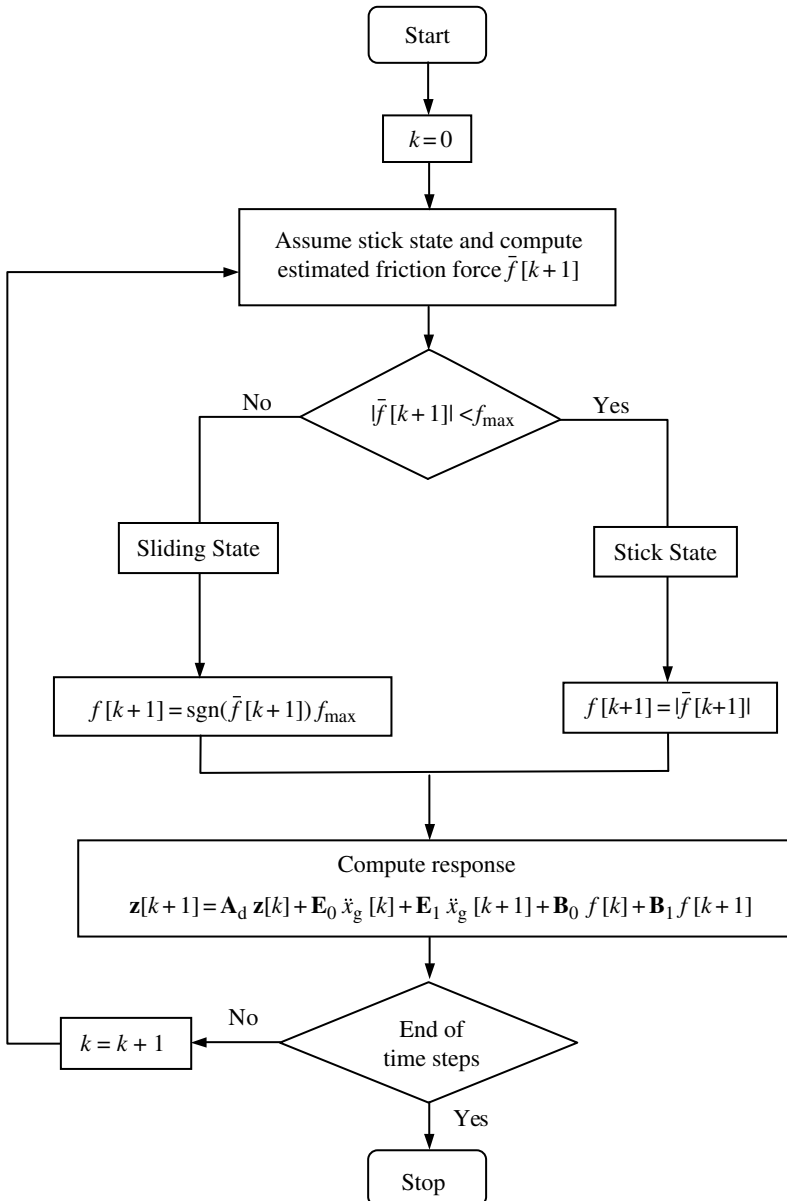


FIGURE 22.18 Computational flow-chart for shear balance method.

mounted on a sliding structure. By this method, a fictitious spring, k_f , is introduced between the base mat and the ground, as in Figure 22.19, to represent the mechanism of sliding or friction. The stiffness, k_f , of the fictitious spring is taken as zero for the sliding state and as a very large value for the stick state. With the introduction of the fictitious spring, the stiffness matrix, \mathbf{K} , in Equation 22.29 should be modified as follows:

$$\mathbf{K} = \mathbf{K}(k_f) = \begin{bmatrix} k_e & -k_e & 0 \\ -k_e & k_e + k_s & -k_s \\ 0 & -k_s & k_s + k_f \end{bmatrix} \quad (22.45)$$

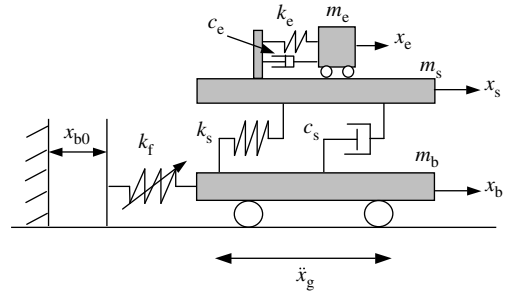


FIGURE 22.19 Model for isolated structures with fictitious spring.

Accordingly, the state-space dynamic equation, Equation 22.31, should be modified as

$$\dot{\mathbf{z}}(t) = \mathbf{A}(k_f)\mathbf{z}(t) + \mathbf{E}\ddot{x}_g(t) + \mathbf{B}\tilde{f}(t) \quad (22.46)$$

where

$$\mathbf{A} = \mathbf{A}(k_f) = \begin{bmatrix} -\mathbf{M}^{-1}\mathbf{C} & -\mathbf{M}^{-1}\mathbf{K}(k_f) \\ \mathbf{I} & \mathbf{0} \end{bmatrix} \quad (22.47)$$

Depending on the current state of the sliding system, the fictitious stiffness, k_f , and the modified friction term, $\tilde{f}(t)$, in Equation 22.46 may take one of the following two sets of values:

- (1) In the stick state

$$k_f = \alpha k_s, \quad \tilde{f}(t) = k_f x_{b0} \quad (22.48)$$

- (2) In the sliding state

$$k_f = 0, \quad \tilde{f}(t) = -\text{sgn}(\dot{x}_b(t))\mu W \quad (22.49)$$

In Equation 22.48, the symbol α represents a constant of very large value, and x_{b0} the initial elongation of the fictitious spring in the current stick state (computation of x_{b0} will be explained later). Note that the modified friction term, $\tilde{f}(t)$, may not be the actual frictional force. The actual frictional force can be determined as follows:

- (1) In the stick state

$$f(t) = k_f(x_b(t) - x_{b0}) \quad (22.50)$$

- (2) In the sliding state

$$f(t) = \tilde{f}(t) \quad (22.51)$$

According to Equation 22.50 and Equation 22.51, the actual frictional force of the isolation system in the stick state is equal to the internal force of the fictitious spring, while in the sliding state it is equal to the modified frictional force, $\tilde{f}(t)$. The frictional force computed from the preceding two equations should obey the conditions given in Equation 22.34a and Equation 22.35a as well.

With the conditions imposed for the stick and sliding states in Equation 22.48 and Equation 22.49, respectively, the equation of motion in Equation 22.46 actually represents two different sets of equations.

Specifically, Equation 22.46 and Equation 22.48 collectively describe the motion of the structure in the stick state, while Equation 22.46 and Equation 22.49 represent the motion of the structure in the sliding state. Owing to the fact that a sliding system may switch between the two states at certain instants, the behavior of the entire system should undoubtedly be regarded as a nonlinear one. Nevertheless, within each particular state, the behavior of the system as represented either by Equation 22.46 and Equation 22.48 or Equation 22.46 and Equation 22.49 is a linear one.

In the following, a numerical solution scheme based on the concept of fictitious spring will be introduced. Let Δt denote a time increment, which is usually taken as a very small value, and assume that the ground excitation and frictional force are constant within each time increment, Δt (see Figure 22.20). Accordingly, the discrete-time solution of Equation 22.46 can be rewritten in an incremental form (Meirovitch, 1990) as

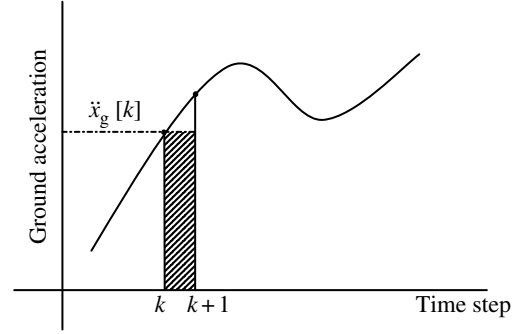


FIGURE 22.20 Constant force integration scheme.

$$\mathbf{z}[k+1] = \mathbf{A}_d \mathbf{z}[k] + \mathbf{E}_d \ddot{x}_g[k] + \mathbf{B}_d \tilde{f}[k] \quad (22.52)$$

where

$$\mathbf{A}_d = \mathbf{A}_d(k_f) = e^{\mathbf{A}(k_f)\Delta t} = \sum_{i=0}^{\infty} \frac{\Delta t^i}{i!} \mathbf{A}(k_f)^i \quad (22.53)$$

$$\mathbf{E}_d = \mathbf{E}_d(k_f) = \mathbf{A}(k_f)^{-1} (\mathbf{A}_d(k_f) - \mathbf{I}) \mathbf{E} \quad (22.54a)$$

$$\mathbf{B}_d = \mathbf{B}_d(k_f) = \mathbf{A}(k_f)^{-1} (\mathbf{A}_d(k_f) - \mathbf{I}) \mathbf{B} \quad (22.54b)$$

For the case where the system matrix \mathbf{A} is invertible, \mathbf{B}_d and \mathbf{E}_d may be computed instead using the following formulas:

$$\mathbf{E}_d = \mathbf{E}_d(k_f) = \left[\sum_{i=0}^{\infty} \frac{\Delta t^i}{i!} \mathbf{A}(k_f)^{i-1} \right] \mathbf{E} \quad (22.55)$$

$$\mathbf{B}_d = \mathbf{B}_d(k_f) = \left[\sum_{i=0}^{\infty} \frac{\Delta t^i}{i!} \mathbf{A}(k_f)^{i-1} \right] \mathbf{B} \quad (22.56)$$

Equation 22.52 is the solution of the sliding system given in incremental form, because the response, $\mathbf{z}[k+1]$, can be computed from the solution of the previous step, $\mathbf{z}[k]$. Note that, in Equation 22.53 and Equation 22.54, the coefficient matrices \mathbf{A}_d , \mathbf{E}_d , and \mathbf{B}_d have two possible sets of values, as the fictitious spring constant, k_f , may take different values for the sliding and stick states. Nevertheless, once the time step size, Δt , is chosen, the coefficient matrices \mathbf{A}_d , \mathbf{E}_d , and \mathbf{B}_d , remain constant for each state. As such, they need only be calculated once at the beginning of the incremental procedure. The computational flow-chart for the fictitious spring method described above has been given in Figure 22.21.

The dynamic equation and its discrete-time solution for the sliding structure in the two states have been presented above. In the following, we shall describe how to determine the *transition time* for the sliding structure to switch from one state to the other. Once the transition time is determined, the original step size should be scaled down accordingly to reflect the transition point (Yang et al., 1990).

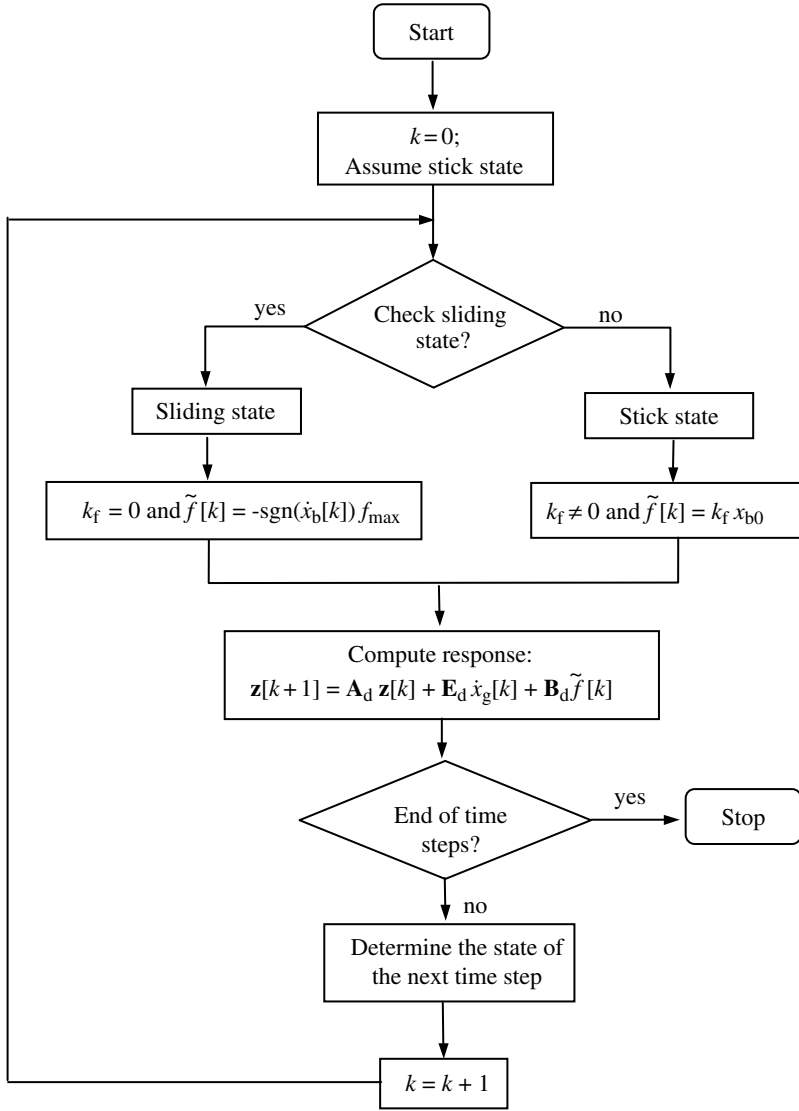


FIGURE 22.21 Computational flow-chart for fictitious spring method.

Transition from stick to sliding state. As stated in Equation 22.34a, the condition for a sliding isolated structure to remain in the stick state is that the static frictional force under the base mat be less than its maximum value, f_{\max} . Once the frictional force exceeds this maximum value, the system starts to slide. With the fictitious spring method, the static frictional force is computed as the internal force of the fictitious spring, as in Equation 22.50. Based on the above considerations and Equation 22.50, the condition for the sliding system to transfer from the stick to the sliding state is

$$|f(t_0)| = |k_f(x_b(t_0) - x_{b0})| = f_{\max} = \mu W \quad (22.57)$$

where t_0 denotes the transition time at which the structure starts to slide and k_f is the spring constant given in Equation 22.48 for the stick state. Because a very large value has been used for the fictitious spring constant, k_f , in the stick state, the deviation in base displacement due to spring elongation is very small in this state, which can just be neglected. In practice, the transition time, t_0 may not occur precisely

at the discrete points of time considered. It is likely that the spring force is less than f_{\max} at the current time step, say, the k th step, but exceeds f_{\max} at the following time step. If this is the case, numerical methods such as the bisection method should be employed to locate the transition time, t_0 within the time interval $(k\Delta t, (k+1)\Delta t)$ considered based on Equation 22.57.

Transition from sliding state to stick state. The structure in the sliding state may return to the stick state whenever the following two conditions are satisfied. (1) The relative velocity of the base mat to the ground reaches zero, that is, $\dot{\xi}_b(t_0) = 0$ where t_0 is the transition time; (2) the estimated static frictional force, denoted by $\tilde{f}(t_0)$, is less than the maximum static frictional force, that is, $\tilde{f}(t_0) < f_{\max}$. Here, the estimated static frictional force, $\tilde{f}(t_0)$, is defined as the shear force required to balance the motion of the superstructure if the system is assumed to be in the stick state, similar to the one given in Equation 22.42 for $\tilde{f}[k+1]$. By letting the relative velocity and relative acceleration between the base mat and the ground be equal to zero, that is, $\ddot{\xi}_b(t_0) = \dot{\xi}_b(t_0) = 0$, the estimated frictional force can be calculated from the free-body diagram of the base mat as

$$\tilde{f}(t_0) = m_b \ddot{x}_g(t_0) - k_s(x_s(t_0) - x_b(t_0)) - c_s \dot{x}_s(t_0) \quad (22.58)$$

For the sliding structure to transfer from the sliding to the stick state, both the aforementioned conditions must be satisfied simultaneously. Once the structure enters the stick state, the term $f(t_0)$ should be set equal to $\tilde{f}(t_0)$ and used as the initial frictional force. For the sake of equilibrium, the initial base mat displacement, x_{b0} , should be computed as

$$x_{b0} = x_b(t_0) - (\tilde{f}(t_0)/k_f) \quad (22.59)$$

where the value of k_f is the one given for the stick state in Equation 22.48.

Concerning the two conditions mentioned above, it may happen that only the first condition, $\dot{\xi}_b = 0$ is satisfied, while the computed $\tilde{f}(t_0)$ is still larger than f_{\max} . If this is the case, the sliding system should not be regarded as a transition to the stick state. Rather, the situation should be regarded as an indication for reversing the direction of sliding in the next time step. Correspondingly, the frictional force, $f(t_0)$, should be set equal to the sliding frictional force, rather than the estimated one, $\tilde{f}(t_0)$.

22.4.3 Simulation Results for Sliding Isolated Systems

22.4.3.1 Numerical Model and Ground Excitations

In this section, the dynamic behavior of the sliding isolated structure–equipment system shown in Figure 22.16 will be analyzed using the shear balance method. Although the sliding structure and equipment considered are both of single-DoF, there exists no difficulty for use of the method to solve problems with multi-DoF systems. In Table 22.3, the material properties adopted for the present model have been listed, which are intended to simulate a small, five-story, reinforced concrete frame. For the present purposes, two types of ground excitation are considered, namely, harmonic and earthquake excitations. The harmonic excitation is considered primarily for studying the frequency response of the sliding system, while the earthquake excitation is considered for the effect of earthquake intensity. For the

TABLE 22.3 System Parameters Used in Simulation (Section 22.4.3)

Equipment		Superstructure		Isolation System	
Parameter	Value	Parameter	Value	Parameter	Value
Mass m_e	3 t ($= m_s/100$)	Mass m_s	300 t	Mass m_b	100 t ($= m_s/3$)
Frequency ω_e	$5\omega_s$ or a variable	Frequency ω_s	1.67 Hz	Frictional coefficient μ	0.05, 0.1, 0.25
Damping ratio ζ_e	5%	Damping ratio ζ_s	5%	—	—

harmonic excitation, a sinusoidal ground acceleration of the following form is adopted:

$$\ddot{x}_g(t) = 0.5g \sin \omega_g t \quad (22.60)$$

where ω_g denotes the excitation frequency and g is the gravitational acceleration. For the earthquake excitation, the 1940 El Centro earthquake (NS component) is considered, for which the waveform has been given in Figure 22.10. The PGA level of the earthquake will be adjusted for reasons of research. Concerning the effectiveness of response reduction, three quantities are chosen as the indices, namely, the base displacement (base drift), structural acceleration, and equipment acceleration. For all the figures shown in Section 22.4.3 below, the symbol μ in the legend is used to denote the frictional coefficient of the sliding isolation system and the word “fixed” denotes the response of the corresponding fixed-base structure.

22.4.3.2 Harmonic Response of Structure

Time history. For the isolated system subjected to a harmonic excitation of $\omega_g = 1$ Hz, the base displacements computed for different coefficients of friction were plotted in Figure 22.22 and Figure 22.23. As can be seen, the base displacements quickly reach the steady-state response within the first few cycles. Meanwhile, the use of a smaller frictional coefficient results in a larger permanent displacement before the steady state is reached. From the structural accelerations plotted in Figure 22.24, one observes that, for a sliding structure with a smaller coefficient of friction, the steady-state response is achieved in a faster way, accompanied by a larger reduction on structural acceleration. Of interest in Figure 22.24 is that the response of the fixed-base case shows a clear period of 1 sec, while in the sliding case, the response is contaminated by high-frequency signals caused by the sliding-stick transitions.

Hysteretic behavior. In order to understand the mechanical characteristics of a nonlinear device used for vibration control, it is common to present a diagram showing the force–deformation relation of the device, also referred to as the *hysteretic diagram* (Soong and Dargush, 1997). Figure 22.25 shows the hysteresis loops of the sliding isolation system (the sliding layer) for $\mu = 0.1$ and 0.25, when the system is subjected to a harmonic excitation of $\omega_g = 1$ Hz. In the figure, the horizontal and vertical axes, respectively, represent the base displacement and shear force, that is, the frictional force, under the mat. Just like many other frictional elements or devices, the shape of the hysteresis loop of a sliding bearing is rectangular. The height of the rectangle is equal to the maximum frictional force that depends on the coefficient of friction, while the width of the hysteresis loop is determined by the base-sliding displacement. As the coefficient of friction decreases, the height of the loop decreases, while the width increases. The total area of the hysteresis loop is equivalent to the portion of the energy dissipated by the sliding bearing.

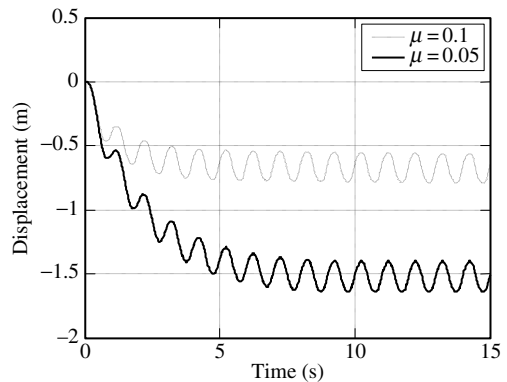


FIGURE 22.22 Comparison of base displacements ($\omega_g = 1$ Hz; $\omega_e = 5\omega_s$).

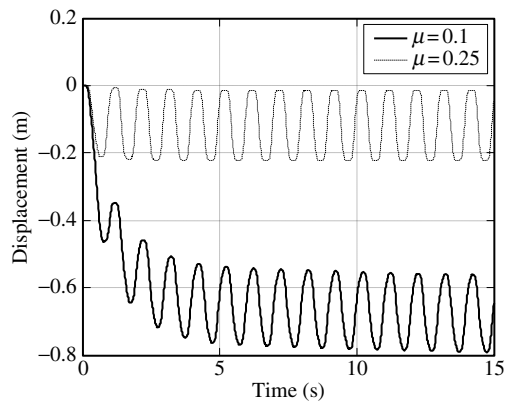


FIGURE 22.23 Comparison of base displacements ($\omega_g = 1$ Hz; $\omega_e = 5\omega_s$).

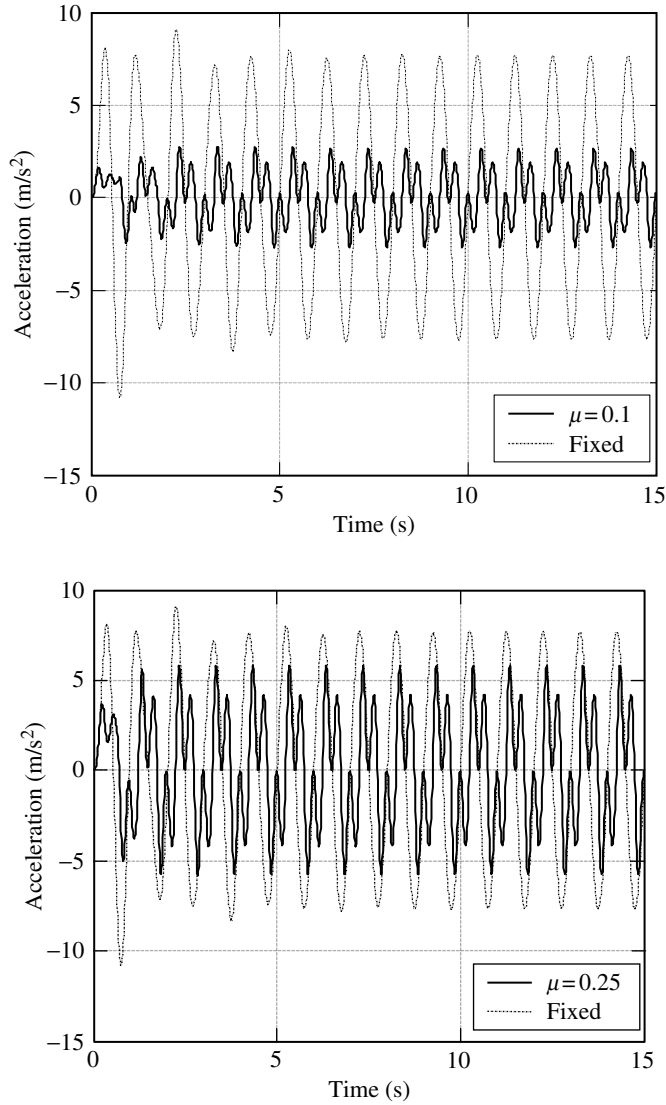


FIGURE 22.24 Comparison of structural accelerations ($\omega_g = 1$ Hz; $\omega_e = 5\omega_g$).

Frequency response. Figure 22.26 shows the maximum structural acceleration with respect to the excitation frequency for four different frictional coefficients, $\mu = 0.05, 0.1, 0.25$ and ∞ (for the fixed-base case). Here, the maximum acceleration means the steady-state acceleration response. The following observations can be made from Figure 22.26: (1) Compared with the fixed-base case, the use of a smaller frictional coefficient can reduce the structural acceleration for the frequency range considered. (2) The sliding mechanism can effectively suppress the main resonant response, associated with the natural frequency of 1.67 Hz of the superstructure system. (3) As the coefficient of friction, μ , decreases from ∞ to 0.05, the main resonant frequency associated with the structural natural frequency drifts from the fixed-base frequency of 1.67 Hz toward a higher value. (4) For the sliding cases of $\mu = 0.05, 0.1, 0.25$, there exist some minor peaks in the range of lower excitation frequencies, besides the main resonant peak. Such a phenomenon is called the *subharmonic resonance*. For a large frictional coefficient, say, with $\mu = 0.25$, the subharmonic resonant response may be even larger than that of the main resonance.

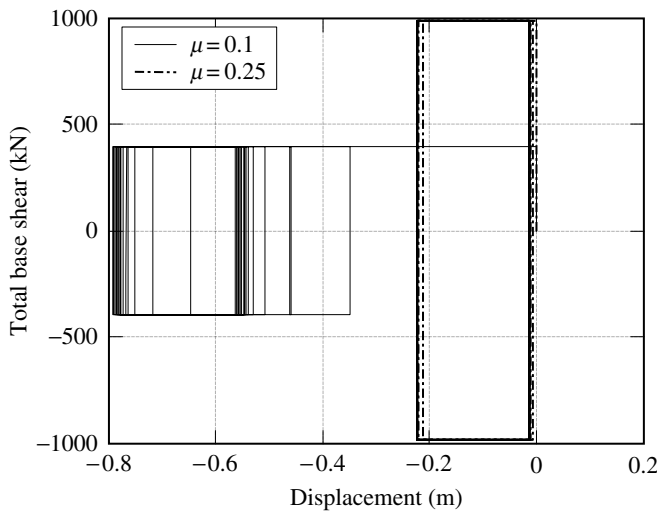


FIGURE 22.25 Hysteresis loops of a sliding bearing ($\omega_g = 1 \text{ Hz}$; $\omega_e = 5\omega_s$).

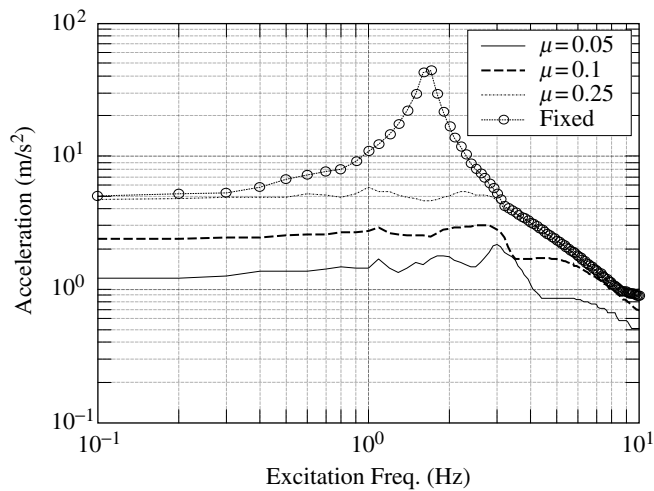


FIGURE 22.26 Maximum structural acceleration vs. ground excitation frequency ($\omega_e = 5\omega_s$).

Figure 22.27 shows the frequency responses of the maximum base displacement for various frictional coefficients. The following are observed: (1) The larger the frictional coefficient, the smaller the base drift is. (2) The base displacement has very large magnitudes in the lower excitation frequencies and decreases monotonically as the excitation frequency increases. (3) The extremely large base drift exhibited in the lower excitation frequency range is due to the initial permanent displacement observed in Figure 22.22.

22.4.3.3 Harmonic Response of Equipment

Time history. Consider an equipment item of a natural frequency equal to five times of the structural frequency, that is, $\omega_e = 5\omega_s$. For the case of a harmonic excitation of $\omega_g = 1 \text{ Hz}$, the accelerations solved for the equipment mounted on the structure with $\mu = 0.1$ and 0.25 , along with the fixed-base case, have

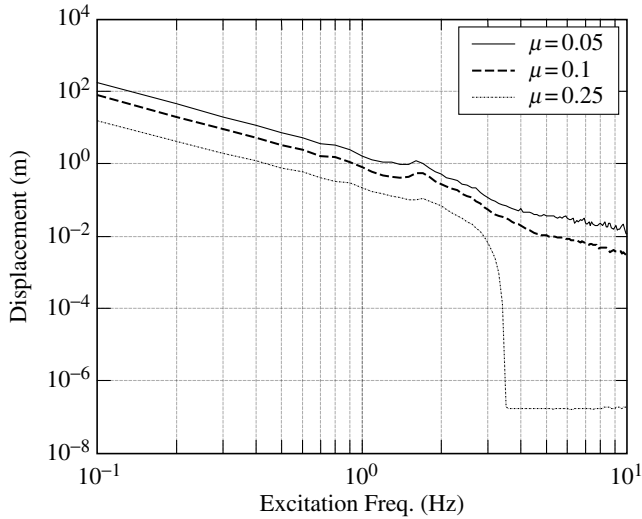


FIGURE 22.27 Maximum base displacement vs. ground excitation frequency ($\omega_e = 5\omega_s$).

been plotted in Figure 22.28. As can be seen, the equipment quickly reaches the steady state within a few cycles of oscillation. The equipment response is effectively suppressed for the case with a smaller frictional coefficient. Additionally, the waveforms shown in Figure 22.28 for the equipment appear to be marginally higher than those of the primary structure shown in Figure 22.24, which can be attributed to the use of a relatively stiff equipment, that is, with $\omega_e = 5\omega_s$.

Frequency responses. For an equipment item of the frequency $\omega_e = 5\omega_s$ ($= 8.34$ Hz), the maximum acceleration response has been plotted as a function of the excitation frequency in Figure 22.29. By comparing Figure 22.29 with Figure 22.26, one observes that the frequency response curves of the equipment and primary structure are generally similar, except that a secondary resonant peak occurs around the equipment natural frequency of 8.34 Hz in Figure 22.29. The other observations from Figure 22.29 are as follows: (1) In comparison with the fixed-base case, the sliding isolation alleviates both the structural and equipment resonant peaks around the frequencies of 1.67 and 8.34 Hz, respectively. However, the level of alleviation is more apparent for the former than for the latter. (2) The equipment also exhibits the same subharmonic resonance behavior as that of the primary structure, in terms of the resonance peaks and frequencies. (3) As the frictional coefficient μ decreases from ∞ (for the fixed-base case) to 0.05, the main resonant frequency associated with the structure drifts toward a higher value. However, the resonant frequency associated with the equipment remains the same.

Effect of equipment tuning. The effect of equipment tuning refers to the case when the equipment frequency is tuned to the structural frequency, that is, $\omega_e = \omega_s$. Figure 22.30 shows the frequency response of the equipment when the equipment tuning occurs. Compared with Figure 22.29, this figure shows the following: (1) When equipment tuning occurs, the sliding isolation system can still mitigate the main resonant peak of the equipment, but the effectiveness of mitigation is drastically reduced. (2) Although the subharmonic resonance can still be observed, the relevant frequencies of the equipment are different from those of the primary structure. (3) The frequency of the maximum resonant response remains equal to the tuned equipment's natural frequency of 1.67 Hz, regardless of the change in the frictional coefficient, μ , from ∞ to 0.05.

22.4.3.4 Earthquake Response of Structure

Time history. For the isolated system subjected to the El Centro earthquake with a PGA of 0.5g, the structural acceleration and base displacement of the sliding system have been plotted in Figure 22.31 and Figure 22.32, respectively, together with the response for the fixed-base case in Figure 22.31. As can be

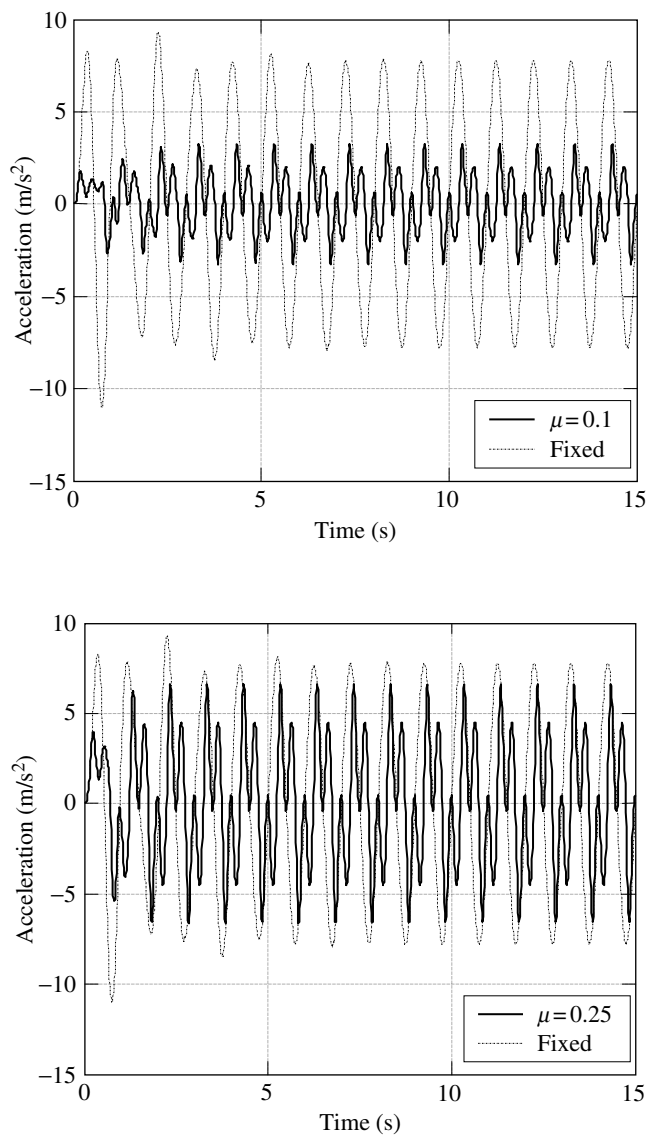


FIGURE 22.28 Comparison of equipment accelerations ($\omega_g = 1$ Hz; $\omega_e = 5\omega_s$).

seen from Figure 22.31, the main-shock response occurring between 0 and 10 sec for the fixed-base structure has been effectively suppressed by the sliding isolators with $\mu = 0.1$ and 0.25. About 80 and 60% of the maximum structural acceleration have been suppressed by the isolators with $\mu = 0.1$ and 0.25, respectively. On the other hand, Figure 22.32 demonstrates that the better suppression effect for the case with $\mu = 0.1$ is achieved at the expense of a larger base displacement. It is interesting to note that the horizontal segments in the curves of Figure 22.32 actually represent the stick state of the sliding system, which is useful for unveiling the sliding-stick mechanism involved.

Effect of earthquake intensity. The maximum structural acceleration and base displacement vs. the PGA have been plotted in Figure 22.33 and Figure 22.34, respectively. As can be seen from Figure 22.33, the maximum structural acceleration for the fixed-base case is proportional to the earthquake intensity, while in all the sliding cases it remains essentially as a constant after the PGA reaches a certain level. In other words, the reduction in structural maximum response and the efficiency of isolation have increased

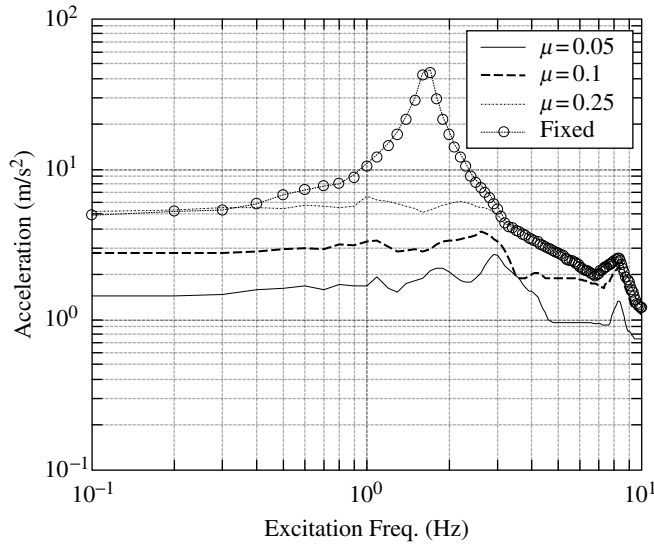


FIGURE 22.29 Maximum equipment acceleration vs. ground excitation frequency ($\omega_e = 5\omega_s$).

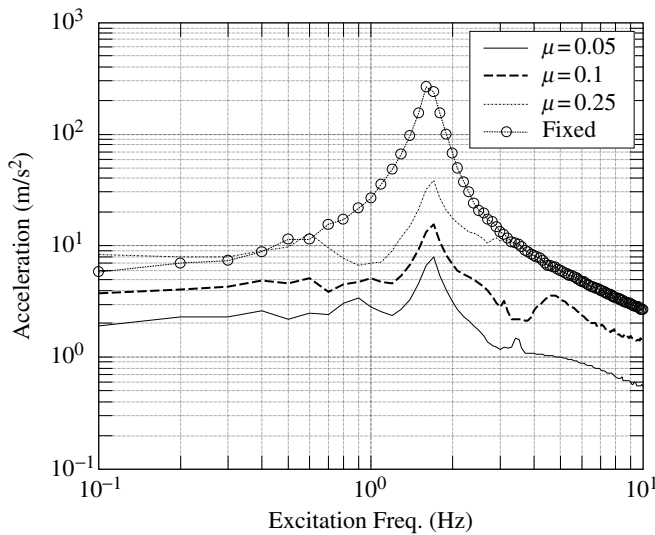


FIGURE 22.30 Maximum equipment acceleration vs. ground excitation frequency for equipment tuning ($\omega_e = \omega_s$).

with the increase in earthquake intensity. For example, for the case of $\mu = 0.1$, Figure 22.33 shows that the structural acceleration is reduced by around 60% at $\text{PGA} = 0.2g$, while it is reduced by more than 90% at $\text{PGA} = 1.0g$. However, as indicated by Figure 22.34, the above reduction in structural response has been achieved at the expense of increased base displacements. For the same PGA level, a sliding system with a smaller frictional coefficient has a better effect of vibration reduction, but this is accompanied by a larger base displacement.

Residual base displacement. The residual base displacement is defined as the permanent base displacement of the structure after it stops vibrating. This quantity is important in the study of sliding structures. Figure 22.35 shows the residual base displacement as a function of the earthquake PGA level. A first look at the figure reveals that no clear relation exists between the earthquake intensity and residual

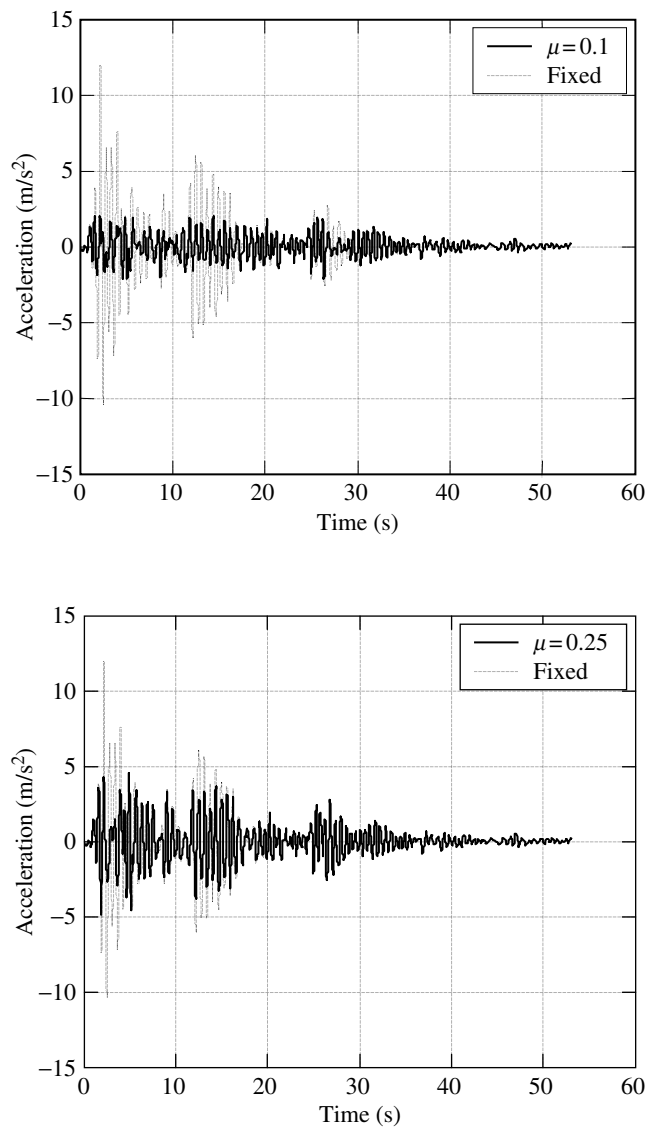


FIGURE 22.31 Comparison of structural accelerations ($\omega_c = 5\omega_s$, PGA = 0.5g).

displacement, because a larger PGA may lead to a smaller residual base displacement. Nevertheless, after taking the average of the residual displacements over the PGA range of 0.1 to 1g, we obtain $x_{res} = 0.083, 0.084, 0.084$ m for the case of $\mu = 0.05, 0.1, 0.25$, respectively. These values indicate that a smaller frictional coefficient leads to a larger residual base displacement in general. However, when the frictional coefficient, μ , approaches zero, the residual displacement approaches a constant equal to the permanent ground displacement.

22.4.3.5 Earthquake Response of Equipment

Time history. Consider an equipment item with a natural frequency equal to five times the structural frequency, that is, $\omega_c = 5\omega_s$ ($= 8.34$ Hz). For the isolated system subjected to the El Centro earthquake

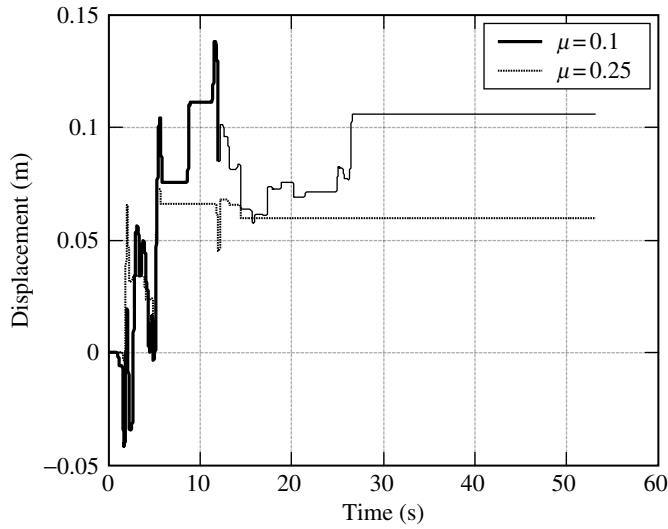


FIGURE 22.32 Comparison of base displacements ($\omega_e = 5\omega_s$, PGA = 0.5g).

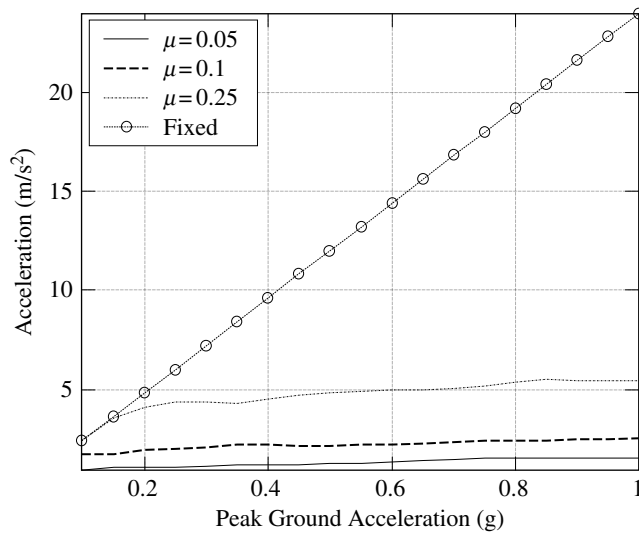


FIGURE 22.33 Maximum structural acceleration vs. PGA ($\omega_e = 5\omega_s$).

with PGA = 0.5g, the time histories computed for the equipment acceleration for the cases with $\mu = 0.1$ and 0.25, along with the fixed-base case, have been plotted in Figure 22.36a and b. As can be seen, the main-shock response of the fixed-base structure occurring for the first 10 sec has been effectively suppressed through installation of the sliding isolator with $\mu = 0.1$ and 0.25. A higher level of reduction can be achieved if a smaller frictional coefficient is chosen.

Effect of earthquake intensity. Figure 22.37 shows the maximum equipment acceleration as a function of the PGA level. Because of the use of a relatively stiff equipment ($\omega_e = 5\omega_s$), the curves shown in Figure 22.37 are similar to those for the primary structure in Figure 22.33, but with slightly higher values. Therefore, the observations made previously for Figure 22.33 are applicable to Figure 22.37. The maximum response of equipment items with other frequencies will be discussed below.

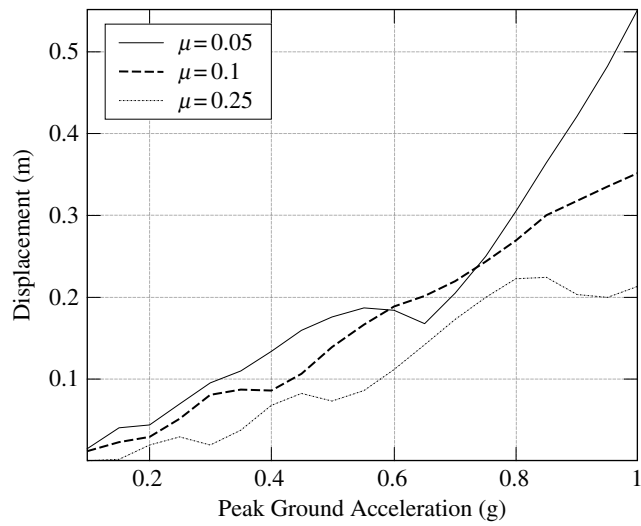


FIGURE 22.34 Maximum base displacement vs. PGA ($\omega_c = 5\omega_s$).

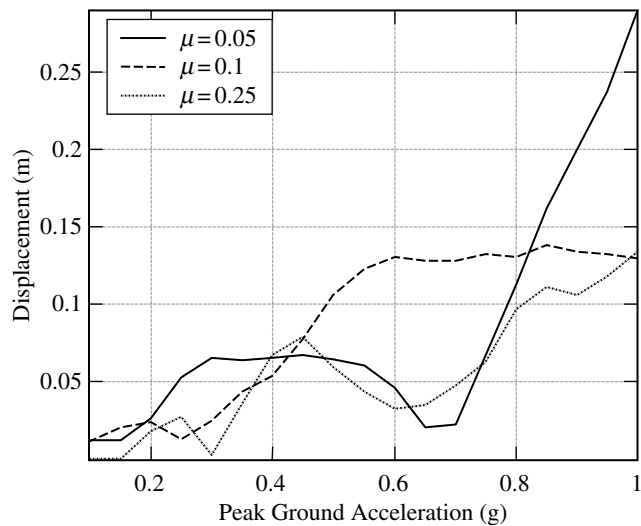


FIGURE 22.35 Residual base displacement vs. PGA ($\omega_c = 5\omega_s$).

Effect of equipment tuning. In order to study the equipment tuning effect, the maximum equipment acceleration has been plotted as a function of the equipment frequency in Figure 22.38. As can be seen, for all the values of μ considered, the equipment response is amplified when the equipment frequency moves close to the structural frequency of 1.67 Hz for the fixed-base case. Note that, since the resonant frequency of a sliding structure shifts to a higher value as the frictional coefficient decreases (see Figure 22.26), the frequency for which the most severe tuning effect occurs in Figure 22.38 also shifts from 1.67 Hz to a higher value as μ decreases. Nevertheless, it is concluded that, by choosing a smaller μ , the amplification of the equipment response due to tuning effect can be effectively suppressed.

22.4.4 Concluding Remarks

The dynamic behavior of a sliding isolated structural system with an attached equipment item was investigated in this section. A sliding isolated structure is classified as a nonlinear dynamic system, as the

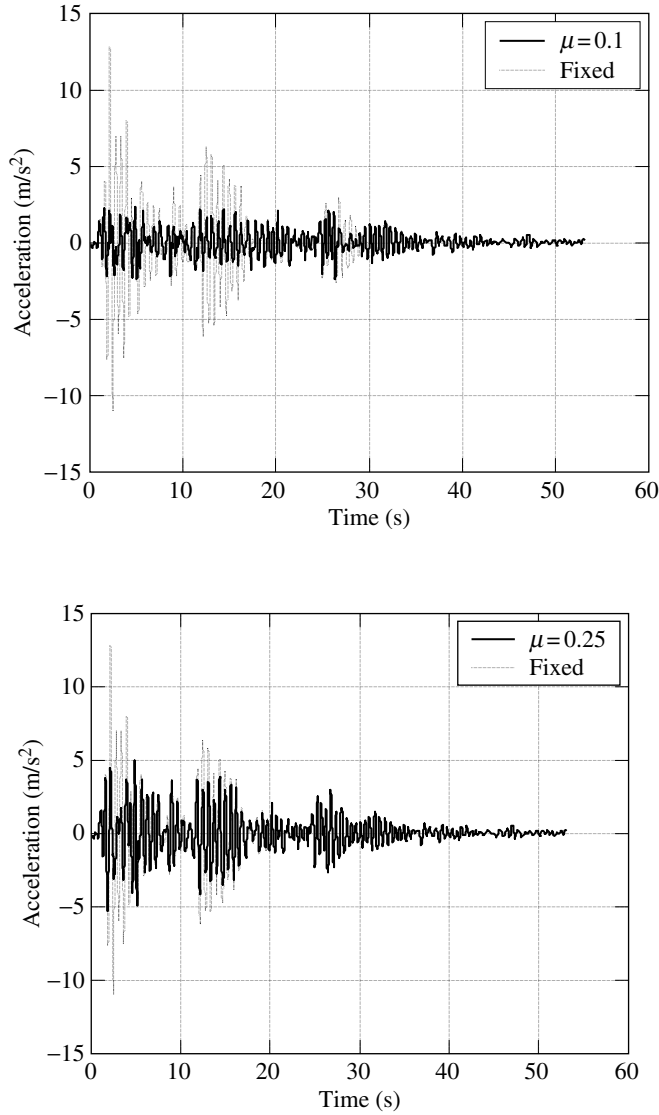


FIGURE 22.36 Comparison of equipment accelerations ($\omega_c = 5\omega_s$, PGA = 0.5g).

frictional forces induced on the sliding surface do not remain constant. To deal with such nonlinear systems, two analysis methods were formulated, the shear balance method and the fictitious spring method, both of which were presented in an incremental form that is suitable for direct implementation. Through the selection of a sliding isolated structure–equipment model, the responses of the structure and equipment subjected to both harmonic and earthquake excitations were analyzed. For the case of harmonic excitation, the results showed that the resonant responses of both the structure and attached equipment can be effectively suppressed, which remains good even when the equipment frequency is tuned to the structural frequency. For the case of seismic excitation, the results indicated that the level of reduction on the structural and equipment responses increases as the PGA level of the earthquake increases. Moreover, a sliding system with a smaller frictional coefficient has a higher isolation efficiency, at the expense of a larger base displacement.

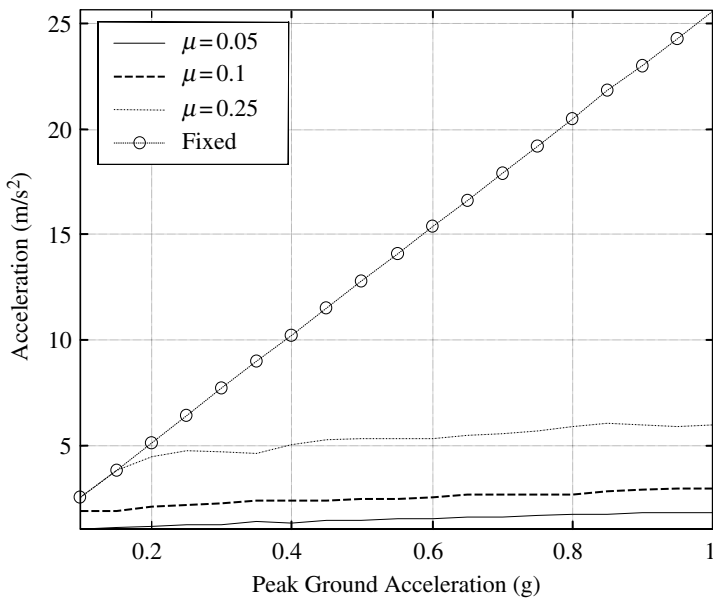


FIGURE 22.37 Maximum equipment acceleration vs. PGA ($\omega_e = 5\omega_s$).

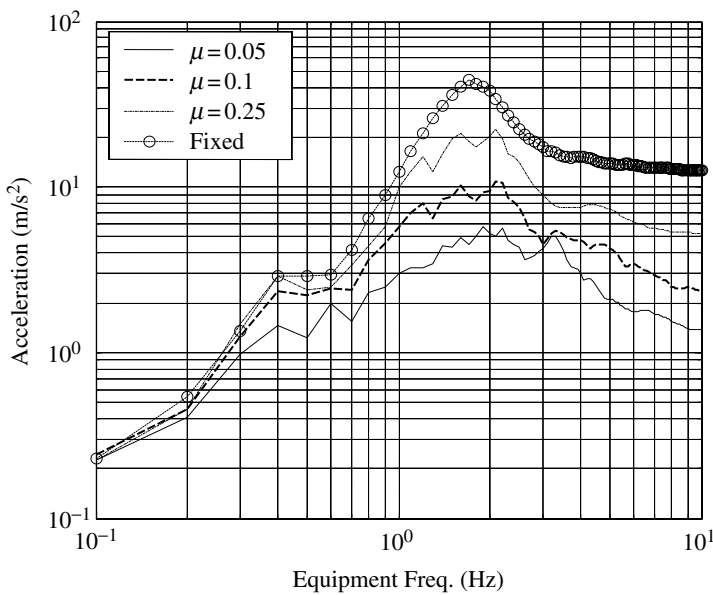


FIGURE 22.38 Maximum equipment acceleration vs. equipment frequency (PGA = 0.5g).

22.5 Sliding Isolation Systems with Resilient Mechanism

In Section 22.4, the relevant equations of analysis have been presented for a sliding isolated structural system, with no consideration made for the resilient (or recentering) mechanism. Because of this, rather large residual displacements may occur on the sliding isolation system, as have been numerically illustrated. If the concept of sliding isolators is to be applied to a real structure, it is important that the residual base displacements be controlled within certain limits, since they are not tolerable for some

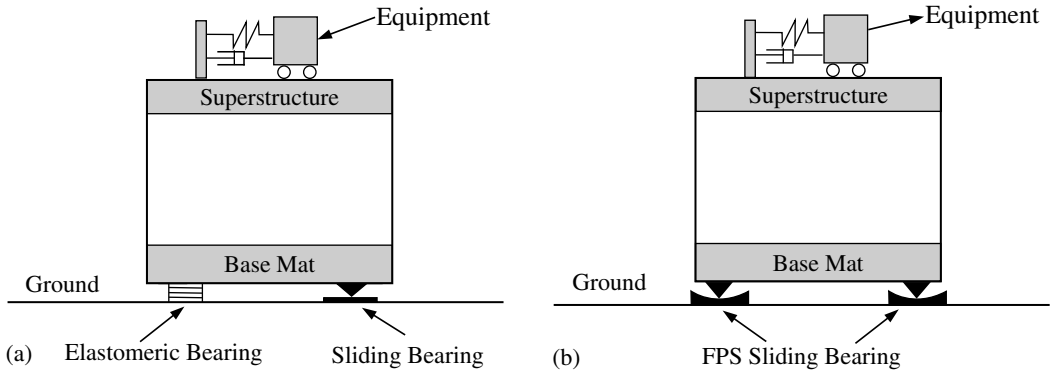


FIGURE 22.39 Schematic for a structure–equipment system isolated by a sliding bearing with resilience capability: (a) combined isolation system; (b) friction pendulum system (FPS).

engineering applications. For example, residual base displacements may distort the networking of water and power lines, change the space between the isolated structure and adjacent buildings, and widen the gaps at building entrances. Therefore, in practice, a sliding isolation system is usually enhanced through inclusion of mechanisms that can provide some resilient force. However, for certain ground motions, the added resilient force may also present some negative effects not readily transparent to structural designers, as will be illustrated in the numerical studies later on.

As shown in Figure 22.39, there are at least two ways of implementing the resilient mechanism in a sliding isolation system. Figure 22.39a shows an isolation system that combines the elastomeric bearings with sliding bearings (Chalhoub and Kelly, 1990), in which the elastomeric bearings are used to provide the resilient force, and the sliding bearings to uncouple the structural system from the ground motion. On the other hand, the resilient mechanism can also be incorporated into each single sliding bearing, in a way similar to that in the RFBI described in Section 22.2.3 (Mostaghel and Khodaverdian, 1987) or the FPS shown in Figure 22.39b (Mokha et al., 1991). The FPS isolation system has been implemented in many existing buildings and bridges. A typical FPS bearing consists a spherical sliding surface and a slider, which usually has a smooth coating of very low friction. When an FPS device is implemented under a structure, the slider will slide on the spherical surface during an earthquake, and the gravitational load of the structure, together with the curved sliding surface, will provide the resilient force for the system to return to its original position. The resilient stiffness of an FPS bearing depends on the radius of curvature of the sliding surface and the structural weight carried by the bearing.

This section is aimed at investigating the behavior of a structure–equipment system isolated by a sliding system with resilient device. For convenience of discussion, a system with resilient device will be referred to as the *resilient sliding isolation* (RSI), and a sliding system without resilient device, as the one studied previously, as the *pure sliding isolation* (PSI).

22.5.1 Mathematical Modeling and Formulation

Both the RSI systems shown in Figure 22.39 can be represented by the mathematical model given in Figure 22.40, for which the symbols used have been defined in Table 22.1. The RSI model shown in Figure 22.40 differs from the PSI model shown Figure 22.16 in that a linear spring of stiffness, k_b , is added to simulate the resilient force of the isolator. Obviously, an RSI model can be considered as the composition of a friction element and a spring element in parallel. Owing to addition of resilient stiffness, the number of vibration frequencies of the system is increased by one. The newly introduced frequency, which depends on the resilient stiffness, is called the *isolation frequency*, which can be approximated by

$$\omega_b = \sqrt{k_b/(W/g)} \quad (22.61)$$

where W is the total weight of the isolated structure–equipment system. The isolation frequency commonly used in design is between 0.33 and 0.5 Hz, which implies a period of 2 to 3 sec (Naeim and Kelly, 1999).

For the type of combined sliding system shown in Figure 22.39(a), the actual value of resilient stiffness, k_b , is decided by the total horizontal stiffness of the elastomeric bearings implemented. On the other hand, for the FPS shown in Figure 22.39(b), the resilient stiffness, k_b , is approximated by the following equation for small isolator displacements:

$$k_b = \frac{W}{R} \quad (22.62)$$

where R denotes the radius of curvature of the sliding surface. By substituting Equation 22.62 into Equation 22.61, one can verify that the isolation period of an FPS is equal to the oscillation period of a pendulum; that is

$$T_b = \frac{2\pi}{\omega_b} = \frac{2\pi}{\sqrt{k_b/(W/g)}} = 2\pi\sqrt{R/g} \quad (22.63)$$

When the sliding isolated system of Figure 22.40 is excited by a ground motion, its equation of motion may be written in exactly the same form as that of Equation 22.27; that is

$$\mathbf{M}\ddot{\mathbf{x}}(t) + \mathbf{C}\dot{\mathbf{x}}(t) + \mathbf{K}\mathbf{x}(t) = -\mathbf{M}\mathbf{L}_1\ddot{x}_g(t) + \mathbf{L}_2f(t) \quad (22.64)$$

All the variables used in the preceding equation are the same as those defined in Equation 22.28 to Equation 22.30, except that the stiffness matrix, \mathbf{K} , should be modified as

$$\mathbf{K} = \begin{bmatrix} k_e & -k_e & 0 \\ -k_e & k_e + k_s & -k_s \\ 0 & -k_s & k_s + k_b \end{bmatrix} \quad (22.65)$$

Note that, in Equation 22.64, the frictional force, $f(t)$, which does not remain constant, is placed on the right-hand side, while the resilient stiffness, k_b , which remains constant, is absorbed by the stiffness matrix, \mathbf{K} , as in Equation 22.65. However, if the total shear force, $s(t)$ of the isolation system is of interest, it should be computed as the summation of the frictional force and resilient force (see Figure 22.40); that is

$$s(t) = k_b x_b(t) + f(t) \quad (22.66)$$

The equation of motion as given in Equation 22.64 can be recast in the following form of the first-order state-space equation:

$$\dot{\mathbf{z}}(t) = \mathbf{A}\mathbf{z}(t) + \mathbf{E}\ddot{x}_g(t) + \mathbf{B}f(t) \quad (22.67)$$

The definitions of the matrices $\mathbf{z}(t)$, \mathbf{E} , \mathbf{A} , and \mathbf{B} are the same as those defined in Equation 22.32 and Equation 22.33, except that the system matrix, \mathbf{A} , should be modified to account for the addition of the resilient stiffness k_b in the stiffness matrix, \mathbf{K} .

22.5.2 Methods for Numerical Analysis

If one compares the equation of motion for the RSI system in Equation 22.67 with that for the PSI system in Equation 22.31, one will conclude that the only source of nonlinearity in both equations comes from

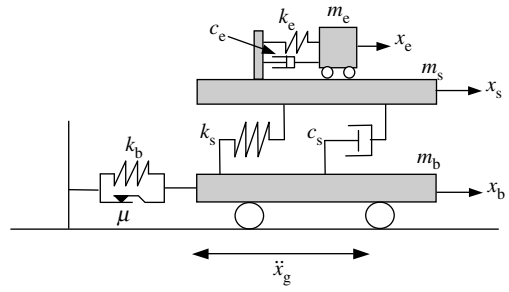


FIGURE 22.40 Model for a structure–equipment system isolated by a sliding bearing with resilience capability.

the same term, namely, the frictional force, $f(t)$. As a result, the two methods of solution mentioned in Section 22.4.2, the shear balance method (Wang et al., 1998) and fictitious spring method (Yang et al., 1990), remain valid for the analysis of the RSI systems, with no modification required. Moreover, owing to inclusion of the resilient stiffness, k_b , in the structural stiffness matrix, \mathbf{K} , the system matrix, \mathbf{A} , becomes nonsingular and invertible. This introduces some advantage in computation of relevant coefficient matrices, including the \mathbf{B}_0 and \mathbf{B}_1 matrices in Equation 22.38a and Equation 22.38b. In Section 22.5.3, the shear balance method will be employed to simulate the response of an RSI system.

22.5.3 Simulation Results for Sliding Isolation with Resilient Mechanism

22.5.3.1 Numerical Model and Ground Excitations

In this section, the dynamic behavior of a sliding system represented by the model shown in Figure 22.40 will be investigated. The data adopted in the analysis for the equipment, structure, and the isolator have been listed in Table 22.4. To facilitate comparison, some of the data are selected to be the same as those in Table 22.3. In particular, the isolation frequency chosen is $\omega_b = 0.4$ Hz, falling in the common range of 0.33 to 0.5 Hz. Again, two types of ground excitations are considered, namely, the harmonic and earthquake excitations. For the harmonic excitation, a waveform of ground acceleration identical to the one given in Equation 22.60 is used. And for the earthquake excitation, the 1940 El Centro earthquake with different levels of PGA will be used, of which the acceleration waveform has been given in Figure 22.10. The harmonic excitation is adopted mainly for studying the frequency response of the sliding isolated system, while the earthquake excitation is for studying the effect of earthquake intensity. The dynamic responses computed for the RSI system, including the structure and equipment, will be presented, with emphasis placed on comparison with the PSI system of the same parameters. Similar to what was done in Section 22.4.3, the symbol μ will be used to denote the frictional coefficient of the sliding isolation system in all figures, and the word “fixed” denotes the fixed-base structure.

22.5.3.2 Harmonic Response of Structure

Time history. Consider an RSI system subjected to a harmonic excitation of $\omega_g = 1$ Hz. The base displacement and structural acceleration of the RSI system have been plotted in Figure 22.41 and Figure 22.42, respectively. Clearly, both the base displacement and structural acceleration of the RSI system reach their steady-state harmonic responses in the first few cycles. Moreover, a smaller sliding frictional coefficient ($\mu = 0.1$) is more effective for suppressing the structural acceleration, as indicated by Figure 22.42. However, this is achieved only at the expense of a larger base displacement, as indicated by Figure 22.41. By comparing the result for the RSI system in Figure 22.41 with those for the PSI system in Figure 22.23, the effect of resilient mechanism in eliminating the permanent base displacement for the case with a small frictional coefficient of $\mu = 0.1$ can be clearly appreciated. In spite of the large difference in base displacement, the structural accelerations for the RSI and PSI systems shown in Figure 22.42 and Figure 22.24, respectively, appear to be quite similar, when interpreted in terms of the waveform and response amplitude. This implies that, for the harmonic excitation considered, the resilient mechanism in RSI has little influence on the isolation effectiveness.

Hysteretic behavior. In Figure 22.43, the hysteresis loops for RSI systems with $\mu = 0.1$ and 0.25 subjected to a harmonic excitation of $\omega_g = 1$ Hz have been plotted, in which the vertical axis represents

TABLE 22.4 System Parameters Used in Simulation (Section 22.5.3)

Equipment		Superstructure		Isolation System	
Parameter	Value	Parameter	Value	Parameter	Value
Mass m_e	3 t ($= m_s/100$)	Mass m_s	300 t	Mass m_b	100 t ($= m_s/3$)
Frequency ω_e	$5\omega_s$ or a variable	Frequency ω_s	1.67 Hz	Frictional coefficient μ	0.05, 0.1, 0.25
Damping ratio ζ_e	5%	Damping ratio ζ_s	5%	Isolation frequency ω_b	0.4 Hz

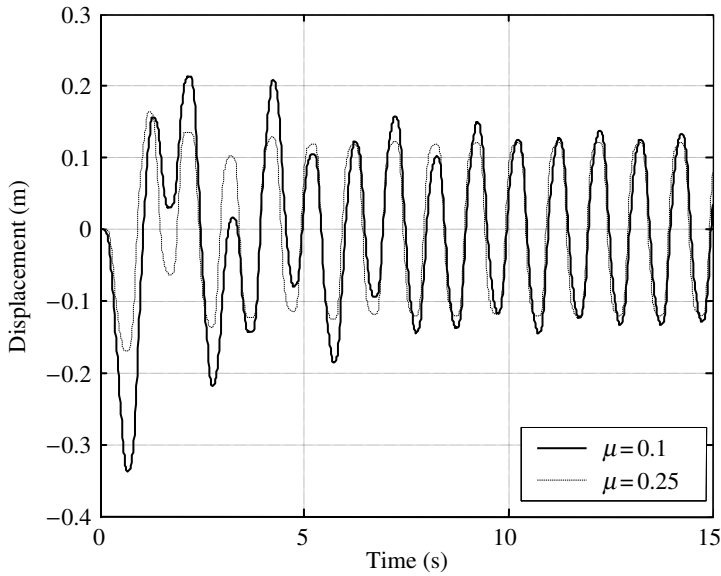


FIGURE 22.41 Comparison of base displacements ($\omega_g = 1$ Hz, $\omega_c = 5\omega_s$).

the total shear, $s(t)$, of the bearing computed from Equation 22.66. It is interesting to note that, for an RSI system, the hysteresis loop is a parallelogram, of which the slope of the inclined upper and lower sides exactly represents the total resilient stiffness, k_b , and the height and width, respectively, are decided by the maximum frictional force and maximum base displacement. As the frictional coefficient decreases, the height of the parallelogram decreases, but the width increases. The total area of the hysteresis loop represents the portion of energy dissipated by the RSI system. Noteworthy is the fact that, when the resilient stiffness, k_b , reduces to zero, the hysteresis parallelogram reduces to a square as well, identical to the one shown in Figure 22.25 for the PSI system.

Frequency responses. The maximum accelerations of the steady-state response of the structure for four different frictional coefficients, that is, $\mu = 0.05, 0.1, 0.25$ and ∞ (fixed-base), have been plotted in Figure 22.44. From this figure, the following observations can be made: (1) Compared with the fixed-base case, the resonant peak occurring around the structural frequency, ω_s , of 1.67 Hz was effectively suppressed by the RSI system, but a resonance of higher amplitude was induced in the lower frequency range (with frequencies lower than 0.6 Hz for the case studied). A further investigation reveals that the newly induced resonance is associated with the isolation frequency, ω_b , of 0.4 Hz. Such an observation remains valid for all values of frictional coefficients, μ . (2) The use of a lower frictional coefficient, μ , will result in a smaller response in the high-frequency range for the RSI system, for example, with frequencies higher than 0.6 Hz, but a larger response for the low-frequency range. (3) Although both the RSI and PSI systems can effectively remove the resonant peak around the structural frequency of 1.67 Hz, the RSI system has the side effect of creating a low-frequency resonant peak at the isolation frequency, ω_b . This implies that the RSI system is more sensitive to the excitation frequency.

The frequency responses of the maximum base displacement for the RSI system with various frictional coefficients have been plotted in Figure 22.45. When compared with the results for the PSI system in Figure 22.27, it is clear that the resilient mechanism of the RSI system considerably reduces the base displacement in the nonresonant excitation range, but it also amplifies the base displacement in the region when the excitation frequency is close to the isolation frequency, ω_b . From Figure 22.44 and Figure 22.45, we observe that both the structural acceleration and base displacement of an RSI system may resonate at the isolation frequency, which is usually designed to be less than 0.5 Hz. This implies that an RSI system may be ineffective or unsafe for a ground motion with enriched low-frequency

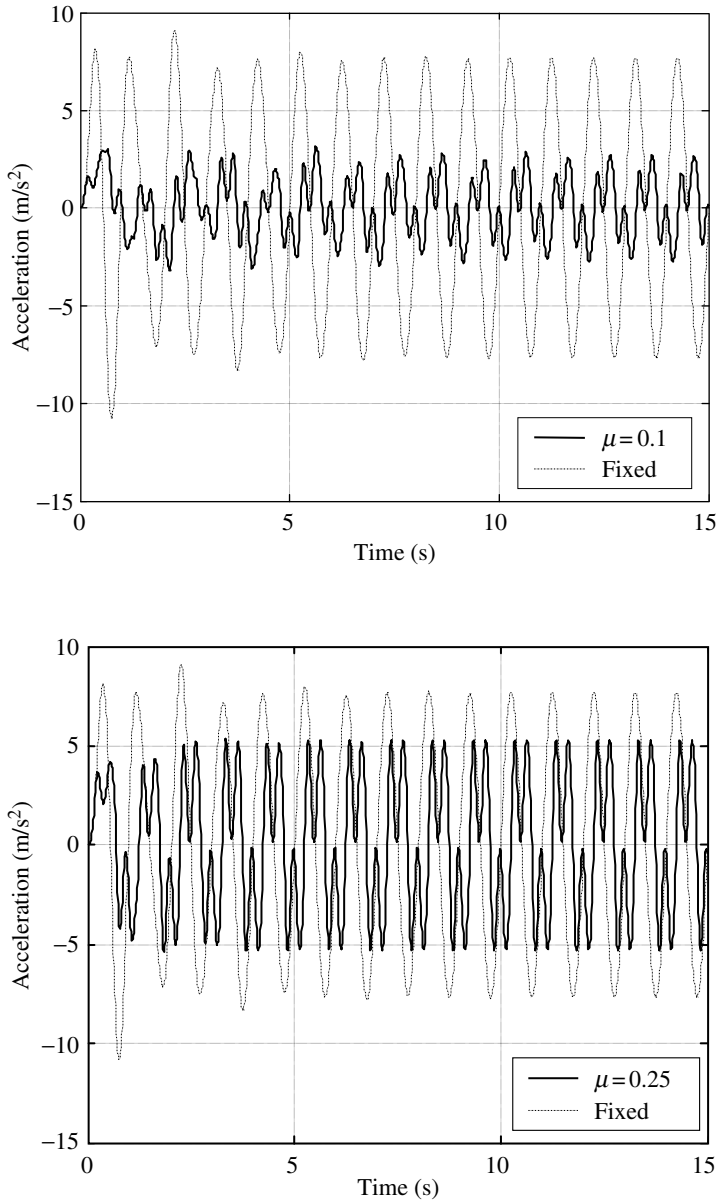


FIGURE 22.42 Comparison of structural accelerations ($\omega_g = 1$ Hz, $\omega_e = 5\omega_g$).

(long-period) vibrations, such as the case with a near-fault earthquake containing a long-period, pulse-like waveform (Jangid and Kelly, 2001; Lu et al., 2003). Structural designers should be aware of such a side effect when designing an RSI system.

22.5.3.3 Harmonic Response of Equipment

Time history. Consider an equipment item with a frequency of $\omega_e = 5\omega_g$ ($= 8.34$ Hz), attached to the RSI system. The harmonic acceleration responses of the equipment for the case with $\mu = 0.1$ and 0.25 have been plotted in Figure 22.46a and b, respectively, together with those for the fixed-base case. As can be seen, the equipment acceleration has been effectively suppressed by the RSI with the smaller frictional coefficient ($\mu = 0.1$). Moreover, the acceleration waveforms shown in Figure 22.46 are similar to those of

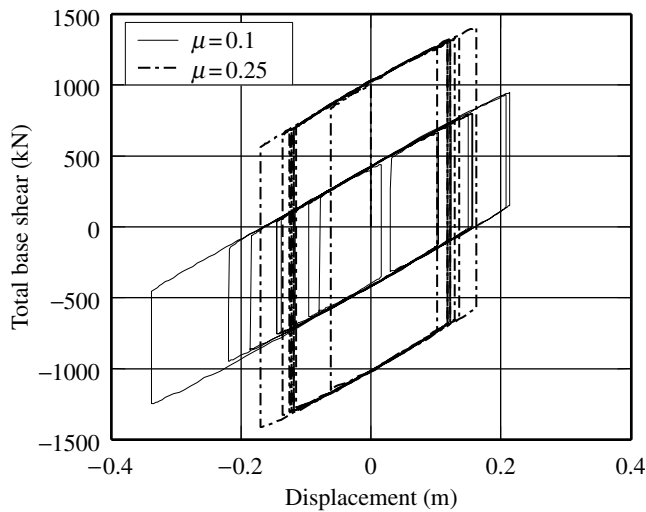


FIGURE 22.43 Hysteresis loops of a sliding bearing with resilience capability ($\omega_g = 1$ Hz, $\omega_e = 5\omega_s$).

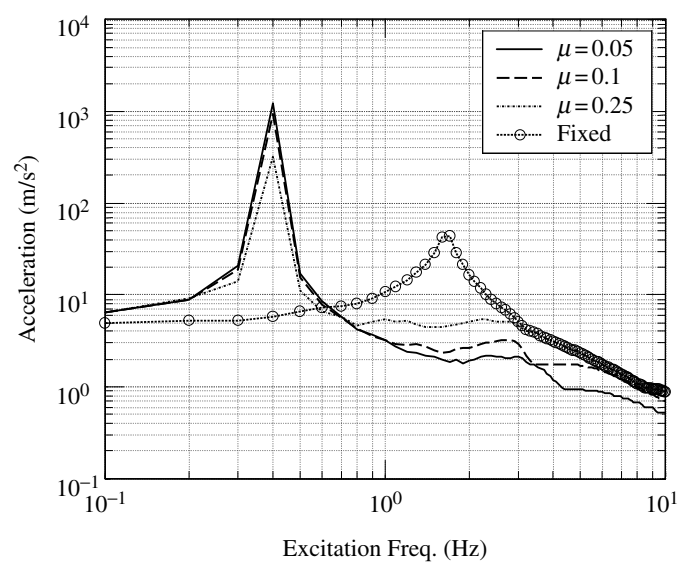


FIGURE 22.44 Maximum structural acceleration vs. ground excitation frequency ($\omega_e = 5\omega_s$).

the PSI system shown in Figure 22.28. This implies that for the given excitation, the behavior of the equipment was not altered by introduction of the resilient mechanism in the RSI system.

Frequency responses. Figure 22.47 shows the acceleration frequency response curve of the attached equipment with a frequency of $\omega_e = 5\omega_s$ (8.34 Hz). A comparison of Figure 22.47 with Figure 22.44 indicates that the frequency responses of the equipment and primary structure are generally similar, except that a resonant peak associated with the equipment frequency around 8.34 Hz appears in Figure 22.47. Owing to such a similarity, the observations made previously for Figure 22.44 are applicable to Figure 22.47 for the attached equipment.

Effect of equipment tuning. Figure 22.48 shows the frequency response of the attached equipment for the case when the equipment frequency is tuned to the structural frequency, that is, with $\omega_e = \omega_s$. Similar to

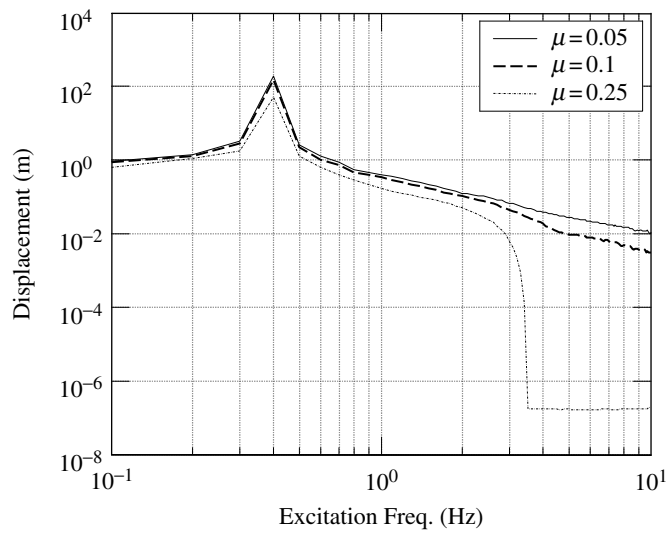


FIGURE 22.45 Maximum base displacement vs. ground excitation frequency ($\omega_e = 5\omega_s$).

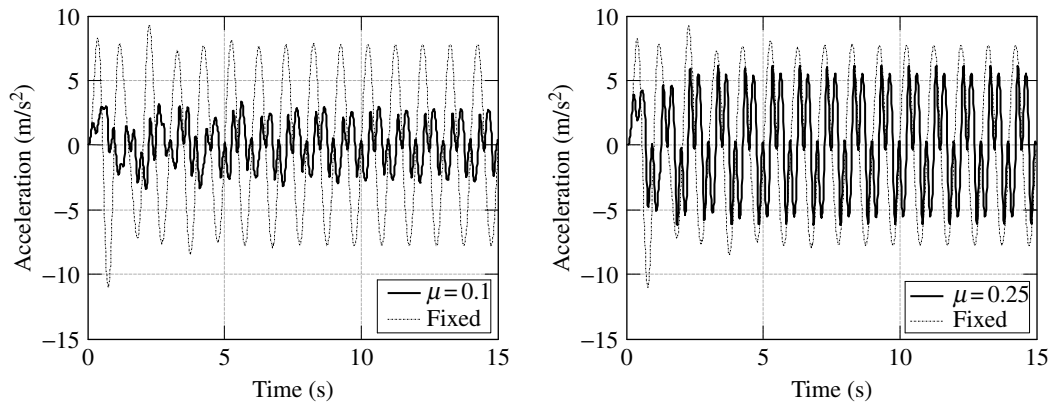


FIGURE 22.46 Comparison of equipment accelerations ($\omega_b = 1$ Hz, $\omega_e = 5\omega_s$).

the structural frequency response shown in Figure 22.44, the equipment attached to the RSI system also resonates at the isolation frequency ω_b of 0.4 Hz. Such a resonance does not occur for the equipment attached to the PSI system (see Figure 22.30). Through comparison of the tuned case in Figure 22.48 with the detuned case in Figure 22.47, the following observations can be made: (1) Even when the equipment tuning occurs, an RSI system mitigates the equipment's resonant peak associated with the structural frequency at 1.67 Hz, although the effectiveness of isolation has been reduced. (2) The tuning effect has no influence on the resonant response associated with the isolation frequency of 0.4 Hz.

22.5.3.4 Earthquake Response of Structure

Time history. For an RSI system subjected to the El Centro earthquake with $\text{PGA} = 0.5g$, the structural acceleration and base displacement have been shown in Figure 22.49 and Equation 22.50, respectively. By comparing Figure 22.49 with Figure 22.31 for the corresponding PSI system, one observes that the structural accelerations of the RSI and PSI systems are generally similar, in terms of the response waveform and the response magnitude. Both systems reduce the maximum structural acceleration quite effectively, for example, by about 80% for $\mu = 0.1$. However, significant difference does exist between the

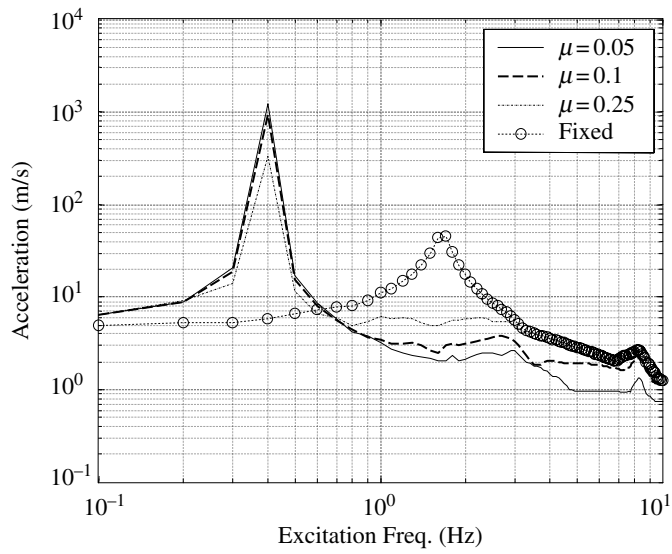


FIGURE 22.47 Maximum equipment acceleration vs. ground excitation frequency ($\omega_e = 5\omega_s$).

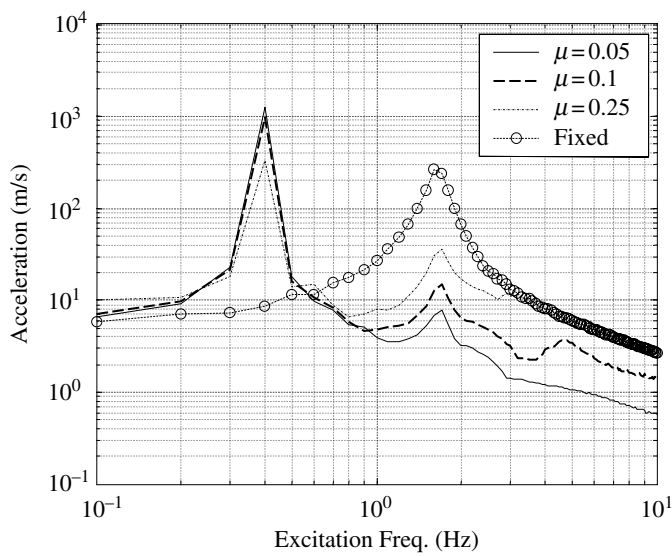


FIGURE 22.48 Maximum equipment acceleration vs. ground excitation frequency under tuning condition ($\omega_e = 5\omega_s$).

base displacements for the RSI system in [Figure 22.50](#) and those for the PSI system in [Figure 22.32](#). For example, for $\mu = 0.1$, the maximum base displacement experienced by the RSI system has been reduced by about 30%, while the residual base displacement has been reduced by about 70%, as can be seen by comparing [Figure 22.50](#) with [Figure 22.32](#). This implies that the resilient mechanism of the RSI system plays an important role in reducing the maximum and residual base displacements, especially the latter.

In spite of the observations made above, one should not forget that the frequency content of one earthquake may be different from another. As was demonstrated in [Figure 22.44](#) and [Figure 22.45](#), an RSI system is generally sensitive to low-frequency excitations and may resonate at the isolation frequency.

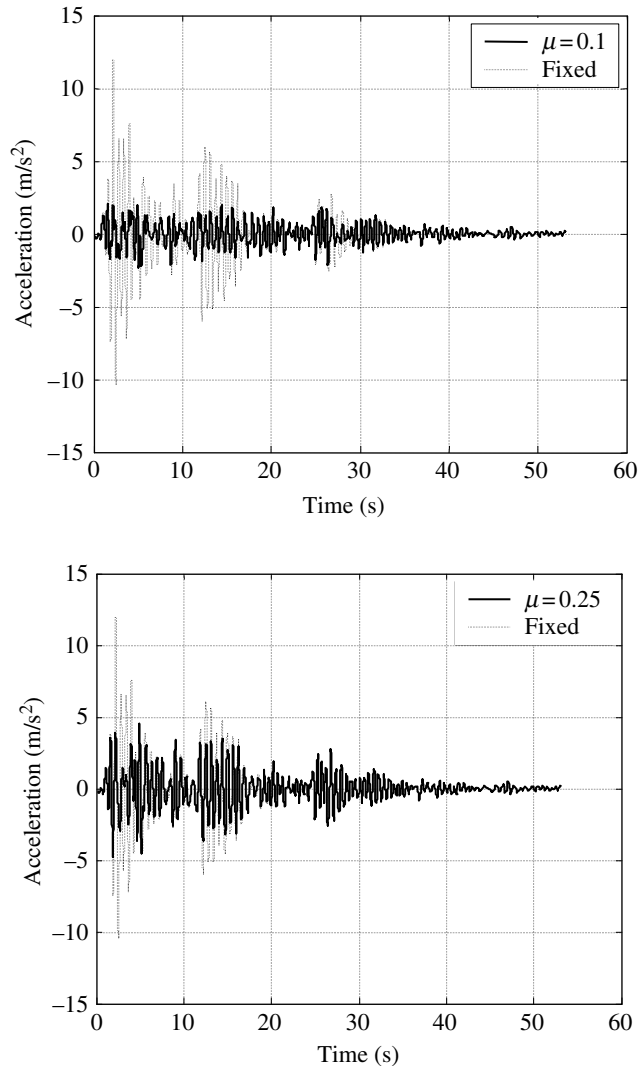


FIGURE 22.49 Comparison of structural accelerations ($\omega_c = 5\omega_s$, PGA = 0.5g).

Therefore, if the RSI system is subjected to an earthquake containing more low-frequency components, unlike the El Centro earthquake, it is likely that the maximum structural responses induced exceed those of the PSI system.

Effect of earthquake intensity. The maximum structural acceleration and base displacement of the RSI system have been plotted with respect to the PGA in Figure 22.51 and Figure 22.52, respectively. These figures indicate that as the earthquake intensity increases from 0.1 to 1g, the structural acceleration is reduced by an increasing amount by the RSI system, while the maximum base displacement also increases. By comparing Figure 22.51 and Figure 22.52 with Figure 22.33 and Figure 22.34 for the PSI system, one observes that both the RSI and PSI systems perform equally well for the El Centro earthquake, although the PSI system induces a slightly larger base displacement. On the other hand, unlike the response for the PSI system, the use of a smaller frictional coefficient for the RSI system does not always lead to a lower structural acceleration, as can be verified by comparing the responses for $\mu = 0.1$ and 0.05 with a PGA greater than 0.8g in Figure 22.33 and Figure 22.51. This can be attributed to the large resilient force induced by the large base displacement under higher PGA levels.

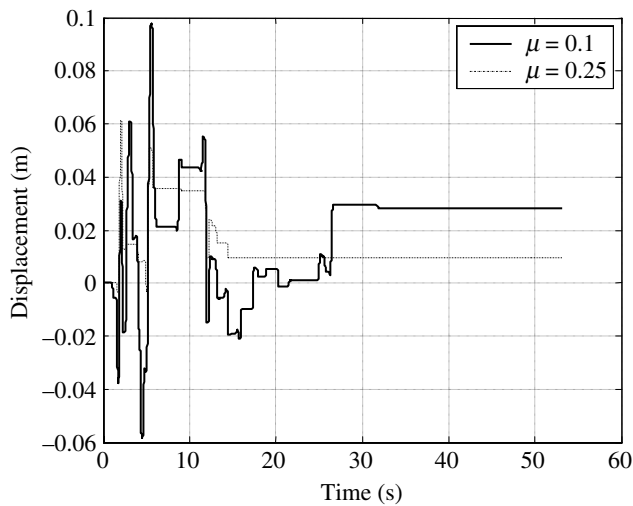


FIGURE 22.50 Comparison of base displacements ($\omega_e = 5\omega_s$, $\text{PGA} = 0.5g$).

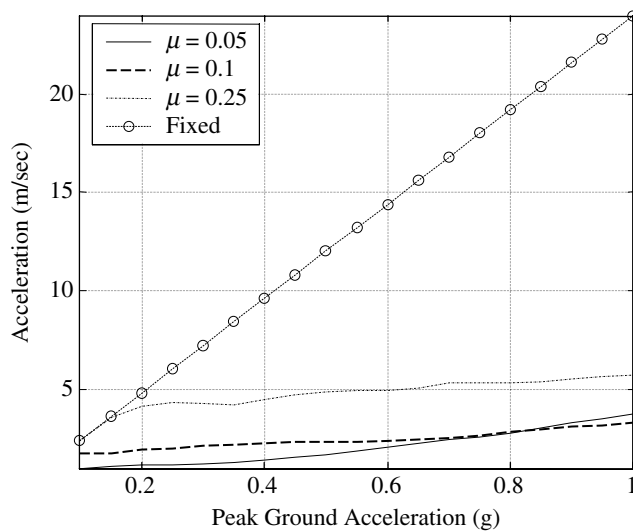


FIGURE 22.51 Maximum structural acceleration vs. PGA ($\omega_e = 5\omega_s$).

Residual base displacement. Figure 22.53 shows the residual base displacement of the RSI system vs. the PGA of the earthquake. For a given μ , it is difficult to establish a relation between the earthquake intensity and residual displacement, because a larger PGA may result in a smaller residual base displacement in some cases. However, if one takes the average of residual displacements over the PGA range from 0.1 to 1g, the following can be computed: $x_{\text{res}} = 0.0065, 0.011$, and 0.014 m for $\mu = 0.05, 0.1$, and 0.25 , respectively. These values indicate that a smaller frictional coefficient leads to a smaller residual base displacement, which can be attributed to the fact that for a SRI system with a smaller coefficient of friction, it is easier for the resilient mechanism to return the structure to its initial position after an earthquake. On the other hand, a comparison of Figure 22.53 with Figure 22.35 for the PSI system indicates that for the same value of μ , the residual displacement was reduced substantially by the RSI system. This is certainly an advantage offered by the resilient mechanism of the RSI system.

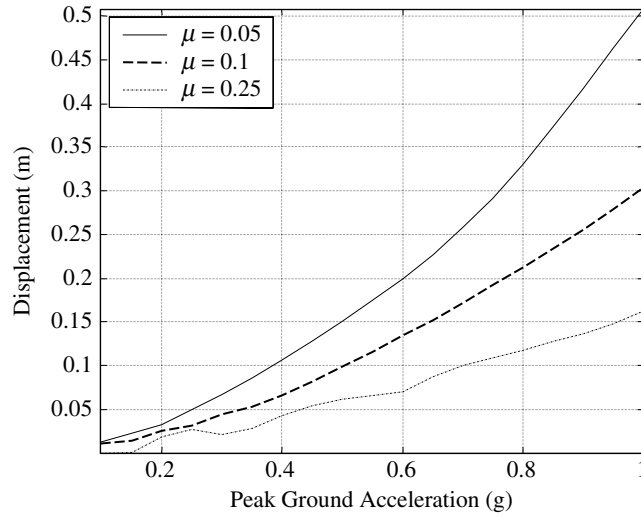


FIGURE 22.52 Maximum base displacement vs. PGA ($\omega_e = 5\omega_s$).

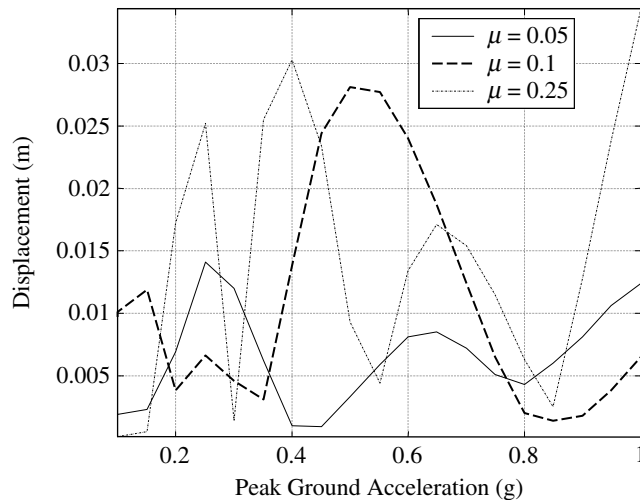


FIGURE 22.53 Residual base displacement vs. PGA ($\omega_e = 5\omega_s$).

22.5.3.5 Earthquake Response of Equipment

Time history. Let us consider an equipment item of natural frequency equal to five times the structural frequency, that is, $\omega_e = 5\omega_s$ ($= 8.34$ Hz). The acceleration responses of the equipment mounted on the RSI system that were subjected to the El Centro earthquake with a PGA of $0.5g$ for $\mu = 0.1$ and 0.25 have been plotted in Figure 22.54a and b, respectively, along with those for the fixed-base cases. As can be seen, the main-shock response of the equipment appearing during the first 10 sec for the fixed-base system was effectively suppressed by the RSI system with $\mu = 0.1$ or 0.25 . The level of reduction is more pronounced for the case with a smaller frictional coefficient, that is, with $\mu = 0.1$. By comparing Figure 22.54 with Figure 22.36 for the PSI system, one concludes that the effect of the resilient mechanism of the RSI system on the equipment response is insignificant for the earthquake and equipment frequency considered.

Effect of earthquake intensity. Figure 22.55 shows the maximum equipment acceleration vs. the PGA of the earthquake. This figure illustrates that for all values of the frictional coefficient, μ , considered, an

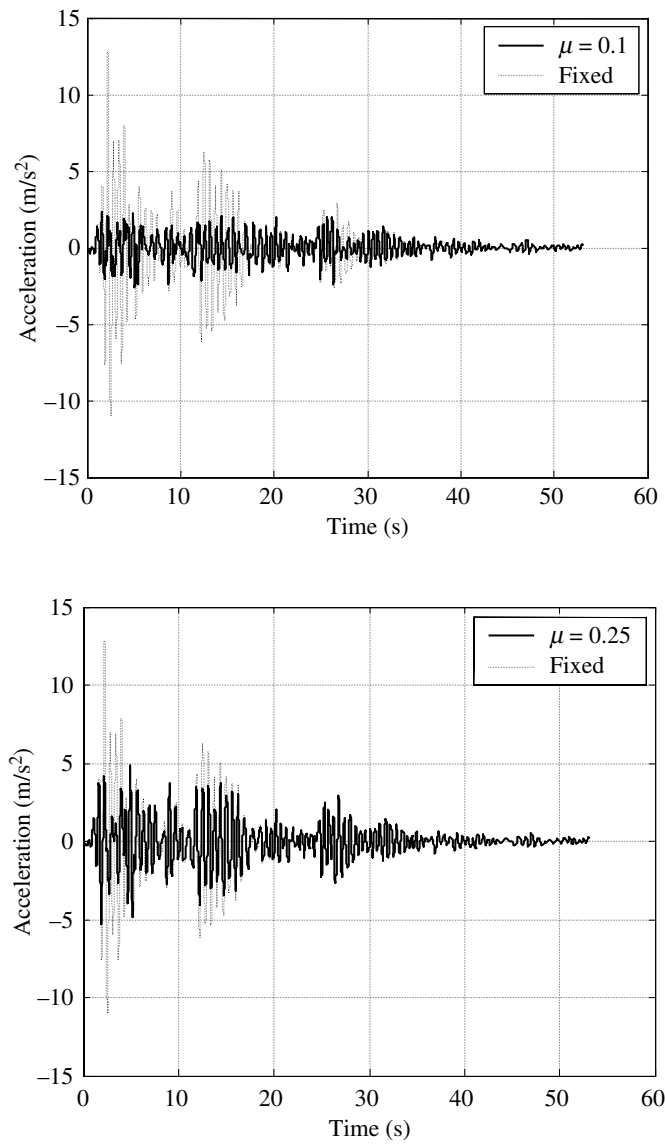


FIGURE 22.54 Comparison of equipment accelerations ($\omega_e = 5\omega_s$, PGA = 0.5g).

increasing amount of reduction can be achieved by the RSI system as the earthquake intensity increases from 0.1 to 1g. Because relatively stiff equipment (i.e., with $\omega_e = 5\omega_s$) was assumed in the simulation, the curves shown in Figure 22.55 are similar to those of Figure 22.51 for the primary structure. Therefore, the observations made previously for Figure 22.51 apply here. The maximum response of equipment items with other natural frequencies will be discussed below. Moreover, a comparison of Figure 22.55 with Figure 22.37 (for the PSI system) reveals that the resilient mechanism can have some minor effect on the equipment response, but only when a smaller frictional coefficient (i.e., $\mu = 0.05$ or 0.1) is used and when the PGA level is high.

Effect of equipment tuning. In order to study the effect of equipment tuning, the maximum acceleration of the equipment has been plotted in Figure 22.56 for equipment frequencies ranging from 0.1 to 10 Hz.

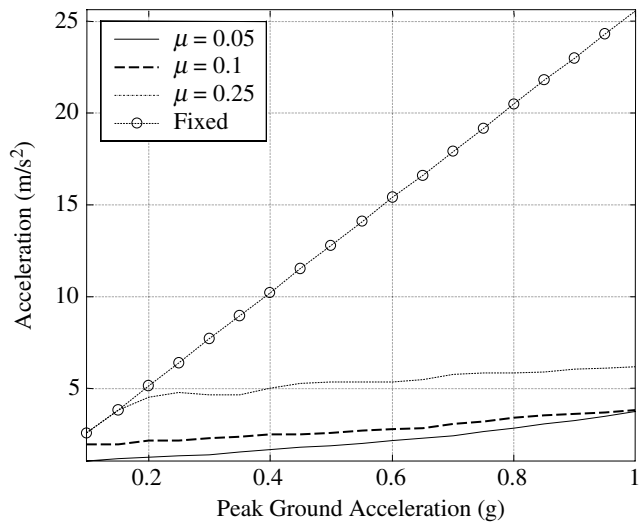


FIGURE 22.55 Maximum equipment acceleration vs. PGA ($\omega_e = 5\omega_s$).

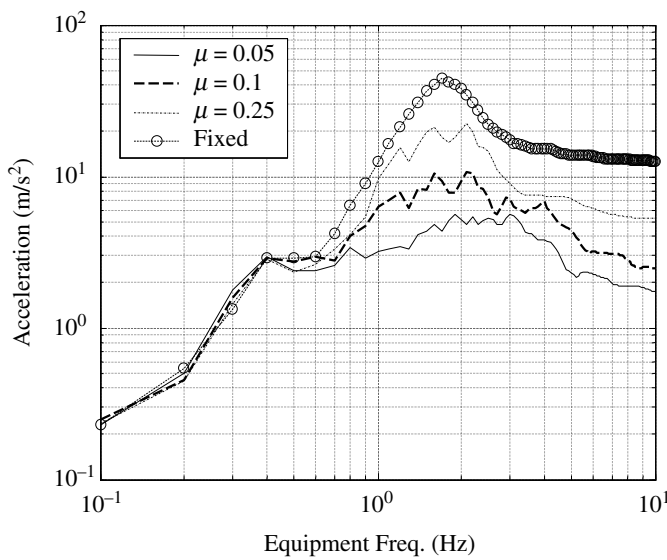


FIGURE 22.56 Maximum equipment acceleration vs. equipment frequency (PGA = 0.5g).

As can be seen, for all the values of μ considered, the equipment response is amplified when the equipment frequency is close to the structural frequency, ω_s , of 1.67 Hz, which means that the tuning effect tends to enlarge the equipment response. However, the use of a smaller μ can help in reducing the amplification of the equipment response resulting from the tuning effect. Finally, a comparison between Figure 22.56 and Figure 22.38 (for the PSI system) shows that the two diagrams are quite similar for an equipment item with a frequency higher than 1 Hz, but are different for that with a lower frequency. This implies that for the earthquake considered, the resilient mechanism of the RSI system has little effect on the response of the equipment with a higher stiffness.

22.5.4 Concluding Remarks

In this section, the behavior of a structure–equipment system isolated by an RSI system under both the harmonic and earthquake excitations has been investigated. Both the responses of the structure and equipment were studied, with special attention given to the effect of the resilient mechanism that characterizes an RSI system. The numerical results demonstrated that when subjected to a harmonic excitation, an RSI system is able to effectively suppress the resonant peaks associated with the structural frequency for both the structure and equipment, but it may also induce some resonant response near the isolation frequency due to the presence of resilient stiffness. Therefore, an RSI system is more sensitive to the frequency content of the ground excitation than a PSI system, especially to excitations of low-frequency components. As for the earthquake responses, the numerical results showed that the resilient mechanism of an RSI system can considerably reduce the residual base displacement. The resilient mechanism has a minor effect on the acceleration response of the structure and equipment, as long as no resonance is induced by the RSI system at the isolation frequency. By and large, both the RSI and PSI systems can be used as effective devices for reducing the acceleration responses of a structure and equipment.

22.6 Issues Related to Seismic Isolation Design

22.6.1 Design Methods

Having been developing for over 30 years, the technology of seismic isolation has matured. Many earthquake-prone countries, including the U.S., Japan, New Zealand, Taiwan, China, and European countries, have developed their own design codes, regulations, or guidelines (Fujita, 1998; Kelly, 1998; Martelli and Forni, 1998). Although most of the codes were developed based on the theory of structural dynamics, the design details outlined in the codes vary from one country to another. While a comprehensive explanation of the various design codes is not the purpose of this section, a brief overview of the concept underlying the design codes will be given. For more details, interested readers should refer to each code or to the books by Naeim and Kelly (1999) or Skinner et al. (1993). The design concept introduced herein is based on the series of Uniform Building Code (UBC, 1994, 1997).

Given the fact that base isolation devices are diverse, most design codes or regulations have been written in such a way as not to be specific with respect to the isolation systems. For instance, in the UBC (1997), no particular isolation system is identified as being acceptable; rather, it requires that every isolation system is stable for required displacement, has properties that do not degrade under repeated cyclic loadings, and provides increasing resistance with increasing displacement.

The design methods for base isolation can be classified as static analysis and dynamic analysis. The static analysis is applicable for stiff and regular buildings (in vertical and horizontal directions) that are constructed on soil of a relatively stiff condition. On the other hand, dynamic analysis is usually required for isolation systems with an irregular or long-period superstructure, or constructed on relatively soft soils. For a sophisticated design case, static analysis may be used in the preliminary design phase in order to draft or initiate the isolation design parameters, while dynamic analysis is employed in the final design phase for tuning or finalizing the design details of the isolation system. For simple design cases, static analysis alone is considered sufficient.

22.6.2 Static Analysis

For static analysis, a number of formulas have been specified in the design codes, so that engineers can easily calculate the following design parameters (shown in the design sequence): maximum isolator displacement, D ; isolator total shear, V_b ; total base shear, V_s , of superstructure; and seismic load, F_i , applied on each floor. These formulas were usually derived based on a simplified isolation model,

assuming the isolation system can be linearized (even though most isolation systems are nonlinear) and the superstructure can be modeled as a rigid block. Such a simplified model is considered reasonable, since the displacements of an isolated structure are concentrated at the isolation level, which implies that the superstructure behaves as a rigid block. Based on such a model, only the first vibration mode with the superstructure treated as a rigid body has been considered in deriving the formulas. This explains why static analysis is suitable only for rigid and regular structures.

22.6.2.1 Computation of Maximum Isolator Displacement

An isolation design by static analysis usually starts with the calculation of the maximum isolator displacement, D , which depends on several factors:

$$D = D(Z, N, S, T_{\text{ef}}, \zeta_{\text{ef}}) \quad (22.68)$$

where Z denotes the earthquake zone factor, N the near-fault factor, S the soil condition factor, T_{ef} the effective isolation period, and ζ_{ef} the effective isolation damping. For example, in the UBC (1994), the formula derived from the constant-velocity spectra over the period range of 1.0 to 3.0 sec has been given in the following form:

$$D = \frac{0.25ZNST_{\text{ef}}}{B} \quad (22.69)$$

where B is the damping factor, given as

$$B = B(\zeta_{\text{ef}}) \approx 0.25(1 - \ln \zeta_{\text{ef}}) \quad (22.70)$$

In the above equations, the factors Z , N , and S depend on conditions of the construction site of the isolated structure; however, the factors T_{ef} and ζ_{ef} depend solely on the properties of the chosen isolation system. The factors T_{ef} and ζ_{ef} are called the “effective” period and damping of the isolation system, because they are frequently obtained by linearizing a nonlinear isolation system. The way to linearize an isolation system will be explained below, along with the formulas for computing T_{ef} and ζ_{ef} . Suppose that for a nonlinear isolation system, the force-displacement relation (hysteresis loop) obtained from a component test is shown in Figure 22.57. The effective stiffness of this isolation system can be computed by

$$K_{\text{ef}} = \frac{F^+ - F^-}{2D} \quad (22.71)$$

where F^+ and F^- , respectively, denote the largest positive and negative forces in the test. After the linearized stiffness is obtained from Equation 22.71, the corresponding effective quantities T_{ef} and ζ_{ef} can be computed from the dynamic theory for a single DoF oscillation system; that is

$$T_{\text{ef}} = 2\pi\sqrt{\frac{W}{K_{\text{ef}}g}} \quad (22.72)$$

$$\zeta_{\text{ef}} = \frac{1}{2\pi} \left(\frac{A}{K_{\text{ef}}D^2} \right) \quad (22.73)$$

where W is the structural weight, g the gravitational acceleration, and A the total area enclosed by the hysteresis loop in Figure 22.57.

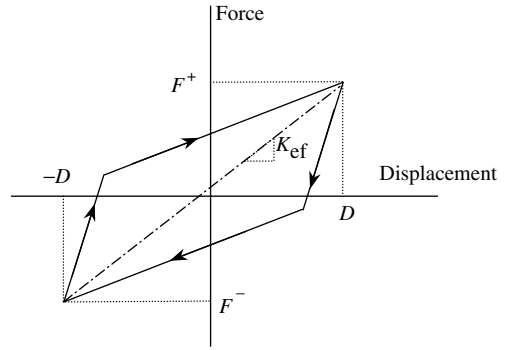


FIGURE 22.57 Typical force-displacement diagram for an isolation system.

22.6.2.2 Computation of Maximum Isolator Shear

After the maximum isolator displacement, D , is obtained, the maximum isolator shear, V_b , can be estimated by the following formula:

$$V_b = K_{ef}D \quad (22.74)$$

Obviously, the above equation represents an equivalent static force exerted on the isolation system, when the system is displaced by an amount, D . In some design codes, V_b has also been referred to as the design force beneath the isolation system.

22.6.2.3 Computation of Total Base Shear

The total base shear, V_s , of the superstructure can be given as

$$V_s = \frac{K_{ef}D}{R_1} \quad (22.75)$$

where R_1 is a reduction factor (ductility factor) to account for structural ductility, which will be developed when the structure is subjected to an earthquake with intensity above the design level. In some codes, V_s has also been referred to as the design force above the isolation system.

22.6.2.4 Computation of Shear Force for Each Floor

Having computed the above total base shear, V_s , a formula is employed to distribute this total shear to each floor of the isolated structure. For instance, in the, UBC (1997), the shear force, F_i , exerted on each floor is computed by

$$F_i = V_s \frac{h_i w_i}{\sum_{j=1}^n h_j w_j} \quad (22.76)$$

where n denotes the number of floors, w_i the weight of the i th floor, and h_i the height of the i th floor above the isolation level. Note that the sum of F_i ($i = 1$ to n) must be equal to V_s .

The general procedure for static analysis was illustrated in [Figure 22.58](#). Once the design parameters, D , V_b , V_s , and F_i , are all determined according to the code, they can be used in the detailed design of structural elements as well as of isolator elements. Nevertheless, in most applications, because the test data of the isolation system may not be available in the beginning of design, the values of K_{ef} , T_{ef} , and ζ_{ef} , which are required in computing D , are not known to the designer. If this is the case, the design can begin with assumed values of K_{ef} , T_{ef} , and ζ_{ef} , which may be obtained from experience or previous test data on similar isolators. After the preliminary design is completed, prototype isolators will be fabricated and tested. The actual values of K_{ef} , T_{ef} , and ζ_{ef} , obtained from the tests will be used in the aforementioned code formulas to update the design parameters D , V_b , V_s . Moreover, one observes from Equation 22.71 that the linearized isolator stiffness, K_{ef} , is a function of the design parameter, D , itself, and so are T_{ef} , and ζ_{ef} , obtained from Equation 22.72 and 22.73. In order to obtain K_{ef} , as well as T_{ef} , and ζ_{ef} , an initial guess of D is required at the beginning of design. As a result, the design procedure may have to be repeated iteratively until the difference between the final value of D and the value D_0 computed in the last iteration is less than a preset tolerance. Such an iterative process is illustrated in [Figure 22.58](#).

22.6.3 Dynamic Analysis

The dynamic analysis may be carried out in one of the two forms: response spectrum analysis and time-history analysis. Response spectrum analysis usually involves application of the concepts of response spectrum and modal superposition, and so on. Since these concepts primarily come from the dynamics of linear systems, the response spectrum analysis is only suitable for isolation systems with linear

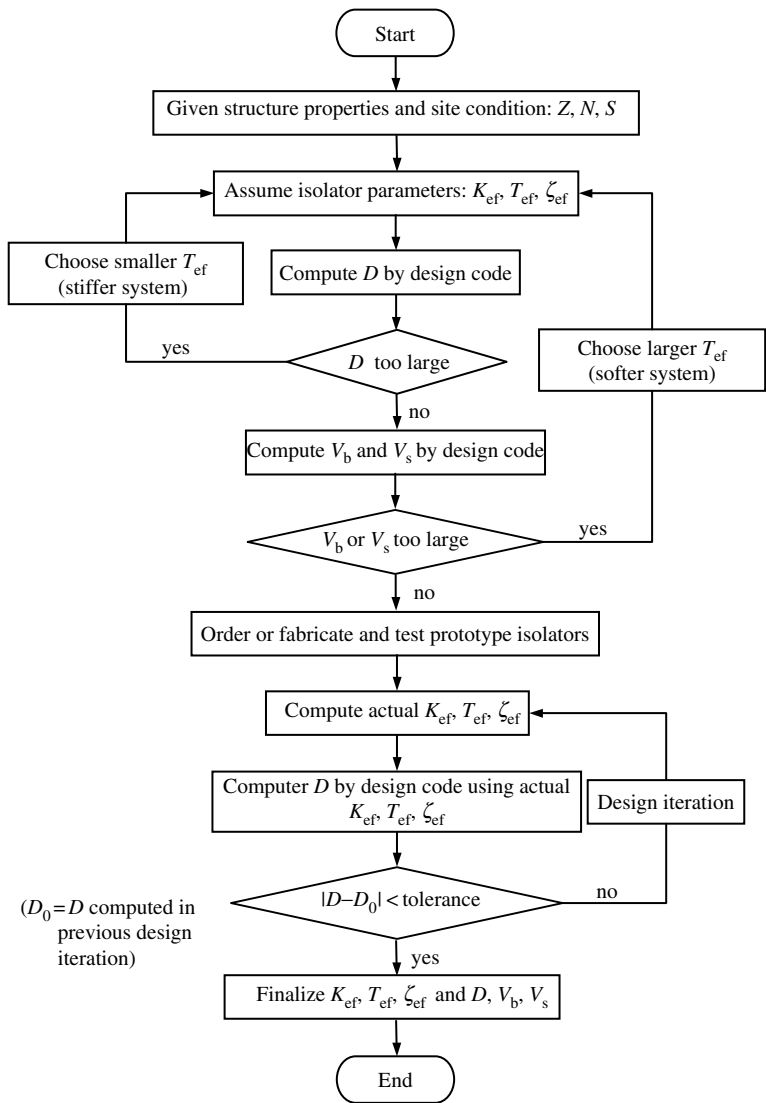


FIGURE 22.58 Flow chart of static analysis.

properties. For the case when the isolation system or the superstructure appears to be highly nonlinear, a time-history analysis is generally required.

Because dynamic analysis depends generally on the usage of computer programs, relatively few formulas have been given in the dynamic analysis sections of design codes. Nevertheless, for a successful time-history analysis, the designer must prepare the following three basic elements: (1) a set of representative input ground motions, (2) accurate mathematic models for isolators and superstructures, and (3) a computer program that is capable of performing the nonlinear time-history analysis. These three elements are explained below.

22.6.3.1 Input Ground Motions

The response of an isolated system depends greatly on the chosen input ground motions, which are usually expressed in the form of ground accelerations. Each ground motion is called one record event.

The chosen events must be representative of the site conditions and soil characteristics. Design codes usually specify the minimum number of events required for analysis. Each ground motion event must be scaled so that all events are compatible with each other and also with the code specified target spectrum. In the UBC (1997), the scaling factor for each event is obtained in response spectra, and then applied to the time domain of the record data. In particular, site specific ground motions are required in the UBC for the following cases: (1) an isolated structure located on a soft soil, (2) an isolated structure located within certain distance (e.g., 10 km) of an active fault, (3) an isolated structure with very long period of vibration (e.g., greater than 3 sec).

22.6.3.2 Mathematic Models

Before any time-history analysis can be carried out, a mathematic model that can accurately reflect the mechanical behavior of the isolation system and the superstructure must be constructed. If the isolation system is nonlinear, the nonlinear parameters must be identified so that the constructed mathematic model can correctly describe the hysteretic behavior of the isolation system. In many cases, the isolation system is assumed to be nonlinear, but the superstructure linear. Establishing an accurate mathematic model is curial for obtaining reliable results in a time-history analysis.

22.6.3.3 Computer Programs

In practice, the task of time-history analysis is executed through the use of a computer program. The mathematic model properties mentioned above will be input to the program for analysis. The computer program selected should be capable of simulating the three-dimensional behavior of structures with selected nonlinear elements. To serve the purpose of isolation design and analysis, several structural analysis programs running on the platform of personal computers have been developed for easy access. Some of the widely used programs include (but are not limited to): ETABS (ETABS, 2004), SAP-2000 Nonlinear (SAP, 2000), and 3D-BASIS (Nagarajaiah et al., 1993). Most of these programs provide a set of imbedded mathematic models for the widely used isolator elements with linear or nonlinear parameters. The designers using these programs can easily build up the mathematic model for the isolated structure considered, specify the parameters of the isolator elements selected, and execute a nonlinear time-history analysis on a personal computer.

22.6.4 Concluding Remarks

In this section, the design concept of seismic isolation for structures was briefly reviewed. The design methods can be based either on static or dynamic analysis. The fundamental issues that should be considered in each design method were highlighted, along with some relevant formulas for computing the relevant parameters. It is believed that, with the concepts and procedures presented in this section, the readers should have a general knowledge of the procedure for base isolation design of structures and equipment.

Acknowledgments

The authors are indebted to the graduate student, Cheng-Yan Wu, at the Department of Construction Engineering, National Kaohsiung First University of Science and Technology, for preparing some of the graphs presented in this chapter.

Nomenclature

Symbol	Quantity	Symbol	Quantity
c, c_s	damping coefficients of superstructure	V_b	total shear force of isolation system
c_e	damping coefficients of equipment	V_s	total base shear of superstructure
c_{EDF}	damping of the EDF system	w_i	weight of the i th floor
D	maximum isolator displacement	W	total weight of superstructure
f_r	interfacial frictional force	$x, x_s(t)$	relative-to-the-ground displacements of superstructure
F_i	seismic load applied on the i th floor	$x_b(t)$	relative-to-the-ground displacements of base mat
k, k_s	stiffness of superstructure	$x_e(t)$	relative-to-the-ground displacements of equipment
k_b	stiffness of isolation system	$\ddot{x}_g(t)$	ground acceleration
k_e	stiffness of equipment	Z	zone factor
k_{EDF}	stiffness of the EDF system	μ	frictional coefficient of sliding isolation system
k_f	stiffness of the fictitious spring in sliding isolation	ω_b	frequency of isolation system
K_{ef}	effective stiffness of isolation system	ω_e	frequencies of equipment
m, m_s	mass of superstructure	ω_g	frequency of ground excitation
m_b	mass of base mat	ζ_e	damping ratios of equipment
m_e	mass of equipment	ζ_{ef}	effective damping ratios of isolation system
n	number of building stories	ζ, ζ_s	damping ratios of superstructure
N	near fault factor	Ω_d	damped natural frequency
R_l	ductility factor	Ω, ω_s	frequencies of superstructure
S	soil factor		
T	natural period of superstructure		
T_d	damped period of superstructure		
T_{ef}	effective isolation period		

References

- Agrawal, A.K., Behaviour of equipment mounted over a torsionally coupled structure with sliding support, *Eng. Struct.*, 22, 72–84, 2000.
- Chalhoub, M.S. and Kelly, J.M. 1990. Earthquake simulator test of a combined sliding bearing and rubber bearing isolation system, Report No. UCB/EERC-87/04, Earthquake Engineering Research Center, University of California, Berkeley, CA.
- Chaudhuri, S.R. and Gupta, V.K., A response-based decoupling criterion for multiply-supported secondary systems, *Earthquake Eng. Struct. Dyn.*, 31, 1541–1562, 2002.
- Chen, G. and Soong, T.T., Energy-based dynamic analysis of secondary systems, *J. Eng. Mech.*, ASCE, 120, 514–534, 1994.
- Chen, G. and Soong, T.T., Exact solutions to a class of structure–equipment systems, *J. Eng. Mech.*, ASCE, 122, 1093–1100, 1996.
- Dey, A. and Gupta, V.K., Response of multiply supported systems to earthquakes in frequency domain, *Earthquake Eng. Struct. Dyn.*, 27, 187–201, 1998.
- Dey, A. and Gupta, V.K., Stochastic seismic response of multiply-supported secondary systems in flexible-base structures, *Earthquake Eng. Struct. Dyn.*, 28, 351–369, 1999.
- ETABS, Integrated Analysis, Design and Drafting of Building Systems, Version 8, Software by Computers and Structures Inc., Berkeley CA, 2004.
- Fujita, T., Seismic isolation of civil buildings in Japan, *Prog. Struct. Eng. Mater.*, 1, 295–300, 1998.
- Gueraud, R., Noel-Leroux, J.P., Livolant, M., and Michalopoulos, A.P., Seismic isolation using sliding-elastomer bearing pads, *Nucl. Eng. Des.*, 84, 363–377, 1985.

- Huang, C.D., Zhu, W.Q., and Soong, T.T., Nonlinear stochastic response and reliability of secondary systems, *J. Eng. Mech.*, ASCE, 120, 177–196, 1994.
- Igusa, T., Response characteristic of inelastic 2-DOF primary–secondary system, *J. Eng. Mech.*, ASCE, 116, 1160–1174, 1990.
- Igusa, T. and Der Kiureghian, A.D., Dynamic characteristic of two-degree-of-freedom equipment–structure systems, *J. Eng. Mech.*, ASCE, 111, 1–19, 1985a.
- Igusa, T. and Der Kiureghian, A.D., Dynamic response of multiply supported secondary systems, *J. Eng. Mech.*, ASCE, 111, 20–41, 1985b.
- Igusa, T. and Der Kiureghian, A.D., Generation of floor response spectra including oscillator–structure interaction, *Earthquake Eng. Struct. Dyn.*, 13, 661–676, 1985c.
- Inaudi, J.A. and Kelly, J.M., Minimum variance control of base-isolation floors, *J. Struct. Eng.*, ASCE, 119, 438–453, 1993.
- Jangid, R.S. and Kelly, J.M., Base isolation for near-fault motion, *Earthquake Eng. Struct. Dyn.*, 30, 691–707, 2001.
- Juhn, G., Manolis, G.D., Constantinou, M.C., and Reinhorn, A.M., Experimental study of secondary systems in base-isolated structure, *J. Struct. Eng.*, ASCE, 118, 2204–2221, 1992.
- Kelly, J.M., Seismic isolation of civil buildings in USA, *Prog. Struct. Eng. Mater.*, 1, 279–285, 1998.
- Kelly, J.M. and Tsai, H.C., Seismic response of light internal equipment in base-isolated structures, *Earthquake Eng. Struct. Dyn.*, 13, 711–732, 1985.
- Lai, M.L. and Soong, T.T., Statistical energy analysis of primary–secondary structural systems, *J. Eng. Mech.*, ASCE, 116, 2400–2413, 1990.
- Lu, L.Y. and Yang, Y.B., Dynamic response of equipment in structures with sliding support, *Earthquake Eng. Struct. Dyn.*, 26, 61–77, 1997.
- Lu, L.Y., Shih, M.H., Tzeng, S.W., and Chang, C.S. 2003. Experiment of a sliding isolated structure subjected to near-fault ground motion, In *Proceedings of the Seventh Pacific Conference on Earthquake Engineering*, February 13–15, Christchurch.
- Martelli, A. and Forni, M., Seismic isolation of civil buildings in Europe, *Prog. Struct. Eng. Mater.*, 1, 286–294, 1998.
- Meirovitch, L. 1990. *Dynamics and Control of Structures*, Wiley, New York.
- Mokha, A.S., Constantinou, M.C., Reinhorn, A.M., and Zayas, V.A., Experimental study of friction-pendulum isolation system, *J. Struct. Eng.*, ASCE, 117, 1201–1217, 1991.
- Mostaghel, N., 1984. *Resilient-friction Base Isolator*, Report No. UTEC 84-097, University of Utah, Salt Lake City, UT.
- Mostaghel, N. and Khodaverdian, M., Dynamics of resilient-friction base isolator (R-FBI), *Earthquake Eng. Struct. Dyn.*, 15, 379–390, 1987.
- Mostaghel, N., Hejazi, M., and Tanbakuchi, J., Response of sliding structures to harmonic support motion, *Earthquake Eng. Struct. Dyn.*, 11, 355–366, 1983.
- Naeim, F. and Kelly, J.M. 1999. *Design of Seismic Isolated Structures: From Theory to Practice*, Wiley, New York.
- Nagarajaiah, S., Li, C., Reinhorn, A.M., and Constantinou, M.C. 1993. 3D-BASIS-TABS: Computer program for nonlinear dynamic analysis of three dimensional base isolated structures, Technical report NCEER-93-0011, National Center for Earthquake Engineering Research, Buffalo, NY.
- Newmark, N.M., A method of computation for structural dynamics, *J. Eng. Mech. Div.*, ASCE, 85, 67–94, 1959.
- Park, K.S., Jung, H.J., and Lee, I.W., A comparative study on aseismic performances of base isolation systems for multi-span continuous bridge, *Eng. Struct.*, 24, 1001–1013, 2002.
- Rivin, E.I., Vibration isolation of precision equipment, *Precision Eng.*, 17, 41–56, 1995.
- SAP 2000. Integrated Structural Analysis and Design Software, Software by Computers and Structures, Inc., Berkeley, CA.
- Skinner, R.I., Robinson, W.H., and Mcverry, G.H. 1993. *An Introduction to Seismic Isolation*, Wiley, New York.

- Soong, T.T. and Dargush, G.F. 1997. *Passive Energy Dissipation Systems in Structural Engineering*, Wiley, New York.
- Steinberg, D.S. 2000. *Vibration Analysis for Electronic Equipment*, 3rd ed., Wiley, New York.
- Suarez, L.E. and Singh, M.P., Floor spectra with equipment–structure–equipment interaction effects, *J. Eng. Mech.*, ASCE, 115, 247–264, 1989.
- UBC 1994. Uniform building code, *International Conference of Building Officials*, Whittier, CA.
- UBC 1997. Uniform building code, *International Conference of Building Officials*, Whittier, CA.
- Veprik, A.M. and Babitsky, V.I., Vibration protection of sensitive electronic equipment from harsh harmonic vibration, *J. Sound Vib.*, 238, 19–30, 2000.
- Villaverde, R., Simplified seismic analysis of secondary systems, *J. Eng. Mech.*, ASCE, 112, 588–604, 1986.
- Wang, Y.P., Chung, L.L., and Liao, W.H., Seismic response analysis of bridges isolated with friction pendulum bearings, *Earthquake Eng. Struct. Dyn.*, 27, 1069–1093, 1998.
- Westermo, B. and Udawadia, F., Period response of a sliding oscillator system to harmonic excitation, *Earthquake Eng. Struct. Dyn.*, 11, 135–146, 1983.
- Xu, Y.L., Liu, H.J., and Yang, Z.C., Hybrid platform for vibration control of high-tech equipment in buildings subject to ground motion. Part 1. Experiment, *Earthquake Eng. Struct. Dyn.*, 32, 1185–1200, 2003.
- Yang, J.N. and Agrawal, A.K., Protective systems for high-technology facilities against microvibration and earthquake, *Struct. Eng. Mech.*, 10, 561–575, 2000.
- Yang, Y.B. and Chen, Y.C., Design of sliding-type base isolators by the concept of equivalent damping, *Struct. Eng. Mech.*, 8, 299–310, 1999.
- Yang, Y.B. and Huang, W.H., Seismic response of light equipment in torsional buildings, *Earthquake Eng. Struct. Dyn.*, 22, 113–128, 1993.
- Yang, Y.B. and Huang, W.H., Equipment–structure interaction considering the effect of torsion and base isolation, *Earthquake Eng. Struct. Dyn.*, 27, 155–171, 1998.
- Yang, Y.B., Lee, T.Y., and Tsai, I.C., Response of multi-degree-of-freedom structures with sliding supports, *Earthquake Eng. Struct. Dyn.*, 19, 739–752, 1990.
- Yang, Y.B., Hung, H.H., and He, M.J., Sliding and rocking response of rigid blocks due to horizontal excitations, *Struct. Eng. Mech.*, 9, 1–16, 2000.
- Yang, Y.B., Chang, K.C., and Yau, J.D. 2002. Base isolation. In *Earthquake Engineering Handbook*, W.F. Chen and C. Scawthorn, Eds., CRC Press, Boca Raton, FL, chap. 17.
- Yang, Z.C., Liu, H.J., and Xu, Y.L., Hybrid platform for vibration control of high-tech equipment in buildings subject to ground motion. Part 2. Analysis, *Earthquake Eng. Struct. Dyn.*, 32, 1201–1215, 2003.

23

Vibration Control

23.1	Introduction	23-1
	Vibration Isolation vs. Vibration Absorption • Vibration Absorption vs. Vibration Control • Classifications of Vibration-Control Systems • Performance Characteristics of Vibration-Control Systems	
23.2	Vibration-Control Systems Concept	23-4
	Introduction • Passive Vibration Control • Active Vibration Control • Semiactive Vibration Control • Adjustable Vibration-Control Elements	
23.3	Vibration-Control Systems Design and Implementation	23-12
	Introduction • Vibration Absorbers • Vibration-Control Systems	
23.4	Practical Considerations and Related Topics	23-38
	Summary of Vibration-Control Design Steps and Procedures • Future Trends and Developments	

Nader Jalili

Clemson University

Ebrahim Esmailzadeh

University of Ontario

Summary

The fundamental principles of vibration-control systems are formulated in this chapter. There are many important areas directly or indirectly related to the main theme of the chapter. These include practical implementation of vibration-control systems, nonlinear control schemes, actual hardware implementation, actuator bandwidth requirements, reliability, and cost. Furthermore, in the process of designing a vibration-control system, in practice, several critical criteria must be considered. These include weight, size, shape, center-of-gravity, types of dynamic disturbances, allowable system response, ambient environment, and service life. Keeping these in mind, general design steps and procedures for vibration-control systems are provided.

23.1 Introduction

The problem of reducing the level of vibration in constructions and structures arises in various branches of engineering, technology, and industry. In most of today's mechatronic systems, a number of possible devices such as reaction or momentum wheels, rotating devices, and electric motors are essential to the system's operation and performance. These devices, however, can also be sources of detrimental vibrations that may significantly influence the mission performance, effectiveness, and accuracy of operation. Therefore, there is a need for vibration control. Several techniques are utilized either to limit or alter the vibration response characteristics of such systems. During recent years, there has been considerable interest in the practical implementation of these vibration-control systems. This chapter presents the basic theoretical concepts for vibration-control systems design and implementation, followed by an overview of recent developments and control techniques in this subject. Some related practical developments in variable structure control (VSC), as well as piezoelectric vibration control of flexible structures, are also provided, followed by a summary of design steps and procedures for vibration-control systems. A further treatment of the subject is found in [Chapter 32](#).

23.1.1 Vibration Isolation vs. Vibration Absorption

In vibration isolation, either the source of vibration is isolated from the system of concern (also called “force transmissibility”; see Figure 23.1a), or the device is protected from vibration of its point of attachment (also called “displacement transmissibility”; see Figure 23.1b). Unlike the isolator, a vibration absorber consists of a secondary system (usually mass–spring–damper trio) added to the primary device to protect it from vibrating (see Figure 23.1c). By properly selecting absorber mass, stiffness, and damping, the vibration of the primary system can be minimized (Inman, 1994).

23.1.2 Vibration Absorption vs. Vibration Control

In vibration-control schemes, the driving forces or torques applied to the system are altered in order to regulate or track a desired trajectory while simultaneously suppressing the vibrational transients in the system. This control problem is rather challenging since it must achieve the motion tracking objectives while stabilizing the transient vibrations in the system. Several control methods have been developed for such applications: optimal control (Sinha, 1998); finite element approach (Bayo, 1987); model reference adaptive control (Ge et al., 1997); adaptive nonlinear boundary control (Yuh, 1987); and several other techniques including VSC methods (Chalhoub and Ulsoy, 1987; de Querioz et al., 1999; de Querioz et al., 2000).

As discussed before, in vibration-absorber systems, a secondary system is added in order to mimic the vibratory energy from the point of interest (attachment) and transfer it into other components or dissipate it into heat. Figure 23.2 demonstrates a comparative schematic of vibration control (both single-input control and multi-input configurations) on translating and rotating flexible beams, which could represent many industrial robot manipulators as well as vibration absorber applications for automotive suspension systems.

23.1.3 Classifications of Vibration-Control Systems

Passive, active, and semiactive (SA) are referred to, in the literature, as the three most commonly used classifications of vibration-control systems, either as isolators or absorbers (see Figure 23.3; Sun et al., 1995). A vibration-control system is said to be active, passive, or SA depending on the amount of

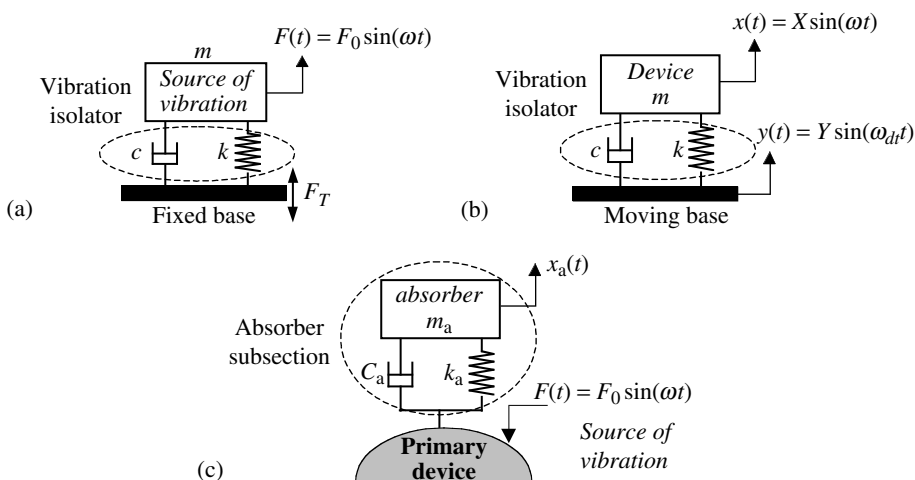


FIGURE 23.1 Schematic of (a) force transmissibility for foundation isolation; (b) displacement transmissibility for protecting device from vibration of the base and (c) application of vibration absorber for suppressing primary system vibration.

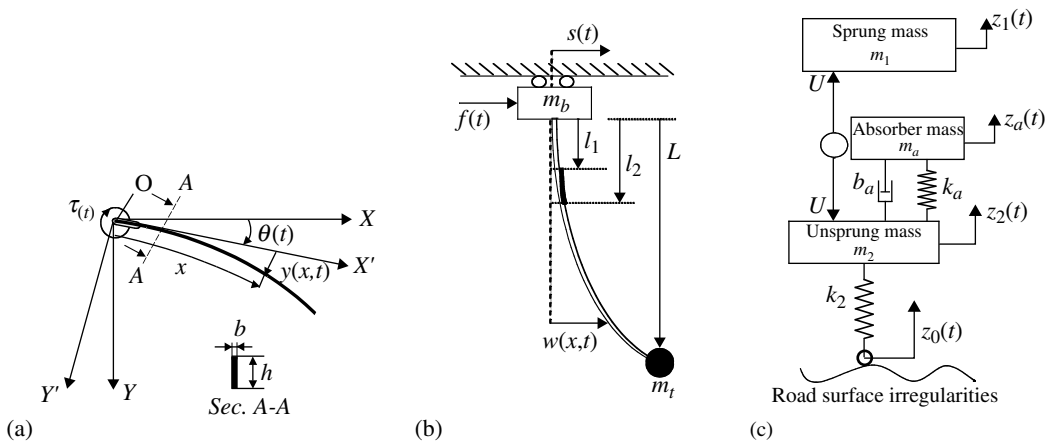


FIGURE 23.2 A comparative schematic of vibration-control systems: (a) single-input simultaneous tracking and vibration control; (b) multi-input tracking and vibration control and (c) a two-DoF vehicle model with dynamic vibration absorber.

external power required for the vibration-control system to perform its function. A passive vibration control consists of a resilient member (stiffness) and an energy dissipater (damper) either to absorb vibratory energy or to load the transmission path of the disturbing vibration (Korenev and Reznikov, 1993; Figure 23.3a). This type of vibration-control system performs best within the frequency region of its highest sensitivity. For wideband excitation frequency, its performance can be improved considerably by optimizing the system parameters (Puksand, 1975; Warburton and Ayorinde, 1980; Esmailzadeh and Jalili, 1998a). However, this improvement is achieved at the cost of lowering narrowband suppression characteristics.

The passive vibration control has significant limitations in structural applications where broadband disturbances of highly uncertain nature are encountered. In order to compensate for these limitations, active vibration-control systems are utilized. With an additional active force introduced as a part of absorber subsection, $u(t)$ (Figure 23.3b), the system is controlled using different algorithms to make it more responsive to source of disturbances (Soong and Constantinou, 1994; Olgac and Holm-Hansen, 1995; Sun et al., 1995; Margolis, 1998). The SA vibration-control system, a combination of active and passive treatment, is intended to reduce the amount of external power necessary to achieve the desired performance characteristics (Lee-Glauser et al., 1997; Jalili, 2000; Jalili and Esmailzadeh, 2002), see Figure 23.3c.

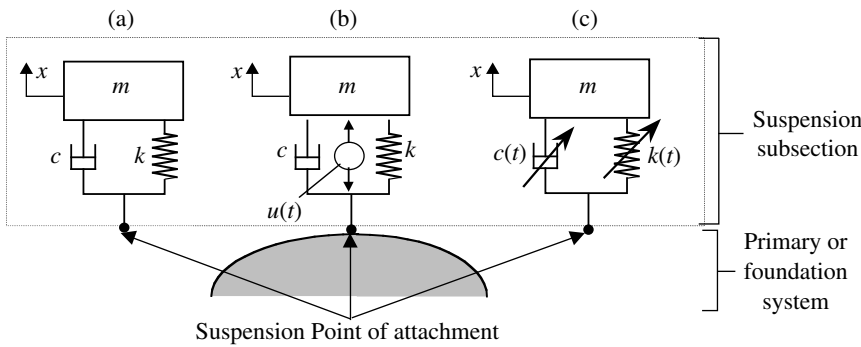


FIGURE 23.3 A typical primary structure equipped with three versions of suspension systems: (a) passive; (b) active and (c) SA configurations.

23.1.4 Performance Characteristics of Vibration-Control Systems

In the design of a vibration-control system, it often occurs that the system is required to operate over a wideband load and frequency range that is impossible to meet with a single choice of required stiffness and damping. If the desired response characteristics cannot be obtained, an active vibration-control system may provide an attractive alternative vibration control for such broadband disturbances. However, active vibration-control systems suffer from control-induced instability in addition to the large control effort requirement. This is a serious concern, which prevents them from the common usage in most industrial applications. On the other hand, passive systems are often hampered by a phenomenon known as “detuning.” Detuning implies that the passive system is no longer effective in suppressing the vibration it was designed for. This occurs due to one of the following reasons: (1) the vibration-control system may deteriorate and its structural parameters can be far from the original nominal design, (2) the structural parameters of the primary device itself may alter, or (3) the excitation frequency or the nature of disturbance may change over time.

A semiactive (also known as adaptive-passive) vibration-control system addresses these limitations by effectively integrating a tuning control scheme with tunable passive devices. For this, active force generators are replaced by modulated variable compartments such as variable rate damper and stiffness (see Figure 23.3c; Hrovat et al., 1988; Nemir et al., 1994; Franchek et al., 1995). These variable components are referred to as “tunable parameters” of the suspension system, which are retailored *via* a tuning control, thus resulting in semiactively inducing optimal operation. Much attention is being paid to these systems because of their low energy requirement and cost. Recent advances in smart materials, and adjustable dampers and absorbers have significantly contributed to applicability of these systems (Garcia et al., 1992; Wang et al., 1996; Shaw, 1998).

23.2 Vibration-Control Systems Concept

23.2.1 Introduction

With a history of almost a century (Frahm, 1911), the dynamic vibration absorber has proven to be a useful vibration-suppression device, widely used in hundreds of diverse applications. It is elastically attached to the vibrating body to alleviate detrimental oscillations from its point of attachment (see Figure 23.3). This section overviews the conceptual design and theoretical background of three types of vibration-control systems, namely the passive, active and SA configurations, along with some related practical implementations.

23.2.2 Passive Vibration Control

The underlying proposition in all vibration control or absorber systems is to adjust properly the absorber parameters such that the system becomes absorbent of the vibratory energy within the frequency interval of interest. In order to explain the underlying concept, a single-degree-of-freedom (single-DoF) primary system with a single-DoF absorber attachment is considered (Figure 23.4). The governing dynamics is expressed as

$$\begin{aligned} m_a \ddot{x}_a(t) + c_a \dot{x}_a(t) + k_a x_a(t) \\ = c_a \dot{x}_p(t) + k_a x_p(t) \end{aligned} \quad (23.1)$$

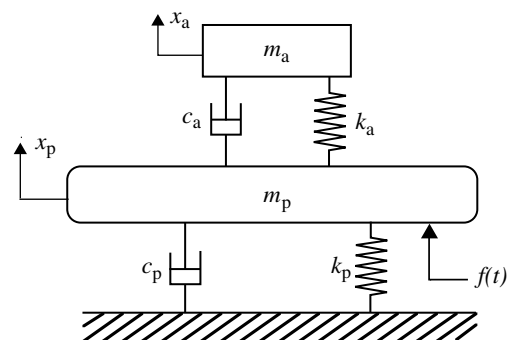


FIGURE 23.4 Application of a passive absorber to single-DoF primary system.

$$m_p \ddot{x}_p(t) + (c_p + c_a) \dot{x}_p(t) + (k_p + k_a)x_p(t) - c_a \dot{x}_a(t) - k_a x_a(t) = f(t) \quad (23.2)$$

where $x_p(t)$ and $x_a(t)$ are the respective primary and absorber displacements, $f(t)$ is the external force, and the rest of the parameters including absorber stiffness, k_a , and damping, c_a , are defined as per Figure 23.4. The transfer function between the excitation force and primary system displacement in the Laplace domain is then written as

$$TF(s) = \frac{X_p(s)}{F(s)} = \left\{ \frac{m_a s^2 + c_a s + k_a}{H(s)} \right\} \quad (23.3)$$

where

$$H(s) = \{m_p s^2 + (c_p + c_a)s + k_p + k_a\}(m_a s^2 + c_a s + k_a) - (c_a s + k_a)^2 \quad (23.4)$$

and $X_a(s)$, $X_p(s)$, and $F(s)$ are the Laplace transformations of $x_a(t)$, $x_p(t)$, and $f(t)$, respectively.

23.2.2.1 Harmonic Excitation

When excitation is tonal, the absorber is generally tuned at the disturbance frequency. For this case, the steady-state displacement of the system due to harmonic excitation can be expressed as

$$\left| \frac{X_p(j\omega)}{F(j\omega)} \right| = \left| \frac{k_a - m_a \omega^2 + j c_a \omega}{H(j\omega)} \right| \quad (23.5)$$

where ω is the disturbance frequency and $j = \sqrt{-1}$. An appropriate parameter tuning scheme can then be selected to minimize the vibration of primary system subject to external disturbance, $f(t)$.

For complete vibration attenuation, the steady state, $|X_p(j\omega)|$, must equal zero. Consequently, from Equation 23.5, the ideal stiffness and damping of absorber are selected as

$$k_a = m_a \omega^2, \quad c_a = 0 \quad (23.6)$$

Notice that this tuned condition is only a function of absorber elements (m_a , k_a , and c_a). That is, the absorber tuning does not need information from the primary system and hence its design is stand alone. For tonal application, theoretically, zero damping in the absorber subsection results in improved performance. In practice, however, the damping is incorporated in order to maintain a reasonable trade-off between the absorber mass and its displacement. Hence, the design effort for this class of application is focused on having precise tuning of the absorber to the disturbance frequency and controlling the damping to an appropriate level. Referring to Snowdon (1968), it can be proven that the absorber, in the presence of damping, can be most favorably tuned and damped if adjustable stiffness and damping are selected as

$$k_{\text{opt}} = \frac{m_a m_p^2 \omega^2}{(m_a + m_p)^2}, \quad c_{\text{opt}} = m_a \sqrt{\frac{3k_{\text{opt}}}{2(m_a + m_p)}} \quad (23.7)$$

23.2.2.2 Broadband Excitation

In broadband vibration control, the absorber subsection is generally designed to add damping to and change the resonant characteristics of the primary structure in order to dissipate vibrational energy maximally over a range of frequencies. The objective of the absorber design is, therefore, to adjust the *absorber parameters* to minimize the peak magnitude of the frequency transfer function ($FTF(\omega) = |TF(s)|_{s=j\omega}$) over the absorber parameters vector $\mathbf{p} = \{c_a, k_a\}^T$. That is, we seek \mathbf{p} to

$$\min_{\mathbf{p}} \left\{ \max_{\omega_{\min} \leq \omega \leq \omega_{\max}} \{|FTF(\omega)|\} \right\} \quad (23.8)$$

Alternatively, one may select the mean square displacement response (MSDR) of the primary system for vibration-suppression performance. That is, the absorber parameters vector, \mathbf{p} , is selected such that

the MSDR

$$E\{\{\tilde{x}_p\}^2\} = \int_0^\infty \{FTF(\omega)\}^2 S(\omega) d\omega \quad (23.9)$$

is minimized over a desired wideband frequency range. $S(\omega)$ is the power spectral density of the excitation force, $f(t)$, and FTF was defined earlier.

This optimization is subjected to some constraints in \mathbf{p} space, where only positive elements are acceptable. Once the optimal absorber suspension properties, c_a and k_a , are determined, they can be implemented using adjustment mechanisms on the spring and the damper elements. This is viewed as a SA adjustment procedure as it adds no energy to the dynamic structure. The conceptual devices for such adjustable suspension elements and SA treatment will be discussed later in Section 23.2.5.

23.2.2.3 Example Case Study

To better recognize the effectiveness of the dynamic vibration absorber over the passive and optimum passive absorber settings, a simple example case is presented. For the simple system shown in Figure 23.4, the following nominal structural parameters (marked by an overscore) are taken:

$$\begin{aligned} \bar{m}_p &= 5.77 \text{ kg}, & \bar{k}_p &= 251.132 \times 10^6 \text{ N/m}, & \bar{c}_p &= 197.92 \text{ kg/sec} \\ \bar{m}_a &= 0.227 \text{ kg}, & \bar{k}_a &= 9.81 \times 10^6 \text{ N/m}, & \bar{c}_a &= 355.6 \text{ kg/sec} \end{aligned} \quad (23.10)$$

These are from an actual test setting, which is optimal by design (Olgac and Jalili, 1999). That is, the peak of the FTF is minimized (see thin lines in Figure 23.5). When the primary stiffness and damping increase 5% (for instance during the operation), the FTF of the primary system deteriorates considerably (the dashed line in Figure 23.5), and the absorber is no longer an optimum one for the present primary. When the absorber is optimized based on optimization problem 8, the retuned setting is reached as

$$k_a = 10.29 \times 10^6 \text{ N/m}, \quad c_a = 364.2 \text{ kg/sec} \quad (23.11)$$

which yields a much better frequency response (see dark line in Figure 23.5).

The vibration absorber effectiveness is better demonstrated at different frequencies by frequency sweep test. For this, the excitation amplitude is kept fixed at unity and its frequency changes every 0.15 sec from

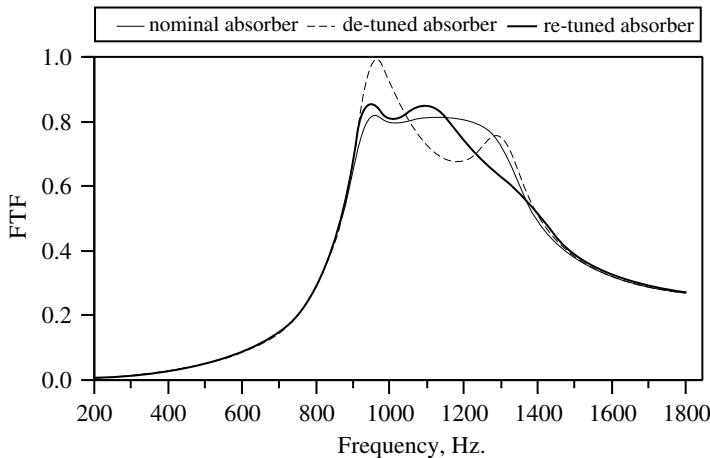


FIGURE 23.5 Frequency transfer functions (FTFs) for nominal absorber (thin-solid line), detuned absorber (thin-dotted line), and retuned absorber (thick-solid line) settings. (Source: From Jalili, N. and Olgac, N., *AIAA J. Guidance Control Dyn.*, 23, 961–970, 2000a. With permission.)

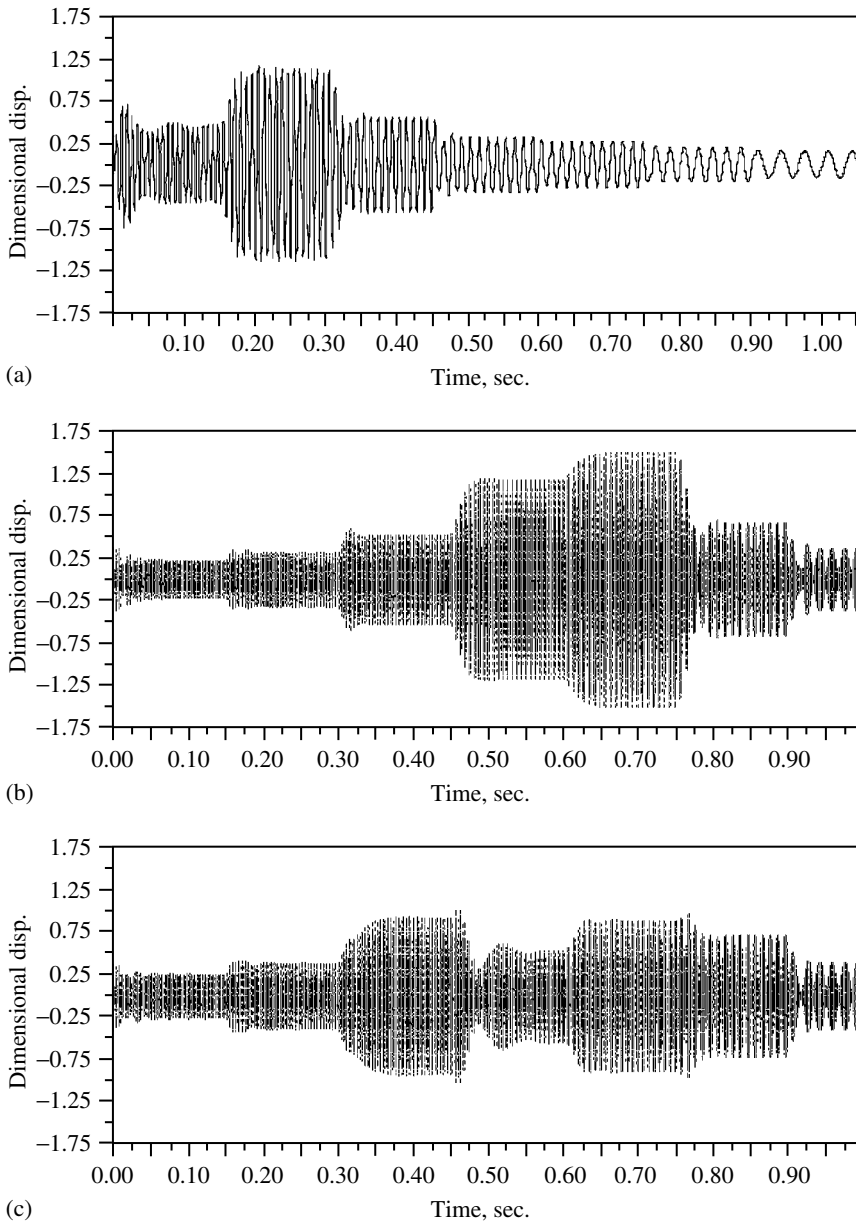


FIGURE 23.6 Frequency sweep each 0.15 with frequency change of 1860, 1880, 1900, 1920, 1930, 1950, and 1970 Hz: (a) nominally tuned absorber settings; (b) detuned absorber settings and (c) retuned absorber settings. (Source: From Jalili, N. and Olgac, N., *AIAA J. Guidance Control Dyn.*, 23, 961–970, 2000a. With permission.)

1860 to 1970 Hz. The primary responses with nominally tuned, with detuned, and with retuned absorber settings are given in Figure 23.6a–c, respectively.

23.2.3 Active Vibration Control

As discussed, passive absorption utilizes resistive or reactive devices either to absorb vibrational energy or load the transmission path of the disturbing vibration (Korennev and Reznikov, 1993; see [Figure 23.7](#), top). Even with optimum absorber parameters (Warburton and Ayorinde, 1980;

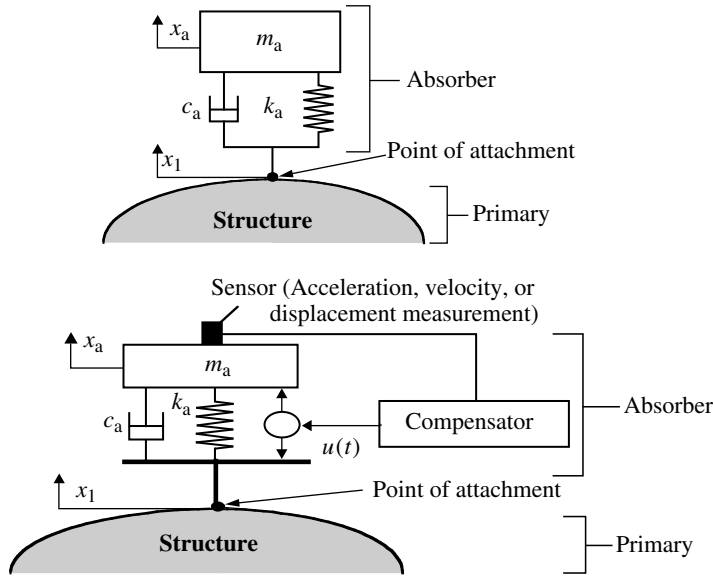


FIGURE 23.7 A general primary structure with passive (top) and active (bottom) absorber settings.

Esmailzadeh and Jalili, 1998a), the passive absorption has significant limitations in structural applications where broadband disturbances of highly uncertain nature are encountered.

In order to compensate for these limitations, active vibration-suppression schemes are utilized. With an additional active force, $u(t)$ (Figure 23.7, bottom), the absorber is controlled using different algorithms to make it more responsive to primary disturbances (Sun et al., 1995; Margolis, 1998; Jalili and Olgac, 1999). One novel implementation of the tuned vibration absorbers is the active resonator absorber (ARA) (Knowles et al., 2001b). The concept of the ARA is closely related to the concept of the delayed resonator (Olgac and Holm-Hansen, 1994; Olgac, 1995). Using a simple position (or velocity or acceleration) feedback control within the absorber subsection, the delayed resonator enforces that the dominant characteristic roots of the absorber subsection be on the imaginary axis, hence leading to resonance. Once the ARA becomes resonant, it creates perfect vibration absorption at this frequency. The conceptual design and implementation issues of such active vibration-control systems, along with their practical applications, are discussed in Section 23.3.

23.2.4 Semiactive Vibration Control

Semiactive (SA) vibration-control systems can achieve the majority of the performance characteristics of fully active systems, thus allowing for a wide class of applications. The idea of SA suspension is very simple: to replace active force generators with continually adjustable elements which can vary and/or shift the rate of the energy dissipation in response to instantaneous condition of motion (Jalili, 2002).

23.2.5 Adjustable Vibration-Control Elements

Adjustable vibration-control elements are typically comprised of variable rate damper and stiffness. Significant efforts have been devoted to the development and implementation of such devices for a variety of applications. Examples of such devices include electro-rheological (ER) (Petek, 1992; Wang et al., 1994; Choi, 1999), magneto-rheological (MR) (Spencer et al., 1998; Kim and Jeon, 2000) fluid dampers, and variable orifice dampers (Sun and Parker, 1993), controllable friction braces (Dowell and Cherry, 1994), and variable stiffness and inertia devices (Walsh and Lamnacula, 1992;

Nemir et al., 1994; Franchek et al., 1995; Abe and Igusa, 1996). The conceptual devices for such adjustable properties are briefly reviewed in this section.

23.2.5.1 Variable Rate Dampers

A common and very effective way to reduce transient and steady-state vibration is to change the amount of damping in the SA vibration-control system. Considerable design work on SA damping was done in the 1960s to the 1980s (Crosby and Karnopp, 1973; Karnopp et al., 1974) for vibration control of civil structures such as buildings and bridges (Hrovat et al., 1983) and for reducing machine tool oscillations (Tanaka and Kikushima, 1992). Since then, SA dampers have been utilized in diverse applications ranging from trains (Stribersky et al., 1998) and other off-road vehicles (Horton and Crolla, 1986) to military tanks (Miller and Nobles, 1988). During recent years, there has been considerable interest in the SA concept in the industry for improvement and refinements of the concept (Karnopp, 1990; Emura et al., 1994). Recent advances in smart materials have led to the development of new SA dampers, which are widely used in different applications.

In view of these SA dampers, ER and MR fluids probably serve as the best potential hardware alternatives for the more conventional variable-orifice hydraulic dampers (Sturk et al., 1995). From a practical standpoint, the MR concept appears more promising for suspension, since it can operate, for instance, on vehicle battery voltage, whereas the ER damper is based on high-voltage electric fields. Owing to their importance in today's SA damper technology, we briefly review the operation and fundamental principles of SA dampers here.

23.2.5.1.1 Electro-Rheological Fluid Dampers

ER fluids are materials that undergo significant instantaneous reversible changes in material characteristics when subjected to electric potentials (Figure 23.8). The most significant change is associated with complex shear moduli of the material, and hence ER fluids can be usefully exploited in SA absorbers where variable-rate dampers are utilized. Originally, the idea of applying an ER damper to vibration control was initiated in automobile suspensions, followed by other applications (Austin, 1993; Petek et al., 1995).

The flow motions of an ER fluid-based damper can be classified by shear mode, flow mode, and squeeze mode. However, the rheological property of ER fluid is evaluated in the shear mode (Choi, 1999). As a result, the ER fluid damper provides an adaptive viscous and frictional damping for use in SA system (Dimarogonas-Andrew and Kollias, 1993; Wang et al., 1994).

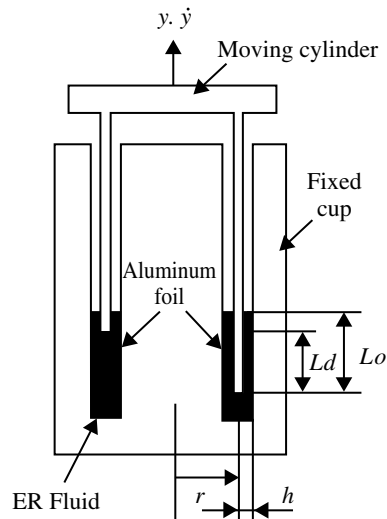


FIGURE 23.8 A schematic configuration of an ER damper. (Source: From Choi, S.B., *ASME J. Dyn. Syst. Meas. Control*, 121, 134–138, 1999. With permission.)

23.2.5.1.2 Magneto-Rheological Fluid Dampers

MR fluids are the magnetic analogies of ER fluids and typically consist of micron-sized, magnetically polarizable particles dispersed in a carrier medium such as mineral or silicon oil. When a magnetic field is applied, particle chains form and the fluid becomes a semisolid, exhibiting plastic behavior similar to that of ER fluids (Figure 23.9). Transition to rheological equilibrium can be achieved in a few milliseconds, providing devices with high bandwidth (Spencer et al., 1998; Kim and Jeon, 2000).

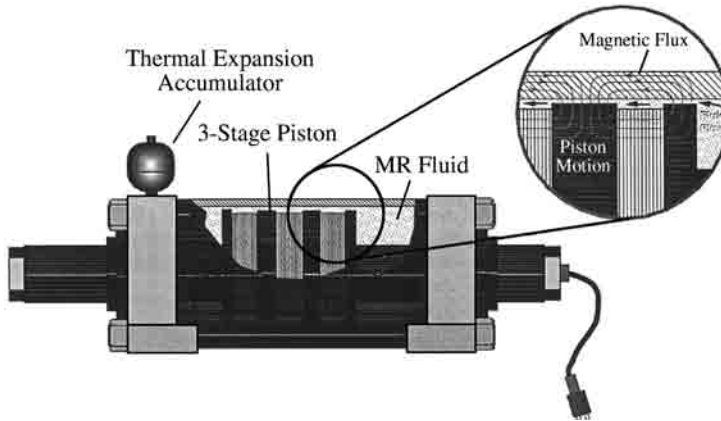


FIGURE 23.9 A schematic configuration of an MR damper. (Source: From Spencer, B.F. et al., *Proc. 2nd World Conf. on Structural Control*, 1998. With permission.)

23.2.5.2 Variable-Rate Spring Elements

In contrast to variable dampers, studies of SA springs or time-varying stiffness have also been geared for vibration-isolation applications (Hubard and Marolis, 1976), for structural controls and for vibration attenuation (Sun et al., 1995 and references therein). The variable stiffness is a promising practical complement to SA damping, since, based on the discussion in Section 23.2, both the absorber damping and stiffness should change to adapt optimally to different conditions. Clearly, the absorber stiffness has a significant influence on optimum operation (and even more compared to the damping element; Jalili and Olgac, 2000b).

Unlike the variable rate damper, changing the effective stiffness requires high energy (Walsh and Lamnaca, 1992). Semiactive or low-power implementation of variable stiffness techniques suffers from limited frequency range, complex implementation, high cost, and so on. (Nemir et al., 1994; Franchek et al., 1995). Therefore, in practice, both absorber damping and stiffness are concurrently adjusted to reduce the required energy.

23.2.5.2.1 Variable-Rate Stiffness (Direct Methods)

The primary objective is to directly change the spring stiffness to optimize a vibration-suppression characteristic such as the one given in Equation 23.8 or Equation 23.9. Different techniques can be utilized ranging from traditional variable leaf spring to smart spring utilizing magnetostrictive materials. A tunable stiffness vibration absorber was utilized for a four-DoF building (Figure 23.10), where a spring is threaded through a collar plate and attached to the absorber mass from one side and to the driving gear from the other side (Franchek et al., 1995). Thus, the effective number of coils, N , can be changed resulting in a variable spring stiffness, k_a :

$$k_a = \frac{d^4 G}{8D^3 N} \quad (23.12)$$

where d is the spring wire diameter, D is the spring diameter, and G is modulus of shear rigidity.

23.2.5.2.2 Variable-Rate Effective Stiffness (Indirect Methods)

In most SA applications, directly changing the stiffness might not be always possible or may require large amount of control effort. For such cases, alternatives methods are utilized to change the effective tuning ratio ($\tau = \sqrt{k_a/m_a}/\omega_{\text{primary}}$), thus resulting in a tunable resonant frequency.

In Liu et al. (2000), a SA flutter-suppression scheme was proposed using differential changes of external store stiffness. As shown in Figure 23.11, the motor drives the guide screw to rotate with slide block, G , moving along it, thus changing the restoring moment and resulting in a change of store

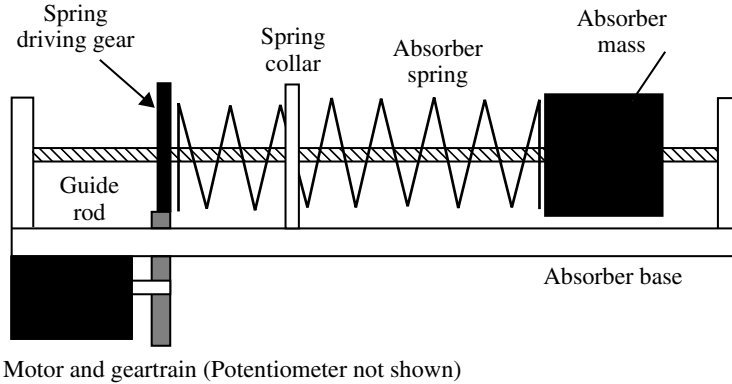


FIGURE 23.10 The application of a variable-stiffness vibration absorber to a four-DoF building. (Source: From Franchek, M.A. et al., *J. Sound Vib.*, 189, 565–585, 1995. With permission.)

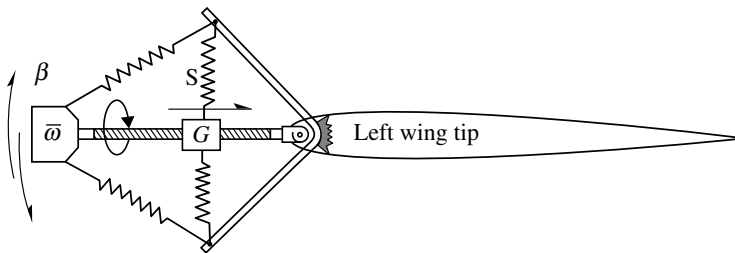


FIGURE 23.11 A SA flutter control using adjustable pitching stiffness. (Source: From Liu, H.J. et al., *J. Sound Vib.*, 229, 199–205, 2000. With permission.)

pitching stiffness. Using a double-ended cantilever beam carrying intermediate lumped masses, a SA vibration absorber was recently introduced (Jalili and Esmailzadeh, 2002), where positions of moving masses are adjustable (see Figure 23.12). Figure 23.13 shows an SA absorber with an adjustable effective inertia mechanism (Jalili et al., 2001; Jalili and Fallahi, 2002). The SA absorber consists of a rod carrying a moving block and a spring and damper, which are mounted on a casing. The position of the moving block, r_v , on the rod is adjustable which provides a tunable resonant frequency.

23.2.5.3 Other Variable-Rate Elements

Recent advances in smart materials have led to the development of new SA vibration-control systems using indirect influence on the suspension elements. Wang et al. used a SA piezoelectric network (1996) for structural-vibration control. The variable resistance and inductance in an external RL circuit are used as real-time adaptable control parameters.

Another class of adjustable suspensions is the so-called hybrid treatment (Fujita et al., 1991). The hybrid design has two modes, an active mode and a passive mode. With its aim of lowering the

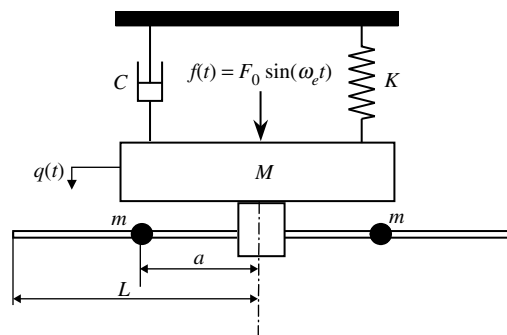


FIGURE 23.12 A typical primary system equipped with the double-ended cantilever absorber with adjustable tuning ration through moving masses, m . (Source: From Jalili, N. and Esmailzadeh, E., *J. Multi-Body Dyn.*, 216, 223–235, 2002. With permission.)

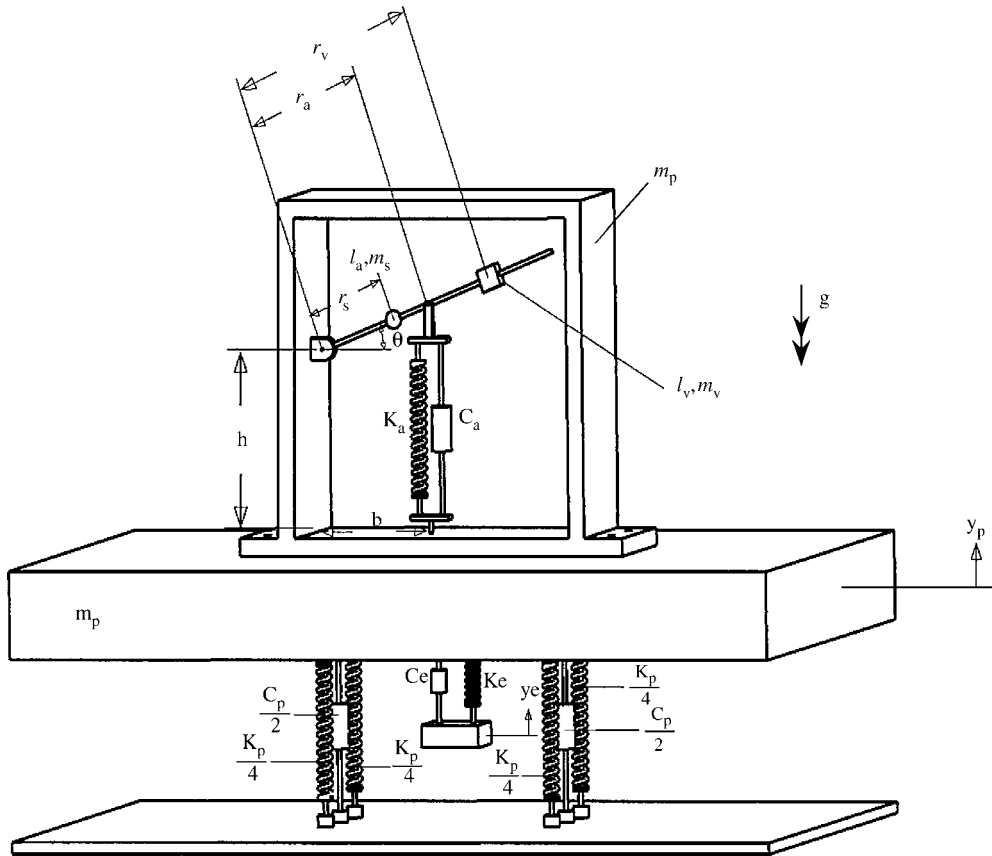


FIGURE 23.13 Schematic of the adjustable effective inertia vibration absorber. (Source: From Jalili, N. et al., *Int. J. Model. Simulat.*, 21, 148–154, 2001. With permission.)

control effort, relatively small vibrations are reduced in active mode, while passive mode is used for large oscillations. Analogous to hybrid treatment, the semiautomated approach combines SA and active suspensions to benefit from the advantages of individual schemes while eliminating their shortfalls (Jalili, 2000). By altering the adjustable structural properties (in the SA unit) and control parameters (in the active unit), a search is conducted to minimize an objective function subject to certain constraints, which may reflect performance characteristics.

23.3 Vibration-Control Systems Design and Implementation

23.3.1 Introduction

This section provides the basic fundamental concepts for vibration-control systems design and implementation. These systems are classified into two categories: vibration absorbers and vibration-control systems. Some related practical developments in ARAs and piezoelectric vibration control of flexible structures are also provided.

23.3.2 Vibration Absorbers

Undesirable vibrations of flexible structures have been effectively reduced using a variety of dynamic vibration absorbers. The active absorption concept offers a wideband of vibration-attenuation

frequencies as well as real-time tunability as two major advantages. It is clear that the active control could be a destabilizing factor for the combined system, and therefore, the stability of the combined system (i.e., the primary and the absorber subsystems) must be assessed.

An actively tuned vibration-absorber scheme utilizing a resonator generation mechanism forms the underlying concept here. For this, a stable primary system (see Figure 23.7, top, for instance) is forced into a marginally stable one through the addition of a controlled force in the active unit (see Figure 23.7, bottom). The conceptual design for generating such resonance condition is demonstrated in Figure 23.14, where the system's dominant characteristic roots (poles) are moved and placed on the imaginary axis. The absorber then becomes a resonator capable of mimicking the vibratory energy from the primary system at the point of attachment. Although there seem to be many ways to generate such resonance, only two widely accepted practical vibration-absorber resonators are discussed next.

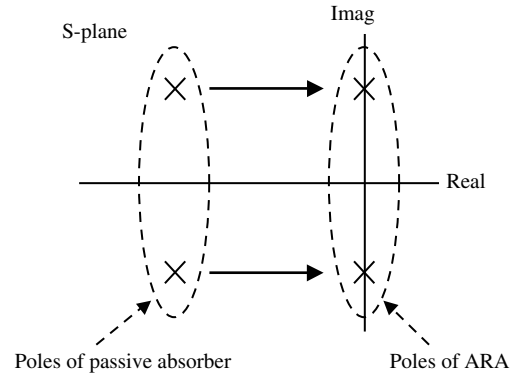


FIGURE 23.14 Schematic of the active resonator absorber concept through placing the poles of the characteristic equation on the imaginary axis.

23.3.2.1 Delayed-Resonator Vibration Absorbers

A recent active vibration-absorption strategy, the delayed resonator (DR), is considered to be the first type of active vibration absorber when operated on a flexible beam (Olgac and Jalili, 1998; Olgac and Jalili, 1999). The DR vibration absorber offers some attractive features in eliminating tonal vibrations from the objects to which it is attached (Olgac and Holm-Hansen, 1994; Olgac, 1995; Renzulli et al., 1999), some of which are real-time tunability, the stand-alone nature of the actively controlled absorber, and the simplicity of the implementation. Additionally, this single-DoF absorber can also be tuned to handle multiple frequencies of vibration (Olgac et al., 1996). It is particularly important that the combined system, that is, the primary structure and the absorber together, is asymptotically stable when the DR is implemented on a flexible beam.

23.3.2.1.1 An Overview of the Delayed-Resonator Concept

An overview of the DR is presented here to help the reader. The equation of motion governing the absorber dynamics alone is

$$m_a \ddot{x}_a(t) + c_a \dot{x}_a(t) + k_a x_a(t) - u(t) = 0, \quad u(t) = g \ddot{x}_a(t - \tau) \quad (23.13)$$

where $u(t)$ represents the delayed acceleration feedback. The Laplace domain transformation of this equation yields the characteristics equation

$$m_a s^2 + c_a s + k_a - g s^2 e^{-\tau s} = 0 \quad (23.14)$$

Without feedback ($g = 0$), this structure is dissipative with two characteristic roots (poles) on the left half of the complex plane. For g and $\tau > 0$, however, these two finite stable roots are supplemented by infinitely many additional finite roots. Note that these characteristic roots (poles) of Equation 23.14 are discretely located (say at $s = a + j\omega$), and the following relation holds:

$$g = \frac{|m_a s^2 + c_a s + k_a|}{|s^2|} e^{\tau a} \quad (23.15)$$

where $|\cdot|$ denotes the magnitude of the argument.

Using Equation 23.15, the following observation can be made:

- For $g = 0$: there are two finite stable poles and all the remaining poles are at $a = -\infty$.
- For $g = +\infty$: there are two poles at $s = 0$, and the rest are at $a = +\infty$.

Considering these and taking into account the continuity of the root loci for a given time delay, τ , and as g varies from 0 to ∞ , it is obvious that the roots of Equation 23.14 move from the stable left half to the unstable right half of the complex plane. For a certain critical gain, g_c , one pair of poles reaches the imaginary axis. At this operating point, the DR becomes a perfect resonator and the imaginary characteristic roots are $s = \pm j\omega_c$, where ω_c is the resonant frequency and $j = \sqrt{-1}$. The subscript “c” implies the crossing of the root loci on the imaginary axis. The control parameters of concern, g_c and τ_c , can be found by substituting the desired $s = \pm j\omega_c$ into Equation 23.14 as

$$g_c = \frac{1}{\omega_c^2} \sqrt{(c_a \omega_c)^2 + (m_a \omega_c - k_a)^2}, \quad \tau_c = \frac{1}{\omega_c} \left\{ \tan^{-1} \left[\frac{c_a \omega_c}{m_a \omega_c^2 - k_a} \right] + 2(\ell - 1)\pi \right\}, \quad \ell = 1, 2, \dots \quad (23.16)$$

When these g_c and τ_c are used, the DR structure mimics a resonator at frequency ω_c . In turn, this resonator forms an *ideal absorber* of the tonal vibration at ω_c . The objective of the control, therefore, is to maintain the DR absorber at this marginally stable point. On the DR stability, further discussions can be found in Olgac and Holm-Hansen (1994) and Olgac et al. (1997).

23.3.2.1.2 Vibration-Absorber Application on Flexible Beams

We consider a general beam as the primary system with absorber attached to it and subjected to a harmonic force excitation, as shown in Figure 23.15. The point excitation is located at b , and the absorber is placed at a . A uniform cross section is considered for the beam and Euler–Bernoulli assumptions are made. The beam parameters are all assumed to be constant and uniform. The elastic deformation from the undeformed natural axis of the beam is denoted by $y(x, t)$ and, in the derivations that follow, the dot ($\dot{\cdot}$) and prime ($'$) symbols indicate a partial derivative with respect to the time variable, t , and position variable x , respectively.

Under these assumptions, the kinetic energy of the system can be written as

$$T = \frac{1}{2} \rho \int_0^L \left(\frac{\partial y}{\partial t} \right)^2 dx + \frac{1}{2} m_a \dot{q}_a^2 + \frac{1}{2} m_e \dot{q}_e^2 \quad (23.17)$$

The potential energy of this system using linear strain is given by

$$U = \frac{1}{2} EI \int_0^L \left(\frac{\partial^2 y}{\partial x^2} \right)^2 dx + \frac{1}{2} k_a \{y(a, t) - q_a\}^2 + \frac{1}{2} k_e \{y(b, t) - q_e\}^2 \quad (23.18)$$

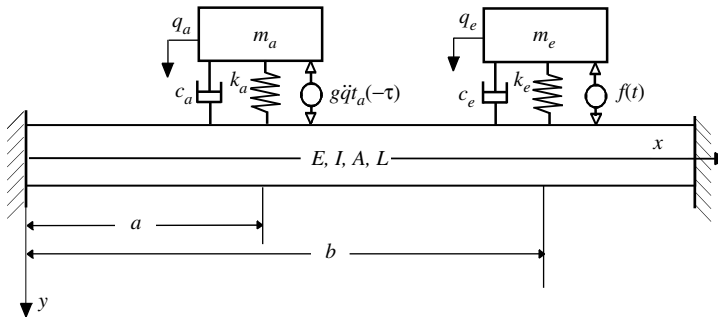


FIGURE 23.15 Beam–absorber–exciter system configuration. (Source: From Olgac, N. and Jalili, N., *J. Sound Vib.*, 218, 307–331, 1998. With permission.)

The equations of motion may now be derived by applying Hamilton's Principle. However, to facilitate the stability analysis, we resort to an assumed-mode expansion and Lagrange's equations. Specifically, y is written as a finite sum "Galerkin approximation":

$$y(x, t) = \sum_{i=1}^n \Phi_i(x) q_{bi}(t) \quad (23.19)$$

The orthogonality conditions between these mode shapes can also be derived as (Meirovitch, 1986)

$$\int_0^L \rho \Phi_i(x) \Phi_j(x) dx = N_i \delta_{ij}, \quad \int_0^L EI \Phi_i''(x) \Phi_j''(x) dx = S_i \delta_{ij} \quad (23.20)$$

where $i, j = 1, 2, \dots, n$, δ_{ij} is the Kronecker delta, and N_i and S_i are defined by setting $i = j$ in Equation 23.20.

The feedback of the absorber, the actuator excitation force, and the damping dissipating forces in both the absorber and the exciter are considered as non-conservative forces in Lagrange's formulation. Consequently, the equations of motion are derived.

Absorber dynamics is governed by

$$m_a \ddot{q}_a(t) + c_a \left\{ \dot{q}_a(t) - \sum_{i=1}^n \Phi_i(a) \dot{q}_{bi}(t) \right\} + k_a \left\{ q_a(t) - \sum_{i=1}^n \Phi_i(a) q_{bi}(t) \right\} - g \ddot{q}_a(t - \tau) = 0 \quad (23.21)$$

The exciter is given by

$$m_e \ddot{q}_e(t) + c_e \left\{ \dot{q}_e(t) - \sum_{i=1}^n \Phi_i(b) \dot{q}_{bi}(t) \right\} + k_e \left\{ q_e(t) - \sum_{i=1}^n \Phi_i(b) q_{bi}(t) \right\} = -f(t) \quad (23.22)$$

Finally, the beam is represented by

$$\begin{aligned} N_i \ddot{q}_{bi}(t) + S_i q_{bi}(t) + c_a \left\{ \sum_{i=1}^n \Phi_i(a) \dot{q}_{bi}(t) - \dot{q}_a(t) \right\} \Phi_i(a) + c_e \left\{ \sum_{i=1}^n \Phi_i(b) \dot{q}_{bi}(t) - \dot{q}_e(t) \right\} \Phi_i(b) \\ + k_a \left\{ \sum_{i=1}^n \Phi_i(a) q_{bi}(t) - q_a(t) \right\} \Phi_i(a) + k_e \left\{ \sum_{i=1}^n \Phi_i(b) q_{bi}(t) - q_e(t) \right\} \Phi_i(b) + g \Phi_i(a) \ddot{q}_a(t - \tau) \\ = f(t) \Phi_i(b), \quad i = 1, 2, \dots, n \end{aligned} \quad (23.23)$$

Equation 23.21 to Equation 23.23 form a system of $n + 2$ second-order coupled differential equations.

By proper selection of the feedback gain, the absorber can be tuned to the desired resonant frequency, ω_c . This condition, in turn, forces the beam to be motionless at a , when the beam is excited by a tonal force at frequency ω_c . This conclusion is reached by taking the Laplace transform of Equation 23.21 and using feedback control law for the absorber. In short,

$$Y(a, s) = \sum_{i=1}^n \Phi_i(a) Q_{bi}(s) = 0 \quad (23.24)$$

where $Y(a, s) = \mathfrak{L}\{y(a, t)\}$, $Q_a(s) = \mathfrak{L}\{q_a(t)\}$ and $Q_{bi}(s) = \mathfrak{L}\{q_{bi}(t)\}$. Equation 23.24 can be rewritten in time domain as

$$y(a, t) = \sum_{i=1}^n \Phi_i(a) q_{bi}(t) = 0 \quad (23.25)$$

which indicates that the steady-state vibration of the point of attachment of the absorber is eliminated. Hence, the absorber mimics a resonator at the frequency of excitation and absorbs all the vibratory energy at the point of attachment.

23.3.2.1.3 Stability of the Combined System

In the preceding section, we have derived the equations of motion for the beam–exciter–absorber system in its most general form. As stated before, inclusion of the feedback control for active absorption is, indeed, an invitation to instability. This topic is treated next.

The Laplace domain representation of the combined system takes the form (Olgac and Jalili, 1998)

$$\mathbf{A}(s)\mathbf{Q}(s) = \mathbf{F}(s) \quad (23.26)$$

where

$$\mathbf{Q}(s) = \begin{Bmatrix} Q_a(s) \\ Q_e(s) \\ Q_{b1}(s) \\ \vdots \\ Q_{bn}(s) \end{Bmatrix}_{(n+2) \times 1}, \quad \mathbf{F}(s) = \begin{Bmatrix} 0 \\ -F(s) \\ 0 \\ \vdots \\ 0 \end{Bmatrix}_{(n+2) \times 1},$$

$$\mathbf{A}(s) = \begin{pmatrix} m_a s^2 + c_a s + k_a - g s^2 e^{-\tau s} & 0 & -\Phi_1(a)(c_a s + k_a) & \cdots & -\Phi_n(a)(c_a s + k_a) \\ 0 & m_e s^2 + c_e s + k_e & -\Phi_1(b)(c_e s + k_e) & \cdots & -\Phi_n(b)(c_e s + k_e) \\ m_a \Phi_1(a) s^2 & m_e \Phi_1(b) s^2 & N_1 s^2 + c s + S_1(1 + j\delta) & \cdots & 0 \\ \vdots & \vdots & \vdots & \ddots & \vdots \\ m_a \Phi_n(a) s^2 & m_e \Phi_n(b) s^2 & 0 & \cdots & N_n s^2 + c s + S_n(1 + j\delta) \end{pmatrix} \quad (23.27)$$

In order to assess the combined system stability, the roots of the characteristic equation, $\det(\mathbf{A}(s)) = 0$ are analyzed. The presence of feedback (transcendental delay term for this absorber) in the characteristic equations complicates this effort. The root locus plot observation can be applied to the entire system. It is typical that increasing feedback gain causes instability as the roots move from left to right in the complex plane. This picture also yields the frequency range for stable operation of the combined system (Olgac and Jalili, 1998).

23.3.2.1.4 Experimental Setting and Results

The experimental setup used to verify the findings is shown in [Figure 23.16](#). The primary structure is a 3/8' in. \times 1' in. \times 12' in. steel beam (2) clamped at both ends to a granite bed (1). A piezoelectric actuator with a reaction mass (3 and 4) is used to generate the periodic disturbance on the beam. A similar actuator-mass setup constitutes the DR absorber (5 and 6). The two setups are located symmetrically at one quarter of the length along the beam from the center. The feedback signal used to implement the DR is obtained from the accelerometer (7) mounted on the reaction mass of the absorber structure. The other accelerometer (8) attached to the beam is present only to monitor the vibrations of the beam and to evaluate the performance of the DR absorber in suppressing them. The control is applied *via* a fast data acquisition card using a sampling of 10 kHz.

The numerical values for this beam–absorber–exciter setup are taken as

- *Beam*: $E = 210$ GPa, $\rho = 1.8895$ kg/m
- *Absorber*: $m_a = 0.183$ kg, $k_a = 10,130$ kN/m, $c_a = 62.25$ N sec/m, $a = L/4$
- *Exciter*: $m_e = 0.173$ kg, $k_e = 6426$ kN/m, $c_e = 3.2$ N sec/m, $b = 3L/4$

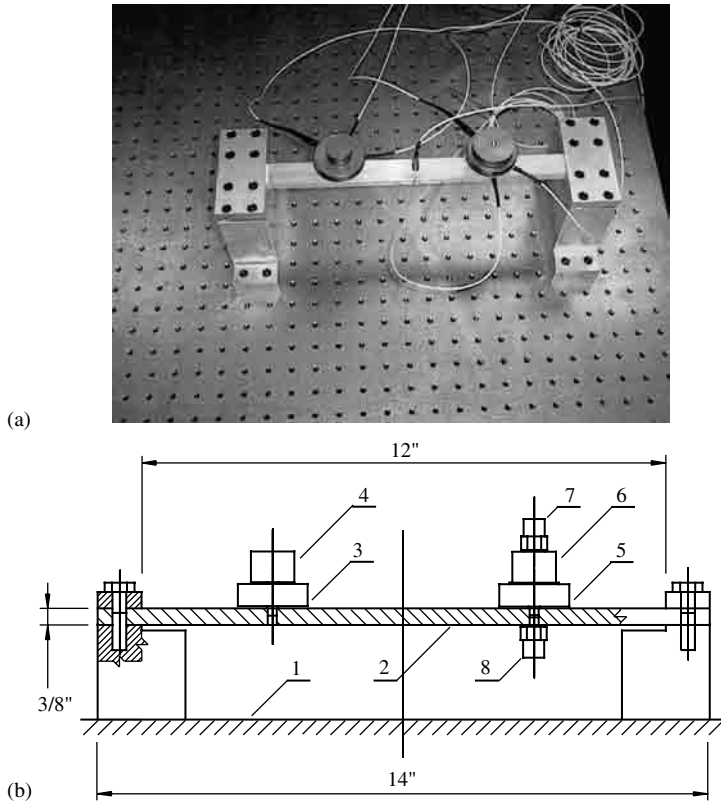


FIGURE 23.16 (a) Experimental structure and (b) schematic depiction of the setup. (Source: From Olgac, N. and Jalili, N., *J. Sound Vib.*, 218, 307–331, 1998. With permission.)

23.3.2.1.5 Dynamic Simulation and Comparison with Experiments

For the experimental set up at hand, the natural frequencies are measured for the first two natural modes, ω_1 and ω_2 . These frequencies are obtained much more precisely than those of higher-order natural modes. Table 23.1 offers a comparison between the experimental (*real*) and analytical (*ideal*) clamped–clamped beam natural frequencies.

The discrepancies arrive from two sources: first, the experimental frequencies are structurally damped natural frequencies, and second, they reflect the effect of partially clamped BCs. The theoretical frequencies, on the other hand, are evaluated for an undamped ideal clamped–clamped beam.

After observing the effect of the number of modes used on the beam deformation, a minimum of three natural modes are taken into account. We then compare the simulated time response vs. the experimental results of vibration suppression. Figure 23.17 shows a test with the excitation frequency $\omega_c = 1270$ Hz. The corresponding theoretical control parameters are $g_{c \text{ theory}} = 0.0252$ kg and $\tau_{c \text{ theory}} = 0.8269$ msec. The experimental control parameters for this frequency are found to be $g_{c \text{ exp.}} = 0.0273$ kg and $\tau_{c \text{ exp.}} = 0.82$ msec. The exciter disturbs the beam for 5 msec, then the DR tuning is triggered. The acceleration of the beam at the point of attachment decays exponentially. For all intents and purposes, the suppression takes effect in approximately 200 ms. These results match very closely with the experimental data, Figure 23.18. The only noticeable difference is in the frequency content of the exponential decay. This property is dictated by the dominant poles of the combined system. The imaginary part, however, is smaller in the analytical study. This difference is a nuance that does not affect the earlier observations.

TABLE 23.1 Comparison between Experimental and Theoretical Beam Natural Frequencies (Hz)

Natural Modes	Peak Frequencies (Experimental)	Natural Frequencies (Clamped–Clamped)
First mode	466.4	545.5
Second mode	1269.2	1506.3

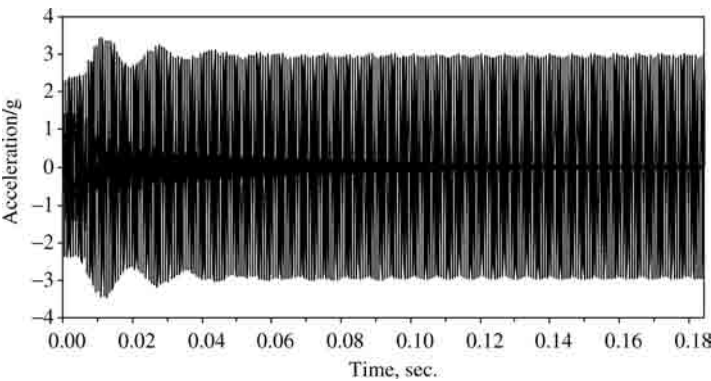


FIGURE 23.17 Beam and absorber response to 1270 Hz disturbance, analytical. (Source: From Olgac, N. and Jalili, N., *J. Sound Vib.*, 218, 307–331, 1998. With permission.)

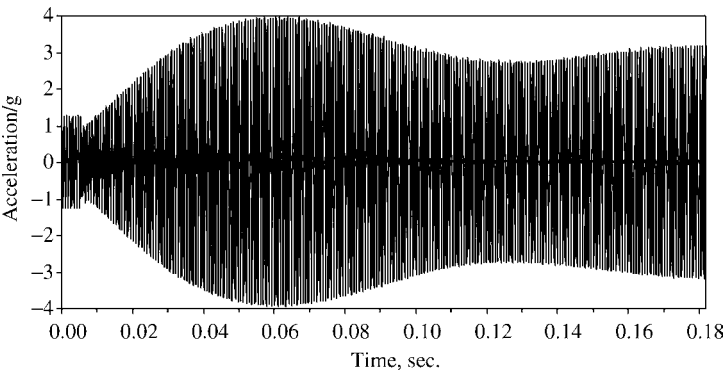


FIGURE 23.18 Beam and absorber response to 1270 Hz disturbance, experimental. (Source: From Olgac, N. and Jalili, N., *J. Sound Vib.*, 218, 307–331, 1998. With permission.)

23.3.2.2 Active Resonator Vibration Absorbers

One novel implementation of the tuned vibration absorbers is the ARA (Knowles et al., 2001b). The concept of the ARA is closely related to the concept of the delayed resonator (Olgac and Holm-Hansen, 1994; Olgac and Jalili, 1999). Using a simple position (or velocity or acceleration) feedback control within the absorber section, it enforces the dominant characteristic roots of the absorber subsection to be on the imaginary axis, and hence leading to resonance. Once the ARA becomes resonant, it creates perfect vibration absorption at this frequency.

A very important component of any active vibration absorber is the actuator unit. Recent advances in smart materials have led to the development of advanced actuators using piezoelectric ceramics, shape memory alloys, and magnetostrictive materials (Garcia et al., 1992; Shaw, 1998). Over the past two decades, piezoelectric ceramics have been utilized as potential replacements for conventional transducers.

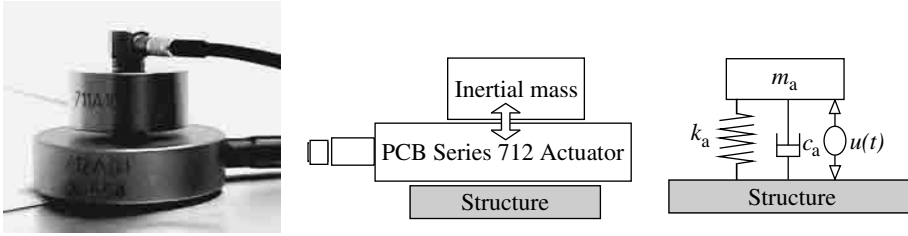


FIGURE 23.19 A PCB series 712 PZT inertial actuator (left), schematic of operation (middle), and a simple single-DoF mathematical model (right). (Active Vibration Control Instrumentation, A Division of PCB Piezotronics, Inc., www.pcb.com.)

These materials are compounds of lead zirconate–titanate (PZT). The PZT properties can be optimized to suit specific applications by appropriate adjustment of the zirconate–titanate ratio. Specifically, a piezoelectric inertial actuator is an efficient and inexpensive solution for active structural vibration control. As shown in Figure 23.19, it applies a point force to the structure to which it is attached.

23.3.2.2.1 An Overview of PZT Inertial Actuators

PZT inertial actuators are most commonly made out of two parallel piezoelectric plates. If voltage is applied, one of the plates expands as the other one contracts, hence producing displacement that is proportional to the input voltage. The resonance of such an actuator can be adjusted by the size of the inertial mass (see Figure 23.19). Increasing the size of the inertial mass will lower the resonant frequency and decreasing the mass will increase it. The resonant frequency, f_r , can be expressed as

$$f_r = \frac{1}{2\pi} \sqrt{\frac{k_a}{m_a}} \quad (23.28)$$

where k_a is the effective stiffness of the actuator, m_a , is defined as

$$m_a = m_{\text{ePZT}} + m_{\text{inertial}} + m_{\text{acc}} \quad (23.29)$$

The PZT effective mass is m_{ePZT} , m_{inertial} is the inertial mass, and m_{acc} is the accelerometer mass. Using a simple single-DoF system (see Figure 23.19), the parameters of the PZT inertial actuators can be experimentally determined (Knowles et al., 2001a). This “parameter identification” problem is an inverse problem. We refer interested readers to Banks and Ito (1988) and Banks and Kunisch (1989) for a general introduction to parameter estimation or inverse problems governed by differential equations.

23.3.2.2.2 Active Resonator Absorber Concept

The concept of ARA is closely related to that of the DR (Olgac, 1995; Olgac and Holm-Hansen, 1995; Olgac and Jalili, 1998). Instead of a compensator, the DR uses a simple delayed position (or velocity, or acceleration) feedback control within the absorber subsection for the mentioned “sensitization.”

In contrast to that of the DR absorber, the characteristic equation of the proposed control scheme is rational in nature and is hence easier to implement when closed-loop stability of the system is concerned. Similar to the DR absorber, the proposed ARA requires only one signal from the absorber mass, absolute or relative to the point of attachment (see Figure 23.7 bottom). After the signal is processed through a compensator, an additional force is produced, for instance, by a PZT inertial actuator. If the compensator parameters are properly set, the absorber should behave as an ideal resonator at one or even more frequencies. As a result, the resonator will absorb vibratory energy from the primary mass at given frequencies. The frequency to be absorbed can be tuned in real time. Moreover, if the controller or the actuator fails, the ARA will still function as a passive absorber, and thus it is inherently fail-safe. A similar vibration absorption methodology is given by Filipović and Schröder (1999) for linear systems. The ARA, however, is not confined to the linear regime.

For the case of linear assumption for the PZT actuator, the dynamics of the ARA (Figure 23.7, bottom) can be expressed as

$$m_a \ddot{x}_a(t) + c_a \dot{x}_a(t) + k_a x_a(t) - u(t) = c_a \dot{x}_1(t) + k_a x_1(t) \quad (23.30)$$

where $x_1(t)$ and $x_a(t)$ are the respective primary (at the absorber point of attachment) and absorber mass displacements. The mass, m_a , is given by Equation 23.29 and the control, $u(t)$, is designed to produce designated resonance frequencies within the ARA.

The objective of the feedback control, $u(t)$, is to convert the dissipative structure (Figure 23.7, top) into a conservative or marginally stable one (Figure 23.7, bottom) with a designated resonant frequency, ω_c . In other words, the control aims the placement of dominant poles at $\pm j\omega_c$ for the combined system, where $j = \sqrt{-1}$ (see Figure 23.14). As a result, the ARA becomes marginally stable at particular frequencies in the determined frequency range. Using simple position (or velocity or acceleration) feedback within the absorber section (i.e., $U(s) = \bar{U}(s)X_a(s)$), the corresponding dynamics of the ARA, given by Equation 23.30, in the Laplace domain become

$$(m_a s^2 + c_a s + k_a)X_a(s) - \bar{U}(s)X_a(s) = C(s)X_a(s) = (c_a s + k_a)X_1(s) \quad (23.31)$$

The compensator transfer function, $\bar{U}(s)$, is then selected such that the primary system displacement at the absorber point of attachment is forced to be zero; that is

$$C(s) = (m_a s^2 + c_a s + k_a) - \bar{U}(s) = 0 \quad (23.32)$$

The parameters of the compensator are determined through introducing resonance conditions to the absorber characteristic equation, $C(s)$; that is, the equations $\text{Re}\{C(j\omega_i)\} = 0$ and $\text{Im}\{C(j\omega_i)\} = 0$ are simultaneously solved, where $i = 1, 2, \dots, l$ and l is the number of frequencies to be absorbed. Using additional compensator parameters, the stable frequency range or other properties can be adjusted in real time.

Consider the case where $U(s)$ is taken as a proportional compensator with a single time constant based on the acceleration of the ARA, given by

$$U(s) = \bar{U}(s)X_a(s), \quad \text{where } \bar{U}(s) = \frac{g s^2}{1 + T s} \quad (23.33)$$

Then, in the time domain, the control force, $u(t)$, can be obtained from

$$u(t) = \frac{g}{T} \int_0^t e^{-(t-\tau)/T} \ddot{x}_a(\tau) d\tau \quad (23.34)$$

To achieve ideal resonator behavior, two dominant roots of Equation 23.32 are placed on the imaginary axis at the desired crossing frequency, ω_c . Substituting $s = \pm j\omega_c$ into Equation 23.32 and solving for the control parameters, g_c and T_c , one can obtain

$$g_c = m_a \left(\frac{c_a^2}{m_a^2 \left(\omega^2 - \frac{k_a}{m_a} \right)} - \frac{k_a}{m_a \omega^2} + 1 \right), \quad T_c = \frac{c_a \sqrt{k_a/m_a}}{\sqrt{m_a k_a} \left(\omega^2 - \frac{k_a}{m_a} \right)}, \quad \text{for } \omega = \omega_c \quad (23.35)$$

The control parameters, g_c and T_c , are based on the physical properties of the ARA (i.e., c_a , k_a , and m_a) as well as the frequency of the disturbance, ω , illustrating that the ARA does not require any information from the primary system to which it is attached. However, when the physical properties of the ARA are not known within a high degree of certainty, a method to autotune the control parameters must be considered. The stability assurance of such autotuning proposition will bring primary system parameters into the derivations, and hence the primary system cannot be totally decoupled. This issue will be discussed later in the chapter.

23.3.2.2.3 Application of ARA to Structural-Vibration Control

In order to demonstrate the effectiveness of the proposed ARA, a simple single-DoF primary system subjected to tonal force excitations is considered. As shown in Figure 23.20, two PZT inertial actuators are used for both the primary (model 712-A01) and the absorber (model 712-A02) subsections. Each system consists of passive elements (spring stiffness and damping properties of the PZT materials) and active compartment with the physical parameters listed in Table 23.2. The top actuator acts as the ARA with the controlled force, $u(t)$, while the bottom one represents the primary system subjected to the force excitation, $f(t)$.

The governing dynamics for the combined system can be expressed as

$$m_a \ddot{x}_a(t) + c_a \dot{x}_a(t) + k_a x_a(t) - u(t) = c_a \dot{x}_1(t) + k_a x_1(t) \quad (23.36)$$

$$m_1 \ddot{x}_1(t) + (c_1 + c_a) \dot{x}_1(t) + (k_1 + k_a) x_1(t) - \{c_a \dot{x}_a(t) + k_a x_a(t) - u(t)\} = f(t) \quad (23.37)$$

where $x_1(t)$ and $x_a(t)$ are the respective primary and absorber displacements.

23.3.2.2.4 Stability Analysis and Parameter Sensitivity

The sufficient and necessary condition for asymptotic stability is that all roots of the characteristic equation have negative real parts. For the linear system, Equation 23.36 and Equation 23.37, when utilizing controller (Equation 23.34), the characteristic equation of the combined system (Figure 23.20, right) can be determined and the stability region for compensator parameters, g and T , can be obtained using the Routh–Hurwitz method.

23.3.2.2.5 Autotuning Proposition

When using the proposed ARA configuration in real applications where the physical properties are not known or vary over time, the compensator parameters, g and T , only provide partial vibration suppression. In order to remedy this, a need exists for an autotuning method to adjust the compensator

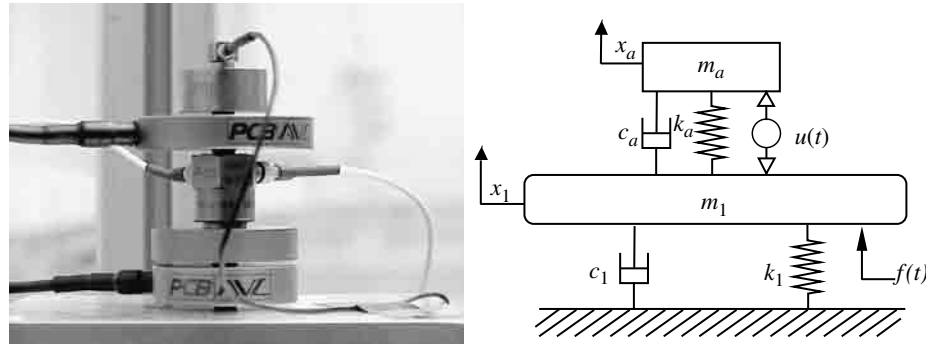


FIGURE 23.20 Implementation of the ARA concept using two PZT actuators (left) and its mathematical model (right).

TABLE 23.2 Experimentally Determined Parameters of PCB Series 712 PZT Inertial Actuators

PZT System Parameters	PCB Model 712-A01	PCB Model 712-A02
Effective mass, m_{ePZT} (gr)	7.20	12.14
Inertial mass, m_{inertial} (gr)	100.00	200.00
Stiffness, k_a (kN/m)	3814.9	401.5
Damping, c_a (Ns/m)	79.49	11.48

parameters, g and T , by some quantities, Δg and ΔT , respectively (Jalili and Olgac, 1998b; Jalili and Olgac, 2000a). For the case of the linear compensator with a single time constant, given by Equation 23.33, the transfer function between primary displacement, $X_1(s)$, and absorber displacement, $X_a(s)$, can be obtained as

$$G(s) = \frac{X_1(s)}{X_a(s)} = \frac{m_a s^2 + c_a s + k_a - \frac{g s^2}{1 + Ts}}{c_a s + k_a} \quad (23.38)$$

The transfer function can be rewritten in the frequency domain for $s = j\omega$ as

$$G(j\omega) = \frac{X_1(j\omega)}{X_a(j\omega)} = \frac{-m_a \omega^2 + c_a j\omega + k_a + \frac{g \omega^2}{1 + Tj\omega}}{c_a j\omega + k_a} \quad (23.39)$$

where $G(j\omega)$ can be obtained in real time by convolution of accelerometer readings (Renzulli et al., 1999) or other methods (Jalili and Olgac, 2000a). Following a similar procedure as is utilized in Renzulli et al. (1999), the numerator of the transfer function (Equation 23.39) must approach zero in order to suppress primary system vibration. This is accomplished by setting

$$G(j\omega) + \Delta G(j\omega) = 0 \quad (23.40)$$

where $G(j\omega)$ is the real-time transfer function and $\Delta G(j\omega)$ can be written as a variational form of Equation 23.39 as

$$\Delta G(j\omega) = \frac{\partial G}{\partial g} \Delta g + \frac{\partial G}{\partial T} \Delta T + \text{higher order terms} \quad (23.41)$$

Since the estimated physical parameters of the absorber (i.e., c_a , k_a , and m_a) are within the vicinity of the actual parameters, Δg and ΔT should be small quantities and the higher-order terms of Equation 23.41 can be neglected. Using Equation 23.40 and Equation 23.41 and neglecting higher-order terms, we have

$$\begin{aligned} \Delta g &= \text{Re}[G(j\omega)] \left[\frac{2Tc_a \omega^2 - k_a + k_a T^2 \omega^2}{\omega^2} \right] + \text{Im}[G(j\omega)] \left[\frac{c_a - T^2 \omega^2 c_a + 2k_a T}{\omega^2} \right], \\ \Delta T &= \text{Re}[G(j\omega)] \left[\frac{c_a - T^2 \omega^2 c_a + 2k_a T}{g \omega^2} \right] + \text{Im}[G(j\omega)] \left[\frac{k_a - 2Tc_a \omega^2 - k_a T^2 \omega^2}{g \omega^3} \right] + \frac{T}{g} \Delta g \end{aligned} \quad (23.42)$$

In the above expressions, g and T are the current compensator parameters given by Equation 23.35, c_a , k_a , and m_a are the estimated absorber parameters, ω is the absorber base excitation frequency, and $G(j\omega)$ is the transfer function obtained in real time. That is, the retuned control parameters, g and T , are determined as follows

$$g_{\text{new}} = g_{\text{current}} + \Delta g \quad \text{and} \quad T_{\text{new}} = T_{\text{current}} + \Delta T \quad (23.43)$$

where Δg and ΔT are those given by Equation 23.42. After compensator parameters, g and T , are adjusted by Equation 23.43, the process can be repeated until $|G(j\omega)|$ falls within the desired level of tolerance. $G(j\omega)$ can be determined in real time as shown in Liu et al. (1997) by

$$G(j\omega) = |G(j\omega)| e^{(j\phi(j\omega))} \quad (23.44)$$

where the magnitude and phase are determined assuming that the absorber and primary displacements are harmonic functions of time given by

$$x_a(t) = X_a \sin(\omega t + \phi_a), \quad x_1(t) = X_1 \sin(\omega t + \phi_1) \quad (23.45)$$

With the magnitudes and phase angles of Equation 23.44, the transfer function can be determined from Equation 23.44 and the following:

$$|G(j\omega)| = \frac{X_1}{X_a}, \quad \phi(j\omega) = \phi_1 - \phi_a$$

23.3.2.2.6 Numerical Simulations and Discussions

To illustrate the feasibility of the proposed absorption methodology, an example case study is presented. The ARA control law is the proportional compensator with a single time constant as given in Equation 23.34. The primary system is subjected to a harmonic excitation with unit amplitude and a frequency of 800 Hz. The ARA and primary system parameters are taken as those given in Table 23.2. The simulation was done using Matlab/Simulink® and the results for the primary system and the absorber displacements are given in Figure 23.21.

As seen, vibrations are completely suppressed in the primary subsection after approximately 0.05 sec, at which the absorber acts as a marginally stable resonator. For this case, all physical parameters are assumed to be known exactly. However, in practice these parameters are not known exactly and may vary with time, so the case with estimated system parameters must be considered.

To demonstrate the feasibility of the proposed autotuning method, the nominal system parameters (m_a , m_1 , k_a , k_1 , c_a , c_1) were fictitiously perturbed by 10% (i.e., representing the actual values) in the simulation. However, the nominal values of m_a , m_1 , k_a , k_1 , c_a , and c_1 were used for calculation of the compensator parameters, g and T . The results of the simulation using nominal parameters are given in Figure 23.22. From Figure 23.22, top, the effect of parameter variation is shown as steady-state oscillations of the primary structure. This undesirable response will undoubtedly be encountered when the experiment is implemented. Thus, an autotuning procedure is needed.

The result of the first autotuning iteration is given in Figure 23.22, middle, where the control parameters, g and T , are adjusted based on Equation 23.43. One can see tremendous improvement in the primary system response with only one iteration (see Figure 23.22, middle). A second iteration is

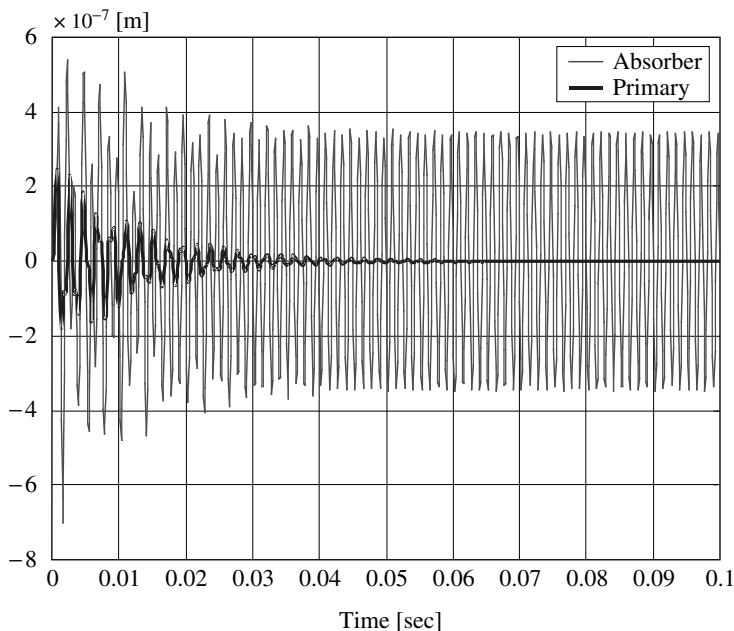


FIGURE 23.21 Primary system and absorber displacements subjected to 800 Hz harmonic disturbance.

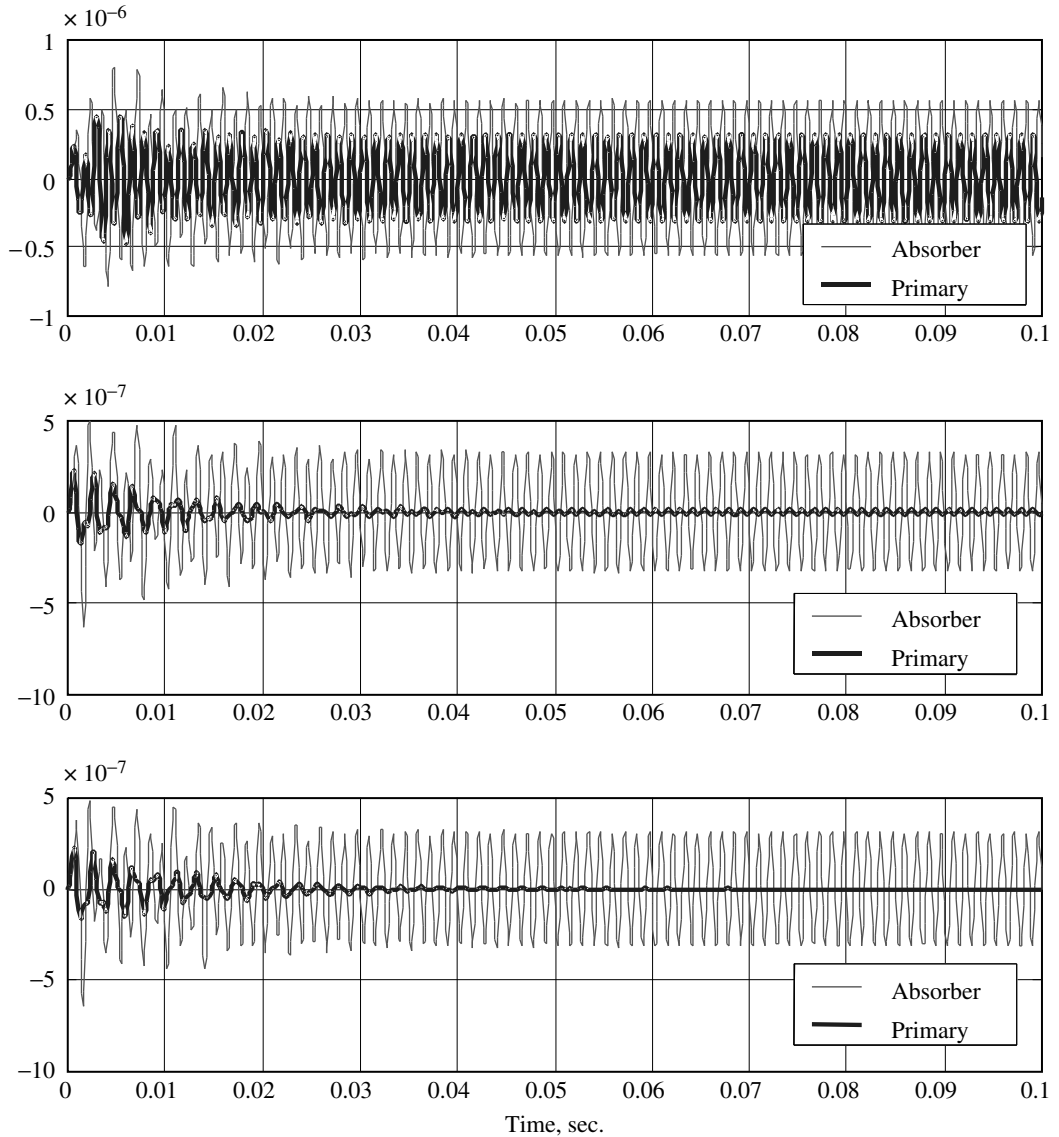


FIGURE 23.22 System responses (displacement, m) for (a) nominal absorber parameters; (b) after first autotuning procedure and (c) after second autotuning procedure.

performed, as shown in Figure 23.22, bottom. The response closely resembles that from Figure 23.21, where all system parameters are assumed to be known exactly.

23.3.3 Vibration-Control Systems

As discussed, in vibration-control schemes, the control inputs to the systems are altered in order to regulate or track a desired trajectory while simultaneously suppressing the vibrational transients in the system. This control problem is rather challenging since it must achieve the motion-tracking objectives while stabilizing the transient vibrations in the system. This section provides two recent control methods developed for the regulation and tracking of flexible beams. The experimental implementations are also discussed. The first control method is a single-input vibration-control system discussed in

Section 23.3.3.1, while the second application utilizes a secondary input control in addition to the primary control input to improve the vibrational characteristics of the system (see Section 23.3.3.2).

23.3.3.1 Variable Structure Control of Rotating Flexible Beams

The vibration-control problem of a flexible manipulator consists in achieving the motion-tracking objectives while stabilizing the transient vibrations in the arm. Several control methods have been developed for flexible arms (Skaar and Tucker, 1986; Bayo, 1987; Yuh, 1987; Sinha, 1988; Lou, 1993; Ge et al., 1997; de Querioz et al., 1999). Most of these methods concentrate on a model-based controller design, and some of these may not be easy to implement due to the uncertainties in the design model, large variations of the loads, ignored high frequency dynamics, and high order of the designed controllers. In view of these methods, VSC is particularly attractive due to its simplicity of implementation and its robustness to parameter uncertainties (Yeung and Chen, 1989; Singh et al., 1994; Jalili et al., 1997).

23.3.3.1.1 Mathematical Modeling

As shown in Figure 23.23, one end of the arm is free and the other end is rigidly attached to a vertical gear shaft, driven by a DC motor. A uniform cross section is considered for the arm, and we make the Euler–Bernoulli assumptions. The control torque, τ , acting on the output shaft, is normal to the plane of motion. Viscous frictions and the ever-present unmodeled dynamics of the motor compartment are to be compensated *via* a perturbation estimation process, as explained later in the text. Since the dynamic system considered here has been utilized in literature quite often, we present only the resulting partial differential equation (PDE) of the system and refer interested readers to Junkins and Kim (1993) and Luo et al. (1999) for detailed derivations.

The system is governed by

$$I_h \ddot{\theta}(t) + \rho \int_0^L x \ddot{z}(x, t) dx = \tau \quad (23.46)$$

$$\rho \ddot{z}(x, t) + EI z''''(x, t) = 0 \quad (23.47)$$

with the corresponding boundary conditions

$$z(0, t) = 0, \quad z'(0, t) = \theta(t), \quad z''(L, t) = 0, \quad z'''(L, t) = 0 \quad (23.48)$$

where ρ is the arm's linear mass density, L is the arm length, E is Young's modulus of elasticity, I is the cross-sectional moment of inertia, I_h is the equivalent mass moment of inertia at the root end of the arm, $I_t = I_h + \rho L^3/3$ is the total inertia, and the global variable z is defined as

$$z(x, t) = x\theta(t) + y(x, t) \quad (23.49)$$

Clearly, the arm vibration equation (Equation 23.47) is a homogeneous PDE but the boundary conditions (Equation 23.48) are nonhomogeneous. Therefore, the closed form solution is very tedious to obtain, if not impossible. Using the application of VSC, these equations and their associated boundary conditions can be converted to a homogeneous boundary value problem, as discussed next.

23.3.3.1.2 Variable Structure Controller

The controller objective is to track the arm angular displacement from an initial angle, $\theta_d = \theta(0)$, to zero position, $\theta(t \rightarrow \infty) = 0$, while minimizing the flexible arm oscillations. To achieve the control

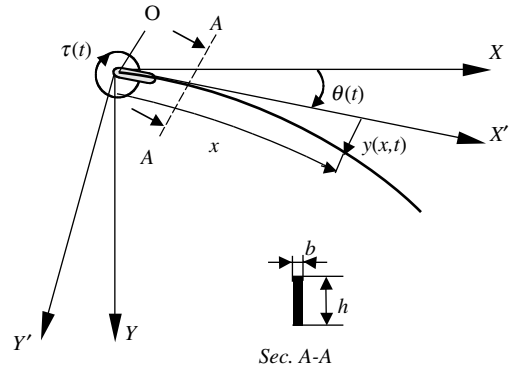


FIGURE 23.23 Flexible arm in the horizontal plane and kinematics of deformation. (Source: From Jalili, N., *ASME J. Dyn. Syst. Meas. Control*, 123, 712–719, 2001. With permission.)

insensitivity against modeling uncertainties, the nonlinear control routine of sliding mode control with an additional perturbation estimation (SMCPE) compartment is adopted here (Elmali and Olgac, 1992; Jalili and Olgac, 1998a). The SMCPE method, presented in Elmali and Olgac (1992), has many attractive features, but it suffers from the disadvantages associated with the truncated-model-base controllers. On the other hand, the infinite-dimensional distributed (IDD)-base controller design, proposed in Zhu et al. (1997), has practical limitations due to its measurement requirements in addition to the complex control law.

Initiating from the idea of the IDD-base controller, we present a new controller design approach in which an online perturbation estimation mechanism is introduced and integrated with the controller to relax the measurement requirements and simplify the control implementation. As utilized in Zhu et al. (1997), for the tip-vibration suppression, it is further required that the sliding surface enable the transformation of nonhomogeneous boundary conditions (Equation 23.48) to homogeneous ones. To satisfy vibration suppression and robustness requirements simultaneously, the sliding hyperplane is selected as a combination of tracking (regulation) error and arm flexible vibration as

$$s = \dot{w} + \sigma w \quad (23.50)$$

where $\sigma > 0$ is a control parameter and

$$w = \theta(t) + \frac{\mu}{L} z(L, t) \quad (23.51)$$

with the scalar, μ , being selected later. When $\mu = 0$, controller (Equation 23.50) reduces to a sliding variable for rigid-link manipulators (Jalili and Olgac, 1998a; Yeung and Chen, 1988). The motivation for such sliding a variable is to provide a suitable boundary condition for solving the beam Equation 23.47, as will be discussed next and is detailed in Jalili (2001).

For the system described by Equation 23.46 to Equation 23.48, if the variable structure controller is given by

$$\tau = \psi_{\text{est}} + \frac{I_t}{1 + \mu} \left(-k \operatorname{sgn}(s) - Ps - \frac{\mu}{L} \ddot{y}(L, t) - \sigma(1 + \mu) \dot{\theta} - \frac{\sigma\mu}{L} \dot{y}(L, t) \right) \quad (23.52)$$

where ψ_{est} is an estimate of the beam flexibility effect

$$\psi = \rho \int_0^L x \ddot{y}(x, t) dx \quad (23.53)$$

k and P are positive scalars $k \geq 1 + \mu/I_t |\psi - \psi_{\text{est}}|$, $-1.2 < \mu < -0.45$, $\mu \neq -1$ and $\operatorname{sgn}(\cdot)$ represents the standard signum function, then, the system's motion will first reach the sliding mode $s = 0$ in a finite time, and consequently converge to the equilibrium position $w(x, t) = 0$ exponentially with a time-constant $1/\sigma$ (Jalili, 2001).

23.3.3.1.3 Controller Implementation

In the preceding section, it was shown that by properly selecting control variable, μ , the motion exponentially converges to $w = 0$ with a time-constant $1/\sigma$, while the arm stops in a finite time. Although the discontinuous nature of the controller introduces a robustifying mechanism, we have made the scheme more insensitive to parametric variations and unmodeled dynamics by reducing the required measurements and hence easier control implementation. The remaining measurements and ever-present modeling imperfection effects have all been estimated through an online estimation process. As stated before, in order to simplify the control implementation and reduce the measurement effort, the effect of all uncertainties, including flexibility effect ($\int_0^L x \ddot{y}(x, t) dx$) and the ever-present unmodeled dynamics, is gathered into a single quantity named perturbation, ψ , as given by Equation 23.53. Noting Equation 23.46, the perturbation term can be expressed as

$$\psi = \tau - I_t \ddot{\theta}(t) \quad (23.54)$$

which requires the yet-unknown control feedback τ . In order to resolve this dilemma of causality, the current value of control torque, τ , is replaced by the most recent control, $\tau(t - \delta)$, where δ is the small time-step used for the loop closure. This replacement is justifiable in practice since such an algorithm is implemented on a digital computer and the sampling speed is high enough to claim this. Also, in the absence of measurement noise, $\ddot{\theta}(t) \cong \ddot{\theta}_{\text{cal}}(t) = [\dot{\theta}(t) - \dot{\theta}(t - \delta)]/\delta$.

In practice and in the presence of measurement noise, appropriate filtering may be considered and combined with these approximate derivatives. This technique is referred to as “switched derivatives”. This backward differences are shown to be effective when δ is selected to be small enough and the controller is run on a fast DSP (Cannon and Schmitz, 1984). Also, $\ddot{y}(L, t)$ can be obtained by attaching an accelerometer at arm-tip position. All the required signals are, therefore, measurable by currently available sensor facilities and the controller is thus realizable in practice. Although these signals may be quite inaccurate, it should be pointed out that the signals, either measurements or estimations, need not be known very accurately, since robust sliding control can be achieved if k is chosen to be large enough to cover the error existing in the measurement/signal estimation (Yeung and Chen, 1989).

23.3.3.1.4 Numerical Simulations

In order to show the effectiveness of the proposed controller, a lightweight flexible arm is considered ($h \gg b$ in Figure 23.23). For numerical results, we consider $\theta_a = \theta(0) = \pi/2$ for the initial arm base angle, with zero initial conditions for the rest of the state variables. The system parameters are listed in Table 23.3. Utilizing assumed mode model (AMM), the arm vibration, Equation 23.47, is truncated to three modes and used in the simulations. It should be noted that the controller law, Equation 23.52, is based on the original infinite dimensional equation, and this truncation is utilized only for simulation purposes.

We take the controller parameter $\mu = -0.66$, $P = 7.0$, $k = 5$, $\varepsilon = 0.01$ and $\sigma = 0.8$. In practice, σ is selected for maximum tracking accuracy taking into account unmodeled dynamics and actuator hardware limitations (Moura et al., 1997). Although such restrictions do not exist in simulations (i.e., with ideal actuators, high sampling frequencies and perfect measurements), this selection of σ was decided based on actual experiment conditions.

The sampling rate for the simulations is $\delta = 0.0005$ sec, while data are recorded at the rate of only 0.002 sec for plotting purposes. The system responses to the proposed control scheme are shown in Figure 23.24. The arm-base angular position reaches the desired position, $\theta = 0$, in approximately 4 to 5 sec, which is in agreement with the approximate settling time of $t_s = 4/\sigma$ (Figure 23.24a). As soon as the system reaches the sliding mode layer, $|\dot{s}| < \varepsilon$ (Figure 23.24d), the tip vibrations stop (Figure 23.24b), which demonstrates the feasibility of the proposed control technique. The control torque exhibits some residual vibration, as shown in Figure 23.24c. This residual oscillation is expected since the system

TABLE 23.3 System Parameters Used in Numerical Simulations and Experimental Setup for Rotating Arm

Properties	Symbol	Value	Unit
Arm Young's modulus	E	207×10^9	N/m ²
Arm thickness	b	0.0008	m
Arm height	h	0.02	m
Arm length	L	0.45	m
Arm linear mass density	ρ	0.06/L	kg/m
Total arm base inertia	I_h	0.002	kg m ²
Gearbox ratio	N	14:1	—
Light source mass	—	0.05	kg
Position sensor sensitivity	—	0.39	V/cm
Motor back EMF constant	K_b	0.0077	V/rad/sec
Motor torque constant	K_t	0.0077	N m/A
Armature resistance	R_a	2.6	Ω
Armature inductance	L_a	0.18	mH
Encoder resolution	—	0.087	Deg/count

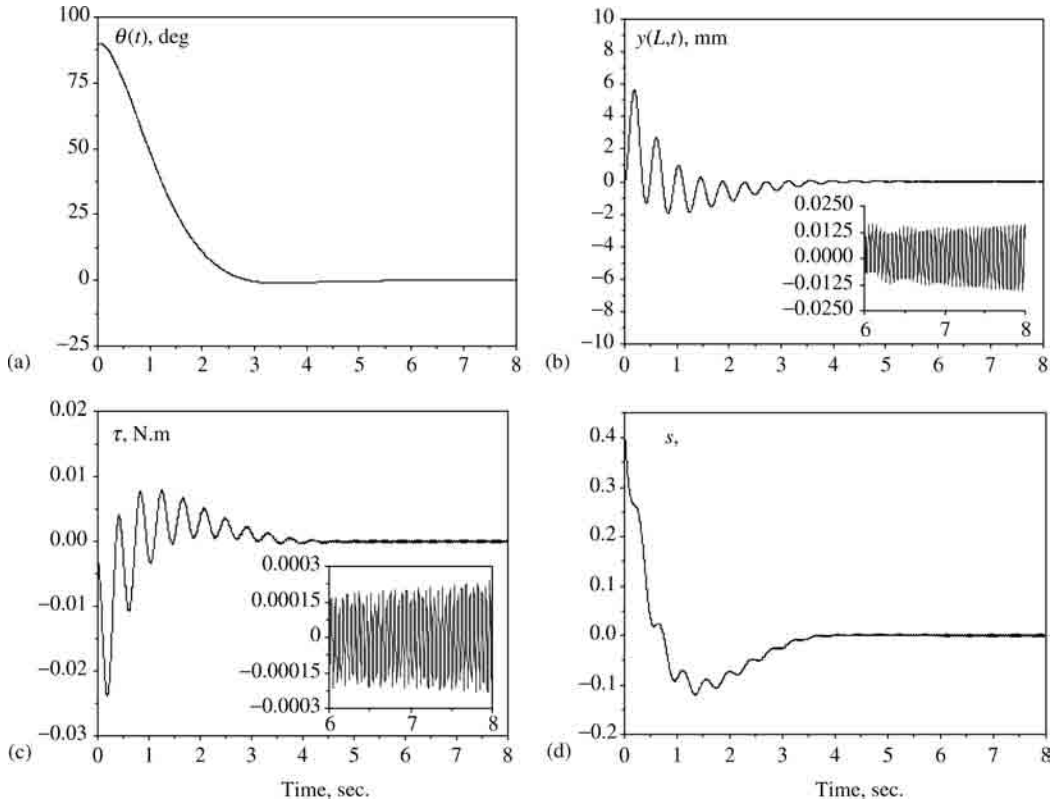


FIGURE 23.24 Analytical system responses to controller with inclusion of arm flexibility, that is, $\mu = -0.66$: (a) arm angular position; (b) arm-tip deflection; (c) control torque and (d) sliding variable sec. (Source: From Jalili, N., *ASME J. Dyn. Syst. Meas. Control*, 123, 712–719, 2001. With permission.)

motion is not forced to stay on $s = 0$ surface (instead it is forced to stay on $|s| < \varepsilon$) when saturation function is used. The sliding variable s is also depicted in Figure 23.24d. To demonstrate better the feature of the controller, the system responses are displayed when $\mu = 0$ (Figure 23.25). As discussed, $\mu = 0$ corresponds to the sliding variable for the rigid link. The undesirable oscillations at the arm tip are evident (see Figure 23.25b and c).

23.3.3.1.5 Control Experiments

In order to demonstrate better the effectiveness of the controller, an experimental setup is constructed and used to verify the numerical results and concepts discussed in the preceding sections. The experimental setup is shown in Figure 23.26. The arm is a slender beam made of stainless steel, with the same dimensions as used in the simulations. The experimental setup parameters are listed in Table 23.3. One end of the arm is clamped to a solid clamping fixture, which is driven by a high-quality DC servomotor. The motor drives a built-in gearbox ($N = 14:1$) whose output drives an antibacklash gear. The antibacklash gear, which is equipped with a precision encoder, is utilized to measure the arm base angle as well as to eliminate the backlash. For tip deflection, a light source is attached to the tip of the arm, which is detected by a camera mounted on the rotating base.

The DC motor can be modeled as a standard armature circuit; that is, the applied voltage, v , to the DC motor is

$$v = R_a i_a + L_a \frac{di_a}{dt} + K_b \dot{\theta}_m \quad (23.55)$$

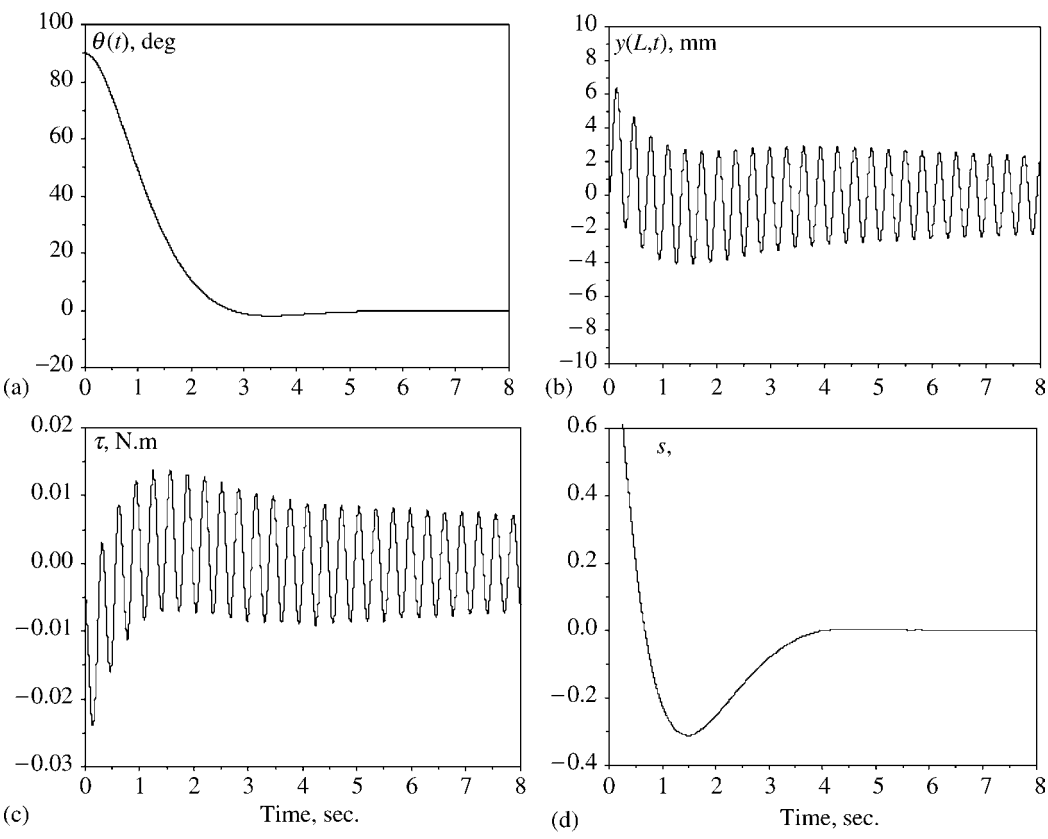


FIGURE 23.25 Analytical system responses to controller without inclusion of arm flexibility, that is, $\mu = 0$: (a) arm angular position; (b) arm-tip deflection; (c) control torque and (d) sliding variable sec. (Source: From Jalili, N., *ASME J. Dyn. Syst. Meas. Control*, 123, 712–719, 2001. With permission.)

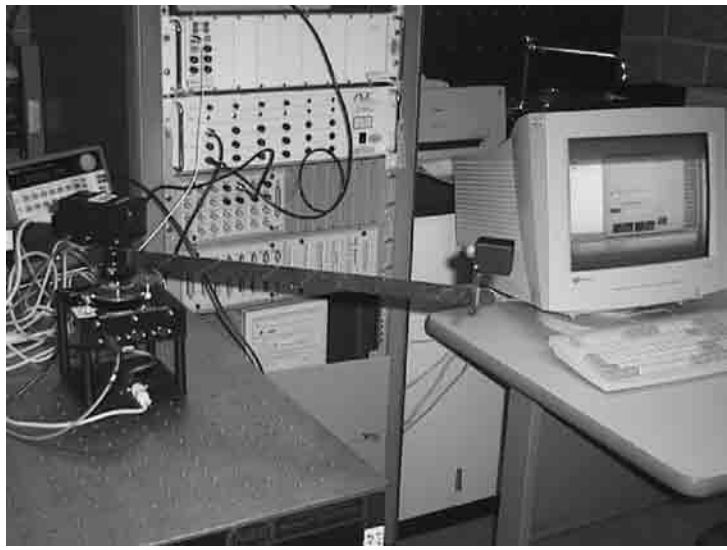


FIGURE 23.26 The experimental device and setup configuration. (Source: From Jalili, N., *ASME J. Dyn. Syst. Meas. Control*, 123, 712–719, 2001. With permission.)

where R_a is the armature resistance, L_a is the armature inductance, i_a is the armature current, K_b is the back-EMF (electro-motive-force) constant, and θ_m is the motor shaft position. The motor torque, τ_m from the motor shaft with the torque constant, K_t , can be written as

$$\tau_m = K_t i_a \quad (23.56)$$

The motor dynamics thus become

$$I_e \ddot{\theta}_m + C_v \dot{\theta}_m + \tau_a = \tau_m = K_t i_a \quad (23.57)$$

where C_v is the equivalent damping constant of the motor, and $I_e = I_m + I_L/N^2$ is the equivalent inertia load including motor inertia, I_m , and gearbox, clamping frame and camera inertia, I_L . The available torque from the motor shaft for the arm is τ_a .

Utilizing the gearbox from the motor shaft to the output shaft and ignoring the motor electric time constant, (L_a/R_a) , one can relate the servomotor input voltage to the applied torque (acting on the arm) as

$$\tau = \frac{NK_t}{R_a} v - \left(C_v + \frac{K_t K_b}{R_a} \right) N^2 \dot{\theta} - I_h \ddot{\theta} \quad (23.58)$$

where $I_h = N^2 I_e$ is the equivalent inertia of the arm base used in the derivation of governing equations. By substituting this torque into the control law, the reference input voltage, V , is obtained for experiment.

The control torque is applied *via* a digital signal processor (DSP) with sampling rate of 10 kHz, while data are recorded at the rate 500 Hz (for plotting purposes only). The DSP runs the control routine in a single-input–single-output mode as a free standing CPU. Most of the computations and hardware commands are done on the DSP card. For this setup, a dedicated 500 MHz Pentium III serves as the host PC, and a state-of-the-art dSPACE® DS1103 PPC controller board equipped with a Motorola Power PC 604e at 333 MHz, 16 channels ADC, 12 channels DAC, as microprocessor.

The experimental system responses are shown in Figure 23.27 and Figure 23.28 for similar cases discussed in the numerical simulation section. Figure 23.27 represents the system responses when controller (Equation 23.52) utilizes the flexible arm (i.e., $\mu = -0.66$). As seen, the arm base reaches the desired position (Figure 23.27a), while tip deflection is simultaneously stopped (Figure 23.27b). The good correspondence between analytical results (Figure 23.24) and experimental findings (Figure 23.27) is noticeable from a vibration suppression characteristics point of view. It should be noted that the controller is based on the original governing equations, with arm-base angular position and tip deflection measurements only. The unmodeled dynamics, such as payload effect (owing to the light source at the tip, see Table 23.3) and viscous friction (at the root end of the arm), are being compensated through the proposed online perturbation estimation routine. This, in turn, demonstrates the capability of the proposed control scheme when considerable deviations between model and plant are encountered. The only noticeable difference is the fast decaying response as shown in Figure 27b and c. This clearly indicates the high friction at the motor, which was not considered in the simulations (Figure 24b and c). Similar responses are obtained when the controller is designed based on the rigid link only, that is, $\mu = 0$. The system responses are displayed in Figure 23.28. Similarly, the undesirable arm-tip oscillations are obvious. The overall agreement between simulations (Figure 24 and Figure 25) and the experiment (Figure 27 and Figure 28) is one of the critical contributions of this work.

23.3.3.2 Observer-Based Piezoelectric Vibration Control of Translating Flexible Beams

Many industrial robots, especially those widely used in automatic manufacturing assembly lines, are Cartesian types (Ge et al., 1998). A flexible Cartesian robot can be modeled as a flexible cantilever beam with a translational base support. Traditionally, a PD control strategy is used to regulate the movement of the robot arm. In lightweight robots, the base movement will cause undesirable vibrations at the arm tip because of the flexibility distributed along the arm. In order to eliminate

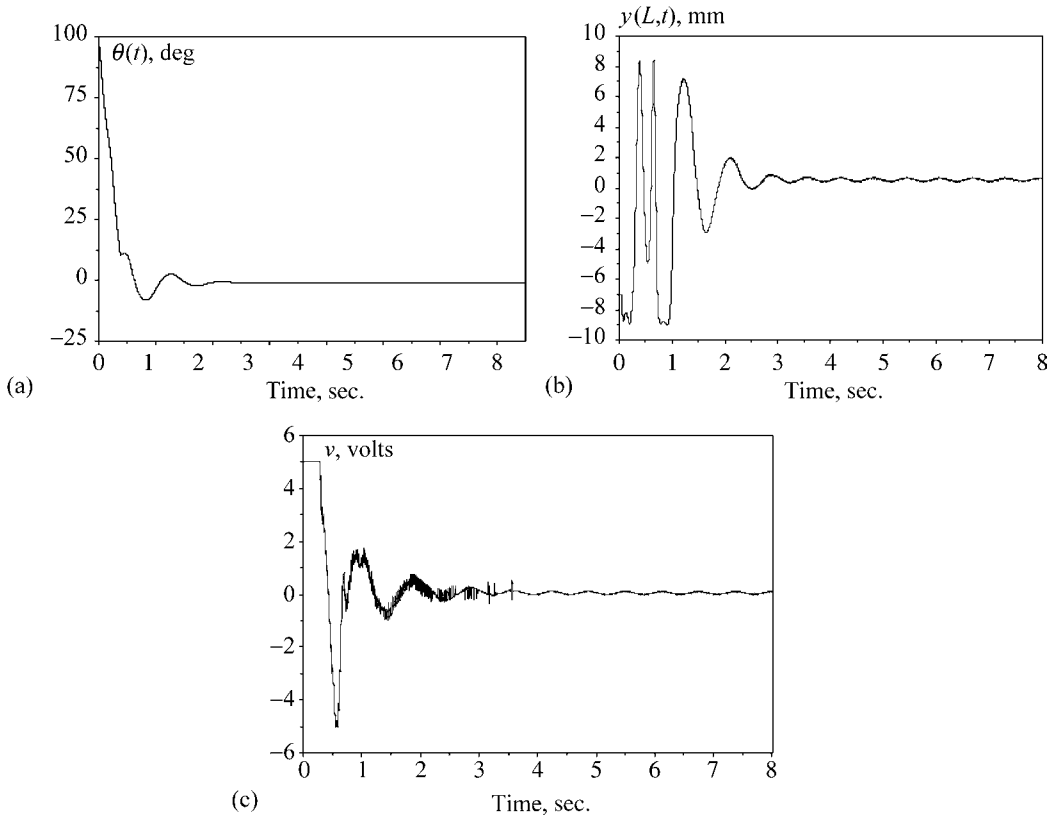


FIGURE 23.27 Experimental system responses to controller with inclusion of arm flexibility, that is, $\mu = -0.66$: (a) arm angular position; (b) arm-tip deflection; (c) control voltage applied to DC servomotor. (Source: From Jalili, N., *ASME J. Dyn. Syst. Meas. Control*, 123, 712–719, 2001. With permission.)

such vibrations, the PD controller must be upgraded with additional compensating terms. In order to improve further the vibration suppression performance, which is a requirement for the high-precision manufacturing market, a second controller, such as a piezoelectric (PZT) patch actuator attached on the surface of the arm, can be utilized (Oueini et al., 1998; Ge et al., 1999; Jalili et al., 2002).

In this section, an observer-based control strategy is presented for regulating the arm motion (Liu et al., 2002). The base motion is controlled utilizing an electrodynamic shaker, while a piezoelectric (PZT) patch actuator is bonded on the surface of the flexible beam for suppressing residual arm vibrations. The control objective here is to regulate the arm base movement, while simultaneously suppressing the vibration transients in the arm. To achieve this, a simple PD control strategy is selected for the regulation of the movement of the base, and a Lyapunov-based controller is selected for the PZT voltage signal. The selection of the proposed energy-based Lyapunov function naturally results in velocity-related signals, which are not physically measurable (Dadfarnia et al., 2003). To remedy this, a reduced-order observer is designed to estimate the velocity related signals. For this, the control structure is designed based on the truncated two-mode beam model.

23.3.3.2.1 Mathematical Modeling

For the purpose of model development, we consider a uniform flexible cantilever beam with a PZT actuator bonded on its top surface. As shown in Figure 23.29, one end of the beam is clamped into

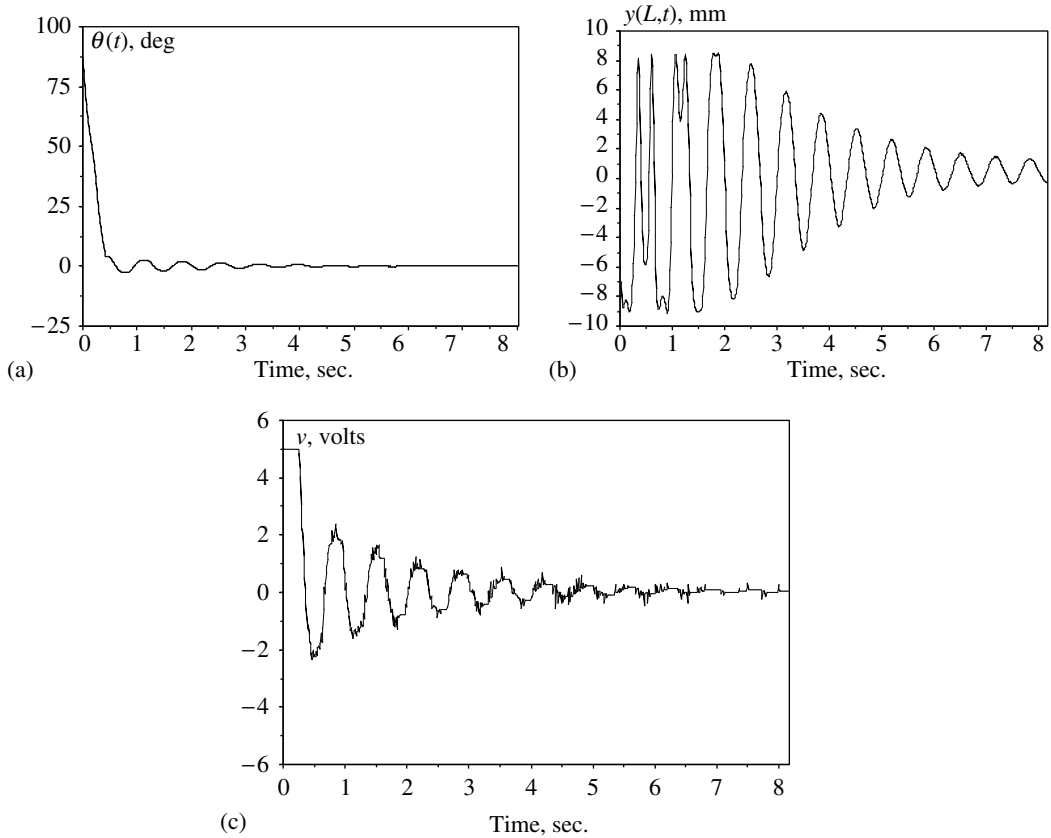


FIGURE 23.28 Experimental system responses to controller without inclusion of arm flexibility, that is, $\mu = 0$: (a) arm angular position; (b) arm-tip deflection; (c) control voltage applied to DC servomotor. (Source: From Jalili, N., *ASME J. Dyn. Syst. Meas. Control*, 123, 712–719, 2001. With permission.)

a moving base with the mass of m_b , and a tip mass, m_t , is attached to the free end of the beam. The beam has total thickness t_b , and length L , while the piezoelectric film possesses thickness and length t_p and $(l_2 - l_1)$, respectively. We assume that the PZT and the beam have the same width, b . The PZT actuator is perfectly bonded on the beam at distance l_1 measured from the beam support. The force, $f(t)$, acting on the base and the input voltage, $v(t)$, applied to the PZT actuator are the only external effects.

To establish a coordinate system for the beam, the x -axis is taken in the longitudinal direction and the z -axis is specified in the transverse direction of the beam with midplane of the beam to be $z = 0$, as shown in Figure 23.30. This coordinate is fixed to the base.

The fundamental relations for the piezoelectric materials are given as (Ikeda, 1990)

$$\mathbf{F} = \mathbf{c}\mathbf{S} - \mathbf{h}\mathbf{D} \quad (23.59)$$

$$\mathbf{E} = -\mathbf{h}^T\mathbf{S} + \boldsymbol{\beta}\mathbf{D} \quad (23.60)$$

where $\mathbf{F} \in \mathcal{R}^6$ is the stress vector, $\mathbf{S} \in \mathcal{R}^6$ is the strain vector, $\mathbf{c} \in \mathcal{R}^{6 \times 6}$ is the symmetric matrix of elastic stiffness coefficients, $\mathbf{h} \in \mathcal{R}^{6 \times 3}$ is the coupling coefficients matrix, $\mathbf{D} \in \mathcal{R}^3$ is the electrical displacement vector, $\mathbf{E} \in \mathcal{R}^3$ is the electrical field vector, and $\boldsymbol{\beta} \in \mathcal{R}^{3 \times 3}$ is the symmetric matrix of impermeability coefficients.

An energy method is used to derive the equations of motion. Neglecting the electrical kinetic energy, the total kinetic energy of the system is expressed as (Liu et al., 2002; Dadfarnia et al., 2004)

$$\begin{aligned}
 E_k &= \frac{1}{2} m_b \dot{s}(t)^2 + \frac{1}{2} b \int_0^{l_1} \rho_b t_b (\dot{s}(t) + \dot{w}(x, t))^2 dx \\
 &+ \frac{1}{2} b \int_{l_1}^{l_2} (\rho_b t_b + \rho_p t_p) (\dot{s}(t) + \dot{w}(x, t))^2 dx \\
 &+ \frac{1}{2} b \int_{l_2}^L \rho_b t_b (\dot{s}(t) + \dot{w}(x, t))^2 dx \\
 &+ \frac{1}{2} m_t (\dot{s}(t) + \dot{w}(L, t))^2 \\
 &= \frac{1}{2} m_b \dot{s}(t)^2 + \frac{1}{2} \int_0^L \rho(x) (\dot{s}(t) + \dot{w}(x, t))^2 dx \\
 &+ \frac{1}{2} m_t (\dot{s}(t) + \dot{w}(L, t))^2 \quad (23.61)
 \end{aligned}$$

where

$$\begin{aligned}
 \rho(x) &= [\rho_b t_b + G(x) \rho_p t_p] b \\
 G(x) &= H(x - l_1) - H(x - l_2) \quad (23.62)
 \end{aligned}$$

and $H(x)$ is the Heaviside function, ρ_b and ρ_p are the respective beam and PZT volumetric densities. Neglecting the effect of gravity due to planar motion and the higher-order terms of quadratic in w' (Esmailzadeh and Jalili, 1998b), the total potential energy of the system can be expressed as

$$\begin{aligned}
 E_p &= \frac{1}{2} b \int_0^{l_1} \int_{-t_b/2}^{t_b/2} \mathbf{F}^T \mathbf{S} dy dx + \frac{1}{2} b \int_{l_1}^{l_2} \int_{-t_b/2}^{t_b/2} \mathbf{F}^T \mathbf{S} dy dx + \frac{1}{2} b \int_{l_1}^{l_2} \int_{t_b/2}^{(t_b/2)+t_p} [\mathbf{F}^T \mathbf{S} + \mathbf{E}^T \mathbf{D}] dy dx \\
 &+ \frac{1}{2} b \int_{l_2}^L \int_{-t_b/2}^{t_b/2} \mathbf{F}^T \mathbf{S} dy dx \\
 &= \frac{1}{2} \int_0^L c(x) \left[\frac{\partial^2 w(x, t)}{\partial x^2} \right]^2 dx + h_l D_y(t) \int_{l_1}^{l_2} \frac{\partial^2 w(x, t)}{\partial x^2} dx + \frac{1}{2} \beta_l (l_2 - l_1) D_y(t)^2 \quad (23.63)
 \end{aligned}$$

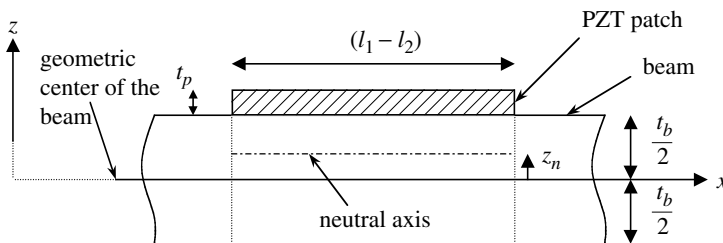


FIGURE 23.30 Coordinate system.

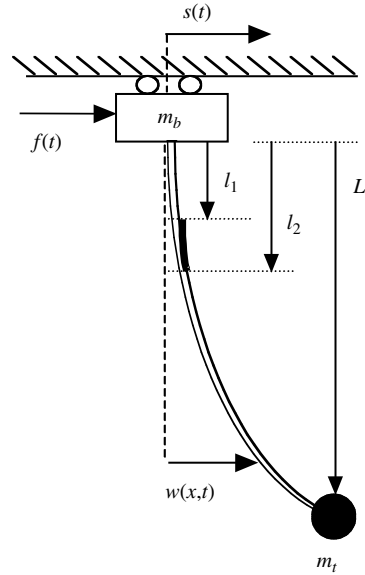


FIGURE 23.29 Schematic of the SCARA/Cartesian robot (last link).

where

$$c(x) = \frac{b}{3} \left\{ \left(\frac{c_{11}^b t_b^3}{4} \right) + G(x) \left\{ 3c_{11}^b t_b z_n^2 + c_{11}^p \left(t_p^3 + 3t_p \left(\frac{t_b}{2} - z_n \right)^2 + 3t_p^2 \left(\frac{t_b}{2} - z_n \right) \right) \right\} \right\} \quad (23.64)$$

$$h_l = h_{12} t_p b (t_p + t_b - 2z_n)/2, \quad \beta_l = \beta_{22} b t_p$$

and

$$z_n = \frac{c_{11}^p t_p (t_p + t_b)}{c_{11}^b t_b + c_{11}^p t_p}$$

The beam and PZT stiffnesses are c_{11}^b and c_{11}^p , respectively.

Using the AMM for the beam vibration analysis, the beam deflection can be written as

$$w(x, t) = \sum_{i=1}^{\infty} \phi_i(x) q_i(t), \quad P(x, t) = s(t) + w(x, t) \quad (23.65)$$

The equations of motion can now be obtained using the Lagrangian approach

$$\left[m_b + m_t + \int_0^L \rho(x) dx \right] \ddot{s}(t) + \sum_{j=1}^{\infty} m_j \ddot{q}_j(t) = f(t) \quad (23.66a)$$

$$m_i \ddot{s}(t) + m_{di} \ddot{q}_i(t) + \omega_i^2 m_{di} q_i(t) + h_l (\phi_i'(l_2) - \phi_i'(l_1)) D_y(t) = 0 \quad (23.66b)$$

$$h_l \sum_{j=1}^{\infty} \{ (\phi_j'(l_2) - \phi_j'(l_1)) q_j(t) \} + \beta_l (l_2 - l_1) D_y(t) = b(l_2 - l_1) v(t) \quad (23.66c)$$

where

$$m_{dj} = \int_0^L \rho(x) \phi_j^2(x) dx + m_t \phi_j^2(L), \quad m_j = \int_0^L \rho(x) \phi_j(x) dx + m_t \phi_j(L) \quad (23.67)$$

Calculating $D_y(t)$ from Equation 23.66b and substituting into Equation 23.66c results in

$$\begin{aligned} m_i \ddot{s}(t) + m_{di} \ddot{q}_i(t) + \omega_i^2 m_{di} q_i(t) - \frac{h_l^2 (\phi_i'(l_2) - \phi_i'(l_1))}{\beta_l (l_2 - l_1)} \sum_{j=1}^{\infty} \{ (\phi_j'(l_2) - \phi_j'(l_1)) q_j(t) \} \\ = - \frac{h_l b (\phi_i'(l_2) - \phi_i'(l_1))}{\beta_l} v(t), \quad i = 1, 2, \dots \end{aligned} \quad (23.68)$$

which will be used to derive the controller, as discussed next.

23.3.3.2.2 Derivation of the Controller

Utilizing Equation 23.66a and Equation 23.68, the truncated two-mode beam with PZT model reduces to

$$\left[m_b + m_t + \int_0^L \rho(x) dx \right] \ddot{s}(t) + m_1 \ddot{q}_1(t) + m_2 \ddot{q}_2(t) = f(t) \quad (23.69a)$$

$$\begin{aligned} m_1 \ddot{s}(t) + m_{d1} \ddot{q}_1(t) + \omega_1^2 m_{d1} q_1(t) - \frac{h_l^2 (\phi_1'(l_2) - \phi_1'(l_1))}{\beta_l (l_2 - l_1)} \\ \times \{ (\phi_1'(l_2) - \phi_1'(l_1)) q_1(t) + (\phi_2'(l_2) - \phi_2'(l_1)) q_2(t) \} \\ = - \frac{h_l b (\phi_1'(l_2) - \phi_1'(l_1))}{\beta_l} v(t) \end{aligned} \quad (23.69b)$$

$$\begin{aligned}
& m_2 \ddot{s}(t) + m_{d2} \ddot{q}_2(t) + \omega_2^2 m_{d2} q_2(t) - \frac{h_l^2 (\phi_2'(l_2) - \phi_2'(l_1))}{\beta_l (l_2 - l_1)} \\
& \quad \times \{(\phi_1'(l_2) - \phi_1'(l_1)) q_1(t) + (\phi_2'(l_2) - \phi_2'(l_1)) q_2(t)\} \\
& = - \frac{h_l b (\phi_2'(l_2) - \phi_2'(l_1))}{\beta_l} v(t)
\end{aligned} \tag{23.69c}$$

The equations in Equation 23.69 can be written in the following more compact form

$$\mathbf{M} \ddot{\Delta} + \mathbf{K} \Delta = \mathbf{F}_e \tag{23.70}$$

where

$$\mathbf{M} = \begin{bmatrix} \psi & m_1 & m_2 \\ m_1 & m_{d1} & 0 \\ m_2 & 0 & m_{d2} \end{bmatrix}, \quad \mathbf{K} = \begin{bmatrix} 0 & 0 & 0 \\ 0 & k_{11} & k_{12} \\ 0 & k_{12} & k_{22} \end{bmatrix}, \quad \mathbf{F}_e = \begin{Bmatrix} f(t) \\ \epsilon_1 v(t) \\ \epsilon_2 v(t) \end{Bmatrix}, \quad \Delta = \begin{Bmatrix} s(t) \\ q_1(t) \\ q_2(t) \end{Bmatrix} \tag{23.71}$$

and

$$\begin{aligned}
\psi &= m_b + m_t + \int_0^L \rho(x) dx, \quad \epsilon_1 = -\frac{h_l b}{\beta_l} (\phi_1'(l_2) - \phi_1'(l_1)), \quad \epsilon_2 = -\frac{h_l b}{\beta_l} (\phi_2'(l_2) - \phi_2'(l_1)), \\
k_{11} &= \omega_1^2 m_{d1} - \frac{h_l^2}{\beta_l (l_2 - l_1)} (\phi_1'(l_2) - \phi_1'(l_1))^2, \\
k_{12} &= -\frac{h_l^2}{\beta_l (l_2 - l_1)} (\phi_1'(l_2) - \phi_1'(l_1)) (\phi_2'(l_2) - \phi_2'(l_1)), \\
k_{22} &= \omega_2^2 m_{d2} - \frac{h_l^2}{\beta_l (l_2 - l_1)} (\phi_2'(l_2) - \phi_2'(l_1))^2
\end{aligned} \tag{23.72}$$

For the system described by Equation 23.70, if the control laws for the arm base force and PZT voltage generated moment are selected as

$$f(t) = -k_p \Delta s - k_d \dot{s}(t) \tag{23.73}$$

$$v(t) = -k_v (\epsilon_1 \dot{q}_1(t) + \epsilon_2 \dot{q}_2(t)) \tag{23.74}$$

where k_p and k_d are positive control gains, $\Delta s = s(t) - s_d$, s_d is the desired set-point position, and $k_v > 0$ is the voltage control gain, then the closed-loop system will be stable, and in addition

$$\lim_{t \rightarrow \infty} \{q_1(t), q_2(t), \Delta s\} = 0$$

See Dadfarnia et al. (2004) for a detailed proof.

23.3.3.2.3 Controller Implementation

The control input, $v(t)$, requires the information from the velocity-related signals, $\dot{q}_1(t)$ and $\dot{q}_2(t)$, which are usually not measurable. Sun and Mills (1999) solved the problem by integrating the acceleration signals measured by the accelerometers. However, such controller structure may result in unstable closed-loop system in some cases. In this paper, a reduced-order observer is designed to estimate the velocity signals, \dot{q}_1 and \dot{q}_2 . For this, we utilize three available signals: base displacement, $s(t)$, arm-tip deflection, $P(L, t)$, and beam root strain, $\epsilon(0, t)$; that is

$$y_1 = s(t) = x_1 \tag{23.75a}$$

$$y_2 = P(L, t) = x_1 + \phi_1(L) x_2 + \phi_2(L) x_3 \tag{23.75b}$$

$$y_3 = \epsilon(0, t) = \frac{t_b}{2} (\phi_1''(0) x_2 + \phi_2''(0) x_3) \tag{23.75c}$$

It can be seen that the first three states can be obtained by

$$\begin{Bmatrix} x_1 \\ x_2 \\ x_3 \end{Bmatrix} = \mathbf{C}_1^{-1} \mathbf{y} \quad (23.76)$$

Since this system is observable, we can design a reduced-order observer to estimate the velocity-related state signals. Defining $\mathbf{X}_1 = [x_1 \ x_2 \ x_3]^T$ and $\mathbf{X}_2 = [x_4 \ x_5 \ x_6]^T$, the estimated value for \mathbf{X}_2 can be designed as

$$\hat{\mathbf{X}}_2 = \mathbf{L}_r \mathbf{y} + \hat{\mathbf{z}} \quad (23.77)$$

$$\dot{\hat{\mathbf{z}}} = \mathbf{F}\hat{\mathbf{z}} + \mathbf{G}\mathbf{y} + \mathbf{H}\mathbf{u} \quad (23.78)$$

where $\mathbf{L}_r \in R^{3 \times 3}$, $\mathbf{F} \in R^{3 \times 3}$, $\mathbf{G} \in R^{3 \times 3}$, and $\mathbf{H} \in R^{3 \times 2}$ will be determined by the observer pole placement. Defining the estimation error as

$$\mathbf{e}_2 = \mathbf{X}_2 - \hat{\mathbf{X}}_2 \quad (23.79)$$

the derivative of the estimation error becomes

$$\dot{\mathbf{e}}_2 = \dot{\mathbf{X}}_2 - \dot{\hat{\mathbf{X}}}_2 \quad (23.80)$$

Substituting the state-space equations of the system (Equation 23.77 and Equation 23.78) into Equation 23.80 and simplifying, we obtain

$$\dot{\mathbf{e}}_2 = \mathbf{F}\mathbf{e}_2 + (\mathbf{A}_{21} - \mathbf{L}_r \mathbf{C}_1 \mathbf{A}_{11} - \mathbf{G}\mathbf{C}_1 + \mathbf{F}\mathbf{L}_r \mathbf{C}_1) \mathbf{X}_1 + (\mathbf{A}_{22} - \mathbf{L}_r \mathbf{C}_1 \mathbf{A}_{12} - \mathbf{F}) \mathbf{X}_2 + (\mathbf{B}_2 - \mathbf{L}_r \mathbf{C}_1 \mathbf{B}_1 - \mathbf{H}) \mathbf{u} \quad (23.81)$$

In order to force the estimation error, \mathbf{e}_2 , to go to zero, matrix \mathbf{F} should be selected to be Hurwitz and the following relations must be satisfied (Liu et al., 2002):

$$\mathbf{F} = \mathbf{A}_{22} - \mathbf{L}_r \mathbf{C}_1 \mathbf{A}_{12} \quad (23.82)$$

$$\mathbf{H} = \mathbf{B}_2 - \mathbf{L}_r \mathbf{C}_1 \mathbf{B}_1 \quad (23.83)$$

$$\mathbf{G} = (\mathbf{A}_{21} - \mathbf{L}_r \mathbf{C}_1 \mathbf{A}_{11} + \mathbf{F}\mathbf{L}_r \mathbf{C}_1) \mathbf{C}_1^{-1} \quad (23.84)$$

The matrix \mathbf{F} can be chosen by the desired observer pole placement requirement. Once \mathbf{F} is known, \mathbf{L}_r , \mathbf{H} , and \mathbf{G} can be determined utilizing Equation 23.82, to Equation 23.84, respectively. The velocity variables, $\hat{\mathbf{X}}_2$, can now be estimated by Equation 23.77 and Equation 23.78.

23.3.3.2.4 Numerical Simulations

In order to show the effectiveness of the controller, the flexible beam structure in Figure 23.29 is considered with the PZT actuator attached on the beam surface. The system parameters are listed in Table 23.4.

First, we consider the beam without PZT control. We take the PD control gains to be $k_p = 120$ and $k_d = 20$. Figure 23.31 shows the results for the beam without PZT control (i.e., with only PD force control for the base movement). To investigate the effect of PZT controller on the beam vibration, we consider the voltage control gain to be $k_v = 2 \times 10^7$. The system responses to the proposed controller with a piezoelectric actuator based on the two-mode model are shown in Figure 23.32. The comparison between the tip displacement, from Figure 31 and Figure 32, shows that the beam vibration can be suppressed significantly utilizing the PZT actuator.

23.3.3.2.5 Control Experiments

In order to demonstrate better the effectiveness of the controller, an experimental setup is constructed and used to verify the numerical results. The experimental apparatus consists of a flexible beam with a PZT actuator and strain sensor attachments, as well as data acquisition,

TABLE 23.4 System Parameters Used in Numerical Simulations and Experimental Setup for Translational Beam

Properties	Symbol	Value	Unit
Beam Young's modulus	c_{11}^b	69×10^9	N/m ²
Beam thickness	t_b	0.8125	mm
Beam and PZT width	b	20	mm
Beam length	L	300	mm
Beam volumetric density	ρ_b	3960.0	kg/m ³
PZT Young's modulus	c_{11}^p	66.47×10^9	N/m ²
PZT coupling parameter	h_{12}	5×10^8	V/m
PZT impermittivity	β_{22}	4.55×10^7	m/F
PZT thickness	t_p	0.2032	mm
PZT length	$l_2 - l_1$	33.655	mm
PZT position on beam	l_1	44.64	mm
PZT volumetric density	ρ_p	7750.0	kg/m ³
Base mass	m_b	0.455	kg
Tip mass	m_t	0	kg

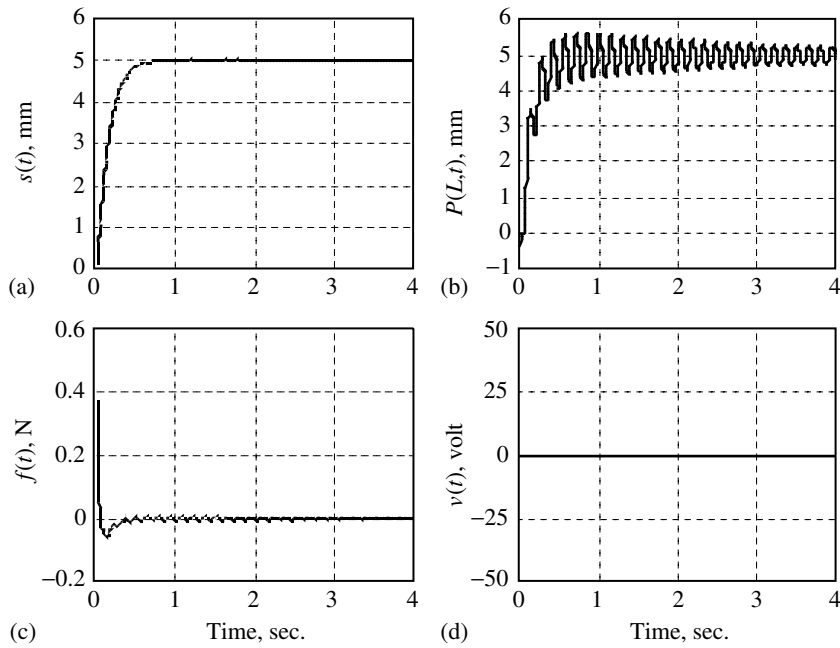


FIGURE 23.31 Numerical simulations for the case without PZT control: (a) base motion; (b) tip displacement; (c) control force and (d) PZT voltage.

amplifier, signal conditioner and the control software. As shown in [Figure 23.33](#), the plant consists of a flexible aluminum beam with a strain sensor and a PZT patch actuator bound on each side of the beam surface. One end of the beam is clamped to the base with a solid clamping fixture, which is driven by a shaker. The shaker is connected to the arm base by a connecting rod. The experimental setup parameters are listed in [Table 23.4](#).

[Figure 23.34](#) shows the high-level control block diagram of the experiment, where the shaker provides the input control force to the base and the PZT applies a controlled moment on the beam. Two laser sensors measure the position of the base and the beam-tip displacement. A strain-gauge sensor, which is attached near the base of the beam, is utilized for the dynamic strain measurement. These three signals

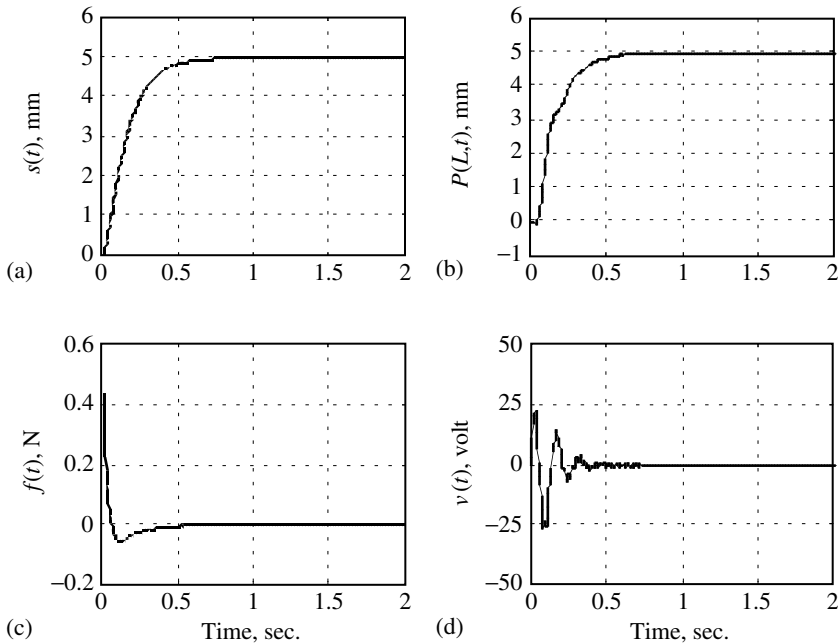


FIGURE 23.32 Numerical simulations for the case with PZT control: (a) base motion; (b) tip displacement; (c) control force and (d) PZT voltage.

are fed back to the computer through the ISA MultiQ data acquisition card. The remaining required signals for the controller (Equation 23.66) are determined as explained in the preceding section. The data acquisition and control algorithms are implemented on an AMD Athlon 1100 MHz PC running under the RT-Linux operating system. The Matlab/Simulink environment and Real Time Linux Target are used to implement the controller.

The experimental results for both cases (i.e., without PZT and with PZT control) are depicted in Figure 35 and Figure 36, respectively. The results demonstrate that with PZT control, the arm vibration is eliminated in less than 1 sec, while the arm vibration lasts for more than 6 sec when PZT control is not used. The experimental results are in agreement with the simulation results except for some differences at the beginning of the motion. The slight overshoot and discrepancies at the beginning of the motion are due to the limitations of the experiment (e.g., the shaker saturation limitation) and unmodeled dynamics in the modeling (e.g., the friction modeling). However, it is still apparent that the PZT voltage control can substantially suppress the arm vibration despite such limitations and modeling imperfections.

23.4 Practical Considerations and Related Topics

23.4.1 Summary of Vibration-Control Design Steps and Procedures

In order to select a suitable vibration-control system, especially a vibration isolator, a number of factors must be considered.

23.4.1.1 Static Deflection

The static deflection of the vibration-control system under the deadweight of the load determines to a considerable extent the type of the material to be used in the isolator. Organic materials, such as rubber

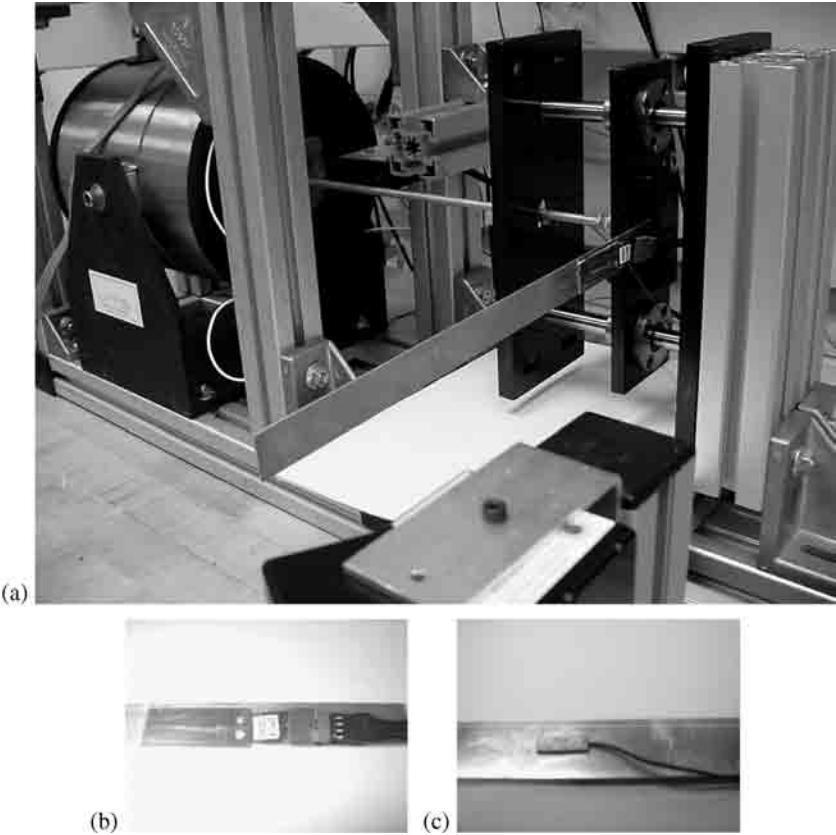


FIGURE 23.33 The experimental setup: (a) the whole system; (b) PZT actuator, ACX model No. QP21B; (c) dynamic strain sensor (attached on the other side of the beam), model No. PCB 740B02.

and cork, are capable of sustaining very large strains provided they are applied momentarily. However, if large strains remain for an appreciable period of time, they tend to drift or creep. On the other hand, metal springs undergo permanent deformation if the stress exceeds the yield stress of the material, but show minimal drift or creep when the stress is maintained below the yield stress.

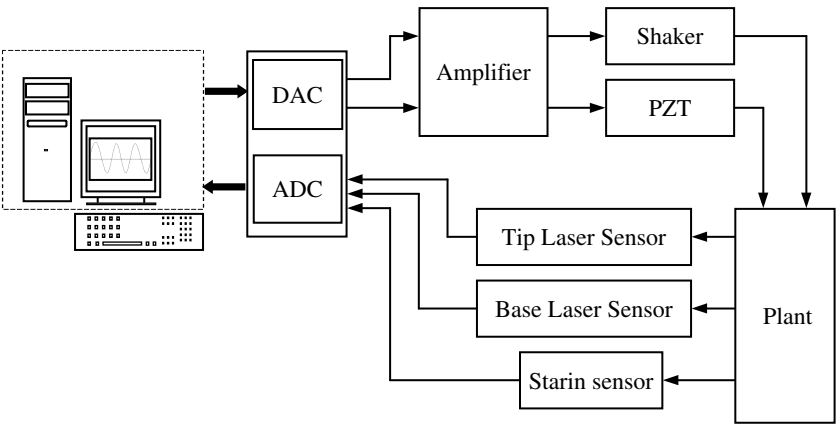


FIGURE 23.34 High-level control-block diagram.

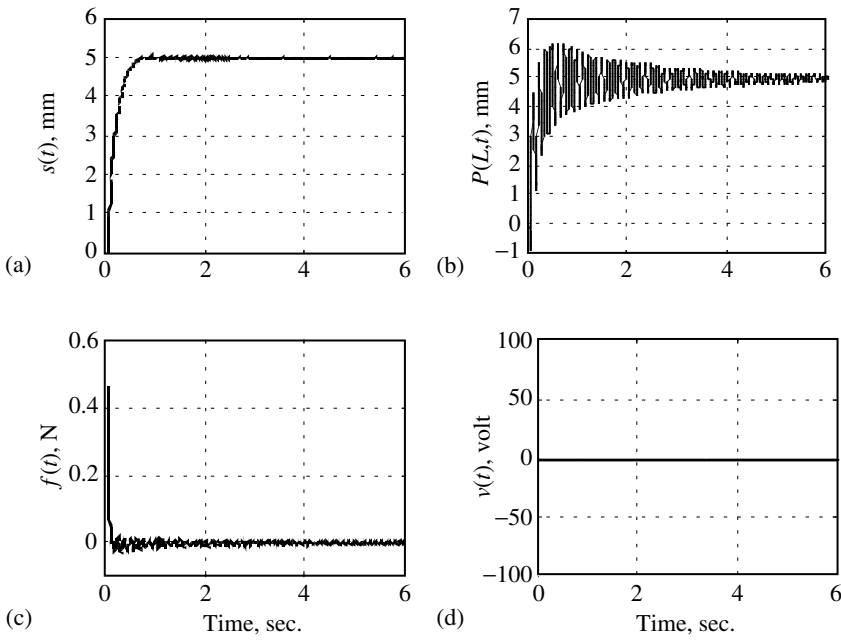


FIGURE 23.35 Experimental results for the case without PZT control: (a) base motion; (b) tip displacement; (c) control force and (d) PZT voltage.

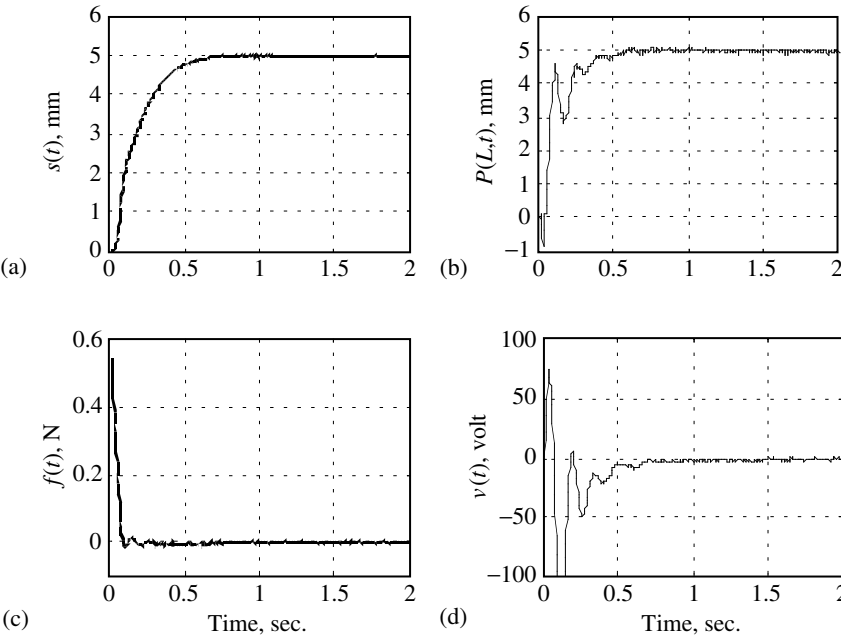


FIGURE 23.36 Experimental results for the case with PZT control: (a) base motion; (b) tip displacement; (c) control force and (d) PZT voltage.

23.4.1.2 Stiffness in Lateral Directions

Resilient materials strained in compression are most useful when the load is relatively large and the static deflection is small. Such applications are difficult to design for a small load, unless the required

static deflection is small. Otherwise, the small area and great thickness tend to cause a condition of instability. To a considerable extent, this limitation can be overcome by using sponge rubber, a material of lower modulus. In general, when the load is small, it is preferable to use rubber springs that carry the load in shear.

23.4.1.3 Environmental Conditions

It is highly common for vibration-control systems to be subjected to harsh environmental conditions. Especially in military applications, extreme ambient temperatures are encountered in addition to exposure to substances like ozone, rocket fuels, and so on. Organic materials are usually more susceptible to these environmental conditions than metal materials. However, owing to the superior mechanical properties of organic materials, such as lighter weight, smaller size, greater damping, and the ability to store large amounts of energy under shock, organic materials that are capable of withstanding the harsh conditions are being developed.

23.4.1.4 Damping Characteristics

In most of the vibration-control applications, the excitations cover a wide range of frequencies and may have random properties requiring the vibration-control systems to possess adequate damping. Elastomers possess very good damping properties when compared with metal springs, and they also eliminate the trouble of standing waves that occurs at high frequencies. If a metal spring is used in vibration-control applications requiring isolation of vibration at high frequencies, it is common to employ rubber pads in series with the metal spring, which also results in the damping of vibrations due to the addition of damping material.

23.4.1.5 Weight and Space Limitations

The amount of load-carrying resilient material is determined by the quantity of energy to be stored. In most of the cases, the vibration amplitude tends to be small relative to the static deflection, and the amount of material may be calculated by equating the energy stored in the material to the work done on the vibration control system.

23.4.1.6 Dynamic Stiffness

In the case of organic materials like rubber, the natural frequency calculated using the stiffness determined from a static-force deflection test of the spring is almost invariably lower than that experienced during vibration; that is, the dynamic modulus is greater than static modulus. The ratio between the dynamic and static modulus is generally between one and two. In many vibration-control applications, it is not feasible to mount the equipment directly upon the vibration-control system (isolator). Instead, a heavy, rigid block, usually made of concrete or heavy steel, supported by the isolator is employed.

23.4.2 Future Trends and Developments

During recent years, there has been considerable interest in the design and implementation of a variety of vibration-control systems. Recent developments in multivariable control design methodology and microprocessor implementation of modern control algorithms have opened a new era for the design of externally controlled passive systems for use in such systems: fuzzy reasoning (Yoshimura, 1998); adaptive algorithms (Venhovens, 1994); observer design (Hedrick et al., 1994); and many others.

Observing these developments combined with the substantial ongoing theoretical advances in the areas of adaptive and nonlinear controls (Astrom and Wittenmark, 1989; Alleyne and Hedrick, 1995), it is expected that the future will bring applications of these techniques in advanced vibration-control system design. For practical implementation, however, it is preferable to simplify these strategies, thus leading to simpler software implementations. Suboptimal policy neglecting some performance requirements can serve as an example of such simplifications.

References

- Abe, M. and Igusa, T., Semiactive dynamic vibration absorbers for controlling transient response, *J. Sound Vib.*, 198, 5, 547–569, 1996.
- Alleyne, A. and Hedrick, J.K., Nonlinear adaptive control of active suspensions, *IEEE Trans. Control Syst. Technol.*, 3, 94–101, 1995.
- Astrom, J.J. and Wittenmark, B. 1989. *Adaptive Control*, Addison-Wesley, Reading, MA.
- Austin, S.A., The vibration damping effect of an electrorheological fluid, *ASME J. Vib. Acoust.*, 115, 136–140, 1993.
- Banks, H.T. and Ito, K., A unified framework for approximation in inverse problems for distributed parameter systems, *Control Theor. Adv. Technol.*, 4, 73–90, 1988.
- Banks, H.T. and Kunisch, K. 1989. *Estimation Techniques for Distributed Parameter Systems*, Birkhauser, Boston, MA.
- Bayo, E., A finite-element approach to control the end-point motion of a single-link flexible robot, *J. Robotic Syst.*, 4, 63–75, 1987.
- Cannon, R.H. Jr. and Schmitz, E., Initial experiments on the end-point control of a flexible one-link robot, *Int. J. Robotics Res.*, 3, 62–75, 1984.
- Chalhoub, N.G. and Ulsoy, A.G., Control of flexible robot arm: experimental and theoretical results, *ASME J. Dyn. Syst. Meas. Control*, 109, 299–309, 1987.
- Choi, S.B., Vibration control of flexible structures using ER dampers, *ASME J. Dyn. Syst. Meas. Control*, 121, 134–138, 1999.
- Crosby, M. and Karnopp, D.C. 1973. The active damper—a new concept for shock and vibration control, *Shock Vibration Bulletin*, Part H, Washington, DC.
- Dadfarnia, M., Jalili, N., Xian, B. and Dawson, D.M. 2003. Lyapunov-based piezoelectric control of flexible cartesian robot manipulators, In *Proceedings of the 22nd American Control Conference (ACC'03)*, Denver, CO.
- Dadfarnia, M., Jalili, N., Liu, Z., and Dawson, D.M., An observer-based piezoelectric control of flexible cartesian robot manipulators: theory and experiment, *J. Control Eng. Practice*, 12, 1041–1053, 2004.
- de Querioz, M.S., Dawson, D.M., Agrawal, M., and Zhang, F., Adaptive nonlinear boundary control of a flexible link robot arm, *IEEE Trans. Robotics Automat.*, 15, 779–787, 1999.
- de Querioz, M.S., Dawson, D.M., Nagarkatti, S.P., and Zhang, F. 2000. *Lyapunov-Based Control of Mechanical Systems*, Birkhauser, Boston, MA.
- Dimarogonas-Andrew, D. and Kollias, A., Smart electrorheological fluid dynamic vibration absorber, *Intell. Struct. Mater. Vib. ASME Des. Div.*, 58, 7–15, 1993.
- Dowell, D.J., Cherry, S. 1994. Semiactive friction dampers for seismic response control of structures, Vol. 1, pp. 819–828. In *Proceedings of the Fifth US National Conference on Earthquake Engineering*, Chicago, IL.
- Elmali, H. and Olgac, N., Sliding mode control with perturbation estimation (SMCPE): a new approach, *Int. J. Control*, 56, 923–941, 1992.
- Emura, J., Kakizaki, S., Yamaoka, F., and Nakamura, M. 1994. Development of the SA suspension system based on the sky-hook damper theory, *SAE Paper No. 940863*.
- Esmailzadeh, E. and Jalili, N., Optimal design of vibration absorbers for structurally damped Timoshenko beams, *ASME J. Vib. Acoust.*, 120, 833–841, 1998a.
- Esmailzadeh, E. and Jalili, N., Parametric response of cantilever timoshenko beams with tip mass under harmonic support motion, *Int. J. Non-Linear Mech.*, 33, 765–781, 1998b.
- Filipović, D. and Schröder, D., Vibration absorption with linear active resonators: continuous and discrete time design and analysis, *J. Vib. Control*, 5, 685–708, 1999.
- Frahm, H., Devices for damping vibrations of bodies, US Patent #989958, 1911.
- Franchek, M.A., Ryan, M.W., and Bernhard, R.J., Adaptive-passive vibration control, *J. Sound Vib.*, 189, 565–585, 1995.

- Fujita, T., Katsu, M., Miyano, H., and Takanashi, S., Fundamental study of active-passive mass damper using XY-motion mechanism and hydraulic actuator for vibration control of tall building, *Trans. Jpn Soc. Mech. Engrs*, Part C, 57, 3532–3539, 1991.
- Garcia, E., Dosch, J., and Inman, D.J., The application of smart structures to the vibration suppression problem, *J. Intell. Mater. Syst. Struct.*, 3, 659–667, 1992.
- Ge, S.S., Lee, T.H., and Zhu, G., A nonlinear feedback controller for a single-link flexible manipulator based on a finite element method, *J. Robot. Syst.*, 14, 165–178, 1997.
- Ge, S.S., Lee, T.H., and Zhu, G., Asymptotically stable end-point regulation of a flexible SCARA/cartesian robot, *IEEE/ASME Trans. Mechatron.*, 3, 138–144, 1998.
- Ge, S.S., Lee, T.H., and Gong, J.Q., A robust distributed controller of a single-link SCARA/cartesian smart materials robot, *Mechatronics*, 9, 65–93, 1999.
- Hedrick, J.K., Rajamani, R., and Yi, K., Observer design for electronic suspension applications, *Vehicle Syst. Dyn.*, 23, 413–440, 1994.
- Horton, D.N. and Crolla, D.A., Theoretical analysis of a SA suspension fitted to an off-road vehicle, *Vehicle Syst. Dyn.*, 15, 351–372, 1986.
- Hrovat, D., Barker, P., and Rabins, M., Semiactive versus passive or active tuned mass dampers for structural control, *J. Eng. Mech.*, 109, 691–705, 1983.
- Hrovat, D., Margolis, D.L., and Hubbard, M., An approach toward the optimal SA suspension, *ASME J. Dyn. Syst. Meas. Control*, 110, 288–296, 1988.
- Hubard, M. and Marolis, D. 1976. The SA spring: is it a viable suspension concept?, pp. 1–6. In *Proceedings of the Fourth Intersociety Conference on Transportation*, Los Angeles, CA.
- Ikeda, T. 1990. *Fundamental of Piezoelectricity*, Oxford University Press, Oxford, New York.
- Inman, D.J. 1994. *Engineering Vibration*, Prentice Hall, Englewood Cliffs, NJ.
- Jalili, N., A new perspective for semi-automated structural vibration control, *J. Sound Vib.*, 238, 481–494, 2000.
- Jalili, N., An infinite dimensional distributed base controller for regulation of flexible robot arms, *ASME J. Dyn. Syst. Meas. Control*, 123, 712–719, 2001.
- Jalili, N., A comparative study and analysis of SA vibration-control systems, *ASME J. Vib. Acoust.*, 124, 593–605, 2002.
- Jalili, N., Dadfarnia, M., Hong, F., and Ge, S.S. 2002. An adaptive non model-based piezoelectric control of flexible beams with translational base, pp. 3802–3807. In *Proceedings of the American Control Conference (ACC'02)*, Anchorage, AK.
- Jalili, N., Elmali, H., Moura, J., and Olgac, N. 1997. Tracking control of a rotating flexible beam using frequency-shaped sliding mode control, pp. 2552–2556. In *Proceedings of the 16th American Control Conference (ACC'97)*, Albuquerque, NM.
- Jalili, N. and Esmailzadeh, E., Adaptive-passive structural vibration attenuation using distributed absorbers, *J. Multi-Body Dyn.*, 216, 223–235, 2002.
- Jalili, N. and Fallahi, B., Design and dynamics analysis of an adjustable inertia absorber for SA structural vibration attenuation, *ASCE J. Eng. Mech.*, 128, 1342–1348, 2002.
- Jalili, N., Fallahi, B., and Kusculuoglu, Z.K., A new approach to SA vibration suppression using adjustable inertia absorbers, *Int. J. Model. Simulat.*, 21, 148–154, 2001.
- Jalili, N. and Olgac, N., Time-optimal/sliding mode control implementation for robust tracking of uncertain flexible structures, *Mechatronics*, 8, 121–142, 1998a.
- Jalili, N. and Olgac, N. 1998b. Optimum delayed feedback vibration absorber for MDOF mechanical structures, In *Proceedings of the 37th IEEE Conference on Decision Control (CDC'98)*, Tampa, FL.
- Jalili, N. and Olgac, N., Multiple identical delayed-resonator vibration absorbers for multi-DoF mechanical structures, *J. Sound Vib.*, 223, 567–585, 1999.
- Jalili, N. and Olgac, N., Identification and re-tuning of optimum delayed feedback vibration absorber, *AIAA J. Guidance Control Dyn.*, 23, 961–970, 2000a.
- Jalili, N. and Olgac, N., A sensitivity study of optimum delayed feedback vibration absorber, *ASME J. Dyn. Syst. Meas. Control*, 121, 314–321, 2000b.

- Junkins, J.L. and Kim, Y. 1993. *Introduction to Dynamics and Control of Flexible Structures*. AIAA Educational Series, Washington, DC.
- Karnopp, D., Design principles for vibration-control systems using SA dampers, *ASME J. Dyn. Syst. Meas. Control*, 112, 448–455, 1990.
- Karnopp, D.C., Crodby, M.J., and Harwood, R.A., Vibration control using SA force generators, *J. Eng. Ind.*, 96, 619–626, 1974.
- Kim, K. and Jeon, D., Vibration suppression in an MR fluid damper suspension system, *J. Intell. Mater. Syst. Struct.*, 10, 779–786, 2000.
- Knowles, D., Jalili, N., and Khan, T. 2001a. On the nonlinear modeling and identification of piezoelectric inertial actuators, In *Proceedings of the 2001 International Mechanical Engineering Congress and Exposition* (IMECE'01), New York.
- Knowles, D., Jalili, N., and Ramadurai, S. 2001b. Piezoelectric structural vibration control using active resonator absorber, In *Proceedings of the 2001 International Mechanical Engineering Congress and Exposition* (IMECE'01), New York.
- Korennev, B.G. and Reznikov, L.M. 1993. *Dynamic Vibration Absorbers: Theory and Technical Applications*, Wiley, Chichester, England.
- Lee-Glauser, G.J., Ahmadi, G., and Horta, L.G., Integrated passive/active vibration absorber for multistory buildings, *ASCE J. Struct. Eng.*, 123, 499–504, 1997.
- Liu, Z., Jalili, N., Dadfarnia, M., and Dawson, D.M. 2002. Reduced-order observer based piezoelectric control of flexible beams with translational base, In *Proceedings of the 2002 International Mechanical Engineering Congress and Exposition* (IMECE'02), New Orleans, LA.
- Liu, J., Schönecker, A., and Frühauf, U. 1997. Application of discrete Fourier transform to electronic measurements, pp. 1257–1261. In *International Conference on Information, Communications and Signal Processing*, Singapore.
- Liu, H.J., Yang, Z.C., and Zhao, L.C., Semiactive flutter control by structural asymmetry, *J. Sound Vib.*, 229, 199–205, 2000.
- Lou, Z.H., Direct strain feedback control of flexible robot arms: new theoretical and experimental results, *IEEE Trans. Automat. Control*, 38, 1610–1622, 1993.
- Luo, Z.H., Guo, B.Z., and Morgul, O. 1999. *Stability and Stabilization of Finite Dimensional Systems with Applications*, Springer, London.
- Margolis, D., Retrofitting active control into passive vibration isolation systems, *ASME J. Vib. Acoust.*, 120, 104–110, 1998.
- Meirovitch, L. 1986. *Elements of Vibration Analysis*, McGraw-Hill, New York.
- Miller, L.R. and Nobles, C.M. 1988. The design and development of a SA suspension for military tank, *SAE Paper No. 881133*.
- Moura, J.T., Roy, R.G., and Olgac, N., Frequency-shaped sliding modes: analysis and experiments, *IEEE Trans. Control Syst. Technol.*, 5, 394–401, 1997.
- Nemir, D., Lin, Y., and Osegueda, R.A., Semiactive motion control using variable stiffness, *ASCE J. Struct. Eng.*, 120, 1291–1306, 1994.
- Olgac, N., Delayed resonators as active dynamic absorbers, US Patent #5431261, 1995.
- Olgac, N., Elmali, H., Hosek, M., and Renzulli, M., Active vibration control of distributed systems using delayed resonator with acceleration feedback, *ASME J. Dyn. Syst., Meas. Control*, 119, 380–389, 1997.
- Olgac, N., Elmali, H., and Vijayan, S., Introduction to dual frequency fixed delayed resonator (DFFDR), *J. Sound Vib.*, 189, 355–367, 1996.
- Olgac, N. and Holm-Hansen, B., Novel active vibration absorption technique: delayed resonator, *J. Sound Vib.*, 176, 93–104, 1994.
- Olgac, N. and Holm-Hansen, B., Tunable active vibration absorber: the delayed resonator, *ASME J. Dyn. Syst., Meas. Control*, 117, 513–519, 1995.
- Olgac, N. and Jalili, N., Modal analysis of flexible beams with delayed-resonator vibration absorber: theory and experiments, *J. Sound Vib.*, 218, 307–331, 1998.

- Olgac, N. and Jalili, N., Optimal delayed feedback vibration absorber for flexible beams, *Smart Struct.*, 65, 237–246, 1999.
- Oueini, S.S., Nayfeh, A.H., and Pratt, J.R., A nonlinear vibration absorber for flexible structures, *Nonlinear Dyn.*, 15, 259–282, 1998.
- Petek, N.K., Shock absorbers uses electrorheological fluid, *Automot. Eng.*, 100, 27–30, 1992.
- Petek, N.K., Romstadt, D.L., Lizell, M.B., and Weyenberg, T.R. 1995. Demonstration of an automotive SA suspension using electro-rheological fluid, SAE Paper No. 950586.
- Puksand, H., Optimum conditions for dynamic vibration absorbers for variable speed systems with rotating and reciprocating unbalance, *Int. J. Mech. Eng. Educ.*, 3, 145–152, 1975.
- Renzulli, M., Ghosh-Roy, R., and Olgac, N., Robust control of the delayed resonator vibration absorber, *IEEE Trans. Control Syst. Technol.*, 7, 683–691, 1999.
- Shaw, J., Adaptive vibration control by using magnetostrictive actuators, *J. Intell. Mater. Syst. Struct.*, 9, 87–94, 1998.
- Singh, T., Golnaraghi, M.F., and Dubly, R.N., Sliding-mode/shaped-input control of flexible/rigid link robots, *J. Sound Vib.*, 171, 185–200, 1994.
- Sinha, A., Optimum vibration control of flexible structures for specified modal decay rates, *J. Sound Vib.*, 123, 185–188, 1988.
- Skaar, S.B. and Tucker, D., Point Control of a one-link flexible manipulator, *J. Appl. Mech.*, 53, 23–27, 1986.
- Snowdon, J.C. 1968. *Vibration and Shock in Damped Mechanical Systems*, Wiley, New York.
- Soong, T.T. and Constantinou, M.C. 1994. *Passive and Active Structural Control in Civil Engineering*, Springer, Wien.
- Spencer, B.F., Yang, G., Carlson, J.D., and Sain, M.K. 1998. Smart dampers for seismic protection of structures: a full-scale study, In *Proceedings of the Second World Conference on Structural Control*, Kyoto, Japan.
- Stribersky, A., Muller, H., and Rath, B., The development of an integrated suspension control technology for passenger trains, *Proc. Inst. Mech. Engrs*, 212, 33–41, 1998.
- Sturk, M., Wu, M., and Wong, J.Y., Development and evaluation of a high voltage supply unit for electrorheological fluid dampers, *Vehicle Syst. Dyn.*, 24, 101–121, 1995.
- Sun, J.Q., Jolly, M.R., and Norris, M.A., Passive, adaptive, and active tuned vibration absorbers — a survey, *ASME Trans.*, 117, 234–242, 1995 (Special 50th Anniversary, Design issue).
- Sun, D. and Mills, J.K. 1999. PZT actuator placement for structural vibration damping of high speed manufacturing equipment, pp. 1107–1111. In *Proceedings of the American Control Conference (ACC'99)*, San Diego, CA.
- Sun, Y. and Parker, G.A., A position controlled disc valve in vehicle SA suspension systems, *Control Eng. Practice*, 1, 927–935, 1993.
- Tanaka, N. and Kikushima, Y., Impact vibration control using a SA damper, *J. Sound Vib.*, 158, 277–292, 1992.
- Venhovens, P.J., The development and implementation of adaptive SA suspension control, *Vehicle Syst. Dyn.*, 23, 211–235, 1994.
- Walsh, P.L. and Lamnacula, J.S., A variable stiffness vibration absorber for minimization of transient vibrations, *J. Sound Vib.*, 158, 195–211, 1992.
- Wang, K.W., Kim, Y.S., and Shea, D.B., Structural vibration control via electrorheological-fluid-based actuators with adaptive viscous and frictional damping, *J. Sound Vib.*, 177, 227–237, 1994.
- Wang, K.W., Lai, J.S., and Yu, W.K., An energy-based parametric control approach for structural vibration suppression via SA piezoelectric networks, *ASME J. Vib. Acoust.*, 118, 505–509, 1996.
- Warburton, G.B. and Ayorinde, E.O., Optimum absorber parameters for simple systems, *Earthquake Eng. Struct. Dyn.*, 8, 197–217, 1980.
- Yeung, K.S. and Chen, Y.P., A new controller design for manipulators using the theory of variable structure systems, *IEEE Trans. Automat. Control*, 33, 200–206, 1988.

- Yeung, K.S. and Chen, Y.P., Regulation of a one-link flexible robot arm using sliding mode control technique, *Int. J. Control*, 49, 1965–1978, 1989.
- Yoshimura, T., A SA suspension of passenger cars using fuzzy reasoning and the filed testing, *Int. J. Vehicle Des.*, 19, 150–166, 1998.
- Yuh, J., Application of discrete-time model reference adaptive control to a flexible single-link robot, *J. Robotic Syst.*, 4, 621–630, 1987.
- Zhu, G., Ge, S.S., Lee, T.H. 1997. Variable structure regulation of a flexible arm with translational base, pp. 1361–1366. In *Proceedings of the 36th IEEE Conference on Decision and Control*, San Diego, CA.

Helicopter Rotor Tuning

24.1	Introduction	24-1
24.2	Neural Network-Based Tuning	24-4
24.3	Probability-Based Tuning	24-5
24.4	Adaptive Tuning	24-8
	The Interval Model • Estimation of Feasible Region • Selection of Blade Adjustments • Learning	
24.5	Case Study	24-12
	Simulation Model • Interval Modeling • Performance Evaluation	
24.6	Conclusion	24-17

Kourosh Danaei

University of Massachusetts

Summary

Before a helicopter leaves the plant, its rotors need to be tuned so that the helicopter vibration meets the required specifications during different flight regimes. For this, three different adjustments can be made to each rotor blade in response to the magnitude and phase of vibration. In this chapter, the basic concepts for determining the blade adjustments are discussed, and three methods with fundamentally different approaches are described. A neural network-based method is described, which trains a feedforward network as the inverse model of the effect of the blade adjustments on helicopter vibrations, and uses the inverse model to determine the blade adjustments. Another is a probability-based method that maximizes the likelihood of success of the selected blade adjustments based on a stochastic model of the probability densities of the vibration components. The third method is an adaptive method that uses an interval model to represent the range of effect of blade adjustments on helicopter vibration, so as to cope with the nonlinear and stochastic nature of aircraft vibration. This method includes the a priori knowledge of the process by defining the initial coefficients of the interval model according to sensitivity coefficients between the blade adjustments and helicopter vibration, but then transforms these coefficients into intervals and updates them after each tuning iteration, to improve the model estimation accuracy. The details of rotor tuning are described through a case study, which demonstrates the application of the adaptive method.

24.1 Introduction

Helicopter rotor tuning (track and balance) is the process of adjusting the rotor blades so as to reduce the aircraft vibration and the spread of rotors. Rotor tuning as applied to Sikorsky's Black Hawk (H-60) helicopters is performed as follows. For initial measurements, the aircraft is flown through six different regimes, during which measurements of rotor track and vibration (balance) are recorded. Rotor track is measured by optical sensors, which detect the vertical position of the blades (see Chapter 15). Vibration is measured at the frequency of once per blade revolution (per rev) by two accelerometers, A and B, attached to the sides of the cockpit (see Figure 24.1, detail B). The vibration data are vectorially combined into two components: $A + B$, representing the vertical vibration of the aircraft, and $A - B$, representing its roll vibration. A sample of peak vibration levels for the six flight regimes, as well as the peak angular positions relative to a reference blade, are given in Table 24.1, along with a sample of track data.

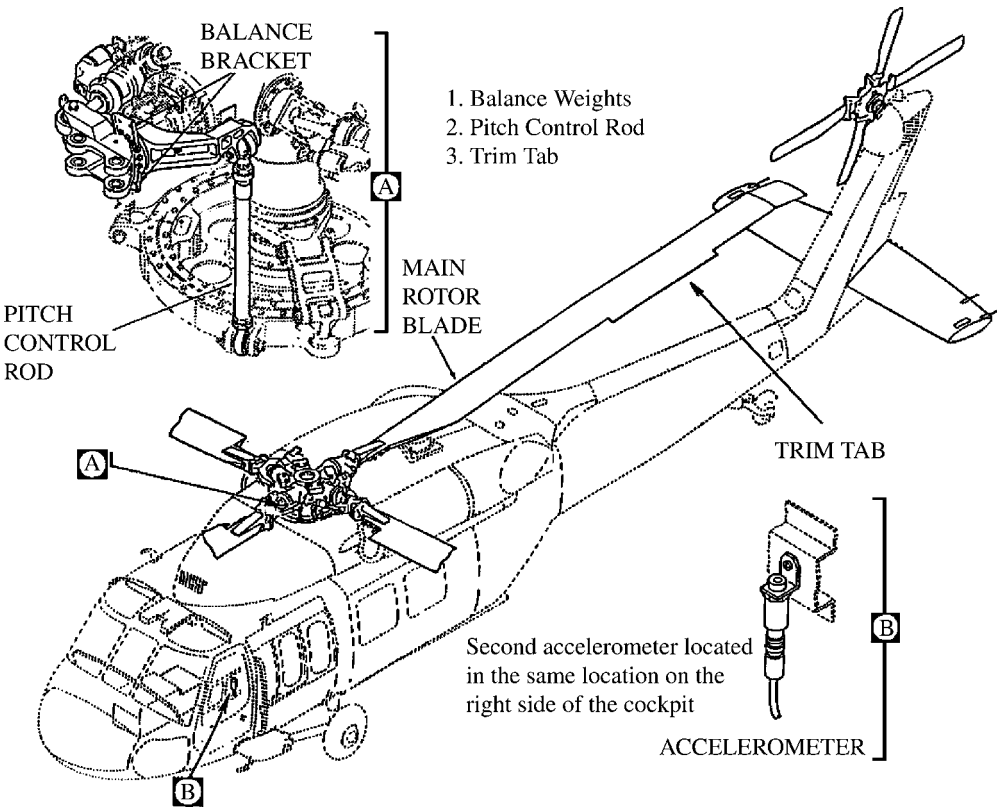


FIGURE 24.1 Illustration of the position of accelerometers A and B on the aircraft, and the rotor blade adjustments (push rod, trim tab, and hub weights).

TABLE 24.1 Typical Track and Balance Data Recorded during a Flight

Flight Regime	Vibration			
	A + B		A - B	
	Magnitude (ips)	Phase (°)	Magnitude (ips)	Phase (°)
fp	0.19	332	0.38	272
h	0.07	247	0.10	217
80	0.02	86	0.04	236
120	0.04	28	0.04	333
145	0.02	104	0.07	162
vh	0.10	312	0.12	211
Track (mm)				
	Blade #			
	1	2	3	4
fp	-2	3	1	-2
h	-1	3	0	-2
80	1	11	1	-13
120	2	13	-1	-14
145	5	18	-3	-20
vh	2	13	-1	-14

The six flight regimes in Table 24.1 are: ground (fpm), hover (hov), 80 knots (80), 120 knots (120), 145 knots (145), and maximum horizontal speed (vh). The track data indicate the vertical position of each blade relative to a mean position.

In order to bring track and one per rev vibration within specification, three types of adjustments can be made to the rotor system: pitch control rod adjustments, trim tab adjustments, and balance weight adjustments (see Figure 24.1). Pitch control rods can be extended or contracted by a certain number of notches to alter the pitch of the rotor blades. Positive push rod adjustments indicate extension. Trim tabs, which are adjustable surfaces on the trailing edge of the rotor blades, affect the aerodynamic pitch moment of the air foils and consequently their vibration characteristics. Tab adjustments are measured in thousandths of an inch, with positive and negative changes representing upward and downward tabbing, respectively. Finally, balance weights can be either added to or removed from the rotor hub to tune vibrations through changes in the blade mass. Balance weights are measured in ounces, with positive adjustments representing the addition of weight. In the case of the Sikorsky H-60 helicopter, which has four main rotor blades, a total of 12 adjustments can be made to tune the rotors (i.e., three adjustments per blade). Among them, balance weights primarily affect the ground vibration, so they are not commonly used for in-flight tuning. Furthermore, since the symmetry of rotor blades in four-bladed aircraft produces identical effects for adjustments to opposite blades, the combined form of blade adjustments to opposite blade pairs can be used as inputs. Accordingly, the input vector can be defined as

$$\Delta \mathbf{x} = [\Delta x_1, \Delta x_2, \Delta x_3, \Delta x_4]^T \quad (24.1)$$

where Δx_1 and Δx_3 denote the combined (condensed) trim tab adjustments (ΔT) to blade combinations one/three and two/four, respectively, and Δx_2 and Δx_4 represent the combined pitch control rod adjustments (ΔP) to blade combinations one/three and two/four, respectively. The relationships between the combined and individual adjustments are in the form:

$$\Delta x_1 = \Delta T_3 - \Delta T_1 \quad (24.2)$$

$$\Delta x_2 = \Delta P_3 - \Delta P_1 \quad (24.3)$$

$$\Delta x_3 = \Delta T_4 - \Delta T_2 \quad (24.4)$$

$$\Delta x_4 = \Delta P_4 - \Delta P_2 \quad (24.5)$$

Ideally, identical adjustments made to any two aircraft with different tail numbers should result in identical changes in vibration. In reality, however, significant inconsistencies in vibration changes may be present for identical adjustments to different tail numbers. This is perhaps due more to nonuniformity of flight conditions from weather or error in implementing the blade adjustments than factors such as dissimilarities between aircraft and rotor blades.

Virtually all of the current systems of rotor track and balance rely on the strategy shown in Figure 24.2, whereby the measurements of the flight just completed are used as the basis of search for the new blade adjustments. The search for blade adjustments is guided by the “process model” (see Figure 24.2), which represents the relationship between vibration changes and blade adjustments. A difficulty of rotor tuning is the excess of equations compared to degrees of freedom (four inputs to control 24 outputs), which translates into one-to-many mapping. Another difficulty is caused by the high level of noise present in the vibration measurements.

The traditional approach to rotor tuning uses linear relationships to define the process model

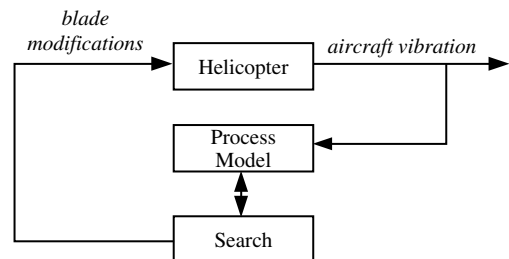


FIGURE 24.2 Tuning strategy of the current methods.

and uses model inversion to streamline the search. The drawback of the traditional approach, therefore, is its neglect of the potential nonlinearity of track and balance, and the vibration noise, as well as its limited capacity to produce comprehensive solutions to facilitate model inversion due to its consideration of the most extreme vibration components. In an attempt to include the potential nonlinearity of the process, Taitel et al. (1995) trained a set of neural networks with actual track and balance data to map vibration measurements to blade adjustments as well as to evaluate the goodness of the solution. In effect, they developed an inverse model based on the solutions available in the historical track and balance data, and provided a forward model to evaluate the solution. The potential advantage of this method is that it can interpolate among the historical solutions to address potential nonlinearity and vibration noise. Its disadvantages are that it is only applicable to helicopters with extensive track and balance history, and that its solutions are constrained by those contained in the historical data.

Another deviation from the traditional approach is introduced by Ventres and Hayden (2000), who define the relationships between blade adjustments and vibration in frequency domain, and provide an extension of these relationships to higher order vibrations. They use an optimization method to search for the adjustments to reduce per rev vibration as well as higher-order vibrations. Accordingly, this approach has the capacity to provide a comprehensive solution, but it too neglects the potential nonlinearity between the blade adjustments and aircraft vibration as well as the noise in the measurements.

The most recent solutions to rotor tuning are those by Wang et al. (2005a, 2005b), which are designed to address both the stochastics of vibration and the potential nonlinearity of the tuning process. In the first solution, which is a probability-based method, the underlying model comprises two components: a deterministic component and a probability component. The method relies on the probability model to estimate the likelihood of the measured vibration satisfying the specifications and to search for blade adjustments that will maximize this likelihood. The likelihood measures in the probability model are computed according to the probability distribution of vibration derived from historical track and balance data. The second solution is an adaptive method that uses an interval model to cope with the potential nonlinearity of the process and to account for vibration noise. This method, which also incorporates learning to provide adaptation to the rotor tuning process, initializes the coefficients of the interval model according to the sensitivity coefficients between the blade adjustments and helicopter vibration. However, it modifies these coefficients after the first iteration to better represent the vibration measurements acquired. This method takes into account vibration data from all of the flight regimes during the search for the appropriate blade adjustments; therefore, it has the capacity to provide comprehensive solutions. The remainder of this chapter describes three of the methods discussed above to provide a representation of various solutions proposed for rotor tuning, followed by a case study to demonstrate the application of the adaptive method.

24.2 Neural Network-Based Tuning

As mentioned earlier, rotor tuning in four-bladed aircraft is performed by first specifying a condensed set of adjustments to reduce vibrations, and then expanding these adjustments into a detailed set to satisfy the track requirements. This same strategy is implemented in the system of neural networks shown in [Figure 24.3](#) (Taitel et al., 1995). The first network in this system, called the selection net, determines the condensed blade adjustments (output) that will bring about a given change in vibration (input). To eliminate vibration, the negatives of the vibration measurements from the flight are utilized as inputs to this network. The validity of the condensed adjustments is then checked by predicting their effect on vibration via the condensed simulation net. Theoretically, these simulated vibration changes should be the negative of the vibration measurements from the aircraft so that their summation will be zero. However, owing to the inexactness of the neural network models and noise, the resultant vibration will most likely not equal zero. In cases where the resultant vibration is not within specifications (usually less than 0.20 inches per second [ips]), the condensed adjustments may be refined by feeding the resultant

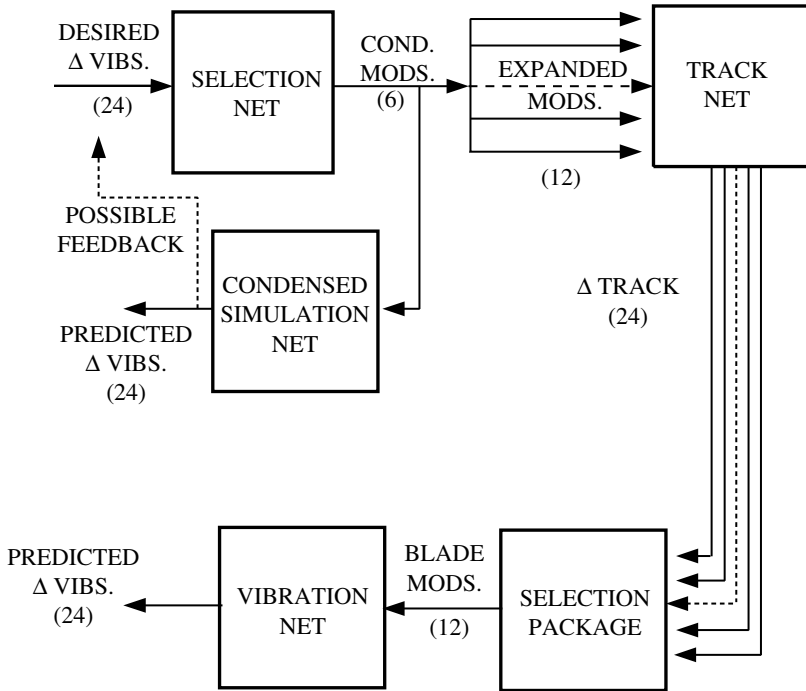


FIGURE 24.3 Schematic of the rotor tuning system. The numbers inside parentheses represent the number of inputs or outputs of individual nets.

vibration back into the selection net. This feedback is depicted by the dashed feedback line in Figure 24.3. It should be noted that the condensed simulation net may also serve as a diagnostic tool by indicating behavior out of the norm. For example, an aircraft with vibrations significantly different from those predicted by this network may suffer from defective components.

Just as with the traditional approach, once the condensed solution has been specified, it needs to be expanded into a detailed form to satisfy the rotor track requirements. As previously mentioned, the condensed set of adjustments may be viewed as the constraint on detailed adjustments so as to ensure that the vibration solution is not compromised for track. Each one of these detailed sets of adjustments is a candidate for the final rotor tuning solution, and it is left to the track net and the selection package to determine which set of detailed adjustments provides the best tracking performance. For selection purposes, the track net simulates the changes in track due to a candidate set of detailed adjustments, and then adds these changes to the initial track measurements from the flight to estimate the resultant track. The set of detailed adjustments that yields the smallest estimated track (i.e., smallest maximum blade spread) is selected as the solution to the rotor tuning problem. The selected set of detailed adjustments is then checked via the vibration net, which, similar to the condensed simulation net, serves as an independent evaluator of the selected adjustments.

24.3 Probability-Based Tuning

The noted contribution of this method is its introduction of the likelihood of success as a criterion in the search for the blade adjustments (Wang et al., 2005). This method speculates the effectiveness of various adjustment sets in reducing the vibration and selects the set with the maximum probability of producing acceptable vibration (see Chapter 5 for useful concepts of random or stochastic vibration). The concept of this method is explained in the context of a simple example. If the measured vibration from the current

flight is denoted by $V_j(k-1)$ and the estimated vibration change according to the model is represented by $\Delta\hat{V}_j(k) = f(\Delta x)$ as a function of the blade adjustments, Δx , then the predicted vibration of the next flight, $\hat{V}_j(k)$, can be defined as

$$\hat{V}_j(k) = V_j(k-1) + \Delta\hat{V}_j(k) \quad (24.6)$$

$$V_j(k) = \hat{V}_j(k) + \hat{e}_j(k) \quad (24.7)$$

where $V_j(k)$ denotes the measured vibration for the next flight. In rotor tuning, the adjustments are selected according to the predicted vibration, $\hat{V}_j(k)$, whereas the objective is defined in terms of the measured vibration. The inclusion of the probability model here is to account for the inevitable uncertainty in the actual position of the measured vibration. According to Equation 24.7, the mean value of the measured vibration is equal to the value of the predicted vibration plus the mean value of the prediction error. However, since the predicted vibration is a deterministic entity, the probability distribution of the measured vibration is the same as that of the prediction error. Accordingly, whereas the nominal value of the measured vibration can be controlled by the blade adjustment, its optimal position within the specification region should be determined according to its probability distribution. For a case where the prediction error, $\hat{e}_j(k)$, is zero-mean and normally distributed, as illustrated in Figure 24.4, placing the predicted vibration at the center of the specification range will be synonymous with maximizing the probability that the measured vibration will be within the range. The likelihood of success of blade adjustments can therefore be measured by the area under the probability density function of prediction error located within the specification region. The blade adjustment set that produces the highest likelihood will be the preferred adjustment.

The main difficulty with rotor tuning, however, is the limited number of DoFs, which precludes perfect positioning of the predicted vibration. This point is illustrated in Figure 24.5 for a case where two vibration components are to be positioned at the center of the specification region with only one adjustment. If one assumes that the effect of adjustment, Δx , on the change in the two vibration components, $\Delta\hat{V}_j(k)$, can be represented by a linear model, as

$$\Delta\hat{V}_j(k) = a_{ij}\Delta x$$

then the position of the predicted vibration components will be constrained to the line L in Figure 24.5. As illustrated in this figure, since it will be impossible to place the predicted vibration components at the center, a compromised position needs to be selected. In this method, the best compromised position for the predicted vibration is that which renders the largest probability of satisfying the specifications for the measured vibration. This position, for the two-component vibration example, is one that maximizes $P_r[(V_1, V_2) \in S] = \int_{(V_1, V_2) \in S} P(V_1, V_2) dV_1 dV_2$. The above formulation indicates that the placement of the predicted vibration requires knowledge of

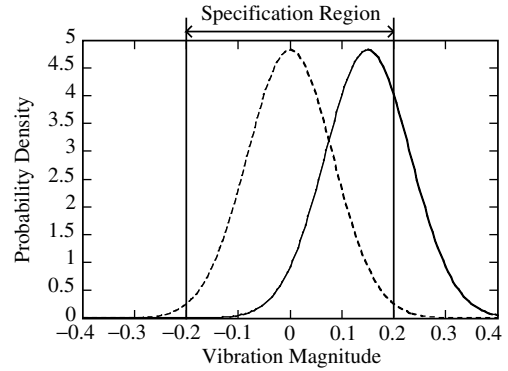


FIGURE 24.4 Illustration of improved placement of the predicted vibration within the specification range.

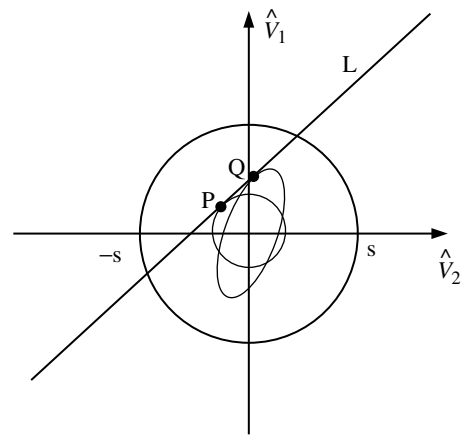


FIGURE 24.5 Restricted placement of vibration components within the specification region for a two-dimensional case.

the joint probability density function, $p(V_1, V_2)$, of the vibration components. In the ideal case of independent vibration components with equal probability distributions, the loci of the points with equal probabilities $P_r[(V_1, \dots, V_n) \in S]$ are surfaces of hyperspheres. Such ideal loci for the two-component vibration example of Figure 24.5 are circles centered at the origin (see Figure 24.5), which lead to point P as the best compromised position closest on line L to the center of the specification circle. Point P, however, does not represent the best position if the two vibration components are dependent or have unequal distributions. The loci of equal probabilities for this more general case are elliptical, as also shown in Figure 24.5, indicating point Q as the best position on line L for placing the predicted vibration. The inadequacy of the DoFs illustrated here is exacerbated in rotor tuning, where 24 correlated vibration components need to be positioned within the specification region using only four condensed blade adjustments. For the 24-component vector of measured vibration $\mathbf{V}(k) = [V_{c1}(k), V_{s1}(k), \dots, V_{c12}(k), V_{s12}(k)]^T$, where V_c and V_s represent the cosine and sine components of each vibration measurement, respectively, the joint probability density function of measured vibration for the k th flight, $\mathbf{V}(k)$, can be characterized as an N -dimensional Gaussian function:

$$p(\mathbf{V}(k)) = \frac{1}{(2\pi)^{N/2} |\Phi|^{1/2}} \exp \left[-\frac{1}{2} \hat{\mathbf{e}}(k)^T \Phi^{-1} \hat{\mathbf{e}}(k) \right] \quad (24.8)$$

$$\hat{\mathbf{e}}(k) = \mathbf{V}(k) - \mathbf{V}(k-1) - C\Delta\mathbf{x}(k) \quad (24.9)$$

where Φ represents the covariance matrix of the prediction error. Now, if $\Gamma = \{|\mathbf{V}_j| = \sqrt{V_{cj}^2 + V_{sj}^2} \leq \alpha, j = 1, \dots, 12\}$ denotes the specification region in 24-dimensional Euclidean space, the blade adjustments, $\Delta\mathbf{x}^*$, can be selected such that the probability that the measured vibration is within the acceptable range is maximized (see also Table 24.2). Formally,

$$\Delta\mathbf{x}^* = \arg_{\Delta\mathbf{x}} \max \left[\Pr(\mathbf{V}(k) \in \Gamma) = \int_{\Gamma} p(\mathbf{V}(k)) d\mathbf{V}(k) \right] \quad (24.10)$$

TABLE 24.2 Summary of Probability-Based Tuning

For the input vector:

$$\Delta\mathbf{x} = [\Delta x_1, \Delta x_2, \Delta x_3, \Delta x_4]^T$$

where Δx_1 and Δx_3 denote the combined trim tab adjustments to blade combinations one to three and two to four, respectively, and Δx_2 and Δx_4 represent the combined pitch control rod adjustments to blade combinations one to three and two to four, respectively, the blade adjustments, $\Delta\mathbf{x}$, can be selected such that the probability that the measured vibration is within the acceptable range is maximized. Formally,

$$\Delta\mathbf{x}^* = \arg_{\Delta\mathbf{x}} \max [\Pr(\mathbf{V}(k) \in \Gamma) = \int_{\Gamma} p(\mathbf{V}(k)) d\mathbf{V}(k)]$$

where $\Pr(\mathbf{V}(k))$ denotes the probability of the measured vibration, Γ denotes the specification region in 24-dimensional Euclidean space, and $p(\mathbf{V}(k))$ represents the joint probability density of the measured vibration for the k th flight characterized as an N -dimensional Gaussian function:

$$p(\mathbf{V}(k)) = \frac{1}{(2\pi)^{N/2} |\Phi|^{1/2}} \exp \left[-\frac{1}{2} \hat{\mathbf{e}}(k)^T \Phi^{-1} \hat{\mathbf{e}}(k) \right]$$

with

$$\hat{\mathbf{e}}(k) = \mathbf{V}(k) - \mathbf{V}(k-1) - C\Delta\mathbf{x}(k)$$

representing the predicted error in vibration.

24.4 Adaptive Tuning

The schematic of this method is shown in Figure 24.6 (Wang et al., 2005). As in the other methods, it uses a process model as the basis of search for the appropriate blade adjustments, but instead of using a linear model, it uses an interval model to accommodate process nonlinearity and measurement noise. According to this model, the feasible region of the process is estimated first, to include the adjustments that will result in acceptable vibration estimates. This feasible region is then used to search for the blade adjustments that will minimize the modeled vibration. If the application of these adjustments does not result in satisfactory vibration, the interval model will be updated to better estimate the feasible region and improve the choice of blade adjustments for the next flight. Important parameters of adaptive tuning are summarized in Table 24.3.

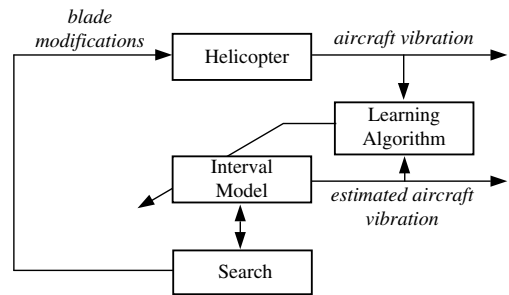


FIGURE 24.6 The strategy of the proposed tuning method.

24.4.1 The Interval Model

In order to account for the stochastics and nonlinearity of vibration, an interval model (Moore, 1979) is defined to represent the range of aircraft vibration caused by blade adjustments. The interval model used here has the form:

$$\Delta \vec{y}_j = \sum_{i=1}^n \vec{C}_{ji} \Delta x_i, \quad j = 1, \dots, m \quad (24.11)$$

where each coefficient is defined as an interval:

$$\vec{C}_{ji} = [C_{Lji}, C_{Uji}]$$

In the above model, the variables with the two-sided arrow, \leftrightarrow , denote intervalled variables, C_{Lji} and C_{Uji} represent, respectively, the current values of the lower and upper bounds of the sensitivity coefficients between each input, Δx_i , and output, $\Delta \vec{y}_j$. The interval $\Delta \vec{y}_j$ denotes the estimated range of change of the j th output caused by the change to the current inputs, $\Delta x_1, \dots, \Delta x_n$.

TABLE 24.3 Summary of Adaptive Tuning

In adaptive tuning, each vibration component is defined as

$$\Delta \vec{y}_j = \sum_{i=1}^n \vec{C}_{ji} \Delta x_i, \quad j = 1, \dots, m$$

where each coefficient is defined as an interval:

$$\vec{C}_{ji} = [C_{Lji}, C_{Uji}]$$

with C_{Lji} and C_{Uji} representing, respectively, the current values of the lower and upper bounds of the sensitivity coefficients between each input, Δx_i , and output, $\Delta \vec{y}_j$. The blade adjustments are then sought by minimizing the objective function:

$$S = \frac{\sum_{e=1}^{N_e} \text{Distance}(x_c, x_e)}{(\prod_{s=1}^{N_s} \text{Distance}(x_c, x_s))^{1/N_s}}$$

where x_c represents a candidate set of blade adjustments within the feasible region, x_e represents any set of blade adjustments within the selection region, x_s denotes each of the previously selected blade adjustments, and N_e and N_s represent the number of the estimated feasible blade adjustments and the previously selected blade adjustments, respectively.

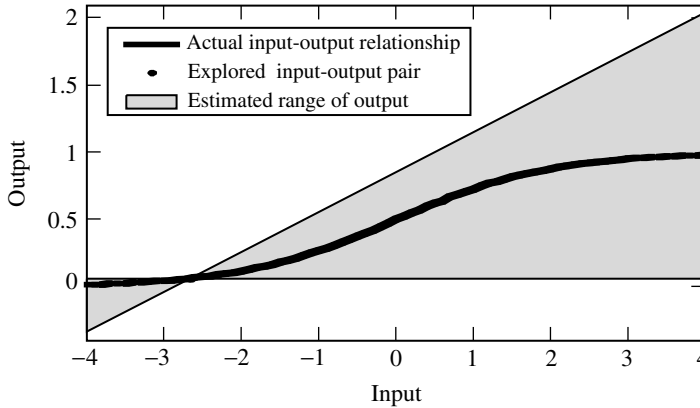


FIGURE 24.7 Estimated range of output by the interval model using one reference input.

The fit provided by the interval model for a mildly nonlinear input/output relationship is illustrated in Figure 24.7, where the output range is estimated relative to one explored input.¹ According to Equation 24.11, the estimated range of the output becomes larger, and therefore less accurate, as the potential input is selected farther from the current input (producing a large Δx_i). This potential drawback of the interval model is considerably reduced when multiple inputs have been explored so that the interval model can take advantage of several inputs for estimating the output range. The estimated output, \tilde{y}_j , at a potential input, x_i , may be computed relative to any set of previously explored inputs, yielding different estimates of \tilde{y}_j (due to different values of Δx_i). In order to cope with the multiplicity of estimates, \tilde{y}_j is defined as the common range among all of the \tilde{y}_j estimates (Yang, 2000). The estimation of \tilde{y}_j using this commonality rule is illustrated in Figure 24.8, which indicates that using this estimation approach enables representation of the system nonlinearities in a piecewise fashion. It can be shown that the lack of commonality between the estimated ranges of output will cause a part of the input–output relationship to not be represented by the interval model. In such cases, however, the lack of compliance between the interval model and the *input–output* relationship can be corrected by adaptation of the coefficient intervals through learning.

24.4.2 Estimation of Feasible Region

The feasible region comprises all sets of blade adjustments that will reduce the aircraft vibration within specifications. The feasible region is estimated here by comparing the individually estimated \tilde{y}_j values with their corresponding constraints, so as to decide whether the corresponding blade adjustments belong to the feasible region. In this method, even when the interval \tilde{y}_j partly overlaps the vibration constraint, the corresponding blade adjustments are included in the estimated feasible region. The above procedure of estimating the feasible region based on individual outputs is then extended to multiple outputs by forming the conjunction of the estimated feasible regions from each output.

24.4.3 Selection of Blade Adjustments

The blade adjustments provide the coordinates of the feasible region, therefore, they need to provide a balanced coverage of the input space. As such, blade adjustment selection becomes synonymous with maximizing the distance of the selected blade adjustments from the previous blade adjustments, as well as

¹An explored input represents an input for which the exact value of the output is available. In rotor tuning, an explored input would denote a blade adjustment that has been applied to the helicopter, and for which the corresponding vibration changes have been measured.

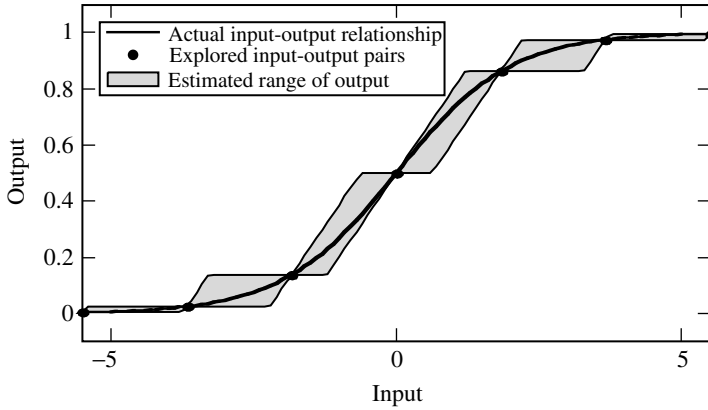


FIGURE 24.8 Estimated range of output by the interval model using seven reference inputs.

bringing them closer to the center of the feasible region. This objective can be pursued by minimizing the following objective function:

$$S = \frac{\sum_{e=1}^{N_e} \text{Distance}(x_c, x_e)}{\left(\prod_{s=1}^{N_s} \text{Distance}(x_c, x_s)\right)^{1/N_s}} \quad (24.12)$$

where x_c represents a candidate set of blade adjustments within the feasible region, x_e represents any set of blade adjustments within the selection region, x_s denotes each of the previously selected blade adjustments, and N_e and N_s represent, respectively, the numbers of the estimated feasible blade adjustments and the previously selected blade adjustments. Note that when the candidate set, x_c , is close to the previously selected blade adjustments, $\left(\prod_{s=1}^{N_s} \text{Distance}(x_c, x_s)\right)^{1/N_s}$ becomes small, and when the candidate set of blade adjustments, x_c , is far from the center of the feasible region, the value of $\sum_{e=1}^{N_e} \text{Distance}(x_c, x_e)$ becomes large. By minimizing S , the candidate blade adjustments are selected such that the above extremes are avoided.

24.4.4 Learning

Although an interval model defined according to the sensitivity coefficients may provide a suitable initial basis for tuning, it may not be the most representative of the rotor tuning process. As such, it may not be able to carry the search process to the end. A noted feature of the proposed method is its learning capability, which enables it to refine its knowledge base. To this end, the coefficients of the model are updated by considering new values for each of the upper and lower limits of individual coefficients. The objective is to make the range of the coefficients as small as possible while making sure that the interval model envelopes the acquired *input-output* data. The learning problem can be defined as

$$\text{Minimize } E = \sum_{m=1}^{K-1} \sum_{k>m}^K \{[y_L(m, k) - y(k)]^2 + [y_U(m, k) - y(k)]^2\} \quad (24.13)$$

subject to

$$y_U(m, k) \geq y(k) \quad (24.14)$$

$$y_L(m, k) \leq y(k) \quad (24.15)$$

$$C_{Ui} - \gamma \geq C_{Li} \quad (24.16)$$

where K represents the total number of sample points collected so far, $y_L(m, k)$ and $y_U(m, k)$ represent, respectively, the lower and upper limits of the estimated output range at the k th sample point relative to

the m th sample point, $y(k)$ denotes the actual output value at the k th sample point, and C_{Ui} and C_{Li} represent the upper and lower limits of the i th coefficient interval, respectively. The parameter γ is a small positive number to control the range of the coefficients.

Most of the approaches that can be potentially used for adapting the coefficient intervals, such as gradient descent (Ishibuchi et al., 1993) or nonlinear programming, cannot be applied to rotor tuning due to their demand for rich training data and their impartiality to the initial value of the coefficients representing the *a priori* knowledge of the process. As an alternative, a learning algorithm is devised here to cope with the scarcity of track and balance data while staying true to the initial values of the coefficients. In this algorithm, the coefficients of the interval model, initially set pointwise at the sensitivity coefficients, are adapted after each flight in two steps: enlargement and shrinkage. First, the vibration measurements from all of the flights completed for the present tail number are matched against the estimated output ranges from the current interval model. If any of the measurements do not fit the upper or lower limits of the estimates, the coefficient intervals are enlarged in small steps, iteratively, and the output ranges are re-estimated at each iteration using the updated interval model. The enlargement of the coefficient intervals stops when the estimated output ranges include all of the measurements. At this point, even though the updated interval model provides a fit for the *input-output* data, it may be overcompensated. In order to rectify this situation, the coefficient intervals are shrunk individually by selecting new candidates for their upper and lower limits.

The shrinkage-enlargement learning algorithm has the form:

$$\Delta C_{Li} = -\eta \delta_L \Delta x_i(m, k) \quad (24.17)$$

$$\Delta C_{Ui} = -\eta \delta_U \Delta x_i(m, k) \quad (24.18)$$

where, during the enlargement phase, δ_L and δ_U are defined as

$$\delta_L = \begin{cases} \Delta y_L & \text{If } \Delta x_i(m, k) > 0 \text{ and } \Delta y_L > 0 \\ \Delta y_U & \text{If } \Delta x_i(m, k) < 0 \text{ and } \Delta y_U < 0 \\ 0 & \text{otherwise} \end{cases} \quad (24.19)$$

$$\delta_U = \begin{cases} \Delta y_U & \text{If } \Delta x_i(m, k) > 0 \text{ and } \Delta y_U < 0 \\ \Delta y_L & \text{If } \Delta x_i(m, k) < 0 \text{ and } \Delta y_L > 0 \\ 0 & \text{otherwise} \end{cases} \quad (24.20)$$

and during the shrinkage phase, they are defined as

$$\delta_L = \begin{cases} \Delta y_L & \text{If } \Delta x_i(m, k) > 0 \text{ and } \Delta y_L < 0 \\ \Delta y_U & \text{If } \Delta x_i(m, k) < 0 \text{ and } \Delta y_U > 0 \\ 0 & \text{otherwise} \end{cases} \quad (24.21)$$

$$\delta_U = \begin{cases} \Delta y_U & \text{If } \Delta x_i(m, k) > 0 \text{ and } \Delta y_U > 0 \\ \Delta y_L & \text{If } \Delta x_i(m, k) < 0 \text{ and } \Delta y_L < 0 \\ 0 & \text{otherwise} \end{cases} \quad (24.22)$$

with

$$\Delta x_i(m, k) = x_i(k) - x_i(m) \quad (24.23)$$

$$\Delta y_L = y_L(m, k) - y(k) \quad (24.24)$$

$$\Delta y_U = y_U(m, k) - y(k) \quad (24.25)$$

This procedure is repeated for each coefficient interval in an iterative fashion until the objective function E (Equation 24.13) is minimized. The minimization of E ensures limited adaptation of the coefficient intervals within the smallest possible range.

At the beginning of tuning, the limited number of *input–output* data available for learning will not provide a comprehensive representation of the process. Therefore, the coefficient intervals should not be shrunk drastically until enough *input–output* data have become available. For this, the length of each coefficient interval $[C_{Li}, C_{Ui}]$ is constrained by the minimal interval length for each tuning iteration as

$$\min L = \{C_{Ui}(0) - C_{Li}(0)\}(1 - \beta)^n \quad (24.26)$$

where $\beta \in [0, 1]$ controls the shrinkage rate of the coefficient interval, and n denotes the number of tuning iterations. The coefficient interval cannot be shrunk when $\beta = 0$ and can be shrunk without limit when $\beta = 1$. Usually, β is selected closer to 0.

24.5 Case Study

The utility of the Interval Model (IM) method is demonstrated in application to Black Hawks. Ideally, the performance of the proposed method should be evaluated side by side against that of the traditional method. However, such an evaluation would require tuning the aircraft with one method, undoing changes, and tuning the aircraft with another. Since such testing is prohibitively costly and infeasible, a compromised approach of evaluating the method in simulation is utilized. A process simulation model is therefore used to represent the block “helicopter” in Figure 24.6, with the block “forward model” represented by an interval model.

24.5.1 Simulation Model

Considering the potential nonlinearity of the effect of blade adjustments on the helicopter vibration and the high level of noise present in vibration measurements, multilayer neural networks offer the most suitable framework for modeling. A series of neural networks were trained with historical balance data to represent the relationships between vibration changes and blade adjustments, and the stochastic aspects of vibration (see Chapter 5) were represented by the addition of random numbers to the outputs of the networks.

A total of 102 sets of vibration data were used to train and test the neural networks. The inputs to these networks were the combined blade adjustments of push rods and trim tabs to opposite blade pairs, and their outputs were the resulting vibration changes between two consecutive flights. Since the vibration data are vector quantities that are represented by both magnitude and phase components (see Table 24.1), the vibration data were transformed into Cartesian coordinates, so that each vector element would denote the change in the cosine or sine component of the $A + B$ or $A - B$ vibration of each of the six flight regimes (see Table 24.1). In this study, each neural network model consisted of four inputs and one output, so a total of 24 networks were trained to represent all of the vibration components. Alternatively, all of the vibration measurements may be represented by one neural network, but such a network is more difficult to train. Formally, the outputs of the neural networks, which represent the cosine and sine components of the vibration at different regimes, $v_{sj}(k)$ and $v_{cj}(k)$, respectively, are defined as

$$\hat{V}_{sj}(k) = V_{sj}(k-1) + \Delta V_{sj}(k) + R_{sj}(k) \quad (24.27)$$

$$\hat{V}_{cj}(k) = V_{cj}(k-1) + \Delta V_{cj}(k) + R_{cj}(k) \quad (24.28)$$

$$\Delta V_{sj}(k) = F_{sj}(\Delta x) \quad (24.29)$$

$$\Delta V_{cj}(k) = F_{cj}(\Delta x) \quad (24.30)$$

$$\hat{V}_j(k) = \sqrt{\hat{V}_{sj}(k)^2 + \hat{V}_{cj}(k)^2} \quad (24.31)$$

where the input vector $\Delta \mathbf{x} = \{\Delta x_1, \Delta x_2, \Delta x_3, \Delta x_4\}$ denotes the set of combined blade adjustments, each of the functionals, F_{sj} and F_{cj} , represent the change in vibration between two consecutive flights as represented by a neural network, and $R_{sj}(k)$ and $R_{cj}(k)$ denote random numbers added to the outputs of the networks to account for measurement noise. Each of the networks consisted of two hidden layers, with four and eight processing elements in the first and second layers, respectively. To avoid overtraining, the 102 sets of data were divided into two equal subsets, one set to train the network and the other to test its performance. The random numbers, R_{cj} and R_{sj} , were generated according to the Gaussian distribution $N(\mu, \sigma^2)$, with the mean μ and variance σ^2 defined as

$$\hat{\mu} = \frac{1}{M} \sum_{i=1}^M e_i \quad (24.32)$$

$$\hat{\sigma}^2 = \frac{1}{M-1} \sum_{i=1}^M (e_i - \hat{\mu})^2 \quad (24.33)$$

In the above formulation, M represents the total number of data sets and e_i denotes the difference between the measured and expected value of vibration, defined as

$$e_j(k) = V_j(k) - V_j(k-1) - \Delta V_j(k) \quad (24.34)$$

A sample of estimated vibration changes generated by the neural network model is compared side by side with the actual vibration changes in Figure 24.9. The results indicate close agreement between the predicted and actual vibration changes.

24.5.2 Interval Modeling

In application to the Black Hawks, a total of 24 interval models need to be constructed to approximate the changes in the cosine and sine components of the A + B and A - B vibrations at each of the six flight regimes. The interval models have the form

$$\tilde{V}_{cj}(k) = V_{cj}(k-1) + \sum_{i=1}^4 \tilde{C}_{cji}(k-1) \Delta x_i(k) \quad (24.35)$$

$$\tilde{V}_{sj}(k) = V_{sj}(k-1) + \sum_{i=1}^4 \tilde{C}_{sji}(k-1) \Delta x_i(k) \quad (24.36)$$

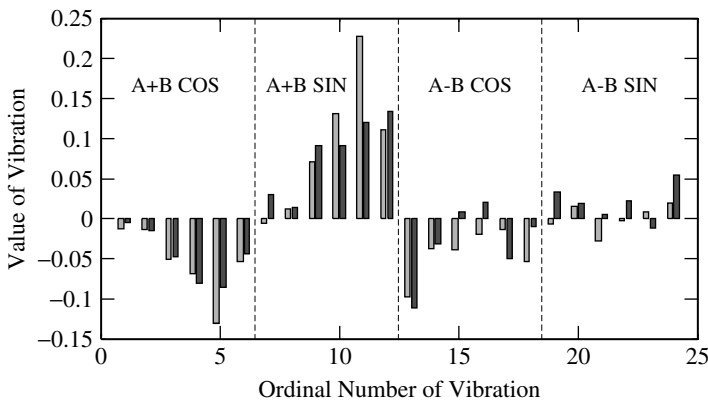


FIGURE 24.9 A sample set of simulated vibration changes shown side by side with the actual vibration changes.

$$\vec{V}_j(k) = \sqrt{\vec{V}_{sj}^2(k) + \vec{V}_{cj}^2(k)}, \quad i = 1, \dots, 4 \text{ and } j = 1, \dots, 12 \quad (24.37)$$

where the $\vec{V}_{cj}(k)$ and $\vec{V}_{sj}(k)$ represent, respectively, the estimated cosine and sine components of $A + B$ or $A - B$ vibration at each of the six flight regimes, $\vec{V}_j(k)$ denotes the magnitude of the vibration, and Δx_i are the same as those in Equation 24.2 to Equation 24.5. For this study, the feasible region was defined to include all of the blade adjustments associated with vibration estimates that satisfied the specification: $\max\{\min(\vec{V}_1), \dots, \min(\vec{V}_{12})\} \leq 0.2$. The above specification ensures that the lower limit of the estimated vibration range of the largest vibration component will be less than 0.2 ips (an industry standard). The selection of the lower limit here is to ensure that the feasible region is as large as possible, so as not to eliminate any potentially good candidate blade adjustments. The computation of the feasible region was based on the range $[-0.015, 0.015]$ for push rods and $[-0.035, 0.035]$ for trim tabs, within which 20,000 random sets of blade adjustments were evaluated for their feasibility. The blade adjustments associated with vibration ranges satisfying the specification were included in the feasible region.

As noted earlier, the proposed method uses the feasible region as the basis of search for the blade adjustments. For this study, the blade adjustments set that produced the smallest value for the objective function S (Equation 24.12) was selected to be applied to the helicopter. It should be noted that, given the stringent constraints on the vibration components, there were cases where the search algorithm could not find any feasible blade adjustments that would satisfy all of the constraints. In such cases, the set of blade adjustments that produced the smallest lower limit of the maximum estimated vibration was used as a compromised solution.

The interval model was updated after each tuning iteration. For shrinkage–enlargement learning, the parameter β in Equation 24.26 was set to 1 and γ to 0, so that the coefficient intervals could be shrunk without limits. Learning was performed separately for each tail number to customize the interval model to individual tail numbers; that is, the interval model was set to the sensitivity coefficients for each tail number and was adapted after the first tuning iteration. Accordingly, the interval model was actually a pointwise model for the first iteration and took the form of an interval model thereafter.

24.5.3 Performance Evaluation

The interval model (IM) method was tested on 39 tail numbers, for which actual track and balance data were available from the field. For each tail number, the IM method was applied iteratively until either the simulated vibrations were within their specifications, or an upper limit of five process iterations had been reached.

Since the stochastic aspects of vibration measurements impose randomness on the rotor tuning process, rotor tuning solutions cannot be evaluated by deterministic measures. This calls for the creation of performance measures that account for uncertainty. One such measure that assesses tuning efficiency is the *average tuning iteration number* (ATIN) which represents the average number of iterations taken for tuning each tail number. The number of flights used by the IM method for the 39 tail numbers is included in Table 24.4 along with those actually performed in the field. The results indicate that the IM method requires a smaller ATIN relative to that actually performed.

Another potentially significant aspect of the IM method is its adaptation capability, which enables it to transform a pointwise model into an IM, and to subsequently update it after the first iteration. Adaptation capability, however, may not be as significant in rotor tuning, which offers limited possibility for training. In order to evaluate the significance of learning in the performance of the IM method, the results in Table 24.4 were reproduced in Table 24.5 with the learning feature turned off. The ATINs indicate that with learning, the IM method requires fewer iterations for tuning each tail number, despite the small number of iterations taken to tune each tail number. This, in turn, indicates that the interval model enhances the performance of the IM method, since without learning, the model remains pointwise at the sensitivity coefficients. However, perhaps an equally interesting set of results in Table 24.5 are those indicating that even without learning, the IM method requires fewer iterations than actually

TABLE 24.4 The Number of Tuning Iterations Required by the Interval Model Method and Those Applied in the Field

Tail # (39)	Number of Tuning Iterations	
	Actual	IM Method
176	1	1
178	1	1
179	3	2
180	1	1
184	2	1
⋮	⋮	⋮
260	4	1
⋮	⋮	⋮
861	1	1
Total	71	48
ATIN	1.82	1.23

TABLE 24.5 The Number of Tuning Iterations Required by the IM Method (with and without Learning) along with Those Actually Applied in the Field

Tail # (39)	Tuning Iteration Number		
	Actual	IM Method	
		With Learning	Without Learning
185	3	2	3
186	3	2	3
208	2	2	3
245	3	2	3
260	4	2	3
802	3	2	3
822	3	2	3
⋮	⋮	⋮	⋮
Total	71	48	62
ATIN	1.82	1.23	1.59

performed in the field. Given that the adjustments associated with both sets of results were selected from the same model (i.e., sensitivity coefficients), the better performance of the IM method can only be attributed to its more effective search strategy that leads to more comprehensive solutions.

A preferred aspect of a system of rotor tuning is its ability to tune the aircraft within one iteration. This aspect of the method was evaluated by checking the number of tail numbers tuned within one iteration. For these results, in order to eliminate the difference between the simulation model and the helicopter, only the vibration estimates from simulation were used to evaluate the suitability of the adjustments. The results of this study are shown in Table 24.6, where the tail numbers tuned within one iteration are shown by a \surd and those requiring more than one iteration are denoted by \times . The results indicate that the IM method satisfies this more stringent criterion better than the actual adjustments, further validating the claim that the IM method benefits from a more effective search engine.

Owing to the randomness of the vibration measurements, repeated applications of an adjustment set may lead to slightly different vibration measurements. This, in turn, may cause a variance in the number of iterations produced by adjustments when the resulting vibration is close to the specified threshold. It would be beneficial, therefore, to devise a measure for the probability of success of adjustments.

TABLE 24.6 Tally of the Tail Numbers Tuned within One Iteration According to Simulated Vibration

Tail # (39)	Tuned within One Iteration	
	Actual	IM Method
176	✓	✓
178	×	✓
179	✓	✓
⋮	⋮	⋮
822	×	✓
858	×	✓
859	✓	✓
861	✓	✓
Total	19	30

The empirical measure, the acceptability index (AI), is defined here as

$$AI = \frac{1}{N} \sum_{l=1}^N s_l \tag{24.38}$$

to denote the percentage of times an adjustment set will result in the vibration satisfying the specification. In the above equation, N represents the total number of flights simulated to represent the repeated applications of the same adjustment set, and

$$s_l = \begin{cases} 1 & \text{if vibration of the } l\text{th simulation flight is acceptable} \\ 0 & \text{if vibration of the } l\text{th simulation flight is unacceptable} \end{cases}$$

The AIs computed for both the actual and selected adjustments at the first iteration are included in Table 24.7. The results indicate that the IM method provides adjustments with a higher probability of success as judged by the acceptability of vibration estimates from the simulation model. These results, which indicate that the selected adjustments from the IM method can more consistently tune the rotors within one iteration, imply the better positioning of the adjustments within the feasible region.

TABLE 24.7 The Values of Acceptability Index (Trial Mode) Computed for Both the Actual and Selected Adjustments at the First Flight

Tail # (39)	Acceptability Index	
	Actual	IM Method
176	0.92	0.87
178	0	0.54
179	0.61	0.52
⋮	⋮	⋮
260	0.40	0.89
261	0.09	0.95
263	0.18	0.12
⋮	⋮	⋮
822	0.00	0.64
857	0.62	0.55
858	0.64	0.93
859	0.94	0.67
861	0.96	0.74
Average	0.581	0.724

TABLE 24.8 Comparison of the First Iteration Solutions of IM Method and Actual Solutions from Sikorsky’s Production Line with the Cumulative Acceptable Adjustments

Tail #	Modifications		
	Actual Iteration 1 Modifications	CAM	IM Iteration 1 Modifications
801	6, -4, -10, 11	2, -4, -4, 14	3, -5, -6, 12
802	5, 2, 0, 0	9, 0, -10, 10	8, -2, -5, 10
822	6, 0, -20, 0	10, -4, -23, 13	8, -4, -22, 6
858	7, 0, -14, 0	9, -2, -10, 3	9, -2, -15, 4

Another evaluation basis for the adjustments can be established by comparing them to the actual cumulative adjustments performed in the field. The cumulative adjustment set, $\sum x$, can be defined as

$$\sum x = \sum_{k=1}^N \Delta x_k \tag{24.39}$$

where N represents the total number of tuning iterations performed in the field for the tail number and Δx_k denotes the adjustments applied at the k th iteration. A sample of actual first iteration adjustments, actual cumulative adjustments, and first iteration adjustments from the IM method is shown in Table 24.8. The results indicate that the adjustments from the IM method are closer to the actual cumulative adjustments than are the actual first iteration adjustments. Although the cumulative adjustments may not be the most desirable ones for the aircraft, they represent an acceptable set that has been proven in the field. The closeness of the IM method’s solutions to the actual cumulative adjustments further validates its effectiveness.

24.6 Conclusion

A logical feature for future rotor tuning systems will be the capability to adjust the blades during the flight. For this, these systems will need to have the capability to learn from their mistakes. They will also need to be able to monitor the condition of the rotor system in-flight, so they will stop modifying the blade parameters when more drastic actions are necessary for saving the aircraft. As such, these systems will need to be used with strong operator interaction to prevent implementation of inappropriate adjustments, and must have the ability to explain the recommended adjustments to the operator.

References

- Ishibuchi, H., Tanaka, H., and Okada, H., An architecture of neural networks with interval weights and its applications to fuzzy regression analysis, *Fuzzy Sets Syst.*, 57, 27–59, 1993.
- Moore, R.E. 1979. *Methods and Applications of Interval Analysis*, Society for Industrial and Applied Mathematics, Philadelphia.
- Taitel, H., Danai, K., and Gauthier, D.G., Helicopter track and balance with artificial neural nets, *ASME J. Dyn. Syst. Meas. Contr.*, 117, 226–231, 1995.
- Ventres, S. and Hayden, R.E. 2000. *Rotor tuning using vibration data only*, American Helicopter Society 56th Annual Forum, Virginia Beach, VA, May 2–4, 2000.
- Wang, S., Danai, K., and Wilson, M., A probability-based approach to helicopter track and balance, *J. Am. Helicopter Soc.*, 50, 1, 56–64, 2005a.
- Wang, S., Danai, K., and Wilson, M., An adaptive method of helicopter track and balance, *ASME J. Dyn. Syst. Meas. Contr.*, 2005b, March, in press.
- Yang, D.Z. 2000. Knowledge-based interval modeling method for efficient global optimization and process tuning, Ph.D. Thesis. Department of Mechanical and Industrial Engineering, University of Massachusetts, Amherst.

VI

Monitoring and Diagnosis

25

Machine Condition Monitoring and Fault Diagnostics

25.1	Introduction	25-2
25.2	Machinery Failure	25-2
	Causes of Failure • Types of Failure • Frequency of Failure	
25.3	Basic Maintenance Strategies	25-4
	Run-to-Failure (Breakdown) Maintenance • Scheduled (Preventative) Maintenance • Condition-Based (Predictive, Proactive, Reliability Centered, On-Condition) Maintenance	
25.4	Factors which Influence Maintenance Strategy	25-7
25.5	Machine Condition Monitoring	25-8
	Periodic Monitoring • Continuous Monitoring	
25.6	Transducer Selection	25-10
	Noncontact Displacement Transducers • Velocity Transducers • Acceleration Transducers	
25.7	Transducer Location	25-14
25.8	Recording and Analysis Instrumentation	25-14
	Vibration Meters • Data Collectors • Frequency-Domain Analyzers • Time-Domain Instruments • Tracking Analyzers	
25.9	Display Formats and Analysis Tools	25-16
	Time Domain • Frequency Domain • Modal Domain • Quefrency Domain	
25.10	Fault Detection	25-21
	Standards • Acceptance Limits • Frequency-Domain Limits	
25.11	Fault Diagnostics	25-25
	Forcing Functions • Specific Machine Components • Specific Machine Types • Advanced Fault Diagnostic Techniques	

Chris K. Mechefske
Queen's University

Summary

The focus of this chapter is on the definition and description of machine condition monitoring and fault diagnosis. Included are the reasons and justification behind the adoption of any of the techniques presented. The motivation behind the decision making in regard to various applications is both financial and technical. Both of these aspects are discussed, with the emphasis being on the technical side. The chapter defines machinery failure (causes, types, and frequency), and describes basic maintenance strategies and the factors that should be considered when deciding

which to apply in a given situation. Topics considered in detail include transducer selection and mounting location, recording and analysis instrumentation, and display formats and analysis tools (specifically, time domain, frequency domain, modal domain, and quefrency domain-based strategies). The discussion of fault detection is based primarily on standards and acceptance limits in the time and frequency domains. The discussion of fault diagnostics is divided into sections that focus on different forcing functions, specific machine components, specific machine types, and advanced diagnostic techniques. Further considerations on this topic are found in [Chapter 26](#) and [Chapter 27](#).

25.1 Introduction

Approximately half of all operating costs in most processing and manufacturing operations can be attributed to maintenance. This is ample motivation for studying any activity that can potentially lower these costs. Machine condition monitoring and fault diagnostics is one of these activities. Machine condition monitoring and fault diagnostics can be defined as the field of technical activity in which selected physical parameters, associated with machinery operation, are observed for the purpose of determining machinery integrity. Once the integrity of a machine has been estimated, this information can be used for many different purposes. Loading and maintenance activities are the two main tasks that link directly to the information provided. The ultimate goal in regard to maintenance activities is to schedule only what is needed at a time, which results in optimum use of resources. Having said this, it should also be noted that condition monitoring and fault diagnostic practices are also applied to improve end product quality control and as such can also be considered as process monitoring tools.

This definition implies that, while machine condition monitoring and fault diagnostics is being treated as the focus of this chapter, it must also be considered in the broader context of plant operations. With this in mind, this chapter will begin with a description of what is meant by machinery failure and a brief overview of different maintenance strategies and the various tasks associated with each. A short description of different vibration sensors, their modes of operation, selection criteria, and placement for the purposes of measuring accurate vibration signals will then follow. Data collection and display formats will be discussed with the specific focus being on standards common in condition monitoring and fault diagnostics. Machine fault detection and diagnostic practices will make up the remainder of the chapter. The progression of information provided will be from general to specific. The hope is that this will allow a broad range of individuals to make effective use of the information provided.

25.2 Machinery Failure

Most machinery is required to operate within a relatively close set of limits. These limits, or operating conditions, are designed to allow for safe operation of the equipment and to ensure equipment or system design specifications are not exceeded. They are usually set to optimize product quality and throughput (load) without overstressing the equipment. Generally speaking, this means that the equipment will operate within a particular range of operating speeds. This definition includes both steady-state operation (constant speed) and variable speed machines, which may move within a broader range of operation but still have fixed limits based on design constraints. Occasionally, machinery is required to operate outside these limits for short times (during start-up, shutdown, and planned overloads).

The main reason for employing machine condition monitoring and fault diagnostics is to generate accurate, quantitative information on the present condition of the machinery. This enables more confident and realistic expectations regarding machine performance. Having at hand this type of reliable information allows for the following questions to be answered with confidence:

- Will a machine stand a required overload?
- Should equipment be removed from service for maintenance now or later?

- What maintenance activities (if any) are required?
- What is the expected time to failure?
- What is the expected failure mode?

Machinery failure can be defined as the inability of a machine to perform its required function. Failure is always machinery specific. For example, the bearings in a conveyor belt support pulley may be severely damaged or worn, but as long as the bearings are not seized, it has not failed. Other machinery may not tolerate these operating conditions. A computer disk drive may have only a very slight amount of wear or misalignment resulting in noisy operation, which constitutes a failure.

There are also other considerations that may dictate that a machine no longer performs adequately. Economic considerations may result in a machine being classified as obsolete and it may then be scheduled for replacement before it has “worn out.” Safety considerations may also require the replacement of parts in order to ensure the risk of failure is minimized.

25.2.1 Causes of Failure

When we disregard the gradual wear on machinery as a cause of failure, there are still many specific causes of failure. These are perhaps as numerous as the different types of machines. There are, however, some generic categories that can be listed. Deficiencies in the original design, material or processing, improper assembly, inappropriate maintenance, and excessive operational demands may all cause premature failure.

25.2.2 Types of Failure

As with the causes of failure, there are many different types of failure. Here, these types will be subdivided into only two categories. Catastrophic failures are sudden and complete. Incipient failures are partial and usually gradual. In all but a few instances, there is some advanced warning as to the onset of failure; that is, the vast majority of failures pass through a distinct incipient phase. The goal of machine condition monitoring and fault diagnostics is to detect this onset, diagnose the condition, and trend its progression over time. The time until ultimate failure can then hopefully be better estimated, and this will allow plans to be made to avoid undue catastrophic repercussions. This, of course, excludes failures caused by unforeseen and uncontrollable outside forces.

25.2.3 Frequency of Failure

Anecdotal and statistical data describing the frequency of failures can be summarized in what is called a “bathtub curve.” Figure 25.1 shows a typical bathtub curve, which is applicable to an individual machine or population of machines of the same type.

The beginning of a machine’s useful life is usually characterized by a relatively high rate of failure. These failures are referred to as “wear-in” failures. They are typically due to such things as design errors, manufacturing defects, assembly mistakes, installation problems and commissioning errors. As the causes of these failures are found and corrected, the frequency of failure decreases.

The machine then passes into a relatively long period of operation, during which the frequency of failures occurring is relatively low. The failures that do occur mainly happen on a random basis. This period of a machine’s life is called the “normal wear” period and usually makes up most of the life of a machine. There should be a relatively low failure rate during the normal wear period when operating within design specifications.

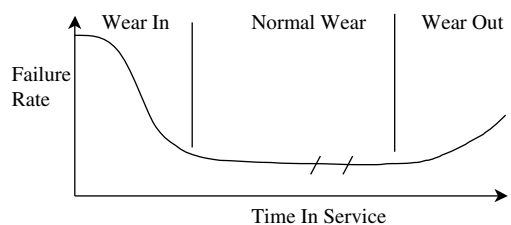


FIGURE 25.1 Typical bathtub curve.

As a machine gradually reaches the end of its designed life, the frequency of failures again increases. These failures are called “wearout” failures. This gradually increasing failure rate at the expected end of a machine’s useful life is primarily due to metal fatigue, wear mechanisms between moving parts, corrosion, and obsolescence. The slope of the wearout part of the bathtub curve is machine-dependent. The rate at which the frequency of failures increases is largely dependent on the design of the machine and its operational history. If the machine design is such that the operational life ends abruptly, the machine is underdesigned to meet the load expected, or the machine has endured a severe operational life (experienced numerous overloads), the slope of the curve in the wearout section will increase sharply with time. If the machinery is overdesigned or experiences a relatively light loading history, the slope of this part of the bathtub curve will increase only gradually with time.

- Generally (outside of start-up and shutdown) machinery is required to operate at constant speed and load.
- Machinery failure is defined based on performance, operating condition, and system specifications.
- Machinery failure can be defined as the inability of a machine to perform its required function.
- Causes of machinery failure can be generally defined as being due to deficiencies in the original design, material or processing, improper assembly, inappropriate maintenance, or excessive operation demands.
- The frequency of failure for an individual machine or a population of similar machines can be summarized using a “bathtub curve.”

25.3 Basic Maintenance Strategies

Maintenance strategies can be divided into three main types: (1) run-to-failure, (2) scheduled, and (3) condition-based maintenance. Each of these different strategies has distinct advantages and disadvantages, which will be described below. Specific situations within any large facility may require the application of a different strategy. Therefore, no one strategy should be considered as always superior or inferior to another.

25.3.1 Run-to-Failure (Breakdown) Maintenance

Run-to-failure, or breakdown maintenance, is a strategy where maintenance, in the form of repair work or replacement, is only performed when machinery has failed. In general, run-to-failure maintenance is appropriate when the following situations exist:

- The equipment is redundant.
- Low cost spares are available.
- The process is interruptible or there is stockpiled product.
- All known failure modes are safe.
- There is a known long mean time to failure (MTTF) or a long mean time between failure (MTBF).
- There is a low cost associated with secondary damage.
- Quick repair or replacement is possible.

An example of the application of run-to-failure maintenance can be found when one considers the standard household light bulb. This device satisfies all the requirements above and therefore the most cost-effective maintenance strategy is to replace burnt out light bulbs as needed.

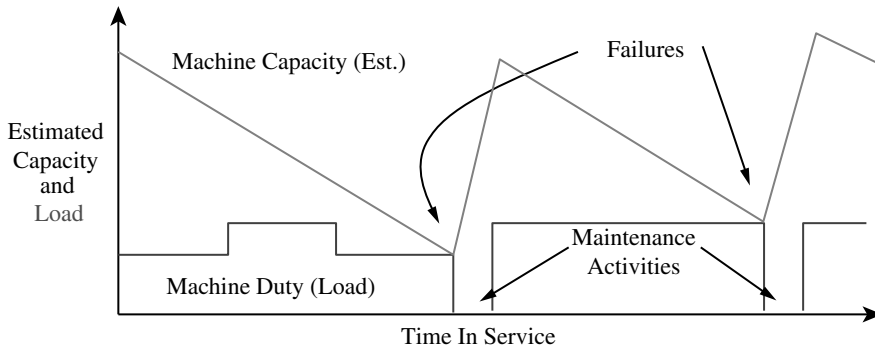


FIGURE 25.2 Time vs. estimated capacity and actual load (run-to-failure maintenance).

Figure 25.2 shows a schematic demonstrating the relationship between a machine's time in service, the load (or duty) placed on the machine, and the estimated remaining capacity of the machine. Whenever the estimated capacity curve intersects with (or drops below) the load curve, a failure will occur. At these times, repair work must be carried out. If the situation that exists fits within the "rules" outlined above, all related costs (repair work and downtime) will be minimized when using run-to-failure maintenance.

25.3.2 Scheduled (Preventative) Maintenance

When specific maintenance tasks are performed at set time intervals (or duty cycles) in order to maintain a significant margin between machine capacity and actual duty, the type of maintenance is called scheduled or preventative maintenance. Scheduled maintenance is most effective under the following circumstances:

- Data describing the statistical failure rate for the machinery is available.
- The failure distribution is narrow, meaning that the MTBF is accurately predictable.
- Maintenance restores close to full integrity of the machine.
- A single, known failure mode dominates.
- There is low cost associated with regular overhaul/replacement of the equipment.
- Unexpected interruptions to production are expensive and scheduled interruptions are not so bad.
- Low cost spares are available.
- Costly secondary damage from failure is likely to occur.

An example of scheduled maintenance practices can be found under the hood of your car. Oil and oil filter changes on a regular basis are part of the scheduled maintenance program that most car owners practice. A relatively small investment in time and money on a regular basis acts to reduce (but not eliminate) the likelihood of a major failure taking place. Again, this example shows how when all, or most, of the criteria listed above are satisfied, overall maintenance costs are minimized.

Figure 25.3 shows a schematic demonstrating the relationship between a machine's time in-service, the load (or duty) placed on the machine and the estimated remaining capacity of the machine when scheduled maintenance is being practiced. In this case, maintenance activities are scheduled at regular intervals in order to restore machine capacity before a failure occurs. In this way, there is always a margin between the estimated capacity and the actual load on the machine. If this margin is always present, there should theoretically never be an unexpected failure, which is the ultimate goal of scheduled maintenance.

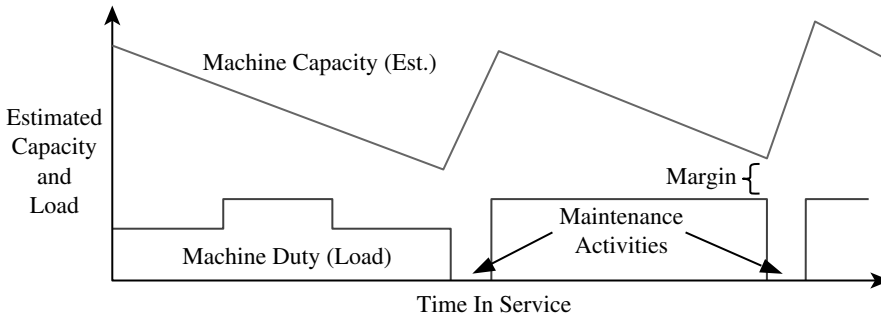


FIGURE 25.3 Time vs. estimated capacity and actual load (scheduled maintenance).

25.3.3 Condition-Based (Predictive, Proactive, Reliability Centered, On-Condition) Maintenance

Condition-based maintenance (which is also known by many other names) requires that some means of assessing the actual condition of the machinery is used in order to optimally schedule maintenance, in order to achieve maximum production, and still avoid unexpected catastrophic failures. Condition-based maintenance should be employed when the following conditions apply:

- Expensive or critical machinery is under consideration.
- There is a long lead-time for replacement parts (no spares are readily available).
- The process is uninterruptible (both scheduled and unexpected interruptions are excessively costly).
- Equipment overhaul is expensive and requires highly trained people.
- Reduced numbers of highly skilled maintenance people are available.
- The costs of the monitoring program are acceptable.
- Failures may be dangerous.
- The equipment is remote or mobile.
- Failures are not indicated by degeneration of normal operating response.
- Secondary damage may be costly.

An example of condition-based maintenance practices can again be found when considering your car, but this time we consider the tires. Regular inspections of the tires (air pressure checks, looking for cracks and scratches, measuring the remaining tread, listening for slippage during cornering) can all be used to make an assessment of the remaining life of the tires and also the risk of catastrophic failure. In order to minimize costs and risk, the tires are replaced before they are worn out completely, but not before they have given up the majority of their useful life. A measure of the actual condition of equipment is used to utilize maintenance resources optimally.

Figure 25.4 shows a schematic drawing that demonstrates the relationship between a machine's time in service, the load (or duty) placed on the machine, and the estimated remaining capacity of the machine when condition-based maintenance is being practiced. Note that the margin between duty and capacity is allowed to become quite small (smaller than in scheduled maintenance), but the two lines never touch (as in run-to-failure maintenance). This results in a longer time between maintenance activities than for scheduled maintenance. Maintenance tasks are scheduled just before a failure is expected to occur, thereby optimizing the use of resources. This requires that there exists a set of accurate measures that can be used to assess the machine integrity.

Each of these maintenance strategies has its advantages and disadvantages and situations exist where one or the other is appropriate. It is the maintenance engineer's role to decide on and justify the use of any one of these procedures for a given machine. There are also instances where a given machine will require more than one maintenance strategy during its operational life, or perhaps even at one

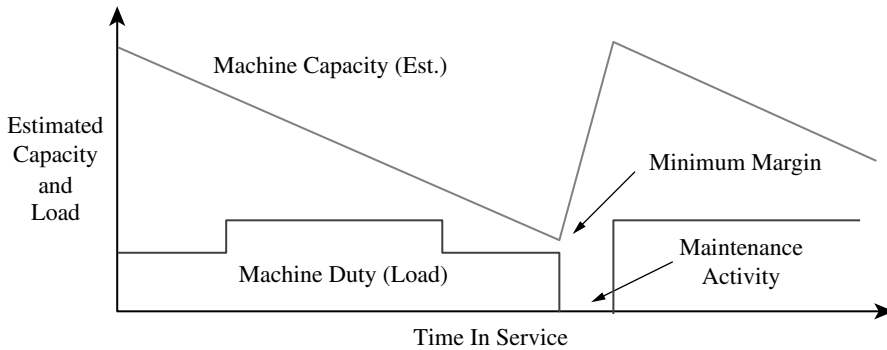


FIGURE 25.4 Time versus estimated capacity and actual load (condition-based maintenance).

time, and situations where more than one strategy is appropriate within a particular plant. Examples of these situations include the need for an increased frequency of monitoring as the age of a machine increases and the likelihood of failure increases, and the scheduling of maximum time between overhauls during the early stages of a machine's useful life, with monitoring in between looking for unexpected failures.

- Maintenance strategies can be divided into three main types: (1) run-to-failure, (2) scheduled, and (3) condition-based maintenance.
- No one strategy should be considered as always superior or inferior to another.
- Run-to-failure, or breakdown maintenance, is a strategy where maintenance, in the form of repair work or replacement, is only performed when machinery has failed.
- When specific maintenance tasks are performed at set time intervals (or duty cycles) in order to maintain a significant margin between machine capacity and actual duty, the type of maintenance is called scheduled or preventative maintenance.
- Condition-based maintenance requires that some means of assessing the actual condition of the machinery is used in order to optimally schedule maintenance, in order to achieve maximum production and still avoid unexpected catastrophic failures.

25.4 Factors which Influence Maintenance Strategy

While there are some general guidelines for choosing the most appropriate maintenance strategy, each case must be evaluated individually. Principal considerations will always be defined in economic terms. Sometimes, a specific company policy (such as safety) will outweigh all other considerations. Below is a list of factors (in no particular order) that should be taken into account when deciding which maintenance strategy is most appropriate for a given situation or machine:

- Classification (size, type) of the machine
- Critical nature of the machine relative to production
- Cost of replacement of the entire machine
- Lead-time for replacement of the entire machine
- Manufacturers' recommendations
- Failure data (history), MTTF, MTBF, failure modes
- Redundancy
- Safety (plant personnel, community, environment)

- Cost and availability of spare parts
- Personnel costs, administrative costs, monitoring equipment costs
- Running costs for a monitoring program (if used)

25.5 Machine Condition Monitoring

With the understanding that condition-based maintenance may not be appropriate in all situations, let us say that some preliminary analysis has been carried out and a decision made to apply machine condition monitoring and fault diagnostics in a selected part of a plant or on a specific machine. The following is a list of potential advantages that should be realized:

- Increased machine availability and reliability
- Improved operating efficiency
- Improved risk management (less downtime)
- Reduced maintenance costs (better planning)
- Reduced spare parts inventories
- Improved safety
- Improved knowledge of the machine condition (safe short-term overloading of machine possible)
- Extended operational life of the machine
- Improved customer relations (less planned/unplanned downtime)
- Elimination of chronic failures (root cause analysis and redesign)
- Reduction of postoverhaul failures due to improperly performed maintenance or reassembly

There are, of course, also some disadvantages that must be weighed in the decision to use machine condition monitoring and fault diagnostics. These disadvantages are listed below:

- Monitoring equipment costs (usually significant).
- Operational costs (running the program).
- Skilled personnel needed.
- Strong management commitment needed.
- A significant run-in time to collect machine histories and trends is usually needed.
- Reduced costs are usually harder to sell to management as benefits when compared with increased profits.

The ultimate goal of machine condition monitoring and fault diagnostics is to get useful information on the condition of equipment to the people who need it in a timely manner. The people who need this information include operators, maintenance engineers and technicians, managers, vendors, and suppliers. These groups will need different information at different times. The task of the person or group in charge of condition monitoring and diagnostics must ensure that useful data is collected, that data is changed into information in a form required by and useful to others, and that the information is provided to the people who need it when they need it. Further general reading can be found in these references: Mitchell (1981), Lyon (1987), Mobley (1990), Rao (1996), and Moubray (1997).

The focus of this chapter will be on vibration-based data, but there are several different types of data that can be useful for assessing machine condition and these should not be ignored. These include physical parameters related to lubrication analysis (oil/grease quality, contamination), wear particle monitoring and analysis, force, sound, temperature, output (machine performance), product quality, odor, and visual inspections. All of these factors may contribute to a complete picture of machine integrity. The types of information that can be gleaned from the data include existing condition, trends, expected time to failure at a given load, type of fault existing or developing, and the type of fault that caused failure.

The specific tasks which must be carried out to complete a successful machine condition monitoring and fault diagnostics program include detection, diagnosis, prognosis, postmortem, and

prescription. Detection requires data gathering, comparison to standards, comparison to limits set in-plant for specific equipment, and trending over time. Diagnosis involves recognizing the types of fault developing (different fault types may be more or less serious and require different action) and determining the severity of given faults once detected and diagnosed. Prognosis, which is a very challenging task, involves estimating (forecasting) the expected time to failure, trending the condition of the equipment being monitored, and planning the appropriate maintenance timing. Postmortem is the investigation of root-cause failure analysis, and usually involves some research-type investigation in the laboratory and/or in the field, as well as modeling of the system. Prescription is an activity that is dictated by the information collected and may be applied at any stage of the condition monitoring and diagnostic work. It may involve recommendations for altering the operating conditions, altering the monitoring strategy (frequency, type), or redesigning the process or equipment.

The tasks listed above have relatively crisp definitions, but there is still considerable room for adjustment within any condition monitoring and diagnostic program. There are always questions, concerning such things as how much data to collect and how much time to spend on data analysis, that need to be considered before the final program is put in place. As mentioned above, things such as equipment class, size, importance within the process, replacement cost, availability, and safety need to be carefully considered. Different pieces of equipment or processes may require different monitoring strategies.

25.5.1 Periodic Monitoring

Periodic monitoring involves intermittent data gathering and analysis with portable, removable monitoring equipment. On occasion, permanent monitoring hardware may be used for this type of monitoring strategy, but data is only collected at specific times. This type of monitoring is usually applied to noncritical equipment where failure modes are well known (historically dependable equipment). Trending of condition and severity level checks are the main focus, with problems triggering more rigorous investigations.

25.5.2 Continuous Monitoring

Constant or very frequent data collection and analysis is referred to as continuous monitoring. Permanently installed monitoring systems are typically used, with samples and analysis of data done automatically. This type of monitoring is carried out on critical equipment (expensive to replace, with downtime and lost production also being expensive). Changes in condition trigger more detailed investigation or possibly an automatic shutdown of the equipment.

- Potential advantages of machine condition monitoring include increased machine availability and reliability, improved efficiency, reduced costs, extended operational life, and improved safety.
- Some of the disadvantages of condition monitoring include monitoring equipment costs, operational costs, and training costs.
- The ultimate goal of machine condition monitoring and fault diagnostics is to get useful information on the condition of equipment to the people who need it, in a timely manner.
- The specific tasks which must be carried out to complete a successful machine condition monitoring and fault diagnostics program include detection, diagnosis, prognosis, postmortem, and prescription.

25.6 Transducer Selection

A transducer is a device that senses a physical quantity (vibration in this case, but it can also be temperature, pressure, etc.) and converts it into an electrical output signal, which is proportional to the measured variable (see Chapter 15). As such, the transducer is a vital link in the measurement chain. Accurate analysis results depend on an accurate electrical reproduction of the measured parameters. If information is missed or distorted during measurement, it cannot be recovered later. Hence, the selection, placement, and proper use of the correct transducer are important steps in the implementation of a condition monitoring and fault diagnostics program.

Considerable research and development work has gone into the design, testing, and calibration of sensors (transducers) for a wide range of applications. The transducer must be:

- Correct for the task
- Properly mounted
- In good working order (properly calibrated)
- Fully understood in terms of operational characteristics

Transducers usually require amplification and conversion electronics to produce a useful output signal. These circuits may be located within the sealed sensor unit or in a separate box. There are advantages and disadvantages to both of these configurations but they will not be detailed here. Traditional vibration sensors fall into three main classes:

- Noncontact displacement transducers (also known as proximity probes or eddy current probes)
- Velocity transducers (electro-mechanical, piezoelectric)
- Accelerometers (piezoelectric)

Force and frequency considerations dictate the type of measurements and applications that are best suited for each transducer. Recently, laser-based noncontact velocity/displacement transducers have become more commonplace. These are still relatively expensive because of their extreme sensitivity, and hence are still predominantly used in the laboratory setting.

Figure 25.5 shows the relationship between the different transducer types in terms of response amplitude and frequency. For constant velocity vibration amplitude across all frequencies, a displacement transducer is more sensitive in the lower frequency range, while an accelerometer is more sensitive at higher frequencies. While it may appear as if the velocity transducer is the best compromise, transducers are selected to optimize sensitivity over the frequency range that is expected to be recorded.

The type of motion sensed by displacement transducers is the relative motion between the point of attachment and the observed surface. Velocity transducers and accelerometers measure the absolute motion of the structure to which they are attached.

25.6.1 Noncontact Displacement Transducers

These types of sensors find application primarily in fluid film (journal) radial or thrust bearings. With the rotor resting on a fluid film there is no way to easily attach a sensor. A noncontact approach is then the best alternative. Noncontact measurements indicate shaft motion and position relative to the bearing. Radial shaft displacements and seal clearances can be conveniently measured. Another advantage of using

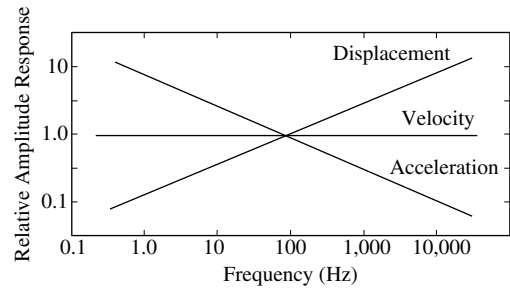


FIGURE 25.5 Frequency versus response amplitude for various sensor types.

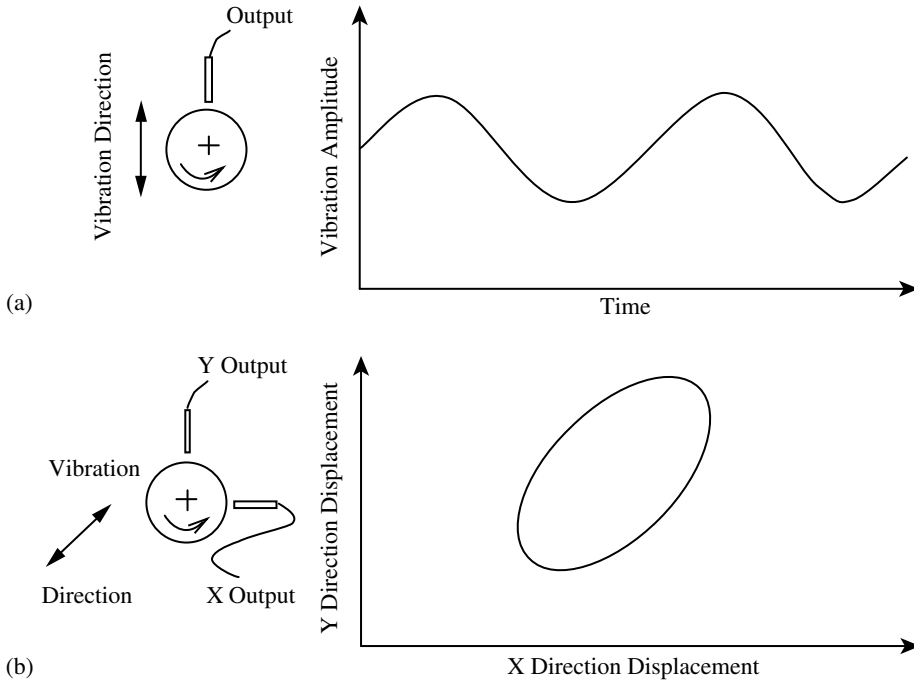


FIGURE 25.6 (a) Shaft displacement with one sensor; (b) shaft orbit with two sensors (x direction versus y direction displacement — assumes shaft is circular).

noncontact displacement probes is that when they are used in pairs, set 90° apart, the signals can be used to show shaft dynamic motion (orbit) within the bearing. Figure 25.6 shows a single channel and dual channel measurement result. When the two channels are plotted against one another, they clearly show what are known as shaft orbits. These orbits define the dynamic motion of the shaft in the bearing, and are valuable fault detection and diagnostic tools.

The linearity and sensitivity of the proximity probe depends on the target conductivity and porosity. Calibration of the probe on the specific material in use is recommended. This type of sensor is capable of both static and dynamic measurements, but temperature and pressure extremes will affect the transducer output. The probe will detect small defects in the shaft (cracks or pits), and these may seem like vibrations in the output signal.

Installation of these sensors requires a rigid mounting. Adaptors for quick removal and replacement without machine disassembly can be useful. The minimum tip clearance from all adjacent surfaces should be two times the tip diameter. Probe extensions must be checked to ensure that the resonant frequency of the extension is not excited during data gathering. As with all sensors, care must be taken when handling the cables and the connections must be kept clean.

25.6.2 Velocity Transducers

There are two general types of velocity transducers. They can be distinguished by considering the mode of operation. The two types are electro-mechanical and piezoelectric crystal based. Piezoelectric crystal-based transducers will be discussed in the next section, so the focus here will be on electro-mechanical (see Chapter 15).

Electro-mechanical velocity transducers function with a permanent magnet (supported by springs) moving within a coil of wire. As the sensor experiences changes in velocity, as when attached to a vibrating surface, the movement of the magnet within the coil is proportional to force acting on the

sensor. The current in the coil, induced by the moving magnet, is proportional to velocity, which in turn is proportional to the force. This type of device is known as “self-generating” and produces a low impedance signal; therefore, no additional signal conditioning is generally needed.

Electro-mechanical velocity sensors require the spring suspension system to be designed with a relatively low natural frequency. These devices have good sensitivity, typically above 10 Hz, but their high-frequency response is limited (usually around 1500 Hz) by the inertia of the system. Some devices may obtain a portion, or all, of their damping electrically. This type must be loaded with resistance of a specific value to meet design constraints. These are usually designed for use with a specific data collection instrument and must be checked and modified if they are to be used with other instruments. Figure 25.7 shows a plot of the sensitivity vs. frequency for an electro-mechanical velocity transducer.

While electro-mechanical velocity transducers can be designed to have good dynamic range within a specific frequency range, there are several functional limitations. Because a damping fluid is typically used to provide most of the damping, this type of transducer is limited to a relatively narrow temperature band, below the boiling point of the damping liquid. The mechanical reliability of these sensors is also limited by the moving parts within the transducer, which may become worn or fail over time. This has resulted in this type of transducer being replaced by piezoelectric sensors in machine condition monitoring applications. The orientation of the sensor is also limited to only the vertical or horizontal direction, depending on the type of mounting used. Finally, as a damped system, such as an electro-mechanical velocity transducer, approaches its natural frequency, a shift in phase relationships may occur (below 50 Hz). This phase shift at low frequencies will affect analysis work.

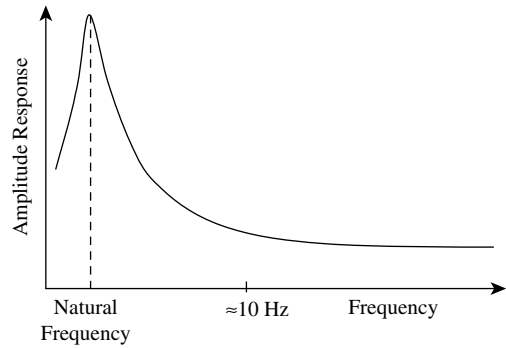


FIGURE 25.7 Output sensitivity vs. frequency for an electro-mechanical velocity transducer.

25.6.3 Acceleration Transducers

By far the most commonly used transducers for measuring vibration are accelerometers (see [Chapter 15](#)). These devices contain one or more piezoelectric crystal elements (natural quartz or man-made ceramics), which produce voltage when stressed in tension, compression or shear. This is the piezoelectric effect. The voltage generated across the crystal pole faces is proportional to the applied force.

Accelerometers have a linear response over a wide frequency range (0.5 Hz to 20 kHz), with specialty sensors linear up to 50 kHz. This wide linear frequency range and the broad dynamic amplitude range make accelerometers extremely versatile sensors. Figure 25.8 shows the sensitivity vs. frequency relationship for a typical accelerometer.

In addition, the signal can be electronically integrated to give velocity and displacement measurements. This type of transducer is relatively resistant to temperature changes, reliable (having no moving parts), produces a self-generating output signal meaning no external power supply is needed unless there are onboard electronics, is available in a variety of sizes, is usually relatively insensitive to nonaxial vibration

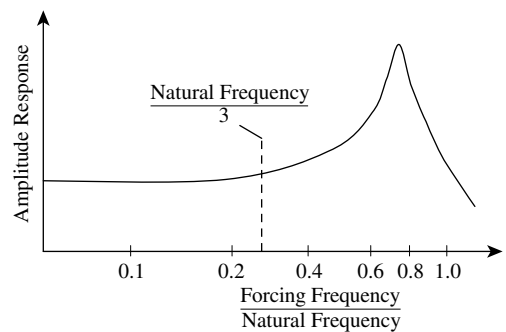


FIGURE 25.8 Typical accelerometer sensitivity vs. frequency.

(<3% of main axis sensitivity), and can function well in any orientation. Signals from this type of transducer contain significantly more vibration components than other types. This means that there is a large amount of information available in the raw vibration signal.

Installation of accelerometers requires as rigid a mount as possible. Permanent installation with studs or bolts is usually best for high speed machinery where high-frequency measurements are required. The close coupling between the machine and the sensor allows for direct transmission of the vibration to the sensor. Stud mounting requires a flat surface to give the best amplitude linearity and frequency response. This type of mounting is expensive and may not be practical if large numbers of measurements are being recorded with a portable instrument. Magnetic mounts have the advantage of being easily movable and provide good repeatability in the lower frequency range, but have limited high-frequency sensitivity (4 to 5 kHz). Hand-held measurements are useful when conducting general vibration surveys, but usually result in significant variation between measurements. The hand-held mount is least expensive but only offers frequency response below 1 kHz. Figure 25.9 shows a plot of the response curves for the same accelerometer with different mounts. For machine condition monitoring and fault diagnostics applications, there will typically be a combination of all three mounting methods used, depending on the equipment being monitored and the monitoring strategy employed.

As with the other types of vibration sensor, accelerometers have certain limitations. Because of their sensitivity and wide dynamic range, accelerometers are also sensitive to environmental input not related to the vibration signal of interest. Temperature (ambient and fluctuations) may cause distortion in the recorded signal. General purpose accelerometers are relatively insensitive to temperatures up to 250°C. At higher temperatures, the piezoelectric material may depolarize and the sensitivity may be permanently altered. Temperature transients also affect accelerometer output. Shear-type accelerometers have the lowest temperature transient sensitivity. A heat sink or mica washer between the accelerometer and a hot surface may help reduce the effects of temperature.

Piezoelectric crystals are sensitive to changes in humidity. Most accelerometers are epoxy bonded or welded together to provide a humidity barrier. Moisture migration through cables and into connections must be guarded against. Large electro-magnetic fields can also induce noise into cables that are not double shielded.

If an accelerometer is mounted on a surface that is being strained (bent), the output will be altered. This is known as base strain, and thick accelerometer bases will minimize this effect. Shear-type accelerometers are less sensitive because the piezoelectric crystal is mounted to a center post not the base.

Accelerometers are designed to remain constant for long periods of time; however, they may need calibrating if damaged by dropping or high temperatures. A known amplitude and frequency source (or another accelerometer that has a known calibration) should be used to check the calibration of accelerometers from time to time.

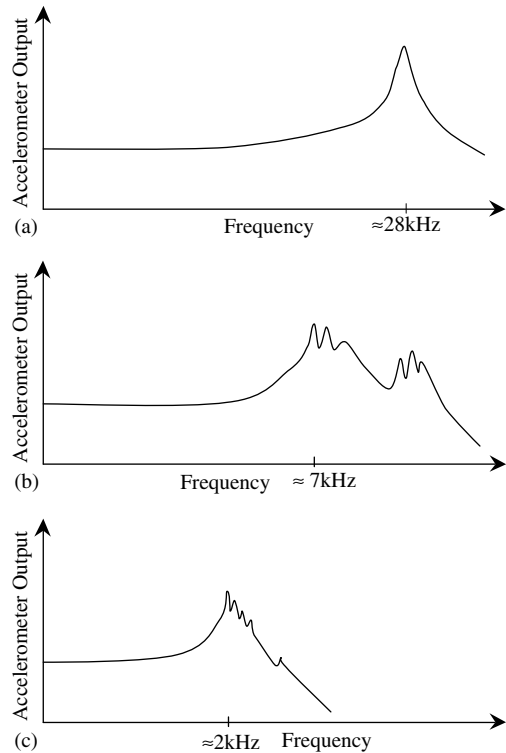


FIGURE 25.9 Accelerometer response vs. frequency for various types of mounts (a — stud; b — magnet; c — hand held).

25.7 Transducer Location

The placement (location) of a vibration transducer is a critical factor in machine condition monitoring and fault diagnostics. Using several locations and directions when recording vibration information is recommended. As always, it depends on the application and whether or not the expense is warranted. If the vibration component which relates to a given fault condition is not recorded, no amount of analysis will extract it from the signal. When selecting sensor locations consider the following:

- Mechanical independence
- The vibration transmission path
- Locations where natural frequency vibrations may be excited (flexible components or attachments)

- A transducer is a device that senses a physical quantity and converts it into an electrical output signal, which is proportional to the measured variable.
- The selection, placement, and proper use of the correct transducer are important steps in the implementation of a condition monitoring and fault diagnostics program.
- The transducer must be correct for the task, properly mounted, in good working order (properly calibrated), and fully understood in terms of operational characteristics.
- Traditional vibration sensors fall into three main classes: noncontact displacement transducers, velocity transducers, and accelerometers.
- Transducers are selected to optimize sensitivity over the frequency range that is expected to be recorded.
- Using several locations and directions when recording vibration information is recommended.
- When selecting sensor locations, one must consider mechanical independence, the vibration transmission path, and locations where natural frequency vibrations may be excited.

25.8 Recording and Analysis Instrumentation

25.8.1 Vibration Meters

Vibration meters are generally small, hand-held (portable), inexpensive, simple to use, self-contained devices that give an overall vibration level reading (see [Chapter 15](#)). They are used for walk-around surveys and measure velocity and/or acceleration. Generally, these devices have no built-in diagnostics capability, but the natural frequency of an accelerometer can be exploited to look for specific machinery faults. As an example, rolling element bearings generally emit “spike” energy during the early stages of deterioration. These are sharp impacts as rollers strike defects (pits, cracks) in the races. A spike energy meter is an accelerometer that has been tuned to have its resonant frequency excited by these impacts, thus giving a very early warning of deteriorating bearings.

25.8.2 Data Collectors

Most vibration data collectors available today for use in machine condition monitoring and fault diagnostics are microcomputer based. They are used together with vibration sensors to measure vibration, to store and transfer data, and for frequency domain analysis. Considerably more data can be recorded in a digital form, but the cost of these devices can also be considerable. Another

advantage of most data collectors is the ability to use these devices to conduct on-the-spot diagnostics or balancing. They are usually used with a PC to provide permanent data storage and a platform for more detailed analysis software. Data collectors are usually used on general-purpose equipment.

25.8.3 Frequency-Domain Analyzers

The frequency-domain analyzer is perhaps the key instrument for diagnostic work. Different machine conditions (unbalance, misalignment, looseness, bearing flaws) all generate characteristic patterns that are usually visible in the frequency domain. While data collectors do provide some frequency domain analysis capability, their main purpose is data collection. Frequency-domain analyzers are specialized instruments that emphasize the analysis of vibration signals. As such, they are often treated as a laboratory instrument. Generally, analyzers will have superior frequency resolution, filtering ability (including antialiasing), weighting functions for the elimination of leakage, averaging capabilities (both in the time and frequency domains), envelope detection (demodulation), transient capture, large memory, order tracking, cascade/waterfall display, and zoom features. Dual-channel analysis is also common.

25.8.4 Time-Domain Instruments

Time-domain instruments are generally only able to provide a time domain display of the vibration waveform. Some devices have limited frequency-domain capabilities. While this restriction may seem limiting, the low cost of these devices and the fact that some vibration characteristics and trends show up well in the time domain make them valuable tools. Oscilloscopes are the most common form. Shaft displacements (orbits), transients and synchronous time averaging (and negative averaging) are some of the analysis strategies that can be employed with this type of device.

25.8.5 Tracking Analyzers

Tracking analyzers are typically used to record and analyze data from machines that are changing speed. This usually occurs during run-up and coast-down of large machinery or turbo-machinery. These measurements are typically used to locate machine resonances and unbalance conditions. The tracking rate is dependent on filter bandwidth, and there is a need for a reference signal to track speed (tachometer input). These devices usually have variable input sensitivity and a large dynamic range.

- Vibration meters are generally small, hand-held (portable), inexpensive, simple to use, self-contained devices that give an overall vibration level reading.
- Most vibration data collectors available today for use in machine condition monitoring and fault diagnostics are microcomputer based. They are used together with vibration sensors to measure vibration, to store and transfer data, and for frequency domain analysis.
- Frequency domain analyzers are specialized instruments that emphasize the analysis of vibration signals, and as such they are perhaps the key instrument for diagnostic work.
- Time domain instruments are generally only able to provide a time domain display of the vibration waveform.
- Tracking analyzers are typically used to record and analyze data (locate machine resonances and unbalance conditions) from machines that are changing speed. This usually occurs during run-up and coast-down of large machinery or turbo-machinery.

25.9 Display Formats and Analysis Tools

Vibration signals can be displayed in a variety of different formats. Each format has advantages and disadvantages, but generally the more processing that is done on the dynamic signal, the more specific information is highlighted and the more extraneous information is discarded. The broad display formats that will be discussed here are the time domain, the frequency domain, the modal domain, and the quefrequency domain. Within each of these display formats, several different analysis tools (some specific to that display format) will be described.

25.9.1 Time Domain

The time domain refers to a display or analysis of the vibration data as a function of time. The principal advantage of this format is that little or no data are lost prior to inspection. This allows for a great deal of detailed analysis. However, the disadvantage is that there is often too much data for easy and clear fault diagnosis. Time-domain analysis of vibration signals can be subdivided into the following sections.

25.9.1.1 Time-Waveform Analysis

Time-waveform analysis involves the visual inspection of the time-history of the vibration signal. The general nature of the vibration signal can be clearly seen and distinctions made between sinusoidal, random, repetitive, and transient events. Nonsteady-state conditions, such as run-up and coast-down, are most easily captured and analyzed using time waveforms. High-speed sampling can reveal such defects as broken gear teeth and cracked bearing races, but can also result in extremely large amounts of data being collected — much of which is likely to be redundant and of little use.

25.9.1.2 Time-Waveform Indices

A time-waveform index is a single number calculated in some way based on the raw vibration signal and used for trending and comparisons. These indices significantly reduce the amount of data that is presented for inspection, but highlight differences between samples. Examples of time-waveform-based indices include the peak level (maximum vibration amplitude within a given time signal), mean level (average vibration amplitude), root-mean-square (RMS) level (peak level/ $\sqrt{2}$; reduces the effect of spurious peaks caused by noise or transient events), and peak-to-peak amplitude (maximum positive to maximum negative signal amplitudes). All of these measures are affected adversely when more than one machinery component contributes to the measured signal. The crest factor is the ratio of the peak level to the RMS level (peak level/RMS level), and indicates the early stages of rolling-element-bearing failure. However, the crest factor decreases with progressive failure because the RMS level generally increases with progressive failure.

25.9.1.3 Time-Synchronous Averaging

Averaging of the vibration signal synchronous with the running speed of the machinery being monitored is called time-synchronous averaging. When taken over many machine cycles, this technique removes background noise and nonsynchronous events (random transients) from the vibration signal. This technique is extremely useful where multiple shafts that are operating at only slightly different speeds and in close proximity to one another are being monitored. A reference signal (usually from a tachometer) is always needed.

25.9.1.4 Negative Averaging

Negative averaging works in the opposite way to time-synchronous averaging. Rather than averaging all the collected data, a baseline signal is recorded and then subtracted from all subsequent signals to reveal changes and transients only. This type of signal processing is useful on equipment or components that are isolated from other sources of vibrations.

25.9.1.5 Orbits

As described above, orbits are plots of the X direction displacement vs. the Y direction displacement (phase shifted by 90°). This display format shows journal bearing relative motion (bearing wear, shaft misalignment, shaft unbalance, lubrication instabilities [whirl, whip], and seal rubs) extremely well, and hence is a powerful monitoring and diagnostic tool, especially on relatively low-speed machinery.

25.9.1.6 Probability Density Functions

The probability of finding the instantaneous amplitude value from a vibration signal within a certain amplitude range can be represented as a probability density function. Typically, the shape of the probability density function in these cases will be similar to a Gaussian (or normal) probability distribution. Fault conditions will have different characteristic shapes. Figure 25.10 shows two probability density functions. One is characteristic of normal machine operating conditions, and the other represents a fault condition. A high probability at the mean value with a wide spread of low probabilities is characteristic of the impulsive time-domain waveforms that are typical for rolling-element-bearing faults. This type of display format can be used for condition trending and fault diagnostics.

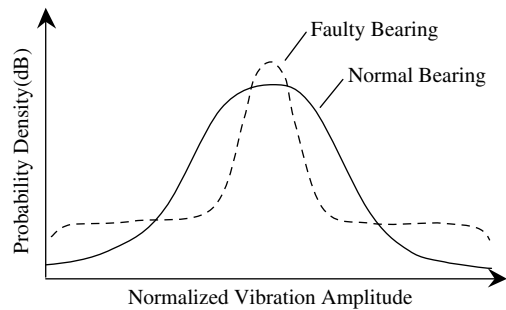


FIGURE 25.10 Normalized vibration amplitude vs. probability density (normal and faulty bearings).

25.9.1.7 Probability Density Moments

Probability density moments are single-number indices (descriptors), similar to the time-waveform indices except they are based on the probability density function. Odd moments (first and third, mean and skewness) reflect the probability density function peak position relative to the mean. Even moments (second and fourth, standard deviation and kurtosis) are proportional to the spread of the distribution. Perhaps the most useful of these indices is the kurtosis, which is sensitive to the impulsiveness in the vibration signal and therefore sensitive to the type of vibration signal generated in the early stages of a rolling-element-bearing fault. Because of this characteristic sensitivity, the kurtosis index is a useful fault detection tool. However, it is not good for trending. As a rolling-element-bearing fault worsens, the vibration signal becomes more random, the impulsiveness disappears, and the noise floor increases in amplitude. The kurtosis then increases in value during the early stages of a fault, and decreases in value as the fault worsens.

25.9.2 Frequency Domain

The frequency domain refers to a display or analysis of the vibration data as a function of frequency. The time-domain vibration signal is typically processed into the frequency domain by applying a Fourier transform, usually in the form of a fast Fourier transform (FFT) algorithm. The principal advantage of this format is that the repetitive nature of the vibration signal is clearly displayed as peaks in the frequency spectrum at the frequencies where the repetition takes place. This allows for faults, which usually generate specific characteristic frequency responses, to be detected early, diagnosed accurately, and trended over time as the condition deteriorates. However, the disadvantage of frequency-domain analysis is that a significant amount of information (transients, nonrepetitive signal components) may be lost during the transformation process. This information is nonretrievable unless a permanent record of the raw vibration signal has been made.

25.9.2.1 Band-Pass Analysis

Band-pass analysis is perhaps the most basic of all frequency-domain analysis techniques, and involves filtering the vibration signal above and/or below specific frequencies in order to reduce the amount of information presented in the spectrum to a set band of frequencies. These frequencies are typically where fault characteristic responses are anticipated. Changes in the vibration signal outside the frequency band of interest are not displayed.

25.9.2.2 Shock Pulse (Spike Energy)

The shock-pulse index (also known as spike energy; Boto, 1979) is derived when an accelerometer is tuned such that the resonant frequency of the device is close to the characteristic responses frequency caused by a specific type of machine fault. Typically, accelerometers are designed so that their natural frequency is significantly above the expected response signals that will be measured. If higher frequencies are expected, they are filtered out of the vibration signal. High-speed rolling-element bearings that are experiencing the earlier stages of failure (pitting on interacting surfaces) emit vibration energy in a relatively high, but closely defined, frequency band. An accelerometer that is tuned to 32 kHz will be a sensitive detection device. This type of device is simple, effective, and inexpensive tool for fault detection in high-speed rolling-element bearings. The response from this type of device is load-dependent and may be prone to false alarms if measurement conditions are not constant.

25.9.2.3 Enveloped Spectrum

Another powerful analysis tool that is available in the frequency domain and can be effectively applied to detecting and diagnosing rolling-element-bearing faults is the enveloped spectrum (Courrech, 1985). When the vibration signal time waveform is demodulated (high-pass filtered, rectified, then low-pass filtered) the frequency spectrum that results is said to be enveloped. This process effectively filters out the impulsive components in signals that have high noise levels and other strong transient signal components, leaving only the components that are related to the bearing characteristic defect frequencies. This method of analysis is useful for detecting bearing damage in complex machinery where the vibration signal may be contaminated by signals from other sources. However, the filtering bands must be chosen with good judgment. Recall also, the impulsive nature of the fault signal at the characteristic defect frequency leaves as the fault deteriorates.

25.9.2.4 Signature Spectrum

The signature spectrum (Braun, 1986) is a baseline frequency spectrum taken from new or recently overhauled machinery. It is then later compared with spectra taken from the same machinery that represent current conditions. The unique nature of each machine and installation is automatically taken into account. Characteristic component and fault frequencies can be clearly seen and comparisons made manually (by eye), using indices, or using automated pattern recognition techniques.

25.9.2.5 Cascades (Waterfall Plots)

Cascade plots (also known as waterfall plots) are successive spectra plotted with respect to time and displayed in a three-dimensional manner. Changing trends can be seen easily, which makes this type of display a useful fault detection and trending tool. This type of display is also used when a transient event, such as a coast-down, is known to be about to occur. Cascade plots can also be linked to the speed of a machine. In this case, the horizontal axis is labeled in multiples of the rotational speed of the machine. Each multiple of the rotational speed is referred to as an "order."

"Order tracking" is the name commonly used to refer to cascade plots that are synchronously linked to the machine rotational speed *via* a tachometer. As the speed of the machine changes, the responses at specific frequencies change relative to the speed, but are still tracked in each time-stamped spectra by the changing horizontal axis scale.

25.9.2.6 Masks

Like negative averaging in the time domain, masks are baseline spectra that are used with an allowable tolerance limit to “filter out,” or block, specific frequencies. This technique is similar to band-pass analysis and requires a good knowledge of the full range of each machine’s operating limits (varying load or speed).

25.9.2.7 Frequency-Domain Indices

It has been noted that frequency spectra are more sensitive to changes related to machine condition (Mathew, 1987). Because of this sensitivity, several single number indices based on the frequency spectra have been proposed. Like the time-waveform indices, frequency-domain indices reduce the amount of information in frequency spectra to a single number. Because they are based on the frequency spectra, they are generally more sensitive to changes in machine condition than time domain indices. They are used as a means of comparing original spectra or previous spectra to the current spectra. Several frequency domain indices are listed below:

- Arithmetic mean (Grove, 1979):

$$20 \log \left\{ \left(\frac{1}{N} \sum_{i=1}^N A_i \right) / 10^{-5} \right\}$$

A_i = amplitude of i th frequency spectrum component

N = total number of frequency spectrum components

- Geometric mean (Grove, 1979):

$$\frac{1}{N} \left\{ \sum_{i=1}^N 20 \log \left(\left(\frac{A_i}{\sqrt{2}} \right) / 10^{-5} \right) \right\}$$

- Matched filter RMS (Mathew and Alfredson, 1984):

$$10 \log \left\{ \frac{1}{N} \sum_{i=1}^N \left(\frac{A_i}{A_{i(\text{ref})}} \right)^2 \right\}$$

$A_{i(\text{ref})}$ = amplitude of i th component in the reference spectrum

- RMS of spectral difference (Alfredson, 1982):

$$\left\{ \frac{1}{N} \sum_{i=1}^N (L_{ci} - L_{oi})^2 \right\}^{1/2}$$

L_{ci} = amplitude (dB) of i th component

L_{oi} = amplitude (dB) of i th reference component

- Sum of squares of difference (Mathew and Alfredson, 1984):

$$\left\{ \frac{1}{N} \sum_{i=1}^N [(L_{ci} + L_{oi}) \times |L_{ci} - L_{oi}|]^{1/2} \right\}$$

25.9.3 Modal Domain

Modal analysis is not traditionally listed as a machine condition monitoring and fault diagnostics tool, but is included here because of the ever-increasing complexity of modern machinery. Often, unless the

natural (free and forced response) frequencies of machinery, their support structure, and the surrounding buildings are fully understood, a complete and accurate assessment of existing machinery condition is not possible. A complete overview of modal analysis will not be provided here, but a specific approach to modal analysis (operational deflection shape [ODS] analysis) will be described.

ODS analysis is like other types of modal analysis in that a force input is provided to a structure or machine and then the response is measured. The response at different frequencies defines the natural frequencies of the structure or machine. Typically, an impact or constant frequency force is used to excite the structure. In the case of ODSs, the regular operation of the machinery provides the excitation input. With vibration sensors placed at critical locations and a reference signal linking together all the recorded signals, a simple animation showing how the machine or structure deflects under normal operation can be generated. These animations, along with the frequency information contained in each individual signal, can provide significant insights into how a machine or structure deforms under a dynamic load. This information, in turn, can be a useful addition to other data when attempting to diagnose problems.

25.9.4 Quefrency Domain

A quefrency-domain (Randall, 1981, 1987) plot results when a Fourier transform of a frequency spectra (log scale) is generated. As the frequency spectra highlight periodicities in the time waveform, so the quefrency “cepstra” highlights periodicities in a frequency spectra. This analysis procedure is particularly useful when analyzing gearbox vibration signals where modulation components in spectrum (sidebands) are easily detected and diagnosed in the cepstrum.

- Generally, the more processing that is done on the dynamic signal, the more specific useful information is highlighted and the more extraneous information is discarded.
- The primary display formats used in machine condition monitoring are the time domain, the frequency domain, the modal domain, and the quefrency domain.
- The time domain refers to a display or analysis of the vibration data as a function of time, allowing for little or no data to be lost prior to inspection.
- Time domain analysis includes: waveform analysis, time waveform indices, time synchronous averaging, negative averaging, orbit analysis, probability density functions, and probability density moments.
- The frequency domain refers to a display or analysis of the vibration data as a function of frequency, where the time domain vibration signal is typically processed into the frequency domain by applying a Fourier transform, usually in the form of a FFT algorithm.
- The principal advantage of frequency-domain analysis is that the repetitive nature of the vibration signal is clearly displayed as peaks in the frequency spectrum at the frequencies where the repetition takes place. This allows for faults, which usually generate specific characteristic frequency responses, to be detected early, diagnosed accurately, and trended over time as the condition deteriorates.
- Frequency-domain analysis includes the use of band pass analysis, shock pulse (spike energy), envelope spectrum, signature spectrum, cascades (waterfall plots), masks, and frequency-domain indices.
- Quefrency-domain analysis involves a Fourier transform of a frequency spectra (log scale). As the frequency spectra highlight periodicities in the time waveform, so the quefrency “cepstra” highlights periodicities in a frequency spectra.

25.10 Fault Detection

In many discussions of machine condition monitoring and fault diagnostics, the distinction between fault detection and fault diagnosis is not made. Here, they have been divided into separate sections in order to highlight the differences and clarify why they should be treated as separate tasks. Fault detection can be defined as the departure of a measurement parameter from a range that is known to represent normal operation. Such a departure then signals the existence of a faulty condition. Given that measurement parameters are being recorded, what is needed for fault detection is a definition of an acceptable range for the measurement parameters to fall within. There are two methods for setting suitable ranges: (1) comparison of recorded signals to known standards and (2) comparison of the recorded signals to acceptance limits.

25.10.1 Standards

One of the best known sources of standards is the International Organization for Standardization (ISO). These standards are technology oriented and are set by teams of international experts. ISO Technical Committee 108, Sub-Committee 5 is responsible for standards for condition monitoring and diagnostics of machines. This group is further divided into a number of working groups who review data and draft preliminary standards. Each working group has a particular focus such as terminology, data interpretation, performance monitoring, or tribology-based machine condition monitoring.

While ISO is perhaps the most widely known standardization organization, there are several others that are focused on specific industries. Examples of these include the International Electrical Commission, which is primarily product oriented, and the American National Standards Institute (ANSI), which is a nongovernment agency. There are also different domestic government agencies that vary from country to country. National defense departments also tend to set their own standards.

25.10.1.1 Standards Based on Machinery Type

Because different machines that are designed to perform approximately the same task tend to behave in a similar manner, it is not surprising that many standards are set based on machinery type. Figure 25.11 shows a generic plot separating vibration amplitude vs. rotating speed into different zones. For a specific type, size, or class of machine, a plot like this can be used to distinguish gross vibration limits relative to the speed of operation. Machines are usually divided into four basic categories:

1. *Reciprocating machinery*: These machines may contain both rotating and reciprocating components (e.g., engines, compressors, pumps).
2. *Rotating machinery (rigid rotors)*: These machines have rotors that are supported on rolling element bearings (usually). The vibration signal can be measured from the bearing housing because the vibration signal is transmitted well through the bearings to the housing (e.g., electric motors, single-stage pumps, slow-speed pumps).

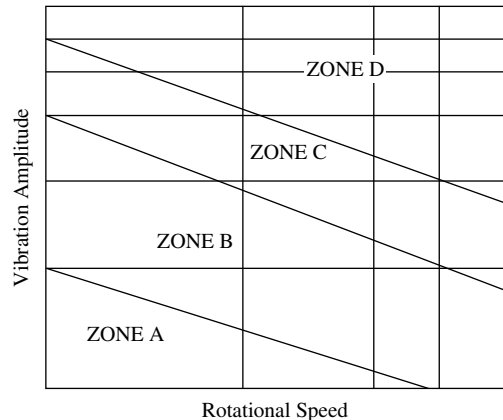


FIGURE 25.11 Normalized vibration amplitude vs. probability density (zone A — new machine; zone B — acceptable; zone C — monitor closely; zone D — damage occurring).

- 3. *Rotating machinery (flexible rotors)*: These machines have rotors that are supported on journal (fluid film) bearings. The movement of the rotor must be measured using proximity probes (e.g., large steam turbines, multistage pumps, compressors). These machines are subject to critical speeds (high vibration levels when the speed of rotation excites a natural frequency). Different modes of vibration may occur at different speeds.
- 4. *Rotating machinery (quasi-rigid rotors)*: These are usually specialty machines in which some vibration gets through the bearings, but it is not always trustworthy data (e.g., low-pressure steam turbines, axial flow compressors, fans).

25.10.1.2 Standards Based on Vibration Severity

It is an oversimplification to say that vibration levels must always be kept low. Standards depend on many things, including the speed of the machinery, the type and size of the machine, the service (load) expected, the mounting system, and the effect of machinery vibration on the surrounding environment. Standards that are based on vibration severity can be divided into two basic categories:

- 1. *Small-to-medium sized machines*: These machines usually operate with shaft speeds of between 600 and 12,000 rpm. The highest broadband RMS value usually occurs in the frequency range of 10 to 1000 Hz.
- 2. *Large machines*: These machines usually operate with shaft speeds of 600 to 1200 rpm. If the machine is rigidly supported, the machine’s fundamental resonant frequency will be above the main excitation frequency. If the machine is mounted on a flexible support, the machine’s fundamental resonant frequency will be below the main excitation frequency.

While general standards do exist, there are also a large number of standards that have been developed for specific machines. Figure 25.12 shows a table with generic acceptance limits based on vibration severity.

25.10.2 Acceptance Limits

Standards developed by dedicated organizations are a useful starting point for judging machine condition. They give a good indication of the current condition of a machine and whether or not a fault exists. However, judging the overall condition of machinery is often more involved. Recognizing the changing machinery condition requires the trending of condition indicators over time. The development and use of acceptance limits that are close to the normal operating values for specific machinery will detect even slight changes in condition. While these acceptance limits must be tight enough to allow even small changes in condition to be detected, they must also tolerate normal operating variations without

Vibration Amplitude Increasing ↓	Vibration Severity for Separate Classes of Machines			
	Class I	Class II	Class III	Class IV
	A	A		
	B	B	A	A
	C	C	B	B
	D	D	C	C
			D	D

FIGURE 25.12 Acceptance limits based on vibration severity levels (zone A — new machine; zone B — acceptable; zone C — monitor closely; zone D — damage occurring).

generating false alarms. There are two types of limits:

1. *Absolute limits* represent conditions that could result in catastrophic failure. These limits are usually physical constraints such as the allowable movement of a rotating part before contact is made with stationary parts.
2. *Change limits* are essentially warning levels that provide warning well in advance of the absolute limit. These vibration limits are set based on standards and experience with a particular class of machinery or a particular machine. Change limits are usually based on overall vibration levels.

It is important to note that the early discovery of faulty conditions is a key to optimizing maintenance effort by allowing the longest possible lead-time for decision making. As well as the overall vibration levels being monitored, the rates of change are also important. The rate of change of a vibration level will often provide a strong indication of the expected time until absolute limits are exceeded. In general, relatively high but stable vibration levels are of less concern than relatively low but rapidly increasing levels.

An example of how acceptance limits may be used to detect faults and trend condition is provided when the gradual deterioration of rolling-element bearings is considered. Rolling-element bearings generate distinctive defect characteristic frequencies in the frequency spectrum during a slow, progressive failure. Vibration levels can be monitored to achieve maximum useful life and failure avoidance. Typically, the vibration levels increase as a fault is initiated in the early stages of deterioration, but then decrease in the later stages as the deterioration becomes more advanced. Appropriately, set acceptance levels will detect the early onset of the fault and allow subsequent monitoring to take place even after the overall vibration level has dropped. However, rapid bearing deterioration may still occur due to a sudden loss of lubrication, lubrication contamination, or a sudden overload. The possibility of these situations emphasizes the need for carefully selected acceptance limits.

It should also be noted that changes in operating conditions, such as speed or load changes, could invalidate time trends. Comparisons must take this into consideration.

25.10.2.1 Statistical Limits

Statistical acceptance limits are set using statistical information calculated from the vibration signals measured from the equipment that the limits will ultimately be used with. As many vibration signals as possible are recorded, and the average of the overall vibration level is calculated. An alert or warning level can then be set at 2.5 standard deviations above or below the average reading (Mechefske, 1998). This level has been found to provide optimum sensitivity to small changes in machine condition and maximum immunity to false alarms. A distinct advantage to using this method to set alarm levels is the fact that the settings are based on actual conditions being experienced by the machine that is being monitored. This process accommodates normal variations that exist between machines and takes into account the initial condition of the machine.

25.10.3 Frequency-Domain Limits

Judging vibration characteristics within the frequency spectra is sometimes a more accurate method of detecting and trending fault conditions. It can also provide earlier detection of specific faults because, as mentioned previously, the frequency domain is generally more sensitive to changes in the vibration signal that result from changes in machine condition. The different specific methods are listed and described below.

25.10.3.1 Limited Band Monitoring

In limited band monitoring, the frequency spectrum is divided into frequency bands. The total energy or highest amplitude frequency is then trended within each band. Each band has its own limits based on experience. Generally, ten or fewer bands are used. Small changes in component-specific frequency

ranges are more clearly shown using this strategy. Bandwidths and limits must be specific to the machine, sensor type, and location. Narrowband monitoring is the same as limited band monitoring, except it has finer definition of the bands.

25.10.3.2 Constant Bandwidth Limits

When limited band monitoring is practiced and the bands have same width at high and low frequencies, the procedure is called constant bandwidth monitoring (see Figure 25.13). This technique is useful for constant speed machines where the frequency peaks in the spectra remain relatively fixed.

25.10.3.3 Constant Percentage Bandwidth Limits

Constant percentage bandwidth monitoring involves using bandwidths that remain a constant percentage of the frequency being monitored (see Figure 25.14). This results in the higher frequency bands being proportionally wider than the lower frequency bands. This allows for small variations

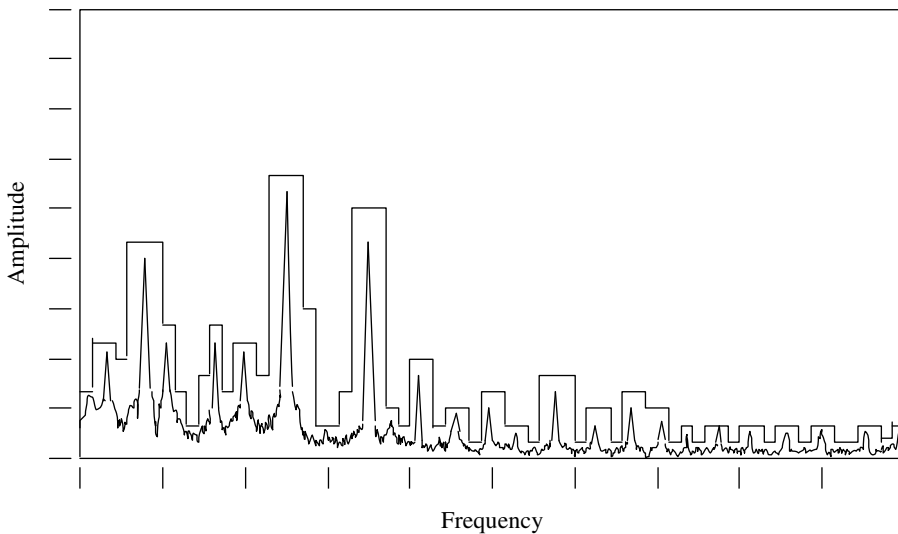


FIGURE 25.13 Constant bandwidth acceptance limits.

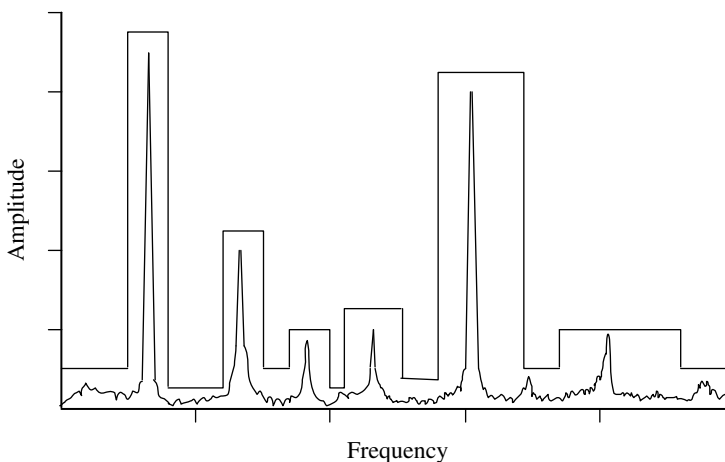


FIGURE 25.14 Constant percentage bandwidth acceptance limits.

in speed without the frequency peaks moving between bands, which may have different acceptance limits.

- Fault detection can be defined as the departure of a measurement parameter from a range that is known to represent normal operation. Such a departure signals the existence of a faulty condition.
- ISO Technical Committee 108, Sub-Committee 5 is responsible for standards for Condition Monitoring and Diagnostics of Machines.
- Standards are based on machinery type or vibration severity.
- The development and use of acceptance limits that are close to normal operating values for specific machinery will detect even slight changes in condition.
- Statistical acceptance limits are set using statistical information calculated from the vibration signals measured from the equipment that the limits will ultimately be used with.
- Judging vibration characteristics within the frequency spectra is sometimes a more accurate method of the early detecting and trending of fault conditions because the frequency domain is generally more sensitive to changes in the vibration signal that result from changes in machine condition.
- Frequency domain limits include limited band monitoring, constant bandwidth limits, and constant percentage bandwidth limits.

25.11 Fault Diagnostics

Depending on the type of equipment being monitored and the maintenance strategy being followed, once a faulty condition has been detected and the severity of the fault assessed, repair work or replacement will be scheduled. However, in many situations, the maintenance strategy involves further analysis of the vibration signal to determine the actual type of fault present. This information then allows for a more accurate estimation of the remaining life, the replacement parts that are needed, and the maintenance tools, personnel, and time required to repair the machinery. For these reasons, and many more, it is often advantageous to have some idea of the fault type that exists before decisions regarding maintenance actions are made.

There are obviously a large number of potential different fault types. The description of these faults can be systemized somewhat by considering the type of characteristic defect frequencies generated (synchronous to rotating speed, subsynchronous, harmonics related to rotating speed, nonsynchronous harmonics, etc.). Such a systemization requires a focus on frequency-domain analysis tools (primarily frequency spectra). While this organization strategy is effective, it inherently leaves out potentially valuable information from other display formats. For this reason, the various faults that usually develop in machinery are listed here in terms of the forcing functions that cause them and specific machine types. In this way, a diagnostic template can be developed for the different types of faults that are common in a given facility or plant. Further reading on machinery diagnostics can be found in these references: Wowk (1991), Taylor (1994), Eisenmann and Eisenmann (1998), Goldman (1999), and Reeves (1999).

25.11.1 Forcing Functions

Listed and described below are a variety of forcing functions that can result in accelerated deterioration of machinery or are the result of damaged or worn mechanical components. The list is not meant to be exhaustive and is in no particular order.

25.11.1.1 Unbalance

Unbalance (also referred to as imbalance) exists when the center of mass of a rotating component is not coincident with the center of rotation. It is practically impossible to fabricate a component that is perfectly balanced; hence, unbalance is a relatively common condition in a rotor or other rotating component (flywheel, fan, gear, etc.). The degree to which an unbalance affects the operation of machinery dictates whether or not it is a problem.

The causes of unbalance include excess mass on one side of the rotor, low tolerances during fabrication (casting, machining, assembly), variation within materials (voids, porosity, inclusions, etc.), nonsymmetry of design, aerodynamic forces, and temperature changes. The vector sum of all the different sources of unbalance can be combined into a single vector. This vector then represents an imaginary heavy spot on the rotor. If this heavy spot can be located and the unbalance force quantified, then placing an appropriate weight 180° from the heavy spot will counteract the original unbalance. If left uncorrected, unbalance can result in excessive bearing wear, fatigue in support structures, decreased product quality, power losses, and disturbed adjacent machinery.

Unbalance results in a periodic vibration signal with the same amplitude each shaft rotation (360°). A strong radial vibration at the fundamental frequency, $1X$, ($1 \times$ rotational speed) is the characteristic diagnostic symptom. If the rotor is overhung, there will also be a strong axial vibration at $1X$. The amplitude of the response is related to the square of the rotational speed, making unbalance a dangerous condition in machinery that runs at high rotational speeds. In variable speed machines (or machines that must be run-up to speed gradually), the effects of unbalance will vary with the shaft rotational speed. At low speeds, the high spot (location of maximum displacement of the shaft) will be at the same location as the unbalance. At increased speeds, the high spot will lag behind the unbalance location. At the shaft first critical speed (the first resonance), the lag reaches 90° , and at the second critical and above, the lag reaches 180° .

A special form of unbalance is caused by a bent shaft or bowed rotor. These two conditions are essentially the same; only the location distinguishes them. A bent shaft is located outside the machine housing, while a bowed rotor is inside the machine housing. This condition is seen on large machines (with heavy rotors) that have been allowed to sit idle for a long time. Gravity and time cause the natural sag in the rotor to become permanent.

The vibration spectrum from a machine with a bent shaft or bowed rotor is identical to unbalance, largely because it is an unbalanced condition. Bent shafts and bowed rotors are difficult to correct (straighten), so they need to be balanced by adding counterweights as described above. The best way to avoid this condition is to keep the shaft/rotor rotating slowly when the machine is not in use.

25.11.1.2 Misalignment

While misalignment can occur in several different places (between shafts and bearings, between gears, etc.), the most common form is when two machines are coupled together. In this case, there are two main categories of misalignment: (1) parallel misalignment (also known as offset) and (2) angular misalignment. Parallel misalignment occurs when shaft centerlines are parallel but offset from one another in the horizontal or vertical direction, or a combination of both. Angular misalignment occurs when the shaft centerlines meet at an angle. The intersection may be at the driver or driven end, between the coupled units or behind one of the coupled units. Most misalignment is a combination of these two types.

Misalignment is another major cause of excessive machinery vibration. It is usually caused by improper machine installation. Flexible couplings can tolerate some shaft misalignment, but misalignment should always be minimized.

The vibration caused by misalignment results in excessive radial loads on bearings, which in turn causes premature bearing failure. Elevated $1X$ vibrations with harmonics (usually up to the third, but sometimes up to the sixth) in the frequency spectrum are the usual diagnostic signatures. The harmonics

TABLE 25.1 Characteristics that Can Help Distinguish between Unbalance and Misalignment

Unbalance	Misalignment
High 1X response in frequency spectra	High harmonics of 1X relative to 1X
Low axial vibration levels	High axial vibration levels
Measurements at different locations are in phase	Measurements at different locations are 180° out of phase
Vibration levels are independent of temperature	Vibration levels are dependent on temperature (change during warm-up)
Vibration level at 1X increases with rotational speed. Centrifugal force increases as the square of the shaft rotational speed	Vibration level does not change with rotational speed. Forces due to misalignment remain relatively constant with changes in shaft rotational speed

allow misalignment to be distinguished from unbalance. High horizontal relative to vertical vibration amplitude ratios (greater than 3:1) may also indicate misalignment.

One final note regarding misalignment is that the heat of operation causes metal to expand resulting in thermal growth. Vibration readings should be taken when the equipment is cold and again after normal operating temperature has been reached. The changes in alignment due to thermal growth may be minimal, but should always be measured since they can lead to significant vibration levels.

Because unbalance and misalignment are perhaps the two most common causes of excessive machinery vibrations and they have similar characteristic indicators, Table 25.1 has been included to help distinguish between them.

25.11.1.3 Mechanical Looseness

While there are many ways in which mechanical looseness may appear, there are two main types: (1) a bearing loose on a shaft and (2) a bearing loose in a housing. A bearing that is loose on a shaft will display a modulated time signal with many harmonics. The time period of modulation will vary and the time signal will also be truncated (clipped). A bearing that is loose in its housing will display a strong fourth harmonic, which can sometimes be mistaken for the blade-pass frequency on a four-blade fan. These faults may also look like rolling-element-bearing characteristic defect frequencies, but always contain a significant amount of wideband noise.

Another way to diagnose mechanical looseness is by tracking the changes in the vibrations signal as the condition worsens. In the early stages, mechanical looseness generates a strong 1X response in the frequency spectrum along with some harmonics. At this stage, the condition could be mistaken for unbalance. As the looseness worsens, the amplitude of the harmonics will increase relative to the 1X response (which may actually decrease). The overall RMS value of the time waveform may also decrease. Further deterioration of the condition results in fractional harmonics ($\frac{1}{2}$, $\frac{1}{3}$, $1\frac{1}{2}$, $2\frac{1}{2}$) increasing in amplitude. These harmonics are most visible in signals taken when the machine is only lightly loaded. These harmonics show up because of the clipping described above.

25.11.1.4 Soft Foot

Another condition that is in fact a type of mechanical looseness, but often masquerades as misalignment, unbalance, or a bent shaft, is soft foot. Soft foot occurs when one of a machine’s hold-down bolts is not tight enough to resist the dynamic forces exerted by the machine. That part of the machine will lift off and set back down as a function of the cyclical forces acting on it. All the diagnostic signs associated with mechanical looseness will be present in the vibration signal.

If the foundation (hold-down points) of a machine does not form a plane, then tightening the hold-down bolts will cause the casing and/or rotor to be distorted. This distortion is what leads to the misalignment, unbalance, and bent shaft vibration signatures. In order to check for a soft foot,

the vibration level must be monitored while each hold-down bolt is loosened and then retightened. The appearance and/or disappearance of the diagnostic indicators mentioned above will determine if soft foot is the problem. When a machine's vibration levels cannot be reduced by realignment or balancing, soft foot could well be the cause.

25.11.1.5 Rubs

Rubs are caused by excessive mechanical looseness or oil whirl. The result is that moving parts come into contact with stationary parts. The vibration signal generated may be similar to that of looseness, but is usually clouded with high levels of wideband noise. This noise is due to the impacts. If the impacts are repetitive, such as occurring each time a fan blade passes, there may be strong spectral responses at the striking frequency.

In many cases, rubs are the result of a rotor pressing too hard against a seal. In these cases, the rotor will heat up unsymmetrically and develop a bowed shape. Subsequently, a vibration signal will be generated that shows unbalance. To diagnose this condition, it will be noted that the unbalance is absent until the machine comes up to normal operating temperature.

25.11.1.6 Resonances

The analysis of resonance problems is beyond the scope of this chapter. However, some basic description is provided here because of the high likelihood that at some time a resonance will be excited by repetitive or cyclic forces acting on or nearby a machine. A resonance is the so-called "natural frequency" at which all things tend to vibrate. A machine's natural resonant frequency is dictated by the relationship $\omega_n = (k/m)^{1/2}$, where ω_n is the natural frequency, k is the spring stiffness, and m is the mass. Most systems will have more than one resonance frequency. These resonances (also called modes) can be excited by any forcing function that is at or close to that frequency. The response amplitude can be 10 to 100 times that of the forcing function. The term "critical speed" is also used to refer to resonances when the machine rotating speed equals the natural frequency.

The amount of response amplification depends on the damping in the system. A highly damped system will not show signs of resonance excitation, while a lightly damped system will be prone to resonance excitations. Resonances can be diagnosed by monitoring the vibration level while the speed of rotation of the machine is changed. A resonance will cause a dramatic increase in the 1X vibration levels as the speed is slowly changed. Most machines are designed to operate well away from known resonance frequencies, but changes to the machine (support structure, piping connections, etc.) and proximity to other machines may excite a resonance.

25.11.1.7 Oil Whirl

Oil whirl occurs when the fluid in a lightly loaded journal bearing does not exert a constant force on the shaft that is being supported and a stable operating position is not maintained. In most journal bearing designs, this situation is prevented by using pressure dams or tilt pads to insure that the shaft rides on an oil pressure gradient that is sufficient to support it. During oil whirl, the shaft pushes a wedge of oil in front of itself and the shaft then migrates in a circular fashion within the bearing clearance at just less than one half the shaft rotational speed. The rotor is actually revolving around inside the bearing in the opposite direction from shaft rotation.

Because of the inherent instability of oil whirl, in many situations where oil whirl occurs, the time waveform will show intermittent whirl events. The shaft makes a few revolutions while whirl is present and then a few revolutions where the whirl is not present. This "beating" effect is often evident in the time waveform and can be used as a diagnostic indicator.

Persistent oil whirl usually requires a replacement of the bearing. However, temporary measures to mitigate the detrimental effects include changing the oil viscosity (changing the operating temperature or the oil), running the machine in a more heavily loaded manner, or introducing a misalignment that will load the bearing asymmetrically. This last course of action is of course not recommended for more than relatively short-term relief.

25.11.1.8 Oil Whip

Oil whip occurs when a subsynchronous instability (oil whirl) excites a critical speed (resonance), which then remains at a constant frequency regardless of speed changes. Oil whip often occurs at two times the critical speed because, at that speed, oil whirl matches the critical speed. Figure 25.15 shows a waterfall (cascade) plot of a mass unbalance that excites oil whirl and oil whip. Note how the oil whip “locks on” to the critical speed resonance.

25.11.1.9 Structural Vibrations

Structural vibrations can range dramatically in amplitude and frequency. Large-amplitude, low-frequency vibrations can be excited in multistory buildings during an earthquake or by the wind. These vibrations are usually the result of a building resonance being excited. While these sources of structural vibration are important, the source that we are concerned with here is that of machinery operating as part of a building’s utility system, as part of the production plant, or construction equipment close-by. Fans, blowers, compressors, piping systems, elevators, and other building service machines all produce vibrations in a building and, if they are not properly isolated they can cause disruption and/or damage to other machines or processes operating close-by. The same is true of heavy machinery operating within a plant (stamping machines, presses, forges, etc.) and construction equipment. High-impact and repetitive vibrations can excite resonances large distances from the source of the excitation.

25.11.1.10 Foundation Problems

Machine foundations provide rigidity and inertia so that the machine stays in alignment. The energy generated by a machine in the form of vibrations is transmitted, reflected, or absorbed by the foundation. Especially on larger machines, the foundation is paramount to successful dynamic behavior. Maximum energy is transmitted through the foundation to the earth when the mechanical impedance of the foundation is well matched to that of the source of vibration. That is, the source of vibration and the foundation should have the same natural frequency. If this is the case, all frequencies of vibration below

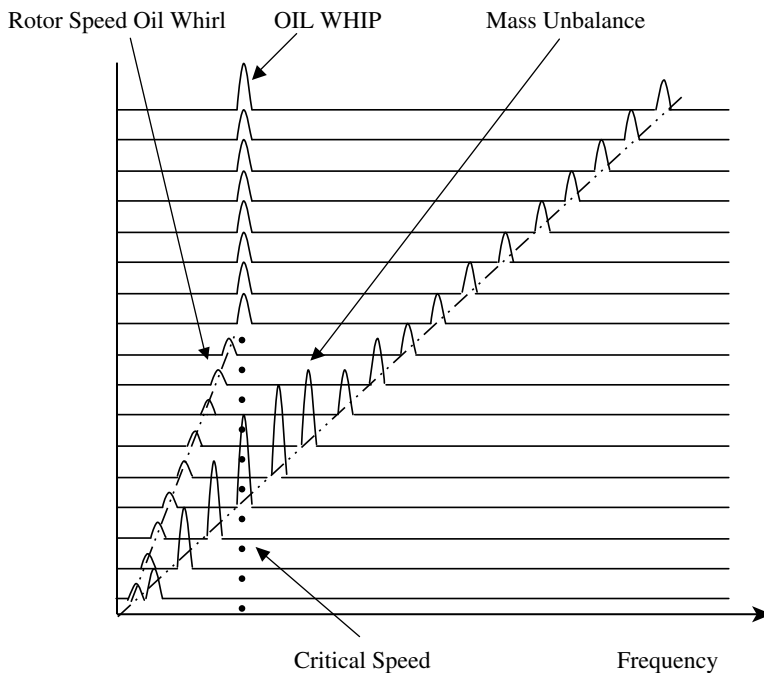


FIGURE 25.15 Waterfall (cascade) plot of a mass unbalance that excites oil whirl and oil whip.

the natural frequency will be transmitted by the foundation to earth. A poor match will mean that more energy is reflected or absorbed by the foundation, which could effect the operation of the machine attached. Changing foundations can grossly affect amplitude and phase measurements, which means that vibration measurements can be used to easily detect a changing foundation or hold-down system.

25.11.2 Specific Machine Components

25.11.2.1 Damaged or Worn Rolling-Element Bearings

Rolling-element bearings produce very little vibration (low level random signal) when they are fault free, and have very distinctive characteristic defect frequency responses (see Eschman, 1985, for the equations for calculation of defect frequencies) when faults develop. This, and the fact that most damage in rolling-element bearings occurs and worsens gradually, makes fault detection and diagnosis on this component relatively straightforward. Faults due to normal use usually begin as a single defect caused by metal fatigue in one of the raceways or on a rolling element. The vibration signature of a damaged bearing is dominated by impulsive events at the ball or roller passing frequency. Figure 25.16 shows the characteristic time waveform and frequency spectra at various stages of damage. As the damage worsens, there is a gradual increase in the characteristic defect frequencies followed by a drop in these amplitudes and an increase in the broadband noise. In machines where there is little other vibration that would contaminate or mask the bearing vibration signal, the gradual deterioration of rolling-element bearings can be monitored by using the crest factor or the kurtosis measure (see above for definitions).

A key factor in being able to accurately detect and diagnose rolling-element-bearing defects is the placement of the vibration sensor. Because of the relatively high frequencies involved, accelerometers should be used and placed on the bearing housing as close as possible to, or within, the load zone of the stationary outer race.

Specific applications can also pose significant challenges to fault diagnosis. Very low-speed machines have bearings that generate low energy signals and require special processing to extract useful bearing condition indications (Mechefske and Mathew, 1992a). Machines that operate at varying speeds also pose a problem because the characteristic defect frequencies are continuously changing (Mechefske and Liu, 2001). Bearings located close to, or within, gearboxes are also difficult to monitor because the high energy at the gear meshing frequencies masks the bearing defect frequencies (Randall, 2001).

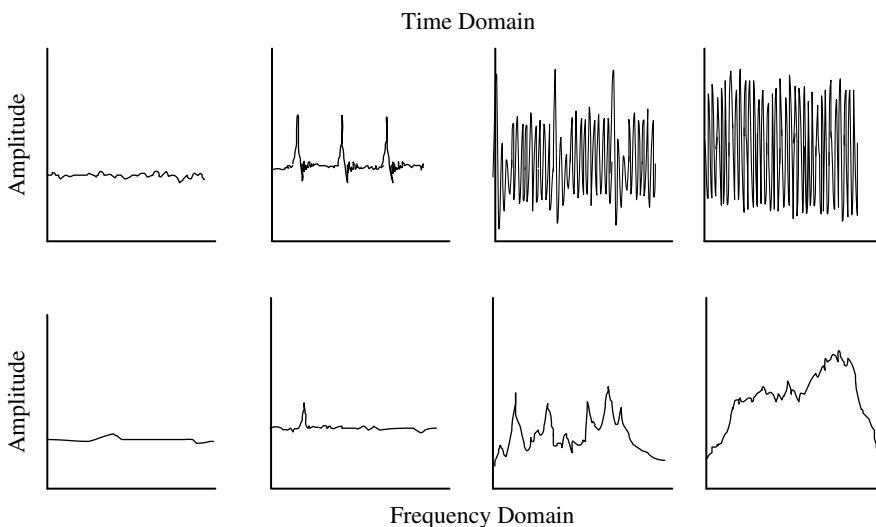


FIGURE 25.16 Characteristic time waveform and frequency spectra at various stages of damage in a rolling-element bearing.

25.11.2.2 Damaged or Worn Gears

Because gears transmit power from one rotating shaft to another, significant forces are present within the mating teeth. While gears are designed for robustness, the teeth do deflect under load and then rebound when unloaded. The local stresses are high at the tooth interface and root, which leads to fatigue damage. Proper design and perfect fabrication of gears (with perfect form and no defects) would result in relatively low vibration levels and a long life. However, the presence of nonperfect gears gives rise to excessive vibration (Smith, 1983).

The time waveform, the frequency spectral, and the cepstral patterns generated by gear vibrations all contain critical information needed to diagnose defects (see Figure 25.17). In relatively simple gearboxes, the time waveform can be used to distinguish impacts due to cracked, chipped, or missing teeth (McFadden and Smith, 1984, 1985). The frequency spectra and cepstra are powerful tools when the gearbox contains several sets of mating gears, which is most often the case.

Even a significant defect on one tooth (or even a missing tooth) often does not produce an abnormally strong frequency spectral response at $1X$. However, the defect will modulate the gear mesh frequency (number of teeth times the shaft rotational speed) and appear as $1X$ sidebands of the gear mesh frequency. That is, smaller spectral responses that appear a distance of $1X$ (and multiples of $1X$ for more severe gear faults) above and below the gear mesh frequency. Because these sidebands occur at multiples of $1X$ and a spectral plot can become quite cluttered with response lines, cepstral analysis is well suited to distinguish the frequency components that are strong fault indicators. Often, a change in the response at two times the gear mesh frequency is a good indicator of developing gear problems. The amplitude of the gear mesh frequency, and its multiples, vary with load. This makes it important to sample the vibration signal at the same load conditions. When unloaded, excessive gear backlash may also cause an increase in the amplitude of the gear mesh frequency.

Because each gear tooth meshes with an impact, structural resonances may be excited in the gears, shafts, and housing. Proper design of a gearbox will minimize this effect, but resonances in gearboxes cause accelerated gear wear and should be monitored.

Gears provide an excellent example of how machines must wear-in during early use. New gears will have defects that are quickly worn away in the machine's early life. Vibration levels will become steady and only increase gradually later in the machine's life as the gears wearout. These gradual increases in vibration level are normal. Sudden changes in vibration levels (at gear mesh frequency, two times gear mesh frequency, or sidebands), especially decreases, are very significant. A drop in the vibration level usually means a decrease in stiffness, and that more of the transmission forces are being absorbed due to bending of the gear teeth. Catastrophic failure is imminent. Premature gear failures are usually a symptom of other problems such as unbalance, misalignment, bent shaft, looseness, improper lubrication, or contaminated lubrication.

25.11.3 Specific Machine Types

25.11.3.1 Pumps

There are two principal types of pumps: (1) centrifugal pumps and (2) reciprocating pumps. Reciprocating pumps will be discussed in a later section. The sources of vibration in pumps are widely

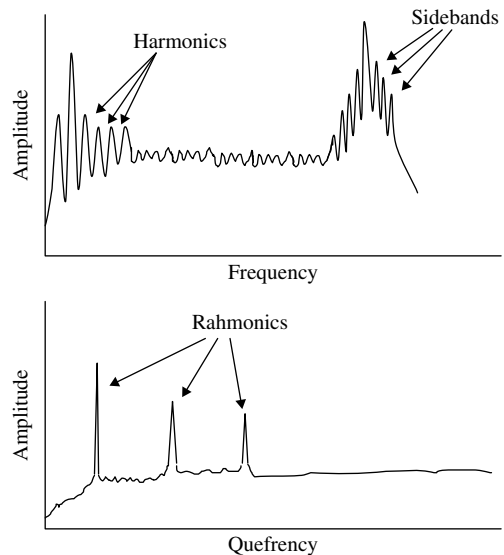


FIGURE 25.17 Frequency and quefrency plots (damaged gear).

varied. In addition to the standard mechanical problems (unbalance, misalignment, worn bearings, etc.), problems that are particular to pumps include vane-pass frequency generating conditions (starvation, impeller loose on the shaft, impeller hitting something) and cavitation.

Starvation occurs when not enough liquid is not present to fill each vane on the impeller every revolution of the shaft. Pump starvation can be confused with unbalance (see Chapter 34). However, it can be distinguished by the varying amplitude 1X vibration at constant speed and the reduced load on the driving motor.

When the vanes on the impeller are striking something, the vane-pass frequency (the number of vanes times the rotational speed) is excited. Because the striking causes a force on the shaft, an unbalance is also present. The frequency spectrum will show a response at 1X and vane-pass frequency. The time waveform will show a high-frequency response (vane pass) riding on a frequency response at 1X. The vane-pass frequency is in phase with the shaft speed. If the impeller is loose on the shaft, the vane-pass frequency will be modulated by the shaft speed.

Cavitation occurs when there is sufficient negative pressure (suction) acting on the liquid in the system that it becomes a gas (it boils). This usually takes place in localized parts of the system. Cavitation usually occurs in a pump when the suction intake is restricted and the liquid vaporizes when coming off the impeller. As the fluid moves past the low pressure region, the gas bubble collapses. If the collapsing bubble is close to a solid surface, it will aggressively erode the surface. Cavitation may be caused by a local decrease in atmospheric pressure, an increase in fluid temperature, an increase in fluid velocity, a pipe obstruction, or abrupt change in direction. The vibration signal that results will have significant vibration levels at 1X with harmonics and strong spectral responses at vane-pass frequency. High-frequency broadband noise is also common. An increase in the system pressure can reduce cavitation.

Hydraulic unbalance will result if there has been poor design of suction piping (elbow close to inlet) or poor impeller design (unsymmetrical). The vibration signal will contain high 1X axial vibration components. Impeller unbalance is a specific form of mechanical unbalance as discussed above. High 1X vibration levels will result. Pipe stresses result from inadequate pipe support and cause stress on the pump casing. This may also cause misalignment. Pipe resonances can also be excited by vane-pass frequency pressure pulsations.

Diagnosis of pump problems can be improved by installing a pressure transducer in the discharge line of the pump. The measured pressure fluctuations can be processed in the same way as vibration signals. The frequencies measured represent the pressure fluctuations and the amplitude is the zero-to-peak pressure change.

25.11.3.2 Fans

Fans account for a significant number of field vibration problems due to their function and construction. Fans move air or exhaust gases that are often laden with grease, dust, sand, ash, and other corrosive and erosive particles (also see Chapter 34). Under these conditions, fans blades gain and lose material resulting in the need to regularly rebalance. The level of balance must also be relatively fine because fans often have large fan-blade diameters and operate at relatively high speeds. Fans are usually mounted on spring/damper systems to help isolate vibrations, but they are also constructed in a relatively flexible manner, which adds to the demands for fine balancing. Along with fine balancing requirements, typical problems include looseness, misalignment, bent shaft, and defective bearings.

Fans also generate a strong response at blade-pass frequency (number of blades times the shaft rotational speed). This frequency response is present during normal operation, but it can become elevated if the blades are hitting something, the fan housing is excessively flexible, or an acoustical resonance is present. Acoustical resonances are relatively common where large volumes of air are being moved through large flexible ducts and/or the fan blades are of an air-foil design.

25.11.3.3 Electric Motors

Electric motors can be divided into two groups: (1) induction motors and (2) synchronous motors. A full description will not be given here as to the differences. Like any machine, electric motors are subject to a

full range of mechanical problems, and vibrations signals can be used to detect and diagnose these problems. Apart from the conditions described elsewhere in this section, there are some problems that occur only in electric motors. For the sake of brevity, these problems and the vibration signals that typically accompany them are summarized in Table 25.2.

25.11.3.4 Steam and Gas Turbines

Steam and gas turbines (and high-speed compressors) require special mention because of the high speeds and temperatures involved. Problems on steam turbines are usually limited to looseness, unbalance, misalignment, soft foot, resonance, and rubs. As discussed above, each of these conditions has a set of characteristic vibration responses that allow for relatively straightforward diagnosis. However, because of the high speeds, this type of machinery is usually designed to be lighter and less rigid than other rotating machines. Excessive vibration can therefore lead to catastrophic failure very quickly. Because of this, high-speed turbines and compressors are designed to closer tolerances than other types of machines, and extra care is taken when balancing rotors. These machines also frequently operate above their first critical speed and sometimes between their second and third critical speeds. At these speeds, the rotor becomes quite flexible and the support bearings become very important in that they must provide the appropriate amount of damping.

Because steam and gas turbines are supported on journal bearings, most monitoring and diagnostics work will be based solely on proximity probe signals. While this is not a problem in and of itself, accelerometer signals should also be taken in order to cover the higher frequencies, which are excited by conditions such as looseness and rubs.

25.11.3.5 Compressors

Compressors act in much the same way as pumps, except that they are compressing some type of gas. They come in many different sizes, but only two principal types: (1) screw-type and (2) reciprocating compressors. Reciprocating compressors will be discussed in a later section. Screw-type compressors have a given number of lobes or vanes on a rotor and generate a vane-passing frequency. Screw compressors with multiple rotors can also generate strong 1X and harmonics up to vane-pass frequency. The close tolerances involved result in relatively high vibration levels, even when the machine is in good condition. As with pumps, signals taken from pressure transducers in the discharge line can be useful for diagnostics.

25.11.3.6 Reciprocating Machines

Reciprocating machines (gas and diesel engines, steam engines, compressors, and pumps) all have one thing in common — a piston that moves in a reciprocating manner. These machines generally have high overall vibration levels and particularly strong responses at 1X and harmonics, even when in good condition. The vibrations are caused by compressed gas pressure forces and unbalance. Vibrations at $\frac{1}{2}X$ may be present in four-stroke engines because the camshaft rotates at one half the crankshaft speed.

TABLE 25.2 Mechanical Problems Particular to Electric Motors

Condition	Vibration Indicator
Motor out of magnetic center	High spectral response at 60 Hz
Motors with broken rotor bars	High spectral response at motor running speed and/or second harmonic
Motor with turn-to-turn shorts in the windings	Motor runs at a slower than expected speed (high slit frequency)
Motor out of magnetic center with broken rotor bars or turn-to-turn shorts in the windings	Side bands of slip frequency times the number of poles centered around the motor running speed and harmonics of the running speed

Many engines operate at variable speeds, which will allow the strong forcing functions to excite resonances of the components and the mounting structure, if it is not designed in a robust manner. Excessive vibrations in reciprocating machines usually occur due to operational problems such as misfiring, piston slap, compression leaks, and faulty fuel injection. These problems result in elevated $\frac{1}{2}X$ vibrations, if only one cylinder is affected, and a decrease in efficiency and power output. Gear and bearing problems may also occur in reciprocating machines, but the characteristic defect frequencies for these faults are significantly higher.

25.11.4 Advanced Fault Diagnostic Techniques

Much of the discussion in the previous sections has highlighted the fact that many machine defects generate distinctive vibration signals. This fact has been exploited recently with the development of a variety of different automatic fault diagnostics techniques (Mechefske and Mathew, 1992b; Mechefske, 1995). The details of these systems will not be provided here, but the goal of automatic diagnostics is to augment and assist, rather than replace, the vibration signal analyst. If characteristic defect indicators can be detected and extracted from a vibration signal without the intervention of a signal analyst, the analyst will have more time for other duties and will also have access to information that may not have been uncovered through normal signal processing and analysis.

There are, however, still many situations where machine defects do not generate distinctive vibration signals or when the vibration signals are masked by large amounts of noise or vibrations from other machinery. In such cases, advanced diagnostic algorithms incorporating new signal processing techniques are currently being developed and implemented. Artificial neural networks (Timusk and Mechefske, 2002) have been found to provide an excellent basis for detecting and diagnosing faults. Wavelet analysis (Lin et al., 2004) and short-time Fourier transforms (STFTs) have also been shown to effectively allow both time domain and frequency domain information to be displayed on the same plot. This provides an opportunity to clearly see short duration transient events as well as detect faults in machinery that is operating in nonsteady-state conditions.

- Analysis of the vibration signal to determine the actual type of fault present will allow for more accurate estimation of the remaining life, the replacement parts that are needed, and the maintenance tools, personnel, and time required to repair the machinery.
- A diagnostic template can be developed for the different types of faults that are common in a given facility or plant by listing various faults that usually develop in machinery in terms of the forcing functions that cause them and specific machine types.
- Common forcing functions include unbalance, misalignment, mechanical looseness, soft foot, rubs, resonances, oil whirl, oil whip, structural vibrations, and foundation problems.
- Specific machine components that need to be monitored include damaged or worn rolling-element bearings and gears.
- Specific machine types that can be treated as common groups include pumps, fans, electric motors, steam and gas turbines, compressors, and reciprocating machines.

References

- Alfredson, R.J. 1982. A computer based system for condition monitoring, *Symposium on Reliability of Large Machines*, The Institute of Engineers Australia, Sydney, pp. 39–46.
- Boto, P.A., Detection of bearing damage by shock pulse measurement, *Ball Bearing J.*, 5, 167–176, 1979.
- Braun, S. 1986. *Mechanical Signature Analysis: Theory and Applications*, Academic Press, London.

- Courrech, J. 1985. New techniques for fault diagnostics in rolling element bearings, In *Proceedings of the 40th Meeting of the Mechanical Failure Prevention Group*, National Bureau of Standards, Gaithersburg, MD, pp. 47–54.
- Eisenmann, R.C. Sr. and Eisenmann, R.C. Jr. 1998. *Machinery Malfunction: Diagnosis and Correction*, Prentice Hall, Newark.
- Eschman, P. 1985. *Ball and Roller Bearings*, 2nd ed., Wiley, New York.
- Goldman, S. 1999. *Vibration Spectrum Analysis*, Industrial Press, New York.
- Grove, R.C. 1979. An investigation of advanced prognostic analysis techniques, Paper USARTL-TR-79-10. Northrup Research and Technology Center, Palos Verdes, CA.
- Lin, J., Zuo, M.J., and Fyfe, K.R., Mechanical fault detection based on the wavelet de-noising technique, *ASME J. Vib. Acoust.*, 126, 9–16, 2004.
- Lyon, R.H. 1987. *Machinery Noise and Diagnostics*, Butterworth, Boston.
- Mathew, J., Machine condition monitoring using vibration analysis, *J. Aust. Acoust. Soc.*, 15, 7–21, 1987.
- Mathew, J. and Alfredson, R.J., The condition monitoring of rolling element bearings using vibration analysis, *Trans. ASME J. Vib. Acoust. Stress Reliab. Des.*, 106, 447–457, 1984.
- McFadden, P.D. and Smith, J.D., A model for the vibration produced by a single point defect in a rolling element bearing, *J. Sound Vib.*, 96, 69–77, 1984.
- McFadden, P.D. and Smith, J.D., A signal processing technique for detecting local defects in a gear from the average of the vibration, *Proc. IMechE*, 199, 99–112, 1985.
- Mechefske, C.K., Fault detection and diagnosis in low speed rolling element bearings using inductive inference classification, *Mech. Syst. Signal Process.*, 9, 275–282, 1995.
- Mechefske, C.K., Objective machinery fault diagnosis using fuzzy logic, *Mech. Syst. Signal Process.*, 12, 855–864, 1998.
- Mechefske, C.K. and Liu, L., Fault detection and diagnosis in variable speed machines, *Int. J. Condition Monit. Diagn. Eng. Manage.*, 5, 29–42, 2001.
- Mechefske, C.K. and Mathew, J., Fault detection in low speed rolling element bearings, part I: the use of parametric spectra, *Mech. Syst. Signal Process.*, 6, 297–308, 1992a.
- Mechefske, C.K. and Mathew, J., Fault detection in low speed rolling element bearings, part II: the use of nearest neighbour classification, *Mech. Syst. Signal Process.*, 6, 309–317, 1992b.
- Mitchell, J.S. 1981. *An Introduction to Machinery Analysis and Monitoring*, Penwell, Los Angeles.
- Mobley, R.K. 1990. *An Introduction to Predictive Maintenance*, Van Nostrand Reinhold, New York.
- Moubray, J. 1997. *Reliability Centered Maintenance*, Industrial Press, New York.
- Randall, R.B. 1981. A new method of modeling gear faults, *ASME Annual Congress*. Paper No. 81-Set-10.
- Randall, R.B. 1987. *Frequency Analysis*, Bruel & Kjaer, Copenhagen.
- Randall, R.B. 2001. Bearing diagnostics in helicopter gearboxes, *Condition Monitoring and Diagnostic Engineering Management Conference*, Manchester, U.K., August 2001.
- Rao, B.K.N. 1996. *The Handbook of Condition Monitoring*, Elsevier, Oxford.
- Reeves, C.W. 1999. *The Vibration Monitoring Handbook*, Coxmoor, Oxford.
- Smith, J.D. 1983. *Gears and Their Vibrations*, Marcel Dekker, New York.
- Taylor, J.I. 1994. *The Vibration Analysis Handbook*, Vibration Consultants, Tampa.
- Timusk, M. and Mechefske, C.K. 2002. Applying neural network based novelty detection to industrial machinery, *6th International Conference on Knowledge-Based Intelligent Information Engineering Systems*, Crema, Italy, November 2002.
- Wowk, V. 1991. *Machinery Vibration: Measurements and Analysis*, McGraw-Hill, New York.

26

Vibration-Based Tool Condition Monitoring Systems

26.1	Introduction	26-1
26.2	Mechanics of Turning	26-2
	General Terms • Chatter Vibrations • Tool Wear	
26.3	Vibration Signal Recording	26-7
	Direct and Indirect Systems • Sensor Requirements for Tool Wear Monitoring • Force Measurement • Acceleration Measurement • Acoustic Emission Measurement • Sensor Comparisons	
26.4	Signal Processing for Sensor-Based Tool Condition Monitoring	26-11
	Feature Extraction • Feature Selection	
26.5	Wear Model/Decision-Making for Sensor-Based Tool Condition Monitoring	26-15
	Trending, Threshold • Neural Networks • Fuzzy Logic • Other Methods	
26.6	Conclusion	26-20

C. Scheffer
University of Stellenbosch

P.S. Heyns
University of Pretoria

Summary

Despite the high level of technology built into every aspect of modern metal cutting operations, the phenomenon of tool wear still hampers the reliability and complete automation of machining processes. Tool wear is the loss of material on the edge of the cutting tool. This chapter concerns sensor-based tool condition monitoring (TCM), and specifically those methods that are based on vibration related properties such as force, acceleration, and acoustic emission (AE). References are made to systems proposed in the literature and also to commercially available hardware. The chapter focuses on turning operations. The mechanics of turning are briefly discussed. Various methods of obtaining vibration signals from turning operations are described. The vibration signal has to be processed in order to estimate the level of wear in the cutting edge of the tool, and several state-of-the-art approaches are discussed. Effective methods of constructing a model relating sensor data and the tool wear, using processed vibration signals, are described. The chapter concludes by indicating some important points that should be considered when using vibration-based systems for TCM, and some interesting topics for future research in this field of study. Chapters 25 and Chapter 27 present further information on the present subject.

26.1 Introduction

Millions of products are manufactured daily by a variety of processes. A basic method to form bulk metal into a desired final shape is through the process of metal cutting, also referred to as machining. Metal cutting is essentially the removal of excess material from a workpiece by moving a working tool over the

surface of the workpiece at a certain depth, speed, and feed rate. Conventional machining operations are turning, milling, and drilling.

Despite the high level of technology built into every aspect of modern metal cutting operations, the phenomenon of tool wear still hampers the reliability and complete automation of machining processes. Tool wear is the loss of material on the edge of the cutting tool. Although tool wear can be minimized, it cannot be eliminated. Unfortunately, excessive or even a small quantity of tool wear may cause a defect in a machined component, and therefore it is always necessary to be aware of the extent of the current tool wear before machining can commence. Economic losses due to tool wear occur as a result of the scrapping of expensive parts and the nonoptimal use of tool inserts. A conservative approach is often taken, and the insert is recycled long before it should have been. Furthermore, secondary damage due to tool wear can be extreme and even catastrophic. For this reason, many approaches to tool condition monitoring (TCM) have been proposed through the years. There exist sensorless and sensor-based TCM approaches. Sensorless approaches are generally tool-life equations and not monitoring methods. Thus, sensorless approaches attempt to determine the optimal tool life under certain machining conditions. These are often extended versions of the famous Taylor equation, which is described by

$$vT^n = C \quad (26.1)$$

where v is the cutting speed, T is the tool life, and n and C are constants that must be determined experimentally for a given tool and workpiece combination.

This chapter is focused on sensor-based TCM, and specifically those methods that are based on vibration related properties such as force, acceleration, and acoustic emission (AE). These sensor types are known to be most effective for TCM. Furthermore, discussions will be focused on the application of TCM in turning operations, though reference will be made to other machining operations as well. Besides vibration-based approaches, other sensor based TCM methods are:

- Use of noncontact capacitive sensors
- Vision systems
- Measurement of the motor current
- Surface roughness monitoring
- Ultrasonic monitoring
- Temperature monitoring
- Laser scatter methods
- Audible emission monitoring

The reader is also referred to other excellent overviews of sensor-assisted TCM, published by Dan and Mathew (1990), Byrne et al. (1995), Scheffer and Heyns (2001a), and Dimla (2000). A TCM database was also published by the CIRP, supervised by Teti (1995), which includes more than 500 research papers focusing only on TCM.

26.2 Mechanics of Turning

26.2.1 General Terms

A typical turning operation is schematically shown in [Figure 26.1](#). The cutting tool moves parallel to the workpiece and spindle, and hence reduces the diameter of the shaft. The most important machining parameters are:

- Cutting speed (usually expressed in m/min)
- Feed rate (usually expressed in mm/rev)
- Depth of cut (usually expressed in mm)

The force response on the tool tip due to the turning operation consists of three components: F_x , F_y , and F_z . These forces consist of a static and a dynamic part, as shown in [Figure 26.2](#). The static forces are governed by the static pressure between the tool and workpiece, and are a function of the machining

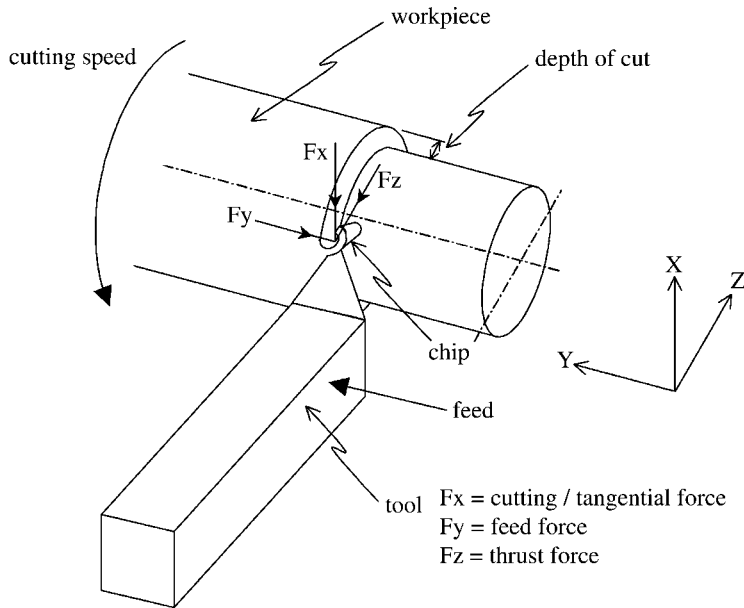


FIGURE 26.1 Turning operation.

parameters. The dynamic forces are governed by forced and free vibrations due to excitation from the cutting operation. Analytical models exist that can describe the static forces for basic machining operations (Merchant, 1945). The dynamic behavior is more difficult to model theoretically, although there is also continuous research in this area (Kapoor et al., 1998).

One of the main difficulties of monitoring tool wear with vibration is to identify the frequency range that is influenced by tool wear, since machining processes entail various mechanisms that produce vibrations that are not related to tool wear. The frequency range of vibrations produced during ordinary machining operations usually falls between 0 and 10 kHz. From the literature, it can be concluded that the frequency range sensitive to tool wear depends entirely on the type of machining operation, and must be determined experimentally for each individual case. There are two important vibration frequencies present during cutting:

- The natural frequencies of the tool holder and its components
- The frequency of chip formation

Dynamic tests should be conducted to identify the dynamic properties of tool holders (Scheffer and Heyns, 2002a). However, the interaction of the working tool engaged into the rotating workpiece complicates the situation, and as a result the dynamic behavior during cutting could be different from the expected behavior obtained from off-line tests. Scheffer and Heyns (2004) compared continuous cantilever models with modal hammer tests for different tool holder overhang lengths. The natural frequency of the first mode as a function of overhang length is plotted in Figure 26.3 (for a specific tool holder). It can be seen that a continuous fixed-free cantilever beam model corresponds well with the results obtained with hammer tests.

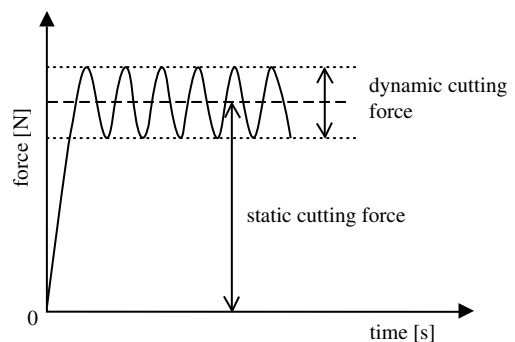


FIGURE 26.2 Static and dynamic forces.

The chip formation frequency can be calculated with simple equations that take the machining conditions into account (Lee et al., 1989). The tool holder natural frequencies and chip formation frequency are independent. Generally, tool wear has a larger effect on the vibration amplitudes at the tool holder natural frequencies but can influence chip formation frequencies as well.

26.2.2 Chatter Vibrations

Another phenomenon important to machining operations is tool chatter vibrations. These are self-excited vibrations resulting from the generation of different chip thicknesses during machining. Initially, cutting forces excite a structural mode of the machine–workpiece system. This leaves a wavy surface finish on the workpiece. During the next revolution, another wavy surface is produced in the same way. Depending on the phase shift between these two waves, the maximum chip thickness can grow and oscillate at a particular frequency that is close to that of a structural mode. This is called the regenerative chatter frequency. Chatter cause a poor surface finish and can also lead to tool breakage.

The analysis and prediction of chatter has been the subject of research for many years. Morimoto et al. (2000) developed a piezoelectric shaker/actuator to regenerate the vibrations of the cutting process. In this way, unwanted vibrations such as chatter can be attenuated. The system is also helpful to determine the dynamic properties of the machine tool. Koizumi et al. (2000) used a very interesting approach called the correlation integral in the time domain to identify chatter onset. Lago et al. (2002) designed a sensor and actuator integrated tool for turning and boring to control chatter. The tool holder shank vibrations are sent to the actuator *via* a digital controller. An adaptive feedback control system is used to perform broadband vibration attenuation up to 40 dB at different frequencies simultaneously.

26.2.3 Tool Wear

26.2.3.1 Tool Failure Mechanisms

Tool wear is caused by mechanical loads, thermal loads, chemical reactions, and abrasive loads. The load conditions are in turn influenced by the cutting conditions and materials. The different loads can cause certain wear mechanisms that may occur in combination. These mechanisms have either a physical or chemical characteristic that causes loss or deformation of tool material. Tool wear mechanisms can be classified into several types, summarized as follows (Du, 1999):

- Abrasive wear resulting from hard particles cutting action
- Adhesive wear associated with shear plane deformation
- Diffusion wear occurring at high temperatures
- Fracture wear due to fatigue

Other wear mechanisms are plastic deformation and oxidation, which are not very common in industry. It is estimated that 50% of all tool wear is caused by abrasion, 20% by adhesion, 10% by chemical reactions and the remaining 20% by the other mechanisms (Kopac, 1998). Abrasion is basically the grinding of the cutting tool material. The volume of abrasive wear increases linearly with the cutting forces. Higher hardness of the tool material can reduce the amount of abrasive wear. During adhesion, the high pressures and temperatures on the roughness peaks on the tool and the workpiece cause

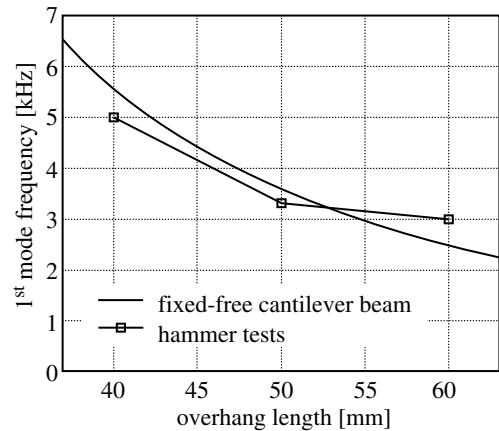


FIGURE 26.3 Frequency of first tool holder mode. (Source: Scheffer, C. and Heyns, P.S., *Mech. Syst. Signal Process*, Elsevier, 2004. With permission.)

welding. These welding points are broken many times every second due to the workpiece movement and as a result cause removal of the tool material (Kopac, 1998). Diffusion wear occurs at even higher cutting speeds, where very high temperatures are present (especially when using hard metal tools).

26.2.3.2 Tool Failure Modes

Tool wear will generally occur as a combination of a number of wear modes, with one mode predominant. The dominant mode will depend on the dominant wear mechanism, which in its turn is influenced by the machining conditions and the choice of tool and workpiece material. For a given tool and workpiece combination, the dominant wear mode can be determined at different cutting speeds using the product of the cutting speed and the undeformed chip thickness (Dimla, 2000). The common wear modes are:

- Nose wear
- Flank wear
- Crater wear
- Notch wear
- Chipping
- Cracking
- Breakage
- Plastic deformation

Figure 26.4 is a graphical representation of the different tool failure modes. The consequences of tool wear are deviations in shape and roughness of the machined part that cause the part to be discarded because it is out of tolerance. Most wear modes cause an increase in cutting forces, although this is not always the case for all tool and workpiece combinations. The most widely researched tool failure modes for turning with single point tools are flank wear, breakage (fracture), and crater wear. Flank and crater wear are accepted as normal tool failure modes, because the other failure modes can be avoided by selecting the proper machining parameters. The growth of flank and crater wear is directly related to the total cutting time, unlike some of the other failure modes, which can occur unexpectedly even with a new tool.

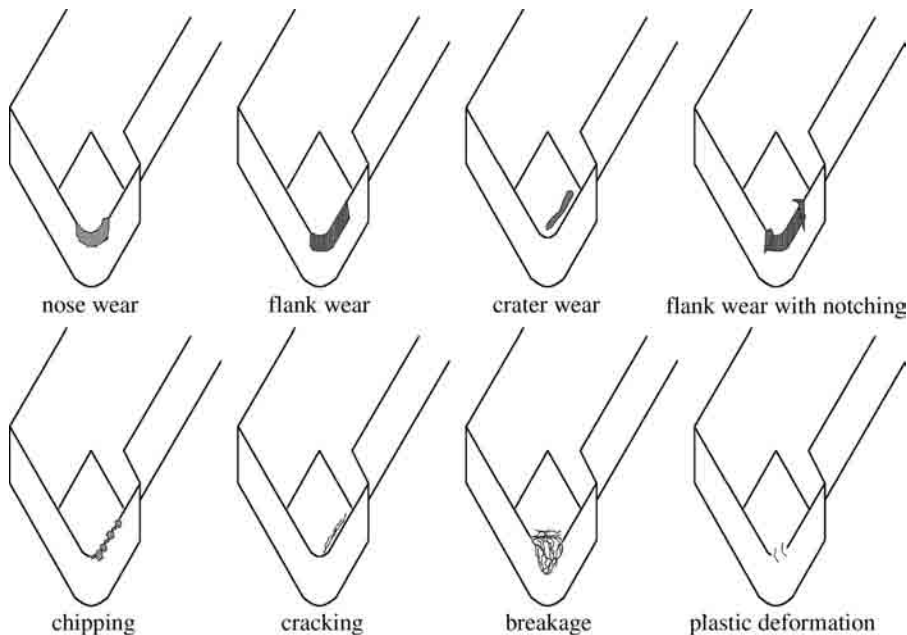


FIGURE 26.4 Tool failure modes. (Source: Scheffer, C. and Heyns, P.S. 2001a. COMA '01, University of Stellenbosch. With permission.)

26.2.3.3 Tool Wear Measurement

Wear measurements of tool inserts are done through the implementation of an appropriate international standard, ISO 3685. Flank wear is quantified in terms of VB, which is the mean of the wear height on the tool flank. The length of flank wear is also measured in terms of b . Crater wear is quantified in terms of the crater depth, K . The parameters are depicted in Figure 26.5, which is a scanning electron microscope (SEM) picture of a worn turning insert.

26.2.3.4 Tool Wear Stages

It is assumed by most authors that tool wear consists of an initial, a regular, and a fast wear stage (Zhou et al., 1995). Some authors divide tool wear into five distinct stages (Bonifacio and Diniz, 1994):

1. Initial stage of wear
2. Regular stage of wear
3. Microbreakage stage of wear
4. Fast wear stage
5. Tool breakage

It has been established by various researchers that the initial and fast (before tool breakage) stages occur more rapidly than the regular stage. Bonifacio and Diniz (1994) explain that, during the fast wear stage with coated carbide tools, the tool loses its coating and the tool substrate (which has less resistance) begins to perform the cut and wears faster. During the initial stage, the tool edge loses its sharp edge rapidly, after this the process stabilizes for a given time. Flank wear in relation to total cutting time will typically appear as depicted in Figure 26.6.

The geometrical growth and rate of wear is unique for every tool insert, even those used with the same machining parameters. Wear measurements conducted on the shop floor of a piston manufacturer by Scheffer and Heyns (2004) are shown in Figure 26.7. It was found that the tools last between 1000 and 6000 components, which makes the optimal use of the tool extremely problematic if the wear is not monitored on-line. The reason for this behavior is mainly attributed to fluctuating conditions on the shop floor, for example, the rate at which components are manufactured. If the time allowed for the tool to cool down between workpieces is not constant, large variations in the tool life can be expected.

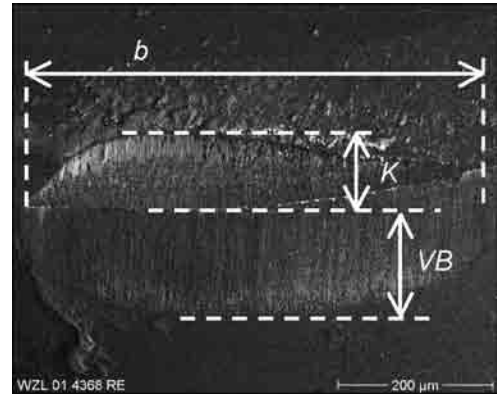


FIGURE 26.5 Tool wear parameters.

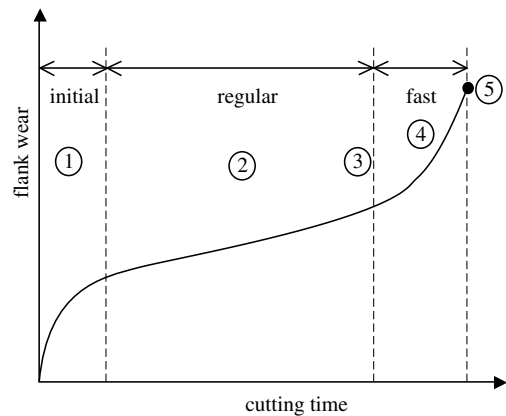


FIGURE 26.6 Flank wear in relation to cutting time.

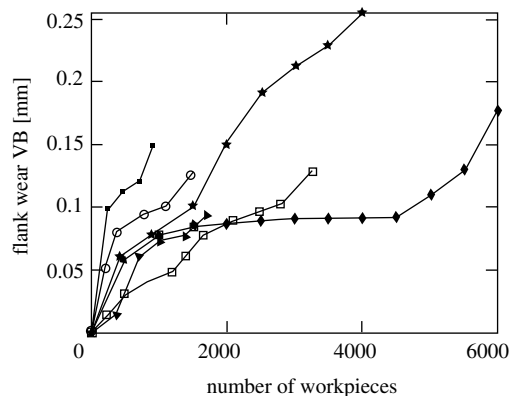


FIGURE 26.7 Typical variations in tool life. (Source: Scheffer, C. and Heyns, P.S., *Mech. Syst. Signal Process*, Elsevier, 2004. With permission.)

26.3 Vibration Signal Recording

The information from vibration sensors can be treated in numerous ways. The overall aim of a tool condition monitoring system (TCMS) is to utilize the best processing techniques to extract the relevant information from sensor signals. Generally, a TCMS consists of the steps depicted in Figure 26.8. Various methods that could be used in each step will be discussed in more detail.

26.3.1 Direct and Indirect Systems

TCMSs can be divided in two categories, namely, direct and indirect. Direct methods are concerned with a measurement of volumetric loss at the tool tip, while indirect methods use a pattern in sensor data to detect a failure mode (Byrne et al., 1995). Direct methods do not utilize vibration and will not be discussed here. In general, direct methods are sensitive to dirt and cutting chips, and consequently they are not commonly accepted in industry. Indirect methods have found more acceptance in industry due to the fact that most indirect methods are easily interpreted, cost-effective, and often more reliable than direct methods. Also, for some applications, it might not be possible to use a direct monitoring method due to the nature of the process.

26.3.2 Sensor Requirements for Tool Wear Monitoring

Machine tools represent very hostile environments for sensors. Sensors used for TCM (also see Chapter 15) must meet certain requirements, such as (Byrne et al., 1995) the following:

- Must measure as close as possible to the point of metal removal
- Must not cause a reduction in the stiffness of the machine tool
- Must not cause a restriction of the working space of the machine
- Should be wear and maintenance free, easy to replace, and of low cost
- Must have resistance to dirt, chips, and electromagnetic and thermal influences
- Should function independent of tool and workpiece
- Must provide reliable signal transmission, e.g., from rotating to fixed machine components

26.3.3 Force Measurement

Worn tools cause an increase in the cutting force components. It is also known that both the dynamic and static components generally increase with tool wear due to frictional effects. The three components of the cutting force each responds uniquely to varying machining parameters and the different wear modes. Depending on the type of process that is investigated and the specific experimental setup, results among researchers vary. This can be attributed to dynamic effects of the machine tool and the measurement equipment. There are a number of different sensor configurations to collect forces from machining operations and these are described below.

26.3.3.1 Direct Measurement Dynamometers

Tool holder dynamometers are by far the most popular method for collecting cutting forces. These sensors utilize the piezoelectric effect and can measure quasistatic and dynamic cutting forces very accurately. However, dynamometers are very expensive and bulky instruments and are not practical for a

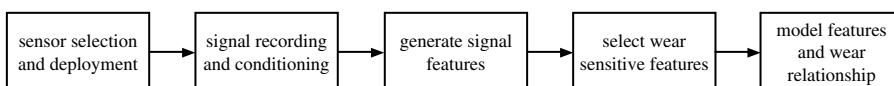


FIGURE 26.8 TCMS steps.

typical shop floor. Furthermore, their usable frequency range is limited to approximately 1 kHz. An example of a tool holder dynamometer is shown in Figure 26.9.

Tarmal and Opavsky (2000) investigated the dynamics of a conventional force dynamometer for machining operations. It was found that the dynamometer has significant amplitude distortion in the frequency range that is quoted as the operating range by the manufacturer. The authors suggest that the dynamic characteristics of the dynamometer (while clamped as it would be during measurements) be identified with a modal test and the effect of dynamometer dynamics be compensated for after measurements are made to obtain the true cutting force.

26.3.3.2 Indirect Force Sensors

There are numerous small force sensors available for the purpose of force measurement on machine tools. These measure forces in load-carrying components of the machine tool and are thus not direct force measurement devices. The advantages of these sensors are their size, low cost, and significantly higher operational frequency range. A disadvantage is that a suitable position for the sensor can only be determined experimentally. These sensors are suitable for tool breakage monitoring in rough machining or detection of other catastrophic events such as collisions. An example of a three-component force sensor is shown in Figure 26.10.

26.3.3.3 Piezoelectric Strain Sensors

The use of piezoelectric strain sensors for wear monitoring of synthetic diamond tool inserts was reported by Scheffer and Heyns (2000a). These sensors are ultrasensitive to changes in cutting forces if they are installed in an appropriate location. The best location for the sensor must once again be determined experimentally, but generally it should be installed on a load-carrying component of the machine as close as possible to the tool tip, for example, on the tool holder itself (Scheffer and Heyns, 2001b). An example of a piezoelectric strain sensor that can be used on machine tools is shown in Figure 26.11.

26.3.3.4 Resistance Strain Gauges

A quite simple method to estimate both the static and dynamic components of cutting forces without any distortion is to use resistance strain gauges (see Chapter 15). These comply with most of the requirements for TCM sensors, and they can accurately follow the static and dynamic response of a system up to



FIGURE 26.9 KISTLER force dynamometer type 9121. (Source: KISTLER Brochure 2002. Courtesy of Kistler Instrumente AG.)



FIGURE 26.10 KISTLER three-component force sensor type 9251A. (Source: KISTLER Brochure 2003. Courtesy of Kistler Instrumente AG.)



FIGURE 26.11 KISTLER strain sensor type 9232A. (Source: KISTLER Brochure 2004. Courtesy of Kistler Instrumente AG.)

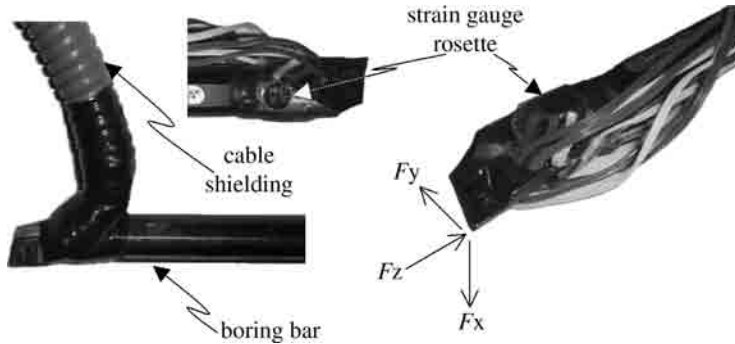


FIGURE 26.12 Application of resistance strain gauges. (Source: Scheffer, C. and Heyns, P. S., *Mech. Syst. Signal Process.*, Elsevier, 2004. With permission.)

50 kHz. Scheffer and Heyns (2002a) developed a sensor-integrated tool holder using strain gauges. It was shown that the system is robust, cost-effective, and fit for an industrial TCMS. The physical layout of the strain gauges on a boring bar is shown in Figure 26.12. The system was calibrated with a special device to directly obtain the three cutting forces from the strain gauge signals.

26.3.3.5 Customized Force Sensors

There are a number of customized force sensors available that can be used with specific machining operations. These are:

- Force measuring plates, pins, and bearings
- Special force measuring bolts
- Force and torque measuring rings that fit on spindles

26.3.4 Acceleration Measurement

Piezoelectric accelerometers can measure the machine vibration caused by oscillations of cutting forces. It is well known that high-frequency vibrations (higher than 1 kHz) yield large acceleration levels, giving accelerometers an advantage over force-based monitoring. Accelerometers fulfill the environmental requirements for tool wear monitoring because they are resistant to the aggressive media present during machining. Accelerometers are also less expensive than force dynamometers and can measure vibration levels within a very wide frequency range, typically 5 Hz to 10 kHz.

Various authors have shown that acceleration levels change with tool wear. Li et al. (1997) found that the coherence function of two crossed accelerations can be used as an easy and effective way to identify tool wear and chatter. They found that with progressive tool wear, the autospectra of the two accelerations and their coherence function increase gradually in magnitude around the first natural frequencies of the cross-bending vibration of the tool shank. As the tool approaches a severe wear stage, the peaks of the coherence function increase to values close to unity. Scheffer et al. (2003) reported on the use of an accelerometer for wear monitoring during hard turning. It was found that certain frequencies show repeatable amplitude increase with increasing tool wear. These frequencies corresponded to the tool holder natural frequencies. Some authors, for example, Bonifacio and Diniz (1994), also found that a wear sensitive frequency will increase with increasing tool wear and then suddenly decrease near the end of tool life. This can be attributed to an increased damping effect due to plastic deformation and microbreakage of the cutting edge.

26.3.5 Acoustic Emission Measurement

Cutting processes produce elastic stress waves that propagate through the machine structure. Different sources in the cutting process generate these stress waves known as acoustic emission (AE). Sources of AE

in metal cutting are:

- Friction on the tool face and flank
- Plastic deformation in the shear zone
- Crack formation and propagation
- Impact of the chip at the workpiece
- Chip breakage

A typical AE sensor for use on machine tools is shown in Figure 26.13.

The fact that crack formation generates AE makes AE ideal for tool breakage detection. Collection of the AE requires special hardware that can bandpass filter the signals to the AE range (between approximately 50 and 250 kHz). Furthermore, amplification is required and an analogue root-mean-square (RMS) circuit with a short time constant is generally also included to collect the AE_{RMS} . The different steps required to collect AE are depicted in Figure 26.14 (adapted from Jemielniak, 2000).

Araujo et al. (2000) investigated sliding friction as a possible source of AE during metal cutting. The AE_{RMS} values in different frequency ranges were collected for different widths of cut and also with the tool rubbing against the workpiece without cutting. It was found that the level of AE remains almost constant for all width of cut conditions, and hence it was concluded that the main mechanism for AE during metal cutting is the sliding friction between the tool and workpiece. Consequently, an increase or decrease of AE can be expected with tool wear depending on the effect on the sliding friction due to that tool wear. Furthermore, it is believed that the cutting temperatures will affect the AE due to thermal expansion effects. Chiou and Liang (2000) investigated AE with tool wear and chatter effects in turning. A model is presented that can predict the chatter AE_{RMS} amplitude with certain levels of flank wear. Good correlation was found between the model and the experimental results. Kim et al. (1999) reported on the use of AE to monitor the tool life during a gear shaping process. The AE_{RMS} is collected and used in a software program to predict the remaining tool life.

Li (2002) presented an overview of using AE for TCM in turning operations. It is stated the AE is heavily dependent on cutting conditions and, as a result, methods should be employed to handle this problem effectively. Some methods are proposed that include advanced signal processing, sensor fusion and modeling techniques. Many other AE-based tool wear and breakage monitoring systems have been implemented successfully in research. One problem still lies with an appropriate interpretation of the AE frequency spectrum. In most studies, an explanation for the choice of certain frequencies and their advantages are not given or not investigated. In fact, Jemielniak (2000) found that using the average value of AE (or AE_{RMS}) is the most suitable. A similar conclusion was made by Scheffer et al. (2003), who compared different processing methods of the AE signal during hard turning.



FIGURE 26.13 Kistler AE sensor type 8152B. (Source: PCB Website 2002. Courtesy of Kistler Instrumente AG.)

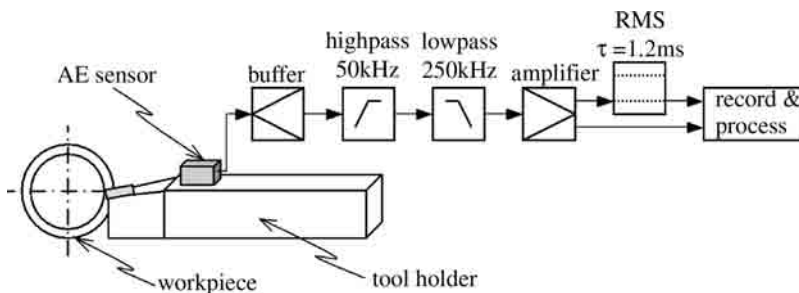


FIGURE 26.14 Steps for collecting AE during turning. (Adapted from Jemielniak, K., *Ultrasonics*, 2000.)

26.3.6 Sensor Comparisons

Future research should be directed towards directly comparing different sensors for tool wear monitoring. Choi et al. (1999) developed a single sensor for parallel measurement of force and AE. A finite element analysis was carried out to determine the optimal position for the sensor away from the tool holder because the sensor obstructed the working space of the machine. The approach was successful for breakage detection but no wear estimations are reported. Barrios et al. (1993) compared AE, vibration, and spindle current for TCM during milling. It was found that the spindle current is the most sensitive sensor for detecting tool wear, with AE the least sensitive. However, contradictory results are reported in other publications, and hence more research would be required to determine ultimately which sensor is the best for which machining operation. Govekar et al. (2000) compared force and AE methods for TCM, and concluded that the best result is achieved when sensory information is combined. Dimla and Lister (2000a) compared the use of force and vibration signals for TCM and also combined the information in a single decision-making technique (Dimla and Lister, 2000b). Similar comparative studies were reported by Scheffer et al. (2003).

26.4 Signal Processing for Sensor-Based Tool Condition Monitoring

Using the sensor information from the different sensor systems described in the previous section, a decision must be made with respect to the tool condition. This decision is generally referred to as the data classification. It is often better to combine sensory information to solve a complex problem such as TCM. Such a combined approach is referred to as sensor fusion. Sick (2002) proposed a generic sensor fusion architecture for TCM, which summarizes the various sensor fusion levels of a TCMS. These are:

- Analogue preprocessing
- Digital preprocessing
- Feature extraction
- Wear model
- Decision making

Fusion of sensor information can occur at any of these levels. Analogue and digital preprocessing are activities such as signal amplification, conditioning, filtering, calibration, and temperature compensation. The feature extraction step is probably the most important step, because here the sensor signals must be condensed and reduced to only a few appropriate wear sensitive values. Many different methods are available to achieve this. The wear model level establishes a relationship between the chosen features and the tool condition. In many cases, neural networks (NNs) are used in this step, and sensor fusion takes place within the NN. A decision level can also be included where a final decision is made with respect to the tool condition, for instance a “competing experts” formulation if a TCMS is used in conjunction with a tool-life equation. Discussions on the various techniques follow.

26.4.1 Feature Extraction

Most decision-making techniques for process monitoring are based on signal features. Through appropriate signal processing, features can be extracted from signals that show consistent trends with respect to tool wear. Features are mainly derived through processing in the time, frequency, or joint time-frequency domain or statistical analysis.

26.4.1.1 Time Domain

Features extracted from the time domain are usually fundamental values such as the signal mean or RMS. Other techniques include the shape of enveloping signals, threshold crossings, ratios between

time-domain signals, peak values, and polynomial approximations of time-domain signals. Examples of time-domain features from an interrupted cutting operation are shown in Figure 26.15.

It has been found that some of the time-domain features show good correlation with tool wear and are easy to implement (Scheffer, 1999). Bayramoglu and Döngel (1998) investigated the use of several different force ratios (calculated from the static cutting forces). It was found that certain force ratios can be used to monitor tool wear under a wide range of cutting conditions. Most commercial TCMS rely on time-domain information. However, time-domain features are known to be sensitive to disturbances and should be complemented with features from another domain.

26.4.1.2 Frequency Domain

The power or energy of certain frequency bands in the fast Fourier transform (FFT) is often suggested as a feature for TCM. It is very challenging to identify spectral bands that are sensitive to tool wear. It is even more difficult to determine exactly why these frequencies are influenced by tool wear. Power in certain bands will often increase due to higher excitation forces because of the increase in friction when the tool starts to wear. Sometimes a peak in the FFT will also shift due to changing process dynamics as a result of tool wear. An early frequency-domain approach is reported by Jiang et al. (1987), in which frequency-band energy is determined from the power spectral density (PSD) function as a feature for tool wear.

Some authors suggest that two frequency ranges be identified from the original signal (Bonifacio and Diniz, 1994). The one range must be sensitive to tool wear, the other must be insensitive. For instance, if the measurement was made from 0 to 8 kHz, it must be split (using appropriate filters) into a 0 to 4 kHz signal and a 4 to 8 kHz signal. If the lower range is more sensitive to tool wear, a ratio between the two ranges can be calculated. If this ratio exceeds a certain pre established value, it can be concluded that the end of the tool life has been reached. This can also apply for a ratio between the signal recorded from a fresh tool to that compared with a worn tool. Examples of frequency-domain features from cutting forces are shown in Figure 26.16.

One difficulty with frequency-domain approaches is that the dynamics of the operation and measurement hardware is not always fully understood. The fact that measurement hardware dynamics instead of process dynamics are often measured was also recently identified by Warnecke and Siems (2002). The response of a force dynamometer is influenced by its clamping condition, which may cause it to experience nonlinearities at relatively low frequencies. There are also some uncertainties when using these instruments, relating to their calibration and other varying parameters. A model for expressing the uncertainties when collecting cutting forces with a dynamometer was proposed by Axinte et al. (2001). These uncertainties might be responsible for the scatter of force components often reported in the

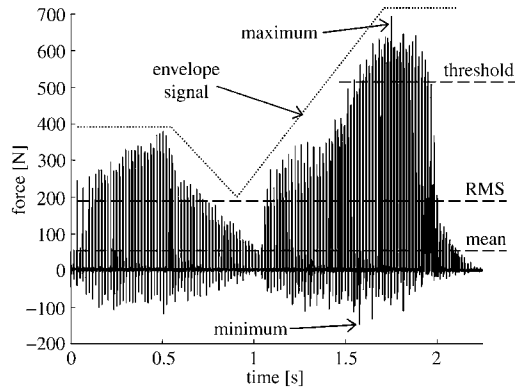


FIGURE 26.15 Simple time-domain features.

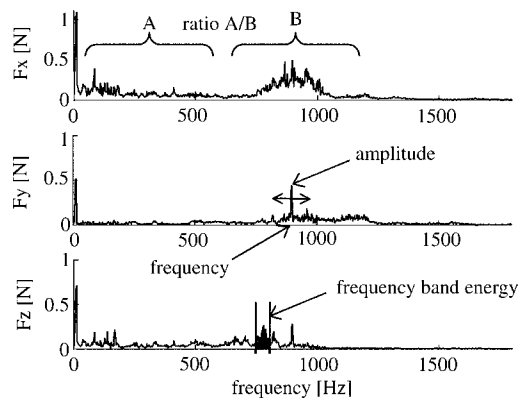


FIGURE 26.16 Frequency-domain features.

literature. An interesting study is also reported by Bähre et al. (1997), concerning determination of the natural frequencies of the machine tool components using the finite element method (FEM). These are taken into account for interpretation of the vibration/AE signal.

26.4.1.3 Statistical Processing

In the case of statistical features, signals are assumed to have a probabilistic distribution, and consequently, useful information can be extracted from the statistics of the distribution. Hence, the signal is regarded as a random process. Generally, machining processes are nonstationary but are assumed to be stationary for the short periods during which features are calculated. Several statistical features have been investigated for TCM and can be applied to several machining operations. The main features are those that describe the probability distribution of a random process (variance, standard deviation, skewness, kurtosis, etc.) and coefficients of time-series models. There are also miscellaneous other statistical features, such as cross-correlations, the coherence function, and the harmonic mean.

One useful approach is the use of autoregressive (AR) and autoregressive moving average (ARMA) coefficients. AR coefficients computed for a signal represent its characteristic behavior. When the signal changes during the cutting operation due to tool wear, the model coefficients also change and can then be utilized to monitor the progressive tool wear. Baek et al. (2000) report on the use of an eighth order AR model for tool breakage detection during end milling. It was found that the AR approach is somewhat more accurate than the frequency band energy method. Yao et al. (1990) used the ARMA method to decompose the dynamic cutting force signals, and wear-sensitive frequencies were identified. This assisted in identifying the importance of certain vibration modes with respect to TCM.

The use of statistical process control (SPC) methods is also reported by some authors. Jun and Suh (1999) considered the X-bar and exponentially weighted moving average (EWMA) for tool breakage detection in milling. Jennings and Drake (1997) used statistical quality control charts for TCM. Different statistical parameters are calculated and examples of one-, two- and three-variable control charts are given.

26.4.1.4 Time–Frequency Domain

The most common time–frequency domain processing method in TCM applications is wavelet analysis. A comprehensive discussion on the advantages and disadvantages of wavelet analysis for TCM is described by Sick (2002). It is often stated that wavelets are used because they provide information about the localization of an event in the time as well as in the frequency domain. However, locating discrete frequency-related events in the time domain is rarely of importance with respect to tool wear (which is a gradually increasing phenomenon). In contrast, tool breakage will have a large localized effect in the time domain, but this can be monitored more effectively using time-domain techniques. Furthermore, wavelets are time variant and the exact contribution of a particular frequency at any given time can never be determined accurately due to Heisenberg's uncertainty principle.

Despite the above arguments, the use of wavelet analysis for TCM is reported in several publications. Lee and Tarng (1999) use the discrete wavelet transform for cutter breakage detection in milling and find that the technique is reliable even under changing machining conditions. Luo et al. (2002) published results of a TCMS using wavelet analysis of vibration signals. In this case, the wavelet is used as a filter to enhance wear-sensitive features in the signals. However, the results are not compared with conventional digital filtering. A comparative study between wavelets and digital filtering for tool wear monitoring was carried out by Scheffer (2002). It was found that, although the wavelet packets act as automated filters, a very similar (if not better) result could be achieved with appropriate digital filtering. The use of wavelets increase the complexity of the TCMS, which is a disadvantage for shop-floor implementations. Furthermore, the results from digital filtering can be physically related to the machining operation and tool wear, whereas the behavior of wavelet packets is more difficult to interpret.

Another method of time–frequency analysis that can be applied for TCM is spectrograms (e.g., the Gabor distribution). Spectrograms are very useful to identify stationarity in dynamic signals, and for detection of disturbances that may be time-localized in signals. The use of the Choi–Williams time–frequency distribution for TCM during multimilling is described by James and Tzeng (2000).

Wear-sensitive regions on the time–frequency distribution are calculated and used as inputs to a NN for wear classification. An example of a change in the dominant chip curl frequency during hard turning is shown in Figure 26.17. It is obvious that, due to some disturbance (perhaps tool wear), the dominant dynamic force frequency “jumps” from 27 to 9 Hz.

26.4.2 Feature Selection

Various authors attempt to generate features that are sensitive to tool wear but insensitive to changing machining parameters. For most operations, the machining parameters can be included in the wear model and hence the sensitivity of the features is not such an important issue. There are also other techniques to normalize sensor data with respect to machining parameters, for instance the use of a theoretical model (Sick, 1998). This is very useful if the machining conditions change so often that not enough data can be collected for training or calibrating a model. Numerous techniques exist to select the most wear-sensitive features or to reduce the input feature matrix to a lower dimension. The main techniques for feature selection and reduction are listed below:

- Principal component analysis (PCA)
- Statistical overlap factor (SOF)
- Genetic algorithm (GA)
- Partial least squares (PLS)
- Automatic relevance determination (ARD)
- Analysis of variance (ANOVA)
- Correlation coefficient
- Simulation error calculations

Al-Habaibeh et al. (2000) presented a TCMS for a parallel kinematics machine tool for high-speed milling of titanium. An interesting approach to feature selection is employed, called self-learning automated sensors and signal processing selection (ASPS). This approach is based on an on-line self-learning methodology, whereby a certain feature will be selected automatically based on a correlation with tool wear. A linear regression is performed on each feature in the sensory feature matrix to detect the sensitivity of each feature with respect to tool wear. A very interesting cost analysis is then performed to determine if the installation of a sensor justifies its costs.

Ruiz et al. (1993) proposed the use of a discrimination power for feature selection in a TCM application. The method is similar to that of the SOF. An automated version is proposed that also checks for linear correlation between features. It is difficult to assess the success rate of the automated procedure because the experiments/simulations are not described in enough detail. Lee et al. (1998) describe the use of ANOVA to determine the best force ratio for TCM statistically. Several ratios between the three main cutting forces are computed and the influence of controllable parameters (e.g., machining conditions) on these ratios are investigated by means of ANOVA.

Du (1999) describes the use of a blackboard system, which is a knowledge-based approach for feature selection and decision-making. An advantage is the fact that a physical interpretation of a feature can be linked to phenomena in the machining operation. The method is also flexible, but suffers from the disadvantage of requiring a large quantity of data and expertise to establish the knowledge-based rules.

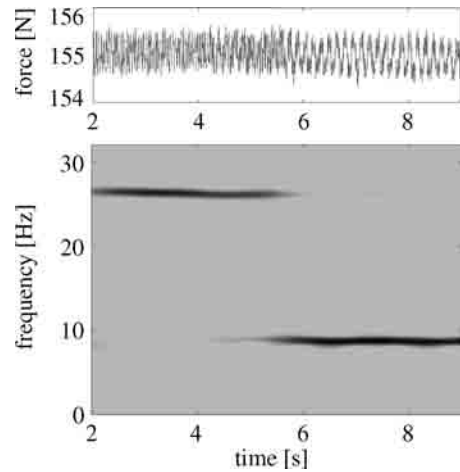


FIGURE 26.17 Time-frequency distribution of cutting force signal. (Source: Scheffer, et al., *Int. J. Mach. Tools Manuf.*, Elsevier, 2003. With permission.)

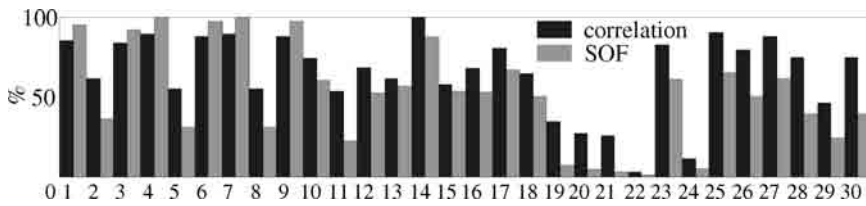


FIGURE 26.18 Comparison of correlation coefficient and SOF for feature selection. (Source: Scheffer, C. and Heyns, P.S., *Mech. Syst. Signal Process*, Elsevier, 2004. With permission.)

Mdlazi et al. (2003) compared the performance of ARD and PCA for feature selection for two damage detection case studies. It was found that the performance of the methods is similar, but one might perform better on a particular data set. Generally speaking, the PCA yields better results for damage detection problems. Scheffer and Heyns (2002b) compared several feature selection methods for TCM, such as SOF, PCA, GA, ANOVA, and the linear correlation coefficient. It was found that the correlation coefficient approach and the SOF should be preferred for TCM applications. PCA could also be of assistance, but the feasibility of PCA for on-line applications is still questionable. The correlation coefficient and SOF is expressed as percentages in Figure 26.18 (from Scheffer and Heyns, 2004) for 30 different wear monitoring features in a turning tool wear case study. Ideally, a feature with a high level of correlation and SOF should be selected.

As a last step, engineering judgment is required for proper feature selection because automated methods will often select features that are dependant on one another, thus not achieving the goals of sensor fusion. The following rules can be used as a guideline for selecting features for TCM:

- Select features from the static and dynamic parts of force signals.
- Select features measured in different directions.
- Use time- and frequency-domain features.
- Features based on simple signal processing methods are preferred.
- There should be a reasonable physical explanation for the behavior of a feature with respect to tool wear.

26.5 Wear Model/Decision-Making for Sensor-Based Tool Condition Monitoring

26.5.1 Trending, Threshold

A very simple decision-making technique is to trend features and to establish threshold values. When a certain feature or set of features crosses a threshold value, an estimation of the tool condition can be made. Unfortunately, these threshold values can only be determined experimentally. The difficulty with this method is to determine the correct threshold value, especially under diverse cutting conditions. Furthermore, the method is extremely sensitive to disturbances. The trend of the mean feed force with increasing flank wear is shown in Figure 26.19, and two thresholds are shown as examples. It is clear that this technique is not very reliable due to the large variance in the trend.

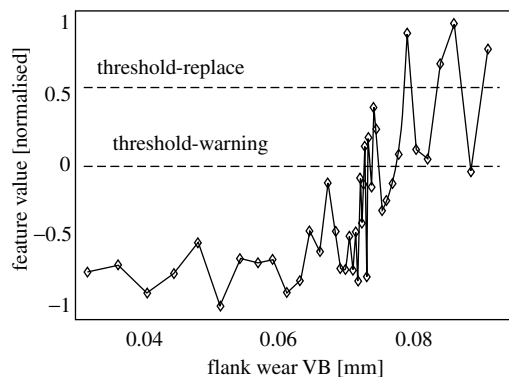


FIGURE 26.19 Example of trend and thresholds.

26.5.2 Neural Networks

The use of NNs as a secondary, more sophisticated signal processing and decision-making technique is often found in TCM applications. The simultaneous utilization of many features and the robustness towards distorted sensor signals are two of the most attractive properties of NNs. Neural networks also assist in the fusion of sensor information for TCM. In other words, combining features from acceleration, AE, and force signals in a NN can result in a method that can predict the tool condition with increased accuracy (Silva et al., 1998). The successful implementation of NNs is dependent on the proper selection of the network structure, as well as the use of the correct training and testing methods.

It is important to make a distinction between supervised and unsupervised NN paradigms. Unsupervised NNs are trained with input data only, and are usually used for discrete classification of different stages of tool wear. Supervised NNs are trained with input and output data, and these are used for continuous estimations of tool wear. Furthermore, a distinction should be made between dynamic and static NNs. In the case of dynamic NNs, temporal (time) information is included in the network with the aim to model a time series. This can be done explicitly by using a time-based feature as an input to the network, or implicitly by using recurrent networks or networks with tapped delay lines (TDLs). Dynamic networks are preferred for TCM because tool wear is time-dependent (tool wear is a monotonically increasing parameter that is partly a function of machining time).

26.5.2.1 Unsupervised Networks

There are two basic network paradigms for unsupervised classifications, namely adaptive resonance theory (ART) and the self-organizing map (SOM). ART is based on competitive learning, addressing the stability–plasticity dilemma of NNs. The main advantage is its ability to adapt to changing conditions. ART networks also have self-stability and self-organization capabilities. The SOM is actually a data-mining method used to cluster multidimensional data automatically. A high-dimensional feature matrix can be displayed on a two-dimensional grid of neurons that are arranged in clusters with similar feature values. Clusters for new and worn tools can be formed, and these are used for automatic classification of the tool condition. A SOM is depicted schematically in Figure 26.20.

There are many practical advantages for using unsupervised networks. One is the fact that the machining operation is not interrupted for tool wear measurements during the training phase. There is also the advantage of practical implementation if machining conditions change very often and appropriate training samples for supervised learning cannot be collected. Furthermore, the numerous different combinations of tool and workpiece materials and geometries can make supervised learning impossible. Normally, unsupervised NNs are used to identify discrete wear classes and cannot be used for a continuous estimation of tool wear.

Silva et al. (2000) investigated the adaptability of the SOM and ART for tool wear monitoring during turning with changing machining conditions. It was found that, with appropriate training, the methods have enough adaptive capabilities to be employed in industrial applications. Govekar and Grabec (1994) use the SOM for drill wear classification, where the SOM is used as a kind of empirical modeler. It was found that the adaptability of the SOM and its ability to handle noisy data makes the technique viable for on-line TCM. Scheffer and Heyns (2000b, 2001b) showed how a TCMS can be adaptable using SOMs. Different network sizes were compared with define discrete classes of new and worn tools. Larger networks yielded more continuous results. The TCMS using SOMs was applied to monitoring synthetic diamond tools for an industrial turning operation. It was found that the SOM can be used for industrial applications, especially if tool wear measurements are not available.

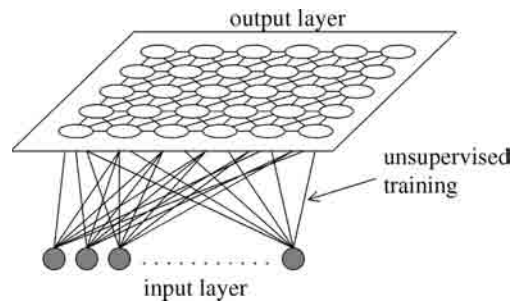


FIGURE 26.20 Schematic representation of the SOM.

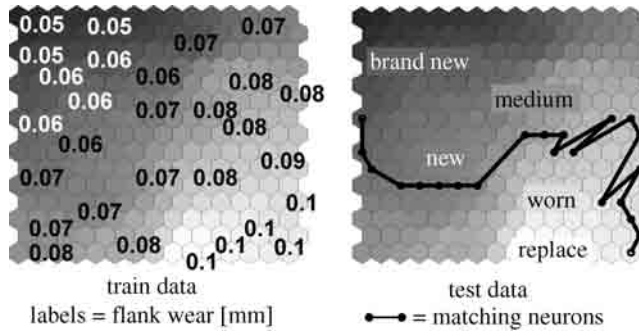


FIGURE 26.21 Unsupervised approach to wear monitoring with the SOM. (Source: Scheffer, C. and Heyns, P.S., *South African Inst. Tribol.* 2002. With permission.)

Different NN paradigms were compared on a wear monitoring application for aluminum turning by Scheffer and Heyns (2002b). It was shown that the SOM is useful to identify discrete wear classes, as shown in Figure 26.21. If an exact value of the tool wear is required, supervised networks will yield better results but will require proper training samples.

26.5.2.2 Supervised Networks

Common supervised NNs used for TCM are the multilayer perceptron (MLP), multilayer feedforward (FF) network, recurrent neural network (RNN), supervised neuro-fuzzy system (NFS-S), time delay neural network (TDNN), single layer perceptron (SLP) and the radial basis function (RBF) network. The use of an SLP for TCM is described by Dimla et al. (1996), using the perceptron learning rule for training. The SLP is useful to identify discrete classes of the tool condition. FF networks are usually trained with the backpropagation algorithm. However, backpropagation should not always be the preferred choice because other methods are known that outperform this technique in terms of training time and generalization. The size of the hidden layers in multilayer networks should be optimized for performance. Many contradictory statements about the use of MLP networks can be found in the literature. One of the main problems is the selection of the number of input features, size of the network, and the number of training examples that should be used.

A multilayer feedforward (FF) network is shown schematically in Figure 26.22. Normally, a nonlinear activation function should be used in the first layer, and linear neurons in the subsequent layers. In the case of the FF networks, the backpropagation algorithm is often used for training. Backpropagation is an optimization algorithm based on steepest gradient descent.

The use of FF networks with the backpropagation training rule is reported by authors such as Zhou et al. (1995), Das et al. (1996), and Zawada-Tomkiewicz (2001). Cutting conditions can also be included in such networks. Lou and Lin (1997) describe the use of a FF network using a Kalman filter to avoid the training problems encountered with backpropagation for a TCM application. The proposed method is less sensitive to the network initializations that often cause convergence problems with backpropagation.

Monitoring a dynamic system such as a cutting process should be done with a dynamic modeling technique such as dynamic NN paradigms, for example, recurrent networks, TDNNs, or explicit

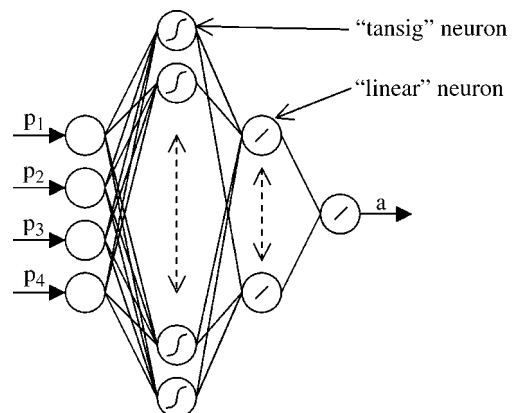


FIGURE 26.22 Multilayer FF network.

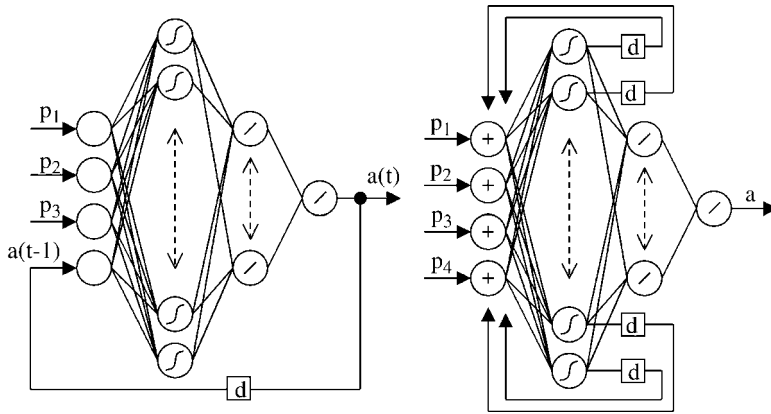


FIGURE 26.23 Recurrent networks: feedback connection (left) and Elman network (right). (Source: Scheffer, C. and Heyns, P.S., *South African Inst. Tribol.* 2002. With permission.)

inclusion of temporal information in static networks. Recurrent NNs have feedback connections from their output to their input. There are various types of recurrent NNs that are useful for specific applications. Elman networks are quite interesting. Generally, they are two-layer networks with feedbacks from the first layer output to the first layer input. This type of network can be used to learn and model temporal patterns. A recurrent network and an Elman network are shown schematically in Figure 26.23.

Liu and Altintas (1999) report on the use of a FF network using a combination of TDLs and recurrent connections. Machining conditions are also included. It is stated that the system was integrated into an industrial TCMS, but was never put to use due to lack of "... robust, practical cutting force sensors ...". (Liu and Altintas 1999). Scheffer and Heyns (2002b) report on the use of an Elman NN for TCM. It was found that the Elman network has a very smooth response and yielded better results than static NN paradigms. It should be mentioned that the Elman network requires more time for training, but because this is done off-line, training time should not be a criterion for evaluating NNs.

Neuro-fuzzy systems (NFS-S) attempts to combine the learning ability of NNs with the interpretation ability of fuzzy logic. A TCMS using an NFS-S can be generated almost automatically because the fuzzy rules can be learned by the NN. A combination of supervised and unsupervised training is used for NFS-S. An in-process NFS-S system to monitor tool breakage was designed and implemented successfully by Chen and Black (1997), concentrating on end milling operations. Xiaoli et al. (1997) as well as Chungchoo and Saini (2002) also propose some of the advantages of using an NFS-S for TCM.

RBF networks are often preferred because of the convergence properties of the training algorithm. In essence, convergence can be guaranteed and is often achieved much faster than in MLPs. The accuracy of RBFs depends on the choice of the centers for the basis functions, and should be treated with care. Pai et al. (2001) reported on the use of a resource allocation network (RAN) for TCM. The RAN is a RBF network utilizing sequential learning. The RAN is compared with the MLP for wear estimation during face milling. It was found that the RAN has faster learning ability but the MLP is more robust.

TDNNs have delay elements in the feedforward connections, called TDLs. One advantage of TDNNs over RNNs is that stability problems are avoided. An investigation towards the inclusion of one and two phase delays for a TCM application was reported by Venkatesh et al. (1997). Different network sizes were also investigated, and it was found that the NNs with temporal memory generally perform better than those without memory. It is also stated that new algorithms should be investigated for training. Sick and Sicheneder (1997) also describe the use of TDNNs for TCM in turning. The TDNN is compared with the MLP and a significant improvement was found when using

TDNNs. In another instance, Sick et al. (1998) compare the SOM, NFS-S, and MLP networks for wear estimation. The following critical questions are used to evaluate the different NN paradigms (Sick et al., 1998):

- Are the generalization capabilities of the NN sufficient (tested on previously unseen data)?
- What rate of correct classification can be achieved for different wear stages?
- Are the results repeatable (e.g., with a new initialization)?

In the case study presented by Sick et al. (1998), the best results were found with MLPs. It is stated, however, that the results can be improved when using TDNNs, and such results are reported in Sick (1998).

A novel combined approach is suggested by Sick (1998) to handle the effect of machining parameters. An empirical model is used to normalize the data with respect to machining parameters before the data are entered into the NN. Thus, machining parameters are not included in the NN itself. This approach solves the extrapolation limitations encountered when an NN is tested with data recorded with machining parameters it was not trained with. Although many authors test their NNs' paradigms in such a way, NNs cannot be expected to extrapolate. NNs should instead be tested with previously unseen data recorded with same machining parameters it was trained with (hence an interpolation effect). This is a problem because training and testing patterns for each condition must be supplied. However, if data can be normalized with respect to machining parameters, training is only required for the normalized condition. This was in effect achieved by Sick (1998). A difficulty still lies with establishing an appropriate model, and in many cases it will also require a large number of experimental tests. A possible solution lies in the incorporation of numerical models, for example, finite element models.

Scheffer (2002) presented another approach to tool wear monitoring of turning operations, using a combination of static and dynamic NNs. Static networks are trained off-line to model selected features from cutting forces. A dynamic NN that uses explicit temporal information is then trained on-line with the particle swarming optimization algorithm (PSOA). The training goal of the dynamic NN is to minimize the errors between the outputs of the static NNs and the on-line measurements. The method was tested on various turning operations and was also tested on an industrial shop floor. It was found that the method is more accurate and reliable than other NN paradigms and can be used with cost-effective hardware (Scheffer and Heyns 2002a, 2004). The method is depicted schematically in Figure 26.24.

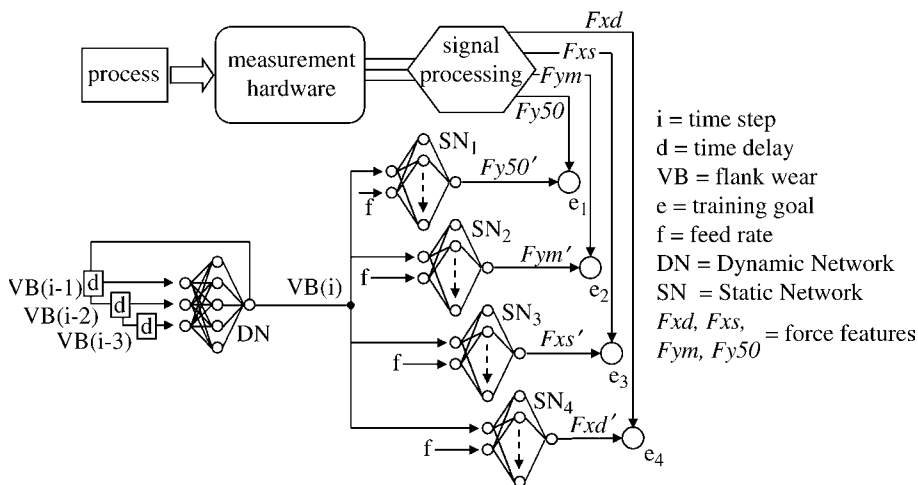


FIGURE 26.24 Combined static and dynamic NN approach for turning. (Source: Scheffer, C. and Heyns, P. S., *Mech. Syst. Signal Process*, Elsevier, 2004. With permission.)

26.5.3 Fuzzy Logic

Many authors have investigated the use of fuzzy logic to classify tool wear. It has been shown that fuzzy logic systems demonstrate great potential for use in intelligent manufacturing applications. While NN models cannot directly encode structured knowledge, it is often stated that fuzzy systems can directly encode structured knowledge in a numerical framework. Additionally, fuzzy systems are capable of estimating functions of a system with only a partial description of the system's behavior.

Du et al. (2002) propose a very interesting method called transition fuzzy probability, which was applied to a boring operation. This formulation can deal with the uncertainty of process conditions. The method performs well because TCM has two uncertainties: that of occurrence and that of appearance. The transition fuzzy probability solves this issue through the use of temporal information, similar to dynamic NNs. The method was shown to outperform a backpropagation NN, although very few details are given. It would be interesting to compare this method with dynamic NNs such as TDNNs.

Fu et al. (1997) combined force, vibration, and AE in a fuzzy classifier for TCM during milling. Time- and frequency-domain features were used, and it was found that combining the sensory information achieved the best result. This is done within the fuzzy classifier. Li and Elbestawi (1996) and Kuo and Cohen (1998) combine fuzzy modeling steps with NNs at different levels for TCM. The latter combined force, vibration and AE in a multisensor approach with satisfactory results.

26.5.4 Other Methods

There are also a number of other decision-making and modeling methods that have been applied to TCM, and these include:

- Knowledge-based expert systems (Du, 1999)
- Pattern recognition algorithms (Kumar et al., 1997)
- Dempster–Shafer theory of evidence (Beynon et al., 2000)
- Hidden Markov models (Ertunc and Loparo, 2001; Ertunc et al., 2001)

Of these four approaches, only hidden Markov models have the potential possibly to outperform NNs and fuzzy systems. However, not enough comparable research has been conducted in this area, and is it certainly a worthwhile topic for future research.

26.6 Conclusion

Techniques for achieving TCM with vibration-based properties were presented in this chapter. The sensing methods that have proved to be effective for TCM are force, acceleration, and AE. The sensors employed must comply with certain requirements such as robustness and cost-effectiveness. Sensors must be installed as close as possible to the point of metal removal in order to avoid signal-to-noise ratio problems. Various techniques exist to condition and process the signals in analogue and digital formats. The aim of signal processing is to generate wear sensitive features from the vibration signals. This could be done by time, frequency, joint time–frequency, and statistical analysis. Feature selection can be automated with a variety of procedures, but care must be taken when using these to avoid selection of linearly dependent data.

The selected features can be used to establish a model of tool wear. Numerous research papers have shown that NNs should be used due to the many advantages of NN modeling. The training and testing procedures of NNs are of utmost importance if the system is considered for industrial implementation. Care must be taken not to overtrain the networks because they will lose their ability to generalize. Furthermore, NNs cannot be expected to perform well if they are tested with previously unseen machining parameters. They should also be trained with the minimum and maximum tool wear that is

expected. Future work should be directed towards incorporating numerical machining models into the wear monitoring system to normalize the data with respect to machining parameters. If this can be achieved, the amount of training data required for an effective TCMS will be reduced, which in turn will provide a better solution to TCM for the manufacturing industry.

References

- Al-Habaibeh, A., Gindy, N., and Radwan, N. 2000. An automated approach for monitoring gradual tool wear in high speed milling of titanium, pp. 371–380. In *Proceedings of the 13th International Congress on Condition Monitoring and Diagnostic Engineering Management (COMADEM 2000)*, Houston, TX, 3–8 December.
- Araujo, A.J.M.M., Wilcox, S.J., and Reuben, R.L. 2000. Sliding friction as a possible source of acoustic emission in metal cutting, pp. 381–387. In *Proceedings of the 13th International Congress on Condition Monitoring and Diagnostic Engineering Management (COMADEM 2000)*, Houston, TX, 3–8 December.
- Axinte, D.A., Belluco, W., and De Chiffre, L., Evaluation of cutting force uncertainty components in turning, *Int. J. Machine Tools Manuf.*, 41, 719–730, 2001.
- Baek, D.K., Ko, T.J., and Kim, H.S., Real time monitoring of tool breakage in a milling operation using a digital signal processor, *J. Mater. Process. Technol.*, 100, 266–272, 2000.
- Bähre, D., Müller, M., and Warnecke, G. 1997. Basic characteristics on cutting effects in correlation to dynamic effects, pp. 21–26. *1997 Technical Papers of the North American Manufacturing Research Institution of SME*.
- Barrios, L.J., Ruiz, A., Guinea, D., Ibanez, A., and Bustos, P., Experimental comparison of sensors for tool-wear monitoring on milling, *Sensors Actuators A*, 37–38, 589–595, 1993.
- Bayramoglu, M. and Düngel, Ü., A systematic investigation on the force ratios in tool condition monitoring for turning operations, *Trans. Inst. Measur. Control*, 20, 92–97, 1998.
- Beynon, M., Curry, B., and Morgan, P., The Dempster–Shafer theory of evidence: an alternative approach to multicriteria decision modelling, *Omega*, 28, 37–50, 2000.
- Bonifacio, M.E.R. and Diniz, A.E., Correlating tool wear, tool life, surface roughness and tool vibration in finish turning with coated carbide tools, *Wear*, 173, 137–144, 1994.
- Byrne, G., Dornfeld, D., Inasaki, I., Ketteler, G., König, W., and Teti, R., Tool Condition Monitoring (TCM) — The status of research and industrial application, *Ann. CIRP*, 44, 541–567, 1995.
- Chen, J.C. and Black, J.T., A Fuzzy-Nets-In-Process (FNIP) system for tool breakage monitoring in end-milling operations, *Int. J. Machine Tools Manuf.*, 37, 783–800, 1997.
- Chiou, R.Y. and Liang, S.Y., Analysis of acoustic emission in chatter vibration with tool wear effect in turning, *Int. J. Machine Tools Manuf.*, 40, 927–941, 2000.
- Choi, D., Kwon, W.T., and Chu, C.N., Real-time monitoring of tool fracture in turning using sensor fusion, *Int. J. Adv. Manuf. Technol.*, 15, 305–310, 1999.
- Chungchoo, C. and Saini, D., On-line tool wear estimation in CNC turning operations using fuzzy neural network model, *Int. J. Machine Tools Manuf.*, 42, 29–40, 2002.
- Dan, L. and Mathew, J., Tool wear and failure monitoring techniques for turning — a review, *Int. J. Machine Tools Manuf.*, 30, 579–598, 1990.
- Das, S., Chattopadhyay, A.B., and Murthy, A.S.R., Force parameters for on-line tool wear estimation: a neural network approach, *Neural Networks*, 9, 1639–1645, 1996.
- Dimla, D.E., Sensor signals for tool-wear monitoring in metal cutting operations — a review of methods, *Int. J. Machine Tools Manuf.*, 40, 1073–1098, 2000.
- Dimla, D.E. and Lister, P.M., On-line metal cutting tool condition monitoring I: force and vibration analyses, *Int. J. Machine Tools Manuf.*, 40, 739–768, 2000a.
- Dimla, D.E. and Lister, P.M., On-line metal cutting tool condition monitoring II: tool-state classification using multi-layer perceptron neural networks, *Int. J. Machine Tools Manuf.*, 40, 769–781, 2000b.

- Dimla, D.E., Lister, P.M., and Leighton, N.J. 1996. Investigation of a single-layer perceptron neural network to tool wear inception in a metal turning process, pp. 3/1–3/4. In *Proceedings of the 1997 IEEE Colloquium on Modelling and Signal Processing for Fault Diagnosis*.
- Du, R., Signal understanding and tool condition monitoring, *Eng Appl. Artif. Intell.*, 12, 585–597, 1999.
- Du, R., Liu, Y., Xu, Y., Li, X., Wong, Y.S., and Hong, G.S. 2002. Tool condition monitoring using transition fuzzy probability. In *Metal Cutting and High Speed Machining*, pp. 375–392, Kluwer Academic/Plenum Publishers, New York.
- Ertunc, H.M. and Loparo, K.A., A decision fusion algorithm for tool wear condition monitoring in drilling, *Int. J. Mach. Tools Manuf.*, 41, 1347–1362, 2001.
- Ertunc, H.M., Loparo, K.A., and Ocak, H., Tool wear condition monitoring in drilling operations using Hidden Markov Models (HMMs), *Int. J. Mach. Tools Manuf.*, 41, 1363–1384, 2001.
- Fu, P., Hope, A.D., and Javed, M.A., Fuzzy classification of milling tool wear, *Insight*, 39, 553–557, 1997.
- Govekar, E. and Grabec, I., Self-organizing neural network application to drill wear classification, *Trans. ASME: J. Eng. Ind.*, 116, 233–238, 1994.
- Govekar, E., Gradisek, J., and Grabec, I., Analysis of acoustic emission signals and monitoring of machining processes, *Ultrasonics*, 38, 598–603, 2000.
- James, L.C. and Tzeng, T., Multimilling-insert wear assessment using non-linear virtual sensor, time–frequency distribution and neural networks, *Mech. Syst. Signal Process.*, 14, 945–957, 2000.
- Jemielniak, K., Some aspects of AE application in tool condition monitoring, *Ultrasonics*, 38, 604–608, 2000.
- Jennings, A.D. and Drake, P.R., Machine tool condition monitoring using statistical quality control charts, *Int. J. Mach. Tools Manuf.*, 37, 1243–1249, 1997.
- Jiang, C.Y., Zhang, Y.Z., and Xu, H.J., In-process monitoring of tool wear stage by the frequency band energy method, *Ann. CIRP*, 36, 45–48, 1987.
- Jun, C. and Suh, S., Statistical tool breakage detection schemes based on vibration signals in NC milling, *Int. J. Mach. Tools Manuf.*, 39, 1733–1746, 1999.
- Kapoor, S.G., DeVor, R.E., and Zhu, R. 1998. Development of mechanistic models for the prediction of machining performance: Model-building methodology, pp. 109–120. In *Proceedings of the International Workshop on Modelling of Machining Operations*, Atlanta, GA, May 19.
- Kim, J., Kang, M., Ryu, B., and Ji, Y., Development of an on-line tool-life monitoring system using acoustic emission signals in gear shaping, *Int. J. Mach. Tools Manuf.*, 39, 1761–1777, 1999.
- Koizumi, T., Tsujiuchi, N., and Matsumura, Y., Diagnosis with the correlation integral in the time domain, *Mech. Syst. Signal Process.*, 14, 1003–1010, 2000.
- Kopac, J., Influence of cutting material and coating on tool quality and tool life, *J. Mater. Process. Technol.*, 78, 95–103, 1998.
- Kumar, S.A., Ravindra, H.V., and Srinivasa, Y.G., In-process tool wear monitoring through time series modeling and pattern recognition, *Int. J. Prod. Res.*, 35, 739–751, 1997.
- Kuo, R.J. and Cohen, P.H., Intelligent tool wear estimation system through artificial neural networks and fuzzy modelling, *Artif. Intell. Eng.*, 12, 229–242, 1998.
- Lago, L., Olsson, S., Hakansson, L., and Claesson, I. 2002. Design of an efficient chatter control system for turning and boring applications, pp. 4–7. In *Proceedings of the 20th International Modal Analysis Conference (IMAC XX)*, Los Angeles, CA, February.
- Lee, B.Y. and Tarng, Y.S., Milling cutter breakage detection by the discrete wavelet transform, *Mechatronics*, 9, 225–234, 1999.
- Lee, L.C., Lee, K.S., and Gan, C.S., On the correlation between dynamic cutting force and tool wear, *Int. J. Mach. Tools Manuf.*, 29, 295–303, 1989.
- Lee, J.H., Kim, D.E., and Lee, S.J., Statistical analysis of cutting force ratios for flank-wear monitoring, *J. Mater. Process. Technol.*, 74, 104–114, 1998.
- Li, X., A brief review: acoustic emission method for tool wear monitoring during turning, *Int. J. Mach. Tools Manuf.*, 42, 157–165, 2002.

- Li, S. and Elbestawi, M.A., Fuzzy clustering for automated tool condition monitoring in machining, *Mech. Syst. Signal Process.*, 10, 533–550, 1996.
- Li, X.Q., Wong, Y.S., and Nee, A.Y.C., Tool wear and chatter detection using the coherence function of two crossed accelerations, *Int. J. Mach. Tools Manuf.*, 37, 425–435, 1997.
- Liu, Q. and Altintas, Y., On-line monitoring of flank wear in turning with multilayered feed-forward neural network, *Int. J. Mach. Tools Manuf.*, 39, 1945–1959, 1999.
- Lou, K. and Lin, C., An intelligent sensor fusion system for tool monitoring on a machining centre, *Int. J. Adv. Manuf. Technol.*, 13, 556–565, 1997.
- Luo, G., Osypiw, D., and Irle, M. 2002. Tool wear monitoring by on-line vibration analysis with wavelet algorithm. In *Metal Cutting and High Speed Machining*, pp. 393–405, Kluwer Academic/Plenum Publishers, New York.
- Mdlazi, L., Marwala, T., Stander, C.J., Scheffer, C., and Heyns, P.S. 2003. The principal component analysis and automatic relevance determination for fault identification in structures. In *Proceedings of the 21st International Modal Analysis Conference (IMAC)*, Kissimmee, FL, Paper 37.
- Merchant, M.E., Mechanics of the cutting process, *J. Appl. Phys.*, 16, 318–324, 1945.
- Morimoto, Y., Ichida, Y., and Sata, R. 2000. Excitation technique by 2-axes shaker of an CNC lathe, pp. 1643–1648. In *Proceedings of the 18th International Conference on Modal Analysis*, San Antonio, TX.
- Pai, P.S., Nagabhushana, T.N., and Rao, P.K.R., Tool wear estimation using resource allocation network, *Int. J. Mach. Tools Manuf.*, 41, 673–685, 2001.
- Ruiz, A., Guinea, D., Barrios, L.J., and Betancourt, F., An empirical multi-sensor estimation of tool wear, *Mech. Syst. Signal Process.*, 7, 105–199, 1993.
- Scheffer, C. 1999. Monitoring of tool wear in turning operations using vibration measurements, Masters dissertation (MEng), Department of Mechanical and Aeronautical Engineering, University of Pretoria, South Africa.
- Scheffer, C. 2002. Development of a tool wear monitoring system for turning using artificial intelligence, Ph.D. thesis, Department of Mechanical and Aeronautical Engineering, University of Pretoria, South Africa.
- Scheffer, C. and Heyns, P.S. 2000a. Synthetic diamond tool wear monitoring using vibration measurements, pp. 245–251. In *Proceedings of the 18th International Modal Analysis Conference*, San Antonio, TX, 7–10 February.
- Scheffer, C. and Heyns, P.S. 2000b. Development of an adaptable tool condition monitoring system, pp. 361–370. In *Proceedings of the 13th International Congress on Condition Monitoring and Diagnostic Engineering Management (COMADEM 2000)*, Houston, TX, 3–8 December.
- Scheffer, C. and Heyns, P.S. 2001a. Tool condition monitoring systems — an overview, pp. 316–323. *International Conference on Competitive Manufacturing (COMA '01)*, Stellenbosch, South Africa, 31 January–2 February.
- Scheffer, C. and Heyns, P.S., Wear monitoring in turning operations using vibration and strain measurements, *Mech. Syst. Signal Process.*, 15, 1185–1202, 2001b.
- Scheffer, C. and Heyns, P.S. 2002a. A robust and cost-effective system for conducting cutting experiments in a production environment, pp. 329–334. In *Proceedings of 3rd CIRP International Conference on Intelligent Computation in Manufacturing Engineering (ICME 2002)*, Ischia (Naples), Italy, 3–5 July.
- Scheffer, C. and Heyns, P. S. 2002b. Neural Network approaches for sensor-based tool wear monitoring, In *Proceedings of Metalworking Tools & Fluids*, South African Institute of Tribology, Johannesburg, South Africa, 7 November.
- Scheffer, C. and Heyns, P. S., An industrial tool wear monitoring system for interrupted turning, *Mech. Syst. Signal Process.*, 18, 1219–1242, 2004.
- Scheffer, C., Kratz, H., Heyns, P.S., and Klocke, F., Development of a tool wear monitoring system for hard turning, *Int. J. Mach. Tools Manuf.*, 43, 973–985, 2003.

- Sick, B., On-line tool wear monitoring in turning using neural networks, *Neural Comput. Appl.*, 7, 356–366, 1998.
- Sick, B., Online and indirect tool wear monitoring in turning with artificial neural networks: a review of more than a decade of research, *Mech. Syst. Signal Process.*, 16, 487–546, 2002.
- Sick, B. and Sicheneder, A. 1997. Time-delay neural networks for on-line tool wear classification and estimation in turning, pp. 461–466. In *Proceedings of the Third Conference on Neural Networks and Their Applications*, Kule, Poland, 14–18 October.
- Sick, B., Sicheneder, A., and Lindinger, H. 1998. A comparative evaluation of different neural network paradigms for tool wear classification in turning, pp. 139–146. In *Proceedings of the 3rd International Workshop Neural Networks in Applications (NN '98)*, University of Magdeburg, Germany, 12–13 February.
- Silva, R.J., Rueben, R.L., Baker, K.J., and Wilcox, S.J., Tool wear monitoring of turning operations by neural network and expert system classification of a feature set generated from multiple sensors, *Mech. Syst. Signal Process.*, 12, 319–332, 1998.
- Silva, R.J., Baker, K.J., Wilcox, S.J., and Reuben, R.L., The adaptability of a tool wear monitoring system under changing cutting conditions, *Mech. Syst. Signal Process.*, 14, 287–298, 2000.
- Tarmal, G.J. and Opavsky, P. 2000. Signal processing in measurement of milling forces, pp. 389–397. In *Proceedings of the 13th International Congress on Condition Monitoring and Diagnostic Engineering Management (COMADEM 2000)*, Houston, TX.
- Teti, R., A review of tool condition monitoring literature database, *Ann. CIRP*, 44, 659–667, 1995.
- Venkatesh, K., Zhou, M., and Caudill, R.J., Design of artificial neural networks for tool wear monitoring, *J. Intell. Manuf.*, 8, 215–226, 1997.
- Warnecke, G. and Siems, S. 2002. Dynamics in high speed machining. *Metal Cutting and High Speed Machining*, pp. 21–30, Kluwer Academic/Plenum Publishers, New York.
- Xiaoli, L., Yingxue, Y., and Zhejun, Y., On-line tool condition neural network with improved fuzzy neural network, *High Technol. Lett.*, 3, 30–38, 1997.
- Yao, Y., Fang, X.D., and Arndt, G., Comprehensive tool wear estimation in finish-machining via multivariate time-series analysis of 3-D cutting forces, *Ann. CIRP*, 39, 57–60, 1990.
- Zawada-Tomkiewicz, A., Classifying the wear of turning tools with neural networks, *J. Mater. Process. Technol.*, 109, 300–304, 2001.
- Zhou, Q., Hong, G.S., and Rahman, M., A new tool life criterion for tool condition monitoring using a neural network, *Eng. Appl. Artif. Intell.*, 8, 579–588, 1995.

Fault Diagnosis of Helicopter Gearboxes

27.1	Introduction	27-1
27.2	Abnormality Scaling	27-5
27.3	The Structure-Based Connectionist Network	27-8
27.4	Sensor Location Selection	27-11
	Coverage Index • Overlap Index • Monitoring Effectiveness	
27.5	A Case Study	27-14
	Structural and Feature Influences • Evaluation of Influences • Fault Detection Results • Fault Diagnostic Results • Sensor Location Evaluation • Sensor Location Validation	
27.6	Conclusion	27-23

Kourosh Danai
University of Massachusetts

Summary

An overview of fault detection and diagnosis of helicopter gearboxes is presented in this chapter. Between oil analysis and vibration monitoring, the two predominant methods of gearbox monitoring, vibration monitoring is much more studied and relied upon because of its ability to reflect a wider variety of faults. In order to cover the concepts used in vibration monitoring, a method of diagnosis is discussed that relies on the knowledge of the gearbox structure and characteristics of the features of vibration for component fault isolation. Since a necessary part of vibration monitoring is selection of accelerometer locations on the housing, a method is also described whereby the suitability of accelerometer locations is quantified based on the structure of the gearbox and the monitoring effectiveness of the locations. Finally, a case study is included to illustrate the application of the concepts presented in the chapter to fault detection and diagnosis, as well as the ranking of suites of accelerometer locations. Some topics related to this chapter are covered in [Chapter 15](#), [Chapter 25](#), and [Chapter 26](#).

27.1 Introduction

Present helicopter power trains are significant contributors to both flight safety incidents and maintenance costs. For example, for large and medium civil transport helicopters in the period 1956 to 1986, gearboxes were the principal cause of 22% of the accidents with potential loss of life and aircraft (Astridge, 1989). To prevent such incidents, routine maintenance is scheduled at a significant ratio of the total maintenance cost for the helicopter. Rapid and reliable detection and diagnosis (isolation) of faults¹ in helicopter gearboxes is therefore necessary to prevent major breakdowns due to progression of undetected faults, and for enhancing personnel safety by

¹Determining whether the overall machinery is healthy is referred to as fault detection, whereas diagnosis is analogous to isolating the source of failure.

preventing catastrophic failures. Fault detection and diagnosis is also necessary for reducing maintenance costs by eliminating the need for routine disassembly of the gearbox, and for saving time during inspection.

Detection and diagnosis of helicopter gearbox faults, like most rotating machinery, is based on oil analysis and vibration monitoring. Oil analysis, which is used to detect the presence of metallic debris, is performed by: (1) magnetic plugs (chip detectors), (2) oil filters, and (3) spectrometric oil analysis (SOA) (Lurton, 1994). Among these, magnetic plugs are the most popular because of their in-flight utility and their ability to quantify the severity of wear by measuring the rate of detected debris. However, magnetic plugs can only collect ferromagnetic particles, and their capture efficiency may be poor. Oil filters used in helicopter gearboxes range between 3 and 150 μm , with finer meshes of 3 μm more common in the recent years. SOA, which is a ground-based technique, is useful for detecting fine debris, typically below 10 μm in size, caused by wear conditions such as rubbing, cutting, and corrosion wear, and fine surface fatigue such as micropitting. Therefore, development of a reliable method of identifying common forms of fatigue such as spalling or wear that generate particles greater than 10 μm in size is of particular interest. The effectiveness of SOA is also affected by the level of filtering performed on the used oil, which often leaves the oil free of particles (Lurton, 1994). The need for improving wear detection has motivated development and use of other analysis methods such as image processing of oil filters, ferrography, thermography, and ultrasonic analysis (Thornton, 1994).

The other method of gearbox fault detection and diagnosis, and by far the more popular one, is based on vibration monitoring. The basic principle behind vibration monitoring is that, under normal operating conditions, each component in the gearbox produces vibrations at specific frequencies related to the component's rotational frequency. In the case of a component fault, the vibration generated by the faulty component is different from the normal vibration, and will be reflected at the component's rotational frequency and its harmonics. As such, monitoring the changes of vibration should theoretically give an indication of the fault. In practice, however, changes in the measured vibration as a

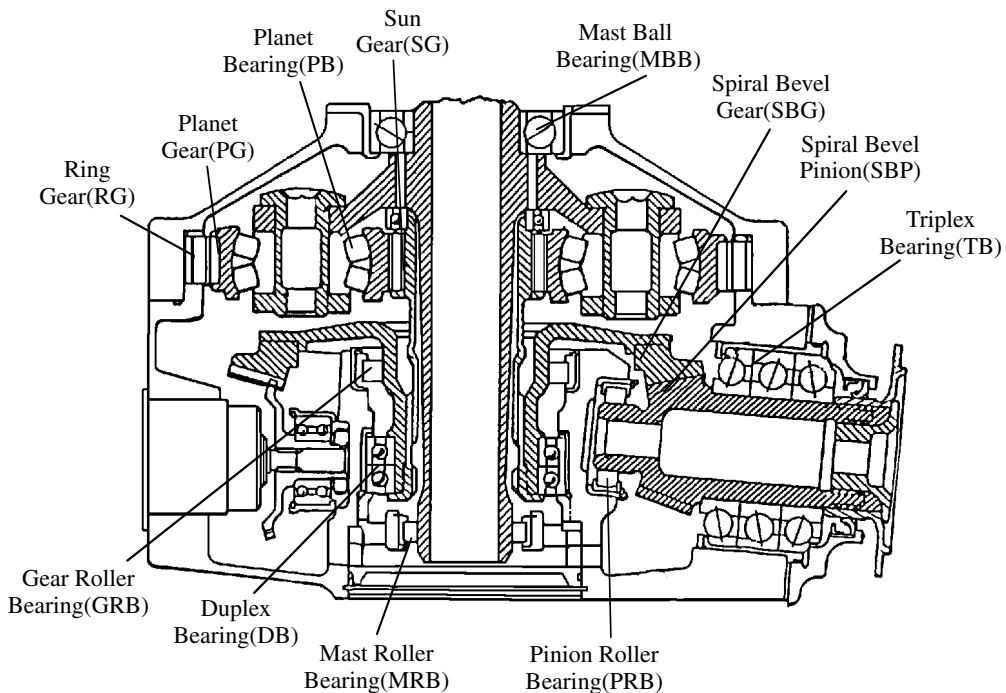


FIGURE 27.1 Layout of various components in a typical helicopter (OH-58A) gearbox.

result of component faults are not always distinct due to the attenuation of vibration by the housing and other components it travels through, as well as the noise in the signal. To provide a more tangible framework for the concepts in vibration monitoring, the layout of a typical helicopter gearbox is shown in Figure 27.1, with the location of the accelerometers on its test stand shown in Figure 27.2.

In order to enhance identification of vibration changes by component faults, the raw vibration is generally processed to obtain “features” that characterize the vibration at the frequencies associated with the gearbox components. Accordingly, the main focus of research in vibration monitoring has been the identification of individual features that consistently reflect specific gearbox faults (Dyer and Stewart, 1978; McFadden and Smith, 1986; Mertaugh, 1986; Zakrajsek et al., 1995). A typical set of vibration features obtained from each vibration measurement is shown in Figure 27.3 (Stewart Hughes Ltd., 1986). Among them, envelope band and tone energies, cepstra, and synchronous-time averaged signals, are associated with various bearing frequencies and gear mesh tones. Envelope band and tone energies, which are the sum of the harmonics of the bearings’ fundamental rolling-element frequencies within a filtered bandwidth, could be used for early detection of failure in rolling-element bearings (Barkov and Barkova, 1995). Similarly, a cepstrum, which is the power spectrum of the logarithm of a power spectrum, is often used because of its insensitivity to transmission path effects for identification of families of uniformly spaced sidebands in gearbox vibration spectra (Randall, 1982). Synchronous-time averaging is a signal processing technique that isolates the fundamental and harmonics of the gear meshing frequency, and is a primary analysis technique for detection of gear and shaft faults (McFadden and Smith, 1986).

The traditional approach to fault diagnosis has relied on human expertise to relate vibration features to faults. In this approach, a diagnostician first identifies abnormalities in vibration features, then relates them to component faults, considering both the proximity of the accelerometer producing the feature to various components and the information about the type of fault characterized by the feature. Using this information, the diagnostician hypothesizes faults in specific components and then verifies or discards the hypothesis by examining features from other accelerometers in the proximity of the suspect component. The disadvantages of this approach arise from: (1) the difficulty in identifying abnormality in features which are contaminated with noise, and (2) the tediousness of examining the numerous features obtained from all of the accelerometers. Owing to the large number of features

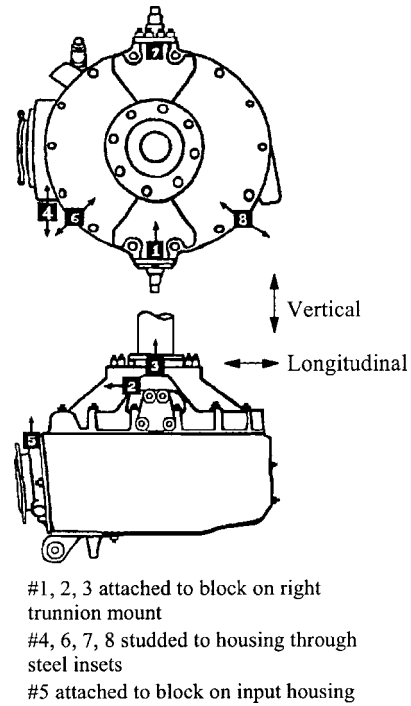


FIGURE 27.2 Location and orientation of the accelerometers on the OH-58A test stand.

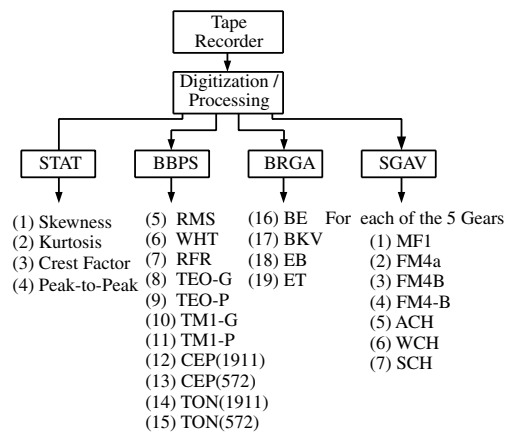


FIGURE 27.3 A typical set of vibration features extracted from each accelerometer.

associated with a gearbox², the diagnostician cannot often pay equal attention to all the features and is likely to ignore information that contradicts the hypothesis.

The most efficient method for integration of features is pattern classification. To this end, artificial neural networks have been widely investigated and shown to provide excellent results (Solorzano et al., 1991; Chin et al., 1993; Kazlas et al., 1993; Chin et al., 1995). Neural networks offer the following advantages in diagnosis: (1) as pattern classifiers, they can efficiently cope with noise in features, (2) through training, they can form the signatures of individual faults in the multidimensional space of features, and (3) they can process vibration features in parallel, so diagnosis is not hindered by the enormity of feature space. The main disadvantage of supervised neural networks, however, is their need for prior training, which requires a comprehensive set of features during normal operation and at various fault instances. While training data can be obtained experimentally through accelerated fatigue tests (Lewicki et al., 1992) or seeded fault studies (Naval Command, Control, and Ocean Surveillance Center, 1995), their cost is considered too high, limiting the utility of supervised neural networks in fault diagnosis. The lack of training data poses a similar restriction for statistical pattern classifiers which need *a priori* statistics of the features.

In the absence of training data required by supervised neural networks, the monitoring system can be formatted as in Figure 27.4 to take advantage of unsupervised pattern classification. The strategy depicted in Figure 27.4 considers fault detection independent of abnormality scaling of features, so it can be performed before or in parallel to this stage, based on the overall deviation of all of the features from their normal state. An example of abnormality scaling based on unsupervised pattern classification is described in the Section 27.2.

For fault diagnosis, the proposed system should have detailed information about the relation between the individual features and component faults. One format for providing that information is expert diagnostic software, which can be developed at two different levels. At one level, “shallow expert systems” can be developed to compile a human diagnostician’s knowledge relating measurements to faults, often as “if ...then” rules, similar to those already developed for simpler rotating machinery (Liddle and Reilly, 1993). The main obstacle in such a development will be the design of a robust inference engine that can resolve conflicting conclusions from the large pool of suspect features. At another level, “deep expert systems” can be developed to represent the diagnostic knowledge derived from the physics of the process. In deep expert systems, measurements need to be related to component faults by a model of the energy flow via the structural connections between components and sensors. A suitable format for defining the relation between components and sensors is the fuzzy set theory, which can address the approximate nature of vibration modeling. An example of a deep expert diagnostic system for helicopter gearboxes is the structure-based connectionist network (SBCN) (Jammu et al., 1998) described in Section 27.3, which takes advantage of the integration capability of neural networks while avoiding the need for supervised training. The salient feature of this connectionist network is that its weights can be determined *a priori*, based on the proximity of components to various accelerometers and the type of faults characterized by individual features. Although this system has been developed on a very approximate model of vibration flow between the gearbox components and accelerometers, it has produced promising results when used for fault diagnosis of helicopter gearboxes (Jammu et al., 1998).

A side benefit of a model of the structural connections between gearbox components and sensors is its use in sensor location selection (Wang et al., 1999). An important issue in helicopter gearbox diagnostics is the determination of the number of accelerometers to be used for monitoring and their location on the gearbox housing. Accelerometers are generally located by experts, based on their

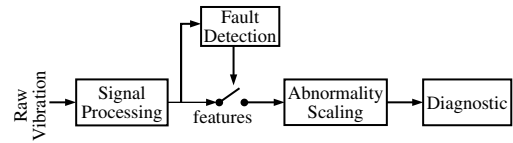


FIGURE 27.4 Generic structure of an unsupervised diagnostic system.

²The large number of frequencies (tones) associated with the various components of the gearbox necessitates a huge number of features (often in excess of a hundred) to be obtained for vibration readings from each of the several accelerometers.

proximity to gearbox components, orientation, and ease of mounting on the housing. However, this approach often leads to too many accelerometers and too high a demand for on-line monitoring on the on-board computer. Another problem with the extra accelerometers is the cost of extra mountings, cabling, and signal conditioning equipment. Sensor location selection based on a gearbox model is discussed in Section 27.4.

27.2 Abnormality Scaling

The abnormality-scaling module described here relies solely on the value of each feature during normal operation. Accordingly, it is referred to as the *single category-based classifier* (SCBC) to signify its independence from feature values associated with faulty conditions (Jammu et al., 1996). In order to perform abnormality scaling, the SCBC compares features with their normal values, and if they are sufficiently different, assigns values between zero and one to characterize their degree of deviation from their normal values. The schematic of the SCBC, which is implemented by a connectionist network, is shown in Figure 27.5. The inputs to SCBC are the raw features from signal processing, $s_i(t)$, $i = 1, \dots, n$, and its outputs are abnormality-scaled features, $f_i(t)$, with values between zero and one. The value of zero indicates normality, and the other extreme of one denotes complete abnormality. The individual weights of the SCBC network, w_i , represent the normal values of the features, which are initially set equal to the first corresponding feature value supplied to the SCBC.

Classification in the SCBC is performed by first measuring the Euclidean distance of each feature, $s_i(t)$, from its weight value, w_i , and normalizing it into the range $[0, 1]$ using a *matching factor*, ϕ_i , defined as (Figure 27.6)

$$\phi_i(t) = 1 - \exp\left(\frac{-(s_i(t) - w_i)}{w_i}\right)^2 \quad (27.1)$$

A ϕ_i value of zero indicates that the feature value matches the weight value precisely, and a value of one denotes that it deviates from it considerably. Note that the exponential function used here is not unique, and that other functions that can map the Euclidean distance into the range $[0, 1]$ can also be used for the *matching factor*. Since during normal operation of the gearbox, noise in the features usually causes them

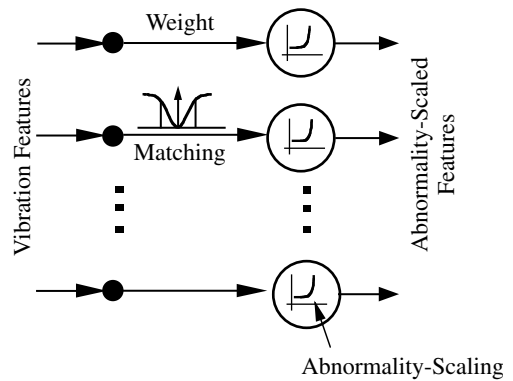


FIGURE 27.5 Schematic of the SCBC network.

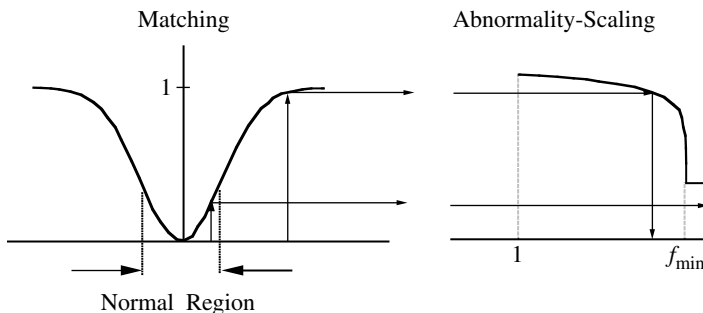


FIGURE 27.6 Matching and abnormality-scaling in SCBC.

to deviate from their normal values, a threshold, θ , is considered to account for deviations by noise. The threshold, θ , is used to hard-limit $\phi_i(t)$ in SCBC as

$$\phi_i(t) = \begin{cases} 0 & \text{(normal)} & \text{if } \phi_i(t) < \theta \\ \phi_i(t) & \text{(hard-limited)} & \text{otherwise} \end{cases} \quad (27.2)$$

In the above relationship, the threshold θ is obtained as

$$\theta = \frac{1}{n} \sum_{i=1}^n \left(1 - \exp \frac{-[\max(s_i) - \mu_i]^2}{\mu_i^2} \right) \quad (27.3)$$

where $\max(s_i)$ denotes the maximum value of the i th feature in a set of κ samples of this feature recorded during normal operation, and μ_i represents its mean, estimated as

$$\mu_i = \frac{1}{\kappa} \sum_{t=1}^{\kappa} s_i(t) \quad (27.4)$$

The matching factor, defined by Equation 27.1, suppresses any positive value in $[0, \infty]$ into the range $[0, 1]$. As such, only very large deviations in the feature values will be scaled to the value of one. Since large deviations in feature values are uncommon for gearboxes, the value of matching factor is further scaled to yield abnormality-scaled feature values $f_i(t)$ as (Figure 27.6)

$$f_i(t) = f_{\min} + \exp(\alpha * \phi_i(t)) \quad (27.5)$$

where f_{\min} represents the minimum abnormality value assigned to any feature that violates the threshold, θ , and α controls the slope of the exponential curve. Since $f_i(t)$ is defined to have a value between zero and one, it is set to one when $f_i(t)$ in Equation 27.5 exceeds the value of one.

After each round of classification of the vibration features, the weight values in the SCBC are updated so as to cope with noise and small variations in the operating conditions. Adaptation is carried out in two stages. In the first stage, called *primary adaptation*, a network weight is adapted if the feature associated with it is classified as normal. In the second stage, referred to as *contrast enhancement* (CE) (Carpenter and Grossberg, 1987), the rest of the weights are adapted to achieve homogeneity in the abnormality-scaled values, thus increasing the likelihood of all of them being classified as normal or abnormal. Homogeneity, however, needs to exist only within specific feature groups, because gearbox faults do not necessarily cause abnormality in all of the features. For example, a gear fault will be reflected only by the features related to the gear, and is not expected to cause abnormality in bearing features. In order to preserve the functionality of individual feature groups (i.e., general features, gear features, and bearing features), CE is performed exclusively for each feature group.

Adaptation in SCBC is performed as follows. Let w_I represent the weight which is presently being updated and w_i the remaining weights in the group. In *primary adaptation*, the weight value w_I is modified according to the relationship

$$w_I = w_I + \delta w_I \quad (27.6)$$

where

$$\delta w_I = \begin{cases} \eta[s_I(t) - w_I] & \text{if } f_I(t) = 0 \\ 0 & \text{otherwise} \end{cases} \quad (27.7)$$

with the parameter η denoting the learning rate.

For CE, if the majority of features are classified as normal, then the weight values associated with the features classified as abnormal will be adjusted such that the likelihood of all of the features being

classified as normal is increased for the same feature. CE is performed as

$$w_i = w_i + \delta w_i \quad \text{for all } i \neq I \quad (27.8)$$

where

$$\delta w_i = \begin{cases} \eta \Lambda[s_i(t) - w_i] & \text{if } f_i(t) = 0 \\ -\eta \Lambda[s_i(t) - w_i] & \text{otherwise} \end{cases} \quad (27.9)$$

In CE, the amount by which the weight values are adjusted is controlled by a *neighborhood function*, Λ (Kohonen, 1989), which is assigned a value between zero and one. A value of zero is used for inputs with no noise, and a value at the other extreme of one is used for unreliable features with large amounts of noise. Usually, in practice, the value of Λ is set less than 0.5. For each round of *primary adaptation* (Equation 27.6 and Equation 27.7), I is varied to include all the features in the group. If the j th group of features contains m_j features, then primary adaptation is applied by varying I from one to m_j , to cover all the weight values w_I in the j th feature group. For each I , the remaining weight values, w_i , in the group ($i = 1$ to m_j and $i \neq I$) are adapted using CE according to Equation 27.8 and Equation 27.9.

The adaptation algorithm presented in Equation 27.6 to Equation 27.9 is biased towards the most recent feature vector if only this vector were used for adaptation, whereas adaptation should be ideally performed using all of the feature vectors that pertain to the current operating conditions. However, as the number of available feature vectors for the operating condition progressively increases, adaptation based on all of the features becomes computationally demanding. As a compromise, in SCBC only the β most recent feature vectors are utilized for each adaptation sweep, such that adaptation is performed iteratively over the β most recent feature vectors. The learning rate, η , is progressively reduced for each adaptation iteration (Equation 27.7 and Equation 27.9). Abnormality scaling formulae are summarized in Table 27.1.

TABLE 27.1 Summary of the Abnormality-Scaling Formulae

Classification in the single category-based classifier is performed by first measuring the Euclidean distance of each vibration feature, $s_i(t)$, from its weight value w_i , and normalizing it into the range $[0, 1]$ using a *matching factor*, ϕ_i , defined as

$$\phi_i(t) = 1 - \exp\left(\frac{-(s_i(t) - w_i)^2}{w_i}\right)$$

The matching factor is then hard-limited by a threshold, θ , as

$$\phi_i(t) = \begin{cases} 0 & \text{(normal)} & \text{if } \phi_i(t) < \theta \\ \phi_i(t) & \text{(hard-limited)} & \text{otherwise} \end{cases}$$

In the above relationship, the threshold, θ , is obtained as

$$\theta = \frac{1}{n} \sum_{i=1}^n \left(1 - \exp\left(\frac{[\max(s_i) - \mu_i]^2}{\mu_i^2}\right)\right)$$

where $\max(s_i)$ denotes the maximum value of the i th feature in a set of κ samples of this feature, recorded during normal operation, and μ_i represents its mean, estimated as

$$\mu_i = \frac{1}{\kappa} \sum_{t=1}^{\kappa} s_i(t)$$

The vibration feature is then abnormality-scaled as

$$f_i(t) = f_{\min} + \exp(\alpha * \phi_i(t))$$

where f_{\min} represents the minimum abnormality value assigned to any feature that violates the threshold, θ , and α controls the slope of the exponential curve.

27.3 The Structure-Based Connectionist Network

The SBCN (Jammu et al., 1998) is developed to take advantage of the integration capability of neural networks, but to avoid the need for supervised training. It defines the weights of the network according to the structural knowledge of the gearbox and the type of fault represented by various vibration features. In the SBCN, the structural influences, which represent the proximity effect of faults on accelerometers, are determined based on the root-mean-square (RMS) value of the frequency response of a simplified lumped-mass model of the gearbox.

Fault diagnosis in SBCN is performed by propagating the abnormality-scaled vibration features from SCBC to produce outputs representing the fault possibility values for each gearbox component as (Figure 27.7)

$$p_k(t) = \sum_{i=1}^n f_i(t)v_{ik} \quad (27.10)$$

In the above equation, $p_k(t)$ represents the fault possibility value for the k th component of the gearbox, $f_i(t)$ denotes the abnormality-scaled value of a feature and v_{ik} represents the weighting factor determined based on the lower and upper bounds of fuzzy influence weights (l_{ik} , u_{ik}) as

$$v_{ik} = l_{ik} + (u_{ik} - l_{ik})f_i(t) \quad (27.11)$$

Note that Equation 27.10 represents propagation of inputs through the weights of the SBCN, similar to a regular connectionist network with v_{ik} as weights (Hertz et al., 1991). The difference is that the weights of the SBCN vary within the range (l_{ik} , u_{ik}) according to the magnitude of the corresponding input, $f_i(t)$. According to Equation 27.11, a higher abnormality-scaled feature value produces a higher weight value, v_{ik} , emulating the reasoning by the human expert who pays more attention to the features that exhibit higher abnormality values. In SBCN, in order to make uniform the interpretation of the fault possibility values $p_k(t)$, they are normalized to have values between zero and one as

$$c_k(t) = \frac{p_k(t)}{\sum_{i=1}^n u_{ik}} \quad (27.12)$$

Accordingly, a $c_k(t)$ equal to one denotes a definite fault, whereas a value of zero represents normality. In this system, fault diagnosis is performed hierarchically. First, the faulty subsystem within the gearbox is identified by using the structural influences as v_{ik} . Then, the faulty components within the suspect subsystem(s) are isolated using the product of structural and featural influences as v_{ik} .

The connection weights of the SBCN are defined based on the influences between the component faults and vibration features. Ideally, the structural influences should represent the strength of component vibration at the particular frequency (frequencies) represented by the feature. For this, the attenuation property of the “travel path” between each component and accelerometer needs to be modeled as a function of the moment of inertia, stiffness, and damping of the components in the path (Badgley and Hartman, 1974; Smith, 1983; Lyon, 1995). In order to appreciate the difficulties associated with vibration modeling of gearboxes, the vibration model of a simple gearbox is considered

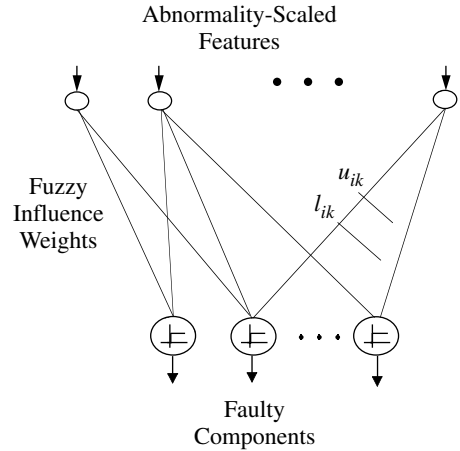


FIGURE 27.7 The structure-based connectionist network (SBCN) with its fuzzy weights for isolating faulty components.

(Choy and Qian, 1993):

$$[M][\ddot{X}] + [\dot{G}_v][\dot{X}] + [G_A][X] + [C_b][\dot{X} - \dot{X}_c] + [K_b][X - X_c] + [K_s][X - X_r] = [F(t)] + [F_G(t)] \quad (27.13)$$

where X represents the generalized displacement vectors in the lateral x , y , and z , and rotational θ_x , θ_y , and θ_z directions, M denotes the inertia matrix, G_v represents gyroscopic forces, G_A denotes the rotor angular acceleration, C_b and K_b represent the damping and stiffness matrices of bearings, respectively, $[X - X_c]$ denotes the casing vibration, $[X - X_r]$ represents the shaft residual bow, and K_s denotes the shaft bow stiffness matrix. The excitation force $[F(t)]$ is due to mass imbalance, and $[F_G(t)]$ represents the nonlinear gear mesh force, which in the x direction has the form (Choy and Qian, 1993)

$$F_{Gxk} = \sum_{i=1, i \neq k}^n K_{tki} [-R_{ci}\theta_{ci} - R_{ck}\theta_{ck} + (X_{ci} - X_{ck})\cos(\alpha_{ki}) + (Y_{ci} - Y_{ck})\sin(\alpha_{ki})][\cos(\alpha_{ki}) + \text{SIGN}(\mu)\sin(\alpha_{ki})] \quad (27.14)$$

where F_{Gxk} denotes the gear mesh force in the x direction on the $(n - 1)$ th gear due to its mesh with $(n - 1)$ other gears, K_{tki} represents the nonlinear gear mesh stiffness between the k th gear and i th gear, R_{ci} denotes the radius of the i th gear, α_{ki} represents the orientation angle between the k th and i th gears, and μ denotes the coefficient of friction. Mathematical relationships similar to Equation 27.14 can be defined to represent the force in the y direction as well as torsional gear mesh forces. Furthermore, the vibration of the casing due to the vibration of the gear–shaft system needs to be represented by a separate set of coupled equations of motion similar to Equation 27.13. The above equations need to be integrated numerically in order to estimate the vibration signal recorded on the housing, but the following difficulties exist. (1) The values of stiffness and damping coefficients for the components are not readily available. (2) The cross-coupling terms in the stiffness matrices in the x , y , and z directions cannot be easily defined (Mitchell and Davis, 1985; Choy and Qian, 1993). (3) It is difficult to take into account the multitude of travel paths and the associated models of attenuation for the many component–accelerometer pairs in the gearbox. For example, K_{tki} , the gear mesh stiffness, which is obtained by considering the gear tooth as a nonuniform cantilever beam (Lin et al., 1988; Boyd and Pike, 1989), is a function of the cross section of the tooth at the point of loading as well as load variation due to changes in the direction of load application (Mark, 1987; Lin et al., 1988; Choy and Qian, 1993), friction between the meshing teeth (Rebbechi et al., 1991), contact ratio (Cornell and Westervelt, 1978), the type of gears (spur, helical, etc.) (Mark, 1987; Lin et al., 1988; Boyd and Pike, 1989), and gear errors such as profile, transmission, and manufacturing errors (Smith, 1983; Mark, 1987). Similarly, the stiffness of bearings is a time-varying, nonlinear function of bearing displacement and the number of rolling elements in the load zone, as well as the bearing type (roller, ball, etc.), axial preload, clearance, and race waviness (Harris, 1966; While, 1979; Walford and Stone, 1983). All these factors make it very difficult to obtain an accurate and computationally inexpensive vibration attenuation model for gearboxes.

In order to avoid the difficulties associated with accurate modeling of vibration transfer, a simplified method is described here that accounts separately for the two main aspects of vibration change by faulty components: (1) the proximity effect of the faulty component on the accelerometer generating the feature (structural influence), and (2) the frequency related information represented by the feature (featural influence). The main simplification in this method is in the definition of structural influences as the average strength of the vibration signal across all frequencies measured by an accelerometer due to a component fault. To compute this average vibration, several simplifications have been adopted:

1. A lumped-mass model of the gearbox is used to model vibration.
2. Only the average static values for the stiffness coefficients are used, to cope with the absence of accurate values for stiffness coefficients.
3. Damping ratios of bearings and shafts are neglected (Lin et al., 1988).
4. A damping ratio of 0.1 is used for all the gears as an approximation to actual gear ratios estimated between 0.03 and 0.17 (Kasuba and Evans, 1981).

5. The cross-coupling terms in the stiffness matrix are neglected.
6. Only the shortest vibration travel path between each component–accelerometer pair is considered.

Using the above simplifications, the average vibration registered by an accelerometer due to a faulty i th component can be simulated by applying an excitation source y at the i th component in the lumped-mass model (Figure 27.8). In order to represent all frequencies in the excitation source, y can be selected to consist of unit amplitude sine waves of all frequencies. The displacement of various components in the travel path due to an excitation exerted at the i th component can be obtained for a typical N -mass path as (James et al., 1994)

$$\begin{bmatrix} a_{11} & a_{12} & 0 & \cdots & 0 \\ a_{21} & a_{22} & a_{23} & \cdots & 0 \\ \vdots & \vdots & \vdots & \cdots & \vdots \\ 0 & \cdots & 0 & a_{N-1,N-1} & a_{NN} \end{bmatrix} \begin{bmatrix} x_1 \\ x_2 \\ \vdots \\ x_N \end{bmatrix} = \begin{bmatrix} y \\ 0 \\ \vdots \\ 0 \end{bmatrix} \quad (27.15)$$

where $[x_1, x_2, \dots, x_N]^T$ represent the displacements of the N components in the path, y denotes the magnitude of excitation at the first component, and the coefficients a_{ij} are defined as

$$\begin{aligned} a_{nn-1} &= -j\omega c_{n-1} - k_{n-1} & a_{nn} &= -m_n \omega^2 + j\omega(c_{n-1} + c_n) + (k_{n-1} + k_n) \\ a_{nn+1} &= -j\omega c_n - k_n \end{aligned} \quad (27.16)$$

In the above equation, m_n denotes the mass of the n th component, k_n and c_n represent the stiffness and damping coefficients between the n th and $(n+1)$ th components, respectively, and ω denotes frequency.

In SBCN, the average vibration representing the overall vibration transferred from the component to the accelerometer is characterized by the RMS value of vibration across all frequencies. RMS values of vibration are readily obtained from Equation 27.15 by numerical integration of the square of displacements across all frequencies. In these calculations, to avoid unnecessary numerical problems at the natural frequencies of the components with negligible damping, the integration is carried out excluding the natural frequencies.

For the purpose of assigning structural influences, the RMS values are scaled so that the component directly adjacent to the accelerometer has the highest influence. Different functions can be used for defining the influences. For example, I_i can be defined as

$$I_i = \frac{\log(r_i)}{\log(r_N)} \quad (27.17)$$

where r_i represents the RMS value of vibration with the excitation source at the i th component, and r_N denotes the RMS value when the excitation is at the N th component. In both cases, the accelerometer is considered at the N th component. The influence for the other components is obtained in a similar fashion, by moving the excitation source to them in the travel path.

The RMS values, r_i , are only approximate estimates due to the simplifications made for their computation. Such approximate RMS values would, in turn, result in approximate influences. To

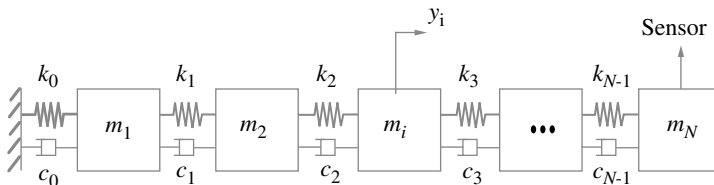


FIGURE 27.8 Illustration of the lumped-mass model of a vibration travel path consisting of N masses.

characterize the approximate nature of influences, they can be defined as fuzzy variables (Zadeh, 1975) by mapping the influences into the range associated with fuzzy variables, such as *nil*: (0, 0.1), *low*: (0.1, 0.4), *medium*: (0.4, 0.6), *high*: (0.6, 0.9) and *definite*: (0.9, 1).

Another body of knowledge commonly used by diagnosticians is that of the type of fault represented by a feature. To incorporate this knowledge, fuzzy featural influences can be defined according to the relation between the frequency content of each feature and the rotational frequencies of various components (McFadden and Smith, 1986; Stewart Hughes Ltd., 1986). For example, a feature such as envelope band energy (BE), which represents the energy at the bearings rotational frequencies and harmonics, is assigned a featural influence of “high” in relation to bearing faults.

The SBCN is designed to provide fault possibility values for gearbox components without any prior training. However, its design does not preclude the possibility of training when confronted with misclassifications, which are in the form of undetected faults, false alarms, and misdiagnoses. Among these, undetected faults are safety hazards that should be avoided at all costs, and false alarms and misdiagnoses, although not as crucial as undetected faults, should be minimized so as to improve the reliability of the diagnostic system. One of the features of the SBCN is its ability to benefit from connectionist learning (Hertz et al., 1991) to improve diagnostic performance after each misdiagnosis. For this purpose, an error-minimizing adaptation algorithm can be considered for adapting the fuzzy influence weights of SBCN so as to avoid reoccurrence of misdiagnosis. This algorithm reduces the error between the outputs of the SBCN $c_k(t)$ and the binary target $T_k(t)$ obtained after inspection. The binary target takes the value of zero for all the normal components and one for the faulty components. Sequential update rules for adapting the fuzzy influences in SBCN have the form

$$l_{ik} = \begin{cases} l_{ik} + \eta_3(T_k(t) - c_k(t))(1 - f_i(t))f_i(t) & \text{if } 0 < l_{ik} < 1 \\ l_{ik} & \text{otherwise} \end{cases} \quad (27.18)$$

$$u_{ik} = \begin{cases} u_{ik} + \eta_3(T_k(t) - c_k(t))f_i(t)^2 & \text{if } 0 < u_{ik} < 1 \\ u_{ik} & \text{otherwise} \end{cases} \quad (27.19)$$

where η_3 represents the learning rate. In this method, in order to allow uniform interpretation of the trained fuzzy influences with respect to their original values, adaptation is stopped when the weight values reach the bound of zero or one.

27.4 Sensor Location Selection

Suitable mounting locations for accelerometers on the housing are generally those that provide both close proximity to gearbox components and ease of mounting (also see Chapter 15). However, considering that only a limited number of accelerometers can be used, the candidate locations need to be selected so as to provide a comprehensive coverage of the components. The method presented here relies on indices to quantify the suitability of various mounting locations. It uses a *coverage index* to define the reach of each accelerometer, and an *overlap index* to represent the overlap of the locations in coverage of the gearbox components. The monitoring effectiveness of various combinations of accelerometer locations can then be estimated as a function of the coverage and overlap indices of the accelerometer locations (Wang et al., 1999).

27.4.1 Coverage Index

The coverage index denotes the reach of each accelerometer in monitoring various components of the gearbox. It can be computed based on an influence matrix such as that defined in the SBCN. It can be defined, for example, as the sum of the corresponding row of the influence matrix, as

$$C_j = \frac{1}{N} \sum_{i=1}^N \frac{u_{ij} + l_{ij}}{2} \quad (27.20)$$

where u_{ij} and l_{ij} represent the upper and lower limits, respectively, of the fuzzy influence coefficients between the gearbox component, i , and accelerometer, j , and N denotes the total number of gearbox components. According to this index, an accelerometer location with a higher coverage index should be considered a better candidate.

27.4.2 Overlap Index

The coverage index can be used to rank accelerometers individually. However, for a complex gearbox where more than one accelerometer is needed for monitoring, the sum of the coverage indices associated with all of the accelerometers in the suite will not provide a correct representation of their overall effectiveness because it will ignore the overlap among them.

Although the overlap between accelerometer pairs may be defined according to the influence coefficients, that definition will only consider the distance of the accelerometers from the components, and will ignore factors such as accelerometer orientation and gearbox size. In order to consider these other factors, the overlap index may be defined independent of the influence coefficients, based on an overlap matrix that represents the level of cocoverage between all of the accelerometer pairs. The individual components O_{jk} in this matrix can be defined as

$$O_{jk} = \frac{E_{jk}}{e^{aD_{jk}}}(1 + S_{jk}) \quad (27.21)$$

where O_{jk} denotes the overlap between the accelerometers, j and k , E_{jk} represents the similarity of orientation between the two accelerometers, a denotes a constant to account for the size of the gearbox, D_{jk} accounts for the physical distance between the two accelerometers, and S_{jk} represents a symmetry factor between the two accelerometers. The formulation of Equation 27.21 is based on the following understanding. The overlap in coverage of two accelerometers depends mainly on their orientation and location, that is, the more identical their orientation is and the closer they are mounted to each other, the higher is their expected level of overlap. In the above equation, the orientation factor, $E_{jk} \in [0, 1]$, is set to one when the accelerometers, j and k , have identical orientation. The distance factor, $D_{jk} \in [0, 1]$, is defined as the normalized shortest geometrical distance between the two accelerometers along the casing, where the term $e^{aD_{jk}}$ approximates the attenuation of vibration due to distance (Lindsay, 1960) and the constant a , with values ranging between zero and two, accounts for the effect of gearbox size on vibration attenuation. Although the main factors in the coverage overlap of two accelerometers are orientation and distance, the accelerometers that are symmetrically positioned are believed to have a larger overlap with each other. In order to account for this factor, a symmetry factor, $S_{jk} \in [0, 1]$, is also included in Equation 27.21, which is set to one when two accelerometers are perfectly symmetrical with respect to the housing. Based on Equation 27.21, the values of O_{jk} would ordinarily fall in the range $[0, 1]$, where the value of one indicates that the two accelerometers, j and k , have 100% overlap with each other and that one of them can be removed. Similarly, when O_{jk} is zero then the two accelerometers are assumed to be covering completely different components. It should be noted, of course, that some overlap between accelerometers is considered useful and is often factored in when selecting accelerometer locations.

The overlap coefficients only represent the level of overlap between pairs of accelerometers and not the specific components covered jointly by each accelerometer pair. As such, defining the level of overlap between several accelerometers is not as straightforward. At one extreme, one can assume that the coverage overlap of each accelerometer pair in the suite does not coincide with the coverage overlap of the other accelerometer pairs, so the total overlap, O_s , for the accelerometer suite can be computed as

$$O_s = \sum_{j=1}^m \min \left(\sum_{k=j+1}^m O_{jk} \frac{C_j + C_k}{2}, C_j \right) \quad (27.22)$$

where m denotes the number of accelerometers in the suite, and the min function ensures that the computed overlap will not exceed the total coverage of accelerometer j . At the other extreme, it can

be assumed that the overlaps of all of the accelerometer pairs coincide, and that the total overlap of the accelerometer suite can be defined as

$$O_s = \sum_{j=1}^m \max \left(O_{jk} \frac{C_j + C_k}{2} \text{ for all } k > j \right) \quad (27.23)$$

The latter formulation only considers the largest overlap between accelerometer j and the other accelerometers in the suite. It is also possible to use the average of the above two extremes as a compromise:

$$O_s = \sum_{j=1}^m \frac{1}{2} \left[\left(\min \left(\sum_{k=j+1}^m O_{jk} \frac{C_j + C_k}{2}, C_j \right) + \left(\max \left(O_{jk} \frac{C_j + C_k}{2} \text{ for all } k > j \right) \right) \right) \right] \quad (27.24)$$

It should be noted that, unlike the coverage index, the overlap index is suite related because the overlap of an accelerometer depends on the other accelerometers in the suite.

27.4.3 Monitoring Effectiveness

As mentioned earlier, the coverage index can be used to evaluate the effectiveness of individual accelerometers in monitoring, but its sum cannot be a sole measure of effectiveness of suites of accelerometers. For instance, a suite consisting of the top three accelerometer locations in terms of coverage may be inferior to another suite of three accelerometer locations with a lower total level of coverage but less overlap among the accelerometers. The best set of accelerometer locations is, therefore, one which provides the highest coverage of the gearbox components and the least overlap among the accelerometers. As such, the monitoring effectiveness (ME) of a suite can be expressed as

$$ME_s = \left(\sum_{j=1}^m C_j \right) - O_s \quad (27.25)$$

where m represents the number of accelerometers in the suite, C_i denotes the coverage of individual accelerometers in the suite, and O_s represents the total overlap among the accelerometers in the suite (Equation 27.24), estimated from Equation 27.22, Equation 27.23, or Equation 27.24. The indices used in sensor location are summarized in Table 27.2.

TABLE 27.2 Summary of Indices Used for Sensor Location Selection

Sensor location is performed according to the following indices:

Coverage index

$$C_j = \frac{1}{N} \sum_{i=1}^N \frac{u_{ij} + l_{ij}}{2}$$

where u_{ij} and l_{ij} represent the upper and lower limits of the fuzzy influence coefficients between the gearbox component, I , and accelerometer, j , and N denotes the total number of gearbox components.

Overlap index

$$O_{jk} = \frac{E_{jk}}{e^{aD_{jk}}} (1 + S_{jk})$$

where O_{jk} denotes the overlap between the accelerometers, j and k , E_{jk} represents the similarity of orientation between the two accelerometers, a denotes a constant to account for the size of the gearbox, D_{jk} accounts for the physical distance between the two accelerometers, and S_{jk} represents a symmetry factor between the two accelerometers.

According to the above indices, the monitoring effectiveness of an accelerometer suite is defined as

$$ME_s = \left(\sum_{j=1}^m C_j \right) - O_s$$

where m represents the number of accelerometers in the suite, C_j denotes the coverage of individual accelerometers in the suite and O_s represents the total overlap among the accelerometers in the suite.

27.5 A Case Study

This case study illustrates the application of the SBCN to an OH-58A main rotor gearbox (Figure 27.1; Jammu et al., 1996). Experimental vibration data for the OH-58A gearbox were collected at the NASA Lewis Research Center as part of a joint NASA/Navy/Army advanced lubricants program (Lewicki et al., 1992). Various component failures in the OH-58A transmission were produced during accelerated fatigue tests. The vibration signals were recorded by eight piezoelectric accelerometers (frequency range of up to 10 kHz) using an FM tape recorder. The signals were recorded once every hour, for about 1 to 2 min per recording (using a bandwidth of 20 kHz). Two magnetic chip detectors were also used to detect the debris caused by component failures. The location and orientation of the accelerometers are shown in Figure 27.2. The OH-58A gearbox was run under a constant load, and was disassembled and inspected periodically or when one of the chip detectors indicated a failure. A total of eleven failures occurred during these tests. They consisted of three cases of planet bearing pitting fatigue, three cases of sun gear pitting fatigue, two cases of top housing cover cracking, and one case each of spiral bevel pinion (SBP) pitting fatigue, mast bearing micropitting, and planet gear pitting fatigue.

In order to extract the vibration features, the vibration signals from the gearbox were digitized and processed by a commercially available signal analyzer (Stewart Hughes Ltd., 1986). Overall, 54 vibration features were extracted from each accelerometer for the OH-58A gearbox. Out of these features, 35 features were gear-related features (7 for each of the five gears). The remaining 19 features were indicators of either general faults (e.g., wear and out-of-balance), or general gear and bearing faults.

27.5.1 Structural and Featural Influences

The structural influences for the OH-58A gearbox were obtained through five primary vibration travel paths: (1) duplex bearing-spiral bevel mesh-triplex bearing, (2) duplex bearing-sun-planet mesh-ring gear, (3) mast roller bearing-main shaft-mast ball bearing, (4) ring gear-planet bearing-mast ball bearing, and (5) duplex bearing-sun planet mesh-mast ball bearing. The first travel path was in connection to accelerometers 4, 5, and 6, whereas all the other paths were connected to accelerometers 1, 2, 3, 6, 7, and 8. The RMS values of vibration were then computed using the lumped-mass model of these paths with excitation sources at each of the gearbox components. These RMS values were then used as the basis for defining the fuzzy structural influences between each component–accelerometer pair (Table 27.3).

The structural influences in Table 27.3 indicate that all of the components in the gearbox are covered by the accelerometers, and that some accelerometers have identical influences with respect to the components. Although these influences are not completely accurate due to their neglect of the orientation of accelerometers and various approximations (Jammu et al., 1998), they can still be used for

TABLE 27.3 Structural Influences between the Components of the OH-58A Gearbox and the Eight Accelerometers

Component/Accelerator	1	2	3	4	5	6	7	8
Triples bearing	—	—	—	H	H	—	—	—
Spiral bevel pinion	—	—	—	H	H	—	—	—
Pinion roller bearing	—	—	—	H	H	—	—	—
Spiral bevel gear	—	—	—	H	H	—	—	—
Duplex bearing	M	M	M	H	H	M	M	M
Gear roller bearing	M	M	M	H	H	M	M	M
Mast roller bearing	M	M	M	—	—	M	M	M
Main shaft	M	M	M	—	—	M	M	M
Mast ball bearing	M	M	M	—	—	M	M	M
Sun gear	H	H	H	L	M	H	H	H
Planet bearing	H	H	H	L	M	H	H	H
Planet gear	H	H	H	L	M	H	H	H
Ring gear	H	H	H	L	M	H	H	H

The influences shown are: “—” nil, “L” low, “M” medium, and “H” high.

an overall assessment of the effectiveness of various accelerometers and their redundancy. For example, the influences in Table 27.3 are identical for accelerometers 1, 2, 3, 6, 7, and 8. This would indicate that one or more of these accelerometers can be discarded without any drastic effect on fault diagnostic effectiveness. However, it should be noted that the strategy used in SBCN relies on the averaging effect of accelerometers, and that it will not function without a certain level of overlap in accelerometer coverage.

The featural influences were defined for individual vibration features according to the type of fault they are supposed to represent. For example, bearing-related features such as envelope band and tone energy were assigned high in association with gearbox bearings. Similarly, the signal averaged features for the five gears in the OH-58A gearbox were assigned high with respect to these gears. Features that are indicators of faults in all rotating elements in the gearbox were assigned an influence of medium for gears as well as bearings.

The structural and featural influences constitute the basis of the SBCN connection weights. As discussed in Jammu et al. (1998), diagnosis in SBCN is performed hierarchically, first isolating the faulty subsystems and then faulty components. As such, only the average of the structural influences associated with each subsystem is used as the connection weights, v_{ik} , of SBCN to yield the fault possibility values, $p_k(t)$, associated with each subsystem, according to Jammu et al. (1998):

$$p_k(t) = \sum_{i=1}^n f_i(t)v_{ik} \quad (27.26)$$

In subsystem diagnosis, $f_i(t)$ denotes the average abnormality-scaled value of general features. In the second stage of fault diagnosis, at the component level, the combination of structural and featural influences are used as v_{ik} , and $f_i(t)$ consist of individual abnormality-scaled features.

27.5.2 Evaluation of Influences

As explained in Jammu et al. (1998), the structural influences representing the proximity effect of component faults on accelerometer readings were obtained from the RMS value of the frequency response of the lumped-mass model of the gearbox. In this case, however, the actual RMS values of the vibration were available at several fault instances for the OH-58A gearbox, which could also be used to yield a set of experimentally obtained structural influences. In order to evaluate the modeled influences, a comparison between these two sets of structural influences was conducted. The experimental influences were obtained by normalizing the experimental RMS values when a faulty component had been detected and using them as the basis for assigning the level of fuzzy influences (Table 27.4). The results in Table 27.4 indicate mixed agreement between experimental and structural influences. For example, the structural influences of sun gear, planet bearing, and planet gear on accelerometers 1, 2, and 3 are close to the experimentally obtained influences, but the influence of mast ball bearing on accelerometers 2 and 3

TABLE 27.4 Influences between Accelerometers and Gearbox Components Obtained from Experimental RMS Values of Vibration for the OH-58A Gearbox

Accelerator/Parts	Influences from RMS Values of Vibration				
	Spiral Bevel Pinion	Mast Ball Bearing	Sun Gear	Planet Bearing	Planet Gear
1	— (—)	— (—)	H (H)	M (H)	M (H)
2	M (—)	— (H)	M (H)	M (H)	M (M)
3	M (—)	— (H)	M (H)	H (H)	M (M)
4	L (H)	— (—)	H (L)	— (—)	M (—)
5	H (H)	— (—)	H (M)	H (M)	— (M)
6	L (—)	— (—)	L (H)	M (H)	L (H)
7	— (—)	— (—)	H (H)	M (H)	L (H)
8	— (—)	— (—)	M (H)	M (H)	M (H)

For comparison, the influences from the lumped-mass model are shown inside parentheses.

TABLE 27.5 Normalized Weight Values of the Supervised Connectionist Network

Accelerator	Subsystem		
	1	2	3
1	* (–)	* (M)	* (H)
2	* (–)	H (M)	H (H)
3	* (–)	* (M)	L (H)
4	H (H)	* (–)	* (L)
5	M (H)	* (–)	H (M)
6	M (M)	* (M)	H (H)
7	M (–)	L (M)	H (H)
8	* (–)	H (M)	M (H)

For comparison, the subsystem influences of the SBCN are included inside parentheses. A “*” indicates a negative weight value.

do not match. In this case, the mismatch between the two sets of influences may be due to (1) the limitation of the RMS value in reflecting the change in vibration as a result of various component faults (e.g., mast ball bearing micropitting), (2) variation in the level of change of the RMS values as a function of the type and size of the fault, and (3) lack of faults in every component of the OH-58A gearbox, which limits the ability to determine the influences for every gearbox component.

Defining influences based on an approximate model of the gearbox was motivated by the need to avoid supervised training of the SBCN. However, given that experimental data were available for the OH-58A gearbox, an evaluation of the structural influences could be performed by comparing them with the weights of a connectionist network structurally similar to SBCN, but trained by supervised learning. For this purpose, the OH-58A gearbox was divided into three subsystems (Figure 27.1), and the supervised network, having three output units for the three subsystems and eight input units for the eight accelerometers, was trained using least-mean-square (LMS) learning. The weights of this network were trained until the number of false alarms and misdiagnoses were reduced to zero. The trained weights were then normalized and converted into fuzzy variables for comparison with the structural influences obtained from the lumped-mass model of the gearbox. Table 27.5 includes the influences of the two networks, where the modeled influences (inside parentheses) represent the average of component influences within each subsystem (Table 27.3). The results in Table 27.3 indicate general agreement between the trained weights and modeled influences. Some of the trained weights had negative values (indicated by “*”), which is inevitable due to the use of LMS learning. However, all of these negative weights were quite small in magnitude, which makes them consistent with their modeled nil counterparts (denoted by “–”). As in the case of influences from the RMS values (Table 27.4), some of the mismatches in Table 27.5 are expected to be due to the limited number of faults represented in the experimental data. For example, the considerably different influence of subsystem 2 on accelerometer 1, or subsystem 3 on accelerometer 1, is attributed to the lack of specific faults in these subsystems that would lead to a more accurate influence on accelerometer 1.

The comparison between the modeled structural influences and those obtained from the supervised neural network indicates that the modeled influences are in good agreement with the trained influences, and that the lumped-mass modeling used here provides an acceptable set of structural influences for the SBCN.

27.5.3 Fault Detection Results

The fault detection network (FDN) in the proposed diagnostic system (Figure 27.4) is used first to identify the presence of faults in the gearbox. Fault diagnosis is then performed when the presence of a fault is prompted. A total of eight FDNs, one for each of the eight OH-58A accelerometers, were used. The inputs to each FDN were the 19 general features not specific to any particular gear or bearing. The initial weight

TABLE 27.6 Fault Detection Results for the OH-58A Gearbox

Day	Fault Detection Network: Predicted and Actual Failures				
	Test 1	Test 2	Test 3	Test 4	Test 5
1	— (—)	— (—)	— (—)	— (—)	— (—)
2	— (—)	— (—)	— (—)	— (—)	— (—)
3	— (—)	— (—)	1 (1)	— (—)	— (—)
4	— (—)	— (—)	1 (1*)	— (—)	— (—)
5	1 (1)	— (—)	— (—)	— (—)	— (—)
6	— (1)	— (—)	— (—)	— (—)	— (—)
7	1 (1)	— (—)	— (—)	— (—)	— (—)
8	1 (1)	— (—)	— (—)	— (—)	— (1)
9	— (1*)	— (—)	— (1*)	— (—)	1 (1)
10			— (—)	1 (1)	— (1)
11			1 (1)	1 (1)	— (1*)
12			1 (1)	1 (1*)	
13			— (1*)	1 (—)	
14				1 (1)	
15				1 (1*)	

A “—” indicates normality and a “1” represents the presence of a fault. For reference, the expected faults determined by an expert are included inside the parentheses, with “*” indicating actual observation of the fault.

values of the FDNs were set as the values of the first set of features for each of the five tests, and were subsequently adapted using 50 adaptation sweeps for each training batch. The occurrence of a fault was prompted when any of the FDNs indicated a fault. The detection results for individual test sets obtained from the FDNs are shown in Table 27.6. A “—” in this table indicates normal conditions, whereas a “1” indicates the presence of a fault. The expected detection results are indicated inside parentheses. The results for test 1 indicate that the presence of faults was detected on days 5, 7, and 8, while faults were expected to be present from days 5 to 9. Of course, it should be noted that the gearbox was not inspected on a daily basis, so the actual condition of the gearbox is unknown for each day of the tests. In test 1, which was run for nine days, a fault was actually observed only on day 9 during a routine inspection of the gearbox (indicated by 1*). However, based on an inspection of the vibration features, it was estimated that the fault could have been present as early as day 5. For the other tests, the days when the faults were actually observed are also indicated by 1*. While it is discouraging to note that day 6 of test 1 was classified as normal though a fault was present on day 5, the results are in agreement with observations by experts who believe that sometimes increased noise levels immediately after the occurrence of faults mask the effect of faults on vibration features. For the other tests, the results indicate that except for an undetected fault in test 3 and a false alarm in test 4, excellent fault detection was obtained. It should also be noted that the fault on day 9 of test 3 was a hairline crack, which was perhaps undetectable through vibration monitoring. The quality of fault detection in the proposed system is particularly important to the overall diagnostic results, since it is only after a fault is detected that SBCN is engaged in diagnosis.

In summary, the detection results obtained (Table 27.6) indicate that the occurrences of most of the faults were identified. This provides assurance that the later stage of diagnostics would not be hampered by the detection phase.

27.5.4 Fault Diagnostic Results

In the proposed system, fault diagnosis is performed by the SBCN only after the presence of a fault is detected. In this system, fault diagnosis is performed in two hierarchies so as to take full advantage of the separation of the structural and featural influences. In the first hierarchy the gearbox is divided into subsystems (Figure 27.1) and the faults in individual subsystems are isolated by the SBCN based on the structural influences alone. For each subsystem, the weights of the SBCN are set equal to the average of the structural influences of the components within that subsystem (Table 27.5). The inputs to the SBCN

for this stage of the diagnosis consist of the averaged values of abnormality-scaled features from each accelerometer, and its outputs are the fault possibility values for each subsystem. In the second hierarchy, the faulty components within each subsystem are isolated. The inputs to the SBCN for this stage of the diagnosis are the abnormality-scaled vibration features, and the weights are the product of featural influences and structural influences of the subsystem containing each component. The averaging of fuzzy influences here was done by taking the average of upper bounds and lower bounds of individual influences separately, and then defining the fuzzy variable that would match the range. The product of fuzzy influences was determined by multiplying the upper bounds and lower bounds of fuzzy variables separately, and then defining the fuzzy variable for the resultant range.

27.5.4.1 Faulty Subsystem Isolation

The fault possibility values for the three subsystems of the OH-58A gearbox are shown in Table 27.7. The results in this table represent the hard-limited fault possibility values (threshold of 0.5) and include, for comparison, the actual condition of the gearbox reported from routine inspection inside parentheses. As before, a “*” indicates actual observation of the fault during inspection of the gearbox. The results in Table 27.7 indicate that in test 1, faults in subsystems 1 and 3 were correctly identified on days 5, 7, and 8. In test 3, the faults in subsystem 3 on days 3 and 4 were correctly identified, along with a possible fault in subsystem 1. The housing crack on day 9 of this test was left unidentified because it was never prompted during the detection phase. In any case, this particular fault (a housing crack) could not be isolated by the current SBCN due to absence of features that reflect this fault. Also for this test, faults in subsystems 2 and 3 were correctly identified on days 11 and 12. In Test 4, the fault in subsystem 3 was correctly diagnosed on days 10, 11, 12, 14, and 15. Moreover, on day 13 of test 4, even though the gearbox was supposed to be normal, the SBCN indicated faults in subsystem 3. This was due to the replacement of the three-planet assembly with a four-planet assembly, which changed the vibration characteristic of subsystem 3. In test 5, the fault in subsystem 3 was correctly identified on day 9. There was also a misdiagnosis in subsystem 1.

In summary, the diagnostic results from the gearbox subsystems indicate that all of the eight subsystem faults were correctly identified in the OH-58A gearbox and that four faults were misdiagnosed. Considering that these results were obtained by using structural influences alone as the connection weights of the SBCN, the results validate the utility of these influences and of lumped-mass modeling as a means of representing the vibration travel path of gearboxes for their model-based fault diagnosis.

TABLE 27.7 Faulty Subsystem Isolation Results for the OH-58A Gearbox

Day	Faulty Subsystems Isolation for OH-58A				
	Test 1	Test 2	Test 3	Test 4	Test 5
1	— (—)	— (—)	— (—)	— (—)	— (—)
2	— (—)	— (—)	— (—)	— (—)	— (—)
3	— (—)	— (—)	1, 3 (3)	— (—)	— (—)
4	— (—)	— (—)	1, 3 (3*)	— (—)	— (—)
5	1, 3 (1, 3)	— (—)	— (—)	— (—)	— (—)
6	— (1, 3)	— (—)	— (—)	— (—)	— (—)
7	1, 3 (1, 3)	— (—)	— (—)	— (—)	— (—)
8	1, 3 (1, 3)	— (—)	— (—)	— (—)	— (3)
9	— (1*, 3*)	— (—)	— (3)	— (—)	1, 3 (3)
10			— (—)	3 (3)	— (3)
11			2, 3 (2, 3)	3 (3)	— (3*)
12			2, 3 (2, 3)	3 (3*)	
13			— (2*, 3*)	3 (—)	
14				3 (3)	
15				3 (3*)	

The three subsystems in the table are the input subsystem (1), the output subsystem (2), and the transmission subsystem (3). For comparison, the actual faults are included inside parentheses with “*” indicating the observed faults.

27.5.4.2 Faulty Component Isolation

Fault possibility values associated with the components of the OH-58A gearbox obtained from the SBCN are included in Table 27.8. The results indicate that the diagnostics associated with individual components are not as accurate as those obtained for the subsystems. Briefly, for test 1, the SBP fault in subsystem 1 and the sun gear (SG) fault in subsystem 3 were correctly identified only on days 5 and 8, respectively, while other components were assigned higher fault possibility values on other days. For test 3, the three bearing faults in subsystems 2 and 3 (BRG2 and BRG3, respectively) were correctly identified on days 3, 4, and 12, but other components were also given high fault possibility values. In test 4, the bearing fault in subsystem 3 (BRG3) was correctly identified only on day 10, while the SG fault remained misdiagnosed. In test 5, the SG fault was correctly identified on day 9, while the planet gear (PG) fault was misdiagnosed.

In view of the promising results obtained at the subsystem level, which confirm the validity of the structural influences, the cause of diagnostic inaccuracies at the component level should be attributed mainly to the deficiency of gear and bearing specific features used in this study. The strong cross-coupling

TABLE 27.8 Faulty Component Isolation by SBCN for the OH-58A Gearbox

Days	Faulty Component Isolation for OH-58A							
	SS1			SS2	SS3			
	SBP	SBG	BRG1		SG	PG	RG	BRG3
Test 1								
1–4	—	—	—	—	—	—	—	—
5	0.90*	0.62	0.89	—	0.52*	0.73	0.12	0.86
6	—*	—	—	—	—*	—	—	—
7	0.68*	0.43	0.79	—	0.67*	1.00	0.23	0.72
8	0.65*	0.74	0.18	—	0.98*	0.70	0.70	0.33
9	—	—	—	—	—	—	—	—
Test 2								
1–9	—	—	—	—	—	—	—	—
Test 3								
1 and 2	—	—	—	—	—	—	—	—
3	0.43	0.77	0.80	—	0.65	0.56	0.71	0.72*
4	0.38	0.60	0.78	—	0.56	0.47	0.04	0.79*
5–10	—	—	—	—	—	—	—	—
11	—	—	—	—	0.67	0.79	0.52	—*
12	—	—	—	0.74*	0.67	0.71	0.55	1.00*
13	—	—	—	—*	—	—	—	—*
Test 4								
1–9	—	—	—	—	—	—	—	—
10	—	—	—	—	0.34	0.41	0.75	0.79*
11	—	—	—	—	0.54	0.53	0.79	—*
12	—	—	—	—	0.59	0.50	0.91	0.64*
13	—	—	—	—	0.72	0.85	0.83	1.00
14	—	—	—	—	0.81*	0.90	0.88	0.68
15	—	—	—	—	0.79*	0.90	0.93	0.48
Test 5								
1–8	—	—	—	—	—	—	—	—
9	0.58	0.24	0.68	—	0.60*	0.54*	0.50	0.58
10 and 11	—	—	—	—	—*	—*	—	—

The components listed are SBP: spiral bevel pinion; SBG: spiral bevel gear; BRG1: bearings in subsystem (SS) 1; BRG2: bearings in SS2; SG: sun gear; PG: planet gear; RG: ring gear; and BRG3: bearings in SS3. As before, “*” indicates observation of the faulty component.

TABLE 27.9 Maximum Values of Correlation Coefficients between Features and Faults

Fault-Feature Correlation Coefficients		
Features/Faults	Gear Faults	Bearing Faults
Gear features	0.49 (1)	0.57 (0)
Bearing features	0.38 (0)	0.44 (1)

The values inside parentheses are the expected ideal values.

between these features is illustrated by the maximum values of the correlation coefficients between the gear and bearing features and gear and bearing faults in Table 27.9. The results indicate reasonable correlation values of 0.49 between the gear features and gear faults, and 0.44 between the bearing features and bearing faults. These numbers, however, are not as impressive when they are compared with the cross-correlation values of 0.57 between gear features and bearing faults, and 0.38 between bearing features and gear faults. The high cross-correlation values in Table 27.9 indicate that the gear and bearing features do not provide the resolution necessary for faulty component isolation. The manifestation of the resolution problem caused by the coupling between gear and bearing features is observed in the similar fault possibility values of 0.9 and 0.89 on day 5 of test 1, in Table 27.8, for the SBP and bearings in subsystem 1 (BRG1). Based on the results in Table 27.8, one can conclude that the unsupervised pattern classification scheme incorporated in this research cannot be a substitute for well-defined features, and that a more effective set of features with smaller cross-correlation values are needed for diagnosis at the component level.

27.5.5 Sensor Location Evaluation

The eight candidate accelerometer locations (see Figure 27.2 for their locations and orientations), which were actually used for vibration measurement during accelerated fatigue tests of the gearbox, were analyzed and ranked for their significance in monitoring. In order to obtain the overlap coefficients for the OH-58A gearbox, the values of the orientation factors, E_{jk} , distance factors, D_{jk} , and symmetry factors, S_{jk} , for the eight accelerometer locations were defined as

$$E_{jk} = \begin{bmatrix} 1 & 0.5 & 0.3 & 1 & 0.4 & 0.8 & 1 & 0.8 \\ 0.5 & 1 & 0.3 & 0.5 & 0.4 & 0.7 & 0.5 & 0.7 \\ 0.3 & 0.3 & 1 & 0.4 & 1 & 0.3 & 0.3 & 0.3 \\ 1 & 0.5 & 0.4 & 1 & 0.4 & 0.5 & 1 & 0.8 \\ 0.4 & 0.4 & 1 & 0.4 & 1 & 0.4 & 0.4 & 0.4 \\ 0.8 & 0.7 & 0.3 & 0.5 & 0.4 & 1 & 0.8 & 0.6 \\ 1 & 0.5 & 0.3 & 1 & 0.4 & 0.8 & 1 & 0.8 \\ 0.8 & 0.7 & 0.3 & 0.8 & 0.4 & 0.6 & 0.8 & 1 \end{bmatrix}, \quad aD_{jk} = \begin{bmatrix} 0 & 0 & 0 & 1.5 & 1.5 & 0.5 & 2.0 & 0.5 \\ 0 & 0 & 0 & 1.5 & 1.5 & 0.5 & 2.0 & 0.5 \\ 0 & 0 & 0 & 1.5 & 1.5 & 0.5 & 2.0 & 0.5 \\ 1.5 & 1.5 & 1.5 & 0 & 0.8 & 1.0 & 0.5 & 2.0 \\ 1.5 & 1.5 & 1.5 & 0.8 & 0 & 1.0 & 0.5 & 2.0 \\ 0.5 & 0.5 & 0.5 & 1.0 & 1.0 & 0 & 1.5 & 1.0 \\ 2.0 & 2.0 & 2.0 & 1.5 & 1.5 & 1.5 & 0 & 1.5 \\ 0.5 & 0.5 & 0.5 & 2.0 & 2.0 & 1.0 & 1.5 & 0 \end{bmatrix}$$

$$S_{jk} = \begin{bmatrix} 0 & 0 & 0 & 0 & 0 & 0 & 1 & 0 \\ 0 & 0 & 0 & 0 & 0 & 0 & 1 & 0 \\ 0 & 0 & 0 & 0 & 0 & 0 & 1 & 0 \\ 0 & 0 & 0 & 0 & 0 & 0 & 1 & 0 \\ 0 & 0 & 0 & 0 & 0 & 0 & 0 & 0 \\ 0 & 0 & 0 & 0 & 0 & 0 & 0 & 1 \\ 1 & 1 & 1 & 1 & 0 & 0 & 0 & 0.5 \\ 0 & 0 & 0 & 0 & 0 & 1 & 0.5 & 0 \end{bmatrix}$$

TABLE 27.10 Best and Worst Accelerometer Suites within Each Suite Size

Suite Size	Best Suites	Worst Suites
1 accelerometer	5	3
2 accelerometers	(5, 8); (2, 5)	(4, 7); (1, 6)
3 accelerometers	(2, 5, 7); (4, 5, 8); (2, 4, 5)	(1, 6, 8); (1, 2, 6); (1, 2, 8)
4 accelerometers	(3, 4, 5, 8); (2, 4, 5, 8); (2, 4, 5, 7)	(1, 2, 7, 8); (1, 4, 7, 8); (1, 6, 7, 8)
5 accelerometers	(2, 3, 4, 5, 8); (2, 3, 5, 7, 8); (2, 3, 5, 6, 7)	(1, 4, 6, 7, 8); (1, 2, 6, 7, 8); (1, 2, 4, 7, 8)
6 accelerometers	(1, 2, 3, 4, 5, 7); (2, 3, 4, 5, 6, 8)	(1, 2, 4, 6, 7, 8); (1, 3, 4, 6, 7, 8)
7 accelerometers	(1, 2, 3, 4, 5, 6, 8)	(1, 2, 3, 4, 6, 7, 8)

Using the above values, the overlap coefficients for the eight locations were determined from Equation 27.21 as

$$O_{jk} = \begin{bmatrix} 1 & 0.50 & 0.3 & 0.2 & 0.089 & 0.485 & 0.271 & 0.485 \\ 0.500 & 1 & 0.3 & 0.112 & 0.089 & 0.425 & 0.135 & 0.425 \\ 0.300 & 0.300 & 1 & 0.089 & 0.223 & 0.182 & 0.081 & 0.182 \\ 0.223 & 0.112 & 0.089 & 1 & 0.180 & 0.184 & 0.446 & 0.108 \\ 0.089 & 0.089 & 0.223 & 0.180 & 1 & 0.147 & 0.089 & 0.054 \\ 0.485 & 0.425 & 0.182 & 0.184 & 0.147 & 1 & 0.179 & 0.441 \\ 0.271 & 0.135 & 0.081 & 0.446 & 0.089 & 0.179 & 1 & 0.268 \\ 0.485 & 0.425 & 0.182 & 0.108 & 0.054 & 0.441 & 0.268 & 1 \end{bmatrix} \quad (27.27)$$

Given the above values of coverage and overlap, the ME values were determined from Equation 27.24 for various suites from the eight candidate accelerometer locations of the OH-58A main rotor gearbox. The ME values can be used, for example, to select the best set of accelerometer locations given a number of accelerometers to be used. A sample set of accelerometer locations with the highest and lowest rankings (from the 254 possible suites of the eight OH-58A locations) are shown in Table 27.10. Note that, for some suite sizes, several combinations of accelerometer locations are selected as the “best” and “worst” suites, because in these cases the ME values were too close to render a suite better or worse than the others.

The ME values can also be used to assess the benefit of additional accelerometers, leading to larger suite sizes. To demonstrate this utility of monitoring effectiveness, the maximum ME value for each suite size was obtained (Figure 27.9). While additional accelerometers are expected to add to monitoring effectiveness, the added coverage they provide will diminish for larger suite sizes due to the increase in overlap between the accelerometers. This is clearly reflected in Figure 27.9 where the maximum ME value of the eight-strong accelerometer suite is the same as that of the seven-strong accelerometer suite, and the suite with five accelerometers has a maximum ME value of 0.90, only 10% less than that of the suite with eight accelerometers.

27.5.6 Sensor Location Validation

The validity of the ME values was evaluated by comparing the rankings they provided for various accelerometer suites to the rankings obtained

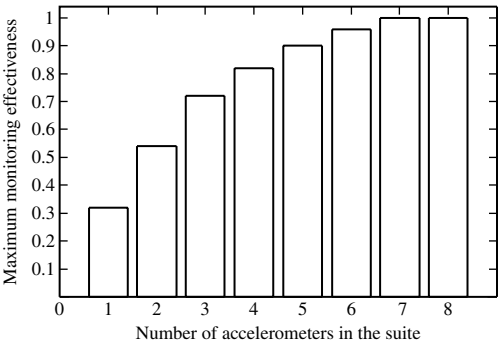


FIGURE 27.9 Maximum values of monitoring effectiveness for different accelerometer suite sizes.

empirically from a series of diagnostic tests. The suites were ranked into four evenly spaced categories. The suites with the highest monitoring effectiveness were ranked as one, and those with the lowest values were ranked into the fourth category. The empirical rankings were obtained from the SBCN according to the fault possibility values, $p_i \in (0, 1)$, of the individual gearbox subsystems (Jammu et al., 1998). For quantification purposes, a performance index, p_s , was obtained for each suite of accelerometers to represent the accuracy of the diagnostic results, as

$$p_s = \sum_{\text{faults}} p_i \quad (27.28)$$

where the summation was carried out over all the available faults that had occurred during the OH-58A experiments. Under ideal conditions and with a perfect accelerometer suite, the values of p_i should be all equal to one (i.e., the value of p_s should be equal to the number of faults). However, in practice, the fault possibility values are smaller than one due to imperfect signal conditioning, presence of noise, and so on. The understanding used here is that, everything else being the same, the value of p_s is only affected by the quality of the accelerometer suite when the vibration features from different suites are used as inputs to the diagnostic system. The value of p_s was computed for various accelerometer suites, and then normalized against the largest value of p_s obtained for the same suite size. These normalized p_s values were then used as the basis for ranking the suites. As with the monitoring effectiveness values, the suite with the highest normalized p_s value was assigned to the first category. It should also be noted that, in both cases, the rankings provide only a relative measure of effectiveness among suites of the same size, and that they should not be perceived as global measures. The normalized p_s values and the associated rankings for suites of seven accelerometers are included in Table 27.11, along with the ME values and their corresponding rankings. The results indicate remarkably close agreement between the estimated and empirical rankings and that, except for one mismatch, the rankings are identical. Similar analyses were performed for suites of other sizes. A summary of matches and mismatches for all the suites is given in Table 27.12. The results indicate that, out of the 254 possible suites, the estimated rankings of 174 suites match exactly the empirical rankings, and 103 mismatch by only one rank.

The results summarized in Table 27.12 indicate that the proposed selection method is effective in assessing the monitoring effectiveness of suites of accelerometers. The experimental data set, although one of the most complete sets available in the industry, is not comprehensive enough to render a complete evaluation of the method. The main limitation is the absence of faults in all of the components of the gearbox. This could result in an overestimation of the significance of accelerometers that cover faulty components during the experiments. Similarly, it could lead to devaluation of accelerometers which cover healthy components during the experiments. For example, there was only a single fault in subsystem 2 (mast bearing micropitting), therefore, accelerometer locations that covered this subsystem were given a lower empirical ranking than they actually deserved.

TABLE 27.11 Rankings Obtained from the Monitoring Effectiveness Values and from the Diagnostic Results for Suites of Seven Accelerometers

Accelerometers Included	Monitoring Effectiveness		Empirical	
	ME _s	Rank	p_s	Rank
2, 3, 4, 5, 6, 7, 8	0.983	1	0.888	1
1, 3, 4, 5, 6, 7, 8	0.791	2	0.702	2
1, 2, 4, 5, 6, 7, 8	0.705	2*	0.844	1
1, 2, 3, 5, 6, 7, 8	0.908	1	0.926	1
1, 2, 3, 4, 6, 7, 8	0.200	4	0.200	4
1, 2, 3, 4, 5, 7, 8	0.990	1	1.000	1
1, 2, 3, 4, 5, 6, 8	1.000	1	0.938	1
1, 2, 3, 4, 5, 6, 7	0.940	1	0.843	1

* indicates a mismatch between the rankings.

TABLE 27.12 Summary Comparison of Rankings Obtained from the Monitoring Effectiveness Values and from the Diagnostic Results for Suites of All sizes

Suites of	Match Exactly	Mismatch by		
		1	2	3
7	7	1	0	0
6	17	11	0	0
5	39	17	0	0
4	48	22	0	0
3	38	18	0	0
2	17	11	0	0
1	8	0	0	0
Total	174	80	0	0

27.6 Conclusion

Commercial fault detection systems developed for helicopter gearboxes, generally as part of a Health and Usage Monitoring System (HUMS)³, follow the traditional approach to fault detection and diagnosis. In these systems, the individual vibration signals obtained from each accelerometer are processed first to extract various features, and are then evaluated statistically or in comparison with established thresholds to identify possible abnormalities. The abnormal features are then scaled and weighted to provide a weighted average “figure of merit” that can be used for fault detection. Once a gearbox is identified as abnormal, diagnosis is performed by evaluating the synchronized time averaged features associated with individual shafts and gears — the signal average of a particular shaft contains the mounted gear meshing characteristics which can be used to determine the gear condition. In HUMS, statistical analysis is usually based on the mean and standard deviation of individual features, and thresholds are established based either on experience or according to base-lines determined from initial data points at the beginning of aircraft operation. It should be noted that the simplistic approach used by major HUMS producers for abnormality identification and fault detection and diagnosis is often due to the stringent restrictions imposed by the certification process⁴; otherwise, much development work has been conducted in the recent years that can be included in commercial systems.

A truly integrated mechanical diagnostic system should have the following characteristics: (1) be able to automatically correlate the information from various sensor suites including accelerometers, oil debris sensors, acoustic emission (AE) transducers, and so on, and to consolidate the results into a reliable solution; (2) be able to “predict” (prognose) a degrading mechanical condition based on trending of the “features” or condition indices; (3) be compatible with the maintenance policies and operational situations, (4) account for the fatigue life of the monitored components; (5) account for flight conditions (such as transmission torque) that would affect the diagnostic results; (6) be based on open systems architecture (both hardware and software) for future technology insertion; and (7) be lightweight (including cabling and sensors) such that no significant extra weight will be added to the aircraft.

Oil analysis will undoubtedly play a more critical role in fault detection and diagnosis. One logical step will be development of more reliable in-flight methods of chip detection based on optical technology and image processing (Lukas and Yurko, 1996). The chip detectors of the future are expected to benefit from the micro-electro-mechanical systems (MEMS) technology, making available microdetectors that can be

³A HUMS generally consists of structural usage monitoring, gearbox, engine, and rotor system fault detection and diagnosis, rotor track and balance, and the associated data processing and maintenance logistics.

⁴No HUMS has been certified by the FAA yet because of the relative newness of the technology and lack of data to verify it. Some HUM systems have been flying in the North Sea area, mostly manufactured by Teledyne-Stewart Hughes and GEC-Bristows, but they need to be developed further before they can be totally reliable.

located practically anywhere within the gearbox. Continued emphasis is also expected on postflight oil analysis such as ferrography, thermography, ultrasonic analysis, and passive electric current analysis (Saba 1996).

As for vibration monitoring, there will be continued need for algorithmic development to produce new features for reliable identification of component faults. In this domain, there will be more focus on acoustic monitoring and stress wave analysis. Accelerometers normally have a frequency response range of a few Hz to over 50 kHz. In acoustic monitoring, a much higher bandwidth is considered — microphones are currently available that have a flat response to over 100 kHz. This provides the possibility of measuring a cleaner signal in higher frequency ranges, which may prove useful in detecting certain bearing faults. Another advantage of microphones is that they do not need to be mounted on the surface of the housing, therefore, unlike accelerometers, they are not affected by mounting resonance. For stress wave monitoring, AE sensors are available that detect the stress waves generated by strain (elastic) energy spontaneously released by materials when they undergo deformation. This type of energy, which has a very broad bandwidth (DC to several MHz) due to the impulse nature of the strain release, propagates away from a crack tip and throughout the structure body. For crack growth monitoring, analysis is usually focused on the high frequency region (> 100 kHz) of the AE signal so that the effect of low frequency noise caused by airframe, gearbox, and/or drive shaft vibration is minimized. Stress wave monitoring through AE signals may, therefore, reveal the presence of cracks, as well as their location and severity (Teller and Kwun, 1994).

Another important area of research and development in fault diagnosis is sensor technology. A generic restriction in vibration monitoring is the limited number of mounting locations for accelerometers on the housing. This restriction, however, is expected to be alleviated with the advancement of the MEMS technology which will eventually make available miniaturized sensors that can be mounted practically anywhere on a housing, and perhaps inside it. These sensors are expected to have the added capability of processing the vibration signal and producing the features locally, so that the central processor can be dedicated solely to integration of features for fault detection and diagnosis.

References

- Astridge, D.G., Helicopter transmission — design for safety and reliability, *Proc. Inst. Mech. Engrs.*, 203, 123–138, 1989.
- Badgley, R.H. and Hartman, R.M., Gearbox noise reduction: prediction and measurement of mesh-frequency vibrations within an operating helicopter rotor-drive gearbox, *J. Engng Ind.*, May, 567–577, 1974.
- Barkov, A. and Barkova, N., Condition assessment and life prediction of rolling element bearings — parts 1 and 2, *Sound Vibr.*, June, 14–20, 1995.
- Boyd, L.S. and Pike, J., Epicyclic gear dynamics, *AIAA J.*, 27, 5, 603–609, 1989.
- Carpenter, G.A. and Grossberg, S., ART2: self-organization of stable category recognition codes for analog input patterns, *Appl. Optics*, 1987.
- Chin, H., Danai, K., and Lewicki, D.G., Pattern classifier for fault diagnosis of helicopter gearboxes, *IFAC J. Control Eng. Practice*, 1, 5, 771–778, 1993.
- Chin, H., Danai, K., and Lewicki, D.G., Fault detection of helicopter gearboxes using the multivalued influence matrix method, *ASME J. Mech. Des.*, 117, 2, 248–253, 1995.
- Choy, F.K. and Qian, W. 1993. *Global Dynamic Modeling of a Transmission System*. NASA Contractor Report 191117, ARL-CR-11. Lewis Research Center, Cleveland, OH.
- Cornell, R.W. and Westervelt, W.W., Dynamic tooth loads and stressing for high contact ratio spur gears, *J. Mech. Des.*, 100, 69–76, 1978.
- Dyer, D. and Stewart, R.M., Detection of rolling element bearing damage by statistical vibration analysis, *ASME J. Mech. Des.*, 100, 229–235, 1978.
- Harris, T.A. 1966. *Rolling Bearing Analysis*, Wiley, New York.

- Hertz, J., Krogh, A., Palmer, R.G., and Palmer, R.G. 1991. *Introduction to the Theory of Neural Computation*, Addison-Wesley, Redwood City, CA.
- James, M.L., Smith, G.M., Wolford, J.C., and Whaley, P.W. 1994. *Vibration of mechanical and structural systems*, Harper Collins College Publishers, New York.
- Jammu, V.B., Danai, K., and Lewicki, D.G., Unsupervised pattern classifier for abnormality scaling of vibration features for helicopter gearbox diagnosis, *Machine Vibr.*, 5, 3, 154–162, 1996.
- Jammu, V.B., Danai, K., and Lewicki, D.G., Structure-based connectionist network for fault diagnosis of helicopter gearboxes, *ASME J. Mech. Des.*, 120, 100–112, 1998.
- Kasuba, R. and Evans, J.W., An extended model for determining dynamic loads in spur gearing, *J. Mech. Des.*, 103, 398–409, 1981.
- Kazlas, P.T., Monsen, P.T., and LeBlanc, M.J. 1993. Neural Network-Based Helicopter Gearbox Health Monitoring System, presented at IEEE-SP Workshop on Neural Networks for Signal Processing, Linthicum, MD, September.
- Kohonen, T. 1989. *Self-Organization and Associative Memory*, Springer, Berlin.
- Lewicki, D.G., Decker, H.J., and Shimski, J.T. 1992. Full-Scale Transmission Testing to Evaluate Advanced Lubricants. Technical Report, NASA TM-105668, AVSCOM TR-91-C-035.
- Liddle, I. and Reilly, S., Automatic analysis of rotating machinery using an expert system, *Sound Vibr.*, February, 7–11, 1993.
- Lin, H.-H., Huston, R.L., and Coy, J.J., On dynamic loads in parallel shaft trans-mission: Part I — modelling and analysis, *J. Mech. Transm. Automation Des.*, 110, 221–229, 1988.
- Lindsay, R.B. 1960. *Mechanical Radiation*, McGraw-Hill, New York.
- Lukas, M. and Yurko, R.J. 1996. Current technology in oil analysis spectrometers and what we may expect in the future, pp. 161–171. *Proceedings of Integrated Monitoring Diagnostics and Failure Prevention*, Mobile, AL.
- Lurton, E.H. 1994. Navy oil analysis program overview, pp. 4–6. In *Proc. JOAP International Condition Monitoring Conference*.
- Lyon, R.H., Structural diagnostics using vibration transfer functions, *Sound Vibr.*, January, 28–31, 1995.
- Mark, W.D., Use of the generalized transmission error in equations of motion of gear systems, *J. Mech. Transm. Automation Des.*, 109, 283–291, 1987.
- McFadden, P.D. and Smith, J.D., Effect of transmission path on measured gear vibration, *J. Vibr. Acoust. Stress Reliabil. Des.*, 108, 377–378, 1986.
- Mertaugh, L.J. 1986. Evaluation of vibration analysis techniques for the detection of gear and bearing faults in helicopter gearboxes, pp. 28–30. In *Proc. of the Mechanical Failure Prevention Group 41th Meeting*, October, 1986.
- Mitchell, L.D. and Davis, J.W., Proposed solution methodology for the dynamically coupled, nonlinear geared rotor mechanics equations, *J. Vibr. Acoust. Stress Reliabil. Des.*, 107, 112–116, 1985.
- Naval Command, Control, and Ocean Surveillance Center. 1995. CH-53E Aft Main Transmission Test Stand Data Set, San Diego, CA.
- Randall, R.B., A new method of modeling gear faults, *ASME J. Mech. Des.*, 104, 259–267, 1982.
- Rebbechi, B., Oswald, F.B., and Townsend, D.P. 1991. *Dynamic measurements of gear tooth friction and load*, NASA Tech. Memorandum 103281, TR-90-C-0023. Lewis Research Center, Cleveland, OH.
- Saba, C.S. 1996. Alternate techniques for wear metal analysis, pp. 151–160. In *Proceedings of Integrated Monitoring Diagnostics and Failure Prevention*, Mobile, AL.
- Smith, J.D. 1983. *Gears and Their Vibrations*, Marcel Dekker/The Macmillan Press Ltd, Network, New York.
- Solorzano, M.R., Ishii, D.K., Nickolaissen, N.R., and Huang, W.Y. 1991. *Detection and Classification of Faults from Helicopter Vibration Data Using Recently Developed Signal Processing and Neural Network Techniques*, Code 535. Advanced Technology Development Branch, Naval Ocean Systems Center, San Diego, CA.
- Stewart Hughes Ltd. 1986. MSDA User's Guide, Technical Report, Southamton, U.K.

- Teller, C.M. and Kwun, H. 1994. Magnetostrictive sensors for structural health monitoring systems, pp. 297–305. In *Proceedings of Mechanical Failure Prevention Group 48th Meeting*, April.
- Thornton, M.G. 1994. Filter debris analysis, a viable alternative to existing spectrometric oil analysis techniques, pp. 108–119. In *Proceedings of JOAP International Condition Monitoring Conference*, 1994.
- Walford, T.L.H. and Stone, B.J. 1983. The sources of damping in rolling element bearings under oscillating conditions, pp. 225–232. In *Proceedings of the Institute of Mechanical Engineers*, Vol. 197c, December.
- Wang, K., Yang, D., Danai, K., and Lewicki, D.G., Model-based selection of accelerometer locations for helicopter gearbox monitoring, *J. Am. Helicopter Soc.*, 44, 4, 269–275, 1999.
- While, M.F., Rolling element bearing vibration transfer characteristics: effect of stiffness, *J. Appl. Mech.*, 46, 677–684, 1979.
- Zadeh, L.A., The concept of a linguistic variable and its application to approximate reasoning-1, *Inf. Sci.*, 8, 199–249, 1975.
- Zakrajsek, J.J., Hanschuh, R.F., Lewicki, D.G., and Decker, H.J. 1995. Detecting gear tooth fracture in a high contact ratio face gear mesh, pp. 91–102. In *Proceedings of 49th Meeting of the Society of Machinery Failure Prevention Technology*, April.

28

Vibration Suppression and Monitoring in Precision Motion Systems

K.K. Tan, T.H. Lee,
K.Z. Tang, and S. Huang
National University of Singapore

S.Y. Lim, W. Lin,
and Y.P. Leow
*Singapore Institute of Manufacturing
Technology*

28.1	Introduction	28-1
28.2	Mechanical Design to Minimize Vibration	28-2
	Stability and Static Determinacy of Machine Structures • Two-Dimensional Structures • Three-Dimensional Structures	
28.3	Adaptive Notch Filter	28-10
	Fast Fourier Transform • Simulation and Experiments	
28.4	Real-Time Vibration Analyzer	28-17
	Learning Mode • Monitoring Mode • Diagnostic Mode • Experiments	
28.5	Practical Insights and Case Study	28-29
28.6	Conclusions	28-35

Summary

Much research and development effort is going on to develop precision motion systems that are used in most production equipment. Market demands for better products (products with much higher performance, higher reliability, longer life, lower cost, and increasing miniaturization) are some of the main driving forces behind these efforts. There are several challenges ahead in order to meet these stringent requirements for precision motion systems. One of the main challenges is to suppress the mechanical vibrations in these motion systems. This chapter provides several possible approaches to this objective. The first approach will focus on a proper mechanical design, based on the determinacy of machine structure, to reduce the mechanical vibration in the motion systems to a minimum. In addition to a good design, a monitoring and suppression mechanism is necessary to cope with additional and usually unpredictable sources of vibration seeping in during the course of operations. An approach, utilizing an adaptive notch filter in the control system, is presented in the chapter, to continuously identify resonant frequencies present and suppress signal transmission into the system at these frequencies. Finally, the development of a low-cost real-time vibration analyzer for precision motion systems is presented. A case study is provided at the end of the chapter to illustrate the effectiveness of a remote vibration monitoring and control system for precision motion systems.

28.1 Introduction

Industrialization, propelled by advances in science and technology in the last millennium, has led to the development of mass-production equipment to satisfy man's relentless pursuit for products such as

automobiles, air-conditioners, audio and video products, and so on. Today, apart from the consumer's demand for more functionality in new product lines, a miniaturization phenomenon is also clearly evident where the physical size of the product can be smaller than its predecessor, even when it has expanded performance. In addition, the ever shortening time-to-market of products and productivity cost factors in today's highly competitive world together pose tough and challenging requirements on the manufacturing and automation systems that produce them. Thus, while high accuracy and precision in production systems are necessary to produce highly delicate parts and products, a high production speed must still be maintained even though speed and precision adversely affect each other. It is not difficult to appreciate this dilemma since a high production speed can lead to excessive mechanical vibration (Fertis, 1995; Uicker et al., 2003), which means inevitably a loss in precision (Tan et al., 2001). This chapter will seek to address the vibration issues in precision motion systems.

Different and numerous sources of vibration can be present in an industrial operating environment (Adams, 2000; Kelly, 2000). Vibration may be generated by rotating or reciprocating machineries such as: engines, motors, and compressors; impact processes such as drilling and PCB printing; the flow of fluid; and many others (Raichel, 2000). The vibration level can reach an excessive level when abnormal operating conditions occur due to unbalanced inertia, bearing failures in rotating systems such as turbines, motors, generators, pumps, drives, and turbofans, component failure and operation outside prescribed load ratings, and poor kinematical design (resulting in a nonrigid and nonisolating support structure). Vibration, whether naturally occurring or induced under abnormal conditions, is undesirable as it usually leads to dynamic stresses that, in turn, causes fatigue and deterioration of the machinery. Other adverse consequences include unnecessary energy losses, deterioration in performance, and an unduly high level of noise produced. These effects can be even more severe for high-precision motion systems with stringent requirements on precision and accuracy, since vibration will lead directly to poor repeatability properties, impeding any effort for systematic error compensation. Thus, it is even more essential that the vibration level in such systems be suppressed as far as possible with an efficient mechanical design and that functionality be included in the control to monitor and possibly adaptively reduce excessive vibration when it occurs.

This chapter provides several possible approaches to this objective. The first approach will focus on a proper mechanical design, based on the determinacy of the machine structure, to reduce the mechanical vibration to a minimum. While the system design approach is certainly a first and key step to minimizing vibration in mechanical systems, a parallel monitoring and suppression mechanism is necessary to cope with additional and usually unpredictable sources of vibration seeping in during the course of operations. An approach, utilizing an adaptive notch filter (narrow bandstop filter) in the control system, will be presented as a means of continuously identifying resonant frequencies present and suppress signal transmission into the system at these frequencies.

Finally, the development of a low-cost real-time vibration analyzer will be presented. This analyzer can be implemented independently of the control system, and as such can be applied to existing equipment without much retrofitting being necessary. A vibration signature is derived from the vibration signal acquired using an accelerometer that is attached to the machine under normal operating conditions. A pattern recognition template is used to compare real-time vibration signals against the normal-condition signature and an alarm can be activated when the difference deviates beyond an acceptable threshold. Actions of rectification can then be invoked before damage is done to the machine. A case study will be provided at the end of the chapter to illustrate the effectiveness of a remote vibration monitoring and control system for precision motion systems.

28.2 Mechanical Design to Minimize Vibration

In the development of high-speed and high-precision motion systems, the notion of determinism is a key consideration (Evan, 1989), which implies that a physical system complies with the law of cause and effect, and this behavior allows the physical system to be modeled mathematically.

The governing equations describing the model can then be used to predict the behavior of the system and thus allow for the compensation for possible errors to meet the demand of a tight error budget. A mechatronic approach, in which the structural design and the control design are to be seamlessly integrated (Rankers, 1997), is one of the possible approaches for machine design. This approach has been adopted efficiently by many scientists and engineers, and the benefits are clearly evident in the end products, such as the wafer scanner and stepper.

In this section, the key issues to address in a sound mechanical design to keep mechanical vibration to a minimum will be highlighted. The issue of mechanical design represents a very large area in precision motion systems. In this section, only key points will be highlighted in general, to enable designers to design “rigid” structures during the initial phase, even before the physical modeling stage. Design, being an iterative process, always requires the designer to revisit the drawing board frequently, until an optimum design is achieved. The section will give qualitative ideas with abundant figures to illustrate key ideas, rather than using a purely quantitative approach. The reason for this is that, during the initial phase of a design, intensive quantification is normally not necessary for decision making. Iteration and optimization, which are normally mathematically intensive, should be addressed during the next stage of the design process.

28.2.1 Stability and Static Determinacy of Machine Structures

A structure can be a supporting framework that houses all the subassemblies that make up a machine, or it can be a collection of many smaller structures, or even a single component. The reaction forces of the high-speed moving parts will excite the structural dynamics resulting in mechanical vibrations. These vibrations can be attenuated by reducing either the excitation or the response of the structure to that excitation (Beards, 1983). The first factor can be overcome by relocating the source within the structure or by isolating it from the structure so that the generated vibration is not transmitted to the structure via the supports. As for the second factor, changing the mass, the stiffness, or the damping can alter the structural response. In order to understand the dynamic responses of the structure, the real structure can be transformed into a physical model, which is usually a simplified model representative of the real structure. For example, a real machine can be modeled as a number of coupled spring–mass systems. A derived physical model of the real system can be translated to a mathematical model which can be solved via software or by hand, thereby allowing engineers from different disciplines to communicate and refine their portion of the design.

Every designer working on the structure for a machine needs to answer a very important question. Is the designed structure rigid and stable? A structure is rigid if its shape cannot be changed without deforming the members in the structure (Fleming, 1997), and a structure is stable if rigid-body translation or rotation cannot occur. A good way to tell whether a structure is stable or not is the degree of indeterminacy. A structure is considered *statically determinate* if all the support reactions and internal forces in the members can be determined solely by the equations of static equilibrium. Otherwise, the structure is considered *statically indeterminate*. Statically indeterminate structures arise owing to the presence of extra supports, members, reaction forces, or reaction moments. For a structure to be statically determinate, it must first be constructed correctly and then supported correctly.

28.2.2 Two-Dimensional Structures

Most machine structures, in practice, are three-dimensional. However, it is useful to look at a two-dimensional problem first, before extending the problem to a three-dimensional one. Generally, machine structures are stationary. Therefore, the sum of the forces and moments acting on it must be zero, which is in accordance with Newton’s Second Law. In mathematical form,

$$\sum \mathbf{F}_x = 0 \quad (28.1)$$

$$\sum F_y = 0 \quad (28.2)$$

$$\sum M_z = 0 \quad (28.3)$$

where F_x and F_y are the forces in the x -axis and y -axis, respectively, while M_z is the moment about the z -axis, where the z -axis is pointing out of the page. For a plane structure, we will make use of the sign conventions as depicted in Figure 28.1.

Since the static determinacy of a structure is a two fold issue, it is possible to proceed without considering the support first. Each structural configuration can be tested to verify if the plane structure satisfies the equation:

$$2j = m + 3 \quad (28.4)$$

where j denotes the number of joints and m denotes the number of members. There are three possible cases, as follows:

1. If $2j = m + 3$, then the structure is statically determinate.
2. If $2j > m + 3$, then the structure is unstable.
3. If $2j < m + 3$, then the structure is statically indeterminate.

The three conditions are depicted in Figure 28.2.

When a structure is unstable due to member deficiency, it appears that the structure becomes a four-bar mechanism with one degree of freedom (DoF), as shown in Figure 28.2c. This DoF is undesirable, since it is the structure that is being designed and not the mechanism. If, however, there are too many members present, the structure becomes statically indeterminate. Under such a condition, it will be difficult to assemble the fifth bar of the structure shown in Figure 28.2d, if the

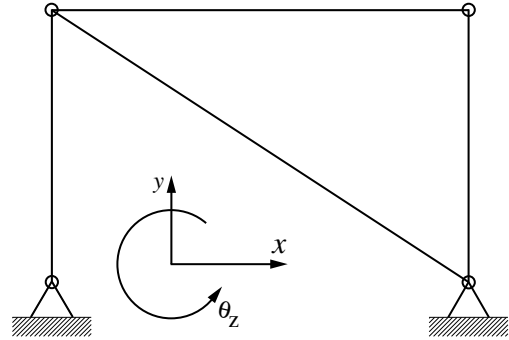


FIGURE 28.1 Sign convention for plane structure.

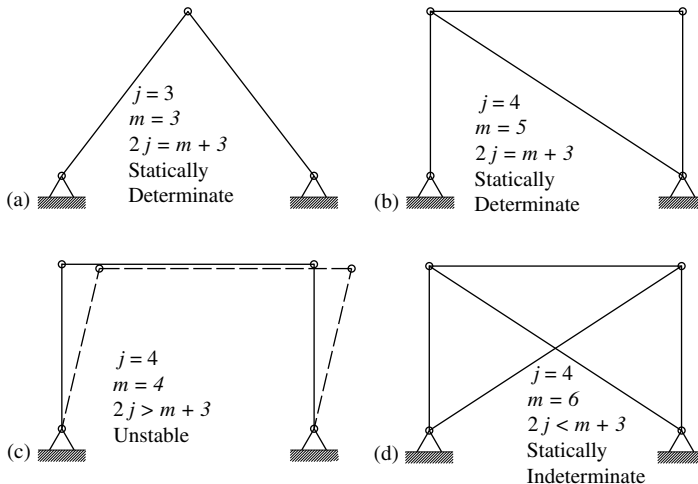


FIGURE 28.2 Plane structure: (a) and (b) statically determinate structure; (c) unstable structure; (d) statically indeterminate structure.

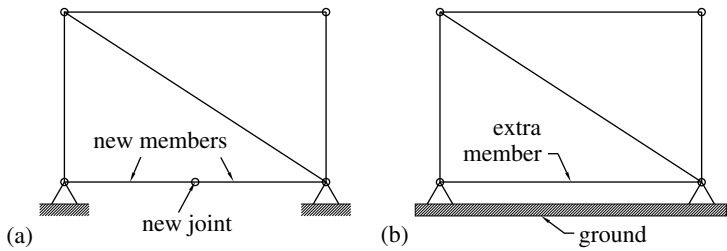


FIGURE 28.3 (a) Unstable structure; (b) extra member.

dimension of the fifth bar is not exact. Assembly is probably possible using brute force, but internal stresses will be built into the structure even without any external loading. When a structure is statically determinate, it will be stress-free when it is not loaded externally other than by its own weight. In the event of thermal expansion of its member, owing to an increase in temperature, statically determinate structures allow expansion of their members, without inducing any stress resulting from an overconstrained condition due to the redundant members.

The triangle is the basic shape for a plane structure as shown in Figure 28.2a. Statically determinate plane structure can be expanded from this basic structure, simply by linking two new members to two different existing joints for every new joint added, as shown in Figure 28.2b. However, the axis of the two new members must not form a line; in other words, the three joints must not be on the same line, as shown in Figure 28.3a. It is also noteworthy that the ground constitutes one member as well, and all joints are pin-joints, as shown in Figure 28.3b.

The second part of structure design lies in its supports. In this aspect, the whole structure can be treated as a rigid body. A plane structure has three DoF; that is, the plane structure is capable of motion in the x and y directions, and rotation about the z -axis. Therefore, three members are needed providing three reactive forces to exactly constrain the plane structure in the plane.

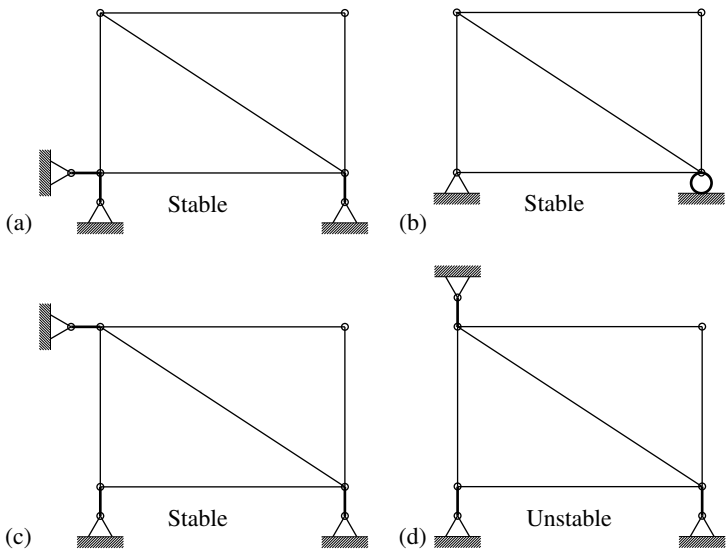


FIGURE 28.4 (a), (b), and (c) Stable and exactly constraint supports; (d) unstable support.

Figure 28.4a–c show some possible support for plane structure, while Figure 28.4d shows an unstable support scenario.

It should be highlighted that the condition of having two support members at the same location can be replaced by a single pin-joint, as shown in Figure 28.5. It is apparent that, in both cases, they constitute two reaction forces and do not constrain the angular motion about the z-axis present in the plane structure.

The correct number of members in a structure, as well as the correct number of supports, must be in place for a stable and statically determinate structure. At this juncture, the issue of where the loads are to be applied on the structure must be addressed. To this end, it is necessary to examine the members that make up the structure. The stiffness of a bar member is affected by the way the load is applied with respect to its axial axis, its cross-sectional geometry (e.g., the diameter, for a round bar) and the modulus of elasticity, E , of its material. In most cases, the bar is either loaded in tension, compression, or bending, as shown in Table 28.1.

It is apparent from examining Table 28.1 that the stiffness of a bar is much better in axial loading than in bending loading. For a value of $d = 0.05$ m and $L = 1.2$ m, the ratio of k_t/k_b is 192. That is, a bar is 192 times stiffer when loaded axially than in bending. Therefore, when designing a rigid and stiff structure, the members must be loaded in tension or compression, never in bending. At times, redesigning the way an external load is applied on a structure can greatly improve the stiffness of the structure. Various configurations are shown in Table 28.2. As a general rule to observe, the loading point should be located at the joints.

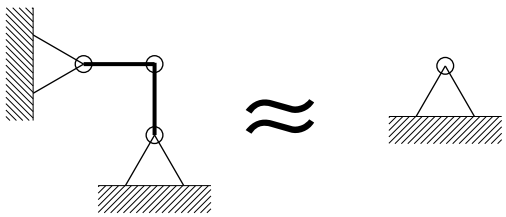


FIGURE 28.5 Equivalent of a two-member support.

28.2.3 Three-Dimensional Structures

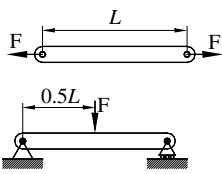
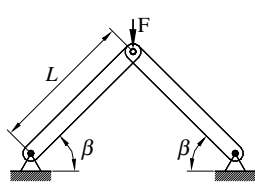
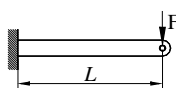
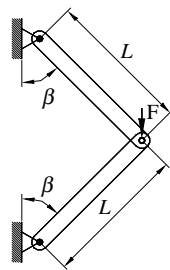
Next, space structures or three-dimensional structures will be considered. These are structures that are of interest in most applications. In a very general sense, space structures can be perceived as a combination of many plane structures, arranged in a manner that all the planes are not coplanar. Therefore, for a space structure to be rigid, every plane structure that makes up the space structure

TABLE 28.1 Comparison of Stiffness for Axial Loading versus Bending Loading

	Configurations	Loading Condition	Stiffness (N/m)	Normalized Stiffness
(a)		Tension	$k_t = 0.25\pi Ed^2/L$	1
(b)		Compression	$k_c = 0.25\pi Ed^2/L$	1
(c)		Bending	$k_b = 0.75\pi Ed^4/L^3$	$3(d/L)^2$

Units: E (N/m²), d (m), L (m), and $L \gg d$.

TABLE 28.2 Comparison of Stiffness for Various Loading Configurations

Configurations	Stiffness (N/m)	Normalized Stiffness	Compare
(a) 	$k_t = 0.25\pi Ed^2/L$	1	1
(c) 	$k_b = 0.75\pi Ed^4/L^3$	$3(d/L)^2$	1/192
(d) 	$k_\Lambda = 0.5\pi Ed^2 \sin^2 \beta/L$	$\sin^2 \beta$	1/2
(e) 	$k_{cl} = 0.047\pi Ed^4/L^3$	$0.1875(d/L)^2$	1/3072
(f)	$k_{>} = 0.25\pi Ed^2/L$	1	1

$\beta = 45^\circ, d = 0.05 \text{ m}, L = 1.2 \text{ m}.$

must be rigid in its own right. This is one reason to have a good understanding of plane structural rigidity.

Since machine structures are stationary, the sum of the forces and moments acting on the machine must be zero, which is in accordance with Newton's Second Law. Mathematically, this implies

$$\sum \mathbf{F} = 0 \tag{28.5}$$

$$\sum \mathbf{M} = 0 \tag{28.6}$$

where **F** and **M** are three-dimensional force and moment vectors, respectively. The sign conventions as depicted in Figure 28.1 will be used.

As before, each structural configuration can be tested to verify if the plane structure satisfies the equation:

$$3j = m + 6 \tag{28.7}$$

where j denotes the number of joints and m denotes the number of members. There are three possible cases, as follows:

1. If $3j = m + 6$, then the structure is statically determinate.
2. If $3j > m + 6$, then the structure is unstable.
3. If $3j < m + 6$, then the structure is statically indeterminate.

In the plane structure, the triangle is the basic shape, and is rigid and statically determinate. In a space structure, the basic form for being rigid and statically determinant is the tetrahedron, which is depicted in Figure 28.6. Adding a new noncoplanar joint to the three existing joints of a triangular plane structure derives the tetrahedron structure. This new joint is connected to the existing joints with three new members. By following this procedure, a rigid and statically determinate space structure can be derived.

Other space structures are shown in Figure 28.7 and Figure 28.8. It is also noteworthy that the members are connected with ball joints.

Thus far, the approach to obtain the tetrahedron space structure from the triangle plane structure, the pyramid from the tetrahedron, and the box from the tetrahedron has been illustrated. The next aspect of the design is to combine some of these structures. The structures can be treated as being coupled together as rigid bodies, and a rigid body in space has six DoF, i.e., the structure is capable of translations in the x , y , and z directions, and rotation about the x , y , and z axes. Therefore, six members are needed, providing six reactive forces to exactly constrain the structure in space. Figure 28.9 shows a typical gantry configuration, which is used extensively in many coordinate-measuring machines (CMM). However, one of the members is bearing a bending load, which has been shown earlier to be very detrimental to the stiffness of the structure. There are alternative structure configurations as shown in Figure 28.10 and Figure 28.11, although some redesign may be needed if such a configuration is to be utilized.

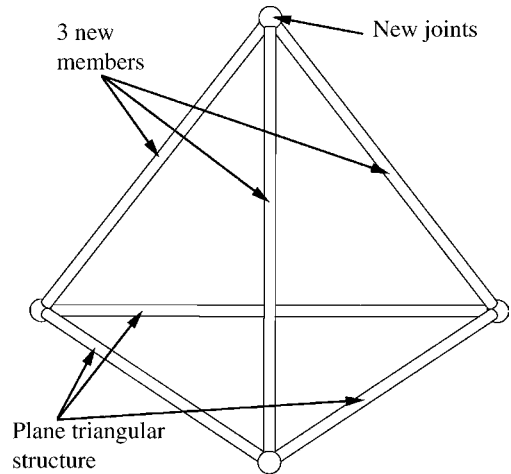


FIGURE 28.6 Basic space structure — the tetrahedron structure.

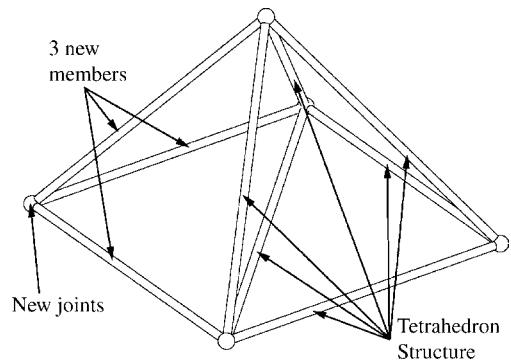


FIGURE 28.7 Pyramid structure derived from a tetrahedron structure.

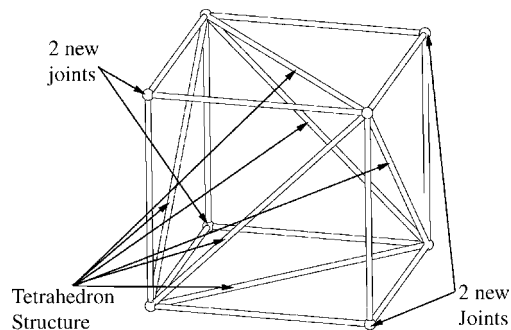


FIGURE 28.8 Box structure derived from a tetrahedron structure.

If the ground is perceived as another rigid body to which the space structure is to be coupled, then the design of the supports for a space structure is similar to those of coupling two space structures together; that is, six reactive forces are needed to exactly constrain the space structure. Some ways to arrange the six supporting members constraining a space structure are suggested in Figure 28.12.

Examples of physical supports offering one, two, or three reactive forces are shown in Figure 28.13.

This method of design, known as kinematical design, requires the use of point contact at the interfaces. Unfortunately, this method has some disadvantages:

- Load carrying limitation.
- Stiffness may be too low for application.
- Low damping.

There are, however, ways to overcome the disadvantages, which are via the semikinematical approach. This approach is a modification of the kinematical approach, and it aims to overcome the limitations of a pure kinematical design. The direct way is to replace all point contact with a small area, as shown in Figure 28.14; doing so decreases the contact stress, but increases the stiffness and load carrying capacity. However, the area contact should be kept reasonably small.

This section has only illustrated some fundamental concepts in designing rigid and statically determinate machine structures. Interested readers may refer to Blanding (1999) for more details on designing a machine using the exact constraints principles.

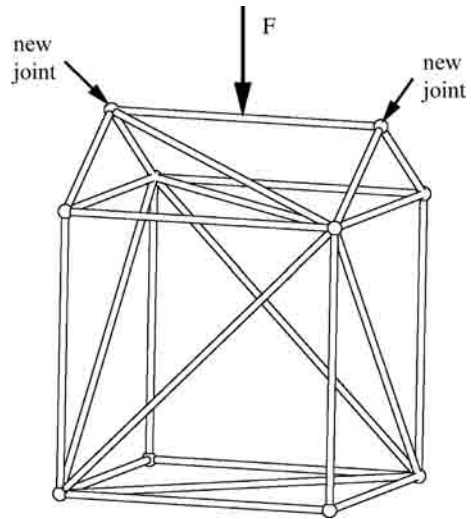


FIGURE 28.9 Gantry space structure.

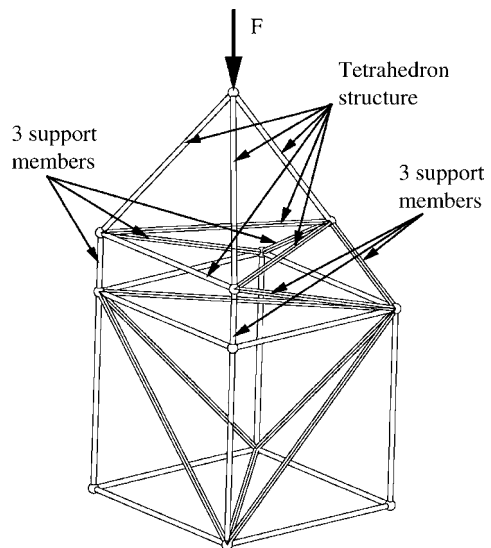


FIGURE 28.10 Coupling of a tetrahedron structure to a box structure with six members.

SUMMARY

The approach taken to reduce the mechanical vibration in precision motion systems is to focus on a proper mechanical design, based on the determinacy of machine structures in this chapter. The aim of this approach is to design systems with stable and statistically determinate structures. Two-dimensional structures and three-dimensional structures are considered.

28.3 Adaptive Notch Filter

The task of eliminating or suppressing undesirable narrowband frequencies can be efficiently accomplished using a notch filter (also known as a narrowband-stop filter), if the frequencies are known. The filter highly attenuates a particular frequency component and leaves the rest of the spectrum relatively unaffected. An ideal notch filter has a unity gain at all frequencies except in the so-called null frequency band, where the gain is zero. A single-notch filter is effective in removing single-frequency or narrowband interference; a multiple-notch filter is useful for the removal of multiple narrowbands, which is necessary in applications requiring the cancellation of harmonics. Digital notch filters are widely used to retrieve sinusoids from noisy signals, eliminate sinusoidal disturbances, and track and enhance time-varying narrowband signals with wideband noise. They have found extensive use in the areas of radar, signal processing, communications, biomedical engineering, and control and instrumentation systems.

To create a null band in the frequency response of a digital filter at a normalized frequency, β_0 , a pair of complex-conjugate zeros can be introduced on the unit circle at phase angles $\pm \beta_0$, respectively. The zeros are defined as

$$z_{1,2} = e^{\pm j\beta_0} = \cos \beta_0 \pm j \sin \beta_0 \tag{28.8}$$

where the normalized null frequency, β_0 , is defined as

$$\beta_0 = 2\pi \frac{f_0}{f_s} \tag{28.9}$$

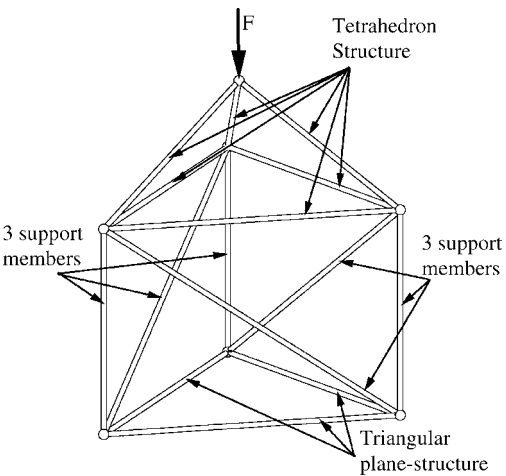


FIGURE 28.11 Coupling of a triangular plane structure to a tetrahedron space structure with six members.

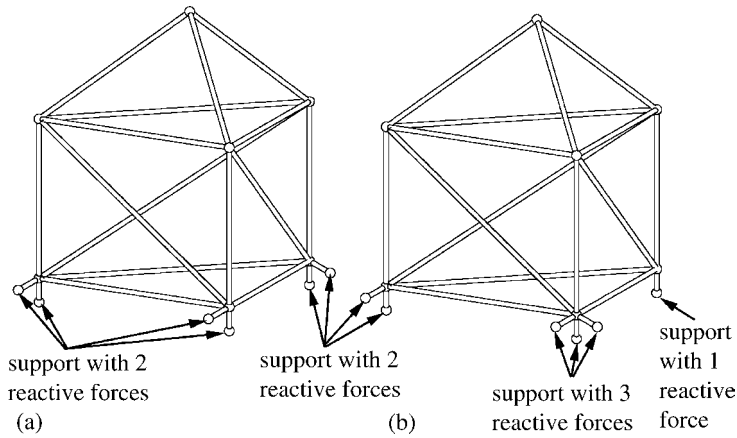


FIGURE 28.12 Examples for applying six constraints to a rigid body: (a) three sets of twin reactive forces; (b) 3–2–1 reactive forces.

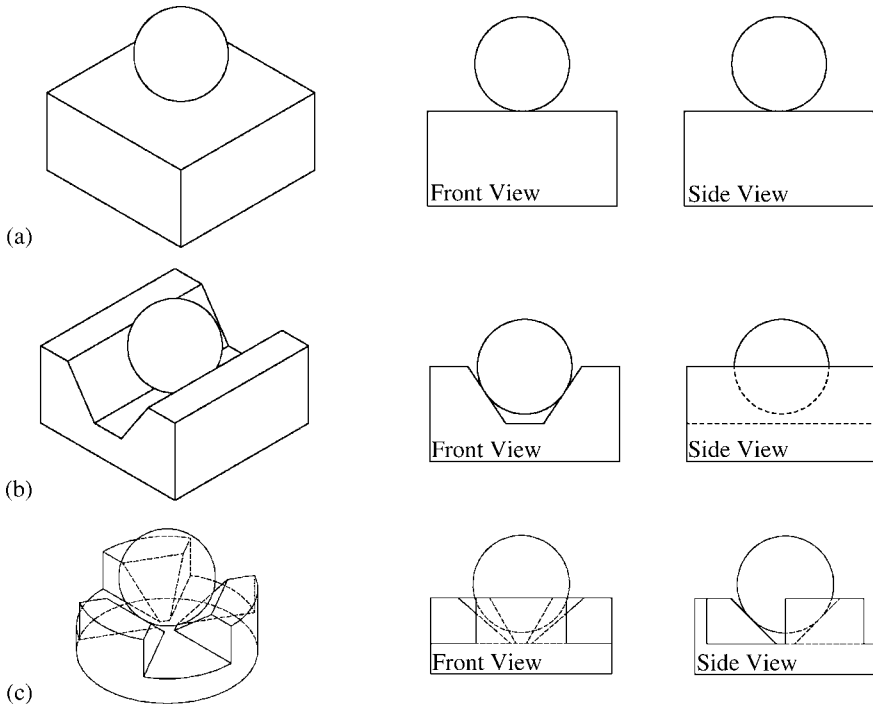


FIGURE 28.13 Examples of support with (a) one reactive force; (b) two reactive forces; and (c) three reactive forces.

Note that f_s is the sampling frequency in Hz (or rad/sec) and f_0 is the notch frequency in Hz (or rad/sec). This yields a finite impulse response (FIR) filter given by the following transfer function:

$$H(z) = 1 - 2 \cos \beta_0 z^{-1} + z^{-2} \quad (28.10)$$

A FIR notch filter has a relatively large notch bandwidth, which means that the frequency components in the neighborhood of the desired null frequency are also severely attenuated as a consequence. The frequency response can be improved by introducing a pair of complex-conjugate poles. The poles are placed inside the circle with a radius of α at phase angles $\pm \beta_0$. The poles are defined as

$$p_{1,2} = \alpha e^{\pm j\beta_0} = \alpha(\cos \beta_0 \pm j \sin \beta_0) \quad (28.11)$$

where $\alpha \leq 1$ for filter stability, and $(1 - \alpha)$ is the distance between the poles and the zeros.

The poles introduce a resonance in the vicinity of the null frequency, thus reducing the bandwidth of the notch. The transfer function of the filter is given by

$$H(z) = \frac{(z - z_1)(z - z_2)}{(z - p_1)(z - p_2)} \quad (28.12)$$

Substituting the expression for z_i and p_i , and dividing throughout by z^2 , the resulting filter has

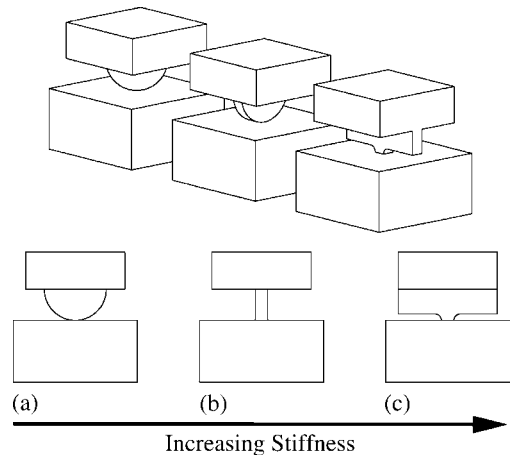


FIGURE 28.14 Kinematical vs. semikinematical design: (a) ideal condition — point contact; (b) line contact; (c) area contact.

the following transfer function:

$$H(z) = \frac{a_0 + a_1 z^{-1} + a_2 z^{-2}}{1 + b_1 z^{-1} + b_2 z^{-2}} \quad (28.13)$$

$$H(z) = \frac{1 - 2 \cos \beta_0 z^{-1} + z^{-2}}{1 - 2\alpha \cos \beta_0 z^{-1} + \alpha^2 z^{-2}} \quad (28.14)$$

Digitally, the filtered signal, y , is thus obtained from the raw signal, u , via the recursive formula in the discrete time domain as follows:

$$y(n) = a_0 u(n) + a_1 u(n-1) + a_2 u(n-2) - b_1 y(n-1) - b_2 y(n-2) \quad (28.15)$$

where the coefficients a_i and b_i are the same as those in Equation 28.13 because z^{-1} corresponds to the time-shift (delay through sampling period) operator.

The bandwidth and the Q-factor of the notch filter are, respectively

$$BW = \frac{2\sqrt{2}(1 - \alpha^2)}{[16 - 2\alpha(1 + \alpha)^2]^{1/2}} \quad (28.16)$$

$$Q = w_0 \frac{[16 - 2\alpha(1 + \alpha)^2]^{1/2}}{2\sqrt{2}(1 - \alpha^2)} \quad (28.17)$$

The filter transfer function, $H(z)$, has its zeros on the unit circle. This implies a zero transmission gain at the normalized null frequency, β_0 . It is interesting to note that the filter structure, Equation 28.14, allows independent tuning of the null frequency and the 3-dB attenuation bandwidth by adjusting β_0 and α , respectively. The performance of the notch filter depends on the choice of the constant, α , which controls the bandwidth, BW, according to Equation 28.16. The bandwidth, which is a function of the distance of the poles and zeros $(1 - \alpha)$, narrows when α approaches unity. Clearly, when α is close to 1, the corresponding transfer function behaves virtually like an ideal notch filter.

Complete narrowband disturbance suppression requires an exact adjustment of the filter parameters to align the notches with the resonant frequencies. If the true frequency of the narrowband interference that is to be rejected is stable and known *a priori*, a notch filter with fixed null frequency and fixed bandwidth can be used. However, if no information is available *a priori*, or when the resonant frequencies drift with time, the fixed notch may not coincide exactly with the desired null frequency, particularly if the bandwidth is too narrow (i.e., $\alpha \approx 1$). In this case, a tunable or adaptive notch filter is highly recommended. In Ahlstrom and Tompkins (1985) and Glover (1987), it is proposed to adapt the null bandwidth of the filter to accommodate the drift in frequency. In Bertran and Montoro (1998), it is suggested that an active compensator be used to suppress the vibration signals. Kwan and Martin (1989) adapt the null frequency, β_0 , while keeping the pole radii, α , constant. In other words, the parameters a_i and b_i of Equation 28.13 are adjusted such that the notch will center at the unwanted frequency while retaining the null bandwidth of the notch filter.

28.3.1 Fast Fourier Transform

The discrete Fourier transform (DFT) is a tool that links the discrete-time domain to the discrete-frequency domain (see Chapter 10, Chapter 21, and Appendix 2A). It is a popular off-line approach, widely used to obtain the information about the frequency distribution required for the filter design. However, the direct computation of the DFT is prohibitively expensive in terms of required computation effort. Fortunately, the fast Fourier transform (FFT) is mathematically equivalent to the DFT, but it is a more efficient alternative for implementation purposes (with a computational speed that is exponentially faster) and can be used when the number of samples, n , is a power of two (which is not a serious constraint). For vibration signals where the concerned frequencies drift with time, the FFT can be continuously applied to the latest n samples to update the signal spectrum. Based on the updated spectrum, the filter characteristics can be continuously adjusted for notch alignment. The block diagram

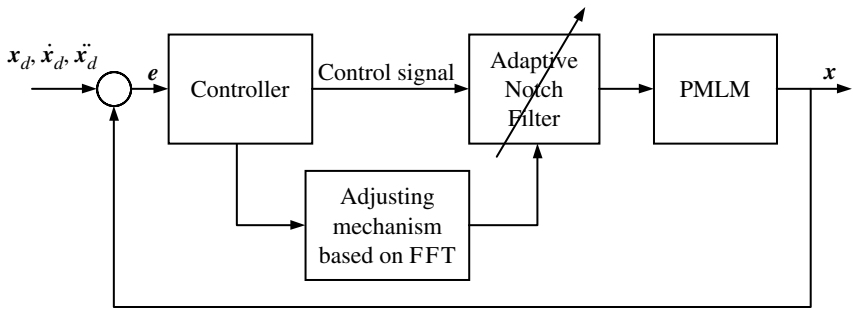


FIGURE 28.15 Block diagram of the adaptive notch filter with adjusting mechanism. (Source: Tan, K.K., Tang, K.Z., de Silva, C.S., Lee, T.H., and Chin, S.J., *J. Intell. Fuzzy Syst.*, 2001, IOS Press. With permission.)

of the adaptive notch filter that has been developed in the present work, with its adjusting mechanism, is shown in Figure 28.15.

28.3.2 Simulation and Experiments

A simulation study is carried out to explore the application of the adaptive notch filter in suppressing undesirable frequency transmission in the control system for a precision positioning system that uses permanent magnet linear motors (PMLM). In the simulation, a sinusoidal trajectory profile is to be closely followed and an undesirable vibration signal is simulated that drifts from a frequency of 500 Hz in the first cycle to a frequency of 1 to 5 Hz in the second cycle of the trajectory. Figure 28.16 shows

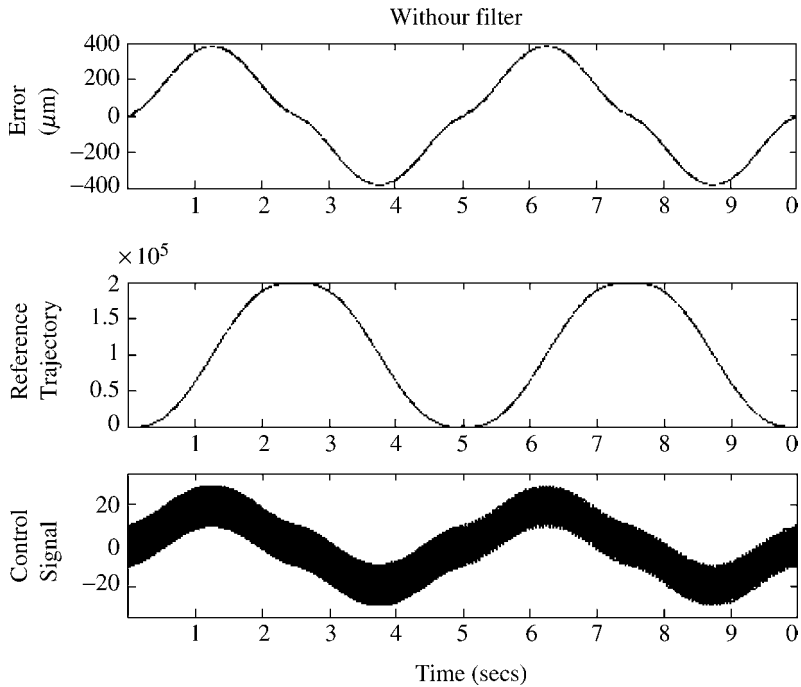


FIGURE 28.16 Simulation results without a notch filter: (a) error (μm); (b) desired trajectory (μm); (c) control signal (V). (Source: Tan, K.K., Tang, K.Z., de Silva, C.S., Lee, T.H., and Chin, S.J., *J. Intell. Fuzzy Syst.*, 2001, IOS Press. With permission.)

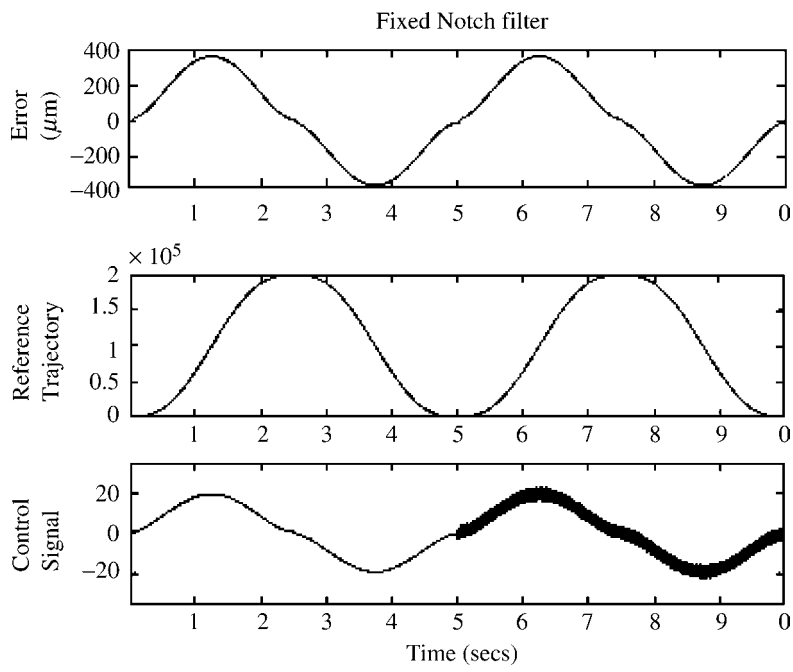


FIGURE 28.17 Simulation results using a fixed notch filter: (a) error (μm); (b) desired trajectory (μm); (c) control signal (V). (Source: Tan, K.K., Tang, K.Z., de Silva, C.S., Lee, T.H., and Chin, S.J., *J. Intell. Fuzzy Syst.*, 2001, IOS Press. With permission.)

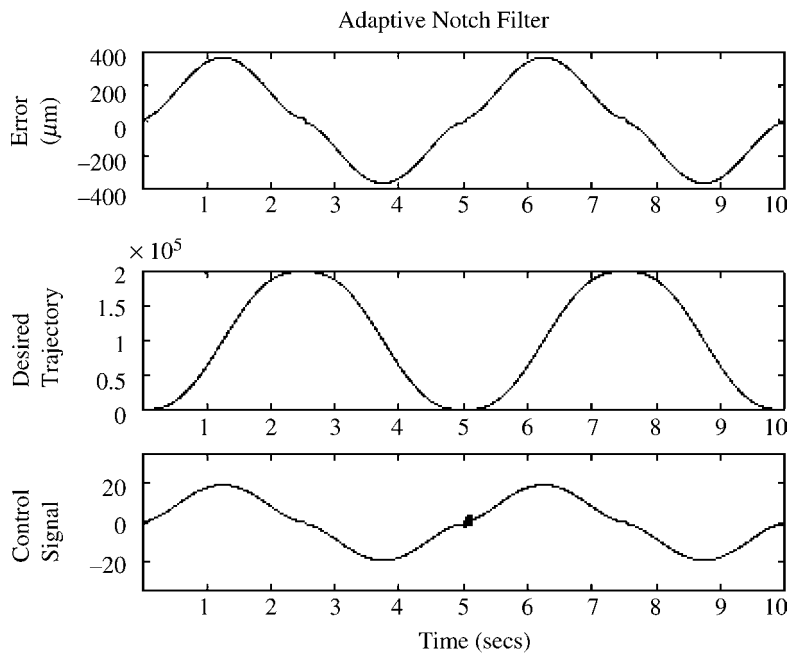


FIGURE 28.18 Simulation results using an adaptive notch filter: (a) error (μm); (b) desired trajectory (μm); (c) control signal (V). (Source: Tan, K.K., Tang, K.Z., de Silva, C.S., Lee, T.H., and Chin, S.J., *J. Intell. Fuzzy Syst.*, 2001, IOS Press. With permission.)

the tracking performance of the precision machine without a notch filter. Figure 28.17 shows the performance when a fixed notch filter is used, and Figure 28.18 shows the performance with an adaptive notch filter. It is clearly evident that a time-invariant narrowband vibration signal can be effectively eliminated using just a fixed notch filter. However, when the vibration frequencies drift, an adaptive notch filter is able to detect the drift and align the notch to remove the undesirable frequencies, with only a short transient period.

The notch filter is subsequently implemented in the control system of a linear drive tubular linear motor (LD3810) equipped with a Renishaw optical encoder having an effective resolution of $1\text{ }\mu\text{m}$. The hardware setup for this experimental study is shown in Figure 28.19 whereas Figure 28.20 shows the linear motor in more detail.

The components of the linear motor consist of the thrust rod, the thrust block, the motor cable, and the optical encoder. The thrust rod is made of a thin-walled stainless steel tube housing high-energy permanent magnets. To enable the smooth translation of the thrust block along the length of the thrust rod, the thrust block is made from an aluminum housing that contains cylindrical coils arranged in a three-phase star pattern. An electromagnetic field is produced by energizing these coils. The interactions between the permanent magnetic field of the thrust rod and the changing magnetic field of the thrust block provide the induced force for the translation of the block. Usually, a sinusoidal or trapezoidal motor commutation is utilized to smoothen the translation of the block. The popular proportional–integral–derivative (PID) control is used in this experimental study. The dSPACE DS1102 (*dSPACE User's Guide*, 1996) digital signal processing (DSP) board is used as the data acquisition and control card. It is a single-board system, which is specifically designed for the development of high-speed multivariable digital controllers and real-time simulations in various fields. The DS1102 is based on the Texas Instruments TMS320C31 third-generation floating-point DSP, which builds the main processing unit, providing fast instruction cycle time for numeric intensive algorithms. It contains 128K words memory that is fast enough to allow zero wait-state operation. Besides these, the DS1102 DSP board supports a total memory space of 16M 32-bit words, including program, data, and I/O space. All off-chip memory and I/O can be accessed by the host, even while the host is running, thus allowing easy system setup and monitoring. The TMS320C31 is object-code compatible to the TMS320C30. The DSP is fully supplemented by a set of on-board peripherals, frequently used in digital control systems. Analog-to-digital and digital-to-analog converters, a DSP-microcontroller-based digital-input/output (I/O) subsystem, and incremental sensor interfaces make the DS1102 an ideal single-board solution for a broad range of digital control tasks.

The DS1102 DSP board is well supported by popular software design and simulation tools, including MATLAB and SIMULINK, which offer a rich set of standard and modular design functions for both classical and modern control algorithms. The SIMULINK model developed for the system (Figure 28.15), with the notch filter, is shown in Figure 28.21. This model is then downloaded to the DS1102 DSP board for real-time implementation using one of the options available from the pull-down menu.

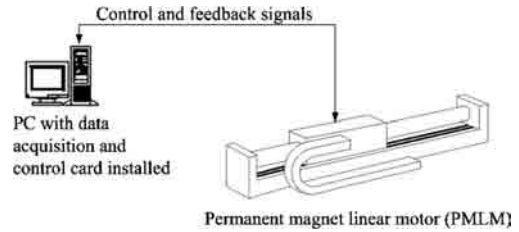


FIGURE 28.19 Hardware setup for the experimental study of the notch filter. (Source: Tan, K.K., Tang, K.Z., de Silva, C.S., Lee, T.H., and Chin, S.J., *J. Intell. Fuzzy Syst.*, 2001, IOS Press. With permission.)

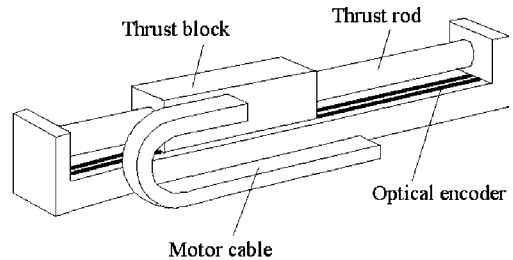


FIGURE 28.20 Experimental platform (LD 3810) — linear drive tubular motor with optical encoder attached. (Source: Tan, K.K., Tang, K.Z., de Silva, C.S., Lee, T.H., and Chin, S.J., *J. Intell. Fuzzy Syst.*, 2001, IOS Press. With permission.)

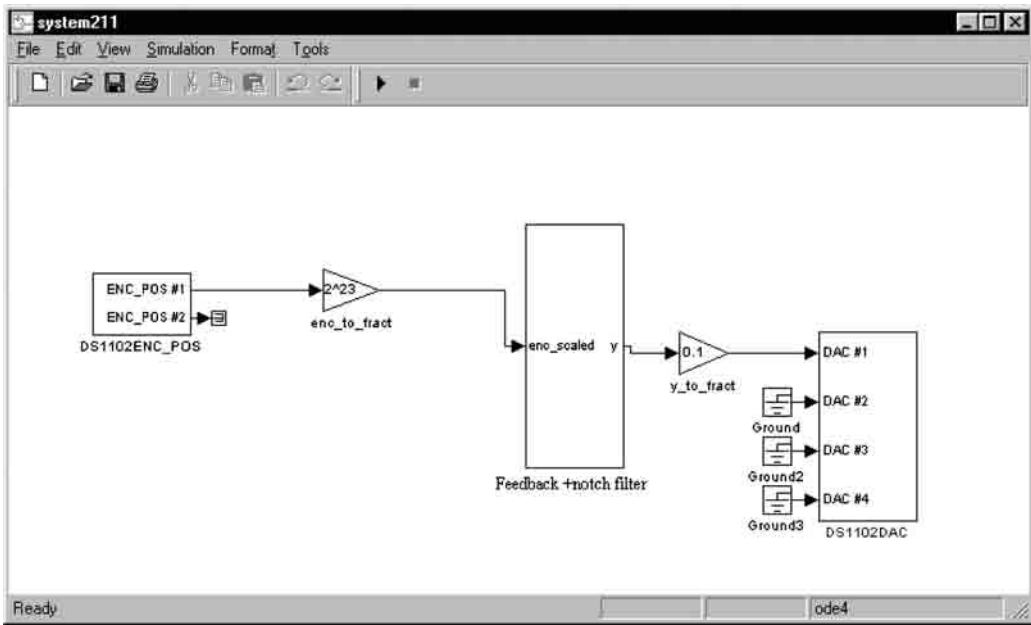


FIGURE 28.21 SIMULINK model created for the system with the notch filter incorporated. (Source: Tan, K.K., Tang, K.Z., de Silva, C.S., Lee, T.H., and Chin, S.J., *J. Intell. Fuzzy Syst.*, 2001, IOS Press. With permission.)

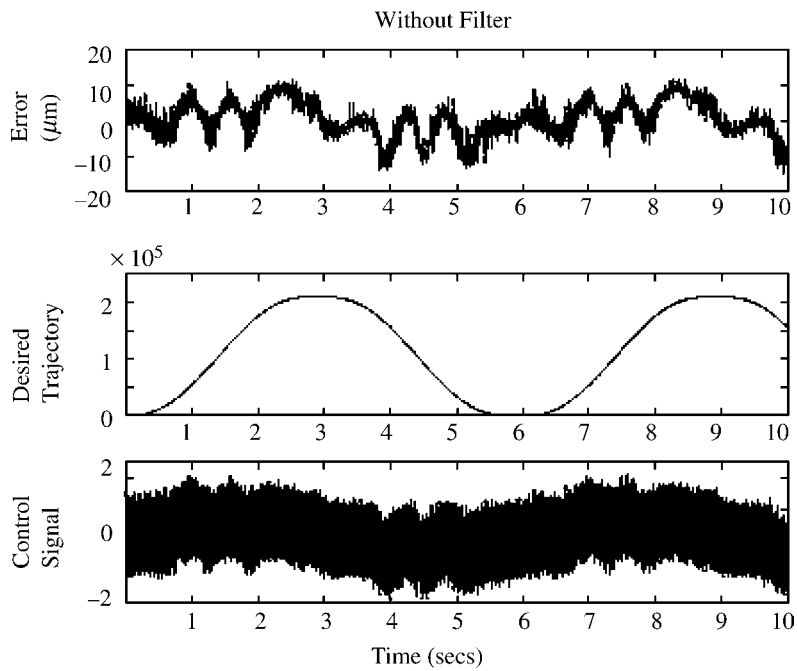


FIGURE 28.22 Experimental results without a notch filter: (a) error (μm); (b) desired trajectory (μm); (c) control signal (V). (Source: Tan, K.K., Tang, K.Z., de Silva, C.S., Lee, T.H., and Chin, S.J., *J. Intell. Fuzzy Syst.*, 2001, IOS Press. With permission.)

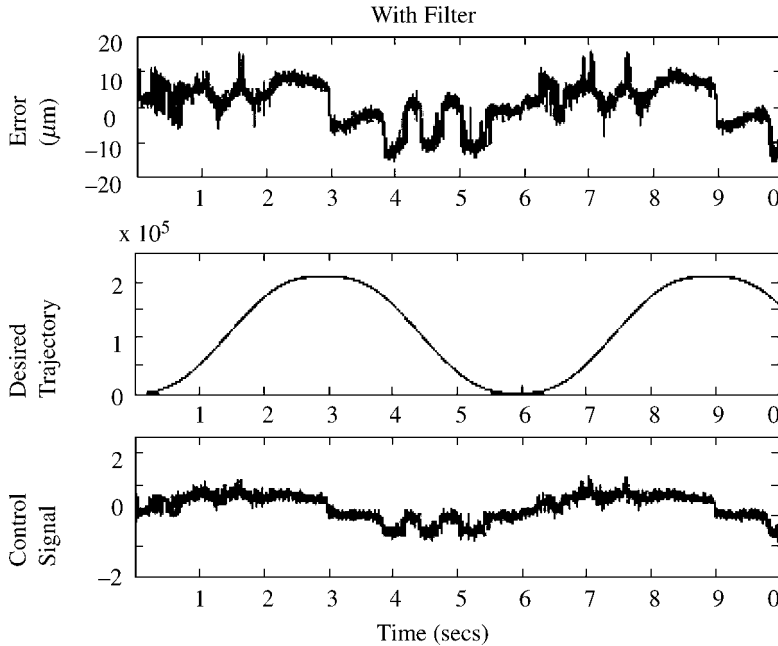


FIGURE 28.23 Experimental results using a notch filter: (a) error (μm); (b) desired trajectory (μm); (c) control signal (V). (Source: Tan, K.K., Tang, K.Z., de Silva, C.S., Lee, T.H., and Chin, S.J., *J. Intell. Fuzzy Syst.*, 2001, IOS Press. With permission.)

It is now in order to present the experimental results utilizing the notch filter in the system. Figure 28.22 shows the performance of the PMLM when no filter is used. Figure 28.23 shows the improvement in the control performance when the notch filter is incorporated into the control system.

SUMMARY

An approach utilizing an adaptive notch filter in the control system is elaborated upon in this section. The notch filter is able to adaptively identify resonant frequencies present in the motion system and suppress vibration signal transmission into the system at these frequencies. The FFT is used to obtain the frequency distribution of the vibration signals. Experimental and simulation results are provided to illustrate the effectiveness of the adaptive notch filter.

28.4 Real-Time Vibration Analyzer

The development of an alternative, low-cost approach towards real-time monitoring and analysis of machine vibration (Vierck, 1979; de Silva, 2000) is described in this section. The main idea behind this approach is to construct a vibration signature based on pattern recognition of “acceptable” or “healthy” vibration patterns. The vibration analyzer can operate in three modes: learning, monitoring, or diagnostic. The learning mode, to be initiated first, will yield a set of vibration signatures based on which the monitoring and diagnostic modes will operate. In the monitoring mode, with the machine

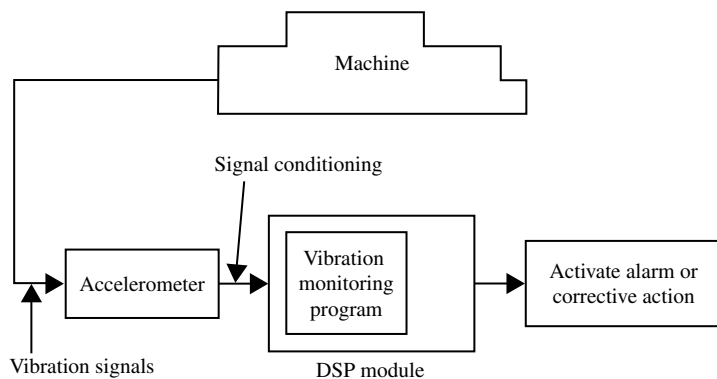


FIGURE 28.24 Schematic diagram of the real-time vibration analyzer. (Source: Tan, K.K., Tang, K.Z., de Silva, C.S., Lee, T.H., and Chin, S.J., *J. Intell. Fuzzy Syst.*, 2001, IOS Press. With permission.)

under normal closed-loop control, the analyzer only uses a naturally occurring vibration signal to deduce the condition of the machine. No test excitation is deliberately added to the input signal of the machine. More than one criterion may be used in the evaluation of the condition of the machine, in which case a fusion approach will generate a combined output (machine condition) based on the multiple inputs. In the diagnostic mode, explicit input signals are applied to the machine and the output signal (vibration) is logged for analysis with respect to the associated vibration signature. In what follows, the details of the various components and functions of the analyzer will be described systematically.

The block diagram of the real-time vibration analyzer system that has been developed is shown in Figure 28.24. It consists of an accelerometer, which is mounted on the machine to be monitored. The accelerometer measures a multifrequency vibration signal and transmits it to an intelligent DSP module after performing appropriate signal conditioning. This module can be a standalone device (Figure 28.25), or one integrated to a personal computer (PC) host. The vibration analysis algorithm is downloaded to this DSP module. With this algorithm, it can be established as to whether the condition of the machine is within a predetermined acceptable threshold. If the condition is determined to be poor, the DSP module will trigger an alarm to the operator who would enable a corrective action, or automatically activate a corrective action (e.g., change the operating conditions of the machine, modify the parameters of the controller or shutdown the machine).

The construction of the real-time vibration analyzer is inexpensive and requires only commercially available, low-cost components. The installation can be hassle free, as the accelerometer is able to gather vibration signals independent of the machine's own control system. Thus, there is no need to disrupt the operation of the machine. In the prototype reported here, a DSP emulator board TMS320C24x model (TMSS320C24x DSP Controllers Evaluation Module Technical References, 1997), from Texas Instruments, is used as the standalone DSP module (Figure 28.25). This C24x series emulator board is built around the F240 DSP controller, operating at

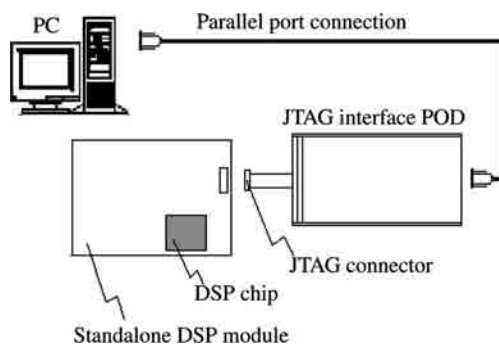


FIGURE 28.25 Hardware setup for the standalone DSP module. (Source: Tan, K.K., Tang, K.Z., de Silva, C.S., Lee, T.H., and Chin, S.J., *J. Intell. Fuzzy Syst.*, 2001, IOS Press. With permission.)

20MIPS with an instruction cycle time of 50 ns. It is optimized for digital motor control and conversion applications. Other key components supported on this DSP module are analog-to-digital converters (ADCs), dual access RAM (DARAM), on-chip flash memory, and an RS-232 compatible serial port. This DSP module and the accelerometer unit (with signal conditioning) constitute the only hardware requirements of the real-time vibration analyzer.

The vibration-analysis algorithm, which is described in the sequel, will be downloaded to the flash ROM on the DSP module after satisfactory evaluation and tests on the PC. The algorithm is programmed using a Visual C++-based compatible environment, that is, a Code Composer integrated environment (IDE). The C-based source code is then compiled into assembly code, using the built-in compiler available in the IDE.

28.4.1 Learning Mode

In the learning mode, with the machine operating under normal conditions, the vibration signals are acquired by the accelerometer and stored in the DSP module. A suitable vibration signature (Ramirez, 1985) is then extracted from the vibration signals. There are many types of vibration signatures that are adequate for the purpose of machine monitoring. For example, one form of vibration signature may be based on the amplitude of the vibration; another form may use a time-series analysis of the vibration; yet another form may employ the spectrum of the vibration, which can be efficiently obtained using the FFT algorithm. Regardless of the type, these vibration signatures are dependent on the nature of the input signals driving the machine. For example, a square wave input will produce a vibration spectrum that can be quite different from that resulting from an input of a chirp signal (i.e., a repeating sine wave of increasing frequency) or a pure sinusoid. Thus, a particular input signal will produce a unique spectrum based on which a unique vibration signature can be derived. Multiple vibration signatures corresponding to the natural vibrations of the machine (useful for the monitoring mode) or corresponding to different input signals (useful for the diagnostic mode) can thus be captured for subsequent diagnosis and monitoring of the machine.

28.4.2 Monitoring Mode

In the monitoring mode, the vibration signals are sampled periodically from the machine to monitor the condition of the machine. No deliberate or additional input signal is required, so the machine operation is not disrupted. The updated spectra are analyzed against the relevant vibration signatures. The analysis and comparison may be done in terms of the shift in the frequency or the amplitude of the spectrum, or a combination of the two. For example, one evaluation criterion (EV) may be based on the mean-square (ms) value of the error between the current real-time vibration spectrum and the vibration signature:

$$EV_1 = \frac{\sum_{q=1}^N (S_q - S_q^*)^2}{M} \quad (28.18)$$

where S_q is the discretized current real-time vibration spectrum, the superscript $*$ represents the vibration signature of the “healthy” machine, subscript q is the index for the data points, N is the total number of frequency points, and M is the total number of data points. Another EV may be formulated based on the difference in the amplitude of the current time series vibration pattern and its corresponding vibration signature:

$$EV_2 = \frac{\max(T_q) - \max(T_q^*)}{M} \quad (28.19)$$

where $\max(T_q)$ represents the highest amplitude of the current time series vibration pattern T_q , and $\max(T_q^*)$ is the highest amplitude of its corresponding vibration signature.

More than one evaluation criterion may be used in the determination of machine condition. In this case, a fusion technique is necessary. The key idea of fusion is to associate the machine with a *HEALTH* attribute, which is computed from multiple evaluation criteria. These criteria are expected to influence, to a varying degree, the *HEALTH* of the machine. The *HEALTH* attribute is thus an appropriate function, \Im , of the various criteria (EV_i s); that is

$$\text{HEALTH} = \Im(EV_1, EV_2, \dots, EV_n) \quad (28.20)$$

where n refers to the number of criteria being evaluated.

A fuzzy weighted approach may be used to realize the \Im function as follows. The *HEALTH* attribute is treated as a fuzzy variable (i.e., $\text{HEALTH} \in [0, 1]$). $\text{HEALTH} = 0$ will represent absolute machine failure, while $\text{HEALTH} = 1$ represents a perfectly normal machine condition. This attribute may be computed from a fuzzy operation on a combination of the evaluation criteria (EV_i s) obtained *via* an analysis of the vibration signals against their signatures. The final decision on the condition of the machine will be derived from the *HEALTH* attribute. Zadeh (1973) provides a comprehensive review on fuzzy logic.

A Takagi and Sugeno (1985) type of fuzzy inference is used in this chapter. Consider the following p rules governing the computation of an attribute:

$$\text{IF } EV_1^i \text{ IS } F_1^i \otimes \dots \otimes EV_n^i \text{ IS } F_n^i, \text{ THEN } u^i = \alpha^i \quad (28.21)$$

$$\sum_{i=1}^p \alpha^i = 1 \quad (28.22)$$

where $u^i \in [0, 1]$ is a crisp variable output representing the extent to which the i th evaluation rule affects the final outcome. Thus, α^i represents the weight of the i th rule, F_j^i represents the fuzzy sets in which the input linguistic variables (EV_i s) are evaluated, and \otimes is a fuzzy operator that combines the antecedents into premises.

The value of the attribute is then evaluated as a weighted average of the u_i s:

$$\text{HEALTH} = \frac{\sum_{i=1}^p w^i u^i}{\sum_{i=1}^p w^i} \quad (28.23)$$

where the weight w^i implies the overall truth value of the premise of rule, i , for the input. It is computed as

$$w^i = \prod_{j=1}^n \mu_{F_j^i}(EV_j^i) \quad (28.24)$$

where $\mu_{F_j^i}(EV_j^i)$ is the membership function for the fuzzy set, F_j^i , related to the input linguistic variable, EV_j^i , (for the i th rule). For example, in this application, EV_j may be the maximum error, MAX_ERR , and F_j^i may be the fuzzy set *HIGH*. The membership function is represented as $\mu_{\text{HIGH}}(\text{MAX_ERR})$. It may have the characteristic shown in Figure 28.26. The decision as to whether any corrective action might be

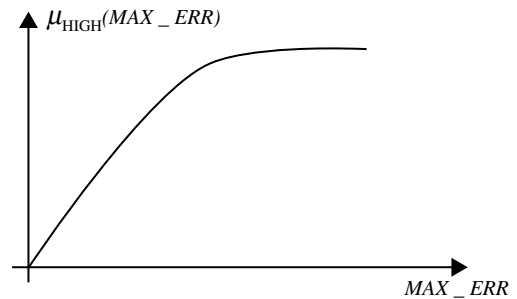


FIGURE 28.26 Membership function for the fuzzy input MAX_ERR . (Source: Tan, K.K., Tang, K.Z., de Silva, C.S., Lee, T.H., and Chin, S.J., *J. Intell. Fuzzy Syst.*, 2001, IOS Press. With permission.)

necessary can then be based on a simple *IF–THEN–ELSE* formulation as follows:

$$\begin{aligned} & \text{IF HEALTH} \leq \gamma, \text{ THEN STRATEGY} = \text{TRIGGER ALARM} \\ & \text{ELSE STRATEGY} = \text{CONTINUE TO MONITOR} \end{aligned}$$

Here, γ is interpreted as a threshold value. Suitable values for γ may be in the range $0.6 \leq \gamma \leq 0.9$. Here, *STRATEGY* is stated to trigger an alarm to the operator who will enable a corrective action, or automatically activate a corrective action (e.g., change the operating conditions of the machine, modify the parameters of the controller, or shutdown the machine).

Under this framework, it is relatively easy to include additional criteria for analysis and decision making to the system. The procedure will involve setting up the membership functions for the criterion, formulating the additional fuzzy rules required, and adjusting the scaling parameters (the α terms in Equation 28.21) to reflect the relative weight of the new criterion as compared with the existing ones. In this manner, in the monitoring mode, foreboding trends can often be spotted long before the vibration condition reaches a level that is seriously detrimental to the machine.

28.4.3 Diagnostic Mode

In the diagnostic mode, the current vibration signal corresponding to each input signal (with standardized amplitude and frequency) is analyzed against the associated signature obtained earlier in the learning mode, depending on the type of machine (also see Chapter 25). Similar to the monitoring mode, there can be multiple evaluation criteria used in the diagnostic mode, so that the fusion technique described earlier is also applicable. The input signals applied to the machine must be designed carefully so as to yield as much information of the machine condition as possible in the operational regime of interest. Two important considerations are the choices of amplitude and frequency.

Machines may have constraints in relation to the amount of travel that is possible. Too large an amplitude for the input signal may be not be viable for the machine owing to the limit of travel, or may even damage the machine. Also, the frequency range of the input should be chosen so that it has most of its energy in the frequency bands that are important for the system. Where input signals cannot be applied to the system in the open loop, the setpoint signal will serve as the input for the closed-loop system since it may not be possible to directly access the system under closed-loop control. Careful considerations of the mentioned issues will ensure that significant information can be obtained from the machine.

The input signals considered here are square wave input (Figure 28.27), chirp input (Figure 28.29), and sine wave input (Figure 28.31), standardized in amplitude to 1 V and in frequency to 5 Hz. The corresponding vibration signatures are shown in Figure 28.28, Figure 28.30, and Figure 28.32, respectively.

28.4.4 Experiments

A shaker table (Figure 28.33) is used as the test platform for the experiments presented here (also see Chapter 15). The shaker table can be used to simulate machine vibrations and evaluate the performance, for example, of active inertial dampers. The shaker table is driven by a high-torque direct-drive motor (which has a maximum torque of 1.11 N m, a maximum design load of 11 kg and generates a maximum force of 175 N). The maximum linear travel of the table is ± 2 cm.

The learning mode is first initiated to obtain the vibration signals with the shaker table operating under normal conditions. It is assumed in the experiments that the normal condition corresponding to the input is a square wave signal (with a standardized amplitude of 1 V and frequency of 5 Hz). For the purpose of implementing the diagnostic mode, the vibration signals are also obtained for the input signals of the sinusoidal and chirp type, with standardized amplitudes of 1 V and

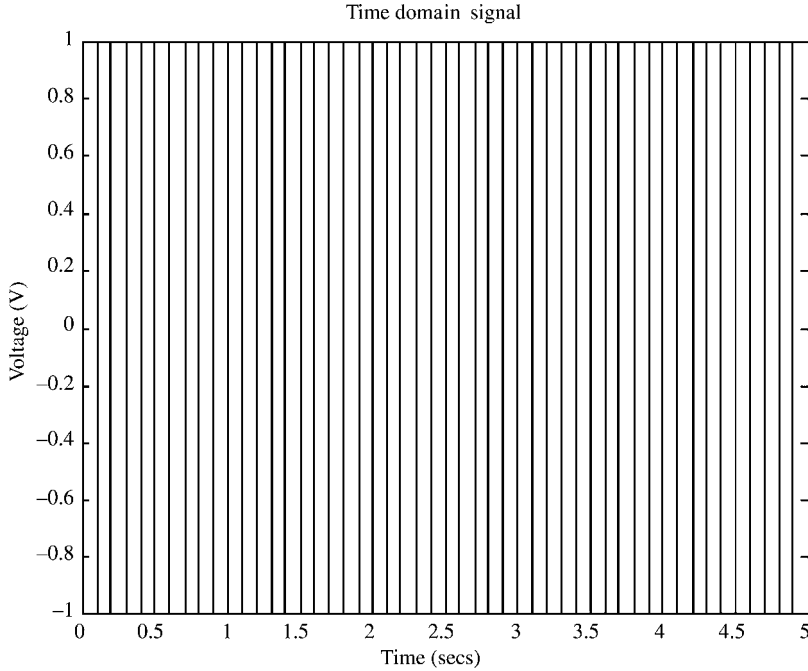


FIGURE 28.27 Square wave input, with a standardized amplitude of 1 V and frequency of 5 Hz. (Source: Tan, K.K., Tang, K.Z., de Silva, C.S., Lee, T.H., and Chin, S.J., *J. Intell. Fuzzy Syst.*, 2001, IOS Press. With permission.)

frequencies of 5 Hz (see Figure 28.27 to Figure 28.32 for the inputs and their corresponding vibration signatures).

28.4.4.1 Input Variables — the Evaluation Criteria

Different types of EV can be used as input variables for the determination of the machine condition. For the present vibration-analysis application, the input variables chosen for the computation of the *HEALTH* attribute are given below.

28.4.4.1.1 Monitoring Mode

$$EV_1 = \frac{\sum_{q=1}^N (S_{sq,q} - S_{sq,q}^*)^2}{M} \quad (28.25)$$

$$EV_2 = \frac{(\max(T_{sq,q}) - \max(T_{sq,q}^*))^2}{M} \quad (28.26)$$

$$EV_3 = \frac{\sum_{q=1}^M (T_{sq,q} - T_{sq,q}^*)^2}{M} \quad (28.27)$$

where $S_{sq,q}$ represents the vibration spectrum for a square wave input (driving the machine) at the q th frequency point and $T_{sq,q}$ represents the time-domain signal of a square wave input at the q th time instant. N refers to the total number of points in the FFT spectrum and M is the number

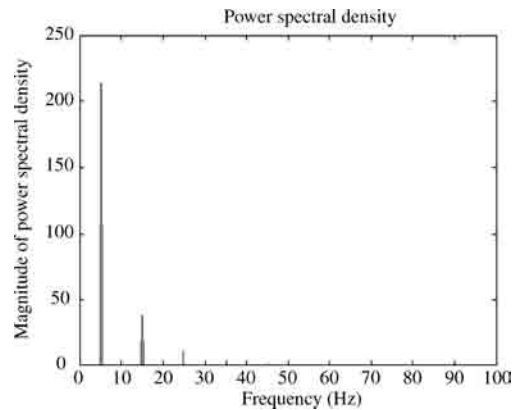


FIGURE 28.28 Vibration signature of the square wave input, with a standardized amplitude of 1 V and frequency of 5 Hz. (Source: Tan, K.K., Tang, K.Z., de Silva, C.S., Lee, T.H., and Chin, S.J., *J. Intell. Fuzzy Syst.*, 2001, IOS Press. With permission.)

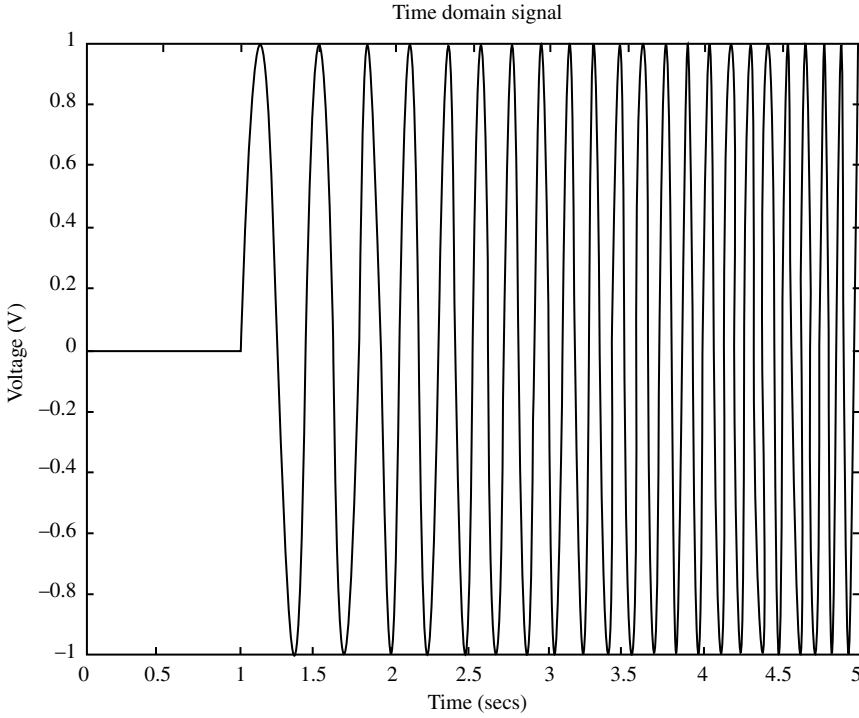


FIGURE 28.29 Chirp wave input, with a standardized amplitude of 1 V and initial frequency of 5 Hz. (Source: Tan, K.K., Tang, K.Z., de Silva, C.S., Lee, T.H., and Chin, S.J., *J. Intell. Fuzzy Syst.*, 2001, IOS Press. With permission.)

of time-series data points over an operational cycle. Hence, EV_1 refers to the ms deviation between the vibration spectrum and its signature; EV_2 refers to the square of the difference between the amplitude of the vibration signal over one operational cycle compared with its signature; EV_3 refers to the ms deviation between the vibration signal and its signature (time domain) over one operational cycle. The superscript $*$ represents the signature of the healthy machine.

28.4.4.1.2 Diagnostic Mode

$$EV_4 = \frac{\sum_{q=1}^N (S_{sq,q} - S_{sq,q}^*)^2}{M} \quad (28.28)$$

$$EV_5 = \frac{\sum_{q=1}^N (S_{cp,q} - S_{cp,q}^*)^2}{M} \quad (28.29)$$

$$EV_6 = \frac{\sum_{q=1}^N (S_{sn,q} - S_{sn,q}^*)^2}{M} \quad (28.30)$$

Here, cp denotes a chirp input signal and sn denotes a sine input signal.

For the monitoring mode, the input attributes are related only to the square input owing to the assumption that the input signal, under normal operating conditions, is the square wave signal (with a standardized amplitude of 1 V and frequency of 5 Hz).

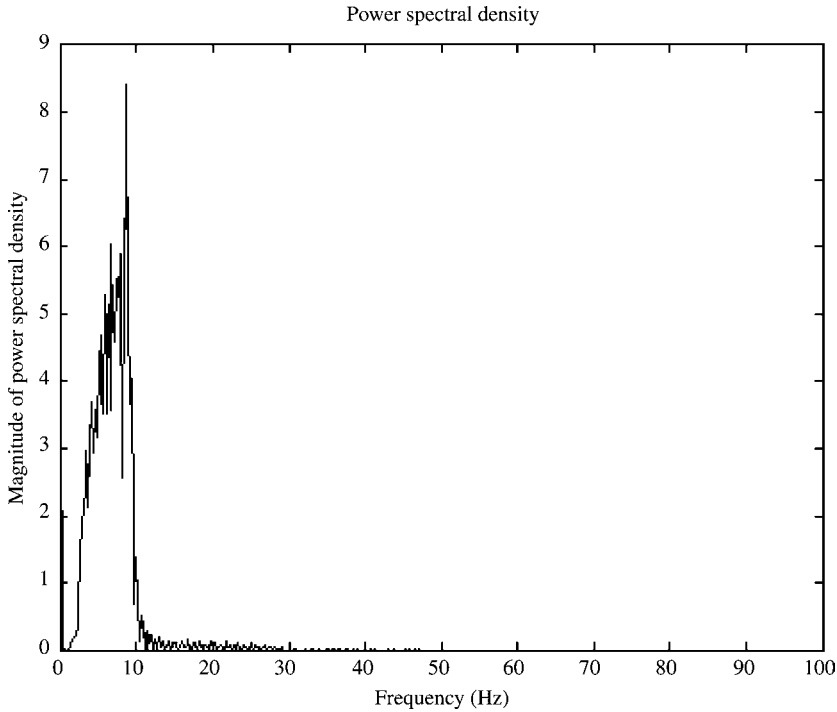


FIGURE 28.30 Vibration signature of the chirp wave input, with a standardized amplitude of 1 V and starting frequency of 5 Hz. (Source: Tan, K.K., Tang, K.Z., de Silva, C.S., Lee, T.H., and Chin, S.J., *J. Intell. Fuzzy Syst.*, 2001, IOS Press. With permission.)

28.4.4.2 Evaluation Rules

The three rules for the computation of the *HEALTH* attribute are given below.

28.4.4.2.1 Monitoring Mode

- IF EV_1 IS LOW, THEN $u = \alpha_1$
- IF EV_2 IS SHORT, THEN $u = \alpha_2$
- IF EV_3 IS LOW, THEN $u = \alpha_3$

The values of the scaling parameters, that is, α terms in Equation 28.21, reflect the relative importance of the fuzzy rules in the determination of the *HEALTH* of the machine. The scaling values of α_1 , α_2 , and α_3 are set at 0.7, 0.2, and 0.1, respectively. The respective membership functions are

$$\mu_i(EV_i) = e^{-n(EV_i)^\beta} \quad (28.31)$$

where n and β are scaling factors for normalization of EV_i . Here, they are selected to be $n = 10$ and $\beta = 0.5$.

28.4.4.2.2 Diagnostic Mode

The three evaluation rules for the computation of the *HEALTH* attribute in the diagnostic mode are

- IF EV_4 IS LOW, THEN $u = \alpha_4$
- IF EV_5 IS LOW, THEN $u = \alpha_5$
- IF EV_6 IS LOW, THEN $u = \alpha_6$

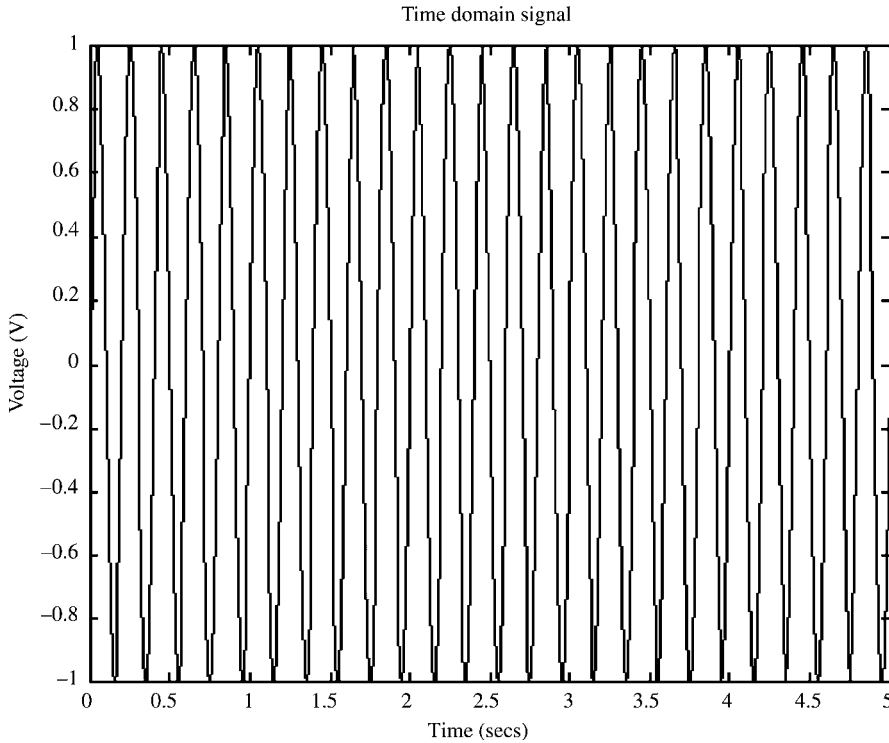


FIGURE 28.31 Sine wave input, with a standardized amplitude of 1 V and frequency of 5 Hz. (Source: Tan, K.K., Tang, K.Z., de Silva, C.S., Lee, T.H., and Chin, S.J., *J. Intell. Fuzzy Syst.*, 2001, IOS Press. With permission.)

The scaling values of α_4 , α_5 , and α_6 are set at 0.4, 0.2, and 0.4, respectively. Similar membership functions as for the monitoring mode are used here. The machine condition attribute *HEALTH* is then computed as in Equation 28.23.

28.4.4.3 Tests

28.4.4.3.1 Monitoring Mode

In the monitoring mode, the normal input signal (i.e., the square wave with standardized amplitude of 1 V and frequency of 5 Hz) is applied to the shaker-table system. At $t = 5$ sec, a sinusoidal signal (with amplitude 0.4 V and frequency $f = 5$ Hz) is also applied to the system to simulate a fault arising in the machine. The time-domain signal of the machine (corresponding to the square input) is shown in Figure 28.34. The spectra of the machine before and after $t = 5$ sec are shown in Figure 28.35. The vibration-analysis algorithm is able to detect the fault in the machine. Before the introduction of the fault, the *HEALTH* attribute of the shaker table is found to be 0.98. After the introduction of the fault, the *HEALTH* attribute falls to 0.63, which is below the threshold value, set at 0.7. As a result, the alarm is triggered.

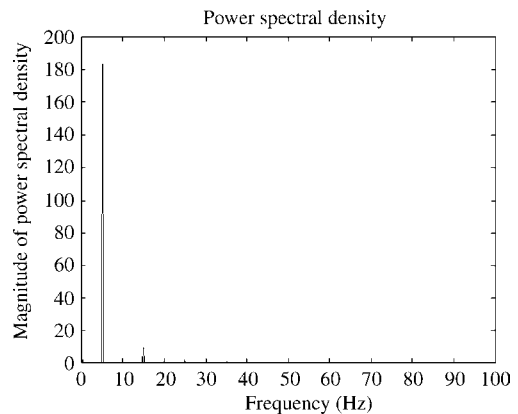


FIGURE 28.32 Vibration signature of the sine wave input, with a standardized amplitude of 1 V and frequency of 5 Hz. (Source: Tan, K.K., Tang, K.Z., de Silva, C.S., Lee, T.H., and Chin, S.J., *J. Intell. Fuzzy Syst.*, 2001, IOS Press. With permission.)

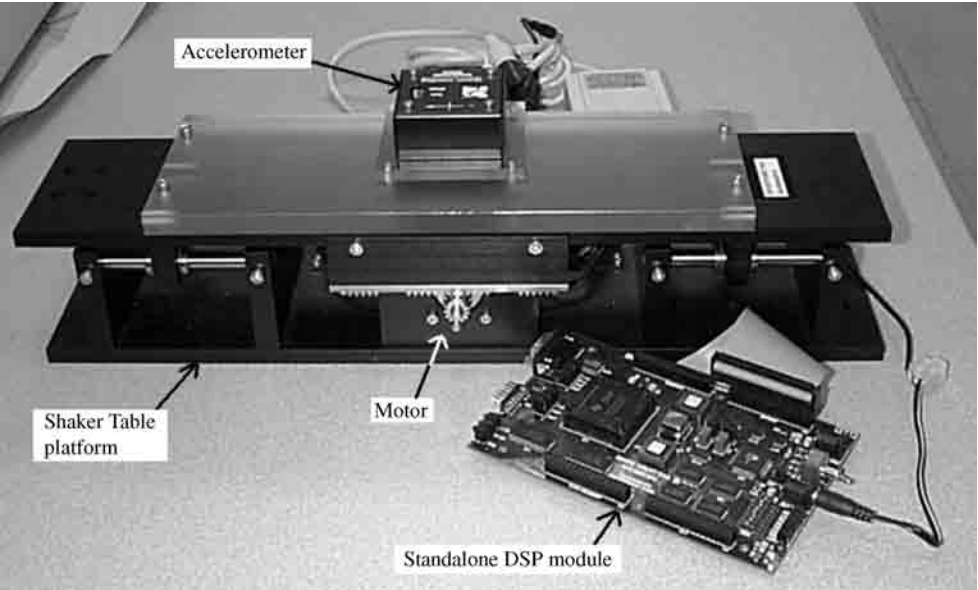


FIGURE 28.33 Test platform: the shaker table. (Source: Tan, K.K., Tang, K.Z., de Silva, C.S., Lee, T.H., and Chin, S.J., *J. Intell. Fuzzy Syst.*, 2001, IOS Press. With permission.)

28.4.4.3.2 Diagnostic Mode

In the diagnostic mode, three input signals (i.e., sine, square, and chirp wave with standardized amplitude and frequency) are selected to be applied to the shaker table system in turn. To simulate a fault arising at $t = 5$ sec, the input gain is increased by a factor of 1.4 times at $t = 5$ sec. The time-domain

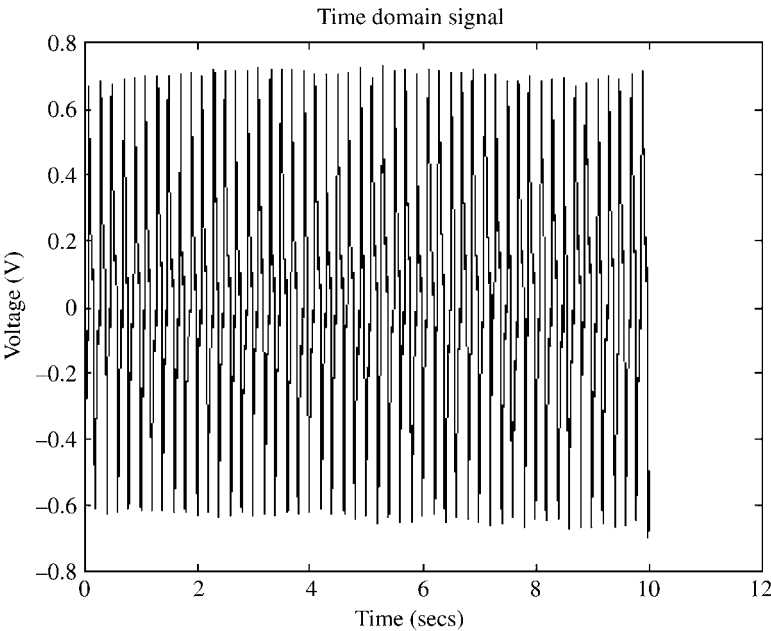


FIGURE 28.34 Time-domain vibration signal corresponding to the square input, with a standardized amplitude of 1 V and frequency of 5 Hz (at $t = 5$ sec, a fault is simulated). (Source: Tan, K.K., Tang, K.Z., de Silva, C.S., Lee, T.H., and Chin, S.J., *J. Intell. Fuzzy Syst.*, 2001, IOS Press. With permission.)

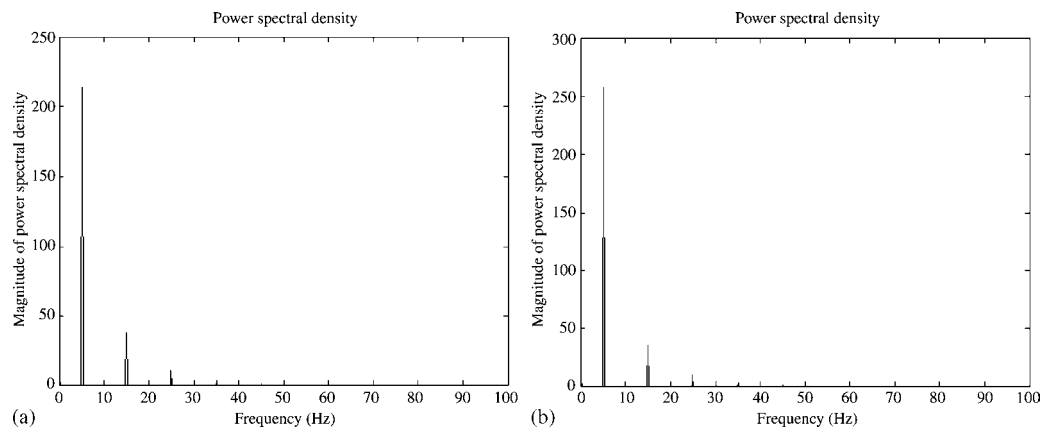


FIGURE 28.35 (a) Vibration signature corresponding to the square input, with a standardized amplitude of 1 V and frequency of 5 Hz; (b) spectrum of the machine corresponding to the square input after fault occurs. (Source: Tan, K.K., Tang, K.Z., de Silva, C.S., Lee, T.H., and Chin, S.J., *J. Intell. Fuzzy Syst.*, 2001, IOS Press. With permission.)

vibration signal of the machine (corresponding to the chirp signal, with a standardized amplitude of 1 V and starting frequency of 5 Hz) is shown in Figure 28.36. The spectra (corresponding to the chirp signal) of the machine before and after $t = 5$ sec are shown in Figure 28.37. The time-domain vibration signal of the machine (corresponding to the sinusoidal wave input, with a standardized amplitude of 1 V and

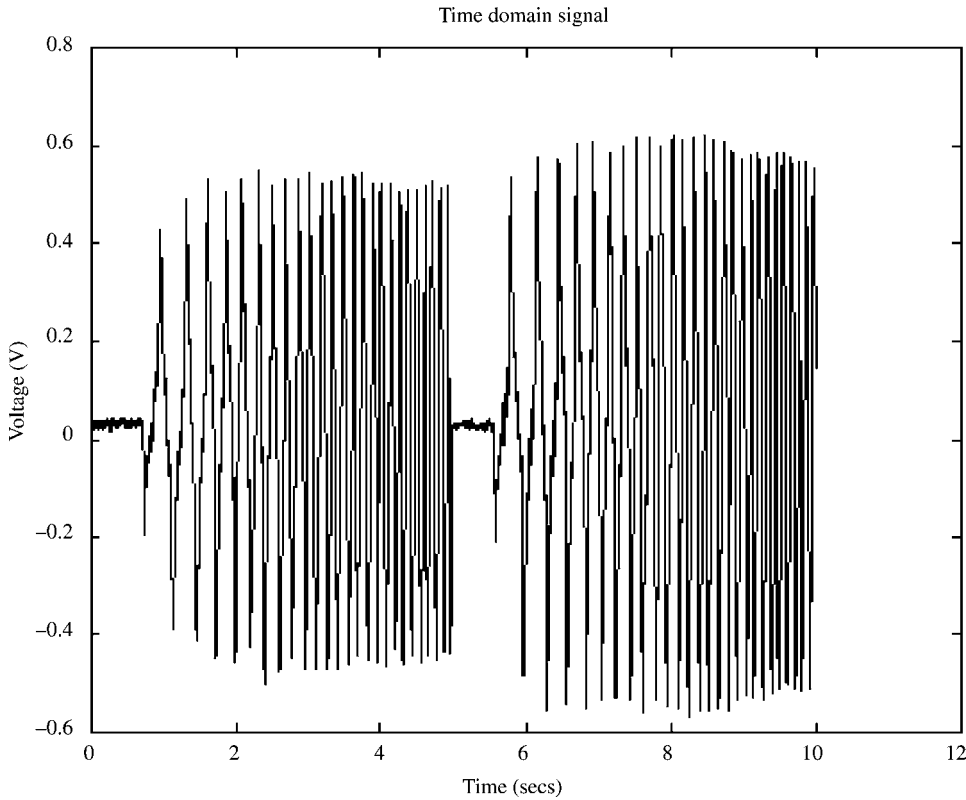


FIGURE 28.36 Time-domain vibration signal corresponding to the chirp input, with a standardized amplitude of 1 V and starting frequency of 5 Hz (at $t = 5$ sec, a fault is simulated).

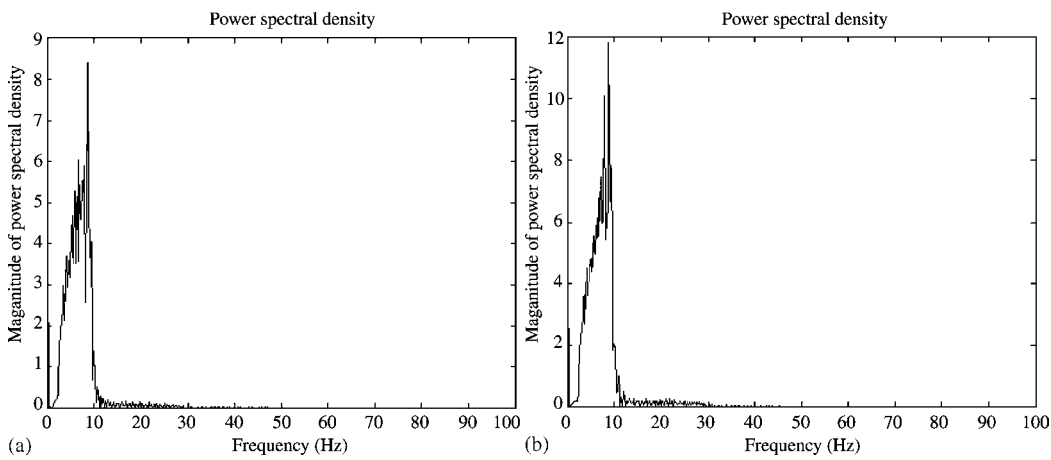


FIGURE 28.37 (a) Vibration signature corresponding to the chirp input, with a standardized amplitude of 1 V and starting frequency of 5 Hz; (b) spectrum of the machine corresponding to the chirp input after a fault occurs.

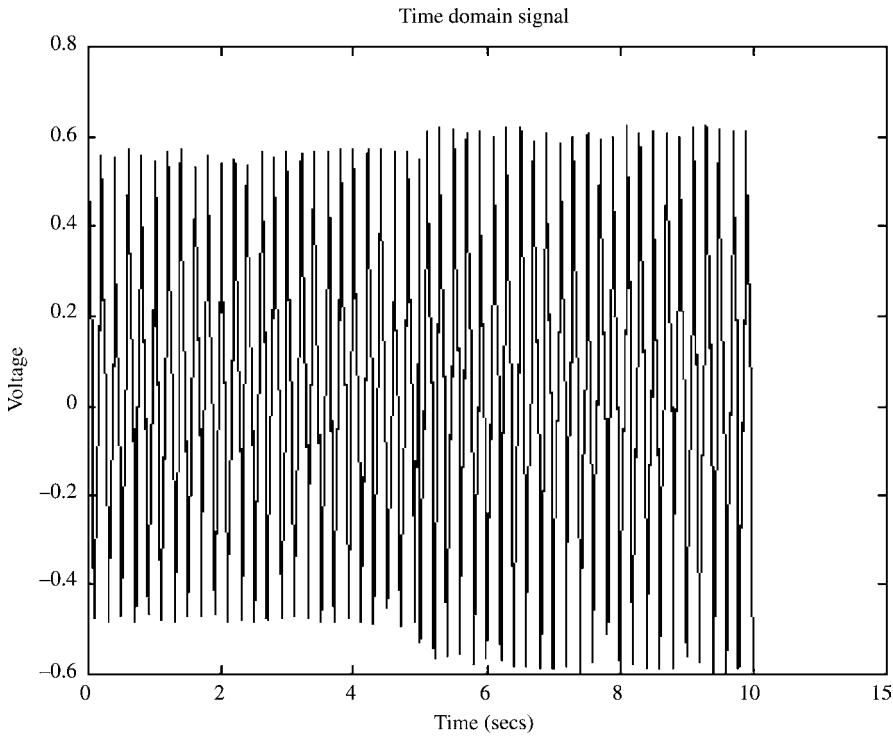


FIGURE 28.38 Time-domain vibration signal corresponding to the sinusoidal input, with a standardized amplitude of 1 V and frequency of 5 Hz (at $t = 5$ sec, a fault is simulated).

frequency of 5 Hz) is shown in Figure 28.38. The spectra (corresponding to the sinusoidal input) of the machine before and after $t = 5$ sec are shown in Figure 28.39.

The vibration-analysis algorithm is able to detect the fault in the machine. Before the introduction of the fault, the *HEALTH* attribute of the shaker table is found to be about 0.97. After the introduction of the fault, the *HEALTH* attribute falls to 0.58, which is below the threshold value, set at 0.7. The alarm is triggered as a result.

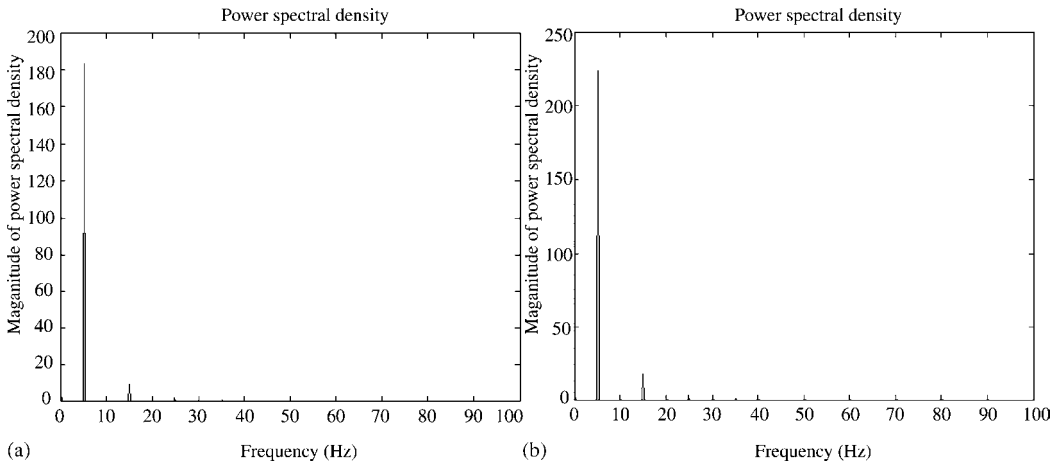


FIGURE 28.39 (a) Vibration signature corresponding to the sinusoidal input, with a standardized amplitude of 1 V and frequency of 5 Hz; (b) spectrum of the machine corresponding to the sinusoidal input after fault occurs.

SUMMARY

In this section, the development of a low-cost approach towards real-time monitoring and analysis of machine vibration is described. A real-time analyzer, based on a fuzzy fusion technique, is used to monitor continuously and compare the actual vibration pattern against a vibration signature. This intelligent knowledge-based real-time analyzer is able to detect excessive vibration conditions much sooner than a resulting fault could be detected by an operator. Subsequently, appropriate actions can be taken. This approach may be implemented independently of the control system and as such can be applied to existing equipment without modification of the normal mode of operation. Experimental and simulation results are provided to illustrate the effectiveness of this real-time vibration analyzer.

28.5 Practical Insights and Case Study

There are currently many companies in the industry that deal with machinery vibrations. Broadly, these companies can be classified into those that produce vibration-related testing products (e.g., FFT analyzers [Steinberg, 2000], vibration data collectors, and end-of-line production test equipment), and those that provide solutions in resolving noise- and vibration-related problems for different industries (e.g., automotive, aerospace, manufacturing, and engineering companies). For instance, if one of the machines in operation on the shop-floor is experiencing unexplained machinery noise or a high level of product failure, vibration analysis (Farrar et al., 2001) may provide some answers.

The case study explores the feasibility of remote vibration monitoring and control of a number of machines or mechanical systems located at different sites. For the sake of generality, "machines" is used as a general term to represent vibrating machines, mechanical systems, and other systems that exhibit vibration behavior. There are strong motivations for such setups. Since the middle of the 1960s, the concept of the distributed system has been widely adopted in the process industries, such

as the chemical industry, manufacturing industry, food processing industry, primary industry, and many others. These distributed systems are also characterized by smart devices. As the costs of manufacturing, that is, labor costs, the cost of raw materials, fixed costs, rental costs, and other production costs, are a major concern for the location of plants, many processes are currently widely distributed geometrically. The layout of an entire plant can be rather extensive, spreading across continents in certain cases.

The extensive distribution of an entire plant requires close coordination and synchronization of the distributed operations, as well as an efficient remote monitoring and control facility in place. The utilization of the Internet for this monitoring and control purpose perfectly complements the trend of distributed intelligence in the field controllers and devices on the shop-floor. As a result, superior control decisions can be made with these readily available resources and information, that is, historical data, knowledge databases, and so on. Internet working has become essential for plant automation. A case study which implements remote vibration monitoring and control of various machines will be illustrated in this section.

This vibration monitoring and control system possesses the structure as shown in Figure 28.40. It is able to monitor continuously the real-time health conditions of multiple machines at different sites, connected via the Internet. The system operates in two modes: the learning mode and the monitoring mode, as mentioned earlier. In the learning mode, vibration signatures, representative of the health of the machines to be monitored, are stored in the supervisory controller. Accelerometers mounted on the machine directly provide measurements of the vibration signals. In the monitoring mode, real-time vibration signals are streamed from the front-end controllers to the supervisory controller. Based on these real-time vibration signals from the various machines, the supervisory controller is able to generate decisions on the health condition of the machines, taking into consideration various criteria based on a fuzzy fusion technique, as mentioned earlier. Alarms will be activated when the health condition of the machines falls below an acceptable threshold level. Subsequently, rectification actions, to provide a warning or automatic corrective action (e.g., changing the operating conditions of the machine,

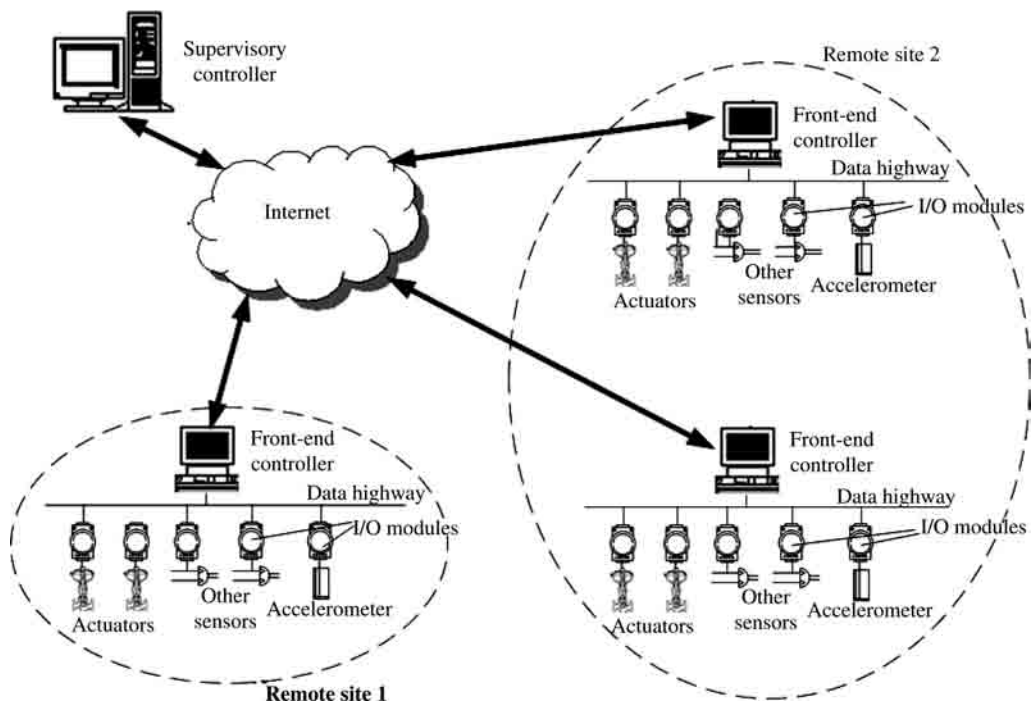


FIGURE 28.40 Remote vibration monitoring and control system.

modifying the parameters of the controller, or shutting down the machine), may be invoked before extensive damage is done to the machines.

Referring to the architecture of the vibration monitoring and control system as shown in [Figure 28.40](#), a data transfer and communication protocol needs to be adopted for such an application. There are several ways of connecting the supervisory controller and the remote machines. One of the possible ways is to apply DataSocket technology; yet another is to use low-level protocols such as TCP/IP and User Datagram Protocol. As can be seen, this vibration monitoring and control system may be applied to existing setups at the shop-floor level, without much modification necessary. The front-end field devices (i.e., actuators, sensors, and other I/O modules) are linked up *via* the field-level data highway. Two popular types of field-level data highway are fieldbus and twisted pair. Access security is a main issue of such remote applications. There is a need to prevent unauthorized users from accessing and modifying the system so as to maintain the integrity and proper functioning of the system. This can be achieved by

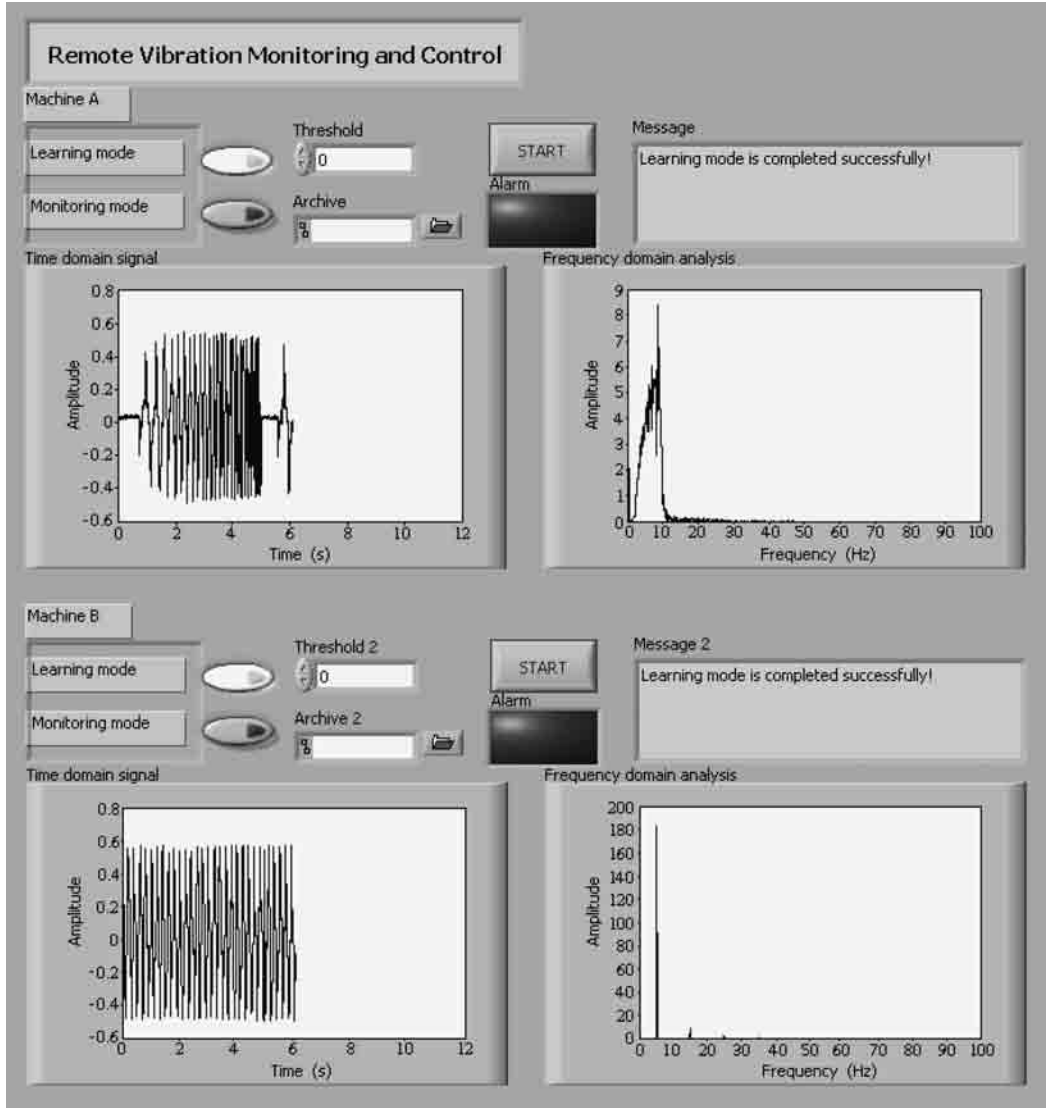


FIGURE 28.41 Learning mode — snapshot of the control panel at the supervisory controller end.

imposing some access authentication scheme. One commonly used basic access authentication scheme is the challenge–response authentication mechanism whereby the operator or user must provide some user logon information (e.g., user identification and a password) before accessing the supervisory controller terminal.

The control panel at the supervisory controller end (Figure 28.40) is as shown in Figure 28.41. At the supervisory controller end, the operator is able to monitor and control the health condition of various machines at different remote sites. As shown here, two machines (i.e., machine A and machine B) are being monitored. The learning mode is first initiated to obtain the vibration signatures of the two machines in the normal operational condition. The vibration signature of machine A resembles a chirp-like signal input whereas that of machine B resembles a sinusoidal-like signal input. At the end of the learning mode, a message is shown in the message box. Figure 28.42 shows a snapshot of the control panel in the monitoring mode. Here, the two machines are in good health, as the health indices

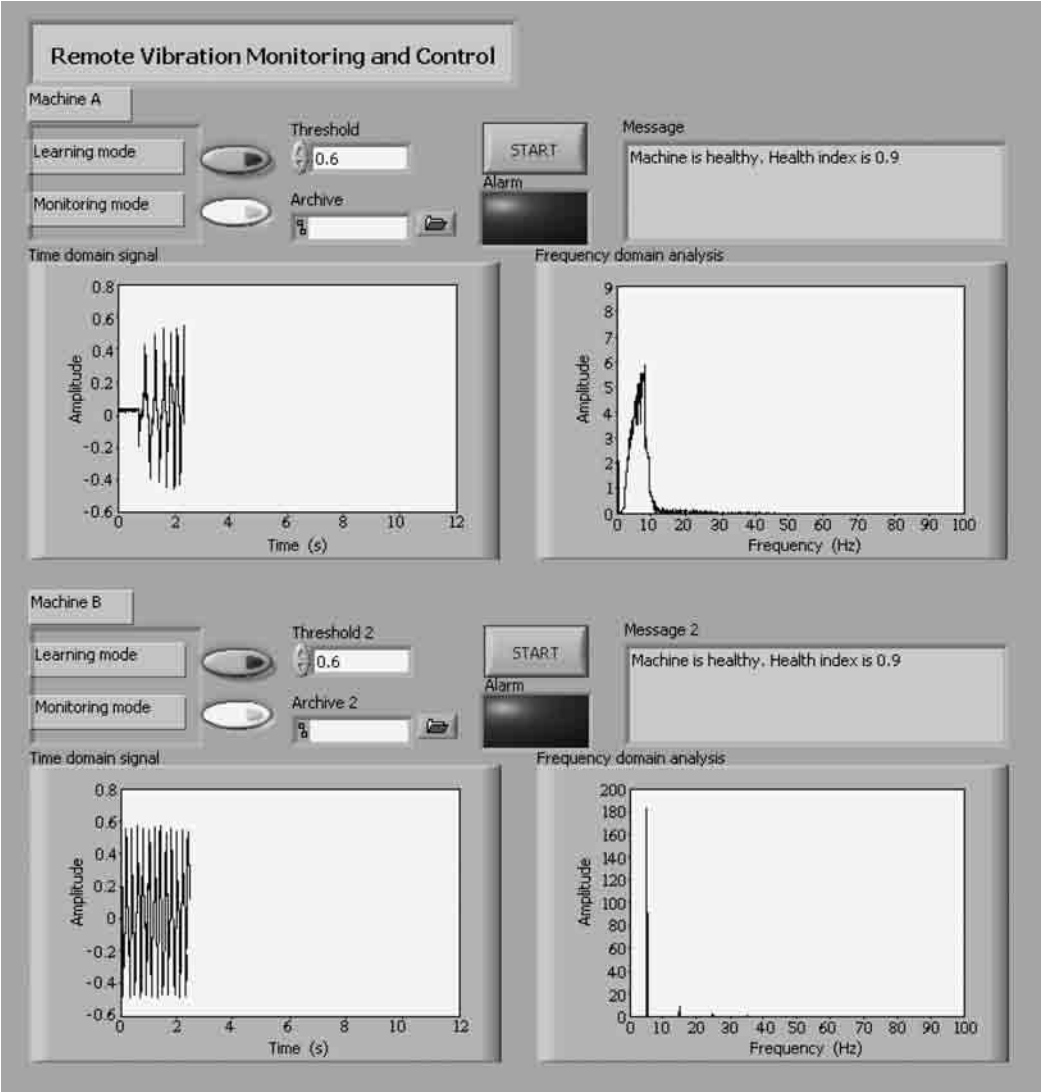


FIGURE 28.42 Monitoring mode — snapshot of the control panel at the supervisory controller end before any fault is invoked on machine A and machine B.

(i.e., current values are at 0.9) of the two machines are above the threshold value of 0.6. To simulate a fault arising in machine A, the input signal to machine A is changed to a sinusoidal input. This causes a simultaneous change in the vibration pattern of Machine A. A snapshot of the control panel at the supervisory controller end is as shown in Figure 28.43 after the fault is invoked to machine A. As can be clearly seen, the vibration pattern of machine A has changed. The message box displays that the health index of machine A (current value is at 0.49) has fallen below the threshold value of 0.6. To signal the deterioration of the health condition of machine A, the alarm LED is lit up. The health condition of machine B remains in the satisfactory region. To simulate a fault arising in machine B, the amplitude of the input signal to Machine B is increased slightly, by 20%. Consequently, this will also cause simultaneous change in the vibration pattern of machine B. A snapshot of the control panel at the supervisory controller end, after the fault is invoked to machine B, is as shown in [Figure 28.44](#).

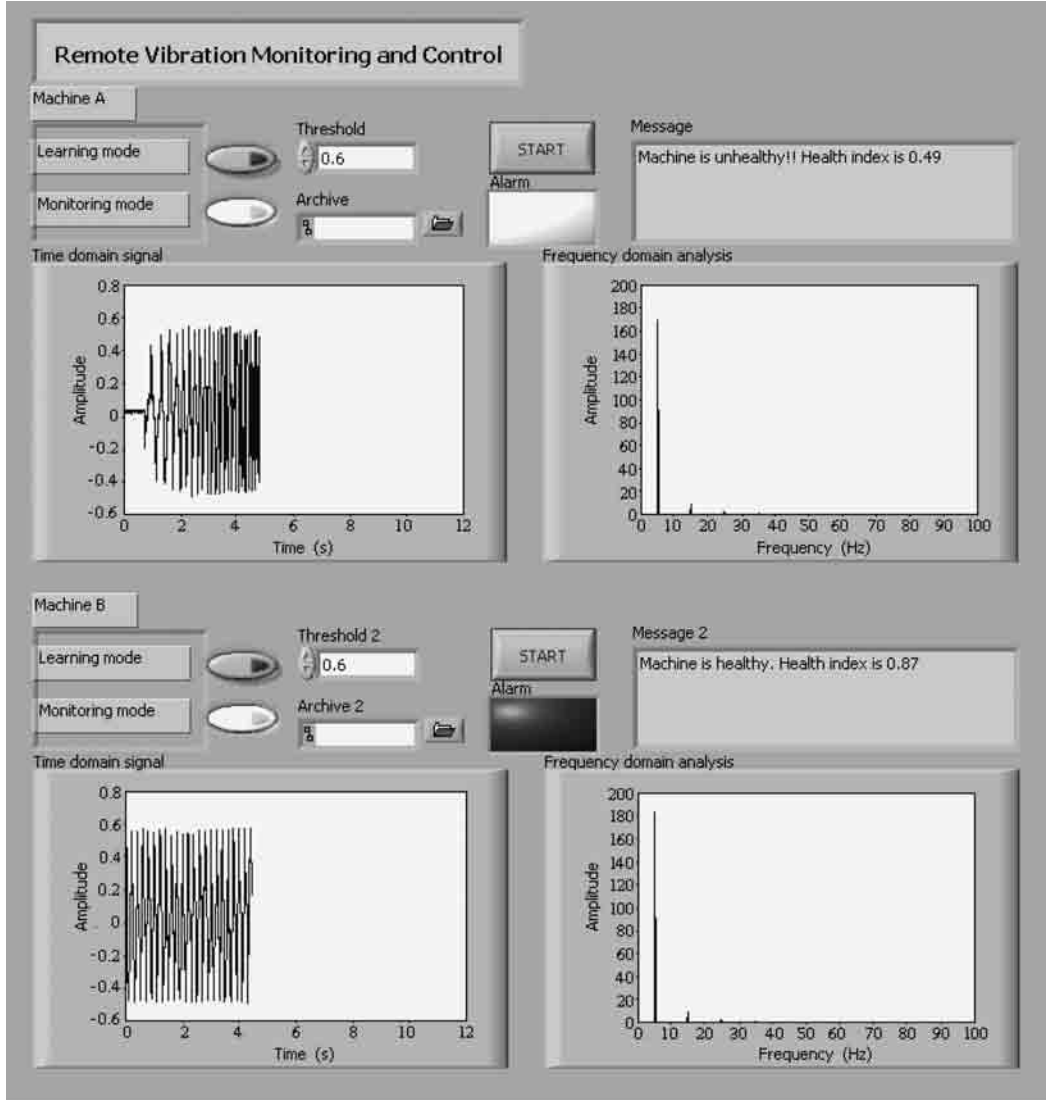


FIGURE 28.43 Monitoring mode — snapshot of the control panel at the supervisory controller end when a fault is invoked on machine A (at $t = 3$ sec).

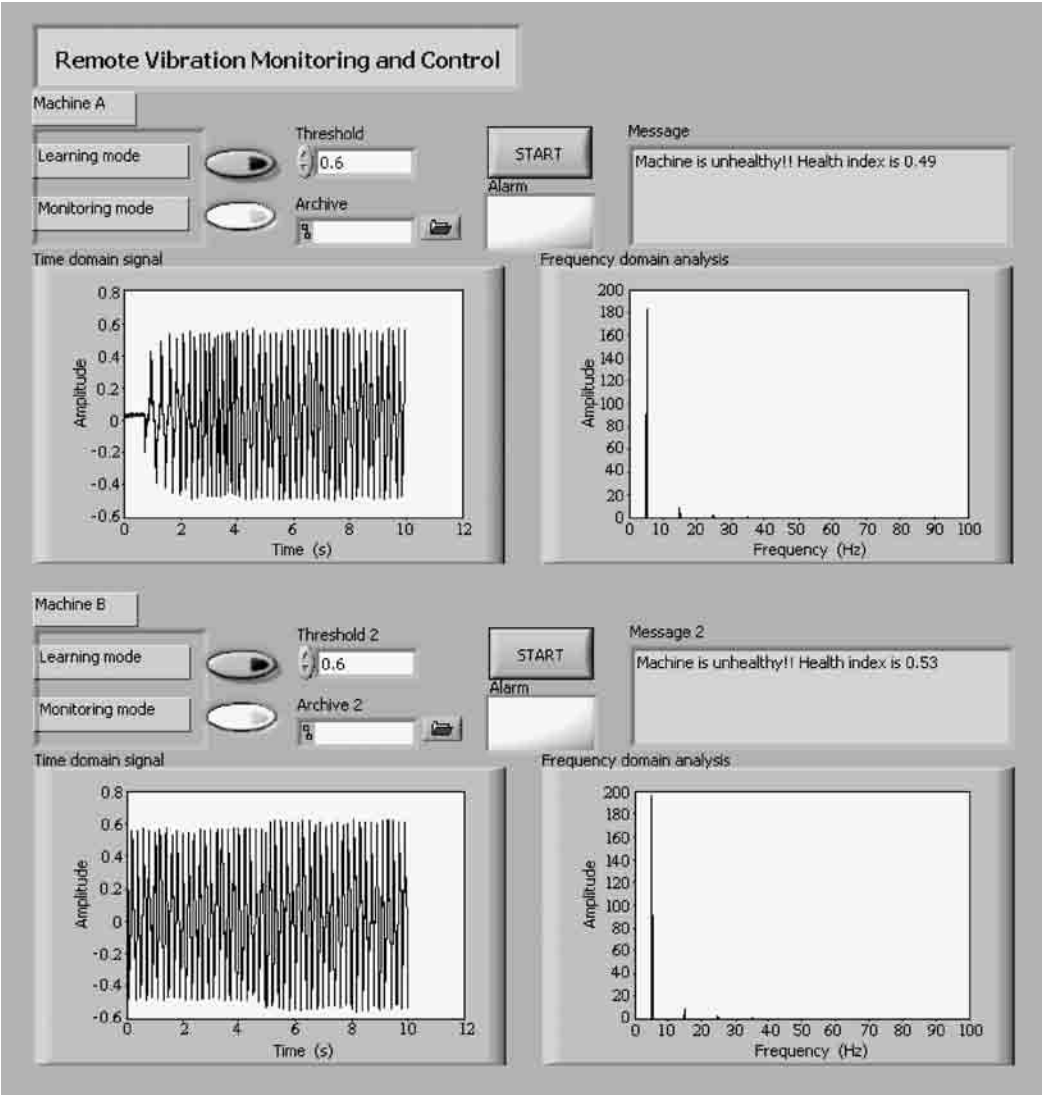


FIGURE 28.44 Monitoring mode — snapshot of the control panel at the supervisory controller end when a fault is invoked on machine B (at $t = 5$ sec).

The vibration pattern of machine B has changed. The message box displays the health index of machine B (current value is at 0.53) has fallen below the threshold value of 0.6. In the same way, the deterioration of the health condition of machine B is highlighted by activating the alarm LED.

SUMMARY

This section gives the reader practical insights into vibration monitoring and control applications in the industry. A case study is provided to explore the feasibility of remote vibration monitoring and control of a number of machines or mechanical systems located at different sites.

28.6 Conclusions

Approaches to address undue vibration arising in mechanical systems have been presented in the chapter. The first approach presented is concerned with a proper mechanical design with a view to reduce the sources of vibration. The second approach is the possibility of including functionalities in the control system to continuously monitor and possibly suppress vibration by terminating transmission at the resonant frequencies. The third approach uses a low-cost monitoring device, which can trigger alarm when excessive vibration is detected to enable corrective actions. Precision motion systems, where the effects due to vibration will directly affect performance, will usually adopt a number of such strategies to keep vibration level to a minimum and acceptable level.

References

- Adams, M.L. Jr. 2000. *Rotating Machinery Vibration: From Analysis to Troubleshooting*, Marcel Dekker, New York.
- Ahlstrom, M.L. and Tompkins, W.J., Digital filters for real-time ECG signal processing using microprocessors, *IEEE Trans. Biomed. Eng.*, 32, 708–713, 1985.
- Beards, C.F. 1983. *Structural Vibration Analysis: Modelling, Analysis and Damping of Vibrating Structures*, Ellis Horwood, Chichester, U.K.
- Bertran, E. and Montoro, G. 1998. *Adaptive suppression of narrow-band vibrations*, 5th International Workshop on Advanced Motion Control, Coimbra, Portugal, June 1998, pp. 288–292.
- Blanding, D.L. 1999. *Exact Constraint: Machine Design Using Kinematic Principles*, ASME Press, New York.
- de Silva, C.W. 2000. *Vibration: Fundamentals and Practice*, CRC Press, Boca Raton, FL.
- dSPACE DS1102 User's Guide, Document Version 3, dSPACE GmbH, Paderborn, Germany, 1996.
- Evan, C. 1989. *Precision Engineering: An Evolutionary View*, Cranfield Press, Bedford, U.K.
- Farrar, C.R., Doebling, S.W. and Duffey, T.A. 2001. *Vibration-based Damage Detection, Structural Dynamics @ 2000: Current Status and Future Directions*, Research Studies Press, Baldock, U.K., pp. 145–174.
- Fertis, D.G. 1995. *Mechanical and Structural Vibrations*, Wiley, New York.
- Fleming, J.F. 1997. *Analysis of Structural Systems*, Prentice Hall, Englewood Cliffs, NJ.
- Glover, J.R. Jr., Comments on digital filters for real-time ECG signal processing using microprocessors, *IEEE Trans. Biomed. Eng.*, 34, 1, 962–963, 1987.
- Kelly, S.G. 2000. *Fundamentals of Mechanical Vibrations*, 2nd ed., McGraw-Hill, Boston, MA.
- Kwan, T. and Martin, K., Adaptive detection and enhancement of multiple sinusoids using a cascade IIR filter, *IEEE Trans. Circuits Syst.*, 36, 7, 937–947, 1989.
- Raichel, D.R. 2000. *The Science and Applications of Acoustics*, Springer-Verlag, New York.
- Ramirez, R.W. 1985. *The FFT Fundamentals and Concepts*, Prentice Hall, Englewood Cliffs, NJ.
- Rankers, A.M. 1997. *The Machine Dynamics in Mechatronic Systems — An Engineering Approach*, In-house Report, Philips, Amsterdam.
- Steinberg, D.S. 2000. *Vibration Analysis for Electronic Equipment*, 3rd ed., Wiley, New York.
- Takagi, T. and Sugeno, M., Fuzzy identification of systems and its applications to modelling and control, *IEEE Trans. Syst. Man Cybern.*, 15, 116–132, 1985.
- Tan, K.K., Lee, T.H., Dou, H.F., Huang, S. 2001. *Precision Motion Control: Design and Implementation*, Springer-Verlag, London.
- TMSS320C24x DSP Controllers Evaluation Module Technical References, Tarrant Dallas Printing, Dallas, TX, 1997.
- Uicker, J.J., Pennock, G.R. and Shigley, J.E. 2003. *Theory of Machines and Mechanisms*, 3rd ed., Oxford University Press, New York.
- Vierck, R.K. 1979. *Vibration Analysis*, Crowell, New York.
- Zadeh, L.A., Outline of a new approach to the analysis of complex systems and decision process, *IEEE Trans. Syst. Man Cybern.*, 3, 28–44, 1973.

VII

Seismic Vibration

Seismic Base Isolation and Vibration Control

Hirokazu Iemura

Kyoto University

Sarvesh Kumar Jain

Madhav Institute of Technology
and Science

Mulyo Harris Pradono

Kyoto University

29.1	Introduction	29-1
	From Ductility Design to Base Isolation and Control Design • The Importance of Reducing Seismic Input and Response	
29.2	Seismic Base Isolation	29-4
	Historical Development of Base Isolation • Basic Principle • Issues in Seismic Base Isolation • Seismic Isolation Devices • Design of Isolation Devices • Verification of Properties of Isolation Systems • Analysis of Base-Isolated Structures • Experimental Methods for Isolated Structures • Implementation of Seismic Isolation • Performance during Past Earthquakes	
29.3	Seismic Vibration Control	29-33
	Historical Development of Seismic Vibration Control • Basic Principles • Important Issues in Vibration Control • Vibration-Control Devices • Control Algorithm • Experimental Performance Verification • Implementations	

Summary

This chapter presents seismic vibration control of civil engineering structures. It is divided into two main sections. The first part of the chapter deals with vibration control by seismic base isolation, whereas the second part covers methods of response control that use passive energy dissipation, active control, semiactive control, and hybrid control, respectively. Each part starts with a brief description of the historical development of these methods, followed by basic principles and important issues in their implementation. Thereafter, devices used for structural response control, their design methods, and recommended experimental procedures for verification of their properties and analytical modeling are discussed. Various methods generally used for analysis of such structures are then discussed in detail followed by a brief description of the implementation of these methods for various types of structures. In addition, performance of existing structures during past earthquakes is also included, to highlight the effectiveness of these methods during real earthquakes. Further information on the general topic of this chapter is found in [Chapter 22](#), [Chapter 30](#), and [Chapter 31](#).

29.1 Introduction

Seismic isolation and vibration-control systems are relatively new and sophisticated concepts that require more extensive design and detailed analysis than do most conventional seismic designs of structures. In general, these systems will be most applicable to structures whose designers seek superior earthquake performance. Seismic base isolation and passive energy-dissipation systems are viable design strategies that have already been used for seismic protection of a number of structures. Other special seismic protective system techniques such as active control, semiactive control, hybrid combinations of active and passive devices, and tuned mass and liquid dampers may also provide practical solutions in the

near future. An innovative challenge is highly expected in this field for the seismic safety enhancement of civil structures.

29.1.1 From Ductility Design to Base Isolation and Control Design

The conventional method of seismic design mainly deals with increasing capacity. The approach is based on designing a strong and ductile structure (see Figure 29.1), which can take care of the inertial forces generated by the earthquake shaking. The approach results in increasing the size of structural members and connections, and providing additional bracing members and shear walls, or other stiffening members. The increase in stiffness then attracts more seismic forces and in turn requires further strengthening, which becomes uneconomical. Therefore, the conventional practice permits safe design of a structure on the premise that inelastic action in a ductility-based designed structure will dissipate significant energy and enable it to survive a severe earthquake without collapse. The conventional designs may permit some structural damage because of inelastic deformation in the members and also in nonstructural elements. Contents of structure can get damaged due to large interstory drift and high-floor accelerations.

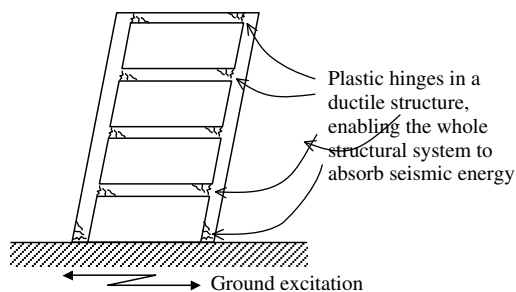


FIGURE 29.1 Schematic of a structure with ductile members.

It is difficult to control structural damage and it may be dangerous in unexpected strong seismic events. It has been observed that, in the event of major seismic events, structures based on the conventional design methods suffered damage, experienced high-floor accelerations, and resulted in disruption of essential services such as transportation, communication, and so on. Thus, for the class of structures like nuclear power plants, museums, hospital buildings, buildings with artifacts, important bridges, and such structures located in high-seismicity regions, this ductility-based design is not suitable. The need to minimize earthquake damage in critical and important structures prompted civil engineers to search for other methods of earthquake-resistant designs, which can not only protect structures from earthquake motions but also keep them functional during and after strong earthquakes. To this end, base isolation and structural control methods are found to be a solution.

Base isolation has the capability to reduce the seismic response of a structure by isolating it from the ground shaking (Figure 29.2a). An isolation system reduces the transmission of ground vibration, thus enabling the structure to experience less shaking from the ground. Therefore, structural damage and occupants' inconvenience can be minimized using this technique. However, at the expense of safety and the convenience of structure, the bearings undergo significant drift during large earthquakes that may disrupt the function of the bearings themselves and supply lines of services such as water and gas.

Another way of reducing seismic response is by using the structural control method. It has the capability of modifying the structural properties, such as stiffness, mass, and damping, and providing passive or active counterforces. Figure 29.2b shows the schematic diagram of the structural control method in a civil structure. It shows some examples of devices generally used for applying control forces.

The seismic safety enhancement of structures using the structural control method can be categorized as active and passive systems. There are also hybrid systems that represent combinations of active and passive, and semiactive systems to represent active controller that employs controllable passive devices.

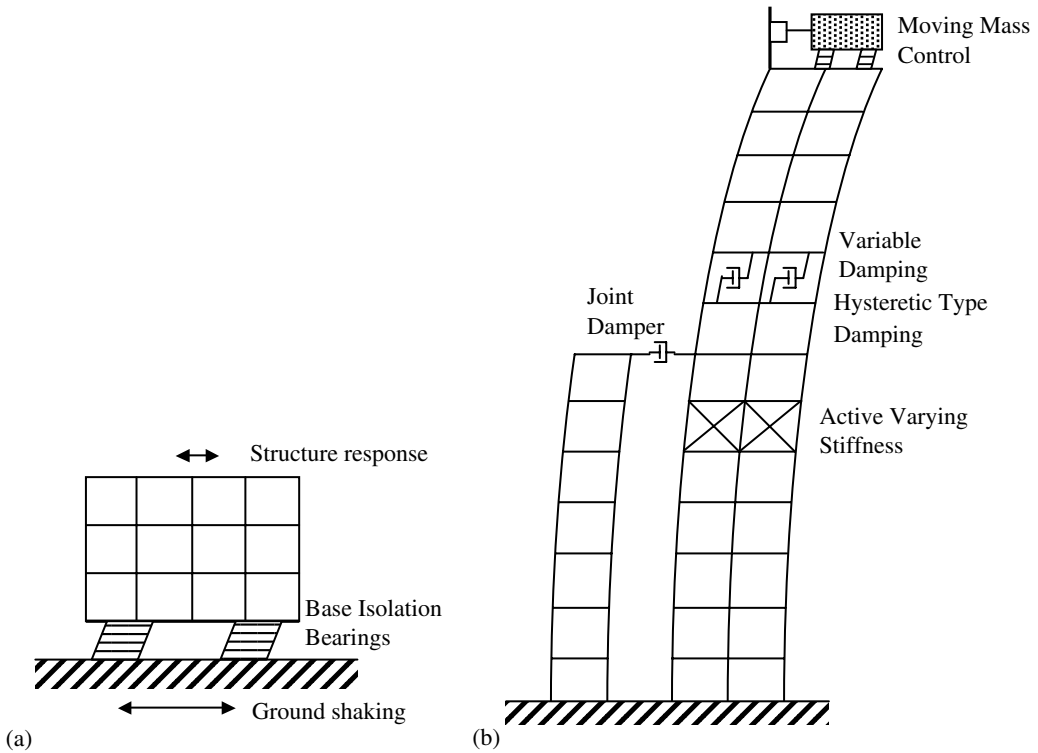


FIGURE 29.2 Schematic of a civil structure with (a) isolation bearings and (b) the structural control method.

Owing to changes in code provisions or upgradation of seismic zones, many structures come into the category of “unsafe” and require retrofiting. Response control strategies are found to be easier than other options, economical, and are often the only alternative for such cases.

29.1.2 The Importance of Reducing Seismic Input and Response

As mentioned above, by using the conventional method of seismic design, the design may permit some structural damage because of inelastic deformation in the members, and also in nonstructural elements, during large earthquakes. The ductility enables the structure as a whole to absorb the seismic energy. Once the structural response goes deeply into the plastic range during a large earthquake, structures may not be operational or repairable.

If the seismic input to the structure and structural response can be reduced, then the structural damage can be minimized. For higher reliability of structures even under very severe earthquake motion, structural control techniques that effectively reduce seismic force to structures are developed. The fast development of technology, particularly in the fields of electronics and computer science, has provoked the researchers in some centers worldwide to intensify development of a new concept with the new philosophy of seismic design. Generally, this concept is known as a design of intelligent structures or smart structures.

Owing to the experience of severe damage due to the Kobe earthquake, public demand for seismic performances of civil infrastructures became relatively clear in Japan. Civil infrastructures are constructed with the tax paid by the public, so a collapse or near collapse with unrepairable damage cannot be accepted, even under a very rare earthquake loading. Infrastructures are also expected to serve as public tools to help rehabilitate the affected society. For this purpose, infrastructures have to be repaired in a relatively short time, even though their functions are temporarily terminated due to severe earthquake loading.

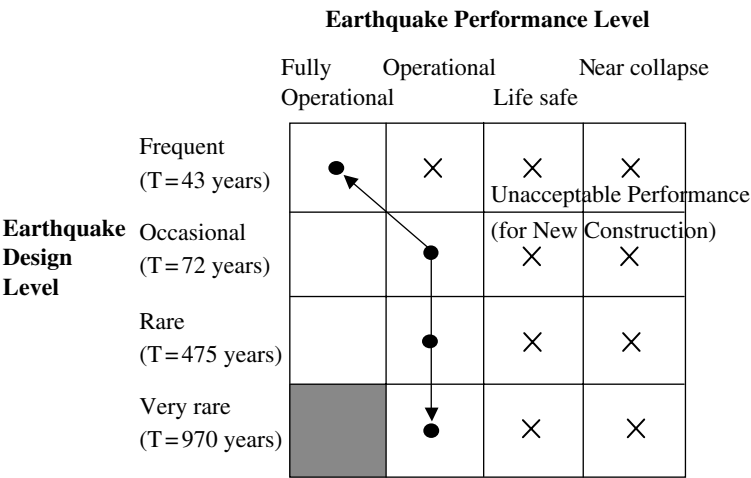


FIGURE 29.3 Public demand for seismic performance of infrastructure.

The public demand for seismic performance objectives of infrastructures shows that structural damage has to be limited even against very rare earthquake loading (Figure 29.3). The figure shows that civil infrastructures must be fully operational during and after frequent, weak earthquakes. They also expected to be operational even after very rare, strong earthquakes. To achieve the objectives, new technologies are to be developed that can result in the desired performance.

29.2 Seismic Base Isolation

29.2.1 Historical Development of Base Isolation

Seismic base isolation is not a very new idea. More than a century ago, John Milne, a professor of engineering in Japan, built a small house of wood and placed it on ball bearings to demonstrate that a structure could be isolated from earthquake shaking (Housner et al., 1997). In 1891, after the Narobi earthquake ($M = 8.0$), Kawai, a Japanese person, proposed a base-isolated structure with timber logs placed in several layers in the longitudinal and transverse direction (Izumi, 1988; see Figure 29.4). In 1906, Jacob Bechtold of Germany applied for a U.S. patent in which he proposed to place building on rigid plate, supported on spherical bodies of hard material (Buckle and Mayes, 1990). In 1909, a medical doctor from England, Calentarients, applied for patents for his invention comprising isolation system for earthquake-proof building (see Figure 29.5). He proposed separating a building from its foundation with a layer of sand or talc (Kelly, 1986). The Imperial Hotel in Tokyo, constructed in 1921, was intended to float on an underlying layer of mud. The building was founded on an 8-ft thick layer of firm soil under which exists a 60- to 70-ft thick layer of soft mud. The building was

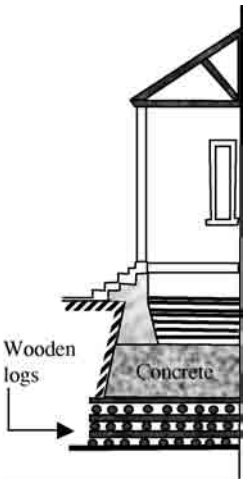


FIGURE 29.4 Base isolation by timber logs. (Source: JSSI, *Introduction of Base Isolated Structures*, Japan Society of Seismic Isolation, Ohmsa, Tokyo, 1995. With permission.)

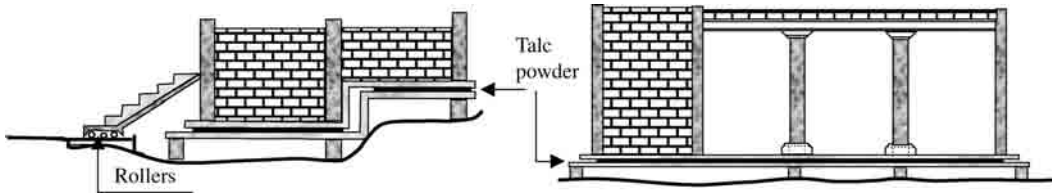


FIGURE 29.5 Calentarients' idea of seismic base isolation. (Source: JSSI, *Introduction of Base Isolated Structures*, Japan Society of Seismic Isolation, Ohmsa, Tokyo, 1995. With permission.)

highly decorative with many appendages. The soft mud acted as isolation system and the building survived the devastating 1923 Tokyo earthquake (Kelly, 1986; Buckle and Mayes, 1990).

Attempts were made in the 1930s to protect the upper floors of multistory buildings by designing very flexible first-story columns. In a later modification of the flexible first-story columns approach, it was proposed that the first-story columns should be designed to yield during an earthquake to produce an energy-absorbing action. However, to produce enough damping, several inches of displacement is required, and a yielded column has greatly reduced buckling load, proving the concept to be impractical. It was then proposed that, if the soft first story is constructed underground, then energy dissipaters can be installed at the top of this story (which approximates ground level) that prevent the superstructure from moving too far, and dissipate the energy of ground motion before it enters the building. The superstructure, from the first floor up, can be an economically braced, nonductile concrete frame requiring no internal shear walls (Arnold, 2001). To overcome the inherent dangers of soft supports at the base, many types of roller-bearing systems have been proposed. The rollers and the spherical bearings are very low in damping and have no inherent resistance to lateral load, and therefore some other mechanism that provides wind restraint and energy-absorbing capacity is needed. A long duration between two successive earthquakes can result in the cold welding of bearings and plates, thus causing the system to become rigid after a time. Therefore, the application of rolling supports was restricted to the isolation of special components of low or moderate weight (Caspe, 1984).

Parallel to the development of the soft first-story approach, the flexibility of natural rubber was also seen as another solution for increasing the flexibility of the system. In 1968, large blocks of hard rubber, 54 in number, were used to isolate the three-story Heinrich Pestalozzi School in Skopje, Republic of Macedonia. The building is constructed of reinforced concrete shear walls. This is the first building for which rubber bearings were used as base isolation against strong earthquakes. These rubber blocks are unreinforced and bulge sideways under the weight of this concrete structure (see Figure 29.6). Owing to having the same stiffness of the isolation system in all the directions, the building bounces and rocks backwards and forwards (Jurukovski and Rakicevic, 1995). These types of bearings are unsuitable for the earthquake protection of structures. The subsequent development of laminated rubber bearings has made base isolation a practical reality (Figure 29.7). Later, a large number of isolation devices were developed, and now base isolation has reached the stage of gaining acceptance and replacing the conventional construction, at least for important structures.

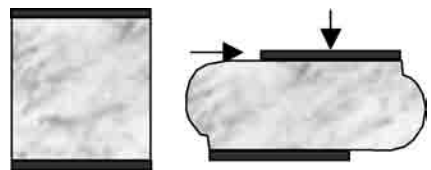


FIGURE 29.6 Unreinforced rubber blocks. (Source: Ohashi, U.G. *Earthquakes and Base Isolation*, Pub. Asakura, Tokyo, 1995. With permission.)

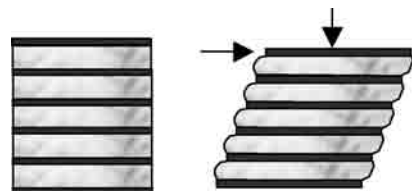


FIGURE 29.7 Rubber bearings with steel shims.

29.2.2 Basic Principle

Seismic base isolation is basically a lengthening of the fundamental time period of the structure with the help of a specially designed system that is placed between its superstructure and substructure (see Figure 29.8). Besides other advantages, the concept gained widespread acceptance due to the fact that most of the earthquake motions around the world have dominating frequencies in the range of 1.0 to 10 Hz, and the majority of conventionally designed structures also has their fundamental frequency of vibration lying in this range. Owing to this unwanted matching of the frequencies, these structures are subjected to high forces during earthquakes. The application of seismic base isolation shifts the fundamental time period away from the dominating frequencies of earthquake motions and thus detunes the frequencies. In other words, base isolation consists in filtering out high-frequency waves from the ground motion, thereby preventing the transmission of high energy in the structure. The effect of base isolation on reduction in force is shown schematically in Figure 29.9. Under favorable conditions, seismic base isolation can reduce drift to 0.2 to 0.5 of that which would occur if the building were fixed base (Figure 29.10). Reduction in acceleration has more influence on the force–deflection characteristics of the isolation system and may not be as significant as the reduction of drift (FEMA 356, 2000). However, the additional flexibility required for this period shift give rise to excessive relative displacement at the isolation level. Additional damping is introduced in the isolation system to limit this displacement response to within feasible limits. Still, it is necessary to provide an adequate seismic gap that can accommodate displacements at the isolation level. Most of the isolators have inherent damping, although sometimes supplemental energy dissipation devices may also be required at the isolation level. Various types of energy dissipation devices like metallic dampers and hydraulic dampers have been developed and can be used for this purpose (Skinner et al., 1993). The isolation damping also suppresses the resonance

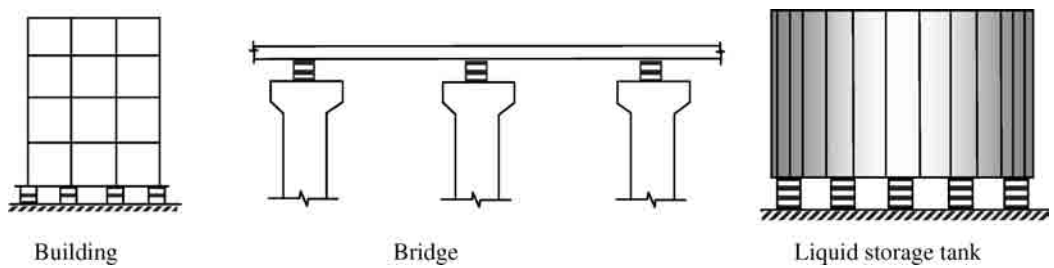


FIGURE 29.8 Application of seismic isolation for different structures.

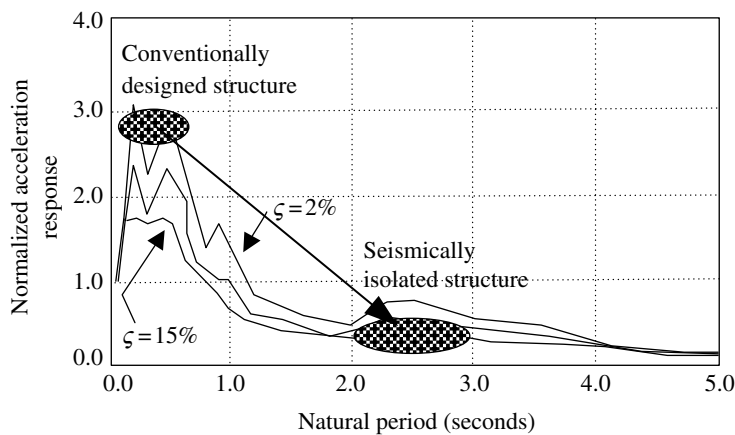


FIGURE 29.9 Conceptual diagram for seismic isolation.

resulting due to higher period contents of the earthquake motion. Although damping is useful in reducing the required seismic gap, excess damping may result in an increase in acceleration that may affect the performance of nonstructural elements and contents. Thus, an isolation system should essentially be able to (1) support a structure, (2) provide horizontal flexibility, and (3) dissipate energy. These three functions can be incorporated in a single device or can be provided by means of different components. In addition, it may be necessary to provide buffers, which can limit the isolator displacements during extreme earthquakes.

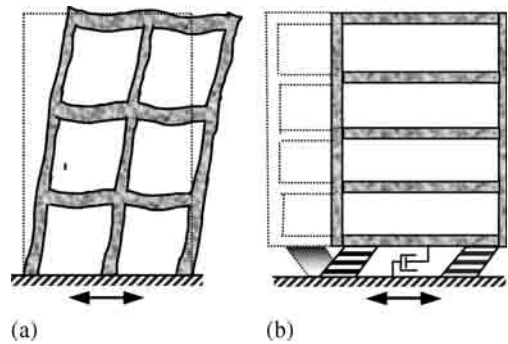


FIGURE 29.10 Behavior of (a) fixed-base and (b) base-isolated building.

29.2.3 Issues in Seismic Base Isolation

A number of issues for seismic isolation design have been identified based on experiences of their behavior. Some of the issues that should be considered before choosing the base-isolation approach for a project are touched in the following sections.

29.2.3.1 Performance Criteria

The performance criteria for the structure needs to be established in order to evaluate alternative seismic resisting systems; for example, it must be established whether the structure is required to be functional during and after major earthquakes, or if it is to be preserved for its historical importance. Whether seismic base isolation is a suitable design strategy for a particular project will depend primarily on the performance required. To achieve the *fully operational* or *operational* performance level, one can consider seismic base isolation as a possible design strategy, but if *life safe* is the required structural performance level, it may not be practical to choose seismic base isolation.

29.2.3.2 Type of Structure

Significant benefits obtained from isolation exist in structures for which the fundamental period of vibration without base isolation is short, that is, less than 1 sec. Certain structures may not be suitable for base isolation because of their shape; for example, this is true for slender high-rise buildings that have a natural period long enough to attract low earthquake forces without isolation. Therefore, seismic isolation is mostly used for low-rise buildings. Historical buildings, which generally are stiff masonry structures, can be appropriate structures for seismic base isolation. Bridges are the structures for which application of seismic isolation is very convenient. The provision of bearings at the tops of piers adds flexibility to stiffer piers and in turn avoids yielding of piers. It is easy to examine these bearings after a seismic event and replace them if needed.

29.2.3.3 Site Characteristics

In base-isolation design, the basic objective is to filter out the high frequencies of the ground motion by lengthening the time period of vibration to approximately 2 sec. Thus, conventional base isolation is not suitable for structures on soft soils where the ground motions are dominated by low frequencies. Therefore, a detailed investigation of the site must be carried out before possible isolation can be considered. Another important aspect is near-fault ground motions. Waves from such motions usually have long-period velocity pulses, which impart lot of momentum to the structure. This is particularly damaging to base-isolated structures because it may cause large horizontal base displacements. The displacement can result in instability of the structure, or it

can result in impact with moat walls, which can affect the sensitive equipment housed in the building. An isolator with bilinear force–displacement behavior and a large ratio of yield-force to supported weight can substantially reduce the displacement. The provision of high damping in an isolation system can also work. However, the degree of isolation during relatively frequent earthquakes without near-fault pulses is much reduced due to these provisions (Skinner and McVerry, 1996).

29.2.3.4 Retrofit Issues

In selecting a suitable retrofit system and properties of seismic isolation system, consideration should be given to the characteristics of the existing building, such as foundation capacity and strength of the superstructure. For retrofit of buildings, successful implementation of a seismic isolation system requires that the sequences of temporary bracing, shoring, cutting of existing columns and walls, and installation of isolators be well planned. Base isolation for the retrofit of bridges is simpler as they usually have thermal bearings, which can easily be replaced by seismic isolation bearings. The retrofitting of monuments or buildings of historical importance requires special efforts to cope with the need of minimum alterations. Provisions must be made to protect them from any seismic event during the retrofitting. Also it must be identified whether workable spaces and access to the work area is available.

29.2.3.5 Design of Building Services

Depending on the base-isolation system, base-isolated structures under earthquake motions can exhibit significant base slab displacements due to the low horizontal stiffness of the isolation elements. This may create problems on the supply lines transitioning between the parts of structure below and above isolation level. Therefore, special attention is to be given to installations of building services such as water supply, sewerage, gas, air-conditioning, and so on in order to prevent any damage to these supply lines, which might cause secondary effects. In the case of isolation of two or more structural units founded on a common foundation and connected by expansion joints, special care is needed regarding the proportions of the expansion joint in order to prevent the pounding of buildings during earthquakes.

29.2.3.6 Expected Life of Isolator

The isolation system should remain operational for the expected lifetime of the isolated structure. It should not require frequent maintenance during this period. Although the functioning of an isolator may be required few times during the lifetime of structure, it must perform well at such times. If life of the isolator is less than the life of structure, then it may be necessary to provide a mechanism for the inspection and replacement of the isolation system. Another related aspect is the protection of isolation elements against fire, and measures should be taken for this. Furthermore, as an isolation system is provided mostly at the base, its resistance to chemical and biological reactions is also important (Jurukovski and Rakicevic, 1995).

29.2.4 Seismic Isolation Devices

The successful seismic isolation of a particular structure is strongly dependent on the appropriate choice of the isolation system. In addition to providing adequate horizontal flexibility and appropriate damping, the isolation system should essentially have the capability of self-centering after deformation, high vertical stiffness to avoid rocking, and enough initial stiffness to avoid frequent vibration from wind and minor seismic events. Different types of isolators have been developed and proposed to achieve these properties, and some of them are discussed below.

29.2.4.1 Laminated Rubber Bearings

Rubber bearings offer the simplest method of seismic base isolation and are relatively easy to manufacture. The bearings are made by vulcanization bonding of sheets of rubber to thin steel reinforcing plates. Initially, the main function of the laminated rubber bearings was to provide flexibility for thermal displacements in bridges. Later, similar bearings found application in the isolation of buildings from vibration due to underground railways, and these bearings have performed well over a substantial period of time (Kelly, 1990). The bearings are very stiff in the vertical direction and flexible in the horizontal direction. High vertical stiffness of these bearings is achieved through the laminated construction of the bearing using steel plates. The cross section of a typical rubber bearing is shown in Figure 29.11. The most common elastomers used in elastomeric bearings are natural rubber, neoprene rubber, butyl rubber, and nitrile rubber. The mechanical (tear strength, high strain fatigue resistance, creep resistance) and low-temperature properties of natural rubber are superior to those of most synthetic elastomers used for seismic isolation bearings. Therefore, natural rubber is the most frequently recommended material for use in elastomeric bearings, followed by neoprene. Butyl rubbers are suitable for low-temperature applications and nitrile rubber has limited application in offshore oil structures (Taylor et al., 1992).

The damping ratio (i.e., the fraction of critical damping) achieved from natural rubber is low, in the order of 0.02 to 0.04, and therefore it is unusual to use it without some other element that is able to provide increased damping. In order to achieve better performance in a single unit, rubber used in the bearing is a compound formed with some filler agents. This compounding results in desired properties, such as (1) high damping and (2) high horizontal stiffness at low values of shear strain. The damping ratio (i.e., the fraction of critical damping) achieved is in the order of 0.10 to 0.20. These *high-damping rubber bearings*, originally developed in England, found several applications in Japan and United States. A number of fillers are employed, such as metal oxides, clay, and cellulose, but the filler that is most commonly used in seismic isolation bearings is carbon black (Taylor et al., 1992). Force–displacement behavior of these bearings depends upon the type of compounding. Figure 29.12 shows the results of cyclic loading test conducted on a four-layer high-damping rubber bearing specimen (Tanzo et al., 1992). In the experiment, the tests were carried out up to 200% (96 mm) shear strain. Vertical load for the tests was kept as 40 tonf (64 kg/cm²).

The application of steel shims in laminated rubber bearings provides necessary vertical stiffness, but at the same time makes these isolators heavy and expensive. Recently, Kelly (2001) proposed a seismic isolation system for developing countries, in which steel plates are replaced by fiber mesh. The *fiber-reinforced isolator* is expected to be significantly lighter and could lead to a much less labor-intensive manufacturing process.

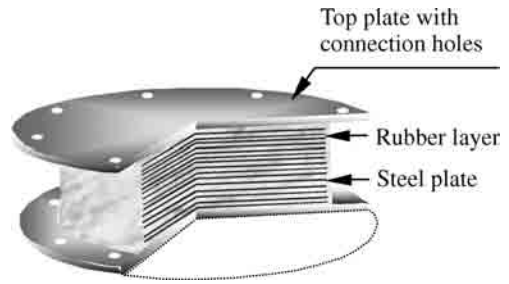


FIGURE 29.11 Laminated rubber bearing.

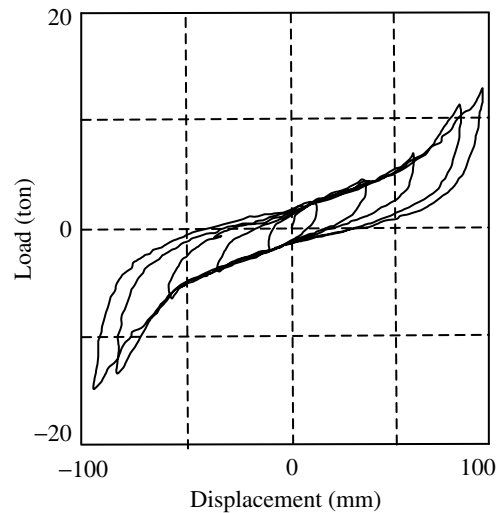


FIGURE 29.12 Load–displacement loops for high-damping rubber bearing. (Source: Tanzo, W. et al. Res. Rpt. 92-ST-01, Kyoto Univ., 1992. With permission.)

29.2.4.2 Lead Rubber Bearing

This isolation system consists of a cylinder of lead enclosed in a rubber bearing. The system is also known as the NZ bearing system, and its components are shown in Figure 29.13. The lead plug produces a substantial increase in damping, from about 3% of critical damping in the natural rubber to 10 to 15%, and also increases the resistance to frequently occurring loads such as minor earthquakes or wind. The reason for choosing lead is that it is a crystalline material, and under normal conditions it changes its crystal structure under deformation but almost instantly regains its original crystal structure when the deformation ceases. Thus, repeated yielding due to cyclic loading does not cause fatigue. Lead yields in shear at the relatively low stress of about 8 to 10 N/mm², and therefore produces stable hysteretic behavior and dissipates significant energy in strong ground motion. Load–displacement behavior of a lead rubber bearing is shown in Figure 29.14 (JSSI, 1995). The hysteretic behavior of lead rubber bearings can be treated as bilinear, with initial stiffness in the range of 9 to 16 times the postyield stiffness. These bearings provide an economical and effective solution, incorporating period shifting, increased damping, and high stiffness at low strains, and providing vertical support in a single device (Skinner et al., 1993). It has found several applications in new constructions as well as for retrofitting of buildings and bridges in different parts of the world.

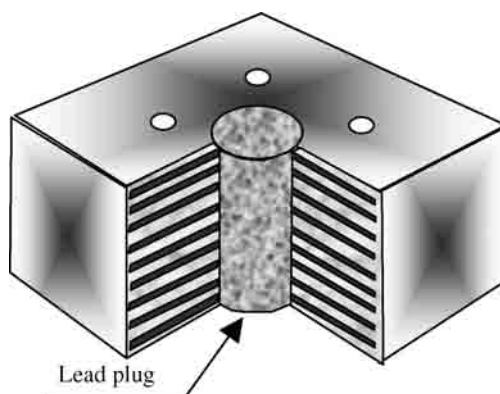


FIGURE 29.13 Lead rubber bearing. (Source: Skinner, R.I. et al. *An Introduction to Seismic Isolation*, Wiley, Chichester, UK, 1993. With permission.)

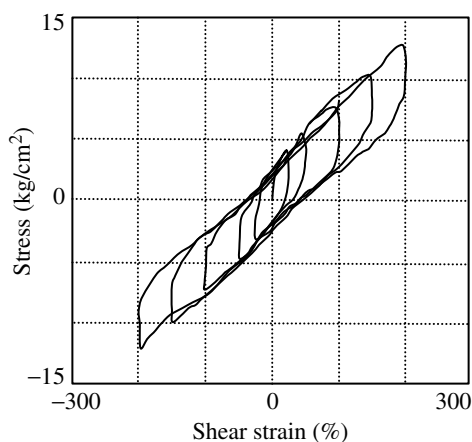


FIGURE 29.14 Behavior of lead rubber bearing under cyclic loading. (Source: JSSI, *Introduction of Base Isolated Structures*, Japan Society of Seismic Isolation, Ohmsa, Tokyo, 1995. With permission.)

29.2.4.3 Friction-Based Systems

In this class of isolators, the superstructure is allowed to slide during major seismic events. The structure slides whenever the lateral force exceeds the friction force at the sliding interface. The horizontal friction force at the sliding surface offers resistance to motion and dissipates energy. Pure sliding systems have no inherent natural period and therefore are insensitive to variations in the frequency content of ground excitation. The acceleration at the base of the structure is limited to the coefficient of friction at the sliding interface. Thus, by keeping this coefficient of friction low, the acceleration felt by the structure can be reduced. Systems based on a Teflon (PTFE) and stainless steel interface have the potential to provide high levels of protection against floor acceleration because of the low friction of the materials. However, the friction coefficient cannot be reduced arbitrarily, as the sliding displacement may exceed the acceptable value. Another feature of this isolation system is that the frictional force is proportional to the vertical load coming on the bearing, and therefore the center of mass and the center of resistance of the sliding support coincide. As a result, the torsional effects produced by the asymmetry of building are diminished.

The main drawback of the system is the absence of restoring force due to which a large residual displacement from the original position of the structure may be left after a major earthquake event. There are other practical problems that can affect the efficiency of sliding isolation, such as cold welding, freezing, and deterioration of the sliding surfaces. Changes may occur in the friction coefficient due to ageing, environmental attack, temperature variation, or wear during use (Skinner et al., 1993).

As the sliding depends upon the coefficient of

friction, the system may require regular inspection to maintain its coefficient of friction. The unsatisfactory predictability of friction coefficient and the absence of any centering force suggest that Teflon bearings should be used as seismic isolators only in combination with some other centering devices like steel dampers or rubber bearings (Priestley et al., 1996). Based on this concept another system called the *resilient friction bearing* (R-FBI) system was developed (Mostaghel and Khodaverdian, 1987). The system consists of several concentric layers of Teflon-coated friction plates that are in friction contact with each other and a central core of rubber. The rubber provides the resilient force while the friction forces dissipate the energy.

An effective mechanism to provide recentering force by gravity has been utilized in a *friction pendulum system* (FPS). In this system, the sliding surface takes a concave spherical shape so that the sliding and recentering mechanisms are integrated in one unit. As the name indicates, there are two mechanisms that are employed to achieve isolation, namely, sliding friction and pendulum motion. The internal components consist of a stainless steel concave surface upon which slides a stainless steel articulated slider surfaced with a high-load capacity and a low friction bearing material composite (see Figure 29.15). The radius of curvature determines the sliding or isolation period of the system. The period of the structure supported on the FPS is independent of the structure mass and therefore the period does not change if the structure weight changes or is different than assumed. This results in better control over the response of the systems, like liquid storage tanks in which weight varies in time because of variable liquid storage level. However, since the restoring force is linearly proportional to the sliding displacement, in case of high-intensity earthquakes or a low coefficient of friction, the additional sliding introduces additional energy in the structure. To overcome this problem, Pranesh and Sinha (2002) proposed the *variable frequency pendulum isolator*, in which the geometry of the concave surface is designed such that its frequency decreases with the increase in sliding displacement and asymptotically approaches zero at very large displacement.

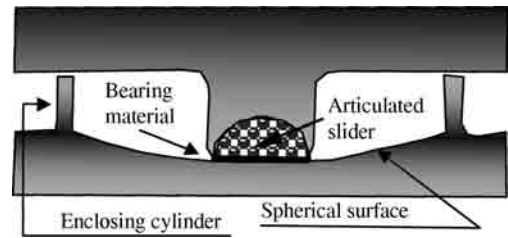


FIGURE 29.15 Schematic diagram of friction pendulum system.

29.2.4.4 Other Systems

A base-isolation system, which has found many applications in Japan, comprises of *low-damping rubber bearings* with *yielding metal devices*. The yielding of metals provides the necessary dissipation of energy. The commonly used dampers are shown in Figure 29.16 (Aoyagi et al., 1988; Takayama et al., 1988; Yasaka et al., 1988).

To standardize the designs of the sensitive structures of nuclear power plants for regions of different seismicity, an isolation system called the *EDF (Electricite de France) system* was developed. This is a laminated rubber bearing with friction plate at the top. An attractive feature of the EDF isolator is that, for the lower amplitude ground excitations, the lateral flexibility of the rubber provides the base isolation. At a high level of excitation, however, sliding will occur assuring maximum acceleration transmissibility of μg , where μ is the coefficient of friction between materials of sliding surface (Constantinou, 1994).

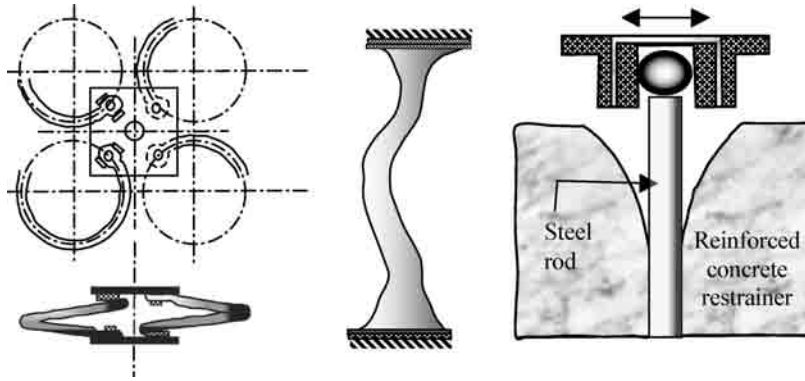


FIGURE 29.16 (a) Elasto-plastic steel damper; (b) lead damper; (c) steel rod damper.

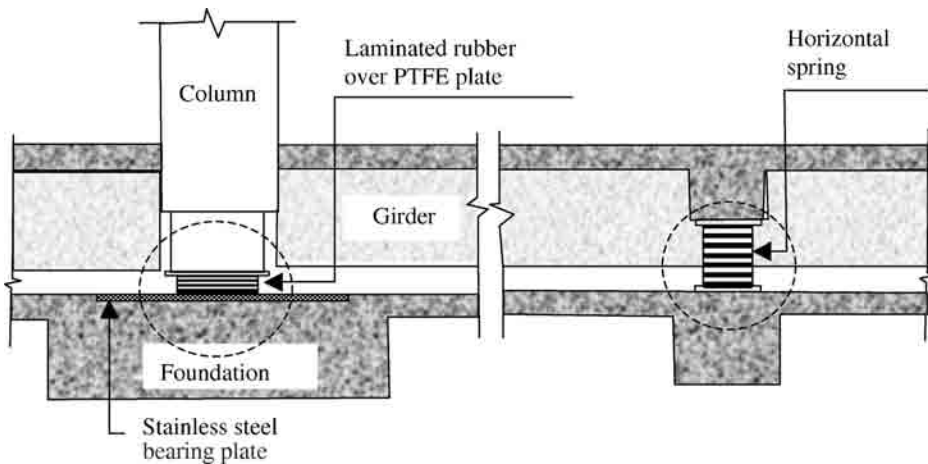


FIGURE 29.17 Elements of a TASS system. (Source: Kawamura, S. et al. 1998. *Proc. IX World Conf. on Earthquake Engineering*, pp. 735–740. Tokyo, Japan. With permission.)

Taisei Corporation, Japan, developed the TASS (TAISEI Shake Suppression) system (Figure 29.17), which is composed of PTFE-elastomeric bearings and neoprene springs (Kawamura et al., 1988). PTFE-elastomeric bearings support the vertical load of the superstructure and reduce the horizontal seismic forces by sliding against severe earthquake motion. Horizontal springs provide weak lateral stiffness and restrain displacement. The TASS system never resonates to any type of excitation, stably supports superstructure, and limits the horizontal force transmitted to the superstructure to that equal to friction force.

In situations where circumstances may result in substantial tension forces on the bearings, it has generally been accepted that elastomeric, sliding, or roller isolators alone are not suitable. For this, a system that controls uplift was developed. The system consists of rubber bearings with a central hole to accommodate a tension device (Kelly and Chalhoub, 1990). Logiadis et al. (1996) proposed a *prestressed bearing* isolation system in which vertical prestressed tendons are located in pairs, symmetrical on both sides of each bearing to avoid tension in the rubber bearing.

Tarics (1996) developed a *composite isolator* to provide equal protection in minor, moderate, or major earthquakes (see Figure 29.18). The composite seismic isolator has two distinctly different stiffnesses, which are activated by the displacement demand. During minor or moderate earthquakes, the upper isolator provides flexibility. In the event of major earthquake, the higher stiffness of the lower isolator prevents excessive displacement. This isolator seems to be a promising alternative for near-fault ground motions. With similar objectives, Shimoda et al. (1992) proposed lead rubber bearings with a stepped lead plug. Several other systems, for example, the *sleeved pile system*, *GERB*, *alexisis-mon*, and so on, were developed by different researchers (Kelly, 1986; Buckle and Mayes, 1990) and the search for new isolation systems, which can give better performance under different conditions, is still continuing.

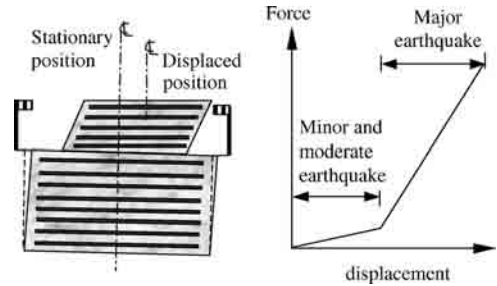


FIGURE 29.18 Composite isolator and its force–displacement diagram. (Source: Tarics, A.G. *Proc. XI World Conf. on Earthquake Engineering*, 1996. With permission.)

29.2.5 Design of Isolation Devices

As discussed above, several types of isolators have been proposed so far. Only a few bearings, namely, laminated rubber bearings, lead rubber bearing, FPS bearings, and Teflon–steel sliding bearings with a restoring device, have been developed to the stage of practical application. These isolators are in general observed to be effective in reducing seismic response; however, their effectiveness depends on the situation and design constraints. For example, rubber bearings are most suitable for high-frequency motions, while friction-type isolators may also be applied at the site where ground motion can have low-frequency content. Buildings with sophisticated electronic equipment and loose contents should preferably be isolated with rubber bearings to avoid transmission of high frequencies to the superstructure. In the case where, for some reason, it is not possible to provide large seismic gaps or for the conditions where light weight structure is to be isolated, the FPS-type isolators are more suitable. The main requirements for the design of a base-isolation system are (1) the ability to sustain gravity loads, (2) low horizontal stiffness that can lengthen the fundamental time period to the desired value, (3) large vertical stiffness to minimize amplification in vertical direction and complications due to rocking, (4) energy dissipation capacity to keep displacements at the isolation level within acceptable limits, and (5) sufficient initial stiffness to avoid unwanted vibrations due to wind loads and frequent minor seismic events. The design procedure of most widely used isolation systems, namely, high-damping rubber bearings, lead rubber bearings, and the FPS, is discussed in the following sections.

29.2.5.1 High-Damping Rubber Bearing

The design of high-damping laminated rubber bearings involves determining the plan size, the number of rubber layers, the thickness of each rubber layer, and steel shim. The steps involved in the design of high-damping rubber bearings are as follows:

1. Specify the design vertical load on the bearing (W), the design period for the isolated structure (T_1), and site conditions.

The load, W , is computed for the dead load and live load combination. The design period, T_1 , depends on site conditions. Its minimum value is usually taken as three times the fundamental time period of the structure when it is fixed base.

2. Find corresponding horizontal stiffness of the bearing, K_h , using

$$K_h = \frac{W}{g} (2\pi/T_1)^2 \quad (29.1)$$

3. Assign the values to quantities such as the maximum permissible shear strain (γ), Young's modulus (E), and the shear modulus (G) for the rubber compound.

Generally, γ is considered to be in the range of 100 to 150%. G can be taken from design specifications provided by the manufacturer. The value of G for this range of shear strains varies from 0.69 to 0.86 MPa, depending on the rubber composition (Kelly, 1997).

4. Specify the effective equivalent damping in the isolation system and allowable pressure on the bearing (p) for vertical loads.

The allowable pressure (p) for bearings with metal reinforcement can be taken as about 6.9 N/mm² (Kelly, 1997). Damping can be taken as 15 to 20%, subject to verification.

5. Using a response spectrum or code formulae, find the maximum horizontal displacement, that is, the design displacement (D). This depends on the spectral coefficient (i.e., the site condition), design period, and damping.
6. The plan area of the rubber (A) in bearing is primarily controlled by the design vertical load (W) and allowable pressure (p), and is determined by the expression

$$A = W/p \quad (29.2)$$

7. The total thickness of rubber, t_r , in the bearing is determined from the following equation:

$$t_r = GA/K_h \quad (29.3)$$

Total thickness, t_r , should not be less than D/γ .

8. Evaluate the shape factor (S) for the desired value of ratio of vertical stiffness (K_v) and horizontal stiffness (K_h) using following expressions:

$$6S^2 = K_v/K_h \quad \text{for circular bearings} \quad (29.4a)$$

$$6.73S^2 = K_v/K_h \quad \text{for square bearings} \quad (29.4b)$$

The minimum recommended value for the stiffness ratio is 400. These expressions are fairly accurate for shape factors of ten or less. However, for higher values of S , the effect of compressibility should also be taken into account (Kelly, 1997).

9. Using a basic definition of shape factor as the ratio of the cross-sectional area of the bearing to the force-free area of a single layer of rubber, the thickness of each rubber layer can now be determined by

$$t = \phi/4S \quad \text{for circular bearings} \quad (29.5a)$$

$$t = b/4S \quad \text{for square bearings} \quad (29.5b)$$

where ϕ is the diameter for circular bearing and b is the side for square bearing. Knowing the values of t_r and t , the number of rubber layers (n) can be computed.

10. The thickness of steel shims provided for laminated construction should be in the range of one tenth to one eighth of an inch (Kelly, 1997).

The material properties for rubber compounds used for isolation devices can be related to the rubber hardness. Properties for the range of rubber hardness normally used in bearing are listed in Table 29.1 (Bridgestone, 1990).

The designed bearing should be checked for the following criteria also.

29.2.5.1.1 Stability against Buckling

Buckling load may become critical in situations where bearings with a high rubber thickness relative to the plan dimension are to be provided. For example, in the case of base isolation for low vertical loads,

TABLE 29.1 Relationship between Rubber Hardness and Other Properties

Rubber Hardness (IRHD ± 2)	Young's Modulus, E (MPa)	Shear Modulus, G (MPa)	Material Constant, k	Minimum Elongation at Break (%)
35	1.18	0.37	0.89	650
40	1.50	0.45	0.85	600
45	1.80	0.54	0.80	600
50	2.20	0.64	0.73	500
55	3.25	0.81	0.64	500
60	4.45	1.06	0.57	400

rubber bearings are generally slender. Average compressive stress in the bearing (W/A) should not exceed the critical stress (p_{cr}) given by Kelly (1997):

$$p_{cr} = \frac{\sqrt{2}\pi GS}{t_r} r \quad (29.6)$$

where r is radius of gyration ($b/2\sqrt{3}$ for a square bearing and $\phi/4$ for a circular bearing).

Maximum shear strain is described as follows. Under vertical loading only, as per AASHTO recommendations for service loads (i.e., for the dead and live load), a factor of safety of three should be adopted for maximum shear strain values. Thus, maximum shear strain (γ_s) should satisfy the following condition:

$$\gamma_s \text{ i.e. } 6S \frac{W}{E_c A} \leq \frac{\varepsilon_b}{3}$$

where ε_b is the minimum tensile strain at which rubber breaks and E_c is compression modulus for bearing and is given by $E_c = E(1 + kS^2)$. E and k , for a given value of rubber hardness, can be taken from Table 29.1.

Under earthquake loading, the following applies. In the case of ultimate load that includes effect of earthquake loads, AASHTO recommends a factor of safety of 1.33. Thus, maximum shear strain (γ_u) due to combined effect of compression (γ_c), torsion (γ_t), and lateral load (γ_{eq}) should not exceed $\varepsilon_b/1.33$; that is, $\gamma_c + \gamma_{eq} + \gamma_t \leq \varepsilon_b/1.33$. γ_{eq} is given by D/t_r , and γ_t can be evaluated by

$$\gamma_t = \frac{b^2}{2tt_r} \frac{12De}{(B^2 + L^2)} \quad (29.7)$$

Here, B and L are dimensions of a structure with rectangular plan and e is the eccentricity. $\gamma_c (= 6SW'/E_c A_r)$ is computed for vertical load (W'), which also includes the effect of earthquake load. In this case, the effective area (A_r) is reduced due to lateral displacement (D) and it is the overlapping area of top and bottom in displaced condition. A_r can be determined using the following expressions:

$$A_r = A \left(1 - \frac{D}{b} \right) \quad \text{for square bearings} \quad (29.8a)$$

$$A_r = \frac{1}{2} \left\{ \phi^2 \sin^{-1} \left(\frac{\sqrt{\phi^2 - D^2}}{\phi} \right) - D \sqrt{\phi^2 - D^2} \right\} \quad \text{for circular bearings} \quad (29.8b)$$

29.2.5.1.2 Stability against Roll Out

Maximum horizontal displacement should not exceed the roll-out displacement (δ) given by

$$\delta = \frac{W_E b}{W_E + K_h h} \quad (29.9)$$

where vertical load (W_E) also includes the effect of earthquake load, b is the side for square and the diameter for the circular bearing, and h is the overall height of the bearing (Figure 29.19).

The check should be made for bearings with bolted connections also, so as to avoid the development of tensile stresses.

29.2.5.2 Lead Rubber Bearings

The design of lead rubber bearings can be split into two parts, namely, (a) the design of the lead plug and (b) the design of the laminated rubber bearing.

29.2.5.2.1 Design of Lead Plug

In fact, the lead rubber bearing can be designed effectively by assuming its force–displacement behavior comprises two distinct stiffnesses, namely, the preyielding and postyielding stiffnesses, as shown in Figure 29.20. The characteristic strength, Q_d , for the desired energy dissipation (W_D) or the known effective damping (ξ_{eff}) can be computed using

$$Q_d = W_D/4(D - d_y) \\ = 2\pi K_{\text{eff}} D^2 \xi_{\text{eff}}/4(D - d_y) \quad (29.10)$$

Q_d and yield displacement (d_y) are the unknowns. So for a first trial, considering d_y is very small as compared with design displacement (D), we have, as a first approximation

$$Q_d = W_D/4D \quad (29.11)$$

Using this approximate value for Q_d , the postyield stiffness (K_p) can be evaluated by

$$K_{\text{eff}}D = Q_d + K_p D \quad (29.12)$$

This may lead to modified value of yield displacement, d_y , given by

$$d_y = Q_d/(K_e - K_p) \quad (29.13)$$

where, depending upon the physical parameters of the laminated rubber bearing, K_e can be assumed to be about ten times the value of K_p .

This value of d_y can be used in the next trial to compute revised values of Q_d , K_p , and d_y . Trials are to be repeated until d_y converges.

Now, the yield force can be evaluated by

$$F_y = K_e d_y \quad (29.14)$$

Thus, the area of lead plug (A_p) can be determined using $A_p = F_y/f_y$, in which f_y is the yield strength of the lead in shear and has a value of 10.5 MPa (Skinner et al., 1993). In design, owing to considerations for the confinement of the plug, a reduced value of 7 to 8 MPa is generally considered.

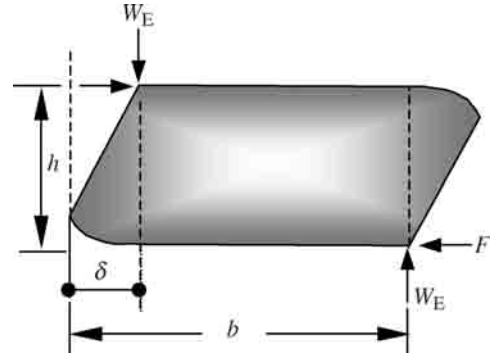


FIGURE 29.19 Stability against roll out. (Source: Kelly, J.M. *Earthquake Resistant Design with Rubber*, Springer, London, 1997. With permission.)

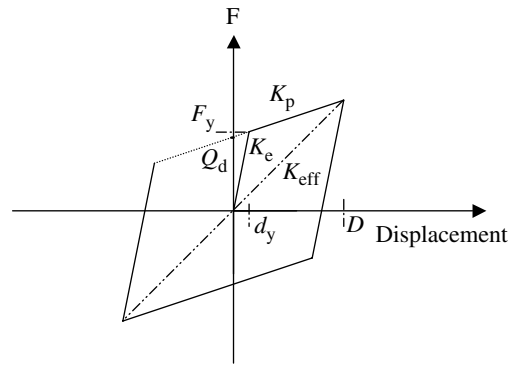


FIGURE 29.20 Design parameters for lead rubber bearing.

29.2.5.2.2 Design of Laminated Rubber Bearing

Postyield stiffness of the bearing (K_p) is typically higher than the corresponding stiffness of the bearing without the lead plug (K_h):

$$K_p = f_L K_h$$

where f_L is a factor that takes into account the effect of lead plug and is always larger than unity. Typically, f_L is 1.15 (FEMA 356, 2000).

Another expression for computing K_p is given by (Yang et al., 2003)

$$K_p = K_h \left[1 + 12 \frac{A_p}{A_0} \right] \quad (29.15)$$

where A_0 is the area of the bearing based on allowable normal stress under the vertical load.

The final value of K_p obtained during design of the lead plug is used in these expressions to find K_h . This contribution (K_h) towards combined stiffness (K_p) controls the design of the laminated rubber bearing. The steps from Step 3 onwards, described earlier in the design of high-damping rubber bearings, can be followed to design this laminated rubber bearing.

One additional check for the lead plug should be applied:

$$1.25 \leq \frac{h_p}{\phi_p} \leq 5.0$$

where h_p is effective height of the lead plug and ϕ_p is its diameter (Yang et al., 2003).

29.2.5.3 Design of Friction Pendulum System

The basic design variables in FPS are (1) the radius of curvature (R), (2) the material friction coefficient (μ), and (3) the plan dimension. The desired isolation period governs the radius of curvature, whereas the plan dimension is controlled by the design displacement. R for a known value of the design period of the isolated structure (T_1) can be computed using

$$R = g(T_1/2\pi)^2 \quad (29.16)$$

where g is acceleration due to gravity.

The coefficient of friction (μ), along with the displacement, controls the energy dissipation. The effective damping (β) for this system is given by expression

$$\beta = \frac{2}{\pi} \left(\frac{\mu}{\mu + D/R} \right) \quad (29.17)$$

The desired damping, depending upon the properties of the system, may vary from 10% to 20% of critical damping. As the design displacement (D) depends upon damping (β), it becomes a trial-and-error process and requires few iterations to get the values of β , μ , and D for desired response.

The effective stiffness of the isolation system at design displacement can be evaluated by

$$K_{\text{eff}} = \frac{W}{R} + \frac{\mu W}{D} \quad (29.18)$$

29.2.6 Verification of Properties of Isolation Systems

As they are the most critical part of the base-isolated structure, the quality of isolation bearings is of paramount importance. Looking into uncertainties in the manufacture, the deformation characteristics and damping values of the isolation system must be verified by tests. Therefore, the selected units of the isolation system have to undergo testing for examining quality control and determining their actual load–deformation behavior. Force–deformation characteristics of the isolation system obtained from tests are used for analyzing the base-isolated structures. These tests also serve as a means to verify the

ability of the isolation bearings to withstand long-term vertical loading and numerous cycles of shear displacement during design basis and maximum capable earthquake. The primary function of an isolation system is called on during major earthquakes only and, for most of its design life, it is subjected to nonseismic loads. Therefore its behavior for such loads should also be verified by tests.

29.2.6.1 Tests for Isolation Systems

System characterization tests, prototype tests, and quality control tests are the three levels of tests that are recommended for an isolation system. The first tests provide the fundamental characteristics of the isolation system; the second allow one to know the design parameters of the isolation system fabricated for the project; and the third verify the quality control and consistency achieved in manufacturing. These tests are briefly discussed in the following sections (Taylor et al., 1995).

29.2.6.1.1 System Characterization Tests

These tests are performed to evaluate the basic characteristics of the isolation systems, especially its dependence on temperature, frequency, bilateral loading, wear and fatigue, and so on. The tests are also intended to provide the ultimate and reserve capacity of a device for various loading conditions. These tests are conducted only once for a system of a given design, material, and construction. However, they should be repeated if there are major changes. These tests are formally not required by codes; however, in practice, they are conducted for a new isolation system and the test results provide some idea about the suitability of the isolation system for a particular project.

29.2.6.1.2 Prototype Tests

These tests are conducted to verify the design properties of an isolation system prior to its construction. Effective stiffness, energy dissipation capacity, stability of hysteretic behavior (in a check for system degradation), and stability at maximum seismic displacement are the properties generally verified through these tests. The stability of an isolation system is verified for maximum and minimum vertical load conditions. Tests are also carried out for nonseismic loads. In the case of isolation systems for buildings, the major nonseismic force is wind load, and for bridges it may be thermal displacements and braking or centrifugal forces. If the isolation system is frequency-dependent, then prototype tests should be performed dynamically for a range of frequency that represents full-scale prototype loading rates. Similarly, if the behavior of the isolation system is significantly different for unilateral and bilateral loadings, then the isolation system should be tested for different combinations of displacements in two orthogonal directions. Specimens in these tests are subjected to extreme conditions and therefore are not to be used for construction.

29.2.6.1.3 Quality Control Tests

These tests are carried out to verify the quality and consistency of the manufacturing process, and to measure the as-built properties of the isolation system prior to installation. The quality control tests are divided into *production tests* and *completed unit tests*. Production tests are carried out on materials or components that are used in the making of the isolation unit. In the case of elastomeric bearings, the elastomer is tested for hardness, tensile strength and elongation at break, bond strength, compression set, low-temperature properties, high-temperature aging, and ozone resistance. Elements used for a sliding system are supposed to be tested for surface roughness, trueness of surface, interface material properties, bearing pad attachment, and sliding interface attachment. All completed units are tested for (1) sustained compression, and (2) combined compression and shear. The purpose of the sustained compression test is to verify (1) the quality of the bond between the elastomer and the steel for laminated elastomeric bearings and (2) the bond between the bearing liner and the metal backing plate for sliding bearings. A combined compression and shear test is conducted to verify that actual values of effective stiffness and damping are in close agreement with design values. After quality control testing, laminated elastomeric bearings are visually inspected for rubber-to-steel bond, surface cracks, laminate placement, and permanent deformation, while sliding bearings should be inspected for bearing liner-to-metal bond,

scoring of the stainless steel plate, leakage, and permanent deformation. In the case that the bearings do not meet the requirements, they should be rejected.

29.2.6.2 Uniform Building Code Recommendations

Uniform Building Code (UBC, 1997) recommends that the deformation characteristics and damping values of the isolation system used in the design and analysis of seismic-isolated structures is based on the sequence of cyclic loading tests of a selected sample of the components (Figure 29.21). First, the specimen is tested under a cyclic load corresponding to the design wind load. Subsequently, it is tested, for a prescribed number of cycles, with cyclic displacements varying from one

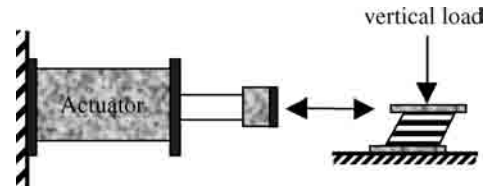


FIGURE 29.21 Schematic diagram for cyclic loading test of bearing.

fifth of the design displacement to the total maximum design displacement. Vertical load (dead load plus 50% of the live load) for all the above tests is prescribed as the average load on all isolators of common type and size. If an isolator unit is also a vertical load-carrying element, the cyclic load tests should be performed for maximum and minimum vertical loads, which includes the effects of an earthquake overturning evaluated corresponding to the test displacement.

29.2.6.2.1 Units Dependent on Loading Rates

If there is greater than 10% difference in effective stiffness values at the design displacement (i) obtained by performing test on an isolator unit at a frequency equal to the inverse of the effective period T_1 of the isolated structure, and (ii) obtained by performing test on the same unit at any frequency in the range of 0.1 to 2.0 times the inverse of T_1 , then the force–deflection properties of the isolator unit are considered to be dependent on rate of loading. In such cases, the tests are prescribed to be performed at a frequency equal to the inverse of T_1 .

29.2.6.2.2 Units Dependent on Bilateral Load

If the bilateral and unilateral force–deflection properties have greater than a $\pm 10\%$ difference in effective stiffness at the design displacement, the force–deflection properties of an isolator unit are considered to be dependent on bilateral load. In such cases, the tests specified above shall be augmented to include bilateral load increments of the total design displacement 0.25 and 1.0, 0.50 and 1.0, 0.75 and 1.0, and 1.0 and 1.0.

29.2.6.2.3 System Adequacy

The performance of the test specimens is assessed as adequate if the following conditions are satisfied:

1. The load–displacement curves for all tests have a positive incremental load-carrying capacity.
2. The difference between the average values of effective stiffness of the two test specimens of a common type and size does not exceed the prescribed value of 10%.
3. The effective stiffness of each test specimen for each cycle of test is within $\pm 10\%$ of the average value of effective stiffness for the specimen.
4. There is no greater than a 20% change in the initial effective stiffness of each test specimen over the prescribed number of cycles.
5. There is no greater than a 20% decrease in the initial effective damping of each test specimen over the prescribed number of cycles.
6. All specimens of vertical load-carrying elements remain stable at the total maximum displacement for the prescribed vertical load.

29.2.7 Analysis of Base-Isolated Structures

Depending upon the code requirements, one can choose the static or dynamic analysis procedure for a particular project. Regarding the static analysis method, codes generally have some bindings, whereas time-history analysis can be used for all types of situations. In UBC (1997), minimum values of some design parameters to be used in dynamic analysis are defined in terms of percentage of values obtained by static analysis and thus most of the steps of static analysis are necessary for a designer, even if the dynamic analysis procedure is followed. These analysis methods require the modeling of the base-isolation system and the superstructure. In most of the cases, the linear model for the superstructure of a base-isolated building is enough. However, the isolation systems generally require nonlinear model.

29.2.7.1 Modeling of a Superstructure

The superstructure of a base-isolated *building* can be modeled as rigid blocks, a two-dimensional and a three-dimensional linear model, or nonlinear models. The rigid block assumption is the simplest one, which is used in the design of isolation system, for preliminary analysis and feasibility studies. Moreover, it can also be used as a tool to crosscheck the results obtained from other rigorous analysis methods. Assuming the superstructure as a single-degree-of-freedom (single-DoF) model and the isolation system as linear spring plus linear viscous damper, Kelly (1990) developed linear theory for a base-isolated structure (Figure 29.22). In general, an isolation system aims at providing significant protection not only to the building but also to nonstructural components and contents. Therefore, a three-dimensional linear model for the superstructure is generally sufficient for analyzing a base-isolated structure. However, for the situations when the response to extreme earthquakes must be investigated, nonlinear models for superstructure should be used.

In case of the analysis of seismically isolated *bridges*, it may be important to take into account the pier masses and their own modes of vibration. The pier can be modeled using a linear beam element with mass, and the deck can be modeled with linear beams with mass. However, for very squat piers, the shear flexibility should also be considered. In the case of a regular structure, the coupling effect of the deck can be neglected, and a bend can be considered independent of the others. However, if a stiff deck is supported on piers of different flexibility, the structure should be modeled as a linear multi-DoF system. To ascertain the response for extreme loading conditions, the piers should be modeled with nonlinear models; however, the deck can still be simulated with linear elements. In such cases, proper account should be made for change in the effective stiffness of piers due to cracks (Priestley et al., 1996). In the case of *equipment*, the modeling depends upon the level of protection; however, the rigid block assumption for equipment generally suffices. *Liquid storage containers* should be modeled with proper consideration to the sloshing affect of liquid during base motion.

29.2.7.2 Modeling of Isolation System

The isolation system can be modeled as a linear or nonlinear element. The linear model of an isolation system consists of effective stiffness and effective damping at the design displacement. These values are derived from force–displacement test data for the isolation system. However, except in preliminary designs, the isolation system is generally modeled as nonlinear. Commonly used isolation systems, namely, high-damping rubber bearings, lead rubber bearings, friction bearings, and FPSs, can be modeled by bilinear model (Figure 29.23). However, for more precise results, the isolation elements should be modeled by their actual force–displacement behavior, for example, in the modeling of

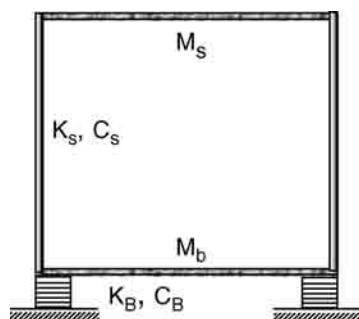


FIGURE 29.22 A two-DoF model of base-isolated building. (Source: Kelly, J.M. *Earthquake Spectra*, 6(2), 223–244, 1990. With permission.)

high-damping rubber bearings, which in extreme conditions follow a trilinear model with stiffening at larger strains. The model used for analysis should be verified with force–displacement characteristics obtained by prescribed tests, discussed in Section 29.2.6. Moreover, the isolation system should be modeled with considerations for the following requirements (UBC, 1997):

1. Account for the spatial distribution of isolator units.
2. Calculate translation, in both horizontal directions, and the torsion of the structure above the isolation interface, considering the most disadvantageous location of mass eccentricity.
3. Assess overturning or uplift forces on individual isolator units.
4. Account for the effects of vertical load, bilateral load, and/or the rate of loading if the force–deflection properties of the isolation system are dependent on one or more of these attributes.

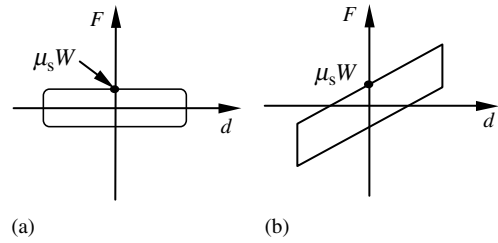


FIGURE 29.23 Analytical models for isolators: (a) pure friction system; (b) friction pendulum system.

29.2.7.3 Static Analysis Procedure

This procedure may be sufficient for analyzing a base-isolated structure that satisfies certain code requirements related to the height of a building, soil conditions, geometry of a structure, effective period of base-isolated building, force–deflection, and restoring-force characteristics of the isolation system, and so on. The procedure involves the use of simple expressions for computing design displacements (D) and lateral forces. Using the response spectrum or code formula, the design displacement is computed for a target period of the isolation system, its effective damping, and site conditions. Since time period and effective damping itself depends on design displacement, it becomes an iterative procedure. Appropriate values of damping and the target time period can be assumed for the first iteration. Force–displacement data for the isolation system, obtained from tests, is used to determine effective stiffness (k_{eff}) and damping at design displacement.

The design lateral seismic force for the isolation system and structural elements at or below the isolation system is simply evaluated as

$$V_b = k_{\text{eff}} D \quad (29.19)$$

Total lateral force for the structure above the isolation system is given by

$$V_s = \frac{k_{\text{eff}} D}{R_1} \quad (29.20)$$

The factor R_1 is based on the type of lateral force resisting system used for the structure above the isolation level.

The value of V_s is not to be taken as less than the following (UBC, 1997):

1. The lateral seismic force required for a fixed-base structure of the same weight, W , and a period equal to the isolated period
2. The base shear corresponding to the design wind load
3. One and a half times the lateral seismic force required to fully activate the isolation system

The total lateral force shall be distributed over the height of the structure in accordance with the formula

$$F_x = \frac{W_x h_x}{\sum_{i=1}^n W_i h_i} V_s \quad (29.21)$$

where W_x is weight at level x and h_x is the distance of level x from the base. F_x , the lateral force at level x , is applied over the area of the building at that level in accordance with the mass distribution. The maximum

displacement of the isolation system is calculated in the most critical direction and for maximum capable earthquake. The total design and maximum displacement of the elements of the isolation system should include the additional displacement due to actual and accidental torsion, calculated by taking into account the spatial distribution of the lateral stiffness of the isolation system and the most disadvantageous location of mass eccentricity.

29.2.7.4 Dynamic Analysis Procedure

The method involves response spectrum or time-history analysis, and is essential when, owing to code requirements, it is not possible to use the static analysis procedure alone. However, for the situations when (1) the structure above isolation system may reach the nonlinear range for the design earthquake motion, (2) the soil is soft or site conditions require site specific evaluation, or (3) the isolation system does not meet certain prescribed code criteria, even the use of the response spectrum method is not sufficient and the time-history analysis procedure becomes essential.

29.2.7.4.1 Response Spectrum Method

This method of analysis is very convenient for the laminated rubber bearing-type isolation system. A design spectrum is constructed for the design basis and the maximum capable earthquake. Total design displacement of the isolation system and the lateral forces and displacements of the isolated structure are computed for the design basis earthquake. Maximum displacement of the isolation system should be obtained for the maximum capable earthquake. In this method of analysis, damping for fundamental mode in the direction of interest is generally restricted to the effective damping of the isolation system or 30% of the critical damping, whichever is less. Damping for higher modes is consistent with those appropriate for the response spectrum analysis of similar fixed-base structure. To take into account the effect of bidirectional excitation, the total maximum displacement includes simultaneous excitation of the model by 100% of the most critical direction of the ground, and not less than 30% of the ground in the orthogonal direction (UBC, 1997). The maximum displacement of the isolation system is calculated as the vector sum of the two orthogonal displacements. The total lateral force shall be distributed over the height of the structure in accordance with Equation 29.21.

29.2.7.4.2 Time-History Analysis

This method of analysis can be used for base-isolated structures under all types of situation. The method is necessary for conditions where (1) isolation systems have a sliding system, (2) the structure is founded on very soft soil, (3) the isolation system allows low displacement, or (4) the force–displacement behavior of the isolation system depends on (a) the rate of loading, (b) the vertical load, or (c) the bilateral load. Appropriate horizontal ground motion time histories are selected, and their magnitudes, fault distances, and source mechanism should be consistent with those that control the design basis (or the maximum capable) earthquake. Where appropriate recorded ground motion time-history pairs are not available, appropriate simulated ground motion time-history pairs may be used. Each pair of time histories is applied simultaneously to the model, considering the most disadvantageous location of mass eccentricity. The maximum displacement of the isolation system is calculated from the vectorial sum of the two orthogonal displacements at each time step.

29.2.7.5 Software for Analysis

The need for an isolation system that is stiff under low levels of frequently occurring loads but flexible under higher levels necessarily leads to a nonlinear system. The force–displacement behavior of most of the isolators can be modeled as bilinear. However, in the case of high-damping rubber bearings, in extreme conditions, a trilinear model with stiffening at large shear strains better represents the behavior. These nonlinear force–displacement relationships of the bearings need the use of specialized computer programs to analyze base-isolated structures. The program should be capable of analyzing base-isolated

buildings with isolator models made of combination of discrete nonlinear elements and superstructure models that are fully elastic or that permit some localized nonlinear behavior.

Several programs are available for this purpose. The computer code NPAD has plasticity-based nonlinear elements that can be used to model certain types of elastomeric bearings. The program simulates the superstructure using a three-DoF per floor model and can analyze base-isolated structures with linear superstructure (Tospelas et al., 1994). The justification behind the approach of considering superstructure as linear is that seismic base isolation is generally provided to reduce the force transmitted to the superstructure to the point where it can be assumed to remain elastic. The computer program SADSAP has the capability to analyze three-dimensional structures with localized nonlinearities. The nonlinear elements available in the software can be combined to simulate the behavior of various types of isolation systems. The program may also be useful in analyzing base-isolated buildings with nonlinear bracing elements provided for supplemental damping (Kelly, 1997). Some general-purpose programs such as the DRAIN series and ANSR have the capability of nonlinear analysis of two- and three-dimensional structures and have provisions that can be used to simulate seismic isolators, which exhibit bilinear behavior (Tospelas et al., 1994). Some commonly used finite element analysis software such as ABAQUS, ANSYS, and COSMOS also have the capability for analyzing complex superstructures on nonlinear isolators (Kelly, 1997). However, sliding bearings cannot be modeled precisely with these programs.

SAP2000 (2002) can be used to analyze these structures and also has the facility to model friction bearings. The 3D-BASIS group of programs is a group of special purpose programs developed for nonlinear dynamic analysis of three-dimensional base-isolated structures, and has been used for the analysis of many base-isolated structures (Constantinou, 1994). The programs assume that the superstructure is elastic and the isolation system is nonlinear. Models used for modeling the isolation elements can also capture precisely frictional behavior. It is not possible to account for stiffening of laminated rubber bearings at higher strain levels using the programs discussed above. The program LPM (lumped parameter model), originally developed for nonlinear three-dimensional analysis of masonry structures, has the capability to model this stiffening and at the same time can also incorporate a nonlinear element in the superstructure (Kelly, 1997).

29.2.8 Experimental Methods for Isolated Structures

Although analytical simulation has progressed tremendously through the use of powerful computers utilizing accumulated theoretical and experimental data on structures, it is not yet possible to analyze and predict the inelastic response of base-isolated structures with total confidence. The responses of base-isolated structures are very much dependent on the characteristics of the input earthquake motion, isolation system, and the supported structures. Experimental tests have been used to verify and calibrate mathematical models, as well as to provide data for the design of structures. However, extensive tests are needed to study the complex behavior of base-isolated structures under realistic conditions that are likely to occur during earthquakes. Different test methods such as quasistatic testing, shaking table testing, online hybrid testing, and substructured online testing have been proposed. A typical problem that appears when performing quasistatic tests on an isolated structure is the alteration of the restoring forces due to strain-rate effect existing for this material. This problem does not exist for shaking table tests performed at the real-size and real-time scale. Shaking table tests of base-isolated specimens have been used successfully for investigating the behavior. However, it requires a large-capacity table for testing a full-scale specimen. The involvement of high cost for large-size shaking tables and the limited capacity of available shaking tables necessitate the structure to be drastically scaled down. This scaling of a structure presents some limitations for the extrapolation of the results to the real scale.

As a promising option, the online hybrid test method seems to be well suited for obtaining the seismic response of isolated structures thanks to available quasistatic loading equipment and high-speed computers. However, this technique involves the fabrication of a complete structural prototype

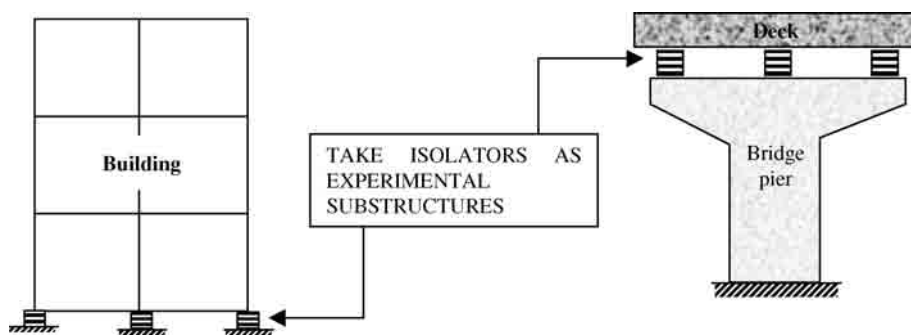


FIGURE 29.24 Substructured hybrid testing for seismically isolated structures. (Source: Tanzo, W. et al. Res. Rpt. 92-ST-01, Kyoto Univ., 1992. With permission.)

for proper modeling. Thus, test models must be simplified, for example, into a single-DoF model, and/or specimens have to be reduced in scale.

By incorporating substructure concepts into the online hybrid test technique, a substructured online hybrid test method can be used, in which a complete system is considered to be divided into analytical substructures and experimental substructures (Tanzo et al., 1992). In the case of seismically isolated structures, inelastic deformations are designed to occur only in isolation system. The isolation system, which is generally difficult to model mathematically, is taken as experimental substructures (Figure 29.24). The remaining part of the structure is taken as analytical substructures in which presently available analytical models are used to describe their restoring-force characteristics. For the experimental substructure, restoring-force information is directly measured from a specimen loaded according to its current deformation state. The substructured online hybrid test procedure for the earthquake response of base-isolated structure is explained in Figure 29.25.

29.2.9 Implementation of Seismic Isolation

29.2.9.1 New Construction

29.2.9.1.1 Buildings

In the early stages of the development of seismic isolation, the main target of the earthquake-resistant design of the structure was the prevention of collapse. However, later, other additional considerations, such as the value of structure or its content, have exerted their importance on the seismic design of structures. For example, facilities of postearthquake importance such as fire stations, police stations, hospitals, communication centers, and so on, have a critical role and are required to remain operational immediately after a major seismic event. Similar reasoning applies to museums housing unique artifacts or buildings that are architecturally important. The required low level of structural and nonstructural damage may be achieved by using an isolation system, which limits structural deformations and ductility demands to low values. The isolation system can be provided at different levels. However, while deciding the isolation level, considerations should be given for (1) the seismic gap, (2) the continuity of supply lines, stairways, and elevators, and (3) details of cladding below the isolation level. In addition, provisions for (1) access to bearings for inspection and replacement, (2) backup system for vertical loads, and (3) full diaphragm for the uniform distribution of lateral load to individual bearings also need to be considered. Figure 29.26 shows typical positions for bearings in buildings (Mayes and Naeim, 2001).

The first building constructed using modern isolation bearings was a government facility, the William Clayton Building in Wellington, New Zealand, which was completed in 1981. After that, a number of seismically isolated buildings have been constructed there, and in most of them the isolation system used is lead rubber bearings. The most widespread use of seismic isolation systems is in Japan. The first seismically isolated structure to be completed in Japan was the Yachiyodai Residential Dwelling, a two-story building completed in 1982. Better performance of seismically isolated buildings during the

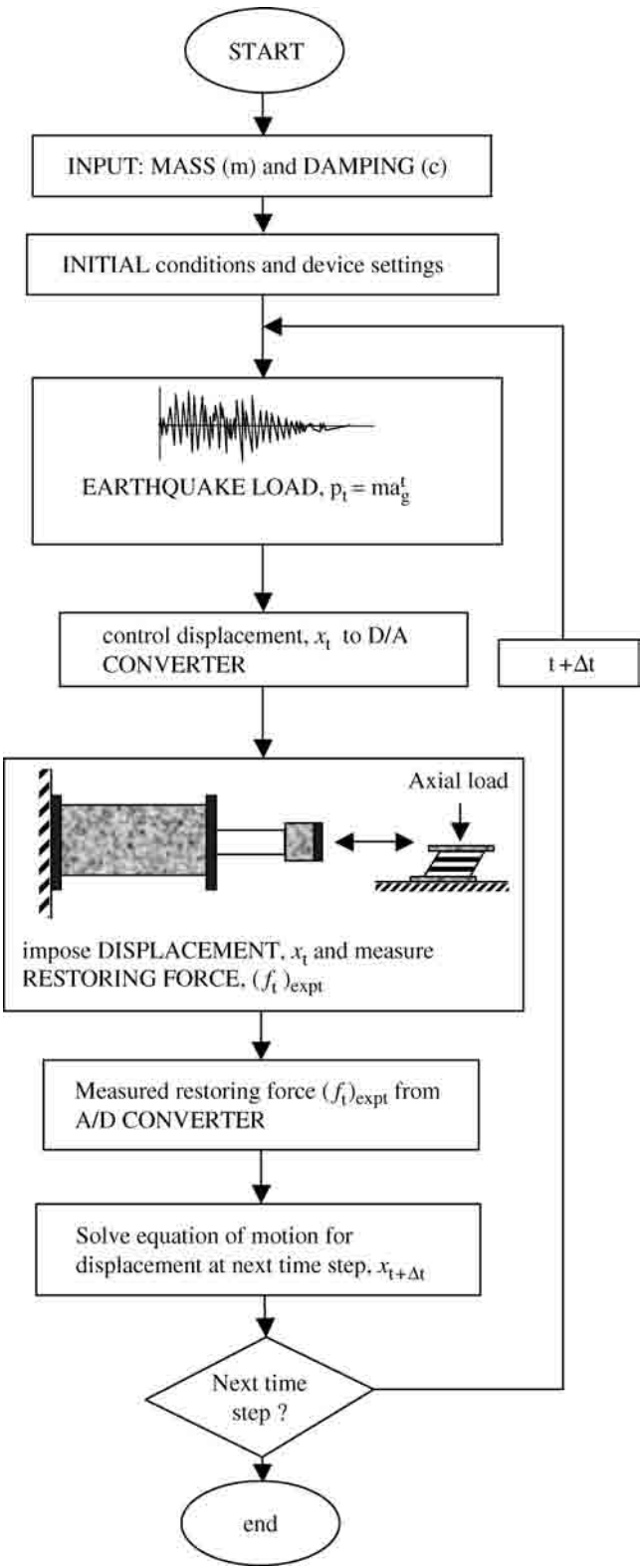


FIGURE 29.25 Procedure for substructured online test method for a base-isolated structure. (Source: Tanzo, W. et al. Res. Rpt. 92-ST-01, Kyoto Univ., 1992. With permission.)

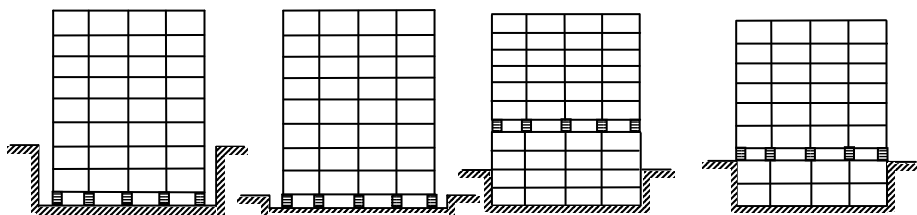


FIGURE 29.26 Typical positions of isolation level for buildings. (Source: Mayes, R.L. and Naeim, F. 2001. *The Seismic Design Handbook*, 2nd ed., Kluwer, Boston. With permission.)

Kobe earthquake of 1995 triggered the rapid increase in number of seismic isolation projects. Before the Kobe earthquake, the number of such buildings in Japan was 82; this suddenly increased to about 650 within 4 years of the earthquake. Besides rubber bearings, there have been some applications of frictional sliding systems also for seismic isolation of buildings (Nishitani, 2000). The first newly constructed base-isolated building in the United States was the Foothill Communities Law and Justice Center in California, which was completed in 1986. Until 1990 there were four isolated buildings. After the good performance of base-isolated buildings during the Northridge earthquake, the number increased and, at the end of 1998, there were approximately 40 isolated buildings completed or in construction in the United States (Clark et al., 2000). Some buildings in other countries, including Italy, France, Canada, Mexico, China, England, Russia, Armenia, Indonesia, Iran, Chile, and India, now use these systems. Until now, the emphasis on base-isolation applications has mostly been for structures with sensitive and expensive contents or high-risk structures like nuclear power plants and computer centers. However, there is an increasing interest in applying this technology to public housing and schools in developing countries (Fuller and Muhr, 1995). Most of the base-isolation projects have made use of laminated rubber bearings and lead rubber bearings. In Japan, laminated rubber bearings are often used with energy-dissipating devices, both with and without provision for recentering.

29.2.9.1.2 Bridges

In most cases, bridges are strategic structures and require a higher degree of protection to ensure their functionality after a seismic event. For many simple bridges, it has been found that seismic isolation of the superstructure gives improved seismic resistance, often at a reduced cost, while it is also effective for thermal expansion of the superstructure (Skinner et al., 1993). The aim of seismically isolating bridge superstructures is usually to protect the piers and their foundations, and sometimes to protect the abutments also. With this approach, bearings are placed between the superstructure and the top of the substructure (the piers and abutments). Under normal conditions, they behave like regular thermal bearings. However, in the event of a strong earthquake, they add flexibility to the structure by elongating its period and dissipating energy. In addition, most of the mass of a bridge is concentrated at the deck level, which is inherently strong and can be assumed to be rigid. This permits the superstructure to oscillate at a lower frequency than its piers, which results in the reduction or elimination of deformation of the substructure components beyond their elastic range, particularly at locations that are difficult to inspect or repair (e.g., the piles). Superstructure isolation systems are designed, as far as is practical, to provide moderate flexibility, high damping, torsional balance, and an appropriate distribution of seismic loads between the superstructure supports.

Isolated bridges in the United States are generally designed for the effects of a design-basis earthquake; however, the components of the isolation system are provided with increased displacement capacity and are tested for the effects of maximum capable earthquake. This design philosophy is based on observations of bridge failures in past earthquakes, which were primarily due to excessive bearing displacement and the loss of bearing support rather than the collapse of substructure. Providing for strong restoring force in this design philosophy prevents the accumulation of significant permanent displacements and allows for a relatively reliable estimation of peak bearing displacement and substructure force.

Isolation systems adopted by Italian engineers restrict the transmission of force to elements of the substructure to a predetermined level, which is independent of seismic action. Thus, the Italian engineers chose to limit the force transmitted to the substructure to a desired level, at the expense, however, of large variation in peak bearing displacements and the development of permanent displacements. In Japan, *men shin* (reduction of response) design is followed for the design of bridges. Although *men shin* design is closely related to the seismic isolation design, the natural period of a bridge is not forcibly elongated in this method, because there are various restrictions in increasing the natural period. Instead of elongating the period, the emphasis in the *men shin* design is on increasing the energy-dissipating capability and distribution of lateral forces to as many substructures as possible in order to decrease the lateral forces for the design of substructures (Iemura, 1994a, 1994b). It is common to restrain the transverse displacement of bridge isolators, and therefore many bridges in Japan are isolated in longitudinal direction only.

The application of seismic isolation for bridges started in the early 1970s. Bridges isolated in New Zealand before 1978 used metallic dampers for seismic isolation. Later, lead rubber bearings replaced the metallic dampers for their seismic isolation. Italian engineers also started the application of modern technology of seismic isolation for bridges in the mid-1970s and now have a long list of isolated bridges. The first seismically isolated bridge in Japan was the Hokuso line viaduct in Chiba Prefecture. The viaduct was completed in 1990 and used lead rubber bearings for its isolation system. The United States also obtained its first seismically isolated new bridge in 1990, when two bridges, namely, Sexton Creek Bridge in Illinois and Toll Plaza Road Bridge in Pennsylvania, were completed. Lead rubber bearings were used as the isolation system for both the bridges (Skinner et al., 1993).

29.2.9.2 Seismic Retrofit

Postearthquake analysis of recent earthquakes around the world shows that the damage was especially concentrated in the buildings and bridge structures that were not designed for earthquake loads or were designed by following the old seismic design guidelines. Moreover, a significant proportion of the damage was due to nonstructural elements and the contents housed in the buildings (Kelly, 1997). In order to prevent the recurrence of damage in such seismically deficient structures, it is vital to understand their vulnerability and retrofit them for expected future seismic events. In the case of important structures, retrofit techniques are required to provide a solution that can also lead to continued functioning during and after major earthquakes, protection of nonstructural components and contents, and, sometimes, to preserve their historic character.

29.2.9.2.1 Buildings

Conventional retrofitting has been the most common way of enhancing the performance of existing, seismically deficient structures. However, to maintain the usability of important structures after a big earthquake and to protect the valuable contents housed in the buildings, conventional methods can help a little. Simple strengthening or stiffening of a structure through reducing inelastic response displacement, however, may increase the response acceleration and the forces. Some of the other demerits of this approach are (i) the large amount of labor required to increase the strength and ductility of critical sections distributed throughout the complex structural system and (ii) damage may occur due to inelastic behavior of structural elements during a major seismic event (Iemura and Adachi, 2003). Besides this, conventional methods of retrofitting often require restricting the use of the building during the retrofit. Some buildings, housing important activities, cannot afford to have their routine usage stopped and therefore require retrofitting through an earthquake-resistance system that enables continued building use even during the retrofit operation.

Seismic isolation has proved to be very effective not only in enhancing the safety of existing seismically deficient buildings, but also to preserve the function and protect the contents. Unlike the conventional approach, this retrofit method aims to reduce the earthquake force to a level lower than the strength of the existing structure (Figure 29.27). Seismic isolation is the method that can mitigate both interstory drift and high-floor accelerations simultaneously, and it has been used in retrofitting of important buildings, buildings housing valuable contents, and structures of postearthquake importance.

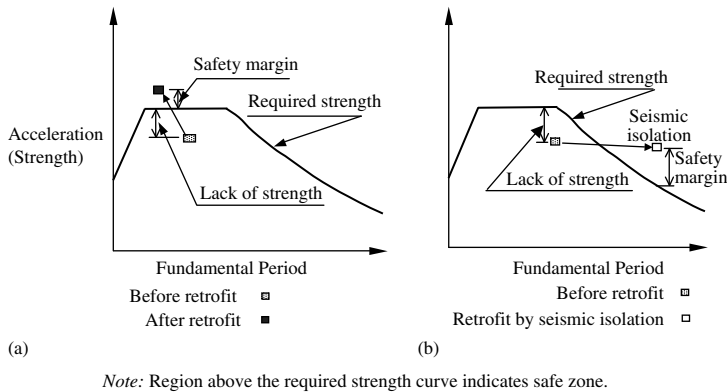


FIGURE 29.27 Concept of retrofitting methods: (a) conventional; (b) seismic isolation. (Source: Sugano, S., *Proc. XII World Conf. on Earthquake Engineering*, 2000. With permission.)

Moreover, as the modification or demolition of building features is minimized, the method has found application in many monuments of historical importance, protecting them from future earthquakes (Buckle, 1995). Recently, the old masonry Chapel of Rikkyo (St Paul's) University, Tokyo, constructed in 1920, was retrofitted with seismic isolation to preserve this historical asset to the university (Seki et al., 2000). Retrofitting using seismic isolation of the 72-year-old Clock Tower, a symbol of Kyoto University, Japan, is presently underway (Ogura et al., 2003).

The seismic isolation method is found to be more appropriate for the retrofitting of seismically vulnerable buildings that are required to function even during retrofit operation. To meet such a demand, the retrofitting method should affect minimum alterations to the existing structures and should produce a low level of noise and vibration. The technique has successfully been applied to a number of such buildings. In the retrofitting of Rankine Brown Building of Victoria University, Wellington, New Zealand, which houses the main library and administration of the university, one of the main requirements was the building's uninterrupted usage during the retrofit operation (Robinson, 2003). Meeting a similar challenge, the government office of Toshima Ward, in Tokyo, has been retrofitted with rubber and sliding isolators below the existing foundation and was used as usual by the officials and citizens even during the retrofit works. Similarly, a building of Nihon University in Tokyo, Japan, in which seismic isolation was applied at the top of the columns of basement floor, was available for research and education during the retrofit operation (Kawamura et al., 2000).

Although seismic isolation reduces earthquake forces, it does not eliminate them. Consequently, the strength and ductility of an existing structure must at least be sufficient to resist the reduced earthquake forces that remain even after isolation. Further, the requirement of space for the seismic gap and provisions for services, elevators, and so on to follow large displacements at isolation level are some issues that need prior attention. Although not applicable to all structures and all site conditions, seismic isolation still has great potential to reduce the risk in existing buildings and bridges that are not capable of resisting expected future earthquakes. This method, in the beginning, was used generally for preservation of cultural assets, but now has many applications in the retrofitting of other buildings also.

29.2.9.2.2 Bridges

A large number of old bridges were constructed with little or no consideration for seismic requirements. Some of them have been retrofitted, mostly by conventional methods. However, the remaining bridges are waiting for the enhancement of their strength to meet the latest code requirements. In existing bridges, bearings have generally been provided to accommodate longitudinal thermal movements between the superstructure and the supports. Therefore, little structural modification is required to use seismic isolation as a retrofit method. A common structural configuration, a continuous deck supported

on bearings at the tops of piers, attracts the option of seismic upgrading of existing bridge structures by seismic isolation and is often practical and relatively inexpensive. Seismic isolation has been used for the retrofitting of number of bridges in New Zealand. During the early period of its application in the United States, seismic isolation was mainly used for the retrofitting of bridges and the isolation system used was mainly lead rubber bearings (Skinner et al., 1993).

However, to replace an existing bearing with an isolation bearing, enough space is required between the deck and pier top. All the jacks used for replacing the bearings should be driven by the same hydraulic pump and raised at the same time to prevent stressing any cross members between girders. The dampers can be connected to the substructure using heavy-duty mechanical or chemical anchorages, with the other end bolted to the girders. Since an earthquake can shift a bridge in any direction, universal joints are recommended on each end of the damping device to prevent the shaft from being bent during movements other than axial ones. The damper should be set to the bridge in its midstroke position or a position that takes full advantage of the free movements (Hippley, 1997).

In situations where rigid connection of footing and piers has made the bearing capacity of existing piles inadequate for the new seismic requirements, seismic isolation bearings can be used at the base of columns. Sometimes, it may be costly to retrofit a seismically deficient pier and foundation by conventional methods due to submerged conditions that may require construction of cofferdams. In such cases, seismic isolation can reduce the demand on the seismically deficient piers by redistributing the force and transferring it to the abutments, which are significantly less expensive to retrofit. Seismic retrofits are intended to bring bridges up to reasonable earthquake standards; however, in some old bridges, the retrofit method is also required to have the least effect possible on the historic appearance and seismic isolation is the appropriate alternative for this requirement.

29.2.9.3 Other Implementations

Apart from in buildings and bridges, seismic isolation has found application in other structures. It has been used for a number of reactor units in France for which the site safe shutdown earthquake acceleration was $0.2g$. An isolation system of neoprene pads with topping of lead-bronze alloy limits the acceleration to a value of $0.2g$. A similar system was used for reactor units in Koeberg, South Africa, where the site safe shutdown earthquake acceleration was $0.3g$ (Tajiran, 1998). Seismic isolation has a lot of potential for the protection of sensitive equipment that can malfunction when the acceleration reaches beyond its allowable limit. Communication centers, hospitals, computer centers, and other facilities housing such sensitive equipment can use seismic isolation to remain functional even after a major seismic event. Proposed systems for the seismic isolation of sensitive equipment are to (1) base isolate the entire building or a portion of the building, (2) isolate essential flooring systems only (raised floors), and (3) isolate individual pieces of equipment by placing them on separate isolation bearing systems (see Figure 29.28). In Japan, there are many buildings that are using the raised floor system to protect computers and other sensitive equipment. Seismic isolation is found to be very useful for semiconductor facilities, in which cost of the delicate items is as high as 75% of the total investment (Amick et al., 1998). Liquid storage tanks are important components of chemical factories and are also used in increasing

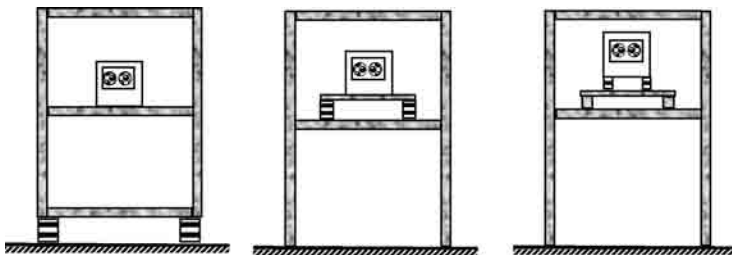


FIGURE 29.28 Seismic isolation for protection of equipment. Unreinforced rubber blocks. (Source: Ohashi, U.G. *Earthquakes and Base Isolation*, Pub. Asakura, Tokyo, 1995. With permission.)

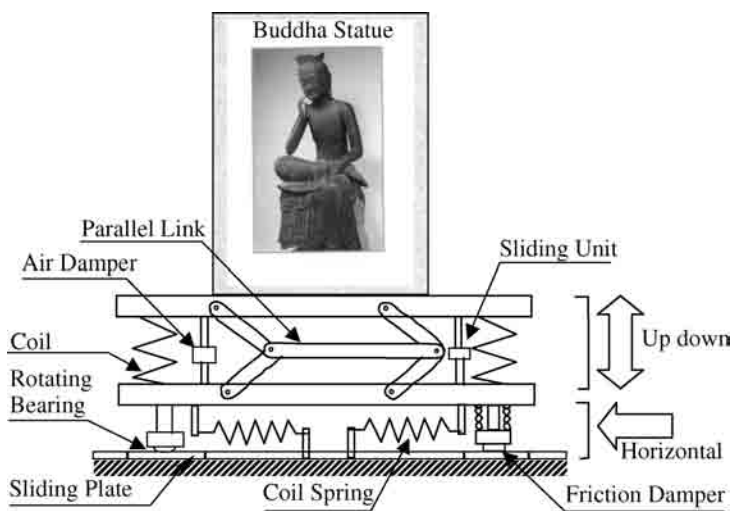


FIGURE 29.29 Three-dimensional base-isolation system for Moroku Bosatsu statue.

TABLE 29.2 Details of Isolation System and Dynamic Characteristics of the Structure

	Horizontal Direction	Vertical Direction
Elastic support	Coil spring	Coil spring
Damping mechanism	Friction damper	Air damper
Natural frequency (Hz)	0.25–0.35	2.0–2.5

number to store liquefied natural gas. The FPS was applied for seismic isolation of a large-size tank in Greece, and steel–rubber bearings were used for another tank in Korea, storing liquefied natural gas (Tajiran, 1998).

Seismic base isolation can also be used for the seismic protection of antique pieces. Iemura and coworkers designed a special seismic isolation system to protect a wooden carved statue of Moroku Bosatsu (Maitreya). It is an antique cultural artifact, considered to be the first wooden carved statue in Japan. The isolation system provides protection in all three directions (Figure 29.29). The details of the isolation system are provided in Table 29.2.

The overall size of the isolation system is shown in Figure 29.30. The shaking table test was also carried out to verify the effectiveness of the isolation system. Results of the experiment are presented in Table 29.3 and clearly show that the isolation system is very effective in reducing the accelerations.

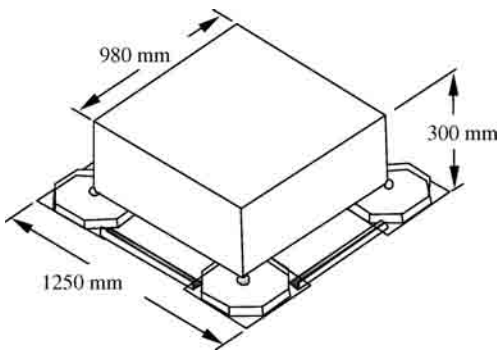


FIGURE 29.30 Overall size of the three-dimensional base-isolation system.

29.2.10 Performance during Past Earthquakes

Analytical models and experimental tools have been developed by researchers to simulate the behavior of a structure under earthquake motion. However, none of these methods can validate the behavior of a structure as does a real earthquake. In fact, many of the concepts of earthquake-resistant design are

TABLE 29.3 Results of Shaking Table Tests of a Three-Dimensional Base Isolation System

Direction	Level		
	Acceleration (gal)		Relative Displacement of Base Isolation (cm)
	Shaking Table	Above Base-Isolation System	
NS	795	166	15.3
EW	505	136	10.0
Vertical	314	250	1.1

the outcome of the analysis of observations made or recorded during past earthquakes. In the case of base isolation, as it is a relatively newer approach, it can help to assess the modeling techniques, existing analysis and design procedures, and methods followed in construction. Such analyses may help in evaluating the effectiveness of base isolation and also exposing weak aspects of designs. Strong motion-recording instrument networks have been installed on some of the base-isolated structures in different parts of the world in order to record the response of those structures during earthquakes. During the Northridge, Kobe, and Turkey earthquakes, a few base-isolated structures had their isolation system reaching nonlinear range, and the recorded performance of these structures can give a fair idea of the behavior of base-isolated structures during strong earthquake motions.

29.2.10.1 Performance of Buildings

The Northridge earthquake of January 1994 saw thousands of conventionally designed buildings and their contents suffer extensive damage and be closed for several days. However, two base-isolated buildings, namely, University of Southern California Hospital building and Fire Command and Control Facility, performed well during the earthquake. During the event, the seven-story base-isolated hospital building experienced a peak ground acceleration of 0.37g. The recorded peak acceleration at the roof was 0.21g. Analytical study showed that presence of the isolation system reduced the peak story shear at the base to about one third of that if the building had its base fixed (Nagarajaiah et al., 1996). “Workers in a large supply room within the hospital reported no disruption of supplies, or material falling off shelves, as a result of the earthquake. In contrast a pharmacy at the ground level in an adjacent medical building with fixed-base reported substantial disruption of the supplies” (EERI, 1996). The two-story base-isolated Fire Command and Control Facility could not perform as per expectation due to minor negligence in detailing the seismic gap. The building is base-isolated by high-damping rubber bearings and experienced peak ground acceleration of 0.19g. The recorded response shows the presence of sharp acceleration spikes that were due to pounding. However, the analytical study by Nagarajaiah et al. (2001) shows that, even with pounding, maximum base story shear of the base-isolated building was half that of the fixed-base case and without pounding it would have been one fourth.

In January 1995, the unexpected earthquake of magnitude 7.2 in Kobe shocked the engineering community. The 7 sec of strong shaking caused a heavy loss of life (over 5000 people died) and a catastrophic loss to infrastructure. The strong earthquake tested two existing base-isolated buildings in the region, namely, the six-story building of West Japan Postal Savings Computer Center (WJPSCC) and the three-story building of Technical Research Institute of Matsumura Gumi Corporation (TRIMGS). The six-story WJPSCC building that is base-isolated with elastomeric isolators, lead rubber bearings, and steel coil dampers experienced peak ground acceleration of 0.306g. A nearby six-story fixed-base building experienced peak ground acceleration of 0.27g. However, during the event, the maximum acceleration recorded at the roof of the fixed-base building was about nine times of that recorded at the roof of the WJPSCC building. Similarly, a

comparison of the roof acceleration of the three-story base-isolated TRIMGS building with that of a nearby three-story fixed-base building reveals that, due to base isolation, the peak accelerations at the roof were reduced by a factor of approximately 4.9 in the north–south direction and 2.5 in the east–west direction. It was later realized that the performance of this base-isolated building might be adversely affected due to freezing cold, when the rubber has a tendency to become stiffer (Izawa et al., 1996).

29.2.10.2 Performance of Bridges

In the year 1999, Turkey faced two major earthquakes, the first one on 17th August and the second on 12th November. At the time of the events, there were two base-isolated structures in the region, namely, Bolu Viaduct and Bolu Bridge. The structures were designed for a peak ground acceleration of 0.4g with isolation system comprising of a friction system and crescent moon-type hysteretic elements. During the earthquake of August 17, 1999, when the estimated ground acceleration at the Bolu viaduct site was 0.39g in the longitudinal direction and 0.31g in the transverse direction, the viaduct survived without any damage. The residual displacement was of the order of 1 mm only. However, the second event produced near-fault, or rather on-fault, pulse-type motion with a peak ground acceleration at the viaduct site in the order of 1.0g. The unexpected level of ground acceleration caused heavy damage to the viaduct. It was reported that the sliding bearings fell down from most of the piers before any cyclic movement. This performance again raised the issue of feasibility of base isolation for such near-fault pulse-type motions. During the same event, Bolu Bridge experienced the estimated peak ground motion of 0.65g, much higher than the design value. However, the only significant damage suffered by the bridge was the failure of some elements of the expansion joints because they were designed for a movement of 100 mm only (corresponding to the earthquake with a return period of 50 years). After the earthquake, the bridge showed a residual displacement in longitudinal direction of 45 mm and in transversal direction varying from 60 to 100 mm (Marioni).

The Eel River Bridge (U.S.), after being retrofitted with lead laminated rubber bearings, was hit by the magnitude 7.0 Cape Mendocino (Petrolia) earthquake in the year 1992. The peak ground acceleration recorded at a nearby recording station was 0.55g. The bridge suffered structural damage limited to the spalling of concrete at joints. Another base-isolated bridge, Sierra Point overpass (U.S.), was subjected to the 1989 Loma Prieta earthquake when peak ground acceleration at the base of bridge columns was 0.090g. The bridge, first constructed in 1956, was later retrofitted with lead rubber bearings in 1985. However, the abutments were not modified for the larger clearance required in isolation. This design weakness was exposed during the Loma Prieta earthquake and caused significant amplification in the steel superstructure of the bridge. However, no damage was sustained (Lee et al., 2001). Rangitaiki River Bridge at Te Teko, New Zealand, with lead rubber bearings on each pier and plain rubber bearings on abutments, suffered minor damage and a small permanent displacement during the 1987 Bay of Plenty earthquake. The peak acceleration, recorded at about 11 km from the bridge site was 0.33g. It was observed that owing to the inadequate fastening details for the isolators, one of the two bearings on abutment was dislocated (McKay et al., 1990). Bai-Ho bridge (Taiwan), a three-span, continuous nonprismatic prestressed concrete girder bridge, was subjected to the magnitude 6.0 Gia-I earthquake in year 1999. The bridge is seismically isolated in its longitudinal direction with lead rubber bearings; however, shear keys and specially designed steel rods are installed on both abutments to restrict the transverse movement of the superstructure. The peak acceleration recorded on the deck in longitudinal direction was slightly higher than that in the foundation while, owing to restraints, the peak acceleration in the transverse direction was 2.5 times than that of foundation (Lee et al., 2001). During the Kobe earthquake, the base-isolated Matsunohama Bridge had good recorded performance; however, the ground acceleration was not profound enough to test the effectiveness of the isolation system (Izawa et al., 1996).

In summary, analysis of the records obtained from a variety of base-isolated structures during real earthquakes presents some very interesting facts. In general, it was observed that, during strong earthquakes, numerous conventionally designed buildings suffered damage and remained closed for several days; however, the base-isolated buildings in the same region not only survived but continued to operate. On the other hand, in some cases, strong earthquakes exposed the lack of attention to minor construction details and the effectiveness of base isolation for near-fault earthquakes. Better performance of base-isolated structures during the Northridge and Kobe earthquakes have now persuaded the structural engineers and owners and triggered a rapid increase in the number of base-isolated buildings. In Japan alone, the number of buildings of this kind constructed during 1995 was almost the same as that of those constructed during the period from 1985 to 1994.

29.3 Seismic Vibration Control

29.3.1 Historical Development of Seismic Vibration Control

It is worth noting that a structural vibration control system for reducing seismic responses was developed several centuries ago in Japan, by an unknown engineer. This was applied to the construction of a Gojunoto (pagoda). The Gojunoto was five stories tall and was constructed of closely fitting mortised wooden beams and columns (Figure 29.31). During an earthquake, the vibrations of such a vertical cantilever structure would produce bending moments that could not be resisted by tension at the mortised joints. To overcome this weakness, a long wooden pole was suspended freely from the upper part of the pagoda so that it could undergo pendular vibrations if the pagoda was excited into motion by an earthquake. The weight of the pole exerted a compressive prestress on the pagoda, thus increasing the bending resistance. The bottom of the pole extended into a cylindrical hole in the ground that was of a larger diameter than the pole. Thus, when the pagoda was excited into vibrations by an earthquake, some of the vibrational energy would be transferred into oscillations of the pole and the impact of the pole on the sides of the hole would dissipate energy.

In 1969, Gupta and Chandrasekaran (1969) studied the effectiveness of a number of tuned mass dampers (TMDs) put in a single-DoF system to reduce seismic responses. The TMD system has both linear and elasto-plastic restoring-force characteristics and viscous-type damping. The study was shown in the Fourth World Conference on Earthquake Engineering (WCEE) in Santiago, Chile. In the Fifth WCEE in 1973, Skinner et al. (1973) presented their studies on energy absorption devices for earthquake-resistant structures. The devices were based on the plastic deformation of mild steel. In 1977, Ohno et al. (1977) introduced optimum tuning of the dynamic damper for civil structures under earthquake

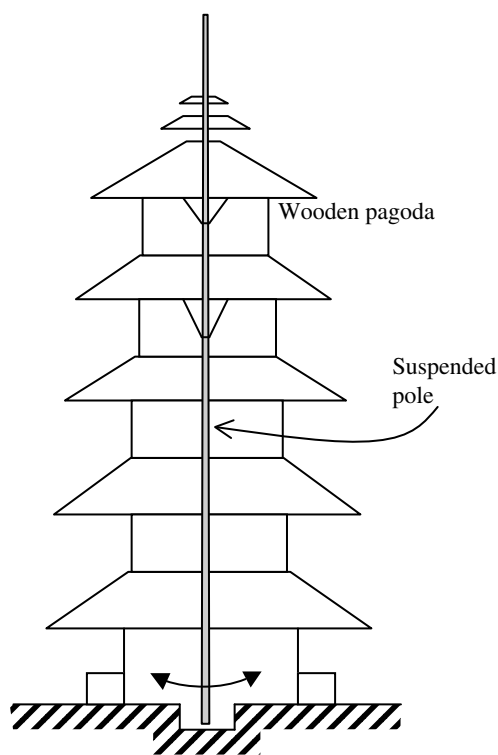


FIGURE 29.31 Sketch of a wooden pagoda with suspended pole that is free to undergo pendular vibration. (Source: Tanabashi, R., *Proc. II World Conf. on Earthquake Engineering*, 1960. With permission.)

excitations. Skinner et al. (1977) showed their works on studying hysteretic dampers for increasing structural earthquake resistance, and Tyler (1978) demonstrated the usefulness of flexural yielding of steel plate energy-dissipation devices in New Zealand.

In the seventh WCEE in 1980, Sladek and Klingner (1980) reported their studies on tuned-mass dampers for seismic response reduction in civil structures, whereas Keightley (1980) presented his work on a dry friction damper for multistory structures. Figure 29.32 shows the schematic of a framed structure with additional friction dampers and the hysteretic loop of the damper.

In 1984, Pall (1984) numerically studied the performance of a framed building equipped with friction devices. The performance was found to be superior to that of a conventional building. Scholl (1984) introduced brace dampers. The stiffness and damping of the damper can be set to alter the stiffness and damping in a structure. It was typically installed at the cross points in braced-frame structure systems. Liu et al. (1984) investigated the effectiveness of an active mass-damper control system for controlling coupled lateral-torsional motions of tall buildings subjected to strong earthquakes.

A special themed session named “Seismic response control of structural systems” was held at the Ninth WCEE in 1988. Some studies on passive systems were reported such as: a hysteretic damper that is put between two adjacent structures (Kobori et al., 1988); a multiple passive TMD (Clark, 1988); viscoelastic materials (Bergman and Hanson, 1988); viscous damping walls (Arima et al., 1988); and magnetic damping (Shimosaka et al., 1988). Also, some studies on active control were reported, such as an experimental study on active mass dampers (Aizawa et al., 1988) and air injection for suppressing sloshing in a liquid tank (Hara and Saito, 1988; Sogabe et al., 1988). Since then, the active vibration control of buildings and other civil structures has attracted a worldwide growing interest as an innovative technology in earthquake engineering.

During the Tenth WCEE in 1992, more thorough studies on structural control were reported such as: predictive control of structures with reduced number of sensors and actuators (Lopez-Almansa et al., 1992); applicability of vibration control to nonlinear structure (Shimada et al., 1992); full-scale implementation of active control (Soong et al., 1992); effects of soil-structure interaction (SSI) on actively controlled structure (Wong and Luco, 1992); the time-delay problem (Hou and Iwan, 1992); and fuzzy logic control (Tani et al., 1992). In this conference, the decision to form an international association and to hold a world conference dedicated to structural control was made. The International Association for Structural Control (IASC) was formed in 1993. The efforts led to the successful First World Conference on Structural Control in 1994 in Pasadena, California (IASC, 1994).

It was followed by the Second World Conference on Structural Control in 1998, which was held in Kyoto, Japan (IASC, 1999). The Third World Conference on Structural Control was held in April 2002, in Como, Italy (IASC, 2003). The conferences showed increasing interest among researchers and an increase of innovations and applications of structural control technologies in civil structures.

29.3.2 Basic Principles

Structural vibration control basically involves the regulation of structural properties in order to achieve structural a desirable response to a given external load and modification of the excitation. The regulation of structural properties includes the modification of mass, damping, and stiffness of the structure so that

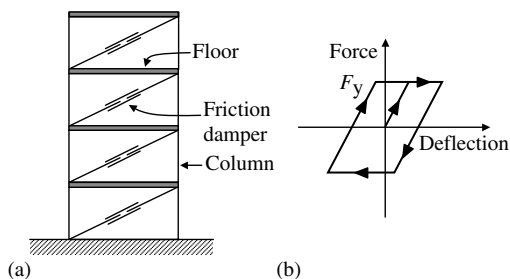


FIGURE 29.32 (a) Friction dampers in a framed structure; (b) hysteretic loop of the damper. (Source: Keightley, W.O. *Proc. VII World Conf. on Earthquake Engineering*, 1980. With permission.)

it can respond more favorably to the external excitation. Moreover, it is also possible to reduce the level of excitation transmitted to the structure. Structural control can be defined as a mechanical system that is installed in a structure to reduce structural vibrations during loadings such as strong earthquakes.

29.3.2.1 Passive Control System

The basic function of a passive control system is to absorb or consume a portion of the input energy, thereby reducing energy-dissipation demand on primary structural members and minimizing the possible structural damage. In the passive system, controlling forces develop at the locations of installation of the mechanism itself. The energy necessary for generation of these forces is provided through the motion of the mechanism during the dynamic excitation. The relative motion of the mechanism defines the amplitude and the direction of the controlling force. Passive control has four main advantages: (1) it is usually relatively inexpensive; (2) it consumes no external energy (energy may not be available during a major earthquake); (3) it is inherently stable; and (4) it works even during a major earthquake.

In the passive system area, structural response control can be divided into two groups. The first group uses supplemental damping to reduce structural responses by conversion of kinetic energy to heat. The second group uses supplemental oscillators to reduce the structural response by transferring energy among vibration modes. The first group includes devices that operate on principles such as frictional sliding, the yielding of metals, phase transformation in metals, deformation of viscoelastic solids or fluids, and fluid orificing. The second group includes dynamic vibration absorbers such as TMDs and tuned liquid dampers.

The major difference between viscous/viscoelastic devices and friction/yielding devices is the maximum force that each device will develop during an earthquake. The maximum earthquake forces developed in viscous/viscoelastic devices are determined by the maximum displacements and velocities across these devices. The maximum earthquake forces in a friction/yielding device equals the design friction force/design yield force plus strain hardening. Thus, the maximum earthquake forces are more easily controlled in the friction/yielding devices.

The effect of increasing damping in a structure can be appreciated by studying the earthquake response spectrum. The earthquake response spectrum of a quantity is a plot of the peak value of the response quantity as a function of the natural vibration period of the system. Each such plot is for single-DoF system having a fixed damping ratio, and several such plots for different values of damping ratio are included to cover the range of damping values. The most commonly used spectra in earthquake engineering are the absolute acceleration response spectrum, the velocity response spectrum, and the displacement response spectrum. For more information on how to develop earthquake response spectrum, readers are referred to Chopra (1995).

Figure 29.33 shows the response spectra of measured ground acceleration during the Kobe, Japan, earthquake on January 17, 1995. The ground acceleration north–south (NS) component was recorded at the Kobe Marine Meteorological Observatory in Chuo-ku. As is shown in the figure, increasing the damping ratio from 5 to 30% decreases the response spectra. Therefore, on a level of ordinary structure that has 5% of damping, the response can be reduced further by increasing the structural damping. In the area of passive systems, a variety of mechanical energy dissipaters to increase structural damping has been developed and tested in the laboratory and, in some cases, in actual structural applications, such as bracing systems, friction dampers, viscoelastic dampers, and other mechanical dampers.

The principle of the TMD dates back to the 1940s when Den Hartog (1947) reintroduced the dynamic absorber invented by Frahm in 1909. Figure 29.34 shows the principle of the TMD. A large system under alternating force $P_0 \sin \omega t$ is represented by a K – M system where K and M are the stiffness and the mass of the system, respectively. The vibration absorber consists of a comparatively small vibratory system with stiffness k and mass m . The natural frequency, $\sqrt{k/m}$, of the attached absorber is chosen to be equal to the frequency, ω , of the disturbing force. It has been shown (Den Hartog, 1947) that the main mass, M , does not vibrate at all and that the small system, k – m , vibrates in such a way that its spring force is at all instants equal and opposite to $P_0 \sin \omega t$. Thus, there is no net force acting on M and therefore that mass

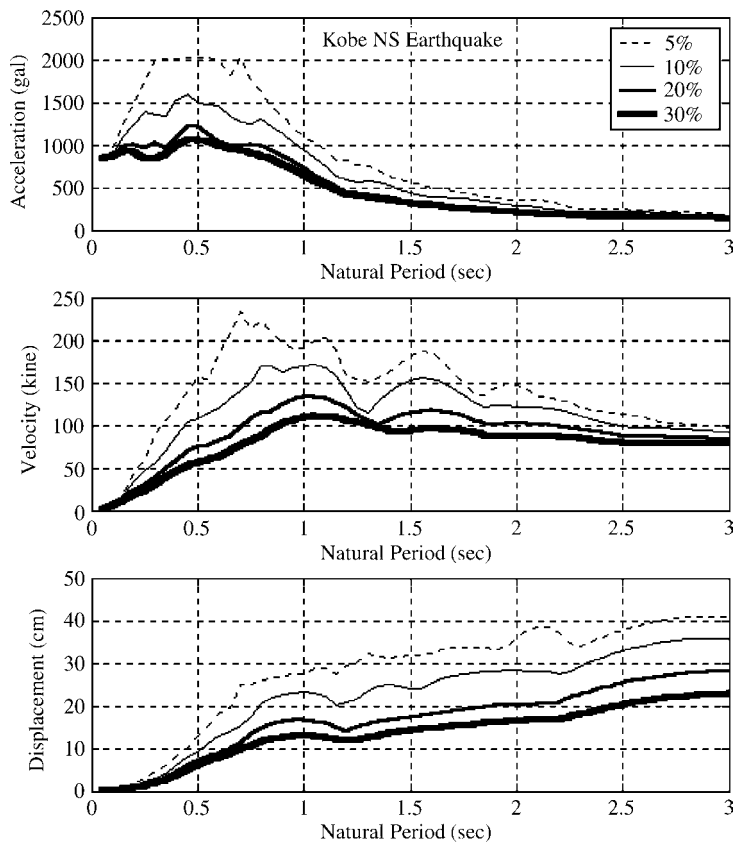


FIGURE 29.33 Effect of damping on earthquake response spectra.

does not vibrate

$$\omega_M = \sqrt{\frac{K}{M}}, \quad \omega_m = \sqrt{\frac{k}{m}}, \quad \mu = \frac{m}{M} \quad (29.22)$$

It is useful to introduce the new notations, above. Assume that $\mu = 0.2$, and $\omega_M = \omega_m$. For this condition, the resonance curve of the system is illustrated in Figure 29.35. At $\omega = \omega_m$ or $\omega/\omega_m = 1$, the motion of the main mass ceases altogether (Chopra, 1995). Since the system has two DoF, two resonant frequencies exist and the response is unbounded at those frequencies.

If the exciting frequency, ω , is close to the natural frequency, ω_m , of the attached absorber, and the operating restrictions make it possible to vary either one, the vibration absorber can be used to reduce the response amplitude of the main system to near zero. It is worth noting that the larger the attached absorber mass, m , the smaller the absorber displacement, $(x_2 - x_1)$, relative to the displacement of main mass, M . However, a large absorber mass presents a practical problem. At the same time, the smaller is the mass, m , the narrower is the operating frequency range of the absorber (Chopra, 1995).

29.3.2.2 Active Control System

Active control systems are used to control the response of structures to internal or external excitation, such as machinery or traffic noise, wind, or earthquakes, where the safety or comfort level of the

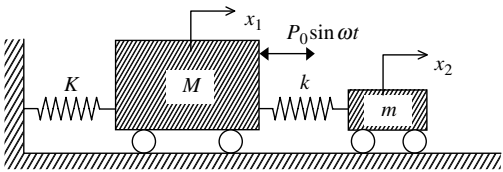


FIGURE 29.34 Additional vibratory k – m system to a larger K – M system to reduce vibration of the larger system.

occupants is of concern. Active control makes use of a wide variety of actuators, which may employ hydraulic, pneumatic, electromagnetic, or motor-driven ball-screw actuation. An essential feature of active control is that external power is used to effect the control action. This makes the system vulnerable to power failure, which is always a possibility during a strong earthquake.

For the actuators properly to apply the desired forces, sensors are placed in the structure in order to measure structural response. The sensors convey response information to a central computer that then uses this information to calculate the desired actuator forces. The advantage of an active control system is that it attains excellent control results. However, there are many drawbacks to using the active control system. It is relatively expensive to design and to operate due to the large amount of power needed. It has the potential to destabilize the structural system. Furthermore, it tends to take up more space than passive control devices.

A fully active structural control system has the basic configuration as shown schematically in Figure 29.36. The structural control system in the figure basically consists of sensors, controllers, and actuators. Sensors are used to measure either external excitations or structural responses, or both. Controllers process the measured information and compute necessary control forces needed based on a given control algorithm. Actuators are used to produce the required forces and are usually powered by external energy sources.

According to the characteristics of the controlling effects, active control can be classified into two categories: open-loop control and closed-loop control. A control system in which the control input is applied without the knowledge of the plant output is called an open-loop control system. Figure 29.37 shows a block diagram of an open-loop control system, where the subsystems (controller and plant) are shown as rectangular blocks. Open-loop control will be successful only if the controller has a reasonably good prior knowledge of the behavior of the plant, which can be defined as the relationship between the control input and the plant output. Mathematically, the relationship between the output of a linear plant and the control input can be described by a transfer function. However, in actuality, the presence of plant behavior uncertainty is unavoidable. Therefore, it is clear that an open-loop control system is unlikely to be successful.

In the case that the controller adjusts the control input according to the actual observed output, the system is called a closed-loop system. In this system, the control input is a function of the plant's output. Since in a closed-loop system the controller is constantly in touch with the actual output, it is likely to succeed in achieving the desired output even in the presence of uncertainty in the linear plant's behavior (the transfer function). The mechanism by which the information about the actual output is conveyed to the controller is called feedback. On a block diagram, the path from the plant output to the controller is called a feedback loop. A block diagram of a possible closed-loop system is given in Figure 29.38.

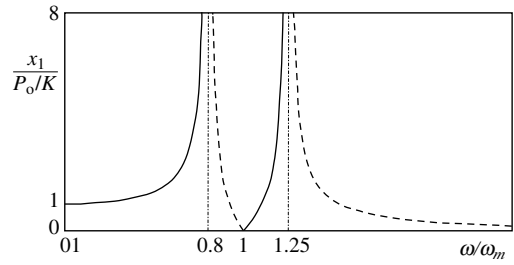


FIGURE 29.35 Resonance curve for the system in Figure 29.34 that shows response amplitude vs. exciting frequency (the dashed curve indicates negative x_2 or phase opposite to excitation) for $\mu = 0.2$ and $\omega_M = \omega_m$. (Source: Chopra, A.K. 1995. *Dynamics of Structures, Theory and Applications to Earthquake Engineering*, Prentice Hall, New York. With permission.)

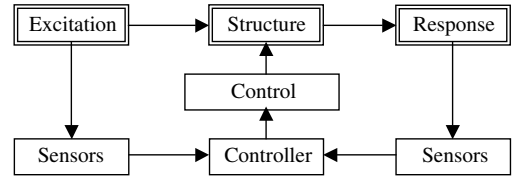


FIGURE 29.36 Schematic diagram of active control system.

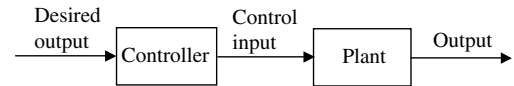


FIGURE 29.37 An open-loop control system; the controller applies control input without knowing the plant output.

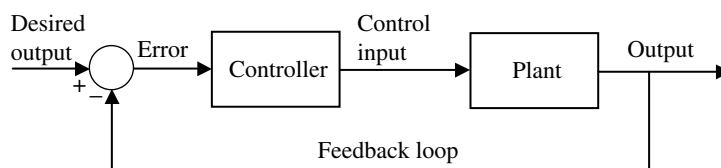


FIGURE 29.38 Example of a closed-loop control system with feedback; the controller applies a control input based on the plant output.

When the desired output is a constant, the resulting controller is called a regulator. If the desired output changes with time, the corresponding control system is called a tracking system. In any case, the principal task of a closed-loop controller is to minimize the “error” as quickly as possible.

29.3.2.3 Semiactive Control System

Semiactive control falls between passive and active on the control spectrum. A semiactive control system is similar to an active system in that the system uses sensors and controllers, and operates on external power. However, the source of external energy is used only for adjustment of the mechanical characteristics of the system (Rakicevic and Jurukovski, 2001). The inherent benefit of a semiactive control device is that the mechanism used does not require large amounts of external power. Many semiactive devices can be powered by batteries protecting them from sudden power loss during earthquakes. Semiactive control systems are basically derived from passive systems; they are modified in such a way that they enable adjustment or correction of their mechanical characteristics.

A typical strategy for a semiactive control system is that an “ideal” actively controlled device is first assumed and appropriate primary controller designs for this device are designed. Then, a secondary controller is used that clips the optimal control force so it is dissipative in a manner consistent with the physical nature of the device. This strategy has been widely used (e.g., Dyke et al., 1996a, 1996b, Jung et al., 2001).

Spencer and Sain (1997) found that many active control systems for civil engineering applications operate primarily to modify structural damping. They claimed that preliminary studies indicate that appropriately implemented semiactive systems perform significantly better than passive devices and have the potential to achieve the majority of the performance of fully active systems, thus allowing for the possibility of effective response reduction during a wide array of dynamic loading conditions. In other words, semiactive control devices offer the adaptability of active control devices without requiring the associated large power sources (Spencer and Sain, 1997).

Moreover, according to presently accepted definitions (Housner et al., 1997), a semiactive control device is one that cannot inject mechanical energy into the controlled structural system (including the structure and the control device), but has properties that can be controlled optimally to reduce the responses of the system. Therefore, in contrast to active control devices, semiactive control devices do not have the potential to destabilize (in the bounded input/bounded output sense) the structural system. Semiactive control devices are often viewed as controllable passive devices.

Semiactive control technologies have recently been widely investigated in terms of the reduction of the dynamic response of structures subjected to earthquake and wind excitations (Housner et al., 1997; Spencer et al., 1997; Patten, 1998; Kurata et al., 1999; He et al., 2001; Iemura et al., 2001; Jung et al., 2001). Various semiactive devices have been proposed that utilize forces generated by surface friction or viscous fluids to dissipate vibratory energy in a structural system.

29.3.2.4 Hybrid Control System

The common usage of the term “hybrid control” implies the combined use of active and passive control systems. For example, this may be a structure equipped with distributed viscoelastic damping

supplemented with an active mass damper on the top of the structure, or a base-isolated structure with actuators actively controlled to enhance performance. The method, which consists of using both passive and active devices, should utilize the merits of both passive and active methods and avoid the demerits of these methods. Thus, higher levels of performance should be achievable. Additionally, the resulting hybrid control system can be more reliable than a fully active system because, should the active control malfunction, the minimum seismic protection of the structure can be done by the passive control.

29.3.2.5 Categorization of Basic Principles

From the above group of structural control systems, there are basically five principles concerning earthquake-induced structural response control that are important to consider. They are listed below:

1. Cutting off the input energy from the earthquake ground motion; examples:
 - (a) Floating structures
 - (b) Frictional structures
2. Isolating the natural frequencies of the structures from the predominant seismic power components; examples:
 - (a) Base-isolated structures
 - (b) Long period structures
3. Providing nonlinear structural characteristics and establishing a nonstationary state nonresonant system; examples:
 - (a) Inelastic structures
 - (b) Varying stiffness and damping structures
4. Utilizing energy absorption mechanism; examples:
 - (a) Viscous damper
 - (b) Viscoelastic damper
 - (c) Inelastic behavior
5. Supplying control force to suppress the structural response; examples:
 - (a) Active mass damper
 - (b) Active tendon
 - (c) Joint damper

29.3.3 Important Issues in Vibration Control

29.3.3.1 Soil–Structure Interaction

Seismic vibration control of a civil structure deals with methods to suppress the response in a structure subjected to earthquake excitation. To control the structural dynamic response, the structural system model must be known. Modeling of a structure is relatively straightforward, using a finite number of DoF, because the dimensions of the structure are finite. However, in general, civil structures are supported on surrounding soil from which the tremor excites the structure. This makes the structure interact with the surrounding soil. Therefore, it is very important to include SSI for controlling the seismic response.

SSI will result in a structural response that may be quite different from the structural response computed for a fixed-base building. The frequency of vibration of the structure may be lower because of the interaction. The change in frequency may also affect the response of the overall structure or its substructures or components. Moreover, soils are notoriously nonlinear when subjected to strong ground motions at the level of engineering interest (Marshall, 2001). Damping of the final system increases because of the radiation of energy of the propagating waves away from the structure (Wolf, 1985).

29.3.3.2 Device–Structure Interaction and Time Delay

Other important effects come from the device–structure dynamic interaction. Dyke et al. (1995) studied the role of control–structure interaction in mitigating dynamic response. Their findings show that accounting for control–structure interaction and actuator dynamics in the design process can improve the performance and robustness of a control system.

Time delay between control command and actual control force also causes problems. A study by Hou and Iwan (1992) showed the problems of time delay in the vibration control of structures. Also, Agrawal and Yang (2000) claimed that applications of unsynchronized control forces due to time delay may result in a degradation of the control performance, and it may even render the controlled structure unstable. Therefore, they provide a state-of-the-art review for available methods of time-delay compensation.

29.3.3.3 Design Guidelines

Since structural control is a new concept in civil structures, design guidelines are now being developed to provide the design engineers with tools for the safe design or seismic rehabilitation of structures. For a passive control system, the American Society of Civil Engineers has prepared for the Federal Emergency Management Agency a “Prestandard and Commentary for the Seismic Rehabilitation of Buildings” (ASCE, 2000), in which requirements for the systematic rehabilitation of buildings using energy-dissipation systems is set forth. In the standard, analysis and design criteria for passive energy dissipation systems are provided.

In this prestandard, two sections deal with structural control technology. First, is “Passive Energy Dissipation Systems,” which contains (1) General Requirements, (2) Implementation of Energy Dissipation Devices, (2) Modeling of Energy Dissipation Devices, (3) Linear Procedures, (4) Nonlinear Procedures, (5) Detailed Systems Requirements, (G) Design Review, and (H) Required Test of Energy Dissipation Devices. Each subsection is explained in detail in the prestandard for the users.

However, in the second section, “Other Response Control Systems,” it is mentioned that analysis and design of response control other than in the passive systems above shall be reviewed by an independent engineering review panel. This is because the technology of active, semiactive, and hybrid control is not sufficiently mature and the necessary hardware is not sufficiently robust to warrant the preparation of general guidelines for the implementation of the technology.

29.3.4 Vibration-Control Devices

29.3.4.1 Passive Control Systems

29.3.4.1.1 *Metallic Yielding Dampers*

One of the effective mechanisms useful for the dissipation of energy input to a structure from an earthquake is through the inelastic deformation of metals. The idea of utilizing added metallic energy dissipaters within a structure to absorb a large portion of the seismic energy began with the conceptual and experimental work of Kelly et al. (1972) and Skinner et al. (1975). Devices considered by them included torsional beams, flexural beams, and U-strip energy dissipaters as shown schematically in [Figure 29.39](#).

During the following years, considerable progress has been made in the development of metallic dampers. For example, many new designs have been proposed, including the hourglass or X-shaped and triangular plate dampers as shown in [Figure 29.40](#).

The X-shaped steel plates form devices called ADAS (Added Damping and Stiffness; see Perry et al., 1993), because the devices essentially add stiffness as well as damping to the element where they are installed. For example, if they are installed between two adjacent floors, then it will increase the stiffness and damping between those two floors. Increasing the stiffness will generally attract more seismic forces. However, since the devices have much lower yielding forces than the elements where they are installed, then the postyield stiffness of the devices is dominant during a strong earthquake.

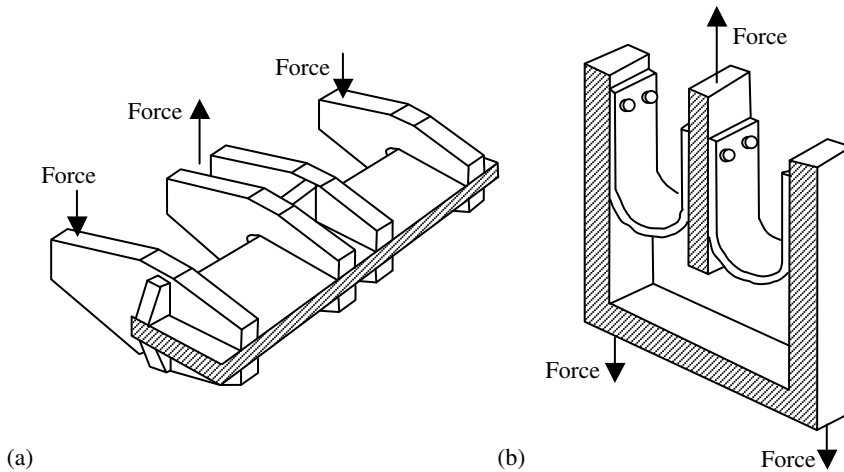


FIGURE 29.39 Schematic of metallic dampers: (a) torsional beam and (b) U-strip, and the directions of alternating forces. (Source: Skinner, R.I. et al. *Earthquake Eng. Struct. Dyn.*, 3, 287–296, 1975. With permission.)

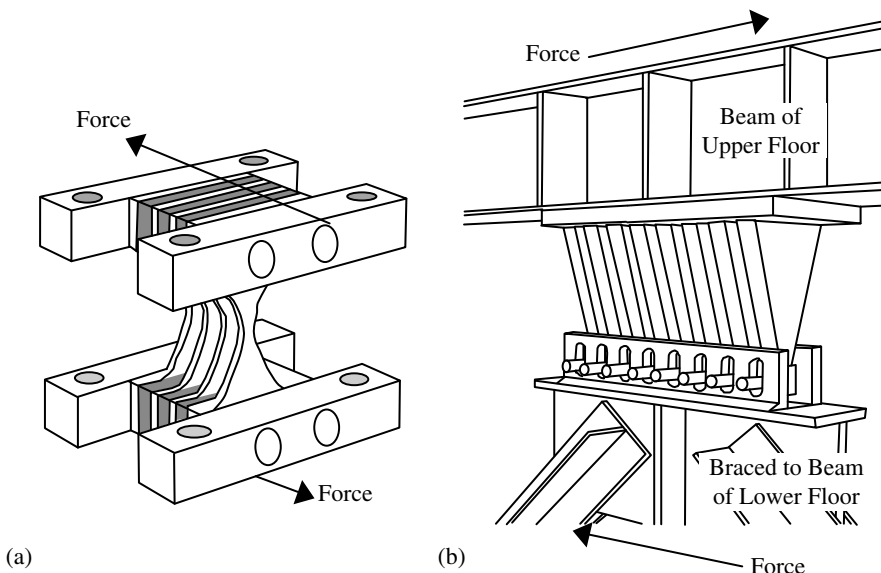


FIGURE 29.40 Schematic of (a) X-shaped (Source: Tsai, K.-C. et al. *Earthquake Spectra*, 9, 505–528, 1993. With permission.) and (b) triangular plate dampers, and the directions of alternating forces. (Source: Perry, C.L. et al. *Earthquake Spectra*, 9, 559–579, 1993. With permission.)

The devices dissipate energy through the flexural yielding deformation of mild steel plates. Each device consists of a series of steel plates arranged in parallel, with boundary elements at the top and bottom to establish end fixity, which bend in double-curvature flexure when subjected to lateral loading. The direction of the lateral loadings is shown in Figure 29.41. The plates are cut in an hour-glass shape to match the moment diagram and thus maximize the uniformity of plastification over the height of the steel plates.

Cyclic loading tests to determine the reliability of the ADAS were performed by Bergman and Goel (1987). The tests demonstrated that the devices maintained stable hysteretic properties, dissipated significant energy with no pinching or slip zones, and continued to have these properties until plate fracture at high strain or high numbers of cycles. The schematic hysteretic loop of ADAS

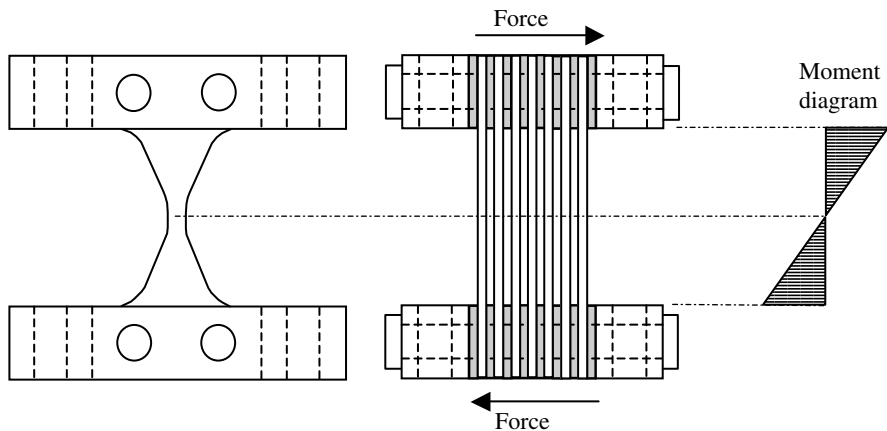


FIGURE 29.41 ADAS element: (a) lateral view; (b) longitudinal view with lateral forces; and (c) moment diagram over the height of the steel plates.

devices tested by Bergman and Goel (1987) is shown in Figure 29.42. It is worth noting that the apparent stiffening of the device in the figure is due to finite deformation, not strain hardening of the material; therefore, the effects of finite deformation should be included in the assessment of a design.

Tsai et al. (1993) have performed cyclic loading tests on TADAS (Triangular-plate ADAS; see Figure 29.40b). The hysteretic loops of the tested TADAS are similar to those of ADAS, such as the apparent stiffening at large displacement, since the mechanism is the same. Although the slotted pin connection at the apex reduces the axial tension force, some friction at the pin location contributes to the stiffening of hysteretic loops (Soong and Dargush, 1997).

29.3.4.1.2 Friction Dampers

Another excellent mechanism for energy dissipation is friction. The mechanism has been used for many years in automotive brakes to dissipate kinetic energy of motion. In friction dampers, stick-slip phenomena must be minimized to avoid introducing high-frequency excitation.

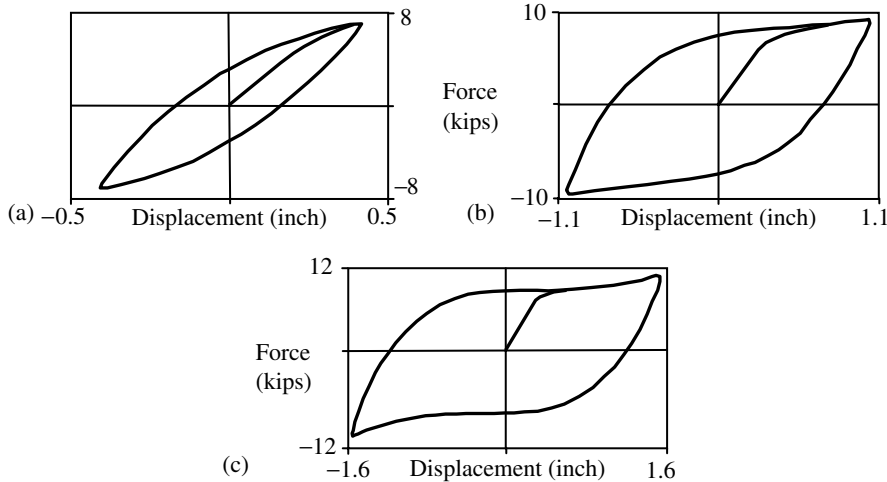


FIGURE 29.42 Schematic hysteresis loop of the ADAS device with maximum displacements of (a) 0.42 in. (10.7 mm); (b) 1.04 in. (26.4 mm); and (c) 1.56 in. (39.6 mm). (Source: Bergman, D. and Goel, S., Rpt. UMCE 87-10, Univ. Michigan, 1987. With permission.)

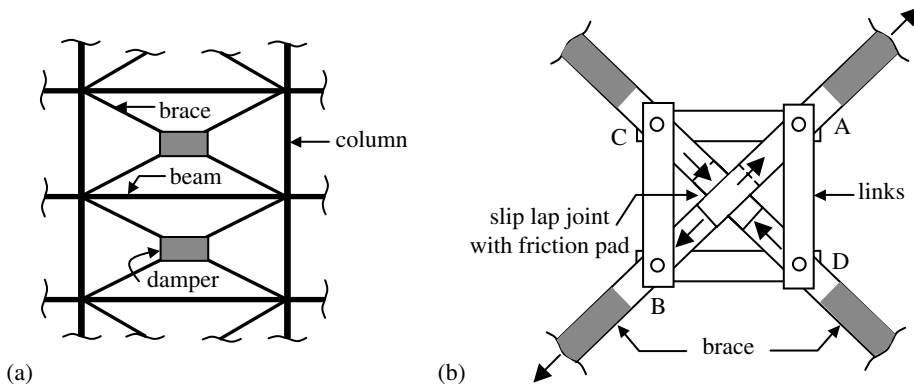


FIGURE 29.43 Pall friction damper: (a) set up in a structure; (b) schematic of the damper.

Furthermore, friction materials should have a consistent coefficient of friction over the intended life of the device (Housner et al., 1997).

The Pall device (Pall and Marsh, 1982) is one of the friction dampers that can be installed in a structure in an X-braced frame as illustrated in Figure 29.43. The mechanism of the damper is that, when there is axial tension force in the bracing system, as shown in the figure by outward arrows, then plates A and B are moving outward from each other. This movement is resisted by some friction force at the slip lap joint between plates A and B. This movement also causes plates C and D to move toward each other because of the existence of the links. This movement is also resisted by some frictional force between plates C and D. Without the existence of the links, the bracing may buckle because of axial compression force. The friction level between plates is designed so that the plates will not slip to each other during wind storms or moderate earthquakes. Under severe loading conditions, the devices slip in order to dissipate energy so that structural response can be reduced. The force–displacement relationship of Pall dampers has been studied extensively. A plot of its typical cyclic response is illustrated in Figure 29.44 (Filiatrault and Cherry, 1987).

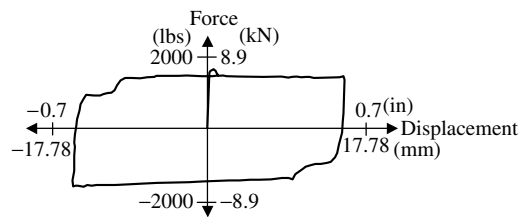


FIGURE 29.44 Schematic of force–displacement hysteresis loop of the Pall friction damper. (Source: Filiatrault, A. and Cherry, S. *Earthquake Spectra*, 3, 57–78, 1987.)

29.3.4.1.3 Viscoelastic Dampers

The application of viscoelastic dampers to civil engineering structures seems to have begun in 1969, when approximately 10,000 viscoelastic dampers were installed in each of the twin towers of the late World Trade Center in New York to reduce wind-induced vibrations. An example of a viscoelastic damper is illustrated in Figure 29.45.

The damper consists of a viscoelastic material bonded to steel plates. The viscoelastic materials used in structural application are typically copolymers or glassy substances, which dissipate energy when subjected to shear deformation (Soong and Dargush, 1997). With induced structural vibration, the damper will absorb and dissipate the vibrational

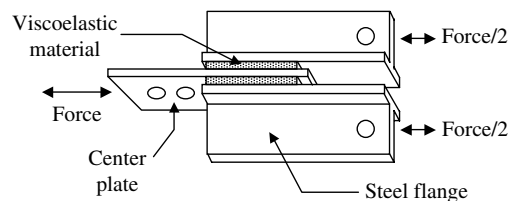


FIGURE 29.45 Typical viscoelastic-damper configuration.

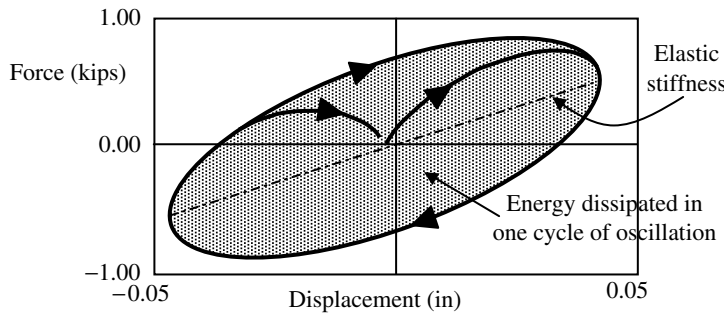


FIGURE 29.46 Typical schematic hysteresis loop of viscoelastic damper. (Source: Shen, K.L. and Soong, T.T. *J. Eng. Mech. ASCE*, 121, 694–701, 1995. With permission.)

energy by shearing deformation within the viscoelastic material. Heat will be generated in the viscoelastic material and released through the steel members of the damper.

A typical hysteresis loop produced by viscoelastic dampers is shown in Figure 29.46. By using viscoelastic dampers, although the structural response is elastic, hysteresis loops are formed because of the viscoelastic material. The area enclosed in the hysteresis loops is the energy dissipated by the viscoelastic dampers during one cycle of oscillation.

The behavior of viscoelastic materials under dynamic loading depends on vibrational frequency, strain, and ambient temperature. In general, the relationship between shear strain, $\gamma(t)$, and shear stress, $\tau(t)$, under harmonic shear strain with frequency, ω , can be expressed as (Zhang et al., 1989)

$$\tau(t) = G'(\omega)\gamma(t) + \frac{G''(\omega)}{\omega} \dot{\gamma}(t) \tag{29.23}$$

$G'(\omega)$ and $G''(\omega)$ are shear storage modulus and shear loss modulus of the viscoelastic material, respectively. The loss factor is defined by $\eta = G''(\omega)/G'(\omega)$. In general, as the vibrational frequency increases, the values of $G'(\omega)$ and $G''(\omega)$ become larger. However, if the ambient temperature increases, those values become smaller. Test results of a typical viscoelastic damper averaged over the first 20 cycles are shown in Table 29.4.

For a viscoelastic damper with shear area, A , and thickness, δ , the corresponding force–displacement relationship is

$$F(t) = k_d(\omega)X + c_d(\omega)\dot{X} \tag{29.24}$$

in which X and \dot{X} are the relative displacement and velocity of the damper, respectively, and

$$k_d(\omega) = \frac{AG'(\omega)}{\delta} \quad c_d(\omega) = \frac{AG''(\omega)}{\omega\delta} \tag{29.25}$$

TABLE 29.4 Typical Viscoelastic Damper Properties

Temperature (°C)	Frequency (Hz)	Strain (%)	k_d^a (lb/in.)	G' (psi)	G'' (psi)	η
24	1	5	2124	142	193	1.36
24	1	20	2082	139	192	1.38
24	3	5	4084	272	324	1.19
24	3	20	3840	256	306	1.20
36	1	5	880	59	67	1.13
36	1	20	873	58	65	1.12
36	3	5	1626	108	119	1.10
36	3	20	1542	103	112	1.09

^a The definition of k_d is shown in the text.
Source: Data from Chang, K.C. et al. *Earthquake Spectra*, 9, 371–387, 1993.

From the above equations, it is clear that a linear system with added viscoelastic dampers remains linear with the dampers contributing to increased viscous damping as well as stiffness. However, it needs to be pointed out that, for viscoelastic material at large strains, there is considerable self-heating due to the large amount of energy dissipated. The heat generated changes the mechanical properties of the material, and the overall behavior becomes nonlinear. This means that a linear analysis utilizing the above equations can only be for approximation of the response.

29.3.4.1.4 Viscous Fluid Dampers

The most convenient and common functional output equation for a damper comes from classical system theory, and is that of the so-called “linear” or “viscous” damping element

$$F(t) = c_d \dot{X}(t) \quad (29.26)$$

in which $F(t)$, c_d , and $\dot{X}(t)$ are the damping force, damping coefficient, and relative velocity across the damper, respectively.

In mechanical engineering, it is difficult to manufacture a useable fluid-filled component having a purely viscous output, because even moderate pressure hydraulic flows through a simple orifice follow a very different output equation, in which differential pressure varies with the fluid velocity squared. Therefore, the output of the basic hydraulic damping element is

$$F(t) = \text{sgn}(\dot{X}(t))c_d|\dot{X}(t)|^2 \quad (29.27)$$

As a result of long research in this area, which was started in the 1960s, the most useful dampers being used in buildings today are the so-called “low exponent” type, with an output equation of the form:

$$F(t) = \text{sgn}(\dot{X}(t))c_d|\dot{X}(t)|^\alpha \quad (29.28)$$

In most cases, α is an exponent having a specified value in the range of 0.3 to 1.0. Values of α that have proven to be the most popular are in the range of 0.4 to 0.5 for building designs with seismic input (Taylor, 2002).

The design elements of a fluid damper are relatively few. However, the detailing of these elements varies greatly. Typical elements for a fluid damper are shown in Figure 29.47. Typical experimentally measured force–displacement loops are shown in [Figure 29.48](#).

29.3.4.1.5 Tuned Mass Dampers

Much of the early development of dynamic vibration absorbers, as mentioned in Section 29.3.2.1, has been limited to the use of dynamic absorbers in mechanical engineering systems in which one operating frequency is in resonance with a machine’s fundamental frequency. However, building structures are subjected to earthquakes which possess many frequency components. The performance of a

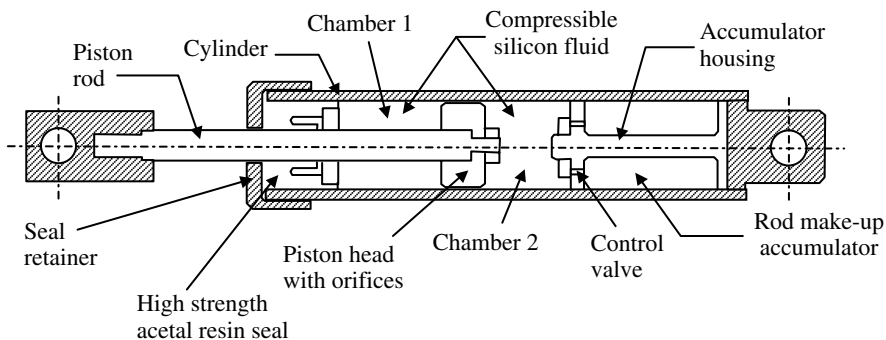


FIGURE 29.47 Typical schematic of a fluid damper. (Source: Taylor, D.P. *Passive Structural Control Symp.*, 2002. With permission.)

dynamic vibration absorber, referred to as the TMD herein, in complex multi-DoF systems is expected to be different. Consider the resonance curve in Figure 29.49 of a system shown in Figure 29.34, but now with different parameters: $\mu = 0.05$, but still $\omega_M = \omega_m$ (see Equation 29.22 for the definition of these parameters). An additional parameter, the damping ratio of TMD, is shown in Equation 29.29. Where c is damping coefficient of a linear viscous damper installed between structural mass, M , and TMD mass, m ,

$$\zeta_{\text{TMD}} = \frac{c}{2m\omega_m} \quad (29.29)$$

When the damping ratio in the TMD equals zero, the response amplitude is infinite at the two resonant frequencies. When the damping ratio becomes infinite, the two masses are virtually stuck to each other; the result is a single-DoF system with mass, $1.05 (M)$ with the amplitude becoming infinite again at a resonant frequency (see Figure 29.49). Therefore, somewhere between these extremes, there must be a value of the TMD damping ratio for which the peak becomes a minimum. Therefore, the objective in adding the TMD herein is to bring the resonant peak of the amplitude to its lowest possible value so that smaller amplifications over a wider frequency bandwidth can be achieved.

There are many types of TMD for implementation and the following are some examples (Figure 29.50). An innovative challenge is highly expected in this field.

There is another type of TMD that uses liquid as the mass; this damper is called the tuned liquid damper (TLD). The TLD has been used in ships for controlling vibrations because of water waves. The TLD uses water or other liquid as the moving mass and the restoring force is generated by gravity. Energy absorption comes from boundaries between liquid and containers and turbulence in the liquid flow. The basic principle of the TLD in absorbing kinetic energy of the main structure is the same as the TMD. Figure 29.51 shows types of TLD. Favorable properties of TLD compared with TMD are as follows:

- Smooth movement in small vibration is possible because of no mechanical friction.
- It is reasonable in cost and maintenance because of no complex mechanism.
- It can be applied easily in two horizontal directions with a single TLD.
- It can be compact and portable if large numbers are used.

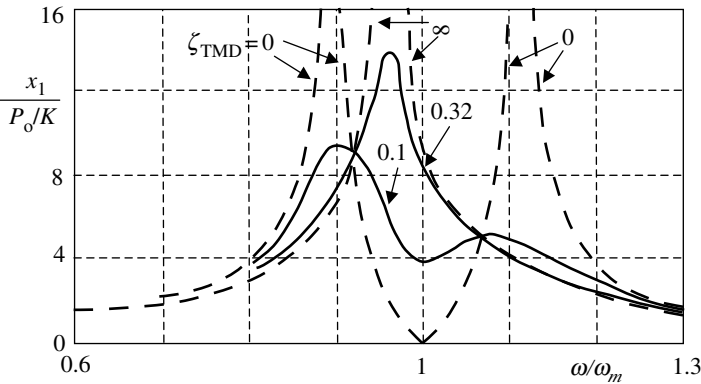


FIGURE 29.49 Resonance curve for the system in Figure 29.34 that shows response amplitude vs. exciting frequency for $\mu = 0.05$ and $\omega_M = \omega_m$.

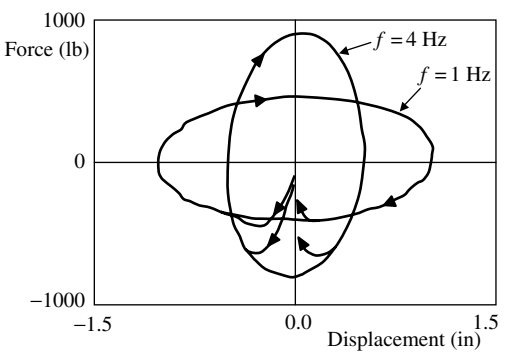


FIGURE 29.48 Typical schematic of fluid damper hysteretic loops. (Source: Constantinou, M.C. and Symans, M.D. *Struct. Des. Tall Build.*, 2, 93–132, 1993. With permission.)

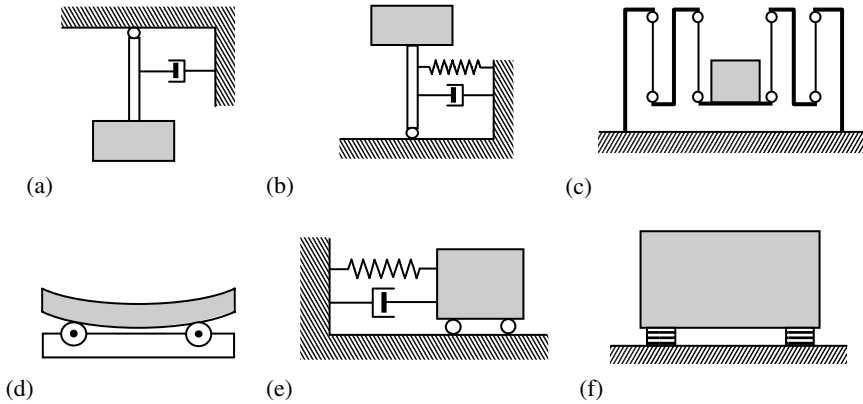


FIGURE 29.50 Examples of different types of TMD: (a) pendulum with damper; (b) inverted pendulum with spring and damper; (c) pendulum of which hangers are wound to save space; (d) swinging mass on rotational bearings; (e) sliding mass with spring and damper; (f) mass on rubber bearings. (Source: Iemura, H. *Passive and Active Vibration Control in Civil Engineering*, Springer, New York, 1994a,b. With permission.)

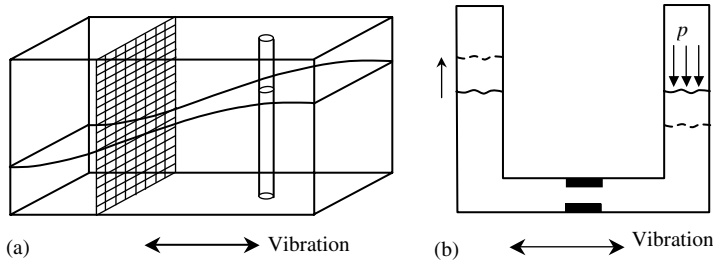


FIGURE 29.51 Types of TLD: (a) tuned sloshing damper with meshes and rods; (b) tuned liquid column damper with orifice. (Source: Iemura, H. *Passive and Active Vibration Control in Civil Engineering*, Springer, New York, 1994a,b. With permission.)

The TLD can be divided into two categories. First, is the sloshing damper as shown in Figure 29.51a. The vibration period is adjusted by the size of the container and the depth of the liquid. The damping capacity is increased by placing meshes or rods in the liquid. The second category is the tuned liquid column damper as shown in Figure 29.51b. The vibration period is adjusted by the shape of the column or the air pressure in the column. The damping capacity is increased by adjusting the orifice in the column, which generates a high turbulence.

29.3.4.2 Active Control System

29.3.4.2.1 Electromagnetic Actuator

An electromagnetic actuator is frequently employed where it is necessary to provide a mechanical force depending on an electric current. Figure 29.52 shows the elements of such a device. A magnetic structure supports a circuit of magnetic flux driven by the coil of N turns carrying current i , in ampere. Part of the magnetic circuit is a movable armature that slides smoothly on the support member. An air gap (or possibly a vacuum gap) of length d m is also in the magnetic circuit. Assume that d is small enough for the magnetic flux density to be essentially constant at B Wb/m² across the face of the armature. The cross-sectional area of the armature face is A m². A tractive force, F , in Newtons, developed on the face of the armature, is related to the area and field strength as

$$F = \frac{AB^2}{2\mu_0} \quad (29.30)$$

where μ_0 is the magnetic permeability of the air gap having a value of $4\pi \times 10^{-7}$ H/m (Henries/meter). The magnetic field intensity is proportional to the magnetomotive force $N \times i$ ampere turns. For an efficient magnetic structure, the magnetic flux density is

$$B = \frac{\mu_0}{d} N \times i \tag{29.31}$$

which, combined with Equation 29.30, gives a useful relationship:

$$F = \left[\frac{A \mu_0 N^2}{2} \right] \left(\frac{i^2}{d^2} \right) \text{ Newton} \tag{29.32}$$

Note that F is positive when i is either positive or negative. This means that the force, F , is always tractive if the current, I , is either positive or negative. The maximum value for magnetic flux density, B , which can be realized using modern magnetic materials in normal environments, is approximately 1 Wb/m² (Clark, 1996).

In most cases, it is necessary to apply force in both the positive and negative directions. In this case, the device is constructed with two air gaps having the corresponding traction forces opposed to one another, as shown in Figure 29.53.

It is interesting to observe how the net force, F , on the armature depends on z and Δi (differential current = $i_L - i_0 = i_R - i_0$; see Figure 29.53 for the parameters) when these are constants. The schematic plot of F vs. z , with Δi as a parameter, is shown in Figure 29.54. It is worth noting that the plot is nonlinear. It is also noted from the figure that, if z is positive, F is also positive. It means that the force developed on the armature due to a small displacement from the equilibrium position is in the direction to increase that small displacement. This characterizes a condition of static instability. Feedback control can be used to stabilize this inherently unstable device when such a device is used as an actuator.

29.3.4.2.2 Hydraulic Actuators

Hydraulic actuators can produce large forces even at large displacements, which is useful for seismic response-control applications. The actuator is usually driven using electrical signals. In other words, an electro-hydraulic device is used to convert the low-powered signals into high-powered hydraulic fluid flow. One example of such a device is an electro-hydraulic servo-valve. The schematic of such a device is shown in Figure 29.55.

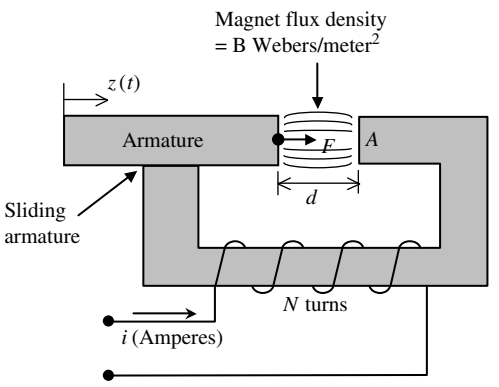


FIGURE 29.52 Elements of an electromagnet. (Source: Clark, R.N. *Control System Dynamics*, Cambridge Univ. Press, U.K., 1996. With permission.)

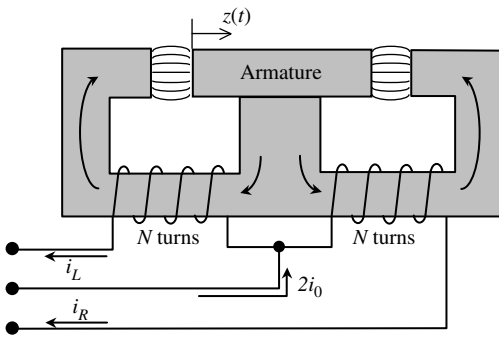


FIGURE 29.53 Push-pull electromagnet. (Source: Clark, R.N. *Control System Dynamics*, Cambridge Univ. Press, U.K., 1996. With permission.)

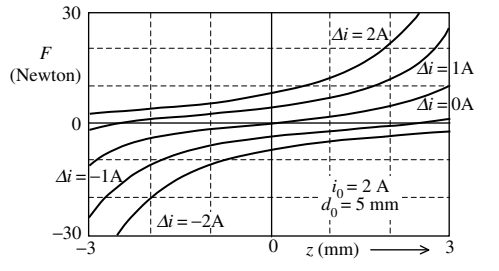


FIGURE 29.54 Force vs. displacement of push-pull electromagnet with differential current as a parameter. (Source: Clark, R.N. *Control System Dynamics*, Cambridge Univ. Press, U.K., 1996. With permission.)

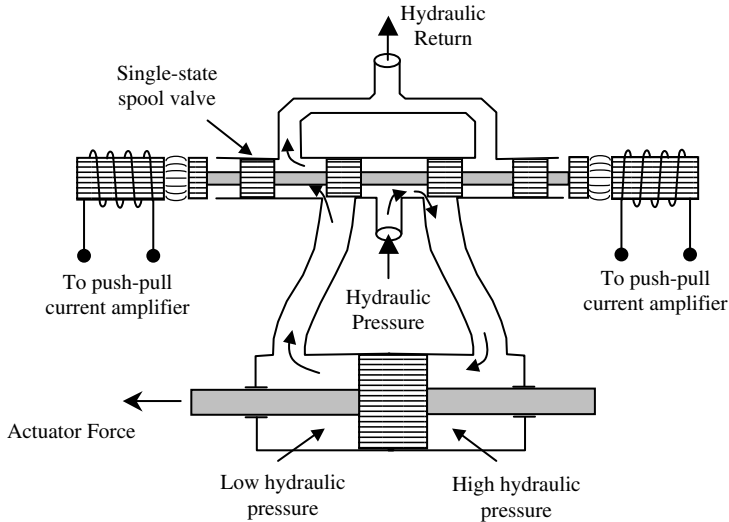


FIGURE 29.55 Schematic of servo-valve actuator. (Source: Clark, R.N. *Control System Dynamics*, Cambridge Univ. Press, U.K., 1996. With permission.)

The valve shown in the figure is a single-stage spool valve. The simple design shown in the figure exhibits the basic principles, inherent in most types of servo-valves, of conversion from electromagnetic to hydraulic energy; in other words, actuating force. By changing the electric signals going to the spool valve, the actuating force can be generated because the hydraulic pressure acting on the piston in one side is greater than the other side (see Figure 29.55). The actuating force can also be altered in real time, enabling real-time control of seismically excited structures.

29.3.4.3 Semiactive Control System

29.3.4.3.1 Variable-Orifice Hydraulic Dampers

A variable damping device used for the semiactive control method can be achieved by using a controllable, electro-mechanical, variable-orifice valve to alter the resistance to flow of a conventional hydraulic fluid damper. Figure 29.56 shows a schematic of such a device. The effectiveness of variable-orifice dampers in controlling seismically excited buildings has been demonstrated through both simulation and small scale experimental studies (Hrovat et al., 1983; Mizuno et al., 1992; Kurata et al., 1994; Patten et al., 1994; Sack et al., 1994; Liang et al., 1995; Niwa et al., 2000).

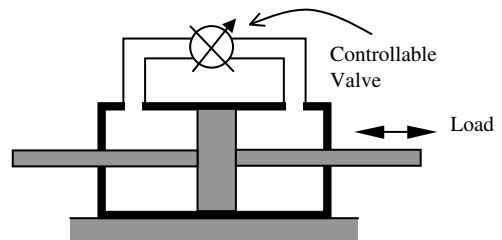


FIGURE 29.56 Schematic diagram of variable-orifice valve oil damper.

29.3.4.3.2 Controllable Fluid Dampers

Another class of semiactive devices use controllable fluids. The advantage of controllable fluid devices over controllable valve devices is that they contain no moving parts other than the piston. The essential characteristic of controllable fluids is their ability to change reversibly from a free-flowing, linear viscous fluid to a semisolid with a controllable yield strength in milliseconds, when exposed to an electric (for electro-rheological fluid) or magnetic (for magneto-rheological [MR] fluid) field (Housner et al., 1997).

MR fluids typically consist of micron-sized, magnetically polarizable particles dispersed in a carrier medium such as mineral or silicone oil. When a magnetic field is applied to the fluid, particle chains form and the fluid becomes a semisolid and exhibits viscoplastic characteristics. Transition to rheological equilibrium can be achieved in a few milliseconds. A schematic diagram of the controllable fluid damper is shown in Figure 29.57.

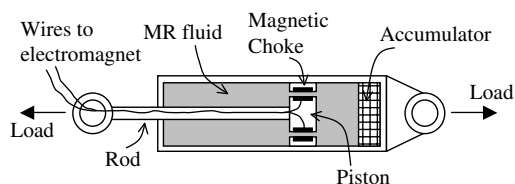


FIGURE 29.57 Schematic diagram of magnetorheological damper. (Source: Spencer, B.F. et al. *J. Eng. Mech.*, 123, 1997. With permission.)

29.3.4.3.3 Controllable Friction Dampers

Various controllable friction devices have been proposed to dissipate vibratory energy in a structural system. Akbay and Aktan (1990, 1991) and Kannan et al. (1995) proposed a variable-friction device in which the force at the frictional interface was adjusted by allowing slippage in controlled amounts. A similar device was also studied by Cherry (1994) and Dowdell and Cherry (1994a, 1994b).

A recent work by He et al. (2003) studied a semiactive electromagnetic friction damper (SAEMFD) for controlling seismic responses. Figure 29.58 shows a schematic diagram of the SAEMFD. The device consists of a friction pad

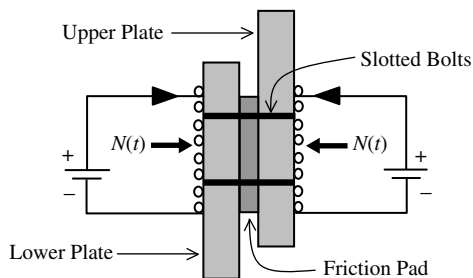


FIGURE 29.58 Schematic drawing of semiactive electro-magnetic friction damper. (Source: He, W.L. et al. *J. Struct. Eng.*, ASCE, 129, 941–950, 2003. With permission.)

sandwiched between two steel plates. These three layers are slot-bolted together so that sliding takes place between the steel plates and the friction pad. The friction force between steel plates and the friction pad depends on the coefficient of friction (μ) and the normal force $N(t)$. Two insulated solenoids are installed on the outer surfaces of the steel plates and the electric current in these solenoids is regulated such that an electromagnetic attractive force exists between the two solenoids. Hence, the normal force $N(t)$ between the steel plates is directly proportional to the square of the current in the solenoids.

29.3.4.4 Hybrid Control System

The hybrid control methods which consist of both passive and active devices have been proposed and implemented, utilizing the merits of both passive and active methods and avoiding the demerits of these methods. Thus, higher levels of performance may be achievable. Additionally, the resulting hybrid control system can be more reliable than a fully active system, although it is also often somewhat more complicated.

One example of a hybrid system is a TMD with actuators that is put between the TMD mass and its support so that the effectiveness of the TMD is increased by this technique. Figure 29.59 shows a schematic diagram of a passive TMD, an active AMD (active mass damper), and a hybrid ATMD (active TMD). Another example of hybrid control is a combination of base isolation with some form of active control to limit excessive displacement (Fujii et al., 1992; Kageyama, M. and Yasui, 1992; Feng et al., 1993; Reinhorn and Riley, 1994).

29.3.5 Control Algorithm

29.3.5.1 Active Control System

The most important part of active control is the algorithm, because the control forces are based on this. Research efforts in active structural control have been focused on a variety of control algorithms based

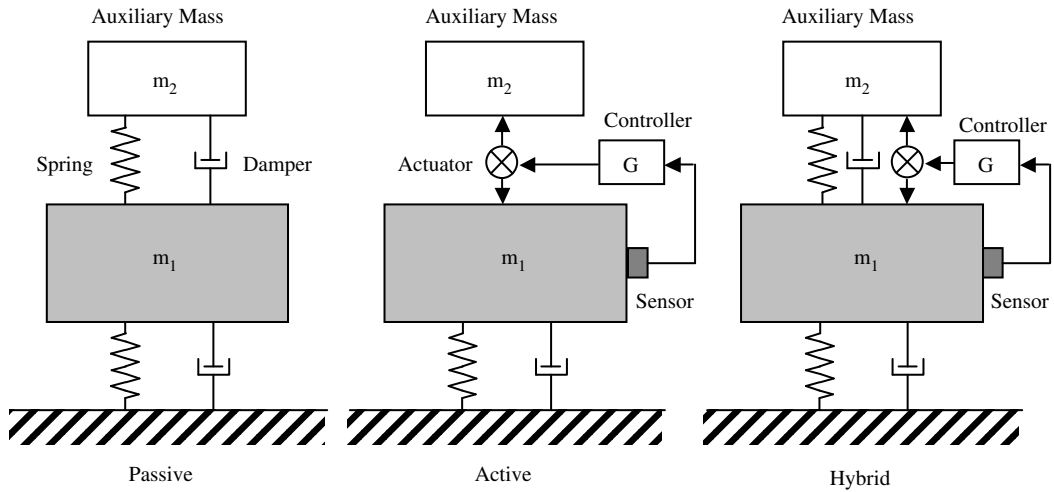


FIGURE 29.59 Schematic diagram of a passive, an active, and a hybrid mass damper system.

on several control design criteria. An example of a famous control algorithm is linear optimal control because all of the control design parameters can be determined for multiinput and multioutput systems. Also, the control allows us to formulate directly the performance objectives of a control system. The adjective optimal above means that a control system can be designed to meet the desired performance objectives with the smallest control energy, which is the energy associated with generating the control inputs. Such a control system that minimizes the cost associated with generating control inputs is called an optimal control system. The optimal control system directly addresses the desired performance objectives, while minimizing the control energy, by formulating an objective function that must be minimized in the design process.

If the transient energy of a system is the total energy of the system when it is undergoing the transient response, then the successful control system must have the capability to decay quickly the transient energy to zero. By including the transient energy and the control energy in the objective function, both parameters can be minimized. The objective function for the optimal control problem is a time integral of the sum of transient energy and control energy expressed as a function of time.

The general, optimal control formulation for regulators can be explained as follows. Consider a structure (Figure 29.60) under dynamic loading that is represented by Equation 29.33:

$$\mathbf{M}\ddot{\mathbf{x}}(t) + \mathbf{C}\dot{\mathbf{x}}(t) + \mathbf{K}\mathbf{x}(t) = \mathbf{D}\mathbf{u}(t) + \mathbf{E}\mathbf{f}(t) \quad (29.33)$$

where \mathbf{M} , \mathbf{C} , \mathbf{K} are, respectively, the $n \times n$ mass, damping, and stiffness matrices, and $\mathbf{x}(t)$ is the n -dimensional displacement vector, $\mathbf{f}(t)$ is an r -vector representing applied load or external excitation, and $\mathbf{u}(t)$ is the m -dimensional control force vector. The $n \times m$ matrix, \mathbf{D} , and $n \times r$ matrix, \mathbf{E} , are location matrices that define locations of the control force and the excitation, respectively.

The equation can be rewritten using the state-space representation in the form

$$\dot{\mathbf{z}}(t) = \mathbf{A}\mathbf{z}(t) + \mathbf{B}\mathbf{u}(t) + \mathbf{H}\mathbf{f}(t), \quad \mathbf{z}(0) = \mathbf{z}_0 \quad (29.34)$$

where

$$\mathbf{z}(t) = \begin{bmatrix} \mathbf{x}(t) \\ \dot{\mathbf{x}}(t) \end{bmatrix} \quad (29.35)$$

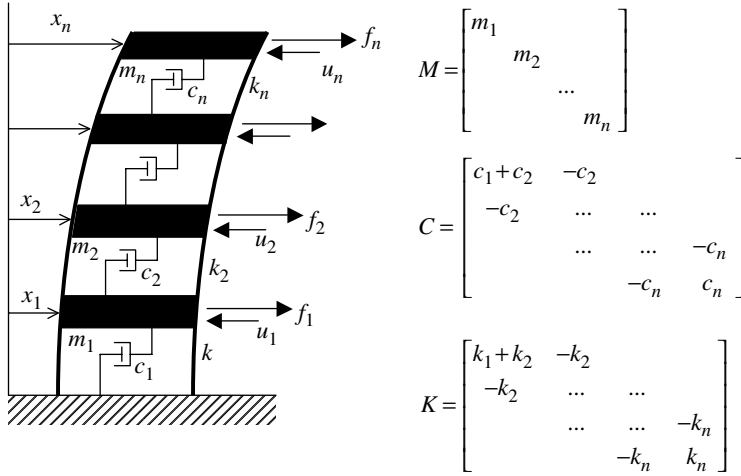


FIGURE 29.60 Typical civil structure with its dynamic properties.

is the $2n$ -dimensional state vector

$$A = \begin{bmatrix} \mathbf{0} & \mathbf{I} \\ -\mathbf{M}^{-1}\mathbf{K} & -\mathbf{M}^{-1}\mathbf{C} \end{bmatrix} \quad (29.36)$$

is the $2n \times 2n$ system matrix, and

$$B = \begin{bmatrix} \mathbf{0} \\ \mathbf{M}^{-1}\mathbf{D} \end{bmatrix} \text{ and } H = \begin{bmatrix} \mathbf{I} \\ \mathbf{M}^{-1}\mathbf{E} \end{bmatrix} \quad (29.37)$$

are $2n \times m$ and $2n \times r$ location matrices specifying, respectively, the locations of controllers and external excitation in the state space. In Equation 29.36, $\mathbf{0}$ and \mathbf{I} denote the null matrix and the identity matrix of appropriate dimensions, respectively.

For simplicity, assume that we have a linear time invariant plant, as shown in Equation 29.34 above, and suppose we would like to design a full-state feedback regulator for the plant such that the control input vector is given by

$$\mathbf{u}(t) = -\mathbf{G}\mathbf{x}(t) \quad (29.38)$$

where \mathbf{G} is a feedback gain matrix. The control law given by the above equation is linear. Since the plant is also linear, the closed-loop control system is linear. The control energy, CE, can be expressed as

$$CE = \mathbf{u}^T(t)\mathbf{R}\mathbf{u}(t) \quad (29.39)$$

where \mathbf{R} is a square, symmetric matrix called the control cost matrix. Such an expression for control energy is called a quadratic form, because the scalar function in Equation 29.39 contains quadratic functions of the elements of $\mathbf{u}(t)$. The transient energy, TE, can also be expressed in a quadratic form as

$$TE = \mathbf{x}^T(t)\mathbf{Q}\mathbf{x}(t) \quad (29.40)$$

where \mathbf{Q} is a square, symmetric matrix called the state weighting matrix. The objective function can then be written as follows:

$$J(t, t_f) = \int_t^{t_f} [\mathbf{x}^T(\tau)\mathbf{Q}\mathbf{x}(\tau) + \mathbf{u}^T\mathbf{R}\mathbf{u}(\tau)]d\tau \quad (29.41)$$

where t and t_f are the initial and final times, respectively; that is, the control begins at $\tau = t$ and ends at $\tau = t_f$, where τ is the variable of integration.

The optimal control problem consists of solving for the feedback gain matrix, \mathbf{G} , such that the scalar objective function, $J(t, t_f)$, given by Equation 29.41, is minimized. Hence, the optimal control problem solves a regulator gain matrix, \mathbf{G} , which minimizes $J(t, t_f)$, subject to the constraint given by Equation 29.34.

MATLAB[®] *Control System Toolbox* (MathWorks, 1998) provides a function “lqr” for the solution of the linear optimal control problem shown above (also see Appendix 32A). By using this command, the gain matrix, \mathbf{G} , can easily be obtained. For a numerical simulation, the matrix, \mathbf{G} , is used for obtaining optimal forces, $\mathbf{u}(t)$, as shown in Equation 29.38. The MATLAB[®] *Control System Toolbox* user manual is a good reference (MathWorks, 1998) for applying this command. For a real application in a structure, the optimal forces, $\mathbf{u}(t)$, must be converted to real forces by actuating devices. Actuating devices are covered in Section 29.3.4.

In the above explanation, the linear optimal controller has been derived with full-state feedback that minimizes a quadratic objective function. The controller robustness to process and measurement noise can only be indirectly ensured by iterative techniques. There are more advanced topics in modern control that directly address the problem of robustness by deriving controllers that maintain system response and error signals to within prescribed tolerances. One example is the H_∞ (pronounced *H-infinity*) optimal control design technique. The reader may refer to control design textbooks, such as that written by Tewari (2002).

29.3.5.2 Semiactive Control System

Because of the intrinsically nonlinear nature of semiactive control devices, development of control strategies that are practically implementable and can fully utilize the capabilities of these unique devices is an important and challenging task. Various nonlinear control strategies have been developed to take advantage of the particular characteristics of semiactive devices, including bang-bang control (Mukai et al., 1994; McClamroch and Gavin, 1995), clipped optimal control (Dyke et al., 1996a), bistate control (Patten et al., 1994), fuzzy control methods (Sun and Goto, 1994), and adaptive nonlinear control (Kamagata and Kōbori, 1994). Caughey (1993) proposed a variable stiffness system that employed a semiactive implementation of the Reid (1956) spring as a structural element. He et al. (2001) proposed a resetting semiactive stiffness damper used for controlling seismically excited cable-stayed bridges. Iemura and Pradono (2003) introduced a pseudonegative stiffness control algorithm used for producing artificially rigid–perfectly plastic force–deformation hysteretic loops by using controllable damper.

29.3.5.2.1 Common Control Schemes for Controllable Dampers

An example will be given here for common control schemes for a controllable damper. Examples of a controllable damper are variable-orifice damper and MR fluid dampers. Both types of dampers are covered in Section 29.3.4. The strategy of a clipped-optimal control algorithm (Dyke et al., 1996a, 1996b) for seismic protection using MR fluid dampers is as follows. First, an “ideal” active control device is assumed, and an appropriate *primary* controller for this active device is designed. Then a *secondary* bang-bang-type controller causes the smart damper to generate the desired active control force, so long as this force is dissipative. The primary controller can be one of active control algorithms shown above. For the general smart damping device, the secondary control strategy is given by

$$f_{sa,i} = \begin{cases} f_{a,i}, & f_{a,i} \times \dot{x}_{dev} < 0 \\ 0, & \text{otherwise} \end{cases} \quad (29.42)$$

where $f_{sa,i}$ is the control force of the i th MR fluid damper, $f_{a,i}$ is the desired control force for the i th device, and \dot{x}_{dev} is the velocity across the i th damper. Since the controllable damper is an energy-dissipative device that cannot add mechanical energy to the structural system, special care must be taken in the design of the primary controller so that the desired control force, $f_{a,i}$, is dissipative during the majority of the seismic event.

29.3.5.2.2 Special Control Schemes for Controllable Damper

The term “special” here refers to control schemes that have certain objectives for the hysteretic loops of the controllable dampers. The control schemes are not centralized, so that each damper is controlled separately in one structure or, in other words, one controller is for one damper. The advantage is that should one controller malfunction, this controller will not affect the other controller.

One example is given by He et al. (2001). A resetting semiactive stiffness damper (RSASD) is used to control the peak seismic response of a structure. The RSASD consists of a cylinder-piston system with an on–off valve in the bypass pipes connecting two sides of the cylinder. Basically, the damper is similar to a variable-orifice oil damper as shown in Figure 29.58; however, the orifice valve is replaced by an on–off valve. This damper serves as a stiffness element in which the stiffness is provided by the bulk modulus of the fluid in the cylinder when the valve is closed. When the valve is open, the piston is free to move, and the hydraulic damper provides only a small damping, without stiffness.

Such a stiffness damper can be operated in the resetting mode. During the operation in this mode, the valve is always closed. The energy is then stored in the hydraulic oil of the damper in the form of potential energy. At an appropriate time, the valve is pulsed to open and close quickly. At that moment, the piston is at the resetting position, and the energy stored in the hydraulic damper is released and converted into the head loss across the damper. Hence, by pulsing the valve at appropriate times, structural response can be reduced by drawing energy from the system (He et al., 2001).

Another example is that of Kurino et al. (2003). They presented a device developed for an actual application whose system employs a decentralized control algorithm that uses information only from built-in sensors.

The pseudonegative stiffness control algorithm (Iemura and Pradono, 2003) is also intended for controlling a variable damper based only on the displacement and velocity sensors located within the damper. The purpose is to control the variable damper’s hysteresis loop. An example of the application of this control algorithm to a bridge model is shown in Section 29.3.7.2.

29.3.6 Experimental Performance Verification

29.3.6.1 Shaking Table Tests of a Flexible Structural Model with TMD, AMD, and ATMD

For practical implementation of TMD, AMD, and ATMD for structures, it is important to find the efficiency of each control system for random excitations. The author has made an analytical and numerical studies on the efficiency of different control methods. To verify the results, a three-DoF structural frame model (Figure 29.61) with and without control devices is tested on a shaking table at Kyoto University, Japan (Iemura et al., 1992).

Natural periods for modes 1, 2, and 3 are 0.6578, 0.2580, and 0.1568 sec, respectively. The relevant participation factors for each mode are 1.2204, 0.3493, and -0.1341 , respectively. The moving mass and other mass of the TMD are 3.5 and 5.5 kg, respectively. The spring constant is 0.581 kg/cm . The damping ratio is 25.06%. These properties are used for the experiment. The masses of the TMD consist of the AC servo-motor, moving mass, driving guides, and velocity meter. At the time of the experiment of the TMD, the moving mass was fixed and the TMD

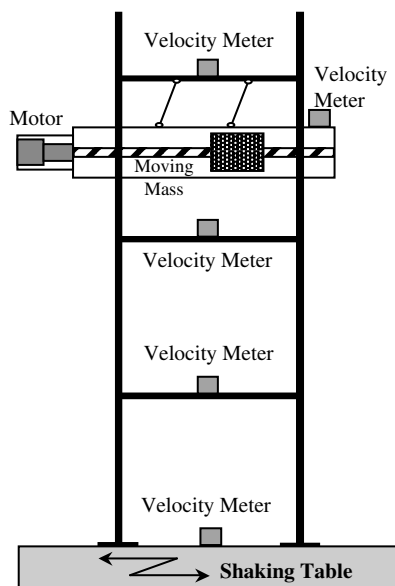


FIGURE 29.61 Three-DoF experimental model with TMD/ATMD.

was hung from the third floor. In order to work as the hybrid type ATMD, the moving mass was driven by the motor. For the pure active control experiment, the motor and the moving mass are set directly on the third floor.

It was clearly found that the second mode response is not reduced by the TMD but is effectively reduced by the AMD and ATMD. The TMD is effective only in the first mode frequency range, while active control force can cover a wide frequency range.

It was also found that the control force of the ATMD is much lower than that of AMD, especially in the first mode frequency range. The first mode response is reduced mainly by the TMD and the second mode response is reduced by the AMD. This verifies the energy efficiency of ATMD. This is the reason that the ATMD concept is now popularly used for practical application.

29.3.6.2 Substructure Hybrid Test

Before introducing additional dampers to a structure for seismic-response reduction, the precise frequency-dependent properties of the damper should be obtained from the damper. These properties will be used for numerical simulation on the effectiveness of the damper in reducing seismic responses. It is quite difficult to work out the appropriate model for a specified device because of the existence of strong nonlinearity. For a more reliable experimental test of structures with structural control devices, so-called “substructure hybrid experiment” techniques have been developed.

The term “substructure hybrid” implies a technique that combines the device loading experiment and numerical simulation of structural response. Why should it be separated? It is because civil structures are relatively large and expensive to construct in a laboratory. Therefore, only the inelastic part is tested experimentally. The elastic part, which is easier to model, is numerically simulated on a computer. Both results are combined in real time at every time step of the simulation. Up until now, various kinds of test methods have been proposed. Most of them can be classified into three categories from the viewpoint of the loading equipment.

29.3.6.2.1 Hybrid Tests Using Hydraulic Actuator

Hydraulic actuators are commonly used for loading experiments. They are advantageous for testing specimens that needs large excitation force and displacements (Tanzo et al., 1992; Igarashi et al., 1993; Igarashi, 1994; Williams and Blakeborough, 2001). Various algorithms and techniques have been proposed in order to conduct precise, real-time experiments such as the “operator splitting numerical integration scheme,” which is suitable for online controlled experiments (Nakashima, 1993). A compensation method based on extrapolation is proposed by Horiuchi and Konno (2001) for the response delay of the actuator. Similar feedforward-based compensation methods are widely used for the numerical algorithm’s development and real-time testing (Nakashima and Masaoka, 1999; Nakashima et al., 1999; Blakeborough et al., 2001).

29.3.6.2.2 Hybrid Tests Using Shaking Table

Substructure hybrid loading test systems have been developed for shaking table equipment. Since most shaking tables are driven by hydraulic actuators, algorithms as well as technologies for the hydraulic actuators system are directly applicable to the shaking table test systems. Iemura et al. (2002) introduced the inverted digital filter of the shaking table for compensating its dynamics, and conducted a real-time hybrid experiment using the electromagnetic mass damper installed in the nonlinear structure. The shaking table test is applicable to a test specimen such as the TMD.

29.3.6.2.3 Hybrid Tests Using Inertia-Force-Driven Loading System

This is a newly developed method for hybrid loading test (Toyooka, 2002; Iemura et al., 2003). The system consists of a large size mass, rubber and roller supports, and active mass driver. The schematic figure of the system is shown in [Figure 29.62](#) and the property of the system is in [Table 29.5](#). The active mass driver is attached to the mass. The test specimen is attached to the mass and the ground. The mass

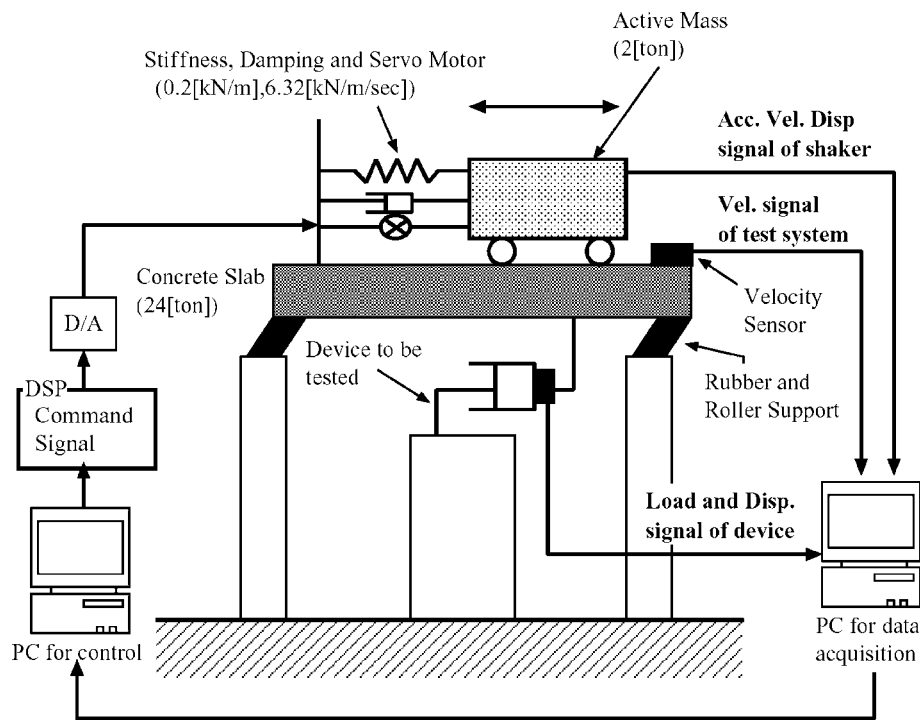


FIGURE 29.62 Test set up of the IFDL system.

TABLE 29.5 Properties of the IFDL System

Weight of slab mass	23.853 tonf
Total stiffness	344.43 kN/m
Total damping	6.32 kN/m/sec
Natural frequency	0.55 Hz
Equivalent damping	3.86%
Stroke limit	± 10 cm

(i.e., the concrete slab) can be excited with large displacement, velocity, and acceleration by making use of the shaker (Iemura et al., 2003). The Inertia-Force-Driven Loading (IFDL) system was developed to allow an economical and accurate loading environment for energy dissipation devices to characterize the dynamic properties and to comprehend the performances of these devices under the realistic loading conditions.

29.3.7 Implementations

29.3.7.1 Semiactive Control of Full-Scale Structures Using Variable Joint Damper System

29.3.7.1.1 Background of Study

In order to verify the effectiveness of the application of the semiactive control technique to the joint damper system (JDS), seismic response control tests using full-scale multistory steel-frame structures, excitation devices, and a variable damper are performed at the Disaster Prevention Research Institute, Kyoto University, Japan. The variable damper allows external control of damping force by the electric servo-valve that regulates the oil flow through the cylinder/piston mechanism. The test results show that the variable damper was successfully controlled with high accuracy, as well as having the advantage of JDS application of the semiactive control in reducing the dynamic response of structures over the

conventional passive control. A comparison of the semiactive control algorithms to JDSs in terms of the feasibility and the advantage in the engineering application is also based on the test results.

Extensive research on the semiactive control approach has been conducted in order to reduce the seismic response of structures, induced especially by strong earthquake ground motions. The JDS, which aims to achieve the dynamic response reduction of adjacent structures through the use of connection devices with energy-absorbing capability, has been considered a promising approach to establish effective semiactive structural systems for earthquakes.

The purpose of this study is to verify experimentally the effectiveness of the application of semiactive control to the JDS. Seismic response control tests using full-scale multistory frame structures, excitation devices, and a variable damper are performed at the Disaster Prevention Research Institute, Kyoto University. The variable damper allows for external control of the damping force using the electric servo-valve that regulates the oil flow through the cylinder/piston mechanism.

Two types of semiactive control algorithms were employed, namely the linear quadratic regulator (LQR) control theory and the newly proposed pseudonegative stiffness control for JDSs. Parameter-setting strategies for the algorithms are studied prior to the tests through numerical simulations based on the modeling of the full-scale steel frame structures and the control device used in the tests.

29.3.7.1.2 Test System Set Up

As shown in Figure 29.63, the test structure of the JDS consists of two full-scale structural steel frames: a five-story frame (1×2 span) and a three-story frame (1×1 span). The dimensions of both frames are shown in Table 29.6. Natural frequencies are also shown in the table.

In this test system, mass-driver devices are used to reproduce the vibration conditions under both sinusoidal and real earthquake inputs. One-directional horizontal earthquake excitation is applied. Although three mass-driver systems can be seen in the figure, two of them are used at the same time. The accuracy of the simulated response using the mass driver devices has been verified by a series of research

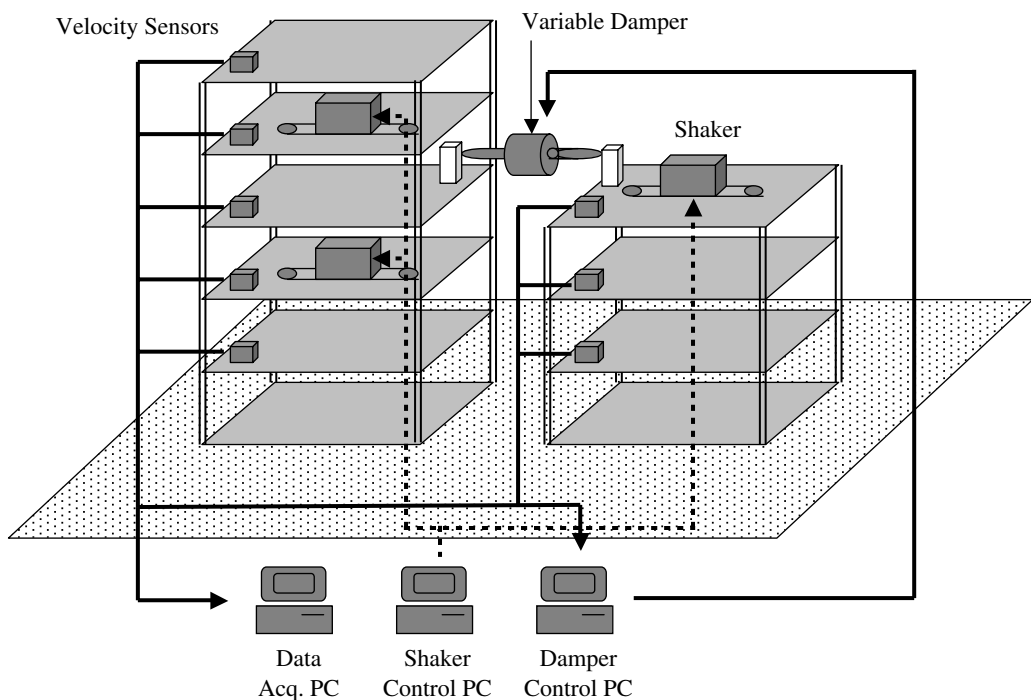


FIGURE 29.63 Schematic diagram of joint damper system.

TABLE 29.6 Test Frames and Mass-Drivers

	Five-Story	Three-Story
Height (m)	17.22	10.65
Weight (tonf)	163.1	62.1
First mode natural frequency (Hz)	1.78	2.41
Mass driver	5 ton mass at the fourth floor	2 ton mass at third floor

conducted prior to this study. Velocities, relative displacements, and absolute accelerations of all floors are measured through instrumentation. All measured responses are sent to a digital signal processing-based system for the feedback control.

As the control device in the JDS, a variable damping device (variable damper) is used in the test system. The variable damper is installed at the third story of the five-story frame so as to connect the two frames. The mechanism of the variable damper is similar to that shown in [Figure 29.56](#). It is a semiactive hydraulic damper consisting of a cylinder/piston mechanism filled with oil, double rods that connect the frames, a by-pass pipe that contains a flow control valve, and an accumulator that keeps the by-pass line pressure constant. The opening ratio of the flow control valve can be changed by a servo-controller using an external signal. The flow volume through the valve can be regulated to control the pressure loss. The delay time for the opening ratio control is sufficiently short to allow real-time control.

29.3.7.1.3 Control Algorithm

In this study, three types of control algorithms are used: linear viscous damper control, LQR control (discussed in Section 29.3.5), and pseudonegative stiffness (PNS) control. The linear viscous damper control algorithm is intended to be the reference response in the case of passive control, and the effectiveness of the semiactive control is demonstrated by comparing the other two cases with the linear viscous damper control case.

In linear viscous control algorithm, the damping force demanded of the variable damper, $F_d(t)$, is

$$F_d(t) = C_c v_r(t) \quad (29.43)$$

where C_c is the connecting damping coefficient and v_r is the relative velocity of the damper position. Real-time control of the valve opening ratio is required to generate the demanded control force, F_d , with the variable damper, even for this simplest control algorithm.

The LQR control theory is used as a semiactive control algorithm in this study, as extensively used in past studies. In the LQR control algorithm, the optimal control force, F_d , is regarded as the demanded force and the variable damper is controlled to track the demanded force as close as possible within the constraint, depending on the piston velocity. The control gain parameters are chosen on the basis of numerical simulation in consideration of the capacity of the variable damper. The control force is calculated in the following manner:

$$F_d(t) = -\mathbf{G}\mathbf{x}(t) \quad (29.44)$$

where \mathbf{G} is the optimal gain matrix given by the LQR theory and $\mathbf{x}(t)$ is the state vector for the structural frames.

If the main purpose of a JDS is the response reduction of the upper floors in the adjacent structures, the most interesting feature of the system is obtained by connecting them at lower stories with a negative stiffness element. Although this characteristic has been reported theoretically and analytically in many studies, there are many problems left in applying the active control device at the present time, mainly owing to the difficulty in realizing the negative stiffness with a passive control device. However, semiactive devices such as the variable damper can generate an apparent negative stiffness by controlling the damping. Therefore, taking into account JDS and negative stiffness, a new, simple control algorithm to realize pseudonegative stiffness with a damping element is proposed in this study. To generate the

negative stiffness, the demanded force of variable damper F_d is defined as follows:

$$F_d(t) = K_c x_r(t) + C_c v_r(t) \quad (29.45)$$

where K_c and C_c are the connecting stiffness (negative value) and the damping coefficient, respectively. The relative displacement and velocity of the damper piston, respectively, are x_r and v_r . It follows that this algorithm simulates the state in which the two frames are connected by a negative stiffness and a positive damping elements. The eigenvalue analysis is used to determine the value of K_c and C_c .

This pseudonegative stiffness algorithm has a great advantage in practical application. Most of the previously proposed control algorithms require direct measurement of the structural system to produce feedback and to calculate the demanded control force. That means that a considerable number of sensors should be installed in the object structure. Considering practical application, it is difficult to install many sensors because of the economical disadvantage. On the other hand, for the pseudonegative stiffness algorithm, only the relative displacement and velocity are used for feedback and a sensor is required only at the damper. In addition to the simplicity in installation, the required parameters are limited to the connecting stiffness and damping.

29.3.7.1.4 Test Results

The response of variable damper to sinusoidal input with 1.8 Hz (max 10 gal), which is approximately the first resonance frequency in the connected state, is shown in Figure 29.64. The five-story top-floor velocity response in the LQR control theory and pseudonegative stiffness are smaller than that in the viscous damper; especially, the peak value in pseudo negative stiffness is improved at 25% compared with that in the viscous damper, though the velocities at the top story of the three-story frame are almost equal for all control algorithms. On the other hand, the LQR control theory can reduce the peak response of both frames as compared with the viscous damper. When the object is to moderate the response of total system, the LQR theory is the most effective algorithm of the three being compared. Based on the test, semiactive controls based on the LQR control theory and pseudonegative stiffness can reduce the peak responses of the total system more effectively than viscous damper-type passive control.

For the earthquake excitation (El-Centro 1940 N–S and Kobe 1995 N–S, scaled to 20 gal max), the influence of the friction of the variable damper appears in the dynamic characteristics of the variable damper in every control algorithm because of the relatively small responses. The relative velocity and displacement responses of the variable damper in both semiactive controls are larger than that in the viscous damper. Judging from the test result, it is confirmed that the variable damper is controlled effectively in the different control algorithm for real earthquake inputs. With respect to the velocity response of the top story of the three-story frame, the responses are not very different when different control algorithms are used. On the other hand, for the five-story top-floor response, both semiactive controls can reduce the response more effectively than the passive control to both real

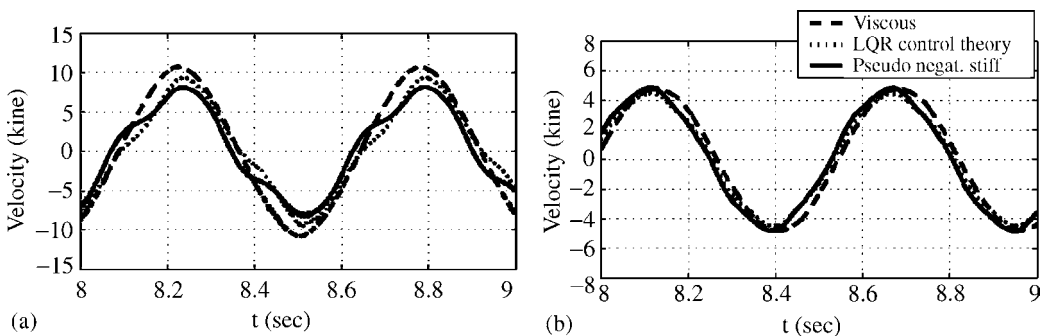


FIGURE 29.64 Variable damper responses in the sinusoidal excitation test: (a) at the top story of five-story frame; (b) at the top story of three-story frame.

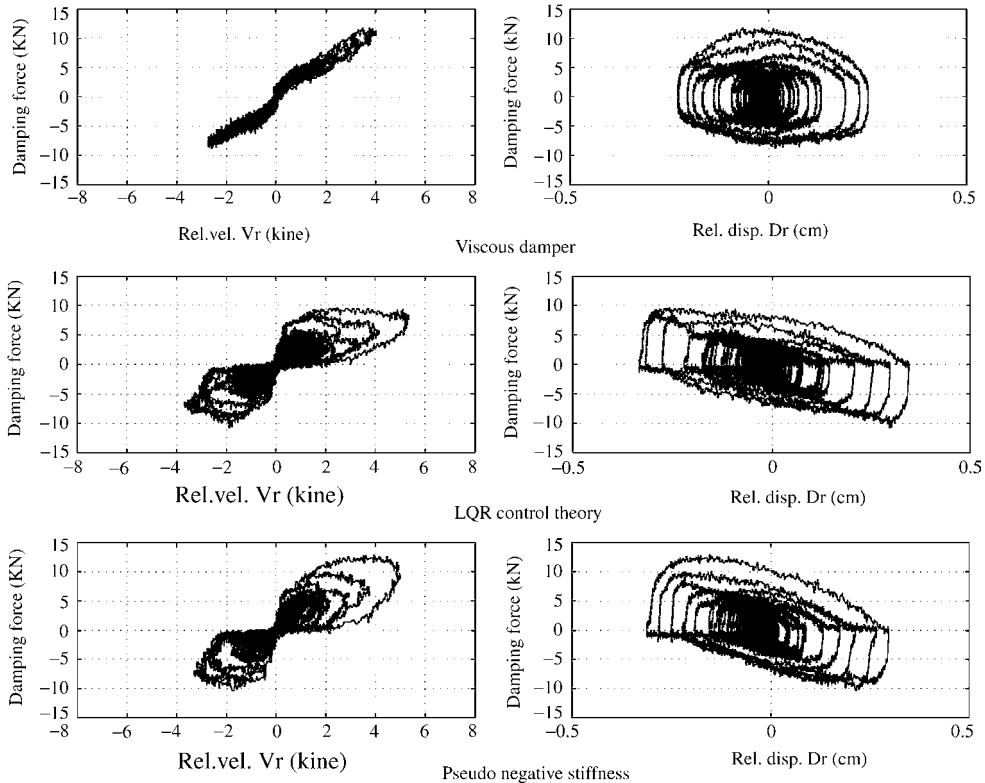


FIGURE 29.65 (a) Viscous-type control, (b) LQR-type control, and (c) pseudonegative stiffness-type control under El-Centro 1940 N–S scaled to 20 gal max.

earthquake excitations. Semiactive controls are more effective than passive control to reduce the response of the top story of the five-story frame in the earthquake excitation cases.

Figure 29.65 shows the hysteretic loops resulting from viscous-type, LQR-type, and pseudonegative stiffness-type controls under El-Centro 1940 N–S, scaled to 20 gal max. It is obvious that the pseudonegative hysteretic loop can be achieved experimentally by using a variable damper.

29.3.7.2 Application of Structural Control Technologies to Seismic Retrofit of a Cable-Stayed Bridge

29.3.7.2.1 Background of Study

Owing to severe damage to bridges caused by the Hyogo-ken Nanbu earthquake in 1995, very high ground accelerations (level II design) are now required in the new bridge design specification set in 1996, in addition to the relatively frequent earthquake motion (level I design) by which old structures were designed and constructed. Hence, the seismic safety of cable-stayed bridges that were built before the present specification has to be reviewed and seismic retrofit has to be done, if it is found necessary.

In order to study the effectiveness of passive and semiactive control on the seismic retrofit of a cable-stayed bridge, numerical analyses on a model is carried out. An existing cable-stayed bridge that has fixed-hinge connections between the deck and towers is modeled and its connections are replaced with isolation bearings and dampers. The isolation bearings are assumed to be elastic or hysteretic type. The dampers are linear and variable type. The objective is to increase the damping ratio of the bridge by using passive and semiactive control technologies. The calculation of the structural damping ratio at the main mode is feasible, as the passive or semiactive control method produces certain hysteretic loops under

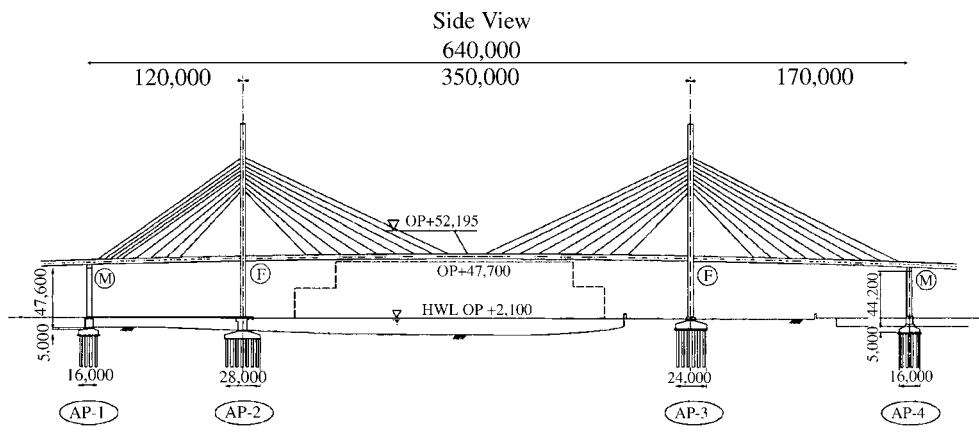


FIGURE 29.66 Side view of the Tempozan Bridge.

harmonic motion, and the main mode has an effective modal mass that is larger than 90% of the total mass. SSI effects on the structural damping ratio are also studied.

The Tempozan Bridge (Hanshin Highway Public Corporation, 1992), built in 1988, is a three-span continuous steel cable-stayed bridge that is situated on reclaimed land and crosses the mouth of the Aji River, Osaka, Japan. The total length of the bridge is 640 m with a center span of 350 m, and the lengths of the side spans are 170 and 120 m (Figure 29.66). The main towers are A-shaped to improve the torsional rigidity. The cable in the superstructure is a two-plane fan pattern multicable system with nine stay cables each plane. The bridge is supported on a 35 m thick soft layer and the foundation consists of cast-in-place RC piles of 2 m in diameter. The main deck is fixed at both towers to resist horizontal seismic forces. The bridge is relatively flexible, with a predominant period of 3.7 sec. As to the seismic design in the transverse direction, the main deck is fixed at the towers and the end piers.

Figure 29.67 shows the original design spectrum used for designing the bridge and the new design spectrum specified in the bridge design specification set in 1996 for level I and level II earthquakes (Japan Roadway Association, 1996). A level II earthquake has type I (interplate type)

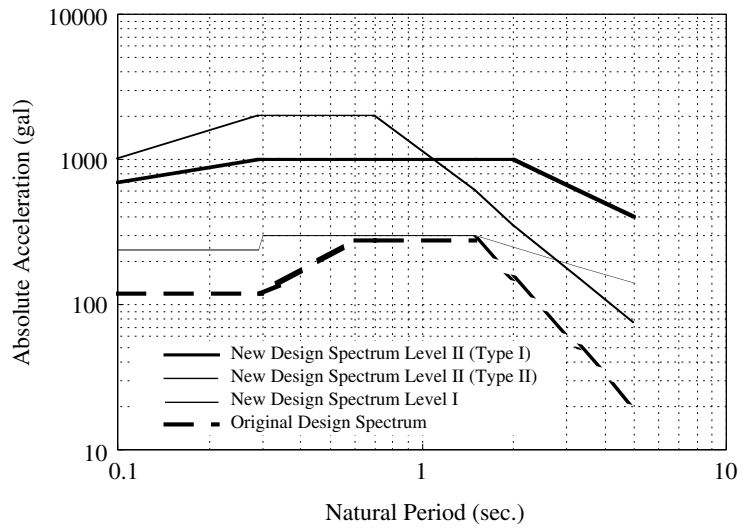


FIGURE 29.67 Design spectra for bridges.

and type II (intraplate type). As can be seen in the figure, the new design spectrum shows higher acceleration response in all period ranges than the original one.

29.3.7.2.2 Basic Concept of Seismic Retrofit

If the deck is connected with very flexible bearings to the towers, the induced seismic forces will be kept to minimum values, but the deck may have a large displacement response. On the other hand, a very stiff connection between the deck and the towers will result in a lower deck displacement response but will attract much higher seismic forces during an earthquake. This is the case in the original bridge structure, the Tempozan Bridge. Therefore, it is important to replace the existing fixed-hinge bearings with special bearings or devices at the deck-tower connection both to reduce seismic forces and to absorb large seismic energy and reduce the response amplitudes. Additionally, energy-absorbing devices may also be put between the deck-ends and piers; however, this will attract relatively large lateral force of the piers, and therefore this kind of method has been avoided for this bridge at this time.

The bridge model that represents the existing Tempozan Bridge is termed the “original bridge model.” The bridge model with the spring and damper (viscous, hysteretic, and semiactive) between the deck and the towers is termed the “retrofitted bridge model.” The original and retrofitted bridge models are shown in Figure 29.68. The original structure system has fixed-hinge connections between the towers and the deck and rollers connection between the deck-ends and piers, so that the deck longitudinal movement is constrained by the towers (Figure 29.68a). For the retrofitted bridge, the isolation bearings and dampers connect the deck to the towers (Figure 29.68b).

The cables are modeled by truss elements. The towers and deck are modeled by beam elements, and the isolation bearings are modeled by spring elements. The models were analyzed by a commercial finite element program (Prakash and Powell, 1993). The moment–curvature relationship of the members is calculated based on the sectional properties of members and material used.

29.3.7.2.3 Modal Shape Analysis

The first modes of the structures are interesting here because these modes have the largest contribution to the longitudinal movement of the bridge (also see Chapters 3 and Chapter 4). The mode shapes of the original bridge and the retrofitted bridge are shown in Figure 29.69. The first mode shape of the original structure is shown in Figure 29.69a. The natural period (T) of this mode is 3.75 sec (frequency = 0.266 Hz), which is close to the design value for the bridge (3.7 sec, frequency = 0.270 Hz; Hanshin Highway Public Corporation, 1992). This first mode shape has the effective modal mass as a percentage of the total mass of 84%.

For the retrofitted structure, the stiffness of the bearings is an important issue, as large stiffness produces a large bearing force. However, very flexible connections produce a large displacement response. Therefore, based on a study on a simplified model of the bridge under seismic motion, the bearing stiffness

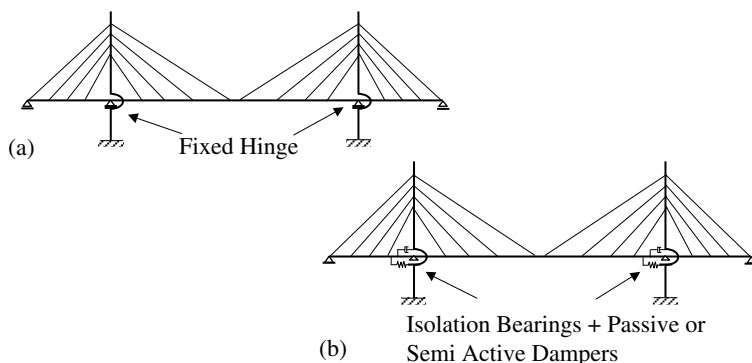


FIGURE 29.68 Cable-stayed bridge models: (a) original structure system; (b) retrofitted structure system.

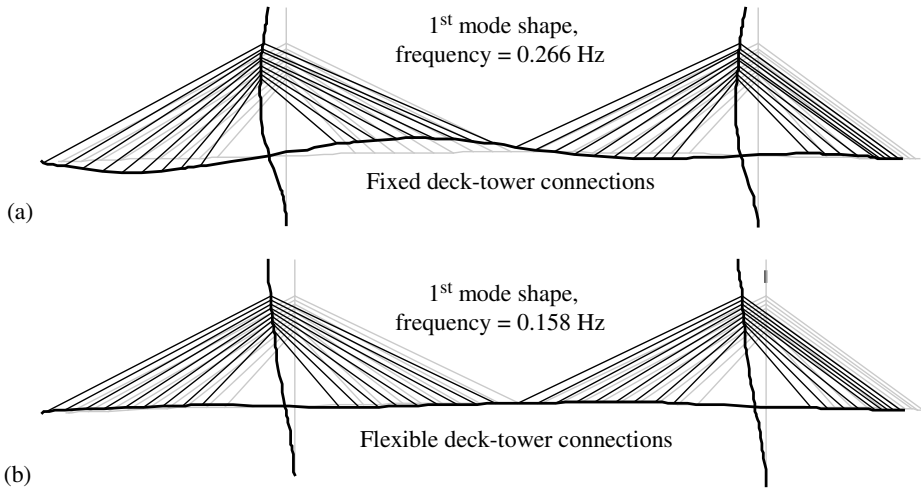


FIGURE 29.69 First mode shapes of (a) original structure and (b) retrofitted structure.

that produces retrofitted main period (T') 1.7 times the original main period (T) was chosen. This bearing stiffness makes the energy-absorbing devices work well in reducing seismic-induced force and displacement. The main natural period (T') of the retrofitted bridge then becomes 6.31 sec and the effective modal mass as a percentage of total mass is 92%.

It is clear from the figures that smaller curvatures are found at the towers and the decks of the retrofitted structure than in the original structure. This shows that the retrofitted structure is expected to produce smaller moments at the towers and the decks than the original structure during a seismic attack.

29.3.7.2.4 Time-History Analysis

The models were analyzed by a commercial finite element program (Prakash and Powell, 1993), which produces a piece-wise dynamic time history using Newmark's constant average acceleration ($\beta = 1/4$) integration of the equations of motion, governing the response of a nonlinear structure to a chosen base excitation. The input earthquake motions were type I-III-3, I-III-2, and I-III-1 earthquakes, which are artificial acceleration data used for design in Japan for soft soil condition. Those data are intended to be type I (interplate type). With numerical comparison (Figure 29.67), type I earthquake motion gives higher effect to the bridge than type II motion, in longer period range.

Table 29.7 shows the seismic response effects because of different kinds of bearings and dampers: fixed-hinge bearings for the original bridge model; elastic bearings, elastic bearings plus viscous dampers, and hysteretic bearings for the retrofitted bridge models. The input earthquake was type I-III-3 earthquake data and was in the longitudinal direction.

From the table, it is clearly seen that if only elastic bearings are used for seismic retrofit, then the sectional forces are reduced to about 40% of the original ones. However, the displacement response is increased to 176% of the original one. By adding viscous dampers to the elastic bearings, the sectional forces can be reduced to about 25% of the original ones, and the displacement response is reduced to 63% of the original. Thus, the viscous dampers together with bearings work to reduce the seismic response of retrofitted bridge. The structural damping ratio is calculated as 35%.

If hysteretic bearings are used for seismic retrofit, the sectional forces are reduced to about 29% of the original ones and the displacement response is reduced to 67% of the original one. The equivalent structural damping ratio is calculated as 13.1% by using pushover analysis to obtain a hysteretic loop at the main mode. The hysteretic bearings are modeled by a bilinear model, and the second stiffness of the hysteretic bearings is 0.03 times the initial stiffness and produces a first mode natural period of 6.31 sec.

TABLE 29.7 Maximum Earthquake Responses and Damping Ratios in Longitudinal Direction

Items	Original Structure	Retrofitted Structure		
		Elastic Bearings	Elastic Bearings + Viscous Damping	Hysteretic Bearings
Deck displacement (m)	2.37	4.17	1.50	1.58
Tower moment ^a (MN m)	3,100	2,000	900	900
Tower axial force ^a (kN)	48,000	15,000	15,000	21,000
Cable force (kN)	24,000	3,440	4,000	5,000
Bearing force ^b (kN)	94,000	44,000	17,000	25,000
Deck moment (MN m)	370	95	75	95
Deck axial force (kN)	56,000	21,000	11,000	15,000
Damping ratio (%)	2	2	35	13.1
Natural period (sec)	3.75	6.31	6.73	3.86 and 6.31 ^c

^a Base of tower AP3.
^b At connection between deck and tower AP3.
^c Initial and postyield stiffness.

29.3.7.2.5 Soil–Structure Interaction Effect

One method to study the SSI effects is to take into account the effects of flexible foundations and the radiation of energy from foundations. In this method, the cable-stayed bridge is idealized as in Figure 29.70 (Kawashima and Unjoh, 1991). The subsoil supporting the foundation was assumed to be an elastic half space. The subsoil was assumed to be elastic with no energy dissipation. The foundation was idealized as a rigid massless circular plate. The radius of the rigid circular plate was simply assumed so that it gives the same surface area as the foundation. Dynamic stiffness of the foundation was assumed in a frequency independent form:

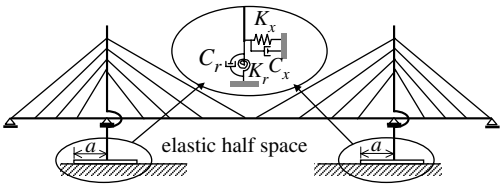


FIGURE 29.70 Cable-stayed bridge model with flexible foundation and energy radiating from foundation.

$$K_x = \frac{8G_s a}{2 - \nu} \quad C_x = \frac{\pi G_s a^2}{V_s} \tag{29.46}$$

$$K_r = \frac{8G_s a^3}{3(1 - \nu)} \quad C_r = \frac{0.25\pi\sqrt{2(1 - \nu)/(1 - 2\nu)}G_s a^4}{V_s} \tag{29.47}$$

in which K_x and C_x represent the spring and damping coefficient for sway motion, and K_r and C_r represent those for rocking motion. V_s and a represent shear wave velocity of subsoils and the radius of foundation, respectively.

The result shows that SSI increases the natural period and the damping ratio of the original structure. However, the damping ratio of the retrofitted structure is reduced and the effectiveness of the bearings and dampers in reducing seismic responses is also reduced (Table 29.8). This is mainly because the SSI model introduces flexibility at the base. A flexible base will reduce the frequency of the structure. A smaller frequency will reduce the effectiveness of viscous damping devices in absorbing earthquake energy. Moreover, a flexible base will increase the elastic strain energy of the structure that reduces the damping ratio. If the SSI model possesses an elemental damping ratio, as is a usual case for the soil, the structural damping ratio will also be influenced by the SSI-model damping characteristics.

29.3.7.2.6 Semiactive Control

The semiactive control herein uses the pseudonegative stiffness control algorithm (Iemura and Pradono, 2003) so that the sum of the damper force and bearing force (plus other connecting stiffness forces) are expected to produce a hysteresis loop that is as close as possible to that of rigid–perfectly plastic

TABLE 29.8 Maximum Earthquake Responses and Damping Ratios (SSI Included)

Items	Original Structure	Retrofitted Structure	
		Elastic Bearings + Viscous Damping	Hysteretic Bearings
Deck displacement (m)	2.78	2.57	2.77
Tower moment ^a (MN m)	1,500	800	882
Tower axial force ^a (kN)	36,200	12,500	19,800
Cable force (kN)	12,300	3,010	4,470
Deck moment (MN m)	228	58	86
Deck axial force (kN)	31,900	9,100	12,300
Foundation displacement (m)	0.171	0.079	0.093
Damping ratio (%)	3.1	23	9.3
Natural period (sec)	5.04	7.66	5.13 and 7.46 ^b

^a Base of tower AP3.
^b Initial and postyielding stiffness.

force–deformation characteristics (Figure 29.71a). Moreover, no residual displacement is expected at the bearings after an earthquake attack, because the hysteresis loop is velocity dependent. Figure 29.71 shows ideal and realistic force–deformation characteristics of the variable damper that can produce artificial rigid–perfectly plastic force–deformation characteristics by using variable damper.

One algorithm that can approach the hysteretic loop in Figure 29.71b requires the following variable-damper force (Iemura et al., 2001):

$$F_{d,t} = K_d u_t + C_d \dot{u}_t \tag{29.48}$$

where K_d is connecting stiffness (negative value) and C_d is damping coefficient (positive value). The algorithm is practical because only displacement and velocity sensors are placed in the dampers. Therefore, each damper can have its own controller. Should a malfunction happen in one damper or controller, it will not affect the other dampers or controllers.

This algorithm produces the hysteretic loop shown in Figure 29.72b under harmonic motion. It is clear from the figure that the variable damper is superior to the linear viscous damper, because the maximum variable damper plus the connecting-stiffness force can be set to be equal to the maximum connecting-stiffness force (Figure 29.72b). One can calculate that the damping ratio of the hysteresis loop in Figure 29.72b is 53.4%. For the same damping ratio, the hysteresis loop in Figure 29.72a produces a total force 1.46 times larger than the connecting-stiffness force (Iemura and Pradono, 2003). The connecting stiffness between the deck and the tower of the retrofitted cable-stayed bridge comes from the contribution of cable stiffness, upper tower stiffness, and bearing stiffness.

The cable-stayed bridge model with isolation bearings and variable dampers controlled with the pseudonegative stiffness algorithm was analyzed by a program developed by the authors under the MATLAB (MathWorks, 2000) and SIMULINK (MathWorks, 1999) environments. The program produces a piece-wise dynamic time-history, using Newmark’s constant average acceleration ($\beta = 1/4$) integration of the equations of motion, governing the response of a nonlinear structure to a chosen base excitation. The input motions were type I-III-1, I-III-2, and I-III-3 earthquakes, which are artificial acceleration data used for design in Japan (Japan Roadway Association, 1996).

The results show that the application of the pseudonegative stiffness control algorithm is effective in reducing seismic response of the bridge model. Figure 29.73 shows the base shear-deck displacement

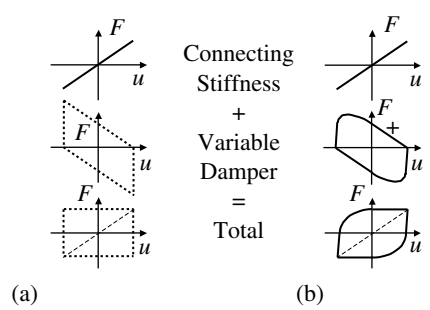


FIGURE 29.71 (a) Ideal and (b) realistic hysteretic loops produced by variable damper.

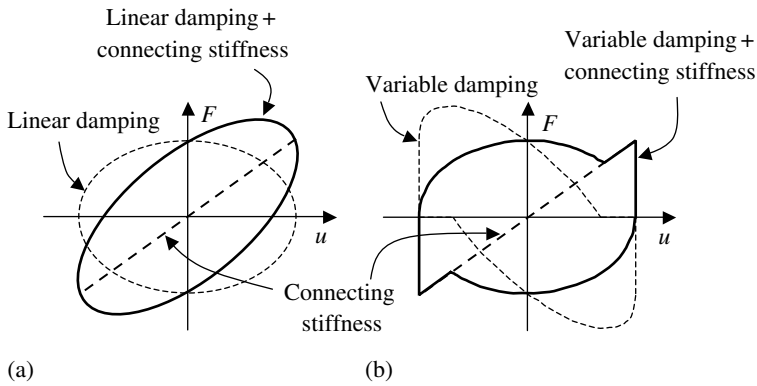


FIGURE 29.72 Hysteresis loops for (a) linear viscous damping and (b) pseudonegative stiffness damping.

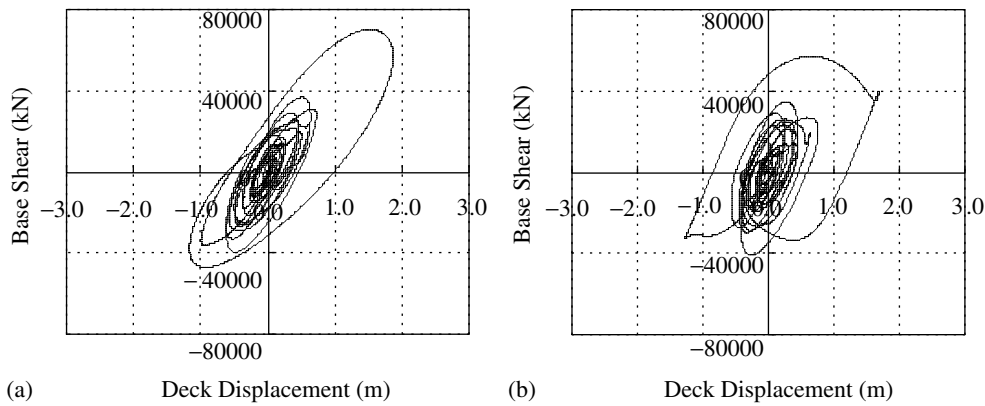


FIGURE 29.73 Base shear vs. deck displacement relationship of a cable-stayed bridge model with (a) linear dampers (b) pseudonegative stiffness dampers (type I-III-1 earthquake).

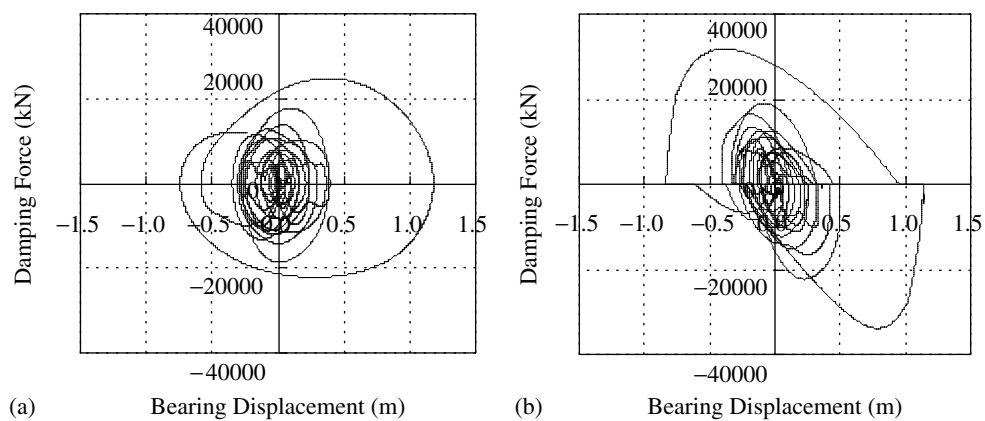


FIGURE 29.74 Damping force vs. damping displacement relationship of a cable-stayed bridge model with (a) linear dampers, (b) pseudonegative stiffness dampers (type I-III-1 earthquake).

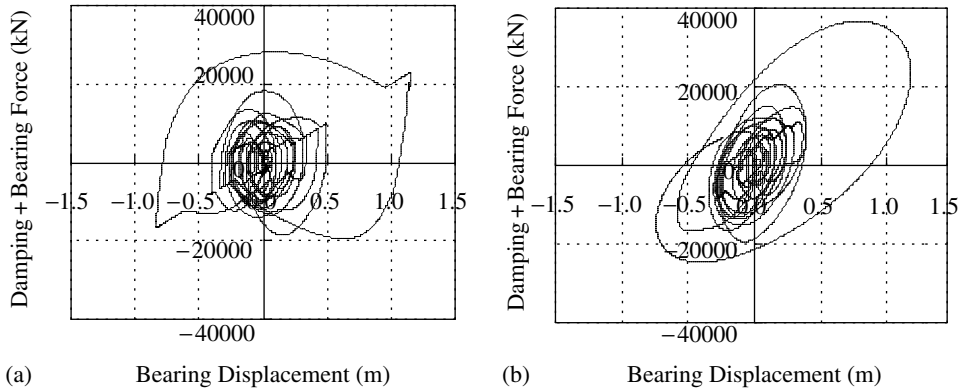


FIGURE 29.75 Damping plus bearing force vs. damping displacement relationship of a cable-stayed bridge model with (a) linear dampers, (b) pseudonegative stiffness dampers (type I-III-1 earthquake).

relationship for both bridges, with a linear damper and pseudonegative stiffness damper, respectively, under type I-III-1 earthquake input. The bridge model with pseudonegative stiffness dampers shows lower base shear than that of the bridge with linear damper.

Figure 29.74 shows the hysteretic loops produced by both linear dampers and pseudonegative stiffness dampers (at tower AP3). The damping force produced by the pseudonegative stiffness damper is larger than that of the linear damper. However, the total force of damping plus the isolation bearing is lower for the pseudonegative stiffness damper (Figure 29.75). Therefore, the base shear of the cable-stayed bridge model is lower for the pseudonegative stiffness dampers.

Bibliography

- Agrawal, A.K. and Yang, J.N., Compensation of time delay for control of civil engineering structures, *Earthquake Eng. Struct. Dyn.*, 29, 37–62, 2000.
- Aizawa, S., Fukao, Y., Minewaki, S., Hayamazu, Y., Abe, H., and Haniuda, N. 1988. An experimental study on active mass damper, Vol. V, pp. 871–876. In *Proceedings of Ninth World Conference on Earthquake Engineering*, Japan.
- Akbaý, Z. and Aktan, H.M., Vibration control of buildings by active energy dissipation, *Proc. U.S. Natl. Workshop Earthquake Eng.*, 3, 427–435, 1990.
- Akbaý, Z. and Aktan, H.M. 1991. Actively regulated friction slip devices, pp. 367–374. In *Proceedings of Sixth Canadian Conference on Earthquake Engineering*, University of Toronto Press, Toronto.
- Amick, H., Bayat, A., and Kemeny, Z.A. 1998. Seismic isolation of semiconductor production facilities, pp. 297–312. In *Proceedings of Seminar on Seismic Design, Retrofit and Performance of Nonstructural Components*, ATC-29-1, Applied Technology Council, San Francisco.
- Aoyagi, S., Mazda, T., Harada, O., and Ohtsuka, S. 1988. Vibration test and earthquake response observation of base-isolated building, Vol. V, pp. 681–686. In *Proceedings of IX World Conference on Earthquake Engineering*, Tokyo, Japan.
- Arima, F., Miyazaki, M., Tanaka, H., and Yamazaki, Y. 1988. A study on buildings with large damping using viscous damping walls, Vol. V, pp. 821–826. In *Proceedings of Ninth World Conference on Earthquake Engineering*, Japan.
- Arnold, C. 2001. Architectural considerations. *The Seismic Design Handbook*, 2nd ed., F. Naeim, Ed., pp. 275–326. Kluwer Academic, Boston.
- ASCE (American Society of Civil Engineers), 2000. *Prestandard and Commentary for the Seismic Rehabilitation of Buildings*, Federal Emergency Management Agency, Washington, DC.

- Bergman, D. and Goel, S. 1987. *Evaluation of Cyclic Testing of Steel-Plate Devices for Added Damping and Stiffness*, Report UMCE 87-10, Department of Civil Engineering, University of Michigan, Ann Arbor, MI.
- Bergman, D.M. and Hanson, R.D. 1988. Characteristics of mechanical dampers, Vol. V, pp. 815–820. In *Proceedings of Ninth World Conference on Earthquake Engineering*, Japan.
- Blakeborough, A., Williams, M.S., Darby, A.P., and Williams, D.M., The development of real-time substructure testing, *R. Soc. Lond.*, 359, 1869–1891, 2001.
- Bridgestone Corporation, 1990. *Multirubber Bearings*, International Industrial Products Department, Tokyo.
- Buckle, I.G. 1995. Earthquake protective systems for civil structures. In *Proceedings of Tenth European Conference on Earthquake Engineering*, G. Duma, Ed., pp. 641–650. Balkema, Rotterdam.
- Buckle, I.G. and Mayes, R.L., Seismic isolation: history, application and performance — a world view, *Earthquake Spectra*, 6(2), 161–201, 1990.
- Caspe, M.S. 1984. Base isolation from earthquake hazards: an idea whose time has come!, pp. 1031–1038. In *Proceedings of VIII World Conference on Earthquake Engineering*, San Francisco, CA.
- Caughey, T.K. 1993. Musings on structural control, pp. 65–75. In *Proceedings of the International Workshop on Structural Control*, Hawaii.
- Chang, K.C., Soong, T.T., Lai, M.L., and Nielsen, E.J., Viscoelastic dampers as energy dissipation devices for seismic applications, *Earthquake Spectra*, 9, 371–387, 1993.
- Cherry, S. 1994. Research on friction damping at the University of British Columbia, pp. 84–91. In *Proceedings of International Workshop on Structural Control*, USC Publication, No. CE-9311.
- Chopra, A.K. 1995. *Dynamics of Structures, Theory and Applications to Earthquake Engineering*, Prentice Hall, New York.
- Clark, A.J. 1988. Multiple passive tuned mass dampers for reducing earthquake induced building motion, Vol. V, pp. 779–784. In *Proceedings of Ninth World Conference on Earthquake Engineering*, Japan.
- Clark, R.N. 1996. *Control System Dynamics*, Cambridge University Press, Cambridge.
- Clark, P.W., Aiken, I.D., Nakashima, M., Miyazaki, M., and Modorikawa, M. 2000. The Hyogo-Ken Nanbu earthquake as a trigger for implementing new seismic design techniques in Japan, Lessons learned over time. *Learning from Earthquake Series*, Vol. III. Earthquake Engineering Research Institute, Oakland, CA, March 2000.
- Constantinou, M.C. 1994. Seismic isolation systems: introduction and overview. In *Passive and Active Vibration Control in Civil Engineering*, T.T. Soong and M.C. Constantinou, eds., pp. 81–96, Springer-Verlag, New York.
- Constantinou, M.C. and Symans, M.D., Experimental study of seismic response of buildings with supplemental fluid dampers, *Struct. Des. Tall Build.*, 2, 93–132, 1993.
- den Hartog, J.P. 1947. *Mechanical Vibration*, 3rd ed., McGraw-Hill, New York.
- Dowdell, D.J. and Cherry, S. 1994a. Semiactive friction dampers for seismic response control of structures, Vol. 1, pp. 819–828. In *Proceedings of Fifth U.S. National Conference on Earthquake Engineering*, Chicago, IL.
- Dowdell, D.J. and Cherry, S. 1994b. Structural control using semiactive friction dampers, pp. 59–68. In *Proceedings of First World Conference on Structural Control*, Los Angeles, CA.
- Dyke, S.J., Spencer, B.F., Quast, P., and Sain, M.K., Role of control–structure interaction in protective system design, *ASCE J. Eng. Mech.*, 121, 322–338, 1995.
- Dyke, S.J., Spencer, B.F., Sain, M.K., and Carlson, J.D. 1996a. A new semiactive control device for seismic response reduction. In *Proceedings of the 11th ASCE Engineering Mechanics Spec. Conference*, Ft. Lauderdale, FL.
- Dyke, S.J., Spencer, B.F., Sain, M.K., and Carlson, J.D. 1996b. Seismic response reduction using magnetorheological dampers. In *Proceedings of IFAC World Congress*, San Francisco, CA.
- Earthquake Engineering Research Institute (EERI), Northridge earthquake of January 17, 1994, Reconnaissance Report, *Earthquake Spectra*, 1996, Supplement C to Vol. 11.

- FEMA 356, 2000. *Prestandard and Commentary for the Seismic Rehabilitation of Buildings*, Federal Emergency Management Agency, Washington DC.
- Feng, Q., Shinozuka, M., and Fujii, S., Friction-controllable sliding isolated systems, *J. Eng. Mech.*, ASCE, 119(9), 1845–1864, 1993.
- Filiatrault, A. and Cherry, S., Comparative performance of friction damped braced frames under simulated earthquake loads, *Earthquake Spectra*, 3, 57–78, 1987.
- Fujii, S., Feng, Q., Kawamura, S., Shinozuka, M., and Fujita, T. 1992. Hybrid isolation system using friction-controllable sliding bearings. *Transactions of Japan National Symposium on Active Structural Control*, March 1992, in Japanese.
- Fuller, K.N.G. and Muhr, A.H. 1995. The design of natural rubber bearing base-isolation systems for apartments blocks in Indonesia and China. In *Proceedings of Tenth European Conference on Earthquake Engineering*, G. Duma, Ed., pp. 739–744. Balkema, Rotterdam.
- Gupta, Y.P. and Chandrasekaran, A.R. 1969. Absorber system for earthquake excitations, pp. 139–148. In *Proceedings of the Fourth World Conference on Earthquake Engineering*, Santiago de Chile, January 13–18, 1969, B-3.
- Hanshin Highway Public Corporation, 1992. *Tempozan Bridge, Structure and Construction Data* (in Japanese).
- Hara, F. and Saito, O. 1988. Active control for earthquake-induced sloshing of a liquid contained in a circular tank, Vol. V, pp. 889–894. In *Proceedings of Ninth World Conference on Earthquake Engineering*, Japan.
- He, W.L., Agrawal, A.K., and Mahmoud, K., Control of seismically excited cable-stayed bridge using resetting semiactive stiffness dampers, *J. Bridge Eng.*, 6, 2001.
- He, W.L., Agrawal, A.K., and Yang, J.N., Novel semiactive friction controller for linear structures against earthquakes, *J. Struct. Eng.*, ASCE, 129, 941–950, 2003.
- Hipley, P. 1997. Bridge retrofit construction techniques. In *Proceedings of the Second National Seismic Conference on Bridges and Highways*, Sacramento, CA.
- Horiuchi, T. and Konno, T., A new method for compensating actuator delay in real-time hybrid experiments, *R. Soc. Lond.*, 359, 1893–1909, 2001.
- Hou, Z. and Iwan, W.D. 1992. Reliability problem of active control algorithms caused by time delay, Vol. 4, pp. 2149–2154. In *Proceedings of Tenth World Conference on Earthquake Engineering*, Madrid, Spain.
- Housner, G.W., Bergman, L.A., Caughey, T.K., Chassiakos, A.G., Claus, R.O., Masri, S.F., Skelton, R.E., Soong, T.T., Spencer, B.F., and Yao, J.T.P., Structural control: past, present, and future, *J. Eng. Mech.*, 123, 1997.
- Hrovat, D., Barak, P., and Rabins, M., Semiactive versus passive or active tuned mass dampers for structural control, *J. Eng. Mech.*, 109(3), 691–705, 1983.
- IASC (International Association for Structural Control), 1994. *First World Conference on Structural Control*, Los Angeles, CA, August 3–5, 1994.
- IASC (International Association for Structural Control). 1999. *Second World Conference on Structural Control*, T. Kobori, Y. Inoue, K. Seto, H. Iemura and A. Nishitani, eds., Wiley, New York.
- IASC (International Association for Structural Control). 2003. *Third World Conference on Structural Control*, F. Casciati, Ed., Wiley, New York.
- Iemura, H. 1994a. Base isolation development in Japan — code provision and implementation. In *Passive and Active Vibration Control in Civil Engineering*, T.T. Soong and M.C. Constantinou, eds., pp. 187–197. Springer Verlag, New York.
- Iemura, H. 1994b. Principles of TMD and TLD — basic principles and design procedure. In *Passive and Active Structural Vibration Control in Civil Engineering*, T.T. Soong and M.C. Constantinou, eds., pp. 241–254. Springer Verlag, New York.
- Iemura, H. and Adachi, Y. 2003. Seismic retrofit of long span bridges with base isolation and structural control techniques (in Japanese), pp. 49–62. In *Proceedings of Symposium on Base Isolation and Structural Control Technologies for Seismic Retrofit of Buildings and Bridges*, Kyoto, Japan, January 2003.

- Iemura, H., Yamada, Y., Izuno, K., Yoneyama, H., and Baba, K. 1992. Comparison of passive, active, and hybrid control techniques on earthquake response of flexural structures — numerical simulations and experiments. In *Proceedings of U.S.–Italy–Japan Workshop/Symposium on Structural Control and Intelligent Systems*, Sorrento, July 1992.
- Iemura, H., Igarashi, A., and Nakata, N. 2001. Semiactive control of full-scale structures using variable joint damper system. *The Fourteenth KKNN Symposium on Civil Engineering*, Kyoto, Japan, November 5–7, 2001.
- Iemura, H., Igarashi, A., and Nakata, N. 2003. Full-scale verification tests of semiactive control of structures using variable joint damper system, Vol. 1, pp. 175–180. In *Proceedings of the Third World Conference on Structural Control*, Como, Italy.
- Iemura, H., Igarashi, A., and Tanaka, H. 2002. Substructure hybrid shake table test using digitally filtered displacement compensation control scheme. In *Proceedings of the 11th Japan Earthquake Engineering Symposium*, No. 304 (in Japanese).
- Iemura, H., Igarashi, A., Toyooka, A., and Suzuki, Y. 2003. Dynamic loading experiment of passive and semiactive dampers using the inertia-force-driven loading system, Vol. 2, pp. 45–50. In *Proceedings of the Third World Conference on Structural Control*, Como, Italy.
- Iemura, H. and Pradono, M.H., Application of the pseudo negative stiffness damper to the benchmark cable-stayed bridge, *J. Struct. Control*, 10, 187–203, 2003 (special issue on the benchmark control problems for cable-stayed bridges).
- Igarashi, A. 1994. On-line computer controlled testing of stiff multi-DoF structural systems under simulated seismic loads. Ph.D. Thesis, University of California, San Diego.
- Igarashi, A., Seible, F., and Hegemier, G.A. 1993. Development of the pseudodynamic technique for testing a full-scale 5-story shear wall structure. *U.S.–Japan Seminar on Development and Future Dimension of Structural Testing Techniques*.
- Izawa, K., Kai, M., and Nishikawa, H. 1996. Effectiveness of base isolated building structure subjected to the Hyogo-Ken Nanbu earthquake. In *Proceedings of XI World Conference on Earthquake Engineering*, Acapulco, Mexico, Paper No. 1533.
- Izumi, M. 1988. State of the art report: base isolation and passive seismic response control, Vol. 8, pp. 385–396. In *Proceedings of IX World Conference on Earthquake Engineering*, Tokyo, Japan.
- Japan Roadway Association. 1996. *The Seismic Design Specification*.
- JSSI. 1995. *Introduction of Base Isolated Structures*, Japan Society of Seismic Isolation, Ohmsa, Tokyo (in Japanese).
- Jung, H.-J., Spencer, B.F., and Lee, I.-W. 2001. Benchmark control problem for seismically excited cable-stayed bridges using smart damping strategies. In *Proceedings of IABSE Conference*, Seoul, Korea, June 2001.
- Jurukovski, D. and Rakicevic, Z. 1995. Vibration base isolation development and application. In *Proceedings of Tenth European Conference on Earthquake Engineering*, Duma, Ed., pp. 667–676. Balkema, Rotterdam.
- Kageyama, M. and Yasui, Y. 1992. Study on super quake free control system of buildings. *Transactions of Japan National Symposium on Active Structural Control*, March 1992 (in Japanese).
- Kamagata, S. and Kabori, T. 1994. Autonomous adaptive control of active variable stiffness system for seismic ground motion, pp. 33–42. In *Proceedings of First World Conference on Structural Control*, Los Angeles, CA, TA4.
- Kannan, S., Uras, H.M., and Aktan, H.M., Active control of building seismic response by energy dissipation, *Earthquake Eng. Struct. Dyn.*, 24(5), 747–759, 1995.
- Kawamura, S., Kitazawa, K., Hisano, M., and Nagashima, I. 1998. Study on a sliding-type base-isolation system — system composition and element properties, pp. 735–740. In *Proceedings of IX World Conference on Earthquake Engineering*, Tokyo, Japan.
- Kawamura, S., Sugisaki, R., Ogura, K., Maezawa, S., Tanaka, S., and Yajima, A. 2000. Seismic isolation retrofit in Japan. In *Proceedings of XII World Conference on Earthquake Engineering*, Auckland, New Zealand, Paper No. 2523.

- Kawashima, K. and Unjoh, S. 1991. Seismic behavior of cable-stayed bridges. In *Cable-Stayed Bridges: Recent Developments and their Future*, M. Ito, Ed., Elsevier, Amsterdam.
- Keightley, W.O. 1980. Dry friction damping of multistory structures, pp. 465–471. In *Proceedings of Seventh World Conference on Earthquake Engineering*, Turkey, Part IV, September 8–13, 1980.
- Kelly, J.M., Aseismic base isolation: review and bibliography, *Soil Dyn. Earthquake Eng.*, 5(3), 202–216, 1986.
- Kelly, J.M., Base isolation: linear theory and design, *Earthquake Spectra*, 6(2), 223–244, 1990.
- Kelly, J.M. 1997. *Earthquake Resistant Design with Rubber*, 2nd ed., Springer Verlag, London.
- Kelly, J.M., Seismic isolation systems for developing countries, *Earthquake Spectra*, 18(3), 385–406, 2001.
- Kelly, J.M. and Chalhoub, M.S. 1990. *Earthquake Simulator Testing of Combined Sliding Bearing and Rubber Bearing Isolation System*, Report No. UCB/EERC-87/04, Earthquake Engineering Research Center, University of California, Berkeley.
- Kelly, J.M., Skinner, R.I., and Heine, A.J., Mechanisms of energy absorption in special devices for use in earthquake resistant structures, *Bull. N.Z. Soc. Earthquake Eng.*, 5(3), 63–68, 1972.
- Kobori, T., Yamada, T., Takenaka, Y., Maeda, Y., and Nishimura, I. 1988. Effect of dynamic tuned connector on reduction of seismic response — application to adjacent office buildings, Vol. V, pp. 773–778. In *Proceedings of Ninth World Conference on Earthquake Engineering*, Japan.
- Kurata, N., Kobori, T., Takahashi, M., Niwa, N., and Kurino, H. 1994. Shaking table experiments of active variable damping system, pp. 108–127. In *Proceedings of First World Conference of Structural Control*, TP2.
- Kurata, N., Kobori, T., Takahashi, M., Niwa, N., and Midorikawa, H., Actual seismic response controlled building with semiactive damper system, *Earthquake Eng. Struct. Dyn.*, 28, 1427–1447, 1999.
- Kurino, H., Tagami, J., Shimizu, K., and Kobori, T., Switching oil damper with built-in controller for structural control, *J. Struct. Eng.*, ASCE, 129, 895–904, 2003.
- Lee, G.C., Kitane, Y., and Buckle, I.G. 2001. *Literature Review of the Observed Performance of Seismically Isolated Bridges*, Report on Research Progress and Accomplishments: 2000–2001, MCEER Publications, State University of New York, Buffalo.
- Liang, Z., Tong, M., and Lee, G.C. 1995. *Real-Time Structural Parameter Modification (RSPM): Development of Innervated Structures*, Technical Report NCEER-95-0012, National Center for Earthquake Engineering Research, Buffalo, New York.
- Liu, S.C., Yang, J.N., and Samali, B. 1984. Control of coupled lateral-torsion motion of buildings under earthquake excitation, Vol. V, pp.1023–1030. In *Proceedings of Eighth World Conference on Earthquake Engineering*, San Francisco, CA, July 21–28, 1984.
- Logiadis, I., Zilch, K., and Meskouris, K. 1996. Prestressed bearings in the seismic isolation of structures. In *Proceedings of XI World Conference on Earthquake Engineering*, Acapulco, Mexico, Paper No. 1895.
- Lopez-Almansa, F., Andrade, R., and Rodellar, J. 1992. Predictive control of structures with reduced number of sensors and actuators, Vol. 4, pp. 2085–2090. In *Proceedings of Tenth World Conference on Earthquake Engineering*, Madrid, Spain.
- Marioni, A. Behavior of large base isolated prestressed concrete bridges during the recent exceptional earthquakes in Turkey. Article from web page of *Civil Engineer, The Internet for Civil Engineers* (<http://192.107.65.2/GLIS/HTML/gn/turchi/g5turchi.htm>).
- Marshall, L. 2001. Geotechnical design considerations. *The Seismic Design Handbook*, 2nd ed., F. Naeim, Ed., Kluwer Academic, Boston, Chap. 3.
- MathWorks. 1998. *Control System Toolbox for Use with MATLAB®*, The MathWorks Inc., Natick, MA.
- MathWorks. 1999. *SIMULINK, Dynamic System Simulation for MATLAB®*, The MathWorks Inc., Natick, MA.
- MathWorks. 2000. *MATLAB, the Language of Technical Computing*, The MathWorks Inc., Natick, MA.
- Mayes, R.L. and Naeim, F. 2001. Design of structures with seismic isolation. *The Seismic Design Handbook*, 2nd ed., F. Naeim, Ed., pp. 723–755. Kluwer Academic, Boston.

- McClamroch, N.H. and Gavin, H.P. 1995. Closed loop structural control using electrorheological dampers, pp. 4173–4177. In *Proceedings of American Control Conference*, Seattle, Washington, DC.
- McKay, G.R., Chapman, H.E., and Korkcaldie, D.K., Seismic isolation: New Zealand applications, *Earthquake Spectra*, 6(2), 203–222, 1990.
- Mizuno, T., Kobori, T., Hirai, J., Matsunaga, Y., and Niwa, N. 1992. Development of adjustable hydraulic dampers for seismic response control of large structures, Vol. 229, pp. 163–170. In *Proceedings of ASME PVP Conference*.
- Mostaghel, N. and Khodaverdian, M., Dynamics of resilient-friction base isolator (R-FBI), *Earthquake Eng. Struct. Dyn.*, 15, 379–390, 1987.
- Mukai, Y., Tachibana, E., and Inoue, Y. 1994. Experimental study of active fin system for wind-induced structural vibration, pp. WP2-52–WP2-61. In *Proceedings of First World Conference on Structural Control*.
- Nagarajaiah, S. and Sun, X. 1996. Seismic performance of base isolated buildings in the 1994 Northridge earthquake. In *Proceedings of XI World Conference on Earthquake Engineering*, Acapulco, Mexico, Paper No. 598.
- Nagarajaiah, S. and Sun, X., Base isolated fcc building: impact response in Northridge earthquake, *Struct. Eng., ASCE*, 127, 1063–1075, 2001.
- Nakashima, M. 1993. Extension of on-line computer control method. *U.S.–Japan Seminar on Development and Future Dimension of Structural Testing Techniques*.
- Nakashima, M., Kato, H., and Takaoka, E., Development of real-time pseudo dynamic testing, *Earthquake Eng. Struct. Dyn.*, 21, 79–92, 1999.
- Nakashima, M. and Masaoka, N., Real-time on-line test for MDOF systems, *Earthquake Eng. Struct. Dyn.*, 28, 393–420, 1999.
- Nishitani, A. 2000. Structural control implementation in Japan. In *Proceedings of XII World Conference on Earthquake Engineering*, Auckland, New Zealand, Paper No. 2840.
- Niwa, N., Kobori, T., Takahashi, M., Midorikawa, H., Kurata, N., and Mizuno, T., Dynamic loading test and simulation analysis of full-scale semiactive hydraulic damper for structural control, *Earthquake Eng. Struct. Dyn.*, 29, 789–812, 2000.
- Ogura, M., Morohoshi, M., Hashimoto, T., and Nakashima, M. 2003. Seismic retrofit of Kyoto University clock tower using base isolation techniques, pp. 83–87. In *Proceedings of Symposium on Base Isolation and Structural Control Technologies for Seismic Retrofit of Buildings and Bridges*, Kyoto, Japan, January 2003 (in Japanese).
- Ohashi, U.G. 1995. *Earthquakes and Base Isolation*, Pub. Asakura, Tokyo, in Japanese.
- Ohno, S., Watari, A., and Sano, I. 1977. Optimum tuning of the dynamic damper to control response of structures to earthquake ground motion, Vol. 2, pp. 3–157. In *Proceedings of Sixth World Conference on Earthquake Engineering*, India.
- Pall, A.S. 1984. Response of friction damped buildings, Vol. V, pp.1007–1014. In *Proceedings of Eighth World Conference on Earthquake Engineering*, San Francisco, July 21–28, 1984.
- Pall, A.S. and Marsh, C., Response of friction damped braced frames, *J. Struct. Div., ASCE*, 108(ST6), 1313–1323, 1982.
- Patten, W.N. 1998. The I-35 Walnut Creek Bridge: an intelligent highway bridge via semiactive structural control, Vol. 1, pp. 427–436. In *Proceedings of Second World Conference on Structural Control*, Kyoto, Japan.
- Patten, W.N., He, Q., Kuo, C.C., Liu, L., and Sack, R.L. 1994. Seismic structural control via hydraulic semiactive vibration dampers, pp. 83–89. In *Proceedings of First World Conference on Structural Control*, CA, FA2.
- Perry, C.L., Fierro, E.A., Sedarat, H., and Scholl, R.E., Seismic upgrade in San Francisco using energy dissipation devices, *Earthquake Spectra*, 9, 559–579, 1993.
- Prakash, V. and Powell, G.H. 1993. *Drain-2DX, Drain-3DX, and Drain-Building: Base Program Design Documentation*, Report No. UCB/SEMM-93/16, University of California, Berkeley, CA, December 1993.

- Pranesh, M. and Sinha, R., Earthquake resistant design of structures using the variable frequency pendulum isolator, *Struct. Eng., ASCE*, 128(7), 870–880, 2002.
- Priestley, M.J.N., Seible, F., and Calvi, G.M. 1996. *Seismic Design and Retrofit of Bridges*, 1st ed., Wiley, New York.
- Rakicevic, Z. and Jurukovski, D. 2001. *Optimum Design of Passive Controlled Steel Frame Structures*, Report IZIIS 2001-59, Project 123/NIST, Skopje, December 2001.
- Reid, T.J., Free vibration and hysteretic damping, *J. Aero. Soc.*, 69, 283, 1956.
- Reinhorn, A. and Riley, M.A. 1994. Control of bridge vibrations with hybrid devices, pp. 50–59. *First World Conference on Structural Control*, California, TA2.
- Robinson, W.H. 2003. Retrofit of seismic isolation in New Zealand, pp. 11–20. In *Proceedings of Symposium on Base Isolation and Structural Control Technologies for Seismic Retrofit of Buildings and Bridges*, Kyoto, Japan, January 2003.
- Sack, R.L., Kuo, C.C., Wu, H.C., Liu, L., and Patten, W.N. 1994. Seismic motion control via semiactive hydraulic actuators. In *Proceedings of U.S. Fifth National Conference on Earthquake Engineering*.
- SAP2000. 2002. *Basic Analysis Reference, Linear and Nonlinear Static and Dynamic Analysis and Design of Three-Dimensional Structures*, Version 8.0, Computer and Structures Inc., Berkeley, CA, June 2002.
- Scholl, R.E. 1984. Brace dampers: an alternative structural system for improving the earthquake performance of buildings, Vol. V, pp.1015–1022. In *Proceedings of Eighth World Conference on Earthquake Engineering*, San Francisco, July 21–28, 1984.
- Seki, M., Miyazaki, M., Tsunaki, Y., and Kataoka, K. 2000. A masonry school building retrofitted by base isolation technology. In *Proceedings of XII World Conference on Earthquake Engineering*, Auckland, New Zealand, Paper No. 1118.
- Shen, K.L. and Soong, T.T., Modeling of viscoelastic dampers for structural application, *J. Eng. Mech., ASCE*, 121(6), 694–701, 1995.
- Shimada, S., Noda, S., Fujinami, T., Nakanowatari, S., and Jodai, S. 1992. A study of applicability of vibration control to nonlinear structure for seismic excitation, Vol. 4, pp. 2125–2130. In *Proceedings of Tenth World Conference on Earthquake Engineering*, Madrid, Spain.
- Shimoda, I., Ikenaga, M., Takenaka, Y., and Yasaka, A. 1992. Development of lead rubber bearing with a stepped plug, Vol. 4, pp. 2327–2332. In *Proceedings of X World Conference on Earthquake Engineering*, Madrid, Spain.
- Shimosaka, H., Ohmata, K., Shimoda, H., Koh, T., and Arakawa, T. 1988. An earthquake isolator effectively controlling the displacement by employing the ball screw type damper with magnetic damping, Vol. V, pp. 827–832. In *Proceedings of Ninth World Conference on Earthquake Engineering*, Japan.
- Skinner, R.I., Heine, A.J., and Tyler, R.G. 1977. Hysteretic dampers to provide structure with increased earthquake resistance, Vol. 2, 3-333, p. 1319. In *Proceedings of Sixth World Conference on Earthquake Engineering*, India.
- Skinner, R.I., Kelly, J.M., and Heine, A.J. 1973. Energy absorption devices for earthquake resistant structures, Vol. 3, pp. 2924–2933. In *Proceedings of Fifth World Conference on Earthquake Engineering*, Rome, June 25–29, 1973.
- Skinner, R.I., Kelly, J.M., and Heine, A.J., Hysteresis dampers for earthquake-resistant structures, *Earthquake Eng. Struct. Dyn.*, 3, 287–296, 1975.
- Skinner, R.I. and McVerry, G.H. 1996. Seismic isolators for ground motions with large displacement and velocities. In *Proceedings of XI World Conference on Earthquake Engineering*, Acapulco, Mexico, Paper No. 1841.
- Skinner, R.I., Robinson, W.H., and McVerry, G.H. 1993. *An Introduction to Seismic Isolation*, 1st ed., Wiley, Chichester, England.
- Sladek, J.R. and Klingner, R.E. 1980. Using tuned-mass dampers to reduce seismic response, pp. 265–271. In *Proceedings of Seventh World Conference on Earthquake Engineering*, Turkey, September 8–13, 1980, Part IV.

- Sogabe, K., Goto, Y., Nakamura, T., and Okada, H. 1988. Basic study on active suppression method of sloshing of liquid in tanks during earthquakes by air injection, Vol. V, pp. 877–882. In *Proceedings of Ninth World Conference on Earthquake Engineering*, Japan.
- Soong, T.T. and Dargush, G.F. 1997. *Passive Energy Dissipation Systems in Structural Engineering*, Wiley, New York.
- Soong, T.T., Reinhorn, A.M., Wang, Y.P., Lin, R.C., and Riley, M. 1992. Full-scale implementation of active structural control, Vol. 4, pp. 2131–2136. In *Proceedings of Tenth World Conference on Earthquake Engineering*, Madrid, Spain.
- Spencer, B.F., Dyke, S.J., Sain, M.K., and Carlson, J.D., Phenomenological model for magnetorheological dampers, *J. Eng. Mech.*, 123, 1997.
- Spencer, B.F. and Sain, M.K., Controlling buildings: a new frontier in feedback, *Spec. Issue IEEE Control Syst. Mag. Emerging Technol.*, 17, 19–35, 1997.
- Sugano, S. 2000. Seismic rehabilitation of existing concrete buildings in Japan. In *Proceedings of XII World Conference on Earthquake Engineering*, Auckland, New Zealand, Paper No. 2324.
- Sun, L. and Goto, Y. 1994. Applications of Fuzzy Theory to variable dampers for bridge vibration control, pp. 31–40. In *Proceedings of First World Conference on Structural Control*, Los Angeles, CA, WP1.
- Tajiran, F.F. 1998. Base isolation design for civil components and civil structures. In *Proceedings of Structural Engineers World Congress*, San Francisco, CA, July 1998.
- Takayama, M., Wada, A., Akiyama, H., and Tada, H. 1988. Feasibility study on base isolated building, pp. 669–674. In *Proceedings of IX World Conference on Earthquake Engineering*, Tokyo, Japan, Vol. 5.
- Tanabashi, R. 1960. Earthquake resistance of traditional Japanese wooden buildings, Vol. 1, pp. 151–163. In *Proceedings of Second World Conference on Earthquake Engineering*, Japan.
- Tani, A., Kawamura, H., and Watari, Y. 1992. optimal adaptive and predictive control of seismic structures by Fuzzy Logic, Vol. 4, pp. 2155–2160. In *Proceedings of Tenth World Conference on Earthquake Engineering*, Madrid, Spain.
- Tanzo, W., Yamada, Y., and Iemura, H. 1992. *Substructured Computer-Actuator Hybrid Loading Tests for Inelastic Earthquake Response of Structures*, Research Report No. 92-ST-01, Department of Civil Engineering, Kyoto University.
- Tarics, A.G. 1996. Composite seismic isolator and method. In *Proceedings of XI World Conference on Earthquake Engineering*, Acapulco, Mexico, Paper No. 1895.
- Taylor, D.P. 2002. History, design, and applications of fluid dampers in structural engineering, pp. 17–34. *Passive Structural Control Symposium*, December 13–14, 2002, Tokyo Institute of Technology, Japan.
- Taylor, A.W., Lin, M., and Martin, J.W., Performance of elastomers in isolation bearings: a literature review, *Earthquake Spectra*, 8(2), 279–303, 1992.
- Taylor, A.W., Shenton, H.W., and Chung, R.M. 1995. Standards for the testing and evaluation of seismic isolation systems, pp. 39–43. In *Proceedings of the ASME/JSME Pressure Vessels and Piping Conference*, Honolulu, Hawaii, Vol. 319.
- Tewari, A. 2002. *Modern Control Design with MATLAB and SIMULINK*, Wiley, England.
- Tospelas, P.C., Nagarajaiah, S., Constantinou, M.C., and Reinhorn, A.M., Nonlinear dynamic analysis of multiple building base isolated structures, *Comput. Struct.*, 50(1), 47–57, 1994.
- Toyooka, A. 2002. Development of the inertia force driven hybrid loading system and pseudonegative stiffness control method of a MR damper. A dissertation submitted to the Faculty of Engineering of Kyoto University in partial fulfillment of the requirements for the degree of Doctor of Engineering, Kyoto, Japan, December 2002.
- Tsai, K.-C., Chen, H.-W., Hong, C.-P., and Su, Y.-F., Design of steel triangular plate energy absorbers for seismic-resistant construction, *Earthquake Spectra*, 9, 505–528, 1993.
- Tyler, R.G., Tapered steel cantilever energy absorbers, *Bull. N.Z. Natl. Soc. Earthquake Eng.*, 11, 1, 1978.
- UBC (Uniform Building Code). 1997. *International Conference of Building Officials*, Whittier, CA.

- Williams, M.S. and Blakeborough, A., Laboratory testing of structures under dynamic loads: an introductory review, *R. Soc. Lond.*, 359, 1651–1669, 2001.
- Wolf, J.P. 1985. *Dynamic Soil–Structure Interaction*, Prentice Hall, New York.
- Wong, H.L. and Luco, J.E. 1992. Effects of soil–structure interaction on the seismic response of structures subjected to active control, Vol. 4, pp. 2137–2142. In *Proceedings Tenth World Conference on Earthquake Engineering*, Madrid, Spain.
- Yang, Y.-B., Chang, K.-C., and Yau, J.-D. 2003. Base isolation. In *Earthquake Engineering Handbook*, 1st ed., W.F. Chen and C. Scawthorn, eds., pp. 17.1–17.31. CRC Press, Boca Raton, FL.
- Yasaka, A., Koshida, H., and Iizuka, M. 1988. Base isolation system for earthquake protection and vibration isolation of structures, Vol. 5, pp. 699–704. In *Proceedings of IX World Conference on Earthquake Engineering*, Tokyo, Japan.
- Zhang, R.H., Soong, T.T., and Mahmoodi, P., Seismic response of steel frame structures with added viscoelastic dampers, *Earthquake Eng. Struct. Dyn.*, 8, 389–396, 1989.

30

Seismic Random Vibration of Long-Span Structures

30.1	Introduction	30-2
	Basic Concepts of Random Vibration • Three Methods for Structural Seismic Analysis	
30.2	Seismic Random-Excitation Fields	30-11
	Power Spectral Density of Spatially Varying Ground Acceleration • Several Coherence Models • Generation of Ground Acceleration Power Spectral Density Curves from Acceleration Response Spectrum Curves • Seismic Equations of Motion of Long-Span Structures • Seismic Waves and Their Geometrical Expressions	
30.3	Pseudoexcitation Method for Structural Random Vibration Analysis	30-16
	Structures Subjected to Stationary Random Excitations • Structures Subjected to Nonstationary Random Vibration • Precise Integration Method	
30.4	Long-Span Structures Subjected to Stationary Random Ground Excitations	30-27
	The Solution of Equations of Motion Using the Pseudoexcitation Method • Numerical Comparisons with Other Methods	
30.5	Long-Span Structures Subjected to Nonstationary Random Ground Excitations	30-34
	Modulation Functions • The Formulas for Nonstationary Multiexcitation Analysis • Expected Extreme Values of Nonstationary Random Processes • Numerical Comparisons with the Corresponding Stationary Analysis	
30.6	Conclusions	30-39

Jiahao Lin

Dalian University of Technology

Yahui Zhang

Dalian University of Technology

Summary

Particular considerations must be made during the design of long-span bridges with regard to safety during earthquakes. These include: the wave-passage effect caused by the different times at which seismic waves arrive at different supports; the incoherence effect due to loss of coherency of the motion caused by either reflections and refractions of the waves in the inhomogeneous ground medium or the difference in the manner of superposition of waves from an extended source arriving at various supports; and the local effect because of the differences in soil conditions at different supports and the manner in which these influence the amplitude and frequency content of the bedrock motion. This chapter deals with the random vibration approach to analyzing these structures, which is based on a statistical characterization of the set of motions at the supports. This approach is particularly suitable for dealing with the above spatially varying input motions. The computational problems may be largely overcome by the pseudo excitation method. This approach is presented here. Numerical comparisons are given to show the

accuracy of the method and its capability of dealing with the spatial effects and nonstationary effects. Further topics related to this chapter are discussed in [Chapter 5](#).

30.1 Introduction

Seismic computations of long-span structures have long been an issue of great concern. Such computations are usually executed numerically using schemes in the time domain (i.e., time history). For short-span bridges, all supports can be assumed to move uniformly and the response-spectrum method (RSM) is a suitable computation tool. For long-span bridges, however, various spatial effects such as the wave-passage effect, the incoherence effect, the local site effect, and so on, may be important. Such spatial effects cannot be dealt with directly by the conventional RSM. Instead, the time-history method (THM) is the most widely used method for these systems. The time-history scheme requires solving the dynamic equations for a number of seismic acceleration samples. The results are then processed statistically to produce the quantities required by the designs. This process is rather complex and requires a considerable computational effort. As a result, more efficient and effective methods are under investigation.

Seismic motions are random (stochastic) in nature (Housner, 1947). Spatial effects of long-span bridges can be analyzed using the random-vibration approach (see also Chapter 5). In the last two decades, many scholars and experts (Lee and Penzien, 1983; Dumanoglu and Severn, 1990; Lin et al., 1990; Berrah and Kausel, 1992; Kiureghian and Neuenhofer, 1992; Ernesto and Vanmarcke, 1994) have made great progress in promoting the seismic random analysis of long-span structures and its engineering applications. Although available computational methods still need further improvement both in precision and efficiency, the random-vibration approach, as a theoretically advanced tool, has been gradually accepted by the earthquake engineering community. For example, it has been adopted by the European Bridge Code (European Committee for Standardization, 1995).

Developed recently (Lin, 1992; Lin et al., 1994a, 1995a, 1995b, 1997a, 1997b; Lin and Zhan, 2003), the pseudoexcitation method (PEM) is an accurate and highly efficient approach to the stationary and nonstationary random seismic analysis of long-span structures. For typical three-dimensional finite element models of long-span bridges with thousands of degrees of freedom (DoF) and dozens of supports, when using 100 to 300 modes for mode-superposition analysis, the seismic responses can be implemented quickly and accurately on a standard personal computer. Numerical results show that the wave-passage effect is of particular importance for the seismic analysis of long-span bridges, and the incoherence effect is of comparatively less importance. The details will be given in this chapter. The PEM has been successfully applied to some practical engineering analyses (Wang et al., 1999; Liu and Liu, 2000; Xue et al., 2000; Fan et al., 2001), and has been proven to be quite effective.

30.1.1 Basic Concepts of Random Vibration

30.1.1.1 Stationary Random Process

The probabilistic properties of stationary random processes are independent of time. A random process is said to be *strictly stationary* (or *strongly stationary*) if its probability density function does not change with time. However, such a condition is very difficult to satisfy in practical engineering problems. Therefore, a *wide-sense stationary* (or *weakly stationary*) process is defined for which only the mean value and autocorrelation function of the process are not permitted to vary with time.

A random variable x is said to be Gaussian-distributed if its probability density can be written in the form

$$p(x) = \frac{1}{\sigma\sqrt{2\pi}} \exp\left(-\frac{(x - \bar{x})^2}{2\sigma^2}\right) \quad (30.1)$$

in which σ is the standard deviation of x , and the variance is given by

$$\sigma^2 = \int_{-\infty}^{\infty} (x - \bar{x})^2 p(x) dx \quad (30.2)$$

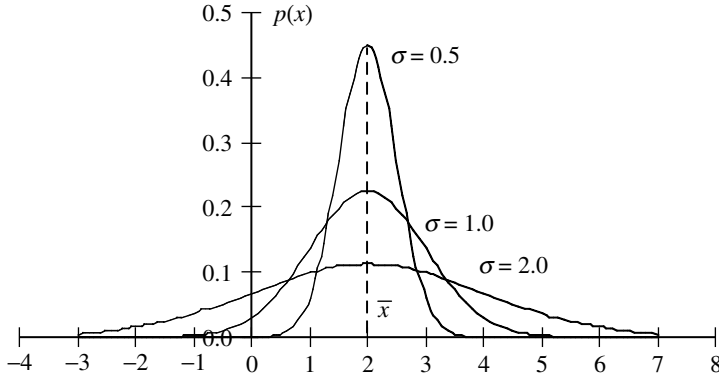


FIGURE 30.1 Probability density functions of Gaussian random variables.

Probability density functions of typical Gaussian random processes are shown in Figure 30.1, in which \bar{x} is the mean value given by the abscissa (horizontal coordinate) of the peak value. A smaller σ corresponds to a narrower and higher peak.

For a random process $x(t)$, if the joint probability density function of its values $x(t_1), x(t_2), \dots, x(t_n)$ at n arbitrary time instants is Gaussian, then $x(t)$ is said to be a Gaussian random process. Since the joint probability density function depends only on the mean values and covariances of the n values, a weakly stationary Gaussian random process is also strongly stationary.

If a stationary random process has statistical properties that can be computed by taking the time average of an arbitrary sample over a sufficiently long period, the process is said to be *ergodic*. A typical seismic ground motion record is usually assumed to be a Gaussian and ergodic stationary random process. Its *expected value* (i.e., mean value) can be computed by

$$E[x(t)] = \bar{x}(t) = \int_{-\infty}^{+\infty} x(t)p(x, t)dx \quad (30.3)$$

in which $p(x, t)$ is the probability density function of $x(t)$.

In order to investigate the relation between the values of a random process $x(t)$ at two different times, the autocorrelation function of $x(t)$ is defined as

$$R_{xx}(\tau) = E[x(t)x(t + \tau)] = \lim_{T \rightarrow \infty} \frac{1}{T} \int_{-T/2}^{T/2} x(t)x(t + \tau)dt \quad (30.4)$$

A stationary random process, denoted as $x(t)$, is not absolutely integrable in a region of $t \in (-\infty, \infty)$. Therefore, a subsidiary function $x_T(t)$ is defined:

$$x_T(t) = \begin{cases} x(t) & \text{when } -T/2 \leq t \leq T/2 \\ 0 & \text{elsewhere} \end{cases} \quad (30.5)$$

Obviously, $x_T(t)$ is absolutely integrable within $t \in (-\infty, \infty)$. Therefore, its *Fourier transformation* (see [Appendix 2A](#) and [Chapter 10](#)) can be computed by

$$X_T(\omega) = \frac{1}{2\pi} \int_{-\infty}^{\infty} x_T(t)\exp(j\omega t)dt \quad (30.6)$$

Let

$$S_{xx}(\omega) = \lim_{T \rightarrow \infty} \frac{1}{T} |X_T(\omega)|^2 \quad (30.7)$$

Equation 30.7 is the definition of the auto-PSD (power spectral density) function of $x(t)$.

Note that the repeated subscripts in R_{xx} or S_{xx} can be represented by just one; that is, they can be denoted as R_x or S_x . When $x(t)$ is a zero-mean stationary random process, its variance is given by

$$\sigma_x^2 = \int_{-\infty}^{\infty} S_{xx}(\omega)d\omega \tag{30.8}$$

Figure 30.2 gives the auto-PSD curves of four typical stationary random processes, which show the energy distribution with frequency for each kind of random process. The energy of a narrowband random process is concentrated within a narrow frequency band (see Figure 30.2b) whereas the energy of a wideband random process is distributed over a rather wide frequency range, as shown in Figure 30.2c. The energy of a *white noise* process is distributed uniformly over an infinite region, $\omega \in (-\infty, \infty)$, as shown in Figure 30.2d. Using such a random process model results in mathematical convenience. However, the white noise process does not physically exist. A single harmonic random wave has nonzero values only at two isolate frequencies $\pm \omega_0$ (see Figure 30.2a), and its initial phase angle φ is usually regarded as uniformly distributed over $[0, 2\pi)$.

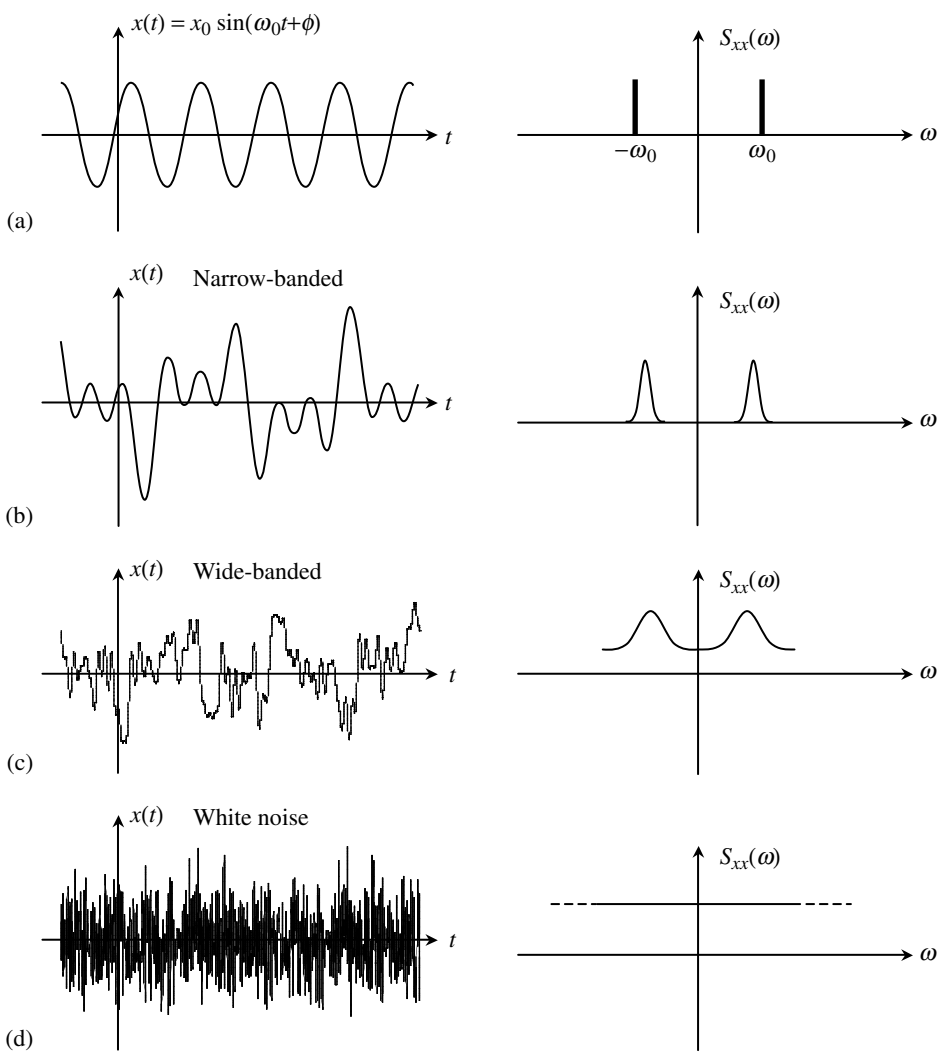


FIGURE 30.2 Auto-PSD curves of four typical stationary random processes.

The auto-PSD $S_{xx}(\omega)$ of a stationary random process $x(t)$ has the following properties:

1. $S_{xx}(\omega)$ is a nonnegative real number; that is

$$S_{xx}(\omega) \geq 0 \quad (30.9)$$

This can be judged from the definition of auto-PSD functions, that is, Equation 30.7.

2. $S_{xx}(\omega)$ is an even function; that is

$$S_{xx}(\omega) = S_{xx}(-\omega) \quad (30.10)$$

This can also be deduced from Equation 30.7.

3. The auto-PSDs of the derivatives of $x(t)$ can be computed from $S_{xx}(\omega)$ directly by

$$S_{\dot{x}\dot{x}}(\omega) = \omega^2 S_{xx}(\omega), \quad S_{\ddot{x}\ddot{x}}(\omega) = \omega^4 S_{xx}(\omega) \quad (30.11)$$

30.1.1.1 Wiener–Khinchine Theorem

Wiener and Khinchine proved that for an arbitrary stationary random process $x(t)$, its auto-PSD $S_{xx}(\omega)$ and autocorrelation function $R_{xx}(\tau)$ are a Fourier transform pair; that is

$$S_{xx}(\omega) = \frac{1}{2\pi} \int_{-\infty}^{\infty} R_{xx}(\tau) \exp(-j\omega\tau) d\tau \quad (30.12)$$

$$R_{xx}(\tau) = \int_{-\infty}^{\infty} S_{xx}(\omega) \exp(j\omega\tau) d\omega \quad (30.13)$$

According to this theorem, if either of $S_{xx}(\omega)$ or $R_{xx}(\tau)$ has been found, the other can be directly obtained.

If stationary random processes $x(t)$ and $y(t)$ are both ergodic, then their cross-correlation function can be computed in terms of their sample functions $\hat{x}(t)$ and $\hat{y}(t)$:

$$R_{xy}(\tau) = \lim_{T \rightarrow \infty} \frac{1}{T} \int_{-T/2}^{T/2} \hat{x}(t) \hat{y}(t + \tau) dt \quad (30.14)$$

$$R_{yx}(\tau) = \lim_{T \rightarrow \infty} \frac{1}{T} \int_{-T/2}^{T/2} \hat{y}(t) \hat{x}(t + \tau) dt \quad (30.15)$$

Also, their cross-PSD functions can be defined by means of the Fourier transforms of the corresponding cross-correlation functions:

$$S_{xy}(\omega) = \frac{1}{2\pi} \int_{-\infty}^{\infty} R_{xy}(\tau) \exp(-i\omega\tau) d\tau \quad (30.16)$$

$$S_{yx}(\omega) = \frac{1}{2\pi} \int_{-\infty}^{\infty} R_{yx}(\tau) \exp(-i\omega\tau) d\tau \quad (30.17)$$

For more details, see Lin (1967).

30.1.1.2 Nonstationary Random Process

Nonstationary random processes are generally short in duration. Their basic characteristic is that the statistical properties vary significantly with time. An example is the process of a typical earthquake record, for which the medium flat segment is often regarded as a stationary random process in order to simplify the structural analysis. However, such simplification sometimes causes significant errors. For instance, some long-span bridges are very flexible, with fundamental periods of approximately 15 to 20 sec. The period of the strong earthquake portion of a typical earthquake record is only approximately 20 to 30 sec. For such slender long-span bridges, the seismic excitations exhibit clear nonstationary characteristics. In order to avoid computational complexities in the structural analyses, such excitations are usually assumed to be stationary random processes. This chapter shows that the analysis of such nonstationary random responses is made very simple by using PEM.

Nonstationary random processes are not ergodic because their statistical properties vary with time. In earthquake engineering, the evolutionary random process defined by Priestly (1967) has been investigated extensively. It is expressed in terms of the Riemann–Stieltjes integration as

$$f(t) = \int_{-\infty}^{\infty} A(\omega, t) \exp(i\omega t) d\alpha(\omega) \quad (30.18)$$

in which $\alpha(\omega)$ satisfies the relations

$$x(t) = \int_{-\infty}^{\infty} \exp(i\omega t) d\alpha(\omega) \quad (30.19)$$

$$E[d\alpha^*(\omega_1) d\alpha(\omega_2)] = S_{xx}(\omega_1) \delta(\omega_2 - \omega_1) d\omega_1 d\omega_2 \quad (30.20)$$

Here, $x(t)$ is a zero-mean stationary random process, with auto-PSD $S_{xx}(\omega)$, $A(\omega, t)$ is a deterministic slowly varying nonuniform modulation function, and δ is a Dirac delta function. The variance of $f(t)$ is

$$\sigma_f^2(t) = \int_{-\infty}^{\infty} S_{ff}(\omega) d\omega = \int_{-\infty}^{\infty} |A(\omega, t)|^2 S_{xx}(\omega) d\omega \quad (30.21)$$

The PSD of $f(t)$ as given by

$$S_{ff}(\omega, t) = |A(\omega, t)|^2 S_{xx}(\omega) \quad (30.22)$$

is known as an evolutionary power spectral density function.

Responses of structures subjected to nonstationary random excitations expressed by Equation 30.18 are not easy to compute. Therefore, the nonuniform modulation assumption is often replaced by a uniform modulation assumption; that is, the nonuniform modulation function $A(\omega, t)$ is replaced by a uniform modulation function $g(t)$. Thus, Equation 30.18 reduces to

$$f(t) = \int_{-\infty}^{\infty} g(t) \exp(i\omega t) dZ(\omega) = g(t)x(t) \quad (30.23)$$

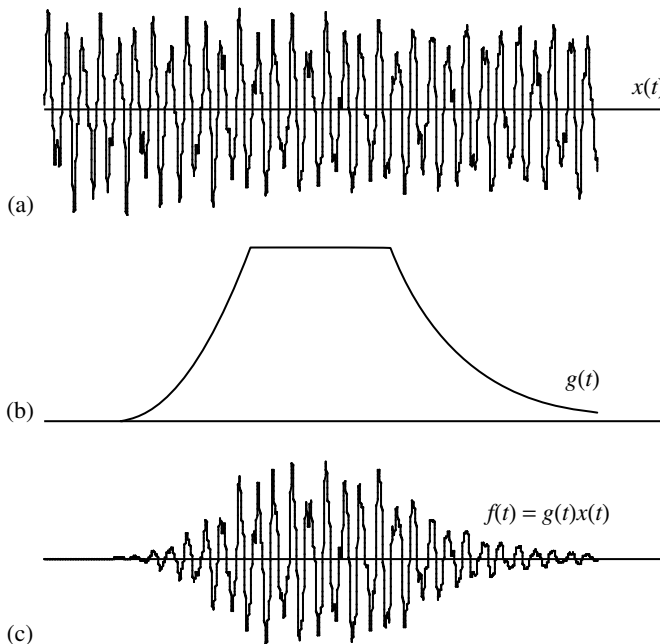


FIGURE 30.3 A uniformly modulated evolutionary random excitation $f(t)$.

Equation 30.18 and Equation 30.23 are known as the nonuniformly modulated and uniformly modulated evolutionary random processes, respectively.

Figure 30.3 shows a stationary random process $x(t)$ and the corresponding uniformly modulated evolutionary random excitation $f(t)$ with a given modulation function $g(t)$.

30.1.2 Three Methods for Structural Seismic Analysis

30.1.2.1 Response Spectrum Method

The equations of motion of a linear multi-DoF structure subjected to a ground acceleration excitation $\ddot{x}_g(t)$ can be written as (see Chapter 3 and Chapter 8)

$$\mathbf{M}\ddot{\mathbf{y}} + \mathbf{C}\dot{\mathbf{y}} + \mathbf{K}\mathbf{y} = -\mathbf{M}\mathbf{e}\ddot{x}_g(t) \quad (30.24)$$

in which \mathbf{M} , \mathbf{C} , and \mathbf{K} are the $n \times n$ mass, damping, and stiffness matrices of the structure, and \mathbf{e} is the index vector of inertia forces. For short-span structures, all supports can be assumed to move uniformly with the same ground acceleration $\ddot{x}_g(t)$. If the structure under consideration has a very large number of DoF, Equation 30.24 can be solved by using the mode-superposition scheme (see Chapter 3). First, the lowest q natural angular frequencies ω_j ($j = 1, 2, \dots, q, q \ll n$) and the corresponding $n \times q$ mass normalized mode matrix Φ should be extracted. Then, $\mathbf{y}(t)$ can be decomposed in terms of these modes:

$$\mathbf{y}(t) = \Phi \mathbf{u}(t) = \sum_{j=1}^q u_j \boldsymbol{\varphi}_j \quad (30.25)$$

With proportional damping assumed (see Chapter 3 and Chapter 19), Equation 30.24 can be decoupled into q single-DoF equations

$$\ddot{u}_j + 2s_j\omega_j\dot{u}_j + \omega_j^2 u_j = -\gamma_j\ddot{x}_g(t) \quad (30.26)$$

in which s_j is the j th damping ratio and γ_j is the j th modal participation factor

$$\gamma_j = \boldsymbol{\varphi}_j^T \mathbf{M} \mathbf{e} \quad (30.27)$$

According to the response spectrum theory, the solution of Equation 30.26 is

$$u_j = \gamma_j \alpha_j g / \omega_j^2 \quad (30.28)$$

in which g is the gravity acceleration and α_j is the value of the ground acceleration response spectrum (ARS) at frequency ω_j . If the k th element of \mathbf{y} , denoted as y_k , is required, then the k th elements of all \mathbf{y}_j ($j = 1, 2, \dots, q$) are taken to compose a vector \mathbf{y}_k , which is then used in the computation of the response (or demand) y_k :

$$y_k = \sqrt{\mathbf{y}_k^T \mathbf{R}_c \mathbf{y}_k} \quad (30.29)$$

Here, \mathbf{R}_c is the correlation matrix representing the degree of correlation between all participating modes. Based on random-vibration theory, Wilson and Kiureghian (1981) have derived the expression for its elements as

$$R_{ij} = \frac{8\sqrt{\xi_i \xi_j}(\xi_i + r\xi_j)r^{3/2}}{(1 - r^2)^2 + 4\xi_i \xi_j r(1 + r^2) + 4(\xi_i^2 + \xi_j^2)r^2} \quad (30.30)$$

in which $r = \omega_j/\omega_i$. This is the widely used Complete Quadratic Combination (CQC) algorithm in the RSM. If the correlation coefficients between all modes are neglected, that is, if $R_{ij} = \delta_{ij}$ (Dirac delta function), then \mathbf{R}_c becomes a unity (identity) matrix and Equation 30.29 reduces to the square root of the sum of squares (SRSS) algorithm.

The RSM, as outlined above, is very popular in the seismic analysis of short-span structures. Some extensions have been published (Lee and Penzien, 1983; Dumanoglu and Severn, 1990; Lin et al., 1990;

Berrah and Kausel, 1992; Kiureghian and Neuenhofer, 1992; Ernesto and Vanmarcke, 1994) in order to deal with the seismic analysis of long-span structures. However, the efficiency and accuracy still need further improvement before they can be widely accepted in engineering practice.

30.1.2.2 Time-History Method

Assume that all supports move uniformly with the same acceleration $\ddot{x}_g(t)$, which is now given in a discrete numerical form. Equation 30.24 can now be solved using the Newmark method, the Wilson- θ method (Clough and Penzien, 1993), or the precise integration method (Zhong and Williams, 1995). In these THMs, the structural parameters can be modified at any time. Therefore, this method is good for nonlinear problems for which structural parameters often vary with time, for example in seismic elastoplastic analysis. A major disadvantage of THMs is that the computational results rely heavily on the selected ground acceleration records. In general, a number of records must be selected for structural analyses, and statistical results are then used in the designs. In order to reduce the computational effort, usually only about three to ten records are used for statistical purposes.

When the wave passage effect needs to be taken into account, the same ground acceleration record is applied to different supports with time lags and this generates \ddot{x}_b on the right-hand side of Equation 30.78. If the incoherence effect between the supports must also be considered, then the process for generating \ddot{x}_b becomes rather complicated (Deodatis, 1990). In fact, real records of this type are difficult to find.

30.1.2.3 Random Vibration Method

The random vibration approach is appealing for seismic random analysis of long-span structures. Previously, because of its high complexity and low efficiency, it was not accepted as a method of analysis by practicing engineers. However, this situation has changed considerably in recent years. Let us still begin with Equation 30.24, which we can also apply to structures subjected to uniform stationary random ground excitations. Now $\ddot{x}_g(t)$ is a zero-mean Gaussian stationary random process with a known auto-PSD $S_a(\omega)$ representing acceleration excitations uniformly applied to all supports of the structure. By means of the modal superposition scheme, that is, Equation 30.25 to Equation 30.27, the traditional CQC method can be established (Clough and Penzien, 1993):

$$S_{yy}(\omega) = \sum_{j=1}^q \sum_{k=1}^q \gamma_j \gamma_k \boldsymbol{\varphi}_j \boldsymbol{\varphi}_k^T H_j^*(\omega) H_k(\omega) S_a(\omega) \quad (30.31)$$

in which $\boldsymbol{\varphi}_j$ and γ_j are the j th mode and the j th modal participation factor, and

$$H_j = (\omega_j^2 - \omega^2 + 2i\zeta_j\omega\omega_j)^{-1} \quad (30.32)$$

is the j th frequency-response function. For a real long-span bridge, the number of structural DoF n usually ranges from 10^3 to 10^4 , and the numbers of ω and q typically range from 10^2 to 10^3 . Equation 30.31 includes all quadratic terms of the participating modes, and it must be repeatedly computed for dozens or hundreds of frequencies. Although it is a simple form of excitation, the computational effort is still considerable. Therefore, in engineering practice, the following SRSS method obtained by neglecting all $j \neq k$ terms in Equation 30.31, is generally used in place of the above CQC method:

$$S_{yy}(\omega) = \sum_{j=1}^q \gamma_j^2 \boldsymbol{\varphi}_j \boldsymbol{\varphi}_j^T |H_j(\omega)|^2 S_a(\omega) \quad (30.33)$$

This is frequently recommended in academic literature. The SRSS formula is an approximation of Equation 30.31 that neglects the cross-correlation terms between participating modes, thereby reducing the computational effort to about $1/q$ of that required by Equation 30.31. However, this approximation can be used only for lightly damped structures for which the participating frequencies must be sparsely spaced. For most structures (in particular their three-dimensional structural models), some participating frequencies are often closely spaced. Hence, the applicability of the SRSS approximation is

somewhat questionable. It will be seen in the next section that PEM will produce results identical to those from Equation 30.31 with much less computational effort.

The random-vibration analysis outlined above is executed in terms of power spectral densities in the frequency domain and therefore it is also referred to as the power-spectrum method.

A diagonal element $S_{\xi\xi}$ in the PSD matrix represents the auto-PSD of a random response ξ . Assume that this response is significant only within the frequency domain $\omega \in [\omega_L, \omega_U]$. Thus, the i th spectral moment of ξ can be computed by

$$\lambda_i = 2 \int_0^\infty \omega^i S_{\xi\xi}(\omega) d\omega \approx 2 \int_{\omega_L}^{\omega_U} \omega^i S_{\xi\xi}(\omega) d\omega \quad (30.34)$$

The PSD values at the negative frequencies do not have any intuitive physical significance and so the single-sided PSD $G_{xx}(\omega)$ is defined for applications in many engineering fields:

$$G_{xx}(\omega) = \begin{cases} 2S_{xx}(\omega) & \omega \geq 0 \\ 0 & \omega < 0 \end{cases} \quad (30.35)$$

Thus, Equation 30.34 becomes

$$\lambda_i = \int_0^\infty \omega^i G_{\xi\xi}(\omega) d\omega \approx \int_{\omega_L}^{\omega_U} \omega^i G_{\xi\xi}(\omega) d\omega \quad (30.36)$$

For general multiple input ($\mathbf{x}(t) = \{x_1(t), x_2(t), \dots, x_n(t)\}^T$) and multiple output ($\mathbf{y}(t) = \{y_1(t), y_2(t), \dots, y_m(t)\}^T$) problems (or MIMO problems), the response (i.e., output) PSD matrix $\mathbf{S}_{yy}(\omega)$ can be computed using the excitation (i.e., input) PSD matrix $\mathbf{S}_{xx}(\omega)$:

$$\mathbf{S}_{yy}(\omega) = \mathbf{H}^* \mathbf{S}_{xx}(\omega) \mathbf{H}^T \quad (30.37)$$

in which \mathbf{H} is the frequency-response function matrix. Also, the cross-PSD matrices between the excitations and responses can be computed from

$$\mathbf{S}_{xy}(\omega) = \mathbf{S}_{xx}(\omega) \mathbf{H}^T \quad (30.38)$$

$$\mathbf{S}_{yx}(\omega) = \mathbf{H}^* \mathbf{S}_{xx}(\omega) \quad (30.39)$$

Equation 30.37 to Equation 30.39 have simple forms and are comparatively convenient for engineering applications. However, they must be executed for dozens or hundreds of discrete frequencies. For complex structures, such matrix operations may require extensive effort. PEM, which will be introduced in the next section, is a better alternative than these equations.

If the first N modes are used in the modal superposition analysis, numerical tests for seven bridges show that taking $[\omega_L, \omega_U] = [0.7\omega_1, 1.2\omega_N]$ seems to be a good choice for the integration interval, where ω_1 and ω_N are the first and the N th natural angular frequencies of the structure.

It is inconvenient for engineers to take such spectral moments for practical designs. However, some approaches have been suggested to estimate structural responses (or demands) in terms of these spectral moments. Two popular approaches are described next.

30.1.2.3.1 Davenport Approach

With the seismic excitations assumed to be zero-mean stationary Gaussian processes, an arbitrary linear response of the structure subjected to such excitations, denoted $y(t)$, will also possess the same probability characteristic. It is also assumed that if a given barrier (threshold) a is sufficiently high, the peaks of $y(t)$ above this barrier will appear independently. Let $N(t)$ be the number of upcrossing of a within the time interval $(0, t]$, then $N(t)$ will be a Poisson process with a stationary increment (Davenport, 1961). Denote the extreme value of $y(t)$, that is, the maximum value of all peaks by their absolute values, within the earthquake duration $[0, T_s]$ as y_e , and the standard deviation of $y(t)$ as σ_y . Define η as the dimensionless parameter of y_e , and ν as the mean zero-crossing rate, which can be

expressed as

$$\eta = y_e/\sigma_y, \quad \nu = \sqrt{\lambda_2/\lambda_0}/\pi \quad (30.40)$$

Based on these assumptions, the probability distribution of η can be derived as

$$P(\eta) = \exp[-\nu T_s \exp(-\eta^2/2)], \quad \eta > 0 \quad (30.41)$$

The expected value of η , known as the peak factor, is approximately given by

$$E(\eta) \approx (2 \ln \nu T_s)^{1/2} + \gamma/(2 \ln \nu T_s)^{1/2} \quad (30.42)$$

and its standard deviation is

$$\sigma_\eta \approx \pi/(12 \ln \nu T_s)^{1/2} \quad (30.43)$$

in which $\gamma = 0.5772$ is the Euler constant, while the expected value of y_e is approximately

$$E[y_e] = E[\eta]\sigma_y \quad (30.44)$$

This quantity is the demand usually required by engineers.

30.1.2.3.2 Vanmarcke Approach

In the preceding paragraph, the barrier a was assumed to be sufficiently high. Therefore, the peaks of $y(t)$ above this barrier will appear independently, and $N(t)$ can be regarded as a Poisson process. Vanmarcke (1972) considered that the barrier a should not be very high. Therefore, the Poisson process assumption should be replaced by the two-state Markov process assumption and the probability distribution of η becomes

$$P(\eta) = \left[1 - \exp\left(-\frac{\eta^2}{2}\right) \right] \exp\left[-\nu T_s \frac{1 - \exp(-\sqrt{\pi/2} q^{1.2} \eta)}{\exp(\eta^2/2) - 1} \right] \quad (30.45)$$

in which ν and T_s have the same meanings as the above, while the shape factor for the response PSD is

$$\delta_0 = (1 - \lambda_1^2/(\lambda_0 \lambda_2))^{1/2} \quad (30.46)$$

Here, δ_0 is a bandwidth parameter with values ranging from zero to one. For a narrowband process, δ_0 is close to zero. Based on the probability distribution function shown in Equation 30.45, Kiureghian (1980) proposes the following approximate expressions for the peak factor $E(\eta)$ and standard deviation σ_η when $10 \leq \nu\tau \leq 1000$ and $0.11 \leq q \leq 1$, which are of interest in earthquake engineering:

$$E(\eta) = (2 \ln \nu_e T_s)^{1/2} + \frac{\gamma}{(2 \ln \nu_e T_s)^{1/2}} \quad (30.47)$$

$$\sigma_\eta = \begin{cases} \frac{1.2}{(2 \ln \nu_e T_s)^{1/2}} - \frac{5.4}{13 + (2 \ln \nu_e T_s)^{3.2}} & \nu_e T_s > 2.1 \\ 0.65 & \nu_e T_s \leq 2.1 \end{cases} \quad (30.48)$$

in which

$$\nu_e = \begin{cases} (1.63q^{0.45} - 0.38)\nu_0 & \delta_0 < 0.69 \\ \nu_0 & \delta_0 \geq 0.69 \end{cases} \quad (30.49)$$

Gupta and Trifunac (1998) made numerical experiments to compare the above two models using 1000 simulated time-history excitations. Their research shows that for most practical purposes in earthquake engineering studies, the effect of the dependence among level crossings is not significant.

30.1.2.4 Comparisons of the Three Seismic-Analysis Methods

The RSM is the most popular method for the seismic analysis of short-span structures. Some extensions have been made to allow this method to be used in the seismic analysis of long-span structures.

However, the accuracy and efficiency still need further improvement for practical applications. The THM can be used in the seismic analysis of long-span structures without theoretical difficulties. However, its major disadvantages are that it requires a good selection of the ground acceleration record samples and its computational cost is very high. The random-vibration method is appealing because of its statistical nature. In the past, the random vibration computation of complex structures has been very costly. This issue has received much attention in the last two decades. As will be described below, PEM has remarkably improved this situation. Now, long-span structures with thousands of DoF and dozens of supports can be computed far more quickly and accurately on a personal computer.

30.2 Seismic Random-Excitation Fields

30.2.1 Power Spectral Density of Spatially Varying Ground Acceleration

For multiple excitation problems, the PSD matrices of ground acceleration excitations have the form

$$\mathbf{S}_{xx}(i\omega) = \begin{bmatrix} S_{\ddot{x}_1\ddot{x}_1}(i\omega) & S_{\ddot{x}_1\ddot{x}_2}(i\omega) & \cdots & S_{\ddot{x}_1\ddot{x}_N}(i\omega) \\ S_{\ddot{x}_2\ddot{x}_1}(i\omega) & S_{\ddot{x}_2\ddot{x}_2}(i\omega) & \cdots & S_{\ddot{x}_2\ddot{x}_N}(i\omega) \\ \cdots & \cdots & \cdots & \cdots \\ S_{\ddot{x}_N\ddot{x}_1}(i\omega) & S_{\ddot{x}_N\ddot{x}_2}(i\omega) & \cdots & S_{\ddot{x}_N\ddot{x}_N}(i\omega) \end{bmatrix} \quad (30.50)$$

in which

$$S_{\ddot{x}_k\ddot{x}_l}(i\omega) = \rho_{kl}(i\omega) \sqrt{S_{\ddot{x}_k}(\omega) S_{\ddot{x}_l}(\omega)} \quad (30.51)$$

$$\rho_{kl}(i\omega) = |\rho_{kl}(i\omega)| \exp[i\theta_{kl}(\omega)] \quad (30.52)$$

and $\rho_{kl}(i\omega)$ is the acceleration coherence function between the k th and l th supports. Its norm must satisfy the relation $|\rho_{kl}(i\omega)| \leq 1$. The values of $S_{\ddot{x}_k}(\omega)$ and $S_{\ddot{x}_l}(\omega)$ in Equation 30.51 can be different due to local effects. However, earthquake records show that the structural responses due to the difference between $S_{\ddot{x}_k}(\omega)$ and $S_{\ddot{x}_l}(\omega)$ are in general of relatively low significance. The factor $\exp[i\theta_{kl}(\omega)]$ expresses the wave passage effect, which can be further expressed as

$$\exp[i\theta_{kl}(\omega)] = \exp[-i\omega d_{kl}^L/v_{\text{app}}] \quad (30.53)$$

in which d_{kl} is the horizontal distance between the two supports; d_{kl}^L is the projection of d_{kl} along the propagation direction of the seismic waves; and v_{app} is the apparent velocity of seismic waves along the surface. Assume that the time lags between the supports and the origin of the reference coordinate system are t_1, t_2, \dots, t_N , respectively. Without losing generality, let $t_l \geq t_k$ (when $l > k$). Then $d_{kl}^L/v_{\text{app}} = t_l - t_k$, and so Equation 30.53 becomes

$$\exp[i\theta_{kl}(\omega)] = \exp[i\omega(t_k - t_l)] \quad (30.54)$$

The factor $|\rho_{kl}(i\omega)|$ reflects the incoherence effect (Kiureghian and Neuenhofer, 1992). Some mathematical models of $\rho_{kl}(i\omega)$ have been established based on practical earthquake records, which will be shown in the next section. Using Equation 30.51 to Equation 30.54, Equation 30.50 can be written as

$$\mathbf{S}(i\omega) = \mathbf{B}^* \mathbf{J} \mathbf{R} \mathbf{J} \mathbf{B} \quad (30.55)$$

in which

$$\mathbf{B} = \text{diag}[\exp(-i\omega t_1), \exp(-i\omega t_2), \dots, \exp(-i\omega t_N)] \quad (30.56)$$

$$\mathbf{J} = \text{diag}[\sqrt{S_{\ddot{x}_1}}, \sqrt{S_{\ddot{x}_2}}, \dots, \sqrt{S_{\ddot{x}_N}}] \quad (30.57)$$

$$\mathbf{R} = \begin{bmatrix} 1 & |\rho_{12}| & \cdots & |\rho_{1N}| \\ |\rho_{21}| & 1 & \cdots & |\rho_{2N}| \\ \cdots & \cdots & \cdots & \cdots \\ |\rho_{N1}| & |\rho_{N2}| & \cdots & 1 \end{bmatrix} \quad (30.58)$$

30.2.2 Several Coherence Models

A number of coherence models have been established based on practical earthquake records. Some of them are outlined below.

30.2.2.1 Feng–Hu Model

$$|\rho_{kl}(\omega, d_{kl})| = \exp[-(\rho_1 \omega + \rho_2) d_{kl}] \quad (30.59)$$

in which ρ_1 and ρ_2 are the coherence parameters. According to the Hai-Cheng earthquake records (China) and the Niigata earthquake records (Japan), the values of these parameters are (Feng and Hu, 1981):

Hai-Cheng: $\rho_1 = 2 \times 10^{-5} \text{ sec/m}$, $\rho_2 = 88 \times 10^{-4} \text{ m}^{-1}$

Niigata: $\rho_1 = 4 \times 10^{-4} \text{ sec/m}$, $\rho_2 = 19 \times 10^{-4} \text{ m}^{-1}$

30.2.2.2 Harichandran–Vanmarcke Model

$$|\rho_{kl}(\omega, d_{kl})| = A \exp\left[-\frac{2d}{\alpha\theta(\omega)}(1 - A + \alpha A)\right] + (1 - A) \exp\left[-\frac{2d}{\alpha\theta(\omega)}(1 - A + \alpha A)\right] \quad (30.60)$$

in which

$$\theta(\omega) = K[1 + (\omega/\omega_0)^b]^{-1/2} \quad (30.61)$$

According to the acceleration records of the SMART-1 array (Harichandran and Vanmarcke, 1986), the parameters in Equations 30.60 and Equations 30.61 are: $A = 0.736$, $\alpha = 0.147$, $K = 5210$, $\omega_0 = 6.85 \text{ rad/sec}$, $b = 2.78$.

30.2.2.3 Loh–Yeh Model

$$|\rho_{kl}(\omega, d_{kl})| = \exp\left[-\alpha \frac{\omega d_{kl}}{2\pi v_{\text{app}}}\right] \quad (30.62)$$

in which α is the wave-number of the seismic waves. According to the 40 acceleration records of the SMART-1 array (Loh and Yeh, 1988), $\alpha = 0.125$ is proposed. Parameters v_{app} and d_{kl} have been explained above.

30.2.2.4 Oliveira–Hao–Penzien Model

$$|\rho_{kl}(\omega, d_{kl})| = \exp(-\beta_1 d_{kl}^L - \beta_2 d_{kl}^T) \exp(-[\alpha_1 \sqrt{d_{kl}^L} - \alpha_2 \sqrt{d_{kl}^T}](\omega/2\pi)^2) \quad (30.63)$$

in which $\alpha_i = (2\pi a_i/\omega) + (\omega b_i/2\pi) + c_i$. d_{kl}^L and d_{kl}^T are the projections of d_{kl} along the propagation direction of the seismic waves and along its normal direction, respectively. Based on 17 acceleration records of the SMART-1 array (Oliveira et al., 1991), parameters $\beta_1, \beta_2, a_1, a_2, b_1, b_2, c_1$, and c_2 are given for each of these records.

30.2.2.5 Luco–Wong Model

$$|\rho_{kl}| = \exp \left[- \left(\frac{\alpha \omega d_{kl}}{v_s} \right)^2 \right] \quad (30.64)$$

in which α is the coherence factor, d_{kl} is the horizontal distance between the k th and l th supports and v_s is the shear wave velocity (Luco and Wong, 1986).

30.2.2.6 Qu–Wang–Wang Model

T. Qu, J. Wang, and Q. Wang (QWW) (Qu et al., 1996) proposed the following model

$$|\rho_{kl}| = \exp \left[-a(\omega) d_{kl}^{b(\omega)} \right] \quad (30.65)$$

in which

$$a(\omega) = a_1 \omega^2 + a_2, \quad b(\omega) = b_1 \omega + b_2 \quad (30.66)$$

$a_1 = 0.00001678$, $a_2 = 0.001219$, $b_1 = -0.0055$, $b_2 = 0.7674$. This model was established based on the statistics of dozens of records from four closely located arrays with SMART-1 as the leading one. This model has given reasonable results in some applications in China.

30.2.3 Generation of Ground Acceleration Power Spectral Density Curves from Acceleration Response Spectrum Curves

In order to carry out the seismic random vibration analysis of important long-span bridges, the local seismic motion PSD (usually the acceleration PSD) must be established by specialists. For bridges of less importance, however, such seismic acceleration PSD can be derived from the local ARS curve. Two methods to perform the transformation are given below.

30.2.3.1 Kaul Method

Kaul (1978) proposed an approximate transformation method that consists of the two equations

$$S(\omega_0) = \frac{4\xi R_a^2(\xi, \omega_0)}{\pi \omega_0 r^2} \quad (30.67)$$

$$r^2 = 2 \ln \left[\left(-\frac{\pi}{\omega_0 T_s} \ln p \right)^{-1} \right] \quad (30.68)$$

in which $R_a(\xi, \omega_0)$ is the ARS curve of the seismic absolute acceleration when the damping ratio is ξ and the natural angular frequency is ω_0 (usually ξ takes 0.05); $S(\omega_0)$ is the equivalent PSD curve corresponding to the given ARS curve; T_s is the seismic duration; and p is the probability of the peaks that do not cross with the given positive or negative barriers — usually $p = 0.85$ is assumed.

30.2.3.2 Iteration Scheme

An iteration-based scheme for the transformation has been proposed (Sun and Jiang, 1990), which produces more accurate equivalent PSD curve than the Kaul method. For a given ARS curve $R_a(\xi, \omega_0)$, in order to transform it into an equivalent PSD curve $S(\omega)$, specify its initial values $S^0(\omega_i) = S_i$, for $i = 1, 2, \dots, N$. Then the standard deviation of the acceleration response for a SDOF system can be computed from

$$\sigma_0(\xi, \omega_0) = \left[\int_0^\infty S(\omega) \frac{1 + 4\xi^2(\omega/\omega_0)^2}{(1 - (\omega/\omega_0)^2)^2 + 4\xi^2(\omega/\omega_0)^2} d\omega \right]^{1/2} \quad (30.69)$$

The peak factor r is

$$r = \sqrt{2 \ln(vT_s)} + 0.5772 / \sqrt{2 \ln(vT_s)} \quad (30.70)$$

in which T_s is the period of the strong earthquake portion. The average zero-crossing rate is approximately $\nu = \sqrt{\lambda_2/\lambda_0}/\pi \approx \omega_0/\pi$.

The acceleration responses computed by means of Equation 30.69 and Equation 30.70 are

$$A_m(\xi, \omega_0) = r\sigma_0(\xi, \omega_0) \quad (30.71)$$

The percentage errors between $R_a(\xi, \omega_0)$ and $A_m(\xi, \omega_0)$ can be computed from

$$E(\omega_0) = \frac{|R_a(\xi, \omega_0) - A_m(\xi, \omega_0)|}{R_a(\xi, \omega_0)} \times 100\% \quad (30.72)$$

Compute $E(\omega_0)$ for each frequency. If $E(\omega_0)$ is found to be greater than the given tolerance ε for at least one frequency, modify all PSD values according to the following equation

$$S^{k+1}(\omega_i) = S^k(\omega_i)R_a^2(\xi, \omega_i)/A_m^2(\xi, \omega_i), \quad i = 1, 2, \dots, N \quad (30.73)$$

and then repeat the computations of Equation 30.69 to Equation 30.72. The above process is continued until Equation 30.72 is satisfied at all frequencies.

30.2.4 Seismic Equations of Motion of Long-Span Structures

For long-span structures subjected to differential ground motion, the equations of motion in the global coordinate system (assumed to be fixed to the center of the Earth) can be written in partitioned form as

$$\begin{bmatrix} \mathbf{M}_s & \mathbf{M}_{sb} \\ \mathbf{M}_{sb}^T & \mathbf{M}_b \end{bmatrix} \begin{Bmatrix} \ddot{\mathbf{x}}_s \\ \ddot{\mathbf{x}}_b \end{Bmatrix} + \begin{bmatrix} \mathbf{C}_s & \mathbf{C}_{sb} \\ \mathbf{C}_{sb}^T & \mathbf{C}_b \end{bmatrix} \begin{Bmatrix} \dot{\mathbf{x}}_s \\ \dot{\mathbf{x}}_b \end{Bmatrix} + \begin{bmatrix} \mathbf{K}_s & \mathbf{K}_{sb} \\ \mathbf{K}_{sb}^T & \mathbf{K}_b \end{bmatrix} \begin{Bmatrix} \mathbf{x}_s \\ \mathbf{x}_b \end{Bmatrix} = \begin{Bmatrix} \mathbf{0} \\ \mathbf{p}_b \end{Bmatrix} \quad (30.74)$$

in which the subscript m represents the master DoF, that is, the support displacements, while the subscript s represents the slave DoF. The absolute displacement vector \mathbf{x}_s can be decomposed into the two parts

$$\mathbf{x}_s = \mathbf{y}_s + \mathbf{y}_r \quad (30.75)$$

where \mathbf{y}_s is the quasi-static displacement vector (Clough and Penzien, 1993), which satisfies

$$\mathbf{y}_s = -\mathbf{K}_s^{-1}\mathbf{K}_{sb}\mathbf{x}_b \quad (30.76)$$

Substituting Equation 30.75 and Equation 30.76 into Equation 30.74 gives

$$\mathbf{M}_s\ddot{\mathbf{y}}_r + \mathbf{C}_s\dot{\mathbf{y}}_r + \mathbf{K}_s\mathbf{y}_r = \mathbf{M}_s\mathbf{K}_s^{-1}\mathbf{K}_{sb}\ddot{\mathbf{x}}_b + (\mathbf{C}_s\mathbf{K}_s^{-1}\mathbf{K}_{sb} - \mathbf{C}_{sb})\dot{\mathbf{x}}_b \quad (30.77)$$

It should be pointed out that Equation 30.77 cannot be reduced to the conventional Equation 30.24 when \mathbf{x}_b represents uniform ground displacements (Clough and Penzien, 1993). This is because Equation 30.74 assumes the damping forces to be proportional to the absolute velocity vector $\{\dot{\mathbf{x}}_s^T, \dot{\mathbf{x}}_b^T\}^T$. In order to avoid this inconsistency, the damping forces should be assumed to be proportional to the relative velocity vector $\{\dot{\mathbf{y}}_r^T, 0\}^T$ in Equation 30.74. This leads to the equations

$$\mathbf{M}_s\ddot{\mathbf{y}}_r + \mathbf{C}_s\dot{\mathbf{y}}_r + \mathbf{K}_s\mathbf{y}_r = \mathbf{M}_s\mathbf{K}_s^{-1}\mathbf{K}_{sb}\ddot{\mathbf{x}}_b \quad (30.78)$$

for uniform ground motion

$$\ddot{\mathbf{x}}_b = \mathbf{e}_b\ddot{\mathbf{x}}_g \quad (30.79)$$

Note that the following rigid displacement condition is satisfied:

$$\begin{bmatrix} \mathbf{K}_s & \mathbf{K}_{sb} \\ \mathbf{K}_{sb}^T & \mathbf{K}_b \end{bmatrix} \begin{Bmatrix} \mathbf{e}_s \\ \mathbf{e}_b \end{Bmatrix} = \begin{Bmatrix} \mathbf{0} \\ \mathbf{0} \end{Bmatrix} \quad (30.80)$$

Its second half gives

$$\mathbf{K}_{sb}\mathbf{e}_b = -\mathbf{K}_s\mathbf{e}_s \quad (30.81)$$

Substituting Equation 30.79 into Equation 30.78 and using Equation 30.81 gives Equation 30.24.

30.2.5 Seismic Waves and Their Geometrical Expressions

Seismic waves can be divided into body waves and surface waves. Body waves include longitudinal waves (or pressure waves, primary waves or P waves) and transverse waves (or shear waves, secondary waves or S waves). Surface waves include Rayleigh waves and Love waves. For P waves, the soil particles move parallel to the traveling direction of waves; for S waves, however, their motion is normal to the wave traveling direction (see Figure 30.4). For horizontal shear waves (SH waves), all particles move horizontally. For vertical shear waves (SV waves), all particles move vertically.

Assume that both x and y axes lie in the horizontal plane. The angle between axis x and the horizontal traveling direction of these waves is β , as shown in Figure 30.5. Thus, the acceleration components along the coordinate axes can be expressed by the components parallel, or normal, to the wave traveling direction, that is, for P waves

$$\begin{aligned} \ddot{x}_i &= \ddot{u}_i \cos \beta, & \ddot{y}_i &= \ddot{u}_i \sin \beta, \\ \ddot{z}_i &= 0 \end{aligned} \quad (30.82)$$

for SH waves

$$\begin{aligned} \ddot{x}_i &= -\ddot{u}_j \sin \beta, & \ddot{y}_i &= \ddot{u}_j \cos \beta, \\ \ddot{z}_i &= 0 \end{aligned} \quad (30.83)$$

and for SV waves

$$\ddot{x}_i = 0, \quad \ddot{y}_i = 0, \quad \ddot{z}_i = \ddot{u}_k \quad (30.84)$$

In the equations of motion of an multi-DoF system under uniform ground excitations, that is, Equation 30.24, \mathbf{e} is the index vector of inertia forces. Its mathematical expressions for the different waves are:

for P waves

$$\mathbf{e} = \mathbf{e}_x \cos \beta + \mathbf{e}_y \sin \beta \quad (30.85)$$

for SH waves

$$\mathbf{e} = -\mathbf{e}_x \sin \beta + \mathbf{e}_y \cos \beta \quad (30.86)$$

for SV waves

$$\mathbf{e} = \mathbf{e}_z \quad (30.87)$$

Clearly, for P waves, $\mathbf{e} = \mathbf{e}_x$ when $\beta = 0$ and $\mathbf{e} = \mathbf{e}_y$ when $\beta = 90^\circ$.

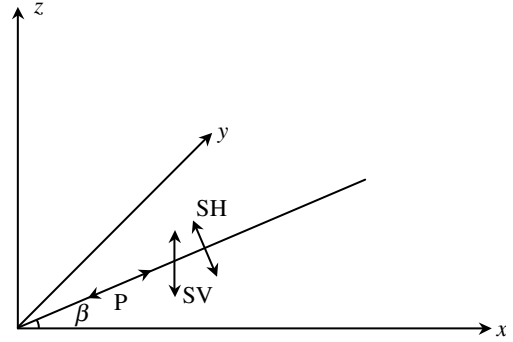


FIGURE 30.4 Particle motion directions for P and S waves.

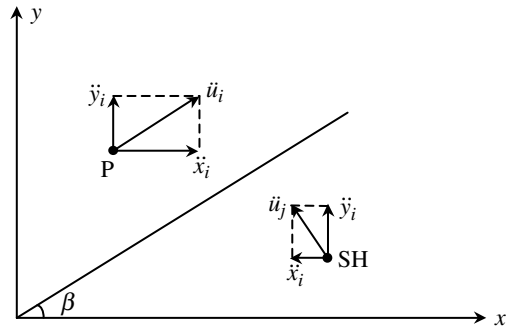


FIGURE 30.5 Transform of ground acceleration components.

If a structure has N supports, its ground acceleration excitations along the wave traveling direction can be expressed by the N -dimensional vector

$$\ddot{\mathbf{u}}_b = \{\ddot{u}_1, \ddot{u}_2, \dots, \ddot{u}_N\}^T \quad (30.88)$$

The m -dimensional ground acceleration vector in Equation 30.78 is

$$\ddot{\mathbf{x}}_b = \{\ddot{x}_1, \ddot{x}_2, \dots, \ddot{x}_m\}^T \quad (30.89)$$

The relation between these two vectors is

$$\ddot{\mathbf{x}}_b = \mathbf{E}_{mN} \ddot{\mathbf{u}}_b \quad (30.90)$$

in which \mathbf{E}_{mN} is a $m \times N$ block-diagonal matrix

$$\mathbf{E}_{mN} = \text{diag}[\mathbf{e}_\beta, \mathbf{e}_\beta, \dots, \mathbf{e}_\beta]_{m \times N} \quad (30.91)$$

If only three translations are considered for each support, then $m = 3N$ and each submatrix \mathbf{e}_β would be

$$\begin{Bmatrix} \cos \beta \\ \sin \beta \\ 0 \end{Bmatrix}, \begin{Bmatrix} -\sin \beta \\ \cos \beta \\ 0 \end{Bmatrix} \text{ and } \begin{Bmatrix} 0 \\ 0 \\ 1 \end{Bmatrix}$$

for the P, SH and SV waves, respectively.

Using Equation 30.90, Equation 30.76 and Equation 30.78 can be rewritten as

$$\mathbf{y}_s = -\mathbf{K}_s^{-1} \mathbf{K}_{sb} \mathbf{E}_{mN} \mathbf{u}_b \quad (30.92)$$

$$\mathbf{M}_s \ddot{\mathbf{y}}_r + \mathbf{C}_s \dot{\mathbf{y}}_r + \mathbf{K}_s \mathbf{y}_r = \mathbf{M}_s \mathbf{K}_s^{-1} \mathbf{K}_{sb} \mathbf{E}_{mN} \ddot{\mathbf{u}}_b \quad (30.93)$$

30.3 Pseudoexcitation Method for Structural Random Vibration Analysis

30.3.1 Structures Subjected to Stationary Random Excitations

30.3.1.1 Single Stationary Random Excitations

The basic principle of the PEM for structural stationary random vibration analysis can be explained by Figure 30.6. Consider a linear system subjected to a zero-mean stationary random excitation $x(t)$

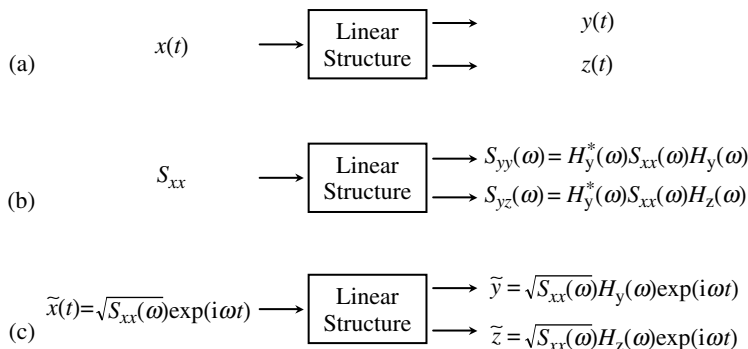


FIGURE 30.6 Basic principle of pseudoexcitation method (stationary analysis).

(see Figure 30.6a) and with a given PSD $S_{xx}(\omega)$. Suppose that for two arbitrarily selected responses $y(t)$ and $z(t)$, the auto-PSD $S_{yy}(\omega)$ and cross-PSD $S_{yz}(\omega)$ are desired. Figure 30.6b gives the conventional formulas for computing these PSD functions. $H_y(\omega)$ and $H_z(\omega)$ are the frequency-response functions, that is, if $x(t)$ is replaced by a sinusoidal excitation $\exp(i\omega t)$, the harmonic responses of $y(t)$ and $z(t)$ would be $H_y(\omega)\exp(i\omega t)$ and $H_z(\omega)\exp(i\omega t)$, respectively. Thus, if $x(t)$ is replaced by a sinusoidal excitation (Lin et al., 1994b)

$$\tilde{x} = \sqrt{S_{xx}(\omega)}\exp(i\omega t) \quad (30.94)$$

the responses of $y(t)$ and $z(t)$ would be $\tilde{y} = \sqrt{S_{xx}(\omega)}H_y(\omega)\exp(i\omega t)$ and $\tilde{z} = \sqrt{S_{xx}(\omega)}H_z(\omega)\exp(i\omega t)$ (see Figure 30.6c). It can be readily verified that

$$\tilde{y}^*\tilde{y} = \sqrt{S_{xx}(\omega)}H_y^*(\omega)\exp(-i\omega t)\sqrt{S_{xx}(\omega)}H_y(\omega)\exp(i\omega t) = |H_y(\omega)|^2 S_{xx}(\omega) = S_{yy}(\omega) \quad (30.95)$$

$$\tilde{y}^*\tilde{z} = \sqrt{S_{xx}(\omega)}H_y^*(\omega)\exp(-i\omega t)\sqrt{S_{xx}(\omega)}H_z(\omega)\exp(i\omega t) = H_y^*(\omega)S_{xx}(\omega)H_z(\omega) = S_{yz}(\omega) \quad (30.96)$$

If $\mathbf{y}(t)$ and $\mathbf{z}(t)$ are two arbitrarily selected random response vectors of the structure, and $\tilde{\mathbf{y}} = \mathbf{a}_y\exp(i\omega t)$ and $\tilde{\mathbf{z}} = \mathbf{a}_z\exp(i\omega t)$ are the corresponding harmonic response vectors due to the pseudo-excitation (30.94), it can also be proven that the PSD matrices of $\mathbf{y}(t)$ and $\mathbf{z}(t)$ are

$$\mathbf{S}_{yy}(\omega) = \tilde{\mathbf{y}}^*\tilde{\mathbf{y}}^T = \mathbf{a}_y^*\mathbf{a}_y^T \quad (30.97)$$

$$\mathbf{S}_{yz}(\omega) = \tilde{\mathbf{y}}^*\tilde{\mathbf{z}}^T = \mathbf{a}_y^*\mathbf{a}_z^T \quad (30.98)$$

This means that the auto- and cross-PSD functions of two arbitrarily selected random responses can be computed using the corresponding pseudoharmonic responses.

Now, consider a structure subjected to a single seismic random excitation. Its equations of motion are

$$\mathbf{M}\ddot{\mathbf{y}} + \mathbf{C}\dot{\mathbf{y}} + \mathbf{K}\mathbf{y} = -\mathbf{M}\mathbf{e}\ddot{x}_g(t) \quad (30.99)$$

in which the ground acceleration $\ddot{x}_g(t)$ is a stationary random process. Its PSD $S_{\ddot{x}_g}(\omega)$ is known and \mathbf{e} is a given constant vector, indicating the distribution of inertia forces. In order to solve Equation 30.99, let the pseudoground acceleration be

$$\ddot{x}_g(t) = \sqrt{S_{\ddot{x}_g}(\omega)}\exp(i\omega t) \quad (30.100)$$

then Equation 30.99 becomes

$$\mathbf{M}\ddot{\tilde{\mathbf{y}}} + \mathbf{C}\dot{\tilde{\mathbf{y}}} + \mathbf{K}\tilde{\mathbf{y}} = -\mathbf{M}\mathbf{e}\sqrt{S_{\ddot{x}_g}(\omega)}\exp(i\omega t) \quad (30.101)$$

and its stationary solution is

$$\tilde{\mathbf{y}}(t) = \mathbf{a}_y(\omega)\exp(i\omega t) \quad (30.102)$$

Using its first q normalized modes for mode-superposition, then (Clough and Penzien, 1993)

$$\mathbf{a}_y(\omega) = \sum_{j=1}^q \gamma_j H_j \boldsymbol{\phi}_j \sqrt{S_{xx}(\omega)} \quad (30.103)$$

in which ω_j , $\boldsymbol{\phi}_j$, \mathbf{s}_j , H_j and γ_j are the j th natural angular frequency, mass normalized mode, damping ratio, frequency-response function, and mode participation factor, respectively. According to PEM, the PSD matrix of \mathbf{y} is

$$\mathbf{S}_{yy}(\omega) = \tilde{\mathbf{y}}^*\tilde{\mathbf{y}}^T = \mathbf{a}_y^*(\omega)\mathbf{a}_y^T(\omega) \quad (30.104)$$

Substituting Equation 30.102 into Equation 30.104 and expanding it also gives Equation 30.31. This means these two equations are mathematically identical. However, the computational effort required by Equation 30.104 is approximately only $1/q^2$ of that required by Equation 30.31. Therefore, Equation 30.104 is also known as the fast CQC algorithm (Lin, 1992).

Example 30.1 Derivation of the Kanai–Tajimi PSD Formula

Consider the system shown in Figure 30.7(a). The single-layered homogeneous soil and the super single-DoF structure can be modeled by the system of Figure 30.7(b). Assume that the horizontal acceleration of the bedrock \ddot{x}_0 is a stationary random process with white noise spectrum S_0 . The ground displacement relative to the bedrock is y , and the displacement of the superstructure (assumed to be an single-DoF system) relative to the ground is x . The effective horizontal shear-resistant stiffness of the soil layer is k_g , while the corresponding damping coefficient is c_g . Assuming that m is very small in comparison with the equivalent ground mass m_g , then the equation of motion of the effective ground mass is

$$m_g \ddot{y} + c_g \dot{y} + k_g y = -m_g \ddot{x}_0 \quad (\text{i})$$

or

$$\ddot{y} + 2\varsigma_g \omega_g \dot{y} + \omega_g^2 y = -\ddot{x}_0 \quad (\text{ii})$$

in which $\omega_g^2 = k_g/m_g$, $2\varsigma_g \omega_g = c_g/m_g$.

Now, form the horizontal pseudoacceleration for the bedrock

$$\ddot{x}_0 = \sqrt{S_0} \exp(i\omega t) \quad (\text{iii})$$

Substituting it into Equation ii gives

$$\ddot{y} + 2\varsigma_g \omega_g \dot{y} + \omega_g^2 y = -\sqrt{S_0} \exp(i\omega t) \quad (\text{iv})$$

Its right-hand side is harmonic. Therefore, the stationary solution of \tilde{y} is

$$\tilde{y} = \frac{-\sqrt{S_0}}{\omega_g^2 - \omega^2 + 2i\varsigma_g \omega_g \omega} \exp(i\omega t) \quad (\text{v})$$

The pseudoabsolute displacement of the ground is

$$\tilde{x}_g = \tilde{x}_0 + \tilde{y} \quad (\text{vi})$$

The corresponding pseudoabsolute acceleration is

$$\ddot{\tilde{x}}_g = \ddot{\tilde{x}}_0 + \ddot{\tilde{y}} = \sqrt{S_0} \exp(i\omega t) \left[1 + \frac{\omega^2}{\omega_g^2 - \omega^2 + 2i\varsigma_g \omega_g \omega} \right] = \sqrt{S_0} \exp(i\omega t) \frac{\omega_g^2 + 2i\varsigma_g \omega_g \omega}{\omega_g^2 - \omega^2 + 2i\varsigma_g \omega_g \omega} \quad (\text{vii})$$

Using PEM, the PSD of $\ddot{\tilde{x}}_g$ is

$$S_{\ddot{\tilde{x}}_g}(\omega) = \ddot{\tilde{x}}_g^* \ddot{\tilde{x}}_g = S_0 \frac{\omega_g^4 + 4\varsigma_g^2 \omega_g^2 \omega^2}{(\omega_g^2 - \omega^2)^2 + 4\varsigma_g^2 \omega_g^2 \omega^2} \quad (\text{viii})$$

This is exactly the Kanai–Tajimi filtered white noise spectrum formula (Clough and Penzien, 1993).

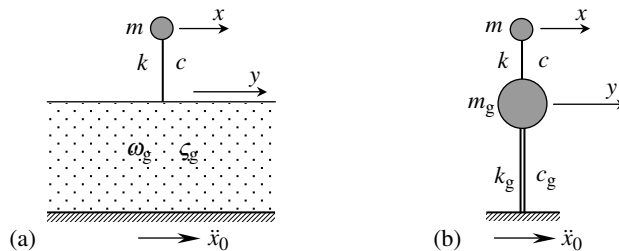


FIGURE 30.7 Structural modeling for Kanai–Tajimi PSD formula.

30.3.1.2 Multiple Stationary Random Excitations

Consider a linear structure subjected to a number of stationary random excitations, which are denoted as an m -dimensional stationary random process vector $\mathbf{x}(t)$ with known PSD matrix $\mathbf{S}_{xx}(\omega)$. It is a Hermitian matrix and so it can be decomposed, for example, by using its eigenpairs $\boldsymbol{\psi}_j$ and d_j ($j = 1, 2, \dots, r$), into

$$\mathbf{S}_{xx}(\omega) = \sum_{j=1}^r d_j \boldsymbol{\psi}_j^* \boldsymbol{\psi}_j^T \quad (r \leq m) \quad (30.105)$$

in which r is the rank of $\mathbf{S}_{xx}(\omega)$. Next, form the r pseudoharmonic excitations

$$\tilde{\mathbf{x}}_j(t) = \sqrt{d_j} \boldsymbol{\psi}_j \exp(i\omega t) \quad (j = 1, 2, \dots, r) \quad (30.106)$$

By applying each of these pseudoharmonic excitations, two arbitrarily selected response vectors $\mathbf{y}_j(t)$ and $\mathbf{z}_j(t)$ of the structure, which can be displacements, internal forces, or other linear responses, may be easily obtained and expressed as

$$\tilde{\mathbf{y}}_j(t) = \mathbf{a}_{yj}(\omega) \exp(i\omega t) \quad (30.107)$$

$$\tilde{\mathbf{z}}_j(t) = \mathbf{a}_{zj}(\omega) \exp(i\omega t) \quad (30.108)$$

The corresponding PSD matrices can be computed by means of the following formulas (Lin et al., 1994a; Zhong, 2004):

$$\mathbf{S}_{yy}(\omega) = \sum_{j=1}^r \tilde{\mathbf{y}}_j^*(t) \tilde{\mathbf{y}}_j^T(t) = \sum_{j=1}^r \mathbf{a}_{yj}^*(\omega) \mathbf{a}_{yj}^T(\omega) \quad (30.109)$$

$$\mathbf{S}_{yz}(\omega) = \sum_{j=1}^r \tilde{\mathbf{y}}_j^*(t) \tilde{\mathbf{z}}_j^T(t) = \sum_{j=1}^r \mathbf{a}_{yj}^*(\omega) \mathbf{a}_{zj}^T(\omega) \quad (30.110)$$

The method used to decompose $\mathbf{S}_{xx}(\omega)$ into the form of Equation 30.105 is not unique. In fact, the Cholesky scheme is perhaps the most efficient and convenient way to do it; that is, $\mathbf{S}_{xx}(\omega)$ is decomposed into

$$\mathbf{S}_{xx}(\omega) = \mathbf{L}^* \mathbf{D} \mathbf{L}^T = \sum_{j=1}^r d_j \mathbf{l}_j^* \mathbf{l}_j^T \quad (r \leq m) \quad (30.111)$$

in which \mathbf{L} is a lower triangular matrix with all its diagonal elements equal to unity and \mathbf{D} is a real diagonal matrix with r nonzero diagonal elements d_j . The implementation of Cholesky decomposition for a Hermitian matrix is very similar to that for a real symmetric matrix (Wilkinson and Reinsch, 1971).

Example 30.2 A Massless Trolley Subjected to Excitations with Phase-Lags

The massless trolley shown in Figure 30.8 is connected to two abutments by springs and viscous dashpots (linear viscous dampers) as shown. The abutments move distances $x_1(t)$ and $x_2(t)$ with spectral densities S_0 (constant), but $x_2(t) = x_1(t - T)$, in which T is a fixed time difference. The response spectral density of the trolley displacement $S_{yy}(\omega)$ is to be determined. The equation of motion of the trolley is (Newland, 1975)

$$(c_1 + c_2)\dot{y} + (k_1 + k_2)y = k_1 x_1 + c_1 \dot{x}_1 + k_2 x_2 + c_2 \dot{x}_2 \quad (i)$$

Since the PSD of $x_1(t)$ is S_0 , the pseudoexcitation corresponding to $x_1(t)$ is

$$\tilde{x}_1(t) = \sqrt{S_0} \exp(i\omega t) \quad (ii)$$

Because $x_2(t) = x_1(t - T)$, we have

$$\tilde{x}_2(t) = \sqrt{S_0} \exp[i\omega(t - T)] \quad (\text{iii})$$

Clearly

$$\dot{\tilde{x}}_1(t) = i\omega\sqrt{S_0} \exp(i\omega t), \quad (\text{iv})$$

$$\dot{\tilde{x}}_2(t) = i\omega\sqrt{S_0} \exp[i\omega(t - T)]$$

Substituting the above equations into Equation i gives the harmonic equation

$$\begin{aligned} (c_1 + c_2)\dot{\tilde{y}} + (k_1 + k_2)\tilde{y} \\ = [(k_1 + i\omega c_1) + (k_2 + i\omega c_2) \\ \exp(-i\omega T)] \exp(i\omega t) \end{aligned} \quad (\text{v})$$

Its solution can be readily obtained as

$$\tilde{y} = \frac{k_1 + i\omega c_1 + (k_2 + i\omega c_2) \exp(-i\omega T)}{k_1 + k_2 + i\omega(c_1 + c_2)} \exp(i\omega t) \quad (\text{vi})$$

Hence,

$$S_{yy} = \tilde{y}^* \tilde{y} = \frac{k_1^2 + k_2^2 + c_1^2 \omega^2 + c_2^2 \omega^2 + 2(k_1 k_2 + c_1 c_2 \omega^2) \cos \omega T + 2(k_1 c_2 \omega - k_2 c_1 \omega) \sin \omega T}{(k_1 + k_2)^2 + (c_1 + c_2)^2 \omega^2} S_0 \quad (\text{vii})$$

This result is identical to that given by Newland (1975). However, the process given here is quite simple.

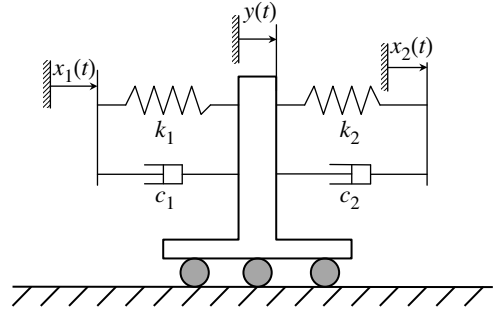


FIGURE 30.8 Two-phase input trolley.

30.3.2 Structures Subjected to Nonstationary Random Vibration

30.3.2.1 Structures Subjected to Uniformly Modulated Evolutionary Random Excitations

30.3.2.1.1 Single Excitation Problems

The basic principle of the PEM for nonstationary random vibration analyses can be described by Figure 30.9. Consider a linear system subjected to an evolutionary random excitation (see Figure 30.9a)

$$f(t) = g(t)x(t) \quad (30.112)$$

in which $g(t)$ is a slowly varying modulation function, while $x(t)$ is a zero-mean stationary random process with auto-PSD $S_{xx}(\omega)$. The deterministic functions $g(t)$ and $S_{xx}(\omega)$ are both assumed to be given.

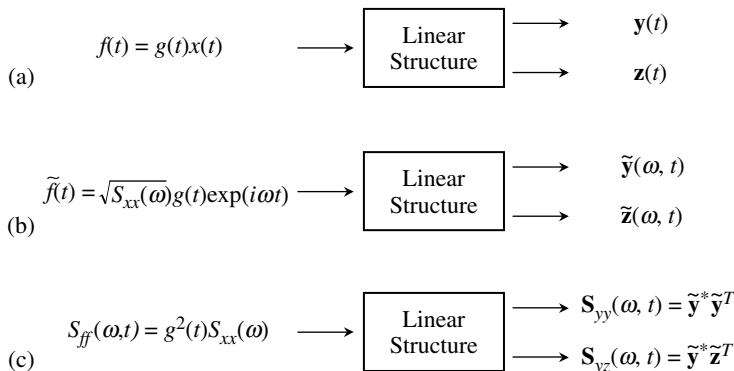


FIGURE 30.9 Basic principle of pseudoexcitation method (nonstationary analysis).

The auto-PSD of $f(t)$ (see Figure 30.9b) is

$$S_{ff}(\omega, t) = g^2(t)S_{xx}(\omega) \quad (30.113)$$

In order to compute the PSD functions of various linear responses due to the action of $f(t)$, we note that the pseudoexcitation has the form

$$\tilde{f}(\omega, t) = g(t)\sqrt{S_{xx}(\omega)}\exp(i\omega t) \quad (30.114)$$

Now suppose that $\mathbf{y}(t)$ and $\mathbf{z}(t)$ are two arbitrarily selected response vectors (see Figure 30.9a) and $\tilde{\mathbf{y}}(\omega, t)$ and $\tilde{\mathbf{z}}(\omega, t)$ are the corresponding transient responses due to the pseudoexcitation $\tilde{f}(\omega, t)$ with the structure initially at rest (see Figure 30.9b). It has been proven (Lin et al., 1994a; Lin et al., 2004) that the desired PSD matrices of $\mathbf{y}(t)$ and $\mathbf{z}(t)$ are

$$\mathbf{S}_{yy}(\omega, t) = \tilde{\mathbf{y}}^*(\omega, t)\tilde{\mathbf{y}}^T(\omega, t) \quad (30.115)$$

$$\mathbf{S}_{yz}(\omega, t) = \tilde{\mathbf{y}}^*(\omega, t)\tilde{\mathbf{z}}^T(\omega, t) \quad (30.116)$$

as shown in Figure 30.9c.

Now, consider the Equation 30.99 of a linear structure subjected to the evolutionary random excitation $\ddot{x}_g(t) = g(t)x(t)$. The pseudoground acceleration is now $\ddot{x}_g(t) = g(t)\sqrt{S_{xx}(\omega)}\exp(i\omega t)$. Substituting this into the right-hand side of Equation 30.99 gives the deterministic equations

$$\mathbf{M}\ddot{\tilde{\mathbf{y}}} + \mathbf{C}\dot{\tilde{\mathbf{y}}} + \mathbf{K}\tilde{\mathbf{y}} = -\mathbf{M}\mathbf{e}g(t)\sqrt{S_{xx}(\omega)}\exp(i\omega t) \quad (30.117)$$

For seismic problems, the structure is initially at rest, that is, $\tilde{\mathbf{y}} = \dot{\tilde{\mathbf{y}}} = 0$ when $t = 0$. Thus, the time history of $\tilde{\mathbf{y}}(\omega, t)$ can be computed using the Newmark or Wilson- θ schemes. Furthermore, any other linear pseudo response vectors, denoted as $\tilde{\mathbf{u}}(\omega, t)$ and $\tilde{\mathbf{v}}(\omega, t)$, can be computed from $\tilde{\mathbf{y}}(\omega, t)$. The response PSD matrices of $\mathbf{u}(t)$ and $\mathbf{v}(t)$ can also be accurately computed by using their pseudoresponses $\tilde{\mathbf{u}}(\omega, t)$ and $\tilde{\mathbf{v}}(\omega, t)$

$$\mathbf{S}_{uu}(\omega, t) = \tilde{\mathbf{u}}^*(\omega, t)\tilde{\mathbf{u}}^T(\omega, t) \quad (30.118)$$

$$\mathbf{S}_{uv}(\omega, t) = \tilde{\mathbf{u}}^*(\omega, t)\tilde{\mathbf{v}}^T(\omega, t) \quad (30.119)$$

Example 30.3 Single-Degree of Freedom System Subjected to Suddenly Applied Stationary Random Excitation

Consider the following single-DoF example, which was first given by Caughey and Stumpf (1961) and has been widely used to compare the efficiency and precision of various methods:

$$\ddot{y} + 2\varsigma\omega_0\dot{y} + \omega_0^2y = f(t) = g(t)x(t), \quad y(0) = \dot{y}(0) = 0 \quad (i)$$

in which

$$g(t) = \begin{cases} 1.0 & t \geq 0 \\ 0 & t < 0 \end{cases} \quad (ii)$$

and $x(t)$ is a zero-mean-valued stationary random process with its PSD $S_{xx}(\omega)$ given. Now, constitute a pseudo excitation

$$\tilde{f}(t) = \sqrt{S_{xx}(\omega)}\exp(i\omega t) \quad (t \geq 0) \quad (iii)$$

Thus, the motion equation that should be solved is

$$\ddot{y} + 2\varsigma\omega_0\dot{y} + \omega_0^2y = \sqrt{S_{xx}(\omega)}\exp(i\omega t), \quad \tilde{y}(0) = \dot{\tilde{y}}(0) = 0 \quad (iv)$$

The solution of this simple equation is

$$\tilde{y}(\omega, t) = H \left\{ \exp(i\omega t) - \exp(-\varepsilon t) \left[\cos \omega_e t + \frac{i\omega + \varepsilon}{\omega_e} \sin \omega_e t \right] \right\} \sqrt{S_{xx}(\omega)} \quad (\text{v})$$

in which

$$H = (\omega_0^2 - \omega^2 + 2i\varsigma\omega_0\omega)^{-1}, \quad \varepsilon = \varsigma\omega_0, \quad \omega_e = \omega_0\sqrt{1 - \varsigma^2} \quad (\text{vi})$$

Therefore, the auto-PSD of y is

$$S_{yy}(\omega, t) = \tilde{y}^* \tilde{y} = |\tilde{y}|^2 = |H|^2 \left\{ \left[\exp(-\varepsilon t) \left(\frac{\varepsilon}{\omega_e} \sin \omega_e t + \cos \omega_e t \right) - \cos \omega t \right]^2 + \left[\exp(-\varepsilon t) \frac{\omega}{\omega_e} \sin \omega_e t - \sin \omega t \right]^2 \right\} S_{xx}(\omega) \quad (\text{vii})$$

This result is identical to the exact solution given by Caughey and Stumpf (1961), who used a more complicated process and expressed it less concisely as

$$S_{yy}(\omega, t) = |H|^2 [1 + \exp(-2\varepsilon t)] \left[1 + \frac{2\omega_0}{\omega_e} \varsigma \sin \omega_e t \cos \omega_e t - \exp(\varepsilon t) \left(2 \cos \omega_e t + \frac{2\omega_0}{\omega_e} \varsigma \sin \omega_e t \right) \cos \omega t - \exp(\varepsilon t) \frac{2\omega}{\omega_e} \sin \omega_e t \sin \omega t + \frac{(\omega_0 \varsigma)^2 - \omega_e^2 + \omega^2}{\omega_e^2} \sin^2 \omega_e t \right] S_{xx}(\omega) \quad (\text{viii})$$

30.3.2.1.2 Multiple Excitation Problems

Fully coherent excitations. In order to include the phase-lags between ground excitations, that is, the wave passage effect, the evolutionary random excitation vector $\mathbf{f}(t)$ to which the structure is subjected should be

$$\mathbf{f}(t) = \begin{Bmatrix} F_1(t) \\ F_2(t) \\ \vdots \\ F_n(t) \end{Bmatrix} = \begin{Bmatrix} a_1 g(t - t_1) F(t - t_1) \\ a_2 g(t - t_2) F(t - t_2) \\ \vdots \\ a_n g(t - t_n) F(t - t_n) \end{Bmatrix} = \mathbf{G}(t) \bar{\mathbf{f}}(t) \quad (30.120)$$

in which

$$\mathbf{G}(t) = \begin{bmatrix} a_1 g(t - t_1) & & & \\ & a_2 g(t - t_2) & & \\ & & \ddots & \\ & & & a_n g(t - t_n) \end{bmatrix}, \quad \bar{\mathbf{f}}(t) = \begin{Bmatrix} F(t - t_1) \\ F(t - t_2) \\ \vdots \\ F(t - t_n) \end{Bmatrix} \quad (30.121)$$

Here, all components of $\bar{\mathbf{f}}(t)$ clearly have the same form, although there are time lags $t_j (j = 1, 2, \dots, n)$ between them; $g(t)$ is the modulation function; $a_j (j = 1, 2, \dots, n)$ are given real numbers; and t_j are given constants. $F(t)$ is a stationary random process, of which the auto-PSD $S_{FF}(\omega)$ is known. The pseudo-excitations corresponding to $\{\mathbf{f}(t)\}$ are (Lin and Zhang, 2004)

$$\tilde{\mathbf{f}}(t) = \mathbf{G}(t) \mathbf{V} \mathbf{q}_0 \sqrt{S_{FF}(\omega)} \exp(i\omega t) \quad (30.122)$$

in which

$$\mathbf{R}_0 = \mathbf{q}_0 \mathbf{q}_0^T = \begin{bmatrix} 1 & 1 & \cdots & 1 \\ 1 & 1 & \cdots & 1 \\ \vdots & \vdots & \ddots & \vdots \\ 1 & 1 & \cdots & 1 \end{bmatrix} \quad (30.123)$$

$$\mathbf{V} = \text{diag}[\exp(-i\omega t_1), \exp(-i\omega t_2), \dots, \exp(-i\omega t_n)]$$

$$\mathbf{q}_0^T = \{1, 1, \dots, 1\}$$

The excitation PSD matrix can be written as

$$\mathbf{S}_{ff}(\omega, t) = \tilde{\mathbf{f}}^*(t) \tilde{\mathbf{f}}^T(t) = S_{FF}(\omega) \mathbf{G}(t) \mathbf{V}^* \mathbf{q}_0 \mathbf{q}_0^T \mathbf{V}^T \mathbf{G}^T(t) = S_{FF}(\omega) \times \begin{bmatrix} g^2(t-t_1) & g(t-t_1)g(t-t_2)\exp(i\omega(t_1-t_2)) & \cdots & g(t-t_1)g(t-t_n)\exp(i\omega(t_1-t_n)) \\ g(t-t_2)g(t-t_1)\exp(i\omega(t_2-t_1)) & g^2(t-t_2) & \cdots & g(t-t_2)g(t-t_n)\exp(i\omega(t_2-t_n)) \\ \vdots & \vdots & \ddots & \vdots \\ g(t-t_n)g(t-t_1)\exp(i\omega(t_n-t_1)) & g(t-t_n)g(t-t_2)\exp(i\omega(t_n-t_2)) & \cdots & g^2(t-t_n) \end{bmatrix} \quad (30.124)$$

An arbitrarily chosen response $\tilde{\mathbf{y}}_k(\omega, t_k)$ excited by $\tilde{\mathbf{f}}(t)$ can be computed using a numerical integration scheme and the results can be expressed as

$$\tilde{\mathbf{y}}_k(\omega, t_k) = \mathbf{a}_{yk}(\omega, t) \sqrt{S_{FF}(\omega)} \quad (30.125)$$

in which

$$\mathbf{a}_{yk}(\omega, t_k) = \int_0^{t_k} \mathbf{H}(t_k - \tau_k) \mathbf{G}(\tau_k) \mathbf{V} \mathbf{q}_0 \exp(i\omega \tau_k) d\tau_k \quad (30.126)$$

Here, $\mathbf{a}_{yk}(\omega, t)$ is the response excited by $\mathbf{G}(t) \mathbf{V} \mathbf{q}_0 \exp(i\omega t)$ and $\mathbf{H}(t)$ is the impulse-response function matrix. The cross-PSD matrix between $\mathbf{y}_k(t)$ and $\mathbf{y}_l(t)$ is

$$\mathbf{S}_{y_k y_l}(\omega, t) = \tilde{\mathbf{y}}_k^*(\omega, t) \tilde{\mathbf{y}}_l^T(\omega, t) \quad (30.127)$$

By letting $k = l$, the auto-PSD matrix of $\mathbf{y}_k(t)$ can be directly computed by Equation 30.127.

Partially coherent excitations. In addition to the time lags between excitations, if the arbitrary coherence between such nonstationary excitations is also taken into account, then the problem is more difficult. According to PEM, however, it is only required that the matrix \mathbf{R}_0 in Equation 30.123 is changed into

$$\mathbf{R} = \begin{bmatrix} 1 & \rho_{12} & \cdots & \rho_{1n} \\ \rho_{21} & 1 & \cdots & \rho_{2n} \\ \vdots & \vdots & \ddots & \vdots \\ \rho_{n1} & \rho_{n2} & \cdots & 1 \end{bmatrix} \quad (30.128)$$

in which ρ_{ij} reflects the coherence between the excitations at points i and j , and matrix \mathbf{R} is usually symmetric and positive definite or semipositive definite. Denoting its rank as $r(r \geq 1)$, \mathbf{R} can be

expressed as

$$\mathbf{R} = \sum_{j=1}^r \alpha_j \boldsymbol{\Psi}_j^* \boldsymbol{\Psi}_j^T \quad (30.129)$$

This means that the global excitation PSD matrix is decomposed into r matrices with rank unity where the j th of them corresponds to the pseudoexcitation

$$\tilde{\mathbf{f}}_j(t) = \mathbf{G}(t) \mathbf{V} \boldsymbol{\Psi}_j \sqrt{\alpha_j S_{FF}(\omega)} \exp(i\omega t) \quad (30.130)$$

If $\tilde{\mathbf{y}}_{kj}(t)$ and $\tilde{\mathbf{y}}_{lj}(t)$ are two arbitrary responses due to $\tilde{\mathbf{f}}_j(t)$, then

$$\mathbf{S}_{y_k y_l}(\omega, t) = \sum_{j=1}^r \tilde{\mathbf{y}}_{kj}^*(t) \tilde{\mathbf{y}}_{lj}^T(t) \quad (30.131)$$

By letting $k = l$, the auto-PSD matrix of $\mathbf{y}_k(t)$ can be directly computed by Equation 30.131.

30.3.2.2 Structures Subjected to Nonuniformly Modulated Evolutionary Random Excitations

30.3.2.2.1 Single Excitation Problems

Consider a nonuniformly modulated evolutionary random excitation $f(t)$ (Priestly, 1967)

$$f(t) = \int_{-\infty}^{\infty} A(\omega, t) \exp(i\omega t) d\alpha(\omega) \quad (30.132)$$

in which $A(\omega, t)$ is a given nonuniform modulation function and α satisfies the equation

$$E[d\alpha^*(\omega_1) d\alpha(\omega_2)] = S_{xx}(\omega) \delta(\omega_2 - \omega_1) d\omega_1 d\omega_2 \quad (30.133)$$

Here, $S_{xx}(\omega_1)$ is the auto-PSD of the stationary random process $x(t)$.

The Riemann–Stieltjes integration in Equation 30.132 causes difficulties in conventional computations. However, this problem can be conveniently solved using PEM as follows. First, constitute the following pseudoexcitation (Lin et al., 1997a, 1997b):

$$\tilde{f}(\omega, t) = A(\omega, t) \sqrt{S_{xx}(\omega)} \exp(i\omega t) \quad (30.134)$$

Second, replace $g(t)$ in Equation 30.117 by $A(\omega, t)$ to yield

$$\mathbf{M}\ddot{\tilde{\mathbf{y}}} + \mathbf{C}\dot{\tilde{\mathbf{y}}} + \mathbf{K}\tilde{\mathbf{y}} = -\mathbf{M}\mathbf{e}A(\omega, t)\sqrt{S_{xx}(\omega)}\exp(i\omega t) \quad (30.135)$$

Third, with the structure initially at rest, compute the time history, $\tilde{\mathbf{y}}(\omega, t)$, for any arbitrary frequency ω , and the required time histories $\tilde{\mathbf{u}}(\omega, t)$ and $\tilde{\mathbf{v}}(\omega, t)$. Finally, the PSD matrices of $\mathbf{u}(t)$ and $\mathbf{v}(t)$ can be computed from

$$\mathbf{S}_{uu}(\omega, t) = \tilde{\mathbf{u}}^*(\omega, t) \tilde{\mathbf{u}}^T(\omega, t) \quad (30.136)$$

$$\mathbf{S}_{uv}(\omega, t) = \tilde{\mathbf{u}}^*(\omega, t) \tilde{\mathbf{v}}^T(\omega, t) \quad (30.137)$$

Evidently, the PEM is nearly identical for uniformly or nonuniformly modulated evolutionary random excitations. The unique difference is the use of either $A(\omega, t)$ or $g(t)$ in the pseudoexcitation expressions, see Equation 30.114 and Equation 30.134.

30.3.2.2.2 Multiple Excitation Problems

For multiple nonstationary random excitation problems, the PEM-based analysis process for uniformly modulated evolutionary random excitations can be immediately extended to that for nonuniformly modulated evolutionary random excitations if the modulation function $g(t)$ is replaced by $A(\omega, t)$.

All other formulas remain exactly the same. The difference in computational effort from using different modulation functions is negligible.

30.3.3 Precise Integration Method

30.3.3.1 Precise Integration of Exponential Matrices

Structural equations of motion, for example, Equation 30.99, can be written as

$$\mathbf{M}\ddot{\mathbf{y}} + \mathbf{G}\dot{\mathbf{y}} + \mathbf{K}\mathbf{y} = \mathbf{f}(t) \quad (30.138)$$

in which \mathbf{M} , \mathbf{G} , and \mathbf{K} are given time-invariant $n \times n$ matrices, respectively, and $\mathbf{f}(t)$ is the given external force vector. The initial displacement $\mathbf{y}(t)$ and the initial velocity $\dot{\mathbf{y}}(t)$ of the system are specified. The equation of motion, Equation 30.138, combined with the identity $\dot{\mathbf{y}} = \dot{\mathbf{y}}$ leads to the first-order equations of motion in the state space being

$$\dot{\mathbf{v}} = \mathbf{H}\mathbf{v} + \mathbf{r} \quad (30.139)$$

in which

$$\mathbf{H} = \begin{bmatrix} \mathbf{0} & \mathbf{I} \\ \mathbf{B} & \mathbf{D} \end{bmatrix}, \quad \mathbf{v} = \begin{Bmatrix} \mathbf{y} \\ \dot{\mathbf{y}} \end{Bmatrix}, \quad \mathbf{r} = \begin{Bmatrix} \mathbf{0} \\ \mathbf{M}^{-1}\mathbf{f}(t) \end{Bmatrix}, \quad \mathbf{B} = -\mathbf{M}^{-1}\mathbf{K}, \quad \mathbf{D} = -\mathbf{M}^{-1}\mathbf{G} \quad (30.140)$$

The homogeneous solution of Equation 30.139 is

$$\mathbf{v}_h(t) = \mathbf{T}(\tau)\mathbf{c} \quad (30.141)$$

in which

$$\mathbf{T}(\tau) = \exp(\mathbf{H}\tau) \quad (30.142)$$

Consider the current integration interval $t \in [t_k, t_{k+1}]$, $\tau = t - t_k$. When $\tau = 0$ or $t = t_k$, $\mathbf{T}(\tau) = \mathbf{I}$ and, therefore, \mathbf{c} is a constant vector. If the particular solution to Equation 30.139, $\mathbf{v}_p(t)$, is temporarily assumed to have been found, then the general solution of Equation 30.139 is

$$\mathbf{v}(t) = \mathbf{T}(\tau)(\mathbf{v}(t_k) - \mathbf{v}_p(t_k)) + \mathbf{v}_p(t) \quad (30.143)$$

In order to compute $\mathbf{T}(\tau)$ accurately, it is desirable to subdivide the step τ into $m = 2^N$ equal intervals, that is,

$$\Delta t = \tau/m = 2^{-N}\tau \quad (30.144)$$

For application purposes, the use of $N = 20$ is sufficient, because it leads to $\Delta t \approx 10^{-6}\tau$. Such a small Δt is, in general, much smaller than the highest natural period of any practical discretized system.

Using the Taylor series expansion, we have

$$\exp(\mathbf{H} \times \Delta t) \approx \mathbf{I} + \mathbf{T}_{a0} \quad (30.145)$$

in which

$$\mathbf{T}_{a0} = (\mathbf{H} \times \Delta t) + (\mathbf{H} \times \Delta t)^2/2! + (\mathbf{H} \times \Delta t)^3/3! + (\mathbf{H} \times \Delta t)^4/4! \quad (30.146)$$

Substituting Equation 30.145 into Equation 30.142 gives

$$\mathbf{T}(\tau) = (\exp(\mathbf{H} \times \Delta t))^m = (\mathbf{I} + \mathbf{T}_{a0})^m \quad (30.147)$$

Note that

$$\mathbf{I} + \mathbf{T}_{ai} = (\mathbf{I} + \mathbf{T}_{a,i-1})^2 = (\mathbf{I} + 2 \times \mathbf{T}_{a,i-1} + \mathbf{T}_{a,i-1} \times \mathbf{T}_{a,i-1}), \quad (i = 1, 2, \dots, N) \quad (30.148)$$

so that

$$\mathbf{I} + \mathbf{T}_{aN} = (\mathbf{I} + \mathbf{T}_{a,N-1})^2 = (\mathbf{I} + \mathbf{T}_{a,N-2})^4 = \dots = (\mathbf{I} + \mathbf{T}_{a0})^m = \mathbf{T}(\tau) \quad (30.149)$$

Equation 30.148 and Equation 30.149 suggest the following computing strategy. In order to avoid the loss of significant digits in the matrix $\mathbf{T}(\tau)$, it is necessary to compute \mathbf{T}_{a1} directly from \mathbf{T}_{a0} , \mathbf{T}_{a2} directly from \mathbf{T}_{a1} , and so on, by using

$$\mathbf{T}_{ai} = 2 \times \mathbf{T}_{a,i-1} + \mathbf{T}_{a,i-1} \times \mathbf{T}_{a,i-1}, \quad (i = 1, 2, \dots, N) \quad (30.150)$$

Then $\mathbf{T}(\tau)$ should be computed from

$$\mathbf{T}(\tau) \approx \mathbf{I} + \mathbf{T}_{aN} \quad (30.151)$$

In Equation 30.151, the approximation is caused by the truncation of the Taylor expansion of Equation 30.146. It is generally negligibly small because when $N = 20$, the first term ignored by the truncation is of the order $O(\Delta t^5) = 10^{-30} O(\tau^5)$, which is on the order of the round-off errors of a typical computer.

30.3.3.2 Particular Solutions and Precise Integration Formulas for Various Forms of Loading

30.3.3.2.1 Linear Loading Form (HPD-L Form)

Assume that the loading varies linearly within the time step (t_k, t_{k+1}) , that is,

$$\mathbf{r} = \mathbf{r}_0 + \mathbf{r}_1 \times (t - t_0) \quad (30.152)$$

in which \mathbf{r}_0 and \mathbf{r}_1 are time-invariant vectors. The particular solution of Equation 30.139 is then (Lin et al., 1995a, 1995b; Zhong, 2004)

$$\mathbf{v}_p(t) = (\mathbf{H}^{-1} + \mathbf{I}t)(-\mathbf{H}^{-1}\mathbf{r}_1) - \mathbf{H}^{-1}(\mathbf{r}_0 - \mathbf{r}_1 t_k) \quad (30.153)$$

Substituting Equation 30.152 into Equation 30.143 gives the HPD-L (High Precision Direct integration-Linear) integration formula

$$\mathbf{v}(t_{k+1}) = \mathbf{T}(\tau)(\mathbf{v}(t_k) + \mathbf{H}^{-1}(\mathbf{r}_0 + \mathbf{H}^{-1}\mathbf{r}_1)) - \mathbf{H}^{-1}(\mathbf{r}_0 + \mathbf{H}^{-1}\mathbf{r}_1 + \mathbf{r}_1 \tau) \quad (30.154)$$

30.3.3.2.2 Sinusoidal Loading Form (HPD-S Form)

If the applied loading is sinusoidal within the time region $t \in (t_k, t_{k+1})$, then

$$\mathbf{r}(t) = \mathbf{r}_1 \sin \omega t + \mathbf{r}_2 \cos \omega t \quad (30.155)$$

in which \mathbf{r}_1 and \mathbf{r}_2 are time-invariant vectors. Substituting Equation 30.155 into Equation 30.139 enables the particular solution to be obtained (Lin et al., 1995a, 1995b; Zhong, 2004)

$$\mathbf{v}_p(t) = \mathbf{v}_1 \sin \omega t + \mathbf{v}_2 \cos \omega t \quad (30.156)$$

in which

$$\mathbf{v}_1 = (\omega \mathbf{I} + \mathbf{H}^2/\omega)^{-1}(\mathbf{r}_2 - \mathbf{H}\mathbf{r}_1/\omega) \quad \mathbf{v}_2 = (\omega \mathbf{I} + \mathbf{H}^2/\omega)^{-1}(-\mathbf{r}_1 - \mathbf{H}\mathbf{r}_2/\omega) \quad (30.157)$$

Substituting Equation 30.156 into Equation 30.143 gives the general solution of Equation 30.139, that is, the HPD-S direct integration formula

$$\mathbf{v}(t_{k+1}) = \mathbf{T}(\tau)(\mathbf{v}(t_k) - \mathbf{v}_1 \sin \omega t_k - \mathbf{v}_2 \cos \omega t_k) + \mathbf{v}_1 \sin \omega t_{k+1} + \mathbf{v}_2 \cos \omega t_{k+1} \quad (30.158)$$

The time interval $\tau = t_{k+1} - t_k$ can cover an arbitrary segment, or even many periods, of a sinusoidal wave because, no matter how large the step size may be, exact responses will be obtained provided the matrix $\mathbf{T}(\tau)$ has been generated accurately, without any instability occurring.

30.3.3.2.3 Exponentially Decaying Sinusoidal Loading Form (HPD-E Form)

Suppose that the applied loading varies according to the following exponentially decaying sinusoidal law within the time region $t \in (t_k, t_{k+1})$:

$$\mathbf{r}(t) = \exp(\alpha t)(\mathbf{r}_1 \sin \omega t + \mathbf{r}_2 \cos \omega t) \quad (30.159)$$

in which \mathbf{r}_1 and \mathbf{r}_2 are time-invariant vectors. Substituting Equation 30.159 into Equation 30.139 enables the particular solution to be obtained (Lin et al., 1995a, 1995b; Zhong, 2004) as

$$\mathbf{v}_p(t) = \exp(\alpha t)(\mathbf{v}_1 \sin \omega t + \mathbf{v}_2 \cos \omega t) \quad (30.160)$$

in which

$$\mathbf{v}_1 = ((\alpha \mathbf{I} - \mathbf{H}^2) + \omega^2 \mathbf{I})^{-1}((\alpha \mathbf{I} - \mathbf{H})\mathbf{r}_1 + \omega \mathbf{r}_2) \quad (30.161)$$

$$\mathbf{v}_2 = ((\alpha \mathbf{I} - \mathbf{H}^2) + \omega^2 \mathbf{I})^{-1}((\alpha \mathbf{I} - \mathbf{H})\mathbf{r}_2 - \omega \mathbf{r}_1)$$

Thus, substituting Equation 30.161 into Equation 30.143 gives the general solution of Equation 30.139, that is, the HPD-E direct integration formula

$$\mathbf{v}(t_{k+1}) = \mathbf{T}(\tau)(\mathbf{v}(t_k) - \exp(\alpha t_k)(\mathbf{v}_1 \sin \omega t_k + \mathbf{v}_2 \cos \omega t_k)) + \exp(\alpha t_{k+1})(\mathbf{v}_1 \sin \omega t_{k+1} + \mathbf{v}_2 \cos \omega t_{k+1}) \quad (30.162)$$

The time interval is $\tau = t_{k+1} - t_k$.

30.4 Long-Span Structures Subjected to Stationary Random Ground Excitations

30.4.1 The Solution of Equations of Motion Using the Pseudoexcitation Method

In Equation 30.93, the PSD matrix of $\ddot{\mathbf{u}}_b$, that is, $\mathbf{S}(i\omega)$ in Equation 30.55, is an N -dimensional Hermitian matrix, while \mathbf{R} is an N -dimensional real symmetric matrix. Both matrices are usually positive definite or semipositive definite. If the rank of \mathbf{R} is r ($r \leq N$), then by using Equation 30.111 it can be readily decomposed into the product of an $N \times r$ matrix \mathbf{Q} and its transposition; that is

$$\mathbf{R} = \mathbf{Q}\mathbf{Q}^T \quad (30.163)$$

Thus, Equation 30.55 can be written as

$$\mathbf{S}(i\omega) = \mathbf{B}^* \mathbf{J} \mathbf{Q} \mathbf{Q}^T \mathbf{J} \mathbf{B} = \mathbf{P}^* \mathbf{P}^T \quad (30.164)$$

in which

$$\mathbf{P} = \mathbf{B} \mathbf{J} \mathbf{Q} \quad (30.165)$$

To solve Equation 30.93, the right-hand side $\ddot{\mathbf{u}}_b$ can be replaced by the pseudoground acceleration

$$\ddot{\mathbf{U}}_b = \mathbf{P} \exp(i\omega t) \quad (30.166)$$

Thus, Equation 30.93 becomes the following sinusoidal equations of motion:

$$\mathbf{M}_s \ddot{\mathbf{Y}}_r + \mathbf{C}_s \dot{\mathbf{Y}}_r + \mathbf{K}_s \mathbf{Y}_r = \mathbf{M}_s \mathbf{K}_s^{-1} \mathbf{K}_{sb} \mathbf{E}_{mN} \mathbf{P} \exp(i\omega t) \quad (30.167)$$

The stable solution of Equation 30.167 is the pseudorelative displacement vector $\tilde{\mathbf{Y}}_r$, whilst the pseudostatic displacement vector $\tilde{\mathbf{Y}}_s$ can be computed by

$$\tilde{\mathbf{Y}}_s = \frac{1}{\omega^2} \mathbf{K}_s^{-1} \mathbf{K}_{sb} \mathbf{E}_{mN} \mathbf{P} \exp(i\omega t) \quad (30.168)$$

Thus, the pseudoabsolute displacement vector is

$$\tilde{\mathbf{X}}_s = \tilde{\mathbf{Y}}_r + \tilde{\mathbf{Y}}_s \quad (30.169)$$

If necessary, any arbitrary pseudointernal force vector $\tilde{\mathbf{N}}_s$ can be computed from $\tilde{\mathbf{X}}_s$ by means of a quasi-static analysis. Then, the corresponding PSD matrix is

$$\mathbf{S}_{N_s N_s}(\omega) = \tilde{\mathbf{N}}_s^* \tilde{\mathbf{N}}_s^T \quad (30.170)$$

If it is assumed that $S_{\ddot{x}_1} = S_{\ddot{x}_2} = \dots = S_{\ddot{x}_N}$, denoted as S_a , then Equation 30.165 becomes

$$\mathbf{P} = \sqrt{S_a} \mathbf{BQ} \quad (30.171)$$

If only the wave passage effect is considered, that is, all $|\rho_{ij}| = 1$ in Equation 30.58, then matrix \mathbf{Q} will reduce to a vector \mathbf{q}_0 with all its elements unity; that is

$$\mathbf{Q} = \mathbf{q}_0 = \{1, 1, \dots, 1\}^T \quad (30.172)$$

Thus, Equation 30.171 reduces to

$$\mathbf{P} = \sqrt{S_a} \mathbf{e}_0 \quad (30.173)$$

in which \mathbf{e}_0 is a complex vector

$$\mathbf{e}_0 = \{\exp(-i\omega t_1), \exp(-i\omega t_2), \dots, \exp(-i\omega t_N)\}^T \quad (30.174)$$

Therefore, when only the wave passage effect is considered, Equation 30.167 reduces to

$$\mathbf{M}_s \ddot{\mathbf{y}}_r + \mathbf{C}_s \dot{\mathbf{y}}_r + \mathbf{K}_s \mathbf{y}_r = \mathbf{M}_s \mathbf{K}_s^{-1} \mathbf{K}_{sb} \mathbf{E}_{mN} \mathbf{e}_0 \sqrt{S_a} \exp(i\omega t) \quad (30.175)$$

Furthermore, if the structure is subjected to a uniform ground motion, then the vector \mathbf{e}_0 in Equation 30.174 should be replaced by \mathbf{q}_0 , and so Equation 30.175 can be further reduced to

$$\mathbf{M}_s \ddot{\mathbf{y}}_r + \mathbf{C}_s \dot{\mathbf{y}}_r + \mathbf{K}_s \mathbf{y}_r = \mathbf{M}_s \mathbf{K}_s^{-1} \mathbf{K}_{sb} \mathbf{E}_{mN} \mathbf{q}_0 \sqrt{S_a} \exp(i\omega t) \quad (30.176)$$

30.4.2 Numerical Comparisons with Other Methods

30.4.2.1 Song-Hua-Jiang Suspension Bridge

The Song-Hua-Jiang suspension bridge (see Figure 30.10) is located in Jilin Province of China. Its overall length is 450 m, with a main span of 240 m and a width of 28 m. The finite element model had 2076 DoF, 445 nodes (including 12 supports) and 574 elements. The static equilibrium position of the bridge included the effects of the initial tensions of the cables. The earthquake action was determined based on the Chinese National Standard (Code for Seismic Design of Buildings GB 50011-2001), which directly gives the ground ARS curve for the bridge. The PSD curve was obtained in terms of the Kaul method from which the samples of the ground acceleration time-history can be produced (Kaul, 1978). For the analyses associated with the SH and SV waves, 100 modes were used for mode-superposition, whereas for the P waves, only 30 modes were used. The apparent wave speeds used were 3 km/s for P waves and 2 km/s for SH or SV waves.

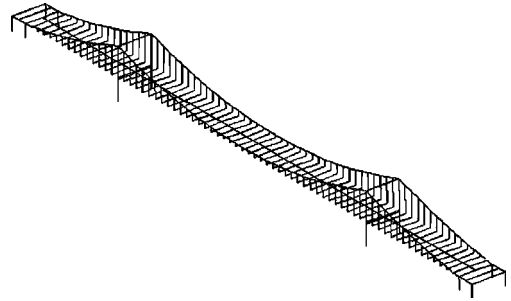


FIGURE 30.10 Song-Hua-Jiang suspension bridge.

30.4.2.1.1 All Supports Move Uniformly

Figure 30.11(a) gives the axial force distribution of this bridge along the deck due to the seismic P waves, which travel along the longitudinal direction of the deck. All supports of the bridges are assumed to move uniformly. The following four computational models were used:

1. Response spectrum method
2. Pseudoexcitation method
3. Time-history method using three samples
4. Time-history method using ten samples

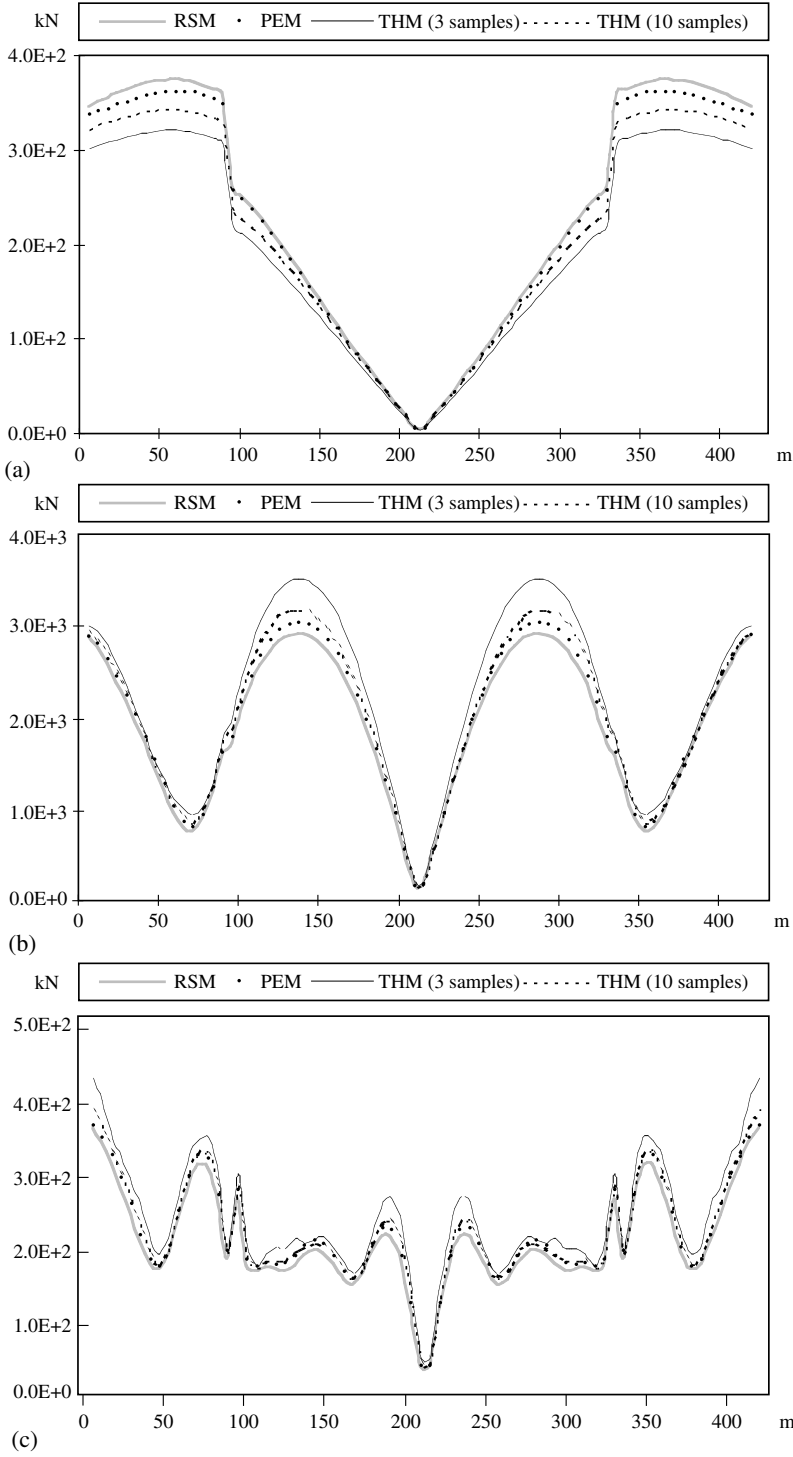


FIGURE 30.11 Deck force distribution of Song-Hua-Jiang bridge due to uniform ground motion: (a) axial force distribution along the deck under P waves; (b) transverse shear force distribution along the deck under SH waves; (c) vertical shear force distribution along the deck under SV waves.

TABLE 30.1 Central Processing Unit (CPU) Times Required by Different Methods for Stationary Analysis

Method Used	RSM (sec)	PEM (sec)	THM (for One Sample) (sec)
Uniform ground motion	80.6	15.1	29.9
Wave passage effect		24.2	36.7
Wave passage effect and incoherence effect		209.1	

Note: the CPU time for mode extraction is not included; extracting 100 modes needs 180.9 sec.

Figure 30.11(b) gives the transverse shear force distribution along the deck due to the seismic SH waves traveling along the deck. All supports move uniformly. The above four computational models were used.

Figure 30.11(c) gives the vertical shear force distribution along the deck due to the seismic SV waves traveling along the deck. All supports move uniformly. The above four computational models were also used here.

All computations were executed on a P3-750 personal computer. The computation times for different methods are listed in Table 30.1.

Figure 30.11 and Table 30.1 show that, when ground motion is assumed uniform, that is, the earthquake spatial effects are not taken into account, the RSM, PEM, and THM (using ten samples) give very close results if the excitations are properly produced. The RSM is the most popular method, but the newly developed PEM may be the more efficient one. The THM needs to be executed for a number of ground acceleration samples and so was inefficient.

30.4.2.1.2 Wave Passage Effect Is Taken into Account

Figure 30.12(a) gives the axial force distribution of the bridge along the deck due to the seismic P waves, which travel along the longitudinal direction of the deck. All supports of the bridges are assumed to move with certain time lags; that is, the wave passage effect is taken into account. The apparent P wave speed is 3 km/sec. The following four computational models were used:

1. RSM (uniform ground motion is assumed for comparison only)
2. PEM (wave passage effect is considered)
3. THM (wave passage effect is considered using three ground-acceleration samples)
4. THM (wave passage effect is considered using ten ground-acceleration samples)

Figure 30.12(b) gives the transverse shear force distribution along the deck due to the seismic SH waves traveling along the deck and Figure 30.12(c) gives the corresponding vertical shear-force distribution. The above four computational models were used.

Figure 30.12 and Table 30.1 show that when the seismic wave-passage effect is taken into account, that is, the earthquake spatial effects are partly taken into account, the PEM and THM (using ten samples) give very close results. The RSM, which does not consider the wave-passage effect, may give quite different results; these may appear larger or smaller than, or very close to, the results by the more reasonable PEM or THM analyses. Therefore, such computations are necessary for evaluating the seismic spatial effects of long-span structures. The PEM gives the most reliable results with the least computational effort and, therefore, this method is strongly recommended.

30.4.2.1.3 Wave-Passage Effect and Incoherence Effect Are Jointly Taken into Account

Figure 30.13(a) gives the axial force distribution of the bridge along the deck due to the seismic P waves, which travel along the longitudinal direction of the deck. All supports of the bridge are assumed to move with certain time lags; that is, the wave passage effect is taken into account. In addition, the incoherence effects are also taken into account. Two coherence models, that is, the Loh–Yeh model

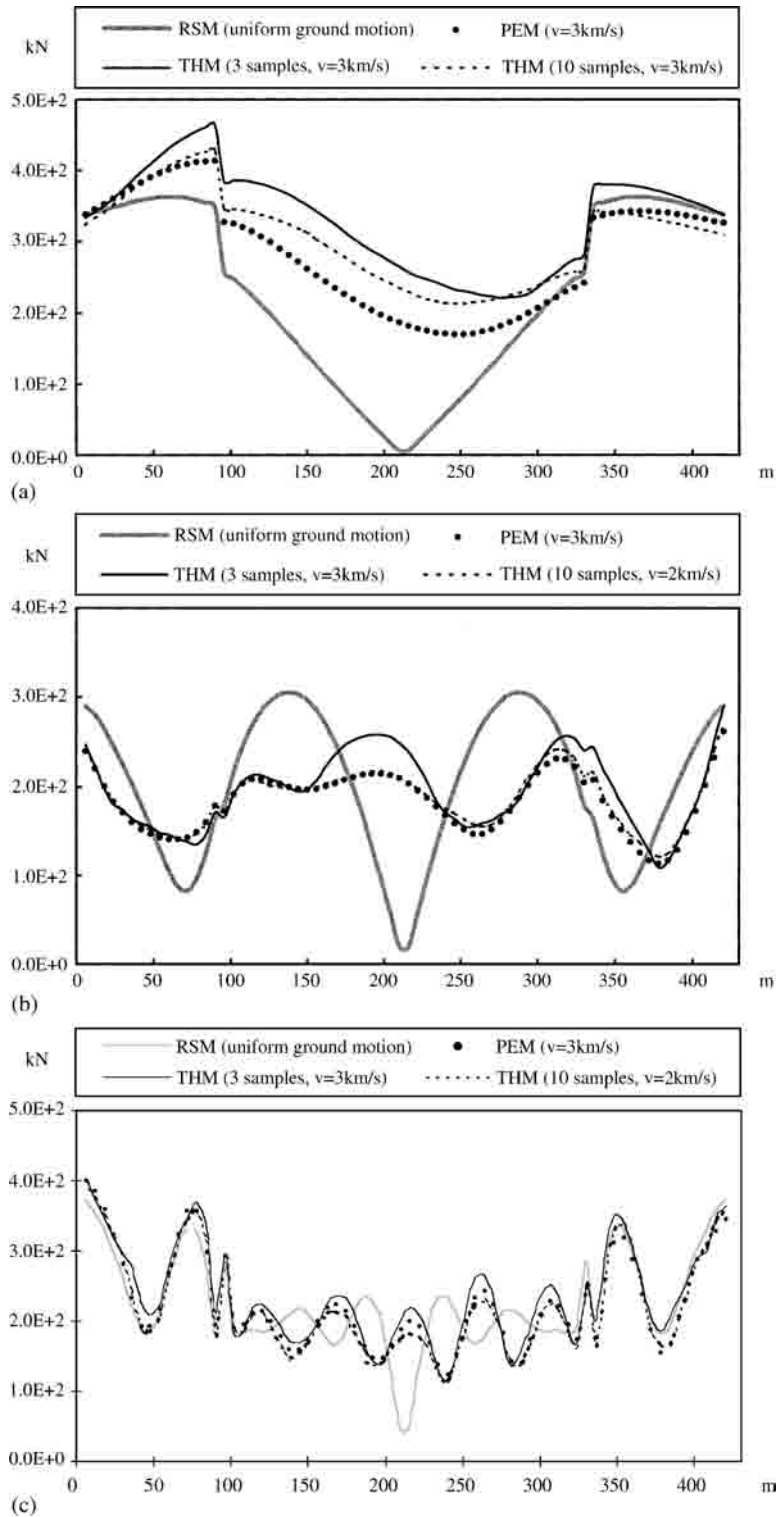


FIGURE 30.12 Deck force distribution of Song-Hua-Jiang bridge due to wave passage effect: (a) axial force distribution along the deck under P waves; (b) transverse shear force distribution along the deck under SH waves; (c) vertical shear force distribution along the deck under SV waves.

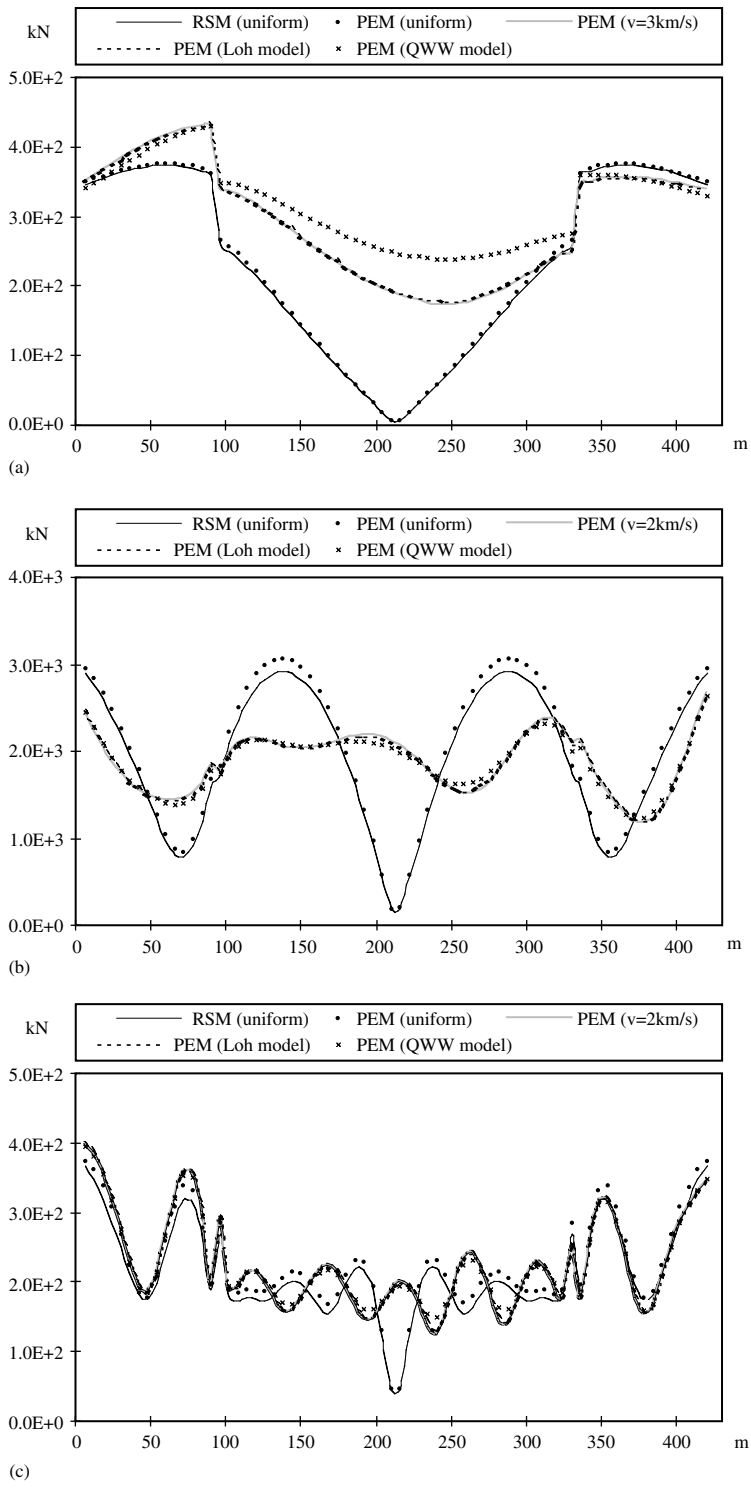


FIGURE 30.13 Deck force distribution of Song-Hua-Jiang bridge due to incoherence effect: (a) axial force distribution along the deck under P waves; (b) transverse shear force distribution along the deck under SH waves; (c) vertical shear force distribution along the deck under SV waves.

and the QWW model were used for evaluating such effects. The following five computational models were used:

1. RSM (uniform ground motion is assumed)
2. PEM (uniform ground motion is assumed)
3. PEM (wave passage effect is considered)
4. PEM (wave passage effect is considered also using the Loh–Yeh coherence model)
5. PEM (wave passage effect is considered also using the QWW coherence model)

Figure 30.13(b) gives the transverse shear force distribution along the deck due to the seismic SH waves traveling along the deck, and Figure 30.13(c) gives the corresponding vertical shear force distribution due to the seismic SV waves. For both analyses the above five computational models were used.

The above computations as well were executed on a P3-750 personal computer, and the computation times required by different methods are listed in Table 30.1.

From Figure 30.13 and Table 30.1, we can conclude that:

1. When ground motion is assumed to be uniform, the RSM and PEM give very close internal force responses (i.e., demands), with the PEM being more efficient.
2. The wave passage effect is an important factor that affects the seismic responses of long-span structures. To execute such seismic analyses, the PEM is not only theoretically quite reasonable, but also very efficient.
3. The incoherence effect appears to diverge when using different coherence models. Herein, the influence caused by the QWW model is more evident than that caused by the Loh–Yeh model. However, compared with the wave passage effect, the influence of the incoherence effect is of less importance.

30.4.2.2 San Joaquin Concrete Bridge

San Joaquin Bridge, located in California (see Figure 30.14), is a reinforced concrete bridge built in 2001. Its length is $36 + 50 + 50 + 50 + 36 = 222$ m, its width is 12 m, and the height of all piers is 16.76 m. The finite element model had 367 nodes (including 10 ground nodes) and 366 elements. Its basic natural period is 0.811s. Twenty modes were used in the mode-superposition analysis with all damping ratios being 0.05. The seismic analysis was carried out using the RSM and PEM, respectively. The RSM analysis was conducted according to the CALTRANS Code (1999) with $ARS = 0.2$ g, Type D soil profile and magnitude $M_w = 7.0$. The equivalent ground-acceleration power spectral density curve was produced by means of the Kaul method. All seismic waves were assumed to travel along the longitudinal direction of the bridge. The apparent P and S wave speeds were 3000 and 2000 m/s, respectively. The internal forces in the deck (i.e., the axial forces due to P waves, the transverse shear forces due to SH waves, and the vertical shear forces due to SV waves) were all computed using the following computational models:

1. RSM (uniform ground motion is assumed)
2. PEM (uniform ground motion is assumed)

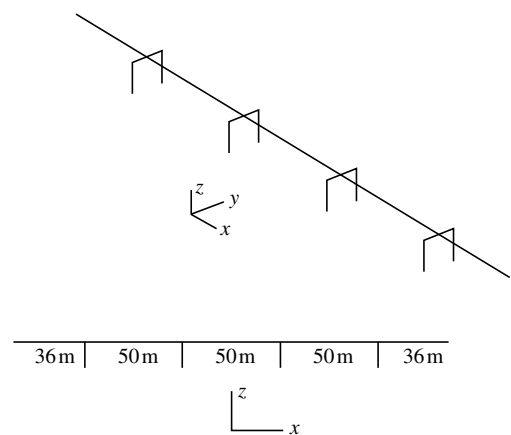


FIGURE 30.14 Structural model of San Joaquin bridge.

3. PEM (wave-passage effect is considered)
4. PEM (wave-passage effect is considered also using the Loh–Yeh coherence model)
5. PEM (wave-passage effect is considered also using the QWW coherence model)

The computational results are shown in Figure 30.15(a)–(c). This bridge is not very long. However, similar phenomena to those found for the bridge of Example 30.1 are still found. Clearly, when the ground motion is assumed to be uniform, the RSM and PEM still give very close results. If the wave-passage effect is taken into account, then the internal force distribution with the PEM will change considerably, particularly at the midpoint of the deck. It is known that, for symmetric bridges, the antisymmetric modes will not participate in the symmetric motions under the assumption of uniform ground motion. However, when the wave-passage effect is taken into account, this conclusion does not hold. It is obvious that, even for this shorter bridge, the wave-passage effect seems to be quite significant. The incoherence effect is comparatively not so important.

30.5 Long-Span Structures Subjected to Nonstationary Random Ground Excitations

A typical strong motion earthquake record consists of three stages. In the first stage, the intensity of the ground motion increases, which mainly reflects the motion of P waves. The intensity of the ground motion remains the strongest in the second stage, which mainly reflects the motion of S waves. The ground motion will die down in the last stage. Such a complete seismic motion is usually regarded as a nonstationary random process. If the nonstationary property is assumed to take place only for the intensity of the motion, then this random process is regarded as a uniformly modulated evolutionary random process. However, if the shape of the ground motion PSD curve also varies with time (in other words, the intensity and the distribution with frequency of the ground motion energy both depend on time), then the ground motion is regarded as a nonuniformly modulated evolutionary random process. It is usually accepted that when the intensity of the seismic motion in the second stage appears quite stationary while the time interval of this stage is much longer (e.g., three times or over) than the basic period of the structure under consideration, a simplified, stationary-based random analysis may be acceptable as a substitute of the nonstationary analysis. In fact, the basic periods of many long-span bridges range from 10 to 20 sec, and the stationary portion of a typical strong earthquake is usually less than 1 min, being only 20 to 30 sec in most cases. Therefore, nonstationary analyses are appropriate for such problems. Previously, such nonstationary random analyses have been considered very difficult. However, by using the recently developed PEM, combined with the precise integration method, such analyses have become relatively easy.

30.5.1 Modulation Functions

Some popular uniform modulation functions are listed below:

$$g(t) = \begin{cases} I_0(t/t_1)^2 & 0 \leq t \leq t_1 \\ I_0 & t_1 \leq t \leq t_2 \\ I_0 \exp\{c(t - t_2)\} & t \geq t_2 \end{cases} \quad (30.177)$$

$$g(t) = \begin{cases} 1 & t \geq 0 \\ 0 & t < 0 \end{cases} \quad (30.178)$$

$$g(t) = a[\exp(-\alpha_1 t) - \exp(-\alpha_2 t)], \quad 0 \leq \alpha_1 < \alpha_2 \quad (30.179)$$

$$g(t) = \sin \beta t \quad (30.180)$$

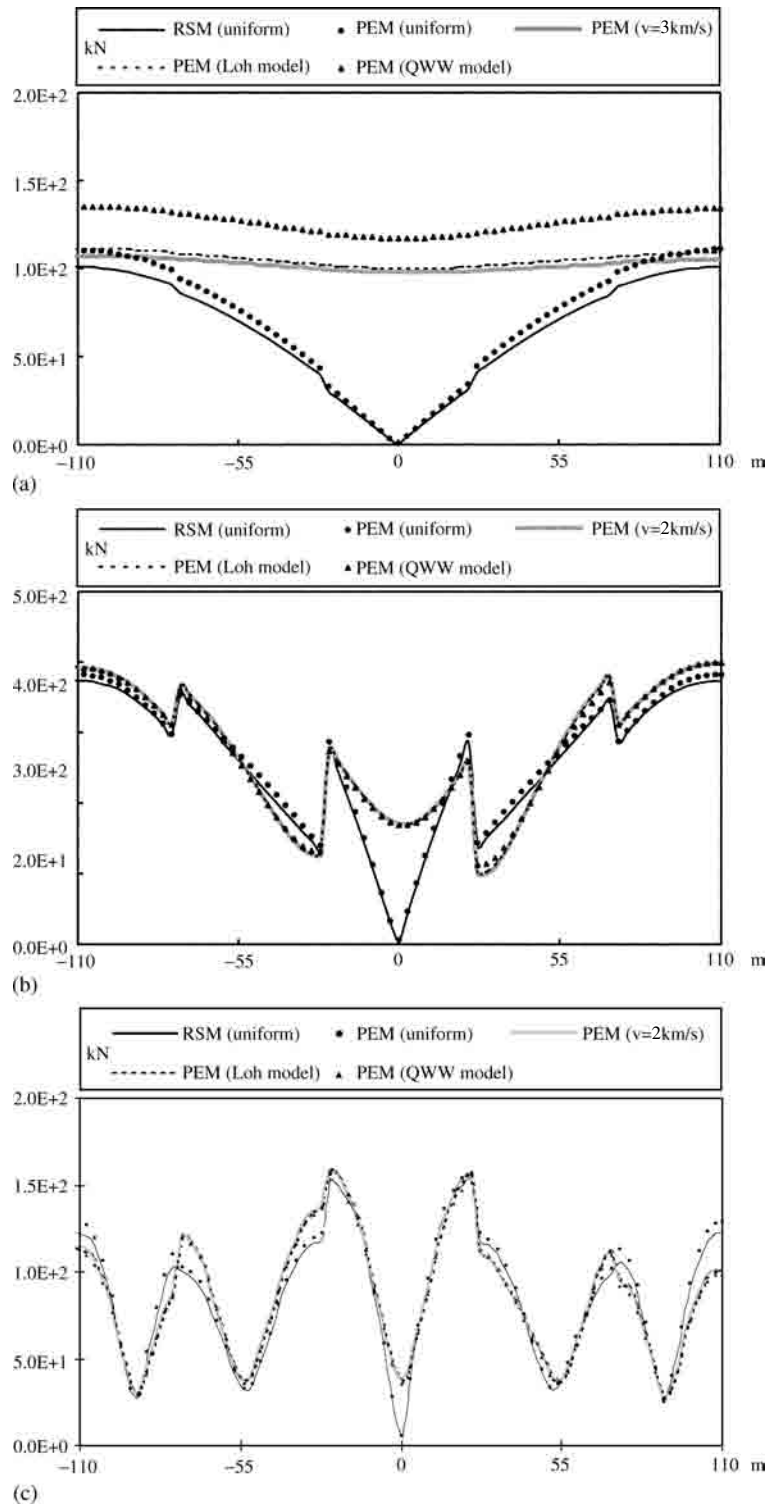


FIGURE 30.15 Deck force distribution of San Joaquin bridge due to incoherence effect: (a) axial force distribution along the deck under P waves; (b) transverse shear force distribution along the deck under SH waves; (c) vertical shear force distribution along the deck under SV waves.

Nonuniform modulation models have rarely been investigated. Lin et al. (1997a, 1997b) suggested the following nonuniform modulation model:

$$A(\omega, t) = \beta(\omega, t)g(t) = \exp\left(-\eta_0 \frac{\omega t}{\omega_\alpha t_\alpha}\right)g(t) \quad (30.181)$$

in which $g(t)$ is an amplitude modulation function; $\beta(\omega, t)$ is a frequency modulation function; and ω_α and t_α are the reference frequency and time, which are introduced to transform ω and t into dimensionless parameters. In principle, ω_α and t_α can be arbitrarily selected. Once they have been selected, the factor η_0 ($\eta_0 > 0$) can be adjusted accordingly to make the high-frequency components of the nonstationary random process decay more quickly than the low-frequency components and, thus, simulate the seismic motion more accurately. When $\eta_0 = 0$, that is, $\beta(\omega, t) = 1$, $A(\omega, t)$ reduces to the uniform modulation function $g(t)$.

30.5.2 The Formulas for Nonstationary Multiexcitation Analysis

For nonuniformly modulated multiexcitation problems, the pseudoexcitation for the corresponding stationary problems, that is, Equation 30.166, is extended to

$$\ddot{\mathbf{U}}_b(\omega, t) = \mathbf{A}(\omega, t)\mathbf{P}\exp(i\omega t) \quad (30.182)$$

in which the k th diagonal element of the $N \times N$ diagonal matrix $\mathbf{A}(\omega, t)$ is the modulation function $A_k(\omega, t)$ of the excitation which is applied to the k th support of the structure. In the case of uniformly modulated excitations, it is only necessary to replace all the nonuniform modulation functions $A_k(\omega, t)$ by the uniform modulation functions $g_k(t)$. Other formulae remain entirely unchanged. The $N \times r$ matrix \mathbf{P} can be generated by means of Equation 30.165 to Equation 30.174. Each column of $\ddot{\mathbf{U}}_b(\omega, t)$ can be regarded as a deterministic acceleration excitation vector. By substituting it into the right-hand side of Equation 30.93 and solving the equations of motion, a column of the matrix $\ddot{\mathbf{Y}}_r(\omega, t)$ can be produced.

Because $A_j(\omega, t)$ is a time-dependent and slowly varying function, the pseudoground displacement matrix can be computed approximately from

$$\tilde{\mathbf{U}}_b(\omega, t) = -\frac{1}{\omega^2}\ddot{\mathbf{U}}_b(\omega, t) \quad (30.183)$$

The pseudoquasi-static displacement matrix $\tilde{\mathbf{Y}}_s(\omega, t)$ can then be computed from Equation 30.92. Then, the PSD matrix of the absolute displacement vector $\mathbf{X}_s(\omega, t)$ is

$$\mathbf{S}_{X_s X_s}(\omega, t) = (\tilde{\mathbf{Y}}_r(\omega, t) + \tilde{\mathbf{Y}}_s(\omega, t))^* (\tilde{\mathbf{Y}}_r(\omega, t) + \tilde{\mathbf{Y}}_s(\omega, t))^T \quad (30.184)$$

If a group of pseudointernal forces, denoted as $\tilde{\mathbf{N}}_e$, has been computed, then the PSD matrix of the corresponding internal forces \mathbf{N}_e can be computed from

$$\mathbf{S}_{N_e N_e}(\omega, t) = \tilde{\mathbf{N}}_e^* \tilde{\mathbf{N}}_e^T \quad (30.185)$$

When the ground acceleration PSD matrix is known, the corresponding pseudoacceleration vector $\ddot{\mathbf{u}}_b$ is easy to generate according to Equation 30.163 to Equation 30.166. If instead, the ground displacement PSD matrix or velocity PSD matrix is known, then the acceleration PSD matrix can be obtained by multiplying the displacement or velocity PSD matrices by ω^4 or ω^2 , respectively.

30.5.3 Expected Extreme Values of Nonstationary Random Processes

The evaluation of the peak amplitude responses of structures subjected to nonstationary seismic excitations has also received much attention (Shrikhande and Gupta, 1997; Zhao and Liu, 2001). Previously, only very simple structures could be computed. However, by using the PEM, complicated structures can be analyzed, as is briefly described below.

To evaluate the expected extreme value responses of a structure subjected to nonstationary Gaussian excitations, the duration of which the intensity of the excitation peaks exceeds 50% of the maximum peak intensity denoted by $[t_0, t_0 + \tau]$ is taken as the equivalent stationary duration in order to use Equation 30.40 to Equation 30.49 to evaluate the desired expected extreme values. Provided that the time-dependent PSD of any arbitrary response $y(t)$, that is $S_{yy}(\omega, t)$, has been computed over that equivalent duration using the PEM, then the equivalent stationary PSD over that duration is

$$S'_{yy}(\omega) = \frac{1}{\tau} \int_{t_0}^{t_0+\tau} S_{yy}(\omega, t) dt \quad (30.186)$$

To compute the extreme value responses based on Equation 30.177, the parameters t_0 and τ are chosen as

$$t_0 = t_1/\sqrt{2}, \quad \tau = t_2 + \ln 2/c - t_1/\sqrt{2} \quad (30.187)$$

Thus, the equivalent stationary random responses are obtained and the subsequent processing can still use Equation 30.40 to Equation 30.49.

30.5.4 Numerical Comparisons with the Corresponding Stationary Analysis

The example of the Song-Hua-Jiang suspension bridge of the last section is used here for the seismic nonstationary random vibration analysis. The results are compared with those from the corresponding stationary random-vibration analyses with the ground assumed to move uniformly (i.e., at an apparent wave speed $v_{app} = \infty$), or to move at a limited apparent wave speed v_{app} (with the wave-passage effect is taken into account), which is 3 km/sec for P waves and 2 km/sec for S waves.

The nonstationary random excitation model $z(t) = g(t)x(t)$ was used in which the auto-PSD of $x(t)$ is assumed to be identical to that used for the stationary excitation in the preceding section. The frequency-domain parameters also remained the same. The modulation function had the form of Equation 30.177 with $t_1 = 8.0$, $t_2 = 20.0$, and $c = 0.20$. The duration of the earthquake was $t \in [0, 25]$, and the time step-size was $\Delta t = 0.5$.

The nonstationary analysis results are shown in Figure 30.16(a) to (c), and are compared with the results of the corresponding stationary random vibration analyses. Clearly, for such a long-span bridge, the wave passage effect is quite significant in its seismic analysis, as seen in Figure 30.11 to Figure 30.13. In addition, whether for uniform ground motion or for differential ground motion (i.e., the wave-passage effect is considered), the nonstationary responses are always smaller than the corresponding stationary responses. The maximum difference between their corresponding peak values may reach up to 23.1% for the present problem, as shown in Table 30.2. For very slender bridges, this nonstationary property will be even stronger.

By means of the PEM combined with the precise integration method (its HPD-E form for the modulation function used in this example), such modification can be fulfilled quickly and conveniently. The computational effort required by the nonstationary analysis is only about 25 min (see Table 30.3).

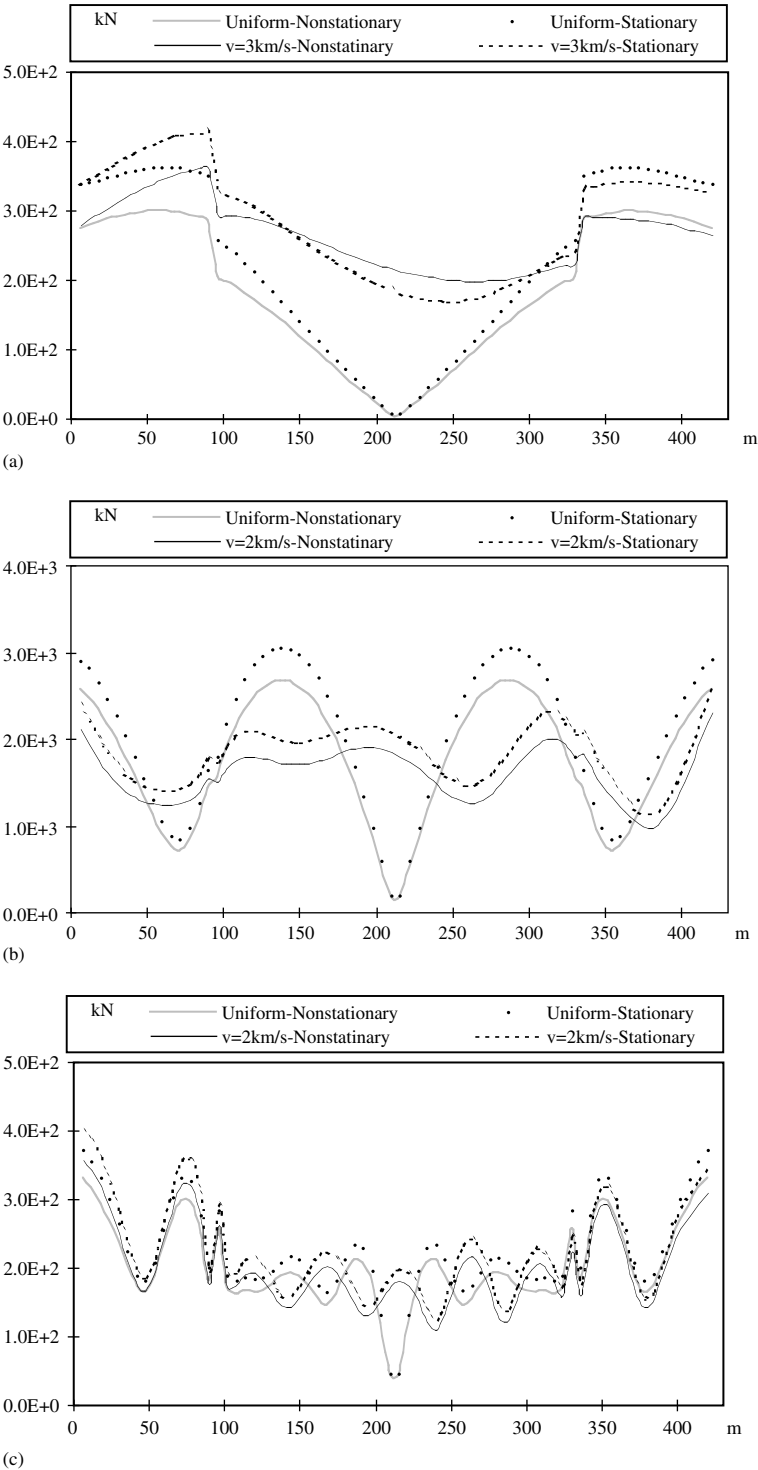


FIGURE 30.16 Deck-force distribution of Song-Hua-Jiang bridge due to uniform and differential, and stationary and nonstationary random ground motion: (a) axial force distribution along the deck under P waves; (b) transverse shear force distribution along the deck under SH waves; (c) vertical shear force distribution along the deck under SV waves.

TABLE 30.2 Comparisons of the Expected Extreme Values of Deck Internal Forces

Ground Motion	Internal Forces in the Deck (kN)	Distance from the Left End (m)	Nonstationary Responses	Stationary Responses	Increases (%)
Uniform ground motion	Axial force N due to P waves	6	274.95	337.60	22.8
	Transverse shear force F_y due to SH waves	72	712.19	832.47	16.9
	Vertical shear force F_z due to SV waves	258	146.00	165.81	13.6
Wave-passage effect	Axial force N due to P waves	420	264.51	325.61	23.1
	Transverse shear force F_y due to SH waves	270	1292.17	1515.75	17.3
	Vertical shear force F_z due to SV waves	246	134.00	152.89	14.1

TABLE 30.3 CPU Times Required by PEM for Nonstationary Analyses (Units: Seconds)

Modes Used	30	100
Uniform ground motion	450	1142
Wave passage effect	543	1479
Extracting modes	143	181

30.6 Conclusions

For short-span structures, the ground spatial effects are negligible, and the seismic analyses using RSM, PEM, or THM (with a sufficient number of samples) are relatively close to one another provided that the ground accelerations have been produced properly, and so are almost equivalent. Although they have almost the same accuracy level, their efficiencies are quite different. Of the three methods, if the structural models are rather complex (e.g., the FEM models have thousands or more DoF and need dozens or hundreds of modes for mode superposition), then the PEM will have the highest computational efficiency.

For long-span structures, the wave passage effect is an important factor for structural seismic responses. The influence may produce more conservative, or more dangerous, designs, which is difficult to predict by intuitive experience. Thus, computer-based analysis is a preferable choice. The PEM is comparatively efficient and accurate, and is recommended. If the apparent seismic wave speed is not available, then a few possible speeds can be taken for computation, with the most unfavorable results being used in the practical design. The reasonable selection of an incoherence model for a special region needs further study, but its influence seems to be much less than that caused by the wave passage effect. Therefore, for less important long-span structures, the incoherence effect can be neglected. The influence of nonstationarity is also significant for very flexible long-span structures, and should be taken into account. The PEM, combined with the precise integration method, provides a powerful tool for such nonstationary analysis.

References

Berrah, M. and Kausel, E., Response spectrum analysis of structures subjected to spatially varying motions, *Earthquake Eng. Struct. Dyn.*, 21, 461–470, 1992.

Caughey, T.K. and Stumpf, H.J., Transient response of a dynamic system under random excitation, *Trans. ASME, JAM*, 28, 563–566, 1961.

Clough, R.W. and Penzien, J. 1993. *Dynamics of Structures*, McGraw-Hill, New York.

Davenport, A.G., Note on the distribution of the largest value of a random function with application to gust loading, *Proc. Inst. Civil Eng.*, 28, 187–196, 1961.

- Deodatis, G., Simulation of ergodic multivariate stochastic processes, *J. Eng. Mech.*, 122, 778–787, 1996.
- Dumanoglu, A. and Severn, R.T., Stochastic response of suspension bridges to earthquake forces, *Earthquake Eng. Struct. Dyn.*, 19, 133–152, 1990.
- Ernesto, H.Z. and Vanmarcke, E.H., Seismic random vibration analysis of multi-support structural systems, *J. Eng. Mech.*, ASCE, 120, 1107–1128, 1994.
- European Committee for Standardization, 1995. Eurocode 8, *Structures in Seismic Regions — Design Part 2: Bridge*, Brussels, Belgium.
- Fan, L.C., Wang, J.J., and Chen, W., Response characteristics of long-span cable-stayed bridges under non-uniform seismic action, *Chin. J. Comput. Mech.*, 18, 358–363, 2001 (in Chinese).
- Feng, Q.M. and Hu, Y.X., Mathematical model of spatial correlative ground motion, *Earthquake Eng. Eng. Vib.*, 1, 1–8, 1981 (in Chinese).
- Gupta, I.D. and Trifunac, M.D., A note on statistic of level crossing and peak amplitude in stationary stochastic process, *Eur. Earthquake Eng.*, 12, 52–58, 1998.
- Harichandran, R.S. and Vanmarcke, E.H., Stochastic variation of earthquake ground motion in space and time, *J. Eng. Mech.*, ASCE, 112, 154–175, 1986.
- Housner, G.W., Characteristic of strong motion earthquakes, *Bull. Seism. Soc. Am.*, 37, 17–31, 1947.
- Kaul, M.K., Stochastic characterization of earthquake through their response spectrum, *Earthquake Eng. Struct. Dyn.*, 6, 497–510, 1978.
- Kiureghian, A.D., Structural response to stationary random excitation, *J. Eng. Mech.*, Div. ASCE, 106, 1195–1213, 1980.
- Kiureghian, A.D. and Neuenhofer, A., Response spectrum method for multi-support seismic excitations, *Earthquake Eng. Struct. Dyn.*, 21, 713–740, 1992.
- Lee, M. and Penzien, J., Stochastic analysis of structures and piping systems subjected to stationary multiple support excitations, *Earthquake Eng. Struct. Dyn.*, 11, 91–110, 1983.
- Lin, Y.K. 1967. *Probabilistic Theory of Structural Dynamics*, McGraw-Hill, New York.
- Lin, J.H., A fast CQC algorithm of PSD matrices for random seismic responses, *Comput. Struct.*, 44, 683–687, 1992.
- Lin, J.H., Li, J.J., Zhang, W.S., and Williams, F.W., Non-stationary random seismic responses of multi-support structures in evolutionary inhomogeneous random fields, *Earthquake Eng. Struct. Dyn.*, 26, 135–145, 1997a.
- Lin, J.H., Shen, W.P., and Williams, F.W., A high precision direct integration scheme for non-stationary random seismic responses of non-classically damped structures, *Struct. Eng. Mech.*, 3, 215–228, 1995a.
- Lin, J.H., Shen, W.P., and Williams, F.W., A high precision direct integration scheme for structures subjected to transient dynamic loading, *Comput. Struct.*, 56, 113–120, 1995b.
- Lin, J.H., Sun, D.K., Sun, Y., and Williams, F.W., Structural responses to non-uniformly modulated evolutionary random seismic excitations, *Commun. Numer. Meth. Eng.*, 13, 605–616, 1997b.
- Lin, J.H., Zhang, Y.H. 2004. *Pseudo Excitation Method of Random Vibration*, Science Press, Beijing (in Chinese).
- Lin, J.H., Zhang, W.S., and Li, J.J., Structural responses to arbitrarily coherent stationary random excitations, *Comput. Struct.*, 50, 629–633, 1994a.
- Lin, J.H., Zhang, W.S., and Williams, F.W., Pseudo-excitation algorithm for non-stationary random seismic responses, *Eng. Struct.*, 16, 270–276, 1994b.
- Lin, Y.K., Zhang, R., and Yong, Y., Multiply supported pipeline under seismic wave excitations, *J. Eng. Mech.*, 116, 1094–1108, 1990.
- Liu, T.Y. and Liu, G.T., Seismic random response analysis of Arch Dams, *Eng. Mech.*, 17, 20–25, 2000, in Chinese.
- Loh, C.H. and Yeh, Y.T., Spatial variation and stochastic modeling of seismic differential ground movement, *Earthquake Eng. Struct. Dyn.*, 16, 583–596, 1988.
- Luco, J.E. and Wong, H.L., Response of a rigid foundation to a spatially random ground motion, *Earthquake Eng. Struct. Dyn.*, 14, 891–908, 1986.

- National Standard of The People's Republic of China, 2001. *Code for Seismic Design of Buildings GB50011-2001*, Chinese Architectural Industry Press, Beijing.
- Newland, D.E. 1975. *An Introduction to Random Vibration and Spectral Analysis*, Longmans, London.
- Oliveira, C.S., Hao, H., and Penjien, J., Ground motion modeling for multiple-input structural analysis, *Struct. Saf.*, 10, 79–93, 1991.
- Priestly, M.B., Power spectral of non-stationary random responses, *J. Sound Vib.*, 6, 86–97, 1967.
- Qu, T.J., Wang, J.J., and Wang, Q.X., A practical power spectrum model for spatially varying seismic motion, *J. Seismol.*, 18, 55–62, 1996.
- Shrikhande, M. and Gupta, V.K., A generalized approach for the seismic response of structural systems, *Eur. Earthquake Eng.*, 11, 3–12, 1997.
- Sun, J.J. and Jiang, J.R., Parameters of Kanai-Tajimi power spectrum according to the response spectrum of Chinese code, *Chin. J. World Earthquake Eng.*, 8, 42–48, 1990 (in Chinese).
- Vanmarcke, E.H., Properties of spectral moments with applications to random vibration, *J. Eng. Mech., Div. Proc. ASCE*, 98, 425–446, 1972.
- Wang, G.W., Cheng, G.D., Shao, Z.M., Chen, H.Q. 1999. *Optimal Fortification Intensity and Reliability of Aseismic Structures, Part 4*, Science Press, Beijing, in Chinese.
- Wilkinson, J.H., Reinsch, G. 1971. *Linear Algebra*, Oxford University Press, London.
- Wilson, E.L. and Kiureghian, A.D., A replacement for the SRSS method in seismic analysis, *Earthquake Eng. Struct. Dyn.*, 9, 187–192, 1981.
- Xue, S.D., Li, M.H., Cao, Z., and Zhang, Y.G. 2000. Random vibration analysis of lattice shells subjected to multi-dimensional earthquake inputs. In *Proceedings of the International Conference on Advances in Structural Dynamics*, December 2000, pp. 777–784. Elsevier, Hong Kong.
- Zhao, F.X. and Liu, A.W., Relationship between power-spectral-density functions and response spectra of earthquake ground motions, *Earthquake Eng. Eng. Vib.*, 21, 30–35, 2001 (in Chinese).
- Zhong, W.X. 2004. *The Dual System in Applied Mechanics and Optimal Control*, Kluwer Academic Publishers, Boston.
- Zhong, W.X. and Williams, F.W., A precise time step integration method, *Proc. Inst. Mech. Engrs*, 208C, 6, 427–430, 1995.

Seismic Qualification of Equipment

31.1	Introduction	31-1
31.2	Distribution Qualification	31-1
	Drive-Signal Generation • Distribution Spectra • Test Procedures	
31.3	Seismic Qualification	31-6
	Stages of Seismic Qualification • Test Preliminaries • Single-Frequency Testing • Multifrequency Testing • Generation of RRS Specifications	

Clarence W. de Silva

The University of British Columbia

Summary

Product qualification is intended for determining the adequacy of a product of good quality for a specific application or a range of applications. A good example is the seismic qualification of a nuclear power plant. This chapter presents test procedures used in product qualification, with emphasis on seismic qualification. Both single-frequency testing and multifrequency testing are described. Generation of test signal specifications is outlined.

31.1 Introduction

Vibration testing is used in product qualification. Here, the objective is to test the adequacy of a product of good quality for a specific use in a typical operating environment. Clearly, the nature of testing and the test requirements, including test specifications, will depend on the type of application and the class of product. In this chapter, we will consider just two types of product qualification: distribution qualification and seismic qualification. Procedures of vibration testing for other types of qualification will be similar.

31.2 Distribution Qualification

The term “distribution qualification” denotes the process by which the ability of a product to withstand a clearly defined distribution environment is established. Dynamic effects on the product due to handling loads, characteristics of packaging, and excitations under various modes of transportation (truck, rail, air, and ocean) must be properly represented in the test specifications used for distribution qualification. If a product fails a qualification test, then corrective measures and subsequent requalification are necessary prior to commercial distribution. Product redesign, packaging redesign, and modification of existing shipping procedures might be required to meet qualification requirements.

Often, the necessary improvements can be determined by analyzing data from prior tests. Proper distribution qualification will result in improved product quality (and associated reliability and performance), reduced wastage and inventory problems, cost-effective packaging, reduced shipping and handling costs, and reduced warranty and service costs.

TABLE 31.1 Comparison of Test Types

	Sine Testing	Random Testing	Narrowband Random Sweep	Broadband Random Sweep
Simultaneous multimodal (multiresonant) excitation possible?	No	Yes	No	Yes
Test duration	Long	Short	Long	Moderate
Power requirements	Low	High	Low	High
Represents a random environment?	No	Yes	Yes	Yes
Test system cost	Low	High	Moderate to high	High
Overtesting possibility	High	Low	High	Low

Random testing can more accurately represent vibrations in distribution environments. Several characteristics make it superior to sine testing. A sine test is a single-frequency test; thus, only one frequency is applied to a test object at a given instant. As a result, failure modes caused by the simultaneous excitation of two or more modes of vibration cannot be realized by sine testing, at least under steady excitations. On the other hand, in random testing, many frequencies are simultaneously applied to the test object. Therefore, conditions are more conducive to multiple-mode excitations and associated complex failures. A comparison of testing with four types of excitation signals is given in Table 31.1.

31.2.1 Drive-Signal Generation

The first step in signal synthesis for driving the exciter is to assign independent and identically distributed, random phase angles to the digitized spectral magnitude (spectral lines) of the drive spectrum. The number of lines chosen is consistent with the fast Fourier transform (FFT) algorithm that is employed and the desired numerical accuracy. The inverse Fourier transform is obtained from the resulting discrete, complex Fourier spectrum. In general, the signal thus obtained would not possess ergodicity and Gaussianity.

Stationarity can be attained by randomly shifting the signal with respect to time and summing the results. The resulting signal would also be weakly ergodic. Ergodicity is improved by increasing the duration of the signal. To obtain Gaussianity, a sufficiently large number of time-shifted signals must be summed as dictated by the central limit theorem. Furthermore, because the magnitude of a Gaussian signal almost always remains within three times its standard deviation (99.7% of the time), Gaussianity can be imposed simply by windowing the time-shifted signal. The amplitude of the window function is governed by the required standard deviation of the drive signal. Unwanted frequency components introduced as a result of sharp end transitions in each time-shifted signal component can be suppressed by properly shaping the window. This process introduces a certain degree of nonstationarity into the synthesized signal, particularly if the windowed signal segments are joined end-to-end to generate the drive signal. A satisfactory way to overcome this problem is to introduce a high overlap from one segment to the next. Because the processing time increases in proportion to the degree of overlap, however, a compromise must be reached.

In summary, for a given drive spectral magnitude the drive signal can be synthesized as follows:

1. Assign independent, identically distributed random phase values to the drive-spectral lines.
2. Perform an inverse Fourier transform of the resulting spectrum using FFT.
3. Generate a set of independent and identically distributed time-shift values.
4. Perform a time-shift of the signal obtained in Step 2 using the values from Step 3.
5. Window the time-shifted signals.
6. Join the windowed signals with a fixed overlap.

The resulting digital drive signal is converted into an analog signal using a digital-to-analog converter (DAC) and passed through a low-pass filter to remove any unwanted frequency components before it is used to drive the shaker. This procedure is illustrated in [Figure 31.1](#).

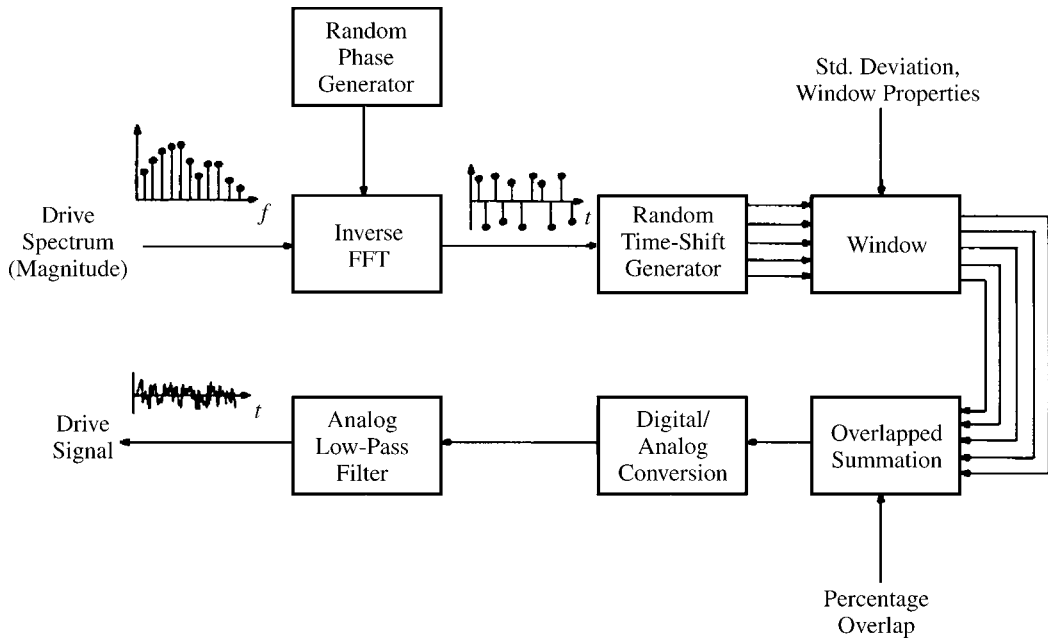


FIGURE 31.1 The synthesis of a random drive signal.

31.2.2 Distribution Spectra

The distribution environment to which a product is subjected depends on several factors. In particular, one must consider (1) the nature and severity of handling prior to and during shipment, (2) the mode of transportation (truck, rail, air cargo, ship), (3) the geographic factors, (4) the environmental conditions, (5) the characteristics of the protective packaging used, and (6) the dynamic characteristics of the product itself. These factors are complex and essentially random in nature. Laboratory simulation of such an environment is difficult even if a combination of several types of tests — e.g., vibration, shock, drop, and thermal cycling — is employed. A primary difficulty arises from the requirement that test specifications should be simple, yet accurately represent the true environment. The test must also be repeatable to allow standardization of the test procedure and to facilitate evaluation and comparison of test data. Finally, testing must be cost effective.

During transportation, a package is subjected to multi-degree-of-freedom (multi-DoF) excitations that can include rectilinear and rotational excitations at more than one location simultaneously. However, test machines are predominantly single-axis devices that generate excitations along a single direction. Thus, any attempt to duplicate a realistic distribution environment in a laboratory setting can prove futile.

An alternative might be to use trial shipments. However, because of the random nature of the distribution environment, many such trials would be necessary before the data would be meaningful. Therefore, trial shipments are not appealing from a cost-benefit point of view and also because test control and data acquisition would be difficult. Data from trial shipments are extremely useful, however, in developing qualification-test specifications and in improving existing laboratory test procedures.

A more realistic goal of testing would be to duplicate possible failure and malfunction modes without actually reproducing the distribution environment. This, in fact, is the underlying principle of testing for distribution qualification. For instance, sine tests can reproduce some types of failure caused during shipment even though the test signal does not resemble the actual dynamic environment; however, random testing is generally superior.

Test specifications are expressed in terms of distribution spectra in distribution qualification where random testing is used. Specification development begins with a sufficient collection of realistic data.

Sources of data include field measurements during trial shipments, computer simulations (e.g., Monte Carlo simulations), and previous specifications for similar products and environments. For best results, all possible modes of transportation, excitation levels, and handling severities should be included. The data, expressed as power spectral density (PSD), must be reduced to a common scale — particularly with respect to the duration of excitation — for comparison purposes. Scaling can be accomplished by applying a similarity law based on a realistic damage criterion. For example, a similarity law might relate the excitation duration and the PSD level such that the value of a suitable damage function would remain constant. Time-dependent damage criteria are developed primarily on the basis of fatigue–strength characteristics of a test product.

Owing to nonlinearities of the environment, spectral characteristics (frequency content) will change with the excitation level. If such changes are significant, then they should be properly accounted for. The influence of environmental conditions, such as temperature and humidity, must be considered as well. The PSD curves conditioned in this manner are plotted on a log–log plane to establish an envelope curve. This curve represents the worst composite environment that is typically expected. The envelope is then fitted with a small number of straight-line segments.

At this point, the PSD curve should be scaled so that the root-mean-square (RMS) value is equal to that before the straight-line segments were fitted. The resulting PSD curve can be used as the test specification. Test duration can be established from the time-scaling criterion. If the corresponding test duration is excessively long, thereby making the test impractical, then the test duration should be shortened by increasing the test level according to a realistic similarity criterion.

Product overtesting can be significant only if one reference spectrum is used to represent all possible distribution environments. Shipping procedures should thus be classified into several groups depending on the dynamic characteristics of the shipping environment and a representative reference spectrum should be determined for each group. If a range of products with significantly diverse dynamic characteristics is being qualified, then reference spectra should be modified and classified according to product type. At the testing stage, a reference spectrum must be chosen from a spectral database depending on the product type and applicable shipping procedures. Alternatively, a general composite spectrum can be developed by assigning weights to a chosen set of reference spectra and computing the weighted sum.

Vibration levels in land vehicles and aircraft can range up to several kilohertz (kHz). Ships are known to have lower levels of excitation. In general, the energy content in vibrations experienced during the distribution of computer products is known to remain within 20 Hz. Consequently, the test specification spectra (reference spectra) used in distribution qualification are usually limited to this bandwidth. The typical specification curve shown in [Figure 31.2](#) can be specified simply from the co-ordinates of the break points of the PSD curve. Intermediate values can be determined easily because the break points are joined by straight-line segments on a log–log plane.

The area beneath the PSD curve gives the required mean-square value of the test excitation. The square root of this value is the RMS value. It is specified along with the PSD curve, even though it can be determined directly from the PSD curve. An acceptable tolerance band for the control spectrum — usually ± 3 db — is also specified. Test duration should be supplied with the test specification.

31.2.3 Test Procedures

Dynamic-test systems with digital control are easy to operate. In menu-driven systems, a routine or mode is activated by picking the appropriate item from a menu that is displayed on the cathode-ray tube screen. The system asks for necessary data, and then necessary parameter values are entered into the system. Typically, the user supplies lower and upper RMS limits for test abort levels, break point co-ordinates of the reference spectrum, and test duration. The tolerance bands for test spectrum equalization and the accelerometer sensitivities are also entered. More than one test setup can be stored, a number being assigned to denote each test.

Preprogrammed tests can be modified using a similar procedure in the edit mode. Any preprogrammed test can be carried out simply by entering the corresponding test number. Computed

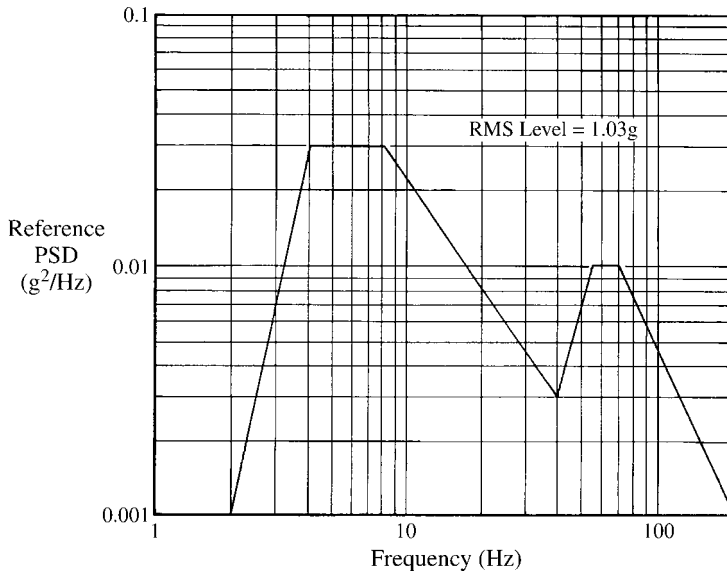


FIGURE 31.2 A reference spectrum for the distribution qualification of personal computers.

results, such as PSD curves and transmissibility functions, are stored for future evaluation. If desired, these results can be displayed, printed, or plotted with proper annotations and scales while the test is in progress.

Main steps of a typical test procedure are as follows:

1. Carefully examine the test object and record obvious structural defects, abnormalities, and hazardous or unsafe conditions.
2. Perform a functional test (i.e., operate the product) according to specifications and record any malfunctions and safety hazards.
Note: The test may be abandoned at this stage if the test object is defective.
3. Mount the test object rigidly on the shaker table so that the loading points and the excitation axis are consistent with standard shipping conditions and the specified test sequence.
4. Perform an exploratory test at half the specified RMS level (one fourth the specified PSD level). Monitor the response of the test package at critical locations including the control sensor location.
5. Perform the full-level test for the specified duration. Record the response data.
6. Change the orientation in accordance with the specified test sequence and repeat the test.
7. After the test sequence is completed, carefully inspect the test object and record any structural defects, abnormalities, and safety hazards.
8. Conduct a functional test and record any malfunctions, failures, and safety problems.

An exploratory test at a fraction of the specified test level is required for new product models that are being tested for the first time, or for older models that have been subjected to major design modifications. Three mutually perpendicular axes are usually tested, including the primary orientation (vertical axis) that is used for shipping. If product handling during distribution is automated, then testing only the primary axis is adequate.

When multiple tests are required, the test sequence is normally stipulated. If the test sequence is not specified, then it can be chosen such that the least-severe orientation (orientation least likely to fail) is tested first. The test is repeated for the remaining orientations, ending with the most severe one. The rationale is that with this choice of test sequence, the aging of the most severe direction would be maximized, thereby making the test more reliable.

The test report should contain the following:

1. *Description of the test object*: Serial number, size (dimensions and weight), product function (e.g., system unit, hard drive, power supply, printer, keyboard, mouse, monitor, and floppy disk drive of a personal computer), and packaging particulars. Descriptive photos are useful.
2. *Test plan*: Usually standard and attached to the report as an appendix.
3. *Test setup*: Test orientations, sensor (accelerometer) locations, details of mounting fixtures, and a brief description of the test apparatus. Photos may be included.
4. *Test procedure*: A standard attachment that is usually given according to corporate specifications.
5. *Test results*: Ambient conditions in the laboratory (e.g., temperature, humidity), pretest observations (e.g., defects, abnormalities, malfunctions), test data (e.g., reference spectrum, equalized control spectrum, drive spectrum, response time histories and corresponding spectra, transmissibility plots, coherence plots) and posttest observations.
6. *Comments and recommendations*: General comments regarding the test procedure and test item and recommendations for improving the test, product or packaging.

Names and titles of the personnel who conducted the test should be given in the test report, with appropriate signatures, dates, and location of the test facility.

Tests for distribution qualification can be conducted on both packaged products and those without any protective packaging, even though it is the packaged product that is shipped. However, the reference spectra used in the two cases are usually not the same. The spectrum used for testing a product without protective packaging is generally less severe. Response spectra that are used for testing an unpackaged product should reflect the excitations experienced by the product during packaging.

31.3 Seismic Qualification

Frequently, it is necessary to determine whether a given piece of equipment is capable of withstanding a pre-established seismic environment in a specific application. This process is known as seismic qualification. For example, electric utility companies should qualify their equipment for seismic capability before installing it in earthquake-prone geographic localities. Safety-related equipment in nuclear power plants also requires seismic qualification. Regulatory agencies usually specify the general procedures to follow in seismic qualification.

Seismic qualification by testing is appropriate for complex equipment, but in such cases, the equipment size is a limiting factor. For large systems that are relatively simple to model, qualification by analysis is suitable. Often, however, both testing and analysis are needed in the qualification of a given piece of equipment. Seismic qualification of equipment by testing is accomplished by applying a dynamic excitation by means of a shaker to the equipment, which is suitably mounted on a test table, and then monitoring structural integrity and functional operability of the equipment. Special attention should be given to the development of the dynamic-test environment, mounting features, the operability variables that should be monitored, the method of monitoring functional operability and structural integrity, and the acceptance criteria used to decide qualification.

In monitoring functional operability, the test facility would normally require auxiliary systems to load the test object or to simulate in-service operating conditions. Such systems include actuators, dynamometers, electrical-load and control-signal circuitry, fluid-flow and pressure loads, and thermal loads. In seismic qualification by analysis, a suitable model is first developed for the equipment, and then static or dynamic analysis (or computer analysis) is performed under an analytically defined dynamic environment. The analytical dynamic environment is developed on the basis of the specified dynamic environment for seismic qualification. By analytically or computationally determining system response at various locations, and by checking for such crucial parameters as relative deflections, stresses, and strains, qualification can be established.

31.3.1 Stages of Seismic Qualification

Consider the construction of a nuclear power plant. In this context, the plant owner is the customer. Actual construction of the plant is done by the plant builder, who is directly responsible to the customer concerning all equipment purchased from the equipment supplier or vendor. Often, the vendor is also the equipment manufacturer. The equipment may be purchased by the customer and handed over to the plant builder or directly purchased by the plant builder. Accordingly, the purchaser could be the plant builder or the plant owner. A regulatory agency might stipulate seismic-excitation capability requirements for the equipment used in the plant, or might specify the qualification requirements for various categories of equipment. The customer is directly responsible to the regulatory agency for adherence to these stipulations. The vendor, however, is responsible to the plant builder and the customer for the seismic capability of the equipment. The vendor may perform seismic qualification on the equipment according to required specifications. More often, however, the vendor hires the services of a test laboratory, which is the contractor, for seismic qualification of equipment in the plant. A reviewer, who is hired by the plant builder or the customer, may review the qualification procedure and the report, which are usually developed by the test laboratory by adhering to the qualification requirements. [Figure 31.3](#) gives a flowchart for test-object movement and for associated information interactions between various groups in the qualification program.

A basic step in any qualification program is the preparation of a qualification procedure. This is a document that describes in sufficient detail such particulars as the tests that will be conducted on the test object, pretest procedures, the nature of test-input excitations and the method of generating these signals, inspection and response-monitoring procedures during testing, definitions of equipment malfunction, and qualification criteria. Where analysis is also used in the qualification, the analytical methods and computer programs that will be used should be described adequately in the qualification procedure. The qualification procedure is prepared by the test laboratory (contractor), equipment particulars are obtained from the vendor or the purchaser, and the purchaser usually supplies the test environment for which the equipment will be qualified.

Before the qualification tests are conducted, the test procedure is submitted to the purchaser for approval. The purchaser normally hires a reviewer to determine whether the qualification procedure satisfies the requirements of both the regulatory agency and the purchaser. There could be several stages of revision of the test procedure until it is accepted by the purchaser upon the recommendation of the reviewer.

The approved qualification procedure is sent to the test laboratory and qualification is performed accordingly. The test laboratory prepares a qualification report that also includes the details of static or dynamic analysis when incorporated. The qualification report is sent to the purchaser for evaluation. The purchaser might obtain the services of an authority to review the qualification report. The report might have to be revised and analysis and tests might have to be repeated before a final decision is made on the qualification of the equipment. Information flow in a typical qualification program is shown in [Figure 31.4](#).

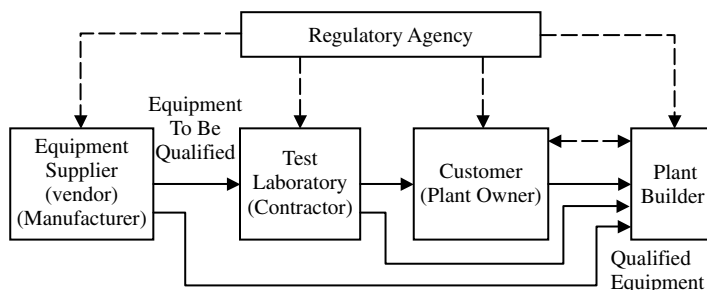


FIGURE 31.3 Test-object movement and information interactions in seismic qualification.

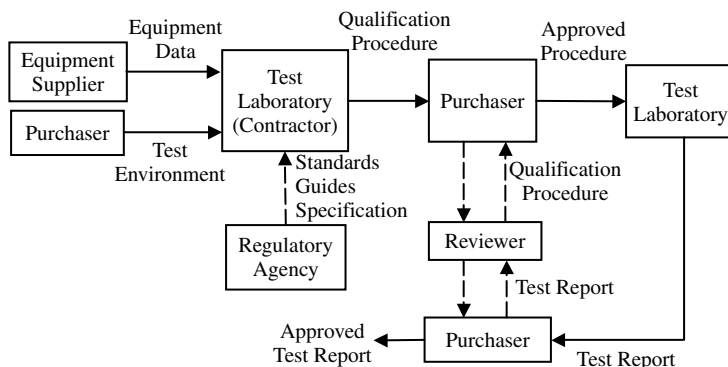


FIGURE 31.4 Information flow in a seismic qualification program.

31.3.2 Test Preliminaries

Seismic qualification tests are usually conducted by one of two methods depending on whether single-frequency or multifrequency excitation inputs are employed in the main tests. The two test categories are (1) single-frequency tests and (2) multifrequency tests. Although the second test method is more common in seismic qualification by testing, the first method is used under some conditions depending on the nature of the test object and its mounting features (for example, line-mounted vs. floor-mounted equipment). Typically, multifrequency excitations are preferred in qualification tests, and single-frequency excitations are favored in design-development and quality-assurance tests.

In single-frequency testing, amplitude of the excitation input is specified by a required input motion (RIM) curve, similar to that shown in Figure 31.5. If single-frequency dwells (e.g., sine dwell, sine beat) are employed, then the excitation input is applied to the test object at a series of selected frequency values in the frequency range of interest for that particular test environment. In such cases, dwell times (and number of beats per cycle where sine beats are employed) at each frequency point should be specified.

If a single-frequency sweep (such as a sine sweep) is employed as the excitation signal, then the sweep rate should be specified. When the single-frequency test-excitation is specified in this manner, the tests are conducted very much like multifrequency tests.

Multifrequency test are normally conducted by employing the response spectra method to represent the test-input environment. Basically, the test object is excited using a signal whose response spectrum, known as the test response spectrum (TRS), envelopes a specified response spectrum, known as the required response spectrum (RRS). Ideally, the TRS should equal the RRS but it is practically impossible to achieve this condition. Hence, multifrequency tests are conducted using a TRS that envelopes the RRS so that in significant frequency ranges, the two response spectra are nearly equal (see Figure 31.6). However, excessive conservatism, which would result in overtesting, should be avoided. It is usually acceptable to have TRS values below the RRS at a few frequency points.

The RRS is part of the data supplied to the test laboratory prior to the qualification tests being conducted. Two types of RRS are provided, representing (1) the operating-basis earthquake (OBE), and (2) the safe-shutdown earthquake (SSE). The response spectrum of the OBE represents the most severe motions produced by an earthquake under which the equipment being tested would remain functional without undue risk of malfunction or safety hazard. However, if the equipment is allowed to operate at a

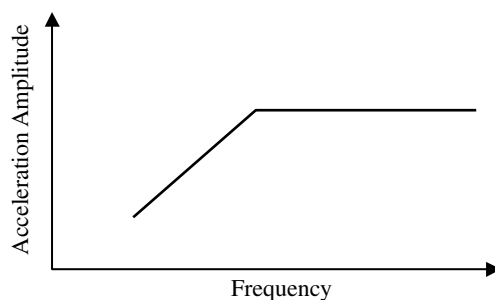


FIGURE 31.5 A typical required input motion curve.

disturbance level higher than the OBE level for a prolonged period then there would be a significant risk of malfunction.

The response spectrum of the SSE represents the most severe motions produced by an earthquake that the equipment being tested could safely withstand while the entire nuclear power plant is being shutdown. However, prolonged operation (i.e., more than the duration of one earthquake) could result in equipment malfunction. In other words, equipment is designed to withstand only one SSE in addition to several OBEs.

A typical seismic qualification test would first subject the equipment to several OBE-level excitations, primarily for aging the equipment mechanically to its end-of-design-life condition, and then would subject it to one SSE-level excitation. When providing RRS test specifications, it is customary to supply only the SSE requirement. The OBE requirement is then taken as a fraction (typically, 0.5 or 0.7) of the SSE requirement.

Test response spectra corresponding to the excitation signals are generated by the test laboratory during testing. The purchaser usually supplies the test laboratory with an FM tape containing frequency components that should be combined in some ratio to generate the test-input signal.

Qualification tests are conducted according to the test procedure approved and accepted by the purchaser. The main steps of seismic qualification testing are outlined in the following subsections.

31.3.3 Single-Frequency Testing

Seismic ground motions usually pass through various support structures before they eventually are transmitted to equipment. For seismic qualification of that equipment by testing, in theory we should apply the actual excitations felt by it, and not the seismic ground motions. In an ideal case, the shaker-table motion should be equivalent to the seismic response of the supporting structure at the point of attachment of the equipment.

The supporting structure would have a particular frequency-response function between the ground location and the equipment-support location (see Figure 31.7). Consequently, it could be considered a filter that modifies seismic ground motions before they reach the equipment mounts.

In particular, the components of the ground motion that have frequencies close to a resonant frequency of the supporting structure will be felt by the equipment at a relatively higher intensity. Furthermore, the ground motion components at very high frequencies will be almost entirely filtered out by the structure. If the frequency response of the supporting structure is approximated by a lightly damped simple oscillator, then the response felt by the equipment will be almost sinusoidal, with a frequency equal to the resonant frequency of the structure.

When the equipment supporting structure has a very sharp resonance in the significant frequency range of the dynamic environment (for example, 1 to 35 Hz for seismic ground motions), it follows from the previous discussion that it is desirable to use a short-duration single-frequency test in seismic qualification of the equipment. Equipment that is supported on pipelines (valves, valve actuators, gauges, and so forth) falls into this category and is termed line-mounted equipment.

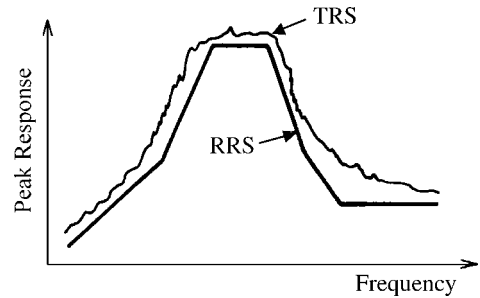


FIGURE 31.6 The TRS enveloping the RRS in a multifrequency test.

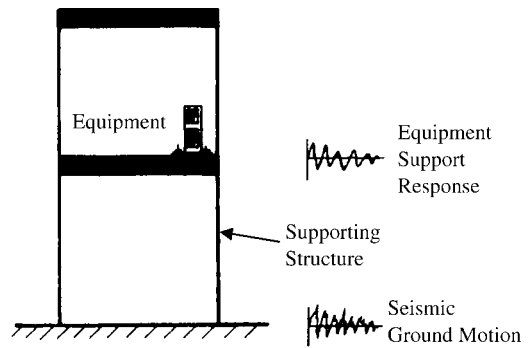


FIGURE 31.7 Schematic representation of the filtering of seismic ground motions by a supporting structure.

Resonant frequency of the supporting structure is usually not known at the time of the seismic qualification test. Consequently, single-frequency testing must be performed over the entire frequency range of interest for that particular dynamic environment.

Another situation in which single-frequency testing is appropriate is when the test object (equipment) itself does not have more than one sharp resonance in the frequency range of interest. In this case, the most prominent response of the test object occurs at its resonant frequency, even when the dynamic environment is an arbitrary excitation. Consequently, a single-frequency excitation would yield conservative test results. Equipment that has more than one predominant resonance may employ single-frequency testing provided that each resonance corresponds to a dynamic DoF (e.g., one resonance along each dynamic principal axis), and that cross coupling between these DoF is negligible.

In summary, single-frequency testing may be used where one or more of the following conditions are satisfied:

1. The supporting structure has one sharp resonance in the frequency range of interest (line-mounted equipment is included).
2. The test object does not have more than one sharp resonance in the frequency range of interest.
3. The test object has a resonance in each DoF, but the DoF are uncoupled (for which adequate verification should be provided in the test procedure).
4. The test object can be modeled as a simple dynamic system (such as a simple oscillator), for which adequate justification or verification should be provided.

Usually, the required SSE excitation level for a single-frequency test over a frequency range is specified by a curve such as the one shown in Figure 31.5. This curve is known as the RIM magnitude curve. The OBE excitation level is usually taken as a fraction (typically, 0.5 or 0.7) of the RIM values given for the SSE. For a sine-sweep test, the sweep rate and the number of sweeps in the test should also be specified. Typically, the sweep rate for seismic qualification tests is less than 1 octave/min. One sweep, from the state of rest to the maximum frequency in the range and back to the state of rest, is normally carried out in an SSE test (for example, 1–35 to 1 Hz). Several sweeps (typically, five) are performed in an OBE test.

In an SSE sine-dwell test, the dwell time for each dwell frequency should be specified. The dwell-frequency intervals should not be high (typically, a half-octave or less). For an OBE test, the dwell times are longer (typically, five times longer) than those specified for an SSE test.

For an SSE test using sine beats, the minimum number of beats and the minimum duration of excitation (with or without pauses) at each test frequency should be specified. In addition, the pause time for each test frequency should be specified when sine beats with pauses are employed. For an OBE test, the duration of excitation should be increased (as in a sine-dwell test).

The dwell time at each test frequency should be adequate to perform at least one functional-operability test. Furthermore, a dwell should be carried out at each resonant frequency of the test object as well as at those frequencies that are specified. Total duration of an SSE test should be representative of the duration of the strong-motion part of a standard safe-shutdown earthquake.

Sometimes, narrow-band random excitations may be used in situations where single-frequency testing is recommended. Narrowband random signals are those that have their power concentrated over a narrow frequency band. Such a signal can be generated for test-excitation purposes by passing a random signal through a narrow-band-pass filter. By tuning the filter to different center frequencies in narrowbands, the test-excitation frequency can be varied during testing. This center frequency of the filter should be swept up and down over the desired frequency range at a

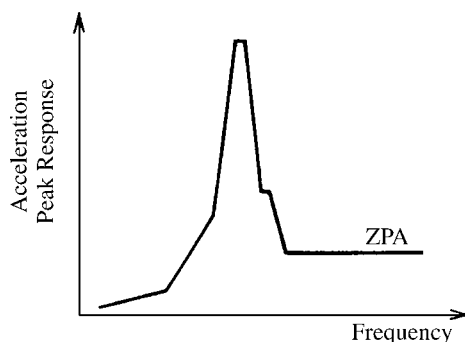


FIGURE 31.8 A typical RRS for a narrow-band excitation test.

reasonably slow rate (e.g., 1.0 octave/min) during the test. Thus, a multifrequency test with a sharp frequency-response spectrum (the RRS), as illustrated in Figure 31.8, is adequate in cases where single-frequency testing is recommended. In this case, a requirement that has to be satisfied by the test-excitation signal is that its amplitude should be equal to or greater than the zero-period acceleration of the RRS for the test.

31.3.4 Multifrequency Testing

When equipment is mounted very close to the ground under its normal operating conditions, or if its supporting structure and mounting can be considered rigid, then seismic ground motions will not be significantly filtered before they reach the equipment mounts. In this case, the seismic excitations that are felt by the equipment will retain broadband characteristics. Multifrequency testing is recommended for seismic qualification of such equipment.

Whereas single-frequency tests are specified by means of an RIM curve along with the test duration at each frequency (or sweep rates), multifrequency tests are specified by means of an RRS curve. The test requirement in multifrequency testing is that the response spectrum of the test excitation (the TRS) felt by the equipment mounts should envelop the RRS. Note that all frequency components of the test excitation are applied simultaneously to the test object. This is in contrast to single-frequency testing, in which only one significant frequency component is applied at a given instant.

When random excitations are employed in multifrequency testing, enveloping of the RRS by the TRS may be achieved by passing the random signal produced by a signal generator through a spectrum shaper. As the analyzing frequency bandwidth (e.g., one-third octave bands, one-sixth octave bands) decreases, the flexibility of shaping the TRS improves. A real-time spectrum analyzer (or a personal computer) may be used to compute and display the TRS curve corresponding to the control accelerometer signal (see Figure 31.9). By monitoring the displayed TRS, it is possible to adjust the gains of the spectrum-shaper filter to obtain the desired TRS that would envelop the RRS.

Most test laboratories generate their multifrequency excitation signals by combining a series of sine beats that have different peak amplitudes and frequencies. Using the same method, many other signal types (such as decaying sinusoids) may be superimposed to generate a required multifrequency excitation signal. A combination of signals of different types could also be employed to produce a desired test input. A commonly used combination is a broadband random signal and a series of sine beats. In this combination, the random signal is adjusted to have a response spectrum that will envelop the broadband portion of the RRS without much conservatism. The narrow-band peaks of the RRS, which generally will not be enveloped by such a broadband response spectrum, will be covered by a suitable combination of sine beats.

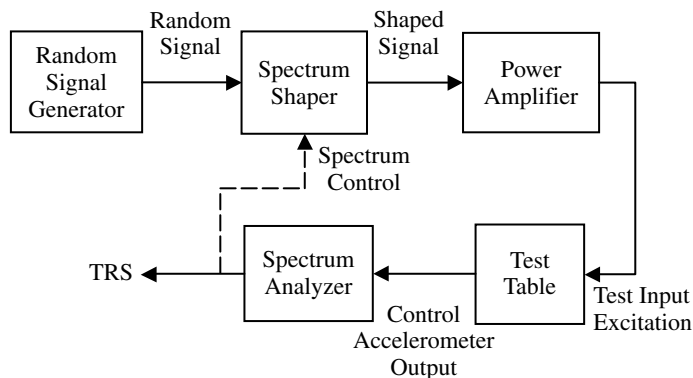


FIGURE 31.9 Matching of the TRS with the RRS in multifrequency testing.

By employing such mixed composite signals, it is possible to envelop the entire RRS without having to increase the amplitude of the test excitation to a value that is substantially higher than the ZPA of the RRS. One important requirement in multifrequency testing is that the amplitudes of the test excitation be equal to or greater than the ZPA of the RRS.

31.3.5 Generation of RRS Specifications

Seismic qualification of an object is usually specified in terms of an RRS. The excitation input that is used in seismic qualification analysis and testing should conservatively satisfy the RRS; that is, the response spectrum of the actual excitation input should envelop the RRS (without excessive conservatism, of course).

For equipment to be installed in a building or on some other supporting structure, the RRS generally cannot be obtained as the response spectrum of a modified seismic ground-motion time-history. The supporting structure usually introduces an amplification effect and a filtering effect on seismic ground motions. This amplification factor alone could be as high as three. Some of the major factors that determine the RRS for a particular seismic qualification test are as follows:

1. Nature of the building that will be qualified
2. Dynamic characteristics of the building or structure and the location (elevation and the like) where the object is expected to be installed
3. In-service mounting orientation and support characteristics of the object
4. Nature of the seismic ground motions in the geographic region where the object would be installed
5. Test severity and conservatism that is required by the purchaser or the regulator agency

The basic steps in developing the RRS for a specific seismic qualification application include the following:

1. Development of representative safe-shutdown earthquake (SSE) ground-motion time histories for the building (or support structure) location
2. Development of a suitable building (or support structure) model
3. Response analysis of the building model, using the time histories that are obtained in Step 1
4. Development of response spectra for various critical locations in the building (or support structure), using the response time histories obtained in Step 3
5. Normalization of the response spectra obtained in Step 4 to unity ZPA (that is, dividing by their individual ZPA values)
6. Identification of the similarities in the set of normalized response spectra that are obtained in Step 5 and grouping them into a small number of groups
7. Representation of each similar group by a response spectrum consisting of straight-line segments that envelop all members in the group, giving a normalized RRS for each group
8. Determination of scale factors for various locations in the building for use in conjunction with the corresponding normalized RRS curves

Representative strong-motion earthquake time histories (SSEs) are developed by suitably modifying actual seismic ground-motion time histories that have been observed in that geographic location (or a similar one), or by using a random-signal-generation (simulation) technique or any other appropriate method. These time histories may be available as either digital or analog records, depending on the way in which they are generated. If computer simulation is used in their development, then a statistical representation of the expected seismic disturbances in the particular geographic region (using geological features in the region, seismic activity data, and the like) should be incorporated in the algorithm. The intensity of the time histories can be adjusted, depending on the required test severity and conservatism.

The normalized response spectra are grouped so that the spectra that have roughly the same shape are put in the same group. In this manner, relatively few groups of normal response spectra (normalized) are

obtained. Then, the response spectra that belong to each group are plotted on the same graph paper. Next, straight-line segments are drawn to envelop each group of response spectra. This procedure results in a normalized RRS for each group of analytical response spectra.

The RRS that is used for a particular seismic qualification scheme is obtained as follows. First, the normalized RRS corresponding to the location in the building where the object would be installed is selected. The normalized RRS curve is then multiplied by the appropriate scaling factor. The scaling factor normally consists of the product of the actual ZPA value under SSE conditions at that location (as obtained from the analytical response spectrum at that location, for example) and a factor of safety that depends on the required test severity and conservatism.

In fact, three RRS curves corresponding to the vertical, east–west and north–south directions might be needed, even for single-degree-of-freedom (single-DoF) seismic qualification tests because, by mounting three control accelerometers in these three directions, triaxial monitoring could be accomplished. If only one control accelerometer is used in the test, then only one RRS curve is used. In this case, the resultant of the three orthogonal RRS curves should be used. One way to obtain the resultant RRS curve is to apply the square root of the sum of squares (SRSS) method to the three orthogonal components. Alternatively, the envelope of the three orthogonal RRS curves is obtained and multiplied by a safety factor (greater than unity).

Note that more than one building (or even many different geographic locations) could be included in the described procedure for developing RRS curves. The resulting RRS curves are then valid for the collection of buildings or geographic locations considered. When the generality of an RRS curve is extended in this manner, the test conservatism increases. This will also result in an RRS curve with a much broader band.

In practice, in a particular seismic qualification project, only a few normalized RRS curves are employed. In conjunction with these RRS curves, a table of data is provided that identifies the proper RRS curves and the scaling factors that should be used for different physical locations (for example, elevations) in various buildings that are situated at several geographic locations.

Bibliography

- Bendat, J.S. and Piersol, A.G. 1971. *Random Data: Analysis and Measurement Procedures*, Wiley-Interscience, New York.
- Brigham, E.O. 1974. *The Fast Fourier Transform*, Prentice Hall, Englewood Cliffs, NJ.
- de Silva, C.W. 1983. *Dynamic Testing and Seismic Qualification Practice*, D.C. Heath and Co., Lexington, MA.
- de Silva, C.W., A dynamic test procedure for improving seismic qualification guidelines, *J. Dyn. Syst. Meas. Control, Trans. ASME*, 106, 143–148, 1984.
- de Silva, C.W., Hardware and software selection for experimental modal analysis, *Shock Vibration Digest*, 16, 3–10, 1984.
- de Silva, C.W., Matrix eigenvalue problem of multiple-shaker testing, *J. Eng. Mech. Div., Trans. ASCE*, 108, 457–461, 1982.
- de Silva, C.W., Optimal input design for the dynamic testing of mechanical systems, *J. Dyn. Syst. Meas. Control, Trans. ASME*, 109, 111–119, 1987.
- de Silva, C.W., Seismic qualification of electrical equipment using a uniaxial test, *Earthquake Eng. Struct. Dyn.*, 8, 337–348, 1980.
- de Silva, C.W., Selection of shaker specifications in seismic qualification tests, *J. Sound Vibration*, 91, 21–26, 1983.
- de Silva, C.W., Shaker test-fixture design, *Meas. Control*, 17, 152–155, 1983.
- de Silva, C.W., Henning, S.J., and Brown, J.D., Random testing with digital control-application in the distribution qualification of microcomputers, *Shock Vibration Digest*, 18, 3–13, 1986.
- de Silva, C.W., Loceff, F., and Vashi, K.M., Consideration of an optimal procedure for testing the operability of equipment under seismic disturbances, *Shock Vibration Bull.*, 50, 149–158, 1980.

- de Silva, C.W. 2000. *Vibration — Fundamentals and Practice*, CRC Press, Boca Raton, FL.
- Ewins, D.J. 1984. *Modal Testing: Theory and Practice*, Research Studies Press Ltd., Letchworth, England.
- McConnell, K.G. 1995. *Vibration Testing*, Wiley, New York.
- Randall, R.B. 1977. *Application of B & K Equipment to Frequency Analysis*, Bruel and Kjaer, Naerum, Denmark.

VIII

Design and Applications

32

Vibration Design and Control

32.1	Introduction	32-2
	Shock and Vibration	
32.2	Specification of Vibration Limits	32-3
	Peak Level Specification • Root-Mean-Square Value Specification • Frequency-Domain Specification	
32.3	Vibration Isolation	32-5
	Design Considerations • Vibration Isolation of Flexible Systems	
32.4	Balancing of Rotating Machinery	32-15
	Static Balancing • Complex Number/Vector Approach • Dynamic (Two-Plane) Balancing • Experimental Procedure of Balancing	
32.5	Balancing of Reciprocating Machines	32-26
	Single-Cylinder Engine • Balancing the Inertia Load of the Piston • Multicylinder Engines • Combustion/ Pressure Load	
32.6	Whirling of Shafts	32-33
	Equations of Motion • Steady-State Whirling • Self-Excited Vibrations	
32.7	Design through Modal Testing	32-39
	Component Modification • Substructuring	
32.8	Passive Control of Vibration	32-45
	Undamped Vibration Absorber • Damped Vibration Absorber • Vibration Dampers	
32.9	Active Control of Vibration	32-61
	Active Control System • Control Techniques	
32.10	Control of Beam Vibrations	32-67
	State-Space Model of Beam Dynamics • Control Problem • Use of Linear Dampers	
	Appendix 32A MATLAB Control Systems Toolbox	32-73

Clarence W. de Silva

The University of British Columbia

Summary

There are desirable and undesirable types and situations of mechanical vibration. Undesirable vibrations are those that cause human discomfort and hazards, structural degradation and failure, performance deterioration and malfunction of machinery and processes, and various other problems. This chapter discusses ways of either eliminating or reducing the undesirable effects of vibration. Specifically, some useful topics on design for vibration suppression and the control of vibration are addressed. General approaches to vibration mitigation may be identified from the dynamic systems point of view. Typically, a set of vibration specifications is given as simple threshold values (bounds) or frequency spectra, and the goal is to either design or control the system to meet these

specifications. Frequency-domain techniques based on transfer functions such as transmissibility and time-domain techniques using the state-space representation, optimal control, and modal control are presented. Applications considered here include vibration isolation, balancing of rotating and reciprocating machinery, whirling suppression, and passive and active control of vibration.

32.1 Introduction

Consider the schematic diagram of a vibratory system shown in Figure 32.1. Forcing excitations $f(t)$ to the mechanical system S cause the vibration responses y . Our objective is to suppress y to a level that is acceptable. Clearly, there are three general ways of doing this:

1. *Isolation.* Suppress the excitations of vibration. This method deals with f .
2. *Design modification.* Modify or redesign the mechanical system so that for the same levels of excitation, the resulting vibrations are acceptable. This method deals with S .
3. *Control.* Absorb or dissipate the vibrations using external devices, through implicit or explicit sensing and control. This method deals with y .

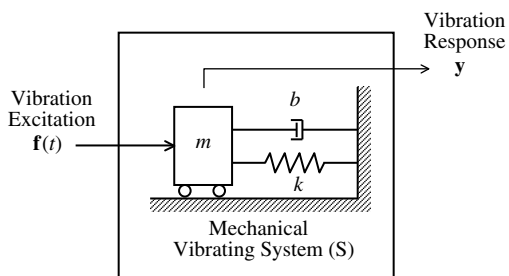


FIGURE 32.1 A vibrating mechanical system.

Within each of these three categories, several approaches can be used to achieve the objective of vibration mitigation. Essentially, each of these approaches involves designing (either complete through redesign or incremental design modification) of the system on the one hand, and controlling the vibration through external means (passive or active devices) on the other. Note that removal of faults (e.g., misalignments and malfunctions by repair or parts replacement) can also remove vibrations. This approach may fall into any of the three categories listed above.

The category of vibration isolation involves “isolating” a mechanical system (S) from vibration excitations (f) so that the excitation signals are “filtered” out or dissipated prior to reaching the system. The use of properly designed suspension systems, mounts, and damping layers falls within this category. The category of design modification will involve making changes to the components and the structure of a mechanical system according to a set of specifications and design guidelines. Balancing of rotating machinery and structural modification through modal analysis and design techniques fall into this category. The category of control will involve either passive devices (which do not use external power), such as dynamic absorbers and dampers, or active control devices (which need external power for operation). In the passive case, the control device implicitly senses the vibration response and dissipates it (as in the case of a damper) or absorbs and stores its energy where it is slowly dissipated (as in the case of a dynamic absorber). In the active case, the vibrations y are explicitly sensed through *sensors* and *transducers*. The forces that should be acted on the system to counteract and suppress vibrations are determined by a controller, and the corresponding forces or torques are applied to the system through one or more *actuators*.

Note that there may be some overlap in the three general categories of vibration mitigation that were mentioned above. For example, the addition of a mount (category 1) may also be interpreted as a design modification (category 2) or as incorporating a passive damper (category 3). It should also be noted that the general approach, commonly known as *source alteration*, may fall into either category 1 or category 2. In this case, the purpose is to alter or remove the source of vibration. The source could either be external (e.g., road irregularities that result in vehicle vibrations) — a category 1 problem, or internal (imbalance or misalignment in rotating devices that results in periodic forces, moments, and vibrations) — a category 2 problem. It can be more difficult to alter external vibration sources (e.g., resurfacing the roadways) than to modify the internal sources (e.g., balancing of rotating machinery).

Furthermore, the external source of vibration may be quite random and may not be accessible for alteration at all (e.g., aerodynamic forces on an aircraft).

32.1.1 Shock and Vibration

Sometimes, response to shock loads is considered separately from response to vibration excitations for the purpose of design and control of mechanical systems. For example, shock isolation and vibration isolation are treated under different headings in some literature. This is actually unnecessary. Even though vibration analysis predominantly involves periodic excitations and responses, transient and random oscillations (vibrations) are also commonly found in practice. The frequency band of the latter two types of signals is much broader than that of a simple periodic signal. A shock signal is transient by definition, and has a very short duration (in comparison to the predominant time constants of the mechanical system to which the shock load is applied). Hence, it will possess a wide band of frequencies. Consequently, frequency-domain techniques are still applicable. Furthermore, time-domain techniques are particularly suited to dealing with transient signals in general and shock signals in particular. In that context, a shock excitation may be treated as an impulse whose effect is to instantaneously change the velocity of an inertia element. Then, in the time domain, a shock load may also be treated as an initial-velocity excitation of an otherwise free (unforced) system.

32.2 Specification of Vibration Limits

Design and control procedures of vibration have the primary objective of ensuring that under normal operating conditions, the system of interest does not encounter vibration levels that exceed the specified values. In this context, then, the ways of specifying vibration limits become important. This section will present some common ways of vibration specification.

32.2.1 Peak Level Specification

Vibration limits for a mechanical system may be specified in either the time domain or the frequency domain. In the time domain, the simplest specification is the peak level of vibration (typically, acceleration in units of g — the acceleration due to gravity). Here, the techniques of isolation, design, or control should ensure that the peak vibration response of the system do not exceed the specified level. In this case, the entire time interval of operation of the system is monitored, and the peak values are checked against the specifications. Note that, in this case, it is the instantaneous peak value at a particular time instant that is of interest, and what is used in representing vibration is an instantaneous amplitude measure rather than an average amplitude or an energy measure.

32.2.2 Root-Mean-Square Value Specification

The root-mean-square (RMS) value of a vibration signal $y(t)$ is given by the square root of the average of the squared signal as

$$y_{\text{RMS}} = \left[\frac{1}{T} \int_0^T y^2 dt \right]^{1/2} \quad (32.1)$$

Note that, by squaring the signal, its sign is eliminated and, essentially, the energy level of the signal is used. The period T , over which the squared signal is averaged, will depend on the problem and the nature of the signal. For a periodic signal, one period is adequate for averaging. For transient signals, several time constants (typically four times the larger time constant) of the vibrating system would be sufficient. For random signals, a value that is as large as feasible should be used.

In the method of RMS value specification, the RMS value of the acceleration response (typically, acceleration in g s) is computed using Equation 32.1 and is compared with the specified value. In this method, instantaneous bursts of vibration do not have a significant effect as they are filtered out because of the integration. It is the average energy or power of the response signal that is considered. The duration of exposure enters into the picture indirectly and in an undesirable manner. For instance, a highly transient vibration signal can initially have a damaging effect. However, the larger the T that is used in Equation 32.1, the smaller the computed RMS value. Hence, in this case, the use of a large value for T would lead to diluting or masking the damage potential. In practice, the longer the exposure to a vibration signal, the greater the harm caused. Hence, when using specifications such as peak and RMS values, they have to be adjusted according to the period of exposure. Specifically, a larger specification should be used for longer periods of exposure.

32.2.3 Frequency-Domain Specification

It is not realistic to specify the limitation to vibration exposure of a complex dynamic system by just a single threshold value. Usually, the effect of vibration on a system depends on at least the following three parameters:

1. Level of vibration (peak, RMS, power, etc.).
2. Frequency content (range) of excitation.
3. Duration of exposure to vibration.

This is particularly true because the excitations that generate the vibration environment may not necessarily be a single-frequency (sinusoidal) signal and may be broadband and random. Furthermore, the response of the system to the vibration excitations will depend on its frequency transfer function, which determines its resonances and damping characteristics. Under these circumstances, it is desirable to provide specifications in a *nomograph* where the horizontal axis gives frequency (Hz) and the vertical axis could represent a motion variable such as displacement (m), velocity (m/s), or acceleration (m/s^2 or g). It is not important which of these motion variables represents the vertical axis of the nomograph. This is true because in the frequency domain

$$\text{Velocity} = j\omega \times \text{displacement}$$

$$\text{Acceleration} = j\omega \times \text{velocity}$$

and one form of motion may be easily converted into one of the remaining two motion representations. In each of the forms, assuming that the two axes of the nomograph are graduated in a logarithmic scale, the constant displacement, constant velocity, and constant acceleration lines are straight lines.

Consider a simple specification of machinery vibration limits as given by the following values:

$$\text{Displacement limit (peak)} = 0.001 \text{ m}$$

$$\text{Velocity limit} = 0.01 \text{ m/sec}$$

$$\text{Acceleration limit} = 1.0g$$

This specification may be represented in a velocity vs. frequency nomograph (log-log) as in Figure 32.2.

Usually, such simple specifications in the frequency domain are not adequate. As noted above, the system behavior will vary depending on the excitation frequency range. For example, motion sickness in humans may be predominant in low frequencies in the range of 0.1 to 0.6 Hz and passenger discomfort in

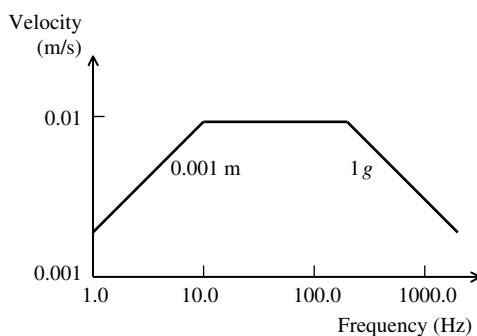


FIGURE 32.2 Operating vibration specification (nomograph) for a machine.

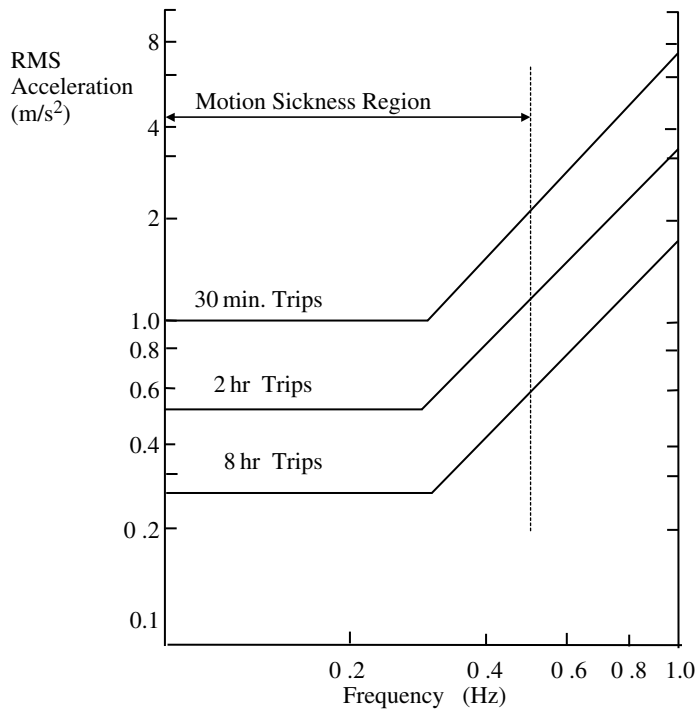


FIGURE 32.3 A severe-discomfort vibration specification for ground transit vehicles.

ground transit vehicles may be most serious in the frequency range of 4 to 8 Hz for vertical motion and 1 to 2 Hz for lateral motion. In addition, for any dynamic system, particularly at low damping levels, the neighborhoods of resonant frequencies should be avoided and, hence, should be specified by low vibration limits in the resonant regions. Furthermore, the duration of vibration exposure should be explicitly accounted for in specifications. For example, Figure 32.3 presents a ride comfort specification for a ground transit vehicle, where lower vibration levels are specified for longer trips.

Finally, it should be noted that the specifications we are concerned with in the present context of design and control are upper bounds of vibration. The system should perform below (within) these specifications under normal operating conditions. Test specifications are lower bounds. The test should be conducted at or above these vibration levels so that the system would meet the test specifications. Some considerations of vibration engineering are summarized in Box 32.1.

32.3 Vibration Isolation

The purpose of vibration isolation is to “isolate” the system of interest from vibration excitations by introducing an *isolator* in between them. Examples of isolators are machine mounts and vehicle suspension systems. Two general types of isolation can be identified:

1. Force isolation (related to force transmissibility)
2. Motion isolation (related to motion transmissibility)

In force isolation, vibration forces that would be ordinarily transmitted directly from a source to a supporting structure (isolated system) are filtered out by an isolator through its flexibility (spring) and dissipation (damping) so that part of the force is routed through an inertial path. Clearly, the concepts of *force transmissibility* are applicable here. In motion isolation, vibration motions that are applied at a moving platform of a mechanical system (isolated system) are absorbed by an isolator through its flexibility and dissipation so that the motion that is transmitted to the system of interest is weakened.

Box 32.1

VIBRATION ENGINEERING

Vibration mitigation approaches:

- Isolation (buffers system from excitation)
- Design modification (modifies the system)
- Control (senses vibration and applies a counteracting force: passive/active)

Vibration specification:

- Peak and RMS values
- Frequency-domain specs on a nomograph
 - *Vibration levels
 - *Frequency content
 - *Exposure duration

Note:

$$|\text{Velocity}| = \omega \times |\text{Displacement}|$$

$$|\text{Acceleration}| = \omega \times |\text{Velocity}|$$

Limiting specifications:

- Operation (design) specifications: specify upper bounds
- Testing specifications: specify lower bounds

The concepts of motion transmissibility are applicable in this case. The design problem in both cases is to select applicable parameters for the isolator so that the vibrations entering the system are below specified values within a frequency band of interest (the operating frequency range).

Let us revisit the main concepts of force transmissibility and motion transmissibility. Figure 32.4(a) gives a schematic model of force transmissibility through an isolator. Vibration force at the source is $f(t)$. In view of the isolator, the source system (with impedance Z_m) is made to move at the same speed as the isolator (with impedance Z_s). This is a parallel connection of impedances. Hence, the force $f(t)$ is split so that part of it is taken up by the inertial path (broken line) of Z_m . Only the remainder (f_s) is transmitted through Z_s to the supporting structure, which is the isolated system. Force transmissibility is

$$T_f = \frac{f_s}{f} = \frac{Z_s}{Z_m + Z_s} \quad (32.2)$$

Figure 32.4(b) gives a schematic model of motion transmissibility through an isolator. Vibration motion $v(t)$ of the source is applied through an isolator (with impedance Z_s and mobility M_s) to the isolated system (with impedance Z_m and mobility M_m). The resulting force is assumed to transmit directly from the isolator to the isolated system and hence, these two units are connected in series. Consequently, we have the motion transmissibility:

$$T_m = \frac{v_m}{v} = \frac{M_m}{M_m + M_s} = \frac{Z_s}{Z_s + Z_m} \quad (32.3)$$

It can be seen that, according to these two models, we have

$$T_f = T_m \quad (32.4)$$

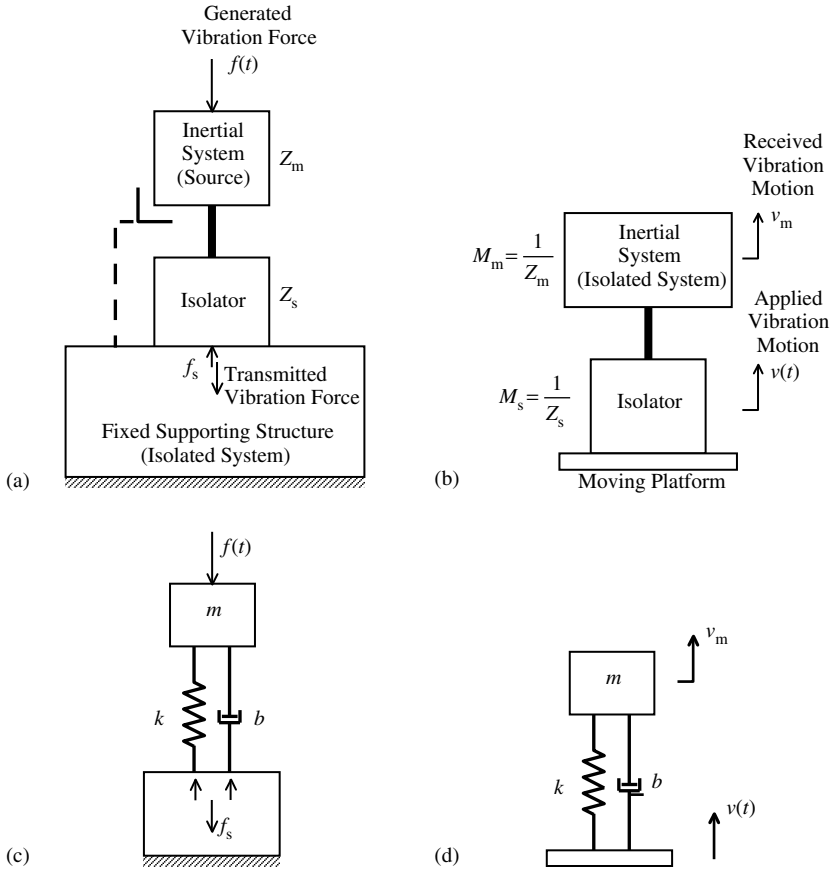


FIGURE 32.4 (a) Force isolation; (b) motion isolation; (c) force isolation example; (d) motion isolation example.

As a result, the concepts of force transmissibility and motion transmissibility may be studied using just one common transmissibility function T .

Simple examples of force isolation and motion isolation are shown in Figure 32.4(c) and (d). For both cases, the transmissibility function is given by

$$T = \frac{k + bj\omega}{(k - m\omega^2 + bj\omega)} \quad (32.5)$$

where ω is the frequency of vibration excitation. Note that the model (Equation 32.5) is not restricted to sinusoidal vibrations. Any general vibration excitation may be represented by a Fourier spectrum, which is a function of frequency ω . Then, the response vibration spectrum is obtained by multiplying the excitation spectrum by the transmissibility function T . The associated design problem is to select the isolator parameters k and b to meet the specifications of isolation.

Equation 32.5 may be expressed as

$$T = \frac{\omega_n^2 + 2\zeta\omega_n\omega}{(\omega_n^2 - \omega^2 + 2\zeta\omega_n\omega)} \quad (32.6)$$

where

$\omega_n = \sqrt{k/m}$ = undamped natural frequency of the system

$\zeta = \frac{b}{2\sqrt{km}}$ = damping ratio of the system

Equation 32.6 may be written in the nondimensional form:

$$T = \frac{1 + 2\zeta rj}{1 - r^2 + 2\zeta rj} \quad (32.7)$$

where the nondimensional excitation frequency is defined as

$$r = \omega/\omega_n$$

The transmissibility function has a phase angle as well as magnitude. In practical applications, the level of attenuation of the vibration excitation (rather than the phase difference between the vibration excitation and the response) is of primary importance. Accordingly, the transmissibility magnitude

$$|T| = \sqrt{\frac{1 + 4\zeta^2 r^2}{(1 - r^2)^2 + 4\zeta^2 r^2}} \quad (32.8)$$

is of interest. It can be shown that $|T| < 1$ for $r > \sqrt{2}$, which corresponds to the isolation region. Hence, the isolator should be designed such that the operative frequencies ω are greater than $\sqrt{2}\omega_n$. Furthermore, a threshold value for $|T|$ would be specified, and the parameters k and b of the isolator should be chosen so that $|T|$ is less than the specified threshold in the operating frequency range (which should be given). This procedure may be illustrated using an example.

Example 32.1

A machine tool and its supporting structure are modeled as the simple mass–spring–damper system shown in Figure 32.5.

1. Draw a mechanical-impedance circuit for this system in terms of the impedances of the three elements: mass (m), spring (k), and viscous damper (b).
2. Determine the exact value of the frequency ratio r in terms of the damping ratio ζ , at which the force transmissibility magnitude will peak. Show that for small ζ , this value is $r = 1$.
3. Plot $|T_f|$ vs. r for the interval $r = [0, 5]$, with one curve for each of the five ζ values 0.0, 0.3, 0.7, 1.0, and 2.0, on the same plane. Discuss the behavior of these transmissibility curves.
4. From part (3), determine for each of the five ζ values and the excitation frequency range with respect to ω_n , for which the transmissibility magnitude is:
 - Less than 1.05
 - Less than 0.5
5. Suppose that the device in Figure 32.5 has a primary, undamped natural frequency of 6 Hz and a damping ratio of 0.2. It is necessary that the system has a force transmissibility magnitude of less than 0.5 for operating frequency values greater than 12 Hz. Does the existing system meet this requirement? If not, explain how you should modify the system to meet the requirement.

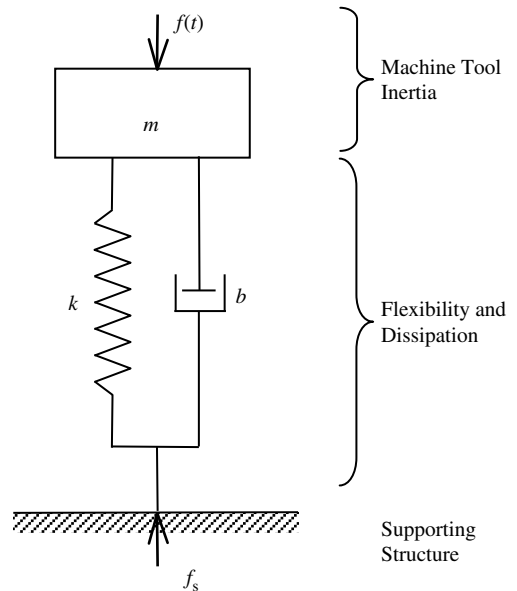


FIGURE 32.5 A simplified model of a machine tool and its supporting structure.

Solution

1. Here, the elements m , b , and f are in parallel with a common velocity v across them, as shown in Figure 32.6. In the circuit, $Z_m = mj\omega$, $Z_b = b$, and $Z_k = k/j\omega$.

Force transmissibility

$$T_f = \frac{F_s}{F} = \frac{F_s/V}{F/V} = \frac{Z_s}{Z_s + Z_0} = \frac{Z_b + Z_k}{Z_m + Z_b + Z_k} \quad (i)$$

Substitute the element impedances. We obtain

$$T_f = \frac{b + \frac{k}{j\omega}}{mj\omega + b + \frac{k}{j\omega}} = \frac{bj\omega + k}{-\omega^2 m + bj\omega + k} = \frac{j\omega b/m + k/m}{-\omega^2 + j\omega b/m + k/m} \quad (ii)$$

The last expression is obtained by dividing the numerator and the denominator by m . Now, use the fact that

$$\frac{k}{m} = \omega_n^2 \quad \text{and} \quad \frac{b}{m} = 2\zeta\omega_n$$

and divide Equation ii throughout by ω_n^2 . We obtain

$$T_f = \frac{\omega_n^2 + 2\zeta\omega_n j\omega}{\omega_n^2 - \omega^2 + 2\zeta\omega_n j\omega} = \frac{1 + 2\zeta r j}{1 - r^2 + 2\zeta r j} \quad (iii)$$

The transmissibility magnitude is

$$|T_f| = \sqrt{\frac{1 + 4\zeta^2 r^2}{(1 - r^2)^2 + 4\zeta^2 r^2}} \quad (32.9)$$

where $r = \omega/\omega_n$ is the normalized frequency.

2. To determine the peak point of $|T_f|$, differentiate the expression within the square-root sign in Equation iv and equate to zero:

$$\frac{[(1 - r^2)^2 + 2\zeta^2 r^2]8\zeta^2 r - [1 + 4\zeta^2 r^2][2(1 - r^2)(-2r) + 8\zeta^2 r]}{[(1 - r^2)^2 + 4\zeta^2 r^2]^2} = 0$$

Hence,

$$4r\{[(1 - r^2)^2 + 2\zeta^2 r^2]2\zeta^2 + [1 + 4\zeta^2 r^2][(1 - r^2) - 2\zeta^2]\} = 0$$

which simplifies to

$$r(2\zeta^2 r^4 + r^2 - 1) = 0$$

The roots are

$$r = 0 \quad \text{and} \quad r^2 = \frac{-1 \pm \sqrt{1 + 8\zeta^2}}{4\zeta^2}$$

The root $r = 0$ corresponds to the initial stationary point at zero frequency. That does not represent a peak. Taking only the positive root for r^2 and then its positive square root, the peak point of the transmissibility magnitude is given by

$$r = \frac{[\sqrt{1 + 8\zeta^2} - 1]^{1/2}}{2\zeta} \quad (iv)$$

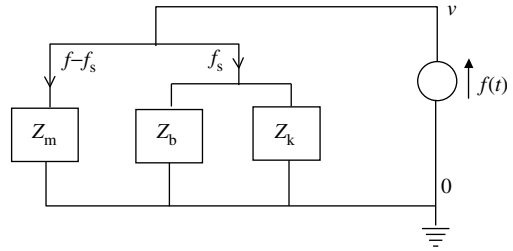


FIGURE 32.6 The mechanical impedance circuit of the force isolation problem.

For small ζ , Taylor series expansion gives

$$\sqrt{1 + 8\zeta^2} \approx 1 + \frac{1}{2} \times 8\zeta^2 = 1 + 4\zeta^2$$

With this approximation, Equation iv equates to 1. Hence, for small damping, the transmissibility magnitude will have a peak at $r = 1$, and from Equation 32.9, its value is

$$|T_f| \approx \frac{\sqrt{1 + 4\zeta^2}}{2\zeta} \approx \frac{1 + \frac{1}{2} \times 4\zeta^2}{2\zeta}$$

or

$$|T_f| \approx \frac{1}{2\zeta} + \zeta \approx \frac{1}{2\zeta} \quad (\text{v})$$

3. The five curves of $|T_f|$ vs. r for $\zeta = 0, 0.3, 0.7, 1.0$, and 2.0 are shown in Figure 32.7. Note that these curves use the exact expression (see Equation 32.9).

From the curves, we observe the following:

1. There is always a nonzero frequency value at which the transmissibility magnitude will peak. This is the resonance.
2. For small ζ , the peak transmissibility magnitude is obtained at approximately $r = 1$. As ζ increases, this peak point shifts to the left (i.e., a lower value for peak frequency).
3. The peak magnitude decreases with increasing ζ .
4. All the transmissibility curves pass through the magnitude value 1.0 at the same frequency $r = \sqrt{2}$.
5. The isolation (i.e., $|T_f| < 1$) is given by $r > \sqrt{2}$. In this region, $|T_f|$ increases with ζ .
6. The transmissibility magnitude decreases for large r .

4. From the curves in Figure 32.7, we obtain:

- For $|T_f| < 1.05$; $r > \sqrt{2}$ for all ζ .
- For $|T_f| < 0.5$; $r > 1.73, 1.964, 2.871, 3.77, 7.075$ for $\zeta = 0.0, 0.3, 0.7, 1.0$, and 2.0 , respectively.

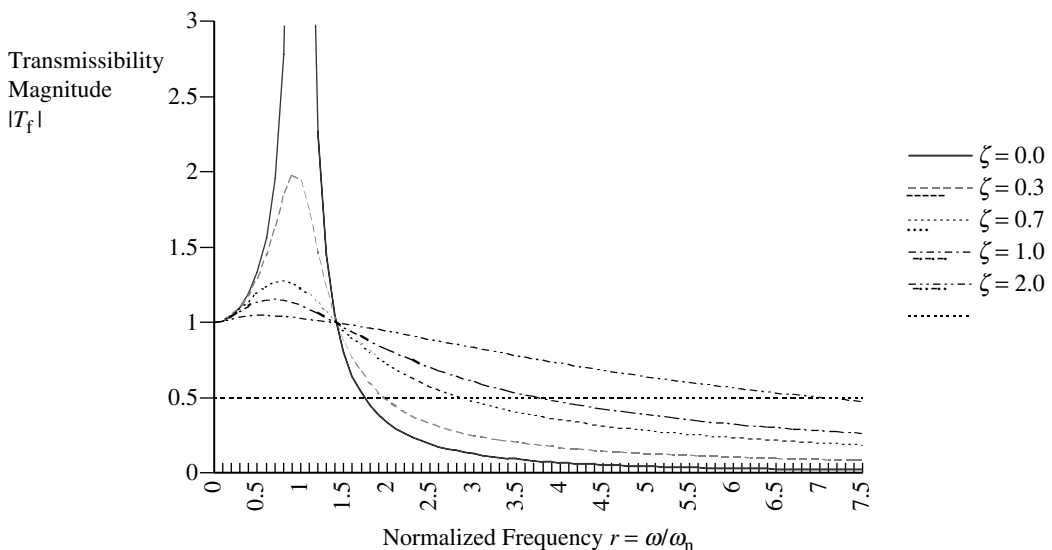


FIGURE 32.7 Transmissibility curves for a simple oscillator model.

5. We need

$$\sqrt{\frac{1 + 4\zeta^2 r^2}{(1 - r^2)^2 + 4\zeta^2 r^2}} < \frac{1}{2}$$

or

$$\frac{1 + 4\zeta^2 r^2}{(1 - r^2)^2 + 4\zeta^2 r^2} < \frac{1}{4}$$

or

$$4 + 16\zeta^2 r^2 < (1 - r^2)^2 + 4\zeta^2 r^2$$

or

$$r^4 - 2r^2 - 12\zeta^2 r^2 - 3 > 0$$

For $\zeta = 0.2$ and $r = 12/6 = 2$, the left-hand-side expression computes to

$$2^4 - 2 \times 2^2 - 12 \times (0.2)^2 \times 2^2 - 3 = 3.08 > 0$$

Hence, the requirement is met. In fact, since, for $r = 2$

$$\text{LHS} = 2^4 - 2 \times 2^2 - 12 \times 2^2 \zeta^2 - 3 = 5 - 48\zeta^2$$

it follows that the requirement would be met for

$$5 - 48\zeta^2 > 0$$

or

$$\zeta < \sqrt{\frac{5}{48}} = 0.32$$

If the requirement was not met (e.g., if $\zeta = 0.4$), the option would be to reduce damping.

32.3.1 Design Considerations

The *level of isolation* is defined as $1 - T$. It was noted that in the isolation region ($r > \sqrt{2}$) the transmissibility decreases (hence, the level of isolation increases) as the damping ratio ζ decreases. Thus, the best conditions of isolation are given by $\zeta = 0$. This is not feasible in practice, but we should maintain ζ as small as possible. For small ζ in the isolation region, Equation 32.8 may be approximated by

$$T = \frac{1}{(r^2 - 1)} \quad (32.10)$$

Note that T is real, in this case, of $\zeta \cong 0$, and also is positive since $r > \sqrt{2}$. However, in general, T may denote the magnitude of the transmissibility function. Substitute

$$r^2 = \omega^2/\omega_n^2 = \omega^2 m/k$$

We get

$$k = \frac{\omega^2 m T}{(1 + T)} \quad (32.11)$$

This equation may be used to determine the design stiffness of the isolator for a specified level of isolation ($1 - T$) in the operating frequency range $\omega > \omega_0$ for a system of known mass (including the isolator mass). Often, the static deflection δ_s of spring is used in design procedures and is

given by

$$\delta_s = \frac{mg}{k} \quad (32.12)$$

Substituting Equation 32.12 into Equation 32.11, we obtain

$$\delta_s = (1 + T) \frac{g}{\omega^2 T} \quad (32.13)$$

Since the isolation region is $\omega > \sqrt{2}\omega_n$ it is desirable to make ω_n as small as possible in order to obtain the widest frequency range of operation. This is achieved by making the isolator as soft as possible (k as low as possible). However, there are limits to this in terms of structural strength, stability, and availability of springs. Then, m may be increased by adding an inertia block as the base of the system, which is then mounted on the isolator spring (with a damping layer) or an air-filled pneumatic mount. The inertia block will also lower the centroid of the system, thereby providing added desirable effects of stability and reducing rocking motions and noise transmission. For improved load distribution, instead of just one spring of design stiffness k , a set of n springs, each with stiffness k/n and uniformly distributed under the inertia block, should be used.

Another requirement for good vibration isolation is low damping. Usually, metal springs have very low damping (typically ζ less than 0.01). On the other hand, higher damping is needed to reduce resonant vibrations that will be encountered during start-up and shutdown conditions when the excitation frequency will vary and pass through the resonances. In addition, vibration energy has to be effectively dissipated, even under steady operating conditions. Isolation pads made of damping material such as cork, natural rubber, and neoprene may be used for this purpose. They can provide damping ratios of the order of 0.01.

The basic design steps for a vibration isolator in force isolation are as follows:

1. The required level of isolation (1 to T) and the lowest frequency of operation (ω_0) are specified. The mass of the vibration source (m) is known.
2. Use Equation 32.11 with $\omega = \omega_0$ to compute the required stiffness k of the isolator.
3. If the component k is not satisfactory, then increase m by introducing an inertia block and recompute k .
4. Distribute k over several springs.
5. Introduce a mounting pad of known stiffness and damping. Modify k and b accordingly and compute T using Equation 32.8. If the specified T is exceeded, then modify the isolator parameters as appropriate and repeat the design cycle.

Box 32.2 gives some relations that are useful in a design for vibration isolation.

Example 32.2

Consider a motor and fan unit of a building ventilation system weighing 50 kg and operating in the speed range of 600 to 3600 rpm. Since offices are located directly underneath the motor room, a 90% vibration isolation is desired. A set of mounting springs, each having a stiffness of 100 N/cm, is available. Design an isolation system to mount the motor-fan unit on the room floor.

Solution

For an isolation level of 90%, the required force transmissibility is $T = 0.1$. The lowest frequency of operation is $\omega = (600/60)2\pi$ rad/sec. First, we try four mounting points. The overall spring stiffness is $k = 4 \times 100 \times 10^2$ N/m. Substitute in Equation 32.11.

$$4 \times 100 \times 100 = \frac{(10 \times 2\pi)^2 \times m \times 0.1}{1.1}$$

Box 32.2

VIBRATION ISOLATION

Transmissibility (force/force or motion/motion):

$$|T| = \sqrt{\frac{1 + 4\zeta^2 r^2}{(1 - r^2)^2 + 4\zeta^2 r^2}} \cong \frac{1}{(r^2 - 1)} \text{ for } r > 1 \text{ and small } \zeta$$

Properties:

1. $T_{\text{peak}} \cong \frac{\sqrt{1 + 4\zeta^2}}{2\zeta} \cong \frac{1}{2\zeta}$ for small ζ
2. T_{peak} occurs at $r_{\text{peak}} = \frac{[\sqrt{1 + 8\zeta^2} - 1]^{1/2}}{2\zeta} \cong 1$ for small ζ
3. All $|T|$ curves coincide at $r = \sqrt{2}$ for all ζ
4. Isolation region: $r > \sqrt{2}$
5. In isolation region:
 $|T|$ decreases with r (i.e., better isolation at higher frequencies)
 $|T|$ increases with ζ (i.e., better isolation at lower damping)

Design formulas:

Level of isolation = $1 - T$

Isolator stiffness:

$$k = \frac{\omega^2 m T}{(1 + T)}$$

where

m = system mass

ω = operating frequency

Static deflection:

$$\delta_s = \frac{mg}{k} = (1 + T) \frac{g}{\omega^2 T}$$

which gives $m = 111.5$ kg. Since the mass of the unit is 50 kg, we should use an inertia block of mass 61.5 kg or more.

32.3.2 Vibration Isolation of Flexible Systems

The simple model shown in Figure 32.4(c) and (d) may not be adequate in the design of vibration isolators for sufficiently flexible systems. A more appropriate model for this situation is shown in Figure 32.8. Note that the vibration isolator has an inertia block of mass m in addition to damped flexible mounts of stiffness k and damping constant b . The vibrating system itself has a stiffness K and damping constant B in addition to its mass M .

In the absence of K , B , and the inertia block (m) as in Figure 32.4(c), the vibrating system becomes a simple inertia (M). Then, y_a and y are the same and the equation of motion is

$$M\ddot{y} + b\dot{y} + ky = f(t) \quad (32.14)$$

with the force transmitted to the support structure, f_s , given by

$$f_s = b\dot{y} + ky \quad (32.15)$$

The force transmissibility in this case is

$$T_{\text{inertial}} = \frac{f_s}{f} = \frac{bs + k}{Ms^2 + bs + k} \quad (32.16)$$

with $s = j\omega$

For the flexible system and isolator shown in Figure 32.8, the equation of motion:

$$M\ddot{y}_a + B(\dot{y}_a - \dot{y}) + K(y_a - y) = f(t) \quad (32.17)$$

$$m\ddot{y} + B(\dot{y} - \dot{y}_a) + K(y - y_a) + b\dot{y} + ky = 0 \quad (32.18)$$

Hence, in the frequency domain, we have

$$(Ms^2 + Bs + K)y_a - (Bs + K)y = f \quad (32.19)$$

$$[ms^2 + (B + b)s + K + k]y = (Bs + K)y_a \quad (32.20)$$

with $s = j\omega$

Substitute Equation 32.20 into Equation 32.19 for eliminating y_a . We obtain

$$\left\{ (Ms^2 + Bs + K) \frac{[ms^2 + (B + b)s + K + k]}{(Bs + K)} - (Bs + K) \right\} y = f$$

which simplifies

$$\left\{ \frac{Ms^2[ms^2 + (B + b)s + K + k] + (Bs + K)(ms^2 + bs + k)}{(Bs + K)} \right\} y = f \quad (32.21)$$

The force transmitted to the supporting structure is still given by Equation 32.15. Hence, the transmissibility with the flexible system is

$$T_{\text{flexible}} = \frac{(Bs + K)(bs + k)}{\{Ms^2[ms^2 + (B + b)s + K + k] + (Bs + K)(ms^2 + bs + k)\}} \quad \text{with } s = j\omega \quad (32.22)$$

From Equation 32.16 and Equation 32.22, the transmissibility magnitude ratio is

$$\frac{T_{\text{flexible}}}{T_{\text{inertial}}} = \left| \frac{(Bs + K)(Ms^2 + bs + k)}{Ms^2[ms^2 + (B + b)s + K + k] + (Bs + K)(ms^2 + bs + k)} \right| \quad \text{with } s = j\omega \quad (32.23)$$

or

$$\frac{T_{\text{flexible}}}{T_{\text{inertial}}} = \left| \frac{(Ms^2 + bs + k)}{Ms^2(ms^2 + bs + k)/(Bs + K) + Ms^2 + ms^2 + bs + k} \right| \quad s = j\omega \quad (32.24)$$

In the nondimensional form, we have

$$\frac{T_{\text{flexible}}}{T_{\text{inertial}}} = \left| \frac{1 - r^2 + 2j\zeta_b r}{-r^2(1 - r_m r^2 + 2j\zeta_b r)/(r_\omega^2 + 2j\zeta_a r_\omega r) + 1 - (1 + r_m)r^2 + 2j\zeta_b r} \right| \quad (32.25)$$

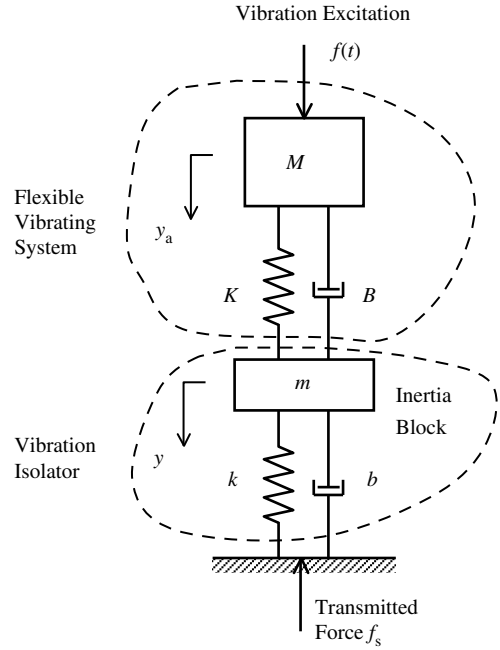


FIGURE 32.8 A model for vibration isolation of a flexible system.

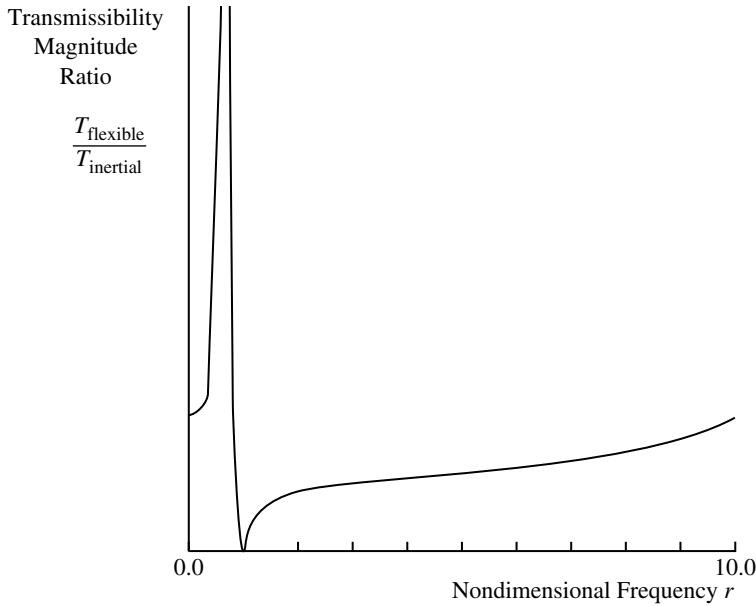


FIGURE 32.9 The effect of system flexibility on the transmissibility magnitude in the undamped case (mass ratio = 1.0; natural frequency ratio = 10.0).

where

$$r = \frac{\omega}{\sqrt{k/M}}$$

$$r_m = \frac{m}{M}$$

$$r_\omega = \frac{\sqrt{K/M}}{\sqrt{k/M}} = \sqrt{\frac{K}{k}}$$

$$\zeta_a = \frac{B}{2\sqrt{KM}}$$

$$\zeta_b = \frac{b}{2\sqrt{kM}}$$

Again, the design problem of vibration isolation is to select the parameters r_m , r_ω , ζ_a , and ζ_b so that the required level of vibration isolation is realized for an operating frequency range of r .

A plot of Equation 32.25 for the undamped case with $r_m = 1.0$ and $r_\omega = 10.0$ is given in Figure 32.9. Generally, the transmissibility ratio will be zero at $r = 1$ (the resonance of the inertial system) and there will be two values of r (the resonances of the flexible system), for which the ratio will become infinity in the undamped case. The latter two neighborhoods should be avoided under steady operating conditions.

32.4 Balancing of Rotating Machinery

Many practical devices that move contain rotating components. Examples are wheels of vehicles, shafts, gear transmissions of machinery, belt drives, motors, turbines, compressors, fans, and rollers. An unbalance (imbalance) is created in a rotating part when its center of mass does not coincide with the axis

of rotation. The reasons for this *eccentricity* include the following:

1. Inaccurate production procedures (machining, casting, forging, assembly, etc.)
2. Wear and tear
3. Loading conditions (mechanical)
4. Environmental conditions (thermal loads and deformation)
5. Use of inhomogeneous and anisotropic material (which does not have a uniform density distribution)
6. Component failure
7. Addition of new components to a rotating device

For a component of mass m , eccentricity e , and rotating at angular speed ω , the centrifugal force that is generated is $m\omega^2 e$. Note the quadratic variation with ω . This rotating force may be resolved into two orthogonal components, which will be sinusoidal with frequency ω . It follows that harmonic forcing excitations are generated due to the unbalance, which can generate undesirable vibrations and associated problems.

Problems caused by unbalance include wear and tear, malfunction and failure of components, poor quality of products, and undesirable noise. The problem becomes increasingly important given the present trend of developing high-speed machinery. It is estimated that the speed of operation of machinery has doubled during the past 50 years. This means that the level of unbalance forces may have quadrupled during the same period, causing more serious vibration problems.

An unbalanced rotating component may be balanced by adding or removing material to or from the component. We need to know both the magnitude and location of the balancing masses to be added to, or removed. The present section will address the problem of component balancing for vibration suppression.

Note that the goal to remove the source of vibration (namely, the mass eccentricity) typically by adding one or more balancing mass elements. Two methods are available:

1. Static (single-plane) balancing
2. Dynamic (two-plane) balancing

The first method concerns balancing of planar objects (e.g., pancake motors, disks) whose longitudinal dimension about the axis of rotation is not significant. The second method concerns balancing of objects that have a significant longitudinal dimension. We will discuss both methods.

32.4.1 Static Balancing

Consider a disk rotating at angular velocity ω about a fixed axis. Suppose that the mass center of the disk has an eccentricity e from the axis of rotation, as shown in Figure 32.10(a). Place a fixed coordinate frame

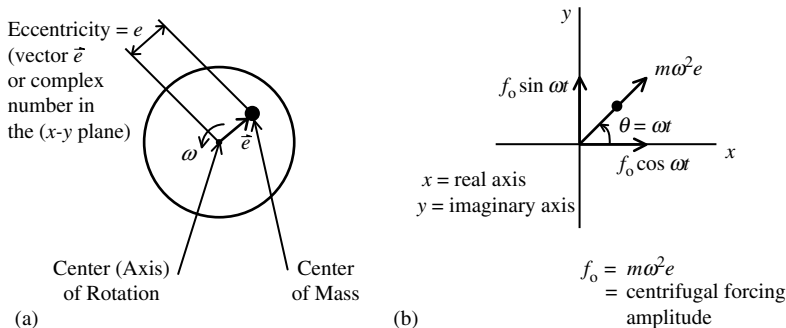


FIGURE 32.10 (a) Unbalance in a rotating disk due to mass eccentricity; (b) rotating vector (phasor) of centrifugal force due to unbalance.

x - y at the center of rotation. The position \vec{e} of the mass center in this coordinate frame may be represented as:

1. A position vector rotating at angular speed ω .
2. A complex number, with x -coordinate denoting the real part and y -coordinate denoting the imaginary part.

The centrifugal force due to the mass eccentricity is also a vector in the direction of \vec{e} , but with a magnitude $f_o = m\omega^2 e$, as shown in Figure 32.10(b). It is seen that harmonic excitations result in both x and y directions, given by $f_o \cos \omega t$ and $f_o \sin \omega t$, respectively, where $\theta = \omega t =$ orientation of the rotating vector with respect to the x -axis. To balance the disk, we should add a mass m at $-\vec{e}$. However, we do not know the value of m and the location of \vec{e} .

32.4.1.1 Balancing Approach

1. Measure the amplitude V_u and the phase angle ϕ_1 (e.g., by the signal from an accelerometer mounted on the bearing of the disk) of the unbalance centrifugal force with respect to some reference.
2. Mount a known mass (trial mass) M_t at a known location on the disk. Suppose that its own centrifugal force is given by the rotating vector \vec{V}_w , and the resultant centrifugal force due to both the original unbalance and the final mass is \vec{V}_r .
3. Measure the amplitude V_r and the phase angle ϕ_2 of the resultant centrifugal force as in step 1, with respect to the same phase reference.

A vector diagram showing the centrifugal forces \vec{V}_u and \vec{V}_w due to the original unbalance and the trial-mass unbalance, respectively, is shown in Figure 32.11. The resultant unbalance is $\vec{V}_r = \vec{V}_u + \vec{V}_w$. Note that $-\vec{V}_u$ represents the centrifugal force due to the balancing mass. Therefore, if we determine the angle ϕ_b in Figure 32.11, it will give the orientation of the balancing mass. Suppose also that the balancing mass is M_b and it is mounted at an eccentricity equal to that of the trial mass M_t . Then,

$$\frac{M_b}{M_t} = \frac{V_u}{V_w}$$

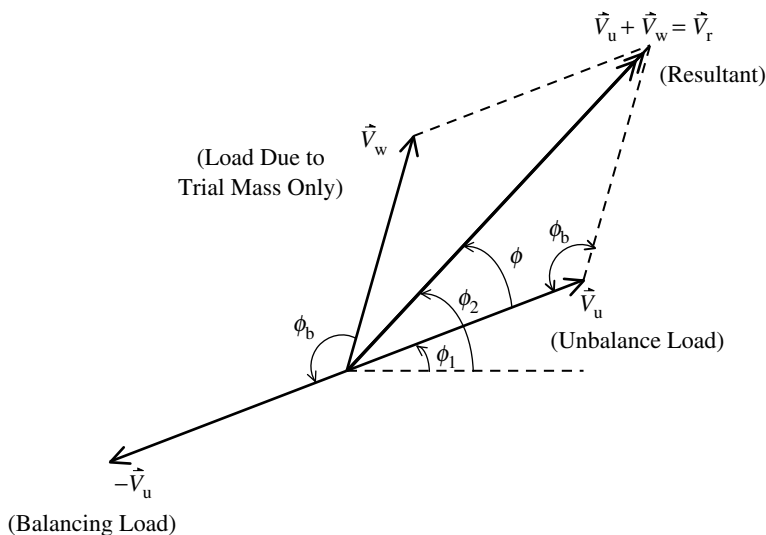


FIGURE 32.11 A vector diagram of the single-plane (static) balancing problem.

We need to determine the ratio V_u/V_w and the angle ϕ_b . These values can be derived as follows:

$$\phi = \phi_2 - \phi_1 \quad (32.26)$$

The cosine rule gives

$$V_w^2 = V_u^2 + V_r^2 - 2V_u V_r \cos \phi \quad (32.27)$$

This will provide V_w since V_u , V_r , and ϕ are known. Apply the cosine rule again:

$$V_r^2 = V_u^2 + V_w^2 - 2V_u V_w \cos \phi_b$$

Hence,

$$\phi_b = \cos^{-1} \left[\frac{V_u^2 + V_w^2 - V_r^2}{2V_u V_w} \right] \quad (32.28)$$

Note: One may think that since we measure ϕ_1 , we know exactly where \bar{V}_u is. This is not the case because we do not know the reference line from which ϕ_1 is measured. We only know that this reference is kept fixed (through strobe synchronization of the body rotation) during measurements. Hence, we need to know ϕ_b , which gives the location of $-\bar{V}_u$ with respect to the known location of \bar{V}_w on the disk.

32.4.2 Complex Number/Vector Approach

Again, suppose that the imbalance is equivalent to a mass of M_b that is located at the same eccentricity (radius) r as the trial mass M_t . Define complex numbers (mass location vectors in a body frame)

$$\bar{M}_b = M_b \angle \theta_b \quad (32.29)$$

$$\bar{M}_t = M_t \angle \theta_t \quad (32.30)$$

as shown in Figure 32.12.

Associated force vectors are

$$\bar{V}_u = \omega^2 r e^{j\omega t} M_b \angle \theta_b \quad (32.31)$$

$$\bar{V}_w = \omega^2 r e^{j\omega t} M_t \angle \theta_t \quad (32.32)$$

or

$$\bar{V}_u = \bar{A} \bar{M}_b \quad (32.33)$$

$$\bar{V}_w = \bar{A} \bar{M}_t \quad (32.34)$$

where $\bar{A} = \omega^2 r e^{j\omega t}$ is the conversion factor (complex) from the mass to the resulting dynamic force (rotating). This factor is the same for both cases since r is the same. We need to determine \bar{M}_b .

From Equation 32.33

$$\bar{M}_b = \frac{\bar{V}_u}{\bar{A}} \quad (32.35)$$

Substitute Equation 32.34:

$$\bar{M}_b = \frac{\bar{V}_u}{\bar{V}_w} \cdot \bar{M}_t \quad (32.36)$$

However, since

$$\bar{V}_r = \bar{V}_u + \bar{V}_w \quad (32.37)$$

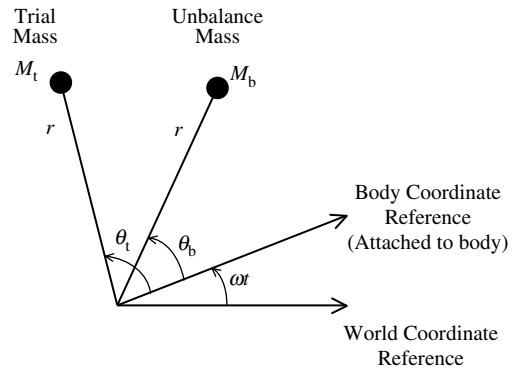


FIGURE 32.12 Rotating vectors of mass location.

we have

$$\vec{M}_b = \frac{\vec{V}_u}{(\vec{V}_r - \vec{V}_u)} \cdot \vec{M}_t \quad (32.38)$$

Since we know \vec{M}_t and we measure \vec{V}_u and \vec{V}_r to the same scaling factor, we can compute \vec{M}_b . Locate the balancing mass at $-\vec{M}_b$ (with respect to the body frame).

Example 32.3

Consider the following experimental steps:

Measured: Accelerometer amplitude (oscilloscope reading) of 6.0 with a phase lead (with respect to strobe signal reference, which is synchronized with the rotating body frame) of 50° .

Added: Trial mass $M_t = 20$ g at angle 180° with respect to a body reference radius.

Measured: Accelerometer amplitude of 8.0 with a phase lead of 60° (with respect synchronized strobe signal).

Determine the magnitude and location of the balancing mass.

Solution

Method 1:

We have the data

$$\phi = 60 - 50^\circ = 10^\circ$$

$$V_u = 6.0; \quad V_r = 8.0$$

Hence, from Equation 32.27:

$$V_w = \sqrt{6^2 + 8^2 - 2 \times 6 \times 8 \cos 10^\circ} = 2.37$$

Balancing mass:

$$M_b = \frac{6.0}{2.37} \times 20 = 50.63 \text{ g}$$

Equation 32.28 gives

$$\phi_b = \cos^{-1} \left[\frac{6^2 + 2.37^2 - 8^2}{2 \times 6 \times 2.37} \right] = \cos^{-1}(-0.787) = 142^\circ \text{ or } 218^\circ$$

Pick the result $0^\circ \leq \phi_b \leq 180^\circ$, as clear from the vector diagram shown in [Figure 32.11](#).

Hence,

$$\phi_b = 142^\circ$$

However,

$$\vec{M}_t = 20 \angle 180^\circ \text{ g}$$

It follows that

$$-\vec{M}_b = 50.63 \angle (180^\circ + 142^\circ) \text{ g} = 50.63 \angle 322^\circ \text{ g}$$

Method 2:

We have

$$\vec{M}_t = 20 \angle 180^\circ \text{ g}$$

$$\vec{V}_u = 6.0 \angle 50^\circ$$

$$\vec{V}_r = 8.0 \angle 60^\circ$$

Then, from Equation 32.38 we obtain

$$\vec{M}_b = \frac{6.0 \angle 50^\circ}{(8.0 \angle 60^\circ - 6.0 \angle 50^\circ)} 20 \angle 180^\circ \text{ g}$$

First, we compute

$$\begin{aligned} 8.0 \angle 60^\circ - 6.0 \angle 50^\circ &= (8.0 \cos 60^\circ + j8.0 \sin 60^\circ) - (6.0 \cos 50^\circ + j6.0 \sin 50^\circ) \\ &= (8.0 \cos 60^\circ - 6.0 \cos 50^\circ) + j(8.0 \sin 60^\circ - 6.0 \sin 50^\circ) = 0.1433 + j2.332 \\ &= 2.336 \angle 86.48^\circ \end{aligned}$$

Hence,

$$\vec{M}_b = \frac{6.0 \angle 50^\circ}{2.336 \angle 86.48^\circ} 20 \angle 180^\circ = \frac{6.0 \times 20}{2.336} \angle (50^\circ + 180^\circ - 86.48^\circ) = 51 \angle 143.5^\circ \text{ g}$$

The balancing mass should be located at

$$-\vec{M}_b = 51 \angle 323.5^\circ \text{ g}$$

Note: This angle is measured from the same body reference as for the trial mass.

32.4.3 Dynamic (Two-Plane) Balancing

Instead of an unbalanced disk, consider an elongated rotating object supported at two bearings, as shown in Figure 32.13. In this case, in general, there may not be an equivalent single unbalance force at a single plane normal to the shaft axis. To show this, recall that a system of forces may be represented by a single force at a specified location and a couple (two parallel forces that are equal and opposite). If this single force (resultant force) is zero, we are left with only a couple. The couple cannot be balanced by a single force.

All the unbalance forces at all the planes along the shaft axis can be represented by an equivalent single unbalance force at a specified plane and a couple. If this equivalent force is zero, then to balance the couple we will need two equal and opposite forces at two different planes.

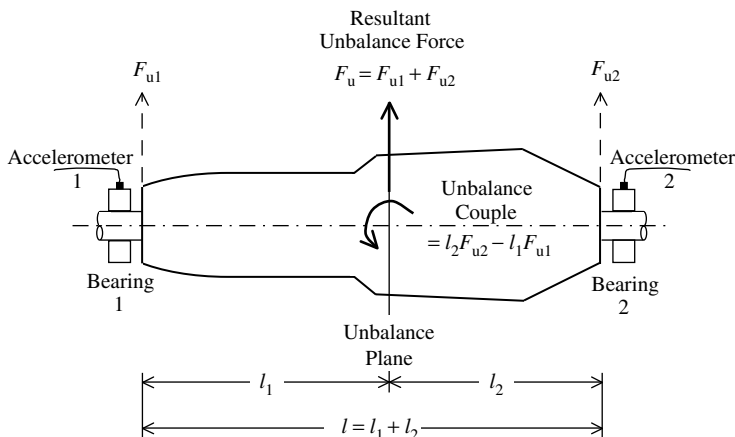


FIGURE 32.13 A dynamic (two-plane) balancing problem.

On the other hand, if the couple is zero, then a single force in the opposite direction at the same plane of the resultant unbalance force will result in complete balancing. However, this unbalance plane may not be reachable, even if it is known, for the purpose of adding the balancing mass.

In the present (two-plane) balancing problem, the balancing masses are added at the two bearing planes so that both the resultant unbalance force and couple are balanced, in general. It is clear from Figure 32.13 that even a sole unbalance mass \bar{M}_b at a single unbalance plane may be represented by two unbalance masses \bar{M}_{b1} and \bar{M}_{b2} at the bearing planes 1 and 2. Likewise, in the presence of an unbalance couple, we can simply add two equal and opposite forces at the planes 1 and 2 so that its couple is equal to the unbalance couple. Hence, a general unbalance can be represented by the two unbalance masses \bar{M}_{b1} and \bar{M}_{b2} at planes 1 and 2, as shown in Figure 32.13. As for the single-plane balancing problem, the resultant unbalance forces at the two bearings (which would be measured by the accelerometers at 1 and 2) are

$$\bar{V}_{u1} = \bar{A}_{11}\bar{M}_{b1} + \bar{A}_{12}\bar{M}_{b2} \quad (32.39)$$

$$\bar{V}_{u2} = \bar{A}_{21}\bar{M}_{b1} + \bar{A}_{22}\bar{M}_{b2} \quad (32.40)$$

Suppose that a trial mass of \bar{M}_{t1} (at a known location with respect to the body reference line) was added at plane 1. The resulting unbalance forces at the two bearings are

$$\bar{V}_{r11} = \bar{A}_{11}(\bar{M}_{b1} + \bar{M}_{t1}) + \bar{A}_{12}\bar{M}_{b2} \quad (32.41)$$

$$\bar{V}_{r21} = \bar{A}_{21}(\bar{M}_{b1} + \bar{M}_{t1}) + \bar{A}_{22}\bar{M}_{b2} \quad (32.42)$$

Next, suppose that a trial mass of \bar{M}_{t2} (at a known location with respect to the body reference line) was added at plane 2, after removing \bar{M}_{t1} . The resulting unbalance forces at the two bearings are

$$\bar{V}_{r12} = \bar{A}_{11}\bar{M}_{b1} + \bar{A}_{12}(\bar{M}_{b2} + \bar{M}_{t2}) \quad (32.43)$$

$$\bar{V}_{r22} = \bar{A}_{21}\bar{M}_{b1} + \bar{A}_{22}(\bar{M}_{b2} + \bar{M}_{t2}) \quad (32.44)$$

The following subtractions of equations are now made.

Equation 32.41 minus Equation 32.39:

$$\bar{V}_{r11} - \bar{V}_{u1} = \bar{A}_{11}\bar{M}_{t1} \quad \text{or} \quad \bar{A}_{11} = \frac{\bar{V}_{r11} - \bar{V}_{u1}}{\bar{M}_{t1}} \quad (32.45)$$

Equation 32.42 minus Equation 32.40:

$$\bar{V}_{r21} - \bar{V}_{u2} = \bar{A}_{21}\bar{M}_{t1} \quad \text{or} \quad \bar{A}_{21} = \frac{\bar{V}_{r21} - \bar{V}_{u2}}{\bar{M}_{t1}} \quad (32.46)$$

Equation 32.43 minus Equation 32.39:

$$\bar{V}_{r12} - \bar{V}_{u1} = \bar{A}_{12}\bar{M}_{t2} \quad \text{or} \quad \bar{A}_{12} = \frac{\bar{V}_{r12} - \bar{V}_{u1}}{\bar{M}_{t2}} \quad (32.47)$$

Equation 32.44 minus Equation 32.40:

$$\bar{V}_{r22} - \bar{V}_{u2} = \bar{A}_{22}\bar{M}_{t2} \quad \text{or} \quad \bar{A}_{22} = \frac{\bar{V}_{r22} - \bar{V}_{u2}}{\bar{M}_{t2}} \quad (32.48)$$

Hence, generally

$$\bar{A}_{ij} = \frac{\bar{V}_{rij} - \bar{V}_{ui}}{\bar{M}_{tj}} \quad (32.49)$$

These parameters A_{ij} are called *influence coefficients*.

Next, in Equation 32.39 and Equation 32.40 eliminate \bar{M}_{b2} and \bar{M}_{b1} separately to determine the other. Thus,

$$\bar{A}_{22} \bar{V}_{u1} - \bar{A}_{12} \bar{V}_{u2} = (\bar{A}_{22} \bar{A}_{11} - \bar{A}_{12} \bar{A}_{21}) \bar{M}_{b1}$$

$$\bar{A}_{21} \bar{V}_{u1} - \bar{A}_{11} \bar{V}_{u2} = (\bar{A}_{21} \bar{A}_{12} - \bar{A}_{11} \bar{A}_{22}) \bar{M}_{b2}$$

or

$$\bar{M}_{b1} = \frac{\bar{A}_{22} \bar{V}_{u1} - \bar{A}_{12} \bar{V}_{u2}}{(\bar{A}_{22} \bar{A}_{11} - \bar{A}_{12} \bar{A}_{21})} \quad (32.50)$$

$$\bar{M}_{b2} = \frac{\bar{A}_{21} \bar{V}_{u1} - \bar{A}_{11} \bar{V}_{u2}}{(\bar{A}_{21} \bar{A}_{12} - \bar{A}_{11} \bar{A}_{22})} \quad (32.51)$$

Substitute Equation 32.45 to Equation 32.48 into Equation 32.50 and Equation 32.51 to determine \bar{M}_{b1} and \bar{M}_{b2} . Balancing masses that should be added are $-\bar{M}_{b1}$ and $-\bar{M}_{b2}$ in planes 1 and 2, respectively.

The single-plane and two-plane balancing approaches are summarized in Box 32.3.

Example 32.4

Suppose that the following measurements are obtained.

Without trial mass:

Accelerometer at 1: amplitude = 10.0; phase lead = 55°.

Accelerometer at 2: amplitude = 7.0; phase lead = 120°

With trial mass 20 g at location 270° of plane 1:

Accelerometer at 1: amplitude = 7.0; phase lead = 120°

Accelerometer at 2: amplitude = 5.0; phase lead = 225°

With trial mass 25 g at location 180° of plane 2:

Accelerometer at 1: amplitude = 6.0; phase lead = 120°

Accelerometer at 2: amplitude = 12.0; phase lead = 170°

Determine the magnitude and orientation of the necessary balancing masses in planes 1 and 2 in order to completely balance (dynamic) the system.

Solution

In the phasor notation, we can represent the given data as follows:

$$\bar{V}_{u1} = 10.0 \angle 55^\circ; \quad \bar{V}_{u2} = 7.0 \angle 120^\circ$$

$$\bar{V}_{r11} = 7.0 \angle 120^\circ; \quad \bar{V}_{r21} = 5.0 \angle 225^\circ$$

$$\bar{V}_{r12} = 6.0 \angle 120^\circ; \quad \bar{V}_{r22} = 12.0 \angle 170^\circ$$

$$\bar{M}_{t1} = 20 \angle 270^\circ \text{ g}; \quad \bar{M}_{t2} = 25 \angle 180^\circ \text{ g}$$

From Equation 32.45 to Equation 32.48, we have

$$\bar{A}_{11} = \frac{7.0 \angle 120^\circ - 10.0 \angle 55^\circ}{20 \angle 270^\circ}; \quad \bar{A}_{21} = \frac{5.0 \angle 225^\circ - 7.0 \angle 120^\circ}{20 \angle 270^\circ}$$

$$\bar{A}_{12} = \frac{6.0 \angle 120^\circ - 10.0 \angle 55^\circ}{25 \angle 180^\circ}; \quad \bar{A}_{22} = \frac{12.0 \angle 170^\circ - 7.0 \angle 120^\circ}{25 \angle 180^\circ}$$

These phasors are computed as below:

$$\begin{aligned} \bar{A}_{11} &= \frac{(7.0 \cos 120^\circ - 10 \cos 55^\circ) + j(7 \sin 120^\circ - 10 \sin 55^\circ)}{20 \angle 270^\circ} = \frac{-9.235 - j2.129}{20 \angle 270^\circ} = \frac{9.477 \angle 193^\circ}{20 \angle 270^\circ} \\ &= 0.474 \angle -77^\circ \end{aligned}$$

Box 32.3

BALANCING OF ROTATING COMPONENTS

Static or single-plane balancing (balances a single equivalent dynamic force)

Experimental approach:

1. With respect to a body reference line of accelerometer signal at bearing, measure magnitude (V) and phase (ϕ):
 - (a) Without trial mass: (V_u, ϕ_1) or $\bar{V}_u = V_u \angle \phi_1$
 - (b) With trial mass M_t : (V_r, ϕ_2) or $\bar{V}_r = V_r \angle \phi_2$.
2. Compute balancing mass M_b and its location with respect to M_t .
3. Remove M_t and add M_b at determined location.

Computation approach 1:

$$V_w = [V_u^2 + V_r^2 - 2V_u V_w \cos(\phi_2 - \phi_1)]^{1/2}$$

$$\phi_b = \cos^{-1} \left[\frac{V_u^2 + V_w^2 - V_r^2}{2V_u V_w} \right] \text{ and } M_b = \frac{V_u}{V_w} M_t$$

Locate M_b at ϕ_b from M_t .

Computation approach 2:

Unbalance mass phasor

$$\bar{M}_b = \frac{\bar{V}_u}{(\bar{V}_r - \bar{V}_u)} \bar{M}_t$$

where $\bar{M}_t = M_t \angle \theta_t$ (trial mass phasor).

Locate balancing mass at $-\bar{M}_b$.

Dynamic or two-plane balancing (balances an equivalent dynamic force and a couple)

Experimental approach:

1. Measure \bar{V}_{ui} at bearings $i = 1, 2$, with a trial mass.
2. Measure \bar{V}_{rij} at bearings $i = 1, 2$, with only one trial mass \bar{M}_{tj} at $j = 1, 2$.
3. Compute unbalance mass phasor \bar{M}_{bi} in planes $i = 1, 2$.
4. Remove trial mass and place balancing masses $-\bar{M}_{bi}$ in planes $i = 1, 2$.

Computations:

Influence coefficients: $\bar{A}_{ij} = (\bar{V}_{rij} - \bar{V}_{ui})/\bar{M}_{tj}$

Unbalance mass phasors:

$$\bar{M}_{b1} = \frac{\bar{A}_{22}\bar{V}_{u1} - \bar{A}_{12}\bar{V}_{u2}}{(\bar{A}_{22}\bar{A}_{11} - \bar{A}_{12}\bar{A}_{21})} \quad \text{and} \quad \bar{M}_{b2} = \frac{\bar{A}_{21}\bar{V}_{u1} - \bar{A}_{11}\bar{V}_{u2}}{(\bar{A}_{21}\bar{A}_{12} - \bar{A}_{11}\bar{A}_{22})}$$

$$\begin{aligned} \bar{A}_{21} &= \frac{(5 \cos 225^\circ - 7 \cos 120^\circ) + j(5 \sin 225^\circ - 7 \sin 120^\circ)}{20 \angle 270^\circ} = \frac{-7.036 - j9.6}{20 \angle 270^\circ} = \frac{11.9 \angle 234^\circ}{20 \angle 270^\circ} \\ &= 0.595 \angle -36^\circ \end{aligned}$$

$$\begin{aligned} \bar{A}_{12} &= \frac{(6 \cos 120^\circ - 10 \cos 55^\circ) + j(6 \sin 120^\circ - 10 \sin 55^\circ)}{25 \angle 180^\circ} = \frac{-8.736 - j3.0}{25 \angle 180^\circ} = \frac{9.237 \angle 199^\circ}{25 \angle 180^\circ} \\ &= 0.369 \angle 19^\circ \end{aligned}$$

$$\begin{aligned}\bar{A}_{22} &= \frac{(12 \cos 170^\circ - 7 \cos 120^\circ) + j(12 \sin 170^\circ - 7 \sin 120^\circ)}{25 \angle 180^\circ} = \frac{-8.318 - j4.0}{25 \angle 180^\circ} = \frac{9.23 \angle 205.7^\circ}{25 \angle 180^\circ} \\ &= 0.369 \angle 25.7^\circ\end{aligned}$$

Next, the denominators of the balancing mass phasors (in Equation 32.50 and Equation 32.51) are computed as

$$\begin{aligned}\bar{A}_{22}\bar{A}_{11} - \bar{A}_{12}\bar{A}_{21} &= (0.369 \angle 25.7^\circ \times 0.474 \angle -77^\circ) - (0.369 \angle 19^\circ \times 0.595 \angle -36^\circ) \\ &= 0.1749 \angle -51.3^\circ - 0.2196 \angle -17^\circ \\ &= (0.1749 \cos 51.3^\circ - 0.2196 \cos 17^\circ) - j(0.1749 \sin 51.3^\circ - 0.2196 \sin 17^\circ) \\ &= -0.1 - j0.0723 = 0.1234 \angle 216^\circ\end{aligned}$$

and, hence

$$-(\bar{A}_{22}\bar{A}_{11} - \bar{A}_{12}\bar{A}_{21}) = 0.1234 \angle 36^\circ$$

Finally, the balancing mass phasors are computed using Equation 32.50 and Equation 32.51 as

$$\begin{aligned}\bar{M}_{b1} &= \frac{0.369 \angle 25.7^\circ \times 10 \angle 55^\circ - 0.369 \angle 19^\circ \times 7.0 \angle 120^\circ}{0.1234 \angle 216^\circ} = \frac{3.69 \angle 80.7^\circ - 2.583 \angle 139^\circ}{0.1234 \angle 216^\circ} \\ &= \frac{(3.69 \cos 80.7^\circ - 2.583 \cos 139^\circ) + j(3.69 \sin 80.7^\circ - 2.583 \sin 139^\circ)}{0.1234 \angle 216^\circ} = \frac{2.546 + j1.947}{0.1234 \angle 216^\circ} \\ &= \frac{3.205 \angle 37.4^\circ}{0.1234 \angle 216^\circ} = 26 \angle -178.6^\circ \\ \bar{M}_{b2} &= \frac{0.595 \angle -36^\circ \times 10 \angle 55^\circ - 0.474 \angle -77^\circ \times 7.0 \angle 120^\circ}{0.1234 \angle 36^\circ} = \frac{5.95 \angle 19^\circ - 3.318 \angle 43^\circ}{0.1234 \angle 36^\circ} \\ &= \frac{(5.95 \cos 19^\circ - 3.318 \cos 43^\circ) - j(5.95 \sin 19^\circ - 3.318 \sin 43^\circ)}{0.1234 \angle 36^\circ} = \frac{3.2 + j0.326}{0.1234 \angle 36^\circ} \\ &= \frac{1.043 \angle 5.8^\circ}{0.1234 \angle 36^\circ} = 8.45 \angle -30.0^\circ\end{aligned}$$

Finally, we have

$$-\bar{M}_{b1} = 26 \angle 1.4^\circ \text{ g}; \quad -\bar{M}_{b2} = 8.45 \angle 150^\circ \text{ g}$$

32.4.4 Experimental Procedure of Balancing

The experimental procedure for determining the balancing masses and locations for a rotating system should be clear from the analytical developments and examples given above. The basic steps are:

1. Determine the magnitude and the phase angle of accelerometer signals at the bearings with and without trial masses at the bearing planes.
2. Using this data, compute the necessary balancing masses (magnitude and location) at the bearing planes.
3. Place the balancing masses.
4. Check whether the system is balanced. If not, repeat the balancing cycle.

A laboratory experimental setup for two-plane balancing is shown schematically in [Figure 32.14](#). A view of the system is shown in [Figure 32.15](#). The two disks rigidly mounted on the shaft are driven by a DC motor. The drive speed of the motor is adjusted by the manual speed controller. The (two) shaft

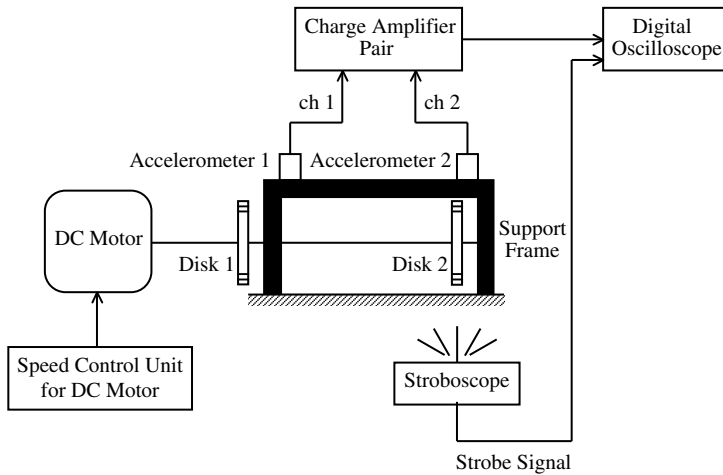


FIGURE 32.14 Schematic arrangement of a rotor balancing experiment.

bearings are located very close to the disks, as shown in Figure 32.14. Two accelerometers are mounted on the top of the bearing housing so that the resulting vertical accelerations can be measured. The accelerometer signals are conditioned using the two-channel charge amplifier and read and displayed through two channels of the digital oscilloscope. The output of the stroboscope (tachometer) is used as the reference signal with respect to the phase angles of the accelerometer signals that are measured.

In Figure 32.15, the items of equipment are seen from left to right. The first item is the two-channel digital oscilloscope. The manual speed controller with control knob for the DC motor follows. Next is the pair of charge amplifiers for the accelerometers. The strobe-light unit (strobe-tacho) is placed on top of the common housing of the charge amplifier pair. The two-disk rotor system with the drive motor is shown as the last item to the right. Also, note the two accelerometers (seen as small vertical projections) mounted on the bearing frame of the shaft directly above the two bearings.

Because this reference always has to be fixed prior to reading the oscilloscope data, the strobe-tacho is synchronized with the disk rotation. This is achieved as follows (note that all the readings are taken with

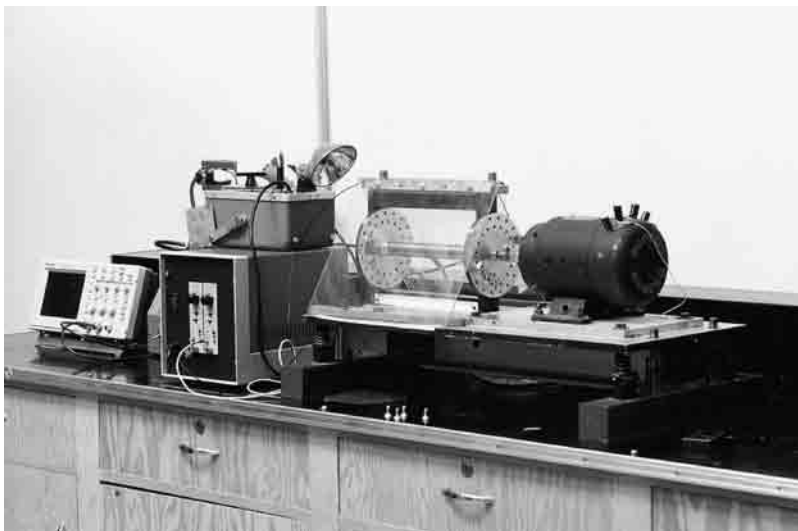


FIGURE 32.15 A view of the experimental setup for two-plane balancing at the University of British Columbia.

the same rotating speed, which is adjusted by the manual speed controller): First, make a physical mark (e.g., a black spot in a white background) on one of the disks. Aim the strobe flash at this disk. As the motor speed is adjusted to the required fixed value, the strobe flash is synchronized such that the mark on the disk “appears” stationary at the same location (e.g., at the uppermost location of the circle of rotation). This ensures not only that the strobe frequency is equal to the rotating speed of the disk, but also that the same phase angle reference is used for all readings of accelerometer signals.

The two disks have slots at locations whose radius is known, and whose angular positions in relation to a body reference line (a radius representing the 0° reference line) are clearly marked. Known masses (typically, bolts and nuts of known mass) can be securely mounted in these slots. Readings obtained through the oscilloscope are:

1. Amplitude of each accelerometer signal
2. Phase lead of the accelerometer signal with respect to the synchronized and reference-fixed strobe signal (note: a phase lag should be represented by a negative sign in the data)

The measurements taken and the computations made in the experimental procedure should be clear from Example 32.4.

32.5 Balancing of Reciprocating Machines

A reciprocating mechanism has a slider that moves rectilinearly back and forth along some guideway. A piston-cylinder device is a good example. Often, reciprocating machines contain rotatory components in addition to the reciprocating mechanisms. The purpose is to either convert a reciprocating motion to a rotary motion (as in the case of an automobile engine), or to convert a rotary motion to a reciprocating motion (as in the opto-slider mechanism of a photocopier). Irrespective of the reciprocating machine employed, it is important to remove the vibratory excitations that arise in order to realize the standard design goals of smooth operation, accuracy, low noise, reliability, mechanical integrity, and extended service life. Naturally, in view of their rotational asymmetry, reciprocating mechanisms with rotary components are more prone to unbalance than purely rotary components. Removing the “source of vibration” by proper balancing of the machine would be especially applicable in this situation.

32.5.1 Single-Cylinder Engine

A practical example of a reciprocating machine with integral rotary motion is the internal combustion (IC) engine of an automobile. A single-cylinder engine is sketched in Figure 32.16. Observe the nomenclature of the components. The reciprocating motion of the piston is transmitted through the connecting rod and crank into a rotatory motion of the crankshaft. The crank, as sketched in Figure 32.16, has a counterbalance mass, the purpose of which is to balance the rotary force (centrifugal).

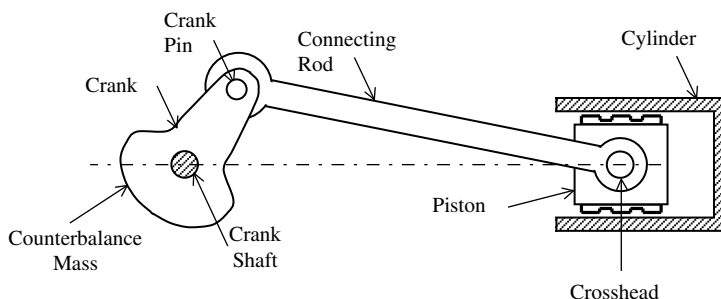


FIGURE 32.16 A single-cylinder reciprocating engine.

We will ignore this in our analysis because the goal is to determine the unbalance forces and ways to balance them.

Clearly, both the connecting rod and the crank have distributed mass and moment of inertia. To simplify the analysis, we approximate as follows:

1. Represent the crank mass by an equivalent lumped mass at the crank pin (equivalence may be based on either centrifugal force or kinetic energy).
2. Represent the mass of the connecting rod by two lumped masses, one at the crank pin and the other at the cross head (piston pin).

The piston itself has a significant mass, which is also lumped at the crosshead. Hence, the equivalent system has a crank and a connecting rod, both of which are considered massless, with a lumped mass m_c at the crank pin and another lumped mass m_p at the piston pin (crosshead).

Furthermore, under normal operation, the crankshaft rotates at a constant angular speed (ω). Note that this steady speed is realized not by natural dynamics of the system, but rather by proper speed control (a topic which is beyond the scope of the present discussion).

It is a simple matter to balance the lumped mass m_c at the crank pin. Simply place a counter-mass m_c at the same radius in the radially opposite location (or a mass in inverse proportion to the radial distance from the crankshaft, but remaining in the radially opposite direction). This explains the presence of the counter-mass in the crank shown in Figure 32.16. Once complete balancing of the rotating inertia (m_c) is thus achieved, we still need to completely eliminate the effect of the vibration source on the crankshaft. To achieve this, we must compensate for the forces and moments on the crankshaft that result from:

1. The reciprocating motion of the lumped mass m_p
2. Time-varying combustion (gas) pressure in the cylinder

Both types of forces act on the piston in the direction of its reciprocating (rectilinear) motion. Hence, their influence on the crankshaft can be analyzed in the same way, except that the combustion pressure is much more difficult to determine.

The above discussion justifies the use of the simplified model shown in Figure 32.17 for analyzing the balancing of a reciprocating machine. The characteristics of this model are as follows:

1. A light crank OC of radius r rotates at constant angular speed ω about O, which is the origin of the x - y coordinate frame.
2. A light connecting rod CP of length l is connected to the connecting rod at C and to the piston at P with frictionless pins. Since the rod is light and the joints are frictionless, the force f_c supported by it will act along its length. (Assume that the force f_c in the connecting rod is compressive, for the purpose of the sign convention). Connecting rod makes an angle ϕ with OP (the negative x axis).
3. A lumped mass m_p is present at the piston. A force f acts at P in the negative x direction. This may be interpreted as either the force due to the gas pressure in the cylinder or the inertia force $m_p a$ where a is the acceleration m_p in the positive x direction. These two cases of forcing are considered separately.
4. A lateral force f_l acts on the piston by the cylinder wall, in the positive y direction.

Again, note that the lumped mass m_c at C is not included in the model of Figure 32.17 because it is assumed to be completely balanced by a counter-mass in the crank. Furthermore, the lumped mass m_p includes both the mass of the piston and also part of the inertia of the connecting rod.

There are no external forces at C. Furthermore, the only external forces at P are f and f_l , where f is interpreted as either the inertia force in m_p or the gas force on the piston. Hence, there should be

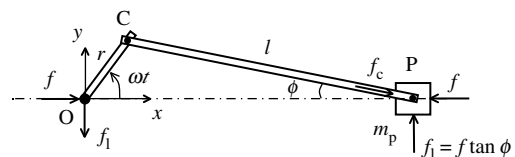


FIGURE 32.17 The model used to analyze balancing of a reciprocating engine.

equal and opposite forces at the crankshaft O, as shown in Figure 32.17, to support the forces acting at P. Now, let us determine f_l .

Equilibrium at P gives

$$f = f_c \cos \phi$$

$$f_l = f_c \sin \phi$$

Hence,

$$f_l = f \tan \phi \quad (32.52)$$

This lateral force f_l acting at both O and P, albeit in the opposite directions, forms a couple $\tau = xf_l$ or, in view of Equation 32.52:

$$\tau = xf \tan \phi \quad (32.53)$$

This couple acts as a torque on the crankshaft. It follows that, once the rotating inertia m_c at the crank is completely balanced by a counterweight, the load at the crankshaft is due only to the piston load f and it consists of:

1. A force f in the direction of the piston motion (x)
2. A torque $\tau = xf \tan \phi$ in the direction of rotation of the crankshaft (z)

As discussed below, the means of removing f at the crankshaft will also remove τ to some extent. Hence, we will discuss only the approach of balancing f .

32.5.2 Balancing the Inertia Load of the Piston

First, consider the inertia force f due to m_p . Here,

$$f = m_p a \quad (32.54)$$

where a is the acceleration \ddot{x} , with the coordinate x locating the position P of the piston (in other words $OP = x$). We notice from Figure 32.17 that

$$x = r \cos \omega t + l \cos \phi \quad (32.55)$$

However,

$$r \sin \omega t = l \sin \phi \quad (32.56)$$

Hence,

$$\cos \phi = \left[1 - \left(\frac{r}{l} \right)^2 \sin^2 \omega t \right]^{1/2} \quad (32.57)$$

which can be expanded up to the first term of Taylor series as

$$\cos \phi \cong 1 - \frac{1}{2} \left(\frac{r}{l} \right)^2 \sin^2 \omega t \quad (32.58)$$

This approximation is valid because l is usually several times larger than r and, hence, $(r/l)^2$ is much small than unity. Next, in view of

$$\sin^2 \omega t = \frac{1}{2} [1 - \cos 2\omega t] \quad (32.59)$$

we have

$$\cos \phi \cong 1 - \frac{1}{4} \left(\frac{r}{l} \right)^2 [1 - \cos 2\omega t] \quad (32.60)$$

Substitute Equation 32.60 into Equation 32.55. We get, approximately

$$x = r \cos \omega t + \frac{l}{4} \left(\frac{r}{l} \right)^2 \cos 2\omega t + l - \frac{l}{4} \left(\frac{r}{l} \right)^2 \quad (32.61)$$

Differentiate Equation 32.61 twice with respect to t to get the acceleration

$$a = \ddot{x} = -r\omega^2 \cos \omega t - l \left(\frac{r}{l} \right)^2 \omega^2 \cos 2\omega t \quad (32.62)$$

Hence, from Equation 32.54, the inertia force at the piston (and its reaction at the crankshaft) is

$$f = -m_p r \omega^2 \cos \omega t - m_p l \left(\frac{r}{l} \right)^2 \omega^2 \cos 2\omega t \quad (32.63)$$

It follows that the inertia load of the reciprocating piston exerts a vibratory force on the crankshaft which has a *primary component* of frequency ω and a smaller *secondary component* of frequency 2ω , where ω is the angular speed of the crank. The primary component has the same form as that created by a rotating lumped mass at the crank pin. However, unlike the case of a rotating mass, this vibrating force acts only in the x direction (there is no $\sin \omega t$ component in the y direction) and, hence, cannot be balanced by a rotating counter-mass. Similarly, the secondary component cannot be balanced by a counter-mass rotating at double the speed. To eliminate f , we use multiple cylinders whose connecting rods and cranks are connected to the crankshaft with their rotations properly phased (delayed), thus canceling out the effects of f .

32.5.3 Multicylinder Engines

A single-cylinder engine generates a primary component and a secondary component of vibration load at the crankshaft, and they act in the direction of piston motion (x). Because there is no complementary orthogonal component (y), it is inherently unbalanced and cannot be balanced using a rotating mass. It can be balanced, however, by using several piston-cylinder units with their cranks properly phased along the crankshaft. This method of balancing multicylinder reciprocating engines is addressed now.

Consider a single cylinder whose piston inertia generates a force f at the crankshaft in the x direction given by

$$f = f_p \cos \omega t + f_s \cos 2\omega t \quad (32.64)$$

Note that the primary and secondary forcing amplitudes f_p and f_s , respectively, are given by Equation 32.63. Suppose that there is a series of cylinders in parallel, arranged along the crankshaft, and the crank of cylinder i makes an angle α_i with the crank of cylinder 1 in the direction of rotation, as schematically shown in Figure 32.18(a). Hence, force f_i on the crankshaft (in the x direction, shown as vertical in Figure 32.18) due to cylinder i is

$$f_i = f_p \cos(\omega t + \alpha_i) + f_s \cos(2\omega t + 2\alpha_i) \quad \text{for } i = 1, 2, \dots, \text{ with } \alpha_1 = 0 \quad (32.65)$$

Not only do the cranks need to be properly phased, but the cylinders should also be properly spaced along the crankshaft to obtain the necessary balance. Consider two examples.

32.5.3.1 Two-Cylinder Engine

Consider the two-cylinder case, as shown schematically in Figure 32.18(b) where the two cranks are in radially opposite orientations (i.e., 180° out of phase). In this case, $\alpha_2 = \pi$. Hence,

$$f_1 = f_p \cos \omega t + f_s \cos 2\omega t \quad (32.66)$$

$$f_2 = f_p \cos(\omega t + \pi) + f_s \cos(2\omega t + 2\pi) = -f_p \cos \omega t + f_s \cos 2\omega t \quad (32.67)$$

It follows that the primary force components cancel out. However, they form a couple $z_0 f_p \cos \omega t$ where z_0 is the spacing of the cylinders. This causes a bending moment on the crankshaft, and it will not vanish

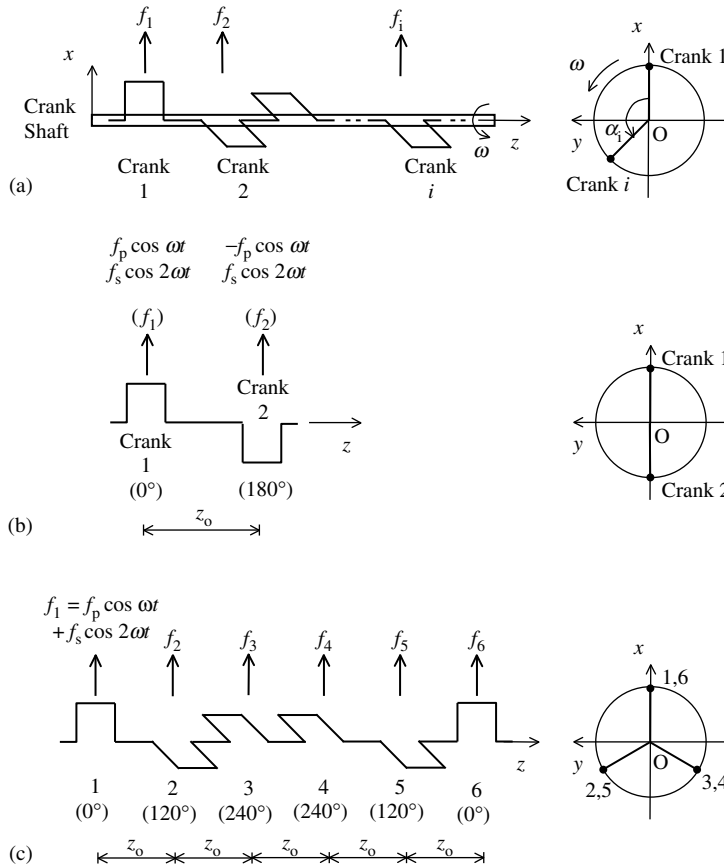


FIGURE 32.18 (a) Crank arrangement of a multicylinder engine; (b) two-cylinder engine; (c) six-cylinder engine (balanced).

unless the two cylinders are located at the same point along the crankshaft. Furthermore, the secondary components are equal and additive to $2f_s \cos 2\omega t$. This resultant component acts at the midpoint of the crankshaft segment between the two cylinders. There is no couple due to the secondary components.

32.5.3.2 Six-Cylinder Engine

Consider the six-cylinder arrangement shown schematically in Figure 32.18(c). Here, the cranks are arranged such that $\alpha_2 = \alpha_5 = 2\pi/3$, $\alpha_3 = \alpha_4 = 4\pi/3$, and $\alpha_1 = \alpha_6 = 0$. Furthermore, the cylinders are equally spaced, with spacing z_0 . In this case, we have

$$f_1 = f_6 = f_p \cos \omega t + f_s \cos 2\omega t \quad (\text{i})$$

$$f_2 = f_5 = f_p \cos(\omega t + 2\pi/3) + f_s \cos(2\omega t + 4\pi/3) \quad (\text{ii})$$

$$f_3 = f_4 = f_p \cos(\omega t + 4\pi/3) + f_s \cos(2\omega t + 8\pi/3) \quad (\text{iii})$$

Now, we use the fact that

$$\cos \theta + \cos\left(\theta + \frac{2\pi}{3}\right) + \cos\left(\theta + \frac{4\pi}{3}\right) = 0 \quad (\text{iv})$$

which may be proved either by straightforward trigonometric expansion or by using geometric interpretation (i.e., three sides of an equilateral triangle, the sum of whose components in any

direction vanishes). The relation iv holds for any θ , including $\theta = \omega t$ and $\theta = 2\omega t$. Furthermore,

$$\cos(2\omega t + 8\pi/3) = \cos\left(2\omega t + \frac{2\pi}{3}\right)$$

Thus, from Equation i to Equation iii, we can conclude that

$$f_1 + f_2 + f_3 + f_4 + f_5 + f_6 = 0 \quad (32.68)$$

This means that the lateral forces on the crankshaft that are exerted by the six cylinders will completely balance. Furthermore, by taking moments about the location of crank 1 of the crankshaft, we have

$$\begin{aligned} (z_0 + 4z_0) \left[f_p \cos\left(\omega t + \frac{2\pi}{3}\right) + f_s \cos\left(2\omega t + \frac{4\pi}{3}\right) \right] \\ + (2z_0 + 3z_0) \left[f_p \cos\left(\omega t + \frac{4\pi}{3}\right) + f_s \cos\left(2\omega t + \frac{8\pi}{3}\right) \right] \\ + 5z_0 [f_p \cos \omega t + f_s \cos 2\omega t] \end{aligned} \quad (v)$$

which also vanishes in view of relation iv. Hence, the set of six forces is in complete equilibrium and, as a result, there will be neither a reaction force nor a bending moment on the bearings of the crankshaft from these forces.

In addition, it can be shown that the torques $x_i f_i \tan \phi_i$ on the crankshaft due to this set of inertial forces f_i will add to zero, where x_i is the distance from the crankshaft to the piston of the i th cylinder and ϕ_i is the angle ϕ of the connecting rod of the i th cylinder. Hence, this six-cylinder configuration is in complete balance with respect to the inertial load.

Example 32.5

An eight-cylinder in-line engine (with identical cylinders that are placed in parallel along a line) has its cranks arranged according to the phasing angles 0, 180, 90, 270, 270, 90, 180, and 0° on the crankshaft. The cranks (cylinders) are equally spaced, with spacing z_0 . Show that this engine is balanced with respect to primary and secondary components of reaction forces and bending moments of inertial loading on the bearings of the crankshaft.

Solution

The sum of the reaction forces on the crankshaft are

$$\begin{aligned} 2 \left[f_p \cos \omega t + f_s \cos 2\omega t + f_p \cos(\omega t + \pi) + f_s \cos(2\omega t + 2\pi) + f_p \cos\left(\omega t + \frac{\pi}{2}\right) + f_s \cos(2\omega t + \pi) \right. \\ \left. + f_p \cos\left(\omega t + \frac{3\pi}{2}\right) + f_s \cos(2\omega t + 3\pi) \right] = 2 \left[f_p \cos \omega t - f_p \cos \omega t - f_p \sin \omega t + f_p \sin \omega t \right. \\ \left. + f_s \cos 2\omega t + f_s \cos 2\omega t - f_s \cos 2\omega t - f_s \cos 2\omega t \right] = 0 \end{aligned}$$

Hence, both primary forces and secondary forces are balanced. The moment of the reaction forces about the crank 1 location of the crankshaft is

$$\begin{aligned} (z_0 + 6z_0) [f_p \cos(\omega t + \pi) + f_s \cos(2\omega t + 2\pi)] + (2z_0 + 5z_0) \left[f_p \cos\left(\omega t + \frac{\pi}{2}\right) + f_s \cos(2\omega t + \pi) \right] \\ + (3z_0 + 4z_0) \left[f_p \cos\left(\omega t + \frac{3\pi}{2}\right) + f_s \cos(2\omega t + 3\pi) \right] + 7z_0 [f_p \cos \omega t + f_s \cos 2\omega t] \\ = 7z_0 [-f_p \cos \omega t + f_s \cos 2\omega t - f_p \sin \omega t - f_s \cos 2\omega t + f_p \sin \omega t - f_s \cos 2\omega t + f_p \cos \omega t + f_s \cos 2\omega t] = 0 \end{aligned}$$

Hence, both primary bending moments and secondary bending moments are balanced. Therefore, the engine is completely balanced.

The formulas applicable for balancing reciprocating machines are summarized in Box 32.4.

Box 32.4

BALANCING OF RECIPROCATING MACHINES

Single cylinder engine:

Inertia force at piston (and its reaction on crankshaft)

$$f = -m_p r \omega^2 \cos \omega t - m_p l \left(\frac{r}{l} \right)^2 \omega^2 \cos 2\omega t = f_p \cos \omega t + f_s \cos 2\omega t$$

where

ω = rotating speed of crank

m_p = equivalent lumped mass at piston

r = crank radius

l = length of connecting rod

f_p = amplitude of the primary unbalance force (frequency ω)

f_s = amplitude of the secondary unbalance force (frequency 2ω)

Multicylinder engine:

Net unbalance reaction force on crankshaft = $\sum_{i=1}^n f_i$

Net unbalance moment on crankshaft = $\sum_{i=1}^n z_i f_i$

where

$$f_i = f_p \cos(\omega t + \alpha_i) + f_s \cos(2\omega t + 2\alpha_i)$$

α_i = angular position of the crank of i th cylinder, with respect to a body (rotating) reference (i.e., crank phasing angle)

z_i = position of the i th crank along the crankshaft, measured from a reference point on the shaft

n = number of cylinders (assumed identical)

Note: For a completely balanced engine, both the net unbalance force and the net unbalance moment should vanish.

Finally, it should be noted that, in the configuration considered above, the cylinders are placed in parallel along the crankshaft. These are termed in-line engines. Their resulting forces f_i act in parallel along the shaft. In other configurations such as V6 and V8, the cylinders are placed symmetrically around the shaft. In this case, the cylinders (and their inertial forces, which act on the crankshaft) are not parallel. Here, a complete force balance may be achieved without having to phase the cranks. Furthermore, the bending moments of the forces can be reduced by placing the cylinders at nearly the same location along the crankshaft. Complete balancing of the combustion/pressure forces is also possible by such an arrangement.

32.5.4 Combustion/Pressure Load

In the balancing approach presented above, the force f on the piston represents the inertia force due to the equivalent reciprocating mass. Its effect on the crankshaft is an equal reaction force f in the lateral direction (x) and a torque $\pi = x f \tan \phi$ about the shaft axis (z). The balancing approach is to use a series of cylinders so that their reaction forces f_i on the crankshaft from an equilibrium set so that no net reaction or bending moment is transmitted to the bearings of the shaft. The torques τ_i also can be balanced by the same approach, which is the case, for example, in the six-cylinder engine.

Another important force that acts along the direction of piston reciprocation is the drive force due to gas pressure in the cylinder (e.g., created by combustion of the fuel–air mixture of an internal combustion engine). As above, this force may be analyzed by denoting it as f . However, several important observations should be made first:

1. The combustion force f is not sinusoidal of frequency ω . It is reasonably periodic but the shape is complex and depends on the firing/fuel-injection cycle and the associated combustion process.
2. The reaction forces f_i on the crankshaft, which are generated from cylinders i , should be balanced to avoid the transmission of reaction forces and bending moments to the shaft bearings (and hence, to the supporting frame — the vehicle). However, the torques τ_i in this case are in fact the drive torques. Obviously, they are the desired output of the engine and should not be balanced, unlike the inertia torques.

Therefore, although the analysis completed for balancing the inertia forces cannot be directly used here, we can employ similar approaches to the use of multiple cylinders for reducing the gas-force reactions. This is a rather difficult problem given the complexity of the combustion process itself. In practice, much of the leftover effects of the ignition cycle are suppressed by properly designed engine mounts. Experimental investigations have indicated that in a properly balanced engine unit, much of the vibration transmitted through the engine mounts is caused by the engine firing cycle (internal combustion) rather than the reciprocating inertia (sinusoidal components of frequency ω and 2ω). Hence, active mounts, where stiffness can be varied according to the frequency of excitation, are being considered to reduce engine vibrations in the entire range of operating speeds (e.g. 500 to 2500 rpm).

32.6 Whirling of Shafts

In the previous two sections, we studied the vibration excitations caused on rotating shafts and their bearings due to some form of mass eccentricity. Methods of balancing these systems to eliminate the undesirable effects were also presented. One limitation of the given analysis is the assumptions that the rotating shaft is rigid and, thus, does not deflect from its axis of rotation due to the unbalanced excitations. In practice, however, rotating shafts are made lighter than the components they carry (rotors, disks, gears, etc.) and will undergo some deflection due to the unbalanced loading. As a result, the shaft will bow out and this will further increase the mass eccentricity and associated unbalanced excitations and gyroscopic forces of the rotating elements (disks, rotors, etc.). The nature of damping of rotating machinery (which is rather complex and incorporates effects of rotation at bearings, structural deflections, and lateral speeds) will further affect the dynamic behavior of the shaft under these conditions. In this context, the topic of whirling of rotating shafts becomes relevant.

Consider a shaft that is driven at a constant angular speed ω (e.g., by using a motor or some other actuator). The central axis of the shaft (passing through its bearings) will bow out. The deflected axis itself will rotate, and this rotation is termed *whirling* or *whipping*. The whirling speed is not necessarily equal to the drive speed ω (at which the shaft rotates about its axis with respect to a fixed frame). However, when the whirling speed is equal to ω , the condition is called *synchronous whirl*, and the associated deflection of the shaft can be quite excessive and damaging.

To develop an analytical basis for whirling, consider a light shaft supported on two bearings carrying a disk of mass m in between the bearings, as shown in Figure 32.19(a). Note that C is the point on the disk at which it is mounted on the shaft. Originally, in the neutral configuration when the shaft is not driven ($\omega = 0$), the point C coincides with point O on the axis joining the two bearings. If the shaft were rigid, then the points C and O would continue to coincide during motion. The mass center (centroid or center of gravity for constant g) of the disk is denoted as G in Figure 32.19. During motion, C will move away from O due to the shaft deflection. The whirling speed (speed of rotation of the shaft axis) is the speed of rotation of the radial line OC with respect to a fixed reference. Denoting the angle of OC with respect to a fixed reference as θ , the whirling speed is $\dot{\theta}$. This is explained in Figure 32.19(b) where an end view of the

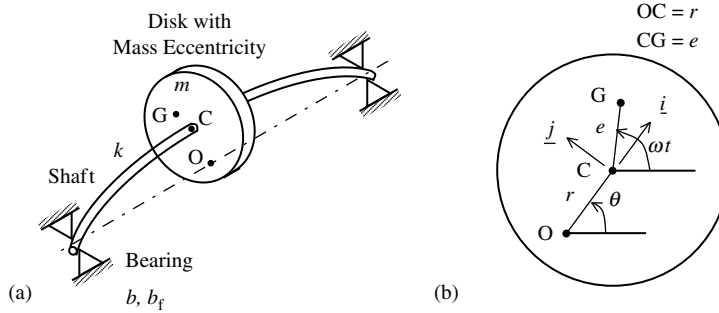


FIGURE 32.19 (a) A whirling shaft carrying a disk with mass eccentricity; (b) end view of the disk and whirling shaft.

disk is given under deflected conditions. The constant drive speed ω of the shaft is the speed of the shaft spin with respect to a fixed reference, and is the speed of rotation of the radial line CG with respect to the fixed horizontal line shown in Figure 32.19(b). Hence, the angle of shaft spin is ωt , as measured with respect to this line. The angle of whirl, θ , is also measured from the direction of this fixed line, as shown.

32.6.1 Equations of Motion

Under practical conditions, the disk moves entirely in a single plane. Hence, its complete set of equations of motion consists of two equations for translatory (planar) motion of the centroid (with lumped mass m), and one equation for rotational motion about the fixed bearing axis. The latter equation depends on the motor torque that drives the shaft at constant speed ω , and is not of interest in the present context. Thus, we will limit our development to the two translatory equations of motion. The equations may be written either in a Cartesian coordinate system (x, y) or a polar coordinate system (r, θ) . Here, we will use the polar coordinate system.

Consider a coordinate frame (\mathbf{i}, \mathbf{j}) that is fixed to the disk with its \mathbf{i} axis lying along OC as shown in Figure 32.19(b). Note that the angular speed of this frame is $\dot{\theta}$ (about the \mathbf{k} axis that is orthogonal to \mathbf{i} and \mathbf{j}). Hence, as is well known, we have

$$\frac{d\mathbf{i}}{dt} = \dot{\theta}\mathbf{j} \quad \text{and} \quad \frac{d\mathbf{j}}{dt} = -\dot{\theta}\mathbf{i} \quad (32.69)$$

The position vector of the mass point G from O is

$$\mathbf{OG} = \mathbf{r}_G = \mathbf{OC} + \mathbf{CG} = r\mathbf{i} + e \cos(\omega t - \theta)\mathbf{i} + e \sin(\omega t - \theta)\mathbf{j} \quad (32.70)$$

The velocity vector \mathbf{v}_G of the mass point G can be obtained simply by differentiating Equation 32.70 with the use of Equation 32.69. However, this can be simplified because ω is constant. Here, line CG has a velocity $e\omega$ that is perpendicular to it about C. This can be resolved along the axes \mathbf{i} and \mathbf{j} . Hence, the velocity of G relative to C is

$$\mathbf{v}_{G/C} = -e\omega \sin(\omega t - \theta)\mathbf{i} + e\omega \cos(\omega t - \theta)\mathbf{j}$$

However, the velocity of point C is

$$\mathbf{v}_C = \frac{d}{dt} r\mathbf{i} = \dot{r}\mathbf{i} + r\frac{d\mathbf{i}}{dt} = \dot{r}\mathbf{i} + r\dot{\theta}\mathbf{j}$$

Hence, the velocity of G, which is given by $\mathbf{v}_G = \mathbf{v}_C + \mathbf{v}_{G/C}$, can be expressed as

$$\mathbf{v}_G = \dot{r}\mathbf{i} + r\dot{\theta}\mathbf{j} - e\omega \sin(\omega t - \theta)\mathbf{i} + e\omega \cos(\omega t - \theta)\mathbf{j} \quad (32.71)$$

Similarly, the acceleration of C is

$$\mathbf{a}_C = \frac{d}{dt} \mathbf{v}_C = \frac{d}{dt} [\dot{r}\mathbf{i} + r\dot{\theta}\mathbf{j}] = \ddot{r}\mathbf{i} + \dot{r}\dot{\theta}\mathbf{j} + \dot{r}\dot{\theta}\mathbf{j} + r\ddot{\theta}\mathbf{j} - r\dot{\theta}^2\mathbf{i} = (\ddot{r} - r\dot{\theta}^2)\mathbf{i} + (r\ddot{\theta} + 2\dot{r}\dot{\theta})\mathbf{j}$$

Also, since line CG rotates at constant angular speed ω about C, the point G has only a radial (centrifugal) acceleration $e\omega^2$ along GC. This can be resolved along \mathbf{i} and \mathbf{j} as before. Hence, the acceleration of G relative to C is

$$\mathbf{a}_{G/C} = -e\omega^2 \cos(\omega t - \theta)\mathbf{i} - e\omega^2 \sin(\omega t - \theta)\mathbf{j}$$

It follows that the acceleration of point G, given by $\mathbf{a}_G = \mathbf{a}_C + \mathbf{a}_{G/C}$, may be expressed as

$$\mathbf{a}_G = (\ddot{r} - r\dot{\theta}^2)\mathbf{i} + (r\ddot{\theta} + 2\dot{r}\dot{\theta})\mathbf{j} - e\omega^2 \cos(\omega t - \theta)\mathbf{i} - e\omega^2 \sin(\omega t - \theta)\mathbf{j} \quad (32.72)$$

The forces acting on the disk are as follows:

Restraining elastic force due to lateral deflection of the shaft = $-kr\mathbf{i}$

Viscous damping force (proportional to the velocity of C) = $-b\dot{r}\mathbf{i} - br\dot{\theta}\mathbf{j}$

In addition, there is a frictional resistance at the bearing, which is proportional to the reaction and, hence, the shaft deflection is r and also depends on the spin speed ω . The following approximate model may be used:

$$\text{Bearing friction force} = -b_f r \omega \mathbf{j}$$

Here,

k = lateral deflection stiffness of the shaft at the location of the disk

b = viscous damping constant for lateral motion of the shaft

b_f = bearing frictional coefficient

The overall force acting on the disk is

$$\mathbf{f} = -b\dot{r}\mathbf{i} - (br\dot{\theta} + b_f r \omega)\mathbf{j} \quad (32.73)$$

The equation of rectilinear motion

$$\mathbf{f} = m\mathbf{a}_G \quad (32.74)$$

on using Equation 32.72 and Equation 32.73, reduces to the following pair in the \mathbf{i} and \mathbf{j} directions:

$$-kr - b\dot{r} = m[\ddot{r} - r\dot{\theta}^2 - e\omega^2 \cos(\omega t - \theta)] \quad (32.75)$$

$$-br\dot{\theta} - b_f r \omega = m[r\ddot{\theta} + 2\dot{r}\dot{\theta} - e\omega^2 \sin(\omega t - \theta)] \quad (32.76)$$

These equations may be expressed as

$$\ddot{r} + 2\zeta_v \omega_n \dot{r} + (\omega_n^2 - \dot{\theta}^2)r = e\omega^2 \cos(\omega t - \theta) \quad (32.77)$$

$$r\ddot{\theta} + 2(\zeta_v \omega_n r + \dot{r})\dot{\theta} + 2\zeta_f \omega_n \omega r = e\omega^2 \sin(\omega t - \theta) \quad (32.78)$$

where the undamped natural frequency of lateral vibration is

$$\omega_n = \sqrt{\frac{k}{m}} \quad (32.79)$$

and

ζ_v = viscous damping ratio of lateral motion

ζ_f = frictional damping ratio of the bearings

Equation 32.77 and Equation 32.78, which govern the whirling motion of the shaft-disk system, are a pair of coupled nonlinear equations, with excitations (depending on ω) that are coupled with a motion variable (θ). Hence, a general solution would be rather complex. A relatively simple solution is possible, however, under steady-state whirling.

32.6.2 Steady-State Whirling

Under steady-state conditions, the whirling speed $\dot{\theta}$ is constant at $\dot{\theta} = \omega_w$, hence, $\ddot{\theta} = 0$. Also, the lateral deflection of the shaft is constant, hence, $\dot{r} = \ddot{r} = 0$. Therefore, Equation 32.77 and Equation 32.78 become

$$(\omega_n^2 - \omega_w^2)r = e\omega^2 \cos(\omega t - \theta) \quad (32.80)$$

$$2\zeta_v \omega_n \omega_w r + 2\zeta_f \omega_n \omega r = e\omega^2 \sin(\omega t - \theta) \quad (32.81)$$

In Equation 32.80 and Equation 32.81, the left-hand side is independent of t . Hence, the right-hand side should also be independent of t . For this, we must have

$$\theta = \omega t - \phi \quad (32.82)$$

where ϕ is interpreted as the phase lag of whirl with respect to the shaft spin (ω), and should be clear from Figure 32.19(b). It follows from Equation 32.82 that, for steady-state whirl, the whirling speed $\dot{\theta} = \omega_w$ is

$$\omega_w = \omega \quad (32.83)$$

This condition is called synchronous whirl because the whirl speed (ω_w) is equal to the shaft spin speed (ω). It follows that under steady-state conditions, we should have the state of synchronous whirl. The equations governing steady-state whirl are

$$(\omega_n^2 - \omega^2)r = e\omega^2 \cos \phi \quad (32.84)$$

$$2\zeta \omega_n \omega r = e\omega^2 \sin \phi \quad (32.85)$$

along with Equation 32.82 and, hence, Equation 32.83. Here, $\zeta = \zeta_v + \zeta_f$ is the overall damping ratio of the system. Note that the phase angle ϕ and the shaft deflection r are determined from Equation 32.84 and Equation 32.85. In particular, squaring these two equations and adding to eliminate ϕ , we obtain

$$r = \frac{e\omega^2}{\sqrt{(\omega_n^2 - \omega^2)^2 + (2\zeta \omega_n \omega)^2}} \quad (32.86)$$

which is of the form of magnitude of the frequency transfer function of a simple oscillator with an acceleration excitation. Divide Equation 32.85 by Equation 32.84 to get the phase angle:

$$\phi = \tan^{-1} \frac{2\zeta \omega_n \omega}{(\omega_n^2 - \omega^2)} \quad (32.87)$$

Using simple calculus (differentiate the square and equate to zero), we can show that the maximum deflection occurs at the critical spin speed ω_c given by

$$\omega_c = \frac{\omega_n}{\sqrt{1 - 2\zeta^2}} \quad (32.88)$$

This *critical speed* corresponds to a resonance. For light damping, we have approximately $\omega_c = \omega_n$. Hence, critical speed for low damping is equal to the undamped natural frequency of bending vibration of the shaft-rotor unit. The corresponding shaft deflection is (see Equation 32.86)

$$r_c = \frac{e}{2\zeta} \quad (32.89)$$

which is also a good approximation of r at critical speed, with light damping. From Equation 32.84 and Equation 32.85, we can see that, at critical speed (with low damping), $\sin \phi = 1$ and $\cos \phi = 0$, which gives $\phi = \pi/2$. Also, note from Equation 32.86 that the steady-state shaft deflection is almost zero at low speeds and approaches e at very high speeds. However, Equation 32.87 shows that, for small ω , $\tan \phi$ is positive and small. We can see from Equation 32.85 that $\sin \phi$ is positive. This means ϕ itself is small for small ω . For large ω , we can see from Equation 32.86 that r approaches e . Thus, we can see from

Equation 32.87 that $\tan \phi$ is small and negative, whereas Equation 32.85 shows that $\sin \phi$ is positive. Hence, ϕ approaches π for large ω .

It is seen from Equation 32.89 that, at critical speed, the shaft deflection increases with mass eccentricity and decreases with damping. This indicates that the approaches for reducing the damaging effects of whirling are:

1. Eliminate or reduce the mass eccentricity through proper construction practices and balancing.
2. Increase damping.
3. Increase shaft stiffness.
4. Avoid operation near critical speed.

There will be limitations to the use of these approaches, particularly making the shaft stiffer. Note also that our analysis did not include the mass distribution of the shaft. A Bernoulli–Euler type beam analysis has to be incorporated for a more accurate analysis of whirling for shafts whose mass cannot be accurately represented by a single parameter that is lumped at the location of the rotor. Formulas related to whirling of shafts are summarized in Box 32.5.

Example 32.6

The fan of a ventilation system has a normal operating speed of 3600 rpm. The blade set of the fan weighs 20 kg and is mounted in the mid-span of a relatively light shaft that is supported on lubricated bearings at its two ends. The bending stiffness of the shaft at the location of the fan is 4.0×10^6 N/m. Equivalent damping ratio that acts on the possible whirling motion of the shaft is 0.05. Owing to fabrication error, the centroid of the fan has an eccentricity of 1.0 cm from the neutral axis of rotation of the shaft:

1. Determine the critical speed of the fan system and the corresponding shaft deflection at the location of the fan at steady state.
2. What is the steady-state shaft deflection at the fan during normal operation?

The fan was subsequently balanced using a mass of 5 kg. The centroid eccentricity was reduced to 2 mm by this means. What is the shaft deflection at the fan during normal operation now? Comment on the improvement that has been realized.

Solution

1. The system is lightly damped. Hence, the critical speed is given by the undamped natural frequency; thus

$$\omega_c \cong \omega_n = \sqrt{\frac{k}{m}} = \sqrt{\frac{4 \times 10^6}{20}} \text{ rad/sec} = 447.2 \text{ rad/sec}$$

The corresponding shaft deflection is

$$r_c = \frac{e}{2\zeta} = \frac{1.0}{2 \times 0.05} \text{ cm} = 10.0 \text{ cm}$$

2. Operating speed $\omega = (3600/60) \times 2\pi \text{ rad/sec} = 377 \text{ rad/sec}$. Using Equation 32.86, the corresponding shaft deflection, at steady state, is

$$r = \frac{1.0 \times (377)^2}{[(447.2^2 - 377^2)^2 + (2 \times 0.05 \times 447.2 \times 377)^2]^{1/2}} \text{ cm} = 2.36 \text{ cm}$$

After balancing, the new eccentricity $e = 0.2 \text{ cm}$.

The new natural frequency (undamped) is

$$\omega_n = \sqrt{\frac{4 \times 10^6}{25}} \text{ rad/sec} = 400 \text{ rad/sec}$$

Box 32.5

WHIRLING OF SHAFTS

Whirling: A shaft spinning at speed ω about its axis, may bend due to flexure. The bent (bowed out) axis will rotate at speed ω_w . This is called whirling.

Equations of motion:

$$\ddot{r} + 2\zeta_v \omega_n \dot{r} + (\omega_n^2 - \dot{\theta}^2)r = e\omega^2 \cos(\omega t - \theta)$$

$$r\ddot{\theta} + 2(\zeta_v \omega_n r + \dot{r})\dot{\theta} + 2\zeta_f \omega_n \omega r = e\omega^2 \sin(\omega t - \theta)$$

where (r, θ) are polar coordinates of shaft deflection at the mounting point of lumped mass.

e = eccentricity of the lumped mass from the spin axis of shaft

$\dot{\theta} = \omega_w$ = whirling speed

ω = spin speed of shaft

$\omega_n = \sqrt{k/m}$ = natural frequency of bending vibration of shaft

k = bending stiffness of shaft at lumped mass

m = lumped mass

ζ_v = damping ratio of bending motion of shaft

ζ_f = damping ratio of shaft bearings

Steady-state whirling (synchronous whirl):

Here, whirling speed ($\dot{\theta}$ or ω_w) is constant and equals the shaft spin speed ω (i.e., $\omega_w = \omega$ for steady-state whirling).

Shaft deflection at lumped mass

$$r = \frac{e\omega^2}{[(\omega_n^2 - \omega^2)^2 + (2\zeta\omega_n\omega)^2]^{1/2}}$$

Phase angle between shaft deflection (r) and mass eccentricity (e)

$$\phi = \tan^{-1} \frac{2\zeta\omega_n\omega}{(\omega_n^2 - \omega^2)}$$

where $\zeta = \zeta_v + \zeta_f$

Note: For small spin speeds ω , we have small r and ϕ . For large ω , we have $r \cong e$ and $\phi \cong \pi$

Critical speed:

$$\begin{aligned} \text{Spin speed } \omega &= \frac{\omega_n}{\sqrt{1 - 2\zeta^2}} \omega_n \text{ for small } \zeta \\ \phi &= \pi/2 \end{aligned}$$

The corresponding shaft deflection during steady-state operation is

$$r = \frac{0.2 \times (377)^2}{[(400^2 - 377^2)^2 + (2 \times 0.05 \times 400 \times 377)^2]^{1/2}} \text{ cm} = 1.216 \text{ cm}$$

Note that, even though the eccentricity has been reduced by a factor of five by balancing, the operating deflection of the shaft has been reduced only by a factor of less than two. The main reason for this is that the operating speed is close to the critical speed. Methods of improving the performance include changing the operating speed, using a smaller mass to balance the fan, using more damping, and making

the shaft stiffer. However, some of these methods may not be feasible. Operating speed is determined by the task requirements. A location may not be available that is sufficiently distant to place a balancing mass that is appropriately small. Increased damping will increase heat generating, cause bearing problems, and will also reduce the operating speed. Replacement or stiffening of the shaft may require too much modification to the system and add cost. A preferable alternative would be to balance the fan by removing some mass. This will move the critical frequency (natural frequency) away from the operating speed rather than closer to it, while reducing the mass eccentricity at the same time. For example, suppose that a mass of 3 kg is removed from the fan, which results in an eccentricity of 2.0 mm. The new natural/critical frequency is

$$\sqrt{\frac{4 \times 10^6}{17}} \text{ rad/sec} = 485.1 \text{ rad/sec}$$

The corresponding shaft deflection during steady operation is

$$r = \frac{0.2 \times (377)^2}{[(485.1^2 - 377^2)^2 + (2 \times 0.05 \times 485.1 \times 377)^2]^{1/2}} \text{ cm} = 0.3 \text{ cm}$$

In this case, the deflection has been reduced by a factor of eight.

32.6.3 Self-Excited Vibrations

Equation 32.77 and Equation 32.78, which represent the general whirling motion of a shaft, are nonlinear and coupled. In these equations, the motion variables (r and θ) occur as (nonlinear) products of the excitation (ω). Such systems are termed self-excited. Note that, in general (before reaching the steady state) the response variables r and θ will exhibit vibratory characteristics in view of the presence of the excitation functions $\cos(\omega t - \theta)$ and $\sin(\omega t - \theta)$. Hence, a whirling shaft may exhibit self-excited vibrations. Because the excitation forces directly depend on the motion itself, it is possible that a continuous energy flow into the system could occur. This will result in a steady growth of the motion amplitudes and represents an *unstable* behavior.

A simple example of self-excited vibration is provided by a pendulum whose length is time variable. Although the system is stable when the length is fixed, it can become unstable under conditions of variable length. Practical examples of self-excited vibrations with possible exhibition of instability include the flutter of aircraft wings due to coupled aerodynamic forces, wind-induced vibrations of bridges and tall structures, galloping of ice-covered transmission lines due to air flow-induced vibrations, and chattering of machine tools due to friction-related excitation forces. Proper design and control methods, as discussed in this chapter, are important in suppressing self-excited vibrations.

32.7 Design through Modal Testing

Experimental modal analysis (EMA) involves extracting modal parameters (natural frequencies, modal damping ratios, mode shapes) of a mechanical system through testing (notably, through excitation-response data) and then developing a dynamic model of the system (mass, stiffness, and damping matrices) on that basis. The techniques of EMA are useful in modeling and model validation (i.e., verification of the accuracy of an existing model that was obtained, for example, through analytical modeling). In addition to these uses, EMA is also a versatile tool for design development. In the context of “design for vibration,” EMA may be employed in the design and design modification of mechanical systems with the goal of achieving desired performance under vibrating conditions. This section will introduce this approach.

In applying EMA for design development of a mechanical system, three general approaches are employed:

1. Component modification
2. Modal response specification
3. Substructuring

The method of component modification allows us to modify (i.e., add, remove, or vary) physical parameters (inertia, stiffness, damping) in a mechanical system, and to determine the resulting effect on the modal response (natural frequencies, damping ratios, and mode shapes) of the system. The method of modal response specification provides the capability to establish the best changes, from the design viewpoint, in system parameters (inertia, stiffness, damping values, and associated directions) in order to realize a specified change in the modal response. In the techniques of substructuring, two or more subsystem models are combined using proper components of interfacing (interconnection), and the overall model of the integrated system is determined. Some of the subsystems used in this approach could be of analytical or computational origin (e.g., finite element models). It should be clear how these methods could be used in the design development of a mechanical system for proper vibration performance. The first method is essentially a trial and error technique of incremental design. Here, some appropriate parameters are changed and the resulting modal behavior is determined. If the resulting performance is not satisfactory, further changes are made in discrete steps until an acceptable performance (with regard to natural frequencies, response magnification factors, etc.) is achieved. The second method is clearly a direct design approach, where the design specifications are first developed in terms of modal characteristics, and then the design procedure will generate the size and type of the physical parameters to meet the specifications. In the third method, a suitable set of subsystems is first designed to meet performance characteristics of each subsystem. Then, these subsystems are linked through suitable mechanical interfacing components, and the performance of the overall system is determined to verify acceptance. In this manner, a complex system may be designed through the systematic design of its subsystems.

32.7.1 Component Modification

The method of component modification involves changing a mass, stiffness, or damping element in the system and determining the corresponding dynamic response, particularly the natural frequencies, modal damping ratios, and mode shapes. This is relatively straightforward because a single modal analysis or modal test (EMA) will give the required information. Because single step of component modification might not be acceptable as an appropriate design (e.g., a natural frequency might be too close to a significant frequency component of a vibration excitation), a number of modifications may be necessary. For such incremental procedures, modal analysis would be more convenient and cost effective than EMA because, in the latter case, physical modification and retesting would be needed, whereas the former involves the same computational steps as before, but with a new set of parameter values.

For example, consider an aluminum I beam that has a number of important modes of vibration, including bending and torsional modes. Figure 32.20(a) shows the fourth mode shape of vibration at natural frequency 678.4 Hz. The dotted line in Figure 32.20(b) shows the transfer function magnitude when the beam is excited at some location in the vertical direction and the response is measured in the vertical direction, at some other location, where neither of the locations are node points. The curve shows the first six natural frequencies.

Next, a lumped mass is added to the top flange at the shown location. The corresponding transfer function magnitude is shown by the solid curve in Figure 32.20(b). Note that all the natural frequencies have decreased due to the added mass, but the effect is larger for higher modes. Similarly, mode shapes also will change. If the new modes are not satisfactory (e.g., a particular natural frequency has not shifted enough) further modification and evaluation will be required.

Consider a mechanical vibrating system whose free response y is described by

$$\mathbf{M}\ddot{\mathbf{y}} + \mathbf{K}\mathbf{y} = 0 \quad (32.90)$$

Damping has been ignored for simplicity, but the following discussion can also be extended to a damped system (quite directly, for the case of proportional damping). If the mass matrix \mathbf{M} and the stiffness matrix \mathbf{K} are modified by $\delta\mathbf{M}$ and $\delta\mathbf{K}$, respectively, the corresponding response (as well as the natural frequencies and mode shapes) will be different from that of the original system. To illustrate, let the

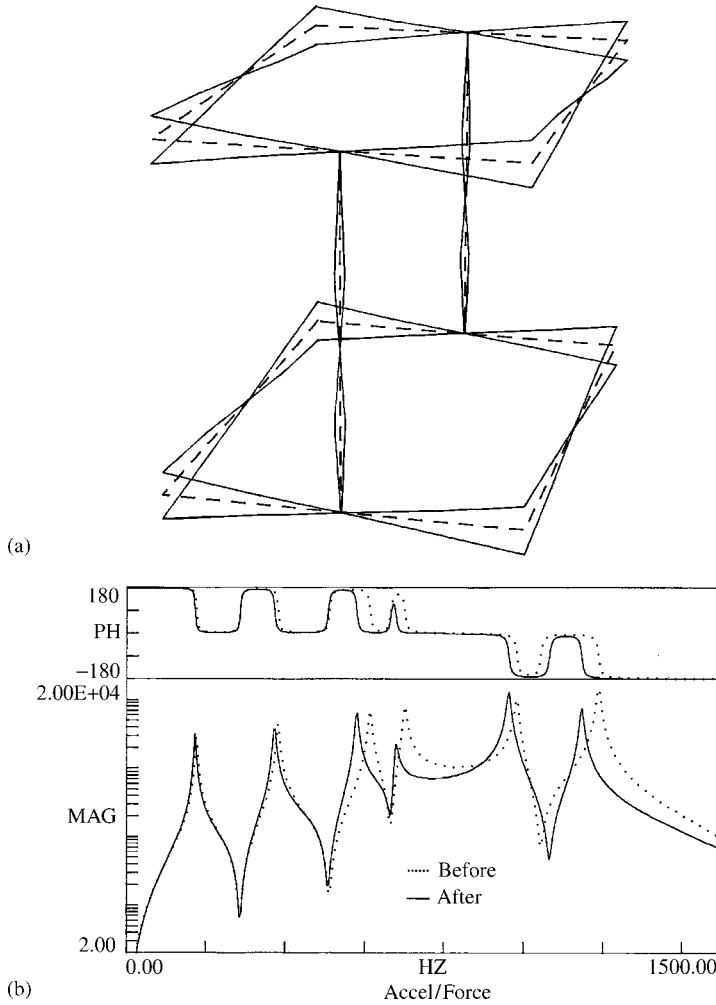


FIGURE 32.20 An example of component modification: (a) the shape of Mode 4 prior to modification; (b) transfer function magnitude before and after modification.

modal matrix (the matrix whose columns are the independent mode shape vectors of the original system) be Ψ . Then, using the modal transformation

$$\mathbf{y} = \Psi \mathbf{q} \quad (32.91)$$

Equation 32.90 can be expressed in the canonical form, with modal generalized coordinates \mathbf{q} , as

$$\bar{\mathbf{M}} \ddot{\mathbf{q}} + \bar{\mathbf{K}} \mathbf{q} = 0 \quad (32.92)$$

where

$$\Psi^T \mathbf{M} \Psi = \bar{\mathbf{M}} = \text{diag}[M_1, M_2, \dots, M_n] \quad (32.93)$$

$$\Psi^T \mathbf{K} \Psi = \bar{\mathbf{K}} = \text{diag}[K_1, K_2, \dots, K_n] \quad (32.94)$$

If the same transformation (Equation 32.91) is used for the modified system

$$(\mathbf{M} + \delta \mathbf{M}) \ddot{\mathbf{y}} + (\mathbf{K} + \delta \mathbf{K}) \mathbf{y} = 0 \quad (32.95)$$

we obtain

$$(\bar{\mathbf{M}} + \mathbf{\Psi}^T \delta \mathbf{M} \mathbf{\Psi}) \ddot{\mathbf{q}} + (\bar{\mathbf{K}} + \mathbf{\Psi}^T \delta \mathbf{K} \mathbf{\Psi}) \mathbf{q} = 0 \quad (32.96)$$

Since both $\mathbf{\Psi}^T \delta \mathbf{M} \mathbf{\Psi}$ and $\mathbf{\Psi}^T \delta \mathbf{K} \mathbf{\Psi}$ are not diagonal matrices in general, $\mathbf{\Psi}$ would not remain the modal matrix for the modified system. Furthermore, the original natural frequencies $\omega_i = \sqrt{K_i/M_i}$ will change due to the component modification. For the special case of proportional modifications ($\delta \mathbf{M}$ proportional to \mathbf{M} and $\delta \mathbf{K}$ proportional to \mathbf{K}), the mode shapes will not change. However, in general, the natural frequencies will change.

The reverse problem is the modal response specification. Here, a required set of modal parameters (ω_{ir} and ψ_{ir}) is specified and the necessary changes $\delta \mathbf{M}$ and $\delta \mathbf{K}$ to meet the specifications must be determined. Note that the solution is not unique and is more difficult than the direct problem. In this case, a sensitivity analysis may initially be performed to determine the directions and magnitudes of the modal shift for a particular physical parameter shift. Then, the necessary magnitudes of physical shift to achieve the specified modal shift are estimated on that basis. The corresponding modifications are made and the modified system is analyzed/tested to check whether it is within specification. If not, further cycles of modification should be performed.

Example 32.7

As an example of component modification, consider the familiar problem of a two-DoF system, as shown in Figure 32.21. The squared nondimensional natural frequencies $r_i^2 = (\omega_i/\omega_0)^2$ of the systems are given by

$$r_1^2, r_2^2 = \frac{1}{2\alpha} \times \{\alpha + \beta + \alpha\beta\} \left\{ 1 \pm \sqrt{1 - \frac{4\alpha\beta}{(\alpha + \beta + \alpha\beta)^2}} \right\}$$

where $\omega_0 = \sqrt{k/m}$. We also showed that the mode shapes, as given by the ratio of the displacement of mass 2 to that of mass 1 at a natural frequency, are

$$\left(\frac{\psi_2}{\psi_1} \right)_i = \frac{1 + \beta - r_i^2}{\beta} \quad \text{for mode } i$$

Consider a system with $\alpha = 0.5$ and $\beta = 0.5$. By direct computation, we can show that $r_1 = 0.71$ and $r_2 = 1.41$. Estimate the modification of β (the relative stiffness of the second spring) that would be necessary to shift the system natural frequencies to approximately $r_1 = 0.8$ and $r_2 = 2.0$. Check the corresponding shift in mode shapes.

Solution

For $\alpha = 0.5$ and $\beta = 0.5$, direct substitution yields $r_1 = 0.71$ and $r_2 = 1.41$ with $(\psi_2/\psi_1)_1 = 2.0$ and $(\psi_2/\psi_1)_2 = -1.0$. Now, consider an incremental change in β by 0.1. Then, $\beta = 0.6$. The corresponding natural frequencies are computed as

$$r_i^2 = \frac{1}{2 \times 0.5} \{0.5 + 0.6 + 0.5 \times 0.6\} \left\{ 1 \mp \left[1 - \frac{4 \times 0.5 \times 0.6}{(0.5 + 0.6 + 0.5 \times 0.6)^2} \right]^{1/2} \right\} = 0.528, 2.272$$

Hence,

$$r_1, r_2 = 0.727, 1.507$$

This step may be interpreted as a way of establishing the sensitivity of the system to the particular component modification. Clearly, the problem of modification is not linear. However, as a first

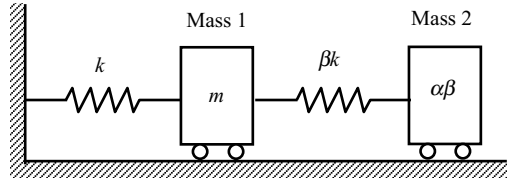


FIGURE 32.21 A two-degree-of-freedom example.

approximation, assume a linear variation of r_i^2 with β , and make modifications according to

$$\frac{\delta\beta}{\delta\beta_0} = \frac{\delta r_i^2}{\delta r_{i0}^2} \quad (32.97)$$

where the subscript 0 refers to the initial trial variation ($\delta\beta_0 = 0.1$). Equation 32.97 is intuitively satisfying given the nature of the physical problem and the fact that, for a single-DoF problem, squared frequency varies with k_0 . Then, we have

For mode 1:

$$\frac{\delta\beta}{0.1} = \frac{0.8^2 - 0.71^2}{0.727^2 - 0.71^2} = 5.634$$

or

$$\delta\beta = 0.56$$

For mode 2:

$$\frac{\delta\beta}{0.1} = \frac{2^2 - 1.41^2}{1.507^2 - 1.41^2} = 7.09$$

or

$$\delta\beta = 0.709$$

Therefore, we use $\delta\beta = 0.71$, which is the larger of the two. This corresponds to

$$\beta = 0.5 + 0.71 = 1.21$$

The natural frequencies are computed as usual:

$$r_1^2, r_2^2 = \frac{1}{2 \times 0.5} \{0.5 + 1.21 + 0.5 \times 1.21\} \left\{ 1 \mp \left[1 - \frac{4 \times 0.5 \times 1.21}{(0.5 + 1.21 + 0.5 \times 1.21)^2} \right]^{1/2} \right\} = 0.60, 4.03$$

or

$$r_1, r_2 = 0.78, 2.01$$

In view of the nonlinearity of the problem, this shift in frequencies is satisfactory. The corresponding mode shapes are

$$\left(\frac{\psi_2}{\psi_1} \right)_1 = \frac{(1 + 1.21) - 0.6}{1.21} = 1.33$$

$$\left(\frac{\psi_2}{\psi_1} \right)_2 = \frac{(1 + 1.21) - 4.03}{1.21} = -1.50$$

It follows that, as the stiffness of the second spring is increased, the motions of the two masses become closer in mode 1. Furthermore, in mode 2, the node point becomes closer to mass 1. Note the limitation of this particular component modification. As $\beta \rightarrow \infty$, the two masses become rigidly linked giving a frequency ratio of $r_1 = \sqrt{k/(m + \alpha m)}/\sqrt{k/m} = 1/\sqrt{1 + \alpha} = 1/\sqrt{1.5} = 0.816$, with $r_2 \rightarrow \infty$. Hence, it is unreasonable to expect a frequency ratio that is closer to this value of r_1 by a change in β alone.

32.7.2 Substructuring

For large and complex mechanical systems with many components, the approach of substructuring can make the process of “design for vibration” more convenient and systematic. In this approach, the system is first divided into a convenient set of subsystems that are more amenable to testing and analysis. The subsystems are separately modeled and designed through the approaches of modal analysis and testing, along with any other convenient approaches (e.g., finite element technique). Note that the performance

of the overall system depends on the interface conditions that link the subsystems, as well as the characteristics of the individual subsystems. Hence, it is not possible to translate the design specifications for the overall system into those for the subsystems without taking the interface conditions into account. The overall system is *assembled* from the designed subsystems by using *compatibility* requirements at the assembly locations together with dynamic equations of the interconnecting components such as spring–mass–damper units or rigid linkages. If the assembled system does not meet the design specifications, then modifications should be made to one or more of the subsystems and interfacing (assembly) linkages, and the procedure should be repeated. Thus, the main steps of using the approach of substructuring for vibration design of a complex system are as follows:

1. Divide the mechanical system into convenient subsystems (substructuring) and represent the interconnection points of subsystems by forces/moments.
2. Develop models for the subsystems through analysis, modal testing, and other standard procedures.
3. Design the subsystems so that their performance is well within the performance specifications provided for the overall system.
4. Establish the interconnecting (assembling) linkages for the subsystems, and obtain dynamic equations for them in terms of the linking forces/moments and motions (displacements/rotations).
5. Establish continuity (force balancing) and compatibility (motion consistency) conditions at the assembly locations.
6. Using matrix methods, eliminate the unknown variables and assemble the overall system.
7. Analyze (or test) the overall system to determine its vibration performance. If satisfactory, stop. If not, make modifications to the systems or assembly conditions and repeat step 4 to step 7.

As a simple example, consider two single-DoF systems that are interconnected by a spring linkage, as shown in Figure 32.22. The two subsystems may be represented by

$$\begin{bmatrix} m_1 & 0 \\ 0 & m_2 \end{bmatrix} \ddot{\mathbf{y}} + \begin{bmatrix} k_1 & 0 \\ 0 & k_2 \end{bmatrix} \mathbf{y} = 0$$

and the corresponding natural frequencies are

$$\omega_{s1} = \sqrt{k_1/m_1} \quad \text{and} \quad \omega_{s2} = \sqrt{k_2/m_2}$$

The overall interconnected system is given by

$$\begin{bmatrix} m_1 & 0 \\ 0 & m_2 \end{bmatrix} \ddot{\mathbf{y}} + \begin{bmatrix} k_1 + k_c & -k_c \\ -k_c & k_2 + k_c \end{bmatrix} \mathbf{y} = 0$$

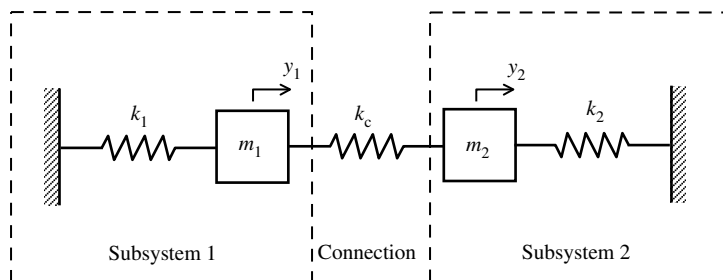


FIGURE 32.22 An example of substructuring.

Its natural frequencies are obtained by solving the equation

$$\det \begin{bmatrix} k_1 + k_c - \omega^2 m_1 & -k_c \\ -k_c & k_2 + k_c - \omega^2 m_2 \end{bmatrix} = 0$$

or

$$(k_1 + k_c - \omega^2 m_1)(k_2 + k_c - \omega^2 m_2) - k_c^2 = 0$$

which simplifies to

$$\omega^4 - \left[\frac{k_1 + k_c}{m_1} + \frac{k_2 + k_c}{m_2} \right] \omega^2 + \frac{k_1 k_2 + k_c(k_1 + k_2)}{m_1 m_2} = 0$$

The sum of the roots is

$$\omega_1^2 + \omega_2^2 = \frac{k_1 + k_c}{m_1} + \frac{k_2 + k_c}{m_2} > \omega_{s1}^2 + \omega_{s2}^2$$

The product of the roots is

$$\omega_1^2 \omega_2^2 = \frac{k_1 k_2 + k_c(k_1 + k_2)}{m_1 m_2} > \omega_{s1}^2 \omega_{s2}^2$$

This does not mean that both frequencies will increase due to the interconnection. Note that the limit on the lower frequency, as $k_c \rightarrow \infty$, is given by that of a single-DoF system with mass $m_1 + m_2$ and stiffness $k_1 + k_2$, which is, $\sqrt{(k_1 + k_2)/(m_1 + m_2)}$. This value can be larger or smaller than the natural frequency of a subsystem depending on the relative values of the parameters. Hence, even for this system, exact satisfaction of a set of design natural frequencies would be somewhat challenging because these frequencies depend on the interconnection as well as the subsystems.

Substructuring is a design development technique where complex designs can be accomplished through parallel and separate development of several subsystems and interconnections. Through this procedure, dynamic interactions among subsystems can be estimated and potential problems can be detected, which will allow redesigning of the subsystems or interfacing linkages prior to building the over prototype. Design approaches using EMA that may be used in vibration problems are summarized in Box 32.6.

32.8 Passive Control of Vibration

The techniques discussed in this chapter for reduction of the effects of mechanical vibration fall into the categories of vibration isolation and design for vibration. The third category, vibration control, is addressed now. Characteristic of vibration control is the use of a sensing device to detect the level of vibration in a system, and an actuation (forcing) device to apply a forcing function to the system to counteract the effects of vibration. In some such devices, the sensing and forcing functions are implicit and integrated together.

Vibration control may be subdivided into the following two broad categories:

1. Passive control
2. Active control

Passive control of vibration employs passive controllers. By definition, passive devices do not require external power for their operation. The two passive controllers of vibration discussed in the present section are vibration absorbers (or dynamic absorbers or Frahm absorbers, named after H. Frahm, who first employed the technique for controlling ship oscillations) and dampers. In both types of devices, sensing is implicit and control is achieved through a force generated by the device from its response to the vibration excitation. A dynamic absorber is a mass–spring-type mechanism with little or no damping,

Box 32.6

TEST-BASED DESIGN APPROACHES FOR VIBRATION

1. Component modification:

Modify a component (mass, spring, damper) and determine modal parameters (natural frequencies, damping ratios, mode shapes).

- Can determine sensitivity to component changes.
- Can check whether a particular change is satisfactory.

2. Modal response specification:

Specify a desired modal response (natural frequencies, damping ratios, mode shapes) and determine the “best” component changes (mass, spring, damper) that will realize the modal specs.

- Can be accomplished by first performing a sensitivity study (as in item 1).

3. Substructuring:

- (i) Design subsystems to meet specs (analytically, experimentally, or by a mixed approach).
- (ii) Establish interconnections between subsystems, and obtain continuity (force balance) and compatibility (motion consistency) at assembly locations.
- (iii) Assemble the overall system by eliminating unknown variables at interconnections.
- (iv) Analyze or test the overall system. If satisfactory, stop. Otherwise, make changes to the subsystems or interconnections, and repeat the above steps.

which can “absorb” the vibration excitation through energy transfer into it, thereby reducing the vibrations of the primary system. The energy received by the absorber will be slowly dissipated due to its own damping. A damper is a purely dissipative device which, unlike a dynamic absorber, directly dissipates the energy received from the system rather than storing it. Hence, it is a more wasteful device, which also may exhibit problems related to wear and thermal effects. However, it has advantages over an absorber, having, for example, a wider frequency of operation.

32.8.1 Undamped Vibration Absorber

A dynamic vibration absorber (or a dynamic absorber, vibration absorber, or Frahm absorber) is a simple mass–spring oscillator with very low damping. An absorber that is tuned to a frequency of vibration of a mechanical system and is able to receive a significant portion of the vibration energy from the primary system at that frequency. In effect, the resulting vibration of the absorber applies an oscillatory force opposing the vibration excitation of the primary system and thereby virtually cancels the effect. In theory, the vibration of the system can be completely removed while the absorber itself undergoes vibratory motion. Since damping is quite low in practical vibration absorbers, we will first consider the case of an undamped absorber.

A vibration absorber may be used for vibration control in two common types of situations, as shown in [Figure 32.23](#). Here, the primary system whose vibration needs to be controlled is modeled as an

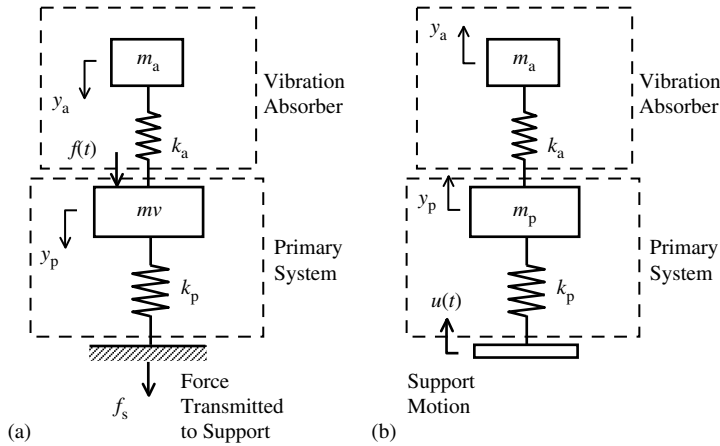


FIGURE 32.23 Two types of applications of a vibration absorber: (a) reduction of the response to forcing excitation (or reducing the force transmitted to support structure); (b) reduction of the response to support motion.

undamped, single-DoF mass–spring system (denoted by the subscript p). An undamped vibration absorber is also a single-DoF mass–spring system (denoted by the subscript a). In the application shown in Figure 32.23(a), the objective of the absorber is to reduce the vibratory response y_p of the primary system as a result of a vibration excitation $f(t)$. The force f_s that is transmitted to the support structure due to the vibratory response of the system is given by

$$f_s = k_p y_p \quad (32.98)$$

Therefore, the objective of reducing y_p may also be interpreted as one of reducing this transmitted vibratory force (a goal of vibration isolation). In the second type of application, represented in Figure 32.23(b), the primary system is excited by a vibratory support motion and the objective of the absorber is to reduce the resulting vibratory motions y_p of the primary system. Note that, in both classes of application, the purpose is to reduce the vibratory responses. Hence, static loads (e.g., gravity) are not considered in the analysis.

Table 32.1 shows the development of the equations of motion for the two systems shown in Figure 32.23. Because we are interested mainly in the control of oscillatory responses to oscillatory excitations, the frequency-domain model is particularly useful. Note from Table 32.1 that the transfer function f_s/f of System a is simply k times the transfer function y_p/f , and is in fact identical to the transfer function y_p/u of System b. The two problems are essentially identical and, thus, we need only address only one of them.

Before investigating the common transfer function for the two types of problems, let us look closely at the frequency-domain equations for the system shown in Figure 32.23(a). We have

$$(k_p + k_a - \omega^2 m_p) y_p - k_a y_a = f \quad (32.99)$$

$$(k_a - \omega^2 m_a) y_a = k_a y_p \quad (32.100)$$

along with Equation 32.98. Here, m_p and k_p are the mass and the stiffness of the primary system, m_a and k_a are the mass and the stiffness of the absorber, f is the excitation amplitude, ω is the excitation frequency, y_p is the primary mass response, and y_a is the absorber response. Now note from Equation 32.100 that if $\omega = \sqrt{k_a/m_a}$ then $y_p = 0$. This means that if the absorber is tuned so that its natural frequency is equal to the excitation frequency (drive frequency), the primary system will not (ideally) undergo any vibratory motion, and is perfectly controlled. The reason for this should be clear from Equation 32.99 which, when $y_p = 0$ is substituted, gives $k_a y_a = -f$. In other words, a tuned absorber applies to the primary system a spring force that is exactly equal and opposite to the excitation force, thereby neutralizing the effect. The absorber mass moves, albeit 180° out of phase with the excitation.

TABLE 32.1 Equations for the Two Types of Absorber Applications

	Absorber Application for the Reduction of Response to a:	
	Forcing Excitation	Support Motion
Time-domain equations	$m_p \ddot{y}_p = -k_p y_p - k_a (y_p - y_a) + f(t)$ $m_a \ddot{y}_a = k_a (y_p - y_a)$	$m_p \ddot{y}_p = k_p (u(t) - y_p) - k_a (y_p - y_a)$ $m_a \ddot{y}_a = k_a (y_p - y_a)$
Frequency-domain equations	$(-\omega^2 m_p + k_p + k_a) y_p = k_a y_a + f$ $(-\omega^2 m_a + k_a) y_a = k_a y_p$	$(-\omega^2 m_p + k_p + k_a) y_p = k_a y_a + k_p u$ $(-\omega^2 m_a + k_a) y_a = k_a y_p$
Matrix form	$\begin{bmatrix} k_p + k_a - \omega^2 m_p & -k_a \\ -k_a & k_a - \omega^2 m_a \end{bmatrix} \begin{bmatrix} y_p \\ y_a \end{bmatrix} = \begin{bmatrix} f \\ 0 \end{bmatrix}$	$\begin{bmatrix} k_p + k_a - \omega^2 m_p & -k_a \\ -k_a & k_a - \omega^2 m_a \end{bmatrix} \begin{bmatrix} y_p \\ y_a \end{bmatrix} = k_p \begin{bmatrix} u \\ 0 \end{bmatrix}$
Transfer-function matrix form	$\begin{bmatrix} y_p \\ y_a \end{bmatrix} = \frac{1}{\Delta} \begin{bmatrix} k_a - \omega^2 m_a & k_a \\ k_a & k_p k_a - \omega^2 m_p \end{bmatrix} \begin{bmatrix} f \\ 0 \end{bmatrix}$	$\begin{bmatrix} y_p \\ y_a \end{bmatrix} = \frac{k}{\Delta} \begin{bmatrix} k_a - \omega^2 m_a & k_a \\ k_a & k_p k_a - \omega^2 m_p \end{bmatrix} \begin{bmatrix} u \\ 0 \end{bmatrix}$
Vibration-control transfer function	$\frac{f_s}{f} = \frac{k_p y_p}{f} = \frac{k_p}{\Delta} (k_a - \omega^2 m_a)$	$\frac{y_p}{u} = \frac{k_p}{\Delta} (k_a - \omega^2 m_a)$
Characteristic polynomial	$\Delta = (k_p + k_a - \omega^2 m_p)(k_a - \omega^2 m_a) - k_a^2$ $= m_p m_a \omega^4 - [k_a(m_p + m_a) + k_p m_a] \omega^2 + k_p k_a$	

The frequency of these motions will be ω (the same as that of the excitation) and the amplitude is proportional to that of the excitation (f) and inversely proportional to the stiffness of the absorber spring. It follows that a vibration absorber “absorbs” vibration energy from the primary system. Furthermore, note from Equation 32.98 that with a tuned absorber the vibration force transmitted to the support structure is (ideally) zero as well. All this information is observed without any mathematical manipulation of the equations of motion.

Note that we are dealing with vibratory excitations and responses. Therefore, static loading (such as gravity and spring preloads) is not considered (we investigate responses with respect to the static equilibrium configuration of the system). In summary, we are now able to state the characteristics of a vibration absorber (undamped) as follows:

1. It is effective only for a single excitation frequency (i.e., a sinusoidal excitation).
2. For the best effect, it should be “tuned” such that its natural frequency $\sqrt{k_a/m_a}$ is equal to the excitation frequency.
3. In the case of forcing vibration excitation, a tuned absorber can (ideally) make the vibratory response of the primary system and the vibratory force transmitted to the support structure zero.
4. In the case of a vibratory support motion, a tuned absorber can make the resulting response of the primary system zero.
5. It functions by acquiring vibration energy from the primary system and storing it (as kinetic energy of the mass or potential energy of the spring) rather than by directly dissipating the energy.
6. It functions by applying a vibration force to the primary system that is equal and opposite to the excitation force, thereby neutralizing the excitation.
7. The amplitude of motion of the vibration absorber is proportional to the excitation amplitude and is inversely proportional to the absorber stiffness. The frequency of the absorber motion is the same as the excitation frequency.

Now, consider the transfer function (f_s/f or y_p/u) of an undamped vibration absorber, as given in Table 32.1. We have

$$G(\omega) = \frac{k_p(k_a - \omega^2 m_a)}{m_p m_a \omega^4 - [k_a(m_p + m_a) + k_p m_a] \omega^2 + k_p k_a} \quad (32.101)$$

It is convenient to use a nondimensional form in analyzing this frequency-transfer function. To that end, we define the following nondimensional parameters and frequency variable:

Fractional mass of the absorber $\mu = m_a/m_p$

Nondimensional natural frequency of the absorber $\alpha = \omega_a/\omega_p$

Nondimensional excitation (drive) frequency $r = \omega/\omega_p$

where

$\omega_a = \sqrt{k_a/m_a}$ = natural frequency of the absorber

$\omega_p = \sqrt{k_p/m_p}$ = natural frequency of the primary system

It is straightforward to divide the numerator and the denominator by $k_p k_a$ and then carry out simple algebraic manipulations to express the transfer function of Equation 32.101 in the nondimensional form as

$$G(r) = \frac{\alpha^2 - r^2}{r^4 - [\alpha^2(1 + \mu) + 1]r^2 + \alpha^2} \quad (32.102)$$

For this undamped system, there is no difference between the resonant frequencies (where the magnitude of the transfer function peaks) and the natural frequencies (roots of the characteristic equation that correspond to the “natural” or free time response oscillations). These are obtained by solving the equation

$$r^4 - [\alpha^2(1 + \mu) + 1]r^2 + \alpha^2 = 0 \quad (32.103)$$

which gives

$$r_1^2, r_2^2 = \frac{1}{2} [\alpha^2(1 + \mu) + 1] \mp \frac{1}{2} \sqrt{[\alpha^2(1 + \mu) + 1]^2 - 4\alpha^2} \quad (32.104)$$

These are squared frequencies, both of which are positive as clear from Equation 32.104. The actual, nondimensional natural frequencies are their square roots. The magnitude of the transfer function becomes infinite at either of these two natural/resonant frequencies. Furthermore, it is clear from Equation 32.102 that the transfer function magnitude becomes zero at $r = \alpha$, where the excitation frequency (ω) is equal to the natural frequency of the absorber (ω_a) as noted above. In the present undamped case, the transfer function $G(r)$ is real but it can be either positive or negative. The magnitude is thus the absolute value of $G(r)$, which is positive. The magnitude plot given in Figure 32.24 shows the resonant and control characteristics of a system with an undamped vibration absorber. Originally, the primary system had a resonance at $r = 1$ (i.e., $\omega = \omega_p$). When the absorber, which also has a resonance at $r = 1$, is added, the original resonance becomes an *antiresonance* with a zero response. Here, however, two new resonances are created, one at $r = 0.854$ and the other at $r = 1.171$, which are on either side of the tuned frequency ($r = 1$) of the absorber.

Owing to these two resonances, the effective region of the absorber is limited to a narrow frequency band centering its tuned frequency. Specifically, the absorber is not effective unless $|G| < 1$. The effective frequency band of a vibration absorber may be determined using this condition.

Example 32.8

A high-precision, yet high-power positioning system uses a hydraulic actuator and a valve. The pressurized oil to this hydraulic servo system is provided by a gear-type rotary pump. The pump and the positioning system are mounted on the same workbench. The mass of the pump is 25 kg. The normal operating speed of the pump is 3600 rpm. During operation, it was observed that the pump exhibits a vertical resonance at this speed and it affects the accuracy of the position servo system. To control the vibrations of the pump at its operating speed, a vibration absorber of mass 1.25 kg tuned to the normal operating speed of the pump is attached, as shown schematically in Figure 32.25. Because the speed of the pump normally fluctuates during operation, we must determine the speed range within which the vibration absorber is effective. What are the new resonant frequencies of the system? (Neglect damping.)

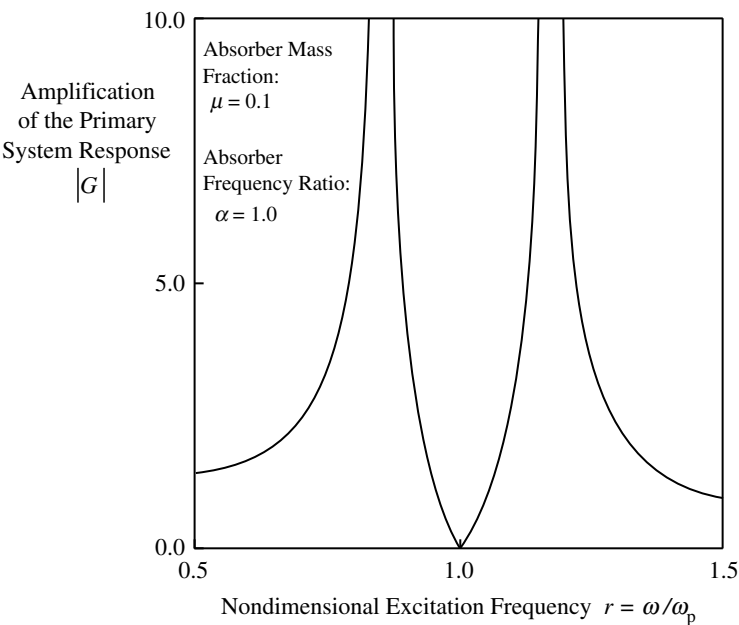


FIGURE 32.24 The effect of an undamped vibration absorber on the vibration response of a primary system.

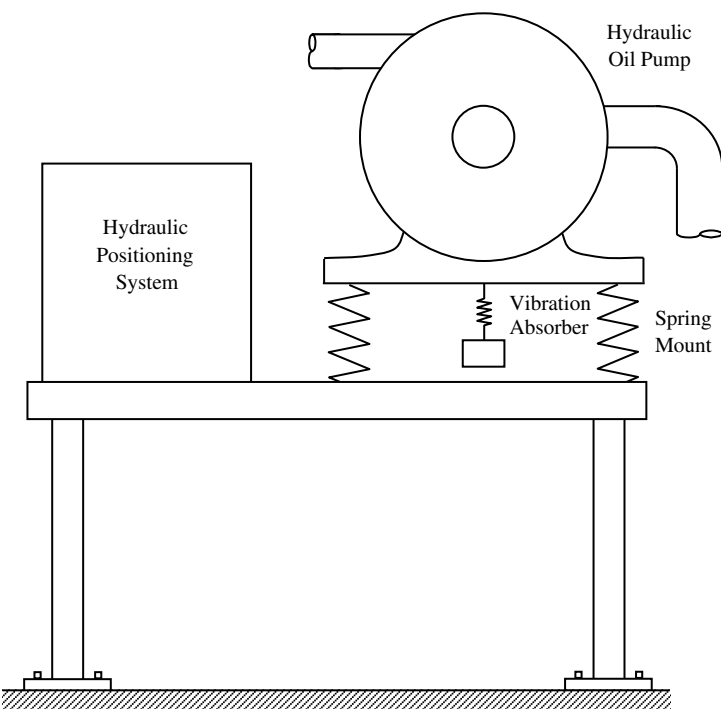


FIGURE 32.25 A hydraulic positioning system with a gear pump.

Solution

For this problem, the fractional mass $\mu = 1.25/25.0 = 0.05$. Since the absorber is tuned to the resonant frequency of the pump, $\alpha = 1.0$. From Equation 32.103, the characteristic equation of the modified system becomes

$$r^4 - 2.05r^2 + 1 = 0$$

which has roots $r_1 = 0.854$ and $r_2 = 1.171$. It follows that the new resonances are at 0.854×3600 and 1.171×3600 rpm. These are 3074.4 and 4215.6 rpm, which should be avoided. From Equation 32.102, the system transfer function is

$$G(r) = \frac{1 - r^2}{(r^4 - 2.05r^2 + 1)}$$

The effective frequency band of the absorber corresponds to $|G(r)| < 1.0$. Since a sign reversal of $G(r)$ occurs at $r = 1$, we need to solve both

$$\frac{1 - r^2}{(r^4 - 2.05r^2 + 1)} = 1 \quad \text{and} \quad -1$$

The first equation gives the roots $r = 0$ and 1.025. The second equation gives the roots $r = 0.977$ and 1.45.

Hence, the effective frequency band corresponds to $\Delta r = [0.977, 1.025]$. In terms of the operating speed of the pump, we have an effective band of 3517.2 to 3690 rpm. Thus, a speed fluctuation of about ± 80 rpm is acceptable.

Finally, recall that the presence of the absorber generates two new resonances on either side of the resonance of the original system (to which the absorber is normally tuned). It is also clear from Equation 32.104 that these two resonances become farther and farther apart as the fractional mass μ of the vibration absorber is increased.

32.8.2 Damped Vibration Absorber

Damping is not the primary means by which vibration control is achieved in a vibration absorber. As noted above, the absorber acquires vibration energy from the primary system (and in turn, exerts a force on the system that is equal and opposite to the vibration excitation), thereby suppressing the vibratory motion. The energy received by the absorber has to be dissipated gradually and, hence, some damping should be present in the absorber. Furthermore, the two resonances that are created by adding the absorber have an infinite magnitude in the absence of damping. Hence, damping has the added benefit of lowering these resonant peaks.

The analysis of a vibratory system with a damped absorber is similar to but somewhat more complex than, that involving an undamped absorber. Furthermore, an extra design parameter — the damping ratio of the absorber — enters into the scene. Consider the model shown in Figure 32.26. Another version of application of a damped absorber, which corresponds to Figure 32.23(b), may also be presented. However, because the two types of application have the same transfer function, it is sufficient to consider Figure 32.26 alone.

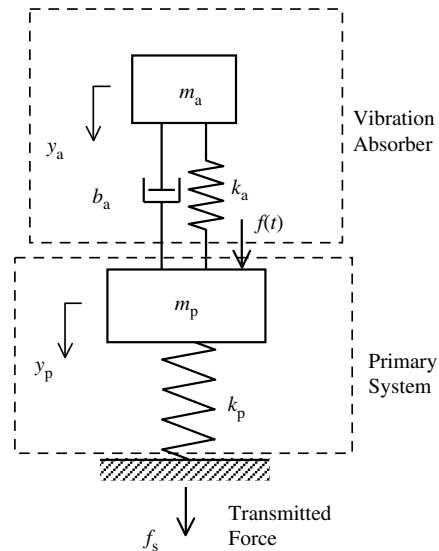


FIGURE 32.26 Primary system with a damped vibration absorber.

Again, the transfer function of vibration control may be taken as either y_a/f or f_s/f , the latter being simply k_p times the former. Although we will consider the dimensionless case of f_s/f , the results are equally valid for y_p/f , except that the responses must be converted from force to displacement by dividing by k_p .

There is no need to derive the transfer function anew for the damped system. Simply replace k_a in Equation 32.101 by the complex stiffness $k_a + j\omega b_a$, which incorporates the viscous damping constant b_a and the excitation frequency ω . Hence, the transfer function of the damped system is

$$G(\omega) = \frac{k_p(k_a + j\omega b_a - \omega^2 m_a)}{m_p m_a \omega^4 - [(k_a + j\omega b_a)(m_p + m_a) + k_p m_a] \omega^2 + k_p(k_a + j\omega b_a)} \quad (32.105)$$

With the parameters defined as before, the nondimensional form of this transfer function is obtained by dividing throughout by $k_p k_a$ and then substituting the appropriate parameters. In particular, we use the fact that

$$\frac{b_a}{k_a} = \frac{2b_a}{2\sqrt{k_a m_a}} \sqrt{\frac{m_a}{k_a}} = \frac{2\zeta_a}{\omega_a} = \frac{2\zeta_a}{\omega_p} \frac{\omega_p}{\omega_a} = \frac{2\zeta_a}{\alpha \omega_p} \quad (32.106)$$

where the damping ratio ζ_a of the absorber is given by

$$\zeta_a = \frac{b_a}{2\sqrt{k_a m_a}} \quad (32.107)$$

as usual. Then, we follow the same procedure that used to derive Equation 32.102 from Equation 32.101 to get

$$G(r) = \frac{\alpha^2 - r^2 + 2j\zeta_a \alpha r}{r^4 - [(\alpha^2 + 2j\zeta_a \alpha r)(1 + \mu) + 1]r^2 + (\alpha^2 + 2j\zeta_a \alpha r)} \quad (32.108)$$

Note that this result is equivalent to simply replacing α^2 by $\alpha^2 + 2j\zeta_a \alpha r$ in Equation 32.102.

It is important to note that the undamped natural frequencies are obtained by solving the characteristics equation with $\zeta_a = 0$. These are the same as before and given by the square roots of Equation 32.104. The damped natural frequencies are obtained by first setting $jr = \lambda$ (hence, $r^2 = -\lambda^2$ and $r^4 = \lambda^4$) and then solving the resulting characteristics equation (see the denominator of Equation 32.108).

$$\lambda^4 + 2\zeta_a \alpha (1 + \mu) \lambda^3 + (\alpha^2 + \alpha^2 \mu + 1) \lambda^2 + 2\zeta_a \alpha \lambda + \alpha^2 = 0 \quad (32.109)$$

and then taking the imaginary parts of the roots of λ . These depend on ζ_a and are different from those obtained from Equation 32.104. The resonant frequencies correspond to the r values where the magnitude of $G(r)$ will peak. Generally, these are not the same as the undamped or damped natural frequencies. However, for low damping (small ζ_a compared with 1), these three types of system characteristics frequencies are almost identical.

The magnitude of the transfer function (Equation 32.108) is plotted in Figure 32.27 for the case $\mu = 1.0$ and $\alpha = 1.0$, as in Figure 32.24, but for damping ratios $\zeta_a = 0.01, 0.1$, and 0.5 . Note that the curve for $\zeta_a = 0.01$ is very close to that in Figure 32.24 for the undamped case. When ζ_a is large, as shown in the case of $\zeta_a = 0.5$, the two masses m_p and m_a tend to become locked together and appear to behave like a single mass. Then, the system tends to act like a single-DoF one, and the primary system is modified only in its mass (which increases). Consequently, only one resonant frequency is produced, which is smaller than that of the original primary system. Furthermore, as expected in this high-damping case, the effect of a vibration absorber is no longer present.

All three curves in Figure 32.27 pass through the two common points A and B, as shown. This is true for all curves corresponding to all values of ζ_a , and particularly for the extreme cases of $\zeta_a = 0$ and $\zeta_a \rightarrow \infty$. Hence, these points can be determined as the points of intersection of the transfer function magnitude curves for the limiting cases $\zeta_a = 0$ and $\zeta_a \rightarrow \infty$.

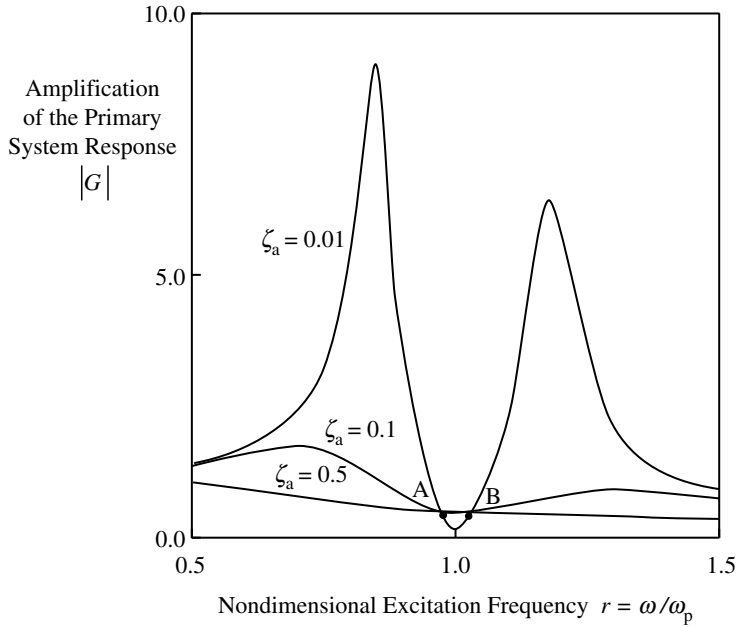


FIGURE 32.27 Vibration amplification (transfer function magnitude) curves for damped vibration absorbers (absorber mass $\mu = 0.1$, absorber resonant frequency $\alpha = 1.0$).

Equation 32.102 gives $G(r)$ for $\zeta_a = 0$. Next, from Equation 32.108, we note that, as $\zeta_a \rightarrow \infty$, all the terms not containing ζ_a can be neglected. Hence,

$$G(r) = \frac{2j\zeta_a\alpha r}{-2j\zeta_a\alpha r(1 + \mu)r^2 + 2j\zeta_a\alpha r}$$

Cancel the common term and we get (for $r \neq 0$)

$$G(r) = \frac{1}{1 - (1 + \mu)r^2} \quad \text{for } \zeta_a \rightarrow \infty \quad (32.110)$$

Note that this is the normalized transfer function of a single-DoF system of natural frequency $1/\sqrt{1 + \mu}$. This result confirms the fact that as $\zeta_a \rightarrow \infty$, the two masses m_p and m_a become locked together and act as a single mass $(m_p + m_a)$ supported on a spring of stiffness k_p . Its natural frequency is $\sqrt{k_p/(m_p + m_a)}$ which, when normalized with respect to $\sqrt{k_p/m_p}$, becomes

$$\sqrt{\frac{k_p}{(m_p + m_a)} \frac{m_p}{k_p}} = \sqrt{\frac{m_p}{(m_p + m_a)}} = \frac{1}{\sqrt{1 + \mu}}$$

In determining the points of intersection between the functions (see Equation 32.102 and Equation 32.110), we should first note that at the first point of intersection (A), the function in Equation 32.102 is negative and positive in Equation 32.110, while the reverse is true for the second point of intersection (B). For either point, this means that the sign of one of the functions should be reversed before equating them. Thus,

$$\frac{\alpha^2 - r^2}{r^4 - [\alpha^2(1 + \mu) + 1]r^2 + \alpha^2} = -\frac{1}{1 - (1 + \mu)r^2}$$

which gives

$$(2 + \mu)r^4 - 2[\alpha^2(1 + \mu) + 1]r^2 + 2\alpha^2 = 0 \quad (32.111)$$

This is the equation whose roots (e.g., r_1 and r_2) give the points A and B. Then, we have the sum of the squared roots equal to the negative coefficient of r^2 in the quadratic (in r^2) Equation 32.111. Thus,

$$r_1^2 + r_2^2 = \frac{2[\alpha^2(1 + \mu) + 1]}{(2 + \mu)} \quad (32.112)$$

In addition, the product of the squared roots is equal to the constant term in the quadratic (r^2) in Equation 32.111. Hence,

$$r_1^2 r_2^2 = \frac{2\alpha^2}{(2 + \mu)} \quad (32.113)$$

32.8.2.1 Optimal Absorber Design

It has been pointed out (primarily by J.P. Den Hartog) that an optimal absorber design should not only have equal response magnitudes at the common points of intersection (i.e., equal ordinates of points A and B in Figure 32.27), but also that the resonances should occur at these points to achieve some balance and uniformity in the response amplification in the region surrounding the tuned frequency of the absorber. It is expected that these (intuitive) design conditions would give relations between the parameters α , μ , and ζ_a , corresponding to an optimal absorber.

Consider the first requirement of equal transfer function magnitudes at A and B. As noted earlier, because these two points do not depend on ζ_a , we use Equation 32.110 to satisfy the requirement. Thus, keeping in mind the sign reversal of the transfer function between A and B (i.e., as the transfer function passes through the resonance), we have

$$\frac{1}{1 - (1 + \mu)r_1^2} = -\frac{1}{1 - (1 + \mu)r_2^2}$$

which gives

$$r_1^2 + r_2^2 = \frac{2}{1 + \mu} \quad (32.114)$$

Substituting this result (for equal ordinates) in the intersection-point condition (see Equation 32.112), we have

$$\frac{2}{1 + \mu} = \frac{2[\alpha^2(1 + \mu) + 1]}{(2 + \mu)}$$

On simplification, we get the simple result

$$\alpha = \frac{1}{1 + \mu} \quad (32.115)$$

Next, we turn to the task of achieving peak magnitudes of the transfer function at the points of intersection (A and B). Generally, when one point peaks the other does not. As reported by Den Hartog, with straightforward but lengthy analysis, we obtain

$$\zeta_a^2 = \frac{\mu[3 - \sqrt{\mu(\mu + 2)}]}{8(1 + \mu)^3} \quad (32.116)$$

for peak at the first intersection point, and

$$\zeta_a^2 = \frac{\mu[3 + \sqrt{\mu(\mu + 2)}]}{8(1 + \mu)^3} \quad (32.117)$$

for peak at the second intersection point.

So, for design purposes, a balance is obtained by taking the average value of the results of Equation 32.116 and Equation 32.117 as

$$\zeta_a^2 = \frac{3\mu}{8(1+\mu)^3} \quad (32.118)$$

Thus, Equation 32.115 and Equation 32.118 correspond to an optimal vibration absorber. In addition, practical requirements and limitations need to be addressed in any design procedure. In particular, since μ is considerably less than unity (i.e., absorber mass is a small fraction of the primary mass), the absorber mass should undergo relatively large amplitudes at the operating frequency in order to receive the energy of the primary system. The absorber spring must be designed accordingly, while meeting the tuning frequency conditions that determine the ratio m_a/k_a .

Example 32.9

The air compressor of a wind tunnel weighs 48 kg and normally operates at 2400 rpm. The first major resonance of the compressor unit occurs at 2640 rpm, with severe vibration amplitudes that are quite dangerous. Design a vibration absorber (damped) for installation on the mounting base of the compressor. What are the vibration amplifications of the compressor unit at the new resonances of the modified system? Compare these with the vibration amplitude of the original system in normal operation.

Solution

As usual, we will tune the absorber to the normal operating speed (2400 rpm). Then, we have the nondimensional resonant frequency of the absorber:

$$\alpha = \frac{\omega_a}{\omega_p} = \frac{2400}{2640} = \frac{12}{13}$$

Now, for an optimal absorber, from Equation 32.115

$$\mu = \frac{1}{\alpha} - 1 = \frac{13}{12} - 1 = \frac{1}{12}$$

Hence, the absorber mass

$$m_a = 48 \times \frac{1}{12} \text{ kg} = 4.0 \text{ kg}$$

Then, from Equation 32.118, the damping ratio of the absorber is

$$\zeta_a = \left[\frac{3/12}{8(1+1/12)^3} \right]^{1/2} = 0.157$$

Now,

$$\omega_a = \sqrt{\frac{k_a}{m_a}} = \sqrt{\frac{k_a}{4.0}} = \frac{2400}{60} \times 2\pi \text{ rad/sec} = 88\pi \text{ rad/sec}$$

Hence,

$$k_a = (88\pi)^2 \times 4.0 \text{ N/m} = 2.527 \times 10^5 \text{ N/m}$$

Also,

$$\zeta_a = \frac{1}{2} \frac{b_a}{\sqrt{m_a k_a}}$$

Then, we have

$$b_a = 2 \times 0.157 \sqrt{4.0 \times 2.527 \times 10^5} \text{ N sec/m} = 315.7 \text{ N sec/m}$$

This gives us the damped absorber. Now, let us check its performance. We know that, in theory, the vibration amplitude at the operating speed should be almost zero now. However, two resonances are created around the operating point. Since damping is small, we use the undamped characteristic Equation 32.103 to compute these resonances:

$$r^4 - \left[\frac{12^2}{13^2} \left(1 + \frac{1}{12} \right) + 1 \right] r^2 + \frac{12^2}{13^2} = 0$$

which gives

$$r^4 - \frac{25}{13} r^2 + \frac{12^2}{13^2} = 0$$

The roots of r^2 are 0.692 and 1.231. The (positive) roots of r are 0.832 and 1.109.

These correspond to compressor speeds of (multiply r by 2640 rpm) 2196 and 2929 rpm. Although they are approximately at -10% and $+20\%$ of the operating speed, the first resonance will be encountered during startup and shutdown conditions. To determine the corresponding vibration amplifications (force/force), use Equation 32.108 which, when the undamped characteristic equation is substituted into the denominator, becomes

$$G(r) = \frac{\alpha^2 - r^2 + 2j\zeta_a \alpha r}{[-2j\zeta_a \alpha r(1 + \mu)r^2 + 2j\zeta_a \alpha r]} = \frac{1 - j(\alpha^2 - r^2)/(2\zeta_a \alpha r)}{1 - (1 + \mu)r^2} \quad (32.119)$$

Substitute the resonant frequencies $r_1 = 0.832$ and $r_2 = 1.109$. We get $|G(r_1)| = 4.223$ and $|G(r_2)| = 4.634$.

Without the absorber, we approximate the system by a simple undamped oscillator with transfer function

$$G_p(r) = \frac{1}{1 - r^2}$$

The corresponding vibration amplification at the operating speed is

$$|G_p(r_0)| = \frac{1}{|1 - 12^2/13^2|} = 6.76$$

It is observed that after adding the absorber, the resonant vibrations are smaller than even the operating vibrations of the original system. Hence, the design is satisfactory. Note that we used the force/force transfer functions. To get the displacement/force transfer functions we divide by k_p . However, we have

$$\sqrt{\frac{k_p}{m_p}} = \frac{2640}{60} \times 2\pi \text{ rad/sec} = 88\pi \text{ rad/sec}$$

Hence,

$$k_p = (88\pi)^2 \times 48 \text{ N/m} = 3.67 \times 10^6 \text{ N/m} = 3.67 \times 10^3 \text{ N/mm}$$

Thus, the amplitude of operating vibrations of the original system is

$$\frac{6.76}{3.67 \times 10^3} \text{ mm/N} = 1.84 \times 10^{-3} \text{ mm/N}$$

The amplitudes of the resonant vibrations of the modified system are

$$\frac{4.223}{3.67 \times 10^3} \quad \text{and} \quad \frac{4.634}{3.67 \times 10^3} \text{ mm/N or } 1.15 \times 10^{-3} \text{ and } 1.26 \times 10^{-3} \text{ mm/N}$$

Vibration absorbers are simple and passive devices, which are commonly used in the control of narrowband vibrations (limited to a very small interval of frequencies). Applications are found in vibration suppression of transmission wires (e.g., a stockbridge damper, which simply consists of a piece of cable carrying two masses at its ends), consumer appliances, automobile engines, and industrial machinery. It should be noted that the concepts presented for a rectilinear vibration absorber may be directly extended to a rotary vibration absorber. Figure 32.28 provides a schematic representation of a rotary vibration absorber. This model corresponds to vibration force excitations (compare with Figure 32.23(a)). The case of rotational support-motion excitations (see Figure 32.23(b)), which has essentially the same transfer function, may also be addressed. Approaches of vibration control are summarized in Box 32.7.

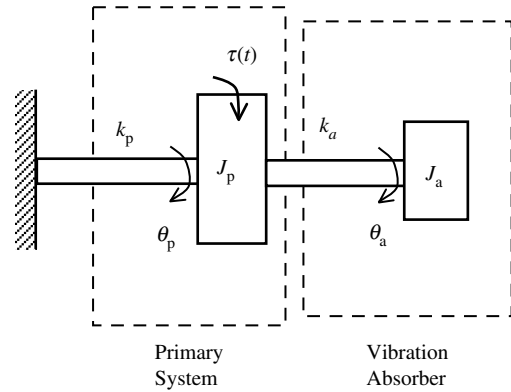


FIGURE 32.28 The application of a rotary vibration absorber.

32.8.3 Vibration Dampers

As discussed above, vibration absorbers are simple and effective passive devices, which are used in vibration control. They have the added advantage of being primarily nondissipative. The main disadvantage of a vibration absorber is that it is only effective over a very narrow band of frequencies enclosing its resonant frequency (tuned frequency). When passive vibration control over a wide band of frequencies is required, a damper would be a preferable choice.

Vibration dampers are dissipative devices. They control vibration through direct dissipation of the vibration energy of the primary (vibrating) system. As a result, however, there will be substantial heat generation, and associated thermal problems and component wear. Consequently, methods of cooling (e.g., use of a fan, coolant circulation, and thermal conduction blocks) may be required in some special situations.

Consider a vibrating system modeled as an undamped single-DoF mass–spring system (simple oscillator). The magnitude of the excitation-response transfer function will have a resonance with a theoretically infinite magnitude in this case. Operation in the immediate neighborhood of such a resonance would be destructive. Adding a simple viscous damper, as shown in Figure 32.29(a), will correct the situation. The equation of motion (about the static equilibrium position) is

$$m\ddot{y} + b\dot{y} + ky = f(t) \quad (32.120)$$

with the dynamic force that is transmitted through the support base (f_s) given by

$$f_s = ky + b\dot{y} \quad (32.121)$$

Hence, the transfer function between the forcing excitation f and the vibration response y is

$$\frac{y}{f} = \frac{1}{k - \omega^2 m + j\omega b} \quad (32.122)$$

and that between the forcing excitation and the force transmitted to the support structure is

$$\frac{f_s}{f} = \frac{k + j\omega b}{k - \omega^2 m + j\omega b} \quad (32.123)$$

Using the nondimensional frequency variable $r = \omega/\omega_n$ where $\omega_n = \sqrt{k/m}$ is the undamped natural frequency of the system and the damping ratio $\zeta = b/(2\sqrt{km})$, we can express Equation 32.122 and

Box 32.7

VIBRATION CONTROL

Passive control (no external power):

1. Dampers
 - A dissipative approach (thermal problems, degradation)
 - Useful over a wide frequency band
2. Vibration absorbers (dynamic absorbers, Frahm absorbers)
 - Absorbs energy from vibrating system and applies counteracting force
 - Useful over a very narrow frequency band (near the tuned frequency)
 - Absorber executes large motions

Undamped absorber design:

$$\text{Transfer function of system with absorber} = \frac{\alpha^2 - r^2}{r^4 - [\alpha^2(1 + \mu) + 1]r^2 + \alpha^2}$$

where

μ = absorber mass/primary system mass

α = absorber natural frequency/primary system natural frequency

r = excitation frequency/primary system natural frequency

The most effective operating frequency $r_{\text{op}} = \alpha$.

Avoid the two resonances.

Optimal damped absorber design:

Mass ratio

$$\mu = \frac{1}{\alpha} - 1$$

Damping ratio

$$\zeta_a = \frac{3\mu}{8(1 + \mu)^3}$$

Active control (needs external power):

1. Measure vibration response using sensors/transducers.
2. Apply control forces to vibrating system through actuators, according to a suitable control algorithm.

Equation 32.123 in the form

$$\frac{y}{f} = \frac{1}{k(1 - r^2 + 2j\zeta r)} \quad (32.124)$$

$$\frac{f_s}{f} = \frac{1 + 2j\zeta r}{(1 - r^2 + 2j\zeta r)} \quad (32.125)$$

When vibration control of the primary system is desired, we use the transfer function in Equation 32.124. However, when force transmissibility is the primary consideration, we use Equation 32.125.

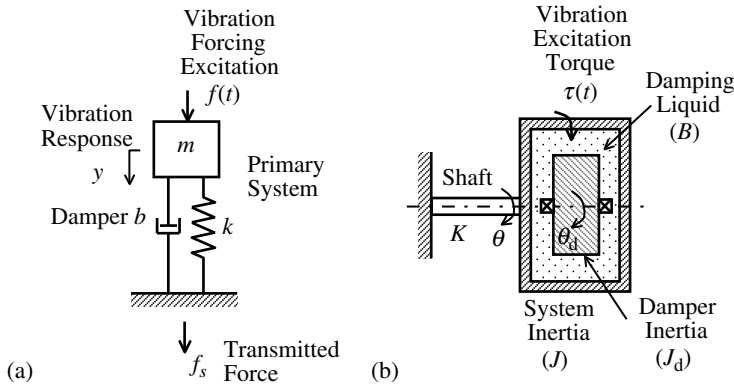


FIGURE 32.29 (a) A system with a linear viscous damper; (b) a rotary system with a Houdaille damper.

Furthermore, it is convenient to use the transfer function in Equation 32.124 in the nondimensional form:

$$\frac{ky}{f} = G(r) = \frac{1}{(1 - r^2 + 2j\zeta r)} \quad (32.126)$$

The magnitude of this transfer function is plotted in Figure 32.30 for several values of damping ratio. Note that the addition of significant levels of damping considerably lowers the resonant peak and flattens the overall response. This example illustrates the broadband nature of the effect of a damper. However, unlike a vibration absorber, it is not possible with a simple damper to bring the vibration levels to a theoretical zero. However, a damper is able to bring the response uniformly close to the static value (unity in Figure 32.30).

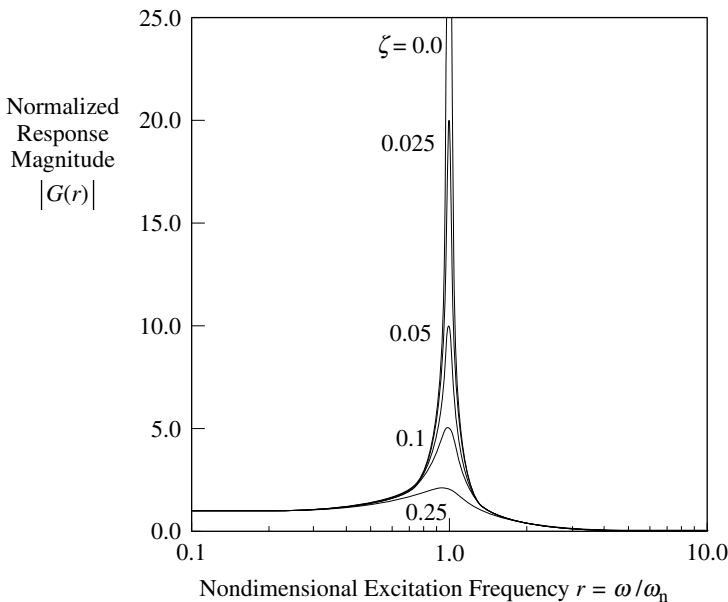


FIGURE 32.30 Frequency response of a system containing a linear damper.

Another common application of damper is connecting it through a free inertia element. For a rotational system, such an arrangement is known as the Houdaille damper, and is modeled as in Figure 32.30(b). The equations of motion are

$$J\ddot{\theta} + B(\dot{\theta} - \dot{\theta}_d) + K\theta = \tau(t) \quad (32.127)$$

$$J_d\ddot{\theta}_d + B(\dot{\theta}_d - \dot{\theta}) = 0 \quad (32.128)$$

In this case, the transfer function between the vibratory excitation torque τ and the response angle θ is given by

$$\frac{\theta}{\tau} = \frac{B + J_d j\omega}{KB - B(J + J_d)\omega^2 - J_d J j\omega^3 + K J_d j\omega} \quad (32.129)$$

Again, we use the normalized form of $K\theta/\tau$. Then, we obtain

$$\frac{K\theta}{\tau} = G(r) = \frac{2\zeta + jr\mu}{2\zeta[1 - (1 + \mu)r^2] + jr\mu(1 - r^2)} \quad (32.130)$$

where $r = \omega/\omega_n$, $\zeta = B/(2\sqrt{KJ})$, $\mu = J_d/J$, and $\omega_n = \sqrt{K/J}$.

Note the two extreme cases. When $\zeta = 0$, the system becomes the original undamped system, as expected. When $\zeta \rightarrow \infty$, the system becomes an undamped simple oscillator, but with a lower natural frequency of $r = 1/\sqrt{1 + \mu}$, instead of $r = 1$ that was present in the original system. This is to be expected because as $\zeta \rightarrow \infty$, the two inertia elements become locked together and act as a single combined inertia $J + J_d$. Clearly, in these two extreme systems, the effect of damping is not present. Optimal damping occurs somewhere in between, as is clear from the curves of response magnitude shown in Figure 32.31 for the case of $\mu = 0.2$.

Proper selection of the nature and values of damping is crucial for the effective use of a damper in vibration control. Damping in physical systems is known to be nonlinear and frequency dependent, as well as time-variant and dependent on the environment (e.g., temperature). Various models are available for different types of damping, but these are only approximate representations. In practice, such considerations as the type of damper used, the nature of the system, the specific application, and the

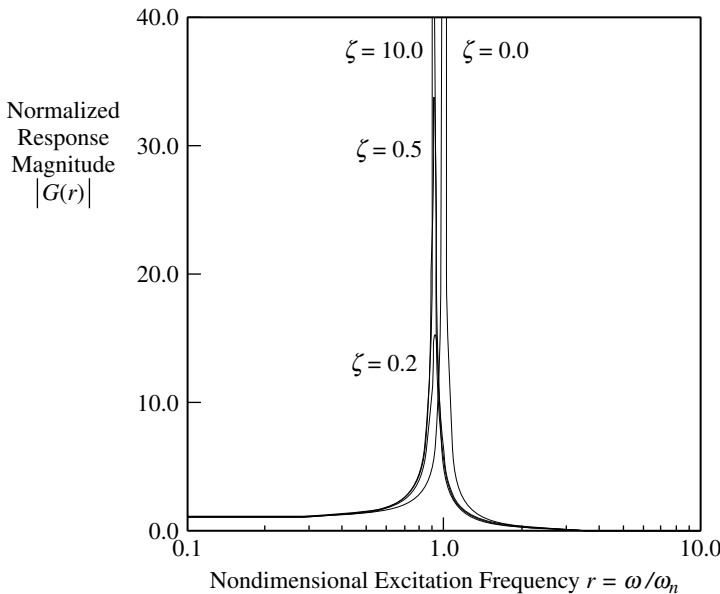


FIGURE 32.31 Response curves for a rotary system with Houdaille damper of inertia ratio $\mu = 0.2$.

speed of operation, determine which particular model (linear viscous, hysteric, Coulomb, Stribeck, quadratic aerodynamic, etc.) is suitable. In addition to the simple linear theory of viscous damper, specific properties of physical damping should be taken into consideration in practical designs.

32.9 Active Control of Vibration

Passive control of vibration is relatively simple and straightforward. Although it is robust, reliable, and economical, it has its limitations. Note that the control force that is generated in a passive device depends entirely on the natural dynamics. Once the device is designed (i.e., after the parameter values for mass, damping constant, stiffness, location, etc. are chosen), it is not possible to adjust the control forces that are naturally generated in real time. Furthermore, in a passive device there is no supply of power from an external source. Hence, even the magnitude of the control forces cannot be changed from their natural values. Since a passive device senses the response of the system as an integral process of the overall dynamics of the system, it is not always possible to directly target the control action at particular responses (e.g., particular modes). This can result in incomplete control, particularly in complex and high-order (e.g., distributed-parameter) systems. These shortcomings of passive control can be overcome using active control. Here, the system responses are directly sensed using sensor-transducer devices, and control actions of specific desired values are applied to desired locations/modes of the system.

32.9.1 Active Control System

Figure 32.32 presents a schematic diagram of an active control system. The mechanical dynamic system whose vibrations need to be controlled is the *plant* or *process*. The controller is the device that generates the signal (or command) according to some scheme (or control law) and controls vibrations of the plant. The plant and the controller are the two essential components of a *control system*. Usually, the plant must

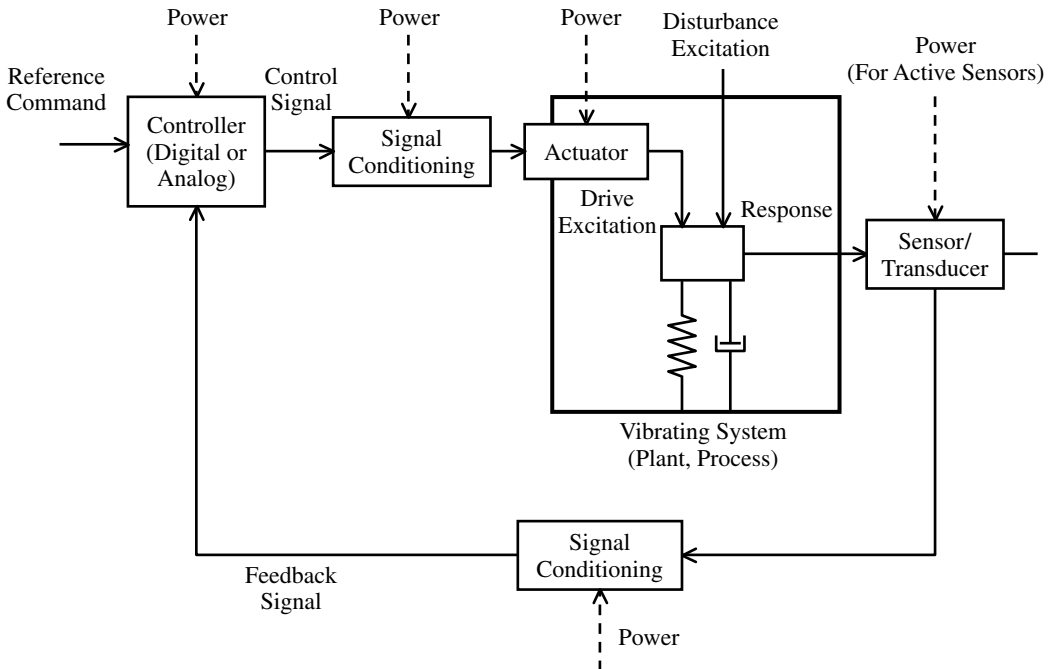


FIGURE 32.32 A system for active control of vibration.

be monitored and its response must be measured using sensors providing feedback into the controller. Then, the controller compares the sensed signal with a desired response specified externally, and uses the error to generate a proper control signal. In this manner, we have a feedback control system. In the absence of a sensor and feedback, we have an open-loop control system. In *feed-forward control*, the excitation (i.e., input signal), not the response (i.e., output signal), is measured and used (i.e., fed forward into the controller) for generating the control signal. Both feedback and feedforward schemes may be used in the same control system.

The actuator that receives a control signal and drives the plant may be an integral part of the plant (e.g., the motor that drives the blade of a saw). Alternatively, it may have to be added specifically as an external component for the control actuation (e.g., a piezoelectric or electromagnetic actuator for controlling blade vibrations of a saw). In the former case, in particular, proper signal conditioning is needed to convert the control signal to a form that is compatible with the existing actuator. In the latter case, both the controller and the actuator must be developed in parallel for integration into the plant. In digital control, the controller is a digital processor. The control signal is in digital form and, typically, it has to be converted into the analog form prior to using in the actuator. Hence, digital-to-analog conversion (DAC) is a form of signal conditioning that is useful here. Furthermore, the analog signal that is generated may have to be filtered and amplified to an appropriate level for use in the actuator. It follows that filters and amplifiers are signal conditioning devices, which are useful in vibration control. In *software control*, the control signal is generated by a computer, which functions as the digital controller. In *hardware control*, the control signal is rapidly generated by digital hardware without using software programs. Alternatively, *analog control* may be used where the control signal is generated directly using analog circuitry. In this case, the controller is quite fast and it does not require DAC. Note that the actuator may need high levels of power. Furthermore, the controller and associated signal conditioning will require some power. The need for an external power source for control distinguishes active control from passive control.

In a feedback control system, sensors are used to measure the plant response, which enables the controller to determine whether the plant operates properly. A sensor unit that “senses” the response may automatically convert (transduce) this “measurement” into a suitable form. A piezoelectric accelerometer senses acceleration and converts it into an electric charge, an electromagnetic tachometer senses velocity and converts it into a voltage, and a shaft encoder senses a rotation and converts it into a sequence of voltage pulses. Hence, the terms *sensor* and *transducer* are used interchangeably to denote a sensor-transducer unit. The signal that is generated in this manner may need conditioning before feeding into the controller. For example, the charge signal from a piezoelectric accelerometer has to be converted to a voltage signal of appropriate level using a charge amplifier, and then it has to be digitized using an analog-to-digital converter (ADC) for use in a digital controller. Furthermore, filtering may be needed to remove measurement noise. Hence, signal conditioning is usually needed between the sensor and the controller as well as between the controller and the actuator. External power is required to operate active sensors (e.g., potentiometer) whereas passive sensors (e.g., electromagnetic tachometer) employ self-generation and do not need an external power source. External power may be needed for conditioning the sensor signals. Finally, as indicated in [Figure 32.32](#), a vibrating system may have unknown disturbance excitations, which can make the control problem particularly difficult. Removing such excitations at the source level through proper design or vibration isolation is desirable, as discussed above. However, in the context of control, if these disturbances can be measured or some information about them is available, then they can be compensated for within the controller itself. This is, in fact, the approach of feedforward control.

32.9.2 Control Techniques

The purpose of a vibration controller is to excite (activate) a vibrating system in order to control its vibration response in a desired manner. In the present context of active feedback control, the controller uses measured response signals and compares them with their desired values in its task of determining an

appropriate action. The relationship that generates the control action from a measured response (and a desired value for the response) is called a *control law*. Sometimes, a *compensator* (analog or digital, hardware or software) is employed to improve the system performance or to enhance the controller so that the task of control is easier. However, for our purpose, we may consider a compensator as an integral part of the controller and thus a distinction between the two is not made.

Various control laws, both linear and nonlinear, have been developed for practical applications. Many of them are suitable in vibration control. A comprehensive presentation of all such control laws is outside the scope of this book. We will give several linear control laws that are common and representative of what is available. These techniques are based on a linear representation (linear model) of the vibrating system (plant). Even when the overall operating range of a plant (e.g., robotic manipulator) is nonlinear, it is often possible to linearize the vibration response (e.g., link vibrations and joint vibrations of a robot) about a reference configuration (e.g., robot trajectory). These linear control techniques would be still suitable even though the overall dynamics of the system is nonlinear.

32.9.2.1 State-Space Models

In applying many types of control techniques, it is convenient to represent the vibrating system (plant) by a state-space model. This is simply a set of ordinary first-order differential equations, which could be coupled or nonlinear, and could have time-varying parameters (time-variant models). Here, we limit our discussion to linear and time-invariant state-space models. Such a model is expressed as

$$\dot{\mathbf{x}} = \mathbf{Ax} + \mathbf{Bu} \quad (32.131)$$

$$\mathbf{y} = \mathbf{Cx} + \mathbf{Du} \quad (32.132)$$

where

$\mathbf{x} = [x_1, x_2, \dots, x_n]^T$ = state vector (n th order column)

$\mathbf{u} = [u_1, u_2, \dots, u_r]^T$ = input vector (r th order column)

$\mathbf{y} = [y_1, y_2, \dots, y_m]^T$ = output vector (m th order column)

\mathbf{A} = system matrix ($n \times n$ square)

\mathbf{B} = input gain matrix ($n \times r$)

\mathbf{C} = measurement gain matrix ($m \times n$)

\mathbf{D} = feedforward gain matrix ($m \times r$)

Usually, for vibrating systems, it is possible to make $\mathbf{D} = 0$, and hence we will drop this matrix in the sequel. Furthermore, although a state variable x_i need not have a direct physical meaning, an output variable y_j should have some physical meaning and, in typical situations, should be measurable as well. The input variables are the “control variables” and are used for controlling the system (plant). The output variables are the “controlled variables,” which correspond to the system response and are measured for feedback control.

It can be verified that the eigenvalues of the system matrix \mathbf{A} occur in complex conjugates of the form $-\zeta_i\omega_i \pm j\sqrt{1 - \zeta_i^2}\omega_i$ in the damped oscillatory case, or as $\pm j\omega_i$ in the undamped case, where ω_i is the i th natural frequency of the system and ζ_i is the corresponding damping ratio (of the i th mode). The mathematical verification requires some linear algebra. An intuitive verification can be made since Equation 32.131 is an equivalent model for a system having the traditional mass–spring–damper model

$$\mathbf{M}\ddot{\mathbf{y}} + \mathbf{C}\dot{\mathbf{y}} + \mathbf{K}\mathbf{y} = \mathbf{f}(t) \quad (32.133)$$

where \mathbf{M} = mass matrix, \mathbf{C} = damping matrix, \mathbf{K} = stiffness matrix, $\mathbf{f}(t)$ = forcing input vector, and \mathbf{y} = displacement response vector. Where both models (Equation 32.131 and Equation 32.133), are equivalent they should have the same characteristic equation, which by its roots determines the natural frequencies and modal damping ratios. This is the case because we are simply looking at two different mathematical representations of the same system. Hence, the parameters of its dynamics, such as ω_i and ζ_i , should remain unchanged. In fact, the state-space mode (Equation 32.131) is not unique, and different versions of state vectors and corresponding models are possible. Of course, all of them should have the

same characteristics polynomial (and hence, the same ω_i and ζ_i). One such state-space model may be derived from Equation 32.133 as follows:

Define the state vector as

$$\mathbf{x} = \begin{bmatrix} y \\ \dot{y} \end{bmatrix} \text{ and } \mathbf{u} = \mathbf{f}(t) \quad (32.134)$$

Since (for nonsingular \mathbf{M} , as required), Equation 32.133 may be written as

$$\ddot{\mathbf{y}} = -\mathbf{M}^{-1}\mathbf{K}\mathbf{y} - \mathbf{M}^{-1}\mathbf{C}\dot{\mathbf{y}} + \mathbf{M}^{-1}\mathbf{f}(t) \quad (32.135)$$

we have

$$\dot{\mathbf{x}} = \begin{bmatrix} \mathbf{0} & \mathbf{I} \\ -\mathbf{M}^{-1}\mathbf{K} & -\mathbf{M}^{-1}\mathbf{C} \end{bmatrix} \mathbf{x} + \begin{bmatrix} \mathbf{0} \\ \mathbf{M}^{-1} \end{bmatrix} \mathbf{u} \quad (32.136)$$

This is a state-space model that is equivalent to the conventional model (Equation 32.133), and can be shown to have the same characteristic equation. The development of a state-space model for a vibrating system can be illustrated using an example.

Example 32.10

Consider a machine mounted on a support structure, modeled as in Figure 32.33. Using the excitation forces $f_1(t)$ and $f_2(t)$ as the inputs and the displacements y_1 and y_2 of the masses m_1 and m_2 as the outputs, develop a state-space model for this system.

Solution

Assume that the displacements are measured from the static equilibrium positions of the masses. Hence, the gravity forces do not enter into the formulation. Newton's Second law is applied to the two masses; thus

$$m_1\ddot{y}_1 = f_1 - k_1(y_1 - y_2) - b_1(\dot{y}_1 - \dot{y}_2)$$

$$m_2\ddot{y}_2 = f_2 - k_1(y_2 - y_1) - b_1(\dot{y}_2 - \dot{y}_1) - k_2y_2 - b_2\dot{y}_2$$

The following state variables are defined:

$$x_1 = y_1; \quad x_2 = \dot{y}_1; \quad x_3 = y_2; \quad x_4 = \dot{y}_2$$

Also, the input vector is $\mathbf{u} = [u_1 \ u_2]^T$ and the output vector is $\mathbf{y} = [y_1 \ y_2]^T$. Then, we have

$$\dot{x}_1 = x_2$$

$$m_1\dot{x}_2 = u_1 - k_1(x_1 - x_3) - b_1(x_2 - x_4)$$

$$\dot{x}_3 = x_4$$

$$m_2\dot{x}_4 = u_2 - k_1(x_3 - x_1) - b_1(x_4 - x_2) - k_2x_3 - b_2x_4$$

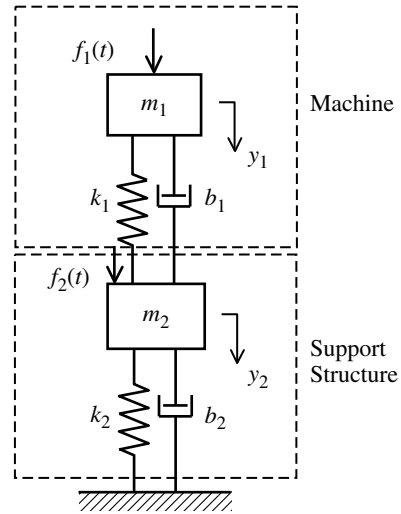


FIGURE 32.33 A model of a machine mounted on support structure.

Accordingly, the state-space model is given by Equation 32.131 and Equation 32.132 with

$$\mathbf{A} = \begin{bmatrix} 0 & 1 & 0 & 0 \\ -k_1/m_1 & -b_1/m_1 & k_1/m_1 & b_1/m_1 \\ 0 & 0 & 0 & 1 \\ k_1/m_2 & b_1/m_2 & (k_1 + k_2)/m_2 & (b_1 + b_2)/m_2 \end{bmatrix}, \quad \mathbf{B} = \begin{bmatrix} 0 & 0 \\ 1/m_1 & 0 \\ 0 & 0 \\ 0 & 1/m_2 \end{bmatrix},$$

$$\mathbf{C} = \begin{bmatrix} 1 & 0 & 0 & 0 \\ 0 & 0 & 1 & 0 \end{bmatrix}, \quad \text{and } \mathbf{D} = 0$$

Also, note that the system can be expressed as

$$\begin{bmatrix} m_1 & 0 \\ 0 & m_2 \end{bmatrix} \ddot{\mathbf{y}} + \begin{bmatrix} b_1 & -b_1 \\ -b_1 & (b_1 + b_2) \end{bmatrix} \dot{\mathbf{y}} + \begin{bmatrix} k_1 & -k_1 \\ -k_1 & (k_1 + k_2) \end{bmatrix} \mathbf{y} = \mathbf{f}(t)$$

Its characteristic equation may be expressed as the determinant equation:

$$\det \begin{bmatrix} m_1 s^2 + b_1 s + k_1 & -b_1 s - k_1 \\ -b_1 s - k_1 & m_2 s^2 + (b_1 + b_2)s + (k_1 + k_2) \end{bmatrix} = 0$$

It can be verified through direct expansion of the determinants that this equation is equivalent to the characteristic equation of the matrix \mathbf{A} , as given by $\det(\lambda \mathbf{I} - \mathbf{A}) = 0$, or

$$\det \begin{bmatrix} \lambda & -1 & 0 & 0 \\ k_1/m_1 & \lambda + b_1/m_1 & -k_1/m_1 & -b_1/m_1 \\ 0 & 0 & \lambda & -1 \\ k_1/m_2 & -b_1/m_2 & -(k_1 + k_2)/m_2 & \lambda - (b_1 + b_2)/m_2 \end{bmatrix} = 0$$

Note that, in the present context, x and y represent the vibration response of the plant and the control objective is to reduce these to zero. We will give some common control techniques that can achieve this goal.

32.9.2.2 Position and Velocity Feedback

In this technique, the position and velocity of each DoF is measured and fed into the system with sign reversal (negative feedback) and amplification by a constant gain. Because velocity is the derivative of position and since the gains are constant (i.e., proportional), this method falls into the general category of proportional-plus-derivative (PD or PPD) control. In this approach, it is tacitly assumed that the degrees of freedom are uncoupled. Then, control gains are chosen so that the DoF in the controlled system are nearly uncoupled, thereby justifying the original assumption. To explain this control method, suppose that a DoF of a vibrating system is represented by

$$m\ddot{y} + b\dot{y} + ky = u(t) \quad (32.137)$$

where y is the displacement (position) of the DoF and u is the excitation input that is applied. Now suppose that u is generated according to the (active) control law

$$u = -k_c y - b_c \dot{y} + u_r \quad (32.138)$$

where k_c is the position feedback gain and b_c is the velocity feedback gain. The implication here is that the position y and the velocity \dot{y} are measured and fed into the controller which in turn generates u according to Equation 32.138. Also, u_r is some reference input that is provided externally to the controller.

Then, substituting Equation 32.138 into Equation 32.137, we obtain

$$m\ddot{y} + (b + b_c)\dot{y} + (k + k_c)y = u_r \quad (32.139)$$

The closed-loop system (the controlled system) now behaves according to Equation 32.139. The control gains b_c and k_c can be chosen arbitrarily (subject to the limitations of the physical controller, signal conditioning circuitry, the actuator, etc.) and may even be negative. In particular, by increasing b_c , the damping of the system can be increased. Similarly, by increasing k_c the stiffness (and the natural frequency) of the system can be increased. Even though a passive spring and damper with stiffness k_c and damping constant b_c can accomplish the same task, once the devices are chosen it is not possible to conveniently change their parameters. Furthermore, it will not be possible to make k_c or b_c negative in this case of passive physical devices. The method of PPD control is simple and straightforward, but the assumptions of linear uncoupled DoF place a limitation on its general use.

32.9.2.3 Linear Quadratic Regulator Control

This is an optimal control technique. Consider a vibrating system that is represented by the linear state-space model:

$$\dot{\mathbf{x}} = \mathbf{A}\mathbf{x} + \mathbf{B}\mathbf{u} \quad (32.131)$$

Assume that all the states \mathbf{x} are measurable and all the system modes are controllable. Then, we use the constant-gain feedback control law:

$$\mathbf{u} = \mathbf{K}\mathbf{x} \quad (32.140)$$

The choice of parameter values for the feedback gain matrix \mathbf{K} is infinite. Therefore, we can use this freedom to minimize the cost function:

$$J = \frac{1}{2} \int_t^\infty [\mathbf{x}^T \mathbf{Q} \mathbf{x} + \mathbf{u}^T \mathbf{R} \mathbf{u}] d\tau \quad (32.141)$$

This is the time integral of a quadratic function in both state and input variables, and the optimization goal may be interpreted as bringing \mathbf{x} down to zero (regulating \mathbf{x} to 0), but without spending a rather high control effort. Hence, the name linear quadratic regulation (LQR). In addition, \mathbf{Q} and \mathbf{R} are weighting matrices, with the former being at least positive semidefinite and the latter positive definite. Typically, \mathbf{Q} and \mathbf{R} chosen as diagonal matrices with positive diagonal elements whose magnitudes are determined by the degree of relative emphasis that should be given to various elements of \mathbf{x} and \mathbf{u} . It is well known that \mathbf{K} that minimizes the cost function (Equation 32.141) is given by

$$\mathbf{K} = -\mathbf{R}^{-1} \mathbf{B}^T \mathbf{K}_r \quad (32.142)$$

where \mathbf{K}_r is the positive-definite solution of the matrix Riccati algebraic equation

$$\mathbf{K}_r \mathbf{A} + \mathbf{A}^T \mathbf{K}_r - \mathbf{K}_r \mathbf{B} \mathbf{R}^{-1} \mathbf{B}^T \mathbf{K}_r + \mathbf{Q} = 0 \quad (32.143)$$

It is also known that the resulting closed-loop control system is stable. Furthermore, the minimum (optimal) value of the cost function (Equation 32.141) is given by

$$J_m = \frac{1}{2} \mathbf{x}^T \mathbf{K}_r \mathbf{x} \quad (32.144)$$

where \mathbf{x} is the present value of the state vector. Major computational burden of the LQR method is in the solution (Equation 32.143). Other limitations of the technique arise due to the need to measure all the state variables (which may be relaxed to some extent). Although stability of the controlled system is guaranteed, the level of stability that is achieved (i.e., stability margin or the level of modal damping) cannot be directly specified. Further, robustness of the control system in the presence of model errors, unknown disturbances and so on, may be questionable. Besides, the cost function incorporates an integral over an infinite time duration, which does not typically reflect the practical requirement of rapid vibration control.

32.9.2.4 Modal Control

The LQR control technique has the serious limitation of not being able to directly achieve specified levels of modal damping, which may be an important goal in vibration control. The method of modal control that accomplishes this objective is *pole placement*, where poles (eigenvalues) of the controlled system are placed at specified values. Specifically, consider the plant (Equation 32.131) and the feedback control law (Equation 32.140). Then, the closed-loop system is given by

$$\dot{\mathbf{x}} = (\mathbf{A} + \mathbf{BK})\mathbf{x} \quad (32.145)$$

It is well known that if the plant (\mathbf{A} , \mathbf{B}) is controllable, then a control gain matrix \mathbf{K} can be chosen that will arbitrarily place the eigenvalues of the closed-loop system matrix $\mathbf{A} + \mathbf{BK}$. Based on the given assumptions, the modal control technique assigns not only the modal damping but also the damped natural frequencies at specified values. The assumptions given above are quite stringent but they can be relaxed to some degree. However, a shortcoming of this method is the fact that it does not place a restriction on the control effort, for example, as the LQR technique does, in achieving a specified level of modal control.

32.10 Control of Beam Vibrations

Beam is a distributed-parameter system, which in theory has an infinite number of modes of vibration with associated mode shapes and natural frequencies. In this sense, it is an “infinite order” system with infinite DoF. Hence, the computation of modal quantities and associated control inputs can be quite complex. Fortunately, however, just a few modes may be retained in a dynamic model without sacrificing a great deal of accuracy, thereby facilitating simpler control. Some concepts of controlling vibrations in a beam are considered in this section. The present treatment is intended as an illustration of the relevant techniques and is not meant to be exhaustive. These techniques may be extended to other types of continuous system such as beams with different boundary conditions and plates. Because the control techniques that were outlined previously depend on a model, we will first illustrate the procedure of obtaining a state-space model for a beam.

32.10.1 State-Space Model of Beam Dynamics

Consider a Bernoulli–Euler-type beam with Kelvin–Voigt-type internal (material) damping. The beam equation may be expressed as

$$ELv(x, t) + E^*L \frac{\partial v(x, t)}{\partial t} + \rho A(x) \frac{\partial^2 v(x, t)}{\partial t^2} = f(x, t) \quad (32.146)$$

in which L is the partial differential operator given by

$$L = \frac{\partial^2 I(x)}{\partial x^2} \frac{\partial^2}{\partial x^2} \quad (32.147)$$

and

$f(x, t)$ = distributed force excitation per unit length of the beam

$v(x, t)$ = displacement response at location x along the beam at time t

$I(x)$ = second moment of area of the beam cross section about the neutral axis

E = Young’s modulus of the beam material

E^* = Kelvin–Voigt material damping parameter

Note that a general beam with nonuniform characteristics is assumed and, hence, the variations of $I(x)$ and $\rho A(x)$ with x are retained in the formulation.

Using the approach of modal expansion, the response of the beam may be expressed by

$$v(x, t) = \sum_{i=1}^{\infty} Y_i(x) q_i(t) \quad (32.148)$$

where $Y_i(x)$ is the i th mode shape of the beam, which satisfies

$$LY_i(x) = \frac{\rho A(x)}{E} \omega_i^2 Y_i(x) \quad (32.149)$$

and ω_i is the i th undamped natural frequency. The orthogonality condition for this general example of a nonuniform beam is

$$\int_{x=0}^l \rho A Y_i Y_j dx = \begin{cases} 0 & \text{for } i \neq j \\ \alpha_j & \text{for } i = j \end{cases} \quad (32.150)$$

Suppose that the forcing excitation on the beam is a set of r point forces $u_k(t)$ located at $x = l_k$, $k = 1, 2, \dots, r$. Then, we have

$$f(x, t) = \sum_{k=1}^r u_k \delta(x - l_k) \quad (32.151)$$

where $\delta(x - l_i)$ is the *Dirac delta function*. Now, substitute Equation 32.148 and Equation 32.151 into Equation 32.146, use Equation 32.149, multiply throughout by $Y_j(x)$, and integrate over $x[0, l]$, using Equation 32.150. This gives

$$\ddot{q}_j + \gamma_j \dot{q}_j(t) + \omega_j^2 q_j = \frac{1}{\alpha_j} \sum_{k=1}^r u_k Y_j(l_k) \quad \text{for } j = 1, 2, \dots \quad (32.152)$$

where

$$\gamma_j = \frac{E^*}{E} \omega_j^2 \quad (32.153)$$

Now, define the state variables x_j according to

$$x_{2j-1} = \omega_j q_j, \quad x_{2j} = \dot{q}_j \quad \text{for } j = 1, 2, \dots \quad (32.154)$$

Assuming that only the first m modes are retained in the expansion, we then have the state equations

$$\dot{x}_{2j-1} = \omega_j x_{2j}, \quad \dot{x}_{2j} = -\omega_j x_{2j-1} - \gamma_j x_{2j} + \frac{1}{\alpha_j} \sum_{k=1}^r u_k Y_j(l_k) \quad \text{for } j = 1, 2, \dots, m \quad (32.155)$$

This can be put in the matrix-vector form of a state-space model

$$\dot{\mathbf{x}} = \mathbf{A}\mathbf{x} + \mathbf{B}\mathbf{u} \quad (32.131)$$

where

$$\mathbf{A} = \begin{bmatrix} 0 & \omega_1 & & & 0 \\ -\omega_1 & -\gamma_1 & & & \\ & & \ddots & & \\ & & & 0 & \omega_m \\ 0 & & & -\omega_m & -\gamma_m \end{bmatrix}_{n \times n} \quad (32.156)$$

and

$$\mathbf{B} = \begin{bmatrix} 0 & & 0 \\ Y_1(l_1)/\alpha_1 & \cdots & Y_1(l_r)/\alpha_1 \\ \vdots & & \vdots \\ 0 & & 0 \\ Y_m(l_1)/\alpha_m & \cdots & Y_m(l_r)/\alpha_m \end{bmatrix}_{n \times r} \quad (32.157)$$

with $n = 2m$, where m is the number of modes retained in the modal expansion. Note that, as the number of modes used in this model increases, both the accuracy and the computational effort that is needed for the control problem increase because of the proportional increase of the system order. At some point, the potential improvement in accuracy by further increasing the model size would be insignificant in comparison with added computational burden. Hence, a balance must be struck in this tradeoff.

32.10.2 Control Problem

The state-space model (Equation 32.131) for the beam dynamics, with matrices (Equation 32.156 and Equation 32.157), is known to be *controllable*. Hence, it is possible to determine a constant-gain feedback controller $\mathbf{u} = \mathbf{K}\mathbf{x}$ that minimizes a quadratic-integral cost function of the form in Equation 32.141. Also, a similar controller can be determined that places the eigenvalues of the system at specified locations thereby achieving not only specified levels of modal damping but also a specified set of natural frequencies. However, there is a practical obstacle to achieving such an active controller. Note that, in the model given in Equation 32.156 and Equation 32.157, the state variables are proportional to the modal variables q_i and their time derivatives \dot{q}_i . They are not directly measurable. However, the displacements and velocities at a set of discrete locations along the beam can usually be measured. Let these locations (s) be denoted by p_1, p_2, \dots, p_s . Thus, in view of the modal expansion (Equation 32.148), the measurements can be expressed as

$$v(p_j, t) = \sum_{i=1}^m Y_i(p_j)q_i(t), \quad \dot{v}(p_j, t) = \sum_{i=1}^m Y_i(p_j)\dot{q}_i(t) \quad \text{for } j = 1, 2, \dots, s \quad (32.158)$$

Now, define the output (measurement) vector \mathbf{y} according to

$$\mathbf{y} = [v(p_1, t), \dot{v}(p_1, t), \dots, v(p_s, t), \dot{v}(p_s, t)]^T \quad (32.159)$$

In view of Equation 32.158 and the definitions of the state variable in Equation 32.154, we can write

$$\mathbf{y} = \mathbf{C}\mathbf{x} \quad (32.160)$$

with

$$\mathbf{C} = \begin{bmatrix} Y_1(p_1)/\omega_1 & 0 & \cdots & Y_m(p_1)/\omega_m & 0 \\ 0 & Y_1(p_1) & \cdots & 0 & Y_m(p_1) \\ \vdots & \vdots & \cdots & \vdots & \vdots \\ Y_1(p_s)/\omega_1 & 0 & \cdots & Y_m(p_s)/\omega_m & 0 \\ 0 & Y_1(p_s) & \cdots & 0 & Y_m(p_s) \end{bmatrix}_{2s \times n} \quad (32.161)$$

Hence, an active controller is possible of the form:

$$\mathbf{u} = \mathbf{H}\mathbf{y} \quad (32.162)$$

which is an output feedback controller. Therefore, in view of Equation 32.160, we have

$$\mathbf{u} = \mathbf{H}\mathbf{C}\mathbf{x} \quad (32.163)$$

This is not the same as complete state feedback $\mathbf{u} = \mathbf{K}\mathbf{x}$ where \mathbf{K} can take any real value (and, hence, the LQR solution in Equation 32.142 and the complete pole placement solution cannot be applied directly). In Equation 32.163, only \mathbf{H} can be arbitrarily chosen, and \mathbf{C} is completely determined according to Equation 32.161. The resulting product $\mathbf{H}\mathbf{C}$ will not usually correspond to either the LQR solution or the complete pole assignment solution. Still, the output feedback controller in Equation 32.162 can provide a satisfactory performance. However, a sufficient number of displacement and velocity sensors (s) have to be used in conjunction with a sufficient number of actuators (r) for active control. This will increase the system complexity and cost. Furthermore, due to added components and their active nature, the reliability of fault-free operation may degrade somewhat. A satisfactory alternative would be to use passive control devices such as dampers and dynamic absorbers, which is illustrated below. Note that in the matrices \mathbf{B} and \mathbf{C} given by Equation 32.157 and Equation 32.161, both the actuator locations l_i and the sensor locations p_j are variable. Hence, there exists an additional design freedom (or optimization parameters) in selecting the sensor and actuator locations in achieving satisfactory control.

32.10.3 Use of Linear Dampers

Now, consider the use of a discrete set of linear dampers for controlling beam vibration. Suppose that r linear dampers with damping constants b_j are placed at locations l_j , $j = 1, 2, \dots, r$ along the beam, as schematically shown in Figure 32.34. The damping forces are given by

$$u_j = -b_j \dot{v}(l_j, t) \quad \text{for } j = 1, 2, \dots, r \quad (32.164)$$

Substituting the truncated modal expansion (m modes)

$$\dot{v}(l_j, t) = \sum_{i=1}^m Y_i(l_j) \dot{q}_i(t) \quad (32.165)$$

we get, in view of Equation 32.154, the passive feedback control action

$$\mathbf{u} = -\mathbf{K}\mathbf{x} \quad (32.166)$$

with

$$\mathbf{K} = \begin{bmatrix} 0 & b_1 Y_1(l_1) & \cdots & 0 & b_1 Y_m(l_1) \\ \vdots & \vdots & \cdots & \vdots & \vdots \\ 0 & b_r Y_1(l_r) & \cdots & 0 & b_r Y_m(l_r) \end{bmatrix}_{r \times n} \quad (32.167)$$

By substituting Equation 32.166 into Equation 32.131, we have the closed-loop system equation

$$\dot{\mathbf{x}} = (\mathbf{A} - \mathbf{F})\mathbf{x} = \mathbf{A}_c \mathbf{x} \quad (32.168)$$

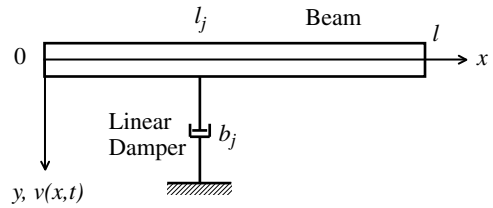


FIGURE 32.34 Use of linear dampers in beam vibration control.

where $\mathbf{F} = \mathbf{BK}$ and is given by

$$\mathbf{F} = \begin{bmatrix} 0 & 0 & \cdots & 0 & 0 \\ 0 & \sum b_i Y_{11}(l_i)/\alpha_1 & \cdots & 0 & \sum b_i Y_{1m}(l_i)/\alpha_1 \\ \vdots & \vdots & \cdots & \vdots & \vdots \\ 0 & 0 & \cdots & 0 & 0 \\ 0 & \sum b_i Y_{m1}(l_i)/\alpha_m & \cdots & 0 & \sum b_i Y_{mm}(l_i)/\alpha_m \end{bmatrix}_{n \times n} \quad (32.169)$$

with

$$Y_{ij}(x) = Y_i(x)Y_j(x) \quad (32.170)$$

In this case, the controller design involves the selection of the damping constants b_i and the damper locations l_j to achieve the required performance. This may be achieved, for example, by seeking to make the eigenvalues of the closed-loop system matrix \mathbf{A}_c reach a set of desired values. This achieves the desired modal damping and natural frequency characteristics. However, given that the structure of the \mathbf{F} matrix is fixed, as seen in Equation 32.169, this is not equivalent to complete state feedback (or complete output feedback). Hence, generally, it is not possible to place the poles of the system at the exact desired locations.

32.10.3.1 Design Example

In realizing a desirable modal response of a beam using a set of linear dampers, one may seek to minimize a cost function of the form

$$J = \text{Re}(\boldsymbol{\lambda} - \boldsymbol{\lambda}_d)^T \mathbf{Q} \text{Re}(\boldsymbol{\lambda} - \boldsymbol{\lambda}_d) + \text{Im}(\boldsymbol{\lambda} - \boldsymbol{\lambda}_d)^T \mathbf{R}(\boldsymbol{\lambda} - \boldsymbol{\lambda}_d) \quad (32.171)$$

where $\boldsymbol{\lambda}$ are the actual eigenvalues of the closed-loop system matrix (\mathbf{A}_c), and $\boldsymbol{\lambda}_d$ are the desired eigenvalues that will give the required modal performance (damping ratios and natural frequencies). “Re” denotes the real part and “Im” denotes the imaginary part. Weighting matrices \mathbf{Q} and \mathbf{R} , which are real and diagonal with positive diagonal elements, should be chosen to relatively weight various eigenvalues. This allows the emphasis of some eigenvalues over others, with real parts and the imaginary parts weighting separately.

Various computational algorithms are available for minimizing the cost function (Equation 32.171). Although the precise details are beyond the scope of this book, we will present an example result. Consider a uniform simply supported 12×5 American Standard beam, with the following pertinent specifications: $E = 2 \times 10^8$ kPa (29×10^6 psi), $\rho A = 47$ kg/m (2.6 lb/in.), length $l = 15.2$ m (600 in.), $I = 9 \times 10^{-5}$ m⁴ (215.8 in.⁴). The internal damping parameter for the j th mode of vibration is given by

$$E^*(\omega_j) = (g_2/\omega_j) + g_2 \quad (32.172)$$

in which ω_j is the j th undamped natural frequency given by

$$\omega_j = (j\pi/l)^2 \sqrt{EI/\rho A} \quad (32.173)$$

The numerical values used for the damping parameters are $g_1 = 88 \times 10^4$ kPa (12.5×10^4 psi) and $g_2 = 3.4 \times 10^4$ kPa s (5×10^3 psi s). For the present problem, $Y_i(x) = \sqrt{2}\sin(j\pi x/l)$ and $\alpha_j = \rho A l$ for all j .

First, ω_j and γ_j are computed using Equation 32.173 and Equation 32.153, respectively, along with Equation 32.172. Next, the open-loop system matrix \mathbf{A} is formed according to Equation 32.156 and its eigenvalues are computed. These are listed in Table 32.2, scaled to the first undamped natural frequency (ω_1). Note that in view of the very low levels of internal material damping of the beam, the actual natural frequencies, as given by the imaginary parts of the eigenvalues, are almost identical to the undamped natural frequencies.

Next, we attempt to place the real parts of the (scaled) eigenvalues all at -0.20 while exercising no constraint on the imaginary parts (i.e., damped natural frequencies) by using: (a) single damper, and

TABLE 32.2 Eigenvalues of the Open-Loop (Uncontrolled) Beam

Mode	Eigenvalue (rad/sec) (Multiply by 26.27)
1	$-0.000126 \pm j1.0$
2	$-0.000776 \pm j4.0$
3	$-0.002765 \pm j9.0$
4	$-0.007453 \pm j16.0$
5	$-0.016741 \pm j25.0$
6	$-0.033.75 \pm j36.0$

(b) two dampers. In the cost function (Equation 32.171), the first three modes are more heavily weighted than the remaining three. Initial values of the damper parameters are $b_1 = b_2 = 0.1$ lbf sec/in. (17.6 N sec/m) and the initial locations $l_1/l = 0.0$ and $l_2/l = 0.5$. At the end of the numerical optimization, using a modified gradient algorithm, the following optimized values were obtained:

1. Single-damper control

$$b_1 = 36.4 \text{ lbf sec/in. } (6.4 \times 10^3 \text{ N sec/m})$$

$$l_1/l = 0.3$$

The corresponding normalized eigenvalues (of the closed-loop system) are given in Table 32.3.

2. Two-damper control

$$b_1 = 22.8 \text{ lbf sec/in. } (4.0 \times 10^3 \text{ N sec/m})$$

$$b_2 = 12.1 \text{ lbf sec/in. } (2.1 \times 10^3 \text{ N sec/m})$$

$$l_1/l = 0.25, \quad l_2/l = 0.43$$

The corresponding normalized eigenvalues are given in Table 32.4.

It would be overly optimistic to expect perfect assignment all real parts at -0.2 . However, note that good levels of damping have been achieved for all modes except for Mode 3 in the single-damper control and Mode 4 in the two-damper control. In any event, because the contribution of the higher modes towards the overall response, is relatively smaller, it is found that the total response (e.g., at point $x = l/12$) is well damped in both cases of control.

TABLE 32.3 Eigenvalues of the Beam with an Optimal Single Damper

Mode	Eigenvalue (rad/sec) (Multiply by 26.27)
1	$-0.225 \pm j0.985$
2	$-0.307 \pm j3.955$
3	$-0.037 \pm j8.996$
4	$-0.119 \pm j15.995$
5	$-0.355 \pm j24.980$
6	$-0.158 \pm j35.990$

TABLE 32.4 Eigenvalues of the Beam with Optimized Two Dampers

Mode	Eigenvalue (rad/sec) (Multiply by 26.27)
1	$-0.216 \pm j0.982$
2	$-0.233 \pm j3.974$
3	$-0.174 \pm j8.997$
4	$-0.079 \pm j15.998$
5	$-0.145 \pm j24.999$
6	$-0.354 \pm j35.989$

Bibliography

- Beards, C.F. 1996. *Engineering Vibration Analysis with Application to Control Systems*, Halsted Press, New York.
- Cao, Y., Modi, V.J., de Silva, C.W., and Misra, A.K., On the control of a novel manipulator with slewing and deployable links, *Acta Astronaut.*, 49, 645–658, 2001.
- Caron, M., Modi, V.J., Pradhan, S., de Silva, C.W., and Misra, A.K., Planar dynamics of flexible manipulators with slewing deployable links, *J. Guid. Control Dyn.*, 21, 572–580, 1998.
- Chen, Y., Wang, X.G., Sun, C., Devine, F., and de Silva, C.W., Active vibration control with state feedback in woodcutting, *J. Vibr. Control*, 9, 645–664, 2003.
- den Hartog, J.P., 1956. *Mechanical Vibrations*, Mc-Graw-Hill, New York.
- de Silva, C.W., Optimal estimation of the response of internally damped beams to random loads in the presence of measurement noise, *J. Sound Vibr.*, 47, 485–493, 1976.
- de Silva, C.W., An algorithm for the optimal design of passive vibration controllers for flexible systems, *J. Sound Vibr.*, 74, 495–502, 1982.
- de Silva, C.W. and Wormley, D.N. 1983. *Automated Transit Guideways: Analysis and Design*, D.C. Heath & Co., Lexington, KY.
- de Silva, C.W. 1989. *Control Sensors and Actuators*, Prentice Hall, Englewood Cliffs, NJ.
- de Silva, C.W. 1995. *Intelligent Control: Fuzzy Logic Applications*, CRC Press, Boca Raton, FL.
- de Silva, C.W. 2000. *Vibration—Fundamentals and Practice*, CRC Press, Boca Raton, FL.
- de Silva, C.W. 2004. *Mechatronics—an Integrated Approach*, CRC Press, Boca Raton, FL.
- Goulet, J.F., de Silva, C.W., Modi, V.J., and Misra, A.K., Hierarchical control of a space-based deployable manipulator using fuzzy logic, *AIAA J. Guid. Control Dyn.*, 24, 395–405, 2001.
- Irwin, J.D. and Graf, E.R. 1979. *Industrial Noise and Vibration Control*, Prentice Hall, Englewood Cliffs, NJ.
- Karray, F. and de Silva, C.W. 2004. *Soft Computing and Intelligent System Design: Theory, Tools, and Applications*, Pearson, England.
- MATLAB Control Systems Toolbox, The MathWorks, Inc., Natick, MA, 2004.
- Van de Vegte, J. and de Silva, C.W., Design of passive vibration controls for internally damped beams by modal control techniques, *J. Sound Vibr.*, 45, 417–425, 1976.

Appendix 32A

MATLAB Control Systems Toolbox

32A.1 Introduction

Modeling, analysis, design, data acquisition, and control are important activities within the field of vibration. Computer software tools and environments are available for effectively carrying out, both at the learning level and at the professional application level. Several such environments and tools are commercially available.

MATLAB¹ is an interactive computer environment with a high-level language and tools for scientific and technical computation, modeling and simulation, design, and control of dynamic systems. SIMULINK¹ is a graphical environment for modeling, simulation, and analysis of dynamic systems, and is available as an extension to MATLAB. The Control Systems Toolbox of MATLAB is suitable in the analysis, design, and control of mechanical vibrating systems.

32A.2 MATLAB

MATLAB interactive computer environment is very useful in computational activities in Mechatronics. Computations involving scalars, vectors, and matrices can be carried out and the results can be

¹MATLAB and SIMULINK are registered trademarks and products of The MathWorks, Inc. LabVIEW is a product of National Instruments, Inc.

graphically displayed and printed. MATLAB toolboxes are available for performing specific tasks in a particular area of study such as control systems, fuzzy logic, neural network, data acquisition, image processing, signal processing, system identification, optimization, model predictive control, robust control, and statistics. User guides, Web-based help, and on-line help from the parent company, MathWorks, Inc., and various other sources. What is given here is a brief introduction to get started in MATLAB for tasks that are particularly related to Control Systems and Mechatronics.

32A.2.1 Computations

Mathematical computations can be done by using the MATLAB command window. Simply type in the computations against the MATLAB prompt “>>” as illustrated next.

32A.2.2 Arithmetic

An example of a simple computation using MATLAB is given below:

```
>> x = 2; y = - 3;
>> z = x^2 - x * y + 4
z =
    14
```

In the first line, we have assigned values 2 and 3 to two variables x and y . In the next line, the value of an algebraic function of these two variables is indicated. Then, MATLAB provides the answer as 14. Note that if you place a “;” at the end of the line, the answer will not be printed/displayed.

Table 32A.1 gives the symbols for common arithmetic operations used in MATLAB. Following example shows the solution of the quadratic equation $ax^2 + bx + c = 0$:

```
>> a = 2; b = 3; c = 4;
>> x = (-b + sqrt(b^2 - 4*a*c))/(2*a)
x =
- 0.7500 + 1.1990i
```

The answer is complex, where i denotes $\sqrt{-1}$. Note that the function `sqrt()` is used, which provides the positive root only. Some useful mathematical functions are given in [Table 32A.2](#).

32A.2.3 Arrays

An array may be specified by giving the start value, increment, and the end value limit. An example is given below.

```
>> x = (0.9:-0.1:0.42)
x =

    0.9000    0.8000    0.7000    0.6000    0.5000
```

TABLE 32A.1 MATLAB Arithmetic Operations	
Symbol	Operation
+	Addition
-	Subtraction
*	Multiplication
/	Division
^	Power

TABLE 32A.2 Useful Mathematical Functions in MATLAB

Function	Description
abs()	Absolute value/magnitude
acos()	Arc-cosine (inverse cosine)
acosh()	Arc-hyperbolic-cosine
asin()	Arc-sine
atan()	Arc-tan
cos()	Cosine
cosh()	Hyperbolic cosine
exp()	Exponential function
imag()	Imaginary part of a complex number
log()	Natural logarithm
log10()	Log to base 10 (common log)
real()	Real part of a complex number
sign()	Signum function
sin()	Sine
sqrt()	Positive square root
tan()	Tan function

Note that MATLAB is case sensitive.

The entire array may be manipulated. For example, all the elements are multiplied by π as below:

```
>> x = x*pi
x =
2.8274 2.5133 2.1991 1.8850 1.5708
```

The second and the fifth elements are obtained by

```
>> x([2 5])
ans =
2.5133 1.5708
```

Next, we form a new array y using x , and then plot the two arrays, as shown in Figure 32A.1:

```
>> y = sin(x);
>> plot(x,y)
```

A polynomial may be represented as an array of its coefficients. For example, the quadratic equation $ax^2 + bx + c = 0$ as given before, with $a = 2$, $b = 3$, and $c = 4$, may be solved using the function “roots” as below:

```
>> p = [2 3 4];
>> roots(p)
ans =
-0.7500 + 1.1990i
-0.7500 - 1.1990i
```

The answer is the same as we obtained before.

32A.2.4 Relational and Logical Operations

Useful relational operations in MATLAB are given in Table 32A.3. Basic logical operations are given in Table 32A.4.

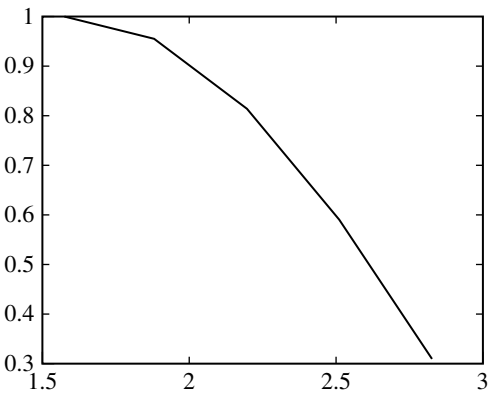


FIGURE 32A.1 A plot using MATLAB.

TABLE 32A.3 Some Relational Operations

Operator	Description
<	Less than
<=	Less than or equal to
>	Greater than
>=	Greater than or equal to
==	Equal to
~=	Not equal to

TABLE 32A.4 Basic Logical Operations

Operator	Description
&	AND
	OR
~	NOT

Consider the following example:

```
>> x = (0:0.25:1)*pi
x =
    0    0.7854    1.5708    2.3562    3.1416
>> cos(x) > 0
ans =
    1     1     1     0     0
>> (cos(x) > 0)&(sin(x) > 0)
ans =
    0     1     1     0     0
```

In this example, first an array is computed. Then the cosine of each element is computed. Next it is checked whether the elements are positive. (A truth value of 1 is sent out if true and a truth value of 0 if false.) Finally, the “AND” operation is used to check whether both corresponding elements of two arrays are positive.

32A.2.5 Linear Algebra

MATLAB can perform various computations with vectors and matrices (see [Appendix 3A](#) and [Appendix 6A](#)). Some basic illustrations are given here.

A vector or a matrix may be specified by assigning values to its elements. Consider the following example:

```
>> b = [ 1.5  -2];
>> A = [2   1;  -1  1];
>> b = b'
b =
    1.5000
   -2.0000
>> x = inv(A) * b
x =
    1.1667
   -0.8333
```

In this example, first a second-order row vector and 2 × 2 matrix are defined. The row vector is transposed to get a column vector. Finally the matrix–vector equation **Ax = b** is solved according to **x = A⁻¹b**. The determinant and the eigenvalues of **A** are determined by

TABLE 32A.5 Some Matrix Operations in MATLAB

Operation	Description
+	Addition
−	Subtraction
*	Multiplication
/	Division
^	Power
'	Transpose

TABLE 32A.6 Useful Matrix Functions in MATLAB

Function	Description
det()	Determinant
inv()	Inverse
eig()	Eigenvalues
[,] = eig()	Eigenvectors and eigenvalues

```
>> det(A)
ans =
    3
>> eig(A)
ans =
    1.5000 + 0.8660i
    1.5000 - 0.8660i
```

Both eigenvectors and eigenvalues of **A** computed as

```
>> [V,P] = eig(A)
V =
    0.7071    0.7071
   -0.3536 + 0.6124i   -0.3536 - 0.6124i
P =
    1.5000 + 0.8660i    0
    0    1.5000 - 0.8660i
```

Here, the symbol **V** is used to denote the matrix of eigenvectors. The symbol **P** is used to denote the diagonal matrix whose diagonal elements are the eigenvalues.

Useful matrix operations in MATLAB are given in Table 32A.5 and several matrix functions are given in Table 32A.6.

32A.2.6 M-Files

The MATLAB commands have to be keyed in on the command window, one by one. When several commands are needed to carry out a task, the required effort can be tedious. Instead, the necessary commands can be placed in a text file, edited as appropriate (using text editor), which MATLAB can use to execute the complete task. Such a file is called an M-file. The file name must have the extension “m” in the form *filename.m*. A toolbox is a collection of such files, for use in a particular application area (e.g., control systems, fuzzy logic). Then, by keying in the M-file name at the MATLAB command prompt, the file will be executed. The necessary data values for executing the file have to be assigned beforehand.

32A.3 Control Systems Toolbox

There are several toolboxes with MATLAB, which can be used to analyze, compute, simulate, and design control problems. Both time-domain representations and frequency-domain representations can be

used. Also, both classical and modern control problems can be handled. The application is illustrated here through several control problems.

32A.3.1 MATLAB Modern Control Examples

Several examples in modern control engineering are given now to illustrate the use of MATLAB in control.

32A.3.1.1 Pole Placement of a Third-Order Plant

A mechanical plant is given by the input–output differential equation $\ddot{x} + \dot{x} = u$, where u is the input and x is the output. Determine a feedback law that will yield approximately a simple oscillator with a damped natural frequency of 1 unit and a damping ratio of $1/\sqrt{2}$.

To solve this problem, first we define the state variables as $x_1 = x$, $x_2 = \dot{x}_1$, and $x_3 = \dot{x}_2$. The corresponding state-space model is

$$\dot{\mathbf{x}} = \begin{bmatrix} \dot{x}_1 \\ \dot{x}_2 \\ \dot{x}_3 \end{bmatrix} = \underbrace{\begin{bmatrix} 0 & 1 & 0 \\ 0 & 0 & 1 \\ 0 & 0 & -1 \end{bmatrix}}_{\mathbf{A}} \begin{bmatrix} x_1 \\ x_2 \\ x_3 \end{bmatrix} + \underbrace{\begin{bmatrix} 0 \\ 0 \\ 1 \end{bmatrix}}_{\mathbf{B}} u$$

$$y = \underbrace{[1 \quad 0 \quad 0]}_{\mathbf{C}} \mathbf{x}$$

The open-loop poles and zeros are obtained using the following MATLAB commands:

```
>> A = [0 1 0; 0 0 1; 0 0 -1];
>> B = [0; 0; 1];
>> C = [1 0 0];
>> D = [0];
>> sys_open = ss(A,B,C,D);
>> [nat_freq_open,damping_open,poles_open] = damp(sys_open)
>> pzmap(sys_open)
```

The open-loop poles are: $[0 \ 0 \ -1]^T$.

The step response of the open-loop system is obtained using the command:

```
>> step(sys_open)
```

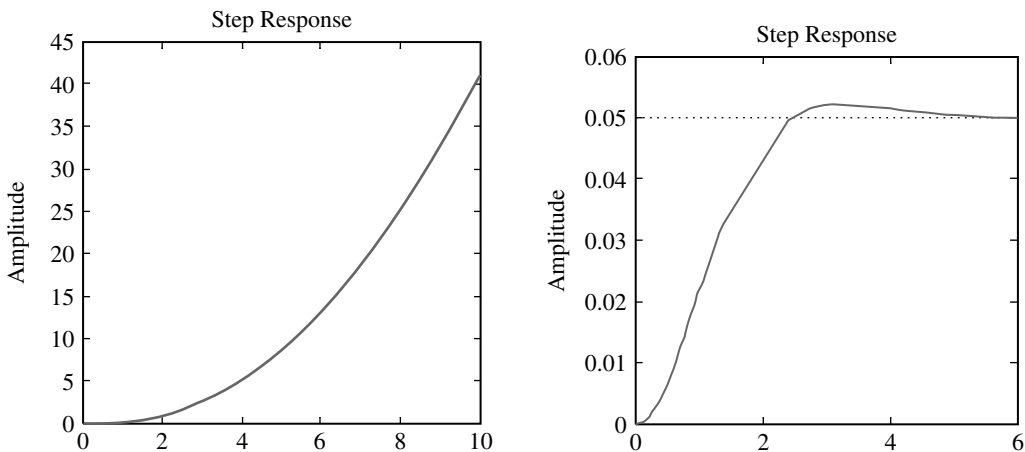


FIGURE 32A.2 (a) Step response of the open-loop system; (b) step response of the third-order system with pole-placement control.

The result is shown in Figure 32A.2(a). Clearly, the system is unstable.

With the desired damped natural frequency $\omega_d = 1$ and damping ratio $\zeta = 1/\sqrt{2}$, we get the undamped natural frequency $\omega_n = \sqrt{2}$ and, hence, $\zeta\omega_n = 1$. It follows that we need to place two poles at $-1 \pm j$. Also the third pole has to be far from these two on the left half plane (LHP); say, at -10 . The corresponding control gain K can be computed using the “place” command in MATLAB:

```
>> p = [-1 + j -1 - j -10];
>> K = place(A,B,p)
place:ndigits = 15
K =
    20.0000    22.0000    11.0000
```

The corresponding step response of the closed-loop system is shown in Figure 32A.2(b).

32A.3.1.2 Linear Quadratic Regulator for a Third-Order Plant

For the third-order plant in the previous example, we design a linear quadratic regulator (LQR), which has a state feedback controller, using MATLAB Control Systems Toolbox. The MATLAB command $K = \text{lqr}(A,B,Q,R)$ computes the optimal gain matrix K such that the state-feedback law $\mathbf{u} = -K\mathbf{x}$ minimizes the quadratic cost function

$$J = \int_0^{\infty} (\mathbf{x}^T \mathbf{Q} \mathbf{x} + \mathbf{u}^T \mathbf{R} \mathbf{u}) dt$$

The weighting matrices \mathbf{Q} and \mathbf{R} are chosen to apply the desired weights to the various states and inputs. The MATLAB commands for designing the controller are

```
>> A = [0 1 0; 0 0 1; 0 0 -1];
>> B = [0; 0; 1];
>> C = [1 0 0];
>> D = [0];
>> Q = [2 0 0; 0 2 0; 0 0 2];
>> R = 2;
>> Klqr = lqr(A,B,Q,R)
>> lqr_closed = ss(A-B*Klqr,B,C,D);
>> step(lqr_closed)
```

The step response of the system with the designed LQR controller is shown in Figure 32A.3.

32A.3.1.3 Modal Analysis Example

Consider the two-DoF mechanical system shown in Figure 32A.4. We now solve the modal analysis problem using MATLAB, for the numerical values

$$\alpha = 0.5, \quad \beta = 0.5, \quad m = 1 \text{ kg}; \quad k = 1 \text{ N/m}$$

For the given mass matrix \mathbf{M} and the stiffness matrix \mathbf{K} , the solution steps for the alternative approach of modal analysis are

1. Determine $\mathbf{M}^{1/2}$ and $\mathbf{M}^{-1/2}$.
2. Solve for the eigenvalues λ and the eigenvectors Φ of $\mathbf{M}^{-1/2} \mathbf{K} \mathbf{M}^{-1/2}$. These eigenvalues are the squares of the natural frequencies of the original system.

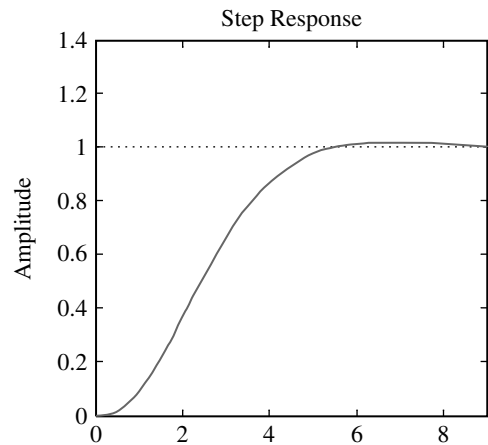


FIGURE 32A.3 Step response of the third-order system with LQR control.

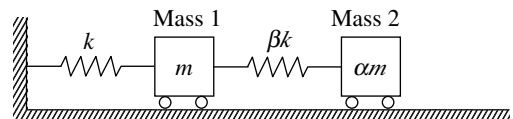


FIGURE 32A.4 A two-DoF system.

3. Determine the modal vectors ψ of the original system using the transformation $\psi = M^{-1/2}\phi$.

The program code is given below:

```
%Modal Analysis Example
clear;
m = 1.0;
k = 1.0;
M = [ m 0; 0 m/2 ];
K = [3/2 * k - k/2;
     - k/2 k/2];
M_sqrt = M^0.5;
M_s_inv = inv(M_sqrt);
lemda = eig(M_s_inv * K * M_s_inv);
[U,D] = eig(M_s_inv * K * M_s_inv);
V = M_s_inv * U;
disp('Natural frequencies')
fprintf('omega1 = %10.3f%14.3f\n',sqrt(lemda(2,1)));
fprintf('\n omega2 = %10.3f%14.3f\n',sqrt(lemda(1,1)));
fprintf('\n')
fprintf('\nMode shapes \n')
fprintf('First mode   Second Mode \n')
for i = 1:2
    fprintf('%10.3f%14.3f\n',V(i,2)/V(1,2),V(i,1)/V(1,1));
end
```

The necessary results are obtained as shown below:

```
>> Natural frequencies
omega1 = 1.414
omega2 = 0.707
```

Mode Shapes	
First Mode	Second Mode
1.000	1.000
- 1.000	2.000

33

Structural Dynamic Modification and Sensitivity Analysis

33.1	Introduction	33-2
33.2	Structural Dynamic Modification of Finite Element Model	33-2
33.3	Perturbation Method of Vibration Modes	33-4
	First-Order Perturbation of Distinct Modes • Second-Order Perturbation of Distinct Modes • Numerical Examples	
33.4	Design Sensitivity Analysis of Structural Vibration Modes	33-8
	Direct Differential Method for Sensitivity Analysis • Perturbation Sensitivity Analysis • Numerical Example • Concluding Remarks	
33.5	High-Accuracy Modal Superposition for Sensitivity Analysis of Modes	33-11
	Method One • Method Two	
33.6	Sensitivity of Eigenvectors for Free–Free Structures	33-13
33.7	Matrix Perturbation Theory for Repeated Modes	33-14
	Basic Equations • The First-Order Perturbation of Eigensolutions • High-Accuracy Modal Superposition for the First-Order Perturbation of Repeated Modes	
33.8	Matrix Perturbation Method for Closely Spaced Eigenvalues	33-16
	Method One of Perturbation Analysis for Close Eigenvalues • Method Two of Perturbation Analysis for Close Eigenvalues • Concluding Remarks	
33.9	Matrix Perturbation Theory for Complex Modes	33-22
	Basic Equations • Matrix Perturbation Method for Distinct Modes • High-Accuracy Modal Superposition for Eigenvector Derivatives • Matrix Perturbation for Repeated Eigenvalues of Nondefective Systems • Matrix Perturbation for Close Eigenvalues of Unsymmetric Matrices	

Su Huan Chen
Jilin University

Summary

The matrix perturbation theory for structural dynamic modification and sensitivity analysis is presented in this chapter. The theory covers a broad spectrum of subjects, specifically, matrix perturbation of real modes of complex structures and matrix perturbation of complex modes. The contents include nine sections. Section 33.2 provides the preliminaries to matrix perturbation and sensitivity analysis. Section 33.3 presents the matrix perturbation method including first-order and second-order perturbation. Section 33.4 presents methods for design sensitivity

analysis. In Section 33.5, high-accuracy modal superposition for sensitivity analysis of modes is given. Section 33.6 presents the sensitivity analysis of eigenvectors for free-free structures. In Section 33.7 and Section 33.8, matrix perturbations for repeated modes and closely spaced modes are discussed. In Section 33.9, the matrix perturbation approach for complex modes is presented.

33.1 Introduction

In modern engineering problems, the dynamic design of structures is becoming increasingly important. In order to achieve an optimal design, we repeatedly have to modify the structural parameters and solve the generalized eigenvalue problem. The iterative vibration analysis can be very tedious for large and complex structures. Therefore, it is necessary to seek a fast computation method for sensitivity analysis and reanalysis. The matrix perturbation method is an extremely useful tool for this purpose.

The matrix perturbation method is concerned with how the natural frequencies and modal vectors change if small modifications are imposed on the parameters of structures. Engineering problems often involve many small modifications in the structural parameters, such as material property variations, manufacturing errors, iterative design of structural parameters, design sensitivity analysis, random eigenvalue analysis, robustness analysis of control systems, and so on.

In this chapter, it is assumed that the reader has an undergraduate knowledge in vibration theory (see Chapter 1 to Chapter 5, and Chapter 14) and a working knowledge in the finite element method (see Chapter 9).

The contents of the chapter include the basic preliminaries: vibration equations of the finite element model, eigenvalue problem, modal vectors, orthogonality conditions, modal expansion theorem, and the power series expansion of eigensolutions. The chapter also covers such topics as: the perturbation method for distinct eigenvalues and corresponding eigenvectors; sensitivities of eigenvalues and eigenvectors; the high-accuracy modal superposition method for eigenvector derivatives; eigenvector derivatives for free-free structures; perturbation method for systems with repeated eigenvalues and close eigenvalues; and perturbation method of the complex modes of systems with real unsymmetric matrices.

33.2 Structural Dynamic Modification of Finite Element Model

The finite element method is an important tool to obtain numerical and computational solutions to problems in structural vibration analysis. By applying the finite element method to a structure, a discrete analysis model to idealize the continuum can be obtained. The finite equation of vibrations of a structure in the global coordinate system is

$$\mathbf{M}\ddot{\mathbf{q}} + \mathbf{C}\dot{\mathbf{q}} + \mathbf{K}\mathbf{q} = \mathbf{Q} \quad (33.1)$$

where \mathbf{M} , \mathbf{K} , and \mathbf{C} are the mass, stiffness, and damping matrices, respectively, $\ddot{\mathbf{q}}$, $\dot{\mathbf{q}}$, and \mathbf{q} are the acceleration, velocity, and displacement vectors, respectively, and \mathbf{Q} is the external load vector.

Neglecting the damping force and external load vector, Equation 33.1 becomes

$$\mathbf{M}\ddot{\mathbf{q}} + \mathbf{K}\mathbf{q} = \mathbf{0} \quad (33.2)$$

This is the natural vibration equation for the structure. Its solution (the natural vibration) is harmonic (see Chapter 30), and is given by

$$\mathbf{q} = \mathbf{u} \cos(\omega t - \varphi) \quad (33.3)$$

where \mathbf{u} is modal vector, and ω the natural frequency of the system. Substituting Equation 33.3 into Equation 33.2, the eigenproblem of structural vibration can be obtained as

$$\mathbf{K}\mathbf{u} = \lambda \mathbf{M}\mathbf{u} \quad (33.4)$$

where λ ($\lambda = \omega^2$) denote the eigenvalues of the system.

In structural vibration analysis, the natural frequencies and the corresponding modal vectors can be obtained by solving the eigenproblem (Equation 33.4). The solutions for n eigenvalues and corresponding eigenvectors satisfy

$$\mathbf{K}\mathbf{U} = \mathbf{M}\mathbf{U}\mathbf{\Lambda} \quad (33.5)$$

where \mathbf{U} , which is called the *modal matrix*, is an $(n \times n)$ matrix with its columns equal to the n eigenvectors, and $\mathbf{\Lambda}$ is an $(n \times n)$ diagonal matrix consisting of the corresponding eigenvalues as the diagonal elements; specifically

$$\mathbf{U} = [\mathbf{u}_1, \mathbf{u}_2, \dots, \mathbf{u}_n] \quad (33.6)$$

$$\mathbf{\Lambda} = \text{diag}(\lambda_i), \quad i = 1, 2, \dots, n \quad (33.7)$$

An important relation for eigenvectors is that of \mathbf{M} orthogonality and \mathbf{K} orthogonality; that is, we have

$$\mathbf{u}_i^T \mathbf{M} \mathbf{u}_j = \delta_{ij} \quad (33.8)$$

$$\mathbf{u}_i^T \mathbf{K} \mathbf{u}_j = \lambda_i \delta_{ij} \quad (33.9)$$

where δ_{ij} is the Kronecker delta. For n eigenpairs, Equation 33.8 and Equation 33.9 can be written as

$$\mathbf{U}^T \mathbf{M} \mathbf{U} = \mathbf{I} \quad (33.10)$$

$$\mathbf{U}^T \mathbf{K} \mathbf{U} = \mathbf{\Lambda} \quad (33.11)$$

Since the modal vectors are independent, an arbitrary displacement vector, \mathbf{u} , can be expressed as a linear combination of \mathbf{u}_i , $i = 1, 2, \dots, n$; that is

$$\mathbf{u} = \sum_{r=1}^n c_r \mathbf{u}_r = \mathbf{U} \mathbf{C} \quad (33.12)$$

where c_r is a constant. Each constant c_r can be determined by

$$c_r = \mathbf{u}_r^T \mathbf{M} \mathbf{u}, \quad r = 1, 2, \dots, n \quad (13.13)$$

This is known as the *expansion theorem*.

Suppose the physical parameter of a given structure is given a small modification. This will cause a small change in the matrices \mathbf{K}_0 and \mathbf{M}_0 ; that is

$$\mathbf{M} = \mathbf{M}_0 + \varepsilon \mathbf{M}_1, \quad \mathbf{K} = \mathbf{K}_0 + \varepsilon \mathbf{K}_1 \quad (33.14)$$

where ε is a small parameter, \mathbf{K}_0 and \mathbf{M}_0 are the original mass and stiffness matrices, respectively, and $\varepsilon \mathbf{M}_1$ and $\varepsilon \mathbf{K}_1$ are the corresponding modifications. It is obvious that if \mathbf{M}_0 and \mathbf{K}_0 are symmetric, the matrices \mathbf{M}_1 and \mathbf{K}_1 are also symmetric.

If $\varepsilon \mathbf{M}_1$ and $\varepsilon \mathbf{K}_1$ are small, the changes of eigenvalues and eigenvectors of the structure are also small. According to the matrix perturbation theory, the eigensolutions of Equation 33.4 can be expressed in the form of a power series in ε ; thus

$$\mathbf{u}_i = \mathbf{u}_{0i} + \varepsilon \mathbf{u}_{1i} + \varepsilon^2 \mathbf{u}_{2i} + \dots \quad (33.15)$$

$$\lambda_i = \lambda_{0i} + \varepsilon \lambda_{1i} + \varepsilon^2 \lambda_{2i} + \dots \quad (33.16)$$

where \mathbf{u}_{0i} and λ_{0i} are the eigensolutions of the original structure, λ_{1i} and λ_{2i} are the first- and the second-order perturbations of the eigenvalues, and \mathbf{u}_{1i} and \mathbf{u}_{2i} are the first- and the second-order perturbation of the eigenvectors.

Since the eigensolutions of the original structure, \mathbf{u}_{0i} and λ_{0i} , are known, only the first- and the second-order perturbations of the eigensolutions are required without solving Equation 33.4.

33.3 Perturbation Method of Vibration Modes

The perturbation methods of vibration modes are well developed (Fox and Kapoor, 1968; Rogers, 1977; Chen and Wada, 1979; Hu, 1987; Chen, 1993). In this section, it is assumed that all eigenvalues of the original structure are distinct.

33.3.1 First-Order Perturbation of Distinct Modes

According to the expansion theorem, the first-order perturbation, \mathbf{u}_{1i} , can be expanded by the modal vectors, \mathbf{u}_{0s} , of the original structure as

$$\mathbf{u}_{1i} = \sum_{s=1}^n c_{1s} \mathbf{u}_{0s} \quad (33.17)$$

where

$$c_{1s} = \frac{1}{\lambda_{0i} - \lambda_{0s}} (\mathbf{u}_{0s}^T \mathbf{K}_1 \mathbf{u}_{0i} - \lambda_{0i} \mathbf{u}_{0s}^T \mathbf{M}_1 \mathbf{u}_{0i}), \quad s \neq i \quad (33.18)$$

$$c_{1i} = -\frac{1}{2} \mathbf{u}_{0i}^T \mathbf{M}_1 \mathbf{u}_{0i} \quad (33.19)$$

The first-order perturbation of the eigenvalues is

$$\lambda_{1i} = \mathbf{u}_{0i}^T \mathbf{K}_1 \mathbf{u}_{0i} - \lambda_{0i} \mathbf{u}_{0i}^T \mathbf{M}_1 \mathbf{u}_{0i} \quad (33.20)$$

33.3.2 Second-Order Perturbation of Distinct Modes

If the parameter modification is fairly large, in order to obtain high computing accuracy, the second-order perturbation must be used. According to the expansion theorem, the second-order perturbation, \mathbf{u}_{2i} , can be expanded by the modal vectors, \mathbf{u}_{0s} , of the original structure as

$$\mathbf{u}_{2i} = \sum_{s=1}^n c_{2s} \mathbf{u}_{0s} \quad (33.21)$$

where

$$c_{2s} = \frac{1}{\lambda_{0i} - \lambda_{0s}} (\mathbf{u}_{0s}^T \mathbf{K}_1 \mathbf{u}_{1i} - \lambda_{0i} \mathbf{u}_{0s}^T \mathbf{M}_1 \mathbf{u}_{1i} - \lambda_{1i} \mathbf{u}_{0s}^T \mathbf{M}_0 \mathbf{u}_{1i} - \lambda_{1i} \mathbf{u}_{0s}^T \mathbf{M}_1 \mathbf{u}_{0i}), \quad s \neq i \quad (33.22)$$

$$c_{2i} = -\frac{1}{2} (\mathbf{u}_{1i}^T \mathbf{M}_0 \mathbf{u}_{1i} + \mathbf{u}_{0i}^T \mathbf{M}_1 \mathbf{u}_{1i} + \mathbf{u}_{1i}^T \mathbf{M}_1 \mathbf{u}_{0i}) \quad (33.23)$$

The second perturbation of the eigenvalues is

$$\lambda_{2i} = \mathbf{u}_{0i}^T \mathbf{K}_1 \mathbf{u}_{1i} - \lambda_{0i} \mathbf{u}_{0i}^T \mathbf{M}_1 \mathbf{u}_{1i} - \lambda_{1i} \mathbf{u}_{0i}^T \mathbf{M}_0 \mathbf{u}_{1i} - \lambda_{1i} \mathbf{u}_{0i}^T \mathbf{M}_1 \mathbf{u}_{0i} \quad (33.24)$$

33.3.3 Numerical Examples

As illustrations of the matrix perturbation method, several numerical examples are given now.

Example 33.1

Consider the five-degree-of-freedom (five-DoF) system shown in [Figure 33.1](#). The physical parameters are given as

$$m_1 = m_2 = m_3 = m_4 = 1.0, \quad m_5 = 0.5, \quad k_1 = k_2 = k_3 = k_4 = k_5 = 1.0$$

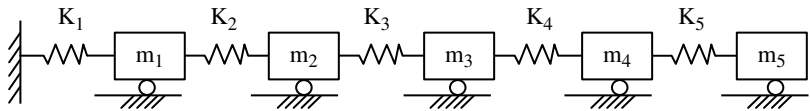


FIGURE 33.1 Mass–spring system for Example 33.1.

In order to study the computing accuracy of first- and second-order perturbations, let us assume that the fifth mass undergoes a decrement of 5 to 30%, and the stiffness of the first spring undergoes a decrement of 5 to 30%.

The computed results for the natural frequencies are presented in Table 33.1, in which the initial solutions mean the eigensolutions of the original structure.

TABLE 33.1 Comparison of Natural Frequencies

Mode Number		Changes of Structural Parameter (%)					
		5	10	15	20	25	30
1	A	0.3022	0.2922	0.2821	0.2724	0.2629	0.2536
	B	0.3128	0.3128	0.3128	0.3128	0.312	0.3128
	C	3.52	7.14	10.9	14.38	18.97	23.3
	D	0.3017	0.2903	0.2783	0.2658	0.2527	0.2388
	C	0.14	0.58	1.34	2.43	3.9	5.81
	E	0.3022	0.2922	0.2827	0.2740	0.2660	0.2588
	C	0.0033	0.068	0.24	0.58	0.93	2.08
2	A	0.8788	0.8512	0.8249	0.7998	0.7756	0.7523
	B	0.9079	0.98079	0.9079	0.98079	0.9079	0.98079
	C	3.31	6.66	10.1	13.52	17.06	20.68
	D	0.8775	0.8460	0.8133	0.7792	0.7435	0.7060
	C	0.15	0.61	1.41	2.58	4.14	6.15
	E	0.3789	0.8518	0.8267	0.8089	0.7835	0.7659
	C	0.0076	0.062	0.21	0.52	0.91	1.80
3	A	1.3732	1.3348	1.2989	1.2650	1.2332	1.2031
	B	1.1421	1.1421	1.1421	1.1421	1.1421	1.1421
	C	2.99	5.94	8.88	11.79	14.7	17.5
	D	1.371	1.3266	1.2806	1.2328	1.1832	1.1313
	C	0.15	0.62	1.41	2.54	4.05	5.96
	E	1.3733	1.3356	1.3015	1.2712	1.2449	1.2231
	C	0.0074	0.060	0.20	0.49	0.74	1.66
4	A	1.7355	1.6923	1.6520	1.6143	1.5790	1.5457
	B	1.7820	1.7820	1.7820	1.7820	1.7820	1.7820
	C	2.68	5.30	7.78	10.38	12.85	15.28
	D	1.7331	1.6828	1.6319	1.5773	1.5209	1.5209
	C	0.14	0.56	1.28	2.29	3.62	5.27
	E	1.7356	1.6933	1.6552	1.6216	1.5830	1.5695
	C	0.0070	0.057	0.19	0.45	0.68	1.53
5	A	1.9273	1.8825	1.8408	1.8017	1.7649	1.7304
	B	1.9753	1.9753	1.9753	1.9753	1.9753	1.9753
	C	2.49	4.93	7.31	9.63	11.92	14.16
	D	1.9248	1.8929	1.896	1.7696	1.7079	1.6492
	C	0.1300	0.51	1.15	2.06	3.23	4.69
	E	1.9274	1.8835	1.8439	1.8090	1.7790	1.7541
	C	0.0064	0.051	0.17	0.41	0.83	1.37

TABLE 33.2 Comparison of Natural Frequencies

Mode No.	A (Hz)	B (Hz)	F (%)	D (Hz)	G (%)	E (Hz)	H (%)
1	27.78	25.45	8.39	29.27	5.36	28.14	1.29
2	109.1	107.7	1.28	110.39	1.18	109.35	0.28
3	157.4	153.2	2.67	159.53	1.35	158.79	0.88
4	230.5	233.2	1.17	231.24	0.32	231.02	0.022
5	320.7	325.6	1.53	320.58	0.04	320.89	0.04
6	391.1	393.7	0.66	392.06	0.24	319.35	0.06

As can be seen from the results, if the change of the structural parameter is 15%, the average change of the natural frequencies is 9.0%. Using the first-order perturbation, the average error of the frequencies is reduced to 1.32%.

If the change of the structural parameter is 30%, the average error of the natural frequencies is 18%. Using the first-order perturbation, the average error of natural frequencies is reduced to 1.6%.

The notation used in Table 33.1 and Table 33.2 is as follows:

- A: the exact solutions of the modified structure
- B: the initial solutions of the original structure
- C: percent error
- D: the first-order perturbation solutions
- E: the second-order perturbation solutions
- F: the percent errors of the initial solutions
- G: the percent errors of the first-order perturbation
- H: the percent errors of the second perturbation

Example 33.2

Consider a truss structure (as shown in Figure 33.2) with 20 rods. The cross section area of the second rod is changed from 1.0 to 2.0 cm². The results calculated are listed in Table 33.2.

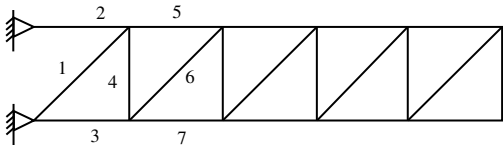


FIGURE 33.2 Truss structure for Example 33.2.

Example 33.3

Consider a torsional vibration system with five disks, as shown in Figure 33.3. The physical parameters of the system are as follows:

- $I_1 = 10.78 \text{ kg cm sec}^2$
- $I_2 = 82.82 \text{ kg cm sec}^2$
- $I_3 = 14.27 \text{ kg cm sec}^2$
- $I_4 = 29.56 \text{ kg cm sec}^2$
- $I_5 = 21.66 \text{ kg cm sec}^2$
- $K_1 = 10.48 \times 10^4 \text{ kg cm/rad}$
- $K_2 = 34.30 \times 10^4 \text{ kg cm/rad}$
- $K_3 = 24.40 \times 10^4 \text{ kg cm/rad}$
- $K_4 = 40.60 \times 10^4 \text{ kg cm/rad}$

The corresponding constrained system is shown in Figure 33.3b, in which the hung stiffness is $K_5 = 4060 \text{ kg cm/rad}$.

The exact eigensolutions of the constrained system are taken as the initial results. Using matrix

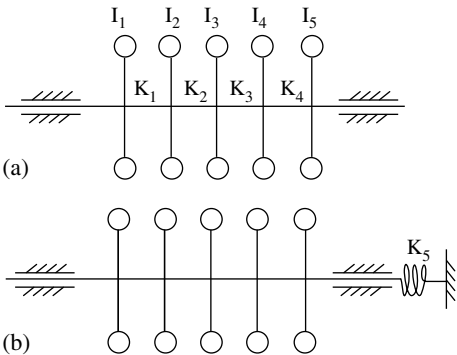


FIGURE 33.3 Torsional vibration system for Example 33.3.

TABLE 33.3 Comparison for Natural Frequencies

	No.				
	1	2	3	4	5
ω_0	0.000000	62.554934	105.668169	177.680405	224.361444
ω_x	1.595950	62.604815	105.669360	177.704224	224.386235
δ		0.079700	0.001070	0.013406	0.011000
$\varepsilon\omega_1$	-1.525707	-0.049895	-0.001132	-0.023834	-0.002508
ω'_0	0.080243	62.554920	105.448168	177.680390	224.383727
δ'		2.24×10^{-5}	9.46×10^{-7}	8.22×10^{-8}	9.93×10^{-5}

TABLE 33.4 Comparison for Eigenvectors

No.	u_0^i	u_x^i	εu_1^i	u_0^i
1	0.079283	0.097363	-0.000080	0.079823
	0.079283	0.079342	-0.000059	0.079283
	0.079283	0.079287	-0.000004	0.079283
	0.079283	0.079198	0.000085	0.079283
	0.079283	0.079189	0.000153	0.079342
2	-0.095647	-0.095611	0.000036	-0.095647
	-0.057148	-0.057064	-0.000084	-0.057148
	0.008612	0.008719	-0.000107	0.008612
	0.099081	0.099192	-0.000111	0.099081
	0.125223	0.125259	0.000036	0.125223
3	0.277894	0.277884	0.000010	0.277894
	-0.041278	-0.041284	0.000005	-0.41279
	-0.027509	-0.027497	-0.000013	-0.027510
	0.009810	0.009840	-0.000030	0.009810
	0.024263	0.024279	-0.000016	0.024263
4	-0.009038	-0.009033	-0.000005	-0.009038
	0.020312	-0.020309	0.000002	0.020312
	-0.125560	-0.125580	0.000024	-0.125556
	-0.098791	0.098735	-0.000053	-0.098788
	0.144375	0.144413	-0.000038	0.144375
5	0.004823	0.004823	0.000001	0.004824
	-0.020156	-0.020154	-0.0000002	-0.020156
	0.217244	0.217227	0.000018	0.217245
	-0.088717	-0.088725	0.000008	-0.088717
	0.052618	0.052652	-0.000034	0.052618

perturbation, the eigensolutions of the free-free system can be obtained. The results are listed in Table 33.3 and Table 33.4.

The notation used in Table 33.3 is as follows:

- ω_0 : exact solution of the natural frequency of the free-free system (l/sec)
- ω'_0 : perturbation solutions of the natural frequency of the free-free system (l/sec)
- ω_x : natural frequency of the constrained system (l/sec)

$\varepsilon\omega_1 = \omega'_0 - \omega_x$ the perturbation of the natural frequency

$$\delta = \frac{|\omega_0 - \omega_x|}{\omega_0} \text{ (%)}$$

$$\delta' = \frac{|\omega_0 - \omega'_0|}{\omega_0} \text{ (%)}$$

The notation used in Table 33.4 is as follows:

- \mathbf{u}_0^i : exact solution of eigenvectors of the free–free system
- $\mathbf{u}_0^{i'}$: perturbation solution of eigenvectors of the free–free system
- \mathbf{u}_x^i : eigenvector of the constrained system
- $\epsilon \mathbf{u}_1^i$: first-order perturbation of eigenvectors

As can be seen from Table 33.3, the natural frequencies of the free–free system are increased by the hung elastic elements. For example, the frequency of the rigid mode is increased to 1.595950 (1/sec), and the frequency of the first elastic mode is increased by 0.8124%. By modifying the eigensolutions with the perturbation method, the frequency of the rigid mode is reduced to 0.079700 (1/sec), which is nearly equal to zero, and all the frequencies of the elastic modes become almost exact solutions. The results in Table 33.4 show that the mode shapes of the free–free system, $\mathbf{u}_0^{i'}$, are close to the exact solution, \mathbf{u}_0^i .

33.4 Design Sensitivity Analysis of Structural Vibration Modes

In the optimization of structural analysis, the design sensitivity analysis of eigenvalues and eigenvectors plays an essential role. The designer can use this information directly in an interactive computer-aided design procedure as a valuable guide. Significant work has been done in this area (Haug et al., 1985; Adelman and Haftka, 1986; Chen and Pan, 1986; Wang, 1991).

33.4.1 Direct Differential Method for Sensitivity Analysis

Design sensitivity analysis of eigenvalues and eigenvectors will reveal how the changes in some design parameters in the system affect the dynamic characteristics of the structure.

Let $\lambda_{i,j}$ and $\mathbf{u}_{i,j}$ denote the sensitivity of the eigenvalue, λ_i , and the eigenvector, \mathbf{u}_i , respectively, with respect to the design variables b_j ($j = 1, 2, \dots, L$), and let \mathbf{K}_j and \mathbf{M}_j denote the derivative of the stiffness and mass matrices, respectively, with respect to b_j . The design sensitivity of the eigenvalue is

$$\lambda_{i,j} = \mathbf{u}_i^T (\mathbf{K}_j - \lambda_i \mathbf{M}_j) \mathbf{u}_i \quad (33.25)$$

The sensitivity of the eigenvector, $\mathbf{u}_{i,j}$, can be expressed as the following series:

$$\mathbf{u}_{i,j} = \sum_{s=1}^n c_{ijs} \mathbf{u}_s \quad (33.26)$$

where

$$c_{ijs} = \frac{1}{\lambda_i - \lambda_s} \mathbf{u}_s^T (\mathbf{K}_j - \lambda_i \mathbf{M}_j) \mathbf{u}_i, \quad i \neq s, \quad i, s = 1, 2, \dots, n, \quad i \neq s \quad (33.27)$$

$$c_{iji} = -\frac{1}{2} \mathbf{u}_i^T \mathbf{M}_j \mathbf{u}_i \quad (33.28)$$

33.4.2 Perturbation Sensitivity Analysis

Let $\Delta \mathbf{K}$ and $\Delta \mathbf{M}$ denote the increments of the stiffness and the mass matrices resulting from an incremental change of the design variable, Δb_j , and let $\Delta \lambda_i$ and $\Delta \mathbf{u}_i$ denote the corresponding perturbations of the eigenvalue and eigenvector, respectively. The direct differential method of design sensitivity analysis of vibration modes can now be put into perturbation form, approximately as

$$\lambda_{i,j} = \frac{\Delta \lambda_i}{\Delta b_j} \quad (33.29)$$

$$\mathbf{u}_{i,j} = \frac{\Delta \mathbf{u}_i}{\Delta b_j} \quad (33.30)$$

where $\Delta\lambda_i$ and $\Delta\mathbf{u}_i$ can be evaluated by the perturbation formulas presented in this chapter. In practical analysis, the design variables could be the cross-sectional area of the truss members, bending moment of inertia, equivalent torsional moment of inertia of a beam, the thickness of a plate, or other variable. In some complex structures, a mass, m_r , may be placed at a node point and moving in the direction of the r th DoF, or an elastic support with spring stiffness, K_r , may be placed at a certain node point. It is also possible that an elastic connector of stiffness, K_j , might exist between two components. They can also be considered as design variables. In finite element analysis, $\Delta\mathbf{K}$ and $\Delta\mathbf{M}$ are known to be the sum of the element increments, $\Delta\mathbf{K}^e$ and $\Delta\mathbf{M}^e$; thus

$$\Delta\mathbf{K} = \sum_e \Delta\mathbf{K}^e \quad (33.31)$$

$$\Delta\mathbf{M} = \sum_e \Delta\mathbf{M}^e \quad (33.32)$$

Hence, the sensitivity formulas of vibration modes as given above can be transformed into the finite element perturbation form (Chen and Pan, 1986)

$$\lambda_{i,j} = \frac{1}{\Delta b_j} \sum_e \bar{\mathbf{u}}_i^T (\Delta\mathbf{K}^e - \lambda_i \Delta\mathbf{M}^e) \bar{\mathbf{u}}_i \quad (33.33)$$

and

$$\mathbf{u}_{i,j} = \frac{1}{\Delta b_j} \sum_e \left(\sum_{\substack{s=1 \\ s \neq i}}^n \frac{1}{\lambda_i - \lambda_s} \bar{\mathbf{u}}_s^T (\Delta\mathbf{K}^e - \lambda_i \Delta\mathbf{M}^e) \bar{\mathbf{u}}_i \mathbf{u}_s - \frac{1}{2} \bar{\mathbf{u}}_i^T \Delta\mathbf{M}^e \bar{\mathbf{u}}_i \mathbf{u}_i \right) \quad (33.34)$$

In these formulas, the overbar signifies that the eigenvector concerned contains only the components needed for the e th finite element. It is important to observe that, in Equation 33.33 and Equation 33.34, calculations are done on the element basis, and as a result, the calculations are greatly simplified.

Using the shorthand notations

$$\lambda_{i,j}^e = \frac{1}{\Delta b_j} \bar{\mathbf{u}}_i^T \Delta\mathbf{K}^e - \lambda_i \Delta\mathbf{M}^e \bar{\mathbf{u}}_i \quad (33.35)$$

$$\mathbf{u}_{i,j}^e = \frac{1}{\Delta b_j} \left(\sum_{\substack{s=1 \\ s \neq i}}^n \frac{1}{\lambda_i - \lambda_s} \bar{\mathbf{u}}_s^T \Delta\mathbf{K}^e - \lambda_i \Delta\mathbf{M}^e \bar{\mathbf{u}}_i \mathbf{u}_s - \frac{1}{2} \bar{\mathbf{u}}_i^T \Delta\mathbf{M}^e \bar{\mathbf{u}}_i \mathbf{u}_i \right) \quad (33.36)$$

Equation 33.33 and Equation 33.34 can be written as

$$\lambda_{i,j} = \sum_e \lambda_{i,j}^e \quad (33.37)$$

and

$$\mathbf{u}_{i,j} = \sum_e \mathbf{u}_{i,j}^e \quad (33.38)$$

where $\lambda_{i,j}^e$ and $\mathbf{u}_{i,j}^e$ are the design sensitivity of the e th element for the eigenvalue λ_i and the eigenvector \mathbf{u}_i , respectively. Let us consider the following important cases.

For a concentrated mass, m_r , placed at a node point and moved in the direction of the r th DoF, Equation 33.33 and Equation 33.34 become

$$\lambda_{i,r} = \frac{\Delta\lambda_i}{\Delta m_r} = -\lambda_i u_{ir}^2 \quad (33.39)$$

and

$$\mathbf{u}_{i,r} = \frac{\Delta \mathbf{u}_i}{\Delta m_r} = \sum_{\substack{s=1 \\ s \neq i}}^n \frac{-\lambda_i}{\lambda_i - \kappa_s} u_{sr} u_{ir} \mathbf{u}_s - \frac{1}{2} u_{ir}^2 \mathbf{u}_i \quad (33.40)$$

where u_{ir} is the r th element of the i th eigenvector \mathbf{u}_i .

For an elastic connector with stiffness K_j between the r th and the l th DoF of two components, Equation 33.33 and Equation 33.34 become

$$\lambda_{i,j} = \frac{\Delta \lambda_i}{\Delta k_j} = (u_{ir} - u_{il})^2 \quad (33.41)$$

and

$$\mathbf{u}_{i,j} = \frac{\Delta \mathbf{u}_i}{\Delta k_j} = \sum_{\substack{s=1 \\ s \neq i}}^n \frac{1}{\lambda_i - \lambda_s} (u_{sr} u_{ir} - u_{sl} u_{ir} - u_{sr} u_{il} + u_{sl} u_{il}) \mathbf{u}_s \quad (33.42)$$

For an elastic support with spring stiffness K_r placed in the direction of the r th DoF, Equations 33.33 and Equation 33.34 become

$$\lambda_{i,r} = \frac{\Delta \lambda_i}{\Delta k_r} = u_{ir}^2 \quad (33.43)$$

and

$$\mathbf{u}_{i,r} = \frac{\Delta \mathbf{u}_i}{\Delta k_r} = \sum_{\substack{s=1 \\ s \neq i}}^n \frac{1}{\lambda_i - \lambda_s} u_{sr} u_{ir} \mathbf{u}_s \quad (33.44)$$

33.4.3 Numerical Example

The design sensitivity analysis of an automotive chassis is presented here as an illustration of the method.

Example 33.4

The finite element model of an automobile chassis consists of 39 beam elements involving 30 nodal points and 180 DoF (Figure 33.4).

The design variables for the sensitivity analysis of eigenvalues in this example are the equivalent torsional moment of inertia, J , and the bending moment of inertia, I_y , of the beam element of

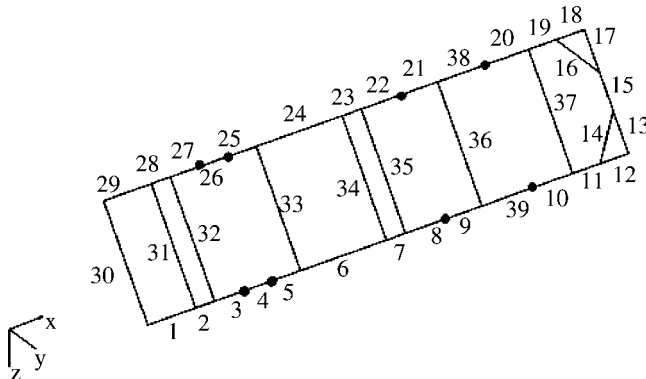


FIGURE 33.4 Finite element model of the automotive chassis for Example 33.4.

TABLE 33.5 Sensitivities of the First Four Chassis Frequencies

1	NE	15	11	19	24	6	37	34	36
	λ_{1J}^e	9.97	5.23	5.23	3.64	3.64	3.34	3.32	3.31
	NE	24	6	23	7	22	8	33	21
	$\lambda_{1I_y}^e$	0.015	0.15×10^{-2}	0.33×10^{-3}	0.33×10^{-3}	0.28×10^{-3}	0.19×10^{-3}	0.11×10^{-3}	0.11×10^{-3}
2	NE	16	14	11	19	18	12	13	17
	λ_{2J}^e	6.67×10^{-2}	0.67×10^{-2}	0.45×10^{-2}	0.45×10^{-2}	0.11×10^{-2}	0.11×10^{-2}	0.53×10^{-3}	0.53×10^{-3}
	NE	38	10	21	9	22	8	24	6
	$\lambda_{2I_y}^e$	2.92	2.92	1.78	1.78	1.49	1.49	1.44	1.44
3	NE	15	19	11	37	31	30	32	1
	λ_{3J}^e	95.9	47.2	47.2	26.5	25.4	25.2	23.8	12.5
	NE	10	38	9	21	8	22	6	24
	$\lambda_{3I_y}^e$	2.96	2.96	1.97	1.97	1.74	1.74	1.70	1.70
4	NE	14	16	19	11	12	18	17	13
	λ_{4J}^e	0.19	0.19	0.12	0.12	0.03	0.03	0.015	0.015
	NE	10	38	39	20	5	25	6	24
	$\lambda_{4I_y}^e$	22.4	22.4	15.7	15.7	11.8	11.8	10.9	10.9

the structure. Results for the sensitivity of eigenvalues with respect to J and I_y are given in Table 33.5, in which NE denotes the number of the element. Only the highest eight values are given, and they are listed in descending order.

From Table 33.5, it is seen that for this particular chassis, the sensitivities of the first natural frequency, $\lambda_{1I_y}^e$, are much smaller than λ_{1J}^e . This indicates that there is very little effect of the change of bending moment of inertia, I_y , of the beams on the vibration of the chassis at its first natural frequency. Thus, we can conclude that the first mode is a torsional mode. Similarly, the results indicate that the third mode is also a torsional mode. On the other hand, the second and the fourth modes are recognized to be bending modes. This information is very useful to the designer when deciding on a change in the design. For example, if he wants to increase the first torsional frequency, the efficient way is for him to increase the equivalent torsional moments of inertia of beam elements 15, 11, 19, 24, 6, and so on.

It should be noted that only the first low-frequency modes are available and can be used as basis vectors of eigenvector derivatives in Equation 33.26. However, modal truncation induces errors, and the errors become significant if more high-frequency modes are truncated. An improvement to truncated modal superposition representation of eigenvector derivatives is presented in the next section.

33.4.4 Concluding Remarks

As can be seen from the numerical examples given above, the matrix perturbation method is an extremely useful tool for fast reanalysis of a modified structure. It is widely used in a range of structural modifications, such as the modification of various types of elements, local modification of structures, sensitivity analysis of vibration modes, and so on. Therefore, matrix perturbation plays an important role in dynamic analysis and optimization of structures.

33.5 High-Accuracy Modal Superposition for Sensitivity Analysis of Modes

The modal superposition method is often used to compute the derivatives of modal vectors. Because of the cost of generating computer solutions for a dynamic analysis, it is impractical to obtain all modes.

Therefore, only the first L low-frequency modes are computed and are used as basis vectors of eigenvector derivatives. However, as noted above, modal truncation induces errors, which can be significant if more high-frequency modes are truncated. An explicit method to improve the truncated modal superposition representation of eigenvector derivatives is presented (Wang, 1991), in which a residual static mode is used to approximate the contribution due to unavailable high-frequency modes (method one).

In this section a more accurate modal superposition method (method two; Chen, 1993a; Liu and Chen, 1994a) than method one is given. In this method, the contribution of the truncated modes to the eigenvector derivatives is expressed exactly, as a convergent series that can be evaluated by a simple iterative procedure.

33.5.1 Method One

The modal sensitivity can be expressed as

$$u_{i,j} = \sum_{s=1}^N c_s u_s = \sum_{j=1}^L c_j \mathbf{u}_j + \mathbf{S}_R \quad (33.45)$$

where

$$\mathbf{S}_R = \sum_{j=L+1}^N c_j \mathbf{u}_j \quad (33.46)$$

Since $\lambda_i \ll \lambda_{L+1}$, Equation 33.46 can be approximated as

$$\mathbf{S}_R \approx \mathbf{S}_{RA} = \bar{\mathbf{H}}_0 - \bar{\mathbf{W}}_0 \quad (33.47)$$

where

$$\bar{\mathbf{H}}_0 = \mathbf{K}^{-1}(-\mathbf{K}_j + \lambda_{i,j} \mathbf{M} + \lambda_i \mathbf{M}_j) \quad (33.48)$$

$$\bar{\mathbf{W}}_0 = \sum_{j=1}^L \frac{1}{\lambda_j} \mathbf{u}_j^T (-\mathbf{K}_j + \lambda_{i,j} \mathbf{M} + \lambda_i \mathbf{M}_j) \mathbf{u}_j \quad (33.49)$$

33.5.2 Method Two

The contribution of $u_{i,j}$, \mathbf{S}_R due to truncated high-frequencies modes is as follows:

$$\mathbf{S}_R = \sum_{j=0}^{\infty} \lambda_i^j (\mathbf{H}_j - \mathbf{W}_j) \quad (33.50)$$

where

$$\mathbf{W}_j = \mathbf{U}_L \mathbf{\Lambda}_L^{-j-1} \mathbf{U}_L^T (-\mathbf{K}_j + \lambda_{i,j} \mathbf{M} + \lambda_i \mathbf{M}_j) \quad (33.51)$$

$$\mathbf{U}_L = [\mathbf{u}_1, \mathbf{u}_2, \dots, \mathbf{u}_L] \quad (33.52)$$

\mathbf{H}_j can be obtained with the following iterative procedure:

$$\left. \begin{aligned} \mathbf{H}_0 &= \mathbf{K}^{-1}(-\mathbf{K}_j + \mathbf{K}_{i,j} \mathbf{M} + \lambda_i \mathbf{M}_j) \\ \mathbf{F}'_{j-1} &= \mathbf{M} \mathbf{H}_{j-1}, \quad j \geq 1 \\ \mathbf{H}_j &= \mathbf{K}^{-1} \mathbf{F}'_{j-1} \end{aligned} \right\} \quad (33.53)$$

Define $\mathbf{S}_R(k)$ as

$$\mathbf{S}_R(k) = \sum_{j=0}^k \lambda_i^j (\mathbf{H}_j - \mathbf{W}_j) \quad (33.54)$$

Using this definition, the given iterative process can be terminated if the following inequality

$$\|\mathbf{S}_R(k) - \mathbf{S}_R(k-1)\|_2 \leq \varepsilon \quad (33.55)$$

is satisfied, where ε is a specified accuracy requirement.

It should be noted that, if only the first term in the series (Equation 33.50) is retained with all the other terms neglected, then method two is reduced to method one. In addition, the series (Equation 33.50) can be used to estimate the errors induced by the modal truncation.

33.6 Sensitivity of Eigenvectors for Free-Free Structures

As can be seen from Equation 33.48 and Equation 33.53, both method one and method two fail to deal with the free-free structures with rigid-body modes because they involve the inversion of the stiffness matrix. However, we can transform the eigenproblem with a singular stiffness matrix into its equivalent eigenproblem with a nonsingular stiffness matrix, in the sense that these two eigenproblems have the same derivatives of eigenvalues and eigenvectors (Liu and Chen, 1994b).

Consider the eigenvalue problem

$$\bar{\mathbf{K}}\bar{\mathbf{u}}_i = \bar{\lambda}_i \bar{\mathbf{M}}\bar{\mathbf{u}}_i \quad (33.56)$$

where

$$\bar{\mathbf{K}} \equiv \mathbf{K} - \mu \mathbf{M} \quad (33.57)$$

Here, μ is a nonzero scalar parameter and $\bar{\mathbf{K}}$ is nonsingular if $\mu \neq \lambda_i$ ($i = 1, 2, \dots, n$)

It can be shown that

$$\bar{\lambda}_i = \lambda_i - \mu \quad (33.58)$$

$$\bar{\mathbf{u}}_i = \mathbf{u}_i, \quad i = 1, 2, \dots, N \quad (33.59)$$

and

$$\frac{d\bar{\lambda}_i}{db} = \frac{d\lambda_i}{db} \quad (33.60)$$

$$\frac{d\bar{\mathbf{u}}_i}{db} = \frac{d\mathbf{u}_i}{db} \quad (33.61)$$

The derivatives $d\mathbf{u}_i/db$ can be obtained from the derivatives $d\bar{\mathbf{u}}_i/db$ of the eigenproblem of Equation 33.56, in which $\bar{\mathbf{K}}$ is nonsingular. In this context, both method one and method two, discussed in Section 33.5.1 and Section 33.5.2, can be applied to deal with the free-free structures with rigid-body modes.

To achieve a faster average convergent speed for all the first m eigenvector derivatives, μ can be determined as

$$\begin{cases} \mu = \frac{\left(\sum_{j=1}^m \lambda_j\right)}{m}, & j = 1, 2, \dots, m \\ \mu \neq \lambda_j, \end{cases} \quad (33.62)$$

33.7 Matrix Perturbation Theory for Repeated Modes

33.7.1 Basic Equations

In this section, let us consider the case of repeated eigenvalues, namely, $\lambda_{0i} = \lambda_{0i+1} = \dots = \lambda_{0i+m-1}$. The system is known as a *degenerate system*. In engineering, many complex and large structures, such as airplanes, rockets, tall towers, bridges, and ocean platforms, often have multiple or cluster eigenvalues. The matrix perturbation for the repeated modes is presented in Haug, et al. (1980), Chen and Pan (1986), Hu (1987), Mills-Curran (1988), Ojalvo (1988), Dailey (1989), Lim et al. (1989) and Shaw and Jayasuriya (1992).

Assume that $\lambda_0 = \lambda_{01} = \lambda_{02} = \dots = \lambda_{0m}$; that is, λ_0 is a repeated eigenvalue with multiplicity equal to m , and $\mathbf{u}_{01}, \mathbf{u}_{02}, \dots, \mathbf{u}_{0m}$ are the eigenvectors associated with λ_0 . Then, a linear combination of \mathbf{u}_{0j} ($j = 1, 2, \dots, m$), denoted as \mathbf{U}_0 , will also be the eigenvector associated with λ_0 :

$$\mathbf{U}_0 = \mathbf{U}_{0m}\boldsymbol{\alpha} \quad (33.63)$$

where

$$\mathbf{U}_{0m} = [\mathbf{u}_{01}, \mathbf{u}_{02}, \dots, \mathbf{u}_{0m}] \quad (33.64)$$

$$\boldsymbol{\alpha}^T \boldsymbol{\alpha} = \mathbf{I} \quad (33.65)$$

and

$$\boldsymbol{\alpha} = [\alpha_1, \alpha_2, \dots, \alpha_m]^T \quad (33.66)$$

Note that $\boldsymbol{\alpha}$ is a constant matrix to be determined.

According to the matrix perturbation method, the eigenvalues and eigenvectors of the structure with repeated eigenvalues for the perturbed structure can be expressed as

$$\boldsymbol{\Lambda}_m = \boldsymbol{\Lambda}_0 + \varepsilon \boldsymbol{\Lambda}_1 \quad (33.67)$$

$$\mathbf{U}_m = \mathbf{U}_{0m}\boldsymbol{\alpha} + \varepsilon(\mathbf{U}_0\mathbf{C}_m + \mathbf{U}_A\mathbf{C}_A) = \mathbf{U}_{0m}\boldsymbol{\alpha} + \varepsilon(\mathbf{U}_{0m}\boldsymbol{\alpha}\mathbf{C}_m + \mathbf{U}_A\mathbf{C}_A) \quad (33.68)$$

where \mathbf{U}_A is the $n \times (n - m)$ modal matrix containing all the eigenvectors except \mathbf{U}_{0m} , $\boldsymbol{\Lambda}_m$ is the $m \times m$ eigenvalue diagonal matrix of the perturbed structure, $\boldsymbol{\Lambda}_1$ is the $m \times m$ diagonal matrix with its diagonal elements equal to the first-order perturbations of eigenvalues, \mathbf{C}_m is an $m \times m$ matrix to be determined, and \mathbf{C}_A is an $(n - m) \times (n - m)$ matrix to be determined.

33.7.2 The First-Order Perturbation of Eigensolutions

$\boldsymbol{\Lambda}_1$ and $\boldsymbol{\alpha}$ can be computed from the following $(m \times m)$ eigenproblem:

$$\mathbf{W}\boldsymbol{\alpha} = \boldsymbol{\alpha}\boldsymbol{\Lambda}_1, \quad \boldsymbol{\alpha}^T \boldsymbol{\alpha} = \mathbf{I} \quad (33.69)$$

where

$$\mathbf{W} = \mathbf{U}_{0m}^T(\mathbf{K}_1 - \lambda_0\mathbf{M}_1)\mathbf{U}_{0m} \quad (33.70)$$

Solving the $m \times m$ eigenproblem of Equation 33.69 can produce $\boldsymbol{\Lambda}_1$ and $\boldsymbol{\alpha}$.

If matrix \mathbf{W} has no repeated eigenvalues, $\boldsymbol{\alpha}$ can be uniquely determined; if matrix \mathbf{W} has repeated eigenvalues, $\boldsymbol{\alpha}$ can be determined using the higher order perturbation equations. Here, we assume that matrix \mathbf{W} has no repeated eigenvalues; that is, $\lambda_{1i} \neq \lambda_{1j}$, ($i \neq j$), where λ_{1k} ($0 < k \leq m$) are the elements of the diagonal matrix $\boldsymbol{\Lambda}_1$.

The matrix \mathbf{C}_A is

$$\mathbf{C}_A = (\boldsymbol{\Lambda}_A - \lambda_0\mathbf{I})^{-1}\mathbf{U}_A^T(\lambda_0\mathbf{M}_1 - \mathbf{K}_1)\mathbf{U}_{0m}\boldsymbol{\alpha} \quad (33.71)$$

The elements of C_m are

$$C_{ij}^m = \frac{R_{ij}}{\lambda_{jm}^{(1)} - \lambda_{im}^{(1)}}, \quad i \neq j, \quad i, j = 1, 2, \dots, m \quad (33.72)$$

where R_{ij} are the elements of \mathbf{R} given by

$$\mathbf{R} = -\boldsymbol{\alpha}^T \mathbf{U}_{0m}^T \mathbf{M}_1 \mathbf{U}_{0m} \boldsymbol{\alpha} \boldsymbol{\Lambda}_1 + \boldsymbol{\alpha}^T \mathbf{U}_{0m} \mathbf{K}_1 \mathbf{U}_A \mathbf{C}_A - \lambda_0 \boldsymbol{\alpha}^T \mathbf{U}_{0m} \mathbf{M}_1 \mathbf{U}_A \mathbf{C}_A - \boldsymbol{\alpha}^T \mathbf{U}_{0m}^T \mathbf{M}_0 \mathbf{U}_A \mathbf{C}_A \boldsymbol{\Lambda}_1 \quad (33.73)$$

and

$$C_{ii}^m = \frac{1}{2} Q_{ii} \quad (33.74)$$

where Q_{ii} is the diagonal elements of \mathbf{Q} , given by

$$\mathbf{Q} = -\boldsymbol{\alpha}^T \mathbf{U}_{0m}^T \mathbf{M}_1 \mathbf{U}_{0m} \boldsymbol{\alpha} \quad (33.75)$$

33.7.3 High-Accuracy Modal Superposition for the First-Order Perturbation of Repeated Modes

In Section 33.5, the high-accuracy modal superposition for the first-order perturbation of eigenvectors of distinct eigenvalues is given. In this section, we extend these methods to the situation with repeated modes.

33.7.3.1 Method One for Computing \mathbf{U}_1

Assuming \mathbf{U}_{AL} and $\boldsymbol{\Lambda}_{AL}$ are the first L modes and eigenvalues excluding the repeated modes, the first-order perturbation of eigenvectors is

$$\mathbf{U}_1 = \mathbf{U}_{0m} \boldsymbol{\alpha} \mathbf{C}_m + \mathbf{U}_{AL} \mathbf{C}_{AL} + \mathbf{S}_R \quad (33.76)$$

$$\mathbf{S}_R = \mathbf{U}_S - [\mathbf{U}_{0m}; \mathbf{U}_{AL}] \text{diag}(\lambda_0^{-1}, \boldsymbol{\Lambda}_{AL}^{-1}) [\mathbf{U}_{0m}; \mathbf{U}_{AL}]^T \mathbf{T} \quad (33.77)$$

where \mathbf{U}_S is the static displacement obtained by

$$\mathbf{K} \mathbf{U}_S = \mathbf{T} \quad (33.78)$$

and

$$\mathbf{T} = \mathbf{M}_0 \mathbf{U}_{0m} \boldsymbol{\alpha} \boldsymbol{\Lambda}_1 + \lambda_0 \mathbf{M}_1 \mathbf{U}_{0m} \boldsymbol{\alpha} - \mathbf{K}_1 \mathbf{U}_{0m} \boldsymbol{\alpha} \quad (33.79)$$

In Equation 33.79, $\boldsymbol{\Lambda}_1$ and $\boldsymbol{\alpha}$ can be obtained from Equation 33.69.

The matrix \mathbf{C}_{AL} is given by

$$\mathbf{C}_{AL} = (\boldsymbol{\Lambda}_{AL} - \lambda_0 \mathbf{I})^{-1} \mathbf{U}_{AL}^T (\lambda_0 \mathbf{M}_1 - \mathbf{K}_1) \mathbf{U}_{0m} \boldsymbol{\alpha} \quad (33.80)$$

and the elements of matrix \mathbf{C}_m are

$$C_{ij}^m = \frac{R_{ij}}{\lambda_{jm}^{(1)} - \lambda_{im}^{(1)}}, \quad i \neq j, \quad i, j = 1, 2, \dots, m \quad (33.81)$$

where \mathbf{R} is given by

$$\mathbf{R} = \boldsymbol{\alpha}^T \mathbf{U}_{0m}^T \mathbf{M}_1 \mathbf{U}_{0m} \boldsymbol{\Lambda}_1 - \boldsymbol{\alpha}^T \mathbf{U}_{0m}^T (\lambda_0 \mathbf{M}_1 - \mathbf{K}_1) (\mathbf{U}_{AL} \mathbf{C}_{AL} + \mathbf{S}_R) - \boldsymbol{\alpha}^T \mathbf{U}_{0m}^T \mathbf{M}_0 \mathbf{S}_R \boldsymbol{\Lambda}_1 \quad (33.82)$$

The diagonal elements of \mathbf{C}_m are

$$C_{ii}^m = \frac{1}{2} Q_{ii} \quad (33.83)$$

where

$$\mathbf{Q} = -\boldsymbol{\alpha}^T \mathbf{U}_{0m}^T \mathbf{M}_1 \mathbf{U}_{0m} \boldsymbol{\alpha} - \boldsymbol{\alpha}^T \mathbf{U}_{0m}^T \mathbf{M}_0 \mathbf{S}_R - \mathbf{S}_R^T \mathbf{M}_0 \mathbf{U}_{0m} \boldsymbol{\alpha} \quad (33.84)$$

33.7.3.2 Method Two for Computing \mathbf{U}_1

The first-order perturbation of eigenvectors can be expressed as

$$\mathbf{U}_1 = \mathbf{U}_{0m} \boldsymbol{\alpha} \mathbf{C}_m + \mathbf{U}_{AL} \mathbf{C}_{AL} + \mathbf{S}_R \quad (33.85)$$

where \mathbf{C}_{AL} can also be calculated using Equation 33.80; that is

$$\mathbf{C}_{AL} = (\boldsymbol{\Lambda}_{AL} - \lambda_0 \mathbf{I})^{-1} \mathbf{U}_{AL}^T (\lambda_0 \mathbf{M}_1 - \mathbf{K}_1) \mathbf{U}_{0m} \boldsymbol{\alpha}$$

and \mathbf{S}_R is given by

$$\mathbf{S}_R = \sum_{j=0}^{\infty} \lambda_0^j (\mathbf{H}_j - \mathbf{W}_j) \quad (33.86)$$

where

$$\mathbf{W}_j = [\mathbf{U}_{0m} \dot{\mathbf{U}}_{AL}] \boldsymbol{\Lambda}_0^{-j-1} [\mathbf{U}_{0m} \dot{\mathbf{U}}_{AL}]^T \mathbf{T}, \quad j \geq 0 \quad (33.87)$$

$$\mathbf{T} = \mathbf{M}_0 \mathbf{U}_{0m} \boldsymbol{\alpha} \boldsymbol{\Lambda}_1 + \lambda_0 \mathbf{M}_1 \mathbf{U}_{0m} \boldsymbol{\alpha} - \mathbf{K}_1 \mathbf{U}_{0m} \boldsymbol{\alpha} \quad (33.88)$$

The iterative method for computing \mathbf{H}_j is as follows:

$$\begin{aligned} \mathbf{H}_0 &= \mathbf{K}^{-1} \mathbf{T}, \\ \mathbf{F}'_{j-1} &= \mathbf{M} \mathbf{H}_{j-1}, \quad j \geq 1 \\ \mathbf{H}_j &= \mathbf{K}^{-1} \mathbf{F}'_{j-1}, \end{aligned} \quad (33.89)$$

This iterative process can be terminated according to the accuracy requirement. If we define $\mathbf{S}_R(k)$ as

$$\mathbf{S}_R(k) = \sum_{j=0}^k \lambda_0^j (\mathbf{H}_j - \mathbf{W}_j) \quad (33.90)$$

the termination condition can be stated as

$$\|\mathbf{S}_R(k) - \mathbf{S}_R(k-1)\|_2 \leq \varepsilon, \quad j = 1, 2, \dots, m \quad (33.91)$$

where ε is a specified accuracy requirement.

The computation method for \mathbf{C}_m in Equation 33.85 is similar to that of Equation 33.81 to Equation 33.84. The only difference is that \mathbf{S}_R in Equation 33.82 and Equation 33.84 can be replaced with $\mathbf{S}_R(k)$ in Equation 33.90.

33.8 Matrix Perturbation Method for Closely Spaced Eigenvalues

The vibration modes with close frequencies, that is, with clusters of frequencies, often occur in certain structural systems including large space structures, multispan beams, and in some nearly periodic structures and symmetric structures. Therefore, it is important here to present the perturbation method for vibration modes with close eigenvalues (Liu, 2000).

The perturbation analysis of close eigenvalues can be transformed into a problem with a repeated eigenvalue, which is equal to the average value of the close eigenvalues (Chen, 1993).

33.8.1 Method One of Perturbation Analysis for Close Eigenvalues

Consider vibration eigenproblem

$$\mathbf{K}_0[\mathbf{U}_0; \dot{\mathbf{U}}_A] = \mathbf{M}_0[\mathbf{U}_0; \dot{\mathbf{U}}_A] \text{diag}(\mathbf{\Lambda}_0, \mathbf{\Lambda}_A) \quad (33.92)$$

$$[\mathbf{U}_0; \dot{\mathbf{U}}_A]^T \mathbf{M}_0[\mathbf{U}_0; \dot{\mathbf{U}}_A] = \mathbf{I} \quad (33.93)$$

where \mathbf{K}_0 and \mathbf{M}_0 are $n \times n$ real symmetric matrices, and $\mathbf{\Lambda}_0$ and \mathbf{U}_0 are the $m \times m$ diagonal matrix of close eigenvalues and the corresponding $n \times m$ modal matrix.

Using the spectral decomposition of \mathbf{K}_0 , the problem can be expressed as

$$\mathbf{K}_0 = \bar{\mathbf{K}}_0 + \varepsilon \delta \mathbf{K}_0 \quad (33.94)$$

where

$$\bar{\mathbf{K}}_0 = \mathbf{M}_0(\lambda_0 \mathbf{U}_0 \mathbf{U}_0^T) \mathbf{M}_0 + \mathbf{M}_0(\mathbf{U}_A \mathbf{\Lambda}_A \mathbf{U}_A^T) \mathbf{M}_0 \quad (33.95)$$

$$\varepsilon \delta \mathbf{K}_0 = \mathbf{M}_0(\mathbf{U}_0(\varepsilon \delta \mathbf{\Lambda}_0) \mathbf{U}_0^T) \mathbf{M}_0 \quad (33.96)$$

$$\varepsilon \delta \mathbf{\Lambda}_0 = \mathbf{\Lambda}_0 - \lambda_0 \mathbf{I} = \mathbf{\Lambda}_0 - \left(\frac{\sum_{i=1}^m \lambda_{0i}}{m} \right) \mathbf{I} \quad (33.97)$$

It can be seen that $\bar{\mathbf{K}}_0$ given by Equation 33.95 satisfies

$$\bar{\mathbf{K}}_0[\mathbf{U}_0; \dot{\mathbf{U}}_A] = \mathbf{M}_0[\mathbf{U}_0; \dot{\mathbf{U}}_A] \text{diag}(\lambda_0 \mathbf{I}, \mathbf{\Lambda}_A) \quad (33.98)$$

$$[\mathbf{U}_0; \dot{\mathbf{U}}_A]^T \mathbf{M}_0[\mathbf{U}_0; \dot{\mathbf{U}}_A] = \mathbf{I} \quad (33.99)$$

This indicates that λ_0 and \mathbf{U}_0 are the repeated eigenvalues and the corresponding eigenvector subspace with multiplicity m of the eigenproblem (Equation 33.92), and $\mathbf{\Lambda}_A$ and \mathbf{U}_A are also the eigensolution of eigenproblem (Equation 33.92).

If $\mathbf{\Lambda}_0 \rightarrow \lambda_0 \mathbf{I}$, $\varepsilon \delta \mathbf{\Lambda}_0 \rightarrow \mathbf{0}$, and $\bar{\mathbf{K}}_0 \rightarrow \mathbf{K}_0$, and if the small parameter modifications $\varepsilon \mathbf{K}_1$ and $\varepsilon \mathbf{M}_1$ are introduced to the matrices \mathbf{K}_0 and \mathbf{M}_0 , the eigenproblem with close eigenvalues becomes

$$(\mathbf{K}_0 + \varepsilon \mathbf{K}_1) \mathbf{U} = (\mathbf{M}_0 + \varepsilon \mathbf{M}_1) \mathbf{U} \mathbf{\Lambda} \quad (33.100)$$

$$\mathbf{U}(\mathbf{M}_0 + \varepsilon \mathbf{M}_1) \mathbf{U}^T = \mathbf{I} \quad (33.101)$$

Substituting Equation 33.94 into Equation 33.100, we obtain

$$(\bar{\mathbf{K}}_0 + \varepsilon \bar{\mathbf{K}}_1) \mathbf{U} = (\mathbf{M}_0 + \varepsilon \mathbf{M}_1) \mathbf{U} \mathbf{\Lambda} \quad (33.102)$$

$$\mathbf{U}(\mathbf{M}_0 + \varepsilon \mathbf{M}_1) \mathbf{U}^T = \mathbf{I} \quad (33.103)$$

where

$$\varepsilon \bar{\mathbf{K}}_1 = \varepsilon \delta \mathbf{K}_0 + \varepsilon \mathbf{K}_1 \quad (33.104)$$

$$\mathbf{\Lambda} = \lambda_0 \mathbf{I} + \varepsilon \mathbf{\Lambda}_1 + \varepsilon^2 \mathbf{\Lambda}_2 + \cdots \quad (33.105)$$

$$\mathbf{U} = \mathbf{U}_0 \alpha + \varepsilon \mathbf{U}_1 + \varepsilon^2 \mathbf{U}_2 + \cdots \quad (33.106)$$

Therefore, the eigenproblem of Equation 33.102 and Equation 33.103 can be considered to be a perturbed eigenproblem with the perturbation matrices equal to $(\delta \mathbf{K}_0 + \mathbf{K}_1)$ and \mathbf{M}_1 , respectively. The eigensolutions, $\mathbf{\Lambda}$ and \mathbf{U} , can be obtained from Equation 33.102 and Equation 33.103 by using the perturbation method for repeated eigenvalues as discussed in Section 33.7. Accordingly, the perturbation problem of modes with close eigenvalues is transformed into one of the repeated eigenvalues.

The complete algorithm for $\mathbf{\Lambda}$ and \mathbf{U} is given below.

- (1) Compute

$$\lambda_0 = \frac{\sum_{i=1}^m \lambda_{0i}}{m}$$

- (2) Compute

$$\mathbf{W} = \mathbf{U}_0^T (\delta \mathbf{K}_0 + \mathbf{K}_1 - \lambda_0 \mathbf{M}_1) \mathbf{U}_0$$

- (3) Solve the eigenvalue problem

$$\mathbf{W} \boldsymbol{\alpha} = \boldsymbol{\alpha} \mathbf{\Lambda}_1$$

$$\boldsymbol{\alpha}^T \boldsymbol{\alpha} = \mathbf{I}$$

- (4) Compute the perturbed eigenvalues of the close eigenvalues

$$\mathbf{\Lambda} = \lambda_0 \mathbf{I} + \mathbf{\Lambda}_1$$

- (5) Compute the new eigenvectors $\mathbf{U}_0 \boldsymbol{\alpha}$ corresponding to λ_0 .

- (6) Compute the matrix \mathbf{C}_A

$$\mathbf{C}_A = (\mathbf{\Lambda}_A - \lambda_0 \mathbf{I})^{-1} \mathbf{U}_A^T (\lambda_0 \mathbf{M}_1 - \mathbf{K}_1 - \delta \mathbf{K}_0) \mathbf{U}_0 \boldsymbol{\alpha}$$

- (7) Compute

$$\mathbf{R} = [R_{ij}]$$

$$\mathbf{R} = -\boldsymbol{\alpha}^T \mathbf{U}_0^T \mathbf{M}_1 \mathbf{U}_0 \boldsymbol{\alpha} \mathbf{\Lambda}_1 - \lambda_0 \boldsymbol{\alpha}^T \mathbf{U}_0^T \mathbf{M}_1 \mathbf{U}_A \mathbf{C}_A - \boldsymbol{\alpha}^T \mathbf{U}_0^T (\delta \mathbf{K}_0 + \mathbf{K}_1) \mathbf{U}_A \mathbf{C}_A - \boldsymbol{\alpha} \mathbf{U}_0^T \mathbf{M}_0 \mathbf{U}_A \mathbf{C}_A \mathbf{\Lambda}_1$$

- (8) Compute

$$\mathbf{C}_m = [C_{ij}^m]$$

$$C_{ij}^m = \frac{R_{ij}}{\lambda_{1j} - \lambda_{1i}}, \quad i \neq j, \quad i, j = 1, 2, \dots, m$$

$$C_{ii}^m = \frac{1}{2} Q_{ii}$$

$$\mathbf{Q} = -\boldsymbol{\alpha}^T \mathbf{U}_0^T \mathbf{M}_1 \mathbf{U}_0 \boldsymbol{\alpha}$$

(9) Compute the perturbed eigenvectors \mathbf{U}

$$\mathbf{U} = \mathbf{U}_0 \boldsymbol{\alpha} + \mathbf{U}_0 \boldsymbol{\alpha} \mathbf{C}_m + \mathbf{U}_A \mathbf{C}_A$$

33.8.2 Method Two of Perturbation Analysis for Close Eigenvalues

Because of the importance of the problem in both theory and practice, we now present method two of perturbation analysis for close eigenvalues, which is equivalent to method one given above.

Using the spectral decomposition of \mathbf{M}_0 , the problem can be expressed as

$$\mathbf{M}_0 = \tilde{\mathbf{M}}_0 + \varepsilon \delta \mathbf{M}_0 \quad (33.107)$$

Then, the following equations hold:

$$\mathbf{K}_0[\mathbf{U}_0; \mathbf{U}_A] = \tilde{\mathbf{M}}_0[\mathbf{U}_0; \mathbf{U}_A] \text{diag}(\lambda_0 \mathbf{I}, \boldsymbol{\Lambda}_A) \quad (33.108)$$

$$[\mathbf{U}_0; \mathbf{U}_A]^T \mathbf{M}_0[\mathbf{U}_0; \mathbf{U}_A] = \mathbf{I} \quad (33.109)$$

where

$$\tilde{\mathbf{M}} = \lambda_0^{-2} \mathbf{K}_0 \mathbf{U}_0 \mathbf{U}_0^T \mathbf{K}_0 + \mathbf{K}_0[\mathbf{U}_A (\boldsymbol{\Lambda}_A^{-1})^2 \mathbf{U}_A^T] \mathbf{K}_0 \quad (33.110)$$

$$\varepsilon \delta \mathbf{M}_0 = \mathbf{K}_0[\mathbf{U}_0 \varepsilon \delta (\boldsymbol{\Lambda}_0^{-1})^2 \mathbf{U}_0^T] \mathbf{K}_0 \quad (33.111)$$

$$\varepsilon \delta \boldsymbol{\Lambda}_0^{-2} = \boldsymbol{\Lambda}_0^{-2} - \lambda_0^{-2} \mathbf{I} \quad (33.112)$$

and

$$\lambda_0 = \frac{\sum_{i=1}^m \lambda_{0i}}{m} \quad (33.113)$$

It can be seen that $\tilde{\mathbf{M}}_0$ and $\varepsilon \delta \mathbf{M}_0$ given by Equation 33.110 and Equation 33.111 satisfy Equation 33.108 and Equation 33.109; that is, λ_0 and \mathbf{U}_0 are the repeated eigenvalues and corresponding modal matrix of Equation 33.108 and Equation 33.109. $\boldsymbol{\Lambda}_A$ and \mathbf{U}_A are the eigenvalue diagonal matrix and the corresponding modal matrix excluding λ_0 and \mathbf{U}_0 , respectively.

If \mathbf{K}_0 and \mathbf{M}_0 are modified to $\mathbf{K}_0 + \varepsilon \mathbf{K}_1$ and $\mathbf{M}_0 + \varepsilon \mathbf{M}_1$, the eigenvalue problem becomes

$$(\mathbf{K}_0 + \varepsilon \mathbf{K}_1) \mathbf{U} = (\mathbf{M}_0 + \varepsilon \mathbf{M}_1) \mathbf{U} \boldsymbol{\Lambda} \quad (33.114)$$

$$\mathbf{U}(\mathbf{M}_0 + \varepsilon \mathbf{M}_1) \mathbf{U}^T = \mathbf{I} \quad (33.115)$$

Substituting Equation 33.107 into Equation 33.114 yields

$$(\mathbf{K}_0 + \varepsilon \mathbf{K}_1) \mathbf{U} = (\tilde{\mathbf{M}}_0 + \varepsilon \tilde{\mathbf{M}}_1) \mathbf{U} \boldsymbol{\Lambda} \quad (33.116)$$

$$\mathbf{U}(\tilde{\mathbf{M}}_0 + \varepsilon \tilde{\mathbf{M}}_1) \mathbf{U}^T = \mathbf{I} \quad (33.117)$$

where

$$\varepsilon \tilde{\mathbf{M}}_1 = \varepsilon \delta \mathbf{M}_0 + \varepsilon \mathbf{M}_1 \quad (33.118)$$

Thus, Equation 33.116 and Equation 33.117 can be considered to be a perturbed eigenproblem with repeated eigenvalues, and the perturbation method for repeated eigenvalues can be used to obtain the perturbed eigensolutions of Equation 33.116 and Equation 33.117:

$$\boldsymbol{\Lambda} = \lambda_0 \mathbf{I} + \varepsilon \boldsymbol{\Lambda}_1 + \cdots \quad (33.119)$$

$$\mathbf{U} = \mathbf{U}_0 \boldsymbol{\alpha} + \varepsilon \mathbf{U}_1 + \cdots \quad (33.120)$$

Example 33.5

For the six-DoF mass–spring system shown in Figure 33.5, the stiffness and mass matrices \mathbf{K}_0 and \mathbf{M}_0 are given by

$$\mathbf{K}_0 = \begin{bmatrix} 1500 & -1000 & & & & \\ -1000 & 1200 & -200 & & & \\ & -200 & 15,200 & -5000 & -5000 & -5000 \\ & & -5000 & 5000 & & \\ & & -5000 & & 5000 & \\ & & -5000 & & & 5000 \end{bmatrix} \text{ (N/m)}$$

$$\mathbf{M}_0 = \text{diag}(200, 300, 50, 20, 20, 20.004) \text{ (kg)}$$

The perturbation eigensolutions are computed for the following three cases:

Case 1

$$\varepsilon \mathbf{K}_1 = \begin{bmatrix} 0 & 0 & 0 & 0 & 0 & 0 \\ 0 & 0 & 0 & 0 & 0 & 0 \\ 0 & 0 & 5 & 0 & -5 & 0 \\ 0 & 0 & 0 & 0 & 0 & 0 \\ 0 & 0 & -5 & 0 & 5 & 0 \\ 0 & 0 & 0 & 0 & 0 & 0 \end{bmatrix} \text{ (N/m)}$$

$$\varepsilon \mathbf{M}_1 = \text{diag}(0, \dots, 0) \text{ (kg)}$$

Case 2

$$\varepsilon \mathbf{K}_1 = \begin{bmatrix} 5.00 & 0 & 0 & 0 & 0 & 0 \\ 0 & 0 & 0 & 0 & 0 & 0 \\ 0 & 0 & 0 & 0 & 0 & 0 \\ 0 & 0 & 0 & 0 & 0 & 0 \\ 0 & 0 & 0 & 0 & 0 & 0 \\ 0 & 0 & 0 & 0 & 0 & 0 \end{bmatrix} \text{ (N/m)}$$

$$\varepsilon \mathbf{M}_1 = \text{diag}(0, 0, 0, 0, 0, 0.5) \text{ (kg)}$$

Case 3

$$\varepsilon \mathbf{K}_1 = \mathbf{0}, \varepsilon \mathbf{M}_1 = \text{diag}(0, 0, 0, 0, 2.0, 0) \text{ (kg)}$$

The unperturbed eigensolutions have a single pair of close eigenvalues given by

$$\Lambda_0 = \text{diag}(249.966642, 250.000000)$$

$$\mathbf{U}_0^T = \begin{bmatrix} 0.00000 & 0.00000 & -0.00012 & -0.091283 & -0.091283 & 0.182560 \\ 0.00000 & 0.00000 & 0.00000 & -0.158114 & 0.158114 & 0.00000 \end{bmatrix}$$

The other unperturbed eigensolutions are as follows:

$$\Lambda_A = \text{diag}(0.594885, 2.478725, 10.234656, 552.175102)$$

U_A

$$= \begin{bmatrix} -0.058595 & -0.027542 & 0.028427 & -0.000001 \\ 0.032047 & -0.027659 & 0.039259 & 0.000127 \\ -0.006732 & 0.074593 & 0.058387 & -0.104793 \\ -0.007020 & 0.075340 & 0.058527 & 0.086699 \\ -0.007020 & 0.075340 & 0.058527 & 0.086699 \\ -0.007020 & 0.075340 & 0.058527 & 0.086667 \end{bmatrix}$$

The perturbed eigensolutions associated with the single pair of close eigenvalues for the three cases are summarized in Table 33.6. These results show that the perturbation analysis of distinct eigenvalues is not only inaccurate but also misleading when applied to close eigenvalues, and that the perturbed eigensolutions given by the present method are in good agreement with the exact solutions.

For example, in Case 3, the eigenvalue errors induced by the present method are reduced to 1.047950 and 0.000000, while the errors induced by the perturbation of distinct eigenvalues are 4.174100 and 3.025595. The eigenvectors obtained by the perturbation method of distinct eigenvalues are not only

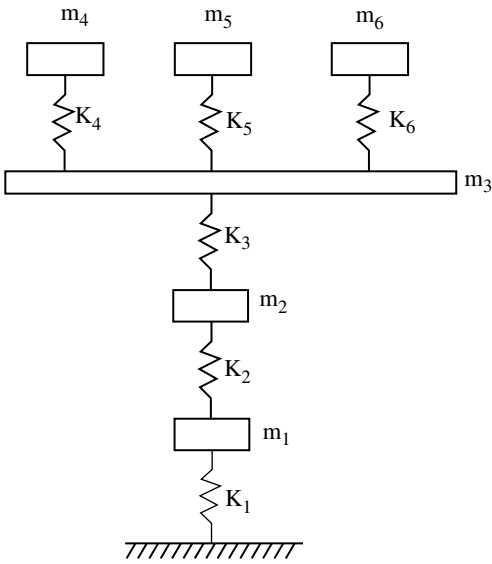


FIGURE 33.5 Six-DoF mass–spring system for Example 33.5.

TABLE 33.6 Comparison of Eigensolutions with Close Eigenvalues

		Exact		Perturbation Method of Distinct Eigenvalues		Perturbation Method of Close Eigenvalues	
Case 1							
Eigenvalues	249.973872	250.159351	250.008324	250.125000	249.973872	250.159451	
Eigenvectors	0.000000	0.000000	0.000000	0.000000	0.000000	0.000000	
	0.000000	0.000000	0.000000	0.000000	0.000000	0.000000	
	0.000018	− 0.000066	− 0.000043	0.000079	0.000011	0.000005	
	0.150492	0.103411	− 0.433574	0.039471	0.150501	− 0.103354	
	0.014254	− 0.181965	0.251058	0.355699	0.014251	0.182015	
	− 0.164753	0.078701	0.182585	− 0.395285	− 0.164745	− 0.078658	
Case 2							
Eigenvalues	243.878599	247.932109	244.759777	246.875000	243.725997	247.908461	
Eigenvectors	0.000000	0.000000	0.000000	0.000000	0.000000	0.000000	
	0.000000	− 0.000004	0.000002	0.000005	0.000000	0.000000	
	− 0.000015	0.001506	− 0.000772	− 0.001976	0.000011	0.000006	
	− 0.000622	0.182090	8.467433	− 5.098718	0.001103	0.183060	
	− 0.155859	− 0.091163	− 8.648272	− 4.784467	− 0.157555	− 0.092069	
	0.156472	− 0.090082	0.180521	9.882118	0.158052	− 0.090988	
Case 3							
Eigenvalues	234.474405	249.975015	245.800915	237.500000	233.326455	249.975015	
Eigenvectors	0.000000	0.000000	0.000000	0.000000	0.000000	0.000000	
	0.000016	0.000000	− 0.000008	0.000021	0.000000	− 0.000000	
	− 0.005558	− 0.000015	0.003030	− 0.007905	0.000006	0.000010	
	− 0.089507	− 0.158189	34.141638	− 19.920531	− 0.091153	0.158189	
	0.175420	0.000158	− 34.321586	− 19.612210	0.182572	− 0.000158	
	− 0.089778	0.158022	0.181586	39.528471	− 0.091415	− 0.158025	

inaccurate but also misleading, while good agreement with the exact eigenvectors has been obtained by the present method.

33.8.3 Concluding Remarks

Perturbation analysis of vibration modes with close frequencies is presented in this section. It can be regarded as a general treatment of perturbation analysis, because the perturbation analysis of both distinct eigenvalues and repeated eigenvalues is contained in the present method. The results obtained by this method allow one to analyze the influence of parameter changes in a system on the dynamic characteristics of the system, which is very important for effective structural design.

33.9 Matrix Perturbation Theory for Complex Modes

In Section 33.2 to Section 33.8, the matrix perturbation for real modes of systems with real symmetric mass and stiffness matrices, \mathbf{M} and \mathbf{K} , was given. However, in many engineering problems such as systems with nonproportional damping (see Chapter 3 and Chapter 19), dynamic systems under nonconservative forces, analysis of aero-elastic flutter, and structural vibration control systems, the system matrices are not symmetric and may not be diagonalizable. In this case, the matrix perturbation for real modes cannot be used, and we must use the matrix perturbation for complex modes (Murthy and Haftka, 1988; Chen, 1993; Liu, 1999; Adhikari and Friswell, 2001). In the following, we assume that the system is not defective; that is, the system has a complete eigenvector set to span the eigenspace. The discussion in this chapter is limited to the nondefective systems.

33.9.1 Basic Equations

The vibration equation of a linear system with n -DoFs is given by

$$\mathbf{M}\ddot{\mathbf{q}} + \mathbf{C}\dot{\mathbf{q}} + \mathbf{K}\mathbf{q} = \mathbf{Q}(t) \quad (33.121)$$

where the matrices \mathbf{M} , \mathbf{C} , and \mathbf{K} , are assumed to be real and unsymmetric. The free vibration equation of the system is

$$\mathbf{M}\ddot{\mathbf{q}} + \mathbf{C}\dot{\mathbf{q}} + \mathbf{K}\mathbf{q} = \mathbf{0} \quad (33.122)$$

The corresponding right eigenvalues problem is

$$(\mathbf{M}s^2 + \mathbf{C}s + \mathbf{K})\mathbf{x} = \mathbf{0} \quad (33.123)$$

and its adjoint eigenvalue problem is

$$\begin{aligned} (\mathbf{M}s^2 + \mathbf{C}s + \mathbf{K})^T \mathbf{y} &= \mathbf{0} \\ \mathbf{y}^T (\mathbf{M}s^2 + \mathbf{C}s + \mathbf{K}) &= \mathbf{0} \end{aligned} \quad (33.124)$$

It is common in literature to call \mathbf{y} the *left eigenvector*, while \mathbf{x} in the original system, a column vector, is called the *right eigenvector*.

Let us introduce a state vector

$$\mathbf{u} = \begin{Bmatrix} s\mathbf{x} \\ \mathbf{x} \end{Bmatrix} = \mathbf{T}\mathbf{x} \quad (33.125)$$

where \mathbf{T} is the state transformation matrix

$$\mathbf{T} = \begin{Bmatrix} s\mathbf{I} \\ \mathbf{I} \end{Bmatrix} \quad (33.126)$$

Similarly, we introduce the state vector

$$\mathbf{v} = \begin{Bmatrix} s\mathbf{y} \\ \mathbf{y} \end{Bmatrix} = \mathbf{T}\mathbf{y} \quad (33.127)$$

Hence, Equations 33.123 and Equation 33.124 become

$$(\mathbf{A}s + \mathbf{B})\mathbf{u} = \mathbf{0} \quad (33.128)$$

$$(\mathbf{A}s + \mathbf{B})^T \mathbf{v} = \mathbf{0} \quad (33.129)$$

or

$$\mathbf{v}^T (\mathbf{A}s + \mathbf{B}) = \mathbf{0}$$

where

$$\mathbf{A} = \begin{bmatrix} -\mathbf{C} & -\mathbf{K} \\ \mathbf{I} & \mathbf{0} \end{bmatrix}$$

$$\mathbf{B} = \begin{bmatrix} \mathbf{M} & \mathbf{0} \\ \mathbf{0} & \mathbf{I} \end{bmatrix}$$

It is well known that the eigenvalues of the adjoint eigenproblem (Equation 33.129) are identical to that of the original eigenproblem (Equation 33.128). The *characteristic equation* is

$$\det(\mathbf{A} + s\mathbf{B}) = 0$$

This characteristic determinant is a polynomial of $2n$ order in s , and $2n$ eigenvalues s_i ($i = 1, 2, \dots, 2n$) can be found in the complex domain. The left and right modal vectors, \mathbf{v}_i and \mathbf{u}_i , corresponding to s_i satisfy

$$\mathbf{A}\mathbf{u}_i = s_i\mathbf{B}\mathbf{u}_i \quad (33.130)$$

and

$$\mathbf{A}^T \mathbf{v}_i = s_i \mathbf{B}^T \mathbf{v}_i \quad (33.131)$$

The *orthogonality conditions* are

$$\mathbf{v}_j^T \mathbf{B}\mathbf{u}_i = \mathbf{0} \quad (33.132)$$

$$\mathbf{v}_j^T \mathbf{A}\mathbf{u}_i = \mathbf{0} \quad (33.133)$$

The *normalization conditions* are

$$\mathbf{v}_i^T \mathbf{B}\mathbf{u}_i = 1$$

$$\mathbf{u}_i^T \mathbf{B}\mathbf{u}_i = 1 \quad (33.134)$$

Therefore, the orthogonality conditions can be written as

$$\mathbf{v}_j^T \mathbf{B}\mathbf{u}_i = \delta_{ij}$$

$$\mathbf{v}_j^T \mathbf{A}\mathbf{u}_i = s_i \delta_{ij} \quad (33.135)$$

33.9.2 Matrix Perturbation Method for Distinct Modes

If small changes are made on the structural parameters, the mass, damping, and stiffness matrices of the system also have small changes given by

$$\begin{aligned} \mathbf{M} &= \mathbf{M}_0 + \varepsilon \mathbf{M}_1 \\ \mathbf{C} &= \mathbf{C}_0 + \varepsilon \mathbf{C}_1 \\ \mathbf{K} &= \mathbf{K}_0 + \varepsilon \mathbf{K}_1 \end{aligned} \quad (33.136)$$

and we have

$$\mathbf{A} = \mathbf{A}_0 + \varepsilon \mathbf{A}_1 \quad (33.137)$$

$$\mathbf{B} = \mathbf{B}_0 + \varepsilon \mathbf{B}_1 \quad (33.138)$$

where ε is a small parameter.

In the following, we first consider the case of distinct eigenvalues, s_{0i} , of the original system. According to the matrix perturbation theory, the eigenvalues and eigenvectors can be expressed as a power series in ε , that is

$$\mathbf{S} = \mathbf{S}_0 + \varepsilon \mathbf{S}_1 + \varepsilon^2 \mathbf{S}_2 + \cdots \quad (33.139)$$

$$\mathbf{U} = \mathbf{U}_0 + \varepsilon \mathbf{U}_1 + \varepsilon^2 \mathbf{U}_2 + \cdots \quad (33.140)$$

$$\mathbf{V} = \mathbf{V}_0 + \varepsilon \mathbf{V}_1 + \varepsilon^2 \mathbf{V}_2 + \cdots \quad (33.141)$$

where \mathbf{S}_0 , \mathbf{U}_0 , and \mathbf{V}_0 are the eigensolutions of the original system; \mathbf{S}_1 , \mathbf{U}_1 , and \mathbf{V}_1 are the first-order perturbations of eigensolutions; and \mathbf{S}_2 , \mathbf{U}_2 , and \mathbf{V}_2 the second-order perturbations.

\mathbf{U}_1 can be expressed as a linear combination of the right eigenvectors of the original system as

$$\mathbf{U}_1 = \mathbf{U}_0 \mathbf{C}^1 \quad (33.142)$$

where \mathbf{C}^1 is to be the determined matrix given by

$$C_{ij}^1 = \frac{1}{S_{0j} - S_{0i}} P_{ij}^1, \quad j \neq i, \quad i, j = 1, 2, \dots \quad (33.143)$$

Also

$$\mathbf{S}_1 = \text{diag}(P_{11}^1, P_{22}^1, \dots) \quad (33.144)$$

where P_{ij}^1 are the elements of \mathbf{P}^1 given by

$$\mathbf{P}^1 = \mathbf{V}_0^T (-\mathbf{A}_1 \mathbf{U}_0 + \mathbf{B}_1 \mathbf{U}_0 \mathbf{S}_0) \quad (33.145)$$

The \mathbf{V}_1 can be expressed as the expansion of \mathbf{V}_0

$$\mathbf{V}_1 = \mathbf{V}_0 \mathbf{D}^1 \quad (33.146)$$

where \mathbf{D}^1 is to be the determined coefficient matrix given by

$$D_{ij}^1 = \frac{1}{S_{0j} - S_{0i}} R_{ij}^1, \quad j \neq i, \quad i, j = 1, 2, \dots \quad (33.147)$$

and R_{ij}^1 are the nondiagonal elements of \mathbf{R}^1

$$\mathbf{R}^1 = \mathbf{U}_0^T (\mathbf{B}_1^T \mathbf{V}_0 \mathbf{S}_0 - \mathbf{A}_1^T \mathbf{V}_0) \quad (33.148)$$

If the modification of the parameter is fairly large, the second-order perturbation must be used to obtain high accuracy. According to the expansion theorem, the second-order perturbation of eigenvectors, \mathbf{U}_2 , can be expressed as

$$\mathbf{U}_2 = \mathbf{U}_0 \mathbf{C}^2 \quad (33.149)$$

In a similar manner, \mathbf{S}_2 and the elements C_{ij}^2 can be obtained as

$$\mathbf{S}_2 = \text{diag}(P_{11}^2, P_{22}^2, \dots) \quad (33.150)$$

$$C_{ij}^2 = \frac{1}{S_{0j} - S_{0i}} P_{ij}^2, \quad j \neq i, i, \quad j = 1, 2, \dots \quad (33.151)$$

where P_{ij}^2 are the nondiagonal elements of \mathbf{P}^2

$$\mathbf{P}^2 = \mathbf{V}_0^T \mathbf{B}_0 \mathbf{U}_1 \mathbf{S}_1 + \mathbf{V}_0^T \mathbf{B}_1 \mathbf{U}_0 \mathbf{S}_1 + \mathbf{V}_0^T \mathbf{B}_1 \mathbf{U}_1 \mathbf{S}_0 - \mathbf{V}_0^T \mathbf{A}_1 \mathbf{U}_1 \quad (33.152)$$

\mathbf{V}_2 can be expressed as

$$\mathbf{V}_2 = \mathbf{V}_0 \mathbf{D}^2 \quad (33.153)$$

where \mathbf{D}^2 is to be the determined coefficient matrix given by

$$D_{ij}^2 = \frac{1}{S_{0j} - S_{0i}} R_{ij}^2, \quad j \neq i, \quad i, j = 1, 2, \dots \quad (33.154)$$

and R_{ij}^2 are the nondiagonal elements of \mathbf{R}^2

$$\mathbf{R}^2 = \mathbf{U}_0^T (\mathbf{B}_0^T \mathbf{V}_1 \mathbf{S}_1 + \mathbf{B}_1^T \mathbf{V}_0 \mathbf{S}_1 + \mathbf{B}_1^T \mathbf{V}_1 \mathbf{S}_0 - \mathbf{A}_1^T \mathbf{V}_1) \quad (33.155)$$

If $j = i$, the coefficients C_{ii}^1 , D_{ii}^1 , C_{ii}^2 , and D_{ii}^2 can be computed as

$$C_{ii}^1 = \frac{-1}{\mathbf{u}_{0i}^T (\mathbf{B}_0 + \mathbf{B}_0^T) \mathbf{u}_{0i}} \left(\mathbf{u}_{0i}^T \mathbf{B}_1 \mathbf{u}_{0i} + \sum_{\substack{j=1 \\ j \neq i}}^n C_{ij} \mathbf{u}_{0j}^T (\mathbf{B}_0 + \mathbf{B}_0^T) \mathbf{u}_{0i} \right) \quad (33.156)$$

$$D_{ii}^1 = Q_{ii}^1 - C_{ii}^1 \quad (33.157)$$

where Q_{ii}^1 is the diagonal element of \mathbf{Q}_1

$$\mathbf{Q}_1 = -\mathbf{V}_0^T \mathbf{B}_1 \mathbf{U}_0 \quad (33.158)$$

$$C_{ii}^2 = \frac{-\mathbf{u}_{1i}^T \mathbf{B}_0 \mathbf{u}_{1i} + \mathbf{u}_{0i}^T \mathbf{B}_1 \mathbf{u}_{1i} + \mathbf{u}_{1i}^T \mathbf{B}_1 \mathbf{u}_{0i} - \sum_{\substack{j=1 \\ j \neq i}}^n C_{ij} \mathbf{u}_{0j}^T (\mathbf{B}_0 + \mathbf{B}_0^T) \mathbf{u}_{0i}}{\mathbf{u}_{0i}^T (\mathbf{B}_0 + \mathbf{B}_0^T) \mathbf{u}_{0i}} \quad (33.159)$$

$$D_{ii}^2 = Q_{ii}^2 - C_{ii}^2 \quad (33.160)$$

and Q_{ii}^2 is the diagonal element of \mathbf{Q}^2

$$\mathbf{Q}^2 = -\mathbf{V}_0^T \mathbf{B}_0 \mathbf{U}_1 - \mathbf{V}_1^T \mathbf{B}_0 \mathbf{U}_1 - \mathbf{V}_1^T \mathbf{B}_1 \mathbf{U}_0 \quad (33.161)$$

33.9.3 High-Accuracy Modal Superposition for Eigenvector Derivatives

For a large-scale structure, only a small number of the first lower L modes are extracted, and the higher modes are truncated in order to reduce the computational cost. The modal superposition method may not only give inaccurate result, but also may be misleading if the truncation is considerable. In this section, we give a high-accuracy modal superposition method for derivatives of the complex mode of nonsymmetric matrices.

33.9.3.1 Improved Modal Superposition

An improved modal superposition (IMS) to reduce the computation errors by modal truncation was proposed (Lim et al., 1989). The derivatives of modes can be expressed as

$$\frac{\partial \mathbf{u}_i}{\partial \mathbf{b}} = \bar{\alpha}_{ii} \mathbf{u}_i + \bar{z}_i \quad (33.162)$$

$$\bar{z}_i = \sum_{\substack{j=1 \\ j \neq i}}^L \frac{\mathbf{v}_j^T \mathbf{F}_i}{S_i - S_j} \mathbf{u}_j + \mathbf{A}^{-1} \mathbf{F}_i + \sum_{j=1}^L \frac{\mathbf{v}_j^T \mathbf{F}_i}{S_j} \mathbf{u}_j \quad (33.163)$$

$$\mathbf{F}_i = \left(\frac{\partial \mathbf{A}}{\partial \mathbf{b}} - \frac{\partial S_i}{\partial \mathbf{b}} \mathbf{B} - S_i \frac{\partial \mathbf{B}}{\partial \mathbf{b}} \right) \mathbf{u}_i \quad (33.164)$$

where $\mathbf{A}^{-1}\mathbf{F}_i$ is the contribution of the truncated higher modes to the derivatives of modes, as given by

$$\bar{\alpha}_{ii} = -\frac{1}{2} \left(\mathbf{u}_i^T \frac{\partial \mathbf{B}}{\partial \mathbf{b}} \mathbf{u}_i + \mathbf{u}_i^T \mathbf{B} \bar{\mathbf{z}}_i + \bar{\mathbf{z}}_i^T \mathbf{B} \mathbf{u}_i \right) \quad (33.165)$$

33.9.3.2 High-Accuracy Modal Superposition

Assume that the eigenvalues are ordered according to their modular magnitude, and satisfy the following condition:

$$|S_i| < |S_j|, \quad j > L \quad (33.166)$$

The derivatives of modes can be expressed as

$$\frac{\partial \mathbf{u}_i}{\partial \mathbf{b}} = \bar{\alpha}_{ii} \mathbf{u}_i + \bar{\mathbf{z}}_i = \bar{\alpha}_{ii} \mathbf{u}_i + \mathbf{z}_{iL} + \mathbf{z}_{iH} \quad (33.167)$$

where

$$\bar{\mathbf{z}}_i = \mathbf{z}_{iL} + \mathbf{z}_{iH} \quad (33.168)$$

$$\mathbf{z}_{iL} = \sum_{\substack{j=1 \\ j \neq i}}^L \frac{\mathbf{v}_j^T \mathbf{F}_i}{S_i - S_j} \mathbf{u}_j \quad (33.169)$$

$$\mathbf{z}_{iH} = - \sum_{j=1}^K \left(\mathbf{A}^{-1} (\mathbf{B} \mathbf{A}^{-1})^{j-1} - \mathbf{U}_L ((\mathbf{S}_L)^{-1})^j \mathbf{V}_L^T \right) \mathbf{F}_i \quad (33.170)$$

Also, $\bar{\alpha}_{ii}$ can be obtained from Equation 33.165, and K denotes the number of terms used in series (Equation 33.170).

It can be shown that for $K = 1$, Equation 33.167 is equivalent to Equation 33.162.

33.9.3.3 Numerical Example

Example 33.6

Consider a 20-DoF system, as shown in Figure 33.6, with the parameters given by

$$m_1 = m_2 = \cdots = m_{19} = 2m, \quad m_{20} = m = 1.0 \text{ kg}$$

$$k_1 = k_2 = \cdots = k_{21} = 1.0 \times 10^3 \text{ N/m}$$

$$c_1 = c_2 = \cdots = c_7 = 3c, \quad c_8 = c_9 = \cdots = c_{14} = 2c$$

$$c_{15} = c_{16} = \cdots = c_{21} = c = 0.1 \text{ N sec/m}$$

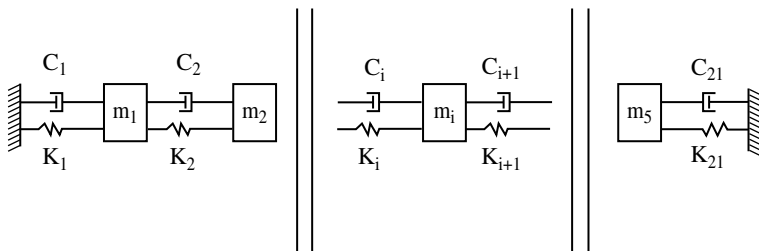


FIGURE 33.6 The 20-DoF system for Example 33.6.

TABLE 33.7 Errors of Eigenvector Derivatives (%)

Modes used		TMS	IMS	HAMS		
				2	3	4
$\partial u_1/\partial b_1$	4	60.18	13.14	1.41	0.01	0.00
	8	26.66	1.01	0.03	0.00	0.00
	12	16.76	0.66	0.01	0.00	0.00
$\partial u_1/\partial b_1$	4	101.00	50.94	27.72	7.64	1.51
	8	48.65	10.32	1.29	0.38	0.03
	12	23.98	3.37	0.35	0.06	0.01
$\partial u_1/\partial b_1$	4	69.74	14.82	3.07	0.02	0.00
	8	26.60	1.39	0.23	0.00	0.00
	12	25.92	0.85	0.12	0.00	0.00
$\partial u_1/\partial b_1$	4	90.63	43.79	21.33	9.01	2.00
	8	44.86	6.65	1.56	0.35	0.04
	12	23.76	3.23	0.37	0.11	0.02
$\partial u_1/\partial b_1$	4	72.52	15.07	8.46	1.11	0.03
	8	37.95	1.22	0.57	0.03	0.00
	12	28.54	0.52	0.03	0.00	0.00
$\partial u_1/\partial b_1$	4	63.33	9.19	1.92	0.42	0.00
	8	27.56	0.75	0.49	0.21	0.00
	12	25.00	0.47	0.15	0.01	0.00

For the purpose of comparison, the errors of the truncation modal superposition (TMS), the IMS, and the high-accuracy superposition (HAMS) in computing the derivatives of eigenvectors are listed in Table 33.7.

For the sake of simplicity, the errors of eigenvector derivatives are represented by

$$\left| \left(\frac{\partial u_i}{\partial b_j} \right)_\varepsilon - \left(\frac{\partial u_i}{\partial b_j} \right)_\alpha \right|$$

where $(\partial u_i/\partial b_j)_\varepsilon$ denotes the exact solution and $(\partial u_i/\partial b_j)_\alpha$ denotes those obtained by the three methods presented above. In the computation of the eigenvector derivatives, the parameters m_1 and m_{10} are functions of the design variable b_1 , the parameters c_8 and c_{15} are functions of design variable b_2 , and K denotes the number of terms used in series (Equation 33.170).

The results in Table 33.7 confirm that the solution accuracy of the high-accuracy modal superposition is much higher than that of the TMS and the IMS. For example, if only the first four modes are used, the errors of $\partial u_2/\partial b_1$ are 101.00 and 50.94% for the truncated modal superposition and the IMS, and the errors are reduced to about 27.27, 7.64, and 1.51% for the high-accuracy modal superposition. If the first 12 modes are used, the error of $\partial u_1/\partial b_1$ is 16.76% for the truncated modal superposition, and the errors are reduced to 0.01, 0.00 and 0.00% for the case of $K = 2, 3, 4$ in the series (Equation 33.170), where the first four modes are used, respectively.

33.9.4 Matrix Perturbation for Repeated Eigenvalues of Nondefective Systems

33.9.4.1 Basic Equation

Consider a system having repeated eigenvalues, $S_0 = S_1 = \cdots = S_{0m}$, with multiplicity m , and the corresponding right and left modal matrices

$$\mathbf{U}_{0m} = [\mathbf{u}_{01} \quad \mathbf{u}_{02} \quad \cdots \quad \mathbf{u}_{0m}] \quad (33.171)$$

$$\mathbf{V}_{0m} = [\mathbf{v}_{01} \quad \mathbf{v}_{02} \quad \cdots \quad \mathbf{v}_{0m}] \quad (33.172)$$

the remaining eigenvalues being distinct.

The repeated eigenvalues satisfy the following equations:

$$\mathbf{A}_0 \mathbf{U}_{0m} = \mathbf{B}_0 \mathbf{U}_{0m} \mathbf{S}_0 \quad (33.173)$$

$$\mathbf{A}_0^T \mathbf{V}_{0m} = \mathbf{B}_0^T \mathbf{V}_{0m} \mathbf{S}_0 \quad (33.174)$$

$$\mathbf{V}_{0m}^T \mathbf{B}_0 \mathbf{U}_{0m} = \mathbf{I} \quad (33.175)$$

$$\mathbf{u}_{0i}^T \mathbf{B}_0 \mathbf{u}_{0i} = 1 \quad (33.176)$$

If small changes are made to the parameters, we have

$$\mathbf{A} = \mathbf{A}_0 + \varepsilon \mathbf{A}_1 \quad (33.177)$$

$$\mathbf{B} = \mathbf{B}_0 + \varepsilon \mathbf{B}_1 \quad (33.178)$$

The eigenvalues and eigenvectors of the perturbed system can be expressed as power series expansions in ε :

$$\mathbf{S}_m = \mathbf{S}_0 + \varepsilon \mathbf{S}_1 + \varepsilon^2 \mathbf{S}_2 + \cdots \quad (33.179)$$

$$\mathbf{U}_m = \mathbf{U}_0 + \varepsilon \mathbf{U}_1 + \varepsilon^2 \mathbf{U}_2 + \cdots \quad (33.180)$$

$$\mathbf{V}_m = \mathbf{V}_0 + \varepsilon \mathbf{V}_1 + \varepsilon^2 \mathbf{V}_2 + \cdots \quad (33.181)$$

where

$$\mathbf{U}_0 = \mathbf{U}_{0m} \boldsymbol{\alpha} \quad (33.182)$$

$$\mathbf{V}_0 = \mathbf{V}_{0m} \boldsymbol{\beta} \quad (33.183)$$

and $\alpha_{m \times m}$ and $\beta_{m \times m}$ are to be determined coefficient matrices.

33.9.4.2 The First-Order Perturbation of Eigenvalues

The first-order perturbation diagonal matrix, \mathbf{S}_1 , of the repeated eigenvalues and the coefficient matrix, $\boldsymbol{\alpha}$, can be obtained from the equations:

$$\mathbf{W} \boldsymbol{\alpha} = \boldsymbol{\alpha} \mathbf{S}_1 \quad (33.184)$$

$$\mathbf{W}^T \boldsymbol{\beta} = \boldsymbol{\beta} \mathbf{S}_1 \quad (33.185)$$

$$\mathbf{W} = \mathbf{V}_{0m}^T (\mathbf{A}_1 - \mathbf{S}_0 \mathbf{B}_1) \mathbf{U}_{0m} \quad (33.186)$$

and the normalization conditions

$$\boldsymbol{\alpha}^T \boldsymbol{\alpha} = \mathbf{I} \quad (33.187)$$

$$\boldsymbol{\beta}^T \boldsymbol{\alpha} = \mathbf{I} \quad (33.188)$$

If matrix \mathbf{W} has no repeated eigenvalues, $\boldsymbol{\alpha}$ and $\boldsymbol{\beta}$ can be uniquely determined. If \mathbf{W} has repeated eigenvalues, we must consider the higher order perturbation equations for determining $\boldsymbol{\alpha}$ and $\boldsymbol{\beta}$. Here, we assume that S_{1i} are distinct eigenvalues, that is, $S_{1i} \neq S_{1j}$ ($i \neq j$), where S_{1i} are the diagonal elements of \mathbf{S}_1 .

33.9.4.3 The First-Order Perturbation of Eigenvectors

According to the modal expansion theorem, the first-order perturbation of the right and left eigenvectors, \mathbf{U}_1 and \mathbf{V}_1 , can be expressed as

$$\mathbf{U}_1 = \mathbf{U}_{0m} \boldsymbol{\alpha} \mathbf{C}_m^1 + \mathbf{U}_A \mathbf{C}_A^1 \quad (33.189)$$

$$\mathbf{V}_1 = \mathbf{V}_{0m} \boldsymbol{\beta} \mathbf{D}_m^1 + \mathbf{V}_A \mathbf{D}_A^1 \quad (33.190)$$

where \mathbf{C}_m^1 and \mathbf{C}_A^1 are coefficient matrices which are to be determined, and \mathbf{U}_A and \mathbf{V}_A are the right and left modal matrices corresponding to the distinct eigenvalues:

$$\mathbf{C}_A^1 = (\mathbf{S}_A - \mathbf{S}_0)^{-1} \mathbf{V}_A^T (\mathbf{S}_0 \mathbf{B}_1 - \mathbf{A}_1) \mathbf{U}_{0m} \alpha \quad (33.191)$$

$$\mathbf{D}_A^1 = (\mathbf{S}_A - \mathbf{S}_0)^{-1} \mathbf{U}_A^T (\mathbf{S}_0 \mathbf{B}_1^T - \mathbf{A}_1^T) \mathbf{V}_{0m} \beta \quad (33.192)$$

The elements of matrix \mathbf{C}_m^1 can be computed by

$$C_{mij}^1 = \frac{R_{ij}^1}{\lambda_{1j} - \lambda_{1i}}, \quad i \neq j, \quad i, j = 1, 2, \dots, m \quad (33.193)$$

where R_{ij}^1 are the nondiagonal elements of \mathbf{R}^1 :

$$\mathbf{R}^1 = \beta^T \mathbf{V}_{0m}^T \mathbf{B}_0 \mathbf{U}_A \mathbf{C}_A^1 \mathbf{S}_1 + \beta^T \mathbf{V}_{0m}^T \mathbf{B}_1 \mathbf{U}_{0m} \alpha \mathbf{S}_1 + \beta^T \mathbf{V}_{0m}^T \mathbf{B}_1 \mathbf{U}_A \mathbf{C}_A^1 \mathbf{S}_0 - \beta^T \mathbf{V}_{0m}^T \mathbf{A}_1 \mathbf{U}_A \mathbf{C}_A^1 \quad (33.194)$$

$$C_{mii}^1 = \frac{-1}{\mathbf{u}_{0i}^T (\mathbf{B}_0 + \mathbf{B}_0^T) \mathbf{u}_{0i}} \left(\mathbf{u}_{0i}^T \mathbf{B}_1 \mathbf{u}_{0i} + \sum_{\substack{j=1 \\ j \neq i}}^m c_{mij}^1 \mathbf{u}_{0j}^T (\mathbf{B}_0 + \mathbf{B}_0^T) \mathbf{u}_{0i} + \sum_{j=m+1}^n c_{Aij}^1 \mathbf{u}_{0j}^T (\mathbf{B}_0 + \mathbf{B}_0^T) \mathbf{u}_{0i} \right) \quad (33.195)$$

$$D_{mij}^1 = \frac{R_{ij}^2}{S_{1j} - S_{1i}}, \quad i \neq j, \quad i, j = 1, 2, \dots, m \quad (33.196)$$

where R_{ij}^2 are the nondiagonal elements of \mathbf{R}^2 :

$$\mathbf{R}^2 = \alpha^T \mathbf{U}_{0m}^T \mathbf{B}_0 \mathbf{V}_A \mathbf{D}_A^1 \mathbf{S}_1 + \alpha^T \mathbf{U}_{0m}^T \mathbf{B}_1^T \mathbf{V}_{0m} \beta \mathbf{S}_1 + \alpha^T \mathbf{U}_{0m}^T \mathbf{B}_1^T \mathbf{V}_A \mathbf{D}_A^1 \mathbf{S}_0 - \alpha^T \mathbf{U}_{0m}^T \mathbf{A}_1^T \mathbf{V}_A \mathbf{D}_A^1 \quad (33.197)$$

$$D_{mii}^1 = Q_{ii}^2 - C_{mii}^1 \quad (33.198)$$

where Q_{ii}^2 are the diagonal elements of \mathbf{Q}^2 :

$$\mathbf{Q}^2 = -\beta^T \mathbf{V}_{0m}^T \mathbf{B}_1 \mathbf{U}_{0m} \alpha \quad (33.199)$$

33.9.5 Matrix Perturbation for Close Eigenvalues of Unsymmetric Matrices

Assume that \mathbf{S}_0 is a diagonal matrix with m close eigenvalues; $\mathbf{U}_{0n \times m}$ and $\mathbf{V}_{0n \times m}$ are the corresponding right and left eigenvectors matrices; \mathbf{S}_A is the remaining distinct eigenvalue diagonal matrix; $\mathbf{U}_{An \times (n-m)}$ and $\mathbf{V}_{An \times (n-m)}$ are the corresponding right and left eigenvector matrices. They satisfy the following equations:

$$\mathbf{A}_0 [\mathbf{U}_0; \mathbf{U}_A] = \mathbf{B}_0 [\mathbf{U}_0; \mathbf{U}_A] \text{diag}(\mathbf{S}_0, \mathbf{S}_A) \quad (33.200)$$

$$\mathbf{A}_0^T [\mathbf{V}_0; \mathbf{V}_A] = \mathbf{B}_0^T [\mathbf{V}_0; \mathbf{V}_A] \text{diag}(\mathbf{S}_0, \mathbf{S}_A) \quad (33.201)$$

$$[\mathbf{V}_0; \mathbf{V}_A]^T \mathbf{B}_0 [\mathbf{U}_0; \mathbf{U}_A] = \mathbf{I} \quad (33.202)$$

$$\mathbf{u}_{0i}^T \mathbf{B}_0 \mathbf{u}_{0i} = 1 \quad (33.203)$$

Construct the matrix $\bar{\mathbf{A}}_0$ as

$$\mathbf{A}_0 = \bar{\mathbf{A}}_0 + \varepsilon \bar{\mathbf{A}}_0 \quad (33.204)$$

where

$$\bar{\mathbf{A}}_0 = \mathbf{B}_0 [\mathbf{U}_0; \mathbf{U}_A] \text{diag}(\mathbf{S}_0 \mathbf{I}, \mathbf{S}_A) [\mathbf{V}_0; \mathbf{V}_A]^T \mathbf{B}_0 \quad (33.205)$$

$$\varepsilon \bar{\mathbf{A}}_0 = \mathbf{B}_0 \mathbf{U}_0 (\varepsilon [\delta \mathbf{S}_0]) \mathbf{V}_0^T \mathbf{B}_0 \quad (33.206)$$

$$\varepsilon [\delta \mathbf{S}_0] = \mathbf{S}_0 - \mathbf{S}_0 \mathbf{I} \quad (33.207)$$

$$S_0 = \frac{1}{m} \left(\sum_{k=1}^n S_{0i} \right) \quad (33.208)$$

Here, S_{0i} are the close eigenvalues, and S_0 is the average of S_{0i} ($i = 1, 2, \dots, m$).

It can be shown that the following equations hold:

$$\bar{\mathbf{A}}_0 \mathbf{U}_0 = \mathbf{B}_0 \mathbf{U}_0 S_0 \mathbf{I} \quad (33.209)$$

$$\bar{\mathbf{A}}_0^T \mathbf{V}_0 = \mathbf{B}_0^T \mathbf{V}_0 S_0 \mathbf{I} \quad (33.210)$$

These equations indicate that S_0 is the repeated eigenvalue with multiplicity, m , for the eigenproblem defined by Equation 33.209 and Equation 33.210, and \mathbf{U}_0 and \mathbf{V}_0 are the corresponding right and left modal matrices, respectively.

If small modifications $\varepsilon \mathbf{A}_1$ and $\varepsilon \mathbf{B}_1$ are imposed on the matrices \mathbf{A}_0 and \mathbf{B}_0 , then the eigenproblems of the perturbed system become

$$(\bar{\mathbf{A}}_0 + \varepsilon \bar{\mathbf{A}}_1) \mathbf{U} = (\mathbf{B}_0 + \varepsilon \mathbf{B}_1) \mathbf{U} \mathbf{S} \quad (33.211)$$

$$(\bar{\mathbf{A}}_0 + \varepsilon \bar{\mathbf{A}}_1)^T \mathbf{V} = (\mathbf{B}_0 + \varepsilon \mathbf{B}_1)^T \mathbf{V} \mathbf{S} \quad (33.212)$$

where

$$\varepsilon \bar{\mathbf{A}}_1 = \varepsilon \bar{\mathbf{A}}_0 + \varepsilon \mathbf{A}_1 \quad (33.213)$$

The eigensolutions of Equation 33.211 and Equation 33.212 are given by

$$\mathbf{U} = \mathbf{U}_0 \boldsymbol{\alpha} + \varepsilon \mathbf{U}_1 \quad (33.214)$$

$$\mathbf{V} = \mathbf{V}_0 \boldsymbol{\alpha} + \varepsilon \mathbf{V}_1 \quad (33.215)$$

$$\mathbf{S} = \mathbf{S}_0 + \varepsilon \mathbf{S}_1 \quad (33.216)$$

It should be noted that Equation 33.211 and Equation 33.212 are the eigenproblem for repeated eigenvalues. That is, the perturbation analysis for close eigenvalues has been transferred into that of repeated eigenvalues. Hence, the methods given by Section 33.9.4 can be used to compute \mathbf{S}_1 , $\boldsymbol{\alpha}$, $\boldsymbol{\beta}$, \mathbf{U}_1 , and \mathbf{V}_1 in Equation 33.214 to Equation 33.216.

References

- Adelmen, H.M. and Haftka, R.T., Sensitivity analysis of discrete structural systems, *AIAA J.*, 24, 823, 1986.
- Adhikari, S. and Friswell, M.I., Eigenderivative analysis of asymmetric non-conservative systems, *Int. J. Numer. Methods Eng.*, 39, 1813, 2001.
- Chen, S.H. 1993. *Matrix Perturbation Theory in Structural Dynamics*, International Academic Publishers, Beijing.
- Chen, S.H. and Liu, Z.S., High accuracy modal superposition for eigenvector derivatives, *Chin. J. Mech.*, 25, 432, 1993a.
- Chen, S.H. and Liu, Z.S., Perturbation analysis of vibration modes with close frequencies, *Commun. Numer. Methods Eng.*, 9, 427, 1993b.
- Chen, S.H. and Pan, H.H., Design sensitivity analysis of vibration modes by finite element perturbation, *Proc. of the Fourth IMAC*, 38, 1986.
- Chen, J.C. and Wada, B.K., Matrix perturbation for structural dynamics, *AIAA J.*, 15, 1095, 1979.
- Dailey, R.L., Eigenvector derivatives with repeated eigenvalues, *AIAA J.*, 27, 486, 1989.
- Fox, R.L. and Kapoor, M.P., Rates of change of eigenvalues and eigenvectors, *AIAA J.*, 12, 2426, 1968.
- Haug, E.J., Komkov, V., and Choi, K.K. 1985. *Design Sensitivity Analysis of Structural Systems*, Academic Press, Orlando, FL.

- Haug, E.J. and Rousselet, B., Design sensitivity analysis in structural dynamics, eigenvalue variations, *J. Struct. Mech.*, 8, 161, 1980.
- Hu, H. 1987. *Natural Vibration Theory for Multi-DoF Structures*, Science Press, Beijing (in Chinese).
- Lim, K.B., Juang, J.N., and Ghaemmaghani, P., Eigenvector derivatives of repeated eigenvalues using singular value decomposition, *J. Guidance Control Dyn.*, 12, 282, 1989.
- Liu, J.K., Perturbation technique for non-self-adjoint systems with repeated eigenvalues, *AIAA J.*, 37, 222, 1999.
- Liu, X.L., Derivation of formulas for perturbation analysis with modes of close eigenvalues, *Struct. Eng. Mech.*, 10, 427, 2000.
- Liu, Z.S. and Chen, S.H., Contribution of the truncated modes to eigenvector derivatives, *AIAA J.*, 32, 1551, 1994a.
- Liu, Z.S. and Chen, S.H., An accurate method for computing eigenvector derivatives for free-free structures, *Int. J. Comput. Struct.*, 52, 1135, 1994b.
- Mills-Curran, W.C., Calculation of eigenvector derivatives for structures with repeated eigenvalues, *AIAA J.*, 26, 867, 1988.
- Murthy, D.V. and Haftka, R.T., Derivatives of eigenvalues and eigenvectors of a general complex matrix, *Int. J. Numer. Methods Eng.*, 26, 293, 1988.
- Ojalvo, E.U., Efficient computation of modal sensitivities for systems with repeated frequencies, *AIAA J.*, 26, 361, 1988.
- Rogers, L.C., Derivatives of eigenvalues and eigenvectors, *AIAA J.*, 8, 943, 1977.
- Shaw, J. and Jayasuriya, S., Modal sensitivities for repeated eigenvalues and eigenvalues derivatives, *AIAA J.*, 30, 850, 1992.
- Wang, B.P., Improved approximate methods for computing eigenvector derivatives in structural dynamics, *AIAA J.*, 29, 1018, 1991.

34

Vibration in Rotating Machinery

34.1	Introduction	34-1
	History of Vibration in Rotating Machinery	
34.2	Vibration Basics	34-6
	Forced Vibration • Self-Excited Vibration • Parametric Instability • Torsional Vibration	
34.3	Rotordynamic Analysis	34-18
	Analysis Methods • Modeling • Design	
34.4	Vibration Measurement and Techniques	34-39
	Units of Measurement • Measured Parameters and Methods	
34.5	Vibration Control and Diagnostics	34-39
	Standards and Guidelines • Vibration Cause Identification • Vibration Analysis — Case Study	

H. Sam Samarasekera
Sulzer Pumps (Canada), Inc.

Summary

This chapter concerns vibration in rotating machinery. Although it is impractical to totally eliminate such vibrations, it is essential that they be controlled to within acceptable limits for safe and reliable operation of such machines. The two major categories of vibration phenomena that occur in rotating machinery are forced vibration and self-excited instability. Monitoring, diagnosis and control of these vibrations requires a sound understanding of rotor dynamics in machinery. Predicting the vibration behavior of a rotating machine by analytical means has become customary in many industries. With the advent of computer technology, several computer-based programs have been developed to accurately predict the behavior of rotating machinery. Significant strides in modeling techniques have also been made over the past century to accurately represent components such as shaft sections, disks, impellers, bearings, seals, rotor dampers, and rotor–stator interactions. This has enhanced the accuracy and reliability of both analytical and computational procedures. The chapter presents useful techniques of analysis, measurement, diagnosis, and control of vibration in rotating machinery.

34.1 Introduction

Vibrations are an inherent part of all rotating machinery. Residual mass imbalance and dynamic interaction forces between the stationary and rotating components, which are practically impossible to eliminate, cause these vibrations. The challenge is to identify the source of vibration and control it to within reasonable limits. Because of economic advantages, the trend in industry has been to move towards high speed, high power, lighter and more compact machinery. This has resulted in machines operating above their first critical speeds, which was unheard of in the past. The new operating parameters have required concurrent development of vibration technology without which it is not

possible to safely and reliably operate such machinery. Industry has also come to realize that *vibration* is an essential phenomenon, which could be used to assess the performance, durability, and reliability of rotating machinery.

Engineers at different levels approach the subject of vibration in rotating machinery differently. The machinery designer has to recognize the potential sources of vibration and control them to within acceptable levels. In the past few decades, owing to the advancement in computers and modeling techniques, better understanding of the dynamics of rotating machinery, including the identification of potential sources of vibration, has been realized. This has enabled designers to accurately predict the rotordynamic behavior of machinery, allowing it to reach higher operating speeds and larger energy capacities safely and reliably.

Approaching vibration from a different perspective, the maintenance engineer uses vibration standards and guidelines to monitor the health of equipment for their timely repair and refurbishment. Reliable vibration monitoring and diagnostics techniques have moved industry into *predictive* rather than *preventive* maintenance practices, which considerably reduce plant downtimes that rely on key rotating machinery. Premature replacement of machinery components has also been minimized. The resulting financial and economic benefits provide an added incentive for the study and understanding of vibration in rotating machinery.

The vibration specialist or troubleshooter has to use his knowledge of rotordynamics and his diagnostic capabilities to solve vibration problems in rotating machinery. In most cases, it is also important to have an understanding of the interfacial dynamics of the rotating machinery with the surrounding system in order to solve a vibration problem.

From a safety and reliability standpoint, the public must be concerned with vibration in rotating machinery. Their concerns are addressed through vibration standards and guidelines. These procedures have been developed for rotating machinery by numerous organizations, both at the national and international levels. Some of these standards are industry specific and some are equipment type specific, while a number of them try to cover a wide range of rotating machinery. The objective of most of these standards is to establish and control quality, safety, durability and reliable performance of rotating machinery for the benefit of those who use or operate it.

34.1.1 History of Vibration in Rotating Machinery

Although various types of rotating machinery have been in use for many centuries, understanding of their rotordynamic behavior did not begin until 1869 (Rankine, 1869). Since that time, there has been steady growth in the development and understanding of the vibration behavior of rotating machinery. A tabulation of major historical events that have contributed to this growth is presented in [Table 34.1](#).

- All rotating machinery vibrates to some degree. For public safety and machine reliability, the vibrations have to be controlled to within acceptable limits.
- Modern trends towards more sophisticated, higher speed compact rotating machinery have contributed to the rapid development in vibration technology through a better understanding of their rotordynamics.
- Vibration technology is integrated into the areas of design, maintenance, and troubleshooting of rotating machinery.
- From a safety and reliability standpoint, the public is protected by the implementation of vibration standards and guidelines.
- The first publicly reported rotordynamic study was made in 1869.

TABLE 34.1 A Chronological Listing of Major Contributions that Have Led to the Development and Understanding of Vibration in Rotating Machinery

Year	Contributor	Description
1869	Rankine, W.J.M.	<p>He examined the equilibrium of a frictionless, uniform shaft disturbed from its initial position. The resulting recorded article is recognized to be the first on the subject of rotor dynamics. He proposed that motion is stable below the first critical speed, is neutral or indifferent at the critical speed, and unstable above the critical speed</p> <p>He also developed numerical formulae for critical speeds for the cases of a shaft resting freely on a bearing at each end and for an overhanging shaft fixed in direction at one end</p>
1883	Greenhill, A.G.	He studied the effect of end thrust and torque on the stability of a long shaft and concluded that they were both unimportant. He also obtained formulae for the cases of an unloaded shaft resting on bearings at each end and fixed in direction at each end
Circa 1890	Reynolds, O.	He extended the theory developed by Rankine and Greenhill for the case of a shaft loaded with pulleys
1893	Dunkerley, S.	<p>He developed formulae for critical speeds for loaded shafts in terms of the diameter of the shaft, weights of pulleys, the manner in which the shaft is supported, and so on, and verified them by experiment</p> <p>He postulated that any degree of unbalance will excite the shaft at the critical speed to very high amplitudes and that it is possible to operate above the first critical speed. The dependence of critical speed on the moment of inertia of the rotating pulley was identified</p>
1894	Rayleigh, J.W.S.	He developed an approximate method to calculate the natural frequency of a continuous beam with distributed mass and flexibility using the energy method
1895	DeLaval, G.	He was responsible for the first experimental demonstration that a steam turbine is capable of sustained operation above the first critical speed
1916	Timoshenko, T.	He discovered the effects of transverse shear deflection on the natural frequency of a continuous beam and applied the principle to the case of the rotating shaft
1919	Jeffcott, H.H.	<p>He examined the effect of unbalance on the whirl amplitudes and the forces transmitted to the bearings. The case of a light uniform shaft supported freely on bearings at its ends and carrying a thin pulley of mass m at the center of the span was studied. He assumed the moment of inertia of the pulley to be negligible. Using this model, later known as the <i>Jeffcott model</i>, a comprehensive theory was developed to explain the behavior of the rotor as it passed through the critical speed</p> <p>The effect of damping on the whirl amplitude, a phase change of angle π as it passes through the critical speed, and the concept of synchronous rotor whirling (precession) were introduced and explained. He also recognized that with a separation margin of 10% on either side of a critical speed, the amplitude of vibration would not be excessive. He demonstrated that it is better from the vibration point of view to design the shaft with its critical speed below the working speed rather than to have a critical speed the same proportion above the working speed. Accordingly, he explained the behavior of the De Laval steam turbine and the economic advantages of operation above the critical speed</p>
1921	Southwell, R.V. and Gough, B.S.	They found that a torque and an end thrust of constant magnitude lowers the critical speed of a rotating shaft, disproving Greenhill's earlier (1883) conclusions

(continued on next page)

TABLE 34.1 (continued)

Year	Contributor	Description
1921	Holzer, H.	He developed a numerical method to calculate torsional critical speeds and mode shapes for a multidisk rotor system
1924	Newkirk, B.L.	<p>He observed that a rotor operating at a speed above the first critical speed can enter into high, violent whirling and the center of the rotor will precess in the forward direction at a rate equal to that of the critical speed. Unlike in the case of synchronous whirling, if the speed is increased beyond the initial whirl speed, the whirl amplitude will continue to increase, eventually leading to failure. This was the first time that it was realized that nonsynchronous unstable motion can exist in a high-speed rotor</p> <p>Based on experiments, he made the following key observations on nonsynchronous whirling. The amplitude and the onset speed of whirling are independent of the rotor balance. Whirling always occurs at speeds above the critical speed, and the whirl speed is always constant at the critical speed, regardless of the rotor speed. The whirl threshold speed can vary even for machines of similar construction. Whirling occurs only in built up rotors, and not in single piece constructions. Increasing the foundation flexibility, distortion or misalignment of the bearing housings, or introducing damping to the foundation or increasing the axial thrust bearing load, increased the threshold speed of whirling</p>
1924	Kimball, A.T.	Suggested that internal friction or viscous action due to bending may cause a shaft to whirl when rotating at any speed above the first critical speed. He postulated that the nonsynchronous whirling observed by Newkirk was due to this phenomenon
1924	Newkirk, B.L.	Based on Mr Kimball's theory, he concluded that similar frictional forces are generated at the mating face between the shrunk on disk and the shaft of a built-up rotor, and the nonsynchronous whirling observed by him was due to this effect. However, he was unable to explain some of his experimental findings, in particular, the effects of bearing or foundation flexibility, damping, and misalignment
1925	Newkirk, B.L.	<p>He experienced another form of nonsynchronous whirling, similar but different to that caused by the frictional effects of a shrink-fit disk. It occurred at rotor speeds just exceeding twice the first critical speed on shafts mounted on journal bearings. He recognized that the oil in the journal bearing was responsible for the violent motion and called it <i>oil whip</i>. The whirl speed and direction of whirling were the same as that for friction induced whirling, that is, the first critical speed in the forward direction. A theory to explain how the oil film can produce the whirling motion of a journal and to account for why it took the same direction as rotation of the shaft was proposed. However, the theory does not explain why whirling does not commence until the rotor speed reaches twice the critical speed value. The influence of foundation flexibility on the rotor stability was also found to be confusing to Newkirk. In the case of friction-induced whirl, he was able to totally eliminate the rotor instability by means of a flexibly mounted bearing. When this was tried with the journal bearings, the whirl amplitudes magnified. External damping at the bearing was found to have a favorable influence on whirl amplitudes</p>
1925	Stodola, A.	He developed an iterative procedure to calculate the fundamental frequency of a vibrating system based on an assumed mode shape
1927	Stodola, A.	He provided an explanation and formulae for the gyroscopic moment effect on the critical speed of a rotor. He also introduced the notion of synchronous and nonsynchronous reverse precession of a rotor under specific conditions

TABLE 34.1 (continued)

Year	Contributor	Description
1933	Robertson, D.	In order to understand oil whip, he studied the stability of the ideal 360° infinitely long journal bearing, and erroneously concluded that the rotor will be unstable at all speeds and not only at speeds above twice the critical speed value
1933	Smith, D.M.	He studied the case of unsymmetrical rotors on unsymmetrical supports and obtained four different critical speed values in comparison to the single value for a symmetrical system. He also discussed the presence of additional critical speeds due to gyroscopic effects of large disks
1944	Myklestad, N.	A lumped parameter transfer matrix method to calculate natural frequencies for airplane wings was developed by him
1945	Prohl, M.	He developed a lumped parameter transfer matrix method for calculating critical speeds of flexible rotors
1953	Poritsky, H.	Using the small displacement theory, he derived a radial stiffness coefficient for the journal bearings and analyzed the rotor behavior under oil whirl conditions. He concluded that the rotor was stable below twice the critical speed and indicated that increasing the rotor or bearing flexibility will reduce the threshold speed of instability. He also proposed a stability criterion for a rotor based on the bearing and rotor stiffness
1953	Miller, D.F.	He introduced a solution to the steady-state forced vibration problem, for a beam or rotating shaft on damped, flexible end supports. The response of the rotor to an unbalance force and the damped resonance frequencies are calculated by this method
1955	Pinkus, O.	He investigated oil whirl in various journal bearing types and made the following major conclusions. The unbalance of the rotor has minimal effect on stability. The threshold of instability occurs at approximately twice the first critical speed of the rotor. In the unstable region, the whirl frequency remained constant at the first critical speed, irrespective of the shaft rotating speed. At speeds nearly equal to three times the first critical speed, whipping motion stops with a heavy shaft rotor, whereas with a light shaft rotor it does not cease. High loads, high viscosity, flexible mountings, and bearing asymmetry favor stability
1958	Lomakin, A.	The influence of the dynamic characteristics of seals on the critical speeds and stability of pump rotors were introduced by him
1958	Thomas, H.	He proposed that an eccentric turbine rotor would generate a destabilizing force due to the circumferential variation in clearance
1966	Gunter, E.J. Jr.	He combined the different theories on whirling developed by the rotor dynamist and the bearing specialist, and elegantly explained some of the conflicting experimental evidence gathered thus far. He emphasized the importance of considering the combined effects of rotor parameters and the bearing and foundation characteristics on rotor stability, and developed more comprehensive criteria for self-excited whirl instability
1969	Black, H.F.	He provided a comprehensive analysis of annular pressure seals on the vibrations of pump rotors
1970	Ruhl, R.	He introduced finite element models for flexible rotors for calculating rotor critical speeds and mode shapes. These models did not take into account gyroscopic effects and axial loading
1974	Lund, J.	A transfer matrix method to calculate damped critical speeds of a rotor taking into account the cross coupling terms as well were introduced by him
1976	Nelson, H. and McVaugh, J.	They extended the finite element model of a rotor to account for rotary inertia, gyroscopic effect, and axial loads

(continued on next page)

TABLE 34.1 (continued)

Year	Contributor	Description
1978–1980	Benckert, H. and Wachter, J.	A method to calculate flow induced spring constants for labyrinth gas seals and the use of <i>swirl breaks</i> to reduce the destabilizing force caused by tangential velocity in labyrinth seals was introduced by them
1980	Nelson, H.	He further developed a finite element model of a rotor to include shear deflection and axial torque effects
1980	Brennen, C. et al.	They recognized the presence of substantial shroud forces, which influences the rotor dynamics of a pump
1986	Muszynska, A.	She demonstrated that oil whirl occurs at about one-half the running speed in a vertical rotor. With further increase in speed, oil whip will commence when the whirl frequency approaches the critical speed of the rotor

34.2 Vibration Basics

The vibration phenomena that manifest in rotating machinery can be divided into two major categories: *forced vibration* and *self-excited instability*. A stimulus or a source of excitation is required to initiate and sustain vibratory motion in a rotor. When the stimulus is a forcing phenomenon such as mass unbalance, it will produce forced flexural vibration in the rotor analogous to linear forced vibration response in a simple spring–mass system. On the other hand, self-excited vibration (instability) does not require a forcing phenomenon for its initiation or sustenance. A description of these phenomena is given next.

34.2.1 Forced Vibration

A rotating force vector (unbalance), a steady directional force (gravity), or a periodic force (pump impeller/diffuser interface action), will cause forced vibration in a rotating machine. The response of the rotor will depend on the nature of the forcing function and how it relates to rotor characteristics. The rotor responses to the most common excitation phenomena are examined below.

34.2.1.1 Unbalance Response — Synchronous Whirling

As an introduction to the theory on rotating machinery vibration and understanding unbalance response, it is most appropriate to examine Jeffcott’s (1919) rotor, which is a simple model that has many of the basic characteristics of more complex rotating machinery. The Jeffcott rotor represents a massless elastic shaft supported freely in bearings at its ends and carrying a disk of mass m at the center of its span. The mass center of the disk is eccentric to its geometric center by a distance e . Refer to Figure 34.1.

C = geometric center of the disk
 β = phase angle

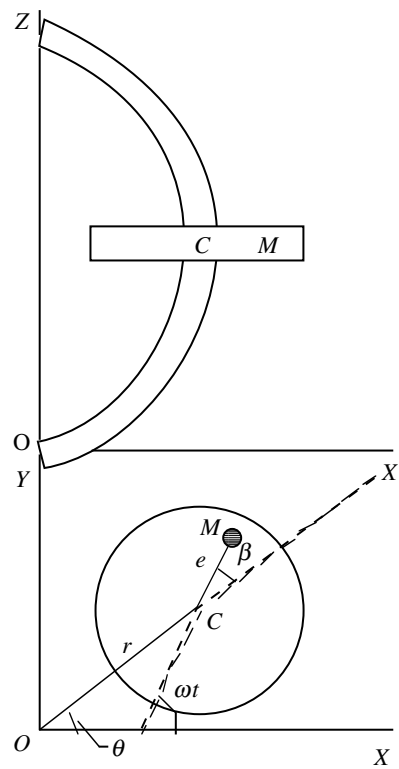


FIGURE 34.1 Jeffcott rotor.

M = mass center of the disk
 c = viscous damping coefficient of on the rotor
 O = bearing center
 r = deflection of rotor from origin
 θ = angle of precession
 k = shaft stiffness
 ω = angular velocity of the rotor = $\dot{\theta} + \dot{\beta}$

Whirling is defined as the angular velocity of rotation of the rotor geometric center (c) or the time derivative ($\dot{\theta}$) of the angle of precession (θ) (also see Chapter 32). *Synchronous whirling* is when the rate of whirling, $\dot{\theta}$, is equal to the total angular velocity, ω , of the system.

Applying Newton's Laws of motion to the rotor, the differential equations of motion in polar coordinates (r, θ) are obtained as

$$\ddot{r} + \frac{c}{m}\dot{r} + \left(\frac{k}{m} - \dot{\theta}^2\right)r = e\omega^2 \cos \beta \quad (34.1)$$

$$r\ddot{\theta} + \left(\frac{c}{m}r + 2\dot{r}\right)\dot{\theta} = e\omega^2 \sin \beta \quad (34.2)$$

For a steady-state condition, the values of r , β , $\dot{\theta}$, and ω are constant. For synchronous whirling, Equation 34.1 and Equation 34.2 reduce to

$$\left(\frac{k}{m} - \omega^2\right)r = e\omega^2 \cos \beta \quad (34.3)$$

$$\frac{c}{m}\omega r = e\omega^2 \sin \beta \quad (34.4)$$

From Equation 34.3 and Equation 34.4

$$r = \frac{e\omega^2}{\sqrt{\left(\frac{k}{m} - \omega^2\right)^2 + \left(\frac{c\omega}{m}\right)^2}} \quad (34.5)$$

$$\beta = \tan^{-1} \frac{c\omega}{m\left(\frac{k}{m} - \omega^2\right)} \quad (34.6)$$

$$F = \frac{kr}{2} = \frac{ke\omega^2}{2\sqrt{\left(\frac{k}{m} - \omega^2\right)^2 + \left(\frac{c\omega}{m}\right)^2}} \quad (34.7)$$

Using the following relationships:

$$\omega_N = \sqrt{\frac{k}{m}} \text{ — Natural frequency of rotor without damping}$$

$$c_{cr} = 2\sqrt{km} \text{ — Critical damping coefficient}$$

$$\zeta = \frac{c}{c_{cr}} \text{ — Damping ratio}$$

Equation 34.6 and Equation 34.7 are reduced to the following nondimensional form:

$$\frac{r}{e} = \frac{2F}{ke} = \frac{(\omega/\omega_N)^2}{\sqrt{(1 - (\omega/\omega_N)^2)^2 + (2\zeta\omega/\omega_N)^2}} \quad (34.8)$$

$$\beta = \tan^{-1} \frac{2\zeta(\omega/\omega_N)}{(1 - (\omega/\omega_N)^2)} \quad (34.9)$$

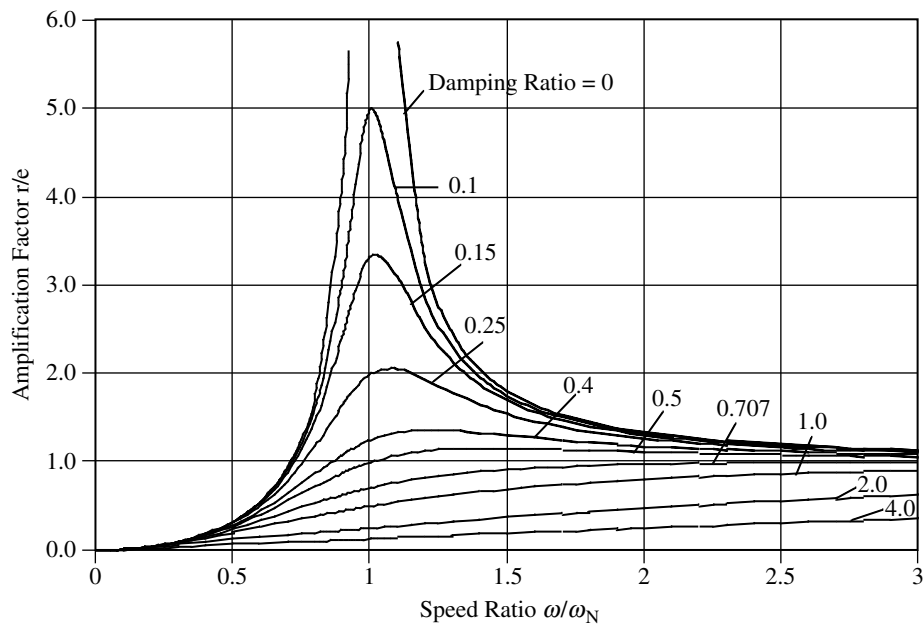


FIGURE 34.2 Jeffcott rotor response with mass eccentricity — amplification vs. speed.

Figure 34.2 is a graphical representation of the unbalance response of the rotor as a function of rotating speed, ω . Upon examination of the phase relationship, it is important to note that the phase angle, β , changes from approximately 0° at low speed to values approaching 180° at the higher speed. At ω_N , $\beta = 90^\circ$. A pictorial illustration of this phenomenon is given in Figure 34.3.

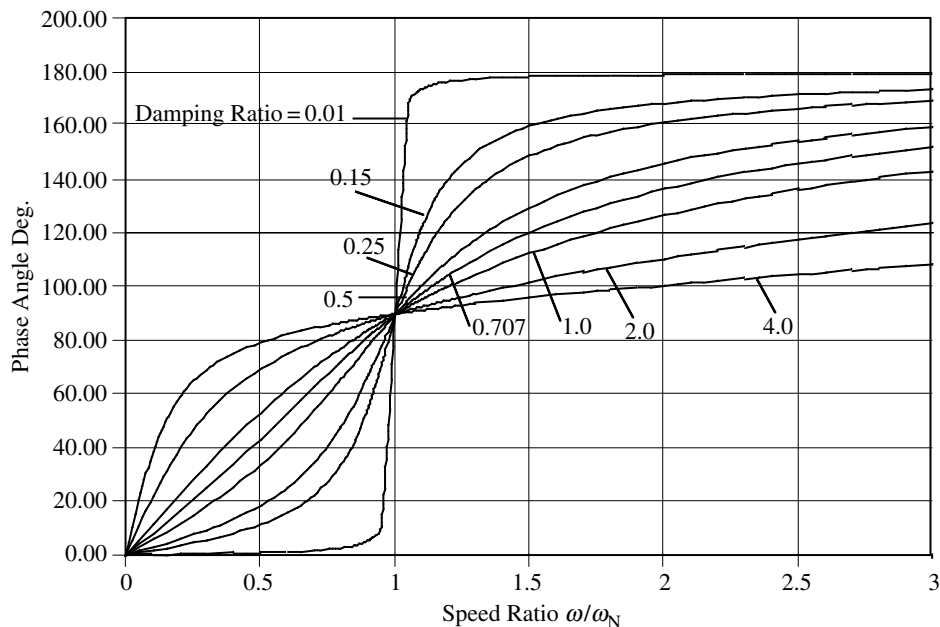


FIGURE 34.3 Jeffcott rotor response to unbalance — phase angle vs. speed.

For the case of zero damping, when $\omega = \omega_N$, the rotor deflection and the bearing forces are unbounded. For all other cases, the rotor deflection and the bearing forces are bounded, and their amplitude depends on the damping ratio. If a shaft is quickly accelerated through its critical speed to a higher working speed, then there may not be enough time for large rotor deflection to take place. At high speeds, $\omega \gg \omega_N$, the amplitude of the rotor deflection decreases and approaches the value e , the eccentricity of the rotor.

The critical speed, ω_{cr} , of a rotor in the general case, is the speed at which the rotor deflection amplitude or the force amplitude transmitted to the bearings is a maximum.

This implies that, at $\omega = \omega_{cr}$

$$\frac{dr}{d\omega} = \frac{dF}{d\omega} = 0$$

Using Equation 34.8, the following relationship between the natural frequency of the rotor and its critical speed is derived:

$$\omega_{cr} = \frac{\omega_N}{\sqrt{1 - 2\zeta^2}} \quad (34.10)$$

From Equation 34.10, it is evident that the critical speed of a rotor is not a fixed value and is dependent on the degree of rotor damping. When $\zeta = 1/\sqrt{2}$, the system is said to be critically damped.

It is important to note that rotor response to unbalance (or imbalance) is recognizable and controllable. The amplitude of the force transmitted to the bearing can be reduced by operation at speeds above the critical speed, reducing unbalance, increasing viscous damping, and avoiding operation close to critical speeds.

34.2.1.2 Shaft Bow

A rotor with a bent shaft will behave in a similar manner to a rotor with an eccentric mass (Ehrich, 1999). At high rotor speeds ($\omega \gg \omega_{cr}$), the shaft will tend to correct the bow as illustrated in Figure 34.4. When shaft bow is combined with mass eccentricity, unique behavior patterns are produced depending on the phase angle between the bow and the eccentric mass (Childs, 1993).

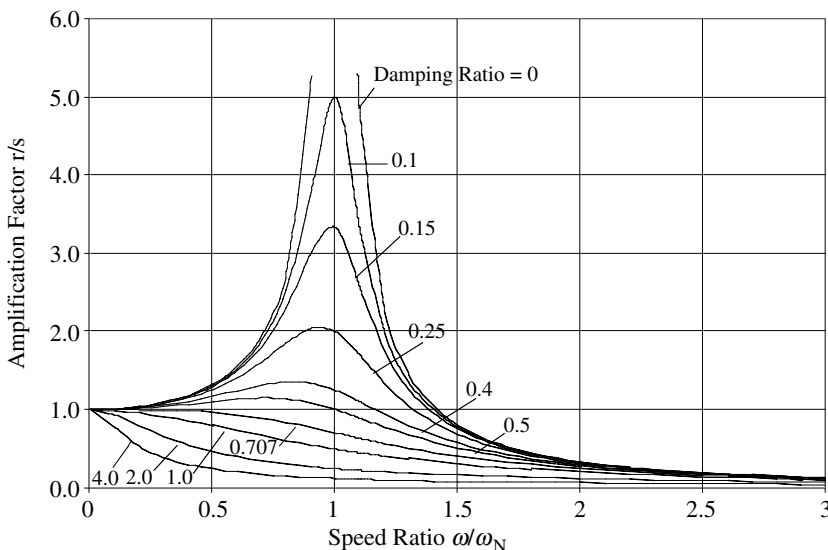


FIGURE 34.4 Jeffcott rotor response with shaft bow — amplification vs. speed.

34.2.1.3 Gravity Critical

A special case of synchronous whirling may occur in certain types of horizontal rotors due to the gravitational force. It is a secondary critical speed commonly called the *gravity critical*, which can occur in a very heavy lightly damped rotor. The critical speed will occur at approximately half the natural frequency of the rotor and its amplitudes of deflection at the critical speed are bounded and approximately twice the static deflection of the rotor (Gunter, 1966).

34.2.1.4 The Influence of Rotor Inertia and Gyroscopic Action

The effect of rotor inertia is ignored in the Jeffcott model. However, in practice, it is recognized that rotor inertia and gyroscopic action has an influence on the natural frequencies, critical speeds, and unbalance response of the rotor, including reverse whirling. In the case of the natural frequency of the rotor (zero speed), the diametral or rotary inertia provides an additional natural frequency associated with the rotational degree of freedom (DoF). Also, the inertia effect lowers the first natural frequency (Childs, 1993). In the rotating case, the effect of inertia generates both forward and reverse whirling critical speeds (Childs, 1993). These forward whirling critical speeds tend to be higher (stiffening effect) and the reverse whirling critical speed lower than the natural frequency of the rotor. At the forward critical speeds, large amplitude whirling motion due to imbalance occurs, whereas the reverse critical speeds are insensitive to imbalance of the rotor.

34.2.1.5 Rotor Housing Response across an Annular Clearance

If the rotor deflection due to imbalance exceeds the uniform annular gap, continuous contact would occur between the rotor and stator resulting in coupled motion between the rotor and stator (Childs, 1993). For low contact frictional forces, synchronous forward whirling driven by the imbalance forces will occur. If the contact friction force is large enough to prevent slipping between the rotor and stator, reverse whirling will take place. For the case of synchronous forward whirling in a certain range of running speeds, instability will occur due to engagement between the rotor and stator (Black, 1968). The zones of instability depend on the coupled natural frequency of the rotor and stator and the degree of rotor deflection with respect to the annular gap.

34.2.1.6 Effect of Nonlinearity and Asymmetry on Forced Vibration Response

The foregoing analysis has assumed that stiffness and damping are linear and symmetric and the resulting forces are proportional to the deflection and velocity of the rotor. However, in reality, rotating machinery components have inherent nonlinearities and asymmetries that can have a profound influence on their rotordynamic behavior. At large amplitudes of motion, stiffness and damping coefficients become nonlinear and result in modifying the response amplitude and critical speeds of the rotor. Nonlinearity in the support stiffness will introduce considerable distortion to the otherwise simple harmonic vibration behavior of a purely linear system. The stiffness and damping coefficients of the bearings and their supports are asymmetric in most cases, in particular in horizontal machines. As a result, the forced vibratory responses in the two principal directions are different and can behave independent of each other. Each principal direction will display a critical speed unique to itself. Ehrich (1999) has presented a discussion on how nonlinearity and asymmetry of stator systems influence forced vibration response.

The influence of rotor stiffness asymmetry and inertia asymmetry on rotor stability is discussed in Section 34.2.3.

34.2.2 Self-Excited Vibration

Instability (nonsynchronous whirling) is a self-induced excitation phenomenon, sometimes described as *sustained transient motion*, that can occur in rotating machinery. At the inception of instability, the rotor deflection will continue to build up with increase in speed, whereas in the case of a critical speed resonance, the amplitude of the deflection reaches a maximum value and then decreases. If the rotor speed is increased above the instability threshold speed, the large amplitudes of motion will normally

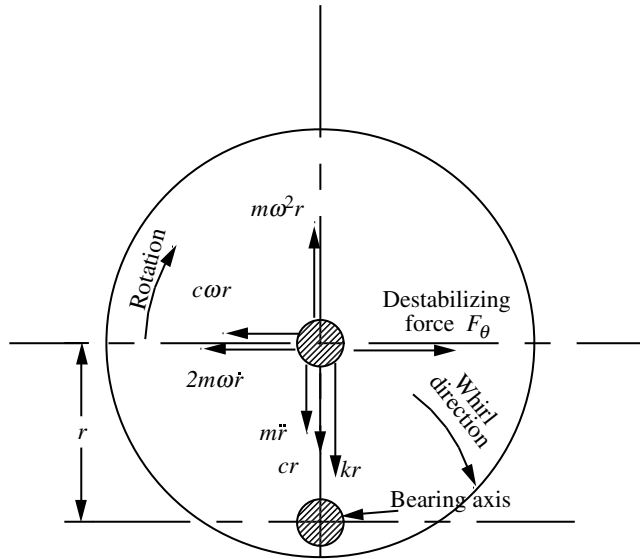


FIGURE 34.5 Rotor instability — general case.

result in damage to the machine. Unlike forced flexural vibration, rotor instability is self-induced and does not require a sustained forcing phenomenon to initiate or maintain the motion. It is known to occur only in machines operating at speeds well above the critical speeds of the rotor. Furthermore, the rotor whirling speed is different to the rotor speed (nonsynchronous whirling), and it is identical to the critical speed irrespective of the rotor speed.

In general, the rotor instability is associated with the existence of a tangential force vector, F_θ , acting at right angles to the deflection vector and directly opposing the damping force vector, as illustrated in Figure 34.5. The nature of F_θ is such that its magnitude increases proportionately with the rotor deflection. At the point where F_θ equals the external damping force, rotor instability will commence due to the nullification of the stabilizing force. This will produce a whirling motion of ever increasing amplitude. Several phenomena inherent in the rotor system that generates such tangential force vectors have been identified and are discussed below. Rotordynamists believe that there still remain more such phenomena to be discovered.

34.2.2.1 Internal Friction Damping

This type of instability was first experienced in the early 1920s in blast furnace compressors made by the General Electric Company. These machines were subject to occasional fits of violent vibration. Newkirk (1924) carried out a series of experiments to understand the unusual behavior of these machines. Based on the *internal friction theory* of Kimball (1924), Newkirk (1924) concluded that the interfacial friction damping forces at the disk shaft interface caused the subsynchronous whirling.

In order to understand the internal friction damping phenomena let us examine the shaft stresses in the whirling Jeffcott rotor (Figure 34.1). Figure 34.6 is a cross section of the shaft disk interface. Owing to its deflection, all of the fibers in the right half of the cross section are in tension, T_e , and those in the left half are in compression, C_e . These fiber stresses tend to straighten the shaft and produce a restoring force, F_r , which opposes the centrifugal force, $m\dot{\theta}r$. Furthermore, a set of frictional forces are generated at the shaft disk interface due to stretching and compression of the fibers. The fibers in the bottom lower half will be stretched and are under frictional tension, T_f , and those in the upper half are being compressed under frictional compression C_f . Similarly to the reaction force, F_r , produced from right to left by T_e and C_e , a reaction force, F_θ , from bottom to top will be produced by the frictional stresses T_f and C_f . The disturbing force, F_θ , is in the same direction as the whirling motion and as a result will increase as

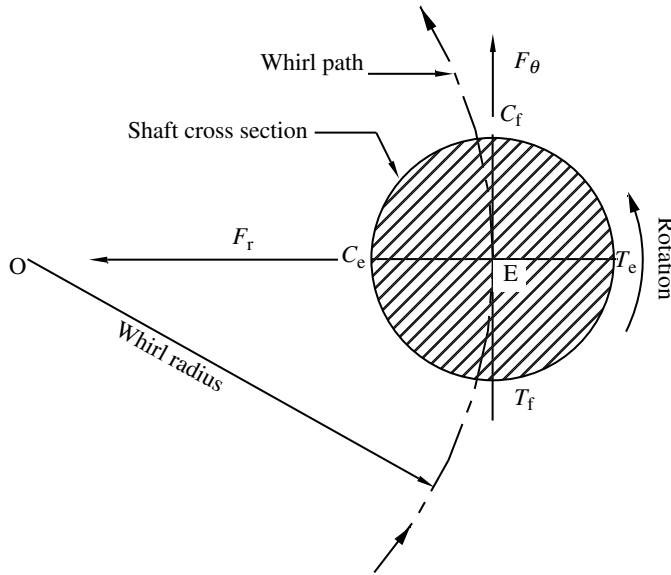


FIGURE 34.6 Internal friction damping forces acting on a rotor.

the whirling motion increases. The force, F_θ , will oppose the external damping force, $c\dot{\theta}r$. At the threshold of instability, the two forces nullify each other. It is also known that the frequency of whirling, $\dot{\theta}$, at the threshold of instability equals the natural frequency, ω_n , of the rotor. Mathematically it can be expressed as follows:

$$F_\theta = c_i r (\omega - \dot{\theta}) \quad (34.11)$$

where c_i is the rotor internal damping coefficient:

$$c\dot{\theta}r = c_i r (\omega - \dot{\theta}) \quad (34.12)$$

$$\dot{\theta} = \omega_N \quad (34.13)$$

Equation 34.12 and Equation 34.13 yield the following relationship between the threshold speed of instability, the first critical speed, and the damping factors (both internal and external):

$$\frac{\omega}{\omega_N} = 1 + \frac{c}{c_i} \quad (34.14)$$

34.2.2.2 Tip Clearance Excitation (Alford's Force, Steam Whirl)

Thomas (1958) investigated the instability of steam turbines and suggested that nonsymmetric radial clearances caused by an eccentric rotor could result in destabilizing forces, and called them *clearance excitation forces*. Subsequently Alford (1965) discovered a similar phenomenon in aircraft gas turbines and, as a result, the destabilizing forces are sometimes referred to as *Alford forces* in North America.

The destabilizing force is created as a result of the variation in the gap between the blade tip and the stator. When the gap decreases, the leakage decreases and consequently the efficiency increases, resulting in a torque higher than the average torque produced by a uniform gap. When the gap increases, there is a corresponding decrease in the torque relative to the average. The variation in torque produced by the eccentricity results in a tangential force, which is normal to the radial deflection and is in the direction of the whirling motion as shown in Figure 34.7. Furthermore, it has been illustrated that the magnitude of the resulting force increases proportionately with the increase in rotor deflection, that is, the decrease

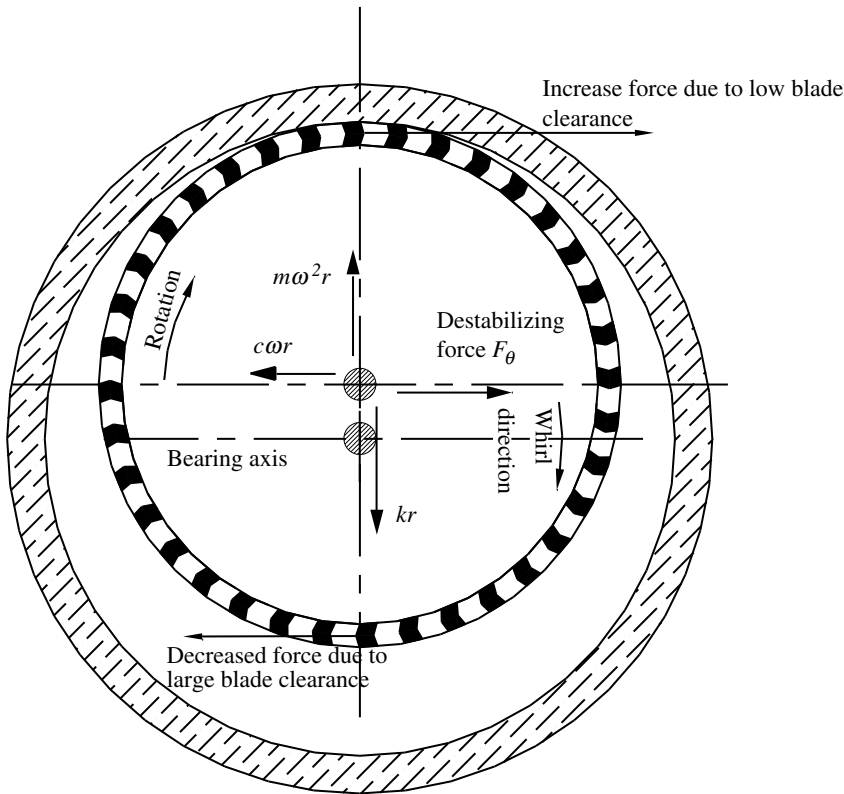


FIGURE 34.7 Tip clearance excitation (Alford forces).

in the gap. The resulting force is a destabilizing force that will oppose the external damping force, and at some point when they balance each other, rotor instability will occur. A detailed analysis of the tip clearance forces has been made by Urlichs (1977).

34.2.2.3 Impeller Diffuser Excitation Forces

Instability experienced in centrifugal compressors provides a strong suspicion that impeller–diffuser interaction phenomena are involved in the development of destabilizing forces. However, to date, no satisfactory destabilizing mechanism or source involving impellers has been identified. In the last two decades there have been several studies related to rotordynamic forces arising from shrouded centrifugal pump impellers, but very little work has been done on compressor impellers. The destabilizing force arising from the impeller–diffuser/volute interaction of a pump has been determined to be relatively small (Jery et al., 1984; Bolleter et al., 1985; Adkins and Brennen, 1986; Ohashi et al., 1986). The major portion of the destabilizing force is known to be generated in the narrow gap region between the casing and shroud of the impeller (Childs, 1986; Bolleter et al., 1989; Baskharone et al., 1994; Moore and Palazzolo, 2001). In the case of centrifugal compressors, an empirical method to determine stability of multistage machines has been proposed (Kirk and Donald, 1983). The stability maps proposed by them for flow through and back-to-back centrifugal compressors are shown in Figure 34.8 and Figure 34.9.

34.2.2.4 Propeller Whirl

Propeller whirl (Taylor and Browne, 1938; Houbolt and Reed, 1961) is another form of instability which occurs in aircraft rotors when there is a mismatch in the angular velocity vector of the propeller and the linear velocity vector of the aircraft. This angular mismatch results in the generation of a moment whose vector has a component of significant magnitude, which contributes to the instability of the

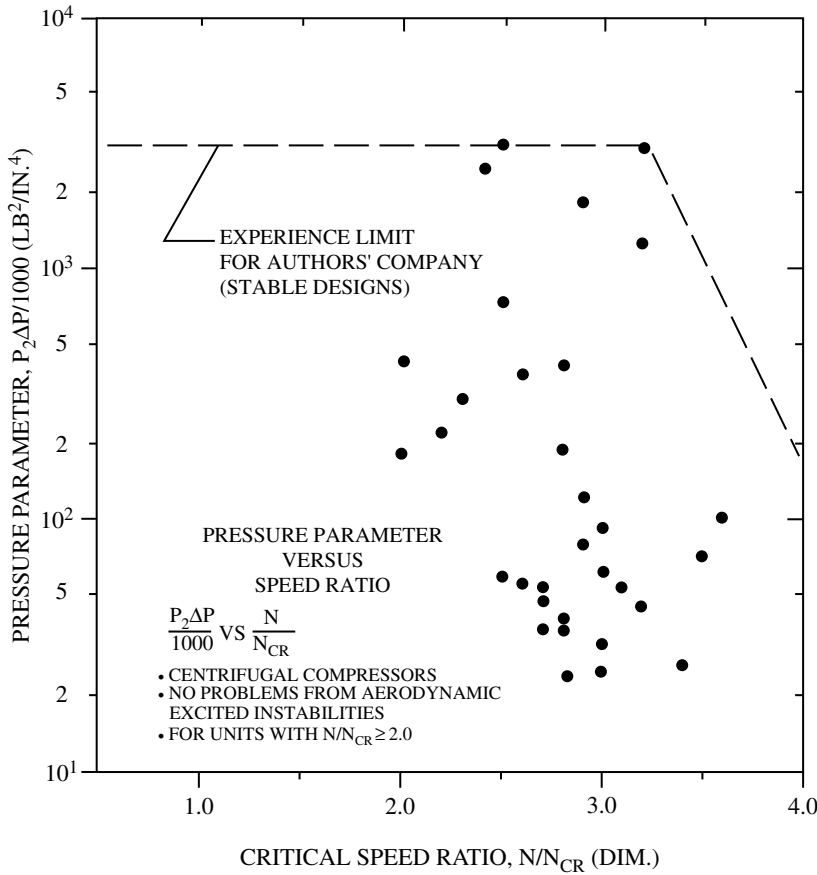


FIGURE 34.8 Proposed stability map for flow through centrifugal compressors. (Source: Rotor Dynamical Instability, 1983. With permission.)

propeller (Vance, 1988). Its magnitude is proportional to both the angular mismatch and the linear speed of the aircraft. With increasing speed, the magnitude of the destabilizing moment will exceed the rotor viscous damping moment and result in propeller instability (refer to Figure 34.5). Since the propeller is supported only from one end, the whirling motion is conical and is found to be in the reverse direction to propeller rotation. The instability is sensitive to the velocity and density of the air and not a function of the torque of the machine.

34.2.2.5 Fluid Trapped in a Hollow Rotor

Wolf (1968) has demonstrated that trapped fluid inside a hollow rotor can produce a force component tangential to the whirl orbit due to viscous drag forces. Under subsynchronous whirling speeds, this force component acts in the same direction of whirling motion and its magnitude is proportional to the rotor deflection. With reference to Figure 34.5, this force has all the markings of a destabilizing force, which can produce instability in the rotor. The threshold speed of instability is reached when the whirling speed equals the first critical speed of the rotor. It has been shown (Ehrich, 1999) that, at the threshold of instability, the rotor speed is less than twice the first critical speed. This results in a ratio of whirl speed to rotor speed in the range of 0.5 to 1.0.

34.2.2.6 Dry Friction Rubs

In Section 34.2.1.5, a dry friction rub situation was identified, where slipping was prevented between the rotor and stator under contact conditions. The contact was made possible by the deflection of the rotor

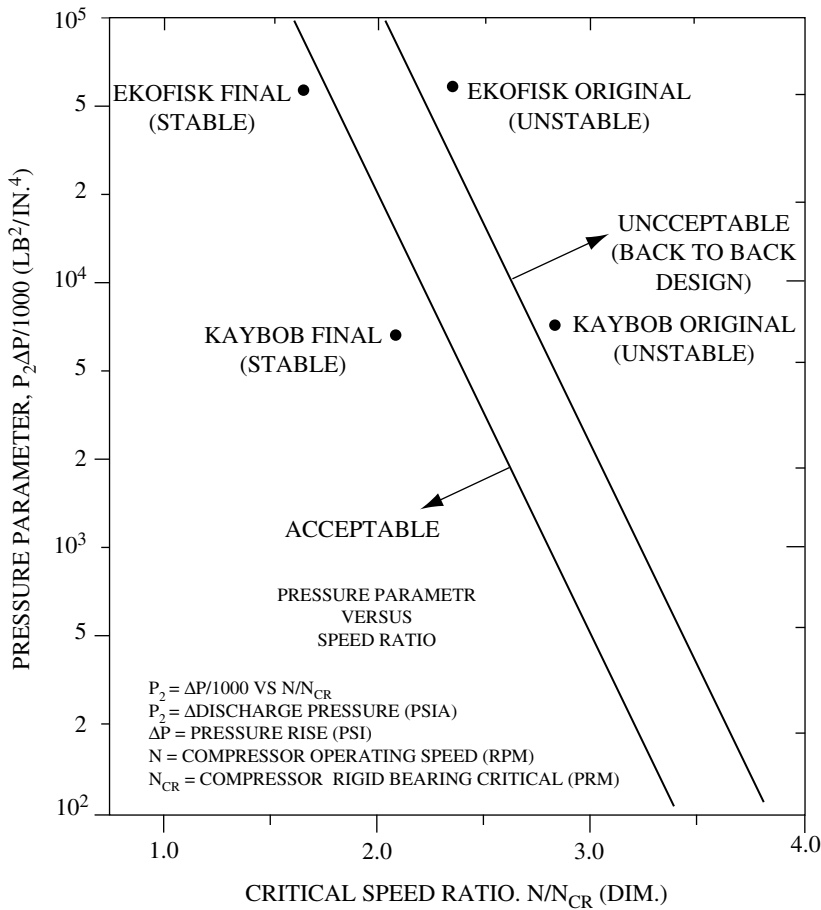


FIGURE 34.9 Proposed stability map for back-to-back centrifugal compressors. (Source: Rotor Dynamical Instability, 1983. With permission.)

due to unbalance forces. When contact is made between the rotor and stator, Coulomb friction produces a tangential force in the direction opposite to shaft rotation. Since the frictional force prevents slipping, whirling in the reverse direction to rotation occurs. The whirling speed is equal to $r\omega/C$, where r is the radius of the rotor, C the radial gap, and ω the speed of the rotor. Since the frictional force is in the same direction of whirling, it will cause the magnitude of whirling to increase, resulting in further increase of the frictional force. When the magnitude of this force exceeds the viscous damping force, rotor instability will occur. Another possibility is for the dry friction whirling speed to approach the coupled natural frequency of the rotor and stator, in which case unstable motion termed *dry friction whipping* takes place (Ehrich, 1999).

In addition to the case described above, dry friction rubs can occur in journal bearings, seals, wear rings, or any situation where a small clearance between a rotor and stator exists. The inadvertent closure of the clearance due to unbalance or lack of proper lubrication can initiate dry friction rub induced instability in these cases as well.

34.2.2.7 Torque Whirl/Load Torque

When the rotor disk axis is not aligned with the bearing axis, as in the case with an overhung rotor, Vance (1988) has shown that nonsynchronous whirling (torque whirl) can occur as a result of the misalignment between the load torque and the driving torque. His findings are based on the analysis of a simple

rotor model. It appears that torque whirl instability can occur only in the case of long slender shafts with high-load torque values. The practical implications of this theory are still to be fully explored.

34.2.2.8 Oil Whirl/Whip

Newkirk and Taylor (1925) first experienced shaft whipping due to oil action in journal bearings during their investigation into internal friction induced whirling of rotors. They found that under certain conditions, a rotor mounted on journal bearings whipped when the rotor was running at any speed above double the critical speed; the whirling motion was in the forward direction and its speed matched the critical speed of the rotor. He provided a qualitative explanation of the phenomenon based on the fact that the oil film rotates at half the velocity of the shaft due to friction drag. Hence, for rotational speeds near twice the critical speed, the oil film provides the stimulus as its speed matches the critical speed value resulting in large displacements and whipping. Others have also drawn similar conclusions based on the suggestion of an oil wedge rotating at half speed, or rotating fluid force fields at half shaft speed. However, the foregoing fails to explain why oil whip persists at speeds greater than twice the critical speed. Ehrich (1999) has also provided a qualitative explanation for oil whirl based on the general theory of rotor instability.

Although a comprehensive explanation of the physical phenomena of oil whirl is still outstanding, numerous analytical models to identify where it could be encountered have been suggested. Gunter (1966) has analytically demonstrated that the instability in a rotor supported on journal bearings can be attributed to the cross coupling bearing coefficients. As a result, most of the research on oil whirl instability has narrowed to accurate estimation of bearing cross coupling coefficients.

34.2.2.9 Influence of Bearings and Supports on Rotor Instability

The results of the Jeffcott model can be easily adopted to include bearing stiffness and bearing support stiffness effects, provided they are both linear and circumferentially symmetric (isotropic). For this particular case, the rotor stiffness, k , is the equivalent stiffness resulting from the series connection of the shaft, bearings, and support stiffness. The resulting values for ω_N and ω_{cr} will be less than those for the simply supported Jeffcott model. This will result in lowering the threshold speed of instability.

If the bearing stiffness or the bearing-support stiffness is not symmetric (orthotropic) then it can be shown (Childs, 1993) that the threshold speed of instability is increased and the maximum amplitude of deflection of the rotor is reduced in comparison to the case with symmetric bearings.

The effect of damping at the bearings or at the bearing-support is very similar to the influence of stiffness. It reduces the amplitude of the synchronous rotor response at the critical speed, and elevates the threshold speed of instability. However, there is a limit to the amount of damping that can be applied. Excessive damping causes a reduction in stability (Childs, 1993).

The mass of the bearings plays a significant role on rotor stability. If the bearing mass is significantly larger than the rotor mass, the threshold speed of instability is lowered.

34.2.3 Parametric Instability

The instability phenomena described in Section 34.2.2 can be represented by linear differential equations where the system parameters such as mass, inertia, stiffness, damping, and natural frequency are assumed to be constants. There is another subcategory of self-excited motion, referred to as *parametric instability*, since it is induced by the periodic variation of the system parameters such as inertia, mass, and stiffness. A discussion of the more common forms of this phenomenon follows.

34.2.3.1 Shaft Stiffness Asymmetry

If the shaft of a rotor contains a sufficient level of stiffness asymmetry in the two principal axis of flexure, rotor instability could occur. Smith (1933) investigated the rotor behavior under unsymmetrical flexibility of the bearing supports and unsymmetrical transverse flexibility of the shaft, taking into consideration the damping effects as well. The following conclusions were derived based on his investigation:

In the presence of stiffness asymmetry, the onset speed of internal-friction induced instability is lowered.

When there is no external damping, the rotor becomes unstable at all speeds between the two undamped natural frequencies in the two orthogonal directions. However, if external damping is significant, parametric instability may be eliminated.

Within the unstable range, the whirling motion is in the forward direction and is synchronous with the shaft speed. Further, unlike in the case of internal-friction induced instability; it is theoretically possible to run through parametric instability. This makes parametric instability quite similar to the case of unbalance response.

When the asymmetric rotor is acted upon by a transverse disturbing steady force such as gravitational force, the rotor whirls at twice the speed of the shaft. This motion exhibits a resonant increase in amplitude at a speed that is approximately half the mean of the two natural frequencies.

34.2.3.2 Rotor Inertia Asymmetry

Crandall and Brosens (1961) analyzed the parametric excitation of a rotor with nonsymmetrical principal moments of inertia. Their results indicate that the rotor behavior is very similar to the case of rotors with stiffness asymmetry described in Section 34.2.3.1, and parametric instability over similar speed ranges occurs.

34.2.3.3 Pulsating Torque

Constant torque acting on a rotor is known to lower its critical speeds because they effectively reduce the rotor's lateral stiffness. A pulsating torque introduces lateral vibrations and instabilities into a rotor. When a combination of a pulsating and constant torque is applied to a rotor, it will induce unstable lateral vibrations in a specific range of rotor speeds and certain combinations of torque amplitudes. In the region of unstable lateral motion, the whirling speed of the rotor will coincide with the first critical speed of the rotor regardless of the rotor speed or the frequency of the pulsating torque. At rotor speeds outside the unstable region, the whirling speed of the rotor will be coincident with the pulsating torque frequency.

34.2.3.4 Pulsating Longitudinal Loads

Pulsating axial forces on a shaft that are in the order of magnitude of the buckling load will effectively cause a periodic variation in its lateral stiffness. This will result in a proportionate reduction of the lateral natural frequency of the shaft. Therefore, pulsating axial loads are capable of inducing parametric instability in a shaft for both the rotating and the stationary cases.

34.2.3.5 Nonsymmetric Clearance Effects

Bentley (1974) recognized that large subsynchronous whirling can occur in rotating machinery due to certain types of nonsymmetric clearance conditions. One such condition is when a rotor's whirling motion causes rubbing with a stationary surface over a portion of the rotor orbit. This effectively results in an increase in the rotor stiffness during the contact portion of the orbit, producing a periodic variation in rotor stiffness during each cycle. Another situation that produces cyclic variation in rotor stiffness can occur in the case of a rotor supported on antifriction bearings mounted with a clearance fit to the housing. The cyclic variation of the effective rotor stiffness produces a subsynchronous whirling motion at exactly half the rotational speed. Occasionally, whirling at one third and one fourth the running speed has also been observed by Childs (1993). Instability will occur when the whirling speed corresponds to a critical speed of the rotor.

34.2.4 Torsional Vibration

Rotating machinery with rotors that have relatively large moments of inertia are susceptible to torsional vibration problems. Torsional vibration is an oscillatory angular motion that is superimposed on the steady rotational motion of the rotor. In practice it can easily go undetected, as standard vibration

monitoring equipment is not geared to measure torsional vibration. Special equipment must be used to detect torsional vibration in rotating machinery. Since the introduction of electric motor variable frequency drives (VFD), the incidence of field torsional vibration problems has increased. This has been attributed to the inherent torsional excitation forces present in current designs of VFDs. An added complication when using VFDs, as compared with using fixed speed drives, is the requirement of eliminating torsional natural frequencies over a wider speed range. Large synchronous electric motors are known to produce a large pulsating torque at a frequency that changes from twice the line frequency at the start, down to zero at the synchronous operating speed. In this case, any torsional natural frequency between zero and twice the line frequency may be subject to excitation. Most industries have come to recognize that torsional vibration is a potential hazard, and therefore, needs to be investigated at the design stage of rotating machinery. Several standard design specifications now require that torsional analysis is part of the design procedure.

The standard design practice in modeling the system for torsional analysis has been to calculate the undamped eigenvalues of the rotor as a free body in space. This practice is acceptable for most types of rotating machinery since the torsional stiffness and damping of bearings is insignificant. Also, in most cases, the torsional damping of the rotors itself is extremely low. Although the absence of damping is favorable from an analysis point of view, it makes it extremely difficult to eliminate a torsional vibration problem when encountered. This deficiency has been partly addressed with the introduction of several new lines of couplings that have a significant degree of torsional damping. Although not commonly used in rotating machinery, several torsional dampers such as the Lanchester damper have been developed for use on reciprocating machines. Dampers of similar design could be developed for use in rotating machinery to solve torsional vibration problems.

The torsional critical speeds of a simple rotor with one or two DoFs can be calculated by analytical methods. Numerical methods are used to calculate critical speeds and mode shapes of more complex systems with higher DoF. The Holzer numerical method (Holzer, 1921) described in Section 34.3.1.11 is one of the common methods used for these analyses.

- The two major categories of vibration phenomena that occur in rotating machinery are forced vibration and self-excited instability.
- Parametric instability is a special case of self-excited instability where some of the normally constant parameters vary, influencing rotor motion.
- Torsional vibrations are similar to lateral vibrations but occur in the planes perpendicular to the shaft axis.

34.3 Rotordynamic Analysis

Rotordynamic analysis is a part of current design procedures for rotating machinery that is carried out to predict the vibration behavior during operation of the machine. Potential problems are identified and eliminated by analytical means well before the manufacturing of components is begun. Furthermore, when a machine in operation displays unusual vibration behavior, analytical means are employed to study, identify, and help resolve the problem. In order for the analysis to be useful, it must be accurate and cost-effective.

During the last 100 years, several analytical procedures have been developed to understand the vibration behavior of rotating machinery. Some of these techniques are of historical interest only, and their usefulness in practical systems is very limited. With the advent of computer technology and advanced modeling techniques, several computer-based procedures have been developed to predict the vibration behavior of rotating machinery quite precisely. Of the most commonly used procedures, two are based on the lumped-parameter model where the distributed elastic and inertial properties are

represented as a collection of rigid bodies connected by massless elastic beam elements. These two procedures are the transfer matrix formulations introduced by Myklestad (1944) and Prohl (1945), and the direct stiffness matrix formulations proposed by Biezeno and Grammel (1954). Ruhl and Booker (1972) introduced the third commonly used method, based on the finite element analysis (FEA) model in which the rotor is represented as an assemblage of elements with distributed elastic and inertial properties. Several of the well-known procedures are discussed next, some of them for historical significance.

34.3.1 Analysis Methods

34.3.1.1 Rankine's Numerical Method

Rankine (1869) proposed that, for a shaft of a given length, diameter, and material, there is a limit of speed, and for a shaft of a given diameter and material, turning at a given speed, there is a limit of length, below which centrifugal whirling is impossible. The limits of length and speed depend on the way the shaft is supported. The critical speed of the shaft is given by the following equation:

$$\omega = \frac{k(Hg)^{1/2}}{b^2} \quad (34.15)$$

where

ω = critical speed in rad/sec

k = radius of gyration of the cross section of the shaft

g = acceleration due to gravity

H = modulus of elasticity expressed in units of height of itself ($H = E/\rho$)

E = Young's modulus

ρ = density of the material

l = shaft length

$b = l/\pi$ for a simply supported shaft

$b = l/0.595\pi$ for an overhanging shaft

34.3.1.2 Greenhill's Formulae

Greenhill (1883) introduced the following differential equation of motion for a uniform shaft slightly deformed from straightness by centrifugal whirling:

$$\frac{d^4 y}{dx^4} - \frac{m\omega^2}{gEak^2} y = 0 \quad (34.16)$$

The general solution to Equation 34.16 is given by

$$y = B \cosh \mu x + A \cos \mu x \quad (34.17)$$

where

$$\mu^4 = m\omega^2/gEak^2$$

m = weight of the shaft per unit length

ω = rotational speed

a = cross-sectional area of the shaft

The constants A and B depend on the boundary conditions at the support locations.

34.3.1.3 Reynolds' Equations

Reynolds extended the differential equation of motion for a uniform rotating shaft (Equation 34.16) to include shafts loaded with pulleys (disks) and for multispan rotors (Dunkerly, 1894).

At a bearing support, the difference in shear force must equal the bearing load P :

$$\frac{dM_r}{dx} - \frac{dM_l}{dx} = P \quad (34.18)$$

where M_r and M_l are bending moments in the right (r) and left (l) sides of the load.

At a load consisting of a revolving weight, W , the above equation becomes

$$\frac{dM_r}{dx} - \frac{dM_l}{dx} = \frac{W}{g} \omega^2 y \quad (34.19)$$

A further equation may be obtained by considering the *centrifugal couple* (gyroscopic moment) as given by

$$M_r - M_l = \omega^2 I' \frac{dy}{dx} \quad (34.20)$$

where I' = moment of inertia of the pulley.

The solution to Equation 34.20 is given by

$$y = A \cosh mx + B \sinh mx + C \cos mx + D \sin mx \quad (34.21)$$

The values of A , B , C , and D will depend on the boundary conditions between any two singular points.

34.3.1.4 Dunkerley Method

When considering the effects of the pulleys and the shaft together, the formulae derived by Reynolds were found to be limited for practical purposes. Dunkerly (1894) proposed an empirical method to consider the effects of the shaft and each of the pulleys separately, and then combine them using the following formula to obtain the critical speed of the rotor:

$$\frac{1}{\omega_c^2} = \frac{1}{\omega_s^2} + \sum_{i=1}^n \frac{1}{\omega_i^2} \quad (34.22)$$

where

ω_c = critical speed of the rotor

ω_s = critical speed of the shaft alone

ω_i = critical speed of the i th disk on a weightless shaft

In the case of the unloaded shaft, the critical speed, ω_s , is given by the following formula

$$\left(\frac{m\omega_s^2}{gEI} \right)^{1/4} l = a \quad (34.23)$$

where

I = sectional inertia of shaft

l = length of the span

a = a coefficient dependent on the manner of support of the shaft

The critical speed of the rotor ω_i with a single disk of weight W_i on a weightless shaft is given by

$$\omega_i = \theta \left(\frac{gEI}{W_i c^3} \right)^{1/2} \quad (34.24)$$

where

c = distance of disk from nearest support

θ = a coefficient dependant on the manner in which the shaft is supported, the position of the disk within the span and the dimensions of the disk

34.3.1.5 Rayleigh Method

The Rayleigh method is based on the premise that, when a system vibrates at its natural frequency, the maximum potential energy stored in the elastic components is equal to the maximum kinetic energy stored in the masses (Rayleigh, 1945).

The first natural frequency of a vibrating uniform beam is given by the following equation:

$$\omega^2 = \frac{EI \int_0^l \left(\frac{d^2 y}{dx^2} \right)^2 dx}{\mu \int_0^l y^2 dx} \quad (34.25)$$

The Rayleigh formula for a lumped mass system is

$$\omega^2 = \frac{\sum_{i=1}^n m_i y_i}{\sum_{i=1}^n m_i y_i^2} \quad (34.26)$$

where

ω = first natural frequency

y = deflection of the beam

x = distance along x -axis

l = length of the beam

m_i = i th lumped mass

y_i = static deflection of i th mass

The accuracy of the Rayleigh method depends upon the selection of a suitable deflection curve that approximates the fundamental mode shape. If the assumed curve represents the true mode shape, then the correct fundamental natural frequency will result. All deviations from the true mode shape will yield frequencies that are higher than the correct value.

34.3.1.6 Ritz Method

The Ritz method is an improvement on the Rayleigh method (Timoshenko et al., 1974) where the mode shape is represented by several orthogonal functions with unknown coefficients that satisfy the boundary conditions. The orthogonal functions are represented by a series of functions, $\Phi_i(x)$, where i varies from 1 to n . The mode shape is represented by the following expression:

$$y = \sum_{i=1}^n a_i \Phi_i(x) \quad (34.27)$$

In order for the coefficients a_i in the above equation to yield minimum values when substituted in the energy balance equation proposed by Rayleigh, the following expression needs to be satisfied:

$$\frac{\partial}{\partial a_i} \frac{\int_0^l \left(\frac{d^2 y}{dx^2} \right)^2 dx}{\int_0^l y^2 dx} = 0 \quad (34.28)$$

From Equation 34.25 and Equation 34.28, we find

$$\frac{\partial}{\partial a_i} \int_0^l \left[\left(\frac{d^2 y}{dx^2} \right)^2 - \frac{\omega^2 \mu}{EI} y^2 \right] dx = 0 \quad (34.29)$$

Substituting Equation 34.27 for y in Equation 34.29 and performing the mathematical operations, a system of linear equations in a_i is obtained. The number of such equations will be equal to n . These equations will yield solutions different from zero only if the determinant of the coefficients of a_i is equal to zero. This condition yields the frequency equation, from which the frequency of each mode can be derived.

34.3.1.7 Stodola–Vianello Method

The Stodola–Vianello method is a numerical iterative process (Timoshenko et al., 1974) that can be used to calculate the natural frequencies and mode shapes of vibrating systems. An approximate mode shape is first assumed and by successive iterations it is refined until convergence is obtained to the desired level of accuracy. This method can be used to refine the assumed mode shape when using the Rayleigh formulae or in the more general case of the matrix iteration process illustrated below.

Using Newton's Second law, the equations of motion for a multi-DoF system in matrix notation are

$$\{Y\} = \omega_i^2 [A][m]\{Y\} \quad (34.30)$$

where

$$[A] = [K]^{-1} \quad (34.31)$$

$[A]$ is the flexibility matrix

$[m]$ is the mass matrix

$[K]$ is the stiffness matrix

To start the iterative process a trial vector, $\{Y\}_1$, representing the mode shape is substituted to both sides of Equation 34.30 and solve for the natural frequency, ω_i . For this reason, let the product of $[A]$, $[m]$, and $\{Y\}_1$ be $\{Y\}'_2$. The first approximation for ω_i may be obtained by dividing any one of the elements on $\{Y\}_1$ by $\{Y\}'_2$ (Note that, if $\{Y\}_1$ was the true mode shape, then the ratio for all such elements will be equal.) The vector $\{Y\}'_2$ is then normalized by dividing all the elements by the first element to produce $\{Y\}_2$. The vector $\{Y\}_2$ is premultiplied by $[m]$ and $[A]$ to produce $\{Y\}'_3$. Once again the ratio of corresponding elements of $\{Y\}'_3$ and $\{Y\}_2$ are compared for equality.

This procedure is repeated until the mode shape and the associated frequency is determined to the desired level of accuracy. In the above iteration procedure, the mode shape converges to the one corresponding to the lowest natural frequency. If the stiffness matrix had been used instead of the flexibility matrix, then convergence at the highest natural frequency is obtained. After the first mode of vibration is determined, it is removed from the system matrices by the use of a sweeping matrix so that higher modes can be obtained. This procedure is repeated until all the desired mode shapes and natural frequencies are determined.

34.3.1.8 Myklestad–Prohl Method (Transfer Matrix Method)

The Myklestad–Prohl transfer matrix formulation (Myklestad, 1944; Prohl, 1945) is commonly used to analyze lumped parameter models of rotating machinery. The distributed elastic and inertial properties of the rotor are represented as a collection of rigid bodies connected by massless elastic beam elements as illustrated in Figure 34.10. This method is best suited to calculate critical speeds and mode shapes of rotors neglecting the effects of viscous damping. The Myklestad–Prohl procedure can also be adopted to perform synchronous response and stability analysis, including for the effects of damping.

In order to demonstrate the transfer matrix procedure, an axisymmetric rotor is analyzed to determine its undamped critical speeds and mode shapes. Referring to Figure 34.10, the rotor is divided into n nodes, and each node is connected to the adjacent node by a massless elastic beam with uniform cross-sectional properties. The mass of components such as disks, impellers, and so on, together with the mass of the adjacent portion of the shaft, is lumped at the nodes. The Myklestad–Prohl method is based on the solution of the Bernoulli–Euler equation and the variables of interest are displacement (y), slope (θ), moment (M), and shear (V). The development of the following procedure follows Childs (1993).

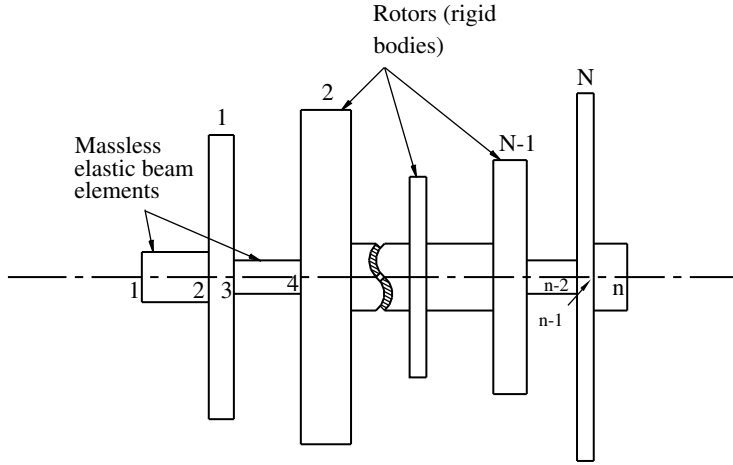


FIGURE 34.10 Lumped-parameter model of rotor.

At a typical nodal point (n), the variables on the left-hand side (l) are related to the variables on the right-hand side (r) by the following relationship:

$$\begin{Bmatrix} y_n^r \\ \theta_n^r \\ M_n^r \\ V_n^r \end{Bmatrix} = \begin{bmatrix} 1 & 0 & 0 & 0 \\ 0 & 1 & 0 & 0 \\ 0 & -J_n \omega^2 & 1 & 0 \\ -m_n \omega^2 & 0 & 0 & 1 \end{bmatrix} \begin{Bmatrix} y_n^l \\ \theta_n^l \\ M_n^l \\ V_n^l \end{Bmatrix} \quad (34.32)$$

For the purpose of abbreviation:

$$(Q)_n^T = (y_n \quad \theta_n \quad M_n \quad V_n) \quad (34.33)$$

and Equation 34.32 can be written in a more compact form as follows:

$$(Q)_n^r = [T_{mn}](Q)_n^l \quad (34.34)$$

where $[T_{mn}]$ represents the transfer mass matrix at node n .

At a massless beam section, connecting node n to node $n+1$ the transfer matrix is given by

$$\begin{Bmatrix} y_{n+1}^l \\ \theta_{n+1}^l \\ M_{n+1}^l \\ V_{n+1}^l \end{Bmatrix} = \begin{bmatrix} 1 & l_n & \frac{l_n^2}{2EI_n} & \frac{-l_n^3}{6EI_n} \\ 0 & 1 & \frac{l_n}{EI_n} & \frac{l_n^2}{2EI_n} \\ 0 & 0 & 1 & -l_n \\ 0 & 0 & 0 & 1 \end{bmatrix} \begin{Bmatrix} y_n^r \\ \theta_n^r \\ M_n^r \\ V_n^r \end{Bmatrix} \quad (34.35)$$

Equation 34.35 may be written in a more abbreviated form as

$$(Q)_{n+1}^l = [T_{bn}](Q)_n^r \quad (34.36)$$

where $[T_{bn}]$ represents the beam element transfer matrix connecting node n to node $n+1$.

From Equation 34.34 and Equation 34.36, we obtain the combined transfer matrix for nodes n and $n+1$:

$$(Q)_{n+1}^l = [T_{bn}][T_{mn}](Q)_n^l = [T_n](Q)_n^l \quad (34.37)$$

Starting with node one, successive matrix multiplications are carried out until node $n + 1$ is reached. The last node ($n + 1$) is a dummy node with the beam length, l , equal to zero, and the mass and inertias also equal to zero. This makes the nodal parameters on the left-hand side of node $n + 1$ equal to those on the right-hand side of node n . The result is as follows:

$$(Q)_n^r = [T_n][T_{n-1}] \cdots [T_1](Q)_1^l \quad \text{or} \quad (Q)_n^r = [T](Q)_1^l \quad (34.38)$$

The matrix $[T]$ is a function of the rotational speed, ω . The Myklestad–Prohl method uses a trial and error solution to determine the values of ω which satisfy the boundary conditions and Equation 34.38 simultaneously. It is not necessary to store and multiply all the matrices together. The transfer matrix procedure is used to proceed from one end to the other without having to store all the nodal matrices. In all cases, two boundary conditions each are known at the two ends of the shaft, and the frequencies that satisfy these boundary conditions are the critical speeds of the rotor. Once the critical speeds are calculated, the corresponding mode shapes can also be determined using the transfer matrix procedure. It should be noted that other types of elements, such as elastic supports, flexible couplings, and so on, could also be introduced very conveniently.

34.3.1.9 Direct Stiffness Method

The direct stiffness method uses a lumped-parameter formulation to evaluate the dynamic characteristics of a flexible rotor. The general differential equation of motion that characterizes its behavior (less the damping and gyroscopic forces) is as follows:

$$\begin{bmatrix} [m] & 0 \\ 0 & [J] \end{bmatrix} \begin{Bmatrix} (\ddot{Y}) \\ (\ddot{\theta}) \end{Bmatrix} + [K] \begin{Bmatrix} (Y) \\ (\theta) \end{Bmatrix} = \begin{Bmatrix} (F) \\ (T) \end{Bmatrix} \quad (34.39)$$

where $[m]$ and $[J]$ are diagonal matrices which contains the nodal masses, m_i , and nodal moments of inertia, J_i , respectively. The stiffness matrix, $[K]$, contains the internal stiffness terms of the beam elements as well as any external spring stiffness at the supports. The vectors (F) and (T) represent external forces and moments acting on the system, respectively.

The stiffness matrix for a typical beam element based on the Bernoulli–Euler equations is as follows (Childs, 1993):

$$[K^i] = \frac{2EI_i}{l_i^3} \begin{bmatrix} 6 & 3l_i & -6 & 3l_i \\ 3l_i & 2l_i^2 & -3l_i & l_i^2 \\ -6 & -3l_i & 6 & -3l_i \\ 3l_i & l_i^2 & -3l_i & 2l_i^2 \end{bmatrix} \quad (34.40)$$

The overall stiffness matrix, $[K]$, has to be assembled by combining the individual component matrices in a systematic manner. The following procedure illustrates the process.

The stiffness matrix of the i th beam element in matrix notation is

$$[K^i] = [k_{j,k}^i] \quad (34.41)$$

where j and k vary from $(2i - 1)$ to $(2i + 2)$.

To form the overall stiffness matrix, the elements with the same subscripts of adjacent beam elements are added over n beam elements as given by the following equation:

$$[K] = [K_{j,k}] = \sum_{i=1}^n \sum_{j=2i-1}^{2i+2} \sum_{k=2i-1}^{2i+2} k_{j,k}^i \quad (34.42)$$

Once the inertia matrix and the stiffness matrix for the entire system are assembled, the eigenvalues and eigenvectors can be evaluated by solving the following homogeneous equation derived

from Equation 34.39:

$$[M](\ddot{Y}) + [K](Y) = 0 \quad (34.43)$$

There are numerous analysis procedures (Meirovitch, 1986) for the solution of Equation 34.43 that yield the eigenvalues and eigenvectors of the system. The method of choice will depend on the complexity and nature of the inertia and stiffness matrices. Perhaps the most widely known is the matrix iteration using the power method in conjunction with the sweeping technique. However, this method is not necessarily the most efficient, particularly for higher-order systems. The Jacobi's method, which uses matrix iteration to diagonalize a matrix by successive rotations, is more commonly used owing to its higher efficiency. Details of these techniques are given in the text by Meirovitch (1986).

When the damping matrix and the gyroscopic matrix is also included in Equation 34.39, the direct stiffness method can be used to calculate damped critical speeds, forced rotor response, and instability of the rotor in addition to the eigenvalues using similar methods of solution.

34.3.1.10 The Finite Element Analysis Method

The basis of the FEA method is to provide formulation for complex and irregular systems that can utilize the automation capabilities of computers (also see Chapter 9). The FEA method considers a rotordynamic system as an assemblage of discrete elements, where every such element has distributed and continuous properties, namely, the consistent representation of both mass and stiffness as distributed parameters. As illustrated in Section 34.3.1.9, the lumped-parameter method uses a consistent stiffness matrix equation (Equation 34.40) in its formulation, and therefore, the identical procedure can be adopted for the finite element method as well. For the distributed mass representation of an element, Archer (1963) procedure, which is based on the assumption that the mass distribution is proportional to the elastic distribution similar to the Rayleigh–Ritz formulation, is utilized. The resulting mass matrix is as follows:

$$[m^i] = \frac{m^i l_i}{420} \begin{bmatrix} 156 & 22l_i & 54 & -13l_i \\ 22l_i & 4l_i^2 & 13l_i & -3l_i^2 \\ 54 & 13l_i & 156 & -22l_i \\ -13l_i & -3l_i^2 & -22l_i & 4l_i^2 \end{bmatrix} \quad (34.44)$$

The overall stiffness matrix, $[K]$, for the entire system is assembled by combining the individual component matrices in a systematic manner according to Equation 34.41 and Equation 34.42. The overall mass matrix can also be assembled in precisely the same manner, as given by Equation 34.45 and Equation 34.46.

The mass matrix of the i th beam element in matrix notation can be represented as

$$[m^i] = [m_{j,k}^i] \quad (34.45)$$

where j and k varies from $(2i - 1)$ to $(2i + 2)$:

$$[M] = [M_{j,k}] = \sum_{i=1}^n \sum_{j=2i-1}^{2i+2} \sum_{k=2i-1}^{2i+2} m_{j,k}^i \quad (34.46)$$

Once the mass matrix and the stiffness matrix for the entire system are assembled, Equation 34.43 that describes the free vibration of the complete system can be solved. The solution methods of the eigenvalue problem, which can be utilized, are the same as those used for the direct stiffness method illustrated in Section 34.3.1.9 above. Details of the FEA methods are given in Ruhl and Booker (1972).

34.3.1.11 Torsional Analysis (Holzer Method)

The development of torsional analysis methods have gone through a similar evolutionary process to lateral vibration methods. Holzer (1921) first introduced the lumped-parameter numerical method to calculate torsional natural frequencies of a multi-DoF system. Even to-date, this is the most commonly used method because of its simplicity and reasonable degree of accuracy. The Holzer method is a transfer matrix formulation that uses a lumped parameter model similar to that used in the Myklestad–Phrol method described in Section 34.3.1.8. The only difference is that the transfer matrices represented by Equation 34.32 and Equation 34.35 are replaced by the equations

$$\begin{Bmatrix} \theta \\ T \end{Bmatrix}_n^r = \begin{bmatrix} 1 & 0 \\ -\omega^2 J & 1 \end{bmatrix}_n \begin{Bmatrix} \theta \\ T \end{Bmatrix}_n^l \quad (34.47)$$

$$\begin{Bmatrix} \theta \\ T \end{Bmatrix}_{n+1}^l = \begin{bmatrix} 1 & \frac{1}{k} \\ 0 & 1 \end{bmatrix}_{n+1} \begin{Bmatrix} \theta \\ T \end{Bmatrix}_n^r \quad (34.48)$$

Starting with node one, successive matrix multiplications are carried out until node $n + 1$ is reached. The result can be represented by Equation 34.38. The matrix $[T]$ is a function of the rotational speed, ω . In all cases, one boundary condition at each end of the rotor is known. A trial-and-error solution to determine the values of ω which satisfy the boundary conditions and Equation 34.38 are simultaneously determined. These values are the torsional critical speeds of the rotor. Once the critical speeds are calculated, the corresponding torsional mode shapes can also be determined using the transfer matrix procedure.

In the case of branched systems and geared systems, particular attention has to be paid to the relative rotational speeds of the components. The rule is quite simple: multiply all stiffness and inertias of the geared shaft by N^2 , where N is the speed ratio of the geared shaft to the reference shaft.

Other methods such as the distributed mass matrix method, direct stiffness method, and finite element method can also be used to determine torsional critical speeds of rotors. These procedures are very similar to those for lateral critical speed analysis.

34.3.2 Modeling

The design and analysis of rotordynamic systems require the development of models that simulate the behavior of the physical system. In the past, the critical speed of the rotor was considered to be the main criterion for stable operation. Today, stable, well-damped rotordynamic response to the exciting forces within a machine is considered to be a necessary condition for high reliability. The accuracy and reliability of the results greatly depends on the credibility of the system model and its adaptability to the analytical procedure. Even the most accurate and efficient analytical method cannot produce good results from a bad model. The methods that are commonly used to model shaft sections and disks and other such elements attached to shafts have been discussed in the previous sections. Useful formulae for calculating critical speeds of simple systems are given in Table 34.2. Models to represent bearings, rotor dampers, seals, and rotor–stator interactions are discussed in the following sections.

34.3.2.1 Journal Bearings

Journal bearings were used in rotating machinery for a long time before their dynamic characteristics were fully understood. Considerable effort has been expended in the last few decades to understand and develop techniques for their accurate representation in rotordynamic analysis. A variety of bearing types with improved characteristics have been developed over the years. Figure 34.11 shows the most commonly used types in rotating machinery. Hagg and Sankey (1958) were amongst the first to provide dynamic stiffness and damping coefficients for a number of these bearing types. However, these coefficients are considered incomplete as cross-coupling terms were not considered. Soon after, there was a flurry of activity related to the analysis of journal bearings; Sternlicht (1959), Warner (1963),

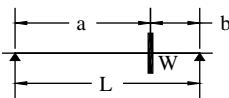
TABLE 34.2 Useful Formulas in Vibration Analysis and Design

Rankine formula	$\omega = \frac{k(Hg)^{1/2}}{b^2}$	Note: This formula is of historical interest only and has limited practical value
Greenhill formula	$\frac{d^4 y}{dx^4} - \frac{m\omega^2}{gEak^2} y = 0$	
Dunkerly equation	$\frac{1}{\omega_c^2} = \frac{1}{\omega_s^2} + \sum_{i=1}^n \frac{1}{\omega_i^2}$	

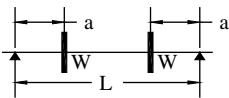
The above equation reduces to

$$\omega_c^2 = \frac{g}{\sum y_{\text{stat}}}$$

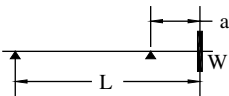
Formulas for natural frequency calculation (Blevins, 2001; Gorman, 1975)



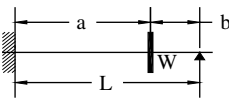
$$\omega_c = \frac{1}{ab} \sqrt{\frac{3EIL}{W}}$$



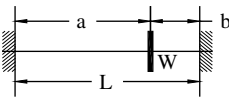
$$\omega_c = \frac{1}{a} \sqrt{\frac{6EI}{W(3L - 4a)}}$$



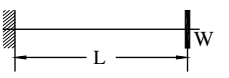
$$\omega_c = \frac{1}{a} \sqrt{\frac{3EI}{WL}}$$



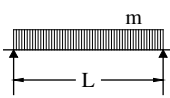
$$\omega_c = \left(\frac{12EIL^3}{Wa^3b^2(3L + b)} \right)^{1/2}$$



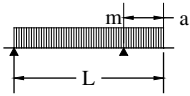
$$\omega_c = \left(\frac{3L^3EI}{Wa^3b^3} \right)^{1/2}$$



$$\omega_c = \left(\frac{3EI}{WL^3} \right)^{1/2}$$



$$\omega_c = \left(\frac{98EI}{mL^4} \right)^{1/2}$$

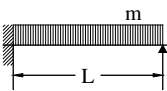


$$\omega_c = \left(\left(\frac{64a}{9L} \right)^2 - \left(\frac{6a}{L} \right) + \frac{16}{3} \right)^{1/2} \left(\frac{EI}{mL^4} \right)^{1/2},$$
$$\frac{a}{L} \geq 0.25$$

(continued on next page)

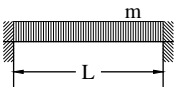
TABLE 34.2 (continued)

Formulas for torsional
natural frequency
calculation

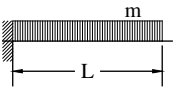

$$\omega_c = \left(\frac{237EI}{mL^4} \right)^{1/2}$$

$$\omega_c = \left(-74.7 \left(\frac{a}{L} \right)^2 + 22.1 \left(\frac{a}{L} \right) + 3.14 \right)^2 \left(\frac{EI}{mL^4} \right)^{1/2},$$

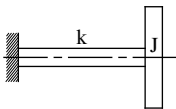
$$\frac{a}{L} < 0.25$$



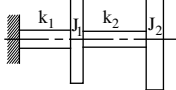
$$\omega_c = \left(\frac{502EI}{mL^4} \right)^{1/2}$$



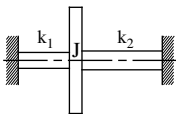
$$\omega_c = \left(\frac{12.4EI}{mL^4} \right)^{1/2}$$



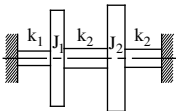
$$\omega_c = \left(\frac{k}{J} \right)^{1/2}$$



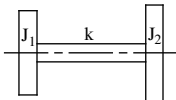
$$\omega_c = \frac{1}{\sqrt{2}} \left[\frac{k_1 + k_2}{J_1} + \frac{k_2}{J_2} \mp \left\{ \left(\frac{k_1 + k_2}{J_1} + \frac{k_2}{J_2} \right)^2 - \frac{4k_1k_2}{J_1J_2} \right\}^{1/2} \right]^{1/2}$$



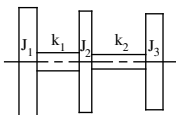
$$\omega_c = \left(\frac{k_1 + k_2}{J} \right)^{1/2}$$



$$\omega_c = \frac{1}{\sqrt{2}} \left[\frac{k_1 + k_2}{J_1} + \frac{k_2 + k_3}{J_2} \mp \left\{ \left(\frac{k_1 + k_2}{J_1} + \frac{k_2 + k_3}{J_2} \right)^2 - \frac{4(k_1k_2 + k_2k_3 + k_1k_3)}{J_1J_2} \right\}^{1/2} \right]^{1/2}$$



$$\omega_c = \left(\frac{k}{J_1} + \frac{k}{J_2} \right)^{1/2}$$



$$\omega_c = \frac{1}{\sqrt{2}} \left[\frac{k_1}{J_1} + \frac{k_1 + k_2}{J_2} + \frac{k_2}{J_3} \mp \left\{ \left(\frac{k_1}{J_1} + \frac{k_1 + k_2}{J_2} + \frac{k_2}{J_3} \right)^2 - \frac{4k_1k_2(J_1 + J_2 + J_3)}{J_1J_2J_3} \right\}^{1/2} \right]^{1/2}$$

Rayleigh equations

$$\omega^2 = \frac{EI \int_0^l \left(\frac{d^2y}{dx^2} \right)^2 dx}{\mu \int_0^l y^2 dx}$$

TABLE 34.2 (continued)

	$\omega^2 = \frac{\sum_{i=1}^n m_i y_i}{\sum_{i=1}^n m_i y_i^2}$	
Ritz method	$y = \sum_{i=1}^n a_i \Phi_i(x)$ $\frac{\partial}{\partial a_i} \frac{\int_0^l \left(\frac{d^2 y}{dx^2} \right)^2 dx}{\int_0^l y^2 dx} = 0$ $\frac{\partial}{\partial a_i} \int_0^l \left[\left(\frac{d^2 y}{dx^2} \right)^2 - \frac{\omega^2 \mu}{EI} y^2 \right] dx = 0$	
Stodola–Vianello method	$\{Y\} = \omega_f^2 [A] [m] \{Y\}, [A] = [K]^{-1}$	
Transfer matrix — Myklestad–Phrol method	$\begin{Bmatrix} y_{n+1}^1 \\ \theta_{n+1}^1 \\ M_{n+1}^1 \\ V_{n+1}^1 \end{Bmatrix} = \begin{bmatrix} 1 & l_n & \frac{l_n^2}{2EI_n} & -\frac{l_n^3}{6EI_n} \\ 0 & 1 & \frac{l_n}{EI_n} & \frac{l_n^2}{2EI_n} \\ 0 & 0 & 1 & -l_n \\ 0 & 0 & 0 & 1 \end{bmatrix} \begin{Bmatrix} y_n^r \\ \theta_n^r \\ M_n^r \\ V_n^r \end{Bmatrix}$	
Stiffness matrix for a beam element	$[K^i] = \frac{2EI_i}{l_i^3} \begin{bmatrix} 6 & 3l_i & -6 & 3l_i \\ 3l_i & 2l_i^2 & -3l_i & l_i^2 \\ -6 & -3l_i & 6 & -3l_i \\ 3l_i & l_i^2 & -3l_i & 2l_i^2 \end{bmatrix}$	
Mass matrix for a beam element	$[m^i] = \frac{m^i l_i}{420} \begin{bmatrix} 156 & 22l_i & 54 & -13l_i \\ 22l_i & 4l_i^2 & 13l_i & -3l_i^2 \\ 54 & 13l_i & 156 & -22l_i \\ -13l_i & -3l_i^2 & -22l_i & 4l_i^2 \end{bmatrix}$	
Squeeze-film damper coefficients	$k = \frac{24R^3 L \mu \omega \varepsilon}{C_r^3 (2 + \varepsilon^2)(1 - \varepsilon^2)}$ $c = \frac{12\pi R^3 L \mu}{C_r^3 (2 + \varepsilon^2)(1 - \varepsilon^2)^{1/2}}$ $k = \frac{2RL^3 \mu \omega \varepsilon}{C_r^3 (1 - \varepsilon^2)^2}$ $c = \frac{\pi RL^3 \mu}{2C_r^3 (1 - \varepsilon^2)^{3/2}}$	
Unbalance sensitivity	$SF = \frac{a}{U} M$	
Rolling element bearing defect frequencies	$f_{bor} = \frac{ND}{60d} \left[1 - \left(\frac{d}{D} \cos \theta \right)^2 \right]$	$N = \text{rotational speed (rpm)},$ $D = \text{rolling element pitch diameter}$

(continued on next page)

TABLE 34.2 (continued)

Lomakin formula for radial stiffness for a close clearance bushing	$f_{ir} = \frac{Nn}{120} \left(1 + \frac{d}{D} \cos \theta \right)$	d = rolling element diameter, N = number of rolling elements
	$f_{or} = \frac{Nn}{120} \left(1 - \frac{d}{D} \cos \theta \right)$	θ = contact angle with respect to axis, bor = ball or roller defect
	$f_c = \frac{N}{120} \left(1 - \frac{d}{D} \cos \theta \right)$	ir = inner race defect, or = outer race defect, c = cage defect
	$k = \frac{\pi}{8} (1 + s) \lambda \mu^4 \left(\frac{l}{b_m} \right)^2 \Delta p D$	
	$\mu^2 = \frac{1}{1 + s + (\lambda l / 2b_m)}$	
	b_m = radial clearance, l = length of bushing,	D = diameter, Δp = differential pressure across bushing,
	ζ = inlet loss coefficient,	λ = friction coefficient

Lund (1964), Lund (1965), Glienicke (1966), Orcutt (1967), Lund (1968), Someya et al. (1988), and several others provided complete bearing coefficients, including cross-coupling terms, for several bearing types. This information is considered to be a valuable resource for those engaged in rotordynamic analysis. The general form of the rotordynamic model for a journal bearing resulting from the above contributions is given by the following equation:

$$\begin{Bmatrix} F_X \\ F_Y \end{Bmatrix} = - \begin{bmatrix} k_{11} & k_{12} \\ k_{21} & k_{22} \end{bmatrix} \begin{Bmatrix} X \\ Y \end{Bmatrix} - \begin{bmatrix} c_{11} & c_{12} \\ c_{21} & c_{22} \end{bmatrix} \begin{Bmatrix} \dot{X} \\ \dot{Y} \end{Bmatrix} \quad (34.49)$$

Since the dawn of the digital computer era, several computer codes have been developed to analyze all aspects of journal bearings, including stiffness and damping coefficients. Many of these codes have been developed by equipment manufactures and research centers for their exclusive use. Several commercially available software codes popularized in North America are given in Table 34.3. Although bearing coefficients given in the form of charts and tables from the earlier studies are still in use, computer-based codes are growing in popularity.

34.3.2.2 Rolling Element Bearings

Rolling element bearings are used in numerous types of rotating machinery which are required to be compact, manage high loads, and have low heat rejection and simple lubrication systems. Unlike journal bearings, their load-carrying capacity is not speed-dependent and as a result is capable of full load capacity down to zero speed. Some of these salient features make rolling element bearings very attractive to many industries.

From a rotordynamic standpoint, rolling element bearings are modeled as linear spring elements with direct spring coefficients only. The damping terms are insignificant and as a result do not attenuate rotor deflections at critical speeds. A typical rolling element bearing is represented by the following equation:

$$\begin{Bmatrix} F_X \\ F_Y \end{Bmatrix} = - \begin{bmatrix} k & 0 \\ 0 & k \end{bmatrix} \begin{Bmatrix} X \\ Y \end{Bmatrix} \quad (34.50)$$

The absence of cross-coupling stiffness and damping terms signifies that bearing induced rotor instability will not occur. Although, for convenience of analysis, the spring stiffness is considered linear, its

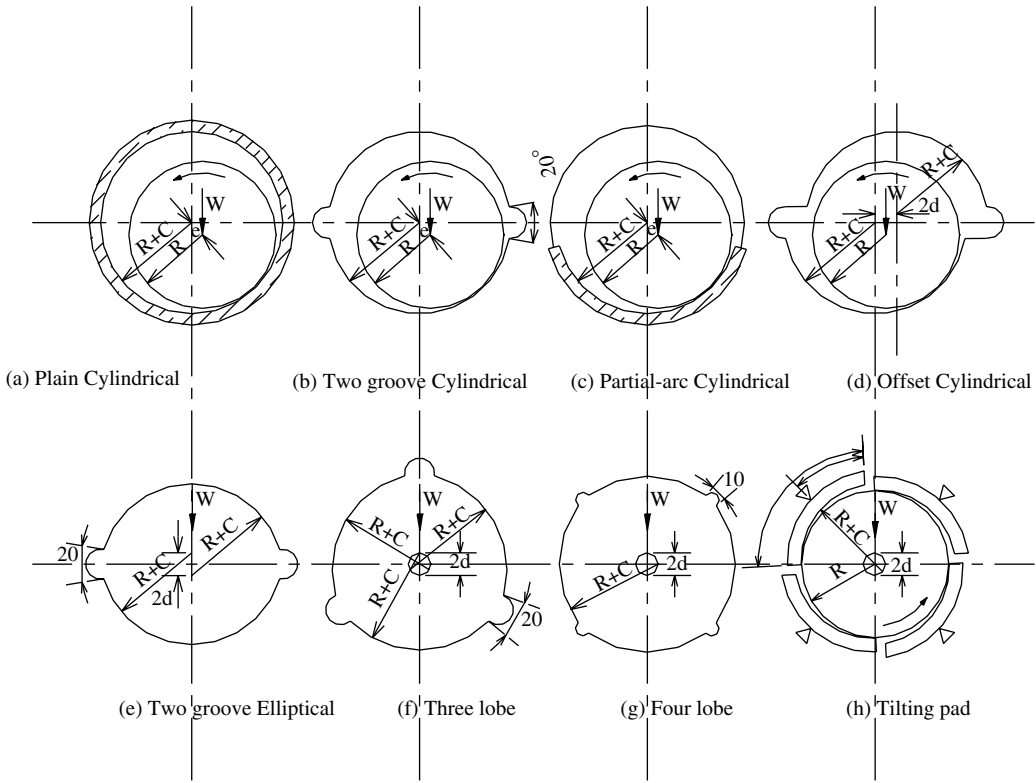


FIGURE 34.11 Common types of journal bearings.

true behavior can be quite the opposite, leading to some calculation inaccuracies. The nonlinearities are most significant where the bearings have no preload and some internal clearance in the bearings exists. Preloaded bearings with little or no internal clearance behave quite linearly. Jones (1960), Harris (1991), and Kramer (1993) have analyzed the bearing stiffness coefficients for the common types of rolling element bearings, and this data can be utilized for rotordynamic study of rotating machinery.

34.3.2.3 Squeeze-Film Dampers

Squeeze-film dampers are used to introduce damping capacity to a rolling element bearing or, in the case of journal bearings, to provide additional damping and stiffness to eliminate rotor instability problems. Squeeze-film dampers have come into prominence through the modern aircraft gas turbine industry where the bearing of choice is the rolling element bearing. In the mid-1970s, several designs were introduced to add damping capacity and predictable stiffness to the rolling element bearings. In its basic form, a squeeze-film damper is very similar to a nonrotating cylindrical journal bearing where the outer race of the rolling element bearing forms the journal as illustrated in Figure 34.12. The addition of end seals (to control leakage) and centering springs are modifications that have been introduced to enhance its performance. The interactive force at a bearing using a squeeze-film damper can be represented by the following equation:

$$\begin{Bmatrix} F_X \\ F_Y \end{Bmatrix} = - \begin{bmatrix} k & 0 \\ 0 & k \end{bmatrix} \begin{Bmatrix} X \\ Y \end{Bmatrix} - \begin{bmatrix} c & 0 \\ 0 & c \end{bmatrix} \begin{Bmatrix} \dot{X} \\ \dot{Y} \end{Bmatrix} \quad (34.51)$$

The stiffness and damping coefficients for the squeeze-film dampers have been derived (Ehrich, 1999), from the solution of the Reynolds' equation for the case of a nonrotating journal bearing. For dampers with end seals, the long journal bearing theory is used to generate the following stiffness and damping

TABLE 34.3 Rotordynamic Analysis Software

Name of Software	Type of Analysis	Supplier
CAD20	Lateral critical speeds of flexible rotors	CADENSE Programs, Foster Miller Technologies Inc., Albany, NY, USA
CAD21	Unbalance response of flexible rotors	
CAD21a	Response of flexible rotors to nonsynchronous sinusoidal excitation	
CAD22	Torsional critical speeds and response of geared systems	
CAD24	Transient torsional critical speeds of geared system	
CAD25	Dynamic stability of flexible rotors	
CAD25a	Transient response of flexible rotors	
CAD26	Lateral critical speeds of multilevel rotors	
CAD27	Unbalance response of multilevel rotors	
CAD30	Dynamic coefficients of liquid lubricated journal bearings	
CAD30a	Dynamic coefficients of ball bearings	
CAD31	Dynamic coefficients of liquid lubricated tilting pad journal bearings	
CAD32	Dynamic coefficients of liquid lubricated axial-groove and single pad journal bearings	
CAD34a	Performance of tilting pad thrust bearings	
CAD34b	Performance of tapered-land thrust bearings	
CAD36	Dynamic coefficients of liquid lubricated pressure dam journal bearings	
CAD38	Dynamic coefficients of liquid lubricated deep-pocket hydrostatic journal bearings	
CAD40	Dynamic coefficients of gas lubricated journal bearings	
CAD41	Dynamic coefficients of gas lubricated tilting pad journal bearings	
CAD42	Dynamic coefficients of gas lubricated spiral groove journal bearings	
CAD42i	Dynamic coefficients of liquid lubricated spiral groove journal bearings	
FEATURE	Rotor bearing system analysis	
COJOUR	Analysis of journal bearings	
DYNROT	A program designed to perform a complete study of the rotordynamic behavior of rotors. It is capable of linear, nonlinear and torsional analysis of rotors	Dipartimento di Meccanica, Politecnico di Torino, Torino, Italy
DyRoBeS	Comprehensive rotordynamic analysis software for lateral and torsional analysis, including bearing analysis of rotor-bearing systems	AGILE SOFTWARE CONCEPTS NREC White River Junction, VT, USA
RotorLab	A software package for agile modeling of rotor systems, bearings, and seals. It combines the tasks of design, modeling, analysis, post processing, and data management into a consistent user interface	
DAMBRG2	Coefficients and rigid rotor stability information for two-lobe isoviscous bearings with a pressure dam in only one pad	ROMAC—Rotating Machinery and Controls Laboratory, University of Virginia, Charlottesville, VA, USA
HYDROB	Predicts the steady state and dynamic operating characteristics of hybrid journal bearings	
PDAM2D	This program can analyze stiffness and damping coefficients, and the rigid rotor stability threshold of multipad pressure dam bearings	
SQFDAMP	Determines stiffness and damping coefficients for short and long squeeze-film bearings with and without fluid film cavitation	
THBRG	Dynamic coefficients of multilobe journal bearings with incompressible fluid	

TABLE 34.3 (continued)

Name of Software	Type of Analysis	Supplier
THPAD	Dynamic coefficients of tilting pad journal bearings with incompressible fluid	Rotordynamics Laboratory, Texas A&M University, College Station, TX, USA
THRUST	Predicts the steady-state operating characteristics of tilting-pad and fixed geometry fluid-film thrust bearings	
CRTSP2	Undamped lateral critical speeds of dual-level rotor systems	
MODFR2	Undamped lateral critical speeds of single or dual-level rotor systems	
TWIST2	Undamped torsional critical speeds and mode shapes of rotor systems	
FRESP2	Predicts the modal frequency forced response of dual rotor systems with a flexible substructure	
RESP2V3	Nonplanar synchronous unbalance response of dual-level multimass flexible rotors	
HCOMB	Dynamic coefficients of straight-through honeycomb seals with a compressible gas	
LABY3	Dynamic coefficients for straight-through and uniform interlocking type labyrinth seals with a compressible fluid	
SEAL2	Stiffness and damping coefficients for plain and grooved seals with incompressible turbulent axial flow	
SEAL3	Stiffness, damping and mass coefficients of both plain and circumferentially grooved seals	
TURSEAL	Stiffness and damping coefficients of turbulent flow annular seals or water lubricated bearings	
FSTB3	Stability, damped critical speeds, and whirl mode shapes of multispool rotor systems	
ROTSTB	Stability, damped critical speeds, and whirl mode shapes of single spool rotor systems	
COTRAN	Nonlinear time transient analysis of multilevel rotors with substructure	
TORTRAN3	Transient torsional rotor response	
hydrosealt	Stiffness and damping coefficients, and threshold speed of instability of cylindrical-pad journal bearings and pad-hydrostatic bearings of arbitrary arc lengths and preloads	
hydroflex	Stiffness and damping coefficients, and threshold speed of instability of a variety of bearing and seal types	
hydrotran	Predicts the transient force response of a rigid rotor supported on fluid film bearings	
hydrojet	Force coefficients for a variety of hybrid bearing and seal types handling process fluids	
hydroTRC	Stiffness and damping coefficients for a variety of bearing and seal types and for different types of fluids	
hseal2p	Stiffness and damping coefficients of seals that operate under two-phase flow conditions	
fembear	Stiffness and damping coefficients of cylindrical and fixed arc pad hydrostatic and hydrodynamic bearings for laminar and isothermal flow conditions	
sdfem	Damping force coefficients of finite length squeeze-film dampers executing circular centered motion	
sdflexs	Instantaneous fluid film forces for arbitrary journal motions and circular centered orbits in multiple pad integral squeeze-film dampers	
hsealm	Stiffness and damping coefficients of cylindrical annular pressure seals	

(continued on next page)

TABLE 34.3 (continued)

Name of Software	Type of Analysis	Supplier
lubsealn	Stiffness and damping coefficients of single-land and multiple-land high pressure oil seal rings and cylindrical journal bearings	
ROTECH	Lateral rotordynamic analysis for critical speeds; unbalance response, linear stability and nonlinear transient response of rotors. Also includes a torsional rotordynamic analysis program	ROTECH Engineering Services, Delmont, PA, USA
ROTOR-E	A comprehensive software package for lateral rotordynamic analysis of rotating equipment	Engineering Dynamics Inc., San Antonio, TX, USA
ROTORINSA	A software package devoted to the prediction of the steady-state lateral dynamic behavior of rotors	Laboratoire de Mecanique des Structures, LMST INSA Lyon, Lyon, France
TURBINE-PAK	A software package for rotordynamic analysis of nonlinear multibearing rotor-bearing-foundation systems	Scientific Engineering Research, Mt Best, Vic., Australia.
TURBINE-PAK NONLINEAR	Designed to study transient responses of rotor-bearing-foundation systems, including the loss of stability of the system	
XLrotor	A complete suite of analysis tools for rotating machinery dynamics. Handles both lateral and torsional analysis of rotors. Also includes codes for calculating coefficients for fluid film and antifriction bearings	Rotating Machinery Analysis Inc., Austin, TX, USA
XLTRC	A suite of codes for executing a complete lateral rotordynamic analysis of rotating machinery	The Turbomachinery Laboratory, Texas A&M University, College Station, TX, USA
XLAnSeal	Force and moment coefficients for annular turbulent seals in the laminar, turbulent, and transition flow regimes	
XLGrv	Coefficients for centered grooved-stator, turbulent flow, annular pump seals	
XLlaby	Stiffness and damping coefficients for tooth-on-rotor or tooth-on-stator gas labyrinth seals	
XLIsotSL	Coefficients for smooth rotor/honeycomb stator annular seals	
XLlbgT	Coefficients for high-pressure oil bushing seals of compressors or smooth pump seals in the laminar flow regime	
XLJrnl	Stiffness and damping coefficients for fixed-arc and tilting-pad bearings	
HLHydPad	Stiffness and damping coefficients for hydrostatic and hybrid journal-pad bearings in the laminar flow regime	
XLTFPBrg	Stiffness and damping coefficients for fixed-arc, tilting-pad and flexure-pivot hydrostatic bearings	
XLPresDm	Stiffness and damping coefficients for multilobed, rigid-pad arc bearings with preload and pressure-dam bearings with relief tracks	
XLBalBrg	Stiffness coefficients for ball bearings	
XLlSFD	Damping and mass coefficients for locally sealed squeeze-film dampers	
XLlOSFD	Damping and mass coefficients for open ended squeeze-film dampers	
XLlSFDfEM	Damping coefficients for squeeze-film dampers with various types of end seals	
XLlPIMPLR	Stiffness, damping, and mass matrices for centrifugal pump impellers	
XLWachel	Destabilizing cross-coupled force coefficients for impellers of centrifugal compressors	
XLClrEx	Destabilizing cross-coupled stiffness coefficients for unshrouded turbines	

coefficients:

$$k = \frac{24R^3 L \mu \omega \varepsilon}{C_r^3 (2 + \varepsilon^2)(1 - \varepsilon^2)} \quad (34.52)$$

$$c = \frac{12\pi R^3 L \mu}{C_r^3 (2 + \varepsilon^2)(1 - \varepsilon^2)^{1/2}} \quad (34.53)$$

where

R = the damper radius

ω = whirl speed

L = length of damper

μ = viscosity of oil

C_r = the radial clearance

ε = eccentricity ratio (orbit radius/ C_r)

Similarly, for a damper without end seals, the short journal bearing theory yields the following stiffness and damping coefficients:

$$k = \frac{2RL^3 \mu \omega \varepsilon}{C_r^3 (1 - \varepsilon^2)^2} \quad (34.54)$$

$$c = \frac{\pi RL^3 \mu}{2C_r^3 (1 - \varepsilon^2)^{3/2}} \quad (34.55)$$

Although the above equations, based on the Reynolds' equation, have been proposed to predict damper characteristics, the experimental evidence does not validate these equations. Therefore, these equations should be used with caution for practical purposes.

34.3.2.4 Annular Seals

Annular seals are primarily used in pumps, compressors, gas turbines, and steam turbines to minimize leakage and thereby improve the volumetric efficiency of the machine. In addition to their basic function, they also play a vital role in the rotordynamics of the machine, especially in multistage machines, providing stiffness and damping and thereby enhancing high-speed operational capability. In fact, in the last few decades, most of the development work on seals has focused on understanding and improving their dynamic vibration characteristics rather than improving their efficiency in sealing.

Lomakin (1958) was the first to publish on the restoring forces in smooth annular clearances in pumps. However, it was more than a decade later that Black (1968) provided the major initial impetus for the understanding and development of seals. Childs (1993) provided an excellent compendium of the research work conducted in the area of seals. His book also provides the most comprehensive coverage of the subject of seal dynamics.

In the present context, seals are handled in the same manner as the stiffness and damping characteristics of journal bearings with some degree of modifications. In particular, fluid inertia effects are included, and it is assumed that the center of the shaft orbit is the same as the center of the stationary seal ring. Assuming rotational symmetry the reaction force-seal motion model can be represented by the following equation:

$$\begin{Bmatrix} F_X \\ F_Y \end{Bmatrix} = - \begin{bmatrix} k & k_c \\ -k_c & k \end{bmatrix} \begin{Bmatrix} X \\ Y \end{Bmatrix} - \begin{bmatrix} c & c_c \\ -c_c & c \end{bmatrix} \begin{Bmatrix} \dot{X} \\ \dot{Y} \end{Bmatrix} - \begin{bmatrix} m & 0 \\ 0 & m \end{bmatrix} \begin{Bmatrix} \ddot{X} \\ \ddot{Y} \end{Bmatrix} \quad (34.56)$$

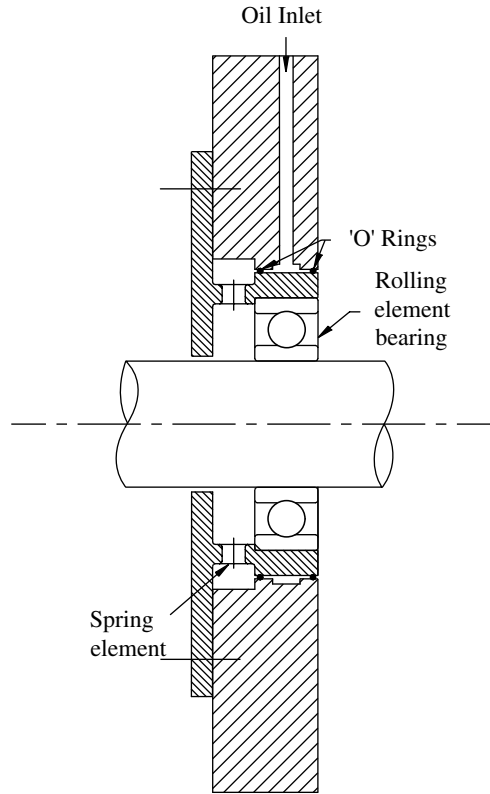


FIGURE 34.12 A squeeze-film damper.

An added complexity is the predominance of turbulent flow in annular seals. This invalidates the use of Reynolds' equation for the derivation of seal coefficients. The highest degree of accuracy can be obtained by the direct solution of the Navier–Stokes and continuity equations. However, at the present moment, such methods are considered to be excessively costly and impractical. As a result, two practical semiempirical methods have been developed to derive seal coefficients. In the first approach, the semiempirical turbulent model is directly substituted in the Navier–Stokes equation and a numerical technique is used for its solution. The second, most commonly used technique uses a bulk flow model together with control volume formulations, namely, the continuity equation and momentum equation, to obtain the desired results. For a detailed discussion of these methods, solution techniques, the influence of various physical parameters on the coefficients, and an excellent compilation of computational and experimental results, the publication by Childs (1993) is recommended.

34.3.2.5 Impeller–Diffuser/Volute Interface

It is widely known that the flow fields within certain types of rotating machinery can significantly influence its vibration behavior. Thomas (1958) recognized and explained the presence of destabilizing clearance excitation forces in axial flow steam turbines. Black (1974) was the first to suggest that centrifugal pump impellers could also develop destabilizing forces. The nature of these forces and their influence on rotor instability has been explained in Section 34.2.2.2 and Section 34.2.2.3 of this chapter. The impeller–diffuser/volute forces assuming rotational symmetry can generally be modeled by an equation of the following form:

$$\begin{Bmatrix} F_X \\ F_Y \end{Bmatrix} = - \begin{bmatrix} k & k_c \\ -k_c & k \end{bmatrix} \begin{Bmatrix} X \\ Y \end{Bmatrix} - \begin{bmatrix} c & c_c \\ -c_c & c \end{bmatrix} \begin{Bmatrix} \dot{X} \\ \dot{Y} \end{Bmatrix} - \begin{bmatrix} m & m_c \\ -m_c & m \end{bmatrix} \begin{Bmatrix} \ddot{X} \\ \ddot{Y} \end{Bmatrix} \quad (34.57)$$

For analytical procedures for the derivation of impeller interaction coefficients and a comparison of experimental data, the work by Childs (1993) is recommended. It is well recognized that a considerable amount of work still needs to be done towards understanding the complex nature of impeller–diffuser/volute interactive forces, especially at off-design conditions.

34.3.3 Design

Since the real machine is not available for tests, at the preliminary design stage it is a common practice to develop an accurate mathematical model of the machine to predict its dynamic behavior in operation. It is also prudent to understand and estimate how the machine will interact with its operating environment and how the environment could influence the operation of the machine. A suitable model of the rotor can be developed using the techniques described in Section 34.3.2, and the rotordynamic characteristics of the machine can be analyzed using one of the methods described in Section 34.3.1, above. Based on these methods, numerous computer-based rotordynamic analysis programs have been developed. A listing of the most widely known computer programs in North America is given in Table 34.3. The objectives of the analysis are to predict the critical speeds, excitation frequencies, the amplitudes of deflection, and the magnitude of the forces of the rotor within its full operating range. In certain situations, evaluation of the energy content of the excitation may also be required.

Once the mathematical model is developed, the eigenvalues of the rotor and the mode shapes can be determined. The results can then be presented in the form of a Campbell diagram, where the eigenvalues along with the excitation frequencies are plotted as a function of rotor speed. Critical speeds occur at the speeds corresponding to the points of intersection of the excitation frequency lines and the eigenvalue lines. The Campbell diagram presentation (Figure 34.13) of the results is very useful since the influence of key parameters such as stiffness, damping, clearances (new and worn conditions), and so on can all be shown on the same diagram. A critical speed, although present, may be of little consequence if it is associated with sufficient damping. As illustrated in Figure 34.4, when the damping ratio $\zeta \geq 0.707$, the system is critically damped and above this level of damping there is no amplification of the rotor deflection. At or near a critical speed the amplification factor is $\approx 1/2\zeta$. Using this estimated value,

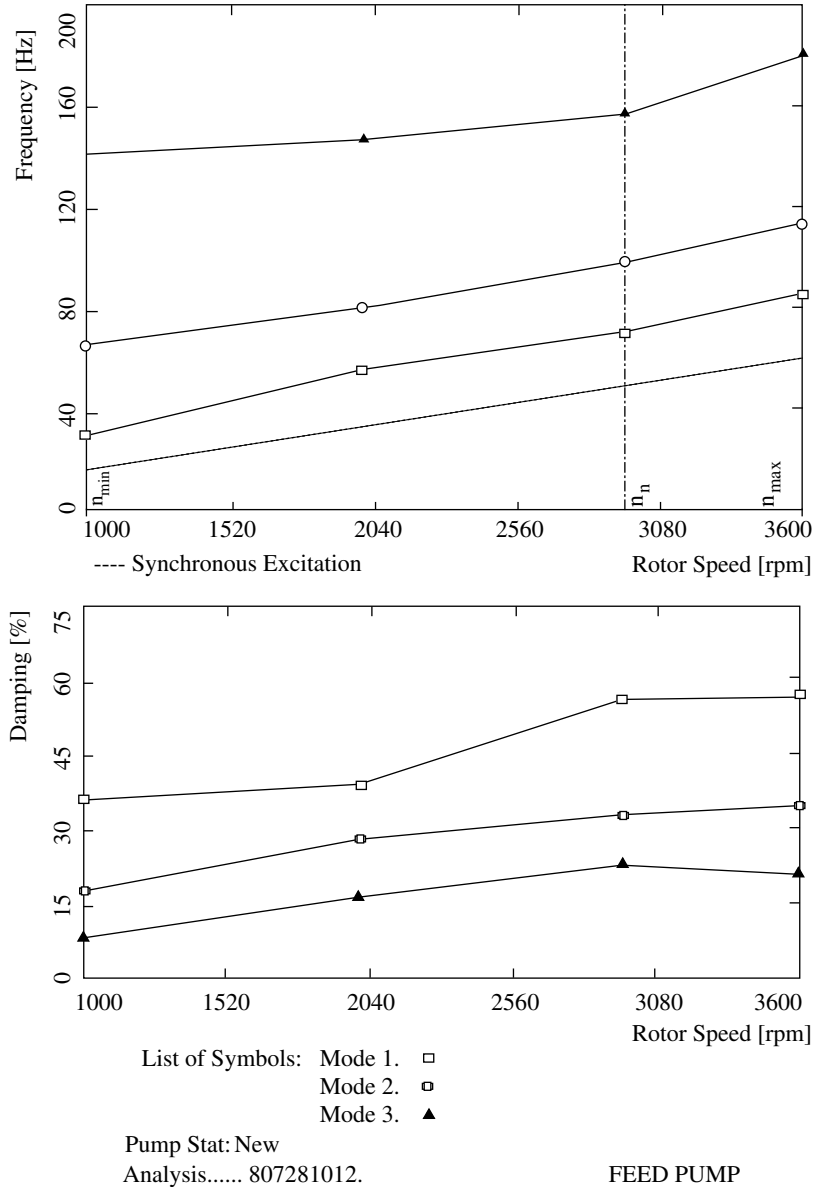


FIGURE 34.13 Campbell diagram for a multistage pump.

depending on the internal clearances of the machine, it is possible to assess if the rotor can pass through a critical speed without causing damage to the components. An amplification factor of 2.5 or below is a typical acceptance limit for centrifugal pumps, even for continuous operation at or near it. However, if the amplification factor exceeds the acceptable limits or the critical speeds are too close to the continuous operating speed, then design modifications have to be made to change the critical speed values. At the design stage, it is considered good practice to ensure that the critical speeds are not within $\pm 10\%$ of the continuous operating speed; these limits are sometimes referred to as *separation margins*. The mode shapes of the rotor are important from the standpoint of identifying where the maximum deflections occur. It also provides a good guide for assessing design modifications to improve damping or reduce sensitivity to unbalance forces.

The eigen analysis only provides relative deflections of the rotor. In order to estimate true deflections, a forced response analysis has to be made. Forcing functions of estimated magnitude are applied at selected locations to determine the resulting deflections at specific points on the rotor. This type of analysis is typically carried out for synchronous excitation forces only. The nature of the forcing function depends on the type of the machine; mechanical unbalance is common to all types of machines, whereas hydraulic unbalance is relevant to centrifugal pumps and electrical unbalance to electric motors. The challenge, of course, is to determine the magnitudes, directions, and locations of the forces to apply and how the resulting rotor response should be judged. Of course, these criteria are machine type-dependent and not necessarily applicable to all types of rotating machinery. An example of how forced response analysis on centrifugal pumps is evaluated is given below (Bolleter et al., 1992):

1. Maximum amplification factors and required separation margins are defined by specifications; example as shown in API 610, 8th edn., 1995.
2. Excitation forces are defined and the response is judged relative to admissible shaft vibration limits, and relative to clearances.
3. Apply unbalance forces of such a magnitude that maximum permissible vibration limits at the vibration probe locations are reached, and then evaluate if the deflections exceed the minimum clearances in the machine.
4. Apply an unbalance force of arbitrary magnitude and determine the resulting response at the same or another location, and calculate the sensitivity factor (SF) using the following formula:

$$SF = \frac{a}{U} M \quad (34.58)$$

where

a = rotor deflection

U = unbalance force

M = rotor mass

The sensitivity factor should then be compared with experimental base values of similar machines for acceptance. The rotor responses to the applied forces can be further analyzed to extract other parameters of interest, such as phase angles and force magnitudes at the bearings, in order to evaluate the design.

In order to optimize the rotating machine design in terms of placement of critical speeds and control of deflections and forces, a parameter sensitivity coefficients analysis (Lund, 1979; Rajan et al., 1986; Rajan et al. 1987) may be carried out. For speed and convenience of analysis, the optimization routine can be automated.

- Rotordynamic analysis is a part of the current rotating machinery design practice used to predict their vibration behavior.
- The most current rotordynamic analytical procedures are computer-based and are derived from the lump-parameter model or the transfer matrix method.
- In the lumped-parameter model method, the distributed elastic and inertial properties of the rotor are represented as a collection of rigid bodies connected by massless elastic beams.
- In the transfer matrix method, commonly called the FEA method, the rotor is represented as an assembly of elements with distributed elastic and inertial properties.
- Accurate modeling and representation of rotor components is vital to the accuracy and reliability of analysis results. As a result, significant advancement in modeling shaft sections, disks, impellers, bearings, seals, rotor dampers, and rotor–stator interactions have been made.

34.4 Vibration Measurement and Techniques

34.4.1 Units of Measurement

The most commonly used units of measurement of vibration are as follows:

- Displacement (peak to peak): millimeter (mm) or micron (10^{-6} m) in metric units, and *thou* or *mil* (0.001 in) in imperial units
- Velocity (peak, RMS or “true peak”): mm/sec or m/sec in metric units, and in./sec in imperial units
- Acceleration (RMS): *g* or m/sec^2 in metric units, and *g* or in./sec^2 in imperial units
- Frequency: hertz (Hz) or cycles/min (cpm) in both systems of units
- Phase angle: degrees in both systems of units

34.4.2 Measured Parameters and Methods

Under steady-state conditions, the vibration from a rotating machine is a periodic signal of a complex waveform. During unstable operation or upset conditions, the signal may become random in nature. In certain types of machines, transient signals that are nonperiodic could also be present due to internal impacts and damping. Based on the simple spring–mass system and the mathematical Fourier analysis procedure, all periodic complex waveforms can be reduced to the sum of a series of sinusoidal functions. In the case of random signals, averaging techniques are used to reduce them to periodic signals for convenience of analysis.

A quantitative assessment of the vibration can be made in terms of the amplitude, velocity, acceleration, or the magnitude of force of the motion. Other key parameters such as frequency, phase angle, and the time-varying nature of the signal are important in fully characterizing it. Because the true signal is not purely sinusoidal, it is important to identify its magnitude as, *peak*, *peak-to-peak* or *root mean square* (RMS). The preferred parameter of measurement varies throughout the industry and depends on the nature, complexity, and type of machine, and the purpose for which it is measured. A general classification of measured parameters and techniques based on industry and rotating machine type is given in [Table 34.4](#).

- The displacement amplitude, velocity, acceleration, frequency, and phase angle of the vibration signal are some of the parameters that can be used to assess the condition of a rotating machine.
 - The vibration signals generated by a typical rotating machine is complex in nature and, therefore, requires various mathematical analysis procedures and signal averaging techniques to reduce them to simple and interpretable forms.

34.5 Vibration Control and Diagnostics

34.5.1 Standards and Guidelines

Given the fact that some degree of vibration is always present in rotating machinery, some means of judging “how much is too much” has to be established so that vibrations can be controlled within reasonable limits. When such a judgment is not based on a scientific method, there is room for speculation and it will depend on the one making the decision, the manufacturer, end user, the governing authority, and so on. Since vibrations are a key indication parameter of the performance of rotating machinery, different interest groups monitor it for a variety of purposes. It can be used as a measure of

TABLE 34.4 Measurement Parameters and Techniques

Measurement/Technique	Description	When/Where Used
Acceleration, RMS	When high frequency or force of the vibration is of interest	Gear boxes, rolling element bearings, gas/steam turbines. Mainly used by defense and aerospace industry
Bode/Nyquist plot	Plot of displacement amplitude and phase angle vs. speed	Observe critical speeds and instability in machines using journal bearings
Cepstrum analysis	Inverse Fourier transform of logarithmic power spectrum	To detect families of harmonics and sidebands in gearboxes, rolling element bearings, and electric motors
Condition monitoring	Analysis of signals generated by the machine to determine its condition on a continuous or periodic basis	On critical equipment where predictive maintenance programs are used. Can reduce equipment redundancy
<i>Displacement peak-to-peak</i>		
(a) Absolute	Absolute displacement amplitude of rotor vibration	Where the rotor mass is very much larger than the stator mass. Large motors, generators, and fans
(b) Relative	Relative displacement amplitude of rotor vibration	Commonly used on machines with journal bearings or in close clearance seals
(c) External	Absolute displacement amplitude of stator component vibration	Low speed machines (less than 1000 rpm)
Modal analysis	To measure the vibration response of a structure to an applied force. The force can be periodic or an impact force	To determine the modal mass, stiffness and damping properties of a structure. Also used to measure structural natural frequencies
Orbit analysis	The path of the shaft centerline motion during rotation	Diagnostics of machines using journal bearings. Provides a picture of the motion of the journal in the bearing
Polar plots	A polar graph of amplitude versus phase at various machine speeds	Similar to Bode plots, can be used to detect critical speeds and instability. Modal properties can also be extracted from polar plots
Phase angle	Phase angle of vibration signal	Useful in balancing, diagnosing critical speeds, and misalignment problems
<i>Rolling element bearing analysis</i>		
(a) Acceleration	Measure the amplitude of all pass and discrete frequency accelerations	When damage has progressed to generate audible noise amplitudes increase. Useful from 5–5 kHz
(b) Shock pulse method	A high frequency resonance technique tuned to the detector natural frequency	Early detection of failure, measures ultrasonic noise. Proprietary technique
(c) Envelope technique	Bearing defects cause periodic impacts, which make bearing components resonate. Demodulation and enveloping techniques are used to detect the impact (fault) frequencies	Used for early failure detection (ultrasonic noise) as well as for advanced stages of damage (audible noise)
(d) Spike energy method	Measure the broadband acceleration over the 5–45 kHz range	Used for early failure detection (ultrasonic noise) as well as for advanced stages of damage (audible noise)
(e) Kurtosis method	The normalized fourth moment of the probability distribution of acceleration over the 2–80 kHz range	Used for early failure detection (ultrasonic noise) as well as for advanced stages of damage (audible noise)
Run-up, run-down analysis (waterfall/cascade plots)	Three-dimensional plot of frequency or time spectrum vs. time or speed	Used for diagnosing a variety of vibration problems. Helpful in analyzing transient signals

TABLE 34.4 (continued)

Measurement/Technique	Description	When/Where Used
Spectrum analysis	Plot of amplitude vs. frequency of vibration	Used for diagnostics, to determine frequency, harmonics, side bands, beats, transfer functions, etc., and to control of vibrations levels at discreet frequencies
Trend analysis	Vibration data collected periodically over an extended time domain	Useful in predictive maintenance programs in assessing machine conditions
Time averaging	Averaging of time records using triggering at the same point of the waveform of a repetitive signal	Used in the analysis of faulty gearboxes. Can reduce asynchronous components in the signal and improve signal-to-noise ratio
Time-domain analysis	Plot of amplitude versus time	To observe amplitude modulation, beats, impacts, transients, and phase angle. Very useful in diagnostics
Velocity-peak or RMS	Velocity amplitude of vibration signal	Parameter most commonly used in many industries to monitor vibrations. Peak readings relate to peak stress levels and rms to energy of vibrations

quality and workmanship or the common basis for acceptance between the user and manufacturer. From a safety point of view, the operator can establish *normal*, *alarm*, and *shutdown levels* based on vibration limits. Vibration levels are also used in making maintenance decisions in rotating machinery.

Rathbone (1939) was the first to publish guidelines for vibration limits for machinery, based on his experience as an insurance agent. Since that time, numerous individuals, organizations, and governing bodies have developed a variety of guidelines and standards for vibration levels in rotating machinery. A listing of the more commonly used guidelines and standards is given in [Table 34.5](#). It should be recognized that these are experience-based standards, and therefore, will grow and develop with technology.

ISO 10816 Part 1 to Part 5 is a comprehensive set of standards that has been developed for the evaluation of vibration of rotating machinery by measuring the vibration response on nonrotating, structural components such as bearing housings. Vibration measuring points as specified by these standards are shown in [Figure 34.14](#). In a similar vein, ISO 7919 Part 1 to Part 5 has been developed for the evaluation of vibration by measuring the vibration on rotating shafts. These standards cover the most widely used types of rotating machinery and they relate to both operational monitoring and acceptance testing of equipment. [Table 34.6](#) and [Table 34.7](#) are derived from these standards and are presented as a general guideline for vibration limits of rotating machinery. For specific details, including the limitations of the standards, the reader is advised to refer to the relevant sections of ISO 10816 and ISO 7919 Standards.

34.5.2 Vibration Cause Identification

Vibrations are an inherent part of all rotating machinery. Vibration can be due to many causes: improper design, practical manufacturing limits, poor installation, the effect of system environment, component deterioration, operation outside of design limits, or a combination of the above. At times, finding the exact cause of vibration can be quite a challenge, as several of the causes have similar symptoms. [Table 34.8](#) is a list of the more commonly known causes of vibration in rotating machinery and their symptoms.

34.5.3 Vibration Analysis — Case Study

In the past, it was common practice to operate centrifugal pumps at a fixed speed and attain required flow changes by means of throttling. This forces the pump to operate at low efficiency conditions

TABLE 34.5 Vibration Guidelines and Standards

Year	Author/ Organization	Reference Number	Title/Description
2002	AGMA	ANSI/AGMA 6000-B96	Specification for Measurement of Linear Vibration on Gear Units
2003	API	ANSI/API std 541-2003	Form-Wound Squirrel-Cage Induction Motors 500 hp and Larger
1997	API	API STD 546, second edition	Brushless Synchronous Machines, 500 kVA and Larger
2004	API	API STD 610/ISO 13709, ninth edition	Centrifugal Pumps for Petroleum, Petrochemical and Natural Gas Industries
1997	API	API STD 611, fourth edition	General Purpose Steam Turbines for Petroleum, Chemical and Gas Industry Services
2005	API	API STD 612/ISO 10437, sixth edition	Petroleum, Petrochemical and Natural Gas Industries – Steam Turbines – Special-Purpose Applications
2003	API	API STD 613, fifth edition	Special Purpose Gear Units for Petroleum, Chemical and Gas Industry Services
1998	API	API STD 616, fourth edition	Gas Turbines for the Petroleum, Chemical, and Gas Industry Services
2002	API	API STD 617, seventh edition	Axial and Centrifugal Compressors and Expander-compressors for Petroleum, Chemical and Gas Industry Services
2000	API	API STD 670, fourth edition	Mechanical Protection Systems
2004	API	API STD 672, fourth edition	Packaged Integrally Geared, Centrifugal Air Compressors for Petroleum, Chemical, and Gas Industry Services
2001	API	API STD 673, second edition	Special Purpose Fans
1997	API	API STD 677, second edition	General Purpose Gear Units for Petroleum, Chemical, and Gas Industry Services
1996	API	API STD 681, first edition	Liquid Ring Vacuum Pumps for Petroleum, Chemical, and Gas Industry Services
2000	API	API STD 685, first edition	Sealless Centrifugal Pumps for Petroleum, Heavy-Duty Chemical, and Gas Industry Services
1965	BDS	BDS 5626-65	Measurement of Vibration on Electrical Rotating Machines
1964	Blake, M.P.	Hydrocarbon Processing, January 1964	New Vibration Standards for Maintenance
1963	CAGI		In-Service Standards for Centrifugal Compressors
1975	CAGI		Standard for Centrifugal Air Compressors
1971	CSN	CSN 011410	Permitted Limits for Unbalanced Solid Machine Elements
1968	Dresser Industrial		General Guidelines for Vibration on Clark Centrifugal Compressors
1966	Gosstandart	GOST 12379-66	Measurement of Vibration on Electrical Rotating Machines
2002	HI	ANSI/HI 9.6.4	Centrifugal and Vertical Pumps — Vibration Measurement and Allowable Values
1996	IEC	IEC 60034-14	Rotating Electrical Machines, Part 14: Mechanical Vibrations of Certain Machines with Shaft Heights 56 mm and Higher — Measurement, Evaluation and Limits of Vibration
1964	IRD	IRD #305D	General Machinery Vibration Severity Chart
1995–2001	ISO		Mechanical Vibration — Evaluation of Machine Vibration by Measurements on Nonrotating Parts:
		ISO 10816-1:1995	Part 1: General Guidelines
		ISO 10816-2:2001	Part 2: Land-Based Steam Turbines and Generators in Excess of 50 MW with Normal Operating Speeds of 1500, 1800, 3000 and 3600 rpm
		ISO 10816-3:1998	Part 3: Industrial Machines with Nominal Power above 15 kW and Nominal Speeds between 120 and 15,000 rpm when Measured <i>In Situ</i>
		ISO 10816-4:1998	Part 4: Gas Turbine Driven Sets Excluding Aircraft Derivations

TABLE 34.5 (continued)

Year	Author/ Organization	Reference Number	Title/Description
2002	ISO	ISO 10816-5: 2000	Part 5: Machine Sets in Hydraulic Power Generating and Pumping Plants
			Mechanical Vibration — Vibration of Active Magnetic Bearing Equipped Rotating Machinery
1996–2001	ISO	ISO 14839-1: 2002	Part 1: Vocabulary
		ISO/CD 14839-2:2004	Part 2: Evaluation of Vibration
			Mechanical Vibrations of Nonreciprocating Machines — Measurement on Rotating Shafts and Evaluation Criteria
		ISO 7919-1: 1996	Part 1 (1996): General Guidelines
		ISO 7919-2: 2001	Part 2 (2001): Land-Based Steam Turbines and Generators in Excess of 50 MW with Normal Operating Speeds of 1500, 1800, 3000 and 3600 rpm
		ISO 7919-3: 1996	Part 3 (1996): Coupled Industrial Machines
		ISO 7919-4: 1996	Part 4 (1996): Gas Turbine Sets
		ISO 7919-5: 1997	Part 5 (1997): Machine Sets in Hydraulic Power Generating and Pumping Plants
1993	ISO	ISO 8579-2	Acceptance Code for Gears, Part 2: Determination of Mechanical Vibration of Gear Units During Acceptance Testing
2004	ISO		Rolling Bearings — Measuring Methods for Vibration
		ISO 15242-1:2004	Part 1: Fundamentals
		ISO 15242-2:2004	Part 2: Radial Ball Bearings with Cylindrical Bore and Outside surface
		ISO/CD 15242-3	Part 3: Spherical and Taper Radial Roller Bearings with Cylindrical Bore and Outside Diameter
1959	Kruglov, N.V.	Teplonerg, 8 (85), 1959	Turbomachine Vibration Standards
1967	Maten, S	Hydrocarbon Processing, January 1967	New Vibration Velocity Standards
1983	McHugh, J.D.	J. Lub. Tech., Trans. ASME, 1983, 105	Estimating the Severity of Shaft Vibration within Fluid Film Journal Bearings
1974	MIL	MIL-STD-167-1	Mechanical Vibration of Shipboard Equipment, Type I: Environmental, Type II: Internally Excited
2003	NEMA	NEMA MG 1-2003	Motors and Generators, Part 7 — Mechanical Vibration — Measurement, Evaluation and Limits
1991	NEMA	NEMA SM 23-1991	Steam Turbines for Mechanical Drive Service
1991	NEMA	NEMA SM 24-1991	Land Based Steam Turbine Generator Sets 0 to 33,000 kW
1965	PKN	PN-65/E-04255	Measurement of Vibration of Electrical Rotating Machines
1939	Rathbone, T.C.	Power Plant Engineering, November 1939	Vibration Tolerances
1964	VDI	VDI 2056	Evaluation Criteria for Mechanical Vibrations in Machines
1982	VDI	VDI 2059 P1	Shaft Vibrations of Turbosets Principles for Measurement and Evaluation
1990	VDI	VDI 2059 P2	Shaft Vibrations of Steam Turbosets for Power Station Measurement and Evaluation
1985	VDI	VDI 2059 P3	Shaft Vibrations of Industrial Turbosets Measurement and Evaluation
1981	VDI	VDI 2059 P4	Shaft Vibrations of Gas Turbosets Measurement and Evaluation
1982	VDI	VDI 2059 P5	Shaft Vibrations of Hydraulic Machinesets Measurement and Evaluation
1949	Yates, H.G.	Trans. N.E. Coast Inst. Engrs Ship Builders, Vol. 65, 1949	Vibration Diagnosis of Marine Geared Turbines

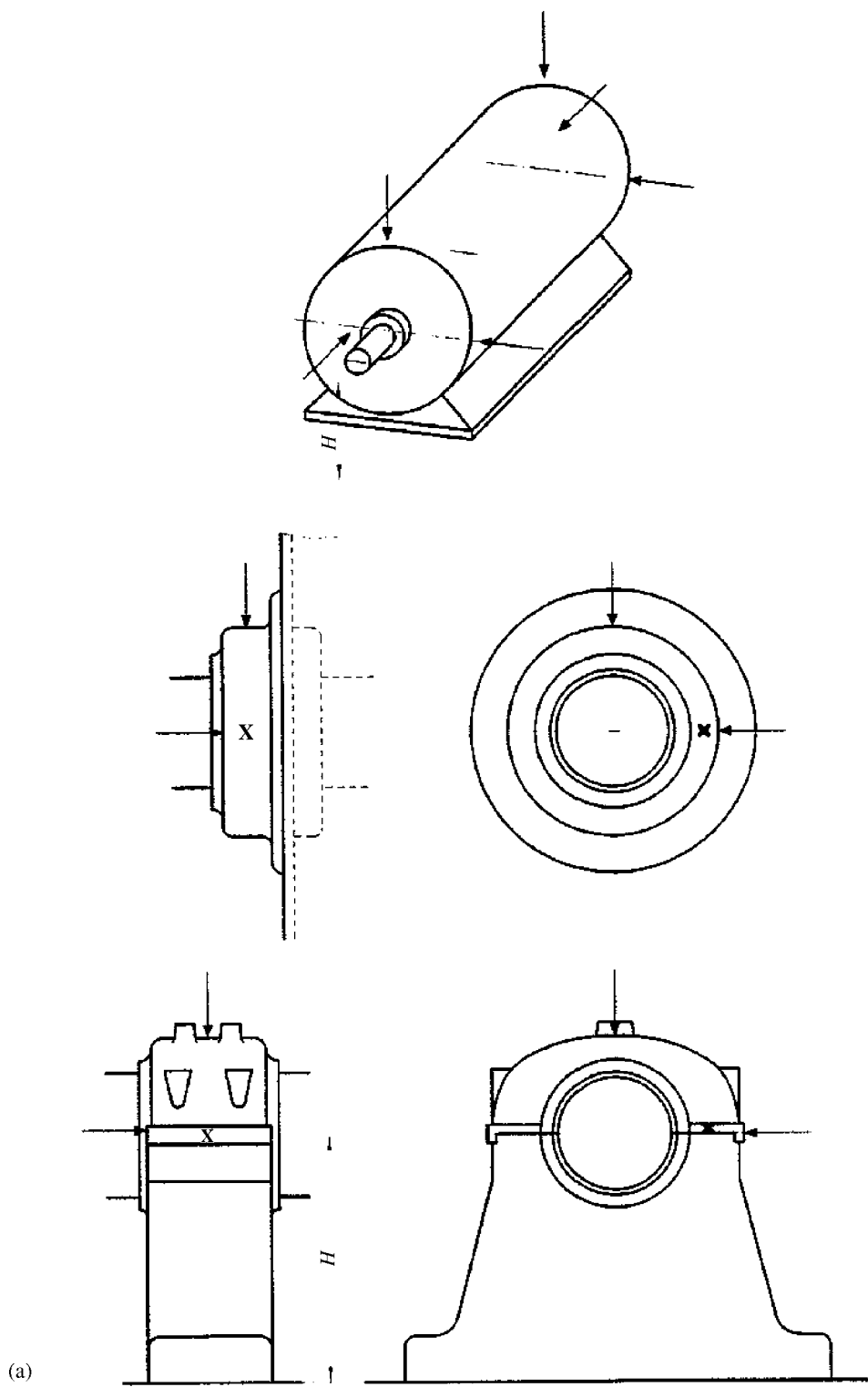


FIGURE 34.14 (a) Measuring points; (b) measuring points for vertical machine sets. (Source: ISO 10816-3, 1998-05-15. With permission.)

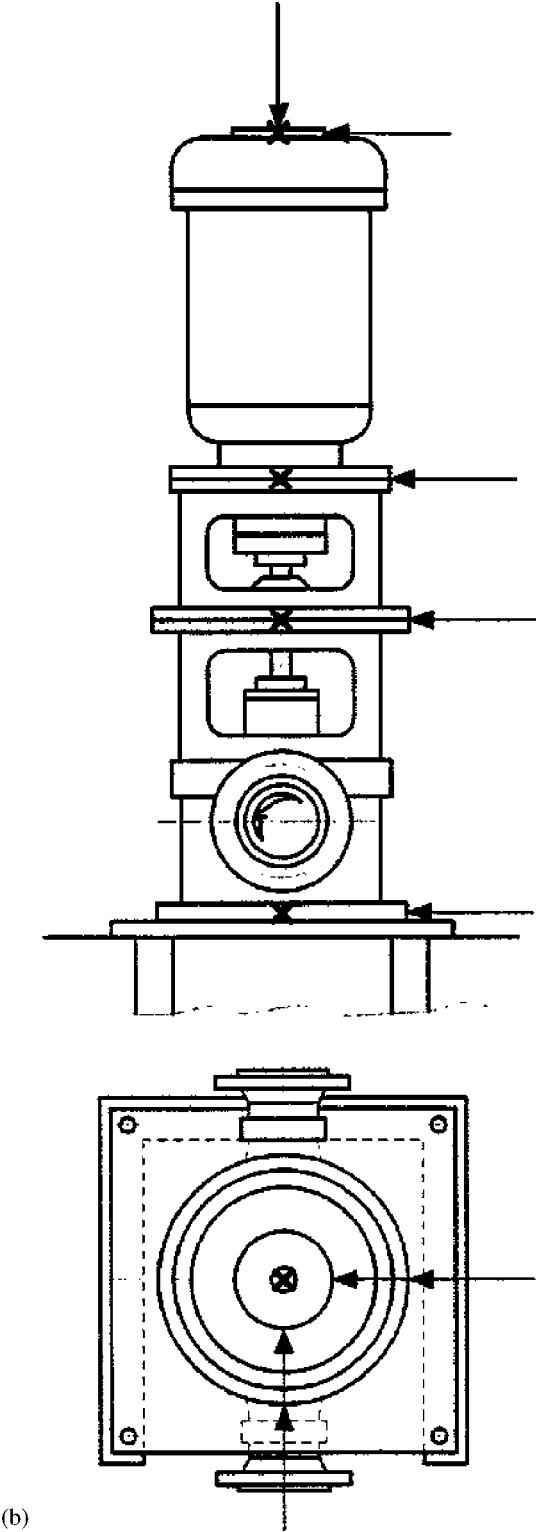


FIGURE 34.14 (continued)

TABLE 34.6A Acceptable Vibration Levels for Rotating Machinery Measured on Nonrotating Parts

Machinery Type	Power Level	Speed Range (rpm)	Applicable Vibration Level	
			Rigid Support	Flexible Support
Steam turbines	$15 \leq P \leq 300$ kW	$120 \leq N \leq 15,000$	V1 and D3	V3 and D7
	$300 \text{ kW} \leq P \leq 50$ MW	$120 \leq N \leq 15,000$	V3 and D5	V6 and D8
	$P > 50$ MW	$N < 1,500$ or $N > 3,600$	V3 and D5	V6 and D8
	$P > 50$ MW	$N = 1,500$ or $1,800$	V5	V5
	$P > 50$ MW	$N = 3,000$ or $3,600$	V7	V7
Gas turbines	$15 \leq P \leq 300$ kW	$120 \leq N \leq 15,000$	V1 and D3	V3 and D7
	$300 \text{ kW} \leq P \leq 3$ MW	$120 \leq N \leq 15,000$	V3 and D5	V6 and D8
	$P > 3$ MW	$3,000 \leq N \leq 20,000$	V8	V8
Hydraulic turbines and pump turbine	Horizontal machines			
	$P > 1$ MW	$60 \leq N \leq 300$	N/A	V4
	$P > 1$ MW	$300 < N \leq 1,800$	V2 and D6	N/A
Vertical machines	$P > 1$ MW	$60 < N \leq 1,800$	V2 and D6	N/A
	$P > 1$ MW	$60 < N \leq 1,000$	V2 and D6	V4 and D9
Centrifugal pumps				
Separate driver	$P > 15$ kW	$120 \leq N \leq 15,000$	V3 and D2	V6 and D4
Integral driver	$P > 15$ kW	$120 \leq N \leq 15,000$	V1 and D1	V3 and D2
Electric motors				
Shaft height $H \geq 315$ mm	$P > 15$ kW	$120 \leq N \leq 15,000$	V3 and D5	V6 and D8
Shaft height $160 \leq H < 315$ mm	$P > 15$ kW	$120 \leq N \leq 15,000$	V1 and D3	V3 and D7
Generators, excluding those used in hydraulic power generation	$15 \leq P \leq 300$ kW	$120 \leq N \leq 15,000$	V1 and D3	V3 and D7
	$300 \text{ kW} \leq P \leq 50$ MW	$120 \leq N \leq 15,000$	V3 and D5	V6 and D8
	$P > 50$ MW	$N < 1,500$ or $N > 3,600$	V3 and D5	V6 and D8
	$P > 50$ MW	$N = 1,500$ or $1,800$	V5	V5
	$P > 50$ MW	$N = 3,000$ or $3,600$	V7	V7
Generators and motors used in hydraulic power generation	Horizontal machines			
	$P > 1$ MW	$60 \leq N \leq 300$	N/A	V4
	$P > 1$ MW	$300 < N \leq 1,800$	V2 and D6	N/A
Vertical machines	$P > 1$ MW	$60 < N \leq 1,800$	V2 and D6	N/A
	$P > 1$ MW	$60 < N \leq 1,000$	V2 and D6	V4 and D9
Compressors, rotary, blowers, and fans	$15 \leq P \leq 300$ kW	$120 \leq N \leq 15,000$	V1 and D3	V3 and D7
	$300 \text{ kW} \leq P \leq 50$ MW	$120 \leq N \leq 15,000$	V3 and D5	V6 and D8

resulting in wasted energy and premature failure of components due to high vibration. The current practice to obtain flow changes in the pump is by means of speed change. This eliminates flow throttling and allows the pump to operate close to its best efficiency point, where energy is not wasted and vibrations are a minimum. However, as illustrated below, variable speed operation of a pump-motor set over a wide speed range could pose several challenging problems.

TABLE 34.6B Maximum Vibration Velocity Limits for Different Levels (mm/sec, RMS)

Vibration Level	Zone A	Zone B	Zone C	Alarm	Trip
V1	1.4	2.8	4.5	3.5	5.6
V2	1.6	2.5	4.0	3.1	5.0
V3	2.3	4.5	7.1	5.6	8.9
V4	2.5	4.0	6.4	5.0	8.0
V5	2.8	5.3	8.5	6.6	10.6
V6	3.5	7.1	11.0	8.9	13.8
V7	3.8	7.5	11.8	9.4	14.8
V8	4.5	9.3	14.7	11.6	18.4

TABLE 34.6C Maximum Vibration Displacement Limits for Different Levels (μm , RMS)

Vibration Level	Zone A	Zone B	Zone C	Alarm	Trip
D1	11	22	36	28	45
D2	18	36	56	45	70
D3	22	45	71	56	89
D4	28	56	90	70	113
D5	29	57	90	71	113
D6	30	50	80	63	100
D7	37	71	113	89	141
D8	45	90	140	113	175
D9	65	100	160	125	200

Zone A: Newly commissioned machines should fall within this zone. *Zone B:* Machines with vibrations within this zone are considered acceptable for long-term operation. *Zone C:* Machines with vibrations within this zone are normally considered unsatisfactory for long-term operation. Such a machine may be operated for a short period in this condition. *Alarm:* The values chosen will normally be set relative to a baseline value determined from experience. However, it is recommended that the alarm value shall not exceed those given herein. *Trip:* The values will generally relate to the mechanical integrity of the machine. They will generally be the same for all machines with similar design. It is recommended that the trip value shall not exceed those given herein. *Notes:* (1) The measured vibration is broadband, and the frequency range will depend on the type of machine being considered. A range from 2 to 1000 Hz is typical except for in high-speed machines, $>10,000$ rpm, where the upper limit should at least be six times the rotational frequency. (2) It is common practice to evaluate rotating machinery based on the broadband RMS vibration velocity, since it can be related to the vibration energy levels. However, other quantities such as vibration displacement or acceleration may be preferred. Especially low speed machines can have unacceptably large vibration displacements when the $1 \times$ rpm component is dominant. Therefore, where specified, both the velocity and displacement criteria are met. (3) Since typical vibration waveforms measured on rotating machinery are complex in nature, there is no simple relationship between broadband velocity, displacement, and acceleration. (4) Vibration measurements shall be taken on bearing support housings, or other structural components, which adequately respond to the dynamic forces of the machine. Recommended locations for bearing housings are shown in Figure 34.14. (5) For certain types of machines, the axial vibration limits may differ from those for radial directions. Also, within the same machine set, in particular hydraulic power-generating sets, the applicable level may differ from bearing to bearing depending on its classification as a rigid or flexible support. (6) Above vibration limits apply to steady-state/normal operating conditions of the machine. If the vibration levels are sensitive to the operational conditions, then evaluation of the machine for operating conditions outside steady-state conditions will have to be based on different criteria. (7) The vibration limits specified herein should not be used to assess the condition of rolling element type bearings although it encompasses machines that may have these types of bearings. (8) It must be recognized that the vibration measurement on nonrotating parts alone does not form the only basis for judging the condition of a machine. In certain types of machines, it is common practice also to judge the vibration based on measurements taken on rotating shafts. (9) A support may be considered as rigid in a specific direction only if its natural frequency in that direction exceeds the main excitation frequency by at least 25%, otherwise it is considered to be flexible. In some cases, a support may be rigid in one direction and flexible in another. (10) In the case of hydraulic machine sets, major differences in radial bearing support arrangement can occur. For evaluation of the support type it is recommended that the reader refer to ISO 10816-5.

Description. The following case study is taken from a petroleum pipeline pump application where pump-motor sets with VFDs were installed in a new pipeline starting in Alberta, Canada and terminating in Minnesota, USA. VFDs are frequently used in the pipeline industry to power high horsepower pumps to eliminate power wasted by throttling, reduce inrush current at motor startup, and to provide greater operating flexibility. However, variable speed operation can cause vibration problems in the pump, motor, and the couplings that are not normally experienced with fixed speed pumps. Unexpected high torsional and lateral vibrations were experienced with these pumps and motors at certain operating speeds. A rotor torsional resonance, motor housing resonance, acoustic resonance in the internals of the pump, and discharge piping were identified to be the causes of the high vibration in the pump-motor set. Details on diagnosing the problems and the corrective measures taken to resolve them are given below:

Pump type: The pump was a centrifugal, two-stage, double volute horizontal pump, with six vane impellers, normally designed to operate at a fixed speed. Generation of pressure pulsations at the vane passing frequencies of $6 \times$ and $12 \times$ rotational speed is normally expected.

TABLE 34.7A Acceptable Vibration Levels for Rotating Machinery, Measured on Rotating Shafts

Machinery Type	Power Level	Speed Range (RPM)	Applicable Vibration Level	
			Relative Displacement	Absolute Displacement
Steam turbines	$P \leq 50$ MW	$1,000 \leq N \leq 30,000$	D8	—
	$P > 50$ MW	$N = 1,500$	D5	D7
	$P > 50$ MW	$N = 1,800$	D4	D6
	$P > 50$ MW	$N = 3,000$	D2	D5
	$P > 50$ MW	$N = 3,600$	D1	D3
Gas turbines	$P > 3$ MW	$3,000 \leq N \leq 30,000$	D8	—
	$P \leq 3$ MW	$1,000 \leq N \leq 30,000$	D8	—
Hydraulic turbines and pumps used in hydraulic power generation and pumping plants	$P > 1$ MW	$60 \leq N \leq 1,800$	D9	D9
Centrifugal pumps	All	$1,000 \leq N \leq 30,000$	D8	—
Electric motors	All	$1,000 \leq N \leq 30,000$	D8	—
Generators, excluding those used in hydraulic power generation	$P \leq 50$ MW	$1,000 \leq N \leq 30,000$	D8	—
	$P > 50$ MW	$N = 1,500$	D5	D7
	$P > 50$ MW	$N = 1,800$	D4	D6
	$P > 50$ MW	$N = 3,000$	D2	D5
	$P > 50$ MW	$N = 3,600$	D1	D3
Generators and motors used in hydraulic power generation	$P > 1$ MW	$60 \leq N \leq 1,000$	D9	D9
	$P > 1$ MW	$1,000 < N \leq 1,800$	D8	—
Compressors, rotary, blowers, and fans	All	$1,000 \leq N \leq 30,000$	D8	—

Motor: The motor was a 3000 hp, two pole horizontal induction motor, designed to operate at 3600 rpm.

Supply: The supply was a VFD of the current source inverter type. These drives are known to generate an oscillatory torque at $6 \times$ and $12 \times$ the operating frequency.

Coupling: Flexible disc type coupling with a spacer was used. These couplings have very little torsional damping capacity.

Speed range: The speed range was from 1440 rpm (24 Hz) to 3900 rpm (65 Hz).

Reference: Refer to [Figure 34.15](#) to [Figure 34.18](#).

As for the resonance at second and third torsional critical speeds ([Figure 34.15](#)) the second and third torsional modes are excited when the $6 \times$ component of rotational speed corresponds to the critical speeds of 92 and 268 Hz, respectively. The $6 \times$ rpm torsional excitation is caused by the pressure pulsations in the pump. The waterfall plot ([Figure 34.15a](#)) was taken during a run down of the set with the power to the motor turned off.

A similar plot taken during run up of the motor ([Figure 34.15b](#)) shows excitations at the same frequencies but having different amplitude. Since both the pump and motor generate $6 \times$ excitation, it suggests a phase difference between the excitation torques.

It is important to note that the conventional vibration monitoring devices cannot detect the torsional resonance problem. The only indication of a problem was the unusual chattering noise emitted by the coupling. Special techniques to measure dynamic torque using strain gauges had to be used to detect the torsional vibrations.

As for the motor housing resonance ([Figure 34.16](#)), the $2 \times$ rotational speed vibration of the motor is dominant and peaks at 118 Hz corresponding to a natural frequency of the motor frame. In the waterfall plot, the natural frequencies corresponds to excitations that are parallel to the axis. Excitation at harmonics, including the $6 \times$ component, is present but is not dominant.

As for the pump vibrations at the vane passing frequency ([Figure 34.17](#)), the $6 \times$ vane passing frequency is dominant at all operating speeds. It peaks at 238 Hz, possibly due to an acoustic resonance in

TABLE 34.7B Maximum Vibration Displacement S_{p-p} Limits (μm) Peak-to-Peak Limits for Different Levels

	Zone A	Zone B	Zone C
D1	75	150	240
D2	80	165	260
D3	90	180	290
D4	90	185	290
D5	100	200	320
D6	110	220	350
D7	120	240	385
D8	$4800/\sqrt{n}$	$9000/\sqrt{n}$	$13,200/\sqrt{n}$
D9	$10^{(2.3381-0.0704 \log n)}$	$10^{(2.5599-0.0704 \log n)}$	$10^{(2.8609-0.0704 \log n)}$

Zone A: Newly commissioned machines should fall within this zone. **Zone B:** Machines with vibrations within this zone are considered acceptable for long-term operation. **Zone C:** Machines with vibrations within this zone are normally considered unsatisfactory for long-term operation. Such a machine may be operated for a short period in this condition. **Alarm:** The values chosen will normally be set relative to a baseline value determined from experience. However, it is recommended that the alarm value shall not exceed those given herein. **Trip:** The values will generally relate to the mechanical integrity of the machine. They will generally be the same for all machines with similar design. It is recommended that the trip value shall not exceed those given herein. **Notes:** (1) The measured vibration is broadband and is shaft vibration displacement peak to peak. Where applicable, vibration limits for both absolute and relative radial shaft vibrations are given in certain cases. (2) Relative displacement is the vibratory displacement between the shaft and an appropriate structural component such as the bearing housing. Absolute displacement is the vibratory displacement of the shaft with reference to an inertial frame of reference. (3) Relative measurements are carried out with a noncontacting transducer. Absolute readings are obtained by one of the following methods: by a shaft riding probe on which a seismic transducer is mounted so that it measures absolute shaft displacement directly, or with the combination of a noncontacting transducer which measures relative shaft displacement and a seismic transducer which measures support vibration. Their conditioned outputs are vectorially added to provide a measure of the absolute shaft motion. (4) The vibration evaluation criteria are dependent upon a variety of factors and the criteria adopted will vary for different types of machines. Some of these factors are the bearing type, clearance, and diameter. The adopted criteria have to be compared with the bearing diametral clearance (C) and adjusted to suit. Typical values are: Zone A $\leq 0.4C$; Zone B $\leq 0.6C$; and Zone C $\leq 0.7C$. (5) Above vibration limits apply to steady state/normal operating conditions of the machine. If the vibration levels are sensitive to the operational conditions then evaluation of the machine for operating conditions outside steady-state conditions will have to be based on different criteria. (6) It is recommended that vibration readings at each location be made with a pair of transducers and that the transducers are mounted perpendicular to the shaft axis and they are at an angle of 90° to one another. The vibration limits apply to each measured direction. (7) The mechanical and electrical run-out at each measurement location must be assessed and should be $<25\%$ of the allowable limit or $6 \mu\text{m}$, whichever is greater. (8) It must be recognized that the vibration measurement on rotating shafts does not form the only basis for judging the condition of a machine. In certain types of machine, it is common practice also to judge the vibration based on measurements taken on nonrotating parts. (9) ALARM levels should be set relative to a baseline value determined from experience for the measurement position, direction and type of machine. It must provide a warning that a defined value, which is significantly above the baseline value, has been reached. The maximum ALARM setting should be $\leq 0.75C$. (10) The TRIP values should be based on protecting the mechanical integrity of the machine. Consideration of damage to bearings is typical; therefore, maximum TRIP setting should be $\leq 0.9C$.

the discharge pipe. It does not seem to correspond to a structural natural frequency due to the absence of excitations at 238 Hz at all speeds.

As for the acoustic resonance in the pump cross-over pipe (Figure 34.18), dynamic pressure pulsation measurements made on the pump cross-over pipe from the first stage discharge to the second stage suction show an acoustic resonance at 540 Hz. The consistent presence of some excitation at 540 Hz at all speeds confirms that it is an acoustic natural frequency of the cross-over pipe. When the $6 \times \text{rpm}$ pressure pulsation frequency coincides with the acoustic natural frequency, a resonance condition occurs and the magnitude of the pressure pulsation increases by almost a factor of 30.

As for corrective action, for a pump that has to operate over a wide speed range, totally eliminating the coincidence of all the frequencies of exciting forces with the system natural frequencies is impractical. Therefore, the system has to be designed such that the resulting magnitudes of the forces are controlled to within tolerable levels so that safe and reliable operation can take place. This can be accomplished by a

TABLE 34.8 Vibration Cause Identification

Cause	Dominant Frequency	Spectrum, Time Domain, Orbit Shape	Characteristics, Corrections, Comments
Mass unbalance	1 ×	High 1 × with much lower harmonics; circular or elliptic orbits	Corrected by shop or field balancing
Shaft bow	1 ×	Run down plot shows decrease of vibration at critical speed	The shaft has to be straightened using an acceptable method
Misalignment	1 × and 2 ×	Equally high 1 × and 2 ×, figure 8 orbits	Realign at operating conditions; loads causing misalignment, such as nozzle loads, may have to be reduced
Worn journal bearings	1 ×, 1/2 ×	Equally high 1 × and 1/2 ×	Difficult to balance
Gravity critical	2 ×	Run down plot will show excitation at 1/2 critical speed	Can be corrected by balancing
Asymmetric shaft	2 ×	Run down plot will show excitation at 1/2 critical speed	Typically occurs on multistage machines when all the keyways lie in the same plane; correct by staggering them
Shaft crack	1 × and 2 ×	High 1 × and run down plots may show excitation at 1/2 critical speed	Confirmation and detection of location of the crack may require NDE techniques
Loose components	1 × and higher orders plus fractional subharmonics	High 1 × with lower level orders and fractional subharmonics	Shimming and peening may be used as temporary methods to fix the problem
Coupling lockup	1 × and 2 ×	Equally high 1 × and 2 ×, figure 8 orbits	Stop starts may change vibration pattern
Thermal instability	1 ×	High 1 × varies with temperature. Phase angle may change	Proper prewarming or compromise balancing can correct the problem
Oil whirl	<1/2 ×, typically 0.35 × to 0.47 ×	Run-up plot will show 1/2 × increasing and locking into fixed value <1/2 ×	Temporary problem may be caused by excess clearances, oil viscosity, or unloading of the bearing; if it is a design problem, correct by changing to tilting pad bearings
Internal rubs	1/4 ×, 1/3 ×, 1/2 ×, 2 ×, 3 ×, 4 ×, etc.	Run down plots may show decreasing amplitudes and disappearance; loops in orbits	May get progressively worse; galling between contact surfaces or heat build-up may cause seizure and shaft failure
Trapped fluids in rotor	0.8 × to 0.9 ×	Time domain signal will show beating	Balancing the rotor may reduce the vibration
Defective rolling element bearings	At bearing defect frequency	Peaks at defect frequencies in spectrum	Shock pulse measurements can also be used to detect problem
Damaged gears	Gear mesh frequency	High peaks at gear mesh frequency with side bands. Time domain may also show pulses	To determine exact nature of damage further analysis may be required

TABLE 34.8 (continued)

Cause	Dominant Frequency	Spectrum, Time Domain, Orbit Shape	Characteristics, Corrections, Comments
Electric motor problems	$1 \times$ (line frequency), $2 \times$ (line frequency)	High peaks at $1 \times$ and $2 \times$ line frequency with side bands; disappears when power to motor is turned off	In the case of two pole motors, it can be confused with mechanical causes as the rotational speed is the same as line frequency
Casing distortion	$1 \times$	High $1 \times$, may change with time	Caused by high nozzle loads, casing not free to expand, soft foot or foundation distortion
Piping forces	$1 \times$, $2 \times$	Equally high $1 \times$ and $2 \times$	Causes misalignment between bearings or between coupled equipment
Rotor and bearing critical	$1 \times$	High $1 \times$, on rundown plot $1 \times$ decreases rapidly, may also show a large phase angle change	More common in machines originally designed for fixed speed operation, later converted to variable speed operation
Structural resonance	$1 \times$, $2 \times$	High $1 \times$ and some $2 \times$; can be easily identified on run down plot	Increase or decrease stiffness of structure or add or remove mass to change natural frequency
Rotor hysteresis	$0.65 \times$ to $0.85 \times$	Spectrum will show high magnitudes at $0.65 \times$ to $0.85 \times$	Occurs in built up rotors with transitional fits
Hydraulic causes	$1 \times$ (vane pass frequency), $2 \times$ (vane pass frequency)	High $1 \times$ and $2 \times$ vane pass frequency	Common in centrifugal pumps due to flow recirculation or inadequate gap between impeller and casing

direct reduction of the exciting force or by means of increased damping. Based on these guidelines, the following modifications were proposed to correct the problem:

1. Torsional resonance

- Use an electrometric type coupling that has a high degree of torsional damping to reduce the magnitude of the torsional excitation forces such that the torsional stresses within the rotors are within acceptable limits.
- Since both the pump and VFD generate excitation at $6 \times$ rpm, their effects could be compounding one another. Introducing either five vane or seven vane impellers into the pump will eliminate this possibility.
- Additional filters could be introduced into the VFD to reduce the $6 \times$ and $12 \times$ component periodic torsional excitation.
- Consider not operating (lock out) the pump within $\pm 10\%$ of the frequency at which torsional resonance occurs.

2. Motor housing resonance at $2 \times$

- Although the $2 \times$ vibration is dominant, its magnitude is within tolerable levels. The fact that some $2 \times$ vibration is also present in the pump indicates that the $2 \times$ vibration is perhaps caused by misalignment between the pump and the motor. This can be corrected by proper

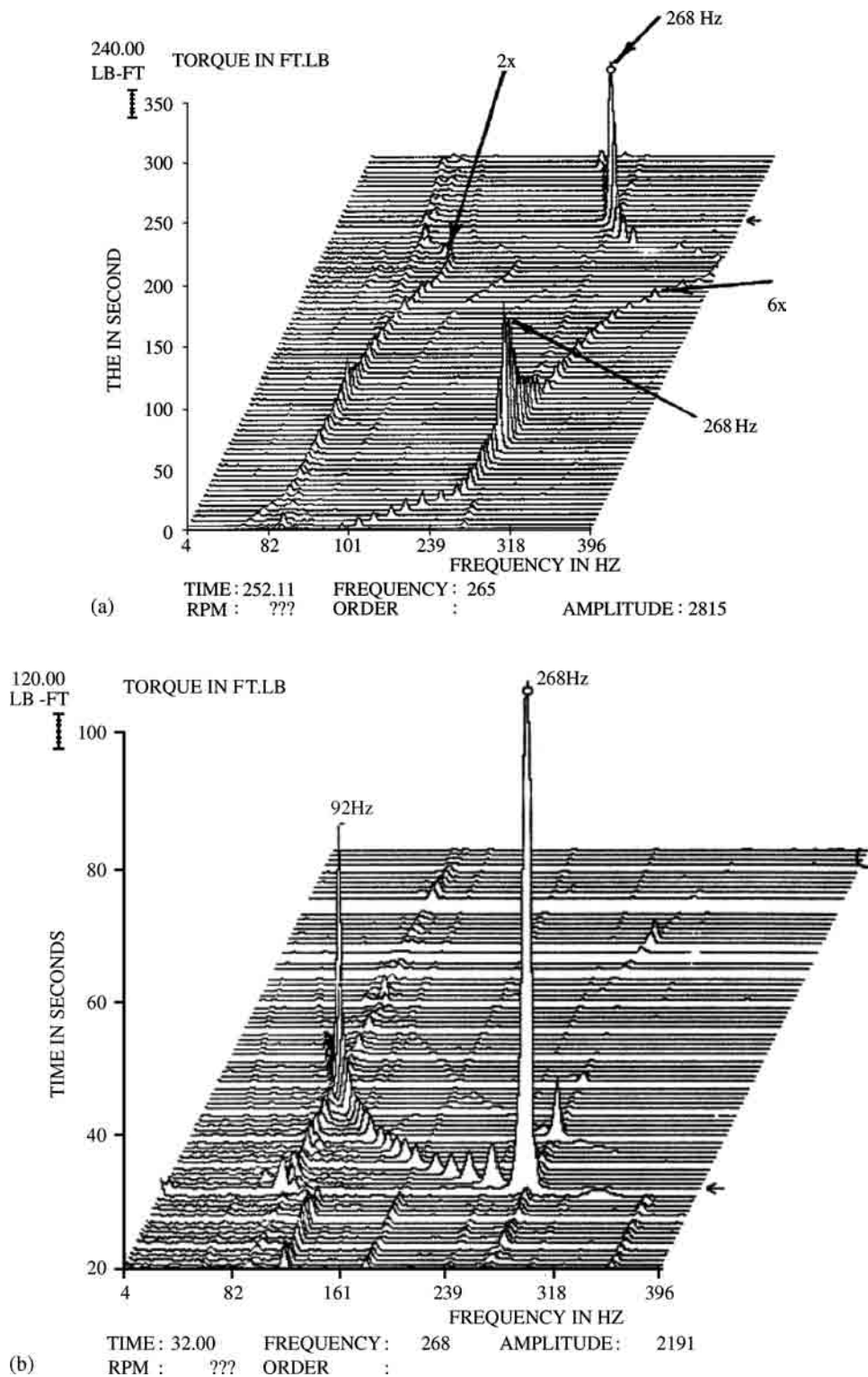


FIGURE 34.15 (a) Torsional resonance run-up and run-down plots; (b) torsional resonance run-down plot. (Source: Private communique, Insight Engineering Services Ltd. Alta., Canada. With permission.)

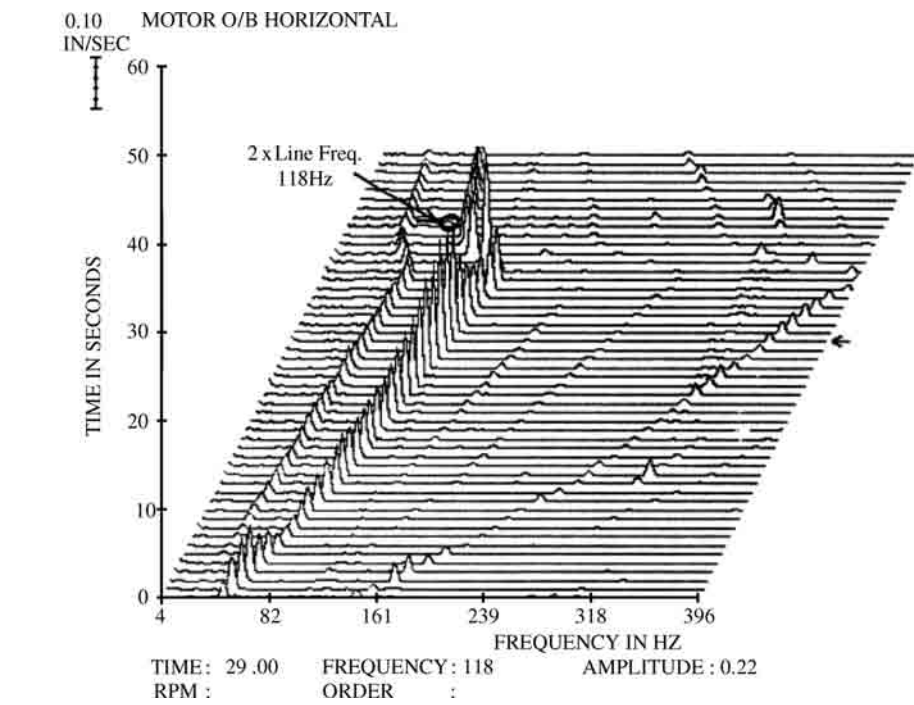


FIGURE 34.16 Motor frame resonance. (Source: Private communique, Insight Engineering Services Ltd., Alta., Canada. With permission.)

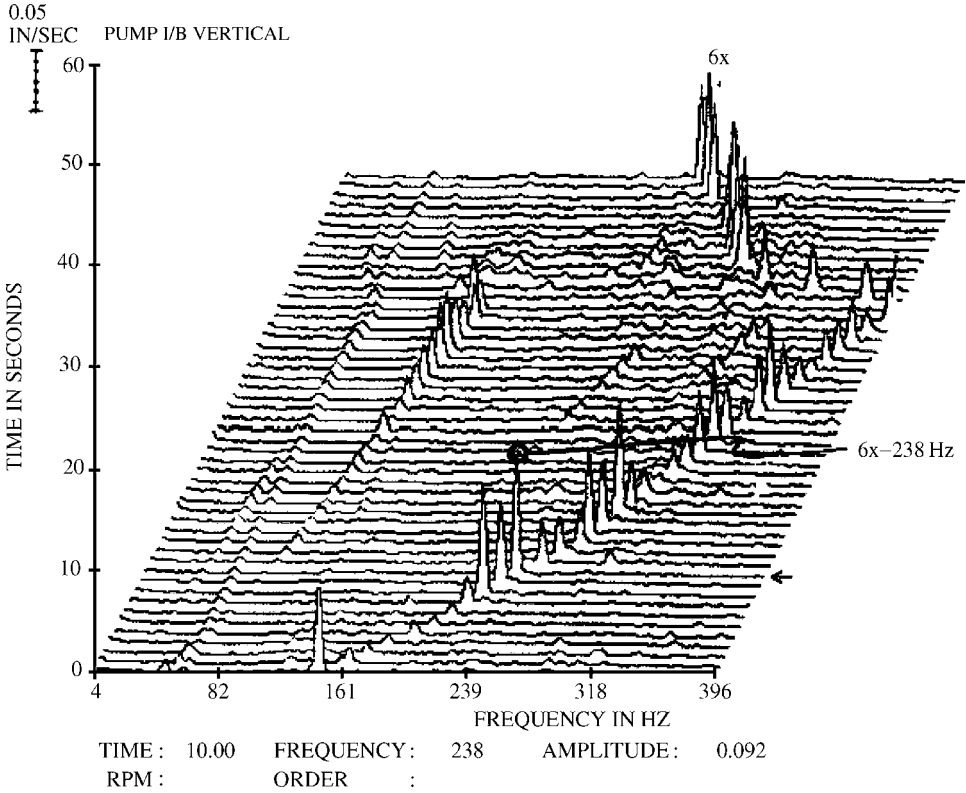


FIGURE 34.17 Pump bearing housing resonance. (Source: Private communique, Insight Engineering Services Ltd., Alta., Canada. With permission.)

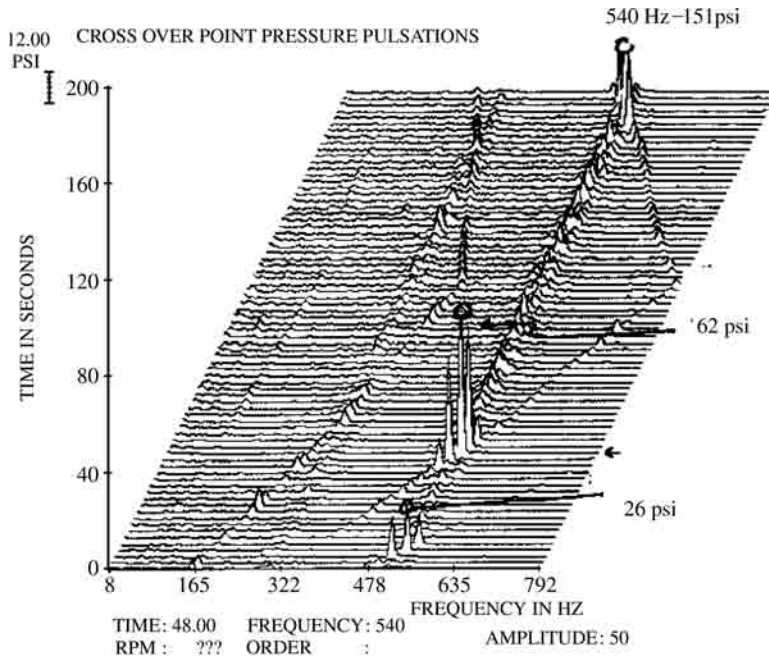


FIGURE 34.18 Pump cross-over pipe acoustic resonance. (Source: Private communicate, Insight Engineering Services Ltd., Alta., Canada. With permission.)

alignment and thus reducing the $2 \times$ excitation forces. In some cases, due to an unequal air gap between the rotor and stator of the motor, the motor could generate the $2 \times$ vibration. Under such conditions, accurate centering of the motor bearings will generally correct the problem.

3. Pump vibrations at vane passing frequency

- Generally, high vibrations at vane passing frequency are caused by pressure pulsations generated at the discharge of the impeller. There are several hydraulic modifications that can be made to the pump to reduce the amplitude of these pulsations that occur at vane passing frequency. The most common method is to increase the gap between the impeller discharge vanes and diffuser/volute. Also, changing the ratio of the number of impeller vanes to diffuser/volute vanes can help in reducing vane passing frequency pressure pulsations and the resulting vibration.

4. Acoustic resonance in the pump cross-over pipe

- Once the pump is constructed, it is not possible to change the acoustic natural frequency of the cross-over pipe. However, the excitation force, pressure pulsations generated at the impeller discharge, can be reduced by the methods outlined above.

- The root cause of a vibration problem in a rotating machine can be determined by careful study and analysis of the vibration signals.
- Industrial and international vibration standards and guidelines have been developed to ensure safe and reliable operation of rotating machinery.
- Equipment manufacturers, users, insurance companies, and public interest groups use vibration standards to control vibration to within acceptable levels.

References

- Adkins, D. and Brennen, C. 1986. Origins of hydrodynamic forces on centrifugal pump impellers, NASA CP No 2443, p. 467, In *Proceedings of a Workshop held at Texas A&M University*, Dallas, TX.
- Alford, J., Protecting turbomachinery from self-excited rotor whirl, *Trans. ASME, J. Eng. Power*, 87, 333, 1965.
- API Standard 610, 8th ed., Centrifugal Pumps for General Refinery Service, 1995.
- Archer, J.S., Consistent mass matrix for distributed mass systems, *J. Struct. Div., Proc. ASCE*, 89, ST4, 161, 1963.
- Baskharone, E.A., Daniel, A.S., and Hensel, S.J., Rotordynamic effects of the shroud-to-housing leakage flow in centrifugal pumps, *Trans. ASME, J. Fluid Eng.*, 116, 558, 1994.
- Benckert, H., Wachter, J. 1980. Flow induced spring coefficients of labyrinth seals for application in turbomachinery, NASA CP No. 2133, p. 189, In *Proceedings of a Workshop held at Texas A&M University*, Dallas, TX.
- Bentley, D. 1974. *Forced Subrotative Speed Dynamic Action of Rotating Machinery*, ASME, Dallas, TX, 74-PET-16.
- Biezeno, C.B. and Grammel, R. 1954. Engineering Dynamics, Steam Turbines, Vol. III. D. Van Nostrand Co. Inc., New York (originally published in German in 1939 as *Technische Dynamik* by Julius Springer, Berlin, Germany).
- Black, H.F., Interaction of a whirling rotor with a vibrating stator across a clearance annulus, *J. Mech. Eng. Sci.*, 10, 1, 1968.
- Black, H.F. 1974. Lateral stability and vibrations of high speed centrifugal pump rotors, p. 56, In *Proceedings IUTAM Symposium on Dynamics of Rotors*, Lyngby, Denmark.
- Blevins, Robert, D. 2001. Formulas for Natural Frequency and Mode Shapes, Krieger Publishing Co. Inc., Melbourne, FL.
- Bolleter, U., Frei, A., Florjancic, S., Leibundgut, E., and Stürchler, R., *Rotordynamic Modeling and Testing of Boiler Feedpumps*, EPRI TR-100980, 1992.
- Bolleter, U., Leibundgut, E., Stürchler, R., and McCloskey, T. 1989. Hydraulic interaction and excitation forces of high head pump impellers, p. 187, In *Proceedings of the Third ASCE/ASME Mechanical Conference*, La Jolla, CA.
- Bolleter, U., Wyss, A., Welte, I., and Stürchler, R., Measurement of hydrodynamic interaction matrices of boiler feed pump impellers, *Trans. ASME, J. Vib. Stress Reliab. Des.*, 1985, SME, 85-DET-147, New York.
- Brennen, C., Acosta, A., and Caughey, T. 1980. A test program to measure cross-coupling forces in centrifugal pumps and compressors, NASA CP No. 2133, p. 229, In *Proceedings of a Workshop held at Texas A&M University*, Dallas, TX.
- Childs, D.W. 1986. Force and moment rotordynamic coefficients for pump-impeller shroud surfaces, NASA CP No. 2443, p. 467, In *Proceedings of a workshop held at Texas A&M University Dallas*, TX.
- Childs, D. 1993. Turbomachinery Rotordynamics, Wiley, New York.
- Chree, C., The whirling and transverse vibration of rotating shafts, *Phil. Mag.*, 7, 504, 1904.
- COJOUR, User's Guide: Dynamic Coefficients for Fluid Film Journal Bearings, EPRI CS-4093.
- Crandall, S.H. and Brosens, P.J., Whirling of unsymmetrical rotors, *J. Appl. Mech.*, 28, 567, 1961.
- Dunkerly, S., On the whirling and vibration of shafts, *Phil. Trans. R. Soc., London A*, 185, 279, 1894.
- Ehrich, F.F. 1999. Handbook of Rotordynamics, Revised ed., Krieger Publishing Co. Inc., Melbourne, FL.
- Foppl, A., Das Problem der Laval'schen Turbinewelle, *Civilingenieur*, 41, 333, 1885.
- Glienicke, J. 1966. Experimental investigation of the stiffness and damping coefficients of turbine bearings and their application to instability prediction, p. 122, In *Proceedings of the Journal Bearings for Reciprocating and Turbo Machinery Symposium*, Nottingham, UK.
- Gorman and Daniel, J. 1975. *Free Vibration Analysis of Beams and Shafts*, Wiley, New York.
- Greenhill, A.G., On the strength of shafting when exposed both to torsion and to end thrust, *Proc. I. Mech. Eng (London)*, 182, 1883.

- Gunter, E.J. Jr., Dynamic stability of rotor-bearing systems, *NASA SP-113*, 1966.
- Hagg, A.C. and Sankey, G.O., Elastic and damping properties of oil-film journal bearings for application to unbalance vibration calculations, *Trans. ASME, J. Appl. Mech.*, 25, 141, 1958.
- Harris, T. 1991. Rolling Bearing Analysis, 3rd ed., Wiley, New York.
- Holzer, H. 1921. Die Berechnung der Drehschwingungen, Springer, Berlin.
- Houbolt, J.C. and Reed, W.H., Propeller nacelle whirl flutter, *Inst. Aerospace Sci.*, 1, 61, 1961.
- ISO 10816-1. *Mechanical vibration—evaluation of machine vibration by measurements on non-rotating parts*. Part 1. General Guidelines, ISO, Geneva, Switzerland, 1995.
- ISO 10816-2. *Mechanical vibration—evaluation of machine vibration by measurements on non-rotating parts*. Part 2. Land-based Steam Turbines and Generators in excess of 50 MW with normal operating speeds of 1500 r/min, 1800 r/min, 3000 r/min and 3600 r/min, ISO, Geneva, Switzerland, 2001.
- ISO 10816-3. *Mechanical vibration—evaluation of machine vibration by measurements on non-rotating parts*. Part 3. Industrial machines with nominal power above 15 kW and nominal speeds between 120 r/min and 15 000 r/min when measured in situ, ISO, Geneva, Switzerland, 1998.
- ISO 10816-4. *Mechanical vibration—evaluation of machine vibration by measurements on non-rotating parts*. Part 4. Gas Turbine Driven Sets Excluding Aircraft Derivations, ISO, Geneva, Switzerland, 1998.
- ISO 10816-5. *Mechanical vibration—evaluation of machine vibration by measurements on non-rotating parts*. Part 5. Machine Sets in Hydraulic Power Generating and Pumping Plants, ISO, Geneva, Switzerland, 2000.
- ISO 7919-1. *Mechanical vibrations of non-reciprocating machines—measurement on Rotating Shafts and Evaluation Criteria*. Part 1. General Guidelines, ISO, Geneva, Switzerland, 1996.
- ISO 7919-2. *Mechanical vibrations of non-reciprocating machines—Measurement on Rotating Shafts and Evaluation Criteria*. Part 2. Land-Based Steam Turbines and Generators in Excess of 50 MW with Normal Operating Speeds of 1500 r/min, 1800 r/min, 3000 r/min and 3600 r/min, ISO, Geneva, Switzerland, 2001.
- ISO 7919-3. *Mechanical vibrations of non-reciprocating machines—Measurement on Rotating Shafts and Evaluation Criteria*. Part 3. Coupled Industrial Machines, ISO, Geneva, Switzerland, 1996.
- ISO 7919-4. *Mechanical vibrations of non-reciprocating machines—Measurement on Rotating Shafts and Evaluation Criteria*. Part 4. Gas Turbine Sets, ISO, Geneva, Switzerland, 1996.
- ISO 7919-5. *Mechanical vibrations of non-reciprocating machines—Measurement on Rotating Shafts and Evaluation Criteria*. Part 5 Machine Sets in Hydraulic Power Generating and Pumping Plants, ISO, Geneva, Switzerland, 1997.
- Jeffcott, H.H., The lateral vibration of loaded shafts in the neighbourhood of a whirling speed—the effect of want of balance, *Phil. Mag.*, 37, 304, 1919.
- Jery, B., Acosta, A., Brennen, C., and Caughey, T. 1984. Hydrodynamic impeller stiffness, damping, and inertia in the rotordynamics of centrifugal flow pumps, NASA CP No. 2338, p. 137, In *Proceedings of a workshop held at Texas A&M University*, Dallas, TX.
- Jones, A., A general theory for elastically constrained ball and radial roller bearings under arbitrary load and speed conditions, *Trans. ASME J. Basic Eng.*, 82, 309, 1960.
- Kimball, A.L. Jr., Internal friction theory of shaft whirling, *Gen. Electr. Rev.*, 27, 244, 1924.
- Kirk, R.G., Donald, G.N. 1983. Design Criteria of Improved Stability of Centrifugal Compressors, AMD-Vol. 55, Rotor Dynamical Instability. ASME, New York, p. 59.
- Kramer, E. 1993. Dynamics of Rotors and Foundations, Springer, Berlin.
- Lomakin, A.A., Calculating the critical speed and the conditions to ensure dynamic stability of the rotors in high pressure hydraulic machines, taking account of the forces in the seals, *Energomashino-troenie*, 4, 1, 1958.
- Lund, J.W., Spring and damping coefficients for the tilting-pad journal bearing, *Trans. ASLE*, 7, 342, 1964.

- Lund, J.W. 1965. Rotor-bearing Dynamics Design Technology. Part III. Design Handbook for Fluid-film Bearings, AFAPL-TR-64-45. Wright-Patterson Air Force Base, Dayton, OH.
- Lund, J.W. 1968. Rotor-bearing Dynamics Design Technology. Part VII. The Three Lobe Bearing and Floating Ring Bearing, AFAPL-TR-65-45. Wright-Patterson Air Force Base, Dayton, OH.
- Lund, J.W., Sensitivity of the critical speeds of a rotor to changes in the design, *Trans. ASME, J. Mech. Des.*, 102, 115, 1979.
- Lund, J.W. and Orcutt, F.K., Calculation and experiments on the unbalance response of a flexible rotor, *Trans. ASME, J. Eng. Ind.*, 89, 785, 1967.
- Meirovitch, L. 1986. Elements of Vibration Analysis, 2nd ed., McGraw-Hill, New York.
- Miller, D.F., Forced lateral vibration of beams on damped flexible end supports, *Trans. ASME, J. Appl. Mech.*, 20, 167, 1953.
- Moore, J.J. and Palazzolo, A.B., Rotordynamic force prediction of Whirling Centrifugal Impeller Shroud passages using Computational Fluid Dynamic techniques, *Trans. ASME, J. Eng. Gas Turbine Power*, 123, 910, 2001.
- Muszynska, A., Whirl and whip—rotor/bearing stability problems, *J. Sound Vib.*, 110, 443, 1986.
- Myklestad, N.O., A new method for calculating natural modes of uncoupled bending vibrations of airplane wings and other types of beams, *J. Aeronaut. Sci.*, 11, 153, 1944.
- Nelson, H., A Finite rotating shaft element using Timoshenko beam theory, *Trans. ASME, J. Mech. Des.*, 102, 793, 1980.
- Nelson, H. and McVaugh, J., The dynamics of rotor-bearing systems using finite elements, *Trans. ASME, J. Eng. Ind.*, 98, 593, 1976.
- Newkirk, B.L., *Shaft Whipping Gen. Electr. Rev.*, 27, 169, 1924.
- Newkirk, B.L. and Taylor, H.D., Shaft whipping due to oil action in journal bearings, *Gen. Electr. Rev.*, 28, 559, 1925.
- Ohashi, H., Hatanaka, R., and Sakurai, A. 1986. Fluid force testing machine for whirling centrifugal impeller, In *Proceedings of the International Federation for Theory of Machines and Mechanisms, International Conference on Rotordynamics*, JSME, Tokyo, Japan.
- Orcutt, F.K., The steady-state and dynamic characteristics of the tilting-pad journal bearing in laminar and turbulent flow regimes, *Trans. ASME, J. Lubricat. Technol.*, 89, 392, 1967.
- Perera, L. 2002. Private communiqué, Insight Engineering Services Ltd, Alta., Canada.
- Pinkus, O. and Sternlicht, B. 1961. Theory of Hydrodynamic Lubrication, McGraw-Hill, New York.
- Poritsky, H., Contribution to the theory of oil whip, *Trans. ASME*, 75, 1153, 1953.
- Prohl, M.A., A general method for calculating Critical Speeds of flexible rotors, *Trans. ASME, J. Appl. Mech.*, 12, A-142, 1945.
- Rajan, M., Nelson, H.D., and Chen, W.J., Parameter sensitivity in the dynamics of rotor-bearing systems, *Trans. ASME, J. Vib. Acoust. Stress Reliab. Des.*, 108, 197, 1986.
- Rajan, M., Rajan, S.D., and Nelson, H.D., and Chen, W.J., Optimal placement of critical speeds in rotor-bearing systems, *Trans. ASME, J. Vib. Acoust. Stress Reliab. Des.*, 109, 152, 1987.
- Rankine, W.J.M., On the centrifugal force of rotating shafts, *Engineer*, 249, 9, 1869.
- Rathbone, T.C., Vibration tolerances, *Power Plant Eng.*, November, 1939.
- Rayleigh, J.W.S. 1945. Theory of Sound, Dover Publications, New York.
- Robertson, D., Whirling of a journal in a sleeve bearing, *Phil. Mag.*, 15, 96, 113, 1933.
- Robertson, D., Transient whirling of a rotor, *Phil. Mag.*, 20, 793, 1935.
- Ruhl, R.L. and Booker, J.F., A finite element model for distributed parameter turborotor systems, *Trans. ASME, J. Eng. Ind.*, 94, 126, 1972.
- Smith, D.M., The motion of a rotor carried by a flexible shaft in flexible bearings, *Proc. R. Soc. London A*, 142, 92, 1933.
- Someya, T. 1989. *Journal Bearing Databook*, Springer, New York.
- Southwell, R.V. and Gough B.S., 1921, *Complex Stress Distributions in Engineering Materials*, British Association For Advancement of Science Reports, 345.

- Sternlicht, B., Elastic and damping properties of cylindrical journal bearings, *Trans. ASME, J. Basic Eng.*, 81, 101, 1959.
- Stodola, A. 1927. *Steam and Gas Turbines*, Vol. I, McGraw-Hill, New York.
- Taylor, E.S. and Browne, K.A., Vibration isolation of aircraft power plants, *J. Aeronaut. Sci.*, 6, 43, 1938.
- Thomas, H.J., Unstable natural vibration of turbine rotors excited by the axial flow in stuffing boxes and blading, *Bull. AIM*, 71, 1039, 1958.
- Timoshenko, S., Young, D.H., and Weaver, W. Jr. 1974. *Vibration Problems in Engineering*, 4th ed., Wiley, New York.
- Urlichs, K., Leakage flow in thermal turbo-machines as the origin of vibration exciting lateral forces, NASA, TT-17409, 1977.
- Vance, J.M. 1988. *Rotordynamics of Turbomachinery*, Wiley, New York.
- Warner, P.C., Static and dynamic properties of partial journal bearings, *Trans. ASME, J. Basic Eng.*, 85, 247, 1963.
- Wolf, J.A. 1968. Whirl Dynamics of a Rotor Partially Filled with Liquids, ASME, New York, 68-WA/APM-25.

35

Regenerative Chatter in Machine Tools

35.1	Introduction	35-1
35.2	Chatter in Turning Operations	35-3
	Example 1	
35.3	Chatter in Face-Milling Operations	35-9
	Example 2	
35.4	Time-Domain Simulation	35-14
	Example 3 • Example 4	
35.5	Chatter Detection	35-18
	Example 5	
35.6	Chatter Suppression	35-20
	Spindle-Speed Selection • Example 6 • Feed and Depth-of-Cut Selection • Spindle-Speed Variation • Example 7	
35.7	Case Study	35-24

Robert G. Landers

University of Missouri at Rolla

Summary

Regenerative chatter, a result of unstable interactions between machining forces and structural deflections, is a great limitation in machining operations. This chapter describes the modeling, analysis, simulation, detection, and control of regenerative chatter in machining operations, and, in particular, turning and face milling. An analytical method is applied to calculate the limiting stable depth-of-cut and corresponding spindle speeds to generate stability lobe diagrams. The method is applied to both turning and face-milling operations. Time-domain simulation is described and applied to turning and face-milling operations. Methods for chatter detection are presented and experimental results from a face-milling operation are given. Chatter suppression techniques, namely spindle-speed selection, feed selection, depth-of-cut selection, and spindle-speed variation, are presented and two simulations of a turning operation are used to illustrate the spindle-speed selection and spindle-speed variation techniques. Finally, a case study of a face-milling operation is presented. The nomenclature used in the presentation is listed at the end of the chapter.

35.1 Introduction

Regenerative chatter is a major limitation in machining operations. This phenomenon is a result of an unstable interaction between the machining forces and the structural deflections. The forces generated when the cutting tool and part come into contact produce significant structural deflections. These structural deflections modulate the chip thickness that, in turn, changes the machining forces. For certain cutting conditions, this closed-loop, self-excited system becomes unstable and regenerative chatter occurs. Regenerative chatter may result in excessive machining forces and tool wear, tool failure, and scrap parts due to unacceptable surface finish, thus severely decreasing operation productivity and part quality.

A typical chatter stability chart, the so-called stability lobe diagram, is shown in Figure 35.1. If the process parameters are above the stability borderline, chatter will occur, and if the process parameters are below the stability borderline, chatter will not occur. The asymptotic stability borderline is the depth-of-cut below which stable machining is guaranteed regardless of the spindle speed. The lobed nature of the stability borderline allows stable pockets to form; thus, at specific ranges of spindle speeds, the depth-of-cut may be substantially increased beyond the asymptotic stability limit. These pockets become smaller as the spindle speed decreases. The stability borderline is “pulled up” for low spindle speeds due to process damping (i.e., the back side of the tool rubbing on the part surface). If accurate models of the structural components and the cutting process are available, the stability lobe diagram may be used to plan chatter-free machining operations.

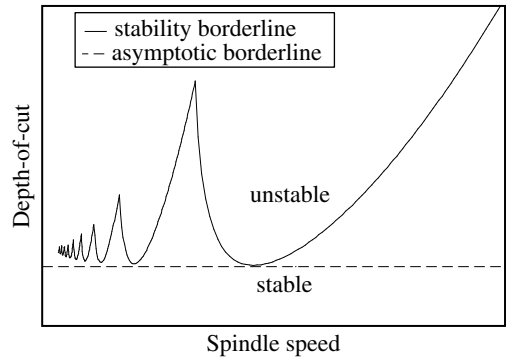


FIGURE 35.1 Stability lobe diagram.

The analysis of regenerative chatter as the interaction between the cutting forces and structural vibrations was established by Tobias (1965) and Koenigsberger and Tlustý (1971). Merritt (1965) used systems theory to determine stability and construct the stability lobe diagram by generating specialized plots from the harmonic solutions of the system's characteristic equation. Chatter analysis reveals a natural delay in the system leading many researchers to use Nyquist techniques to generate stability lobe diagrams (Minis et al., 1990a, 1990b; Lee and Liu, 1991a, 1991b; Minis and Yanushevsky, 1993).

A set of process parameters is selected and the characteristic equation is formed. The Nyquist criterion is applied to determine if the system for this process parameter set is stable. The depth-of-cut is adjusted and the procedure is repeated until the critical depth-of-cut is determined. Another chatter analysis technique capable of generating stability lobe diagrams analytically for linear systems has recently been introduced (Altintas and Budak, 1995; Budak and Altintas, 1998a, 1998b). This technique is utilized in this chapter.

The theoretical analysis of regenerative chatter laid the foundation for developing techniques to automatically detect its occurrence and to automatically suppress it. Since there is a dominant chatter frequency, which is near a structural frequency, that occurs when chatter develops, most monitoring techniques analyze the frequency of a process variable, and chatter is detected when significant energy is present near a structural frequency. Most automatic chatter suppression routines either adjust the spindle speed to be in a pocket of the stability lobe diagram or vary the spindle speed to bring the current and previous tooth passes into phase. While automatic monitoring and control of regenerative chatter shows great promise, it has been mostly limited to laboratory applications. Therefore, commercial tools are not currently available.

While regenerative chatter in turning and face-milling operations is discussed in this chapter, this phenomenon is not limited to these specific manufacturing operations. Other machining operations for which chatter has been analyzed include end milling (Budak and Altintas, 1998a, 1998b), grinding (Inasaki et al., 2001), drilling (Tarng and Li, 1994), and so on. Also, the regenerative chatter phenomenon occurs in other manufacturing operations, most notably in rolling (Yun et al., 1998; Tlustý, 2000).

Section 35.2 and Section 35.3 present an analytical method to examine regenerative chatter in turning and face-milling operations, respectively. Section 35.4 discusses a numerical technique known as time domain simulation that may be used to analyze regenerative chatter for nonlinear systems. The subject of chatter detection is presented in Section 35.5, then methods to perform chatter suppression are discussed and illustrated in Section 35.6. Section 35.7 presents a case study of a face-milling operation.

35.2 Chatter in Turning Operations

A schematic of a turning operation is shown in Figure 35.2. The part structure is assumed to be perfectly rigid, while the cutting-tool structure is capable of vibrations in the longitudinal (i.e., the z) direction only. The machining force in the longitudinal direction is

$$F(t) = Pdf(t) \quad (35.1)$$

The depth-of-cut is assumed to be constant; however, the feed, and hence the machining force, is time-varying due to structural vibrations. It is assumed here that the machining force does not explicitly depend upon the cutting speed.

The feed is the chip thickness in the longitudinal direction. The nominal feed is the distance the tool advances relative to the part each spindle revolution and is constant once the tool fully engages the part. However, the cutting tool vibrates, leaving an undulated surface on the part and, thus, modulates the feed. The instantaneous feed is

$$f(t) = f_{\text{nom}} + \Delta z(t) = f_{\text{nom}} + z(t) - z(t - T) \quad (35.2)$$

The term f_{nom} is the nominal feed, also known as the static feed. The term $\Delta z(t)$ is the feed due to the cutting-tool vibrations and is known as the dynamic feed. The parameter T is the spindle-rotation period. The structural vibration, $z(t)$, known as the inner modulation, is the cutting-tool vibration at the current time. The delayed structural vibration $z(t - T)$, known as the outer modulation, is the cutting-tool vibration as of when the part was at the current angular during the previous spindle rotation. The modulation in feed due to structural vibrations is illustrated in Figure 35.3.

Inserting Equation 35.2 into Equation 35.1:

$$F(t) = Pdf_{\text{nom}} + Pd\Delta z(t) = F_{\text{nom}} + \Delta F(t) \quad (35.3)$$

The force $F_{\text{nom}} = Pdf_{\text{nom}}$ is due to the nominal chip thickness and does not vary since the depth-of-cut and nominal feed are constant. The force $\Delta F(t) = Pd\Delta z(t)$ is due to changes in the nominal feed caused by structural vibrations.

The structural vibrations are related to the machining force by

$$z(s) = -g(s)F(s) \quad (35.4)$$

where $g(s)$ is the transfer function relating the structural vibrations to the machining forces. Since $F(t) - F(t - T) = \Delta F(t) - \Delta F(t - T)$, the structural vibrations are related to the machining

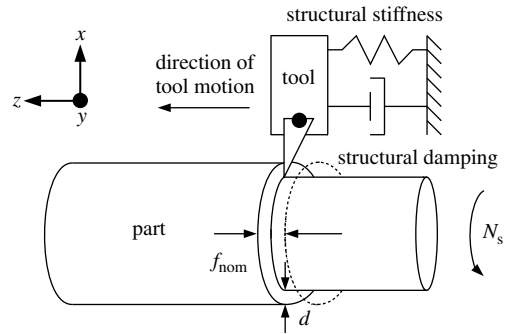


FIGURE 35.2 Turning operation schematic: current pass (solid line) and previous pass (dotted line).

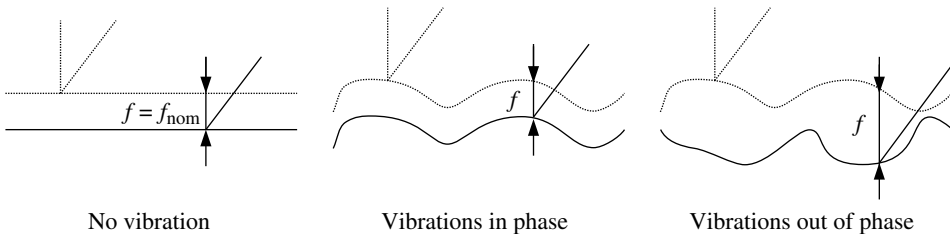


FIGURE 35.3 Modulation in feed due to structural vibrations in a turning operation: current pass (solid line) and previous pass (dotted line).

forces by

$$\Delta z(s) = -(1 - e^{-sT})g(s)\Delta F(s) \quad (35.5)$$

Substituting for Δz in Equation 35.5 and rearranging:

$$\Delta F(s)\{1 + Pd[1 - e^{-sT}]g(s)\} = 0 \quad (35.6)$$

Equation 35.6 is now solved, based on the method presented by Budak and Altintas (1998a, 1998b), to determine the stability lobe diagram. Assuming the steady-state solution is a harmonic function at a single chatter frequency ω_c , Equation 35.6 becomes

$$\Delta F(j\omega_c)e^{j\omega_c T}\{1 + Pd[1 - e^{-j\omega_c T}]g(j\omega_c)\} = 0 \quad (35.7)$$

where $j^2 = -1$. For nontrivial solutions of Equation 35.7, the following eigenvalue problem is derived:

$$\det\{1 + Pd[1 - e^{-j\omega_c T}]g(j\omega_c)\} = 0 \quad (35.8)$$

Since the structural dynamics are one-dimensional, Equation 35.8 reduces to

$$1 + Pd[1 - e^{-j\omega_c T}]g(j\omega_c) = 0 \quad (35.9)$$

The parameter Λ is defined as

$$\Lambda = Pd[1 - e^{-j\omega_c T}] = \Lambda_R + j\Lambda_I \quad (35.10)$$

Using the Euler identity $1 - e^{-j\omega_c T} = 1 - \cos(\omega_c T) + j \sin(\omega_c T)$, the limiting stable depth-of-cut is

$$d_{\lim} = \left(\frac{1}{P}\right) \frac{\Lambda_R + j\Lambda_I}{1 - \cos(\omega_c T) + j \sin(\omega_c T)} \quad (35.11)$$

Equation 35.11 is rewritten as

$$d_{\lim} = \left(\frac{1}{2P}\right) \left\{ \frac{\Lambda_R[1 - \cos(\omega_c T)] + \Lambda_I \sin(\omega_c T)}{1 - \cos(\omega_c T)} + j \frac{\Lambda_R \sin(\omega_c T) + \Lambda_I[1 - \cos(\omega_c T)]}{1 - \cos(\omega_c T)} \right\} \quad (35.12)$$

Since the limiting depth-of-cut must be a real number:

$$\Lambda_R \sin(\omega_c T) + \Lambda_I[1 - \cos(\omega_c T)] = 0 \quad (35.13)$$

The parameter κ is defined as

$$\kappa = \frac{\Lambda_I}{\Lambda_R} = \frac{\sin(\omega_c T)}{1 - \cos(\omega_c T)} \quad (35.14)$$

The limiting stable depth-of-cut is solved explicitly as

$$d_{\lim} = \frac{\Lambda_R}{2P}(1 + \kappa^2) \quad (35.15)$$

Note that Λ_R must be positive for d_{\lim} to be positive. From Equation 35.9, the parameter Λ is

$$\Lambda = -\frac{1}{g(j\omega_c)} \quad (35.16)$$

Equation 35.16 is used to determine Λ_R and Λ_I , and these values are used to solve for d_{\lim} . Next, the spindle speed at which the limiting depth-of-cut occurs is determined. The trivial solution to Equation 35.14 is

$$\omega_c T = 0 + 2l\pi, \quad l = 0, 1, 2, \dots \quad (35.17)$$

The quantity $\omega_c T$ may be interpreted as the number of vibration cycles during a spindle rotation. The trivial solution indicates that the successive vibrations are in phase (i.e., there is no regeneration). The nontrivial solution to Equation 35.14 is

$$\cos(\omega_c T) = \frac{\kappa^2 - 1}{\kappa^2 + 1} \quad (35.18)$$

and may be rewritten as

$$\omega_c T = \varepsilon + 2l\pi, \quad l = 0, 1, 2, \dots \quad (35.19)$$

where

$$\varepsilon = \cos^{-1} \left(\frac{\kappa^2 - 1}{\kappa^2 + 1} \right) \quad (35.20)$$

The parameter ε is the fraction of the vibration cycles during a spindle rotation. The angle of Λ in the complex plane is

$$\varphi = \tan^{-1} \left(\frac{\Lambda_I}{\Lambda_R} \right) = \tan^{-1}(\kappa) \quad (35.21)$$

Substituting $\kappa = \tan(\varphi)$ into Equation 35.18 yields

$$\cos(\omega_c T) = -\cos(2\varphi) \quad (35.22)$$

A solution to Equation 35.22 is

$$\omega_c T = \pi - 2\varphi + 2l\pi, \quad l = 0, 1, 2, \dots \quad (35.23)$$

Comparing Equation 35.19 and Equation 35.23, it is seen that the fraction of vibration cycles is $\varepsilon = \pi - 2\varphi$. Since $0 \leq \varepsilon \leq 2\pi$, one must ensure that $-\pi/2 \leq \varphi \leq \pi/2$ when computing φ . For example, if Equation 35.21 is solved using a four-quadrant inverse tangent function whose solution is bounded between $-\pi$ and π , then $-\pi/2 \leq \varphi \leq \pi/2$ since Λ_R is positive. For milling applications, it will be seen that Λ_R must be negative; therefore, the following conditions must be enforced to ensure $0 \leq \varepsilon \leq 2\pi$:

$$\begin{aligned} \text{if } \Lambda_I < 0 \quad \text{then } \varphi &\rightarrow \varphi + \pi \\ \text{if } \Lambda_I > 0 \quad \text{then } \varphi &\rightarrow \varphi - \pi \end{aligned} \quad (35.24)$$

The spindle speed is

$$N_s = \frac{60}{T} = \frac{60\omega_c}{\varepsilon + 2l\pi}, \quad l = 0, 1, 2, \dots \quad (35.25)$$

To construct a stability lobe diagram, the following steps are implemented:

1. Select a chatter frequency (ω_c) near a dominant structural frequency.
2. Calculate Λ_R and Λ_I using Equation 35.16.
3. Calculate d_{lim} using Equation 35.15.
4. Select a stability lobe number (l) and calculate N_s using Equation 35.25. The point (N_s, d_{lim}) is the point on the stability lobe diagram corresponding to the chatter frequency, ω_c , and the stability lobe number, l .
5. Repeat Step 4 for the desired number of stability lobes. The result is a vector of spindle speeds, $\vec{N}_s = \{N_{s_1} \ N_{s_2} \ \cdots \ N_{s_n}\}$. Each point $\{(N_{s_1}, d_{lim}) \ (N_{s_2}, d_{lim}) \ \cdots \ (N_{s_n}, d_{lim})\}$ corresponds to a different stability lobe, and all of the points correspond to the chatter frequency ω_c .
6. Select another chatter frequency and repeat Steps 2 to 5. In this manner, the stability lobe diagram is constructed. The smaller the difference between successive chatter frequencies, the greater the resolution of the stability lobe diagram. In general, the lobes will overlap. In this case, the

minimum limiting depth-of-cut is the smallest depth-of-cut. If the lobes do not overlap, then the range of chatter frequencies must be increased.

35.2.1 Example 1

The feed force for a turning operation is given by Equation 35.1 and the structural dynamics are given by Equation 35.26. An analytical expression for the limiting depth-of-cut and corresponding spindle speed for a given chatter frequency and stability lobe number is developed. The stability lobe diagram is plotted for $P = 0.6 \text{ kN/mm}^2$, $\omega_n = 600 \text{ Hz}$, $\zeta = 0.2$, and $k = 12 \text{ kN/mm}$. The stability lobe diagram is compared to stability lobe diagrams for $\zeta = 0.1, 0.3$, and 0.4 . The stability lobe diagram is then compared with stability lobe diagrams for $\omega_n = 500, 700$, and 800 Hz . The first ten lobes are included for all stability lobe diagrams:

$$\ddot{z}(t) + 2\zeta\omega_n\dot{z}(t) + \omega_n^2z(t) = -\frac{\omega_n^2}{k}F(t) \quad (35.26)$$

The parameter Λ is

$$\Lambda = \frac{-1}{g(j\omega_c)} = \Lambda_R + j\Lambda_I = \frac{k}{\omega_n^2}(\omega_c^2 - \omega_n^2) - j\frac{k}{\omega_n^2}(2\zeta\omega_c\omega_n) \quad (35.27)$$

The limiting depth-of-cut is

$$d_{\text{lim}} = \frac{k(\omega_c^2 - \omega_n^2)}{2K\omega_n^2} \left[1 + \frac{4\zeta^2\omega_c^2\omega_n^2}{(\omega_c^2 - \omega_n^2)^2} \right] \quad (35.28)$$

The spindle speed is

$$N_s = \frac{60\omega_c}{\pi - 2 \tan^{-1} \left(\frac{-2\zeta\omega_c\omega_n}{\omega_c^2 - \omega_n^2} \right) + 2l\pi}, \quad l = 0, 1, 2, \dots \quad (35.29)$$

where l is the stability lobe number. Note that the chatter frequency must be greater than the structural natural frequency for the limiting depth-of-cut to be positive. The first ten lobes of the

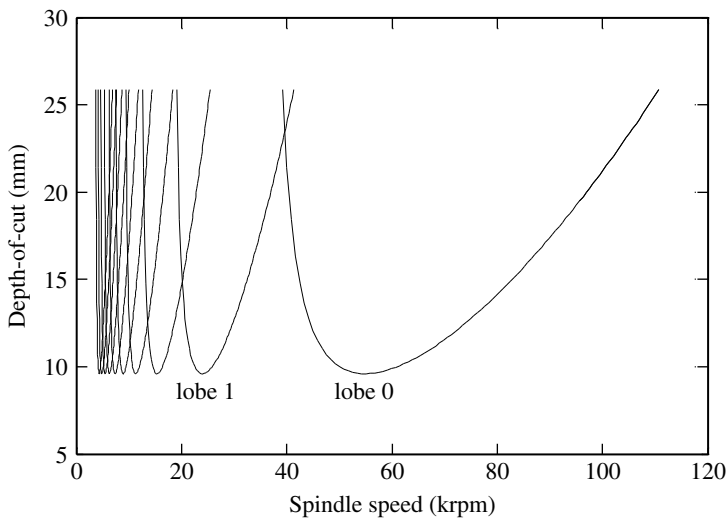


FIGURE 35.4 Unprocessed stability lobe diagram for Example 1.

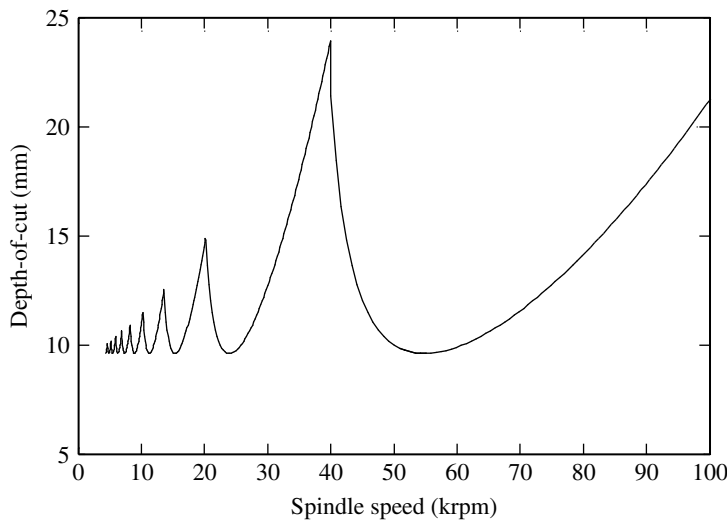


FIGURE 35.5 Processed stability lobe diagram for Example 1.

stability lobe diagram are plotted in Figure 35.4 and Figure 35.5. In Figure 35.4, the entire solution for each of the ten stability lobes is shown. The largest stability lobe is the zeroth lobe on the right. The lobe number increases from right to left on the stability lobe diagram and successive lobes become closer together. The stability lobe diagram is processed in Figure 35.5 such that the minimum depth-of-cut is selected at each spindle speed showing the true stability borderline.

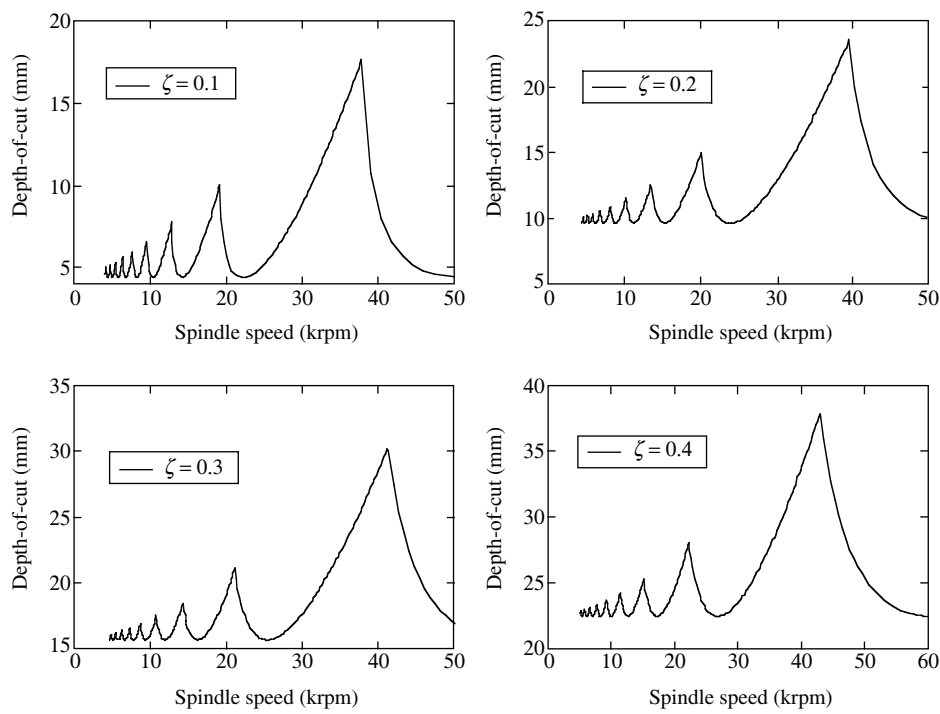


FIGURE 35.6 Stability lobe diagrams for Example 1 with $\zeta = 0.1, 0.2, 0.3,$ and 0.4 .

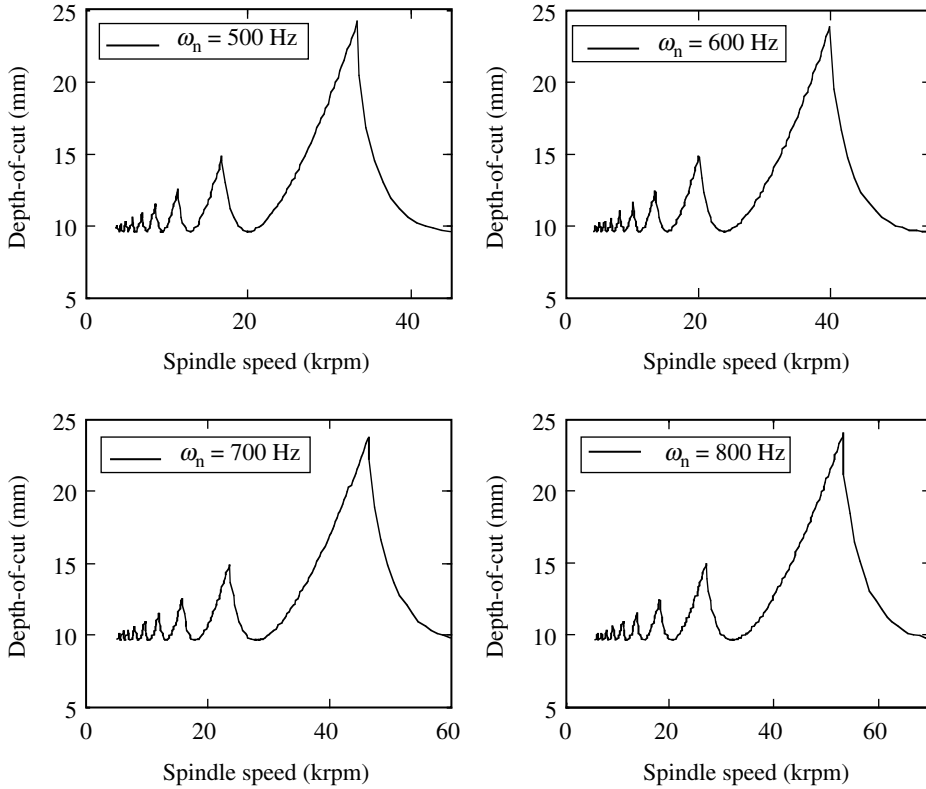


FIGURE 35.7 Stability lobe diagrams for Example 1 with $\omega_n = 500, 600, 700$, and 800 Hz.

In [Figure 35.6](#), the effect of the structural damping ratio is illustrated: as the structural damping ratio increases, the lobes shift slightly to the left and the asymptotic stability boundary shifts up dramatically. The effect of the structural natural frequency is illustrated in [Figure 35.7](#): as the structural natural frequency increases, the lobes shift to the right but the magnitude remains the same.

This section presented an analytical method to generate stability lobe diagrams for turning operations. The limiting depth-of-cut in a turning operation is given by

$$d_{\text{lim}} = \frac{A_R}{2P} (1 + \kappa^2)$$

where A_R is the real part of $-1/g(j\omega_c)$, $g(j\omega_c)$ is the structural transfer function evaluated at the chatter frequency, ω_c , $\kappa = A_I/A_R$, and A_I is the imaginary part of $-1/g(j\omega_c)$. The corresponding spindle speed is

$$N_s = \frac{60\omega_c}{\varepsilon + 2l\pi}$$

where $l = 0, 1, 2, \dots$ is the stability lobe number and

$$\varepsilon = \cos^{-1} \left(\frac{\kappa^2 - 1}{\kappa^2 + 1} \right)$$

35.3 Chatter in Face-Milling Operations

A schematic of a face-milling operation is shown in Figure 35.8. In milling operations, multiple teeth may be in contact with the part simultaneously, the feed naturally varies as a function of the tooth angle even when structural vibrations are not present, and each tooth enters and leaves contact with the part every spindle revolution. The depth-of-cut is the chip thickness in the z direction and is assumed to be constant, since the machine tool and part structures are typically much stiffer in the z direction than in the x and y directions.

The instantaneous feed of the i th tooth, illustrated in Figure 35.9, is

$$f_i(t) = f_t \cos[\theta_i(t)] + \Delta x(t) \cos[\theta_i(t)] + \Delta y(t) \sin[\theta_i(t)] \quad (35.30)$$

where

$$\Delta x(t) = \{x_t(t) - x_t(t - T_t)\} - \{x_p(t) - x_p(t - T_t)\} \quad (35.31)$$

$$\Delta y(t) = \{y_t(t) - y_t(t - T_t)\} - \{y_p(t) - y_p(t - T_t)\} \quad (35.32)$$

The term $f_t \cos[\theta_i(t)]$ in Equation 35.30 represents the feed due to the distance the part advances relative to the cutting tool each tooth rotation and is known as the static feed. The terms $\Delta x(t) \cos[\theta_i(t)]$

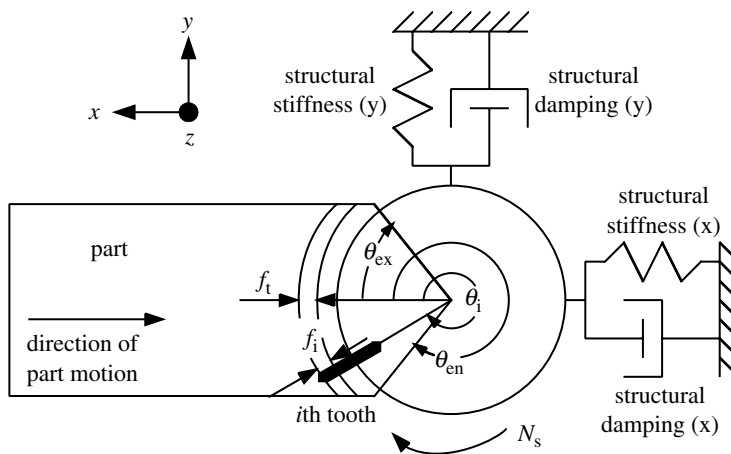


FIGURE 35.8 Face milling operation schematic: current pass (solid line), previous pass (dotted line), and depth-of-cut in z direction.

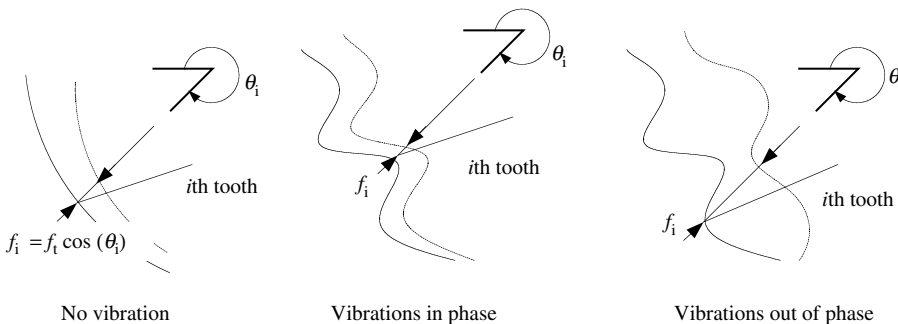


FIGURE 35.9 Modulation in feed due to structural vibrations in a face-milling operation: current pass (solid line) and previous pass (dotted line).

and $\Delta y(t) \sin[\theta_i(t)]$ in Equation 35.30 represent the feed due to tool and part vibrations in the x and y directions, respectively, at the tooth angle $\theta_i(t)$, and are known as the dynamic feed.

The machining forces in the x and y directions, respectively, are

$$\begin{aligned} F_x(t) = & df_t \sum_{i=1}^{N_t} \left\{ -P_T \cos(\psi_r) \cos^2[\theta_i(t)] + P_C \cos[\theta_i(t)] \sin[\theta_i(t)] \right\} \sigma[\theta_i(t)] \\ & + d\Delta x(t) \sum_{i=1}^{N_t} \left\{ -P_T \cos(\psi_r) \cos^2[\theta_i(t)] + P_C \cos[\theta_i(t)] \sin[\theta_i(t)] \right\} \sigma[\theta_i(t)] \\ & + d\Delta y(t) \sum_{i=1}^{N_t} \left\{ -P_T \cos(\psi_r) \sin[\theta_i(t)] \cos[\theta_i(t)] + P_C \sin^2[\theta_i(t)] \right\} \sigma[\theta_i(t)] \end{aligned} \quad (35.33)$$

$$\begin{aligned} F_y(t) = & df_t \sum_{i=1}^{N_t} \left\{ -P_T \cos(\psi_r) \cos[\theta_i(t)] \sin[\theta_i(t)] - P_C \cos^2[\theta_i(t)] \right\} \sigma[\theta_i(t)] \\ & + d\Delta x(t) \sum_{i=1}^{N_t} \left\{ -P_T \cos(\psi_r) \cos[\theta_i(t)] \sin[\theta_i(t)] - P_C \cos^2[\theta_i(t)] \right\} \sigma[\theta_i(t)] \\ & + d\Delta y(t) \sum_{i=1}^{N_t} \left\{ -P_T \cos(\psi_r) \sin^2[\theta_i(t)] - P_C \cos[\theta_i(t)] \sin[\theta_i(t)] \right\} \sigma[\theta_i(t)] \end{aligned} \quad (35.34)$$

where

$$\sigma[\theta_i(t)] = \begin{cases} 1 & \text{if } \theta_{en} \leq \theta_i(t) \leq \theta_{ex} \\ 0 & \text{if } \theta_{en} > \theta_i(t) > \theta_{ex} \end{cases} \quad (35.35)$$

The function $\sigma[\theta_i(t)]$ determines if the i th tooth is in contact with the part at the tooth angle, $\theta_i(t)$. The first terms in Equation 35.33 and Equation 35.34 are the machining forces acting on the tool in the x and y directions, respectively, due to the static feed. The second terms in Equation 35.33 and Equation 35.34 are the machining forces acting on the tool in the x and y directions, respectively, due to the dynamic feed resulting from structural vibrations in the x direction. The third terms in Equation 35.33 and Equation 35.34 are the machining forces acting on the tool in the x and y directions, respectively, due to the dynamic feed resulting from structural vibrations in the y direction.

The dynamic portion of the face milling force process model may be written compactly as

$$\begin{bmatrix} \Delta F_x(t) \\ \Delta F_y(t) \end{bmatrix} = dA(t) \begin{bmatrix} \Delta x(t) \\ \Delta y(t) \end{bmatrix} = d \begin{bmatrix} A_{11}(t) & A_{12}(t) \\ A_{21}(t) & A_{22}(t) \end{bmatrix} \begin{bmatrix} \Delta x(t) \\ \Delta y(t) \end{bmatrix} \quad (35.36)$$

where

$$A_{11}(t) = \sum_{i=1}^{N_t} \left\{ -P_T \cos(\psi_r) \cos^2[\theta_i(t)] + P_C \cos[\theta_i(t)] \sin[\theta_i(t)] \right\} \sigma[\theta_i(t)] \quad (35.37)$$

$$A_{12}(t) = \sum_{i=1}^{N_t} \left\{ -P_T \cos(\psi_r) \sin[\theta_i(t)] \cos[\theta_i(t)] + P_C \sin^2[\theta_i(t)] \right\} \sigma[\theta_i(t)] \quad (35.38)$$

$$A_{21}(t) = \sum_{i=1}^{N_t} \left\{ -P_T \cos(\psi_r) \cos[\theta_i(t)] \sin[\theta_i(t)] - P_C \cos^2[\theta_i(t)] \right\} \sigma[\theta_i(t)] \quad (35.39)$$

$$A_{22}(t) = \sum_{i=1}^{N_t} \left\{ -P_T \cos(\psi_r) \sin^2[\theta_i(t)] - P_C \cos[\theta_i(t)] \sin[\theta_i(t)] \right\} \sigma[\theta_i(t)] \quad (35.40)$$

These coefficients modulate the instantaneous feed as the tooth angular displacement changes. The summation from $i = 1$ to N_t represents the contribution to this modulation for each of the N_t teeth. Note the matrix $A(t)$ is time-varying and periodic with the tooth-passing period, T_t . For chatter analysis, the matrix $A(t)$ is typically expanded in a Fourier series using the zeroth term (Minis and Yanushevsky, 1993; Budak and Altintas, 1998a). The zeroth term of the Fourier expansion of the force process matrix $A(t)$ is

$$A^0 = \frac{N_t}{2\pi} \begin{bmatrix} A_{11}^0 & A_{12}^0 \\ A_{21}^0 & A_{22}^0 \end{bmatrix} \quad (35.41)$$

where

$$A_{11}^0 = \frac{1}{2} \left[-P_T \cos(\psi_r) \left\{ \theta + \frac{1}{2} \sin(2\theta) \right\} + P_C \sin^2(\theta) \right]_{\theta=\theta_{en}}^{\theta=\theta_{ex}} \quad (35.42)$$

$$A_{12}^0 = \frac{1}{2} \left[-P_T \cos(\psi_r) \sin^2(\theta) + P_C \left\{ \theta - \frac{1}{2} \sin(2\theta) \right\} \right]_{\theta=\theta_{en}}^{\theta=\theta_{ex}} \quad (35.43)$$

$$A_{21}^0 = \frac{1}{2} \left[-P_T \cos(\psi_r) \sin^2(\theta) - P_C \left\{ \theta + \frac{1}{2} \sin(2\theta) \right\} \right]_{\theta=\theta_{en}}^{\theta=\theta_{ex}} \quad (35.44)$$

$$A_{22}^0 = \frac{1}{2} \left[-P_T \cos(\psi_r) \left\{ \theta - \frac{1}{2} \sin(2\theta) \right\} - P_C \sin^2(\theta) \right]_{\theta=\theta_{en}}^{\theta=\theta_{ex}} \quad (35.45)$$

The dynamic force process is now approximated by the linear, time-invariant relationship:

$$\begin{bmatrix} \Delta F_x(t) \\ \Delta F_y(t) \end{bmatrix} = dA^0 \begin{bmatrix} \Delta x(t) \\ \Delta y(t) \end{bmatrix} \quad (35.46)$$

The tool and part vibrations, respectively, are related to the machining forces by

$$\begin{bmatrix} x_t(s) \\ y_t(s) \end{bmatrix} = G_t(s) \begin{bmatrix} F_x(s) \\ F_y(s) \end{bmatrix} = \begin{bmatrix} G_{t11}(s) & G_{t12}(s) \\ G_{t21}(s) & G_{t22}(s) \end{bmatrix} \begin{bmatrix} F_x(s) \\ F_y(s) \end{bmatrix} \quad (35.47)$$

$$\begin{bmatrix} x_p(s) \\ y_p(s) \end{bmatrix} = -G_p(s) \begin{bmatrix} F_x(s) \\ F_y(s) \end{bmatrix} = -\begin{bmatrix} G_{p11}(s) & G_{p12}(s) \\ G_{p21}(s) & G_{p22}(s) \end{bmatrix} \begin{bmatrix} F_x(s) \\ F_y(s) \end{bmatrix} \quad (35.48)$$

where $G_t(s)$ and $G_p(s)$ are the transfer functions relating the tool structural and part structural vibrations, respectively, to the machining forces. The negative sign in Equation 35.48 is due to the fact that the forces acting on the part are equal in magnitude and opposite in direction to the machining forces given in Equation 35.33 and Equation 35.34. Since

$$\begin{bmatrix} F_x(t) \\ F_y(t) \end{bmatrix} - \begin{bmatrix} F_x(t - T_t) \\ F_y(t - T_t) \end{bmatrix} = \begin{bmatrix} \Delta F_x(t) \\ \Delta F_y(t) \end{bmatrix} - \begin{bmatrix} \Delta F_x(t - T_t) \\ \Delta F_y(t - T_t) \end{bmatrix}$$

the structural vibrations can be related to the machining forces by

$$\begin{bmatrix} \Delta x \\ \Delta y \end{bmatrix} = (1 - e^{-sT_t}) [G_t(s) + G_p(s)] \begin{bmatrix} \Delta F_x(s) \\ \Delta F_y(s) \end{bmatrix} \quad (35.49)$$

The machine tool and part vibrations are assumed to occur at a chatter frequency, ω_c , when a marginally stable depth-of-cut is taken. Assuming the steady-state solution is a harmonic function at a chatter

frequency, ω_c , and substituting for the structural vibrations, Equation 35.49 becomes

$$\begin{bmatrix} \Delta F_x \\ \Delta F_y \end{bmatrix} e^{j\omega_c t} = \frac{dN_t}{2\pi} (1 - e^{j\omega_c T_t}) G^0(j\omega_c) \begin{bmatrix} \Delta F_x \\ \Delta F_y \end{bmatrix} e^{j\omega_c t} \quad (35.50)$$

where the matrix G^0 is

$$G^0(j\omega_c) = \frac{2\pi}{N_t} A^0 [G_t(j\omega_c) + G_p(j\omega_c)] \quad (35.51)$$

Equation 35.50 is now solved based on the method presented by Budak and Altintas (1998a, 1998b) to determine the stability lobe diagram. The characteristic equation of Equation 35.50 is

$$\det \left[I_2 - \frac{dN_t}{2\pi} (1 - e^{j\omega_c T_t}) G^0(j\omega_c) \right] = 0 \quad (35.52)$$

where I_2 is the 2×2 identity matrix. The solution of Equation 35.52 yields the limiting stable depth-of-cut. The inverse of the eigenvalue of G^0 is defined as

$$\Lambda(j\omega_c) = \Lambda_R(j\omega_c) + j\Lambda_I(j\omega_c) = -\frac{dN_t}{2\pi} (1 - e^{j\omega_c T_t}) \quad (35.53)$$

Expanding the exponential term in Equation 35.53 and noting that the depth-of-cut must be a real number, the limiting stable depth-of-cut may be written as

$$d_{\lim} = -\frac{\pi \Lambda_R}{N_t} (1 + \kappa^2) \quad (35.54)$$

where the parameter κ is defined by the transcendental equation

$$\kappa = \frac{\Lambda_I}{\Lambda_R} = \frac{\sin(\omega_c T_t)}{1 - \cos(\omega_c T_t)} \quad (35.55)$$

Equation 35.55 is solved for the tooth-passing period of the l th stability lobe and the tooth-passing period is related to the spindle speed to yield

$$N_s = \frac{60\omega_c}{N_t[\pi - 2\varphi + 2l\pi]}, \quad l = 0, 1, 2, \dots \quad (35.56)$$

where, again, $\varphi = \tan^{-1}(\kappa)$. A chatter frequency is selected and the limiting stable depth-of-cut is calculated from Equation 35.54 corresponding to the spindle speed on the l th lobe as given by Equation 35.56.

35.3.1 Example 2

The cutting and thrust pressures in a face-milling operation are given by $P_C = 2.0 \text{ kN/mm}^2$ and $P_T = 0.8 \text{ kN/mm}^2$, respectively, and the lead angle is 45° . The part is assumed to be perfectly rigid and the tool structural dynamics for the x and y directions are given by Equation 35.57 and Equation 35.58, respectively. The nominal parameters are $\theta_{\text{en}} = -45^\circ$, $\theta_{\text{ex}} = 45^\circ$, $N_t = 4$, $k_x = 14 \text{ kN/mm}$, $k_y = 17 \text{ kN/mm}$, $\zeta_x = 0.15$, $\zeta_y = 0.1$, $\omega_x = 3000 \text{ rad/sec}$, and $\omega_y = 4000 \text{ rad/sec}$. Stability lobe diagrams are generated for the nominal parameters and $N_t = 1, 2$, and 8 teeth. Next, stability lobe diagrams are generated for the nominal parameters and $\theta_{\text{ex}} = 30^\circ, 60^\circ$, and 75° . The first 15 lobes are included for all stability lobe diagrams.

$$\ddot{x}_t(t) + 2\zeta_x \omega_x \dot{x}_t(t) + \omega_x^2 x_t(t) = \frac{\omega_x^2}{k_x} F_x(t) \quad (35.57)$$

$$\ddot{y}_t(t) + 2\zeta_y \omega_y \dot{y}_t(t) + \omega_y^2 y_t(t) = \frac{\omega_y^2}{k_y} F_y(t) \quad (35.58)$$

The effect of the number of teeth is illustrated in Figure 35.10: as the number of teeth increases, the lobes shift to the left and the asymptotic stability borderline decreases. In Figure 35.11, the effect of the exit angle is illustrated: as the exit angle increases, the asymptotic stability borderline decreases.

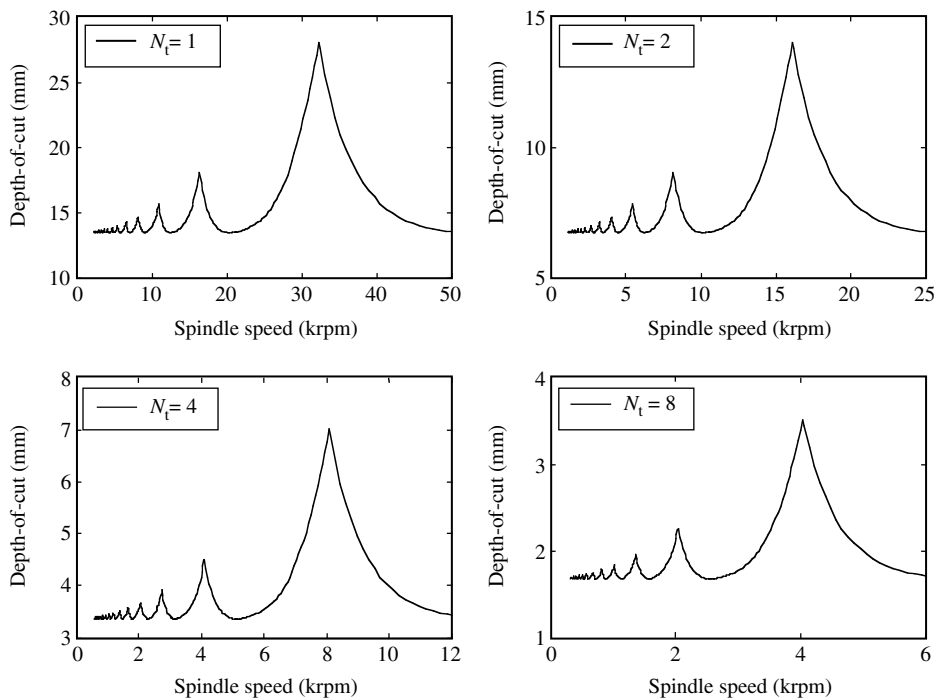


FIGURE 35.10 Stability lobe diagrams for Example 2, with $N_t = 1, 2, 4,$ and 8 .

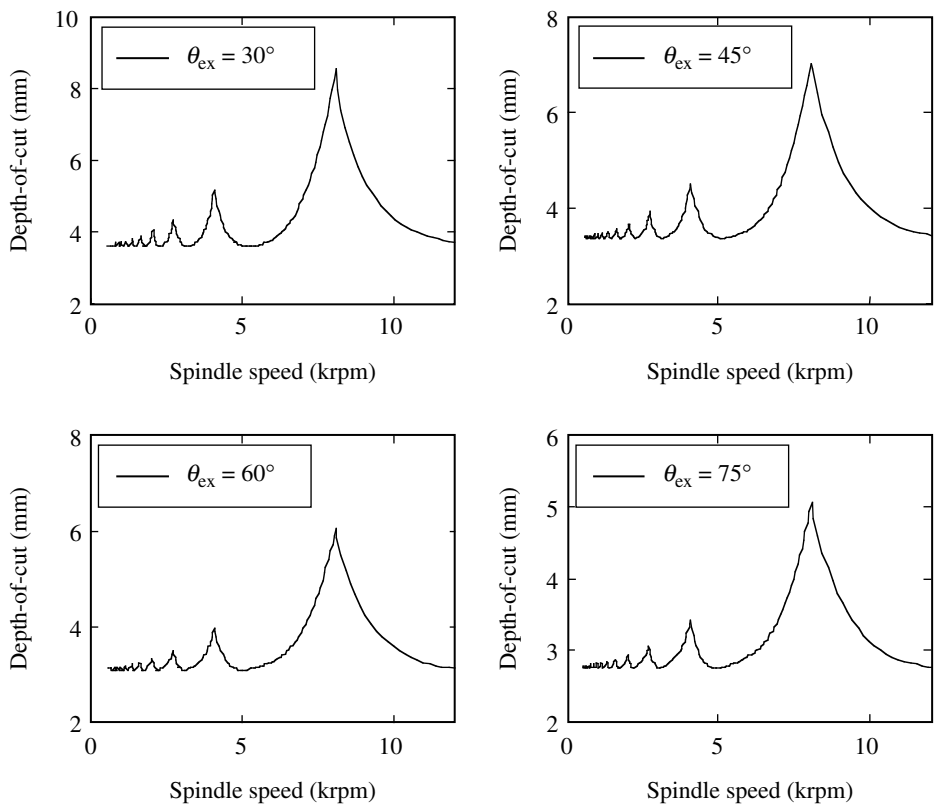


FIGURE 35.11 Stability lobe diagrams for Example 2, with $\theta_{ex} = 30^\circ, 45^\circ, 60^\circ,$ and 75° .

This section presented an analytical method to generate stability lobe diagrams for face-milling operations. The limiting depth-of-cut in a face-milling operation is given by

$$d_{\text{lim}} = -\frac{\pi A_R}{N_t}(1 + \kappa^2)$$

where N_t is the number of teeth, A_R is the inverse eigenvalue of $(2\pi/N_t)A^0[G_t(j\omega_c) + G_p(j\omega_c)]$, A^0 is the zeroth term of the Fourier expansion of the force process matrix, $G_t(j\omega_c)$ and $G_p(j\omega_c)$ are the transfer functions relating the tool structural and part structural vibrations, respectively, to the machining forces evaluated at the chatter frequency ω_c , $\kappa = A_I/A_R$, and A_I is the imaginary part of $(2\pi/N_t)A^0[G_t(j\omega_c) + G_p(j\omega_c)]$. The corresponding spindle speed is

$$N_s = \frac{60\omega_c}{N_t[\pi - 2 \tan^{-1}(\kappa) + 2l\pi]}$$

where $l = 0, 1, 2, \dots$ is the stability lobe number.

35.4 Time-Domain Simulation

Time-domain simulation (Tlusty and Ismail, 1981, 1983; Tlusty, 1986; Tsai et al., 1990; Lee and Liu, 1991a, 1991b; Smith and Tlusty, 1993; Elbestawi et al., 1994; Tarn and Li, 1994; Weck et al., 1994) is an alternative method for determining regenerative chatter. In a time-domain simulation, the machining forces and structural vibrations are simulated in the time domain for a specific set of process parameters and the resulting signals (i.e., forces and displacements) are examined to determine if chatter is present. The analyses presented above for the turning and face-milling operations assume that the tool always maintains contact with the part and that the cutting and thrust pressures are independent of the process parameters. Further, the face milling analysis approximated the time-varying force process matrix, $A(t)$, by the zeroth term of its Fourier expansion. With time domain simulations, nonlinear effects may be directly incorporated into the simulation; thus, more accurate stability prediction is possible. The disadvantage of time-domain simulations is the extreme computational cost that is required. For a specific spindle speed, several simulations must be conducted at different depths-of-cut; thus, the stability boundary for that spindle speed is determined iteratively. This procedure is repeated for a range of spindle speeds to construct a complete stability lobe diagram.

For turning operations, the machining force is calculated using Equation 35.1, the feed is calculated using Equation 35.2, and the tool displacement is calculated using Equation 35.4. For face-milling operations, the feed is calculated using Equation 35.30, the machining forces in the x and y directions are calculated using Equation 35.33 to Equation 35.35, and the tool and part displacements, respectively, are calculated using Equation 35.47 and Equation 35.48. To calculate the machining forces in the face-milling operation, the angular displacement of each tooth is required. The angular displacement of the i th tooth is

$$\theta_i(t) = \frac{2\pi}{60} N_s t + \frac{2\pi}{N_t}(i - 1) \quad (35.59)$$

The feed and force equations are static, while the structural displacement equations are dynamic and must be solved via a numerical integration technique. A sufficiently small time step must be utilized in the numerical integrations to account for the small system time constants associated with the large structural frequencies.

35.4.1 Example 3

The feed force for a turning operation is given by $F(t) = 0.6df^{0.7}(t)$. The structural dynamics are given by Equation 35.26 with the following parameters: $\omega_n = 600$ Hz, $\zeta = 0.2$, and $k = 12$ kN/mm.

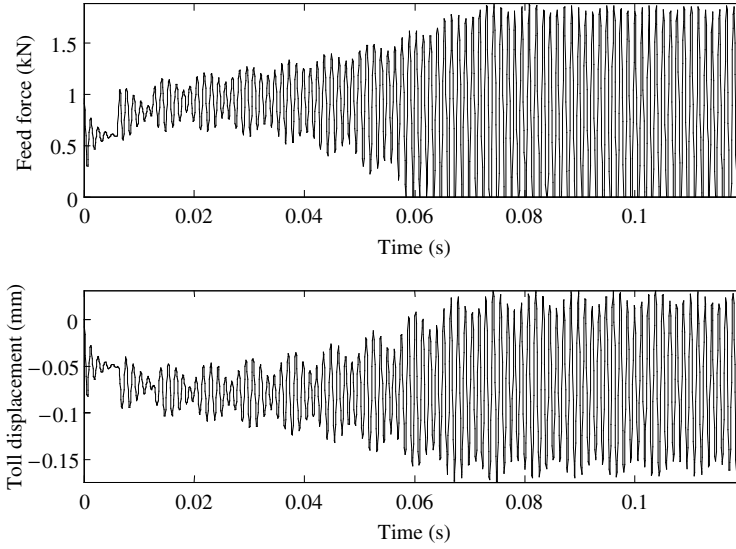


FIGURE 35.12 Time-domain simulations for Example 3 with $f_{\text{nom}} = 0.1$ mm.

A time-domain simulation of the system including the effect of the tool disengaging from the part is constructed, and simulations for $N_s = 10,000$ rpm, $d = 8$ mm, and $f_{\text{nom}} = 0.1$ mm are conducted. The simulation is repeated for $f_{\text{nom}} = 0.2$ mm. For both simulations, the time history of the feed force and the tool displacement are plotted.

To account for the phenomenon of the tool disengaging from the part, the feed in Equation 35.2 must be modified as follows:

$$f(t) = \begin{cases} f_{\text{nom}} + z(t) - f_p(t - T) & \text{if } f_{\text{nom}} + z(t) - f_p(t - T) \geq 0 \\ 0 & \text{if } f_{\text{nom}} + z(t) - f_p(t - T) < 0 \end{cases} \quad (35.60)$$

where

$$f_p(t) = \begin{cases} z(t) & \text{if } f_{\text{nom}} + z(t) - f_p(t - T) \geq 0 \\ -f_{\text{nom}} + f_p(t - T) & \text{if } f_{\text{nom}} + z(t) - f_p(t - T) < 0 \end{cases} \quad (35.61)$$

If the feed at the current time is calculated to be negative, then the cutting tool has disengaged from the part and the feed is zero. The term $f_p(t)$ accounts for feed due to structural vibrations at the previous spindle rotation, even when the cutting tool disengages from the part. The results for $f_{\text{nom}} = 0.1$ mm and $f_{\text{nom}} = 0.2$ mm are shown in Figure 35.12 and Figure 35.13, respectively. As the nominal feed is increased, chatter is suppressed.

35.4.2 Example 4

The cutting and thrust forces in a face-milling operation are given by $F_C(t) = 1.4df^{0.6}(t)$ and $F_T(t) = 0.4df^{0.8}(t)$, respectively. The lead angle is 45° , the entry angle is -60° ; the exit angle is 60° , the number of teeth is four, and the feed per tooth is $f_t = 0.15$ mm. The part is assumed to be perfectly rigid, and tool structural dynamics for the x and y directions are given by Equation 35.58 and Equation 35.59, respectively. A time-domain simulation is developed to determine the limiting stable depth-of-cut for spindle speeds of 1000 and 32,000 rpm. For both spindle speeds, the system is simulated for a depth-of-cut 10% below the limiting stable depth-of-cut and for a depth-of-cut 10% above the limiting stable depth-of-cut. The cutting force, thrust force, x tool displacement, and y tool displacement are plotted.

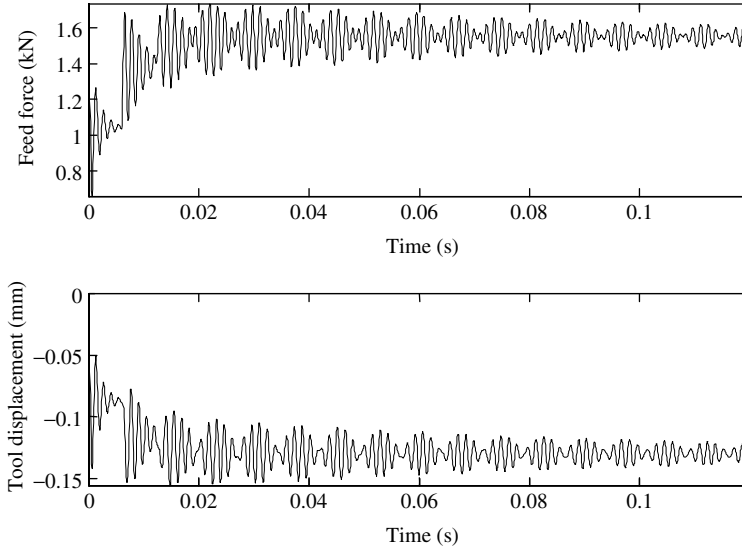


FIGURE 35.13 Time-domain simulations for Example 3 with $f_{\text{nom}} = 0.2$ mm.

The nonlinear effect of tooth disengagement is included:

$$\ddot{x}_t(t) + 2(0.15)(3000)\dot{x}_t(t) + 3000^2 x_t(t) = \frac{3000^2}{15} F_x(t) \quad (35.62)$$

$$\ddot{y}_t(t) + 2(0.1)(4000)\dot{y}_t(t) + 4000^2 y_t(t) = \frac{4000^2}{17} F_y(t) \quad (35.63)$$

To account for the phenomenon of the tool disengaging from the part, the feed in Equation 35.30 must be modified as follows:

$$f_i(t) = \begin{cases} f_{ci}(t) - f_{pi}(t - T_t) & \text{if } f_{ci}(t) \geq 0 \\ 0 & \text{if } f_{ci}(t) < 0 \end{cases} \quad (35.64)$$

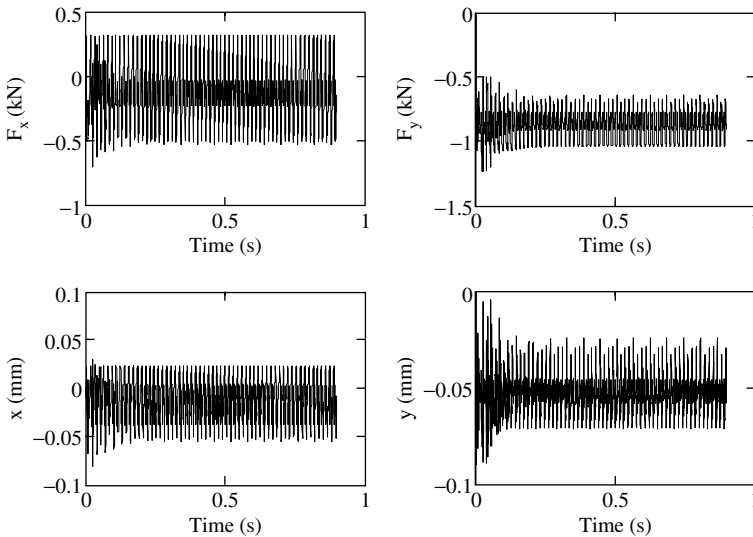


FIGURE 35.14 Time-domain simulation for Example 4 with $N_s = 1000$ rpm and $d = 2.025$ mm.

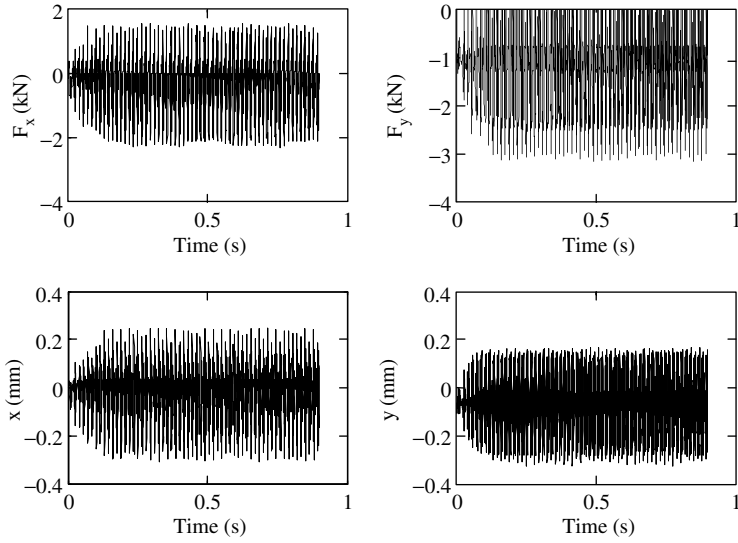


FIGURE 35.15 Time-domain simulation for Example 4 with $N_s = 1000$ rpm and $d = 2.475$ mm.

where

$$f_{ci}(t) = f_t \cos[\theta_i(t)] + \{x_t(t) - x_p(t)\} \cos[\theta_i(t)] + \{y_t(t) - y_p(t)\} \sin[\theta_i(t)] \quad (35.65)$$

$$f_{pi}(t) = \begin{cases} \{x_t(t - T_t) - x_p(t - T_t)\} \cos[\theta_i(t)] + \{y_t(t - T_t) - y_p(t - T_t)\} \sin[\theta_i(t)] & \text{if } f_{ci}(t) \geq 0 \\ -f_t \cos[\theta_i(t)] + f_{pi}(t - T_t) & \text{if } f_{ci}(t) < 0 \end{cases} \quad (35.66)$$

Note that $\theta_i(t) = \theta_{i+1}(t - T_t)$ and $i - 1 \rightarrow N_t$ if $i = 1$. The term $f_{pi}(t)$ represents the contribution to the instantaneous feed when the previous tooth was at the same angular location as the i th tooth. If the tooth and part are in contact, this contribution is due to the tool and part vibrations. If the tooth and part are not in contact, this contribution is the previous contribution added to the static portion and the instantaneous feed is set to zero. Through time-domain simulations, the limiting stable depth-of-cut for

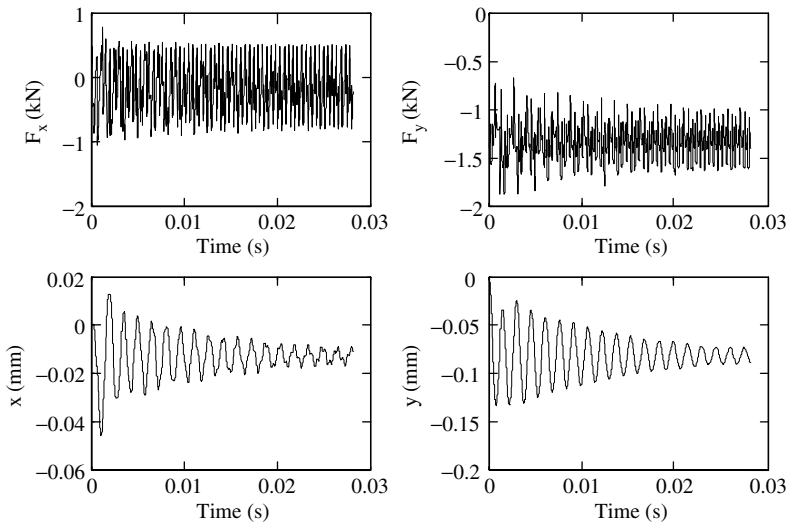


FIGURE 35.16 Time-domain simulation for Example 4 with $N_s = 32,000$ rpm and $d = 3.105$ mm.

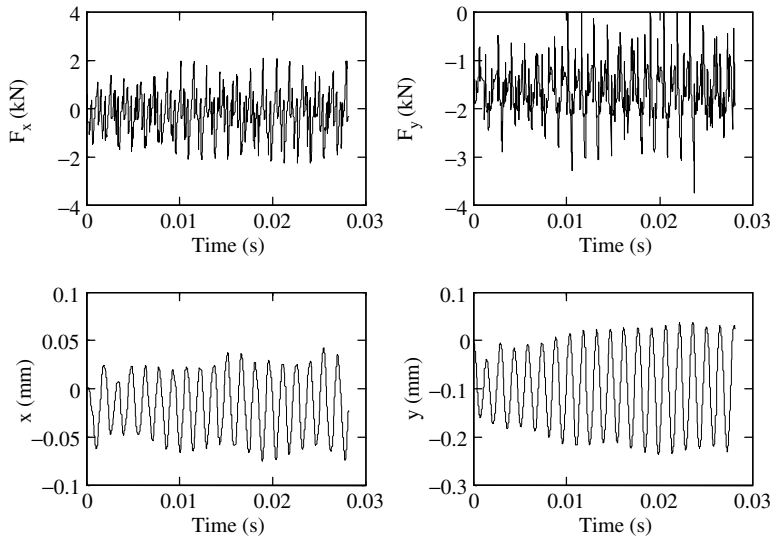


FIGURE 35.17 Time-domain simulation for Example 4 with $N_s = 32,000$ rpm and $d = 3.795$ mm.

$N_s = 1000$ rpm is found to be 2.25 mm and the limiting depth-of-cut for $N_s = 32,000$ rpm is found to be 3.45 mm. The results are shown in Figure 35.14 to Figure 35.17. The system is stable in Figure 35.14 and Figure 35.16, while instability is evidenced in Figure 35.15 and Figure 35.17 by the force in the y direction saturating at 0 kN.

This section presented the technique of time-domain simulation as an alternative means to analyze regenerative chatter. Time-domain simulations are the direct numerical simulations of the force process and structural vibrations. A process parameter is changed iteratively from simulation to simulation to determine the critical value at which chatter occurs. A sufficiently small time step must be utilized in the numerical integrations to account for the small system time constants associated with the large structural frequencies.

35.5 Chatter Detection

Regenerative chatter is easily detected by an operator due to the loud, high-pitched noise it produces and the distinctive “chatter marks” it leaves on the part surface. However, automatic detection is required for intelligent manufacturing (Cho and Ehmann, 1988; Delio et al., 1992). At the onset of chatter, process signals (e.g., force, vibration) contain significant energy at the chatter frequency. It is a well-known fact that the chatter frequency will be close to a dominant structural frequency. The most common method to detect the presence of chatter is to threshold the frequency signal of a process signal. To analyze the frequency content of a signal, a Fourier transform, or fast Fourier transform, is performed. If the frequency content of the resulting signal near a dominant chatter frequency is above a threshold value, then chatter is determined to be present. It should be noted that machining process signals also contain significant energy at the tooth-passing frequency. If the dominant structural frequencies and tooth-passing frequency are sufficiently separated, then the tooth-passing frequency may be ignored when determining the presence of chatter. If the dominant structural frequencies and tooth-passing frequency are close, then the signal must be filtered at the tooth-passing frequency using a notch filter. Also, forced vibrations, such as those resulting from the impact between the cutting tool and part, must not be allowed to falsely trigger the chatter

detection algorithm. These thresholding algorithms all suffer from the lack of an analytical method of selecting a threshold value. This value is typically selected empirically and will not be valid over a wide range of cutting conditions and machining operations.

35.5.1 Example 5

An experimental face-milling operation, a complete description of which is given in Landers (1997), is conducted with a spindle speed of 1500 rpm and a tool with four teeth. The dominant structural frequencies are 334, 414, 653, and 716 Hz. The machining force F_z is sampled at a frequency of 2000 Hz, and the time-domain signal is transformed into the frequency domain via a Fourier transform using 80 points (i.e., one spindle revolution). The power spectral density of the force signal is shown for depths-of-cut of 1.0 and 1.5 mm in Figure 35.18 and Figure 35.19, respectively. In Figure 35.18, there is significant energy at 100 Hz, which is the tooth-passing frequency. There is also significant energy at 750 Hz due to structural vibrations; however, the system did not chatter, as evidenced by the lack of chatter marks on the part and a high-pitched sound during machining. In Figure 35.19, there is significant energy at 665 Hz as well as 100 Hz. Chatter was evidenced by the chatter marks left on the part surface and the high-pitched sound during machining. The results demonstrate that the chatter frequency is 665 Hz, which is near the dominant structural frequency of 653 Hz. Note that the power spectral density at the frequency of 0 Hz is ignored in Figure 35.18 and Figure 35.19. This component is stronger than the components at all other frequencies since the machining force F_z fluctuates about a static, nonzero value. In this application, a thresholding algorithm may ignore the low frequencies where the tooth-passing frequency is strong; however, if the operation were to be performed at a higher spindle speed, say 7500 rpm, or the number of teeth were increased from 4 to 20, the tooth-passing frequency would be 500 Hz, close to the structural frequencies. In this case, the force signal would have to be filtered at the tooth-passing frequency.

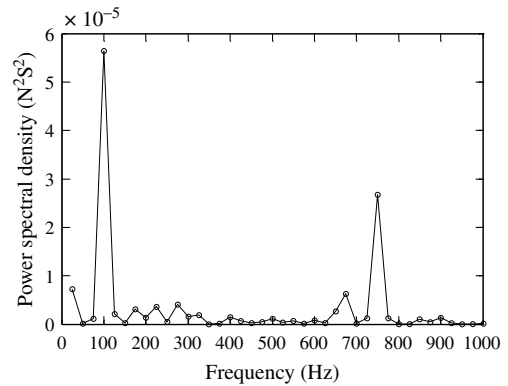


FIGURE 35.18 Power spectral density of F_z in a face-milling operation with $d = 1.0$ mm.

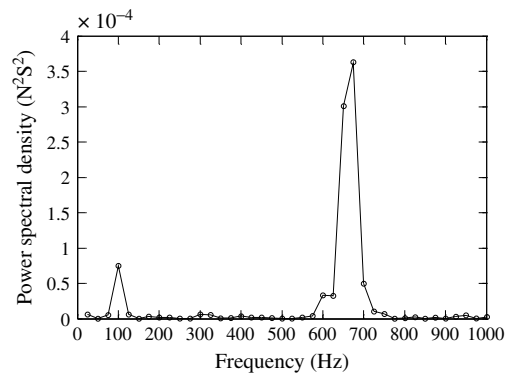


FIGURE 35.19 Power spectral density of F_z in a face-milling operation with $d = 1.5$ mm.

This section presented techniques to detect the occurrence of regenerative chatter. The phenomenon of regenerative chatter is easily detected by an operator due to the loud, high-pitched noise it produces and the distinctive “chatter marks” it leaves on the part surface. The most common method to detect the presence of chatter is to threshold the frequency signal of a process signal. In this case, one must be careful to separate out the spindle rotation and tooth-passing frequencies.

35.6 Chatter Suppression

Most machining process plans are derived from handbooks or from a database. Since these plans do not consider the physical machine that will be used, chatter-free operations cannot be guaranteed. Thus, multiple iterations, where the feed or spindle speed are adjusted using the operator's experience, are typically required. The tool position may also be adjusted (e.g., the depth-of-cut may be decreased) to suppress chatter and, while this is guaranteed to be effective due to the presence of the asymptotic stability borderline, this approach is typically not employed since part program must be rewritten to add multiple passes, thereby drastically decreasing productivity. The stability lobe diagram can be used as a tool to plan chatter-free machining operations and productivity can be greatly increased by selecting the process parameters to lie in a pocket between two lobes. A cutting tool design methodology (Altintas et al., 1999) has also been proposed for milling tools where the pitch is slightly adjusted such that the teeth are not evenly spaced. The variable pitch has the effect of changing the phase difference between successive teeth vibrations and, if designed properly, will suppress chatter. These design techniques are very sensitive to parameter variations and model uncertainty, and may not be used reliably for a large range of operating conditions. This section will describe methods for automatic chatter suppression.

35.6.1 Spindle-Speed Selection

For the stability lobe diagram generated from a system modeled as having a one-dimensional structure, it is seen that the maximum depths-of-cut are located at the tooth-passing frequencies (i.e., the number of teeth multiplied by the spindle speed) corresponding to the dominant structural frequency and integer fractions thereof. If the dominant structural frequency is known, it may be used as an aid in selecting spindle speeds; however, the structural dynamics are often unknown and may be determined only through costly testing. Further, structural dynamics change drastically over time.

It is known, however, that during chatter, the dominant frequency seen in the cutting-process output is close to a dominant structural frequency. This fact is used in Smith and Delio (1992) to suppress chatter automatically. The following steps are taken:

1. Implement a chatter detection routine to determine the presence of chatter.
2. If chatter is detected, determine the chatter frequency, ω_c . This will be the frequency at which the process signal has the greatest energy.
3. Set the new spindle speed to be $N_s = \omega_c / [N_t(N + 1)]$, where N is the smallest positive integer such that the new spindle speed does not violate the maximum spindle speed constraint.
4. Repeat Steps 1 to 3 until the chatter has been suppressed.

The equation $N_s = \omega_c / [N_t(N + 1)]$ may be interpreted as selecting the tooth-passing frequency, or an integer fraction thereof, corresponding to the approximate dominant structural frequency. Note that if the depth-of-cut is too large and the maximum spindle speed is too small, this technique will not be effective and the feed or depth-of-cut must be adjusted, or the spindle speed must be continuously varied.

35.6.2 Example 6

The feed force for a turning operation is given by Equation 35.1, and the structural dynamics are given by Equation 35.26. The system parameters are $P = 0.75 \text{ kN/mm}^2$, $f_{\text{nom}} = 0.1 \text{ mm}$, $\omega_n = 750 \text{ Hz}$, $\zeta = 0.1$, and $k = 15 \text{ kN/mm}$. The depth-of-cut is 5 mm. The spindle speed that should be selected to suppress chatter if the chatter frequency is 725 Hz, when the spindle speed is not constrained, is determined. The spindle speed that should be selected to suppress chatter if the maximum spindle speed is 15,000 rpm is also determined. The system is simulated for a spindle speed of 10,000 rpm for ten spindle revolutions and then for ten spindle revolutions for the spindle

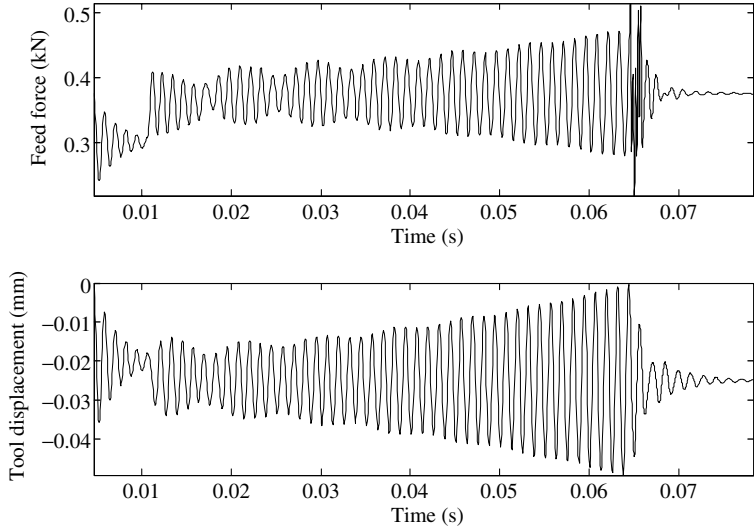


FIGURE 35.20 Time-domain simulations using spindle speed selection with $N_s = 43,500$ rpm.

speed calculated when the spindle speed is not constrained. The simulation is then repeated for the spindle speed calculated when the spindle speed is constrained. Feed force and tool displacement are plotted for both cases.

For a chatter frequency of 725 Hz, the optimal spindle speed is $60(725) = 43,500$ rpm. Other possible spindle speeds are $43,500/2 = 21,750$ rpm, $43,500/3 = 14,500$ rpm, $43,500/4 = 10,875$ rpm, and so on. Therefore, when the maximum spindle speed is 15,000 rpm, a spindle speed of 14,500 rpm is used. The time domain simulations are in Figure 35.20 and Figure 35.21. The results illustrate that a depth-of-cut of 5.3 mm is stable at 43,500 rpm, but not at 14,500 rpm. Therefore, if the spindle speed is limited to 15,000 rpm, spindle-speed selection may not be used to suppress the chatter present in the machining operation.

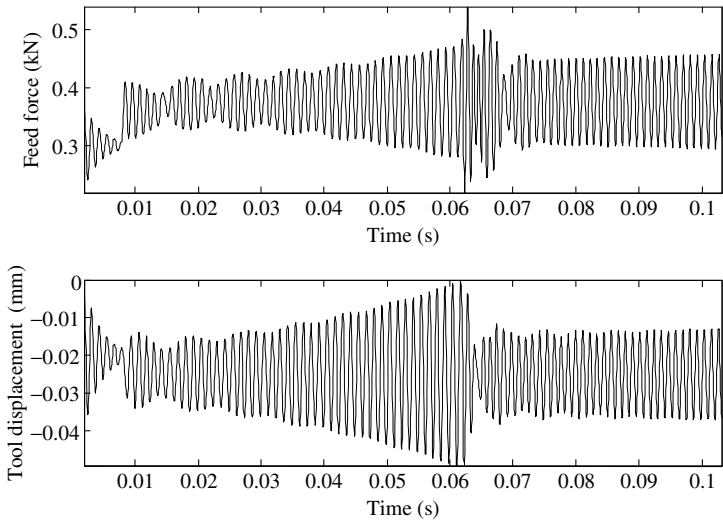


FIGURE 35.21 Time-domain simulations using spindle speed selection with $N_s = 14,500$ rpm.

35.6.3 Feed and Depth-of-Cut Selection

When chatter occurs, operators will sometimes increase the feedrate via the feedrate override button on the machine tool control panel. This has the effect of increasing the feed, assuming the spindle speed remains constant. When linear chatter analysis techniques are employed, the force process gains are linearized about the nominal feed, and stability does not appear to be affected by the nominal feed. However, the stability results are only valid for a small region about the nominal feed. It is well known that there is a nonlinear relationship between the machining forces and the feed of the form $F = P(f)df$. The pressure can be expressed in the form $P(f) = Kf^\alpha$ where $\alpha < 0$; thus, the pressure decreases as the feed increases. Since the stable depth-of-cut is inversely proportional to the pressure, the stability limit will increase as the feed increases, assuming the spindle speed remains constant. An illustration of this phenomenon was shown in Example 3: when the feed was increased from 0.1 to 0.2 mm, chatter was suppressed. While increasing the feed can suppress chatter, the sensitivity of chatter to feed is limited and other adverse phenomenon, such as tooth chippage, may occur.

Another method to suppress chatter is to decrease the depth-of-cut (Weck et al., 1975). This method is guaranteed to work as evidenced by stability lobe diagrams. However, this method is typically not preferred as it dramatically decreases operation productivity by increasing the total number of tool passes that are required to complete the operation.

35.6.4 Spindle-Speed Variation

Spindle speed variation (SSV) is another technique that has shown the ability to suppress chatter (Inamura and Sata, 1974; Lin et al., 1990). The spindle speed is varied about some nominal value, typically in a sinusoidal manner. Although SSV is a promising technique, the theory required to guide the designer in the selection of suitable amplitudes and frequencies is in its infancy (Radulescu et al., 1997a, 1997b; Sastry et al., 2002). Also, in some cases, SSV may create chatter that would not occur when using a constant spindle speed.

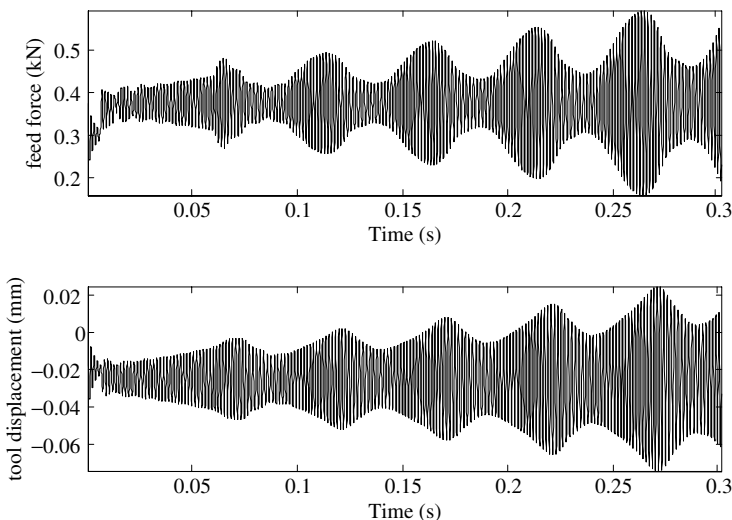


FIGURE 35.22 Time-domain simulations using spindle-speed variation with $A = 0.1$ and $\Omega = 20$ Hz.

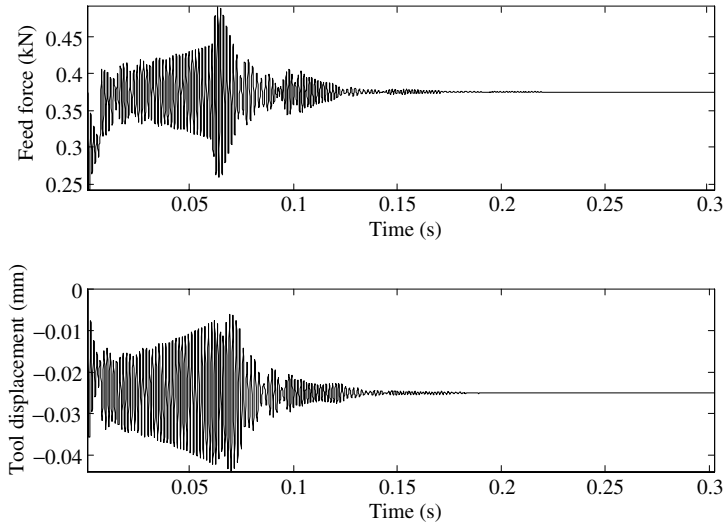


FIGURE 35.23 Time-domain simulations using spindle-speed variation with $A = 0.25$ and $\Omega = 20$ Hz.

35.6.5 Example 7

The feed force for a turning operation is given by Equation 35.1 and the structural dynamics are given by Equation 35.26. The system parameters are $P = 0.75 \text{ kN/mm}^2$, $f_{\text{nom}} = 0.1 \text{ mm}$, $\omega_n = 750 \text{ Hz}$, $\zeta = 0.1$, and $k = 15 \text{ kN/mm}$. The depth-of-cut is 5 mm. The system is simulated for a nominal spindle speed of $N_{\text{nom}} = 10,000 \text{ rpm}$ for 10 spindle revolutions and then for 30 spindle revolutions for the spindle speed calculated from Equation 35.67 for the following three cases: $A = 0.1$ and $\Omega = 20 \text{ Hz}$, $A = 0.25$ and $\Omega = 20 \text{ Hz}$, and $A = 0.25$ and $\Omega = 160 \text{ Hz}$. Feed force and tool displacement are plotted for all three cases.

$$N_s(t) = N_{\text{nom}}[1 + A \sin(\Omega t)] \quad (35.67)$$

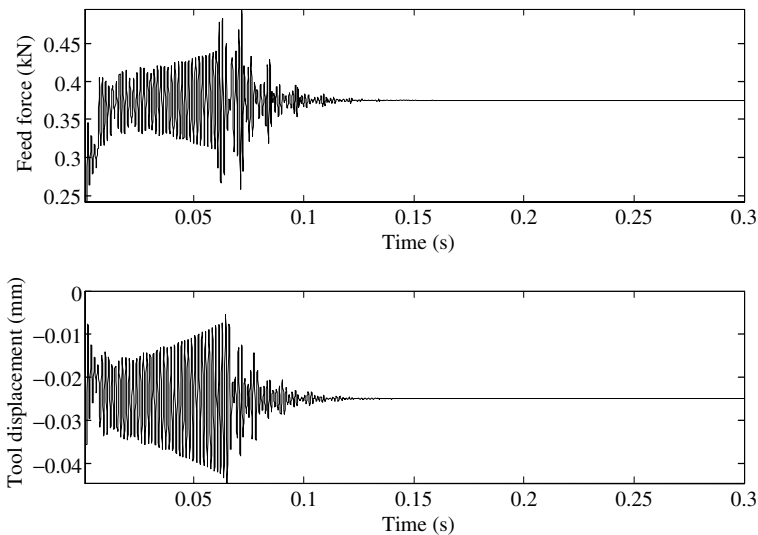


FIGURE 35.24 Time-domain simulations using spindle-speed variation with $A = 0.25$ and $\Omega = 160$ Hz.

The time-domain simulations are in [Figure 35.22](#) to [Figure 35.24](#) for the respective cases. The results illustrate that SSV may be utilized to suppress chatter; however, the amplitude and frequency of the spindle speed vibration must be carefully chosen.

This section presented several techniques to suppress regenerative chatter. The three major techniques to suppress chatter are spindle-speed selection, feed selection, and SSV. In spindle-speed selection, the spindle speed is adjusted to be a multiple of the chatter frequency to place the spindle speed in a pocket of the stability lobe diagram. In feed selection, the feed is increased to suppress chatter. In SSV, the spindle speed is varied in a sinusoidal manner to decrease the phase difference between the current and previous tooth passes.

35.7 Case Study

A case study of regenerative chatter for a face-milling operation is now presented. Further details are presented in Landers (1997). The machine tool is a three-axis vertical milling machine ([Figure 35.25](#)). Each axis has a linear encoder with a resolution of $10\text{ }\mu\text{m}$ mounted on it. The axis motors (186 W) drive pulleys that rotate leadscrews and provide motion to the linear axes. The spindle (2240 W) drives the face mill (Carboloy R/L220.13-02.00-12, 50 mm diameter). The tool holds four carbide inserts (Carboloy SEAN 42AFTN-M14 HX, 45° lead angle). The part is 6061 aluminum. The spindle is run open-loop. A Kistler 9293 piezoelectric three-component dynamometer was utilized for force process modeling and chatter detection. The x and y channels have a natural frequency of 4.5 kHz, rigidity of $0.7\text{ kN}/\mu\text{m}$, and range of -20 to 20 kN . The z channel has a natural frequency of 5 kHz, rigidity of $7\text{ kN}/\mu\text{m}$, and range of -100 to 200 kN . A Bently Nevada 3000 Series Type 190 proximity transducer was utilized to measure the static stiffnesses of the structural components. The sensor gain is 8 V/mm , the response is flat to 10 kHz, and the range is 1.02 mm . A Kistler Quartz Model #802A accelerometer (resonant frequency 36.7 kHz) was utilized to measure the dynamic characteristics of the structural components.

The cutting and thrust pressures, respectively, are

$$P_C = 0.29f^{-0.25}d^{-0.13}\left(\frac{V}{1000}\right)^{-0.72} \quad (35.68)$$

$$P_T = 0.16f^{-0.40}d^{-0.41}\left(\frac{V}{1000}\right)^{-0.58} \quad (35.69)$$

The transfer function matrices, respectively, between the tool structure and machining forces, and the part structure and machining forces are modeled as

$$\begin{bmatrix} x_t(s) \\ y_t(s) \end{bmatrix} = \begin{bmatrix} \frac{(4500^2/14)}{s^2 + 2(0.07)(4500)s + 4500^2} & 0 \\ 0 & \frac{(4100^2/14)}{s^2 + 2(0.11)(4100)s + 4100^2} \end{bmatrix} \begin{bmatrix} F_x(s) \\ F_y(s) \end{bmatrix} \quad (35.70)$$

$$\begin{bmatrix} x_p(s) \\ y_p(s) \end{bmatrix} = - \begin{bmatrix} \frac{(2600^2/9.5)}{s^2 + 2(0.09)(2600)s + 2600^2} & 0 \\ 0 & \frac{(2100^2/9.5)}{s^2 + 2(0.22)(2100)s + 2100^2} \end{bmatrix} \begin{bmatrix} F_x(s) \\ F_y(s) \end{bmatrix} \quad (35.71)$$

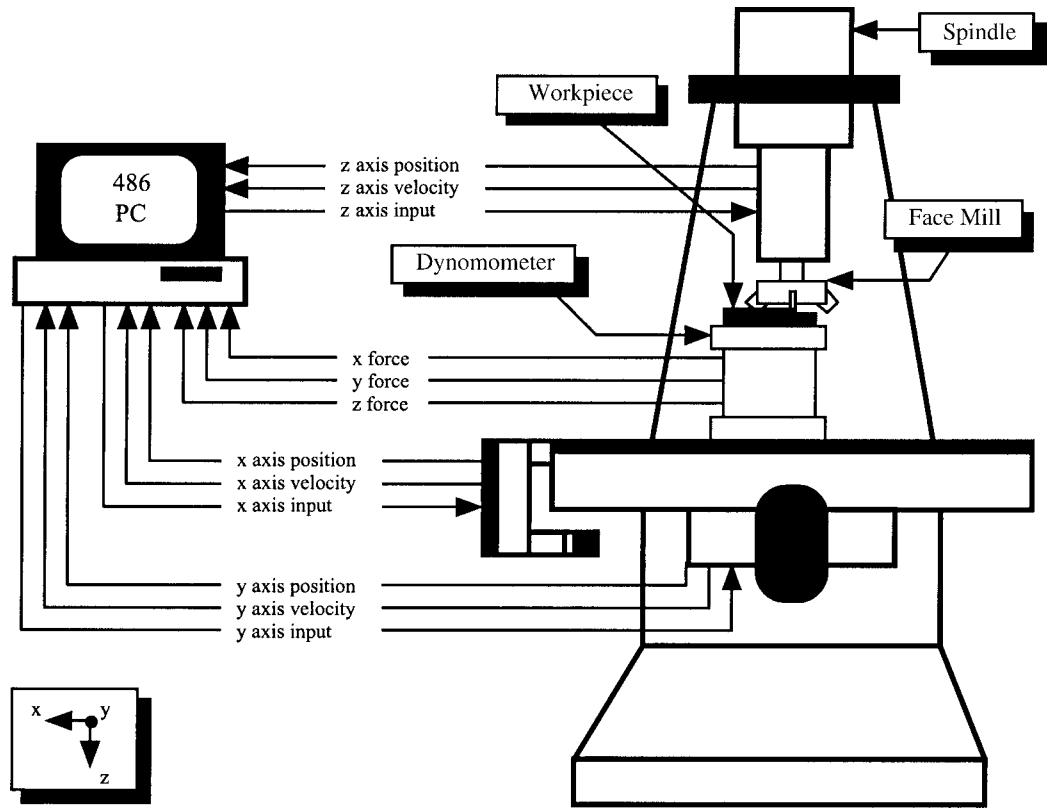


FIGURE 35.25 Three-axis vertical machine tool schematic.

Using the machining force and structural models, a stability lobe diagram was constructed using time domain simulations. Experimental data were collected by adjusting the depth-of-cut in increments of 0.1 mm until chatter occurred. The time-domain simulations and the experimental data are plotted in Figure 35.26. The cutting conditions were $f_t = 0.10$ mm/tooth, $N_t = 4$ teeth, $\theta_{en} = -90^\circ$, and $\theta_{ex} = 90^\circ$. The chatter detection methodology for this system was described in Example 5.

Spindle-speed adjustment is typically a more productive chatter suppression option. However, the machine tool in this case study is not equipped with automatic spindle speed control and, thus, the depth-of-cut is adjusted to suppress chatter. When chatter is detected, the chatter suppressor rewrites the part program to accommodate one additional tool pass (Figure 35.27). Therefore, the new operation depth-of-cut is

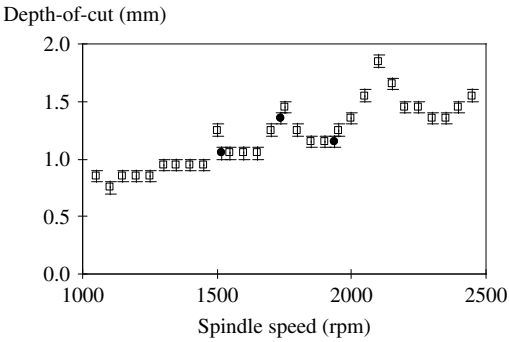


FIGURE 35.26 Stability lobe diagram for a face-milling operation — time-domain simulations (empty boxes) and experimental points (filled circles).

$$d_n = \frac{d_p}{1 + N_c} \tag{35.72}$$

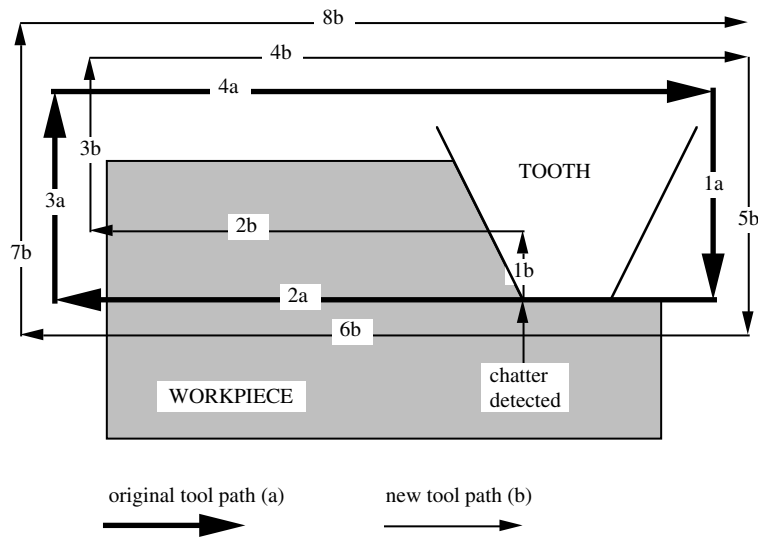


FIGURE 35.27 Original tool path (a) is rewritten when chatter occurs. New tool path (b) contains an additional tool pass.

where d_p is the previous operation depth-of-cut and N_c is the number of times the chatter suppression routine has been invoked. The new value may be well below the stability limit; however, making all passes an equal depth-of-cut provides a good balance between productivity and the search for a stable depth-of-cut. Results of this controller are presented in Landers and Ulsoy (1998, 2001).

Nomenclature

Symbol	Quantity	Symbol	Quantity
d	depth-of-cut (mm)	T	spindle rotational period (sec)
d_{lim}	limiting stable depth-of-cut (mm)	T_t	tooth rotational period (sec)
f	feed (mm)	x_p	part structural displacement in x direction (mm)
f_t	feed per tooth (mm)	x_t	cutting tool structural displacement in x direction (mm)
F	machining force (kN)	y_p	part structural displacement in y direction (mm)
F_C	cutting force (kN)	y_t	cutting tool structural displacement in y direction (mm)
F_T	thrust force (kN)	z	cutting tool structural displacement in z direction (mm)
F_x	force acting on cutting tool in x direction (kN)	θ	tooth angle (rad)
F_y	force acting on cutting tool in y direction (kN)	θ_{en}	tooth entry angle (rad)
F_z	force acting on cutting tool in z direction (kN)	θ_{ex}	tooth exit angle (rad)
k	structural stiffness (kN/mm)	ω_c	chatter frequency (rad/sec)
N_s	spindle speed (rpm)	ω_n	structural natural frequency (rad/sec)
N_t	number of teeth	ψ_r	lead angle (rad)
P	machining pressure (kN/mm ²)	ζ	structural damping ratio
P_C	cutting pressure (kN/mm ²)		
P_T	thrust pressure (kN/mm ²)		
t	time (sec)		

References

- Altintas, Y. and Budak, E., Analytical prediction of stability lobes in milling, *Ann. CIRP*, 44/1, 357–362, 1995.
- Altintas, Y., Engin, S., and Budak, E., Analytical stability prediction and design of variable pitch cutters, *ASME J. Manuf. Sci. Eng.*, 121, 173–178, 1999.
- Budak, E. and Altintas, Y., Analytical prediction of chatter stability in milling, part I: general formulation, *ASME J. Dyn. Syst. Meas. Control*, 120, 22–30, 1998a.
- Budak, E. and Altintas, Y., Analytical prediction of chatter stability in milling, part II: application of the general formulation to common milling systems, *ASME J. Dyn. Syst. Meas. Control*, 120, 31–36, 1998b.
- Cho, D.W. and Ehmann, K.F., Pattern recognition for on-line chatter detection, *Mech. Syst. Signal Process.*, 2, 279–290, 1988.
- Delio, T., Tlustý, J., and Smith, S., Use of audio signals for chatter detection and control, *ASME J. Eng. Ind.*, 114, 146–157, 1992.
- Elbestawi, M.A., Ismail, F., Du, R., and Ullagaddi, B.C., Modeling machining dynamics including damping in the tool–workpiece interface, *ASME J. Eng. Ind.*, 116, 435–439, 1994.
- Inamura, T. and Sata, T., Stability analysis of cutting under varying spindle speed, *Ann. CIRP*, 23/1, 119–120, 1974.
- Inasaki, I., Karpuschewski, B., and Lee, H.-S., Grinding chatter — origin and suppression, *Ann. CIRP*, 50/2, 515–534, 2001.
- Koenigsberger, I., Tlustý, J. 1971. *Structures of Machine Tools*, Pergamon Press, New York.
- Landers, R.G. 1997. Supervisory machining control: a design approach plus force control and chatter analysis components, Ph.D. Dissertation. Department of Mechanical Engineering and Applied Mechanics, University of Michigan, Ann Arbor.
- Landers, R.G. and Ulsoy, A.G., Supervisory machining control: design and experiments, *Ann. CIRP*, 47/1, 301–306, 1998.
- Landers, R.G. and Ulsoy, A.G., Supervisory control of a face-milling operation in different manufacturing environments, *Trans. Control Automat. Syst. Eng.*, 3, 1–9, 2001.
- Lee, A.-C. and Liu, C.-S., Analysis of chatter vibration in a cutter–workpiece system, *Int. J. Mach. Tools Manuf.*, 31, 221–234, 1991a.
- Lee, A.-C. and Liu, C.-S., Analysis of chatter vibration in the end milling process, *Int. J. Mach. Tools Manuf.*, 31, 471–479, 1991b.
- Lin, S.C., DeVor, R.E., and Kapoor, S.G., The effects of variable speed cutting on vibration control in face milling, *ASME J. Eng. Ind.*, 112, 1–11, 1990.
- Merritt, H.E., Theory of self-excited machine tool chatter: contribution to machine-tool chatter research — 1, *ASME J. Eng. Ind.*, 87, 447–454, 1965.
- Minis, I., Magrab, E., and Pandelidis, I., Improved methods for the prediction of chatter in turning, Part III: a generalized linear theory, *ASME J. Eng. Ind.*, 112, 28–35, 1990a.
- Minis, I. and Yanushevsky, R., A new theoretical approach for the prediction of machine tool chatter in milling, *ASME J. Eng. Ind.*, 115, 1–8, 1993.
- Minis, I., Yanushevsky, R., and Tembo, A., Analysis of linear and nonlinear chatter in milling, *Ann. CIRP*, 39/1, 459–462, 1990b.
- Radulescu, R., Kapor, S.G., and DeVor, R.E., An investigation of variable spindle speed face milling for tool work structures with complex dynamics, part 1: simulation results, *ASME J. Manuf. Sci. Eng.*, 119, 266–272, 1997a.
- Radulescu, R., Kapor, S.G., and DeVor, R.E., An investigation of variable spindle speed face milling for tool work structures with complex dynamics, part 2: physical explanation, *ASME J. Manuf. Sci. Eng.*, 119, 273–280, 1997b.
- Sastry, S., Kapor, S.G., and DeVor, R.E., Floquet theory based approach for stability analysis of the variable speed face-milling process, *ASME J. Manuf. Sci. Eng.*, 124, 10–17, 2002.

- Smith, S. and Delio, T., Sensor-based chatter detection and avoidance by spindle speed selection, *ASME J. Dyn. Syst. Meas. Control*, 114, 486–492, 1992.
- Smith, S. and Tlusty, J., Efficient simulation programs for chatter in milling, *Ann. CIRP*, 42/1, 463–466, 1993.
- Tarn, Y.S. and Li, T.C., Detection and suppression of drilling chatter, *ASME J. Dyn. Syst. Meas. Control*, 116, 729–734, 1994.
- Tlusty, J., Dynamics of high-speed milling, *ASME J. Eng. Ind.*, 108, 59–67, 1986.
- Tlusty, J. 2000. *Manufacturing Processes and Equipment*, Prentice Hall, Upper Saddle River, NJ.
- Tlusty, J. and Ismail, F., Basic nonlinearity in machining chatter, *Ann. CIRP*, 30/1, 299–304, 1981.
- Tlusty, J. and Ismail, F., Special aspects of chatter in milling, *ASME J. Vib. Acoust. Stress Reliab. Des.*, 105, 24–32, 1983.
- Tobias, S.A. 1965. *Machine Tool Vibration*, Wiley, New York.
- Tsai, M.D., Takata, S., Inui, M., Kimura, F., and Sata, T., Prediction of chatter vibration by means of a model-based cutting simulation system, *Ann. CIRP*, 39/1, 447–450, 1990.
- Weck, M., Altintas, Y., and Beer, C., CAD assisted chatter-free NC tool path generation in milling, *Int. J. Mach. Tools Manuf.*, 34, 879–891, 1994.
- Weck, M., Verhagg, E., and Gather, M., Adaptive control of face-milling operations with strategies for avoiding chatter-vibrations and for automatic cut distribution, *Ann. CIRP*, 24/1, 405–409, 1975.
- Yun, I.S., Wilson, W.R.D., and Ehmann, K.F., Review of chatter studies in cold rolling, *Int. J. Mach. Tools Manuf.*, 38, 1499–1530, 1998.

36

Fluid-Induced Vibration

36.1	Description of the Ocean Environment	36-1
	Spectral Density • Ocean Wave Spectral Densities •	
	Approximation of Spectral Density from Time Series •	
	Generation of Time Series from a Spectral Density •	
	Short-Term Statistics • Long-Term Statistics • Summary	
36.2	Fluid Forces	36-16
	Wave Force Regime • Wave Forces on Small Structures —	
	Morison Equation • Vortex-Induced Vibration • Summary	
36.3	Examples	36-23
	Static Configuration of a Towing Cable • Fluid Forces on an	
	Articulated Tower • Distribution of Significant Wave	
	Heights — Weibull and Gumbel Distributions •	
	Reconstructing Time Series for a Given Significant Wave	
	Height • Available Numerical Codes	

Seon M. Han

Texas Tech University

Summary

This chapter gives an overview on the subject of fluid-induced vibration in an ocean environment. The main objective is to show how the fluid forces on an offshore structure due to current and random waves are modeled. The chapter is divided into three sections. The first section describes the ocean environment, especially the currents and random waves. The second section is dedicated to obtaining fluid forces utilizing the results from the first section and the third section gives some examples to show how the results from the first two sections can be used in practice. In the first section, the concept of spectral density is introduced. For a given spectrum, methods to obtain a sample time series are given. In the second section, the forces that the fluid can exert on a body are discussed. The regimes in which inertia, drag, or diffraction forces are dominant are shown in terms of the ratio of the wave height to the structural diameter and the ratio of the structural diameter to the wavelength. The Morison equation is extended to the case of a moving inclined cylinder. The Morison equation requires the use of experimentally determined fluid coefficients such as added mass, inertia, and drag coefficients. Plots of these fluid coefficients for various values of the fluid parameters are reproduced here. The vortex shedding force is discussed briefly. In the third section, four examples are given to show how fluid forces affect the static and dynamics of ocean structures, how the significant wave height can be chosen to represent the condition in a certain area for a long time, and how the time series can be constructed from a given spectrum. Finally, the available numerical codes for modeling slender flexible bodies in fluids are listed.

36.1 Description of the Ocean Environment

In modeling offshore structures, one needs to account for the forces exerted by the surrounding fluid. In-depth studies are given in Kinsman (1965), Sarpkaya and Isaacson (1981), Wilson (1984), Chakrabarti (1987), and Faltinsen (1993). The vibration characteristics of a structure can be significantly altered when it is surrounded by water. For example, damping by the fluid (or the added mass) lowers the natural

frequency of vibration. When considering the dynamics of an offshore structure, one must also consider the forces due to the surrounding fluid. The two important sources of fluid motion are ocean waves and ocean currents.

Most steady large currents are generated by the drag of the wind passing over the surface of the water, and they are confined to a region near the ocean surface. Tidal currents are generated by the gravitational attraction of the sun and the moon, and they are most significant near coasts. The ultimate source of the ocean circulation is the uneven radiation heating of the Earth by the Sun.

Isaacson (1988) suggested an empirical formula for the current velocity in the horizontal direction as a function of depth:

$$U_c(x) = (U_{\text{tide}}(d) + U_{\text{circulation}}(d)) \left(\frac{x}{d} \right)^{1/7} + U_{\text{drift}}(d) \left(\frac{x - d + d_0}{d_0} \right) \quad (36.1)$$

where U_{drift} is the wind-induced drift current, U_{tide} is the tidal current, $U_{\text{circulation}}$ is the low-frequency long-term circulation, x is the vertical distance measured from the ocean bottom, d is the depth of the water, and d_0 is the smaller of the depth of the thermocline and 50 m. The value of U_{tide} is obtained from tide tables, and U_{drift} is about 3% of the 10 min mean wind velocity at 10 m above the sea level.

It should be noted that these currents evolve slowly compared with the time scales of engineering interests. Therefore, they can be treated as a quasisteady phenomenon. Waves, on the other hand, cannot be treated as a steady phenomenon. The underlying physics that govern wave dynamics are too complex and, therefore, waves must be modeled stochastically. The subsequent section discusses the concept of the spectral density, available ocean wave spectral densities, a method to obtain the spectral density from wave time histories, methods to obtain a sample time history from a spectral density, the short-term and long-term statistics, and a method to obtain fluid velocities and accelerations from wave elevation using linear wave theory.

36.1.1 Spectral Density

Here, we will consider only surface gravity waves. Let us first consider a regular wave in order to familiarize ourselves with the terms that are used to describe a wave. The wave surface elevation is denoted as $\eta(x, t)$ and can be written as $\eta(x, t) = A \cos(kx - \omega t)$, where k is the wave number, and ω is the angular frequency. Figure 36.1 shows the surface elevation at two time instances ($t = 0$ and $t = \tau$) and the surface elevation at a fixed location ($x = 0$). A is the amplitude, H is the wave height or the distance between the maximum and minimum wave elevation or twice the amplitude, and T is the period given by $T = 2\pi/\omega$.

In practice, waves are not regular. Figure 36.2 shows a schematic time history of an irregular wave surface elevation. The wave height and frequency are not easy to find. Therefore, we rely on a statistical description for the wave elevation such as the wave spectral density. The spectral density tells us how the energy of the system is distributed among frequencies. The random surface elevation $\eta(t)$ can be thought of as a summation of regular waves with different frequencies. The surface elevation $\eta(t)$ is related to its Fourier transform $X(\omega)$ by

$$\eta(t) = \frac{1}{2\pi} \int_{-\infty}^{\infty} X(\omega) \exp(-i\omega t) d\omega$$

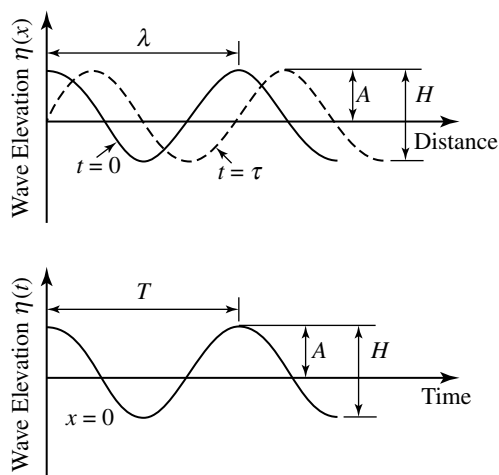


FIGURE 36.1 Regular wave.

Suppose that the energy of the system is proportional to $\eta^2(t)$ so that we can write the energy as

$$E = \frac{1}{2} C \eta^2(t)$$

where C is the proportionality constant.

Let us assume that the expected value of the energy is given by

$$E\{E\} = \frac{1}{2} C E\{\eta^2(t)\}$$

where $E\{\eta^2(t)\}$ is the mean square of $\eta(t)$. If $\eta(t)$ is an *ergodic process* (see Chapter 5 and Chapter 30), then the mean square of $\eta(t)$ can be approximated by the time average over a long period of time:

$$E\{\eta^2(t)\} = \lim_{T_s \rightarrow +\infty} \frac{1}{T_s} \int_{-T_s/2}^{T_s/2} \eta^2(t) dt = \lim_{T_s \rightarrow +\infty} \frac{1}{T_s} \frac{1}{2\pi} \int_{-\infty}^{\infty} |X(\omega)|^2 d\omega \quad (36.2)$$

where we have used Parseval's theorem

$$\int_{-\infty}^{\infty} \eta^2(t) dt = \frac{1}{2\pi} \int_{-\infty}^{\infty} |X(\omega)|^2 d\omega \quad (36.3)$$

where

$$|X(\omega)|^2 = X(\omega)X^*(\omega), \quad X(\omega) = \int_{-\infty}^{\infty} \eta(t) \exp(-i\omega t) dt, \quad X^*(\omega) = \int_{-\infty}^{\infty} \eta(t) \exp(i\omega t) dt$$

We define the power spectral density (or simply the spectrum) as (see Chapter 5 and Chapter 30)

$$S_{\eta\eta}(\omega) \equiv \frac{1}{2\pi T_s} |X(\omega)|^2 \quad (36.4)$$

so that $E\{\eta^2(t)\}$ is given by

$$E\{\eta^2(t)\} = \int_{-\infty}^{\infty} S_{\eta\eta}(\omega) d\omega \quad (36.5)$$

For a zero-mean process, $E\{\eta^2(t)\}$ is also the variance σ_η^2 . The spectral density has units of $\eta^2 t$. Where η is the wave elevation, the spectral density has a unit of $m^2 \text{ sec}$.

It can also be shown that $S_{\eta\eta}(\omega)$ is related to the autocorrelation function, $R(\tau)$, by the Wiener–Khinchine relations (Wiener, 1930; Khinchine, 1934):

$$S_{\eta\eta}(\omega) = \frac{1}{2\pi} \int_{-\infty}^{\infty} R_{\eta\eta}(\tau) \exp(-i\omega\tau) d\tau, \quad R_{\eta\eta}(\tau) = \int_{-\infty}^{\infty} S_{\eta\eta}(\omega) \exp(i\omega\tau) d\omega \quad (36.6)$$

It should be noted that, in some textbooks, the factor $1/2\pi$ appears in the second equation instead of the first. Figure 36.3 shows some important pairs of $S_{\eta\eta}(\omega)$ and $R_{\eta\eta}(\tau)$.

There are a few properties of the spectral density that readers should become familiar with. The first property is that the spectral density function of a real-valued stationary process is both real and symmetric. That is, $S_{\eta\eta}(\omega) = S_{\eta\eta}(-\omega)$ (Equation 36.4). Secondly, the area under the spectral density is equal to $E\{\eta^2(t)\}$ (Equation 36.5) and is also equal to $R_{\eta\eta}(0) = \sigma_\eta^2 - \mu_\eta^2$, where σ_η^2 is the variance and μ_η^2 is the mean of $\eta(t)$. In most cases, we only consider a zero-mean process so that the area under the spectral density is just σ_η^2 . If the process does not have a zero mean, the mean can be subtracted from it so that the process has a zero mean.

For ocean applications, a one-sided spectrum in terms of cycles per second (cps) or hertz is often used. We will denote the one-sided spectrum with a superscript “o”. The one-sided spectrum can be obtained from the two-sided spectrum by

$$S_{\eta\eta}^o(\omega) = 2S_{\eta\eta}(\omega), \quad \omega \geq 0$$

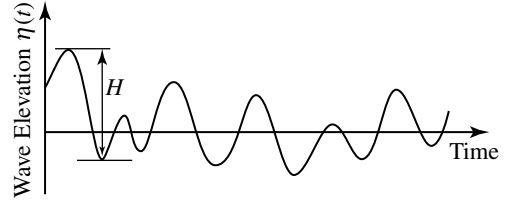


FIGURE 36.2 Time history of random wave.

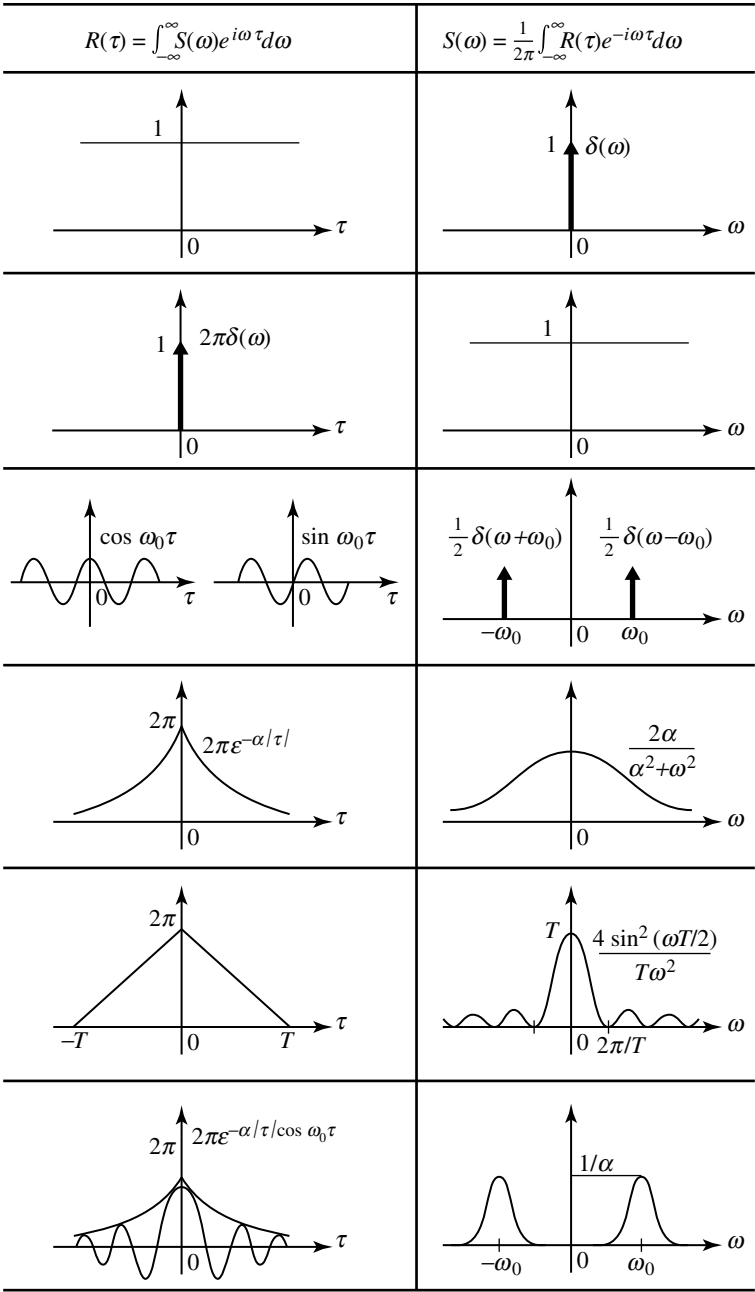


FIGURE 36.3 Relationship between the autocorrelation function and the power spectral density.

The two-sided spectrum in terms of ω can be transformed to the spectrum in terms of f (where $\omega = 2\pi f$) by

$$S_{\eta\eta}(f) = 2\pi S_{\eta\eta}(\omega), \quad f, \omega \geq 0$$

Then, the two-sided spectrum in terms of ω can be transformed to the one-sided spectrum in terms of cps (or hertz) by

$$S_{\eta\eta}^o(f) = 4\pi S_{\eta\eta}(\omega), \quad f, \omega \geq 0$$

It should be noted that the spectral density that we have defined here is the *amplitude half-spectrum*. The amplitude, height, and height double spectra are related to the amplitude half-spectrum by

$$S^A(\omega) = 2S(\omega), \quad S^H(\omega) = 8S(\omega), \quad S^{2H}(\omega) = 16S(\omega)$$

36.1.2 Ocean Wave Spectral Densities

In this section, we will discuss spectral density models to describe a random sea. An excellent review of existing spectral density models is given in [Chapter 4](#) of Chakrabarti (1987).

The ocean wave spectrum models are semiempirical formulas. That is, they are derived mathematically but the formulation requires one or more experimentally determined parameters. The accuracy of the spectrum depends significantly on the choice of these parameters.

In formulating spectral densities, the parameters that influence the spectrum are *fetch limitations*, *decaying vs. developing seas*, *water depth*, *current*, and *swell*. The fetch is the distance over which a wind blows in a wave-generating phase. Fetch limitation refers to the limitation on the distance due to some physical boundaries so that full wave development is prohibited. In a developing sea, the sea has not yet reached its stationary state under a stationary wind. In contrast, a wind has blown for a sufficient time in a fully developed sea, and the sea has reached its stationary state. In a decaying sea, the wind has dropped off from its stationary value. Swell is the wave motion caused by a distant storm and persists even after the storm has died down or moved away.

The Pierson–Moskowitz (P–M) spectrum (Pierson and Moskowitz, 1964) is the most extensively used spectrum for representing a fully developed sea. It is a one-parameter model in which the sea severity can be specified in terms of the wind velocity. The P–M spectrum is given by

$$S_{\eta\eta}^o(f) = \frac{8.1 \times 10^{-3} g^2}{\omega^5} \exp\left(-0.74 \left(\frac{g}{U_{w,19.5 \text{ m}}}\right)^4 \omega^{-4}\right)$$

where g is the gravitational constant and $U_{w,19.5 \text{ m}}$ is the wind speed at a height of 19.5 m above the still water. The P–M spectrum is also called the wind-speed spectrum because it requires wind data. It can also be written in terms of the modal frequency ω_m as

$$S_{\eta\eta}^o(f) = \frac{8.1 \times 10^{-3} g^2}{\omega^5} \exp\left(-1.25 \left(\frac{\omega_m}{\omega}\right)^4\right) \quad (36.7)$$

Note that the modal frequency is the frequency at which the spectrum is the maximum.

In some cases, it may be more convenient to express the spectrum in terms of significant wave height rather than the wind speed or modal frequency. For a narrowband Gaussian process¹, the significant wave height is related to the standard deviation by $H_s = 4\sigma_\eta$. The standard deviation is the square root of the area under the spectral density, $\int_{-\infty}^{\infty} S_{\eta\eta}(\omega) d\omega = \sigma_\eta^2$. Then, the spectrum can be written as

$$S_{\eta\eta}^o(f) = \frac{8.1 \times 10^{-3} g^2}{\omega^5} \exp\left(-\frac{0.0324 g^2}{H_s^2} \omega^{-4}\right) \quad (36.8)$$

and the peak frequency and the significant wave height are related by

$$\omega_m = 0.4 \sqrt{g/H_s} \quad (36.9)$$

The P–M spectrum is applicable for deep water, unidirectional seas, fully developed and local-wind-generated seas with unlimited fetch, and was developed for the North Atlantic. The effect of swell is not accounted for. Although it was developed for the North Atlantic, the spectrum is valid for other locations. However, the limitation that the sea is fully developed may be too restrictive because it cannot model the

¹See Section 36.1.5 for details.

effect of waves generated at a distance. Therefore, we consider a two-parameter spectrum, such as the Bretschneider spectrum, in order to model a sea that is not fully developed as well as a fully developed sea.

The Bretschneider spectrum (Bretschneider, 1959, 1969) is a two-parameter spectrum in which both the sea severity and the state of development can be specified. The Bretschneider spectrum is given by

$$S_{\eta\eta}^o(f) = 0.169 \frac{\omega_s^4}{\omega^5} H_s^2 \exp\left(-0.675 \left(\frac{\omega_s}{\omega}\right)^4\right)$$

where $\omega_s = 2\pi/T_s$ and T_s is the significant period. The sea severity can be specified by H_s and the state of development can be specified by ω_s . It can be shown that the relationship $\omega_s = 1.167\omega_m$ (equivalent to $\omega_s = 1.46/\sqrt{H_s}$) renders the Bretschneider spectrum and the P-M spectrum equivalent. Figure 36.4 shows the Bretschneider spectra for $H_s = 4$ m. When $\omega_s = 0.731$ rad/sec, the P-M and the Bretschneider spectra are identical. It should be noted that the developing sea will have a slightly higher modal frequency than the fully developed sea, and can be described by ω_s greater than $1.46/\sqrt{H_s}$.

Other two-parameter spectral densities that are often used are the International Ship Structures Congress (ISSC) and the International Towing Tank Conference (ITTC) spectra. The ISSC spectrum is written in terms of the significant wave height and the mean frequency, where the mean frequency is given by

$$\bar{\omega} = \sqrt{\frac{\int_0^\infty \omega S(\omega) d\omega}{\int_0^\infty S(\omega) d\omega}} = 1.30\omega_m$$

Thus, the ISSC spectrum is given by

$$S_{\eta\eta}^o(f) = 0.111 \frac{\bar{\omega}^4}{\omega^5} H_s^2 \exp\left(-0.444 \left(\frac{\bar{\omega}}{\omega}\right)^4\right)$$

The ITTC spectrum is based on the significant wave height and the zero crossing frequency and is given by

$$S_{\eta\eta}^o(f) = 0.0795 \frac{\omega_z^4}{\omega^5} H_s^2 \exp\left(-0.318 \left(\frac{\omega_z}{\omega}\right)^4\right)$$

where the zero crossing frequency, ω_z , is given by

$$\omega_z = \sqrt{\frac{\int_0^\infty \omega^2 S(\omega) d\omega}{\int_0^\infty S(\omega) d\omega}} = 1.41\omega_m$$

The Bretschneider, ITTC, and ISSC spectra are called two-parameter spectra, and they can be written as

$$S_{\eta\eta}^o(f) = \frac{A}{4} \frac{\bar{\omega}^4}{\omega^5} H_s^2 \exp\left(-A \left(\frac{\bar{\omega}}{\omega}\right)^4\right)$$

with A and $\bar{\omega}$ given in Table 36.1.

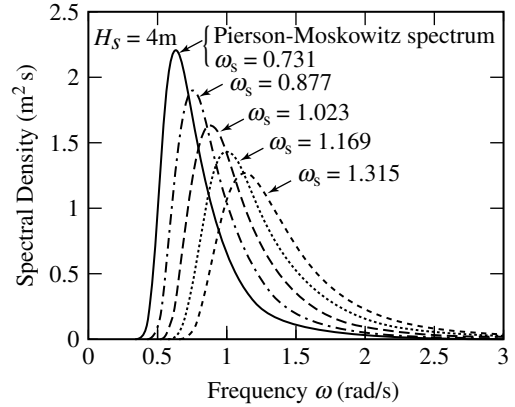


FIGURE 36.4 Bretschneider spectrum with various values of ω_s .

TABLE 36.1 Two-Parameter Spectrum Models

$$S_{\eta\eta}^o(\omega) = (A/4)H_s^2\bar{\omega}^4/\omega^5 \exp(-A(\omega/\bar{\omega})^{-4})$$

Model	A	$\bar{\omega}$
Bretschneider	0.675	ω_s
ITTC	0.318	ω_z
ISSC	0.4427	$\bar{\omega}$

The spectra that we have discussed so far do not allow us to generate spectra with two peaks to represent local or distant storms or to specify the sharpness of the peaks. The Ochi–Hubble (O–H) spectrum (Ochi and Hubble, 1976) is a six-parameter spectrum with the form:

$$S_{\eta\eta}^o(\omega) = \frac{1}{4} \sum_{i=1}^2 \frac{((4\lambda_i + 1)\omega_{mi}^4/4)^{\lambda_i}}{\Gamma(\lambda_i)} \frac{H_{si}^2}{\omega^{4\lambda_i+1}} \exp\left(-\left(\frac{4\lambda_i + 1}{4}\right)\left(\frac{\omega_{mi}}{\omega}\right)^4\right)$$

where $\Gamma(\lambda_i)$ is the Gamma function, H_{s1} , ω_{m1} , and λ_1 are the significant wave height, modal frequency, and shape factor for the lower frequency components, respectively, and H_{s2} , ω_{m2} , and λ_2 are those for the higher frequency component. Assuming that the entire spectrum is that of a narrow band, the equivalent significant wave height is given by

$$H_s = \sqrt{H_{s1}^2 + H_{s2}^2}$$

For $\lambda_1 = 1$ and $\lambda_2 = 0$, the spectrum reduces to the P–M spectrum. With the assumption that the entire spectrum is narrowband, the value of λ_1 is much higher than λ_2 . The O–H spectrum represents unidirectional seas with unlimited fetch. The sea severity and the state of development can be specified by H_{si} and ω_{mi} , respectively. In addition, λ_i can be selected to control the frequency width of the spectrum. For example, a small λ_i (wider frequency range) describes a developing sea, and a large λ_i (narrower frequency range) describes a swell condition. Figure 36.5 shows the O–H spectrum with $\lambda_1 = 2.72$, $\omega_{m1} = 0.626$ rad/sec, $H_{s1} = 3.35$ m, $\lambda_2 = 2.72$, $\omega_{m2} = 1.25$ rad/sec, and $H_{s2} = 2.19$ m.

Finally, another spectrum that is commonly used is the Joint North Sea Wave Project (JONSWAP) spectrum developed by Hasselmann et al. (1973). It is a fetch-limited spectrum because the growth over a limited fetch is taken into account. The attenuation in shallow water is also taken into account. The JONSWAP spectrum is written as

$$S_{\eta\eta}^o(\omega) = \frac{\alpha g^2}{\omega^5} \exp\left(-1.25\left(\frac{\omega_m}{\omega}\right)^4\right) \gamma^{\exp(-(\omega - \omega_m) / 2\tau^2 \omega_m^2)}$$

where γ is the peakedness parameter and τ is the shape parameter. The peakedness parameter γ is the ratio of the maximum spectral energy to the maximum spectral energy of the corresponding P–M spectrum. That is, when $\gamma = 7$, the peak spectral energy is seven times that of the P–M spectrum.

$$\gamma = \begin{cases} 7.0 & \text{for very peaked data} \\ 3.3 & \text{for mean of selected JONSWAP data} \\ 1.0 & \text{for P–M spectrum} \end{cases}$$

$$\tau = \begin{cases} 0.07 & \text{for } \omega \leq \omega_m \\ 0.09 & \text{for } \omega > \omega_m \end{cases}$$

$$\alpha = 0.076(\bar{X})^{-0.22} \text{ or } 0.0081 \text{ if fetch independent}$$

$$\bar{X} = gX/U_w^2$$

$$X = \text{fetch length (nautical miles)}$$

$$U_w = \text{wind speed (knots)}$$

$$\omega_m = 2\pi \times 3.5(g/U_w)\bar{X}^{-0.33}$$

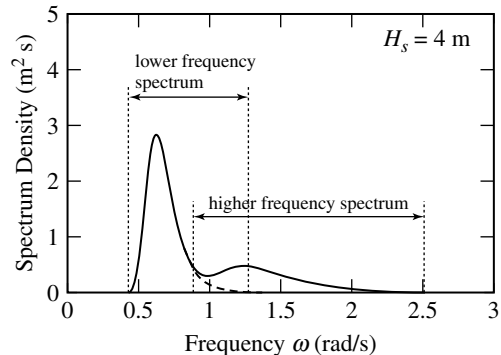


FIGURE 36.5 Ochi–Hubble spectrum.

Figure 36.6 shows the JONSWAP spectrum when $\alpha = 0.0081$ and $\omega_m = 0.626$ rad/sec for three peakedness parameters.

36.1.3 Approximation of Spectral Density from Time Series

From the time history of the wave elevation, the spectral density function can be obtained by two methods.

The first method is to use the autocorrelation function $R_{\eta\eta}(\tau)$, which is related to the spectral density function $S_{\eta\eta}(\omega)$ by the Wiener–Khinchine relations (Equation 36.6).

The autocorrelation $R_{\eta\eta}(\tau)$ is the expected value of $\eta(t)\eta(t + \tau)$ or $R_{\eta\eta}(\tau) = E\{\eta(t)\eta(t + \tau)\}$, where t is an arbitrary time and τ is the time lag. For a weakly stationary process, the autocorrelation is a function of the time lag only.

Assuming that the process is ergodic, the autocorrelation function for a given time history of length T_s can be approximated as

$$\hat{R}_{\eta\eta}(\tau) = \lim_{T_s \rightarrow \infty} \frac{1}{T_s - \tau} \int_0^{T_s - \tau} \eta(t)\eta(t + \tau) dt \quad \text{for } 0 < \tau < T_s$$

Note that the superscript \wedge is used to emphasize that the variable is an approximation based on a sample time history of length T_s . The spectral density is then obtained by taking the Fourier cosine transform of $\hat{R}_{\eta\eta}(\tau)$,

$$\hat{S}_{\eta\eta}(\omega) = \frac{1}{\pi} \int_0^{T_s} \hat{R}_{\eta\eta}(\tau) \cos \omega\tau d\tau \quad (36.10)$$

The second method for obtaining the spectral density function is to use the relationship between the spectral density and the Fourier transform of the time series. They are related by

$$\hat{S}_{\eta\eta}(\omega) = \lim_{T_s \rightarrow \infty} \frac{1}{2\pi T_s} |\hat{X}(\omega)\hat{X}^*(\omega)| \quad (36.11)$$

where $\hat{X}(\omega)$ is given by

$$\hat{X}(\omega) = \int_0^{T_s} \eta(t) \exp(-i\omega t) dt$$

and $\hat{X}^*(\omega)$ is the complex conjugate given by

$$\hat{X}^*(\omega) = \int_0^{T_s} \eta(t) \exp(i\omega t) dt$$

In order to obtain the Fourier transforms of the time series (see Chapter 2, Chapter 10, Chapter 21, and Appendix 2A), the discrete Fourier transform (DFT) or the fast Fourier transform (FFT) procedure can be used. For detailed descriptions of how this is done, see Appendix 1 in Tucker (1991). Nowadays, spectral analysis is almost always carried out via FFTs because it is easier to use and faster than the formal method via correlation function.

It should be noted that the length of the sample time history only needs to be long enough so that the limits converge. Taking a longer sample will not improve the accuracy of the estimate. Instead, one should take many samples or break one long sample into many parts. For n samples, the spectral densities

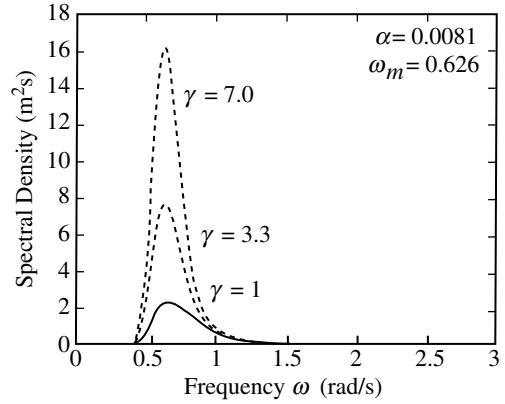


FIGURE 36.6 JONSWAP spectrum for $\gamma = 1.0, 3.3$, and 7.0 .

are obtained for each sample time history using either Equation 36.10 or Equation 36.11, and they are averaged to give the estimate.

The determination of the spectral density from wave records depends on the details of the procedure such as the length of the record, sampling interval, degree and type of filtering and smoothing, and time discretization.

36.1.4 Generation of Time Series from a Spectral Density

In a nonlinear analysis, the structural response is found by a numerical integration in time. Therefore, one needs to convert the wave elevation spectrum into an equivalent time history. The wave elevation can be represented as a sum of many sinusoidal functions with different angular frequencies and random phase angles. That is, we write $\eta(t)$ as

$$\eta(t) = \sum_{i=1}^N \cos(\omega_i t - \varphi_i) \sqrt{2S_{\eta\eta}(\omega_i)\Delta\omega_i} \quad (36.12)$$

where φ_i is a uniform random number between 0 and 2π , ω_i are discrete sampling frequencies, $\Delta\omega_i = \omega_i - \omega_{i-1}$, and N is the number of partitions. Recall that the area under the spectrum is equal to the variance, σ_η^2 . The incremental area under the spectrum, $S_{\eta\eta}(\omega_i)\Delta\omega_i$, can be denoted as σ_i^2 such that the sum of all the incremental area equals the variance of the wave elevation or $\sigma_\eta^2 = \sum_{i=1}^N \sigma_i^2$. The time history can be written as

$$\eta(t) = \sum_{i=1}^N \cos(\omega_i t - \varphi_i) \sqrt{2}\sigma_i$$

The sampling frequencies, ω_i , can be chosen at equal intervals such that $\omega_i = i\omega_1$. However, the time history will then have the lowest frequency of ω_1 and will have a period of $T = 2\pi/\omega_1$. In order to avoid this unwanted periodicity, Borgman (1969) suggested that the frequencies are chosen so that the area under the spectrum curve for each interval is equal or $\sigma_i^2 = \sigma^2 = \sigma_\eta^2/N$. The time history is written as

$$\eta(t) = \sqrt{\frac{2}{N}}\sigma_\eta \sum_{i=1}^N \cos(\bar{\omega}_i t - \varphi_i) \quad (36.13)$$

where $\bar{\omega}_i = (\omega_i + \omega_{i-1})/2$. The discrete frequencies, ω_i , are chosen such that the area between the interval $0 < \omega < \omega_i$ is equal to i/N of the total area under the curve between the interval $0 < \omega < \omega_N$ or

$$\int_0^{\omega_i} S_{\eta\eta}(\omega) d\omega = \frac{i}{N} \int_0^{\omega_N} S_{\eta\eta}(\omega) d\omega \quad \text{for } i = 1, \dots, N$$

where it is assumed that the area under the spectrum beyond ω_N is negligible. If $\eta(t)$ is a narrowband Gaussian process, the standard deviation can be replaced by $\sigma_\eta = H_s/4$, and the time history can be written as

$$\eta(t) = \frac{H_s}{4} \sqrt{\frac{2}{N}} \sum_{i=1}^N \cos(\bar{\omega}_i t - \varphi_i)$$

Shinozuka (1972) proposed that the sampling frequencies, $\bar{\omega}_i$, in Equation 36.13 should be randomly chosen according to the density function, $f(\omega) \equiv S_{\eta\eta}^o(\omega)/\sigma_\eta^2$. This is equivalent to performing an integration using the Monte Carlo method. The random frequencies ω distributed according to $f(\omega)$ can be obtained from uniformly distributed random numbers, x , by $\omega = F^{-1}(x)$, where $F(\omega)$ is the cumulative distribution of $f(\omega)$.

The random frequencies obtained this way are used in Equation 36.13 to generate a sample time series. It should be noted that many sample time histories should be obtained and averaged to synthesize a time history for use in numerical simulations.

36.1.5 Short-Term Statistics

In discussing wave statistics, we often use the term *significant wave* to describe an irregular sea surface. The significant wave is not a physical wave that can be seen but rather a statistical description of random waves. The concept of significant wave height was first introduced by Sverdrup and Munk (1947) as the average height of the highest one third of all waves. Usually, ships co-operate in programs to find sea statistics by reporting a rough estimate of the storm severity in terms of an observed wave height.

This observed wave height is consistently very close to the significant wave height.

Stationarity and ergodicity are two assumptions that are made in describing short-term waves statistics. These assumptions are valid only for “short” time intervals — approximately two hours or the duration of a storm — but not for weeks or years. The wave elevation is assumed to be weakly stationary so that its autocorrelation is a function of time lag only. As a result, the mean and the variance are constant, and the spectral density is invariant with time. Therefore, the significant wave height and the significant wave period are constant when we consider short-term statistics. In this case, the individual wave height and wave period are the stochastic variables. We then need to determine certain statistics for the analysis and design of offshore structures when we consider short time intervals.

Consider a sample time history of a zero-mean random process, as shown in Figure 36.7. The questions that we ask are how often is a certain level (e.g., z in the figure) exceeded, and how are the maxima distributed? Likewise, we can ask when we can expect to see that a certain level is exceeded for the first time, and what are the values of the peaks of a random process? The first question is important when a structure may fail due to a one-time excessive load, and the second question is important when a structure may fail due to cyclic loads.

It is found that the rate at which a random process $X(t)$ crosses Z with a positive slope (zero up-crossing) may be calculated from

$$\nu_{z^+} = \int_0^\infty \nu f_{X\dot{X}}(z, \nu) d\nu$$

where $f_{X\dot{X}}(x, \dot{x})$ is the joint probability density function of X and $\dot{X}(t)$. The expected time of the first up-crossing is then the inverse of the crossing rate or

$$E\{T\} = 1/\nu_{z^+}$$

The probability density function of the maxima, A , can be calculated from

$$f_A(a) = \frac{\int_{-\infty}^0 -\omega f_{X\ddot{X}}(a, 0, \omega) d\omega}{\int_{-\infty}^0 -\omega f_{X\ddot{X}}(0, \omega) d\omega}$$

where $f_{X\dot{X}\ddot{X}}(x, \dot{x}, \ddot{x})$ is the joint probability density function of X , \dot{X} , and \ddot{X} .

If $X(t)$ is a Gaussian process, then we can write the joint probability density functions as

$$f_{X\dot{X}}(x, \dot{x}) = \frac{1}{2\pi\sigma_X\sigma_{\dot{X}}} \exp\left[-\frac{1}{2}\left(\frac{x}{\sigma_X}\right)^2 - \frac{1}{2}\left(\frac{\dot{x}}{\sigma_{\dot{X}}}\right)^2\right], \quad -\infty < x < \infty, \quad -\infty < \dot{x} < \infty$$

and

$$f_{X\dot{X}\ddot{X}}(x, \dot{x}, \ddot{x}) = \frac{1}{(2\pi)^{3/2}|M|^{1/2}} \exp\left[-\frac{1}{2}(\{x\} - \{\mu_X\})^T [M]^{-1} (\{x\} - \{\mu_X\})\right]$$

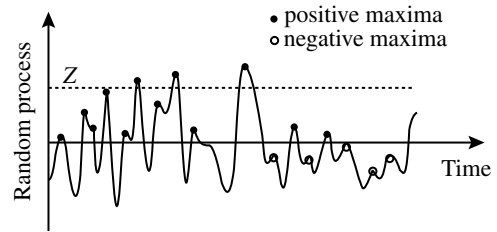


FIGURE 36.7 A sample time history.

where

$$[M] = \begin{bmatrix} \sigma_X^2 & 0 & \sigma_{\dot{X}}^2 \\ 0 & \sigma_{\dot{X}}^2 & 0 \\ \sigma_{\dot{X}}^2 & 0 & \sigma_{\ddot{X}}^2 \end{bmatrix} \quad \text{and} \quad \{x\} - \{\mu_X\} = \begin{bmatrix} x - \mu_X \\ \dot{x} - \mu_{\dot{X}} \\ \ddot{x} - \mu_{\ddot{X}} \end{bmatrix}$$

Then, for a stationary Gaussian process, the up-crossing rate is given by

$$\begin{aligned} \nu_z^+ &= \int_0^\infty f_{\dot{X}\ddot{X}}(Z, \dot{x}) \dot{x} \, d\dot{x} = \frac{1}{2\pi\sigma_X\sigma_{\dot{X}}} \exp\left[-\frac{1}{2}\left(\frac{Z}{\sigma_X}\right)^2\right] \int_0^\infty \exp\left[-\frac{1}{2}\left(\frac{\dot{x}}{\sigma_{\dot{X}}}\right)^2\right] \dot{x} \, d\dot{x} \\ &= \frac{\sigma_{\dot{X}}}{2\pi\sigma_X} \exp\left[-\frac{1}{2}\left(\frac{Z}{\sigma_X}\right)^2\right] \end{aligned} \quad (36.14)$$

and the probability density function of maxima is given by the Rice density function (Rice, 1954)

$$f_A(a) = \frac{\sqrt{1-\alpha^2}}{\sqrt{2\pi}\sigma_\eta} \exp\left[-\frac{1}{2} \frac{\alpha^2}{\sigma_\eta^2(1-\alpha^2)}\right] + a \frac{\alpha}{\sigma_\eta^2} \Phi\left(\frac{a\alpha}{\sigma_\eta\sqrt{\alpha^2-1}}\right) \exp\left(-\frac{1}{2} \frac{a^2}{\sigma_\eta^2}\right) \quad \text{for } -\infty < a < \infty$$

where $\Phi(x)$ is the cumulative distribution function of standard normal random variable

$$\Phi(x) = \frac{1}{\sqrt{2\pi}} \int_{-\infty}^x \exp(-z^2/2) dz$$

and α is the irregularity factor equivalent to the ratio of the number of zero up-crossings (number of times that $\eta[t]$ crosses zero with a positive slope) to the number of peaks. α ranges from 0 to 1, and it is also equal to

$$\alpha = \frac{\sigma_\eta^2}{\sigma_\eta^2 \sigma_\eta^2}$$

If $X(t)$ is a broadband process, $\alpha = 0$ and the Rice distribution is reduced to the Gaussian probability density function given by

$$f_A(a) = \frac{1}{\sqrt{2\pi}\sigma_\eta} \exp\left[-\frac{1}{2} \frac{a^2}{\sigma_\eta^2}\right] \quad \text{for } -\infty < a < \infty$$

If $X(t)$ is a narrowband process, it is guaranteed that it will have a peak whenever $\eta(t)$ crosses its mean. In this case, the irregularity factor is close to unity, and the Rice distribution is reduced to the Rayleigh probability density function given by

$$f_A(a) = \frac{a}{\sigma_\eta^2} \exp\left[-\frac{1}{2} \frac{a^2}{\sigma_\eta^2}\right] \quad \text{for } 0 < a < \infty$$

In other words, the amplitudes of a narrowband stationary Gaussian process are distributed according to the Rayleigh distribution.

Figure 36.8 shows the Rice distribution for various values of α . Note that the Rice distribution includes both positive and negative maxima except when $\alpha = 1$, in which case all the maxima are positive. The positive maxima are the local maxima that occur above the mean of $X(t)$, and the negative maxima are the local maxima that occur below the mean, as shown in Figure 36.7. In some cases, the negative maxima may not mean

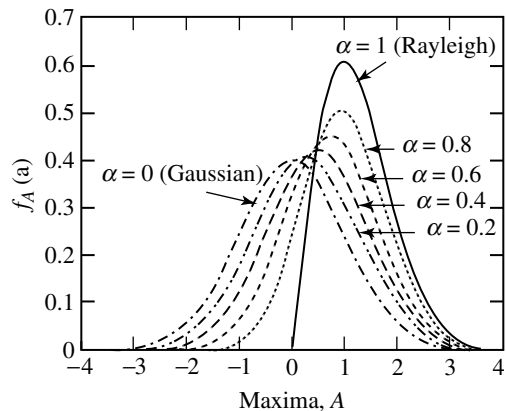


FIGURE 36.8 Rice distribution for maxima.

much physically. In those cases, we can use the truncated Rice distribution, where only the positive portion of $f_A(a)$ is used. $f_A(a)$ is normalized by the area under the probability density for positive maxima (Longuet-Higgins, 1952; Ochi, 1973):

$$f_A^{\text{trunc}}(a) = \frac{f_A(a)}{\int_0^\infty f_A(a) da}, \quad a \geq 0$$

The truncated Rice distribution is shown in Figure 36.9.

If $X(t)$ is the wave elevation, its maxima, A , are the amplitudes of the wave elevation. The wave height, $H = 2A$, is then distributed according to

$$f_H(h) = f_A(H/2) \frac{dA}{dH} = \frac{h}{4\sigma_\eta^2} \exp\left[-\frac{1}{2} \frac{h^2}{4\sigma_\eta^2}\right] \quad \text{for } 0 < h < \infty$$

For any given wave, the probability that the height is less than h (the cumulative distribution) is

$$F_H(h) = 1 - \exp\left[-\frac{1}{2} \frac{h^2}{4\sigma_\eta^2}\right] \quad \text{for } 0 < h < \infty$$

If $\eta(t)$ is a stationary narrowband process so that the peaks are distributed according to the Rayleigh distribution, we find that the root-mean-square wave height, $\sqrt{E\{H^2\}}$, is given by

$$\sqrt{E\{H^2\}} = \int_0^\infty h^2 f_H(h) dh = 2\sqrt{2}\sigma_\eta$$

In addition, it can be shown that the average and the significant wave heights are given by

$$H_0 \equiv E\{H\} = \sqrt{2\pi}\sigma_\eta, \quad H_s \equiv E\{H_{1/3}\} = 4\sigma_\eta \quad (36.15)$$

where $E\{H_{1/3}\}$ means that it is the expectation of the highest one third of the waves.

36.1.6 Long-Term Statistics

Because offshore structures are designed for long life spans, we must also consider long-term wave statistics. Previously, when we considered the short-term statistics, the significant wave height and spectrum were assumed to be invariant with time. This assumption is valid only over time periods of days at most. For longer time periods, the significant wave height has its own statistics and is a random variable.

When one uses short-term statistics to describe long-term events, improbable events seem unjustifiably probable. For example, let us consider the probability that the wave height, distributed according to the Rayleigh distribution, exceeds a certain extreme value. Let us assume that the mean period of this wave is 10 sec and the probability that the height of any given wave is greater than 300 ft is 10^{-10} . The value is small and the occurrence of a 300 ft wave seems improbable. However, the probability that the height will exceed 300 ft at least once in 10 years (3×10^8 sec) is given by

$$1 - (1 - 10^{-10})^{3 \times 10^8 / 10} = 0.997$$

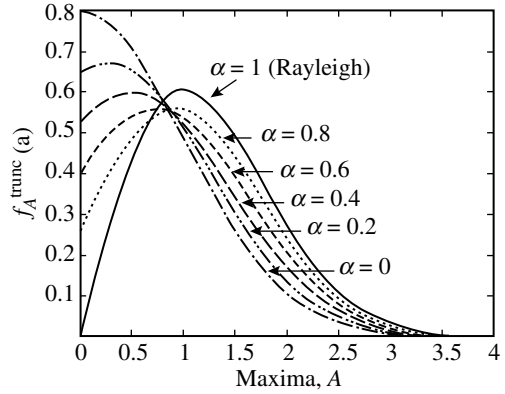


FIGURE 36.9 Truncated Rice distribution.

Thus, the statistical description states that it is almost certain that the wave height will exceed 300 ft at least once in 10 years. This prediction is a shortcoming of the short-term statistics since waves of this magnitude do not arrive at this probability.

In order to compute the probability that a wave height will exceed a certain extreme value, we require statistics for these extreme events. The actual maximum amplitude in a sequence of random amplitudes is a random variable itself. It has a probability distribution with mean value, standard deviation and other statistical properties. In fact, the distributions of these maximum values are called the extreme value distributions (EVDs). Gumbel (1958) obtained three methods of extrapolation known as three asymptotes. They are the Gumbel, Fretchet, and Weibull distributions. We will discuss the Gumbel and Weibull distributions in the next section. For the moment, we will discuss the concept of the N -year storm.

In long-term statistics, we often speak of an N -year storm. It means that, for any given year, the probability that we will have an N -year storm is

$$p = \frac{1}{N}$$

It follows that the probability that we will have m storms in n years is given by

$$\Pr\{mN\text{-year storms in } n \text{ years}\} = {}_n P_m \left(\frac{1}{N}\right)^m \left(1 - \frac{1}{N}\right)^{n-m}$$

where ${}_n P_m$ is the permutation given by

$${}_n P_m = \frac{n!}{(n-m)!}$$

The probability that we will have at least one N -year storm in n years is

$$\Pr\{\text{at least one } N\text{-year storms in } n \text{ years}\} = 1 - \left(1 - \frac{1}{N}\right)^n$$

For a large N , the probability can be approximated as $1 - \exp(n/N)$. It should be noted that the probability that we will have exactly one N -year storm in N years is not one, but

$$\Pr\{\text{one } N\text{-year storm in } N \text{ years}\} = \left(1 - \frac{1}{N}\right)^{N-1}$$

As $N \rightarrow \infty$, we find that

$$P = 1/e \approx 0.3679$$

The probability that we will have at least one N -year storm in N years is

$$\Pr\{\text{at least one } N\text{-year storms in } n \text{ years}\} = 1 - \left(1 - \frac{1}{N}\right)^N$$

As $N \rightarrow \infty$, we find that

$$P = 1 - 1/e \approx 0.6321 \quad (36.16)$$

36.1.6.1 Weibull Distribution

The Weibull distribution fits probabilities of extremes quite satisfactorily. In long-term statistics, the significant wave height follows the Weibull distribution closely. The probability density and the cumulative distribution are given by

$$f(h) = \frac{m}{\beta} \left(\frac{h-\gamma}{\beta}\right)^{m-1} \exp\left(-\left(\frac{h-\gamma}{\beta}\right)^m\right), \quad F(h) = 1 - \exp\left(-\left(\frac{h-\gamma}{\beta}\right)^m\right) \text{ for } \gamma < h \quad (36.17)$$

where m is called the shape parameter. Manipulating the cumulative distribution, we can write

$$\ln(-\ln\{1 - F(h)\}) = m\{\ln(h - \gamma) - \ln(\beta)\}$$

where the left-hand side is known from data. If we let $y = \ln(-\ln\{1 - F(h)\})$ and $x = \ln(h - \gamma)$, y is a straight line with slope of m and a y -intercept of $-m \ln \beta$:

$$y = mx - m \ln \beta$$

Suppose we have significant wave height data over a long period of time, and our goal is to find the Weibull parameters, γ , β , and m that best fit the distribution of the significant wave heights. These parameters can be determined by the least-squares method or using the Weibull paper. Using the latter method, we first guess γ so that the discrete points (x, y) or $(\ln(h - \gamma), \ln(-\ln\{1 - F(h)\}))$ form a straight line. The slope of this line is m , and the value of y when the line intersects the y axis is $-m \ln \beta$. This method will be illustrated in Section 36.3.3.

The Gumbel distribution is given by

$$\begin{aligned} f(h) &= \alpha \exp(-\alpha(h - \beta)) \exp\{\exp[-\alpha(h - \beta)]\} \\ F(h) &= \exp\{-\exp[-\alpha(h - \beta)]\} \quad \text{for } -\infty < h < \infty \end{aligned} \quad (36.18)$$

When $\ln[-\ln F(h)]$ is plotted against h , the result is a line with a slope of $-\alpha$ and y intercept of $\alpha\beta$.

Another distribution that may be used is the lognormal distribution given by (Jasper, 1954)

$$f(h) = \frac{1}{\sqrt{2\pi}\sigma h} \exp\left[-\frac{1}{2} \frac{(\ln h - \mu)^2}{\sigma^2}\right], \quad F(h) = \Phi\left(\frac{\ln h - \mu}{\sigma}\right) \quad \text{for } 0 \leq h \quad (36.19)$$

36.1.6.2 Wave Velocities via Linear Wave Theory

The wave velocities that correspond to the wave elevation given in Equation 36.12 can be obtained by *linear wave theory*. Linear wave theory, also called *airy wave theory*, *sinusoidal wave theory*, and *small-amplitude theory*, is the simplest wave theory. It is also the most important wave theory because it forms the basis for the probabilistic spectral description of waves.

Linear wave theory assumes that the wave height is small compared with the wavelength and wave depth. In addition, fluid particles are assumed to follow a circular orbit. The readers should refer to Kinsman (1965) and LeMehaute (1976) for detailed descriptions.

In linear wave theory, the surface elevation is given by

$$\eta(y, t) = A \cos(\omega t - ky) \quad (36.20)$$

which is a plane wave traveling to the right in Figure 36.10. Linear wave theory relates this sinusoidal surface elevation to the wave velocities given by

$$w_y(x, y, t) = A\omega \frac{\cosh kx}{\sinh kd} \cos(\omega t - ky), \quad w_x(x, y, t) = A\omega \frac{\sinh kx}{\sinh kd} \sin(\omega t - ky) \quad (36.21)$$

where k , ω , and A are wave number, angular frequency, and amplitude of a surface wave, respectively. The velocities vary with time, horizontal coordinate y , and depth x measured from the ocean floor. The wave velocities are sinusoidal in y and t , but exponentially decrease with the distance from the surface.

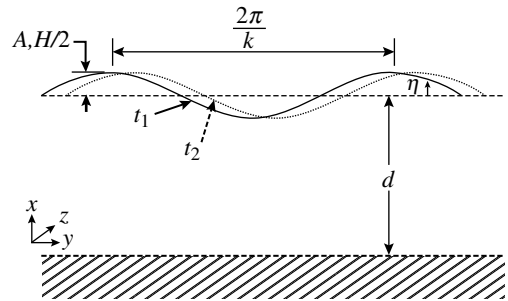


FIGURE 36.10 A schematic of a simple sinusoidal wave shown at two different times.

The frequency ω is related to the wave number k by the dispersion relation given by

$$\omega^2 = gk \tanh kd$$

where d is the water depth. For deep water, $\tanh kd$ approaches unity and the frequency is given by

$$\lim_{d \rightarrow \infty} \omega^2 = gk$$

For the surface elevation given in Equation 36.12, the surface elevation and the wave velocities are given by

$$\begin{aligned} \eta(y, t) &= \sum_{i=1}^N \cos(\omega_i t - k_i y - \varphi_i) \sqrt{2S_{\eta\eta}(\omega_i) \Delta\omega_i} \\ w_y(x, y, t) &= \sum_{i=1}^N \omega_i \frac{\cosh k_i x}{\sinh k_i d} \cos(\omega_i t - k_i y - \varphi_i) \sqrt{2S_{\eta\eta}(\omega_i) \Delta\omega_i} \\ w_x(x, y, t) &= \sum_{i=1}^N \omega_i \frac{\sinh k_i x}{\sinh k_i d} \sin(\omega_i t - k_i y - \varphi_i) \sqrt{2S_{\eta\eta}(\omega_i) \Delta\omega_i} \end{aligned} \quad (36.22)$$

The wave accelerations can be obtained by differentiating the wave velocities with respect to time. Sample time histories of the wave velocity and acceleration can be obtained using either Borgman's or Shinozuka's method.

36.1.7 Summary

In this section, the concept of spectral density is introduced. It is then shown how the concept is used to describe the ocean wave heights. The spectral density or spectrum is related to the autocorrelation function by the Wiener–Khinchine relations:

$$\begin{aligned} S_{\eta\eta}(\omega) &= \frac{1}{2\pi} \int_{-\infty}^{\infty} R_{\eta\eta}(\tau) \exp(-i\omega\tau) d\tau \\ R_{\eta\eta}(\tau) &= \int_{-\infty}^{\infty} S_{\eta\eta}(\omega) \exp(-i\omega\tau) d\omega \end{aligned}$$

In addition, the spectral density function of a real-valued stationary process is also real and symmetric, or

$$S_{\eta\eta}(\omega) = S_{\eta\eta}(-\omega) \quad (36.23)$$

and the area under the spectral density is given by

$$\int_{-\infty}^{\infty} S_{\eta\eta}(\omega) d\omega = R_{\eta\eta}(0) = \sigma_{\eta}^2 - \mu_{\eta}^2 \quad (36.24)$$

If the spectral density is given only for $\omega \geq 0$, then this one-sided spectrum is related to the two-sided spectrum by

$$S_{\eta\eta}^o(\omega) = 2S_{\eta\eta}(\omega), \quad \omega \geq 0$$

When the frequency is given in Hertz instead of in rad/sec, the spectra are related by

$$S_{\eta\eta}(f) = 2\pi S_{\eta\eta}(\omega), \quad \omega \geq 0$$

The spectra that are often used to describe wave heights are the P–M, Bretschneider, ITTC, ISSC, O–H, and JONSWAP spectra. The most widely used spectrum is the P–M spectrum, which is a single parameter spectrum. The P–M spectrum is applicable for deep water, unidirectional seas, fully developed and local-wind-generated sea with unlimited fetch, and was originally developed for the North Atlantic. The single parameter for this spectrum can be expressed as the wind velocity at 19.5 m above sea level or the significant wave height that specifies the sea severity. When it is written

in terms of the significant wave height, it is given by

$$S_{\eta\eta}^o(f) = \frac{8.1 \times 10^{-3} g^2}{\omega^5} \exp\left(-\frac{0.0324 g^2}{H_s^2} \omega^{-4}\right)$$

Bretschneider, ITTC, and ISSC spectra are two-parameter spectra in which the state of development as well as the sea severity can be specified. The O–H spectrum is a six-parameter spectrum that allows us to represent local and distant storm effects and to specify sharpness of the peaks as well as to specify the sea severity and the state of development. The JONSWAP spectrum allows us to account for growth over a limited fetch.

For a given ocean spectrum, a sample time history can be obtained by

$$\eta(t) = \sqrt{\frac{2}{N}} \sigma_\eta \sum_{i=1}^N \cos(\bar{\omega}_i t - \varphi_i)$$

In Borgman's method, the sampling frequencies $\bar{\omega}_i = (\omega_i + \omega_{i-1})/2$ are chosen so that the area between ω_{i-1} and ω_i are equal. In Shinozuka's method, the sampling frequencies are chosen randomly. The traditional method of choosing the sampling frequency at even intervals is not recommended.

When a relatively short interval of time is considered, for example, about two hours or the duration of a storm, it can be assumed that the spectrum and its statistics are invariant with time. In this case, the distribution of local maxima or peaks of a stationary Gaussian process is described by the Rice distribution. The Rice distribution can be reduced to the Rayleigh distribution when the process is narrowband and to the Gaussian distribution when the process is broadband. In the long-term statistics, the spectrum and its statistics may vary with time. In this case, the term “*N*-year storm” is often used to indicate the sea severity, and the significant wave heights closely follow the Weibull distribution.

Finally, the wave velocities and accelerations are related to the wave velocities using linear wave theory.

36.2 Fluid Forces

The following is a list of several types of forces that the fluid can exert on a body:

1. *Drag force.* This is due to the pressure difference between the downstream and upstream flow region. It can be thought of as the force required to hold a body stationary in a fluid of constant velocity. The drag force is proportional to the square of the velocity of the fluid relative to the structure.
2. *Inertia force.* This is the force exerted by the fluid while it accelerates and decelerates as it passes the structure. It is also the force required to hold a rigid structure in a uniformly accelerating flow, and it is proportional to the fluid acceleration. The concept of the inertia force in an inviscid flow was first formulated by Lamb (1945).
3. *Added mass.* As the body accelerates or decelerates in a stationary fluid, the body carries a certain amount of the surrounding fluid along with it. This entrained fluid is called the *added, apparent, or virtual mass*. In order to accelerate the body, additional force is required to accelerate or decelerate the added mass.
4. *Diffraction force.* This is due to the scattering of an incident wave on the surface of the structure. It is important when the body is large compared with the wavelength of the incident wave.
5. *Froude–Kryloff force.* This is the pressure force on the structure due to the incident wave, assuming that the structure does not exist and does not interfere with the incident wave.
6. *Lift force.* This is due to nonsymmetrical separation of the fluid or due to vortices that are shed in a nonsymmetrical way. The component of the force perpendicular to the flow direction is the lift force.

7. *Wave slamming force.* This is due to a single occasional wave with a particularly high amplitude and energy, and it may be important at the free surface. Sarpkaya and Isaacson (1981) reviewed the research on slamming of water against circular cylinders. Miller (1977, 1980) found that the peak wave slamming force on a rigidly held horizontal circular cylinder is proportional to the square of the horizontal water particle velocity.

36.2.1 Wave Force Regime

Previously, we discussed various types of forces caused by waves and currents. In some cases, one type of force may be dominant. Hogben (1976) gave a literature review of the fluid force in various regimes. The load regime of importance can be demonstrated for the case of a vertical cylinder in Figure 36.11 in terms of H/D and $\pi D/\lambda$, where H is the wave height, D is the cylinder diameter, and λ is the wavelength. When linear wave theory is used, H/D is related to the Keulegan–Carpenter number by

$$K = \pi H/D$$

The Keulegan–Carpenter number gives a measure of the importance of drag force relative to the inertia force. The term $\pi D/\lambda$ is called the diffraction parameter, and it determines the importance of the diffraction effect. As H/D increases, the drag force becomes more important and the inertia force becomes less important. As $\pi D/\lambda$ increases, the diffraction force becomes important.

Using linear wave theory, the maximum drag force to the maximum inertia force can be written as

$$\frac{f_{\text{drag}}}{f_{\text{inertia}}} = \frac{1}{2\pi} \frac{H}{D} = \frac{K}{2\pi^2}$$

From the last relation, we find that the drag force is 5% of the inertial force when $H/D = 0.314$. The Morison equation may be used for $D/\lambda < 0.2$ and $f_{\text{drag}}/f_{\text{inertia}} > 0.1$ or thereabouts. It should be noted that Figure 36.11 is valid only near the surface. The drag force is predominant for a cylinder that extends from the bottom to the near surface, so that the Morison equation may be used.

For example, consider a fixed jacket platform with legs with a diameter of 10 m and bracings with a diameter of 0.8 m. For a 10-year storm with $\lambda = 100$ m and $H = 8$ m, the ratios H/D and D/λ for the leg are 0.8 and 0.1, respectively. Similarly, the ratios H/D and D/λ for the bracings are 10 and 0.08, respectively. Figure 36.11 shows that the inertia force is dominant for the legs, and both inertia and the drag forces are important for the bracings.

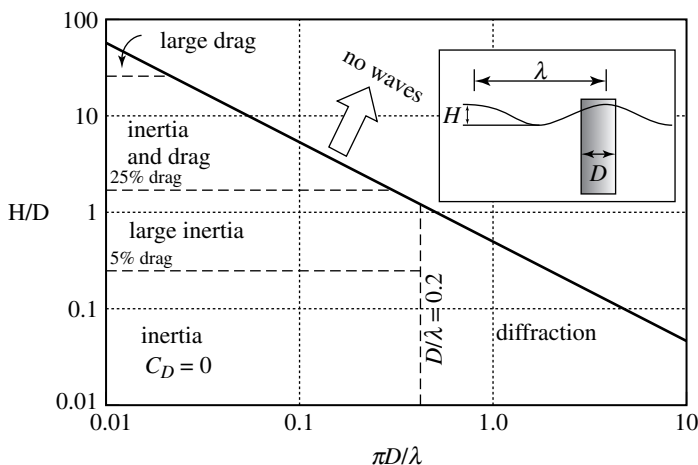


FIGURE 36.11 Load regimes near surface.

36.2.2 Wave Forces on Small Structures — Morison Equation

The added mass, M_A , can be written as

$$M_A = C_A M_{\text{disp}}$$

where C_A is called the *added mass coefficient* and M_{disp} is the mass of the fluid displaced by the structure. For a cylinder with a diameter, D , and height, h , the displaced fluid mass is $\pi D^2 h/4$. It should be noted that the added mass is a tensor quantity. That is, we can speak of the added mass force in the x_i direction due to the acceleration of the body in the x_j direction, denoted as M_{ij}^A . M_{ij}^A is symmetric so that the added mass force in the x_i direction due to the acceleration in the x_j direction is equal to the added mass force in the x_j direction due to the acceleration in the x_i direction. The off-diagonal terms are not zero if the cross-section is not symmetric.

Similarly, the inertia force can be written as

$$F_M = C_M M_{\text{disp}} \dot{w} \quad (36.25)$$

where the proportionality constant, C_M , is called the *inertia coefficient*.

It should be noted that the added mass and the inertia effects are often neglected for a body vibrating in air since the displaced air mass is negligible.

The drag force is proportional to the square of the fluid velocity, w , the density of the fluid, ρ , and the area of the body projected onto the plane perpendicular to the flow direction, A_f ,

$$F_D = \frac{1}{2} C_D \rho A_f w |w|$$

where C_D is the *drag coefficient*. The absolute value sign is used to ensure that the drag force always acts in the direction of the flow. For a cylinder with a diameter D and height h , the projected area A_f is Dh .

For a body with nonzero velocity, the drag force is given by

$$F_D = \frac{1}{2} C_D \rho A_f (w - v) |w - v| \quad (36.26)$$

where $w - v$ is the velocity of the fluid relative to the body.

Morison et al. (1950) combined the inertia and drag terms (Equation 36.25 and Equation 36.26) so that the fluid force on a body is given by

$$f = \frac{1}{2} C_D \rho A_f w |w| + C_M M_{\text{disp}} \dot{w}$$

For a cylinder, the fluid force per unit length can be written as

$$f = \frac{1}{2} C_D \rho D w |w| + C_M \rho \pi \frac{D^2}{4} \dot{w}$$

For a moving cylinder with velocity v , the Morison force is given by

$$f = \frac{1}{2} C_D \rho D (w - v) |w - v| + C_M \rho \pi \frac{D^2}{4} \dot{w}$$

36.2.2.1 Inclined Cylinder

Let us now consider the inclined cylinder shown in [Figure 36.13](#). The direction of the flow makes an angle of θ with the cylinder. Often, only the fluid force in the normal direction is considered. The normal component is given by

$$f^n = \frac{1}{2} C_D \rho D (w^n - v^n) |w^n - v^n| + C_M \rho \pi \frac{D^2}{4} \dot{w}^n \quad (36.27)$$

where the superscript is used for the normal component. The term, $w^n - v^n$, is the normal component of the relative velocity of the fluid with respect to the structure. Suppose that fluid is flowing to the right,

and the cylinder is also moving to the right, as shown in Figure 36.12. The normal components of the fluid and cylinder velocities are

$$w^n = |w| \cos \theta, \quad v^n = |v| \cos \theta$$

In three dimensions, it may be difficult to picture what the normal component should be. Here, we can find the normal component using the formula

$$(w^n - v^n)\vec{n} = \vec{t} \times (\vec{w} - \vec{v}) \times \vec{t} \quad (36.28)$$

where \vec{t} is the unit vector tangent to the cylinder and \vec{n} is the unit vector normal to the cylinder.

Note that the normal direction depends on the direction of the flow as well as the inclination of the cylinder.

In some cases, the tangential drag force may be included, and it can be written as

$$f^t = \frac{1}{2} C_T \rho D (w^t - v^t) |w^t - v^t| \quad (36.29)$$

where C_T is the tangential drag coefficient. Note that C_T is usually a very small number.

The normal component of the fluid force is more dominant than the tangential component. It may seem strange that the fluid force does not act in the direction of the fluid motion. Instead, the force is predominantly in the normal direction defined by Equation 36.28. In Section 36.3.1, we will demonstrate what this means by considering a towing cable.

36.2.2.1.1 Determination of Fluid Coefficients

The drag, inertia, and added mass coefficients must be obtained by experiment. However, for a long cylinder, C_M approaches its theoretical limiting value (uniformly accelerated inviscid flow) of 2, and C_A approaches unity (Lamb, 1945; Wilson, 1984). In reality, the inertia and drag coefficients are functions of at least three parameters (Wilson, 1984):

$$C_M = C_M(\text{Re}, K, \text{cylinder roughness})$$

$$C_D = C_D(\text{Re}, K, \text{cylinder roughness})$$

where Re is the Reynolds number and K is the Keulegan–Carpenter number given by

$$\text{Re} \equiv \frac{\rho_f U D}{\mu}, \quad K \equiv \frac{U T}{D} \quad (36.30)$$

where ρ_f is the density of the fluid, U is the free stream velocity, D is the diameter of the structure, μ is the dynamic or absolute viscosity, and T is the wave period.

Sarpkaya looked at the variation of these hydrodynamic coefficients extensively and obtained the plots shown in Figure 36.13 to Figure 36.15 (Sarpkaya, 1976; Sarpkaya et al., 1977). Figure 36.13 shows the inertia and drag coefficients for a smooth cylinder as a function of K for various values of Re and the reduced frequency β , defined by $\beta = \text{Re}/K$. From this figure, we find that for low Re and β , the inertial coefficient decreases and the drag coefficient increases at about $10 < K < 15$. It is found that the drop and the increase in these coefficients are due to shedding vortices, which also exert forces perpendicular to the structure and the flow.

Figure 36.14 and Figure 36.15 show the inertia and drag coefficients for a rough cylinder, whose roughness is measured by k/D . Figure 36.14a shows a drop in the drag coefficient for Re between 10^4 and 10^5 , and this is called the “drag crisis.” For a larger Re , the drag coefficient stays constant. As the surface becomes rougher, the drop occurs at lower Re and the drag coefficients for the larger Re increases.

Figure 36.14 to Figure 36.16 can be used to obtain proper values of the drag and inertia coefficients for fluid with known Re , Keulegan–Carpenter number, and cylinder roughness.

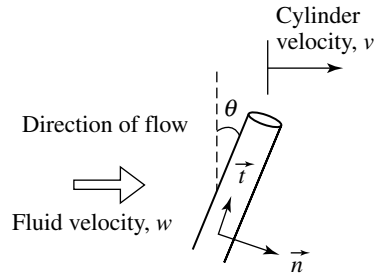


FIGURE 36.12 Inclined cylinder.

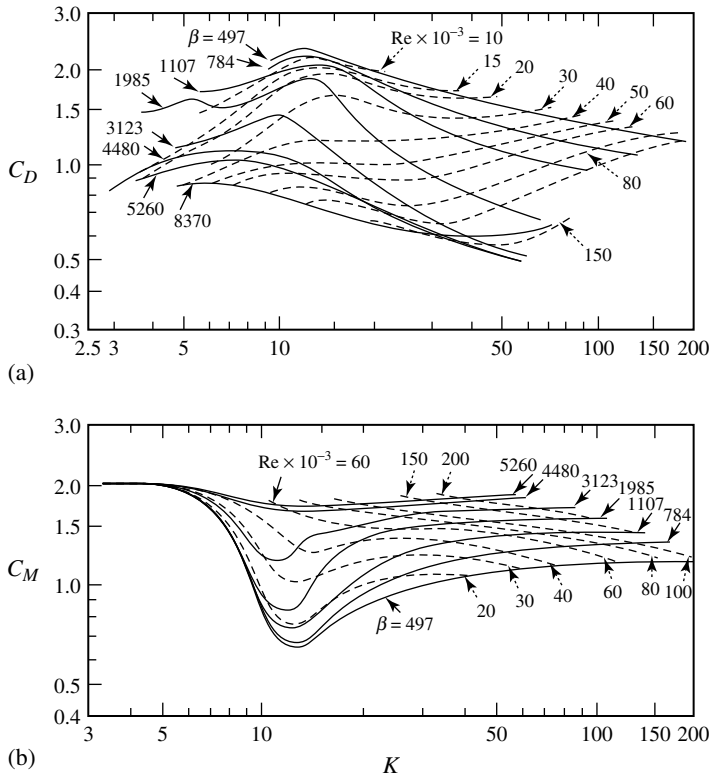


FIGURE 36.13 Drag and inertia coefficients as functions of K for various values of Re and β . (Source: Sarpkaya, 1976, *Proceedings of the Eighth Offshore Technology Conference*. With permission.)

36.2.3 Vortex-Induced Vibration

When the flow passes around a fixed cylinder, for a very low Re ($0 < Re < 4$), the flow separates and reunites smoothly. When the Re is between 4 and 40, eddies are formed and are attached to the downstream side of cylinder. They are stable and there is no oscillation in the flow. For a flow with a Reynolds number greater than about 40, the fluid near the cylinder starts to oscillate due to shedding vortices. These shedding vortices exert an oscillatory force on the cylinder in the direction perpendicular to both the flow and the structure. The frequency of oscillation is related to the nondimensionalized parameter, the Strouhal number, defined by

$$St = \frac{f_v D}{U} \quad (36.31)$$

where f_v is the frequency of oscillation, U is the steady velocity of the flow, and D is the diameter of the cylinder. For circular cylinders, the Strouhal number stays roughly at 0.22 for laminar flow ($10^3 < Re < 2 \times 10^5$) and 0.3 for turbulent flow (Patel, 1989).

The lift force due to these shedding vortices can be written as

$$f_L = \frac{1}{2} C_L \rho A_f U^2 \cos 2\pi f_v t \quad (36.32)$$

where C_L is the lift coefficient, which is also a function of Re , K , and the surface roughness. The experimental data of the lift coefficients show considerable scatter with typical values ranging from 0.25 to 1. For smooth cylinders, the lift coefficient approaches about 0.25 as Re and K increase.

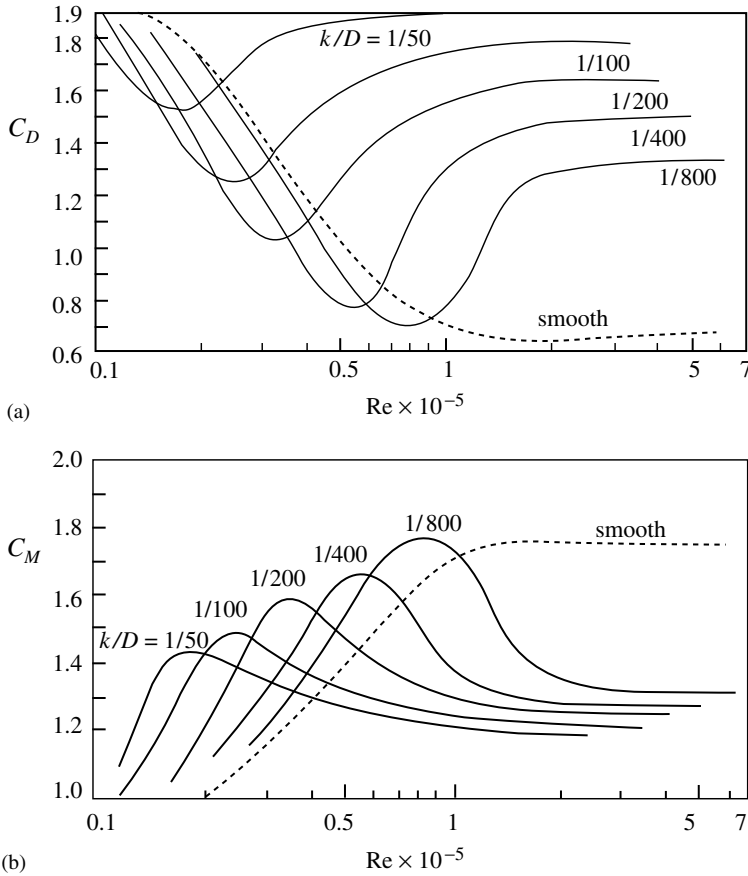


FIGURE 36.14 Drag and inertia coefficients for a rough cylinder as functions of Re for various values of cylinder roughness (as measured by k/D) for $K = 20$. (Source: Sarpkaya et al., 1977, *Proceedings of the Ninth Offshore Technology Conference*. With permission.)

It should be noted that the vortex forces are not generally correlated on the entire cylinder length. That is, the phase of the vortex shedding forces varies over the length. The correlation length — the length over which vortex shedding is synchronized — for a stationary cylinder is about three to seven diameters for laminar flow. If sectional forces are randomly phased, the net effect will be small. The total force on a cylinder of length L will be only a fraction of Lf_L . This fraction is called the joint acceptance and depends on the ratio of the correlation length to the total length.

When the flow passes by a cylinder that is free to vibrate, the shedding frequency is also controlled by the movement of the cylinder. When the shedding frequency is close to the first natural frequency of the cylinder (± 25 to 30% of the natural frequency [Sarpkaya and Isaacson, 1981]), the cylinder takes control of the vortex shedding. The vortices will shed at the natural frequency instead of at the frequency determined by the Strouhal number. This is called lock-in or synchronization, which is a result of nonlinear interaction between the oscillation of the body and the action of the fluid. Figure 36.16 shows the shedding frequency, as a function of flow velocity in the presence of a structure. f_1 and f_2 are the natural frequencies of the structure.

The amplitude of the structural response and the range of the fluid velocity over which the lock-in phenomenon persists are functions of a reduced damping parameter — the ratio of the damping force to the exciting force (Vandiver, 1985, 1993). If the reduced damping parameter is small, the lock-in can persist over a greater range of flow velocity.

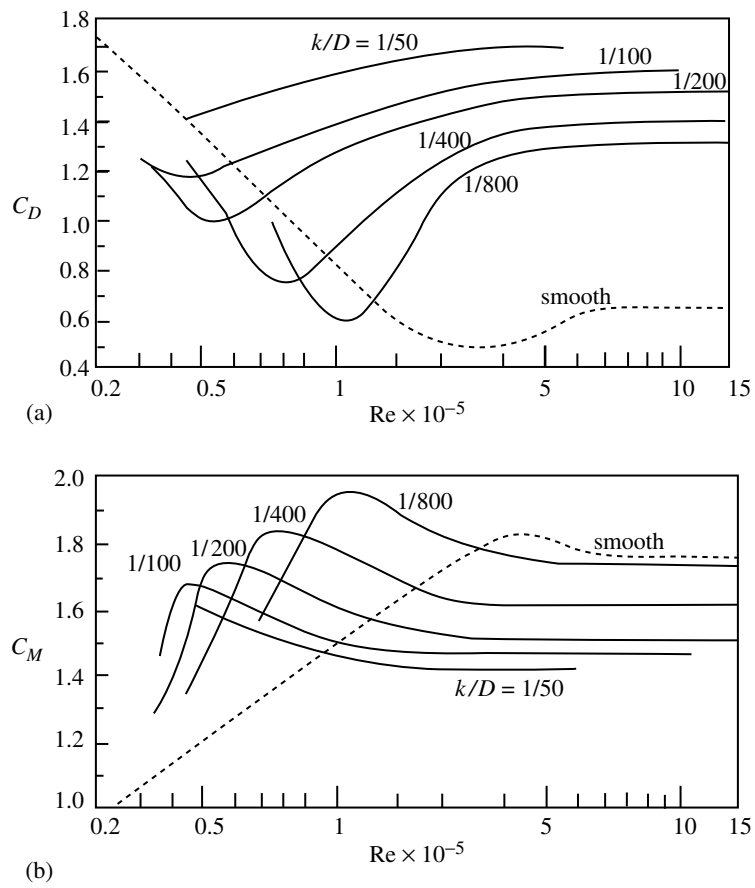


FIGURE 36.15 Drag and inertia coefficients for a rough cylinder as functions of Re for various values of cylinder roughness (as measured by k/D) for $K = 60$. (Source: Sarpkaya et al., 1977, *Proceedings of the Ninth Offshore Technology Conference*. With permission.)

The existing models for vortex-induced oscillation for a rigid cylinder include single-degree-of-freedom models and coupled models. The single-DoF models assume that the effect of vortex shedding is an external forcing function, which is not affected by the motion of the body. The coupled models assume that the equations that govern the motion of the structure and the lift coefficients are coupled so that the fluid and the structure affect each other (Billah, 1989).

36.2.4 Summary

Some of the fluid forces are discussed briefly, and the regimes where inertia, drag, and diffraction forces are important are shown as functions of the ratio of the structural diameter to the wave

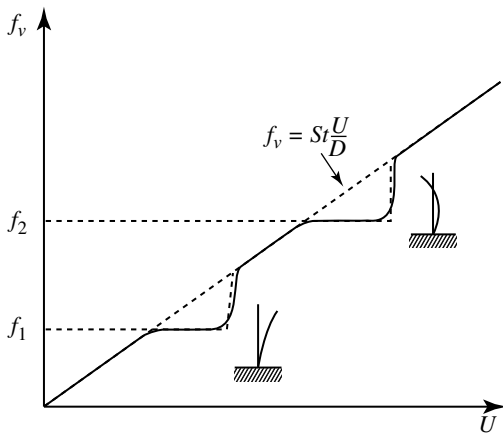


FIGURE 36.16 An example of fluid elastic resonance.

length, D/λ , and the ratio of the wave height to the structural diameter, H/D . The wave forces on small structures are modeled by the Morison equation, and it is valid for $D/\lambda < 0.2$ and $H/D > 0.63$ or thereabouts. The Morison equation includes the effects of added mass, inertia, and drag. The added mass is simply

$$M_A = C_A M_{\text{disp}}$$

For a cylinder with transverse velocity, v , the normal and the tangential components of the drag and the inertia forces are given by

$$\begin{aligned} f^n &= \frac{1}{2} C_D \rho D (w^n - v^n) |w^n - v^n| + C_M \rho \pi \frac{D^2}{4} \dot{w}^n \\ f^t &= \frac{1}{2} C_T \rho D (w^t - v^t) |w^t - v^t| \end{aligned}$$

The fluid coefficients are at least functions of three parameters: the Reynolds number, the Keulegan–Carpenter number, and the cylinder roughness. The plots of these coefficients are reproduced in [Figure 36.13](#) to [Figure 36.15](#).

The frequency of the lift force that is exerted by shedding vortices is closely related to the Strouhal number given by

$$St = \frac{f_v D}{U}$$

The lift force due to these shedding vortices can be written as

$$f_L = \frac{1}{2} C_L \rho A_f U^2 \cos 2\pi f_v t$$

If the structure is free to vibrate, then lock-in or synchronization may occur when the shedding frequency is close to the structure's natural frequency. The structure takes control of the vortex shedding. Many nonlinear models are available to capture this phenomenon.

36.3 Examples

Four examples are given in this section. The first example illustrates the roles of the normal and the tangential components of the drag force in the static configuration of a towing cable. The second example shows how the equation of motion of an articulated tower can be formulated in the presence of surrounding fluid. The third example shows how to choose a single significant wave height to represent a certain condition from significant wave height data over a long period of time. The final example shows how to reconstruct time series data from a given spectrum.

36.3.1 Static Configuration of a Towing Cable

For the purpose of ocean surveillance, oceanographic or geographic measurements, or ocean exploration, marine cables with instrument packages or Remotely Operated Vehicles are often towed behind ships or submarines. For example, the goal of the VENTS program by the National Oceanic and Atmospheric Administration (NOAA) is to conduct research on the impacts and consequences of submarine volcanoes and hydrothermal venting on the global ocean. In attempts to locate and map the distributions of hydrothermal plumes in the Mid-Ocean Ridge system, an instrument package called a CTD (Conductivity, Temperature and Depth Sensors) is towed behind a ship.

Let us consider a cable and a body towed behind a ship at a constant velocity with no current as shown in Figure 36.17. What kind of shape will the cable take? What will be the distance between the ship and the towed body?

We immediately recognize that this is equivalent to having a stationary ship with a steady current in the opposite direction. The equation of motion is given by

$$\sum \vec{F} = m\vec{a}(s, t) = \vec{0} = \frac{\partial}{\partial s}(T\vec{t}) + f^n\vec{n} + f^t\vec{t} + mg\vec{k}$$

where m is the mass of the cable per unit length, $\vec{a}(s, t)$ is the acceleration of the cable, s is the coordinate along the cable, T is the tension which is a function of s , $(\vec{t}, \vec{n}, \vec{b})$ is the set of unit vectors of the curvilinear coordinate system, \vec{k} is the unit vector downward in the direction of gravity, g is the gravitational acceleration, f^n is the normal drag force, and f^t is the tangential drag force. The added mass and the inertial terms are zero because the fluid acceleration and the cable acceleration are zero. The normal and tangential drag forces are given in Equation 36.27 and Equation 36.29. In our case, they are given by

$$f^n = C_D \rho \frac{D}{2} U^2 \cos^2 \theta, \quad f^t = -C_T \rho \frac{D}{2} U^2 \sin^2 \theta$$

The corresponding scalar equations are given by

$$\begin{aligned} \frac{dT}{ds} - C_T \rho \frac{D}{2} U^2 \sin^2 \theta - mg \cos \theta &= 0 \\ -T \frac{d\theta}{ds} + C_D \rho \frac{D}{2} U^2 \cos^2 \theta - mg \sin \theta &= 0 \end{aligned} \quad (36.33)$$

where θ is the angle that the tangential vector makes with the vertical and measured positive clockwise. Note that we have used $\partial \vec{t} / \partial s = (-\partial \theta / \partial s) \vec{n}$ and $\vec{k} = -\cos \theta \vec{t} - \sin \theta \vec{n}$. Equation 36.33 shows that the tangential components of the external forces act to increase the tension, while the normal components cause the towline to bend. Because the normal component of the drag force is much larger than the tangential component, most of the fluid force is used to turn the cable.

From the force diagram (in Figure 36.17), the angle that the cable makes with the vertical where it is connected to the towed body is given by

$$T(0) \cos \theta(0) = W, \quad T(0) \sin \theta(0) = \text{Drag}$$

Once we know the weight and the drag force on the towed body, the tension and the angle at $s = 0$ can be found. If the drag is negligible compared with the weight, then the cable must be near vertical and the tension must be equal to the weight of the towed body at $s = 0$:

$$T(0) \approx W \quad \text{and} \quad \theta(0) \approx 0$$

For now, let us assume that this is the case. Then, with these initial conditions, the system of ordinary differential equations (Equation 36.33) can be solved numerically for $T(s)$ and $\theta(s)$. For example,

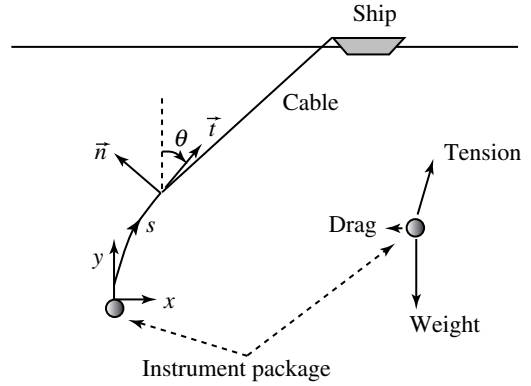


FIGURE 36.17 Towed system in equilibrium and the forces acting on the towed body.

even very simple finite difference equations will work. A set of equations

$$T_{i+1} = T_i + \left(mg \cos \theta_i - C_T \rho \frac{D}{2} U^2 \sin^2 \theta_i \right) \Delta s \quad (36.34)$$

$$\theta_{i+1} = \theta_i - \left(mg \sin \theta_i + C_D \rho \frac{D}{2} U^2 \cos^2 \theta_i \right) \Delta s / T_i \quad (36.35)$$

where $T_i = T(i\Delta s)$, are used here, and it works very well for $\Delta s = 0.05$.

The Cartesian coordinates, x and y , are related to θ by

$$\frac{dx}{ds} = \sin \theta \quad \text{and} \quad \frac{dy}{ds} = \cos \theta$$

and can also be obtained by integrating them numerically.

Figure 36.18 shows the results when $mg = 1.5$ N/m, $C_D \rho D U^2 / 2 = 10$ N/m, $C_T \rho D U^2 / 2 = 0.1$ N/m, $W = 100$ N, and the cable is 100 m long. Care is taken so that the ship is located at $x = 0$ and $y = 0$.

It is interesting to note that θ approaches a critical value, and the shape gradually becomes linear toward the ship. Mathematically, $d\theta/ds$ becomes zero. This is when the drag force is completely balanced by the normal component of the cable weight. The angle at which this occurs, θ_{cr} , can be obtained from the second governing equation and

$$mg \sin \theta_{cr} = -f^n, \quad \frac{\sin \theta_{cr}}{\cos \theta_{cr}} = C_D \rho \frac{D}{2} U^2 \frac{1}{mg}$$

In our case, $\theta_{cr} = 1.184$ rad, and this value agrees with Figure 36.18.

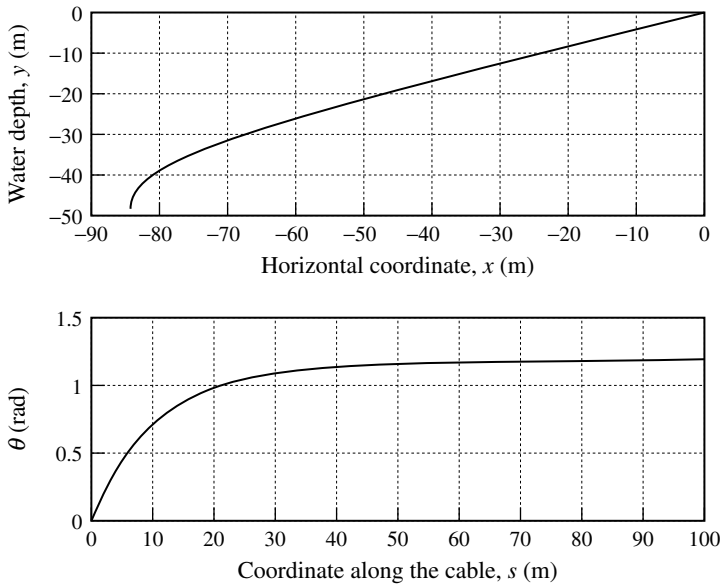


FIGURE 36.18 The equilibrium configuration of a towed cable and the angle that the cable makes with the vertical when $mg = 1.5$ N/m, $C_D \rho D U^2 / 2 = 10$ N/m, $C_T \rho D U^2 / 2 = 0.1$ N/m, and $W = 100$ N.

36.3.2 Fluid Forces on an Articulated Tower

Offshore structures are used in the oil industry as exploratory, production, oil storage, and oil landing facilities. They are designed to be self-supporting and sufficiently stable for offshore activities such as drilling and production of oil. An articulated tower as seen in Figure 36.19 is an example of an offshore platform that consists of a base, shaft, universal joint that connects the base and the shaft, ballast chamber, buoyancy chamber, and deck. The ballast chambers provide the extra weight so that the tower's bottom stays on the ocean floor, and the buoyancy chamber adds the necessary buoyancy so that the tower does not fall.

An articulated tower can be effectively modeled as a rigid inverted pendulum, where the deck is modeled as a point mass, the shaft as a uniform rigid bar, and the buoyancy chamber by a point buoyancy. In two dimensions, motion of the tower can be described with a single DoF (Chakrabarti and Cottor, 1979; Bar-Avi, 1996). The equation of motion in terms of the tower's deflection angle is obtained by summing the moment about the point O in Figure 36.20 and is given by

$$I \frac{d^2 \theta}{dt^2} = \sum M_O = mg \frac{L}{2} \sin \theta + MgL \sin \theta - Bl \sin \theta + \int_0^L f^n x dx$$

where I is the mass moment of inertia about the point O given by $I = mL^2/3 + ML^2$, m is the mass of the shaft, g is the gravitational acceleration, L is the length of the shaft, M is the point mass at the top, B is the buoyancy provided by the buoyancy chamber, l is its moment arm, f^n is the normal fluid force per unit length, and x is the coordinate along the shaft from O.

The fluid force per unit length in the normal direction is given by

$$f^n = C_D \rho \frac{D}{2} (w^n - v^n) |w^n - v^n| + C_M \rho \pi \frac{D^2}{4} \dot{w}^n - C_A \rho \pi \frac{D^2}{4} a^n$$

where the last term is the force in the normal direction due to the added mass. v^n and a^n are the velocity and the acceleration of the body in the normal direction and are given by

$$v^n = x \frac{d\theta}{dt} \quad \text{and} \quad a^n = x \frac{d^2 \theta}{dt^2}$$

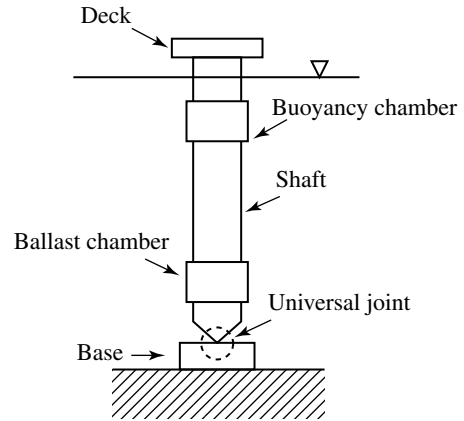


FIGURE 36.19 Schematic of an articulated tower.

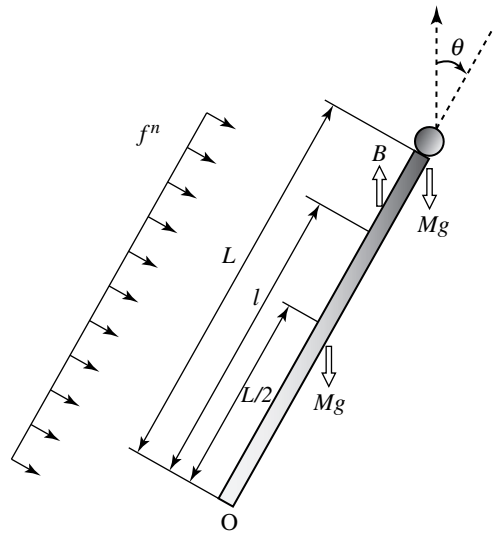


FIGURE 36.20 Free-body diagram.

If we assume that the surrounding fluid is stationary, then the normal velocity and the acceleration of the fluid (w and \dot{w}) are zeros. Thus, the moment due to the fluid force is given by

$$\begin{aligned}\int_0^L f^n x \, dx &= \int_0^L \left(-C_D \rho \frac{D}{2} x^2 \left(\frac{d\theta}{dt} \right)^2 \text{sign} \left(\frac{d\theta}{dt} \right) + C_A \rho \pi \frac{D^2}{4} x \frac{d^2 \theta}{dt^2} \right) x \, dx \\ &= -C_D \rho \frac{D}{2} \frac{L^4}{4} \left(\frac{d\theta}{dt} \right)^2 \text{sign} \left(\frac{d\theta}{dt} \right) + C_A \rho \pi \frac{D^2}{4} \frac{L^3}{3} \frac{d^2 \theta}{dt^2}\end{aligned}$$

and the equation of motion is given by

$$\left(m \frac{L^2}{3} + ML^2 + C_A \rho \pi \frac{D^2}{4} \frac{L^3}{3} \right) \frac{d^2 \theta}{dt^2} = \left(mg \frac{L}{2} + MgL - Bl_b \right) \sin \theta - C_D \rho \frac{D}{2} \frac{L^4}{4} \text{sign} \left(\frac{d\theta}{dt} \right) \left(\frac{d\theta}{dt} \right)^2$$

Note that the normal fluid drag force adds directly to the restoring moment in the case of a rigid bar. The equation of motion can be solved numerically once the initial conditions ($\theta[0]$ and $d\theta/dt[0]$) are given.

The equation of motion can be simplified if we assume that the angle of rotation θ is small. More specifically, if we assume that θ^2 is negligible when compared with 1, then we find that²

$$\sin \theta \approx \theta$$

The equation of motion can be simplified to

$$\left(m \frac{L^2}{3} + ML^2 + C_A \rho \pi \frac{D^2}{4} \frac{L^3}{3} \right) \frac{d^2 \theta}{dt^2} - \left(mg \frac{L}{2} + MgL - Bl_b \right) \theta + C_D \rho \frac{D}{2} \frac{L^4}{4} \text{sign} \left(\frac{d\theta}{dt} \right) \left(\frac{d\theta}{dt} \right)^2 = 0$$

which resembles the equation for a linear oscillator with a nonlinear damping term. Note that the system becomes unstable when the stiffness term (the coefficient of θ) becomes negative. This occurs when the buoyancy is not sufficient or

$$B < \frac{1}{l_b} \left(mg \frac{L}{2} + MgL \right)$$

36.3.3 Distribution of Significant Wave Heights — Weibull and Gumbel Distributions

The National Buoy Data Center (NBDC) run by NOAA collects ocean data such as wind, current, wave, pressure, and temperature data in various locations and the records are made public. Let us say that we are to design an articulated tower (in Section 36.3.2) in one of these locations where the data are available. The first task is to characterize the environment. Using all of the information that is collected is inefficient and impractical. Instead, we are interested in choosing a single number that can represent typical and extreme situations such as 10- and 50-year storms. For now, let us only consider random waves. We are then interested in finding the significant wave heights representing 10- and 50-year storms.

From NBDC data for a buoy outside Monterey Bay, the number of occurrences for ranges of significant wave heights is constructed in Table 36.2. The measurements were taken every hour for about 12 years. We first construct the corresponding Weibull distribution using the method described in Section 36.1.6. We first guess γ so that a pair of $\ln(-\ln\{1 - F(h)\})$ and $\ln(h - \gamma)$ form a

²This is called the small angle assumption.

TABLE 36.2 Number of Occurrences of Various Sea States

Significant Wave Height, h (m)	Number of Occurrences	Sum
< 1	2,367	2,367
1–2	46,353	48,720
2–3	3,4285	83,005
3–4	1,3181	96,186
4–5	3,813	99,999
5–6	716	100,715
6–7	145	100,860
7–8	32	100,892
8–9	8	100,900
9–10	2	100,902
Total	100,902	

straight line. Figure 36.21 shows that the pair yields nearly a straight line when $\gamma \approx 0.84$. The slope and the γ intercept of this line are 1.6 and -0.78 , respectively. The Weibull parameters are then $m = 1.6$ and $\beta = 1.6$.

Similarly, we can find the corresponding Gumbel probability density function by plotting pairs of $(h, \ln(-\ln\{F(h)\}))$ to form a line. For the data shown in Table 36.2, the line has a slope of -1.52 and γ intercept of 2.84 so that $\alpha = -1.52$ and $\beta = 1.87$.

Figure 36.22 shows the Weibull probability density and the cumulative distribution (Equation 36.17) in solid lines, the Gumbel probability density and the cumulative distribution in dotted lines (Equation 36.18), and the discrete probability density and the cumulative distribution derived from Table 36.2 in symbols.

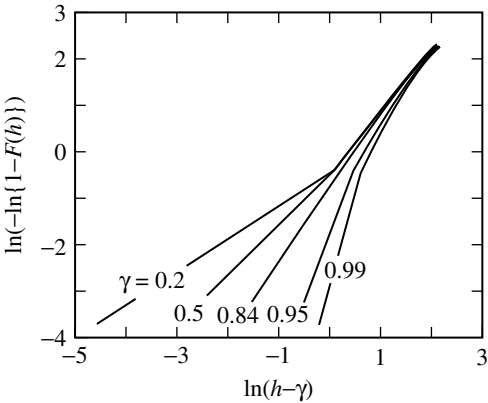


FIGURE 36.21 Plots of $(\ln(h - \gamma), \ln[-\ln\{1 - F(h)\}])$ for various values of γ .

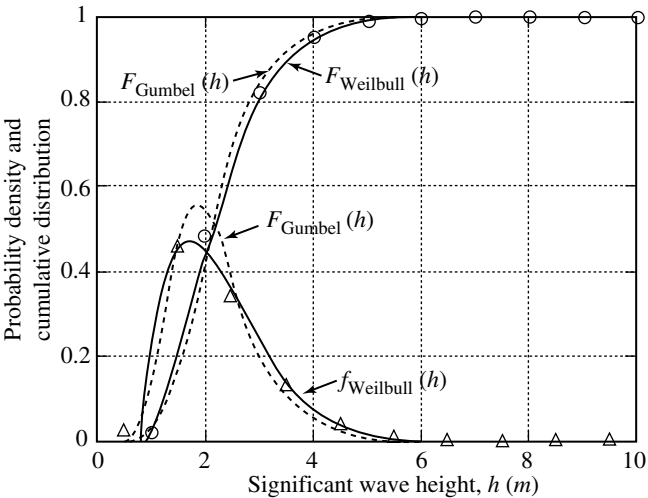


FIGURE 36.22 Weibull approximations of the probability density and cumulative distribution of significant wave heights measured in the outer Monterey Bay area. The symbols are the values given in Table 36.2.

TABLE 36.3 Comparison of Representative Significant Wave Heights for Long-Term Predictions from Gumbel and Weibull Distributions

	5-Year (m)	10-Year (m)	50-Year (m)
Weibull	7.84	8.15	8.79
Gumbel	8.83	9.33	10.4

The next step is to find a significant wave height that can represent an N -year storm, h_N . The probability that we will not have an N -year storm in any given year is $1 - 1/N$ and is equivalent to the probability that the significant wave height will not exceed h_N in the same year. The probability that $h < h_N$ in a single measurement is $F(h_N)$, and the probability that $h < h_N$ in every measurement taken in a year is $F(h_N)^{24 \times 365}$. Then, we have

$$1 - \frac{1}{N} = F(h_N)^{24 \times 365}$$

Table 36.3 shows significant wave heights that represent 5-, 10-, and 50-year storms obtained using the Weibull and Gumbel distributions.

The Gumbel probability distribution gives higher significant wave heights. For this particular set of data, the Weibull distribution seems to fit the data better (Figure 36.22), and the Weibull distribution is the most often used distribution in the offshore industry.

36.3.4 Reconstructing Time Series for a Given Significant Wave Height

Previously, we found significant wave heights that could represent 5-, 10-, and 25-year storms for a given site. Recall that the significant wave height can entirely characterize the Pierson–Moskowitz spectra. Once the spectral density is determined, a sample time history of the wave profile, $\eta(t)$, can be determined using either Borgman's or Shinozuka's method (Section 36.1.4). Here, Shinozuka's method is used to generate the random wave elevations.

Let us first find the random frequencies distributed according to $S_{\eta\eta}^o(\omega)/\sigma_\eta^2$. The P–M spectrum in terms of the significant wave height is given by Equation 36.8.

$$S_{\eta\eta}^o(\omega) = 0.7795\omega^{-5} \exp\left(-\frac{3.118}{H_s^2}\omega^{-4}\right)$$

The variance is given by

$$\sigma_\eta^2 = \int_0^\infty S_{\eta\eta}^o(\omega) d\omega = \frac{H_s^2}{16}$$

The probability density and the cumulative distribution functions are given by

$$f(\omega) = S_{\eta\eta}^o(\omega)/\sigma_\eta^2 = \frac{12.472}{H_s^2}\omega^{-5} \exp\left(-\frac{3.118}{H_s^2}\omega^{-4}\right), \quad F(\omega) = 1 - \exp\left(-\frac{3.118}{H_s^2}\omega^{-4}\right)$$

The inverse of the cumulative distribution function is given by

$$F^{-1}(x) = \left(-\frac{H_s^2}{3.118} \ln(1-x)\right)^{-1/4}$$

The random frequencies distributed according to $f(\omega)$ can be obtained from uniformly distributed random numbers x from 0 and 1. Table 36.4 shows uniform random numbers between

TABLE 36.4 Generation of Random Frequencies Distributed According to $f(\omega)$ from Uniform Random Numbers

Uniform Random Numbers $0 < x < 1$	Random Frequencies ω Distributed According to $f(\omega)$
0.950	$(-19.713 \ln[1 - 0.950])^{-1/4} = 0.360$
0.231	$(-19.713 \ln[1 - 0.231])^{-1/4} = 0.662$
0.606	$(-19.713 \ln[1 - 0.606])^{-1/4} = 0.483$
\vdots	\vdots

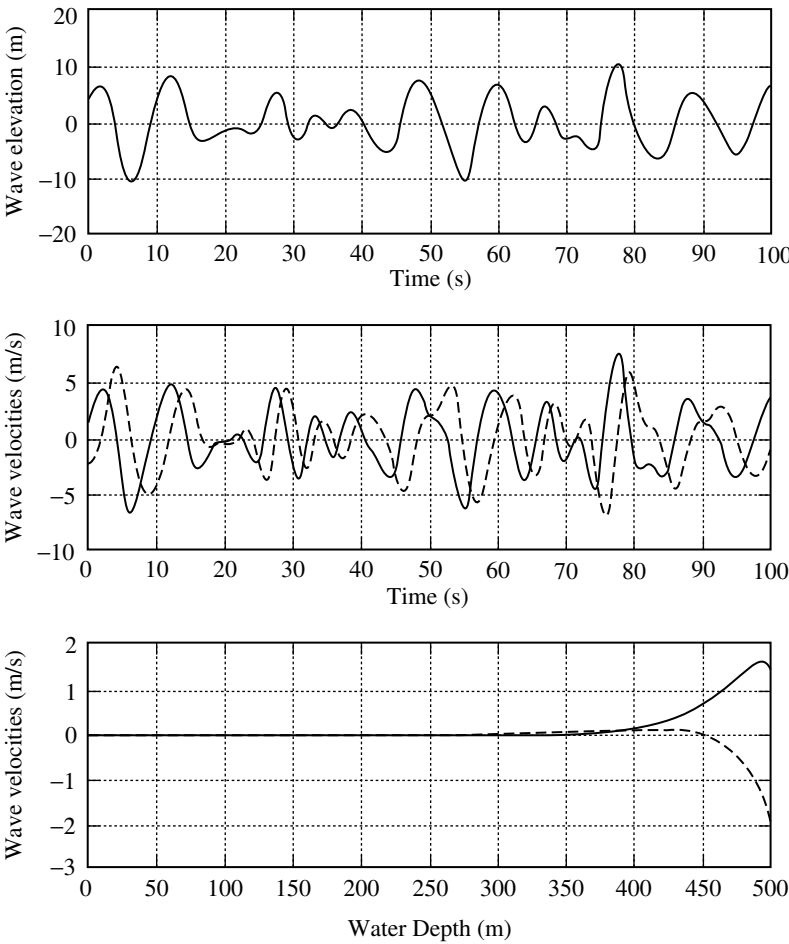


FIGURE 36.23 Wave elevation and velocities.

0 and 1 and the random frequencies distributed according to $f(\omega)$ ³. The significant wave height of 7.84 m is used.

We can obtain 100 in this way, and the wave elevation is also obtained using Equation 36.13. The random phase φ_i is obtained by multiplying uniform random numbers (different from the ones used to generate the random frequencies) by 2π .

Figure 36.23 shows the surface elevation as a function of time, the corresponding wave velocities at the water surface (Section 36.1.7) as functions of time, and the wave velocities at $t = 0$ as functions of the water depth. Note that the wave velocities decay with depth.

³The uniform random numbers can be generated by the MATLAB rand function.

36.3.5 Available Numerical Codes

Many numerical codes are available for modeling the dynamics of slender structures such as risers, tether, umbilicals, and mooring lines. The first example in this section was solved by a numerical code, WHOI Cable, developed at Woods Hole Oceanographic Institution. WHOI Cable is a time-domain program that can be used for analyzing the dynamics of towed and moored cable systems in both two and three dimensions. It takes into account bending and torsion as well as extension.

Comparative studies investigating flexible risers were carried out by ISSC Committee V7 from computer programs developed by 11 different institutions in the period between 1988 and 1991, and the results were reported by Larsen (1992). More recently, Brown and Mavrakos (1999) conducted a comparative study on the dynamic analysis of suspended wire and chain mooring lines and reported results from 15 different numerical codes. The participants included engineering consultancies, and academic and research institutions involved in marine technology. Some of the time-domain programs that were included in the comparative study are MODEX by Chalmers University of Technology, FLEXAN-C by Institut Français du Pétrole, DYWIDAG 95 by MARIN, R.FLEX by MARINTEK, CABLEDYN by National Technical University of Athens, DMOOR by Noble Denton Consultancy Services Ltd, VORCAFLEX by Orcina Ltd Consulting Engineers, ANFLEX by Petrobras SA, TDMOOR-DYN by University College London, FLEXRISER by Zentech International. Some of these programs are available to academic institutions and government laboratories at no cost.

Acknowledgments

The author wishes to express gratitude for the funding from the Woods Hole Oceanographic Institution and the Department of Mechanical Engineering at Texas Tech University.

References

- Bar-Avi, P. 1996. Dynamic response of an offshore articulated tower, Ph.D. thesis, The State University of New Jersey, Rutgers, May 1996.
- Billah, K. 1989. A study of vortex induced vibration, Ph.D. thesis, Princeton University, May 1989.
- Borgman, L., Ocean wave simulation for engineering design, *J. Waterway Harbors Div.*, 95, 557–583, 1969.
- Bretschneider, C. 1959. *Wave variability and wave spectra for wind-generated gravity waves*. Technical Memorandum No.118, Beach Erosion Board, U.S. Army Corps of Engineers, Washington D.C.
- Bretschneider, C. 1969. Wave forecasting. In *Handbook of Ocean and Underwater Engineering*, Ed. J.J. Myers, McGraw-Hill, New York.
- Brown, D. and Mavrakos, S. Comparative study on mooring line dynamic loading, *Marine Structures*, 12, 131–151, 1999.
- Chakrabarti, S.K. 1987. *Hydrodynamics of Offshore Structures*, Computational Mechanics Publications, Southampton, U.K.
- Chakrabarti, S.K. and Cottor, D., Motion analysis of articulated tower, *J. Waterway Port Coast. Ocean Div.*, 105, 281–292, 1979.
- Faltinsen, O.M. 1993. *Sea Loads on Ships and Offshore Structures*, Cambridge University Press, Cambridge.
- Gumbel, E. 1958. *Statistics of Extremes*, Columbia University Press, New York.
- Hasselmann, K., Barnett, T., Bouws, E., Carlson, H., Cartwright, D., Enke, K., Ewing, J., Gienapp, H., Hasselmann, D., Kruseman, P., Meerburg, A., Muller, P., Olbers, D., Richter, K., Sell, W., and Walden, H. 1973. Measurement of wind-wave growth and swell decay during the joint North Sea wave project (JONSWAP), *Technical Report 13 A*. Deutschen Hydrographischen Zeitschrift.
- Hogben, N. 1976. Wave loads on structures, *Behavior of Offshore Structures (BOSS)*, Oslo, Norway.

- Isaacson, M., Wave and current forces on fixed offshore structures, *Can. J. Civil Eng.*, 15, 937–947, 1988.
- Jasper, N., Statistical distribution patterns of ocean waves and of wave induced ship stresses and motions with engineering applications, *Trans. Soc. Nav. Arch. Mar. Engrs*, 64, 375–432, 1954.
- Khinchine, A., Korrelations theorie der stationaren stochastischen prozesse, *Math. Ann.*, 109, 604–615, 1934.
- Kinsman, B. 1965. *Wind Waves*, Prentice Hall, Englewood Cliffs, NJ.
- Lamb, H. 1945. *Hydrodynamics*, 6th Ed., Cambridge University Press, New York.
- Larsen, C. Flexible riser analysis — comparison of results from computer programs, *Marine Structure*, 5, 103–119, 1992.
- LeMehaute, B. 1976. *Introduction to Hydrodynamics and Water Waves*, Springer-Verlag, New York.
- Longuet-Higgins, M., On the statistical distribution of the height of sea waves, *J. Mar. Res.*, 11, 3, 245–266, 1952.
- Miller, B., Wave slamming loads on horizontal circular elements of offshore structures, *Nav. Arch.*, 3, 81–98, 1977.
- Miller, B. 1980. Wave slamming on offshore structures, *Technical Report No. NMI-R81*. National Maritime Institute.
- Morison, J., O'Brien, M., Johnson, J., and Schaaf, S., The force exerted by surface waves on piles, *Pet. Trans., AIME*, 189, 149–157, 1950.
- Ochi, M., On prediction of extreme values, *J. Ship Res.*, 17, 29–37, 1973.
- Ochi, M. and Hubble, E. 1976. Six parameter wave spectra. ASCE pp. 301–328. *Proceedings of the Fifteenth Coastal Engineering Conference*, Honolulu, HI.
- Patel, M. 1989. *Dynamics of Offshore Structures*, Butterworths, London.
- Pierson, W. and Moskowitz, L., A proposed spectral form for fully developed wind seas based on the similarity theory of S.A. Kitaigorodskii, *J. Geophys. Res.*, 69, 24, 5181–5203, 1964.
- Rice, S.O. 1954. Mathematical analysis of random noise. In *Selected Papers on Noise and Stochastic Processes*, N. Wax, Ed., Dover Publications, New York.
- Sarpkaya, T. 1976. In-line and transverse forces on cylinders in oscillating flow at high Reynolds numbers, OTC 2533, pp. 95–108. *Proceedings of the Eighth Offshore Technology Conference*, Houston, TX.
- Sarpkaya, T., Collins, and N., Evans, S. 1977. Wave forces on rough-walled cylinders at high Reynolds numbers, OTC 2901, pp. 175–184. In *Proceedings of the Ninth Offshore Technology Conference*, Houston, TX.
- Sarpkaya, T., and Isaacson, M. 1981. *Mechanics of Wave Forces on Offshore Structures*, Van Nostrand Reinhold, New York.
- Shinozuka, M., Monte Carlo Solution of structural dynamics, *Comput. Struct.*, 2, 855–874, 1972.
- Sverdrup, H., and Munk, W. 1947. Wind, sea, and swell: theory of relations for forecasting, *Technical Report 601*. U.S. Navy Hydrographic Office.
- Tucker, M. 1991. *Waves in Ocean Engineering: Measurements, Analysis, and Interpretation*, Ellis Horwood, Chichester, U.K.
- Vandiver, J. 1985. Prediction of lockin vibration on flexible cylinders in sheared flow, May 1985. In *Proceedings of the 1985 Offshore Technology Conference*, Paper No. 5006, Houston, TX.
- Vandiver, J., Dimensionless parameters important to the prediction of vortex-induced vibration of long, flexible cylinders in ocean currents, *J. Fluids Struct.*, 7, 5, 423–455, 1993.
- Wiener, N., Generalized harmonic analysis, *Acta Math.*, 55, 117–258, 1930.
- Wilson, J. 1984. *Dynamics of Offshore Structures*, Wiley, New York.

IX

Acoustics

37

Sound Levels and Decibels

37.1	Introduction	37-1
37.2	Sound Wave Characteristics	37-1
	Velocity of Sound	
37.3	Levels and Decibels	37-3
	Sound Power Level • Sound Pressure Level • Overall	
	Sound Pressure Level	

S. Akishita

Ritsumeikan University

Summary

In this chapter, the basic characteristics of sound and sound propagation are described. Levels and decibels, which represent the magnitude of sound waves, are defined and explained.

37.1 Introduction

Sound is related to vibration, and is described as a propagating perturbation through a fluid, which is air or water in most cases. A very wide variety of noise sources exists. Each source is peculiar to its generation mechanism, which may cover a wide range of phenomena including fluid mechanics and the vibration of structures. Sound is perceived by the ear of the listener as a pressure wave superimposed upon the ambient air pressure. The *sound pressure* is the incremental variation about the ambient atmospheric pressure. Generally, it is detected by a microphone and expressed as oscillatory electric signal output from an audio measurement instrument. We shall present a mathematical description of these pressure waves that are known as sound. The field of acoustics concerns sound and vibration, and is treated in Chapter 37 to [Chapter 45](#) of this book.

37.2 Sound Wave Characteristics

The characteristics of a sound wave are described by a pressure oscillation of a pure tone. A “pure tone” is a sinusoidal pressure wave of a specific frequency and amplitude, propagating at a velocity determined by the temperature and pressure of the medium (air).

Let us consider a hypothetical sound field in a duct with constant cross-sectional area, as shown in [Figure 37.1a](#). A reciprocating piston at the left end emits the sound wave and it propagates toward the right-side end along the indicated axis. It is detected by a microphone at the right end. [Figure 37.1b](#) shows the instantaneous pressure distribution in a duct at time $t = t_0$. [Figure 37.1c](#) shows the pressure variation of the time history detected by the microphone at $x = x_0$.

The wavelength, λ , is the distance between successive two peaks in the waveform in Figure 37.1b. Wavelength is related to the frequency, f , and the velocity of wave propagation, c , by

$$\lambda = \frac{c}{f} \quad (\text{ft or m}) \quad (37.1)$$

The period, T , of the sinusoidal wave is the time interval required for one complete cycle, as depicted in Figure 37.1b. The period, T , is related to the frequency, f , by

$$T = \frac{1}{f} \quad (\text{sec}) \quad (37.2)$$

37.2.1 Velocity of Sound

The velocity of sound is identical to the velocity of wave propagation, c , and in air it is given by

$$c = \sqrt{\frac{\gamma p_0}{\rho}} \quad (\text{ft/sec or m/sec}) \quad (37.3)$$

where γ denotes the ratio of specific heat, p_0 denotes the ambient or equilibrium pressure, and ρ denotes the ambient or equilibrium density. For air, γ is taken as 1.4. Equation 37.3 then becomes

$$c = \sqrt{\frac{1.4 p_0}{\rho}} \quad (\text{ft/sec or m/sec}) \quad (37.4)$$

which can be further simplified by the fact that the ratio p_0/ρ is related to the temperature of the gas. On assuming that the air behaves virtually as an ideal gas, the velocity, c , is related to the absolute temperature in degrees Kelvin (K) by

$$c = 20.05\sqrt{T} \quad (\text{m/sec}) \quad (37.5)$$

where T , the temperature in degrees Kelvin, is

$$T = 273.2^\circ + (^\circ\text{C}) \text{ K} \quad (37.6)$$

Example 37.1

Calculate the velocity of sound, c , giving the temperature of 15°C .

Solution

$$T = 273.2^\circ + 15^\circ = 288.2 \text{ K, then}$$

$$c = 20.05\sqrt{288.2} = 340.4 \text{ m/sec}$$

is obtained. This value means a typical velocity of sound in the air.

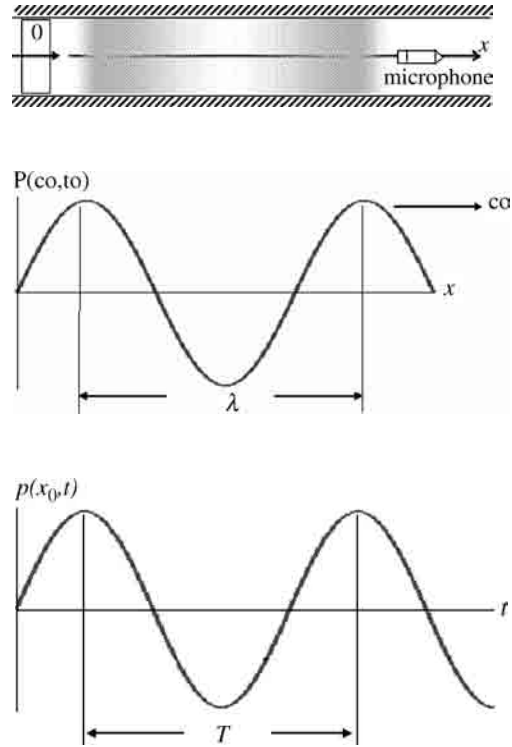


FIGURE 37.1 (a) Propagating sound wave in a duct; (b) instantaneous pressure distribution; (c) pressure variation in time history detected by a microphone at $x = x_0$.

37.3 Levels and Decibels

Sound pressure and power are commonly expressed in terms of *decibel levels*. This allows us to use a logarithmic rather than a linear scale. It provides the distinct advantage of allowing accurate computations using small numerical values, while accommodating a wide range of numerical values.

37.3.1 Sound Power Level

Sound power level describes the acoustical power radiated by a given source with respect to the international reference of 10^{-12} W. The sound power level, L_W , is defined as

$$L_W = 10 \log\left(\frac{W}{W_{re}}\right) \text{ (dB)} \quad (37.7)$$

where W denotes sound power in question and $W_{re} = 10^{-12}$ W (reference).

Example 37.2

Determine the sound power level of a small ventilation fan that generates 10 W of sound power.

Solution

$$L_W = 10 \log\left(\frac{W}{W_{re}}\right) = 10 \log\left(\frac{10}{10^{-12}}\right) = 130 \text{ dB}$$

37.3.2 Sound Pressure Level

Sound pressure levels are expressed in decibels, as are sound power levels. The sound pressure level, L_p , is defined as

$$L_p = 10 \log\left(\frac{\bar{p}^2}{p_{re}^2}\right) = 20 \log\left(\frac{\bar{p}}{p_{re}}\right) \text{ (dB)} \quad (37.8)$$

where \bar{p} denotes root-mean-square (RMS) sound pressure in question Pa or N/m² and $p_{re} = 20 \times 10^{-6}$ Pa = 0.0002 μ bar. The pressure of 20×10^{-6} Pa has been chosen as a reference because it has been found that the average young adult can perceive a 10^3 Hz tone at this pressure. This reference is often referred to as the threshold of hearing at 10^3 Hz.

Example 37.3

Giving $L_p = 50$ dB for the Aeolian tone of 200 Hz, determine the RMS pressure of the tone.

Solution

Given L_p as 50 dB, then \bar{p} is determined by using Equation 37.8.

$$50 = 20 \log\left(\frac{\bar{p}}{p_{re}}\right)$$

then

$$\begin{aligned} \bar{p} &= 10^{50/20} p_{re} = 316.2 p_{re} \\ \bar{p} &= 6.32 \times 10^{-3} \text{ Pa} = 0.0632 \mu\text{bar} \end{aligned}$$

Note that this value is very small, contradicting the magnitude of the sensory impression of the human ear.

37.3.3 Overall Sound Pressure Level

The sound pressure level is defined assuming “pure tone” sound. However, practically any real sound contains various components of pure tone sound. Let us consider a set of n components of pure tone, denoted by

$$\begin{cases} p_1(t) = a_1 \sin(2\pi f_1 t + \phi_1) \\ \vdots \\ p_n(t) = a_n \sin(2\pi f_n t + \phi_n) \end{cases} \quad (37.9)$$

$$p(t) = p_1(t) + \cdots + p_n(t) \quad (37.10)$$

If L_p of $p(t)$ is evaluated in RMS pressure, \bar{p} , we have

$$\bar{p} = \left[\lim_{T \rightarrow \infty} \frac{1}{T} \int_0^T p^2(t) dt \right]^{1/2} = \left[\lim_{T \rightarrow \infty} \frac{1}{T} \int_0^T (p_1(t) + \cdots + p_n(t))^2 dt \right]^{1/2} \quad (37.11)$$

Since

$$\lim_{T \rightarrow \infty} \frac{1}{T} \int_0^T p_i(t) p_j(t) dt = 0, \quad i \neq j$$

is valid, \bar{p} is obtained as

$$\bar{p} = \left[\overline{p_1(t)^2} + \cdots + \overline{p_n(t)^2} \right]^{1/2} = \left[\bar{p}_1^2 + \cdots + \bar{p}_n^2 \right]^{1/2} \quad (37.12)$$

where

$$\bar{p}_i^2 \equiv \overline{p_i(t)^2} \equiv \lim_{T \rightarrow \infty} \frac{1}{T} \int_0^T p_i^2(t) dt = \frac{1}{2} a_i^2 \quad (37.13)$$

Let us define $L_{pi} \equiv 10 \log(\bar{p}_i^2/p_{re}^2)$ ($i = 1, 2, \dots, n$). Then the overall sound pressure level, L_p , of $p(t)$ is expressed by

$$L_p \equiv 20 \log \frac{\bar{p}}{p_{re}} = 10 \log \frac{1}{p_{re}^2} (\bar{p}_1^2 + \cdots + \bar{p}_n^2)$$

or L_p is expressed by L_{pi} ($i = 1, 2, \dots, n$) as follows:

$$L_p = 10 \log(10^{L_{p1}/10} + 10^{L_{p2}/10} + \cdots + 10^{L_{pn}/10}) \quad (37.14)$$

Example 37.4

Determine the overall sound pressure level of the combination of three pure tones, the sound pressure levels of which are expressed by

$$L_{p1} = 60 \text{ dB } (f_1 = 250 \text{ Hz}), \quad L_{p2} = 65 \text{ dB } (f_2 = 500 \text{ Hz}), \quad L_{p3} = 55 \text{ dB } (f_3 = 1000 \text{ Hz})$$

Solution

We have $10^{L_{p1}/10} = 10^6$, $10^{L_{p2}/10} = 10^{6.5}$, and $10^{L_{p3}/10} = 10^{5.5}$. Then the overall level, L_p , is determined by using Equation 37.14 as follows:

$$\begin{aligned} L_p &= 10 \log(10^6 + 10^{0.5} \times 10^6 + 10^{-0.5} \times 10^6) \\ &= 10 \log 10^6 (1 + 10^{0.5} + 10^{-0.5}) = 60 + 10 \log 4.479 = 66.5 \text{ dB} \end{aligned}$$

Note that the sum of 65, 60 and 55 dB is just 66.5 dB.

Hearing and
Psychological Effects

S. Akishita
Ritsumeikan University

38.1 Introduction 38-1
38.2 Structure and Function of the Ear 38-1
38.3 Frequency and Loudness Response 38-2
38.4 Hearing Loss 38-4
38.5 Psychological Effects of Noise 38-4
Loudness Interpretation • Noise-Criteria Curves • Sound Level

Summary

In this chapter, first the characteristics of human hearing are discussed, including a brief description of the anatomy and function of the hearing mechanisms. Next, the frequency and loudness responses of the human hearing are explained, and then hearing loss causing permanent damage is described. Finally, the psychological response to noise is discussed by defining the indices, loudness (sones), noise-criteria curves, and sound level.

38.1 Introduction

This chapter considers the characteristics of human hearing. After a brief description of the anatomy and function of the hearing mechanism, those aspects of hearing that are important in noise control are discussed. The perception of sound by the human ear is a complicated process, dependent both on the frequency and pressure amplitude of the sound. We shall consider the structure of the ear and hearing mechanism. We will also briefly discuss various means of measuring the psychological effects of noise.

38.2 Structure and Function of the Ear [1]

The main components of the human ear are depicted in [Figure 38.1\(a\)](#). The ear is commonly divided into three main components: (1) the outer ear, (2) the middle ear, and (3) the inner ear.

The visible portion of the ear is called the *pinna*. Because of its small size compared with the primary wavelengths that we hear, the pinna serves only to produce a small enhancement of the sounds that arrive from the front of the listener as compared to those which arrive from behind; that is, the human sound reception system has a small frontal directivity. The remainder of the outer ear, which consists of the ear canal terminated in the ear drum, forms a resonant cavity at about 3 kHz. This resonant or near-resonant condition allows for a nearly reflection-free termination of the *ear canal* and thus a good impedance match of the *ear drum* to the air in which the sound wave was propagated.

The middle ear consists of three small *ear bones*, the hammer, anvil, and stirrup. The middle ear serves as an impedance transformer, which matches the low impedance of the air in which sound travels and in

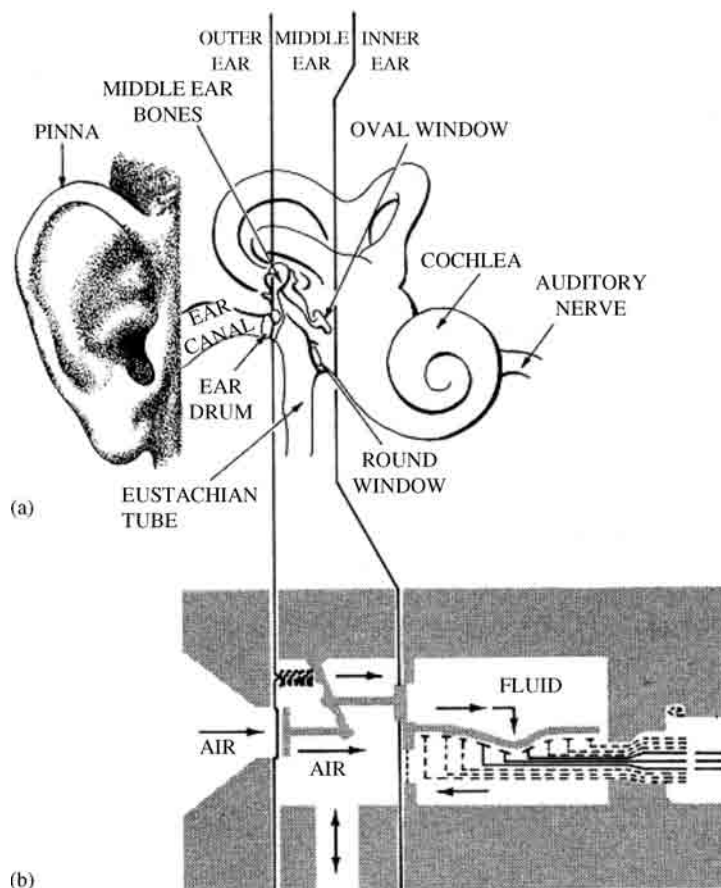


FIGURE 38.1 (a) Main components of the human ear; (b) functional diagram of the ear.

which the ear drum is located to the high impedance of the lymphatic fluid of the *cochlea* beyond the *oval window*. Without this impedance-matching transformation, a mismatch would occur, resulting in a loss of approximately 30 dB.

In the inner ear, the cochlea is the main component where the actual reception of sound takes place. The schematic extended structure of the cochlea is depicted in Figure 38.1(b). The cochlea, which is located in extremely hard temporal bone, is divided almost its entire length by the *basilar membrane*. At the end of the cochlea, the two canals are connected by the *helicotrema*, which allows for the flow of the *lymphatic fluid* between the two sections. The basilar membrane, which is about 3 cm long and 0.02 cm wide, has about 24,000 nerve ends terminated in *hair cells* located on the membrane. The motion of the oval window is transmitted to the basilar membrane and its associated sensing cells. This motion is sensed as sound.

38.3 Frequency and Loudness Response

The threshold of hearing, defined for binaural listening, is that sound pressure in the free field which one can just still hear as the signal is decreased. The threshold of hearing, for what is considered normal hearing, is shown in Figure 38.2. As seen from the curve, human hearing is most sensitive in the range of 2000 to 5000 Hz; furthermore, we note that the response in this range is very close to 0 dB, or 20×10^{-6} Pa. At the other end of the scale, there is the threshold of pain, which is usually taken as about 135 to 140 dB. Thus, there is a dynamic range of normal hearing of approximately 140 dB.

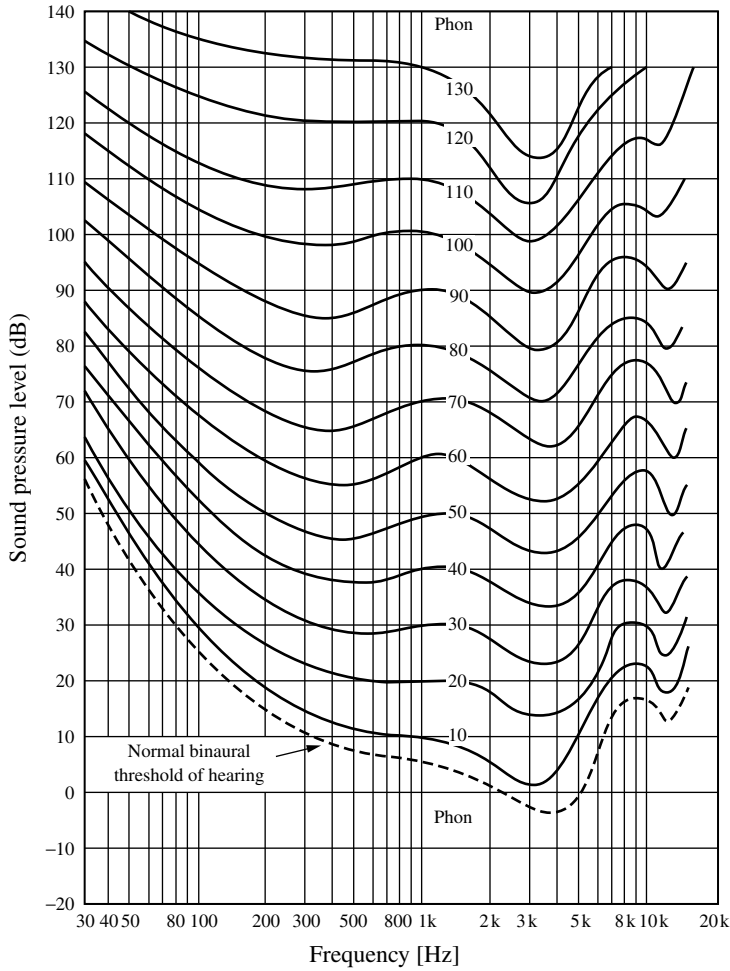


FIGURE 38.2 Equal-loudness contour for free-field binaural listening.

One also readily notes from the curve of Figure 38.2 that the threshold of hearing is a function of frequency. For example, with normal hearing, one would just be able to hear a 2000-Hz tone at a 0-dB level. However, one would require a pressure level of about 15 dB to be able to barely hear a 200-Hz tone. Thus, in describing the subjective loudness of sound, it is necessary to consider the characteristics of the human ear. This concept of loudness is quantized by the loudness level.

The *loudness* level of a particular sound is determined by the subjective comparison of the loudness of the sound to that of a 1000-Hz pure tone. The level, measured in *phons*, is equal numerically to the sound pressure level, in dB, of the 1000-Hz tone, which was regarded to be of equal loudness. A set of internationally standardized equal loudness contours is plotted in Figure 38.2. In keeping with the definition of loudness level, note that at 1000-Hz, all the equal loudness contours are equal in phons to the sound pressure level in dB.

Example 38.1

Determine the sound pressure level of a 100-Hz tone with a loudness level of 30 phon.

Solution

From Figure 38.2, we find the sound pressure level to be 44 dB.

38.4 Hearing Loss

Excessive and prolonged noise exposure causes permanent hearing loss. Various theories have been put forth in an effort to characterize and predict the possible damage that might be caused by a given exposure. Absolute proof of any theory concerning such a complex biological phenomenon is virtually impossible to achieve. However, reliable data have been collected, which deal with situations where workers have been continuously exposed to more or less the same noise environment for many years.

It is well established that excessive noise exposure causes permanent hearing damage by destroying the auditory sensor cells. These cells are hair cells located on the basilar membrane. Furthermore, other types of inner ear damage include harm to the auditory neurons, as well as damage to the structure of the organ of Corti. In all, the various theories and data have been taken advantage of establishing the noise-exposure criteria set forth in the noise exposure regulations.

38.5 Psychological Effects of Noise

In this section, certain generally accepted aspects of the psychological effects of noise will be discussed and quantified. Various indexes have been proposed that quantify the psychological effects of noise. However, only a few of indices, *loudness (sones)*, *noise-criteria (NC) curve*, and *sound level*, are introduced in the following presentation.

38.5.1 Loudness Interpretation

As was discussed relating to Figure 38.2, loudness level is measured in phons, and the related quantity, loudness, is measured in *sones*. A sone is defined as the loudness of a 1000 Hz pure tone with a sound pressure level of 40 dB. On recalling the definition of loudness level, or by referring to Figure 38.2, one notes that 40 phon have a loudness equal to 1 sone. This relationship may be simply expressed as

$$S = 2^{(L_L - 40)/10} \text{ sone} \quad (38.1)$$

where S = loudness (sones), L_L = loudness level (phons), or conversely

$$L_L = 33.2 \log S + 40 \text{ phon} \quad (38.2)$$

Example 38.2

Make the following two conversions using the appropriate equation (Equation 38.1 or Equation 38.2): (1) convert 80 phon to sone, (2) convert 100 sone to phon.

Solution

1. To convert phons to sones, use Equation 38.2:

$$S = 2^{(L_L - 40)/10} = 2^{(80 - 40)/10} = 2^4 = 16 \text{ sone}$$

2. To convert sones to phons, use Equation 38.2:

$$L_L = 33.2 \log S + 40 = 33.2 \log 100 + 40 = 66.4 + 40 = 106.4 \text{ phon}$$

How should we determine the “total loudness” (sones), when the sound is composed of multiple frequency components? Probably the most widely used method for establishing the loudness of a complex noise is that developed by Stevens [2]. The method is based on the measurement of the 1-octave, 1/3-octave, or 1/2-octave band pressure levels. The measured band pressure levels are used

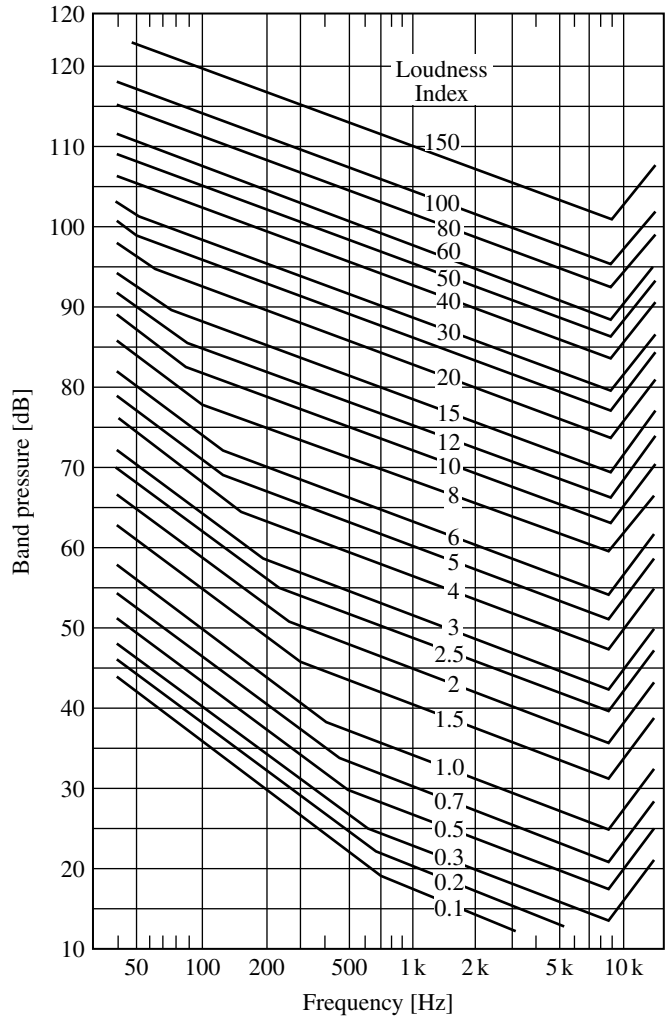


FIGURE 38.3 Equal loudness index contour [2].

in conjunction with the equal loudness index contours shown in Figure 38.3 to determine the loudness or loudness level by means of a simple calculation.

A step-by-step outline of the procedure is as follows:

1. Measure the band pressure levels (1-octave, 1/2-octave, or 1/3-octave) over the frequency range of interest. Usually, the range chosen is from about 50 to 10,000 Hz.
2. Enter the center frequency and band pressure level for each band in the contour of Figure 38.3, and determine the loudness index for each band.
3. Calculate the total loudness, S_t , in sones, by using

$$S_t = I_m(1 - K) + K \sum_{i=1}^n I_i \text{ (sone)} \tag{38.3}$$

where S_t = the total loudness (sones), I_m = the largest of the loudness indices, I_i = the loudness indices, including I_m , K = weighting factor for the bands chosen. $K = 0.3$ for 1-octave bands, $K = 0.2$ for 1/2-octave bands, $K = 0.15$ for 1/3-octave bands.

4. If so desired, one may calculate the loudness level in phons using Equation 38.2, or one may convert to loudness level by means of the conversion curve of [Figure 38.3](#).

Example 38.3

A particular complex noise was measured to yield the one-octave band pressure given in the following table

Center Frequency (Hz)	Band Pressure Level (dB)	Loudness Index (sone)
63	66	2.5
125	63	3.2
250	65	4.8
500	70	7.5
1000	73	10.6
2000	76	15.2
4000	81	25.1
8000	79	29.0

Compute the loudness level using the procedure described before.

Solution

As a first step, the loudness indices are determined from Figure 38.3 and recorded in tabular form with the band pressure levels. Next, we note that one-octave bands have been used. Therefore $K = 0.3$ in Equation 38.3, and

$$S_t = I_m(1 - 0.3) + 0.3 \sum_{i=1}^8 I_i$$

From the table above, we find that $I_m = 29.0$ sone and, summing up, find $\sum I_i = 97.9$ sone. Therefore,

$$S_t = 29(1 - 0.3) + 0.3(97.9) = 49.67 \text{ sone}$$

We find that the loudness, $S_t \cong 50$ sone. The loudness level may now be calculated by means of Equation 38.2 as

$$L_L = 33.2 \log S_t + 40 = 33.2 \log 50 + 40 = 96.4 \text{ phon}$$

Therefore, L_L , the loudness level, is 96 phon.

38.5.2 Noise-Criteria Curves

Noise-criteria curves, which are neglected here, were established in 1957 for rating indoor noise. The curves have been utilized as one method of rating background noise level in a room. Each curve specifies the maximum octave-band sound pressure level for a given NC rating. If the octave band levels for a given noise spectrum are known, the rating of that noise in terms of the NC curves is given by plotting the noise spectrum on the set of NC curves to determine the point of highest penetration.

In 1971, some objections to the NC curves led to their modification. The new curves, which are shown in [Figure 38.4](#), are called the *preferred noise-criteria* (PNC) curves. Although these curves differ from the NC curves, they are used in exactly the same manner.

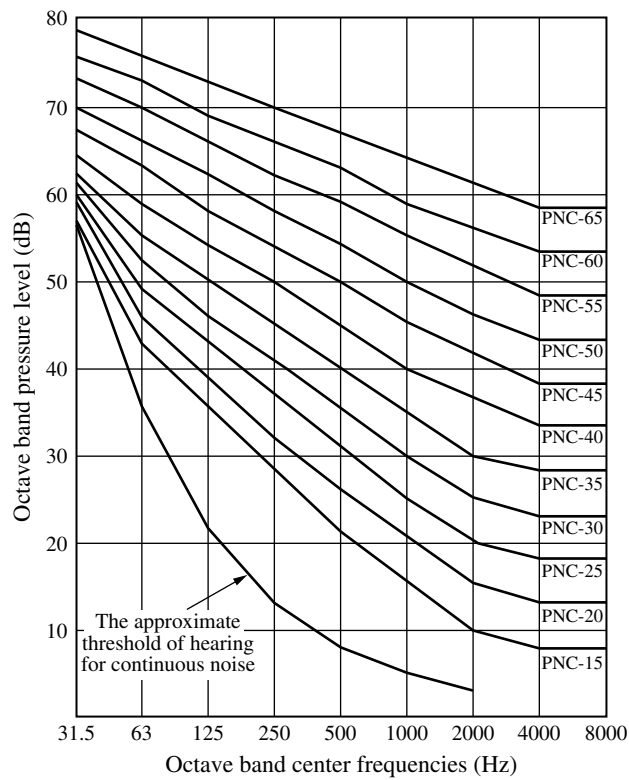


FIGURE 38.4 1971 preferred noise-criteria curves.

Example 38.4

Determine the PNC rating for the octave-band noise spectrum tabulated below.

Center frequency (Hz)	63	125	250	500	1000	2000	4000	8000
Band pressure level (dB)	65	60	60	63	55	50	45	40

Solution

The highest penetration is found at 500 Hz on PNC-60. Hence, the answer is PNC-60.

38.5.3 Sound Level

Sound levels are sound pressure levels that have been weighted according to a particular weighting curve. Three weightings, A, B, and C, and associated sound levels, have been developed as a method to subjectively evaluate the impact of noise upon the human ear, in a proper manner. The frequency response and decibel conversions from a flat response for each of these weightings are given in [Figure 38.5](#) and [Table 38.1](#), respectively.

The A-weighting network is now used almost exclusively in measurements that relate directly to the human response to noise, both from the viewpoint of hearing damage and of annoyance. Such measurements are referred to as *sound level measurements*. Sound level is designated by **L** and the designated unit is the dBA. Similarly, dBB and dBC are used to designate sound level weighted by B weighting and C weighting networks, respectively.

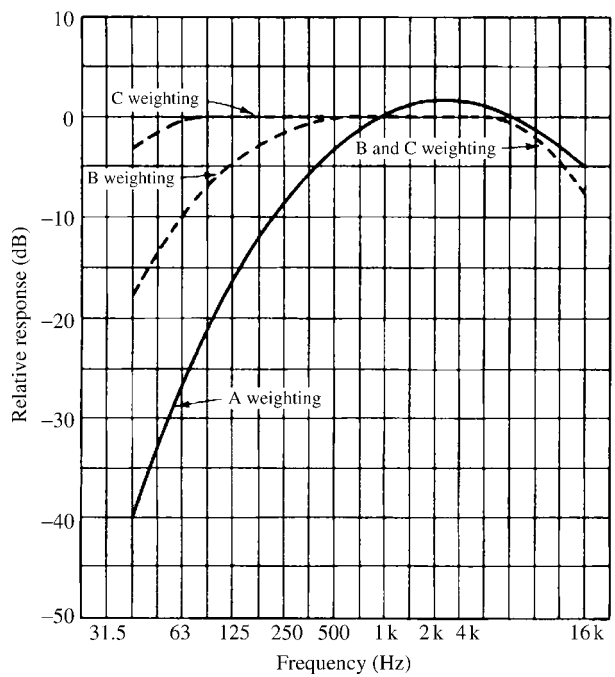


FIGURE 38.5 Frequency response for the A, B, and C weighting networks.

TABLE 38.1 Sound Level Conversion Chart from Flat Response to A Weighting

Frequency (Hz)	A Weighting (dB)
50	-30.2
63	-26.2
80	-22.5
100	-19.1
125	-16.1
160	-13.4
200	-10.9
250	-8.6
315	-6.6
400	-4.8
500	-3.2
630	-1.9
800	-0.8
1,000	0
1,250	+0.6
1,600	+1.0
2,000	+1.2
2,500	+1.3
3,150	+1.2
4,000	+1.0
5,000	+0.5
6,300	-0.1
8,000	-1.1
10,000	-2.5
12,500	-4.3
16,000	-6.6

TABLE 38.2 Octave-Band Sound Pressure Levels

f_c (Hz)	L_{flat} (dB)	ΔL_A (dB)	$L_A = L_{\text{flat}} + \Delta L$ (dB)	I_{iA}
63	74	− 26.2	47.8	0.60×10^5
125	71	− 16.1	54.9	3.09
250	61	− 8.6	52.4	1.74
500	60	− 3.2	56.8	6.31
1000	62	0	62.0	1.585×10^6
2000	60	1.2	61.2	1.318
4000	62	1.0	63.0	1.995
8000	69	− 1.1	67.9	6.166
Sum				12.238×10^6

Note:

- f_c : band center frequency
- L_{flat} : sound pressure level with flat weighting
- ΔL_A : A-weighting level
- I_{iA} : sound pressure intensity with A weighting.

In noise-abatement problems, it is often necessary to convert calculated a 1-octave-band or 1/3-octave-band sound pressure level to a total sound level in dBA. Table 38.1 gives sound level conversion by A weighting from flat response pressure.

Example 38.5

Determine the total A weight sound level, L , of the set of octave-band sound pressure levels given in Table 38.2.

Solution

Refer Table 38.1 for the dB conversion from a flat response level, L_{flat} , for each of the octave bands to a sound pressure intensity with A weighting I_{iA} , and then the sum of I_{iA} . Finally, the total sound level with A weighting $L_{\text{total,A}}$ is given by

$$L_{\text{total,A}} = 10 \log \sum_{i=1}^n I_{iA} = 10 \log 12.238 \times 10^6 = 70.9 \text{ (dB)}$$

References

1. Irwin, J.D. and Graf, E.R. 1979. *Industrial Noise and Vibration Control*, Prentice Hall, Englewood Cliffs, NJ.
2. American National Standard USAS S3.4-1968. 1968. *Procedure for the Computation of Loudness of Noise*, America National Standards Institute, New York, NY.

Noise Control Criteria and Regulations

39.1	Introduction	39-1
39.2	Basic Ideas behind Noise Policy	39-1
39.3	Legislation	39-2
	Action Plans • Publication of Data by the European Commission • Proposal for Further European Union Action	
39.4	Regulation	39-4
39.5	Measures of Noise Evaluation	39-5

S. Akishita

Ritsumeikan University

Summary

In this chapter, the basic ideas behind the development of noise control criteria and regulations are discussed, taking into consideration that the standards and criteria vary from country to country and depend on governments in power. Legislations in the European Union and regulations in Japan are introduced as typical examples. Some indexes as measures of noise evaluation are described.

39.1 Introduction

In order to protect people from being exposed to excessive noise, different communities have implemented different types of legislative control. While the controls vary in scope, control mechanisms, and technical requirements, and are based on different control philosophies, they are intended to achieve a balance between the demand for a tranquil environment and the need for maintaining economic and social activities. In general, the noise standards vary according to the time of day and the use of the land concerned, with the more stringent standards applied to rest periods and areas where the noise sensitivity is high, such as those with schools and hospitals, and exclusive residential areas. Different countries have adopted different noise standards and regulations to meet their local situations and requirements. This chapter cannot describe all major control criteria and regulations in the world, or even in the major industrialized countries. Only the main issues of legislation on noise emission and reception are briefly introduced in the chapter. More details in the on-going noise control issues are found in Refs. [2,3].

39.2 Basic Ideas behind Noise Policy

Every noise policy originates from the idea of protecting the quality of life from noise pollution of all kinds. When establishing a noise policy, it is useful to consider the distinction between noise *emission* and *immission* (or *reception*) [6]. The former means literally emitting or radiating

sound energy or power from a noise source, whereas the latter means receiving, perceiving, or observing radiated noise, which leads to the extent of the noise exposure at a position near the noise source. Therefore, noise emission is controlled with noise regulation law by the government, whereas noise immission is legislated with environmental quality standards. The measure of the extent describing the former is the “sound power level,” and that describing the latter is the sound pressure level.

The global professional organization on noise control, the International Institute of Noise Control Engineering (I-INCE) recently started its activities to develop a global noise policy [5]. In response to the question “is noise policy a global issue, or is it a local issue?” I-INCE had a common theme presented in special session. It was felt that noise is primarily a global policy issue, but many noise problems can only be solved with the active participation of local authorities. The task of the technical study group is to take a global approach to noise in order to define the requirements for an international noise control policy to be effective, stated as follows:

All vehicles, devices, machinery, and equipment that emit audible sound are manufactured products; most are entered into world trade and many are produced in two or more different countries by companies with worldwide operations. The *noise emission* of these products is an appropriate subject of international agreements and regulations. The *noise immisions* resulting from the operation of these products are growing in severity as traffic flow and the pace of industrialization continues to increase in many parts of the globe.

The technical study group reports the classification of noise areas as follows:

1. OCCUPATION NOISE — noise received at the workplace, indoors and outdoors, caused by all noise sources in the vicinity of the workplace.
2. ENVIRONMENTAL NOISE — noise perceived by individuals in the domestic environment, indoors and outdoors, caused by sources controlled by others.
3. CONSUMER PRODUCT NOISE — noise perceived by users and bystanders of noise generating products over which the individual has some control, including noise in the passenger compartment of vehicles, excluding occupational and environmental noise.

39.3 Legislation

The World Health Organization (WHO) published the historic “Guidelines for Community Noise” in 2000, which has been accepted as the most significant recommendations for noise exposure criteria. The bodies that are responsible for enacting the regulations as law include the Federal Government in the USA, the European Union (EU) in Europe, and the Japanese Government in Japan. In the following, the EU’s legislation on noise immission is shown, as an example of the flow of legislation process [8].

On July 18th, 2002, a European Directive on the assessment and management of environmental noise was published in the *Official Journal of European Communities*. It was required to be implemented in the national legislation of the EU Member States no later than July 18th, 2004. From then on, a program was to start, containing periodic noise mapping, the making of action plans, and information of the public. The directive also has strengthened the position of the European Commission regarding the reduction of noise emission.

In 2002, the development of the European Directive on environmental noise resulted in an approved directive relating to the assessment and management of environmental noise, for which the acronym “DAMEN” is used. According to Article 1 of the DAMEN its objective is to “define a common approach to avoid, prevent or reduce harmful effects, including annoyance, due to exposure to environmental noise.” A rough description of actions in the DAMEN is shown in [Figure 39.1](#). Brief notes are given next to supplement Figure 39.1.

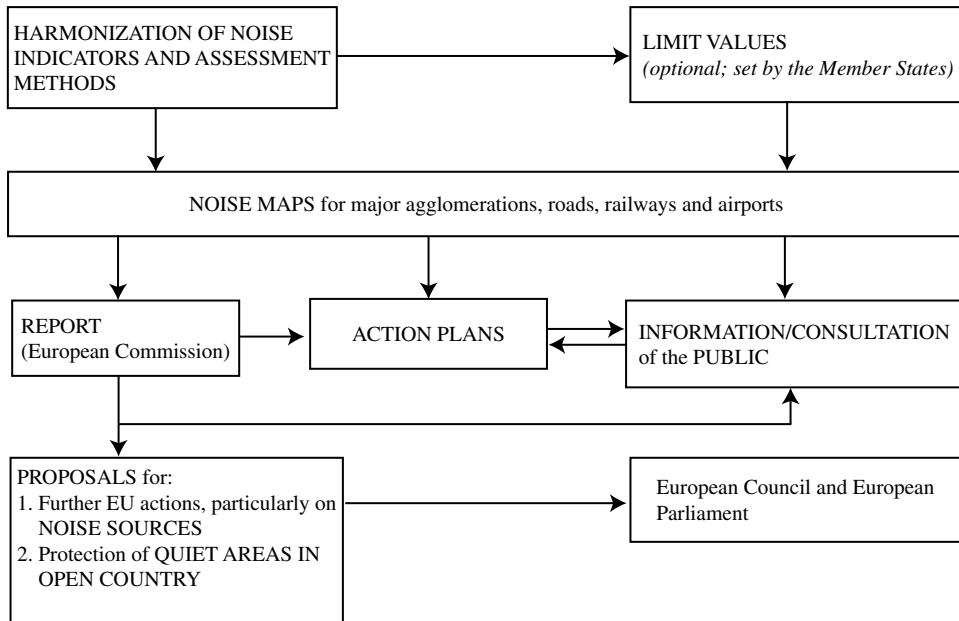


FIGURE 39.1 Overview of the DAMEN. (Source: Wolde, T.T. 2003. The European Union's legislation on noise immission, pp. 4367–4371. In *Proceedings of Inter-noise 2003* (N832). With permission.)

39.3.1 Action Plans

In a case where the mapping results are such that they violate the local or national limit value, or are found unsatisfactory for other reasons, action plans shall be developed for the improvement of the situation. These action plans shall be discussed with the citizens involved. A summary of the action plans shall be sent to the European Commission.

39.3.2 Publication of Data by the European Commission

Every five years, starting in 2009, the Commission shall publish a summary report from the noise maps and the action plans.

39.3.3 Proposal for Further European Union Action

In 2004, the European Commission was to submit a report to the European Parliament and the Council containing a review of existing EU measures relating to sources of environmental noise and present proposals for improvement, if appropriate. In 2009, the European Commission will submit to the European Parliament and the Council a report on the implementation of the directive. That report will in particular assess the need for further EU action and, if appropriate, propose implementing strategies on aspects such as:

- Long-term and medium-term goals for the reduction of the number of persons harmfully affected by environmental noise
- Additional measures on noise emission by specific sources
- The protection of quiet areas on the open country

39.4 Regulation

Noise regulation is executed by local governments once the central government enacts a noise regulation law. The law is considered the “national minimum.” For example, factory noise, construction work noise, and road traffic noise are under the purview of the Noise Control Act, which means the central government is responsible of regulating these kinds of noise. On the other hand, community noise and factory noise are under the purview of the original regulation of local governments. It can be said that local governments are responsible for a great part of the noise policy, although they may not always fully understand the situations concerned. In what follows, an outline of the legal system for environmental noise problem in Japan is given as an example of a typical legal system for noise regulation [6].

In Japan, the “Environmental Quality Standards for Noise” was revised in 1999 after 27 years with the old law. Figure 39.2 outlines of the legal system in Japan.

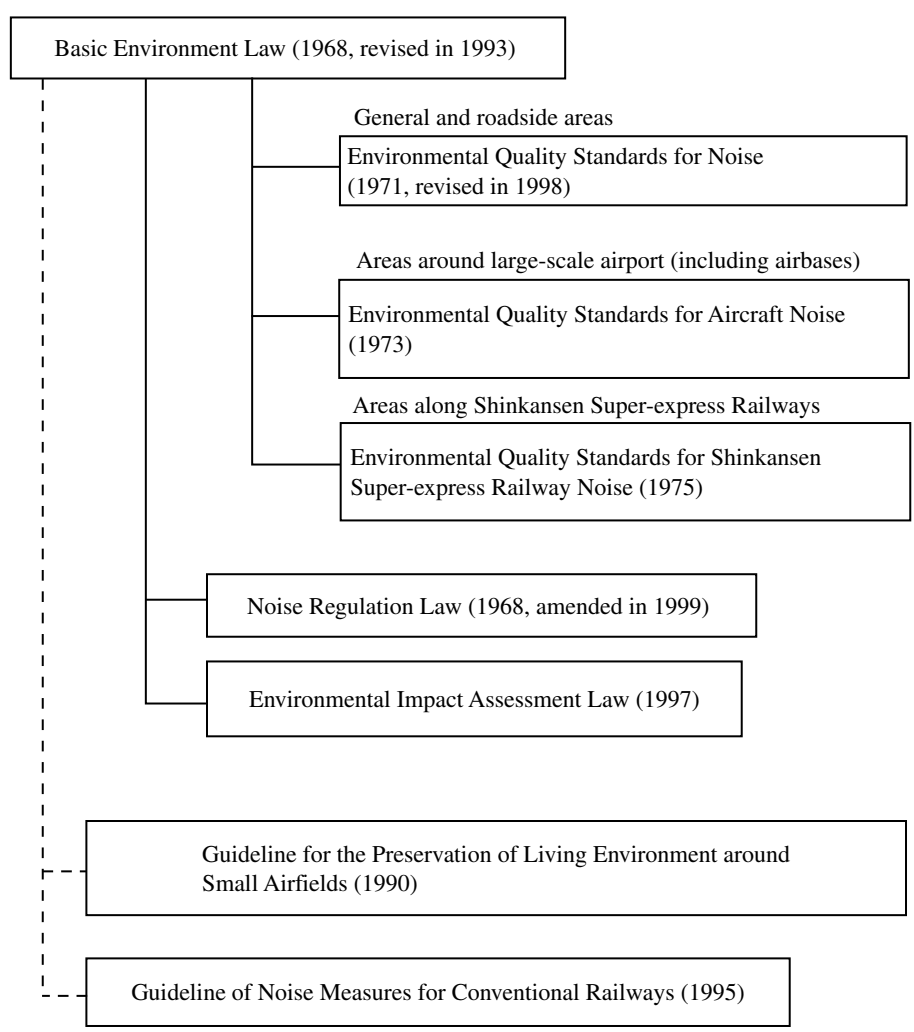


FIGURE 39.2 Legal system for environmental noise in Japan. (Source: Tachibana, H. and Kaku, J. 2003. Acoustic measures for the environmental noise assessment in Japan, pp. 3317–3322. In *Proceedings of Inter-noise 2003* (N1007). With permission.)

Each of these laws and standards is legislated for a specific noise problem (a noise source), and therefore different noise indices are specified according to the respective noise problems. To review this situation from a historical viewpoint, it can be said that each law or standard responds to a specific noise problem promptly, through the use of available measurement technology at that time. However, some laws and standards have become outdated since their establishment, when considering the current situation, international dynamics, and the current acoustic measurement technology.

39.5 Measures of Noise Evaluation

Basically, the A weighting networks are applied to obtain a measure of noise evaluation. As the measures are legislated by governments, they are dependent on the legislative regulations and standards. In what follows, the measure of noise evaluation legislated in Japan is given to show the concepts behind the legislation [6].

In the regulations and standards for environmental noise problems, a variety of noise measures are used. In order to improve these legislative regulations and standards in the future, the present measures shall be reviewed considering the difference between noise emission and immission and the difference between noise measurement and monitoring, and impact assessment and prediction. These measures legislated in Japan are listed and classified in Table 39.1 by considering the difference between noise characteristics.

TABLE 39.1 Assessment Methods Specified in Laws and Standards for Environmental Noises in Japan

Noise Sources	Law and Standards	Noise Indices	Assessment Time
Roads	Environmental Quality Standards for Noise	$L_{Aeq,T}^a$	Daytime (6:00–22:00); nighttime (22:00–6:00)
Shinkansen superexpress railways	Environmental Quality Standards for Shinkansen Superexpress Railways	$L_{A,Smax}^b$	Every event
Conventional railways	Guideline of Noise Measures for Conventional Railways	$L_{Aeq,T}$	Daytime (7:00–22:00); nighttime (22:00–7:00)
Aircrafts	Environmental Quality Standards for Aircrafts Noise	WECPNL ^c	Time weighting
	Guideline for the Preservation of Living Environment around Small Airfields	L_{den}^d	
Construction works	Noise Regulation Law (specific noise sources)	According to time variation:	Not specified; every event
Factories			
Large-scale retail stores	Law concerning the measures by large scale retail stores for preservation of living environment	L_A^e ; $L_{A,Fmax}^f$; L_{A5}^g ; $L_{A,Fmax,5}^h$	

^a $L_{Aeq,T}$ equivalent continuous A-weighted sound pressure level.

^b $L_{A,Smax}$ SLOW maximum value of A-weighted sound pressure level.

^c WECPNL, weighted equivalent continuous perceived noise level(calculated from $L_{A,Smax}$).

^d L_{den} , day/evening/night equivalent continuous A-weighted sound pressure level.

^e L_A , FAST maximum value of A-weighted sound pressure level.

^f $L_{A,Fmax}$, A-weighted sound pressure level.

^g L_{A5} , upper value of the 90% range of A-weighted sound pressure level.

^h $L_{A,Fmax,5}$, upper value of the 90% range of the FAST maximum Aweighted sound pressure level.

Source: Tachibana, H. and Kaku, J. 2003. Acoustic measures for the environmental noise assessment in Japan, pp. 3317–3322. In *Proceedings of Inter-noise 2003* (N1007). With permission.

When considering the consistency between noise measurement and monitoring, and noise prediction for impact assessment, it is most reasonable to use energy based indices such as L_{Aeq} . Of course, L_{Aeq} is not a panacea and some secondary adjustment may be needed for the exact assessment of environmental noise with different characteristics. Nevertheless, the possibility of unification by L_{Aeq} should be considered in the near future in Japan. Although L_{Aeq} is now being widely used for the assessment of aircraft noise in almost all countries, WECPNL is still being used in Japan. WECPNL is very close to L_{Aeq} in concept and it is not difficult to change the assessment index from WECPNL to L_{Aeq} .

The aim of the laws and standards shown in Figure 39.2 is to measure and assess the environmental noise for prevention or maintenance of the present situation. Therefore, any noise index should be appropriately used for each of noise problems, as shown in Table 39.1, which presents assessment methods specified in laws and standards for environmental noise in Japan. In particular, when predicting the future noise situation in environmental impact assessments, the indices should be suitable for theoretical calculation. The statistical noise indices such as the percentile level (L_{A5}) and maximum level ($L_{A,Fmax}$ or $L_{A,Smax}$) specified in the laws and standards have to be predicted statistically. It is difficult to predict these quantities by a simple physical calculation model, in principle. In this respect, the energy-based noise indices such as L_{Aeq} can be easily treated in energy based calculation, and the prediction model becomes simple and clear in physical meaning. In an environmental impact assessment, the predicted results are to be compared with the related laws or standards. In the case of road traffic noise, L_{Aeq} has been adopted in the new environmental quality standards, and therefore prediction has become very simple in theory, founded on energy-based indices.


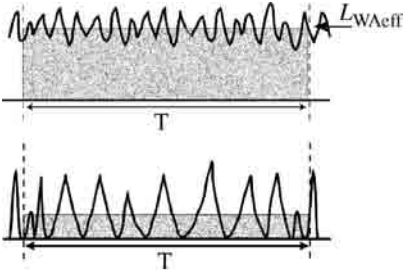
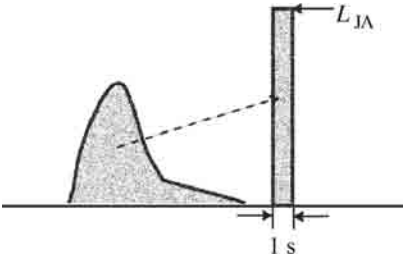
In the prediction of road traffic noise, a motor vehicle as the noise source can be treated as a stationary sound sources of a constant sound power for a limited path. On the other hand, in the case of predicting construction noise, there are many complicated problems because various kinds of machines and equipment with various temporal variations of characteristics must be treated. Therefore, in the construction noise prediction method given in the "Acoustic Society of Japan CN-model 2002" [7], various noise indices for describing the acoustic output of various types of noise sources are specified as given in Table 39.2, which presents classification of noise sources and indices for expressing their acoustic output. Finally, Table 39.3 presents definitions and indices of measurement for acoustical output of noise sources.

TABLE 39.2 Classification of Noise Sources and Indices for Expressing Their Acoustic Output

Temporal Variation	Indices for Expressing Acoustic Output Sign	Terms
Stationary	L_{WA} $L_A(r_0)$	A-weighted sound power level A-weighted sound power level at the reference distance ($r_0 = 1$ m)
Fluctuating randomly and widely	L_{WAeff} $L_{Aeff}(r_0)$ $L_{A,Fmax,5}(r_0)$	Effective A-weighted sound power level Effective A-weighted sound pressure level at the reference distance ($r_0 = 1$ m) 5% value of A-weighted sound pressure level at the reference distance ($r_0 = 1$ m)
Intermittent impulsive	L_{IA} L_{WAeff} $L_{AE}(r_0)$ $L_{A,Fmax}(r_0)$	A-weighted sound energy level Effective A-weighted sound power level Single event sound exposure level at the reference distance ($r_0 = 1$ m) FAST max. of A-weighted sound pressure level at the reference distance ($r_0 = 1$ m)

Source: Tachibana, H. and Kaku, J. 2003. Acoustic measures for the environmental noise assessment in Japan, pp. 3317–3322. In *Proceedings of Inter-noise 2003* (N1007). With permission.

TABLE 39.3 Definitions and Measurements of Indices for Acoustical Output of Noise Sources

Indices	Definition	Measurement Method
L_{WA}	$L_{WA} = 10 \log \frac{P_A}{P_0} \quad (1)$ <p>Here, $P_0 = 1 \text{ pW}$</p> 	$L_{WA} = L_A(r) + 20 \log \frac{r}{r_0} + 8 \quad (2)$ <p>Here, $L_A(r)$ is the A-weighted sound pressure level measured at a distance of r, $r_0 = 1 \text{ m}$</p>
L_{WAeff}	<p>Effective A-weighted sound power level applied to fluctuating, intermittent and impulsive sounds</p> 	$L_{WAeff} = L_{Aeff}(r) + 20 \log \frac{r}{r_0} + 8 \quad (3)$ <p>Here, L_{Aeff} is the A-weighted sound pressure level measured at a distance of r</p> $L_{Aeff} = 10 \log \left[\frac{1}{T} \int_1^2 \frac{p_A^2(t)}{p_0^2} dt \right] \quad (4)$ <p>Here, $T(t_1 - t_2)$ is averaging time (sec), $p_0 = 20 \text{ μPa}$</p>
L_{JA}	$L_{JA} = 10 \log \frac{E_A}{E_0} \quad (5)$ <p>Here, $E_0 = 1 \text{ pJ}$</p> 	$L_{JA} = L_{AE}(r) + 20 \log \frac{r}{r_0} + 8 \quad (6)$ <p>Here, L_{AE} is the single event sound exposure level measured at a distance of r</p> $L_{AE} = 10 \log \left[\frac{1}{T} \int_1^2 \frac{p_A^2(t)}{p_0^2} dt \right] \quad (7)$ <p>Here, $T_0 = 1 \text{ sec}$, $t_1 - t_2$ is the time including the event (sec)</p>
$L_A(r_0)$ $L_{A,Fmax}(r_0)$	<p>A-weighted sound pressure level converted to the value at the reference distance (r_0) = 1 m</p>	$L_A(r_0) = L_A(r) + 20 \log \frac{r}{r_0} + 8 \quad (8)$ <p>Here, $L_A(r)$ is the A-weighted sound pressure level measured at a distance of r</p>

Source: Tachibana, H. and Kaku, J. 2003. Acoustic measures for the environmental noise assessment in Japan, pp. 3317–3322. In *Proceedings of Inter-noise 2003* (N1007). With permission.

References

1. Fahy, F. 1985. *Sound and Structural Vibration, Radiation, Transmission and Response*, Academic Press, New York, chap. 2.
2. Fields, J.M. and de Jong, R.G., Standardized general-purpose noise reaction questions for community noise survey: research and a recommendation, *J. Sound Vib.*, 242, 641–679, 2001.
3. Harris, C.M., Ed. 1979. *Handbook of Noise Control*, 2nd ed., McGraw-Hill, New York, chap. 37.
4. Irwin, J.D. and Graf, E.R. 1979. *Industrial Noise and Vibration Control*, Prentice Hall, New York, chap. 5.
5. Lang, W.W. and Wolde, T.T. 2003. Progress report for TSG#5 ‘Global Noise Policy’, pp. 98–101. In *Proceedings of Inter-noise 2003* (N872).

6. Tachibana, H. and Kaku, J. 2003. Acoustic measures for the environmental noise assessment in Japan, pp. 3317–3322. In *Proceedings of Inter-noise 2003* (N1007).
7. Tachibana, H. and Yamamoto, K. 2003. *Construction Noise Prediction Model*, ASJ CN-Model 2002, proposed by the Acoustical Society of Japan, EURONOISE, in Naples (2003.5).
8. Wolde, T.T. 2003. The European Union's legislation on noise immission, pp. 4367–4371. In *Proceedings of Inter-noise 2003* (N832).

40.1	Sound Intensity Measurement	40-1
	Theoretical Background • Measurement Method • Errors in Measurement of Sound Intensity • Applications	
40.2	Mirror–Microphone System	40-4
	Principle of Measurement • Applications	
40.3	Microphone Array	40-6
	Principle of Microphone Array • Array’s Directivity Pattern • Applications	

Kiyoshi Nagakura

Railway Technical Research Institute

Summary

This chapter describes some measuring methods for the identification and ranking of noise source that are of benefit in noise control projects. Sound intensity measurement and directional measuring devices such as the mirror–microphone system and microphone array are introduced and their principles and applications are described.

40.1 Sound Intensity Measurement

Every noise control project starts with the identification and ranking of the noise sources. Several methods have been proposed for the purpose and have proved to be useful and widely utilized. In this chapter, sound intensity measurement and directional measuring devices such as the mirror–microphone system and microphone array are introduced and their principles and applications are described. Other useful measurements, such as acoustic holography method [1,2] and spatial transformation of sound fields [3], are described in the literature.

40.1.1 Theoretical Background

Sound intensity is a measure of the magnitude and direction of the flow of sound energy. The instantaneous intensity vector, $\mathbf{I}(t)$, is given by the product of the instantaneous sound pressure, $p(t)$, and the corresponding particle velocity, $\mathbf{u}(t)$, that is, $\mathbf{I}(t) = p(t)\mathbf{u}(t)$.

In practice, the time-averaged intensity, $\bar{\mathbf{I}}$, is more important, and is given by the equation:

$$\bar{\mathbf{I}} = \lim_{T \rightarrow \infty} \frac{1}{T} \int_{-T/2}^{T/2} p(t)\mathbf{u}(t)dt \quad (40.1)$$

The intensity vector denotes the net rate of flow of energy per unit area (watts/m²). Thus, the acoustic power, W , of the source located in a closed surface, S , is given by the integral of the intensity passing through the surface, S , as

$$W = \int_S \bar{\mathbf{I}} \cdot d\mathbf{S} \quad (40.2)$$

Equation 40.2 indicates that the measurement of sound intensity over a surface enclosing a source enables the estimation of its sound power, which shows the usefulness of the sound intensity concept.

40.1.2 Measurement Method

The principle of intensity measurement systems in commercial production employs two closely spaced pressure microphones [4,5], as shown in Figure 40.1.

The particle velocity, $u_r(t)$, in a particular direction, r , can be approximated by integrating over time the difference of sound pressures at two points separated by a distance Δr in that direction:

$$u_r(t) = -\frac{1}{\rho_0} \int_{-\infty}^t \frac{p_2(\tau) - p_1(\tau)}{\Delta r} d\tau \quad (40.3)$$

where p_1 and p_2 are the sound pressure signals from the two microphones. The sound pressure at the center of two microphones is approximated by

$$p(t) = \frac{p_1(t) + p_2(t)}{2} \quad (40.4)$$

Thus, the intensity in the direction r can be calculated as

$$I_r(t) = -\frac{1}{2\rho_0\Delta r} [p_1(t) + p_2(t)] \int_{-\infty}^t [p_2(\tau) - p_1(\tau)] d\tau \quad (40.5)$$

Some commercial intensity analyzers use Equation 40.5 to measure the intensity. Another type of analyzer uses the equation in the frequency domain:

$$I_r(\omega) = -\frac{\text{Im}[G_{12}]}{\omega\rho_0\Delta r} \quad (40.6)$$

where G_{12} is the cross spectrum between the two microphone signals. Equation 40.6 makes it possible to calculate sound intensity with a dual-channel fast fourier transform (FFT) analyzer.

40.1.3 Errors in Measurement of Sound Intensity

The principal systematic error of the two-microphone method is due to the approximation of the pressure gradient by a finite pressure difference. When the incident sound is a plane wave, the ratio of the measured intensity, \hat{I}_r , and the true intensity, I_r , is given by

$$\hat{I}_r/I_r = \frac{\sin(k\Delta r \cos \theta)}{k\Delta r \cos \theta} \quad (40.7)$$

where the angle θ is as defined in Figure 40.1 and k is the wave number. Equation 40.7 indicates that the upper frequency limit is inversely proportional to the distance between the microphones.

Another serious error is caused by the phase mismatch between the two measurement channels. In the calculation of intensity from Equation 40.5, the phase difference, φ , between the two microphone signals, p_1 and p_2 , is very important. Hence, the phase mismatch between the two measurement channels, $\Delta\varphi$, must be much smaller than φ . Since φ increases with frequency, this error is serious in lower frequencies. Other possible errors, such as in the sensitivity of microphones and random errors associated with a given finite averaging time, are usually less serious.

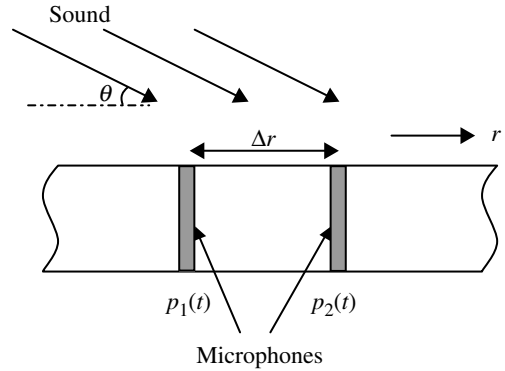


FIGURE 40.1 Microphone arrangement used to measure sound intensity.

40.1.4 Applications

One important application of sound intensity measurement is the determination of the sound power level using Equation 40.2. Furthermore, measurement of the intensity in the very near field of a source surface makes it possible to identify and rank the noise-sources. Plots of the sound intensity measured on a surface near a sound source are useful for investigating noise source distributions. Figure 40.2 shows sound intensity of noise from a wheel of a railway car. An intensity probe is located in the vicinity of the wheel and the normal component of sound intensity is measured by traversing the probe on a plane 100 mm away from the side surface of the wheel. These figures show a free vibration behavior of the wheel at each frequency; the wheel vibrates with one nodal diameter at 700 Hz and with three nodal diameters at 1150 Hz. Visualization by intensity vectors also gives valuable information about a noise source. Figure 40.3 shows the sound intensity vectors at each octave band measured in the vicinity of a railway car running at 120 km/h. These results suggest that the main radiator of rolling noise is the rail at the 500 Hz to 1 kHz band and the wheels at the 2 to 4 kHz band.

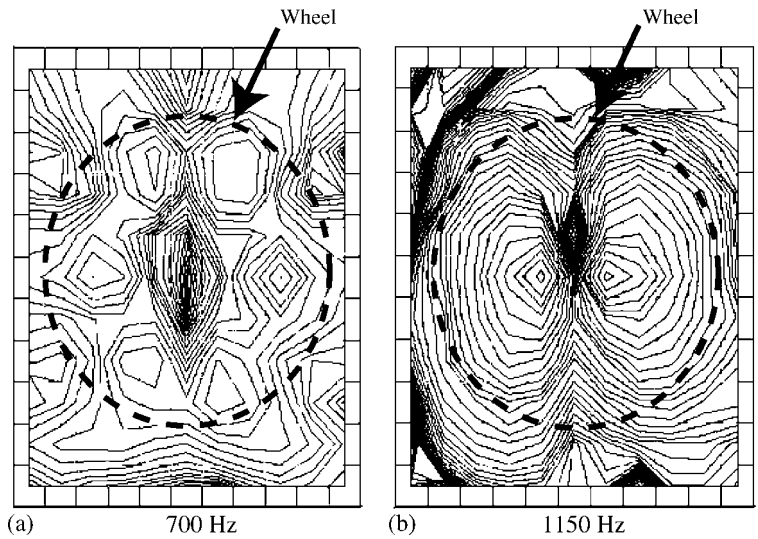


FIGURE 40.2 Measurements of the sound intensity radiated by a wheel of a railway car (1 dB contour).

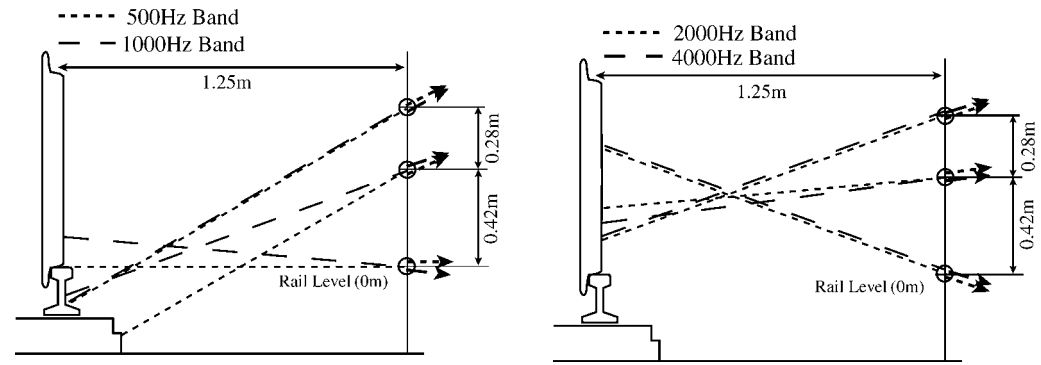


FIGURE 40.3 Sound intensity vectors measured in the vicinity of a railway car running at 120 km/h.

40.2 Mirror–Microphone System

40.2.1 Principle of Measurement

A mirror–microphone system consists of a reflector of elliptic or parabolic shape and an omnidirectional microphone located at its focus [6,7]. Figure 40.4 shows the layout of a reflector of elliptic shape, an omnidirectional microphone, and a noise source. Here, S and S' denote the front and back surfaces of the mirror, respectively; $P(\mathbf{r})$ denotes the pressure field on this configuration; $P_i(\mathbf{r})$ denotes the pressure field of free space; \mathbf{r}_m is the position of the microphone; \mathbf{r} is a point on the mirror surface. The normal, \mathbf{n}_0 , directs toward the medium.

Using Green's theorem, the pressure at the microphone position $P(\mathbf{r}_m)$ is obtained by

$$P(\mathbf{r}_m) = P_i(\mathbf{r}_m) + \iint_{(s+s')} P(\mathbf{r}) \frac{\partial}{\partial \mathbf{n}_0} \times \left[\frac{e^{ikR_m}}{4\pi R_m} \right] d^2\mathbf{r} \quad (40.8)$$

where $k = 2\pi f/c_0$ is the wave number, f is the frequency of sound, c_0 is the speed of sound, and $R_m = |\mathbf{r} - \mathbf{r}_m|$ is the distance between the microphone and the mirror surface. If the wavelength is sufficiently smaller than the diameter of the reflector, the pressure field $P(\mathbf{r})$ is approximated by $2P_i(\mathbf{r})$ on the front surface, S , and by zero on the back surface, S' . In such a frequency range, the incident field term $P_i(\mathbf{r}_m)$ can be ignored. With these approximations, assuming that the noise source is a monopole type point source located at a position, \mathbf{r}_s , Equation 40.8 reduces to

$$P(\mathbf{r}_m) = -\frac{m(f)}{8\pi^2} \iint_s \frac{e^{ik(R_m+R_s)}}{R_m R_s} \left(ik - \frac{1}{R_m} \right) \times \cos \theta(\mathbf{r}) d^2\mathbf{r} \quad (40.9)$$

Here, $m(f)$ is the amplitude of the mass-flux rate of the source, $R_s = |\mathbf{r} - \mathbf{r}_s|$ is the distance between the sound source and the mirror surface and the angle $\theta(\mathbf{r})$ is defined in Figure 40.4. When the noise source is located at the far focus of the mirror, the sound pass length $R_m + R_s$ is constant with respect to \mathbf{r} , and a strong signal is obtained. As the noise source is moved away in the direction perpendicular to the mirror axis, the variance of the sound pass length, $R_m + R_s$, due to the position \mathbf{r} increases, and thus the microphone signal drops off due to interference (see Figure 40.5, which we call the “directivity pattern”). The ratio of the peak level to the free field level at the microphone, G , is referred to as the “gain factor.” The spatial resolution of the mirror is characterized by the displacement of the mirror position, w , at which the microphone signal drops off by a given relative amount, such as 3 dB. The quantities G and w

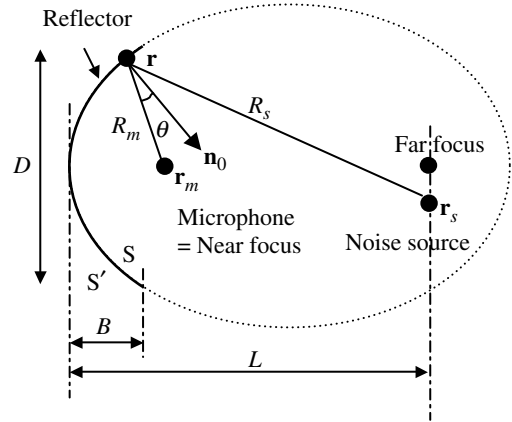


FIGURE 40.4 Layout of a reflector, microphone, and noise source.

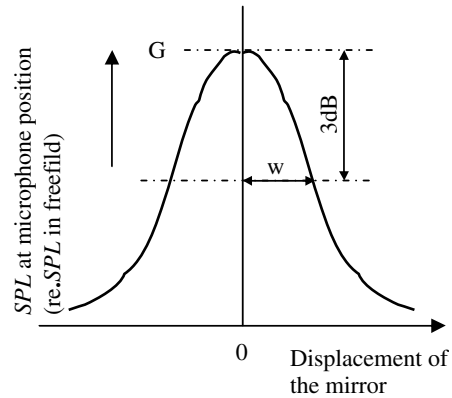


FIGURE 40.5 Directivity pattern of a mirror–microphone system.

can be related to the mirror geometries in Figure 40.4 by

$$G \approx 10 \log(CD^4/\lambda^2 B^2) \quad (C = \text{const.}) \quad (40.10)$$

$$w \propto \lambda L/D \quad (40.11)$$

The gain factor, G , increases with frequency at the rate of 6 dB per octave, and the spatial resolution, w , is inversely proportional to the frequency. The lower frequency limit is decided by the size of the mirror. On the other hand, there is no higher frequency limit, except for the capacity of an omnidirectional microphone itself. Thus, measurements with the mirror–microphone system are more suited to a scaled model test.

40.2.2 Applications

The mirror–microphone system has proved useful for identification of a noise source because of its directional property [8–10]. A scan of the source region produces a noise source map. It has an advantage in that the measurement is possible at a far field and it needs only one sensor, but has a disadvantage in that the measuring process is a time-consuming task.

Figure 40.6 shows an example of source maps of aerodynamic noise generated by a one-fifth scale high-speed train model, obtained from measurements by a mirror–microphone system, in a wind tunnel test. The surface of the car model is divided into several noise-source areas and the noise-source distribution in each area is measured by traversing the mirror–microphone system over the surface. The diameter and focal distance of the reflector are 1.7 and 3 m, respectively. Detailed maps of noise-source strength are obtained, which show that aerodynamic noise from high-speed trains is generated in relatively localized areas, namely, the local surface structures. The mirror–microphone system can be used for the measurement of the source distribution of a moving noise source. Figure 40.7 gives a time

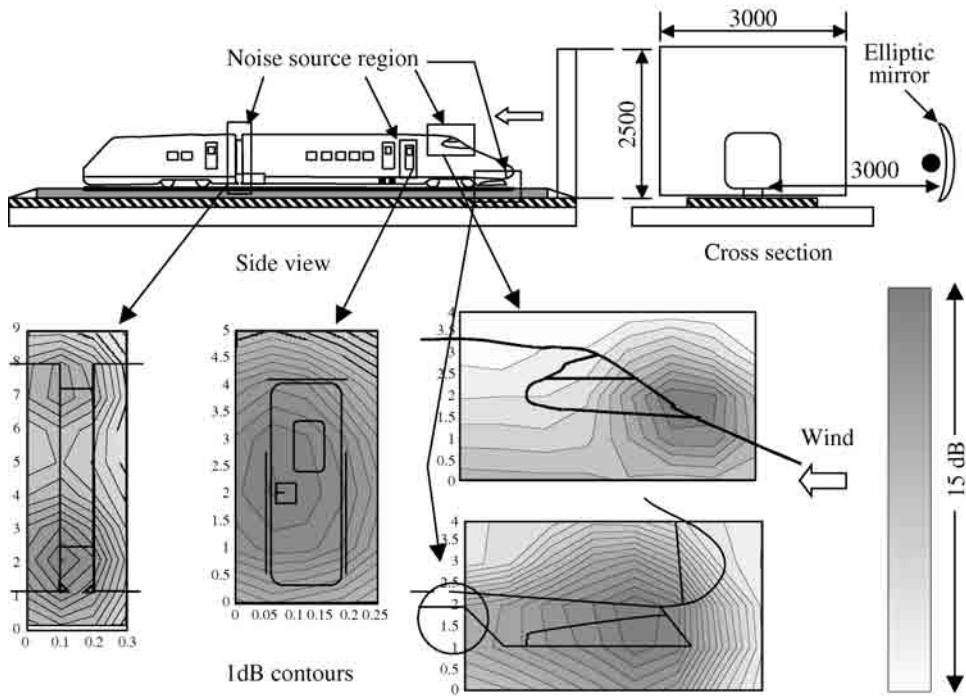


FIGURE 40.6 Noise-source distribution of a one-fifth scale Shinkansen car model in a wind tunnel test measured with an elliptic mirror–microphone system.

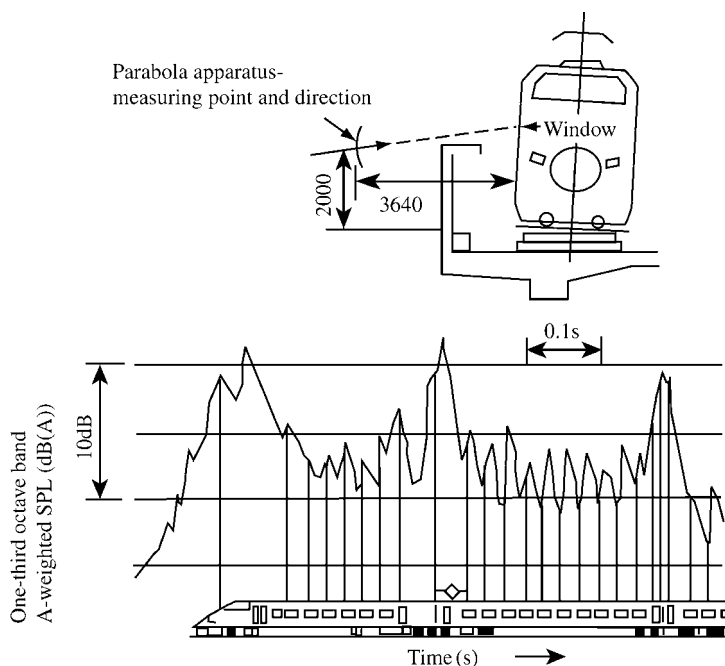


FIGURE 40.7 Time history of the A-weighted one-third octave band ($f_0 = 8$ kHz) sound pressure level measured with a parabolic mirror–microphone system ($D = 1$ m, train speed = 274 km/h).

history of noise from a high-speed train measured with a parabolic mirror–microphone system, the diameter of which is 1 m. Peaks of the time history correspond to pantographs, doors, gaps between cars and the step-up of windows, which shows that they are main noise sources.

40.3 Microphone Array

40.3.1 Principle of Microphone Array

A microphone array [11] consists of several microphones distributed spatially to measure an acoustic field. The time signals from each microphone are added, accounting for the time delay between sound sources and microphones, and a directional output signal can be obtained as a result. The algorithm is called “beamforming.” Now, consider M omnidirectional microphones distributed in a far field of noise sources. The output signal of the array focused to a particular location in the source region, \mathbf{r} , and $z(\mathbf{r}, t)$, is calculated as a sum of delayed and weighted signals of each microphone:

$$z(\mathbf{r}, t) = \sum_{m=1}^M w_m p_m(t - \Delta_m) \quad (40.12)$$

Here, $p_m(t)$ is the signal from the m th microphone, w_m is a weighting factor, and Δ_m is a time delay applied to signal of the m th microphone, as given by

$$\Delta_m = \frac{r_o - r_m}{c_0} \quad (40.13)$$

where r_o and r_m are the distances from the focus point to the reference point o and the m th microphone, respectively. When the focus location coincides with the source location, a strong signal is obtained (see Figure 40.8). If this process is repeated for various focus locations, \mathbf{r} , on the source surface, then a noise-source map can be obtained.

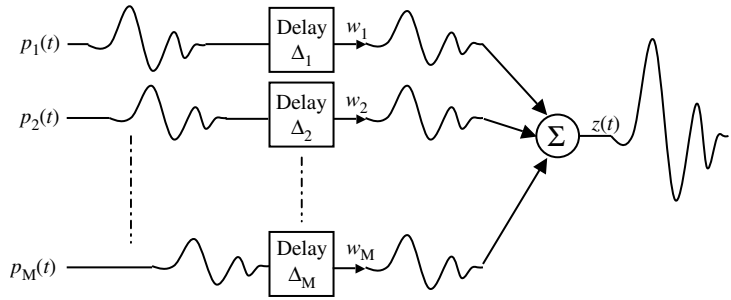


FIGURE 40.8 Principle of a microphone array. Individual time delays are chosen such that signals arriving from a given point will be added up coherently.

40.3.2 Array's Directivity Pattern

The performance of a microphone array is characterized by the spatial resolution and signal-to-noise ratio. For simplicity, consider a linear array of $M = 2N + 1$ microphones spaced equally by d . When a harmonic plane wave is propagating with an incident angle θ , and weighting factors all equal $1/M$, the ratio of the output signal of the array to that of the center microphone is computed using

$$W(\theta) = \frac{1}{M} \frac{\sin((M/2)kd \sin \theta)}{\sin((1/2)kd \sin \theta)} \quad (40.14)$$

where k is the wave number. Figure 40.9 shows the directivity patterns for different values of the product kd based on Equation 40.14. The highest peak appears at $\theta = 0$, which we call a "main lobe," and lower peaks also appear at some locations that are separate from a true source direction, which we call "side lobes." The width of the main lobe decides the performance of the array to separate two closely lying sources (which we call spatial resolution), and the ratio of main lobe to side lobe decides the signal-to-noise ratio of the array. The spatial resolution improves as kd increases, that is, in proportion to the ratio of the array length to the wavelength. However, when $kd = 2\pi$, a peak of the same strength as the true source appears due to a spatial aliasing at $\theta = 90^\circ$, which occurs when $d > \lambda/2$, where λ is the wavelength. Thus, the acoustic frequency, f , is restricted by $f < c_0/2d$, to avoid aliasing.

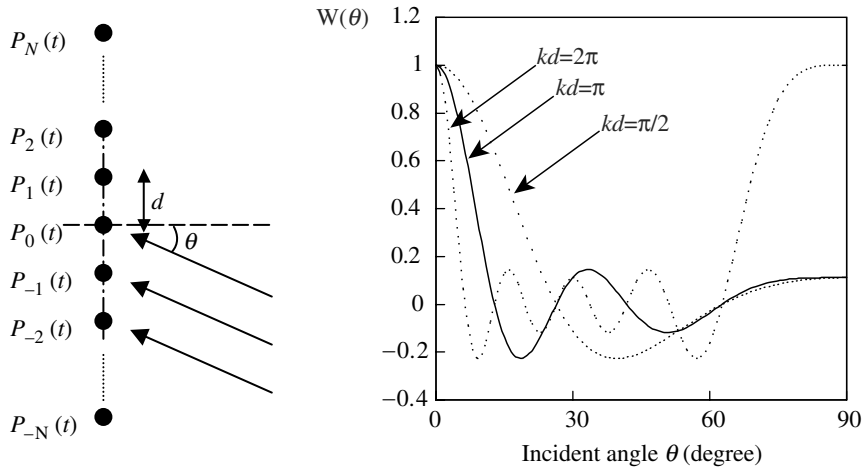


FIGURE 40.9 Directivity patterns of a linear array for different values of the product kd ($M = 2N + 1 = 9$).

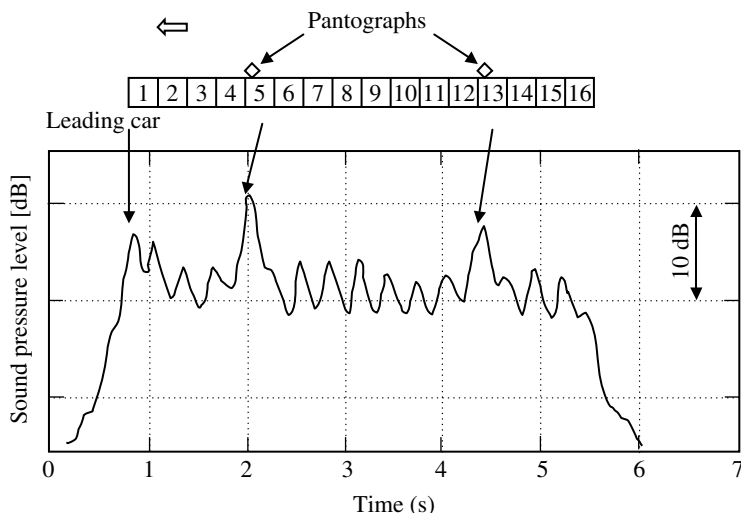


FIGURE 40.10 Time history of sound pressure level for a passing train measured with a linear microphone array located at a point 25 m away from a track (train velocity = 285 km/h).

In the above case of the linear array, the directivity exists only in the direction of the array (one-dimensional). If microphones are arranged in a two-dimensional plane, a two-dimensional directivity can be obtained. Recently, many microphone arrangements have been proposed that obtain better spatial resolution and to reduce side lobes [12–15].

40.3.3 Applications

Microphone arrays have been used for identification of the noise source in various situations, for example, in wind tunnel tests. Many actual examples can be found in published literature [10,16–18]. The measurement with a microphone array has the advantage of much shorter measuring time than that of a mirror–microphone system. Furthermore, the lower frequency limit is not so serious because the size of the apparatus can be easily extended.

Another fundamental example is given now. Nine microphones are arranged equally spaced by $d = \lambda/2$ for each one-third octave band, and their signals are summed without time delay. In this case, the array is focused to a fixed direction, perpendicular to the array axis. Figure 40.10 shows a time history of noise generated by a high-speed train, measured with a linear microphone array located at a point 25 m away from the track. It is found that pantographs, the leading car, and gaps between cars are the main noise sources in this example.

References

1. Ferris, H.G., Computation of far field radiation patterns by use of a general integral solution to the time independent scalar wave equation, *J. Acoust. Soc. Am.*, 41, 1967.
2. Maynard, J.D., Nearfield acoustic holography: theory of generalized holography and the development of NAH, *J. Acoust. Soc. Am.*, 78, 1985.
3. Ginn, K. and Hald, J., The effect of bandwidth on spatial transformation of sound field measurements, *Inter-Noise*, 87, 1987.
4. Fahy, F.J., Measurement of acoustic intensity using the cross-spectral density of two microphone signals, *J. Acoust. Soc. Am.*, 62, 1977.

5. Chung, J.Y., Cross-spectral method of measuring acoustic intensity without error caused by instrument phase mismatch, *J. Acoust. Soc. Am.*, 64, 1978.
6. Grosche, F.R., Stiewitt, H., and Binder, B., On aero-acoustic measurements in wind tunnels by means of a highly directional microphone system, *Paper AIAA-76-535*, 1976.
7. Sen, R., Interpretation of acoustic source maps made with an elliptic-mirror directional microphone system, *Paper AIAA-96-1712*, 1996.
8. Blackner, A.M. and Davis, C.M., Airframe noise source identification using elliptical mirror measurement techniques, *Inter-Noise 95*, 1995.
9. Dobrzynski, W., Airframe noise studies on wings with deployed high-lift devices, *Paper AIAA-98-2337*, 1998.
10. Dobrzynski, W., Research into landing gear airframe noise reduction, *Paper AIAA-2002-2409*, 2002.
11. Johnson, D.H. and Dudgeon, D.E. 1993. *Array Signal Processing*, Prentice Hall, Englewood Cliffs, NJ.
12. Elias, G., Source localization with a two-dimensional focused array: optimal signal processing for a cross-shaped array, *Inter-Noise 95*, 1995.
13. Dougherty, R.P. and Stoker, R.W., Sidelobe suppression for phased array aeroacoustic measurements, *Paper AIAA-98-2242*, 1998.
14. Nordborg, A., Optimum array microphone configuration, *Inter-Noise 2000*, 2000.
15. Hald, J. and Christensen, J.J., A class of optimal broad band phased array geometries designed for easy construction, *Inter-Noise 2002*, 2002.
16. Piet, J.F. and Elias, G., Airframe noise source localization using a microphone array, *Paper AIAA-97-1643*, 1997.
17. Hayes, J.A., Airframe noise characteristics of a 4.7% scale DC-10 model, *Paper AIAA-97-1594*, 1997.
18. Stoker, R.W., Underbrink, J.R., and Neubert, G.R., Investigation of airframe noise in pressurized wind tunnels, *Paper AIAA-2001-2107*, 2001.

41

Source of Noise

S. Akishita

Ritsumeikan University

41.1	Introduction	41-1
41.2	Radiation of Sound	41-1
	Point Source • Sources of Finite Volume • Radiation from a Plane Surface • Estimation of Noise-Source Sound Power	

Summary

In this chapter, a mathematical description of sound radiation is briefly presented accompanied by an introduction to sound sources, monopole, and dipole. The modeling of a simple source of noise is discussed, introducing Green's function. As an example of simple sound radiation, the sound field generated by a source embedded in a plane surface is described. Finally, an estimation of noise-source sound power is presented by introducing the power conversion factor of actual machinery.

41.1 Introduction

A careful examination of noise measurement data reveals that there exists a very wide variety of noise sources. Each source is peculiar to its generation mechanism, which can be any of a wide range of phenomena including fluid mechanics and the vibration of structures. However, in analysis, sources are normally simplified to rather simple and typical models in their generation mechanism.

The vibration of a solid body, which may be in contact with the fluid medium, generates sound waves or vibratory forces acting directly on a fluid, will result in the emission of acoustic energy in the medium. In the next section, an expression for an idealized sound source is introduced. We will assume that the fluid medium outside the source region is initially uniform and at rest. Also, we will concentrate on wave propagation in an infinite medium.

Generally, acoustic waves sensed as a sound represent a very small energy density in the medium. Only a very small fraction of the mechanical energy of a source body is converted into acoustic energy. The conversion factor, defined as the ratio of sound power to the mechanical power of the source, is in the order of 10^{-7} to 10^{-5} . Some examples of estimated sound power conversion factor are given for typical common noise sources.

41.2 Radiation of Sound

41.2.1 Point Source

41.2.1.1 Simple Source: Spherical Wave by a Monopole

Propagation of sound pressure wave $p(x, y, z, t)$ is described by the following partial differential equation for a medium where a field point is expressed by orthogonal coordinate system O -xyz, as shown

in Figure 41.1(a):

$$\nabla^2 p - \frac{1}{c^2} \frac{\partial^2 p}{\partial t^2} = 0, \quad (41.1)$$

$$\nabla^2 \equiv \left(\frac{\partial^2}{\partial x^2} + \frac{\partial^2}{\partial y^2} + \frac{\partial^2}{\partial z^2} \right)$$

where c denotes the velocity of sound propagation. If the source region is compact and the generating motion has no preferred direction, it will produce a wave, which spreads spherically outwards. As the medium is assumed infinite in extent, the waveform will depend on the distance, r , from the center of the source. The wave equation in this case is

$$\frac{1}{r^2} \frac{\partial}{\partial r} \left(r^2 \frac{\partial p}{\partial r} \right) - \frac{1}{c^2} \frac{\partial^2 p}{\partial t^2} = 0 \quad (41.2)$$

When a monopole source of angular frequency ω is assumed, the simplest solution for the outward propagating waveform is expressed as

$$p(r, t) = p_\omega(\mathbf{r}) e^{-i\omega t},$$

$$p_\omega(\mathbf{r}) = \frac{-\omega \rho}{4\pi r} S_\omega e^{ikr}, \quad k = \frac{\omega}{c} = \frac{2\pi}{\lambda} \quad (41.3)$$

where ρ denotes the density of the medium and k denotes the wave number. Here, p_ω is used to denote the sinusoidal component of the sound pressure with angular frequency, ω . The subscript ω on a variable typically indicates the sinusoidal component of a variable, but the variables related to sound energy and sound power, such as w , I , W , do not have the subscript ω even if they mean the sinusoidal component. In this case, the source of sound is taken as a “pulsating globe” of radius a and radial velocity U_ω on the surface. Therefore, the flow outward from the origin, S_ω , is related to U_ω as follows, and as shown in Figure 41.1(a):

$$S_\omega = 4\pi a^2 U_\omega \quad (41.4)$$

We should note that, while a pulsating globe with a finite radius a is assumed as the physical sound source, the sound field by a monopole with infinitesimal small size and finite magnitude, as expressed mathematically in Equation 41.3, is used.

The other quantities related to the spherical wave are described next [1]:

$$\left\{ \begin{array}{ll} u_{r\omega} = \frac{-1}{4\pi r^2} (ikr - 1) S_\omega e^{ik(r-ct)}; & \text{radial velocity} \\ w = \rho \left(\frac{1}{4\pi r^2} \right)^2 |S_\omega|^2 \left[(kr)^2 + \frac{1}{2} \right]; & \text{energy density} \\ I = \rho c \left(\frac{k}{4\pi r} \right)^2 |S_\omega|^2 = \frac{|p|^2}{\rho c}; & \text{energy flux intensity} \\ W = (4\pi r^2) I = \rho c \frac{\pi}{\lambda^2} |S_\omega|^2 = \frac{\rho \omega^2}{4\pi c} |S_\omega|^2; & \text{total power} \end{array} \right. \quad (41.5)$$

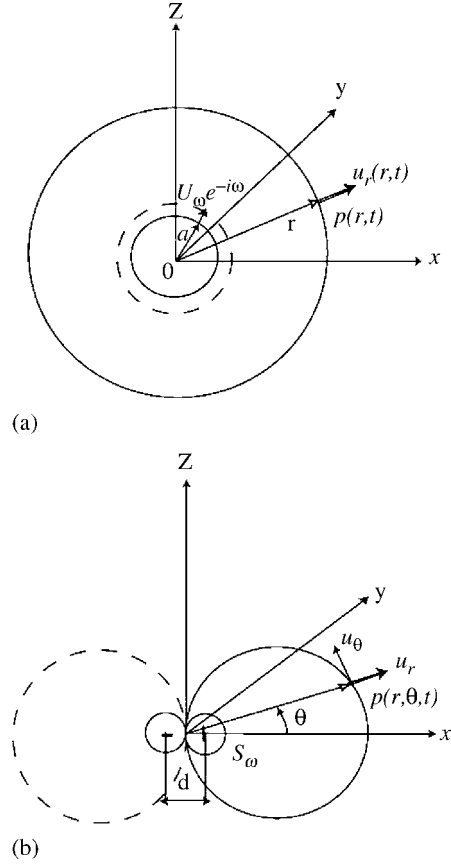


FIGURE 41.1 Directivity of monopole and dipole, (a) Spherical sound field by a monopole; (b) Axis-symmetric sound field by a dipole.

We should note that the first term in the parentheses, kr , is negligible in the region where $|kr| \ll 1$ is valid. Hence,

$$w = \frac{\rho}{2} (|S_\omega|/4\pi r^2)^2 = \frac{\rho}{2} u_{r\omega}^2 = \left(\frac{\lambda}{\omega}\right) \frac{I}{4\pi r^2}$$

is reduced. Conversely, when $|kr| \gg 1$ is valid, then $w = \rho(k/4\pi r)^2 |S_\omega|^2 = I/c$ is valid.

41.2.1.2 Simple Source: Plane Wave by an Alternating Piston

Another example of simple sound wave is generated in the one-dimensional field of fluid medium, as shown in Figure 41.1. Let us set the coordinate x along the axis of wave propagation, for example, the axis of duct with a constant cross-sectional area. Then the wave equation is

$$\frac{\partial^2 p}{\partial x^2} - \frac{1}{c^2} \frac{\partial^2 p}{\partial t^2} = 0 \quad (41.6)$$

The solution for a periodic source is given by

$$p(x, t) = p_\omega(x) e^{-i\omega t}, \quad p_\omega(x) = \rho c u_\omega e^{ikx} \quad (41.7)$$

This is known as a *plane wave*, which is generated by the piston motion at the origin, the velocity of which is expressed by

$$u(t) = u_\omega(x) e^{-i\omega t} \quad (41.8)$$

The other quantities related with the plane wave are given below:

$$\begin{cases} u_\omega(x) = u_\omega e^{ikx}, & \text{particle velocity} \\ w = I = \rho c |u_\omega|^2 = |p_\omega|^2 / \rho c^2; & \text{energy density, sound intensity} \\ W = SI \text{ (S; cross-sectional area);} & \text{total power} \end{cases} \quad (41.9)$$

A plane wave is generated in very limited situations, but its utility is rather wide since the sound wave propagating through a duct or duct-like space with a gradually varying cross section is approximated as the plane wave. Network theory is applied to the sound wave propagating through a branch and junction by using the description of a plane wave.

41.2.1.3 Dipole and Multipoles and Their Sound Field

Let us return to the three-dimensional sound field. The second simple solution to Equation 41.1 is the “dipole” sound field. Suppose that a pair of monopoles, close together, opposite in sign, and equal in magnitude, S_ω , are located along the x -axis as shown in Figure 41.1(b). Since only a preferred direction is assigned along the x -axis, the sound field is axisymmetric as represented by

$$p(r, \theta, t) = -k^2 D_\omega \frac{\rho c \cos \theta}{4\pi r} \left(1 + \frac{i}{kr}\right) e^{-i(\omega t - kr)} \quad (41.10)$$

D_ω is defined by

$$D_\omega = S_\omega d \quad (41.11)$$

where d denotes the separation of the monopoles as shown in Figure 41.1(b). Mathematically, d tends to zero, keeping D_ω finite, and the preferred axis is the x -axis. Physically, a sound field is commonly realized by a pair of monopoles with a finite separation that is short compared with the wavelength, λ , as illustrated next with realistic examples.

The characteristic quantities relating with dipole sound field are described below [1]:

$$\left\{ \begin{array}{ll} u_{r\omega} = -\frac{k^2 D_\omega \cos \theta}{4\pi r} \left(1 + \frac{2i}{kr} - \frac{2}{k^2 r^2}\right) e^{-i\omega t + kr}; & \text{radial velocity} \\ u_{\theta\omega} = i\frac{k^2 D_\omega \sin \theta}{4\pi r^2} \left(1 + \frac{i}{kr}\right) e^{-i\omega t + kr}; & \text{peripheral velocity} \\ w = \rho \left(\frac{k^2 |D_\omega|}{4\pi r}\right)^2 \left[\cos^2 \theta + \frac{1}{2} \left(\frac{1}{kr}\right)^2 + \frac{1}{2} \left(\frac{1}{kr}\right)^4 (1 + 3 \cos^2 \theta) \right]; & \text{energy density} \\ I_r = \rho c \left(\frac{k^2 |D_\omega|}{4\pi r}\right)^2 \cos^2 \theta, \quad I_\theta = 0; & \text{sound intensity} \\ W = \frac{\rho \omega^4}{12\pi c^3} |D_\omega|^2; & \text{total power} \end{array} \right. \quad (41.12)$$

We should add the following notes on the dipole sound field.

When $|kr| \gg 1$ is assumed, the second term in parentheses in Equation 41.10 is negligible. Then the directivity for $p(r, \theta, t)$ is expressed by $\cos \theta$. A similar directivity is found on I_r and on $u_{r\omega}$, $u_{\theta\omega}$, and w with the assumption $|kr| \gg 1$.

A pair of dipoles produces a *quadrupole*, a pair of quadrupoles produce an *octopole*, and so on. These are called *multipole* in general. Out of multipoles, the quadrupole is common in representing a sound field generated by mixing fluid flow, especially jet flow. More details on multipoles are found in Ref. [1].

41.2.2 Sources of Finite Volume

41.2.2.1 Description of Sound Field by Green's Function

In order to describe the sound field from distributed sources, source terms are introduced to the right side of Equation 41.1. The partial differential equation with source term is derived from the equation system representing the dynamics of fluid flow with periodic motion at angular frequency ω :

$$\nabla^2 p_\omega + k^2 p_\omega = -m_\omega + \text{div } \mathbf{F}_\omega \quad (41.13)$$

where p_ω denotes the acoustic pressure amplitude according to $p(x, y, z, t) = p_\omega(x, y, z)e^{-i\omega t}$, m_ω denotes the effective monopole source density expressed by $-i\omega \rho s_\omega$, s_ω denotes the generalization of the point source strength, S_ω , of Equation 41.4 for a distributed source, and \mathbf{F}_ω denotes the vector representation of point force-density in the fluid. Introduction of Green's function, g_ω , of angular frequency, ω , satisfying the following equation is useful in general:

$$\nabla^2 g_\omega + k^2 g_\omega = -\delta(x - x_0)\delta(y - y_0)\delta(z - z_0)e^{i\omega t_0} \quad (41.14)$$

Here, $\delta(z)$ denotes the Dirac impulse (delta) function of the variable z ; the coordinate (x_0, y_0, z_0) denotes the position of unit source, r_0 , with periodic angular velocity, ω , and t_0 denotes the time pertaining to the source. The solution of Equation 41.14 is

$$g_\omega(\mathbf{r}, \mathbf{r}_0) = \frac{1}{4\pi R} e^{ikr}, \quad |\mathbf{r} - \mathbf{r}_0| = \sqrt{(x - x_0)^2 + (y - y_0)^2 + (z - z_0)^2} \quad (41.15)$$

where \mathbf{r} denotes the position vector of sound field with coordinates (x, y, z) . The solution of Equation 41.13 is described by using $g_\omega(\mathbf{r}, \mathbf{r}_0)$ as follows:

$$p_\omega(\mathbf{r}) = \iiint [m_\omega(\mathbf{r}_0) - \text{div } \mathbf{F}_\omega(\mathbf{r}_0)] g_\omega(\mathbf{r}, \mathbf{r}_0) dx_0 dy_0 dz_0 \quad (41.16)$$

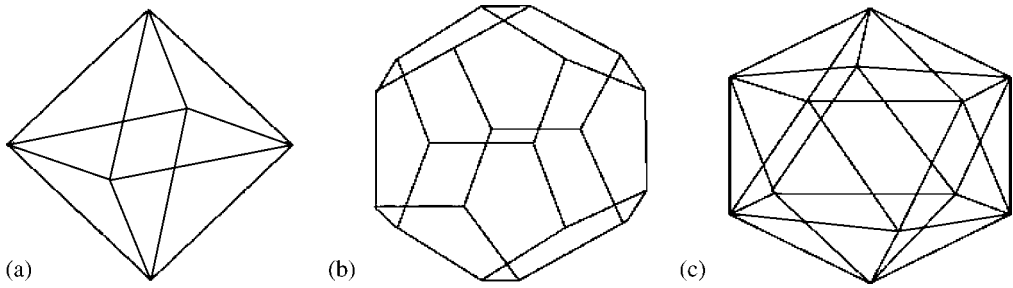


FIGURE 41.2 Practical monopole sources.

41.2.2.2 Radiation from Vibrating Small Body

A pulsating globe, as the simplest sound source, is rarely realized in the real world. The approximated monopole source required in most measurements is an eight-sided polyhedron, as depicted in Figure 41.2, where a loud speaker is installed on each of the surfaces. The sound field radiated by a thus approximated source is almost the same as that by a pulsating globe at the far field, where $kr \gg 1$ is valid.

In this case, the sound field is represented by Equation 41.16, assuming that $F_\omega(\mathbf{r}_0) = 0$, $m_\omega(\mathbf{r}_0) = -i\omega\rho U_\omega \delta(n)$, and $dx_0 dy_0 dz_0 = dn dS$, where the source $m_\omega(\mathbf{r}_0)$ is distributed on a thin layer of thickness, dn , on the spherical surface element, dS . Substitution of these relationships into Equation 41.16 yields the formula

$$\begin{aligned} p_\omega(\mathbf{r}) &= - \iint_S \frac{i\omega\rho U_\omega}{4\pi R} e^{ikR} dS \\ &= - \frac{i\omega\rho}{4\pi R_0} (4\pi a^2) U_\omega e^{ikR_0} \quad (41.17) \end{aligned}$$

where $\iint_S dS$ means integration on the approximately spherical surface, and then $R \equiv |\mathbf{r} - \mathbf{r}_0| \cong R_0 = \sqrt{x^2 + y^2 + z^2}$ is applied. The final reduction of Equation 41.17 gives the same expression as is deduced from Equation 41.3 and Equation 41.4.

The sound field generated by a monopole source is illustrated in Figure 41.1. This field is unchanged with the presence of a rigid plane AB in Figure 41.3. It is clear, on account of symmetry, that the presence of the rigid plane does not alter the sound field in any way, because only the tangential component of particle velocity is induced on the plane. This utilization of the symmetry and construction of the semi-infinite field is applied to the expression of the sound field generated by the baffled structure, as shown in Figure 41.4.

Let us imagine a sound field generated by an oscillating small body in an infinite medium, as shown in Figure 41.4(a). Since the oscillation is caused by an external force, the sound source is modeled by the force $-\mathbf{F}_\omega(\mathbf{r}_0)$. Therefore, the sound field is described by Equation 41.16, assuming $m_\omega(\mathbf{r}_0) = 0$. After applying a law of vector analysis, such as $g_\omega(\mathbf{r}, \mathbf{r}_0) \text{div } \mathbf{F}_\omega(\mathbf{r}_0) \cdot \text{grad}_0 g_\omega + \text{div}_0(g_\omega \mathbf{F}_\omega)$, the sound field is

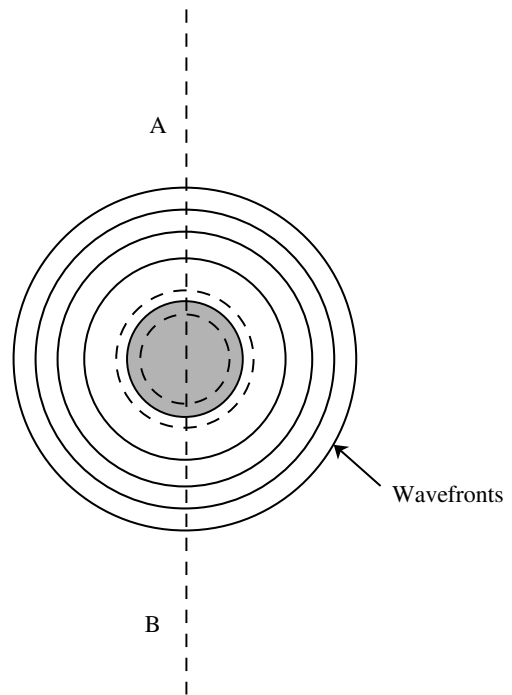


FIGURE 41.3 Field of a pulsating spherical source.

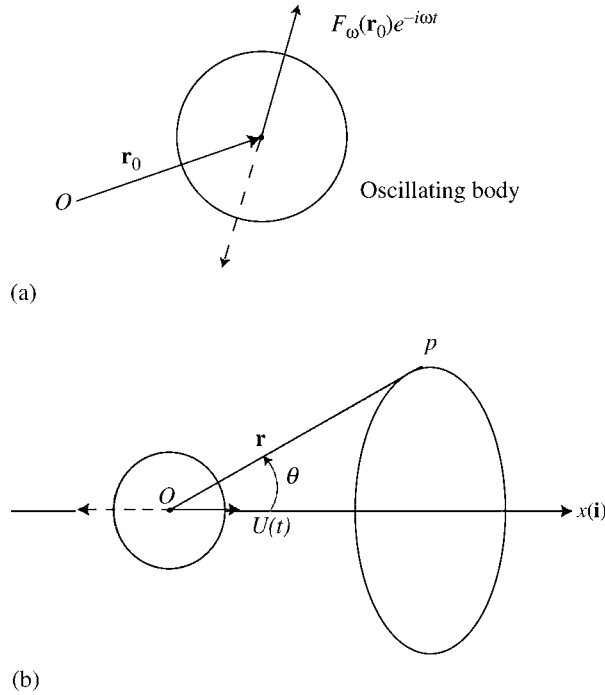


FIGURE 41.4 Dipole field generated by an oscillating small body: (a) oscillating small body; (b) oscillating sphere along x -axis.

represented by

$$p_{\omega}(\mathbf{r}) = \iiint \mathbf{F}_{\omega}(\mathbf{r}_0) \cdot \nabla_0 g_{\omega}(\mathbf{r}, \mathbf{r}_0) dx_0 dy_0 dz_0 \quad (41.18)$$

where $\iiint \text{div}_0(g_{\omega} \mathbf{F}_{\omega}) dx_0 dy_0 dz_0 = \iint_S g_{\omega} \mathbf{F}_{\omega} dS_n(x_0, y_0, z_0) = 0$ is applied. Assume that a small sphere of radius a_0 is oscillating along the x -axis with angular frequency ω . Instead of an oscillating sphere with velocity $U_t = U_{\omega} e^{-i\omega t}$, the sound field is generated by the concentrated body force, $F(t) = -m(d/dt)U(t) = i\omega m U_{\omega} e^{-i\omega t}$, (m is the mass of the sphere), at the origin, $\mathbf{r}_0 = 0$. Then $\mathbf{F}_{\omega}(\mathbf{r}_0)$ is expressed by $F_{\omega}(\mathbf{r}_0) = (F_{x\omega} \mathbf{i}) \delta(x_0) \delta(y_0) \delta(z_0)$; $F_{x\omega} = i\omega m U_{\omega}$. This approximate reduction is appropriate when $ka_0 \ll 1$ is valid. Substituting the approximation, Equation 41.18 is rewritten as

$$p_{\omega}(\mathbf{r}) \cong F_{x\omega} \frac{\partial}{\partial x_0} g_{\omega}(\mathbf{r}, \mathbf{r}_0, \theta) = -k^2 D_{\omega} \frac{\rho c}{4\pi r} \cos \theta \left(1 + \frac{i}{kr}\right) e^{ikr} \quad (41.19a)$$

$$D_{\omega} = \frac{i}{k\rho c} F_{\omega x} \quad (41.19b)$$

As the sound field is axisymmetric about x -axis, the sound pressure, $p_{\omega}(\mathbf{r}, \theta)$, depends only on \mathbf{r} and θ , where \mathbf{r} and θ are defined in Figure 41.4(b). The expression is applicable to the sound field generated by an oscillating small body in a free space.

41.2.3 Radiation from a Plane Surface

41.2.3.1 Radiation from a Small Body in Infinite Plane Surface

The introduction of an infinite rigid plane surface to the sound field, as shown in Figure 41.3, simplifies the formulation of the sound field generated by an oscillating body adjacent to a large plane.

The configuration discussed in this section relates to a source in the presence of an infinite plane barrier, so that the medium is confined to one side of the plane.

By taking the effect of the image caused by the rigid plane surface, the Green's function, $g_\omega(\mathbf{r}, \mathbf{r}_0)$, in this case simplifies as given below, to what is called Rayleigh's formula [2]:

$$g_\omega(\mathbf{r}, \mathbf{r}_0) = \frac{1}{2\pi R} e^{ikr}, \quad R = |\mathbf{r} - \mathbf{r}_0| \quad (41.20)$$

where \mathbf{r}_0 denotes the projection position of the source on the surface. Therefore, Equation 41.16 is rewritten as follows:

$$p_\omega(\mathbf{r}) = \iint \int \frac{e^{ikR}}{2\pi R} [m_\omega(\mathbf{r}_0) - \text{div } \mathbf{F}_\omega(\mathbf{r}_0)] dx_0 dy_0 dz_0 \quad (41.21)$$

41.2.3.2 Radiation from a Circular Piston

Let us consider the sound field generated by a rigid circular piston of radius a mounted flush with the surface of an infinite baffle and vibrating with simple harmonic motion of angular frequency, ω . The solution of this example is applicable to a number of related problems, including the radiation from the open end of a flanged organ pipe.

The coordinate system is shown in Figure 41.5, where the infinite baffle and the piston are placed in the Oxy -plane. Note that the observation point, P , is denoted by $\mathbf{r} = \overrightarrow{OP}$, while the source point, Q , is denoted by $\mathbf{r}_0 = \overrightarrow{OQ}$.

Since sound is observed only in the semi-infinite plane where $z > 0$ is valid, only $m_\omega(\mathbf{r}_0)$ remains nonzero in Equation 41.21. As the velocity of the piston is denoted by $U_\omega e^{-i\omega t}$ along the z -axis, $m_\omega(\mathbf{r}_0) = -i\omega\rho U_\omega \delta(z_0)$, is distributed only on the circular piston. Finally, Equation 41.21 is rewritten as

$$p_\omega(\mathbf{r}) = \frac{-i\omega\rho U_\omega}{2\pi} \iint_S \frac{e^{ikR}}{R} dx_0 dy_0 \quad (41.22)$$

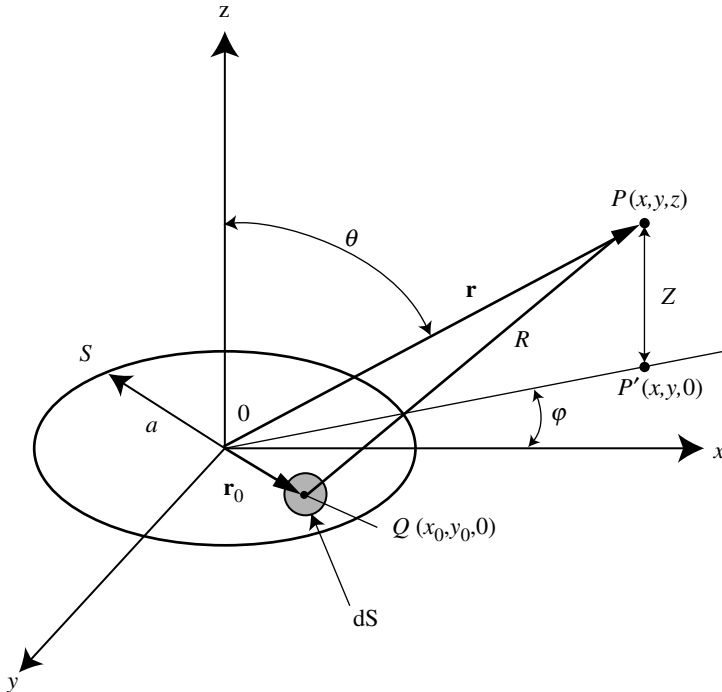


FIGURE 41.5 The rigid circular piston and the coordinate system.

Assuming $a \ll r$, the following approximation can be made:

$$R \cong r - (x_0 \cos \varphi + y_0 \sin \varphi) \sin \theta, \quad (41.23)$$

$$\frac{1}{R} \cong \frac{1}{r}$$

where φ and θ denote the angles defining the observation point, P , as shown in Figure 41.5. By changing from Cartesian coordinates, x_0, y_0 , to polar coordinates, ρ, φ_0 , such that $x_0 = \rho \cos \varphi_0$, $y_0 = \rho \sin \varphi_0$ in the integral above, we rewrite Equation 41.22 as

$$p_\omega(\mathbf{r}) = -\frac{i\omega\rho U_\omega}{2\pi R} e^{ikr} \int_0^{2\pi} d\varphi_0 \times \int_0^a \exp[-k\rho \cos(\varphi_0 - \varphi) \sin \theta] \rho d\rho \quad (41.24)$$

The integration is performed by introducing the Bessel function of the first order, $J_1(z)$ as follows:

$$p_\omega(\mathbf{r}) = -\frac{i\omega\rho e^{ikr}}{2\pi r} f_\omega(\theta), \quad (41.25)$$

$$f_\omega(\theta) = \pi a^2 U_\omega \left[\frac{2J_1(ka \sin \theta)}{ka \sin \theta} \right]$$

Note that dependency on φ has disappeared in the integration process, which follows from the axisymmetry of the sound field. The corresponding intensity at \mathbf{r} is given by

$$I_r(\theta) \cong \frac{|p_\omega|^2}{\rho c} = \frac{\rho c U_\omega^2 a^2}{4r^2} (ka)^2 \left[\frac{2J_1(ka \sin \theta)}{ka \sin \theta} \right]^2 \quad (41.26)$$

Figure 41.6 illustrates the dependency of I_r on θ for two cases of ka . Note that, for the smaller $ka = 2\pi a/\lambda$, I_r is almost independent on θ , which is similar to the dependence of the monopole.

41.2.3.3 Radiation from a Rectangular Plate

An normal velocity distribution, $u_\omega(x_0, y_0)$, is prescribed over a baffled planar radiator located in the plane $z_0 = 0$ in the region $-L_x \leq x_0 \leq L_x, -L_y \leq y_0 \leq L_y$, as shown in Figure 41.7.

In this case, the sound pressure field is represented by the following equation, similar to the previous section:

$$p_\omega(\mathbf{r}) = \frac{-i\omega\rho}{2\pi} \int_{-L_y}^{L_y} dy_0 \int_{-L_x}^{L_x} \frac{U_\omega(x_0, y_0) e^{ikR}}{R} dx_0 \quad (41.27)$$

Assuming $2L_x, 2L_y \ll r$, the same approximation in as Equation 41.23 is acceptable. Therefore, $p_\omega(\mathbf{r}) = p_\omega(r, \theta, \phi)$ takes the form [2]:

$$p_\omega(r, \theta, \phi) = \frac{-i\omega\rho e^{ikr}}{2\pi r} \int_{-L_y}^{L_y} dy_0 \int_{-L_x}^{L_x} U_\omega(x_0, y_0) \exp[-ik \sin \theta (x_0 \cos \phi + y_0 \sin \phi)] dx_0 \quad (41.28)$$

The result of the above integration, assuming $U_\omega(x_0, y_0) = U_\omega = \text{const}$, which means the rigid rectangular piston oscillates with amplitude U_ω along the z -axis, is

$$p_\omega(r, \theta, \phi) = \frac{i\omega\rho U_\omega}{2\pi r} (4L_x L_y) e^{ikr} S(kL_x \sin \theta \cos \phi) S(kL_y \sin \theta \sin \phi) \quad (41.29a)$$

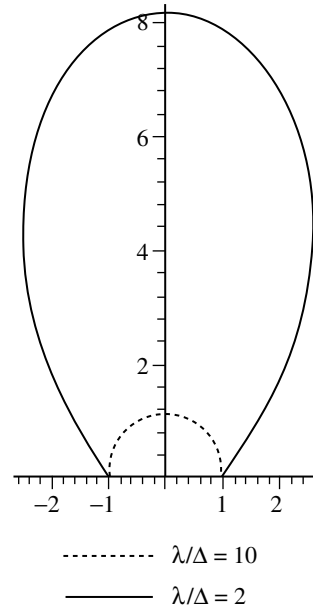


FIGURE 41.6 Directivity of sound intensity generated by an oscillating piston.

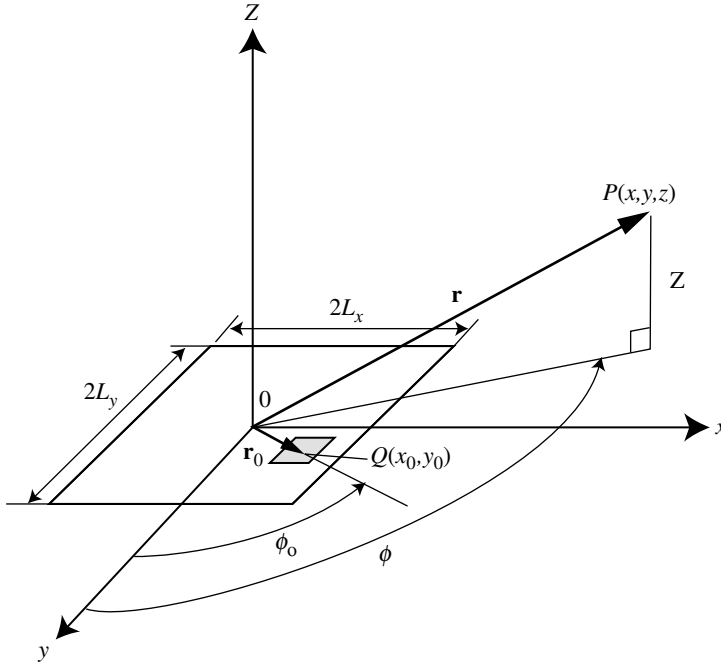


FIGURE 41.7 A flexural rectangular plate and the coordinate system.

where the function $S(z)$ is defined by

$$S(z) = \frac{\sin z}{z} \quad (41.29b)$$

Now, let us discuss the case of flexural plate, which has the same lengths, $2L_x$ and $2L_y$, but $U_\omega(x_0, y_0)$ represents the flexural vibration mode. Flexural mode patterns of rectangular panels take the general form of contiguous regions of roughly equal area and shape, which vary alternately in vibration phase, and are separated by nodal lines of zero vibration.

For simply supported edges, the normal vibration velocity distribution is (see Chapter 4)

$$U_\omega(x_0, y_0) = U_{mn} \sin\left(\frac{m\pi x}{2L_x}\right) \sin\left(\frac{n\pi y}{2L_y}\right), \quad (0 \leq x \leq 2L_x, 0 \leq y \leq 2L_y) \quad (41.30)$$

Note that the coordinate system $O-x_0y_0z_0$ shifts its origin from the center point of the panel to the edge at the leftmost and frontmost point in Figure 41.7.

The approximation represented by Equation 41.23 is valid as well in this case. The result of integration is rather simple as given below [3]:

$$p_\omega(r, \theta, \phi) = \frac{-i\omega\rho U_{mn} e^{kr}}{2\pi r} \frac{4L_x L_y}{mn\pi^2} \left[\frac{(-1)^m e^{i\alpha} - 1}{(\alpha/m\pi)^2 - 1} \right] \left[\frac{(-1)^n e^{i\beta} - 1}{(\beta/n\pi)^2 - 1} \right] \quad (41.31)$$

where α and β are defined by

$$\alpha = 2kL_x \sin \theta \cos \phi, \quad \beta = 2kL_y \sin \theta \sin \phi \quad (41.32)$$

The corresponding intensity, $I_r(\theta, \phi)$, at \mathbf{r} is expressed by

$$I_r(r, \theta, \phi) = \frac{|p_\omega|^2}{\rho c} = 4\rho c |U_{mn}|^2 \left(\frac{4kL_x L_y}{\pi^3 r mn} \right)^2 \left\{ \frac{\cos\left(\frac{\alpha}{2}\right) \cos\left(\frac{\beta}{2}\right)}{[(\alpha/m\pi)^2 - 1][(\beta/n\pi)^2 - 1]} \right\} \quad (41.33)$$

where $\cos(\alpha/2)$ is used when m is an odd integer, and $\sin(\beta/2)$ is used when m is an even integer; $\cos(\beta/2)$ is used for even n and $\sin(\beta/2)$ for odd n .

41.2.4 Estimation of Noise-Source Sound Power

41.2.4.1 Power Conversion Factor of Machinery

It is often necessary to estimate the expected sound power that a particular machine might introduce into an environment [4]. One way where such an estimate may be approached for a particular class of machine is by means of the sound power conversion factor, η_n . This factor is defined as

$$\eta_n = \frac{P}{P_m}$$
 (41.34)

where P = sound power of the machine (W), and P_m = power of the machine (W). This relationship is valid for both mechanical and electrical machinery. The conversion factors for some common noise sources are given in Table 41.1.

Example 41.1

Estimate the sound power level of a typical 1-kW electric motor that operates at 1200 rpm.

Solution

From Table 41.1, we find that for typical electric motors, $\eta_n = 1 \times 10^{-7}$. Thus, using Equation 41.34, we obtain

$$P = \eta_n P_m = (1 \times 10^{-7}) \times 1000 = 10^{-4} \text{ (W)}$$

as the total sound power of motor. Then using Equation 37.7, L_W is given by

$$L_W = 10 \log \left(\frac{10^{-4}}{10^{-12}} \right) = 80 \text{ (dB)}$$

41.2.4.2 Fan Noise

We are familiar with noise nuisance caused by a domestic ventilating fan. The mechanical power of the fan is expressed by

$$P_m = p_T Q$$
 (41.35)

where p_T denotes the total pressure rise through the fan and Q denotes the volumetric flow rate. According to the law of sixth power of flow velocity deduced by the aeroacoustics theory, sound power of the fan is proportional to $p_T^{2.5} Q$. Therefore, the specific ratio k_T defined below is more useful than η_n for the fan:

$$k_T = \frac{P_m}{p_T^{2.5} Q}$$
 (41.36)

TABLE 41.1 Estimated Sound Power Conversion Factors for Common Noise Sources^a

Noise Source	Conversion Factor		
	Low	Midrange	High
Compressor, air (1–100 hp)	3×10^{-7}	5.3×10^{-7}	1×10^{-6}
Gear trains	1.5×10^{-8}	5×10^{-7}	1.5×10^{-6}
Loud speakers	3×10^{-2}	5×10^{-2}	1×10^{-1}
Motors, diesel	2×10^{-7}	5×10^{-7}	2.5×10^{-6}
Motors, electric (1200 rpm)	1×10^{-8}	1×10^{-7}	3×10^{-7}
Pumps, over 1600 rpm	3.5×10^{-6}	1.4×10^{-5}	5×10^{-5}
Pumps, under 1600 rpm	1.1×10^{-6}	4.4×10^{-6}	1.6×10^{-5}
Turbines, gas	2×10^{-6}	5×10^{-6}	5×10^{-5}

^a Total sound power for the four octave bands from 500 to 4000 Hz.
Source: Irwin, J. D. and Graf, E. R. 1979. *Industrial Noise and Vibration Control*, Prentice Hall, Englewood Cliffs, NJ.

TABLE 41.2 Specific Fan Noise Level for Low-Pressure Fans

Type	K_T (dB)
Axial	− 87.5 to − 70.7
Centrifugal/cirroco	− 87.5 to − 85.7
Centrifugal/radial	− 98.7 to − 84.7
Centrifugal/turbo	− 104.7 to − 89.7
Cross-flow	− 76.7 to − 68.7

Furthermore, usually the specific fan noise level, K_T , as given below is more useful than k_T .

$$K_T = L_W - 10 \log(p_{T^{2.5}} Q) \text{dB} \quad (41.37)$$

where p_T denotes the total pressure rise in mmAg, Q denotes the flow rate in m^3/min , L_W denotes the total sound power level in dB, and K_T represents the radiation efficiency of the fan noise. This efficiency varies with the type of the fan and with the flow rate when the model is assigned. In particular, K_T will be the lowest at the flow rate at which the aerodynamic power efficiency is the highest. Therefore, we will have the best advantage on the sound environment when the fan is operated at the highest efficiency. For convenience of design, the L_W is often evaluated by A-weighted total sound level (dB-A) not by linear total level (dB). Table 41.2 gives the specific fan noise level evaluated with dB-A for five types of the low-pressure fans.

Example 41.2

Consider a ventilating axial-flow fan, the specifications of which are: $p_T = 10$ mmAg, $Q = 30$ m^3/min , $D = 30$ cm (diameter of the duct containing fan rotor). Estimate the directional distribution of intensity $I_r(\theta)$, assuming $r = 3$ m and $f = 150$ Hz for the main component of the fan noise, and $K_T = -79.0$ dB-A from Table 41.2. The fan noise is assumed to be radiated as a plane sound wave at the mouth of the duct.

Solution

First, we modify the K_T in dB-A to that of linear scale. From the frequency response for A-weighting network shown in Figure 2.5, for $f = 150$ Hz, the modification is found as $\Delta K_T = 15$ dB. Then, the modified specific fan noise level is $K_T = -79.0 + 15.0 = -64.0$ dB. By using Equation 41.37, $L_W = K_T + 25 \log p_T + 10 \log Q = -64 + 25 + 15 = -24$ dB is obtained. This means the emitted total sound power is $W = 10^{-24/10} = 3.98 \times 10^{-3}$ W. Since we assume a plane sound wave at the mouth of the duct for the fan noise, we can use the sound radiation model of a circular piston with $a = 15$ cm for the radiated sound wave. In our case $k_a = 2\pi a/(c/f) = 0.415$, or $\lambda/a = 15.1$. A monopole model will be valid for the directional distribution of intensity from Figure 41.6. Therefore, $I_r = W/2\pi r^2 = 0.704 \times 10^{-4}$ W/m² or $|p|^2 = I_r \rho c = 2.92 \times 10^{-2}$ (Pa²). This is the same as the sound pressure level $L_p = 10 \log |p|^2 / p_{\text{ref}}^2 = 78.6$ dB or $L_p(A) = L_p - 15 = 63.6$ dB-A.

References

1. Morse, P.M. and Ingard, K.U. 1986. *Theoretical Acoustics*, Princeton University Press, Princeton, NJ, chap. 7.
2. Junger, M.C. and Feit, D. 1986. *Sound, Structures, and Their Interaction*, 2nd ed., MIT Press, Cambridge, chap. 4.
3. Fahy, F. 1985. *Sound and Structural Vibration. Radiation, Transmission and Response*, Academic Press, New York, chap. 2.
4. Irwin, J.D. and Graf, E.R. 1979. *Industrial Noise and Vibration Control*, Prentice Hall, Englewood Cliffs, NJ, chap. 5.

42

Design of Absorption

42.1	Introduction	42-1
42.2	Fundamentals of Sound Absorption	42-2
	Attenuation of Sound	
42.3	Sound-Absorbing Materials	42-3
	Porous Material • Tubular Material • Membrane Material • Perforated Plate • Acoustic Resonator	
42.4	Acoustic Characteristic Computation of Compound Wall	42-6
	Absorption Coefficient of Combined Plate with Porous Blanket • Transmission Loss through a Single Porous Board • Transmission Loss through a Sandwich Board	
42.5	Attenuation of Lined Ducts	42-10
	Computation of Attenuation in a Lined Duct • Attenuation in a Lined Bend • Attenuation in Splitter Lined Duct	
42.6	Attenuation of Dissipative Mufflers	42-12
	Transmission Loss of Lined Expansion Chamber • Transmission Loss of a Plenum Chamber	
42.7	General Considerations	42-15
	Surface Treatment with Lining of Acoustic Material • Gas Flow Velocity • Gas Temperature • Dust and Water Exposure	
42.8	Practical Example of Dissipative Muffler	42-17

Teruo Obata
Teikyo University

Summary

This chapter presents the basics of designing devices for sound absorption. The absorption coefficient and acoustic impedance are introduced. Characteristic properties and parameters of sound absorption material and basic elements are presented. Acoustic modeling, analysis, and design considerations of components, such as ducts, and noise attenuation devices, such as mufflers, are presented. A practical design example is presented for illustration of the concepts presented in the chapter.

42.1 Introduction

Sound-absorption equipment is used for multiple purposes in architectural acoustics, mechanical noise countermeasures, and so on. In this context, the necessity for designing sound-absorption equipment from the viewpoint of noise control is explained. Architectural acoustics is an important area of study, which involves architecture, sound-absorption design, and sound-measurement facility.

In the area of noise reduction, the characteristics of sound are important, and proper sound-absorbing material should be selected based on how much attenuation is necessary for each frequency of sound. In particular, acoustic characteristics of sound-absorbing material such as the type of material and the

sound-absorption mechanism are important. In this chapter, the basics of sound absorption are given, and the prediction and calculation methods for attenuation of lined or dissipative mufflers are outlined.

42.2 Fundamentals of Sound Absorption

42.2.1 Attenuation of Sound

When an acoustic wave propagates in a medium, the sound energy attenuates due to such reasons as viscosity, heat conduction, and the effects of molecular absorption. In a medium of small volume surrounded by a boundary surface, the attenuation is particularly considerable, for example, when the medium is a thin tube. This is because there is the dissipation of the energy controlled by the viscosity of the medium and heat conduction between the material and the medium of tube wall. A sound-absorbing material may be utilized to adjust such dissipation of acoustic energy.

42.2.1.1 Absorption Coefficient and Normal Acoustic Impedance

Some amount of energy is lost when an acoustic wave hits the surface of a sound-absorbing material. Figure 42.1 illustrates an infinite medium of absorbing material separated by air and the reflected wave (sound pressure p_r) from the boundary surface with the air where a plane wave of sound pressure p_i is emitted in the direction indicated by an arrow, at an angle θ . When $\theta = 0$, sound pressure p in air is given by

$$p = p_i + p_r = (Ae^{-jkx} + Be^{jkx})e^{j\omega t} \quad (42.1)$$

where

A, B = the amplitude of sound pressure of incident and reflected waves (in Pa),

$j = \sqrt{-1}$,

$k = 2\pi f/c$; wave number (1/m),

ω = angular frequency (rad/sec).

The sound pressure, p_m , in the absorbing material may be expressed using a complex propagation constant, by the equation:

$$p_m = p_{x=0} e^{-\gamma x} e^{j\omega t} \quad (42.2)$$

where

γ = the propagation constant in the absorbing material (m^{-1}). *Note:* $\gamma = \delta + j\beta$. γ is a property of the material itself and is not dependent on the mounting conditions when large areas of material are considered.

δ = attenuation constant. *Note:* δ tells us how much of the sound wave will be reduced as it travels through the material.

β = phase constant. *Note:* β is a measure of the velocity of propagation of the sound wave through the material.

The relation for determining the velocity of sound in the material is given by

$$c_m = \omega/\beta \quad (42.3)$$

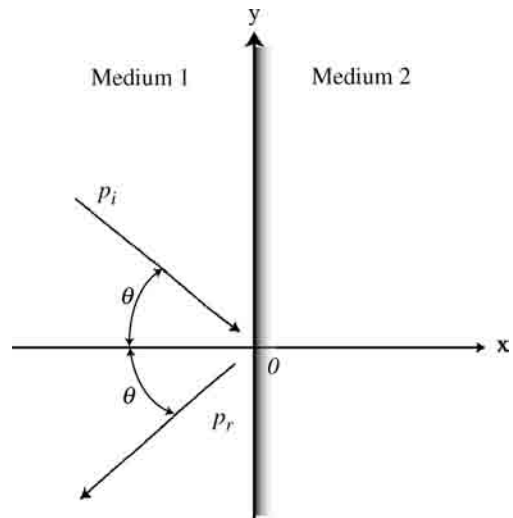


FIGURE 42.1 Plane wave incidence on an infinite absorbing material.

Boundary conditions must be satisfied on the boundary surface. The acoustic impedance of a unit area of air and of absorbing material are, respectively, denoted by z and z_a . The pressure and the particle velocity on both sides of the boundary are equal. We have

$$\left. \begin{aligned} p_i + p_r &= p_{x=0} \\ \frac{p_i - p_r}{z_a} &= \frac{p_{x=0}}{z} \end{aligned} \right\} \quad (42.4)$$

The amplitude of reflectance of sound pressure, r , is obtained from Equation 42.4, and is given by

$$r = \frac{p_r}{p_i} = \frac{z_a - z}{z_a + z} \quad (42.5)$$

The reflectivity is the energy reflection rate. The absorption coefficient, α , of an absorbing material is defined as

$$\alpha = 1 - |r|^2 \quad (42.6)$$

The impedance, z_n , through a surface is the quantity that represents the dissipation of energy of sound as well as the absorption coefficient. It is given as a ratio between sound pressure and particle velocity on boundary surface in the reflecting acoustic wave:

$$z_n = \left(\frac{p}{u} \right)_{x=0} = \left(\frac{\rho c}{\cos \theta} \right) \frac{p_i + p_r}{p_i - p_r} \quad (42.7)$$

Note that z_n is a complex quantity and involves both amplitude and phase, both of which depend on the sound pressure at the boundary surface in the reflecting acoustic wave.

In the case of oblique incidence, the surface impedance can be expressed by following equation:

$$z_n = Z \gamma z / q \quad (42.8)$$

where z = the acoustic impedance (Pa sec/m³). Here,

$$Z = \frac{z_1 \cosh(ql) + (\gamma z/q) \sinh(ql)}{z_1 \sinh(ql) + (\gamma z/q) \cosh(ql)}$$

$$q = \sqrt{\gamma^2 + k^2 \sin^2 \theta}$$

The absorption coefficient, $\alpha(\theta)$, for an oblique incidence with angle θ may be expressed by

$$\alpha(\theta) = 1 - \left| \frac{z_n \cos \theta - \rho c}{z_n \cos \theta + \rho c} \right|^2 \quad (42.9)$$

42.3 Sound-Absorbing Materials

42.3.1 Porous Material

Porous acoustical materials are a special category of a more general class of gas–solid mixtures. They range from porous solids, for example, porous rocks, fibrous granular solids, expanded plastics, and form materials, to porous or turbid gases, for example, suspensions and emulsions. Sound is attenuated in a gas-saturated porous solid due to the restriction on the gas movement within it. A convenient microstructure model for such materials is one of a rigid solid matrix through which run cylindrical, capillary pores (tubing) with constant radius, normal to its surface. This model enables the use of Kirchoff's theory of sound propagation in narrow tubes with rigid walls. Accordingly, this mechanism of dissipation may be identified as (1) a viscous loss in the boundary layer at the wall of each capillary tube

associated with the relative motion between the viscous gas and the solid wall, or (2) heat conduction between compressions and rarefactions of the gas and the conducting solid walls.

42.3.2 Tubular Material

Consider the absorption of low-frequency sound using the tubular absorbing material. By itself, sound absorption is not satisfactory with the tubular absorbing material. The material produces bending vibration due to an acoustic wave through it, and sound absorption occurs by the internal friction of the material. For hard plywood and gypsum boards, there is a natural frequency in the range 100 to 200 Hz, and the absorption coefficient ranges from 0.3 to 0.5. It is possible to increase the absorption coefficient by coating the board surface with fibrous absorbing material.

42.3.3 Membrane Material

For membrane material, the sound-absorption mechanism makes use of resonant vibration. Hence, resonant frequency is a governing parameter. The imaginary part (the reactance term) of the acoustic impedance of a membrane gives rise to a resonance. The associated natural frequency is given by

$$f_r = \frac{1}{2} \left\{ \frac{1}{m} \left(\frac{1.4 \times 10^5}{L} \right) + K_m \right\} \quad (42.10)$$

where

f_r = natural frequency (Hz)

m = surface density (kg/m^2)

L = thickness of air space (m)

K_m = board rigidity ($\text{kg/m}^2 \text{sec}^2$)

The K_m values of some boards are shown in Figure 42.2. The absorption coefficient is approximately 0.3 to 0.4 in the frequency range of 300 to 1000 Hz, when the thickness of the air space between the membrane and the rigid wall behind it is 50 to 100 mm.

42.3.4 Perforated Plate

A perforated board of sound absorbing material (i.e., a board with holes) is placed over a rigid wall at a fixed clearance, as shown in Figure 42.3. The sound-absorption characteristics depend on the board thickness, t , the hole diameter of the perforations, d , the clearance, L , between the perforated board and the rigid wall, and so on. The absorption coefficient becomes a maximum at resonant frequency. In the present case, the resonant frequency is given by

$$f_r = \frac{c}{2\pi} \sqrt{\frac{\varepsilon}{(t + 0.8d)L}} \quad (42.11)$$

where sound speed is c , the airspace thickness is L (typically, 300 mm or less), and the ratio of the total area of holes to the total area of the board is ε . The absorption coefficient is approximately 0.3 to 0.4.

42.3.5 Acoustic Resonator

Yet another method of achieving sound absorption is using an acoustic resonator of Helmholtz type, which consists of a vessel of any shape containing a volume air, as shown in Figure 42.4. The air volume is in direct communication with the ambient air in the room through an interconnecting tube, which may be long or short and of any cross-sectional shape. An example of a resonator of Helmholtz type may be a 1 gal jar. When a sound wave impinges on the aperture of neck of the jar, the air in the neck will be set in oscillation, periodically expanding and compressing the air in the vessel.

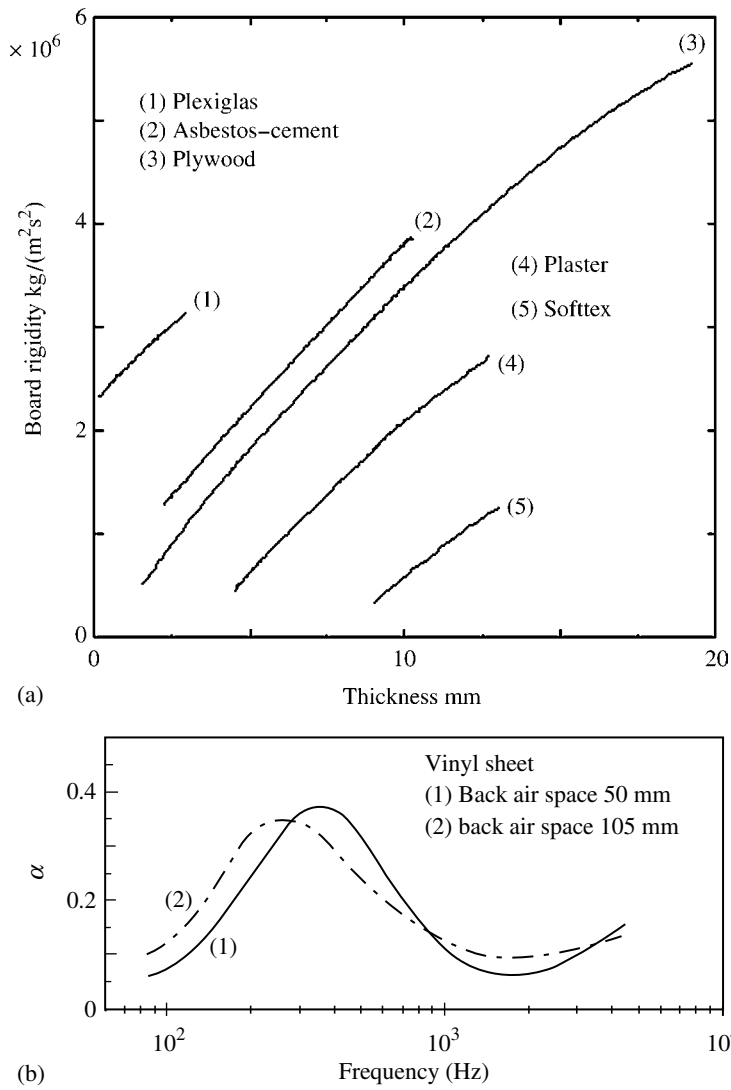


FIGURE 42.2 Some K_m values for membrane absorbing materials.

The resulting amplified motion of the air particles in the neck of the jar, due to phase cancellation between the air plug in the neck and the air volume in the vessel, causes energy dissipation due to friction in and around the neck. This type of absorber can be designed to produce maximum absorption over a very narrow frequency band or even a wide frequency band. The resonant frequency of a Helmholtz resonator may be expressed as

$$f_r = \frac{c}{2m} \sqrt{\frac{\varepsilon}{(t + 0.8d)L}} \tag{42.12}$$

where

- c = speed of sound (m/sec)
- S_n = cross-sectional area of neck of jar (m²)
- d_n = diameter of neck of jar (m)
- V = volume of vessel (m³)

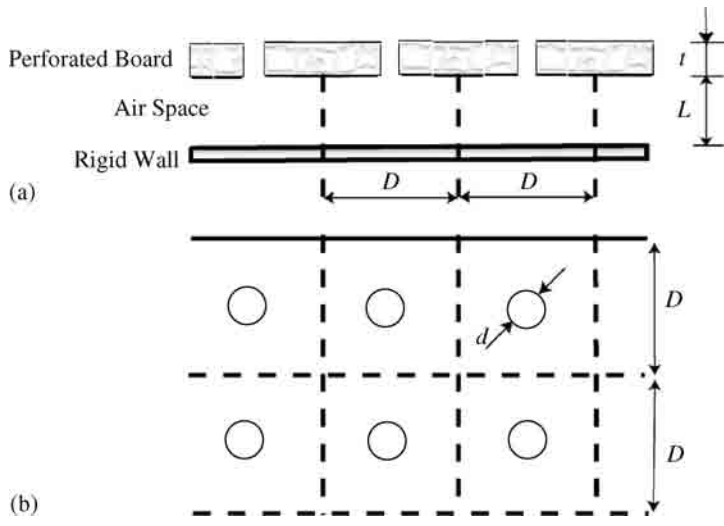


FIGURE 42.3 Sound-absorption characteristics of a perforated plate structure: (a) cross sectional view; (b) plan view.

42.4 Acoustic Characteristic Computation of Compound Wall

42.4.1 Absorption Coefficient of Combined Plate with Porous Blanket

A common form of problem in noise control is the need to reduce the sound radiated from a duct or some other object. A way to achieve this is by lining the duct with several centimeters of porous acoustic material, and covering it with a solid plate of some type, as indicated in Figure 42.5.

Consider the case of normal incidence with the sound-absorbing structure of Figure 42.5. Assume that the boundary conditions for the sound pressure and the volume flow-rate are identical. For plane wave incidence on the hard wall, the magnitude of reflection coefficient is -1 [1]. The following equation is obtained:

$$\begin{bmatrix} 1 & -1 & -1 & 0 \\ -1 & -m_1 & m_1 & 0 \\ 0 & e^{-\gamma l_1} & e^{\gamma l_1} & -(1 + e^{-2jkl_2}) \\ 0 & m_2 e^{-\gamma l_1} & m_2 e^{\gamma l_1} & -(1 - e^{-2jkl_2}) \end{bmatrix} \begin{bmatrix} B_1 \\ A_1 \\ B_1 \\ B_2 \end{bmatrix} = \begin{bmatrix} -1 \\ -1 \\ 0 \\ 0 \end{bmatrix} \quad (42.13)$$

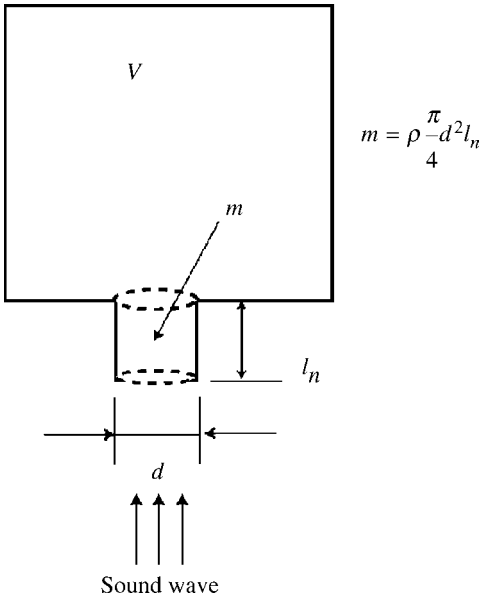


FIGURE 42.4 Geometry of a Helmholtz resonator. Volume, V , is connected to an infinitely open area by a neck tube of diameter d and length l_n .

where

$$j = \sqrt{-1}$$

$$m_1 = z_0/z_1, m_2 = z_1/z_2$$

z_0, z_1, z_2 : acoustic impedance of each medium
(Pa sec/m³)

γ = complex propagation constant (1/m)

The absorption coefficient for normal incidence is given by the following equation:

$$\alpha_0 = 1 - \left| \frac{B_0}{A_0} \right|^2 = 1 - |B_0|^2 \quad (42.14)$$

The absorption coefficient for random incidence may be approximated by

$$\alpha = \frac{1}{n} \sum_{i=1}^n \alpha(\theta)_i \quad (42.15)$$

where θ = the incident angle of sound, $0 < \theta < \pi/2$.

It is known that the propagation speed of the sound in fibrous materials changes with air, and the following equation holds on the boundary surface:

$$\sin \theta / \sin \theta' = c/c_m \quad (42.16)$$

Here, c_m is the sound speed in fibrous materials, which is calculated from the imaginary part of Equation 42.18, given later. The angle of reflection, θ' , in the boundary surface of the back air space is obtained in a similar way. Hence, the following equation is substituted in Equation 42.13 instead of the thickness of the absorber, l_1 , and the thickness of the air space, l_2 , to obtain the absorption coefficient in oblique incidence:

$$l'_1 = l_1 / \cos \theta', \quad l'_2 = l_2 / \cos \theta'' \quad (42.17)$$

The complex propagation constant, γ , is an important physical quantity in absorbing material of propagated sound, which is given per unit length of acoustic attenuations, and phase changes. Between the aeroelasticity rate, K_a , of absorbing material and the bulk modulus, Q , of absorbing material, γ is given by the following equation, for $K_a > 20 Q$ [2,3]:

$$\gamma = j\omega\sqrt{Y/K}\sqrt{\langle\rho_1\rangle - j\langle R_1\rangle/\omega} \quad (42.18)$$

$$\langle R_1 \rangle = \frac{R_1[1 - \rho_0(1 - Y)/\rho_m]}{\left[1 + \frac{\rho_0(\kappa - 1)}{\rho_m}\right]^2 \left[1 + \frac{R_1^2}{\rho_m^2 \omega^2 [1 + \rho_0(\kappa - 1)/\rho_m]^2}\right]}$$

$$\langle\rho_1\rangle = \rho_0\kappa - \frac{\frac{R_1^2(Y/\kappa + \rho_m/\rho_0\kappa)}{\rho_m^2 \omega^2 [1 + \rho_0(\kappa - 1)/\rho_m]^2} + \frac{1 + \rho_0 Y(\kappa - 1)/\rho_m \kappa}{1 + \rho_0(\kappa - 1)/\rho_m}}{1 + \frac{R_1^2}{\rho_m^2 \omega^2 [1 + \rho_0(\kappa - 1)/\rho_m]^2}}$$

where

ρ_m = density of acoustical material (kg/m³)

ρ_0 = density of air (kg/m³)

c_0 = speed of sound in air (m/sec)

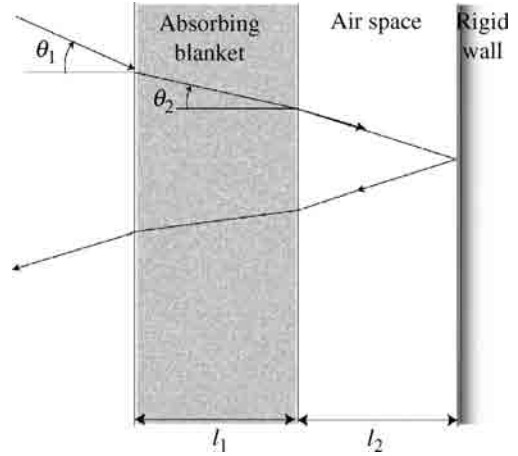


FIGURE 42.5 Structure for sound absorption using a blanket and an air space showing angles θ_1 in the air and θ_2 in the blanket.

K = volume coefficient of elasticity of air (N/m²)
 R_1 = alternating flow resistance for unit thickness of material due to the difference between the velocity of the skeleton and the velocity of air in the interstices (Pa sec/m²). R_1 values are given in Table 42.1
 Y = porosity = the ratio of the volume of the voids in the material to the total volume; porosity equals the total volume minus the fiber volume, all divided by total volume
 $\kappa = 5.5 - 4.5Y$, the structure factor of the interstices in the skeleton
 $\omega = 2\pi f$, the angular frequency (radians/sec)

The acoustic impedance, z_1 , of absorbing material is given by

$$z_1 = R + jX = -\frac{jK\gamma}{\omega Y} \tag{42.19}$$

in which

$$R = \rho_0 c_0 \left\{ 1 + 0.0571(\rho_0 f / R_f)^{-0.754} \right\}$$
$$X = -\rho_0 c_0 \left\{ 0.0870(\rho_0 f / R_f)^{-0.732} \right\}$$

42.4.2 Transmission Loss through a Single Porous Board

Assume that a sound wave impinges on the left side of a porous board at normal incidence and emerges with a reduced amplitude from the right side. The associated transmission loss of the porous board is obtained from

$$\left. \begin{aligned} & TL_0 = 10 \log_{10}(X + Y) \\ & X = \left\{ 1 + \frac{\omega^2 m^2 P R_f}{2 \rho_0 c_0 (\omega^2 m^2 P^2 + R_f^2)} \right\}^2 \\ & Y = \left\{ \frac{\omega m R_f^2}{2 \rho_0 c_0 (\omega^2 m^2 P^2 + R_f^2)} \right\}^2 \end{aligned} \right\} \tag{42.20}$$

where

m = surface density of the blanket (kg/m²)
 P = porosity of the blanket (porosity = the total volume minus the fiber volume, all divided by the total volume)
 R_f = specific flow resistance of material (Pa sec/m)

TABLE 42.1 Flow Resistance Values of Glass-Wool Board (Quality Regulation Range by JIS)

Board Type	K value	Gross Specific Gravity (kg/m ³)	Specific Flow Resistance ($\times 10^{-3}$ N sec/m ⁴)	Standard of JIS for Glass Wool
#1 Glass-wool board	8	8 \pm 2	1.5 ~ 7.0	JIS A 9505-A
	12	12 \pm 2	2.5 ~ 12.0	
	16	16 \pm 2	4.7 ~ 17.0	
	20	20 \pm 3	5.0 ~ 22.0	
	24	24 \pm 3	6.5 ~ 27.0	
#2 Glass-wool board	12	12 \pm 2	1.5 ~ 7.0	JIS A 9505-B
	16	16 \pm 2	2.5 ~ 10.0	
	20	20 \pm 3	3.0 ~ 13.0	
	24	24 \pm 3	4.0 ~ 16.0	
	32	32 \pm 4	6.0 ~ 22.0	
	48	48 \pm 5	11.0 ~ 38.0	
	64	64 \pm 6	18.0 ~ 60.0	
	96	96 \pm 10	27.0 ~ 95.0	
#3 Glass-wool board	96	96 \pm 10	15.0 ~ 40.0	JIS A 9505-C

ρ_0 = density of air (kg/m³)
 c_0 = sound speed in air (m/sec)

42.4.3 Transmission Loss through a Sandwich Board

Consider a wide wall formed by two panels (sheets) of infinite area separated with a homogeneous filling of fibrous acoustical material, as shown in Figure 42.6. Suppose that a plane wave impinges at an angle θ . As the pressure of both sides of the wall is equal with regard to the amplitude of the progressing wave and the reflected wave in each boundary surface, the following result may be established [4]:

$$\left. \begin{aligned} A_0 + B_0 &= A_1 + B_1 \\ (A_0 - B_0)/z_0 &= (A_1 - B_1)/z_1 \\ A_1 e^{-jkl'_1} + B_1 e^{jkl'_1} &= A_2 + B_2 \\ (A_1 e^{-jkl'_1} - B_1 e^{jkl'_1})/z_1 &= (A_2 - B_2)/z_2 \\ A_2 e^{-\gamma l'_2} + B_2 e^{\gamma l'_2} &= A_3 + B_3 \\ (A_2 e^{-\gamma l'_2} - B_2 e^{\gamma l'_2})/z_2 &= (A_3 - B_3)/z_3 \\ A_3 e^{-\gamma l'_3} + B_3 e^{\gamma l'_3} &= A_4 + B_4 \\ (A_3 e^{-\gamma l'_3} - B_3 e^{\gamma l'_3})/z_3 &= (A_4 - B_4)/z_0 \end{aligned} \right\} \quad (42.21)$$

where A and B are the amplitude of sound pressures.

From Equation 42.17, $l'_1 = l_1/\cos \theta_1$, $l'_2 = l_2/\cos \theta'_2$, and l'_1 and l'_2 may be calculated.

The speed of sound in the walls is given by the following equation in terms of the modulus of longitudinal elasticity, E_i :

$$c_i = \sqrt{E_i/\rho_i} \quad (42.22)$$

The real part of acoustic impedance, z_i ($i = 1, 3$), is given by $R_i = r_i/\cos \theta$, and of the imaginary part is given at $X_i = m_i\omega$. The internal resistances, r_i , are functions of such factors as the material, frequency, temperature, and density. Some typical values are given in Table 42.2.

If the space of the transmission side is infinite, B_4 in Equation 42.21 becomes equal to zero. Then, the transmission loss is given is given by

$$TL(\theta) = 10 \log_{10} \left| \frac{A_4}{A_0} \right|^2 \quad (42.23)$$

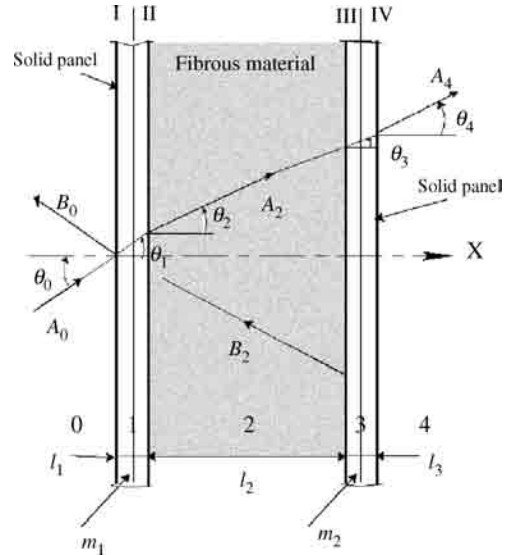


FIGURE 42.6 Cross-sectional view of a sandwich panel.

TABLE 42.2 Internal Resistance Values of Several Useful Materials

Material	Thickness (mm)	Internal Resistance (Pa sec/m ³)
Aluminum	0.4	3.0
Plywood	3.0	7.5
Plaster board	7.0	15.0

42.5 Attenuation of Lined Ducts

42.5.1 Computation of Attenuation in a Lined Duct

A lined duct is an air passage with one or more of the interior surfaces covered with an acoustical material such as a glass or mineral fiber blanket. The parallel baffles are merely a series of side-by-side ducts that generally have a rectangular or round cross section. If the walls are covered with absorptive material, attenuation will occur because of the viscous motion of the air in and out of the porous of blanket.

Figure 42.7 shows an isometric illustration of a lined duct. The attenuation of sound for a lined duct is dependent primarily on the duct length, l_e , the thickness of the lining, b , the density of the lining, ρ , the width of the air passage, l , and the wavelength of sound, λ . At low frequencies ($l/\lambda < 0.1$), the attenuation of sound in a lined duct may be calculated from the following empirical formula:

$$ATT = K_1 P/S \tag{42.24}$$

where

K_1 = the coefficient, which is determined from the random incidence absorption coefficient of lined material, given in the chart of Figure 42.8

P = acoustically lined perimeter of duct (m)

S = cross-sectional open area of duct (m²)

If the absorbing material is lined in the rectangular cross section as shown in Figure 42.9 to Figure 42.11, the attenuation can be estimated using the formulas given in Table 42.3 [5].

42.5.2 Attenuation in a Lined Bend

A lined bend duct is shown in Figure 42.12. The insertion loss, IL, of a lined bend results from two mechanisms: the reflection of sound back toward the source side, and the scattering of sound energy into the high-frequency region is rapidly attenuated by the lining beyond the bend. Higher-frequency modes will be attenuated by even an unlined duct for frequencies below the ratio of the air passage between the linings to the wavelength of sound equal to 0.5. At frequencies well above this ratio, the insertion loss of a lined bend is expected to be comparable to the reverberant-field

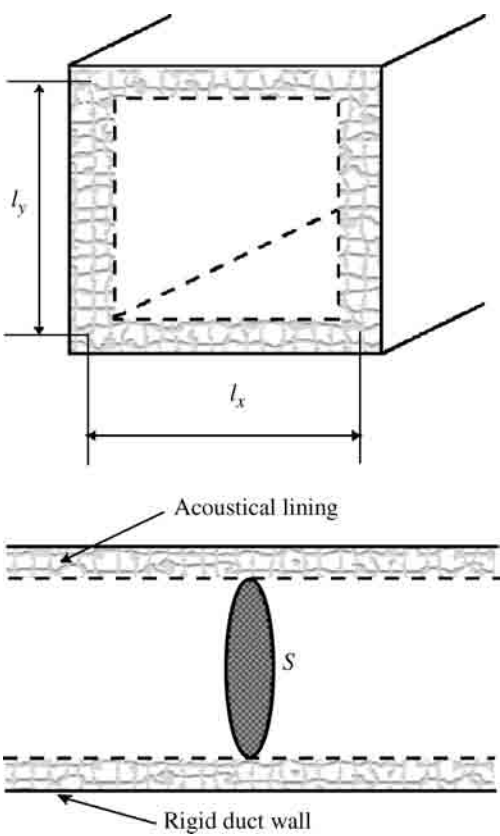


FIGURE 42.7 Illustration of a lined duct.

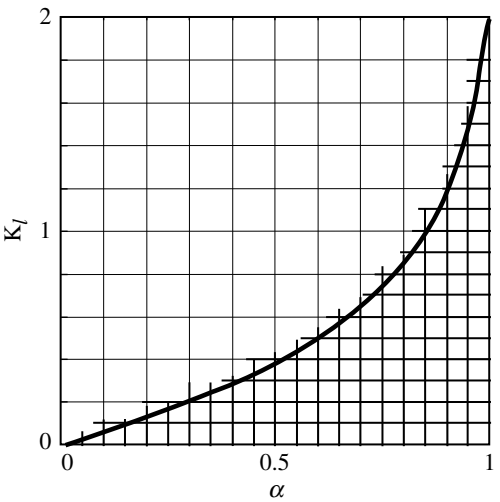


FIGURE 42.8 K_1 value for sound-absorption coefficient by reverberation room method.

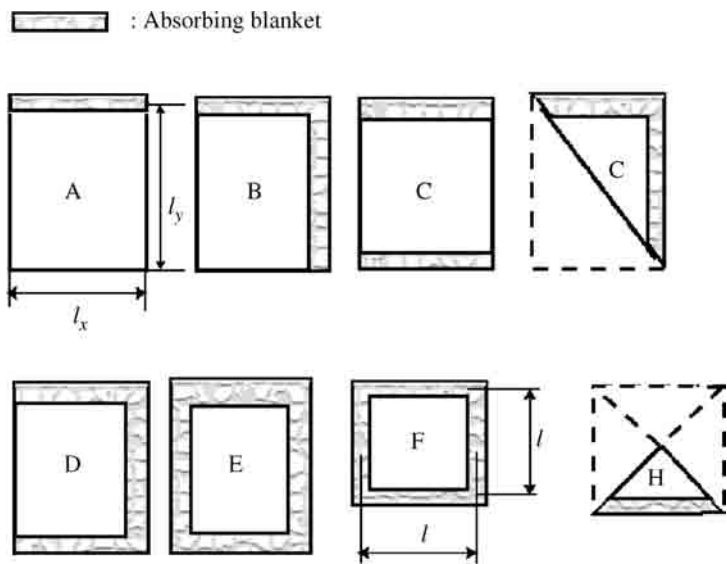


FIGURE 42.9 Duct-liner configurations corresponding to Table 42.3.

end correction derived for the duct. The insertion loss of a lined bend may be obtained as following equation [6]:

$$IL = \frac{K_1 P}{S} + (l_1 + l_2) + \Phi \tag{42.25}$$

where Φ is obtained from Figure 42.13.

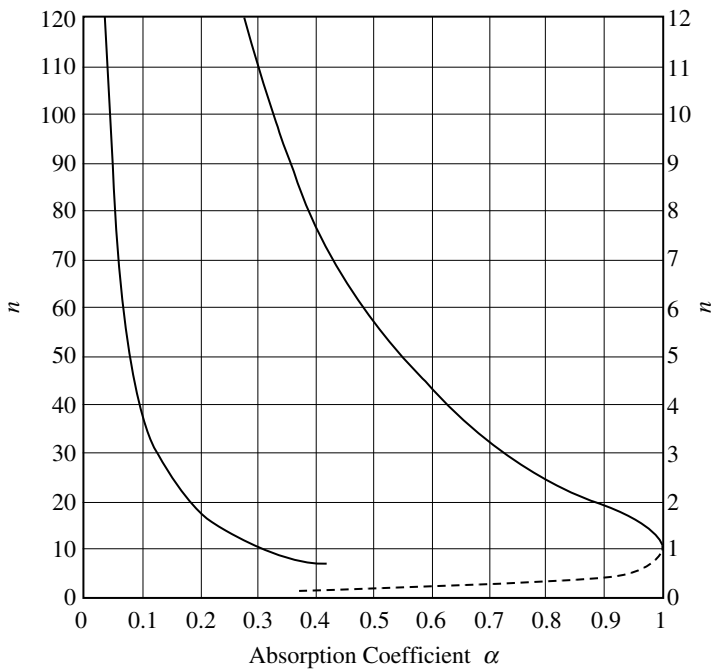


FIGURE 42.10 Relationship between absorption coefficient and stationary wave factor, n .

The total insertion loss for a lined bend is given in Figure 42.13 along with the attenuation of the lining beyond the bend.

42.5.3 Attenuation in Splitter Lined Duct

The use of parallel or zigzag baffle-type separators (splitters) to increase the perimeter–area ratio results in more compact attenuators. In rock-wool blankets, the attenuation of a parallel type splitter duct may be obtained directly from Figure 42.14. The peak value of the attenuation is related to wavelength of sound and the splitter interval. With the zigzag arrangement of acoustic blankets, the attenuation of high frequencies is improved over that of the parallel splitter [7].

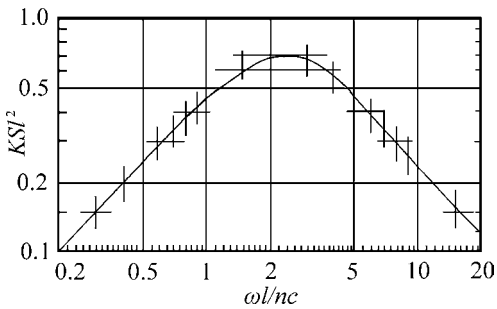


FIGURE 42.11 Damping function KSL^2 as a function of dimensionless frequency, $\omega l / nc$.

42.6 Attenuation of Dissipative Mufflers

42.6.1 Transmission Loss of Lined Expansion Chamber

The geometry and nomenclature for a dissipative muffler are given in Figure 42.15. For $f < 1.2c/D$, the assumption of plane wave is acceptable where D = the diameter of the muffler.

The transmission loss for the light lining in the chamber may be obtained using [8,9]:

$$TL = 10 \log_{10} \left[\left\{ \cosh(\delta_e l_e / 2) + \frac{m+1}{2m} \sinh(\delta_e l_e / 2) \right\}^2 \cos^2 kl_e + \left\{ \sinh(\delta_e l_e / 2) + \frac{m+1}{2m} \cosh(\delta_e l_e / 2) \right\}^2 \sin^2 kl_e \right] \quad (42.26)$$

TABLE 42.3 Formulas for Attenuation of Several Lined Ducts

See Figure 42.7	Low-Frequencies Range: $\frac{\omega l}{nc} < 1$	Middle-Frequencies Range ($K_y S_y l_y$; see Figure 42.7)	High-Frequencies Range: $\frac{\omega l}{nc} > 5$
(A)	$\beta = \frac{4.34}{nl_y}$	$\beta = \frac{8.7c}{l_y^2 \omega} (K_y S_y l_y^2)$	$\beta = 21.4 \frac{c^2 n}{\omega^2 l_y^3}$
(B)	$\beta = 4.34 \left(\frac{1}{n_y l_y} + \frac{1}{n_x l_x} \right)$	$\beta = \frac{8.7c}{\omega} \left(\frac{K_y S_y l_y^2}{l_y^2} + \frac{K_x S_x l_x^2}{l_x^2} \right)$	$\beta = 21.4 \frac{c^2}{\omega^2} \left(\frac{n_y}{l_y^3} + \frac{n_x}{l_x^3} \right)$
(C)	$\beta = \frac{8.7}{nl_y}$	$\beta = \frac{34.7c}{l_y^2 \omega} \left(\frac{K_y S_y l_y^2}{4} \right)$	$\beta = 171 \frac{c^2}{\omega^2} \frac{n_y}{l_y^3}$
(D)	$\beta = 4.34 \left(\frac{2}{n_y l_y} + \frac{1}{n_x l_x} \right)$	$\beta = \frac{8.7c}{\omega} \left(\frac{K_y S_y l_y^2}{l_y^2} + \frac{K_x S_x l_x^2}{l_x^2} \right)$	$\beta = 21.4 \frac{c^2}{\omega^2} \left(\frac{8n_y}{l_y^3} + \frac{n_x}{l_x^3} \right)$
(E)	$\beta = 8.7 \left(\frac{1}{n_y l_y} + \frac{1}{n_x l_x} \right)$	$\beta = \frac{34.7c}{\omega} \left(\frac{K_y S_y l_y^2}{4l_y^2} + \frac{K_x S_x l_x^2}{4l_x^2} \right)$	$\beta = \frac{171c^2}{\omega^2} \left(\frac{n_y}{l_y^3} + \frac{n_x}{l_x^3} \right)$
(F)	$\beta = \frac{17.4}{nl}$	$\beta = \frac{69.5c}{4l^2 \omega} KSL^2$	$\beta = \frac{341c^2 n}{\omega^2 l^3}$

β is attenuation (dB/m), n is absorbing factor plotted in Figure 42.7, $K_y S_y l_y$ is damping function, plotted in Figure 42.8, c is sound speed, l is the width of the duct, $\omega = 2\pi f$: angular frequency, x, y : coordinates, see Figure 42.7.

Source: Brüel, P.V. 1951. *Sound Insulation and Room Acoustics*, Chapman & Hall, London, p.159. With permission.

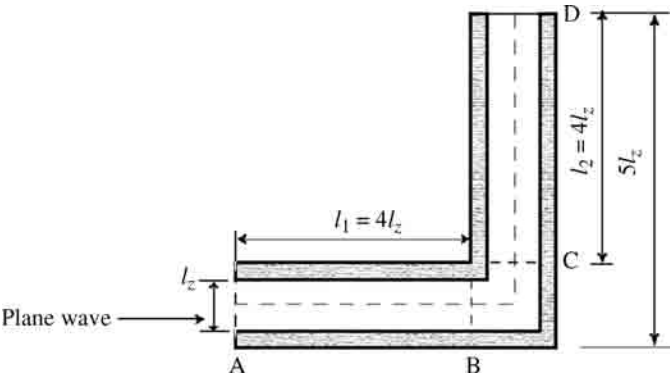


FIGURE 42.12 Sketch of a typical lined bend with plane wave incidence. (Source: Beranek, L.L. *Noise Reduction*, McGraw-Hill, 1960. With permission.)

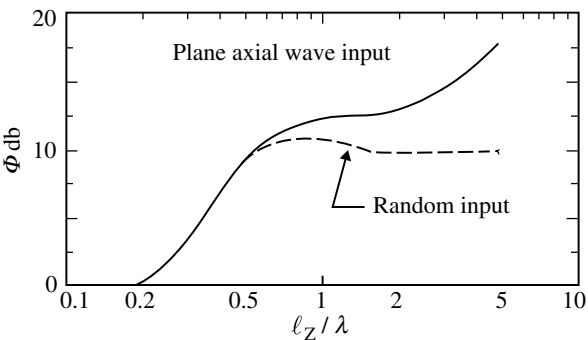


FIGURE 42.13 Insertion loss for lined bend. (The lining must extend two to four duct widths beyond the bend for this data to be valid.) (Source: Beranek, L.L. *Noise Reduction*, McGraw-Hill, 1960. With permission.)

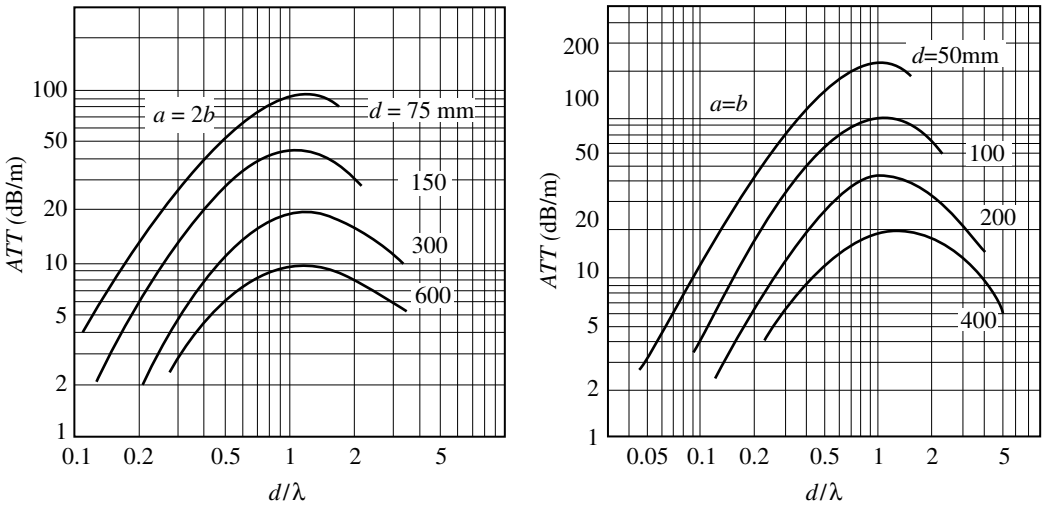


FIGURE 42.14 Sound attenuation for a splitter duct. Each baffle is constructed with two sheets of perforated metal filled with mineral wool, with about 100 to 140 kg/m³ gross density; a = the width of the open space, b = the width of the baffle, d = the center-to-center distance of baffles, λ = the wavelength of the sound.

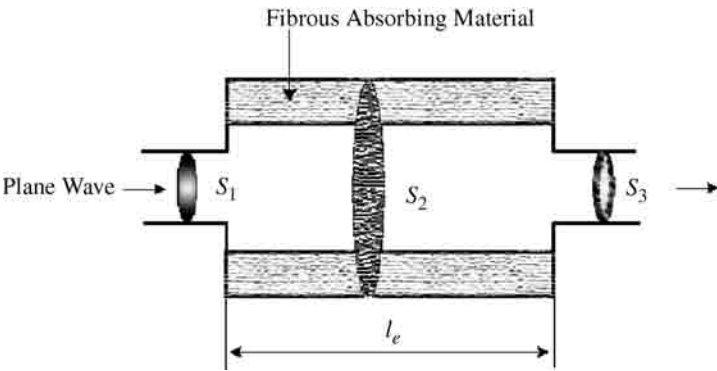


FIGURE 42.15 A dissipative muffler.

TABLE 42.4 Filled up Factor of Glass Wool, α_g

V_g/V	0.05	0.10	0.15	0.20	0.30	0.40	0.50	0.60	0.70	0.80	0.90	1.00
α_g	0.106	0.124	0.288	0.365	0.529	0.677	0.794	0.885	0.935	0.960	0.987	1.0

V_g = Filled up volume (factors of 100 kg/m³), V = Volume of chamber

in which δ_e = the attenuation per unit length for the lined duct, which is given by the following equation:

$$20 \log_{10}(\delta_e l_e) = \frac{K_1 P l_e}{S} \tag{42.27}$$

The K_1 values are obtained from the absorption coefficient, as shown earlier (see Figure 42.8). In particular, δ_e is given by

$$\delta_e = \frac{1}{l_e} 10^{0.05 K_1 P l_e / S} \tag{42.28}$$

where m = the ratio of the area of expanded or lined sections to the area of inlet or outlet sections of muffler; $k = 2\pi f/c$, and l_e = the length of the muffler.

The transmission loss for the case of a thick lining of glass wool in the chamber is obtained using the empirical formula [10]

$$TL = 10 \log_{10} \left[1 + \left\{ \frac{1}{2} \alpha_g m k l_e \right\}^2 \right] \tag{42.29}$$

where

α_g = the coefficient, which is obtained from Table 42.4, using the filling volume and the density of glass wool

m = the ratio of the area of expanded or lined sections to the area of inlet or outlet sections of muffler

$k = 2\pi f/c$

l_e = the length of muffler

42.6.2 Transmission Loss of a Plenum Chamber

The geometry and nomenclature for a plenum chamber are given in Figure 42.16. A plenum chamber is similar in many ways to a lined expansion chamber. The main difference is that the inlet and outlet of a plenum chamber are not located in line. Generally, there is an offset to direct transmission of sound. Sound is reflected at the square-cornered bend as the cross section dimension of the duct is

sufficiently large. Particularly at high frequencies, almost all of the sound energy may reflect many times off the lined sides when propagating from the inlet to the outlet. The transmission loss of a single plenum chamber can be obtained approximately from [11]:

$$TL = 10 \log_{10} \left\{ S_w \left(\frac{\cos \theta}{2\pi d^2} + \frac{1}{R} \right) \right\} \quad (42.30)$$

where

- $S_w = IW =$ area of the inlet and outlet
- $d = \{(L - l)^2 + H^2\}^{1/2} =$ the slant distance from inlet to outlet
- $\cos \theta = H/d$
- $R = a/(1 - \alpha_m)$
- $a =$ the total lined area in chamber times absorption coefficient
- $\alpha_m =$ the statistical absorption coefficient of the lining

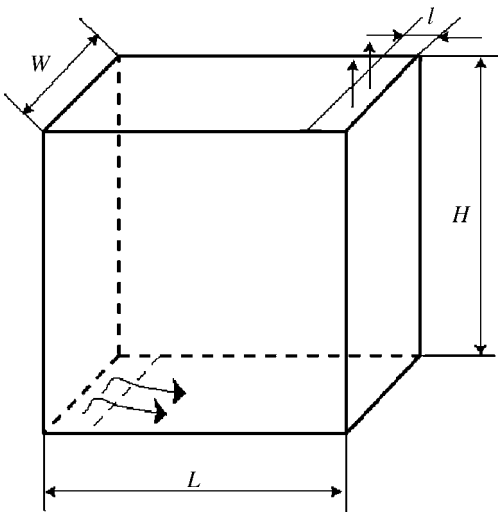


FIGURE 42.16 A single-plenum chamber showing the nomenclature used in Equation 42.26.

42.7 General Considerations

In order to carry out the design of noise-control measures for a particular problem, we must consider not only the fundamental acoustical properties of the material as discussed before, but also such practical aspects of the problem as (1) gas flow velocities, (2) temperature of gas, (3) moisture exposure, and (4) head losses for gas-flow. The client depends heavily on the expertise of the designer to realize adequate protection of the noise-control equipment under operating conditions.

42.7.1 Surface Treatment with Lining of Acoustic Material

Fibrous material in the market has some form of resin binder. Comparatively long fiber flocculent and comparatively short fiber are available. The packaging density of flocculent is about 60 to 100 kg/m³. It is necessary to cover with perforated thin metal or wire netting so that an arbitrary shape may be maintained in the absorbing material. The perforated metal does not take into account the numerical aperture, hole shape, hole diameter, and metal thickness. From the acoustic viewpoint, a suitable numerical aperture is given in Table 42.5.

42.7.2 Gas Flow Velocity

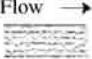




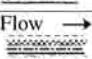
Noise control problems often involve the use of an acoustical material in high-velocity gas-flow such as those found in the exhaust of engines or ventilating systems. Deterioration of the acoustical

TABLE 42.5 Perforated Metal for Treatment of Absorbing Material (Gas Flow Velocity is 25 m/sec or Less)

Perforation rate: 30 to 50%
Hole diameter: 5 to 10 mm
Hole shape: round, plus, slit and interminglement
Metal: iron, stainless steel (used in case of the corrosive gas)

material due to high-velocity gas flowing past it can be a serious problem. In addition, turbulence in the gas flow subjects the materials to vibration and can cause further deterioration. One solution to this problem is to install the acoustical material behind some form of protective facing, which will vary in complexity depending on the gas velocity.

A limited amount of information on this subject is available through field experience, as shown in Figure 42.17 [12]. However, the parameters of the treatment structure are not well established, for example, those concerning perforated metal, wire net, absorbing material, and gas flow. Multiple layers are used under conditions of flow velocity exceeding 25 m/sec, and the associated performance analysis can become rather complex.

Surface Treatments with Gas Flow		
$u < 8 \text{ m/s}$	Flow → 	
$8 < u < 10$	Flow → 	
$10 < u < 25$	Flow → 	Perforated metal Glass fiber cloth
$25 < u < 40$	Flow → 	Wire screen
$40 < u < 60$	Flow → 	Two corrugated steel sheets
$60 < u < 100$	Flow → 	Blanket

42.7.3 Gas Temperature

In many noise-control problems, temperature is a very important factor. Sometimes high-temperature ducts that are radiating noise, for example, in diesel engines, and induced draft fans, must be wrapped. With a proper choice, it is possible to combine thermal and acoustical insulations using one single material. Under extremely high temperatures, the tensile strength of materials tends to decrease, and the material may be subjected to thermal shock.

Examples of absorbing materials that are currently available for use where temperature is an important consideration are given in Table 42.6.

FIGURE 42.17 Protective surface for absorbing material subjected to high-velocity gas flow.

42.7.4 Dust and Water Exposure

The holes of perforated metal can be blocked if a dust treatment is not carried out, and the sound absorption performance will deteriorate with adhesion to the surface of the absorbing material. Methods of dust accumulation and removal may be designed into cavity type mufflers used on the sound absorption equipment.

A fan of a cooling tower, for example, experiences a considerable amount of moisture. Precautions must be taken so that water droplets are not deposited on the sound absorbing material. The underside of the equipment should be treated with rust prevention material. Figure 42.18 shows the degradation

TABLE 42.6 Fibrous Materials of Use in Hot Gas Flows

Materials	Maximum Allowable Temperature (°C)
Glass fibers with binder	320 ~ 360
Glass wool	960 ~ 1060
Mineral wool felts	1160
Mineral wool	1660
Asbestos fibers	760
Alumina-silica	1900

of the acoustic characteristic of absorbing material due to moisture, using the normal incidence absorption coefficient [13].

42.8 Practical Example of Dissipative Muffler

An example is given on the design of a dissipative muffler for noise reduction in an axial-flow fan for a ventilation system.

1. Specification of the axial-flow fan

- Volume flow rate: $Q = 125 \text{ m}^3/\text{min}$
- Wind pressure: $p = 80 \text{ mm Aq}$
- Rotor blade number: $Z = 10$
- Stationary blade number: $Z_s = 5$
- Rotational speed: $N = 2580 \text{ rpm}$
- Shaft horsepower: $P = 3.75 \text{ kW}$

2. The desired values of attenuation and head loss with the muffler installation follow. The noise of the fan propagates both intake and discharge sides. A performance level (noise reduction) of about 37.5 dB is required, when specific sound level K_s is obtained on the basis of the axial-flow fan specification given by

$$K_s = L_A - 10 \log_{10}(p^2 Q) \quad (42.31)$$

3. Figure 42.19 gives the noise spectrum for the axial-flow fan. The blade passing frequency, BPF, is a fundamental component of the velocity fluctuation as the flow passes the blades. It is seen in the noise spectrum in Figure 42.19 at 430 Hz ($Q \times Z = (2580/60) \times 10$). By adding the background noise spectrum to this spectrum, it is seen that a muffler that provides an attenuation over 20 dB near 430 Hz, and about 15 dB in the frequency range of 800 to 1000 Hz is necessary. The head loss value of the muffler is to be maintained within 4 mm Aq.

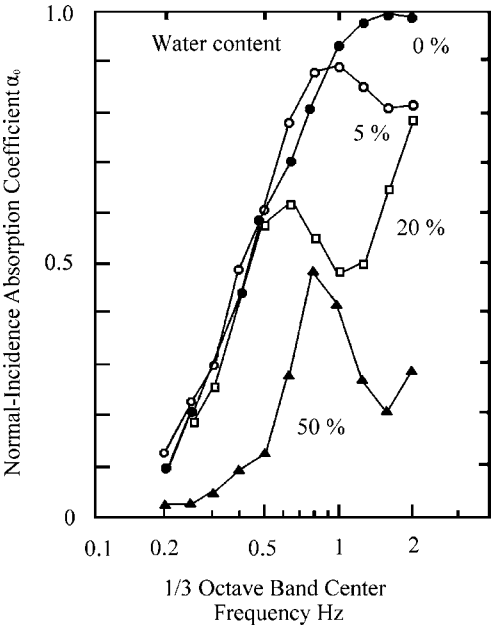


FIGURE 42.18 Degradation of the absorption coefficient by water content.

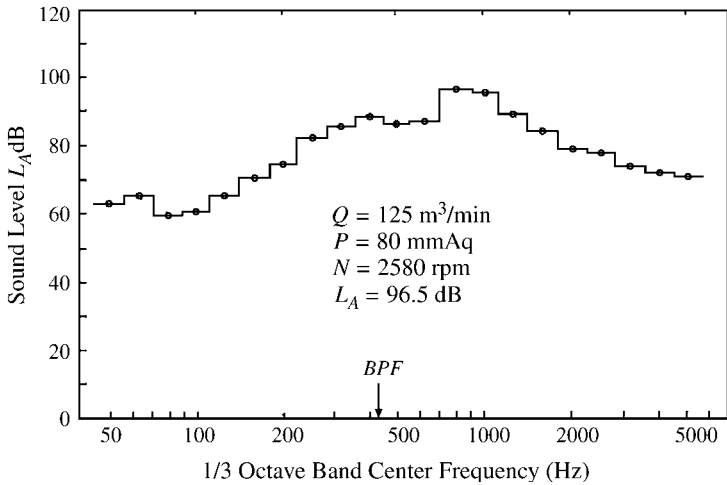


FIGURE 42.19 Noise spectrum of the axial flow fan of a factory ventilation system.

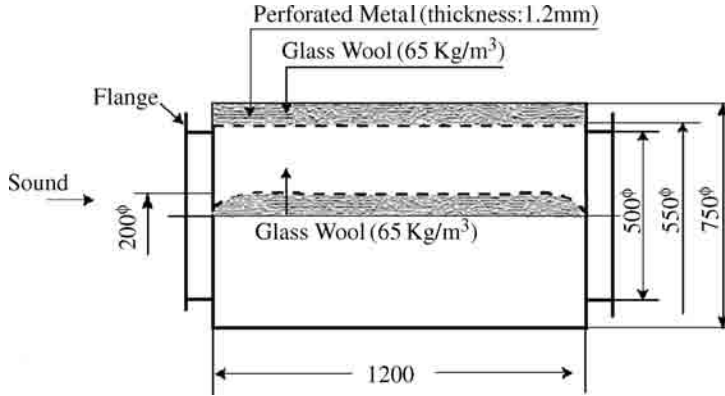


FIGURE 42.20 Half cross-sectional view of dissipative muffler for the axial flow fan.

4. The structure of the dissipative muffler is shown in Figure 42.20. The maximum value of outer diameter of the muffler is 750 mm, and the length chosen to optimize the performance.
5. The packing density of glass wool is chosen as 65 kg/m^3 . The surface treatment of glass wool uses perforated metal with 1 mm thickness, 36% open area with 6 mm hole diameter. A sound absorption body of 200 mm diameter is supported in the center part, and it is welded to the outside cylinder by three props in the flow direction, and two in the circumferential direction.
6. The attenuation characteristics of the dissipative muffler may be calculated using Equation 42.27

$$TL = 10 \log_{10} \left[1 + \left\{ \frac{1}{2} \alpha_g m k l_e \right\}^2 \right]$$

The proportion of the volume of glass wool filled into the muffler is approximately $(0.75^2 - 0.55^2 + 0.2^2)/0.75^2 = 0.53$. For a packing density of 100 kg/m^3 , we have $0.53 \times 65/100 = 0.347$. The value of $\alpha_g \approx 0.6$ is obtained from Table 42.2.

The required expansion ratio, m , length, l_e , and wave number, k , are given by

$$m = (750/500)^2 = 2.25, \quad l_e = 1.2 \text{ m}, \quad k = 2\pi f/c$$

The speed of sound c depends on the environmental temperature. For a temperature of 25°C , we get 346.5 m/sec ($= 331.5 + 0.6 \times 25$). The TL values at 100 to 1000 Hz are calculated. We have

$$f = 100 \text{ Hz}; \quad TL = 5.0 \text{ dB}$$

$$f = 430 \text{ Hz}; \quad TL = 16.1 \text{ dB}$$

$$f = 1000 \text{ Hz}; \quad TL = 23.4 \text{ dB}$$

The flow velocity satisfies desired value of head loss p_{loss} (in mm Aq), and is calculated by following empirical equation [12]:

$$p_{\text{loss}} = \left\{ 0.142 m_f^{-0.1} \left(\frac{l_e}{d_1} \right)^{3/4} \left(\frac{d_m}{d_1} \right)^{-1/3} \right\} \frac{u^2}{g} \quad (42.32)$$

Use the numerical values as follows:

- $m_f = (550/500)^2 = 1.21$, ratio of cross-sectional area between air passage and muffler.
- $d_1 = 500 \text{ mm}$, diameter of inlet.
- $l_e = 1.2 \text{ m}$, length of muffler.
- $d_m = 200 \text{ mm}$, diameter of absorption body.
- $u = 10 \text{ m/sec}$ or less, flow velocity at inlet.
- $g = 9.8 \text{ m/sec}^2$, acceleration of gravity force.

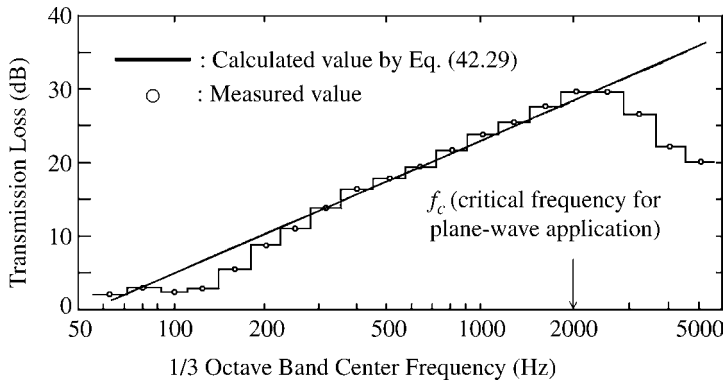


FIGURE 42.21 Noise-reduction characteristics of the designed dissipative muffler.

The corresponding head loss is 3.25 mm Aq, which corresponds to JIS B 833, and nearly agrees with the predicted value. Specifically, the condition of 4 mm Aq or less of the designed value is satisfied. The connection of axial-flow fan and the muffler uses vibration isolation, using the thick synthetic rubber.

7. The result of the attenuation realized from the spectrum after the muffler installation is shown in Figure 42.21. It is proven that the attenuation characteristics almost parallel the designed value. The frequency range where the approximation is valid is given by

$$f < c/d = 346.5/0.175 = 1980 \text{ Hz}$$

For frequencies below 250 Hz, the estimated result of the attenuation becomes slightly overestimated.

References

1. Obata, T., Hirata, M., Nishiwaki, N., Ohnaka, I., and Kato, K., Noise reduction characteristics of dissipative mufflers, 1st report, acoustical characteristics of fibrous materials, *Trans. Japan Soc. Mech. Eng.*, 42, 363, 3500, 1976.
2. Zwicker, C. and Kosten, C.W. 1949. *Sound Absorbing Materials*, Elsevier, New York.
3. Beranek, L.L., Acoustical properties of homogeneous isotropic rigid tiles and flexible blankets, *J. Acoust. Soc. Am.*, 19, 4, 556, 1947.
4. Obata, T. and Hirata, M., Estimation of acoustical transmission loss for combined walls, *Proc. Japan Soc. Mech. Eng. Annu. Meet.*, 780, 1, 42, 1978.
5. Brüel, P.V. 1951. *Sound Insulation and Room Acoustics*, Chapman & Hall, London, p. 159.
6. Beranek, L.L. 1971. *Noise and Vibration Control*, McGraw-Hill, New York, chap. 17, p. 390.
7. King, A.J., Attenuation of lined ducts, *J. Acoust. Soc. Am.*, 30, 6, 505, 1958.
8. Davis, D.D. Jr. and Stokes, G.M., 1954. *Natl. Advisory Comm. Aeronaut. Ann. Rept.*, 1192.
9. Davis, D.D. Jr. 1957. *Acoustical Filters and Mufflers. Handbook of Noise Control*, C.M. Harris, Ed., McGraw-Hill, New York, chap. 21.
10. Hagi, S., Studies on Silencer for Ventilating System, A Doctoral Thesis of University of Tokyo, 1961.
11. Wells, R.J., Acoustical plenum chambers, *Noise Control*, 4, 4, 9, 1958.
12. Obata, T. and Hirata, M., Estimation of acoustic power of flow-generated noise within silencer and head losses, *J. Acoust. Soc. Japan*, 34, 9, 532, 1978.
13. Koyasu, M., Acoustical properties of fibrous materials, personal letter, RC-SC35, *Japan Soc. Mech. Eng. Div. Meet.*, 15, 1975.

43

Design of Reactive Mufflers

43.1	Introduction	43-1
43.2	Fundamental Equations	43-2
	Analytical Model • Boundary Conditions	
43.3	Effects of Reactive Mufflers	43-3
	Insertion Loss • Transmission Loss	
43.4	Calculation Procedure	43-5
43.5	Application Range of Model	43-6
	Condition for Approximation of Plane Wave • Effect of Temperature • Effect of Gas Flow in Pipe • Effect of Friction Loss in Pipe	
43.6	Practical Example	43-13
	Expansion-Type Muffler for Reciprocating Compressor	

Teruo Obata
Teikyo University

Summary

This chapter concerns the design of noise suppression devices such as mufflers. In particular, reactive mufflers that are inserted into long ducts are considered in detail. Analytical and empirical equations and information that are useful in the modeling and analysis of mufflers are presented, with an indication of their application ranges and limitations. A design procedure, complete with the necessary computations, is given. Methodologies and parameters of the performance analysis of acoustic systems with mufflers are indicated. An illustrative example of a muffler for a double-acting reciprocating compressor is presented.

43.1 Introduction

In noise-reduction applications, the need for a reactive muffler usually arises when transporting gas through a duct. For sound transmission through the duct to be minimized, an acoustic suppression device must be incorporated into the duct system. For example, in internal-combustion engines, it is required to reduce the intake and exhaust noise to acceptable levels. This may be accomplished by inserting a muffler in the intake and exhaust ducting to attenuate the pressure pulsations before they reach the environment.

A successful muffler design must satisfy at least the following three criteria: (1) muffler performance as a function of frequency (the maximum permissible noise generated by the gas flow through the muffler may have to be specified as well); (2) the maximum permissible average pressure drop through the muffler at a given temperature and mass flow; (3) the maximum allowable volume and restrictions on space utilization.

The customer may ask for a muffler with unrealistically high noise attenuation, virtually no backpressure, and very small size. In addition, it is important to the customer that the muffler is inexpensive and durable, and presents no maintenance problems. Needless to say, in practice, these

criteria for muffler design are unrealistic, and have to be modified to practical levels. In this chapter, we will present some of the analytical and empirical tools that are helpful in muffler design.

43.2 Fundamental Equations

43.2.1 Analytical Model

The physical behavior of a reactive muffler may be adequately modeled by linear differential equations. The law of conservation of mass must hold, while three simultaneous equations, Newton's, Boyle–Charles, and that of conservation, must be satisfied. When these equations are combined, we obtain the wave equation for the plane, one-dimensional sound-pressure wave:

$$\frac{\partial^2 \xi}{\partial t^2} = c^2 \frac{\partial^2 \xi}{\partial x^2} \quad (43.1)$$

$$p = \rho c^2 \frac{\partial \xi}{\partial x} \quad (43.2)$$

where

ξ = displacement of particle motion (m)

c = velocity of sound (m/sec)

p = sound pressure (Pa)

ρ = density of air (kg/m³)

t = time (sec)

x = coordinate system along which wave travels (m)

The stationary solutions for angular frequency ω of Equation 43.1 and Equation 43.2 are given by

$$\xi = (A e^{-jkx} - B e^{jkx}) e^{j\omega t} \quad (43.3)$$

$$p = -\rho c^2 k (A e^{-jkx} + B e^{jkx}) e^{j\omega t} \quad (43.4)$$

where A, B = amplitudes of sound pressure or particle motion for traveling and reflecting waves, $k = 2\pi f/c$, wave number, and $j = \sqrt{-1}$.

43.2.2 Boundary Conditions

The boundary conditions are given below.

(1) *Sound source.* The sound source is assumed to be independent of the existence of the muffler, and the volume rate of the particles is assumed constant, as given by

$$S \dot{\xi} = \text{const} \quad (43.5)$$

in which $\dot{\cdot}$ denotes the time derivative.

(2) *Open end of duct.* The reflection coefficient, R , at the open end of an unflanged circular pipe is available, and is given by

$$R = \frac{B e^{jkx}}{A e^{-jkx}} \quad (43.6)$$

The magnitude of the reflection coefficient, $|R|$, is shown in Figure 43.1a as a function of ka , where a is the pipe radius. The phase shift can be determined from Figure 43.1b, which is a plot of α/a as a function of ka . Also, the reflection coefficient is [1]:

$$R = -|R| e^{-2jk\alpha} \quad (43.7)$$

For the small values of ka that are most often encountered in reactive muffler design, $|R| \approx 1$ and $\alpha/a = 0.613$.

(3) *Closed end.* The displacement of particle motion is zero at a rigid wall. Hence, we have

$$\xi = 0 \quad (43.8)$$

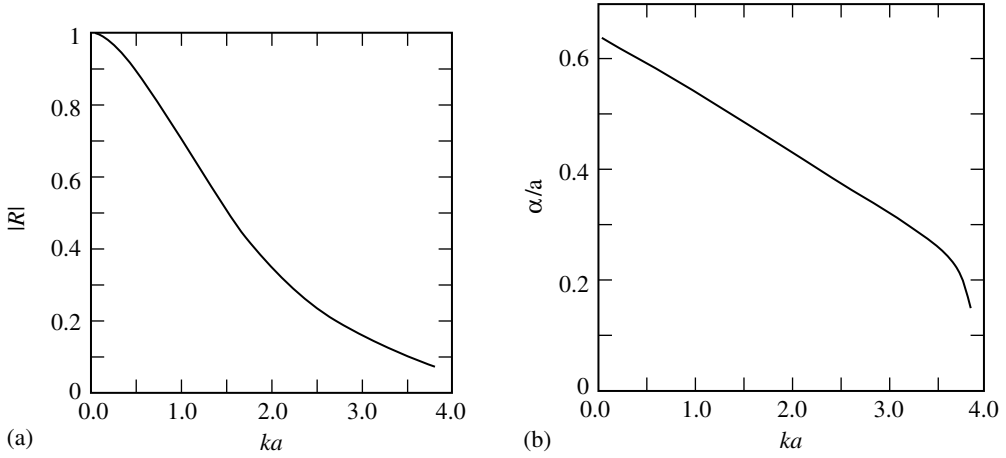


FIGURE 43.1 (a) Magnitude of the reflection coefficient at open end of an unflanged circular pipe; (b) End correction for an unflanged circular pipe. (Source: Levine, H. and Schwinger, J., On the radiation of sound from an unflanged circular pipe, *J. Phys. Rev.*, 73, 383, 1948. With permission.)

(4) *Junction conditions.* The following equations correspond to the continuity of volume flow rate of the particles and the continuity of pressure, even if the cross section changes suddenly:

$$S_i \dot{\xi}_i = S_{i+1} \dot{\xi}_{i+1} \quad (43.9)$$

$$p_i = p_{i+1} \quad (43.10)$$

43.3 Effects of Reactive Mufflers

The acoustic behavior of a reactive muffler may be expressed in term of the insertion loss, the difference in the noise levels measured at some external point with and without the muffler in the system. The transmission loss is defined as the insertion loss for a nonreflecting source and the end of exhaust duct.

43.3.1 Insertion Loss

A single expansion-type muffler installation is shown schematically in Figure 43.2. At the open end of a pipe, as in Figure 43.2, the traveled and reflected waves of the source become $A_0 e^{-jkl}$, $B_0 e^{jkl}$, over a length l , where the amplitudes are denoted by A_0 , B_0 . The reflective coefficient for length l_0 is given by

$$R_0 = \frac{B_0 e^{jkl_0}}{A_0 e^{-jkl_0}} \quad (43.11)$$

This is obtained from Equation 43.6 with $x = l_0$.

The energy, W_0 , of the acoustic wave escaping from the open end of the pipe is given by

$$W_0 \propto \frac{S_0 A_0^2 (1 - R_0^2)}{\rho_0 c_0} \quad (43.12)$$

in which ρ_0 = density of air, and c_0 = speed of sound in air. The equation of the sound-pressure level measured at an open point at some distance is given by

$$p_0 = 10 \log_{10} \left(\frac{Q_d}{4\pi r_0^2} + \frac{4}{R_r} \right) + PWL_{r_0} \quad (43.13)$$

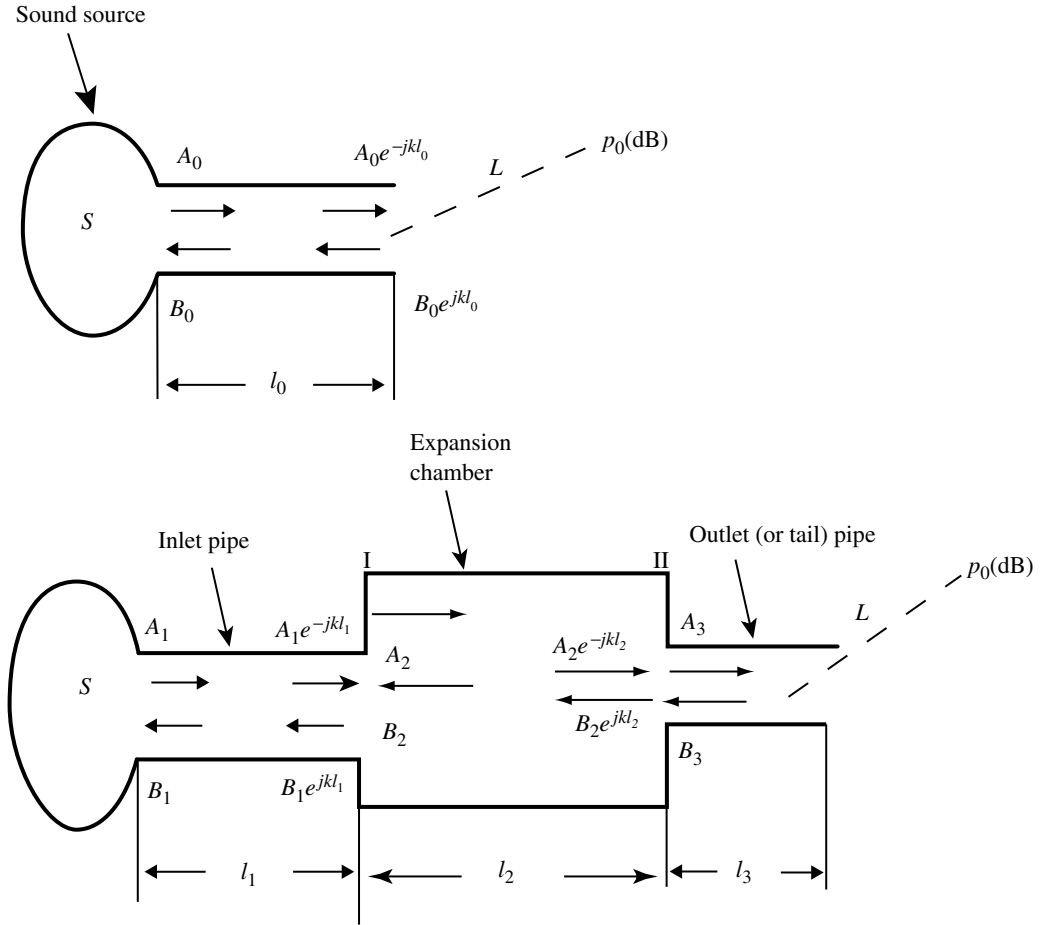


FIGURE 43.2 Measurement of insertion loss.

where

r_0 = distance

$R_r = A/(1 - \alpha)$, room constant

A = the indoor sound absorbing power (indoor surface area times indoor average absorption coefficient)

α = the indoor average absorption coefficient

Q_d = the directivity factor from the open end

Therefore, the measured value of insertion loss can be obtained from Equation 43.14, when Q_d values are equal. Power level is defined as

$$\text{PWL} = 10 \log_{10} \left(\frac{W}{10^{-12}} \right)$$

Now,

$$\text{IL} = \text{PWL}_{r_0} - \text{PWL}_r \quad (43.14)$$

Using Equation 43.14, it can be shown that IL can be expressed by

$$\text{IL} = 10 \log_{10} \left| \frac{S_0}{S_3} \left| \frac{A_0}{A_3} \right|^2 \right| \left| \frac{1 - R_0^2}{1 - R_3^2} \right| \quad (43.15)$$

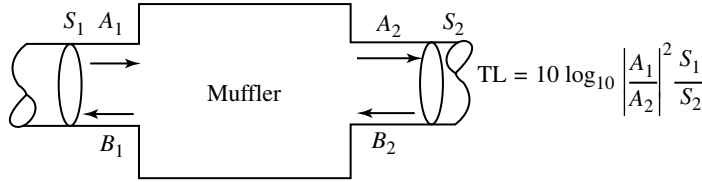


FIGURE 43.3 Definition of transmission loss for a muffler.

3.2 Transmission Loss

It is desirable to eliminate the source and radiation characteristics from the system in Figure 43.3, and to look only at some property of the muffler itself. This may be accomplished by defining a quantity called “transmission loss” (TL) as follows:

$$TL = 10 \log_{10} \left| \frac{A_1}{A_2} \right|^2 \frac{S_1}{S_2} \quad (43.16)$$

In the measurement of TL, it is difficult to separate the reflected wave. The theoretical calculation is easy and useful.

43.4 Calculation Procedure

For the reactive muffler shown in Figure 43.2, the following equations are obtained from Equation 43.5 to Equation 43.7 and Equation 43.9. The inlet pipe, cavity, and tail pipe are denoted by suffix in the figure [2].

- (1) The sound source:

$$S_0(A_0 - B_0) = S_1(A_1 - B_1) \quad (43.17)$$

- (2) The open end of pipes:

$$\left. \begin{aligned} B_0 e^{jkl_0} &= A_0 e^{-jkl_0} R_0 \\ B_3 e^{jkl_3} &= A_3 e^{-jkl_3} R_3 \end{aligned} \right\} \quad (43.18)$$

- (3) The sudden expansion (junction I):

$$\left. \begin{aligned} A_1 e^{-jkl_1} + B_1 e^{jkl_1} &= A_2 + B_2 \\ S_1(A_1 e^{-jkl_1} - B_1 e^{jkl_1}) &= S_2(A_2 - B_2) \end{aligned} \right\} \quad (43.19)$$

- (4) The sudden contraction (junction II):

$$\left. \begin{aligned} A_2 e^{-jkl_2} + B_2 e^{jkl_2} &= A_3 + B_3 \\ S_2(A_2 e^{-jkl_2} - B_2 e^{jkl_2}) &= S_3(A_3 - B_3) \end{aligned} \right\} \quad (43.20)$$

From these linear equations, the following equation can be obtained:

$$\frac{A_0}{B_0} = \frac{m_{10}}{1 - R_0 e^{-2jkl_0}} \left\{ j \left(1 + R_3 e^{-2jkl_3} \right) (\sin kl_1 \cos kl_2 + m_{21} kl_1 \sin kl_2) \right. \\ \left. + m_{32} \left(1 - R_3 e^{-2jkl_3} \right) (m_{21} \cos kl_1 \cos kl_2 - \sin kl_1 \sin kl_2) \right\} \quad (43.21)$$

When the reflection coefficients are absent, $R_0 = R_3 = 0$, we have

$$IL = 10 \log_{10} m_{03} \left\{ m_{10}^2 (\sin kl_1 \cos kl_2 + m_{21} \cos kl_1 \sin kl_2)^2 + m_{10}^2 m_{32}^2 \right. \\ \left. \times (m_{21} \cos kl_1 \cos kl_2 - \sin kl_1 \sin kl_2)^2 \right\} \quad (43.22)$$

where $m_{10} = S_0/S_1$, $m_{21} = S_2/S_1$, $m_{32} = S_3/S_2$, $m_{03} = S_0/S_3$, which are ratios of cross-sectional areas of the pipes.

For the reflection factors, $R_0 = R_3 = -1$, $S_0 = S_1 = S_3$, and $m_{21} = m$, the equation of insertion loss becomes

$$IL = 20 \log_{10} \left\| \frac{\cos kl_1}{\cos kl_0} \left\{ \cos kl_{21} \cos kl_3 - m \sin kl_2 \sin kl_3 - \tan kl_1 \left(\cos kl_2 \sin kl_3 + \frac{1}{m} \sin kl_2 \cos kl_3 \right) \right\} \right\| \quad (43.23)$$

The ratio $|A_1/A_3|$ may also be obtained from Equation 43.17 to Equation 43.20. When the magnitude of reflection coefficients $R_0 = R_3 = 0$, $S_0 = S_1 = S_3$, and expansion ratio of the cross-sectional open area of the pipes $m_{21} = m$, the transmission loss is given by

$$TL = 10 \log_{10} \left\{ 1 + \frac{1}{4} \left(m - \frac{1}{m} \right)^2 \sin^2 kl_2 \right\} \quad (43.24)$$

When $R_0 = R_3 = -1$, $S_0 = S_1 = S_3$, and $m_{21} = m$, TL is obtained from the following equation:

$$TL = 10 \log_{10} \left| 1 + \frac{1}{m^2} (m^2 - 1) \{ (m^2 + 1) \sin^2 kl_3 - 1 \} \sin^2 kl_2 + \frac{1}{2} \left(-m + \frac{1}{m} \right) \sin 2kl_2 \sin 2kl_3 \right| \quad (43.25)$$

Computation formulas of insertion loss and transmission loss for the case of an expansion chamber with insertion pipe and resonator are shown in [Table 43.1](#).

The principal structures of several reactive mufflers are shown in [Figure 43.4](#).

43.5 Application Range of Model

43.5.1 Condition for Approximation of Plane Wave

The frequency range where the approximation of a plane wave is valid is given by

$$f_c < 1.22 \frac{c}{D} \quad (43.26)$$

where

f_c = critical frequency of plane wave (Hz)

c = speed of sound (m/sec)

D = diameter of muffler (m)

It is seen that the expansion ratio of an open area of a pipe increases with IL or TL. However, the application range of the analytical model decreases with increasing diameter of chamber.

43.5.2 Effect of Temperature

Under conditions of high-temperature and high-speed gas flow, as in an engine exhaust system, the primary effect of a change in pipe temperature is the corresponding change in the speed of sound, which is proportional to the square root of the absolute temperature. In the design of a reactive muffler, it is necessary to use the actual speed of sound in the gas inside the pipe. The most accurate values available for density (ρ_0) and the speed of sound (c_0) at each element should be used in calculating the impedance

TABLE 43.1 Transmission Loss of Reactive Mufflers and Insertion Loss of Reactive Mufflers

Muffler (see Figure 43.4)	TL (dB)	Application Limits and Comments
<i>Transmission loss of reactive mufflers</i>		
(a)	$TL = 10 \log_{10} \left\{ 1 + \left(\frac{kS}{4a} \right)^2 \right\}$ <p>a: radius of orifice</p>	$a/\lambda < 0.1, R = 0$
(b)	$TL = 20 \log_{10} \left \begin{array}{l} (1 + R_3 e^{-2jkl_3})(\cos kl_2 + jm_{21} \sin kl_2) \\ + m_{32}(1 - R_3 e^{-2jkl_3})(j \sin kl_2 + m_{21} \cos kl_2) \end{array} \right $ <p> $m_{10} = S_1/S_0, m_{21} = S_2/S_1, m_{32} = S_3/S_2, R_0, R_3$: the reflection coefficient of the open end, l_3 = length of the tail pipe (1) when $R_0 = R_3 = 0, S_0 = S_1 = S_3$ $TL = 10 \log_{10} \left\{ 1 + \frac{1}{4} \left(m_{21} - \frac{1}{m_{21}} \right)^2 \sin^2 kl_2 \right\}$ (2) when $R_0 = R_3 = -1, S_0 = S_1 = S_3$ $TL = 10 \log_{10} \left[1 + \left(\frac{m_{21}^2 - 1}{m_{21}^2} \right) \{ (m_{21}^2 + 1) \sin^2 kl_3 - 1 \} \sin^2 kl_2 + \frac{1}{2} \left(\frac{1}{m_{21}} - m_{21} \right) \sin 2kl_2 \sin 2kl_3 \right]$ </p>	$f < 1.22c/D$
(c)	$TL = 10 \log_{10} \left[\left\{ 2 \cos k(l_1 - l_{11} - l_{22}) - \frac{m-1}{m} \sin k(l_1 - l_{11} - l_{22})(\tan kl_{11} + \tan kl_{22}) \right\}^2 \right. \\ \left. + \left\{ \left(m + \frac{1}{m} \right) \sin k(l_1 - l_{11} - l_{22}) + (m-1) \cos(l_1 - l_{11} - l_{22})(\tan kl_{11} + \tan kl_{22}) \right. \right. \\ \left. \left. - \frac{(m-1)^2}{m} \tan kl_{11} \tan kl_{22} \sin k(l_1 - l_{11} - l_{22}) \right\}^2 \right]$ <p>$M = S_1/S_0$</p>	$R \approx 0$
(d)	$TL = 10 \log_{10} \left\{ 1 + \frac{1}{4} \left(\frac{m}{\frac{kS_2}{C_0} - \cot kl} \right)^2 \right\}$ <p> $C_0 = NC_i$; N: number of holes, $C_i = 2\pi a_i^2/(l_b + \pi a_i)$, l_b, l_b: thickness of the pipe, a_i: radius of a hole, $m = S_{12}/S$ </p>	$R \approx 0$

(continued on next page)

TABLE 43.1 (continued)

Muffler (see Figure 43.4)	TL (dB)	Application Limits and Comments
(e)	$TL = 10 \log_{10} \left[1 + \frac{1}{4} \left \frac{\frac{\sqrt{C_0 V}}{S}}{\frac{f}{f_r} - \frac{f_r}{f}} \right ^2 \right]$ $f_r = \frac{c}{2\pi} \sqrt{\frac{C_0}{V}},$ $C_0 = \frac{2\pi a^2}{2l_b + \pi a}$ <p>l_b: length of the neck or thickness of the pipe, a: radius of the neck or hole</p>	$R \approx 0, l_b \ll \lambda$ Resonator size $\ll \lambda$
(f)	$TL = 10 \log_{10} \left\{ 1 + \frac{m^2}{4} \left(\frac{\tan kl_b - \frac{S_b}{kV}}{\frac{S_b}{kV} \tan kl_b + 1} \right)^2 \right\}$ $m = S_b/S$	$R \approx 0, l_b \ll \lambda$ Resonator size $\ll \lambda$
(g)	$TL = 20 \log_{10} \frac{1}{16m^2} \left [4m(m+1)^2 \cos 2k(l+l_c) - 4m(m-1)^2 \cos 2k(l-l_c)] \right. \\ \left. + j \left\{ 2(m^2+1)(m+1)^2 \sin 2k(l+l_c) - 2(m^2+1)(m-1)^2 \sin 2k(l-l_c) \right. \right. \\ \left. \left. - 4(m^2-1)^2 \sin 2kl_c \right\} \right $ $m = S_2/S_1$	$R \approx 0$
(h)	$TL = 10 \log_{10} \left \cos 2kl - (m-1) \sin 2kl_c \tan kl_c \right ^2 + \left\{ \frac{j}{2} \left(m + \frac{1}{m} \right) \sin 2kl \right. \\ \left. + (m-1) \tan kl_c \left(\left(m + \frac{1}{m} \right) \cos 2kl - \left(m - \frac{1}{m} \right) \right) \right\}^2 \right $ $m = S_2/S_1$	$R \approx 0$

(i)

$$TL = 10 \log_{10} \left\{ \frac{1}{4} \left| \frac{A_1 + jB_1}{A_2 + jB_2} \right|^2 \right\}$$

$$A_1 = Y_3 X_1^2 + Z_0 Y_3^2 + Z_0 (X_1 + X_3)^2$$

$$B_1 = X_1 Y_3^2 + X_1 X_3 (X_1 + X_3)$$

$$A_2 = Y_3 X_1^2 \cos kl + Z_0 X_1 Y_3 \sin kl$$

$$B_2 = X_1 Y_3^2 + X_1 X_3 (X_1 + X_3) \cos kl - Z_0 X_1 (X_1 + X_3) \sin kl$$

$$X_1 = \frac{\omega \rho}{C_0} - \frac{\rho c^2}{\omega V_1},$$

$$X_2 = \frac{\omega \rho}{C_0} - \frac{\rho c^2}{\omega V_2}$$

$$X_3 = \frac{Z_0^2 (X_2 \cos 2kl + \frac{1}{2} Z_0 \sin^2 kl)}{(X_2 \sin kl - Z_0 \cos kl)^2 + X_2^2 \cos^2 kl}$$

$$Y_3 = \frac{Z_0 X_2^2}{(X_2 \sin kl - Z_0 \cos kl)^2 + X_2^2 \cos^2 kl}$$

$$Z_0 = \frac{\rho c}{S_0},$$

$$C_0 = \frac{2\pi a^2}{2l_b + \pi a}$$

l_b : thickness of the pipe, a : radius of hole

(j)

$$TL = 10 \log_{10} \left\{ \left(\cos kl + \frac{\rho c}{4S_0 X} \left(m + \frac{1}{m} \right) \sin kl - \frac{\rho c}{4S_0 X} \left(m - \frac{1}{m} \right) \cos 2kl_b \sin kl \right)^2 \right. \\ \left. + \left(\frac{1}{2} \left(m + \frac{1}{m} \right) \sin kl + \frac{\rho c}{4S_0 X} \left(m - \frac{1}{m} \right) \sin 2kl_b \sin kl - \frac{\rho c}{2S_0 X} \cos kl \right)^2 \right\}$$

$$X = \frac{\omega \rho}{C_0} - \frac{\rho c^2}{\omega V},$$

$$m = \frac{S}{S_0}$$

$R \approx 0$ Resonator size $\ll \lambda$

$R \approx 0$

(continued on next page)

TABLE 43.1 (continued)

Muffler (see Figure 43.4)	IL (dB)	Application Limits and Comments
Insertion loss of reactive mufflers (b)	$IL = 10 \log_{10} \frac{1}{m_{30}}$ $\times \left \frac{m_{10}}{1 - R_0 e^{-2jkl_0}} \{j(1 + R_3 e^{-2jkl_3} (\sin kl_1 \cos kl_2 + m_{21} \cos kl_1 \sin kl_2)) \right.$ $\left. + m_{32}(1 - R_3 e^{-2jkl_3})(m_{21} \cos kl_1 \cos kl_2 - \sin kl_1 \sin kl_2) \} \right ^2$	$f < 1.22c/D$, R is plotted in Fig.43.1
	$(1) IL = 10 \log_{10} \left\{ \left[1 + (m_{21}^2 - 1) \right] \left(1 - \frac{m_{21}^2 + 1}{m_{21}^2} \sin^2 kl_1 \right) \sin^2 kl_2 \right.$ $\left. + \frac{1}{2} \left(m_{21} - \frac{1}{m_{21}} \right) \sin 2kl_1 \sin 2kl_2 \right $	$R_0 = R_3 = 0$, $S_0 = S_1 = S_3$
	$(2) IL = 10 \log_{10} \left\{ \left(\frac{\cos kl_1}{\cos kl_0} \{ \cos kl_2 \cos kl_3 - m_{21} \sin kl_2 \sin kl_3 - \tan kl_1 (\cos kl_2 \sin kl_3 \right. \right.$ $\left. \left. + \frac{1}{m_{21}} \sin kl_2 \cos kl_3 \} \right) \right\}^2$	$R_0 = R_3 = -1$, $S_0 = S_1 = S_3$
(c)	$IL = 20 \log_{10} \left \frac{\cos kl_1 \cos kl_2 - m \sin kl_1 \sin kl_2}{\cos kl_{11} \cos kl_{22}} \right $ $m = S_1/S_0$	$R = -1$
(d)	$IL = 20 \log_{10} \left[\cos^2 kl_2 + \frac{m}{\frac{kS_2}{C_0} - \cot kl} \sin 2kl_2 + \left(\frac{m}{\frac{kS_2}{C_0} - \cot kl} \right)^2 \sin^2 kl_2 \right]$	$R = -1$, $kl_0 \ll 1$
$C_0 = NC_i$; $C_i = 2\pi a_i^2/(l_b + \pi a_i)$, N : number of holes, l_b : thickness of the pipe, a_i : radius of a hole, $m = S_{12}/S$		

- (e)
$$IL = 10 \log_{10} \left| \frac{\frac{\sqrt{C_0 V}}{S}}{\frac{f}{f_r} - \frac{f_r}{f}} \sin 2kl_2 + \frac{\frac{C_0 V}{S^2}}{\left(\frac{f}{f_r} - \frac{f_r}{f}\right)^2} \sin^2 kl_2 + \cos^2 kl_2 \right|$$

$$f_r = \frac{c}{2\pi} \sqrt{\frac{C_0}{V}},$$

$$C_0 = \frac{2\pi a^2}{2l_b + \pi a}$$

$$l_b: \text{length of the neck or thickness of pipe, } a: \text{radius of the neck or hole}$$

$$R = -1, kl_0 \ll 1$$
- (f)
$$IL = 10 \log_{10} \left[\cos^2 kl_2 + m \sin 2kl_2 \frac{\frac{S_b}{kV} \tan kl_b + 1}{\tan kl_b - \frac{S_b}{kV}} + \left(m \frac{\frac{S_b}{kV} \tan kl_b + 1}{\tan kl_b - \frac{S_b}{kV}} \right)^2 \sin^2 kl_2 \right]$$

$$f_r = \frac{c}{2\pi} \sqrt{\frac{C_0}{V}},$$

$$C_0 = \frac{2\pi a^2}{2l_b + \pi a}$$

$$l_b: \text{length of the neck or thickness of the pipe, } a: \text{radius of the neck or hole}$$

$$R = -1, kl_0 \ll 1$$
- (k)
$$IL = 20 \log_{10} [(\cos kl_1 \cos kl_{11} - m_1 \sin kl_1 \sin kl_{11}) + (\cos kl_2 \cos kl_{22} - m_2 \sin kl_2 \sin kl_{22}) + \dots + (\cos kl_i \cos kl_{ii} - m_i \sin kl_i \sin kl_{ii})]$$

$$R = -1, kl_0 \ll 1$$
- (l)
$$IL = 20 \log_{10} \left\{ \frac{\cos kL_1 \cos kl_1 - m \sin kL_1 \sin kl_1}{\cos kl_{11}} + \frac{\cos kL_2 \cos kl_2 - m \sin kL_2 \sin kl_2}{\cos kl_{12} \cos kl_{21}} + \dots + \frac{\cos kL_n \cos kl_n - m \sin kL_n \sin kl_n}{\cos kl_{(n-1)2}} \right\}$$

$$R = -1, kl_0 \ll 1$$

A is the radius of tube in orifice hole or diameter of side branch, c is the sound speed, C_0 is the conductivity, D is the diameter of chamber, f is the frequency, f_r is the resonant frequency of the resonator, $k = 2\pi f/c$ is the wave number, L is the length, $m = S_i/S_{i+1}$ is the ratio of the cross section, IL is the insertion loss, N is the number of holes, R is the reflection coefficient, S is the cross section, TL is the transmission loss, V is the volume of chamber, Z is the acoustic impedance, ρ is the density, λ is the wavelength, $\omega = 2\pi f$, angular frequency.

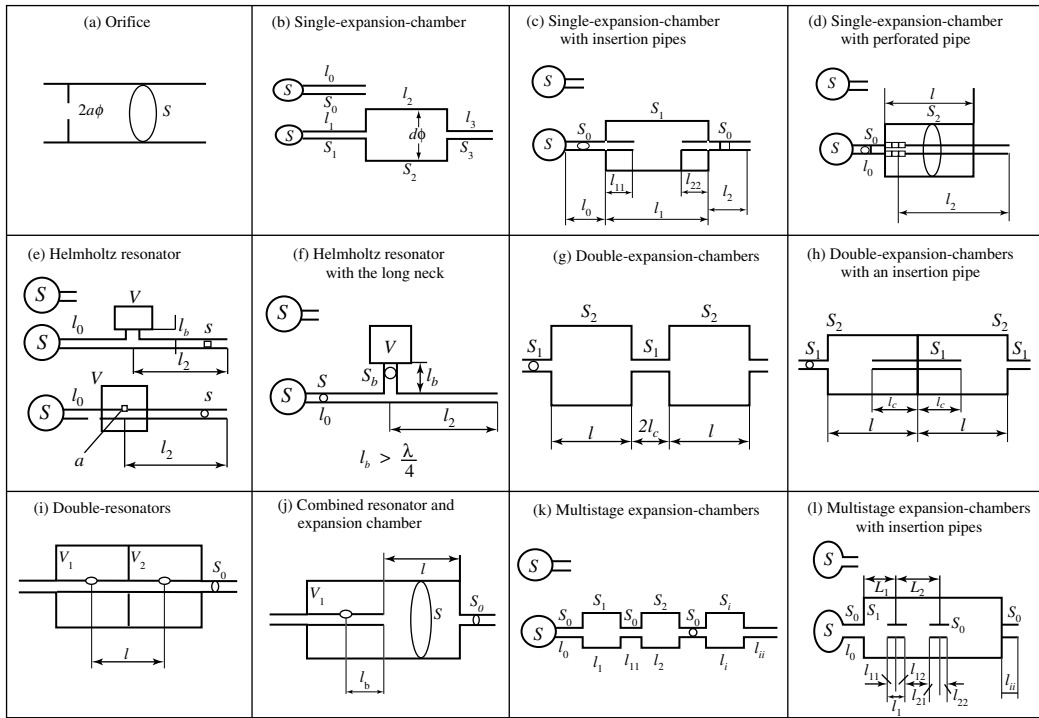


FIGURE 43.4 Sketches of the 12 principal structures of reactive mufflers.

of the elements. The impedance, z , is given by

$$z = -j \frac{\rho_0 c_0}{S} \frac{1}{kl} \quad (43.27)$$

where

S = the cross-sectional open area of pipe

$k = 2\pi f/c_0$, wave number

l = the length of the pipe element

Note that the impedance of the resonator chamber is proportional to $\rho_0 c_0^2$. However, c_0^2 is proportional to the absolute temperature of gas (T) and ρ_0 is proportional to $1/T$. Hence, the chamber impedance is independent of temperature. The connector impedance is a function of T , but in most cases the connector will be at the pipe temperature. For a resonator-type muffler, a temperature difference between the pipe and chamber is expected to have little effect on the performance of the muffler.

43.5.3 Effect of Gas Flow in Pipe

Under conditions of high-temperature and high-speed gas flow in a pipe, the pressure amplitude in the pipe is large, and is larger than what is predicted by theory. Analysis by the characteristic curve method is desirable under such conditions.

In a reactive muffler where the pipe flow passes through a sudden pipe expansion or an orifice, the computed transmission loss or insertion loss tends to be an overestimate because of new noise that is generated due to the resulting irregular air-flow within the muffler.

43.5.4 Effect of Friction Loss in Pipe

When an acoustic wave propagates in a pipe, it will attenuate due to viscous friction. The effect is large for long pipes of small diameter. Friction damping in a pipe may be incorporated into the propagation constant, γ , such that

$$\gamma = \delta + jk \quad (43.28)$$

where δ is the attenuation constant per unit length of pipe. By substituting Equation 43.28 into Equation 43.3 and Equation 43.4, we obtain

$$\xi = (A e^{-\gamma l} - B e^{\gamma l}) e^{j\omega t} \quad (43.29)$$

$$p = -\rho c^2 k (A e^{-\gamma l} + B e^{\gamma l}) e^{j\omega t} \quad (43.30)$$

Empirical formulas are given below for two cases of the attenuation coefficient δ [3].

(1) The formula for seamless steel or chloride-ethylene pipes (regression formula when the inside roughness is 4 to 8 μm and length under 3 m) is

$$\delta = 26,100 \lambda^{-0.5} \frac{\mu}{\rho c d} \quad (43.31)$$

where

λ = wavelength of sound (m)

μ = viscosity of gas in the pipe (Pa sec)

ρ = density of gas (kg/m^3)

d = diameter of the pipe (m)

(2) The equations for lining with glass wool are

$$\left. \begin{aligned} \delta_2 &= 2491 \lambda^{-0.476} \left(\frac{\rho c d}{\mu} \right)^{-1.068} \\ \delta_6 &= 5175 \lambda^{-0.476} \left(\frac{\rho c d}{\mu} \right)^{-1.303} \\ \delta_6 &= 11596 \lambda^{-0.476} \left(\frac{\rho c d}{\mu} \right)^{-1.270} \end{aligned} \right\} \quad (43.32)$$

The suffix of δ gives the thickness of absorbing material in mm.

43.6 Practical Example

43.6.1 Expansion-Type Muffler for Reciprocating Compressor

Consider a double-acting (i.e., fluid on both sides of the piston in the cylinder) reciprocating compressor for supplying high-pressure air to a machine shop of a factory, for example.

The specifications of the reciprocating compressor follow:

- Delivery pressure: 6.9×10^5 Pa
- Rotational speed of driving shaft: 600 rpm
- Power of driving shaft: 450 kW
- Diameter of inlet pipe: 380 mm

Pressure pulsations of 10 and 20 Hz are produced by the compressor due to the rotational speed, as seen in Figure 43.5. The pressure wave from the inlet propagates the free space and can the damage nearby private houses. Wooden doors with glass paneling, wooden sliding-doors, and leaves of plants and foliage, and have been found to vibrate due to low-frequency audible sound. An attenuation of 15 to 20 dB was

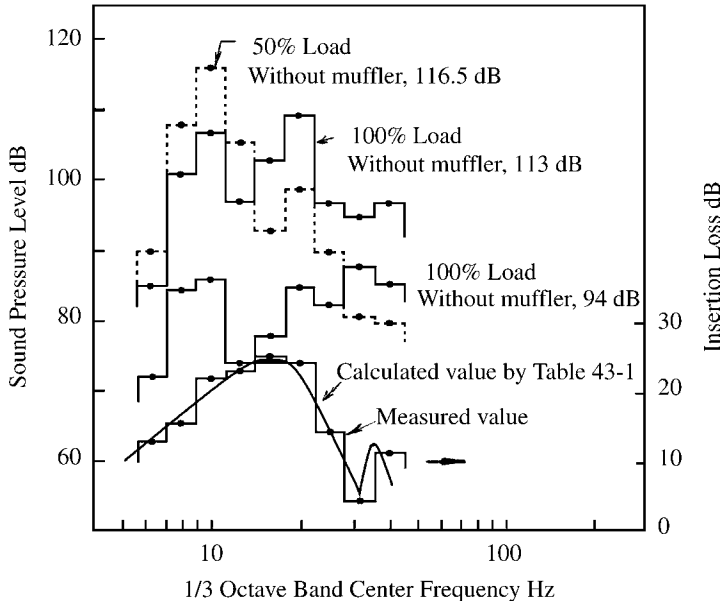


FIGURE 43.5 Noise spectrum at inlet of reciprocating compressor and insertion loss of designed muffler.

necessary at the frequencies 10 and 20 Hz. A muffler using an expansion and tail pipe type was suggested to handle the problem. The reflection coefficient of the tail pipe is approximately $R = -1$ and $ka = 2\pi fa/c = 2\pi \times 20 \times 0.19/345 = 0.0692$.

$$IL = 20 \log_{10} |\cos kl_2 \cos kl_3 - m \sin kl_2 \sin kl_3|$$

where

$k = 2\pi f/c$; wave number (1/m)

l_2 = the length of the chamber (m)

l_3 = the length of the tail pipe (m)

m = the expansion ratio of the cross section between the chamber and inlet

With $kl_2 = kl_3 = \pi/2$, we have

$$IL = 20 \log_{10} |m|$$

We need $m > 10$ in order to satisfy the desired value of IL. For 20 Hz, we use $kl_2 = kl_3 = \pi$. When $kl_2 = kl_3 = \pi/2$ at $f = 10$ Hz, we have $IL = 0$. Then, using $kl_2 = kl_3 = \pi/2$ at frequency 15 Hz, we can satisfy the IL condition of 20 dB at both frequencies. Hence, $l_2 = l_3 = 345/(4 \times 15) = 5.75$ (m) is chosen at a speed of sound $c = 345$ m/s.

The noise spectrum at the inlet of the reciprocating compressor under study and insertion loss of the muffler design in this example are shown in Figure 43.5.

The diameters or the lengths of the chamber and the tail pipe are properly selected, as shown and in Figure 43.6. At 10 Hz, IL is determined as

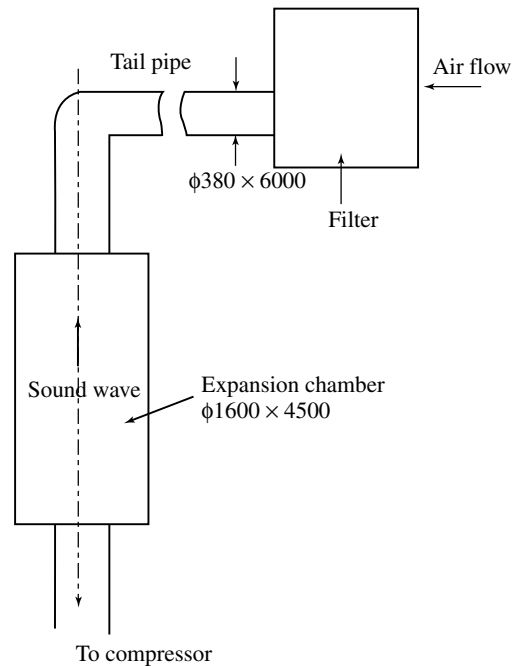


FIGURE 43.6 The muffler designed for the noise control of a reciprocating compressor.

indicated below:

$$\begin{aligned} \text{IL} &= 20 \log_{10} |\cos(2\pi \times 10 \times 4.5/345) \cos(2\pi \times 10 \times 6/345) - (1.6/0.38)^2 \sin(2\pi \times 10 \times 4.5/345) \\ &\quad \times \sin(2\pi \times 10 \times 6/345)| \\ &= 20 \log_{10} |0.6825 \times 0.4600 - 17.728 \times 0.7308 \times 0.8879| = 21.0 \text{ (dB)} \end{aligned}$$

Similarly, at 20 Hz, we have

$$\begin{aligned} \text{IL} &= 20 \log_{10} |\cos(2\pi \times 20 \times 4.5/345) \cos(2\pi \times 20 \times 6/345) - (1.6/0.38)^2 \sin(2\pi \times 20 \times 4.5/345) \\ &\quad \times \sin(2\pi \times 20 \times 6/345)| \\ &= 20 \log_{10} |(-0.0682) \times (-0.5767) - 17.728 \times 0.9977 \times 0.8170| = 23.2 \text{ (dB)} \end{aligned}$$

Clearly, the attenuation at both frequencies satisfies the desired lower limit of 20 dB. Calculated values of IL at low frequencies are shown by a curved continuous line in [Figure 43.5](#).

References

1. Levine, H. and Schwinger, J., On the radiation of sound from an unflanged circular pipe, *J. Phys. Rev.*, 73, 383, 1948.
2. Ohnaka, I., Lecture for noise reduction of machines, no. 2, *J. Marine Eng. Soc. Jpn.*, 4, 179, 1969.
3. Suyama, E. and Hirata, M., Attenuation constant of plane wave in a tube, *J. Acoust. Soc. Jpn.*, 35, 152, 1979.

44

Design of Sound Insulation

44.1	Theory of Sound Insulation	44-1
	Expressions of Sound Insulation • Transmission Loss of a Single Wall • Transmission Loss of Multiple Panels • Transmission Loss of Double Wall with Sound Bridge	
44.2	Application of Sound Insulation	44-13
	Acoustic Enclosure • Sound Insulation Lagging	

Kiyoshi Okura
Mitsuboshi Belting Ltd.

Summary

This chapter presents useful theory and design procedures for sound insulation. Related concepts and representations of transmission loss, the transmission coefficient, and impedance are given. Analysis and design procedures for sound insulation structures such as single and multiple panels and walls with sound absorption material are presented. Practical applications for the design of sound insulation components and systems are described.

44.1 Theory of Sound Insulation

44.1.1 Expressions of Sound Insulation [1]

44.1.1.1 Transmission Coefficient

Let us denote by I_i the acoustic energy incident on a wall per unit area and unit time. Some energy is dissipated in the wall, and, apart from the energy that is reflected by the wall, the rest is transmitted through the wall. Using I_t to denote the transmitted acoustic energy, the transmission coefficient of the wall is defined as

$$\tau = \frac{I_t}{I_i} \quad (44.1)$$

44.1.1.2 Transmission Loss

As an expression for sound insulation performance, we may use transmission loss (TL), which is defined as (also see Chapter 42 and Chapter 43)

$$TL = 10 \log\left(\frac{1}{\tau}\right) = 10 \log\left(\frac{I_i}{I_t}\right) \quad (44.2)$$

44.1.2 Transmission Loss of a Single Wall

Consider a plane sound wave incident on a impermeable infinite plate at angle θ , which is placed in a uniform air space as shown in Figure 44.1. The sound pressure of the incident, reflected, and transmitted

waves, denoted by p_i , p_r , and p_t , respectively, are given by

$$\begin{aligned} p_i &= P_i e^{j\omega t - jk(x \cos \theta + y \sin \theta)} \\ p_r &= P_r e^{j\omega t - jk(-x \cos \theta + y \sin \theta)} \\ p_t &= P_t e^{j\omega t - jk(x \cos \theta + y \sin \theta)} \end{aligned} \quad (44.3)$$

where P_i , P_r , and P_t are the sound pressure amplitudes of incident, reflected, and transmitted waves, respectively; ω is angular frequency; k is the wave number of the sound wave; c is the speed of sound, respectively in the air. Assuming that the plate is sufficiently thin compared with the wavelength of the incident sound wave, the vibration velocities on the incident and transmitted surfaces of the plate are equal. Then vibration velocity, u , of the plate in the x direction is equal to the particle velocity of the incident and transmitted sound waves, and we obtain relations

$$u = -\frac{1}{j\omega\rho} \frac{\partial(p_i + p_r)}{\partial x} = -\frac{1}{j\omega\rho} \frac{\partial p_t}{\partial x} \quad (44.4)$$

$$\frac{p_i + p_r - p_t}{u} = Z_m \quad (44.5)$$

where ρ is the air density and Z_m is the *mechanical impedance* of the plate per unit area. From these equations, the transmission coefficient, τ_θ , and then the transmission loss, TL_θ , at the incident angle, θ , are obtained according to

$$TL_\theta = 10 \log \frac{1}{\tau_\theta} = 10 \log \left| \frac{p_i}{p_t} \right|^2 = 10 \log \left| 1 + \frac{Z_m \cos \theta}{2\rho c} \right|^2 \quad (44.6)$$

44.1.2.1 Coincidence Effect

Consider the vibration of the plate in the x - y plane shown in Figure 44.1. Denoting by m the surface density, and by B the bending stiffness per unit length of the plate, the equation of motion of the plate is given by

$$m \frac{\partial^2 \xi}{\partial t^2} + B(1 + j\eta) \frac{\partial^4 \xi}{\partial y^4} = p_i + p_r - p_t, \quad B = \frac{Eh^3}{12(1 - \nu^2)} \cong \frac{Eh^3}{12} \quad (44.7)$$

where

ξ = displacement in the x direction
 E = Young's modulus of the plate
 h = thickness of the plate
 η = loss factor of the plate
 ν = Poisson's ratio of the plate

The plane sound wave of angular frequency, ω , and of incidence angle, θ , causes a bending wave in the plate where displacement is assumed to be $\xi = \xi_0 e^{j(\omega t - k_1 y)}$, as a solution of Equation 44.7. Hence, the mechanical impedance per unit area is obtained:

$$Z_m = \frac{p_i + p_r - p_t}{\partial \xi / \partial t} = \eta \frac{Bk_1^4}{\omega} + j \left(\omega m - \frac{Bk_1^4}{\omega} \right) \quad (44.8)$$

where $k_1 = k \sin \theta$ ($k = \omega/c$) is the wave number of the bending wave in y direction caused by the incident sound wave. Propagation speed of the forced bending wave, c_1 , and a free bending wave of

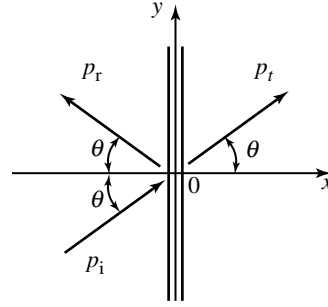


FIGURE 44.1 Plane sound wave incidence on an infinite plate.

the plate, c_B , are given by

$$c_1 = \omega/k_1, \quad c_B = \left(\frac{\omega^2 B}{m} \right)^{1/4} \quad (44.9)$$

Equation 44.9 reduces Equation 44.8 to

$$Z_m = \eta \omega m \left(\frac{c_B}{c_1} \right)^4 + j \omega m \left[1 - \left(\frac{c_B}{c_1} \right)^4 \right] \quad (44.10)$$

When the speed of forced bending wave, c_1 , and the speed of free bending wave, c_B , are equal in Equation 44.10, the imaginary part of Z_m becomes 0, and a form of “resonance” occurs. Then the transmission loss decreases rapidly. This phenomenon is called the *coincidence effect*, and the resonant frequency dependent on the incident angle is given by

$$f = \frac{c^2}{2\pi \sin^2 \theta} \sqrt{\frac{m}{B}} \quad (44.11)$$

The minimum of the resonant frequency is called coincidence critical frequency, or critical frequency for short, and it reduces to

$$f_c = \frac{c^2}{2\pi} \sqrt{\frac{m}{B}} \cong \frac{c^2}{1.8 c_L h} \quad (44.12)$$

where $c_L = \sqrt{E/\rho_P}$ is the speed of longitudinal wave in the plate, and ρ_P denotes the density of the plate.

Let us show the relations of the critical frequency and the plate thickness of typical material of sound insulation shown in Figure 44.2. Using the relation $c_B/c_1 = \sqrt{f/f_c} \sin \theta$, Equation 44.10

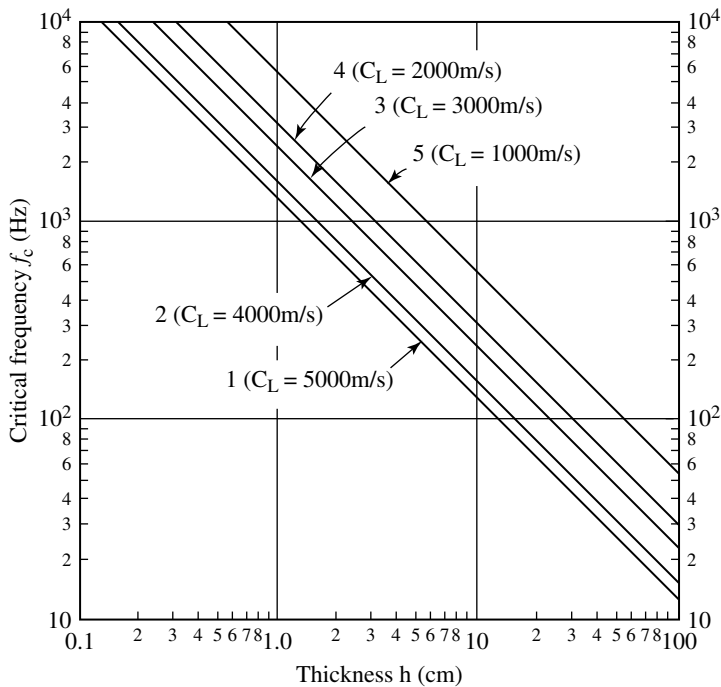


FIGURE 44.2 Critical frequency vs. plate thickness of typical sound insulation materials: (1) aluminum, steel, or glass; (2) hardboard or copper; (3) dense concrete, plywood, or brick; (4) gypsum board; (5) lead or light weight concrete. (Source: Beranek, L.L. 1988. *Noise and Vibration Control*, INCE/USA. With permission.)

becomes

$$Z_m = \eta \omega m \left(\frac{f}{f_c} \right)^2 \sin^4 \theta + j \omega m \left[1 - \left(\frac{f}{f_c} \right)^2 \sin^4 \theta \right] \quad (44.13)$$

44.1.2.2 Mass Law of Transmission Loss

When $f \ll f_c$, Equation 44.13 becomes $Z_m \cong j \omega m$. Then, the transmission loss depends on the incident angle, the frequency and the surface density of the plate. This is called the mass law of transmission loss.

Mass law of normal incidence represents the transmission loss at the incident angle $\theta = 0$, as given by

$$TL_0 = 10 \log \left[1 + \left(\frac{\omega m}{2 \rho c} \right)^2 \right] \quad (44.14)$$

For $\omega m \gg 2 \rho c$, it becomes

$$TL_0 \cong 10 \log \left(\frac{\omega m}{2 \rho c} \right)^2 = 20 \log mf - 42.5; \text{ for air} \quad (44.15)$$

Mass law of random incidence represents the transmission loss at the angle averaged over a range of θ from 0 to 90° , which is realized for perfectly diffused sound field. We have

$$TL_r = 10 \log(1/\tau_r) \cong TL_0 - 10 \log(0.23 TL_0) \quad (44.16)$$

where the random incident transmission coefficient, τ_r , is defined as

$$\tau_r = \int_0^{\pi/2} \tau_\theta \cos \theta \sin \theta d\theta / \int_0^{\pi/2} \cos \theta \sin \theta d\theta \quad (44.17)$$

An approximation for Equation 44.16, as given below, is generally used for a practical use and this is often useful.

$$TL_r = 18 \log mf - 44 \quad (44.18)$$

Mass law of field incidence represents the transmission loss at the angle averaged over a range of θ from 0 to about 78° , which is said to agree with actual sound field. We have

$$TL_f = TL_0 - 5 \quad (44.19)$$

The three types of transmission loss presented above are compared in [Figure 44.3](#).

44.1.2.3 Stiffness Law of Transmission Loss [2]

The plate described above is assumed to be infinite. However, an actual plate is always supported by some structures at its boundaries and the plate size is finite. Transmission loss of a finite plate is considered to be related to the nature of excitation of vibration in the plate, for example, sound wave incidence, modes of vibration and characteristics of sound radiation. Therefore, the governing relationships become very complex. However, in the following frequency range, it is known that the transmission loss conforms to the mass law

$$\frac{c}{2a} < f < f_c \quad (44.20)$$

where a is length of shorter edge for rectangular plate.

When $f < c/2a$, the whole plate is excited in phase, and stiffness effects from the supports of its edges will appear. If we denote the equivalent stiffness of the plate as K and assume a loss factor of 0,

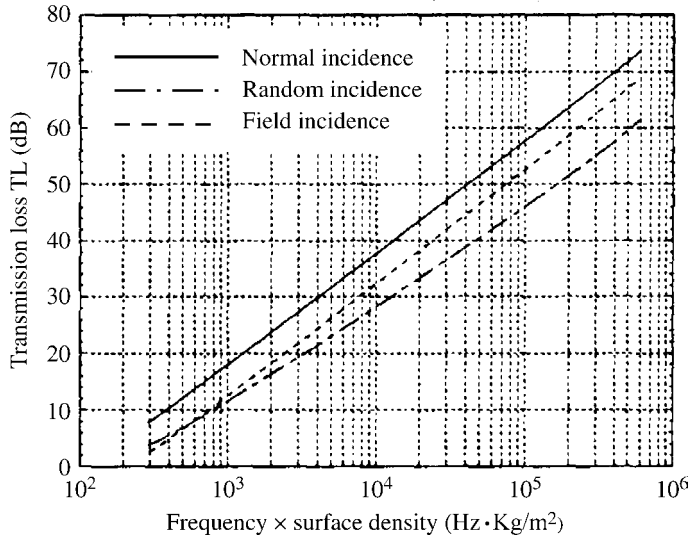


FIGURE 44.3 Theoretical transmission loss based on mass law.

the mechanical impedance of the plate is obtained by using Equation 44.8; thus

$$Z_m = j\left(\omega m - \frac{K}{\omega}\right) \quad (44.21)$$

The frequency at $Z_m = 0$ corresponds to the first mode natural frequency, f_{11} , of the plate (see Chapter 4), and consequently, the equivalent stiffness of rectangular plate with simple edge-support is given by

$$f_{11} = \frac{1}{2\pi} \sqrt{\frac{K}{m}} \equiv \frac{\pi}{2} \sqrt{\frac{B}{m}} \left[\left(\frac{1}{a}\right)^2 + \left(\frac{1}{b}\right)^2 \right] \quad (44.22)$$

Then,

$$K = B\pi^4 \left(\frac{1}{a^2} + \frac{1}{b^2} \right)^2$$

where a and b are the length of the short and long edges for the rectangular plate, respectively. When $f \ll f_{11}$ is assumed in Equation 44.21, the mass term can be neglected, and from Equation 44.6 the normal incidence transmission loss, TL_{s0} , is given by

$$\begin{aligned} TL_{s0} &= 10 \log \left| 1 - j \frac{K}{2\omega\rho c} \right|^2 \\ &= 10 \log \left[1 + \left(\frac{K}{2\omega\rho c} \right)^2 \right] \\ &\cong 20 \log(K/f) - 74.5 \end{aligned} \quad (44.23)$$

This is called the stiffness law of the transmission loss, and it shows a 6 dB decay per octave.

The characteristics mentioned above for single wall transmission loss are shown in Figure 44.4 and summarized below.

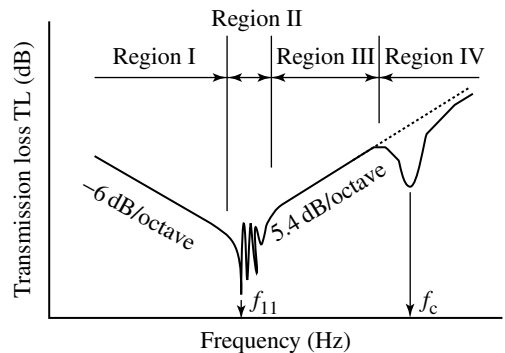


FIGURE 44.4 Transmission loss characteristics of a single wall.

1. Region I ($f \ll f_{11}$). Transmission loss is controlled by the stiffness of the panel:

$$TL = TL_0 - 40 \log\left(\frac{f}{f_{11}}\right) \quad (44.24)$$

2. Region II ($f \approx f_{11}$). Transmission loss is controlled by the lower-mode natural frequencies of the panel, and the estimation becomes very complex.
3. Region III ($f_{11} \ll f \leq f_c/2$). Transmission loss is controlled by the mass (surface density) of the panel:

$$TL = 18 \log mf - 44 \quad (44.25)$$

4. Region IV ($f > f_c/2$). Transmission loss is controlled by the mass and the damping of the panel, and it is reduced by coincidence effects.

For $f_c/2 < f \leq f_c$:

TL is represented by a straight line connecting the value at $f = f_c/2$ of Equation 44.25 and the value at $f = f_c$ of Equation 44.26.

For $f > f_c$:

$$TL = TL_0 + 10 \log\left(\frac{2\eta}{\pi} \frac{f}{f_c}\right) \quad (44.26)$$

44.1.3 Transmission Loss of Multiple Panels

To realize sound insulation of high performance, we often use a double wall or a multiple panel composed of insulation materials like steel plates and absorbing materials like fiber-glass. In this subsection, transmission loss of a multiple panel is described [3].

44.1.3.1 Calculation Method

Consider a multiple panel of infinite lateral extent as shown in Figure 44.5, which is composed of n acoustic elements, each element consisting of three basic materials, an impermeable plate, air space, and an absorption layer. Furthermore, consider a plane wave incident on the left-hand side surface of the n th element at angle θ . Let the sound pressure of the incident wave be p_i , and of the reflected wave be p_r , and the wave be propagating through the structure, and then radiating from the right-hand side of the first element as a plane wave of pressure p_t into a free field at transmission angle θ .

In the analysis, we append the subscript $k(= 1, 2, \dots, n)$ to the physical parameters of the k th element, and “2” and “1” to the left- and right-hand side values of these parameters, respectively, as shown in Figure 44.5. The ratio of the sound pressure at the incident surface, p_{n2} , to the incident wave, p_i , is given by

$$\frac{p_{n2}}{p_i} = \frac{p_i + p_r}{p_i} = \frac{2Z_{n2}}{Z_{n2} + \rho c / \cos \theta} \quad (44.27)$$

where Z_{n2} is the acoustic impedance of the left-hand side normal to the surface of the n th element and $\rho c / \cos \theta$ is the acoustic impedance normal to the surface, which is equal to the radiation impedance of the

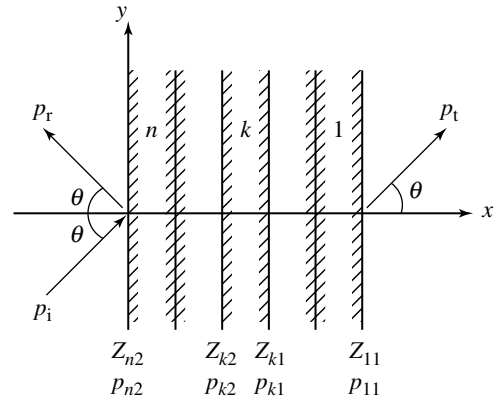


FIGURE 44.5 Calculation model of n -element multiple panel.

first element, Z_{11} , shown in Figure 44.5. Using the usual condition of pressure matching at each interface, we can write the expression for the oblique incidence transmission coefficient as

$$\tau(\theta) = \left| \frac{p_t}{p_i} \right|^2 = \left| \frac{p_{11}}{p_i} \right|^2 = \left| \frac{p_{n2}}{p_i} \right|^2 \left| \frac{p_{n1}}{p_{n2}} \dots \frac{p_{k1}}{p_{k2}} \dots \frac{p_{11}}{p_{12}} \right|^2 \quad (44.28)$$

Hence, we obtain the following expression for the random incidence transmission loss:

$$TL = 10 \log \left(\frac{\int_0^{\theta_1} \cos \theta \sin \theta d\theta}{\int_0^{\theta_1} \tau(\theta) \cos \theta \sin \theta d\theta} \right) \quad (44.29)$$

where θ_1 is the limiting angle above which no sound is assumed to be received, and it varies between 78° and 85° .

If we know Z_{n2} in Equation 44.27 and the pressure ratio across each of the single elements in Equation 44.28, we can calculate the TL using Equation 44.29. We can obtain Z_{n2} by using the conditions of impedance matching at each interface from the rightmost to the leftmost element in order, if we know the impedance relations across each of the single elements.

Now, we present the pressure ratios and the acoustic impedance relations across three basic elements.

44.1.3.2 Impermeable Plate

Consider the vibration of an infinite impermeable plate of thickness, h , induced by the sound pressure difference on each side of the plate, as illustrated in Figure 44.6. In this case, the particle velocity on both sides of the plate must be the same as the plate vibration velocity. Then, from Equation 44.8, the following expressions are obtained:

$$Z_2 = Z_1 + Z_m \quad (44.30)$$

$$\frac{p_2}{p_1} = \frac{Z_2}{Z_1} \quad (44.31)$$

where p_2, p_1 are the sound pressure at the incident surface $x = 0$ and at the transmitted surface $x = h$,

respectively, Z_m is the mechanical impedance of the plate, and Z_2, Z_1 are the acoustic impedance normal to the incident surface at $x = 0$ and the transmitted one at $x = h$, respectively.

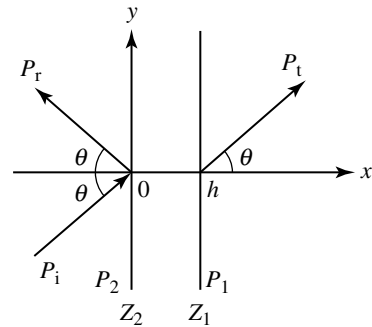


FIGURE 44.6 Excitation of infinite plate by a plane sound wave.

44.1.3.3 Sound Absorbing Material

For a sound absorbing material layer of thickness d and infinite lateral extent, consider a plane wave incident at an angle θ to the normal, as shown in Figure 44.7. Deriving the wave equation in the sound absorbing material and applying the continuity conditions of the sound pressure across the surface at $x = 0$ and $x = d$, with some mathematical manipulation we get the following results:

$$Z_2 = \frac{\gamma Z_0}{q} \coth(qd + \varphi) \quad (44.32)$$

$$\frac{p_2}{p_1} = \frac{\cosh(qd + \varphi)}{\cosh \varphi} \quad (44.33)$$

$$q = \gamma \sqrt{1 + \left(\frac{k}{\gamma}\right)^2 \sin^2 \theta}, \quad \varphi = \coth^{-1} \left(\frac{q Z_1}{\gamma Z_0} \right) \quad (44.34)$$

where γ is a propagation constant and Z_0 is a characteristic impedance of a homogeneous, isotropic absorbing material.

If porous material is used as the absorbing material, the following relations are applicable for γ and Z_0 [4]:

$$Z_0 = R + jX$$

$$R/\rho c = 1 + 0.0571(\rho f/R_1)^{-0.754} \quad (44.35)$$

$$X/\rho c = -0.0870(\rho f/R_1)^{-0.732}$$

$$\gamma = \alpha + j\beta$$

$$\alpha/k = 0.189(\rho f/R_1)^{-0.595} \quad (44.36)$$

$$\beta/k = 1 + 0.0978(\rho f/R_1)^{-0.700}$$

$$(0.01 \leq \rho f/R_1 \leq 1)$$

where ρ is the air density, f is the frequency, and R_1 is the flow resistivity, respectively. Specifically, note that R_1 is defined as the flow resistance of the porous absorbing material per unit thickness. With data measured with a measuring tube of flow resistance, we can write

$$R_1 = \frac{\Delta p}{l \cdot u} \quad (44.37)$$

where Δp is pressure difference between the inlet and the outlet of the absorbing material in the tube, u is the mean flow velocity in the tube, and l is the thickness of the absorbing material. It is known that the flow resistivity of porous absorbing material such as fiber-glass or rock wool is related to the bulk density, as shown in Figure 44.8.

44.1.3.4 Air Space

For an air space, $Z_0 = \rho c$ and $\gamma = jk$. Hence, Equation 44.32 to Equation 44.34 reduce to

$$Z_2 = \frac{\rho c}{\cos \theta} \coth(jkd \cos \theta + \delta) \quad (44.38)$$

$$\frac{p_2}{p_1} = \frac{\cosh(jkd \cos \theta + \delta)}{\cosh \delta} \quad (44.39)$$

$$\delta = \coth^{-1} \left(\frac{Z_1 \cos \theta}{\rho c} \right) \quad (44.40)$$

44.1.3.5 Double Wall [2]

Applying the theory formulated above, we can easily obtain the transmission loss of a double wall composed of the three elements: impermeable plate, air space, and impermeable plate, as shown in Figure 44.9. Assume that the two impermeable plates have the same surface density, m , and the mechanical impedance of the plates is $j\omega m$. Then, we can obtain following equations for element

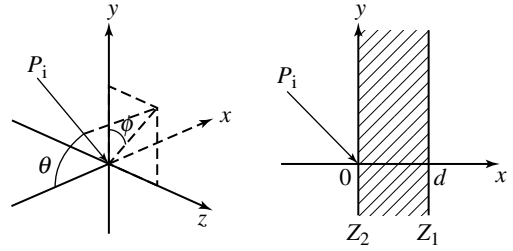


FIGURE 44.7 Schematic relation of sound wave directions.

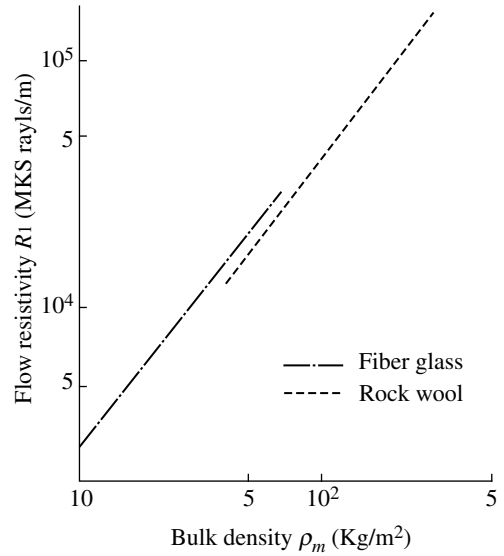


FIGURE 44.8 Flow resistivity vs. bulk density for porous, sound absorbing materials.

one and element three:

$$Z_{12} = Z_{11} + Z_m = \frac{\rho c}{\cos \theta} + j\omega m, \quad (44.41)$$

$$\frac{p_{12}}{p_{11}} = \frac{Z_{12}}{Z_{11}} = 1 + j \frac{\omega m \cos \theta}{\rho c}$$

$$Z_{32} = Z_{31} + Z_m = Z_{22} + j\omega m, \quad (44.42)$$

$$\frac{p_{32}}{p_{31}} = \frac{Z_{32}}{Z_{22}} = 1 + j \frac{\omega m}{Z_{22}}$$

For element two:

$$Z_{22} = \frac{\rho c}{\cos \theta} \coth (jkd \cos \theta + \delta'), \quad (44.43)$$

$$\frac{p_{22}}{p_{21}} = \frac{\cosh (jkd \cos \theta + \delta')}{\cosh \delta'}$$

where, by applying impedance matching

conditions at the interface of element one and element two, the following definition is introduced:

$$\delta' = \coth^{-1} \left(\frac{Z_{21} \cos \theta}{\rho c} \right) = \coth^{-1} \left(\frac{Z_{12} \cos \theta}{\rho c} \right) = \coth^{-1} \left(1 + j \frac{\omega m \cos \theta}{\rho c} \right) \quad (44.44)$$

In this case, Equation 44.27 reduces to

$$\frac{p_i}{p_{32}} = \frac{Z_{32} + \rho c / \cos \theta}{2Z_{32}} = \frac{Z_{22} + j\omega m + \rho c / \cos \theta}{2(Z_{22} + j\omega m)} \quad (44.45)$$

Substituting Equation 44.41 to Equation 44.45 into Equation 44.28, we obtain the transmission loss of the double wall:

$$TL_\theta = 10 \log[1/\tau(\theta)] = 10 \log[1 + 4a^2 \cos^2 \theta (\cos \beta - a \cos \theta \sin \beta)^2] \quad (44.46)$$

$$a = \omega m / 2\rho c, \quad \beta = kd \cos \theta$$

In Equation 44.46, the transmission loss is zero, and full passage (i.e., “all-pass” in the filter terminology) of sound occurs when the following equation holds:

$$\cos \beta - a \cos \theta \sin \beta = 0 \quad (44.47)$$

When $\beta \ll 1 (kd \ll 1)$, the frequency of full passage for normal incidence is given by

$$f_r = \frac{1}{2\pi} \sqrt{\frac{2\rho c^2}{md}} \quad (44.48)$$

This is the natural frequency of a vibrating system consisting of two masses, m , connected by a spring of spring constant, $\rho c^2/d$.

When $\beta \gg 1 (kd \gg 1)$, the solution of Equation 44.47 for β is $\beta \cong n\pi$, and the frequency of all passage for normal incidence is given by

$$f_n = \frac{nc}{2d} \quad (n = 1, 2, 3, \dots) \quad (44.49)$$

These are the acoustic resonant frequencies of the air space d .

Characteristics of the transmission loss given by Equation 44.46, in case of normal incidence ($\theta = 0$), are as follows:

$$1. f < f_r (\beta < \sqrt{2\rho d/m})$$

$$TL \cong 10 \log(4a^2) = TL_0 + 6 \quad (44.50)$$

This is equal to the transmission loss of a single wall of surface density $2m$.

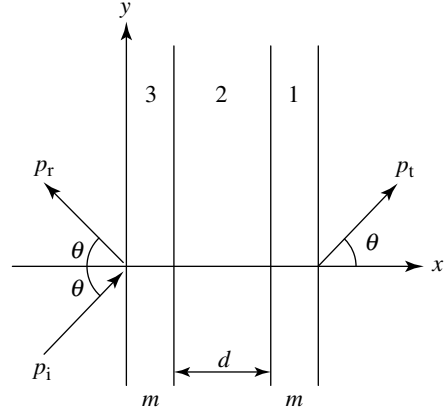


FIGURE 44.9 Calculation model of a double wall with air space.

$$2. f_r \leq f < f_1/\pi \left(\sqrt{2\rho d/m} \leq \beta < 1 \right)$$

$$TL \cong 10 \log(4a^4\beta^2) = 2TL_0 + 20 \log(2kd) \quad (44.51)$$

This transmission loss indicates an 18 dB increase per octave.

$$3. f = (2n - 1)c/4d (\beta = n\pi - \pi/2)$$

$$TL \cong 10 \log(4a^4) = 2TL_0 + 6 \quad (44.52)$$

A straight line connecting the transmission losses at these frequencies in Figure 44.10 indicates a 12 dB increase per octave. When the two impermeable plates have different surface densities, m_1 and m_2 , Equation 44.41 to Equation 44.52 reduce to

$$1. f < f_r (\beta < \sqrt{2\rho d/m})$$

$$TL = 20 \log[\omega(m_1 + m_2)/2\rho c] \quad (44.53)$$

$$2. f_r \leq f < f_1/\pi (\sqrt{2\rho d/m} \leq \beta < 1)$$

$$TL = TL_1 + TL_2 + 20 \log(2kd) \quad (44.54)$$

$$3. f = (2n - 1)c/4d (\beta = n\pi - \pi/2)$$

$$TL = TL_1 + TL_2 + 6 \quad (44.55)$$

In these equations, TL_1 and TL_2 are the transmission losses of each plate, which are given by Equation 44.15.

The transmission loss of a double wall, as mentioned above, is shown schematically in Figure 44.10. An actual double wall, however, is finite in size and the air space forms a closed acoustic field, which

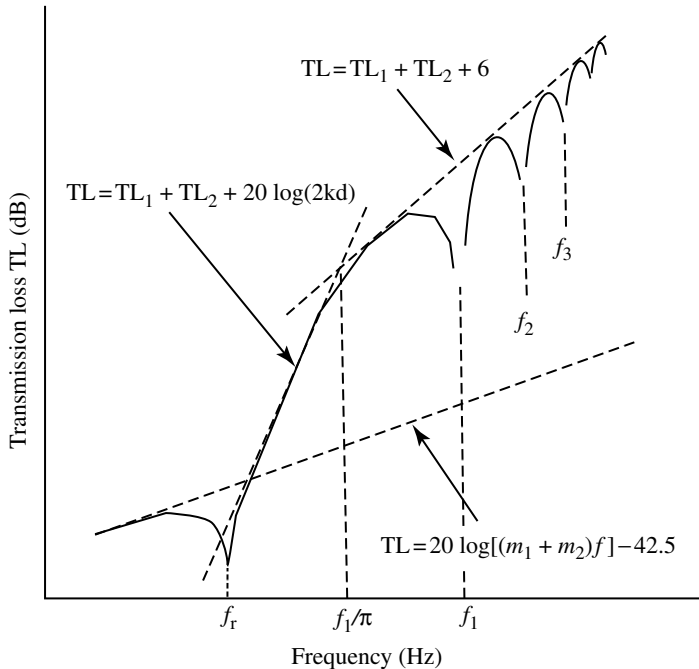


FIGURE 44.10 Transmission loss of a double wall with air space.

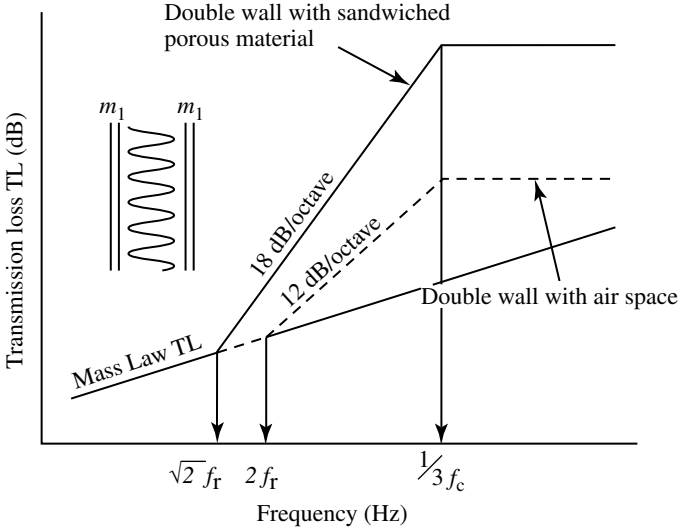


FIGURE 44.11 Design chart for estimating the transmission loss of a double wall with sandwiched porous material or air space.

makes the transmission loss deviate from the theoretical value. Figure 44.11 gives a design chart of an actual double wall, which is based on theory and experiments.

44.1.4 Transmission Loss of Double Wall with Sound Bridge [5]

In the previously presented theory, each plate of the multiple panel is considered to be structurally independent. In actual multiple panels, such as partitions of a building or sound insulation laggings of a duct, however, each plate is connected with steel sections, stud bolts, and the like, which are called sound bridges. This is illustrated in Figure 44.12.

The sound pressure of the transmitted wave through a double wall with sound bridges is given by the summation of radiated sound pressure from the vibration of the transmitted side plate excited by the sound in the air space and that mechanically excited by the sound bridges.

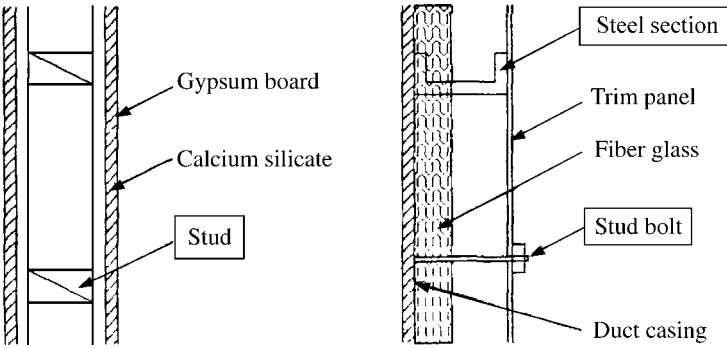


FIGURE 44.12 Examples of actual double wall with sound bridges.

The acoustic power radiated from the area, S , of an infinite plate excited by sound pressure is given by

$$W_p = \rho c S v_2^2 \quad (44.56)$$

where v_2^2 is the space averaged mean square vibration velocity over the plate. The acoustic power radiated from the plate mechanically excited by a point force or a line force is

$$W_B = \rho c \chi v^2 (f < f_c) \quad (44.57)$$

$$\chi = \begin{cases} \frac{8}{\pi^3} \lambda_c^2 & \text{(point force excitation)} \\ \frac{2}{\pi} l \lambda_c & \text{(line force excitation)} \end{cases} \quad (44.58)$$

where v^2 is the mean square vibration velocity of the plate at the excitation point, $\lambda_c = c/f_c$ is the wavelength of the bending wave at the critical frequency, and l is the length of the line force. By comparing Equation 44.56 and Equation 44.57, it is noted that χ is the effective area of the acoustic power radiated from the infinite plate excited by the point or line force. Acoustic power, W_B , is the power radiated from a small area near the excitation point, because a free bending wave propagating in an infinite plate can radiate little sound when $f < f_c$.

From the equations given above, the total acoustic power radiated from the transmitted side plate is obtained as

$$W_T = W_p + W_B = \rho c S v_2^2 \left[1 + \frac{n\chi}{S} \left(\frac{v}{v_2} \right)^2 \right] \quad (44.59)$$

where n is the number of excitation forces applied to the area, S . Then, transmission loss TL_T of the double wall with sound bridges is given by

$$TL_T = 10 \log \left(\frac{W_I}{W_T} \right) = 10 \log \left(\frac{W_I}{W_p} \cdot \frac{W_p}{W_T} \right) = TL - TL_B \quad (44.60)$$

where W_I is the acoustic power incident on the double wall, TL is the transmission loss of the double wall without a sound bridge, and TL_B denotes the transmission loss reduction by the sound bridges, and is given by

$$TL_B = 10 \log \left(\frac{W_T}{W_p} \right) = 10 \log \left[1 + \frac{n\chi}{S} \left(\frac{v}{v_2} \right)^2 \right] \quad (44.61)$$

We assume the following:

1. The vibration velocity of the incident side plate is not affected by the sound bridges.
2. The vibration velocity of the transmitted side plate at the excitation points (connecting points) is equal to the velocity v_1 of the incident side plate, and consequently, the next equation holds

$$\frac{v}{v_2} \cong \frac{v_1}{v_2}$$

With these assumptions, we apply the method presented in section 44.1.3, to determine v/v_2 as

$$\frac{v}{v_2} \cong \frac{v_1}{v_2} = \frac{\omega^2 m_2 d}{\rho c^2} \quad (f_r < f < f_1/\pi) = \frac{\omega m_2}{\rho c} \quad (f > f_1/\pi) \quad (44.62)$$

Using Equation 44.60 and Equation 44.53, we can obtain the increase in transmission loss, ΔTL , from the transmission loss of mass law based on the total mass of the double wall, as presented below.

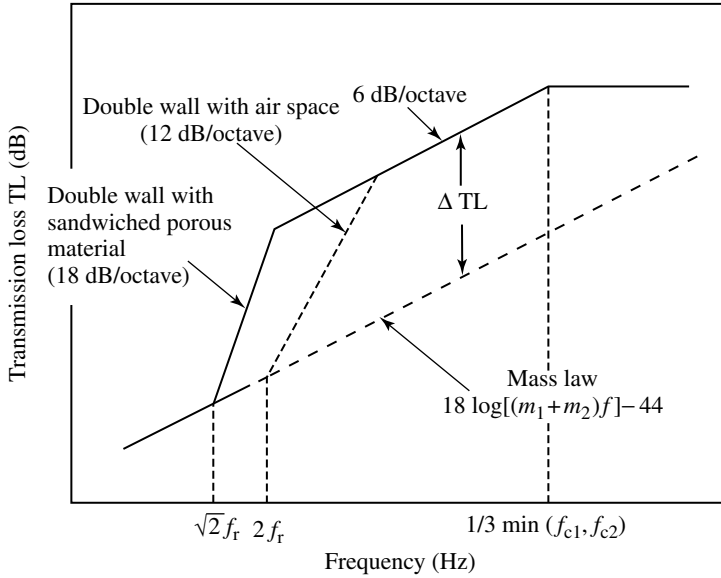


FIGURE 44.13 Design chart for estimating the transmission loss of a double wall with sound bridges.

1. Point connection

$$\begin{aligned}\Delta TL &= TL - TL_B - 20 \log \left[\frac{\omega(m_1 + m_2)}{2\rho c} \right] \\ &= 20 \log(e f_c) + 20 \log \left(\frac{m_1}{m_1 + m_2} \right) + 10 \log \left(\frac{\pi^3}{8c^2} \right)\end{aligned}\quad (44.63)$$

2. Line connection

$$\begin{aligned}\Delta TL &= TL - TL_B - 20 \log \left[\frac{\omega(m_1 + m_2)}{2\rho c} \right] \\ &= 10 \log(b f_c) + 20 \log \left(\frac{m_1}{m_1 + m_2} \right) + 10 \log \left(\frac{\pi}{2c} \right)\end{aligned}\quad (44.64)$$

where $e = \sqrt{S/n}$ is the distance between point forces and $b = S/nl$ is the distance between line forces.

Figure 44.13 presents a practical and useful design chart of the transmission loss for a double wall with sound bridges, which is based on Figure 44.11 and Equation 44.63 and 44.64.

44.2 Application of Sound Insulation

44.2.1 Acoustic Enclosure

Performance of an enclosure may be represented by the insertion loss (IL), which is the difference of acoustic power level before and after installation of the enclosure. When we assume a noise source and also an enclosure with one-dimensional model as shown in Figure 44.14a, the insertion loss through frequency is shown in Figure 44.14b. It is divided into the following four regions:

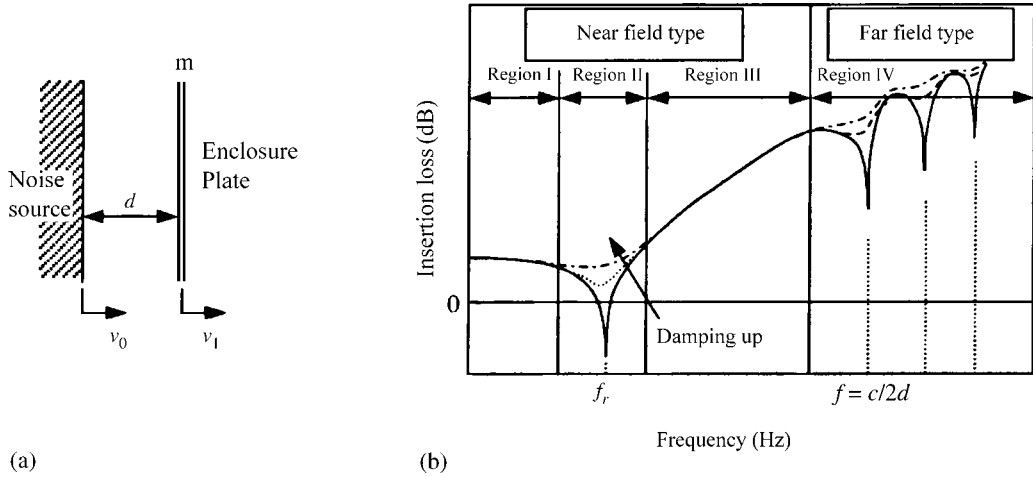


FIGURE 44.14 One-dimensional model for calculating the insertion loss characteristics of an acoustic enclosure: (a) One-dimensional model; (b) insertion loss of an enclosure.

1. Region I ($f < f_r$) is controlled by the stiffness of the enclosure plate and air space.
2. Region II ($f \cong f_r$) is the resonance region for a vibrating system consisting of the mass, the stiffness of the enclosure plate, and the capacitance of air space.
3. Region III ($f_r < f < c/2d$) is controlled by the mass of the enclosure plate.
4. Region IV ($f > c/2d$) is controlled by the diffused sound field. This region cannot be represented by a one-dimensional model.

44.2.1.1 Near Field Type [4]

When the distance between the noise source and the enclosure is less than half of a wavelength of the emitted sound from the source, insertion loss corresponds to the characteristics of the regions I to III, and we can represent them with a one-dimensional acoustic model, as shown in Figure 44.14a.

Consider an infinite flat enclosure plate with distance d from a noise source of plane sound wave, as shown in Figure 44.14a. The insertion loss of the plate is given by

$$IL = 10 \log \left(\frac{v_0}{v_1} \right)^2 = 10 \log \left[1 - \frac{2 \sin \theta (X \cos \theta - R \sin \theta)}{\rho c} + \frac{\sin^2 \theta (X^2 + R^2)}{\rho^2 c^2} \right] \quad (44.65)$$

$$\theta = kd = \omega d/c, \quad R = \eta \omega m, \quad X = (\omega m - K/\omega) = \omega m [1 - (\omega_{11}/\omega)^2], \quad \omega_{11} = \sqrt{K/m}$$

where m and K are the density and equivalent stiffness of the plate per unit area, respectively, and η is the loss factor of the plate. If the enclosure is a rectangular plate of size $a \times b$ and is simply supported at its edges, the equivalent stiffness is given by Equation 44.22, and ω_{11} is the natural (angular) frequency of the first mode.

In Equation 44.65, the conditions in which the brackets of the right-hand side are equal to zero or $IL = -\infty$ are satisfied by following frequencies:

- (1) $\theta \ll \pi$

$$f_r = \frac{1}{2\pi} \sqrt{\frac{K + \rho c^2/d}{m}} = \frac{1}{2\pi} \sqrt{\omega_{11}^2 + \frac{\rho c^2}{md}} \quad (44.66)$$

This is the natural frequency of vibration of the one-degree-of-freedom (one-DoF) system determined by the stiffness of the plate, the spring constant of the air space, and the surface density of the plate, as shown in Figure 44.15.

$$(2) \theta = n\pi \quad (n = 1, 2, \dots)$$

$$f_n = \frac{nc}{2d} \quad (n = 1, 2, \dots) \quad (44.67)$$

These are the resonant frequencies of the air space.

The frequency characteristics of the IL given by Equation 44.65 are shown in Figure 44.16, where the normal incidence transmission losses are shown by broken lines, as a reference. Equation 44.65 is approximated by

$$1. f < f_r$$

$$IL \cong 10 \log \left(1 + \frac{2Kd}{\rho c^2} \right) \quad (44.68)$$

$$2. f_r \leq f < f_1$$

$$IL \cong 20 \log(mdf^2) + 20 \log \left(\frac{4\pi^2}{\rho c^2} \right) \quad (44.69)$$

$$= 20 \log(mdf^2) - 71$$

44.2.1.2 Far Field-Type (Absorption Type) Enclosure [1]

When the distance between the noise source and the enclosure is larger than half of a wavelength of the emitted sound, insertion loss may be represented by the characteristics of Region IV, and it can be analyzed using the theory of room or hall acoustics.

Consider the enclosure shown in Figure 44.17, with a noise source of power level L_{W0} .

From the theory of room acoustics, the average sound pressure level, L_{p0} , on the inner surface of the enclosure plate is obtained as the sum of the direct and reverberant sound pressures:

$$L_{p0} = L_{W0} + 10 \log \left(\frac{1}{S} + \frac{4}{R} \right)$$

$$= L_{W0} - 10 \log S + 10 \log \left(1 + \frac{4S}{R} \right) \quad (44.70)$$

$$R = \frac{\bar{\alpha}S}{(1 - \bar{\alpha})} \quad (44.71)$$

where S is the inner surface area of the enclosure and $\bar{\alpha}$ is the average absorption coefficient on the inner surface of the enclosure. In Equation 44.70, the first and the second terms of the right-hand side represent the influence of the direct sound field, and the third term represents the buildup caused by the covering.

When we use S_p for the area of the enclosure plate and $S_O (= S - S_p)$ for the area of the enclosure opening, and assume diffusing condition for the sound field in the enclosure, acoustic power levels

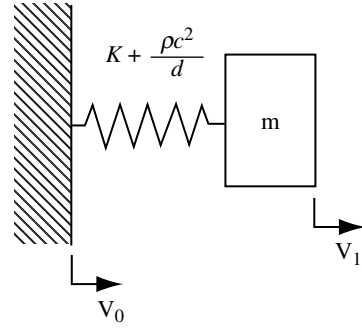
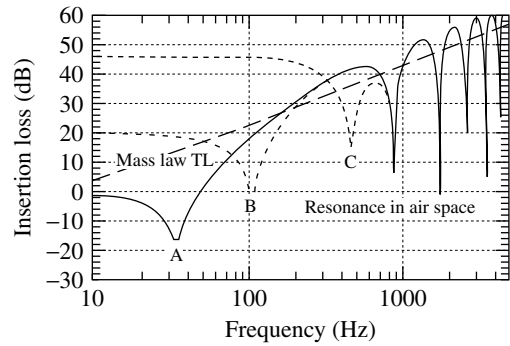


FIGURE 44.15 One-degree-of-freedom vibrating system.



$$m = 16 \text{ Kg/m}^2, d = 0.19 \text{ m}$$

$$\text{Curve A: } f_{11} = 0 \text{ Hz, } \eta \cong 0.033 \text{ (at 33 Hz)}$$

$$\text{Curve B: } f_{11} = 100 \text{ Hz, } \eta \cong 0.033 \text{ (at 105 Hz)}$$

$$\text{Curve C: } f_{11} = 475 \text{ Hz, } \eta \cong 0.033 \text{ (at 475 Hz)}$$

FIGURE 44.16 Example of theoretical insertion loss of a near field-type enclosure.

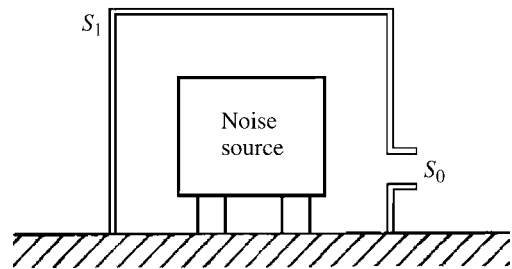


FIGURE 44.17 Calculation model of a far field type enclosure.

radiated from the plate and the opening are given, respectively, by

$$L_{WP} = L_{P0} - (TL + 6) + 10 \log S_P, \quad (44.72)$$

$$L_{W0} = L_{P0} - 6 + 10 \log S_O$$

where TL is the random incident transmission loss of the enclosure plate. Then, the insertion loss of the enclosure is

$$IL = L_{W0} - 10 \log(10^{L_{WP}/10} + 10^{L_{W0}/10}) \quad (44.73)$$

In the design of an acoustic enclosure, special attention should be paid to the following points:

1. *Buildup* increases the sound pressure in the enclosure and also the power level radiated from the enclosure. We must treat the inner surface of the enclosure with sound absorbing materials to reduce the absorption coefficient and to decrease the buildup.
2. *Opening* radiates more acoustic power than the enclosure plate by TL, as is clear from Equation 44.72. It is desirable to make the opening as small as possible within the range given by

$$\frac{S_O}{S_P} \leq 10^{-TL/10} = \tau \quad (44.74)$$

This equation means that the acoustic power from the opening is less than that from the enclosure plate. If the relation in Equation 44.74 cannot be satisfied because of ventilation requirements, and so on, some type of silencers should be provided at the opening, as shown in Figure 44.18.

3. *Structure-borne noise*, which is caused by the vibration propagating from the base of the machine (noise source) to the enclosure plate, significantly decreases the insertion loss of the enclosure. In this case, some means of noise/vibration suppression should be provided, for example, the following:
 - Place supporting structures of the enclosure at the points of lowest vibration level, and the vibrations of the machine should be prevented from propagating to the enclosure plate, using vibration isolation materials.
 - Add damping materials to the enclosure plate so as to reduce the vibration level of the plate.

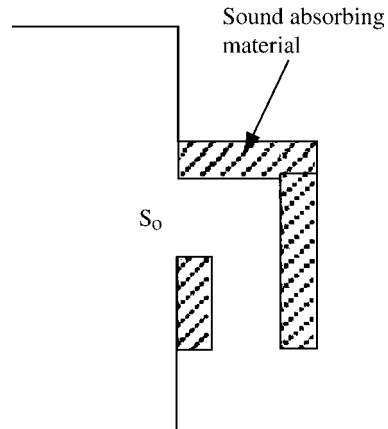


FIGURE 44.18 Example of a silencer at the opening.

44.2.2 Sound Insulation Lagging

In electric power plants and chemical plants, for example, piping for high-pressure water or steam, and ducts for air or gas flow form major noise sources. For controlling these noise sources, we usually use sound insulation laggings, which cover the noise sources with heavy and impermeable plates or sheets with sound absorbing materials, as shown in Figure 44.19.

44.2.2.1 Pipe Lagging [2]

Approximate the cylindrical piping and pipe lagging with a one-dimensional model as shown in Figure 44.20. The insertion loss of one-layered lagging approximated by a one-DoF system is given by Equation 44.69 in the frequency region $f_r \leq f < f_1$, as mentioned before. It is not practical, however, to directly apply Equation 44.69 to actual laggings, and we approximate the insertion loss of actual laggings by

$$IL = a \log(mdf^2) + b$$

where a and b are constants.

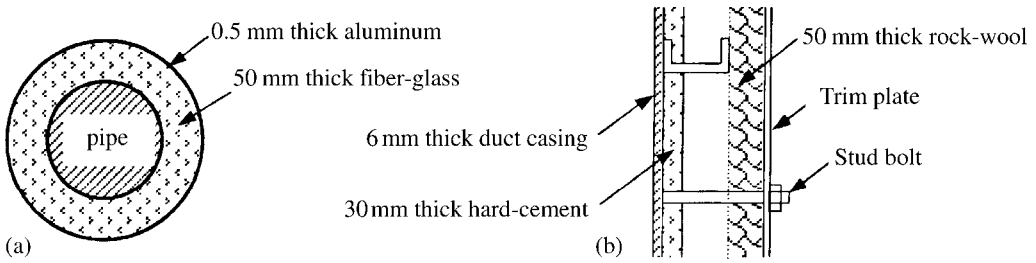


FIGURE 44.19 Examples of typical sound insulation laggings: (a) pipe lagging, (b) duct lagging.

By taking mdf^2 as the horizontal axis and plotting the insertion loss data from laboratory tests and field tests (the vertical coordinates), we obtain Figure 44.21. Apply regression analysis to the data in Figure 44.21 to obtain the insertion loss of one layered lagging as

$$IL = 11.7 \log(mdf^2) - 43.3 \quad (5 \times 10^3 \leq mdf^2 \leq 10^8) \quad (44.75)$$

Applying the same method to double layered lagging, approximated by a two-DoF vibrating system, we get Figure 44.22, and the insertion loss

$$IL = 6.9 \log(m_1 m_2 d_1 d_2 f^4) - 40.3 \quad (10^6 \leq m_1 m_2 d_1 d_2 f^4 \leq 10^{15}) \quad (44.76)$$

where the subscripts “1” and “2” denote the first layer and the second layer, respectively.

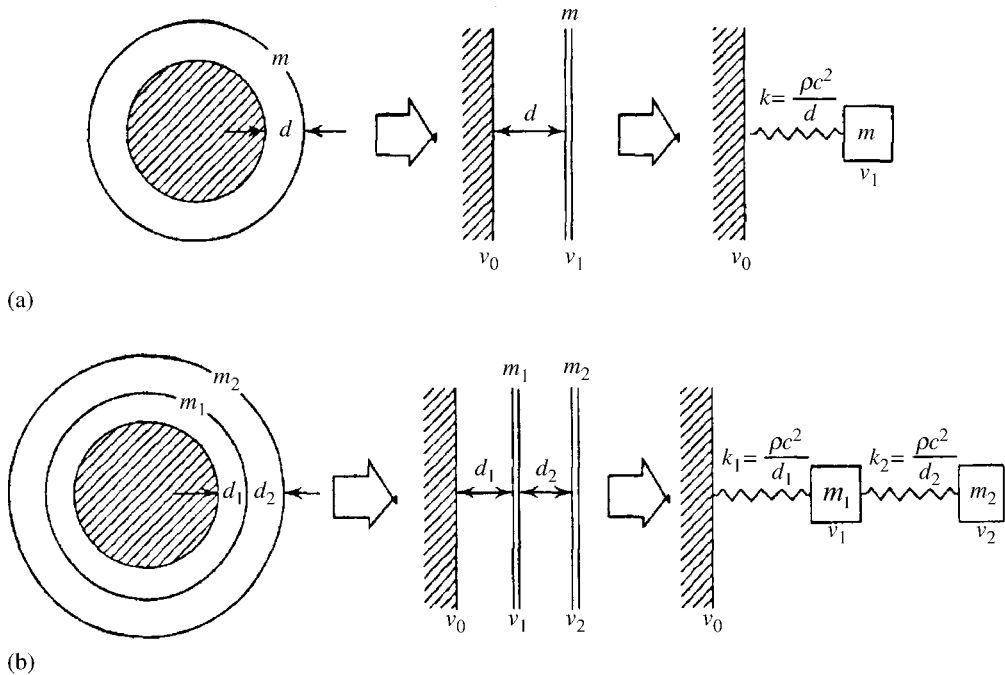


FIGURE 44.20 Examples of pipe laggings and calculation model: (a) one-layered lagging; (b) double-layered lagging.

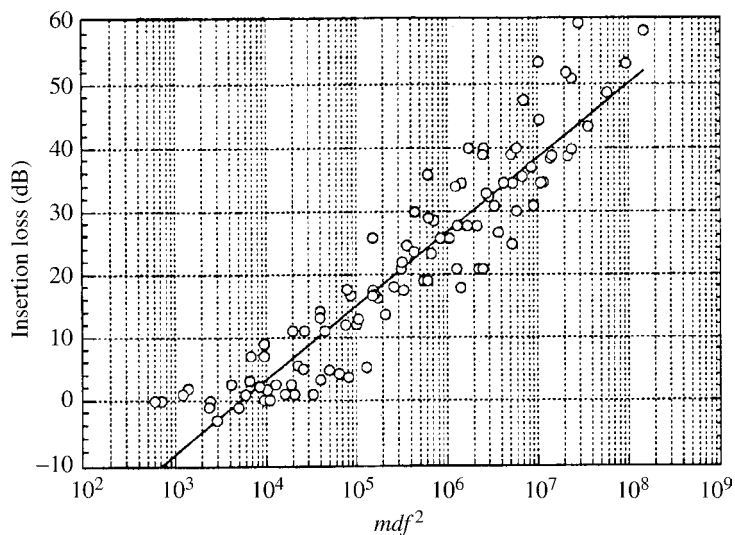


FIGURE 44.21 Measured insertion loss data obtained from laboratory and field tests for one-layered laggings and regression analysis.

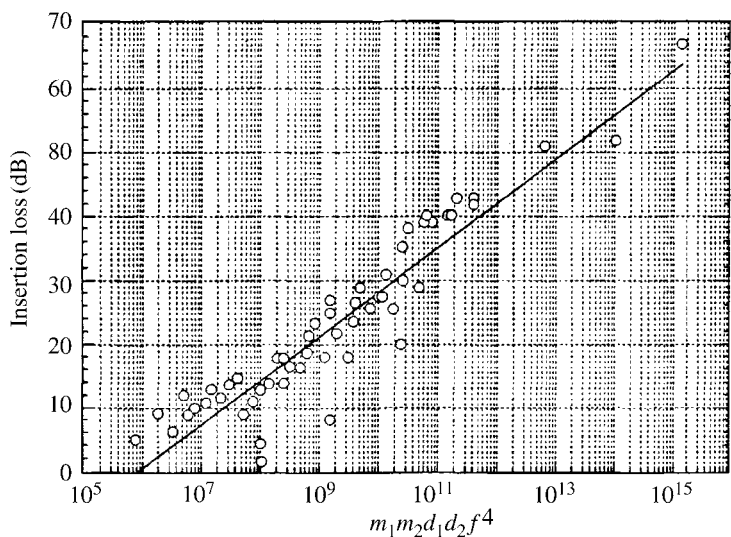


FIGURE 44.22 Measured data of insertion loss obtained from laboratory and field tests for double-layered laggings and regression analysis.

44.2.2.2 Duct Lagging [4]

Various types of the duct laggings are used according to the need, for example, as shown in Figure 44.19. A simpler and more practical approach is to place a thin plate on the duct casing through absorbing materials, as shown in Figure 44.23. In this case, assuming that vibration of the duct casing is not affected by the placed plate, the insertion loss of the duct lagging is obtained by following equations, which can be deduced from the method used in the transmission loss of double wall with sound bridges.

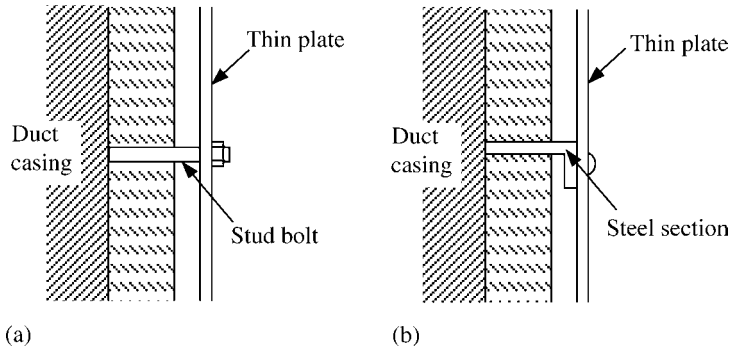


FIGURE 44.23 Examples of duct laggings and connection types of thin plate to the duct casing: (a) point connection; (b) line connection.

1. Point connection

$$IL = -10 \log \left[\beta^2 \frac{8}{\pi^3} n_p \frac{c^2}{f_c^2} + \left(\frac{f_r}{f} \right)^4 \right] + 10 \log \sigma \quad (44.77)$$

2. Line connection

$$IL = -10 \log \left[0.64 n_L \frac{c}{f_c} + \left(\frac{f_r}{f} \right)^4 \right] + 10 \log \sigma \quad (44.78)$$

where

β = vibration isolation factor of the flexible support ($\beta = 1$ for rigid support)

n_p = number of attachment points per unit area

n_L = number of studs per unit length

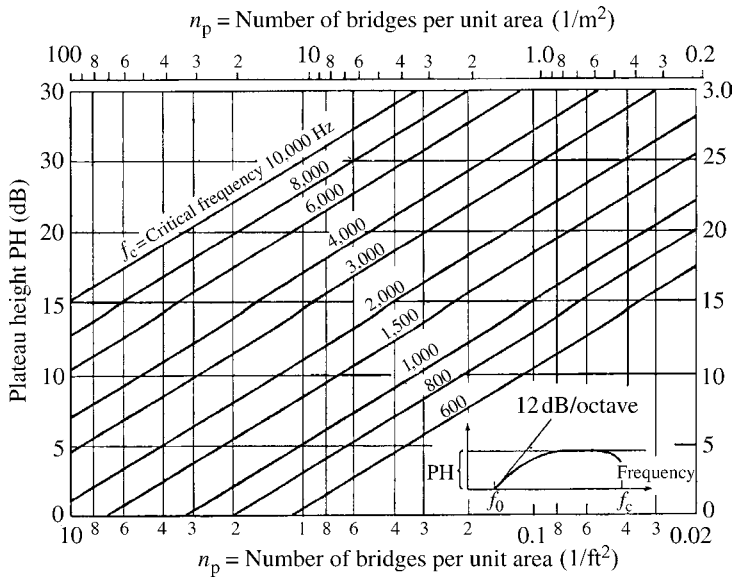


FIGURE 44.24 Plateau height for point connection as a function of the number of bridges per unit area [4]. (Source: Beranek, L. L. 1988. *Noise and Vibration Control*, INCE/USA. With permission.)

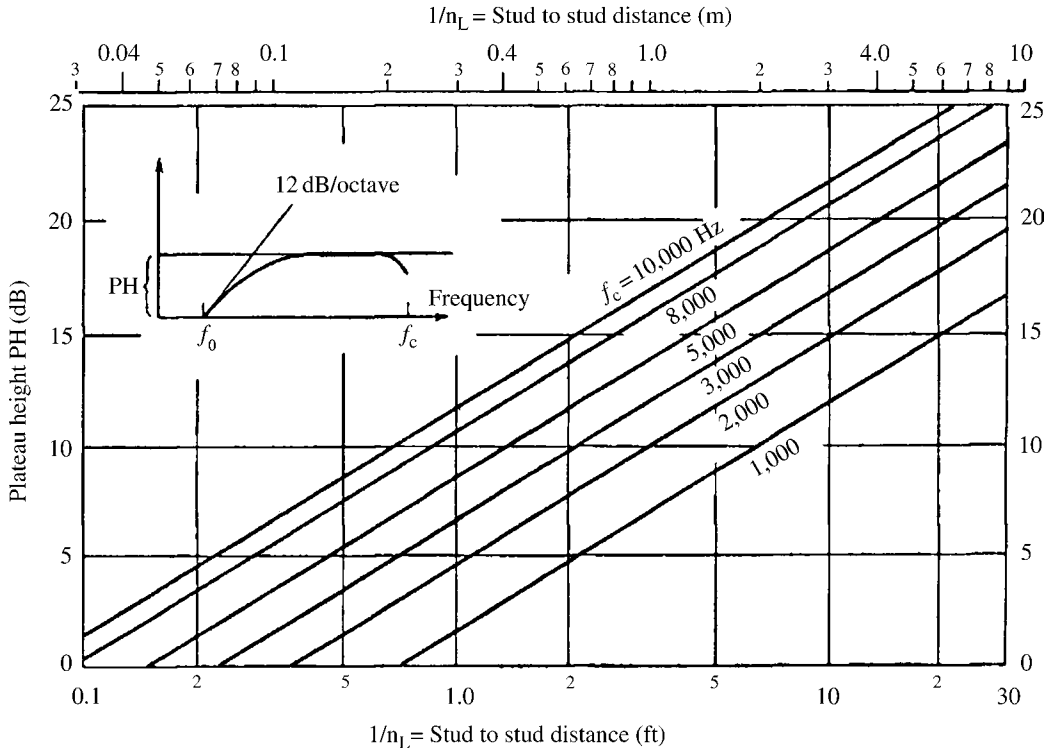


FIGURE 44.25 Plateau height for line connection as a function of the number of studs per unit length [4]. (Source: Beranek, L. L. 1988. *Noise and Vibration Control*, INCE/USA. With permission.)

f_c = critical frequency of the thin plate given by Equation 44.12

f_r = resonant frequency given by Equation 44.66

σ = sound radiation efficiency of the thin plate

Knowing the critical frequency, f_c , and the resonant frequency, f_r , we can obtain the insertion loss from the charts given in Figure 44.24 and Figure 44.25 instead of using Equation 44.77 and Equation 44.78. In Figure 44.24 and Figure 44.25, it is assumed that $\sigma = 1$. Note from Equation 44.77 and Equation 44.78 that we must consider the following measures to obtain a higher insertion loss.

1. Make the distance between attachment points or studs as large as possible (decrease n_p and n_L).
2. Make the air space as large as possible (decrease f_r).

References

1. Shiraki, K., ed. 1987. *From Designing of Noise Reduction to Simulation* (in Japanese), Ouyou-gijutsu Shuppan, Chiyoda-ku, Tokyo.
2. Tokita, Y., ed. 2000. *Sound Environment and Control Technology, Vol. I, Basic Engineering* (in Japanese), Fuji-techno-system, Bunkyo-ku, Tokyo.
3. Okura, K. and Saito, Y., Transmission loss of multiple panels containing sound absorbing materials in a random incidence field, *Inter-noise*, 78, 637, 1978.
4. Beranek, L.L., ed. 1988. *Noise and Vibration Control*, INCE/USA, Ames, IA.
5. Sharp, B.H. 1973. A study of techniques to increase the sound insulation of building elements, Wyle Laboratory Report WR 73-5, El Segundo, CA.

45

Statistical Energy Analysis

45.1	Introduction	45-1
45.2	Power Flow Equations	45-2
	Power Flow Equations of a Two-Subsystem Structure •	
	Power Flow Equations of a Multiple Subsystem Structure	
45.3	Estimation of SEA Parameters	45-4
	Modal Density • Internal Loss Factor • Coupling Loss	
	Factor • Input Power	
45.4	Application in Structures	45-7
	Application for Prediction of Noise in a Tractor Cabin •	
	Application for Prediction of Noise and Vibration in a	
	Building	

Takayuki Koizumi
Doshisha University

Summary

This chapter presents the basics of statistical energy analysis (SEA) as applied to acoustic problems in structural systems. Power flow equations for structures consisting of two or more subsystems are described. The modeling and analysis procedures for the structural subsystems and acoustic subsystems are given. An estimation procedure of the necessary SEA parameters is given. The practical application of the SEA procedure in structures is illustrated using a two-story building as an example.

45.1 Introduction

This chapter describes the basic concepts of the method of statistical energy analysis (SEA) and presents its application to structures. The analysis and computation techniques for vibration response and radiating sound in instruments and structures vary according to the characteristics of the physical object and the frequency range of interest. Here, we analyze vibration and noise in relation to a rather large-scale structure over a wide frequency band. Extensive computations are usually required, when, for example, the finite element method (see Chapter 9) is used for the computations, with respect to a given oscillation mode. In particular, when the computations must be performed in the high-frequency range and when many modes are included in the frequency band, the level of computation becomes considerable, generally resulting in reduced computational accuracy. To supplement the weak point of the traditional approach, it is necessary to redistribute statistically the energy equally from all modes in the analytical frequency band. This allows computed results to be compared with experimental results for a structure across a wide frequency band. This is the SEA method [1]. Early in its development, the objective of this analytical method was to predict the vibration response of artificial satellites and rockets that receive sound excitation when the jet discharges, and to predict the response of vibration stress in the boundary layer noise of an aircraft's airframe. It also became a model that allows an

exciting force to be statistically (randomly) diffused (distributed) over a wide frequency band. This technique considers energy of excitation of a diffused (distributed) sound field and its variables that represent the sound pressure, acceleration, and force. Thus, it can be applied to problems of solid-borne sound in which vibration propagates through each element [2] and problems of air-borne sound in which multiple barriers exist [3], even when more excitation points than one are present.

45.2 Power Flow Equations

With the SEA method, we do not deal with specific characteristic modes (see Chapter 3 and Chapter 4) of the analyzed structure. Instead, we consider the structural components as a set of equivalent vibrating elements, and evaluate the vibration condition of the components as a macroscopic quantity averaged statistically over the frequency band and space (by describing the energy). We assume that the vibration modes within a given frequency band are distributed uniformly and are excited to the same degree.

Using the SEA method, we can formalize the relationships of power flows between subsystems, and by solving these relationships, we can compute the energy stored in each subsystem. Next, the equations of such basic power flow [4] are explained.

45.2.1 Power Flow Equations of a Two-Subsystem Structure

The power flow relationships of a structure consisting of a two-subsystem structure are shown in Figure 45.1. The equations for the power flows between subsystem 1 and subsystem 2 under typical conditions are expressed as

$$\text{Subsystem 1: } P_{i1} = P_{l1} + P_{12} \quad (45.1)$$

$$\text{Subsystem 2: } P_{i2} = P_{l2} + P_{21} \quad (45.2)$$

where P_{i1} is the input power to subsystem 1 from outside, P_{l1} is the internal power loss of subsystem 1, and P_{12} is the transmitted power from subsystem 1 to subsystem 2.

The internal power loss, P_{l1} , is written as

$$P_{l1} = \omega \eta_1 E_1 \quad (45.3)$$

where ω is the central angular frequency in the band, E_1 is the energy in the bandwidth $\Delta\omega$ of subsystem 1, and η_1 is the internal loss factor (ILF).

The average modal energy E_{m1} in subsystem 1, and E_{m2} in subsystem 2, are given by

$$E_{m1} = \frac{E_1}{N_1}, \quad E_{m2} = \frac{E_2}{N_2} \quad (45.4)$$

where N_1 is number of modes in the bandwidth $\Delta\omega$ of subsystem 1, and N_2 is number of modes in the bandwidth $\Delta\omega$ of subsystem 2.

The transferred power, P_{12} , between subsystems 1 and 2 is expressed as

$$P_{12} = -P_{21} = P'_{12} - P'_{21} \quad (45.5)$$

$$P'_{12} = \omega \eta_{12} E_1 = \omega \eta_{12} N_1 E_{m1} \quad (45.6)$$

$$P'_{21} = \omega \eta_{21} E_2 = \omega \eta_{21} N_2 E_{m2} \quad (45.7)$$

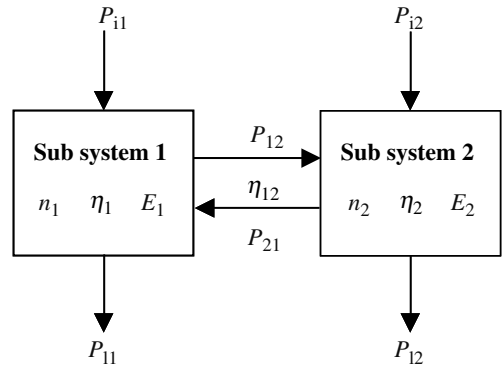


FIGURE 45.1 Power flow relationships between two subsystems.

where η_{12} and η_{21} are the coupling loss factors (CLFs) from subsystem 1 to subsystem 2, and from subsystem 2 to subsystem 1. They satisfy the reciprocity relationship $\eta_{12}n_1 = \eta_{21}n_2$. Therefore, transferred power, P_{12} , becomes

$$P_{12} = \omega\eta_{12}N_1(E_{m1} - E_{m2}) = \omega\eta_{12}N_1\left(\frac{E_1}{N_1} - \frac{E_2}{N_2}\right) \quad (45.8)$$

Consequently, the power flow equations (Equation 45.1 and Equation 45.2) can be expressed as follows:

$$P_{11} = \omega\eta_1E_1 + \omega\eta_{12}N_1\left(\frac{E_1}{N_1} - \frac{E_2}{N_2}\right) \quad (45.9)$$

$$P_{12} = \omega\eta_2E_2 + \omega\eta_{21}N_2\left(\frac{E_2}{N_2} - \frac{E_1}{N_1}\right) \quad (45.10)$$

If the SEA parameters (i.e., the modal density, intrinsic loss factor, CLF, and input power) are given, then each subsystem's energy condition can be easily computed.

45.2.2 Power Flow Equations of a Multiple Subsystem Structure

By expanding the formulation in the previous section, it is possible to formalize the power flow relationships of a structure composed of multiple subsystems in the same way. The power flow equation for a structure composed of N subsystems is expressed by the following equation in the matrix form:

$$\omega \begin{bmatrix} \left(\eta_1 + \sum_{i \neq 1}^N \eta_{1i}\right)n_1 & -\eta_{12}n_1 & \cdots & -\eta_{1N}n_1 \\ -\eta_{21}n_2 & \left(\eta_2 + \sum_{i \neq 2}^N \eta_{2i}\right)n_2 & \cdots & -\eta_{2N}n_2 \\ \vdots & \vdots & \ddots & \vdots \\ -\eta_{N1}n_n & \cdots & \cdots & \left(\eta_N + \sum_{i \neq N}^{N-1} \eta_{Ni}\right)n_N \end{bmatrix} \times \begin{bmatrix} E_1/n_1 \\ E_2/n_2 \\ \vdots \\ E_N/n_N \end{bmatrix} = \begin{bmatrix} P_{11} \\ P_{12} \\ \vdots \\ P_{1N} \end{bmatrix} \quad (45.11)$$

From Equation 45.11, if the SEA parameters are given in the same way as for the structure of two subsystems, then the energy equation of each subsystem can be obtained.

The average energy of a subsystem is expressed by the following equations by using the vibration velocity and sound pressure:

$$E = M\langle v^2 \rangle \quad (45.12)$$

$$E = \frac{M\langle p^2 \rangle}{Z_0^2} \quad (45.13)$$

where M is the mass of the subsystem, $\langle v^2 \rangle$ is the average spatial square of the vibration velocity, $\langle p^2 \rangle$ is the average spatial square of the sound pressure, and Z_0 is the specific acoustic impedance of air.

Accordingly, if each condition of component's energy is determined from Equation 45.11, it is possible to compute the vibration variable and the sound pressure with Equation 45.12 and Equation 45.13.

45.3 Estimation of SEA Parameters

To solve the power flow equations, it is necessary to determine the SEA parameters (i.e., the modal density, ILF, CLF, and input power). In this subsection, a method is given for computing the SEA parameters.

45.3.1 Modal Density

45.3.1.1 Structural Subsystem

Modal density is a key parameter for determining the dynamic characteristic of a structure. The number of modes, N , included in the frequency band (for estimation), is a factor denoting how easily energy, in transferring between subsystems, can be obtained. To determine N in the prescribed frequency band, it is first necessary to determine the modal density $n(f)$, that is, the gradient of N in the frequency band.

The modal density of a structural subsystem is computed by using the following equation [4,5]:

$$n(f) = \frac{dN}{df} = \frac{1}{f_0} = \frac{A}{2t} \sqrt{\frac{12\rho(1-\nu^2)}{E}} \quad (45.14)$$

where A is the area of cross section, t is the thickness of the structural subsystem, ρ is the mass density, ν is the Poisson's ratio, E is the Young's modulus, and f_0 is the fundamental natural frequency of the structural subsystem.

45.3.1.2 Acoustic Subsystem

The modal density of an acoustic subsystem is determined by the following analytical equation [6]:

$$n(f) = \frac{dN}{df} = \frac{4\pi V}{c^3} f^2 \quad (45.15)$$

where c is the speed of sound propagation within the acoustic subsystem, and V denotes the volume of the acoustic subsystem.

Modal density of the cavity in the low frequency band is deduced in a similar manner to that in the two-dimensional space. Define the depth of the cavity by d , and the frequency of the standing wave in the cavity by $f_d = c/2d$. If $f < f_d$, then the modal density is assumed to be uniformly distributed, and is estimated by

$$n(f) = \frac{2\pi S}{c^2} f \quad (45.16)$$

where S is the area of the cavity.

If $f > f_d$, modal density can be estimated using Equation 45.15, because the cavity is designated as acoustically three dimensional.

45.3.2 Internal Loss Factor

45.3.2.1 Structural Subsystem

The ILF, η_1 , of a subsystem gives the loss ratio when the input power to the subsystem from the outside is converted to kinetic energy of the subsystem. An excitation test to measure the damping ratio is employed to estimate the ILF of the structural subsystem. There are several methods for estimating the internal loss factor. The ILF applied in the SEA method is estimated by measuring input energy and output energy simultaneously, or by measuring the attenuation ratio within a given period of time. Both methods require the same setup to conduct an excitation test, and one is able to improve the measurement precision by conducting both methods.

With the energy measuring methods mentioned above, the ILF can be estimated by

$$\eta = \frac{\int_{f_1}^{f_2} \text{Re}(Y) F^2 df}{\omega_0 M \left\langle \int_{f_1}^{f_2} v^2 df \right\rangle} \quad (45.17)$$

where Y is the complex mobility at the driving point in the range of f_1 to f_2 , F^2 is the power spectrum of the input vibration force, and v^2 is the power spectrum of the response speed. In addition, $\langle \rangle$ denotes the space average operator.

45.3.2.2 Acoustic Subsystem

The ILF of an acoustic subsystem is determined by [7]

$$\eta = \frac{cS\bar{\alpha}}{4V\omega} \quad (45.18)$$

where $\bar{\alpha}$ is the average acoustic absorption coefficient, V is the volume of the acoustic subsystem, and S denotes the surface area. The acoustic absorption coefficient can be estimated by measuring the reverberation time.

Both the ILF of the cavity in the low-frequency band and the modal density are deduced similar to that in two-dimensional spaces. For $f < f_d$, the ILF is estimated using

$$\eta = \frac{cS_p\alpha_p}{\pi\omega V_c} \quad (45.19)$$

where α_p is the acoustic absorption coefficient in the cavity, S_p is the peripheral area of the cavity, and V_c is the volume of the cavity.

For $f > f_d$, the modal density can be estimated using Equation 45.18 because the cavity is taken as an acoustic subsystem.

45.3.3 Coupling Loss Factor

45.3.3.1 Between Structural Subsystems

The CLF η_{ij} gives the loss ratio when power transmits between two subsystems [4]. For example, the CLF between two flat plates can be estimated using

$$\eta_{ij} = \frac{c_{gi}L_c\tau}{\pi\omega S_i} \quad (45.20)$$

where c_{gi} is the group velocity of the bending waves, L_c is the coupled length, S_i is the surface area, and τ_{ij} is the energy transmission factor from subsystem i to subsystem j . The transmission factor varies with the type of coupling, for example, I-type, L-type, or T-type shown in Figure 45.2. In this section, we use energy transmission efficiency of vertical incidence, reported by Cremer [7].

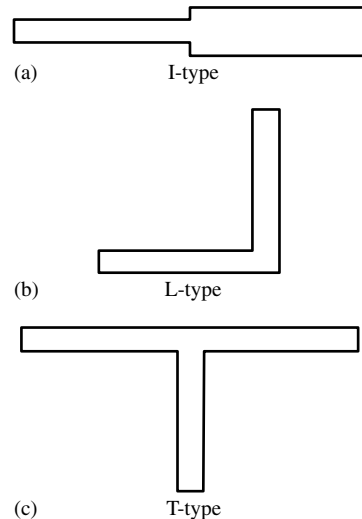


FIGURE 45.2 Coupled type.

45.3.3.2 Between a Structural Subsystem and an Acoustic Subsystem

Coupling power between a structural subsystem and an acoustic subsystem is the power flow based on resonance at transmission. The CLF between a structural subsystem and an acoustic subsystem is given by

$$\eta_{ij} = \frac{Z_0 S_c \sigma}{\omega M_i} \quad (45.21)$$

where Z_0 is the specific acoustic impedance of air, S_c is the surface area of coupling, σ is the acoustical radiation efficiency, and M_i is the mass of the structural subsystem.

45.3.3.3 Between an Acoustic Subsystem and a Cavity

Coupling power between an acoustic subsystem and a cavity is power flow based on resonance in transmission. The CLF between an acoustic subsystem and a cavity is given by [8]

$$\eta_{sc} = \frac{c_s S_{cs} \tau_m}{4\omega V_s} \quad (45.22)$$

where c_s is the sound velocity in the acoustic space, V_s is the volume in the acoustic space, τ_m is the transmission factor at random incidence depending on mass flow through the partition, and S_{cs} is the coupling area.

45.3.4 Input Power

45.3.4.1 Vibration Input Power

The vibration input power P_{iN} is given by

$$P_{iN} = \omega M_i \langle v_i^2 \rangle \quad (45.23)$$

where M_i is the equivalent mass, $\langle v_i^2 \rangle$ is the spatial average of square of the vibration velocity, and ω is the central angular frequency.

45.3.4.2 Acoustical Input Power

The acoustical input power P_s is given by

$$P_s = \frac{\langle p^2 \rangle S^2 n(f)}{4M} \sigma_{\text{rad}} \frac{c^2}{2\pi S f^2} \quad (45.24)$$

where $\langle p^2 \rangle$ is the square average of the input sound pressure, S is the surface area of the component, M is the mass of the component, $n(f)$ is the modal density, and σ_{rad} is the sound radiation factor [2].

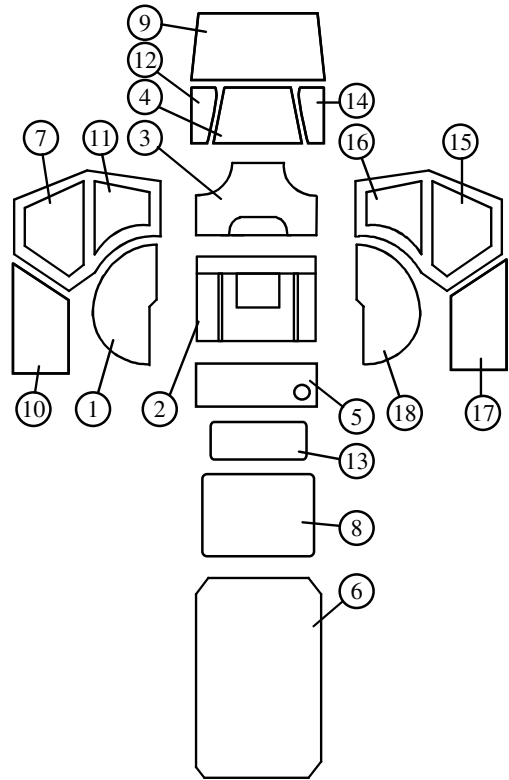


FIGURE 45.3 Modeling of the tractor cabin.

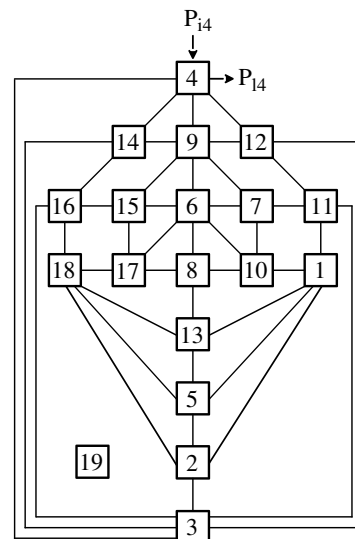


FIGURE 45.4 Power flows in the tractor cabin.

45.4 Application in Structures

In this section, we present an example of modeling with significant analytical accuracy, and discuss the application of the SEA method for structures.

45.4.1 Application for Prediction of Noise in a Tractor Cabin

Figure 45.3 shows a model of the tractor cabin. This figure shows that the cabin consists of a floor, a door, a ceiling, and other components. Figure 45.4 presents the power flow relationships within the cabin [9,10].

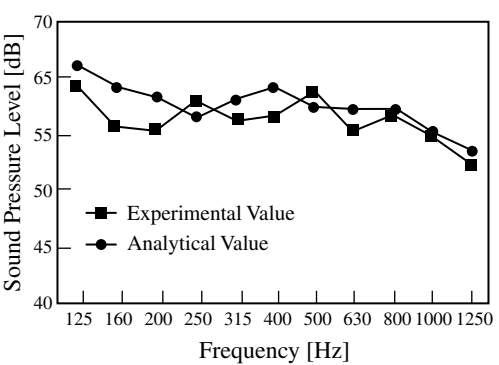


FIGURE 45.5 Results of estimating the sound pressure level in a cabin.

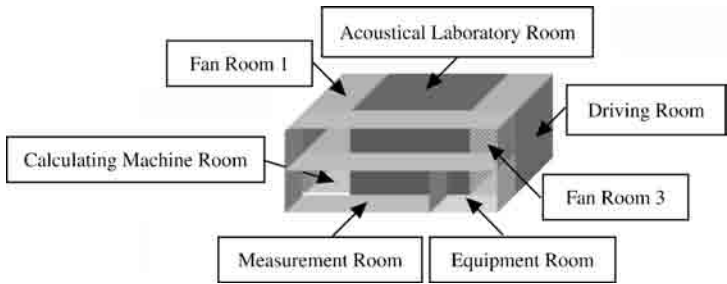


FIGURE 45.6 The configuration of the building.

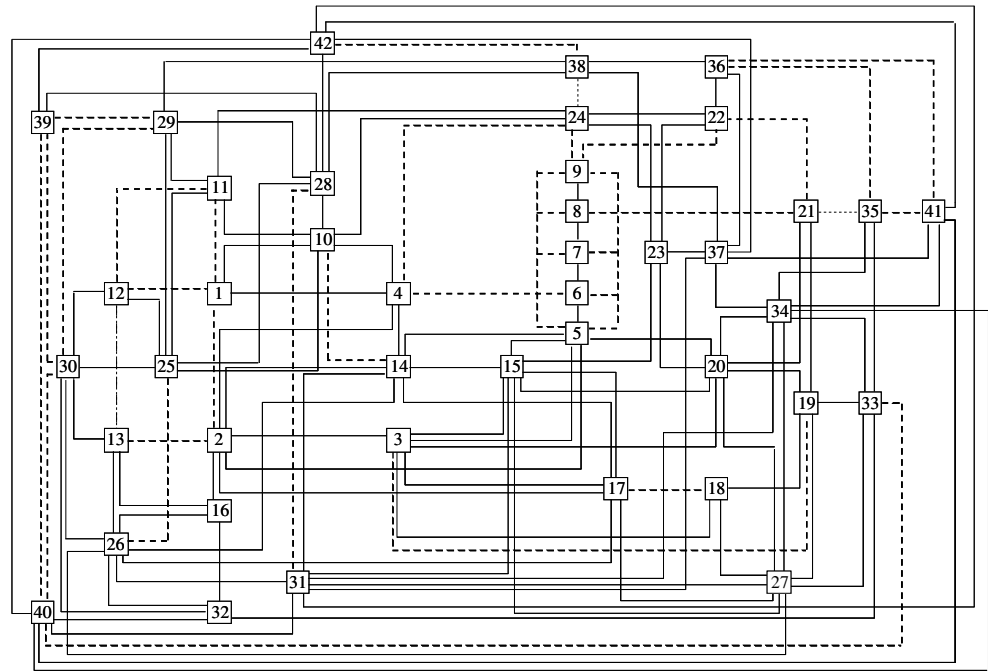


FIGURE 45.7 The power flow relationships between structural subsystems in the entire building.

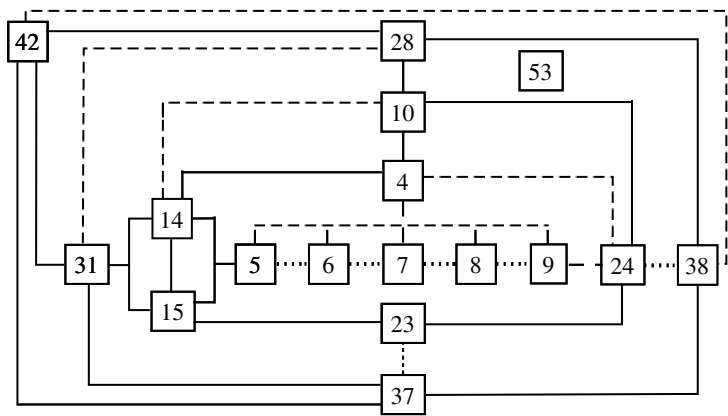


FIGURE 45.8 The power flow relationships in the acoustical laboratory room.

The results obtained for the cabin are shown in Figure 45.5. According to this figure, the disagreement between the computation and the measurement was found about 2 dB in the medium- to high-frequency band.

45.4.2 Application for Prediction of Noise and Vibration in a Building

Consider a two-story laboratory reinforced with concrete [11]. The building configuration is shown in Figure 45.6. This building comprises a driving room, an acoustical laboratory room, a computer room, a measurement room, an equipment room, and others.

We modeled the structural subsystem using I-, L-, or T-type connected points, and the acoustic subsystem as an element shown in Figure 45.6.

The SEA model constructed in this manner is composed of 61 elements, and has 244 connecting points. Subsystems 1 to 17 and subsystems 19 to 42 are concrete components. Subsystem 18 and subsystems 43 to 48 are plasterboard components; subsystems 49 to 55 are room components; and subsystems 56 to 61 are cavity components. For example, Figure 45.7 shows the power flow relationships between structural subsystems in the entire building, while Figure 45.8 shows them in the acoustical laboratory room. Here, the thin-dotted, dotted, and solid lines indicate the I-, L-, and T-type combinations, respectively. Subsystem 53 is the room component, and it is connected with all structural components shown in Figure 45.8. The plasterboards located between the computer room and the measurement room are considered as a partition; therefore, connections between subsystem 49 and subsystems 56 to 59 (cavity components), and subsystem 50 and subsystems 60 and 61 (cavity components) are derived from nonresonant modes.

The results obtained for some other rooms are shown in Figure 45.9. Computing accuracy in this building is worse than in the cabin because the structure of this building is complicated, although the differences between the computed values and the measured values were approximately 4 dB in the medium- to high-frequency band.

The computations take approximately 10 sec, so the workload on the personal computer is quite light.

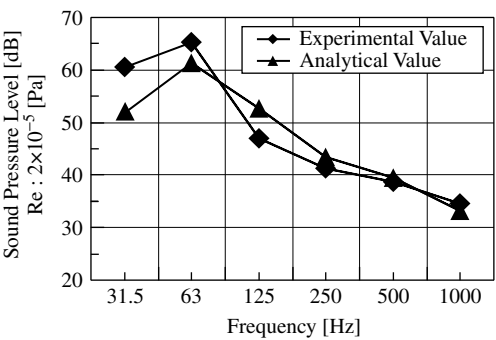


FIGURE 45.9 Estimated sound pressure level results for other rooms.

References

1. Lyon, R.H. 1975. *Statistical Energy Analysis of Dynamical Systems: Theory and Applications*, MIT Press, Cambridge, MA.
2. Irie, Y., Solid propagation sound analysis by SEA, *Mitsubishi Heavy Ind. Tech. Rev.*, 21, 4, 571–578, 1984.
3. Crocker, M.J., Sound transmission using statistical energy method, *AIAA J.*, 15, 2, 75–83, 1977.
4. Irie, Y., Solid propagation sound analysis by SEA, *Nihon Onkyo Gakkai-shi*, 48, 6, 433–444, 1992.
5. Lyon, R.H. and Dejong, R.G. 1995. *Theory and Applications of Statistical Energy Analysis*, 2nd ed., Butterworth-Heinemann, Oxford.
6. Craik, R.J.M. 1996. *Sound Transmission Through the Buildings Using Statistical Energy Analysis*, Gower Press, England.
7. Cremer, L., Heckle, M., and Unger, E.E. 1973. *Structure Borne Sound*, Springer, New York, pp. 347–370.
8. *Mechanical Noise Handbook*, JSME, Japan Society of Mechanical Engineers, pp. 179–181, 1991 (in Japanese).
9. Koizumi, T., Tsujiuchi, N., Kubomoto, I., and Ishida, E., Estimation of the noise and vibration response in a tractor cabin using statistical energy analysis, *JSAE Paper*, 28, 4, 49–54, 1997.
10. Koizumi, T., Tujiuchi, N., Kubomoto, I., and Ishida, E., Estimation of the noise and vibration response in a tractor cabin using statistical energy analysis, *SAE Paper*, 1999-01-2821, 1999.
11. Koizumi, T., Tujiuchi, N., Tanaka, H., Okubo, M., and Shinomiya, M., Prediction of the vibration in building using statistical energy analysis, *IMAC Paper*, 7–13, 2002.

Glossary

A + B vibration

Vertical vibration of an aircraft represented by the sum of the vibrations measured at the two sides of the cockpit.

A – B vibration

Roll vibration of an aircraft represented by the difference in the vibrations measured at the two sides of the cockpit.

A-weighted sound level

Sound pressure level that has been weighted according to A-weighting networks, commonly used in measurements that relate to human response to noise (dBA). [See Sound level.](#)

Abnormality scaling

The process of scaling the level of abnormality in each vibration feature between 0 and 1 to signify the degree of deviation from its normal value.

Absolute acceleration shock response spectrum

This is an SRS for acceleration. [See Response spectrum \(RS\)](#) and [Shock response spectrum \(SRS\)](#).

Absolute error

The absolute value of the difference between the exact solution and the computed solution, or between the true value and the measured value.

Absolute limit

Conditions that could result in catastrophic failure.

Absorber

[See Vibration absorber.](#)

Absorption coefficient

Fraction of the incident energy absorbed by a sound surface.

AC

Alternating current.

AC bridge

A bridge circuit that uses an AC excitation. It is more stable than a DC bridge.

AC motor

A motor that uses an AC excitation. Single-phase and multiphase, induction, and synchronous varieties are available.

Acceleration

Rate of change of velocity with respect to time along a specified axis (m/sec^2 or g) or about an axis (rad/sec^2). Second derivative of displacement. Gives both magnitude and direction (vector).

Accelerogram

A recording of the acceleration of the ground during an earthquake.

Accelerograph

An instrument (accelerometer) that records the acceleration of the ground during an earthquake.

Accelerometer

Sensor or transducer measuring acceleration; output (typically voltage) is proportional to acceleration. A piezoelectric accelerometer contains one or more piezo-electric crystal elements, which produce electric charges or voltages when stressed in tension, compression, or shear. Can be two or three axial. The output can be in digital in some cases, with proper transducers.

Acceptability index

The percentage of times an adjustment set will result in the vibration satisfying the specification.

Accuracy

How well a measurement (reading) or a computed result represents the true (correct) value. Accuracy of a value and accuracy of an instrument are related because the latter can determine the former.

Acoustic absorption coefficient

A ratio (fraction) expressing the ability of a material to absorb acoustic power.

Acoustic emission (AE)

Sound or ultrasound pulses generated during crack initiation or propagation in materials and coatings from being subjected to stress.

Acoustic enclosure

A rigid box surrounding noise sources to provide noise isolation for machinery or equipment.

Acoustic holography

A method using phase and amplitude information over a closed surface to reconstruct a sound field in the region outside the surface.

Acoustic impedance

Acoustic pressure acting on a surface divided by the volume (or particle) velocity at the surface. Assumes a plane wave is falling perpendicular to the surface. May assume acoustic material of infinite depth on which the wave is applied.

Acoustic power

The rate of acoustic energy flow emitted or radiated by a specified sound or noise source (W).

Acoustic resonance

Condition of peak (maximum) response of a fluid-borne system to a periodic driving pressure oscillation. Typically, the frequency at which the system tends to oscillate naturally.

Across wind response

Response perpendicular to the direction of wind.

Action plan

When measured values of noise or vibration violate the local or national regulatory limits, “action plans” shall be developed for correcting of the situation.

Active bridge

A bridge circuit (with four bridges; e.g., Wheatstone bridge) that uses an operational amplifier (an active device, which uses an external power source).

Active control

[See Active vibration control.](#)

Active damping

Controlled damping where the damping force is generated by an actuator (with an external power source) in response to sensing (e.g., active suspensions and magnetorheology).

Active device

A device (hardware) that needs an external power source to operate.

Active filter

Uses an operational amplifier (an active device), as opposed to a passive filter, which uses only passive devices.

Active gauge

The strain gauge mounted on the deforming member and forms a part of the bridge circuit. [See Dummy gauge.](#) The bridge output is proportional to the change in the active gauge (automatically compensated for ambient changes by the dummy gauges).

Active mount

An engine mount that uses actuators (with external power) for providing proper suspension and isolation (force and motion).

Active resonator absorber

[See Vibration absorber](#) and [Resonator absorber](#). A resonator absorber that utilizes an active device to generate resonance ([see Resonance](#)) within the absorber subsection.

Active suspension

A suspension system (of a vehicle) that uses actuators (with external power) with feedback control for providing proper suspension.

Active vibration control

A vibration control method in which an external force (utilizing external power) is applied to control vibrations.

ADC

An analog-to-digital converter, which samples an analog signal at some frequency (sampling rate) and converts the sampled data into a digital form.

Adiabatic process

A process that takes place with no heat transfer with the environment.

Adjustable suspension element

Typically includes variable rate damper and stiffness.

Aeroelastic model

The model that simulates the dynamic properties of buildings to capture the motion-dependent loads.

Air-borne sound

A sound that is transmitted from one structure to another.

Aliasing distortion

The error that results due to sampling (discretization) of an analog signal.

Along-wind response

Response in the direction of wind.

Amplitude

Peak magnitude of variation (displacement, velocity, acceleration, etc.) of each oscillation of vibration. The maximum value of a sinusoidal quantity. A measure of floor vibration.

Amplitude-dependent damping

Nonlinear form of damping where its value depends on the amplitude but not frequency of motion, e.g., fluid friction or aerodynamic damping or whose magnitude is proportional to the square of the velocity; nonhysteretic internal damping.

Amplitude ratio

The ratio of forced vibration amplitude to the static amplitude.

Analog device

A device with analog circuitry (hardware) but no digital components. It deals with analog or time-continuous signals but not digital signals.

Analog-to-digital conversion

See [ADC](#).

Anelasticity

Property of real solids responsible for internal friction (prefix “an” means “other than”). Anisotropic damping where there are differences depending on directions relative to crystalline axes.

Angular frequency

Frequency of a periodic quantity, measured in radians per unit time. Cyclic frequency multiplied by 2π . The usual symbol is ω .

Angular velocity

The rate of change of angular position (i.e., orientation) of an object (radians per second [rad/sec], revolutions per minute [rpm], etc.).

Annular clearance

The uniform gap between the rotor and stator of a turbine or compressor motor or some rotating machine.

Antialiasing filter

A low-pass filter with its cut-off set near half the sampling rate of the filtered signal in order to minimize the aliasing error.

Appendages

Additional secondary devices. Additional nonstructural elements to the main structure to increase the building's function to the occupants.

Asymptotic stability

Stability representation where the response naturally decays to zero.

Asymptotic stability borderline

Maximum depth-of-cut below which chatter will not occur for all spindle speeds.

Attenuate

Decrease. To make small.

Attenuation of muffler

Decrease in sound power between two points in a muffler system (noise suppressor).

Autocorrelation

Correlation of a signal with itself, with a phase shift (reference time shift) expressed as a function of the shift. Inverse Fourier transform of the power spectrum.

Autonomous system

Self-contained system with internal control (no external control). A system whose parameters are time-invariant (i.e., do not vary with time).

Autotuning

Automatic tuning ([see tuning](#)) of controller parameters to achieve desired performance (e.g., in vibration control).

Average tuning iteration number (ATIN)

The average number of iterations taken for tuning an aircraft.

Average value

A representative value of a data set. The centroid of the data. The approximate point at which the sum of moments of all the data values is zero. A first-order statistic of random data. Mean value. Expected value. Mathematical expectation.

Axi-symmetric wave

A sound wave generated by a point dipole. When propagation of sound wave is described by polar coordinates, its magnitude is independent of the angle about the given axis.

Axial

Along the shaft centerline. Along the axis.

Back e.m.f.

An electromotive force (e.m.f.) is a voltage generated in a conductor located in a magnetic field when there is a relative motion (in an orthogonal direction). The back e.m.f. is the voltage generated in a moving coil that is connected to a voltage source (like motor rotor windings) and located in a magnetic field, where the generated e.m.f. opposes the applied voltage.

Backlash

Mechanical looseness in between meshed gear wheels due to unavoidable clearances between meshing teeth.

Baffled space

The idealized boundary condition to model the sound field generated by a compact source embedded in a plane large in size compared to wavelength, e.g., a radiation field generated by a circular vibrating piston mounted flush with the surface.

Balance

A condition where the rotating centerline between bearings coincides with that which defines the center of mass distribution. See [Static balancing](#) and [Dynamic balancing](#).

Balance weight adjustments

Weights added to or removed from the rotor hub to tune vibrations through changes in blade mass. Balance weights are measured in grams or ounces, with positive adjustments representing the addition of weight.

Balancing

A procedure for adjusting the mass distribution of a rotor by adding or removing weight, with the goal of achieving less vibration amplitude at rotational speed. See [Static balancing](#) and [Dynamic balancing](#).

Band-pass filter

A filter that allows through the signal components within a given range of frequencies, stopping (filtering) those above and below that band.

Bandstop filter

A filter that suppresses a given range of frequencies, transmitting only those above and below that band. Also called band-elimination filter. Also called a notch filter when the band is very small.

Bandwidth

Operating frequency range of a device. The difference between the upper- and lower-cut-off frequencies at which the signal is attenuated by 3 dB. The difference between the limiting frequencies within which performance of a device falls within specified limits with respect to some characteristic. A measure of speed of response of a device.

Barkhausen effect

Jerkiness in the magnetization curve of a ferrous specimen.

Base isolation

See [Isolation](#). An engineering technology that uncouples the motion of a structural system from the ground motion by inserting an isolation layer under the structure.

Basis

Countable set of linearly independent functions or vectors that can represent a general function or a vector space.

Bathtub curve

Curve (based on anecdotal and statistical data) describing the frequency of failures. Applicable to an individual machine or population of machines of the same type.

Beam

A structural (vibrating) component that is long and slender and has some flexibility (bending or flexure). Commonly modeled by Euler–Bernoulli equation or Timoshenko equation.

Bearing

A support for the ends of a shaft, a rotating member, etc. May be dry or lubricated. Will introduce some damping, but it should be minimized for proper operation. Linear bearing is one that provides a guideway for rectilinear motion (rather than rotary motion).

Beats

The alternating and significant rise and fall of vibration amplitude caused by two sources vibrating at nearly equal frequencies (or engines or rotating machines rotating at nearly equal speeds).

Bernoulli–Euler beam

A common analytical model (partial differential equation with respect to time and length coordinate) used to analyze slender beams. Rotatory inertia and deformation due to shear are neglected in this model (holds for slender beams), unlike the Timoshenko beam model.

Bicoherence

Second-order correlation measure between signals.

Biorthogonal wavelets

Symmetric wavelets with compact support created by two sets of wavelets; one set for decomposition and one set for reconstruction.

Bisection method

A nonlinear root-finding method which repeatedly bisects the interval to find a root. For this method to be successful, the initial interval has to be such that the function is positive at one endpoint and negative at the other.

Blast mitigation

Physical defensive measures taken to reduce the damaging effects of explosions from devices introduced by hostile parties. Includes both exterior hardening (wall, etc.) and internal measures taken to improve the survival of the protected resources (e.g., using more stable chemicals in a protected process).

Bode plot

The pair of plots of amplitude versus frequency and phase versus frequency. Usually, the amplitude is given in dB (or in log scale) as a nondimensional magnification factor of a transfer-function magnitude. The frequency is given in log scale.

Boom

A long, overhanging pole or beam like structure. As in a crane or a robot, a boom can be used to position and manipulate objects at a remote location.

Boundary conditions (BCs)

The conditions (force, moment, motion, deformation, etc.) at the boundary locations of an object (e.g., beam, plate, structure) used for solving the governing equations of the object. These are conditions expressed with respect to spatial coordinates (space) rather than time. Also require initial conditions (ICs) which are conditions at the initial time, for a complete solution of the system equations.

Boundary layer

A thin stationary layer of liquid with a hypothetical boundary next to a solid surface where much of the velocity changes (gradients) occur.

Bracing

Temporary supports of a structure using struts in vertical and lateral directions during seismic rehabilitation of the structure.

Bridge circuit

An electric circuit with four arms having resistances or impedances, and input (source) and an output. Where pure resistances are used, we have a Wheatstone bridge. Hydraulic circuits also may be represented as bridge circuits, and analyzed using similar techniques.

Bridge balance

The condition (the relation between bridge resistances or impedances) such that the output of the bridge circuit is zero (even when the source provides an excitation).

Bridge constant

The constant parameter relating a variation in a bridge arm (resistance or impedance) to the corresponding bridge output, starting with a balanced bridge.

Broadband (wideband) process

A random process where most of the energy is in a wideband of frequency.

Broadband excitation

An excitation with a significant range of frequency (almost a white noise spectrum).

Buffer

A device provided at an isolation bearing which will be hit by the moving plate of an isolation bearing to limit the bearing displacement during extreme earthquakes.

Bulk modulus

Change in volume divided by initial volume gives the bulk strain. The bulk stress (or pressure) divided by the bulk strain is the bulk modulus.

Bump

Simple shock that is generally repeated many times when testing, e.g., half-sine, 10g, 16 msec, 3000 bumps (shock) per axis, 3 bumps per second.

Bump test

See Bump. An impact test. A test carried out on an object (equipment, structure, etc.) using a bump impact.

Butterworth filter

A low-pass filter with many poles (i.e., high order) to provide good roll-off (i.e., sharp cut-off).

Calibration

Adjusting some parameters or conditions (using knobs, keys, computer interface, etc.) of a device so that its performance (output or reading) is accurate with known engineering units.

Cantilever

A flexible beam fixed at one end (zero displacement and zero slope) and free at the other (zero bending moment and zero shear force).

Carrier

A sufficiently high-frequency signal that can carry another (transient) signal of lower frequency for maintaining the accuracy of the carried signal during signal transmission and analysis.

Carrier frequency

Frequency of the carrier signal.

Carrier signal

[See Carrier.](#)

Cartesian coordinates

Orthogonal (perpendicular) coordinates in a rectangular coordinate frame with a common origin.

Cascade connection

Connection in series of two or more devices.

Cascade plots

Successive spectra plotted with respect to time and displayed in a three-dimensional manner. Also known as Waterfall plots.

Catastrophic failure

Sudden and complete failure of a machine. Cannot be analyzed by conventional methods of nonlinear system analysis.

Causality

Cause–effect behavior of a dynamic system. The numerator order (or the input order) cannot be greater than the denominator order (or the output order) of the system transfer function. This determines the physical realizability of the system.

Center of gravity

The point representing the average position of weight in a body. The point of intersection of orthogonal axes, relative to which the first moment of weight is zero. Typically the same as the center of mass. Denoted by COG or CG.

Center of mass

The point representing the average position of matter (mass) in a body. The point of intersection of orthogonal axes, relative to which the first moment of mass is zero. Typically the same as the center of gravity, denoted by COG or CG.

Center of stiffness

The point of intersection of orthogonal axes relative to which the first moment of stiffness is zero.

Centered difference

Finite difference approximation that uses the Taylor series expansions on either side of the point in question.

Centrifugal acceleration

Acceleration of a rotating mass (e.g., attached to a string or arm) directed towards the center rotation. Equal to $\omega^2 r$ where ω is the angular speed of rotation and r is the radius of rotation.

Centrifugal compressor

A compressor (a machine in which air or gas is compressed) by the mechanical action of rotating vanes or impellers. The flow is in a radial direction through the impeller, which imparts velocity (kinetic energy) to the fluid. Passing through a diffuser section at exit, the kinetic energy is converted into pressure (potential energy).

Centrifugal pump

See [Centrifugal compressor](#). As the impeller of the pump (enclosed in a casing or volute with an inlet and a discharge connection), kinetic energy is imparted to the fluid by the rotating impeller and is converted into pressure at the outlet.

Centripetal acceleration

See [Centrifugal acceleration](#) (synonymous).

Centroid

Same as the center of mass or center of gravity for practical purposes.

Cepstra

Plural of cepstrum. Equivalent to spectra, but in the “quefrency domain” rather than the frequency domain.

Cepstrum

The inverse Fourier spectrum of the logarithm of the Fourier spectrum of a signal.

Change limit

Warning levels that provide early warning well in advance of the absolute limit.

Channel

A signal line in a piece of equipment or hardware. Both input channels and output channels are important. The capability and complexity increase as the number of channels increases.

Chaos

Deterministic form involving the “butterfly effect” (work of E. Lorenz).

Characteristic equation

See Characteristic polynomial.

Characteristic polynomial

The polynomial, when set to zero (characteristic equation) and solved, gives the eigenvalues (or poles or characteristic roots) of a dynamic system. The denominator polynomial of the transfer function of a dynamic system. The roots are complex in general. The imaginary parts give the natural frequencies. The real parts give the reciprocal of time constants or damping level.

Charge amplifier

An electronic amplifier used to convert the high-output impedance of a device (e.g., piezoelectric accelerometer) into low-output impedance so that it is compatible with common signal acquisition and readout devices (processors, controllers, displays, recorders, etc.).

Chatter

An instability in a machine tool, which occurs at high frequencies, causing poor machining quality, increasing tool wear, generating noise, and causing other problems to the machine.

Chatter frequency

Dominant frequency of vibration during the occurrence of chatter (unstable vibration in a machine tool).

Chatter marks

Distinctive undulating patterns left on a part after machining that are indicative of chatter.

Cholesky decomposition

A symmetric positive definite matrix may be written as the product of a lower triangular matrix and its transpose (an upper triangular matrix): $A = U^t U$.

Circle fit

Fitting vibration test data to a transfer function that approximates to a circle on the complex plane (horizontal real axis and vertical imaginary axis). True for a single degree-of-freedom (single-DoF) in relation to some specific transfer functions (e.g., mobility) with some types of damping. Parameters of the system (damping, natural frequency) can be extracted from the fitted circle. Used in experimental modal analysis or modal testing.

Cofferdam

A temporary watertight enclosure that is pumped dry to expose the bottom of a body of water so that construction (e.g., of piers) may be undertaken.

COG

Centre of gravity (or center of mass). See their definitions.

Coherence

First-order correlation measure (normalized) between different signals, expressed in the frequency domain (as a function of frequency). It has a magnitude and a phase.

Coincidence effect

A form of acoustic resonance phenomena where the transmission loss decreases rapidly when the acoustically forced bending wave speed is equal to the free bending wave speed (flexural natural frequency) in a structure (plate).

Cold welding

Bonding between two parts of seismic isolation bearings (which are supposed to move relatively to each other during earthquake attacks) because of long durations of contact.

Color centers

Defects introduced into a crystal such as lithium fluoride by ionizing radiation.

Combined adjustments

The net adjustments to opposite blade-pairs in a four-bladed aircraft.

Common-mode rejection

Improvements in signal-to-noise ratio (SNR) by the reduction of noise signals that are common to both inputs of a differential amplifier.

Commutator

A device that provides power to a set of coil segments (circuits) in a rotating electric machine (motor). Analogous methods may be used in linear actuators (which perform rectilinear motion rather than rotary motion). A commutator with a slip-ring with split segments connected to the circuit segments, and brushes (carbon blocks) in contact to provide the power, is called a "slip-ring brush commutator." Alternatively, electronic commutation may be used where the power is switched into to different circuit segments by electronic means.

Compact source condition

When the scale of the source region is small (compared with the wavelength of generated sound wave), the compact source condition is mathematically valid for modeling the sound field. [See Monopole and Dipole.](#)

Compensating element

A resistor or a coil in a circuit (e.g., eddy-current sensor, bridge circuit, potentiometer circuit), which is used to compensate for environmental changes (e.g., change in temperature).

Complex modes

In some vibrating systems with some complex types of damping, the mode shapes (eigenvectors) obtained analytically ([see mode shapes](#)) can be complex (as opposed to real). Strictly then, these mode shapes are not realizable in practice. In fact, some distinct shapes will appear (similar to real modes) but with some changes (e.g., movements of nodes, small changes in phase of the moving elements) at the corresponding natural frequencies.

Complex propagation constant

This constant γ has two parts; the real part, δ , called the attenuation constant in decibels per meter (dB/m), and the imaginary part, β , called the phase constant in radians per meter (rad/m).

Compound pendulum

[See Pendulum.](#) A pendulum having more than one degree of freedom (e.g., two swinging degrees and one twisting degree).

Compressor circuit

In controlling a vibration shaker, this circuit ensures that the drive signal to the shaker satisfies the required spectrum of the test signal that needs to be applied to the test object. It compresses the frequency components that exceed the specification.

Condition-based maintenance

A strategy where maintenance is performed after assessing the actual condition of the machinery (rather than scheduling it at fixed intervals) in order to optimally schedule maintenance, thereby achieving maximum production and still avoiding unexpected catastrophic failures.

Condition monitoring

Monitoring the operation of a machine or other dynamic system, for the purpose of checking proper operation and possible faults or malfunction. Vibration signal analysis is one approach to condition monitoring.

Confined concrete

Concrete confined by transverse reinforcement, commonly using closely spaced steel spirals or hoops to increase the ductility.

Consistent mass

Representation of the mass of a system based on the virtual work principle and that results in a nondiagonal mass matrix.

Constant percentage bandwidth

Frequency bandwidths over the entire frequency range that remain a constant percentage of the frequency being monitored.

Consumer product noise

Noise perceived by a user or bystander of a noise generating product over which the individual has some control. Excludes occupational noise and environmental noise.

Contrast enhancement

Adaptation of the weights associated with features classified as normal or abnormal to enhance the contrast.

Continuous monitoring

Constant or very frequent data collection and analysis, usually with a permanently installed monitoring system.

Continuous wavelet transform

Wavelet transform on continuous ranges of scale-shift parameters.

Controllability

The ability of a controller to drive the response of the dynamic system, which it controls, to any desired value in a finite time, using a finite input (excitation).

Convolution integral

Integral of the product of two functions (usually of time), where one function is the shifted complement of the other (i.e., one is a function of τ and the other is a function of $t - \tau$, and the integration is done over τ). If one function is the system input and the other is the response of the system to a unit impulse, then the convolution integral gives the system response to the given input. The Fourier transform of a convolution integral is the product of the Fourier spectra of the individual time functions. In general, a product in the frequency (or Laplace) domain is a convolution integral in the time domain, and vice versa.

Correlation function

The correlation function is the mathematical expectation of a random function with another random function in the time domain. It is a measure of how two random functions correlate with each other over various time differences.

Coulomb damping

Friction force that is constant in magnitude, and acts on a body in the opposite direction to the velocity of the body relative to the surface in contact.

Coupling loss factor

The fraction of the original vibrating energy between two subsystems that is lost when interconnected.

Coverage index

The reach of each sensor (accelerometer) location in reflecting faulty components. It is defined in terms of the structural influences that represent the proximity of each sensor (accelerometer) to various system (gearbox) components.

Creep

Slow dimensional changes of a specimen due to structural defects. They progress through three distinctive phases called primary, secondary, and tertiary.

Crest factor

The ratio ($\frac{\text{Peak Level}}{\text{RMS Level}}$) of a waveform. It can indicate early stages of rolling element (bearing) failure.

Critical damping

The minimum value of damping that produces a nonoscillatory decaying motion of a system under free vibration. Value of damping that provides most rapid response to a step function without overshoot. When this occurs, damping ratio = 1.

Critical damping coefficient

Damping coefficient corresponding to critical damping. [See Damping coefficient](#) and Critical damping. This occurs when $(c/2m)^2 = k/m$, where k = spring constant, m = mass, and c = damping coefficient or damping constant. At this value, damping ratio = 1.

Critical frequency

The minimum frequency at which the coincidence effect occurs when the propagation speed of a bending wave in a plate equals the speed of sound in air.

Critical speed

The rotational speed that is equal to a natural frequency of bending of a rotor–shaft–bearing system (rotor dynamic resonant frequency). It can cause large amplitude vibration or whirling with only slight excitation.

Cross sensitivity

The sensitivity of a device (e.g., sensor) in a direction orthogonal (perpendicular) to the direction of direct sensitivity. Normally, the cross sensitivity of a sensor has to be minimized and the direct sensitivity maximized.

Crust

The outermost major layer of the Earth, ranging from about 10 to 65 km in thickness worldwide. The uppermost 15 to 35 km of crust is brittle enough to produce earthquakes.

Cumulative modification set

The total number of tuning iterations performed in the field on an aircraft.

Curve-fitting

Fitting a set of data to an analytical curve, as accurately as possible. [See Circle fit](#), which is a single-DoF fit. Multi-DoF curve-fitting is used for complex systems with closely-spaced modes. Used in experimental modal analysis and modal testing.

Cut-off frequency

The frequency of a filter beyond which the signal entering it is cut-off (filtered out).

Cycle

The full range of states or values through which a periodic (cyclic) phenomenon or function passes before completely repeating itself. The complete sequence of values of a periodic quantity that occur during one period. For a periodic waveform (signal), this corresponds to one period (or 1/frequency).

Cyclic frequency

Frequency of a periodic variation in cycles per unit time (Units: Hertz or Hz, or cycles or cycles). Typical symbol is f . [See also Angular frequency](#).

D'Alembert's principle

An equivalent version of Newton's Second Law where the acceleration is multiplied by mass, and the resulting "inertia force" is applied in the direction opposite to that of the acceleration. The dynamic systems become an equivalent static system in this manner.

DAC

Digital-to-analog conversion. Digital data from a digital device (e.g., computer) are interpolated and converted by a DAC into an analog signal for use with analog instruments.

Damage boundary curve

For a given acceleration, curve giving the critical velocity change and, for a given velocity change, the critical maximum shock acceleration that leads to a damage on the material (deformation, fracture, faulty operation after the shock, etc.).

Damped natural frequency

The natural frequency of free vibration of a damped linear system.

Damper

A device that dissipates mechanical energy and progressively diminishes the response of a mechanical system (in free motion). In the case of linear viscous damping, this device is sometimes called a dashpot. The resulting damping force is the product of the damping coefficient and the relative velocity of the two components of the damper.

Damping

The dissipation of energy of a mechanical system, which progressively diminishes (dampens) the magnitude of response (or the amplitude of vibration) of the system in free motion. The damping process converts and dissipates mechanical energy into other forms of energy such as thermal energy (heat transfer) and noise.

Damping capacity

Energy loss per cycle of the motion.

Damping coefficient

The constant by which the relative velocity of a body is multiplied to yield the viscous damping force acting on the body.

Damping constant

The same as damping coefficient.

Damping ratio

Ratio of actual damping coefficient to the critical damping coefficient in a system with viscous damping. Expressed mathematically, the damping ratio $\zeta = c/c_c$. If less than 1, the system will be underdamped and will exhibit oscillations when disturbed or excited. If larger than 1, the system will be overdamped and the system response will diminish and die out with no oscillations.

Damping redshift

Change in frequency of a harmonic oscillator due to damping. Predicted by the viscous damping model, it is virtually immeasurable because of the small size of the shift.

Dashpot

Same as “damper” but assumes a linear viscous damping model and generally has three orthogonal damping forces.

Daubechies wavelets

A family of orthogonal wavelets with compact support and a specified number of vanishing moments.

DC

Direct current.

DC bridge

A bridge circuit using a DC excitation. Compare with an AC bridge.

DC motor

An electric motor that uses a DC excitation. Requires a commutator for operation. Commonly used as a servomotor, where motion sensing and feedback control are employed for accurate generation of motion trajectories.

DC tachometer

A speed sensor that uses the principle of an electric generator (electromagnetic induction). The excitation is DC. The output DC voltage is proportional to the measured speed.

Detuning

Deviation of a passive vibration control system ([see passive vibration control](#)) from its original design due to structural parameters changes, change in the excitation frequency, or change in nature of disturbance.

Deflection

Movement (or deformation) of a structure or parts of a structure under applied loads. In the case of an elastic body or spring, the distance it moves when subjected to a static or dynamic force.

Degrees of freedom

Denoted by DoF or dof or df. Minimum number of independent coordinates necessary to determine completely the state (position and orientation) of the considered system. This definition assumes a holonomic system. For a general (nonholonomic) system, the definition must use “incremental” coordinates and corresponding “incremental” displacements. Often used to classify mechanical structures, such as robotic arms. In the finite element analysis, DoF may be associated with nodes or elements. Three-dimensional shell and beam elements have six DoF per node (three translations and three rotations).

Delayed resonator (DR) absorber

A form of a resonator absorber ([see resonator absorber](#)) to optimally utilize the effect of time-delay in the processed signal.

Delta function

Dirac delta function. A unit impulse function. A function whose value is infinity at one point and zero elsewhere, with the integral of the function equal to 1.

Demodulation

Recovering the original signal from a modulated signal by removing the carrier signal. A common method is to multiply (by digital or analog means) the modulated signal by the carrier signal and then low-pass filter the result.

Depth-of-cut selection

Technique where the depth-of-cut is chosen to avoid or suppress chatter in a machine tool. [See Chatter.](#)

Design (basis) earthquake

Denoted by DBE. The earthquake (as defined by various parameters, such as peak ground acceleration or PGA, response spectra, etc.) for which the structure will be, or was, designed.

Desorption

Release of gas molecules from a solid undergoing evacuation.

Determinacy of machine structure

A degree at which a physical structure complies with the law of cause and effect ([see causality](#)). This allows the system dynamic behavior to be modeled and analyzed mathematically, and the modeled system to be physically realizable.

Detonation

An explosive reaction that consists of the propagation of a shock wave through the explosive, accompanied by a chemical reaction that furnishes energy to sustain the shock propagation in a stable manner, with gaseous formation and pressure expansion following shortly thereafter.

DFT

Discrete Fourier transform or digital Fourier transform. A discrete version of the Fourier integral for use in numerical computation. The fast Fourier transform (FFT) uses a much more efficient algorithm for this computation.

Dielectric constant

A parameter of a capacitive material indicating the degree of its ability to store electric charges. Also known as permittivity.

Differential transformer

[See LVDT](#) and [RVDT](#). A transformer with a movable ferromagnetic element in its core. Serves as a noncontact displacement sensor.

Difference equation

A discrete version of a differential equation. Used in computer simulation of dynamic systems. In the nonhomogeneous case (i.e., when there is an input function) there is an equivalent z-transform transfer function (just like a nonhomogeneous differential equation having an equivalent Laplace transfer function or a frequency response function).

Diffraction parameter

This indicates the importance of the diffraction force. A larger parameter value means that the diffraction force is more important than the drag or inertia forces.

Diffuser

A component in a centrifugal pump adjacent to the impeller exit, which has multiple passages of increasing area for converting velocity (kinetic energy) to pressure (potential energy).

Digital filter

In contrast to an analog filter, it uses a digital processor and a filter algorithm to perform filtering on digital data.

Digital Fourier analysis

[See DFT](#) and [FFT](#). Fourier analysis using digital data. Converts time-domain information into frequency-domain (spectral) information. Can determine Fourier spectra, transfer functions, power spectra densities, coherence functions, etc. through this analysis.

Digital oscilloscope

An instrument that has the usual oscilloscope capabilities (acquisition and display of one or more signals) together with a variety of other capabilities such as extraction of signal parameters (mean, time constants, periods) and even FFT and spectral analysis.

Digital signal analyzer

Signal analyzer. Digital spectrum analyzer. A hardware digital device that carries out Fourier analysis and related operations on signals at very high speed (almost real time). Faster than a software-based analyzer.

Digital-to-analog conversion

[See DAC.](#)

Digital transducer

A transducer that can sense a signal and present it as a pulse sequence (pulse count or pulse rate) or digital data. It is generally very accurate, but necessarily introduces a quantization error.

Dilation

The squeezing or stretching of the mother wavelet in the time domain in order to analyze the signal in different scales.

Dipole

[See Monopole.](#) The second basic sound source where a pair of monopoles, close together, opposite in sign, and equal in magnitude are located along one axis. The sound sources like a compact vibrating body, with a characteristic axis or a point force acting in the medium that may be modeled as a dipole.

Dirac delta function

[See Delta function.](#)

Direct sensitivity

[See Cross sensitivity.](#)

Directivity

The dependency of a sound field on the angular position. Although the monopole sound field has no preferred direction, the dipole and the multipole sound fields have a particular dependency on the angular position. The dependency varies with the condition of the compactness of the sound source.

Discrete Fourier transform

[See DFT.](#) A mathematical transformation used to transform a discrete time signal (sampled data) into a discrete set of spectral values equally spaced in the discrete frequency domain. It can be used to numerically (computationally) determine the spectrum of any general (e.g., nonperiodic) time signal.

Discrete wavelet transform

Wavelet transform on a discrete set of scale-shift parameters.

Dislocation

Disruption to the order of an ideal crystal, e.g., by an extra plane of atoms inserted partway into the crystal to form an edge dislocation. Edge and screw dislocations are described by means of the Burgers vector.

Displacement

Change of position of a body, usually measured from the mean position or position of rest. Usually applies to the uniaxial case. In the case of angular motions, it may be termed a “rotation.” In a general multidimensional case, this is a vector quantity that specifies the change of a body or particle, and is usually measured from the mean position or position of rest. In general, it can be represented as a translation vector, a rotation vector, or both.

Dissipative muffler

A muffler where the acoustic performance is determined mainly by the presence of sound absorbing (e.g., flow-resistive) material. See [Muffler](#) and [Reactive muffler](#).

Distinct eigenvalues

The case where there are no repeated eigenvalues. All the eigenvalues are unequal.

Distributed-parameter system

A system where at least one member is continuous (e.g., beam, plate), needing one or more spatial coordinates to analytically represent (model) it. A partial differential equation in time and space is needed. Compare with lumped-parameter system.

Doppler effect

When the wave source moves towards the receiver, the received frequency increases. When it moves away from the receiver, the received frequency decreases. True for both sound and light.

Drag force

Force on a body in the direction of wind or any other fluid (liquid or gas).

Drift

The undesirable variation of the output of an instrument when the input conditions are kept constant.

Ductile detailing

Special requirements for civil engineering structures, such as close spacing of lateral reinforcement to attain confinement of a concrete core in reinforced concrete and masonry, appropriate relative dimensioning of beams and columns, hooks on main beam reinforcement within the column, etc.

Ductile structure

A structure that is able to undergo a repeated large displacement after yielding, without significant degradation of yield strength.

Ductility factor

The ratio of the total displacement (elastic plus inelastic) to the elastic (i.e., yield) displacement.

Duffing oscillator

Classic nonlinear elastic (mechanical) oscillator characterized by a double-well potential.

Dummy gauge

A strain gage in a bridge that is not active. Used for bridge completion and compensation (for temperature changes, etc.). Active gauge is the strained gauge, which is mounted on the deforming member.

Dunkerley's formula

A formula that provides a lower bound for the fundamental (first or lowest) natural frequency of a mechanical (vibrating) system.

Duration of shock pulse

The time required for the acceleration of a shock pulse to rise from some specified fraction of the maximum amplitude (peak) of the pulse and to decay to this value (see [Shock pulse](#)).

Dwell frequency

The frequency at which a "sine-dwell" test is carried out.

Dyadic

Follows a geometric sequence of ratio 2.

Dynamic absorber

See [Absorber](#) or [Vibration absorber](#).

Dynamic balancing

See [Balancing](#). Balancing achieved on two parallel planes of vibration perpendicular to the axis of rotation.

Dynamic magnification factor

The ratio of the maximum displacement of a single-DoF system excited by a harmonic force to the deflection that would result if a force of that magnitude was applied statically.

Eccentric mass

An equivalent point mass in a rotary device, located at a radial offset (eccentricity) from the axis of rotation such that the corresponding centrifugal force is equal to the imbalance force of the original device. The mass that needs to be placed on a rotor (eccentrically) in order to balance it.

Eccentricity

The distance between the geometric center and the center of mass of a rotor.

Eddy current damping

Damping due to eddy currents generated in a conducting surface and associated dissipation of the energy through electrical resistance to eddy currents.

Eddy current sensor

Eddy currents are generated on the surface of a conducting medium when a high frequency (e.g., radio frequency in the MHz level) magnetic field is applied to it. An eddy current sensor is a proximity sensor where the probe emits a high-frequency magnetic field towards the monitored object, which acts as a thin conducting layer. The inductance change caused by the eddy currents in the probe coil is a measure of the intensity of eddy currents and the distance (proximity) of the object. The inductance change can be measured using an inductance bridge circuit.

Effective isolation period

A linearized equivalent isolation period of a nonlinear isolation system.

Eigenfrequencies

Natural frequencies determined by an eigenvalue analysis.

Eigenfunctions

Mode-shape functions, in a general sense, including complex modes.

Eigenvalue analysis

Analysis carried out to obtain the roots of the characteristic equation of the matrix formulation of an engineering problem. In system dynamics and vibration problems, the imaginary parts of the eigenvalues are the natural frequencies of the system. The reciprocal of the imaginary parts are the time constants of the system. Imaginary parts divided by the corresponding undamped natural frequencies provide the modal damping ratios. The analysis also provides eigenvectors, which give the mode shape information. The analysis that provides both natural frequencies and mode shapes is called modal analysis. See [Eigenvalue problem](#). In stress analysis, the eigenvalues and eigenvectors give the values and the directions

of the principal stresses or principal strains. In other engineering problems, there are eigenvalue problems with corresponding interpretations.

Eigenvalues

The equation of motion for undamped free vibrations of a system with n DoF can be represented in matrix notation as the product of the characteristic matrix and the vector representing the corresponding displacement coordinates. For nontrivial solutions, the determinant of the characteristic matrix is set equal to zero, yielding a characteristic equation. The roots of the characteristic equation of the system are called eigenvalues. See [Eigenvalue analysis](#) for the interpretation of eigenvalues.

Eigenvalue problem

The mathematical formulation of the dynamics of a system as a problem of determining eigenvalues and eigenvectors of a matrix. This matrix is $M^{-1}K$, where M is the mass matrix and K is the stiffness matrix in the undamped case, giving natural frequencies, time constants and modal damping ratios. See [Eigenvalue analysis](#). In stress analysis, the eigenvalue analysis gives the values and directions of the principal stresses or principal strains. In other engineering problems, there are eigenvalue problems with corresponding interpretations.

Eigenvectors

Many engineering problems can be cast as the solution of eigenvalues and eigenvectors of a characteristic matrix. In vibrations problems, this matrix is $M^{-1}K$, where M is the mass matrix and K is the stiffness matrix, in the undamped case. The corresponding eigenvectors give mode shape vectors (see [Eigenvalue analysis](#)). In stress analysis, the eigenvectors give the direction of the principal stresses or strains.

Elastomer

A generic term that encompasses all types of rubber, natural or synthetic.

Elastomeric bearing

One type of base isolators, which are usually made of rubber or soft materials.

Elastomeric coupling

A flexible shaft coupling, which employs nonmetallic elastomeric elements for transmitting power, and accommodates shaft misalignment from one rotating shaft to another.

Electricite de France (EDF)

One type of seismic isolators, which consists of an elastomeric component and a sliding bearings in series.

Electrical impedance

The transfer function (voltage or current), in the frequency domain.

Electro-rheological (ER) fluid

Materials that undergo significant instantaneous reversible changes in characteristics when subjected to electric field.

Element

In finite element analysis, this is a small portion or a sub domain of a system having small but finite dimensions and bounded by straight or curved boundaries. Elements are connected to each other via a set of connection points called nodes. The minimum number of nodes for an element would be the corner nodes defining its shape.

EMA

See [Experimental modal analysis](#).

e.m.f.

Electromotive force. See [Back e.m.f.](#)

Emission

Emitting or radiation of sound energy or power from a noise source. Noise emission is controlled through noise government legislation.

Energy equivalence

A simplified analysis method of a dynamic system where a simplified (e.g., lumped-parameter) model (of reduced number of degrees of freedom) is established such that its energy (kinetic energy and potential energy) is equal to that of the original system. Information about the original system can be derived (approximately) by analyzing the equivalent system.

Ensemble average

The average of ensembles or samples (records) of possible outcomes. This is different from averaging a single record or signal (temporal average).

Enveloped spectrum

The envelope of a set of spectra obtained by different records of a vibration signal.

Environmental noise

Noise received by individuals indoors and outdoors, caused by noise sources that are controlled by others.

Environmental quality standard

World Health Organization (WHO) is the world body that recommends this regulatory standard of noise exposure. E.g., see *Guideline for Community Noise* published by WHO in 2000.

Epicenter

The projection on the surface of the earth directly above the hypocenter of an earthquake.

Equalization

In vibration testing, the spectrum of the actual excitation signal applied to the test object has to be (approximately) equal to the specified test spectrum. The process of achieving this by examining small frequency band of the actual spectrum and changing the spectral values (by adjusting the gains) is called equalization.

Equalizer

A device that achieves equalization in a dynamic test system.

Equipment interaction

Feedback effect between the motions of the structure and attached equipment.

Equipment tuning

When the natural frequency of a piece of equipment is such that undesirable resonances occur in vibratory response and equipment tuning may be necessary to avoid this condition. One option is to tune a vibration absorber (dynamic absorber) to this frequency.

Equivalent static acceleration

Steadily applied acceleration producing the same deformation of the structure as that resulting from the action of a shock. Also termed pseudoacceleration.

Equivalent mass

[See Energy equivalence.](#) The mass of a single-DoF model, in the “energy equivalence” method.

Equivalent stiffness

[See Energy equivalence.](#) The stiffness of a single-DoF model, in the “energy equivalence” method.

Equivalent viscous damping

The value of viscous damping assumed to analyze a vibratory motion, such that the dissipation of energy per cycle is the same for the viscous and the actual cases.

Ergodic hypothesis

For a stationary process, the assumption that the ensemble average can be approximated by the time (temporal) average.

Ergodic process

A stationary process where the ensemble average can be approximated by the time (temporal) average. This assumption is known as the ergodic hypothesis.

Euclidean norm

Square root of sum of squares (SRSS) of a set of independent values.

Euclidean space

[See Cartesian coordinates.](#) Space represented by a general Cartesian coordinate system with n coordinate axes. Cannot be represented in a physical space when $n > 3$.

Euler angles

A set of orthogonal rotation angles normally used to describe orientation of bodies in three-dimensional (3-D) space.

Euler–Bernoulli beam

[See Bernoulli–Euler beam.](#)

Euler’s method

First-order Runge–Kutta method of numerical integration.

Excel

Microsoft® spreadsheet software.

Excitation

Force (or even a motion such as support motion) applied to a mechanical system. This is the input to the system. The resulting response is the output.

Exciter

Shaker. The device that generates and applies an excitation to the test object in dynamic (vibration) testing.

Expansion joint

A connection between two or more seismically-isolated structures for the passage of occupants from one building to another, and also to let the adjacent buildings move relatively to each other during a seismic excitation.

Expected value

Also known as “mathematical expectation” of a random function. It is the integral of that function weighted by its probability density function. If the function is the random variable X , then the expected value gives the mean value (\bar{X}), which is the first moment statistic. If it is X^2 , then we get the second moment statistic. If it is $(X - \bar{X})^2$, then we get the variance, the square root of which is the standard deviation of a random parameter. Other higher-order statistics of X can be derived similarly.

Experimental modal analysis (EMA)

A method of determining a model of a dynamic (vibrating system) through testing and modal parameter extraction. A signal is applied to the system using an exciter. Various responses are acquired and analyzed (usually by Fourier analysis methods in the frequency domain) to determine the natural frequencies, damping ratios, and mode shapes of the system, and using these an analytical model (mass matrix, stiffness matrix, and a damping matrix) is computed for the system.

Explosion interaction

Two structures collide during an explosion.

Extrinsic

Opposite of intrinsic. A method where the device is used as the medium (or vehicle) in transmitting the objective (e.g., signal), rather than generating the objective. Some types of fiber-optic and ultrasound sensors use the extrinsic approach as well as the intrinsic approach.

Fast Fourier Transform (FFT)

A fast and efficient computer algorithm to calculate the discrete Fourier transform (DFT). The input data are samples of a time waveform from (e.g., digitized voltage measurements). The result is a display of discrete spectral points giving amplitude versus frequency, and phase versus frequency. The frequency interval is so small that the spectrum appears continuous in the display or printout.

Fatigue

Failure of a structural member exposed to a repeated load whose amplitude is well under the member's strength.

Fault

A zone of the Earth's crust within which the two sides have moved. Faults may be hundreds of miles long, from 1 to over 100 miles deep, and not readily apparent on the ground surface.

Fault detection

The process of determining if the overall machinery is healthy or a fault has occurred. Fault detection may be performed by such methods as oil analysis and vibration monitoring. Data gathering, data analysis (e.g., FFT, cepstrum, wavelet analysis), comparison to standards, comparison to limits set in-plant for specific equipment, etc., may be involved when detecting whether machinery is developing a faulty condition.

Fault diagnosis

The process of identifying the type, source, and severity of a failure (e.g., a faulty gearbox) for a detected fault. Vibration-based fault diagnosis may be performed by studying the abnormality of vibration features combined with the locations of the accelerometers generating those features.

Fault prognosis

Estimating the expected time to failure, and trends in the condition of the equipment being monitored, and planning and scheduling appropriate maintenance procedures.

FEA

Finite element analysis. [See also Finite element method \(FEM\)](#). A computational technique that starts by discretizing the continuum equations of the problem.

Feasible region

All sets of blade adjustment in jet engines that will reduce the aircraft vibration to within specifications.

Featural influence

The coefficients representing the weight of each vibration feature in the structure-based connectionist network.

Feed selection

Technique where the feed is chosen to avoid or suppress chatter.

Feedback control

A common control procedure where a sensor measures or monitors the system response and feeds the information into the controller. The controller compares the measurement with the desired value. If there is an error, then a correcting signal is generated by the controller, which is then applied to the system by the drive unit (or actuator).

Feedback resistor

The resistance element in the feedback path of an operational amplifier. It makes the device stable.

Feedforward action

A control signal generated without monitoring the response. Using a model of the system or measurement of unknown inputs may be used to generate it.

Feedforward control

See Feedforward action.

FEM

Finite element method. See FEA.

Ferromagnetic core

A member (e.g., rod or disk made of laminations) made of ferromagnetic material for use in a magnetic circuit (e.g., windings) to concentrate the field and reduce losses.

FFT

[See Fast Fourier transform.](#)

Fiber-optic

Devices made using optical fibers (a bundle of thin and flexible fibers that can carry light or laser signals).

Fictitious spring method

An analysis method for sliding isolated structures, in which a fictitious spring is introduced between the base mat and ground to simulate nonlinear behavior of friction.

Filter

An analog-hardware or software (programmed) device used to filter out some frequency bands of a signal (while allowing through the other bands).

Final peak sawtooth shock (FPS)

See [Terminal peak sawtooth shock \(TPS\)](#).

Finite difference

Computational methods involving a difference approximation for the derivatives.

Finite element method

A method for solving differential equations by approximating the solution by a linear combination of trial functions, which are typically polynomials.

Finite element method (FEM)

A numerical technique to solve the equations of an engineering (e.g., vibration) problem. A continuum is divided into a number of relatively small regions called elements that are interconnected at selected nodes. The kinetic energy or potential energy of the entire continuum is expressed as the sum of the element kinetic or potential energy. The solution is approximated by a linear combination of trial functions, which are typically polynomials. This leads to the assembled mass matrix and the assembled stiffness matrix, and finally to the finite element equations of the problem (vibration).

Fixed end

A boundary condition where the displacement and slope are zero (bending moment and shear force are not zero). Cantilever is obtained by fixing one end of a beam.

Flexible mount

An engine mount made of flexible material (e.g., elastomer or spring) to provide vibration or shock isolation.

Flexibility matrix

The a_{ij} element of this matrix is the displacement at i due to a unit force at j with all other forces equal to zero. Inverse of the stiffness matrix.

Flexural vibration

Bending vibration. The oscillatory motion of a flexible shaft (possibly with a rotor) or a beam or plate in any transverse plane of bending.

Flow resistance

Resistance due to friction between a fluid and some constriction (e.g., a pipe or duct) or between a gas and fibers in acoustic problems. The energy loss may take place in a very narrow layer of air adjacent to each fiber of acoustic material.

Flow resistivity

Unit area flow resistance per unit thickness of a porous material. Given by the applied air pressure difference across the two sides of the material divided by particle velocity through the material.

Fluid damping

Force of external friction whose magnitude is proportional to the square of the velocity, and whose direction is opposite the velocity.

Foil-type strain gauge

A strain gauge consisting of a thin metallic foil. As it is stretched (strained), its resistance increases, which can be measured using a bridge circuit to provide a strain reading.

Force isolation

[See Isolation](#). Vibration isolation of a system from a force source.

Force transmissibility

[See Transmissibility](#). Transmitted vibration force divided by an applied vibration force (or actuator force).

Forced vibration

The steady-state vibration caused by an external excitation (force or input). Typically (in linear problems in particular), forced vibration occurs at the frequency of the exciting force.

Forcing frequency

The frequency of the excitation function (force).

Fourier analysis

Analysis carried out using the Fourier transform. This provides frequency domain information (magnitude and phase with respect to frequency) of a time signal.

Fourier integral

See Fourier transform.

Fourier series expansion

Expressing a general periodic signal into a series (sum) of harmonic (sinusoidal, real or complex) components of integer multiples of a fundamental frequency.

Fourier spectrum

Frequency spectrum of a signal. The spectrum of a signal, as obtained by Fourier transform.

Fourier transform

An integral transform (weighted by a complex exponential function). This converts time-domain information (time signals) into frequency-domain information (frequency spectra) and vice versa.

Frahm absorber

[See Absorber](#). A dynamic (vibration) absorber.

Frame

Countable set of linearly dependent functions.

Free-body diagram

Diagram showing the basic components of an object and all the forces acting on them.

Free vibration

Vibration that occurs in a system after the removal of excitation. Typically, free vibrations occur at one or more natural frequencies.

Free vibration

The oscillatory motion (vibration) of a system that occurs in the absence of an external forcing function (excitation).

Frequency

The repetition rate or periodicity of a periodic event, usually expressed in cycles per second (hertz or Hz), or revolutions per minute (rpm). This is the cyclic frequency, which is the reciprocal of the period. The angular frequency (radians per second or rad/sec) is obtained by multiplying cyclic frequency by 2π .

Frequency domain

The representation of the system variables (including inputs and outputs) as functions of frequency. Related to the time domain through the Fourier transform. Vibration data or results are displayed or usually analyzed as a function of frequency. The independent variable is frequency (ω).

Frequency-domain analysis

Response analysis of a dynamic system with respect to frequency. Typically, uses Fourier analysis, frequency spectra, and transfer functions.

Frequency-domain index

A single number calculated from the frequency spectrum and used for trend analysis and comparison.

Frequency modulation (FM)

A signal modulation method, where a carrier signal is used to transmit another signal (modulating signal, carried signal) over a long distance without distortion. In this method, the amplitude of the carrier is fixed, but its frequency is varied according to the amplitude of the carried (modulating) signal. Typically, radio signals are transmitted by this FM method.

Frequency response

The amplitude and phase response characteristics of a system as functions of frequency under external excitation.

Frequency response function (FRF)

Output or input in the frequency domain, assuming zero initial conditions. Laplace transfer function can be converted into FRF by simply changing the Laplace variable into complex frequency variable $j\omega$. The FRF has amplification and phase change information of a response with respect to an input at various frequency values. It may be plotted as a Bode diagram or a Nyquist diagram.

Frequency transfer function (FTF)

Same as Frequency response function (FRF).

Friction pendulum system (FPS)

One type of sliding isolators, which has a spherical concave sliding surface to produce a recentering force for the isolated structure under excitations.

Fringes

A pattern of dark and light lines obtained when two light waves of nearly equal frequency are mixed. This method is used in some sensors, for example, for measuring small velocity changes (by Doppler effect).

Full bridge

A bridge circuit with four arms. It can be used to sense small changes in one of the arms (consisting of a resistor, inductor, capacitor, etc.). A half bridge contains two arms.

Full-scale drift

The drift (undesirable variation of the output when the input conditions are kept constant) of an instrument, when the input conditions correspond to its full-scale (maximum) value.

Fully differential capacitive sensor

A bridge in which all four components change in symmetric manner.

Fully operational

The highest performance level at which a structure is expected to operate with all functions, after an earthquake attack, if there is no (or at least very little) structural and nonstructural damage.

Fundamental frequency

Fundamental natural frequency. The lowest (first) natural frequency of a (vibrating) system.

Fundamental natural mode of vibration

The mode of vibration of a system having the lowest natural frequency.

Fuzzy logic

An approach to computing (soft computing) and knowledge-based decision making, based on the “degrees of membership” in a set, rather than the conventional binary membership (member or nonmember). Fuzzy data are matched with a fuzzy knowledge base to generate fuzzy inferences (decisions). A more general form of “true or false” boolean logic on which the modern computer is based, and incorporates such logic states as slightly true or very true.

FVC

Frequency to voltage converter.

***g* units**

Units of acceleration due to the Earth’s gravity (by international agreement, $g = 9.80665 \text{ m/sec}^2$ or 386.087 in/sec^2 or 32.1739 ft/sec^2). Divide an acceleration value by the value of g to obtain (as a ratio) the acceleration in g units.

Gabor transform

A sampled short-time Fourier transform.

Gaussian elimination

The process by which a matrix is converted by elementary row operations to an upper triangular matrix.

Generalized coordinates

A coordinate system, which does not necessarily use physical coordinates to represent the dynamics of the system. An example is the modal coordinates.

Generalized forces

See Generalized coordinates. When multiplied by the increment of the corresponding generalized coordinate, the product is equal to the actual incremental work done by that force in moving through that incremental motion.

Geometric modeling

The process of transcribing the geometry of a system into a finite element or CAD data base.

Geometric nonlinearity

Nonlinearity caused by geometrical constraints, such as rubber mount casing, or by trigonometric functions in the kinematic equations of the system (e.g., robot).

Gradient wind

Wind velocity above the boundary layer.

Green's function

The solution that represents the sound field generated by an impulsive source in space and in time. Useful in describing the sound field generated by a continuously distributed source, with convolution integration, both in free space and bounded space.

Ground vibration

A wave transmitted through the ground that causes the surface particles of ground to oscillate as it passes.

Guyan reduction

A procedure to reduce the model scale for vibration analysis by removing those DoF (called slave DoF) that can be approximately expressed by the rest of the DoF (called master DoF) through a static relation.

Gyroscopic action

A torque (or moment) is necessary to change the direction of angular momentum vector (the product of inertia and angular velocity vector) of a spinning member. Without such a torque, the member will remain oriented in a fixed direction.

Gyroscopic motion

Motion of bodies in 3-D space subjected to multiple angular rotations, causing gyroscopic effects.

Gyroscopic sensor

A sensor based on the gyroscopic principle, commonly used to measure angles from a fixed reference, when a physical surface representing such a reference is not available.

h-conversion

The process of achieving convergence or improving the accuracy of a finite element solution through increasing the number of elements, while keeping the element order the same.

Haar wavelet

The first known wavelet derived from a step function.

Half bridge

[See Full bridge.](#)

Half-power bandwidth

The frequency interval in a spectrum where the magnitude drops to $1/\sqrt{2}$ the peak, resonant value (i.e., half the power).

Half-power points

See Half-power bandwidth. The two frequency points representing the half-power bandwidth.

Half-sine shock

Simple shock for which the acceleration-time curve has the form of a half-period (positive or negative part) of a sinusoid.

Hamilton's principle

Variation of the difference of the system kinetic energy and the system potential energy plus the line integral of the virtual work done by the nonconservative forces during any time interval must be equal to zero.

Hammer test

An impact test where the test object is impacted with an instrumented hammer and the corresponding excitation and response signals of the object are measured. It can be used to determine natural frequencies and damping ratios.

Harmonic

A sinusoidal quantity having a frequency that is an integral multiple of the frequency of a periodic quantity to which it is related (normally the fundamental frequency).

Harmonic oscillator

This oscillator produces periodic oscillation described mathematically by either of the harmonic trigonometric functions (sine or cosine), which has only one frequency component (undamped natural frequency of the oscillator). Similar to an undamped simple oscillator.

Harmonic response analysis

Harmonic response analysis is used to determine the response of a vibration system to a harmonic (i.e., sinusoidal) excitation force. A typical output is a graph showing response (usually displacement of a certain degree of freedom) vs. frequency. The response has an amplitude (amplification) and a phase change with respect to the harmonic excitation, which are characteristics of the system itself.

Hearing loss

Permanent hearing loss is caused by excessive and prolonged noise exposure, which destroys the auditory sensor cells.

High-tech facility

Production lines for printed circuit boards, high precision devices, semiconductor devices, electronic appliances, etc., employing robotics, automation, and other modern and advanced technologies.

Holonomic system

A mechanical dynamic system where all of the constraints can be represented by algebraic equations (not differential equations). In this case, the number of DoF is equal to the number of independent coordinates needed to represent an arbitrary position and orientation of the system.

Homogeneous equation

An unforced ordinary differential equation. For a dynamic system with zero input, the right-hand side of the system differential equation will be zero, giving a homogeneous equation.

Hooke's Law

Linear spring equation. Deflection is proportional to the applied force. Strain is proportional to stress in one dimension.

Hydraulic actuator

A piston-cylinder (i.e., ram) device to which a controlled and pressurized fluid is sent, thereby moving the piston. This motion can be used to move another object. This describes a linear (rectilinear) actuator, although rotary hydraulic actuators are also available.

Hyperpatch or Volume

A portion of tri-cubic solid completely bounded by four areas (for tetrahedron volumes) or six areas (for brick volumes).

Hypocenter

The location of initial radiation of seismic waves (i.e., the first location of dynamic rupture).

Hysteresis

Greek word meaning “arrive late,” used to describe a specific nonlinear processes where the response curve when the input is increasing is different from that when the input is decreasing, resulting in a hysteresis loop. Examples include magnetic systems (due to residual magnetism) and plastic systems (due to residual stresses and strains).

Hysteresis loop

A diagram that describes the force–deformation relation of a nonlinear device of the hysteresis type. See Hysteresis. Vibration isolator with hysteretic damping produces a hysteresis loop, the area of which gives the energy dissipation in one cycle of vibration.

Hysteretic damping

Internal friction type damping in material where the energy dissipation per cycle is independent of frequency.

Imbalance

The eccentricity that exists between the center of mass of a rotor and the axis of rotation that generates centrifugal forces, resulting in vibrations and undesirable forces at the bearings.

IC engine

Internal combustion engine. A mixture of fuel and air is ignited in a cylinder, causing the piston of the cylinder to move.

Imission

Receiving, perceiving or observing radiated noise, causing noise exposure at a location near the noise source. Noise imission is legislated using an Environmental Quality Standard.

Impedance

Resistance exhibited by a “flow” variable (e.g., current, velocity) to an applied “effort” variable (e.g., voltage, force), expressed as a transfer function in the frequency domain. See [Mechanical impedance](#) and [Electrical impedance](#).

Impedance bridge

A bridge circuit with inductor or capacitor elements in addition to resistors in at least one of its four arms.

Impedance transformer

A device with a very high input impedance and very low output impedance. Typically, an operational amplifier with feedback.

Impeller

A bladed member of the rotor of a pump or compressor that imparts principal energy into the fluid that is being pumped or compressed.

Impulse

The product of the force on a body and the time during which that force acts, equal to the change in momentum.

Impulse response function

The response of a system to a unit impulse input. Inverse Fourier transform of the frequency response function (or inverse Laplace transform of the transfer function) of the system.

Incipient failures

Partial and usually gradual failure of a machine.

Inelastic response

A structure subjected to large excitations, resulting in yielding of longitudinal rebars.

Inertia

A property of matter where it resists a change in motion, including resistance to change from a position at rest.

Inertia asymmetry

The moments of inertia in two orthogonal planes are not equal.

Inertia block

A block or a heavy plate attached to the base of a machine in order to achieve good vibration isolation.

Inertia matrix

A matrix consisting of direct and cross moment of inertia terms in three dimension of a rigid body. Mass matrix. The matrix multiplied by the acceleration vector of a multi-DoF system in its Newtonian equations of motion expressed in the vector-matrix form.

Inertial actuator

A class of actuators in which the actuation force is generated through the addition of inertial masses and applying the resulting inertial forces on the system at the actuator point of attachment.

Influence coefficient

A coefficient representing the effect at a particular point of an action some other point.

Initial conditions (ICs)

The conditions of the response of a dynamic system at time $t = 0$. These are temporal conditions, different from boundary conditions, which are special conditions. The required number of ICs is equal to the “order” of the system, or the number of state variables needed for the system, or the order of the highest derivative of the input–output differential equation.

Inner ear

Cochlea is the main component of inner ear, where the actual reception of sound takes place. The mechanical motion caused by the sound wave is transmitted to basilar membrane and its associated sensing cells, where this motion is sensed as sound.

Inner modulation

Current structural vibration.

Input

The force or energy (or a motion such as support motion) applied to a mechanical system.

Input–output equation

A single differential equation with the response as the dependent variable and the input as the independent variable.

Insertion loss

The insertion loss of a muffler is defined as the difference between the sound pressure or acoustic power level at the same point in space before and after the muffler is connected to the noise source.

Instability

A self-induced excitation that can occur in rotating machinery, which does not require a sustained forcing phenomenon to initiate or maintain the motion. At the inception of instability, the rotor deflection will continue to build up with speed, and if further increased the large amplitudes of motion will normally result, causing damage to the machine.

Intensity

A metric of the effect, or the strength, of an earthquake hazard at a specific location, commonly measured on qualitative scales such as MMI, MSK, and JMA.

Internal friction

Damping that derives from structural defects internal to structural components of a vibrating system.

Interplate

Processes between the Earth's crustal plates.

Interval model

A linear regression model with interval coefficients to represent the range of aircraft vibrations caused by blade adjustments. This model can account for the stochastic and nonlinear nature of aircraft vibration.

Intraplate

Processes within the plates.

Intrinsic

Opposite of extrinsic. A method where the device is used to directly generate the objective (e.g., signal) rather than simply to transmit it. Some types of fiber-optic and ultrasound sensors use the intrinsic approach (as well as extrinsic approach).

Intrinsic loss factor

Factor in a subsystem to represent the loss of vibration power with respect to the total power.

ISO

International Organization for Standardization. Technical Committee 108, Subcommittee 5 is responsible for standards for Condition Monitoring and Diagnostics of Machines.

Isolation

Diminishing the transfer of vibration amplitude from a machine to another machine or a structure by the judicious selection of barrier materials and barrier configuration. Vibration isolation of a system from a vibration source. Inverse of "transmissibility."

Isolation period

Vibration period of the isolation system.

Isotropic

Being the same in all directions. [See Orthotropic.](#)

Jerk

The rate of change of acceleration with time (third derivative of displacement with respect to time).

Johnson noise

White noise (approx.), whose value depends on both bandwidth and resistance.

Journal bearings

Journal bearings consist of a circular section of shaft, called the journal, rotating inside a cylindrical bush, called the bearing. The space between the two is partially filled by the lubricating fluid, which is drawn up around the journal due to the effect of elasto-hydrodynamic lubrication.

Jump phenomenon

A nonlinearity where the frequency response of a system sharply shifts up or down (jumps) at a particular frequency, as the frequency of excitation to the system increases or decreases through this frequency.

K-normal

A modal vector z that is normalized with respect to the stiffness matrix K , such that $z^T K z = 0$

Keulegan–Carpenter number

The Keulegan–Carpenter number indicates the relative importance of the drag and inertia forces for small (small compared to the wavelength) diameter structures. A small Keulegan–Carpenter number means that the inertia force is more important than the drag force.

Key point

A coordinate location in space.

Kinematic design

Design of a structure by its motion, independent of mass and force.

Kinematics

Motion geometry of bodies.

Kinetic energy

Energy associated with motion (velocity).

Kronecker delta

A function of two indices, which is equal to one when the two indices are identical, and zero otherwise. It may be used to represent a unit matrix (or identity matrix), a diagonal matrix with unity diagonal elements.

Kurtosis

Fourth probability density moments sensitive to the impulsiveness in the vibration signal and, therefore, sensitive to the type of vibration signal generated in the early stages bearing fault of a rolling element.

LabVIEW

Industry standard equipment, software, and hardware marketed by National Instruments.

LaCoste zero-length spring

Spring of a vertical seismometer, which would collapse to zero length if wire of the coil was of infinitesimal diameter.

Lagrange's equations

Differential equations of motion of a dynamic system, obtained using the Lagrangian energy approach, in terms of a set of generalized coordinates. There are as many Lagrange's equations as there are generalized coordinates. The forcing terms are generalized forces.

Lagrangian

Equal to total kinetic energy minus the total potential energy of the system.

Laminated rubber bearing (LRB)

A type of elastomeric isolators that is usually composed of alternating layers of steel and hard rubber ensuring it is stiff enough to sustain the vertical loads, yet flexible under the lateral forces.

Laplace transform

An integral transform weighted by an exponential function of the Laplace variable s . It converts a derivative into a power of s , of the same order. Hence, a differential equation is converted into an algebraic equation. Related through the Fourier transform through $s = j\omega$, where ω = angular frequency and $j = \sqrt{-1}$. An input–output equation is converted into a transfer function.

Lateral force resisting system

A structural system for resisting horizontal forces due, for example, to earthquake or wind (as opposed to the vertical force resisting system, which provides support against gravity).

Learning

Adaptation of the interval coefficients to represent the range of vibration caused by blade adjustments more effectively.

Life safety

The third performance level in which a structure is expected to survive an earthquake. The life safety of occupants is not endangered either by structural collapse or the presence of heavy falling debris, although substantial damage may occur to both structural and nonstructural building components.

LIGO

Laser Interferometer Gravitational Wave Observatories of the U.S.

Limit cycle

An instability in a nonlinear system that is exhibited as a steady oscillation of amplitude that is independent of the input amplitude.

Limiting stable depth-of-cut

Depth-of-cut below which chatter will not occur for a given spindle speed of a machine tool.

Line noise

Noise at the frequency of the voltage signal in a power line (60 or 50 Hz) caused by the power lines in the vicinity of a system (e.g., through ground loops).

Line or line segment

A portion of a cubic spline curve bounded on both ends by a key point. A line may be straight or curved.

Linear quadratic regulator (LQR)

A linear feedback controller with constant gains, which minimizes a cost function consisting of the time integral of the sum quadratic functions (positive definite and semidefinite) in the state variables and input variables.

Linear system

A system is linear if it can be represented by a set of linear differential equations. The principle of superposition holds. Its magnitude of response is directly proportional to its magnitude of excitation for every part of the system.

Linear-variable differential transformer

See LVDT.

Load–displacement relationship

The relationship between the load on a structure and the corresponding displacement.

Logarithmic Decrement

Measure of damping. Equal to the natural logarithm of the ratio of successive amplitudes of free decay. It is inversely proportional to the magnification factor (quality factor), Q .

Long-term statistics

Statistics of the short-term parameters such as the significant wave height.

Lorentzian

Resonant response of a driven harmonic oscillator with damping. Also, the shape of spectral lines in atomic physics.

Lorenz force

Force on a current-carrying wire located orthogonally in a magnetic field.

Loudness level

The loudness of sound is determined by subjective comparison with the loudness of a pure tone of 1000 Hz. The level, measured in “phons,” is numerically equal to the sound pressure level, in decibels (dB), of the 1000 Hz tone.

LPA

Last point algorithm for performing numerical integration. Will not become unstable like Euler’s first point approximation does.

Lumped mass

A point presentation of the mass of a system. Results in a diagonal matrix.

Lumped mass matrix

The diagonal mass matrix obtained by lumping the inertia of a system by element masses at the nodes finite element mesh.

Lumped-parameter model

A model where the system components are represented by parameters (e.g., mass, stiffness, damping coefficient) concentrated at a finite number of points. An approximation of a distributed-parameter system.

LVDT

Linear variable differential transformer. A popular noncontact sensor for measuring linear (rectilinear) displacements. Operates by the transformer effect, with a movable ferromagnetic core element (attached to the sensed object).

M-normal

A modal vector z that is normalized with respect to the mass matrix M , such that $z^T M z = 0$.

Machinery failure

The inability of a machine to perform its required function due to some defect in the machine components.

Machining

Removal of excess material from a piece of material (workpiece) by moving a working tool over the surface of the workpiece to achieve a desired shape.

Magneto-rheological (MR) fluid

A magnetic fluid analogous to electro-rheological (ER) fluid. Typically consists of micron-sized, magnetically polarizable particles dispersed in a carrier medium such as mineral or silicon oil. When a magnetic field is applied to the fluid, particle chains are formed, and the fluid becomes a semisolid and exhibits viscoplastic characteristics.

Magnetorheological damping

Damping associated with a magnetic fluid and a magnetic field.

Magnitude

A measure of an earthquake's release of strain energy, measured on a variety of scales, of which the moment magnitude MW (derived from seismic moment) is preferred. The absolute value of a complex quantity (e.g., FRF).

Masks

Baseline spectra that are used with an allowable tolerance limit to "filter out" or block specific frequencies. Optical plates with windows for concentrating light from a source to generate better contrast in an optical pulse-generating transducer (e.g., optical encoder).

Masonry structure

A structure built from bricks and cement mortar that has relatively small lateral and tensile strength, which is vulnerable to an earthquake attack.

Mass law

For a single plate, the transmission loss depends on frequency and the surface density of the plate in the frequency range from the fundamental (lowest) natural frequency to the critical frequency of the plate.

Mass matrix

The matrix multiplied by the acceleration vector of a multi-DoF system, which, in its Newtonian equations of motion, is expressed in the vector-matrix form. Typically, a diagonal matrix with its diagonal elements giving the masses corresponding to various DoF of the system.

Mathematical expectation

Also known as "expected value." The mathematical expectation of a random function is the integral of that function weighted by its probability density function. If the function is the random variable X , the expected value gives the mean value (\bar{X}), which is the first moment statistic. If it is X^2 , we get the second moment statistic. If it is $(X - \bar{X})^2$ we get the variance, the square root of which is the standard deviation of a random parameter. Other higher order statistics of X can be derived similarly.

Matlab

MATLAB[®] is a commercial software package (tool) for numerical computation, visualization and symbolic manipulation. Various toolboxes are available for specialized computation on important subjects such as control and signal analysis.

Maximax shock response spectrum

Envelope of the absolute values of the positive and negative shock response spectra. [See Response spectrum.](#)

Mechanical design

Design of a structure or building utilizing the properties of electronic and mechanical subassemblies and parts.

Mechanical impedance

Force or velocity in the frequency domain. This transfer function is one of many used in the analysis and design of vibrating systems.

Mechanical looseness

A condition where two or more mechanical components, which are designed to be rigidly connected or in firm contact, can move relative to one another. See [Backlash](#) (in gears).

Mechatronics

Synergistic integration of electronic and electrical engineering, computer technology and control engineering with mechanical engineering, using concurrent and integrated design techniques. This area forms a crucial part in the design, manufacture, and maintenance of a wide range of engineering products and processes.

Mean free path

Distance a molecule travels on average in a gas between molecular collisions.

Measure of noise evaluation

Energy based indices like L_{Aeq} (equivalent A-weighted sound pressure level) for noise evaluation. All of these measures are legislated by the government, and are dependent on legislative regulations or standards.

Member

Any individual component of a structural frame. An element is within a set (membership = 1).

MEMS

Microelectromechanical systems. A relatively new and important field concerned with modeling, analysis, design, and development of very small mechanical devices with electrical or electronic features.

Mesodynamics

A new term to describe complex behavior of otherwise harmonic mechanical oscillators with energies approximating 10^{-11} J.

Mesomechanics

Focused on the complex behavior of granular materials.

Mexican hat wavelets

Obtained by calculating the second derivative of a Gaussian.

Meyer wavelets

Wavelets associated with enveloped trigonometric functions.

Microdynamics

Dynamics describing complex features of contact friction, largely advanced by NASA.

Microphone

A device for producing an electrical signal from an acoustic pressure (sound or voice). Standard equipment in acoustic or sound acquiring and generating systems.

Microphone array

A directional measuring device that consists of an array of miniature microphones distributed spatially in an acoustic field.

Middle ear

Consists of three small ear bones, the hammer, anvil and stirrup. Serves as an impedance transformer, which matches the low impedance of the air in ear canal with the high impedance of inner ear.

MIMO

Multi-input–multioutput system. A system with many inputs and many outputs. A multivariable system.

Mirror microphone system

A directional measuring device that consists of a reflector of elliptic or parabolic shape and an omnidirectional microphone located at its focus.

Misalignment

A condition when two rotating machines (or components) are not coupled together along a single axis (straight line) of rotation.

Mobility

The transfer function (velocity or force) in the frequency domain. The inverse of mechanical impedance.

Modal analysis

The dynamics of a system may be formulated as a problem of determining eigenvalues and eigenvectors of a matrix. This matrix is $M^{-1}K$, where M is the mass matrix and K is the stiffness matrix in the undamped case giving natural frequencies, time constants and modal damping ratios. See [Eigenvalue analysis](#) and [Eigenvalue problem](#). The imaginary parts of the eigenvalues are the natural frequencies of the system. The reciprocal of the imaginary parts are the time constants of the system. Imaginary parts divided by the corresponding undamped natural frequencies provide the modal damping ratios. The eigenvectors provide the mode shape information. The analysis that provides both natural frequencies and mode shapes is called modal analysis. This is the process of decomposing the vibrations (or response) of a complex system into its component modes of vibration (motion). One goal may be to find the locations and frequencies of maximum (undesirable) response for application of vibration control or suppression methods (e.g., stiffener and dampers).

Modal density

The number of mode shapes present in a unit spatial area or the number of natural frequencies in a unit frequency interval.

Modal matrix

The square matrix formed by placing all the independent mode shape vectors as column vectors.

Modal vector

A mode shape vector expressed as a column vector.

Mode

The condition where a mechanical system moves at one natural frequency while maintaining a characteristic shape (mode shape). Can also apply to nonmechanical systems.

Mode mixing

Transfer of energy among modes of different frequencies. This assumes nonlinearity and is not the same as beating.

Mode shape

The deflected characteristic shape, usually normalized, that a system would take when it vibrates at one of its natural frequencies. All elements move in step at this frequency while maintaining a specific shape. Some points will remain stationary throughout, which and they are called nodes. Only the shape of the curve would be known from a modal analysis. If the mode shapes are real, they correspond to natural modes. Otherwise, we have complex modes, which is the case in the presence of some types of damping.

Model identification

Experimental modeling. Determining an analytical model of a dynamic system using input–output test data. [See Experimental modal analysis.](#)

Model reduction

Reduction of the order or the number of DoF (of a vibrating system) by using some accuracy limits (error tolerance). Modal truncation is used, where modes above a specific frequency are neglected. Means of simplification and idealization based on the nature of the vibration problem.

Modulation

Embedding a signal within a carrier signal so that the original signal (carried signal or modulating signal) does not lose accuracy during transmission. Examples are amplitude modulation (AM), frequency modulation (FM), and pulse-width modulation (PWM).

Modulus of elasticity

Young's modulus. Direct stress divided by direct strain in one dimension.

Mohr's circle

A circle for representing stresses, strains, or moments of inertia at a particular point of system in different directions. The horizontal axis indicates the direction of the principal values and the vertical axis the shear (or cross) values. The angle around the circle is double the physical angle in the system.

Moment of inertia

A mass parameter that is measure of the resistance (inertia) of a body to angular acceleration about a given axis. Equal to the sum of (or integral to) the products of each element of mass in the body and the square of the element's distance from the axis.

Momentum

A property of a moving body that exists by virtue of its mass and motion, to resist any change to that motion. Equal to the product of the body's mass and velocity. It is a vector (with a direction as well as a magnitude) in the same direction as the velocity.

Monopole

An acoustic source with energy density concentrated at a single point in space. The most basic sound source, where the source region is compact and the generating motion has no preferred direction. Monopole produces a wave that spreads spherically outwards.

Mother wavelet

The function used to generate all the basis functions of the space by dilation and translation.

Motion isolation

[See Isolation](#). Vibration isolation of a system from a motion source.

Motion transmissibility

[See Transmissibility](#). Transmitted vibration motion divided by an applied vibration motion (or support motion).

Mounts

Usually, vibration mounts used for vibration isolation.

Muffler

A structural device that suppresses noise when fluid (e.g., hot and high-speed gas) flows through it. [See Dissipative muffler](#) and [Reactive muffler](#).

MTBF

Mean time between failures.

MTTF

Mean time to failure.

Multibody-spring-dashpot

Collection of rigid bodies joined together by springs and dashpots.

Multiresolution analysis

The process of studying a signal at different scales by use of different time windows to capture characteristics varying from coarse to fine.

Narrowband

Corresponding to a narrow (small) frequency interval (band).

Narrowband process

A random process where most of the energy is concentrated in a narrow band (interval) of frequency.

Natural frequency

The frequency of free vibrations of a system without the influence of an external forcing, except for an initial excitation to start the motion. Also a self-induced phenomenon. For a single-DoF system, $\omega_n = (k/m)^{1/2}$, where ω_n is the undamped natural frequency, k is the spring stiffness, and m is the mass. When damping is present, the natural frequency decreases to ω_d , which is the damped natural frequency given by $\omega_d = \sqrt{1 - \zeta^2} \omega_n$, where ζ = damping ratio. For a multi-DoF system, the natural frequencies are the frequencies of the normal modes of vibration.

Natural mode

[See Mode shape](#).

Natural period

The time period of one complete cycle of free vibration. The inverse of the natural frequency (cyclic).

Natural vibration analysis

[See Modal analysis](#). The natural vibration analysis is to determine the natural vibration frequencies and the associated mode shapes of a vibration problem when the excitation forces are zero. They are intrinsic characteristics of the vibration problem and independent of the excitation forces.

Near-fault ground motions

Ground motions, typically assumed to be within a distance of about 20 to 60 km from a ruptured fault, which usually have long-period velocity pulses that impart considerable momentum to a long-period structure.

Negative averaging

A baseline signal that is recorded and then subtracted from subsequent signals before analysis to reveal changes and transients.

Negative definite

A symmetric matrix is negative definite if $\mathbf{x}^t \mathbf{A} \mathbf{x} < 0$ for every nonzero vector \mathbf{x} .

Negative shock response spectrum

[See Shock response spectrum \(SRS\)](#). SRS plotted, considering the highest negative response due to the shock, without reference to the duration of the shock. It is the envelope of the negative primary and residual spectra.

Neural Network (NN)

A nonanalytical (computational) modeling technique, inspired by the human nervous system. Considered as a “learning” network. A network of massively parallel network is trained (by adjusting the network weights, etc.) to yield a known (correct) output for a given input. Once trained, it may be used as a computational model of the system. Further training and adaptations may be done subsequently. Several variations of this feed-forward network architecture are available (e.g., feedback, recurrent, dynamic, reinforcement learning).

Neutral axis

The axis along a bending beam where the stress and strain are zero. Undeformed axis when a beam is bent.

Nodal point

In finite elements: a point of connection between elements. A node will have a specific number of degrees of freedom, indicating its ability to move or rotate. In vibrations: a point or a line in the mode shape of a structure that does not move (see Node).

Node

[See Mode shape](#). Points that are stationary in a modal vibration. The mode shape curve passes through the relaxed configuration of the structure at these points.

Noise (1/f)

Also known as pink or flicker noise. Common in complex systems of both electronic and mechanical type.

Noise Criteria (NC)

NC curves are utilized for rating the background noise level in a room. Each curve specifies the maximum octave-band sound pressure level for a given NC rating. [See Preferred noise criteria \(PNC\)](#).

Noise regulation law

This regulatory standard defines the national minimum for noise suppression, for example, factory noise, construction work noise, and road traffic noise. The central government is the regulating agency. [See Emission](#).

Nomograph

A logarithmic frequency–velocity plotting graph sheet. The sheet gives constant displacement, constant velocity, and constant acceleration lines, properly graduated. A period axis (period = $1/\text{cyclic frequency}$) is given for convenience of plotting.

Nonclassical damping

Damping that cannot lead to modal decoupling of a structural system. For this case, the mode shapes of a structure can only be expressed in terms of complex (not real-valued) functions.

Nonholonomic system

A mechanical dynamic system where one or more of its constraints need differential relations (not algebraic equations) for mathematical representation. In this case, the number of DoF is equal to the number of independent “incremental” coordinates needed to represent an arbitrary increment (change) in position and orientation of the system, and is less than the number of independent coordinates needed to represent an arbitrary position and orientation of the system.

Nonlinearity

A characteristic that is not linear (e.g., hysteresis, saturation, deadband, jump phenomenon, nonlinear or nonproportional force–motion relationship). Represented by nonlinear equations. The principle of superposition does not hold. [See Linear system.](#)

Normal modes

[See Natural mode.](#) In a multiple DoF system, the normal modes are the free natural configurations in which the system vibrates. A mode is characterized by its natural frequency and mode shape. The mode shape depends only on the mass and stiffness of the system and how they are distributed, and not on damping. Normal modes exist for all undamped systems and only for a selected class of damped systems (e.g., proportional damping).

Normal wear period

A relatively long period of operation during which the frequency of failure occurrence is relatively low.

Notch filter

A bandstop filter when the band is very small.

Nyquist frequency

Half the sampling rate. The frequency above which the spectrum of a digital signal has no significance and should be ignored.

Nyquist plot

Plot of frequency transfer function (FTF) on a complex plane where the horizontal axis gives the real part, and the vertical axis gives the imaginary part of the FTF.

OBE

Operating basis earthquake. An earthquake representation (e.g., response spectrum) under which a nuclear power plant can operate safely.

Occupational Noise

Noise received at the workplace, indoors and outdoors, caused by all noise sources in the vicinity of the workplace.

ODS

Operational deflection shape of a structure.

Offset

Steady-state error in response of a device.

Oil whip

A condition that occurs when a subsynchronous instability (oil whirl) excites a critical speed (resonance), which then remains at a constant frequency regardless of speed changes.

Oil whirl

A condition that occurs when the lubrication in a lightly loaded journal bearing does not exert a constant force on the supported shaft, and a stable operating position is not maintained.

Oil whirl/whip

[See Whirling](#). The whirling motions that occur due to oil action in journal bearings when operated at or above double the critical speed of the rotor. The whirling motion is in the forward direction and its speed will match the critical speed of the rotor. The oil film is believed to rotate at half the velocity of the shaft due to friction drag. At rotational speeds near twice the critical speed, the oil film provides the stimulus as its speed matches the critical speed value resulting in large displacements and whipping.

Omnidirectional microphone

A microphone whose response does not depend on the direction of the incident sound.

Operating basis earthquake

[See OBE](#).

Operational

The second performance level in which a structure is expected to function in a limited manner after an earthquake because of some damage to structural or nonstructural members.

Optical encoder

A digital transducer that measures displacement. The encoder plate (disk) has light-passing areas (windows) on one or more tracks, with a light source on one side and a light sensor on the other side. As the plate moves, a pulse signal is generated by the light sensor. The pulse count gives displacement and a pulse rate gives speed.

Orbit

A plot of the displacement Y -direction (ordinate) versus the displacement in X -direction (abscissa).

Order

The order of the highest derivative of a differential equation (DE) and the highest difference in a difference equation. The order of a dynamic system corresponds to the number of first-order DEs needed to represent the system. Factor of rotational speed of a machine used to represent nondimensional frequency in tracking (monitoring) its spectral response (in the frequency domain). See also order tracking.

Order tracking

Cascade plots of machine response (vibration) spectra that are synchronously linked to the machine rotational speed via a tachometer.

Orthogonality

Generalized perpendicularity. If the vectors x and y are orthogonal, then $\mathbf{x}^T \mathbf{y} = \mathbf{y}^T \mathbf{x} = 0$. If the vectors x and y are orthogonal with respect to matrix P , then $\mathbf{x}^T P \mathbf{y} = \mathbf{y}^T P \mathbf{x} = 0$.

Orthotropic

Not uniform in all directions (not isotropic).

Oscillation

A periodically increasing and decreasing variation of a response. In forced oscillation, the force itself oscillates causing an oscillatory response. In free oscillations, the cause is the continuous interchange of energy between two forms (e.g., kinetic energy and potential energy), where the variation can be either constant amplitude (undamped) or decaying amplitude (damped). If the amplitude progressively increases, it is an unstable oscillation. No oscillations occur in overdamped systems because energy is more rapidly dissipated than it is interchanged, leaving no energy for a returning (reversed) response.

Outer modulation

Structural vibration delayed by one tooth passing period.

Outer ear

Composed of pinna, ear canal, and eardrum. Pinna produces only a small enhancement of the sounds arriving from the front of the listener. Ear canal works as a resonant cavity allowing for a nearly reflection-free termination, and thus a good impedance match of eardrum. Eardrum transforms sound wave to vibration in the membrane.

Overdamped response

No oscillations occur in overdamped systems because energy is more rapidly dissipated than it is interchanged between two forms (e.g., kinetic and potential), leaving no energy for a returning (reversed) response. For a simple DoF mass (m)–spring (k)–damper (c) system, the condition for overdamped behavior is $4k/m < (c/m)^2$.

Overall sound pressure level

The pressure is evaluated as the root mean square (RMS) of all components of pure tones. Can be converted into decibels (dB) as for any sound pressure.

Overlap index

Denotes the overlap in coverage of more than one gearbox component by one accelerometer location.

***p*-conversion**

The process of achieving convergence or improving the accuracy of a finite element solution through increasing the order of the elements, while keeping the number of elements the same.

Parametric instability

A self-excited motion, representing an instability that is induced by the periodic variation of the system parameters such as inertia, mass, and stiffness. The system cannot be represented by linear differential equations with constant coefficients.

Particle velocity

The fluctuating velocity of a material particle associated with a sound field (units: m/s). Using Newton's Second Law, we can solve for the particle velocity u in terms of sound pressure p .

Particular integral

A particular solution (just one solution) that is satisfied by a nonhomogeneous differential equation.

Particular solution

Same as particular integral.

Passive vibration control

A vibration control method in which a resilient member (stiffness) and an energy dissipater (damper) are utilized to either absorb the vibratory energy or dissipate it inside the damper. By definition, no external power source is needed in a “passive” system.

Patch or area

A portion of a bicubic surface completely bounded by three line segments (for triangular patches) or four line segments (for quadrilateral ones).

Peak

Maximum value of a varying quantity (or a spectrum) measured from the zero or mean value.

Peak ground acceleration (PGA)

The maximum amplitude of a recorded acceleration (similar to the ZPA, or zero period acceleration, which is the acceleration at infinite frequency).

Peak level

The highest absolute value in a vibration signal.

Peak-to-peak value

For an oscillating quantity, this is the algebraic difference between the maximum and minimum extremes of the quantity.

Pendulum

A simple pendulum. A point mass suspended from a fixed point by a string. A mechanical-swing oscillator whose motion is harmonic at small amplitudes, but nonlinear otherwise — an archetype of deterministic chaos. These are assumed to have just one DoF (the angle of swing). More complex pendula such as compound pendulum and double pendulum, which have more than one DoF, are available.

Perimeter

The edge or boundary of an area.

Period

Duration of one complete cycle in a cyclic waveform (e.g., vibration signal, pressure or particle local velocity in an acoustic system). The inverse of the cyclic frequency (Hz).

Period shift effect

Reducing the structural response by increasing the structural period.

Periodic monitoring

Regular and intermittent data gathering and analysis with portable and removable, monitoring equipment.

Periodic quantity

An oscillating quantity whose value repeats itself in cyclic (periodic) manner.

Phase

The fractional part of a period through which a variable (signal) has advanced, measured from an arbitrary reference. A time difference, expressed in degrees, between two signals gives their phase difference. A shift of one period of the signal is considered a phase shift of 2π (or 360°). Phase lag corresponds to a time delay and phase lead corresponds to a time advance of the signal.

Phase angle

The fractional part of a period through which the quantity has advanced as a measure from a reference independent variable.

Phase difference

[See Phase](#). The differences between the phase angles of two periodic quantities. In theory, only those components with the same frequency can be compared for phase.

Phase noise

See Phasor. In phasor representation, the noise vector that is perpendicular, rather than parallel, to the oscillator (primary signal) vector.

Phasor

A rotating vector of length (magnitude) a and angular speed ω . Its projection on the vertical axis gives a sinusoidal wave of amplitude a and angular frequency ω . The phase angle may be represented by the starting angle of the phasor from a reference line (e.g., vertical axis).

Phons

Unit of loudness level. [See Loudness level](#).

Photogate

Infrared beam device used for time interval measurement.

Physical pendulum

[See Pendulum](#). Contrasted with a simple pendulum, its motion at very small amplitudes is not harmonic — an archetype of mesodynamic complexity.

Physical realizability

Whether an analytical model is physically realizable (whether the cause–effect condition or causality is satisfied).

Pierson–Moskowitz spectrum

A parameter ocean-wave spectrum first derived for the North Atlantic, which is applicable for deep water, fully developed, and unidirectional seas.

Piezoelectric

A phenomenon exhibited by some materials in which application of a strain (or stress) causes the establishment of an electric field (or charge) and vice versa. The forward principle is used in piezoelectric accelerometers and the reverse principle is used in piezoelectric actuators.

Pinned beam

[See Simply supported beam](#).

Pitch control rod adjustments

Extension or contraction of pitch control rods by a number of notches to alter the pitch of the rotor blades. Positive pitch rod adjustments indicate extension.

Plane wave

A sound wave that is uniform over any plane normal to a specified axis. This is applicable when propagation of sound wave is one-dimensional and the amplitude of the sound pressure variation is constant. This is approximately valid locally for a sound field very far from the source region.

Poisson's ratio

Lateral strain divided by the direct strain (absolute value, disregarding the sign) in a member in tension in one dimension.

Poles

Eigenvalues of a system. The roots of the characteristic equation. The characteristic polynomial is the denominator of the transfer function.

Portevin–LeChatelier Effect

“Jerky” strain of a loaded specimen as a result of internal friction arising from mesoscale structural changes.

Post mortem

The investigation of root cause failure mechanisms.

Postprocessing

The process of calculating and graphically representing additional quantities and results (e.g., stresses, reactions) from the primary finite element solution results (e.g., displacements).

Positive definite

A symmetric matrix is positive definite if $\mathbf{x}^T \mathbf{A} \mathbf{x} > 0$ for every nonzero vector \mathbf{x} .

Positive shock response spectrum

SRS plotted, considering the highest positive response due to the shock, without reference to the duration of the shock. It is about the envelope of the positive primary and residual spectra.

Postshock

Shock pulses added after the specified shock test carried out on a shaker to cancel the velocity and displacement of the shaker table at the end of its movement (return to the rest position with a zero velocity).

Potential energy (PE)

Energy due to deformation of a spring or other flexible member (elastic PE) or due to elevated state (gravitational PE).

Potentiometer (Pot)

A displacement sensor consisting of a conductor with a constant voltage applied to it and a slider moving along it. The voltage of the slider is proportional to the displacement.

Power conversion factor

The ratio is sound power generated from a machine divided by the total power of the machine. This factor ranges from 10^{-8} to 10^{-5} for both mechanical and electrical machinery.

Power flow

Acoustic power translation from a subsystem to the next connected subsystem.

Power spectral density

The Fourier transform of the autocorrelation function of a signal. Also called power spectrum. It is a measure of how energy is distributed as a function of frequency for a random signal. A cross spectrum is similarly defined corresponding to the cross-correlation function of two signals.

Power supply

A device that supplies DC power to instruments and circuits. In a regulated power supply, the output voltage does not drop when connected to an external instrument.

Predictive maintenance

An equipment maintenance strategy based on measuring the condition of equipment in order to assess whether it will fail during some future period, and then taking appropriate action to avoid the consequences of that failure. The performance of the equipment is assessed using such approaches as condition monitoring, statistical process control, or the human experience. See also Preventive maintenance.

Preferred noise criteria (PNC)

See [Noise criteria \(NC\)](#). PNC curves are used to modify NC curves and are utilized in exactly the same manner as NC curves.

Preprocessing

The process of building up the geometric and finite element model for a physical system.

Preshock

Shock pulses added before the specified shock test carried out on a shaker to cancel the velocity and displacement of the shaker table at the end of its movement (return to the rest position with a zero velocity).

Pressure of sound

Incremental variation of pressure due to a sound wave, about the ambient atmospheric pressure, with an accompanying variation of the air density.

Pressure pulsations

The oscillatory pressure variations that occur at a point in a fluid system.

Preventive maintenance

An equipment maintenance strategy based on replacing, overhauling or refurbishing machine parts and components at a fixed interval, regardless of its state or condition at that time. See also Predictive maintenance.

Primary adaptation

In feature classification: the process of adapting each weight of the single-category-based classifier (SCBC) closer to the current value of the feature if the corresponding feature is classified as normal.

Primary (or initial) negative shock response spectrum

Shock response spectrum (SRS) plotted using the highest negative response observed during the shock.

Primary (or initial) positive shock response spectrum

Shock response spectrum (SRS) plotted using the highest positive response observed during the shock.

Principal axes of inertia

Orthogonal axes relative to which no cross inertia exist. The inertia matrix will be diagonal in this coordinate frame.

Principal axes of stiffness

Axes along which any deflection will not create resultant loading in any other direction. The stiffness matrix will be diagonal in this coordinate frame.

Principal directions

See [Principal axes](#).

Principal inertia

Moment of inertia about a principal axis where the cross inertia are zero and the inertia matrix is diagonal.

Principal stresses

Stresses along the principal axes where the shear stresses are zero.

Probability density function

A function that defines the likeliness (or probability) that a random parameter will take a particular value of the function variable. Derivative of the “probability distribution function.” This function completely defines the random parameter. In vibration, this can be used to determine the probability of realizing a particular instantaneous amplitude value from a vibration signal within a certain amplitude range.

Probability density moments

See [Expected value](#). Single number indices expressed as moments weighted by the probability density function.

Probability distribution function

A function that defines the probability that a random parameter will take a value less than or equal to a particular value of the function variable. Integral of the probability density function. This function completely defines the random parameter.

Process damping

In machining, damping due to the rubbing between the back side of tool and the surface of the machined part. This decreases chatter.

Propeller

Rotor with blades or a screw like device that imparts kinetic energy to a fluid (which can be converted into pressure and thrust). Used in compressors, pumps, jet engines. Provides thrust to push a boat through the water, or an aircraft through air.

Proportional damping

The damping matrix of a mechanical (vibrating) system is such that the modal vectors are real. The damping matrix is proportional to the mass matrix, stiffness matrix or both.

Pseudoacceleration

Product of the squared natural frequency $(2\pi f_n)^2$ and the highest relative displacement response of a linear one degree of freedom system to a shock input. This product has the dimension of acceleration but does not represent the acceleration of the mass, except when damping is zero. In such cases, this term is then strictly equal to the absolute acceleration of the mass.

Pseudovelocitv

Product of the natural frequency $(2\pi f_n)$ and the highest relative displacement response of the mass of a linear one degree of freedom system to a shock input. This product has the dimension of velocity but does not represent the velocity of the mass.

Pulse rise time

Interval of time required for a shock pulse to rise from some specified small fraction to a large fraction (typically 10% to 90%) of its maximum value.

Pyrotechnic shock (or pyroshock)

Transient response of a structure to loading induced by the ignition of pyrotechnic (explosive or propellant activated) devices. Pyroshocks are characterized by high peak acceleration, short duration and high-frequency content.

Quadrature error

The secondary signal that is at 90° phase to the primary signal, produced by an LVDT when the slider is symmetrically placed, while in theory it should be zero.

Quadrature signals

The two signals from a shaft encoder that are 90° out of phase, which are used to determine the direction of motion.

Quality factor (Q-factor)

A measure of the sharpness of a resonance or frequency selectivity of a vibratory linear one-degree-of-freedom system. Assuming a lightly damped single-DoF system, the Q-factor is related to damping ratio by $Q = 1/(2\zeta)$. Other approximate relations for Q are:

1. Transmissibility at resonance
2. $\pi/\text{logarithmic decrement}$
3. $2\pi W/\Delta W$ where W is the stored energy and ΔW the energy dissipation per cycle
4. $f_r/\Delta f$ where f_r is the resonant frequency and Δf is the bandwidth between the half-power points

Nonlinear damping causes it to vary with time. The concept is applicable to both mechanical and electrical systems.

Quantization error

The error created by the finite representation of numbers (i.e., finite number of digits or bits) within a computer (i.e., for a digital quantity).

Quefrency

[See Cepstrum](#). Similar to frequency, but in the Quefrency domain. The independent variable of a cepstrum (similar to spectrum).

Quefrency domain

[See Cepstrum](#). The domain of a cepstrum — inverse Fourier transform of a log of the Fourier transform of a signal.

Radiational sound

Sound in an acoustic field generated from a radiating source.

Random vibration

A vibration whose magnitude cannot be precisely predicted for any given instant of time.

Range of normal hearing

Human hearing is most sensitive in the range 2000 to 5000 Hz, where the threshold response is very close to 0 dB. At the other end of the scale, we have the threshold of pain, which is usually about 135 to 140 dB.

Reactive muffler

A muffler where there are one or more chambers, resonators, or finite sections of pipe, which collectively provide impedance mismatch for the acoustic energy traveling along the duct, causing noise suppression.

[See Muffler](#) and [Dissipative muffler](#).

Real-time

Refers to the relative response time for a particular process under computer control to occur after an action is taken. Should be consistent with the response time of the physical system.

Receptance

The transfer function of displacement or force in the frequency domain.

Rectangular shock

Simple shock for which the acceleration–time curve increases instantaneously up to a given value, remains constant throughout the signal and decreases instantaneously to zero. Practically, trapezoidal shocks are rather carried out.

Rectilinear

Along a straight line. Often (incorrectly) called “linear.”

Recurrence relation

Discrete equation (difference equation) that allows the computation of numbers in a series one by one.

Regenerative chatter

Unstable, self-excited interaction between machining forces and structural vibrations.

Relative displacement shock spectrum

[See Shock response spectrum.](#) SRS plotted, taking its ordinate (y -axis) the pseudoacceleration of the mass of a linear one DoF system.

Relaxation

Process characterized by an exponential variation, for example, sample strain response to a constant load.

Reluctance

Magnetic resistance. Resistance to magnetic field in a magnetic circuit (magnetic path).

Repeatability

The ability of a transducer to reproduce output readings accurately when the same measured value is applied to it repeatedly, under the same conditions (in the same direction, etc.). Repeatability is expressed as the maximum difference between output readings as a percent of full scale. This concept is also applicable to the operation of other instruments and machinery such as robots.

Required response spectrum

[See RRS.](#)

Residual base displacement

A permanent base displacement of an isolated structure after an earthquake.

Resilient friction base isolator (RFBI)

One type of sliding isolator, which is made of a central rubber core and Teflon-coated steel plates.

Resilient mechanism

An automatic recentering mechanism of isolators by which the isolated structure can return to its original position after an earthquake.

Resolution

The smallest change (in a parameter, signal, instrument output, etc.) that can be meaningfully detected and used.

Resonance

A resonance occurs in a mechanical system excited by a harmonic force if the excitation frequency is equal to the resonant frequency of the system. A small change in the frequency of excitation in either direction will cause the system response to decrease rapidly if the system damping is low. At a resonance, very little energy input into a structure results in a very large displacement (for low damping levels). Resonant frequency is almost equal to (but less than) the undamped natural frequency when the damping is low. Although the resonant frequency is nearly equal to natural frequency, the two concepts are not the same. Resonant frequency is excited by a harmonic forcing function at that frequency. The natural frequency is excited by an initial condition (corresponding the particular mode shape) followed by a free (unforced) response.

Resonance search

A vibration testing procedure whose objective is to identify and observe various resonances in a test object. A harmonic excitation with variable frequency may be used for this. [See Sine sweep](#).

Resonator absorber

A method in which a vibration absorber ([see Vibration absorber](#)) is tuned to have a natural frequency equal to the external excitation frequency to mimic optimally the vibratory energy from the primary system (system of concern). The absorber then “absorbs” the energy of vibration of the primary system, thereby suppressing those vibrations. Actually, the absorber generates a force in the opposite direction to the force of vibration of the primary system.

Response

The response of a device or system is the motion (or other output) resulting from an excitation (force, stimulus, or input) under specified conditions.

Response spectrum (RS)

A plot of maximum amplitudes (acceleration, velocity, or displacement) of a single-DoF oscillator (Single-DOF) as the natural period (or natural frequency) of the Single-DOF is varied across a spectrum of engineering interest (typically, for natural periods from 0.03 to 3 or more seconds, or frequencies of 0.3 to 30 Hz; in seismic applications). One RS curve is obtained for a specified damping ratio of the Single-DOF system.

Response spectrum analysis

Computation of the response spectrum (RS) of a given signal ([see Response spectrum](#)). This is quite different from spectral analysis (or spectrum analysis), which is to compute the Fourier spectrum of a signal. These are different from spectral density analysis, which determines the power spectral density function of a “random” signal.

Reverse whirling

Whirling is the rotation of a spinning rotor center of mass, which has an offset (due to shaft deflection) with respect to the axis through the bearings of its shaft. Reverse whirling occurs if the direction of this rotation about the bearing axis is in the opposite direction to the angular speed of spinning of the rotor with respect to a fixed frame of reference.

Reynolds number

A dimensionless parameter (that depends on viscosity and velocity), whose value determines if a fluid flow is laminar or turbulent.

Ridge

Curve of local maxima in a mean-square wavelet map.

Rigid bodies

Bodies exhibiting no deformation under acceleration or forces.

Rigid-body mode

A mode of motion that corresponds to zero natural frequency. Such a mode will exist in an unrestrained structure (no end fixtures) that is free to move as a rigid body without any deformation.

Rigid-body motion

A structural motion that results in no deformations or strains. By definition, these are zero frequency motions.

Rigid–perfectly plastic force–deformation characteristics

Characteristics of hysteretic loops produced by an ideal friction-damping device.

Rigid structure

A structure that cannot be deformed and whose shape cannot be changed.

RMS value

Root-mean-square value. Square root of the arithmetical average of a set of squared instantaneous values of a response quantity.

Rolling element bearings

A rolling element bearing generally consists of two rings (races or raceways) with a set of rolling elements running in their tracks. The rolling elements take the form of balls or various types of rollers. The outer race is located in a housing and the inner race on the shaft.

Root cause failure

The basic cause for a given failure.

Root Mean Square

See RMS value.

Rotating machinery

The group of electrical or mechanical machinery composed of a rotating component that rides on some form of bearings encased in a stationary casing (housing).

Rotor

The rotating part (as opposed to the stator) of an electrical or mechanical machine.

Rotor instability

An excitation mode, which is self-induced and does not require a sustained forcing phenomenon to initiate or maintain the motion. It occurs in machines operating at speeds well above the critical speeds of the rotor, and the rotor whirling speed is identical to the critical speed irrespective of the rotor (spinning) speed.

Rotor internal damping

A damping phenomenon, which occurs within the internal fibers of a material due to friction when there is relative movement between the fibers.

Rotor track

The vertical position of the blades of a rotor, usually measured by optical sensors.

Rotor tuning

The process of adjusting the rotor blades of a jet engine to reduce the system vibration (e.g., aircraft) and the spread of rotors.

Rotordynamics

The dynamics of rotating machinery.

Round-off error

The error created by the finite representation of numbers (i.e., finite number of digits) within a computer. Similar to Quantization error.

RRS

In a dynamic test, the response spectrum specification that has to be satisfied (enveloped) by the excitation signal.

Rub

A condition when a moving part comes into contact with, and slides against, a stationary part.

Run-to-failure maintenance

A strategy where maintenance is performed only when machinery has failed. [See Scheduled maintenance](#), Predictive maintenance, Preventive maintenance, and Condition-based maintenance.

Runge–Kutta

Numerical methods (integration schemes) based on approximating the solution by a Taylor series, and weighted averages of corresponding differences.

RVDT

Rotary variable differential transformer. [See LVDT](#). Similar to an LVDT, but for measuring angular displacements.

Safe shutdown earthquake (SSE)

An earthquake representation (e.g., by a response spectrum) for which a nuclear reactor can be safely shutdown without causing damage or fault in equipment due to the earthquake.

Sampling

The process of converting continuous signals into discrete values for digital processing.

Sampling frequency

The rate at which samples of a continuous time signal is recorded in discrete fixed time periods.

Sampling theorem

When a signal is sampled, its spectrum has no meaning beyond half the sampling frequency, called Nyquist frequency.

Saturation

A nonlinearity state in a device where a further increase in input no longer changes the output.

Scaling

To stretch or compress a function.

Scheduled maintenance

A strategy where maintenance is performed at set time intervals (or duty cycles) in order to maintain a significant margin between machine capacity and actual duty.

SEA

Statistical energy analysis.

Second moment of area

Similar to moment of inertia, except uses area elements rather than mass elements. (The two are proportional for uniform material density and constant thickness along the axis.)

Secondary (or Residual) negative shock response spectrum

SRS plotted, considering the highest negative response observed after the end of the shock.

Secondary (or Residual) positive shock response spectrum

SRS plotted, considering the highest positive response observed after the end of the shock.

Secondary system

A general term for equipment attached to a primary structural system.

Seismic

Measurements and activity concerning earth motion, such as earthquakes.

Seismic gap

A gap provided between a seismically isolated building and the ground so that the ground-level story can move in relation to the ground during earthquake excitations.

Seismic hazards

The phenomena or expectation of an earthquake-related agent of damage, such as fault rupture, vibratory ground motion (i.e., shaking), inundation (e.g., tsunami, seiche, dam failure), various kinds of permanent ground failure (e.g., liquefaction), fire, or hazardous material release.

Seismic isolation

Application of base isolation technology to structures subjected to earthquake motions.

Seismic risk

The product of the hazard and the vulnerability (i.e., the expected damage or loss, or associated full probability distribution).

Seismicity

The geographic and historical distribution of earthquakes.

Self excited instability

Same as Rotor instability.

Self-induced

Created within itself and does not require an external influence.

Self-organizing map (SOM)

A type of unsupervised neural network that yields a graphical representation of input data where similar input vectors are placed in close proximity.

Semiactive vibration control

A vibration control system in which both active and passive (see [Active vibration control](#) and [Passive vibration control](#)) treatments are combined to reduce the amount of external power necessary to achieve the desired vibration control performance.

Shaker

[See Exciter.](#)

Shape function

Is a spatial function (i.e., function of position vectors) describing the change of a variable within an element domain.

Shear balance method

An analysis method for sliding isolated structures, which uses the force balance condition of total shear under the isolation system to compute the friction force.

Shear force

An internal force acting normal to the longitudinal axis given by the algebraic sum of all forces to one side of the section chosen.

Shear wall

A structural wall between stories of a building to increase shear strength but at the expense of increasing stiffness.

Shifting

The process of translating (moving) a function with respect to some reference (coordinate system).

Shock

Transient condition where the equilibrium of a system is disrupted by a sudden applied force or by a sudden change in the direction or magnitude of a velocity vector. The time duration of this change is shorter than about twice the natural period of the excited mechanical system.

Shock duration

Interval of time during which the shock pulse has a higher acceleration value than some specified small fraction of its maximum value (usually 10%).

Shock machine (or shock test machine)

Device for subjecting a system to controlled and reproducible mechanical shock. Two principal categories are usually distinguished. Impulse machines: increase the velocity of the test item during the shock. The initial velocity is generally zero. Impact machines: decrease the velocity of the test item throughout the shock or change its direction.

Shock motion

An excitation involving motion of a foundation.

Shock programmer

Same as Shock simulator. Device on a shock machine that is used to format the applied shock waveform according to a desired shape during impact (usually half-sine, terminal peak sawtooth, and rectangular pulses).

Shock pulse

A substantial disturbance characterized by a rise of acceleration from a constant value to a substantial peak value, and decay of acceleration to the constant value in a very short period of time. Shock pulses are normally displayed graphically as curves of acceleration as functions of time.

Shock pulse index

An accelerometer tuned to have its resonant frequency excited by a specific shock can provide early warning of fault (e.g., deteriorating bearings). The sensor output level is the shock pulse index (also known as spike energy).

Shock response spectrum (SRS)

The response of an array of single-DoF systems to a shock input represented as the maximum response versus the natural frequency of single-DoF systems for a specified damping ratio. This response may be expressed in units of acceleration, velocity, or displacement.

Shock simulator

Same as shock programmer. Device on a shock machine that is used to format the applied shock waveform during impact according to a desired shape (usually half-sine, terminal peak sawtooth, and rectangular pulses).

Shock spectrum

See shock response spectrum. A plot (amplitude vs. natural frequency) of the response of a natural-frequency-variable single-DoF system to an applied shock for a specified damping ratio. This response may be expressed in units of acceleration, velocity, or displacement.

Shock wave

A strong pressure wave produced by explosions or other phenomena that create violent changes in pressure.

Shoring

Temporary support at the base floors of a structure during replacement of its originally fixed support to seismically isolated support.

Short-term statistics

Statistics of a random process that are only good for a few hours or a few days at the most. It is assumed that the significant wave height and the wave spectrum are invariant with time.

Short time FFT

Time sequence of concatenated FFT of short-period records of a signal.

Shroud of impeller

The circular section that forms a sidewall of a pump or compressor impeller.

Signal-to-noise ratio (SNR)

Determined by both electronic and mechanical noise (but not thermal noise due to the fluctuation–dissipation theorem).

Signature spectrum

A base-line frequency spectrum taken from new or recently overhauled machinery.

Significant wave height

A statistical description of random waves. Average of the highest one third of all waves or four times the variance. Consistently very close to the observed wave height.

Simple beam

See Simply supported beam. A beam restrained at its end only against vertical movement.

Simple harmonic motion

See Simple harmonic vibration.

Simple harmonic vibration

A motion such that the displacement, velocity and acceleration are pure sinusoidal functions of time. Sometimes called “harmonic motion.”

Simple oscillator

A single-DoF mass–spring–damper system (or an LRC electric circuit), which can produce damped oscillations at one frequency (damped natural frequency). An undamped simple oscillator is a harmonic oscillator, which can produce a periodic oscillation described mathematically by either of the harmonic trigonometric functions (sine or cosine), and has only one frequency component (undamped natural frequency).

Simple (or perfect) shock

Shock whose signal can be represented exactly in simple mathematical terms. Standards specify generally one of the three following: half-sine (approached by a versed sine waveform); terminal peak sawtooth; and rectangular shock (approached by a trapezoid waveform).

Simply supported beam

A beam pinned (or simply supported) at its ends so that the displacement and bending moment at these ends will be zero. Slopes and shear forces will not be zero.

Sine beat

A signal formed by adding two sine signals whose frequencies nearly equal, so as to generate beats. Such a signal is used for excitation in some types of vibration testing.

Sine-dwell

A vibration test where a shake applies a sinusoidal excitation of a specific frequency to the test object over a specific duration, changes the frequency, and repeats the dwell in specific frequency steps.

Sine sweep

A vibration test procedure where a harmonic excitation is applied to a test object (using an exciter or shaker) and the frequency of excitation is slowly and continuously varied at a specified rate.

Single-category-based classifier (SCBC)

The pattern classifier that performs abnormality scaling by comparing the value of its feature with its no-fault value.

Single-degree-of-freedom (single-DoF) system

A system with only one coordinate (strictly, one incremental coordinate to include nonholonomic systems) to define completely the configuration of the system at any instant.

Single plane balancing

See [Static balancing](#), which is synonymous.

SISO

Single-input–single-output system. A system with just one input and one output.

Skeleton

Wavelet transform values along a ridge.

Sliding bearing

A type of base isolator that protects a structure from ground excitations by using a sliding frictional interface at the base.

SNR

Signal-to-noise ratio, determined by both electronic and mechanical noise (but not thermal noise due to the fluctuation–dissipation theorem).

Soft foot

A condition that occurs when one of a machine's hold-down bolts are not tight enough to resist the dynamic forces exerted by the machine.

Soft story

A story of a building that is more flexible than the other stories so that the stories above this story are isolated from the ground shaking.

Softened compression stress–strain relationship

Viewing the shear action on a membrane element as a two-dimensional problem, the compressive strength of concrete in one direction is reduced by cracking due to tension in the perpendicular direction.

Softening parameter

When a membrane element is subjected to shear, the compressive strength of concrete is reduced to approximately 40 to 60%.

Soil–structure interaction

A dynamic interaction between a structure and its supporting soil, in which dynamic properties of one will affect the response of the other.

Solenoid

A linear (rectilinear) two-position (on–off) actuator. A ferromagnetic rod surrounded by a coil of many turns. An electric current through the coil will generate a flux that will move the rod, thereby turning on the solenoid. A version (linear motor) is able to provide continuous movements.

Sone

Unit of the loudness that is defined as the loudness of a 1000 jHz pure tone with a sound pressure level of 40 dB. This relationship is expressed as $S = 2^{(L_L - 40)/10}$, S (sone) and L (phons).

Sound absorbing material

Porous materials such as glass fiber blankets used to attenuate sound propagating in ducts to improve sound transmission loss and to reduce standing waves in air spaces.

Sound bridge

Structures such as studs or stud bolts connecting the plates added to a noise source in insulation lagging or the plates of a double wall. They can considerably reduce insertion loss of the lagging or transmission loss of the double wall.

Sound insulation lagging

Thin plates separated by airspace or sound absorbing materials added to noise sources such as pipes, ducts and machines to isolate their noise.

Sound intensity

The time-average rate of energy flow per unit area, denoted by the vector I (W/m^2).

Sound level

Sound pressure level that has been weighted according to particular weighting curves: A- B-, C-weighting networks and associated levels. The frequency response and decibel conversions from a flat response for each of these weightings are available.

Sound power level

The acoustic power radiated by a source with respect to the international reference of 10^{-12} (watts), expressed in decibels (dB).

Sound pressure

The difference between the instantaneous pressure at a fixed point in a sound field and the pressure at the same point without the sound (Pa). Alternatively, this may be defined as the ratio (dB) of the instantaneous pressure at a fixed point in a sound field with respect to a reference of 2×10^{-6} (Pa), for which a pure tone of sound is assumed.

Span

The distance between two consecutive supports of a beam, truss, bridge, guideway, etc.

Spatial coupling

Effect of multiple support motions occurring when the attached equipment is mounted at multiple locations of the structure.

Specific fan noise level

Ratio (dB) of sound power generated from a fan due to its pressurized flow with respect to some standard power level.

Specifications

Conditions that must be satisfied by operating or design parameters during operation or design of a product in order to satisfy the objectives of the product.

Spectral density

[See Power spectral density](#). Fourier transform of the autocorrelation function of a random signal (random process). It shows how the variance of the system is distributed over frequency. It may also be expressed as a “spectral energy density” since the unit of the variance often has the unit of energy.

Spectrogram

A graph of time vs. frequency, e.g., the Gabor distribution.

Spectrum

A description of a quantity as a function of frequency or wavelength. Fourier transform of a signal is called the Fourier spectrum (or simply a spectrum).

Spherical wave

When propagation of sound wave is described by radial (polar) coordinates, the sound field is represented by a “spherical wave,” which is generated by a point monopole.

Spike energy meter

An accelerometer tuned to have its resonant frequency excited by the impacts in a deteriorating bearing, thus giving an early warning of an impending failure.

Spindle speed selection

In machining: a technique where the spindle speed is chosen to avoid or suppress chatter.

Spindle speed variation

In machining: a technique where the spindle speed is continuously adjusted to suppress chatter.

Spring

The basic flexibility element characterized by its stiffness, force, or deflection. Stores elastic potential energy. In three-dimensional problems, a spring may assume three orthogonal stiffness parameters.

SRSS

Square-root of sum of squares of a set of values.

SSE

[See Safe shutdown earthquake.](#)

Stability

Stability of a dynamic system: If the natural (unforced) response of a system decays to zero, then the system is asymptotically stable. If for a finite excitation, the system response is bounded, we have bounded-input–bounded-output (BIBO) input. Stability of a numerical method: Numerical errors do not grow without bound.

Stability lobe diagram

Chatter stability chart in the process parameter space.

Standardized shock response spectrum

[See Shock response spectrum \(SRS\).](#) Standardized or reduced SRS plotted in dimensionless coordinates. The abscissa is the product of natural frequency and shock duration. The ordinate is the ratio spectrum value or shock pulse amplitude.

Standoff distance

Distance away from a specific structure that determines the amount of damage that would occur if an explosion of a specific size was detonated. For standoff threats, the distance away from a potential vantage point with direct line of sight to the asset.

State space formulation

A generalized analytical model for a dynamic system expressed as a minimum set of first-order ordinary differential equations (state equations). The associate variables are the state variables that may include structural displacements and velocities, which will represent the dynamic state of the system.

Static balancing

[See Balancing.](#) Balancing achieved on a single plane of vibration perpendicular to the axis of rotation.

Static loading

Constant loading of a member.

Stationary process

A random process where the statistics can be considered independent of time. Stationary process is used synonymously with weakly stationary process where the first-order statistics such as the mean and the variance are independent of time, and the second-order statistics such as the autocorrelation function depend on the difference in time.

Statistically determinate

A structure is considered statistically determinate if all the support reactions and internal forces in the members can be determined solely by the equations of static equilibrium.

Stator

The stationary structure surrounding the rotating member (rotor) of a rotating electrical or mechanical machine.

Steady-state error

Offset. The error in the response of a system under steady-state conditions.

Steady-state vibration

Steady-state vibration exists in a system if the velocity of each particle is a continuous periodic quantity.

Stiffness

Characteristic parameter of a spring element. Ratio of change of force (or torque) to the corresponding change in translational (or rotational) deflection of an elastic element, i.e., force required to deflect an elastic element through a unit distance. Typical units are Newtons/meter (N/m).

Stiffness asymmetry

The stiffness (or flexibility) is not symmetrical in two or more orthogonal directions.

Stiffness law

Transmission loss characteristic of a single plate that the transmission loss depends on frequency and equivalent stiffness of the plate below the first-order natural frequency of the plate.

Stiffness matrix

The matrix multiplied by the displacement vector in the Newtonian form of differential equations of motion of a mechanical (vibrating) system, expressed in the vector-matrix form.

Stochastic process

An indexed collection of correlated (in general) random variables.

Stochastic resonance

Counterintuitive increase of SNR when the noise level is raised. Only possible in nonlinear systems.

Stokes law

Viscous friction force on a sphere of radius R , given by $6\mu Rv$, where μ is the fluid's viscosity.

Strain

Change in length divided by length. A nondimensional measure of the physical deformation or deflection resulting from stress (force per unit area).

Strain gauge

A miniature resistive element (metal foil or semiconductor) whose resistance changes when stretched (deformed), which can be measured using a Wheatstone bridge circuit. When properly mounted on (i.e., bonded to) a structural member, it can measure the local direct strain in the member.

Stress–strain curve of a steel bar in concrete

A steel bar in concrete is stiffened by tensile stress of concrete. It relates the average stress to the average strain of a large length of bar crossing several cracks.

Stretched exponentials

Discovered with Leyden jars (capacitors), a multiexponential model used by some to explain features of anelasticity.

Stribeck damping

A sophisticated friction model where the coefficient of friction drops rapidly and then increases gradually (somewhat linearly) as the relative velocity increases from zero.

Stroke

The maximum rectilinear movement that is possible in a device.

Strouhal frequency

Frequency at which the vortices are shed from a fixed cylinder subjected to a constant velocity flow. It is proportional to the diameter of the structure and inversely proportional to the stream velocity.

Structural influence

The coefficient that represents the proximity effect of the accelerometer generating a feature of a machine (gearbox) component.

Structural wall

An in-plane wall to reduce the relative interstory distortions of a building caused by seismic-induced motions.

Structure-based connectionist network (SBCN)

In machine monitoring for fault detection, this network takes advantage of the integration capability of neural networks, but avoids the need for supervised training. In the SBCN, the network weights are defined according to the “structural” knowledge of the monitored machine (e.g., gearbox) and the type of fault represented by various vibration features. The structural influences in the SBCN, which represent the proximity effect of faults on accelerometers, are determined according to the RMS value of the frequency response of a simplified lumped-mass model of the monitored machine (e.g., gearbox).

Structure-borne noise

Type of noise that is based on the generation and propagation of timewise varying motions and forces in solid bodies, as well as on the associated sound radiation.

Subharmonic

Sinusoidal quantity of a frequency that is an integral submultiple of a fundamental frequency.

Subharmonic resonancy

A phenomenon observed in sliding isolation where the isolated system possesses extra harmonic resonant frequencies in the low-frequency range in addition to the original ones as a result.

Substructured online hybrid test

A test in which only inelastic parts of a structure are experimentally tested, while the remaining elastic parts are modeled in a computer. Both parts are interconnected using online communications so that the complete structural responses are obtained.

Substructuring

Modeling, analysis and design development method where subsystems are developed first and assembled together (interconnected) through appropriate connecting elements. The analysis is simplified by using interconnection laws and making use of the results for the subsystems.

Subsystem structure

A structure that is regarded as a subsystem in the analyzing process of statistical energy analysis (SEA).

Sweep rate

The rate at which the frequency is changed in a sine-sweep test.

Symmetric matrix

The corresponding elements of a symmetric matrix about its main diagonal are identical. Specifically, $a_{ij} = a_{ji}$ where a is an element, i is the row number, and j is the column number. The transpose does not change the matrix in this case.

Synchronous averaging

Averaging of the vibration signal synchronous with the running speed of the machinery being monitored.

Synchronous whirling

[See Whirling](#). The angular velocity of whirling rotation of the rotor geometric center is equal to the rotational speed (spin) of the rotor shaft.

Tachometer

A speed sensor. [See DC tachometer](#). AC tachometers have a primary coil with an AC signal (carrier signal), a secondary coil whose induced signal is demodulated to determine the speed, and a rotor that is either a permanent magnet of a closed conduction (as in induction motor).

Thermal bearings

Flexible bearings used in long span bridges for accommodating the changes of deck length due to varying temperature to protect bridge piers from receiving large lateral forces.

Terminal peak sawtooth shock (TPS)

Same as Final peak sawtooth shock (FPS). A simple shock for which the acceleration–time curve has the shape of a triangle where acceleration increases linearly up to a maximum value and then instantly decreases to zero.

Test factor

Where the shock test specification is derived from measurements of the real environment, this is the coefficient applied to mean SRS of the measured shock pulses to take into account the variability of the resistance of the test item and the very small number of specimens tested (often only one specimen).

Test response spectrum

[See TRS](#).

Thermoelastic damping

Energy dissipation (damping) due to the anharmonic, interatomic potential independent of defects.

Threshold

The minimum value a stimulus may have to create a desired effect.

Threshold of hearing

This is defined for binaural listening as the lowest sound pressure in free field that one can just hear as the signal reduced.

Threshold speed

The speed at which a stimulus is perceptible or can produce an effect.

Throttling

Reducing the fluid flow in a system by a valve or regulator.

Time constant

The inverse of the real part (disregarding the negative sign) of an eigenvalue. Inversely proportional to the speed of response and the level of stability.

Time-dependent effects

Normally referred to material properties that are influenced by motion history.

Time domain

Domain of analysis of a dynamic (vibrating) system where the independent variable is time (t). In this domain, vibration data (and systems) are represented, displayed or analyzed as a function of time.

Time-domain analysis

Analysis of dynamic (vibration) systems and response (motion) results, which are described with respect to time.

Time-domain simulation

Computer simulation of the response of a dynamic system as a function of time. Technique to analyze chatter where delay-differential equations defining the machining forces and structural vibrations are numerically simulated in the time domain.

Time-history analysis

The analysis of a response of a dynamic system (e.g., structure) with respect to time.

Time waveform index

A single number representative of a waveform, calculated using a raw vibration signal and used for trending and comparisons.

TNT equivalent

The weight of trinitrotoluene (TNT) that has an equivalent energy output to that of a specified weight of another explosive compound.

Tool chatter

Self-excited vibration between the cutting tool and the workpiece due to a cutting tooth machining over a portion of the workpiece that was machined by a previous tooth of the cutter. This causes uneven chip thickness and consequently, excessive self-excited vibrations.

Tool condition monitoring (TCM)

A method by which the condition or state of cutting tools can be monitored.

Tool condition monitoring system (TCMS)

A combination of sensors and algorithms to achieve TCM.

Tool wear

The loss of material on the edges of a cutting tool due to machining.

Tooth passing frequency

Frequency at which the cutting tool teeth pass a given point during a spindle revolution.

Tooth passing period

Time interval for two successive cutting tool teeth to pass a given point during a spindle revolution.

Tornado

A violently rotating column of air in contact with, and extending between, a convective cloud and the surface of the Earth. It is the most destructive of all storm-scale atmospheric phenomena. They can occur anywhere in the world given the right conditions, especially after landfall of hurricanes.

Torque whirl

A whirling instability that can occur in overhung, long, slender, rotors with high load torque values. [See Whirling.](#)

Torsional response

Response causing a twisting motion.

Torsional stiffness

Torque applied to a member divided by the resulting angular displacement (twist) of the member.

Torsional vibrations

Oscillatory angular motion causing twisting of a shaft (carrying a rotor) in a rotating machine.

Tracking analyzer

Device used to record and analyze data from machines with variable speed.

Transducer

A device that senses a physical quantity is called a sensor. A transducer is a device that converts the sensed signal (measurand) into a form (typically, an electrical output signal of sufficient value) proportional to the measured variable. Often, the terms sensor and transducer are used interchangeably.

Transfer function

The ratio of the output of a dynamic system to its input in the Laplace domain or frequency domain ([see Frequency domain](#) and [FRF](#)) assuming zero initial conditions.

Transient-response analysis

Sometimes called time-history analysis, this determines the dynamic response of a dynamic system (e.g., structure, machine) under the action of time-varying excitation. Excitation forces are explicitly defined in the time domain. Computed response usually includes the time-varying displacements, velocities, accelerations, strains, and stresses.

Transient vibration

The vibratory motion of a mechanical system as it changes from one state to another as a function of time. This may be a decaying or growing signal but not a steady vibration. It may consist of forced or free vibration or both.

Transmissibiliy

Transmitted vibration (force or motion) divided by an applied vibration (force or motion). Inverse of Isolation.

Transmission loss

The difference between incident and transmitted acoustic intensity levels. It is used to rate the sound insulating properties of a wall or some other structure or device. For a muffler, this is the ratio between the energy in incident sound wave at the muffler inlet and energy transmitted at the muffler outlet into perfectly absorbing termination.

Transmitted power

An acoustic power that is transmitted from a subsystem to another subsystem.

Trapezoidal shock

Simple shock for which the acceleration–time curve grows linearly up to a given value, remains constant during a certain time, and then decreases linearly to zero.

Trim tab adjustments

Trim tabs are adjustable surfaces on the trailing edge of the rotor blades of a rotating machine (e.g., jet engine). They affect the aerodynamic pitch moment of their foils and consequently, their vibration characteristics. Tab adjustments are measured in thousandths of an inch (thou), with positive and negative changes representing upward and downward tabbing, respectively.

TRS

Test-response spectrum. The response spectrum of the excitation signal that is applied to a test object during testing.

Truncation error

The error created by deleting a signal after a finite time period to obtain a finite segment before digitally analyzing it. This is equivalent to multiplying the signal by a rectangular window. The error can be reduced (or ripples in the frequency spectrum of the truncated signal can be suppressed) by using other types of window functions with smoothing at the two ends.

Tuning

The process of adjusting the controller parameters in order to achieve the required performance (e.g., vibration control).

Unbalance (or imbalance)

A condition when the center of mass of a rotating component is not coincident with the center of rotation.

Unbalance response

The displacement vibratory response of a rotor to its mass imbalance as a function of rotor speed.

Uncertainty factor

Where the shock test specification is derived from measurements of a real environment, this is the coefficient applied to the mean SRS of the measured shock pulses to take into account the variability of the shock environment and the variability of the resistance of the material.

Uncertainty principle

The product of uncertainties of conjugate variables is greater than or equal to a constant, which in quantum mechanics is Planck's constant. Also known by the name Heisenberg.

Undamped natural frequency

The frequency of free vibration resulting from only elastic and inertial forces of the system while neglecting damping.

Undamped system

A system where there is no energy dissipation. It has energy storage capability (e.g., inertia elements to store kinetic energy and springs to store elastic potential energy). If there is no external force applied on the system, then the system will experience free steady vibrations. Motion of the system are established by an initial disturbance (i.e., initial conditions).

Undetermined coefficient method

Use a trial solution consisting of the sum of possible set of functions multiplied by unknown coefficients. Substitute in the equation to be solved and equate like terms to determine the unknown coefficients.

Uplift force

Force perpendicular to the flow.

Van der Pol oscilaltor

Classic nonlinear electronic oscillator.

Variable frequency drives

A controlling device to vary the frequency of AC supplied to an electric motor in order to vary proportionately the speed of rotation of the motor.

Variable structure control (VSC)

A class of nonlinear switching controllers whose structure consists of different phases. Typically associated with a discontinuity function (e.g., signum function). When the system response enters a different phase, a different controller (corresponding to the particular phase) is switched on.

VCC

Voltage to current converter.

Velocity

A vector quantity that specifies the magnitude and direction of the rate of change of displacement with time along a specified axis with respect to a reference frame (m/sec). First derivative of displacement with respect to time. It may refer to angular motion as well as to uniaxial (rectilinear) motion. Where the reference frame is not inertial, the velocity is often designated "relative velocity."

Velocity change

Variation of the velocity during a shock, i.e., integral of the acceleration time-history signal over the shock duration.

Velocity of sound

Velocity of sound wave propagation. In air, it is proportional to the square root of ambient pressure and of the inverse of ambient density, or it is proportional to the square root of the absolute temperature. For example, in stationary air, the velocity is 340.4 m/sec at 15°C.

Velocity shock

Shock motion characterized by a sudden velocity change of the support (base) of a system.

Versed-sine (or Haversine) shock

Simple shock for which the acceleration–time curve has the form of one period of the curve representative of the function $[1 - \cos(\quad)]$, with this period starting from the zero value of the function. It is thus a signal ranging between two minima of a sine wave.

VFC

Voltage to frequency converter.

Vibration

The oscillating, reciprocating, or other periodic motion of a rigid or elastic body or medium (such as a floor) when its position or state of equilibrium has been changed.

Vibration absorber

A secondary system (usually a mass–spring–damper trio with zero or low damping) to protect the primary device from vibrating. Typically, the secondary system vibrates at its natural frequency (resonance) generating an opposing force to suppress vibration in the primary system.

Vibration absorption

Addition of a vibration absorber to protect the primary device from vibrating.

Vibration analyzer

The device that could monitor and analyze the machine conditions using the machine's vibration signals.

Vibration control

Means of controlling vibration using external or internal forces and loads.

Vibration features

Aspects of vibration that can illuminate the effect of individual faulty components of a machine (e.g., gearbox) on vibration. Usually, vibration features are defined as functions of specific frequencies affected by the components.

Vibration isolation

[See Isolation.](#) Isolating the source of vibration from the concerned system protecting a device from vibration of its point of attachment. Motion isolation and force isolation are of interest.

Vibration measurements

For a bladed rotating machine (e.g., jet engine, turbine, compressor), obtained at the frequency of once per blade revolution (1 per rev) by two accelerometers, A and B, attached to the sides of the cockpit. The vibration data is vectorially combined into two components: $A + B$, representing the vertical (heave) vibration of the system (e.g., aircraft), and $A - B$, representing its roll vibration.

Vibration meter

Small, handheld, inexpensive, simple-to-use, self-contained device that gives an overall vibration level reading.

Vibration mode

[See Mode shape.](#) For a flexible plate, the vibration represents the particular spatial configuration of vibration amplitude (i.e., mode shape) with phase information of the moving elements, and the associated natural frequency. The actual vibration of the plate is obtained by the superposition of the

distinct vibration modes. For continuous (i.e., distributed-parameter) systems (e.g., plate), there are infinite distinct modes, many of which at the high-frequency end can be neglected depending on the frequency range of operation.

Vibration modeling

The process of converting an engineering vibration problem into a mathematical model, whereby the major vibration characteristics of the original problem can be accurately predicted.

Vibration mounts

Devices that are placed at the base (or legs) of a machine or equipment to reduce its vibration problems and specifically, to reduce the vibration forces transmitted from the machine or equipment to the support structure and its environment. A key purpose is vibration isolation. Inertia blocks may be attached to the machine base and the mounts.

Vibration response

The output of a vibrating system for an arbitrary input.

Vibration signature

A unique frequency response or pattern that corresponds to a particular input or excitation signal.

Vibration standards

National and international vibration standards and guidelines published by recognized professional organizations and regulatory agencies. The objective of these publications is to establish and control quality, safety, durability and reliable performance of rotating machinery.

Viscoelasticity

Model of anelasticity where an elastic solid also has fluid like (viscous) properties.

Viscous damping

The dissipation of energy that occurs when a particle in a vibrating system is resisted by a force that has a magnitude proportional to the magnitude of the relative velocity of the particle and a direction opposite to the direction of the particle.

Volume coefficient of elasticity of air

Generally, isothermal conditions prevail for frequencies below 100 Hz, whereas adiabatic conditions prevail above 1 kHz. In between these limits, there is a volume coefficient of elasticity (similar to bulk modulus) that varies between 1.0×10^5 and 1.4×10^5 N/m².

Volute

One of the major components of a centrifugal pump forming the casing around the impeller, which channels the flow exiting the impeller into the outlet of the pump while converting the velocity energy generated by the impeller into pressure energy.

Vortex

Any circular or rotary flow in the atmosphere that possesses vorticity.

Vulnerability

The expected damage given a specified value of a hazard parameter.

Wake

Region surrounded by the shear layers originating from separation points.

Wake excitation

Excitation caused by the vortices in the wake.

Waterfall plots

Successive spectra plotted with respect to time and displayed in a three-dimensional manner. Also known as Cascade plots.

Wavelength

In acoustics, the distance between successive two peaks in the repetitive spatial variation of the pressure or the particle local velocity.

Wavelet

Functions having representations in the time and frequency domains of small support set.

Wavelet analysis

Similar to Fourier analysis, wavelet analysis is the breaking up of a time waveform into shifted and scaled versions of a wavelet. A wavelet is a waveform of limited duration with an average value of zero.

Wavelet transform

Representation of a function as a series of wavelets.

Wear-in failures

Failures that occur at the beginning of a machine's useful life, usually characterized by a relatively high rate of failure.

Wearout failures

Failures that occur as a machine reaches the end of its design life.

WECPNL

Acronym of weighted equivalent continuous perceived noise level. It is very close to L_{Aeq} in concept and it would not be difficult to change the assessment index from WECPNL to L_{Aeq} . WECPNL is used for the assessment of aircraft noise.

Whipping

A term used to describe relatively large motion associated with whirling of a rotor. Typically, occurs when the whirling speed matches the critical speed of the rotor.

Whirling

Condition when the rotor shaft bends so that the center of mass of the rotor rotates about the fixed axis through the bearings while spinning about the shaft geometric axis. [See Synchronous whirl.](#)

White noise process

A random process where the energy is equally distributed over the entire frequency domain. It is a mathematical simplification rather than a real process.

Wideband

Corresponding to a wide (large) frequency band.

Wideband process

A random process where most of the energy is in a wideband of frequency.

Wiener–Khinchine relationship

Relates the autocorrelation function to the spectral density of a random process.

Young's modulus

[See Modulus of elasticity.](#)

Zener model

Classic description of damping that involves relaxation processes — named after the individual who also contributed to a well-known voltage controlling diode.

Zero drift

[See Drift.](#) The drift in a device under conditions of zero output.

Zero period acceleration

See ZPA.

Zero shift

Slow variation of the average of a signal due to the fact that high accelerations make the crystal of the accelerometer work in a temporarily nonlinear field. This shift can affect the calculation of the shock response spectrum.

Zeros

The roots of the numerator polynomial equation of a transfer function. Together with poles, they represent the entire system (transfer function) and govern the system behavior (stability, phase, speed of response, percentage overshoot, rise time, etc.).

ZPA

Zero period acceleration. The acceleration shown on a RS or shock SRS at infinite frequency. This can be used as a representative parameter of a signal (e.g., earthquake ground motion) for testing and designing a system.